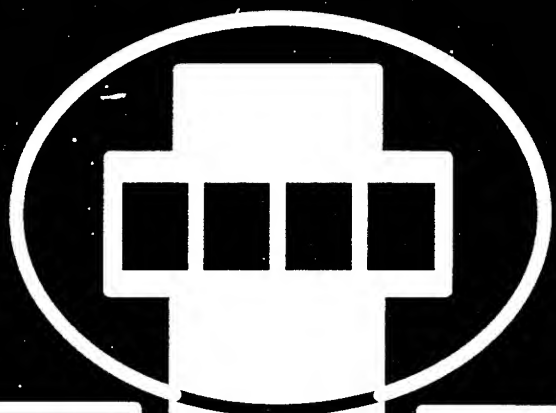
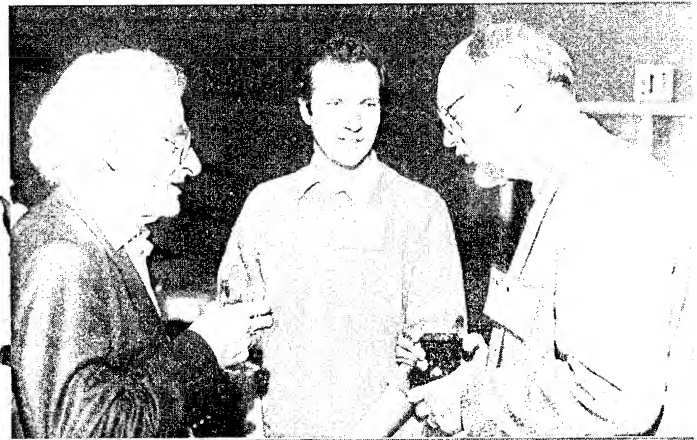


**Proceedings of the 1995
Particle Accelerator Conference
and International Conference
on High-Energy Accelerators**



1995 PARTICLE ACCELERATOR CONFERENCE
AND INTERNATIONAL CONFERENCE
ON HIGH-ENERGY ACCELERATORS
JULY 1-5, 1995
AT THE UNIVERSITY OF TEXAS AT AUSTIN





The
American
Physical
Society

Proceedings of the 1995 Particle Accelerator Conference

NO 0014-95-1-0791

Volume 5 of 5

DTIC QUALITY INSPECTED 4

Papers from the sixteenth biennial Particle Accelerator Conference, an international forum on accelerator science and technology held May 1-5, 1995, in Dallas, Texas, organized by Los Alamos National Laboratory (LANL) and Stanford Linear Accelerator Center (SLAC), jointly sponsored by the Institute of Electrical and Electronics Engineers (IEEE) Nuclear and Plasma Sciences Society (NPSS), the American Physical Society (APS) Division of Particles and Beams (DPB), and the International Union of Pure and Applied Physics (IUPAP), and conducted with support from the US Department of Energy, the National Science Foundation, and the Office of Naval Research.

19960705 130

PROCEEDINGS OF THE 1995 PARTICLE ACCELERATOR CONFERENCE

Abstracting is permitted with credit to the source. Libraries are permitted to photocopy beyond the limits of U. S. copyright law for private use of patrons those articles in this volume that carry a code at the bottom of the first page, provided the per-copy fee indicated in the code is paid through the Copyright Clearance Center, 222 Rosewood Drive, Danvers, MA 01923. Instructors are permitted to photocopy isolated articles for noncommercial classroom use without fee. For other copying, reprint, or republication permission, write to the IEEE Copyright Manager, IEEE Operations Center, 445 Hoes Lane, Piscataway, NJ 08855-1331. All rights reserved. Copyright © 1996 by the Institute of Electrical and Electronic Engineers, Inc.

IEEE Catalog Number: 95CH35843 (softbound)
95CB35843 (casebound)

Library of Congress Number: 88-647453

ISBN Softbound: 0-7803-2934-1
ISBN Casebound: 0-7803-2935-X
ISBN Microfiche: 0-7803-2936-8
ISBN CD-ROM: 0-7803-2937-6

Additional copies of this publication are available from

IEEE Operations Center
445 Hoes Lane
P. O. Box 1331
Piscataway, NJ 08855-1331 USA

Phone: 1-800-678-IEEE (1-800-678-4333)
1-908-981-1393
FAX: 1-908-981-9667
Telex: 833-233
e-mail: customer.service@ieee.org

The CD-ROM version is available from

Dan Rusthoi, PAC95 Treasurer
Los Alamos National Laboratory
P. O. Box 1663 - M/S H811
Los Alamos, NM 87545 USA

Phone: 505-667-2796
FAX: 505-667-0919
e-mail: drusthoi@lanl.gov

Volume 1

Plenary and Special Sessions

CEBAF Commissioning and Future Plans (<i>Invited</i>) — Hermann A. Grunder.....	1	MAD01
The Advanced Photon Source (<i>Invited</i>) — John N. Galayda.....	4	MAD02
Commissioning and Performance of the HIMAC Medical Accelerator (<i>Invited</i>) — S. Yamada.....	9	MAD03
Accelerator Field Development at Novosibirsk (History, Status, Prospects) (<i>Invited</i>) — A. Skrinsky.....	14	MAD04
A Personal Perspective of High Energy Accelerators (<i>Invited</i>) — Gustav-Adolf Voss.....	27	FPD01
Photon-Photon Colliders (<i>Invited</i>) — Andrew M. Sessler.....	30	FPD02
Transmutation and Energy Production with High Power Accelerators (<i>Invited</i>) — G.P. Lawrence.....	35	FPD03
The Large Hadron Collider (<i>Invited</i>) — L.R. Evans.....	40	FPD04
Frontiers of Particle Physics (<i>Invited</i>) — L. Okun.....	45	FPD05
R. R. Wilson Prize Lecture: Pretzels (<i>Invited</i>) — R. Littauer.....	manuscript not submitted	MXG01
Experimental Studies of Longitudinal Dynamics of Space-Charge Dominated Electron Beams (<i>Invited</i>) — D.X. Wang.....	48	MXG02
High-Energy High-Luminosity $\mu^+ \mu^-$ Collider Design (<i>Invited</i>) — Robert B. Palmer, Richard Fernow, Juan C. Gallardo, Y.Y. Lee, Yagmur Torun, David Neuffer, David Winn.....	53	MXG03
Cosmic Acceleration Mechanisms (<i>Invited</i>) — J. Arons.....	manuscript not submitted	MXG04

Accelerator Applications

Hadron Particle Therapy (<i>Invited</i>) — Jose R. Alonso.....	58	WPE01
Micromechanics via Synchrotron Radiation (<i>Invited</i>) — H. Guckel.....	63	WPE02
Radionuclide Production for the Biosciences (<i>Invited</i>) — Thomas J. Ruth.....	67	WPE03
X-Ray Lithography - Status and Projected Use (<i>Invited</i>) — W.A. Johnson.....	manuscript not submitted	WPE04
Microelectronic Applications for RF Sources and Accelerators (<i>Invited</i>) — Cha-Mei Tang.....	70	WPE05
A High-Gradient Electron Injector to an X-Ray Lithography Ring (<i>Invited</i>) — D. Yu.....	manuscript not submitted	FAG01
X-Ray Holography (<i>Invited</i>) — I. McNulty.....	manuscript not submitted	FAG02
Medical and Surgical Applications of FELs (<i>Invited</i>) — Benedikt Jean.....	75	FAG03
Medical Uses of Monochromatic X-Rays (<i>Invited</i>) — Frank E. Carroll.....	80	FAG04
Texas Regional Medical Technology Center — R. Sah, T.D. Cain, E.K. Cleveland, K. Saadatmand, M.E. Schulze, R.A. Winje.....	83	FAG05
A Proposed 100-400 MeV Beam Facility at Fermilab — C. Johnstone, C. Ankenbrandt, S. Bjerklie, D. Boehnlein, M. Foley, T. Kroc, J. Lackey, A. Lennox, A. Leveling, E. McCrory, M. Popovic, C. Schmidt, K. Vaziri.....	86	FAG06
Cyclotrons for Isotope Production — B.F. Milton, N.R. Stevenson.....	89	FAG07
European Heavy Ion ICF Driver Development — G. Plass.....	92	FAG08
A 3-Stage Cyclotron Complex for Driving the Energy Amplifier — P. Mandrillon, N. Fietier, C. Rubbia.....	95	FAG09
Accelerator-Based Gamma Neutron Transmutation of Radionuclides as a New Technology for the Nuclear Fuel Cycle — I.P. Ereemeev.....	98	FAG10
A High-Average-Power FEL for Industrial Applications — H.F. Dylla, S. Benson, J. Bisognano, C.L. Bohn, L. Cardman, D. Engwall, J. Fugitt, K. Jordan, D. Kehne, Z. Li, H. Liu, L. Meringa, G.R. Neil, D. Neuffer, M. Shinn, C. Sinclair, M. Wiseman, L.J. Brillson, D.P. Henkel, H. Helvajian, M.J. Kelley.....	102	FAG11
X-Ray Radiation by Relativistic Electrons in Condensed Media on Base of MSU Race-Track Microtron — V.K. Grishin, A.S. Chepurnov, K.A. Gudkov, B.S. Ishkhanov, S.A. Kosterin, E.V. Lasutin, S.V. Blazhevich, N.N. Nasonov.....	105	FAG12
Applications of MeV Proton and Deuteron Linear Accelerators — George H. Gillespie, Gerald E. McMichael.....	107	FAG13
Accelerator Requirements for Fast-Neutron Interrogation of Luggage and Cargo — B.J. Micklich, C.L. Fink, T.J. Yule.....	110	FAG14

Energy Varying Resonant Beam Extraction from the Synchrotron — K. Hiramoto, <i>M. Tadokoro, J.I. Hirota, M. Nishi, K. Noda</i>	113	TAB03
Radiotherapy Process Integration Using a Compact Photon Source Together with Fluence Control and Patient Imaging — D. Tronc, F. Dugardin, J.P. Georges, R. Letoumelin, <i>J.L. Pourre</i>	116	TAB04
A 1.5 GeV Compact Light Source with Superconducting Bending Magnets — A.A. Garren, <i>D.B. Cline, M.A. Green, D.E. Johnson, J.J. Kolonko, E.M. Leung, D.D. Madura,</i> <i>L.C. Schachinger</i>	119	TAB06
Applications of Industrial Electron Accelerators at Samsung Heavy Industries — <i>Bumsoo Han, Keeman Kim, Kihun Joh, Sungmyun Kim, Byungmun Kim, Heunggyu Park,</i> <i>Jongpil Park, Jinsoo Kim, Wongu Kang, Kyungwoo Kang, Yuri Kim, Sangil Lee, Younghee Kim</i>	122	TAB09
Application of Accelerated Electron Beams for Rubber and Polymer Modification — <i>A. Shalnov, B.Yu. Bogdanovich, A. Ignatyev, V. Senyukov</i>	125	TAB13
Status on Low Energy (10 MeV Range) X-band Linacs Developed Worldwide — <i>A.V. Michine</i>	128	TAB15
Linear Accelerator for Radiation Chemistry Research at Notre Dame — K. Whitham, <i>S. Lyons, R. Miller, D. Nett, P. Treas, A. Zante, R.W. Fessenden, M.D. Thomas, Y. Wang</i>	131	TAB17
IREN Status: New Electron Linac Driven Intense Resonance Neutron Source — A. Krasnykh	134	TAC01
A Cost Estimation Model for High Power FELs — George R. Neil	137	TAC03
Details of the Initial Part of the Tungsten Ion Linac for Particle Track Membranes Production — V. Kushin, T. Kulevoy, N. Nesterov, A. Oreshnikov, S. Plotnikov, D. Seleznev, <i>V. Zubovskiy</i>	140	TAC05
A Series of Ion Accelerators for Industry — B.N. Sukhina, N.I. Alinovsky, I.L. Chertok, <i>S.N. Chumakov, N.S. Dikansky, A.D. Goncharov</i>	143	TAC06
A Pulsed Source of Neutron Focus for Fundamental and Applied Research in High-Energy Electron Accelerator Centres — I.P. Ereemeev	146	TAC11
Moderator/Collimator for a Proton/Deuteron Linac to Produce a High-Intensity, High-Quality Thermal Neutron Beam for Neutron Radiography — R.C. Singleterry Jr., <i>G.R. Imel, G.E. McMichael</i>	149	TAC12
Experimental Set-up for Multiplication Coefficient Fluctuation Study vs Accelerator Parameter Deviations on the JINR Pulsed Accelerator Driven Neutron Source — <i>V. Belkovets, A. Ivanov, A. Kaminsky, A. Krasnykh, N. Malakhov, L. Menshikov, Yu. Popov,</i> <i>V. Piataev, N. Pilyar, V. Rudenko, L. Somov, A. Sumbaev, V. Tarabrin</i>	152	TAC16

Synchrotron Light Sources and Free Electron Lasers

European Synchrotron Radiation Storage Rings (Invited) — H. Zyngier	155	TPG01
Development of the JAERI FEL Driven by a Superconducting Accelerator (Invited) — <i>E.J. Minehara, M. Sugimoto, M. Sawamura, R. Nagai, N. Kikuzawa</i>	159	TPG02
Status of New Light Sources in Russia (Invited) — G. Kulipanov	manuscript not submitted	TPG03
Free Electron Laser Research in China (Invited) — Jialin Xie	162	TPG04
Accelerator Physics Trends at the ESRF — A. Ropert, L. Farvacque, J. Jacob, J.L. Laclare, <i>E. Plouviez, J.L. Revol, K. Scheidt</i>	167	TPG05
Commissioning of the PLS 2 GeV Storage Ring — M. Yoon, J.Y. Huang, J.S. Jang, M. Kwon, <i>T. Lee, S.H. Nam</i>	171	TPG06
Femtosecond X-Rays from 90° Thomson Scattering — W. Leemans, R. Schoenlein, A. Chin, <i>E. Glover, R. Govil, P. Volfbeyn, S. Chattopadhyay, K.-J. Kim, C.V. Shank</i>	174	TPG07
Design of a Diffraction Limited Light Source (DIFL) — D. Einfeld, J. Schaper, M. Plesko	177	TPG08
Updated Plans for DIAMOND, a New X-ray Light Source for the UK — V.P. Suller, <i>J.A. Clarke, J.B. Fitzgerald, H.L. Owen, M.W. Poole, X. Queralti, S.L. Smith</i>	180	TPG09
Design Optimization for an X-Ray Free Electron Laser Driven by SLAC Linac — Ming Xie	183	TPG10

The FERMI FEL Project at Trieste — <i>D. Bulfone, F. Cargnello, G. D'Auria, F. Daclon, M. Ferianis, M. Giannini, G. Margaritondo, A. Massarotti, A. Rindi, R. Rosei, C. Rubbia, R. Visintini, R.P. Walker, A. Wrulich, D. Zangrando, F. Ciocci, G. Dattoli, A. De Angelis, A. Dipace, A. Doria, G.P. Gallerano, F. Garosi, L. Giannessi, E. Giovenale, L. Mezi, P.L. Ottaviani, A. Renieri, E. Sabia, A. Segreto, A. Torre, M. Castellano, P. Patteri, S. Tazzari, F. Tazzioli, F. Cevenini, A. Cutolo</i>	186	TPG11
Studies on a Free Electron Laser for the TESLA Test Facility — <i>J. Rossbach</i>	189	TPG12
MIT Microwiggler for Free Electron Laser Applications — <i>P. Catravas, R. Stoner, J. Blastos, D. Sisson, I. Mastovsky, G. Bekefi, X.-J. Wang, A. Fisher</i>	192	TPG14
DORIS III as a Dedicated Source for Synchrotron Radiation — <i>H. Neseemann, W. Brefeld, F. Brinker, W. Decking, O. Kaul, B. Sarau</i>	195	FAA02
Beam Lifetime and Beam Brightness in ALS — <i>C. Kim, A. Jackson, A. Warwick</i>	198	FAA03
Asynchronized Energy Ramping at SRRS Storage Ring — <i>Gwo-Huei Luo, L.H. Chang, Y. Cheng, K.T. Hsu, C.C. Kuo, W.C. Lau, Ch. Wang, P.K. Tseng, Y.C. Liu</i>	201	FAA04
Emittance Measurements in the ALS Booster Synchrotron — <i>D. Massoletti, C.H. Kim, A. Jackson</i>	204	FAA05
Compton Scattering in the ALS Booster — <i>D. Robin, C. Kim, A. Sessler</i>	207	FAA06
Beam Stability at SRRS Storage Ring — <i>W.T. Weng, H.P. Chang, J.R. Chen, Y. Cheng, K.T. Hsu, C.C. Kuo, J.C. Lee, K.K. Lin, Y.C. Liu, G.H. Luo, K.L. Tsang</i>	210	FAA07
Commissioning of the Duke Storage Ring — <i>V.N. Litvinenko, Y. Wu, B. Burnham, J.M.J. Madey, F. Carter, C. Dickey, M. Emamian, J. Gustavsson, N. Hower, P. Morcombe, S.H. Park, P. O'Shea, R. Sachtshale, D. Straub, G. Swift, P. Wang, J. Widgren</i>	213	FAA08
Pulsed VUV Synchrotron Radiation Source — <i>S.H. Kim, Y.S. Cho, T.Y. Kim, K.H. Chung</i>	216	FAA10
Merits of a Sub-Harmonic Approach to a Single-Pass, 1.5-Å FEL — <i>W.M. Fawley, H.-D. Nuhn, R. Bonifacio, E.T. Scharlemann</i>	219	FAA12
Operation of the ELETTRA Injection Linac in the FEL Mode — <i>G. D'Auria, C.J. Bocchetta, M. Plesko, C. Rossi, L. Tosi, R.P. Walker, A. Wrulich</i>	222	FAA13
Free Electron Laser - FEL - Study in Institute of Nuclear Physics of MSU — <i>V.K. Grishin, B.S. Ishkhanov, T.A. Novikova, V.I. Shvedunov</i>	225	FAA14
A Chirped-Pulse Regenerative-Amplifier FEL for the Gamma-Gamma Collider — <i>K.C.D. Chan, J.C. Goldstein, D.C. Nguyen, H. Takeda</i>	228	FAA16
Alignment and Magnet Error Tolerances for the LCLS X-Ray FEL — <i>H.-D. Nuhn, E.T. Scharlemann, R. Schlüter</i>	231	FAA17
Electron Transport and Emittance Diagnostics in CIRFEL — <i>J. Krishnaswamy, I.S. Lehrman, R. Hartley, R.H. Austin</i>	234	FAA19
Study on Accelerator Noise Effects on a Far-Infrared FEL Oscillator — <i>Shinian Fu, Yinbao Chen, Zhibin Huang</i>	237	FAA21
Status of the UCLA High-Gain Infrared Free Electron Laser — <i>M. Hogan, C. Pellegrini, J. Rosenzweig, G. Travish, A. Varfolomeev</i>	240	FAA23
Accelerator Design for the High-Power Industrial FEL — <i>D.V. Neuffer, S. Benson, J. Bisognano, D. Douglas, H.F. Dylla, D. Kehne, J. Fugitt, K. Jordan, Z. Li, H.-X. Liu, L. Merminga, G. Neil, M. Shinn, C. Sinclair, M. Wiseman, M. Cornacchia</i>	243	FAA25
Free Electron Laser Amplifier Experiment Based on 3.5 MeV Linear Induction Accelerator — <i>Ding Bainan, Deng Jianjun, Hu Shenzong, Shi Jinsui, Zhu Wenjun, Li Qing, He Yi</i>	246	FAA26
A High Duty Factor Electron Linac for FEL — <i>T.D. Hayward, D.H. Dowell, A.M. Vetter, C. Lancaster, L. Milliman, D. Smith, J. Adamski, C. Parazzoli</i>	248	FAA27
A Kilowatt Class Visible Free Electron Laser Facility — <i>J.L. Adamski, D.H. Dowell, T.D. Hayward, C.G. Parazzoli, A.M. Vetter</i>	251	FAA28
Self-Consistent Analysis of Radiation and Relativistic Electron Beam Dynamics in a Helical Wiggler Using Lienard-Wiechert Fields — <i>M. Tecimer, L.R. Elias</i>	254	FAA29
First Lasings at Visible and IR Range of Linac-Based FELs at the FELI — <i>T. Tomimasu, E. Oshita, S. Okuma, K. Wakita, K. Saeki, A. Zako, T. Suzuki, Y. Miyauchi, A. Koga, S. Nishihara, A. Nagai, E. Tongu, K. Wakisaka, A. Kobayashi, M. Yasumoto</i>	257	FAA30
The Northrop Grumman Compact Infrared FEL (CIRFEL) — <i>I.S. Lehrman, J. Krishnaswamy, R.A. Hartley, R.H. Austin</i>	260	FAA31
A Proposed NSLS X-Ray Ring Upgrade Using B Factory Technology — <i>E.B. Blum</i>	263	FAR01
A Low Emittance Lattice for the NSLS X-Ray Ring — <i>J. Safranek</i>	266	FAR02

Design of a 1.2 GeV Synchrotron Light Source for X-Ray Lithography at Samsung Heavy Industries — Keeman Kim, Bumsoo Han, Kihun Joh, Sungmyun Kim, Byungmun Kim, Heunggyu Park, Jongpil Park, Jinsoo Kim, Wongu Kang, Kyungwoo Kang, Yuri Kim, Sangil Lee, Younghee Kim.....	269	FAR03
ANKA, A Synchrotron Light Source for Microstructure Fabrication and Analysis — H.O. Moser, M. Ballauff, V. Bechtold, H. Bertagnolli, J. Bialy, P. v. Blanckenhagen, C. Bocchetta, W. Bothe, C. Coluzza, A.N. Danilewsky, K.D. Eichhorn, B. Eigenmann, D. Einfeld, L. Friedrich, M. Haller, N. Holtkamp, V. Honecker, K. Hümmer, E. Huttel, J. Jacob, V. Kashikin, J. Kircher, H. Klewe-Nebenius, A. Knöchel, A. Krüssel, G. Kumpe, K.D. Möller, J. Mohr, M. Nagaenko, F.J. Pantenburg, M. Plesko, J. Schaper, K. Schlösser, G. Schulz, S. Schuppler, H. Schweickert, I. Seidel, Y. Severgin, I. Shukeilo, L. Steinbock, R. Steininger, M. Svandrlik, G. Williams, K. Wilson, J. Zegenhagen.....	272	FAR06
An Undulator at PETRA II - A New Synchrotron Radiation Source at DESY — K. Balewski, W. Brefeld, U. Hahn, J. Pflüger, R. Rossmanith.....	275	FAR07
Electron Storage Ring, KSR for Light Source with Synchrotron Radiation — A. Noda, H. Dewa, H. Fujita, M. Ikegami, Y. Iwashita, S. Kakigi, M. Kando, K. Mashiko, H. Okamoto, T. Shirai, M. Inoue.....	278	FAR08
A Lattice for the Future Project of VUV and Soft X-Ray High Brilliant Light Source — H. Takaki, Y. Kobayashi, K. Matsuda, Y. Kamiya.....	281	FAR09
Millimeter Wave Coherent Synchrotron Radiation in a Compact Electron Storage Ring — J.B. Murphy, E. Blum, R. Heese, J. Keane, S. Krinsky.....	284	FAR10
Commissioning of the Argonne Positron Accumulator Ring — M. Borland.....	287	FAR11
APS Storage Ring Commissioning and Early Operational Experience — G. Decker.....	290	FAR13
New Specifications for the SOLEIL Project — M.-P. Level, P. Brunelle, A. Nadji, M. Sommer, H. Zyngier, J. Faure, P. Nghiem, J. Payet, A. Tkatchenko.....	293	FAR14
A Combined Magnet Lattice of the Synchrotron Light Source ISI-800 — I. Karnaukhov, S. Kononenko, A. Shcherbakov, V. Nemoshkalenko, V. Molodkin, A. Shpak.....	296	FAR16
Progress of the ISI-800 Project — E. Bulyak, S. Efimov, A. Gevchuk, P. Gladikh, I. Karnaukhov, S. Kononenko, V. Kozin, V. Markov, N. Mocheshnikov, A. Mytsykov, A. Shcherbakov, Yu. Telegin, A. Zelinsky, V. Molodkin, V. Nemoshkalenko, A. Shpak.....	299	FAR17
Reduction of Open-Loop Low Frequency Beam Motion at the APS — G. Decker, Y.G. Kang, S. Kim, D. Mangra, R. Merl, D. McGhee, S. Sharma.....	303	FAR19
Horizontal-Vertical Coupling Correction at Aladdin — R.A. Bosch, W.S. Trzeciak.....	306	FAR20
One and a Half Years of Experience with the Operation of the Synchrotron Light Source ELETTRA — C.J. Bocchetta, D. Bulfone, F. Daclon, G. D'Auria, A. Fabris, R. Fabris, M. Ferianis, M. Giannini, F. Iazzourene, E. Karantzoulis, A. Massarotti, R. Nagaoka, N. Pangos, R. Richter, C. Rossi, M. Svandrlik, L. Tosi, R. Visintini, R.P. Walker, F. Wei, A. Wrulich.....	309	FAR21

Low and Intermediate Energy Accelerators

First Generation ISOL Radioactive Ion Beam Facilities (Invited) — D.K. Olsen.....	312	RPG01
Latest Developments in Superconducting Cyclotrons (Invited) — H.W. Schreuder.....	317	RPG02
Synchrotron-Driven Spallation Sources (Invited) — P.J. Bryant.....	322	RPG03
Heavy Ion Cooling Rings (Invited) — J.S. Hangst.....	manuscript not submitted	RPG04
Commissioning the MIT-Bates South Hall Ring — K. Jacobs, R. Averill, S. Bradley, A. Carter, G. Dodson, K. Dow, M. Farkhondeh, E. Ihloff, S. Kowalski, B. McAllister, W. Sapp, C. Sibley, S. Sobczynski, D. Tieger, C. Tschalaer, E. Tsentalovich, W. Turchinets, A. Zolfaghari, T. Zwart.....	327	RPG05
The AmPS Ring: Actual Performance and Future Plans — G. Luijckx, R. Bakker, H. Boer Rookhuizen, C. de Jager, F. Kroes, J. van der Laan, R. Maas, J. Noomen, Y. Wu.....	330	RPG06
Feasibility Study for Using the FNAL Antiproton Source as a Low Energy Proton-Antiproton Collider — Mike Church, Stephan Maury.....	333	RPG07
CIS, A Low Energy Injector for the IUCF Cooler — D.L. Friesel, S.Y. Lee.....	336	RPG08
The R&D Works on the High Intensity Proton Linear Accelerator for Nuclear Waste Transmutation — N. Ito, M. Mizumoto, K. Hasegawa, H. Oguri, J. Kusano, Y. Okumura, M. Kawai, H. Ino, H. Murata, Y. Touchi.....	339	RPG09
Development of the RFD Linac Structure — D.A. Swenson, K.R. Crandall, F.W. Guy, J.W. Lenz, A.D. Ringwall, L.S. Walling.....	342	RPG10

Proposed Upgrade of the NSCL — R.C. York, H. Blosser, T. Grimm, D. Johnson, D. Lawton, F. Marti, J. Vincent, X. Wu, A.F. Zeller.....	345	RPG11
ISAC-1: Radioactive Ion Beams Facility at TRIUMF — P.G. Bricault, R. Baartman, J.L. Beveridge, G.S. Clark, J. Doornbos, G. Dutto, T. Hodges, S. Koscielniak, L. Root, P.W. Schmor, H.R. Schneider.....	348	RPG12
First Beam Tests of the INS Split Coaxial RFQ for Radioactive Nuclei — S. Arai, A. Imanishi, K. Niki, M. Okada, Y. Takeda, E. Tojyo, N. Tokuda.....	351	RPG13
Accelerator Complex for a Radioactive Ion Beam Facility at ATLAS — J.A. Nolen.....	354	RPG14
The Lattice Design of Indiana University Cyclotron Facility Cooler Injector Synchrotron — D. Li, X. Kang, D.L. Friesel, S.Y. Lee, J.Y. Liu, A. Pei, A. Riabko, L. Wang.....	357	TAP03
Design Study of AntiProton Accumulation and Deceleration Ring in the KEK PS Complex — S. Machida, M. Yoshii, Y. Mori, N. Tokuda, Y. Ishi.....	360	TAP04
Feasibility Study of a 1-MW Pulsed Spallation Source — Y. Cho, Y.-C. Chae, E. Crosbie, M. Fathizadeh, H. Friedsam, K. Harkay, D. Horan, S. Kim, R. Kustom, E. Lessner, W. McDowell, D. McGhee, F. Mills, H. Moe, R. Nielsen, G. Norek, K.J. Peterson, A. Rauchas, K. Symon, K. Thompson, D. Warner, M. White.....	363	TAP05
ORIC Central Region Calculations — J.D. Bailey, D.T. Dowling, S.N. Lane, S.W. Mosko, D.K. Olsen, B.A. Tatum.....	366	TAP07
An Internal Timing Probe for Use in the MSU K1200 Cyclotron — J.D. Bailey, J. Kuchar, F. Marti, J. Ottarson.....	369	TAP08
Axial Injection and Phase Selection Studies of the MSU K1200 Cyclotron — J.D. Bailey.....	372	TAP09
Study and Redesign of the NSCL K500 Central Region — S.L. Snyder, F. Marti.....	375	TAP10
Heavy Ion Acceleration Strategies in the AGS Accelerator Complex -- 1994 Status Report — L.A. Ahrens, J. Benjamin, M. Blaskiewicz, J.M. Brennan, C.J. Gardner, H.C. Hseuh, Y.Y. Lee, R.K. Reece, T. Roser, A. Soukas, P. Thieberger.....	378	TAP11
Observation of Intensity Dependent Losses in Au(15+) Beams — M. Blaskiewicz, L.A. Ahrens, H.C. Hseuh, T. Roser, Y. Shoji, K. Zeno.....	381	TAP12
High Intensity Proton Operations at the Brookhaven — M. Blaskiewicz, L.A. Ahrens, E.J. Bleser, J.M. Brennan, C.J. Gardner, J.W. Glenn, R.K. Reece, T. Roser, M.J. Syphers, W. VanAsselt, S.Y. Zhang.....	383	TAP13
Fast Extracted Proton Beams at Low Energies in the CPS East Experimental Area — R. Cappi, L. Durieu, J.-Y. Hémy, M. Martini, J.-P. Riunaud, Ch. Steinbach.....	386	TAP14
Ion-Optics Systems Of Multiply Charged High-Energy Ions For High Emittance Beams — V.O. Naidenov, L.A. Baranova, G.M. Gusinskii, A.V. Matyukov, S.Ya. Yavor.....	389	TAP16

High Energy Hadron Accelerators and Colliders

The Status of the Fermilab Main Injector Project (Invited) — D. Bogert, W. Fowler, S. Holmes, P. Martin, T. Pawlak.....	391	MPG01
Status and Future of the Tevatron (Invited) — V. Bharadwaj.....	396	MPG02
The RHIC Project - Status and Plans (Invited) — M. Harrison.....	401	MPG03
HERA Status and Plans (Invited) — R. Brinkmann.....	406	MPG04
The CERN Heavy Ion Accelerating Facility (Invited) — H.D. Haseroth.....	411	MPG05
UNK Status and Plans (Invited) — G. Gurov.....	416	MPG06
Reduction of Particle Losses in HERA by Generating an Additional Harmonic Tune Modulation — O.S. Brüning, F. Willeke.....	420	MPG07
Acceleration of Lead Ions in the CERN PS Booster and the CERN PS — F. Blas, P. Bossard, R. Cappi, G. Cyvoct, R. Garoby, G. Gelato, H. Haseroth, E. Jensen, D. Manglunki, K. Metzmacher, F. Pedersen, N. Rasmussen, K. Schindl, G.C. Schneider, H. Schöner, L. Sermeus, M. Thivent, M. van Rooij, F. Völker, E. Wildner.....	423	MPG09
Highly Efficient Deflection of the Divergent Beam by Bent Single Crystal — V.I. Baranov, V.M. Biryukov, A.P. Bugorsky, Yu.A. Chesnokov, V.I. Kotov, M.V. Tarakanov, V.I. Terekhov, S.V. Tsarik, O.L. Fedin, M.A. Gordeeva, M.P. Gur'yev, Yu.P. Platonov, A.I. Smirnov.....	426	MPG10
Potential Accelerator Improvements Required for the Tevatron Upgrade at Fermilab — G. Jackson, G.W. Foster.....	428	MPG11
Beyond the LHC: A Conceptual Approach to a Future High Energy Hadron Collider — M.J. Syphers, M.A. Harrison, S. Peggs.....	431	MPG12

132 nsec Bunch Spacing in the Tevatron Proton-Antiproton Collider — S.D. Holmes, <i>J.A. Holt, J. Johnstone, J. Marriner, M. Martens, D. McGinnis</i>	434	WAP01
Aluminum Beam Tube for the Super Collider: An Option for No-Coating & No-Liner — <i>W. Chou</i>	437	WAP02
Variable Bunch Spacing in Super Collider — W. Chou	440	WAP03
Fermilab Collider Run 1B Statistics — V. Bharadwaj, J. Crawford, R. Mau	443	WAP04
Optimizing the Luminosity in the Tevatron by Independently Moving the Horizontal and Vertical Beta Stars Longitudinally — M.A. Martens, G.P. Goderre	446	WAP05
A Model of the Fermilab Collider for Optimization of Performance — Elliot S. McCrory, <i>Peter W. Lucas</i>	449	WAP06
Coupling in the Tevatron — Norman M. Gelfand	452	WAP07
Calculating Luminosity for a Coupled Tevatron Lattice — J.A. Holt, M.A. Martens, <i>L. Michelotti, G. Goderre</i>	455	WAP08
Remarks Concerning the γ-Production Probability of High Relativistic Dirac-Electrons in the Positron Bunch — Huschang Heydari	458	WAP09
Field Quality Evaluation of the Superconducting Magnets of the Relativistic Heavy Ion Collider — J. Wei, R.C. Gupta, A. Jain, S.G. Peggs, C.G. Trahern, D. Trbojevic, P. Wanderer	461	WAP10
High Intensity Proton Beams in a Multi-cycled SPS — A. Faugier, X. Altuna, R. Bailey, <i>R. Blanchard, T. Bohl, H. Burkhardt, P. Collier, K. Cornelis, N. Garrel, A. Hilaire, M. Jonker,</i> <i>R. Keizer, M. Lamont, T. Linnecar, G. de Rijk, G. Roy, H. Schmickler, J. Wenninger</i>	464	WAP12
The SPS as Accelerator of Pb^{82+} Ions — A. Faugier, X. Altuna, R. Bailey, R. Blanchard, T. Bohl, <i>E. Brouzet, H. Burkhardt, P. Collier, K. Cornelis, G. de Rijk, F. Ferioli, A. Hilaire, M. Lamont,</i> <i>T. Linnecar, M. Jonker, C. Niquille, G. Roy, H. Schmickler</i>	467	WAP13
Experimental Evidence for Multi-pass Extraction with a Bent Crystal — B. Dehning, <i>K. Elsener, G. Fidecaro, M. Gyr, W. Herr, J. Klem, W. Scandale, G. Vuagnin, E. Weisse,</i> <i>S. Weisz, S.P. Møller, E. Uggerhoj, A. Freund, R. Hustache, G. Carboni, M.P. Bussa, F. Tosello</i>	470	WAP14
Storage Ring for Enhanced Antiproton Production at Fermilab — G. Jackson, G.W. Foster	473	WAP16

Circular Electron Accelerators and Colliders

LEP Status and Plans (Invited) — S. Myers	476	WPG01
CESR Status and Plans (Invited) — David L. Rubin	481	WPG02
PEP II Status and Plans (Invited) — John T. Seeman	486	WPG03
KEKB Status and Plans (Invited) — Shin-ichi Kurokawa	491	WPG04
DAΦNE Status and Plans (Invited) — G. Vignola	495	WPG05
Electron-Positron Colliders at Novosibirsk (Invited) — N. Dikansky	500	WPG06
BEPC Status and Plans (Invited) — Shu-Hong Wang	506	WPG07
The First Attainment and Routine Use of Longitudinal Spin Polarization at a High Energy Electron Storage Ring — D.P. Barber	511	WPG08
Experiments with Bunch Trains in LEP — O. Brunner, W. Herr, G. von Holtey, E. Keil, <i>M. Lamont, M. Meddahi, J. Poole, R. Schmidt, A. Verdier, C. Zhang</i>	514	WPG09
Trapped Macroparticles in Electron Storage Rings — F. Zimmermann, J.T. Seeman, <i>M. Zolotarev, W. Stoeffl</i>	517	WPG10
A Compact-High Performance NLC Damping Ring Using High Magnetic Field Bending Magnets — D.B. Cline, A. Garren, M. Green, J. Kolonko, D. Madura	520	WPG11
Application of Precision Magnetic Measurements for Control of the Duke Storage Ring — <i>B. Burnham, V.N. Litvinenko, Y. Wu</i>	524	RAA01
Wiggler Insertion of the PEP-II B-Factory LER — J. Heim, L. Bertolini, J. Dressler, O. Fackler, <i>B. Hobson, M. Kendall, T. O'Connor, W. Stoeffl, T. Swan, A. Zholents, M.S. Zisman</i>	527	RAA03
Status of the High Energy Ring of the PEP II B-Factory — U. Wienands, E. Reuter, <i>J.T. Seeman, W. Davies-White, A. Fisher, J. Fox, L. Genova, J. Gracia, C. Perkins,</i> <i>M. Pietryka, H. Schwarz, T. Taylor, T. Jackson, C. Belser, D. Shimer</i>	530	RAA04
Design of the PEP-II Low-Energy Ring — M.S. Zisman, R.B. Yourd, H. Hsieh	533	RAA05
Injection Envelope Matching in Storage Rings — M.G. Minty, W.L. Spence	536	RAA06
A Mathematical Model for Investigating Chromatic Electron Beam Extraction from a Pulse Stretcher Ring — Yu.N. Grigor'ev, A.Yu. Zelinsky	539	RAA07

The Dynamical Aperture of ISI - 800 — S. Efimov, I. Karnaukhov, S. Kononenko, A. Shcherbakov, A. Tarasenko, A. Zelinsky.....	542	RAA08
The Influence of Residual Vertical Dispersion on LEP Performance — P. Collier, H. Schmickler.....	545	RAA10
Operational Procedures to Obtain High Beam-Beam Tune Shifts in LEP Pretzel Operation — R. Bailey, P. Collier, T. Bohl, H. Burkhardt, K. Cornelis, G. De Rijk, A. Faugier, M. Jonker, M. Lamont, G. Roy, H. Schmickler, J. Wenninger.....	548	RAA11
Synchrotron Phase Space Injection into LEP — P. Collier.....	551	RAA12
Systematic Studies of the LEP Working Point — P. Collier, H. Schmickler.....	554	RAA13
Modification of the LEP Electrostatic Separator Systems for Operation with Bunch Trains — B. Balhan, A. Burton, E. Carlier, J.-P. Deluen, J. Dieperink, N. Garrel, B. Goddard, R. Guinand, W. Kalbreier, M. Laffin, M. Lamont, V. Mertens, J. Poole, H. Verhagen.....	557	RAA15
Low Emittance Lattice for LEP — Y. Alexahin, D. Brandt, K. Cornelis, A. Hofmann, J.P. Koutchouk, M. Meddahi, G. Roy, A. Verdier.....	560	RAA17
Radiation Damping Partitions and RF-Fields — M. Cornacchia, A. Hofmann.....	564	RAA18
Experiments on Beam-Beam Depolarization at LEP — R. Assmann, A. Blondel, B. Dehning, A. Drees, P. Grosse-Wiesmann, H. Grote, M. Placidi, R. Schmidt, F. Tecker, J. Wenninger.....	567	RAA19
Measurements of Impedance Distributions and Instability Thresholds in LEP — D. Brandt, P. Castro, K. Cornelis, A. Hofmann, G. Morpurgo, G.L. Sabbi, J. Wenninger, B. Zotter.....	570	RAA20
A Preliminary Lattice Design of a Tau-Charm Factory Storage Ring in Beijing — N. Huang, L. Jin, Y. Wu, G. Xu.....	573	RAA21
Low Energy Ring Lattice of the PEP II Asymmetric B-Factor — Y. Cai, M. Donald, R. Helm, J. Irwin, Y. Nosochkov, D.M. Ritson, Y. Yan, E. Forest, A. Zholents.....	576	RAA22
Damping Rates of the SRRC Storage Ring — K.T. Hsu, C.C. Kuo, W.K. Lau, W.T. Weng.....	579	RAA23
Performance of the SRRC Storage Ring and Wiggler Commissioning — C. Kuo, K.T. Hsu, G.H. Luo, W.K. Lau, Ch. Wang, H.P. Chang, L.H. Chang, M.H. Wang, J.C. Lee, C.S. Hsue, W.T. Weng, Y.C. Liu.....	582	RAA24
Detector Solenoid Compensation in the PEP-II B-Factor — Y. Nosochkov, Y. Cai, J. Irwin, M. Sullivan, E. Forest.....	585	RAA25
Swamp Plots for Dynamic Aperture studies of PEP-II Lattices — Y.T. Yan, J. Irwin, Y. Cai, T. Chen, D. Ritson.....	588	RAA26
Lattice Design for the High Energy Ring of the SLAC B-Factor (PEP-II) — M.H.R. Donald, Y. Cai, J. Irwin, Y. Nosochkov, D.M. Ritson, J. Seeman, H.-U. Wienands, Y.T. Yan.....	591	RAA27
The APS Booster Synchrotron: Commissioning and Operational Experience — S.V. Milton.....	594	RAA28
A Preliminary Design for a Tau-Charm Factory — J. Norem, E. Crosbie, J. Repond, L. Teng.....	597	RAA29
A Spin Control System for the South Hall Ring at the Bates Linear Accelerator Center — T. Zwart, P. Ivanov, Yu. Shatunov, R. Averill, K. Jacobs, S. Kowalski, W. Turchinets.....	600	RAA31
Beam-Based Alignment of Sextupoles with the Modulation Method — M. Kikuchi, K. Egawa, H. Fukuma, M. Tejima.....	603	RAA33

Linear Colliders and Advanced Accelerator Concepts

The Stanford Linear Collider (Invited) — Paul Emma.....	606	WAG01
Options and Trade-Offs in Linear Collider Design (Invited) — J. Rossbach.....	611	WAG02
Test Facilities for Future Linear Colliders — Ronald D. Ruth.....	616	WAG03
Channel Guided Lasers for Plasma Accelerators (Invited) — H.M. Milchberg, C.G. Durfee III, T.M. Antonsen, P. Mora.....	621	WAG04
Inverse Cerenkov Accelerator Results (Invited) — W.D. Kimura.....	626	WAG05
Measurements of Plasma Wake-Fields in the Blow-Out Regime — N. Barov, M. Conde, J.B. Rosenzweig, P. Schoessow, G. Cox, W. Gai, R. Konecny, J. Power, J. Simpson.....	631	WAG06
Experimental Study of Electron Acceleration by Plasma Beat-Waves with Nd Lasers — F. Amiranoff, F. Moulin, J. Fusellier, J.M. Joly, M. Juillard, M. Bercher, D. Bernard, A. Debraine, J.M. Dieulot, F. Jacquet, P. Matricon, Ph. Miné, B. Montès, R. Morano, P. Poilleux, A. Specka, J. Morillo, J. Ardonneau, B. Cros, G. Matthieussent, C. Stenz, P. Mora.....	634	WAG07
A Broadband Electron Spectrometer and Electron Detectors for Laser Accelerator Experiments — C.E. Clayton, K.A. Marsh, C. Joshi, C.B. Darrow, A.E. Dangor, A. Modena, Z. Najmudin, V. Malka.....	637	WAG08

Photon Acceleration from Rest to the Speed of Light — C.H. Lai, T. Katsouleas, R. Liou, W.B. Mori, C. Joshi, P. Muggli, R. Brogle, J. Dawson.....	640	WAG09
A Constant Gradient Planar Accelerating Structure for Linac Use — Y.W. Kang, P.J. Matthews, R.L. Kustom.....	643	WAG10
Pulse to Pulse Stability Issues in the SLC — C. Adolphsen, R. Assmann, F.J. Decker, P. Emma, J. Frisch, L.J. Hendrickson, P. Krejcik, M. Minty, N. Phinney, P. Raimondi, M.C. Ross, T. Slaton, W. Spence, R. Stege, H. Tang, F. Tian, J. Turner, M. Woodley, F. Zimmermann.....	646	WAG11
HOM-Free Linear Accelerating Structure for e+e- Linear Collider at C-Band — T. Shintake, K. Kubo, H. Matsumoto, O. Takeda.....	649	WAG12
SLAC/CERN High Gradient Tests of an X-Band Accelerating Section — J.W. Wang, G.A. Loew, R.J. Loewen, R.D. Ruth, A.E. Vlieks, I. Wilson, W. Wuensch.....	653	WAG13

Linear Colliders

Performance of the 1994/95 SLC Final Focus System — F. Zimmermann, T. Barklow, S. Ecklund, P. Emma, D. McCormick, N. Phinney, P. Raimondi, M. Ross, T. Slaton, F. Tian, J. Turner, M. Woodley, M. Placidi, N. Toge, N. Walker.....	656	RPB01
Direct Measurement of Transverse Wakefields in the SLC Linac — P. Krejcik, R. Assmann, F.-J. Decker, S. Hartman, R. Miller, T. Raubenheimer.....	659	RPB02
Feedback Performance at the Stanford Linear Collider — M.G. Minty, C. Adolphsen, L.J. Hendrickson, R. Sass, T. Slaton, M. Woodley.....	662	RPB03
Vibration Studies of the Stanford Linear Accelerator — J.L. Turner, C. Adolphsen, G.B. Bowden, F.J. Decker, S.C. Hartman, S. Matsumoto, G. Mazaheri, D. McCormick, M. Ross, R. Stege, S. Virostek, M. Woodley.....	665	RPB04
SLAC Modulator Availability and Impact on SLC Operation — A.R. Donaldson, J.R. Ashton.....	668	RPB05
The SLC as a Second Generation Linear Collider — J.E. Spencer.....	671	RPB06
Status of the Design for the TESLA Linear Collider — R. Brinkmann.....	674	RPB07
The TESLA Test Facility (TTF) Linac - A Status Report — H. Weise.....	677	RPB08
The Infrastructure for the TESLA Test Facility (TTF) - A Status Report — S. Wolff.....	680	RPB09
The Status of the S-Band Linear Collider Study — N. Holtkamp.....	683	RPB12
The S-Band Linear Collider Test Facility — N. Holtkamp.....	686	RPB13
Beam Dynamics Studies for the SBLC — M. Drevlak, R. Wanzenberg.....	689	RPB14
S-Band HOM-Damper Calculations and Experiments — M. Dohlus, M. Marx, N. Holtkamp, P. Hülsmann, W.F.O. Müller, M. Kurz, H.-W. Glock, H. Klein.....	692	RPB15
The S-Band 36-Cell Experiment — B. Krietenstein, O. Podebrad, U. v.Rienen, T. Weiland, H.-W. Glock, P. Hülsmann, H. Klein, M. Kurz, C. Peschke, M. Dohlus, N. Holtkamp.....	695	RPB16

Volume 2

Linear Colliders (cont'd)

Parameters for the SLAC Next Linear Collider — T. Raubenheimer, C. Adolphsen, D. Burke, P. Chen, S. Ecklund, J. Irwin, G. Loew, T. Markiewicz, R. Miller, E. Paterson, N. Phinney, M. Ross, R. Ruth, J. Sheppard, H. Tang, K. Thompson, P. Wilson.....	698	RPC01
A Damping Ring Design for the SLAC Next Linear Collider — T.O. Raubenheimer, J. Byrd, J. Corlett, R. Early, M. Furman, A. Jackson, P. Krejcik, K. Kubo, T. Mattison, M. Minty, W. Moshhammer, D. Robin, B. Scott, J. Spencer, K. Thompson, P. Wilson.....	701	RPC02
A Bunch Compressor for the Next Linear Collider — P. Emma, T. Raubenheimer, F. Zimmermann.....	704	RPC03
A Final Focus System for the Next Linear Collider — F. Zimmermann, K. Brown, P. Emma, R. Helm, J. Irwin, P. Tenenbaum, P. Wilson.....	707	RPC06
Optimization of the NLC Final Focus System — F. Zimmermann, R. Helm, J. Irwin.....	710	RPC07
The SLAC NLC Extraction & Diagnostic Line — J. Spencer, J. Irwin, D. Walz, M. Woods.....	713	RPC08

CLIC - A Compact and Efficient High Energy Linear Collider — <i>H. Braun, R. Corsini, J.-P. Delahaye, G. Guignard, C. Johnson, J. Madsen, W. Schnell, L. Thorndahl, I. Wilson, W. Wuensch, B. Zotter</i>	716	RPC09
CLIC Test Facility Developments and Results — <i>R. Bossart, H. Braun, F. Chautard, M. Comunian, J.P. Delahaye, J.C. Godot, I. Kamber, J.H.B. Madsen, L. Rinolfi, S. Schreiber, G. Suberlucq, I. Wilson, W. Wuensch</i>	719	RPC10
Generation of a 30 GHz Train of Bunches Using a Magnetic Switch-Yard — <i>B. Autin, R. Corsini</i>	722	RPC11
A New Family of Isochronous Arcs — <i>G. Guignard, E.T. d'Amico</i>	725	RPC12
Updating of Beam Dynamics in the CLIC Main Linac — <i>G. Guignard</i>	728	RPC13
Improved CLIC Performances Using the Beam Response for Correcting Alignment Errors — <i>C. Fischer</i>	731	RPC14
Experimental Studies of a CERN-CLIC 32.98 GHz High Gradient Accelerating Structure Driven by the MIT Free Electron Laser Amplifier — <i>P. Volfbeyn, I. Mastovsky, G. Bekefi, I. Wilson, W. Wuensch</i>	734	RPC15
Design of a Relativistic Klystron Two-Beam Accelerator Prototype — <i>G. Westenskow, G. Caporaso, Y. Chen, T. Houck, S. Yu, S. Chattopadhyay, E. Henestroza, H. Li, C. Peters, L. Reginato, A. Sessler</i>	737	RPC16
Beam Dynamics Issues in an Extended Relativistic Klystron — <i>G. Giordano, H. Li, N. Goffeney, E. Henestroza, A. Sessler, S. Yu, T. Houck, G. Westenskow</i>	740	RPC17
Engineering Conceptual Design of the Relativistic Klystron Two-Beam Accelerator Based Power Source for 1-TeV Next Linear Collider — <i>L. Reginato, C. Peters, D. Vanecek, S. Yu, F. Deadrick</i>	743	RPC18
Design of Inductively Detuned RF Extraction Cavities for the Relativistic Klystron Two Beam Accelerator — <i>E. Henestroza, S.S. Yu, H. Li</i>	746	RPC19
Beam-Based Optical Tuning of the Final Focus Test Beam — <i>P. Tenenbaum, D. Burke, S. Hartman, R. Helm, J. Irwin, R. Iverson, P. Raimondi, W. Spence, V. Bharadwaj, M. Halling, J. Holt, J. Buon, J. Jeanjean, F. Le Diberder, V. Lepeltier, P. Puzo, K. Oide, T. Shintake, N. Yamamoto</i>	749	RPC20
Fermilab Contributions to the FFTB — <i>V. Bharadwaj, A. Braun, M. Halling, J.A. Holt, D. Still</i>	752	RPC21
HV Injection Phase Orbit Characteristics for Sub-Picosecond Bunch Operation with a High Gradient 17 GHz Linac — <i>J. Haimson, B. Mecklenburg</i>	755	RPC22

New Acceleration Techniques

Electron Acceleration in Relativistic Plasma Waves Generated by a Single Frequency Short-Pulse Laser — <i>C.A. Coverdale, C.B. Darrow, C.D. Decker, W.B. Mori, K.-C. Tzeng, C.E. Clayton, K.A. Marsh, C. Joshi</i>	758	RAB01
Theory and Simulation of Plasma Accelerators — <i>W.B. Mori, K.-C. Tzeng, C.D. Decker, C.E. Clayton, C. Joshi, T. Katsouleas, P. Lai, T.C. Chiou, R. Kinter</i>	761	RAB02
An Injector-prebuncher for a Plasma Electron Accelerator — <i>M. Lampel, C. Pellegrini, R. Zhang, C. Joshi, W.M. Fawley</i>	764	RAB03
Measurements of the Beatwave Dynamics in Time and Space — <i>A. Lal, K. Wharton, D. Gordon, M.J. Everett, C.E. Clayton, C. Joshi</i>	767	RAB04
A Novel Technique for Probing the Transverse Interactions Between an Electron Beam and a Plasma — <i>D. Gordon, A. Lal, C.E. Clayton, M. Everett, C. Joshi</i>	770	RAB05
Studies of Intense Laser Propagation in Channels for Extended Length Plasma Accelerators — <i>T. Katsouleas, T.C. Chiou, W.B. Mori, J.S. Wurtele, G. Shvets</i>	773	RAB08
UV Laser Ionization and Electron Beam Diagnostics for Plasma Lenses — <i>R. Govil, P. Volfbeyn, W. Leemans</i>	776	RAB10
Plasma Wakefield Acceleration Experiments in Overdense Regime Driven by Narrow Bunches — <i>T. Kozawa, T. Ueda, T. Kobayashi, M. Uesaka, K. Miya, A. Ogata, H. Nakanishi, T. Kawakubo, M. Arinaga, K. Nakajima, H. Shibata, N. Yugami, Y. Nishida, D. Whittum, Y. Yoshida</i>	779	RAB13
The Wake-Field Excitation in a Plasma-Dielectric Structure by a Sequence of Short Bunches of Relativistic Electrons — <i>I.N. Onishchenko, V.A. Kiseljov, A.K. Berezin, G.V. Sotnikov, V.V. Uskov, A.F. Linnik, Ya.B. Fainberg</i>	782	RAB15

A Beam Focusing System for a Linac Driven by a Traveling Laser Focus — A.A. Mikhailichenko.....	784	RAB18
2 x 2 TeV $\mu^+\mu^-$ Collider: Lattice and Accelerator-Detector Interface Study — N.M. Gelfand, N.V. Mokhov.....	787	RAB19
Muon Cooling and Acceleration Experiment at TRIUMF — S.A. Bogacz, D.B. Cline, P.H. Sandler, D.A. Sanders.....	790	RAB20
Helical Siberian Snakes — E. Ludmirsky.....	793	RAB21
Performance of Achromatic Lattice with Combined Function Sextupoles at Duke Storage Ring — V.N. Litvinenko, Y. Wu, B. Burnham, J.M.J. Madey, S.H. Park.....	796	RAB22

Accelerators and Storage Rings, Misc.

Matreshka High-Intensity Accelerator of Continuous Particle Beams — F.A. Vodopianov.....	799	TAR02
The Amplitude and Phase Control of the ALS Storage Ring RF System — C.C. Lo, B. Taylor, K. Baptiste.....	801	TAR03
Integral Dipole Field Calibration of the SRRC Storage Ring Combined Function Bending Magnets — J.C. Lee, Peace Chang, C.S. Hsue.....	804	TAR04
Improved Mobile 70 MeV Race-Track Microtron Design — V.I. Shvedunov, A.I. Karev, V.N. Melekhin, N.P. Sobenin, W.P. Trower.....	807	TAR05
The Improvement of Energy Measurement in BTS Transport Line by Using Beam Tracing Method — M.H. Wang, J.C. Lee.....	810	TAR06
Design Study of PAL-Stretcher Ring — I.S. Ko, G.N. Kim, J. Choi, M.H. Cho, W. Namkung.....	813	TAR07
Thermomechanical Analysis of a Compact-Design High Heat Load Crotch Absorber — I.C. Sheng, S. Sharma, R. Rotela, J. Howell.....	816	TAR08
Novosibirsk Tau-Charm Factory Design Study — N. Dikansky, V. Parkhomchuk, A. Skrinsky, V. Yakimenko.....	819	TAR11
Development of a RAMI Program for LANSCE Upgrade — K.C.D. Chan, A. Browman, R.L. Hutson, R.J. Macek, P.J. Tallerico, C.A. Wilkinson.....	822	TAR12
Accelerator Waveform Synthesis and Longitudinal Beam Dynamics in a Small Induction Recirculator — T.J. Fessenden, D.P. Grote, W.M. Sharp.....	825	TAR13
Progress Toward a Prototype Recirculating Induction Accelerator for Heavy-Ion Fusion — A. Friedman, J.J. Barnard, M.D. Cable, D.A. Callahan, F.J. Deadrick, S. Eylon, T.J. Fessenden, D.P. Grote, D.L. Judd, H.C. Kirbie, D.B. Longinotti, S.M. Lund, L.A. Natrass, M.B. Nelson, M.A. Newton, T.C. Sangster, W.M. Sharp, S.S. Yu.....	828	TAR14
Three Dimensional Simulations of a Small Induction Recirculator Accelerator — D.P. Grote, A. Friedman, I. Haber.....	831	TAR15
A Dynamic Momentum Compaction Factor Lattice in the FERMILAB DEBUNCHER Ring — D.N. Olivieri, M. Church, J. Morgan.....	834	TAR16
Mechanical Design of Recirculating Accelerator Experiments for Heavy-Ion Fusion — V. Karpenko, J. Barnard, F. Deadrick, A. Friedman, D. Grote, S. Lund, J. Meredith, L. Natrass, M. Nelson, G. Repose, C. Sangster, W. Sharp, T. Fessenden, D. Longinotti, C. Ward.....	837	TAR17
The PEP-II Project-Wide Database — A. Chan, S. Calish, G. Crane, I. MacGregor, S. Meyer, J. Wong, A. Weinstein.....	840	TAR18
Chromaticity Compensation - Booster Sextupoles — S.A. Bogacz, K.-Y. Ng, J.-F. Ostiguy.....	843	TAR20
Overview of $\mu^+\mu^-$ Collider Options — D.B. Cline.....	846	TAR21
HIRFL Status and HIRFL-CSR Proposal — Ye Fang, Wang Yifang.....	850	TAR22

Particle Sources and Injectors

A Review of Polarized Ion Sources (Invited) — P.W. Schmor.....	853	MPE01
Sources for Production of Radioactive Ion-Beams (Invited) — Helge L. Ravn.....	858	MPE02
The TRIUMF High-Curent DC Optically -Pumped Polarized H⁺ Ion Source — A.N. Zelenski, C.D.P. Levy, K. Jayamanna, M. McDonald, P.W. Schmor, W.T.H. van Oers, J. Welz, G.W. Wight, G. Dutto, Y. Mori, T. Sakae.....	864	MPE03

Lifetime Test on a High-Performance DC Microwave Proton Source — J. Sherman, <i>D. Hodgkins, P. Lara, J.D. Schneider, R. Stevens Jr.</i>	867	MPE04
Performance Enhancement of a Compact Radio Frequency Ion Source by the Injection of Supplemental Electrons — R.F. Welton, G.D. Alton, D. Becher, G.D. Mills, J. Dellwo, <i>S.N. Murray</i>	871	MPE05
A High-Current Position Source — V.V. Gorev	874	MPE06
Polarized Electron Sources (Invited) — J.E. Clendenin	877	MPE08
High Brightness Electron Sources (Invited) — Richard L. Sheffield	882	MPE09
Polarization Studies of Strained GaAs Photocathodes at the SLAC Gun Test Laboratory — <i>P. Sáez, R. Alley, J. Clendenin, J. Frisch, R. Kirby, R. Mair, T. Maruyama, R. Miller,</i> <i>G. Mulhollan, C. Prescott, H. Tang, K. Witte</i>	887	MPE10
Experimental Results of the ATF In-line Injection System — X.J. Wang, T. Srinivasan-Rao, <i>K. Batchelor, M. Babzien, I. Ben-Zvi, R. Malone, I. Pogorelsky, X. Qiu, J. Sheehan, J. Skaritka</i>	890	MPE11
High Power Testing of a 17 GHz Photocathode RF Gun — S.C. Chen, B.G. Danly, J. Gonichon, <i>C.L. Lin, R.J. Temkin, S.R. Trotz, J.S. Wurtele</i>	893	MPE12
Analytical Model for Emittance Compensation in RF Photo-Injectors — L. Serafini, <i>J.B. Rosenzweig</i>	896	MPE13
Emission, Plasma Formation, and Brightness of a PZT Ferroelectric Cathode — <i>S. Sampayan, G. Caporaso, D. Trimble, G. Westenskow</i>	899	MPE14

Radio Frequency Guns and Linac Injectors

Design and Testing of the 2 MV Heavy Ion Injector for the Fusion Energy Research Program — W. Abraham, R. Benjegerdes, L. Reginato, J. Stoker, R. Hipple, C. Peters, J. Pruyn, <i>D. Vanecek, S. Yu</i>	902	WPA01
K⁺ Diode for the LLNL Heavy Ion Recirculator Accelerator Experiment — S. Eylon, <i>E. Henestroza, F. Deadrick</i>	905	WPA02
A Single Bunch RFQ System for Heavy Ions — J. Madlung, A. Firjahn-Andersch, A. Schempp	908	WPA03
The Design of Low Frequency Heavy Ion RFQ Resonators — A. Schempp, H. Vormann, <i>U. Beisel, H. Deitinghoff, O. Engels, D. Li</i>	911	WPA04
A VE-RFQ-Injector for a Cyclotron — A. Schempp, O. Engels, F. Marhauser	914	WPA05
Fermilab Linac Injector, Revisited — M. Popovic, L. Allen, C.W. Schmidt	917	WPA06
New RF Structures for the Fermilab Linac Injector — M. Popovic, A. Moretti, R.J. Nobel	920	WPA07
High-Power RF Operations Studies with the CRITS RFQ — G.O. Bolme, D.R. Keffeler, <i>V.W. Brown, D.C. Clark, D. Hodgkins, P.D. Lara, M.L. Milder, D. Rees, P.J. Schafstall,</i> <i>J.D. Schneider, J.D. Sherman, R.R. Stevens, T. Zaugg</i>	923	WPA08
Beam Dynamics Studies of the Heavy Ion Fusion Accelerator Injector — E. Henestroza, <i>S.S. Yu, S. Eylon, D.P. Grote</i>	926	WPA09
First Tests at Injector for the S-Band Test Facility at DESY — M. Schmitz, W. Herold, <i>N. Holtkamp, W. Kriens, R. Walther</i>	929	WPA12
RF Phasing of the Duke Linac — Ping Wang, Nelson Hower, Patrick G. O'Shea	932	WPA13
Simulations and Measurements of the TTF Phase-1 Injector Gun — T. Garvey, M. Omeich, <i>M. Jablonka, J.M. Joly, H. Long</i>	935	WPA14
Experimental Studies on Cold Cathode Magnetron Gun — A.N. Dovbnya, V.V. Zakutin, <i>V.F. Zhiglo, A.N. Opanasenko, V.P. Romasko, S.A. Cherenshchikov</i>	938	WPA15
Secondary Emission in Cold-Cathode Magnetron Injection Gun — S.A. Cherenshchikov, <i>A.N. Dovbnya, A.N. Opanasenko</i>	939	WPA16
Design of a High Charge CW Photocathode Injector Test Stand at CEBAF — H. Liu, <i>D. Kehne, S. Benson, J. Bisognano, L. Cardman, F. Dylla, D. Engwall, J. Fugitt, K. Jordan,</i> <i>G. Neil, D. Neuffer, C. Sinclair, M. Wiseman, B. Yunn</i>	942	WPA17
CANDELA Photo-Injector Experimental Results With a Dispenser Photocathode — <i>C. Travier, B. Leblond, M. Bernard, J.N. Cayla, P. Thomas, P. Georges</i>	945	WPB01
A Multi-Cell RF Photoinjector Design — Sanghyun Park	948	WPB02
On the Frequency Scalings of RF Guns — Leon C.-L. Lin, J.S. Wurtele, S.C. Chen	951	WPB03
Waveguide Broad-Wall Coupling for RF Guns — Leon C.-L. Lin, S.C. Chen, J.S. Wurtele	954	WPB04

Charge and Wavelength Scaling of RF Photoinjectors: A Design Tool — J. Rosenzweig, E. Colby.....	957	WPB05
A Photocathode RF Gun Design for a mm-Wave Linac-Based FEL — A. Nassiri, T. Berenc, J. Foster, G. Waldschmidt, J. Zhou.....	961	WPB06
The RF Gun Development at SRRC — C.H. Ho, W.K. Lau, J.I. Hwang, S.Y. Hsu, Y.C. Liu	964	WPB07
Design and Construction of High Brightness RF Photoinjectors for TESLA — E. Colby, V. Bharadwaj, J.F. Ostiguy, T. Nicol, M. Conde, J. Rosenzweig.....	967	WPB08
Jitter Sensitivity in Photoinjectors — Patrick G. O'Shea	970	WPB09
Asymmetric Emittance Beam Generation Using Round Beam RF Guns and Non-linear Optics — G. Fiorentini, C. Pagani, L. Serafini.....	973	WPB10
The Argonne Wakefield Accelerator High Current Photocathode Gun and Drive Linac — P. Schoessow, E. Chojnacki, G. Cox, W. Gai, C. Ho, R. Konecny, J. Power, M. Rosing, J. Simpson, N. Barov, M. Conde.....	976	WPB11
Witness Gun for the Argonne Wakefield Accelerator — J. Power, J. Simpson, E. Chojnacki, R. Konecny.....	979	WPB12
Microwave Measurements of the BNL/SLAC/UCLA 1.6 Cell Photocathode RF Gun — D.T. Palmer, R.H. Miller, H. Winick, X.J. Wang, K. Batchelor, M. Woodle, I. Ben-Zvi.....	982	WPB13
Subpicosecond, Ultra-Bright Electron Injector — Bruce E. Carlsten, Martin L. Milder, John M. Kinross-Wright, Donald W. Feldman, Steven Russell, John G. Plato, Alan Shapiro, Boyd Sherwood, Jan Studebaker, Richard Lovato, David Warren, Carl Timmer, Ronald Cooper, Ronald Sturges, Mel Williams.....	985	WPB15
Energy Spread Compensation in an Electron Linear Accelerator — Yu.D. Tur, A.N. Dovbnya, V.A. Kushnir, V.V. Mitrochenko, D.L. Stepin	988	WPB16
On Enhancement of Limited Accelerating Charge — Yu. Tur.....	990	WPB17
Magnetic Pulse Compression Using a Third Harmonic RF Linearizer — D.H. Dowell, T.D. Hayward, A.M. Vetter	992	WPB20
A Comparison of L-Band and C-Band RF Guns as Sources for Inline-Injection Systems — Juan C. Gallardo, Harold G. Kirk, Thomas Meyer.....	995	WPB21
Progress in the Study and Construction of the TESLA Test Facility Injector — R. Chehab, M. Bernard, J.C. Bourdon, T. Garvey, B. Jacquemard, M. Mencick, B. Mouton, M. Omeich, J. Rodier, P. Roudier, J.L. Saury, M. Taurigna-Quere, Y. Thiery, B. Aune, M. Desmons, J. Fusellier, F. Gougnaud, J.F. Gournay, M. Jablonka, J.M. Joly, M. Juillard, Y. Lussignol, A. Mosnier, B. Phung, S. Buhler, T. Junquera.....	998	WPB22

Particle Sources

Hollow Beam Profile in the Extraction System of ECR Ion Source — Y. Batygin, A. Goto, Y. Yano.....	1001	WPC01
Ion Sources for Use in Research and Applied High Voltage Accelerators — S. Nikiforov, V. Golubev, D. Solnyshkov, M. Svinin, G. Voronin	1004	WPC03
Direct Fast Beam Chopping of H⁻ Ion Beam in the Surface-Plasma H⁻ Ion Source — K. Shinto, A. Takagi, Z. Igarashi, K. Ikegami, M. Kinsho, S. Machida, M. Yoshii, Y. Mori	1007	WPC07
Emittance Measurements of the High Intensity Polarized Ion Source at IUCF — V. Derenchuk, R. Brown, H. Petri, E. Stephenson, M. Wedekind.....	1010	WPC08
Report on EBIS Studies for a RHIC Preinjector — E. Beebe, A. Herscovitch, A. Kponou, K. Prelec, J. Alessi, R. Schmieder.....	1013	WPC09
Development of a Volume H⁻ Ion Source for LAMPF — D.R. Swenson, R.L. York, R.R. Stevens Jr., C. Geisik, W. Ingalls, J.E. Stelzer, D. Fitzgerald.....	1016	WPC10
Generation of High Purity CW Proton Beams from Microwave-Driven Sources — David Spence, Keith R. Lykke	1019	WPC11
Computational Studies for an Advanced Design ECR Ion Source — G.D. Alton, J. Dellwo, R.F. Welton, D.N. Smithe.....	1022	WPC12
Pulsed Ion Sources of Duoplasmatron Type with Cold and Hot Cathodes — A. Glazov, V. Krasnopolsky, R. Meshcherov, V. Masalov	1025	WPC13
Double Pulse Experiment with a Velvet Cathode on the ATA Injector — G. Westenskow, G. Caporaso, Y. Chen, T. Houck, S. Sampayan.....	1027	WPC16

Emittance Measurements for the Illinois/CEBAF Polarized Electron Source — <i>B.M. Dunham, L.S. Cardman, C.K. Sinclair</i>	1030	WPC17
The NLC Positron Source — <i>H. Tang, A.V. Kulikov, J.E. Clendenin, S.D. Ecklund, R.A. Miller, A.D. Yeremian</i>	1033	WPC18
Ferroelectric Cathodes as Electron Beam Sources — <i>D. Flechtner, G.S. Kerslick, J.D. Ivers, J.A. Nation, L. Schächter</i>	1036	WPC19
Studies of Linear and Nonlinear Photoelectric Emission for Advanced Accelerator Applications — <i>R. Brogle, P. Muggli, P. Davis, G. Hairapetian, C. Joshi</i>	1039	WPC20
A Derivative Standard for Polarimeter Calibration — <i>G. Mulhollan, J. Clendenin, P. Sáez, D. Schultz, H. Tang, A.W. Pang, H. Hopster, K. Trantham, M. Johnston, T. Gay, B. Johnson, M. Magugumela, F.B. Dunning, G.K. Walters, G.F. Hanne</i>	1043	WPC21
Analysis of Positron Focusing Section for SPring-8 Linac — <i>A. Mizuno, S. Suzuki, H. Yoshikawa, T. Hori, K. Yanagida, H. Sakaki, T. Taniuchi, H. Kotaki, H. Yokomizo</i>	1046	WPC22
R & D Activity on High QE Alkali Photocathodes for RF Guns — <i>P. Michelato, A. Di Bona, C. Pagani, D. Sertore, S. Valeri</i>	1049	WPC23
Development of an Accelerator-Ready Photocathode Drive Laser at CEBAF — <i>S. Benson, M. Shinn</i>	1052	WPC24

Linear Accelerators

Analytical Formulae for the Loss Factors and Wakefields of a Disk-loaded Accelerating Structure — <i>J. Gao</i>	1055	RPA03
Design Parameters for the Damped Detuned Accelerating Structure — <i>K. Ko, K. Bane, R. Gluckstern, H. Hoag, N. Kroll, X.T. Lin, R. Miller, R. Ruth, K. Thompson, J. Wang</i>	1058	RPA04
Operation of PLS 2-GeV Linac — <i>W. Namkung, I.S. Ko, M.H. Cho, J.S. Bak, J. Choi, H.S. Lee</i>	1061	RPA06
Radiation Measurements at the Advanced Photon Source (APS) Linear Accelerator — <i>H.J. Moe, J.H. Vacca, V.R. Veluri, M. White</i>	1064	RPA07
Positron Focusing in the Advanced Photon Source (APS) Linear Accelerator — <i>Y.L. Qian, M. White</i>	1067	RPA08
Bunch Length Measurements at the Advanced Photon Source (APS) Linear Accelerator — <i>N.S. Sereno, R. Fuja, C. Gold, A.E. Grelick, A. Nassiri, J.J. Song, M. White</i>	1070	RPA10
Performance of the Advanced Photon Source (APS) Linear Accelerator — <i>M. White, N. Arnold, W. Berg, A. Cours, R. Fuja, J. Goral, A. Grelick, K. Ko, Y.L. Qian, T. Russell, N.S. Sereno, W. Wesolowski</i>	1073	RPA11
TW Accelerating Structures with Minimal Surface Electric Field — <i>O. Nezhevenko, D. Myakishev, V. Tarnetsky, V. Yakovlev</i>	1076	RPA12
A 100 MeV Injector for the Electron Storage Ring at Kyoto University — <i>T. Shirai, M. Kando, M. Ikegami, Y. Iwashita, H. Okamoto, S. Kakigi, H. Dewa, H. Fujita, A. Noda, M. Inoue, K. Mashiko</i>	1079	RPA13
Phase Control and Intra-Pulse Phase Compensation of the Advanced Photon Source (APS) Linear Accelerator — <i>A.E. Grelick, N. Arnold, K. Ko, N. Sereno, M. White</i>	1082	RPA14
Error Sensitivity Study for Side Coupled Muffin Tin Structures using a Finite Difference Program — <i>Warner Bruns</i>	1085	RPA15
Design of Input Couplers and Endcells for Side Coupled Muffin-Tin Structures — <i>Warner Bruns</i>	1088	RPA16
Accelerator Archeology - The Resurrection of the Stanford MARKIII Electron Linac at Duke — <i>P.G. O'Shea, F. Carter, C. Dickey, N. Hower, V.N. Litvinenko, R. Sachtschale, G. Swift, P. Wang, Y. Wu, J.M.J. Madey</i>	1090	RPA17
Cold Model Test of Biperiodic L-Support Disk-and-Washer Linac Structure — <i>Y. Iwashita, A. Noda, H. Okamoto, T. Shirai, M. Inoue</i>	1093	RPA18
Compact Low Energy CW Linac with High Beam Current — <i>A. Alimov, A. Chepurinov, O. Chubarov, D. Ermakov, K. Gudkov, B. Ishkhanov, I. Piskarev, V. Shvedunov, A. Shumakov</i>	1096	RPA19
C-Band Linac RF-System for e+e- Linear Collider — <i>T. Shintake, N. Akasaka, K.L.F. Bane, H. Hayano, K. Kubo, H. Matsumoto, S. Matsumoto, K. Oide, K. Yokoya</i>	1099	RPA20
Initial Operation of the UCLA Plane Wave Transformer (PWT) Linac — <i>R. Zhang, P. Davis, G. Hairapetian, M. Hogan, C. Joshi, M. Lampel, S. Park, C. Pellegrini, J. Rosenzweig, G. Travish</i>	1102	RPA21

The UCLA Compact High Brightness Electron Accelerator — P. Davis, G. Hairapetian, M. Hogan, C. Joshi, M. Lampel, S. Park, C. Pellegrini, J. Rosenzweig, G. Travish, R. Zhang	1105	RPA22
A Semi-Automated System for the Characterization of NLC Accelerating Structures — S.M. Hanna, G.B. Bowden, H.A. Hoag, R. Loewen, A.E. Vlieks, J.W. Wang	1108	RPA23
SLAC Accelerator Operations Report: 1992-1995 — R. Erickson, C.W. Allen, T.K. Inman, W. Linebarger, M. Stanek.....	1111	RPA24
Beam Current Limitation in Microwave Accelerators — A.V. Mishin, I.S. Shchedrin.....	1114	RPA25
Installation and Commissioning of the e+/e- Injector for DAFNE at Frascati — K. Whitham, H. Amankath, J. Edighoffer, K. Fleckner, E. Gower, S. Lyons, D. Nett, D. Palmer, R. Sheppard, S. Sutter, P. Treas, A. Zante, R. Miller, R. Boni, H. Hsieh, F. Sannibale, M. Vescovi, G. Vignola.....	1116	RPA26
Recent Studies of Linac for Production of Radioactive Beams in the INR — I.N. Birukov, I.V. Gonin, D.V. Gorelov, A.N. Iljinov, V.A. Moiseev, P.N. Ostroumov, A.V. Tiunov.....	1119	RPR01
RFQ Cold Model Studies — P.G. Bricault, D. Joffe, H.R. Schneider.....	1122	RPR02
Simulation of the TRIUMF Split-Ring 4-Rod RFQ with MAFIA — P.G. Bricault, H.R. Schneider.....	1125	RPR03
A Low-charge-state Injector Linac for ATLAS — K.W. Shepard, J.W. Kim.....	1128	RPR05
Progress of the Heidelberg High Current Injector — C.-M. Kleffner, S. Auch, M. Grieser, D. Habs, V. Kößler, M. Madert, R. Repnow, D. Schwalm, H. Deitinghoff, A. Schempp, E. Jaeschke, R. von Hahn, S. Papureanu.....	1131	RPR06
The New Concepts in Designing the CW High-current Linacs — B.P. Murin, G.I. Batsikh, V.M. Belugin, B.I. Bondarev, A.A. Vasiljev, A.P. Durkin, Yu.D. Ivanov, V.A. Konovalov, A.P. Fedotov, I.V. Shumakov.....	1134	RPR07
A Versatile, High-Power Proton Linac for Accelerator Driven Transmutation Technologies — J.H. Billen, S. Nath, J.E. Stovall, H. Takeda, R.L. Wood, L.M. Young.....	1137	RPR08
A Compact High-Power Proton Linac for Radioisotope Production — H. Takeda, J.H. Billen, S. Nath, J.E. Stovall, R.L. Wood, L.M. Young.....	1140	RPR09
Potentialities of Electron and Ion Beam Accelerators for Long-Lived Nuclear Waste Transmutation — A. Shalnov, N. Abramenko, B. Bogdanovich, M. Karetnikov, A. Nesterovich, A. Puchkov.....	1143	RPR10
RFQ Design for High-Intensity Proton Beams — R. Ferdinand, J.-M. Lagniel, P. Mattei	1146	RPR11
Methods for Increasing of Beam Intensity in Undulator Linear Accelerator — E.S. Masunov.....	1149	RPR12
Linac Integrated Scheme Using RF Energy Storage and Compression — A.V. Smirnov	1152	RPR13
Magnetic Field Influence on RF-Structures Electrodynamical Characteristics and Sparking Limit — A. Shalnov, N. Abramenko, B. Bogdanovich, M. Karetnikov, A. Nesterovich, M. Tubaev	1155	RPR15
Calculations on the Possibility of the Simultaneous Acceleration of Ions with Different Charge States in a RFQ — H. Deitinghoff.....	1158	RPR18
Phase-Scan Analysis Results for the First Drift Tube Linac Module in the Ground Test Accelerator: Data Reproducibility and Comparison to Simulations — K.F. Johnson, O.R. Sander, G.O. Bolme, S. Bowling, R. Connolly, J.D. Gilpatrick, W.P. Lysenko, J. Power, E.A. Wadlinger, V. Yuan.....	1161	RPR19
Accelerator Systems Optimizing Code — C.C. Paulson, A.M.M. Todd, M.A. Peacock, M.F. Reusch, D. Bruhwiler, S.L. Mendelsohn, D. Berwald, C. Piasczyk, T. Meyers, G.H. Gillespie, B.W. Hill, R.A. Jamison.....	1164	RPR20
Unexpected Matching Insensitivity in DTL of GTA Accelerator — V.W. Yuan, O.R. Sander, R.C. Connolly, J.D. Gilpatrick, K.F. Johnson, W.P. Lysenko, D.P. Rusthoi, M. Smith, R. Weiss.....	1167	RPR22
Current Losses and Equilibrium in RF Linear Accelerators — Nathan Brown, Martin Reiser.....	1170	RPR23
MMF Linac Upgrade Possibilities for the Pulsed Neutron Source — S.K. Esin, L.V. Kravchuk, A.I. Kvasha, P.N. Ostroumov, V.L. Serov.....	1173	RPR24
Moscow Meson Factory DTL RF System Upgrade — S.K. Esin, L.V. Kravchuk, A.I. Kvasha, V.L. Serov.....	1175	RPR25

Pulsed and High Intensity Beams and Technology

Heavy Ion Fusion 2 MV Injector (Invited) — S. Yu, S. Eylon, E. Henestroza, C. Peters, L. Reginato, D. Vanecek, F. delaRama, R. Hipple, J.D. Stoker, D. Grote, F. Deadrick	1178	TAE01
Linac-Driven Spallation-Neutron Source (Invited) — Andrew J. Jason	1183	TAE02

High Average Power, High Current Pulsed Accelerator Technology (Invited) — <i>Eugene L. Neau</i>	1188	TAE03
Studies of Localized Space-Charge Waves in Space-Charge Dominated Beams (Invited) — <i>J.G. Wang, M. Reiser</i>	1193	TAE04
Design of the Jupiter Accelerator for Large X-ray Yields — J.J. Ramirez	1198	TAE05
Design and Power Flow Studies of a 500-TW Inductive Voltage Adder (IVA) Accelerator — <i>M.G. Mazarakis, J.W. Poukey, J.P. Corley, D.L. Smith, L. Bennett, J.J. Ramirez, P. Pankuch,</i> <i>I. Smith, P. Corcoran, P. Spence</i>	1201	TAE06
COBRA Accelerator for Sandia ICF Diode Research at Cornell University — David L. Smith, <i>Pete Ingwersen, Lawrence F. Bennett, John D. Boyes, David E. Anderson, John B. Greenly,</i> <i>Ravi N. Sudan</i>	1204	TAE07
Beam Injector and Transport Calculations for ITS — Thomas P. Hughes, David C. Moir, <i>Paul W. Allison</i>	1207	TAE08
Status of the AIRIX Induction Accelerator — Ph. Eyharts, Ph. Anthouard, J. Bardy, <i>C. Bonnafond, Ph. Delsart, A. Devin, P. Eyl, J. Labrousche, J. Launspach, J. De Mascureau,</i> <i>E. Merle, A. Roques, P. Le Taillandier, M. Thevenot, D. Villate, L. Voisin</i>	1210	TAE09
Pulse Modulators for Ion Recirculator Cells — T.F. Godlove, L.K. Len, F.M. Mako, <i>W.M. Black, K. Sloth</i>	1213	TAE10
A High Charge State Heavy Ion Beam Source for HIF — S. Eylon, E. Henestroza	1216	TAE11
Design and Operation of a 700kV, 700A Modulator — J.D. Ivers, G.S. Kerslick, J.A. Nation, <i>L. Schüchter</i>	1219	TAE12
The 3 MEV, 200 KW High Voltage Electron Accelerator for Industrial Application — <i>N.G. Tolstun, V.S. Kuznetsov, A.S. Ivanov, V.P. Ovchinnikov, M.P. Svinjin</i>	1222	TAE13
Klystron Modulator for Industrial Linac — Yu.D. Tur, V.I. Beloglazov, E.A. Khomyakov, <i>V.P. Krivchikov, V.B. Mufel, V.V. Zakutin</i>	1225	TAE14
Optimization of High-Current Ion Beam Acceleration and Charge Compensation in Two Cusps of Induction Linac — Vyacheslav I. Karas', Nadya G. Belova	1227	WAA01
2,5-Dimensional Numerical Simulation of Propagation of the Finite Sequence of Relativistic Electron Bunches (REB) in Tenuous and Dense Plasmas — V.I. Karas', Ya.B. Fainberg, <i>V.D. Levchenko, Yu.S. Sigov</i>	1230	WAA02
Kinetic Simulation of Fields Excitation and Particle Acceleration by Laser Beat Wave in Non-Homogeneous Plasmas — V.I. Karas', Ya.B. Fainberg, V.D. Levchenko, Yu.S. Sigov	1233	WAA03
An Upgraded Proton Injection Kicker Magnet for the Fermilab MIR — J. Dinkel, R. Reilly	1236	WAA05
Fermilab Main Injector Abort Kicker System — C.C. Jensen, J.A. Dinkel	1239	WAA07
Analysis of the Electrical Noise from the APS Kicker Magnet Power Supplies — <i>J.A. Carwardine, J. Wang</i>	1242	WAA08
Design and Test Results of Kicker Units for the Positron Accumulator Ring at the APS — <i>J. Wang</i>	1245	WAA09
Development of a Modular and Upgradeable Fast Kicker Magnet System for the Duke Storage Ring — R.J. Sachschtale, C. Dickey, P. Morcombe	1248	WAA10
High Current High Accuracy IGBT Pulse Generator — V.V. Nesterov, A.R. Donaldson	1251	WAA11
Analysis and Design Modifications for Upgrade of Storage Ring Bump Pulse System Driving the Injection Bump Magnets at the ALS — G.D. Stover	1254	WAA14
Eddy Currents Induced in a Muon Storage Ring Vacuum Chamber Due to a Fast Kicker — <i>W.Q. Feng, E.B. Forsyth</i>	1257	WAA15
High Pulse Power Modulator for a S-Band Transmitter — J. DeCobert, B. Binns, R. Campbell, <i>A. Hawkins, D. Wang, A. Zolfaghari</i>	1260	WAA16
Modulator for Klystron 5045 — N.S. Dikansky, V. Akimov, B. Estrin, K. Gubin, I. Kazarezov, <i>V. Kokoulin, N. Kot, A. Novokhatsky, Yu. Tokarev, S. Vasserman</i>	1263	WAA17
High Voltage Nanosecond Generators for SIBERIA - 2 — A. Kadnikov, V. Deviatilov, <i>V. Korchuganov, Yu. Matveev, D. Shvedov</i>	1266	WAA18
High Gradient Insulator Technology for the Dielectric Wall Accelerator — S. Sampayan, <i>G. Caporaso, B. Carder, Y. Chen, C. Holmes, E. Lauer, D. Trimble, J. Elizondo, M. Krogh,</i> <i>B. Rosenblum, C. Eichenberger, J. Fockler</i>	1269	WAA19
Status of the First Stage of Linear Induction Accelerator SILUND-21 — A.A. Fateev, <i>G.V. Dolbilov, I.I. Golubev, I.N. Ivanov, V.V. Kosukhin, N.I. Lebedev, V.A. Petrov,</i> <i>V.N. Razuvakin, V.S. Shvetsov, M.V. Yurkov</i>	1272	WAA20

EMIR-M Installation in the Mode of Operation with Plasma Opening Switch — <i>V.P. Kovalev, V.M. Korepanov, B.M. Lavrent'ev, R.N. Munasypov, B.A. Filatov</i>	1274	WAA21
--	------	-------

Magnet Technology

New Developments in Niobium Titanium Superconductors (Invited) — D.C. Larbalestier, <i>P.J. Lee</i>	1276	TPE01
Superconducting Magnets (Invited) — R. Perin	1282	TPE02
Assembly and Commissioning of the LHC Test String (Invited) — P. Faugeras	1288	TPE03
Construction and Testing of Arc Dipoles and Quadrupoles for the Relativistic Heavy Ion Collider (RHIC) at BNL (Invited) — P. Wanderer, J. Muratore, M. Anerella, G. Ganetis, A. Ghosh, A. Greene, R. Gupta, A. Jain, S. Kahn, E. Kelly, G. Morgan, A. Prodell, M. Rehak, W. Sampson, R. Thomas, P. Thompson, E. Willen	1293	TPE04
Permanent Magnet Design for the Fermilab Main Injector Recycler Ring — G.W. Foster, K. Bertsche, J.-F. Ostiguy, B. Brown, H. Glass, G. Jackson, M. May, D. Orris, Dick Gustafson	1298	TPE05
Recent Advances in Insertion Devices (Invited) — E. Gluskin, E.R. Moog	1301	TPE06
Permanent Magnet Beam Transport (Invited) — R.F. Holsinger	1305	TPE07
Statistical Analyses of the Magnet Data for the Advanced Photon Source Storage Ring Magnets (Invited) — S.H. Kim, D.W. Carnegie, C. Doose, R. Hogrefe, K. Kim, R. Merl	1310	TPE08
The Magnet System for the BESSY II Injector Synchrotron — T. Knuth, D. Krämer, E. Weihreter, I. Chertok, S. Michailov, B. Sukhina	1316	TPE09
Segmented High Quality Undulators — J. Chavanne, P. Elleaume, P. Van Vaerenbergh	1319	TPE10
Design of the PEP-II Low-Energy Ring Arc Magnets — T. Henderson, N. Li, J. Osborn, J. Tanabe, D. Yee, R. Yourd, W. Du, Y. Jiang, Y. Sun	1322	FAP01
Prototype Development of the BESSY II Storage Ring Magnetic Elements — T. Becker, D. Krämer, S. Kuchler, U. Strönisch, V. Korchuganov, N. Kuznetsov, E. Levichev	1325	FAP02
Design, Construction, and Procurement Methodology of Magnets for the 7-GeV Advanced Photon Source — A. Gorski, J. Argyrakis, J. Biggs, E. Black, J. Humbert, J. Jagger, K. Thompson	1328	FAP03
The Main Injector Trim Dipole Magnets — R. Baiod, D.J. Harding, D.E. Johnson, P.S. Martin, S. Mishra	1331	FAP04
The Main Injector Chromaticity Correction Sextupole Magnets: Measurements and Operating Schemes — C.M. Bhat, A. Bogacz, B.C. Brown, D.J. Harding, Si J. Fang, P.S. Martin, H.D. Glass, J. Sim	1334	FAP05
Magnetic Field Measurements of the Initial Fermilab Main Injector Production Quadrupoles — D.J. Harding, R. Baiod, B.C. Brown, J.A. Carson, N.S. Chester, E. Desavouret, J. DiMarco, J.D. Garvey, H.D. Glass, P.J. Hall, P.S. Martin, P.O. Mazur, C.S. Mishra, A. Mokhtarani, J.M. Nogiec, D.F. Orris, J.E. Pachnik, A.D. Russell, S.A. Sharonov, J.W. Sim, J.C. Tompkins, K. Trombly-Freytag, D.G.C. Walbridge, V.A. Yarba	1337	FAP06
Magnetic Field Measurements of the Initial Fermilab Main Injector Production Dipoles — D.J. Harding, R. Baiod, B.C. Brown, J.A. Carson, N.S. Chester, E. Desavouret, J. DiMarco, J.D. Garvey, H.D. Glass, P.J. Hall, P.S. Martin, P.O. Mazur, S. Mishra, A. Mokhtarani, J.M. Nogiec, D.F. Orris, J.E. Pachnik, A.D. Russell, S.A. Sharonov, J.W. Sim, J.C. Tompkins, K. Trombly-Freytag, D.G.C. Walbridge, V.A. Yarba	1340	FAP07
The Fermilab Main Injector Dipole and Quadrupole Cooling Design and Bus Connections — J.A. Satti	1343	FAP08
Design of the Fermilab Main Injector Lambertson — D.E. Johnson, R. Baiod, D.J. Harding, P.S. Martin, M. May	1346	FAP09
Three-Dimensional End Effects in Iron Septum Magnets — J.-F. Ostiguy, D.E. Johnson	1349	FAP10
Design and B-field Measurements of a Lambertson Injection Magnet for the RHIC Machine — N. Tsoupas, E. Rodger, J. Claus, H.W. Foelsche, P. Wanderer	1352	FAP11
The APS Direct-Drive Pulsed Septum Magnets — S. Sheynin, F. Lopez, S.V. Milton	1355	FAP12
Development of the Pulse Magnets for the Booster Synchrotron of SPring-8 — H. Yonehara, H. Suzuki, T. Nagafuchi, M. Kodaira, T. Aoki, N. Tani, S. Hayashi, Y. Ueyama, T. Kaneda, Y. Sasaki, H. Abe, H. Yokomizo	1358	FAP13
Magnetic Design of the LNLS Transport Line — R.H.A. Farias, Liu Lin, G. Tosin	1361	FAP14
Construction and Characterization of Combined Function Quadrupoles — G. Tosin	1364	FAP15

Dipole Magnets for the SLAC 50 GeV A-Line Upgrade — R. Erickson, S. DeBarger, C.M. Spencer, Z. Wolf.....	1366	FAP16
Design and Testing of the Magnetic Quadrupole for the Heavy Ion Fusion Program — R. Benjegerdes, A. Faltens, W. Fawley, C. Peters, L. Reginato, M. Stuart	1369	FAP17
Design and Construction of a Large Aperture, Quadrupole Electromagnet Prototype for ILSE — M. Stuart, A. Faltens, W.M. Fawley, C. Peters, M.C. Vella.....	1372	FAP18
A Permanent Race-Track Microtron End Magnet — A.I. Karev, V.N. Melekhin, V.I. Shvedunov, N.P. Sobenin, W.P. Trower.....	1375	FAP19
Planar Permanent Magnet Multipoles: Measurements and Configurations — T. Cremer, R. Tatchyn.....	1378	FAP20
Temperature Considerations in the Design of a Permanent Magnet Storage Ring — K. Bertsche, J.-F. Ostiguy, W.B. Foster.....	1381	FAP21
3D Numerical Analysis of Magnets and the Effect of Eddy Current on Fast Steering — T. Nagatsuka, T. Koseki, Y. Kamiya, Y. Terada	1384	FAP22
MEB Resitive Magnets Prototypes Manufacturing — G. Batsikh, G. Mamaev, T. Latypov, I. Tenyakov, Y. Tereshkin.....	1387	FAP24

Volume 3

Magnet Technology (cont'd)

Quench Antennas for RHIC Quadrupole Magnets — T. Ogitsu, A. Terashima, K. Tsuchiya, G. Ganetis, J. Muratore, P. Wanderer.....	1390	FAQ02
Superconducting 8 cm Corrector Magnets for the Relativistic Heavy Ion Collider (RHIC) — A. Morgillo, J. Escallier, G. Ganetis, A. Greene, A. Ghosh, A. Jain, E. Kelly, A. Marone, G. Morgan, J. Muratore, W. Sampson, P. Thompson, P.J. Wanderer, E. Willen.....	1393	FAQ03
Superconducting Sextupoles and Trim Quadrupoles for RHIC — P. Thompson, M. Anerella, G. Ganetis, A. Ghosh, A. Greene, R. Gupta, A. Jain, E. Kelly, M. Lindner, G. Morgan, J. Muratore, W. Sampson, P. Wanderer, E. Willen.....	1396	FAQ04
Study of UNK Quench Protection System on the String of 4 UNK Superconducting Magnets — A. Andriishchin, O. Afanasiev, V. Gridasov, A. Erochin, E. Kachtanov, K. Myznikov, V. Sytchev, L. Vassiliev, O. Veselov, N. Yarygin.....	1399	FAQ06
Two Alternate High Gradient Quadrupoles; An Upgraded Tevatron IR and a "Pipe" Design — A.D. McInturff, J.M. van Oort, R.M. Scanlan.....	1402	FAQ07
Superconducting Focusing Solenoid for X-band Klystron — T. Ogitsu, T. Higo, H. Mizuno, Y. Imai, T. Inaguchi, T. Minato, T.H. Kim, T. Uemura, S. Yokoyama, Z. Wolf, D. Jensen, P. Radusewicz.....	1405	FAQ08
A High Gradient Superconducting Quadrupole for a Low Charge State Ion Linac — J.W. Kim, K.W. Shepard, J.A. Nolen.....	1408	FAQ09
Status of the High Brilliance Synchrotron Radiation Source BESSY-II — E. Jaeschke, S. Khan, D. Krämer, D. Schirmer	1411	FAQ12
Harmonic Generation FEL Magnets: Measured B-fields Compared to 3D Simulations — W.S. Graves, L. Solomon.....	1414	FAQ13
Measurement of Ramp Rate Sensitivity in Model Dipoles with Ebanol-Coated Cable — C. Haddock, V. Kovachev, D. Capone.....	1417	FAQ14
Combined Element Magnet Production for the Relativistic Heavy Ion Collider (RHIC) at BNL — S. Mulhall, H. Foelsche, G. Ganetis, A. Greene, E. Kelly, S. Plate, E. Willen	1420	FAQ15
Field Quality Control Through the Production Phase of the RHIC Arc Dipoles — R. Gupta, A. Jain, S. Kahn, G. Morgan, P. Thompson, P. Wanderer, E. Willen	1423	FAQ16
The Elliptical Multipole Wiggler Project — E. Gluskin, D. Frachon, P.M. Ivanov, J. Maines, E.A. Medvedko, E. Trakhtenberg, L.R. Turner, I. Vasserman, G.I. Erg, Yu.A. Evtushenko, N.G. Gavrilov, G.N. Kulipanov, A.S. Medvedko, S.P. Petrov, V.M. Popik, N.A. Vinokurov, A. Friedman, S. Krinsky, G. Rakowsky, O. Singh	1426	FAQ17
Results of Magnetic Measurements and Field Integral Compensation for the Elliptical Multipole Wiggler — D. Frachon, P.M. Ivanov, E.A. Medvedko, I. Vasserman, O. Despe, Y.G. Kang	1429	FAQ18

Status of ELETTRA Insertion Devices — R.P. Walker, R. Bracco, A. Codutti, B. Diviacco, D. Millo, D. Zangrando	1432	FAQ19
Expected Radiation Spectra of a 30-m Long Undulator in SPring-8 — M. Takao, Y. Miyahara.....	1435	FAQ20
Analytical Formulation of a Quasi-periodic Undulator — M. Takao, S. Hashimoto, S. Sasaki, Y. Miyahara.....	1438	FAQ21
High-Field Strong-Focusing Undulator Designs for X-Ray Linac Coherent Light Source (LCLS) Applications — S. Caspi, R. Schlueter, R. Tatchyn.....	1441	FAQ23
Wigglers at the Advanced Light Source — E. Hoyer, J. Akre, D. Humphries, T. Jackson, S. Marks, Y. Minamihara, P. Pipersky, D. Plate, G. Portmann, R. Schlueter.....	1444	FAQ24
Design of End Magnetic Structures for the Advanced Light Source Wigglers — D. Humphries, J. Akre, E. Hoyer, S. Marks, Y. Minamihara, P. Pipersky, D. Plate, R. Schlueter.....	1447	FAQ25
Passive End Pole Compensation Scheme for a 1.8 Tesla Wiggler — L.H. Chang, Ch. Wang, C.H. Chang, T.C. Fan.....	1450	FAQ26
Insertion of Helical Siberian Snakes in RHIC — A. Luccio, F. Pilat	1453	FAQ28
Modeling of WLS Field with Piecewisely Constant Magnets — Zuping Liu, Aihua Zhao.....	1456	FAQ29
A BESSY-1 6 Tesla WLS Effect Compensation Scheme — Zuping Liu, Aihua Zhao.....	1459	FAQ30
16 Tesla Block-Coil Dipole for Future Hadron Colliders — Peter M. McIntyre, Weijun Shen.....	1462	FAQ31
Automated Methods of Field Harmonic Signal Extraction and Processing for the Magnets in Superconducting Supercollider — T.S. Jaffery, J. Butteris, M. Wake.....	1465	FAQ32

Radio Frequency Technology

Review of the Development of RF Cavities for High Currents (Invited) — J. Kirchgessner.....	1469	F AE01
Performance of Normal Conducting Structures for Linear Colliders (Invited) — Toshiyasu Higo.....	1474	F AE02
High Gradient Superconducting RF Systems (Invited) — J. Graber.....	1478	F AE03
Development and Advances in Conventional High Power RF Systems (Invited) — P.B. Wilson.....	1483	F AE04
The Upgraded RF System for the AGS and High Intensity Proton Beams (Invited) — J.M. Brennan.....	1489	F AE05
Phase-Stable, Microwave FEL Amplifier — Bruce E. Carlsten, Michael V. Fazio, W. Brian Haynes, Lisa M. May, James M. Potter.....	1494	F AE06
1.2 MW Klystron for Asymmetric Storage Ring B Factory — W.R. Fowkes, G. Caryotakis, E. Doyle, E. Jongewaard, C. Pearson, R. Phillips, J. Sackett, E. Wright, H. Bohlen, G. Huffman, S. Lenci, E. Lien, E. McCune, G. Miram	1497	F AE07
Analysis of Multipacting in Coaxial Lines — E. Somersalo, P. Ylä-Oijala, D. Proch.....	1500	F AE08
An Accelerator Resonantly Coupled with an Energy Storage (ARES) for the KEKB — Y. Yamazaki, K. Akai, N. Akasaka, E. Ezura, T. Kageyama, F. Naito, T. Shintake, Y. Takeuchi.....	1503	F AE09
Non Integer Harmonic Number Acceleration of Lead Ions in the CERN SPS — D. Boussard, T. Bohl, T. Linnekar, U. Wehrle.....	1506	F AE10
Analysis and Results of the Industrial Production of the Superconducting Nb/Cu Cavities for the LEP2 Project — E. Chiaveri, C. Benvenuti, R. Cosso, D. Lacarrere, K.M. Schirm, M. Taufer, W. Weingarten.....	1509	F AE11
Performance Experience with the CEBAF SRF Cavities — C. Reece, J. Benesch, M. Drury, C. Hovater, J. Mammosser, T. Powers, J. Preble.....	1512	F AE12
Beam Test of a Superconducting Cavity for the CESR Luminosity Upgrade — H. Padamsee, P. Barnes, S. Belomestnykh, K. Berkelman, M. Billing, R. Ehrlich, G. Flynn, Z. Greenwald, W. Hartung, T. Hays, S. Henderson, R. Kaplan, J. Kirchgessner, J. Knobloch, D. Moffat, H. Muller, E. Nordberg, S. Peck, M. Pisharody, J. Reilly, J. Rogers, D. Rice, D. Rubin, D. Sagan, J. Sears, M. Tigner, J. Welch.....	1515	F AE13

Radio Frequency Power Sources

Development of Input & Output Structures for High Power X-Band TWT Amplifiers — S. Naqvi, Cz. Golkowski, G.S. Kerslick, J.A. Nation, L. Schächter.....	1518	TAQ01
Characterization of a Klystron as a RF Source for High-Average-Power Accelerators — D. Rees, D. Keffeler, W. Roybal, P.J. Tallerico.....	1521	TAQ02
Choppertron II — T.L. Houck, G.A. Westenskow, J. Haimson, B. Mecklenburg.....	1524	TAQ03

The Resistive-Wall Klystron as a High-Power Microwave Source — Han S. Uhm.....	1527	TAQ04
Operating Conditions of High-Power Relativistic Klystron — Han S. Uhm	1530	TAQ05
Spurious Oscillations in High Power Klystrons — B. Krietenstein, K. Ko, T. Lee, U. Becker, T. Weiland, M. Dohlus.....	1533	TAQ06
In-House Repair of a 30 Megawatt S Band Klystron — R. Sachtschale, P.G. O'Shea, M. Ponds, G. Swift	1536	TAQ07
Development of a High Power 1.2 MW CW L-Band Klystron — K. Hirano, Y.L. Wang, T. Emoto, A. Enomoto, I. Sato	1539	TAQ08
Ultrarelativistic Klystron - a Future Super Power UHF Generator — F.A. Vodopianov	1542	TAQ10
A 200 KW Power Amplifier and Solid State Driver for the Fermilab Main Injector — J. Reid, H. Miller	1544	TAQ11
A 476 MHz RF System for the Storage Mode of the AmPS Ring — F. Kroes, P. de Groen, E. Heine, B. Heutenik, A. Kruijer, B. Munneke, R. Pirovano, T. Sluijk, J. Verkooyen.....	1547	TAQ12
Lifetime Experience with Low Temperature Cathodes Equipped in Super Power Klystrons — Rudolf Backmor.....	1550	TAQ13
Microwave System of PLS 2-GeV Linac — H.S. Lee, O.H. Hwang, S.H. Park, C.M. Ryu, W. Namkung	1553	TAQ14
Klystron-Modulator System Performances for PLS 2-GeV Linac — M.H. Cho, J.S. Oh, S.S. Park, W. Namkung.....	1556	TAQ15
Klystron Modulator Operation and Upgrades for the APS Linac — Thomas J. Russell, Alexander Cours	1559	TAQ16
Prospects for Developing Microwave Amplifiers to Drive Multi-TeV Linear Colliders — V.L. Granatstein, G.S. Nusinovich, J. Calame, W. Lawson, A. Singh, H. Guo, M. Reiser	1561	TAQ17
Design of 100 MW, Two-Cavity Gyroklystrons for Accelerator Applications — J.P. Calame, W. Lawson, J. Cheng, B. Hogan, M. Castle, V.L. Granatstein, M. Reiser.....	1563	TAQ18
Design of Three-Cavity Coaxial Gyroklystron Circuits for Linear Collider Applications — W. Lawson, G. Saraph, J.P. Calame, J. Cheng, M. Castle, B. Hogan, M. Reiser, V.L. Granatstein, H. Metz	1566	TAQ19
Numerical Simulation of Magnicon Amplifier — V. Yakovlev, O. Danilov, O. Nezhevenko, V. Tarnetsky.....	1569	TAQ21
RF-Power Upgrade Systems with Energy Compression for Electron Linacs — A. Shalnov, B.Yu. Bogdanovich, A. Ignatyev, V. Senyukov.....	1572	TAQ23
RF-Power Upgrade System with Resonant Loading — A. Shalnov, B. Bogdanovich, A. Ignatyev, V. Senyukov.....	1575	TAQ24
High-Power Test of Traveling-Wave-Type RF-Pulse Compressor — S. Yamaguchi, A. Enomoto, I. Sato, Y. Igarashi.....	1578	TAQ25
Active Radiofrequency Pulse Compression Using Switched Resonant Delay Lines — Sami G. Tantawi, Ronald D. Ruth, A.E. Vlieks.....	1581	TAQ26
Design of a Multi-Megawatt X-Band Solid State Microwave Switch — Sami G. Tantawi, Terry G. Lee, Ronald D. Ruth, A.E. Vlieks, Max Zolotarev	1584	TAQ27
Reduced Field TE01 X-Band Traveling Wave Window — W.R. Fowkes, R.S. Callin, S.G. Tantawi, E.L. Wright.....	1587	TAQ28
Design and High-Power Test of a TE11-Mode X-Band RF Window with Taper Transitions — Y. Otake, S. Tokumoto, H. Mizuno.....	1590	TAQ29
Feasibility Study of Optically Coupling RF-Power at mm Waves — B. Littmann, H. Henke.....	1593	TAQ30
A Low-Frequency High-Voltage RF-Barrier Bunching System for High-Intensity Neutron Source Compressor Rings — T.W. Hardek, D. Rees, C. Ziomek.....	1596	TAQ31
Temporal Evolution of Multipactor Discharge — R. Kishek, Y.Y. Lau, R.M. Gilgenbach.....	1599	TAQ32
Stabilizing a Power Amplifier Feeding a High Q Resonant Load — A.K. Mitra, R.L. Poirier, J.J. Lu, R. Hohbach.....	1602	TAQ33
Study of 14 GHz VLEPP Klystron With RF Absorbing Drift Tubes — G.V. Dolbilov, N.I. Azorsky, A.A. Fateev, N.I. Lebedev, V.A. Petrov, V.P. Sarantsev, V.S. Shvetsov, M.V. Yurkov.....	1605	TAQ34
24-MW, 24-μs Pulse RF Power Supply For Linac-Based FELs — E. Ohshita, Y. Morii, S. Abe, S. Okuma, K. Wakita, T. Tomimasu, I. Ito, Y. Miyai, K. Nakata, M. Hakota	1608	TAQ35
Initial Operation of an X-Band Magnicon Amplifier Experiment — S.H. Gold, A.K. Kinkad, A.W. Fliflet, B. Hafizi	1611	TAQ37

Superconducting RF

The Effects of Tuning and Terminating on the Operating Mode of Multi-Cell Coupled Cavity — Zubao Qian	1614	TPP01
Response of Superconducting Cavities to High Peak Power — T. Hays, H. Padamsee	1617	TPP02
Development of HOM Damper for B-Factory (KEKB) Superconducting Cavities — T. Tajima, K. Asano, T. Furuya, M. Izawa, S. Mitsunobu, T. Takahashi, N. Gamo, S. Iida, Y. Ishi, Y. Kijima, S. Kokura, M. Kudo, K. Sennyu, S. Tachibana, H. Takashina, N. Taniyama	1620	TPP03
Microscopic Examination of Defects Located by Thermometry in 1.5 GHz Superconducting Niobium Cavities — J. Knobloch, R. Durand, H. Muller, H. Padamsee	1623	TPP04
RF System for the NSLS Coherent Infrared Radiation Source — W. Broome, R. Biscardi, J. Keane, P. Mortazavi, M. Thomas, J.M. Wang	1626	TPP06
Development of TESLA-type Cavity at KEK — M. Ono, E. Kako, S. Noguchi, K. Saito, T. Shishido, M. Wake, H. Inoue, T. Fujino, Y. Funahashi, M. Matsuoka, T. Suzuki, T. Higuchi, H. Umezawa	1629	TPP07
Study of Luminous Spots Observed on Metallic Surfaces Subjected to High RF Fields — T. Junquera, S. Maïssa, M. Fouaidy, A. Le Goff, B. Bonin, M. Luong, H. Safa, J. Tan	1632	TPP09
Test Results for a Heat-Treated 4-Cell 805-MHz Superconducting Cavity — Brian Rusnak, Alan Shapiro	1636	TPP10
An Advanced Rotating T-R Mapping & its Diagnoses of TESLA 9-Cell Superconducting Cavity — Q.S. Shu, G. Deppe, W-D. Möller, M. Pekeler, D. Proch, D. Renken, P. Stein, C. Stolzenburg, T. Junquera, A. Caruette, M. Fouaidy	1639	TPP11
Improvements to Power Couplers for the LEP2 Superconducting Cavities — J. Tückmantel, C. Benvenuti, D. Bloess, D. Boussard, G. Geschonke, E. Haebel, N. Hilleret, S. Juras, H.P. Kindermann, J. Uythoven, C. Wyss, M. Stirbet	1642	TPP12
Arcing Phenomena on CEBAF RF-Windows at Cryogenic Temperatures — Tom Powers, Peter Kneisel, Ray Allen	1645	TPP13
Surface Scanning Thermometers for Diagnosing the TESLA SRF Cavities — T. Junquera, A. Caruette, M. Fouaidy, Q.S. Shu	1648	TPP14
Microwave Surface Resistance of YBaCuO Superconducting Films Laser-Ablated on Copper Substrates — J. Liu, K. Asano, E. Ezura, M. Fukutomi, S. Inagaki, S. Isagawa, K. Komori, S. Kumagai, H. Nakanishi, M. Tosa, K. Yoshihara	1652	TPP16

Room Temperature RF

Transverse Coupling Impedance Measurement Using Image Current — D. Sun, P. Colestock, M. Foley	1655	WPP01
Decreasing Transient Beam Loading in RF Cavities of U-70 Accelerator — O.P. Lebedev	1658	WPP02
RF System for Bunch Lengthening — R. Biscardi, G. Ramirez	1660	WPP03
Electromagnetic Field Vector Components Precise Measurements in Accelerating Structures — M.A. Chernogubovsky, M.F. Vorogushin	1663	WPP04
A New Tuning Method for Traveling Wave Structures — T. Khabiboulline, V. Puntus, M. Dohlus, N. Holtkamp, G. Kreps, S. Ivanov, K. Jin	1666	WPP05
RF Systems for RHIC — J. Rose, J. Brodowski, R. Connolly, D.P. Deng, S. Kwiatkowski, W. Pirkel, A. Ratti	1669	WPP07
A New RF System for Bunch Coalescing in the Fermilab Main Ring — J. Dey, I. Kourbanis, D. Wildman	1672	WPP08
Higher Order Modes of the Main Ring Cavity at Fermilab — J. Dey, D. Wildman	1675	WPP09
RF Measurements and Control of Higher Order Modes in Accelerating Cavities — V. Veshcherevich, S. Krutikhin, I. Kuptsov, S. Nosyrev, A. Novikov, I. Sedlyarov	1678	WPP10
RF System of VEPP-4M Electron-Positron Collider — E. Gorniker, P. Abramsky, V. Arbutov, S. Belomestnykh, A. Bushuyev, M. Fomin, I. Kuptsov, G. Kurkin, S. Nosyrev, V. Petrov, I. Sedlyarov, V. Veshcherevich	1681	WPP11
Storage Ring Cavity Higher-Order Mode Dampers for the Advanced Photon Source — Paul Matthews, Yoon Kang, Robert Kustom	1684	WPP12

Reduction of Multipactor in RF Ceramic Windows Using a Simple Titanium-Vapor Deposition System — <i>K. Primdahl, R. Kustom, J. Maj</i>	1687	WPP13
Cooling the APS Storage Ring Radio-Frequency Accelerating Cavities Thermal/Stress/Fatigue Analysis and Cavity Cooling Configuration — <i>K. Primdahl, R. Kustom</i>	1690	WPP14
RF Cavities for the Positron Accumulator Ring (PAR) of the Advanced Photon Source (APS) — <i>Y.W. Kang, A. Nassiri, J.F. Bridges, T.L. Smith, J.J. Song</i>	1693	WPP16
The Proposal of Complex Impedance Termination for Versatile HOM Damper Cavity — <i>V.V. Paramonov</i>	1696	WPP17
The Magnetron-Type Varactor for Fast Control in Accelerator RF Systems — <i>M.I. Kuznetsov, V.V. Paramonov, Yu.V. Senichev, I.B. Enchevich, R.L. Poirier</i>	1699	WPP18
The Distortion of the Accelerating Field Distribution in Compensated Structures due to Steady-State Beam Loading — <i>V.G. Andreev, V.V. Paramonov</i>	1702	WPP19
The Indiana University Cooler Injector Synchrotron RF System — <i>A. Pei, M. Ellison, D. Friesel, D. Jenner, X. Kang, S.Y. Lee, D. Li, J. Liu, A. Riabko, L. Wang, K. Hedblom</i>	1705	WPP20
The Indiana University Cooler Injection Synchrotron RF Cavity — <i>A. Pei, M. Ellison, D. Friesel, D. Jenner, X. Kang, S.Y. Lee, D. Li, J. Liu, A. Riabko, L. Wang, K. Hedblom</i>	1708	WPP21
Determination of Resonant Frequency and External Q Values for the Bessy II HOM-Damped Cavity — <i>Frank Schönfeld, Bengt Littmann</i>	1711	WPP22
106 MHz Cavity for Improving Coalescing Efficiency in the Fermilab Main Ring — <i>J. Dey, I. Kourbanis, D. Wildman</i>	1714	WPP23
On the Higher Order Mode Coupler Design for Damped Accelerating Structures — <i>Jie Gao</i>	1717	WPQ01
High Power Window Tests on a 500 MHz Planar Window for the CESR Upgrade — <i>M. Pisharody, P. Barnes, E. Chojnacki, R. Durand, T. Hays, R. Kaplan, J. Kirchgessner, J. Reilly, H. Padamsee, J. Sears</i>	1720	WPQ02
Operational Performances and Future Upgrades for the ELETTRA RF System — <i>A. Fabris, A. Massarotti, C. Pasotti, M. Svandrlik</i>	1723	WPQ04
X-Band High Power Dry Load for NLCTA — <i>K. Ko, H. Hoag, T. Lee, S. Tantawi</i>	1726	WPQ05
Development of a High-Power RF Cavity for the PEP-II B Factory — <i>R.A. Rimmer, M.A. Allen, J. Saba, H. Schwarz, F.C. Belser, D.D. Berger, R.M. Franks</i>	1729	WPQ06
A Design of Input Coupler for RF-Cavity — <i>T. Nagatsuka, T. Koseki, Y. Kamiya, M. Izawa, Y. Terada</i>	1732	WPQ07
Design of the KEKB RF System — <i>K. Akai, E. Ezura, Y. Yamazaki</i>	1735	WPQ08
RF Characteristics of ARES Cold Models — <i>N. Akasaka, K. Akai, T. Kageyama, T. Shintake, Y. Yamazaki</i>	1738	WPQ09
Design of Traveling Wave Windows for the PEP-II RF Coupling Network — <i>N.M. Kroll, C.-K. Ng, J. Judkins, M. Neubauer</i>	1741	WPQ10
Impedance Spectrum for the PEP-II RF Cavity — <i>X.E. Lin, K. Ko, C.-K. Ng</i>	1744	WPQ12
Measurement and Analysis of Higher-Order-Mode (HOM) Damping in B-Factory R-F Cavities — <i>D.A. Goldberg, M. Irwin, R.A. Rimmer</i>	1747	WPQ13
Planar Structures for Electron Acceleration — <i>H. Henke</i>	1750	WPQ14
Precise Fabrication of X-Band Detuned Accelerating Structure for Linear Collider — <i>T. Higo, H. Sakai, Y. Higashi, T. Takatomi, S. Koike</i>	1753	WPQ15
Development of a Beam-Pipe HOM Absorber for the ATF Damping Ring — <i>F. Hinode, S. Sakanaka</i>	1756	WPQ16
Development of a HOM-Damped Cavity for the KEK B-Factory (KEKB) — <i>T. Kageyama, K. Akai, N. Akasaka, E. Ezura, F. Naito, T. Shintake, Y. Takeuchi, Y. Yamazaki, T. Kobayashi</i>	1759	WPQ17
Possible Cavity Construction Techniques for the DIAMOND Storage Ring — <i>D.M. Dykes, D.S.G. Higgins</i>	1762	WPQ18
The Design of the 26.7 MHz RF Cavity for RHIC — <i>J. Rose, J. Brodowski, D.P. Deng, S. Kwiatkowski, W. Pirkel, A. Ratti</i>	1765	WPQ19
A Design Upgrade of the RF Cavity and Its Power Window for High Current Operation of the NSLS X-Ray Storage Ring — <i>P. Mortazavi, M. Thomas</i>	1768	WPQ20
A Ferrite Loaded Untuned Cavity for a Compact Proton Synchrotron — <i>J.I. Hirota, K. Hiramoto, M. Nishi, Y. Iwashita, A. Noda, M. Inoue</i>	1770	WPQ21
On the Theory of Two Coupled Cavities — <i>N.I. Aizatsky</i>	1773	WPQ22

Measurement of Multipacting Currents of Metal Surfaces in RF Fields — D. Proch, <i>D. Einfeld, R. Onken, N. Steinhäuser</i>	1776	WPQ24
Optimization of CLIC Transfer Structure (CTS) Design to Meet New Drive Beam Parameters — A. Millich	1779	WPQ25
A High-Power Multiple-Harmonic Acceleration System for Proton- and Heavy-Ion Synchrotrons — P. Ausset, G. Charruau, F.J. Etzkorn, C. Fougeron, H. Meuth, S. Papureanu, <i>A. Schnase</i>	1781	WPQ26
A Bunch Lengthening RF Cavity for Aladdin — K.J. Kleman	1785	WPR01
Design of a High-Power Test Cavity for the ATF Damping Ring — S. Sakanaka, F. Hinode, <i>M. Akemoto, S. Tokumoto, T. Higo, J. Urakawa, T. Miura, Y. Hirata, K. Satoh</i>	1788	WPR02
Design of an RF System for the ATF Damping Ring — S. Sakanaka, F. Hinode, M. Akemoto, <i>H. Hayano, H. Matsumoto, K. Kubo, S. Tokumoto, T. Higo, J. Urakawa</i>	1791	WPR03
Development of a Damped Cavity with SiC Beam-Duct — T. Koseki, M. Izawa, Y. Kamiya	1794	WPR04
HOM Absorber for the KEKB Normal Conducting Cavity — Y. Takeuchi, K. Akai, <i>N. Akasaka, E. Ezura, T. Kageyama, F. Naito, T. Shintake, Y. Yamazaki</i>	1797	WPR05
PEP-II B-Factory Prototype Higher Order Mode Load Design — R. Pendleton, K. Ko, C. Ng, <i>M. Neubauer, H. Schwarz, R. Rimmer</i>	1800	WPR07
High-Power RF Window and Coupler Development for the PEP-II B Factory — M. Neubauer, <i>K. Fant, J. Hodgson, J. Judkins, H. Schwarz, R.A. Rimmer</i>	1803	WPR08
Input Coupler for the KEKB Normal Conducting Cavity — F. Naito, K. Akai, N. Akasaka, <i>E. Ezura, T. Kageyama, T. Shintake, Y. Takeuchi, Y. Yamazaki</i>	1806	WPR09
Minimum Wakefield Achievable by Waveguide Damped Cavity — Xintian E. Lin, <i>Norman M. Kroll</i>	1809	WPR10
PLS RF System Operation During the Commissioning — M. Kwon, I.H. Yu, H.J. Park, <i>D.H. Han, M. Yoon, Y.S. Kim</i>	1812	WPR11
Acoustic Experimental Studies of High Power Modes in Accelerating Structure of Kurchatov SR Source — M. Gangeluk, A. Kadnikov, Yu. Krylov, S. Kuznetsov, V. Moiseev, <i>V. Petrenko, V. Ushkov, Yu. Yupinov</i>	1815	WPR13
Computer Simulations of a Wide-Bandwidth Ferrite-Loaded High-Power Waveguide Termination — J. Johnson, R. Rimmer, J. Corlett	1818	WPR14
Effects of Temperature Variation on the SLC Linac RF System — F.-J. Decker, R. Akre, <i>M. Byrne, Z.D. Farkas, H. Jarvis, K. Jobe, R Koontz, M. Mitchell, R. Pennacchi, M. Ross,</i> <i>H. Smith</i>	1821	WPR15
Broadband Coax-Waveguide Transitions — T. Rizawa, R. Pendleton	1824	WPR16
Rectangular Microtron Accelerating Structure — N.P. Sobenin, V.N. Kandrugin, <i>V.N. Melekhin, A.I. Karev, V.I. Shvedunov, W.P. Trower</i>	1827	WPR17
Investigation of the Biparabolic Accelerating Structure For The Free Electron Laser Buncher — N.P. Sobenin, S.N. Yarygin, D.V. Kostin, A.A. Zavadtsev	1830	WPR18
Ferromagnetic Cores Made from Amorphous Material for Broad-Band Accelerating System — I. Bolotin, V. Budilin, A. Glazov, V. Krasnopol'sky, V. Skuratov	1833	WPR19
A New Structure with Continuous RF Acceleration and Focusing — J.J. Manca, M.C. Fallis, <i>J.P.J. Manca</i>	1835	WPR20
Spark Location in RF Cavities — Q. Kerns, M. Popovic, C. Kerns	1838	WPR21
RF System for the Duke 1 GeV Storage Ring — Ping Wang, Peter Morcombe, Ying Wu, <i>Grigori Kurkin</i>	1841	WPR22

Injection, Extraction and Targetry

Matching Section to the RFQ Using Permanent Magnet Symmetric Lens — M. Kando, <i>M. Ikegami, H. Dewa, H. Fujita, T. Shirai, H. Okamoto, Y. Iwashita, S. Kakigi, A. Noda,</i> <i>M. Inoue</i>	1843	WAQ01
Conceptual Designs of Beam Choppers for RFQ Linacs — Subrata Nath, Ralph R. Stevens Jr, <i>Thomas P. Wangler</i>	1846	WAQ02
The Role of Space Charge in the Performance of the Bunching System for the ATLAS Positive Ion Injector — R.C. Pardo, R. Smith	1849	WAQ03

Experimental Investigations of Plasma Lens Focusing and Plasma Channel Transport of Heavy Ion Beams — A. Tauschwitz, S.S. Yu, S. Eylon, L. Reginato, W. Leemans, J.O. Rasmussen, R.O. Bangerter.....	1852	WAQ04
A Low Energy Ion Beam Transport System with Variable Field Permanent Magnetic Quadrupoles — Y. Mori, A. Takagi, M. Kinsho, T. Baba, K. Shinto.....	1855	WAQ06
A Comparison of Two Injection Line Matching Sections for Compact Cyclotrons — T. Kuo, R. Baartman, L. Root, B. Milton, R. Laxadal, D. Yuan, K. Jayamanna, P. Schmor, G. Dutto, M. Dehnel, K. Erdman	1858	WAQ07
Stripping Injection Into the New Booster Ring at IUCF — K. Hedblom, D.L. Friesel.....	1861	WAQ08
Accurate Tuning of 90° Cells in a FODO Lattice — K. Bertsche, N. Mao	1864	WAQ09
Design Principles for High Current Beam Injection Lines — H. Liu, D. Neuffer.....	1867	WAQ11
Survey and Analysis of Line-Frequency Interference in the CEBAF Accelerator — M.G. Tiefenback, Rui Li	1870	WAQ12
Location and Correction of 60 Hz in the CEBAF Injector — R. Legg, D. Douglas, G.A. Krafft, Q. Saulter.....	1873	WAQ14
PEP-II Injection Transport Construction Status and Commissioning Plans — T. Fieguth, E. Bloom, F. Bulos, T. Donaldson, B. Feerick, G. Godfrey, G. Leyh, D. Nelson, M. Ross, D. Schultz, J. Sheppard, P. Smith, C. Spencer, J. Weinberg.....	1876	WAQ15
Beam Transport Lines at BESSY-II — D. Schirmer, M. v.Hartrott, S. Khan, D. Krämer, E. Weihreter.....	1879	WAQ17
Matching the Emittance of a Linac to the Acceptance of a Racetrack Microtron — R.W. de Leeuw, M.C.J. de Wijs, J.I.M. Botman, G.A. Webers, W.H.C. Theuws, C.J. Timmermans, H.L. Hagedoorn.....	1882	WAQ19
The Extraction Orbit and Extraction Beam Transport Line for a 75 MeV Racetrack Microtron — R.W. de Leeuw, H.R.M. van Greevenbroek, J.I.M. Botman, G.A. Webers, C.J. Timmermans, H.L. Hagedoorn	1885	WAQ20
Electromagnetic, Thermal and Structural Analysis of the Fermilab Antiproton Source Lithium Collection Lens — S. O'Day, K. Anderson	1888	WAQ22
A New Concept in the Design of the LHC Beam Dump — J.M. Zazula, M. Gyr, G.R. Stevenson, E. Weisse.....	1891	WAQ24
Loss Concentration and Evacuation by Mini-Wire-Septa from Circular Machines for Spallation Neutron Sources — H. Schönauer	1894	WAQ25
Status of the Radioactive Ion Beam Injector at the Holifield Radioactive Ion Beam Facility — D.T. Dowling, G.D. Alton, R.L. Auble, M.R. Dinehart, D.L. Haynes, J.W. Johnson, R.C. Juras, Y.S. Kwon, M.J. Meigs, G.D. Mills, S.W. Mosko, D.K. Olsen, B.A. Tatum, C.E. Williams, H. Wollnik.....	1897	WAQ26
A New Fast Rise Time Kicker System For Antiproton Injection Into The Tevatron — B. Hanna, J. Dinkel, C. Jensen, D. Qunell, R. Reilly, D. Tinsley, J. Walton.....	1900	WAR01
Design of the MI40 Beam-Abort Dump — C.M. Bhat, P.S. Martin, A.D. Russell.....	1903	WAR02
Study on the Metallic Coating of the Ceramic Chamber for the ATF Damping Ring Kicker Magnets — N. Terunuma, H. Nakayama, J. Urakawa.....	1906	WAR03
Prospect of the Fast Extraction from KEK-PS for the Long Base Line Neutrino Experiment — H. Sato, Y. Shoji, T. Kawakubo.....	1909	WAR04
Helium Beam Acceleration in the KEK Proton Synchrotron with a Newly Developed Injection System for Positive/Negative Ions — I. Sakai, A. Takagi, Y. Mori, S. Machida, M. Yoshii, T. Toyama, M. Shirakata, Y. Shoji, H. Sato.....	1912	WAR05
Fast and Reliable Kicker Magnets for the SLC Damping Rings — T.S. Mattison, R.L. Cassel, A.R. Donaldson, G. Gross.....	1915	WAR06
Status of the Nuclotron Slow Extraction System — V.I. Chernikov, I.B. Issinsky, O.S. Kozlov, V.A. Mikhailov, S.A. Novikov.....	1918	WAR09
The RHIC Injection Fast Kicker — E.B. Forsyth, G.C. Pappas, J.E. Tuozzolo, W. Zhang	1921	WAR10
The Active Filter Voltage Ripple Correction System of the Brookhaven AGS Main Magnet Power Supply — I. Marneris, R. Bonati, J. Geller, J.N. Sandberg, A. Soukas.....	1924	WAR11
The Injection Kicker System for the Muon G-2 Experiment — G.C. Pappas, E.B. Forsyth, W. Feng	1927	WAR12
The AGS Accelerator Complex with the New Fast Extraction System — M. Tanaka, E.J. Bleser, J.W. Glenn, Y.Y. Lee, A. Soukas	1930	WAR13
DESY III - Dump System with One Fast Kicker — J. Ruemmler.....	1933	WAR14

Utilizing a Pulsed Deflector for Extraction of Pulsed Beams from the TRIUMF Cyclotron — <i>R.E. Laxdal</i>	1936	WAR15
Requirements for a Beam Sweeping System for the Fermilab Antiproton Source Target — <i>F.M. Bieniosek, K. Anderson, K. Fullett</i>	1939	WAR17
Measurement and Reduction of Quadrupole Injection Oscillations in the Fermilab Antiproton Accumulator — <i>F.M. Bieniosek, K. Fullett</i>	1942	WAR18
Results from Experiments of Crystal Extraction of 900 GeV Proton Beams from the Tevatron Collider — <i>G. Jackson, D. Carrigan, D. Chen, C.T. Murphy, A. Bogacz, S. Ramachandran, J. Rhoades, A. McManus, S. Baker</i>	1945	WAR19
High Energy Beam Line Based on Bending Crystal — <i>V.M. Biryukov, Yu.A. Chesnokov, V.N. Greth, A.A. Ivanov, V.I. Kotov, V.S. Selesnev, M.V. Tarakanov, V.I. Terekhov, S.V. Tsarik</i>	1948	WAR20
Observation of the Influence of the Crystal Surface Defects on the Characteristics of the High Energy Particle Beam Deflected With a Bent Monocrystal — <i>V.I. Baranov, V.M. Biryukov, Yu.A. Chesnokov, V.I. Kotov, M.V. Tarakanov, S.V. Tsarik</i>	1949	WAR21
Beam Extraction with Using of Volume Reflection Effect in Crystals — <i>I. Yazynin</i>	1952	WAR22
Use of a Bent Crystal for Beam Extraction in a Slow Extraction Mode — <i>A.A. Asseev, M.Yu. Gorin</i>	1955	WAR23
Computer Simulation of the Tevatron Crystal Extraction Experiment — <i>Valery Biryukov</i>	1958	WAR24

Power Supplies

PEP-II Magnet Power Conversion Systems — <i>L.T. Jackson, A.H. Saab, D.W. Shimer</i>	1961	RPP01
The AGS Main Magnet Power Supply Upgrade — <i>J.N. Sandberg, R. Casella, J. Geller, I. Marneris, A. Soukas, N. Schumburg</i>	1964	RPP02
Performance of the Ramping Power Supplies for the APS Booster Synchrotron — <i>J.A. Carwardine, S.V. Milton, D.G. McGhee</i>	1967	RPP03
A Distributed Dipole Power Supply System for the EUTERPE Electron Ring — <i>A.H. Kemper, Boling Xi, R.W. de Leeuw, W.H.C. Theuws, J.I.M. Botman, C.J. Timmermans, H.L. Hagedoorn, R.G.J. Oude Velthuis</i>	1970	RPP04
A 20 Ampere Shunt Regulator for Controlling Individual Magnets in a Seriesed String — <i>E.J. Martin, N. Dobeck, G.S. Jones, M.K. O'Sullivan</i>	1973	RPP06
A Multi-Channel Corrector Magnet Controller — <i>G.E. Leyh, A.R. Donaldson, L.T. Jackson</i>	1976	RPP07
Advances in Power Supply and Control System for Electrostatic Accelerators — <i>S.N. Chumakov, A.D. Goncharov, A.N. Malygin, V.P. Ostanin, B.N. Sukhina, V.S. Tupikov</i>	1979	RPP08
Mode Analysis of Synchrotron Magnet Strings — <i>M. Kumada</i>	1982	RPP09
Autotransformer Configurations to Enhance Utility Power Quality of High Power AC/DC Rectifier Systems — <i>Sewan Choi, Prasad N. Enjeti, Ira J. Pitel</i>	1985	RPP11
Performance of a 2-Megawatt High Voltage Test Load — <i>D. Horan, R. Kustom, M. Ferguson</i>	1988	RPP12
Early Operating and Reliability Experience with the CEBAF DC Magnet Power Supplies — <i>W. Merz, R. Flood, E.J. Martin, M. O'Sullivan</i>	1991	RPP13

Cryogenics, Vacuum, Alignment and Other Technical Systems

CEBAF Cryogenic System (Invited) — <i>Claus H. Rode</i>	1994	RPE01
The Large Hadron Collider Vacuum System (Invited) — <i>B. Angerth, F. Bertinelli, J.-C. Brunet, R. Calder, F. Caspers, P. Cruikshank, J.-M. Dalin, O. Gröbner, N. Kos, A. Mathewson, A. Poncet, C. Reymermier, F. Ruggiero, T. Scholz, S. Sgobba, E. Wallén</i>	1999	RPE02
Large Medical Gantries (Invited) — <i>J.B. Flanz</i>	2004	RPE03
Alignment Considerations for the Next Linear Collider (Invited) — <i>Robert E. Ruland</i>	2009	RPE04
Reliability of the LEP Vacuum System: Experience and Analysis — <i>P.M. Strubin, J.-P. Bojon</i>	2014	RPE06
On the Electron Beam Lifetime Problem in HERA — <i>D.R.C. Kelly, W. Bialowons, R. Brinkmann, H. Ehrlichmann, J. Kouptsidis</i>	2017	RPE08
Design and Testing of a High Power, Ultra-High Vacuum, Dual-Directional Coupler for the Advanced Photon Source (APS) Linear Accelerator — <i>S.O. Brauer, A.E. Grelick, J. Grimmer, R.D. Otocky, Y.W. Kang, J. Noonan, T. Russell</i>	2020	RPE09
A Pulse Septum Magnet with Low Outgassing Rate — <i>Yuan Ji Pei, W.M. Li, D.M. Jiang, X.Q. Wang</i>	2023	RPE10

Surveying the Monument System at Lawrence Berkeley Laboratory's Advanced Light Source Accelerator — <i>W. Thur, T. Lauritzen</i>	2026	RPE12
Induced Radioactivity of Thick Copper and Lead Targets Irradiated by Protons, ^4He and ^{12}C Nuclei with Energy 3.65 GeV/Nucleon — <i>A.A. Astapov, V.P. Bamblevski</i>	2029	RPE13
The PEP-II High Power Beam Dumping System — <i>A. Kulikov, J. Seeman, M. Zolotorev</i>	2032	RPE14
Cryogenic Thermometry in Superconducting Accelerators — <i>V.I. Datskov, J.A. Demko, J.G. Weisend, M. Hentges</i>	2034	MPP01
Cryogenic Operation and On-line Measurement of RF Losses in the SC Cavities of LEP2 — <i>G. Winkler, Ph. Gayet, D. Güsewell, Ch. Titcomb</i>	2037	MPP02
Pressure Measurement for the UNK-1 Vacuum System — <i>A. Kiver, V. Komarov, K. Mirzoev, V. Terekhov, A. Vasilevsky</i>	2040	MPP03
Total Pressure Measurements in the ELETTRA Storage Ring According to the Performance of the Sputter-Ion Pumps — <i>F. Giacuzzo, J. Miertusova</i>	2042	MPP04
Insertion Device Vacuum Chamber for the ELETTRA Storage Ring — <i>J. Miertusova, N. Pangos</i>	2045	MPP05
Bellows Design for the PEP-II High Energy Ring Arc Chambers — <i>M.E. Nordby, N. Kurita, C.-K. Ng</i>	2048	MPP07
A Zero-Length Bellows for the PEP-II High-Energy Ring — <i>M. Nordby, E.F. Daly, N. Kurita, J. Langton</i>	2051	MPP08
Processing of O.F.E. Copper Beam Chambers for PEP-II High Energy Ring — <i>E. Hoyt, M. Hoyt, R. Kirby, C. Perkins, D. Wright, A. Farvid</i>	2054	MPP09
Stretchforming Vacuum Chambers for the PEP-II B-Factory High Energy Storage Ring — <i>E.F. Daly, D. Bostic, A. Lisin, M. Palrang, C. Perkins, K. Skarpaas</i>	2057	MPP10
Beam Vacuum Chambers for Brookhaven's Muon Storage Ring — <i>H.C. Hseuh, L. Snyderstrup, W.S. Jiang, C. Pai, M. Mapes</i>	2060	MPP11
Test Results of Pre-Production Prototype Distributed Ion Pump Design for the PEP-II Asymmetric B-Factory Collider — <i>F.R. Holdener, D. Behne, D. Hathaway, K. Kishiyama, M. Mugge, W. Stoeffl, K. van Bibber, C. Perkins, E.F. Daly, E. Hoyt, M. Hoyt, M. Nordby, J. Seeman, D. Wright</i>	2064	MPP12
Design of the PEP-II Low Energy Ring Vacuum System — <i>D. Hunt, K. Kennedy, T. Stevens</i>	2067	MPP13
The Vacuum Upgrade of the CERN PS and PS Booster — <i>M. van Rooij, J.-P. Bertuzzi, M. Brouet, A. Burlet, C. Burnside, R. Gavaggio, L. Petty, A. Poncet</i>	2069	MPP15
The Vacuum System for Insertion Devices at the Advanced Photon Source — <i>E. Trakhtenberg, E. Gluskin, P. Den Hartog, T. Klippert, G. Wiemerslage, S. Xu</i>	2072	MPP16
Test Results of a Combined Distributed Ion Pump/Non-Evaporable Getter Pump Design Developed as a Proposed Alternative Pumping System for the PEP-II Asymmetric B-Factory Collider — <i>F.R. Holdener, D. Behne, D. Hathaway, K. Kishiyama, M. Mugge, W. Stoeffl, K. van Bibber, C. Perkins, E.F. Daly, E. Hoyt, M. Hoyt, M. Nordby, J. Seeman, D. Wright</i>	2075	MPP20

Volume 4

Cryogenics, Vacuum, Alignment and Other Technical Systems (cont'd)

Ground Motion Measurements in HERA — <i>V. Shiltsev, B. Baklakov, P. Lebedev, C. Montag, J. Rossbach</i>	2078	TAA01
Alignment of Duke Free Electron Laser Storage Ring — <i>M. Emamian, N. Hower, Y. Levashov</i>	2081	TAA02
Beamline Smoothing of the Advanced Photon Source — <i>H. Friedrich, M. Penicka, S. Zhao</i>	2084	TAA03
Improvement of the Alignment System for the KEK 2.5-GeV Electron Linac — <i>Y. Ogawa, A. Enomoto, I. Sato</i>	2087	TAA04
A Mechanical Feedback System for Linear Colliders to Compensate Fast Magnet Motion — <i>C. Montag, J. Rossbach</i>	2090	TAA06
A Microstrip Based Position System for the Alignment of the TTF Cryostat — <i>D. Giove, A. Bosotti, C. Pagani, G. Varisco</i>	2093	TAA07
Beam-Based Magnetic Alignment of the Final Focus Test Beam — <i>P. Tenenbaum, D. Burke, R. Helm, J. Irwin, P. Raimondi, K. Oide, K. Flöttmann</i>	2096	TAA08

Alignment and Survey of the Elements in RHIC — D. Trbojevic, P. Cameron, G.L. Ganetis, M.A. Goldman, R. Gupta, M. Harrison, M.F. Hemmer, F.X. Karl, A. Jain, W. Louie, S. Mulhall, S. Peggs, S. Tepikian, R. Thomas, P. Wanderer.....	2099	TAA09
RF Radiation Measurement for the Advanced Photon Source (APS) Personnel Safety System — J.J. Song, J. Kim, R. Ostocki, J. Zhou	2102	TAA11
Radiation Shielding of the Main Injector — C.M. Bhat, P.S. Martin.....	2105	TAA12
The Safety Interlock System of Synchrotron Radiation Research Center — T.F. Lin, J.P. Wang.....	2108	TAA14
Radiological Protection Policy Aspects Concerning the Preliminary Design and Operation Modus of the Athens RT Microtron Facility — B. Spyropoulos	2111	TAA15
SLAC Synchronous Condenser — C. Corvin.....	2114	TAA16
Printed-Circuit Quadrupole Design — Terry F. Godlove, Santiago Bernal, Martin Reiser.....	2117	TAA17
Microprocessor Controlled Four-Axis Goniometer — A. Bortnyansky, M. Klopenkov, M. Pavlovets, M. Svinin, P. Kovach, J. Dobrovodsky.....	2120	TAA18
Optically Induced Surface Flashover Switching for the Dielectric Wall Accelerator — S. Sampayan, G. Caporaso, B. Carder, M. Norton, D. Trimble, J. Elizondo.....	2123	TAA20
Measurements of Magnet Vibrations at the Advanced Photon Source — V. Shiltsev	2126	TAA21
The Vacuum System for the PEP II High Energy Ring Straight Sections — U. Wienands, E. Daly, S.A. Heifets, A. Kulikov, N. Kurita, M. Nordby, C. Perkins, E. Reuter, J.T. Seeman, F.C. Belser, J. Berg, F.R. Holdener, J.A. Kerns, M.R. McDaniel, W. Stoeffl.....	2129	TAA22
Compact X-band High Power Load Using Magnetic Stainless Steel — Sami G. Tantawi, A.E. Vliks.....	2132	TAA27
Progress on Plasma Lens Experiments at the Final Focus Test Beam — P. Kwok, P. Chen, D. Cline, W. Barletta, S. Berridge, W. Bugg, C. Bula, S. Chattopadhyay, W. Craddock, I. Hsu, R. Iverson, T. Katsouleas, P. Lai, W. Leemans, R. Liou, K.T. McDonald, D.D. Meyerhofer, K. Nakajima, H. Nakanishi, C.K. Ng, Y. Nishida, J. Norem, A. Ogata, J. Rosenzweig, M. Ross, A. Sessler, T. Shintake, J. Spencer, J.J. Su, A.W. Weidemann, G. Westenskow, D. Whittum, R. Williams, J. Wurtele.....	2135	TAA28
Measurement of the Electric Field Uniformity in an Electrostatic Separator — Weiran Lou, James J. Welch.....	2138	TAA29
Analysis and Redesign of RF Filter Bar to Relieve Thermal Stresses — E.G. Schmenk, K.W. Kelly, V. Saile, H.P. Bluem	2141	TAA32
Loaded Delay Lines for Future R.F. Pulse Compression Systems — R.M. Jones, P.B. Wilson, N.M. Kroll.....	2144	TAA33

Controls and Computing

Integrating Industrial and Accelerator Control Systems (Invited) — R. Saban	2147	WAE01
Control System for Fermilab's Low Temperature Upgrade (Invited) — B.L. Norris.....	2152	WAE02
Databases for Accelerator Control - An Operations Viewpoint (Invited) — J. Poole.....	2157	WAE03
Taking an Object-Oriented View of Accelerators (Invited) — Hiroshi Nishimura	2162	WAE04
The CEBAF Control System (Invited) — William A. Watson III.....	2167	WAE05
MECAR (Main Ring Excitation Controller and Regulator): A Real Time Learning Regulator For The Fermilab Main Ring Or The Main Injector Synchrotron — R. Flora, K. Martin, A. Moibenko, H. Pfeffer, D. Wolff, P. Prieto, S. Hays.....	2172	WAE07
Framework for a General Purpose, Intelligent Control System for Particle Accelerators — R.T. Westervelt, W.B. Klein, G. Luger.....	2175	WAE08
Automatic Beam Steering in the CERN PS Complex — B. Autin, G.H. Hemelsoet, M. Martini, E. Wildner.....	2178	WAE09
Integrated On-Line Accelerator Modeling at CEBAF — B.A. Bowling, H. Shoaee, J. van Zeijts, S. Witherspoon, W. Watson.....	2181	WAE10
A Self-Describing File Protocol for Simulation Integration and Shared Post-Processors — M. Borland.....	2184	WAE11
Analytic Computation of Beam Impedances in Complex Heterogenous Accelerator Geometries — S. Petracca, I.M. Pinto, F. Ruggiero.....	2187	WAE12
Comparison of CONDOR, FCI and MAFIA Calculations for a 150MW S-Band Klystron with Measurements — U. Becker, T. Weiland, M. Dohlus, S. Lütgert, D. Sprehn	2190	WAE13

Controls

The BEPC Control System Upgraded — J. Zhao, X. Geng, Y. Yu, B. Wang, C. Wang, J. Xu, W. Liu, H. Luo, Y. Wang, M. Zhan.....	2193	MPA01
Control System of PLS 2-GeV Linac — I.S. Ko, W. Namkung.....	2196	MPA02
Control System of the Synchrotron Radiation Source SIBERIA-2 — A. Valentinov, A. Kadnikov, Y. Krylov, S. Kuznetsov, Y. Yudinov.....	2199	MPA04
Control System for the Holifield Radioactive Ion Beam Facility — B.A. Tatum, R.C. Juras, M.J. Meigs.....	2202	MPA05
Control System Design for KEKB Accelerators — S.-I. Kurokawa, T. Katoh, T.T. Nakamura, T. Mimashi, N. Yamamoto.....	2205	MPA06
Design of SPring-8 Linac Control System Using Object Oriented Concept — H. Sakaki, H. Yoshikawa, Y. Itoh, A. Kuba, T. Hori, A. Mizuno, H. Yokomizo.....	2208	MPA07
The Slow Control System of the Muon g-2 Experiment — Arnold Stillman.....	2211	MPA09
The Duke Storage Ring Control System — Y. Wu, B. Burnham, V.N. Litvinenko.....	2214	MPA10
EPICS at Duke University — C. Dickey, B. Burnham, F. Carter, R. Fricks, V. Litvinenko, A. Nagchoudhuri, P. Morcombe, R. Pantazis, P. O'Shea, R. Sachschaale, Y. Wu.....	2217	MPA11
The Integration of Two Control Systems — M. Bickley, K. White.....	2220	MPA12
Upgrade of NSLS Timing System — O. Singh, S. Ramamoorthy, J. Sheehan, J. Smith.....	2223	MPA15
Accelerator Timing at Brookhaven National Laboratory — B. Oerter, C.R. Conkling.....	2226	MPA16
The RHIC General Purpose Multiplexed Analog to Digital Converter System — R. Michnoff.....	2229	MPA17
The Datacon Master - Renovation of a Datacon Field Bus Communications System for Accelerator Control — T.M. Kerner, R. Warkentien.....	2232	MPA18
Upgrade of the Controls for the Brookhaven Linac — W.E. Buxton.....	2235	MPA19
Commissioning Software Tools at the Advanced Photon Source — L. Emery.....	2238	MPR01
Rapid Application Development Using the Tcl/Tk Language — Johannes van Zeijts.....	2241	MPR02
Accelerator Operation Management Using Objects — H. Nishimura, C. Timossi, M. Valdez.....	2244	MPR03
Orbit Control at the ALS Based on Sensitivity Matrices — H. Nishimura, L. Schachinger, H. Ohgaki.....	2247	MPR04
Error Handling in the NSLS Control System — Susila Ramamoorthy, Pauline Pearson, John Smith.....	2250	MPR07
History Data Collection, Retriving and Display in the NSLS Control System — Y.N. Tang, J.D. Smith.....	2253	MPR08
Virtual Instrumentation Interface for SRRC Control System — Jenny Chen, C.H. Kuo, Gloria Huang, J.S. Chen, C.J. Wang, K.T. Hsu, G.J. Jan.....	2256	MPR10
User-Friendly Interface for Operator in the Controls of UNK Beam-Transfer Line. — Yu. Karshev, Yu. Fedotov, V. Komarov, I. Lobov.....	2259	MPR11
Macmon: A Monitoring Program for ELETTRA — Emanuel Karantzoulis, Mark Plesko.....	2262	MPR12
Device Control at CEBAF — S. Schaffner, D. Barker, V. Bookwalter, B. Bowling, K. Brown, L. Doolittle, T. Fox, S. Higgins, A. Hofler, G. Lahti, P. Letta, B. Montjar, N. Patavalis, J. Tang, W. Watson, C. West, D. Wetherholt, K. White, S. Witherspoon, M. Wise.....	2265	MPR13
Automated Frequency Tuning of SRF Cavities at CEBAF — M. Chowdhary, L. Doolittle, G. Lahti, S.N. Simrock, R. Terrell.....	2268	MPR14
Operational Monitoring of the CEBAF RF System — J. Karn, B. Dunham, M. Tiefenback.....	2271	MPR15
Operating Experience with the New TRIUMF RF Control System — K. Fong, M. Lavery, S. Fang.....	2273	MPR16
Managing Control Algorithms with an Object-Oriented Database — M. Bickley, W. Watson.....	2276	MPR19
Design of the Commissioning Software for the AGS to RHIC Transfer Line — C.G. Trahern, C. Saltmarsh, T. Satogata, J. Kewisch, S. Sathe, T. D'Ottavio, S. Tepikian, D. Shea.....	2279	MPR20

Computer Codes

A Relational Database for Magnets and Measurement Systems at the Fermilab Magnet Test Facility — J.W. Sim, B.C. Brown, H.D. Glass, D.J. Harding, C.S. Mishra, A.D. Russell, K. Trombly-Freytag, D.G.C. Walbridge.....	2282	MPB05
---	------	-------

Software for a Database-Controlled Measurement System at the Fermilab Magnet Test Facility — J.W. Sim, R. Baiod, B.C. Brown, E. Desavouret, H.D. Glass, P.J. Hall, D.J. Harding, C.S. Mishra, J.M. Nogiec, J.E. Pachnik, A. Russell, K. Trombly-Freytag, D.G.C. Walbridge	2285	MPB06
BBAT: Bunch and Bucket Analysis Tool — D.-P. Deng.....	2288	MPB08
MASTAC - New Code for Solving Three-Dimensional Non-linear Magnetostatic Problems — M. Rojak, E. Shurina, Yu. Soloveichik, A. Grudiev, M. Tiunov, P. Vobly	2291	MPB09
The Computer Code BPERM for Wakepotential & Impedance Calculations — T. Barts, W. Chou.....	2294	MPB10
RESOLVE at CEBAF — Byung C. Yunn, Rui Li, Stefan Simrock.....	2297	MPB11
New Graphic User Interface for the Charged Particle Beam Program PARMILA — George H. Gillespie, Barrey W. Hill.....	2300	MPB14
XWAKE 1.1: A New Impedance and Wake Field Software Package — G.W. Saewert, T.G. Jurgens.....	2303	MPB15
The Los Alamos Accelerator Code Group — Frank L. Krawczyk, James H. Billen, Robert D. Ryne, Harunori Takeda, Lloyd M. Young.....	2306	MPB16
Beam Simulation and Radiation Dose Calculation at the Advanced Photon Source with SHOWER, an Interface Program to the EGS4 Code System — L. Emery.....	2309	MPB17
An Interactive Version of the PBGUNS Program for the Simulation of Axisymmetric and 2-D, Electron and Ion Beams and Guns — Jack E. Boers.....	2312	MPB18
Vector Computer Used for Calculation of 3D Magnetostatic Fields — E.P. Zhidkov, M.B. Yuldasheva, I.P. Yudin, O.I. Yuldashev	2314	MPB19
Impedance Study for the PEP-II B-factory — S. Heifets, A. Chao, E. Daly, K. Ko, N. Kurita, X. Lin, C. Ng, M. Nordby, C. Perkins, J. Seeman, G. Stupakov, U. Wienands, D. Wright, M. Zolotarev, E. Henestroza, G. Lambertson, J. Corlett, J. Byrd, M. Zisman, T. Weiland, W. Stoeffl, C. Bolser	2317	MPC01
Pressure Stability under a Pump Failure — S.A. Heifets, J. Seeman, W. Stoeffl	2319	MPC02
Investigation of the Beam Impedance of a Slowly Varying Waveguide — R.M. Jones, S.A. Heifets.....	2321	MPC03
Optimal Transport of Low Energy Particle Beams — Christopher K. Allen, Samar K. Guharay, Martin Reiser.....	2324	MPC04
Simulation of the Space Charge Effect in RHIC — G.F. Dell, S. Peggs	2327	MPC05
Magnetic Shielding for the D0 Detector Solenoid Upgrade — J.-F. Ostiguy, R. Yamada.....	2330	MPC07
Trapped Modes in the PEP-II B-Factor Interaction Region — E. Henestroza, S. Heifets, M. Zolotarev.....	2333	MPC08
A Proof of Principle of a Storage Ring with Fifth-Order Achromatic Bending Arcs — Weishi Wan, Martin Berz	2336	MPC09
Analytic Electrostatic Solution of an Axisymmetric Accelerator Gap — John K. Boyd.....	2339	MPC13
3D-Finite Difference Analysis of Planar Loop Couplers as Beam Electrodes in Stochastic Cooling Systems — R. Schultheis, H.L. Hartnagel, B. Franzke.....	2342	MPC15
Some Remarks on the Location of Higher Order Modes in Tapered Accelerating Structures with the Use of a Coupled Oscillator Model — G. Romanov, S. Ivanov, M. Dohlus, N. Holtkamp.....	2345	MPC16
The New Possibilities of SuperLANS Code for Evaluation of Axisymmetric Cavities — D.G. Myakishev, V.P. Yakovlev.....	2348	MPC17
Transverse EM Fields in a Detuned X-band Accelerating Structure — S.A. Heifets, S.A. Kheifets, B. Woo.....	2351	MPC18
RF Cavity Computer Design Codes — P.A. McIntosh.....	2353	MPC19
Arbitrary Order Transfer Maps for RF Cavities — Johannes van Zeijts.....	2356	MPC20
The Computation of the Dynamic Inductance of Magnet Systems and Force Distribution in Ferromagnetic Region on the Basis of 3-D Numerical Simulation of Magnetic Field — N. Doinikov, V. Kukhtin, E. Lamzin, B. Mingalev, Yu. Severgin, S. Sytchevsky.....	2359	MPC21
Advanced Electromagnetic Design of Cavities for High Current Accelerators — Frank L. Krawczyk.....	2361	MPC22
Modified PARMILA Code for New Accelerating Structures — H. Takeda, J.E. Stovall.....	2364	MPC23
Tracking Particles with Wake Fields and Space Charge Effects — A.J. Riche	2367	MPC24
On the Importance of Fourth Order Effects on Wakefield Calculations for Short Bunches — Zenghai Li, Joseph J. Bisognano.....	2370	MPC25

Coupling Impedances of Muffin-Tin Structures with Closed and Open Sides — <i>M. Filtz</i>	2373	MPC28
Explicit Soft Fringe Maps of a Quadrupole — <i>John Irwin, Chun-xi Wang</i>	2376	MPC31

Instrumentation and Feedback

Bunched Beam Cooling for the Fermilab Tevatron (<i>Invited</i>) — <i>Ralph J. Pasquinelli</i>	2379	RAE01
Fast Digital Dampers for the Fermilab Booster (<i>Invited</i>) — <i>James M. Steimel Jr.</i>	2384	RAE02
Fast Feedback for Linear Colliders (<i>Invited</i>) — <i>L. Hendrickson, C. Adolphsen, S. Allison, T. Gromme, P. Grossberg, T. Himel, K. Krauter, R. MacKenzie, M. Minty, R. Sass, H. Shoaee, M. Woodley</i>	2389	RAE03
Instrumentation in Medical Systems (<i>Invited</i>) — <i>W.T. Chu</i>	2394	RAE04
Laser Diagnostics of a One-Dimensional Ordered Ion Beam — <i>R. Calabrese, V. Guidi, P. Lenisa, U. Tambini, E. Mariotti, L. Moi</i>	2399	RAE05
Determining Electron Beam Parameters from Edge Radiation Measurement Results on Siberia-1 Storage Ring — <i>O.V. Chubar</i>	2402	RAE06
Absolute Energy Measurement in e- e+ Linear Colliders — <i>Blaine E. Norum, Robert Rossmanith</i>	2405	RAE07
INR Activity in Development and Production of Bunch Shape Monitors — <i>S.K. Esin, A.V. Feschenko, P.N. Ostroumov</i>	2408	RAE08
Conceptual design of a Charged Particle Beam Energy Spectrometer Utilizing Transition Radiation Grating — <i>X.Z. Qiu, X.J. Wang, K. Batchelor, I. Ben-Zvi</i>	2411	RAE09
An Analysis of the Operational Performance of the Automatic Global Horizontal Beam Position Control System on the SRS at Daresbury — <i>J.B. Fitzgerald, B.G. Martlew, P.D. Quinn, S.L. Smith</i>	2414	RAE10
A Prototype Fast Feedback System for Energy Lock at CEBAF — <i>M. Chowdhary, G.A. Krafft, H. Shoaee, S.N. Simrock, W.A. Watson</i>	2417	RAE11
Operation and Performance of the PEP-II Prototype Longitudinal Damping System at the ALS — <i>D. Teytelman, R. Claus, J. Fox, H. Hindi, J. Hoeflich, I. Linscott, J. Olsen, G. Oxoby, S. Prabhakar, W. Ross, L. Sapozhnikov, A. Drago, M. Serio, J. Byrd, J. Corlett, G. Stover</i>	2420	RAE12
Commissioning of the ALS Transverse Coupled-Bunch Feedback System — <i>W. Barry, J. Byrd, J. Corlett, J. Johnson, G. Lambertson, J. Fox</i>	2423	RAE13
Operation of a Fast Digital Transverse Feedback System in CESR — <i>J.T. Rogers, M.G. Billing, J.A. Dobbins, C.R. Dunnam, D.L. Hartill, T. Holmquist, B.D. McDaniel, T.A. Pelaia, M. Pisharody, J.P. Sikora, C.R. Strohman</i>	2426	RAE14
Measuring and Adjusting the Path Length at CEBAF — <i>G.A. Krafft, M. Crofford, D.R. Douglas, S.L. Harwood, R. Kazimi, R. Legg, W. Oren, K. Tremblay, D. Wang</i>	2429	WXE01
Simulations of the BNL/SLAC/UCLA 1.6 Cell Emittance Compensated Photocathode RF Gun Low Energy Beam Line — <i>D.T. Palmer, R.H. Miller, H. Winick, X.J. Wang, K. Batchelor, M. Woodle, I. Ben-Zvi</i>	2432	WXE03
Small Gap Undulator Experiment on the NSLS X-Ray Ring — <i>P.M. Stefan, S. Krinsky, G. Rakowsky, L. Solomon</i>	2435	WXE04
Measurements of Longitudinal Dynamics in the SLC Damping Rings — <i>R.L. Holtzapfel, R.H. Siemann, C. Simopoulos</i>	2438	WXE05
Single Bunch Collective Effects in the ALS — <i>J.M. Byrd, J.N. Corlett, T. Renner</i>	2441	WXE06
Experiments of Nanometer Spot Size Monitor at FFTB Using Laser Interferometry — <i>T. Shintake, K. Oide, N. Yamamoto, A. Hayakawa, Y. Ozaki, D. Burke, R.C. Field, S. Hartman, R. Iverson, P. Tenenbaum, D. Walz</i>	2444	WXE07
Transverse Electron Beam Size Measurements Using the Lloyd's Mirror Scheme of Synchrotron Light Interference — <i>O.V. Chubar</i>	2447	WXE08

Instrumentation

Charge Balancing Fill Rate Monitor — <i>J.L. Rothman, E.B. Blum</i>	2450	MPQ01
Sensitivity and Offset Calibration for the Beam Position Monitors at the Advanced Photon Source — <i>Y. Chung, D. Barr, G. Decker, K. Evans Jr., E. Kahana</i>	2452	MPQ03
An Sampling Detector for the RHIC BPM Electronics — <i>W.A. Ryan, T.J. Shea</i>	2455	MPQ04
RHIC Beam Position Monitor Characterization		

— P.R. Cameron, M.C. Grau, M. Morvillo, T.J. Shea, R.E. Sikora.....	2458	MPQ05
Duke Storage Ring Tune Measurements System using Razor Blade and Photomultiplier — V.N. Litvinenko, B. Burnham, N. Hower, P. Morcombe, Y. Wu	2461	MPQ06
The Development of Beam Current Monitors in the APS — X. Wang, F. Lenkszus, E. Rotela.....	2464	MPQ07
Overall Design Concepts for the APS Storage Ring Machine Protection System — A. Lumpkin, R. Fuja, A. Votaw, X. Wang, D. Shu, J. Stepp, N. Arnold, G. Nawrocki, G. Decker, Y. Chung	2467	MPQ08
Status of the Synchrotron Radiation Monitors for the APS Facility Rings — A. Lumpkin, B. Yang	2470	MPQ09
Initial Diagnostics Commissioning Results for the Advanced Photon Source (APS) — A. Lumpkin, D. Patterson, X. Wang, E. Kahana, W. Sellyey, A. Votaw, B. Yang, R. Fuja, W. Berg, M. Borland, L. Emery, G. Decker, S. Milton.....	2473	MPQ10
Initial Tests of the Dual-Sweep Streak Camera System Planned for APS Particle-Beam Diagnostics — A. Lumpkin, B. Yang, W. Gai, W. Cieslik.....	2476	MPQ11
A Transverse Tune Monitor for the Fermilab Main Ring — P.J. Chou, B. Fellenz, G. Jackson.....	2479	MPQ13
Recalibration of Position Monitors With Beams — Kotaro Satoh, Masaki Tejima	2482	MPQ14
Simulation of PEP-II Beam Position Monitors — C.-K. Ng, T. Weiland, D. Martin, S. Smith, N. Kurita.....	2485	MPQ15
Prototype Bunch Killer System At SRRRC — G.J. Jan, Jenny Chen, C.H. Kuo, T.F. Lin, K.T. Pan, Glory Lin, K.T. Hsu.....	2488	MPQ16
Beam Diagnostics for the Amsterdam Pulse Stretcher AmPS — J.G. Noomen, H. Boer-Rookhuizen, N. Dobbe, J. v. Es, E. Heine, F. Kroes, J. Kuijt, J. v.d. Laan, A. Poelman, H. Nieuwenkamp, T. Sluijk.....	2491	MPQ17
Non-Destructive Beam Profile Measuring System Observing Fluorescence Generated by Circulating Beam — T. Kawakubo, E. Kadokura, T. Kubo, T. Ishida, H. Yamaguchi	2494	MPQ18
The Closed Orbit Measurement of SRRRC Booster During Ramping — T.S. Ueng, K.T. Hsu, K.H. Hwu, K.K. Lin	2497	MPQ19
Lattice Function Measurement with TBT BPM Data — Ming-Jen Yang.....	2500	MPQ20
Optimal Placement of Profile Monitors in a Mismatched FODO Lattice — K. Bertsche	2503	MPQ21
SSRL Beam Position Monitor Detection Electronics — J. Sebek, R. Hettel, R. Matheson, R. Ortiz, J. Wachter	2506	MPQ22
Single-Turn Beam Position Monitor for the NSLS VUV Electron Storage Ring — R.J. Nawrocky, S.L. Kramer.....	2509	MPQ23
Design of the Button Beam Position Monitor for PEP-II — N. Kurita, D. Martin, S. Smith, C. Ng, M. Nordby, C. Perkins.....	2512	MPQ25
Study of Fast Electron Beam Profile Monitor System — Ian Hsu, C.I. Yu, C.C. Chu.....	2515	MPQ26
The Average Orbit System Upgrade for the Brookhaven AGS — D.J. Ciardullo, J.M. Brennan	2518	MPQ30
Feasibility Study of an Orbit Feedback System for the KEKB Facility — Y. Funakoshi, M. Tejima, H. Ishii	2521	MPQ31
Turn-by-Turn Beam Position Measurement for 1.3 GeV Booster Synchrotron — T.S. Ueng, K.T. Hsu, C.S. Fang, Y.M. Chang, K.K. Lin	2524	MPQ32
Beam Position Monitor for the LNSL UVX Synchrotron Light Source — F.S. Rafael, E.K.C.S. Hayashi	2527	MPQ33
Transition Radiation Electron Beam Diagnostic Study at ATF — X.Z. Qiu, X.J. Wang, K. Batchelor, I. Ben-Zvi.....	2530	TPB01
Machine Parameter Measurement of the Amsterdam Pulse Stretcher AmPS — Y.Y. Wu, R. Maas.....	2533	TPB03
Wire Setup Calibration of Beam Position Monitors — D. Wang, B. Binns, M. Kogan, A. Zolfaghari	2536	TPB04
Beam profile data analysis for the RHIC Injection Line — Ping Zhou.....	2539	TPB05
Energy Spread of Ion Beams Generated in Multicusp Ion Sources — M. Sarstedt, P. Herz, W.B. Kunkel, Y. Lee, K.N. Leung, L. Perkins, D. Pickard, M. Weber, M.D. Williams, E. Hammel.....	2542	TPB07
A 2 MHz 3-Port Analog Isolation and Fanout Module — Edward R. Beadle	2545	TPB08
A General Purpose Fiber Optic Link with Radiation Resistance — Edward R. Beadle	2548	TPB09
DSP Based Data Acquisition for RHIC — T.J. Shea, J. Mead, C.M. Degen.....	2551	TPB12

Ion-Chamber Beam-Loss-Monitor System for the Los Alamos Meson Physics Facility — <i>M. Plum, D. Brown, A. Browman, R. Macek</i>	2554	TPB13
Development of Beam Position Monitors for Heavy Ion Recirculators — F.J. Deadrick, <i>J.J. Barnard, T.J. Fessenden, J.W. Meredith, J. Rintamaki</i>	2557	TPB14
Laser Compton Polarimetry of Proton Beams — A. Stillman	2560	TPB15
Phase and Synchronous Detector Theory as Applied to Beam Position and Intensity Measurements — J.D. Gilpatrick	2563	TPB16
Testing Coaxial Switches of BPM using a High-Resolution RF Detector — Takao Ieiri	2566	TPB17
A Beam Size Monitor Based on Appearance Intensities for Multiple Gas Ionization — <i>T. Katsouleas, J. Yoshii, W.B. Mori, C. Joshi, C. Clayton</i>	2569	TPB18
Beam Profile Measurement in the Presence of Noise — K. Bertsche, J. Palkovic	2572	TPB19
Beam Shaping Using a New Digital Noise Generator — H. Stockhorst, G. Heinrichs, <i>A. Schnase, S. Papureanu, U. Bechstedt, R. Maier, R. Tölle</i>	2574	TPB20
The RHIC Transfer Line Cable Database — E.H. Scholl, T. Satogata	2577	TPB21
Characterization of Beam Position Monitors for Measurement of Second Moment — <i>S.J. Russell, J.D. Gilpatrick, J.F. Power, R.B. Shurter</i>	2580	TPB22
Beam Diagnostic Systems and Their Use in the New IUCF Beam Line — W.P. Jones, M. Ball, <i>J. Collins, T. Ellison, B. Hamilton</i>	2583	TPB24
Tomographic Method of Experimental Research of Particle Distribution in Phase Space — <i>V.V. Kalashnikov, V.I. Moiseev, V.V. Petrenko</i>	2586	TPB25
Design of the Beam Profile Monitor System for the RHIC Injection Line — R.L. Witkover	2589	TPB26
Beam Intensity Observation System at SRRC — C.J. Wang, C.H. Kuo, J.S. Chen, Jenny Chen, <i>K.T. Hsu, G.J. Jan</i>	2592	TPB29
Performance of the Advanced Photon Source (APS) Linac Beam Position Monitors (BPMs) with Logarithmic Amplifier Electronics — R.E. Fuja, M. White	2595	TPC01
Preliminary Calculations on the Determination of APS Particle-Beam Parameters Based on Undulator Radiation — A. Lumpkin, B. Yang, Y. Chung, R. Dejus, G. Voykov, G. Dattoli	2598	TPC03
Coherent Synchrotron Radiation Detector for a Non-Invasive Subpicosecond Bunch Length Monitor — G.A. Krafft, D. Wang, E. Price, E. Feldl, D. Porterfield, P. Wood, T. Crowe	2601	TPC04
A Beam Test of Button-Type Beam Position Monitor for the ATF Damping Ring — <i>F. Hinode, H. Hayano, M. Tejima, N. Terunuma, J. Urakawa</i>	2604	TPC05
Application of a Transverse Phase-Space Measurement Technique for High-Brightness, H- Beams to the GTA H- Beam — K.F. Johnson, R.C. Connolly, R.C. Garcia, D.P. Rusthoi, <i>O.R. Sander, D.P. Sandoval, M.A. Shinas, M. Smith, V.W. Yuan</i>	2607	TPC06
Precision Intercomparison of Beam Current Monitors at CEBAF — R. Kazimi, B. Dunham, <i>G.A. Krafft, R. Legg, C. Liang, C. Sinclair, J. Mammoser</i>	2610	TPC07
Damped Button Electrode for B-Factory BPM System — T. Obina, T. Shintake, Y.H. Chin, <i>N. Akasaka</i>	2613	TPC08
Beam Monitors for the S-Band Test Facility — W. Radloff, M. Wendt	2616	TPC09
Low Energy Regime for Optical Transition Radiation Emission — D. Giove, C. De Martinis, <i>M. Pullia, P. Mangili</i>	2619	TPC10
Recovery of CTF Beam Signals from a Strong Wakefield Background — Yan Yin, <i>Elmar Schulte, Tord Ekelöf</i>	2622	TPC11
A Low-Cost Non-Intercepting Beam Current and Phase Monitor for Heavy Ions — <i>J.M. Bogaty, B.E. Clift</i>	2625	TPC12
Transverse Emittance Systematics Measured for Heavy-Ion Beams at ATLAS — J.A. Nolen, <i>T.A. Barlow, K.A. Beyer, K.A. Woody</i>	2628	TPC13
Beam Position Monitors in the TESLA Test Facility Linac — R. Lorenz	2631	TPC14
Energy Measurement of Relativistic Electrons by Compton Scattering — Ian Hsu, C.-C. Chu, <i>C.-I. Yu, C.-I. Chen, A.-T. Lai, Y.-C. Liu, P.-K. Tseng, G.-Y. Hsiung, R.-C. Hsu, C.-P. Wang, R.-</i> <i>C. Chen</i>	2634	TPC15
Tests of a High Resolution Beam Profile Monitor — J. Norem, J. Dawson, W. Haberichter, <i>R. Lam, L. Reed, X.-F. Yang, J. Spencer</i>	2637	TPC16
Airix Alignment and High Current Beam Diagnostics — D. Villate, Ch. Bonnafond, A. Devin, <i>E. Merle</i>	2640	TPC17
A New Beam Intensity Monitoring System with Wide Dynamic Range for the Holifield Radioactive Ion Beam Facility — M.J. Meigs, D.L. Haynes, C.M. Jones, C.T. LeCroy	2643	TPC18

Diagnostic Beam Pulses for Monitoring the SLC Linac — F.-J. Decker, M. Stanek, H. Smith, F. Tian.....	2646	TPC20
Observation of Thermal Effects on the LEP Wire Scanners — J. Camas, C. Fischer, J.J. Gras, R. Jung, J. Koopman	2649	TPC21
CEBAF Beam Loss Accounting — R. Ursic, K. Mahoney, C. Hovater, A. Hutton, C. Sinclair.....	2652	TPC26
Nanometer Resolution BPM Using Damped Slot Resonator — S.C. Hartman, T. Shintake, N. Akasaka.....	2655	TPC29
An Automatic Tune-Measurement System for the CELSIUS Ring — T. Lofnes	2658	TPC31

Feedback

Software Architecture of the Longitudinal Feedback System for PEP-II, ALS and DAΦNE — R. Claus, J. Fox, I. Linscott, G. Oxoby, W. Ross, L. Sapozhnikov, D. Teytelman, A. Drago, M. Serio	2660	RPQ01
Digital I/Q Demodulator — C. Ziomek, P. Corredoura.....	2663	RPQ02
RF Feedback Simulation Results for PEP-II — R. Tighe, P. Corredoura.....	2666	RPQ03
TM0,1.5,0 Mode Cavity for Longitudinal Bunch Feedback Kicker — T. Shintake	2669	RPQ04
Low Level RF System Design for the PEP-II B Factory — P. Corredoura, R. Claus, L. Sapozhnikov, H. Schwarz, R. Tighe, C. Ziomek	2672	RPQ05
Experiment of the RF Feedback using a Parallel Comb Filter — S. Yoshimoto, E. Ezura, K. Akai, T. Takashima.....	2675	RPQ06
Digital Transverse Beam Dampers for the Brookhaven AGS — G.A. Smith, V. Castillo, T. Roser, W. Van Asselt, R. Witkover, V. Wong.....	2678	RPQ07
Design of the PEP-II Transverse Coupled-Bunch Feedback System — W. Barry, J. Byrd, J. Corlett, M. Fahmie, J. Johnson, G. Lambertson, M. Nyman, J. Fox, D. Teytelman	2681	RPQ08
Simulations of the PEP-II Transverse Coupled-Bunch Feedback System — J.M. Byrd	2684	RPQ09
Fermilab Booster Low Level RF System Upgrades — Robert C. Webber.....	2687	RPQ10
Energy Stability in a High Average Power FEL — L. Merminga, J.J. Bisognano.....	2690	RPQ11
Automated Beam Based Alignment of the ALS Quadrupoles — G. Portmann, D. Robin, L. Schachinger.....	2693	RPQ13
First Results with a Nonlinear Digital Orbit Feedback System at the NSLS — Eva Bozoki, Aharon Friedman, Susila Ramamoorthy.....	2696	RPQ14
Local Beam Position Feedback Experiments on the ESRF Storage Ring — Y. Chung, E. Kahana, J. Kirchman, A. Lumpkin, J. Meyer, E. Plouviez, K. Scheidt, E. Taurel, A. Ando, S. Sasaki, A. Taketani	2699	RPQ15
Implementation of the Global and Local Beam Position Feedback Systems for the Advanced Photon Source Storage Ring — Y. Chung, D. Barr, G. Decker, J. Galayda, J. Kirchman, F. Lenkszus, A. Lumpkin, A.J. Votaw.....	2702	RPQ16
The RHIC Accelerating Cavity Prototype Tuner — A. Ratti, J.M. Brennan, J. Brodowski, E. Onillon, J. Rose	2705	RPQ17
Ramp Tuning of the APS Booster Synchrotron Magnet Power Supplies — S.V. Milton, J.A. Carwardine.....	2708	RPQ18
Orbit Stability Improvements at the NSLS X-Ray Ring — J. Safranek, O. Singh, L. Solomon	2711	RPQ19
Digital Orbit Feedback Compensation for SPEAR — J. Corbett, R. Hettel, D. Keeley, D. Mostowfi	2714	RPQ21
Digital Orbit Feedback Control for SPEAR — R. Hettel, J. Corbett, D. Keeley, I. Linscott, D. Mostowfi, J. Sebek, C. Wermelskirchen.....	2717	RPQ22
Beam Position Feedback Systems for the PF Storage Ring — N. Nakamura, K. Haga, T. Honda, T. Kasuga, M. Katoh, Y. Kobayashi, M. Tadano, M. Yokoyama	2720	RPQ23
The New Booster Synchronization Loop — E. Onillon, J.M. Brennan.....	2723	RPQ25
Recent Progress in the Development of the Bunch Feedback Systems for KEKB — E. Kikutani, T. Kasuga, Y. Minagawa, T. Obina, M. Tobiyama.....	2726	RPQ26
60 Hz Beam Motion Reduction at NSLS UV Storage Ring — Om V. Singh	2729	RPQ27
The CEBAF Fiber Optic Phase Reference System — K. Crawford, S. Simrock, C. Hovater, A. Krycuk	2732	RPQ29
RF System Modeling for the High Average Power FEL at CEBAF — L. Merminga, J. Fugitt, G. Neil, S. Simrock.....	2735	RPQ30

Beam Positioning and Monitoring in the Racetrack Microtron Eindhoven — W. Theuws, <i>R.W. de Leeuw, G.A. Webers, J.I.M. Botman, C.J. Timmermans, H.L. Hagedoorn</i>	2738	RPQ31
Multi-Bunch Systems at DESY — Rolf-Dieter Kohaupt	2741	RPQ32

High Energy Accelerator Beam Dynamics

Results of Final Focus Test Beam (Invited) — V.A. Alexandrof, V. Balakin, A. Mikhailichenko, <i>K. Flöttmann, F. Peters, G.-A. Voss, V. Bharadwaj, M. Halling, J.A. Holt, J. Buon, J. Jeanjean,</i> <i>F. LeDiberder, V. Lepeltier, P. Puzo, G. Heimlinger, R. Settles, U. Stierlin, N. Akasaka,</i> <i>H. Hayano, N. Ishihara, H. Nakayama, K. Oide, T. Shintake, Y. Takeuchi, N. Yamamoto,</i> <i>F. Bulos, D. Burke, R. Field, S. Hartman, R. Helm, J. Irwin, R. Iverson, P. Raimondi, S. Rokni,</i> <i>G. Roy, W. Spence, P. Tenenbaum, S.R. Wagner, D. Walz, S. Williams</i>	2742	TAG01
Comparison of Measured and Calculated Dynamic Aperture (Invited) — F. Willeke	2747	TAG02
Ion Effects in Future Circular and Linear Accelerators (Invited) — T.O. Raubenheimer	2752	TAG03
Nonlinear Wave Phenomena in Coasting Beams (Invited) — P.L. Colestock, L.K. Spentzouris, <i>F. Ostiguy</i>	2757	TAG04
The Cure of Multibunch Instabilities in ELETTRA — M. Svandrlik, C.J. Bocchetta, A. Fabris, <i>F. Iazzourene, E. Karantzoulis, R. Nagaoka, C. Pasotti, L. Tosi, R.P. Walker, A. Wrulich</i>	2762	TAG05
Nonlinear Analyses of Storage Ring Lattices Using One-Turn Maps — Y.T. Yan, J. Irwin, <i>T. Chen</i>	2765	TAG06
Precise Determination and Comparison of the SPS Dynamic Aperture in Experiment and Simulation — W. Fischer, F. Schmidt	2768	TAG07
Coherency of the Long Range Beam-Beam Interaction in CESR — Alexander B. Temnykh, <i>James J. Welch</i>	2771	TAG08
Effect of Quadrupole Noise on the Emittance Growth of Protons in HERA — T. Sen, <i>O. Brüning, F. Willeke</i>	2774	TAG09
Nonlinear Mode Coupling Analysis in the Tevatron — S. Assadi, C.S. Mishra	2777	TAG10
Lattice Design for KEKB Colliding Rings — H. Koiso, K. Oide	2780	TAG11
Entropy and Emittance Growth — Patrick G. O'Shea	2783	TAG12
Analysis of Optical Stochastic Cooling Including Transverse Effects — K.-J. Kim	2786	TAG13

Volume 5

Linear and Nonlinear Orbit Theory

Reduction of Non Linear Resonance Excitation from Insertion Devices in the ALS — <i>D. Robin, G. Krebs, G. Portmann, A. Zholents, W. Decking</i>	2789	FAB01
Sum Betatron Resonances under Linear Coupling of Oscillations — P.N. Chirkov, <i>I.I. Petrenko</i>	2792	FAB02
Linear Orbit Parameters for the Exact Equations of Motion — G. Parzen	2795	FAB03
Tune Modulation Due to Synchrotron Oscillations and Chromaticity, and the Dynamic Aperture — G. Parzen	2798	FAB04
Normal Mode Tunes for Linear Coupled Motion in Six Dimensional Phase Space — <i>G. Parzen</i>	2801	FAB05
Fast Symplectic Mapping and Quasi-invariants for the Large Hadron Collider — <i>R.L. Warnock, J.S. Berg, E. Forest</i>	2804	FAB06
Nonlinear Dependence of Synchrotron Radiation on Beam Parameters — G.H. Hoffstätter	2807	FAB07
Effects of Imperfections on the Dynamic Aperture and Closed Orbit of the IPNS Upgrade Synchrotron — E. Lessner, Y.-C. Chae, S. Kim	2811	FAB09
Paraxial Expansion of a Static Magnetic Field in a Ring Accelerator — Lee C. Teng	2814	FAB10
Experimental Determination of Linear Optics Including Quadrupole Rotations — <i>J. Safranek</i>	2817	FAB11
Perturbation of Beam Energy Due to Steering and Pretzel Orbit — W. Lou, M. Billing, <i>D. Rice</i>	2820	FAB12
Lattice Studies for a High-Brightness Light Source — D. Kaltchev, R.V. Servranckx, <i>M.K. Craddock, W. Joho</i>	2823	FAB14

Transfer Maps Through Ideal Bends (Again?) — <i>Leo Michelotti</i>	2826	FAB15
Skew Chromaticity in Large Accelerators — <i>S. Peggs, G.F. Dell</i>	2829	FAB20
The Effect and Correction of Coupling Generated by the RHIC Triplet Quadrupoles — <i>F. Pilat, S. Peggs, S. Tepikian, D. Trbojevic, J. Wei</i>	2832	FAB22
The Beam Envelope Equation - Systematic Solution for a FODO Lattice with Space Charge — <i>Edward P. Lee</i>	2835	FAC01
Analytic Second- and Third-Order Achromat Designs — <i>Chunxi Wang, Alex Chao</i>	2838	FAC02
Measurement of Chromatic Effects in LEP — <i>D. Brandt, P. Castro, K. Cornelis, A. Hofmann,</i> <i>G. Morpurgo, G.L. Sabbi, A. Verdier</i>	2841	FAC03
The Lattice of the CERN Large Hadron Collider — <i>W. Scandale, B. Jeanneret, J.-</i> <i>P. Koutchouk, X. Luo, F. Méot, R. Ostojic, T. Risselada, C. Rufer, T. Taylor, T. Trenkler,</i> <i>S. Weisz</i>	2844	FAC04
Sorting Strategies for the LHC Based on Normal Forms — <i>W. Scandale, M. Giovannozzi,</i> <i>R. Grassi, E. Todesco</i>	2847	FAC06
Algorithms to get a Circulating Beam — <i>André Verdier, Frank Richard</i>	2850	FAC07
Non-Linear Chromaticity Correction with Sextupole Families — <i>André Verdier</i>	2853	FAC08
Simulation of Charged Particle Transport in Nonlinear Axisymmetrical Electrostatic Potential — <i>I.P. Yudin, V.V. Andreev</i>	2856	FAC09
Stochastic Effects in Real and Simulated Ion Beams — <i>Jürgen Struckmeier</i>	2860	FAC10
Magnetic Field Correction in Nuclotron — <i>I.B. Issinsky, V.A. Mikhailov, V.A. Shchepunov</i>	2863	FAC12
Effects of the CHESS Wigglers on a Beam with an Angular Offset — <i>James J. Welch</i>	2866	FAC14
Particle Tracking with Generating Functions of Magnetic Fringing Fields — <i>Godehard Wüstefeld</i>	2868	FAC16
Computation of Lattice Maps Using Modular BCH and Similarity Composition Rules — <i>J. Irwin</i>	2871	FAC18
Treatment of Wiggler and Undulator Field Errors in Tracking Codes — <i>W. Decking,</i> <i>O. Kaul, H. Neemann, J. Roßbach</i>	2874	FAC19
Experimental Study of the Duke Storage Ring Dynamic Aperture — <i>Y. Wu, V.N. Litvinenko,</i> <i>B. Burnham, J.M.J. Madey</i>	2877	FAC20

Beam-Beam Interaction and Beam Cooling

A New Model of the e+e- Beam-Beam Interaction — <i>K.D. Cromer, B.E. Norum</i>	2880	RAP01
A Study of Beam-Beam Interactions at Finite Crossing Angles for a B-Factory — <i>K. Hirata,</i> <i>K. Ohmi, N. Toge</i>	2883	RAP02
Simulation of Beam-Beam Effects in Tevatron — <i>C.S. Mishra, S. Assadi, R. Talman</i>	2886	RAP03
The Dynamic Beta Effect in CESR — <i>David Sagan</i>	2889	RAP04
Lifetime and Tail Simulations for Beam-Beam Effects in PEP-II B Factory — <i>D.N. Shatilov,</i> <i>A.A. Zholents</i>	2892	RAP05
Gamma Ray Sources Based on Resonant Backscattering of Laser Beams With Relativistic Heavy Ion Beams — <i>E.G. Bessonov, Kwang-Je Kim</i>	2895	RAP06
Observations of the Effects of the Beam-Beam Interaction on the Orbits of Stored Beams in CESR — <i>E. Young</i>	2898	RAP07
Calculations on Depolarization in HERA due to Beam-Beam Effects — <i>M. Böge, T. Limberg</i>	2901	RAP08
A Map for the Thick Beam-Beam Interaction — <i>J. Irwin, T. Chen</i>	2904	RAP09
Transient Beam Loading in the SLC Damping Rings — <i>M.G. Minty, R.H. Siemann</i>	2907	RAP10
Studies of Halo Distributions Under Beam-Beam Interaction — <i>T. Chen, J. Irwin,</i> <i>R.H. Siemann</i>	2910	RAP11
The Effect of Phase Advance Errors Between Interaction Points on Beam Halos — <i>T. Chen,</i> <i>J. Irwin, R.H. Siemann</i>	2913	RAP12
Compensation of the "Pacman" Tune Spread by Tailoring the Beam Current — <i>Miguel A. Furman</i>	2916	RAP14
Disruption Effects on the Beam Size Measurement — <i>P. Raimondi, F.-J. Decker, P. Chen</i>	2919	RAP15
Flat Beam Spot Sizes Measurement in the SLC-Final Focus — <i>P. Raimondi, F.-J. Decker</i>	2922	RAP16
Polarization Correlations in the SLC Final Focus — <i>F.-J. Decker</i>	2925	RAP17
Supercooling of Bunched Beams by Coherent Synchrotron Radiation — <i>M. Bergher</i>	2928	RAP19

Analysis of the Tevatron Collider Beam Spectrum for Bunched Beam Stochastic Cooling — <i>G. Jackson</i>	2931	RAP20
Asymmetric Hopf Bifurcation for Proton Beams with Electron Cooling — <i>X. Kang, M. Ball, B. Brabson, J. Budnick, D.D. Caussyn, P. Colestock, G. East, M. Ellison, B. Hamilton, K. Hedblom, S.Y. Lee, D. Li, J.Y. Liu, K.Y. Ng, A. Pei, A. Riabko, M. Syphers, L. Wang, Y. Wang</i>	2934	RAP21
Space Charge Effects and Intensity Limits of Electron-Cooled Bunched Beams — <i>S. Nagaitsev, T. Ellison, M. Ball, V. Derenchuk, G. East, M. Ellison, B. Hamilton, P. Schwandt</i>	2937	RAP22
Stability Conditions for a Neutralised Electron Cooling Beam — <i>J. Bosser, S. Maury, D. Möhl, F. Varenne, I. Meshkov, E. Syresin, E. Mustafin, P. Zenkevich</i>	2940	RAP23
Neutralisation of the LEAR Electron-Cooling Beam: Experimental Results — <i>J. Bosser, F. Caspers, M. Chanel, R. Ley, R. Maccaferri, S. Maury, G. Molinari, G. Tranquille, F. Varenne, I. Meshkov, V. Polyakov, A. Smirnov, O. Stepashkin, E. Syresin</i>	2943	RAP24
Crystalline Beam Properties as Predicted for the Storage Ring ASTRID and TSR — <i>Jie Wei, Xiao-Ping Li, Andrew Sessler</i>	2946	RAP25

Instabilities and Cures

Impedance Matrix - an Unified Approach to Longitudinal Coupled-Bunch Feedbacks in a Synchrotron — <i>S. Ivanov</i>	2949	TPQ01
The Coupling Impedance of Toroidal Beam Pipe with Circular Cross Section — <i>H. Hahn</i>	2952	TPQ02
Bunch Lengthening Study in BEPC — <i>Z. Guo, Q. Qin, G. Xu, C. Zhang</i>	2955	TPQ03
Practical Criterion of Transverse Coupled-Bunch Head-Tail Stability — <i>S. Ivanov, M. Pozdeev</i>	2958	TPQ04
A Code to Compute the Action-Angle Transformation for a Particle in an Arbitrary Potential Well — <i>J. Scott Berg, Robert L. Warnock</i>	2962	TPQ07
Study of Longitudinal Coupled-Bunch Instabilities in the SRRC Storage Ring — <i>W.K. Lau, M.H. Wang, K.T. Hsu, L.H. Chang, Ch. Wang, C.C. Kuo</i>	2965	TPQ08
Suppression of the Transverse Oscillation in the SRRC Storage Ring by RF Knockout Method — <i>J.C. Lee, M.H. Wang, K.T. Hsu, R.J. Sheu, G. Lin, C.S. Hsue</i>	2968	TPQ09
The Observation of Longitudinal Coupled Bunch Motion on Streak Camera at SRRC — <i>M.H. Wang, K.T. Hsu, W.K. Lau, C.S. Hsue, H.J. Tsai, H.P. Chang, J.C. Lee, C.C. Kuo</i>	2971	TPQ10
Resistive-Wall Instability Experiment in Space-Charge Dominated Electron Beams — <i>H. Suk, J.G. Wang, M. Reiser</i>	2974	TPQ11
Mode-Coupling Instability and Bunch Lengthening in Proton Machines — <i>K.Y. Ng</i>	2977	TPQ12
Longitudinal Wakefield for Synchrotron Radiation — <i>J.B. Murphy, S. Krinsky, R.L. Gluckstern</i>	2980	TPQ14
Review of Beam Instability Studies for the SSC — <i>W. Chou</i>	2983	TPQ15
Collective Effects in the NLC Damping Ring Designs — <i>T. Raubenheimer, K.L.F. Bane, J.S. Berg, J. Byrd, J. Corlett, M. Furman, S. Heifets, K. Kubo, M. Minty, B. Scott, K.A. Thompson, P.B. Wilson, F. Zimmermann</i>	2986	TPQ16
Emittance and Energy Control in the NLC Main Linacs — <i>C. Adolphsen, K.L.F. Bane, K. Kubo, T. Raubenheimer, R.D. Ruth, K.A. Thompson, F. Zimmermann</i>	2989	TPQ17
Digital Signal Processing for the APS Transverse and Longitudinal Damping System — <i>D. Barr, W. Sellyey</i>	2992	TPQ19
Longitudinal Coupling Impedance of a Hole in an Infinite Plane Screen — <i>Yong-Chul Chae</i>	2995	TPQ20
Investigation of Resistive Wall Instability in the 7-GeV APS Storage Ring — <i>Yong-Chul Chae</i>	2998	TPQ21
Longitudinal Instability Analysis for the IPNS Upgrade — <i>K. Harkay, Y. Cho, E. Lessner</i>	3001	TPQ22
Transverse Instability Analysis for the IPNS Upgrade — <i>K. Harkay, Y. Cho</i>	3004	TPQ23
Longitudinal Emittance Measurements in the Fermilab Booster — <i>D.A. Herrup</i>	3007	TPQ25
Analog Dampers in the Fermilab Booster — <i>D.A. Herrup, D. McGinnis, J. Steimel, R. Tomlin</i>	3010	TPQ26
A Study of the Longitudinal Coupled Bunch Instability in the Fermilab Main Ring — <i>K. Junck, J. Marriner, D. McGinnis</i>	3013	TPQ28
Inference of Wake Field Structure by Driving Longitudinal Coupled Bunch Modes in Main Ring — <i>S. Assadi, K. Junck, P. Colestock, J. Marriner</i>	3016	WAB01
Simulation of Transverse Coupled Bunch Instabilities — <i>S. Khan</i>	3019	WAB03
The Transition Jump System for the AGS — <i>W.K. van Asselt, L.A. Ahrens, J.M. Brennan, A. Dunbar, E. Keith-Monnia, J.T. Morris, M.J. Syphers</i>	3022	WAB04

Measurements of Longitudinal Phase Space in the SLC Linac — R.L. Holtzapple, <i>F.-J. Decker, R.K. Jobe, C. Simopoulos</i>	3025	WAB05
Observation of Induced Beam Oscillation from Actively Displaced RF Accelerating Structures — John T. Seeman, Henk Fischer, William Roster	3028	WAB06
Measurement of the Effect of Collimator Generated Wakefields on the Beams in the SLC — <i>K.L.F. Bane, C. Adolphsen, F.-J. Decker, P. Emma, P. Krejcik, F. Zimmermann</i>	3031	WAB07
Beam Trajectory Jitter in the SLC Linac — Chris Adolphsen, Tim Slaton	3034	WAB08
Emittance Growth due to Decoherence and Wakefields — M.G. Minty, A.W. Chao, <i>W.L. Spence</i>	3037	WAB09
A Weak Microwave Instability with Potential Well Distortion and Radial Mode Coupling — <i>Alex Chao, Bo Chen, Katsunobu Oide</i>	3040	WAB10
Wake Field and the Diffraction Model Due to a Flat Beam Moving Past a Conducting Wedge — A.W. Chao, H. Henke	3043	WAB11
Operating Experience with High Beam Currents and Transient Beam Loading in the SLC Damping Rings — M.G. Minty, R. Akre, P. Krejcik, R.H. Siemann	3046	WAB12
Deflecting Forces for the Case of Multi Mode Beam - RF Cavity Interaction in Linear Accelerators — V.G. Kurakin	3049	WAB14
Photoelectron Trapping Mechanism for Transverse Coupled Bunch Mode Growth in CESR — J.T. Rogers	3052	WAB15
Electron Cooler Impedances — A. Burov	3055	WAB16
Wall Impedances for Low and Moderate Energies — A. Burov	3058	WAB17
Impedance Analysis of the PEP-II Vacuum Chamber — C.-K. Ng, T. Weiland	3061	WAB18
Microwave Instabilities in Electron Rings with Negative Momentum Compaction Factor — <i>S.X. Fang, K. Oide, K. Yokoya, B. Chen, J.Q. Wang</i>	3064	WAB20
Microwave Stability at Transition — J.A. Holt, P.L. Colestock	3067	WAC01
Experimental Observations of Nonlinear Coupling of Longitudinal Modes in Unbunched Beams — Linda Klamp Spentzouris, Patrick L. Colestock, Francois Ostiguy	3070	WAC02
Damping Rate Measurements in the SLC Damping Rings — C. Simopoulos, R.L. Holtzapple	3073	WAC04
Transverse Multibunch Instabilities for Non-Rigid Bunches — J. Scott Berg, Ronald D. Ruth	3076	WAC05
Simulations of Transition Crossing in the Main Injector — C.M. Bhat, J.A. MacLachlan	3079	WAC06
Impedance Budget for the KEK B-Factor — Y.H. Chin, K. Satoh	3082	WAC07
Single-Beam Collective Effects in the KEK B-Factor — Y.H. Chin, K. Akai, Y. Funakoshi, <i>K. Oide, K. Satoh</i>	3085	WAC08
Beam Transfer Function and Transverse Impedance Measurements in the Fermilab Main Ring — P.J. Chou, G. Jackson	3088	WAC09
Experimental Studies of Transverse Beam Instabilities at Injection in the Fermilab Main Ring — P.J. Chou, G. Jackson	3091	WAC10
Longitudinal Multibunch Feedback Experiment with Switched Filter Bank — A. Pei, <i>M. Ball, M. Ellison, X. Kang, S.Y. Lee, D. Li, J. Liu, A. Riabko, L. Wang</i>	3094	WAC12
Field Propagation Effects and Related Multibunch Instability in Multicell Capture Cavities — M. Ferrario, A. Mosnier, L. Serafini, F. Tazzioli, J.-M. Tessier	3097	WAC13
Cure of Transverse Instabilities by Chromaticity Modulation — T. Nakamura	3100	WAC14
A Fast Beam-Ion Instability — F. Zimmermann, T.O. Raubenheimer, G. Stupakov	3102	WAC15
Simulations of the Longitudinal Instability in the New SLC Damping Rings — K.L.F. Bane, <i>K. Oide</i>	3105	WAC16
High-Intensity Single Bunch Instability Behavior In The New SLC Damping Ring Vacuum Chamber — K. Bane, J. Bowers, A. Chao, T. Chen, F.J. Decker, R.L. Holtzapple, P. Krejcik, <i>T. Limberg, A. Lisin, B. McKee, M.G. Minty, C.-K. Ng, M. Pietryka, B. Podobedov,</i> <i>A. Rackelmann, C. Rago, T. Raubenheimer, M.C. Ross, R.H. Siemann, C. Simopoulos,</i> <i>W. Spence, J. Spencer, R. Stege, F. Tian, J. Turner, J. Weinberg, D. Whittum, D. Wright,</i> <i>F. Zimmermann</i>	3109	WAC17
Alignment Tolerance of Accelerating Structures and Corrections for Future Linear Colliders — K. Kubo, C. Adolphsen, K.L.F. Bane, T.O. Raubenheimer, K.A. Thompson	3112	WAC18
Refinements to Longitudinal, Single Bunch, Coherent Instability Theory — S.R. Koscielniak	3115	WAC19
Simulations of Sawtooth Instability — R. Baartman, M. D'Yachkov	3119	WAC20
Characterisation of a Localised Broad-Band Impedance Phenomenon on the SRS — <i>S.F. Hill</i>	3122	WAC21
Cavity-Beam Instabilities on the SRS at Daresbury — P.A. McIntosh, D.M. Dykes	3125	WAC22

Bunch Lengthening Thresholds on the Daresbury SRS — J.A. Clarke.....	3128	WAC23
Estimation of Collective Instabilities in RHIC — W.W. MacKay, M. Blaskiewicz, D. Deng, V. Mane, S. Peggs, A. Ratti, J. Rose, T.J. Shea, J. Wei.....	3131	WAC24
RHIC Injection Kicker Impedance — V. Mane, S. Peggs, D. Trbojevic, W. Zhang.....	3134	WAC25
KRAKEN, a Numerical Model of RHIC Impedances — S. Peggs, V. Mane.....	3137	WAC26
Lattice Design of Beijing Light Source — N. Huang, L. Jin, D. Wang, L. Wang, A. Xiao, G. Xu.....	3140	WAC27
A Theoretical Study of the Electron-Proton Instability in a Long Proton Pulse — Tai-Sen F. Wang.....	3143	WAC28
Recent Progress on Beam Stability Study in the PSR — T. Wang, P. Channell, R. Cooper, D. Fitzgerald, T. Hardek, R. Hutson, A. Jason, R. Macek, M. Plum, C. Wilkinson, E. Colton.....	3146	WAC29

Low Energy Accelerator Beam Dynamics

Halos of Intense Proton Beams (Invited) — Robert D. Ryne, Salman Habib, Thomas P. Wangler.....	3149	RAG01
Polarized Proton Beams (Invited) — T. Roser.....	3154	RAG02
Beam Dynamics in Heavy Ion Fusion (Invited) — Peter Seidl.....	3159	RAG03
Crystalline Beams (Invited) — John P. Schiffer.....	3164	RAG04
Injecting a Kapchinskij-Vladimirskij Distribution into a Proton Synchrotron — E. Crosbie, K. Symon.....	3167	RAG05
Halo of a High-Brightness Electron Beam — G. Haouat, N. Pichoff, C. Couillaud, J.P. De Brion, J. Di Crescenzo, S. Joly, A. Loulergue, C. Ruiz, S. Seguin, S. Striby.....	3170	RAG06
Studies on Halo Formation in a Long Magnetic Quadrupole FODO Channel First Experimental Results — P.-Y. Beauvais, D. Bogard, P.-A. Chamouard, R. Ferdinand, G. Haouat, J.-M. Lagniel, J.-L. Lemaire, N. Pichoff, C. Ruiz.....	3173	RAG07
Radial Mode Evolution in Longitudinal Bunched Beam Instability — S.Y. Zhang, W.T. Weng.....	3176	RAG08
Stability of a Breathing K-V Beam — Robert L. Gluckstern, Wen-Hao Cheng.....	3179	RAG09
Hamiltonian Formalism for Space Charge Dominated Beams in a Uniform Focusing Channel — A. Riabko, M. Ellison, X. Kang, S.Y. Lee, J.Y. Liu, D. Li, A. Pei, L. Wang.....	3182	RAG10
Simulation Studies of the LAMPF Proton Linac — R.W. Garnett, E.R. Gray, L.J. Rybarczyk, T.P. Wangler.....	3185	RAG11
Functional Dependence of Wakefunctions for $v < c$ — Zenghai Li, Joseph J. Bisognano.....	3188	RAG12
Betatron Transients Caused by Rapid Changes in the Closed Orbit — James J. Welch.....	3191	RAG13
Phenomenology of Crystalline Beams in Smooth Accelerators — A.F. Haffmans, D. Maletic, A.G. Ruggiero.....	3194	RAG14
Beam Dynamics in the 1.3 GeV High Intensity ESS Coupled Cavity Linac — M. Pabst, K. Bongardt.....	3197	TPA01
Final Bunch Rotation and Momentum Spread Limitation for the ESS Facility — K. Bongardt, M. Pabst.....	3200	TPA02
Design Criteria for High Intensity H ⁺ -Injector Linacs — K. Bongardt, M. Pabst.....	3203	TPA03
Measurements of Vacuum Chamber Impedance Effects on the Stored Beam at CESR — M. Billing, Z. Greenwald, W. Hartung, W.R. Lou, M. Pisharody, J. Rogers, D. Sagan, J. Sikora.....	3206	TPA04
The Study of Nonlinear Effects Influenced by Space Charge in High Intensity Linac — A.A. Kolomiets, S.G. Yaramishev, P.R. Zenkevich, A.P. Korolev.....	3209	TPA05
Beam Size Versus Intensity for Resonant Extracted Beam at the Brookhaven AGS — K.A. Brown, R. Thern, H. Huang.....	3212	TPA06
Review of Longitudinal Perturbation Formalism — S.Y. Zhang.....	3214	TPA08
Klystron Power Specifications Based on Transient Beam Loading Analysis in Damping Rings — M.G. Minty, R.H. Siemann.....	3217	TPA09
Transverse Combining of Four Beams in MBE-4 — C.M. Celata, W. Chupp, A. Faltens, W.M. Fawley, W. Ghiorso, K.D. Hahn, E. Henestroza, C. Peters, P. Seidl.....	3220	TPA10
Ion Core Parameters in the Bending Magnets of Electron Storage Rings — E. Bulyak.....	3223	TPA12
Ion Driven Effects in the Intence Electron Beam Circulating in Storage Rings — E. Bulyak.....	3226	TPA13
Disk-Loaded Waveguides for Accelerating High Intensity Short Pulse Electron Beams — N.I. Aizatsky.....	3229	TPA14
The Description of High Current Beam Dynamics Using Lie Algebraic Methods — A.I. Borodich, A.A. Khrutchinsky, V.I. Stolyarsky.....	3232	TPA15

Chaos, a Source of Charge Redistribution and Halo Formation in Space-Charge Dominated Beams — Jean-Michel Lagniel, David Libault.....	3235	TPA17
Transport of a Partially-Neutralized Ion Beam in a Heavy-Ion Fusion Reactor Chamber — Debra A. Callahan, A. Bruce Langdon	3238	TPR01
Emittance Growth from Rotated Quadrupoles in Heavy Ion Accelerators — John J. Barnard.....	3241	TPR02
Wakefield Effects on the Beam Accelerated in a Photoinjector: Perturbation Due to the Exit Aperture — J.-M. Dolique, W. Salah	3245	TPR04
Influence of the Photoinjector Exit Aperture on the Wakefield Driven by an Intense Electron Beam Pulse: a Theoretical Approach — J.-M. Dolique	3248	TPR05
Invariability of Intense Beam Emittance in Nonlinear Focusing Channel — Y.K. Batygin.....	3251	TPR06
Beam Transport for Uniform Irradiation: Nonlinear Space Charge and the Effect of Boundary Conditions — D. Bruhwiler, Yuri K. Batygin.....	3254	TPR07
Transport of Bunched Beams with Space Charge Through a Periodic Lattice — M.F. Reusch, D.L. Bruhwiler.....	3257	TPR08
Modeling Space Charge in Beams for Heavy-Ion Fusion — W.M. Sharp	3260	TPR09
Impedance of Periodic Irises in a Beam Pipe — Shicheng Jiang, Robert L. Gluckstern, Hiromi Okamoto	3263	TPR11
Frequency Dependence of the Polarizability and Susceptibility of a Circular Hole in a Thick Conducting Wall — Wen-Hao Cheng, Alexei V. Fedotov, Robert L. Gluckstern	3266	TPR12
Spatial-Temporal Hysteresis Effects in an Intense Electron Beam — A.V. Agafonov, A.N. Lebedev, V.S. Voronin	3269	TPR13
General Wave Equation in the Electrostatic Approximation — A.V. Agafonov.....	3272	TPR14
Space Charge Effects at KEK-Booster Synchrotron — Chihiro Ohmori, Toshikazu Adachi, Tadamichi Kawakubo, Motohiro Kihara, Isao Yamane	3275	TPR16
On the Relaxation of Semi-Gaussian and K-V Beams to Thermal Equilibrium — S.M. Lund, J.J. Barnard, J.M. Miller.....	3278	TPR18
Transverse-Longitudinal Energy Equilibration in a Long Uniform Beam — I. Haber, D.A. Callahan, A. Friedman, D.P. Grote, A.B. Langdon	3282	TPR19

Beam Dynamics, Misc.

Variants of Optics Schemes and Accelerator Configurations for Athens Microtron: Preliminary Considerations — A.V. Tiunov, V.I. Shvedunov, I.V. Surma, K. Hizanidis, C. Kalfas, C. Trikalinos, J. Tigelis.....	3285	RAQ01
Study of Beam Decoherence in the Presence of Head-Tail Instability Using a Two-particle Model — G.V. Stupakov, A.W. Chao.....	3288	RAQ02
Beam Distribution Function after Filamentation — T.O. Raubenheimer, F.-J. Decker, J.T. Seeman.....	3291	RAQ03
Measurement of the Interaction Between a Beam and a Beam Line Higher-Order Mode Absorber in a Storage Ring — W. Hartung, P. Barnes, S. Belomestnykh, M. Billing, R. Chiang, E. Chojnacki, J. Kirchgessner, D. Moffat, H. Padamsee, M. Pisharody, D. Rubin, M. Tigner.....	3294	RAQ04
A New Analytical Model for Axi-symmetric Cavities — D. Burrini, C. Pagani, L. Serafini.....	3297	RAQ05
Impurity Growth in Single Bunch Operation of PF — M. Tobiyama, A. Higuchi, T. Mitsuhashi, T. Kasuga, S. Sakanaka.....	3300	RAQ06
Coupling Impedance of a Periodic Array of Diaphragms — G.V. Stupakov.....	3303	RAQ09
Coupling Impedance of a Long Slot and an Array of Slots in a Circular Vacuum Chamber — G.V. Stupakov.....	3306	RAQ10
Dark Currents for CEBAF Linacs — Byung C. Yunn	3309	RAQ11
Improvements in Bunch Coalescing in the Fermilab Main Ring — J. Dey, I. Kourbanis, D. Wildman	3312	RAQ13
Slow Extraction of Particles Using a Thin Target for Driving for Resonance — Yu. Severgin, W. Belov, A. Makarov, M. Tarovik.....	3315	RAQ14
Properties of a Transverse Damping System, Calculated by a Simple Matrix Formalism — S. Koscielniak, H.J. Tran.....	3317	RAQ15
A Concept for Emittance Reduction of DC Radioactive Heavy-Ion Beams — J.A. Nolen, J.C. Dooling.....	3320	RAQ16

Measurements of the Octupole-Induced Amplitude-Dependent Frequency Shift in SPEAR — <i>P. Tran, C. Pellegrini, J. Yang, M. Cornacchia, J. Corbett</i>	3323	RAQ17
Radiation Damping in Focusing-Dominated Systems — <i>Zhirong Huang, Pisin Chen, Ronald D. Ruth</i>	3326	RAQ18
Colliding Crystalline Beams — <i>A.F. Haffmans, D. Maletic, A.G. Ruggiero</i>	3329	RAQ20
Helical Spin Rotators and Snakes for RHIC — <i>V.I. Ptitsin, Yu.M. Shatunov, S. Peggs</i>	3331	RAQ21
Effects of Enhanced Chromatic Nonlinearity during the AGS gt-Jump — <i>J. Wei, J.M. Brennan, L.A. Ahrens, M.M. Blaskiewicz, D.-P. Deng, W.W. MacKay, S. Peggs, T. Satogata, D. Trbojevic, A. Warner, W.K. van Asselt</i>	3334	RAQ22
Effect of Parametric Resonances on the Bunched Beam Dilution Mechanism — <i>L. Wang, M. Ball, B. Brabson, J. Budnick, D.D. Caussyn, G. East, M. Ellison, X. Kang, S.Y. Lee, D. Li, J.Y. Liu, K.Y. Ng, A. Pei, A. Riabko, D. Rich, T. Sloan, M. Syphers</i>	3337	RAQ23
Parametric Resonances and Stochastic Layer Induced by A Phase Modulation — <i>J.Y. Liu, M. Ball, B. Brabson, J. Budnick, D.D. Caussyn, P. Colestock, V. Derenchuk, G. East, M. Ellison, D. Friesel, B. Hamilton, W.P. Jones, X. Kang, S.Y. Lee, D. Li, K.Y. Ng, A. Pei, A. Riabko, T. Sloan, M. Syphers, L. Wang</i>	3340	RAQ24
Nonlinear Space Charge Effect of Gaussian Type Bunched Beam in Linac — <i>Yinbao Chen, Shinian Fu, Zhibin Huang, Zhenhai Zhang</i>	3343	RAQ25
Emittance Growth Caused by Bunched Beam with Nonuniform Distributions in Both Longitudinal and Transverse Directions in Linac — <i>Zhibin Huang, Yinbao Chen, Shinian Fu</i>	3346	RAQ26
The Envelopes of Beam Motion in the Charged Particle Cyclic Accelerator — <i>Yu.P. Virchenko, Yu.N. Grigor'ev</i>	3349	RAQ28
A Semi-analytical Approach to the Design of Low Energy Cylindrically Symmetric Transport Lines — <i>Pedro F. Tavares</i>	3352	RAQ29
Stability of Trapped Ions in Electron Storage Rings in View of Parametric Resonance — <i>Y. Miyahara</i>	3355	RAQ30
Entropy and Emittance of Particle and Photon Beams — <i>K.-J. Kim, R.G. Littlejohn</i>	3358	RAR02
Effect of the Coupling Slots on Beam Dynamics in Accelerator Structure of Moscow CW RTM — <i>V.I. Shvedunov, A.S. Alimov, A.S. Chepurinov, O.V. Chubarov, D.I. Ermakov, A.V. Tiunov, P.L. Tkachev</i>	3361	RAR04
The Electron Beam Orbit Sensitivity on the Photon Flux of the Photon Beam Line — <i>Ian Hsu, G.H. Luo, K.L. Tsang, C.C. Chu, C.I. Yu, W.T. Weng, S.C. Chung</i>	3364	RAR05
Ground Motion in LEP and LHC — <i>L. Vos</i>	3367	RAR07
Cosmic Particle Acceleration at Very High Energies — <i>K.O. Thielheim</i>	3370	RAR09
Trapped Modes in the Vacuum Chamber of an Arbitrary Cross Section — <i>Sergey S. Kurennoy, Gennady V. Stupakov</i>	3373	RAR11
A General Approach for Calculating Coupling Impedances of Small Discontinuities — <i>Sergey S. Kurennoy, Robert L. Gluckstern, Gennady V. Stupakov</i>	3376	RAR12
Polarizabilities of an Annular Cut and Coupling Impedances of Button-Type Beam Position Monitors — <i>Sergey S. Kurennoy</i>	3379	RAR13
The Effect of Coupling on Luminosity — <i>D. Sagan</i>	3382	RAR15
RFQ-DTL Matching Solutions for Different Requirements — <i>D. Raparia</i>	3385	RAR16
Low-Dispersion γ Jump for the Main Injector — <i>K.Y. Ng, A. Bogacz</i>	3388	RAR17
Wakefields and HOMs Studies of a Superconducting Cavity Module with the CESR Beam — <i>S. Belomestnykh, W. Hartung, G. Flynn, J. Kirchgessner, H. Padamsee, M. Pisharody</i>	3391	RAR18
Comparison of the Predicted and Measured Loss Factor of the Superconducting Cavity Assembly for the CESR Upgrade — <i>S. Belomestnykh, W. Hartung, J. Kirchgessner, D. Moffat, H. Muller, H. Padamsee, V. Veshcherevich</i>	3394	RAR19
Control of Trapped Ion Instabilities in the Fermilab Antiproton Accumulator — <i>Steven J. Werkema</i>	3397	RAR20
Longitudinal Emittance Oscillation in a Superconducting Drift Tube Linac — <i>J.W. Kim, K.W. Shepard</i>	3400	RAR21
Electric Fields, Electron Production, and Electron Motion at the Stripper Foil in the Los Alamos Proton Storage Ring — <i>M. Plum</i>	3403	RAR22
Electron Clearing in the Los Alamos Proton Storage Ring — <i>M. Plum, J. Allen, M. Borden, D. Fitzgerald, R. Macek, T.S. Wang</i>	3406	RAR23

Advanced Photon Source Insertion Device Field Quality and Multipole Error Specification — <i>Yong-Chul Chae, Glenn Decker</i>	3409	RAR24
Study of Field Ionization in the Charge Exchange Injection for the IPNS Upgrade — <i>Yong-Chul Chae, Yanglai Cho</i>	3412	RAR25
Lattice Considerations for a Tau-Charm Factory — <i>L.C. Teng, E.A. Crosbie</i>	3415	RAR26
Effects of Vertical Aperture on Beam Lifetime at the Advanced Photon Source (APS) Storage Ring — <i>Hana M. Bizek</i>	3418	RAR27
Rebucketing After Transition in RHIC — <i>D.-P. Deng, S. Peggs</i>	3421	RAR29
Closed-Orbit Drifts in HERA in Correlation with Ground Motion — <i>V. Shiltsev, B. Baklakov,</i> <i>P. Lebedev, C. Montag, J. Rossbach</i>	3424	RAR30
Simulation of the Acceleration of Polarized Protons in Circular Accelerators — <i>Yu. Shatunov, V. Yakimenko</i>	3427	RAR31

REDUCTION OF NON LINEAR RESONANCE EXCITATION FROM INSERTION DEVICES IN THE ALS*

D. Robin, G. Krebs, G. Portmann, A. Zholents, Lawrence Berkeley Laboratory, Berkeley CA 94720 USA, and W. Decking, DESY, Hamburg, Germany

Abstract

Theoretical studies of Lawrence Berkeley Laboratory's Advanced Light Source (ALS) storage ring predict strong field insertion devices will break the rings symmetry, increasing resonance excitation that may reduce the dynamic aperture and thus the beam lifetime. We have embarked on an experimental program to study the strength of nonlinear resonance excitation in the ALS when insertion devices are present. We observe an enhancement in the resonance excitation of a third-order resonance when the gap of the insertion device is narrowed. We also find that it is possible to suppress this resonance by detuning two quadrupoles on either side of the insertion device. The results of this study are presented in this paper.

I. INTRODUCTION

The ALS is one of the first members of a new family of synchrotron light sources called third-generation light sources. These new light sources are designed to generate a small beam emittance to enhance the brightness of the radiation emitted from insertion devices. In these rings the natural chromaticity is very large. This is due to the strong focussing quadrupole magnets that provide the small emittances. As a result strong sextupole magnets are necessary to correct the rings natural chromaticity.

The effects of alignment errors, magnetic field imperfections and insertion devices (undulators and wigglers) on the size of the dynamic aperture has been studied theoretically[1][2][3]. These studies have shown that the single most important parameter in causing the reduction in dynamic aperture is the distortion of the periodic betatron phase between the sextupole magnets. The linear focussing of an insertion device can distort the betatron phase to a such a degree that the resulting reduction in the dynamic aperture is greater than a lattice with random magnetic errors but no insertion device. Several linear compensation schemes were studied showing that the dynamic aperture can be restored to a large degree by using a global matching technique to minimize the distortion of the betatron phase[4]. In a earlier study [5] we observed the onset of resonances when the symmetry of the lattice was broken by deliberately detuning one quadrupole.

In this paper we report on the results of an experiment where we observe the onset of resonances when an insertion device is closed. By carefully adjusting a few select quadrupoles near the insertion device we were able to suppress a third order resonance to the same level when the undulator gap was fully open.

II. OBSERVING STRUCTURAL RESONANCES

When excited, structural resonances may alter the behavior of particles in the beams tail. Resonances may cause particles to increase and decrease their transverse amplitudes or to be trapped at large amplitudes. Therefore by monitoring changes in the beam tails as the betatron tunes are varied, it is possible to observe the onset of resonances.

The way in which we monitor the tails is by limiting the transverse physical aperture with a beam scraper and measuring the beam lifetime as a function of betatron tunes. If resonances are present in the vicinity of the tunes, more particles will hit the scraper when they make large amplitude excursions resulting in a shorter beam lifetime. If resonances are not present, fewer particles will hit the scraper resulting in a longer beam lifetime. Thus if we vary the betatron tunes while simultaneously observing the beam lifetime we will see the lifetime drop when we move onto excited resonances.

A. Experimental Method and Apparatus

The experimental technique was very similar to that used in VEPP-4 [6]—to measure the effect of the beam-beam force on the tails of the beam. A detector consisting of two plastic scintillators with photomultiplier tube outputs in coincidence (γ -telescope) was located just down-stream of a horizontal scraper. The γ -telescope detected gamma radiation emitted when electrons hit the scraper. The count rate detected is proportional to the rate at which particles hit the scraper and is related to the beam lifetime in the following way:

$$\text{Beam Lifetime} \propto \frac{\text{Beam Current}}{\text{Detector Count Rate}} \quad (1)$$

We measure beam lifetime versus beam current and γ -telescope count rate and found that equation 1 was valid between beam lifetimes of 1 to 12 hours (see figure 1). Therefore by observing the change in the ratio of the beam current to the detector count rate as a function of betatron tune we were able to observe the onset of resonances. Because of the high counting rate of the detector ($\sim 1\text{MHz}$), this technique is a faster and more accurate method of measuring changes in the beam lifetime than the more direct lifetime measurement of beam current verses time.

Our experimental procedure was the following. We would first change the tunes by changing two families of quadrupoles according to a previously measured transfer matrix. After the quadrupole fields settled we measured the beam current and the count rate in the detector for a 1 second interval. The whole process was automated and took about 2 seconds per tune point. In order to check how well our predicted tunes agreed with the measured tunes we periodically measured the tunes.

*Work supported by the Director, Office of Energy Research, Office of Basic Energy Sciences, Material Sciences Division, U.S. Department of Energy, under Contract No. DEAC03-76SF00098

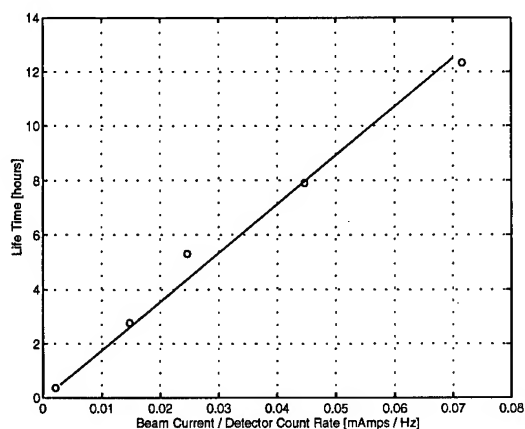


Figure 1. Relationship between the beam lifetime and the detector count rate.

III. TUNE SCANS

We chose to scan in a region of tune space where two resonances are present: $5\nu_x = 72$ and $3\nu_x = 43$ (see figure 2). The resonance $5\nu_x = 72$ is allowed by the rings natural 12-fold symmetry. However the resonance $3\nu_x = 43$ is unallowed unless the 12-fold symmetry is broken. The $3\nu_x$ resonance is very sensitive to lattice errors because the strength of the resonance is linearly proportional to the strength of the sextupoles. Therefore even small lattice errors can cause an observable enhancement in that resonance.

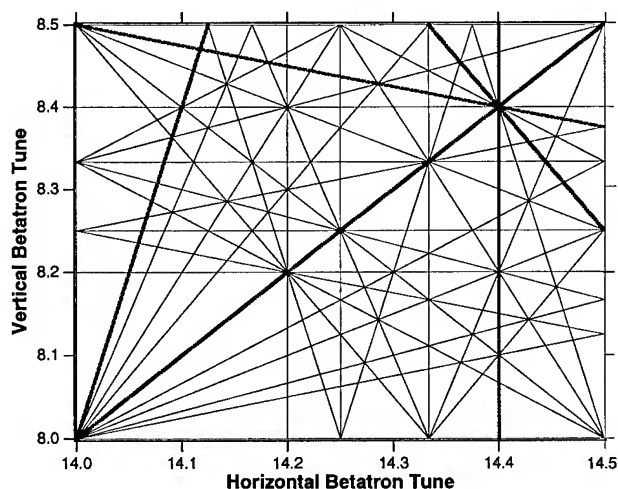


Figure 2. Tune portrait of all betatron resonances up to fifth order. The thicker lines are the allowed resonances.

A. The "Unperturbed" Machine

The first scan was made with the undulator gaps fully open. The scan covered a rectangular region in tune space ($14.3 < \nu_x < 14.45$ and $8.155 < \nu_y < 8.270$). Within this region we scanned 150 horizontal tune values by 10 vertical tune values ($\Delta\nu_x$ steps of 0.001 by $\Delta\nu_y$ steps of 0.012).

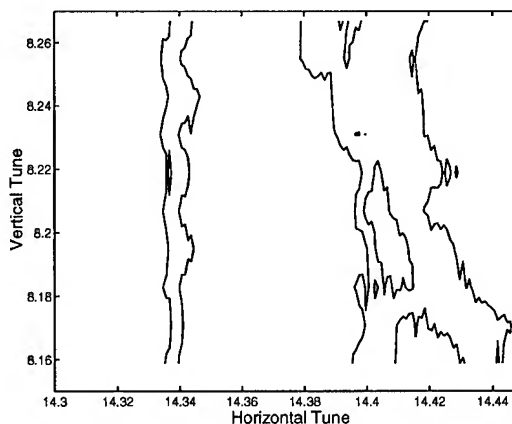


Figure 3. Contour plot of the tune scan. Three resonances were clearly seen.

All the quadrupoles in each family were set to the same current value and all the insertion device gaps were open. Figure 3 shows the results of the scan. Three resonances can be seen in the scan:

$5\nu_x = 72$	(allowed)
$3\nu_x = 43$	(unallowed)
$2\nu_x + \nu_y = 37$	(unallowed)

B. Symmetry Breaking by Detuning 2 Quadrupoles

Next we investigated the effect of detuning two quadrupoles symmetrically on either side of the sector 7 straight section. We scanned horizontally in tune ($\Delta\nu_x$ steps of 0.001) keeping the vertical tune constant ($\nu_y = 8.15$). We found that as the amount of quadrupole detuning increases there was an enhancement in the $3\nu_x$ resonance (see figure 4). In fact when the magnets were detuned by more than $\pm 2.5\%$, it was not possible to cross the $3\nu_x$ resonance without losing a good fraction of the beam.

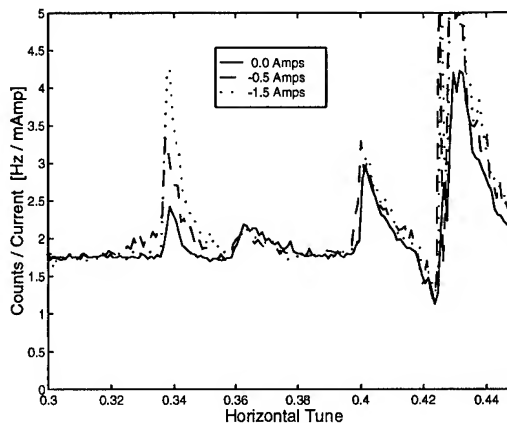


Figure 4. Horizontal tune scans ($\nu_y = 8.15$) for undulator 7 gap open, closed and closed with QDs detuned.

C. Resonance Excitation from the Sector 7 Undulator

We then investigated the effect of narrowing the gap of the U5 undulator in straight section 7. This undulator consists of 89 periods of 5 cm each. When the undulator is at its minimum gap (14 mm) there is a peak field on axis of ~ 1 T.

When the undulator gap was narrowed to 14mm we measured orbit, tunes, beta-functions, and resonance excitations and compared them with measurements taken when the gap was fully open. We found that the change in orbit was less than $100\text{ }\mu\text{m}$ in both planes. We measured a horizontal tune shift of $\Delta\nu_x = 0.003$ and a vertical tune shift of $\Delta\nu_y = 0.02$. By changing individual quadrupole fields and measuring tune changes we found a 10% change in the beating of the vertical beta function. (We were unable to measure the change in the horizontal beta function because the change was smaller than the resolution of our measurement.) At minimum gap there was an enhancement of the $3\nu_x$ resonance (see figure 5). However there is no enhancement of the $5\nu_x$ resonance.

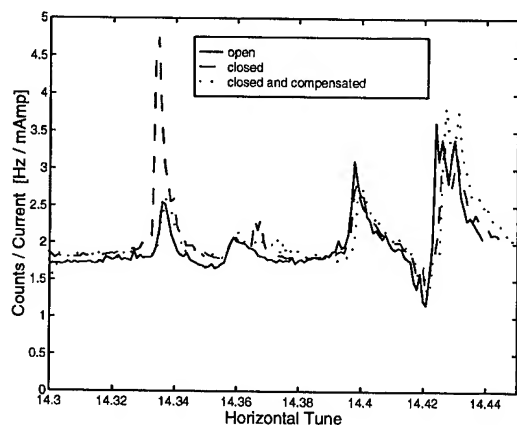


Figure 5. Compensation of the $3\nu_x$ resonance ($\nu_x = 14.3333$).

In order to suppress the excited $3\nu_x$ resonance we detuned two quadrupoles on either side of the undulator. (These are the same quadrupoles which were discussed in the previous section.) These two quadrupoles were chosen because simulations predicted they would be very effective at suppressing the beta beat and phase distortion.

We found that by detuning the quadrupoles we are able to suppress the resonance (see figure 5). The optimal value of detuning the quadrupoles was found to be about -1% . The resonance was suppressed to the same level when the undulator gaps were fully open (see figure 5).

IV. INTERPRETATION OF THE RESULTS

The condition for minimum resonance excitation corresponded to a quadrupole detuning of -1% . Since we did not have a direct measurement of the distortion of the horizontal betatron function we tried to infer the distortion indirectly by introducing a quadrupole component in the model of our undulator which generated the measured horizontal tune shift. From the model we then extracted the distortion of the betatron function, about $+2\%$. Furthermore from the model we predict the settings for the quadrupoles which minimized this distortion. To minimize the distortion the model predicted that the quadrupoles should be detuned by $+2\%$. This optimal detuning is opposite in sign from what was found experimentally (-1%).

We repeated these measurements on several occasions with similar results. Moreover we found a similar result on another undulator in the ring (U8 in sector 9). In order to resolve this

conflict we intend to look at the effects of vertical resonances because the distortion of the betatron amplitude and phase is larger in the vertical plane and are directly measurable.

Acknowledgments

We would like to thank M. Chin for helping us to automate the tune measurement system and A. Jackson for useful discussions and encouragement.

References

- [1] A. Jackson, "Effects of Undulators on the ALS-Early work at LBL", LBL-25888, May 1988.
- [2] M. Zisman, "Full Linear Compensation of ALS Undulators", LBL-ESG Note-65, December 1988.
- [3] A. Jackson, et. al., "The effects of Insertion Devices on Beam Dynamics in the ALS", Proceedings of the Particle Accelerator Conference, 1752-1754, (1989).
- [4] J. Bengtsson and E. Forest, "Global Matching of the Normalized Ring", Advanced Beam Dynamics Workshop on Effects of Errors in Accelerators, Their Diagnosis and Corrections, AIP Conference Proceedings No. 255, 229-233, (1991).
- [5] D. Robin, et. al. "Observation of Non Linear Resonances in the ALS", Proceedings of the Workshop on Non Linear Dynamics in Particle Accelerators: Theory and Experiments, Arcidosso, Italy (1994)—to be published.
- [6] A. B. Temnykh, "Observation of Beam-beam Effects on Vepp-4", Third Advanced ICFA Beam Dynamics Workshop on Beam-Beam Effects in Circular Colliders", Akademgorodok, Novosibirsk, 5 - 11 (1989).

SUM BETATRON RESONANCES UNDER LINEAR COUPLING OF OSCILLATIONS

P.N. Chirkov and I.I. Petrenko, IHEP, Protvino, Moscow Region, 142 284, Russia

Abstract

The joint effect of an arbitrary sum resonance and a linear coupling resonance $Q_y - Q_x = 0$ on stability of betatron oscillations in a circular accelerator is studied. The presence of linear coupling is shown to result in splitting of the cluster of sum resonance straight-lines into a family of hyperbolic curves. The analytic results obtained are verified by numerical simulations.

I. INTRODUCTION

At present, the design employed of SC dipoles for high energy accelerators does not ensure the small enough values of the skew quadrupole field errors, Refs.[1],[2]. This gradient brings about the major contribution to linear coupling between horizontal (x) and vertical (y) betatron oscillations.

The effect of this coupling on the motion has been studied in many papers (refer, say, to Refs.[3]–[8]) of which we would distinguish quite a rigorous and consistent Ref.[8]. These papers treat the problem in terms of normal oscillation modes and the relevant tunes $Q_{1,2}$, the latter being quite distinct from the unperturbed betatron tunes $Q_{x,y}$. However, to analyze the joint effect of linear coupling and magnetic nonlinearities, it might be more convenient to employ x, y -modes of the unperturbed oscillations.

In frames of the first-order perturbation approach, linear coupling shows itself up as an excitation of sum and difference resonances $Q_y \pm Q_x = k$. Being treated isolately from the other resonances, the linear difference resonance is, by itself, not dangerous for the motion of beam with equal betatron x - and y -emittances. The total energy of 2-D oscillations being kept intact, this resonance gives rise to energy exchange between x - and y -directions. Nonetheless, such a resonance can result in an unstable motion in the presence of an additional sum resonance (not necessarily driven by the skew quadrupole) which is far enough from the working point not to inflict any danger, provided the 'switched-off' linear difference resonance.

The common vision that the loss of stability occurs only on the condition $\vec{n}\vec{Q} = k$ being satisfied seems to be not quite the case. It does hold true for the isolated sum resonance, given there exists only one such a resonant straight line in plane $\{Q_x, Q_y\}$ near the working point. By a simple example of joint action of an arbitrary n -th order sum resonance and a linear difference resonance, it would be shown here that there exists a family of $(n+1)$ hyperbolic curves in the betatron tune plane at which the loss of stability is possible.

II. ANALYTIC RESULTS

A. Betatron Oscillations of the Reference Particle

Components $h_{x,y}$ of the magnetic field imperfections are expressed in terms of the longitudinal vector potential A_s :

$$h_x = -\partial A_s / \partial y, \quad h_y = \partial A_s / \partial x,$$

$$A_s(x, y, s) = \sum_{n=0}^{\infty} \frac{\Delta H_{y,n} + i\Delta H_{x,n}}{2r^n(n+1)} (x + iy)^{n+1} + \text{c.c.}$$

where $\Delta H_{y,n}(s), \Delta H_{x,n}(s)$ are additions to the field introduced by the n -th order normal and skew nonlinearities, respectively, taken at $(x = r, y = 0)$; r is a reference radius.

Up to the first order in perturbation, equations of betatron motion of the on-momentum particle in such a field acquire the canonical form, Ref.[9]:

$$\begin{aligned} \frac{dI_\zeta}{d\theta} &= -\frac{\partial \langle D \rangle}{\partial \eta_\zeta}, & \frac{d\eta_\zeta}{d\theta} &= \frac{\partial \langle D \rangle}{\partial I_\zeta}, \\ D &= \frac{2\beta_{max} R_0}{r^2 H R} A_s(\zeta, \theta), \\ \zeta &= r \sqrt{\beta_\zeta(\theta) / \beta_{max}} \sqrt{I_\zeta} \cos(\mu_\zeta(\theta) + \eta_\zeta) \end{aligned} \quad (1)$$

where ζ is an equation symbol for either x or y ; R_0 and R are the average and curvature radii, respectively, of the reference orbit in field H ; θ is a generalized azimuth which may be expressed by the longitudinal coordinate s as $\theta = s/R_0$; $\beta_\zeta(\theta)$ is beta-function and $\mu_\zeta = Q_\zeta \theta + \chi_\zeta$ is unperturbed phase with a periodic part $\chi_\zeta(\theta)$. Thus, $\sqrt{I_\zeta}$ is the ζ -oscillation amplitude normalized to r and taken at azimuth where $\beta_\zeta = \beta_{max}$. The operator $\langle \dots \rangle$ denoting the averaging over θ removes fast harmonics.

By taking into account the periodic dependence of D on $\vec{\mu} = (\mu_x, \mu_y)$ and azimuth θ , one can put down

$$\begin{aligned} D &= \sum_{k=-\infty}^{\infty} \sum_{\vec{n}} D_{\vec{n},k}(I_x, I_y) \exp\{i(\vec{n}\vec{Q} - k)\theta + i\vec{n}\vec{\eta}\} \\ D_{\vec{n},k} &= \frac{1}{(2\pi)^3} \int_0^{2\pi} \int_0^{2\pi} \int_0^{2\pi} D \left\{ r \sqrt{\frac{\beta_\zeta(\theta)}{\beta_{max}}} \sqrt{I_\zeta} \cos \alpha_\zeta, \theta \right\} \\ &\times \exp\{i[k\theta + \vec{n}\vec{\chi}(\theta) - \vec{n}\vec{\alpha}]\} d\alpha_x d\alpha_y d\theta \end{aligned}$$

where $\vec{n} = (n_x, n_y)$, $n_{x,y}, k$ are integers.

The resonant harmonics enter $\langle D \rangle$ as complex conjugated pairs, $\{\vec{n}, k\}$ and $\{-\vec{n}, -k\}$, which are responsible for excitation of $\vec{n}\vec{Q} = k$ resonance. The infinite increase of the total energy $I = I_x + I_y$ is possible under the impact of the isolated sum resonance \vec{n} with $n_x \cdot n_y > 0$. Due to this reason, the 1-D resonances $\vec{n} = (n_x, 0)$ and $\vec{n} = (0, n_y)$ should rather be treated as sum ones. Simplify expression for amplitude $D_{\vec{n},k}$ of the resonant harmonic by retaining the contribution only from the nonlinearity of minimal power allowed for the given order of resonance. Then

$$D_{\vec{n},k} = P_{\vec{n},k} \sqrt{I_x^{n_x} I_y^{n_y}},$$

$$P_{\vec{n},k} = \frac{\beta_{max} R_0}{\pi r n} \binom{n}{|n_y|} \int_0^{2\pi} W_{\vec{n}} \sqrt{\frac{\beta_x^{n_x} \beta_y^{n_y}}{(4\beta_{max})^n}} e^{i(k\theta + \vec{n}\vec{x})} d\theta$$

$$W_{\vec{n}} = \left\{ \frac{\Delta H_{y,n-1}}{RH} \cos \frac{\pi}{2} |n_y| - \frac{\Delta H_{x,n-1}}{RH} \sin \frac{\pi}{2} |n_y| \right\}$$

where $n = |n_x| + |n_y|$ is the order of a resonance.

Let the cross-point \vec{Q}_* of the n -th order sum resonance with the line of difference resonance $\vec{m}\vec{Q} = p$, $\vec{m} = (-1, 1)$ be referred to as the n -th order cluster. No more than $(n+1)$ sum resonances of n -th order can cross such a node: $\vec{n} = (n-j, j)$ where $j = 0, \dots, n$. All these resonances can be driven by the same $(n-1)$ -th power field nonlinearity.

The joint effect of a sum resonance \vec{n} and a difference resonance \vec{m} near \vec{Q}_* is described in terms of variables $\{\vec{I}, \vec{\eta}\}$ through the canonical Eqs.1 with Hamiltonian:

$$\langle D \rangle = \{P_{\vec{m},p} e^{i\vec{m}\vec{w}} + \text{c.c.}\} \sqrt{I_x I_y} + \{P_{\vec{n},k} e^{i\vec{n}\vec{w}} + \text{c.c.}\} \sqrt{I_x^{n_x} I_y^{n_y}} \quad (2)$$

where $\vec{w} = \vec{\delta}\theta + \vec{\eta}$; $\vec{\delta} = (\vec{Q} - \vec{Q}_*)$ is the working point detuning from the cluster; $n_{x,y} \geq 0$.

B. Effect of Isolated Difference Resonance \vec{m}

Study of motion in the vicinity of the isolated difference resonance \vec{m} shows that any particle has its $I_{x,y}$ varying harmonically with a frequency $2\omega = 2\sqrt{|P_{\vec{m},p}|^2 + (\vec{m}\vec{\delta}/2)^2}$. Frequency ω does not depend on oscillation phase and amplitude, which allows one to transfer to new variables $I_{1,2}$ and $\eta_{1,2}$, the latter being the integrals of motion,

$$\begin{pmatrix} \sqrt{I_x} e^{i\eta_x} \\ \sqrt{I_y} e^{i\eta_y} \end{pmatrix} = T(\psi) M(\alpha) T(-\omega\theta) \begin{pmatrix} \sqrt{I_1} e^{i\eta_1} \\ \sqrt{I_2} e^{i\eta_2} \end{pmatrix} \quad (3)$$

$$T(\psi) = \begin{pmatrix} e^{i\psi} & 0 \\ 0 & e^{-i\psi} \end{pmatrix}, \quad M(\alpha) = \begin{pmatrix} \cos \alpha & \sin \alpha \\ -\sin \alpha & \cos \alpha \end{pmatrix}$$

$$2\psi = \vec{m}\vec{\delta}\theta + \arg P_{\vec{m},p}, \quad \tan \alpha = \frac{|P_{\vec{m},p}|}{\omega + \vec{m}\vec{\delta}/2}, \quad 0 < \alpha < \pi/2.$$

Transformation by Eq.3 does not change expression for the total energy $I = I_x + I_y = I_1 + I_2$.

C. Effect of Difference Resonance and Sum Resonance

Whenever simultaneous effect of a sum, \vec{n} , and a difference, \vec{m} , resonances in the neighborhood of the n -th order cluster is taken into account, the quantities $I_{1,2}$, $\eta_{1,2}$ would no longer be integrals of motion. Still, the use of these variables as independent ones allows us to transfer from Hamiltonian, Eq.2, to a new one, \mathcal{K} , in terms of which the resonance \vec{m} would be formally absent. According to Eqs.1, 3, on being put down in terms of new variables, the Eqs. of motion would retain their canonical nature:

$$\frac{dI_i}{d\theta} = -\frac{\partial \mathcal{K}}{\partial \eta_i}, \quad \frac{d\eta_i}{d\theta} = \frac{\partial \mathcal{K}}{\partial I_i}, \quad i = 1, 2 \quad (4)$$

$$\mathcal{K} = \sum_{j=0}^n \mathcal{K}_{\vec{n},j} = \sum_{j=0}^n \sqrt{I_1^j I_2^{n-j}} \times$$

$$\times \{ \mathcal{F}_{\vec{n},j} \exp\{i[n\varepsilon_{n,j}\theta + j\eta_1 + (n-j)\eta_2]\} + \text{c.c.}\}$$

$$\mathcal{F}_{\vec{n},j} = P_{\vec{n},k} \rho_{\vec{n},j} \exp\{i(n_x - n_y)(\arg P_{\vec{m},p})/2\}$$

$$\rho_{\vec{n},j} = \sum_{l=l_{\min}}^{l_{\max}} (-1)^l \binom{n_y}{l} \binom{n_x}{j-l} \times$$

$$\times (\cos \alpha)^{n_y+j-2l} (\sin \alpha)^{n_x-j+2l}$$

$$l_{\min} = \max\{0; j - n_x\}, \quad l_{\max} = \min\{j; n_y\}$$

$$\varepsilon_{n,j} = (\delta_x + \delta_y)/2 + \omega(1 - 2j/n)$$

Any of $\mathcal{K}_{\vec{n},j}$ can result in an infinite increase of the total energy of oscillations, given certain resonant conditions are fulfilled. In absence of a difference resonance \vec{m} there would have been a single straight line $\vec{n}\vec{\delta} = 0$ in the plane $\{\delta_x, \delta_y\}$. However, on this resonance being taken into account, a set of $(n+1)$ resonant curves $\varepsilon_{n,j} = 0$ emerge. These curves are given parametrically through Eqs. to follow,

$$\begin{pmatrix} \delta_x \\ \delta_y \end{pmatrix} = -\frac{|P_{\vec{m},p}|}{\sin 2\alpha} \left\{ \begin{pmatrix} +1 \\ -1 \end{pmatrix} \cos 2\alpha + \begin{pmatrix} 1 \\ 1 \end{pmatrix} (1 - 2j/n) \right\}$$

Depending solely on the cluster order n , these curves form a family of hyperboles with asymptotes being given by $\delta_y + \delta_x + |\delta_y - \delta_x|(1 - 2j/n) = 0$. It can be easily found that the asymptotes coincide with resonant lines of all the n -th order sum resonances which may cross the cluster in question. Thus, the 'switching-on' of the difference resonance yields splitting of the sum resonance's cluster.

Figs.1a,b, where Δ_c designates $\delta_c/|P_{\vec{m},p}|$, show the splitting of sum resonances $\vec{n} = (1, 1)$ and $\vec{n} = (3, 0)$ driven by a skew field gradient and a normal sextupole, respectively. The width of split resonant lines is chosen as proportional to $\rho_{\vec{n},j}$.

III. COMPUTER SIMULATION

Assume the field imperfections that excite resonances \vec{n} and \vec{m} under study be localized at the quadrupole centers of all N cells of an accelerator. Suppose, that at these centers the following conditions are met: $\beta_{x,foc} = \beta_{y,def} = \beta_{max}$, $\beta_{x,def} = \beta_{y,foc} = \beta_{min}$, betatron phase advance between centers of adjacent F- and D-quads being the same. Take the following parameter values appropriate to the UNK case: $N = 160$, $r = 35$ mm, $\beta_{max} = 152$ m, $\beta_{min} = 32$ m. Distribute field imperfections along the lattice so as to excite in the vicinity of the working point only a sum resonance \vec{n} and a linear difference resonance \vec{m} with $\arg P_{\vec{n},k} = 0$ and $\arg P_{\vec{m},p} = 0$.

A. Joint Effect of $\vec{n} = (1, 1)$ and $\vec{m} = (-1, 1)$

Effect of these two resonances treated in variables $I_{1,2}$, $\eta_{1,2}$ results in emerging of three split resonant lines in plane $\{\delta_x, \delta_y\}$, see Fig.1a. Take the split resonance $j = 2$ and treat it separately from the others. In such a case

$$\mathcal{K} \simeq \mathcal{K}_{\vec{n},2} = -I_1 \{|P_{\vec{n},k}| \cdot \sin 2\alpha\} \cos(2\varepsilon_{2,2}\theta + 2\eta_1) \quad (5)$$

and, thus, I_2 and η_2 are kept intact, i.e. $I_2(\theta) = I_2(0)$ and $\eta_2(\theta) = \eta_2(0)$. Put the working point exactly at the resonant

curve $\varepsilon_{2,2}(\alpha) = 0$. Then Eqs.4, 5 with $\eta_1(0) = \pm\pi/4$ yield $\eta_1(\theta) = \eta_1(0)$ and total energy at $I_2(0) = 0$ varying in accordance with

$$I(\theta) = I(0) \exp\{\pm 2|P_{\vec{n},k}| \sin 2\alpha \cdot \theta\} \quad (6)$$

For the preset values of $|P_{\vec{n},k}|$ and $|P_{\vec{m},p}|$ the skew gradient in l -th period is given by

$$\left(\frac{\Delta H_{x,1} \Delta s}{H R r}\right)_l = -\frac{2\pi/N}{\sqrt{\beta_{\max} \beta_{\min}}} \times \{ |P_{\vec{m},p}| + 2|P_{\vec{n},k}| \cos(\frac{2\pi k}{N}(l-t)) \} \quad (7)$$

where $t = 1/2$ and $t = 1$ for F- and D-quads, respectively. Fig.2 shows the values of $I(\theta)$ calculated via Eq.6, and via the numerical tracking during a hundred of turns with $|P_{\vec{n},k}| = 0.01$, $|P_{\vec{m},p}| = 0.1$, $I(0) = 1.0$ for $k = 73$, $p = 0$, $\alpha = 80^\circ$, i.e. $\delta_x = 0.56713$, $\delta_y = 0.01763$. The agreement of results is fairly well.

B. Joint Effect of $\vec{n} = (3, 0)$ and $\vec{m} = (-1, 1)$

As in the previous example, for isolated split resonance $j = 3$ one has

$$\mathcal{K} \simeq \mathcal{K}_{\vec{n},3} = I_1^{3/2} \{ |P_{\vec{n},k}| \cdot \cos^3 \alpha \} \cos(3\varepsilon_{3,3}(\alpha) \cdot \theta + 3\eta_1)$$

Herefrom, $I_2(\theta) = I_2(0)$, $\eta_2(\theta) = \eta_2(0)$, and, given the position of the working point exactly at the resonance line $\varepsilon_{3,3}(\alpha) = 0$ with initial values $\eta_1(0) = \pm\pi/6$, one gets $\eta_1(\theta) = \text{const.}$, while the expression for the total energy of oscillations at $I_2(0) = 0$ acquires the form of

$$I(\theta) = I(0) \cdot \{ 1 \mp 3\sqrt{I_0} |P_{\vec{n},k}| \cos^3 \alpha \cdot \theta \}^{-2} \quad (8)$$

For the preset values of $|P_{\vec{n},k}|$ and $|P_{\vec{m},p}|$ the distribution of the skew gradient is still given by Eq.7, provided a single difference resonance \vec{m} is excited, while the distribution of quadratic nonlinearity acquires the form of

$$\left(\frac{\Delta H_{y,2} \Delta s}{H R r}\right)_l = \frac{48\pi}{N} \frac{|P_{\vec{n},k}|}{\beta_{\max}^2 - \beta_{\min}^2} \times \begin{cases} \sqrt{\beta_{\max}^2} \cos\{\frac{2\pi k}{N}(l - \frac{1}{2})\} & \text{for F} \\ -\sqrt{\beta_{\max} \beta_{\min}} \cos\{\frac{2\pi k}{N}(l - 1)\} & \text{for D} \end{cases}$$

Fig.2b shows the values of the total energy $I(\theta)$ calculated with Eq.8 and numerical tracking results at $|P_{\vec{n},k}| = 0.01$, $|P_{\vec{m},p}| = 0.1$, $I(0) = 0.33$ for $k = 110$, $p = 0$, $\alpha = 80^\circ$, i.e. $\delta_x = 0.56713$, $\delta_y = 0.01763$. The quantitative disagreement of theory against the numerical results can be accounted for by the second-order effect introduced by the quadratic nonlinearity which were omitted in the analytical treatment. Nevertheless, at least the qualitative agreement is still satisfactory.

IV. CONCLUSION

The presence of linear difference resonance changes the location and shape of resonant lines in plane of unperturbed betatron tunes. Namely, the cluster of sum resonances is split into family of hyperbolic resonant curves. These split resonances are capable of increasing the total energy of oscillations and, thus, can decrease the dynamic aperture, which has been found in Ref.[8].

References

- [1] P.Schmüser, IEEE 1991 PAC, p.37, (1991).
- [2] S.Wolff, Preprint DESY, PMAG-90-01, (1990).
- [3] E.Courant, H.Snyder, Ann. of Physics, 3, p.1, (1958).
- [4] D.A.Edwards, L.C.Teng, IEEE Trans. on Nucl. Sci., NS-20, No.3, 1973.
- [5] G.Parzen, Proc. of the 3rd EPAC, V.1, p.655, (1992).
- [6] G.Parzen, ibid, p.658.
- [7] F.Willeke, G.Ripken, DESY 88-114, Hamburg (1988).
- [8] G.Ripken, F.Willeke, DESY 90-001, Hamburg (1990).
- [9] P.Chirkov, JINR: D9-89-801, p.109, Dubna (1989).

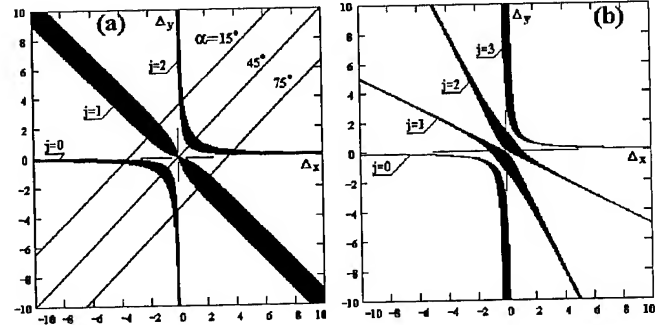


Figure 1. Splitting of sum resonances: $\vec{n} = (1, 1)$ (a), $\vec{n} = (3, 0)$ (b)

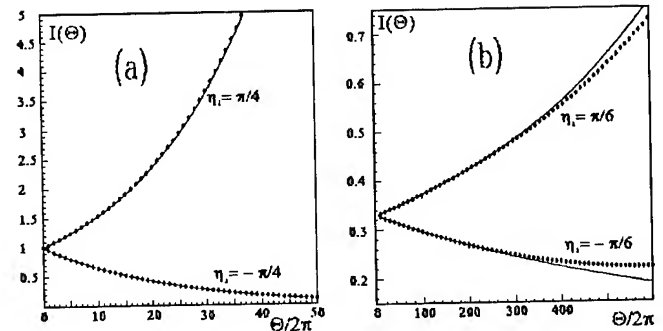


Figure 2. Comparison of theory (—) against tracking (o) for $\vec{n} = (1, 1)$ (a) and $\vec{n} = (3, 0)$ (b)

LINEAR ORBIT PARAMETERS FOR THE EXACT EQUATIONS OF MOTION*

G. Parzen, Brookhaven National Laboratory, Upton, NY 11973 USA

Abstract

This paper defines the beta function and other linear orbit parameters using the exact equations of motion. The β , α and ψ functions are redefined using the exact equations. Expressions are found for the transfer matrix and the emittance. The differential equations for $\eta = x/\beta^{1/2}$ is found. New relationships between α , β , ψ and ν are derived.

I. INTRODUCTION

This paper defines the beta function and the other linear orbit parameters using the exact equations of motion. The usual treatment [1] of the linear orbit parameters is based on the approximate equation of motion

$$\frac{d^2x}{ds^2} + K(s)x = 0 \quad (1)$$

Approximations are made in obtaining Eq. (1) which are usually valid for large accelerators.

The exact linearized equations of motion can be written as

$$\begin{aligned} \frac{dx}{ds} &= A_{11}x + A_{12}p_x \\ \frac{dp_x}{ds} &= A_{21}x + A_{22}p_x \end{aligned} \quad (2)$$

x and p_x are the canonical coordinates in a curvilinear coordinate system based on a reference orbit and the $A_{ij}(s)$ are periodic in s with period L . The approximate Eq. (1) assumes that $A_{11} = A_{22} = 0$, $A_{12} = 1$ and $A_{21} = -K(s)$. The exact values of the A_{ij} are given in [2].

A treatment of the linear orbit parameters based on the exact equations, Eqs. (2), rather than the approximate Eq. (1) may be desirable in the following situations:

1. Symplectic long term tracking using a procedure where the magnets are replaced by a sequence of point magnets and drift spaces. For the tracking to be symplectic, one has to use the solutions of the exact equations of motion. The linearized equations of motion then have the form of Eq. (2).
2. Small accelerators where the approximations made in deriving Eq. (1) may not be valid.

Many of the results found using the approximate equations carry over for the exact equations. A few of the changed results are the following:

$$\begin{aligned} \alpha &= \frac{1}{A_{12}} \left(-\frac{1}{2} \frac{d\beta}{ds} + A_{11}\beta \right) \\ \psi &= \int_0^s A_{12} \frac{ds}{\beta} \end{aligned} \quad (3)$$

$$\nu = \frac{1}{2\pi} \int_0^C ds \frac{A_{12}}{\beta}$$

where C is the circumference of the accelerator.

II. EIGENFUNCTIONS OF THE EXACT LINEAR EQUATIONS OF MOTION AND THE LINEAR ORBIT PARAMETERS

The problem now is, given the exact linear equations of motion, Eq. (2), how does one define the linear orbit parameters β , α , γ , ψ , ν and the emittance ϵ , and what are the relationships that hold between them. To do this, one has to repeat the well known treatment of the linear orbit parameters, and see where the definitions and relationships change for the exact equations. The treatment given below is believed to reduce the amount of algebraic manipulation required, and makes few assumptions about the A_{ij} coefficients in the linear equations.

For the x motion, the linear equations are written as

$$\begin{aligned} \frac{dx}{ds} &= A_{11}x + A_{12}p_x \\ \frac{dp_x}{ds} &= A_{21}p_x + A_{22}x \end{aligned} \quad (4)$$

The transfer matrix $M(s, s_0)$ obeys

$$\begin{aligned} x &= M(s, s_0)x_0 \\ x &= \begin{pmatrix} x \\ p_x \end{pmatrix} \\ \frac{d}{ds}M &= AM \end{aligned} \quad (5)$$

One may note that the symbol x is used in 2 different ways. The meaning of x should be clear from the context. The matrix M is symplectic as the equations of motions are derived from a hamiltonian. [1,3] Thus

$$\begin{aligned} M\bar{M} &= I \\ \bar{M} &= \tilde{M}^T S \\ S &= \begin{pmatrix} 0 & 1 \\ -1 & 0 \end{pmatrix}, \quad I = \begin{pmatrix} 1 & 0 \\ 0 & 1 \end{pmatrix} \end{aligned} \quad (6)$$

\tilde{S} is the transverse of S . Also $|M| = 1$; $|M|$ is the determinant of M .

The one period transfer matrix is defined by

$$\hat{M}(s) = M(s + L, s) \quad (7)$$

where L is the period of the A_{ij} in Eq. (4). One can show that $\hat{M}(s)$ and $\hat{M}(s_0)$ are related by

$$\hat{M}(s) = M(s, s_0)\hat{M}(s_0)M(s_0, s) \quad (8)$$

*Work performed under the auspices of the U.S. Department of Energy.

The eigenfunctions and eigenvalues of $\hat{M}(s)$ are defined by

$$\begin{aligned}\hat{M}(s)x &= \lambda x, \\ |\hat{M} - \lambda I| &= 0, \\ \lambda^2 - (m_{11} + m_{22})\lambda + 1 &= 0\end{aligned}\quad (9)$$

where m_{ij} are the elements of \hat{M} , and using $|\hat{M}| = 1$.

Eqs. (9) shows that the two eigenvalues λ_1, λ_2 obey

$$\lambda_1 \lambda_2 = 1, \quad (10)$$

and for stable motion, $|\lambda| = 1$ and $\lambda_2 = \lambda_1^*$, and we can write

$$\lambda_1 = \exp(i\mu) \quad (11)$$

Given the eigenfunction at s_0 , $x_1(s_0)$ one can find the eigenfunction or any other point s using

$$x_1(s) = M(s, s_0)x_1(s_0), \quad (12)$$

and $x_1(s)$ has the same eigenvalue λ_1 . This follows from Eq. (9), using Eq. (8) to relate $\hat{M}(s)$ and $\hat{M}(s_0)$. Also $x_1(s)$ obeys the linear equations of motion,

$$\frac{d}{ds}x_1 = Ax_1, \quad (13)$$

which follows from Eq. (12) and Eq. (5). One can show that

$$x_1(s)/\lambda_1^{s/L} = f_1(s), \quad (14)$$

where $f_1(s+L) = f_1(s)$. This follows from

$$\begin{aligned}f_1(s+L) &= x_1(s+L)/\lambda_1^{s/L+1} \\ &= \hat{M}(s)x_1(s)/\lambda_1^{s/L+1} = x_1(s)/\lambda_1^{s/L}\end{aligned}$$

Thus, one can write

$$\begin{aligned}x_1(s) &= \exp(i\mu s/L) f_1(s) \\ f_1(s+L) &= f_1(s)\end{aligned}\quad (15)$$

Eq. (15) can be rewritten as

$$\begin{aligned}x_1(s) &= \beta(s)^{1/2} \exp(i\psi) \\ \psi(s) &= \mu s/L + g_1(s) \\ g_1(s+L) &= g_1(s), \quad \beta(s+L) = \beta(s)\end{aligned}\quad (16)$$

Eq. (16) defines the beta functions, $\beta(s)$, except for a normalization multiplier, for the eigenfunction $x_1(s)$. The normalization multiplier will be defined below. It will be shown first that ψ and β are related. To find this relation, one uses the Lagrange invariant [1]

$$W = \tilde{x}_2 S x_1 \quad (17)$$

where x_1, x_2 are two solutions of the equations of motion. Eq. (17) corresponds to the Wronskian in the treatment of the approximate equations of motion. For x_1 and x_2 , we use the two eigenfunctions x_1 and $x_2 = x_1^*$.

$$x_1 = \begin{pmatrix} x_1 \\ p_{x1} \end{pmatrix} \quad (18)$$

For x_1 one uses Eq. (16) and for p_{x1} one finds from the equations of motion

$$p_{x1} = \frac{1}{A_{12}} \left(\frac{dx_1}{ds} - A_{11}x \right) \quad (19)$$

$$\begin{aligned}W &= x_2 p_{x1} - p_{x2} x_1 \\ W &= \left[x_2 \frac{dx_1}{ds} - x_1 \frac{dx_2}{ds} \right] \frac{1}{A_{12}} \\ W &= \frac{2i}{A_{12}} \beta \frac{d\psi}{ds}\end{aligned}\quad (20)$$

The beta function β is normalized by normalizing the eigenfunctions so that

$$W = \tilde{x}_1^* S x_1 = 2i \quad (21)$$

which gives

$$\frac{d\psi}{ds} = \frac{A_{12}}{\beta} \quad (22)$$

Eq. (22) replaces the familiar result $d\psi/ds = 1/\beta$ which is obtained when $A_{12} = 1$. From Eq. (22) one can find a result for the tune. Using $2\pi\nu = \psi(C) - \psi(0)$ where C is the circumference of the accelerator, one finds

$$\nu = \frac{1}{2\pi} \int_0^C ds \frac{A_{12}}{\beta} \quad (23)$$

From Eq. (19) we now find for p_{x1} ,

$$p_{x1} = \frac{1}{\beta^{1/2}} (i - \alpha) \exp(i\psi) \quad (24)$$

$$\alpha = \frac{1}{A_{12}} \left(-\frac{1}{2} \frac{d\beta}{ds} + A_{11}\beta \right) \quad (25)$$

Eq. (25) provides the new definition for the α parameter, which replaces the familiar result $\alpha = -\frac{1}{2} d\beta/ds$. At this point the definition of α may seem arbitrary. It will be seen to be the convenient definition of α when the emittance and transfer matrix are considered.

The eigenfunctions can now be written as, using Eq. (16) and Eq. (25),

$$\begin{aligned}x_1 &= \left[\frac{\beta^{1/2}}{\beta^{-1/2}(-\alpha + i)} \right] \exp(i\psi) \\ x_2 &= x_1^*\end{aligned}\quad (26)$$

For the results for the emittance and transfer matrix, see [2].

III. DIFFERENTIAL EQUATIONS FOR THE LINEAR ORBIT PARAMETERS

This section finds differential equations for β , and η

A. Second Order Differential Equation for x

From the first order differential equation for x, p_x , Eq. (4), one can eliminate p_x to find a second order equation for x . See [2] for details

$$\frac{d}{ds} \left(\frac{1}{A_{12}} \frac{dx}{ds} \right) + x \left(-A_{21} - \frac{d}{ds} \left(\frac{A_{11}}{A_{12}} \right) - \frac{A_{11}^2}{A_{12}} \right) = 0 \quad (27)$$

It has been assumed that $A_{11} = -A_{22}$.

B. Differential Equation for β

To find a differential equation for β , into Eq. (27) for x put the eigenfunction

$$\begin{aligned} x &= b \exp(i\psi) \\ b &= \beta^{1/2} \end{aligned} \quad (28)$$

We find then, see [2] for details,

$$\frac{d}{ds} \left(\frac{1}{A_{12}} \frac{db}{ds} \right) - \frac{A_{12}}{b^3} + b \left(-A_{21} - \frac{d}{ds} \left(\frac{A_{11}}{A_{12}} \right) - \frac{A_{11}^2}{A_{12}} \right) = 0 \quad (29)$$

Eq. (29) is a second order differential equation for $b = \beta^{1/2}$. It can be compared to the result found when $A_{12} = 1$ and $A_{11} = 0$,

$$\frac{d^2 b}{ds^2} - \frac{A_{12}}{b^3} = 0 \quad (30)$$

C. Differential Equation for η

η and x are related by

$$x = b \eta, \quad b = \beta^{1/2} \quad (31)$$

In the differential equation for η the independent variable is ψ or θ which are related to s by

$$\begin{aligned} d\psi &= A_{12} \frac{ds}{\beta} \\ d\theta &= A_{12} \frac{ds}{v\beta} \end{aligned} \quad (32)$$

We find dx/ds and $d(A_{12}^{-1} dx/ds)/ds$ which are then substituted into Eq. (27) to get the equation for η , using Eq. (29) to eliminate derivatives of b . This gives, see [2] for details,

$$\frac{d^2 \eta}{d\theta^2} + v^2 \eta = 0 \quad (33)$$

The differential equation for η is unchanged.

IV. PERTURBATION THEORY USING THE DIFFERENTIAL EQUATION FOR η

The equation for η , Eq. (33) is often used as a starting point in finding the effects of a perturbing field. The particle coordinates are measured relative to a reference orbit which is the particle motion in a known magnetic field with components B_i . The exact equations of motion can then be written as

$$\frac{dx_i}{ds} = \sum_j A_{ij} x_j + f_i \quad i = 1, 4, j = 1, 4 \quad (34)$$

where the f_i includes all the terms not included in $\sum A_{ij} x_j$. These include terms due to fields not included in the reference field B_i , which may be referred as ΔB_i , and nonlinear terms due to the terms in the exact equations of motion that do not depend on B_i .

One can see from the exact equations of motion, that the contributions to f_i which depend explicitly on ΔB_i , when $\Delta B_s = 0$,

are given by

$$\begin{aligned} f_2 &= \frac{1}{B\rho} (1 + x/\rho) \Delta B_y \\ f_4 &= -\frac{1}{B\rho} (1 + x/\rho) \Delta B_x \end{aligned} \quad (35)$$

Repeating the above derivation of Eq. (33) for η , including the f_i terms, one finds the η equation for the x -motion

$$\begin{aligned} \frac{d^2 \eta}{d\theta^2} + v_x^2 \eta &= \frac{v_x^2 \beta_x^{3/2}}{A_{12}} f_x \\ f_x &= f_2 + \frac{A_{11}^2}{A_{12}} f_1 + \frac{d}{ds} \left(\frac{f_1}{A_{12}} \right) \\ d\theta &= A_{12} \frac{ds}{v_x \beta_x} \end{aligned} \quad (36)$$

A similar equation can be found for the y motion,

$$\begin{aligned} \frac{d^2 \eta}{d\theta^2} + v_y^2 \eta &= \frac{v_y^2 \beta_y^{3/2}}{A_{34}} f_y \\ f_y &= f_4 + \frac{A_{33}^2}{A_{34}} f_3 + \frac{d}{ds} \left(\frac{f_3}{A_{34}} \right) \end{aligned} \quad (37)$$

For the case of a gradient perturbation

$$\Delta B_y = -Gx \quad (38)$$

one can use Eq. (36) to find the change in v_x , Δv_x . One finds

$$\Delta v_x = \frac{1}{4\pi} \int ds \beta_x \frac{G}{B\rho} \quad (39)$$

This well known result for Δv_x is not changed by using the exact linear equations.

References

- [1] E.D. Courant and H.S. Snyder, Theory of the Alternating Gradient Synchrotron, Annals. of Physics, Vol. 3, p. 1 (1958).
- [2] G. Parzen, Linear Orbit Parameters for the Exact Equations of Motion, BNL Report AD/RHIC-127, BNL-60090 (1994).
- [3] F.T. Cole, Notes on Accelerator Theory, MURA report, TN-259 (1961).

TUNE MODULATION DUE TO SYNCHROTRON OSCILLATIONS AND CHROMATICITY, AND THE DYNAMIC APERTURE*

G. Parzen, Brookhaven National Laboratory, Upton, NY 11973 USA

Abstract

A tracking study was done of the effects of a tune modulation, due to synchrotron oscillations and the tune dependence on momentum (chromaticity), on the dynamic aperture. The studies were done using several RHIC lattices and tracking runs of about 1×10^6 turns. The dynamic aperture was found to decrease roughly linearly with the amplitude of the tune modulation. Lower order non-linear resonances, like the 1/3 and 1/4 resonance are not crossed because of the tune modulation. Three different cases were studied, corresponding to RHIC lattices with different β^* , and with different synchrotron oscillation amplitudes. In each case, the tune modulation amplitude was varied by changing the chromaticity. In each case, roughly the same result, was found. The result found here for the effect of a tune modulation due to chromaticity may be compared with the result found for the effect of a tune modulation due to a gradient ripple in the quadrupoles. The effect of a tune modulation due to a gradient ripple appears to be about 4 times stronger than the effect of a tune modulation due to chromaticity and synchrotron oscillations.

I. INTRODUCTION

A tracking study was done of the effects of a tune modulation, due to synchrotron oscillations and the tune dependence on momentum (chromaticity), on the dynamic aperture. The studies were done using several RHIC lattices and tracking runs of about 1×10^6 turns. The dynamic aperture was found to decrease roughly linearly with the amplitude of the tune modulation and may be represented by

$$A = A_0(1 - 10 \Delta\nu) \quad (1)$$

where A_0 is the dynamic aperture for $\Delta\nu = 0$, and $\Delta\nu$ is the tune modulation amplitude. In Eq. (1), the range of $\Delta\nu$ is such that lower order non-linear resonances, like the 1/3 and 1/4 resonance are not crossed because of the tune modulation.

Three different cases were studied, corresponding to RHIC lattices with different β^* , and with different synchrotron oscillation amplitudes. In each case, the tune modulation amplitude was varied by changing the chromaticity. In each case, roughly the same result, Eq. (1), was found.

The result found here for the effect of a tune modulation due to chromaticity may be compared with the result found [1] for the effect of a tune modulation due to a gradient ripple in the quadrupoles, which was

$$A = A_0(1 - 42 \Delta\nu) \quad (2)$$

The effect of a $\Delta\nu$ due to a gradient ripple appears to be about 4 times stronger than the effect of a $\Delta\nu$ due to chromaticity and synchrotron oscillations.

*Work performed under the auspices of the U.S. Department of Energy.

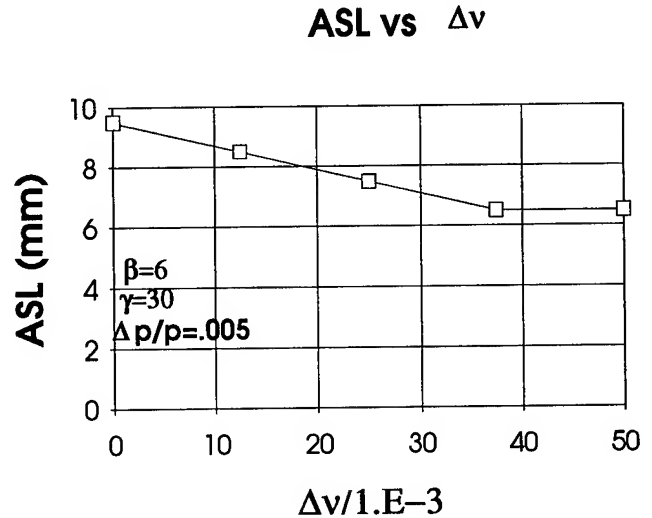


Figure 1. A plot of the dynamic aperture, A_{SL} , versus the tune modulation amplitude, $\Delta\nu$.

II. TRACKING RESULTS

The tune of the particle is modulated with time due to the chromaticity and the synchrotron oscillations. If the chromaticity is given by C_x, C_y and the amplitude of the synchrotron oscillation in momentum is given by $\pm \Delta p/p$, then the tune is modulated with time with a tune oscillation amplitude given by

$$\begin{aligned} \Delta\nu_x &= C_x \Delta p/p \\ \Delta\nu_y &= C_y \Delta p/p \end{aligned} \quad (3)$$

The frequency of the tune modulation is that of the synchrotron oscillation. For one case that was studied, the synchrotron oscillation frequency is about 260 hz.

Figure 1 shows the dynamic aperture A_{SL} versus $\Delta\nu$ for a RHIC lattice with $\beta^* = 6$ at all 6 insertions. The synchrotron oscillation amplitude is held constant at $\Delta p/p = 0.005$, $\Delta\nu$ is varied by varying the chromaticity $C_x = C_y$ from 0 to 10 producing a maximum $\Delta\nu$ of 50×10^{-3} . The nominal tune is $\nu_x = 28.826$, $\nu_y = 28.821$ and with this range of $\Delta\nu$ low order resonances like the 1/3 or 1/4 resonances, are not crossed. Figure 1 shows a roughly linear decrease of the dynamic aperture with $\Delta\nu$ from $A_{SL} = 9.5$ mm at $\Delta\nu = 0$ to $A_{SL} = 6.5$ mm at $\Delta\nu = 50 \times 10^{-3}$.

Three cases were studied with the same RF system which at the energy corresponding to $\gamma = 30$ has a synchrotron oscillation frequency of about 260 hz. These three cases are listed in Table 1. Case 2 has $\beta^* = 6$ and $\Delta p/p = 0.0025$. Case 3 has $\beta^* = 2$

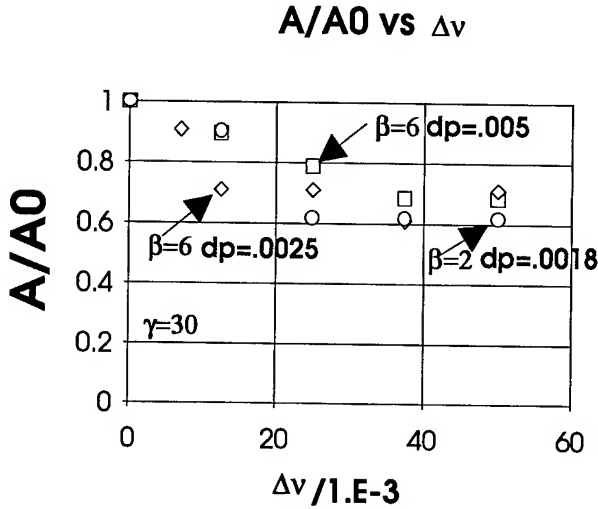


Figure 2. A plot of A/A_0 versus $\Delta\nu$ for three different cases. A is the dynamic aperture, A_0 is the dynamic aperture for $\Delta\nu = 0$.

and $\Delta p/p = 0.0018$. The height of the RF bucket in $\Delta p/p$ is $\Delta_B = 0.006$ in the 3 cases at $\gamma = 30$.

Table 1: A table of 3 cases studied where the synchrotron oscillation frequency was held constant at $f_s = 260$ Hz.

Case	β^* (m)	$\Delta p/p$ Synch. Osc. Amp.
1	6	0.005
2	6	0.0025
3	2	0.0018

Figure 2 plots the tracking results for A/A_0 against $\Delta\nu$ for the 3 cases. A is the dynamic aperture, A_0 is the dynamic aperture for $\Delta\nu = 0$, and $\Delta\nu$ is the amplitude of the tune modulation, which is varied by changing the chromaticity $C_x = C_y$. Figure 2 indicates that the data for all 3 cases lie roughly on the straight line

$$A = A_0(1 - 10 \Delta\nu) \quad (4)$$

In the range of $\Delta\nu$ covered in Fig. 2 there is only one low order resonance, which is below tenth order, that is reached by the tune modulation. This is the 5/6 resonance at $\nu = 28.83333$. The unperturbed tune is at $\nu_x = 28.826$ $\nu_y = 28.821$. The 5/6 resonance is reached at a tune modulation of $\Delta\nu \geq 7 \times 10^{-3}$. The results in Fig. 2 do not clearly show the presence of this resonance. The runs done with $\Delta\nu \geq 7 \times 10^{-3}$ sweep over the 5/6 resonance many times in 10^6 turns, yet the dynamic aperture found for $\Delta\nu \geq 7 \times 10^{-3}$ does not show much effect from the 5/6 resonance.

One may speculate as to under what conditions the result, Eq. (4) may be roughly valid. One may conjecture that Eq. (4) for the dependence of the dynamic aperture on the amplitude of the tune modulation may be roughly valid under the following conditions:

1. The tune modulation does not sweep over the lower order resonances like the 1/3 or 1/4 resonances.
2. The field error multipoles, b_n or a_n , are roughly given by b_0/R^n , where $b_0 \approx 2 \times 10^{-4}$ and, usually, R is roughly the magnet coil radius.
3. The tune modulation is generated by the presence of a tune dependence on momentum (chromaticity) and synchrotron oscillations, and the frequency of the synchrotron oscillations is small compared to the particle revolution frequency in the accelerator.

The result found for the decrease in dynamic aperture, Eq. (4), may be compared with the result found for the effect on the dynamic aperture due to a tune modulation generated by a ripple in the gradient of the quadrupoles, which is given by

$$A = A_0(1 - 42 \Delta\nu), \text{ gradient ripple.} \quad (5)$$

One sees that a $\Delta\nu$ due a gradient ripple is more effective in reducing the dynamic aperture than a $\Delta\nu$ due to chromaticity and synchrotron oscillation by about a factor of 4.

III. DEPENDENCE OF DYNAMIC APERTURE ON THE SYNCHROTRON OSCILLATION FREQUENCY

The frequency of the synchrotron oscillation frequency can be varied by varying the voltage, V , and the harmonic number, h , of the RF cavity. If this is done holding V/h constant, then the height of the RF bucket in $\Delta p/p$ is not changed.

The dependence of the dynamic aperture on the synchrotron oscillation frequency f_s was studied for the case $\Delta\nu = 50 \times 10^{-3}$, $\Delta p/p = 0.005$, $C_x = C_y = 10$, $\beta^* = 6$. This case has the largest tune oscillation amplitude studied. The results for the dynamic aperture A_{SL} vs. f_s for this case are shown in Figure 3. f_s was varied from $f_s = 16.25$ hz to 520 hz. Figure 3 does not show much dependence of A_{SL} on f_s over this range in f_s . A_{SL} is given by 5.5 ± 1 mm over the range in f_s . There appears to be a small decrease in A_{SL} for lower f_s . One should note that the tracking results for A_{SL} become more doubtful at lower values f_s . At $f_s = 16.25$, there is time for about 250 synchrotron periods in 1 million turns. This effect would probably reduce the dynamic aperture at lower values of f_s .

IV. COMMENTS ON THE TRACKING

It is important that the tracking be symplectic. To achieve this, the ORBIT program was changed [2] to allow the use of point magnets. The methods used are similar to those used in the TEAPOT [3] program, with some modifications, including the choice of the reference orbit [4].

One 160 MHz RF cavity with an RF voltage of 4.5 MV was used in the tracking. The bucket height is $\Delta p/p = 6 \times 10^{-3}$ at $\gamma = 30$ and $\Delta p/p = 2 \times 10^{-3}$ at $\gamma = 100$.

Random and systematic field errors were present in each magnet at the level given in Ref. 5. Field error multipoles up to order 10 were included. The studies done in this paper were done for a particular set of field errors which gave the smallest dynamic aperture, out of ten different distributions of the random field errors, in the absence of tune modulation.

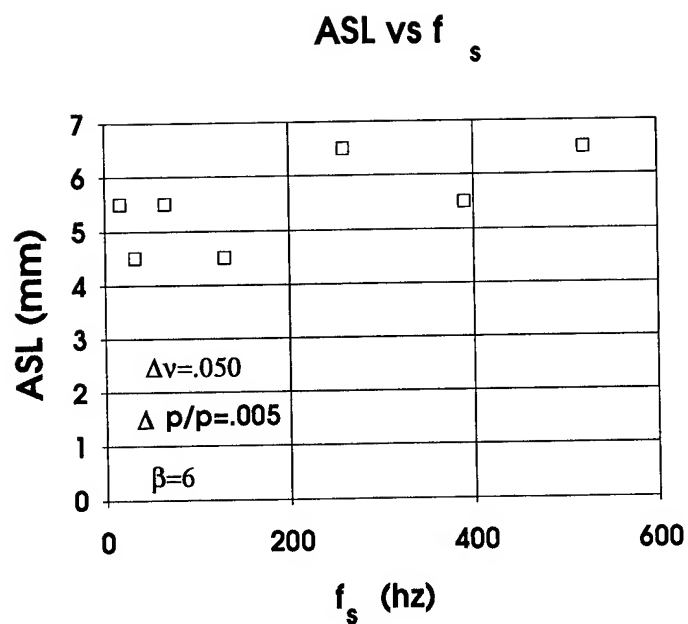


Figure. 3. A plot of A_{SL} versus f_s , the synchrotron oscillation frequency.

The dynamic aperture is computed by doing a series of runs with the starting conditions $\epsilon_x = \epsilon_y$, $x' = y' = 0$, and finding the largest betatron oscillation amplitude that is stable for 800,000 turns.

References

- [1] G. Parzen, Tune Modulation due to Gradient Ripple and the Dynamic Aperture, BNL Report AD/RHIC-124 (1993).
- [2] G. Parzen, Effect of Synchrobetatron Coupling on the Dynamic Aperture, BNL Report AD/RHIC-119 (1993).
- [3] L. Schachinger and R. Talman, TEAPOT, A Thin Element Tracking Program, SSC Report SSC-52 (1985).
- [4] G. Parzen, Symplectic Tracking Using Point Magnets and a Reference Orbit Made of Circular Arcs and Straight Lines, BNL Report AD/RHIC-120 (1993).
- [5] RHIC Conceptual Design, BNL Report BNL-52195 (1989).

NORMAL MODE TUNES FOR LINEAR COUPLED MOTION IN SIX DIMENSIONAL PHASE SPACE*

G. Parzen, Brookhaven National Laboratory, Upton, NY 11973 USA

Abstract

The motion of a particle in 6-dimensional phase space in the presence of linear coupling can be written as the sum of 3 normal modes. A cubic equation is found for the tune of the normal modes, which allows the normal mode tunes to be computed from the 6×6 one turn transfer matrix. This result is similar to the quadratic equation found for the normal mode tunes for the motion of a particle in 4-dimensional phase space. These results are useful in tracking programs where the one turn transfer matrix can be computed by multiplying the transfer matrices of each element of the lattice. The tunes of the 3 normal modes for motion in 6-dimensional phase space can then be found by solving the cubic equation. Explicit solutions of the cubic equation for the tune are given in terms of the elements of the 6×6 one turn transfer matrix.

I. INTRODUCTION

The motion of a particle in 6-dimensional phase space in the presence of linear coupling can be written as the sum of 3 normal mode. A cubic equation is found for the tune of the normal modes, which allows the normal mode tune to be computed from the 6×6 one turn transfer matrix.

This result is similar to the quadratic equation [1] found for the normal mode tune for the motion of a particle in 4-dimensional phase space. These results are useful in tracking programs where the one turn transfer matrix can be computed by multiplying the transfer matrices of each element of the lattice. The tune of the 3 normal modes for motion in 6-dimensional phase space can then be found by solving the cubic equation. Explicit solutions of the cubic equation for the tune are given in terms of the elements of the 6×6 one turn transfer matrix.

II. A CUBIC EQUATION FOR NORMAL MODE TUNES

The particle coordinates are assumed to be x, p_x, y, p_y, z, p_z . Then the linear motion of the particle about some central orbit can be described by a 6×6 transfer matrix $T(s, s_0)$.

$$x(s) = T(s, s_0)x(s_0)$$

$$x = \begin{bmatrix} x \\ p_x \\ y \\ p_y \\ z \\ p_z \end{bmatrix} \quad (1)$$

Note that the symbol x is used to denote the column vector x and also the first element of this column vector. The meaning of x

should be clear from the context. This notation is used in several places in this paper.

It is assumed that the equations of motions can be derived from a hamiltonian, and the matrix T is symplectic:

$$\begin{aligned} T\bar{T} &= I \\ \bar{T} &= \tilde{S} \tilde{T} S \end{aligned} \quad (2)$$

\tilde{T} is the transpose of T .

I is the 6×6 identity matrix, and S can be written in terms of 2×2 matrices as

$$S = \begin{bmatrix} S & 0 & 0 \\ 0 & S & 0 \\ 0 & 0 & S \end{bmatrix} \quad (3)$$

The 2×2 matrix, also called S , is given by

$$S = \begin{pmatrix} 0 & 1 \\ -1 & 0 \end{pmatrix} \quad (4)$$

It is convenient to also write T in terms of 2×2 matrices

$$T = \begin{bmatrix} T_{11} & T_{12} & T_{13} \\ T_{21} & T_{22} & T_{23} \\ T_{31} & T_{32} & T_{33} \end{bmatrix} \quad (5)$$

One may note that the 2×2 matrices of \bar{T} are $(\bar{T})_{ij} = \bar{T}_{ji}$. The eigenfunctions of the one turn transfer matrix $T(s+L, s)$, where L is the period of the forces acting on the particle, obey

$$T(s+L, s)x = \lambda x$$

Because T is symplectic then if λ is an eigenvalue, $1/\lambda$ is also an eigenvalue [1,2] and the 6 eigenvalue can be arranged in 3 pairs of λ and $1/\lambda$. For stable motion, $|\lambda| = 1$ and λ can be written as

$$\begin{aligned} \lambda &= \exp(i\mu) \\ \mu &= 2\pi\nu, \end{aligned} \quad (6)$$

where it is assumed that the period is one turn.

To find the tunes of the normal modes, one has to find the eigenvalues of T , λ , which are given by $|T - \lambda I| = 0$, where $|T|$ indicates the determinant of T . It is more convenient to find the eigenvalues of the matrix C defined by

$$C = \frac{1}{2}(T + \bar{T}) \quad (7)$$

The eigenvalues of C , Λ , are

$$\begin{aligned} \Lambda &= \frac{1}{2}(\lambda + 1/\lambda), \\ \Lambda &= \cos \mu \end{aligned} \quad (8)$$

*Worked performed under the auspices of the U.S. Department of Energy.

and the Λ are determined by

$$|C - \Lambda I| = 0 \quad (9)$$

It is convenient to write C in terms of 2×2 matrices. Note that the 2×2 elements of C are

$$C_{ij} = (T_{ij} + \bar{T}_{ji})/2 \quad (10)$$

and thus

$$\begin{aligned} C_{ii} &= \frac{1}{2} \text{Tr}(T_{ii}) I \\ C_{ij} &= \bar{C}_{ji} \end{aligned} \quad (11)$$

We can then write C as

$$C = \begin{bmatrix} t_1 I & C_{12} & C_{13} \\ C_{21} & t_2 I & C_{23} \\ C_{31} & C_{32} & t_3 I \end{bmatrix} \quad (12)$$

$$t_i = \frac{1}{2} \text{Tr}(T_{ii})$$

To evaluate $|C - \Lambda I|$, $C - \Lambda I$ will be multiplied from the left by a sequence of matrices, each with determinant 1, to produce a matrix which is upper triangular; that is, the elements of this matrix below the diagonal are all zero. This triangular matrix has the same determinant as $C - \Lambda I$, and its determinant can be found by multiplying all the diagonal elements of this matrix.

First, multiply $C - \Lambda I$ from the left by the matrix

$$\begin{bmatrix} 1 & 0 & 0 \\ -C_{21}/\bar{t}_1 & 1 & 0 \\ 0 & 0 & 1 \end{bmatrix} \quad (13)$$

$$\bar{t}_1 = t_1 - \Lambda$$

This matrix is designed to eliminate C_{21} and the multiplication gives the result

$$\begin{bmatrix} \bar{t}_1 I & C_{12} & C_{13} \\ 0 & (\bar{t}_2 - |C_{12}|/\bar{t}_1)I & C_{23} - C_{21}C_{13}/\bar{t}_1 \\ C_{31} & C_{32} & \bar{t}_3 I \end{bmatrix} \quad (14)$$

The result $C_{12}\bar{C}_{12} = |C_{12}|$ has been used. Note that $C_{21} = \bar{C}_{12}$. Now multiply the matrix Eq. (14) by the matrix

$$\begin{bmatrix} 1 & 0 & 0 \\ 0 & 1 & 0 \\ -C_{31}/\bar{t}_1 & 0 & 1 \end{bmatrix} \quad (15)$$

which replaces the third row in Eq. (14) by the third row plus $-C_{31}/\bar{t}_1$ times the first row giving

$$\begin{bmatrix} t_1 I & C_{12} & C_{13} \\ 0 & (\bar{t}_2 - |C_{12}|/\bar{t}_1)I & C_{23} - C_{21}C_{13}/\bar{t}_1 \\ 0 & C_{32} - C_{31}C_{12}/\bar{t}_1 & (\bar{t}_3 - |C_{13}|/\bar{t}_1)I \end{bmatrix} \quad (16)$$

One more matrix multiplication is required to reduce $C - \Lambda I$ to an upper triangular matrix. Multiply matrix Eq. (16) by the matrix

$$\begin{bmatrix} 1 & 0 & 0 \\ 0 & 1 & 0 \\ 0 & -(C_{32} - C_{31}C_{12}/\bar{t}_1)/(\bar{t}_2 - |C_{12}|/\bar{t}_1) & 0 \end{bmatrix} \quad (17)$$

This gives

$$\begin{bmatrix} \bar{t}_1 I & C_{12} & C_{13} \\ 0 & (\bar{t}_2 - |C_{12}|/\bar{t}_1)I & C_{23} - C_{21}C_{13}/\bar{t}_1 \\ 0 & 0 & \bar{t}_3 I \end{bmatrix} \quad (18)$$

$$\bar{t}_3 = [\bar{t}_3 - |C_{13}|/\bar{t}_1 - |C_{23} - C_{21}C_{13}/\bar{t}_1|/(\bar{t}_2 - |C_{12}|/\bar{t}_1)]$$

The matrix Eq. (18) is a triangular matrix with zero elements below the diagonal and its determinant, and thus $|C - \Lambda I|$, can be computed by multiplying the diagonal elements which gives

$$\begin{aligned} |C - \Lambda I|^{1/2} &= \bar{t}_1 (\bar{t}_2 - |C_{12}|/\bar{t}_1) [\bar{t}_3 - |C_{13}|/\bar{t}_1 \\ &\quad - |C_{23} - C_{21}C_{13}/\bar{t}_1|/(\bar{t}_2 - |C_{12}|/\bar{t}_1)] \\ |C - \Lambda I|^{1/2} &= \bar{t}_1 [(\bar{t}_2 - |C_{12}|/\bar{t}_1)(\bar{t}_3 - |C_{13}|/\bar{t}_1) \\ &\quad - |C_{23} - C_{21}C_{13}/\bar{t}_1|] \\ |C - \Lambda I|^{1/2} &= (1/\bar{t}_1) [(\bar{t}_1\bar{t}_2 - |C_{12}|)(\bar{t}_1\bar{t}_3 - |C_{13}|) \\ &\quad - |C_{23}\bar{t}_1 - C_{21}C_{13}|] \end{aligned} \quad (19)$$

To simplify Eq. (19), note the following result

$$\begin{aligned} |C_{23}\bar{t}_1 - C_{21}C_{13}|I &= (C_{23}\bar{t}_1 - C_{21}C_{13})(\bar{C}_{23}\bar{t}_1 - \bar{C}_{13}\bar{C}_{21}) \\ &= [|C_{23}|^2\bar{t}_1^2 - \text{Tr}(C_{23}\bar{C}_{13}\bar{C}_{21})\bar{t}_1 + |C_{21}||C_{13}|]I \end{aligned} \quad (20)$$

which gives

$$|C - \Lambda I|^{1/2} = \bar{t}_1\bar{t}_2\bar{t}_3 - \bar{t}_2|C_{13}| - \bar{t}_3|C_{12}| - \bar{t}_1|C_{23}| + \text{Tr}(C_{23}C_{31}C_{12}) \quad (21)$$

Finally, the normal modes tunes, which are given by $|C - \Lambda I| = 0$ are determined by the cubic equation

$$\begin{aligned} (\Lambda - t_1)(\Lambda - t_2)(\Lambda - t_3) - (\Lambda - t_1)|C_{23}| - (\Lambda - t_2)|C_{31}| - (\Lambda - t_3)|C_{12}| \\ - \text{Tr}(C_{12}C_{23}C_{31}) = 0 \\ \Lambda = \cos \mu, \quad \mu = 2\pi\nu \end{aligned}$$

$$t_1 = \frac{1}{2} \text{Tr}(T_{11}), \quad t_2 = \frac{1}{2} \text{Tr}(T_{22}), \quad t_3 = \frac{1}{2} \text{Tr}(T_{33}) \quad (22)$$

$$C = \frac{1}{2}(T + \bar{T})$$

$$C_{ij} = \frac{1}{2}(T_{ij} + \bar{T}_{ji})$$

The T_{ij} are the 2×2 elements of T and C_{ij} are the 2×2 elements of C .

Equation (22) is a cubic equation, and the 3 roots of this equation $\Lambda_i = \cos \mu_i$, $i = 1, 3$ will give the 3 tunes of the normal modes, $\nu_i = \mu_i/2\pi$. If μ_i is real the mode is stable; if μ has an imaginary part then the mode may be unstable.

To get a result for 4-dimensional coupled motion, we put $C_{23} = C_{31} = 0$ and Eq. (22) then gives

$$(\Lambda - t_1)(\Lambda - t_2) - |C_{12}| = 0$$

$$C_{12} = \frac{1}{2}(T_{12} + \bar{T}_{21}), \quad t_1 = \frac{1}{2} \text{Tr}(T_{11}), \quad t_2 = \frac{1}{2} \text{Tr}(T_{22}) \quad (23)$$

Eq. (23) is the known result [1,3] for the tunes of the 2 normal modes for coupled motion in 4-dimensional phase space.

In the 4-dimensional case, Eq. (23) can be solved to find the two $\cos \mu_i$ of the normal modes. This gives the result for $\cos \mu$

$$\begin{aligned}\cos \mu &= \frac{1}{2}(t_1 + t_2) \pm \frac{1}{2}[(t_1 - t_2)^2 + 4|C_{12}|]^{\frac{1}{2}} \\ t_1 &= \frac{1}{2}T_r(T_{11}), \quad t_2 = \frac{1}{2}T_r(T_{22}) \\ |C_{12}| &= |T_{12} + \bar{T}_{21}|/4\end{aligned}\quad (24)$$

where T_{ij} are the 2×2 elements of the one turn transfer matrix. If one computes T by multiplying the transfer matrices of all the elements in the accelerator, then one can find $\cos \mu$, and the ν values, using Eq. (24).

Equation (24) is useful in tracking programs for finding the normal mode tunes, from the one turn transfer matrix, for coupled motion in 4-dimensional phase space.

A similar result can be found for coupled motion in 6-dimensional phase space by solving the cubic equation, Eq. (22).

Equation (22) can be written as

$$\begin{aligned}\Lambda^3 + a_2\Lambda^2 + a_1\Lambda + a_0 &= 0 \\ a_2 &= -(t_1 + t_2 + t_3) \\ a_1 &= t_1t_2 + t_2t_3 + t_3t_1 - |C_{12}| - |C_{23}| - |C_{31}| \\ a_0 &= -t_1t_2t_3 - T_r(C_{12}C_{23}C_{31}) + t_1|C_{23}| + t_2|C_{31}| + t_3|C_{12}| \\ t_1 &= \frac{1}{2}T_r(T_{11}), \quad t_2 = \frac{1}{2}T_r(T_{22}), \quad t_3 = \frac{1}{2}T_r(T_{33}) \\ C_{ij} &= \frac{1}{2}(T_{ij} + \bar{T}_{ji})\end{aligned}\quad (25)$$

The solutions of Eq. (25) when the 3 roots are all real, can be written as [4]

$$\begin{aligned}\cos \mu_i &= (t_1 + t_2 + t_3)/3 + 2(r^2 + b^2)^{1/6} \cos(\alpha/3 + \delta_i) \\ \delta_i &= 0, 2\pi/3, -2\pi/3 \\ b &= |r^2 + q^3|^{1/2} \\ r &= \frac{1}{6}(a_1a_2 - 3a_0) - \frac{1}{27}a_2^3 \\ q &= \frac{1}{3}a_1 - \frac{1}{9}a_2^2 \\ \tan \alpha &= b/r\end{aligned}\quad (26)$$

Note that the 3 values of δ_i , $\delta_i = 0, 2\pi/3, -2\pi/3$ will give the 3 roots from Eq. (26).

The condition for the 3 roots to be real is [4]

$$q^3 + r^2 \leq 0 \quad (27)$$

If $(q^3 + r^2) > 0$, then 2 roots are imaginary and the motion may be unstable. In order to get $q^3 + r^2 \leq 0$ and stable motion, one has to have $q < 0$.

Equation (26) can be used in a tracking program to find the 3 normal mode tunes from the one turn transfer matrix. The one turn transfer matrix can be computed by multiplying the transfer matrices for each element in the lattice.

References

- [1] E.D. Courant and H.S. Snyder, *Annals of Physics*, **3**, p. 1 (1958).
- [2] F. Willeke and G. Ripken, *Methods of Beam Optics*, DESY 88-114, 1988.
- [3] D.A. Edwards and L.C. Teng, *Parameterization of Linear Coupled Motion*, Proc. IEEE PAC of 1973, p. 885, 1973.
- [4] M. Abramowitz and I.A. Stegun, *Handbook of Mathematical Functions*, National Bureau of Standards, p. 17 (1964).

Fast Symplectic Mapping and Quasi-invariants for the Large Hadron Collider*

R. L. Warnock and J. S. Berg,

Stanford Linear Accelerator Center, Stanford University, Stanford, CA 94309

É. Forest†,

Lawrence Berkeley Laboratory, University of California, Berkeley, CA 94720

Abstract

Beginning with a tracking code for the LHC, we construct the canonical generator of the full-turn map in polar coordinates. For very fast mapping we adopt a model in which the momentum is modulated sinusoidally with a period of 130 turns (very close to the synchrotron period). We achieve symplectic mapping of 10^7 turns in 3.6 hours on a workstation. Quasi-invariant tori are constructed on the Poincaré section corresponding to multiples of the synchrotron period. The possible use of quasi-invariants in deriving long-term bounds on the motion is discussed.

I. Introduction

In [1], we showed how to construct the mixed-variable generating function for the full-turn map, using only single-turn data from a symplectic tracking code. The generator is represented as a Fourier series in angle variables, the Fourier coefficients being B-spline functions of action variables. The symplectic map induced by this generator gives a good representation of the dynamics defined by the tracking code (according to physical criteria to be stated presently), even with moderate numbers of Fourier modes and spline knots. There are two special features of the B-spline-Fourier basis that promote fast map iterations: (i) the B-spline basis functions have "limited support," which is to say that only a few of the functions are non-zero at a particular point, and (ii) among all Fourier amplitudes with mode numbers less than some cutoff, a great many are found to be negligible.

A method to set long-term bounds on nonlinear motion was proposed in [2]. The idea is to make a canonical transformation to new action-angle variables (J, Ψ) , such that the action J is nearly invariant, and then examine the residual variation of J . In [2] the method was illustrated only in a simple example of transverse motion.

In this paper we construct maps for a realistic injection lattice of the LHC. The maps are sufficiently fast so that one can economically follow single orbits for 10^7 turns, and also construct quasi-invariant surfaces with account of synchrotron oscillations. We make the first steps toward derivation of long-term bounds, but find that the method of [2] must be elaborated if one is to find good bounds at large amplitudes.

II. Poincaré section at the synchrotron period

Long-term behavior of transverse coordinates is strongly affected by momentum oscillations, but the synchrotron motion itself remains roughly harmonic. For a first view of the full six-dimensional system, it is then reasonable to modulate the momentum externally, and ignore the coordinate conjugate to momentum (time-of-flight). Experience with tracking shows that such a model gives results rather similar, if not identical, to those of the full six-dimensional treatment. The synchrotron period of the LHC injection lattice is nearly 130 turns. We suppose it to be exactly 130, and take the momentum deviation at the m th turn to be

$$\delta = \frac{p - p_0}{p_0} = \delta_0 \sin \frac{2\pi m}{130}, \quad \delta_0 = 5 \cdot 10^{-4}. \quad (1)$$

The momentum change is localized at a single r.f. cavity. For the rest of the ring we have a 4-dimensional map for fixed δ , which is represented in terms of coordinates centered at its δ -dependent fixed point [1]. To save computing time in map iteration, we store the coefficients that determine the 4-d generating function, for each of the 130 values of δ .

The Hamiltonian is periodic in s with period $130C$, where C is the circumference of the reference orbit. The surface $s = 0 \pmod{130C}$ is then a Poincaré section on which there exist two-dimensional invariant surfaces and resonances that can be studied in the usual way. In comparison to the situation for the single-turn map at fixed δ , we find many more low-order resonances. This is not surprising, since even without modulation of δ the 130-th power of the map will have many more resonances than the first power. The resonance condition for the N -th power, $N\mathbf{m} \cdot \boldsymbol{\nu} = P$, has more solutions than that for the first power, $\mathbf{m} \cdot \boldsymbol{\nu} = p$, where P, p and the components of \mathbf{m} are any integers.

III. Construction and Validation of Full-turn Map for the LHC

In contrast to the approach based on Taylor series, we do not look for a map to be valid over all of the relevant phase space. Rather, we concentrate our approximative power in a small region of action space, over which the map has relatively little variation in action. We can then get high accuracy from a small set of spline basis functions, and that allows fast iteration of the map. For a global study of stability we string together several overlapping regions, and make a map for each region.

To set the scale, we first run the tracking code to determine the short term (2000 turn) dynamic aperture. In the plane of our action variables (I_1, I_2) , described in units of $10^{-7}m$, this

*Work supported by DOE contracts DE-AC03-76SF00515 and DE-AC03-76SF00098

†Current address: National Laboratory for High Energy Physics, KEK, Tsukuba, Japan

aperture roughly follows the straight line from (6, 0) to (0, 9). To illustrate map construction, we discuss a map that is valid for initial actions $I_1(0), I_2(0)$ (with initial angles being zero) in the region R such that $1 \leq I_1(0), I_2(0) \leq 1.5$. This region is located at about one half of the short-term aperture in the plane of displacements x_1, x_2 . The generator is determined in a larger region R_1 , to allow for smear of orbits (as determined by short-term tracking) and an extra "apron" to account for possible long-term drift. The map iteration is programmed to stop if the orbit leaves R_1 .

The map in question has 10 Fourier modes for each angle, 10 spline interpolation points for each action, and 6 for δ . The splines are cubic polynomials locally. The construction of the generator requires 264600 turns of tracking, with 68ms per turn (thus 5 hours) on an IBM RS6000 Model 590 workstation. The resulting implicit map (made explicit by Newton's method) can be iterated in 1.2ms on the same machine, giving 10^7 turns in 3.6 hours. The map agrees with the tracking code to about 1 part in 10^4 at one turn. The accuracy of agreement can be increased essentially at will by increasing the number of Fourier modes and spline points, or the order of the splines. The time for iteration does not increase with the number of spline points if the spline order is fixed (thanks to the limited support of B-splines), but the construction time is proportional to that number.

Rather than trying for higher accuracy, we consider it most interesting to work with a map of modest accuracy (hence short iteration time) and try to show that it gives essentially the same physical picture as the underlying tracking code. We do that by comparing resonances and quasi-invariant surfaces of the map and the tracking code. An easy way to find resonances (on our Poincaré surface at the synchrotron period) is to look for orbits confined to narrow bands in the plane of angles Φ_1, Φ_2 ; see [2]. In the case of relatively broad resonances, of which there are great many at moderate amplitudes, we always find that an initial condition giving a resonance of the map also gives the same one in tracking. In trying the same test for narrow, high-order resonances, we found a 62-nd order resonance of the map at $(I_1(0), I_2(0)) = (1.1, 1.1)$. This did not appear in tracking from the same initial condition, but another 59-th order resonance did appear. Readjusting slightly the initial condition of the map trajectory, we found the 59-th order in the map, at $(I_1(0), I_2(0)) = (1.09983, 1.1)$. This orbit of the map is plotted for 10000 synchrotron periods in Fig. 1. The corresponding orbit of tracking for 5000 synchrotron periods agrees very well on visual inspection; (quantitative comparison is difficult, since the points fill the "curves" differently in the two cases).

To compare quasi-invariant tori of the map and tracking, again on the Poincaré surface, we constructed a torus by the method of [2] in which a nonresonant orbit is fitted to a Fourier series in angle variables. Taking 20 modes for each angle, a few quasi-invariant tori of the map were computed. It typically took about 7000 synchrotron periods of mapping to compute a torus, requiring about 20 minutes on the Model 590. We check invariance under the map or under tracking by starting orbits at many randomly chosen points on the torus, and see how close the orbit is to the torus after one synchrotron period. With 50 randomly chosen points, a typical surface was invariant to one part in 10^5 under the map from which it was constructed, and invariant to

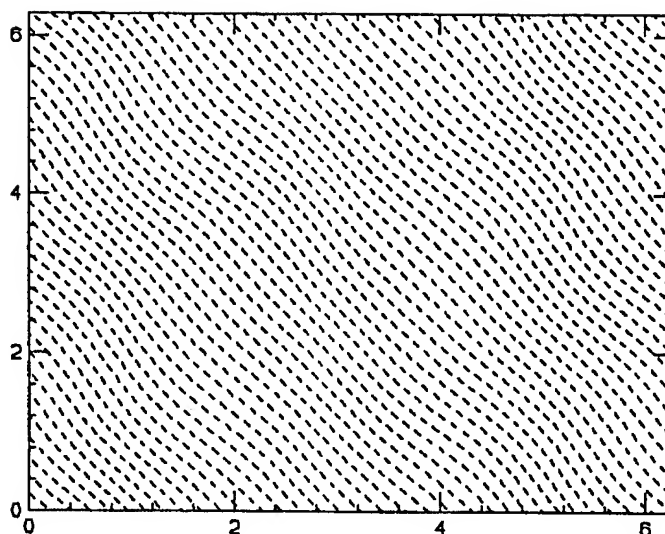


Figure. 1. Φ_2 vs. Φ_1 on a 59th order resonance of the map, $33\nu_1 \pm 26\nu_2 = p$, for 10000 synchrotron periods. Initial conditions: $I_1(0), I_2(0) = (1.09983, 1.1) \cdot 10^{-7}$ m.

one part in 10^4 under the tracking code.

These and other tests convince us that the Hamiltonian system represented by symplectic maps of modest one-turn accuracy (1 part in 10^4) represent a physical system very similar to that of the underlying tracking code, at least at amplitudes not too close to the dynamic aperture. At very large amplitudes it is not easy to validate the map by the above arguments, since one finds large-scale chaotic behavior rather than clean resonances and quasi-invariants.

IV. A String of Large-amplitude Maps and Long-term Mapping

In one over-night run, using a small fraction of available CPU time on a "farm" of workstations at SLAC, we produced a string of five maps in partially overlapping rectangular regions. Numbers of modes and spline knots were the same as in the example above. This gives a continuous strip of allowable initial conditions (with $\Phi_1 = \Phi_2 = 0$), between two lines running parallel to the short-term aperture. The outer border of the strip is at 70% of the aperture. The outer corners of the rectangles go beyond the strip, and allow orbits that go within at least 85% of the aperture. At the time of writing we have done a few runs of 10^7 turns using these maps. Fig. 2 shows a plot of I_1 at every eighth synchrotron period in such a run. The vertical frame size of the graph indicates the domain of the splines in I_1 . The domain of the maps does not include the coordinate axis, $I_1 = 0, I_2 = 0$. The map construction fails in a small neighborhood of each axis, since the polar coordinate system becomes inappropriate.

V. A First Try at Long-term Bounds

Here we are concerned solely with the dynamics defined by the map. For a first attempt at long-term bounds we work at smaller amplitudes, in a region with $0.4 < I_1(0), I_2(0) < 0.6$ (in units of 10^{-7} m). Following the method of [2], we construct

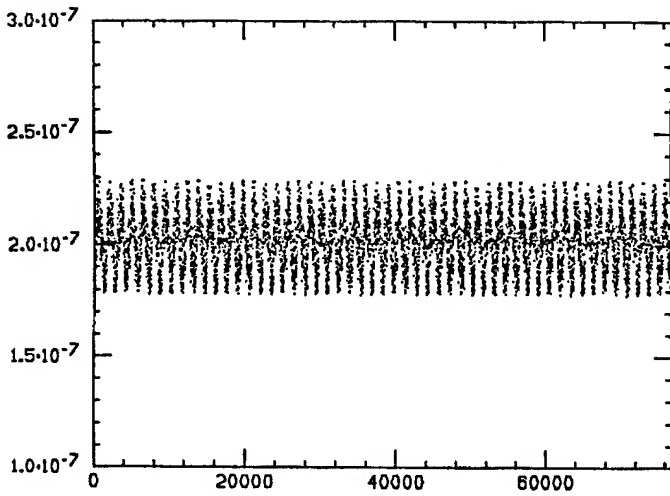


Figure 2. I_1 vs. number of synchrotron periods, for 10^7 turns. Initial conditions: $I_1(0), I_2(0) = (1.87, 0.937) \cdot 10^{-7}$ m.

a set of 9 tori on the Poincaré section, for points close to a 3×3 rectangular grid in $I_1(0), I_2(0)$. These tori have twenty Fourier modes in each variable, and are invariant to about 1 part in 10^5 . We next interpolate the tori in actions, so as to define a smooth canonical transformation to new action-angle variables \mathbf{J}, Ψ . Although \mathbf{J} is fairly constant on and near the original tori, it remains to be seen how much it varies in the region of interpolation.

Let Ω denote the region in which \mathbf{J} is defined. Suppose that δJ is an upper bound for the change in $|J_i|$ during m synchrotron periods, for any orbit beginning in Ω . Let Ω_o be a subregion of Ω , and let ΔJ be the minimum distance from Ω_o to the boundary of Ω . Then an orbit beginning in Ω_o cannot leave Ω in fewer than $n\delta J$ synchrotron periods, where $n\delta J = \Delta J$. Then we have stability (in the sense of being confined to Ω) for $N = 130m\Delta J/\delta J$ turns.

We take $m = 1000$ and try 1000 randomly chosen initial conditions in Ω to estimate δJ . We find that δJ is about 0.01, which is much larger than the variation of J for orbits starting on the original tori. If we take Ω_o to be a small box in the middle of Ω , then ΔJ is about 0.1, and we can predict stability only for $N = 1.3 \cdot 10^6$ turns, a disappointingly small number.

The reason for the large variation of \mathbf{J} is the presence of a fairly broad resonance inside Ω . A sufficiently isolated resonance in mode $\mathbf{m} = (m_1, m_2)$ can be identified by plotting the change of $\mathbf{m} \cdot \mathbf{J}$ against $\mathbf{m} \cdot \Psi$ at constant $K = m_1 J_2 - m_2 J_1$ [2]. As is shown for a (6, 1) resonance in Fig. 3, these variables perform a pendulum-like motion. Note that this motion would be hard to see without first transforming to \mathbf{J}, Ψ . The resonance could be quite stable, but still lead to large oscillations in \mathbf{J} . In order to make our argument for long-term bounds, it will be necessary to find quasi-invariants of resonant orbits. Preliminary work by Armando Antillón showed that a simple pendulum-type Hamiltonian $H(\mathbf{m} \cdot \mathbf{J}, \mathbf{m} \cdot \Psi, K)$ could be fitted to orbit data so as to provide at least a rough quasi-invariant; K is a second quasi-invariant. We hope to use H and K in place of J_1, J_2 in our argument for long-term bounds. It may be nec-

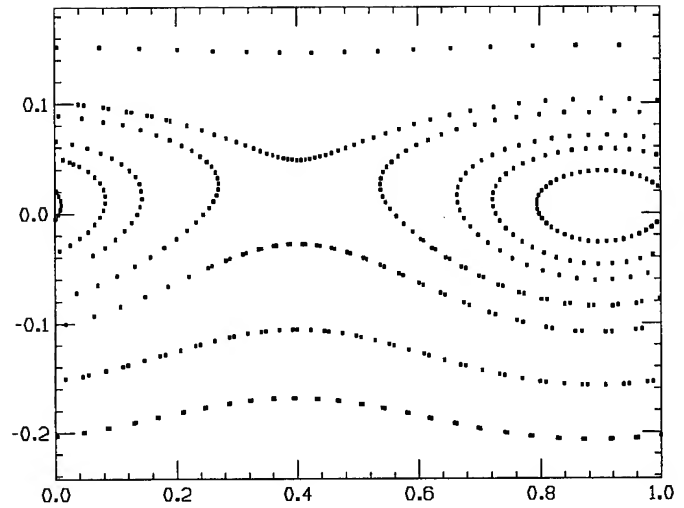


Figure 3. Plot of $\hat{\mathbf{m}} \cdot d\mathbf{J}$ vs. $[\mathbf{m} \cdot \Psi \pmod{2\pi}]/2\pi$, where $\hat{\mathbf{m}}$ is the unit vector in the direction of $\mathbf{m} = (6, 1)$, and $d\mathbf{J}$ is the deviation of \mathbf{J} from a fixed "average action," \mathbf{J}_0 . Each of the 9 orbits plotted is started at the same value of $K = m_2 J_1(0) - m_1 J_2(0)$. The action unit is 10^{-7} m.

essary to refine the definition of these quantities, so that they are functions of all the canonical variables \mathbf{J}, Ψ .

VI. Acknowledgment

This work was made possible by the kind help of Frank Schmidt, who provided lattice information for the LHC and assistance in verifying our tracking code.

References

- [1] J. S. Berg, R. L. Warnock, R. D. Ruth, and É. Forest. *Physical Review E*, 49:722–739, January 1994.
- [2] R. L. Warnock and R. D. Ruth. *Physica D*, 56:188–215, 1992.

NONLINEAR DEPENDENCE OF SYNCHROTRON RADIATION ON BEAM PARAMETERS

G. H. Hoffstätter*

Deutsches Elektronen-Synchrotron DESY, Notkestr. 85, 22603 Hamburg, Germany

Abstract

Synchrotron radiation has been traditionally treated as an effect which only depends on the linear beam dynamics. Electrons in advanced accelerators and storage rings, however, can lose several percent of their energy in one turn, especially when the ring incorporates synchrotron radiation sources or free electron lasers. In these machines nonlinear effects can become important, not only because of the high variation of the particle's energy around the ring, but also because of the necessity to have very good beam quality in wigglers, undulators, and free electron lasers. Since these instruments can have helical structure, a general reference frame with torsion is used and the Lorentz-Dirac radiation reaction of the charged particle is taken into account. We will utilize the Differential Algebra technique to compute nonlinear transfer maps of general optical elements. Applications include radiation damping in multipoles, its effect on closed orbit distortion in a storage ring, and nonlinear tune shifts due to various radiating devices. The software provided will also be useful in simulating Siberian snakes.

I. INTRODUCTION

If the energy of a charged particle is conserved, the equations of motion are Hamiltonian. The Hamiltonian structure of these equations implies that their flows are symplectic. The symplectic symmetry poses several constraints on the motion. Liouville's theorem is an especially famous consequence of this property. If energy is lost during the motion, as in the case of electrons in a storage ring, the equations of motion are not Hamiltonian and knowledge about symplectic flows cannot be applied. If one sets out to describe high energy electron motion, it is therefore best not to start with a Hamiltonian but directly with the equation of motion. It is, however, not sufficient to solve the Hamiltonian equations of motion without radiation and to simulate an effective loss of energy after each dipole, since the phase space dependence of the lost energy is essential even in the linear theory [1]. The general equation of motion for charged particle optics, especially when used to compute highly energetic electron motion, should therefore include the energy loss due to radiation and the reaction of the particle to its own electromagnetic field.

The behavior of a charged particle in the superposition of an external field and its own retarded field cannot be described without problems [2], [3], [4], the classical limit is discussed in [5].

After an appropriate average in the Lorentz-Dirac equation, we reformulate the equations in such a way that they have a suitable form for the conventional description of particle optics. We will keep the argumentation completely general and allow reference curves with torsion. Thus we obtain the equations of motion

with path length along some space curve as the independent parameter. These are the general equations of motion for describing charged particle optics.

To solve these equations of motion, we implemented the method of Taylor maps, which are computed with the Differential Algebraic (DA) technique. In standard devices like dipoles, quadrupoles, and higher order multipoles the equation of motion can be integrated with an exponential operator, such that the full power and speed of the DA method is obtained even with radiation effects.

II. THE LORENTZ-DIRAC EQUATION

To analyze the influence of radiation effects on particle motion consistently, we have to consider the field produced by a moving charged particle. Then we can compute the particle motion under the influence of its own field and an external field. To derive this equation, one can proceed in the following steps:

1. Derive the small velocity limit.
2. Write the general and covariant form of the equations of motion which satisfies the low velocity limit.
3. Reformulate the differential equation into an integral equation.
4. Approximate the integral equation.
5. Transform the covariant equation into a specific inertial frame.

These steps can be extracted from the references mentioned. As a result one obtains the equation of motion

$$m \frac{d}{d\tau} u^\mu = e \sqrt{\frac{\mu_0}{4\pi}} F^{\mu\nu} u_\nu + \frac{e^2 \mu_0}{6\pi c^3} u^\mu \frac{d}{d\tau} u_\nu \frac{d}{d\tau} u^\nu \quad (1)$$

which in the lab frame is

$$\frac{d}{dt} \vec{p} = \vec{F} - \frac{e^2 \mu_0 \gamma^4}{6\pi c^3} [\vec{a}^2 + \frac{\gamma^2}{c^2} (\vec{a} \cdot \vec{v})^2] \vec{v}. \quad (2)$$

with the external force $\vec{F} = q(\vec{E} + \vec{v} \times \vec{B})$. In particle optics we require an equation of motion of the form $\vec{z}' = \vec{f}(\vec{z}, s)$ for phase space variables \vec{z} . It indeed turns out that such a formulation is possible. After introduction of

$$\frac{d}{dt} \vec{p} = m\gamma \vec{a} + m \frac{\gamma^3}{c^2} (\vec{v} \cdot \vec{a}) \vec{v} \quad (3)$$

and several algebraic manipulations one is led to

$$\delta = \frac{e^2 \mu_0 \gamma^2 v}{6\pi m^2 c^3}, \quad (4)$$

$$\frac{d}{dt} \vec{p} = \vec{F}_\perp + \vec{n} \frac{\gamma^2}{2\delta} \left[\sqrt{1 + 4 \frac{\delta}{\gamma^2} (\vec{n} \cdot \vec{F} - \delta (\vec{n} \times \vec{F})^2)} - 1 \right].$$

*e-mail: hoff@desy.de

We can expand to the first power of $\delta|\vec{F}|$ and obtain

$$\frac{d}{dt}\vec{p} = \vec{F} - \vec{n}\delta[(\vec{n} \times \vec{F})^2 + \frac{1}{\gamma^2}(\vec{n}\vec{F})^2]. \quad (5)$$

This expansion is valid even for very high energy. For an electric field of $10^7 \frac{V}{m}$, this electron energy would be around 2700 GeV. For a magnetic field of 10T, this energy is about 150 GeV.

III. THE CURVILINEAR COORDINATE SYSTEM

We want to introduce a coordinate system with which particle motion close to some reference curve $\vec{R}(s)$ parameterized by its path length s can be described well. For that purpose one defines s dependent unit vectors \vec{e}_x and \vec{e}_y in such a way that close to this curve space points \vec{r} can be expressed as

$$\vec{r} = \vec{R}(s) + x\vec{e}_x(s) + y\vec{e}_y(s) \quad (6)$$

and the unit vectors $\vec{e}_x = \partial_s \vec{R}$, \vec{e}_x , and \vec{e}_y build a right handed coordinate frame. The reference curve's curvature κ can have x and y components κ_x and κ_y . There are three reasonable possibilities with different forms for their s derivatives.

1. The horizontal system in which one chooses \vec{e}_x always perpendicular to one fixed space direction \vec{e}_1 :

$$\begin{aligned} \frac{d}{ds}\vec{r} &= (x' + \frac{y\kappa_x}{\tan(\angle \vec{e}_1 \vec{e}_s)})\vec{e}_x \\ &+ (y' - \frac{x\kappa_x}{\tan(\angle \vec{e}_1 \vec{e}_s)})\vec{e}_y + (1 + x\kappa_x + y\kappa_y)\vec{e}_s. \end{aligned} \quad (7)$$

2. The Frenet coordinate system in which one chooses the \vec{e}_x direction always parallel to the curvature vector, which rotates around the reference curve with the torsion T :

$$\frac{d}{ds}\vec{r} = (x' - yT)\vec{e}_x + (y' + xT)\vec{e}_y + (1 + x\kappa)\vec{e}_s. \quad (8)$$

3. The curvilinear system in which the effect of the torsion is compensated by a reversed rotation [6]. In this case the orientation of the coordinate system at s depends on the history of the torsion between 0 and s and is therefore not defined locally. This disadvantage can be compensated by the simplicity of

$$\frac{d}{ds}\vec{r} = x'\vec{e}_x + y'\vec{e}_y + (1 + x\kappa_x + y\kappa_y)\vec{e}_s. \quad (9)$$

IV. THE LORENTZ-DIRAC EQUATION IN CURVILINEAR COORDINATES

In this coordinate system we therefore have

$$\begin{aligned} h &= 1 + x\kappa_x + y\kappa_y, \\ \frac{d}{ds}\vec{r} &= x'\vec{e}_x + y'\vec{e}_y + h\vec{e}_s, \\ \vec{p} &= p_x\vec{e}_x + p_y\vec{e}_y + p_s\vec{e}_s, \\ \frac{d}{ds}\vec{p} &= (p'_x - p_s\kappa_x)\vec{e}_x + (p'_y - p_s\kappa_y)\vec{e}_y \\ &+ (p'_s + p_x\kappa_x + p_y\kappa_y)\vec{e}_s. \end{aligned} \quad (10)$$

We use standard particle optical phase space coordinates

$$a = \frac{p_x}{p_0}, \quad b = \frac{p_y}{p_0}, \quad \tau = (t_0 - t)\frac{K_0}{p_0}, \quad \delta = \frac{K}{K_0} \quad (11)$$

where subscripts 0 refer to a reference particle, which in general does not have to follow the reference curve $\vec{R}(s)$ however. By defining

$$\mathcal{E} = E_x a + E_y b + E_s \frac{p_s}{p_0}, \quad (12)$$

$$\mathcal{B} = B_x a + B_y b + B_s \frac{p_s}{p_0},$$

the general equations of motion which are obtained with $ds/dt = v/h \cdot p_s/p$ simplify to

$$x' = ha \frac{p_0}{p_s}, \quad y' = hb \frac{p_0}{p_s}, \quad (13)$$

$$\tau' = \left(\frac{h_0 p_0}{v_0 p_s} - \frac{hp}{vp_s} \right) \frac{K_0}{p_0},$$

$$a' = \frac{qh}{p_s p_0} \{ m\gamma E_x + p_0(bB_s - \frac{p_s}{p_0} B_y) \} + \frac{p_s}{p_0} \kappa_x - \zeta a,$$

$$b' = \frac{qh}{p_s p_0} \{ m\gamma E_y - p_0(aB_s - \frac{p_s}{p_0} B_x) \} + \frac{p_s}{p_0} \kappa_y - \zeta b,$$

$$\delta' = \frac{qh p_0}{p_s K_0} \mathcal{E} - \xi.$$

where the damping terms are

$$\zeta = \frac{\mu_0 q^4 v}{6\pi m^2 c^3} \left(\frac{p_0}{p} \right)^3 \{ \mathcal{E}^2 + \gamma^2 ($$

$$\begin{aligned} &[bE_s - \frac{p_s}{p_0} E_y - \frac{p_0}{m\gamma} \{ B_x (\frac{p}{p_0})^2 - a\mathcal{B} \}]^2 \\ &+ [\frac{p_s}{p_0} E_x - aE_s - \frac{p_0}{m\gamma} \{ B_y (\frac{p}{p_0})^2 - b\mathcal{B} \}]^2 \\ &+ [aE_y - bE_x - \frac{p_0}{m\gamma} \{ B_s (\frac{p}{p_0})^2 - \frac{p_s}{p_0} \mathcal{B} \}]^2 \} \}, \end{aligned}$$

$$\xi = \zeta \frac{p^2}{m\gamma K_0}.$$

It is worth mentioning that the right hand side can be chosen origin preserving and s independent in standard devices like dipoles, quadrupoles, and multipoles. The transfer map can therefore be computed with the exponential operator $\exp(L_{\vec{r}})$ [7] and the full speed and power of the DA technique can be used even with radiation effects.

V. THE IMPLEMENTATION

Routines were written which integrate the equation of motion with the 8th order Runge Kutta integrator of the DA program COSY INFINITY[8]. By integrating with DA techniques, one obtains the phase space curve of the reference particle $\vec{z}_0(s)$ simultaneously with the Taylor map \vec{M} to arbitrary order such that $\vec{z}(s) = \vec{z}_0(s) + \vec{M}[\vec{z}(0) - \vec{z}_0(0)]$ for particles starting in phase space at $\vec{z}(0)$ close to the reference particle at $\vec{z}_0(0)$.

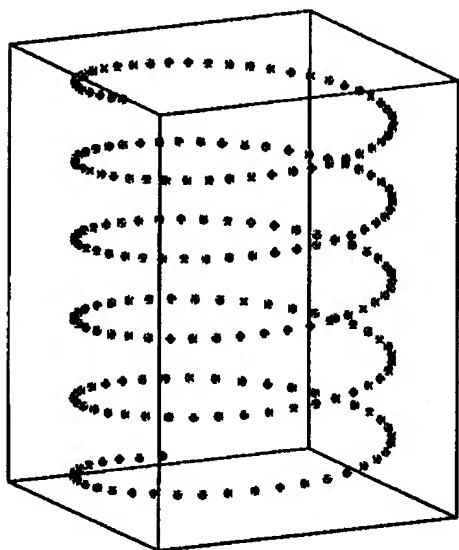


Figure 1. No radiative energy loss: $|\partial_z \vec{M}^T| = 1$

The figures (1) and (2) show an electron's path through a constant magnetic field with and without synchrotron radiation. The second order transfer maps are displayed in the adjacent tables. The Jacobians of the linear transfer maps are 1 for the energy conserving calculations and 0.023 for the calculations with radiation. This test manifests what is known as phase space damping in electron synchrotrons.

Our main purpose in using the constructed software will be the analysis of nonlinear effects in helical structures in proton machines (Siberian snakes) and electron machines (wigglers). Also the possibilities of influencing damping distributions with multipole wigglers should be analyzed.

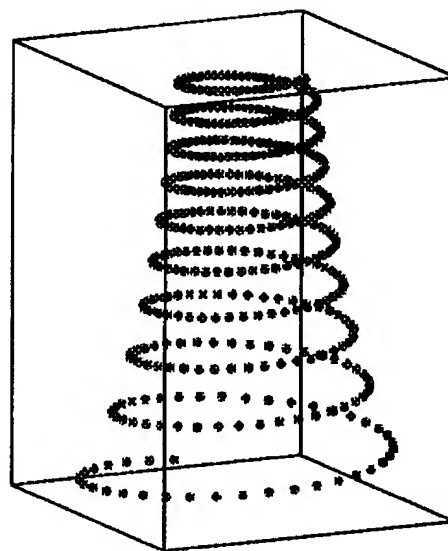


Figure 2. With radiative energy loss: $|\partial_z \vec{M}^T| = 0.023$

x	a	y	b	τ	δ	powers
-6.59	-.252	52.4	-.171	0	-.6	000000
1	0	0	0	0	0	100000
-3301	45.1	-2189	-65.7	-3704	-1	010000
0	0	1	0	0	0	001000
-65.5	.214	-8.24	-.316	0	0	000100
0	0	0	0	1	0	000010
3066	-41.9	2077	60.9	2963	1.0	000001
3E5	8774	-4E5	5646	-1E4	-.5	020000
2818	81.9	-4116	56.8	0	0	010100
-5E5	-2E4	8E5	-1E4	3E4	1.1	010001
-2058	28.4	-1409	-40.9	-2315	-.7	000200
-2596	-76.2	3833	-52.4	0	0	000101
2E5	7545	-4E5	4859	-1E4	-.7	000002

References

- [1] M. Sands. The physics of electron storage rings, an introduction. Technical Report SLAC-121, UC-28, (ACC), Stanford Linear Accelerator Center, 1970.
- [2] A. A. Sokolov and I. M. Ternov. *Radiation from Relativistic Electrons*. American Institutes of Physics, New York, 1986.
- [3] F. Rohrlich. *Classical Charged Particles*. Addison-Wesley, Mass., 1965.
- [4] L. D. Landau and E. M. Lifschitz. *Klassische Feldtheorie*. Lehrbuch der Theoretischen Physik. Akademie-Verlag, Berlin, 1966.
- [5] J. D. Jackson. *Classical Electrodynamics*. John Wiley & Sons, New York, 1975.
- [6] H. Rose. Hamiltonian magnetic optics. *Nuclear Instruments and Methods in Physics Research*, A258:374-401, 1987.
- [7] M. Berz. Arbitrary order description of arbitrary particle optical systems. *Nuclear Instruments and Methods*, A298:426-440, 1990.
- [8] M. Berz. COSY INFINITY version 6 reference manual. Technical Report MSUCL-869, National Superconducting

x	a	y	b	τ	δ	powers
37.9	-.253	52.7	.758	0	0	000000
1	0	0	0	0	0	100000
-893	-56.4	2876	-17.8	-3704	0	010000
0	0	1	0	0	0	001000
-65.9	-.948	47.4	-.317	0	0	000100
0	0	0	0	1	0	000010
1176	70.1	-3512	23.4	2963	1	000001
-1E5	403	-2E4	-2176	-2E4	0	020000
-3512	23.4	-1176	-70.1	0	0	010100
.3E6	-1183	.6E5	5382	.3E5	0	010001
-587	-35.1	1756	-11.7	-2315	0	000200
4390	-29.3	1469	87.7	0	0	000101
-2E5	829	-4E4	-3333	-1E4	0	000002

Cyclotron Laboratory, MSU, East Lansing, MI, 1992.

Effects of Imperfections on the Dynamic Aperture and Closed Orbit of the IPNS Upgrade Synchrotron*

E. Lessner, Y.-C. Chae, S. Kim

Argonne National Laboratory, 9700 So. Cass Ave., Argonne, Illinois 60439, U.S.A.

Abstract

Magnet imperfections and misalignments are analyzed in terms of their effects on the dynamic aperture and closed orbit of the IPNS Upgrade synchrotron. The dynamic aperture is limited primarily by the presence of chromaticity-correcting sextupoles. With the sextupoles energized to the values required to adjust the chromaticities to zero, further reductions of the dynamic aperture caused by dipole strength and roll errors, quadrupole strength and alignment errors, and higher-order multipole errors are studied by tracking. Design specifications for the dipole corrector magnets are obtained and the dynamic aperture is studied before and after correction of the closed orbit. The use of harmonic-correcting sextupoles to reduce the amplitude-dependent tune shifts driven by the chromaticity-correcting sextupoles is investigated.

I. INTRODUCTION

The proposed IPNS Upgrade is a dedicated source for neutron scattering experiments that uses a rapid-cycling synchrotron (RCS) to accelerate 1.04^{14} protons per pulse from 400 MeV to 2 GeV. A summary description of the machine is given elsewhere in these proceedings [1]. The RCS lattice is 190.4 m long and contains four superperiods. Each superperiod consists of three FODO cells of about 90° advance in each transverse plane, two dispersion-suppressor cells, and two dispersion-free straight cells. The orbit functions for one superperiod are shown in Figure 1, which has mirror symmetry at both ends.

The key design feature of the RCS is the prevention of beam losses during the injection, capture, and acceleration processes. Beam loss prevention in the transverse phase space is achieved by providing large dynamic aperture in both transverse planes. We have performed tracking studies to ensure that the RCS has a dynamic aperture larger than the physical aperture of the vacuum chamber, taking into account magnetic field imperfections due to fabrication tolerances and misalignments caused by surveying tolerances. In this paper, we present the results of tracking studies of closed-orbit distortions and dynamic aperture reduction in the RCS.

II. CLOSED-ORBIT DISTORTIONS

We investigated closed-orbit distortions (COD) caused by quadrupole misalignments, $(\delta z)_Q$, field deviations in dipole magnets, $(\delta B/B)_B$, and dipole roll angle misalignments, $(\delta\theta)_B$. The nominal tolerance values for these quantities were estimated based on the actual measured data from the 7-GeV Advanced Photon Source (APS) booster synchrotron [2], and are shown in Table 1. In the table, $(\delta z)_Q$ denotes quadrupole misalignments

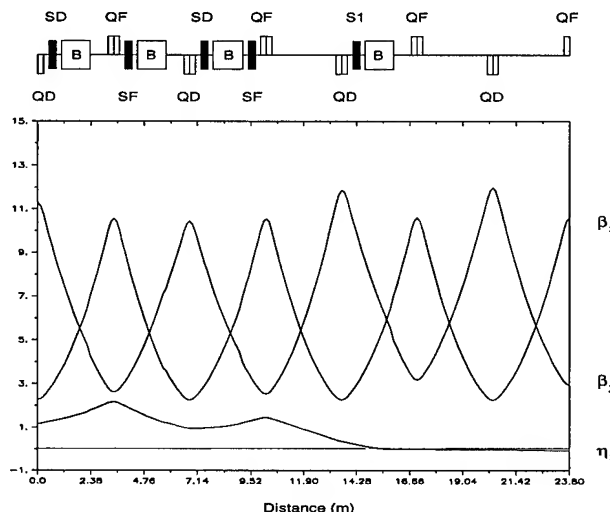


Figure 1
Lattice Functions for One-Half of a Superperiod.

in either the x - or y - plane.

Table 1
Nominal Alignment and Field Quality Tolerances

$(\delta z)_Q$	$(\delta B/B)_B$	$(\delta\theta)_B$
0.2 mm rms	0.1% rms	1 mrad rms

The analytically derived amplification factors for quadrupole misalignments in the RCS lattice are:

$$A_x = (\Delta x)_{\max}/(\delta x)_Q = 33, \quad A_y = (\Delta y)_{\max}/(\delta y)_Q = 24,$$

where $(\Delta z)_{\max}$ is the maximum COD in the horizontal or vertical direction, $(\Delta z)_{\max} = 2(\Delta z)_{\text{rms}}$, and a Gaussian distribution is assumed.

The amplification factors for field deviations in dipole magnets are:

$$A_x = \frac{(\Delta x)_{\max}}{(\delta B/B)_B} = 19 \text{ m}, \quad A_y = \frac{(\Delta y)_{\max}}{(\delta B/B)_B} = 12 \text{ m},$$

where orbit distortions in the vertical direction are caused by dipole roll angle misalignments.

Using these amplification factors, the estimated maximum orbit distortions are $(\Delta x)_{\max} = 18 \text{ mm}$ and $(\Delta y)_{\max} = 14 \text{ mm}$. An effective scheme to reduce the orbit distortions is therefore needed.

The orbit corrections were simulated by using the program MAD [3]. Since the number of simulations is finite, we used relaxed tolerances of $(\delta z)_Q = 0.4 \text{ mm rms}$ to cover the worst cases and increase the level of confidence on the results. The

*Work supported by U.S. Department of Energy, Office of Basic Energy Sciences under Contract No. W-31-109-ENG-38.

corresponding specification of the required corrector strengths is conservative.

The simulations were carried over 30 different machines. In the RCS, horizontal and vertical beam position monitors (BPMs) are located in the focusing and defocusing quadrupoles, respectively. Similarly, horizontal and vertical correctors are located near the focusing and defocusing quadrupoles. There are a total of 28 BPMs and 28 correctors in each plane. Horizontal and vertical correctors of up 85 and 71 G-m, respectively, permit correction of the orbit to within the rms BPM accuracy of 0.1 mm. The maximum dipole corrector strength is specified as 110 G-m. The engineering design for corrector magnets with an effective length of 15 cm is detailed in [4].

III. DYNAMIC APERTURE

The dynamic aperture in the RCS is limited primarily by the presence of chromaticity-correcting sextupoles. The natural normalized chromaticities of the lattice are $\xi_x = -1.06$ and $\xi_y = -1.20$. Chromaticity is adjusted by 16 horizontal focusing and 16 horizontal defocusing sextupoles. With the sextupoles energized to the values required to adjust the chromaticities to zero, we investigated further reductions of the dynamic aperture caused by random misalignments and magnet fabrication imperfections. Dynamic aperture limitations were simulated by using the symplectic kick code RACETRACK [5].

The dynamic aperture was defined as the limiting stable betatron amplitude of a particle that survived 2,000 turns in a static field. This corresponds to about two synchrotron periods at injection. Tests carried out up to 10,000 turns showed very little difference from the results obtained with 2,000 turns. The distribution of errors was assumed to be Gaussian, with a cutoff of $\pm 5\sigma$, and the simulations were performed for 10 different machines.

Dynamic aperture reductions caused by closed-orbit distortions, arising from the alignment tolerances discussed in the previous section, with and without closed-orbit corrections, are shown in Figure 2. The lines in the figure are the averages and the error bars are the standard deviations for the 10 machines. The dynamic apertures are displayed at the focusing quadrupole. The dynamic aperture of the perfect machine and the beam-stay-clear region (BSC), defined as $\sqrt{\frac{2\epsilon\beta}{\pi} + \frac{\eta}{\delta p/p}} + COD$, where η is the dispersion function, ϵ is the emittance, and $\delta p/p$ is the momentum deviation, are also shown. The closed-orbit was corrected to 0.1 mm rms, as described in Section II. Before orbit correction, the dynamic aperture is still sufficient to permit beam injection. Correction of the orbit restores the dynamic aperture to that of the perfect machine.

Dynamic aperture reductions due to magnetic field imperfections were studied by using the multipole coefficients a_n and b_n , shown in Table 2. The coefficient values were obtained by scaling the measured data of the APS booster synchrotron magnets to the RCS magnets. The magnetic field expressed in terms of these coefficients is:

$$B = B_0 \sum_{n=0}^{\infty} (b_n + i a_n)(x + iy)^n, \quad (1)$$

where a_n and b_n are the normal and skew coefficients in units of cm^{-n} .

Table 2
Multipole Coefficients of RCS Magnets

Multipole*	Random cm^{-n}	Systematic cm^{-n}
b_{1D}	2.60E-6	-7.10E-6
b_{2D}	3.90E-8	-0.70E-6
b_{1Q}	4.90E-4	2.50E-4
a_{1Q}	1.70E-4	-0.40E-4
b_{2Q}	4.80E-6	-1.20E-6
a_{2Q}	0.13E-4	0.28E-6
b_{3Q}	1.20E-6	-5.50E-6
a_{3Q}	0.62E-6	0.22E-6
b_{4Q}	3.60E-8	0.30E-8
a_{4Q}	4.50E-8	-0.80E-8
b_{5Q}	0.24E-8	1.95E-8
b_{2S}	1.36E-3	5.00E-4
a_{2S}	3.30E-4	-4.90E-4
b_{3S}	0.17E-4	-2.40E-6
a_{3S}	0.61E-4	3.20E-6
* D = dipole	Q = quadrupole	S = sextupole

There were no appreciable effects on the dynamic aperture for multipoles up to twice the values depicted in Table 2. A reduction of 15% was observed for multipoles at four times those values.

Finally, misalignments were included along with multipole components. Reductions, both before and after closed-orbit corrections, were studied. The results are shown in Figure 3. The dynamic aperture before COD corrections is still as large as the BSC, thus permitting the establishment of a closed-orbit solution at injection. The dynamic aperture after correction is very close to that obtained for multipole components only, as expected.

IV. Harmonic Correction

The tunes of the bare lattice are $\nu_x = 6.821$ and $\nu_y = 5.731$. However, the tune shift due to space charge forces moves the working point to the proximity of the $3\nu_x = 20$ resonance line [4]. This resonance can be driven by the chromaticity-correcting sextupoles and can have a deleterious effect on the circulating beam. The 20th harmonic of the sextupole component is suppressed by placing harmonic-correcting sextupoles (denoted by S1 in Figure 1) in the dispersion-free sections. Horizontally defocusing sextupoles with integrated strength of $0.4m^{-2}$, placed in the eight dispersion-suppressor cells, eliminate the 20th harmonic. The phase spaces with and without harmonic-correcting sextupoles are shown in Figure 4. The dynamic apertures with and without harmonic-correcting sextupoles are shown in Figure 5.

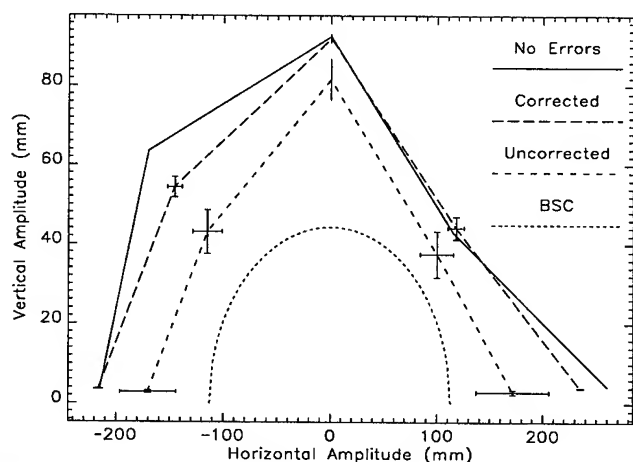


Figure 2

Dynamic Aperture in the Presence of Quadrupole Misalignments, Dipole Field Deviations and Dipole Roll Angle Misalignments. (The dynamic aperture for the perfect machine is shown for comparison. The ellipse represents the BSC region at the focusing quadrupole.)

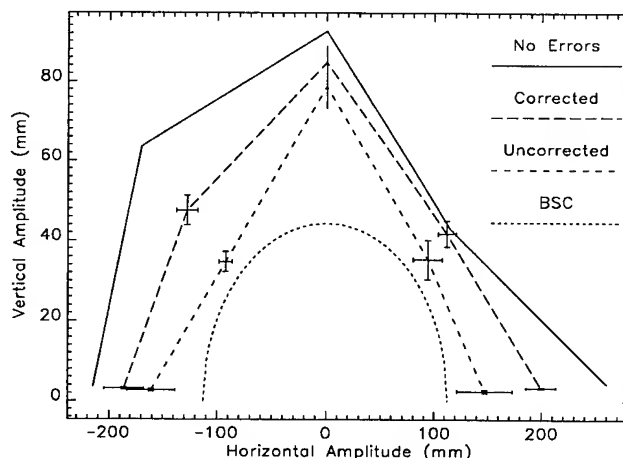


Figure 3

Dynamic Aperture Reductions Caused by Misalignments and Multipoles, Plotted before and after Corrections of the Closed Orbit.

V. Conclusion

Linear and nonlinear effects on the lattice of the IPNS Upgrade RCS were studied in terms of the closed orbit, dynamic aperture, and harmonic-correction techniques. The simulations showed that the closed orbit distortions can be corrected within the desired accuracy, and the dynamic aperture is large enough to contain the beam-stay-clear region. Harmonic-correcting sextupoles, properly placed in the lattice, can effectively remove the dangerous resonance line $3\nu_x = 20$ driven by the chromaticity-correcting sextupoles, without degrading the dynamic aperture.

VI. References

- [1] Y. Cho *et al*, "Feasibility Study of a 1-MW Spallation Source," in these proceedings.
- [2] H. Friedsam, "A New Accelerator Alignment Concept Using Laser Trackers," *Proceedings of the European Particle Conference 3*, 2570-2572 (1994).
- [3] H. Grote and F. C. Iselin, "The MAD Program, User's Reference Manual," CERN Report No. CERN/SL/90-13 (AP), Rev. 4, (1994).
- [4] "IPNS Upgrade: A Feasibility Study," ANL-95/13, (April 1995).
- [5] A. Wrulich, "RACETRACK: A Computer Code for the Simulation of Nonlinear Particle Motion in Accelerators," Report No. DESY 84-026, (1984).

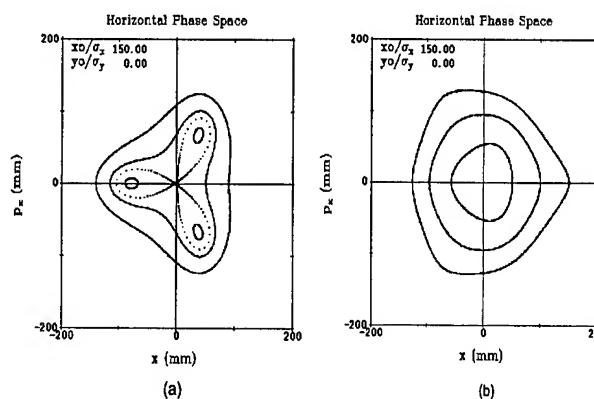


Figure 4

Horizontal Phase Space Motion with $\nu_x = 6\frac{2}{3}$ without (a) and with (b) Harmonic-Correcting Sextupoles.

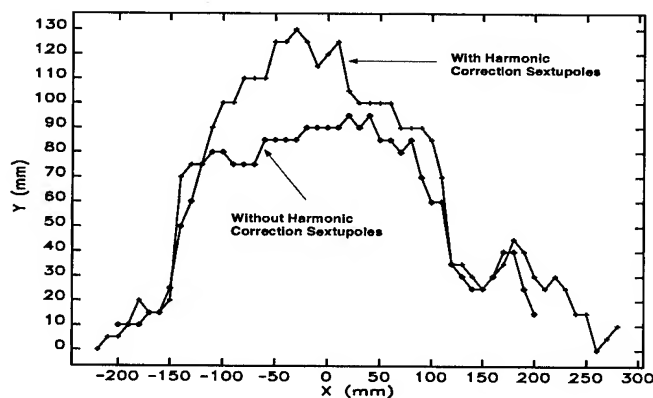


Figure 5

Dynamic Apertures with and without Harmonic-Correcting Sextupoles.

Paraxial Expansion of a Static Magnetic Field in a Ring Accelerator*

Lee C. Teng

Argonne National Laboratory, 9700 So. Cass Ave., Argonne, Illinois 60439, U.S.A.

Abstract

In the paraxial approximation, trajectories of beam particles in a ring accelerator are computed expanded in powers of lateral displacements and slopes from a closed reference orbit. To do this, one needs first the expanded expressions of the magnetic field and potentials producing the particle motion. This is derived here in a most general form.

I. Introduction

In a storage ring or a ring accelerator the ideal closed orbit is generally a planar curve. All particles in the beam travel near to the closed orbit. Thus, for the study of the particle motion it is convenient to use the closed orbit as the reference axis and compute the particle trajectories in the paraxial approximation. The right-handed coordinates used are shown in Fig. 1 and are described below. Also shown in Fig. 1 is the local radius of

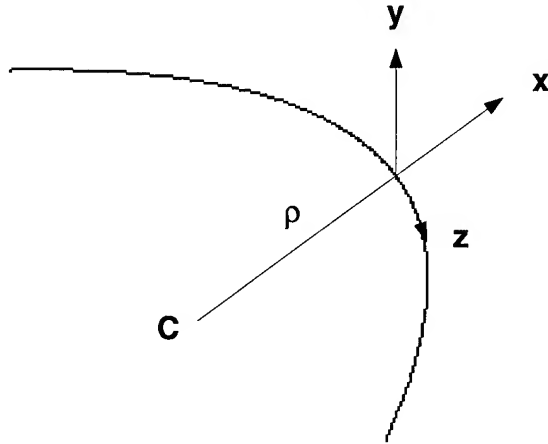


Figure 1

x: horizontal (in orbit plane) along the outward normal of the closed orbit, y: vertical, z: horizontal and along the forward tangent of the closed orbit.

curvature $\rho(z)$ and the center of curvature "C." The metric of these rotating coordinates is

$$ds^2 = dx^2 + dy^2 + (1 + kx)^2 dz^2, \quad (1)$$

where

$$k = k(z) = 1/\rho(z) = \text{curvature}.$$

II. Scalar Potential

To expand the paraxial particle trajectory in powers of x and y (and x' and y' with prime indicating d/dz) we need to first write the magnetic field (considered static) in an expanded form. In vacuum, the magnetic field can be expressed in terms of either a scalar potential ϕ or a vector potential A . It is simpler to start with the scalar potential. We shall write

$$\phi = \sum_{n=0}^{\infty} \sum_{m=0}^n a_{n,m} \frac{x^{n-m}}{(n-m)!} \frac{y^m}{m!} \equiv \sum_{n=0}^{\infty} \phi^{(n)}, \quad (2)$$

where the coefficients $a_{n,m} = a_{n,m}(z)$ are functions of z and the parenthesized superscript (n) indicates that the quantity is a homogeneous expression in x and y of total degree n .

The Laplace equations, $\nabla^2 \phi = 0$, to be satisfied by ϕ is, in these coordinates,

$$-\frac{\partial^2 \phi}{\partial y^2} = \frac{1}{1 + kx} \frac{\partial}{\partial x} \left[(1 + kx) \frac{\partial \phi}{\partial x} \right] + \frac{1}{1 + kx} \frac{\partial}{\partial z} \left(\frac{1}{1 + kx} \frac{\partial \phi}{\partial z} \right). \quad (3)$$

Straightforward but laborious expansions of $(1 + kx)^{-p}$ factors and realignments of indices give the following recursion formula on index m

$$-a_{n+m+2,m+2} = a_{n+m+2,m} + \sum_{l=0}^n (-k)^l \frac{n!}{(n-l)!} [ka_{n-l+m+1,m} + (l+1)a''_{n-l+m,m} - \frac{(l+1)(l+2)}{2} (n-l)k'a'_{n-l+m-1,m}], \quad (4)$$

where, as before, prime means d/dz . This is a rather messy and obscure formula. It is instructive to look at the first two recursions for $n = 0$ and 1,

$$\underline{n = 0}$$

$$-a_{m+2,m+2} = a_{m+2,m} + ka_{m+1,m} + a''_{m,m}, \quad (5)$$

$$\underline{n = 1}$$

$$-a_{m+3,m+2} = a_{m+3,m} + ka_{m+2,m} + a''_{m+1,m} - k'a'_{m,m} - k^2 a_{m+1,m} - 2ka''_{m,m}. \quad (6)$$

These relations reveal clearly the hierarchy of the recursion. Because of the double step recursion in m , there are two sets of solutions. The field with odd m values starting with $m = 1$ is symmetric with respect to the orbit plane and is the normal design field. The field with even m values starting with $m = 0$ is anti-symmetric with respect to the orbit plane and is the skew field arising only from construction imperfections.

* Work supported by U.S. Department of Energy, Office of Basic Energy Sciences under Contract No. W-31-109-ENG-38.

III. Magnetic Field Components

The components of the field \mathbf{B} are given by $\mathbf{B} = \nabla\phi$, or

$$B_x = \frac{\partial\phi}{\partial x} = \sum_{n=1}^{\infty} \sum_{m=0}^{n-1} a_{n,m} \frac{x^{n-m-1}}{(n-m-1)!} \frac{y^m}{m!} \equiv \sum_{n=1}^{\infty} B_x^{(n-1)},$$

$$B_y = \frac{\partial\phi}{\partial y} = \sum_{n=1}^{\infty} \sum_{m=1}^n a_{n,m} \frac{x^{n-m}}{(n-m)!} \frac{y^{m-1}}{(m-1)!} \equiv \sum_{n=1}^{\infty} B_y^{(n-1)}, \quad (7)$$

or

$$B_z = \frac{1}{1+kx} \frac{\partial\phi}{\partial z}$$

$$= \sum_{n=0}^{\infty} \sum_{l=0}^n \sum_{m=0}^{n-l} (-k)^l \frac{(n-m)!}{(n-m-l)!} a'_{n-l,m} \frac{x^{n-m}}{(n-m)!} \frac{y^m}{m!}$$

$$\equiv \sum_{n=0}^{\infty} B_z^{(n)}.$$

On the orbit plane $y = 0$, for the normal field ($m = \text{odd}$) we have

$$B_y(y=0) = \sum_{n=1}^{\infty} a_{n,1} \frac{x^{n-1}}{(n-1)!}, \quad (8)$$

$$B_x(y=0) = B_z(y=0) = 0,$$

and for the skew field ($m = \text{even}$) we have

$$B_x(y=0) = \sum_{n=1}^{\infty} a_{n,0} \frac{x^{n-1}}{(n-1)!},$$

$$B_y(y=0) = 0, \quad (9)$$

$$B_z(y=0) = \sum_{n=0}^{\infty} \sum_{l=0}^n (-k)^l \frac{n!}{(n-l)!} a'_{n-l,0} \frac{x^n}{n!}.$$

The standard (American) multipole coefficients defined by

$$B_y + iB_x = B_0 \sum (b_n + ia_n)(x + iy)^n, \quad i = \sqrt{-1}, \quad (10)$$

are related to the double indexed coefficient $a_{n,m}$ by

$$a_{n,0} = \left(\frac{\partial^{n-1} B_x}{\partial x^{n-1}} \right)_{x=y=0} = B_0(n-1)!a_{n-1}, \quad (11)$$

$$a_{n,1} = \left(\frac{\partial^{n-1} B_y}{\partial x^{n-1}} \right)_{x=y=0} = B_0(n-1)!b_{n-1}.$$

IV. Vector Potential

In the vector potential \mathbf{A} we choose the gauge $x A_x + y A_y = 0$ (the equivalent of $A_r = 0$ in the case of a linear reference orbit and cylindrical coordinates (r, θ, z)). Then we can write

$$A_x = -yF, \quad A_y = xF, \quad A_z = \frac{G}{(1+kx)}, \quad (12)$$

where $F = F(x, y, z)$ and $G = G(x, y, z)$. The relation $\mathbf{B} = \nabla \times \mathbf{A}$ is, then

$$B_x = \frac{1}{1+kx} \left(\frac{\partial G}{\partial y} - x \frac{\partial F}{\partial z} \right),$$

$$B_y = \frac{1}{1+kx} \left(-\frac{\partial G}{\partial x} - y \frac{\partial F}{\partial z} \right), \quad (13)$$

$$B_z = x \frac{\partial F}{\partial x} + y \frac{\partial F}{\partial y} + 2F,$$

$$x \frac{\partial G}{\partial x} + y \frac{\partial G}{\partial y} = (1+kx)(yB_x - xB_y),$$

$$x \frac{\partial F}{\partial x} + y \frac{\partial F}{\partial y} + 2F = B_z. \quad (14)$$

This shows that G or A_z is given by B_x and B_y , and that F , hence A_x and A_y , are given by B_z . Applying Euler's theorem for homogenous forms to give $F^{(p)}$ and $G^{(p)}$ in terms of $B_x^{(p)}$, $B_y^{(p)}$ and $B_z^{(p)}$, then substituting from Eq. (7) we get

$$F = \sum_{n=0}^{\infty} \frac{1}{n+2} B_z^{(n)}$$

$$= \frac{1}{2} a'_{0,0} + \sum_{n=1}^{\infty} \sum_{m=0}^n \frac{a'_{n,m}}{n+2} \frac{x^{n-m}}{(n-m)!} \frac{y^m}{m!}, \quad (15)$$

and

$$G = \sum_{n=1}^{\infty} \left(\frac{1}{n} + \frac{kx}{n+1} \right) (yB_x^{(n-1)} - xB_y^{(n-1)})$$

$$= \sum_{n=1}^{\infty} \left(\frac{1}{n} + \frac{kx}{n+1} \right) \times$$

$$\sum_{m=0}^n a_{n,m} \left[(n-m) \frac{y}{x} - m \frac{x}{y} \right] \frac{x^{n-m}}{(n-m)!} \frac{y^m}{m!}. \quad (16)$$

Eqs. (12), (14), and (15) give the necessary expanded forms of the vector potential components for insertion into either the Lagrangian or the Hamiltonian function of the particle motion.

V. Lagrangian Formulation

To proceed we could employ either the Lagrangian or the Hamiltonian formulation. Here we present the simpler and more symmetric Lagrangian formulation. The orbit Lagrangian is

$$L(x, x', y, y'; z) = [(1+kx)^2 + x'^2 + y'^2]^{1/2}$$

$$+ \frac{e}{p} [x'A_x + y'A_y + (1+kx)A_z]$$

$$\equiv K(\text{kinematic term}) + D(\text{dynamic term}), \quad (17)$$

where e and p are the charge and the momentum of the particle. The expanded forms of K and D are

$$K = (1+kx) \left[1 + \frac{x'^2 + y'^2}{(1+kx)^2} \right]^{1/2}$$

$$\begin{aligned}
&= 1 + kx + \frac{1}{2} \left[\sum_{m=0}^{\infty} (-1)^m (kx)^m \right] (x'^2 + y'^2) \\
&\quad - \frac{1}{8} \left[\sum_{m=0}^{\infty} (-1)^m \frac{(m+1)(m+2)}{2} (kx)^m \right] (x'^2 + y'^2)^2 \\
&\quad + \dots \tag{18}
\end{aligned}$$

$$\begin{aligned}
D &= \frac{1}{B\rho} [(y'x - x'y)F + G] \\
&= \frac{1}{B\rho} (y'x - x'y) \sum_{n=0}^{\infty} \sum_{m=0}^n \frac{a'_{n,m}}{n+2} \frac{x^{n-m}}{(n-m)!} \frac{y^m}{m!} \\
&\quad + \frac{1}{B\rho} \sum_{n=1}^{\infty} \left(\frac{1}{n} + \frac{kx}{n+1} \right) \\
&\quad \times \sum_{m=0}^n a_{n,m} \left[(n-m) \frac{y}{x} - m \frac{x}{y} \right] \frac{x^{n-m}}{(n-m)!} \frac{y^m}{m!}, \tag{19}
\end{aligned}$$

where

$$B\rho \equiv \frac{P}{e} = \text{rigidity of the particle.}$$

It is easy to show that to the first degree terms one gets the well-known linear equations. To get the second- and higher-order terms the procedure is equally straightforward but increases progressively in complexity.

EXPERIMENTAL DETERMINATION OF LINEAR OPTICS INCLUDING QUADRUPOLE ROTATIONS*

J. Safranek

National Synchrotron Light Source, Brookhaven National Laboratory, Upton, NY 11973

Abstract

The measured response matrix giving the change in orbit at beam position monitors (BPMs) with changes in steering magnet excitation can be used to accurately determine many important parameters in a storage ring. Using the NSLS X-Ray Ring measured response matrix we have determined the gradients in all 56 quadrupole magnets; the calibration of the steering magnets and BPMs; the rotational mis-alignments of the quadrupoles, steering magnets, and BPMs about the electron beam direction; the longitudinal magnetic centers of the orbit steering magnets; and the transverse mis-alignments of the sextupoles. Random orbit measurement error of the BPMs propagated to give 0.04% rms error in determination of individual quadrupole gradients and 0.4 mrad rms error in the determination of quadrupole rotational alignment. Small variations of a few parts in a thousand in the quadrupole gradients within an individual family were resolved. The improved understanding of the X-Ray Ring has enabled us to better control the electron beam size.

I. INTRODUCTION

A precise understanding of the linear optics, including coupling, in a storage ring is critical to achieving maximum performance. Recent results from Fermilab [1] illustrate the importance of understanding and controlling coupling in colliding beam machines. Careful coupling control will also be crucial in damping rings for linear colliders. In synchrotron light sources, minimization of coupling minimizes the vertical electron beam size and produces the brightest possible photon beam. Here we will present a method for experimentally determining the sources of coupling in a storage ring.

Previous work [2-7] has shown that it is possible to accurately derive the normal gradient distribution in a storage ring by analyzing the orbit response matrix. In this paper this technique will be extended to include a derivation of the skew gradient distribution in the NSLS X-Ray Ring. The X-Ray Ring BPM system permits fast, highly accurate measurement of the orbit response matrix [8]. In less than one second, the orbit at all 48 horizontal and vertical BPMs is read 256 times and averaged. The result is a reading of the orbit limited mostly by the 2.5 μm digital resolution. These accurate orbit response measurements yield detailed information concerning the X-Ray Ring optics.

II. METHOD

The MAD [9] accelerator optics modeling program was used to calculate the model response matrix. The parameters in the MAD model were varied to minimize the χ^2 deviation between

the model and measured orbit response matrices (M_{mod} and M_{meas}).

$$\chi^2 = \sum_{i,j} \frac{(M_{meas,ij} - M_{mod,ij})^2}{\sigma_i^2},$$

where the sum is over the 90 orbit steering magnets (51 horizontal and 39 vertical) and the 96 BPMs (48 horizontal and 48 vertical). The matrices include the coupling terms (i.e. the shift in vertical orbit with horizontal steering magnets and horizontal orbit shifts with vertical steering). The σ_i are the measured noise levels for the BPMs. The χ^2 minimization was achieved by iteratively solving the linear system of equations,

$$-V_k = \frac{dV_k}{dx_n} \Delta x_n, \quad (1)$$

where $V_k = (M_{meas,ij} - M_{mod,ij})/\sigma_i$ with k ranging from 1 to 8640 for the 8640 elements of the orbit response matrix. The x_n are the parameters varied to fit M_{meas} to M_{mod} . Solving equation 1 for Δx_n gives the change in the parameters to minimize $\sum_k V_k^2$ which is equivalent to χ^2 .

The parameters varied to fit M_{meas} to M_{mod} include each of the gradients in the 56 X-Ray Ring quadrupoles; the small gradients in the dipole magnets; the gains of the 96 BPMs; the calibrations of the 90 orbit steering magnets; and the rotational alignment of the quadrupoles, steering magnets, and BPMs. Also included in the fit is the energy shift associated with changing each orbit steering magnet. When a steering magnet strength is changed, the total path length around the ring must stay constant to keep the electron bunches in synchronism with the rf, so there is an energy shift of the stored beam with an associated shift in the closed orbit proportional to the dispersion.

A fourth parameter was varied for each BPM. Three parameters for each BPM were already mentioned: the horizontal gain, the vertical gain, and the rotational alignment. By adding a fourth parameter we are varying all the possible parameters of a two-dimensional linear fit between the two signals from the BPM and the actual horizontal and vertical orbit. This is necessary, because there is significant variation of the linear mapping from BPM to BPM. The BPMs in the X-Ray Ring were constructed by welding a disk with two pick-up electrodes to the top of the vacuum chamber and another such disk to the bottom of the vacuum chamber. Due to the tolerances in this welding process, there is significant variation in the response of the BPMs. The following gives the full linear transformation used in fitting the orbit measurements for each BPM:

$$\begin{pmatrix} \bar{x} \\ \bar{y} \end{pmatrix} = \frac{1}{\sqrt{1-C^2}} \begin{pmatrix} \cos\theta & \sin\theta \\ -\sin\theta & \cos\theta \end{pmatrix} \begin{pmatrix} 1 & C \\ C & 1 \end{pmatrix} \begin{pmatrix} g_x x \\ g_y y \end{pmatrix}.$$

The four parameters varied for each BPM are horizontal gain (g_x), vertical gain (g_y), rotation (θ), and C which is a parameter

*Work performed under the auspices of the U.S. Department of Energy

associated with errors in the construction of the BPM in which one diagonal pair of pick-up electrodes is closer together than the other diagonal pair.

Even with the above parameters varied, the orbit response of certain orbit steering magnets could not be fit to the BPM measurement noise level. The magnets with the poorest fit were the ones closest to other ferromagnetic material in the ring. The steering magnets have long end-fields. When they are located near other ferromagnetic material, the end fields are clipped and the longitudinal magnetic center of the steering magnet is shifted from its physical center. We varied the positions of the steering magnets in the MAD model, so the fitting converged to give the longitudinal magnetic centers of the magnets. As expected, we found that the closer a steering magnet was to some other ferromagnetic ring element, the more the fit for its magnetic center deviated from its measured physical center. With the corrected longitudinal position, the model and measured responses agreed to about the noise level of the BPMs.

In all, 626 parameters were varied to fit the 8640 elements in the X-Ray Ring response matrix. When the fit had converged, the rms difference between M_{mod} and M_{meas} was 1.2 μm which is primarily due to the digital accuracy (one bit is 2.5 μm) of the BPM readings. The fit converged to values to each of the 626 parameters. In the next sections we discuss how accurately these parameters reflect the real gradients, rotations, and calibrations of the elements in the X-Ray Ring.

III. ERROR ANALYSIS

Random errors on measured data, such as the random noise on the orbit response matrix measurement, propagate in a predictable way to give well-defined error bars on fit parameters. Unknown systematic errors, on the other hand, propagate in unknown ways, making it difficult to determine the size of the error bars. Every effort was made to ensure that the difference between the model and measured response matrices converged to the noise level of the BPMs, because this ensures that there is no remaining systematic error in the model. If all 626 parameters were not included in the fit, the rms difference between the model and measured response matrices would not have converged to 1.2 μm . The additional error would have been due to systematic error and would have contributed an unknown amount to the error bars.

The number of data points, 8640, is much greater than the number of parameters, 626, but this does not in itself guarantee that the solution is unique. One way to test for uniqueness is to look at the eigenvalues associated with the matrix, dV_k/dx_n , in equation 1. If this matrix is singular, it will have eigenvalue(s) equal to zero, and there will be an infinite region in parameter space over which the fit gives the minimum χ^2 . In such a case, our fit parameters would have infinite error bars regardless of how small the BPM noise is. There is actually one singularity in dV_k/dx_n , which is due to the fact that if all the steering magnet calibrations and all the BPM gains were increased together, the response matrix would not change. This means that when analyzing the orbit response matrix data alone, only the relative calibrations of the BPMs and steering magnets can be derived. The absolute calibrations have infinite error bars. The absolute calibrations, however, can be derived by comparing the shift in orbit

with rf frequency to the model dispersion. The model dispersion is well known from the quadrupole calibration, so the absolute gain calibration of the BPMs can be derived. The singularity in dV_k/dx_n was avoided by inverting the matrix using singular value decomposition (SVD) [10]. The SVD threshold was adjusted to eliminate the one very small eigenvalue. The eigenvalue associated with the steering magnet/BPM degeneracy was 15 times smaller than the next smallest eigenvalue. That all the other eigenvalues were much larger indicates that there are no other degeneracies in dV_k/dx_n (see [10]).

The easiest way to determine how much the fit parameters vary due to random errors in the measurements is simply to take many data sets, analyze each one separately, and see how much variation there is between fit parameters for the different data sets. We measured the response matrix ten times, and fit a model to each response matrix. Then, for each of the parameters we took the average over the ten data sets and calculated the rms variation from the average. The results are shown in table 1.

Table 1. These rms variations are the error bars on the fit parameters due to random orbit measurement errors.

Parameter	rms variation
quadrupole gradients	.04 %
quadrupole rotations	.4 mrad
BPM gain	.05 %
BPM rotations	.5 mrad
BPM C-parameter	.0004
steering magnet calibration	.05 %
steering magnet rotations	.8 mrad
steering magnet longitudinal center	2 mm
steering magnet fractional energy shift	3.4E-7

The size of the error bars in table 1 is determined by the signal-to-noise ratio of the orbit response matrix measurement. To decrease the error bars, the signal-to-noise must be increased. The size of the signal is the size of the orbit shifts when measuring the response matrix. Orbit shifts of .8 mm were used when measuring the 10 response matrices used for table 1. We also measured response matrices with 1.6 mm rms orbit shifts to double the signal to noise. With 1.6 mm rms orbit distortions, however, we could only fit M_{mod} to M_{meas} to an rms difference of 1.4 μm , not the 1.2 μm with which we could fit the .8 mm rms orbit distortions. This means there were systematic errors in the measurement, most likely due to nonlinearities in the BPM electronics. Thus BPM-electronics nonlinearities limit the size of the signal we can fit. Improved BPM electronics have been developed [11], and will be available for orbit measurements in the future. The present limit on the noise of the orbit response matrix measurement is the 2.5 μm digital resolution.

IV. RESULTS

The error analysis showed that the fit parameters are very close to the real parameters in the X-Ray Ring. As discussed previously [3], the fit quadrupole gradients agreed well with the magnetic measurements we were able to find. Also other measured lattice parameters such as dispersion and tunes agreed well with the MAD model the fitting generated.

Table 2 shows the rms size of the fit rotations as well as the maximum rotations found. The BPM rotations are quite large due to the construction method described above.

Table 2. This table shows the rms rotations of the 56 quadrupoles, the 48 BPMs, and the 90 steering magnets. Also shown are the maximum rotations and the resolution with which we could determine the rotations. The resolutions come from table 1.

FIT ROTATIONS	rms	maximum	resolution
quadrupole	1.4 mrad	3.6 mrad	.4 mrad
BPM	10 mrad	31 mrad	.5 mrad
steering magnet	6 mrad	21 mrad	.8 mrad

The first work that was a direct application of the better understanding of the X-Ray Ring optics was the development of a low emittance lattice [12]. The response matrix fit was done using response matrices measured while the sextupole magnets were turned off. We then turned on the sextupoles and remeasured the response matrix. Starting with the MAD model which was generated by fitting the response matrix with the sextupoles off, we varied gradients in each sextupole to fit the matrix measured with the sextupoles on. In this way we were able to derive the gradients in each of the sextupoles due to horizontal orbit offsets in the sextupoles. We then adjusted the strengths of the quadrupoles adjacent to the sextupoles in order to compensate for the sextupole gradients. Thus we were able to correct a large break in periodicity of the dispersion, and reduce the horizontal emittance.

Another application of the results will be in the X-Ray Ring coupling correction algorithm [13]. The coupling algorithm is limited by previously unknown corrector and BPM rotational misalignments. Now that these rotations are known, they will be used to improve the coupling correction.

V. CONCLUSION

Analysis of the measured orbit response matrix has yielded a great deal of detailed information concerning the X-Ray Ring including the normal and skew gradients in each quadrupole. This information has already proven useful for lowering the horizontal emittance. The BPM, steering magnet, and quadrupole rotation information should improve the X-Ray Ring coupling correction. The results from this analysis would be useful for colliding beam storage rings and damping rings as well as synchrotron light sources.

VI. ACKNOWLEDGEMENTS

I would like to thank Jeff Corbett, Sam Krinsky, and Martin Lee for stimulating discussions. Susila Ramamoorthy's improved fast averaged orbit readings helped provide the accurate orbit measurements necessary for this work. John Smith's help providing cpu time for the lengthy calculations was appreciated, as was Yong Tang's help integrating the program with the NSLS control system. Thanks to Julie Leader for her patient editing.

References

- [1] N.M. Gelfand, Coupling in the Tevatron, FERMILAB-TM-1916, Dec, 1994.
- [2] J. Safranek and M.J. Lee, Calibration of the X-Ray Ring Quadrupoles, BPMs, and Orbit Correctors Using the Measured Orbit Response Matrix, AIP Conference Proceedings, Vol 315, 1994.
- [3] J. Safranek and M.J. Lee, Proceedings of the 1994 European Particle Accelerator Conference, pg 1027.
- [4] W.J. Corbett, M.J. Lee and V. Ziemann, "A Fast Model-Calibration Procedure for Storage Rings," SLAC-PUB-6111, May, 1993.
- [5] M.J. Lee, Y. Zambre, W.J. Corbett, "Accelerator Simulation Using Computers," SLAC-PUB-5701A, 1991.
- [6] S. Kamada, Proceedings of the Workshop on Non Linear Dynamics in Particle Accelerators, 1994.
- [7] J. Bengtsson and M. Meddahi, Modeling of Beam Dynamics and Comparison with Measurements for the Advanced Light Source, Proceedings of the 1994 European Particle Accelerator Conference, pg 1021.
- [8] R. Biscardi and J.W. Bittner, Switched Detector for Beam Position Monitor, Proceedings of the 1989 IEEE Particle Accelerator Conference, pg 1516.
- [9] H. Grote, F.C. Iselin, The MAD Program, Version 8.1, CERN/SL/90-13, June 17, 1991.
- [10] W. Press, B. Flannery, S. Teukolsky, W. Vetterling, Numerical Recipes, Cambridge, 1990.
- [11] R. Nawrocky, to be published.
- [12] J. Safranek, A Low Emittance Lattice for the X-Ray Ring, these proceedings.
- [13] J. Safranek and S. Krinsky, Plans to Increase Source Brightness of NSLS X-Ray Ring, Proceedings of the 1993 Particle Accelerator Conference, pg 1491.

PERTURBATION OF BEAM ENERGY DUE TO STEERING AND PRETZEL ORBIT*

W. Lou, M. Billing, D. Rice, Lab of Nuclear Studies, Cornell University, Ithaca, NY 14853

Abstract

The energy calibration of the beam directly effects the precision of the mass measurement of particles produced in collision. The beam path length changes due to the pretzel orbit, steering, bumps and quadrupole survey. To provide reasonable extrapolation of energy measurement, this path length change needs to be included in the energy calculation.

I. Introduction

The energy calibration of the beams in CESR directly effect the precision of the mass measurement of particles produced in collision. There are three methods to measure the beam energy (nmr*, Ecleo and B mass) in CESR. It has been seen that there is a 2 MeV shift between nmr*, Ecleo, and B mass measurement from run by run. To provide reasonable extrapolation of energy measurement, there is a need to analyze the effect of machine hardware components (such as steering, bumps, quad survey, pretzels, etc) on the energy.

The energy information could be calculated from the CESR beam trajectory/orbit and the dipole magnetic field throughout the ring. The path length change due to the dipole field error or kicks plays an important roles in energy calculation.

II. The Off-Energy Orbit and Energy Change

The linear transverse particle motion could be described by the differential equations[1]:

$$x'' + [K_1(s) + G^2(s)]x = G(s)\delta - \frac{ec\Delta B_y}{E_0} \quad (1)$$

where: δ is the momentum deviation; e and c are electron charge and speed of light. $ec\Delta B_y/E_0$ is the normalized dipole field imperfection or the quadrupole misalignment; $G(s) = ecB_y(s)/E_0$ is the curvature function; $K_1(s) = ec(\partial B_y/\partial x)/E_0$ is the quadrupole strength.

The coupling terms and high order terms were neglected in Equation.1. The solutions of linear motion of Equation.1 are to be a superposition of periodic forced solutions (energy displacement and closed orbits) with the free oscillation (the betatron oscillation). The total displacement from the ideal orbit could be written as,

$$x(s) = x_\beta(s) + \eta(s)\delta + x_c(s) \quad (2)$$

The betatron oscillation $x_\beta(s)$ is well known and could be represented by

$$x_\beta(s) = a\sqrt{\beta_x}\cos\{\phi_x(s) - \vartheta\} \quad (3)$$

where $\phi_x(s)$ is the horizontal phase, β_x is betatron function, and a and ϑ are constants for a particular trajectory.

The energy displacement term $\eta(s)\delta$ is easy to get by solving the differential equation

$$\eta''(s) + [K_1(s) + G^2(s)]\eta(s) = G(s) \quad (4)$$

$\eta(s)$ is called dispersion function and its solution can be expressed as

$$\eta(s) = \frac{\sqrt{\beta_x(s)}}{2\sin\pi\nu_x} \oint G(s_x)\sqrt{\beta(s_x)}\cos\{|\phi_x(s) - \phi_x(s_x)| - \pi\nu_x\}ds_x \quad (5)$$

If the beam has a slight momentum deviation of δ_0 in relative value, the horizontal closed orbit is displaced to first order:

$$x_{\delta 0}(s) = \eta(s)\delta_0 \quad (6)$$

Since the particles lose a significant fraction of their energy due to the synchrotron radiation in the dipoles while the compensating acceleration only occurs at a few points, the instantaneous momentum therefore varies along the circumference. If the dispersion and its derivative not vanish at the RF cavities, the second order orbit distortion may not be neglected. For simplicity, we neglect all second order terms. There are 98 beam position monitors (BPM) throughout the ring, and be used to take orbits from run to run. By averaging the closed orbit data, the average momentum deviation δ_0 could be extracted.

An important consequence of an energy deviation is associated change in the circumference of the closed orbit. This effect can be expressed by the orbit length dilation factor.

$$\frac{\Delta L_\delta}{L_0} = \alpha_p \delta \quad (7)$$

where $\alpha_p = \frac{1}{L_0} \oint G(s)\eta(s)ds$ is the momentum compaction factor.

The closed orbit derivation term x_c due to the dipole field error or kick could be calculated by solving the equation

$$x'' + [K_1(x) + G^2(x)]x = -\frac{ec\Delta B_y}{E_0} \quad (8)$$

Define the kick $\Delta x'$ by the following equation,

$$\Delta x' = -\frac{ec\Delta B_y \cdot \Delta L}{E_0} \quad (9)$$

By solving Equation.8, the closed orbit displacement due to a kick $\Delta x'(s_x)$ at the location of s_x could be expressed as follows[1],

$$x_c(s) = \frac{\sqrt{\beta(s)}}{2\sin\pi\nu_x} \Delta x'(s_x)\sqrt{\beta(s_x)}\cos(|\phi(s) - \phi(s_x)| - \pi\nu_x) \quad (10)$$

*Work supported by the National Science Foundation

Obviously the total path length will change due to this closed orbit distortion and can be written as

$$L_{total} = \oint (1 + G(s)\Delta x(s))ds = L_0 + \oint G(s)x_c(s)ds \quad (11)$$

The changed path length δL_β could thus be easily derived,

$$\delta L_\beta = \frac{\Delta x'(s_x)\sqrt{\beta(s_x)}}{2 \sin \pi \nu_x} \oint G(s)\sqrt{\beta(s)} \cos(|\phi(s) - \phi(s_x)| - \pi \nu_x) ds \quad (12)$$

Replace the right side of Equation.12 by the definition of dispersion, the δL_β could be very simple,

$$\delta L_\beta = \Delta x'(s_x)\eta(s_x) \quad (13)$$

Since the RF system frequency determines the circumference so that any lengthening of the path due to the betatron closed orbit error must result in an equal and opposite change in path length due to a change in beam energy.

$$\Delta L_\beta = -\Delta L_\delta \quad (14)$$

The energy deviation due to this kick then could be expressed as:

$$\delta = \frac{\Delta L_\delta}{\alpha_p L_0} = -\frac{\Delta L_\beta}{\alpha_p L_0} = -\frac{\eta(s_x)\Delta x'(s_x)}{\alpha_p L_0} \quad (15)$$

For many kicks around the ring, the total energy change is simply the sum of the energy change of each kick.

$$\frac{\delta E}{E_0} = -\sum \frac{\Delta x'(s_x)\eta(s_x)}{\alpha_p L_0} \quad (16)$$

CESR is designed to operate over a range of electron energies by arranging all dipole magnetic fields be varied together (scaled in proportion to the desired operating energy). The design orbit is not changed by varying all fields together which only changes the beam energy associated with the design orbit. This could also be verified by Equation.16. Let's assume the fraction of dipole field change $F = \Delta B(s_x)/B_0(s_x)$ is a constant throughout the ring,

$$\Delta x'(s_x) = -\frac{ec\Delta B\Delta L}{E_0} = -\Delta G(s_x)\Delta L = -FG(s_x)\Delta L \quad (17)$$

and it is demonstrated that the beam energy deviation is also equal to F .

$$\delta = \oint \frac{\eta(s_x)FG(s_x)}{\alpha_p L_0} ds_x = \frac{F}{\alpha_p L_0} \oint G(s)\eta(s)ds = F \quad (18)$$

III. Discussion of the Effect on Energy in CESR

Now, let's discuss the effect of steering, bumps, quadrupole survey, pretzels on energy in CESR. We choose the present high energy physics (HEP) lattice with small crossing angle of 2.5 mrad as an example. The main parameter of the lattice is listed in Table.1. The crossing angle optics are designed to accommodate 9 trains of 2 bunches separated by 28 ns.

Steering: There are total 83 horizontal steering coils in CESR. The total magnetic length of all the horizontal steering coils is

Table.1 Some Parameters of HEP Lattice

Lattice Name	N9A18A600.FD92S_4S
Nominal Energy	5.289 GeV
α	0.011256
ϵ_x	0.20×10^{-6}
Horizontal Tune ν_x	10.5235
Vertical Tune ν_y	9.5971
β_y^*	0.18 m
β_x^*	1.09 m
Energy Spread	0.6149×10^{-3}
Circumference L_0	768.426 m
Average Dispersion	1.38 m

450 m. Most single steering coil have magnetic length of 6.504 m, except the steering coils between the IP and Quadrupole Q8. In principal, we could measure the the excitation curve for all the steering coil, and read the the coil current from the CESR save set. The energy change due to the steering coil could be simply calculated according to the Equation.16.

In CESR, two pairs of electrostatic separators are used to separate the two beams (electron and positron beam) at the parasitic points. The orbits of positron and electron are oppositely distorted in pretzels fashion by these two pairs of separators. In the present high energy physics running optics with crossing angle, the horizontal separators are powered antisymmetrically. Since CESR is a symmetric machine, the energy change due to these two pair of antisymmetrically powered separator kicks should be canceled each other and the energy deviation should be zero. If these two pair of separators are powered symmetrically as we did in the head-on collision running before, the energy change could be calculated by Equation.16.

There could be many horizontal bumps throughout the ring. The effect on the energy should be similar as steering. The local bumps are usually closed, but the beta function at each individual bump is not always the same, and the dispersion difference can be large for bumps in areas with varying dispersion (i.e., when bending magnets are in the bump region). The effect on energy could be large. Bumps in long drift spaces, such as the IR, have a smaller effects on the energy.

Quadrupole Survey Misaligned quadrupoles can cause energy changes also. It is important to distinguish the misalignment of a quadrupole relative to the ideal "design" orbit from the passage of the beam off the magnetic center due to a kick somewhere else in the ring. In the second case, the kick given to the beam by the quad is just part of the focusing action of the storage ring optics and, as implied by the treatment above, does not cause any additional energy change since Equation.16 takes into account the kicks from all the quads.

Misaligned quads are properly treated as dipole kicks using Equation.16. The value of the kick must be computed from the displacement of the quad center from the design orbit. In practice this can be determined only from a survey, which puts definite limits on our knowledge of energy changes due to misaligned quads. If we are interested primarily in a reproducible energy measurement, keeping track of quads moved during a down pe-

riod is very important. The unplanned movements of quads must be determined by some other means if we are to understand their effect on the machine energy.

The kick received by the beam from a misaligned quad could be calculated by:

$$\Delta x' = -x_d K_1 L_{quad} \quad (19)$$

where the L_{quad} is the magnetic length of the quad, x_d is the offset of the quad axis away from the ideal design orbit. K_1 is the quad strength. Assume that the beam offset x_d is 0.1 mm at Q2 ($K_1 L \approx 0.5$), the kick received by the beam at Q2 is -0.05 mrad, which lead to the energy change ($\Delta E/E_0$) of 0.43×10^{-7} from Equation.16, since the dispersion at Q2 is very low (0.0075 m). Another example, if we assume that the beam offset x_d is 0.1 mm at Q6 ($K_1 L \approx 0.25$) where the dispersion is 2.35 m, the kick received by the beam could be calculated to be -0.025 mrad and energy change δ to be 0.68×10^{-5} . For the nominal energy of 5.289 GeV, the energy deviation is about 0.036 MeV.

Miscellaneous Orbit Distortion The closed orbit file could be taken from run to run. The miscellaneous orbit distortion could be gotten by subtracting this orbit with the known orbit distortions introduced by steering, pretzels, bumps, etc. The average momentum displacement due to the miscellaneous orbit distortion then could be calculated by averaging this orbit. The average dispersion function of present HEP running optics is 1.38 m and the average displacement of miscellaneous orbit distortion is at the order of 0.02 mm, so the momentum displacement due to this orbit distortion could be at the order of 1.45×10^{-5} .

References

- [1] M. Sand, The Physics of Electron Storage Rings - An Introduction, SLAC-121, UC-28, 1970.
- [2] R. Johnson, Absolute Luminosity and Energy Determination in Bunched Colliding-beam Machines, Lecture Notes in Physics, V343, p167, 1988.
- [3] J.-P. Koutchouk, Trajectory and Closed Orbit Correction, Lecture Notes in Physics, V343, p46, 1988.

LATTICE STUDIES FOR A HIGH-BRIGHTNESS LIGHT SOURCE

D. Kaltchev*, R.V. Servranckx, M.K. Craddock†
TRIUMF, 4004 Wesbrook Mall, Vancouver, B.C., Canada V6T2A3
W. Joho, PSI, CH-5232 Villigen, Switzerland

Abstract

A number of lattices have been studied for use in a high-brightness Canadian synchrotron light source. In particular we have investigated some designs similar to the proposed 1.5 - 2.1 GeV Swiss Light Source, which incorporates superconducting dipoles in multi-bend achromats, but providing 8 or 10 rather than the original 6 straight sections. Similar emittances to those of the original (1.6 nm-rad at 1.5 GeV) can be obtained, but to achieve similar dynamic apertures great care has to be taken in placing the chromaticity- and resonance-correcting sextupoles, because of their unusual strength. A scheme is described which allows the dynamic apertures to be more than doubled to ~ 100 mm-mrad in both planes.

I. INTRODUCTION

A number of lattices have been studied for use in a very-high-brightness Canadian synchrotron light source. In particular we have investigated, in collaboration with PSI, some designs with similar structures to the proposed 1.5 - 2.1 GeV Swiss Light Source, but with 8 or 10, rather than the original 6, straight sections. The SLS has a number of features superior to, or not available on, existing machines:

- a factor 2 better emittance and brightness,
- superconducting dipoles to provide hard x rays,
- two very long straight sections for advanced i.d.'s,
- a flexible lattice allowing several operating modes,
- individual tuning capability to match each i.d.

The SLS proposal uses a hexagonal lattice with four short (7 m) and two long (19 m) straight sections; there are seven focusing cells per arc tuned to provide an extremely low emittance (1.4 nm-rad at 1.5 GeV). The new lattices use the same basic cell in order to obtain the same low emittance, but fewer cells per arc (4, 5 or 6), allowing the number of arcs and straight sections available for insertion devices to be increased for only a small rise in ring circumference.

In very-low-emittance lattices the region of stable transverse motion is limited by nonlinearities introduced by the rather strong sextupoles needed for chromatic correction. This also makes it difficult to obtain the necessary dynamic acceptance independent of the machine working point. These difficulties increase for the new lattices because there is less flexibility with fewer cells per arc and because the lattice functions are in some cases asymmetric - with alternating high and low beta functions in the straight sections.

Efforts have therefore been focused on correcting the sextupole-driven resonances and finding better sextupole configurations. The algorithm used is based

on simultaneous minimization of linear chromaticities and third- and fourth-order resonance strengths with the code COSY ∞ [5]. The solutions obtained for the original hexagon lattice are very similar to those found at PSI.

Two approaches have been taken, as detailed in the following sections. In the first, the phase advance per cell was set solely to obtain low emittance, as in the original SLS design. One decagon and two octagon lattices of this kind were considered. The best dynamic acceptance (~ 40 mm-mrad in both planes) was found for a periodicity-4 octagon with four long and four short straight sections.

The second approach was to apply the achromat concept to the chromatic corrections. With an appropriate phase advance per cell and the correct distribution of several families of sextupoles, the second-order geometric aberrations can be made vanishingly low or zero. This results in rather high dynamic acceptance, in some cases exceeding the physical aperture of the vacuum chamber. On the other hand, the tuneability of these lattices is more limited.

Lattice Structure

As for the SLS hexagon, each repeat section is an N-bend achromat (NBA) consisting of N-2 bending cells ("C cells" with $\theta \simeq 10^\circ$) with a half-bend dispersion suppressor and a half-straight (together forming an "H section") on each side. Figure 1 illustrates this basic structure for a 5-bend achromat consisting of three C cells and two H sections. The F and D quadrupoles in each cell form independent families.

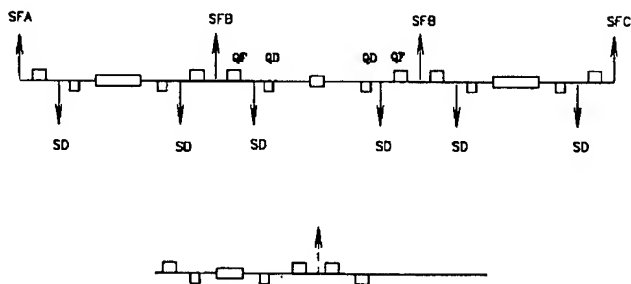


Figure 1. Lattice elements: (above) 3 C cells with a central superconducting dipole; (below) H section composed of dispersion suppressor and half straight.

II. HIGHER-PERIODICITY LATTICES SIMILAR TO SLS

The distinguishing feature of these lattices is that resonance correcting sextupoles are installed both in dispersive (C cell) and nondispersive (H section) locations.

* On leave from INRNE, Sofia, Bulgaria.
† Also at Physics Dept, UBC, Vancouver, Canada.

The octagon lattice OCT4, composed of 4 superperiods of a 45° arc and its mirror image, has been considered both at TRIUMF and PSI[3]. Each arc consists of three C cells with 11° dipoles and one long and one short H section with 6° dipoles. The highest transverse and longitudinal dynamic apertures (units $\mu\text{m.rad}$, %) so far obtained are hor./vert./energy = $65/35/\pm 4\%$ and $45/41/\pm 1\%$, corresponding to natural emittances of 4.7 nm.rad and 2.7 nm.rad respectively at 1.5 GeV. (Although these rings are designed to run up to 2.1 GeV, we quote emittances at the lower energy throughout, to facilitate comparison with existing machines.)

In the decagon lattice DEC288 each 180° superperiod consists of three 5BA 40° arcs and two 4BA 30° arcs. The performance achieved so far is inferior to that of SLS (see Table 1).

III. SECOND-ORDER ACHROMAT LATTICES

To implement the second-order achromat principle groups of cells are created with integer- π total phase advance. This ensures that a sextupole is always paired with a member of the same family exactly in antiphase, thereby canceling some of the driving terms of third-order betatron resonances in a "selfcompensating" scheme. In the lattices discussed here, this is achieved for the focusing sextupoles by making the horizontal tune advance by an integer fraction $n/2m$ (n odd) in each C cell, so a sequence of m C cells has phase advance $n\pi$. In addition, each H section is tuned to π , so that the back-to-back pairs forming insertions (H,-H) are transparent. Any sextupoles m C cells apart are then exactly in antiphase, even if insertions intervene (no sextupoles are installed in the H sections in these lattices). To ensure a non-integer tune around the whole ring, the self-compensating condition is relaxed in selected sections, often in the long straights.

The lattice OCT_5/12 has 2 superperiods, each consisting of 1 long straight, 3 short straights and 4 identical 5BA 45° arcs with three 11.25° dipoles and two 5.625° dipoles; the lattice functions are shown in Fig. 2. In this case $n/2m = 5/12$ and the phase advance over any 90° bend is 9π . The sextupoles are arranged in five separately powered families. All the defocusing sextupoles form one family while the focusing sextupoles are divided into four families (0,1,2,3) arranged (Fig. 2) ABBC = 0113 and 3220 in alternate octants. A number of other groupings were tried, but this proved to be the most effective. Dividing the sextupoles into more families did not provide any significant benefit.

For the lattice OCT_7/16 each octant contains 4 C cells with 9° dipoles and two H sections with 4.5° dipoles. With $n/2m = 7/16$ the phase advance over any 90° bend is 11π . The focusing sextupoles are arranged 01113 and 32220 in alternate octants. With the number of dipoles per octant being even (6 in this case) inclusion of a s.c. dipole breaks the symmetry of the octant a little. The large on-momentum dynamic apertures shown in Table 1 were obtained at optimum conditions - C cells tuned to $(7/8)\pi$ and the horizontal beta functions of the ring having an exact 8-fold symmetry.

A. Resonance Correction and Nonlinear Dynamics

For the self-compensating choice of horizontal tunes described above some of the driving terms of the lowest order nonlinear resonances are automatically zero no matter how the different families are excited. The rest of the third-order resonance

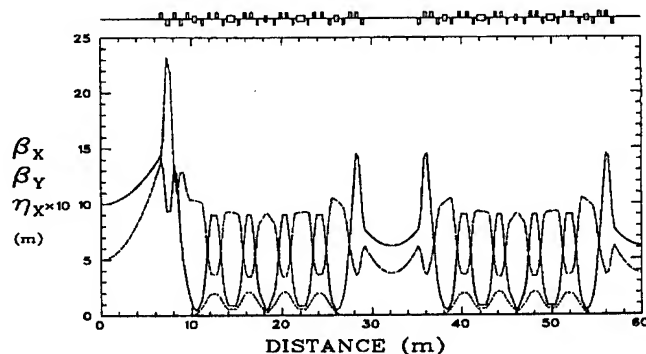


Figure 2. Lattice OCT_5/12 (1/4 ring) with tunes $\nu_x=18.37$, $\nu_y=6.4$, emittance 3.6 nm.

terms, and also some selected fourth-order terms, were minimized using COSY ∞ to improve the dynamic aperture and the chromatic stability.

In principle further improvement of the nonlinear behavior is possible if a similar self-compensating scheme is applied in the vertical plane. The lattice OCT_5/12 provides such a choice for the vertical phase advances, namely:

- for the C-cell $\mu_x = 2\pi/6$
- for the (H,-H) cell $\mu_y = 2\pi$.

Due,

however, to increased chromaticity and sextupole strengths we did not obtain a better acceptance.

For a full cancellation of the terms driving third-order resonances, the phase advances of C cells must satisfy

$$\mu_x = \mu_y \text{ or } \mu_x = \pi - \mu_y$$

The first condition cannot be achieved for this kind of cell. The second implies a vertical phase advance $\mu_y = 2\pi/12$ and looks possible, but has not been tried yet.

B. Lattice Flexibility

Several working points within a half-integer square of the tune diagram gave horizontal on-momentum dynamic aperture A_x equal to or even slightly larger than the geometric acceptance of the vacuum chamber. For the "self-compensating" horizontal tunes in OCT_5/12 the sextupole strengths required for chromaticity and resonance correction were calculated at the working point $\nu_x=18.2$, $\nu_y=6.4$. The natural emittance at this point is 3.6 nm.rad with hor./vert. dynamic aperture 70/70 $\mu\text{m.rad}$. A shift of the working point towards higher horizontal tunes in the interval 18.2 - 18.4 allows the emittance to be decreased to 2.8 nm.rad (the C cell tune increasing from 150° to 155°) and/or the beta values in the middle of the short straight sections to be lowered. The lattice optics also improves because, in order to compensate the increased horizontal tune of the C cells and/or short straight sections, that in the long straights approaches unity. A maximum horizontal error-free dynamic acceptance $A_x = 100 \mu\text{m.rad}$ was obtained if the long straight-section tune was exactly unity horizontally with the fractional part of the machine tune equally distributed over the short straight sections.

The three short (6 m) straight sections in a half ring can have

Table I
Parameters for the various lattices (working points corresponding to largest acceptance)

Lattice	SLS	OCT4	DEC288	OCT_5/12	OCT_7/16
Periodicity	2	4	2	2	4
Circumference, m	240	280.8	288	240	259.2
Straight sections	2× 18.5 m, 4× 7 m	4× 14.2m, 4× 6 m	2× 12.6m, 2× 7 m, 4× 6m	2× 13m, 6× 6 m	8× 6.4m
Dipole bending angle	10°	11°	10°	11.25°	9°
Number of s.c. bends	6	8	6	8	8
Lattice tunes ν_x/ν_y	22.2/5.4	19.2/6.72	22.2/7.4	18.32/6.4	22.3/7.4
Hor. emittance at 1.5 GeV (nm.rad)	1.6	4.7	2.2	3.5	1.25
Dyn. aperture on-momentum, ($\mu\text{m.rad}$)	55/50	65/35	30/35	100/70	60/70
Momentum acceptance (no errors)	4%	4%	2%	6%	3%

different horizontal beta values at the i.d. position, leading to a small but acceptable loss of dynamic acceptance.

Shorter straight sections allow better matching to the insertion devices and even better optics. The maximum dynamic apertures obtained were 130/110 $\mu\text{m.rad}$ (energy acceptance $\pm 6\%$) for an 8.5 m long straight section (ring length 230.4 m).

C. Lattice Errors

The sensitivity of OCT_5/12 to field errors, misalignments and higher-order multipole errors was studied at the working point $\nu_x, \nu_y=18.32, 6.4$ (emittance 3.5 nm.rad, error-free acceptance 100/70 $\mu\text{m.rad}$, $\beta_x=16$ m, $\beta_y=4$ m in the middle of the long straight section). Fig. 3 shows the horizontal dynamic aperture, calculated by binary search for the outermost stable particle, assuming the same r.m.s. errors as the SLS [1]: transverse displacement 0.1 mm, rotation about beam axis 1 mrad; field deviation (except dipoles) 0.1%. Both the horizontal acceptance and the momentum acceptance are about 50% larger than those of the SLS hexagon.

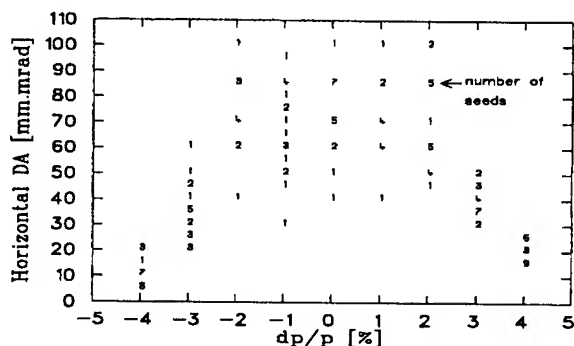


Figure 3. Horizontal dynamic aperture of OCT_5/12

The dynamic aperture has also been studied for the tolerances used in the ALS design [4]:

- r.m.s. misalignments for all elements (cut at 2σ): transverse 0.15 mm, rotation 0.5 mrad, tilt rotation 1 mrad, field deviation 0.1%.

- multipole content as quoted in [4] with only one exception - no random octupole component is generated; the systematic octupole in the quadrupoles is one half the tolerance limit quoted in [1]: $b_{oct}/b_{quad} = 3 \cdot 10^{-3}$ at 35 mm.

With these errors the on-momentum dynamic apertures (hor./vert.) were as follows: with sextupoles only - 100/70 $\mu\text{m.rad}$; with added multipole content to quadrupoles and bends - 85/55 $\mu\text{m.rad}$; with all multipoles and misalignments and after closed-orbit correction - 37/25 $\mu\text{m.rad}$ (assuming minimum values obtained from 20 seeds).

IV. CONCLUSIONS

In summary, new lattices have been found with comparable or better optical performance than the original SLS and with more straight sections.

References

- [1] Conceptual Design of the Swiss Synchrotron Light Source, PSI (1993).
- [2] A.Streun, Status of SLS Lattice design, SLS-Note 2/94.
- [3] A.Streun, SLS Dynamic Aperture Optimization, Proc. of Workshop on Nonlinear Dynamics in Particle Accelerators, Arcidosso (1994).
- [4] ALS Conceptual Design Report, LBL PUB-5172 (1986).
- [5] M. Berz, COSY INFINITY Version 5, User's Guide and Reference Manual, MSUCL-811 (1991).
- [6] A.Streun, OPTICK User's Guide, SLS 3/94, PSI (1994).

EXACT MAP THROUGH IDEAL BENDS (AGAIN?)

Leo Michelotti

Fermi National Accelerator Laboratory*
P. O. Box 500, Batavia, IL 60510, USA

Abstract

There are three logically independent facets to calculating the transfer map through a bend magnet: physics, geometry, and representation. We will derive the exact map for transit through ideal bends while separating these three, esp., isolating the geometry problem from the other two.

I. INTRODUCTION

Writing the exact transfer map through ideal bend magnets requires considerations of physics, geometry, and the particular representation in which a particle's state is expressed. Although logically independent, these are frequently mixed together. We will attempt to separate them. It is likely that many people have already gone through this exercise for themselves, but it may be worth repeating.¹

II. PHYSICS

We all learned the relevant physics as undergraduates. A charged particle in a constant magnetic field, \vec{B} , travels at constant speed on a helix aligned along the field. Since the particle experiences no acceleration in the direction of \vec{B} ,

$$z_{||}(t_f) = z_{||}(t_i) + v_{||}\Delta t, \quad (1)$$

where the subscript "||" stands in for the appropriate coordinate projection, and $\Delta t = t_f - t_i$ is the time spent in the magnetic environment. The (radial) frequency of travelling around the helix is,

$$\omega = |eB/\gamma m|,$$

in rationalized mks units, where, e is the charge of the particle, m is its mass, and $\gamma = 1/\sqrt{1-\beta^2} = E/mc^2$ is the usual relativistic factor. Projected onto a plane orthogonal to \vec{B} , the helical orbit becomes a circle of radius ρ ,

$$\rho = |p_{\perp}/eB|,$$

where p_{\perp} is the projection of the particle's momentum onto the plane orthogonal to \vec{B} .

This is all we need. In the sections to follow we will complete the derivation by (a) solving a few elementary geometry problems and (b) writing the answers in the accelerator physicists' representation.

III. GEOMETRY

The natural Cartesian chart for expressing the geometry, which we will call the "Z-chart," has its origin on the helical

axis with one coordinate axis parallel to it. Following a standard convention, for bending magnets we choose the z_2 -axis parallel to \vec{B} , while for solenoids, we would align z_3 along the \vec{B} , so that in both cases the largest component of momentum is along the z_3 axis. (Please refer to Figures 1 through 3 repeatedly for visualization of the charts in this paper.) Because it is easiest to work with the transverse equations in terms of spinors, we define complex coordinates $z \equiv z_3 + iz_1$, for bend magnets, or $z \equiv z_1 + iz_2$, for solenoids, and write the transversely projected dynamics in either case as follows.²

$$z = \rho e^{i\theta}, \quad \theta \in [-\pi, \pi), \quad (2)$$

$$\dot{z} = -i\omega z. \quad (3)$$

The time taken to cross the magnetic environment is clearly $\Delta t = -\Delta\theta/\omega$, and we will address below the purely geometric problem of calculating $\Delta\theta$.

A difficulty arises because the orbit is not viewed from the Z-chart but from two local charts, say U_i and U_f , which we will call the "initial" and "final" charts, or, alternatively, the "in" and "out" charts. Although these are, in principle, arbitrary, for practical applications, each typically has an axis aligned along \vec{B} : u_2 for bends, and u_3 for solenoids.³ In the treatment that follows we will handle only the bend-magnet configuration explicitly, leaving the easier problem of solenoids to the reader.

For bending magnets, then, the (u_1, u_2) plane (i.e., $u_3 = 0$) is considered the "transverse plane" or "face" of the chart, called so because it is usually considered to be transverse to the local fiducial reference curve, not to the magnetic field. Normally one thinks of the in-face and out-face as located at the edges of the magnet, but this need not be the case; they could be within the body. All that is necessary is that in traversing the region between the faces, the particle is exposed to the environment of a constant magnetic field. We need to establish chart coordinates for two events, viz., the orbit's intersecting the in- and out-faces, the transverse planes of U_i and U_f . The function which converts coordinates of the first event, on U_i , to those of the second, on U_f , is the transfer map for the region.

The time Δt appearing in Eq. 2 is nothing but the time interval between these events,

²This definition does have the disadvantage of making $\dot{\theta}$ negative in Eq. 3, and, later, $\Delta\theta = \theta_f - \theta_i$ negative rather than positive. I've chosen this rather than the less awkward $z \equiv z_1 + iz_3$ for three reasons, not one of which is particularly compelling: (a) it preserves the cyclic ordering of the (z_1, z_2, z_3) triplet, (b) at least in the U.S., accelerator physicists align the "3" axis along the (fiducial) beam current and the "1" axis outward, (c) being at Fermilab, I am accustomed to thinking of beam current as circulating clockwise, and (d) physicists think of time dependence as $e^{-i\omega t}$.

³This restriction could be removed, but the resulting equations would then have to be solved numerically. In any case, it would not conform to any practical application.

*Operated by the Universities Research Association, Inc., under contract with the U.S. Department of Energy

¹The point of doing something this simple is to be reminded that it is simple.

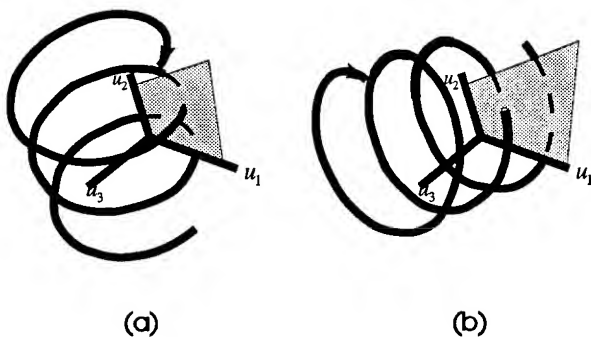


Figure 1. Helical orbit in a constant magnetic field, as viewed from a local chart in (a) a bend magnet and (b) a solenoid.

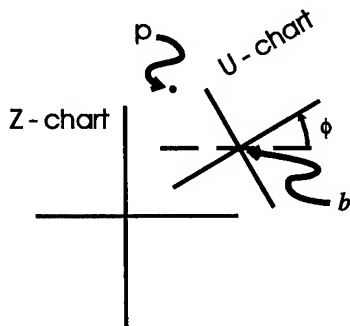


Figure 2. Complex parameters b and ϕ .

Since motion along \vec{B} is taken care of, we can confine our attention to the projection of the orbit on a plane orthogonal to \vec{B} in order to calculate Δt and everything else that we need. The geometric problem we must solve requires nothing more complicated than representing circles and lines in a plane. The transformation which takes us from a U -chart to the Z -chart is written easily in the spinor notation, using $u \equiv u_3 + iu_1$. Referring to Figure 2, we have

$$z = b + ue^{i\phi}, \quad (4)$$

$$\dot{z} = i\dot{u}e^{i\phi}, \quad (5)$$

where b is the Z -chart spinor coordinate of the U -chart's origin, and ϕ is the angle of the u_3 axis relative to the z_3 . Our task now is to represent the very simple motion embodied in Eq. 3 on the U charts and thereby obtain the transfer map $U_i \rightarrow U_f$. This proceeds in two steps, each of which is a simple geometrical problem: (A) obtaining $be^{-i\phi}$ given u and \dot{u} , and (B) finding the intersection of a line with a circle.

A. What is $be^{-i\phi}$?

First, using Eq. 4 and Eq. 3, we have

$$\dot{z} = -i\omega z = -i\omega(b + ue^{i\phi}).$$

Combining this with Eq. 5 yields

$$\dot{u} = \dot{z}e^{-i\phi} = -i\omega u - i\omega be^{-i\phi},$$

from which we obtain $be^{-i\phi}$.

$$be^{-i\phi} = i\dot{u}/\omega - u \quad (6)$$

B. Point of intersection between a line and a circle

We must solve for the point of intersection between the u_1 axis of a U -chart and the orbit projection, which is the circle written in Eq. 2. An arbitrary line $L(z_o, \eta)$ passing through a point z_o with direction η is the subset,

$$L(z_o, \eta) = \{z_o + we^{i\eta} \mid w \in \mathbb{R}\}$$

We easily solve for its intersection with a circle as follows.

$$\begin{aligned} z_o + we^{i\eta} &= \rho e^{i\theta} \\ w &= e^{-i\eta}(\rho e^{i\theta} - z_o) \end{aligned}$$

Of course, w must be real, so that, by setting $\text{Im } w = 0$, we can find θ .

$$\sin(\theta - \eta) = \frac{1}{\rho} \text{Im}(z_o e^{-i\eta}) \quad (7)$$

Applying this to a U -chart, we use the line $L(b, \phi + \pi/2)$; that is, L lies along the imaginary axis of the spinor u . In such cases Eq. 7 becomes,

$$\theta = \phi + \pi/2 - \arcsin\left(\frac{1}{\rho} \text{Re}(be^{-i\phi})\right), \quad (8)$$

when \dot{u} is attached to $L(b, \phi + \pi/2)$. We can write this yet another way by applying Eq. 6 to u and \dot{u} evaluated along $L(b, \phi + \pi/2)$. Thus, u will be pure imaginary, so that

$$\theta = \phi + \pi/2 + \arcsin(\text{Im}(\dot{u})/|\dot{u}|).$$

IV. OF MAGNETS AND MAPS

We are now ready to complete the construction of a transfer map. Of course, on the Z -chart the "initial" and "final" spinor coordinates are trivially related by a phase rotation.

$$z_f = z_i e^{i\Delta\theta}, \quad \dot{z}_f = \dot{z}_i e^{i\Delta\theta}. \quad (9)$$

Eq. 4 and Eq. 5 can now be used to obtain u_f and \dot{u}_f .

$$\dot{u}_f = \dot{u}_i e^{i(\Delta\theta - \Delta\phi)} \quad (10)$$

$$\begin{aligned} u_f &= u_i e^{i(\Delta\theta - \Delta\phi)} + (be^{-i\phi})_i e^{i(\Delta\theta - \Delta\phi)} \\ &\quad - (be^{-i\phi})_f \end{aligned} \quad (11)$$

The complete transfer map, $(u_i, \dot{u}_i) \mapsto (u_f, \dot{u}_f)$ is now constructed according to the following procedure.

Bend algorithm

Step 1. Use Eq. 6 to evaluate $(be^{-i\phi})_i$.

$$(be^{-i\phi})_i = i\dot{u}_i/\omega - u_i.$$

Step 2. Given $(be^{-i\phi})_i$, from Step 1, construct $(be^{-i\phi})_f$ using the relative in-face to out-face geometry. We will illustrate below how to do this.

Step 3. Calculate $\Delta\theta - \Delta\phi$ by applying Eq. 8 to both faces.

$$\begin{aligned} \Delta\theta - \Delta\phi &= \arcsin(\text{Re}(be^{-i\phi})_i/\rho) \\ &\quad - \arcsin(\text{Re}(be^{-i\phi})_f/\rho) \end{aligned} \quad (12)$$

Step 4. Finally, use Eqs. 10 and 11 to complete the map. Notice that $\Delta\theta - \Delta\phi$ appears only in the argument of an exponent. Rather than use Eq. 12 directly we can employ

$$e^{i(\Delta\theta - \Delta\phi)} = \frac{\sqrt{1 - (\text{Re}(be^{-i\phi})_i/\rho)^2} + i\text{Re}(be^{-i\phi})_i/\rho}{\sqrt{1 - (\text{Re}(be^{-i\phi})_f/\rho)^2} + i\text{Re}(be^{-i\phi})_f/\rho}.$$

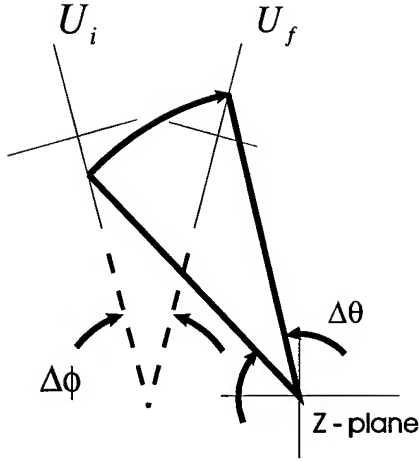


Figure 3. Relationships between the U_i , U_f , and Z charts.

A. Rectangular bends

Detailed information about the magnet's geometry, embodied in the relative placements of the in- and out-faces, is used in Step 2. The simplest possibility is the rectangular bend. We take the "in" and "out" faces to be parallel, so that $\phi_i = \phi_f \equiv \phi$. From the obvious relation, $b_f = b_i + Le^{i\phi}$, where L is the length of the magnet, we obtain the result,

$$(be^{-i\phi})_f - (be^{-i\phi})_i = L, \quad (13)$$

which is to be fed directly into Step 3.

B. Sector bends

Sector bends are only a little more complicated but easily handled by representing, on the Z chart, the point of intersection between the imaginary axes of the U_i and U_f charts. To position these, we place the face of each orthogonal to a local, fiducial path that would be followed by an "ideal" particle. Let $\bar{\rho}$ symbolize its radius of curvature. Further, placing the origins of the U -charts on the fiducial path the intersection point has coordinate $-i\bar{\rho}$ on each chart. Thus, using Eq. 4, we have,

$$(be^{-i\phi})_f - (be^{-i\phi})_i = (1 - e^{-i\Delta\phi})(i\bar{\rho} - (be^{-i\phi})_i). \quad (14)$$

We note in passing the usual relation between $\Delta\phi$, $\bar{\rho}$, and magnet length, L , recalling that, by our convention, $\Delta\phi < 0$,

$$e^{-i\Delta\phi} = \left(\sqrt{1 - (L/2\bar{\rho})^2} + iL/2\bar{\rho} \right)^2. \quad (15)$$

Keeping L fixed and letting $\bar{\rho} \rightarrow \infty$ then reproduces Eq. 13.

C. Arbitrarily angled faces

The in- and out- faces can be rotated through additional angles. If we use the MAD convention for specifying angles e_1 and e_2 , effectively we must replace $\phi_i \rightarrow \phi_i + e_1$ and $\phi_f \rightarrow \phi_f - e_2$ in Eq. 14. The result then looks as follows.

$$(be^{-i\phi})_f = (be^{-i\phi})_i e^{-i\Delta\phi} + i\bar{\rho}(e^{-ie_2} - e^{ie_1} e^{-i\Delta\phi})$$

Setting $e_1 = -e_2 = \Delta\phi/2$ and using Eq. 15 again reproduces Eq. 13.

V. REPRESENTATION

The final complication arises when we insert the accelerator physicists' coordinate representation into these expressions. A particle's crossing the plane of a "face" is typically recorded using momentum and energy coordinates normalized by the fiducial. The position sector is recorded by transverse coordinates x_1, x_2 , and a time offset, $c\Delta\tau$, while the momentum sector is represented by normalized transverse components⁴ of $\vec{q} \equiv \vec{p}/\bar{p}$, and a total momentum offset, and $\delta \equiv |\bar{p}|/\bar{p} - 1$. To apply the bend algorithm, we need only write \vec{v} in terms of these and then use the spinor $\dot{u} = v_3 + iv_1$.

Starting from,

$$\vec{\beta} = \vec{v}/c = \vec{p}c/E = \vec{q} \cdot \bar{p}c/E,$$

we substitute

$$E^2 = \vec{p}^2 c^2 + m^2 c^4 = (\bar{p}c)^2 (1 + \delta)^2 + m^2 c^4,$$

to obtain

$$\vec{\beta} = \vec{q} / \sqrt{(1 + \delta)^2 + (mc/\bar{p})^2}.$$

We can obtain v_1 and v_2 from this directly, but since q_3 is not recorded, we must get v_3 by using the following.

$$\begin{aligned} E^2 &= \vec{p}^2 c^2 + m^2 c^4 = \bar{p}_\perp^2 c^2 + p_3^2 c^2 + m^2 c^4 \\ \frac{E^2 - m^2 c^4}{\bar{p}^2 c^2} &= (\vec{q}_\perp)^2 + (q_3)^2 \\ \beta_3 &= q_3 / \sqrt{\dots} \\ &= \sqrt{\frac{(1 + \delta)^2 - (\vec{q}_\perp)^2}{(1 + \delta)^2 + (mc/\bar{p})^2}} \end{aligned}$$

Of course, there's even more fascinating material to wade through, but we're already up against the three page limit and have no more space (see edge of page below). A finished version will follow somewhere, sometime, but not here, and not now.

⁴That is, the projections into the in- and out-faces.

Skew Chromaticity in Large Accelerators

S. Peggs, G.F. Dell,
Brookhaven National Laboratory, *
Upton, NY 11973, USA

Abstract

The 2-D "skew chromaticity" vector \mathbf{k} is introduced when the standard on-momentum description of linear coupling is extended to include off-momentum particles. A lattice that is well decoupled on-momentum may be badly decoupled off-momentum, inside the natural momentum spread of the beam. There are two general areas of concern:

- 1) The free space in the tune plane is decreased.
- 2) Collective phenomena may be destabilised.

Two strong new criteria for head-tail stability in the presence of off-momentum coupling are derived, which are consistent with experimental and operational observations at the Tevatron, and with tracking data from RHIC.

I. OFF-MOMENTUM COUPLING

A skew quad i is represented by a 2-D vector \mathbf{q}_i with components along the orthogonal axes $\hat{\mathbf{a}}$ and $\hat{\mathbf{b}}$,

$$\mathbf{q}_i = \frac{\sqrt{\beta_x \beta_y}}{2\pi f} (\cos(\phi_y - \phi_x) \hat{\mathbf{a}} + \sin(\phi_y - \phi_x) \hat{\mathbf{b}}) \quad (1)$$

where f is the focal length, β_x and β_y are the beta functions, and ϕ_y and ϕ_x are the betatron phases. The closest approach of the eigentunes Q_- and Q_+ is given by the length of \mathbf{q} , the sum of all skew quad vectors[1], [2].

$$\Delta Q_{min} = |\mathbf{q}| = \left| \sum_i \mathbf{q}_i \right| \quad (2)$$

The eigentunes depend on the design tunes, Q_x and Q_y ,

$$Q_{\pm} = \frac{1}{2}(Q_x + Q_y) \pm \frac{1}{2} |\mathbf{r}| \quad (3)$$

$$\mathbf{r} = \mathbf{q} + (Q_x - Q_y) \hat{\mathbf{c}} \quad (4)$$

and on a vector \mathbf{r} with a component along a third axis $\hat{\mathbf{c}}$. Eqn. 3 also describes the off-momentum eigentunes, $Q_{\pm}(\delta)$ and $Q_{\pm}(\delta)$, if the tunes and the vector \mathbf{r} are chromatically expanded in $\delta = \Delta p/p$ (to arbitrary order)[3], [4], [5]

$$Q_x(\delta) = Q_{x0} + \chi_x \delta \quad (5)$$

$$Q_y(\delta) = Q_{y0} + \chi_y \delta \quad (6)$$

$$\mathbf{r}(\delta) = \mathbf{q} + \mathbf{k}\delta + [(Q_{x0} - Q_{y0}) + (\chi_x - \chi_y)\delta] \hat{\mathbf{c}} \quad (7)$$

These equations introduce the "normal chromaticities" χ_x and χ_y , and also the important new "skew chromaticity" vector \mathbf{k} , which, like \mathbf{q} , lies in the (a,b) plane.

*Operated by Associated Universities Incorporated, under contract with the U.S. Department of Energy.

The eigenchromaticities χ_- and χ_+ are defined as

$$\chi_{\pm} \equiv \frac{dQ_{\pm}}{d\delta} \quad (8)$$

leading to the simple general result,

$$\chi_{\pm} = \frac{1}{2}(\chi_x + \chi_y) \pm \frac{1}{2} \frac{\mathbf{r} \cdot \mathbf{v}}{|\mathbf{r}|} \quad (9)$$

$$\mathbf{v} \equiv \frac{d\mathbf{r}}{d\delta} \quad (10)$$

where it is convenient to introduce the vector \mathbf{v} . If the chromatic expansion of \mathbf{r} is just linear, then \mathbf{v} is a constant

$$\mathbf{v} = \mathbf{k} + (\chi_x - \chi_y) \hat{\mathbf{c}} \quad (11)$$

in which case \mathbf{r} is straight line that advances smoothly

$$\mathbf{r}(\delta) = \mathbf{r}(0) + \mathbf{v}\delta \quad (12)$$

as the off-momentum parameter is scanned.

II. Examples in 2-D

It is pedagogically useful to consider the case when the design tunes and the chromaticities are equal ($Q_{x0} = Q_{y0} \equiv Q_0$, $\chi_x = \chi_y \equiv \chi_0$), since then

$$\mathbf{r} = \mathbf{q} + \mathbf{k}\delta \quad (13)$$

$$\mathbf{v} = \mathbf{k} \quad (14)$$

and all vectors are confined to the (a,b) plane.

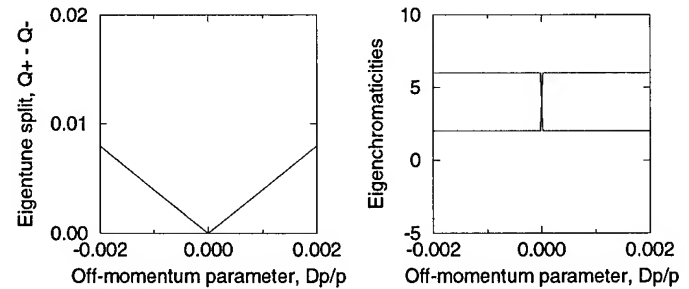


Figure 1. Eigentune split and eigenchromaticities after perfect global decoupling ($\mathbf{q} = 0$), with a typical Tevatron skew chromaticity ($|\mathbf{k}| = 4.0$).

A. Perfect global decoupling.

"Global decoupling" is routinely performed in most contemporary storage rings[2]. Typically, two skew quad families and one erect quadrupole family are adjusted to minimise ΔQ_{min} .

Perfect global decoupling, with $\mathbf{q} = 0$, is the simplest possible case to consider. Substitution into Eqns. 3 and 9 gives

$$Q_{\pm} = Q_0 \pm \frac{1}{2} |\mathbf{k} \delta| \quad (15)$$

$$\chi_{\pm} = \chi_0 \pm \frac{1}{2} |\mathbf{k}| \frac{\delta}{|\delta|} \quad (16)$$

as shown in Fig. 1 with $\chi_0 = |\mathbf{k}| = 4.0$. The eigentune split at a given momentum is just $|\mathbf{k} \delta|$, so that, if $|\mathbf{k}| = 4$ and $\sigma_p/p = 10^{-3}$, the eigentune split of a typical particle is 0.004. This is significant when compared to a typical design tune separation of 0.01. Table I summarises \mathbf{k} measurements made at the Tevatron[4], at CESR[6], and (in tracking) at RHIC[7]. By coincidence, $\sigma_p/p \simeq 0.001$ at all of these machines. The last column of Table I is therefore in good agreement with the approximate prediction

$$\Delta Q_{min}(\text{observed}) \approx |\mathbf{k}| \frac{\sigma_p}{p} \quad (17)$$

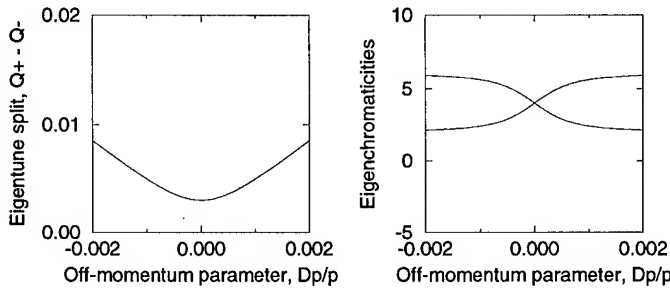


Figure 2. Eigentune split and eigenchromaticities with $|\mathbf{q}| = 0.003$ and $\hat{\mathbf{q}} \cdot \hat{\mathbf{k}} = 0$. Sharp features are broadened.

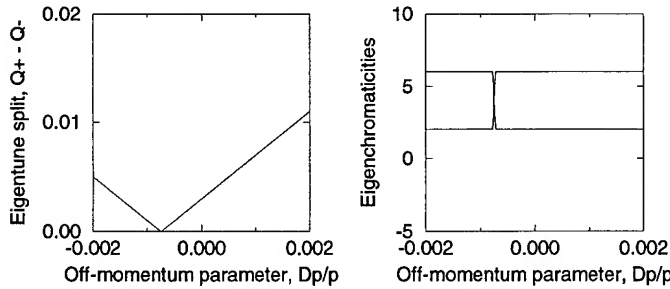


Figure 3. Eigentune split and eigenchromaticities with the same conditions as Fig. 2, except that $\hat{\mathbf{q}} \cdot \hat{\mathbf{k}} = 1$.

Table I

Skew chromaticity observations at three colliders. High luminosity optics were used in all cases.

machine	$ \mathbf{k} $	ΔQ_{min} (observed)
CESR	0.5 ± 0.5	0.001
Tevatron	3.8 ± 0.2	0.003
RHIC	2.1	

B. Realistic global decoupling.

Measurements in the Tevatron found that $|\mathbf{q}| = 0.0032 \pm 0.0008$, $|\mathbf{k}| = 3.8 \pm 0.2$, and $\hat{\mathbf{q}} \cdot \hat{\mathbf{k}} \approx 1$, after a careful round of global decoupling[4]. Note that the angle between $\hat{\mathbf{q}}$ and $\hat{\mathbf{k}}$ can be measured. Figs. 2 and 3 shows what happens in the more realistic situation when $|\mathbf{q}| = 0.003$ and when either $\hat{\mathbf{q}} \cdot \hat{\mathbf{k}} = 0$ or $\hat{\mathbf{q}} \cdot \hat{\mathbf{k}} = 1$. Sharp features in Fig. 1 are broadened when $\hat{\mathbf{q}}$ and $\hat{\mathbf{k}}$ are perpendicular, and are shifted when $\hat{\mathbf{q}}$ and $\hat{\mathbf{k}}$ are parallel. According to Eqn. 3, the closest approach of eigentunes occurs when \mathbf{r} is shortest: when

$$\mathbf{r} \cdot \mathbf{v} = 0 \quad (18)$$

In the current 2-D context this is solved by

$$\delta_c = -\frac{|\mathbf{q}|}{|\mathbf{k}|} \hat{\mathbf{q}} \cdot \hat{\mathbf{k}} \sim \frac{\sigma_p}{p} \quad (19)$$

which is consistent with the figures.

III. STABILITY CRITERIA

Extreme values of the eigenchromaticities χ_+ and χ_- (with respect to changes in δ , \mathbf{q} , Q_{x0} and Q_{y0}) occur when

$$\frac{\mathbf{r} \cdot \mathbf{v}}{|\mathbf{r}|} = \pm |\mathbf{v}| \quad (20)$$

This occurs when \mathbf{r} and \mathbf{v} are collinear: for example, when the design tunes are set equal after perfect global decoupling ($\mathbf{q} = 0$, $Q_{x0} = Q_{y0}$). The extreme values are

$$\chi_{\pm \text{extreme}} = \frac{1}{2}(\chi_x + \chi_y) \pm \frac{1}{2} \sqrt{\mathbf{k}^2 + (\chi_x - \chi_y)^2} \quad (21)$$

Insisting that both of the extreme eigenchromaticities are positive leads to the **new and strong criteria**[5], [8]

$$\chi_x + \chi_y > 0 \quad (22)$$

$$4\chi_x \chi_y > \mathbf{k}^2 \quad (23)$$

If true, neither eigenchromaticity can ever become negative. As such, these criteria are "sufficient but often not necessary". Both χ_x and χ_y must be positive to meet the criteria, even when $\mathbf{k} = 0$, thereby recovering the standard uncoupled head-tail result (above transition).

IV. EXPLANATION OF TEVATRON OBSERVATIONS

In 1989-1990, high intensity Tevatron bunches ($N_{\text{bunch}} > 6 \times 10^{10}$) occasionally became head-tail unstable. Sometimes the beam losses were spontaneous. At other times they were induced when the operators corrected persistent current tune and chromaticity drifts, *often when the tunes were being separated*. Beam studies investigated head-tail stability with different design tunes and chromaticities[4]. The skew quad strengths were held fixed, after a preparatory global decoupling. Entirely different behavior was observed when the chromaticities were equal, and when they were grossly different.

First, the horizontal design tune Q_{x0} was scanned across the diagonal, with equal chromaticities ($\chi_x = \chi_y = \chi_0$). This was repeated for $\chi_0 = 4, 3, 2$, and 1, with significant beam loss observed *as the diagonal was approached* for the last two values. This is consistent with Eqn. 23, which predicts unequivocal stability when $\chi_0 > 1.9 \pm 0.1$. Figs. 4 and 5 show that, when $\chi_0 = 1.5$, both eigenchromaticities are positive for all momentum offsets when the design tunes are 0.007 apart, but that one is negative for all positive momenta when $Q_{x0} - Q_{y0} \approx 0.001$. Simulation confirms this behaviour [5], [8].

The behavior was quite different when $(\chi_x, \chi_y) = (8, -3)$, values that become plausible after persistent current effects have forced the horizontal and vertical chromaticities in opposite directions for several hours. Total beam loss was observed *as the design tunes were separated*. Figures 6 and 7 show that one of the two eigenchromaticities is negative for all positive momentum offsets when the tunes are separated by 0.007, while both are positive when the tunes are only 0.001 apart, at least in a small vicinity around zero momentum offset.

V. Acknowledgements

Sincere thanks to Gerry Annala, Pat Colestock, Glenn Goderre, Tom Pelaia, Stu Peck, Dave Rubin, and the Fermilab operations group, for their encouragement, assistance, and collaboration.

References

- [1] D. Edwards and L. Teng, "Parameterization of Linear Coupled Motion in Periodic Systems", IEEE Trans. Nucl. Sci., Vol. NS-20, No. 3, 1973.
- [2] S. Peggs, "Coupling and Decoupling in Storage Rings", IEEE Trans. Nucl. Sci. Vol. NS-30, No. 4, Santa Fe, 1983, p. 2460.
- [3] S. Peggs, "Head-Tail Stability and Linear Coupling", Fermilab AP Note 90-007, 1990.
- [4] G.P. Goderre et al, "Head-Tail Stability and Linear Coupling in the Tevatron", IEEE Particle Accelerator Conference, San Francisco, 1991, p. 1848.
- [5] S. Peggs and G.F. Dell, "Skew Chromaticity", Proceedings of the LHC Collective Effects Workshop, Montreux, 1994; RHIC/AP/57, 1994.
- [6] Cornell Electron Storage Ring log book 116, unpublished 1994, pp. 123-125.
- [7] G.F. Dell and S. Peggs. TEAPOT tracking studies of the RHIC92.0.4 lattice tuned for luminosity conditions, unpublished, 1994.
- [8] S. Peggs and V. Mane, "KRAKEN, a numerical model of RHIC beam impedances", these proceedings.

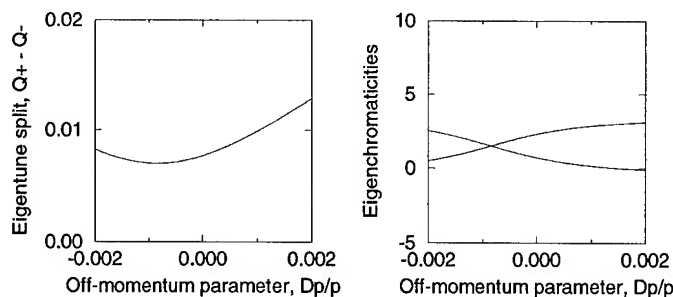


Figure 4. Tevatron eigentune split and eigenchromaticities with equal chromaticities, and design tunes 0.007 apart ($\chi_x = \chi_y = 1.5$, $Q_{x0} = .425$, $Q_{y0} = .418$). The beam was stable.

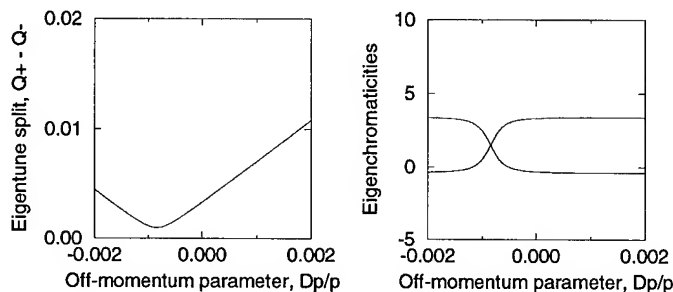


Figure 5. Eigentune split and eigenchromaticities as in Fig. 4, with design tunes 0.001 apart ($Q_{x0} = .419$, $Q_{y0} = .418$). Some beam loss was observed. One eigenchromaticity was negative for all positive momentum offsets.

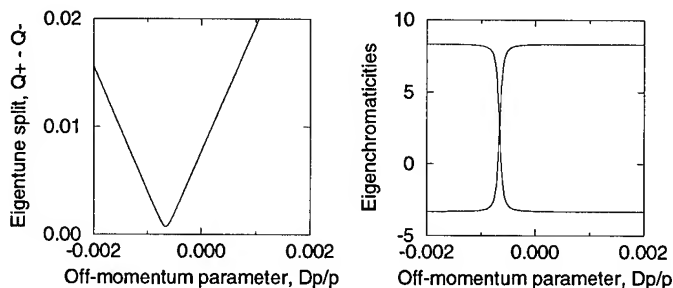


Figure 6. Eigentune split and eigenchromaticities with very unequal chromaticities and design tunes 0.007 apart ($\chi_x = 8.0$, $\chi_y = -3.0$, $Q_{x0} = .425$, $Q_{y0} = .418$). Total beam loss was observed.

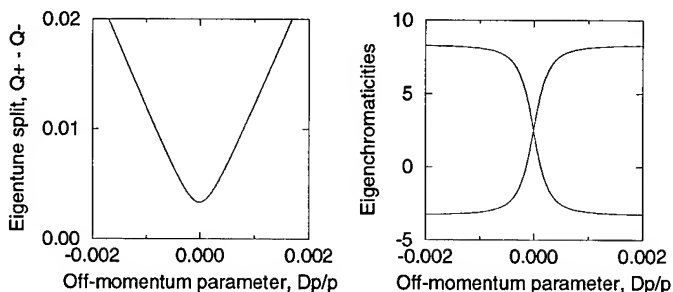


Figure 7. Eigentune split and eigenchromaticities as in Fig. 6, but with design tunes 0.001 apart ($Q_{x0} = .417$, $Q_{y0} = .418$). Remarkably, the beam was stable.

The Effect and Correction of Coupling generated by the RHIC Triplet Quadrupoles

F. Pilat, S. Peggs, S. Tepikian, D. Trbojevic, J. Wei
Brookhaven National Laboratory

I. INTRODUCTION

This study explores the possibility of operating the nominal RHIC coupling correction system in local decoupling mode, where a subset of skew quadrupoles are independently set by minimizing the coupling as locally measured by beam position monitors. The goal is to establish a correction procedure for the skew quadrupole errors in the interaction region triplets that does not rely on a priori knowledge of the individual errors.

After a description of the present coupling correction scheme envisioned for RHIC, the basics of the local decoupling method will be briefly recalled in the context of its implementation in the TEAPOT simulation code as well as operationally.

The method is then applied to the RHIC lattice: a series of simple tests establish that single triplet skew quadrupole errors can be corrected by local decoupling. More realistic correction schemes are then studied in order to correct distributed sources of skew quadrupole errors: the machine can be decoupled either by pure local decoupling or by a combination of global (minimum tune separation) and local decoupling. The different correction schemes are successively validated and evaluated by standard RHIC simulation runs with the complete set of errors and corrections. The different solutions and results are finally discussed together with their implications for the hardware.

II. THE ORIGINAL RHIC COUPLING CORRECTION SYSTEM

The main sources of coupling in RHIC are systematic and random a_1 (skew quadrupole) multipoles in the dipoles and roll alignment errors in the quadrupoles. In particular, the triplet quadrupoles, strong and at a lattice position where the beta functions can be as large as 1300m, are a major source of coupling.

The coupling correction system for RHIC consists of 6 skew quadrupole families (8 quadrupoles in each family) located near the Interaction Regions (IRs) and 12 triplet correctors (1 skew quadrupole per triplet). It is worth noticing that the 6 families have in reality 12 independent power supply circuits, as described in [1]. The correction scheme presently envisioned for RHIC relies on 4 families of skew quadrupoles set up to minimize the tune separation at the nominal operating tunes of 28.19 and 29.18. A detailed description of this method can be found in [2]. The coupling effect of the triplets is corrected locally by the triplet skew quadrupole correctors by "dead reckoning" assuming that the error is known. The triplet coupling correction is part of the general triplet correction scheme, which locally compensates for triplet multipole errors. Further details about the nonlinear triplet correction system can be found in [3] and [4].

The "dead reckoning" method works well, provided we know the

errors. This may not always be the case: even if the triplet quadrupoles are carefully measured and aligned at the beginning, conditions may drift and cause uncorrected residual coupling errors. An operational way of removing the coupling caused by the triplets is desirable and will be discussed below.

III. LOCAL DECOUPLING TECHNIQUE

The local decoupling technique is part of a general method for operational corrections of errors in accelerators. The general underlying concept is to determine the settings of correctors by minimization of a *badness function* that quantifies the effect to be corrected and that is built up by *measurable quantities*. The specific badness function will vary for the different correction operations that can be performed, like closed orbit correction, decoupling, correction of beta functions and vertical dispersion. A complete discussion of this general correction approach can be found in [5]. All the correction techniques are implemented in the TEAPOT simulation code [6] in an operational way that can be easily translated into application software procedures.

A coupling badness function, that measures coupling and goes to zero in absence of coupling, is defined as:

$$B^C = \sum_{d=1}^{N^d} e_A^2 \frac{\beta_x(d)}{\beta_y(d)}$$

The summation is taken over the number of detectors (BPMs) N^d . The measurable quantity e_A is a function of the off diagonal matrix elements R_{A11} and R_{A12} , which can be expressed in terms of the N_a skew quadrupole corrector strengths q_a^{skew} . When $N^d > N^a$ one can determine the skew quadrupole corrector strengths by a fitting procedure so that the following conditions are met:

$$\frac{\partial}{\partial q_a^{skew}} B^C(q_1^{skew}, \dots, q_{N_a}^{skew}) = 0 \quad a = 1, \dots, N_a$$

The local coupling algorithm has been successfully applied to correct coupling in various lattices, the SSC Boosters and Collider, and LEP. Experimental work towards the application of the method in existing machines has been carried out at HERA and LEP [7][8]. A typical criterion for coupling correction is to obtain eigenangles less than 10 degrees everywhere in the machine.

IV. APPLICATION TO RHIC

A. Tests

The decoupling algorithm has been tested in one simple case when a *single roll error* is applied to one triplet quadrupole. If we roll one of the triplet quadrupoles Q by an angle θ , the integrated skew multipole strength in the nearby corrector needed to compensate the error, can be calculated by:

$$kL = a_1(\text{corr}) = \frac{-2\theta b_1(Q) \sqrt{\beta_x(Q) \beta_y(Q)}}{\sqrt{\beta_x(\text{corr}) \beta_y(\text{corr})}}$$

The test consists of applying a 1 mrad roll to the Q3 triplet quadrupole (and similarly to Q1 and Q2) in an otherwise ideal RHIC lattice, and checking the local coupling result versus the analytical one. The results for the Q3 quadrupole in IR6 are summarized in Table 1 below.

Table 1: Q3 triplet quadrupole rolled by 1 mrad in the 6 o'clock (1 m β^*) interaction region.

configuration	eigenangle max [degrees]	max vertical dispersion [m]	skew quad strength [m^{-1}]
no correction	45.0	~0.1	0
calculated setting	4.6	~0	$-0.2119 \cdot 10^{-3}$
local decoupling (1 skew)	0.11	~0	$-0.2232 \cdot 10^{-3}$
local decoupling (24 skews)	0.03	~0	$-0.2205 \cdot 10^{-3}$

The first entry describes the uncorrected effect of 1 mrad roll error in the Q3 triplet quadrupole when the optics is tuned to $\beta^*=1\text{m}$ (in the 6 o'clock and 8 o'clock IRs). The *minimum tune separation* in this case is 0.034. The second row shows the effect of dead reckoning the correction, assuming the error known. As seen in the third row, the local decoupling algorithm can pinpoint the right correction setting when we use only the adjacent corrector strengths as a variable (1 skew case). If we activate other skew correctors distributed in the lattice (24 skew case), their strengths can be optimized to suppress virtually all coupling in the machine. The same analysis has been repeated for the Q2 and Q1 triplet quadrupoles giving similar results: it demonstrates that the local decoupling algorithm can reproduce and improve the "dead-reckoning" triplet correction without relying on a priori knowledge of the individual error.

B. Local decoupling schemes

In order to study possible decoupling schemes, a random generation of skew quadrupole errors has been used in the lattice quadrupoles (triplet, IRs, arc) for the otherwise ideal RHIC lattice, in the storage configuration where 2 IRs (6 and 8 o'clock) are tuned to $\beta^*=1\text{m}$ and the remaining 4 IRs to $\beta^*=10\text{m}$. At injection all the IRs are tuned to the higher β^* and hence the coupling caused by the triplets is lower. For this study the assumptions are that we can measure coupling at every RHIC beam position monitor and that we have 12 independently powered skew quadrupole correctors located in the 12 triplets in the 6 RHIC IRs. Several solutions

of the following types have been investigated:

"pure" local solutions: *all skew errors* are corrected by local decoupling, with the 12 skew triplet correctors (local_12) or with 24 skew correctors (local_24: 12 triplet correctors and 12 correctors from the families circuits).

"hybrid" solutions: *arc-like errors* are corrected with 2 families set up to minimize the tune separation (global_2) and *triplet errors* are corrected with local decoupling (local_12 or local_4, where only the correctors in IR6 and IR8 are used).

When all errors, triplet included, are corrected by global decoupling, the typical residual eigenangles and minimum tune separation are 34 degrees and 10^{-2} , confirming that the triplet correction is necessary.

Tables 2 and 3 summarize results for different seeds for the *pure local decoupling* correction and the 'hybrid' correction scheme.

Table 2: Correction of arc-like and triplet skew errors with 12 triplet skew correctors (local_12)

SEED	max eigenangle [degrees]	max vertical dispersion [m]	max skew quad kL [m^{-1}]
0	1.7	0.70	$0.813 \cdot 10^{-3}$
1	1.1	0.36	$0.829 \cdot 10^{-3}$
2	2.3	0.12	$0.217 \cdot 10^{-2}$
3	1.0	0.40	$0.993 \cdot 10^{-3}$
4	3.4	0.31	$0.483 \cdot 10^{-3}$
5	1.7	0.37	$0.834 \cdot 10^{-3}$

Table 3: "Hybrid" solution: correction of arc-like skew errors with 2 families (global_2) and triplet skew errors with local decoupling (local_12 or local_4)

SEED	max eigenangle [degrees]	max vertical dispersion [m]	max skew quad kL [m^{-1}]
0	0.9	1.01	$0.948 \cdot 10^{-3}$
1	1.1	0.25	$0.610 \cdot 10^{-3}$
2	3.4	0.34	$0.188 \cdot 10^{-2}$
3	1.0	0.52	$0.974 \cdot 10^{-3}$
4	1.7	0.40	$0.817 \cdot 10^{-3}$
5	1.1	0.24	$0.873 \cdot 10^{-3}$

A pure local decoupling solution or a hybrid solution with 12 triplet skew quadrupole correctors are feasible on the basis of these results.

The maximum excitation allowed in the triplet C2 skew quadrupole correctors, 50 Amps, corresponds to a maximum integrated

strength of $1.46 \cdot 10^{-3} \text{ m}^{-1}$. For the hybrid solution with 12 triplet skew quadrupoles operated in local decoupling mode, the quadrupole setting statistics over 6 seeds are:

mean: $\langle |k_L| \rangle = 0.420 \cdot 10^{-3} \text{ m}^{-1}$ or $\langle |I| \rangle = 14.38 \text{ A}$

sigma: $\sigma_{k_L} = 0.295 \cdot 10^{-3} \text{ m}^{-1}$ or $\sigma_I = 10.10 \text{ A}$

All the correctors are well within the system capability.

V. SIMULATION WITH ALL ERRORS

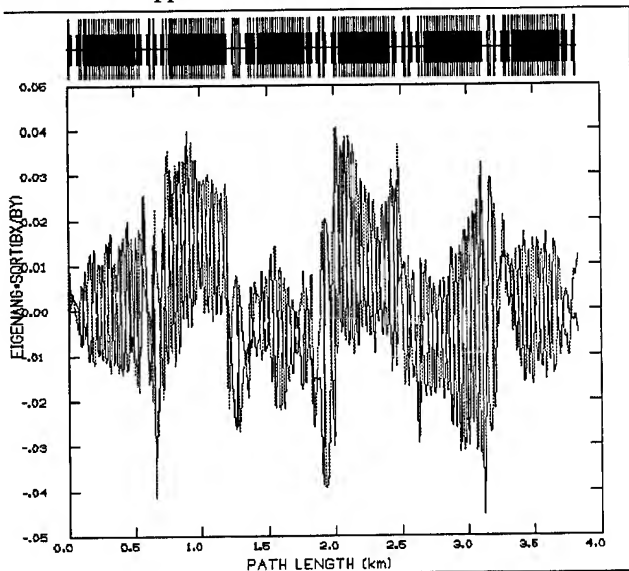
The local coupling correction of the triplet errors has been tested in the context of the full RHIC simulation, when all other errors and correction are also modelled.

The baseline 'MAC94.2' set of alignment and multipole errors, as well as the RHIC standard set of corrections (tuning, chromaticity, triplet corrections) has been used, with the "dead reckoning" compensation of triplet skew quadrupole errors substituted by local decoupling. The results for 4 error distributions are summarized in Table 4. Both the residual coupling and vertical dispersion are acceptable for RHIC, and the skew quadrupole strengths required are within the present system specifications. The resulting eigenangles are shown in Figure 1.

Table 4: Simulation with the full set of errors and corrections

SEED	max eigenangle [degrees]	max vertical dispersion [m]	max skew quad $ k_L $ [m^{-1}]
0	3.1	0.34	$0.771 \cdot 10^{-3}$
1	2.6	0.51	$0.782 \cdot 10^{-3}$
2	3.7	0.62	$0.778 \cdot 10^{-3}$
3	4.7	0.82	$0.144 \cdot 10^{-3}$

Figure 1. The final result for the eigenangles after all error and corrections are applied (seed 1).



VI. CONCLUSIONS

The local decoupling technique proved effective in correcting triplet skew quadrupole errors by relying only on measurable quantities. The simulation results also showed that all coupling sources in the machine could be corrected by local decoupling, should that be desirable. RHIC is adopting the solution to correct the skew quadrupole errors caused by the triplet with the 12 skew quadrupole correctors that are part of the C2 triplet corrector packages, and to rely on the minimum tune separation correction (2+2 skew quadrupole families) for correction of other coupling sources in the machine.

The old baseline corrector configuration for RHIC included power supplies only for the C2 correctors in the 6 and 8 o'clock interaction regions (low β^* triplets). The 12 skew scheme presented here would require 8 more power supplies for the high β^* C2 triplet correctors, a modest investment that will greatly improve the correction quality and flexibility.

For the systematic study conducted here, the assumption was made that we can measure coupling at every beam position monitor (BPM) in the machine. Only a subset of RHIC BPMs are double view, the ones located in the interaction region areas, while the BPMs in the arcs are single plane. However, it was verified that the existing 2 plane BPMs provide enough coupling information for the preferred scheme (12 skew triplet correctors) to work. In order to correct all coupling locally, coupling information from the arc is required: the local coupling algorithm implementation in TEAPOT is being extended so that the coupling at 1 arc horizontal (vertical) BPM can be inferred by measurements at the 2 adjacent vertical (horizontal) BPMs.

VII. REFERENCES

- [1] RHIC Design Manual
- [2] D.Trbojevic, S.Tepikian, S.Peggs, "Decoupling Correction System in RHIC", Proc. of the "Orbit Correction and Analysis in Circular Accelerators" Workshop, BNL, December 1993
- [3] J.Wei, R.Gupta, S.Peggs, "Magnetic Correction of RHIC Triplets", Proceedings of the Particle Accelerator Conference (p. 258-260), Washington, May 1993
- [4] S. Tepikian, S.Peggs, "Skew Quadrupole Errors in the RHIC IR Triplets", Proc. of the "Orbit Correction and Analysis in Circular Accelerators" Workshop, BNL, December 1993
- [5] R.Talman, "A Universal Algorithm for Accelerator Correction", Proceedings of the "Advanced Beam Dynamics Workshop on effect of errors in accelerators, their diagnosis and correction", Corpus Christi, October 1991.
- [6] L.Schachinger, R.Talman, "Manual for the program TEAPOT", November 1994
- [7] G.Bourianoff, "Accelerator Simulation Activities at the SSCL", Proceedings of the "Stability of Particle Motion in Storage Rings" Workshop, BNL, October 1992
- [8] G.Bourianoff, S.Hunt, D.Mathieson, F.Pilat, R.Talman, G.Morpurgo, "Determination of coupled-lattice properties using turn-by-turn data", Proceedings of the "Stability of Particle Motion in Storage Rings" Workshop, BNL, October 1992

THE BEAM ENVELOPE EQUATION - SYSTEMATIC SOLUTION FOR A FODO LATTICE WITH SPACE CHARGE

Edward P. Lee, Lawrence Berkeley Laboratory, Berkeley, CA 94720

ABSTRACT

Many approximate solutions for matched beam envelope functions with space charge have been developed; they generally have errors of 2 - 10% for the parameters of interest and cannot be reliably improved. The new, systematic approach described here provides the K-V envelope functions to arbitrarily high accuracy as a power series in the quadrupole gradient. A useful simplification results from defining the sum and difference of the envelope radii; $S = (a+b)/2$ varies only slightly with distance z along the system axis, and $D = (a-b)/2$ contains most of the envelope oscillations. To solve the coupled equations for S and D , the quadrupole strength $K(z)$ is turned on by replacing K with αK_1 and letting α increase continuously from 0 to 1. It is found that S and D may be expanded in even and odd powers of α , respectively. Equations for the coefficients of powers of α are then solved successively by integration in z . The periodicity conditions and tune integration close the calculation. Simple low order results are typically accurate to 1% or better.

I. INTRODUCTION

The matched (periodic) solution of the coupled Kapchinskij-Vladimirskij (K-V) beam envelope equations is used extensively in the design of quadrupole transport systems.⁽¹⁾ Exact results for a specified set of beam and lattice parameters are readily obtained numerically. However to perform scoping studies, scaling, cost optimization, and to gain physical understanding, it is very desirable to have simple analytical formulas for the envelope functions. The general problem may be stated as follows. For specified quadrupole strength $K(z)$ with period (P), beam edge emittance (ϵ), and beam perveance (Q), find the matched envelope radii $a(z)$ and $b(z)$. The depressed phase advance per period or tune (σ) is then determined from the mean of a^{-2} , and the undepressed phase advance (σ_0) is determined in similar fashion in the limit $Q = 0$.

The simplest rough design formulas are obtained by assuming that the quadrupoles effectively act like a confining harmonic well with frequency $\sigma_0/2\pi P$ and that the envelope radii are approximated by their mean values (\bar{a}). The perveance and emittance are then related to the tunes, σ_0 and σ (expressed in radians) by the "smooth limit" formulas

$$\frac{QP^2}{\bar{a}^2} = \sigma_0^2 - \sigma^2, \quad \frac{\sigma P}{\bar{a}^2} = \sigma, \quad (1,2)$$

These formulas are correct in the limit $\sigma_0 \rightarrow 0$, but are in error by up to 40% for the typical design case of $\sigma_0 = 72^\circ$. Furthermore the smooth limit, by itself, does not provide formulas for σ_0 , the maximum edge radius, or the envelope slopes. The evaluation of the latter quantities requires a definite prescription for $K(z)$ and treatment of the associated envelope oscillations. A new approach to solving for matched envelope functions is described here. Essentially, an expansion in powers of $K^2 P^4$ is made for various envelope quantities, and the low order non-trivial formulas are typically accurate to about 1% or better. Details are contained in an LBL report by the author⁽²⁾.

II. THE K-V ENVELOPE EQUATIONS

The x and y radii, $a(z)$ and $b(z)$, are assumed to satisfy the coupled, non-linear envelope equations of Kapchinskij and Vladimirskij:

$$\frac{d^2 a}{dz^2} = -K(z)a + \frac{\epsilon^2}{a^3} + \frac{2Q}{a+b}, \quad (3)$$

$$\frac{d^2 b}{dz^2} = +K(z)b + \frac{\epsilon^2}{b^3} + \frac{2Q}{a+b}. \quad (4)$$

Here the quadrupole strength $K(z)$ is the ratio of the transverse magnetic field gradient $G(z)$ and particle rigidity $[B\rho] = \beta\gamma mc/q$. The perveance is the dimensionless constant proportional to current as defined by Lawson: $Q = 2qI[(\beta\gamma)^3 mc^3 4\pi\epsilon_0]^{-1}$, and the (un-normalized) edge emittance $\epsilon = \epsilon_x = \epsilon_y$ is the occupied $(x, dx/dz)$ phase space area divided by π .

By assumption, $K(z+P) = K(z)$. We also assume the mean of K vanishes, and K is antisymmetric around $z=0$; $K(-z) = -K(z)$. Denoting the half period length $L = P/2$, it follows that $K(z)$ is also antisymmetric around $z = \pm L, \pm 2L, \dots$. No additional symmetry is assumed, so a system of unsymmetrical quadrupole doublets is accommodated by the general formulation.

The matched envelope radii exhibit the periodicity of the lattice: $a(z+P) = a(z)$, $b(z+P) = b(z)$, and at mid-drift points $z = 0, \pm L, \pm 2L, \dots$, it is easily shown that $a = b$, $da/dz = -db/dz$.

We define the sum and difference of envelope radii: $S(z) = (a+b)/2$, $D(z) = (a-b)/2$. From the symmetries of a and b , it follows that S is symmetric and D is antisymmetric around $z = 0, \pm L, \pm 2L, \dots$. Hence, $S'(0) = S'(L) = 0$, $D(0) = D(L) = 0$.

Next we define the dimensionless envelope functions $s(z)$ and $d(z)$:

$$S(z) = \bar{a}(1 + s(z)), \quad D(z) = \bar{a} d(z). \quad (5a,b)$$

Denoting d/dz by a superscript prime, eqns (3) and (4) are added and subtracted to yield

* This work was supported by the Director, Office of Energy Research, Office of Fusion Energy, U.S. Dept. of Energy, under Contract No. DE-AC03-76SF00098.

$$s'' = -Kd + \frac{\epsilon^2}{\bar{a}^4} \frac{1}{2} \left[\frac{1}{(1+s+d)^3} - \frac{1}{(1+s-d)^3} \right] + \frac{Q}{\bar{a}^2} \frac{1}{1+s} \quad (6)$$

$$d'' = -K(1+s) + \frac{\epsilon^2}{\bar{a}^4} \frac{1}{2} \left[\frac{1}{(1+s+d)^3} - \frac{1}{(1+s-d)^3} \right] \quad (7)$$

The functions $s(z)$ and $d(z)$ satisfy the same symmetry conditions as S and D respectively. Since the envelope radii are periodic, we have the condition

$$\bar{K}d = \frac{\epsilon^2}{\bar{a}^4} \frac{1}{2} \left[\frac{1}{(1+s+d)^3} + \frac{1}{(1+s-d)^3} \right] + \frac{Q}{\bar{a}^2} \frac{1}{(1+s)} \quad (8)$$

In general, the rate of phase advance in the x or y plane is the inverse of the respective β function (defined by $\beta_x = a^2/\epsilon$). A useful expression for the tune is:

$$\sigma = \left(\frac{P\epsilon}{\bar{a}^2} \right) \frac{1}{2} \left[\frac{1}{(1+s+d)^2} + \frac{1}{(1+s-d)^2} \right] \quad (9)$$

Recall that in the initial formulation of the matched envelope calculation $K(z)$, ϵ and Q are considered to be specified and the matched radii are to be determined. However in eqns (6) - (9), \bar{a} actually gets absorbed into combinations with ϵ and Q ; only $K(z)$, ϵ/\bar{a}^2 , and Q/\bar{a}^2 appear. Due to the matched envelope condition (8), these three quantities cannot be specified independently. Intuitively this is clear since, for example, if we set $\epsilon = 0$ then the transport is space-charge-dominated and we would expect the current density J , Q/\bar{a}^2 to be determined by $K(z)$ alone.

III. METHOD OF SOLUTION

We turn on $K(z)$ proportional to a continuous variable (α); $K(z) = \alpha K_1(z)$, where $K_1(z)$ is the full quadrupole strength function and α increases from 0 to 1. For small α , we expect to recover the smooth limit formulas. As α increases the envelope radii become lumpy, i.e. $d(z)$ becomes appreciable. As $K(z)$ turns on it is also necessary that ϵ/\bar{a}^2 and Q/\bar{a}^2 turn on. A natural dependence suggested by the smooth limit formulas (1) is $\epsilon/\bar{a}^2 \sim \alpha$ and $Q/\bar{a}^2 \sim \alpha^2$, so that $\sigma_0 \sim \alpha$ and σ_0/σ is independent of α . Due to the condition (8), it cannot be quite this simple; the system would be overdetermined beyond the lowest two orders in α . A consistent, but not unique, turn-on procedure is to hold the ratio $(Q/\bar{a}^2/\epsilon^2)$ fixed and define the angle (ϕ) : $\cos^2 \phi = (1 + Q/\bar{a}^2/\epsilon^2)^{-1}$. Then convenient forms ϵ/\bar{a}^2 and Q/\bar{a}^2 are

$$\epsilon^2/\bar{a}^4 = \cos^2 \phi (A_2 \alpha^2 + A_4 \alpha^4 + \dots) \quad (10)$$

$$Q/\bar{a}^2 = \sin^2 \phi (A_2 \alpha^2 + A_4 \alpha^4 + \dots) \quad (11)$$

where A_2, A_4, \dots are determined from eqn (8). The consistent expansions for $s(z)$ and $d(z)$ are found to be of the form

$$s(z) = s_2(z)\alpha^2 + s_4(z)\alpha^4 + \dots \quad (12)$$

$$d(z) = d_1(z)\alpha + d_3(z)\alpha^3 + \dots \quad (13)$$

Inserting the expansions (10) - (13) into eqns (6) and (7), expanding all expressions in powers of α , and equating coefficients of each power of α , we get

$$d_1'' = -K_1(z) \quad (14)$$

$$s_2'' = -K_1 d_1 + A_2 \cos^2 \phi + A_2 \sin^2 \phi \quad (15)$$

$$d_3'' = -K_1 s_2 - 3A_2 d_1 \cos^2 \phi \quad (16)$$

and so forth. We are now able to solve sequentially for $d_1, s_2, d_3, s_4, \dots$, by a straightforward program of integration. The associated constants (A_n) are determined from averages ($\bar{s}_n'' = 0$) and can always be evaluated using lower order s and d functions. The first two A_n are

$$A_2 = \bar{K}_1 d_1 \quad (17)$$

$$A_4 = \bar{K}_1 d_1 s_2 - 3\bar{K}_1 d_1 \bar{d}_1^2 \cos^2 \phi \quad (18)$$

For most applications $\sigma_0 \leq 90^\circ$, and it is found that $|d_5| \ll 0.1$ and $|s_4| \ll 0.001$, so they are not included in further calculations here. Typically $|s_2| \approx 0.1$, and $|d_3|$ increases from .01 to .05 as $\cos \phi \rightarrow 1$. Although the formalism developed so far is self-contained, it is of interest to calculate the tunes σ and σ_0 associated with the matched envelopes. The expansion of eqn (9) in powers of α yields

$$\frac{\sigma \bar{a}^2}{P\epsilon} = 1 + 3\bar{d}_1^2 \alpha^2 + \left(3\bar{s}_2^2 + 6\bar{d}_1 \bar{d}_3 - 12\bar{s}_2 \bar{d}_1^2 + 5\bar{d}_1^4 \right) \alpha^4 + \dots \quad (19)$$

The quantity ϵ/\bar{a}^2 may be eliminated using eqn (10) to obtain

$$\sigma^2 = P^2 \cos^2 \phi \left[\bar{K}_1 d_1 \alpha^2 + \bar{K}_1 d_1 s_2 \alpha^4 + 3\bar{K}_1 d_1 \bar{d}_1^2 (2 - \cos^2 \phi) \alpha^4 + \dots \right] \quad (20)$$

Improved convergence is obtained for the expansion of $\cos \sigma$ as compared with σ^2 . Similarly, the expansion of $(\bar{a}^2 \sin \sigma)/P\epsilon$ converges more rapidly than that of $\bar{a}^2 \sigma/P\epsilon$. This behavior of expansions is not surprising because the trigonometric functions of σ appear in the full period transfer matrix. We evaluate the expansions

$$\begin{aligned} \cos \sigma &= 1 - \frac{\sigma^2}{2} + \frac{\sigma^4}{24} - \dots \\ &= 1 - \left(\frac{P^2 \bar{K}_1 d_1 \cos^2 \phi}{2} \right) \alpha^2 + \left[\frac{P^4 (\bar{K}_1 d_1)^2 \cos^4 \phi}{24} \right. \\ &\quad \left. - \frac{P^2 \bar{K}_1 d_1 s_2 \cos^2 \phi}{2} - \frac{3}{2} P^2 \bar{K}_1 d_1 \bar{d}_1^2 (2 - \cos^2 \phi) \cos^2 \phi \right] \alpha^4 + \dots \quad (21) \end{aligned}$$

$$\begin{aligned} \frac{\bar{a}^2 \sin \sigma}{P\epsilon} &= \left(\frac{\bar{a}^2 \sigma}{P\epsilon} \right) \left(1 - \frac{\sigma^2}{6} + \dots \right) \\ &= 1 + \left(3\bar{d}_1^2 - \frac{P^2 \bar{K}_1 d_1}{6} \cos^2 \phi \right) \alpha^2 + \dots \quad (22) \end{aligned}$$

The undepressed tune (σ_0) is obtained from eqn (21) by setting $\cos \phi$ equal to unity. Note that d_1 and s_2 do not depend on ϕ , so that terms of $\cos \sigma_0$ through (α^4) may be immediately written down:

$$\cos \sigma_0 = 1 - \frac{P^2 \overline{K_1 d_1}}{2} \alpha^2 + \left[\frac{P^4 (\overline{K_1 d_1})^2}{24} - \frac{P^2 \overline{K_1 d_1 s_2}}{2} - \frac{3P^2 \overline{K_1 d_1} \overline{d_1^2}}{2} \right] \alpha^4 + \dots \quad (23)$$

Unfortunately, the expansion of tunes in powers of α becomes very cumbersome beyond the lowest non-trivial order. Some simplification is achieved by combining formulas in such a way that some of the higher order terms cancel. A spectacular cancellation of terms may be verified for the combination

$$2(\cos \sigma - \cos \sigma_0) - \left(\frac{QP^2}{\bar{a}^2} \right) + \left(\frac{QP^2}{\bar{a}^2} \right) \left[\frac{\cos \sigma - \cos \sigma_0}{6} - \left(\frac{\bar{a}^2 \sin \sigma}{P\epsilon} - 1 \right) \right] = O(\alpha^6) \quad (24)$$

It is recommended that this equation be used in place of eqn (21).

IV. FLAT TOP QUADRUPOLE FIELDS

A very useful set of design formulas is derived for the simple FODO lattice with drifts of length $(1-\eta)L$ centered at $z = 0, \pm L, \pm 2L, \dots$, and flat-topped quadrupoles of strength $\pm k$ and length ηL centered at $z = \pm L/2, -3L/2, \dots$.

In the interval $0 < z < L/2$, we have

$$d_1'' = \begin{cases} 0 & 0 < z < (1-\eta)\frac{L}{2} \\ -k & (1-\eta)\frac{L}{2} < z < \frac{L}{2} \end{cases} \quad (25)$$

Integrating eqn (14) twice yields

$$d_1 = \begin{cases} \frac{k\eta L}{2} z & 0 < z < (1-\eta)\frac{L}{2} \\ \frac{\eta k L^2}{4} \left(1 - \frac{\eta}{2}\right) - \frac{k}{2} \left(\frac{L}{2} - z\right)^2 & (1-\eta)\frac{L}{2} < z < \frac{L}{2} \end{cases} \quad (26)$$

The maximum value of d_1 is

$$d_{1m} = d_1(L/2) = \frac{\eta k L^2}{4} \left(1 - \frac{\eta}{2}\right) \quad (27)$$

and the useful averages over d_1 are

$$\overline{K_1 d_1} = \frac{\eta^2 k^2 L^2}{4} \left(1 - \frac{2}{3}\eta\right) \quad (28)$$

$$\overline{d_1^2} = \frac{\eta^2 k^2 L^4}{48} \left(1 - \eta^2 + \frac{2}{5}\eta^3\right) \quad (29)$$

Equation (15) is also integrated twice, making use of the condition $\overline{s_2} = 0$, to obtain the minimum and maximum values

$$s_2(0) = -\frac{\eta^2 k^2 L^4}{24} \left(\frac{1}{4} - \frac{\eta}{6} - \frac{\eta^2}{4} + \frac{\eta^3}{5}\right) \quad (30)$$

$$s_2(L/2) = \frac{\eta^2 k^2 L^4}{24} \left(\frac{1}{2} - \frac{13}{12}\eta + \frac{13}{16}\eta^2 - \frac{\eta^3}{5}\right) \quad (31)$$

A double integration of eqn (19) gives the maximum of $d_3(z)$:

$$d_3(L/2) = \frac{\eta^3 k^3 L^6}{192} \left(1 - \frac{19}{6}\eta + \frac{463}{120}\eta^2 - \frac{511}{240}\eta^3 + \frac{9}{20}\eta^4\right) + \frac{\eta^3 k^3 L^6}{64} \left(1 - \frac{2}{3}\eta\right) \left(1 - \frac{\eta^2}{2} + \frac{\eta^3}{8}\right) \cos^2 \phi \quad (32)$$

Using the averages $\overline{K_1 d_1}$, $\overline{d_1^2}$, and $\overline{K_1 d_1 s_2}$, we get the tune formulas from eqns (22) and (23):

$$2(1 - \cos \sigma_0) = \eta^2 k^2 L^4 \left(1 - \frac{2\eta}{3}\right) - \eta^4 k^4 L^8 \left(\frac{\eta^2}{90} - \frac{\eta^3}{63} + \frac{\eta^4}{180}\right) + \dots \quad (33)$$

$$\left(\frac{\bar{a}^2 \sin \sigma}{2L\epsilon} - 1\right) = \eta^2 k^2 L^4 \left[\frac{1}{16} \left(1 - \eta^2 + \frac{2}{5}\eta^3\right) - \frac{\cos^2 \phi}{6} \left(1 - \frac{2}{3}\eta\right)\right] \quad (34)$$

Equation (24), relating Q to other parameters, does not depend on the specific form of $K_1(z)$ in the order of approximation included here and is therefore not repeated in this section.

REFERENCES

- [1] I.M. Kapchinskij and V.V. Vladimirkij, Proc. Intern. Conf. on High Energy Accelerators, CERN, Geneva, 1959, p. 274.
- [2] E. Lee, LBL-37050, April 1995.

ANALYTIC SECOND- AND THIRD-ORDER ACHROMAT DESIGNS

Chunxi Wang and Alex Chao

Stanford Linear Accelerator Center, Stanford University, Stanford, CA 94309 USA

I. INTRODUCTION

An achromat is a transport system that carries a beam without distorting its transverse phase space distribution. In this study, we apply the Lie algebraic technique [1-6] to a repetitive FODO array to make it either a second-order or a third-order achromat. (Achromats based on reflection symmetries [7,8] are not studied here.) We will consider third-order achromats whose unit FODO cell layout is shown in Fig.1. The second-order achromat layout is the same except the octupoles are absent.

For the second-order achromats, correction terms (due to the finite bending of the dipoles) to the well-known formulae for the sextupole strengths are derived. For the third-order achromats, analytic expressions for the five octupole strengths are given. The quadrupole, sextupole and octupole magnets are assumed to be thin-lens elements. The dipoles are assumed to be sector magnets filling the drift spaces. More details of the analysis have been reported elsewhere.[9] We thank Y. Yan, H. Ye, J. Irwin and A. Dragt for their help.

II. ANALYSIS

We first calculate the Lie maps of each of the magnet elements. The map for a magnet element of length L is given by $e^{-L:H}$, where H is the Hamiltonian of the element. For a particle with $\delta = \Delta P/P_0$, we use (we ignore the path-length dynamics)

$$\begin{aligned} \text{thin quadrupole : } HL &= \frac{1}{2F_k}(x^2 - y^2)(1 - \delta + \delta^2) \\ \text{thin sextupole : } HL &= \frac{S_k}{3}(x^3 - 3xy^2)(1 - \delta) \\ \text{thin octupole : } HL &= \frac{O_k}{4}(x^4 - 6x^2y^2 + y^4) \\ \text{sector dipole : } H &= \frac{P_x^2 + P_y^2}{2} + \frac{x^2}{2R^2} - \frac{x\delta}{R} + \frac{x(P_x^2 + P_y^2)}{2R} \\ &\quad - \frac{x^2\delta}{2R^2} + \frac{x\delta^2}{R} + \frac{(P_x^2 + P_y^2)^2}{8} - \frac{x\delta^3}{R} + \frac{x^2\delta^2}{2R^2} \end{aligned} \quad (1)$$

where R is the bending radius; F_k is the focal length of the k -th quadrupole; S_k and O_k are the k -th integrated sextupole and octupole strengths. Fringe fields are ignored.

Given the Hamiltonian H of an element, we factorize the element map as

$$e^{-L:H} = e^{H_2+H_3+H_4+\dots} = e^{f_2}e^{f_3}e^{f_4}e^{\mathcal{O}(X^5)} \quad (2)$$

where H_n and f_n are polynomials of order n in the variables $X = (x, P_x, y, P_y, \delta)$. We performed this factorization [3,5] and obtained

thin quadrupole :

$$f_3 = \frac{1}{2F_k}(x^2 - y^2)\delta, \quad f_4 = -\frac{1}{2F_k}(x^2 - y^2)\delta^2$$

thin sextupole :

$$f_3 = -\frac{S_k}{3}(x^3 - 3xy^2), \quad f_4 = \frac{S_k}{3}(x^3 - 3xy^2)\delta$$

thin octupole : $f_3 = 0, \quad f_4 = -\frac{O_k}{4}(x^4 - 6x^2y^2 + y^4)$

sector dipole :

$$\begin{aligned} f_3 &= -\frac{1}{6R^2}\sin^3\frac{L}{R}x^3 - \frac{1}{4R}\sin\frac{L}{R}\sin\frac{2L}{R}x^2P_x \\ &\quad - \frac{1}{4}\cos\frac{L}{R}\sin\frac{2L}{R}xP_x^2 + \frac{R}{6}(1 - \cos^3\frac{L}{R})P_x^3 \\ &\quad - \frac{1}{2}\sin\frac{L}{R}xP_y^2 + \frac{x^2\delta}{2R}\sin\frac{L}{R}(\cos\frac{L}{R} + \sin^2\frac{L}{R}) \\ &\quad + R\sin^2\frac{L}{2R}P_xP_y^2 - 2\sin^2\frac{L}{2R}\sin^2\frac{L}{R}xP_x\delta \\ &\quad - \frac{R}{2}\sin^2\frac{L}{2R}\sin\frac{2L}{R}P_x^2\delta - \frac{1}{2}(L - R\sin\frac{L}{R})P_y^2\delta \\ &\quad - \frac{x\delta^2}{2}(\sin^3\frac{L}{R} + \sin\frac{2L}{R}) + \frac{R}{2}(2 - \cos\frac{L}{R})\sin^2\frac{L}{R}P_x\delta^2 \\ &\quad + \frac{1}{12}(-6L + 2R\sin^3\frac{L}{R} + 3R\sin\frac{2L}{R})\delta^3 \\ f_4 &= \left[-\frac{x^2}{8R}\sin^3\frac{L}{R} - \frac{xP_x}{8}\sin\frac{L}{R}\sin\frac{2L}{R} \right. \\ &\quad \left. - \frac{R}{8}\cos^2\frac{L}{R}\sin\frac{L}{R}P_x^2 - \frac{R}{8}\sin\frac{L}{R}P_y^2 \right](P_x^2 + P_y^2) \\ &\quad + \frac{x^3\delta}{12R^2}\sin^3\frac{L}{R} + \left(\frac{1}{2} + \cos\frac{L}{R}\right)\sin^2\frac{L}{2R}\sin\frac{L}{R}xP_x^2\delta \\ &\quad + \left[\frac{R}{12}(3 + 4\cos\frac{L}{R} + 5\cos\frac{2L}{R})P_x^3\delta \right. \\ &\quad \left. + \frac{xP_y^2\delta}{4}\sin\frac{2L}{R} + \frac{R}{4}(3 + \cos\frac{2L}{R})P_xP_y^2\delta \right]\sin^2\frac{L}{2R} \\ &\quad - \frac{1}{4R}(\sin^3\frac{L}{R} + \sin\frac{2L}{R})x^2\delta^2 + \frac{1}{2}\sin^2\frac{L}{R}xP_x\delta^2 \\ &\quad - \frac{R}{4}(1 + 3\cos\frac{L}{R})\sin^2\frac{L}{2R}\sin\frac{L}{R}P_x^2\delta^2 \\ &\quad + \left[\frac{R}{2}\sin^4\frac{L}{2R}P_y^2 + (\cos\frac{L}{R} + \frac{1}{4}\sin^2\frac{L}{R})x\delta\right]\sin\frac{L}{R}\delta^2 \\ &\quad - \frac{R}{2}\sin^2\frac{L}{R}P_x\delta^3 + \frac{\delta^4}{12}(6L - R\sin^3\frac{L}{R} - 3R\sin\frac{2L}{R}) \end{aligned} \quad (3)$$

Having factorized the maps of all magnets, the total map $\mathcal{M}_{\text{cell}}$ of a cell is obtained by multiplying and concatenating the maps of the component elements:[3,9]

$$\mathcal{M}_{\text{cell}} = \prod_{i=1}^N (e^{i f_2^i} e^{i f_3^i} e^{i f_4^i}) = e^{i h_2} e^{i h_3} e^{i h_4} e^{i \mathcal{O}(X^5)} \quad (4)$$

where

$$\begin{aligned} \mathcal{R} &= e^{i h_2} = \prod_{i=1}^N e^{i f_2^i}, \quad h_3 = \sum_{i=1}^N \tilde{f}_3^i \\ h_4 &= \sum_{i=1}^N \tilde{f}_4^i + \frac{1}{2} \sum_{j>i=1}^N [\tilde{f}_3^i, \tilde{f}_3^j] \end{aligned} \quad (5)$$

In Eq.(5), \tilde{f}^i means $\tilde{f}^i(X) = f^i(R_{N \rightarrow i} X)$ with $R_{N \rightarrow i}$ the linear map from the last element to the i -th element. The map of the N -cell achromat is $\mathcal{M} = \mathcal{M}_{\text{cell}}^N$. The number of cells N is so that $\mu_{x,y}$ (the total phase advances in x are y) are both multiples of 2π , but avoiding resonances.

We now make a canonical coordinate transformation from (x, P_x, y, P_y) to $(\phi_x, A_x, \phi_y, A_y)$ by $x = \sqrt{2A_x \beta_x} \sin \phi_x + \eta \delta$, $P_x = \sqrt{\frac{2A_x}{\beta_x}} (\cos \phi_x - \alpha_x \sin \phi_x) + \eta' \delta$, and similarly for y and P_y without the η and η' terms, where $\beta_{x,y}$, $\alpha_{x,y}$ and η, η' are the Courant-Snyder and the dispersion functions.[10] The linear map generator h_2 becomes $h_2 = -\mu_x A_x - \mu_y A_y - \frac{1}{2} \bar{\alpha}_c \delta^2$ where $\bar{\alpha}_c$ is the momentum compaction factor. We then decompose h_n in terms of the eigenmodes of h_2 : as[5]

$$\begin{aligned} h_n &= \sum_{a+b+c+d+e=n} C_{abcd,e}^n |abcd, e\rangle \\ |abcd, e\rangle &\equiv A_x^{(a+b)/2} A_y^{(c+d)/2} e^{i(a-b)\phi_x} e^{i(c-d)\phi_y} \delta^e \end{aligned} \quad (6)$$

To reduce a nonlinear map to its normal form, it can be shown[11] that (in the absence of resonances)[2] all the non-secular terms can be transformed away via a symplectic similarity transformation leaving only terms with $a = b$ and $c = d$, i.e., terms depending on A_x, A_y and δ only. In particular, we have

$$\begin{aligned} h_3 &= C_{1100,1}^3 A_x \delta + C_{0011,1}^3 A_y \delta + C_{0000,3}^3 \delta^3 \\ h_4 &= C_{2200,0}^4 A_x^2 + C_{0022,0}^4 A_y^2 + C_{1111,0}^4 A_x A_y \\ &\quad + C_{1100,2}^4 A_x \delta^2 + C_{0011,2}^4 A_y \delta^2 + C_{0000,4}^4 \delta^4 \end{aligned} \quad (7)$$

III. SECOND-ORDER ACHROMATS

For a second-order achromat, we follow Eqs.(6-7) and find the normal form of the unit cell is given by h_3 of Eq.(7) where

$$\begin{aligned} C_{1100,1}^3 &= \sum_{k=1,2}^{\text{quads}} \left[\frac{1}{2F_k} - \lambda_k \eta(k) \right] \beta_x(k) + w_x \\ C_{0011,1}^3 &= - \sum_{k=1,2}^{\text{quads}} \left[\frac{1}{2F_k} - \lambda_k \eta(k) \right] \beta_y(k) + w_y \end{aligned} \quad (8)$$

and

$$\begin{aligned} w_x &= \sum_{k=1,2}^{\text{dipoles}} \frac{1}{2} \sin^2 \left(\frac{L}{R} \right) \left\{ \frac{\beta_x(k)}{R} \left[\sin \frac{L}{R} + \cot \frac{L}{R} \right. \right. \\ &\quad \left. \left. - \frac{\eta(k)}{R} \sin \frac{L}{R} - \eta'(k) \cos \frac{L}{R} \right] + 2\alpha_x(k) \left[1 - \cos \frac{L}{R} \right. \right. \\ &\quad \left. \left. + \frac{\eta(k)}{R} \cos \frac{L}{R} + \eta'(s) \cos \frac{L}{R} \cot \frac{L}{R} \right] \right\} \end{aligned}$$

$$\begin{aligned} &+ \gamma_x(k) R \left[-\cos \frac{L}{R} \tan \frac{L}{2R} - \frac{\eta(k)}{R} \cos \frac{L}{R} \cot \frac{L}{R} \right. \\ &\quad \left. + \left(\cos \frac{L}{R} + \frac{1}{2} \sec^2 \frac{L}{2R} \right) \eta'(k) \right] \} \\ w_y &= \sum_{k=1,2}^{\text{dipoles}} \frac{1}{2} \gamma_y(k) R \left[\sin \frac{L}{R} - \frac{L}{R} - \eta(k) \sin \frac{L}{R} \right. \\ &\quad \left. + \eta'(k) \left(1 - \cos \frac{L}{R} \right) \right] \end{aligned} \quad (9)$$

The lattice functions are evaluated at the two quadrupoles in Eq.(8) and at the ends of the two dipoles in Eq.(9). In the limit of weak bending with $\epsilon_1 = \frac{L}{R} \ll 1$, we have

$$\begin{aligned} w_x &\simeq \epsilon_1 \sum_s^D \alpha_x(s) \eta'(s) + \frac{1}{4} \gamma_x(s) (3L \eta'(s) - 2\eta(s)) \\ w_y &\simeq \epsilon_1 \sum_s^D \frac{1}{4} \gamma_y(s) (L \eta'(s) - 2\eta(s)) \end{aligned} \quad (10)$$

To form a second-order achromat, we set the two C -coefficients to zero, and obtain

$$\begin{aligned} S_1 &= \frac{1}{2\eta(1)F_1} + \frac{\beta_y(2)w_x + \beta_x(2)w_y}{\eta(1)[\beta_x(1)\beta_y(2) - \beta_x(2)\beta_y(1)]} \\ S_2 &= \frac{1}{2\eta(2)F_2} - \frac{\beta_y(1)w_x + \beta_x(1)w_y}{\eta(2)[\beta_x(1)\beta_y(2) - \beta_x(2)\beta_y(1)]} \end{aligned} \quad (11)$$

The first terms usually dominate and give the well-known results. The correction terms with w_x and w_y are normally but not always small.

IV. THIRD-ORDER ACHROMATS

We also studied the case of a third-order achromat. An algebraic program using Mathematica was developed to do the analysis. Here we only report our results. The normal form of the third-order generator for a unit cell is given by Eq.(9) with

$$\begin{aligned} C_{2200,0}^4 &= -\frac{3}{8} \sum_{k=1}^5 \beta_x(k)^2 O_k + w_{xx} \\ C_{1111,0}^4 &= \frac{3}{2} \sum_{k=1}^5 \beta_x(k) \beta_y(k) O_k + w_{xy} \\ C_{0022,0}^4 &= -\frac{3}{8} \sum_{k=1}^5 \beta_y(k)^2 O_k + w_{yy} \\ C_{1100,2}^4 &= -\frac{3}{2} \sum_{k=1}^5 \beta_x(k) \eta(k) O_k + w_{xd} \\ C_{0011,2}^4 &= \frac{3}{2} \sum_{k=1}^5 \beta_y(k) \eta(k) O_k + w_{yd} \end{aligned} \quad (12)$$

and (when $\epsilon_1 = \frac{L}{R} \ll 1$)

$$\begin{aligned} w_{xx} &\simeq \csc \frac{3\mu_x}{2} (2 + 3 \cos \mu_x) \prod_s^S \frac{S_s}{4} \beta_x(s)^{\frac{3}{2}} - \frac{3L}{16} \sum_s^D \gamma_x(s)^2 \\ &\quad + \frac{1}{8} \csc \frac{3\mu_x}{2} (3 \cos \frac{\mu_x}{2} + 2 \cos \frac{3\mu_x}{2}) \sum_s^S S_s^2 \beta_x(s)^3 \end{aligned}$$

$$w_{xy} \simeq -\frac{L}{4} \sum_s \gamma_x(s) \gamma_y(s) - \frac{1}{2} \cot \frac{\mu_x}{2} \sum_s S_s^2 \beta_x(s)^2 \beta_y(s) \\ - \csc(\frac{\mu_x}{2} + \mu_y) \csc(\frac{\mu_x}{2} - \mu_y) \sin 2\mu_y \sum_s \frac{S_s^2}{4} \beta_x(s) \beta_y(s)^2 \\ + \left[\csc(\frac{\mu_x}{2} + \mu_y) - \csc(\frac{\mu_x}{2} - \mu_y) - \csc \frac{\mu_x}{2} \sum_s \frac{\beta_x(s)}{\beta_y(s)} \right] \\ \times \frac{1}{2} \prod_s S_s \sqrt{\beta_x(s)} \beta_y(s)$$

$$w_{yy} \simeq -\frac{3L}{16} \sum_s \gamma_y^2(s) + \frac{1}{16} \sum_s S_s^2 \beta_x(s) \beta_y(s)^2 \\ \times \left[4 \cot \frac{\mu_x}{2} + \sin \mu_x \csc(\frac{\mu_x}{2} + \mu_y) \csc(\frac{\mu_x}{2} - \mu_y) \right] \\ + \frac{1}{8} \left[4 \csc \frac{\mu_x}{2} + \csc(\frac{\mu_x}{2} + \mu_y) + \csc(\frac{\mu_x}{2} - \mu_y) \right] \\ \times \prod_s S_s \sqrt{\beta_x(s)} \beta_y(s)$$

$$w_{xd} \simeq -\frac{3L}{4} \sum_s \gamma_x(s) \eta'(s)^2 - \sum_s \beta_x(s) \left(\frac{1}{2F_s} - S_s \beta_x(s) \right) \\ + \frac{1}{2} \cot \mu_x \sum_s \left[\beta_x(s) \left(\frac{1}{2F_s} - S_s \beta_x(s) \right) \right]^2 \\ + \csc \mu_x \prod_s \beta_x(s) \left(\frac{1}{2F_s} - S_s \beta_x(s) \right) \\ + \csc \frac{\mu_x}{2} \sum_{1,2} \frac{S_2}{2} \beta_x(2) \eta(1) (S_1 \eta(1) - \frac{1}{F_1}) \sqrt{\beta_x(1) \beta_x(2)} \\ + \frac{1}{2} \cot \frac{\mu_x}{2} \sum_s S_s \eta(s) (S_s \eta(s) - \frac{1}{F_s}) \beta_x(s)^2$$

$$w_{yd} \simeq -\frac{L}{4} \sum_s \gamma_y(s) \eta'(s)^2 + \sum_s \beta_y(s) \left(\frac{1}{2F_s} - S_s \beta_x(s) \right) \\ + \frac{1}{2} \cot \mu_y \sum_s \left[\beta_y(s) \left(\frac{1}{2F_s} - S_s \beta_x(s) \right) \right]^2 \\ + \csc \mu_y \prod_s \beta_y(s) \left(\frac{1}{2F_s} - S_s \beta_x(s) \right) \\ - \csc \frac{\mu_x}{2} \sum_{1,2} \frac{S_2}{2} \beta_y(2) \eta(1) (S_1 \eta(1) - \frac{1}{F_1}) \sqrt{\beta_x(1) \beta(2)} \\ - \frac{1}{2} \cot \frac{\mu_x}{2} \sum_s S_s \eta(s) (S_s \eta(s) - \frac{1}{F_s}) \beta_x(s) \beta_y(s)$$

(13)

Exact expressions of the w -coefficients are too lengthy to be included here.

The required octupole strengths are such that the five C -coefficients in Eq.(12) are equal to zero. For the case when two of the octupoles are located next to the two sextupoles and the

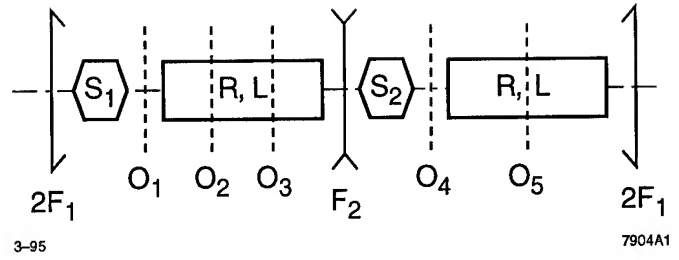


Figure 1. Unit cell of an achromat layout.

other three are at the $\frac{1}{3}$, $\frac{2}{3}$, and the $\frac{1}{2}$ locations of the two bending magnets, we find

$$O_1 \simeq \frac{a+b}{6f^3D}, \quad O_2 \simeq \frac{81(c+d)}{2fD}, \quad O_3 \simeq \frac{81(c-d)}{2fD}$$

$$O_4 \simeq \frac{a-b}{6f^3D}, \quad O_5 \simeq \frac{128e}{3(2f^2-1)D}$$

$$a = 2f(1360 - 22846f^2 - 74476f^4 + 695809f^6 \\ - 1438146f^8 + 1200096f^{10} - 326592f^{12})$$

$$b = -352 - 3360f^2 + 233290f^4 - 1070910f^6 \\ + 1917603f^8 - 1364850f^{10} + 361584f^{12}$$

$$c = 6f(-42 + 1076f^2 - 7409f^4 + 16306f^6 - 14368f^8 \\ + 4032f^{10})$$

$$d = 8 - 394f^2 + 5322f^4 - 16907f^6 + 14866f^8 - 4464f^{10}$$

$$e = -368 + 10536f^2 - 92342f^4 + 307222f^6 - 470547f^8 \\ + 330642f^{10} - 81648f^{12}$$

$$D = (4f^2 - 1)^2(3f^2 - 4)(10 - 173f^2 - 261f^4 + 324f^6)L^3\epsilon_1^2 \quad (14)$$

We have defined the dimensionless parameter $f = \frac{2F_1}{L}$ and have assumed that $\epsilon_1 = \frac{L}{R} \ll 1$ and $|\frac{F_1+F_2}{L}| \ll 1$.

References

- [1] K.L. Brown, SLAC-PUB-3381 (1984).
- [2] E. Forest, D. Douglas and B. Leemann, Nucl. Instr. Meth. A258, 355 (1987).
- [3] A.J. Dragt, AIP conf. Proc. No.87, Phys. high energy part. accel., 1982, p.147.
- [4] A.J. Dragt and J.M. Finn, J. Math. Phys. 17, 2215 (1976).
- [5] A.J. Dragt and E. Forest, J. Math. Phys. 24, 12 (1983).
- [6] A.J. Dragt, Nucl. Instr. Meth. A258, 339 (1987).
- [7] W. Wan, E. Goldmann and M. Berz, AIP Proc. 297 (1994), p.143.
- [8] W. Wan and M. Berz, Proc. Part. Accel. Conf., 1993, p.155.
- [9] Chunxi Wang and Alex Chao, SLAC internal report AP-100 (1995).
- [10] E.D. Courant and H.S. Snyder, Ann. Phys. 3,1 (1958).
- [11] E. Forest, SSC Report 29 (1985).

MEASUREMENT OF CHROMATIC EFFECTS IN LEP

D. Brandt, P. Castro, K. Cornelis, A. Hofmann, G. Morpurgo, G.L. Sabbi and A. Verdier,
CERN, CH-1211 Geneva 23, Switzerland

Abstract

The chromaticity produced by the insertions and the lattice of LEP is corrected in the FODO lattice of the arcs which has horizontal and vertical phase advances of 90° and 60° for the LEP optics presently used. This is done with two horizontal and three vertical sextupole families. To check this correction scheme the non-linear chromaticities have been measured by observing the betatron tunes as a function of RF-frequency, i.e. of momentum deviation. The differences between the results and the expected effects of the sextupoles are interpreted in terms of octupole and decapole components in the dipole magnets. To check the distribution around the ring of the chromaticities and their corrections the betatron phase advances have been measured as a function of momentum deviation. This was done by observing an excited betatron oscillation for 1024 turns in all beam position monitors for different RF-frequencies. The results clearly show the negative chromaticity produced in the straight sections and its correction in the arcs. The parasitic sextupole components are found to be spread uniformly in the arcs within the measurement errors. Under this condition one finds that they have a negligible effect on the dynamic aperture.

I. INTRODUCTION

The non-linear chromaticity of the LEP machine at CERN is corrected with sextupole families. For the optics used from 1993 to 1995, there are five sextupole families. This number is linked with the phase advances in the arc cells where the sextupoles are located. Three families are used for the vertical plane where the phase advance is 60° and two families are used for the horizontal plane where the phase advance is 90° . Detailed specifications concerning sextupole families are given in another paper at this conference [1]. The basic motivation to use more than two sextupole families is to compensate the off-momentum mismatch of the low- β insertions. For instance if the chromaticity is corrected with two sextupole families in the arcs only, the off-momentum betatron motion becomes unstable for a momentum deviation of about 0.003.

Due to the dependence of the radiation damping partitions on Δp , the measurement of the variation of the tunes with momentum can only be used to check the chromaticity correction in a small range of momentum deviations. This is still sufficient to validate the correction done. However what has not been done up to now is to measure the distribution of the parasitic sextupole, octupole and decapole components in the dipoles of the arc cells. Although it should be possible to predict the chromaticity and the tune dependence on amplitude from the known average value of the sextupole and octupole components, it is interesting to check this and see that the distribution of these components in the arc cells is smooth enough and not to make higher order effects. This is what has been done and is reported here.

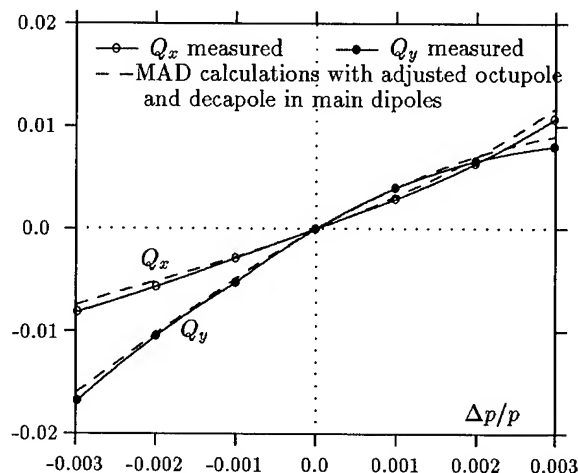


Figure 1. Measured and calculated tunes vs. $\Delta p/p$

II. MEASUREMENT OF THE NON-LINEAR CHROMATICITY BY CHANGING THE RF FREQUENCY.

This method is very well known. For a given value of the RF frequency, there is a momentum of the beam such that its centre of gravity corresponds to the synchronous particle. The momentum deviation $\Delta p/p$ from the central value and the relative RF frequency change $\frac{\Delta f_{RF}}{f_{RF}}$ are related by :

$$\frac{\Delta f_{RF}}{f_{RF}} = \left(\frac{1}{\gamma^2} - \alpha_c \right) \frac{\Delta p}{p} \quad (1)$$

where α_c is the momentum compaction factor.

In the case of LEP some care has to be taken for such a measurement because of the tune change due to the SPS pulsing. In order to eliminate it, a phase-lock loop (PLL) is used to record permanently the machine tunes [2]. By inspecting this record, it is easy to distinguish peaks due to the SPS pulsing and to take the right tune value outside of the perturbed areas. The accuracy of this measurement itself is better than the LEP stability (power supplies and mechanical stability), it is of the order of 0.0001. In order to eliminate tune drifts due to the LEP stability, the PLL record is done while the RF frequency is incremented and decremented by the same value. This makes it possible to obtain an accuracy of the tune measurement of about 0.0002. Given this high accuracy, a correction of the measurement due to the change of the bunch length with $\Delta p/p$ and due to the coupling has been investigated [3]. It was found that a small correction has to be applied to the value of the first derivative of the tunes but no correction from these effects have to be applied to the higher order derivatives as they are well below the measurement errors. The corrected values of the tunes versus momentum deviation are shown in Fig. 1. If the measured octupole and decapole errors in

the dipoles are used directly, a large discrepancy between measurement and calculation would occur. To reduce it to the small values shown in Fig. 1 these components had to be multiplied by large factors of -45 and 630 respectively. This corresponds to a total relative field error of about 0.007, which should have showed up in the magnetic measurements. On the other hand the measurement of the chromatic phase advance shown below rules out non-uniform sextupole errors which could produce higher order effects. Thus we are left with a large discrepancy not yet understood.

III. MEASUREMENT OF THE CHROMATIC PHASE ADVANCE

A. Introduction

The dependence of the betatron tunes on momentum is called "Q-prime" and is given by $Q' = dQ/(dp/p)$. Sometimes the above quantities are divided by the tune and called chromaticities. Since the quadrupole focusing strength decreases with energy, the normal focusing structure produces a negative contribution to the chromaticity. This has to be corrected with sextupole magnets located at finite dispersion. In LEP the eight long straight sections containing the interaction regions have vanishing dispersion and do not contain sextupoles. They give negative contributions to the chromaticities. The sextupoles in the eight arcs have a strength adjusted to compensate the negative chromaticity contributions of the focusing structures in the arc itself and in the long straight sections. This results in a local overcompensation of the chromaticity.

To describe these local effects we use the dependence of the phase advance on momentum deviation [4], [5] which we will call chromatic phase advance

$$\frac{d\mu_x}{dp/p}, \frac{d\mu_y}{dp/p} \text{ or normalized: } \frac{d\mu_x/2\pi}{dp/p}, \frac{d\mu_y/2\pi}{dp/p} \quad (2)$$

The integral over the latter quantities around the ring gives again Q' . A measurement of the chromatic phase advance is an excellent check of the chromaticity and its correction in the ring.

B. Measurement method

The phase advance is measured at the beam position monitors (BPM) using the "1000-turns" system [6]. With this system the beam position is recorded for 1024 revolutions i at each BPM k while one specific bunch is excited in one plane (horizontal or vertical) with the betatron tune frequency by the tune-measurement shaker [2]. The amplitude of the oscillations depends on the proximity of the exciting frequency to the tune and on the strength of the excitation. In order to extract the amplitude A and the phase ϕ of the betatron oscillations, a harmonic fit is made through the 1024 beam position measurement $\{x_i\}_{i=1}^{1024}$ of each BPM k with the known frequency of excitation

$$C_k = \sum_{i=1}^N x_i \cos(2\pi Q_x i) \quad , \quad S_k = \sum_{i=1}^N x_i \sin(2\pi Q_x i) \quad (3)$$

to obtain

$$A_k = \frac{2\sqrt{C_k^2 + S_k^2}}{N} \quad , \quad \phi_k = -\arctan\left(\frac{S_k}{C_k}\right) \quad (4)$$

where $N = 1024$ is the number of samples. ϕ_k corresponds to the phase advance μ_x at the BPM k plus an arbitrary constant for all BPM. For precise phase measurements, the beam must be excited to high amplitude in order to achieve the highest signal-to-noise ratio. Typical oscillation amplitudes are in the order of a few millimeters. The error of the phase is [7]

$$\sigma_\mu = \frac{1}{A} \sqrt{\frac{2}{N}} \sigma_x \quad (5)$$

with σ_x being the beam position error. The phase error is typically about 2-3 mrad for a signal of 2 mm of amplitude (4 mm peak-to-peak) and 1024 points.

C. The experiment

A positron beam of about 0.1 mA per bunch was accumulated on the nominal RF-frequency with the injection optics K21P20 which has detuned low-beta insertions. The horizontal and vertical phase advances were measured in all the BOM monitors using the "1000-turn" system described above for the RF-frequency deviations of -100 Hz, 0 Hz, and +100 Hz. The corresponding energy deviations are obtained with the relation (1) and are listed together with the measured tunes in Table 1. For each measurement the phase advance calculated with MAD [8] for the central orbit was subtracted. All the measurements used for analysis were taken with about the same betatron oscillation amplitude to avoid effects of non-linearities.

Δf_{RF}	$\Delta E/E$	Q_x	Q_y
-100 Hz	0.00153	0.255	0.219
0 Hz	0.0	0.255	0.219
100 Hz	-0.00153	0.255	0.217

Table I
Parameters of the phase advance measurements

D. Analysis of the measured data

A first look at the experimental results indicated that some selection of the data had to be made. A few monitors gave values which were far outside the range of the remaining ones. The corresponding data were ignored. This was the case for 8 monitors in the horizontal plane and for 6 monitors in the vertical plane. Since the absolute phase is not known, the average phase of all the accepted monitors was set to zero for each measurement. For each monitor a linear fit through the three points taken at different energy deviations was made and the quantity $(d\mu/2\pi)/(dp/p)$ calculated.

E. Results

The measured normalized phase advance per relative energy change and the corresponding calculations with MAD are plotted in Fig. 2 against the normalized phase. Clearly visible are the chromaticity contributions of the different parts. The four straight sections containing interaction points IP2, IP4, IP6, and IP8 give large negative contributions of about $\Delta Q_x = -16.4$ and $\Delta Q_y = -12.1$ each, being within 4% of the calculated values. The other straight sections have smaller effects $\Delta Q'_x =$

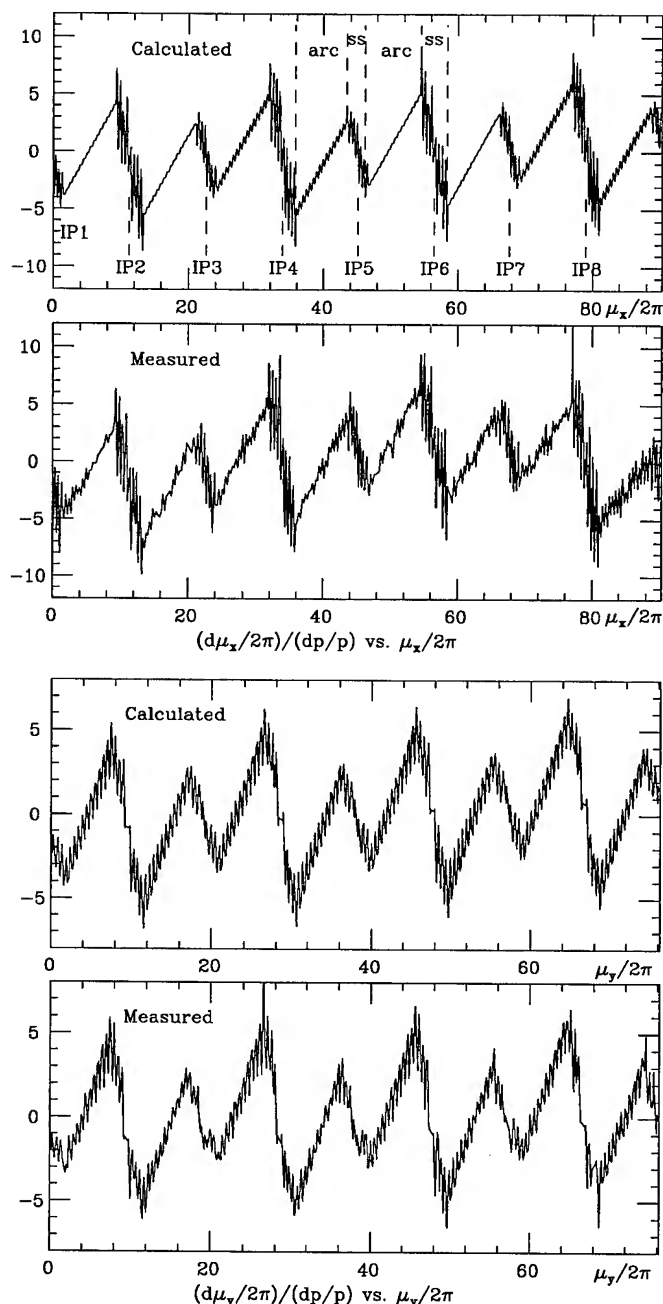


Figure 2. Chromatic phase advances ('ss': straight sections)

-7.7 and $\Delta Q'_y = -6.1$ each, which agree within 12 % with expectations. The measured variation of the individual sections is about 10%. Also the positive contributions of the arcs containing the sextupoles are clearly visible. We measure $\Delta Q'_x = 8.6$ and $\Delta Q'_y = 8.5$ per octant. The horizontal value is about 6% larger than expected whereas the vertical one agrees within 1%. The variation of the individual octants is smaller than 9% for Q'_x and smaller than 2% for Q'_y . All these discrepancies are probably due to measurement errors with the exception that the absolute values of the individual horizontal contributions are in average about 5% too large. Strong localized sextupole errors can be ruled out by these measurements.

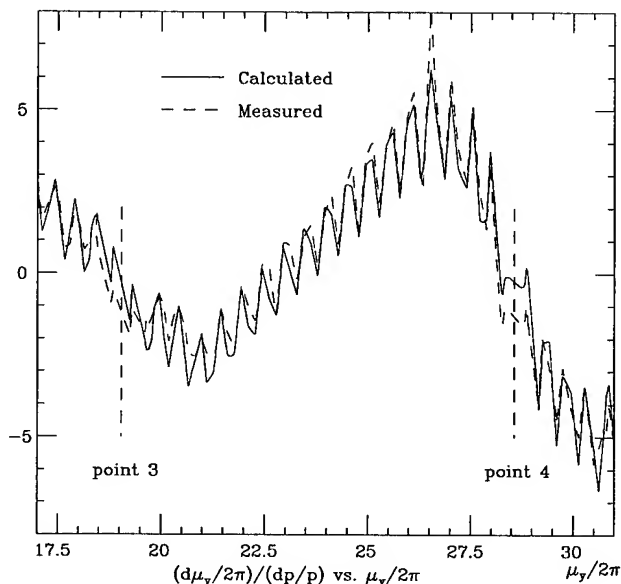


Figure 3. Details of the calculated and measured vertical chromatic phase advance

In general the agreement between experiment and calculation is very good not only for the global behavior of the chromatic phase advance but also for its details as shown in Fig. 3. The fast oscillation of the calculated and measured chromatic phase advance is due to a mismatch of the off-energy optics resulting in a beating both of the beta function and the phase advance. As expected this beating goes with twice the betatron phase advance.

References

- [1] A. Verdier "Chromaticity correction with sextupole families", This conference.
- [2] K.D.Lohmann, M. Placidi and H. Schmickler; "Design and Functionality of the LEP Q-meter"; Proc. of the 2nd European Part. Accel. Conf., EPAC; Nice, June 1990, p. 774.
- [3] A. Verdier, "Measurement of the non-linear chromaticity at 46 GeV (G05P46hv2)", CERN SL-MD Note 117, 1994.
- [4] H. Zyngier; "Strategy for Chromaticity Correction", Orsay LAL Note 77/35, 1977.
- [5] B.W. Montague; "Linear Optics for Improved Chromaticity Correction"; LEP note 165, 1979.
- [6] J. Borer, C. Bovet, A. Burns and G. Morpurgo; "Harmonic Analysis of Coherent Bunch Oscillations In LEP"; Proc. of the 3rd European Part. Accel. Conf., EPAC; Berlin, March 1992, p. 1082.
- [7] A. Burns, P. Castro, G. Morpurgo and R. Schmidt, "Betatron Function Measurement at LEP Using the BOM 1000 Turns Facility"; Proc. of the 1993 IEEE Part. Accel. Conf., PAC; Washington, 17-20 May 1993, p. 2103.
- [8] H. Grote, F.C. Iselin "The Mad Program"; CERN/SL/90-13.

THE LATTICE OF THE CERN LARGE HADRON COLLIDER

W. Scandale, B. Jeanneret, J.-P. Koutchouk, X. Luo, F. Méot, R. Ostojic,
T. Risselada, C. Rufer, T. Taylor, T. Trenkler, S. Weisz

CERN, CH-1211 Geneva 23 Switzerland

The lattice of the CERN Large Hadron Collider is designed with 23 regular cells per arc, each containing 6 tightly packed 14.2 m long dipoles. This allows to reach 7 TeV per beam with a dipole field of 8.4 Tesla. There are four experimental insertions, two of which are devoted to high luminosity experiments with ± 23 m of free space for the detector. The other two experimental insertions are combined with injection. The value of β^* at the interaction points is tunable from 6 m at injection to 0.5 m in collision. The energy deposition in the inner triplets is carefully reduced to sustain the nominal luminosity of $10^{34} \text{ cm}^{-2}\text{s}^{-1}$. Two insertions are devoted to collect the halo particles with large emittance and momentum spread surrounding the beam core: escaping rates of the protons are estimated to be less than $4 \cdot 10^6 \text{ sec}^{-1}\text{m}^{-1}$. Finally, one insertion is used to extract the particles in the vertical direction with a minimized deflecting strength.

I. OVERALL LATTICE

The LHC geometry is dictated by the existing LEP tunnel, and the peak LHC beam energy is broadly given by the maximum magnetic field sustainable by the superconducting dipoles. The present optimization of the optical layout, called *version 4*, aims to increase the bending length of the standard cell, and to use the same cell design in all arcs. The energy of 7 TeV per beam can now be reached with a 8.4 Tesla dipole field. The lattice is designed to lie in a beam plane parallel to that of LEP and the two machines are almost collinear in plane view (the arcs tend to be at the exterior of the LEP theoretical position by up to 4 cm, while the dispersion suppressors - DS- are up to 10 cm on the interior, a price to be paid for standard length dipoles and longer straight sections in the DS).

The two beams of the LHC pass through the same twin bore magnets separated horizontally by 180 mm. They are exchanged from inner to outer circle four times around the circumference in order to avoid any difference in total path length. There are four interaction points (IPs), with the assignment of Fig. 1. The high luminosity insertions are located in points 1 and 5. The combined experimental and injection insertions are in points 2 and 8. There are two cleaning insertions in points 3 and 7, a dump insertion in point 6, and an insertion devoted to the RF in point 4. The betatron phase advance has different values in the insertions: 2.43 in points 1 and 5, 2.57 in points 2 and 8, and 1.80 in the other points. The machine is thus mirror

symmetric about the axis IP1-IP5 and its superperiodicity is 1.

The two-in-one design of the magnets means that the optical polarities of adjacent quadrupoles in the two LHC rings are opposite. This is also true for the first triplet on either side of the IPs, made of single bore quadrupoles. The most natural design of each ring is thus antisymmetric, so that on either side of an IP corresponding quadrupoles have equal and opposite strength. At the IPs, the horizontal and the vertical β functions have equal values and both beams are round.

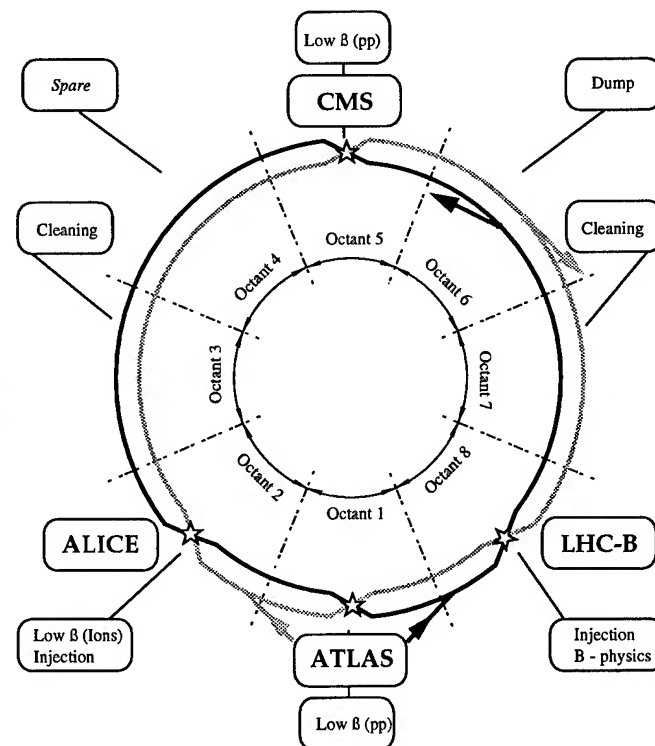


Fig. 1 Layout of the LHC

Equal horizontal and vertical tunes is a feature of the antisymmetric design. The arcs are then adapted to separate slightly the tunes, $Q_x = 63.28$, $Q_y = 63.31$. With a superperiodicity of 1, the choice of the integral part of the tunes is based on the estimated strength of resonances close to the working point. With respect to the betatron coupling, the working point is equivalent to that of the version 1 of the LHC lattice [1]. The necessary changes to make it more robust against dynamic variations of the coupling are the subject of ongoing studies.

II. LATTICE MODULES

The regular cell: the regular cell is 106.92 m long and contains six 14.2 m dipoles and two 3 m quadrupoles. The quadrupoles are centered w.r.t. the bending center of the dipoles in order to have identical cells in every arc, irrespective of its polarity. The cryostat assembly of the quadrupole is symmetrical w.r.t. the quadrupole center. On its left is an octupole corrector and a beam position monitor, and on the right a nested dipole and sextupole corrector. Next to each dipole, in the shadow of the magnet ends, a sextupole and a decapole windings are located on either side. These correctors compensate locally the main systematic imperfections due to persistent currents, which affect the beam stability at the injection plateau and at the beginning of the ramp. The precise magnetic strength of the various correctors will depend on the final optics and should include requirements from the dynamic behaviour of the machine, yet to be estimated.

The nominal betatron phase advance is 90° . It is in practice slightly adjustable with separate power supplies for the F and the D quadrupoles of each ring, needed to control the horizontal and vertical betatron tunes. With the maximum quadrupolar gradient of 250 T/m, it is possible to shift and/or split the tune by ± 2 integers in each ring. The peak values of β and of the horizontal dispersion D are 182.7 m and 2.15 m respectively. The regular arc is made of 23 cells, for a total length of 2456.16 m.

The dispersion suppressors: The lay-out of the 16 DS is identical, except for a small difference in length of the short straight section next to the odd and even arcs (the LEP tunnel has a slightly irregular octagonal shape). The four quadrupoles of the DS (Q7-Q10) are interleaved with four blocs of two dipoles each. The dipoles have the same length as in the cell (14.2 m). The separation between the dipole blocs is not regular in order to obtain exact superposition of the LHC and LEP interaction points, and to get sufficient free space for the quadrupoles and the associated correctors. The quadrupoles are split in two sections. The main sections, 3.25 m long, are powered in series with the cell quadrupoles of the same polarity. The 1.5 m tuning sections, with a maximum gradient of 120 T/m, have all independent power supplies. As the number of parameters in the straight sections of the insertions is smaller than the number of matching constraints, the quadrupoles of the DS contribute to the global matching of the insertions. Therefore, the exact optics of the DS in the various insertions are all somewhat different even if their layouts are the same. The orbit functions are sufficiently smooth and of moderate value to allow the use of magnets with the same aperture as in the regular cell.

The high luminosity experimental insertions: The high luminosity insertions in points 1 and 5 comprise the inner triplet of quadrupoles (Q1, Q2, Q3) close to the interaction point for focusing the beam size in both planes, and the

outer triplet (Q4, Q5, Q6), placed close to the DS for tuning the betatron functions. Between the inner and outer triplets, a doublet of separation-recombination dipoles (D1, D2) brings the two counter-rotating beams to almost collinear trajectories. The position of the lenses is adjusted to minimize the β -functions at all stages of the β -squeeze, especially in the region of the outer triplets, so that magnets with regular aperture can be used. D1 and D2 are 10.2 m long medium-field superconducting dipoles (4.5 T) spaced by 35.7 m. The inner triplet is designed to minimize the irradiation effects due to particle losses in collision. The single-bore quadrupoles Q1, Q2, Q3 are built of identical 5.5 m, 70 mm aperture units. They are powered in series for an operational gradient of 225 T/m. Two additional independently powered quadrupoles, Q01 and Q03, are used for fine tuning of the triplet. Appropriate absorbers are located in front of Q1 and Q2 to reduce the energy deposit to below 25 W per quadrupole. The free space for the detectors, absorbers and associated infrastructure is ± 23 m. The insertions are tunable for a range of β^* from 0.3 m up to 10 m; the nominal β^* at injection is 6 m, and 0.5 m in collision. The change of the gradients during the β -squeeze is smooth. The orbit functions in collision are shown in Fig. 2.

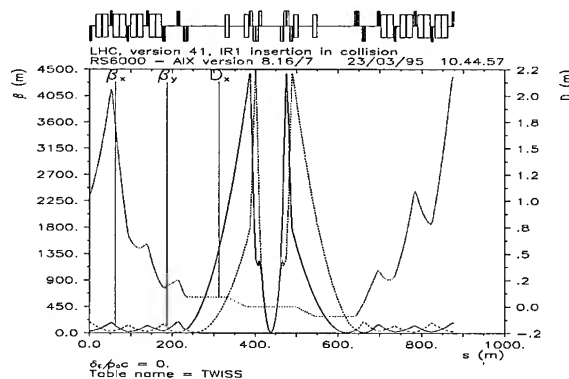


Fig. 2. Orbit functions of the high luminosity insertion in collision

The combined experimental and injection insertions: The layout of the insertions in points 2 and 8 is conceptually identical to that of the high-luminosity insertions. The free space around the interaction point is ± 21 m, while a free space of 100 m between Q4 and D2 is provided for the injection system (kickers and septa). A low waist of the horizontal β -function is needed close to the inner triplet, where protection stoppers intercept badly injected beams. It has been chosen to inject the beams into the outer ring. The insertion are tunable over the same range of β^* as the high-luminosity insertion with a smooth variation of the quadrupole gradients. However, the value of the β -function in the outer triplet is somewhat larger.

The cleaning insertion: Two insertions are used for collimation, one in point 3 for betatron cleaning, and the other in point 7 for momentum cleaning. Their layout is almost identical: a 500 m straight section with a FODO-like structure of warm two-in-one quadrupoles is matched to the DS on each side by a superconducting quadrupole Q6. Immediately downstream of Q6, two dogleg dipoles increase the horizontal beam separation from 180 mm to 220 mm, sweeping away the neutral secondaries from inelastic interactions. This also makes the design the cross section of the warm two-in-one quadrupoles easier. The FODO-like structure contains three pseudo-cells with a total phase advance of 216° for a maximum β around 350. The normal-conducting quadrupoles are built of 3.55 m, 30 T/m modules, resulting in total quadrupole lengths of 10.5, 14 and 17.5 m. Corresponding quadrupoles on either side of the center of the insertion are powered in series with opposite polarities to provide the required optical antisymmetry.

The entire 500 m straight section is free of superconducting magnets and thus available for cleaning. Collimation of the particles circulating in the halo of the stored beams causes scattering in both transverse planes. The primary collimators must be placed at large β values to maximize the impact parameters and thus reduce the out-scattering probability. They have to be backed by secondary collimators placed at suitable phase advances in order to intercept the out-scattered particles.

The dump insertion: The dump insertion is located in point 6. Its purpose is to dispose of the circulating beam at the end of the runs and to protect the machine in case of hardware failure or beam instability. The design benefits from the fact that the two beams do not cross in this point.

Horizontal kickers are used to deflect the circulating beams into a Lambertson type septum which bends vertically the extracted protons to the external absorbers. The antisymmetry of the optics allows to optimize simultaneously the extraction of both beams with a common septum magnet placed at the center of the insertion. On each side of the septum there are four superconducting quadrupoles Q3, Q4, Q5, Q6 to match the optical constraints. The fast kicker is located between Q4 and Q3. In the upstream side, the quadrupole Q3 is horizontally defocusing to enhance the deflection of the kicker and thus the displacement in the septum. On the other hand, the septum must be strong enough to deviate the extracted beam away from Q3 in the downstream side. The position of Q3 thus results from a compromise between the kick enhancement and the required strength of the septum, taking into account realistic assumptions about the aperture of Q3 and the outer radius of its cryostat. In the preferred solution there is a very long drift of about 340 m between the upstream and downstream positions of Q3. Because of this the value of β rises above 600 m, by far the largest around the LHC at injection.

The quadrupoles Q3 and Q4 will need an increased aperture of 70 mm, whilst their length is still standardized to modules of 3.25 m. Enlarged quadrupoles could be used also in the outer triplets of the combined experimental/injection insertions. Like in other insertions, the field quality of the quadrupoles needs to be assessed to ensure that the insertions do not limit the dynamic aperture at injection. Alternatively, it should be possible to reduce the β function at injection to about 450 m by introducing a small warm quadrupole at either end of the septum.

The insertion for the RF: The insertion in point 4 will probably be used to house the two 15 m long superconducting RF modules (one per beam). The optics could be similar to the layout of the dump insertion.

III. APERTURE

The mechanical aperture in the LHC is limited by the collimators in order to localize the beam loss in the cleaning section. The inner coil diameter of the regular magnets is 56 mm. However, the free space for the circulating particles is reduced by the beam screen for synchrotron radiation. Realistic tolerances for the sagitta and alignment of the beam pipe, and for the closed orbit deviations have to be taken into account as well. The available aperture in units of the rms beam size is 10σ . It allows to accommodate 3σ for the beam distribution, 2σ for the transverse and longitudinal injection errors, and 1σ for drifts in time of the orbit. The remaining 4σ is the clearance needed between the primary collimators and the beam screen.

At the nominal LHC luminosity, the proton losses per beam are expected to be $4 \cdot 10^9$ proton sec^{-1} , while it is estimated that at 7 TeV a longitudinal flux of $4 \cdot 10^6$ protons $\text{sec}^{-1} \text{m}^{-1}$ falling onto the vacuum chamber induces a quench. The cleaning system must therefore trap the protons at an amplitude smaller than the aperture of the ring, with an efficiency much better than 10^3 . This will be achieved by installing circular collimators in point 3, approximated by eight jaws forming an octagon. A set of primary collimators made of beryllium or aluminum is followed by three secondary collimators made of copper located at optimized phase advance. Detailed simulations, including nuclear and electromagnetic scattering in the jaws and tracking around the ring indicate that the needed performance can be reached with a good margin.

At injection, momentum losses will be trapped by a system located in point 7. Simulations indicate that the expected efficiency is sufficient even in the case of a large fraction of RF-uncaptured protons.

VI. REFERENCES

- [1] Design Study of the Large Hadron Collider (LHC), CERN 91-03, (1991).

SORTING STRATEGIES FOR THE LHC BASED ON NORMAL FORMS

W. Scandale, M. Giovannozzi, R. Grassi and E. Todesco *
CERN-1211 GENEVA 23

Abstract

Sorting strategies for superconducting dipoles are discussed, in view of maximizing the dynamic aperture in hadron colliders like the CERN LHC. Quality factors based on the perturbative tools of nonlinear maps and normal forms are evaluated with tracking simulations. The best of them is retained and maximized by an appropriate permutation of the magnets. The effectiveness of the proposed ordering is checked again through tracking. This technique is used to sort the sextupolar errors in a lattice that contains a small number of LHC-like cells.

I. INTRODUCTION

One of the main issues in the construction of large hadron colliders like the CERN LHC is the effect of the nonlinear field-shape errors. They fluctuate randomly from magnet to magnet, and considerably reduce the stability domain of the circulating particles. Installing the magnets in ordered sequences can provide a self compensation of the random imperfections i.e. an increase of the dynamic aperture. Due to the huge number of magnet permutations it is not feasible to characterize them by computing the related dynamic aperture. Therefore we propose to use quality factors (QF) based on analytical tools. Intuitive rules based on local compensation and symmetry considerations, which have been shown to be effective in the case of the LHC lattice [1], [2], have also been considered.

In this paper we present strategies based on analytical tools (normal forms [3]) and numerical simulations (element-by-element tracking) [4]. Firstly we introduce three QF: the norm of the nonlinear part of the map, the norm of the amplitude-dependent tunes, computed through nonresonant normal forms, and the resonance strength evaluated through resonant normal forms. Secondly we determine numerically which QF has the best correlation with the dynamic aperture for our accelerator model. Thirdly we use the QF to select the best ordering among a limited set of magnet permutations, chosen either randomly or using local compensation rules. As a final check we compute with tracking the dynamic aperture of our selected case. This procedure is repeated for 100 different realizations of the random errors.

II. QUALITY FACTORS

The indicators of nonlinearity, that we use as QF are listed below with the conventions of Ref. [3].

Q₁: Norm of the map Terms of different orders are added, neglecting possible compensations; the amplitude A gives the weight for the various contributions.

$$Q_1(A, N) = \sum_{n=2}^N A^n \sum_{j_1+j_2+j_3+j_4=n} \sum_{i=1,2} |F_{i;j_1,j_2,j_3,j_4}| \quad (1)$$

Q₂: Norm of the tunes A nonresonant normal form truncated at the order N provides the perturbative series at the order $M = (N - 1)/2$ for the sum of the squares of the tunes:

$$t_{2M}(\rho_1, \rho_2) = \frac{1}{2} \left[\left(\sum_{i=1}^M [\nu_x(\rho_1, \rho_2)]_i \right)^2 + \left(\sum_{i=1}^M [\nu_y(\rho_1, \rho_2)]_i \right)^2 \right] \quad (2)$$

Q_2 is obtained by averaging this quantity over the invariant amplitude A :

$$Q_2(A; M) = \sqrt{\frac{2}{\pi} \int_0^{\pi/2} t_{2M}(A \cos \phi, A \sin \phi) d\phi} \quad (3)$$

Q_2 is to be used with caution, since in absence of detuning (i.e. $Q_2 \circ 0$) all the resonances are unstable.

Q₃: Norm of the resonances The strength of a single resonance $[p, q]$ of order $r = p + q$ can be computed by taking the norm of the resonant part of the interpolating Hamiltonian, truncated at an order L such that $L \geq r$:

$$Q_3([p, q], A; L) = \sum_{l \geq 1} \sum_{2(k_1+k_2)+lr \leq L} |h_{k_1,k_2,l}| A^{2(k_1+k_2)+lr} \quad (4)$$

In all the three QFs, the amplitude A is fixed to the estimated value of the dynamic aperture.

III. RESULTS

The model Our analysis has been carried out on a simplified lattice made of 8 LHC cells and a phase trombone. Each cell has 6 dipoles and a phase advance of 90° . The linear tunes are $\nu_x = 2.28$ and $\nu_y = 2.31$. The peak value of the orbit function is $\beta_{max} = 169m$. The chromaticity sextupoles are ignored. Only the random part of the normal sextupolar errors in the dipoles is considered. Its integrated gradient is distributed according to a gaussian truncated at three sigma, where $\sigma = 8.5872 \times 10^{-3} m^{-2}$ is the expected value for the LHC dipoles.

QF correlation We have computed the correlation between the dynamic aperture and the QF's for 100 realizations of the random errors. The dynamic aperture is computed over 1000 turns and it is expressed in meters normalized at $\beta_{max} = 169m$. The norm of the map Q_1 is evaluated up to order $N = 6$; the tunes Q_2 at the order $M = 2$, and Q_3 has been evaluated for resonances up to order seven, with $L \leq 7$. The parameter A is equal

* INFN, Sezione di Bologna, Via Imerio 46, I-40126 Bologna.

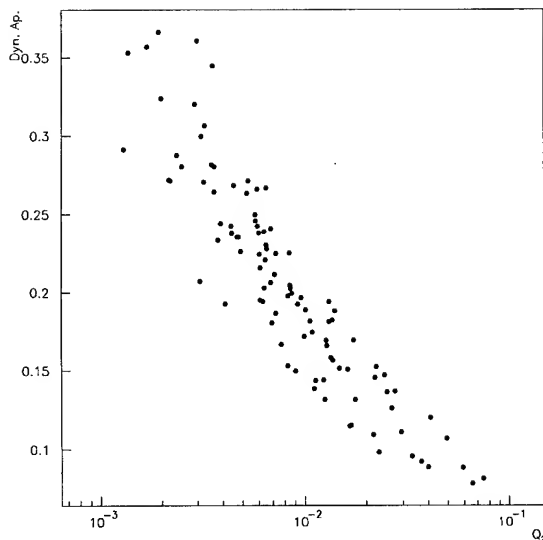


Figure 1. Correlation between the quality factor Q_2 and the dynamic aperture for 100 seeds.

to the average dynamic aperture of the 100 unsorted machines, i.e. 0.2 m .

The tuneshift norm Q_2 shows the best correlation with the dynamic aperture (Fig. 1), while the norm of the map Q_1 has a poor correlation. Among all the resonances the $[3, 0]$, which is the first resonance excited by sextupoles, shows a rather good correlation, and has been used for further tests.

Sorting and tracking check We consider two optimization strategies and for each of them we use two different rules of permutation of the dipoles. The first strategy (SORT1) is based on the norm of the tuneshift Q_2 , the second one (SORT2) on the strength of the resonance $[3, 0]$. In the first rule (SORT11 for Q_1 , SORT21 for Q_2) we consider 500 random permutations. In the second rule (SORT12 for Q_1 , SORT22 for Q_2) we split the 48 dipoles in 24 pairs such that in each pair the sum of the sextupoles errors is minimized, to create a 'first-order local compensation'; then, we consider 500 random permutations of the 24 pairs. The number of permutations P is fixed to 500 as a result of a compromise. For larger values of P one finds better machines, however, the improvement saturates quite rapidly, probably due to the fact that the correlation between the QF and the dynamic aperture is better for bad machines than for good ones (see Fig. 1). This means that the QF easily recognizes bad machines, but it is not very efficient in selecting good machines. The effect of sorting rules based on local compensation as described in [1] has also been computed for comparisons (SORT0).

In Fig. 2 we consider the dynamic aperture for 100 unsorted seeds, to which we apply the sorting rule SORT0. The dynamic aperture increases by a factor 2.7.

In Fig. 3 we show the distributions of the dynamic aperture for 100 seeds for the rule SORT12 and for SORT22. With the rule SORT12 the gain is in average of a factor 3.1 and for the worst machines of a factor two. With SORT22 the gain is lower.

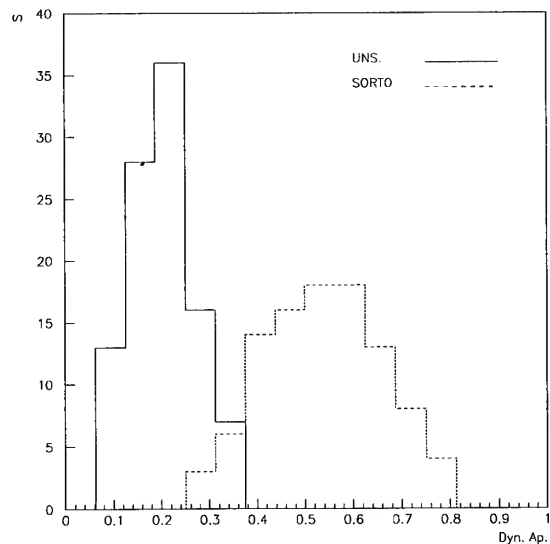


Figure 2. Comparison between the distribution of dynamic aperture for the unsorted machine and SORT0.

In any case, the permutations of pairs of dipoles has been shown to be more efficient than the random permutations. From this we conclude that, in our lattice model, the tuneshift minimization over pair permutations, is to be considered the most efficient algorithm to improve the beam stability. However, we have indications that this conclusion cannot be simply extrapolated to any lattice model.

IV. EFFECT OF THE SORTING PROCEDURE ON THE GLOBAL DYNAMICS

A check of the effect of the sorting procedure has been carried out through the analysis of the dynamics both in phase space and in frequency space, according to the numerical techniques of frequency analysis originally developed for celestial mechanics [5]. A stability diagram and its related tune footprint gives a description of the stability domain in phase space and in frequency space. This second diagram provides the tune distribution, and brings into evidence the most dangerous resonances and their effect on the stability of motion.

We consider particles with initial conditions given by $(r \cos \alpha, 0, r \sin \alpha, 0)$, with $r \in [0, R]$ and $\alpha \in [0, \pi/2]$, and we track them over 1000 turns. If the motion is stable, we compute the related nonlinear frequencies as the average phase advance per turn.

In Fig. 4 we show the frequency distribution for the random machine with an average value of the dynamic aperture, while in Fig. 5 we consider the same machine sorted with the rule SORT12. The analysis of the Figs. 4 and 5 leads to the following observations.

- Tune footprint diagrams show that the ordering procedure not only minimizes the tuneshift, but also changes the low order tuneshift coefficients so that different zones of the frequency space are occupied by the random and sorted ma-

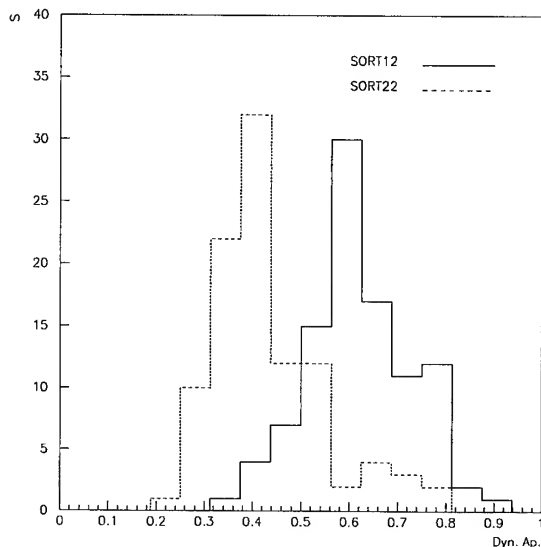


Figure 3. Comparison between the distribution of dynamic aperture for the SORT12 and SORT22.

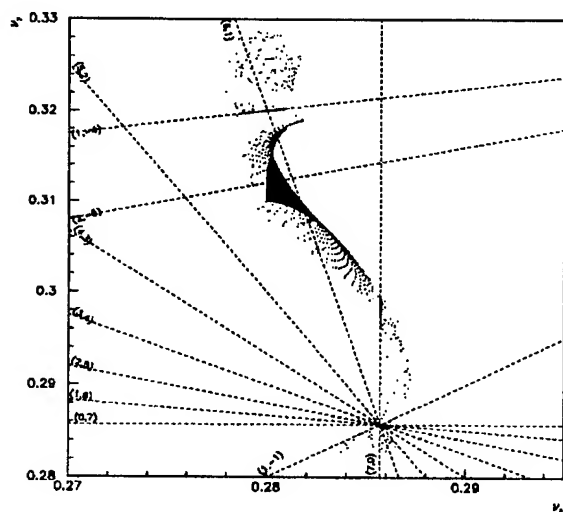


Figure 4. Tune footprint for an average unsorted seed.

chine.

- In the sorted machine the effect of resonances is stronger and more clearly visible: this happens because, having minimized the tunes shift, the islands become larger. Notwithstanding this effect, the stability domain of the sorted machine is three times bigger than the unsorted one. The island width is clearly shown in the tune footprint as an high density of initial conditions on resonance lines, and an empty region around them (e.g. $[1, -4]$ and $[7, 0]$ in Fig. 5). On the other hand, some resonances seem to be not excited (e.g. resonances $[2, -5]$ and $[6, 1]$ in the same Figure).
- Although the resonance $[3, 0]$ is very far from the tune footprint, it shows the best correlation with the dynamic aper-

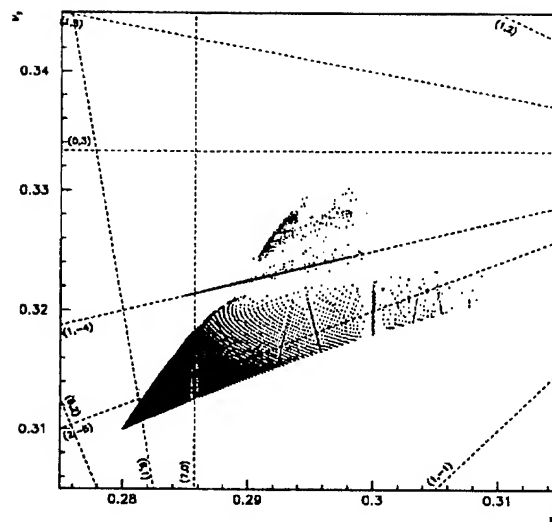


Figure 5. Tune footprint for an average seed sorted according to the rule SORT12.

ture. This fact needs deeper investigations.

V. CONCLUSIONS

We have defined a sorting strategy which has the fundamental property of being very flexible. The proposed approach is based on a mixed technique which exploits both tracking simulations for determining the best quality factor, and analytical techniques to evaluate in a fast way the best permutation of the magnets. This technique can be integrated by other intuitive criteria based on the symmetries of the lattice. The outlined approach has been successfully applied to an LHC cell lattice, finding gains which are very good also compared to other known methods. Although we applied our analysis to a simplified cell lattice with only sextupolar errors, there are no restrictions to extend it to a realistic lattice including a set of arbitrary multipolar imperfections. It remains to be checked if the improvement due to the sorting persists when the operational conditions are changed or when long-term stability is considered.

VI. ACKNOWLEDGEMENTS

We would like to thank A. Bazzani, J. Gareyte, J. Miles, F. Schmidt, G. Turchetti and V. Ziemann. The work of J. Laskar has been determinant for drawing our attention on the importance of frequency analysis of global dynamics.

References

- [1] W. Scandale, L. Wang, CERN SPS (AMS) **89-22** (1989).
- [2] V. Ziemann, CERN SL (AP) **94-59** (1944).
- [3] A. Bazzani, E. Todesco, G. Turchetti and G. Servizi, CERN **94-02** (1994).
- [4] M. Giovannozzi, R. Grassi, W. Scandale and E. Todesco, CERN SL (AP) **95-11** (1995).
- [5] J. Laskar, Physica D **67**, 257-81 (1992).

ALGORITHMS TO GET A CIRCULATING BEAM

André Verdier, Frank Richard
CERN CH1211 Geneva 23

Abstract

Two algorithms based on trajectory fitting have been used to obtain rapidly a circulating beam in LEP with strong focusing lattices.

A new algorithm called "orbit closure" uses the beam positions measured at the first and the second turn. From their difference, it computes two corrector strengths per plane such that the second turn passes at the same place as the first turn at about ten BPM locations. This produces a closed orbit amplitude with an r.m.s. value close to that of the first turn trajectory.

A new 'first turn threader' has been tried. It detects places where an oscillation with an r.m.s. amplitude larger than a specified value starts, and computes two corrector strengths to cancel it. By iterating this process, it should be possible to correct by steps the first turn trajectory so that its r.m.s. amplitude is below a specified value.

The orbit closure has been applied with success to a very low emittance lattice (135° in the horizontal plane) in LEP.

I. The principles

These algorithms are based on the fitting method. This method assumes that the linear optics of the machine is well known. It relies on the description of betatron oscillations with an expression like :

$$y_i = a\sqrt{\beta_i} \cos(\mu_i) + b\sqrt{\beta_i} \sin(\mu_i) + c + \eta_i$$

where y_i stands for the i^{th} measurement of the beam position, β_i and μ_i for the corresponding TWISS parameters and η_i for a realization of a null-mean additive noise. Given this definition of η_i , we must put in the equation the average of the noise which is c . This parameter can be interpreted also as an offset of the measurements.

The values of a , b and c , are computed by means of the least-squares algorithm. In fact what is interesting is not the values of a , b or c themselves, but how relevant is the fit, i.e. whether the measurements follow a betatron oscillation or not. To answer this question, the residual F_n of the fit done with n measurements is computed. Its expression is :

$$F_n = \sqrt{\frac{1}{n-3} \sum_{i=1}^n (\tilde{y}_i - y_i)^2}$$

where \tilde{y}_i is the estimation of y_i obtained once the constants a , b and c have been computed.

A very important feature of the fitting method is the possibility to discard the measurements considered as bad, i.e. those such that $|\tilde{y}_i - y_i|$ is larger than a certain number of standard deviations. Usually this number is between two and three as we discard measurements because they are at the edge of a normal distribution of random variables. Note that the best estimate of the

standard deviation is F_n . Once the bad measurements have been discarded, the computation is remade until no measurement is considered as bad.

II. Orbit closure

A. The algorithm

The first step for operating a circular machine is to get a first turn. However this usually does not guaranty that the beam circulates because the closed orbit distortion may be too large. Furthermore, in the case of strong focusing lattices, the chromaticity sextupoles are strong because the dispersion is small and this makes large anharmonicities which can make a linear instability if one of the tunes comes close to an integer. This may well happen for a closed orbit distortion which would not prevent the beam to circulate with a weak focusing lattice. This is precisely the case where the orbit closure algorithm is the most useful.

When a first turn is obtained in a machine, the beam position can be measured at several places close to the point where it enters the machine, both during the first and the second turn. Then the fitting method is applied to the difference between these beam positions, and this difference is canceled out with two closed orbit correctors in each plane. Once it is made small enough, it is possible to obtain a circulating beam.

Practically twenty positions are measured downstream of the place where the injected beam enters LEP. After elimination of wrong measurements, only ten which are considered good from the fitting of the difference between first and second turn are kept for the computation. It is worth noting that the BPM's which suffer from a mere offset are not considered as bad usually.

B. Experience with a strong focusing lattice

An illuminating example of the efficiency of the closure algorithm is provided by a machine experiment done with a low-emittance lattice in LEP. The LEP machine at CERN is made from eight arc, each containing thirty FODO cell with dipoles and sextupoles, and eight insertions which contain only dipoles and quadrupoles. The super-periodicity is four. All the nonlinear elements (sextupoles) are in the arc cells. Low-emittance lattices have been envisaged for LEP as a mean to increase the luminosity at low current [1]. In one of these lattices, which was found to be difficult to operate, the arc FODO cells have an horizontal phase advance of 135° and a vertical phase advance of 60°. The horizontal tune is 125.28 and the vertical tune is 75.18. Given the machine super-periodicity, such tunes guaranty that no problem is expected from the non-linear chromaticity [4].

During year 1993, two eight hours shifts had been done where no circulating beam was obtained. This led us to an extensive analysis of the problems associated with this lattice in order to understand why it was so difficult. A report on this study is available [2] and some of the results concerning this lattice can be found at this conference [1]. One interesting outcome of this

study was that it is not possible to correct both third order resonances and horizontal anharmonicity. It was felt that it was easier to try to cope with the anharmonicity than with the third order resonances. The horizontal anharmonicity, i.e. the derivative of the horizontal tune with respect to the horizontal emittance, has a value of $-1.6 \times 10^5 m^{-1}$ for the lattice under consideration. For an r.m.s. closed orbit amplitude of 4mm at the BPM's where β_x is about 10m, the associated emittance is about $1.6 \mu rad.m$, which makes an associated horizontal tune-shift is -0.26. As the fractional part of the horizontal tune of our machine is 0.28, we see that a badly corrected closed orbit can easily lead to an horizontal instability due to the fact that the horizontal tune becomes an integer. In practice it can be observed that the horizontal tune, estimated from a Fourier analysis of several turns measurements, wanders considerably depending on the corrections applied to the first turn trajectory.

In the successful experiment, a great care was taken first to correct the first turn trajectory so that its r.m.s. value was between 3 and 2mm. This took about five hours and this is why a more powerful algorithm, described in the next section, was studied. When the first turn was corrected, the orbit closure algorithm was applied but no circulating beam was obtained although the goal was not far, according to the signal of the RF pick-up indicating that some particles were trapped in the RF buckets for several turns. It took us some time to realize that in fact corrector increments of the order of $10 \mu rad$ had to be applied. Indeed usually closed orbit corrections of this importance are not vital as a kick of $10 \mu rad$ at a place where β_x is 10m makes a closed orbit distortion of less than 0.1mm if the fractional part of the tune is close to 0.3. In the present case, if the first turn trajectory has an r.m.s. amplitude above 3mm, the horizontal anharmonicity brings the horizontal tune close to an integer, which in turn amplifies the closed orbit distortion due to this small kick and makes the betatron oscillations unstable.

III. First turn threader

A. Why a new threader?

A new algorithm is in the process of being developed. In fact there is already a usable facility in LEP, but it is extremely lengthy to make a small r.m.s. oscillation amplitude. In order to develop more easily strong focusing lattices, a faster automatic algorithm, which produces a first turn trajectory with an r.m.s. deviation as small as possible, is needed as mentioned above.

Before a first turn is done, the injected beam is steered as well as possible, so that its oscillation amplitude just after its entrance in the machine can be reduced to some tenths of millimeters. However as soon as it encounters field defects, the oscillation amplitude increases and the beam is eventually lost.

The idea underlying the new threader was to detect these growing oscillations and to correct them one after the other using a single trajectory measurement. In this process, after a correction is computed, its contribution is subtracted from the trajectory measurement and the next correction is computed with the corrected trajectory. It is clear that, if the beam is lost in the first turn, this can only be partially applied and this algorithm is not valid close to the places where the beam is lost. The aim was in fact to improve a first turn trajectory from a full turn measure-

ment.

B. What has been achieved

The first part of the new process was to establish a simple algorithm to detect field defects. The algorithm is similar to that used for the defect search from a closed orbit measurement [3], but simpler. A fit of the measured trajectory was done from the injection point starting at each BPM and the residue of each fit was computed. A threshold was set for these residues, above which it was considered that a defect must be there.

This looks simple minded but in practice, it is not possible to determine the location of discontinuities in the measured trajectory by merely looking at the first large residue and deciding that the defect lies close to the last BPM used to do the fit. It was noticed that, instead of this, the detected defect was close to the first BPM used to do the fit. As ten BPM's are used, this can make quite a difference in the location! Once the location of a defect is found, even approximately, two closed orbit correctors upstream of the detected defect are chosen to cancel the downstream oscillation. This complete procedure which consists of identifying defects and making corrections was the main outcome of the first study of the algorithm in the LEP control system.

The next step of the algorithm was to compute a correction for several successive defects. After a first defect has been found, a correction is computed and its contribution to the oscillation is subtracted from the measurements. Then the next defect is sought and the process is iterated. Applying this in practice shown us that it was not possible to go further than about four defects because the algorithm is linear and the machine is not. Another complication came from the existence of the experimental solenoids which make a coupling between the two oscillation planes. Although this can be handled with a formalism based on 4×4 transfer matrices, this is not yet available in the LEP control system. Thus the only possibility is to enter the coupled sections with very low oscillation amplitudes. This was not done in the program we used, therefore the algorithm was not successful.

Nevertheless the two above conclusions are already extremely useful to carry on a study on a fast threader for strong focusing lattices.

IV. Conclusion

The orbit closure algorithm, which was already recommended for the LEP startup in 1989, proved to be extremely useful to obtain a circulating beam with a very strongly focusing lattice.

Devising a fast threader algorithm is far from being an easy task. In fact our study is only at its starting stage and we arrived already at useful recommendations to develop it.

References

- [1] Y. Alexahin, D. Brandt, K. Cornelis, A. Hofmann, J.P. Koutchouk, M. Meddahi, G. Roy, A. Verdier, *Low emittance lattice for LEP*. This conference.
- [2] Y. Alexahin, *A study of the low emittance lattice for LEP2*. CERN SL/94-46(AP). Divisional report.

- [3] **A. Verdier and J.C. Chappelier,**
An automatic finder of field defects in large A.G. machines.
PAC Washington D.C. 1993.
- [4] **A. Verdier,**
Higher order tune derivatives due to low- β insertions. 1993
Part. Acc. Conf., Washington D.C., 17-20 May 1993.

Non-linear Chromaticity Correction with Sextupole Families

André Verdier, CERN CH1211 Geneva 23

Abstract

The correction of the non-linear chromaticity with sextupoles families is explained by means of a simple perturbation theory. The advantages and limitations of such systems are shown, as well as the constraints they put on machine optics.

I. Introduction

The non-linear chromaticity of the LEP machine at CERN has been successfully corrected with sextupole families for a large variety of different lattices. It works actually so well that the subtleties in this correction have been completely forgotten.

As this type of correction was proposed a long time ago, it is presently felt that more modern systems are better. At the Washington conference in 1993, it was stated that non-linear chromaticity correction of the B-factory PEP2 project with sextupole families was not possible [1]. In fact such a statement might mean that the machine lattice was simply not suitable for such a correction or that the sextupole families were wrongly chosen.

In what follows, the computation of the second derivative of the tune with respect to momentum is recalled first. Then the contribution of periodic chromatic perturbations are estimated. Finally practical applications on how to use sextupole families as well as tolerances concerning the optics to make this use possible are given.

II. Second derivative of the tune with respect to momentum.

When low- β insertions sit at places where the dispersion function is zero, a local correction of their chromaticity is not possible. Consequently an off-momentum mismatch of the insertions appears. For certain tune values, this makes a very large second order derivative of the tune with respect to momentum [2].

A. General expression of the second order tune derivative.

It is relatively straightforward to compute the chromatic dependence of the linear optics parameters by computing the one-turn 2×2 transfer matrix of a machine perturbed by chromatic effects. The calculation is based on the change of the transforms of the β -function due to gradient perturbations, which make it possible to express easily the one-turn transfer matrix. This has been shown in a previous accelerator conference [2]. We call μ the phase advance for one super-period in the machine $\mu = 2\pi Q$ if Q is the super-period tune. The ' indicates the derivative with respect to the relative momentum deviation. The second derivative of μ with respect to momentum deviation δ is given by :

$$\mu'' = \mu^{t''} + \left[\frac{\alpha\beta'}{\beta} - \alpha' \right]' - \frac{1}{4} \cot \mu \left[\left(\frac{\beta'}{\beta} \right)^2 + \left(\frac{\alpha\beta' - \alpha'\beta}{\beta} \right)^2 \right] \quad (1)$$

(Note that in reference [2], there was a miss-print in the μ'' formula : there was one term in excess. The correct formula is the above one). In this formula, the terms on the first line come from the first order tune-shift formula applied to the second order chromatic perturbation per element, i.e. their value is of the same order as the natural μ' . α and β are the standard TWISS parameters [3] taken at an arbitrary origin in the lattice. It is assumed that we are able to compute the transforms of these parameters taking into account chromatic perturbations.

For the computation of the term containing squares, which is the important one, what is needed is the first derivative of the transform of the β -function with respect to δ . This is an important point which had been suspected a long time ago [4], [5] but only formalized only recently [2]. This first derivative is obtained from the derivatives with respect to δ of the integrated gradients at the points of index i , which are $\frac{\partial k_i l_i}{\partial \delta}$. We obtain [4] :

$$\frac{1}{\beta} \frac{\partial \beta}{\partial \delta} = \frac{\beta'}{\beta} = \sum_i \frac{\partial k_i l_i}{\partial \delta} \beta_i \sin 2(\mu - \mu_i)$$

Taking the derivative of this expression with respect to the longitudinal coordinate, we obtain :

$$\frac{\alpha\beta' - \beta\alpha'}{\beta} = \sum_i \frac{\partial k_i l_i}{\partial \delta} \beta_i \cos 2(\mu - \mu_i)$$

These two expressions are exactly what is needed to compute the important terms in formula (1). It is essential to recall that β' and α' are not the derivatives of the optics functions with respect to δ , but they are related (not needed here).

In reference [2], the emphasis was put on the contributions of the low- β quadrupoles which make Q'' large. It was simply mentioned that the contributions of periodic cells was negligible. We examine it now.

B. Contribution of periodic chromatic perturbations to the second order tune derivative.

To obtain these contributions, we merely compute the sums in equation (1) for $\frac{\partial k_i l_i}{\partial \delta}$ constant, i.e. not depending on the index i . We obtain readily, keeping only the important term, i.e. that one with $\cot \mu$:

$$\mu'' \approx -\frac{1}{4} \cot \mu \left[\frac{\partial k l}{\partial \delta} \beta \right]^2 \times \quad (2)$$

$$\left[\left(\sum_i \sin 2(\mu - \mu_i) \right)^2 + \left(\sum_i \cos 2(\mu - \mu_i) \right)^2 \right]$$

The periodicity of the chromatic perturbation appears in its phase μ_i which is given by :

$$\mu_i = \mu_0 + (i-1)\mu_c$$

μ_0 being the phase of the first perturbation and μ_c the phase between two successive perturbations. The sum of trigonometric functions can be done easily, we obtain finally for n periodic perturbations :

$$\mu'' \approx -\frac{1}{4} \cot \mu \left[\frac{\sin n\mu_c}{\sin \mu_c} \frac{\partial kl}{\partial \delta} \beta \right]^2 \quad (3)$$

Such contributions to μ'' produced for instance by the arc quadrupoles and sextupoles are very small compared with that of the low- β quadrupoles which is [2] :

$$\mu'' \approx -(Kl\beta)^2 \cot \mu \quad (4)$$

as the term $\left[\frac{\partial kl}{\partial \delta} \beta \right]^2$ associated with the quadrupoles or the sextupoles of the regular cells is usually smaller than $(Kl\beta)^2$ by two order of magnitude and $\sin n\mu_c$ is smaller than one. Obviously this only is true as long as $\sin \mu_c$ is non zero. This is the case when the chromaticity is corrected with one sextupole family per plane in periodic cells, provided the cell phase advance is different from π .

III. Making sextupole families.

From the preceding argument, we see that if the periodicity of the gradient perturbation is a multiple of π , the fraction $\frac{\sin n\mu_c}{\sin \mu_c}$ is equal to n , so that their contribution is multiplied by n^2 . If n is of the order of 10, we see that two order of magnitude can be gained. This can be achieved by forcing the sextupole periodicity to be an odd multiple of π . To make this possible, μ_c must be an odd multiple of $\frac{\pi}{k}$, where k is a small integer different from 1. Then it is possible to assign the same strength to sextupoles separated by k cells, i.e. to build up k sextupole families and to force the sextupole periodicity to be π by assigning different strengths to the families. Under those conditions, sextupole families are an efficient way of making large higher order tune derivatives, especially in large machines thanks to the factor n^2 .

For the particular case where it is possible to distribute the sextupoles in families with equal numbers of members, their contribution to μ'' , forgetting the quadrupole contributions, is given by :

$$\mu'' \approx -\frac{1}{4} \cot \mu \left[\frac{\sin nk\mu_c}{\sin k\mu_c} \right]^2 \times \left[\left(\sum_j \chi_j \sin 2(\mu - \mu_{0j}) \right)^2 + \left(\sum_j \chi_j \cos 2(\mu - \mu_{0j}) \right)^2 \right] \quad (5)$$

with : $\chi_i = k'_j l_j D_j \beta_i$

j is the index of the sextupole families which contain n sextupoles each, D_j is the value of the dispersion function at the sextupole locations and μ_{0j} is the phase of the first sextupole of each family. For $k\mu_c$ multiple of π , we find the factor n^2 in front of the formula. For χ_i independent of i , the sums of trigonometric functions are zero.

This formula gives a good idea on the mechanism of second order chromaticity correction with sextupole families. For a practical correction of the non-linear chromaticity, it is necessary to go to a higher order expansion. In fact other perturbation

formalisms have been developed for a long time, as [6]. Nevertheless the above formulae tells us that it is important to compensate the first order derivatives of the β -functions when such a correction of the higher order tune derivatives is computed.

IV. Tolerance on the phase advance per cell for periodic sextupole families.

A. General conditions

If the phase advance per cell is not an odd multiple of $\frac{\pi}{k}$ where k is any integer, the factor n^2 disappears. This is what happens for instance if the phase of the regular cells are used to adjust the tunes. The sextupole families have been constructed for a certain value of the phase advance of the regular and this phase advance per cell is subsequently "slightly changed". As a consequence, $nk\mu_c$ may become close to a multiple of π , $k\mu_c$ being not a multiple of π , and the sextupole families loose completely their efficiency as their important contribution to the non-linear chromaticity becomes close to zero.

B. The LEP example

A first good example of non working periodic sextupole families is that of the first LEP lattice [7]. In a superperiod of this machine there was one arc with 30 FODO cells with dipoles and one low- β insertion. The phase advance of the arc cells was "about 60° ". It was in fact exactly 60° in the horizontal plane but it was close to 55° in the vertical plane. The number of cells between two successive sextupoles in a given family was set to 3 because of the "about 60° " per cell. This makes 10 sextupoles per family. Then, for the vertical plane, $nk\mu_c$ is 550° which is very close to 3π . The factor $\left[\frac{\sin nk\mu_c}{\sin k\mu_c} \right]^2$ becomes 3.7 instead of 100, which annihilates the effect of the sextupole families in the vertical plane. This was noticed at the time of the first LEP study and non periodic sextupole families were used to correct the non-linear chromaticity of this lattice.

A second good example is that of the second LEP lattice [8]. The horizontal phase advance per cell was 60° and the vertical one was 62.1° . The latter is closer to 60° than in the first design, which made it possible to use periodic families with five sextupoles per family (12 families total).

These cases of phase advances per cell slightly different from 60° for the case of 10 sextupole per family is instructive. For phase of 57.3° or 62.7° , a factor two is lost in the contribution of the sextupole families. This makes sextupoles increments twice as large for correcting the same effect. Consider a case where the increments of the sextupole strength of the family which has to be increased are about 30% with a 60° phase advance. For 57.3° , they have to be increased by 30% more, which makes the dynamic aperture decrease substantially. For the case of 55° quoted above, the factor $\frac{100}{3.7}$ is so large that the correction of the non-linear chromaticity becomes marginal even for a large increase of the sextupole strengths, with the consequence that the dynamic aperture becomes dramatically low [7].

C. Number of sextupoles per family

From formula (5), it is clear that the larger the number of sextupoles per family, the smaller the tolerance on the phase ad-

vance per cell to make the correction of the non-linear chromaticity possible. For instance, for 100 sextupoles per family and a phase advance per cell close to 60° , the efficiency, defined for instance by the ratio $\frac{\sin n\mu_c}{n \sin \mu_c}$, goes to zero for a phase advance per cell of 59.4° . Such a tight tolerance can be avoided by increasing arbitrarily the total number of sextupole families in the case where the number of cells per superperiod is large.

On the opposite, for a small number of cells, the tolerance on the phase advance is much relaxed. For three sextupoles per family, the efficiency of the system losses is reduced by 10% for a phase of about 55° !

V. Sextupole families for out of phase cells

For a case where there it is absolutely necessary to have a phase advance per cell incompatible with periodic families, non-periodic families can be a solution. The best example known to the author is that of the first LEP design [7] quoted above. For this case, the families arrangement is like :

1 2 x 1 2 2 1 x 2 1 1 2 3 1 2 3 1 3 2 1 3

where 1 to 3 refer to the family number and x to a missing sextupole. Such an arrangement has been obtained by inspecting the modulation of the β_y function at the sextupole location on an off-momentum closed orbit and assigning the sextupoles with the same modulation to the same family. An additional rule to obtain a satisfactory system is to make pairs of sextupoles separated by about π phase advance, in order not to produce too much geometric aberrations. It is clear that such a system works only for a given phase advance once it is built, which reduces the lattice flexibility.

VI. Conclusion

Correcting the non-linear chromaticity with sextupole families is easy and powerful when a machine is designed with a number of regular cells having a phase advance equal to an odd number of $\frac{\pi}{k}$ where k is any integer. On top of the designed correction, they provide a simple knob to adjust experimentally the second order tune derivative. Depending on the number of sextupoles per super-period, there is more or less flexibility for changing the machine tune by means of the quadrupoles in the regular cells. The best lattice design to fully exploit the potentialities of sextupole families is always to make tunable insertions to avoid changing the machine tune with the quadrupoles in the regular cells.

With the phase advance per cell chosen as specified above, the second order geometric aberrations are automatically zero provided there is an even number of sextupoles per family and the same phase advance in both planes [9]. The remaining problem is then the anharmonicities. From the experience with LEP, this is a serious problem only for strong focusing lattices. Some examples can be found at this conference [10].

References

[1] **M. Donald et al.**, *Localized chromaticity correction of low-beta insertions in storage rings*. PAC93, Washington DC, May 1993.

[2] **A. Verdier**, *Higher order tune derivatives due to low- β insertions*. 1993 Part. Acc. Conf., Washington D.C., 17-20 May 1993.

[3] **E. D. Courant and H. S. Snyder**, *Theory of the alternating-gradient synchrotron*. Annals of Physics, vol. 3, 1-48 (1958).

[4] **B. Autin and A. Verdier**, *Focusing perturbations in alternating gradient structures*. CERN ISR-LTD/76-14, (1976).

[5] **B. Montague**, *Linear optics for improved chromaticity correction*, LEP note 165 (30.7.1979).

[6] **M. Donald and D. Schofield**, *A users guide to the HARMON Program*, LEP note 420 (1982).

[7] **J.R.J. Bennett et al.**, *Design concept for a 100GeV e^+e^- storage ring (LEP)*, CERN 77-14, (1977).

[8] **The LEP study group**, *Design study of a 15 to 100GeV e^+e^- colliding beam machine (LEP)*. CERN/ISR-LEP/78-17. Report known as "the blue book".

[9] **K. Brown**. SLAC-PUB 2257.

[10] **Y. Alexahin et al.**, *Low emittance lattice for LEP*, this conference.

SIMULATION OF CHARGED PARTICLE TRANSPORT IN NONLINEAR AXISYMMETRICAL ELECTROSTATIC POTENTIAL

I.P. Yudin, V.V. Andreev

Joint Institute for Nuclear Research, Dubna 141980, Moscow region, Russia

Abstract

We describe the procedure within transfer matrix formalism to obtain the solution of nonlinear charge particle motion equation in the electrostatic fields (with axis-symmetrical potential) up to third-order aberrations.

I. INTRODUCTION

In this paper we describe the procedure within transfer matrix formalism to obtain the solution of nonlinear charge particle motion equation up to third-order aberrations in the electrostatic fields.

The matrix elements are given with the coefficients in the Taylor expansion,

$$X_i(z) = \sum_{j=1}^4 R_{ij}(z) X_j^0 + \sum_{j=1}^4 \sum_{k=j}^4 T_{ijk}(z) X_j^0 X_k^0 + \sum_{j=1}^4 \sum_{k=j}^4 \sum_{l=k}^4 U_{ijkl}(z) X_j^0 X_k^0 X_l^0 + \dots \quad (1)$$

where \vec{X} is the usual 4-vector of the TRANSPORT [1] coordinates, $\vec{X} = (r, r', l, \delta)$. The same description of our method can be found in [2] for magnetic solenoid lenses. This paper brings up the investigation that it concludes in [3, 4].

I. NONLINEAR MOTION EQUATION

In cylindrical coordinate system with the Z - axis directed straight along the \vec{E} axial field, the nonlinear motion equation originates from the Lorentz force equation for the charged particles in the external axis-symmetric field [5].

$$\begin{cases} \frac{d}{dt}(\gamma m \dot{r}) - \gamma m r \dot{\theta}^2 - q E_r = 0, & (1.1a) \\ \frac{d}{dt}(\gamma m \dot{z}) - q E_z = 0, & (1.1b) \\ \frac{d}{dt}(\gamma m r^2 \dot{\theta}) = 0, & (1.1c) \end{cases}$$

where m is the particle rest mass, q is the particle charge, $\gamma = 1/\sqrt{1-\beta^2}$, $\beta = v/c$, v - the particle velocity, c - the speed of light in vacuum, E_r & E_z are the radial and axial components of the electrostatic field:

$$\begin{cases} E_z(r, z) = -\Phi'(z) + r^2/4 \Phi'''(z) - \dots, & 1.2a \\ E_r(r, z) = r/2 \Phi''(z) - r^3/16 \Phi''''(z) + \dots. & 1.2b \end{cases}$$

Eqs. (1.2a) - (1.2b) were written from known relation $\vec{E} = -\nabla\phi$ and the decomposition $\phi(r, z)$ on degree r and z with the axis-symmetrical condition $\phi(r, z) = -\phi(-r, z)$:

$$\phi(r, z) = \Phi(z) - \frac{r^2}{4} \Phi''(z) + \frac{r^4}{64} \Phi''''(z) - \dots, \quad (1.3)$$

$\Phi(z) = \phi(0, z)$ is the axial electrostatic potential. The differentiation is held on z . For this investigation we describe $\Phi(z)$ as a piece-uninterrupted (linear and square) function. To obtain the nonlinear motion equation, we have written the conservation law of the energy from behind a nonconservation of our investigation system:

$$V^2 = \dot{r}^2 + \dot{z}^2 = \frac{2|q|}{\gamma m} \phi(r, z). \quad (1.4)$$

We suppose

$$\begin{cases} V_z > V_r, \text{ and} \\ r' = \frac{\dot{r}}{\dot{z}} < 1. \end{cases} \quad (1.5)$$

then Eq. (1.4) can be written in the following form

$$\dot{z}^2 = \frac{2|q|}{\gamma m} \phi(r, z) [1 - r'^2], \quad (1.6)$$

taking into account that the decomposition up to the third order. Thus, by the elimination of a time dependence in (1.1b), and then by the substitution of Eq. (1.6) with the decomposition of Eq. (1.3) truncated after r^3 , the main nonlinear equation of the particle trajectory in the electrostatic field with axial potential $\Phi(z)$ (on closed interval $[0, D]$) can be written in the form:

$$\begin{aligned} 2 \text{sign}(q) \cdot \Phi r'' - \Phi' r' - \frac{\Phi''}{2} r = & \left(\frac{\Phi''^2}{8\Phi} - \frac{\Phi''''}{16} \right) r^3 + \\ & + \left(\frac{\Phi' \Phi''}{4\Phi} + \frac{\Phi'''}{4} \right) r^2 r' + \frac{\Phi''}{2} r r'^2 + \Phi' r'^3. \end{aligned} \quad (1.7)$$

In the case the magnitudes of r and r' have remained small (near the axis), we obtain the paraxial particle linear equation:

$$2 \text{sign}(q) \cdot \Phi r'' - \Phi' r' - \frac{\Phi''}{2} r = 0. \quad (1.8)$$

In further we are limited the $\text{sign}(q) = -1$ in Eq. (1.7), i.e., we describe the motion of an electron far from the axis. Into the decreasing electrostatic field the trajectory of a proton will be the same as one for an electron in the increasing (in the same of a degree) field. It follows from Eq. (1.7), thus one is not dependent explicitly on the q/m ratio.

The basis of our solution method of Eq. (1.7) is the expression (1). Independent variables are $\vec{X} = (r, r', l, \delta)$. Here is the l -definition:

$$l = \int_0^z \left(\sqrt{1 + r'^2 + r^2 \theta'^2} - 1 \right) dz \approx \frac{1}{2} \int_0^z r'^2 dz. \quad (1.9)$$

The appearance of a transverse velocity is to influence on the beam dispersion increment:

$$p = p_0 \cdot (1 + \delta) = mv_z \cdot \left(1 + \frac{1}{2} \left(\frac{v_r}{v_z}\right)^2\right) = p_0 \cdot \left(1 + \frac{r'^2}{2}\right). \quad (1.10)$$

After substituting Eq. (1.2) into Eqs. (1.1a) and (1.1b) and then the result – into Eq. (1.10) we can write in third order:

$$\delta = \frac{\Phi''}{8\Phi} \cdot r^2. \quad (1.11)$$

The aberration coefficients R_{ij} , T_{ijk} and U_{ijkl} define the first, the second and the third orders of transfer matrix and of system properties at all. We shall use some useful relations for "primes" and "nonprimes":

$$R_{2j}(z) = R'_{1j}(z), \quad T_{2jk}(z) = T'_{1jk}(z), \quad U_{2jkl}(z) = U'_{1jkl}(z). \quad (1.12)$$

To define f_{ijk}^T , f_{ijkl}^U as the appropriate right parts of the main trajectory Eq. (1.7), it can be written the beginning condition for the definition of aberration coefficients:

$$\begin{cases} T_{1jk}(0) = T'_{1jk}(0) = 0, & T_{2jk}(0) = T'_{1jk}(0) = 0, \\ T'_{2jk}(0) = T'_{1jk}(0) = f_{1jk}^T(0), \\ U_{1jkl}(0) = U'_{1jkl}(0) = U_{2jkl}(0) = 0, \\ U'_{2jkl}(0) = U'_{1jkl}(0) = f_{1jkl}^U(0). \end{cases} \quad (1.13)$$

II. LINEAR POTENTIAL

Let observe the potential of the view:

$$\Phi(z) = \Phi_0 \cdot (1 + z/z_0) = \Phi_0 \cdot \bar{z}, \quad (2.1)$$

where $z_0 = D/\sqrt{n^2 - 1}$, $n = \sqrt{\Phi_1/\Phi_0}$, D is the length of the acting field region, Φ_0 and Φ_1 are initial and final potential values, n – electron-optics [5] index of the reflection that appropriate by the Snellius law. Naturally it impose a constraint on n that electrostatic potential is equal to zero where the particle velocity is equal to zero.

2.1. Third-order optics in an accelerating (decelerating) tube with a linear potential

The first-order optics is described in [4,6].

The main Eq. (1.7) with a linear potential (2.1) is adopted here as:

$$2\Phi r'' + \Phi' r' = -\Phi' r'^3. \quad (2.1.1)$$

From that follows explicitly the contribution into r and r' it gives only in the third order, i.e., $T_{1jk}(z) = T_{2jk}(z) = 0$. By the substitution of linear solution [4, 6] into Eqs. (1.9) – (1.10), we obtain the following non-zero components of the matrix T (with $\zeta = \sqrt{1 + z/z_0}$):

$$\begin{cases} T_{322}(z) = z_0/2 \cdot \ln \zeta^2, & T_{422}(z) = 1/(2\zeta^2). \end{cases} \quad (2.1.2)$$

We find the accurate analytical solution of Eq. (1.7) with the potential (2.1). In this case the initial equation of the third order can be written to substitute the linear potential (2.1) once into Eqs. (1.2)-(1.3) and then into Eq. (1.1):

$$2\bar{z}r'' + (1 + r'^2/z_0^2) = 0, \quad (2.1.3)$$

where we are accounting the obvious condition (1.5). The directly integration Eq. (2.1.3) on z with the initial conditions (r_0, r'_0) gives us the following nonlinear solution:

$$\begin{cases} r'(z) = \frac{r'_0}{\sqrt{\zeta^2(1 + r_0'^2) - r_0'^2}}, \\ r(z) = r_0 + \frac{2z_0 r'_0}{1 + r_0'^2} \cdot \left[\sqrt{\zeta^2(1 + r_0'^2) - r_0'^2} - 1 \right]. \end{cases} \quad (2.1.4)$$

By using Eq. (1.5), to reduce this result solution to view (1) we have the accurate solution of Eq. (2.1.3):

$$\begin{cases} r'(z) = \frac{r'_0}{\zeta} \cdot \left(1 - \frac{r_0'^2}{2} \cdot \frac{z/z_0}{1 + z/z_0} \right), \\ r(z) = r_0 + 2z_0 r'_0 [\zeta - 1] \left(1 - r_0'^2/2 \cdot (\zeta - 1)/\zeta \right). \end{cases} \quad (2.1.5)$$

is written as

$$\begin{pmatrix} r \\ r' \end{pmatrix} = \begin{bmatrix} \mathbf{R} + \mathbf{U}_{22} \cdot r_0'^2 \end{bmatrix} \cdot \begin{pmatrix} r_0 \\ r'_0 \end{pmatrix}, \quad (2.1.6)$$

where $\mathbf{R} = \begin{pmatrix} R_{11} & R_{12} \\ 0 & R_{22} \end{pmatrix}$, $\mathbf{U}_{22} = \begin{pmatrix} 0 & U_{1222} \\ 0 & U_{2222} \end{pmatrix}$.

Fringe region focusing effects change also in the third order.

III. SQUARE POTENTIAL

Further we shall take into account the following potential:

$$\Phi(z) = \Phi_0 (1 \pm \bar{z}^2), \quad (3.1)$$

where $\bar{z} = z/z_0$, $z_0 = D/\sqrt{n^2 - 1}$, $n \neq 1$. We choose this potential so, that all derivatives of $\Phi(z)$ in the point $z=0$ were equal 0. Sign (\pm) in this case corresponds to electron acceleration (+) or deceleration (-).

3.1. The third-order beam optics of the acceleration tube with the square potential

For first-order optics, the acceleration tube transfer matrix $R^+(z)$ and the deceleration tube transfer matrix $R^-(z)$ are described in [4].

In order to obtain nonzero elements of T-matrix we substitute the equation for $r'(z)$ to the definition of the value δ from (1.13),

$$z_0 = D/\sqrt{n^2 - 1} (n > 1), \quad \zeta = 1/\sqrt{2} \cdot \text{Arsh } \bar{z}, \text{ then:}$$

$$\begin{cases} T_{412}^+(\bar{z}) = \frac{\sin^2 \zeta}{4z_0^2(1 + \bar{z}^2)}, \\ T_{412}^+(\bar{z}) = -\frac{\sin \zeta \cos \zeta}{2z_0(1 + \bar{z}^2)}, & T_{422}^+(\bar{z}) = \frac{\cos^2 \zeta}{4(1 + \bar{z}^2)}. \end{cases} \quad (3.1.1)$$

Integrating with the definition (1.9) gives the following nonzero elements of the third line of the T-matrix:

$$\begin{cases} T_{311}^+(\bar{z}) = \frac{1}{4z_0^2} \cdot \int_0^{\bar{z}} \frac{\sin^2 t}{1+\tau^2} d\tau = \frac{1}{4z_0^2} \cdot (\arctg \bar{z} - I_1), \\ T_{312}^+(\bar{z}) = -\frac{1}{4z_0} \cdot \int_0^{\bar{z}} \frac{\sin t \cos t}{1+\tau^2} d\tau = -\frac{I_3}{4z_0}, \\ T_{322}^+(\bar{z}) = \frac{1}{4} \cdot \int_0^{\bar{z}} \frac{\cos^2 t}{1+\tau^2} d\tau = \frac{I_1}{4}, \end{cases} \quad (3.1.2)$$

where $t = 1/\sqrt{2} \cdot \text{Arsh } \tau$. Eq. (1.7) with the square potential (3.1) can be written in the form:

$$2\Phi r'' + \Phi' r' + \frac{\Phi''}{2} r = -\frac{\Phi'^2}{8\Phi} r^3 - \frac{\Phi' \Phi''}{4\Phi} r^2 r' - \frac{\Phi''}{2} r r'^2 + \Phi' r'^3 \quad (3.1.3)$$

After substituting Eq. (3.1) into Eq. (3.1.3), combining same order members, we shall find *driving forces* to obtain third order aberration coefficients:

$$\begin{cases} f_{1111}^U(\bar{z}) = -\frac{\Phi_0}{2z_0^4(1+\bar{z}^2)} \cdot \left(\cos \zeta - \frac{\sqrt{2} \cdot \bar{z}}{\sqrt{1+\bar{z}^2}} \cdot \sin \zeta \right), \\ f_{1112}^U(\bar{z}) = -\frac{\Phi_0}{2z_0^3(1+\bar{z}^2)} \cdot \left(\sin \zeta + \frac{\sqrt{2} \cdot \bar{z}}{\sqrt{1+\bar{z}^2}} \cdot \cos \zeta \right). \end{cases} \quad (3.1.4)$$

Integrating with the Green's function gives us:

$$\begin{cases} U_{1111}^+(\bar{z}) = z_0^2 \cdot U_{1122}^+(\bar{z}), \\ U_{1112}^+(\bar{z}) = z_0^2 \cdot U_{1122}^+(\bar{z}). \end{cases} \quad (3.1.5)$$

We introduce some useful formulas for beam parameters:

$$\begin{pmatrix} r \\ r' \end{pmatrix} = \begin{bmatrix} \mathbf{R}^+ + \mathbf{U}_{11}^+ \cdot (r_0^2 + r_0'^2 \cdot z_0^2) \end{bmatrix} \cdot \begin{pmatrix} r_0 \\ r_0' \end{pmatrix}, \quad (3.1.6)$$

$$\text{Where } \mathbf{R}^+ = \begin{pmatrix} R_{11}^+ & R_{12}^+ \\ R_{21}^+ & R_{22}^+ \end{pmatrix}, \quad \mathbf{U}_{11}^+ = \begin{pmatrix} U_{1111}^+ & U_{1112}^+ \\ U_{2111}^+ & U_{2112}^+ \end{pmatrix}.$$

Further, we shall integrate Eqs. (3.1.4) with the Green's function (4) according to relations (1.13). We obtained:

$$U_{1111}^+(\bar{z}) = -\frac{\Phi_0}{2z_0^2} \cdot [\sin \zeta \arctg \bar{z} - I_1 \sin \zeta + I_3 \cos \zeta],$$

$$U_{1112}^+(\bar{z}) = -\frac{\Phi_0}{2z_0} \cdot [\sqrt{2} \sin \zeta - I_1 \cos \zeta - I_3 \sin \zeta]$$

$$U_{2111}^+(\bar{z}) = -\frac{\Phi_0}{2z_0^3 \sqrt{2(1+\bar{z}^2)}} \cdot [\cos \zeta \arctg \bar{z} + \sin \zeta \cdot \sqrt{2/(1+\bar{z}^2)} - I_2 \cos \zeta - I_3 \sin \zeta],$$

$$U_{2112}^+(\bar{z}) = -\frac{\Phi_0}{2z_0^2 \sqrt{2(1+\bar{z}^2)}} \cdot \left[\sqrt{2} \cos \zeta \cdot \left(1 - \frac{1}{\sqrt{1+\bar{z}^2}} \right) + I_1 \sin \zeta - I_3 \cos \zeta \right], \quad (3.1.7)$$

3.2. The third-order beam optics of the deceleration tube with the square potential

After the same substitutions (see Section 3.1) we shall obtain following nonzero elements of the T-matrix:

$$\begin{cases} T_{411}^-(\bar{z}) = \frac{sh^2 \zeta}{4z_0^2(1-\bar{z}^2)}, \\ T_{412}^-(\bar{z}) = -\frac{sh \zeta ch \zeta}{2z_0(1-\bar{z}^2)}, T_{422}^-(\bar{z}) = \frac{ch^2 \zeta}{4(1+\bar{z}^2)}. \end{cases} \quad (3.2.1)$$

$$\begin{cases} T_{311}^-(\bar{z}) = \frac{1}{4z_0^2} \cdot \int_0^{\bar{z}} \frac{sh^2 t}{1-\tau^2} d\tau = \frac{1}{4z_0^2} \cdot (I_1 - \text{Arth} \bar{z}), \\ T_{312}^-(\bar{z}) = \frac{1}{4z_0} \cdot \int_0^{\bar{z}} \frac{sh t ch t}{1-\tau^2} d\tau = \frac{I_4}{4z_0}, \\ T_{322}^-(\bar{z}) = \frac{1}{4} \cdot \int_0^{\bar{z}} \frac{ch^2 t}{1-\tau^2} d\tau = \frac{I_2}{4}, \end{cases} \quad (3.2.2)$$

where $z_0 = D/\sqrt{1-n^2}$ ($n < 1$), $\zeta = 1/\sqrt{2} \cdot \arcsin \bar{z}$, and $t = 1/\sqrt{2} \cdot \arcsin \tau$.

We shall find *driving forces* to obtain third order aberration coefficients:

$$\begin{cases} f_{1111}^U(\bar{z}) = -\frac{\Phi_0}{2z_0^4(1-\bar{z}^2)} \cdot \left(ch \zeta + \frac{\sqrt{2} \cdot \bar{z}}{\sqrt{1-\bar{z}^2}} \cdot sh \zeta \right), \\ f_{1112}^U(\bar{z}) = -\frac{\Phi_0}{2z_0^3(1-\bar{z}^2)} \cdot \left(sh \zeta + \frac{\sqrt{2} \cdot \bar{z}}{\sqrt{1-\bar{z}^2}} \cdot ch \zeta \right). \end{cases} \quad (3.2.3)$$

Integrating with the Green's function gives us:

$$\begin{cases} U_{1111}^-(\bar{z}) = -z_0^2 \cdot U_{1122}^-(\bar{z}), \\ U_{1112}^-(\bar{z}) = -z_0^2 \cdot U_{1122}^-(\bar{z}), \end{cases} \quad (3.2.4)$$

According to (1), we introduce some useful formula for beam parameters:

$$\begin{pmatrix} r \\ r' \end{pmatrix} = \begin{bmatrix} \mathbf{R}^- + \mathbf{U}_{11}^- \cdot (r_0^2 - r_0'^2 \cdot z_0^2) \end{bmatrix} \cdot \begin{pmatrix} r_0 \\ r_0' \end{pmatrix}, \quad (3.2.5)$$

$$\text{where } \mathbf{R}^- = \begin{pmatrix} R_{11}^- & R_{12}^- \\ R_{21}^- & R_{22}^- \end{pmatrix}, \quad \mathbf{U}_{11}^- = \begin{pmatrix} U_{1111}^- & U_{1112}^- \\ U_{2111}^- & U_{2112}^- \end{pmatrix}.$$

Further, we shall integrate Eqs. (3.2.4) with the Green's function [4] according to relations (1.13). We found:

$$\begin{aligned}
U_{1111}^{-}(\bar{z}) &= -\frac{\Phi_0}{2z_0^2} \cdot [sh \zeta \operatorname{Arth} \bar{z} - I_2 sh \zeta + I_4 ch \zeta], \\
U_{1112}^{-}(\bar{z}) &= -\frac{\Phi_0}{2z_0} \cdot [-\sqrt{2} sh \zeta + I_2 ch \zeta - I_4 sh \zeta], \\
U_{2111}^{-}(\bar{z}) &= -\frac{\Phi_0}{2z_0^3 \sqrt{2(1-\bar{z}^2)}} \cdot [ch \zeta \operatorname{Arth} \bar{z} + \\
&\quad + sh \zeta \cdot \sqrt{2/(1-\bar{z}^2)} - I_2 ch \zeta + I_4 sh \zeta], \\
U_{2112}^{+}(\bar{z}) &= -\frac{\Phi_0}{2z_0^2 \sqrt{2(1-\bar{z}^2)}} \cdot \left[-\sqrt{2} ch \zeta \cdot \left(1 - \frac{1}{\sqrt{1-\bar{z}^2}} \right) + \right. \\
&\quad \left. + I_2 sh \zeta - I_4 ch \zeta \right], \quad (3.2.6)
\end{aligned}$$

IV. CONCLUSION

In this paper we describe the third-order beam optics of the acceleration (deceleration) tube, created with axis-symmetrical potential. We describe the linear and square electrostatic field models with nonlinear transfer matrices. The described procedure was taken into account to obtain numerical results of investigation of the 0.5 MeV proton beam transport through the SPIN superconducting synchrotron injection channel [7]. Some modification of construction and channel parameters by choosing an optimal installation operation regime was proposed. A possibility of increasing the beam intensity at the entrance into the synchrotron ring was established by a computer simulation.

V. REFERENCES

- [1] K.L. Brown *et al.* "TRANSPORT. A Computer Program for Designed Charged Particle Beam Transport Systems." SLAC-91, Rev. 2, UC-28 (II/A), May 1977.
- [2] V.V. Andreev, I.P. Yudin. "Third-order Beam Optics of Real Solenoid Lens" in: Proc. 5-th International Symposium on Electron Beam Ion Sources and Their Applications, (Dubna, USSR, Sept. 24-28, 1991), pp. 279-290. Editors: E.D. Donets, I.P. Yudin. JINR, Dubna, 1992.
- [3] V.V. Andreev, I.P. Yudin. "The Full Matrices Construction of Linear Transformations of Accelerating Tube and Solenoid Magnetic Lens." JINR Communication B3-1-92-31, Dubna, January 1992.
- [4] V.V. Andreev, I.P. Yudin. "Linear Optics in Accelerating (Decelerating) Tube with a Piece-Unterrupted Potential," in: Proc. of Conference on Charged Particle Accelerators, (Dubna, Oct. 13-15, 1992), JINR D9-92-455, vol. II, pp. 81-88, Dubna, 1993.
- [5] M. Sziladyi. "Electron and Ion Optics," New York, Plenum Press, 1988.
- [6] J.R. Pierce. "Theory and Design of Electron Beams," Princeton: Van Nostrand, 1949, 1954.
- [7] V.V. Andreev *et al.* "Proton Beam Loss Evaluation in the Injection channel of SPIN Synchrotron." JINR Communication P9-87-763, Dubna, October 1987.

Stochastic Effects in Real and Simulated Ion Beams

Jürgen Struckmeier

Gesellschaft für Schwerionenforschung (GSI)

Postfach 11 05 52, D-64220 Darmstadt, Germany

Abstract

Emittance growth due to intra-beam scattering effects in charged particle beams is estimated using a second order moment description based on the Vlasov-Fokker-Planck equation. It is furthermore shown that numerical emittance growth phenomena in computer simulations of particle beams can also be described by this approach.

1 INTRODUCTION

If we want to analyze emittance growth phenomena in charged particle beams, we must distinguish the following sources:

- a non-self-consistent charge density distribution of the beam, which leads to a redistribution of the beam charges within a few plasma periods. In case that a more homogeneous charge density evolves, this results in a rapid increase of the rms-emittance.
- a temperature imbalance between different degrees of freedom within the beam. This can also be interpreted as a transition from a non-stationary to a stationary solution of the Vlasov equation, usually designated as the equipartitioning effect. The related time constants are considerably smaller, hence the time the beam needs to reach a temperature balance is much larger than the time needed for the charge readjustment.
- various orders of resonances between the beam and the external focusing devices. Since usually only a fraction of the beam particles is in resonance, these effects lead to a degradation of the beam emittance due to halo formation.

All these effects have in common that they can be calculated – at least in principle – by integrating the Vlasov equation, which is a strictly deterministic formulation. In other words, all these phenomena could also be observed if the space charge fields were smooth functions of the spatial coordinates, i.e. in a rigid continuous description.

However, there are effects which originate in the fact that the charge distribution is granular on a microscopic scale. The individual particle motion is thus no longer only governed by the smooth macroscopic space charge field, but also by a rapidly fluctuating field caused by neighboring beam particles. Obviously, these effects can only be tackled by means of statistical methods.

We restrict ourselves to cases where these effects can be classified as a chain of 'Markov' processes. Considering beam

dynamics, this is always a good approximation. The dynamics of these processes can then be described by the Fokker-Planck equation. Additionally taking into account stochastic effects means that the Vlasov equation has to be replaced by the combined Vlasov-Fokker-Planck equation. It forms the starting point for any physical process, where the macroscopic (smooth) aspect is described by the Liouville equation and where in addition a chain of Markov processes cannot be neglected.

2 FOKKER-PLANCK APPROACH

We start our analysis writing down formally the generalized Liouville theorem:

$$\frac{df}{dt} = \left[\frac{\partial f}{\partial t} \right]_{\text{FP}} \quad (1)$$

Herein $f = f(\vec{x}, \vec{p}; t)$ denotes the normalized 6-dimensional μ -phase space density function that represents a charged particle beam. The l.h.s. of (1) can be expressed in terms of the Vlasov equation

$$\frac{\partial f}{\partial t} + \vec{p} \cdot \vec{\nabla}_x f + \frac{1}{m} \left(\vec{F}^{\text{ext}} + q \vec{E}^{\text{sc}} \right) \cdot \vec{\nabla}_p f = \left[\frac{\partial f}{\partial t} \right]_{\text{FP}} \quad (2)$$

The r.h.s. of (1) is supposed to describe additional stochastic effects not covered by the Vlasov approach. If these effects constitute a Markov process, we can describe it with the help of the Fokker-Planck equation:

$$\left[\frac{\partial f}{\partial t} \right]_{\text{FP}} = \sum_i \frac{\partial}{\partial p_i} \{ \beta_{f,i} \cdot p_i f \} + \sum_{i,j} \frac{m^2 \partial^2}{\partial p_i \partial p_j} \{ D_{ij}(\vec{p}, t) f \} \quad (3)$$

The Fokker-Planck coefficients, namely the diffusion tensor elements D_{ij} and the drift vector components F_i must be determined in an appropriate way depending on the nature of the stochastic process.

3 SECOND ORDER MOMENT EQUATIONS

Applying Sacherer's formalism[1] to the Vlasov-Fokker-Planck equation (2), we get the following coupled set of second order moment equations[5]:

$$\frac{d}{ds} \langle x^2 \rangle - 2 \langle x x' \rangle = 0 \quad (4)$$

$$\frac{d}{ds} \langle x x' \rangle - \langle x'^2 \rangle + k_x^2(s) \langle x^2 \rangle - \frac{q \langle x E_x \rangle}{m c^2 \beta^2 \gamma^3} + \frac{\beta_{f,x}}{c \beta \gamma} \langle x x' \rangle = 0$$

$$\frac{d}{ds} \langle x'^2 \rangle + 2 k_x^2 \langle x x' \rangle - \frac{2 q \langle x' E_x \rangle}{m c^2 \beta^2 \gamma^3} + \frac{2 \beta_{f,x}}{c \beta \gamma} \langle x'^2 \rangle - \frac{2 \langle D_{xx} \rangle}{c^3 \beta^3 \gamma^3} = 0$$

The similar sets of equations hold for the y - and z -directions.

A useful measure for the beam quality is given by the rms-emittance $\varepsilon_x(s)$, defined as

$$\varepsilon_x^2(s) = \langle x^2 \rangle \langle x'^2 \rangle - \langle xx' \rangle^2. \quad (5)$$

On the basis of Eqs. (4), the derivative of the rms-emittance (5) is readily calculated to give

$$\frac{1}{\langle x^2 \rangle} \frac{d}{ds} \varepsilon_x^2(s) = -2 \left(\frac{\beta_{f;x}}{c\beta\gamma} \frac{\varepsilon_x^2(s)}{\langle x^2 \rangle} - \frac{\langle D_{xx} \rangle}{c^3 \beta^3 \gamma^3} \right), \quad (6)$$

neglecting the “excess field energy” terms. For intrinsically matched beams, this quantity is approximately a constant of motion. The remaining terms are related to the Fokker-Planck coefficients to be discussed now.

4 GROWTH RATES

If the diffusion as well as the friction effects can be approximately treated as isotropic, then only one diffusion coefficient D in conjunction with a single friction coefficient β_f appears in our equations:

$$D \equiv \langle D_{xx} \rangle = \langle D_{yy} \rangle = \langle D_{zz} \rangle, \quad \beta_f \equiv \beta_{f;x} = \beta_{f;y} = \beta_{f;z}$$

Under these circumstances, D turns out to be proportional to the “dynamical friction coefficient” β_f [3]:

$$D = \beta_f \cdot \frac{kT}{m} \quad (7)$$

If we define the ratio r_{xy} of the y - to the x -“temperature” as

$$r_{xy}(s) = \frac{T_y}{T_x} = \frac{\varepsilon_y^2(s) \langle x^2 \rangle}{\langle y^2 \rangle \varepsilon_x^2(s)}, \quad (8)$$

Eq. (6) can be written in an alternative form:

$$\frac{d}{ds} \ln \varepsilon_x^2(s) = \frac{2k_f}{3} (r_{xy}(s) + r_{xz}(s) - 2), \quad (9)$$

wherein $k_f = \beta_f / c\beta\gamma$. Adding Eq. (9) to the corresponding equations for $\ln \varepsilon_y^2$ and $\ln \langle \delta^2 \rangle$, after integration we get the following simple expression for the e -folding time τ_{ef} of the total phase space volume

$$\tau_{ef}^{-1} = \frac{1}{9} \beta_f (I_{xy} + I_{xz} + I_{yz}), \quad (10)$$

with I_{xy} , I_{xz} , and I_{yz} denoting the three possible integrals of the temperature ratio functions. For example, the dimensionless quantity I_{xy} is given by:

$$I_{xy} = \frac{1}{S} \int_0^S \frac{[1 - r_{xy}(s)]^2}{r_{xy}(s)} ds \geq 0. \quad (11)$$

If the transverse particle dynamics can be decoupled from the longitudinal one, the e -folding time for the transverse emittance evaluates to:

$$\tau_{\perp,ef}^{-1} = \frac{1}{4} \beta_f I_{xy}. \quad (12)$$

This condition is fulfilled if – for example – we simulate the transformation of an unbunched charged particle beam using a x , y -Poisson solver.

5 INTRA-BEAM SCATTERING EFFECTS IN STORAGE RINGS

The elementary events for the global process of emittance growth due to intra-beam scattering are Coulomb collisions of individual beam particles. The dynamics of these collisions thus forms the starting point to determine the Fokker-Planck coefficients contained in Eq. (3) for this process. Integrating the coupled set of equations (4) will enable us to study the evolution of the beam properties including intra-beam scattering effects. Explicitly, the coefficients are determined by averaging the velocity change of a test particle over all impact parameters, and subsequently by averaging over all particle velocities assuming that the velocity distribution is Maxwellian.

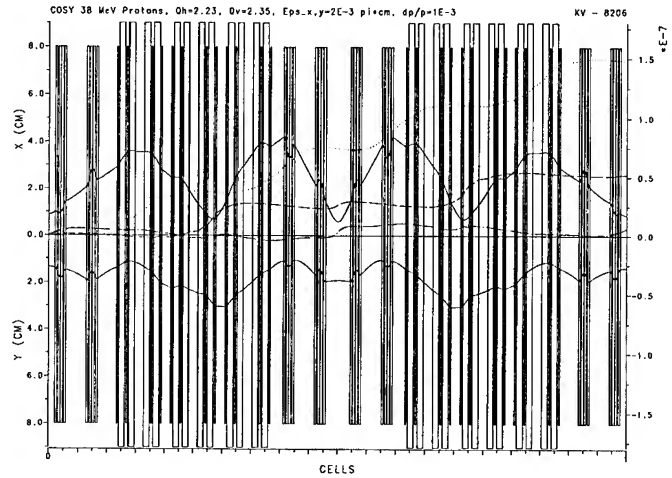


Figure 1: Envelopes and emittance growth functions of a matched beam passing through the Cooler Synchrotron (COSY) at KFA-Jülich. (The scale on the right-hand side applies to the dimensionless emittance growth functions.)

As the result of the averaging procedures, β_f is given by [2, 4]:

$$\beta_f = \frac{16\sqrt{\pi}}{3} n c \left(\frac{q^2}{4\pi\epsilon_0 mc^2} \right)^2 \cdot \left(\frac{mc^2}{2kT} \right)^{3/2} \cdot \ln \Lambda. \quad (13)$$

In order to gain a better physical insight, this quantity can be expressed alternatively as

$$\beta_f = \sqrt{\frac{2}{\pi}} \cdot (\Delta t_{\text{scattering}})^{-1} \cdot \Gamma^2 \cdot \ln \Lambda,$$

with $\Delta t_{\text{scattering}}$ denoting the average time between two successive scattering events of a beam particle, and Γ the coupling constant of the beam plasma.

As an example, we present an integration of the coupled set (4) based on the structure data of the Jülich Cooler Synchrotron (COSY). The beam parameters used in that calculation are listed in Tab. 1. The results, namely the envelopes and the emittance growth functions along one turn, are plotted in Fig. 1. We observe that the maximum growth of the rms-emittance occurs in the x -direction, whereas for these initial conditions practically no growth occurs in the longitudinal direction.

Table 1: List of Parameters for the COSY intra-beam scattering estimation

ion species	H ¹⁺
energy	38 MeV/amu
period length S	183.47 m
horizontal tune Q_h	2.23
vertical tune Q_v	2.35
$\eta_{av} = \gamma^{-2} - \gamma_t^{-2}$	0.371
average beam current I	55 mA
initial RMS emittances $\varepsilon_{x,y}(0)$	5×10^{-6} m
initial RMS momentum spread $\Delta p/p$	5.8×10^{-4}
ellipticity I_{xy}	3.252
ellipticity I_{xz}	2.286
ellipticity I_{yz}	0.997
friction coefficient β_f	4.1935 s^{-2}
horiz. emittance e -folding time $\tau_{x,ef}$	15.0 s
vert. emittance e -folding time $\tau_{y,ef}$	43.0 s
momentum spread e -folding time $\tau_{z,ef}$	336.1 s
total emittance e -folding time τ_{ef}	32.8 s

6 BEAM TRANSPORT SIMULATIONS

As has been mentioned in the introduction, the Fokker-Planck description of stochastic phenomena in the physics of charged particle beams is not restricted to the effect of intra-beam scattering, but applies to any beam dynamical Markov process. As a consequence, the coupled set of moment equations (4) can also be used to explain effects due to random errors generated by the necessarily limited accuracy of computer simulations of particle beams. Especially the problem of calculating the self-fields of arbitrary charge distributions escapes an analytical treatment. The major sources of random errors common to all simulation codes come from the fact that

- the continuously varying self-fields must be replaced by stepwise constant ones,
- the number of simulation particles is much smaller than the real beam particle number.

The joint effect of all these simplifications necessary to keep the computing time finite can be visualized in the way that an additional 'error field' of a certain amplitude is added to the 'true field' of the real beam. This causes a specific 'simulation friction coefficient' $\beta_{f,sim}$ to emerge. Unfortunately, it seems to be impossible to derive a general formula relating globally $\beta_{f,sim}$ to the various sources of 'numerical noise'.

In Fig. 2, the emittance growth factors obtained by numerical simulations of a quadrupole channel are plotted for different numbers of space charge calculations (SSC) per cell and different numbers P of simulation particles. It can be observed that the calculated growth rates do not depend very much on the number of space charge calculations. This indicates that in this case the number of 50 space charge calculations suffices to approximate the continuously varying self-fields. On the other hand, the growth rate is halved if we double the number of sim-

ulation particles from 5000 to 10000, i.e.

$$\beta_{f,sim} \propto P^{-1}.$$

This shows that in our case the concept of representative particles constitutes the major source of numerical noise.

For a comparison, the lower curve in Fig. 2 displays the calculated growth rates for a matched beam transformed under the same conditions through a periodic solenoid channel. Consequently, $\beta_{f,sim}$ must have the same value as for the corresponding quadrupole channel transformation. Nevertheless, no rms-emittance growth at all is observed in this simulation. This outcome is explained by Eq. (12), which states that even a positive β_f does not lead to an increase of the rms-emittance if the ellipticity integral (11) vanishes. We conclude that numerical noise phenomena occurring in computer simulations of charged particle beams can adequately be described by the Fokker-Planck approach.

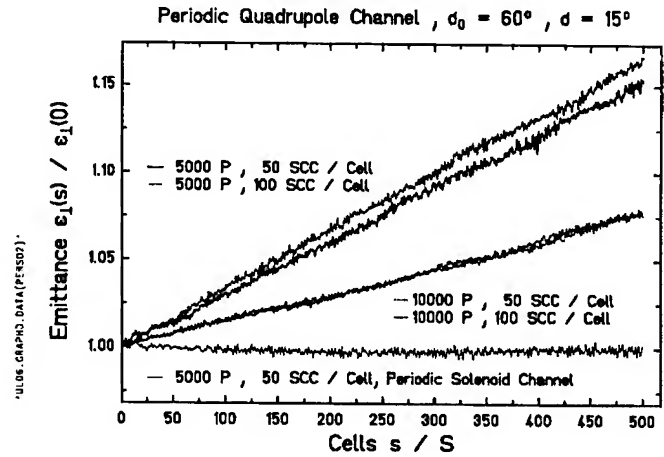


Figure 2: Emittance growth functions obtained by different numerical simulations of a matched beam passing through the GSI experimental quadrupole channel.

7 CONCLUSIONS

The moment description of a charged particle beam has been demonstrated to be useful even if additional stochastic effects must be taken into account. It has been shown that this approach leads to a fairly simple formula which can be used to estimate the growth rates of the beam emittances caused by intra-beam scattering effects. Moreover, since the Fokker-Planck equation describes any Markov process, certain effects of rms-emittance growth in computer simulations can also be explained by this approach.

8 REFERENCES

- [1] F.J. Sacherer, *IEEE Trans. Nucl. Sci.* NS-18, 1105 (1971)
- [2] G.H. Jansen, *Coulomb Interaction in Particle Beams*, Academic Press, New York (1990)
- [3] A. Einstein, *Ann. Physik* 17, 549 (1905) and 19, 371 (1906)
- [4] M. Reiser, *Theory and Design of Charged Particle Beams*, John Wiley & Sons, New York (1994)
- [5] J. Struckmeier, *Particle Accelerators* 45, 229-252 (1994)

MAGNETIC FIELD CORRECTION IN NUCLOTRON

I. B. Issinsky, V. A. Mikhailov, V. A. Shchepunov

Laboratory of High Energies

Joint Institute for Nuclear Research, Dubna, Russia 141980

Abstract

The description of the Nuclotron magnetic field correction is presented. The influence of the structure magnet misalignments and the field imperfections obtained from magnet measurements on the beam dynamical parameters is considered, and the correction schemes are reviewed. This influence and the correction efficiency are investigated with numerical methods.

I. INTRODUCTION

To provide long-term prospects in the area of both relativistic nuclear and applied physics a project of accelerator facilities named Nuclotron has been developed in the Laboratory of High Energies JINR [1]. This project includes a superconducting synchrotron (under commissioning now) and a booster synchrotron [2]. The existing linac used as an injector can accelerate ions from deuterium to xenon with charge to mass ratio Z/A in the range 0.33-0.50. In the Nuclotron ions are accelerated up to relativistic energies of 6 GeV/u. General parameters of the Nuclotron ring [3] are given in the table 1. The lattice of Nuclotron includes 8 superperiods. The structure of one superperiod and its optical functions are shown in fig. 1. Each superperiod contains 3 regular FODO cells with dipole magnets and 1 cell with large drift spaces occupied with elements of the injection-extraction systems, RF-voltages, the internal target equipment etc. Small drift spaces at the lattice quadrupoles are used for the diagnostic elements and multipolar magnets of the magnetic field correction systems.

The correction system includes 20 pick-up electrodes, tune and intensity measurement systems, 29 superconducting multipolar correcting magnets correcting closed orbit (C.O.) [5], chromaticity and octupolar detuning [6], betatron resonances up to the 4-th order [9]. Nuclotron operates with the horizontal and vertical tunes (Q_x and Q_z) between 6 and 7 with the nominal operating point at $Q_x=6.80$, $Q_z=6.85$ (see fig.2).

II. MULTIPOLAR CORRECTOR

Multipolar corrector [4] has 4 superconducting windings. Two of them, skew and right dipoles, are used for the C.O. correction. Other windings are of quadrupolar, sextupolar or octupolar types (skew or regular). All windings are placed on a cylindrical framework wrapped with the hollow tube. Helium flow inside the tube cools the windings due to a thermal contact. The iron cylindrical yoke around the windings allows to encrease the maximal field in the center of a corrector by a factor of 1.7-1.8. The yoke and windings are placed in a cryostat cooled with liquid nitrogen.

III. CLOSED ORBIT CORRECTION

Table 2 presents calculated and measured maximal values of C.O. distortions. It can be seen that at injection ($B_{inj}=291$

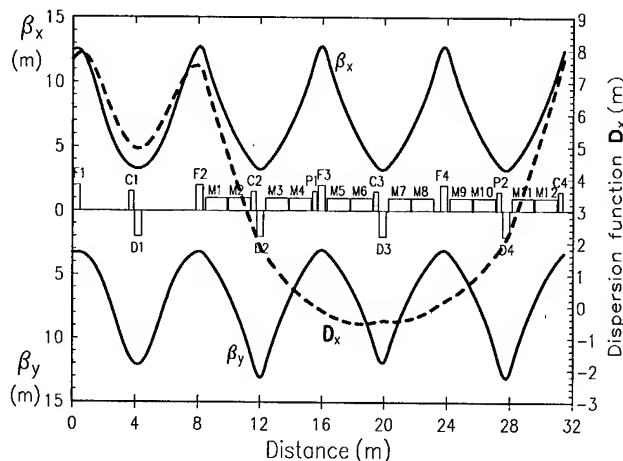


Figure 1. Twiss $\beta_{x,z}$ and dispersion D_x functions of the Nuclotron superperiod. F, D – focusing and defocusing quadrupoles respectively; M – dipole magnets; C – multipolar correctors; P – pick-ups. The positions of the correctors and pick-ups are shown for the 1-st superperiod.

Gauss) remanent fields give the main contribution to the vertical orbit distortions, while the horizontal distortions are mainly determined by the dispersion of integrated fields in dipole magnets. Four conventional C.O. correction algorithms are used for Nuclotron: least squares, harmonical, bump correction and MICADO method. It was found in numerical simulation studies [5] that 3.5 mm maximal orbit distortions could be reached with corrections in both planes.

IV. TUNE, CHROMATICITY AND AMPLITUDE DETUNING CORRECTIONS

Dipoles, F and D quadrupoles of the lattice have 3 independent power supplies. To keep tunes constant for the cycle of acceleration the ratios $I_{F,D}/I_{Dip}$ of the currents $I_{F,D}$ in F and D quadrupoles to the current I_{Dip} in dipoles are changed to compensate for the changing the values $(BL)_{F,D}/(BL)_{Dip}$, where (BL) -average integrated fields in quadrupoles and dipoles (that is mainly due to the saturation phenomena). At constant $I_{F,D}/I_{Dip}$, the tune shifts can be as large as +0.45 in the range of the main field $B_0=1.7-2.0$ T.

For the chromaticity ($\chi_x = -7.7$, $\chi_z = -7.9$) correction there are 2 families of sextupolar windings placed in the multipolar correctors of each superperiod. The same correctors also contain 2 families of octupolar windings to compensate for the amplitude detunings. The currents of the families are chosen so that the tunes of particles move away from the line of the resonance $Q_x - Q_z = 0$ with the increase of the amplitudes of their oscillations. It is also possible to use complicated sextupolar-octupolar

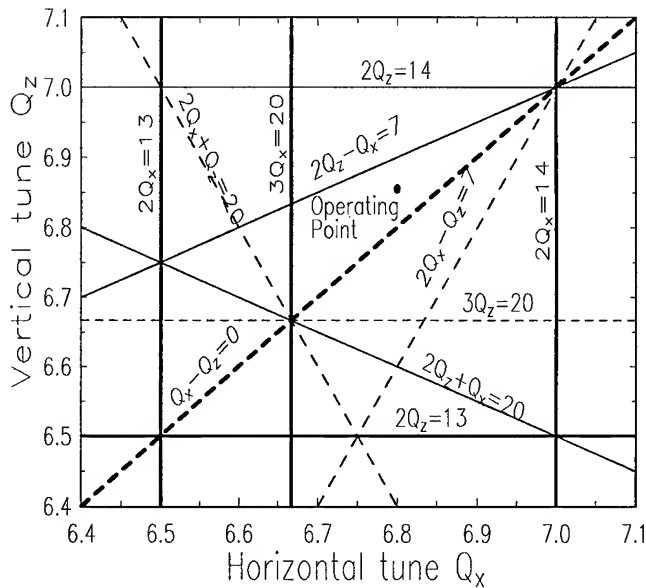


Figure. 2. 2-nd and 3-d order resonances and Nuclotron operating point (O.P.).

correction schemes that take into account the 2-nd order sextupolar effects [6].

V. CORRECTION OF BETATRON RESONANCES

Table 3 gives the list of resonances up to the 4-th order to be corrected (see the diagram in fig.2) and their r.m.s. stopbands estimated with the magnet measurements [7] and geodesic data. The correction system is capable of correcting resonances 1-2 and 3-4 simultaneously, i.e. it can correct each of these resonances without affecting the correction of the others. For the 3-d and the 4-th order resonances such simultaneous corrections are possible only for the combinations of sum and difference ones: 5-6 or 5-7; 8-9 or 8-10; 11-12 or 11-13; 14-15 or 14-16. Generally, correctors of the resonance $mQ_x + nQ_z = N$ create the N-th appropriate multipole harmonic. The sinus S and cosinus C components of this harmonic have the following dependence on the main filed B_0 :

$$C = C_r + C_b B_0 + C_t (dB_0/dt), \quad S = S_r + S_b B_0 + S_t (dB_0/dt),$$

where the constant terms C_r and S_r are due to remanent fields, while those proportional B_0 and the derivative dB_0/dt are presumably due to misalignments and/or field imperfections, and eddy currents respectively. It is the terms proportional to B_0 that were taken into account in the estimations of the stopbands given in the table 2. The eddy current terms have been estimated according to [8]. For the Nuclotron vacuum chamber width $a=0.5$ mm and $(dB_0/dt)_{max}=20$ kG/s they were found to be quite small in comparison with the others. The remanent field contribution is considerable and should be carefully taken into account. Full experimental data on the betatron resonance corrections will be obtained in the planned Nuclotron runs. The detailed description of the resonance correction schemes and the possible sources of relevant magnetic imperfections are discussed in [9].

Table I
General Nuclotron parameters

Injection energy for nuclei	5 MeV/u
for protons	20 MeV
Max energy for nuclei ($q/A=0.5$)	6 GeV/u
for protons	12.8 GeV
Circumference	251.52 m
Duration of acceleration	(0.5-1.5) sec
Max accelerating voltage	50 kV
Transition energy	8.6 GeV
Field in dipoles at injection	0.029 T
maximum	2.083 T
Gradient in quads at injection	0.490 T/m
maximum	34.6 T/m
Betatron tunes $Q_{x,z}$	6.8, 6.85
Chromaticity $\chi_{x,z} = \delta Q_{x,z} / \delta p/p$	-7.7, -7.9
Compaction factor	0.0135
Max closed orbit (after correction)	3.5 mm
Acceptance horizontal	40π mm mrad
vertical	45π mm mrad
Emittance at injection	30π mm mrad
minimum	2π mm mrad
Maximum momentum spread	$\pm 4 \times 10^{-3}$

Table II

Calculated values of maximal closed orbit distortions [mm] due to different sources of imperfections and measured distortions.

$B_0=471$ Gauss.

Source of imperfection	Vertical distortion	Horizontal distortion
Lense misalignments	1.3	2.0
Dipole tilts	0.6	0.0
(BL) dispersion in dipoles	0.0	11.0
Season ground motion	2.1	3.6
Remanent fields	18.2	4.2
Measured values	18	20

VI. ALGORITHMS FOR THE NUMERICAL INVESTIGATION OF THE CORRECTION EFFICIENCY

The correction efficiencies have been investigated numerically with Monte-Carlo simulation algorithms. Generally, one step of the simulation includes: 1) random generation of multipolar field components or magnet misalignments according to their measured average and r.m.s. values; 2) calculation of the maximum values of C.O. distortions, or tracking test particles to determine tune spreads and/or increase of effective emittance; 3) calculation of corrector strengths according to a correction algorithm; 4) repetition of the step 2 taking into account fields in correctors. At the end of the cycle the statistical distributions of the maximal C.O. distortions, tune spreads or effective emittances before and after correction are plotted.

Figure 3 gives an example of the symultaneous correction of the resonances $2Q_x=13$ and $2Q_z=13$. The resonances are driven

Table III
Corrected betatron resonances and estimated r.m.s. stopbands (d) at $Q_x=6.80$, $Q_z=6.85$, emittances $E_{x,z}=30 \pi$ mm mrad and $B_0=2.33$ kG.

N	Resonance	100 (d)	Type of field	Number of correctors
1	$2Q_x=13,14$	10.5	regular quad.	8
2	$2Q_z=13,14$	10.5	quad.	
3	$Q_x - Q_z=0$	6.0	skew quad.	4
4	$Q_x + Q_z=13$	6.5	quad.	
5	$2Q_z - Q_x=7$	0.55	regular sext.	4
6	$2Q_z + Q_x=20$	0.60	sext.	
7	$3Q_x=20$	0.30		
8	$2Q_x - Q_z=7$	0.35	skew sext.	4
9	$2Q_x + Q_z=20$	0.41	sext.	
10	$3Q_z=20$	0.20		
11	$2Q_x - 2Q_z=0$	0.10	regular oct.	4
12	$4Q_{x,z}=27$	0.03	oct.	
13	$2Q_x + 2Q_z=27$	0.08		
14	$3Q_z - Q_x=13$	0.09	skew oct.	4
15	$3Q_x + Q_z=27$	0.11	oct.	
16	$3Q_z + Q_x=27$	0.11		

by the dispersion $\langle dL/L \rangle$ of the effective lengths of the structure quadrupoles at the fields of injection. I_x denotes the linear invariant $[x^2 + (x'b + x\alpha)^2]/2\beta_x$ in the horizontal plane, and I_z in the vertical. To determine the values of $(\delta I/I)_{x,z}^{max}$ 4 test particles were tracked for 20 revolutions for each of the 100 random sets of quadrupolar magnets.

VII. ACKNOWLEDGMENTS

The authors would like to thank A. M. Donyagin and M. A. Voyevodin for magnetic measurements data, A. P. Tsarenkov for the closed orbit measurements, O. S. Kozlov and A. P. Tsarenkov for fruitful discussions of the problem.

References

- [1] Baldin A. M. et al., Nuclotron Status Report, IEEE Trans. on Nucl. Sci., NS-30, 4:3247 (1983).
- [2] Issinsky I. B., Mikhailov V. A., Shchepunov V. A., Nuclotron Lattice, In: Proc. of the 2-nd EPAC, Nice, 1990, Vol.1, 458.
- [3] Issinsky I. B., Mikhailov V. A., Conception of the 200 MeV/u booster for the Nuclotron, In: Proc. of IEEE PAC, San-Francisco, California, May 6-9 1991, Vol.5, 2886.
- [4] Anishchenko N. G. et al., The Model of the Superconducting Multipolar Corrector for Nuclotron, In: Proc. of XI All-Union Conf. on Particle Accelerators, vol.II, Dubna, 1989, p.221.
- [5] Mikhailov V. A., Shchepunov V. A., Magnetic Field Correction System of Nuclotron, In: Proc. of XIII Russian Conf. on Particle Accelerators, Dubna, 1992, p.253.
- [6] Shchepunov V. A., Betatron Tune Spread Corrections in Nuclotron, JINR, P9-92-203, Dubna, 1992.

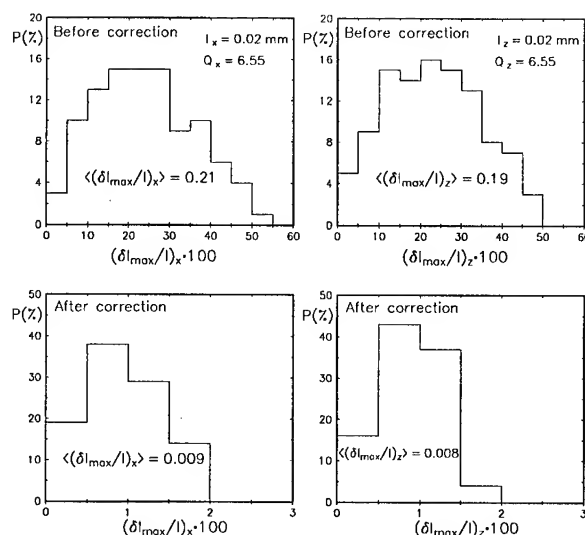


Figure 3. Statistical distributions for maximal distortions $(\delta I/I)_{x,z}^{max}$ of linear invariants $I_{x,z}$ under the influence of resonances $2Q_{x,z}=13$ before and after correction with 4 correctors. The simulation was performed for 100 random sets of effective lengths of the lattice quadrupoles with dispersion $\langle dL/L \rangle = 4.5 \times 10^{-3}$.

- [7] Donyagin A. M., Eliseeva I. A., Kovalenko A. D., Analysis and Corrections of the Magnetic Field Imperfections of the Nuclotron SC Dipole Magnets, JINR, P9-88-644, Dubna, 1988.
- [8] Orlov Yu. F. and Heifets S. A., The Distortion of the Magnetic Field of a Strong Focusing Accelerator Due to a Metal Vacuum Chamber, PTE, N1, 1959, p.21.
- [9] Mikhailov V. A., Shchepunov V. A., Correction of Betatron Resonances in Nuclotron, JINR, P9-92-204, Dubna, 1992.

Effects of the CHES Wigglers on a Beam with an Angular Offset

James J. Welch, *Cornell University, Ithaca NY **

Introduction

The magnetic field due to a single pole of a wiggler is, by normal accelerator magnet standards, both very strong and very nonuniform. Because the poles alternate sign and are made to have the same strength the effects of the nonuniform fields on the beam largely cancel from one pole to another. In an ideal case where there are no mechanical or magnetic errors, the net integrated dipole field along a path parallel to the wiggler axis and on the midplane would be exactly zero.

In this note I estimate the integrated field along a path not parallel to the axis but still in the midplane. Such a path is typical of the closed orbit during electron injection or luminosity optics. When the path of integration is at an angle to the wiggler axis, the horizontal or vertical position in one pole is not precisely the same as the horizontal or vertical position in any other pole. Because of the relatively strong variation of field strength with position the integration over one pole does not cancel with the integration over another pole. Based on approximate expressions for the field in the wiggler, I will show that the size of this effect is substantially smaller than the actual integrated dipole field measured parallel to the axis. This means the beam dynamical effects due to the angle the closed orbit takes through the wiggler are probably not important compared with those due to the actual field errors due to mechanical and magnetic imperfections, at least for the present wigglers and optics.

An expression for integral of the vertical magnetic field along a horizontally tilted straight path $x(z)$ is:

$$\int_{-\frac{L_w}{2}}^{\frac{L_w}{2}} B_y(x(z))dz = \int_{-\frac{L_w}{2}}^{\frac{L_w}{2}} \left\{ B_y\big|_{x=0} + \frac{\partial B_y}{\partial x}\bigg|_{x=0} x + \frac{1}{2} \frac{\partial^2 B_y}{\partial x^2} x^2 + \dots \right\} dz \quad (1)$$

For a perfect wiggler the odd order x derivatives are zero for $x = 0$ by symmetry. For a wiggler with an even number of poles, such as we now have at CESR, the vertical magnetic field is an odd function of z . When $x = x_0 + x'z$ is put into equation 1 the only terms left are:

$$\int_{-\frac{L_w}{2}}^{\frac{L_w}{2}} B_y(x(z))dz = \int_{-\frac{L_w}{2}}^{\frac{L_w}{2}} \frac{\partial^2 B_y}{\partial x^2}\bigg|_{x=0} x_0 x' z + \frac{1}{3} \frac{\partial^4 B_y}{\partial x^4}\bigg|_{x=0} x_0 x' z + \dots \quad (2)$$

In our case the lowest order term $\partial^2 B_y / \partial x^2$ is dominate and we will no longer consider the higher order terms.

Work Supported by the National Science Foundation

A simple estimate of the integral may be made from an approximate expression for the wiggler field. This is what I will develop in the next section assuming that we have N identical periods ($2N$ poles), and the end effects are negligible. Later I will deal with the end effects.

In general the magnetic field in the wiggler may be derived from gradient of a scalar potential with $\nabla^2 \Phi = 0$ everywhere of interest. From the symmetry the lowest order term must be of the form

$$\Phi \sim \sinh(k_y y) \sin(k_x x) \sin(k_z z) \quad (3)$$

Applying $\nabla^2 \Phi = 0$ and utilizing the independence of the x, y, z coordinates, yields:

$$k_y^2 = k_z^2 + k_x^2 \quad (4)$$

So the magnetic field of a wiggler with an even number of identical poles can be approximately described,

$$B_y = B_0 \cosh(k_y y) \cos(k_x x) \sin(k_z z) \quad (5)$$

Now, using the equation 5 we can evaluate the integral equation 2. On the wiggler axis $\partial^2 B_y / \partial x^2 = -k_x^2 B_y$ so we have,

$$\int_{-\frac{L_w}{2}}^{\frac{L_w}{2}} B_y(x(z))dz = -k_x^2 \int_{-\frac{L_w}{2}}^{\frac{L_w}{2}} B_y(x=0, z) x_0 x' z dz \quad (6)$$

$$= -k_x^2 x_0 x' B_0 \int_{-\frac{L_w}{2}}^{\frac{L_w}{2}} z \sin(k_z z) dz \quad (7)$$

$$= k_x^2 x_0 x' B_0 L_w^2 \frac{(-1)^N}{2\pi N} \quad (8)$$

I have used the relation that:

$$\int_{-\frac{L_w}{2}}^{\frac{L_w}{2}} z \sin(k_z z) dz = -\frac{L_w^2 (-1)^N}{2\pi N} \quad (9)$$

which can be verified by direct substitution of $k_z = 2\pi N / L_w$ and integrating.

Equation 8 represents an estimate for a wiggler with N identical periods. The wigglers at CESR have 22 more or less identical poles with two poles the ends with roughly half the strength. The effect of these end poles can be estimated by assuming the magnetic field contribution from the end has the same shape as a normal strength pole. To see how to include this effect first consider how much adding one more period of *normal strength* poles would increase the total field integral. Using equation 8 the change would be:

$$\frac{k_x^2 x_0 x' B_0 L_w^2}{2\pi} \left[\left(\frac{N+1}{N} \right)^2 \frac{(-1)^{N+1}}{N+1} - \frac{(-1)^N}{N} \right] \quad (10)$$

The weaker end poles would produce a proportionally weaker change to the integral since I assume the shape is the same.¹ To get the addition to the integral of the field due to the weaker end poles I simply replace B_0 with B_{end} in equation 10 where B_{end} is the peak magnitude of the field in the end poles. The change in the integral caused by adding the end poles to N identical poles reduces to

$$-k_x^2 x_0 x' L_w^2 B_{end} \frac{(-1)^N}{2\pi} \frac{2N+1}{N} \quad (11)$$

The net integral of N full strength poles plus the change due to two end poles of strength B_{end} is obtained from equations 11 and 8:

$$\int_{total} B_y(x(z)) = k_x^2 x_0 x' L_w^2 B_0 \frac{(-1)^N}{2\pi} \frac{1}{N} \left(1 - \frac{B_{end}}{B_0} \left(2 + \frac{1}{N} \right) \right) \quad (12)$$

Measurements of the field indicate that $k_x \approx 6 \text{ m}^{-1}$.² The longitudinal wavenumber k_z is about 32 m^{-1} and is determined by the spacing between the poles. Therefore k_y works out to 33 m^{-1} . The peak vertical field is $B_0 = 1.2 \text{ T}$ at the nominal closed gap of 4 cm.

Some typical numbers for the present crossing angle conditions and existing wigglers at CESR are:

x	0.01	m
x'	0.0005	$radians$
L_w	2.3	m
B_0	12000	G
B_{end}	7600	G
N	11	$full \text{ strength poles}$

For these values the net integral for one full strength adjacent poles, equation 12,

$$\int_{total} B_y(x(z)) = -5.3 \times 10^{-2} \text{ Gm} \quad (13)$$

per wiggler. This is substantially smaller than the variation in the measured integrated field over for both the east and west wigglers. Over the interval from $x = 0$ to $x = 1 \text{ cm}$ the variation of the integrated field for the wigglers measured parallel to the axis is:^{3 4}

East	$\sim 1 - 2$	Gm
West	$\sim < 1$	Gm

An analogous argument can be made for vertical offsets and angles. The result is obtained by replacing k_x with k_y in equation 8 and substituting y for x and y' for x' . Thus the sensitivity to vertical offsets and angles is higher by a factor of $(k_y/k_x)^2 \approx 30$ but the size of such offsets is quite a bit smaller than those due

to the pretzel. For example, a 1 mm offset in y with an angle of 5×10^{-4} would give a net integrated field of only -0.127 Gm .

Hence the beam dynamical effects due to the angle and offset of the closed orbit through the wiggler are probably not as important as those due to physical and magnetic imperfection, for the present crossing angle lattice. In the future the angular and offset effects can be made stronger or weaker proportional to the product $x_0 x'$.

¹The iron pole shape is identical though the permanent magnet material is less in the end poles and is perturbed by a field clamp.

²This value was derived from measurements reported by Ken Finkelstein in a memo by him dated October 23, 1992.

³Measurements of the west wiggler are reported in CBN 93-7, (1993) by D. Frachon, I. Vasserman from Advanced Photon Source, ANL and J. Welch and A. Tenmykh, CESR.

⁴Measurements of the west wiggler are reported in CON 94-16 (1994) by A. Tenmykh and J. Welch, CESR.

PARTICLE TRACKING WITH GENERATING FUNCTIONS OF MAGNETIC FRINGING FIELDS *

Godehard Wüstefeld, BESSY II Project
Rudower Chaussee 5, Geb. 15.1, 12489 Berlin, Germany

Abstract

A construction scheme for generating functions (*GFs*) suitable for particle tracking across arbitrary magnetic fields is presented. The *GF* is approximated by a power series solution of the Hamilton-Jacobi differential equation [1] with analytical expressions for the coefficients. This approach is applied to magnetic fringing fields, which are presented as simplified analytical expressions. A short REDUCE [2] code transforms the vector potentials automatically into an expanded *GF*.

I. Construction of Generating Functions

Generating functions (*GFs*) are an excellent tool for particle tracking across magnetic fields. They perform a canonical transformation over a finite path length. Even if they are not exactly known and approximate expressions are used, they still preserve the Hamiltonian character of the transformation.

Power series with analytical coefficients as approximations for *GFs* of given magnetic fields were discussed in [3], with special applications to simulate wigglers and undulators, as used in synchrotron light sources [4]. The present approach is much more direct and transparent. It requires less effort in manipulating power series. A short REDUCE code is sufficient to obtain the *GF*; using a general method to construct approximated, analytical expressions for *GFs*, based on the Hamilton-Jacobi equation. Starting with a given vector potential of the magnetic field, the code generates automatically a power series, where the coefficients are analytic functions of the vector potential and the particle coordinates.

The *GF* is calculated by starting with a Hamiltonian in a fixed cartesian coordinate system, where x , y and z are the horizontal, vertical and longitudinal axes, respectively (for a general discussion see for example [5]):

$$H = -\sqrt{1 - (p_x - A_x)^2 - (p_y - A_y)^2} - A_z,$$

where p_x and p_y are the transverse canonical momenta, normalized to the full particle momentum and A_x , A_y and A_z are the vector potentials of the fields, normalized to the beam rigidity parameter $B\rho$ which is proportional to the full particle momentum. Expanding the square root of the Hamiltonian yields:

$$H = (p_x - A_x)^2/2 + (p_y - A_y)^2/2 - A_z.$$

This approximated form of the Hamiltonian used for the present scheme is not a severe restriction, because higher order terms of the expansion could be taken into account. In most cases, the

transverse momenta and the vector potentials are small and a Taylor expansion with respect to these variables is justified.

The *GFs* used in this paper depend on the initial particle momenta p_{xi} , p_{yi} and on the final position variables x , y and z . They are special kinds of *GFs* of a more general type, that is often abbreviated as F_2 . Particle coordinates are derived from partial derivatives of the *GF*:

$$p_x = \partial F / \partial x, p_y = \partial F / \partial y, x_i = \partial F / \partial p_{xi}, y_i = \partial F / \partial p_{yi},$$

where x_i, y_i are the initial coordinates and p_x, p_y are the final particle momenta. In this paper the *GF* is defined always at the starting point $z = 0$ and at the end point z of the transformation in a fixed cartesian coordinate system. The *GF* yields implicit expressions for the transverse coordinate relations; using them as a tool for tracking requires normally a Newton-Raphson root-finding method for solving the transformation.

The Hamilton-Jacobi equation is a first order differential equation, which gives a local relation between the Hamiltonian (H) and the *GF* (F):

$$H + \partial F / \partial z = 0.$$

In this equation the momenta are replaced by derivatives of the *GF*, $p_x = \partial F / \partial x$, $p_y = \partial F / \partial y$. To solve it with respect to F , a series expansion of F is chosen with respect to p_{xi} , p_{yi} and a variable x_3 which counts the order of the A_x , A_y and A_z terms:

$$F = \sum_{l,m,n} f_{lmn} p_{xi}^l p_{yi}^m x_3^n,$$

where the f_{lmn} are dependent on x , y and z . The expansions with respect to the vector potentials are not written explicitly; this is included in the f_{lmn} terms and counted by the variable x_3 . The order of the expansion is the sum $l + m + n$.

The Hamilton-Jacobi equation relates different derivatives of the coefficients f_{lmn} and can be easily solved by a recursive method with an algebraic code such as REDUCE. To demonstrate the method, a REDUCE input code for the *GF* of a quadrupole is given. The code has a PASCAL like input language and is easily readable:

```
% quadrupole example, g = gradient [m-2]
% input of vector potential:
az := g*(x**2-y**2)/2 ; ax := 0 ; ay := 0
;
% 4th order generating function:
ord := 4 ;
fgen:= 0 ;
for ic:=1:ord do for ix:=0:ord do
for iy:=0:ord do for i3:=0:ord do
if ix+iy+i3=ic then
<< depend f(ix,iy,i3),x,y,z ;
fgen := fgen +
```

*funded by the Bundesministerium für Bildung, Wissenschaft, Forschung und Technologie and by the Land Berlin

```

f(ix,iy,i3)*pxi**ix*pyi**iy*x3**i3 >> ;
% initial values of the series:
f(1,0,0) := x ; f(2,0,0) := -z/2 ;
f(0,1,0) := y ; f(0,2,0) := -z/2 ;
% limitation of terms:
for ix:=0:ord+1 do for iy:=0:ord+1 do
for i3:=0:ord+1 do if ix+iy+i3>ord then
let pxi**ix*pyi**iy*x3**i3 = 0 ;
% Hamiltonian:
ham:=(px-x3*ax)**2/2+(py-x3*ay)**2/2-x3*az
;
% substitution of the momenta:
ham:=sub(px=df(fgen,x),py=df(fgen,y),ham)
;
% Hamilton-Jacobi equation:
hamjac := ham + df(fgen,z) ;
% iterative solution of the equation:
for ic:=1:ord do for ix:=0:ord do
for iy:=0:ord do for i3:=0:ord do
if ix+iy+i3=ic then
<< term := coeffn(coeffn(coeffn(hamjac,
pxi,ix),pyi,iy),x3,i3) ;
if term neq 0 then <<
sol1 := solve(term=0,df(f(ix,iy,i3),z)) ;
sol2 := rhs(part(sol1,1)) ;
sol3 := int(sol2,z) ;
f(ix,iy,i3) := sol3-sub(z=0,sol3) >> >> ;
% printing of the generating function:
sub(x3=1,fgen) ;
;end;

```

The code prints the 4th order power series for the GF as:

$$\begin{aligned}
F = & x^2 g z (1/2 - g z^2/6 + g^2 z^4/15 - 17 g^3 z^6/630) \\
& - y^2 g z (1/2 + g z^2/6 + g^2 z^4/15 + 17 g^3 z^6/630) \\
& + p_{xi} x (1 - g z^2/2 + 5 g^2 z^4/24 - 61 g^3 z^6/720) \\
& + p_{yi} y (1 + g z^2/2 + 5 g^2 z^4/24 + 61 g^3 z^6/720) \\
& + p_{xi}^2 z (-1/2 + g z^2/6 - g^2 z^4/15) \\
& + p_{yi}^2 z (-1/2 - g z^2/6 - g^2 z^4/15).
\end{aligned}$$

From this GF the linear transfer matrix can be calculated, which agrees at least to the 3rd order in g with the well known transfer matrix of a quadrupole. For example, the matrix element m_{11} derived from the GF yields $m_{11} = 1 + g z^2/2 + g^2 z^4/24 + g^3 z^6/720 + 11 g^4 z^8/320$. The expanded form of the correct solution differs in the g^4 term: $m_{11} = \cosh(\sqrt{g}z) = 1 + g z^2/2 + g^2 z^4/24 + g^3 z^6/720 + g^4 z^8/40320 \dots$

This simple code can calculate the GF s for most two dimensional normal and skew magnetic fields. One only needs to replace $az := \dots$ in the first line by the appropriate longitudinal vector potential. Wigglers and undulators can be simulated by the three dimensional field approximation:

```

ax:=cos(kx*x)*cosh(ky*y)*sin(k*z)*b0/k ,
ay:=sin(kx*x)*sinh(ky*y)*sin(k*z)*b0*
kx/(k*ky)
and az:=0. However, this last example requires a lot of REDUCE
working space; because many terms are generated, a 3rd

```

order run is recommended.¹ For more complicated vector potentials one has to modify the code. A practical way is to solve the Hamilton-Jacobi equation for a general vector potential and insert it afterwards into the solution of the explicit vector potential [7].

As an example the second order result of the general expansion of the GF is presented here:

$$\begin{aligned}
f_{001} &= \int A_z dz \\
f_{002} &= - \int ((A_x - \int \partial A_z / \partial x dz)^2 \\
&\quad + (A_y - \int \partial A_z / \partial y dz)^2) dz / 2 \\
f_{101} &= \int (A_x - \int \partial A_z / \partial x dz) dz \\
f_{011} &= \int (A_y - \int \partial A_z / \partial y dz) dz \\
f_{100} &= x \quad f_{010} = y \\
f_{200} &= -z/2 \quad f_{020} = -z/2
\end{aligned}$$

where the integration ranges from 0 to z . In a similar form the 3rd and 4th order expansions can be constructed [7].

Using the REDUCE code, the GF can be further manipulated to find a form appropriate for a Newton-Raphson fit routine.

As a special application of this method, GF s for magnetic fringing fields can be calculated.

II. Description of Fringing Fields

Magnets such as dipoles, quadrupoles, sextupoles and so on are described by two dimensional multipoles. This two dimensional approximation fails at the ends of these magnets, where the particle beam enters or exits the magnet, and the field strength approaches zero. Three dimensional fields are necessary to describe their longitudinal dependencies. A simple analytical description of the vector potentials of fringing fields is necessary for manipulations with the REDUCE code when constructing the GF . The analytical description discussed here is a simplification and takes into account only the first leading term of the three dimensional field.

Expressions for the fringing fields are derived by starting with the magnetic scalar potential in an expanded form in cylindrical coordinates as:

$$V = \sum_{i=0}^{\infty} a_i(z) r^i \sin m\psi,$$

where r is the radial coordinate with $x = r \cos \psi$, $y = r \sin \psi$. The number m describes the rotational symmetry around the longitudinal z -axis, and ψ is azimuthal angle with respect to the z axis. Quadrupole symmetry is obtained for $m = 2$. If a is independent of z , the two dimensional multipoles are generated. Replacing the $\sin m\psi$ by a $\cos m\psi$ function yields the skew field terms. From the Maxwell condition $\Delta V \equiv 0$ follows (with $a'_i = \partial a_i / \partial z$):

¹this requires 1 minute cpu time on the DEC 3000 machine (alpha)

$$\sum_{i=0}^{\infty} a_i (i^2 - m^2) r^i + a_i'' r^{i+2} \equiv 0,$$

which yields for the coefficients the condition: $a_0 = 0$, $a_1(1 - m^2) = 0$ and $a_i(i^2 - m^2) + a_{i-2}'' = 0$. This gives a construction law for the series; if the z -dependence of one coefficient a_i is known the higher order terms can be calculated. The coefficients a_0 and a_1 are zero, if the dipole case ($m=1$) is excluded.

A 3rd order function will be used to describe the z -dependence of a_m . This will limit the series to the first term of the higher order three dimensional multipole. For the dipole, the leading term of higher order is y^3 dependent, and for quadrupoles it is a r^4 term. At least a 3rd order function is required to transform the constant, z -independent field inside of the multipole by a smooth, analytic function to zero, at the end of the multipole:

$$a_m = a_{m0}(u^3 - 3u + 2)/4,$$

where $-1 < u = (z - z_0)/z_0 < +1$, and z_0 is an adjustable, characteristic length of the fringing field extension, typically the magnet aperture radius.

The factor a_{m0} has to be adjusted to the strength of the magnetic field. At the positions $z = 0$, $z = z_0$ and $z = 2z_0$ the function a_m yields a_{m0} , $a_{m0}/2$ and 0. Outside of this interval a_m is fixed to a_{m0} for $z < 0$ and to 0 for $z > 2z_0$. This derivation is valid for one side of the multipole, the fringing field of the other side has to be constructed in a similar way.

For the scalar potential a superposition of the two and three dimensional field terms is given as:

$$V = a_{m0} r^m \sin m\psi \{ u^3 - 3u + 2 - 3ur^2/(2z_0^2(m+1)) \}.$$

and for the dipole:

$$V = a_{10} y (u^3 - 3u + 2 - uy^2/z_0^2)/4.$$

The scalar potential of the pseudo-multipole is proportional to a_m'' . The integrated value of a_m'' over the full fringing field area is zero, because a_m' vanishes at the boundaries of the fringing field. Integrating only over half of the area, yields a nonvanishing contribution:

$$-\int_0^{z_0} a_m'' dz = \int_{z_0}^{2z_0} a_m'' dz = a_m'|_{z_0}^{2z_0} = a_m'(z = z_0).$$

A particle that crosses this area will experience two successive kicks around $z = 0$, in opposite directions. Particles circulating many turns in a storage ring, will experience an accumulated effect, if, on the average, their trajectory is inclined with respect to the z -axis, which is the case if the Twiss parameter α differs from zero. Also chromatic effects could be seen if the dispersion function in the fringing field differs from zero.

For the construction of the GF the vector potential is required; it is not uniquely defined. Choosing $A_z = 0$ one obtains from the scalar potential in cartesian coordinates:

$$A_x = - \int \partial V / \partial y dz, \quad A_y = \int \partial V / \partial x dz.$$

These vector fields can be used for the REDUCE input code. If the number of terms becomes too large, one has to use a modified version of the presented code. In case of quadrupole end fields, for example, one expects influences from fourth order terms. A fourth order expansion of the GF with respect to x , y , p_{xi} and p_{yi} should be sufficient to study typical nonlinear effects of these fringe fields.

III. Applications

Fringing field terms of quadrupoles were included into a standard optics code, based on the analytical representation of the GF . The routines were modulated as invisible insertions for the linear optics, following the scheme proposed by [6]. The linear transformation becomes exactly invisible, if the inverse linear transformation is derived from the GF . The BESSY II optics [8] was checked using these routines. The dynamic aperture and the chromatic behavior show only minor changes, when these routines are activated. From the dipoles no further effect on the optics are expected because the vertical Twiss α at their locations is too small.

References

- [1] H. Goldstein, Klassische Mechanik, Akademische Verlagsgesellschaft, Frankfurt, Germany, 1963, page 302 ff
- [2] A. C. Hearn, REDUCE 3.5, A General Purpose Algebra System, ©A.C.Hearn, RAND, Santa Monica, CA 90407-2138, USA (reduce@rand.org)
- [3] J. Bahrtdt, G. Wüstefeld, A Taylor-Expanded Generating Function for Particle Motion in Arbitrary Magnetic Fields, Proceedings of the 3rd European Particle Accelerator Conference, Berlin, 1992, p. 670
- [4] G. Wüstefeld, J. Bahrtdt, Canonical Particle Tracking in Undulator Fields, Proceedings of the 1991 IEEE Particle Accelerator Conference, San Francisco, 1991, p. 266
- [5] R. D. Ruth, Single Particle Dynamics and Nonlinear Resonances in Circular Accelerators, Proceedings of the Joint US-CERN School on Particle Accelerators, pp. 37-63, Lecture Notes in Physics vol. 247, Springer-Verlag Berlin Heidelberg (1986)
- [6] É. Forest et al., The Correct Local Description For Tracking In Rings, Particle Accelerators, Vol. 45, pp. 65-94 (1994)
- [7] available from the author, internet adress: WUESTEFELD@BESSY.DE
- [8] E. Jaeschke, Status of the High Brilliance Synchrotron Radiation Source BESSY II, see these proceedings.

COMPUTATION OF LATTICE MAPS USING MODULAR BCH AND SIMILARITY COMPOSITION RULES

J. Irwin, Stanford Linear Accelerator Center, Stanford University, Stanford, CA 94309 USA

A beam line map construction method for linear and circular high-energy colliders is described which avoids truncated power-series maps through systematic use of a two-term Baker-Campbell-Hausdorff (BCH) formula in combination with similarity transformations. The beam line map ultimately assumes the form of a product of a linear map and a single-exponential Lie-operator map. The method i) provides insight into map generator sources, ii) is accurate, iii) is complete in that all effects, such as edges and soft fringes, mis-alignments and mis-powerings, multipole errors, and input beam errors can be simply included, iv) permits faster map computation times, and v) bypasses truncated power-series map methods allowing for higher order, and even non-polynomial generators.

I. INTRODUCTION

There are many possible motives for creating and using maps in conjunction with accelerator lattice design and analysis, and the method chosen for creating the map will depend on this motive. We describe four distinct primary motives.

1. **Structure.** It is highly desirable to have maps that correspond exactly with the algorithm used for single particle tracking. This allows the user to establish the validity of these maps by comparing map tracking with element-by-element tracking. The map creation algorithms developed by E. Forest and collaborators, represented in the code DESPOT [1], have focused on this objective. A symplectic integrator must be found for each lattice element or sub-element to represent it in element-by-element tracking. The map creation can then be carried out by "tracking" a power series through the lattice. Reliability is also enhanced by the methodical nature in which elements are pieced together, referred to by Forest as "lego like". The resultant power series map for the lattice is guaranteed to be symplectic and may be exponentiated, if desired, by using the Dragt-Finn factorization algorithm [2]. The major disadvantage of this method is that it becomes very computer intensive for large lattices, high order or many additional variables. However tools in the LIELIB package which accompanies DESPOT do allow the user to implement other map composition methods.

2. **Accuracy.** A second motive places primary emphasis on machine precision accuracy. The programs developed by A. Dragt and represented by MARYLIE [3] and M. Berz in COSY-Infinity [4] are examples. MARYLIE uses a generator based map-concatenation in which each element or element part is represented by an ordered generator-based factorization, and map concatenation is based on an algorithm that can take the product of two such factorizations and produce a single factorization of the same form. The program "Genmap" accomplishes this task for continuously varying Hamiltonians, such as those occurring in fringe-field regions. To do a corresponding element-by-element tracking requires use of mixed variable generators for each element. Correspondence with mapping is not exact. The COSY-Infinity uses power series maps by direct expansion of the original Lie generators, operating on coordinates or polynomials.
3. **Insight.** A third motive, is the creation of maps in a transparent way, that yield analytical results and provide insight into lattice function. In principle analytical results can be obtained by the previous methods, but a BCH based map concatenation provides better insight into map composition. BCH composition and has been carried out by N. Walker in the code LAMA [5] using a symbolic manipulation program. This method is especially useful for lattice modules such as linear collider final focus or collimation systems. One can allow all lattice and error parameters as well as incoming beam conditions to be variables. This method is far too slow for use with large lattices.
4. **Speed.** Speed becomes an issue in a large lattice design project because the number of lattice variations encountered is so very large: variations of a multitude of error types and strengths; inclusion of fringes, kinetic nonlinearities, and/or parasitic crossings; changes in section phase relations, changes in chromatic correction techniques, tune-shift-with-amplitude control, insertion devices, solenoid with skew compensation schemes, beam line geometry changes, and so on. For each of these lattice changes one would like to have a map to assess performance with a tune-space scan [6]. Another advantage of a fast map algorithm is the ability to introduce many lattice parameters as variables, and fit or optimize these variables to achieve desired aberration coefficients or performance. A map composition

process whose primary motive is speed is described below. It is based on experience with method 3 above, and hence can also provide insight into lattice dynamics.

II. MAP COMPOSITION METHOD

We summarize the steps of a composition method based on similarity transformations and a low order BCH composition formula. The first six steps describe the conceptual setup. Computation begins with step 7.

- 1) Represent each element as an infinite Lie product corresponding to cutting the elements into thin slices. The generators will be s -dependent when necessary, as for example in fringe regions. Lie maps may be inserted at the ends of the magnets to provide for translations and rotations of the magnet [7].
- 2) In each slice, separate the linear design part of the generator from the remainder and write the map of each slice as a product of two maps. This is possible because the generator strengths are infinitesimal.
- 3) Use similarity transformations to move all design linear maps (2nd order in transverse variables) to the front of the beam line product. This can be accounted for by replacing x (or y , or p_x or p_y) in each slice by x_i where it is understood that x_i is x at the i th element written as a linear function of the particle position and momentum at the end of the beam line.
- 4) Use a 2nd order BCH algorithm to integrate the map factors for each element into a single generator [8]. If the element is particularly long or strong, this can be done for sections of the element rather than the whole element. If fringes effects are to be considered, the integral for the fringe region is done by first expressing the x_i as function of position and slope at a place within the fringe [9], and later expressing the coordinates there as functions of coordinates at the end of the line. To do the body integral, x_i is written as a function of the momentum and position at the center of the element. The results for the body integrals will be a function of x_k and y_k the transverse coordinates at the center of the k th element, plus a function which depends also on $p_{x,k}$ and $p_{y,k}$.
- 5) Factor the map for the element body integrals found above into a central term surrounded by two side factors so that the central term has a generator containing terms depending on x_k and y_k alone.

Now "big" terms are either in a central factor, which depends only on transverse coordinates (hence are kicks),

or in the translation and rotation generators surrounding the element. The central factors can be totally factored because all terms in the generator "commute" (have zero Poisson brackets with one another). The translations and rotations are steering elements: For translations the generator is $\Delta y p_y$, and for small vertical rotations the generator is $\Delta\theta(y+L/2 p_y)$ where L is the length of the element. Next we remove the main dispersion generators.

- 6) Perhaps the largest of the body terms are the sources of design dispersion coming from the main dipole magnets. These terms can be removed using similarity transformations, very much like the design linear terms. The net effect of removing these terms will be that x_k and $p_{x,k}$ are replaced by $x_k + \eta_{x,k} \delta$ and $p_{x,k} + \eta'_{x,k} \delta$ where $\eta_{x,k}$ is the horizontal design dispersion.

We now have the basic factored representation of the lattice with the linear design, including linear dispersion, removed. We proceed to consolidate this representation into a few factors after taking care of the steering terms, which can be quite large.

- 7) Starting at the end of the beam line, use similarity transformations to move all the first-order (steering) generators to the front of the beam line. Intermediate transformed generators will have feed down terms some of which will be steering terms. For the large central factors these are easily factored out and added to the steering generator. This is not as simple for the side-factors. If the feed down steering in the side factors is thought to be significant, these factors can be further factored, pulling the steering terms into side factors. One then brings the two steering terms to the front side by a subsequent similarity transformation. Further feed down terms are formed, but these are now due to steering from the side factor itself, and can be assumed to be small. (Solenoid fringes can contain important steering terms, but these are already present in the linear model.) Since the exact values of steering correctors throughout the ring are not exactly known, there is a limit to the precision one can or should attempt to achieve. It should also be noted that one must implement a steering correction algorithm to determine corrector strengths before embarking on the map generation process, or algorithms can be used which calculate the steering corrector strengths during this step.

We are ready to begin the map consolidation process. The exact procedure must be chosen to suit the particular

situation. If there are especially large sextupole and/or chromatic correction terms, these should be flagged for a similarity composition process and will define ends of a module. In the next step the maps for the modules are assembled.

- 8) The lattice will consist of several modules which may either be what is normally understood as a module, like an arc, a straight section, a chromatic correction section, a beta-match section, and so on, or just the lattice between two large higher order elements that one intends to collapse using the similarity composition rule.

In this step the map for each module is assembled either as a single exponential map, or as a factored map consisting of a product of three maps: the first with a generator that is of first order in transverse variables (dispersion terms), the second with a generator of 2nd order in transverse variables (linear terms), and the third whose generator contains higher order terms. For a factored map the dispersion terms are found for the module using a similarity process to move these terms to the front of the module as was described for steering (7) or dispersion (6) above. This is followed by using a similarity process to move the linear terms to the front.

The final step uses the BCH formula to assemble all remaining generators into a single generator. Note that all of the large terms have been (or will be) handled with similarity transforms. Thus the BCH process is expected to converge quite rapidly, and in most cases a second order BCH formula is sufficient. A third order BCH formula may be used to check the sufficiency of the second order formula. It is important to distinguish BCH order from map order. Map order can be, and is, much higher than BCH order.

- 9) Strong sextupole terms in the lattice are "collapsed" using similarity transformations. The details of this will depend on the design phases between the sextupoles. Use of the similarity transformation is especially important in systems such as final focus systems, or in local chromaticity correction modules of low beta insertions in storage rings. If strong sextupoles are interleaved, special attention is required. One collapses the paired sextupoles, transforming the enclosed sextupole. The transformed sextupole generator is now factored with the central factor being the sextupole and the remainder placed in the side factors. If the interleaving is too strong to do this in one step, the original enclosed sextupole is factored into two

halves, and each half is factored as described above. This process converges quite rapidly: the approximation represented by the three factors improving by a factor of 8 with each halving of the sextupole.

- 10) Strong chromaticity terms are "collapsed" using similarity transformations. This is very similar to the process of step 9). Many of the strong chromatic generators will be at the sextupole locations. Additional generators of this type will be in final doublets. The doublets will have been split into several pieces in the integration of those elements.
- 11) Use the BCH rule to assemble the generator for the various beam line modules.
- 12) Use the BCH rule to assemble the generator for the total beam line.

IV. REFERENCES

- [1] E. Forest, The correct local description for tracking in rings, Part. Accel. 45, p65 (94). There is no published manual for the program DESPOT which is being used at SLAC for PEP-II lattice design.
- [2] A. Dragt and J. Finn, J. Math. Phys. 20, 22649 (1979).
- [3] D. Douglas and A. Dragt, MARYLIE, the Maryland Lie Algebraic Beam Transport and Particle Tracking Program, IEEE Trans. Nucl. Sci. NS-30, 2442 (1983).
- [4] M. Berz, New features in COSY Infinity, In Los Alamos 1993, Proceedings, Computational accelerator physics, p267 (94).
- [5] N. Walker, J. Irwin, M. Woodley, Analysis of higher order optical aberrations in the SLC final focus using Lie algebra techniques, SLAC-PUB-6205 (93) and Proceedings of the 1993 Part. Accel. Conf (PAC93).
- [6] J. Irwin, T. Chen, and Y. Yan, A fast tracking method using resonance basis Hamiltonians, SLAC-PUB-95-6727, and Conference on nonlinear dynamics in particle accelerators proceedings, Arcidosso, Italy (94). Also Y. T. Yan et. al., Swamp plots for PEP-II lattices, RAA26, these proceedings.
- [7] For a further exposition of the notation we use as well as Hamiltonian and generator details see J. Irwin, to be published in Nucl. Instr. and Methods, and SLAC-PUB-_____.
- [8] J. Irwin, The application of Lie algebra techniques to beam transport design, Nucl. Instr. and Methods, A298, 460 (90).
- [9] C-X Wang and J. Irwin, Explicit maps for soft-edge fringe fields, MPC31, these proceedings

TREATMENT OF WIGGLER AND UNDULATOR FIELD ERRORS IN TRACKING CODES

W. Decking*, O. Kaul, H. Nesemann, J. Roßbach

Deutsches Elektronen-Synchrotron DESY, Notkestr. 85, 22603 Hamburg, Germany

Abstract

Wigglers and undulators produce intense synchrotron radiation, used for dedicated experiments or to control beam dimensions. To obtain tolerance criteria for wiggler and undulator field errors, this paper presents a treatment which takes into account the special geometry of wigglers and undulators and the undulating beam trajectory. This is done by creating a nonlinear transfer map of the beam motion through the (measured) magnetic fields. To verify the method, results of tracking calculations using data from magnetic field measurements are compared with dedicated experiments performed at DESY's synchrotron radiation source DORIS III. Measurements of tune shifts with closed orbit amplitudes and of the dynamic acceptance agree with the results of the tracking.

I. INTRODUCTION

The treatment of wigglers¹ in accelerator theory and numerical beam dynamics investigations is focused on the proper description of the combined nonlinear effects of the oscillating fields and particle trajectories. Field errors are commonly described like in 'normal' lattice magnets, i.e. by adding appropriate multipole kicks describing the field error of the magnets.

This procedure does not account for the influence of field errors acting along the undulating particle path. We will present in this paper a possible treatment of this problem, based on a sufficient modeling of the wiggler magnets and their field errors by a current sheet model [1]. The tracking calculations are performed using a numerical evaluated generating function [2][3] of the wiggler, which guarantees the simplicity of the tracking calculations. The combination of these methods allows the treatment of periodicity errors and transversal field gradient errors as well as the investigation of other features of the wiggler fields like the influence of the pole width.

The numerical analysis is exemplarily done for the DORIS III storage ring, DESY's state of the art 1st generation synchrotron light source. It is equipped with 10 wigglers and undulators, covering 10 % of the ring length (for more details see [4][5]). The dynamic acceptance and tune shifts with closed orbit amplitudes in the wiggler have been investigated at DORIS (see also [6]) to verify the numerical results obtained for transversal field gradient errors and the pole width influence.

*e-mail: mpywin@ips102.desy.de

¹We will in general not distinguish between wigglers and undulators in this text.

II. NUMERICAL METHOD

A. The generating function

The concept of generating functions is used to obtain a symplectic transformation of the particle coordinates through the wiggler. An appropriate generating function $F(x_i, p_{x,f}, y_i, p_{y,f})$ maps the canonical variables $x_i, p_{x,f}, y_i, p_{y,f}$ into $x_f, p_{x,i}, y_f, p_{y,i}$, where x, y are the transversal coordinates, p_x, p_y the canonical impulses and the suffixes i, f symbolize initial respective final coordinates. The generating function is expanded in a Taylor series. By tracking a set of particles distributed in phase space through the magnetic field to be investigated, the coefficients of the expansion can be evaluated numerically from the initial and final coordinates. For more details on this method see [2][3]. This procedure guarantees fast, symplectic tracking and allows in principle the investigation of any magnetic field.

B. The current sheet model

The current sheet model was invented to calculate the magnetic fields of pure permanent magnet wigglers [1]. Due to the special properties of the permanent magnet material - a magnetic permeability of ≈ 1.0 over a large range of the magnetization curve - the field of a permanent magnet block can be calculated by assuming current sheets only on the surfaces of the block. Field contributions of different blocks can be superimposed leading to the total field produced by a permanent magnet array. This model is extended to be used also for hybrid wigglers by scaling the remanent fields and block dimensions to fit the measured magnetic fields of the considered devices. Transversal field gradients, measured as multipole contents of the first field integrals, are thus distributed over the whole device length. The three dimensional field distribution producing this multipole content is now taken into account.

The current sheet model can also be used to investigate the effects of pole width by decreasing the horizontal dimensions of the blocks or to simulate periodicity errors by varying the longitudinal block positions and remanent fields.

III. NUMERICAL ANALYSIS OF FIELD ERRORS

A. Periodicity error

The influence of periodicity errors of a DORIS wiggler and an undulator [7] has been investigated by evaluating the dynamic acceptance in the presence of the wiggler/undulator and the machine sextupoles. The error is parameterized by the rms-variation of the magnetic field maxima $\Delta B_{rms} = \left(\frac{B_{y,max.}}{\langle B_{y,max.} \rangle} \right)_{rms}$ and the rms-variation of the period length $\Delta \lambda_{rms} = \left(\frac{\Delta \lambda}{\lambda} \right)_{rms}$, measured from maxima to maxima of the

magnetic field. The chosen error sets ensure that the first and second field integrals are small compared to those usually measured in wigglers. The results show no decrease of dynamic acceptance for $\Delta B_{rms} = 6.0\%$ and $\Delta \lambda_{rms} = 2.0\%$. Values of $\Delta B_{rms} = 15.0\%$, $\Delta \lambda_{rms} = 3.0\%$ give a slight decrease of $\approx 15\%$. The requirements set by synchrotron radiation users due to the quality of the emitted light are much stronger, so periodicity errors should not be important under beam dynamics aspects.

B. Pole width

Although not a field error, the effects of pole width are mentioned since they can be treated with the same tools as field errors. The half pole width is measured in units of the beam size σ , and the field properties are characterized by the peak field, which decreases with decreasing pole width, and the relative field decrease at a horizontal position corresponding to 10σ . Again the dynamic acceptance was evaluated for a DORIS wiggler, with the results given in table I. The acceptance decreases

Table I
Relative dynamic acceptance for DORIS with a wiggler with different pole width inserted

half pole width [σ]	$B_{y,max.}$ [T]	$\frac{\Delta B_y}{B_{y,max.}}$ at 10σ %	acceptance [arbitrary units]	
			horizontal	vertical
24	1.16	1.7	1.0	1.0
19	1.15	6.1	1.0	1.0
14	1.12	19.6	0.85	0.88
9.5	1.01	46.5	0.71	0.88
5	0.75	72.0	0.71	0.88

at a half pole width between 14σ and 19σ , but even a half pole width of 5σ leads only to a 30% reduction of the acceptance. A half pole width of 20σ ensures no influence on the beam dynamics due to the finite width of the poles.

C. Transversal field gradient errors

We have chosen the asymmetric wiggler (ASYH) as an example for the investigation of field gradient errors. The ASYH has an asymmetric field distribution with weak but long positive field contributions and strong and short negative ones along the wiggler axis. The field integral measurements showed strong sextupole (b_2) and decapole (b_4) multipole components [8], the former being four times stronger than the normal storage ring sextupoles.

The ASYH was modeled by the current sheet model with varying block dimensions, leading to the following multipole coefficients for the first field integral:

name of model	b_2 [T/m]	b_4 [T/m ³]	corresponding multipole
ASYH-0	0.03	80	
ASYH-1	4.6	4000	multipole-1
ASYH-2	20	18000	multipole-2

The ASYH-2 corresponds roughly to the original device before a correction with pole shims, while the multipole contents of the ASYH-1 are similar to the maximum acceptable values for these components.

The tune shift with horizontally displaced closed orbit in the wiggler as well as the dynamic acceptance has been calculated:

- The generating functions for the three models.
- The generating function for the ASYH-0 and a thin lens multipole kick of the same strength as the field integrals (multipole-1 or multipole-2).

The tune shift in dependence on the horizontally displaced closed orbit is shown in figure 1 for the ASYH-0 with multipole-1 and the ASYH-1. It is in good agreement in the inner parts of the wiggler but starts to differ at amplitudes of $\approx 25\text{ mm}$, which is the border of the good field region for both the numerical investigations and the real wiggler.

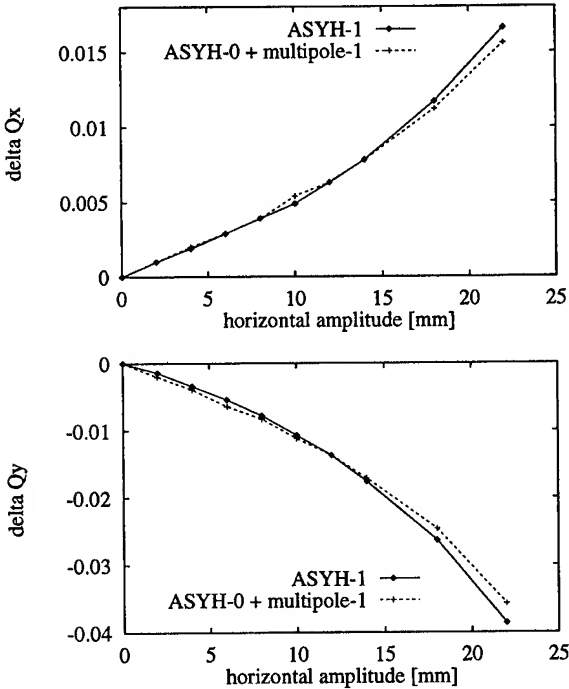


Figure 1. Horizontal (upper) and vertical (lower) tune shift versus horizontal closed orbit amplitude within the wiggler. solid line: ASYH-0 and multipole-1; dashed line: ASYH-1

The dynamic acceptance, measured as the stable horizontal and vertical amplitudes is displayed in figure 2. The dynamic acceptance remains unchanged for the ASYH-0 and the ASYH-1. The ASYH-2 decreases the dynamic acceptance down to 3 mm, a value which would lead to lifetimes of less than 1 hour. The dynamic acceptance calculated by the generating functions for the ASYH-1 and ASYH-2 does not differ from those obtained from the ASYH-0 and multipole lens.

From this analysis follows that the multipole description of the integrated fields is a sufficient treatment of transversal gradient errors in wigglers, if the field integral evolves (more or less) continually along the longitudinal axis.

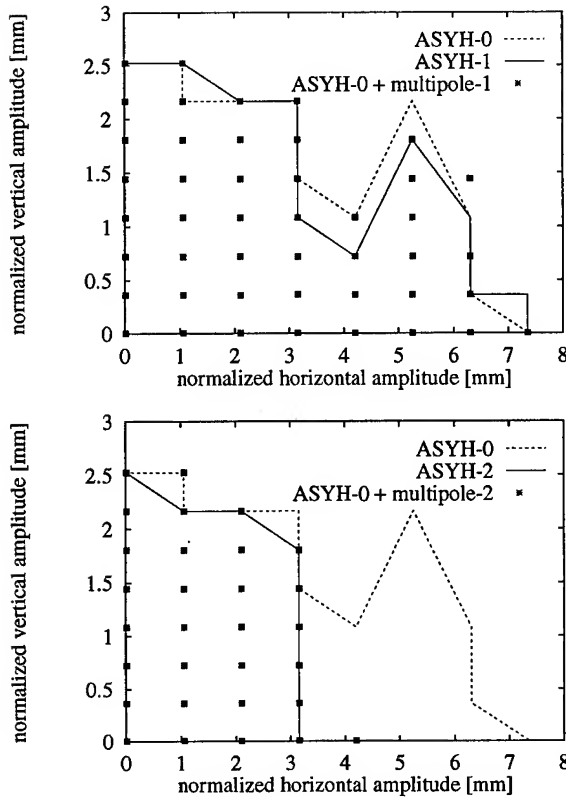


Figure 2. Stable amplitudes (normalized to $\beta = 1m$) for the ASYH-1 (upper) and ASYH-2 (lower). The envelope of the stable amplitudes for the ASYH-0 is plotted as dashed line, for the ASYH-1 and ASYH-2 as solid line. The stable amplitudes for ASYH-0 and appropriate multipole lens (multipole-1 or multipole-2) are plotted as filled boxes.

IV. EXPERIMENTAL VERIFICATIONS

The tune shift with horizontal closed orbit amplitude within the wiggler has been measured for the ASYH. The wiggler was in a different set up during the measurements with respect to the cases investigated above. The measured multipole coefficients for this set up were $b_2 = 0.75T/m$ and $b_4 = -6500T/m^3$, which agrees with the ones obtained from a fit on the tune shift measurements (see figure 3).

Although the dynamic acceptance has not been measured in dependence on the gap, i.e. the multipole strength of the ASYH, the observations made on lifetime and free area in the tune space agree with the multipole limits set by the numerical investigations.

The dynamic acceptance calculated with all wigglers including field errors treated as multipole lenses agrees with the measured ones. The vertical acceptance should not decrease due to the closing of the wigglers. It is determined by the vertical geometric aperture. The horizontal acceptance decreases slightly due to the wiggler field errors. Tracking calculations without field errors show no influence of the wigglers on the dynamic acceptance at all.

A dedicated experiment on the pole width influence was performed by mounting a wiggler off axis in the storage ring. The closed orbit in the wiggler was changed with a bump involving

four steering magnets. Thus the beam center was moved from the wiggler axis up to 30 mm outward, corresponding to 60% of the pole width. The outermost position corresponds to a half pole width of 10σ . No vertical and only a slight horizontal dynamic acceptance reduction was observed, verifying the small effect expected due to the finite wiggler pole width.

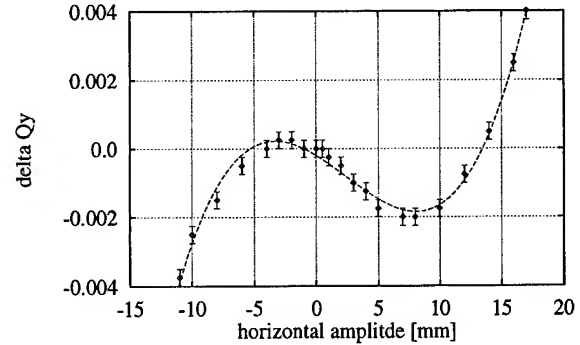


Figure 3. Measured tune shift with horizontal amplitude in the wiggler ASYH. The multipole coefficients obtained from the fit are $b_2 = 1.0 \pm 0.25T/m$ and $b_4 = -6000 \pm 1000T/m^3$.

V. CONCLUSION

Effects of wiggler field errors and other field characteristics have been investigated with the current sheet model and numerical evaluated generating functions. Limits for the periodicity error and the wiggler pole width could be obtained. The field gradient error is well enough described by the usual multipole treatment of the field integrals, as has been shown by numerical investigations and is verified by the experimental results.

References

- [1] M.W. Fan and M.W. Poole. "PMU3D - A program for three dimensional field calculations on periodic permanent magnet systems." *Daresbury Laboratory DL/SCI/TM 29 A*, 1982.
- [2] M. Scheer. "Effects of a Superconducting Wavelength Shifter on the Planned Storage Ring BESSY II — Part I: Canonical Tracking Calculations." *BESSY TB 92-169-A*, 1992.
- [3] J. Bahrtdt and G. Wüstefeld. "A Taylor-Expanded Generating Function for Particle Motion in Arbitrary Magnetic Fields." *Proc. EPAC 92*, 1992.
- [4] H. Neesemann *et al.* "First Experience with DORIS III". *Proc. HEACC 92*, 1992.
- [5] H. Neesemann *et al.* "DORIS III as a Dedicated Source for Synchrotron Radiation". This conference.
- [6] W. Decking. "Influence of Insertion Devices on the Beam Dynamics of DORIS III." *Proc. EPAC 94*, 1994.
- [7] J. Pflüger. "Insertion Devices for DORIS III." *Rev. Sci. Instr.* 63, 1992.
- [8] J. Pflüger. "Magnetic Measurements on the Asymmetric Hybrid Structure (ASYH) for DORIS III," *Proc. Workshop on Magnetic Measurements of Insertion Devices, Argonne*, 1993.

Experimental Study of the Duke Storage Ring Dynamic Aperture *

Y. Wu, V. N. Litvinenko, B. Burnham, and J. M. J. Madey

FEL laboratory, Box 90319, Duke University, Durham, NC 27708-0319, USA

Abstract

The Duke storage ring was designed with a large dynamic aperture for UV-VUV Free Electron Laser (FEL) operations. During commissioning of the Duke storage ring, experiments were performed to measure the horizontal, vertical, and energy apertures. The experimental methods used for the aperture measurements are presented in this paper. The measured results are discussed and compared with the computer simulations.

I. INTRODUCTION

The Duke storage ring lattice was designed with a large 6-D dynamic aperture [1], [2], [3]. The success of the Duke storage ring commissioning [4] has indicated a large 6-D aperture. These indications include:

- after accomplishing the one-turn injection, the stored electron beam current was achieved at the first attempt without using any correctors.
- 115 mA of stored beam current was stacked at the injection energy of 283 MeV using one kicker which kicks both the stored and injected beams.
- the captured beam current per shot was not significantly affected by the change of the RF voltage.

To confirm the observation of the large aperture, experiments were performed to measure it directly.

The measured aperture is determined by either the dynamic aperture or the physical aperture, whichever is smaller. The physical aperture of the real lattice strongly depends on the closed orbit. The dynamic aperture can not be directly measured if the physical aperture is smaller.

From the computer simulations [1], the transverse dynamic aperture of the Duke storage ring lattice is large than the physical aperture defined by the vacuum chambers. For the ideal design orbit, the horizontal physical aperture is 56 mm-mrad, and the vertical physical aperture is 16 mm-mrad. At 1 GeV, the energy dynamic aperture from simulations is larger than 5% depending on the transverse orbit. The energy aperture is therefore limited by the physical aperture defined by the RF voltage (the RF energy acceptance).

II. TRANSVERSE APERTURES

A. Experimental Setup

The transverse apertures are measured using a kicker, a screen, and a vertical dipole (septum) as shown in Fig. 1. The injection kicker provides a horizontal kick to both the injected and stored beams. The inserted screen at the northwest corner is used for the kicker calibration. To measure the horizontal aperture, we use the injection kicker to kick the stored beam horizontally.

The septum [5] is the last dipole in the four-dipole injection chicane. The septum bends the injected beam vertically 9 degrees into the horizontal plane of the stored beam. At the same time the septum allows the stored beam to pass through its V-shape notch without experiencing any magnetic fields. To measure the vertical aperture, we vary the septum current to inject electron beams with different vertical angles.

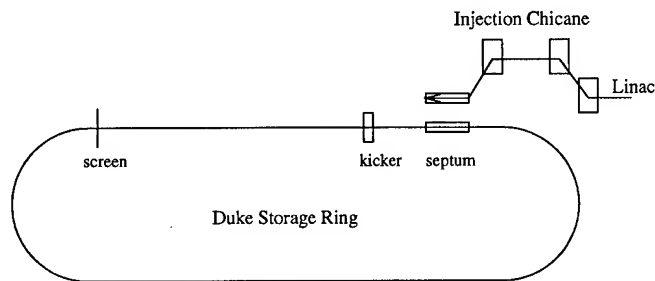


Figure 1. Experimental setup for the transverse aperture measurement.

B. Horizontal Aperture

The horizontal aperture measurement requires the calibration of the injection kicker. To calibrate the kicker, we insert a screen at the northwest corner to measure the injected beam position while varying the kicker voltage. The horizontal kick generated by the kicker is calculated in Eq. 1, where M is the transfer matrix between the kicker and the screen. According to our transfer matrix measurements [6], the measured matrix is very close to the designed one. We can approximate m_{12} with its designed value.

$$\begin{pmatrix} x \\ x' \end{pmatrix}_{screen} = (M) \begin{pmatrix} x \\ x' \end{pmatrix}_{kicker} \quad (1)$$

$$(\Delta x)_{screen} = m_{12} (\Delta x')_{kicker}$$

From the kicker calibration measurement, the horizontal kick $(\Delta x')_{kicker}$ is approximately a linear function of the kicker voltage (Fig. 2.)

The horizontal aperture is measured with a reasonable amount of stored beam current (a few milliamperes). After adjusting the kicker voltage, the stored beam is kicked horizontally. The beam loss is measured after the kick. The horizontal aperture is defined by the kick which kills all the beam during the kicker turn-on time.

Since the stored beam contains many bunches, its envelope usually exceeds the kicker turn-on time. To ensure that the beam is killed by the kicker, the longitudinal profile of the stored beam is therefore also monitored during the measurement.

From the measurement, we find that a stored beam with energy 278 MeV is killed by a kicker voltage of 11.75 kV, which

*Work supported by Office of Naval Research Grant N00014-94-1-0818

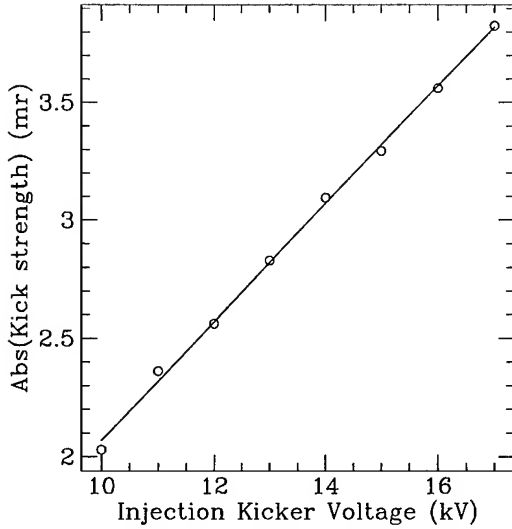


Figure 2. Injection kicker calibration at 278 MeV.

corresponds to a kick of 2.94 mili-radian. Assuming that the stored beam passes through the center of the kicker, the horizontal aperture can be calculated using Eq. 2. The measured horizontal aperture is 43 mm-mrad, which is about 77% of the ideal physical aperture limited by the vacuum chamber.

$$\begin{aligned}
 A_x &= (\beta_x x'^2 + 2\alpha_x x x' + \gamma_x x^2)_{kicker} \\
 &= (\beta_x x'^2)_{kicker} \quad \text{if } x = 0 \\
 \text{where } \beta_x &= 4.911 \text{ m}
 \end{aligned} \tag{2}$$

The measured horizontal aperture is probably limited by the physical aperture due to the closed orbit distortions, rather than by the dynamic aperture. As indicated by the preliminary closed orbit measurements, the horizontal orbit offset in the arc focusing quadrupole (QF) is about 3 mm. With the vacuum chamber opening of 13.5 mm and $\beta_x = 2.5$ m, the estimated available physical aperture is about 44 mm-mrad.

C. Vertical Aperture

The vertical aperture is measured by observing the captured beam current per shot in the storage ring while varying the septum current. The experimental procedures are summarized here:

- optimize the injection and the storage ring configuration.
- measure the average captured beam current per shot from injection.
- repeat the above measurement while varying the septum current to provide a vertical angle to the injected beam.
- record the range of the septum settings which allows the injected beam to be captured.

The range of septum settings which allows beam capture is used to compute the vertical aperture. The maximum vertical angle of the injected beam is calculated in Eq. 3. Note that the septum setting is calibrated in terms of the electron energy in MeV, so that the range in angle $\Delta y'$ is:

$$\Delta y' = \frac{\frac{\Delta E}{2}}{E_0} \times \frac{\pi}{20} \tag{3}$$

Assuming the vertical displacement of the injected beam is small, the vertical aperture can be calculated from Eq. 4. :

$$A_y (\text{mm} - \text{mrad}) = \beta_y (\Delta y')^2, \quad \text{where } \beta_y = 5.949 \text{ m} \tag{4}$$

In our measurement, the injected beam has the energy of 280.5 MeV and $\Delta E = 4$ MeV. From Eq. 4, the measured vertical aperture is 7.5 mm-mrad, which is 47% of the ideal vertical physical aperture.

Similar to the horizontal aperture, we believe that the measured vertical aperture is limited by the physical aperture due to the orbit distortion, not by the vertical dynamic aperture. From the orbit measurement, the vertical orbit offset in dipoles is about 3 mm. With vacuum chamber opening of 8.5 mm and $\beta_y \approx 4$ m, the estimated vertical physical aperture is about 7.6 mm-mrad.

III. ENERGY APERTURE

A large energy aperture is one of the main design requirements for the Duke storage ring lattice, for it determines the maximum FEL efficiency and the electron beam Toucek life time. As we have seen in the simulation [1], the Duke storage ring is designed to provide a large energy dynamic aperture.

To measure the energy aperture, we utilize the synchrotron oscillation of the stored beam (see Fig. 3). The S-band injection linac (at 2.8 GHz) injects a train of macro pulses separated by 350 ps. The injected macro pulses are captured by the 5.6 ns longitudinal phase space RF buckets of the storage ring. Each RF bucket captures up to 16 macro pulses. The captured beam then circulates in the RF bucket. If the energy dynamic aperture is smaller than the RF energy acceptance, it will cause part of the circulating beam be lost.

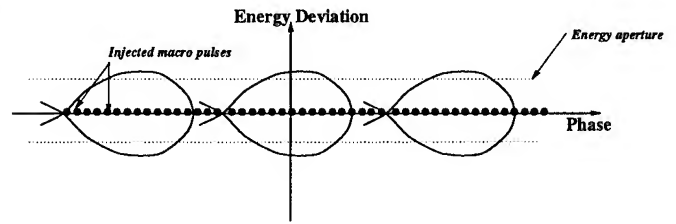


Figure 3. Energy aperture in the longitudinal phase space.

The energy aperture measurement was performed with a 280.5 MeV beam. We first optimized the transverse orbit and the injection conditions. Then we varied the RF cavity voltage to increase the RF energy acceptance and measured the average captured beam current per shot. The result is plotted vs. the RF cavity voltage in Fig. 4.

At a RF voltage of 50 kV, the average captured beam per shot is slightly lower than the maximum. This is because at this low RF voltage, the separation between two neighboring RF buckets is large, about 230 ps. This separation causes some of the injected S-band macro pulses to miss the RF buckets. With increased RF voltage, the bucket separation decreases and the captured beam current per shot increases. As the RF voltage reaches 250 kV, we observe that the captured beam current per shot falls by about 9% from the maximum value. It indicates that more than one injected macro pulse is lost due to the loss at the energy aperture

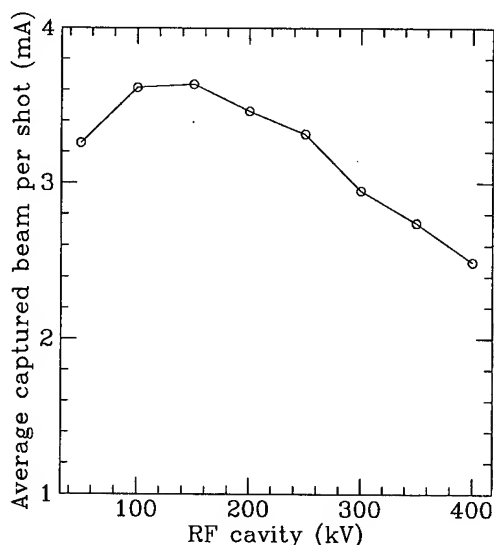


Figure. 4. Measurement on the captured beam per shot at 280.5 MeV.

at the extrema of the macro pulses synchrotron motion. This limitation corresponds to a 3.3% energy aperture.

The measured energy aperture of 3.3% is smaller than the available RF acceptance and the calculated energy dynamic aperture. However the energy aperture depends on the closed orbit and the physical limitation of the vacuum chambers. With improved closed orbit, larger energy aperture is expected.

IV. CONCLUSION AND FUTRUE WORK

From the above measurements, we can conclude that the horizontal dynamic aperture is larger than 43 mm-mrad, the vertical dynamic aperture is larger than 7.5 mm-mrad, and the energy dynamic aperture is larger than 3.3%. These measurements have confirmed that the Duke storage ring does have a large 6-D aperture as designed. The large aperture has helped to speed up the commissioning process and will certainly facilitate FEL operations in the future.

Due to the lack of the beam position monitors (BPMs) electronics, the closed orbit was not optimized during commissioning. The existing closed orbit distortion has limited the physical aperture, thus the measured aperture. In the future, we will improve the closed orbit with the help of BPMs, and experiments will be repeated to verify that the dynamic aperture is not the limiting factor to the available aperture.

V. ACKNOWLEDGEMENTS

We are grateful to the RF engineer Ping Wang for helping us with the RF system setup. We also would like to thank operators James Gustavsson and Jim Widgren for preparing the linac injector for our measurements.

References

- [1] Y. Wu, V. N. Litvinenko, E. Forest, and J. M. J. Madey, "Dynamic Aperture Study for the Duke FEL Storage Ring," Nucl. Instr. and Meth. A 331 (1993), pp.287-292.

- [2] Y. Wu, V. N. Litvinenko, and J. M. J. Madey, "Lattice and Dynamic Aperture of the Duke FEL Storage Ring," Proceedings of the 1993 PAC conference, Volume 1, pp.218-220.
- [3] Y. Wu, V. N. Litvinenko, and J. M. J. Madey, "Study of Undulator Influence on the Dynamic Aperture for the Duke FEL Storage Ring," Nucl. Instr. and Meth. A 341 (1994), pp.363-366.
- [4] V. N. Litvinenko, *et al.*, "Commissioning of the Duke Storage Ring," these proceedings.
- [5] B. Burnham, *et al.*, "Specific Features of Magnet Design for the Duke FEL Storage Ring," Proceedings of the 1993 PAC conference, Volume 4, pp.2889-2891.
- [6] Y. Wu, *et al.*, "The performance of the Duke FEL Storage Ring," Submitted to the 17th International Free Electron Laser Conference, 1995.

A NEW MODEL OF THE e^+e^- BEAM-BEAM INTERACTION *

K. D. Cromer, B. E. Norum, Department of Physics, University of Virginia, Charlottesville, VA 22901 USA
R. Rossmanith, DESY, Hamburg, Germany

Abstract

A new program to simulate the beam-beam interaction between asymmetric e^+ and e^- beams is being developed. Beam bunch distributions are expanded in terms of orthogonal basis functions constructed from solutions to the two-dimensional quantum mechanical harmonic oscillator. Including all solutions corresponding to oscillator energies up to the N^{th} level yields a basis which spans the set of functions composed of a product of a Gaussian times a Hermite polynomial of order N or lower. A consistent and economical description of non-Gaussian beam shapes is thus made possible. In addition, the use of continuous density functions effectively eliminates statistical fluctuations which may arise when beam bunches are modeled by tracking particles. The beam dynamics are encapsulated in matrices which operate on the expansion coefficients of the bunches. These matrices are computed once for each beam with any given set of basis functions and for any particular accelerator. The evolution of a beam distribution is computed by matrix multiplication.

I. INTRODUCTION

Currently used algorithms for the calculation of the effects of the beam-beam interaction in e^+e^- colliders [1], [2], [3] involve tracking representative particles through the machine. An advantage of this approach is that the physics of the bunch dynamics is modeled in a straightforward, clear manner. Also, the freedom of motion of the individual tracked particles permits arbitrary bunch distributions to evolve. However, their use of a finite number of particles allows for the possibility of statistical fluctuations, the magnitudes of which are sensitive to the number of particles tracked. In addition, it is difficult to model with particle tracking the behavior of the bunch core [$\leq \mathcal{O}(\sigma)$] and the behavior of the tails [$> \mathcal{O}(\sigma)$] simultaneously in a self-consistent manner. We have been developing a new description of a bunched beam in which the shapes the bunches can assume are constrained (albeit in an orderly and physically reasonable way) but can be described by a relatively small number of parameters. In addition, model-dependent statistical fluctuations are removed.

The new approach to modeling the time evolution of colliding bunched e^+ and e^- beams is outlined as follows:

- A bunch distribution is expanded in terms of orthogonal basis functions which are constructed from solutions to the two-dimensional quantum harmonic oscillator problem.
- A coordinate transformation is made to a normalized system in which each phase space ellipse of the beam is a circle. This removes the dominant, uncoupled first-order optics.
- The beam-beam interaction is modeled by dividing each beam into transverse slices and then colliding the beams

slice by slice. For a given slice, the effect of its interaction with each slice in the other beam is assumed to be small so that a Taylor series expansion of the distribution can be used.

- The extreme relativistic limit is taken to model the electric field of a slice.
- The luminosity is the sum of the luminosities calculated for each slice-slice collision.

The development of a new code is motivated by the need to reliably evaluate the effects of the beam-beam interaction under highly disruptive conditions such as those in a linac-ring collider. In such a collider, a relatively low energy e^- beam from a linac collides with a relatively high energy e^+ beam in a ring. [4] Because the current in the linac beam is necessarily low compared to the stored beam, very tight focusing is required to achieve a useful luminosity. The configuration is, accordingly, sensitive to beam blowup due to the beam-beam interaction. A reliable calculation of this effect is essential to any assessment of this alternative.

II. THE MODEL

A. Normalized coordinates

We wish to remove the effects of first-order optics on the beam distribution by making a transformation into normalized coordinates. The phase ellipse of a particle, which in one dimension is described by

$$\gamma x^2 + 2\alpha x\theta + \beta\theta^2 = \frac{A_x}{\pi}, \quad (1)$$

is skewed by an angle φ , where A_x is the particle's action in x and θ . The principal axes of the ellipse, $(\bar{x}, \bar{\theta})$, are rotated by this angle and then normalized. The rotation to the principal axes is

$$\bar{\mathbf{x}} = R^T \mathbf{x}, \quad (2)$$

where

$$R = \begin{pmatrix} \cos \varphi & -\sin \varphi \\ \sin \varphi & \cos \varphi \end{pmatrix}. \quad (3)$$

The Twiss parameters transform according to

$$\begin{pmatrix} \bar{\gamma} & 0 \\ 0 & \bar{\beta} \end{pmatrix} = R^T \begin{pmatrix} \gamma & \alpha \\ \alpha & \beta \end{pmatrix} R. \quad (4)$$

Equation 1 in these coordinates becomes

$$\bar{\gamma}\bar{x}^2 + \bar{\beta}\bar{\theta}^2 = \frac{A_x}{\pi}. \quad (5)$$

Then the normalized coordinates, (μ, ν) , are defined such that

$$\mu^2 + \nu^2 = \frac{A_x}{\pi}, \quad (6)$$

*Work supported by the US Department of Energy

and

$$\begin{pmatrix} \mu \\ \nu \end{pmatrix} = \begin{pmatrix} \sqrt{\gamma} \cos \varphi & \sqrt{\gamma} \sin \varphi \\ -\sqrt{\beta} \sin \varphi & \sqrt{\beta} \cos \varphi \end{pmatrix} \begin{pmatrix} x \\ \theta \end{pmatrix}. \quad (7)$$

In all six dimensions, the transformation at a location s in the accelerator is given by

$$\begin{pmatrix} \mu \\ \nu \\ \epsilon \\ \omega \\ \zeta \\ \xi \end{pmatrix} = \begin{pmatrix} a_{11} & a_{12} & 0 & 0 & 0 & 0 \\ a_{21} & a_{22} & 0 & 0 & 0 & 0 \\ 0 & 0 & b_{11} & b_{12} & 0 & 0 \\ 0 & 0 & b_{21} & b_{22} & 0 & 0 \\ 0 & 0 & 0 & 0 & c_{11} & c_{12} \\ 0 & 0 & 0 & 0 & c_{21} & c_{22} \end{pmatrix} \begin{pmatrix} x \\ \theta \\ y \\ \phi \\ l \\ \delta \end{pmatrix}. \quad (8)$$

B. Beam description

The distribution of a single bunch of an electron or positron beam is represented by

$$\rho = \sum_{nmhki} C_{nmhki} \rho_{nmhki}(\mu, \nu, \epsilon, \omega, \zeta, \xi; s), \quad (9)$$

where

$$\begin{aligned} \rho_{nmhki}(\mu, \nu, \epsilon, \omega, \zeta, \xi; s) &= N_{nmhki} H_n(\mu/b_x) H_m(\nu/b_x) \\ &\times H_h(\epsilon/b_y) H_k(\omega/b_y) H_i(\zeta/b_z) H_j(\xi/b_z) \\ &\times \exp \left[-\frac{(\mu^2 + \nu^2)}{2b_x^2} - \frac{(\epsilon^2 + \omega^2)}{2b_y^2} - \frac{(\zeta^2 + \xi^2)}{2b_z^2} \right]. \end{aligned} \quad (10)$$

These are the basis functions of the beam, which are the solutions to the two-dimensional quantum harmonic oscillator problem [5]. The functions $H_p(q)$ are Hermite polynomials in q of order p , and b_x , b_y , and b_z are arbitrary oscillator parameters chosen to yield the most compact description of a bunch. The normalization of the basis functions N_{nmhki} is defined by

$$\int_0^\infty d^6\mu \rho_{nmhki}(\mu, \nu, \epsilon, \omega, \zeta, \xi; s) = \left(\frac{1}{2}\right)^6, \quad (11)$$

so that

$$\int_{-\infty}^\infty d^6\mu \rho(\mu, \nu, \epsilon, \omega, \zeta, \xi; s) = \sum_{nmhki} C_{nmhki} = \begin{cases} 1 & n, m, h, k, i, \text{ and } j \text{ even} \\ 0 & n, m, h, k, i, \text{ or } j \text{ odd} \end{cases} \quad (12)$$

Including s as an argument of ρ is a reminder that the transformation from normalized to unnormalized coordinates is a function of the Twiss parameters evaluated at s .

The sum of the indices $\{n, m, h, k, i, j\}$ is limited by the order of the expansion of basis functions,

$$n + m + h + k + i + j \leq N. \quad (13)$$

Because the solutions are that of the two-dimensional harmonic oscillator, the indices for each two-dimensional pair will share the relation

$$n = N' - m, \quad (14)$$

where N' is an integer less than or equal to N . The number of C_{nmhki} coefficients for an order N is given in Table I.

Table I
Number of basis function coefficients for order N

N	N	N
0	1	3
1	7	4
2	28	5
		84
		210
		462
		924
		1716
		3003

C. Slicing the beam

To calculate the effects of the beam-beam interaction between the colliding bunches, it is necessary to divide each beam into slices and to calculate the incremental changes as the beams pass through each other. The transverse beam distribution for each slice is given by

$$\begin{aligned} \rho_\lambda(\mu, \nu, \epsilon, \omega; s) &= \sum_{nmhki} C_{nmhki}^\lambda \rho_{nmhki}(\mu, \nu, \epsilon, \omega; s) \\ &\times \sum_{ij} \int_{s_\lambda - t/2}^{s_\lambda + t/2} dl \int_{-\infty}^\infty d\delta \rho_{ij}(\zeta, \xi; s) \end{aligned} \quad (15)$$

where t is the thickness of the slice. The value of the integral for each i and j is tabulated and the constant C_{nmhki} becomes C_{nmhki}^λ to distinguish the slices from one another. After the two beams have been stepped through one another, the sliced distribution is reassembled into a single bunch with a functional form describing the dependence on l and δ . The new coefficients of the reassembled bunch are determined by a χ^2 fit, which gives the expression

$$C_{nmhki} = \frac{\sum_\lambda C_{nmhki}^\lambda \int_{s_\lambda - t/2}^{s_\lambda + t/2} dl \int_{-\infty}^\infty d\delta \rho_{ij}(\zeta, \xi; s)}{\sum_\lambda \int_{s_\lambda - t/2}^{s_\lambda + t/2} dl \int_{-\infty}^\infty d\delta \rho_{ij}(\zeta, \xi; s)}. \quad (16)$$

D. The beam-beam interaction

The effects of the beam-beam interaction are determined by making a Taylor expansion of each slice, keeping only the linear terms in the expansion. This is justified if the disruption of a single slice is small for each slice-slice interaction. Each time a slice collides with another slice, the resulting particle distribution, ρ' , is

$$\rho' = \rho + \frac{\partial \rho}{\partial \theta} \delta \theta + \frac{\partial \rho}{\partial \phi} \delta \phi. \quad (17)$$

The extreme relativistic limit is taken such that the electric field lines are entirely transverse. Each slice in the oncoming beam $\tilde{\rho}_\lambda(\mathbf{x}; s)$ is treated as part of an infinite line charge to calculate the transverse impulse on a beam [6],

$$(\delta \theta, \delta \phi) = -\frac{e^2}{2\pi\epsilon_0 E_0} \int \tilde{\rho}_\lambda(\mathbf{x}'; s) \frac{\mathbf{x} - \mathbf{x}'}{|\mathbf{x} - \mathbf{x}'|^2} d^2 x', \quad (18)$$

where all but horizontal and vertical coordinates have been integrated over,

$$\tilde{\rho}_\lambda(\mathbf{x}; s) = \int d\theta d\phi \rho_\lambda(\mu, \nu, \epsilon, \omega; s). \quad (19)$$

A new set of coefficients describes the changed slice. Substituting Equation 15 into Equation 17 gives

$$\begin{aligned} \sum_{nmhki} C'^{\lambda(1)}_{nmhki} \rho_{nmhk} = & \sum_{nmhki} C^{\lambda(1)}_{nmhki} \left\{ \rho_{nmhk} \right. \\ & - \frac{e^2}{2\pi\epsilon_0 E_0} \left[\frac{\partial \mu}{\partial \theta} \frac{\partial}{\partial \mu} \rho_{nmhk} + \frac{\partial \nu}{\partial \theta} \frac{\partial}{\partial \nu} \rho_{nmhk} \right] \\ & \times \int \tilde{\rho}_{\lambda'}^{(2)}(\mathbf{x}'; s) \frac{x - x'}{|\mathbf{x} - \mathbf{x}'|^2} d^2 x' \\ & - \frac{e^2}{2\pi\epsilon_0 E_0} \left[\frac{\partial \epsilon}{\partial \phi} \frac{\partial}{\partial \epsilon} \rho_{nmhk} + \frac{\partial \omega}{\partial \phi} \frac{\partial}{\partial \omega} \rho_{nmhk} \right] \\ & \left. \times \int \tilde{\rho}_{\lambda'}^{(2)}(\mathbf{x}'; s) \frac{y - y'}{|\mathbf{x} - \mathbf{x}'|^2} d^2 x' \right\}, \quad (20) \end{aligned}$$

where we have labeled the beams 1 and 2. A similar equation will exist for beam 2. The closure relationship between Hermite polynomials allows the solution of $C'^{\lambda(1)}_{nmhki}$ to take the form

$$\begin{aligned} C'^{\lambda(1)}_{nmhki} = & C^{\lambda(1)}_{nmhki} \\ & + \sum_{\tilde{n}\tilde{m}\tilde{h}\tilde{k}} \sum_{n'\dots j'} C^{\lambda(1)}_{\tilde{n}\dots\tilde{j}} C^{\lambda'(2)}_{n'\dots j'} F_{\tilde{n}\dots\tilde{k}, n'\dots j', n'\dots j'}(s). \quad (21) \end{aligned}$$

$F_{\tilde{n}\dots\tilde{k}, n'\dots j', n'\dots j'}(s)$ is the tabulated result of the integral. The integral of Equation 20 can be broken down into several integrals of exponentials times polynomials, except for a separable one-dimensional integral which is integrated numerically and tabulated. The evolution of the beam distribution due to the beam-beam interaction is reduced to a sum over the coefficients of the basis functions.

The luminosity, \mathcal{L} , can now be calculated as the sum of the luminosities for each interaction between all pairs of slices. We also utilize the closure of the Hermite polynomials to reduce the luminosity to a form containing tabulated integrals, $G_{nmhk}(s_{\lambda\lambda'})$, and expansion coefficients,

$$\begin{aligned} \mathcal{L} = & f \sum_{\lambda\lambda'} \int d^4 \mu \rho_{\lambda}^{(1)}(\mu, \nu, \epsilon, \omega; s_{\lambda\lambda'}) \rho_{\lambda'}^{(2)}(\mu, \nu, \epsilon, \omega; s_{\lambda\lambda'}) \\ = & f \sum_{\lambda\lambda'} \sum_{nmhki} \sum_{i'j'} C^{\lambda(1)}_{nmhki} C^{\lambda'(2)}_{nmhki'j'} G_{nmhk}(s_{\lambda\lambda'}). \quad (22) \end{aligned}$$

Equation 22 is a sum over all slices interacting at the point $s_{\lambda\lambda'}$ where the λ^{th} slice of beam 1 collides with the λ'^{th} slice of beam 2.

E. Longitudinal phase space

Four effects which directly influence the longitudinal bunch distribution are being included in the model: synchrotron radiation damping (in both transverse and longitudinal phase spaces), quantum excitation, RF acceleration, and beam energy changes during beam-beam collisions. Longitudinal damping is being modeled by a convolution of the beam distribution and the radiation distribution functions. [7] Only terms contained in a description of the beam to a fixed order N are retained. Quantum excitation is being modeled in a parallel fashion. Transverse damping is modeled using a longitudinal momentum impulse at the RF

cavity. The magnitude of the kick is a function of l only. Finally, we have begun to investigate the inclusion of energy changes during the beam-beam collisions following the approach of Hirata *et al.* [6] as far as applicable.

III. SUMMARY

By expressing the distribution of a single beam bunch as an expansion of the two-dimensional quantum harmonic oscillator basis functions in normalized coordinates, the beam dynamics for Gaussian and non-Gaussian beams can be calculated. The beam blowup due to the beam-beam interaction and the luminosity can be computed directly as a sum over the coefficients in the expansion and tabulated integrals. The characteristics of this approach complement those of currently used algorithms.

References

- [1] R. Li, "A Strong-Strong Simulation of the Beam-Beam Effect in a Linac/Ring B-Factory," unpublished.
- [2] An Asymmetric B Factory Based on PEP, LBL-PUB-5303, SLAC-PUB-372, February 1991
- [3] R. Siemann, "The Beam-Beam Interaction in e^+e^- Storage Rings," SLAC-PUB-6073, March 1993.
- [4] K. D. Cromer, B. E. Norum, "High-Luminosity Linac/Ring e^+e^- Colliders," unpublished.
- [5] M. Deady, "Some Properties of the One-Dimensional and Two-Dimensional Quantum Harmonic Oscillator," unpublished.
- [6] K. Hirata, H. Moshhammer, F. Ruggiero, "A Symplectic Beam-Beam Interaction With Energy Change," *Particle Accelerators*, 1993, Vol. 40, pp. 205-228.
- [7] M. Sands, "The Physics of Electron Storage Rings," SLAC-121, November 1970.

A STUDY OF BEAM-BEAM INTERACTIONS AT FINITE CROSSING ANGLES FOR A B-FACTORY

K. HIRATA, K. OHMI, N. TOGE, National Laboratory for High Energy Physics, Tsukuba, Ibaraki 305, JAPAN

Abstract

Feasibility of adopting a finite beam crossing angle at the interaction point of KEKB B-factory has been studied. Various aspects of beam behaviors, such as sensitivities to resonances and development of bunch tails, have been investigated with computer simulations. It is shown that an acceptable operating condition can be found with a suitable combination of machine parameters that are envisioned at KEKB.

I. INTRODUCTION

KEKB is a high-luminosity asymmetric electron-positron (8×3.5 GeV) collider for studies of productions and decays of B mesons at $E_{CM} = 10.5$ GeV [1] [2]. At KEKB it has been planned to adopt a finite-angle beam crossing scheme (2×11 mrad) at its interaction point [3]. This paper reports some recent results of studies that have been done to investigate the beam dynamics in this collision condition. Table I summarizes the KEKB parameters that are pertinent to discussions of beam-beam interactions.

β_x at the IP	0.33	m
β_y at the IP	0.01	m
ϵ_x	1.8×10^{-8}	m
ϵ_y	3.6×10^{-10}	m
σ_z	0.004	m
(ν_x, ν_y, ν_s)	(0.52, 0.08, 0.017)	
Particles / bunch	1.4×10^{10}	electrons
	3.2×10^{10}	positrons
Total number of bunches	5120	per ring

Table I

Working parameter set for the half crossing angle $\phi = 11$ mrad, determined from considerations on beam-beam effects, dynamic apertures and others.

A new beam-beam simulation algorithm has been developed for this study [4] [5]. As indicated in Figure 1, the bunches which are colliding at a crossing angle are first Lorentz-transformed into a frame where their momentum vectors appear parallel. In this "head-on" frame a symplectic synchro-beam mapping is applied to calculate the beam-beam forces and their effects on the bunches. When the mapping is finished, the two bunches are Lorentz-transformed back to the laboratory frame, where the beam tracking code takes over the rest of simulation.

The model is fully symplectic in the 6-dimensional phase space, and it incorporates all known effects such as the energy loss due to the traverse of transverse electric fields at an angle, energy loss due to longitudinal electric fields, and effects due to

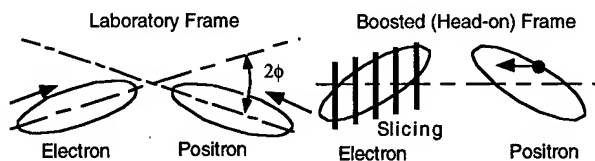


Figure 1. Lorentz transformation from the laboratory frame to the "head-on" frame, which is used for applying synchro-beam mapping to calculate beam-beam interactions with finite crossing angles.

the variation of β along the bunch length during collision (hour-glass effect).

II. BEAM-BEAM SIMULATION WITH LINEAR LATTICE FUNCTIONS

Dependence of beam sizes and the luminosity on the wide range of machine parameters have been investigated with a simplified lattice model, where the beam transfer through the ring is represented by a linear matrix [5].

A weak-strong beam formalism is used to implement the beam-beam interaction algorithm outlined in the previous section. Typically the strong bunch is longitudinally sliced into 5 slices, and the weak bunch is represented by 50 super-particles. Effects of radiation damping is taken into consideration. The beam-beam collision and revolutions through the ring are simulated for up to 10 radiation damping time. Then the equilibrium beam size is examined. The expected luminosity is calculated from a convolution of the distribution functions of the two beams.

Initial beam parameters are specified so that they would give the design luminosity of $1 \times 10^{34} \text{ cm}^2\text{s}^{-1}$ or somewhat higher values, with collisions of 5120 bunches per ring in the absence of aberrations and a beam blow-up.

Figure 2 shows a calculated luminosity contour plot in the ν_x - ν_y plane, with the crossing angle of 2×10 mrad, in the vicinity of the working point: $(\nu_x, \nu_y) = (0.52, 0.08)$.

Notable observations are summarized as follows:

1. A finite crossing angle at the interaction point (IP) certainly causes a reduction of usable area in the ν_x - ν_y plane, because of synchro-betatron and other resonances.
2. However, when ν_s is kept small *i.e.* below 0.02, a fair amount of areas in the ν_x - ν_y plane is still free from resonances. This requirement is compatible with the overall KEKB design. Some of such acceptable ν_x - ν_y areas are compatible with the conditions preferred from dynamic aperture considerations.

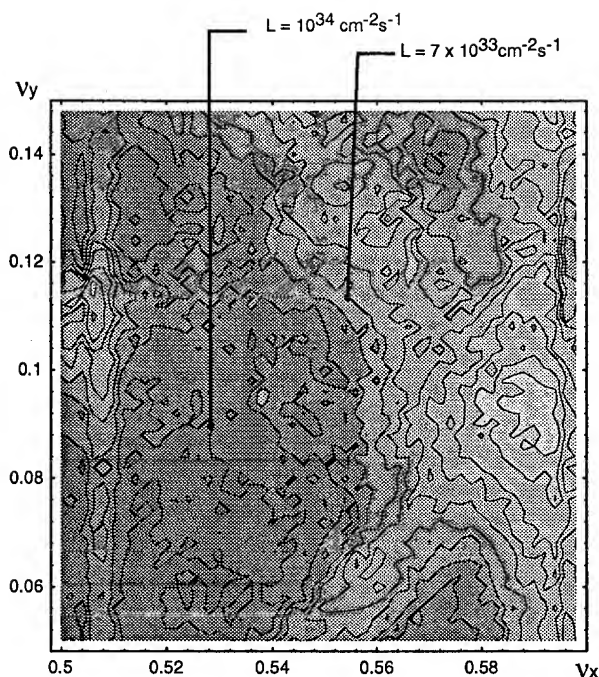


Figure 2. Calculated luminosity contour diagram in the case of crossing angle = 2×11 mrad. Expected luminosity in the ν_x - ν_y plane is shown. The contour spacing is $10^{33} \text{ cm}^{-2} \text{ s}^{-1}$.

3. With the beam intensity of a few $\times 10^{10}$ per bunch or below, no intensity-dependent beam blow-up is seen with finite crossing angles.
4. When the ν_s is small, and when a resonance free condition of ν_x - ν_y is chosen, the predicted luminosity there is roughly consistent with naive expectations from the geometric and linear effects. Occasionally the simulated luminosity exceeds naive expectations which only consider geometric effects. This is because of effects of the dynamic beta and dynamic emittance.

III. SIMULATIONS WITH THE LATTICE WHICH INCLUDES NONLINEARITY AND ERRORS

The beam-beam simulation algorithm based on the weak-strong model has been incorporated in the beam tracking software SAD at KEK [6]. This provides a tool to study effects of finite crossing angles at the IP, combined with the nonlinearity of the KEKB machine lattice[7] and its possible errors.

Simulations with SAD have been conducted with realistic assumptions on lattice errors. Presence of detector solenoid field and its partial compensation near the interaction point is taken into account. Finite alignment and excitation errors of bend (B), quadrupole (Q), sextupole (SX), and steering correction magnets (ST) are simultaneously considered. Typical magnitudes of assumed errors, which we consider realistic, are summarized as follows:

Element	BPM	B	Q	SX	ST
Horiz. shift (μm)	75	0	100	100	0
Vert. shift (μm)	75	100	100	100	100
x-y roll (mrad)	0	0.1	0.1	0.1	0.1
Field error	0	10^{-4}	10^{-3}	10^{-3}	0

Gaussian errors are produced according to the rms values given in the table above. For each series of generated errors, the orbit and tune corrections are done in the tracking code as if it were in an actual machine operation. Then the scale of assumed errors is re-normalized so that the expected vertical spot size σ_y agrees with the design value. We call it "error normalization factor" f . With such renormalized errors in the machine, the orbit and tune corrections are, once again, performed. The expected luminosity is evaluated by using the beam-beam code, plus the tracking with SAD. Different random seeds used for generating lattice errors result in different values of f (error normalization factor) and different expected luminosity values. Some of the obtained results are:

$$\text{Luminosity}(\text{cm}^{-2} \text{s}^{-1})/10^{34} = \begin{cases} 1.21 & f = 1.4 \\ 0.9 & f = 0.8 \\ 1.34 & f = 0.5 \end{cases}$$

It is seen that the lattice nonlinearity and likely machine errors do not lead to fatal degradations of the estimated luminosity.

IV. QUASI STRONG-STRONG SIMULATION

To address issues which may be overlooked in the strong-weak formalism, while not spending a prohibitive amount of CPU time, a quasi strong-strong formalism has been developed. Here, every once in 500 turns of revolution, the average electron and positron bunch sizes are "registered." During the next 500 turns, a weak-strong model calculations are performed, while this "registered" electron (positron) bunch size is used as the "strong bunch size" for calculating the development of positron (electron) bunch size. Then the "strong bunch sizes" are updated again, and the simulation continues.

Figure 3 shows the expected luminosity as function of revolution number obtained from this simulation. A linear matrix is used to represent the lattice beam transfer. No indications of a bunch core blow-up are seen. Figure 4 shows that the horizontal beam size obtained in the simulation is $\sigma_x = 6.2 \times 10^{-5} \text{ m}$. It is somewhat smaller than the nominal value $7.56 \times 10^{-5} \text{ m}$. It is consistent with the dynamic beta and dynamic emittance effect.

V. BUNCH TAILS EXCITED BY BEAM-BEAM INTERACTIONS

The presence of non-Gaussian bunch tails causes an extra synchrotron radiation (SR) background to the detector facility. The fractional bunch tail population should be kept less than 10^{-5} for $> 10\sigma_x$ and 10^{-5} for $> 30\sigma_y$, according to design considerations on SR masks near the interaction point. The bunch tail growth due to beam-beam interactions has been studied with a long-term strong-weak calculation with a linear lattice model. Typically the simulation is done by tracking 50 super particles over 10^8 turns of revolution. This means 1000 seconds for 50 particles, and 14 hours for a single particle in an actual machine.

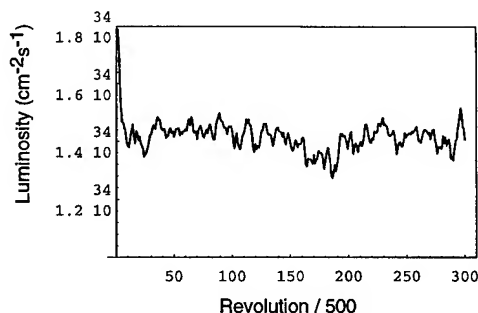


Figure 3. The expected luminosity as function of revolution number in the quasi strong-strong model calculation.

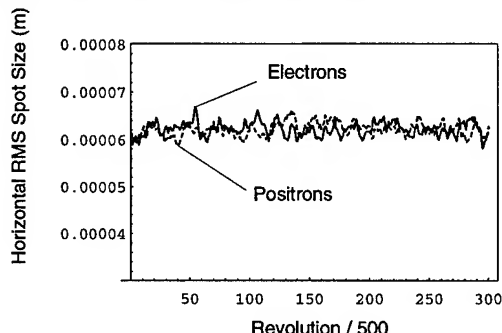


Figure 4. Behavior of σ_x as function of revolution number. The solid line shows the electron bunch size. The broken line shows the positron bunch size.

Figure 5 shows the particle distribution, predicted by this simulation, as function of action variables (I_x and I_y) in the horizontal and vertical planes. The canonical beam parameters, as given in Table I, have been used in this case. From this data, the particle population in the bunch tail has been calculated. It was found that the probability that a particle has the vertical amplitude larger than $30\sigma_y$, where σ_y is the design bunch size, is approximately 10^{-12} . Since the bunch population is $O(10^{10})$, no particle is likely to have such a large vertical amplitude. Tails in the horizontal direction have been also studied, and it has been found that its development is much slower than in the vertical direction. Preparations are under way to evaluate bunch tails with tracking calculations which include non-linear effects of the lattice and possible machine errors.

VI. CONCLUSIONS

It is seen that within the simulation studies conducted so far, the design luminosity goal can be achieved with the finite angle crossing of 2×11 mrad at the interaction point. Naturally this cannot be fully confirmed until operating the real-life machine. As a back-up safety measure, the use of crab crossing scheme to combine with the finite angle collision is being considered [2]. In the meanwhile, more elaborate studies of beam-beam effects will be continued. Some of the major projects include:

- In the tail simulation, nonlinear effects in the lattice should be included in the calculation.
- A strong-strong simulation will be updated so that it evaluates the beam envelopes in each turn, using a Gaussian approximation to calculate beam-beam forces.

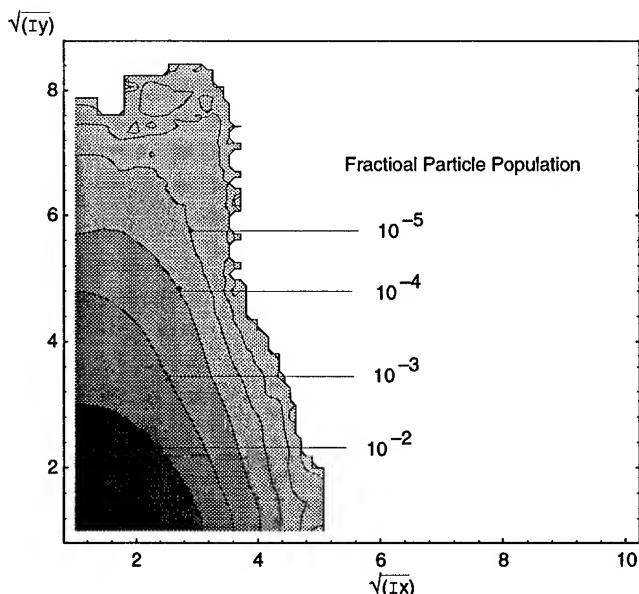


Figure 5. Expected bunch tail distribution as function of action variables (I_x and I_y) in the two planes.

- More ambitious strong-strong simulation which does not rely on the Gaussian approximation for calculating the beam-beam force.

References

- [1] S. Kurokawa, "KEKB Status and Plans," Talk presented at 1995 Particle Accelerator Conference, Dallas, U.S.A. (1995).
- [2] KEKB Accelerator Design Report. In preparation for publication as KEK report (1995).
- [3] N. Toge, KEK Preprint 94-181. Talk presented at 1994 Int'l Workshop on B Physics, Nagoya, Japan.
- [4] K. Hirata, Phys. Rev. Lett. **74**, 2238 (1995), and KEK Preprint 93-160 (1994).
- [5] N. Toge and K. Hirata, KEK Preprint 94-160 (1994), Published in Proc. Workshop on Beam Instabilities in Storage Rings, ed. by W. Chou, et al, Hefei, China (1994).
- [6] Strategic Accelerator Design Code (SAD) is a beam transport and simulation software, which has been developed at KEK. See, K. Oide, Nucl. Instr. Meth. **A176**, 427 (1989).
- [7] H. Koiso and K. Oide, "Lattice Design for KEKB Colliding Rings," Talk presented at 1995 Particle Accelerator Conference, Dallas, U.S.A. (1995).

SIMULATION OF BEAM-BEAM EFFECTS IN TEVATRON[†]

C. S. Mishra and S. Assadi, Fermi National Accelerator Laboratory, Batavia, IL -60510, USA.

R. Talman, Cornell University, Ithaca, NY 14853, USA.

The Fermilab accelerator complex is in the middle of an upgrade plan Fermilab III. In the last phase of this upgrade the luminosity of the Tevatron will increase by at least one order of magnitude. In order to keep the number of interactions per crossing manageable for experiments, the number of bunches will be increased from 6X6 to 36X36 and finally to ~100X100 bunches. The beam dynamics of the Tevatron has been studied from Beam-Beam effect point of view in a "Strong-Weak" representation with a single particle being tracked in presence of other beam. This paper describes the beam-beam effect in 6X6 operation of Tevatron.

I. INTRODUCTION

The Fermilab Tevatron is a 1.8 TeV/c center of momentum proton-antiproton collider, delivering a peak luminosity greater than $2. \times 10^{31}$ cm⁻²sec⁻¹. In the current collider operation six proton and six antiproton bunches collide at B0(CDF) and D0 interaction points. The two beams are kept separated in a helical orbit at ten other possible interaction locations by electrostatic separators, with approximately 5 σ separation. Average intensity of proton and antiproton bunches are about 2.5×10^{10} and 8×10^{10} respectively. Current Tevatron performance does not seem to be limited by beam-beam effects. In the current operating condition each detector sees on average about 2 interactions per crossing.

The Fermilab III accelerator complex upgrade, including the Main Injector will increase the peak luminosity to 10×10^{32} cm⁻²sec⁻¹. Higher luminosity is needed to better understand several high pt physics, including top quark physics, reducing uncertainty in W mass and extend the B Physics CP violation reach. Higher luminosity will be achieved by injecting more proton and antiproton bunches with similar intensities to present bunches. Number of bunches will increase from 6X6 to 36X36 and eventually to ~100X100, to keep the number of interactions per crossing at each high energy physics detectors at a manageable level.

In this paper we describe the calculations which are being performed to study the beam-beam interaction in the current Tevatron. These calculations will be extended to 36X36 and ~100X100 bunch crossing scenarios of upgraded Fermilab accelerator complex. A modified version of thin element tracking program TEAPOT[1] has been used for these simulations.

II. LATTICE

The Tevatron lattice includes standard magnetic elements dipoles, quadrupoles, sextupoles and correction elements. The lattice includes measured higher order multipoles for dipoles and quadrupoles. The higher order multipoles include both normal and skew components up to 14 poles for dipole and 16 poles for quadrupoles. There are electrostatic separators in the lattice which are used to put the beam on a helical orbit. In TEAPOT there is no direct provision for electrostatic separator, so its function is achieved by providing a horizontal and vertical kick to the particles at separator locations. The misalignment of all the magnetic elements and beam position monitors has been included in this calculation. The sigma of the alignment error with respect to close a orbit is 0.25 mm in both horizontal and vertical directions. In addition dipole magnets have a roll angle of 0.5 mrad sigma. The horizontal and vertical dipole correction elements are used to correct the closed orbit error due to these errors. The Tevatron has four RF cavities, each operating at $V_{rf} = 0.2125$ MV. The RF frequency is set to 53 MHz corresponding to a harmonic number of 1113.

The two sextupole families are used to set the chromaticity of the Tevatron to a desired value. The Tevatron has four sets of skew quadrupoles. These skew quadrupoles are used to globally decouple the Tevatron.

III. CALCULATIONS

The calculations of Beam-Beam effect is performed by using a thin element tracking code TEAPOT. The code simulates the passage of a single particle in the presence of an oncoming beam by a BEAM-BEAM element. This is necessarily a "weak-strong" representation with the single particle being tracked seeing the constant field of the other beam like those of any other fixed beam-line element. The code takes as an input the transverse beam size, number of particle in the fixed beam, and horizontal and vertical offset from the ideal orbit.

In the 6X6 bunch operation of the Tevatron the single tracked antiproton crosses the proton bunches at twelve locations

* Operated by University Research Association Inc.,
under contract with the U.S. Department of Energy.

around the ring. We have performed calculations for two operating conditions of the Tevatron at 900 GeV. In the first case the two beams are not colliding at B0 and D0 and in the second case they are. The base tune of the Tevatron is set to $(Q_x, Q_y) = (20.583, 20.574)$ and chromaticity is adjusted to 20., 24. for the first case. The base tune is set to $(Q_x, Q_y) = (20.582, 20.577)$ and chromaticity is lowered to 10.0 and 12.0. The launched particles have $Dp/p = 0.0001$.

We have the effects number of particles in the strong beam, no coupling in Tevatron, global decoupling of Tevatron, effects of higher order multipoles in dipoles and quadrupoles and electrostatic separators off. In this paper we present some general feature of the data.

Fig. 1 shows the change in the x and y tune of a small amplitude particle as a function of beam intensity. Simulation clearly shows the beam-beam tune shift.

Fig. 2 is the phase space plot of a particle with initial amplitude of $x=3.5\text{mm}$ $y=5\text{mm}$ at the maximum beta. Maximum beta is considered away from the low beta region. In this simulation all the higher order multipoles in dipoles and quadrupoles are present and beam-beam effect has been turned off. Fig. 3 shows the phase space of the same particle when the beam-beam effect has been turned on. Clearly, addition of beam-beam increases the occupied phase space.

The inclusion of beam-beam effect also changes the location in x and y plane a particle occupies. Fig 4 and 5 shows the turn by turn plots of a particle without and with beam-beam.

The Tevatron spends most of its time colliding beam at B0 and D0. We have looked at the phase space of a small amplitude particle in the presence of Beam-Beam. Fig 6. shows the phase space of that particle.

IV. OUTLOOK

In this paper we have presented initial results of a long simulation program we are about to undertake to study the Beam-Beam effects in the Fermilab Tevatron. These studies will be extended to 36X36 and ~100X100 bunches operations of the Tevatron and will be published elsewhere[2].

V. REFERENCES

- [1] L. Schachinger and R. Talman, Particle Accl 22, 35 (1987).
- [2] C. S. Mishra and S. Assadi to be submitted to Phy Rev E.

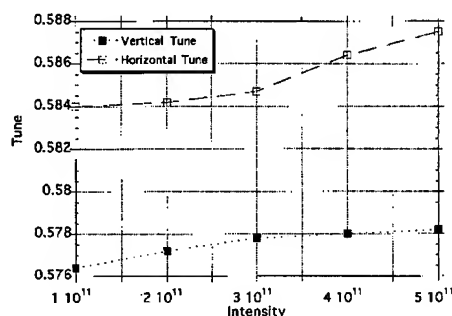


Fig. 1) Betatron tune shift increases as intensity

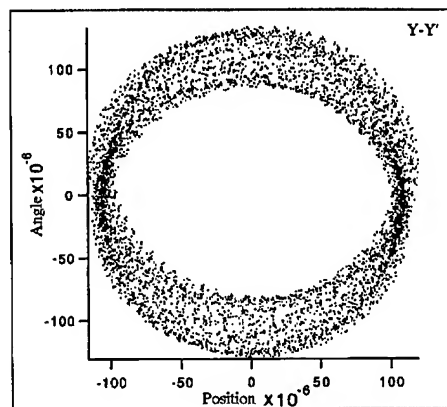
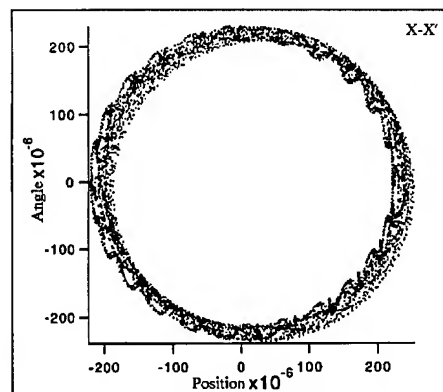


Fig. 2) Normalized horizontal and vertical phase space plots; single beam with higher order multipoles.

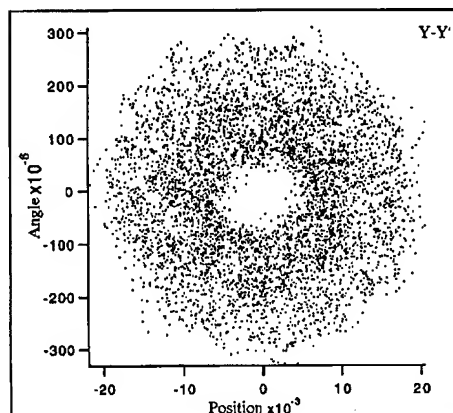
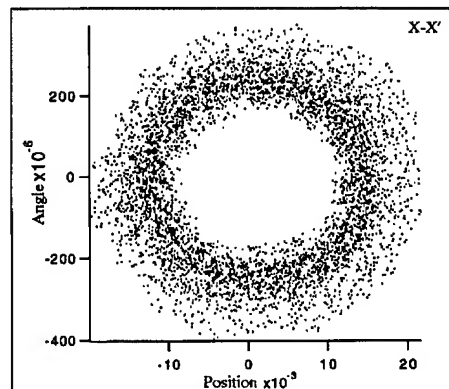


Fig.3) Horizontal (upper) and vertical (lower) normalized phase space plots for beam-beam with higher order multipoles is shown.

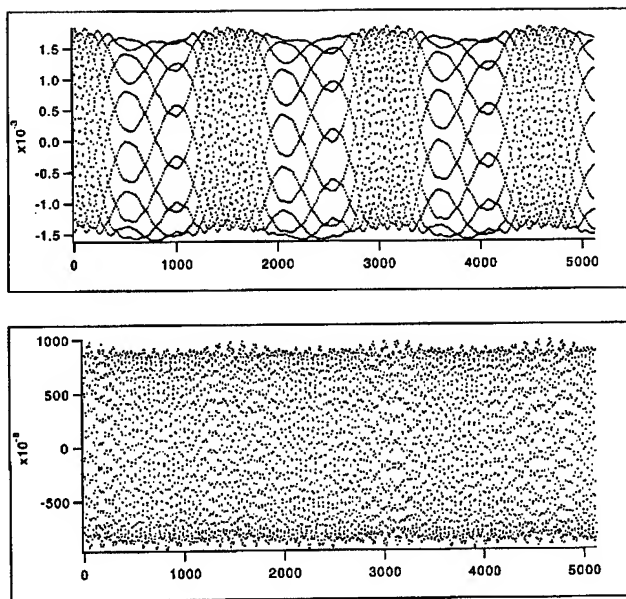


Fig. 4) Turn by turn plots of a particle without beam-beam but all higher order multiples present; (top plot is horizontal and the bottom plot is vertical).

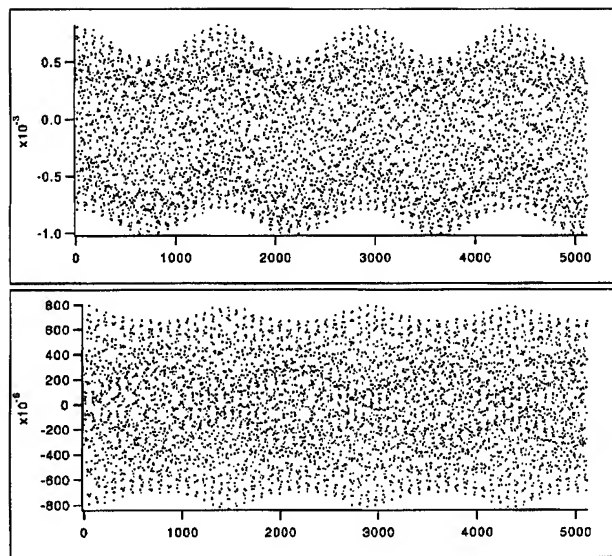


Fig. 6) Turn by turn plots of a particle with beam-beam and all higher order multiples at lowbeta; (top plot is horizontal and the bottom plot is vertical).

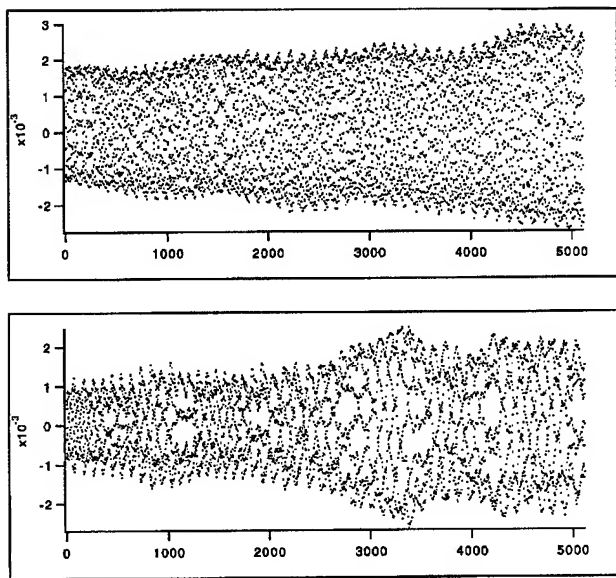


Fig. 5) Turn by turn plots of a particle with beam-beam and all higher order multiples present; (top plot is horizontal and the bottom plot is vertical).

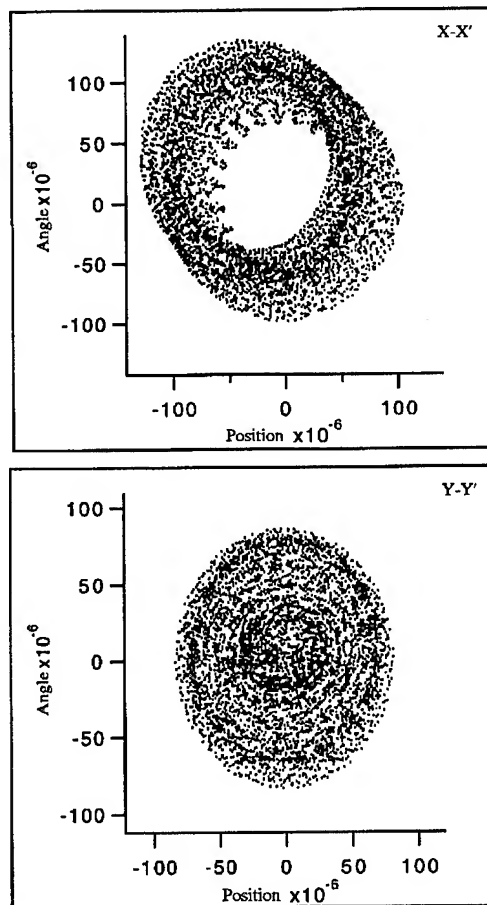


Fig.7) Normalized phase space plots; beam-beam with higher order multipoles at lowbeta location.

THE DYNAMIC BETA EFFECT IN CESR*

David Sagan

Laboratory of Nuclear Studies, Cornell University, Ithaca, NY 14853

Abstract

The change in beta due to the beam-beam interaction — the 'dynamic beta effect' — has been observed in the Cornell Storage Ring CESR by comparing the observed luminosity with the observed vertical beam heights. Under current colliding beam conditions the resulting changes in horizontal beta around the ring have exceeded $\Delta\beta_x/\beta_x = 0.5$ and the horizontal tune shift parameter ξ_x has exceeded 0.05.

I. ANALYSIS

In a colliding beam storage ring the Twiss parameters are affected by the quadrupolar focusing of the beam-beam interaction. Like any quadrupole error this 'dynamic beta' effect is enhanced by running near a half-integer or integer resonance. Following Chao[1], the dynamic beta effect can be analyzed by writing the 1-turn transfer matrix from IP to IP as

$$\begin{pmatrix} \cos \mu & \beta \sin \mu \\ -\frac{1}{\beta} \sin \mu & \cos \mu \end{pmatrix} = \begin{pmatrix} 1 & 0 \\ -\frac{1}{2f} & 1 \end{pmatrix} \cdot \begin{pmatrix} \cos \mu_0 & \beta_0 \sin \mu_0 \\ -\frac{1}{\beta_0} \sin \mu_0 & \cos \mu_0 \end{pmatrix} \cdot \begin{pmatrix} 1 & 0 \\ -\frac{1}{2f} & 1 \end{pmatrix}, \quad (1)$$

where β_0 and μ_0 are the 'unperturbed' beta and tune without the beam-beam interaction. In Eq. (1) the beam-beam interaction strength of $1/f$ is given by

$$\frac{1}{f_{x+}} = \frac{2N_- r_e}{\gamma \sigma_{x-} (\sigma_{x-} + \sigma_{y-})}, \quad (2)$$

with analogous formulas for f_{x-} , f_{y+} , and f_{y-} where x and y refer to the horizontal and vertical planes and $+$ and $-$ refer to the positrons and electrons respectively. In Eq. (2) N is the number of particles in a beam, r_e is the classical electron radius, γ is the usual relativistic factor, and σ is the beam size. The beam-beam parameter ξ is defined by

$$\xi \equiv \frac{\beta_0}{4\pi f}, \quad (3)$$

ξ is just the focusing strength of one beam on the other normalized by β_0 . It is sometimes convenient to define another beam-beam parameter κ by

$$\kappa \equiv \frac{\beta}{4\pi f} = \frac{\beta}{\beta_0} \xi. \quad (4)$$

Combining Eqs. (1), (2), (3), and (4) gives

$$\cos \mu = \cos \mu_0 - 2\pi \xi \sin \mu_0 \quad (5)$$

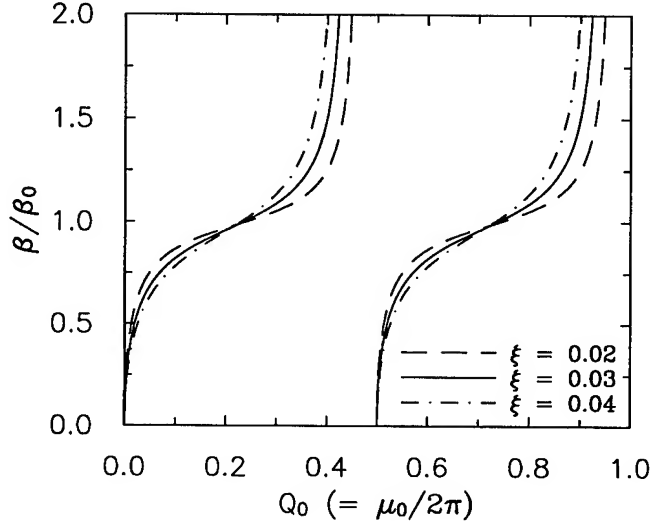


Figure 1. β relative to β_0 as a function of tune for three different values of ξ . The top scale shows the tune in kHz.

$$= \cos \mu_0 - 2\pi \kappa \frac{\beta_0}{\beta} \sin \mu_0, \quad (6)$$

$$\sin \mu = \frac{\beta_0}{\beta} \sin \mu_0. \quad (7)$$

Eliminating μ from Eqs. (5) and (7) gives

$$\frac{\beta}{\beta_0} = (1 - (2\pi \xi)^2 + 2(2\pi \xi) \cot \mu_0)^{-1/2}. \quad (8)$$

Alternatively, in terms of κ , one finds

$$\frac{\beta}{\beta_0} = \sqrt{1 + \frac{(2\pi \kappa)^2}{\sin^2 \mu_0} - (2\pi \kappa) \cot \mu_0}. \quad (9)$$

Figure 1 shows β/β_0 as calculated from Eq. (8) as a function of $Q_0 \equiv \mu_0/2\pi$ for three different values of ξ . As can be seen from the figure, for tunes just above an integer or half-integer resonance, the dynamic beta effect causes a reduction in β . This, of course, is what is desired for increased luminosity. As an example, the Cornell Electron/positron Storage Ring CESR is currently operating with a design horizontal tune of 9.52. Under the assumption that ξ is in the vicinity of 0.03 (see below) this implies that there is a large reduction in beta of $\beta_x/\beta_{x0} \sim 0.5$. Additionally, with the present CESR vertical tune of 9.60, the reduction in vertical beta is $\beta_y/\beta_{y0} \sim 0.8$.

Along with the change in β at the IP there will also be a beta-wave throughout the ring. If the beam-beam interaction is small enough, one can use first order perturbation theory (cf. Sands[2] Eq. 2.105) to obtain

$$\frac{\Delta\beta(s)}{\beta_0(s)} = \frac{\Delta\beta(\text{IP})}{\beta_0(\text{IP})} \cdot \frac{\cos(2\phi_0(s) - \mu_0)}{\cos \mu_0}, \quad (10)$$

*Work supported by the National Science Foundation

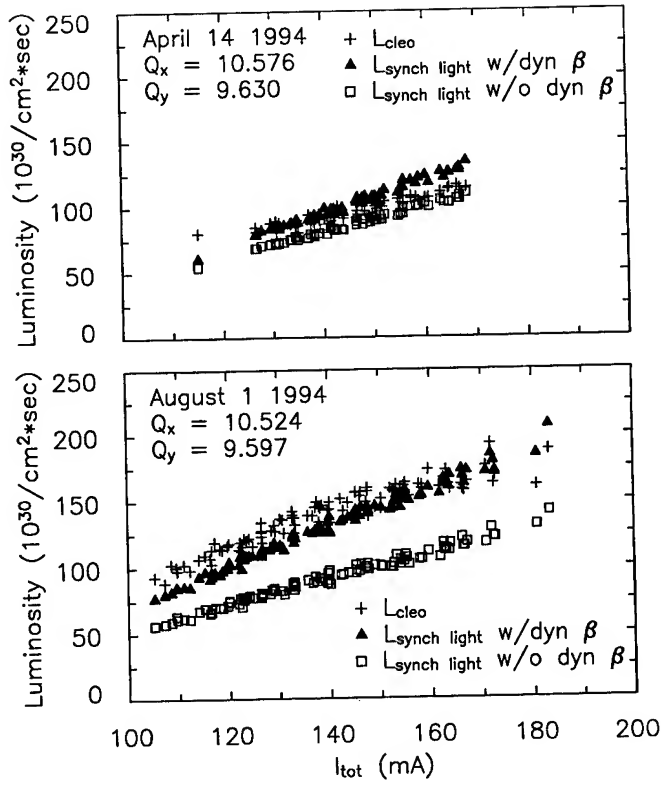


Figure 2. Luminosity as a function of total current for two days of HEP running.

where $\phi_0(s)$ is the phase advance from the IP to point s . With the present CESR horizontal tune of 9.52 this translates into a horizontal beta-wave with amplitude $|\Delta\beta_x|_{max}/\beta_{0x} \approx 0.5$. One consequence of this beta-wave is that it changes the horizontal emittance function $\mathcal{H}_x(s)$ (cf. Sands[2] Eq. 5.71) and this will affect the horizontal emittance.

II. SYNCH LIGHT LUMINOSITY

As a fast tuning aid in CESR the luminosity is monitored via a calculation that uses the observed electron and positron beam heights. The observed beam heights are obtained via the synchrotron light generated at two specific locations in the arcs. Since it modifies the betas the neglect of the dynamic beta effect can throw off the 'synch light' luminosity calculation. Conversely by comparing the synch light luminosity with the actual luminosity recorded by the CLEO detector the presence of the dynamic beta effect can be verified.

The synch light luminosity is calculated from the equation

$$\mathcal{L} = \frac{f_{rev}}{4\pi\sigma_x\sigma_y} \sum_{i=1}^{n_b} N_{i+} N_{i-}, \quad (11)$$

where f_{rev} is the revolution frequency, n_b is the number of bunches, N_{i-} and N_{i+} are the number of positrons and electrons respectively in the i^{th} bunch, and the beam sigmas are calculated from the equations

$$\sigma_x = \sqrt{\epsilon_x \beta_x}, \quad \text{and} \quad (12)$$

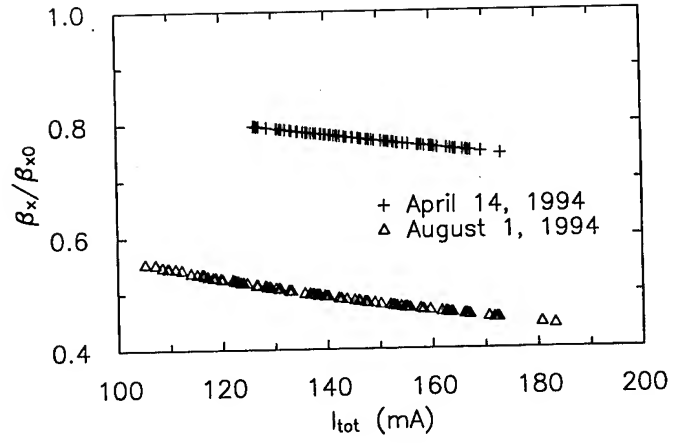


Figure 3. β_x/β_{x0} as a function of total current.

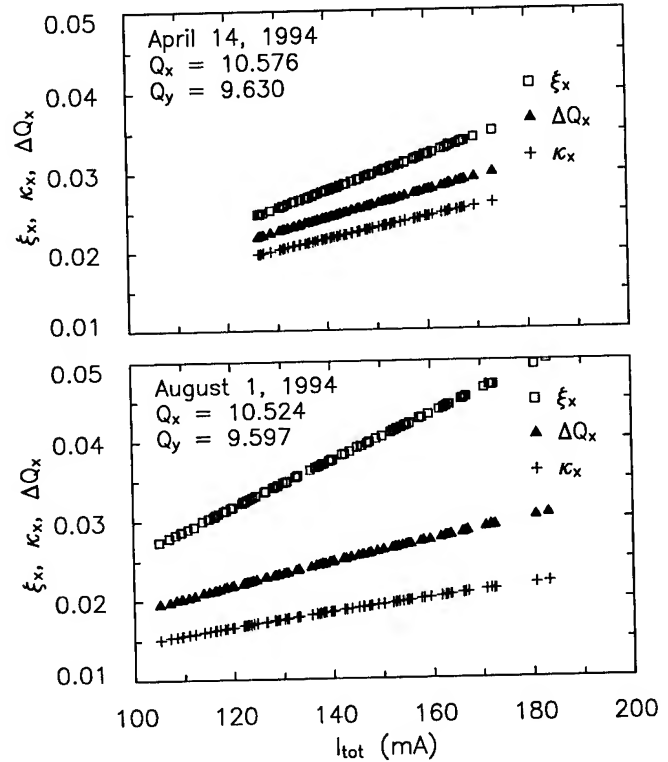


Figure 4. ξ_x , κ_x , and ΔQ_x as a function of total current.

$$\sigma_y = \sigma_y(ls) \cdot \sqrt{\frac{\beta_y(IP)}{\beta_y(ls)}}, \quad (13)$$

where (ls) stands for the light source point.

Figures 2 through 4 show data from two days of normal HEP running: April 14, 1994 and August 1, 1994. [for a complete report see Sagan[4].] The April 14 run was at an old operating point with tunes of $Q_{x0} = 10.574$ and $Q_{y0} = 9.632$ while the August 1 run had tunes of $Q_{x0} = 10.523$ and $Q_{y0} = 9.597$. Figure 2 shows the luminosity as a function of total electron and positron current. The three sets of data shown correspond to: (A) Data from the CLEO detector, (B) The luminosity as calculated from the synchrotron light monitors neglecting the dynamic beta effect, and (C) The luminosity as calculated from the syn-

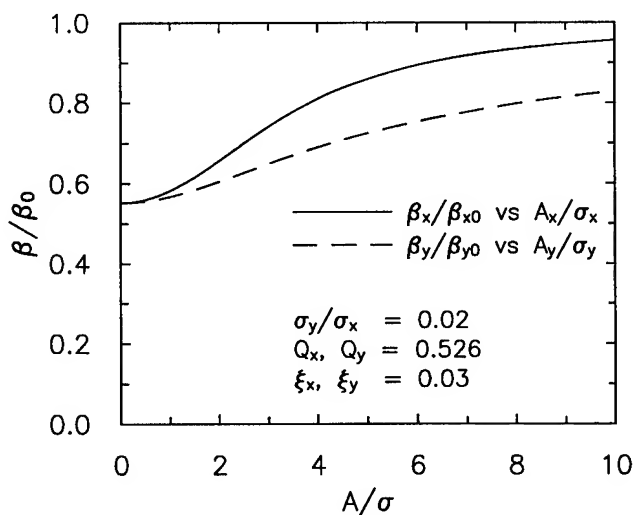


Figure 5. Relative β/β_0 as a function of oscillation amplitude for the horizontal plane (solid line) and the vertical plane (dashed line).

chrotron light monitors including the dynamic beta effect. For the April 14 run the three curves are too close together to decide whether including the dynamic beta effect gives a better fit to the CLEO data. However, for the August 1 run, since the horizontal tune is closer to a half-integer, it is clear that one must take the dynamic beta effect into account. For the August 1 run the change in ϵ_x with beam current was significant exceeding 50% at the highest currents. The fact that there is still a discrepancy between the synch light calculation and CLEO can be explained by the neglect of other effects such as the hourglass effect[3].

Figure 3 shows β_x normalized by the unperturbed β_{x0} as a function of total current. For the August 1 run the reduction in β_x is quite dramatic, being over a factor of 2 at the larger currents.

The difference between ξ_x , κ_x , and $\Delta Q_x \equiv (\mu_x - \mu_{x0})/2\pi$ is shown in figure 4 which shows ξ_x , κ_x , and ΔQ_x as a function of total current. For the April 14 run the tunes are far enough away from the half-integer resonance so that the dynamic beta effect is small and $\kappa_x \approx \xi_x \approx \Delta Q_x$. On the other hand, for the August 1 run, there is a large difference between the three. For the August 1 run ξ_x varies linearly with current up to the largest currents where it exceeds 0.05. ΔQ_x and κ_x however, are significantly lower than ξ_x and they show some slight signs of 'saturation' at the highest currents.

III. AMPLITUDE DEPENDENCE

In terms of single particle dynamics the beam-beam force is nonlinear beyond 1σ either horizontally or vertically. The fact that the beam-beam force starts to fall off beyond 1σ results in a monotonic decrease of the effective quadrupolar focusing strength with increasing particle oscillation amplitude. This results in the dynamic beta effect being amplitude-dependent with large amplitude particles being relatively unaffected by the dynamic beta effect. This implies that the deleterious effects of reduced single particle lifetime that are associated with a lower $\beta(IP)$ are not present with dynamic beta. In other words, the dynamic beta effect is materially different from using a lattice with

a lower $\beta(IP)$.

The amplitude dependence of the dynamic beta effect was explored with a simple 1-dimensional particle tracking program which used linear arcs and the full nonlinear beam-beam kick[4]. Particles were seeded at different amplitudes and tracked for 300 turns. For a single particle the resulting motion in phase space was fitted to an ellipse and a value for β extracted. Figure 5 shows the dependence of β/β_0 on oscillation amplitude A for both the horizontal and vertical planes under the conditions $Q = 0.526$, $\sigma_y/\sigma_x = 0.02$, and, in the linear region, $\xi = 0.3$. As can be seen, β is insensitive to changes in amplitude for the particles with oscillation amplitudes below about 2σ . This implies that the amplitude dependent effects on the luminosity are small. In the tails of the beam, where $A_x \gtrsim 10\sigma_x$ or $A_y \gtrsim 50\sigma_y$, the dynamic beta effect is seen to be small.

References

- [1] Alexander Chao, "Beam-Beam Instability," from Physics of High Energy Particle Accelerators, p. 201, AIP Conference Proceedings No. 127, Melvin Month et. al, eds. (1985).
- [2] Matthew Sands, *The Physics of Electron Storage Rings, An Introduction*, SLAC-121 Addendum.
- [3] Stephen Milton, "Calculation of How the Ratio β^*/σ_z Affects the Maximum Luminosity Obtainable: The HourGlass Effect," Cornell CBN 89-1 (1989).
- [4] David Sagan, "The Dynamic Beta Effect in CESR," Cornell internal note CBN 94-06 (1994).
- [5] J. Seeman, "Observations of the Beam-Beam Interaction," Proc. Joint US-CERN school on Part. Acc., Nonlinear Dynamics Aspects of Part. Acc, Sardinia, 121, (1985).

LIFETIME AND TAIL SIMULATIONS FOR BEAM-BEAM EFFECTS IN PEP-II B FACTORY*

D. N. Shatilov^a and A. A. Zholents^b

^{a)} Budker Institute of Nuclear Physics, 630090 Novosibirsk 90, Russia

^{b)} Center for Beam Physics, Accelerator and Fusion Research Division, Lawrence Berkeley Laboratory,
University of California, Berkeley, CA 94720

Abstract

A fast tracking technique for doing beam tail simulations has been applied to a study of beam-beam effects in the SLAC/LBL/LLNL PEP-II B Factory. In particular, the dependence of beam lifetime and particle density distribution due to vacuum pressure, damping times, machine nonlinearity and parasitic crossings has been analyzed. Effects of accidental orbit separation and dispersion function at the interaction point (IP) have also been considered.

I. BEAM PARAMETERS AND MODEL

Beam and machine parameters for PEP-II B factory are described elsewhere [1]. For the sake of completeness, we reproduce in the Table I all parameters we need for a discussion of beam-beam effects. Our notation for most of the parameters has a standard and obvious meaning. Only a few definitions need explanation. In the PEP-II B factory, electron and positron bunches collide head-on at the IP. After the IP, beam orbits are magnetically separated in the horizontal plane. However, before entering its own vacuum pipe, each electron bunch and each positron bunch experiences four more interactions with other bunches of the opposite beam. We refer to these interactions as parasitic crossings (PC's). A parameter d_{sep} defines orbit separation at the first PC. Orbit separation at the remaining PCs is much larger and, consequently, the effect of beam-beam interactions at these PC is negligible. We will ignore them in our model and will consider only the first parasitic crossing on either side of the IP. Parameters $\Delta\nu_x$ and $\Delta\nu_y$ define horizontal and vertical betatron phase advance, in units of the betatron tune, from the main IP to the first PC.

A goal of our study was understanding the mechanisms leading to a beam lifetime limitation in electron-positron colliders. According to experimental observations [2], these mechanisms are fairly insensitive to particle density distribution in the beam core. Thus, a weak-strong model of beam-beam effects seems adequate to our task.

All our simulations were carried out with the beam-beam program LIFETRAC [3]. This program allows the following physics to be included in the simulation:

1. Beam-beam kick.
2. One turn, six-dimensional linear map.
3. Chromaticity up to the third order:

$$\nu_x = \nu_{0x} + C_x \delta + C_{xx} \delta^2 + C_{xxx} \delta^3$$

*Work supported by DOE under Contract DE-AC03-76SF00098 and by Budker INP of the Russian Academy of Science.

Table I
Beam parameters

	weak beam (e^+)	strong beam (e^-)
E [GeV]	3.1	9.0 ^{a)}
ν_{0x}, ν_{0y}	34.57, 35.64	34.57, 35.64 ^{a)}
ν_s	0.037	0.052 ^{a)}
ξ_{0x}, ξ_{0y}	0.03, 0.03	0.03, 0.03 ^{a)}
$\tau_{x,y}$ [turns]	7200, 7200	5014, 5014 ^{a)}
τ_z [turns]	3600	2507 ^{a)}
$\sigma_{\Delta p/p}$	0.80×10^{-3}	0.62×10^{-3} ^{a)}
σ_z [cm]	1.0	1.0
ε_x [m×rad]	6.4×10^{-8}	4.8×10^{-8} ^{a)}
ε_y [m×rad]	1.9×10^{-9}	1.4×10^{-9} ^{a)}
Main crossing		
$\beta_{x,y}^*$ [m]	0.50, 0.015	0.667, 0.02
$D_{x,y}^*$ [m]	0, 0	0, 0 ^{a)}
$\sigma_{0x}^*, \sigma_{0y}^*$ [μ m]	177, 5.3 ^{a)}	177, 5.3
Parasitic crossing		
d_{sep} [mm]	3.5	
σ_x, σ_y [μ m]	284, 223 ^{a)}	243, 167
$\Delta\nu_x, \Delta\nu_y$	0.143, 0.246	0.117, 0.245 ^{a)}

^{a)} These parameters do not enter the weak-strong simulation

$$\nu_y = \nu_{0y} + C_y \delta + C_{yy} \delta^2 + C_{yyy} \delta^3.$$

Here $\delta = \Delta p/p$ and $C_x, C_{xx}, C_{xxx}, C_y, C_{yy}, C_{yyy}$ are parameters of chromaticity.

4. Machine nonlinearity in the form of an amplitude-dependent betatron tune:

$$\begin{aligned} \nu_x &= \nu_{0x} + \varepsilon_x a_{xx} A_x^2 + \varepsilon_y a_{xy} A_y^2 \\ \nu_y &= \nu_{0y} + \varepsilon_x a_{xy} A_x^2 + \varepsilon_y a_{yy} A_y^2. \end{aligned}$$

Here A_x and A_y are normalized amplitudes and a_{xx}, a_{xy} and a_{yy} are coefficients.

5. Elastic scattering on nuclei of the residual gas.
6. Parasitic crossings.
7. Dispersion functions at the IP and at the PC.
8. Slicing of a bunch with an arbitrary number of slices (typically, we use 5 pancake-like slices).
9. Orbit separation at the IP.

II. SIMULATION TECHNIQUE

The fast tracking technique developed in LIFETRAC [3] emerged from a concept proposed earlier in [4] and realized later

in [5]. It allows a determination of beam lifetime on a level of 10 hours with a statistical confidence of a few percent by tracking only about 10^7 particle-turns. Along with the lifetime, this technique is able to provide information on the particle density distribution in the beam tails.

The idea of the algorithm is based on the presence of a random component (such as quantum fluctuation noise) in the particle motion [4]. It turns out that a particle's trajectory in phase space depends only on current coordinates and momenta (and noise). A history of the particle's motion is irrelevant for its future trajectory. After accumulating rich statistics of a particle's motion in a certain region of phase space, one can ignore the exact knowledge of a particle trajectory in this region and replace it by statistical information. This information could contain particle coordinates and momenta recorded at the moment when the particle leaves the region. Then, each time the particle's trajectory goes inside that region, one can interrupt tracking and begin a new trajectory from one of the pre-recorded points. By this technique, we force actual tracking to go on only in a region with poor statistics rather than tediously tracking in a region with well-defined statistics.

This algorithm was recently checked against 'brute-force' calculations performed with the program TRS [6] and we found excellent agreement in the results [7]. It is worth mentioning that the 'brute-force' calculations took 818 minutes of CPU time on a Cray-2S, while LIFETRAC reached the same accuracy in the tail distribution in 55 minutes of CPU time on a VAX-6610.

III. RESULTS

A result of the simulation of beam-beam effects in PEP-II for the nominal conditions without PC's is presented in Figure 1a. This plot (and other similar plots) shows particle distribution contours in amplitude space. The first contour corresponds to a particle density a factor \sqrt{e} below the peak and all the following contours correspond to successive reduction with a factor of e . Amplitudes A_x, A_y are normalized amplitudes, i.e. $A_x = 1$ corresponds to a physical amplitude of $1\sigma_{0x}$ and $A_y = 1$ corresponds to a physical amplitude of $1\sigma_{0y}$.

The particle density distribution is obviously perturbed by nonlinear resonances $\ell\nu_x + m\nu_y + n\nu_s = k$. The identified resonances are shown by arrows. On top of each arrow we draw numbers, which correspond to the ℓ, m, n resonance identification. Particularly strong is the resonance $14\nu_x = k$. It is partly overlapped with some other resonances, which we were not able to identify.

For the lifetime determination we assumed a limiting aperture of $A_x = 10$ and $A_y = 25$. With that aperture we were not able to determine the lifetime, because it was very long. We interrupted calculations when the lifetime exceeded 8 years. We also did not find any blow-up of the beam core.

A. Parasitic Crossings

Adding PC's did not affect beam lifetime. It was still very long to be determined. But PC's did affect the beam core (we found a 26% increase in the vertical beam size) and particle density distribution (see Figure 1b). The main factors giving rise to the effect of the PC's are strong resonances: $6\nu_y + 3\nu_s = k$ and $-4\nu_x + 2\nu_y = k$. At the same time, we found that resonances

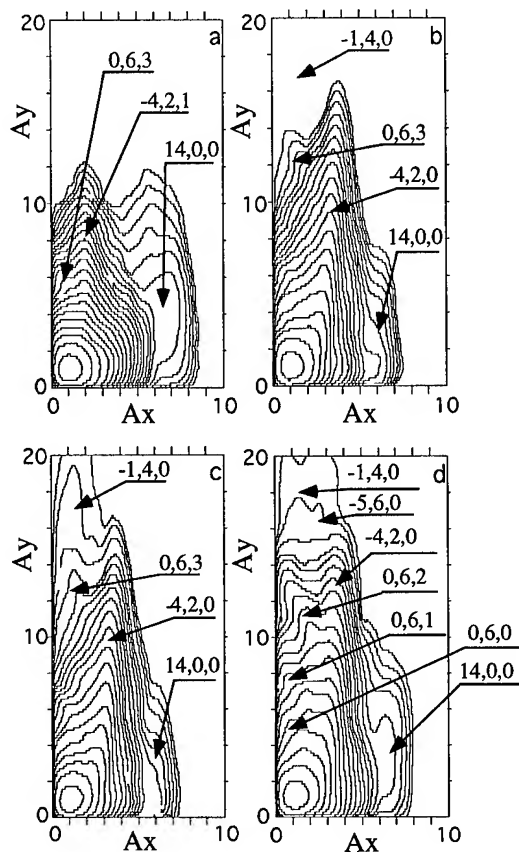


Figure 1. Particle distribution contours: a) nominal case without parasitic crossings; b) the same as a) plus PC; c) the same as b) plus elastic scattering; d) the same as c), but with $\xi_{0x} = \xi_{0y} = 0.05$ and $a_{xx} = -200 \text{ m}^{-1}$.

$-4\nu_x + 2\nu_y + \nu_s = k$ and $14\nu_x = k$ became weaker. This resonance restructuring is a result of a new beam footprint in tune space in the case with PC's.

B. Vacuum

Aside from beam-beam effects, the leading mechanism defining the beam lifetime in PEP-II on a level of 23 hours is elastic scattering on nuclei of the residual gas [1]. Since the beam-beam lifetime defined above is much larger, one might think that the beam-beam interaction will have no noticeable effect on the beam lifetime, but this is not right. The interference of beam-beam effects and elastic scattering could be significant. Imagine that the beam-beam interaction creates some resonance islands in phase space close to the aperture limit. Then, particles scattered inside these islands from the beam core, could be trapped there. As a result, the growing population of particles in the tails will decrease beam lifetime. This is exactly what we found when we included elastic scattering [3] in our simulation for PEP-II. The lifetime dropped from 22.9 hours (vacuum lifetime) to 16.7 hours. We attribute this to the elastic scattering into the resonance $-\nu_x + 4\nu_y = k$, which perturbs the particle density distribution at large vertical amplitudes (compare Figure 1c with Figure 1b).

Table II
Orbit separation

$\Delta x/\sigma_{0x}^*$	$\Delta y/\sigma_{0y}^*$	$\sqrt{x^2}/\sigma_{0x}^*$	$\sqrt{y^2}/\sigma_{0y}^*$	Lifetime,[h]
0	0	1.10	1.46	18.9
0.2	0	1.07	1.71	18.4
0.4	0	1.12	1.93	18.4
0	0.2	1.07	1.99	19.9
0	0.4	1.07	2.57	18.6

C. Damping Time

We compared beam-beam effects for two damping times. First we used a damping time of 5400 turns as it is in [1]; second we took a damping time of 7200 turns, as proposed in [8]. In Figure 2, we show the dependence of the lifetime versus beam-beam parameters for our two cases. The difference between two cases is less than the statistical error expected in the calculations.

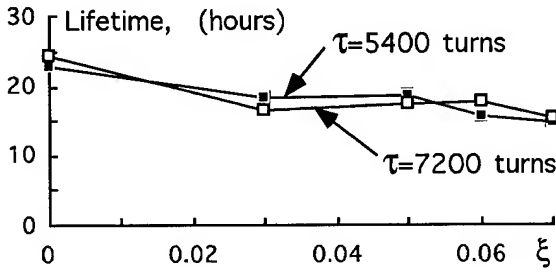


Figure 2. Beam lifetime versus $\xi = \xi_{0x} = \xi_{0y}$ for two damping times. Arrows indicate damping time.

D. Machine Imperfections

In order to be more sensitive to the beam-beam effects, we did all the rest of our simulations with $\xi_{0x} = \xi_{0y} = 0.05$.

Chromaticity. We did not find any significant effect of chromaticity when we varied C_{xx}, C_{yy} in the range of ± 500 and C_{xxx}, C_{yyy} in the range of $\pm 10^4$, which are larger values than we anticipate for the machine.

Tune shifts with amplitude. In our notation, typical dependence of betatron tunes from amplitudes for PEP-II corresponds to $a_{xx}=a_{yy}\sim -200\text{m}^{-1}$ and $a_{xy}\sim -1000\text{m}^{-1}$ [9]. Simulations with these coefficients gave qualitatively similar results to those with zero nonlinearity. By adjusting a_{xx} with $a_{yy}=a_{xy}=0$ we could slightly increase the strength of the resonance $14\nu_x = k$ at $a_{xx}=-200\text{m}^{-1}$ or significantly reduce it at $a_{xx}=400\text{m}^{-1}$ (compare Figure 1d and Figure 3a), but both the beam lifetime and the beam core remained fairly insensitive to this change. For the rest of the simulations we used $a_{xx}=-200\text{m}^{-1}$.

Orbit separation at the IP. Table II contain all results. One can see that only the vertical beam size was sensitive to the orbit separation $\Delta x, \Delta y$.

Dispersion at the IP. Simulations with non-zero horizontal and vertical dispersions at the IP showed that the lifetime began to drop below 10 hours when $D_x^* \geq 4\text{ cm}$ or $D_y^* \geq 0.5\text{ cm}$. An

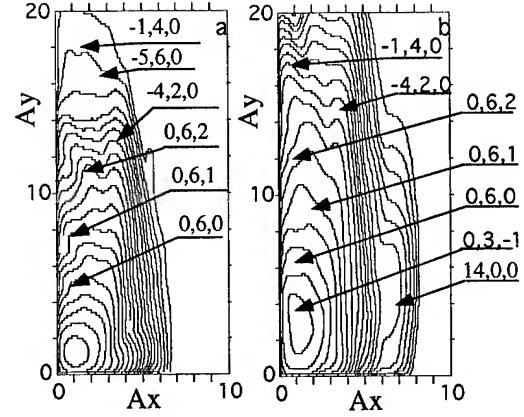


Figure 3. Particle distribution contours: a) the same as Figure 1d, but with $a_{xx}=400\text{ m}^{-1}$; b) the same as Figure 1d plus $D_y^* = 0.53\text{ cm}$.

example with $D_y^* = 0.53\text{ cm}$ is shown in the Figure 3b. Moreover, we found that a dispersion $D_x^* = 2.2\text{ cm}$ already reduced the lifetime below 10 hours when combined with an accidental orbit separation of $\Delta x/\sigma_{0x}^* = 0.4$.

IV. CONCLUSION

Our study demonstrated that beam-beam effects should not affect the performance of the PEP-II B factory if $\xi_{0x} = \xi_{0y} = 0.03$. We did not find significant reduction in the beam lifetime even for larger beam-beam parameter, but we did see in many occasions a large increase in the vertical beam size.

Acknowledgment. We are grateful to M. Furman and M. Zisman for many useful discussions.

References

- [1] PEP-II Design Report, SLAC-Report-418, 1993.
- [2] A. Temnykh, Third Advance ICFA Beam Dynamics Workshop, INP, Novosibirsk, 1989, p.5.
- [3] D.Shatilov, Preprint BINP 92-79, Novosibirsk, 1992, (in russian), unpublished.
- [4] J. Irwin, ref.2, p.123.
- [5] T. Chen et al., Phys. Rev. E49, 1994, p.2323.
- [6] J. Tennyson, unpublished code 'TRS', 1989.
- [7] M. Furman et al., CBP Note-59 (1995).
- [8] J. Heim et al., Wiggler Insertion of the PEP-II B Factory LER, these proceedings.
- [9] E. Forest et al., EPAC 1994, London, 1994, p.1033.

GAMMA RAY SOURCES BASED ON RESONANT BACKSCATTERING OF LASER BEAMS WITH RELATIVISTIC HEAVY ION BEAMS*

†E.G.Bessonov and *Kwang-Je Kim

†*Lebedev Phys. Inst. of the Russian Academy of Sciences, Moscow, Russia.*

**Lawrence Berkeley Laboratory, Berkeley, CA 94720 USA*

Abstract

Resonant backscattering of high-power laser beam with non-fully stripped, ultra-relativistic ion beams in storage rings is studied as a source for γ -ray beams for elementary particle physics experiments. The laser frequency is chosen to be resonant with one of the transition frequencies of the moving ions, and the bandwidth is chosen to cover the full Doppler broadening of the ions in the beam. Due to the resonance, the scattering cross section is enhanced by a large factor compared to the Thomson cross section, of the order 10^8 for some examples considered here. The performance of the LHC as a possible γ -generator or a γ - γ collider is estimated. We study the case where hydrogen-like Pb ions with 2.8 TeV per nucleon are scattered by a train of 1100 Å, 20 mJ laser pulses with the same pulse time format as the ion beam. A free electron laser can be designed satisfying the requirements. It is estimated that γ -rays of maximum quantum energy of 0.4 GeV at an average rate of $0.67 \cdot 10^{18}$ are generated in this scheme. The luminosity of the corresponding γ - γ collider will be about $0.9 \cdot 10^{33} \text{ cm}^{-2} \text{ s}^{-1}$

I. INTRODUCTION

Compared to the case of Thomson scattering on free electrons, the scattering cross section of laser photons on bound electrons, when the photon energy is at resonance with one of the transition energies of non-fully stripped ions, is larger by many orders of magnitudes up to a factor $\lambda/4\pi r_e^2 \sim 10^{15}$ where λ is the laser wavelength and r_e is the classical electron radius [1-4]. Radiative cooling of ion beams has been recently proposed based on this observation [5]. With the large hadron storage rings currently being proposed or under construction, which can store high-Z ions such as Pb with an energy of several TeV per nucleon, the mechanism could also be the basis for a copious source of γ rays. As an example, we study the performance of the LHC [6] as a γ -ion or γ - γ collider when it operates as a collider for Pb ions at CM energy of 1120 TeV. The transition energy is about 60 keV, which corresponds to a laser wavelength of about 1100 Å in the laboratory frame. The laser intensity is chosen to be the saturation intensity. The Rayleigh length is chosen to be about the rms pulse length of the ion beam. It is found that several thousands γ -photons are generated per ion. With a distance about 15 cm between the ion- γ conversion point and the interaction point, which is sufficient to deflect the ion beam by two sigmas of the beam spot size, we estimate that the luminosity of

a γ - γ collider based on the resonant backscattering at the LHC will be about $0.9 \cdot 10^{33}$

II. SPONTANEOUS INCOHERENT γ -RAY SOURCES

Let a laser beam is directed against and scattered by an ion beam. Let $\hbar\omega_0$ be the transition energy in the ion's rest frame between two electronic states 1 and 2, and $\hbar\omega_0^L$ and $\hbar\omega_0^s$ be the corresponding energies of the incoming laser photons and the scattered photons in the laboratory frame, respectively. These quantities are related by

$$\begin{aligned}\hbar\omega_0^L &= \frac{\hbar\omega_0}{\gamma(1 - \beta \cos \psi)}, \\ \hbar\omega_0^s &= \frac{\hbar\omega_0}{\gamma(1 - \beta \cos \theta)},\end{aligned}\quad (1)$$

where $\gamma = E/Mc^2 = 1/\sqrt{1 - \beta^2}$, E is the ion energy, M its mass $\beta = v/c$, v the ion velocity, c the speed of light ψ the angle between the initial photon velocity and ion velocity, and θ the angle between final photon velocity and ion velocity. In this paper, we restrict to the case $\psi \simeq \pi$, $\beta \simeq 1$, $\gamma \gg 1$, in which case the above equations become

$$\hbar\omega_0^L \simeq \frac{\hbar\omega_0}{2\gamma}, \quad \hbar\omega_0^s \simeq \frac{2\gamma\hbar\omega_0}{1 + (\gamma\theta)^2}. \quad (2)$$

The frequency of the incoming laser photons and the scattered photons in the general case will be written as ω and ω^s respectively. Since we are considering the case near resonance in this paper, we have $\omega \simeq \omega_0^L$ and $\omega^s \simeq \omega_0^s$.

The scattering cross section of laser photons by an ion is given by [7]

$$\sigma_\omega = \frac{2\pi r_e c f \Gamma}{(\gamma\omega(1 - \beta \cos \psi) - \omega_0)^2 + \Gamma^2}, \quad (3)$$

where r_e is the classical electron radius, f the oscillator strength, Γ the spontaneous linewidth given by $\Gamma = \omega_0^2 r_e c f g_1 / c g_2$, g_1 and g_2 are respectively the degeneracy factors of the state 1 (ground state) and state 2 (excited state) between which the transition occurs, and $\beta_z = \beta \cos \psi \simeq 1$.

The maximum cross-section at exact resonance $\omega = \omega_0^L$ is

$$\sigma_{max} = \frac{g_2 \lambda_0^2}{2\pi g_1}, \quad (4)$$

where $\lambda_0 = 2\pi c/\omega_0$ is the resonance wavelength corresponding to ω_0 . Note that this is larger than the Thomson cross section by a factor of about $(\lambda_0/r_e)^2$, which is a very large factor.

*This work was supported by the Director, Office of Energy Research, Office of Basic Energy Sciences, of the U.S. Department of Energy under Contract No. DE-AC03-76SF00098.

When the ion beam has an angular spread, $\Delta\psi$, and energy spread, $\Delta\gamma$, then, for effective interaction of all ions with the photon beam, the bandwidth $\Delta\omega$ of the incoming laser should satisfy

$$\frac{\Delta\omega}{\omega} \simeq \frac{(\Delta\psi)^2}{4} + \frac{\Delta\gamma}{\gamma}. \quad (5)$$

This follows from eq(1). The bandwidth $\Delta\omega$ given by eq(5) is usually much larger than the width of the transition frequency in the laboratory frame, i.e., $\Delta\omega \gg \Gamma/2\gamma$. Assuming for simplicity that the spectral intensity of the laser beam I_ω (power per unit area per unit frequency) is distributed uniformly in the frequency range $\Delta\omega$ so that the $I_\omega = I/\Delta\omega$, where I is the intensity (power per unit area), then the average cross-section of the photon scattering by ions is

$$\bar{\sigma} = \frac{1}{I} \int \sigma_\omega I_\omega d\omega = \pi r_e f \lambda_0 \frac{\omega}{\Delta\omega}. \quad (6)$$

The enhancement of the resonant cross section over the Thomson cross section for a broad band laser is about a factor $(\lambda_0/r_e)(\omega/\Delta\omega)$, which is smaller than that in the case of exact resonance, but is still very large. It is about 10^8 in our example later.

The number of scattered photons per ion is given by

$$\Delta n_\gamma = 2 \frac{\bar{\sigma}}{(1+D)} \left[\frac{I}{\hbar\omega} \right] \left[\frac{l_{eff}}{c} \right]. \quad (7)$$

The factor of 2 is due to the fact that relativistic particle and laser photons are making a head-on collision. The factor $(1+D)$ in the denominator is due to the saturation effect, i.e., the fact that the level populations reach an equilibrium via competition between the absorption, stimulated emission and the spontaneous emission[6]. The quantity $D = I/I_{sat}$ is the saturation parameter, $I_{sat} = (\pi c g_1 \hbar \omega_0 / \gamma^2 g_2 \lambda_0^3) (\Delta\omega/\omega)$ and l_{eff} is the effective interaction length of the laser and ion beams, which is assumed to be much longer than the spontaneous decay length $c\tau_{spont} = c\gamma/2\Gamma$ in the laboratory frame. If there are N_i number of ions in the pulse, the total number of γ -ray photons generated per ion pulse is given by $N_\gamma = \Delta n_\gamma N_i$.

Let us now consider the transition between the first excited state (principal quantum number $n = 2$) to the ground state ($n = 1$) to the ground state of a hydrogen-like ion with atomic number Z . In this case, we have $f = 0.42$, $g_1 = 1$, $g_2 = 2^2 = 4$, $\hbar\omega_0 = 3\alpha^2 m_e c^2 Z^2/8 \simeq 10.19 Z^2$ [eV], $\lambda_0 \simeq 1.22 \cdot 10^{-5}/Z^2$ [cm], $c\tau_{spont} \simeq 63.4\gamma/Z^4$ [cm], $I_{sat} = 21.2(Z^8/\gamma^2)(\Delta\omega/\omega)$ [MW/cm²], and $\Delta n_\gamma = 7.85 \cdot 10^{-3} Z^4 l_{eff} [\text{cm}] / \gamma(1+D)$.

The scattered radiation will be polarized if we will use polarized initial laser radiation. It will be possible to change the kind of polarization by changing the kind of initial polarization.

The spectral distribution of the scattered power is of the form

$$\bar{P}_\omega^s = \frac{d\bar{P}^s}{d\omega^s} = \frac{3\bar{P}^s}{\omega_{max}^s} \xi(1 - 2\xi + 2\xi^2), \quad (8)$$

where $0 \leq \xi = \omega^s/\omega_{max}^s \leq 1$, $\omega_{max}^s \simeq 2\gamma\omega_0$ is the maximum energy of the scattered photons.

III. A γ - γ and γ -ION COLLIDER BASED ON THE LHC

Consider now γ -ray generation in straight sections of high energy ion storage ring. A counter propagating laser beam is focused with a waist close to the ion beam waist. Since the γ -ray production rate, is proportional to $D/(1+D)$, as can be seen from eq(7), the laser intensity I is optimized at $I \simeq I_{sat}$. When the ion beam emittance is, as is usually the case, much smaller than the radiation emittance, $\simeq \lambda/4\pi$, the effective interaction length l_{eff} is about twice the Rayleigh length z_R of the laser beam. For most efficient interaction, we choose z_R to be about the rms bunch length of the ion beam σ_{iz} . We also choose the length of the laser pulse to be about $2\sigma_{iz}$. Given these parameters, we obtain the peak laser power by $P_L = (z_R \lambda/2)I$ and the laser pulse energy by $W_L \simeq (2\sigma_{iz})P_L$.

The relevant parameters for the LHC operating as a collider for hydrogen-like Pb ions are[6]; $Z = 82$, $\gamma \simeq 3000$, $N_i = 9.4 \cdot 10^7$, bunch separation 135 ns, the rms beam transverse size $\sigma_{ix} = 1.2 \cdot 10^{-5}$ m, $\sigma_{iz} = 7.5$ cm, $\Delta\gamma/\gamma = 2 \cdot 10^{-4}$.

Following the above procedure, we find the following laser parameters: $\lambda = 1100$ Å, the pulse energy $W_L = 20$ mJ, pulse length $\simeq 500$ ps, peak power $P_L = 40$ MW, average power $\bar{P}_L = 150$ kW, and the required bandwidth $\Delta\omega/\omega \simeq 2 \cdot 10^{-4}$. A free electron laser can be designed that can meet these requirements. The only extension of the current technology would be in the mirror reflectivity at 1100 Å, but the problem could be solved by grazing incident cavity design, etc.

With these parameters, the maximum photon energy of the γ -rays is 0.4 GeV, Δn_γ is $0.9 \cdot 10^3$, and that per pulse is $0.85 \cdot 10^{11}$, and time averaged rate is $0.67 \cdot 10^{18}$ photons per second. This is indeed a very copious source of γ -rays.

A high energy ion-ion collider can therefore be converted to a γ - γ or γ -ion collider with the photon energy in the GeV range, just as a high energy electron linear collider in TeV range can be converted to a TeV γ - γ collider[8]. Assuming 1T magnetic field, a distance $b \simeq 14$ cm is required to deflect the ion beams by a distance of twice the rms spotsize. This will be the distance between the conversion point to the γ - γ interaction point. Due to the opening angle $\simeq 1/\gamma$ of the γ -rays, the cross sectional area at the interaction point is $S_\gamma \simeq \pi(b/\gamma)^2$. The luminosities $L_{\gamma\gamma}$, and $L_{\gamma i}$ of γ - γ , and γ -ion collisions are given by:

$$L_{\gamma\gamma} = \frac{N_\gamma^2 f}{S_\gamma}, \quad L_{\gamma i} = \frac{N_i N_\gamma f}{S_\gamma}, \quad (9)$$

where f is the collision frequency. For the above example, we find $L_{\gamma\gamma} \simeq 0.9 \cdot 10^{33}$ and $L_{\gamma i} \simeq 0.93 \cdot 10^{30}$.

IV. CONCLUSION

In this paper, we have studied the performance of highly relativistic ion storage rings as a γ - γ collider, when laser photons are converted into γ photons through resonant backscattering process. The perturbation on ion beam in such a process extremely gentle, and will not affect the ion beam dynamics. Nevertheless, we have seen that it gives rise to a very intense γ -ray source.

In this paper, we have only considered the example of hydrogen-like Pb ions at the LHC. Similar calculations can clearly be repeated for other ions and also for other machines

such as RHIC. Lower energy machines or lower Z ions may be interesting as high intensity x-ray generator. We will report on these calculations in a future publication.

References

- [1] K.A.Ispirian and A.T.Margarian, Phys. Lett. 44A (5) (1973), 377
- [2] N.G.Basov, A.N.Oraevsky, B.N.Chichkov, Sov. Phys. JETP, Vol.62(1), (1985), 37.
- [3] L.D.Miller, Optics communications, 30 (1979), 87.
- [4] G.C.Baldvin and N.J.DiCiacomo, IEEE Transactions on Nucl. Sci., Vol. NS-30, No 2 (1983), 891.
- [5] E.G.Bessonov, Preprint FIRAS No 6, 1994;
E.G.Bessonov and Kwang-Je Kim, in preparation.
- [6] G. Brianti, Proceedings of PAC-93, pp 3917(1993).
- [7] See, for example, R.Loudon, The quantum theory of light (Clarendon Press, Oxford, 1973).
- [8] V. Telnov, Nucl. Instr. Meth., A 355, 3 (1995)

OBSERVATIONS OF THE EFFECTS OF THE BEAM-BEAM INTERACTION ON THE ORBITS OF STORED BEAMS IN CESR[§]

E. Young, Wilson Synchrotron Laboratory, Cornell University, Ithaca, NY 14853 USA

Luminosity in the Cornell Electron Storage Ring (CESR) depends critically on the degree of overlap of the counter-rotating beams at the interaction point (IP). However, due to the pretzel[†], this overlap is sensitive to changes in quadrupole and sextupole strengths. The beam-beam interaction (BBI) perturbs the closed orbits and depends on the transverse distance between the opposing beams as they pass each other. If a real time measurement of this small orbit change were possible, then this effect could be used to determine whether the bunches remain in collision while tuning CESR for high luminosity. Our purpose was to determine whether this would be possible with the present beam position detector system.

I. THE BEAM-BEAM INTERACTION FOR FLAT BEAMS

The vertical kick felt by a test particle due to the transverse electric field of a two-dimensional Gaussian charge distribution is given by the equation below. Complete derivations are available in the references [1], [2], [3], and [4].

$$\Delta y' = A \operatorname{Re} \left\{ w \left(\frac{\mu + i\rho v}{d} \right) - e^{-\left(\frac{\mu^2}{2} - \frac{v^2}{2} \right)} w \left(\frac{\rho\mu + iv}{d} \right) \right\} \quad (1)$$

where A , d , μ , v , and ρ are

$$A = -\frac{\sqrt{2\pi} N r_e}{\gamma \sqrt{(\sigma_x^2 - \sigma_y^2)}}, \quad d = \sqrt{2(1 - \rho^2)} \quad (2)$$

$$\mu = \frac{x}{\sigma_x}, \quad v = \frac{y}{\sigma_y}, \quad \rho = \frac{\sigma_y}{\sigma_x},$$

N is the number of particles in the distribution, σ_x and σ_y are the transverse sizes of the distribution, and x and y are the horizontal and vertical distances of the test particle from the center of the Gaussian charge distribution. $w(z)$ is the complex error function defined by the following equation.

$$w(z) = \exp \left\{ -z^2 \left(1 + \frac{2i}{\pi} \int_0^z \exp(u^2) du \right) \right\} \quad (3)$$

[§] Work supported by funding from the National Science Foundation.

[†] The pretzel in CESR is a closed orbit with kinks in the horizontal plane in order to insure that counter-rotating beams of electrons and positrons remain separated at parasitic crossing points. Thus, the beams are off axis horizontally through most of the magnets.

The complex error function must be evaluated numerically, and we have used a computer program [5] to do so based on the routines developed in reference [1]. Figure 1 shows the vertical beam-beam kick as a function vertical displacement for a beam aspect ratio of $\sigma_y/\sigma_x = 1/10$.

For fitting measured data to the theory a simpler expression for the kick would be convenient. We can expand the error function and the exponential in equation (1) about the origin and keep as many terms as necessary to obtain good agreement with equation (1). For small vertical displacements and assuming that the horizontal displacement is zero, the linear approximation of equation (1) is

$$\Delta y' = -\frac{2Nr_e}{\gamma(\sigma_x + \sigma_y)\sigma_y} y \quad (4)$$

To 3rd order the approximation is

$$\Delta y' = A \left\{ \left[\frac{2(1-\rho)}{\sqrt{\pi}d} - \frac{2(1-\rho)^2}{\sqrt{\pi}d^3} \mu^2 \right] v + \frac{2(-1+3\rho^2-2\rho^3)}{3\sqrt{\pi}d^3} v^3 \right\} \quad (5)$$

where A , d , ρ , μ , and v are the same as in equation (2). Equation (4) and the first term of equation (5) are the same for $\mu = 0$. These approximations are also plotted in figure 1.

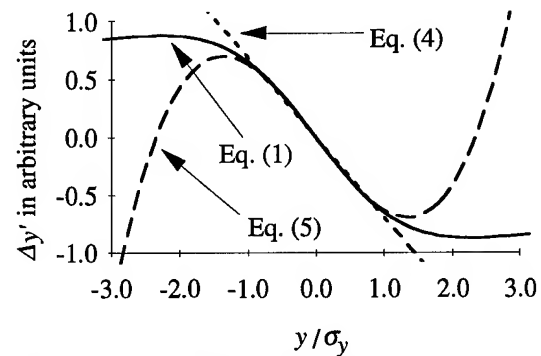


Figure 1: The vertical beam-beam kick from a flat, Gaussian electron beam as a function of vertical distance from the center of the beam.

As is discussed in the references [2], [6], and [7], if the current of one bunch is significantly smaller than that of the other bunch (the weak-strong approximation), the strong beam remains undisturbed by the presence of the weak beam, while the weak beam can be considered a group of non-interacting particles. The disturbed orbit of the weak beam can then be obtained by substituting the kick from equation (1) in the usual formula for a closed orbit distortion (using the N , σ_x , and σ_y of the strong beam).

The above equations apply for the weak-strong case, i.e. one beam has a much smaller current than the other so that its orbit is perturbed, but the strong beam is essentially unperturbed. This is a special case; normally when tuning luminosity in CESR, the bunches have nearly equal currents, so the beams feel kicks of approximately equal strengths, and both beams' orbits and transverse sizes are affected. This will complicate any attempt to measure the closed orbit distortion due to the beam-beam interaction as a function of the overlap at the IP during luminosity conditions and fit that measurement to the theory. In fact, the strong-strong case is usually approached via simulations. However, the qualitative features of the orbit distortion due to the beam-beam interaction in the strong-strong case are the same as in the weak-strong case, i.e. as the displacement between the beams increases, the effect of the beam-beam force increases to a maximum then decreases.

II. MEASURING THE EFFECT OF THE BEAM-BEAM INTERACTION ON CLOSED ORBITS

The measurement of the orbit distortion due to the beam-beam interaction was performed in a lattice which had a vertical tune of $Q_y = 9.6298$ and a vertical beta-function at the IP of $\beta_y^* = 0.0172$ meters. Normally, CESR operates with nine bunches each of electrons and positrons, but for these experiments we filled two positron bunches and one electron bunch; the positron bunches will hereafter be referred to as the colliding and reference bunches. We then brought the beams into collision and measured the difference between the orbits of the positron bunches at 10 different detectors around CESR. Table 1 shows the beam parameters during these measurements. The BBI's at parasitic crossing points were negligible, so the only difference between the orbits of the two positron beams should be due to the BBI at the IP.

Table 1: Beam parameters during the experiments.[‡]

Data set	I ₁₋	I ₁₊	I ₅₊	σ_e	σ_{e+}
#1	7.18	7.33	7.59	15.4	11.7
#2a	6.84	7.51	7.73	14.3	9.7
#2b	6.30	3.40	5.64	7.4	9.8

Since the size of the orbit distortion is different at each detector, we should not average the measured orbit differences directly. Doing so would weight the data from each detector by the beta-function at that detector. Instead we will use Equation (6) to normalize the measured orbit distortion at each detector to β_y^* , then average them. The three sets of normalized, averaged data are plotted in Figures 2,3, and 4.

[‡] The current, I, is in mA, and the vertical beam size, σ , is in μm . The subscripts refer to the bunch number and species. The currents are averages over the measurements. The beam sizes are also averages over the measurements, and for the positrons, an average of the two bunches as well.

$$\Delta y(\text{IP}) = \Delta y(\text{arc}) \sqrt{\frac{\beta_y^*}{\beta_y^{\text{arc}}}} \quad (6)$$

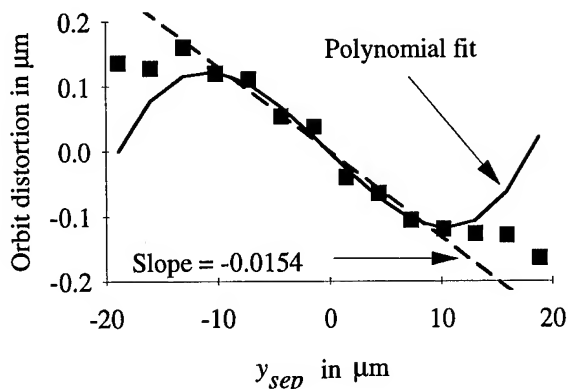


Figure 2: Data set #2b (unequal bunch currents).

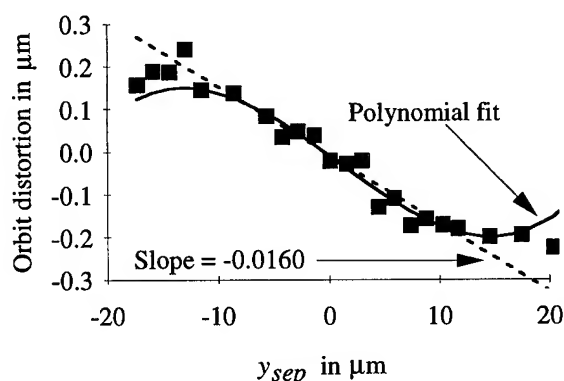


Figure 3: Data set #2a (equal bunch currents).

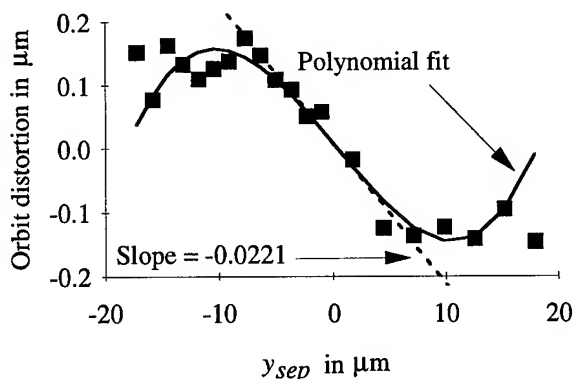


Figure 4: Data set #1 (equal bunch currents).

To vary the vertical separation at the IP we used two electrostatic separators located on the opposite side of the ring from the IP. Ideally, the vertical betatron phase between these separators is π creating a closed vertical bump at the parasitic crossing point opposite the IP and no vertical separation at the IP; however, coupling plus the presence of the pretzel[†] may create a vertical separation at the IP even if the bump is closed. Changing the phase advance uncloses the

bump creating a vertical ripple which changes the vertical separation at the IP. A "knob" in the control room controls a combination of quadrupoles such that we can change the phase advance between these separators without disturbing the rest of the machine. Before attempting to measure the effect of the BBI, we measured the change in the orbit at several points as we varied the phase advance, and calculate the corresponding change in the displacement of the orbit at the IP. To measure the effect of the BBI, we varied the vertical separation at the IP over $35 \mu\text{m}$ or about $4\sigma_y$.

III. DATA ANALYSIS

To find the phase advance which corresponded to $y_{sep} = 0$, we used the fact that $y_{sep} = 0$ occurs at the inflection point of Equations (1) and (5). Using data set #2b, we fit a cubic polynomial to the data versus $-\sigma_y < y_{sep} < \sigma_y$ with an arbitrary zero then found the inflection point of that fit. This point was set to $y_{sep} = 0$. When data sets #2a and #1 were treated in the same way, their inflection points corresponded to the same setting for the phase advance within the errors of the fit. The coefficients of the fit were scaled accordingly, and are listed in Table 2. The slope of the fitted line and m_1 of the fitted polynomial agree with each other within the limit of the errors of the fits in all cases. As a further check, we compared the ratio m_1/m_3 of the polynomial fit to that predicted by equation (5); they agreed within the limits of error.

Table 2: Coefficients of the fits shown in figures (2)-(4).

Data set	Fit to a line	Fit to a cubic polynomial	
	$m_1 (x 10^{-3})$	$m_1 (x 10^{-3})$	$m_3 (x 10^{-5})$
#1	$-(1.54 \pm 0.17)$	$-(1.70 \pm 0.19)$	3.5 ± 1.4
#2a	$-(1.60 \pm 0.10)$	$-(1.88 \pm 0.17)$	5.0 ± 1.5
#2b	$-(2.21 \pm 0.17)$	$-(2.18 \pm 0.10)$	7.6 ± 1.5

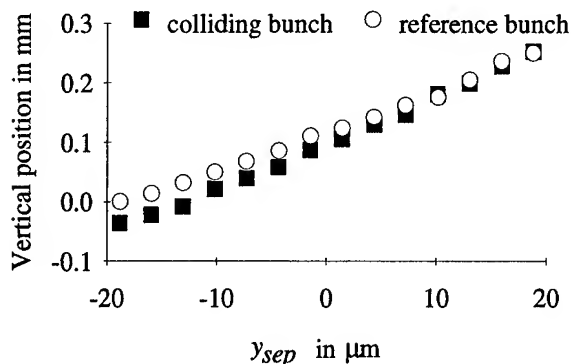


Figure 5: Vertical positions of the colliding and reference positron bunches at one detector from data set #2b.

Our results suggest that in theory this method could be used to determine whether the beams are in collision, however, these measurements were not done under normal

luminosity conditions. Under normal conditions there would not be an extra, non-colliding beam available to use as a reference, and having such an extra bunch during high energy physics runs is undesirable. Figure 5 shows the actual vertical positions of the colliding and reference positron bunches in data set #2b at one detector. Due to limitations of the present beam detector system, the effect of the beam-beam interaction is visible only in the difference between the two bunches. Fitting a cubic polynomial to the colliding bunch's position and finding the inflection point does not agree with the inflection point of the difference data. In fact, adding the quadratic and cubic terms does not significantly improve the "goodness" of the fit.

IV. CONCLUSION

The experiment was successful in that the effects of the beam-beam interaction on the closed orbit were observed and measured, and the measurements were consistent with the formulae in section II. However, the need for a reference bunch as demonstrated in figure 5 makes this method impractical for use during normal operating conditions. Two pairs of dedicated detectors on either side of the interaction point (to measure both the position and slope of the electron and positron orbits separately) might be a more reliable method of determining the overlap of the beams at the IP.

V. REFERENCES

- [1] Yuko Okamoto and Richard Talman, "Rational Approximation of the Complex Error Function and the Electric Field of a Two-Dimensional Gaussian Charge Distribution," CBN 80-13, (1980).
- [2] J. F. Scholnfeld, "The Effects of Beam-Beam Collisions on Storage Ring Performance - A Pedagogical Review," *Physics of High Energy Particle Accelerators*, AIP Conference Proceedings No. 105, American Institute of Physics: New York, 1983.
- [3] M. Bassetti and G. A. Erskine, "Closed expression for the electrical field of a two-dimensional Gaussian charge," CERN-ISR-TH/80-06, (1980).
- [4] K. Takayama, "A New Method for the Potential of a 3-Dimensional Nonuniform Charge Distribution," *Lettre Al Nuovo Cimento*, Vol. 34, No. 7, (1982).
- [5] The FORTRAN routines used to evaluate equation (1) were provided by David Rubin and David Sagan.
- [6] S. Milton, "The Beam-Beam Interaction in Electron Storage Rings: A Study of the Weak/Strong Case," Thesis, 1990.
- [7] J. T. Seeman, "Observations of the Beam-Beam Interaction," *Nonlinear Dynamics Aspects of Particle Accelerators*, Lecture Notes in Physics, No. 247, Springer-Verlag: Berlin, 1986.

CALCULATIONS ON DEPOLARIZATION IN HERA DUE TO BEAM-BEAM EFFECTS

M. Böge and T. Limberg, DESY

Abstract

Polarized beams will play an important role in the HERA physics program in the next years. First, the HERMES experiment will use longitudinally polarized electrons (or positrons) for collisions with a polarized gas target while at the detectors H1 and ZEUS these particles undergo collisions with the proton beam in a transversely polarized state. Later, spin rotators will be installed around the H1 and ZEUS experimental regions, allowing for collisions of longitudinally polarized electrons/positrons with the proton beam. Measurements show that for present HERA beam intensities the beam-beam effect does not reduce polarization by more than 5%. We present calculations using the spin tracking code SITROS which explore depolarization due to beam-beam effects towards higher beam intensities and luminosity.

I. INTRODUCTION

Beam collisions in HERA occur at the two interaction points of the experiments H1 and ZEUS. The transverse dimensions of electron¹ and proton beams have to be matched, otherwise the lifetime of the proton beam would suffer. Especially the naturally small vertical size of the electron beam has to be increased. For that purpose, vertical beam bumps are used to increase vertical dispersion at bending magnets and thus vertical emittance. About 10% of emittance coupling (ratio between vertical and horizontal emittance) is needed to match the height of the proton beam.

The strength of the beam-beam interaction is characterized by the vertical tune-shift parameter of the electron beam:

$$\xi_z = \frac{Nr_e}{\gamma} \cdot \frac{\beta_{zIP}}{2\pi\sigma_{zIP}(\sigma_{xIP} + \sigma_{zIP})}$$

where x and z are the horizontal and vertical coordinates, N denotes the number of particles per proton bunch, r_e is the classical electron radius and γ the Lorentz factor.

A beam-beam tune shift of $\xi_z = 0.04$ is generally considered to be the performance limit, at present luminosities typical values of 0.01-0.02 are reached. For the calculations presented in this paper, the optics and beam sizes at the IP remain constant, so ξ_z is only a function of the bunch charge. For the optics we used, a tune shift of 0.04 corresponds to single bunch currents of 0.5 mA.

II. THE COMPUTER MODEL

The spin tracking code SITROS[3] traces an ensemble of particles through sections of the storage ring, simulating the emission of synchrotron radiation between sections. Orbit motion and the variation of the spin rotation axis and angle through a section are calculated to second order, the rotation of the spins around these

axes is treated correctly to all orders. The polarization is calculated as a function of time by taking the vector sum of the tracked particles spins. An exponential fit to these numbers then yields a depolarization time constant τ_d . The equilibrium polarization is then calculated from

$$P_{eq} = P_{ST} \frac{1}{1 + \frac{\tau_p}{\tau_d}}$$

where P_{ST} is the Sokolov-Ternov level[2] and τ_p the polarization rise time.

In SITROS, a so called 'weak-strong' model is used to describe the beam-beam interaction. The particles of the tracked beam experience the oncoming beam as a fixed gaussian charge distribution. The resulting particle deflections are treated in a thin lense approximation:

$$\begin{aligned} \Delta x' &= \frac{2Nr_e}{\gamma} x \int_0^\infty \sqrt{q_x^3 \cdot q_z} \exp\left(-\frac{x^2}{q_x} - \frac{z^2}{q_z}\right) dq \\ \Delta z' &= \frac{2Nr_e}{\gamma} z \int_0^\infty \sqrt{q_x \cdot q_z^3} \exp\left(-\frac{x^2}{q_x} - \frac{z^2}{q_z}\right) dq \end{aligned} \quad (1)$$

with $q_x = 2\sigma_x^2 + q$ and $q_z = 2\sigma_z^2 + q$.

Since the 820 GeV proton beam is much more rigid than the 27.5 GeV electron beam and the particle deflections per bunch crossing are small, this model should be adequate.

III. SIMULATION RESULTS

The following results are calculated for the HERA electron ring with an energy of 27.52 GeV, the betatron tunes are 47.1 in the horizontal plane and 47.2 in the vertical. The synchrotron tune is 0.06 with a total gap voltage of 125 MV. The optics is the luminosity optics used in this years running period. One pair of spin rotators provides longitudinal polarization for the HERMES experiment.

Care was taken not to be dominated by vertical emittance growth due to orbit resonances. For each calculation, the tunes were empirically fine-tuned to keep the vertical emittance stable and matched to the proton beam as close as possible, just as it would be done in real machine operation.

The results are presented as energy scans over a range of about 440 MeV around the operating energy, corresponding to a spin tune range of one integer. The spin tune, which is plotted on the horizontal axes, is, in an ideal planar storage ring without spin rotators, the number of spin precessions around the magnetic field axis in the bending magnets and is given by $\nu_s = a\gamma$. On the vertical axes, the results for equilibrium polarization are plotted. The dotted lines are first order polarization calculations using a matrix algorithm[4]. The points with error bars connected with a solid line are tracking results from SITROS.

In figure 1 the HERA electron storage ring is modeled with realistic imperfections, the simulation with the present running

¹HERA collides electrons or positrons with protons. Throughout the paper, we will only refer to electrons, but everything also holds for positrons.

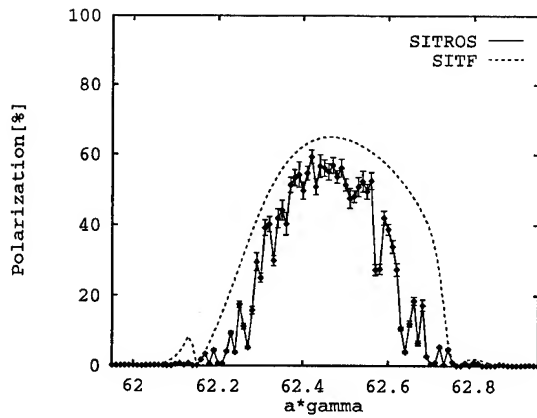


Figure 1. HERA electron ring with realistically modeled imperfections with a beam-beam tune shift of 0.01

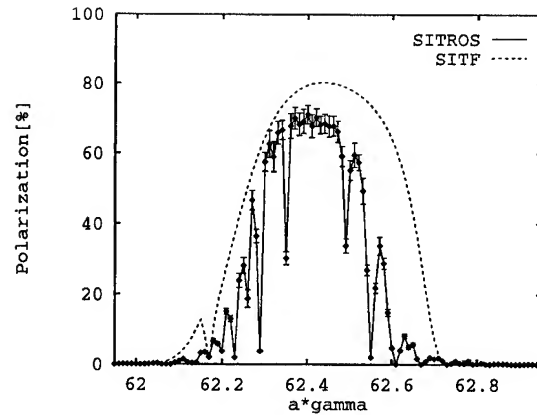


Figure 3. HERA electron ring without imperfections but with dispersion generating vertical bump. No beam-beam effect.

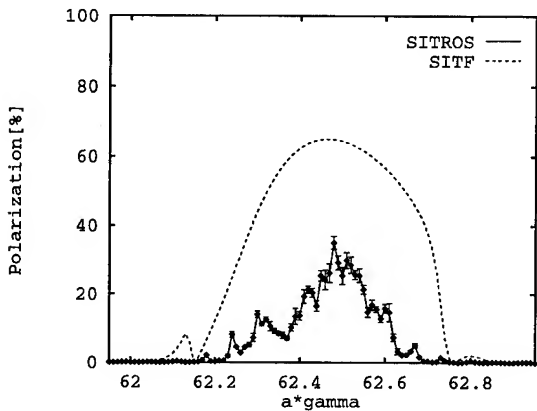


Figure 2. HERA electron ring with realistically modeled imperfections at the beam-beam limit ($\xi_z=0.04$).

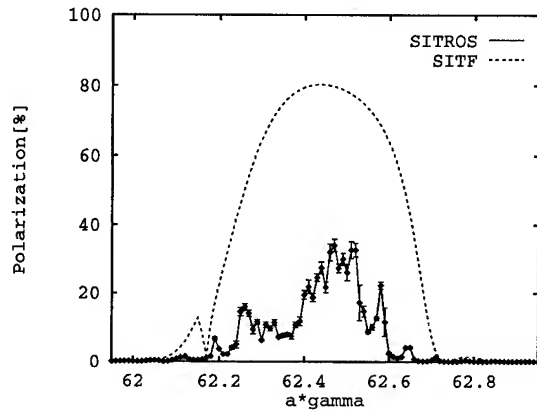


Figure 4. HERA electron ring without imperfections but with dispersion generating vertical bump at the beam-beam limit ($\xi_z=0.04$).

conditions agree within a few percent with polarization measurements. The beam-beam tune shift is 0.01. Figure 2 shows the same machine operating at the beam-beam limit, with 0.5 mA current per proton bunch and a beam-beam tune shift of $\xi_z=0.04$.

Figure 3 shows a calculation for the HERA electron ring without imperfections, only the vertical dispersion bump presently used in the real machine generates vertical emittance. The beam-beam effect is less than 0.01 in this calculation. Although polarization is improved at low currents (compared to the realistic machine in figure 1), figure 4 shows that at the beam-beam limit the equilibrium polarization is not higher than in the realistic machine (figure 2).

In figure 3, the linear calculation shows that the first order synchrotron resonances are strong. We optimized the harmonic content of the dispersion trajectories[5] to weaken the synchrotron resonances and side bands. Figure 5 indeed shows a further improvement for the low current case, both width and height of the polarization plateau improved compared to figure 3. The curve labeled 'SITF Ideal' is the first order result for a perfect machine with one spin rotator pair without dispersion bumps.

Figure 6 shows a somewhat artificial result in that only one of the two ways the beam-beam force acts on the spins is taken into account: the spins of the particles are rotated according to fields experienced in the colliding bunch, but the particle orbit is

artificially left untouched. Therefore, the spins do not experience additional fields and rotations in the quadrupoles and sextupoles around the ring due to a slightly changed particle trajectories.

In figure 7, the full effect of the beam-beam force is applied, like in figures 2 and 4. Still an improvement can be seen in comparison with figure 4. The polarization peaks at 45% instead of 35%.

Figure 8 gives an overview of measured and simulated equilibrium polarization versus beam-beam tune shift in the HERA electron ring. The simulation results are averaged values for the polarization 'plateaus'. The simulation results indicated with circles are calculated for the machine with realistic imperfections like in figures 1 and 2. The triangular point is the improved result with an optimized harmonic content of the vertical dispersion trajectories.

IV. CONCLUSION AND OUTLOOK

Without measures taken SITROS indicates a loss of about 20% of polarization if the operating currents of HERA are increased towards reaching the beam-beam limit with the present optics. An optimization of the harmonic content of the vertical dispersion trajectories improves polarization by about 10%. Further work will concentrate on pushing this gain further and to inves-

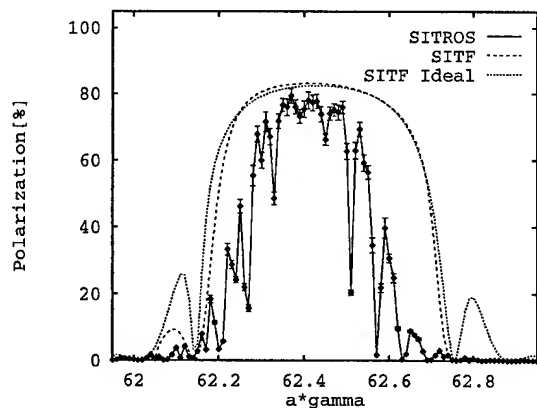


Figure 5. HERA electron ring with improved dispersion generating vertical bump with optimized spin harmonic content, no beam-beam effect.

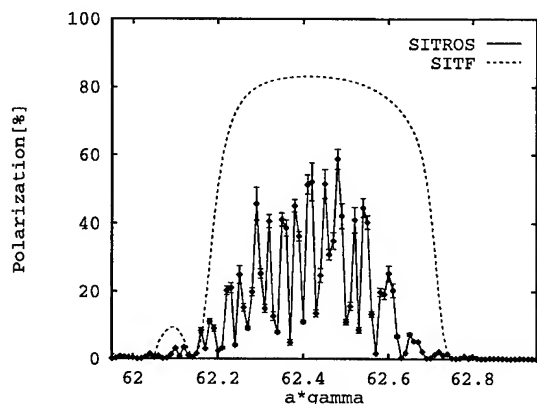


Figure 6. HERA electron ring with improved dispersion generating vertical bump with optimized spin harmonic content at the beam-beam limit ($\xi_z=0.04$). Only the spins are deflected by the beam-beam force, not the particle trajectories.

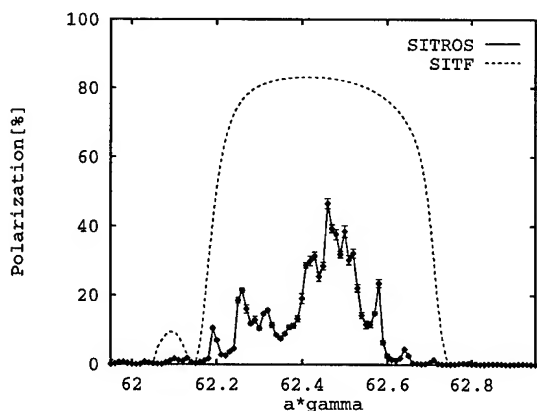


Figure 7. HERA electron ring with improved dispersion generating vertical bump with optimized spin harmonic content, at the beam-beam limit ($\xi_z=0.04$).

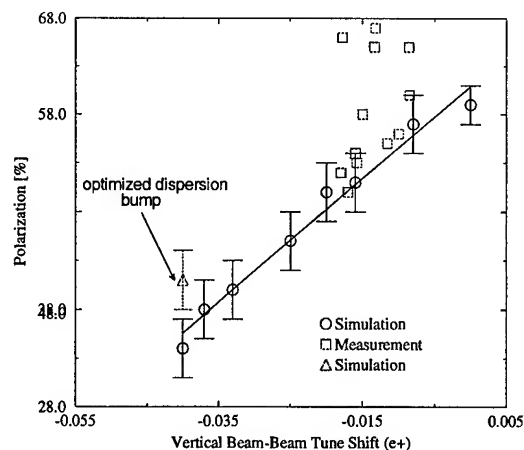


Figure 8. Polarization versus ξ_z for a machine with realistic distortions. Simulation (SITROS) results and measurements made in 1994 [1] are shown.

tigate a possible cancellation between the direct spin kick at the IP and the integrated kick due to the subsequently different orbit [6].

V. ACKNOWLEDGMENTS

We would like to thank Drs. D.P. Barber and R. Brinkmann for fruitful discussions.

References

- [1] Brinkmann, R., in: Willeke, F. (ed.), "HERA Seminar Bad Lauterberg/Harz" (1995) (to be published).
- [2] A.A. Sokolov and I.M. Ternov, Sov. Phys. Doklady 8 (1964) 1203.
- [3] J. Kewisch et al., Phys. Rev. Lett. 62 (1989) 419.
- [4] A.W. Chao, Nucl. Instr. Meth. 180 (1981) 29.
- [5] R. Rossmanith and R. Schmidt, Nucl. Instr. Meth. A 236 (1985) 231.
- [6] D.P. Barber, private communication

A MAP FOR THE THICK BEAM-BEAM INTERACTION†

J. Irwin, T. Chen, Stanford Linear Accelerator Center, Stanford University, Stanford, CA 94309 USA

We give a closed-form expression for the thick beam-beam interaction for a small disruption parameter, as typical in electron-positron storage rings. The dependence on transverse angle and position of the particle trajectory as well as the longitudinal position of collision and the waist-modified shape of the beam distribution are included. Large incident angles, as are present for beam-halo particles or for large crossing-angle geometry, are accurately represented. The closed-form expression is well approximated by polynomials times the complex error function. Comparisons with multi-slice representations show even the first order terms are more accurate than a five slice representation, saving a factor of 5 in computation time.

I. INTRODUCTION

S. Krishnagopal and R. Siemann[1] have established that it is essential to retain the finite longitudinal thickness of the beam when simulating the beam-beam interaction. Present beam-beam simulation codes[2] represent the thick interaction as a set of thin beam-beam kicks. Since the thin beam-beam kick for a bi-Gaussian distribution is usually represented by the Erskine-Bassetti[3] formula involving the evaluation of two complex error functions, the calculation is computer intensive and the representation of the thick beam-beam interaction as a set of slices slows down the simulation by a factor roughly equal to the number of slices. To find a thick beam-beam generator, we represent the thin beam-beam kick by an exponential Lie map, and the thick beam-beam interaction by an infinite product of thin beam-beam kicks. We then use the Cambell-Baker-Hausdorff formula to compose this product to a single exponential map.

II. THE THIN BEAM-BEAM KICK

S. Kheifets[4] has shown that the potential for the Erskine-Bassetti thin beam-beam kick is given by

$$dV(x, y, \sigma_x^2, \sigma_y^2) = dN \frac{2r_e}{\gamma} I(x, y, \sigma_x^2, \sigma_y^2) \quad (1)$$

where dN is the number of electrons in the thin sheet, r_e is the classical electron radius, γ is the Lorentz factor of the particle, and $I(x, y, \sigma_x^2, \sigma_y^2)$ is the (dimensionless) integral

$$I(x, y, \sigma_x^2, \sigma_y^2) = \int_0^\infty d\lambda \cdot g(x, \sigma_x^2, \lambda) \cdot g(y, \sigma_y^2, \lambda) \quad (2)$$

The function

$$g(x, \sigma_x^2, \lambda) = \frac{1}{\sqrt{\pi}} \cdot \frac{e^{-\frac{x^2}{(2\sigma_x^2 + \lambda)}}}{\sqrt{2\sigma_x^2 + \lambda}} \quad (3)$$

is a normalized Gaussian distribution of rms width $(\sigma_x^2 + \lambda/2)^{1/2}$ and a solution of the diffusion equation,

$$\frac{1}{2} \frac{\partial^2}{\partial x^2} g(x, \sigma_x^2, \lambda) = \frac{\partial}{\partial \sigma_x^2} g(x, \sigma_x^2, \lambda) \cdot \quad (4)$$

The vertical and horizontal kicks from the potential dV are given by the Erskine-Bassetti formula[3] as

$$\Delta y' + i\Delta x' = dN \frac{4r_e}{\gamma} \frac{\sqrt{\pi}}{\sigma} \left[w(z_1) - e^{-\frac{x^2}{2\sigma_x^2} + \frac{y^2}{2\sigma_y^2}} w(z_2) \right] \quad (5)$$

where

$$\sigma = \sqrt{2(\sigma_x^2 - \sigma_y^2)}, \quad z_1 = \frac{1}{\sigma} (x + iy), \quad z_2 = \frac{1}{\sigma} \left(\frac{\sigma_y}{\sigma_x} x + i \frac{\sigma_x}{\sigma_y} y \right)$$

and $w(z) = e^{-z^2} \left(1 + \frac{2i}{\pi} \int_0^z du \cdot e^{u^2} \right)$ (6)

is the complex error function. The map for this kick may be represented as an exponential Lie map by[5] $M = e^{-i dV}$. (7)

III. THE THICK BEAM-BEAM MAP

We assume the longitudinal particle density is also Gaussian and given by

$$\rho(s - s_0, \sigma_s) = \frac{1}{\sqrt{2\pi\sigma_s^2}} e^{-\frac{(s-s_0)^2}{2\sigma_s^2}} \quad (8)$$

The potential for a small slice of thickness ds at position s will be given by

$$dV = \rho(s - s_0, \frac{\sigma_s}{2}) ds \frac{2Nr_e}{\gamma} I(x(s), y(s), \sigma_x^2(s), \sigma_y^2(s)) \quad (9)$$

since the beam distribution as seen by the counter-moving particle is fore-shortened by a factor of 2. The coordinate $s_0 = c\tau/2$ is the location of the center of the bunch as experienced by a counter-moving particle whose time of arrival at the interaction point (IP) is delayed by τ . The map through a set of n slices is given by

$$M = \prod_{j=1}^n e^{-\left[\rho(s_j - s_0, \frac{\sigma_s}{2}) ds_j \frac{2Nr_e}{\gamma} I(x(s_j), y(s_j), \sigma_x^2(s_j), \sigma_y^2(s_j)) \right]} \quad (10)$$

where s_j is the longitudinal position of the center of the slice of width ds_j .

The first-order Cambell-Baker-Hausdorff (CBH) formula can be invoked to obtain, in the limit of very small slices,

$$M \approx e^{-G_1} = \prod_{j=1}^n e^{-\left[\frac{2Nr_e}{\gamma} \int ds \rho(s - s_0, \frac{\sigma_s}{2}) \cdot ds \cdot I(x(s), y(s), \sigma_x^2(s), \sigma_y^2(s)) \right]} \quad (11)$$

† Work supported by Department of Energy contracts DE-AC03-76SF00515 and DE-AC05-84ER40150

The transverse position of the particle may be written $x(s) = x_0 + (s-s_0)x'_0$ and $y(s) = y_0 + (s-s_0)y'_0$, where x_0 , x'_0 , y_0 and y'_0 are the particle's position and slope at $s=s_0$. Also $\sigma_x(s)^2 = \sigma_x^2 + s^2\sigma_{x'}^2$ and $\sigma_y(s)^2 = \sigma_y^2 + s^2\sigma_{y'}^2$ describe the longitudinal shape of the waist with σ_x , $\sigma_{x'}$, σ_y , and $\sigma_{y'}$ being the rms values of the position and slope of the beam distribution at the interaction point (IP).

The first-order CBH formula implicitly assumes that the trajectory of the particle is not changed by the interaction, and hence it represents an integrated impulse approximation. The accuracy of this impulse approximation may be estimated by noting that for electron storage rings we have

$$\frac{\Delta y'_{\max}}{\sigma_{y'}} = \Delta\theta_{y,\max} = 4\pi\xi_y \leq 0.4$$

where we have taken the beam-beam tune-shifts $\xi_y = 0.03$. The second-order correction can be estimated through a two-slice approximation as:

$$\Delta y'_2 = \Delta y \cdot \frac{\partial}{\partial y} \left[\frac{1}{2} \Delta y'_1 \right] \equiv \sigma_s \left[\frac{1}{2} \Delta y'_1 \right] \cdot \frac{\partial}{\partial y} \left[\frac{1}{2} \Delta y'_1 \right] \leq \frac{1}{4} \sigma_s \Delta y'_1 \cdot \frac{\Delta y'_{\max}}{\sigma_{y'}}$$

from which we deduce that

$$\frac{\Delta y'_2}{\Delta y'_1} \leq \frac{1}{4} \frac{\Delta y'_{\max}}{\sigma_{y'}} \leq 0.1 \quad \text{implying} \quad \frac{\Delta y'_2}{\sigma_{y'}} \leq 0.04$$

To achieve better than 4% accuracy it will be necessary to include second-order effects.

1. The first-order CBH integral

To find the generator for the thick beam-beam interaction we must perform the integral in equation (11). If we begin by assuming $x'_0 = \sigma_{x'} = \sigma_{y'} = 0$ the integral to be performed, after changing the order of the s and λ integration, is

$$Q_1 = \int ds \cdot \rho(s-s_0, \frac{\sigma_s}{2}) \cdot g(y_0 + (s-s_0)y'_0, \sigma_y^2, \lambda) \quad (12)$$

For simplicity we introduce the variables

$$\hat{s} = \frac{(s-s_0)}{(\frac{\sigma_s}{2})} \quad \text{and} \quad \hat{y}'_0 = y'_0 \cdot (\frac{\sigma_s}{2}).$$

We evaluate this integral, in a way that will later allow us to manage the full s dependence, by introducing a translation operator to represent

$$g(y_0 + \hat{s} \cdot \hat{y}'_0, \sigma_y^2, \lambda) = e^{\hat{s} \cdot \hat{y}'_0 \frac{\partial}{\partial y_0}} g(y_0, \sigma_y^2, \lambda). \quad (13)$$

We combine the \hat{s} dependence of the translation operator

$e^{\hat{s} \cdot \hat{y}'_0 \frac{\partial}{\partial y_0}}$ with the \hat{s} dependence of $\rho(\hat{s}, 1)$ and then complete the square, to obtain

$$\rho(\hat{s}, 1) \cdot e^{\hat{s} \cdot \hat{y}'_0 \frac{\partial}{\partial y_0}} = \rho(\hat{s} - \hat{y}'_0 \frac{\partial}{\partial y_0}, 1) \cdot e^{\frac{1}{2} \hat{y}'_0^2 \frac{\partial^2}{\partial y_0^2}} \quad (16)$$

The integral over $d\hat{s}$ can now be performed by translating ρ :

$$\begin{aligned} \int d\hat{s} \cdot \rho(\hat{s} - \hat{y}'_0 \frac{\partial}{\partial y_0}, 1) &= \int d\hat{s} \cdot e^{-\hat{y}'_0 \frac{\partial}{\partial y_0} \frac{\partial}{\partial \hat{s}}} \rho(\hat{s}, 1) \\ &= \int d\hat{s} \cdot \sum_{n!} \frac{1}{n!} (-\hat{y}'_0 \frac{\partial}{\partial y_0})^n \frac{\partial^n}{\partial \hat{s}^n} \rho(\hat{s}, 1) = 1 \end{aligned} \quad (17)$$

Hence we have

$$Q_1 = e^{\frac{1}{2} \hat{y}'_0^2 \frac{\partial^2}{\partial y_0^2}} \cdot g(y_0, \sigma_y^2, \lambda) \quad (18)$$

Since g is a solution of the diffusion equation

$$Q_1 = e^{\frac{1}{2} \hat{y}'_0^2 \frac{\partial^2}{\partial y_0^2}} \cdot g(y_0, \sigma_y^2, \lambda) = g(y_0, \sigma_y^2 + \hat{y}'_0^2, \lambda) \quad (19)$$

This result for Q_1 implies that the thick beam-beam potential for the case $x'_0 = \sigma_{x'} = \sigma_{y'} = 0$ is just the original potential with σ_y^2 replaced by $\sigma_y^2 + \hat{y}'_0^2$.

Next we perform the integral with only $\sigma_{x'} = \sigma_{y'} = 0$.

$$\begin{aligned} Q_2 &= \int d\hat{s} \cdot \rho(\hat{s}, 1) \cdot g(x_0 + \hat{s}\hat{x}', \sigma_x^2, \lambda) \cdot g(y_0 + \hat{s}\hat{y}', \sigma_y^2, \lambda) \\ &= e^{\hat{x}'\hat{y}' \frac{\partial}{\partial x_0} \frac{\partial}{\partial y_0}} g(x_0, \sigma_x^2 + \hat{x}'^2, \lambda) \cdot g(y_0, \sigma_y^2 + \hat{y}'^2, \lambda) \end{aligned} \quad (20)$$

The integral with only $\sigma_{x'} = 0$ is:

$$\begin{aligned} Q_3 &= \int ds \cdot \rho(s-s_0, \frac{\sigma_s}{2}) \cdot g(x_0 + (s-s_0)x'_0, \sigma_x^2, \lambda) \\ &\quad \cdot g(y_0 + (s-s_0)y'_0, \sigma_y^2 + s^2\sigma_{y'}^2, \lambda) \end{aligned} \quad (21)$$

In changing s to \hat{s} it is convenient to introduce

$$\hat{s}_0 = \frac{s_0}{(\frac{\sigma_s}{2})}, \quad \sigma_{y'} = \frac{\sigma_s}{2} \sigma_{y'}, \quad \text{and} \quad \sigma_{y_0}^2 = \sigma_y^2 + s_0^2 \sigma_{y'}^2.$$

Using these definitions

$$\begin{aligned} &g(y_0 + \hat{s}\hat{y}'_0, \sigma_{y_0}^2 + \sigma_{y'}^2 (2\hat{s}_0\hat{s} + \hat{s}^2), \lambda) \\ &= e^{\frac{\sigma_{y'}^2}{2} (2\hat{s}_0 \frac{\partial}{\partial y_0} \frac{\partial}{\partial y_0} + \frac{\partial^2}{\partial y_0^2})} e^{\hat{s}\hat{y}'_0 \frac{\partial}{\partial y_0}} g(y_0, \sigma_{y_0}^2, \lambda) \end{aligned} \quad (22)$$

The first factor has no \hat{s} dependence and can be taken out of the integral. The remaining integral, after translating x_0 , is just Q_2 . We can now write down an expression for the double integral in the generator of eq. 11 with no assumptions on x'_0 , y'_0 , $\sigma_{x'}$, and $\sigma_{y'}$:

$$\begin{aligned} G_1 &= \frac{2Nr_e}{\gamma} e^{\frac{\sigma_x^2}{2} (2\hat{s}_0 \frac{\partial}{\partial x_0} \frac{\partial}{\partial x_0} + \frac{\partial^2}{\partial x_0^2})} e^{\frac{\sigma_y^2}{2} (2\hat{s}_0 \frac{\partial}{\partial y_0} \frac{\partial}{\partial y_0} + \frac{\partial^2}{\partial y_0^2})} e^{\hat{x}'\hat{y}' \frac{\partial}{\partial x_0} \frac{\partial}{\partial y_0}} \\ &\quad I(x_0, y_0, \sigma_{x_0}^2 + \hat{x}'^2, \sigma_{y_0}^2 + \hat{y}'^2) \end{aligned} \quad (23)$$

2. First-order symplectification

To obtain a symplectic evaluation of G_1 one can introduce a mixed-variable generator

$$F_1(x, y, X', Y') = xX' + yY' + G_1(x, y, X', Y'). \quad (24)$$

The implicit equations can be solved approximately by expanding F_1 in a Taylor series about the point (x, x', y, y') .

3. Evaluation of the derivatives of the generator

The calculation can be arranged so that the derivatives of G_1 required to compute coordinate changes can be found from derivatives of the complex error function. Derivatives of $I(x_0, y_0, \sigma_{x_0}^2 + \hat{x}'^2, \sigma_{y_0}^2 + \hat{y}'^2)$, with

respect to \hat{x}' or \hat{y}' may be replaced by derivatives with respect to σ_{x0}^2 and σ_{y0}^2 which may in turn be replaced by derivatives with respect to x_0 and y_0 . Thus the computation reduces to derivatives of the Erskine-Bassetti formula with respect to x_0 and y_0 . These derivatives become polynomials times the complex error function by using the relationship

$$\frac{\partial w(z)}{\partial z} = -2zw(z) + \frac{2i}{\sqrt{\pi}} \quad (25)$$

The order of this polynomial depends on the accuracy with which the waist effects are represented. The largest corrections to the thin beam-beam kick, arising from the slope y' , are accounted for by replacing σ_y^2 by $\sigma_y^2 + \hat{y}'^2$.

4. The second-order CBH integral

The second order CBH may also be computed. The result is

$$G_2 = \frac{1}{2} \left(\frac{2Nr_e}{\gamma} \right)^2 \frac{1}{\sqrt{\pi}} \left[\left(\frac{\partial I}{\partial y} \right)^2 + \hat{y}'^2 \left(\frac{\partial^3 I}{\partial y^3} \frac{\partial I}{\partial y} - \left(\frac{\partial^2 I}{\partial y^2} \right)^2 \right) + \dots \right] \quad (26)$$

where $I = I(x, y, \sigma_x^2, \sigma_y^2 + \hat{y}'^2)$.

G_2 can be inserted into equation

$$F_{12}(x, y, X', Y') = xX' + yY' + G_1(x, y, X', Y') + \frac{1}{2} \frac{\partial G_1(x, y, X', Y')}{\partial x} \frac{\partial G_1(x, y, X', Y')}{\partial X'} + \frac{1}{2} \frac{\partial G_1(x, y, X', Y')}{\partial y} \frac{\partial G_1(x, y, X', Y')}{\partial Y'} \quad (27)$$

to obtain a second order implicit generator.

IV. NUMERICAL RESULTS

We compare the results calculated by the thick beam-beam interaction with the multiple slice approach for the vertical plane, since the horizontal plane has little thick beam-beam effect. We scanned the range of $y=0$ to 10σ , $y'=-10$ to 10σ , in $1/4\sigma$ steps. In Table 1, the maximum and r.m.s. differences from a 21-slice results are listed.

The thick beam-beam integral may be calculated for various orders. The 1st order includes the lowest order of correction of G_1 —up to the 1st order derivatives of single beam-beam kick, and the 5th order includes up to 5th order derivatives. Then, 2nd order CBH correction, G_2 , is included respectively. Finally, both 2nd order Poisson Bracket of G_1 and CBH corrections are included.

One can see that even the 1st order thick beam-beam calculation gives better result than 5 slices. Notice that in this approximation, the y' kick requires essentially the same computation time as a single slice, implying a factor of 5 can be saved in beam-beam simulation. In addition, the maximum errors occur at about 1σ in thick beam-beam,

unlike the multi-slices methods which have larger error at large y' .

Table 1. Comparison of beam-beam kick with $s_0=0$

		location of maximum error (σ)		Errors: * $(\Delta z - \Delta z_{21})/\max(\Delta z_{21})$ $z=y$ or y'	
		y	y'	max (%)	r.m.s.(%)
1 slice	y	0	9.25	100	.032
	y'	1.75	-10	60	.233
3 slices	y	4.5	-10	34	.009
	y'	4.75	-10	14	.05
5 slices	y	5.75	-10	20	.005
	y'	5.75	-10	7.4	.024
thick BB 1st order	y	1.5	-1.5	4.9	.001
	y'	1	-1	5.1	.017
thick BB 5th order	y	.75	5.5	5.5	.002
	y'	1	1.25	3.5	.015
thick BB w/ 2nd CBH†	y	2	4.75	4.9	.002
	y'	1.25	1.75	3.0	.015
thick BB w/ 2nd PB& CBH†	y	7.75	10	4.8	.001
	y'	1.25	1.75	3.0	.014

* z_{21} indicates the Δz calculated with a 21-slice method.

† These results should be considered as preliminary.

V. CONCLUSION

We represent the thick beam-beam interaction as the infinite product of thin kicks. When the disruption parameter is small it is valid to compose this product to a single map defined by a generator given by the CBH formula. The largest effect by far in typical beam-beam situations is the dependence on the vertical slope. The first order computation for this case results in the replacement of σ_y^2 by $\sigma_y^2 + (\sigma_s/2 y')^2$ in the Erskine-Bassetti formula. The numerical comparison shows the thick beam-beam method, especially the 1st order approach, can replace the multi-slice method which has been used in most of beam-beam simulations, and save substantial CPU time.

VI. REFERENCES

- [1]. S. Krishnogopal and R. Siemann, Phys. Rev. D **41**, 2312 (1990).
- [2]. T. Chen, J. Irwin and R. Siemann, Physical Review E, Vol. 49, No. 3, p2323, March 1994; A. Zholents and DN Shatilov, this proceeding; J. L. Tennyson, ABC-29, (1991).
- [3]. Erskine-Bassetti, CERN-ISR-TH/80-06 (1980).
- [4]. S. Kheifets, PETRA NOTE 119, DESY (Jan., 1976)
- [5]. J. Irwin, SLAC-PUB-6713, submitted to Nuclear Instruments and Methods (1995).

TRANSIENT BEAM LOADING IN THE SLC DAMPING RINGS*

M.G. Minty, R.H. Siemann

Stanford Linear Accelerator Center, Stanford University, Stanford, CA 94309 USA

Abstract

Effects arising from heavy beam loading in the Stanford Linear Collider (SLC) Damping Rings are described. The stability of the rf system and particle beam is studied using a numerical model of the beam cavity interaction with multiple feedback loops. Nonlinearities of the power source are also considered. The effects of beam-induced transients and intensity jitter on the rf system are analyzed and used to determine stability tolerances for both high current and low current pulses.

I. INTRODUCTION

When a particle beam is injected into or extracted from a circular accelerator, beam-induced electromagnetic fields cause the accelerating cavity voltage to oscillate at the synchrotron frequency. For fast cycling storage rings like the SLC damping rings, the magnitude of these oscillations depends on the time between extraction and injection of beam pulses, the cavity fill time, and on the beam current. At the SLC where the single bunch beam current was increased by 20% for the recent run, transient loading occasionally caused rf system and beam instabilities. To better understand the sources of these instabilities, simulations^{1,2} were performed using Matrix_x³, a program developed for the analysis of dynamic stability. The simulations included a detailed model² of the rf system for which a block diagram is shown in Fig. 1.

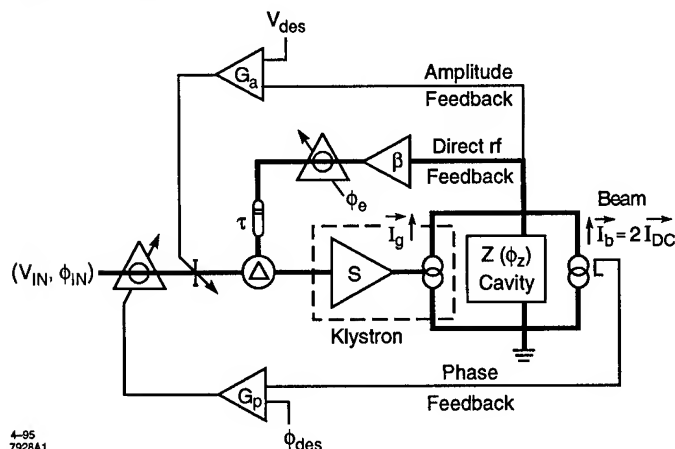


Figure. 1. Circuit model of a beam loaded rf system including amplitude, phase, and direct rf feedback. The thick solid lines indicate paths for phasors which have both an amplitude and phase.

II. TRANSIENT BEAM LOADING

Large oscillations in the cavity voltages induced by injection of a high current beam in the SLC damping rings resulted in

*Work supported by Department of Energy contract DE-AC03-76SF00515.

substantial beam losses⁴, which were reduced using direct rf feedback⁵. Figure 2 shows simulation results with direct rf feedback (open loop gain $H = 6$) and without. With feedback, the cavity fill time is reduced by $1 + H$. The cavity therefore responds quickly to the voltage and phase errors resulting from the absence of beam. Residual oscillations still persist however because the klystron is saturated when the beam is injected.

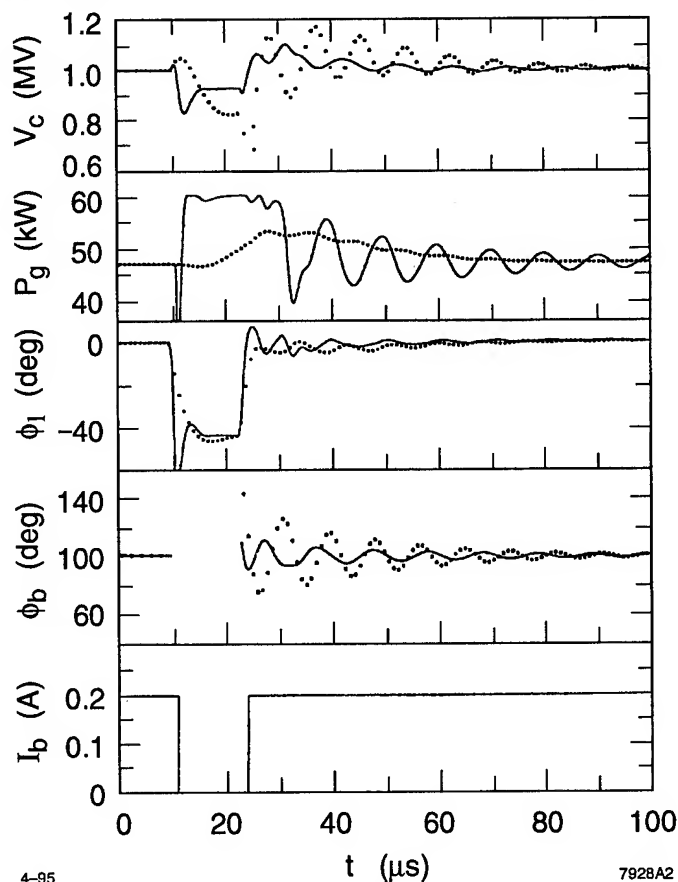


Figure 2. Simulations of transient beam loading. The cavity voltage V_c , the klystron output power P_g , the loading angle ϕ_l , the beam phase ϕ_b , and current I_b are plotted as a function of time for a direct rf feedback open loop gain of $H = 0$ (dotted curves) and $H = 6$ (solid curves).

A second problem during operation was poor regulation of the cavity voltage. Loss of regulation can result from beam-induced transients: if the klystron input power is not properly limited, there exist two solutions for the feedback loops. One solution, on the rising edge of the klystron power curve is stable. The other, beyond saturation, is unstable. Simulation results are shown in Fig. 3 (compare with experimental data in Ref. 4). At each beam current, the tuning angle was adjusted to maintain a zero loading angle, $\phi_l = 0$, in the steady state with beam. At high beam current more power is required in the steady state and

the small signal gain approaches zero; just below saturation, any change in the klystron input power produces little effect on the output power. At high beam current the klystron is unable to return to a condition of positive small signal gain and the cavity voltage is not maintained as a result.

Intensity fluctuations of the incoming beam are considered tolerable provided the rf cavity voltage can regulate. For a fast cycling storage ring with a store time much smaller than the bandwidth of the tuner feedback loops, the effect of injecting a pulse of different current is a change in the steady state loading angle ϕ_l . This in turn requires more klystron power. As discussed previously, the rf system is stable provided that the combined effects of the transients induced by extraction and injection of the beam are such that the klystron returns to a state of positive small signal gain.

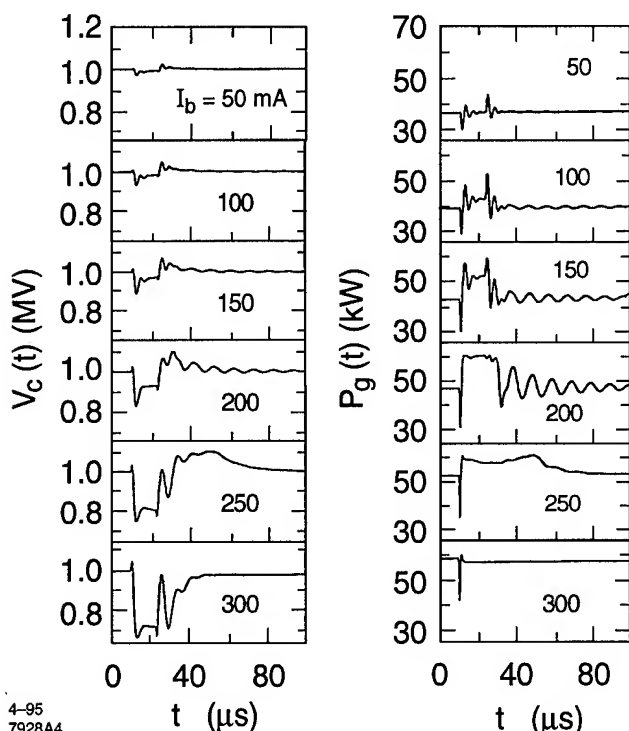


Figure 3. Transient beam loading as a function of I_b with $\phi_l = 0$ in the steady state.

III. STABILITY TOLERANCES

The percentage tolerable current jitter $|\frac{\delta I_b}{I_b}|$ as a function of I_b when $\phi_l = 0$ is plotted in Fig. 4. In these simulations the steady state current I_b is extracted, and a new pulse of current $\delta I_b + I_b$ is injected. The rf system is easily able to regulate for large fluctuations in the beam current except at the highest currents. With $I_b = 0.20$ A for example, the rf system would remain stable if a subsequent pulse of 40% above nominal, or 0.28 A, were injected into the ring. The vertical line at $I_b = I_m$, however, indicates a hard limit due to a missing pulse. With $I_b > I_m$ the klystron is driven towards saturation when the beam is absent. A subsequent pulse may then experience an arbitrary cavity voltage. The time required for the system to become

stable depends on the response time of the slow tuner feedback loops and on the output of low level amplifiers which may limit the maximum klystron input power. This hard limit presents a strict limit on the maximum current. At the SLC with a cavity voltage of 1 MV, a 60 kW maximum klystron output power, and the cavities tuned to $\phi_l = 0$, stability against missing pulses is ensured for $I_b < 0.16$ A. To accommodate 0.22 A rf currents for the 1994 run, the available operating region was expanded by lowering the rf gap voltage from 1 MV to 800 kV.

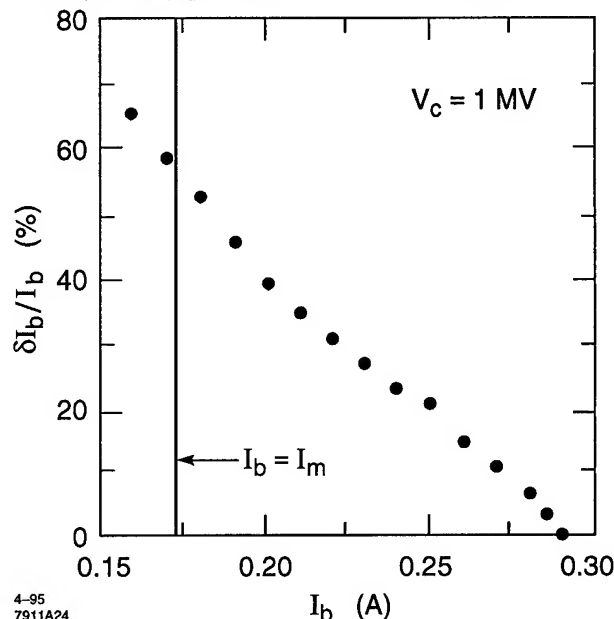


Figure 4. Tolerable current jitter $\frac{\delta I_b}{I_b}$ as a function of nominal current I_b with $\phi_l = 0$ in the steady state.

The parameter space for voltage regulation in the steady state is shown in Fig. 5 for the rf operating conditions of the past 3 years. The solid curve is an analytic result⁶ for the contour of constant klystron power at the indicated power and cavity voltage. The small circles are simulation² results using a nonlinear klystron and a power limiter. The large dots indicate the operating current and tuning angle. In general, the highest beam currents are obtainable for $\phi_l = 0$. The limitation due to low current or missing pulses is representable by a vertical line intersecting the contour of maximum klystron output power and $I_b = 0$. If not properly compensated, the rf system can be unstable for operation to the left of this line. Alternatively, the performance requirements of the klystron can be specified using this analysis⁶.

A. Cavity Detuning

Provided that the additional power reflected from the cavities is absorbed in an isolator between the cavities and klystron, intentional detuning ($\phi_l \neq 0$) is advantageous for two reasons. First, it provides stability against beam-induced transients as shown in Fig. 6. Notice that the peak-to-peak amplitude of the voltage oscillations is largest for $\phi_l = 0$. This is due to the large difference in the klystron output power in the steady state and in saturation. Second, cavity detuning may be used to relax the hard limit from low current or missing pulses as evidenced by the change (see Fig. 5) in operating point, from $\phi_l = 0$ to $\phi_l = 10^\circ$, for the 1994 run.

B. RF Conditioning

To achieve higher beam currents for the same maximum klystron output power and cavity voltage, the klystron must be made to operate more efficiently; the hard limit due to missing pulses or absence of beam must be overcome. This can be accomplished by changing the voltage and phase references to the direct rf feedback loop. The required changes are calculable⁶. In practice, with a power limited klystron, the amount by which to lower the voltage reference would be to that value for which the control voltage from the amplitude feedback loop is unchanged by the change in beam current at injection. The amount by which to change the phase reference would be to minimize the change in the cavity voltage phase angle.

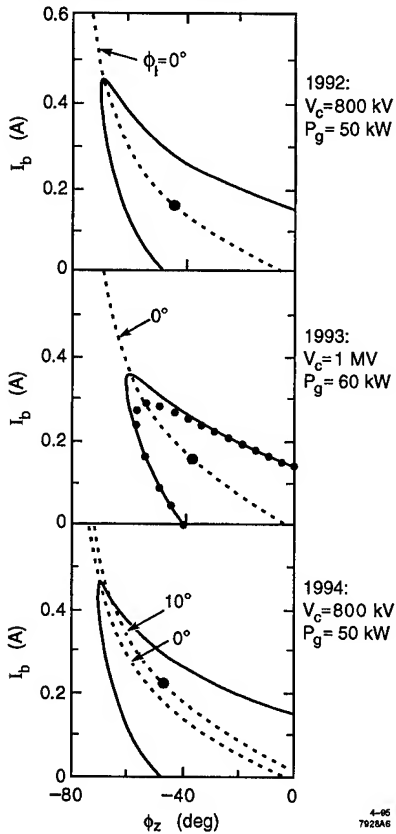


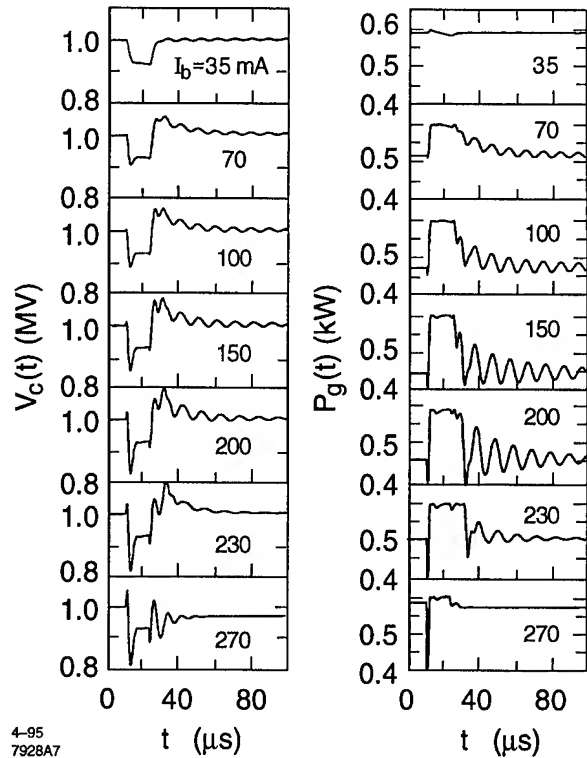
Figure 5. Parameter space for voltage regulation for SLC damping ring parameters for the past 3 years.

IV. CONCLUSION

Simulation results were used to explain performance and performance limits and to suggest changes that could be made. At the SLC, rf system and beam instabilities were shown to result from the interaction of rf feedback loops and a power limited klystron. Rf conditioning was suggested for future operations at even higher beam currents.

References

- [1] M.G. Minty *et al*, Proc. 1993 PAC 2373.
- [2] M. G. Minty, R.H. Siemann, "Heavy Beam Loading in Storage Ring RF Systems", to be submitted to Nucl. Instr. and Methods.



4-95

7928A7

Figure 6. Transient beam loading as a function of I_b with $\phi_z = -45^\circ$ in the steady state.

- [3] Matrix_x by Integrated System, Santa Clara, CA 95054.
- [4] M. G. Minty, *et al.*, WAB12 1995 PAC.
- [5] F. Pederson, *IEEE Tran. on Nucl. Sci.*, NS-32, No. 3 (1985) 2138.
- [6] M.G. Minty, R. H. Siemann, TPA09 1995 PAC.

STUDIES OF HALO DISTRIBUTIONS UNDER BEAM-BEAM INTERACTION†

T. Chen, J. Irwin, R. H. Siemann, Stanford Linear Accelerator Center, Stanford University, Stanford, CA 94309 USA

The halo distribution due to the beam-beam interaction in circular electron-positron colliders is simulated with a program which uses a technique that saves a factor of hundreds to thousands of CPU time^[1,2]. The distribution and the interference between the beam-beam interaction and lattice nonlinearities has been investigated. The effects on the halo distribution due to radiation damping, misalignment at the collision point, and chromatic effect are presented.

I. INTRODUCTION

The leap-frog simulation method^[1] makes the study of the beam-beam halo distribution much more efficient, provides the ability to look into many problems that were difficult or impossible. Using a simulation code, we have studied various beam-beam effects for two existing colliders and for PEP-II B-factory design. In this paper, we present the results of these efforts.

II. THE LATTICE NONLINEARITIES—TUNE SHIFT WITH AMPLITUDES

In previous studies, we have shown that resonances are the dominant effect in tail formation^[2], as evidenced by the fact that the distributions follow resonance locations. The locations of resonances are not only determined by the beam-beam kick potential, but also by the nonlinearities of the lattice, primarily the tune shifts with amplitudes.

Figure 1(a) shows the tail distribution of PEP-II HER from the beam-beam interaction. The lattice is linear and the parameters can be found in [3]. The beam distribution contour lines are steps of the logarithm of numbers in transverse amplitude space. The symbols plotted over the distribution contour lines are the locations of resonances. The few selected resonances believed to be relevant are plotted. The locations of the resonances are calculated by first order perturbation theory using beam-beam potential.

When lattice nonlinearities are added, the tune shifts with amplitudes from the beam-beam interaction and the lattice nonlinearities must be combined. As a result, resonance lines move. It is easy to imagine that the tail distribution will follow the move, and this has been observed in most of our simulations.

However, the lattice tune shift can do more than change the ridge locations at large amplitudes, and the

change of the tail distribution can be dramatic. The change at medium amplitudes is important also. One example of PEP-II HER is shown in figure 1. In figure 1(b), the lattice tune shifts are included. At large vertical amplitude, resonances $2Q_x+6Q_y=5$ and $6Q_y+3Q_s=4$ are at almost the same location. The tune shift terms dQ_x/dA_x^2 and dQ_y/dA_y^2 are small, but the larger crossing terms $dQ_x/dA_y^2=dQ_y/dA_x^2$ are large. They move the two resonances close to the core where there are many more particles that now stream to large amplitudes. This produces the dramatic change in the distribution, that we see in figure 1(b).

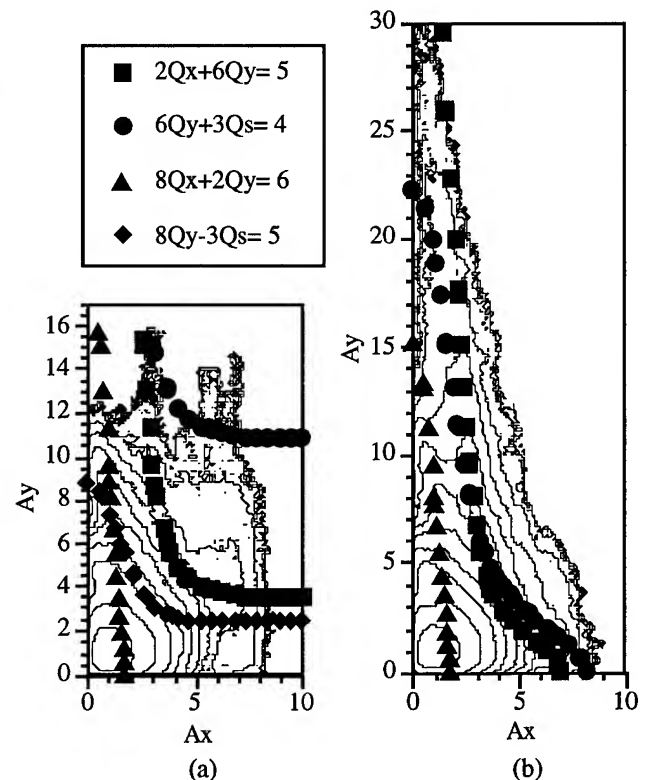


Figure 1: The beam tail distributions of PEP-II HER (a) with linear lattice, and (b) with nonlinear tune shift with amplitudes: $dQ_x/dA_x^2=-85.6$, $dQ_x/dA_y^2=dQ_y/dA_x^2=-3931$, $dQ_y/dA_y^2=-2.1$.

III. ACTION OF MULTIPLE RESONANCES

The resonance streaming and phase convection theory^[4,5] have predicted the role of resonances in forming the tail and are verified by our simulation. In addition, we found that in many cases the same particle may be trapped

† Work supported by Department of Energy contracts DE-AC03-76SF00515 and DE-AC05-84ER40150

in a few resonances simultaneously, rather than streaming in a single resonance. This is shown in an investigation for the PEP-II HER with a linear lattice, the case in figure 1(a).

Study concentrates on the ridge in the distribution at about $1 \sigma_x$ and extending from 8 to $12 \sigma_y$. A single particle was launched at $1 \sigma_x$ and $9 \sigma_y$, and tracked for 1000 turns. The location of the particle in amplitude space turn by turn is plotted in figure 2. One can see this particle is roaming around the ridge, and presumably it is a typical particle contributing to it. The particle's phases are found on every turn. They are plotted in Φ_y versus Φ_x and Φ_s versus Φ_y in figure 2. The phase relationship indicates the particle is trapped in the $4Q_x + Q_y$ resonance most of the time, and $8Q_y - 3Q_s$ all the time. Due to the symmetry of the beam-beam force, there should be no odd order transverse resonances. So, we believe the resonance $4Q_x + Q_y$ should be $8Q_x + 2Q_y$. Both resonances are plotted in the distribution plot. One can see the particle has been moving between them.

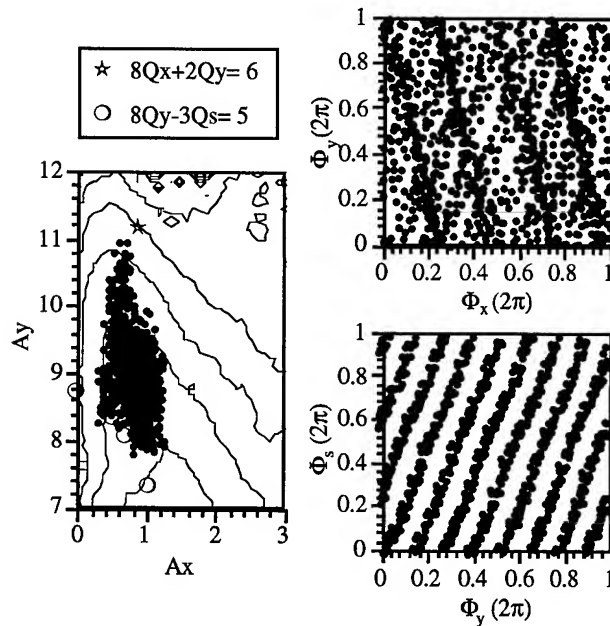


Figure 2: A particle trapped in two resonances. Plots show the particle motion in amplitude and phases.

It is also interesting to see a particle switch between resonances and change behavior. Take the case of figure 1(b), and launch a test particle at $A_x = 2.5 \sigma_x$ and $A_y = 13.5 \sigma_y$ to study the large tail. We found in the first 260 turns, the particle dropped from $13.5 \sigma_y$ to $8.5 \sigma_y$. Then, the particle climbed up to $12 \sigma_y$ in the next 250 turns. The phases of the particle is plotted in figure 3. A cross is used for the time when the vertical amplitude was falling and a circle for when it was increasing. One can see the particle certainly has different resonance features. In addition, multiple resonances acting together may form an "island"

structure in phase plot, as shown in the Φ_s versus Φ_y plot for the falling period.

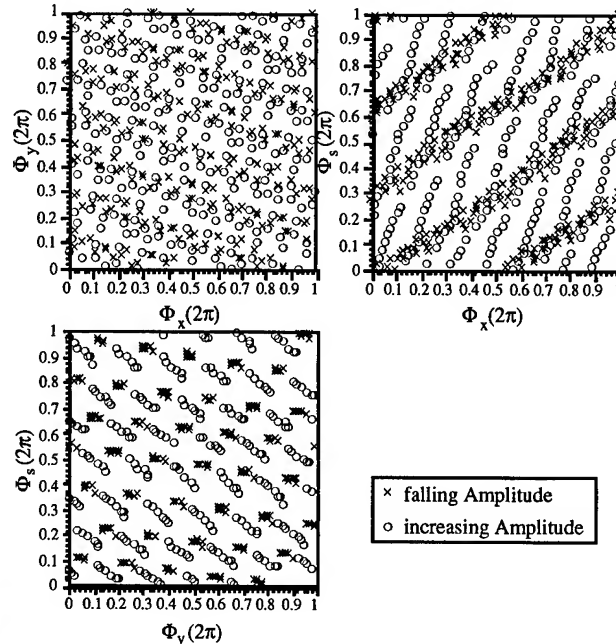


Figure 3: Phase plots of a particle during the period of falling and increasing amplitude. Different resonances are shown for each period.

IV. THE EFFECT OF SYNCHROTRON RADIATION

We know that the synchrotron radiation plays an important role in the tail distribution. It may damp the amplitude of a particle, but it may also help resonance streaming. With our program, the effect of radiation on the beam halo is simulated for the first time. Generally

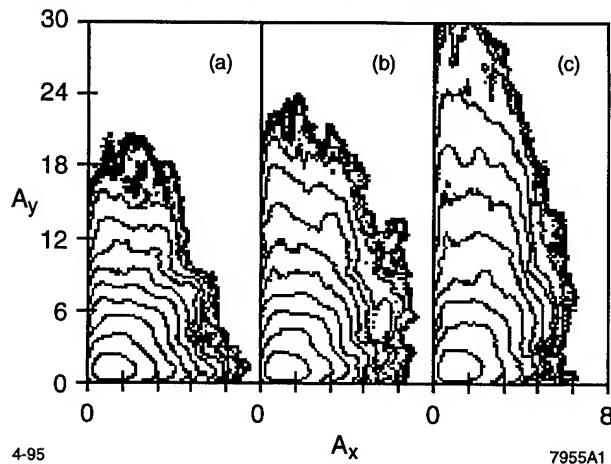


Figure 4: Beam-beam tail distributions with different radiation damping: (a) 5,000 turns; (b) 10,000 turns; (c) 20,000 turns.

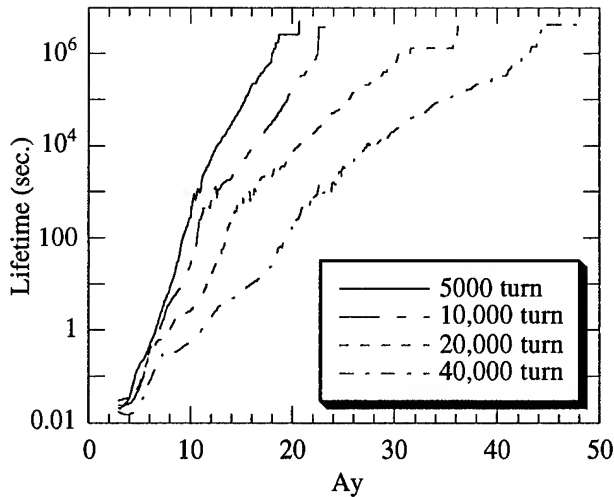


Figure 5. Lifetime as a function of vertical aperture with different radiation damping times (5000-40,000 turns).

speaking, the stronger the radiation, the shorter the vertical tail. The radiation damping seems to have little effect in the horizontal tail.

We studied the radiation effect of PEP-II LER. The parameters used are the same as CDR [3] except the tunes were $Q_x=0.63$, $Q_y=0.552$, $Q_s=0.2477$, and momentum compaction factor was $\alpha=0.00131$. In figure 4, the tail distributions are plotted for different radiation damping times. Figure 4(a) has the design damping time of 5000 turns. With less radiation damping, the vertical tail extends farther. The lifetime as a function of vertical aperture is shown in figure 5.

V. EFFECT OF MISALIGNMENT AT IP

In order to achieve high luminosity, PEP-II is designed with two rings to carry the counter-rotating beams. Unlike other circular electron-positron colliders, which have a common closed orbit for both beams, PEP-II depends on mechanical alignment to bring two beams together at the interaction point. This introduces the problem of beams colliding with an offset. Simulations were performed to investigate this.

Figure 6 gives the PEP-II LER tail distribution for various misalignments. Again, the parameters are from the PEP-II CDR. The beam sizes at the IP is $6\ \mu\text{m}$ in vertical and $155\ \mu\text{m}$ in horizontal. In figure 6(a) there is no offset at the collision point. In figure 6(b) and (c), the vertical offset is $2\ \mu\text{m}$ and $6\ \mu\text{m}$ respectively, and the horizontal offset is zero. In 6(d) through 6(f), the vertical offset is zero but horizontal offsets were set to 30, 50, and $150\ \mu\text{m}$, respectively. From figure 6, one can draw the conclusion that the horizontal offset drives large horizontal tails, while the vertical offset blows up the vertical core. The offsets

are not a problem if alignment errors are controlled to a fraction of the beam sizes.

The essential physics behind this result is a breaking of the symmetry of the beam-beam force, that allows odd order resonances to be excited. Therefore, the conclusion from this particular case is not general, since it depends on near-by resonances.

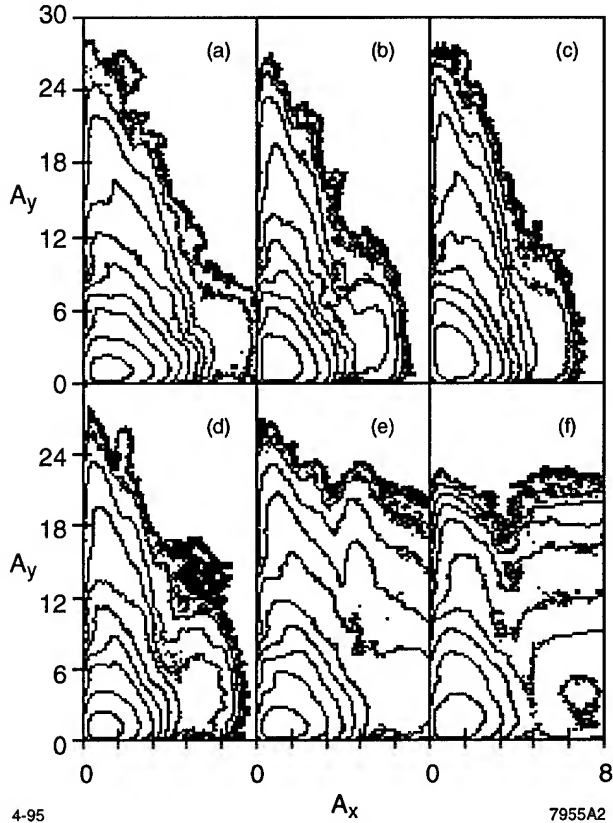


Figure 6. Beam-beam tail distribution of PEP-II LER with offset at the IP. (a): $x_{\text{off}}=0, y_{\text{off}}=0$; (b): $x_{\text{off}}=0, y_{\text{off}}=2\ \mu\text{m}$; (c): $x_{\text{off}}=0, y_{\text{off}}=6\ \mu\text{m}$; (d): $x_{\text{off}}=30\ \mu\text{m}, y_{\text{off}}=0$; (e): $x_{\text{off}}=50\ \mu\text{m}, y_{\text{off}}=0$; (f): $x_{\text{off}}=150\ \mu\text{m}, y_{\text{off}}=0$.

VI. REFERENCES

- [1] J. Irwin, *Proc. of the 3rd Advanced ICFA Beam Dynamics Workshop*, Novosibirsk, USSR, 123 (1989) /SLAC-PUB-5743, Feb. 1992.
- [2] T. Chen, J. Irwin and R. Siemann, *Physical Review E*, Vol. 49, No. 3, p2323, March 1994.
- [3] PEP-II Conceptual Design Report, LBL-PUB-5379 /SLAC-418/CALT-68-1869/UCRL-ID-114055/UC-IIRPA-93-01, (1993).
- [4] J. Tennyson, *Physica* **5D**, 123 (1982).
- [5] A.L. Gerasimov and N. Dikansky, *Nucl. Instr. Meth.* **A292**, 209 (1990); A.L. Gerasimov and N. Dikansky, *Nucl. Instr. Meth.* **A292**, 221 (1990); A.L. Gerasimov and N. Dikansky, *Nucl. Instr. Meth.* **A292**, 233 (1990).

THE EFFECT OF PHASE ADVANCE ERRORS BETWEEN INTERACTION POINTS ON BEAM HALOS†

T. Chen, J. Irwin, R. H. Siemann, Stanford Linear Accelerator Center, Stanford University, Stanford, CA 94309 USA

Phase advance errors between interaction points (IP) break the symmetry of multi-IP colliders. This symmetry breaking introduces new, lower order resonances which may change the halo from the beam-beam interaction dramatically. In this paper, the mechanism of introducing new resonances is discussed. Simulation results showing the changes due to phase advance errors are presented. Simulation results are compared with experimental measurements at VEPP-2M.

I. INTRODUCTION

The luminosity of circular $e^+ e^-$ colliders is usually limited by the lifetime caused by the beam-beam interaction. The mechanism that drives particles into the halo has been a puzzle, because factors combine in complex ways.

Understanding has been hampered by the amount of CPU time required to simulate the halo. A method[1] was proposed to look into rare particles in the beam tail while saving a factor of hundreds, or even thousands, on CPU time. A program based on this method was written, tested and applied to PEP-II, LEP, CESR, and VEPP-2M to understand the halo from the beam-beam interaction. This study concluded that resonance streaming dominates the beam-beam lifetime[2].

The program has been upgraded to model multiple IP machines, such as LEP and VEPP-2M. The lattices between each individual IP are completely independent. Therefore, it can be used to investigate the effects of errors in each section. The results show the important role of the errors. Hamiltonian analysis has been extended to interpret the simulation results.

II. HAMILTONIAN ANALYSIS FOR MULTIPLE IP'S WITH LATTICE ERRORS

In existing multiple IP $e^+ e^-$ colliders, the IPs are symmetrically arranged so that, the collider can be treated as a few single IP colliders in cascade. However, when errors are introduced, especially when the phase advances between IPs are different, this treatment is no longer valid. Because the differences are relatively small, we take them as the perturbations to the symmetric lattice.

The Hamiltonian including the beam-beam interaction can be written as

$$H(x, p_x, y, p_y, s) = H_0 + V_{BB}(x, y, s) \quad (1)$$

where H_0 is the unperturbed Hamiltonian of the storage ring, and V_{BB} is the beam-beam potential[3]. With B_{IP} interaction points, the beam-beam potential is

$$V_{BB}(x, y, s) = \frac{-Nr_e}{\gamma} \sqrt{\frac{2}{\pi\sigma_L^2}} \sum_{n=-\infty}^{\infty} \sum_{b=0}^{B_{IP}-1} V_F(b, x, y, s) \times \exp \left\{ -\frac{2}{\sigma_L^2} \left[s - \left(nC + b \frac{C}{B_{IP}} + c\tau \right) \right]^2 \right\} \quad (2)$$

$$\tau = \frac{\hat{t}}{2} \cos(2\pi Q_s(n + \frac{b}{B_{IP}})), \quad (3)$$

and V_F is defined in [3] with the additional feature that it depends on the parameters of the interaction point, b . By applying Fourier analysis, equation (1) becomes

$$H = H_0 - \frac{Nr_e}{C\gamma} \sum_{b=0}^{B_{IP}-1} \sum_{m,n,p,r=-\infty}^{\infty} T_{pr}^b \exp\{2\pi i(p\Delta Q_x^b + r\Delta Q_y^b) - (k_{pr}^b \sigma_L)^2 / 8\} \times i^m J_m(k_{pr}^b \hat{t}c / 2) \exp\{i(p\psi_x + r\psi_y - 2\pi(n - mQ_s)s / C) + i2\pi nb / B_{IP}\} \quad (4)$$

where T_{pr}^b is a function of transverse actions and strong-beam size at each IP, and k_{pr}^b is a wave number that also depends on IP parameters. The ΔQ^b 's are the phase advance errors from one interaction point to the next one relative to the standard phase advance Q/B_{IP} .

Let's examine the phase in the second exponential function in equation (4). The last exponential function averages to zero, except when the resonance condition

$$pQ_x + rQ_y + mQ_s = n, \quad (5)$$

is satisfied. If there are no errors, i.e., all the IP's are identical and there are no phase advance differences, the superscript b in eq. (4) can be dropped and the sum over b

is reduced to the factor $\sum_{b=0}^{B_{IP}-1} \exp\{i2\pi bn / B_{IP}\}$. This factor,

which can be viewed as a sum of unit-length phasors, equals zero unless n is a multiple of B_{IP} . Resonances with n not equal to a multiple of B_{IP} are eliminated because the phasors cancel each other. The resonances left are

$$p \frac{Q_x}{B_{IP}} + r \frac{Q_y}{B_{IP}} + m \frac{Q_s}{B_{IP}} = \text{integer}. \quad (6)$$

This is equivalent to a storage ring with one IP and $1/B_{IP}$ of the size. If the IP's are not identical, or there are phase advance errors, or both, the cancellation does not

† Work supported by Department of Energy contracts DE-AC03-76SF00515 and DE-AC05-84ER40150

occur. When the IP's are not identical, the phasors have unequal magnitudes, so that they will not cancel completely. When the phase advances between IP's are different, the phasors are no longer evenly spaced, and the cancellation is incomplete.

The above analysis gives two consequences for multiple IP colliders with errors: First, more resonances are introduced. The resonance condition with errors is $pQ_x + rQ_y + mQ_s = n$, or, in terms of tune per IP, the condition is

$$p \frac{Q_x}{B_{IP}} + r \frac{Q_y}{B_{IP}} + m \frac{Q_s}{B_{IP}} = \frac{\text{integer}}{B_{IP}}. \quad (7)$$

Comparing eq. (7) with eq. (6), one can see that many more resonances are allowed in this case. Second, among those resonances, some are possibly of lower order. They can dramatically change the tail distribution and the lifetime.

III. SIMULATION OF A 4-IP MACHINE—LEP

The first multi-IP machine are studied was LEP, which has 4 interaction points symmetrically distributed. Large synchrotron radiation energy losses and chromatic effects naturally break the symmetry. The tune errors can be as large as 0.015 to 0.04 because only two arcs have RF cavities[4]. The errors introduced in the simulation include errors in the β -functions and dispersion functions at each IP, and phase advance errors between IP's. When phase advance errors are included, the total tunes of the storage ring are held constant.

The beam distribution from simulations is plotted in transverse amplitude space. The amplitudes are normalized to beam sizes. The contour lines indicate equal number density and are spaced logarithmically. Figure 1 gives the beam distribution with a linear lattice and 4 symmetric IP's. Resonance lines allowed by symmetry up to 8th order are plotted over the distribution. One can see that the sixth order resonance $2Q_x - 2Q_y - 2Q_s = 1$ dominates the tail formation.

When lattice errors are included, the tail distribution changes dramatically, as shown in figure 2. About 40 resonances appeared inside the footprint of the beam-beam interaction. We have plotted four of those that appear related to the halo distribution. The 6 resonances in figure 1 are still present, but they now appear to have little effect on the tail distribution. The resonances $2Q_x + 2Q_y + 0Q_s = 5/4$ and $4Q_x + 0Q_y - 3Q_s = 9/4$ seem responsible for the vertical tail. The resonance $2Q_x + 2Q_y - 1Q_s = 5/4$ also has an effect at the upper left corner. Notice that all these resonances are forbidden in the symmetrical case.

The horizontal tail is believed to be related to the resonance $4Q_x = 9/4$, another low order resonance forbidden by symmetry. As a result, a peak at $A_x = 5.5$, $A_y = 1$ is formed. The horizontal tune of LEP is 0.2756, which is

close to the 4th integer resonance, making this resonance strong. Figure 3 plots the lifetime as a function of horizontal aperture for the symmetric lattice and the lattice with errors. The $4Q_x = 9/4$ would cause a short lifetime if the horizontal aperture was below $A_x \sim 9$.

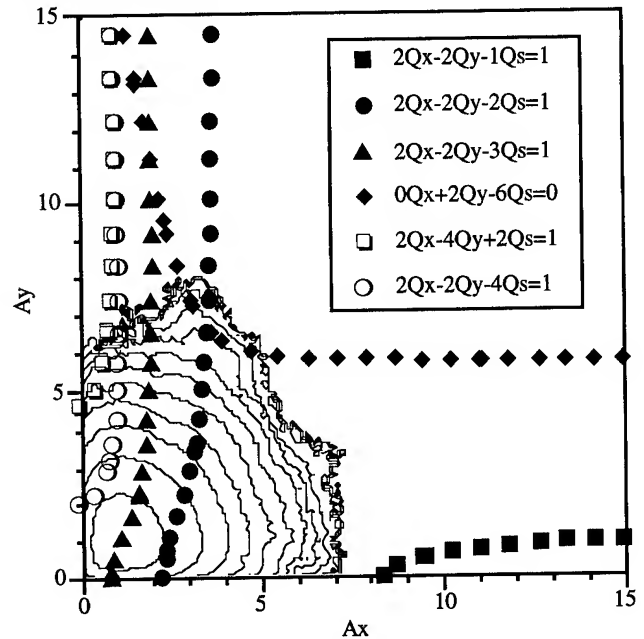


Figure 1. LEP beam-beam tail distribution and resonances. A linear, symmetric lattice is used. The tunes in the legend refer to 1/4 of the total ring tunes.

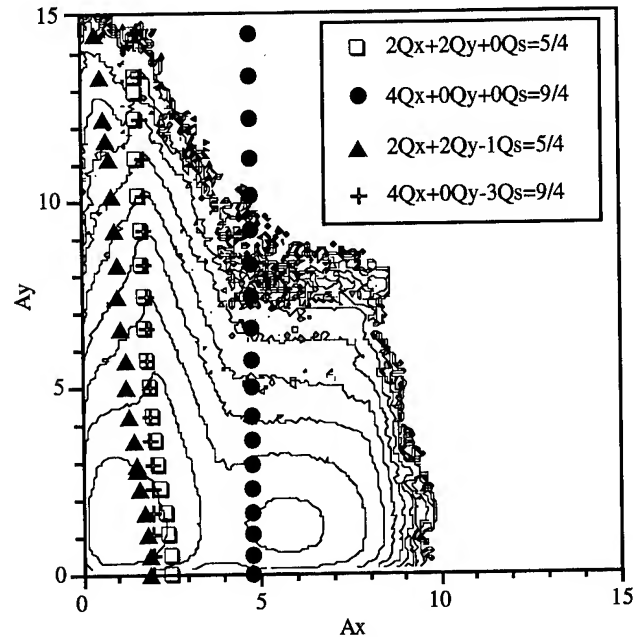


Figure 2. LEP beam-beam tail distribution when lattice errors are included. The tunes in the legend refer to 1/4 of the total ring tunes.

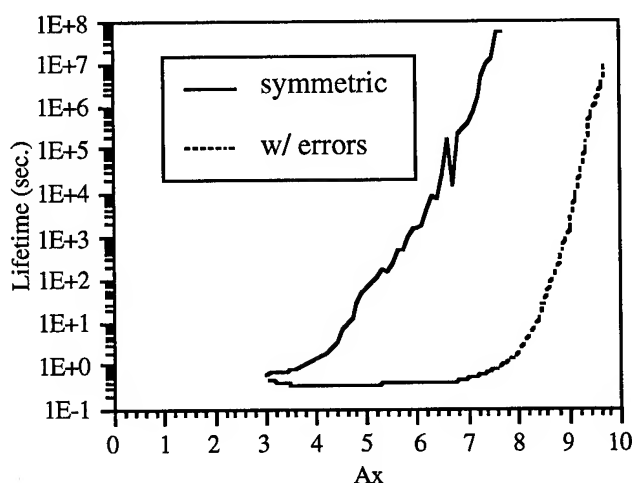


Figure 3. Lifetime versus horizontal aperture for LEP with and without errors.

IV. SIMULATION RESULTS COMPARED WITH VEPP-2M MEASUREMENT

The effects of phase advance errors have been measured in VEPP-2M[5] which has a two-fold symmetry. This offers the opportunity to compare our simulation with data. Parameters are given in Table 1[5,6]. The maximum beam-beam tune-shift was determined by the lifetime falling to about 500 sec, and it was measured as a function of phase advance error.

The first step of the simulation was to set the phase advance error to zero and set the beam current to give a beam-beam tune-shift of 0.045 as measured. The lifetime versus vertical aperture was calculated under these conditions, and the vertical aperture for a 500 second lifetime was determined. It was $A_y=29$. Then phase advance errors were introduced and the current adjusted until the lifetime was 500 second with $A_y=29$. The beam-beam tune-shift at this current is plotted in figure 4.

Table 1. VEPP-2M parameters

Q_x	0.059	E_0 (MeV)	510
Q_y	0.097	U_0 (KeV)	9.17
Q_s	0.0085	ϵ_x (m*rad)	4.6×10^{-7}
β_x^* (m)	0.48	ϵ_y (m*rad)	4.1×10^{-9}
β_y^* (m)	0.048	T_0 (sec.)	6×10^{-8}
η_x^* (m)	0.4	α	0.33

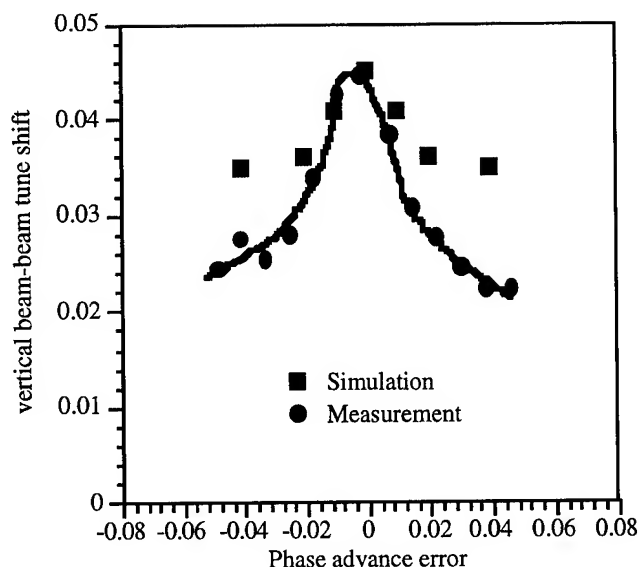


Figure 4 The maximum beam-beam tune-shift as a function of phase advance errors, simulation and measurement[5].

The simulation and the measurement show that the best performance is obtained with no errors. The quantitative agreement is not good, with the simulation giving more optimistic results than the experiment. This may be due to lattice nonlinearities which are not included in the present simulation.

V. REFERENCES

- [1] J. Irwin, *Proc. of the 3rd Advanced ICFA Beam Dynamics Workshop*, Novosibirsk, USSR, 123 (1989) /SLAC-PUB-5743, Feb. 1992.
- [2] T. Chen, J. Irwin and R. Siemann, *Physical Review E*, Vol. 49, No. 3, p2323, March 1994.
- [3] R. Siemann, in *Frontiers of Particle Beams with e^+e^- Rings* edited by M. Dienes, M. Month, B. Strasser and S. Turner (Springer-Verlag, Berlin, 1994), p. 327.
- [4] J. P. Koutchouk, *Proc. of the 1987 Particle Accelerator Conference*, Washington D.C., 1987/CERN LEP-TH/87-16.
- [5] P. M. Ivanov, *et al*, *Proc. of the 3rd Advanced ICFA Beam Dynamics Workshop*, Novosibirsk, USSR, 26 (1989) /SLAC-PUB-5743, Feb. 1992.
- [6] P. M. Ivanov, private communication.

Compensation of the "Pacman" Tune Spread by Tailoring the Beam Current[†]

Miguel A. Furman
Accelerator and Fusion Research Division
Lawrence Berkeley Laboratory
Berkeley, CA 94720, USA

Abstract

"Factory"-like e^+e^- colliders presently under design or construction achieve high luminosity by resorting to large numbers of closely-spaced bunches. The short bunch spacing implies that there are unavoidable parasitic collisions (PCs) in the neighborhood of the interaction point (IP). Since the bunch population of the beam is not uniform due to an intentional ion-clearing gap, the bunches at the head or tail of the train ("pacman bunches") experience different beam-beam tune shifts than those away from the edges ("typical bunches"). We present here a method to minimize the vertical tune spread at the expense of increasing the horizontal tune spread (we assume that there is only one IP). Since the beam-beam dynamics for flat beams typically tolerates a significantly higher horizontal tune spread than a vertical tune spread, this method implies a net advantage. We present our discussion in the context of the PEP-II collider.

I. INTRODUCTION

The PEP-II design [1] calls for head-on collisions with magnetic separation in the horizontal plane. This separation scheme entails unavoidable PCs near the IP whose effects on the beam-beam dynamics have been studied quite extensively [1,2]. The design also calls for an ion-clearing gap equivalent to ~5% of the total beam length. The gaps in the two beams have the same length and are positioned such that head bunch in one beam collides at the IP with the head bunch of the other beam (the two beams have the same bunch spacing and overall length).

The interaction region (IR) is such that a typical bunch experiences four PCs on either side of the IP (for a total of 9 collisions). On the other hand, the pacman bunches (those at the head or tail of the train) do not experience all the collisions, as sketched in Fig. 1.

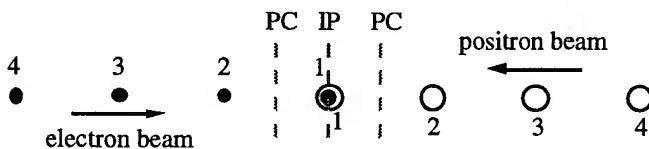


Fig. 1. Sketch of the collision schedule. The dashed lines indicate the location of the IP and first PC. Bunch #1 is at the head of the train in its respective beam.

[†]Work supported by the Director, Office of Energy Research, Office of High Energy and Nuclear Physics, High Energy Division, of the US. Department of Energy under Contract no. DE-AC03-76SF00098.

As a result, the particles in these bunches have different closed orbits [3] and different beam-beam tune shifts [4] than those in typical bunches. This "pacman tune spread" implies that a working point that may be appropriate for typical bunches might not be good for the pacman bunches and vice versa. In this note we show how to compensate this tune spread for both beams in first order approximation by tailoring the bunch currents. The difference in sign and magnitude between the vertical and horizontal beam-beam parameters at the PCs makes it impossible to compensate vertical and horizontal tune spreads simultaneously. In our particular case, we choose to compensate the vertical tune spreads, which are larger than the horizontal. As a result, the horizontal tune spread is *increased* relative to the nominal (even-bunch-current) case. This increase, however, is not expected to be detrimental, as explained below.

II. COMPENSATION PRINCIPLE

Let us consider only one PC on either side of the IP, as we will in the case of PEP-II (our analysis is extended in a straightforward fashion to the case with more PCs). As a result, there is only one pacman bunch at the head of the train and one at the tail.

Let us focus on the vertical tune shift of the positron beam. Neglecting the dynamical beta function effect [4], the vertical tune experienced by a positron at the center of a bunch is (refer to Fig. 1)

$$\begin{aligned} \nu_{y+} &= \nu_{y+}^{(0)} + \xi_{y+}^* + 2\xi_{y+}^{PC} \quad (\text{typical bunch}) \\ \nu_{y+} &= \nu_{y+}^{(0)} + \xi_{y+}^* + \xi_{y+}^{PC} \quad (\text{pacman bunch}) \end{aligned} \quad (1)$$

Similar expressions apply to the electron beam, and to the horizontal counterparts of both beams. Here $\nu^{(0)}$ is the lattice (bare) tune and the ξ 's are the beam-beam tune shifts at the IP and the PC. The absolute difference between these two equations is the vertical "pacman tune spread" for the positrons, namely

$$\Delta\nu_{y+} = \xi_{y+}^{PC} \quad (2)$$

It is this tune spread (and its counterpart in the opposing beam) that we show here how to eliminate.

Let N_{n-} be the number of particles in electron bunch n and d be the separation between the beams at the PC. Then the well-known expressions for the vertical beam-beam parameters of the positron bunch n are written as

$$\xi_{ny+}^* = a_+ N_{n-} \quad \text{and} \quad \xi_{ny+}^{PC} = b_+ N_{n-} \quad (3)$$

where, using standard notation,

$$a_+ = \frac{r_e \beta_{y+}^*}{2\pi\gamma_+ \sigma_{y-}^* (\sigma_{x-}^* + \sigma_{y-}^*)} \quad \text{and} \quad b_+ = \frac{r_e \beta_{y+}^{PC}}{2\pi\gamma_+ d^2} \quad (4)$$

The schedule of the collisions is shown in Fig. 1. We label the bunches so that #1 is at the head of the train in both beams. Thus we see that bunch #1 experiences only one PC with bunch #2 in the opposing beam, in addition to the main collision at the IP. From Fig. 1 we can read off the beam-beam parameter for each bunch as follows:

$$\begin{aligned} \xi_{1y+} &= a_+ N_{1-} + b_+ N_{2-} \\ \xi_{2y+} &= a_+ N_{2-} + b_+ (N_{1-} + N_{3-}) \\ \xi_{3y+} &= a_+ N_{3-} + b_+ (N_{2-} + N_{4-}) \\ &\vdots \end{aligned} \quad (5)$$

where we assume that the bunch sizes σ_x and σ_y remain at their nominal values under colliding conditions. If we now equate all beam-beam parameters to their nominal value (i.e., in the absence of any beam gap), we obtain

$$\begin{aligned} a_+ N_{1-} + b_+ N_{2-} &= (a_+ + 2b_+) N_- \\ a_+ N_{2-} + b_+ (N_{1-} + N_{3-}) &= (a_+ + 2b_+) N_- \\ a_+ N_{3-} + b_+ (N_{2-} + N_{4-}) &= (a_+ + 2b_+) N_- \\ &\vdots \end{aligned} \quad (6)$$

where N_- is the nominal number of electrons per bunch. Thus we obtain the matrix equation

$$\begin{bmatrix} 1 & \varepsilon_+ & 0 & 0 & \cdots \\ \varepsilon_+ & 1 & \varepsilon_+ & 0 & \cdots \\ 0 & \varepsilon_+ & 1 & \varepsilon_+ & \cdots \\ 0 & 0 & \varepsilon_+ & 1 & \cdots \\ \vdots & \vdots & \vdots & \vdots & \ddots \end{bmatrix} \begin{bmatrix} y_{1-} \\ y_{2-} \\ y_{3-} \\ y_{4-} \\ \vdots \end{bmatrix} = (1 + 2\varepsilon_+) \begin{bmatrix} 1 \\ 1 \\ 1 \\ 1 \\ \vdots \end{bmatrix} \quad (7)$$

where we have defined

$$y_{n-} \equiv N_{n-}/N_- \quad \text{and} \quad \varepsilon_+ \equiv b_+/a_+ \quad (8)$$

Eq. (7) has as many entries as there are bunches in the train (1658 in the case of PEP-II). The solution is symmetrical about the middle bunch and is readily found in perturbation theory,

$$\begin{bmatrix} y_{1-} \\ y_{2-} \\ y_{3-} \\ \vdots \end{bmatrix} = \begin{bmatrix} 1 + \varepsilon_+ + \cdots \\ 1 - \varepsilon_+^2 + \cdots \\ 1 + \cdots \\ \vdots \end{bmatrix} \quad (9)$$

where \cdots represents in all entries terms of $O(\varepsilon_+^3)$ or higher.

IV. APPLICATION TO PEP-II AND DISCUSSION

Let us apply our analysis to the case of PEP-II [1], whose basic parameters are listed in Table 1 (LEB=low-energy beam, HEB=high-energy beam). The optics in the IR is symmetrical about the IP and is such that the 1st PC at either side of the IP is much stronger than the others. We are therefore justified in

neglecting all other PCs.

From Eq. (2) and Table 1 we see that the nominal vertical pacman tune spread of the positron beam is 0.004, which is $\sim 14\%$ of the main beam-beam parameter at the IP, i.e.,

$$\varepsilon_+ = \xi_{y+}^{PC} / \xi_{y+}^* \approx 0.14 \quad (10)$$

Thus Eq. (9) says that, in order to compensate this tune spread we must increase the number of particles in the first and last bunches of the *electron* train by 14% relative to the nominal value, and decrease the number of particles in the second and next-to-last bunch by 2% relative to the nominal value. These numbers are within the precision reach with which the linac can inject beam [1].

Table 1. Selected PEP-II parameters.

	LEB (e ⁺)	HEB (e ⁻)
E [GeV]	3.1	9.0
N	5.63×10^{10}	2.59×10^{10}
β_x^* [m]	0.375	0.50
β_y^* [m]	0.015	0.02
β_x^{PC} [m]	1.433	1.293
β_y^{PC} [m]	26.46	19.85
σ_x^* [μ m]	152	152
σ_y^* [μ m]	6.1	6.1
ξ_x^*	0.03	0.03
ξ_y^*	0.03	0.03
ξ_x^{PC}	-0.00022	-0.00015
ξ_y^{PC}	0.0041	0.0023
d [mm]	3.5	

A calculation for the electron beam yields a similar solution, obtained from Eq. (9) by replacing $+\leftrightarrow-$. Because the beam energies in PEP-II are sufficiently high, the beam-beam parameter in one beam does not depend on its own charge; therefore the positron and electron pacman tune spreads can be compensated simultaneously. From Table 1 we obtain $\varepsilon_- = 0.08$, which implies that the number of positrons in the first and last bunches of the train must be increased by 8% relative to the nominal value, while the number of positrons in the second and next-to-last bunches must be decreased by 0.6% relative to the nominal value.

If we were to carry out the same calculation for the horizontal tune spreads we would obtain $\varepsilon_+ = -0.0075$ and $\varepsilon_- = -0.005$. Since both magnitude and sign are different from the solutions presented above for the vertical tune spread, it is obvious that one cannot simultaneously compensate for the vertical and horizontal tune spreads.

As a corollary we conclude that, if we choose to compensate the vertical tune spreads, the horizontal tune spreads become larger than their nominal values. For the LEB

we obtain

$$\begin{aligned}\Delta v_{x+} &= |\xi_{1x+} - \xi_{x+}| \\ &= \left| (1 + \varepsilon_+) \xi_{x+}^* + (1 - \varepsilon_+^2) \xi_{x+}^{PC} - \xi_{x+}^* - 2\xi_{x+}^{PC} \right| \quad (11) \\ &\approx |\varepsilon_+ \xi_{x+}^*|\end{aligned}$$

which evaluates to ~ 0.004 . The corresponding calculation for the horizontal pacman tune spread of the HEB yields ~ 0.002 . These numbers are a factor ~ 15 – 20 larger than their nominal values (see Eq. (2)) and, in fact, are equal to the uncompensated vertical tune spreads. Thus we can say that our method transfers the pacman tune spread from the vertical plane to the horizontal. However, for PEP-II, the horizontal beam dynamics is much less sensitive than the vertical to beam-beam parameter strengths of the same magnitude for an extended region of the tune plane [2]. Therefore, transferring the tune spread from the vertical plane to the horizontal implies a net advantage.

In the more general case, when there are more than two PCs, the method generalizes in a straightforward fashion. If there are altogether n PCs, and if the beam orbits are not symmetrical about the IP, Eq. (6) will couple the currents of $n+1$ bunches in the opposing beam, there will be n different ε parameters in Eq. (7), and the matrix will have n secondary diagonals. If all the ε parameters are small, as is likely to be the case in any realistic IR design, the solution can be found in perturbation theory.

The increase in the bunch current for the pacman bunches will affect their closed orbit distortion [3]. Here, again, the effects are quite small. In the nominal (non-compensated) case, the closed orbits of the pacman bunches are displaced horizontally from the optical IP by $\sim 5 \mu\text{m}$. However, for most values of the horizontal tune, both the LEB and HEB pacman bunches are displaced *to the same side* of the optical IP. As a result, the relative displacement of their centers is ~ 1 – $2 \mu\text{m}$, which is very small compared to the horizontal beam size $\sigma_x^* = 152 \mu\text{m}$. If the vertical pacman tune spread is compensated as discussed above, the relative displacement of the pacman bunch centers at the collision point will not increase by more than $\sim 20\%$ from the nominal value of ~ 1 – $2 \mu\text{m}$ quoted above, and therefore will remain small.

The tailored beam current will also have an effect on the induced transient voltages on the RF cavities, and on the stability of the coherent dipole mode of the beams. The ideal case, in which there is no beam gap and all bunches have the same charge is, of course, the simplest. We do not expect that the beam-beam interaction will drive a coherent dipole instability for any reasonable value of the tune. The design of the RF system does take into account the gap. Although these issues remain to be evaluated in detail, we believe that an increase of $\sim 14\%$ in the current of the first and last bunches should not entail serious difficulties, if any.

V. CONCLUSIONS

We have presented a method for the compensation of the

vertical pacman tune spread in PEP-II. The method consists in tailoring the beam current in such a way that the pacman bunches have slightly larger charge than the typical bunches. The compensation can be carried out simultaneously in both beams but not in both planes. In fact, a generic feature of the method is a trading off of the vertical tune spread for the horizontal. Thus if the vertical tune spread is compensated, the horizontal tune spread becomes roughly equal to the uncompensated vertical tune spread, which is typically larger than its nominal value. However, the horizontal beam dynamics is much more tolerant than the vertical, so tune spreads of this magnitude should not cause any problems, and the method therefore implies a net advantage. We believe that this beneficial trade-off is a generic feature of flat beams. Thus our technique seems unlikely to be applicable to round beams, such as those encountered in multibunch proton colliders.

VI. ACKNOWLEDGMENTS

I am grateful to A. Zholents for valuable comments.

VII. REFERENCES

- [1] "PEP-II: An Asymmetric B Factory Conceptual Design Report," June 1993, LBL-PUB-5379/SLAC-418/CALT-68-1869/UCRL-ID-114055/UC-IIRPA-93-01.
- [2] M. A. Furman and J. R. Eden, "Beam-Beam Effects for the PEP-II B Factory," Proc. Part. Accel. Conf., Washington, DC, May 17–20, 1993, p. 3485 and references therein.
- [3] M. A. Furman, "Closed Orbit Distortion from Parasitic Collisions in PEP-II," Proc. European Particle Accelerator Conference, London, England, June 27 - July 1, 1994, p. 1147.
- [4] M. A. Furman, "Beam-Beam Tune Shift and Dynamical Beta Function in PEP-II," Proc. European Particle Accelerator Conference, London, England, June 27 - July 1, 1994, p. 1145.

Disruption Effects on the Beam Size Measurement*

P.RAIMONDI, F.-J. DECKER and P. CHEN

Stanford Linear Accelerator Center, Stanford University, CA94309 USA

Abstract

At the SLC Final Focus with higher currents and smaller beam sizes, the disruption parameter D_y is close to one and so the pinch effect should produce a luminosity enhancement. Since a flat beam-beam function is fit to deflection scan data to measure the beam size, disruption can affect the measurement. Here we discuss the quantitative effects of disruption for typical SLC beam parameters. With $3.5 \cdot 10^{10}$ particles per pulse, bunch length of 0.8 mm and beam sizes of 2.1 μm horizontally and 0.55 μm vertically, the measured vertical size can be as much as 25% bigger than the real one. Furthermore during the collision the spot size actually decrease, producing an enhancement factor H_D of about 1.25. This would yield to a true luminosity which is 1.6 times that which is estimated from the beam-beam deflection fit.

Disruption Effects

The disruption originates several desired and undesired effects. The desired one is the extra focusing that the two beam exercises during their interaction due to their attractive fields and the finite bunch lengths.

Of course the extra focusing produces a direct increase of the luminosity, however, since the fields are not linear (radially) and do vary during the interaction, the angular spread and emittance of the beam do increase during the interaction. This can affect the extraction of the two beams, increasing the current losses in the extraction-lines.

The extra focusing is desired, but the related luminosity enhancement becomes very difficult to measure. On top of that the beam-beam deflection scans [1] are also distorted by the disruption, in such a way that the spot sizes measured with this technique are in general bigger than the original, undisturbed ones.

Furthermore it is also possible that the disruption alters the optimization of the beam spots leading to a luminosity lower than the optimal.

Experimental Evidence

In the last SLC-SLD run the discrepancy between the estimated luminosity by using beam-beam deflection scans (SLC) and the effective one by counting the number of Z_0 effectively found (SLD) has become evident.

In particular, this discrepancy has become quite large (about 30%) after an improvement of the beam-beam deflection fits was made, in order to make it insensitive to beam position jitter at the IP. The estimated luminosity measurement has become much more stable since then, permitting a much more reliable comparison with the SLD data. In Fig. 1 the SLD/SLC luminosity ratio for the last two months of run is shown.

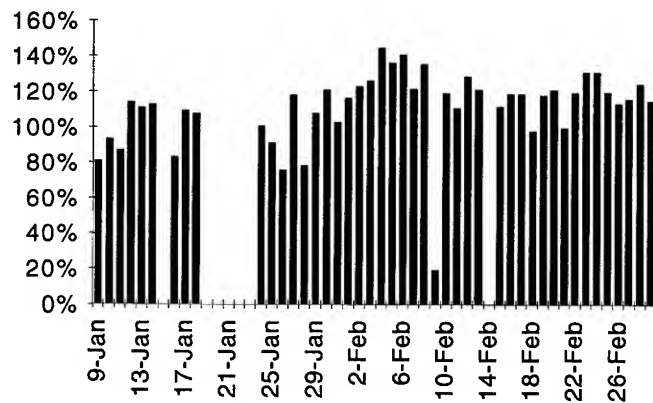


Fig. 1: SLD/SLC luminosity ratio history

Moreover one expects that the discrepancy has to become bigger for higher luminosity, Fig.2 shows the SLD/SLC ratio as a function of the luminosity itself.

*. Work supported by the Department of Energy, contract DE-AC03-76SF00515

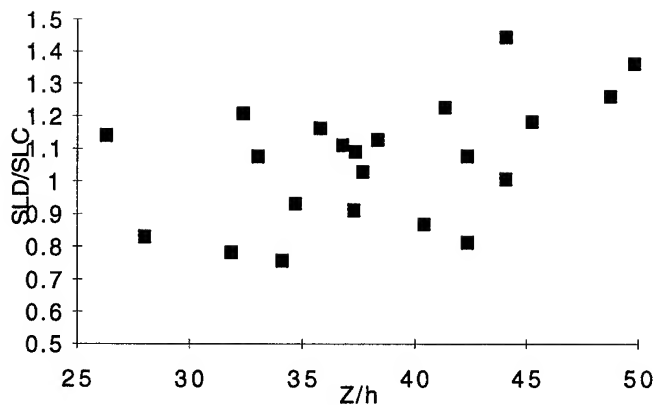


Fig. 2: SLD/SLC luminosity ratio vs luminosity

Theoretical Estimates

In order to estimate the pinch effect, a full tracking code to simulate the beams dynamics during the interaction has been developed [2]. The simulation predicts typical luminosity enhancement of about 25% for our normal running conditions.

Moreover with the same code it is possible to simulate a beam-beam scan. Fig.3 shows the theoretical beam-beam deflection as function of the y offsets of the two beam and the fit with the beam-beam formula. It is noticeable that the fit is not perfect, and the fitted Σ_y is 25% bigger than the original one, while the other plane Σ_x is 20% smaller. For a horizontal scan the difference is negligible.

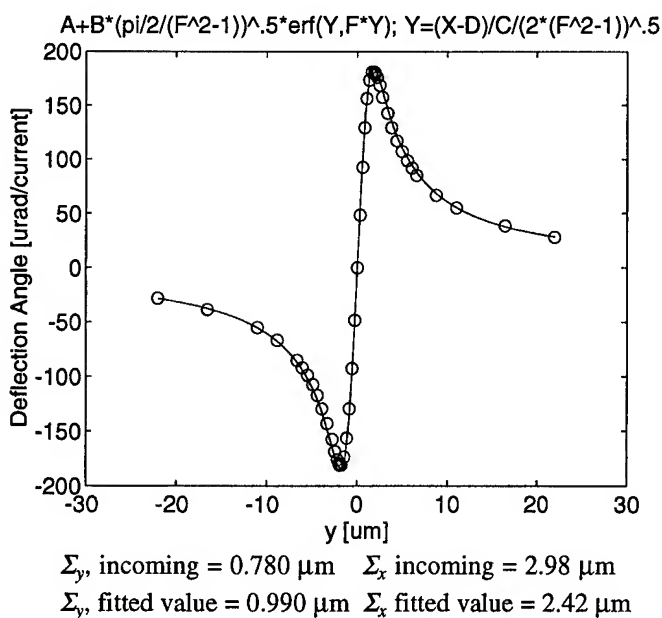


Fig. 3: Simulated *Disrupted* b-b scan, and deflection fit

Fig. 4 shows the relative increase in the overestimation of the unfocused Σ_y , while the effective Σ_y (the average spot size during the interaction) decreases proportionally more and more for smaller spots, leading to a large underestimate of the luminosity. A similar effect is visible for Σ_y when Σ_x changes (see Fig. 5).

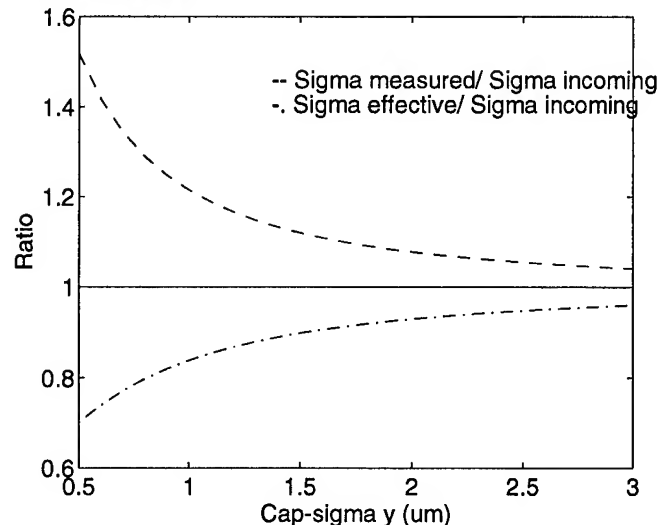


Fig. 4: Σ_y , (measured) / Σ_y , (incoming) and Σ_y , (effective) / Σ_y , (incoming) versus Σ_y ,

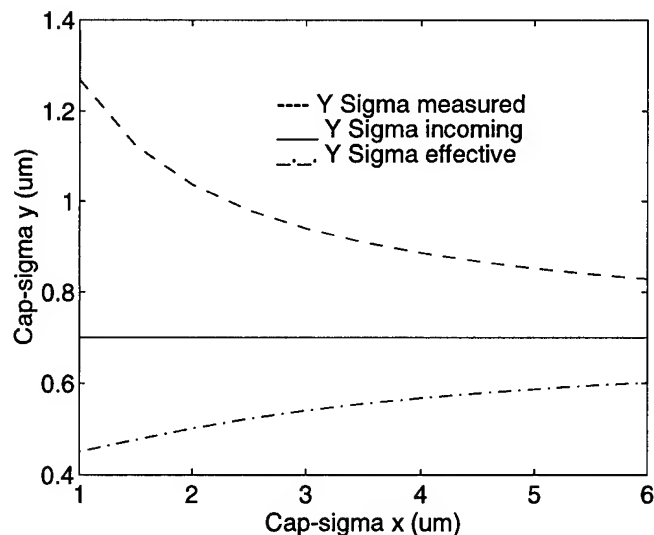


Fig. 5: Σ_y , (measured) and Σ_y , (effective) versus Σ_x

In order to get in real time the correct beam spot sizes, it has been developed a b-b deflection expression that, with some approximations, takes into account for the disruption.

The following assumptions are made:

a) the fields seen by the two beams are always the linear expansion of the true fields around the centroid beam positions,

b) the fields are constant during the interactions, in other words the focusing effects does not change them appreciably.

c) the beam longitudinal distribution is rectangular (in the real case the longitudinal distribution is something between rectangular and gaussian).

With this assumption, it is straightforward to compute the luminosity enhancement. Indeed the focusing effect is now simply like a pure linear focusing lens, and the effective average beam spot size during the interaction can be estimated according to:

$$\sigma_{yEFF} = \sigma_y \frac{\sqrt{2+\sin(2\phi)}}{4\phi}$$

ϕ is the phase advance in the interaction region:

$$\phi = \sqrt{K} \sigma_b$$

K is the derivative of the electric field (colliding beams):

$$K = \frac{631 N}{\sigma_y (\sigma_y + \sigma_x)}$$

N is the target beam number of particles (10^{10} units),
 σ_b the bunch length (in meters),
 σ_y and σ_x the target beam spot sizes (in μm).

The luminosity enhancement so evaluated differs from the one estimated with full tracking by less the 5% up to luminosities of 3 times bigger than the achieved ones.

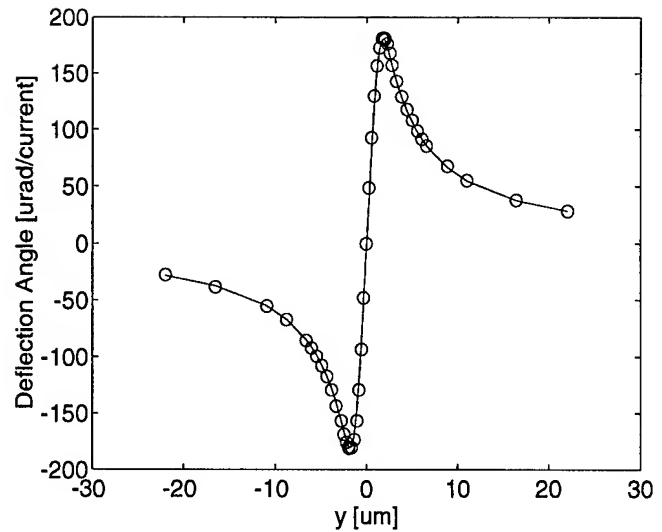
The deflection angle can be evaluated starting from the fields generated by the effective spot sizes (at the relative distance) and considering that the beams do move in a focusing lens, hence:

$$\theta_{yEFF} = \theta_y \frac{\sin(2\phi_{EFF})}{2\phi_{EFF}}$$

being θ_y the deflection angle computed using the effective beam spot sizes and zero bunch length.

With such formulas (see Fig. 6) the fit of the beam-beam deflection computed with the tracking gives much better agreement for the on plane and off plane sigmas and in general the function fits the points much better than the previous one.

Unfortunately the difference between the undisrupted and disrupted deflection is not impressive and probably difficult to see in a fit of real data.



Σ_y , incoming = $0.780 \mu\text{m}$ Σ_x incoming = $2.98 \mu\text{m}$
 Σ_y , fitted value = $0.781 \mu\text{m}$ Σ_x fitted value = $2.98 \mu\text{m}$

Fig. 6: Simulated *Disrupted* b-b scan, and *Disrupted* deflection fit

Conclusions

The disruption has been shown to be a possible cause of the discrepancy between the SLC estimated luminosity and the SLD one. Moreover it can explain a part of the degradation in the measured luminosity as a function of the beam current. In the next run we hope to have a clearer signature of the effect taking accurate data of the beam beam deflection at low and high beam current.

Moreover the use of the disrupted formula probably will lead to a better estimate of the luminosity and better tuning of the final focus.

References

- [1] P. Raimondi, F.-J. Decker, "FLAT BEAM SPOT SIZES MEASUREMENT IN THE SLC - FINAL FOCUS", submitted to PAC95.
- [2] K. Yokoya, P. Chen, "BEAM-BEAM PHENOMENA IN LINEAR COLLIDERS", US-CERN School on Particle Accelerators, Nov. 1990.

FLAT BEAM SPOT SIZES MEASUREMENT IN THE SLC-FINAL FOCUS*

P. Raimondi and F. J. Decker

Stanford Linear Accelerator Center, Stanford University, Stanford, CA 94309 USA

With the switch to flat beam operation in the SLC during the 1993 run [1], it has become necessary to develop an algorithm that is capable of measuring the beam spot sizes at the Final Focus Interaction Point (IP). This algorithm uses the correct beam-beam deflection formula for the more general flat-beam case, since the round beam approximation is no longer valid [2]. The application of this formula to the IP spot size measurements in the SLC Final Focus is the subject of this paper.

I. DERIVATION OF THE BEAM-BEAM DEFLECTION FORMULA IN THE FLAT BEAM CASE

The assumptions used in the theoretical evaluation of the beam-beam deflection are:

- (a) Gaussian and upright distributed beams with sigmas in the three dimensions $\sigma_{z-}, \sigma_{x-}, \sigma_{y-}$ for electrons, and $\sigma_{z+}, \sigma_{x+}, \sigma_{y+}$ for positrons
- (b) $y = 0$ (on plane colliding beams)
- (c) $\alpha_{\max} \times \sigma_{z-} \ll 2\sigma_{x-}$ (no disruption)

It can be proved that the overall deflection angle is proportional to the electric field generated by the convolutions of the two beam space distributions [3]. Moreover, the Bassetti expression for the electric field $E(x)$ is valid for Gaussian distributed beam [4]. Hence, after some algebra, the total deflection angle $\alpha(x)$ in the x -plane of the e^- beam, due to the interaction with the e^+ beam, as a function of their distance x is:

It can be proved that the overall deflection angle is proportional to the electric field generated by the convolutions of the two beam space distributions [3]. Moreover, the Bassetti expression for the electric field $E(x)$ [4] is valid for the Gaussian distributed beam. Hence, after some algebra, the total deflection angle $\alpha(x)$ in the x -plane of the e^- beam (due to the interaction with the e^+ beam) as a function of their distance x is

$$\alpha(x) = 2\sqrt{\pi} \frac{N_{e+} r_e}{\gamma} \frac{x_n e^{x_n^2}}{x} \times \left[\operatorname{erfc}\left(\frac{\Sigma_y}{\Sigma_x} x_n\right) - \operatorname{erfc}(x_n) \right], \quad (1)$$

*Work supported by DE-AC03-76SF00515.

where

$$x_n = \frac{x}{\sqrt{2(\Sigma_y^2 - \Sigma_x^2)}},$$

$$\operatorname{erfc}(x) = \frac{2}{\sqrt{\pi}} \int_x^{+\infty} dt e^{-t^2},$$

N_{e+} is the number of particles in the positron bunch

r_e is the classical electron radius

γ is the beam energy over the electron mass, and

$$\Sigma_y = \sqrt{\sigma_{y-}^2 + \sigma_{y+}^2}, \text{ and } \Sigma_x = \sqrt{\sigma_{x-}^2 + \sigma_{x+}^2},$$

with some further algebra, we can also express the deflection in an integral form simpler than the one used in [2]:

$$\alpha(x) = \frac{N_{e+} r_e}{\gamma} \frac{x}{\Sigma_x^2} \int_0^1 dt \frac{e^{-(x^2/2\Sigma_x^2)t}}{\sqrt{1+(a^2-1)t}}, \quad (2)$$

where

$$a = \Sigma_y / \Sigma_x.$$

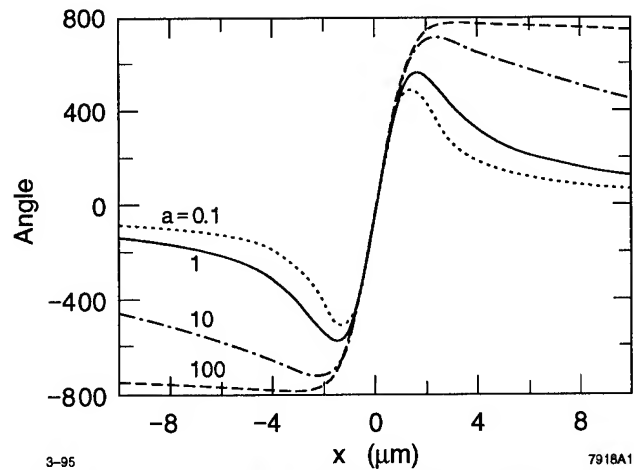


Figure 1. Beam-beam deflection at different aspect ratios (not in scale), $a = \Sigma_y / \Sigma_x$.

It can be shown that in the limit $\Sigma_x \sim \Sigma_y$, Eq.(1) becomes the "round beam-beam deflection" expression [2], and in the limit $\Sigma_y \gg \Sigma_x$ it becomes the "error function" as expected in the infinite flatness case (see Fig. 1). This behavior is much more evident in the integral expression for $\alpha(x)$, since in the case $\Sigma_x = \Sigma_y$, the integral is solvable

in terms of elementary functions; whereas, in the case $\Sigma_y \gg \Sigma_x$, it is simply expressible as an error function.

II. MEASUREMENT OF BEAM SPOT SIZES AT THE SLC INTERACTION POINT

The typical beam sigmas at the SLC-IP are: $\sigma_{z-}, \sigma_{z+} \sim 600 \mu\text{m}$, $\sigma_{x-}, \sigma_{x+} \sim 2.5 \mu\text{m}$, and $\sigma_{y-}, \sigma_{y+} \sim 0.8 \mu\text{m}$. Furthermore, the maximum deflection angle α_{max} is of the order of $300 \mu\text{rad}$.

It can be shown that $\alpha(x)$ is finite and real for any Σ_x and $\Sigma_y > 0$.

Since conditions (b) and (c) are satisfied [condition (a) is assumed to be correct], Eq. (1) was applied to fit the beam-beam deflection in the SLC 1993 run [1]. It is possible to notice from (1) that the deflection in one plane is a function of the distance between the two beams, and of both Σ_x and Σ_y , so that, in principle, the deflection in one plane is able to give information on both spot sizes.

A further advantage of (1) is that the overall scale factor of the deflection angle is a known quantity, depending only by the other-beam charge (measured elsewhere); specifically:

$$2\sqrt{\pi} \frac{N_{e+} r_e}{\gamma} = 1118.4 N_{e+},$$

with the given SLC-beam energy (45.64 GeV), and expressing the deflection angle in μrad , the sigmas in μm and the number of e^+ in 10^{10} units.

The fitting of the beam-beam deflection therefore involves only four free parameters: the two beam spot-sizes, the absolute distance between the two beams, and the overall offset of the measured deflection angle. The last two parameters are mainly caused by the residual offsets of the beam-position-monitor readings.

Figure 2 shows two typical beam-beam scans in the two planes, fitted with the round-beam formula and with the flat formula. Also shown in Fig. 2 are the beam sigmas,

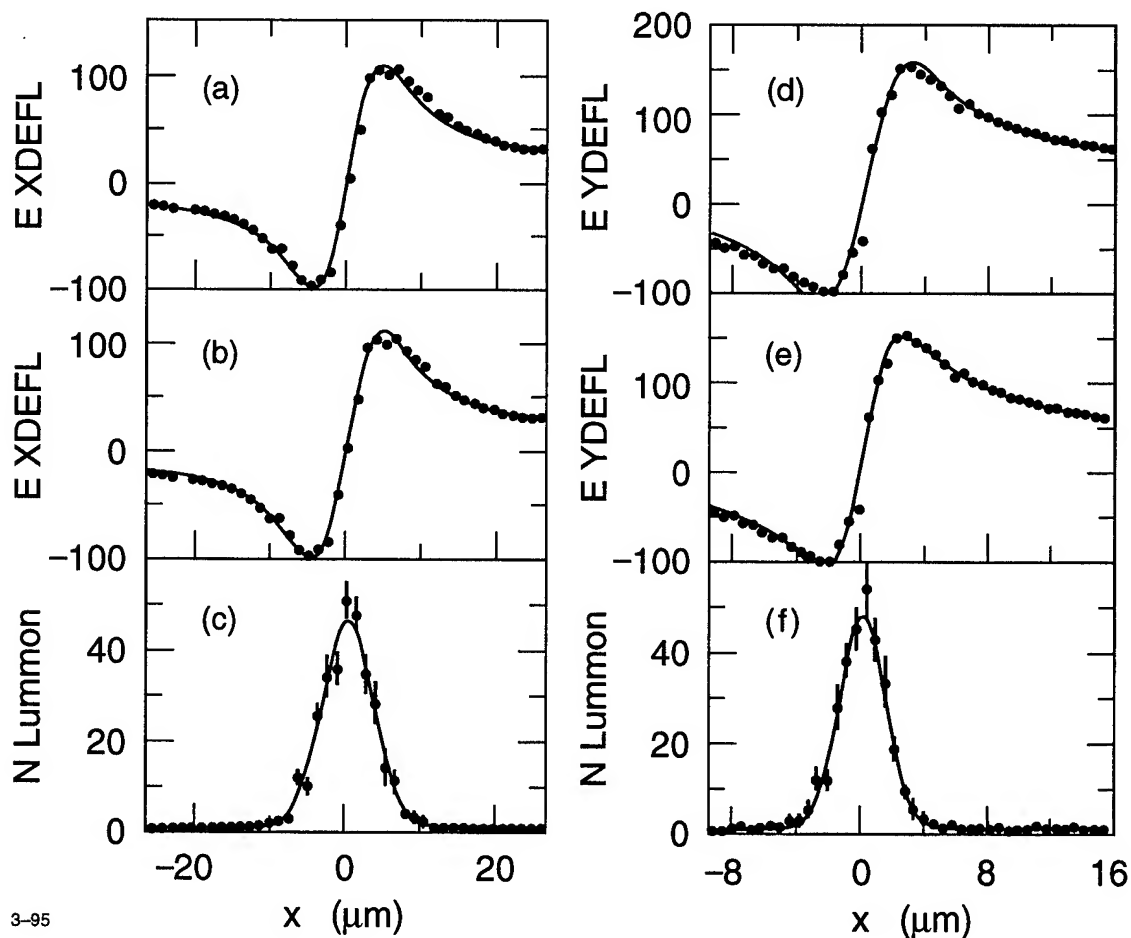


Figure 2. Beam-beam scan fits in a typical SLC running conditions: (a) fit of the x-deflection using the round beam-beam formula, (b) fit of the x-deflection using the flat beam-beam formula, (c) fit of Σ_x using the Bhabha-counts, (d) fit of the y-deflection using the round beam-beam formula, (e) fit of the y-deflection using the flat beam-beam formula, (f) fit of Σ_y using the Bhabha-counts; where A = deflection offset, B = scale factor, C = on plane beam spot size, D = position offset, F = other plane beam spot size.

as measured by using a signal proportional to the Bhabha scattering at low angle. The measured spot sizes using the two techniques are in good agreement.

The accuracy in determining both beam spot sizes with a single beam-beam scan is typically better than 5%.

III. CONCLUSIONS

The use of the Eq. (1) to fit the beam-beam deflection at the SLC IP gives us a very accurate spot-size monitor to tune SLC Final Focus, and to optimize and estimate the SLC luminosity. The agreement of the data with the theory is excellent showing that the assumption (a) is also correct. Furthermore, the disruption effect can be estimated to be still small enough to affect the behavior of the beam-beam scans at the typical 1993 running condition, leading to an underestimate of the real SLC luminosity of about 8%, while it has been a more serious problem in the SLC 1994 where the Σ_y was of the order of $0.9 \mu\text{m}$ and condition (c)

was no longer valid, causing an appreciable difference in the behavior of the measured beam-beam deflection with respect to (1). Corrections of the flat beam-beam formula (1) must be included to take this effect into account.

IV. REFERENCES

- [1] C. Adolphsen et al., "Flat beams in the SLC," PAC93.
- [2] W. Koska et al., "Beam-Beam Deflection as a Beam Tuning Tool at the SLAC Linear Collider", SLAC-PUB-4919.
- [3] V. Ziemann, "Beam beam deflection and signature curves for elliptic beams", SLAC-CN-382.
- [4] M. Bassetti and G.A. Erskine, "Closed Expression for the Electrical field of a Two-Dimensional Gaussian Charge," CERN-ISR-TH/80-06.
- [5] C. Pisin, "SLC Flat Beam Disruption Effects," SLAC Memorandum, April 1993.

POLARIZATION CORRELATIONS IN THE SLC FINAL FOCUS

F.-J. Decker, Stanford Linear Accelerator Center*, Stanford University, Stanford, CA 94309 USA

ABSTRACT

At the SLC, the electron beam polarization (P) is measured by a Compton polarimeter downstream of the Interaction Point. This measurement averages over the entire beam distribution and must be corrected for various correlations to calculate the luminosity (L) weighted polarization. Because the spin rotation in the ARC is energy dependent, off energy particles have lower polarization. These particles may also be poorly focused and contribute less luminosity due to the higher order chromatic optics of the final focus. The small vertical β function at the interaction point also causes an hour-glass effect, where particles at the head and tail of the bunch have less luminosity. Since there is an energy-z correlation due to the compensation of longitudinal wakefields in the linac, these particles may also have lower polarization. The correlations are: $z \longleftrightarrow E$ (linac), $E \longleftrightarrow P$ (ARC), $z \longleftrightarrow L$ (hour-glass) and $E \longleftrightarrow L$ (chromaticity). The contributions from the $z \longleftrightarrow E$ and $z \longleftrightarrow L$ correlations are discussed.

I. INTRODUCTION

At the Stanford Linear Collider (SLC) highly polarized (80%) electrons collide with positrons at the Z mass. The asymmetry in the measured cross section for left and right handed electrons (A_{LR}) determines important high energy parameters like $\sin^2 \theta_w$ and the top mass range [1]. The statistical error of the A_{LR} up to this year is about $\pm 3\%$ and the systematic around 1.5%. Any additional systematics should be carefully checked. The big correction of about 2% for a low energy tail in 1993 [2] is much reduced for the 94/95 run since there are less low energy tails due to over-compression [3]. The number of effective spin rotations in the ARCs was not reduced considerably (from 17 to 13 turns), so other effects have to be investigated. Here we will discuss the effect of the energy spread, which has a certain correlation with the z distribution due to longitudinal wakefields in the linac. This longitudinal distribution correlates with the luminosity at the interaction point (IP), due to the hour-glass effect, where earlier and later particles contribute less to the luminosity. Since these particles are off in energy and the effective polarization of the collisions will be slightly higher.

*Work supported by the Department of Energy, contract DE-AC03-76SF00515.

II. ENERGY-Z CORRELATION

The correlation for the energy in the longitudinal dimensions comes mainly from the rf sinus curve and the longitudinal wakefield. By choosing the bunch length to about 1.2 mm (σ) at $3.5 \cdot 10^{10}$ particles per bunch, the generated wakefield compensates the rf sinus curve roughly. The bunch shaping with over-compression reduced the long low energy tails, so that the energy distribution was about Gaussian with an energy spread of 0.10–0.15%. Since the intrinsic energy spread is about 0.04%, there is some correlation with z . The front has normally a higher energy than the back. This leads also to a compression in the ARCS. A term of $R_{56} = 150$ mm gives about a compression of 0.15–0.23 mm or an IP bunch length of 1.0 ± 0.05 mm at the IP.

A simulation of the longitudinal wakefield effect showed a big sensitivity to the overall phase of the linac. Small variations of 1° in phase will vary the bunch length at the IP by 20% (see Fig. 1).

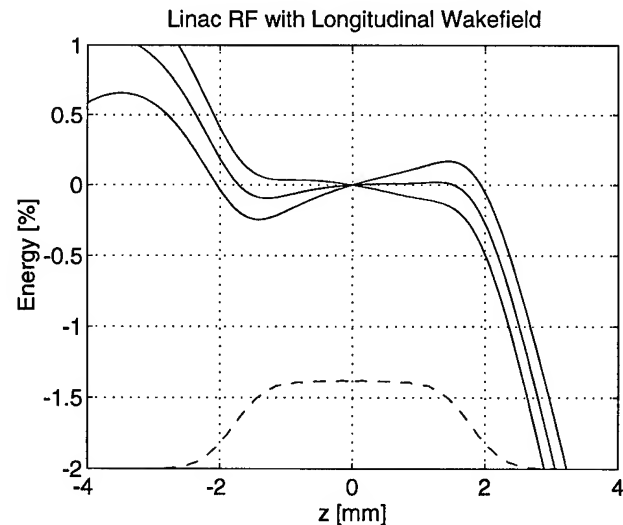


Fig. 1: Energy-z correlation for different linac phase. Small phase changes of $\pm 1^\circ$ influence the energy-z correlation which changes the IP bunch length. The beam distribution (dashed) is generated by over-compression.

III. HOUR-GLASS EFFECT

The strong focussing of the beams at the IP result in a beam envelope which has the form of an hour-glass.

A. Description

At the IP there are two effects which produce different luminosity for different longitudinal positions. One is the hour-glass effect, where particles in the head and the tail of the bunch collide mainly past or in front of the IP with the smallest spot size. The other is the disruption, where the strong beam-beam forces bend the beams towards each other shifting the beam waist somewhat downstream. More sophisticated correlations like traveling focusing, where different longitudinal parts of the bunch have their focus at different z locations, are not considered in this paper.

The hour-glass effect comes mainly from y . With an IP beam size of $0.5 \mu\text{m}$ and an angular divergence of $250 \mu\text{rad}$, the spot size at $z = 0.5 \text{ mm}$ (one effective sigma away) will be $0.515 \mu\text{m}$ or 3% bigger (12% at $2\sigma_{z\text{eff}}$):

$$\sigma_y = \sqrt{\sigma_{y0}^2 + (\theta_{yz})^2}. \quad (1)$$

Figure 2 shows the behavior of the this formula with a correction for the disruption effect.

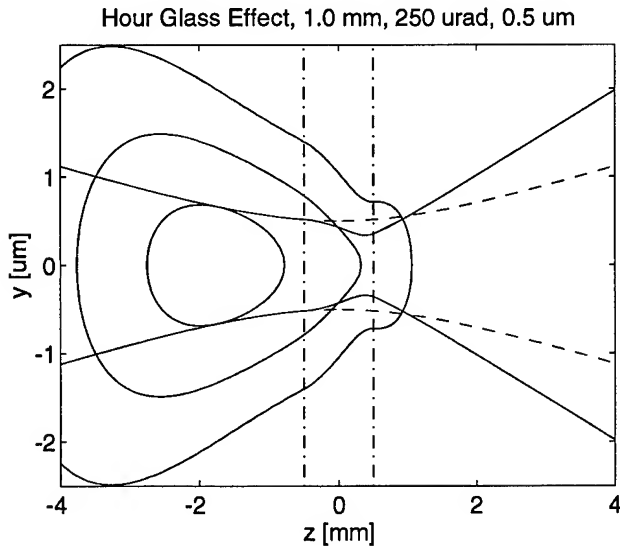


Fig. 2: Hour glass effect with disruption.

The beam enters from the left with a y - z distribution indicated by a 1, 2, and 3 sigma contour lines. The beam-beam forces from the other bunch were assumed to be constant over $\pm\sigma_z/2$ (dash-dotted line). The smaller spot and the bigger outgoing angular divergence is visible from the 1-sigma envelope lines. The dashed curve is the not disrupted case.

The beam-beam disruption [4] or pinch effect focuses the beam even further. The approximation was used, that

the forces were locally fixed and change the beam match in the following way:

$$\sigma_{yod} = \sqrt{\sigma_{y0}^2 \cdot \cos^2(kz) + \theta_{y0}^2 \cdot \sin^2(kz) / k^2} \quad \text{and} \\ \theta_{yd} = \theta_y \cdot \sigma_y / \sigma_{yod} \quad \text{for } -\sigma_z < 2z < \sigma_z \\ \text{with } k = \sqrt{\frac{k_b}{\sigma_z}} \quad \text{and } k_b = \frac{633 \cdot N / 10^{10}}{\sigma_y(\sigma_x + \sigma_y)}.$$

The spot size in x is $2.1 \mu\text{m}$ and $N = 3.5 \cdot 10^{10}$. The beam spot is reduced while the angular divergence increases, keeping the emittance constant in this linearized approach.

B. Estimate

The effective turn in the ARCs set the scale of the problem. With 25 turns and 1% energy offset the spin of these particles will rotate 0.25 turns or 90° , which means they would not have any longitudinal polarization at the IP. For $n = 13$ turns and a $\Delta E/E = 0.3\%$ energy offset the loss in polarization is 3%:

$$\Delta P = 1 - \cos\left(2\pi n \frac{\Delta E}{E}\right).$$

Since there are not too many particles out there the correction will be small. If all the particles outside of 2 sigma (4.6%) would be about 4% off in polarization, but still giving about 80% of the IP luminosity, the effect would cause only a correction of 0.04%. The highly non-linear behavior (quadratic in E and z) can give bigger values especially if the cosine curves are not perfectly centered. To quantify the effect a small simulation program was written.

C. Simulations

The energy spread is assumed to be Gaussian and totally correlated with z . The energy spread is 0.15% and the effective bunch length at the IP is 0.5 mm, half the real value and totally correlated with energy (assumption). The angular divergence in y is $250 \mu\text{rad}$ and the spot size $0.5 \mu\text{m}$. Due to the hour-glass effect (Eq. 1) the spot is bigger and will give less luminosity (3%). An off-energy particle will be sitting off the core and gives even less luminosity. Fig. 3 shows the luminosity versus energy offset and gives for comparison the chromatic effect of $U_{3246} = 850 \text{ m}$.

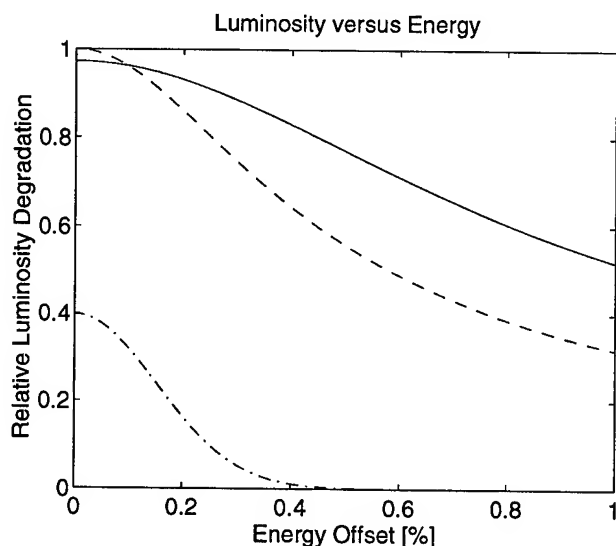


Fig. 3: Luminosity versus Energy Offset

The hour-glass effect (solid) on the luminosity versus energy is less than the direct chromatic effect from a higher order term (dash). A typical (0.15%) energy distribution is given dash-dotted.

IV. HIGHER ORDER CHROMATICS

For the 1994/95 run the higher order chromatics consist mainly of the term $U_{3246} = 850$ m. The effect on the spot size is as follow:

$$\sigma_y = \sqrt{\sigma_{y0}^2 + (2 \cdot U_{3246} \cdot \theta_x \cdot \theta_y \cdot \delta)^2}$$

where the initial size is enlarged by a term which depends on the angular divergences in x (350 μ rad) and y , and the energy spread δ .

V. DISCUSSION OF RESULTS

The hour-glass and direct chromatic effect on the polarization at the interaction point give small corrections of 0.04 % and 0.09 %. For 17 turns the chromatic number is 0.16% which is half the value calculated a year ago with a different program and somewhat different parameters, e.g. real, non-gaussian bunch distribution in z , with more weight in the tails. Taking into account the quadratic effects and any mistuning an overall corrections of about plus 0.2 ± 0.1 % from the apparently lost polarization of -0.75 % from the ARCs seems reasonable.

VI. ACKNOWLEDGMENT

I would like to thank M. Fero for his interest and his careful reading of the manuscript.

VII. REFERENCES

- [1] SLD Collaboration, *Precise Measurement of the Left-Right Cross Section Asymmetry in Z Boson Production by e^+e^- Collisions*, Phys. Rev. Letters, 4 July 1994, Vol. 73, Number 1, p. 25.
- [2] F.-J. Decker, J.T. Seeman, *Luminosity Polarization Correlation in the SLC*, EPAC, London, June 94.
- [3] F.-J. Decker, R. Holtzapple, T. Raubenheimer, *Over-Compression, a Method to Shape The Longitudinal Bunch Distribution for a Reduced Energy Spread*, LINAC94, Tsukuba, Aug. 1994, p. 47.
- [4] P. Raimondi, P. Chen, F.-J. Decker, *Disruption Effects on the Beam Size Measurement*, PAC95, Dallas, May 1995.

SUPERCOOLING OF BUNCHED BEAMS BY COHERENT SYNCHROTRON RADIATION

M. Bergher, LURE, Bât. 209D, Centre Universitaire Paris-Sud, 91405 Orsay Cedex, France

ABSTRACT

Longitudinal and transverse dimensions of bunched beams may be cooled by coherent synchrotron radiation in storage rings. The cooling starts if the bunches are short enough. Coherent synchrotron radiation with wavelengths of the order of the length of the bunch will propagate in the vacuum chamber of the bending magnet. Achievement of such condition, linked to the bunch dimensions, is generally not possible if only the main RF system is used. Therefore it is necessary to add a tunable idle or powered extra RF cavity, whose frequency depends on the transverse dimensions of the vacuum chamber of the bending magnet and on the radius of the orbit curvature. By this mean, a self-consistent effect can be achieved. The energy transfer among particles of the same bunch leads to a dynamic reduction of all bunch dimensions. For these reasons the whole radiated spectrum becomes coherent. This should be true for all storage rings with particles which emit synchrotron radiation. Our experimental results observed on a e^+/e^- storage ring are described.

MICRO-BUNCHING

Coherent synchrotron radiation can propagate when the particle bunch length is smaller or equal to the cutoff wavelength of the vacuum chamber of the bending magnet. This cutoff wavelength depends on the transverse size of the vacuum chamber and the curvature of the bending magnet [1], according to the formula:

$$\lambda_c \approx 2h(h/R)^{1/2} \quad (1)$$

where h is the vertical dimension of the vacuum chamber, and R the radius of curvature. In order to attain the desired bunch length by using only a single RF system, one needs to increase the RF potential. If g represents the length gain (shortening), and σ_0 and σ_d the initial and desired bunch length respectively, $g = \sigma_0 / \sigma_d$, then the increase in RF potential is related to g^2 and the RF power to g^4 , which rapidly becomes limiting.

One can overcome this problem by using a second RF system with a cavity tuned to a higher harmonic. The bunch length gain is then characterized by the formula:

$$g = [(n_1 V_1 \cos \phi_1 + n_2 V_2 \cos \phi_2) / n_1 V_0 \cos \phi_0]^{1/2} \quad (2)$$

where V and ϕ are the potential and phase of the RF systems, and the indexes 0, 1 and 2 refers to the initial, first and second cavity respectively, and n is the number of the harmonic. In the special case when the characteristics of the main RF are maintained, in order to permit the acceptance energy at injection, and to compensate the losses at each turn, one has $V_1 \cos \phi_1 = V_0 \cos \phi_0$. In addition if the second cavity does not procure energy to the beam (at $\phi_2 \approx \pi$) equation (2) becomes:

$$g = [1 - (n_2 V_2 / n_1 V_0 \cos \phi_0)]^{1/2} \quad (3)$$

and each bunch will be replaced by a group of micro-bunches (MB). The length of the MB will depend on the gain (g) defined above, and the number of MB will depend on the length of the bunch provided by the main RF system.

The energy acceptance (ϵ) of the two RF systems must be higher than the dispersion energy of the particles after dumping $\epsilon = r(\sigma E/E)$. This determines the minimum level for V_2 described by:

$$V_2 = [2\pi r V_0 n_1 (g^2 - 1) \alpha E (\sigma E/E)^2]^{1/2} \quad (4)$$

where α is the momentum compression, and E the energy. The potential on the second cavity must increase with the dumping of the particles, which implies that the second cavity must be passive. If the shunt resistance is sufficient to procure the needed potential, then the idle cavity can be excited directly by the beam, otherwise it has to be via a pick-up followed by an amplifier.

It should be mentioned that with a double RF system with different harmonics, the MB are not equally separated and therefore the slope at the loss potential seen by each MB is different. In case of phase oscillations, this gives a synchrotron spectrum with groups of closely spaced lines around the synchrotron main frequency side band and it's "harmonics", the later depending only on the main cavity. This was already seen on several rings, ACO, LEP [2,3], SuperACO (see below), which means that there is an inherent resonant element in these rings that induces MB.

SUPERCOOLING

When the MB becomes sufficiently short, coherent synchrotron radiation can also propagate in the vacuum chamber of the bending magnet. Because of the different

path in the bending magnet for the particles (along the arc of circle) and for the coherent synchrotron radiation that they emit (along the cord), the particles at the rear of the bunch will interact with the particles in front of them by stimulated absorption. The former will transfer energy to the later and therefore they will accelerate them. The phenomenon will propagate gradually, from the tail to the front of the MB.

The resulting energy change can be calculated from the Lorentz force:

$$\delta \gamma m c^2 = - e \int \int v E dt d\lambda \quad (5)$$

where e is the electronic charge, v is the speed of electrons, E is the transverse electric field of the plane light wave, t is the time of interaction, and λ are the coherent wavelengths. The absorption will occur if this energy change is positive. From the energetic point of view, this phenomenon leads to a decrease in energy dispersion in the MB as a whole, which brings to a proportional reduction of the length of the MB, and to a dumping of the transverse horizontal and vertical movements, because of coupling. The shortening of the MB starts very slowly and accelerate with the increase in number of coherent wavelengths which are participating and which becomes shorter and shorter. The transferred energy increased faster than the sum of wavelengths, because the shorter ones transfer more energy. Concomitantly, the yield of the transfer increases with the increase in MB density. The phenomenon is cumulated in all bending magnets, and during a great number of turns in the ring. The overall synchrotron spectrum emitted in the magnets becomes totally coherent and is seen as a line spectrum with the separation among the lines corresponding to the higher harmonic of the idle cavity frequency. The beam becomes "single-energetic" with very shortened transverse and longitudinal dimensions.

As opposed to what happens in free electron lasers, here the MB are cooled down. Only the particles at the front, which have the lowest energy, gain energy by stimulated absorption of different wavelengths, higher or equal to the length of the MB. In free electron lasers stimulated emission and absorption occur at the wavelength of the laser, which is very short compared to that of the bunch, leading to heating.

RESULTS OBTAINED ON e^+ / e^- STORAGE RINGS

Measurements performed on the SuperACO storage ring, related to synchrotron oscillations, showed that the movement of particles is only dipolar, whatever the frequency of oscillation (figure 1). This result is in contradiction to current concepts. It confirms the presence of a passive cavity, which could be either a higher-order mode

of the main cavity, or could be at any other position of the vacuum chamber. This idle cavity is close to a much higher harmonic than the main RF of the ring. If it is exactly tuned to a harmonic of rotation, the RF level permits to obtain very short and stable MB, leading to the presence of first wavelengths of coherent synchrotron radiation.

These exceptional conditions which were met on the old ACO ring, allowed us to see the self-consistent phenomenon of supercooling of MB. The synchrotron spectrum became totally coherent. The light leaving the magnet windows consisted of a succession of stable longitudinal slices of light, that were thin, vertical and perpendicular to the output axis. These slices of light were equally spaced without any light between them. Although partially unexplained, this phenomenon is a representation of the total coherence of the spectrum. The measurements of the emitted light, using a streak camera [4,5], revealed the presence of a discrete structure of the bunch of particles that had a period corresponding to the distance between two slices of light.

Two other features, which we think are related to total coherence, were also recorded under the mentioned conditions. The lifetime of the beam was independent of the current stored in the ring, and corresponded to the one usually seen at small currents. The beam-beam limit was one order of magnitude higher than the usual limit.

In order to confirm the results obtained on the ACO ring, test should be performed on rings that have similar characteristics, similar or smaller energy and curvature radius. Our results indicate that coherent radiation and supercooling of the beam could be implemented to all existing storage rings producing synchrotron radiation, which would extend noticeably their usage.

REFERENCES

- [1] R.L. Warnock, Shielded Coherent Synchrotron Radiation and its Possible Effect in the Next Linear Collider, Proc. IEEE PAC 91, Vol. 3, pp. 1824-1826, (1991)
- [2] G. Da Silva, R. Bernier, M. Bergher, and R. Belbeoch, Mesure et Stabilisation des Oscillations de Phase sur ACO, LAL, Orsay, NI-46, (1973)
- [3] D. Brandt, K. Cornelis and A. Hofmann, Experimental Observations of Instabilities in the Frequency Domain at LEP, Proc. EPAC 92, Vol. 1, pp. 345-347, (1992)
- [4] M. Bergher, M. Velghe, and J.C. Mialocq, Observation of the Substructure in the Electron Bunch on the ACO Storage Ring, Nuclear Instruments and Methods, A 237, pp. 259-262, (1985)
- [5] Yoshihimo Funakoshi, et al., Observation of Multibunch Phenomena in Tristan Accumulation Ring, Particle Accelerators, Vol. 27, pp. 89-94 (1990)

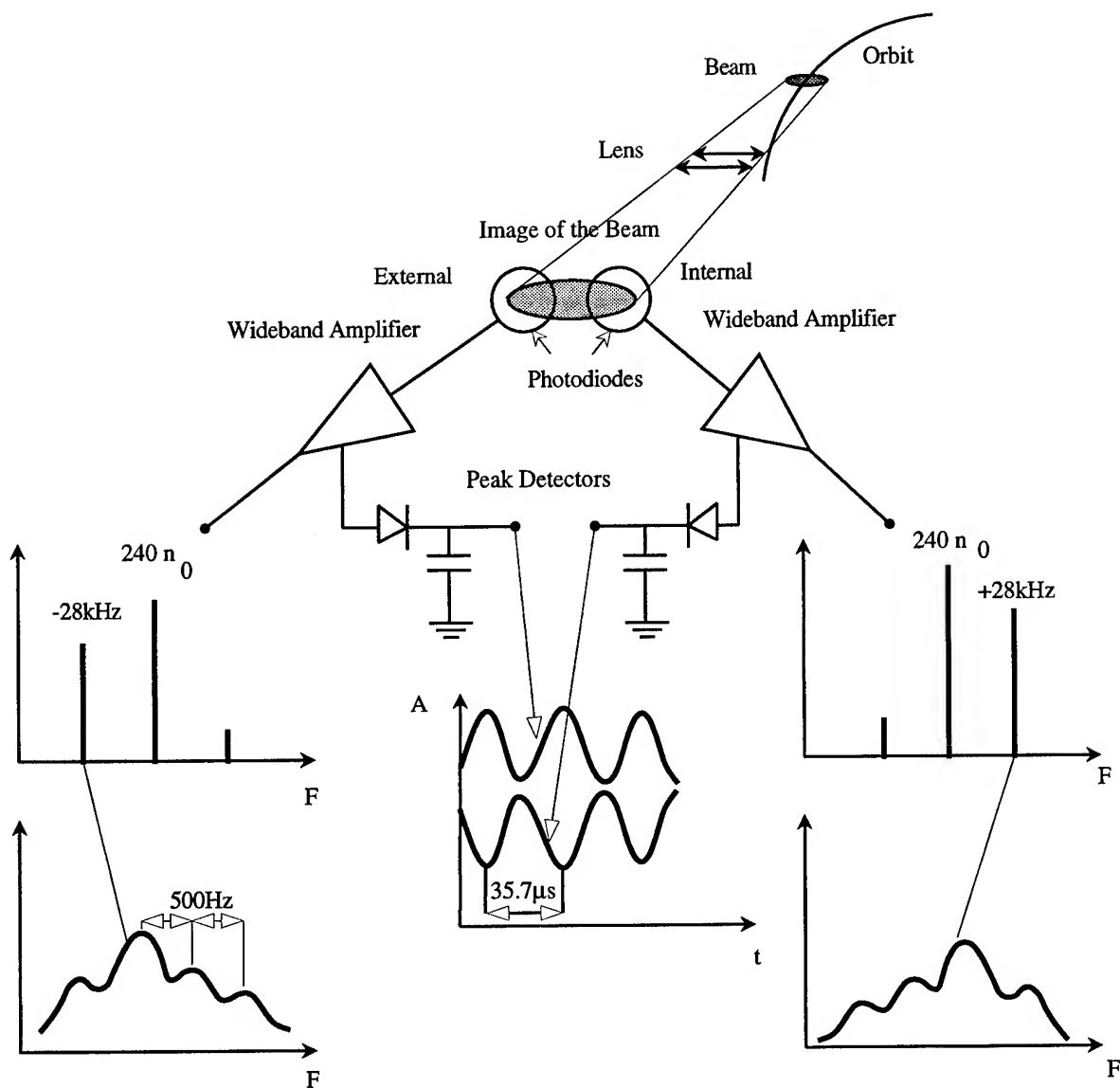


Figure 1. Spectral analysis of the synchrotron oscillations and the demonstration that the movement of the beam is only dipolar.

Measures were performed on the SuperACO storage ring, using two ultra fast PIN photodiodes (35 ps rise time, PD15, Opto-Electronics, Oakville, Canada). The photodiodes were positioned to see the internal and external part of the image of the horizontal synchrotron beam behind the optics at the exit of a magnet. Each circuit consisted of one photodiode followed by a wideband amplifier with two outputs, one for measurements with a spectrum analyzer, the other for peak detection. This second output permitted to detect and extract the amplitude modulation of the pulses which represent the bunches. This modulation is the consequence of oscillations in energy of the particles of the beam. The modulations detected were of opposite phase, as expected for dipolar movements of the particles. This was true for different frequencies of synchrotron oscillations. The recorded spectrum shows that the dipolar movement consists of a series of closely spaced frequencies, which indicates the presence of micro-bunches. For a theoretical and measured synchrotron oscillation frequency of 14.6 kHz, two dipolar frequency oscillations were detected: one at 28 kHz for a current between 72 mA and ≈ 100 mA, and an other one at 39 kHz for a current above 100 mA to the limit of 200 mA. The limit is determined by the high temperature tolerance of the sapphire window. All measurements were performed with two equal "bunches" of particles at the opposite sides of the storage ring.

ANALYSIS OF THE TEVATRON COLLIDER BEAM SPECTRUM FOR BUNCHED BEAM STOCHASTIC COOLING

G. Jackson

Fermi National Accelerator Laboratory¹, MS 345, P.O.Box 500, Batavia, IL 60510 USA

ABSTRACT

The leading cause of the delay in the successful completion of the Tevatron Collider bunched beam stochastic cooling project was the existence of large coherent longitudinal spectral lines at harmonics of the revolution frequency (47.7 kHz) in the frequency range of 4-8 GHz. The preamplifiers of the cooling system would saturate, distorting the betatron Schottky signals to the extent that they were not suitable for stochastic cooling. The results of extensive measurement of these unexpected spectral lines are described and analyzed in this paper.

I. DISCUSSION

The Tevatron bunched beam stochastic cooling project [2] has been stalled because of large coherent revolution harmonic lines in its bandwidth. As seen in figure 1, these lines dominate the power in the system, and cause the TWT driving the kicker array to run at reduced loop gain.

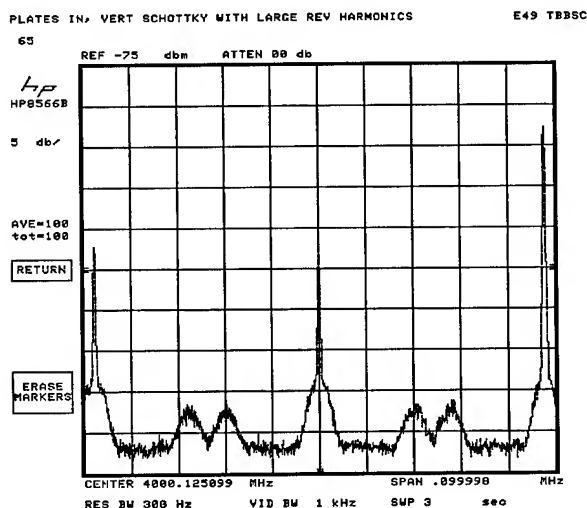


Figure 1: Measured beam spectrum from a vertical proton pickup. Note the large coherent lines at revolution harmonic frequencies at the left, center, and right. The betatron Schottky lines are clearly visible above the noise floor. The center frequency is 4 GHz and the scale is 10 kHz/div.

In order to look systematically at the power in these lines over a broad frequency range, it is necessary to look at harmonics of the RF frequency. This is true because the 6 proton bunches in the ring are not equally spaced. In addition, the bunches are usually quite different in intensity. Therefore, the only way to assure measuring the microwave properties of the beam and not a form factor modulation, measurements are

restricted to the RF frequency harmonics. Figure 2 shows the results of such a survey using the Tevatron resistive wall monitor [3]. Given that there is no beam calibration of the response of the stochastic cooling pickup electrodes, they are not a reliable means of accurately measuring such a spectrum.

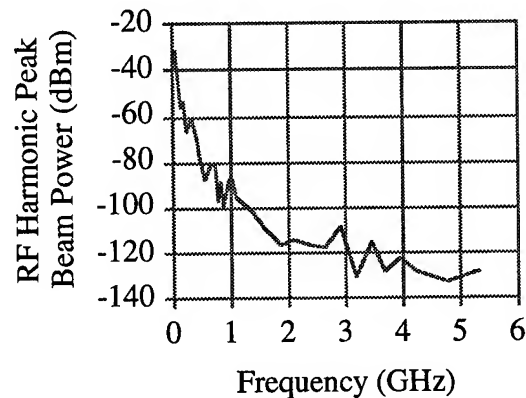


Figure 2: Beam current power spectrum, measured at each harmonic of the RF frequency.

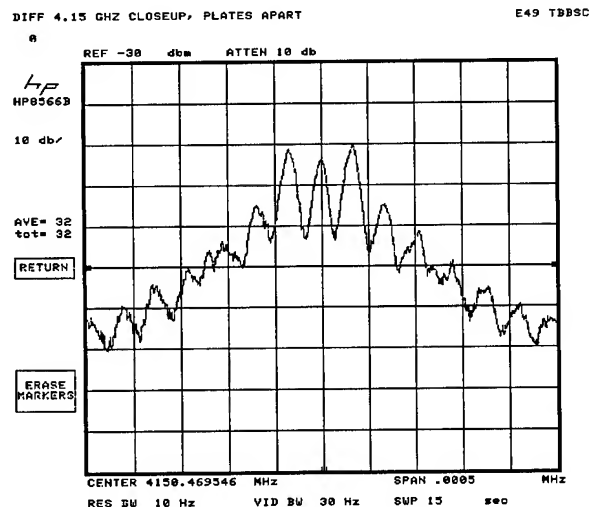


Figure 3: Power spectrum of a single revolution harmonic line at 4.15 GHz. The frequency scale is 50 Hz/div.

Upon closer inspection of the longitudinal lines, as seen in figure 3, there is obviously a modulation at the synchrotron frequency of the beam. Since the vertical dispersion is negligible, this must be the result of phase (arrival time) modulation. Indeed, the Bessel function distribution of the sidebands confirms that hypothesis. By measuring the relative strengths of the various lines, it was found that they could be

explained by a bulk coherent synchrotron oscillation of amplitude 60 psec [4].

If the opposing array were perfectly centered (vertically) around the beam and the signal differencing hybrid were perfect, then in principle a coherent synchrotron oscillation can not be the problem. To convince oneself of this fact, just look in the time domain. Figure 4 shows the result of a measurement of the longitudinal beam profile using the resistive wall monitor, which has a bandwidth ranging from 3 kHz to 6 GHz. The oscilloscope measuring this signal is a Tektronix 11801 fitted with a 20 GHz analog bandwidth sampling head. The beam is composed of the central collider bunch surrounded by satellites formed by the process of coalescing [5].

Beam Signal from Resistive Wall Monitor

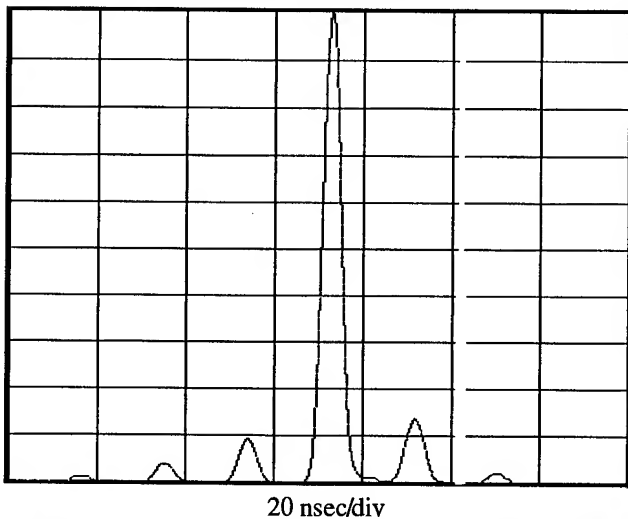


Figure 4: Longitudinal beam signal from a 1 W resistive wall monitor which has a 6 GHz bandwidth. The scope has an analog bandwidth of 20 GHz.

The effect of this waveform on the bunched beam stochastic cooling electronics is apparent in figure 5. The two satellites before the main bunch are visible and are not saturated, but the main bunch clear sends the microwave electronics into shock. The disruption is so pronounced that the trailing satellite bunches are not even visible.

Figure 5 shows the effect of attempting to center the pickup arrays vertically around the beam. This is accomplished by using the motor control on the cooling vacuum tank, where the arrays are fixed with respect to the tank itself. Table 1 contains a summary of the vertical position and scope scale for each of the tank positions. Note that even though the main bunch signal does show a minimum, the amount of signal change with tank position is minimal compared to the amplitude change of the signals from the leading satellite bunches. By comparing the amplitudes of the satellite and main bunch signals, it is clear that the electronics are compressed by almost an order of magnitude, even the arrays are centered as well as possible. Use of the longitudinal inchworm motor to align the arrays longitudinally

may be a possible method to improve this situation a bit. This will be one of the next studies undertaken.

Table 1: Summary of information related to the data shown in figure 5. The scale data is the full range vertical scale of the scope image.

Data	Position (")	Scale (mV)
A	233	972
B	218	964
C	204	940
D	193	900
E	185	860
F	169	944

One of the problems with doing these measurements is the fact that the closed orbit of the beam moves vertically at a frequency of 60 Hz. As far as the electronics are concerned, that is DC. Therefore, if nothing can be done to eliminate the coherent power at this 4-8 GHz frequency band, then the only way to null out the signal would be to build a filter in which the sum signal from the differencing hybrid if fed back into the difference signal with a fast gain modulation to compensate for the beam motion. This has been tried without success [6].

Therefore, the fundamental problem is the existence of coherent longitudinal energy at these high frequencies. Diagnosing the cause of these signals is hampered by the fact that the beam is so dynamic, undergoing closed orbit shifts and coherent synchrotron oscillations. The real challenge for making progress will be on the instrumentation and filter front.

II. REFERENCES

- [1] Operated by Universities Research Association Inc., under contract with the U.S. Department of Energy.
- [2] G. Jackson, "Bunched Beam Stochastic Cooling", Proc. IEEE Part. Acc. Conf., San Francisco (1991) 2532.
- [3] C. Moore, et al., "Single Bunch Intensity Monitoring System Using an Improved Wall Current Monitor", Proc. IEEE Part. Acc. Conf., Vol. 3 (1989), 1513.
- [4] G. Jackson, et al., "Bunched Beam Stochastic Cooling in the Fermilab Tevatron Collider", Proc. IEEE Part. Acc. Conf., Washington D.C. (1993), 3533.
- [5] J. Dey, et al., "Improvements in Bunch Coalescing in the Fermilab Main Ring", this proceedings.
- [6] R. Pasquinelli, "Bunched Beam Cooling for the Fermilab Tevatron", this conference.

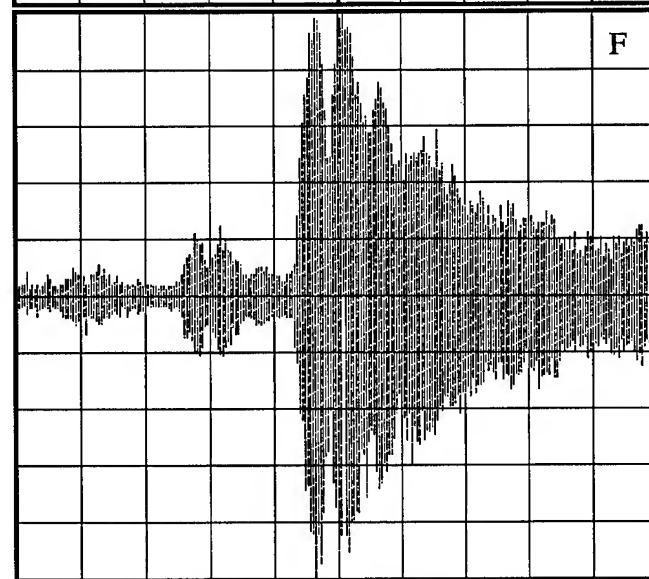
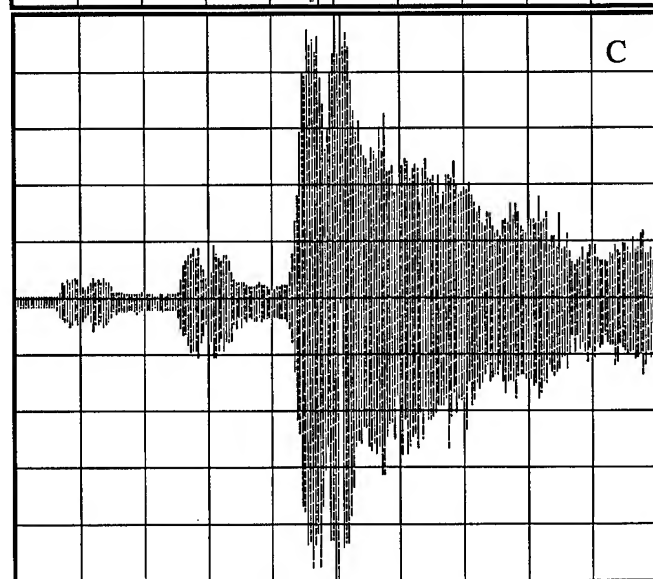
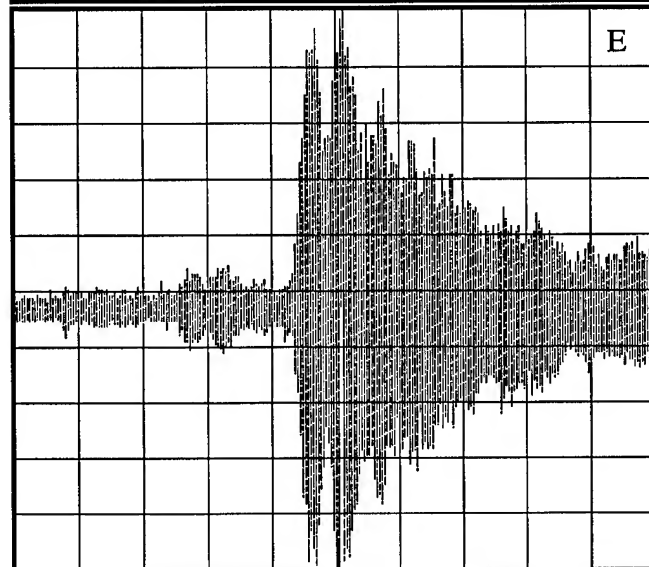
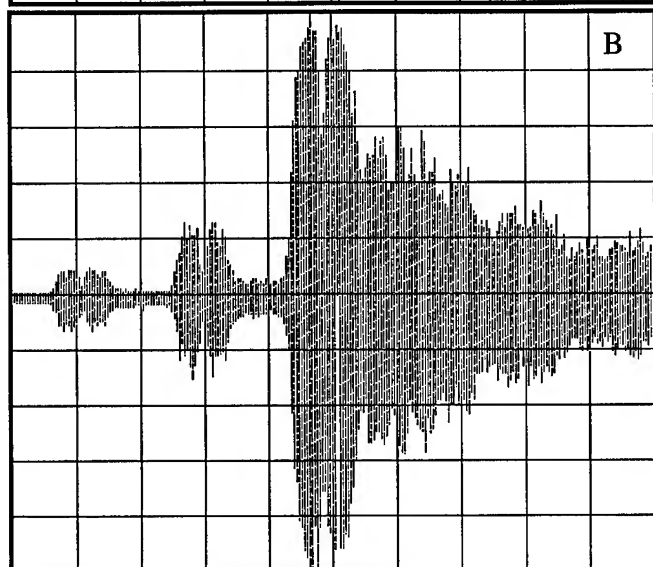
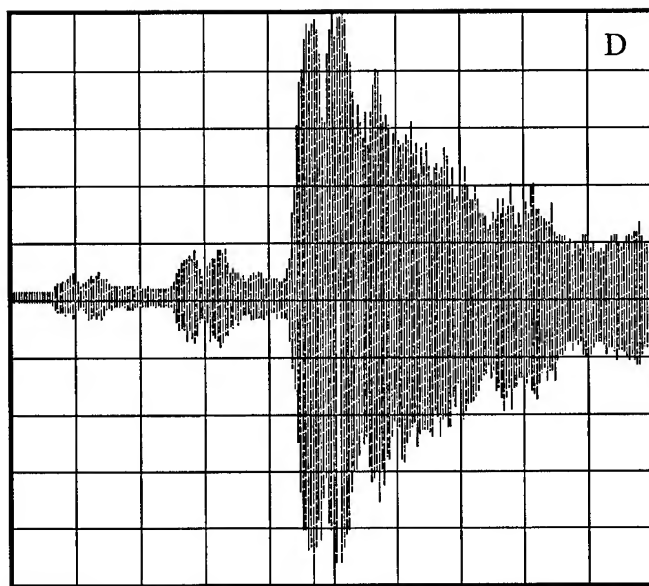
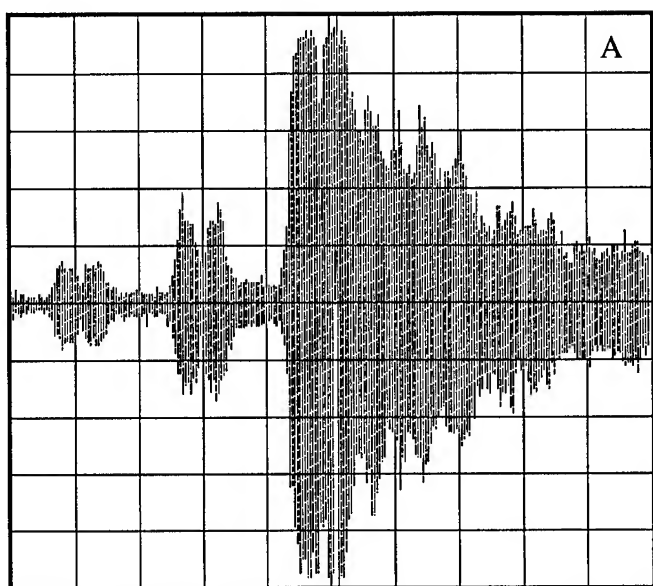


Figure 5: Results of a tank position scan. The horizontal scale is 10 nsec/div, vertical full scale is in table 1.

Asymmetric Hopf bifurcation for proton beams with electron cooling*

X. Kang, M. Ball¹, B. Brabson¹, J. Budnick¹, D.D. Caussyn^{2 †}, P. Colestock³, G. East¹
M. Ellison¹, B. Hamilton¹, K. Hedblom⁴, S.Y. Lee¹,

D. Li¹, J.Y. Liu¹, K.Y. Ng³, A. Pei¹, A. Riabko¹, M. Syphers⁵, L. Wang¹, Y. Wang¹

¹Indiana University Cyclotron Facility, 2401 Milo B. Sampson Lane, Bloomington IN 47408

²Department of Physics, University of Michigan, Ann Arbor, Michigan

³Fermilab, P.O. Box 500, Batavia, Illinois 60510

⁴Uppsala University, The Svedberg Laboratory Box 533, S-75121, Uppsala, Sweden

⁵Alternate Gradient Synchrotron, Brookhaven National Laboratory, Upton, N.Y. 11973

Abstract

We observed maintained longitudinal limiting cycle oscillations, which grew rapidly once a critical threshold in the relative velocity between the proton beam and the cooling electrons was exceeded. The threshold for the bifurcation of a fixed point into a limit cycle, also known as a Hopf bifurcation, was found to be asymmetric with respect to the relative velocity. This asymmetry of Hopf bifurcation was found to be related to the electron beam alignment with respect to the stored proton beam.

I. Introduction

Recently, we have reported an experimental observation of the Hopf bifurcation in the synchrotron phase space when the relative velocity between the proton beam and the cooling electrons is greater than a threshold value [1], [2]. We have found that the threshold of bifurcation is related to the "temperature" of the cooling electrons, or equivalently the rms velocity spread of cooling electrons seen by the proton beams. In these observations, we were puzzled by the asymmetry of the bifurcation with respect to the relative velocities (See Fig. 1 of Ref. [1] and Figs. 4 and 5 of Ref. [2]).

This paper reports results of experimental studies on beam motion when the energy of the synchronous proton is varied, while holding the electron energy constant and varying the electron beam direction relative to the proton beam. In particular, we investigate the effect of electron beam alignment on the asymmetry of Hopf bifurcation and the shape of the cooling drag force on Hopf bifurcation amplitude. Our experimental results are compared with results from numerical simulations, where the onset of the limit cycle instability is related to the temperature of the electron beam.

II. Experimental Methods and Results

The IUCF Cooler Ring is a hexagonal shaped storage ring with a circumference of 86.8 m. The experiment was done with a 45 MeV proton beam injected and then stored in a 10 s cycle time. After 5 s from the start of the cycle, the 6-D phase space coordinates were digitized at 10-revolution intervals for 16384 points. The nominal rf cavity frequency was 1.03168 MHz with the harmonic number $h = 1$. At this energy, the phase slip factor

η of the Cooler Ring was about -0.86 . The beam was typically a single bunch of about 4×10^9 protons with a typical length of about 100 ns FWHM at a rf peak voltage of about 41 V. For experimental results reported in this paper, the rf voltages were set at 85 V and 128 V respectively. Since measurements of longitudinal motion were being made, the phase lock feedback loop for the rf, which is normally on, was switched off. Damping of synchrotron oscillations while operating under these conditions occurred entirely due to the electron cooling.

The difference equations describing the longitudinal motion are

$$\delta_{n+1} = \delta_n - \frac{2\pi v_s^2}{h\eta} (\sin \phi_n - \sin \phi_s) - f(\delta_n) \quad (1)$$

$$\phi_{n+1} = \phi_n + 2\pi h\eta\delta_{n+1}, \quad (2)$$

where η is the phase slip factor, ϕ_s is the phase of the synchronous particle, h is the harmonic number, $f(\delta)$ is the damping force, provided in our case by electron cooling, v_s is the small amplitude synchrotron tune at a zero synchronous phase, and the subscripts n refer to the revolution number.

A. The damping force

The damping force $f(\delta)$ produced by the electron cooling is the result of a statistical exchange of energy in Coulombic collisions between the protons and relatively cold electrons as they travel together at the same velocity in the accelerator. In practice, electron cooling in synchrotrons is normally done in relatively short straight sections due to cost and space limitations. At IUCF the electron beam is mixed with the proton beam for distance of only 2.2 m or about 2.5% of the circumference of the ring. The electron beam radius is about 1.27 cm and the cathode temperature is about 1300°K or $kT_{\text{cath}} = 0.11$ eV, where k is the Boltzmann constant. The maximum electron beam current is 4 A.

Assuming an electron beam with an isotropic phase space Maxwellian velocity distribution, the damping force in the non-magnetized binary collision theory is given by

$$f(\delta) = \frac{4\pi\alpha\Delta_{e\parallel}}{\omega_0} g(\zeta), \quad (3)$$

with a kinematic factor given by

$$g(\zeta) = \frac{3\sqrt{\pi}}{4\zeta^2} \left[\text{erf}(\zeta) - \frac{2\zeta}{\sqrt{\pi}} e^{-\zeta^2} \right], \quad (4)$$

*Work supported by grants from NSF PHY-9221402 and DOE DE-FG02-93ER40801.

[†]Present Address: Department of Physics, Florida State University, Florida

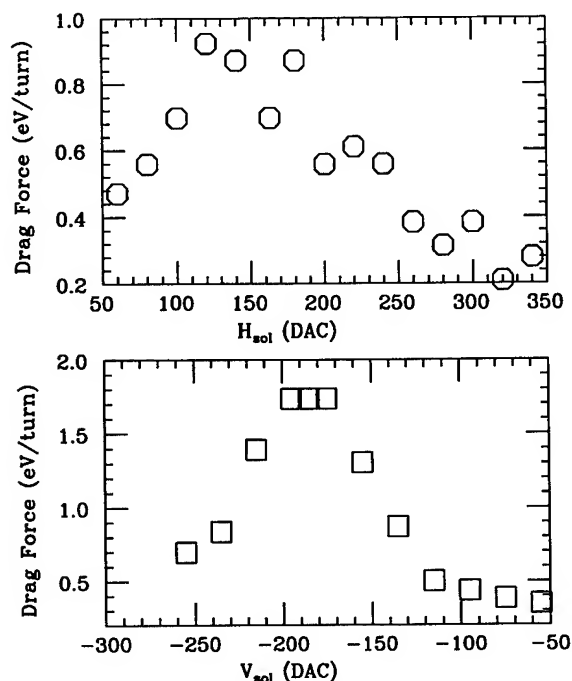


Figure 1. The drag force measured with respect to electron beam alignment by using the horizontal and vertical dipoles H_{sol} and V_{sol} .

where $\Delta_{e\parallel} = \sigma_e/\beta c$, $\zeta = (\delta - \delta_e)/\Delta_{e\parallel}$, α is the $1/e$ damping rate per relative velocities with units s^{-1} . From our previous measurements [1], [2], we have $\Delta_{e\parallel} \approx 3 \times 10^{-4}$ for the IUCF electron cooling system at 45 MeV of proton kinetic energy.

The effective temperature of the electron beam is related to the rms electron velocity spread by

$$kT_{\text{eff}} = \frac{1}{2}m_e\sigma_e^2 = \frac{1}{2}m_e\beta^2c^2\Delta_e^2. \quad (5)$$

Because of the adiabatic acceleration, the longitudinal effective electron temperature is much smaller than that of the cathode temperature. Since there is no adiabatic damping in the transverse phase space, the effective transverse temperature remains 0.11 eV. The equivalent momentum deviation is $\Delta_{e\perp} = 2.1 \times 10^{-3}$. For comparison, the bucket height of the synchrotron phase space at a rf voltage of 128 V is about 1.0×10^{-3} . The cooling drag force for relative velocities between protons and cooling electrons lying between the longitudinal and transverse rms values is of particular interest.

In machines where the electron beam is magnetically confined by a solenoidal field, as it is in the IUCF Cooler Ring, the damping force can be enhanced by an effect called magnetized cooling. Magnetized cooling can be substantial for small relative velocities, where electrons are trapped in magnetic field lines, the effective longitudinal and transverse cooling rates can be greatly enhanced.

B. Optimization of electron cooling system

Since the threshold of Hopf bifurcation is related to the rms velocity spread of cooling electrons along the proton trajectory in the cooling electron cloud, the asymmetry of the Hopf bifurcation

can easily be explained by different velocity spreads seen by the proton beam having different momentum closed orbit. Since electrons having identical speed as that of protons have a much smaller momentum rigidity, the electron beam alignment can easily be adjusted by superimposing a horizontal or a vertical dipole field to the solenoidal field. A method to obtain optimal alignment is described as follows.

When the rf frequency is shifted, the beam, which is originally at the center of the rf bucket (i.e., $\delta = 0$ and $\phi = 0$), will be dragged away from the origin and begin to undergo a synchrotron oscillation. If the damping force were linear over the entire range of v_{rel} , the proton beam would damp to a new fixed point attractor ϕ_{FP} , i.e. the synchronous phase angle, where

$$\phi_{\text{FP}} \approx \frac{2\alpha}{\omega_0 v_s} \frac{h\eta\delta_e}{v_s}, \quad (6)$$

where δ_e is the fractional momentum spread of the proton traveling at the velocity of cooling electrons with respect to the synchronous particle of the rf cavity. This would correspond to the situation where the proton beam was continually losing energy due to the damping force, but with it continually being made back by the rf cavity, or vice versa. Because $\alpha \ll \omega_0 v_s$, the resulting ϕ_{FP} , which is equivalent to the synchronous phase angle ϕ_s of the beam, is very small.

In order to increase the sensitivity of measuring the synchronous phase angle ϕ_{FP} shown in Eq. 6, we choose the rf voltage with $V_{\text{rf}} = 10$ V, where The corresponding synchrotron tune is 1.25×10^{-4} at $h = 1$. The rf synchronous phase angle is measured by stepping away from the reference frequency by 200 Hz. Figure 1 shows the drag force, which is $eV_{\text{rf}} \sin \phi_{\text{FP}}$, vs the horizontal and vertical alignment, where the lower plot shows the drag force vs the vertical alignment with $H_{\text{sol}} = 160$ dac. We obtained a maximum drag force at about 1.8 eV/turn. From Eq. 6, we obtain $\alpha = 45 s^{-1}$, which agrees well with the value of $40 s^{-1}$ obtained from an earlier measurement by using the harmonic modulation to the HVPS (see Sec. III A of Ref. [2]).

C. Hopf Bifurcation amplitude with a Nonlinear Damping Force

To investigate Hopf bifurcation due to the nonlinear damping force, the electron velocity was displaced from the proton velocity to produce a nonzero relative velocity. This was done by changing the rf cavity frequency, where a step of 1 Hz resulted in changing the fractional proton velocity by about 1×10^{-6} . If the electron velocity is equal to the proton velocity when the rf cavity frequency is f_0 , then the fractional momentum deviation of the electron beam from the proton beam, δ_e , at the new rf frequency f is given by

$$\delta_e = \frac{(f - f_0)}{\eta f_0}. \quad (7)$$

The maximum synchrotron phase amplitude $\hat{\phi}$, and the maximum fractional momentum deviation $\hat{\delta}$ are measured at 5 s after the start of an injection cycle to allow the initial transient oscillations to damp out. As shown in our earlier reports [1], [2], the Hopf bifurcation amplitudes can also be measured with a BPM sum signal on an oscilloscope.

Choosing the optimal drag force with $H_{\text{sol}} = 160$ dac and $V_{\text{sol}} = -185$ dac, the measured bifurcation amplitude is shown

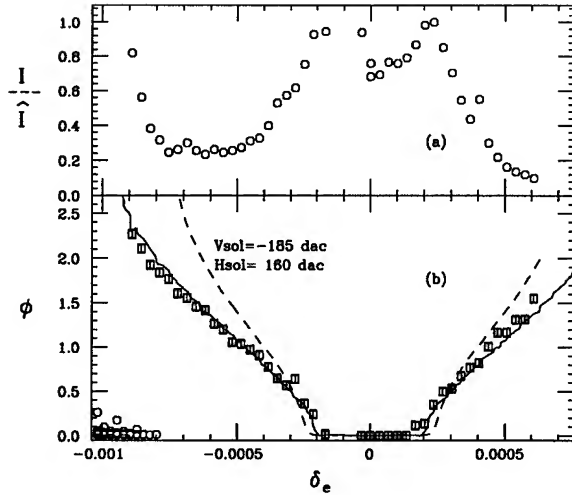


Figure 2. The stored beam current and the stable synchrotron amplitudes vs δ_e . Note the close correlation between the stored beam current and the Hopf bifurcation threshold. The dashed line corresponds to numerical simulations with non-magnetized cooling force while the solid line is obtained from a parameterization with a magnetized cooling force.

in Fig. 2b and the corresponding beam intensity is shown in Fig. 2a. In particular, Fig. 2b shows a nearly symmetric Hopf bifurcation amplitude vs δ_e .

More significantly, a close correlation between the storage beam current and the Hopf bifurcation threshold indicates the importance of this phenomena in realistic beam operation. It is worth pointing out that the dashed line in Fig. 2b shows the theoretical prediction of Hopf bifurcation amplitude based on the kinematic factor of Eq. 4 with $\Delta_{e\parallel} = 3 \times 10^{-4}$. Two obvious disagreements are (1) the experimental threshold is lower than that predicted by theory and (2) the Hopf bifurcation amplitudes observed are much lower than those predicted by theory.

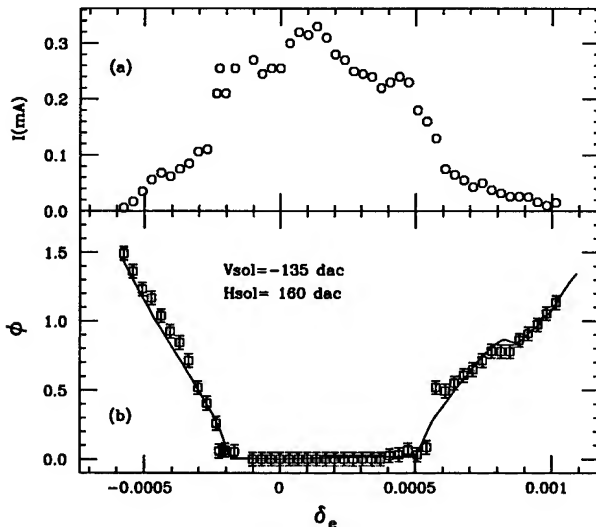


Figure 3. Similar to that of Fig. 2 except with a non-aligned electron beam. Note that the asymmetric Hopf bifurcation is evident.

Using the values of $H_{\text{sol}} = 160$ dac and $V_{\text{sol}} = -135$ dac that do not optimize the drag force, the measured Hopf bifurcation curve is shown in Fig. 3b. It is evident that the Hopf bifurcation amplitude is asymmetric with respect to relative momentum deviation. Similarly, We have also observed a close correlation between the loss of beam intensity with respect to the Hopf bifurcation threshold shown in Fig. 3a.

A strong asymmetry in the Hopf bifurcation threshold may indicate that the off momentum closed orbit of the proton beam would experience different electron “temperature”, or equivalently different velocity spread of the cooling electron cloud. In order to increase the momentum aperture of proton beam, alignment between the proton and the electron beams is important.

III. Conclusion

In conclusion, we have studied the effect of electron beam alignment on the Hopf bifurcation. When the electron and proton beams were aligned, the Hopf bifurcation amplitudes became symmetric with respect to the relative velocity between the cooling electrons and the synchronous proton. The non-magnetized drag force model with the kinematic factor of Eq. (4) fails to fit the data of Hopf bifurcation amplitudes. The data may be employed to determine the slope of drag force in the region $(\Delta_{e\parallel}, \Delta_{e\perp})$, which can provide essential characteristics of the magnetized cooling.

References

- [1] D.D. Caussyn *et al.*, Phys. Rev. Lett. **73**, 2696 (1994).
- [2] D.D. Caussyn *et al.*, Phys. Rev. E **51**, (1995).

Space Charge Effects and Intensity Limits of Electron-Cooled Bunched Beams

S. Nagaitsev, T. Ellison¹, M. Ball, V. Derenchuk, G. East, M. Ellison, B. Hamilton, P. Schwandt
Indiana University Cyclotron Facility, 2401 Milo B. Sampson Ln., Bloomington, IN 47406 USA

¹Present address: Energy Conversion Devices, Inc., 1675 West Maple Rd., Troy, MI 48084 USA

For stripping injection of proton beams in the IUCF Cooler, electron cooling permits us to accumulate beam currents several times higher than what can be obtained without cooling. Paradoxically, the electron cooling system also appears to be responsible for limiting peak currents in the ring at 45 MeV to about 6 mA. Thus the tool which allows us to accumulate beam also prevents us from accumulating more beam. At this point we can account for some of the observed beam features when we include space charge effects. Presently, we do not, however, have any techniques to counteract the space charge effects and thus raise this intensity limit.

I. INTRODUCTION

The IUCF Cooler[1], an electron cooling[2] storage ring-synchrotron of a 3.6 T·m maximum rigidity, has been operating, primarily for internal target experiments in nuclear and particle physics, since 1988. The low beam current from the IUCF cyclotrons used for injection requires a current gain by beam accumulation of order one thousand to obtain useful event rates in experiments. The typical cyclotron beam current is about 0.5 μ A. The time microstructure is a stream of 0.4 ns pulses normally spaced at 1/6 of the Cooler circumference (86.8 m). The cyclotron beam normalized rms emittance is about 1 π mm·mrad and the relative rms momentum spread about $3 \cdot 10^{-4}$. To fill the Cooler ring, a beam pulse of 5 ms duration is diverted down the Cooler injection line by a splitter magnet with timing and repetition rate selected by the Cooler operator. At 0.5 μ A, a 5 ms pulse of H_2^+ after stripping is expected to deliver about 3×10^{10} (5 mA) protons into ring. In practice, however, it takes up to 50 such pulses to reach the current of 5 mA. The maximum cooled proton beam peak current stored in the IUCF Cooler at 45 MeV is about 6 mA (i.e., 6 mA coasting beam or about 1 mA for rf bunched beams with bunching factor $BF = I_{peak}/I_{average}$ of about 6). These currents have been obtained using a combination of stripping injection of a 90 MeV H_2^+ beam with electron cooling accumulation and transverse damping. This paper elaborates on this accumulation inefficiency as well as on the cooled beam intensity limitations[3].

II. INTENSITY LIMITATIONS

A. Peak Current Limit

As might be expected, the intensity limit in the IUCF Cooler is a peak current (I_{peak}) limit, rather than an average current (I_{ave}) limit. Since to first order we expect the bunch length to vary as $I_{ave}^{1/3}$ in the space charge dominated regime[4] for a constant rf voltage, V_{rf} , it can be easily shown that for a constant peak current I_{peak} should vary as $(h/V_{rf})^{1/2}$,

where h is the harmonic number. Such is indeed the case in the Cooler, as illustrated in Fig. 1, where the measured maximum-achievable average beam current is plotted as a function of the $h = 1$ rf voltage.

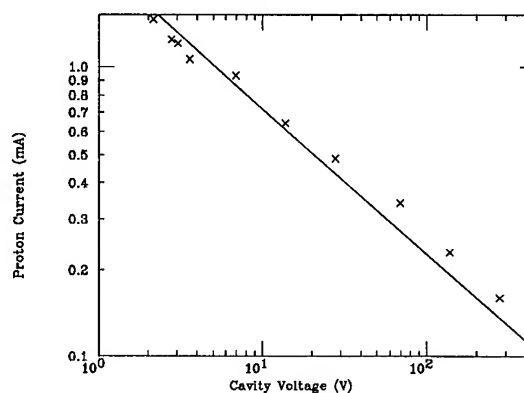


Figure 1. I_{ave} vs. V_{rf} ($h = 1$) in the IUCF Cooler. Solid line is $V_{rf}^{1/2}$.

This suggests an operating mode which would increase I_{ave} without actually addressing the I_{peak} limit: for highly cooled beams, the balance between the space charge and rf forces determines the required rf voltage for fixed frequency operation and the required energy gain per turn determines the voltage requirements during ramping. This is in contrast to the bucket area ($\propto h^{-1/2}$) requirements for emittance dominated beams in many other machines. We thus operate in a regime where the required V_{rf} is not a function of h for beam acceleration, and should be able to increase I_{ave} by a factor of 2 to 3 by operating with a larger value for h (we presently operate at $h = 1$ for historical reasons).

B. Coherent Transverse Instabilities

Although coherent transverse instabilities have been observed, they do not appear to be a limit:

--Coherent transverse instabilities are usually observed only when the Cooler is operated in a non standard mode (i.e., cooling the beam after injection for many seconds before beginning acceleration).

--A transverse feedback (damping) system can damp these instabilities at rates up to two orders of magnitude faster than the measured growth rates.

C. Injection Efficiency

The I_{peak} limit is, within limits, independent of both the injected beam current and the injection repetition rate. We thus conclude that the limit is not related to beam lifetime. This is illustrated in Figure 2 which shows the stored average current as a function of time during the process of cooling

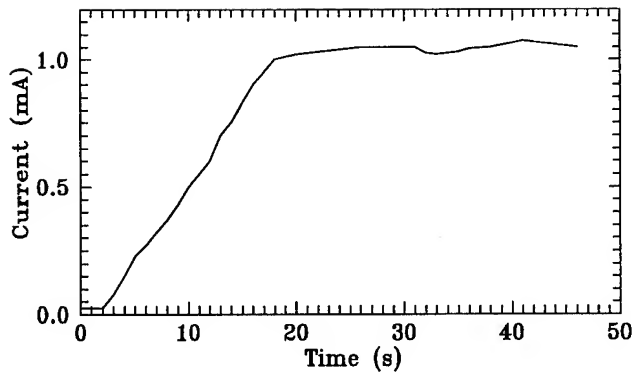


Figure 2. Beam current as a function of time during continuous stripping injection with cooling accumulation. $V_{rf} \approx 10$ V.

accumulation using stripping injection. The beam current does not increase as $I_{limit}(1 - e^{-t/\tau})$, where τ is the beam lifetime; rather the current increases with no significant change in rate until just below the limiting current. Beam is lost continuously between injections rather than suddenly; thus there is no indication of an easily-correctable hardware problem. The manner in which the beam approaches its limiting current can be explained by the beam lifetime being a highly nonlinear function of the beam intensity.

D. Increased Transverse Beam Size

One could conjecture that the intensity limit is due to an increase in the beam size with increasing current. This conjecture was verified by measuring transverse beam profile using a new "flying wire" profile monitor installed in the

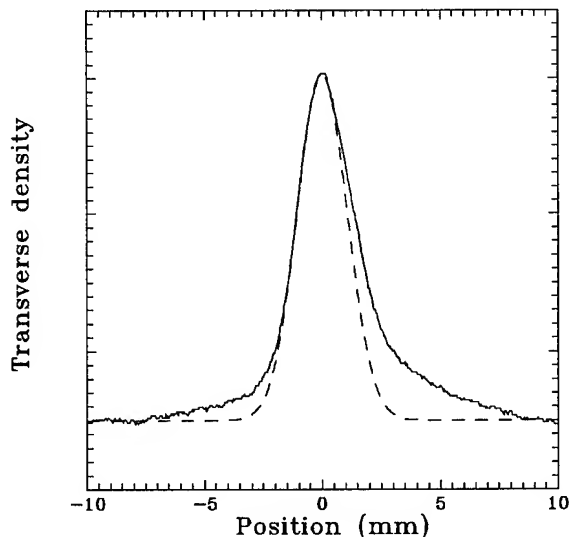


Figure 3. Transverse beam profile (solid) and Gaussian fit (dashed). Average (peak) beam current: 460 (2,000) μ A; rms size from the fit: 1.05 mm.

region of the Cooler where the dispersion function is nominally zero and the measured horizontal beta-function is 13.2 m. A rotary pneumatic actuator swings a 6.4 μ m diameter carbon

filament through the beam at a speed of 8.1 m/s. Secondary electrons produced by the protons passing through the filament are collected by an electrode surrounding the fiber holder. This current is amplified by a low-noise current-to-voltage converter, recorded by a digitizing oscilloscope, and transferred to storage on a PC for offline analysis. Approximately 200 to 500 beam revolution periods are necessary to measure the profile, and consequently the monitor cannot differentiate between coherent betatron oscillations and the beam size due to incoherent oscillations.

Figure 3 is an example of a transverse beam profile. The long tail on the right-hand side of the profile is due to the interaction of the wire with the proton beam. One can also observe a relatively long tail on the left-hand side. This tail corresponds to an emittance ≈ 60 times larger than the rms emittance of the bright central core; such tails develop for relatively high (> 1 –2 mA) peak beam currents and are believed to be related to the beam intensity limit in the IUFC Cooler.

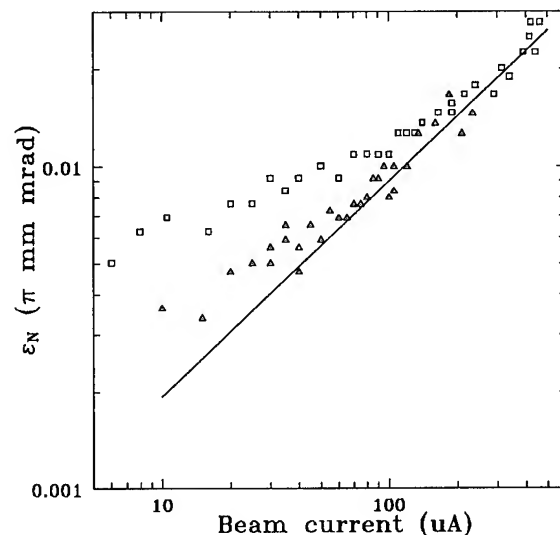


Figure 4. Normalized rms emittance as a function of the average bunched proton beam current before (\square) and after (Δ) the alignment of electron and proton beams. Solid line is $I^{2/3}$.

Recent measurements of the transverse beam size as a function of beam current indicate that even at high currents the non-normalized emittance ($\approx 0.1\pi$ mm·mrad) is still only a small fraction of the ring acceptance ($\approx 15\pi$ mm·mrad). Figure 4 shows the measured equilibrium horizontal rms normalized emittance as a function of the average beam current. Note that the measurements were made with bunched beams and that the horizontal scale is the average beam current. One observes that the beam size varies approximately proportional to the 1/3 power of the beam current. Since the bunch length, to first order, also varies as the 1/3 power of the beam current, we see that the particle beam density to first order stays constant as does the ratio of the longitudinal and transverse beam temperatures.

E. Space Charge Effects

The peak current limit appears to be due to space-charge effects. Space-charge effects in synchrotrons are usually quantified by the space-charge tune shift, ΔQ_{SC} which can be expressed as:

$$\Delta Q_{SC} = \frac{BF \cdot I_{ave} C r_p}{4\pi e c \beta^2 \gamma^2 \epsilon_N}, \quad (1)$$

where C is the ring circumference, r_p is the classical proton radius, e is the proton charge, c is the speed of light, β and γ are the usual relativistic parameters, and ϵ_N is the normalized rms beam emittance. ΔQ_{SC} is the amount the incoherent betatron tune is reduced due to defocusing effects from the beam space charge. Note that ΔQ_{SC} is not directly measured; in this case the tune shift is a mathematical quantity which can be exactly calculated but does not necessarily accurately represent what is happening physically. Fig. 5 shows this calculated space-charge tune shift as a function of a 45 MeV proton beam current.

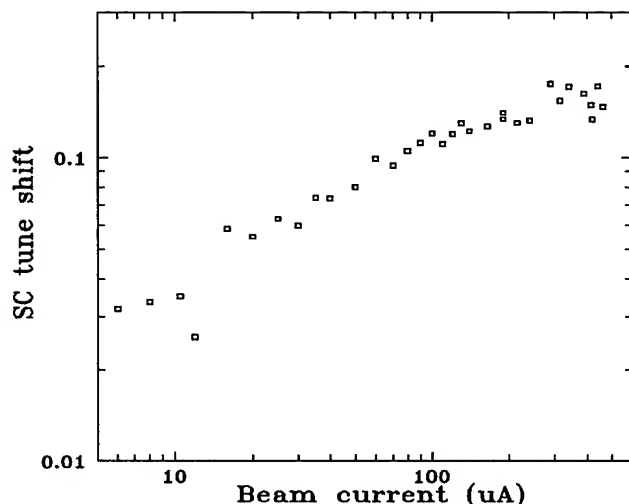


Figure 5. Space charge tune shift as a function of I_{ave} .

It is easy to understand how a large ΔQ_{SC} can lead to emittance growth: the small amplitude particles, which have the largest tune shift, can be shifted onto major resonance lines. It is less easy to understand why a large tune shift should lead to beam loss. It may be that particles with large amplitudes are lost; these particles experience a smaller tune shift, but also experience more nonlinear fields from the beam space charge which may drive higher order resonances.

We have observed that very small (< 0.01) changes in the coherent betatron tunes ($Q_x \approx 3.8$, $Q_y \approx 4.8$) can cause more than order of magnitude changes in the equilibrium beam intensity; this is somewhat unexpected for situations in which the incoherent tune shift is presumed to be more than an order of magnitude larger.

One of the mechanisms which could be responsible for this current limit is a halo formation[5]. Both non-uniform transverse density distribution (Fig. 3) and periodic density

fluctuations of the cold beam core due to changes in beta-functions could be a halo-producing mechanism. According to computer simulations[5] large energy transfer can occur in a single interaction of the particle with the cold core, thus the particle with initial betatron motion can be slowed, stopped, or accelerated in one betatron oscillation period. However, the subject of halo formation is not yet well understood, especially in systems where space charge and emittance play approximately equal roles. Nevertheless, one could make a cautious suggestion of how to possibly avoid the losses if they were associated with the halo formation. One suggestion for future machine designs is to make the machine lattice functions smooth in order to avoid large periodic density fluctuations. Another suggestion is to increase the emittance of the cold core by, perhaps, heating it in a controlled way.

F. Beam heating

Our attempts to heat the beam with white noise applied to a transverse kicker resulted only in reduced lifetime. We found that the beam lifetime is inversely proportional to the total power of applied transverse white band (50 MHz-300 MHz) noise without any noticeable changes in a transverse beam size.

One of the possible heating techniques could be a hollow electron beam created by a ring-shaped cathode. This would create a cooling-free phase space region within available acceptance. If one now places the proton beam closed orbit into this region by aligning the proton beam with the axis of the electron beam, proton beam emittance would be increased to the dimensions of this cooling-free area. Since the available acceptance is at least two orders of magnitude greater than the typical beam emittance, this technique could lead to an order of magnitude increase in the current limit.

III. CONCLUSION

Thus far, we have identified no techniques that can substantially increase the limiting beam current without compromising our ability to accumulate beam quickly by stripping injection. In the future, kick injection of beam from a new Cooler injector synchrotron[6] at significantly higher energy should reduce space charge limits. This work is supported by the National Science Foundation (Grant No. NSF PHY 93-14783).

REFERENCES

- [1] R.E. Pollock, Proc. of the 1989 Part. Accel. Conf.(Chicago), p. 17.
- [2] G. Budker, Atomnaya Energiya 22(5), 246-248(1967).
- [3] Some of the findings presented in this paper were reported in D. Anderson *et al.*, Proc. of the 1993 Workshop on Beam Cooling, CERN94-03, p. 377.
- [4] T. Ellison *et al.*, Phys. Rev. Lett. 70, 790 (1993).
- [5] R. Jameson, Proc. of the 1993 Part. Accel. Conf. (Washington, D.C.), p. 3926.
- [6] D.L. Friesel and S.Y. Lee, "CIS, a Low Energy Injector for IUCF Cooler" in these proceedings.

STABILITY CONDITIONS FOR A NEUTRALISED ELECTRON COOLING BEAM

J. Bosser, S. Maury, D. Möhl, and F. Varenne, CERN, CH-1211 Geneva 23

I. Meshkov and E. Syresin, JINR, Dubna, Russia

E. Mustafin, IHEP, Protvino, Russia

P. Zenkevich, ITEP, Moscow, Russia

Charge neutralisation of the cooling electron beam, e.g. by stationary ions produced from the residual gas, is desirable to compensate the space-charge induced velocity spread which tends to reduce the cooling force. However, it has been demonstrated by Parkhomchuk and collaborators that two-stream instabilities, especially transverse dipole modes, are a serious threat to the stability. In the present report we analyse stabilising mechanisms including Landau damping, external feedback and clearing of reflected electrons. Experimental results at LEAR (the Low Energy Antiproton Ring at CERN) are discussed in a companion paper at this conference.

I. INTRODUCTION

It is known that the maximum current in a neutralised electron cooling system is constrained by transverse instabilities [1,2]. In previous papers Nezhlin's theory for completely neutralised beams [3] was used. However, experiments at LEAR [4] with a vacuum of 10^{-11} torr show that the neutralisation is less than unity and therefore damping of the ion oscillations connected with reflections from the Debye boundary is absent. In such a system it is necessary to take into account the classical Landau damping due to the velocity spread of the neutralising ions.

We derive a dispersion relation to include this spread and discuss resulting stability conditions. Moreover, the influence of external forces on the beam motion is examined.

II. EQUATIONS OF MOTION

Let us consider a system including only the cooling electrons and the slow (neutralising) ions. For simplicity, we assume that the beams have uniform transverse densities. Then the equations of motion are :

$$\frac{d^2 \tilde{U}_e}{dt^2} + i\omega_{Le} \frac{d\tilde{U}_e}{dt} - \omega_{eL}^2 (\tilde{U}_e - U_e) + \eta\gamma^2 \omega_{eL}^2 (\tilde{U}_e - U_i) = F_e(z)e^{-i\omega t} \quad (1.1)$$

$$\frac{d^2 \tilde{U}_i}{dt^2} + i\omega_{Li} \frac{d\tilde{U}_i}{dt} - \eta\omega_{ion}^2 (\tilde{U}_i - U_i) + \omega_{ion}^2 (\tilde{U}_i - U_e) = F_i(z)e^{-i\omega t} \quad (1.2)$$

Here the subscripts e and i refer to electrons and ions respectively, $U = x + iy$ describes the horizontal (x) and vertical (y) displacement in complex notation, \tilde{U} denotes the motion of a single ion and U the motion of the beam centre of charge: $U = (1/N) \sum \tilde{U}$, or, if the dispersion is mainly due to the velocity spread $U = \int \tilde{U} f(v) dv$ where $f(v)$ is the velocity distribution normalized to $\int f(v) dv = 1$. The derivatives in Eq. (1) have to be taken along the particle orbit: $d/dt = (\partial/\partial t) + v_z(\partial/\partial z)$, etc. The different frequencies have the following significance:

$\omega_{Le} = eB/\gamma m_e$ is the Larmor frequency (= cyclotron frequency) of the electrons in the longitudinal magnetic field of the cooler, $m_e\gamma$ is the relativistic mass of the electrons ($\omega_{Le} = 2\pi \times 1.75$ GHz),

$\omega_{Li} = ZeB/M$ is the Larmor frequency of the ions with charge number Z and mass $M = A m_p$ ($\omega_{Li} = 2\pi \times 957$ kHz),

$\omega_{eL}^2 = (2\pi n_e / \gamma^3) r_e c^2$ describes the electron space-charge effect on an electron, n_e is the electron density (electrons/ m^3), r_e is the classical electron radius, c is the velocity of light ($\omega_{eL} = 2\pi \times 35$ MHz),

$\omega_{ion}^2 = (2\pi n_e Z/A) r_p c^2$ with ω_{ion} the ion frequency in the space-charge potential of the electrons, r_p is the classical proton radius ($\omega_{ion} = 2\pi \times 835$ kHz).

In the following we will use three more frequencies which we define here for convenience :

$\omega_e^2 = (\eta\gamma^2 - 1) \omega_{eL}^2$ describes the incoherent space-charge effect experienced by the electrons, $\eta = Z n_i / n_e$ is the neutralisation factor with n_i the density of the trapped ions ($\omega_e = 2\pi \times 27.4$ MHz),

$\omega_i^2 = (1 - \eta) \omega_{ion}^2$ describes the incoherent space-charge effect experienced by the ions, ($\omega_i = 2\pi \times 646$ kHz),

$\omega_d = \gamma^2 \eta \omega_{eL}^2 / \omega_{Le}$ is the electron drift frequency in the space-charge field of the ions ($\omega_d = 2\pi \times 291$ kHz).

The values for the frequencies given in parenthesis above are for "LEAR standard conditions" as defined in Table 1 (where for simplicity trapped hydrogen ions are assumed).

The r.h.s. of Eqs. (1.1) and (1.2) describe the external excitation by kicker electrodes (used e.g. for diagnostics). For a short electrostatic kicker of length l at $z = 0$ with a horizontal electric field $E e^{-i\omega t}$ one has e.g.:

$$F_e = \frac{e}{m_e \gamma} E l \delta(z), \quad F_i = \frac{-eZ}{M} E l \delta(z).$$

Table 1 : LEAR cooler "standard parameters".

Electron energy	E_e	2.8 keV
Velocity factor	$\beta = v_e/c$	0.1
Electron current	I_e	0.3 A
Electron density	n_e	$3.2 \times 10^{13} \text{ m}^{-3}$
Longitudinal B-field	B	0.063 T
Length of neutral. section	L	3.2 m
Neutralisation factor	η	0.4
Ion charge to mass ratio	Z/A	1

For an infinitely long system we seek solutions of Eqs. (1) in the following form:

$$U_{e,i} = a_{e,i} \exp(ikz - i\omega t), \quad \tilde{U}_{e,i} = \tilde{a}_{e,i} \exp(ikz - i\omega t)$$

We obtain :

$$\begin{aligned} a_e \left[(1/I_e) + \omega_{el}^2 \right] - a_i (\eta \gamma^2 \omega_{el}^2) &= f_e \\ -a_e (\omega_{ion}^2) + a_i \left[(1/I_i) + \eta \omega_{ion}^2 \right] &= f_i \end{aligned} \quad (2)$$

Here the dispersion integrals are:

$$\begin{aligned} I_i &= \int \frac{f(v_i)}{\omega_i^2 - \omega_{Li}(kv_i - \omega) - (kv_i - \omega)^2} dv_i \\ &= \frac{1}{2\sqrt{(\omega_{Li}/2)^2 + \omega_i^2}} \left\{ \int \frac{f(v_i)}{\omega_{i1} - (\omega - kv_i)} dv_i - \int \frac{f(v_i)}{\omega_{i2} - (\omega - kv_i)} dv_i \right\} \\ I_e &= \int \frac{f(v_e)}{\omega_e^2 - \omega_{Le}(kv_e - \omega) - (kv_e - \omega)^2} dv_e \\ &\approx \int \frac{f(v_e)}{\omega_e^2 + (\omega - kv_e)\omega_{Le}} dv_e \end{aligned} \quad (3)$$

Note that in the second expression for I_i

$$\omega_{i1,2} \equiv \frac{\omega_{Li}}{2} \pm \sqrt{\left(\frac{\omega_{Li}}{2}\right)^2 + \omega_i^2}$$

is introduced and in the approximation for I_e it is assumed that $\omega_{Le} \gg |\omega_e - kv_e|$

The quantities $f_{e,i}(k) = \frac{1}{L} \int_0^L F_{e,i} e^{-ikz} dz$ (with $k = n\pi/L$, $n = 0, 1, 2, \dots$, and L the length of the neutralisation section) in Eq. (2) are the Fourier expansion coefficients of the kicker fields $F_{e,i}(z)$. Only the leading harmonic (close to the resonance to be determined below) is retained. For large L the spectrum of k values is practically continuous.

The behaviour of the system (2) is given by the determinant:

$$D = \begin{vmatrix} \left[(1/I_e) + \omega_{el}^2 \right] & -\eta \gamma^2 \omega_{el}^2 \\ -\omega_{ion}^2 & \left[(1/I_i) + \eta \omega_{ion}^2 \right] \end{vmatrix} \quad (4)$$

The solution of the homogenous equation ($F_e = F_i = 0$) is determined by $D = 0$.

With external excitation a solution of the system (2) is

$$\begin{aligned} a_e &= \frac{f_e \left[(1/I_i) + \eta \omega_{ion}^2 \right] + f_i (\eta \gamma^2 \omega_{el}^2)}{D} e^{-ikz} \\ a_i &= \frac{f_e (\eta \omega_{ion}^2) + f_i \left[(1/I_e) + \omega_{el}^2 \right]}{D} e^{-ikz} \end{aligned} \quad (5)$$

It exhibits resonant behaviour for $D(k, \omega) \rightarrow 0$. For a system of finite length, the situation becomes very complex because boundary conditions have to be satisfied, which can e.g. be accomplished by adding solutions corresponding to reflections at the borders [3]. This will not be discussed any further here. Rather we content ourselves with the solution of the homogenous equation for an unbounded system.

III. STABILITY CONDITIONS

We discuss the solution of the homogeneous equation for the case of negligible dispersion of the electrons, $f(v_e) = \delta(v_e)$. Then the characteristic equation $D = 0$ is approximated by:

$$\left\{ \omega_d - (kv_e - \omega) \right\} \left\{ (1/I_i) + \eta \omega_{ion}^2 \right\} - \omega_{ion}^2 \omega_d = 0 \quad (6)$$

For negligible ion velocity spread, the term $\left\{ (1/I_i) + \eta \omega_{ion}^2 \right\}$ becomes $\omega_{ion}^2 + \omega_{Li}\omega - \omega^2$. The roots of this expression define the "coherent ion frequencies"

$$\omega_{icoh1,2} = \left| \frac{\omega_{Li}}{2} \pm \sqrt{\left(\frac{\omega_{Li}}{2}\right)^2 + \omega_{ion}^2} \right|$$

(which for the parameters of Table 1 have the values $\omega_{icoh1} = 2\pi \times 1.4$ MHz, $\omega_{icoh2} = 2\pi \times 0.48$ MHz). With finite spread of the ion velocity, developing the denominator of I_i into a Taylor series up to second-order in kv and using $\int f(v_i) v dv = 0$, $\int f(v_i) v^2 dv = \sigma^2$, Eq. (6) yields a third-order equation for $k(\omega)$. An estimate of the growing solution can be made by putting $\omega = \omega_d$ and $\omega = \omega_{icoh2}$. Then we obtain for the imaginary part of k

$$\lambda = \text{Im}(-k) = \frac{\sqrt{3}}{2} \sqrt{\frac{\omega_{ion}^2 \omega_d}{v_e \sigma^2 F}} \quad (7)$$

with $F = [4 + (\omega_{Li}^2 / \omega_{ion}^2) - \eta] / \eta \approx 4 / \eta$. Thus perturbations can be amplified by a factor of $K = e^{\lambda L}$ over the length (L) of the neutralisation section. If this is too large [$\lambda L \geq \ln(K_c)$] the system is unstable. The limiting amplification K_c depends on the initial perturbation and/or on the "internal feedback", e.g. by reflected electrons, to be discussed below.

The upper limit for the stable neutralisation (substituting ω_{ion} , ω_d , etc. in Eq. (7)) can be expressed as:

$$1.27 \times 10^{-9} \left[\frac{m^6 T}{s^3} \right] \frac{n_e^2}{v_e B} \left(\frac{Z}{A} \right) \frac{\eta^2}{\sigma^2} \cdot L^3 \leq |\ell n K_c|^3$$

We conclude that a large spread σ , a large field B and ions of large (A/Z) ensure a high degree of neutralisation η .

A crucial parameter is the longitudinal velocity spread (σ) of the ions. Heating due to collisions with the electrons yields a relatively low (≤ 1 eV) ion temperature compared to the transverse energy spread (typically 100 eV) in the Coulomb field of the electron beam. For a long ion lifetime (ultra high vacuum) one can (perhaps) assume that this transverse spread couples into the longitudinal plane. One potential mechanism for this involves the reflections in the field of the trapping electrodes at either end of the neutralisation section. Thus we estimate $\sigma^2 = c^2 \frac{k\Delta T_e}{Mc^2}$ where $k\Delta T_e [\text{eV}] = (30/\beta) I_e [\text{A}]$ is the potential difference (centre to edge) in the electron beam.

Reflected electrons escaping from the collector or the migrating ions themselves can feed the perturbation back to the upstream end. Stability of the system requires $\alpha K \leq 1$ where α is the "feedback coefficient" i.e. the fraction of the perturbation taken back to the entrance. For typical conditions (Table 1) and taking an ion temperature $0.5 M\sigma^2$ of 50 eV, Eq. (7) yields $\lambda \approx 2.1$, $\lambda L \approx 6.7$, $K \approx 800$. Thus only a very small "internal feedback" ($\alpha < 1/800$) is tolerable. The current loss $\Delta I_e/I_e$ from the collector can be as high as 2×10^{-3} if the beam is badly adjusted, but probably only a fraction of the reflected electrons will get back to the upstream end with the right phase for the growth. Thus we expect $\alpha < \Delta I_e/I_e$. Nevertheless, a high collector efficiency and/or clearing of reflected electrons is important. This has been confirmed both at the test-bench at the CAPT in Russia and at the LEAR electron cooler. In addition, any other internal feedback has to be small to ensure stable neutralisation.

IV. EXTERNAL FEEDBACK AND "SHAKING"

To suppress the instability in the regime where the "internal feedback" or the initial perturbations are strong, an external feedback system has been implemented at LEAR. The signal is taken from a pickup, near one end of the cooling section. It is duly amplified and phase shifted before being applied to a kicker at the other end of the cooler.

The preliminary tests are commented in Ref. [4]. So far we have been unable to stabilise a strongly unstable beam by this system. It was however possible to obtain a stable primary e-beam by "shaking" with a pure sine-wave signal applied to a transverse kicker. We observe from the examples given above that all the characteristic ion frequencies are in the 0.1 to 2 MHz region. By exciting at these frequencies we expect strong response. This was confirmed by the experiments. The response showed abrupt discontinuities at frequencies corresponding to the resonances of ions of the different masses which can thus be selectively expelled. In this way we have been able to obtain stable neutralisation at values

which could be chosen between zero ("clearing by shaking") and a maximum somewhat lower than the one reached during fluctuations without shaking (Table 2).

Table 2 : An example of the effect of shaking

Electron energy	2.8 keV	
Electron current	0.3 A	
Voltage on trapping electrodes	0	6 kV
Neutralisation without shaking fluctuating between	0 - 0.2	0.5 - 0.7
Neutralisation with shaking stable at	0	0.4

The response of the beam ion system both with and without external excitation is also a powerful diagnostic tool [1,4]. The onset of the instability is accompanied by strong RF signals at the coherent frequencies of one or several ion species. It appears that ions of $(A/Z) \approx 4 - 6$ remain trapped. The relatively large width of the resonance supports the hypothesis of a large velocity spread which is an essential ingredient of the theory described in the present paper.

V. CONCLUSIONS

The theory sketched above explains - at least in a qualitative way - the observations made at LEAR. Several refinements, e.g. the non-linearity of the space-charge fields as well as initial and boundary conditions for the finite system, have to be included before quantitative agreement can be expected. Stable electron beams of 0.3 A at 2.8 keV have been achieved with a neutralisation of up to 40%. A more detailed analysis of the internal and external feedback is required to see whether further improvements are feasible.

VI. REFERENCES

- [1] A.V. Burov, V.I. Kudelainen, V.A. Lebedev, V.V. Parkhomchuk, A.A. Sery, V.D. Shiltsev, Experimental Investigation of an Electron Beam in Compensated State, CERN/PS 93-03 (AR), 1993 (Translation of Novosibirsk Preprint 89-116).
- [2] A.V. Burov, Secondary Particle Instabilities in the Storage Rings with Electron Cooling, Proc. Workshop on Beam Cooling ..., CERN 94-03, 1994, p.230.
- [3] M.V. Nezlin, Physics of Intense Beams in Plasmas, Institute of Physics, Bristol 1993.
- [4] J. Bosser, F. Caspers, M. Chaneil, R. Ley, R. Maccaferri, S. Maury, I. Meshkov, G. Molinari, V. Polyakov, A. Smirnov, O. Stepashkin, A. Syresin, G. Tranquille, F. Varenne, Neutralisation of the LEAR Electron Cooling Beam ..., this conference.

NEUTRALISATION OF THE LEAR ELECTRON-COOLING BEAM: EXPERIMENTAL RESULTS

J. Bosser, F. Caspers, M. Chanel, R. Ley, R. Maccaferri, S. Maury,
G. Molinari, G. Tranquille, and F. Varenne
CERN, CH-1211 Geneva 23

I. Meshkov, V. Polyakov, A. Smirnov, O. Stepashkin, and E. Syresin
JINR, Dubna, Russia

The LEAR electron cooler uses dense electron beams. Because of this high density the large space-charge potential induces significant drawbacks for the cooling process itself. As a consequence a space-charge neutralisation system has been implemented on the cooler. It consists of two positively polarised pairs of electrodes, placed on the outside of the drift space, which aim to store the ionised positive ions of charge Z . The major difficulty arises in the neutralisation instabilities [1]. This paper reports on the technological aspects, the measurement techniques and the results.

I. INTRODUCTION

In the frame of the electron cooling (ECOOOL) it is worth having at our disposal large electron beam intensities, I_b . In such a case, mainly for low-velocity beams ($\beta = v/c \ll 1$), the space-charge effects induce some drawbacks.

In the drift space, at ground potential, where the electrons and the ions to be cooled are merged, the space-charge potential U_{sp} [V] as a function of the radius r is given by (Fig. 1a,b):

$$U_{sp}(r) \cong -\frac{30I_b}{\beta} (1-\eta) \left[1 + 2\ln\left(\frac{b}{a}\right) - \left(\frac{r}{a}\right)^2 \right], \quad r \leq a \quad (1)$$

where:

a, b are the e-beam and beam-pipe radii respectively,
 $\eta = Zn_i/n_e$ = stored-ion density/electron-beam density
= neutralisation factor
 I_b (A) is the electron-beam current.

Therefore the radial electrical field

$$E_r = -\frac{\partial U_{sp}}{\partial r} = -\frac{60I_b}{\beta} (1-\eta) \frac{r}{a^2}, \quad r \leq a \quad (2)$$

will induce a transverse force on the electron at radius r . This force, though compensated to a certain extent by the longitudinal magnetic field B_0 , will tend to increase the e-beam transverse velocity spread. Even partial neutralisation ($0 < \eta < 1$) will reduce this unwanted force.

Another difficulty stems from the fact that, the electron kinetic energy is given by

$$E_c = (\gamma - 1)m_e c^2 = e(U_c + U_{sp}) \cong \frac{1}{2} m_e v_e^2$$

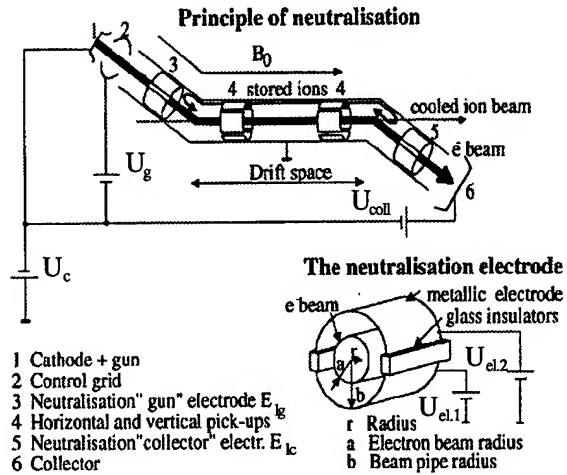


Figure 1: a) ECOOL principle, b) Neutralisation electrode.

[where $-U_c$, the cathode potential (Fig. 1a)], is a function of the radius r . Defining the nominal velocity v_0 (which is equal to the average velocity of the cooled ions) as

$$v_0 = \sqrt{\frac{2e}{m_e} (U_c + U_{sp}(r=0))} \quad (3)$$

then

$$v_e(r) \cong v_0 \left[1 + \frac{1}{2} \frac{U_{sp}(r) - U_{sp}(r=0)}{U_c + U_{sp}(r=0)} \right] \quad (4)$$

has the parabolic shape represented in Fig. 2. In the drift space where the dispersion function of the ion storage ring is D and the betatron function β_H the ion velocity is given by

$$v_i(x_i) \cong v_0 \left[1 + \frac{dv_i(t)}{v_0} \right]$$

with x_i the mean horizontal position of an ion with momentum deviation Δp_i

$$x_i = D \frac{\Delta p_i}{p} = D \gamma^2 \frac{dv_i(t)}{v_0},$$

The horizontal velocity distribution is shown in Fig. 2. It must be noted that to the mean horizontal position the betatron oscillation has to be added. At LEAR with $D = 3.5$ m, $\beta_H = 2$ m for $\beta = 0.1$, $I_e = 0.5$ A, $\eta = 0$, the two velocities v_e and v_i intersect at $x_i \approx 2$ mm \ll a such that relatively large emittance ion beams can be heated rather than cooled.

It is therefore essential either to reduce the dispersion ($D \rightarrow 0$) at the cooler and/or to neutralise the e-beam such that the

electron velocity becomes independent of its radius ($\eta \rightarrow 1 \Rightarrow U_{sp}(r) \rightarrow 0$).

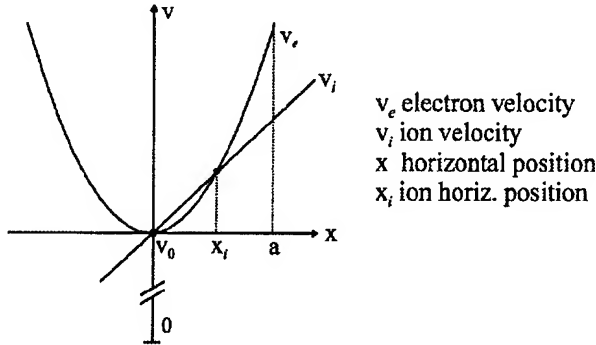


Figure 2: Electron and ion velocity versus horizontal position.

II. PRINCIPLE OF NEUTRALISATION [2,3]

For the purpose of neutralisation, two neutralisation electrodes, El_g and El_c , consisting of two metallic half cylinders separated by a high-resistive-glass insulator (Fig. 1b), have been installed outside the drift space (Fig. 1a). They are polarized by independent positive power supplies named U_{el1} and U_{el2} ($0 \leq U_{el} \leq 6$ kV). Usually, the voltages on opposite electrodes are not equal such that a transverse E -field also exists.

On their way from the cathode to the collector the energetic primary electrons, e_1 , will ionize the residual gas molecules. The ionized low energy, ions, i_2 , and electrons, e_2 , will be submitted to the space charge and to the longitudinal magnetic field forces. They will move towards the cathode or the collector. At the level of the neutralisation electrodes (El_g or El_c) the ions, i_2 , will be reflected, and therefore stored, whilst the low-energy ionized electrons, e_2 which drift in the crossed electric and magnetic fields will be collected on the glass insulators. Consequently, the ion density n_i , and therefore η , will increase with time.

It should be mentioned that in the case of LEAR the beam-chamber diameter, at the level of El_g and El_c , is 100 mm while in the drift space: $b = 140$ mm. This will induce a "natural neutralisation" due to the potential well (Eq. 1).

III. PHYSICAL CONSIDERATIONS

Many physical issues are the subject of intense studies, e.g.

- The physical and mathematical description of the evolution of η versus time, namely what brings the ion escape rate to be equal to the ionization rate ($0 < \eta \leq 1$).
- The conditions for the neutralisation-factor stability. These are discussed in Ref. [4].

Under certain conditions the neutralisation factor becomes unstable, which is detrimental to the cooling process since this implies an instability in the cooled beam velocity [consider the

influence of η jumps in Eqs. (4) and (1)]. This instability is also of concern for natural neutralisation.

IV. EXPERIMENTAL RESULTS

A. Neutralisation factor

The main parameter to be measured is the neutralisation factor η whose final values will depend on many parameters such as the polarisation voltages $U_{el1,2,3,4}$, the electron current I_b , the magnetic field B_0 , etc.

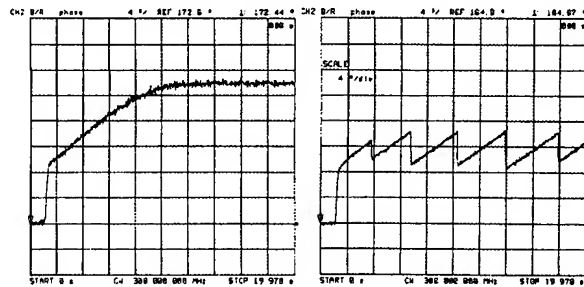
When the ions to be cooled, i_1 , are circulating in LEAR, the signal from a longitudinal Schottky pickup is used. It is displayed on a spectrum analyser at a given harmonic of the revolution frequency f_0 . When the neutralisation is effective, the space-charge potential $U_{sp}(r = 0)$ is reduced [Eq. (1)], which entails an increase of the i_1 velocity. From the correction to be applied to U_c in order to retrieve v_0 [Eq. (3)] the value of η can be deduced.

A second way to measure η is the time of flight method [3]. A high-frequency signal ($200 \leq f \leq 300$ MHz) is applied e.g. to El_g . This signal slightly modulates the longitudinal or transversal density of the e-beam i_1 . The modulated signal is detected by a pair of electrodes at a distance L from the excitation electrode. The phase difference between signals

$$\phi = \frac{2\pi fL}{v_e(\eta)} \quad (5)$$

allows us to deduce v_e and therefore the neutralisation factor [Eqs. (3),(1)]. The phase ϕ can be calibrated by the previous method with ion beams.

Figure 3a shows a measured value of ϕ versus time. The time it takes to reach the final value of ϕ is the neutralisation time. The initial jump is thought to be due to the stored electrons which are expelled when the electrodes are polarized.



a) Stable η .

b) Unstable η .

Figure 3: Time of flight or phase ϕ measurement versus time.

An unstable neutralisation is easily detected through the observation of the phase discontinuity as in Fig. 3b.

B. The Use of Position Pickup Electrodes

Usually, the pickup electrodes in the drift space (4 in Fig. 1a) are used to measure both the electron (e_1) and cooled ion (i_1) beam horizontal and vertical positions. In the present case, they are used to observe the neutralisation ion (i_2) transverse oscillations. Figure 4a shows the transverse

oscillations versus time on both pickups during the instability. No longitudinal oscillations have been observed. Figure 4b shows the oscillation frequency distribution. The results of these measurements are coherent with the theoretical computations [4].

The instability occurs simultaneously with a discontinuity in the time-of-flight measurement (Fig. 3b).

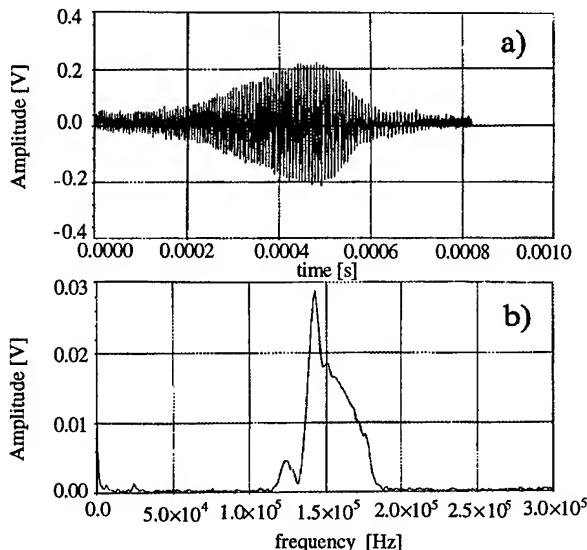


Figure 4: a) Observed instabilities on PUs, b) Frequency distribution.

C. Attempts for Feedback, the "Shaker"

In order to damp the neutralisation instabilities, a feedback system has been developed. The signal from one of the position pickups (where the instability is observed), is amplified and phase delayed in such a way as to be applied with the correct phase on an electrode upstream of the measurement pickup. In the present state of experiments, we did not succeed in damping the instabilities. Nevertheless, ions have been "shaken" out of the e-beam in order to render the e-beam velocity stable. An example is given in Fig. 5 where the neutralisation factor ($\eta = 1 \Rightarrow \varnothing = 100^\circ$) has been recorded under 4 different conditions. Condition 1: no feedback (shaker) at natural neutralisation, the neutralisation factor is unstable. Condition 2: the shaker is ON, the natural neutralisation factor is reduced, but stable. Condition 3: an induced neutralisation is introduced (for El_g : $U_{el1} = 0$ V, $U_{el2} = 6$ kV; for El_c : $U_{el1} = 0$ V, $U_{el2} = 6$ kV, see Fig. 1b) while the shaker is still ON. Condition 4: the shaker is OFF while the neutralisation voltages are maintained, the neutralisation factor increases, but becomes unstable.

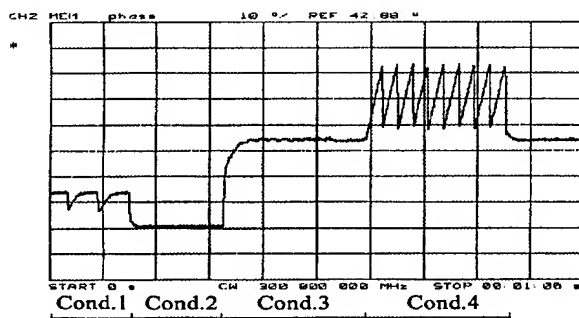


Figure 5: Different uses of the "shaker".

V. CONCLUSION

Neutralisation of the electron beam can be achieved. Nevertheless, under certain conditions it becomes unstable. In order to cancel these instabilities a so-called "shaker" rf voltage has been applied to one pair of position pick-up electrodes; this reduces but stabilises the neutralisation factor. More investigations and experiments are under way.

VI. REFERENCES

- [1] J. Bosser, R. Ley, I. Meshkov, G. Molinari, V. Polyakov, A. Smirnov, E. Syresin, G. Tranquille, and F. Varenne, Electron Cooling with Neutralised Electron Beams, EPAC'94, London, p. 1211.
- [2] A.V. Burov, V.I. Kudelainen, V.A. Lebedev, V.V. Parkhomchuk, A.A. Sery, V.D. Shiltsev, Experimental Investigation of an Electron Beam in Compensated State, CERN/PS 93-03 (AR), 1993.
- [3] J. Bosser, I. Meshkov, D. Möhl, V.V. Parkhomchuk, E. Syresin, and G. Tranquille, Neutralisation of the LEAR-ECool Electron Beam Space Charge, CERN/PS/AR Note 93-08, 1993.
- [4] J. Bosser, D. Möhl, F. Varenne, I. Meshkov, E. Syresin, E. Mustafin, P. Zenkevich. Stability conditions for a Neutralised Electron Cooling Beam. This Conference.

CRYSTALLINE BEAM PROPERTIES AS PREDICTED FOR THE STORAGE RINGS ASTRID AND TSR*

Jie Wei, Brookhaven National Laboratory, P.O. Box 5000, Upton, New York 11973-5000, USA
Xiao-Ping Li, BIOSYM Technologies Inc., 9685 Scranton Rd. San Diego, CA92121, USA
Andrew Sessler, Lawrence Berkeley Laboratory, Berkeley, California 94720, USA

Abstract

Employing a previously developed formalism¹, we have performed ground-state and melting calculations of the expected crystalline beams in ion storage rings ASTRID and TSR.

I. INTRODUCTION

During recent years, significant progress has been made in understanding the formation of crystalline beams in circular accelerators and storage rings.¹⁻⁴ No crystalline beam exists in a constant gradient storage ring, but in an alternating gradient (AG) ring crystalline beams exist at all densities as long as the beam energy is smaller than the transition energy of the machine. The ground-state structure depends upon the machine lattice property, the beam energy, and the beam intensity (line density). At low density, the ground state is a one-dimensional (1D) chain with particles equally spaced along the azimuthal axis. As the density increases, the ground state first becomes a 2D zig-zag in the plane of weaker transverse focusing, and then becomes 3D single- and multi-shell helices. The maximum spatial density of the crystal, on the other hand, is determined only by the machine lattice property and beam energy, independent of the beam intensity.

When circulating in an AG-focusing machine, the total energy of the beam is not a constant of motion. As a result, the crystalline beam will gradually heat up and eventually melt if not refrigerated. Previously, we have shown that if the machine lattice periodicity is lower than twice the maximum betatron tune, heat will generally transfer into the system extremely fast so that a crystalline beam can not last a meaningful period of time (except at very low density). On the other hand, if the lattice periodicity is significantly higher than twice the maximum betatron tune, the heat transfer is slow, and the crystalline beam can last for a long time.^{1,4}

II. CRYSTALLINE BEAM IN THE ASTRID

ASTRID is a charged-ion storage ring of circumference $C_0 = 40$ m. Laser cooling has been used to reduce the velocity spread of the beam, currently achieving a rest frame temperature $T = 1$ mK in longitudinal dimension. The lattice has a super-periodicity of 4.

Employing the previously developed formalism,¹ we perform the molecular dynamics (MD) calculation and analysis with the 100 keV $^7\text{Li}^+$ ion beam. The transverse tunes of the machine are $\nu_x = 2.62$ and $\nu_y = 1.13$. The characteristic distance is¹

$$\xi \equiv \left(\frac{q^2 r_0 \rho^2}{A \beta^2 \gamma^2} \right)^{1/3} \approx 2.2 \times 10^{-5} \text{ m}, \quad (1)$$

*Work performed under the auspice of the U.S. Department of Energy, Office of High Energy and Nuclear Physics under Contract No. DE-AC03-76SF00098.

where $r_0 = e^2/m_0 c^2 = 1.53 \times 10^{-18}$ m is the proton classical radius, $\rho = 1.2$ m is the bending radius, $\beta c = 5.54 \times 10^{-3} c$ is the beam velocity, $\gamma = (1 - \beta^2)^{-1/2}$, $q = 1$ is the charge, and $A \approx 7$ is the atomic mass number.

At low density, the ground state is a 1D chain. MD calculation shows that the transition from 1D to 2D occurs when the inter-particle distance $\Delta_z \approx 5.5$ in reduced units,¹ i.e. when the number of particles in the machine is

$$N = \frac{\gamma C_0}{\Delta_z \xi} \approx 3.4 \times 10^5. \quad (2)$$

When the total number of particles exceeds this value, the ground state first becomes a 2D zig-zag in the vertical plane where the focusing is relatively weak. Fig. 1 shows the trajectory of the

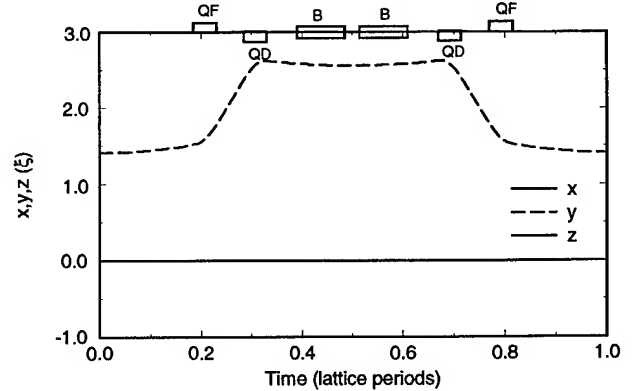


Figure 1. A vertical zig-zag structure at density $\Delta_z = 3$ formed with the ASTRID lattice. The displacement in both x and z is zero at all time. B, QF, and QD denote dipole, focusing quadrupole, and defocusing quadrupole, respectively.

particle with positive y in such a structure at $\Delta_z = 3$ (i.e. $N = 6.1 \times 10^5$). The breathing of the structure can be seen as the particles encounter the focusing and defocusing elements of the machine.

Due to the AG focusing, the crystalline structure absorbs energy (heat) from the lattice. The dots in Fig. 2 shows the heating rate as a function of the temperature T in the reduced units¹ for a 1D crystal of density $\Delta_z = 10$ ($N = 1.8 \times 10^5$). The conventional rest-frame temperature can be conveniently obtained by the relation

$$T_{\text{rest}} = \frac{A m_0 c^2 \beta^2 \gamma^2 \xi^2}{2 k_B \rho^2} T = 0.38 T \text{ (K)}, \quad (3)$$

where k_B is the Boltzmann constant. At low temperature, the heating rate is low. Fig. 3 shows that although the horizontal tune ($\nu_x = 2.62$) is larger than half the lattice periodicity (4),

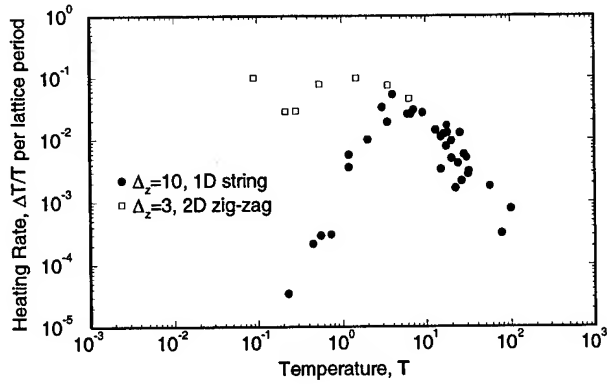


Figure 2. Heating rates as functions of the temperature T for a 1D ($\Delta_z = 10$) and a 2D ($\Delta_z = 3$) ground state in the ASTRID lattice.

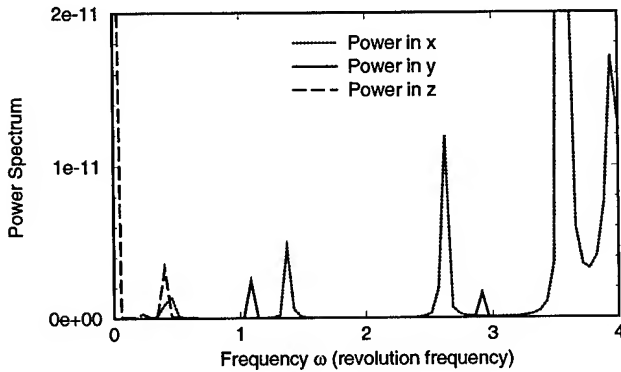


Figure 3. Power spectrum for the 1D ($\Delta_z = 10$) structure in the ASTRID lattice at extremely low temperature. The machine tunes are $\nu_x = 2.62$, $\nu_y = 1.13$.

the phonon spectrum does not extend to twice the revolution frequency (ω_0), thus avoiding the two-phonon process which leads to immediate heat-up.⁴

As the temperature increases, the heating rate increases due to the increased probability of multi-phonon processes. The maximum heating rate is $\Delta T/T \approx 4 \times 10^{-2}$ per lattice period, which corresponds to an e-folding growth time of 0.15 ms. The break up of the crystal occurs at the temperature that corresponds to the maximum heating rate, i.e. $T \approx 4$ (total rest-frame temperature $T_{rest} = 1.5$ K). As the temperature increases further, the heating rate decreases due to the reducing spatial density. The MD calculation quantitatively agrees with the conventional intra-beam scattering calculation at the high-temperature limit (approximately $T > 20$).

The squares in Fig. 2 shows that the 2D structure heats up quickly even at very low temperature. Fig. 4 shows that the phonon spectrum of the 2D structure extends over a broad range including $2\omega_0$. The immediate heat up occurs at any temperature through the two-phonon process.

III. CRYSTALLINE BEAM IN THE TSR

TSR is an ion storage ring of circumference $C_0 = 55.4$ m. The lattice has a super-periodicity of 2. We perform MD calculation with the 7.3 MeV $^9\text{Be}^+$ ion beam. The transverse tunes of the machine are $\nu_x = 2.57$ and $\nu_y = 2.21$. The characteristic

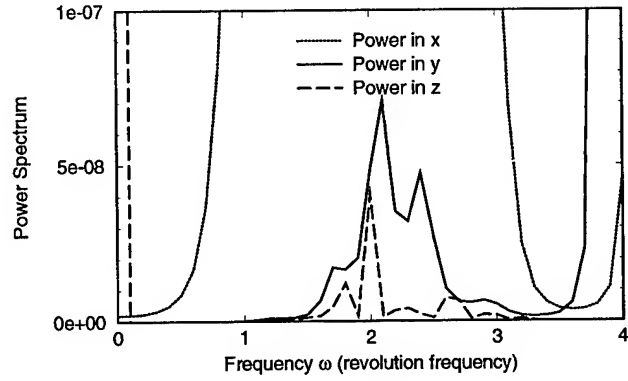


Figure 4. Power spectrum for the 2D ($\Delta_z = 3$) structure in the ASTRID lattice at extremely low temperature.

distance is $\xi \approx 5.1 \times 10^{-6}$ m ($\rho = 1.15$ m).

At low density, the ground state is again a 1D chain. The transition from 1D to 2D occurs approximately at $\Delta_z = 6$, or $N = 1.8 \times 10^6$. When the total number of particles N exceeds this value, the ground state becomes a zig-zag. The structure makes one rotation per lattice period around its longitudinal axis, having a horizontal orientation in the middle of the straight sections with particle separation of 2.5ξ , and a vertical orientation in the middle of the bending region with particle separation 8.7ξ . The rotation is produced by the shear motion when the particle crosses the bending magnetic field and is shown in Fig. 5 for $\Delta_z = 5$ ($N = 2.2 \times 10^6$). The direction of the rotation is determined by

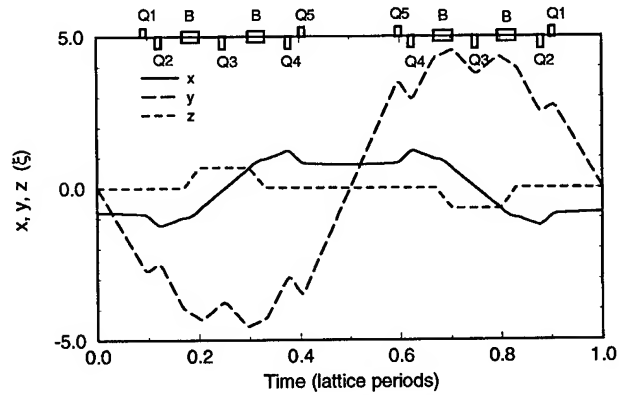


Figure 5. A rotating zig-zag structure at density $\Delta_z = 5$ formed with the TSR lattice with the displacements in x , y , and z changing with time during one lattice period.

the orientation of the bending magnetic field.

The dots and squares in Fig. 6 show the heating rates as functions of the temperature T in reduced units¹ for a 1D crystal of density $\Delta_z = 10$ ($N = 1.1 \times 10^6$) and the 2D rotating zig-zag of $\Delta_z = 5$. The conventional rest-frame temperature can be obtained by the relation $T_{rest} = 1.64 T$ (K). At low temperature, the heating rate for both structure is low. Fig. 7 shows the phonon spectrum of the 2D structure. The gigantic peak at $2\omega_0$ results from the periodic ground-state motion, while the spread is partially due to the finite length of steps used for spectrum analysis. Although the transverse tunes are larger than half the lattice periodicity (2), the phonon spectrum luckily avoids the

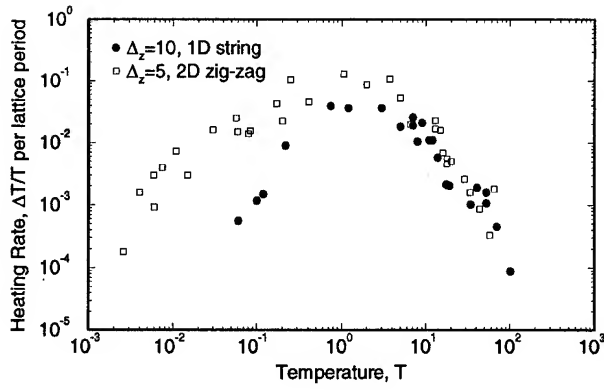


Figure 6. Heating rates as functions of the temperature T for a 1D ($\Delta_z = 10$) and a 2D ($\Delta_z = 5$) ground-state structure in the TSR lattice.

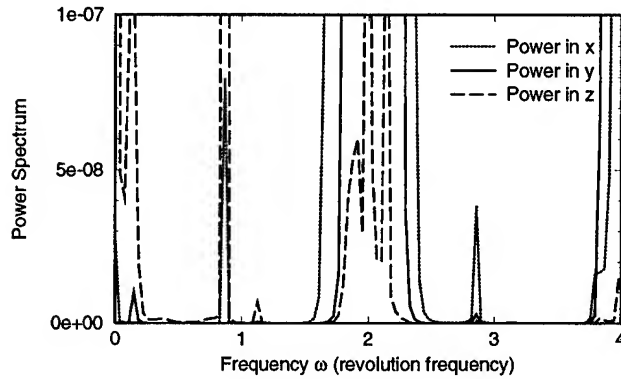


Figure 7. Power spectrum for the 2D ($\Delta_z = 5$) structure in the TSR lattice at extremely low temperature. The machine tunes are $\nu_x = 2.57$, $\nu_y = 2.21$.

dangerous points (integral multiple of ω_0) which would lead to immediate heat-up.

The maximum heating rate $\Delta T/T \approx 1.2 \times 10^{-1}$ per lattice period (e-folding growth time of 0.018 ms) for the 2D state is about twice of the 1D state $\Delta T/T \approx 6 \times 10^{-2}$. The break up of the crystal occurs at the temperature that corresponds to the maximum heating rate, i.e. $T \approx 1.3$ ($T_{rest} = 2.1$ K).

IV. QUANTUM LIMIT

The classical MD calculation fails only at very low temperature when quantum effects become important. The threshold temperature T_{sh} is given by the relation

$$k_B T_{sh} \sim \hbar \omega_{max}, \quad (4)$$

where ω_{max} is the maximum phonon frequency of the crystal. For the ASTRID 1D ($\Delta_z = 10$) structure, $T_{sh} \approx 5 \times 10^{-6}$ K, as shown in Fig. 8.

V. CONCLUSIONS AND DISCUSSION

Employing the previously developed formalism¹, we have performed MD calculations of the expected crystalline beams in ASTRID and TSR. The crystalline structure and the melting conditions depend on the beam energy, density, and the machine properties. For both ASTRID and TSR, we find that 1D and 2D

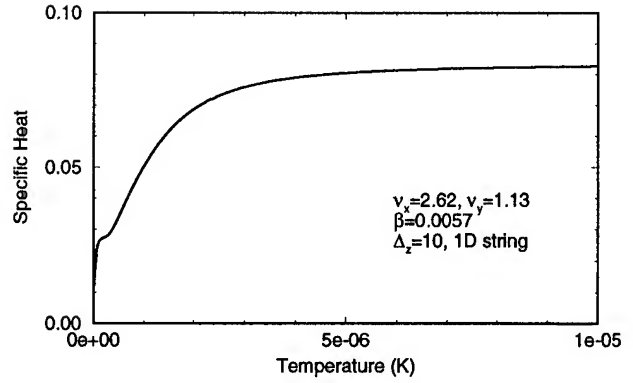


Figure 8. Specific heat (in reduced units) for the 1D ($\Delta_z = 10$) structure in the ASTRID lattice.

crystals can be formed when the total rest-frame temperature is less than about 1 K.

For 1D and occasional 2D crystalline structure, the maximum rate at which the crystalline state absorbs energy from the lattice occurs at the (break-up) temperature when the crystal starts to form (or break). The maximum rate is found to be linearly proportional to the beam intensity. With a given cooling rate, crystalline state of sufficiently low density can in principle be achieved if the external system noise is sufficiently low.

Because of the relatively low machine lattice periodicity, crystals of 2D or higher dimension typically absorb energy from the lattice and heat up extremely fast. In order to obtain crystalline beam of complex structure, storage rings should be designed with lattice periodicity significantly higher than twice the maximum transverse tune.

Acknowledgment We thank J. Hangst and D. Habs for many useful discussions, and A. Draeseke for making the computer program more efficient.

VI. REFERENCES

1. J. Wei, X-P Li, and A.M. Sessler, Phys. Rev. Lett. **73**, 3089 (1994).
2. J.P. Schiffer and P. Kienle, Z. Phys. A321, 181 (1985); J.P. Schiffer and O. Poulsen, Europhys. Lett. **1**, 55 (1986); J.P. Schiffer, Phys. Rev. Lett. **57**, 1133 (1986).
3. For example, J. Beebe-Wang, et al., Nucl. Instrum. Methods **B79**, 806 (1993); CRYSTAL LNL-INFN (REP) 59/92, Laboratori Nazionale di Legnaro.
4. X-P Li, A.M. Sessler, and J. Wei, Proc. European Part. Accel. Conf. 1994, London, p.1379 (1994).

IMPEDANCE MATRIX — AN UNIFIED APPROACH TO LONGITUDINAL COUPLED-BUNCH FEEDBACKS IN A SYNCHROTRON

S. Ivanov, Institute for High Energy Physics, Protvino, Moscow Region, 142284, Russia

Abstract

Characteristic Eq. of coupled-bunch motion of beam governed by a feedback (FB) is given to find FB's stabilizing effect against coherent instabilities or, say, injection error damping rates. Quite a general FB's schematics is involved: (i) it has two paths, the in-phase and quadrature (or amplitude and phase in a small-signal approach), with unequal gains; (ii) may employ distinct RF-bands to pick-up beam data and feed correction back to the beam. To account for cross-talk between various field and beam current harmonics inflicted by frequency down- and up-mixing, an impedance matrix (with, at most, three non-trivial elements per row) is introduced as a natural concept to gain insight into 'FB & beam' dynamics. The important class of FBs to counteract heavy beam loading of accelerating cavities is included into analysis as a particular case.

I. INTRODUCTION

Let $\vartheta = \Theta - \omega_0 t$ be azimuth in a co-rotating frame, where Θ is azimuth around the ring in the laboratory frame, ω_0 is the angular velocity of a reference particle, t is time. The beam current $J(\vartheta, t)$ and longitudinal electric field $E(\vartheta, t)$ are decomposed into $\sum_k J_k e^{ik\vartheta} - i\Omega t$ with Ω being the frequency of Fourier transform w.r.t. the co-rotating frame. In the laboratory frame Ω is seen as $\omega = k\omega_0 + \Omega$.

Interacting with passive components inside the vacuum chamber, the beam drives E -field with amplitude

$$E_k(\Omega) = -L^{-1} Z_{kk}(\omega) J_k(\Omega), \quad \omega = k\omega_0 + \Omega, \quad (1)$$

where L is the orbit length, $Z_{kk}(\omega)$, $\text{Re } Z_{kk}(\omega) \geq 0$ is the standard longitudinal impedance. Its main-diagonal element is cut from the entire matrix $Z_{kk'}(\omega)$ (it describes the lumped nature of the beam environment) due to a narrow-band response appropriate to, as a matter of fact, slowly perturbed bunched beams,

$$J_{k'}((k-k')\omega_0 + \Omega) \simeq J_k(\Omega) \delta_{kk'}, \quad |\Omega| \ll \omega_0, \quad (2)$$

with $\delta_{kk'}$ being the Kronecker's delta-symbol.

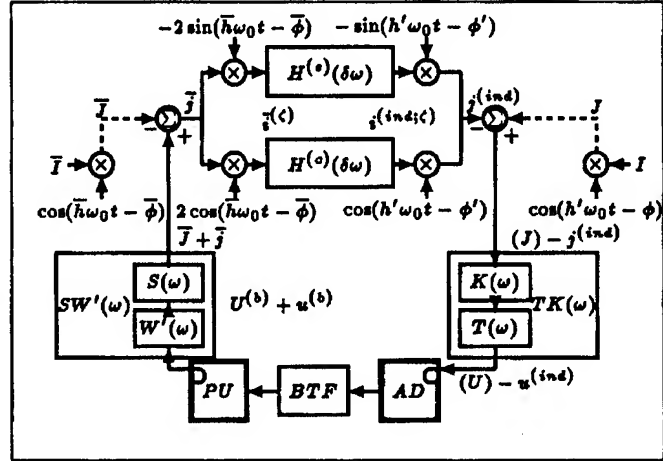
II. FEEDBACK

A. Circuitry with PU \neq AD

To simplify the matters, let a Pick-Up unit and an Acting Device of the FB in question be cavity-like resonant objects which excite longitudinal E -field

$$E^{(a)}(\Theta, t) = L^{-1} G^{(a)}(\Theta) u_a(t); \quad a = \text{PU, AD}, \quad (3)$$

where $u_a(t)$ is voltage across the gap, $G^{(a)}(\Theta)$ specifies the field localization and is normalized as $\int_0^{2\pi} |G^{(a)}(\Theta)| d\Theta = 2\pi$. Its



decomposition into $\sum_k G_k^{(a)} e^{ik\Theta}$ provides $G_k^{(a)}$, the complex transit-time factors at $\omega = k\omega_0$ with $|G_k^{(a)}| \leq 1$ and $\arg G_k^{(a)}$ being proportional to $\Theta^{(a)}$, the object's coordinate along the ring.

Quite a general coupled-bunch FB circuit employing filter methods is shown in the above Fig., Ref.[1]. The circuitry extracts beam data as a band-pass signal at $\omega \simeq \pm \bar{h}\omega_0$, processes it at IF $\omega = 0$ after frequency down-mixing, and then feeds an up-mixed band-pass correction back to the beam at $\omega \simeq \pm h'\omega_0$. Here \bar{h}, h' are integers, and, generally, $\bar{h} \neq h'$; $\bar{h}, h' \neq h$ where h is the main RF harmonic number. The FB has the in-phase (c) and quadrature (s) paths with unequal gains. Treated in a small-signal approach near the FB's set-point, the former one controls an amplitude, while the latter — a phase, of the accelerating voltage seen by the beam. Either of the paths may be switched off altogether, say, $H^{(c)} = 0$ for an injection error damping system, or in case of a dedicated phase control loop.

On neglecting the PU's (small) impact on the beam, the net voltage imposed by the FB can be put down as

$$u_{AD}^{(tot)}(t) = u_{AD}^{(b)}(t) - u_{AD}^{(ind)}(t) \quad (4)$$

where (b) and (ind) denote beam-excited and FB-induced voltages, correspondingly; $u_{AD}^{(ind)}(t)$ is a linear functional of $u_{PU}^{(b)}(t')$ taken at $t' \leq t$ due to causality.

Let $\delta\omega$ be a frequency deviation with $|\delta\omega| \ll (\bar{h}, h')\omega_0$. Whenever $H^{(c,s)}(\pm 2\bar{h}\omega_0 + \delta\omega) = 0$, the state of the system is given by 2-D column-vectors

$$\vec{u}_{PU}(\delta\omega) = (u(\bar{h}\omega_0 + \delta\omega); u(-\bar{h}\omega_0 + \delta\omega))_{PU}^T, \quad (5)$$

$$\vec{u}_{AD}(\delta\omega) = (u(h'\omega_0 + \delta\omega); u(-h'\omega_0 + \delta\omega))_{AD}^T. \quad (6)$$

The in-out gain through the linear FB is

$$\vec{u}_{AD}^{(ind)}(\delta\omega) = \hat{\chi}(\delta\omega) \vec{u}_{PU}^{(b)}(\delta\omega) \quad (7)$$

where $\hat{\chi}(\delta\omega)$ is a 2×2 FB's 'susceptibility' matrix,

$$\chi_{11}(\delta\omega) = 0.25 TK(h'\omega_0 + \delta\omega) S(\bar{h}\omega_0 + \delta\omega) \times \quad (8)$$

$$\times \left(H^{(c)}(\delta\omega) + H^{(s)}(\delta\omega) \right) e^{i(\phi' - \bar{\phi})};$$

$$\chi_{12}(\delta\omega) = 0.25 TK(h'\omega_0 + \delta\omega) S(-\bar{h}\omega_0 + \delta\omega) \times \quad (9)$$

$$\times \left(H^{(c)}(\delta\omega) - H^{(s)}(\delta\omega) \right) e^{i(\phi' + \bar{\phi})};$$

$$\chi_{21}(\delta\omega) = \chi_{12}(-\delta\omega^*)^*; \chi_{22}(\delta\omega) = \chi_{11}(-\delta\omega^*)^*.$$

Carrier phases $\bar{\phi}$, ϕ' of to beam and accelerating voltage so as to comply with the FB's particular purpose and its layout along the ring.

The beam-excited voltages at the PU and AD are

$$u_a^{(b)}(\omega) = - \left(\frac{W'(\omega)}{T'(\omega)} \right) \sum_{k=-\infty}^{\infty} G_{-k}^{(a)} J_k(\omega - k\omega_0) \quad (10)$$

where W' , $T'(\omega)$ are the gap-voltage responses to the beam current of PU and AD, respectively. Generally, the response of AD to external RF-drive $T(\omega) \neq T'(\omega)$.

Insert Eqs.10 into Eqs.7,4 and extract synchronous-to-beam E -field harmonics from Eq.3. Use Eq.2 to truncate \sum_k . Then, to generalize the commonly used impedance concept introduced by Eq.1, the FB can be treated as imposing the E -field harmonics

$$E_k^{(fb)}(\Omega) = -L^{-1} (Z_{kk}(\omega) J_k(\Omega) + \quad (11)$$

$$+ Z_{k,k-h'+\bar{h}}^{(fb)}(\omega) J_{k-h'+\bar{h}}(\Omega) + Z_{k,k-h'-\bar{h}}^{(fb)}(\omega) J_{k-h'-\bar{h}}(\Omega))$$

through coupling impedances

$$Z_{kk}(\omega) = T'(\omega) |G_k^{(AD)}|^2, \quad (12)$$

$$Z_{k,k-h'+\bar{h}}^{(fb)}(\omega) = -\chi_{11}(\omega - h'\omega_0) \times \quad (13)$$

$$\times W'(\omega - h'\omega_0 + \bar{h}\omega_0) G_k^{(AD)} G_{-k+h'+\bar{h}}^{(PU)},$$

$$Z_{k,k-h'-\bar{h}}^{(fb)}(\omega) = -\chi_{12}(\omega - h'\omega_0) \times \quad (14)$$

$$\times W'(\omega - h'\omega_0 - \bar{h}\omega_0) G_k^{(AD)} G_{-k+h'+\bar{h}}^{(PU)}.$$

Here $\omega = k\omega_0 + \Omega$, $k \sim h' > 0$, $|\Omega| \ll \omega_0$. The negative-frequency domain of $k \sim -h' < 0$ is arrived at with the reflection property $Z_{-k,-k'}(-\omega^*)^* = Z_{kk'}(\omega)$.

Eq.12 yields the coupling impedance of AD itself treated as a passive device in line with Eq.1. Eqs.13,14 represent an active response of the FB and account for cross-talk between harmonics E_k , $J_{k'}$ with $k \neq k'$ caused by down- and up-mixing of frequencies. Impedances $Z_{kk'}^{(fb)}(\omega)$ are no longer subject to restriction $\text{Re } Z_{kk'}^{(fb)}(\omega) \geq 0$, which is to introduce damping into the beam motion. The balance $H^{(c)}(\delta\omega) = H^{(s)}(\delta\omega)$ of the FB's path gains results in matrix $\hat{\chi}$ becoming diagonal, and in $Z_{kk'}^{(fb)}(\omega)$ with $|k - k'| = h' + \bar{h}$ vanishing. In injection error damping systems, the FB's path gains and, hence, $Z_{kk'}^{(fb)}(\omega)$ may be scaled reciprocally to, say, the average beam current J_0 .

B. Circuitry with PU = AD

Take $h', \bar{h} = h$, $W'(\omega) = T'(\omega)$ with PU and AD being merged into a single device AC, an Accelerating Cavity. This

particular case represents an RF FB around the final power amplifier which is responsible for the reduction of periodic beam-loading transients and coupled-bunch instability damping, Ref.[2]. Now, Eq.4 is kept intact while the PU detects both, the beam-imposed and correction signals. Therefore, Eq.7 have to undergo an essential modification:

$$\vec{u}_{AC}^{(ind)}(\delta\omega) = \hat{\chi}(\delta\omega) \vec{u}_{AC}^{(tot)}(\delta\omega) \quad (15)$$

due to which the coupling impedances to enter Eq.11 acquire the form other than that given by Eqs.12-14,

$$Z_{kk}(\omega) + Z_{kk}^{(fb)}(\omega) = \epsilon_{11}^{-1}(\omega - h\omega_0) \times \quad (16)$$

$$\times T'(\omega) |G_k^{(AC)}|^2,$$

$$Z_{k,k-2h}^{(fb)}(\omega) = \epsilon_{12}^{-1}(\omega - h\omega_0) \times \quad (17)$$

$$\times T'(\omega - 2h\omega_0) G_k^{(AC)} G_{-k+2h}^{(AC)}$$

where $\omega = k\omega_0 + \Omega$, $k \sim h > 0$, $|\Omega| \ll \omega_0$ and

$$\hat{\epsilon}(\delta\omega) = \hat{I} + \hat{\chi}(\delta\omega), \quad (18)$$

$$\hat{\epsilon}^{-1}(\delta\omega) = \frac{1}{\text{Det } \hat{\epsilon}(\delta\omega)} \begin{pmatrix} 1 + \chi_{22}(\delta\omega) & -\chi_{12}(\delta\omega) \\ -\chi_{21}(\delta\omega) & 1 + \chi_{11}(\delta\omega) \end{pmatrix}. \quad (19)$$

Here \hat{I} , $\hat{\epsilon}(\delta\omega)$ and $\hat{\epsilon}^{-1}(\delta\omega)$ are 2×2 matrix unit, FB's 'permeability' matrix and its inverse, correspondingly.

This FB may turn self-excited, which is avoided technically by putting zeros of $\text{Det } \hat{\epsilon}(\delta\omega)$ into the lower half-plane $\text{Im } \delta\omega < 0$ through a proper tailoring of $H^{(c,s)}(\delta\omega)$.

It is evident hereof that by substituting Eqs.16-17 for Eqs.12-14 the formulae to follow can be extended to treat the important case of $h', \bar{h} = h$; PU, AD = AC as well.

III. CHARACTERISTIC EQUATION

A. General Case

The total E -field at the orbit is a sum of two terms

$$E_k^{(tot)}(\Omega) = E_k^{(ext)}(\Omega) + E_k^{(fb)}(\Omega). \quad (20)$$

The former one, (ext) is imposed from the outside, say, by an external RF drive. The latter, (fb) is the induced response of the environment to the coherent motion of the beam: its perturbed current harmonics $J_k(\Omega)$ drive the FBs, both unintentional (Eq.1) and issued (Eq.11 with its negative-frequency counterpart), to yield

$$E_k^{(fb)}(\Omega) = -L^{-1} \sum_{k'=-\infty}^{\infty} z_{kk'}(k\omega_0 + \Omega) J_{k'}(\Omega), \quad (21)$$

$z_{kk'}(\omega)$ having, at most, three non-trivial elements per row:

$$z_{kk'}(\omega) = Z_{kk'}(\omega) \delta_{k'k} + \quad (22)$$

$$+ Z_{kk'}^{(fb)}(\omega) (\delta_{k',k-(h'-\bar{h})k/|k|} + \delta_{k',k-(h'+\bar{h})k/|k|}).$$

The first member in r.h.s. of Eq.22 incorporates effect of all the passive devices available.

From now on, one enters a standard route of instability analysis, and via the Vlasov's linearized Eq. finds

$$J_k(\Omega) = L \sum_{k'=-\infty}^{\infty} y_{kk'}(\Omega) E_{k'}^{(tot)}(\Omega). \quad (23)$$

Here $y_{kk'}(\Omega)$ is the beam 'admittance' matrix which, say, for the beam of average current J_0 in $M \leq h$ (h/M is an integer) identical and equispaced bunches is equal to

$$y_{kk'}(\Omega) = C J_0 (Y_{kk'}(\Omega)/k') \sum_{l=-\infty}^{\infty} \delta_{k-k', lM}, \quad (24)$$

$$Y_{kk'}(\Omega) = -i \sum_{m=-\infty}^{\infty} \int_0^{\infty} \frac{m}{\Omega - m\Omega_s(\mathcal{J})} \times \frac{\partial F_0(\mathcal{J})}{\partial \mathcal{J}} I_{mk}(\mathcal{J}) I_{mk'}^*(\mathcal{J}) d\mathcal{J}. \quad (25)$$

Here (ψ, \mathcal{J}) are the longitudinal angle-action variables introduced in the phase-plane $(\vartheta, \vartheta' \equiv d\vartheta/dt)$ with the origin $\vartheta = 0$ being put on the reference particle of a bunch; $\Omega_s(\mathcal{J}) = d\psi/dt$ is the non-linear synchrotron frequency; F_0 is unperturbed bunch distribution normalized to unit; functions $I_{mk}^*(\mathcal{J})$ are the coefficients of series which expand a plane wave $e^{ik\vartheta(\mathcal{J}, \psi)}$ into sum over multipoles: $\sum_m I_{mk}^*(\mathcal{J}) e^{im\psi}$. The leftmost factor C in Eq.24 is

$$C = \Omega_0^2 / (h V_0 \sin \varphi_s), \quad (26)$$

where Ω_0 is the small-amplitude synchrotron frequency (circular), V_0 is the nominal amplitude of accelerating voltage, φ_s is the stable phase angle ($\varphi_s > 0$ below transition, the synchronous energy gain being $eV_0 \cos \varphi_s$).

Insert Eq.23 into Eq.21 and use Eq.20 to get

$$E_k^{(ext)}(\Omega) = \sum_{k'=-\infty}^{\infty} \epsilon_{kk'}(\Omega) E_{k'}^{(tot)}(\Omega), \quad (27)$$

$$\epsilon_{kk'}(\Omega) = \delta_{kk'} + \chi'_{kk'}(\Omega), \quad (28)$$

$$\chi'_{kk'}(\Omega) = \sum_{k''=-\infty}^{\infty} z_{kk''}(k\omega_0 + \Omega) y_{k''k'}(\Omega). \quad (29)$$

Here $\chi'_{kk'}(\Omega)$, $\epsilon_{kk'}(\Omega)$ are 'susceptibility' and 'permeability' matrices of 'beam & FB' medium. Zeros of the characteristic Eq.

$$\text{Det } \hat{\epsilon}(\Omega) = 0 \quad (30)$$

are the eigen-frequencies of beam coherent oscillations which must be located in the lower half-plane $\text{Im } \Omega \leq -1/\tau_\epsilon < 0$. Here τ_ϵ is the sought-for damping time of beam coherent oscillations which, as well, determines duration of beam injection transients under the FB showing themselves up, mainly, at the dipole side-bands $\Omega \simeq \pm \Omega_0$.

B. Narrow-Band Case

Label the normal coupled-bunch modes by $n = 0, 1, \dots, M-1$, phase shift between adjacent bunches being $2\pi n/M$. Suppose h'/M and \bar{h}/M be integers, due to which the FB would not couple beam modes whose $n' \neq n$. Let band-width of the FB be $\Delta\omega \ll M\omega_0$. Hence, there would be only four resonant harmonics $J_k(\Omega)$ of beam current perturbation which belong to the given mode n and cross-talk through the FB. Their subscripts are

$$k'_{1,2} = n + l'_{1,2}M \simeq \pm h', \quad \bar{k}_{1,2} = n + \bar{l}_{1,2}M \simeq \pm \bar{h} \quad (31)$$

with $l'_{1,2}, \bar{l}_{1,2}$ the integers. The essential E -field harmonics $E_k(\Omega)$ to occur within $\Delta\omega$ are the two with $k = k'_{1,2}$. In this

2×2 case $\text{Det } \hat{\epsilon}(\Omega)$ can be found, which results in characteristic Eq. to follow,

$$1 + \chi'_{k'_1 k'_1}(\Omega) + \chi'_{k'_2 k'_2}(\Omega) + \left[\chi'_{k'_1 k'_1}(\Omega) \chi'_{k'_2 k'_2}(\Omega) - \chi'_{k'_1 k'_2}(\Omega) \chi'_{k'_2 k'_1}(\Omega) \right] \simeq 0. \quad (32)$$

L.h.s. of Eq.32 involves dispersion integrals $Y_{kk'}$ whose subscripts are $k = k'_{1,2}, \bar{k}_{1,2}$ and $k' = k'_{1,2}$. Given $\Delta\omega \Delta\vartheta_0/\omega_0 \ll \pi$, where $\Delta\vartheta_0$ is bunch half-width, $Y_{kk'}$ become slow functions of k, k' , which allow substitutions $k'_{1,2} \simeq \pm h'$, $\bar{k}_{1,2} \simeq \pm \bar{h}$ be performed in subscripts of all the essential $Y_{kk'}$ that enter the characteristic Eq.32.

Usually, at $\Omega \simeq m\Omega_0 + i0$ a single resonant term $Y_{kk'}^{(m)}$ dominates in \sum_m of Eq.25. Hereof, one arrives at the reflection properties of $Y_{kk'} \simeq Y_{kk'}^{(m)}$,

$$Y_{-k, k'} \simeq Y_{k, -k'} \simeq (-1)^m Y_{kk'}, \quad Y_{-k, -k'} \simeq Y_{kk'}. \quad (33)$$

Up to these two assumptions, expression in square brackets of Eq.32 vanishes, while the characteristic Eq. itself reduces to much a simpler form

$$1 + C J_0 \left(\zeta_n(\Omega) Y_{h'h'}(\Omega) + \zeta_n^{(fb)}(\Omega) Y_{\bar{h}\bar{h}}(\Omega) \right) \simeq 0, \quad (34)$$

being put down in terms of the effective, or instability driving, impedances at side-bands $\Omega \simeq m\Omega_0$ of coupled-bunch mode n ,

$$\zeta_n(\Omega) \simeq Z_{k'_1 k'_1}(k'_1 \omega_0 + \Omega)/k'_1 + \dots \quad k'_1 \rightarrow k'_2, \quad (35)$$

$$\begin{aligned} \zeta_n^{(fb)}(\Omega) &\simeq Z_{k'_1, k'_1 - h' + \bar{h}}^{(fb)}(k'_1 \omega_0 + \Omega)/k'_1 + \\ &+ (-1)^m Z_{k'_1, k'_1 - h' - \bar{h}}^{(fb)}(k'_1 \omega_0 + \Omega)/k'_1 + \\ &+ \dots \quad k'_1 \rightarrow k'_2, \quad h' \rightarrow -h', \quad \bar{h} \rightarrow -\bar{h}. \end{aligned} \quad (36)$$

Items with $(-1)^m$, if any, are responsible for the intrinsic asymmetry in damping of within-bunch multipole modes m with opposite parity inherent in FBs with the unbalanced path gains, $H^{(c)} \neq H^{(s)}$.

References

- [1] F. Pedersen, CERN PS/90-49(AR), CERN, Geneva, 1990.
- [2] D. Boussard, CAS Proceed., CERN/87-03, Vol. 2, Geneva, 1987, pp. 626-646.

THE COUPLING IMPEDANCE OF A TOROIDAL BEAM PIPE WITH CIRCULAR CROSS SECTION*

H. Hahn, Brookhaven National Laboratory, Upton, New York 11973-5000

Abstract

An analytic expression for the non-resonant longitudinal coupling impedance in a toroidal beam pipe with circular cross section is derived using a perturbation treatment carried out in a local orthogonal coordinate system.

I. INTRODUCTION

In this paper, the topic of coupling impedances and beam-induced forces in a toroidal beam pipe is revisited. In straight, smooth accelerator beam pipe configurations, the space charge forces on a charged test particle due to beam-induced electric and magnetic fields are subject to a near perfect cancellation in the ultra-relativistic limit. It is well known that in toroidal geometries the cancellation is imperfect, resulting in residual, "energy-independent" longitudinal and transverse forces which can impact the accelerator performance. Whereas the present-day designs of high-energy hadron accelerators/colliders are based on beam pipes with circular cross section, essentially all theoretical studies assume rectangular geometries, the notable exception being the report by Zotter.¹ The expressions here presented are intended to amend this deficiency.

The primary objective of this paper is the derivation of an expression for the residual longitudinal Z/n of a toroidal beam pipe with circular cross section, with b representing the beam pipe radius and R the curvature radius of the central arc as shown in Fig. 1. The results are obtained via the perturbation method developed by Jouguet² for the analysis of the electromagnetic wave propagation in curved waveguides, which recently has been successfully applied to the derivation of expressions for the longitudinal coupling impedance in toroidal beam pipes with rectangular cross section.^{3,4} Using the Serret-Frenet frame, an appropriate "local" orthogonal coordinate system (r, φ, θ) can be erected around the central arc of the torus. This choice is superior to the use of toroidal coordinates, since the local coordinate system reduces to the usual circular-cylinder coordinates $r, \varphi, s = R\theta$ as required for the perturbation treatment of the problem. Since the residual longitudinal coupling impedance of an on-axis beam must be independent of the direction of curvature, an expansion to second order in $1/R$ is required. It is known from previous studies that the residual coupling impedance does not exhibit a logarithmic divergence, if the transverse beam size is reduced to zero. Consequently, the study can be limited to filamentary beams. Since wall losses are themselves a small perturbation, they can be ignored in deriving the perturbation results due to the curvature.

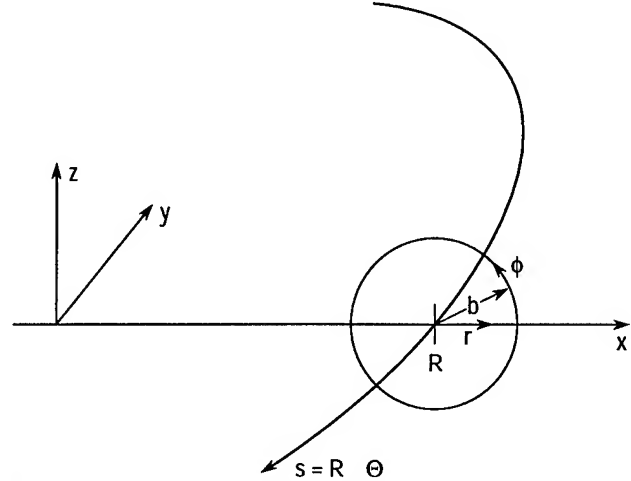


Figure 1. Local coordinate system (r, φ, θ) for toroidal beam tube with circular cross section.

II. PERTURBATIVE SOLUTION OF MAXWELL'S EQUATIONS

The "local" orthogonal curvilinear coordinate system r, φ, θ appropriate to the toroidal beam pipe geometry is defined in terms of the Cartesian coordinates x, y, z

$$\begin{aligned} x &= (R + r \cos \varphi) \cos \theta \\ y &= -(R + r \cos \varphi) \sin \theta \\ z &= r \sin \varphi \end{aligned} \quad (1)$$

Assuming time harmonic fields of the general form $\mathcal{F}(r, \varphi) e^{-jn\theta} e^{j\omega t}$ with $\omega = \nu v$ and $\nu = n/R$ (in natural units where $c = 1, \mu_0 = 1$) one can write Maxwell's equations in the source free regions as

$$\begin{aligned} \frac{\partial g \mathcal{E}_\theta}{r \partial r} + j\nu \mathcal{E}_\varphi &= -j\omega g \mathcal{H}_r \\ j\nu \mathcal{E}_r + \frac{\partial g \mathcal{E}_\theta}{\partial r} &= j\omega g \mathcal{H}_\varphi \\ \frac{\partial r \mathcal{E}_\varphi}{r \partial r} - \frac{\partial \mathcal{E}_r}{r \partial \varphi} &= -j\omega \mathcal{H}_\theta \\ \frac{\partial g \mathcal{H}_\theta}{r \partial \varphi} + j\nu \mathcal{H}_\varphi &= j\omega g \mathcal{E}_r \\ j\nu \mathcal{H}_r + \frac{\partial g \mathcal{H}_\theta}{\partial r} &= -j\omega g \mathcal{E}_\varphi \\ \frac{\partial r \mathcal{H}_\varphi}{r \partial r} - \frac{\partial \mathcal{H}_r}{r \partial \varphi} &= j\omega \mathcal{E}_\theta \end{aligned} \quad (2)$$

with $g = 1 + (r/R) \cos \varphi$.

Perturbative solutions can be found by expanding the fields in inverse powers of the curvature radius, or explicitly

$$\mathcal{E}_{r,\varphi} = E_{r,\varphi} + \frac{1}{R} e_{r,\varphi} + \dots$$

*Work performed under the auspices of the U.S. Department of Energy

$$\begin{aligned}
\mathcal{E}_\theta &= j \left(E_\theta + \frac{1}{R} e_\theta + \dots \right) \\
\mathcal{H}_{r,\varphi} &= H_{r,\varphi} + \frac{1}{R} h_{r,\varphi} + \dots \\
\mathcal{H}_\theta &= j \left(H_\theta + \frac{1}{R} h_\theta + \dots \right)
\end{aligned} \quad (3)$$

The resulting expressions for Maxwell's equations to first order in R^{-1} are given as follows

$$\begin{aligned}
\frac{1}{r} \frac{\partial e_\theta}{\partial \varphi} + \nu e_\varphi + \omega h_r &= -\frac{\partial}{\partial \varphi} (\cos \varphi E_\theta) - \omega r \cos \varphi H_r \\
\nu e_r + \frac{\partial e_\theta}{\partial r} - \omega h_\varphi &= -\cos \varphi \frac{\partial}{\partial r} (r E_\theta) + \omega r \cos \varphi H_\varphi \\
\frac{\partial}{\partial r} (r e_\varphi) - \frac{\partial e_r}{\partial \varphi} - \omega r h_\theta &= 0 \\
\frac{1}{r} \frac{\partial h_\theta}{\partial \varphi} + \nu h_\varphi - \omega e_r &= -\frac{\partial}{\partial \varphi} (\cos \varphi H_\theta) + \omega r \cos \varphi E_r \\
\nu h_r + \frac{\partial h_\theta}{\partial r} + \omega e_\varphi &= -\cos \varphi \frac{\partial}{\partial r} (r H_\theta) - \omega r \cos \varphi E_\varphi \\
\frac{\partial}{\partial r} (r h_\varphi) - \frac{\partial h_r}{\partial \varphi} + \omega r e_\theta &= 0
\end{aligned} \quad (4)$$

Decoupling Maxwell's equations and reducing them to two independent partial differential equations in the azimuthal components e_θ and h_θ can be achieved by introducing complex transverse fields and differential operators.⁵

After some manipulations, one finds the independent differential equations for the azimuthal perturbations

$$\begin{aligned}
\Delta_T e_\theta - \kappa^2 e_\theta &= -\Delta_T (r \cos \varphi E_\theta) \\
&\quad + \frac{1}{r} \frac{\partial}{\partial r} \{ r^2 \cos \varphi (\nu E_r + \omega H_\varphi) \} \\
&\quad + \frac{\partial}{\partial \varphi} \{ \cos \varphi (\nu E_\varphi - \omega H_r) \} \\
\Delta_T h_\theta - \kappa^2 h_\theta &= -\Delta_T (r \cos \varphi H_\theta) \\
&\quad + \frac{1}{r} \frac{\partial}{\partial r} \{ r^2 \cos \varphi (\nu H_r - \omega E_\varphi) \} \\
&\quad + \frac{\partial}{\partial \varphi} \{ \cos \varphi (\nu H_\varphi + \omega E_r) \}
\end{aligned} \quad (5)$$

with $\kappa^2 = \nu^2 - \omega^2 = (1 - v^2)\nu^2 = (\nu/\gamma)^2$ and the transverse Laplacian operator

$$\Delta_T = \frac{1}{r} \frac{\partial}{\partial r} \left(r \frac{\partial}{\partial r} \right) + \frac{1}{r^2} \frac{\partial^2}{\partial \varphi^2}$$

The solution is uniquely determined by imposing boundary and continuity conditions. Having determined e_θ and h_θ , the remaining transverse components can be obtained as follows

$$\begin{aligned}
\kappa^2 e_r &= -\nu \frac{\partial e_\theta}{\partial r} - \nu \cos \varphi \frac{\partial r E_\theta}{\partial r} + \omega^2 r \cos \varphi E_r \\
&\quad - \frac{\omega}{r} \frac{\partial h_\theta}{\partial \varphi} - \omega \frac{\partial}{\partial \varphi} \cos \varphi H_\theta + \omega \nu r \cos \varphi H_\varphi \\
\kappa^2 h_r &= -\nu \frac{\partial h_\theta}{\partial r} - \nu \cos \varphi \frac{\partial r H_\theta}{\partial r} + \omega^2 r \cos \varphi H_r \\
&\quad + \frac{\omega}{r} \frac{\partial e_\theta}{\partial \varphi} + \omega \frac{\partial}{\partial \varphi} \cos \varphi E_\theta - \omega \nu r \cos \varphi E_\varphi
\end{aligned}$$

$$\begin{aligned}
\kappa^2 e_\varphi &= -\frac{\nu}{r} \frac{\partial e_\theta}{\partial \varphi} - \nu \frac{\partial}{\partial \varphi} \cos \varphi E_\theta + \omega^2 r \cos \varphi E_\varphi \\
&\quad + \omega \frac{\partial h_\theta}{\partial r} + \omega \cos \varphi \frac{\partial r H_\theta}{\partial r} - \omega \nu r \cos \varphi H_r \\
\kappa^2 h_\varphi &= -\frac{\nu}{r} \frac{\partial h_\theta}{\partial \varphi} - \nu \frac{\partial}{\partial \varphi} \cos \varphi H_\theta + \omega^2 r \cos \varphi H_\varphi \\
&\quad - \omega \frac{\partial e_\theta}{\partial r} - \omega \cos \varphi \frac{\partial r E_\theta}{\partial r} + \omega \nu r \cos \varphi E_r
\end{aligned} \quad (6)$$

The internal consistency of the results can be checked by testing for a divergence free solution using $\text{div } \vec{E} = 0$:

$$\frac{\partial r e_r}{\partial r} + \frac{\partial e_\varphi}{\partial \varphi} + \nu r e_\theta = -r \cos \varphi \left(E_r + \frac{\partial r E_r}{\partial r} \right) - r \frac{\partial \cos \varphi E_\varphi}{\partial \varphi} \quad (7)$$

and $\text{div } \vec{H} = 0$:

$$\frac{\partial r h_r}{\partial r} + \frac{\partial h_\varphi}{\partial \varphi} + \nu r h_\theta = -r \cos \varphi \left(H_r + \frac{\partial r H_r}{\partial r} \right) - r \frac{\partial \cos \varphi H_\varphi}{\partial \varphi} \quad (8)$$

III. THE CURVATURE-INDUCED RESIDUAL COUPLING IMPEDANCE

First order perturbation results in R^{-1} are the required first step towards finding the curvature-induced longitudinal coupling impedance. In order to prevent a logarithmic divergence of the result, the beam must be given a finite transverse size. Solving the case of a tubular beam located at the radius ρ avoids the divergence. The tubular beam is assumed to travel in the θ direction with velocity v and has the current density

$$i_\theta = \frac{I}{2\pi\rho} \delta(r - \rho) e^{-jn\theta} e^{j\omega t} \quad (9)$$

Perturbative solutions to Maxwell's equations are found as described above separately for inner ($r < \rho$) and outer region ($\rho < r < b$) and by field matching at $r = \rho$, while imposing Ampere's law on H_φ and satisfying the boundary condition at $r = b$, assuming lossless walls.

The field components in the limit of filamentary ($\rho \rightarrow 0$) and ultra-relativistic ($v \rightarrow 1$) beams required in the derivation of \mathcal{E}_θ to second order can be written as

$$\begin{aligned}
\mathcal{E}_r &= \frac{I}{2\pi r} + \frac{1}{R} e_{r1} \cos \varphi + \frac{1}{R^2} \dots \\
\mathcal{E}_\theta &= j \left\{ \frac{1}{R} e_{\theta 1} \cos \varphi + \frac{1}{R^2} (e_{\theta 2} + e_{\theta 22} \cos 2\varphi) + \frac{1}{R^3} \dots \right\} \\
\mathcal{H}_\varphi &= \frac{I}{2\pi r} + \frac{1}{R} h_{\varphi 1} \cos \varphi + \frac{1}{R^2} \dots
\end{aligned} \quad (10)$$

with

$$\begin{aligned}
e_{\theta 1} &= -\frac{I}{2\pi} \nu r \ln \frac{b}{r} \\
e_{r1} &= -\frac{I}{2\pi} \left\{ \frac{1}{2} - \frac{1}{2} \ln \frac{b}{r} - \frac{\nu^2 b^2}{16} \left(7 - \frac{r^2}{b^2} + 4 \frac{r^2}{b^2} \ln \frac{b}{r} \right) \right\} \\
h_{\theta 1} &= -\frac{I}{2\pi} \left\{ \frac{1}{2} + \frac{1}{2} \ln \frac{b}{r} - \frac{\nu^2 b^2}{16} \left(7 - \frac{r^2}{b^2} + 4 \frac{r^2}{b^2} \ln \frac{b}{r} \right) \right\}
\end{aligned} \quad (11)$$

The second order field perturbations of an on-axis filamentary beam are excited by first-order perturbations with pure dipole, i.e. 1φ -dependence. The factor $\cos^2 \varphi = \frac{1}{2} + \frac{1}{2} \cos 2\varphi$ in the forcing term implies that the second order fields have only φ independent and quadrupole, i.e. 2φ , dependent terms. Only the φ -independent term $e_{\theta 2}$ leads to an on-axis electric field component in θ -direction which is responsible for the residual coupling impedance. The differential equation for the relevant φ -independent $e_{\theta 2}$ component thus reduces in the ultra-relativistic limit, i.e. $\kappa = 0$, to

$$\frac{1}{r} \frac{\partial}{\partial r} \left(r \frac{\partial e_{\theta 2}}{\partial r} \right) = -\frac{1}{2r} \frac{\partial}{\partial r} \left(r \frac{\partial r e_{\theta 1}}{\partial r} \right) + \frac{\nu}{2r} \frac{\partial}{\partial r} \left(r^2 (e_{r1} + h_{\varphi 1}) \right) \quad (12)$$

together with the boundary conditions on the beam pipe wall $(e_{\theta 2})_{r=b} = 0$ and, replacing the matching condition, $(\partial e_{\theta 2} / \partial r)_{r=0} = 0$.

The solution is found to be

$$e_{\theta 2} = \frac{I \nu b^2}{2\pi} \frac{1}{4} \left\{ \left(1 - \frac{7}{8} \nu^2 b^2 \right) \left(1 - \frac{r^2}{b^2} \right) + 2 \left(1 + \frac{\nu^2 r^2}{8} \right) \frac{r^2}{b^2} \ln \frac{b}{r} \right\} \quad (13)$$

from which follow the expression for the residual longitudinal coupling impedance seen by a filamentary beam in the ultra-relativistic case, $\gamma \rightarrow \infty$ ($Z_o = c\mu_o$, in SI units)

$$\frac{Z}{n} = -j \frac{b^2 Z_o}{4R^2} \left(1 - \frac{7}{8} \nu^2 b^2 \right) \quad (14)$$

The full second-order expression for the curvature-induced longitudinal coupling impedance and mathematical details of its derivation can be found in a journal paper,⁶ where the impedance in the long-wavelength limit is given as

$$\frac{Z}{n} = -j\beta Z_o \frac{b^2}{4R^2} \left(1 - \frac{7}{8} \nu^2 b^2 \right) + j \frac{Z_o}{16\beta\gamma^2} \frac{b^2}{R^2} \left(1 - 2\nu^2 b^2 + \frac{109}{48} \nu^4 b^4 \right) \quad (15)$$

with $\beta = v/c$.

References

- [1] B. Zotter, Report CERN/ISR-TH/77-56 (1977).
- [2] M. Jouguet, *Cables & Transmissions*, **1**, 133 (1947).
- [3] H. Hahn and S. Tepikian, Proc. 1991 IEEE Particle Accelerator Conf., San Francisco, CA, p. 1707.
- [4] H. Hahn, S. Tepikian and G. Dôme, *Particle Accelerators* (to be published).
- [5] L. Lewin, *Theory of Waveguides*, Chapter 4.4 (J. Wiley & Sons, New York 1975).
- [6] H. Hahn, *Particle Accelerators* (submitted).

BUNCH LENGTHENING STUDY IN BEPC

Z. Guo, Q. Qin, G. Xu, C. Zhang

Institute of High Energy Physics, Chinese Academy of Sciences

P.O.Box 918, Beijing 100039, China

Abstract

The bunch lengthening in the Beijing Electron - Positron Collider (BEPC) is investigated systematically with streak camera and the method of beam spectrum analysis. Many available results are obtained from the measurement and the corresponding scaling law is summarized in the light of the existing theoretical explanation. Due to its importance for BEPC upgrades, the related parameters and effects of bunch lengthening are studied in details.

I. INTRODUCTION

In electron - positron storage rings, bunch length and its lengthening are so important that people should cope with them much carefully as they will influence on the luminosity and machine performance directly. A high luminosity is the destination of every electron - positron collider, due to which, one can reduce the β functions at the interaction point while shortening the bunch length, especially for the lower RF frequency like 200 MHz in BEPC. Small coupling impedance is also considered attentively in the design of colliders in order to avoid bunch lengthening. In BEPC, an electron - positron collider running at the energy of 1.3~2.8 GeV, bunch length is also significant to the machine performance and the luminosity upgrades, it is of course a probe of bunched beam instability. From the data of bunch length and its lengthening, we can fit them as a scaling law and deduce the beam current threshold, coupling impedance and some further understanding of the theories.

II. THEORETICAL ASPECTS

Some theories have been developed to explain the phenomena of bunch lengthening up to now. They are the potential well distortion model and the instability model. At very low currents the bunch length equals the natural bunch length σ_{l0} , which is determined by RF voltage, beam energy and other machine parameters.

The incoherent frequency shift and bunch length distortion (lengthening or shortening) will be caused by potential well effect with beam current. The incoherent tune shift is [1]

$$\left(\frac{\omega_s}{\omega_0}\right) = [1 - \Delta \sum_p j \frac{Z_{||}(p)}{p} p^2 \sigma_0(p)] \quad (1)$$

where $Z_{||}$ is the broad band impedance, Δ is a scaling factor as a function of RF voltage and beam current, $\sigma_0(p)$ is the amplitude of the stationary spectrum of Gaussian distribution at the frequency of $p\omega_0$. The energy spread is not affected by the potential well distortion in electron machines. So $\sigma_l/\sigma_{l0} = \omega_s/\omega_s$

and for a long bunch ($\sigma_l > b$)

$$\left(\frac{\sigma_{l0}}{\sigma_l}\right)^2 = 1 + \delta \frac{b^3}{\sigma_l^3} \quad (2)$$

where b is the radius of vacuum pipe and δ is proportional to Δ . One can see that the distortion (lengthening or shortening) of bunch length depends on δ , i.e. the impedance and the momentum compaction factor.

Due to the microwave instability, bunch lengthening happens on energy spread increasing when beam current is above the threshold. According to Boussard [2], the bunch lengthens with the following relation:

$$\sigma_l = \left(\frac{\sqrt{2\pi} e R^3 I_b \alpha_p}{F E \nu_s^2} \left| \frac{Z_{||}}{n} \right|_0 \right)^{1/3} \quad (3)$$

where I_b is the bunch current, α_p the momentum compaction factor, R the radius of collider, e the charge of electron, E the beam energy, ν_s the synchrotron tune, F the distribution factor and $\left| \frac{Z_{||}}{n} \right|_0$ the longitudinal coupling impedance at lower frequency. From this formula, one can see that the bunch length is proportional to the cubic root of a scaling parameter ξ , which is defined as $\xi = I_b \alpha_p / E \nu_s^2$. It can be written as

$$\sigma_l \propto (\xi \left| \frac{Z_{||}}{n} \right|_0)^{1/3} \quad (4)$$

One can calculate the particle longitudinal distortion in phase space with and without potential well distortion and microwave instability then compare it with the measurement. It is expected to better understand the mechanism of bunch lengthening and energy spread widening.

In reference [3], a scaling law for SPEAR had been concluded. It predicts the bunch length σ_l depends on the parameter ξ as

$$\sigma_l \propto (\xi Z_0 R^3)^{\frac{1}{1+\alpha}} \quad (5)$$

$$Z(\omega) = 2\pi R Z_0 \omega^\alpha. \quad (6)$$

Here, Z_0 is the impedance parameter and (6) assumes a power law behaviour of the coupling impedance responsible for the instability.

In the real case, the behaviour of bunch lengthening over the whole beam current range is as a synthesis affected by the potential well distortion and the microwave instability.

III. INSTRUMENTATION AND DATA ACQUISITION

Two ways of bunch length measurement have been adopted in the BEPC: streak camera and beam spectrum analysis. With the streak camera, the longitudinal particle distribution is gained by

looking at the light of synchrotron radiation from a bending magnet. The light pulse is picked up by the streak camera with a time resolution of a few picoseconds at the end of the synchrotron radiation beam line. The cable used in the instrument was calibrated before measurements. The overall measurement error of this set of apparatus is less than 20 % [4].

Another way to measure the bunch length in BEPC is the beam spectrum analysis. In this method [5], a technique of measuring bunch length by the comparison of two Fourier components of the beam has been applied to an electron bunch. A monitor for real time measurement of the bunch length has been set up with a stripline electrode of 277 mm in length. Assuming a Gaussian longitudinal distribution of rms bunch length σ_l , the Fourier component of the n -th harmonic is given by

$$V(n\omega_0) = 2V_0 \exp[-n^2\omega_0^2\sigma_l^2/2] \quad (7)$$

Here n is an integer, ω_0 the revolution frequency, $V(n\omega_0)$ the induced voltage on an ideal beam pickup and V_0 the DC component. The rms bunch length is obtained from the ratio between two Fourier components as

$$\sigma_l = \frac{1}{\omega_0} \sqrt{\frac{2}{(n_2^2 - n_1^2)} \cdot \ln \frac{V_1(n_1\omega_0)}{V_2(n_2\omega_0)}} \quad (8)$$

where V_1 and V_2 are Fourier components at n_1 -th and n_2 -th harmonics of the revolution frequency and $n_2 > n_1$. The measurement of bunch length by this way has an accuracy of 10 % relatively with a dynamic range of 25dB - 35dB.

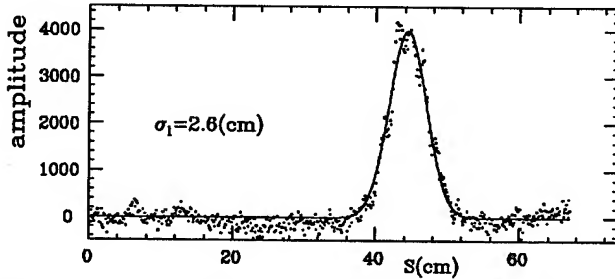


Fig. 1 Longitudinal Distribution at Low Current

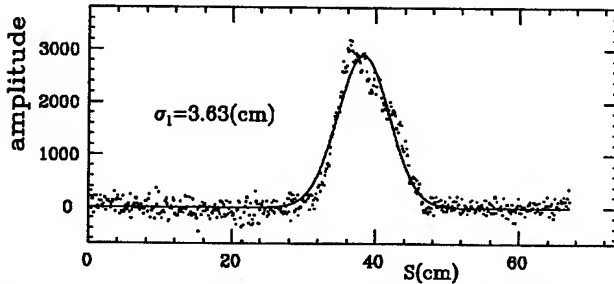


Fig. 2 Longitudinal Distribution at High Current

IV. EXPERIMENTAL RESULTS

A. Data analysis

More than 250 effective experimental points were obtained with various beam energies, RF voltages and beam currents. Fig. 1 and Fig. 2 display the longitudinal distribution of bunches

measured with the streak camera at low and high intensity respectively. Fig. 3 and Fig. 4 show some prototype data of bunch length changing with beam current under different RF voltages. Fig. 5 and Fig. 6 give the variation of the bunch length versus current at different energy and momentum compaction factor. In these figures, one can see that RF voltage determines the bunch length and its lengthening as the beam currents increase. In different energy E and momentum compaction factor α_p , bunch length varies in the same way, i.e., E and α_p do not change the bunch lengthening principle. This is because that the longitudinal tune dependence on the beam current is very weak in the BEPC operation region [6].

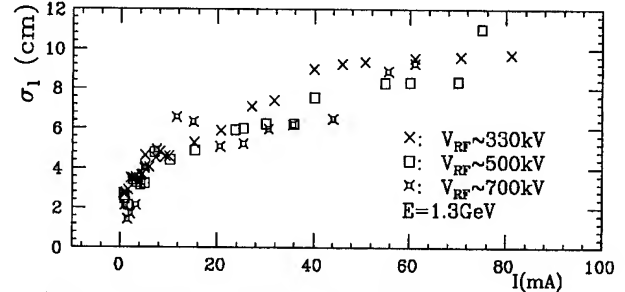


Fig. 3 Bunch Length vs. Beam Current

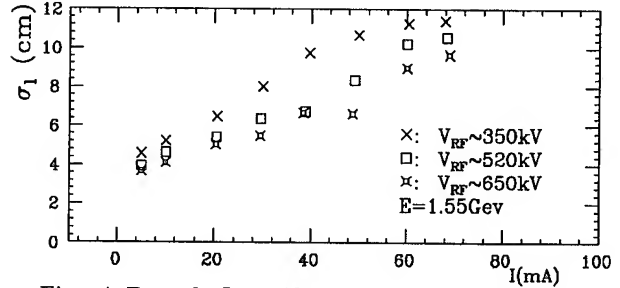


Fig. 4 Bunch Length vs. Beam Current

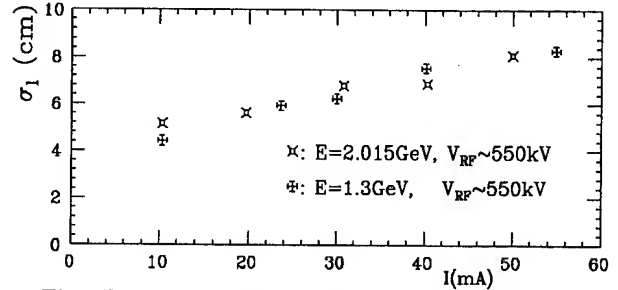


Fig. 5 Bunch Length vs. Beam Current

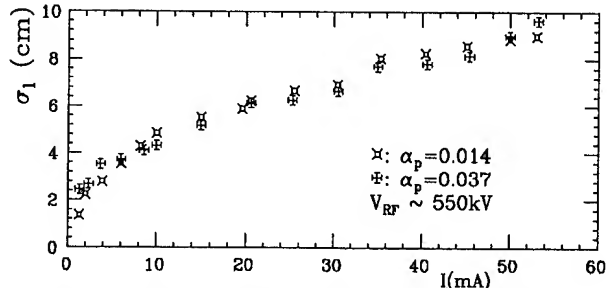


Fig. 6 Bunch Length vs. Beam Current

The variation of energy spread with beam current increase at different RF voltages and different energies are given in Fig. 7.

It seems that the energy spread is almost independent on RF voltage and that the threshold of the microwave instability is around 6 mA at 1.3 GeV and 15 mA at 2.015 GeV.

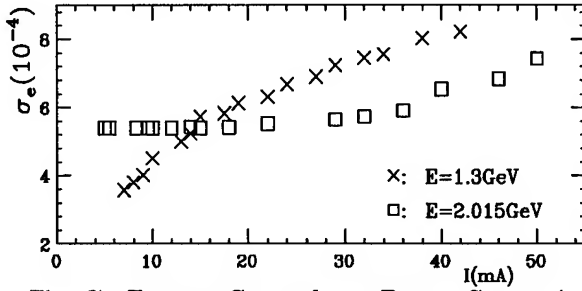


Fig. 7 Energy Spread vs. Beam Current

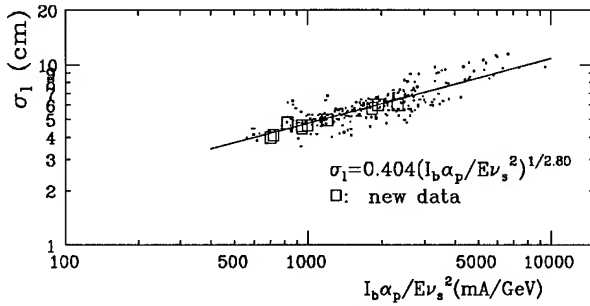


Fig. 8 Bunch Length vs. Scaling Parameter

According to the simulation study, the bunch shape should deviate from Gaussian distribution by the potential well effect. However, it can not be distinguished clearly in our observation. The reason might be this effect is too weak in BEPC and it was covered within the measurement error.

B. The scaling law

When fitting all bunch length data to calculate the scaling parameter ξ and plotting them as σ_l versus ξ in Fig. 8, the frequency dependent factor can be determined as $a=0.80$ for the long bunch. The scaling law of BEPC is given as

$$\sigma_l(\text{cm}) = 0.404 \times \left(\frac{I_b(\text{mA})\alpha_p}{E(\text{GeV})\nu_s^2} \right)^{1/2.80} \quad (9)$$

which looks like agreeable with the theoretical prediction of eq.(3). Some new measurement points measured at higher RF voltage fit the scaling law fairly well. However, the bunch lengths of the recent measurement are somewhat shorter than that predicted by the scaling law. This might be due to removing two extra kickers from the ring for reducing the impedance last summer.

To all measured data, we calculated their rms error as follows:

$$\delta(\text{rms}) = \sqrt{\frac{\sum (\frac{\sigma_c - \sigma_i}{\sigma_c})^2}{N}} \quad (10)$$

Here, σ_c is the value calculated from eq.(10), σ_i the measured value and N the number of measured points. Being compared with the method of beam spectrum, whose rms error is 16.1 %, the

rms error from the streak camera is 12.5 %, and the total rms error is 17.5 %. It stands for the deviation between the measured points and fitting points. The errors include not only systematic and random errors, but also the fluctuation of bunch length due to longitudinal dipole and quadrupole oscillation.

The measurement result shows that the bunch length is 4.0 cm at 2.015 GeV, 35 mA and 2.0 MV of RF voltage. From eq.(10), we also deduce that bunch length is about 4.5 cm at 2.015 GeV, 50 mA and 2.4 MV of RF voltage. The BEPC luminosity upgrades, especially the success of mini- β scheme, are mainly constrained by the bunch length.

C. Threshold current and impedance

Using eq.(10) and equating σ_l to the natural unperturbed bunch length σ_{l0} , current threshold can be predicted as

$$I_{th} = 13.18 \alpha_p^{1.80} E^{3.80} \nu_s^{-0.80} \quad (11)$$

Furthermore, from eq.(10) we can get the value of the impedance driving the potential well distortion and the microwave instability to $|\frac{Z_{||}}{n}|_0 = 3.54 \Omega$. It is in good agreement with the impedance measured with other methods.

V. CONCLUSION

Bunch length and its lengthening are very important, especially for the BEPC luminosity upgrades. From the bunch length measurement, we get a scaling law of BEPC and then estimated the coupling impedance. Different beam energy and α_p do not affect the bunch length. The mechanism of the bunch lengthening in BEPC could be clarified by comparing the measurement results to the analytical calculation in the longitudinal phase space with the improved measurement accuracy.

ACKNOWLEDGEMENTS

The authors gratefully acknowledge all the members of the BEPC operation group and the beam diagnostics group for their collaboration. They would like to thank China Institute of Atomic Energy who provided the streak camera and joined the measurement. They also thank Prof. S. Fang, Dr. J. Wang, Dr. Rossa and Dr. Ieiri for their stimulating discussions.

References

- [1] Q. Qin et al., Proc. of the International Workshop on Particle Dynamics in Accelerator, Tsukuba, Japan, 1994.
- [2] D. Boussard, CERN LABII/RF/Int./75-2, 1975.
- [3] A. W. Chao and J. Gareyte, PEP Note 224, 1976.
- [4] W. Liu, Bunch Length Measurement with a Picosecond Streak Camera in the BEPC, Internal report, 1993.
- [5] T. Ieiri, Proc. of the Workshop on Advanced Beam Instrumentation, 1991.
- [6] Z. Guo et al., Proc. of IEEE PAC93, 1993.

PRACTICAL CRITERION OF TRANSVERSE COUPLED-BUNCH HEAD-TAIL STABILITY

S. Ivanov and M. Pozdeev, IHEP, Protvino, Moscow Region, 142284, Russia

Abstract

Analytical outcome of the paper is a few formulae to simplify practical threshold calculations of transverse coupled-bunch head-tail instability caused by narrow-band impedances in a proton synchrotron, which provide a useful quantitative view on how to keep the instability under control with chromaticity and cubic-nonlinearity correctors of the magnetic field. The formulae include: (i) the envelopes of head-tail mode formfactors expressed via a pair of averages over a bunch longitudinal distribution, and (ii) expressions of the effective betatron tune spread introduced by partial spreads in 2-D function $\omega_y(\mathcal{J}_x, \mathcal{J}_z)$ of transverse action variables in x, z -directions, $y = x, z$. The tolerable values of transverse coupling impedances at parasitic higher-order E_{1np} -modes of the UNK accelerating cavities are estimated as an example of application.

I. INTRODUCTION

Let x, z be horizontal and vertical displacements from the orbit, $\vartheta = \Theta - \omega_0 t$ be azimuth in a co-rotating frame, where Θ is azimuth around the ring in the laboratory frame, ω_0 is the angular velocity of a reference particle, t is time. For definiteness, only x -oscillations are studied, the results being applicable to z -direction by $x \rightarrow z$ and v.v. Introduce a 6-D phase-space of variables $(y, y' \equiv dy/dt)$ with $y = \vartheta, x, z$. Let the unperturbed motion be integrable, x, z -oscillations being assumed uncoupled by the optics and treated in a 'smooth' approximation. Pass from (y, y') to angle-action variables (ψ_y, \mathcal{J}_y) , $y = \vartheta, x, z$ with $\omega_y(\mathcal{J}_y) = d\psi_y/dt$ being frequency of nonlinear oscillations. Let the unperturbed bunch be given by its distribution function $F(\mathcal{J}_\vartheta, \mathcal{J}_x, \mathcal{J}_z)$ normalized to unit.

II. BASIC SET OF EQUATIONS

Beam dipole moment $D_y(\vartheta, t)$ and deflecting Lorentz force $e\bar{S}_y(\vartheta, t)$ averaged over beam transverse distribution are decomposed into $\sum_k D_{y;k}, e\bar{S}_{y;k}(\Omega)e^{ik\vartheta - i\Omega t}$, $y = x, z$ with Ω being the frequency of Fourier transform w.r.t. the co-rotating frame. In the laboratory frame Ω is seen as $\omega = k\omega_0 + \Omega$. Functions $f(\psi_y)$ of cyclic variables ψ_y are decomposed into Fourier series $\sum_{m_y} f_{m_y} e^{im_y \psi_y}$ with m_y being the multipole index of direction $y = \vartheta, x, z$.

According to Maxwell's Eqs., the beam interacts with the vacuum chamber elements and drives horizontal deflecting S -field with

$$\bar{S}_{x;k}(\Omega) = \frac{i\beta\omega_0}{2\pi R_0} \sum_{y=x,z} Z_k^{(xy)}(k\omega_0 + \Omega) D_{y;k}(\Omega) \quad (1)$$

where R_0 is the orbit radius, β is beam reduced velocity, $Z_k^{(xy)}(\omega)$ is the transverse (dipole) coupling impedance. Its

(xy) -matrix nature accounts for the vacuum chamber cross-section anisotropy, if any. It may result in coupling of coherent motions along x, z . Here we study the standard, axisymmetric case $Z_k^{(xy)}(\omega) = Z_k(\omega)\delta_{x,y}$, $y = x, z$.

Consider a beam of average current J_0 in $M \leq h$ identical and equispaced bunches, h is the main RF harmonic number, h/M is an integer. As it follows from the Vlasov's linearized Eq., the transverse BTF is

$$D_{x;k}(\Omega) = \frac{i\pi R_0 \langle \beta_x \rangle e J_0}{2\omega_0 \beta^2 E} \times \sum_{k', l=-\infty}^{\infty} \delta_{k-k', lM} Y_{kk'}^{(x)}(\Omega) \bar{S}_{x;k'}(\Omega) \quad (2)$$

where $\langle \beta_x \rangle \simeq R_0 \omega_0 / \omega_x(0)$ is β -function averaged along the ring, E is the total energy of the beam, $\delta_{kk'}$ is the Kronecker's delta-symbol. The dispersion integrals $Y_{kk'}^{(x)}(\Omega)$ are put down in terms of multipole decomposition series

$$Y_{kk'}^{(x)}(\Omega) = -(i\omega_0/\pi) \sum_{m_x=\pm 1} m_x \sum_{m_\vartheta=-\infty}^{\infty} \times \int \int \int_0^\infty d\mathcal{J}_\vartheta d\mathcal{J}_x d\mathcal{J}_z \frac{\partial F(\mathcal{J}_\vartheta, \mathcal{J}_x, \mathcal{J}_z)}{\partial \mathcal{J}_x} \mathcal{J}_x \times \frac{I_{m_\vartheta, k-m_x \Delta k}(\mathcal{J}_\vartheta) I_{m_\vartheta, k'-m_x \Delta k}^*(\mathcal{J}_\vartheta)}{\Omega - m_\vartheta \omega_\vartheta(\mathcal{J}_\vartheta) - m_x \omega_x(\mathcal{J}_x, \mathcal{J}_z)}. \quad (3)$$

Here $\Delta k = \chi_x/\eta - \omega_x(0)/\omega_0$; $\chi_x \equiv (p_s/\omega_0)(\partial\omega_x(0)/\partial p)$ is chromaticity of the ring; $\eta = \alpha - \gamma^{-2}$, α is orbit compaction factor, γ is relativistic factor; functions $I_{m_\vartheta, k}^*(\mathcal{J}_\vartheta)$ are the coefficients of series which expand a plane wave $e^{ik\vartheta(\mathcal{J}_\vartheta, \psi_\vartheta)}$ into sum over longitudinal multipoles: $\sum_{m_\vartheta} I_{m_\vartheta, k}^*(\mathcal{J}_\vartheta) e^{im_\vartheta \psi_\vartheta}$.

Treated jointly, Eqs.1,2 yield M eigenvalue problems

$$\lambda(\Omega) D_{x;k} = R_x^{-1} \sum_{l'=-\infty}^{\infty} Y_{kk'}^{(x)}(\Omega) Z_{k'}(k'\omega_0 + \Omega) D_{x;k'}, \quad (4)$$

$(k, k') = n + (l, l')M$, $-\infty < l, l' < +\infty$. Each of these stands for one of M normal coupled-bunch modes labeled by, say, $n = 0, 1, \dots, M-1$. R_x has the dimension Ohm/m of a transverse impedance,

$$R_x = -(4\beta E) / (e J_0 \langle \beta_x \rangle) < 0. \quad (5)$$

Generally, the characteristic Eq. of coherent oscillations is

$$1 = \lambda_\ell(\Omega), \quad \ell = (n, \dots), \quad (6)$$

$\lambda_\ell(\Omega)$ being an eigenvalue of Eq.4. On solving this Eq. w.r.t. Ω , one arrives at an eigenfrequency of the ℓ -th coherent mode, the unstable ones having $\text{Im}\Omega > 0$.

III. A SINGLE-MODE APPROACH

To simplify the problem, we make specific the within-bunch mode subindices m_z, m_x, m_ϑ, r that follow the coupled-bunch mode index n in $\ell = (n, \dots)$, and state conditions under which such a mode can exhibit itself solely.

1. Derivation of Eq.3 tacitly implies $m_z = 0$ which is due to the 'smooth' treatment of the uncoupled betatron x, z -oscillations. Herefrom, BTF is diagonal: $Y_{kk'}^{(xy)}(\omega) = Y_{kk'}^{(x)}(\omega)\delta_{x,y}$, $y = x, z$ (i.e., excitation by deflecting force $e\bar{S}_z$ would not drive D_x , etc).

2. Put the working point far from 2-nd order SBRs,

$$2\omega_x(\mathcal{J}_x, \mathcal{J}_z) + (m_\vartheta - m'_\vartheta)\omega_\vartheta(\mathcal{J}_\vartheta) = lM\omega_0, \quad (7)$$

where $l = 0, 1, 2, \dots$ ($\omega_\vartheta \ll \omega_x$); $-\infty < m_\vartheta, m'_\vartheta < +\infty$. Hence, resonant frequencies of the dipole modes $m_\vartheta = \pm 1$ would not overlap, and either can be treated separately. For definiteness, we take the upper sideband $m_x = +1$, the lower one providing no extra information on beam stability unless a SBR, Eq.7 is encountered.

3. Take bunches with a small nonlinearity,

$$|\delta\omega_\vartheta| \ll |\delta\omega_x| < \omega_\vartheta(0) \ll \omega_x(0). \quad (8)$$

Then, at each sideband $\omega \simeq k\omega_0 + \omega_x(0) + m'_\vartheta\omega_\vartheta(0)$ near instability threshold ($\text{Im}\omega \rightarrow +0$) a single resonant term whose $m_\vartheta = m'_\vartheta$ would dominate in the BTF. On dropping the rest, nonresonant items, the so called approximation of uncoupled head-tail modes m_ϑ is arrived at.

4. Assume $F(\mathcal{J}_\vartheta, \mathcal{J}_x, \mathcal{J}_z) = F_\vartheta(\mathcal{J}_\vartheta) \cdot F_{xz}(\mathcal{J}_x, \mathcal{J}_z)$. On applying to Eq.8, ignore the longitudinal tune spread, $\omega_\vartheta(\mathcal{J}_\vartheta) \simeq \omega_\vartheta(0)$. Then, characteristic Eq.6 factorizes to

$$1 = R_x^{-1} Y_x(\Omega) \zeta_r(\Omega) \quad (9)$$

with $Y_x(\Omega)$ denoting a purely transverse dispersion integral

$$Y_x(\Omega) = -(i\omega_0/\pi) \iint_0^\infty d\mathcal{J}_x d\mathcal{J}_z \frac{\partial F_{xz}(\mathcal{J}_x, \mathcal{J}_z)}{\partial \mathcal{J}_x} \mathcal{J}_x \times \\ \times 1 / ((\Omega - m_\vartheta\omega_\vartheta(0)) - \omega_x(\mathcal{J}_x, \mathcal{J}_z)). \quad (10)$$

Effective (instability driving) impedance $\zeta_r(\Omega)$ of mode $\ell = (n, m_z=0, m_x=1, m_\vartheta, r)$ is the r -th eigenvalue of

$$\zeta(\Omega) D_k = \sum_{l'=-\infty}^\infty A_{kk'} Z_{k'}(k'\omega_0 + \Omega) D_{k'}, \quad (11)$$

$$A_{kk'} = \int_0^\infty F_\vartheta(\mathcal{J}_\vartheta) I_{m_\vartheta, k-\Delta k}(\mathcal{J}_\vartheta) I_{m_\vartheta, k'-\Delta k}^*(\mathcal{J}_\vartheta) d\mathcal{J}_\vartheta, \quad (12)$$

$(k, k') = n + (l, l')M$, $-\infty < l, l' < +\infty$.

5. Index r that emerges from this eigenvalue problem specifies the 'radial' (i.e., along direction \mathcal{J}_ϑ in the plane (ϑ, ϑ')) pattern of the head-tail mode m_ϑ . To ensure that only a single 'radial' mode shows itself up, consider a narrow band HOM resonance

$$Z_k(\omega) = \frac{\omega}{\omega_\zeta} R_\zeta \left(1 - i \frac{\omega^2 - \omega_\zeta^2}{2\omega \Delta\omega_\zeta} \right)^{-1} \quad (13)$$

with coupling resistance R_ζ , resonant frequency ω_ζ and bandwidth $\Delta\omega_\zeta$, the latter two complying the restrictions

$$\omega_\zeta \neq lM\omega_0/2, \quad l = 1, 2, \dots; \quad \Delta\omega_\zeta \ll M\omega_0. \quad (14)$$

In this case only one ($k_1 \gtrsim -\omega_x/\omega_0$ or $k_2 \lesssim -\omega_x/\omega_0$) azimuthal harmonic of coupled-bunch mode n would fall inside the HOM bandwidth. Thus, Eq.11 reduces to

$$\zeta_r(\Omega) = A_{kk} Z_k(k\omega_0 + \Omega), \quad r = 1, \quad k = k_{1,2}, \quad (15)$$

the unstable harmonic being k_2 (the slow betatron wave). As $\text{Re}Z_k^{-1}(\omega) \simeq \text{const}$ at $\omega \simeq \pm\omega_\zeta$, the point $R_x/\zeta_1(\Omega)$ which represents HOM's effect at $k_2 = n + Ml$ in the threshold map moves almost parallel to imaginary axis of the complex plane (Y), the distance from the axis being $|R_x|/(A_{k_2 k_2} R_\zeta)$ (it does vary insignificantly due to $A_{k_2 k_2}^{-1}$). Thus, the beam stability is surely guaranteed given

$$|R_x|/(A_{k_2 k_2} R_\zeta) > \Lambda_x \quad (16)$$

where Λ_x is a maximal $\text{Re}Y$ -extension of threshold map,

$$\Lambda_x = \omega_0 \max_{\omega} \int_0^\infty \delta(\omega - \omega_x(\mathcal{J}_x, \mathcal{J}_z)) \times \\ \times (-\partial F_{xz}(\mathcal{J}_x, \mathcal{J}_z)/\partial \mathcal{J}_x) \mathcal{J}_x d\mathcal{J}_x d\mathcal{J}_z. \quad (17)$$

Being a sufficient stability criterion, inequality Eq.16 becomes a necessary one in large rings with $\omega_0 \lesssim \Delta\omega_\zeta$. Up to HOM bandwidth $\Delta\omega_\zeta$ and $\omega_\vartheta \ll \omega_x$, one can insert $k_2 \simeq -(\omega_\zeta + \omega_x)/\omega_0$ into $A_{k_2 k_2}$ to transform it into the longitudinal formfactor,

$$\Lambda_\vartheta^{(m_\vartheta)} = \int_0^\infty F_\vartheta(\mathcal{J}_\vartheta) |I_{m_\vartheta, -k_*}(\mathcal{J}_\vartheta)|^2 d\mathcal{J}_\vartheta \simeq A_{k_2 k_2} \quad (18)$$

where $k_* = \omega_\zeta/\omega_0 + \chi_x/\eta$ and $0 < \Lambda_\vartheta^{(m_\vartheta)} \leq 1$. To account for all head-tail modes available, introduce the envelope

$$\Lambda_\vartheta = \max_{m_\vartheta} (\Lambda_\vartheta^{(m_\vartheta)}) \quad (19)$$

which is a function of the external parameters only: $F_\vartheta(\mathcal{J}_\vartheta)$, ω_ζ/ω_0 , χ_x/η . On adopting the above assumptions, one finally arrives at the stability criterion

$$R_\zeta \leq \frac{|R_x|}{\Lambda_\vartheta \Lambda_x} = \frac{1}{\Lambda_\vartheta \Lambda_x} \times \frac{4\beta E}{eJ_0 \langle \beta_x \rangle} \quad (20)$$

with two bunch formfactors $\Lambda_\vartheta, \Lambda_x$ left to be estimated.

IV. FORMFACTORS

A. Longitudinal Formfactor

According to Eq.8, $|\delta\omega_\vartheta| \ll \omega_\vartheta(0)$ and the law of motion along ϑ is just $\vartheta(\mathcal{J}_\vartheta, \psi_\vartheta) \simeq \sqrt{\mathcal{J}} \cos(\psi_\vartheta + \psi_{\vartheta 0})$. Hence,

$$|I_{m_\vartheta k}(\mathcal{J}_\vartheta)|^2 \simeq J_{m_\vartheta}^2 \left(k \Delta\vartheta_0 \sqrt{\mathcal{J}_\vartheta/\mathcal{J}_{\vartheta 0}} \right) \quad (21)$$

with $J_m(y)$ denoting Bessel functions of the m -th order, $\Delta\vartheta_0 = \Delta\vartheta(\mathcal{J}_{\vartheta 0})$ being longitudinal half-width of the bunch (in

other words, oscillation amplitude along ϑ at a phase-plane trajectory $\mathcal{J}_\vartheta = \mathcal{J}_{\vartheta 0}$. It implies the following reflection properties

$$\Lambda_\vartheta^{(-m_\vartheta)} = \Lambda_\vartheta^{(m_\vartheta)}; \Lambda_\vartheta^{(m_\vartheta)}(-k_* \Delta \vartheta_0) = \Lambda_\vartheta^{(m_\vartheta)}(k_* \Delta \vartheta_0). \quad (22)$$

Globally, formfactor $\Lambda_\vartheta^{(0)}$ of the rigid-bunch head-tail mode $m_\vartheta = 0$ dominates, envelope Λ_ϑ , Eq.19 thus coinciding with $\Lambda_\vartheta^{(0)}$ (except for a small region near $|k_* \Delta \vartheta_0| \simeq 3-5$ where mode $|m_\vartheta| = 1$ may exhibit itself).

Replace $J_m^2(y)$ in Eq.18 by their quadratic small-argument and trigonometric large-argument (with $1/2$ substituted for $\cos^2(\dots)$) asymptotes. On integrating, one obtains with accuracy sufficient for practical purposes,

$$\Lambda_\vartheta \simeq \Lambda_\vartheta^{(0)} \simeq \begin{cases} 1 - \frac{1}{2} \langle \theta^2 \rangle |k_* \Delta \vartheta_0|^2, & |k_* \Delta \vartheta_0| \lesssim 2; \\ \frac{1}{\pi} \langle \theta^{-1} \rangle |k_* \Delta \vartheta_0|^{-1}, & |k_* \Delta \vartheta_0| \gtrsim 3. \end{cases} \quad (23)$$

Here, numerical factors $\langle \theta^2 \rangle \leq 1$ and $\langle \theta^{-1} \rangle \geq 1$ with $\theta = \vartheta / \Delta \vartheta_0$ are, respectively, mean-square and mean-reciprocal reduced half-widths of a bunch,

$$\frac{\langle \theta^2 \rangle}{\langle \theta^{-1} \rangle} = \int_0^\infty \frac{(\mathcal{J}_\vartheta / \mathcal{J}_{\vartheta 0})}{(\mathcal{J}_\vartheta / \mathcal{J}_{\vartheta 0})^{-1/2}} F_\vartheta(\mathcal{J}_\vartheta) d\mathcal{J}_\vartheta. \quad (24)$$

B. Transverse Formfactor

Let us introduce normalized to unit 1-D transverse distributions $F_x(\mathcal{J}_x)$ and $F_z(\mathcal{J}_z)$ where, say, $F_x(\mathcal{J}_x)$ is

$$F_x(\mathcal{J}_x) = \int_0^\infty F_{xz}(\mathcal{J}_x, \mathcal{J}_z) d\mathcal{J}_z. \quad (25)$$

Take into account the cubic nonlinearity of the magnetic field which results in betatron tune spread

$$\omega_x(\mathcal{J}_x, \mathcal{J}_z) \simeq \omega_x(0) + \frac{\partial \omega_x}{\partial \mathcal{J}_x}(0) \mathcal{J}_x + \frac{\partial \omega_x}{\partial \mathcal{J}_z}(0) \mathcal{J}_z, \quad (26)$$

coefficients at \mathcal{J}_x and \mathcal{J}_z being controlled with the octupole correctors.

Formfactor Λ_x is amenable to straightforward calculations in two particular cases. Indeed, for $\partial \omega_x / \partial \mathcal{J}_z = 0$

$$\Lambda_x = \frac{b_{xx}}{|\delta \omega_{xx} / \omega_0|}, \quad \delta \omega_{xx} = \frac{\partial \omega_x}{\partial \mathcal{J}_x}(0) \mathcal{J}_{x0}, \quad (27)$$

$$b_{xx} = \mathcal{J}_{x0} \max_{\mathcal{J}_x \geq 0} (\mathcal{J}_x (-\partial F_x(\mathcal{J}_x) / \partial \mathcal{J}_x)). \quad (28)$$

On the other hand, for $\partial \omega_x / \partial \mathcal{J}_x = 0$ it follows that

$$\Lambda_x = \frac{b_{xz}}{|\delta \omega_{xz} / \omega_0|}, \quad \delta \omega_{xz} = \frac{\partial \omega_x}{\partial \mathcal{J}_z}(0) \mathcal{J}_{z0}, \quad (29)$$

$$b_{xz} = \mathcal{J}_{z0} \max_{\mathcal{J}_z \geq 0} (F_z(\mathcal{J}_z)) = \mathcal{J}_{z0} F_z(0). \quad (30)$$

Here $\mathcal{J}_{x0}, \mathcal{J}_{z0}$ are the action variables at the (effective) edge of the bunch; $\delta \omega_{xx}, \delta \omega_{xz}$ are the partial betatron tune spreads, both having an arbitrary sign.

On inserting Eq.26 into Eq.17, one sees that Λ_x is kept intact by a simultaneous reversal of signs in $\delta \omega_{xx}$ and $\delta \omega_{xz}$. Therefore, taking into account the exact Eqs.27-30 and inflicting no loss to generality, rewrite Λ_x as

$$\Lambda_x = f_x \left(\frac{\delta \omega_{xx}}{\delta \omega_{xz}}; \dots \right) \times \left(\left(\frac{\delta \omega_{xx}}{\omega_0 b_{xx}} \right)^2 + \left(\frac{\delta \omega_{xz}}{\omega_0 b_{xz}} \right)^2 \right)^{-1/2}, \quad (31)$$

$$f_x(\pm\infty; \dots) = f_x(0; \dots) = 1.$$

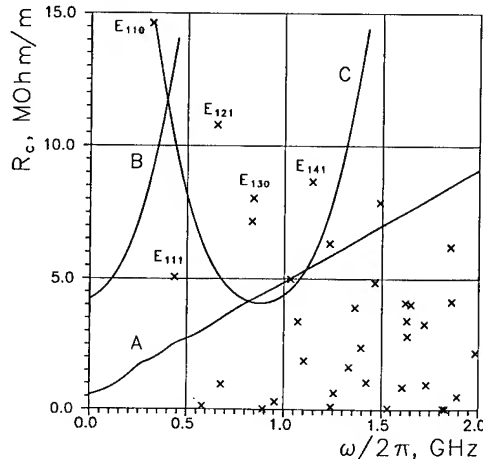
Dots in f_x show its dependence on details of joint distribution $F_{xz}(\mathcal{J}_x, \mathcal{J}_z)$. Fortunately, the calculations show that f_x is rather insensitive to $\delta \omega_{xx} / \delta \omega_{xz}$ for realistic distributions. With a good accuracy Eq.31 can be used with $f_x \simeq 1$, which plainly puts down transverse formfactor as a reciprocal of an effective betatron tune spread,

$$\Lambda_x \simeq \left(\left(\frac{\delta \omega_{xx}}{\omega_0 b_{xx}} \right)^2 + \left(\frac{\delta \omega_{xz}}{\omega_0 b_{xz}} \right)^2 \right)^{-1/2}. \quad (32)$$

Eqs.20, 23, 32 are the sought-for tool for practical estimates of head-tail instability thresholds.

V. EXAMPLE OF APPLICATION

Consider the UNK 1-st Stage which is to be equipped with $N = 8 \times 2 = 16$ conventional copper cavities, their length being $L = 0.5$ m; radius $r_0 = 0.577$ m; surface resistance $\sigma^{-1} = 1.7 \cdot 10^{-8}$ Ohm·m. The figure shows coupling impedances per one cavity for dipole HOMs E_{1np} . Tolerable values of R_c are found with Eqs.20,23,32; $J_0 = 1.4$ A; $\alpha = 4.95 \cdot 10^{-4}$; $\omega_x / \omega_0 = 55.7$; $\delta \omega_{xx} / \omega_0 = \delta \omega_{xz} / \omega_0 = 0.5 \cdot 10^{-2}$; $\langle \beta_x \rangle = 93.5$ m. Curve A: injection at $E = 65$ GeV with $h \Delta \vartheta_0 / \pi = 0.54$ and standard $\chi_x \simeq +3$. Curve B: the same for $\chi_x \simeq +3$ at $E = 600$ GeV, $h \Delta \vartheta_0 / \pi = 0.38$. Curve C: large negative $\chi_x \simeq -30$ as required by a slow extraction scheme.



Evidently, at least nine of the UNK cavity transverse HOMs are to be damped with a dedicated system.

More details on the topic can be found in Ref.[1].

References

- [1] S. Ivanov, M. Pozdeev, IHEP Preprint 94-110, Protvino, 1994 (in Russian).

A Code to Compute the Action-Angle Transformation for a Particle in an Arbitrary Potential Well*

J. Scott Berg and Robert. L. Warnock

Stanford Linear Accelerator Center; Stanford University; Stanford, CA 94309

Abstract

For a Vlasov treatment of longitudinal stability under an arbitrary wake field, with the solution of the Haissinski equation as the unperturbed distribution, it is important to have the action-angle transformation for the distorted potential well in a convenient form. We have written a code that gives the transformation $q, p \rightarrow J, \Phi$, with $q(J, \Phi)$ as a Fourier series in Φ , the Fourier coefficients and the Hamiltonian $H(J)$ being spline functions of J in C^2 (having continuous second derivatives).

I. The Canonical Transformation

We suppose that the Hamiltonian has the form

$$H = \frac{p^2}{2} + V(q), \quad (1)$$

where $V(q)$ is a potential well with continuous derivative. We discuss only values of the constant H such that the motion consists entirely of oscillations between two turning points at which $p = 0$. We denote the turning points by q_0 and q_1 , with $q_0 < q_1$, and exclude values of H for which either $V'(q_0)$ or $V'(q_1)$ is zero. We define

$$p(q, H) = \pm \sqrt{2[H - V(q)]}, \quad (2)$$

where $p > 0$ as q moves from q_0 to q_1 , and $p < 0$ as it returns from q_1 to q_0 . The action integral, which extends over a full period of the motion, is

$$J(H) = \frac{1}{2\pi} \oint p(q, H) dq = \frac{1}{\pi} \int_{q_0}^{q_1} p(q, H) dq. \quad (3)$$

Thanks to our assumption that $V'(q_i) \neq 0$, there is a well-defined inverse function $H(J)$.

Hamilton's equations imply that $p = dq/dt$. If $t = 0$ at $q = q_1$, the time t for displacement q is

$$t = \int_{q_1}^q \frac{dq'}{p(q', H)} \quad (4)$$

where the integration path is understood to follow all oscillations that occur by time t : $q_1 \rightarrow q_0 \rightarrow q_1 \rightarrow \dots \rightarrow q(t)$. Since H depends only on J , Hamilton's equations in action-angle variables give $\Phi = \Phi_0 + H'(J)t$. Choosing $\Phi(q_1) = 0$, we have

$$\Phi(q, H) = H'(J(H)) \int_{q_1}^q \frac{dq'}{p(q', H)} \quad (5)$$

We wish to find the functions $q(J, \Phi)$, $p(J, \Phi)$, and $H(J)$ in a form that will be convenient for repeated and fast numerical

evaluations, with 2π -periodicity in Φ guaranteed. We also want these functions to have continuous second derivatives in both variables. These requirements arise from an intended application in solutions of the Vlasov equation with Fokker-Plank term, as discussed below. A convenient expression of the functions is

$$q(J, \Phi) = \sum_{m=0}^{\infty} q_m(J) \cos m\Phi \quad (6)$$

$$p(J, \Phi) = \frac{\partial q(J, \Phi)}{\partial \Phi} H'(J) \quad (7)$$

with $q_m(J)$ and $H(J)$ expanded in terms of some C^2 basis functions $B_k(J)$ and $C_k(J)$:

$$q_m(J) = \sum_k q_{mk} B_k(J) \quad (8)$$

$$H(J) = \sum_k h_k C_k(J) \quad (9)$$

The formula (7) follows from the derivative of (5) with respect to Φ , if we recall that H is only a function of J when written in action-angle coordinates.

If the series (6), (8), and (9) are truncated at a finite number of terms, the resulting transformation $J, \Phi \rightarrow q, p$ will not be precisely canonical (i.e., symplectic). A measure of symplecticity is the agreement of p as given in (7) with

$$p(J, \Phi) = \pm \sqrt{2[H(J) - V(q(J, \Phi))]} \quad (10)$$

If p is given by (10), a calculation of the Poisson bracket yields

$$[q, p] = \frac{1}{p} \frac{\partial q}{\partial \Phi} \frac{dH}{dJ}. \quad (11)$$

Thus, if p from (7) agrees with p from (10), we have a canonical transformation, since $[q, p] = 1$. With a moderate number of terms in the series (6), (8), and (9), the transformation can be made to satisfy the canonical condition with sufficient precision for our purposes.

II. The Primary Integrations

We first evaluate the integrals (3) and (5) on a regular mesh in H : $\{H_i | i = 1, \dots, K\}$. The turning points $q_0(H_i)$ and $q_1(H_i)$ are easily found by a Newton iteration. The factor $H'(J(H_i))$ is defined at each i by

$$\pi = H'(J(H_i)) \int_{q_1}^{q_0} \frac{dq}{p(q, H_i)}. \quad (12)$$

For numerical integration, it is useful to change the variable to

$$u = \cos^{-1} \frac{q_1 + q_0 - 2q}{q_0 - q_1}. \quad (13)$$

*Work supported by the Department Energy, contract DE-AC03-76SF00515.

The inverse of this transformation is

$$q = \frac{q_0 + q_1}{2} + \frac{q_1 - q_0}{2} \cos u. \quad (14)$$

Then (5) becomes

$$\Phi(q, H_i) = \frac{q_1 - q_0}{2} H'(J(H_i)) \int_0^{u(q)} \frac{\sin u' du'}{\sqrt{2[H_i - V(q(u'))]}}. \quad (15)$$

The integrand is now free of singularities. For a nearly quadratic potential, Φ is close to u . The same change of variable is used to compute $J(H_i)$ by (3).

Now $u = \pi$ corresponds to $q = q_0$. We divide the interval $[0, \pi]$ into N intervals, and integrate by Simpson's rule [1]. The first and last intervals are treated by an open Newton-Cotes formula [1], to avoid taking the limit of the integrand at the end-points. We evaluate the integrand (15) for upper limit u at all of the mesh points u_i . The value of N is increased until the integral on $[0, \pi]$ converges to machine precision.

III. Finding the Fourier Coefficients

After the integrations, the angles $\Phi^{(j)} = \Phi(q(u_j), H_i)$ are known, with the u_j on a large regular mesh of $N + 1$ points. To evaluate the Fourier coefficients q_m for $|m| \leq M$, we search through the $\Phi^{(j)}$ to find those that are closest to the points one would normally use in a discrete Fourier transform, namely the points

$$\frac{\pi k}{M}, \quad k = 0, \dots, M. \quad (16)$$

Denoting those angles by Φ_k , and the corresponding values of $q(u_j)$ by $q^{(k)}$, we solve the following linear equations for the Fourier coefficients:

$$q^{(k)} = \sum_{m=0}^M q_m \cos m \Phi_k, \quad k = 0, \dots, M \quad (17)$$

We solve this system as follows: if we assume that the function $q(\phi)$ can be expressed exactly as

$$q(\phi) = \sum_{m=0}^M q_m \cos m \phi, \quad (18)$$

then we can write $q(\Phi_k)$ in terms of the values $x_k = q(\pi k/M)$ as

$$\begin{aligned} q(\Phi_k) = & \frac{1}{2M} \left\{ x_0 \cot \frac{\Phi_k}{2} \sin M \Phi_k \right. \\ & + x_M \cot \frac{\Phi_k - \pi}{2} \sin M(\Phi_k - \pi) \\ & \left. + \sum_{n=1}^{M-1} x_n \frac{\sin \Phi_k}{\sin(\Phi_k + \pi k/M)} \frac{\sin M(\Phi_k - \pi k/M)}{\sin[(\Phi_k - \pi k/M)/2]} \right\} \end{aligned} \quad (19)$$

This linear system can then be solved for the x_k , the function values at the mesh points. The discrete Fourier transform of the x_k then gives the coefficients q_m . The advantage of this is that the system (19) is very well conditioned if the Φ_k are close to the mesh points (16); this is why we chose the mesh points Φ_k as described above.

The system (17) can also be solved as a Vandermonde system. There are $O(n^2)$ direct methods for solving such a system which should work very well [2].

IV. Expressing the Transformation as a Function of J

Let $q_m^{(i)}$ and $J^{(i)}$ denote the values of q_m and J at $H = H_i$, as determined by the procedure just described. To get the required functions of J , we invoke the expansions (8) and (9), and determine the coefficients by solving the linear systems

$$q_m^{(i)} = \sum_k q_{mk} B_k(J^{(i)}) \quad (20)$$

$$H^{(i)} = \sum_k h_k C_k(J^{(i)}), \quad (21)$$

where $i = 1, \dots, K$. A possible improvement is to use the values of $H'(J^{(i)})$ as determined in (12) for an additional constraint on the function $H(J)$. One would then use a larger set of basis functions C_k , and augment (21) with the additional equations

$$H'(J^{(i)}) = \sum_k h_k C'_k(J^{(i)}), \quad i = 1, \dots, K \quad (22)$$

This step should make the whole scheme more self-consistent, and could be quite worthwhile.

V. Example

We have written a code which finds the transformation described for an arbitrary differentiable potential V . It computes the transformation from $J = 0$ (which is found by finding the minimum of the potential) up through the J corresponding to a given value of H . The basis functions B_j and C_j are both taken to be B-Splines [3] in \sqrt{J} , whose knots t_i are chosen to be

$$t_0 = \dots = t_{k-1} = 0 \quad (23)$$

$$t_{i+k} = \frac{1}{k-1} \sum_{j=i+1}^{i+k-1} \sqrt{J^{(j)}} \quad i = 0, \dots, n-k-1 \quad (24)$$

$$t_n = \dots = t_{n+k-1} = \sqrt{J^{(n-1)}} \quad (25)$$

as described on pp. 218-9 of [3]. The code computes q_m for $m \leq M$ for a given integer M . We do not use the data for $H'(J^{(i)})$ as described above.

We take as an example the potential $V(q) = 1 - \cos q$. We know the transformation for this potential:

$$J = \frac{8}{\pi} \left[\frac{H}{2} K\left(\frac{H}{2}\right) - K\left(\frac{H}{2}\right) + E\left(\frac{H}{2}\right) \right] \quad (26)$$

$$\Phi = \begin{cases} \frac{\pi}{2} \left\{ 1 - \frac{F(\sin^{-1}[\sqrt{H/2} \sin q/2] | H/2)}{K(H/2)} \right\} & p < 0 \\ \frac{\pi}{2} \left\{ \frac{F(\sin^{-1}[\sqrt{H/2} \sin q/2] | H/2)}{K(H/2)} - 1 \right\} & p > 0. \end{cases} \quad (27)$$

Here F and K are elliptic integrals [4].

We will check the accuracy of our transformation by computing q and H on a uniform mesh in J of $10K$ points and a uniform mesh in Φ of $10M$ points (excluding $\Phi = 0$ and $\Phi = \pi$). First, we compute $H(J)$ at each J mesh point, then substitute that value in Eq. (26) and compare to the original J . We give the maximum value of $\Delta J = |J(H(J_i)) - J_i|/J_i$ in table I. Next, we take $H(J_i)$ and $q(J_i, \Phi_j)$ on the grid described and compute Φ using Eq. (27) for each of these values. These results are then compared to the original Φ . We record the maximum value

M	K	ΔJ	$\Delta \Phi$	ϵ_S
4	8	2×10^{-5}	8×10^{-4}	4×10^{-3}
4	16	6×10^{-7}	8×10^{-4}	3×10^{-3}
4	32	2×10^{-8}	8×10^{-4}	3×10^{-3}
4	64	8×10^{-10}	8×10^{-4}	3×10^{-3}
4	128	2×10^{-11}	8×10^{-4}	3×10^{-3}
8	8	2×10^{-5}	8×10^{-4}	2×10^{-2}
8	16	6×10^{-7}	4×10^{-5}	9×10^{-4}
8	32	2×10^{-8}	2×10^{-6}	3×10^{-5}
8	64	8×10^{-10}	8×10^{-7}	7×10^{-6}
8	128	2×10^{-11}	8×10^{-7}	7×10^{-6}
16	8	2×10^{-5}	2×10^{-3}	1×10^{-1}
16	16	6×10^{-7}	2×10^{-5}	1×10^{-3}
16	32	2×10^{-8}	5×10^{-7}	2×10^{-5}
16	64	8×10^{-10}	9×10^{-9}	5×10^{-7}
16	128	2×10^{-11}	5×10^{-10}	8×10^{-9}

Table I

Accuracy of the transformation. Quartic B-splines are used throughout. Maximum value of H is 1.

of $\Delta \Phi = |\Phi(H(J_i), q(J_i, \Phi_j)) - \Phi_j|$ in the second column of table I. Finally, we check the symplecticity of the resulting transformation by computing

$$\epsilon_S = \left| \frac{\frac{\partial q}{\partial \Phi} \frac{dH}{dJ}}{\sqrt{2[H - V(q)]}} - 1 \right| \quad (28)$$

for values where neither the square root nor $\partial q / \partial \Phi$ is zero. The maximum value of this is recorded in the third column of table I.

VI. Conclusion

We have described a method for determining a transformation of a one-dimensional system described by a Hamiltonian of the form (1) to action-angle variables. A computer program to implement this method has been written, and gives satisfactory results regarding convergence.

We note that this method can be applied even to a $V(q)$ which is only given at a finite number of points q_i . We simply define $V(q)$ to be a function which passes through these values. Any interpolation method may be used to define such a $V(q)$.

This work was motivated by the desire to give a more thorough treatment of the Vlasov equation for longitudinal instabilities, along the lines followed by Oide and Yokoya [5]. These authors linearize the Vlasov equation about the stationary distribution derived from the Haïssinski equation, and then use the action-angle variables J, Φ of the "distorted potential well" implied by that distribution. The perturbed distribution function $\Psi_1(J, \Phi)$ is represented as a Fourier series in Φ with the coefficients being step functions in J . The step function technique has some deficiencies. It gives at best slow convergence as the steps are refined, and makes it difficult to treat the Fokker-Planck term, $-2\delta(\partial/\partial p)(p\Psi_1 + \partial\Psi_1/\partial p)$. We think that it would be better to use a C^2 spline basis for the J dependence of Ψ_1 . Then the Fokker-Planck term can be han-

dled easily with the help of our Fourier series (6) for q , since $\partial/\partial p = -(\partial q/\partial J)(\partial/\partial \Phi) + (\partial q/\partial \Phi)(\partial/\partial J)$. Oide's rough treatment of the Fokker-Planck term by a perturbative method suggests that it is very important in determining thresholds of instabilities.

References

- [1] F. B. Hildebrand, *Introduction to Numerical Analysis*. New York: McGraw-Hill, 1956.
- [2] G. H. Golub and C. F. Van Loan, *Matrix Computations*. Baltimore: Johns Hopkins University Press, 1989.
- [3] C. de Boor, *A Practical Guide to Splines*. New York: Springer-Verlag, 1978.
- [4] M. Abramowitz and I. A. Stegun, eds., *Handbook of Mathematical Functions*. New York: Dover Publications, 1972.
- [5] K. Oide and K. Yokoya, "Longitudinal single-bunch instability in electron storage rings," Tech. Rep. KEK Preprint 90-10, KEK, April 1990.

STUDY OF LONGITUDINAL COUPLED-BUNCH INSTABILITIES IN THE SRRC STORAGE RING

W. K. Lau, M. H. Wang, K. T. Hsu, L. H. Chang, Ch. Wang, C. C. Kuo,
Synchrotron Radiation Research Center, No.1, R & D Road VI, Hsinchu, Taiwan, R. O. C.

Longitudinal coupled-bunch instabilities in the SRRC 1.3 GeV storage ring have been studied by analyzing the signals picked up from the stripline electrodes and rf power reflected from the cavities. The current dependence of the instability strengths was measured. As a cross check, the bunch phase jitters as a function of beam current has also been measured by using sampling optical oscilloscope. Threshold currents of a few milliamperes have been determined from both measurements. They agree with each other very well. It is also found that the strength of the instabilities can be reduced significantly by randomly distributing electron bunches around the ring.

I. INTRODUCTION

In a storage ring, longitudinal coupled-bunch instabilities of an electron beam are driven by the interaction of the beam with its environment, especially with the high Q components in the ring. They are the main obstacles in achieving high beam intensity with low emittance. In a synchrotron radiation facility, the poor emittance due to the instabilities will deteriorate the quality of light emission from undulators. In this study, we report the observations of the instabilities in the SRRC 1.3 GeV storage ring. A list of relevant parameters in this study is in Table 1.

Table 1. Parameters of the SRRC 1.3 GeV storage ring.

E	Beam Energy	1.3 GeV
I_b	Nominal Beam Current	200 mA
α	Momentum Compaction Factor	0.00678
f_{rf}	RF Frequency	499.668 MHz
f_0	Revolution Frequency	2.49834 MHz
h	Harmonic Number	200
R_s	Shunt Impedance (two cavities)	6 M Ω
V_c	Cavity Gap Voltage	800 kV
σ_τ	FWHM Bunch Length	58 psec
f_s	Synchrotron Freq. @800 kV	28.73 kHz
τ	Longitudinal Damping Time	8.708 msec

Observation was done in the frequency domain by analyzing beam signals picked up from the stripline electrodes. The stripline was installed in one of the straight sections where the beam dispersion is low. The instabilities are characterized by the synchrotron sidebands near the harmonics of revolution frequency (unequal bunch lines). Some modes were found significantly stronger than the others. Current

dependence of these modes was measured. From such measurement, threshold beam current and the saturated amplitude of the instability can be determined. Excitation of high order modes can be monitored from the cavity reverse powers. For a coherent longitudinal beam motion, electron bunches jitter about synchronous phase. By using a sampling optical oscilloscope triggered at revolution frequency, bunch phase jitters can be measured from the synchrotron light emitted by the electron bunches. The bunch phase jitters as a function of beam current was also measured. There exists a threshold above which the bunch phase jitters increase with beam current. The threshold currents obtained from both measurements agree with each other.

A simple method has been tried to reduce the strengths of the longitudinal coupled-bunch instabilities by distributing electron bunches randomly around the ring such that the bunch spacings are not fixed. In such scheme, the symmetry of bunch spacing does not hold and thereby reduce the strength of the beam coherent motions that are excited by cavities high order modes. In a preliminary experiment, the strengths of the instabilities were reduced significantly.

II. LINE SPECTRUM OF LONGITUDINAL COUPLED-BUNCH INSTABILITIES

A. Identification of The Beam Modes

Each line in the spectrum represents a specific mode of coherent beam motions. The signal spectrum consists of lines with frequencies

$$f_{\mu,m}^{\pm} = nf_{rf} \pm (\mu f_0 + mf_s)$$

that represent longitudinal coupled-bunch modes. Where f_{rf} is the rf frequency, f_0 the revolution frequency and f_s the synchrotron oscillation frequency; $n=0,1,2,\dots,\infty$; μ and m are the coupled-bunch mode and the within bunch mode numbers respectively.

A 740 MHz signal was observed from the reverse power of one cavity. This frequency coincides with the resonant frequency of TM₀₁₁-like cavity mode. Beam modes close to this frequency were ~20 dB larger than the others. It is believed that these modes have been excited by the TM₀₁₁-like mode. At 700 kV gap voltage, a typical spectrum picked up from the stripline is shown in Fig.1

In the figure, the measured central peak frequency

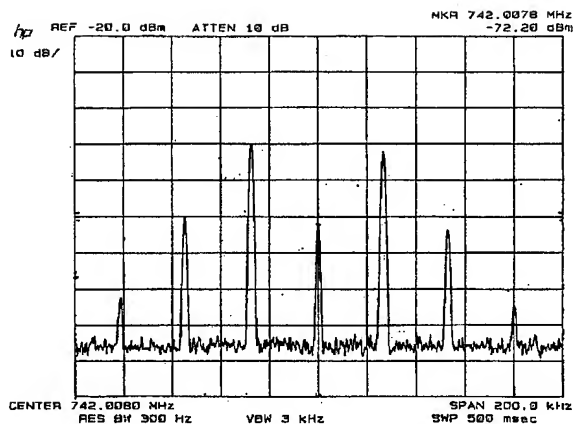


Figure 1: Synchrotron sidebands near the 97th harmonics of the revolution frequency.

is exactly the 97th harmonics of revolution frequency. It has sidebands at 27.5 kHz separations. The first synchrotron sidebands of the central peak correspond to the coupled-bunch dipole mode with mode number $\mu=97$ (right hand side) and $\mu=103$ (left hand side). The second harmonics of synchrotron frequency correspond to the quadruple modes. And the third harmonics of synchrotron sidebands correspond to the sextuple modes. Since the dipole modes are ~ 20 dB larger than the quadruple modes, we expect the bunches will mainly execute coherent rigid bunch synchrotron oscillations as observed by streak camera in an independent study [1].

B. Instability strengths and Threshold Current

Current dependence of the $\mu=97$ dipole mode was measured at 700 kV gap voltage. The amplitudes of the mode with respect to the strengths of the rf carrier at the same current, I_s/I_{rf} , are plotted in Figure 2.

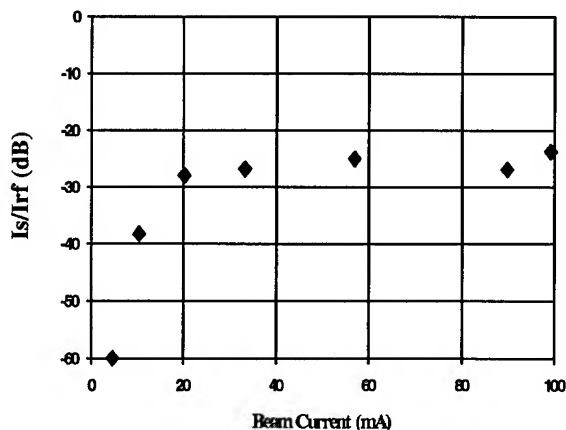


Fig.2 Relative amplitude of the $\mu=97$ longitudinal coupled-bunch mode versus beam current.

At beam current lower than the 4 mA threshold, no oscillations are observed. Above 4 mA, the

instability built up rapidly and saturated beyond 30 mA. The saturated amplitude was 25 dB lower than the rf carrier. It is equivalent to a phase modulation to the rf carrier of about 6° . It is believed that the instability was stabilized by the Landau damping. However, the overall effect of all longitudinal coupled-bunch modes is equivalent to $\sim 12^\circ$ phase modulation to the rf carrier.

C. Random Bunch Distribution

A simple method has been proposed to reduce the longitudinal coupled-bunch instabilities by filling the bunches into buckets and leaving the gap between bunches arbitrarily. In a first test, sixty out of two hundred buckets were chosen by a random number generator and each of these buckets was filled at ~ 0.3 mA by single bunch injection. At 18 mA, the measured amplitude of the $\mu=97$ dipole mode was ~ 15 dB lower than the previous observation at the same current. Unfortunately, further studies are limited by the slow injection process. In further studies, multibunch injection will be employed and individual bunches can be knock out randomly by using an impulse kicker. Since the randomness of the bunch distributions depends on the harmonic number and the maximum current depends on number of bunches in the ring and the threshold current of single bunch instabilities.

III. AMPLITUDES OF BUNCH PHASE OSCILLATIONS

Bunch phase jitters can be measured from a synchrotron light monitor which is installed for the measurement of beam size in the middle of a long straight section. In such setup, a HAMAMATSU OOS-01/VIS sampling optical oscilloscope triggered at revolution frequency has been used. Time structure of the electron beam can also be studied.

A. Current Dependence of Bunch Phase Oscillations

The experiment were performed under following conditions. A beam current of 200 mA was accumulated with $\sim 20\%$ gap. The bunch current was kept below the microwave instabilities threshold such that bunch length would not be affected. During the measurements, beam current was varied by inserting the scraper into the chamber gradually and pulled it all the way out during data collections. The current dependence of the bunch phase jitters are depicted in Figure 3. At high beam current of about 180 mA, the averaged FWHM bunch phase jitters was about 240 picosecond. Amplitude of the jitters decreases as the beam current decreases until the beam current drops to about 6 mA. As the current went below 6 mA, the jitters stayed constant at ~ 80 picoseconds.

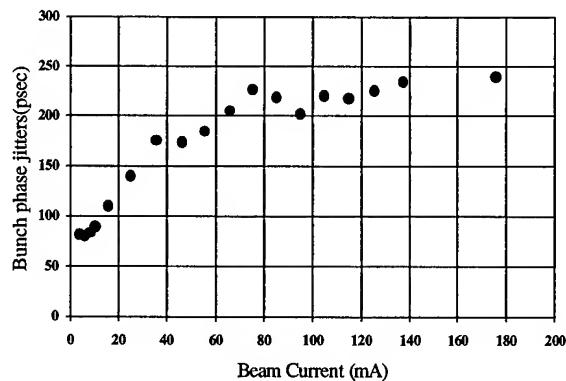


Figure3: Measured bunch phase jitters versus beam current.

B. Systematic Error

Since the measured value (we called it bunch phase jitters for simplicity) is the square root sum of "real" bunch phase jitters, natural bunch length and the systematic error. In order to determine the threshold current for the phase jitters, systematic error of the setup should be calibrated. Calibration can be done by measuring the bunch length as a function of synchrotron frequency at low beam current. Synchrotron frequency can be controlled by changing the cavity gap voltage (Figure 4). An offset of about 50 picoseconds were found by comparing the measured values with the theoretical values at 1 mA.

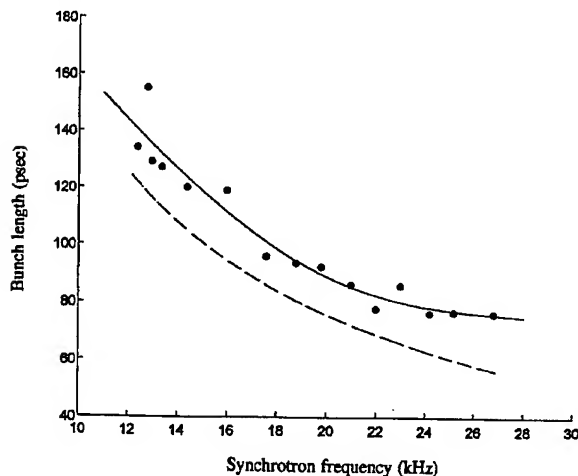


Figure 4: Measured bunch length (dots) versus synchrotron oscillation frequency at 1 mA beam current. Solid line represents the fitted curve from the measured data. Theoretical curve (dashed line) is drawn to compare with the measurements.

It shows that the system has an error of 50 picoseconds contribute to the measured values. Therefore, by subtracting systematic error and assuming no bunch

phase jitters, the values at very low current in the bunch phase measurements are ~60 picoseconds. They are consistent with the theoretical bunch length. This result justified the assumption of no bunch phase jitters at beam currents lower than 6 mA. We concluded that the threshold determined in this measurement is 6 mA. It agrees very well with the previous frequency domain measurement.

IV. SUMMARY AND DISCUSSIONS

In summary, observations on longitudinal coupled-bunch instabilities have been performed. The current dependent characteristics of certain modes were measured. The threshold currents of the instabilities are rather low. The instabilities can be excited by electron beam of a few milliamperes and saturated at about few tens of milliamperes. The sole effect of these instabilities is equivalent to ~12° phase modulation to the rf carrier at 200 mA. As observed in the spectrum, dipole modes dominate over quadruple modes by ~20 dB. Excitations of dipole modes in the SRR storage ring have been predicted by Juinn-Ming Wang [2]. The bunch phase jitters was measured by sampling optical oscilloscope. At 200 mA beam current, bunch phase jitters can be as high as 240 picoseconds. Threshold current measured in such experiment was 6 mA. It agrees with the frequency domain measurement.

A simple way to reduce the amplitudes of the instabilities by random bunch distribution was tested. A reduction of ~15 dB have been observed at 18 mA in compare with the ordinary bunch distribution. The effectiveness and the usefulness of this approach have to be justified in further studies. The feasibilities of implementing longitudinal feedback to damp the bunch phase oscillations[3] and frequency control of high order modes by changing cavity temperature to avoid the excitations of the instabilities [4] are under study also.

V. REFERENCES

- [1] M.H. Wang et al., "The Observation of Longitudinal Coupled Bunch Motion on Streak Camera at SRR" (these proceedings).
- [2] Juinn-Ming Wang, "Symmetrical Coupled-Bunch Modes in SRR Storage Ring", SRR Internal report, SRR/BD/92-01, January 1992.
- [3] J. D. Fox et al., "Feedback Control of Coupled-Bunch Instabilities" Proceedings of the 1993 Particle Accelerator Conference, pp.1432-1435.
- [4] E. Karantzoulis et al., "Observation of Instabilities in the ELETTRA Storage Ring", Proceedings of the Fourth European Particle Accelerator Conference, June 1994.

SUPPRESSION OF THE TRANSVERSE OSCILLATION IN THE SRRC STORAGE RING BY RF KNOCKOUT METHOD

J. C. Lee, M. H. Wang, K. T. Hsu, R. J. Sheu, G. Lin, and C. S. Hsue *
Synchrotron Radiation Research Center

Abstract

Transverse oscillations are observed in the SRRC storage ring as the empty filling gap or the chromaticity is not big enough. The source of transverse oscillations are mostly coming from ions. From experimental evidence the beam quality will be improved as transverse oscillation is suppressed. The RF knockout method is employed to cure the transverse oscillations by shaking at the frequency of betatron sideband. The details of the shaking and the improvement on beam quality are discussed as RF knockout method is applied.

I. INTRODUCTION

The SRRC storage ring is dedicated for synchrotron radiation from 1.3GeV electrons. It is routinely operated at 200mA for the users. The vacuum pressure of this routine operation condition is around 2 ntorr. Since the commissioning of storage ring, transverse oscillation of the electron beam has been observed. The behavior of this oscillation is coherent. Figure 1 shows the spontaneous peaks in spectrum analyzer for both transverse planes. It is clear the first harmonics (dipole mode) of the vertical is much stronger than the others and in most cases only this peak shows up. It is also found frequency of the first harmonics for both transverse planes coincide with or is very close to the betatron tune respectively. Synchrotron satellite peaks also show up in the spectrum.

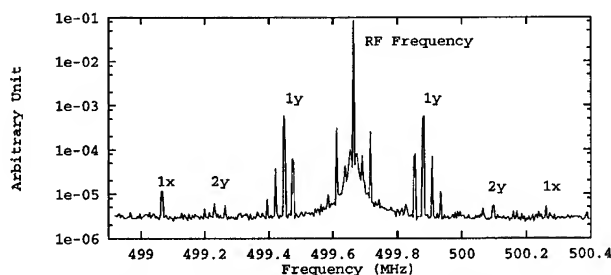


Figure 1. Transverse oscillation spectrum

After a series study the transverse oscillation is found to be cured by leaving a big enough empty gap or by applying strong enough chromaticity. The vacuum pressure is also found to be a critical parameter for this oscillation. The spontaneous peak can be generated by the high vacuum pressure, 10 ntorr locally will produce vertical peak and higher vacuum pressure will in addition excite horizontal peak. During the commissioning of 1.8 tesla wiggler at February this year, a new chamber was installed in the wiggler section and the local pressure is increased up to 100 ntorr with current of 20mA. Drastic transverse oscillation was found in this high vacuum. It is gradually reduced as the

vacuum is continuously cleaned by synchrotron radiation. This indicates the transverse oscillation is mostly generated by ions and some of its effect has been studied^[1]. At present the beam is stored with a big enough empty gap and strong enough chromaticity is also applied to minimize and to damp the transverse oscillation. While stronger chromaticity means larger nonlinear field on the beam, which will reduce the dynamic aperture and lifetime. If the chromaticity increased from zero to +3, the reduction of lifetime is around three hours. This fact motivates the cleaning study for ions by RF knockout method.

In this paper we approach the study from experimental point of view. The betatron sideband frequency is chosen for the shaking frequency. The effectiveness of the shaking is discussed. Improvements of the beam quality are also shown in lifetime, beam size and in the suppression of transverse oscillation.

II. THE EXPERIMENTAL SETUP

As ions are trapped, the electron beam and the ions interact with each other and two beam instability appears^[2,3]. The transverse oscillation is excited by ion kick and the beam performance is then deteriorated^[4,5,6,7]. As ion oscillation amplitude is shaken to larger and goes out of trapping, its effect on the beam will be reduced and minimized. This is the spirit of ion shaking.

In this paper, details of the ion cleaning study by RF knockout method are described. The shaking field is applied from Anritsu MG 3601A signal generator to the excitation electrode. Response signal from the electron beam is obtained from stripline and analyzed by HP8568B spectrum analyzer. HP 34401 DVM converts the spectrum analyzer signal to a PC station. IEEE-488 cable is used for the connection between experimental devices. The shaking and the data acquiring process are program controlled in the PC station. Figure 2 shows the setup for this experiment.

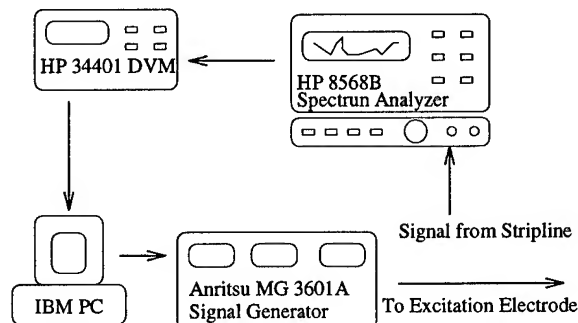


Figure 2. Experimental setup for the shaking and data acquisition system

*Permanent address: Dept. of Phys., National Tsing Hua Univ.

III. THE EXPERIMENTAL RESULTS

Theoretically ions can be driven to resonance by shaking its oscillation frequency directly. It is also possible to shake ions by shaking the betatron sideband of the electron beam^[8,9] indirectly. The shaking frequency, controlled by PC station, can be swept in a desired range with chosen step. Since vertical dipole mode is the most harmful and obvious one of the instability, this peak was picked up in the spectrum analyzer with zero span to observe the shaking effectiveness as the shaking frequency is swept through.

Since single charged hydrogen molecule ion contributes about 93% in the residual gas and could play an important role in ion effect^[1], hydrogen oscillation frequency of around 34MHz at 200mA was applied at the beginning. While no effective improvement was found. The shaking effectiveness is then checked by sweeping from 0.1 to 36MHz with step size of 500 or 700Hz. It is found some of the betatron sideband frequency can suppress the vertical dipole mode. The effective range for the horizontal is from 6 to 20MHz and is not obvious for the rest frequency. The behavior in vertical is much strange. Enhancement of the spontaneous peak has been observed with the application of vertical betatron sideband frequency from 0.1 to 7MHz. As the sweeping frequency goes up, the suppression ability shows up gradually. In the range of 7 to 13MHz the vertical sideband enhances the spontaneous peak first and then suppresses it. For the frequency of 13 to 36MHz, suppression on the spontaneous peaks is obvious.

To check more detail on shaking effectiveness, the beam response signal is input into HP89440A spectrum analyzer instead of HP8568B with a wide enough span to take all of the horizontal and vertical spontaneous peaks. Since the HP89440A has the spectrogram function, it can record the time information of the spectrum during shaking. There is a clear suppression on all of the spontaneous peaks as the effective betatron sideband applied, which indicates the effectiveness of shaking. Since effective frequency is always located at betatron sideband in the horizontal or the vertical in some range, it indicates the effective shaking is shaking beam process indirectly.

The next step is to investigate the detail behavior of the spontaneous peak as effective sideband frequency is applied. The frequency step of the shaking is down to below 50Hz in this case, usually 14Hz frequency step is used. The shaking results for one of the horizontal betatron sideband is shown in figure 3 in which the vertical dipole mode spectrum is suppressed as the frequency of around 11.9MHz is applied. The effective bandwidth for this frequency is around 2KHz.

Suppression ability for the vertical betatron sideband are also shown in figure 4 as the frequency applied around 32.69 and 32.26MHz, which are the fast and slow wave of one high harmonic of the revolution frequency. From what shown in figure 4, the effective bandwidth of around 4KHz is wider than the horizontal. However there is a small range of 1.5KHz within which the vertical dipole mode is not fully suppressed. The feature of the vertical dipole mode not fully suppressed is more obvious for the slow wave. This indicates the shaking ability of fast wave vertical betatron sideband is more effective than the slow one, which can be also found in other literatures^[9,10,11]. The effective shaking pattern for the fast and slow wave seems hav-

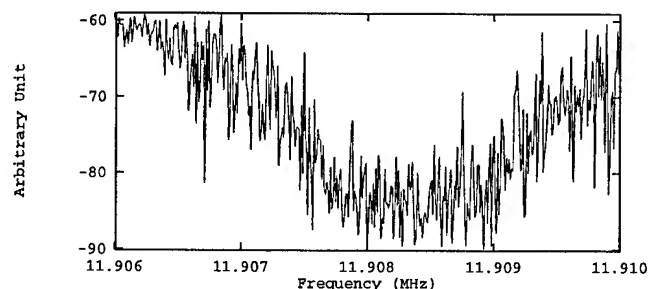


Figure 3. Suppression of vertical dipole mode by horizontal betatron sideband frequency.

ing mirror symmetry w.r.t. one high harmonic of the revolution frequency. Since the effective bandwidth for both transverse betatron sideband is larger than 2KHz, the previous searching of effective frequency from 0.1 to 36MHz with the step of 500 or 700Hz should not lost any information.

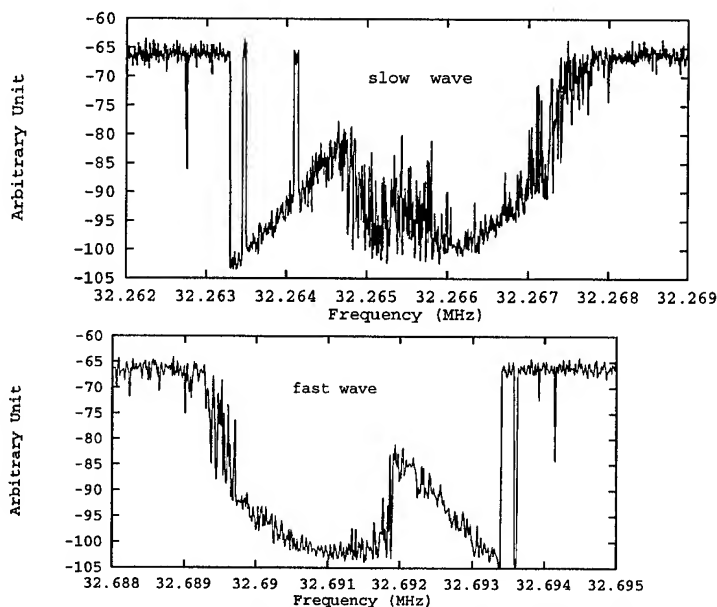


Figure 4. Suppression of vertical dipole mode by vertical betatron sideband frequency

As the effective frequency was found out, the improvement on the beam is also investigated. The suppression on the transverse oscillation indicates the minimalization of ion effect on the beam. The improvement reveals in the increasing of beam lifetime, the reduction of beam size (emittance) and the stabilization of photon beam etc. The lifetime of the SRRC storage ring is dominated by Touschek effect. As transverse oscillation happens, the beam size dilutes, which results to a bigger lifetime. The lifetime can be larger than 25 hours at the zero chromaticity in this deteriorated performance. At present user run, strong chromaticity was applied to damp transverse oscillation. The beam size is around one thirds of the diluted one, which increases the Touschek scattering process within bunches and reduces the lifetime. As effective betatron sideband was applied to suppress the transverse oscillation, the reduction of the beam size is also found. While there could have an increasing of beam lifetime instead of reduction. The lifetime increase-ment is around 2 hours, which proves the benefit of this method.

When the shaking is applied as the machine operated at strong chromaticity, i.e the transverse oscillation has been damped, the improvement on lifetime is not obvious. Figure 5 shows the image of the synchrotron light from one of the photon beamline, which can be traced back to get the beam size information at the source point. It is clear the photon beam size is diluted as the transverse oscillation occurs and the improvement is also found if strong chromaticity or effective shaking frequency applied.

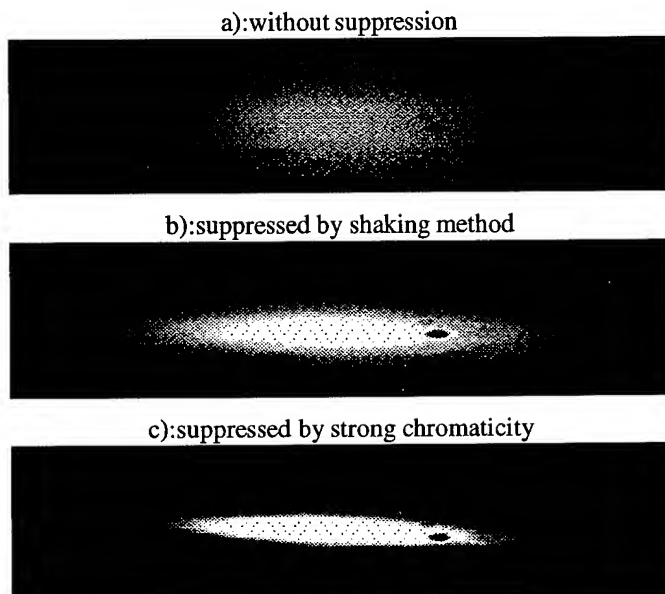


Figure 5. Photon beam size with and without suppression with abscissa the horizontal size and ordinate the vertical size in arbitrary unit

Though the shaking method can suppress transverse instability from ions and increases the lifetime instead of decreasing, it also has difficulty during application, i.e the lock on of resonance frequency. As ions are shaken to larger amplitude its resonance frequency is decreasing^[9,10,11,12] which makes the shaking frequency out of lock. In this case the transverse instability comes in again.

IV. CONCLUSION

The transverse oscillation caused by the ions deteriorate the beam performance in many aspects. At least three spontaneous peaks were found among which the vertical dipole mode is the most harmful and obvious one of this instability. The SRRC storage ring is now operated with a big enough empty gap and with a strong chromaticity to damp the oscillation. While a reduction of the lifetime is found as strong chromaticity is applied. The RF knockout method is also possible to clean the trapped ions from electron beam and to suppress the transverse oscillation as effective horizontal or vertical betatron sideband frequency applied. The effective range was searched from 0.1 to 36MHz and it was found has obvious effect from 6 to 20MHz for the horizontal. Vertical effective range is from 13 to 36MHz. The effective bandwidth for the horizontal is around 2KHz and it is wider for the vertical. However there is a 1.5KHz range for the vertical, within which the vertical dipole mode is not fully suppressed. It is also found the vertical fast wave sideband is more effective than the slow one. The beam lifetime could be

increased for around 2 hours and the beam size (emittance) is reduced as the proper frequency applied. The pulsation of the beam size is basically canceled and the photon beam of the synchrotron radiation is stabilized. If the shaking frequency is out of lock, the instability could appear again. From the experimental results the RF knockout shaking beam method basically can cure the instability coming from ions. While lock on of the shaking frequency with the ion resonance becomes a critical issue in practical application.

References

- [1] J. C. Lee et al., Proc. of the fourth Europe Part. Accel. Conf., London, P1159, 1994.
- [2] E. Keil and B. Zotter, CERN-ISR-TH/71-58, 1971.
- [3] Y. Baconnier and G. Brianti, CERN/SPS/80-2 (DI), 1980.
- [4] P. Zhou et al., Proc. of the 1993 IEEE Part. Accel. Conf., p3303.
- [5] M. E. Biagini et al., 11th Int. Conf. on High Energy Accel., Geneva, p687, 1980.
- [6] H. Kobayakawa et al., Nucl. Instr. and Meth. A248, p565, 1986.
- [7] Pedro F. Tavers, Part. Accel., V43, p107, 1993.
- [8] R. Alves-Pires and R. Dilao, IST-DF-6/91.
- [9] E. Bozoki and D. Sagan, Nucl. Instr. and Meth. A340, p259, 1994.
- [10] A. Poncet, CERN/MT/90-1 (ES), 1990.
- [11] J. Marriner and A. Poncet, Fermi National Lab. \bar{P} Note 481, 1989.
- [12] T. Kasuga, Jpn. J. Appl. Phys. 25, p1711, 1986.

THE OBSERVATION OF THE LONGITUDINAL COUPLED BUNCH MOTION ON STREAK CAMERA AT SRRC

M. H. Wang, K. T. Hsu, W. K. Lau, C.S. Hsue, H. J. Tsai, H. P. Chang, J. C. Lee and C. C. Kuo

Synchrotron Radiation Research Center
Hsinchu Science-Based Industrial Park, Hsinchu, Taiwan, R.O.C.

Abstract

A Hamamatsu C5680 streak camera was set up to observe the beam motion at one of the synchrotron light ports at SRRC. The single bunch, two bunches and a few bunches longitudinal beam motion were observed by the streak camera. The longitudinal dipole mode motion was seen in some cases. The oscillation amplitude was measured and compared with the signal from stripline on spectrum analyzer. The experimental observation was also compared with theoretical predictions.

I. EXPERIMENTAL SETUP

The experimental setup is shown in fig.1. Synchrotron light from one of the bending magnet is guided by optical elements into the streak camera through the pin hole or slit at the head of streak camera. The main body of the Hamamatsu C5680 streak camera is mainly composed of one photocathode, 2 pairs of sweeping electrodes, one in vertical and another one in horizontal, MCP(micro channel plate) streak tube, phosphor screen and a high sensitive camera. The synchrotron light is first converted into electron by the photocathode. The electron is deflected when passing through the electrodes and then is multiplied by the MCP streak tube. The MCP gain can be controlled according to the experimental needs. Finally the electrons hit on the phosphor screen after streak tube and are converted into light again. By using the CCD, the image, usually called the streak image, can be displayed on a TV monitor. By measuring the time structure of the synchrotron light the longitudinal information of the beam can be derived.

There are optional plug-ins for the sweeping voltage of the vertical electrode. At SRRC we use two kind of plug-ins for the vertical electrode sweeping voltage. One is M5676 fast single

sweep unit with maximum sweep repetition rate 10 kHz and vertical range from 200 ps to 50 ns. The sweeping voltage used for this unit is linear. Another plug-in used is M5675 synchroscan unit with 125 MHz sinusoidal sweeping voltage. Considering the linearity of the sweeping voltage of M5675 only a limited vertical time scale up to 1.4 ns is used. By applying a M5679 Dual Time Base Extender unit to the horizontal sweep electrode the display of the image can be extended in the horizontal direction to make a two dimensional time display of streak image. This makes the single shot measurement of the beam possible. The maximum repetition rate of the unit is 10 Hz and the horizontal sweep range is from 100 ns to 100 ms. Because of the different time scale of the two dimensional display the vertical axis is called fast axis and the horizontal slow axis, respectively.

The signal from the master clock (500 MHz) is used as the source of the trigger signal to the streak camera. For synchroscan operation mode the signal from the master clock is put into a prescaler unit to divide the frequency down to 125 MHz. At every sweep of the sinusoidal wave there will be 4 bunches. But as mentioned above considering the linearity of the sweeping only the bunches located at the approximately linear region will be displayed. Hence in the synchroscan operation mode only the streak image of two bunches displayed on the monitor and the two bunches are not successive bunches but first and third or second and fourth bunches. A 2 ns delay is used to select which pair of bunches to observe. For fast single sweep the signal from the master clock need to be divided by two hundred to match the revolution frequency of 2.5 MHz. The revolution frequency is put into a C4547-01 trigger unit to generate a trigger and a pretrigger signal. These two signals are then put into fast single sweep unit for streak trigger and gate mode trigger. The gate mode operation will filter out unwanted noise and enhance the measurements. In single bunch experiment a delay unit is needed to delay the trigger signal to coincide with the single bunch event.

The streak image can be displayed on a TV monitor. A frame grabber board is used to acquire the image data and an image data processing software is implemented on a power Macintosh to analyze the data. Through the GPIB the power MAC can also be used to control the operation of the streak camera instead of using a local controller.

II. THE EXPERIMENTAL RESULTS

A. Synchroscan Operation

Because of the high repetition rate of the sweeping voltage, the synchroscan operation mode can be used to observe the bunch motion in successive turn. By choosing the horizontal sweeping time longer than the period of synchrotron motion,

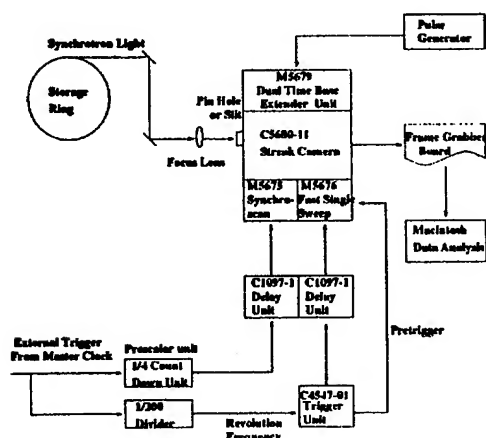


Figure 1. The set up of streak camera system

one can observe the longitudinal coupled bunch motion on the streak camera. At SRRC the period of synchrotron motion is 37 μ s at RF gap voltage of 700 kV. Different bunch patterns such as single bunch, two symmetric bunches, two equal bunches with different spacing, three equal successive bunches and three unequal successive bunches were observed. The bunch pattern was shown on a Tektronic 602 digitizing signal analyzer by putting the signal of stripline electrodes to the analyzer. The spectrum of synchrotron sideband was measured by spectrum analyzer and was compared with the results on streak camera. The time domain longitudinal bunch motion was observed on the streak camera. The results are shown in fig.2, 3 and 4. The full scale of the slow (horizontal) axis is 500 μ s except in fig.4 which is 50 μ s. The full scale of the fast axis is 1.4 ns. In fig.2 we see no obvious longitudinal beam oscillation for single bunch at current of 12 mA. For two successive bunch each with current of 3 mA, again no obvious longitudinal oscillation was observed. The same results were obtained for two equal bunch with different spacing, 4 ns, 6 ns, 8 ns, 10 ns, 100 ns and 200 ns (symmetric bunches). The longitudinal bunch motion of three equal successive bunches are shown in fig.3. Here a very small fourth bunch is shown. The bunches performed longitudinal periodic motion as is shown in the figure. The period of the motion is around 37 μ s which is consistent with the frequency of the first synchrotron sideband as measured from the spectrum analyzer. The longitudinal dipole mode motion was observed on the streak camera. The oscillation amplitudes of the bunches were first <second <third \leq fourth. The total current of the bunches was 8mA. Fig.4 shows the motion of three unequal successive bunches. It shows clear sign of dipole mode oscillation of the beam. One can even observe the periodic changing of bunch length in twice the frequency of dipole mode motion. This is believed to be the quadrupole mode motion. The observation on streak camera was consistent with the results showed on the spectrum analyzer where the second synchrotron sideband showed. The oscillation amplitude went smaller when beam current was smaller. This tendency showed both on streak camera and spectrum analyzer.

B. Fast Single Sweep

The fast single sweep unit can be used to measure the single shot bunch population and bunch length. Due to the repetition rate of this unit, it can't be used to observe the turn by turn motion. Further works on the investigation of the longitudinal beam instability by using this unit are in progressing. Here we show in fig.5 the results of single bunch length versus RF gap voltage with current around 2 mA. It is compared with the natural bunch length at the same gap voltage. The measured bunch length is consistent with the calculation except at gap voltage 150 kV. The streak image get at this mode is shown in fig.6. The vertical axis of the figure is 1 ns, the horizontal is 1 ms and the rate of the vertical sweeping is 10 kHz.

III. DISCUSSION

The longitudinal beam instability was also investigated at SRRC¹ by using the spectrum analyzer. The frequency for the longitudinal symmetric coupled bunch motion is²:

$$f_{s,\mu}^{\pm} = nBf_{rev} \pm Sf_{rev} \pm \mu f_s \quad (1)$$

Where $S=0,1,\dots,B-1$, B is the number of bunches, $(2\pi/B)S$ is the phase difference of adjacent bunches and μ is the coupled bunch mode number. For longitudinal dipole mode μ equals to 1. From the observation the beam mode with frequency close to the resonant frequency of TM_{011} —higher order cavity mode was found. The resonant frequency of this mode is around 743 MHz, which close to mode of $n=1$, $B=200$, $S=97$ for 200 bunches, or $n=148$, $B=2$, $S=1$ for two symmetric bunches. The longitudinal beam instability of symmetrical coupled bunch of SRRC had been calculated². The contribution of the growth time of the TM_{011} mode in the worst case with 0.2 mA per bunch is 0.4 ms. Comparing with the synchrotron damping time 8.7 ms, it can cause beam instability. So an attempt was made to characterize on streak camera the effect of TM_{011} and other high Q mode by using a single bunch and two symmetric bunches operation. As showing in fig.2 there is no obvious oscillation for single bunch. The same result is shown for two symmetric bunches. We had tried to change the spectrum of the bunch population by changing the spacing of the two bunches. But still no obvious beam oscillation was seen at that time. An interesting phenomena is shown in fig.3. The oscillation amplitudes of the bunches are different and increasing one by one. The possible reason is that the motion is caused by a short wake field. The leading bunch can't see the wake field due to the latter bunch since the field already decays when leading bunch arrives. The wake field will effect only several near bunches and will add up. So the latter bunch sees the larger wake field thus operates bigger oscillation.

References

- [1] W. K. Lau, M. H. Wang, K. T. Hsu, L. H. Chang, C. H. Wang, and C. C. Kuo, "Study of the Longitudinal Coupled Bunch Instabilities in the SRRC Storage Ring", these proceedings.
- [2] Jiunn Ming Wang, "Symmetrical Coupled Bunch Modes in SRRC Storage Ring", SRRC/BD/92-01.

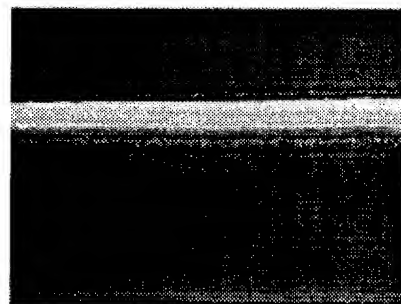


Figure 2. The streak image of single bunch. The full vertical scale is 1.4 ns and is 500 μ s for the horizontal.

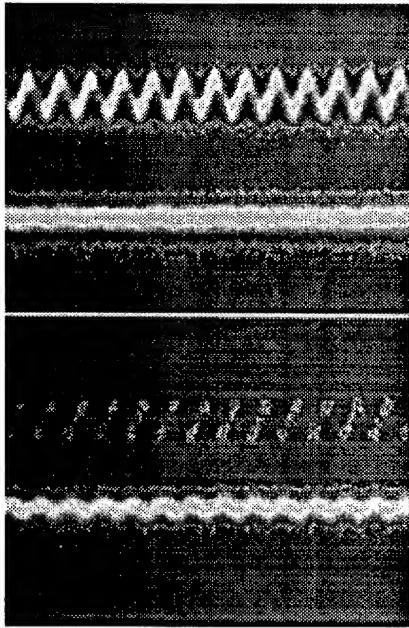


Figure 3. The streak image of four successive bunches. The bunch sequence from top to bottom is third, first, fourth and second. The vertical scale is 1.4 ns and is 500 μ s for the horizontal.

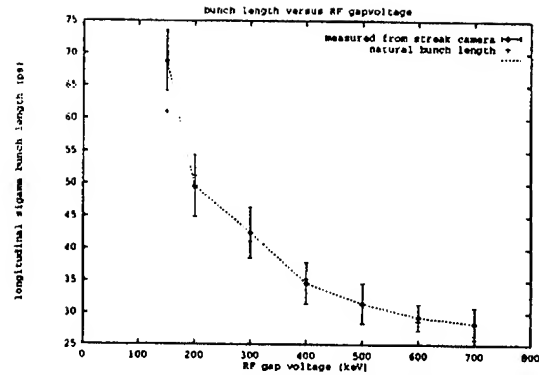


Figure 5. The single bunch length versus RF gap voltage.

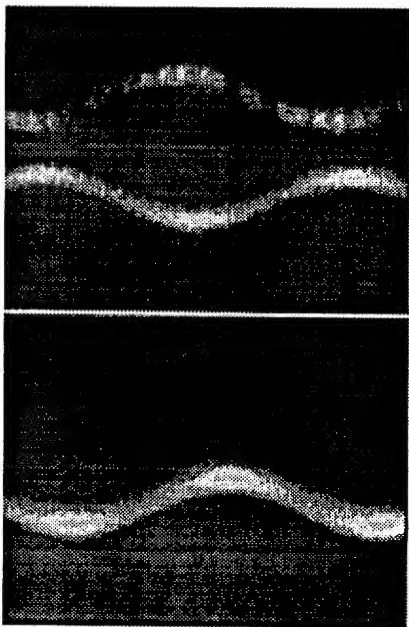


Figure 4. The streak image of three successive unequal bunches. The bunch sequence from top to bottom is third, first and second. The vertical scale is 1.4 ns and is 50 μ s for the horizontal.

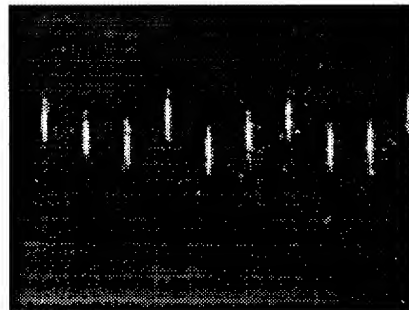


Figure 6. The streak image of single bunch on fast single sweep mode. The vertical scale is 1 ns and the is 1 ms for the horizontal.

RESISTIVE-WALL INSTABILITY EXPERIMENT IN SPACE-CHARGE DOMINATED ELECTRON BEAMS*

H. Suk, J.G. Wang, and M. Reiser

Institute for Plasma Research, University of Maryland
College Park, MD 20742, USA

Abstract

The resistive-wall instability of charged particle beams has been experimentally studied in space-charge dominated electron beams. The beam energy is in the range of 3 to 8.5 keV, the beam current is between 25 mA and 62 mA. In the experiment, electron beams produced from a thermionic cathode are passed through a 0.96 m long glass tube coated with a resistive material, and localized space-charge waves are launched in the beams. The first preliminary experiment clearly shows the growth of slow space-charge waves and the decay of fast space-charge waves. More systematic measurements and analysis of the growth(decay) rate are in progress.

I. INTRODUCTION

Charged particle beams with high brightness and low energy spread have many important applications such as high-current linear accelerators, free electron lasers, heavy-ion fusion drivers, etc. Such high quality beams should be accelerated and transported without serious beam quality deterioration due to instabilities and other effects. One potential problem is the resistive-wall instability which causes an increase of the longitudinal beam energy spread. The increase of the longitudinal energy spread, in turn, may lead to transverse emittance growth due to coupling between the longitudinal and transverse forces acting on the particles.

Historically, the resistive-wall instability was first studied by Birdsall *et al.*^{[1],[2]} Their main interest was in the generation of microwaves. Later, Neil and Sessler^[3] studied the effect of the longitudinal instability on the relativistic beams in circulator accelerators. More recently, theoretical and simulation works for the longitudinal instability were done in connection with heavy-ion fusion induction linacs.^{[4]–[9]} However, a direct experimental verification for the growth and decay rates of short perturbations has not been reported so far. Recently we have started a series of experiments to investigate the resistive-wall instability by launching localized space-charge waves in beams. The first experiments show very clearly the growth of slow space-charge waves and the decay of fast space-charge waves.

In the following sections of this paper, these experiments on the resistive-wall instability are discussed.

II. EXPERIMENTAL SETUP

Figure 1 shows the experimental setup for the resistive-wall instability studies. As shown in the figure, the experimental system consists of the electron beam injector, the resistive-wall

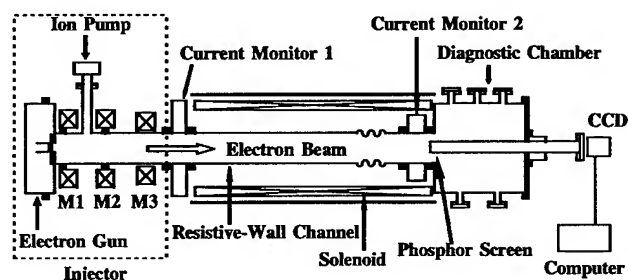


Figure 1. Experimental setup.

channel, and the diagnostic chamber. The electron beam injector includes the variable-perveance gridded electron gun and the three matching lenses. The resistive-wall channel is a glass tube of which the inner surface is coated with SnO_2 . The length of the resistive part is 0.96 m, the total resistance is 5.4 k Ω , and the inner tube radius is 1.9 cm. The beams from the electron gun are accelerated by high voltage (3–8.5 keV), and then matched with the aid of the three solenoid lenses into the resistive transport channel. The beams inside of the resistive transport channel are uniformly focused by a long solenoid surrounding the glass tube. The magnetic field of the solenoid is in the range of 46 to 66 G. The beam current signals at the entrance and exit of the channel are measured with two wall-current monitors which are 1.48 m apart from each other. The diagnostic chamber is placed at the end of the channel. An one-inch diameter phosphor screen in the diagnostic chamber can be alternatively inserted into the resistive transport channel for fluorescent beam image formation. The beam images from the phosphor screen are captured by the CCD (Charge Coupled Device) camera through a window and transferred to a computer for analysis. For studies of the resistive-wall effect on fast space-charge waves, beams with energies in the range of 6 to 8.5 keV and currents in the range of 56 to 60 mA are used. The generalized beam perveance, $K = (I/I_0)(2/\beta_0^3\gamma_0^3)$, is calculated to be between 1.1×10^{-3} and 2.0×10^{-3} , with $I_0 = 1.7 \times 10^4 \text{ A}$ and β_0, γ_0 the usual relativistic velocity and energy factors. For instability studies of slow space-charge waves, beams with energies of 3 to 5 keV and currents of 25 to 62 mA are used. In this case, the generalized beam perveance is about 2.9×10^{-3} .

*This work was supported by the U.S. Department of Energy

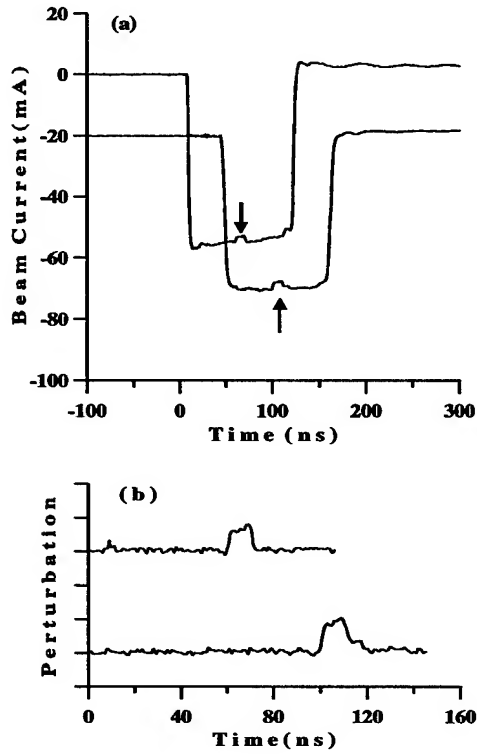


Figure 2. (a) Typical current profiles with a slow space-charge wave in the middle of the beam pulse. (b) Zoom-in view of the perturbation part of the beam pulses. The square-shaped slow wave with a width of about 10 ns is shown to grow. The vertical scale is 2.5 mA/div.

The beam pulses produced with a rectangular grid voltage pulse have a typical width of about 110 ns. In order to launch localized space-charge waves, small square-shaped current perturbations with a width of about 10 ns are generated in the middle of these beam pulses. In the beam frame, the current perturbation can propagate in forward direction as a fast wave or it can propagate in backward direction as a slow wave.^[10] Generations of fast and slow waves depend on electron gun conditions such as anode-cathode distance, cathode temperature, cathode-anode voltage, etc.^[11] In some intermediate conditions, the perturbation can exist as a mixture of fast and slow waves. In our resistive-wall instability experiments, such mixed waves are avoided to obtain separate measurements of the behavior of individual fast and slow waves.

III. RESULTS OF MEASUREMENTS

A typical current profile with a slow space-charge wave is shown in Figure 2(a). The small square-shaped perturbation in the middle of the beam pulse, indicated by the arrow in the figure, moves in the backward direction in the beam frame. Figure 2(b) shows the net perturbation signal produced by subtracting the beam pulse with the perturbation from the beam pulse without the perturbation. It is evident that the amplitude of the perturbation grows as it propagates in the beam.

Numerical calculations of the growth for slow space-charge waves were done for comparison with the experimental results.

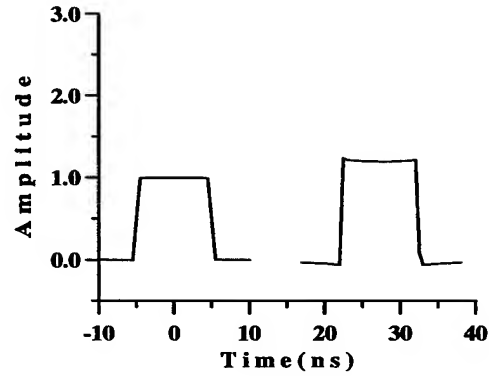


Figure 3. Numerical result of the growth of a square-shaped perturbation. The perturbation is a slow wave in the beam with an energy of 4 keV and a current of 48 mA.

The calculation is based on the linear resistive-wall instability theory in the long-wavelength limit.^[12] In our experiment, the space-charge impedance is not much greater than the wall resistance of the transport channel. In this case, the growth rate is a function of frequency. The square-shaped perturbation in the beam contains a broad range of frequencies so that many frequency components of the perturbation should be taken into account. Figure 3 shows a numerical calculation result for a perturbation in the beam. In the figure, the left signal is an initial perturbation at the location of the first current monitor, and the right signal is a numerically calculated output at the location of the second current monitor. As shown in the figure, the amplitude of the perturbation increases and the perturbation is a little deformed due to the dispersion. In the calculation, the capacitive effect of the transport channel is not included, and a beam with an energy of 4 keV and a current of 48 mA is used.

The experimental result for the growth rate of the slow space-charge waves is shown in Figure 4. The round data points are from the experiment and the cross points are from numerical calculation. The triangular points are the spatial growth rates from the conventional long-wavelength limit formula^[12]

$$k_i = 2\pi \frac{R_w^*}{Z_0} \left(\frac{I}{I_0} \frac{1}{g\beta_0\gamma_0} \right)^{1/2}, \quad (1)$$

where R_w^* is a wall-resistance per unit length, Z_0 a characteristic impedance of free space, I the beam current, I_0 the characteristic current, g the geometry factor. The formula is valid if the space-charge impedance dominates over the wall impedance. As shown

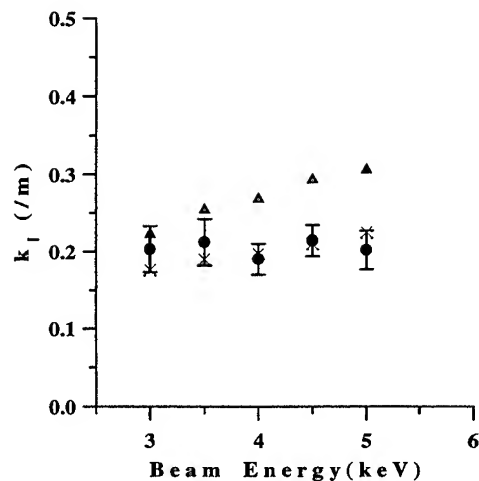


Figure 4. Spatial growth rate of slow space-charge waves. The round data points are from the experiment, cross points are from numerical calculation, and the triangular points are from Eq. (1).

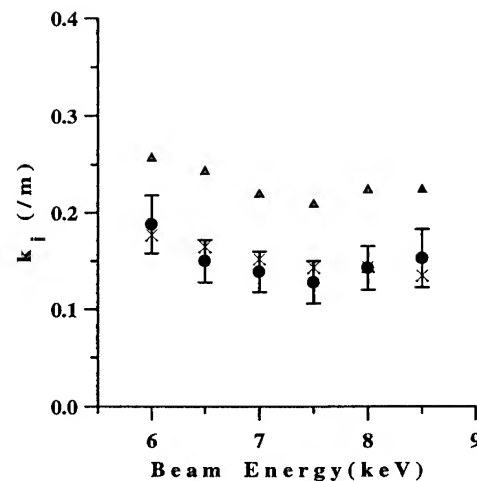


Figure 5. Spatial growth rate of fast space-charge waves. The round data points are from the experiment, cross points are from numerical result, and the triangular points are from Eq. (1).

in the figure, the experimental amplitude growth of the perturbation agrees with the numerical result.

In the experiment of fast space-charge waves, various beam energies between 6 keV and 8.5 keV are used. The experimental results of the spatial decay rates are shown in Figure 5 (round data points). The cross points are from numerical calculations and the triangular points are from Eq. (1). As shown in the figure, the experimental data agrees with the numerical result. For analysis of localized space-charge waves in a resistive transport channel, it is necessary to take into account of wide range of frequencies in the localized perturbations.

IV. SUMMARY

Localized slow space-charge waves are clearly observed to grow as they propagate in a transport channel with wall-resistivity. The measured amplitude growth of the square-shaped perturbations is significantly smaller than that of the long wavelength limit formula which applies to sinusoidal perturbations. Similarly the decay of localized fast space-charge waves are observed, and the measured amplitude decay is smaller than the formula for sinusoidal perturbations.

As pointed out in the introduction, the instability will cause beam quality deterioration. For better understanding and experimental verification of beam quality deterioration, further experiments and analysis are needed. Our next experiments for time-resolved beam energy spread and emittance measurements will provide more information about the resistive-wall instability.

References

- [1] C. K. Birdsall, G. R. Brewer, and A. V. Haeff, Proc. of I.R.E. **41**, July 1953.
- [2] C. K. Birdsall and J. Whinnery, J. Appl. Phys. **24**, 314(1953).
- [3] V. K. Neil and A. M. Sessler, Rev. Sci. Instr. **36**, 429(1965).
- [4] S. Humphries, Jr., J. Appl. Phys. **51**, p. 2338, May 1980.
- [5] E. Lee, Proc. of the 1981 Linear Accelerator Conference, Santa Fe, NM, October 19-23, 1981, pp. 263-265.
- [6] J. Bisognano, I. Haber, L. Smith, and A. Sternlieb, IEEE Trans. on Nuclear Science, Vol. NS-28, No. 3, pp. 2513-2515, June 1981.
- [7] J. G. Wang and M. Reiser, Phys. Fluids B5, 2286(1993).
- [8] E. Lee, Nouvo Cimento **106A**, 1679(1993).
- [9] D. A. Callahan, A. B. Langdon, A. Friedman, and I. Haber, in the Proceedings of the 1993 Particle Accelerator Conference, Vol. 1, p. 730, Washington D.C., May 17-20, 1993.
- [10] J. G. Wang and M. Reiser, in this proceedings.
- [11] J. G. Wang, D. X. Wang, and M. Reiser, Phys. Rev. Lett. **71**, 1836(1993).
- [12] M. Reiser, *Theory and Design of Charged Particle Beams*(Wiley, New York, 1994), Sec. 6.3.2.

Mode-Coupling Instability and Bunch Lengthening in Proton Machines

K.Y. Ng

Fermi National Accelerator Laboratory,* P.O. Box 500, Batavia, IL 60510

Abstract

In proton machines, potential-well distortion leads to small amount of bunch lengthening with minimal head-tail asymmetry. Longitudinal mode-mixing instability occurs at higher azimuthal modes. When the driving resonance is of broad-band, the threshold corresponds to Keil-Schnell criterion for microwave instability. [1] When the driving resonance is narrower than the bunch spectrum, the threshold corresponds to a similar criterion derived before. [2]

I. Introduction

Proton bunches are very much different from electron bunches. First, electron bunches have a length roughly equal to the radius of the beam pipe, whereas proton bunches are usually very much longer. Second, the momentum spread of the electron bunches is determined by the heavy synchrotron radiation. Protons do not radiate and behave quite differently in the longitudinal phase space, with the bunch area conserved instead. These differences lead to different results in potential-well distortion and mode mixing, which we will discuss briefly below. The details are given in a separate paper. [3]

II. Potential-Well Distortion

As an example, the bunches in the Fermilab Main Ring have a typical full length of ~ 60 cm or $\tau_L \approx 2$ ns. The spectrum has a half width of ~ 0.5 GHz. Therefore, the static bunch profile is hardly affected by the resistive part of the broad-band impedance which is centered at $1.5 \sim 2$ GHz. As a result, the inductive part of the broad-band will only lead to a symmetric broadening (shortening) of the bunch above (below) transition. Numerically solving the Haissinski equation [4] confirms this conjecture. Strictly speaking, the Haissinski equation does not apply to proton bunches where the bunch area is conserved and the momentum spread is not a fixed Gaussian.

Since the driving impedance is inductive, the wake potential is the derivative of the δ -function. For a parabolic bunch, the wake force will be linear and can be superimposed onto the linearized rf force easily. We use for the distribution in longitudinal z - δ phase space, [5]

$$\psi(z, \delta) = \frac{3\eta c N}{2\pi \omega_{s0} \hat{z}_0^3} \sqrt{\hat{z}_0^2 - \frac{1}{\kappa} \left(\frac{\eta c}{\omega_{s0}} \delta \right)^2 - \kappa z^2}, \quad (2.1)$$

where η is the phase-slip parameter, c the velocity of light, $\omega_{s0}/2\pi$ the unperturbed synchrotron frequency, and N the number of particles in the bunch. The original half length of the bunch \hat{z}_0 has been lengthened to $\hat{z}_0/\sqrt{\kappa}$, whereas the momentum spread δ is shortened by $\sqrt{\kappa}$, so that the bunch area remains

the same. The Hamiltonian is modified to

$$H = \frac{\eta^2 c^2}{2\omega_{s0}} \delta^2 + \frac{\omega_{s0}}{2} (1 - D\kappa^{3/2}) z^2, \quad (2.2)$$

where

$$D = \frac{3e^2 N \eta c^3}{4\pi \omega_{s0}^2 E \hat{z}_0^3} \frac{Z}{n} \bigg|_{\text{ind}}. \quad (2.3)$$

The incoherent synchrotron angular frequency is therefore $\omega_s = \omega_{s0}(1 - D\kappa^{3/2})^{1/2}$. Since the distribution $\phi(z, \delta)$ must be a function of the Hamiltonian, we obtain the constraint $\kappa^2 = 1 - D\kappa^{3/2}$. Take a Fermilab Main Ring bunch with $N = 2.5 \times 10^{10}$ at $E = 150$ GeV, bunch area 0.15 eV-sec, and synchrotron tune $\nu_{s0} = 0.0030$. The accelerator ring has a revolution frequency $f_0 = 47.7$ kHz, a phase-slip parameter $\eta = 0.0028$, and the inductive impedance is believed to be $Z/n|_{\text{ind}} \approx 10$ Ohms. Then $D = 0.204$, indicating that the bunch has been lengthened by $\kappa^{-1/2} = 1.05$ and the momentum spread flattened by 5% . This implies that we cannot infer the momentum spread by naively measuring the bunch length and the synchrotron frequency through the relation $\hat{\delta} = \omega_{s0} \tau_L / \eta$, because the answer will be 10% too large, giving a wrong idea about the amount of Landau damping. Instead, the momentum spread should be measured from Schottky signals or inferred through dispersion from the measurement of the transverse profile of the bunch using a flying wire.

III. Mode-Mixing

The shifts of the synchrotron side-bands can be derived using Vlasov equation. Here, we follow the Sacherer's approach. [6] The coherent side-band synchrotron angular frequencies ω can be obtained from the determinant

$$|(\omega - m\omega_s)\delta_{mm'} - M_{mm'}| = 0. \quad (3.1)$$

The longitudinal impedance $Z(n)$ in the matrix elements $M_{mm'} = \bar{\epsilon} \omega_s A_{mm'}$ is responsible for the coupling of the azimuthal modes, with

$$A_{mm'} = \frac{m}{m+1} \frac{\sum_n [j_{n_r} \hat{Z}(n)/n] h_{mm'}(n)}{\sum_n h_{mm}(n)}, \quad (3.2)$$

where $h_{mm'}(n) = \tilde{\lambda}_m^*(n) \tilde{\lambda}_{m'}(n)$ are the overlap of the spectral function $\tilde{\lambda}_m(n)$ of the bunch obtained by solving the matrix $M_{mm'}$. In the above, $\bar{\epsilon} = \epsilon(\omega_{s0}/\omega_s)^2$, $\epsilon = I_b(R_s/n_r)/(3B_0^3 h V \cos \phi_s)$, I_b the average bunch current, \hat{Z} the resonant impedance centered at $f_r = n_r f_0$ and normalized to the shunt impedance R_s , V unperturbed rf voltage, ϕ_s the synchronized phase, h the rf harmonic, $B_0 = \tau_L f_0$ the bunching factor, and τ_L the full bunch length in sec.

Potential-well distortion has been neglected in the formulation, because the effect is small for proton machines. We will use a prescribed set of $\tilde{\lambda}_m(p)$ instead of the eigenvectors. Although

* Operated by the Universities Research Association under contracts with the U.S. Department of Energy.

self-consistency will be lost, we do think that the essence of the results will not be affected. We use Sacherer's sinusoidal bunch profiles. The spectral functions are

$$\tilde{\lambda}_m(p) = (-j)^m \frac{m+1}{2\pi} \frac{\cos \pi x/2}{x^2 - (m+1)^2}, \quad (3.3)$$

when m is even and with cosine replaced by sine when m is odd. A dimensionless frequency parameter $x = 2nf_0\tau_L$ has been introduced, so that, with the exception of $m = 0$, the spectrum for the m th mode peaks at $x \approx m + 1$. Continuing with the example of the Fermilab Main Ring which has a broad band impedance centered at $x_r = 7.5$ or $f_r \sim 1.88$ GHz and $Q \approx 1$, we find the colliding of modes 6 and 7 in Fig. 1, and the bunch becomes unstable at $\epsilon = 0.94$. This is expected, because the symmetries of Eqs. (3.2) and (3.3) show that $\text{Re}Z$ is responsible for the coupling between two adjacent modes. Note that the ordinate of Fig. 1 is normalized with respect to the unperturbed synchrotron frequency ω_{s0} , and an adjustment for the incoherent tune shift has been made.

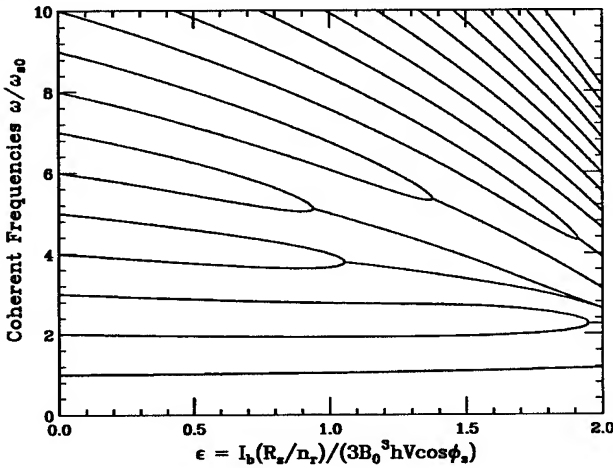


Fig. 2. Coupling of modes $m = 6$ and 7 in the presence of a resonance at $x_r = 7.5$ and $Q = 1$.

We vary Q and compute the threshold ϵ_{th} in each case. The result is plotted in Fig. 2 versus $z = \Delta f_r \tau_L = x_r/4Q$, where $\Delta f_r = f_r/2Q$ is the HWHM of the resonance. Also plotted are threshold curves at different resonant frequencies x_r . Note that all the curves approach a minimum threshold of $\epsilon_{th} \approx 0.92$ at $z \approx 0.6$. The latter has the physical meaning of the resonance peak just wide enough to cover only two coupling modes. A smaller z implies that the resonance peak is too narrow and interacts with only parts of the two mode spectra, thus giving a higher instability threshold. A larger z means that the resonance will cover more than two mode spectra. For $x_r = 7.5$ say, modes 6 and 7 will then be pulled and pushed also by the other modes, so the threshold for their collision is expected to be higher also. However, Eq. (2.2) reveals that the coupling comes in not through $\text{Re}Z(n)$ but through $\text{Re}Z(n)/n$, whose peak value becomes larger and the peak frequency smaller when Q is small, as illustrated in Fig. 3. As a result, the lower modes start to collide first (Fig. 4). Thus the threshold for large z remains small, which is very much different from what Sacherer stated in his paper.

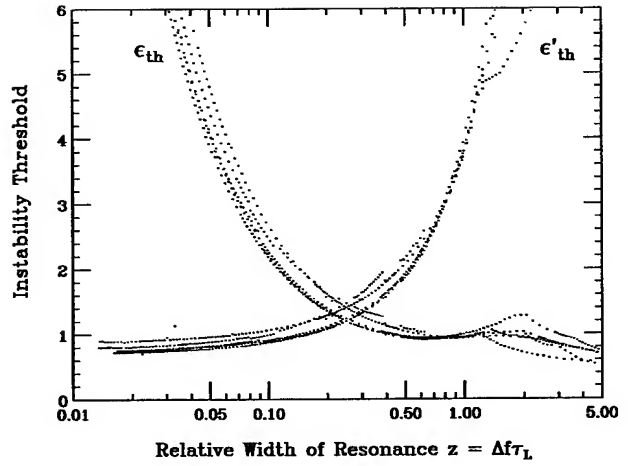


Fig. 2. Instability thresholds ϵ_{th} and ϵ'_{th} for various widths of the resonance impedance located at $x_r = 3.5$ to 11.5 .

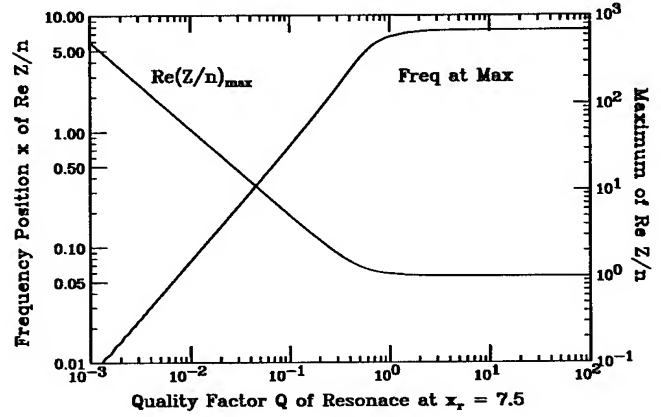


Fig. 3. Enhancement of $(\text{Re}Z/n)_{\max}$ (normalized to R_s) and its frequency position x as the quality factor Q of the resonance centered at $x_r = 7.5$ decreases.

IV. Microwave Instability Driven by Broad Resonances

Microwave instability can occur when the resonance is much wider than the bunch spectrum. When this happens, many coherent modes are excited. Therefore the threshold at the $z \gg 1$ end, $\epsilon_{th} \approx 0.75$, is the threshold of microwave instability. This threshold condition can be easily rewritten in terms of the energy spread $(\Delta E)_{\text{FWHM}} = \frac{3}{2}(\Delta E)_{\text{full}}$ and peak bunch current $I_p = \pi I_b/2\tau_L f_0$ of the sinusoidal profile as

$$\frac{R_s}{n_r} = \frac{3}{4} \epsilon_{th} \frac{\eta(E/e)}{I_p} \left(\frac{\Delta E}{E} \right)_{\text{FWHM}}^2. \quad (4.1)$$

This is the familiar Boussard-modified Keil-Schnell criterion [1] of microwave instability driven by a broad resonance. The form factor for this type of bunch shape should be slightly bigger than unity, which is very close to $\frac{27}{16} \epsilon_{th} = 1.3$ obtained here. The equivalence of mode-coupling and microwave instability had been pointed out by Sacherer [6] and Laclare. [7]

When $z \approx 0.6$, $\text{Re}Z$ is just wide enough to cover two adjacent azimuthal modes m and $m' = m + 1$, and the excitation is one with

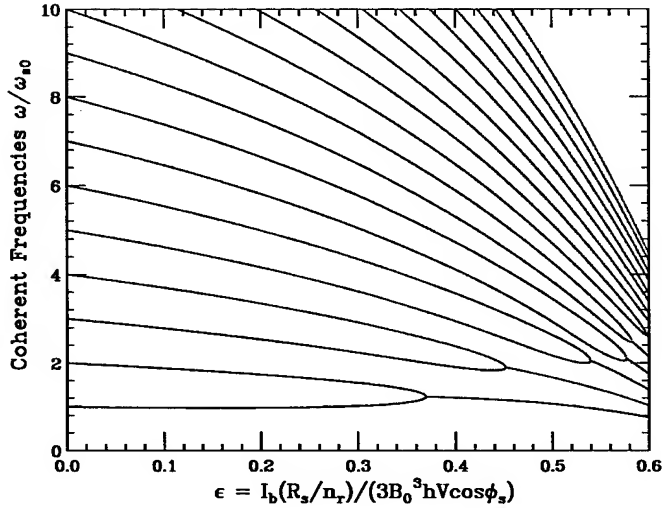


Fig. 4. Mode coupling starts at the lowest modes when the driving resonance is much wider than the bunch spectrum. Here $x_r = 7.5$, $Q = 0.2$, $\tau_L = 2$ ns, or $z = 37.5$.

$x_r = \frac{1}{2}(m+3)$ nodes along the bunch. The coupling matrix can be truncated to include only these two modes. From Eq. (3.1), the eigen modes are

$$\frac{\omega}{\omega_s} = \frac{1}{2} \left[(v_m + v_{m'}) \pm \sqrt{(v_{m'} - v_m)^2 - 4\bar{\epsilon}^2 A_{mm'}^2} \right], \quad (4.2)$$

where $v_k = k + \bar{\epsilon} A_{kk}$, $k = m$ or m' . The threshold of instability ϵ_{th} is therefore given by

$$|\bar{\epsilon}_{th} A_{mm'}| = \frac{1}{2} |\bar{\epsilon}_{th} (A_{m'm'} - A_{mm}) - 1|. \quad (4.3)$$

The matrix elements A_{mm} , $A_{m'm'}$, and $A_{mm'}$ have been computed numerically for any two adjacent m, m' , with the resonance peak centered at $x_r = \frac{1}{2}(m+3)$. The result is actually very close to $\epsilon_{th} = 0.92$ and depends on m very weakly. It can also be estimated easily. Since $A_{m'm'} \approx A_{mm}$, we have $|\epsilon_{th} A_{mm'}| \approx \frac{1}{2}$. If we further approximate the resonance and adjacent spectra by rectangular curves, we get $|A_{mm'}| \approx 0.5$.

V. Microwave Instability Driven by Narrow Resonances

When the resonance is much narrower than the width of the bunch spectrum, we have $z \ll 1$. Then, the summation over frequency in Eq. (3.2) can be approximated by

$$\sum_n \frac{x_r \hat{Z}(n)}{n} h_{mm'}(n) \approx \frac{\pi x_r}{Q} \tilde{\lambda}_m^* \tilde{\lambda}_{m'}|_{x=x_r}. \quad (5.1)$$

For this, we need a new dimensionless current parameter $\epsilon' = 2I_b(R_s/Q)/(3B_0^2 h V \cos \phi_s)$. This new threshold ϵ'_{th} is now plotted versus z in Fig. 2. For small z , we obtain $\epsilon'_{th} \approx 0.75$ which is almost independent of x_r . Again, this threshold can be computed numerically using the truncated 2×2 coupling matrix, or estimated by approximating the spectral functions by rectangular curves. When it is cast into the form

$$\frac{R_s}{Q} = \frac{27}{16\pi} \epsilon'_{th} \frac{\eta(E/e)}{I_b} \left(\frac{\Delta E}{E} \right)_{FWHM}^2, \quad (5.2)$$

it is just the criterion of microwave instability driven by an impedance resonance that is narrower than the bunch spectrum. [2] The form factor is 0.41, which agrees very well with $\frac{27}{16\pi} \epsilon'_{th} \approx 0.40$. This may be a more appropriate microwave instability threshold for electron machines, since electron bunches are short.

VI. Going Below Transition

Figure 1 shows that the coherent frequencies tend to cluster together when the current ϵ increases. This is because we are above transition, $\cos \phi_s < 0$. Looking into the diagonal elements of Eq. (3.2), modes with $m < x_r - 1$ ($> x_r - 1$) sample the inductive (capacitive) part of the impedance and are shifted upward (downward). Below transition, the shifts will be in the opposite direction; i.e., diverging outward with increasing ϵ . In other words, the mode-mixing threshold ϵ_{th} will be increased, or the bunch becomes more stable. We tried to reverse the sign of $\cos \phi_s$ in the example of Fig. 1 and found ϵ_{th} increases from 0.94 to 1.88. Therefore, a bunch in a machine with a negative momentum-compaction factor [8] will be more stable. This idea had been pointed out by Fang et al [9] in shortening electron bunches.

References

- [1] D. Boussard, CERN/LAB II/RF/75-2 (1975); E. Keil and W. Schnell, CERN/ISR/TH/RF/69-48 (1969)
- [2] K.Y. Ng, Proc. 1986 Summer Study on Phys. of SSC, ed. R. Donelson and J. Marx, 1986, p.590.
- [3] K.Y. Ng Fermilab Internal Report FN-630, 1995.
- [4] J. Haissinski, Nuovo Cimento B18, 72 (1973).
- [5] A.W. Chao, *Physics of Collective Beam Instabilities in High Energy Accelerators*, Wiley, p.284.
- [6] F.J. Sacherer, IEEE Trans. Nucl. Sc. 24, No.3, 1393 (1977).
- [7] J.L. Laclare, CERN Accel. School, Queen's College, Oxford, England, 1985, p.264.
- [8] S.Y. Lee, K.Y. Ng, and D. Trbojevic, Phys. Rev. E48, 3040 (1993).
- [9] S.X. Fang, K. Oide, Y. Yokoya, B. Chen, and J.Q. Wang, KEK Preprint 94-190, 1995.

Longitudinal Wakefield for Synchrotron Radiation

J.B. Murphy & S. Krinsky, NSLS, Brookhaven National Laboratory, Upton, NY 11973,
R.L. Gluckstern, University of Maryland, College Park, MD 20742

ABSTRACT

It is of interest to determine how short a bunch can be maintained in a storage ring. Some aspects of this problem depend on specific details of the storage ring design. Instability thresholds depend on the strength of the wakefields. In this paper we determine the longitudinal wakefield due to curvature of the electron orbit, both in free space and between parallel plates with infinite conductivity. Our study leads to the conclusion that as long as the vertical aperture of the vacuum chamber is not too small, the wakefield due to image charges does not significantly vary along a short bunch. Therefore, we suggest that in the determination of the equilibrium bunch length of very short bunches, the effect of the conducting plates can be neglected. The starting point for bunch lengthening calculations should be the free space wakefield.

I. INTRODUCTION

In his pioneering book, published in 1912, Schott [1] calculated many of the properties of the radiation due to a relativistic point charge moving with uniform speed on a circular orbit. In particular, Schott determined the electromagnetic field at all points on the circular orbit, yielding what we now refer to as the wakefield of the point charge. Here, it is our goal to extend Schott's work in several directions, considering a highly relativistic particle whose velocity is close to the speed of light c . In this case the longitudinal wakefield simplifies and is large in front of the point charge and reduced by a factor of $1/\gamma^4$ behind. Working in the time domain, we obtain an analytic expression for the longitudinal wake in front of the charge. Next, we use the method of image charges to derive the longitudinal wake due to a point charge moving on a circular orbit lying between two parallel plates of infinite conductivity.

II. WAKEFIELD IN FREE SPACE

The retarded Lienard-Wiechert potentials and fields for a point particle are derivable from the time dependent Green function [2],

$$G(\vec{x}, t; \vec{x}', t') = \delta(t' - t + |\vec{x} - \vec{x}'|/c) / |\vec{x} - \vec{x}'|. \quad (1)$$

In Lorentz gauge, the scalar and vector potentials are,

$$\Phi(\vec{x}, t) = \int d^3x' dt' \rho(\vec{x}', t) G(\vec{x}, t; \vec{x}', t'), \quad (2a)$$

$$\vec{A}(\vec{x}, t) = \int d^3x' dt' \vec{j}(\vec{x}', t) G(\vec{x}, t; \vec{x}', t'). \quad (2b)$$

For a point particle following a trajectory $\vec{r}_0(t)$ the charge and current densities are $\rho(\vec{x}', t) = e\delta(\vec{x}' - \vec{r}_0(t))$ and $\vec{j}(\vec{x}', t) = e\vec{v}_0\delta(\vec{x}' - \vec{r}_0(t))$, where $\vec{v}_0 = c\vec{\beta}_0(t) = d\vec{r}_0/dt$ is the instantaneous velocity.

Choosing $\vec{r}_0(t)$ to be the trajectory of an electron moving with uniform velocity on a circle of radius ρ , Schott determined the tangential electric field at the observation point \vec{x} using

$$E_\phi(\vec{x}, t) = -\frac{1}{\rho} \frac{\partial}{\partial \phi} \Phi(\vec{x}, t) - \frac{1}{c} \frac{\partial}{\partial t} A_\phi(\vec{x}, t). \quad (3)$$

Starting from Schott's result we consider its simplification in the limit as $\beta \rightarrow 1$. The tangential electric field on the circular orbit is written as the sum of the singular Coulomb term and a non-singular term, \tilde{E}_ϕ due to synchrotron radiation:

$$E_\phi = \frac{e}{4\rho^2\gamma^2} \frac{\cos\xi}{\sin^2\xi} + \tilde{E}_\phi. \quad (4)$$

Here, γ is the electron energy measured in units of its rest mass and $\xi = s/\rho$ is the angle between the electron and the observation point. Directly in front of the electron $\xi = 0$ and directly behind $\xi = \pi$. Introducing the scaled angle, $\mu \equiv 3\gamma^3\xi$, the non-singular term is given by,

$$\tilde{E}_\phi(\mu) = -\frac{2U_0}{2\pi\rho e} \frac{d\Psi(\mu)}{d\mu} = \quad (5)$$

$$-\frac{4e\gamma^4}{3\rho^2} \begin{cases} 0, & \mu < 0 \\ \frac{1}{2}, & \mu = 0 \\ \frac{d}{d\mu} \left[\frac{9}{4} \frac{\cosh\left[\frac{5}{3}\sinh^{-1}\mu\right] - \cosh[\sinh^{-1}\mu]}{\sinh[2\sinh^{-1}\mu]} \right], & \mu > 0 \end{cases}$$

where $U_0 = 4\pi e^2\gamma^4/3\rho$ is the energy loss per turn for a single electron. Since $\Psi(\mu)$ vanishes at $\mu = 0$ and $\mu = \infty$, the

function $d\Psi(\mu)/d\mu$ has the additional property, $\int_0^\infty d\Psi(\mu) = 0$;

a plot of $\Psi(\mu)$ & $d\Psi(\mu)/d\mu$ is given in Figure 1. Useful asymptotic expansions for small and large $\mu > 0$ are [3-5],

$$\frac{d\Psi(\mu)}{d\mu} \equiv W(\mu) = \begin{cases} 1 - \frac{14}{9}\mu^2 + \dots, & \mu \ll 1 \\ -\frac{3}{4 \cdot 2^{1/3}} \frac{1}{\mu^{4/3}} + \dots, & \mu \gg 1 \end{cases} \quad (6)$$

The wake function is discontinuous at the position of the point charge. The choice, $d\Psi(0)/d\mu = 1/2$, represents an average of the electric field immediately in front and behind the charge, and results in the power loss being correctly given by $ec\tilde{E}_\phi(0)$. The total power radiated by an individual electron is $P = I_0 \cdot U_0 = 2ce^2\gamma^4/3\rho^2$.

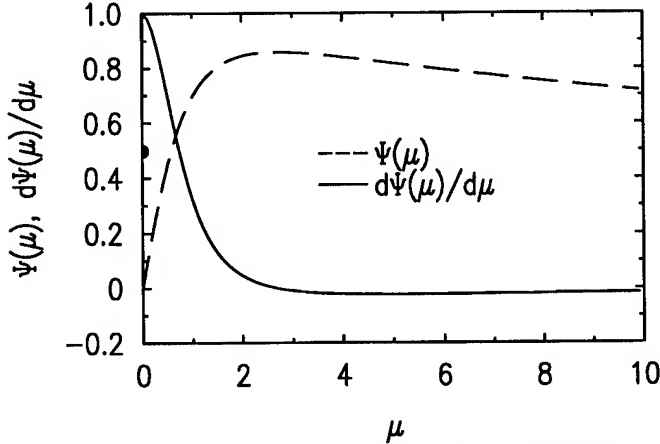


Figure 1: Free space potential function Ψ and wakefield function $d\Psi/d\mu$.

The wake potential due to synchrotron radiation that is generated by a beam of electrons is then given as,

$$\tilde{V}(s) = \int_{-\infty}^{\infty} \tilde{E}_\phi(s-s') \cdot I(s') ds'. \quad (7)$$

For a Gaussian electron beam the curvature wake potential, which is plotted in Figure 2, scales as [5],

$$\tilde{V}(s) \propto \frac{1}{\sigma^{4/3}} \exp\left[-\frac{s^2}{4\sigma^2}\right] D_{1/3}(-s/\sigma), \quad (8)$$

where $D_{1/3}(x)$ is a parabolic cylinder function.

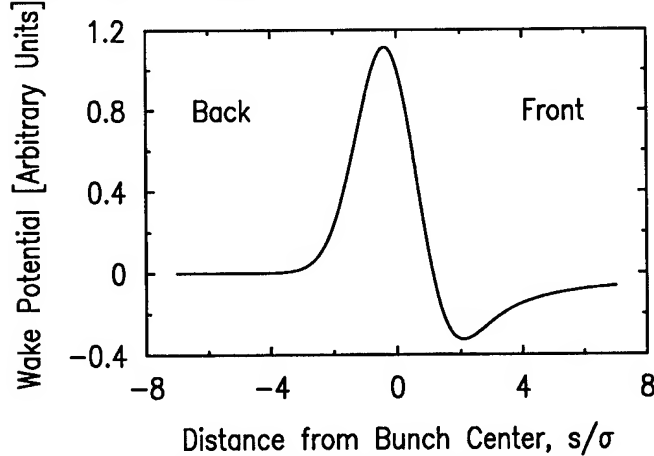


Figure 2: Wake Potential for a Gaussian bunch.

III. WAKEFIELD FOR PARALLEL PLATES

Let us now consider an electron moving with uniform speed on a circular orbit in the horizontal midplane, between two parallel plates of infinite conductivity located at $z = \pm h$. Using the method of image charges we easily see that

the free space Green function of equation (1) should be replaced by the parallel plate Green function,

$$G_{pp}(\bar{x}, t; \bar{x}', t') = \sum_{n=-\infty}^{\infty} \frac{(-1)^n \delta\left(t' - t + \frac{|\bar{x} - \bar{x}' - 2nh\hat{z}|}{c}\right)}{|\bar{x} - \bar{x}' - 2nh\hat{z}|}. \quad (9)$$

Here the observation point \bar{x} and the source point \bar{x}' lie in the midplane and \hat{z} is a unit vector in the vertical direction perpendicular to the plates.

Using the Green function of equation (9) together with equation (2-3), we proceed in a manner analogous to that of the free space calculation. Introducing the parameter $\Delta \equiv h/\rho$, the tangential electric field on the orbit is found to be given by ($\Delta \ll 1, \gamma^2 \Delta \gg 1$):

$$E_\phi \approx \frac{e}{4\rho^2\gamma^2} \left[\frac{\cos\xi}{\sin^2\xi} + \frac{1}{\Delta^3} G_1(\xi/\Delta^{3/2}) \right] - \frac{4}{3} \frac{e\gamma^4}{\rho^2} \left[W(3\gamma^3\xi) - \frac{3}{8} \frac{1}{\Delta^2\gamma^4} G_2(\xi/\Delta^{3/2}) \right] \quad (10)$$

where $W(\mu) \equiv d\Psi(\mu)/d\mu$, and the scaling functions G_1 and G_2 are plotted in Figure 3.

In free space the radiation travels along a chord to another point on the circle, thereby always arriving before (in front) of the exciting charge. With the plates in place the radiation can bounce off the plates once or numerous times and arrive behind the exciting charge resulting in a trailing wakefield, which we have described using image charges. For $\gamma^2 \Delta \gg 1$, the G_1 term is smaller than the G_2 term and for small ξ they are both small compared to the free space wakefield, $W(3\gamma^3\xi)$. The main effect of G_2 is to cancel the tail of $W(3\gamma^3\xi)$ at large distances (times), which is the time domain analog of the suppression of low frequencies in the impedance due to the parallel plates. The G_1 term cancels the long distance tail of the Coulomb term. When $\gamma^2 \Delta \approx 1$, the G_1 , G_2 and W term become comparable in magnitude, and the situation is more complicated.

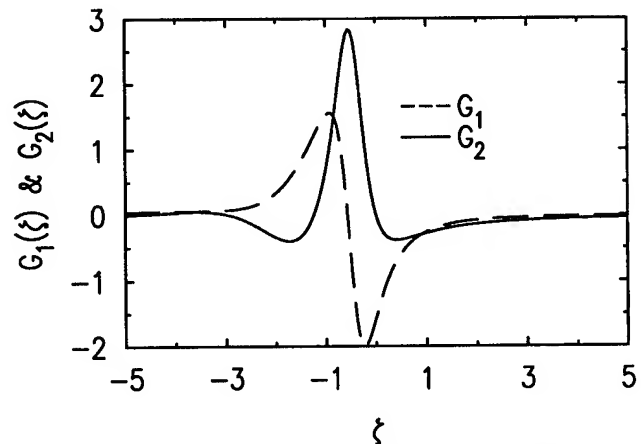


Figure 3: Plot of scaling functions G_1 and G_2 .

The expression for E_ϕ in equation (10) is given in the time domain. Results in the frequency domain were obtained in references [6,7]. We believe that the time domain results are more directly applicable to the study of the bunch lengthening instability.

We have also calculated the tangential electric field at the position of the charge itself for $\Delta \ll 1, \gamma^2 \Delta \gg 1$, we have found the radiated power loss $P = ecE_\phi(0)$ to be given by,

$$P \equiv \frac{2}{3} \frac{ce^2 \gamma^4}{\rho} \left[1 + \frac{3\sqrt{3}K_1}{8} \frac{1}{\gamma^6 \Delta^3} + \frac{3\sqrt{3}K_2}{10} \frac{1}{\gamma^4 \Delta} \right], \quad (11)$$

where $K_1 \equiv \sum_{n=1}^{\infty} \frac{(-1)^{n+1}}{n^3}$ and $K_2 \equiv \sum_{n=1}^{\infty} \frac{(-1)^{n+1}}{n} = \ln 2$.

In equation (11) we have averaged the singular free space contribution to the electric field immediately in front and behind the point charge. The second term, proportional to K_1 , is in agreement with the G_1 term in equation (10). The third term cannot be obtained from equation (10) because $G_2(0) = 0$. It was necessary to go to higher order in Δ . The correction due to the conducting plates is small in magnitude and has the sign indicating that the electron radiates more energy between the conducting plates than it would in free space. This is the case despite the fact that the plates cut off the lowest frequencies.

IV. LONGITUDINAL COUPLING IMPEDANCE

The longitudinal coupling impedance due to synchrotron radiation is related to the Fourier transform of the non-singular function wake, $Z_n \equiv 2\pi\rho \cdot \tilde{E}_n / I_n$, where

$$\tilde{E}_n = \frac{1}{2\pi} \int_0^{2\pi} d\theta e^{-in\theta} \tilde{E}_\phi(\theta) \text{ and for a single circulating charge,}$$

$I_n = ec\beta / 2\pi\rho$. In free space the impedance associated with this wake is computed to be in MKS units [8],

$$Z_n = Z_0 \pi \beta n \left\{ \begin{aligned} & [J'_{2n}(2n\beta) - iE'_{2n}(2n\beta)] \\ & - \frac{n}{\beta^2 \gamma^2} \int_0^\beta [J_{2n}(2nx) - iE_{2n}(2nx)] dx \\ & - \frac{i}{\pi \gamma^2 \beta^2} \ln \gamma \end{aligned} \right\} \quad (12)$$

where the Weber function, $E_n(z)$, is defined as

$$E_n(z) \equiv \frac{1}{\pi} \int_0^\pi \sin(nt - z \sin t) dt.$$

The real part of the impedance is proportional to the synchrotron radiation power emitted at a frequency $n\omega_0$ and integrated over all vertical angles for a single electron,

$$\text{Re } Z_n = Z_0 \pi \beta \left[n J'_{2n}(2n\beta) - \frac{n^2}{\beta^2 \gamma^2} \int_0^\beta J_{2n}(2nx) dx \right] = \frac{2P_n}{I_n^2} \quad (13)$$

For $1 \ll n \ll \gamma^3$, only the first two terms in the expression for the impedance are significant which implies the far field radiation term is dominant. Using the expressions for J_n and E_n when the order and argument are nearly equal one can recover the well known result of Faltens & Laslett [9],

$$Z_n \approx Z_0 \cdot \frac{\Gamma(2/3)}{3^{1/3}} \cdot \left(\frac{\sqrt{3}}{2} + i \frac{1}{2} \right) \cdot n^{1/3}, \quad (14)$$

except the sign of the reactive part is opposite to that given by them since the wake is in front of the exciting charge and not behind.

For $n \gg \gamma^3$, the first four terms in the expression for the impedance are now significant which implies that at very high frequencies, characteristic of very short distances, the near field also contributes to the impedance.

V. ACKNOWLEDGMENTS

The authors would like to thank Dr. J.M. Wang of BNL and Dr. R. Warnock of SLAC for useful discussions. Work performed under DOE contract DEAC02-76CH00016.

VI. REFERENCES

- [1] G.A. Schott, *Electromagnetic Radiation*, Cambridge, (1912).
- [2] J.D. Jackson, *Classical Electrodynamics*, Wiley, New York, (1975).
- [3] L.V. Iogansen & M.S. Rabinovich, "Coherent Electron Radiation in the Synchrotron II", *Sov. Phys. JETP*, Vol. 37 (10), No. 1, p. 83, (1960).
- [4] M. Bassetti & D. Brandt, "Some Properties of the Azimuthal Component of the Electric Field of a Particle on a Circular Trajectory", *CERN/LEP-TH/83-1*, (1983).
- [5] P. Goldreich & D.A. Keeley, "Coherent Synchrotron Radiation", *Astrophysical Journal*, 170, p.463, (1971).
- [6] J.S. Nodvick & D.S. Saxon, "Suppression of Coherent Radiation by Electrons in a Synchrotron", *Phys. Rev.*, Vol. 96, No. 1, p.180, (1954).
- [7] R.L. Warnock, "Shielded Coherent Synchrotron Radiation and Its Effect on Very Short Bunches", *SLAC PUB 5375* (1990).
- [8] A similar but not totally equivalent expression was given earlier by: B.G. Shinov, A.G. Bonch-Osmolovski, V.F. Manakov & V.N. Tsytovich, *Plasma Physics*, 15, p. 211 (1973).
- [9] A. Faltens & L.J. Laslett, "An Estimate of Limits to the Longitudinal Coupling Impedance", *BNL 20550*, p. 486, (1975).

REVIEW OF BEAM INSTABILITY STUDIES FOR THE SSC

W. Chou, Fermi National Accelerator Laboratory,* P.O. Box 500, Batavia, IL 60510, USA

Abstract

Beam instability studies for the SSC during the period 1989-1993 are briefly reviewed in this paper. Various topics are covered: single bunch and multi-bunch, single beam and beam-beam, parasitic heating and active feedback, *etc.* Although the SSC will not be built, many of the results obtained from these studies remain as useful references to the accelerator community.

I. INTRODUCTION

Studies on beam instability problems for the SSC started in the early 1980s. A set of preliminary results were included in Reference [1]. Since the establishment of the SSC Laboratory in 1989, these studies have been further pursued and numerous new results have been obtained. In this paper we will briefly review these results. For details the readers are referred to Ref. [2] and the references therein.

The SSC is a low beam current machine. The beam intensity is primarily limited by the cryogenic system for absorbing the synchrotron radiation power. Generally speaking, therefore, collective effects — such as single bunch instability, parasitic heating and beam-beam interactions — do not present a threat to machine operations. However, the coupled-bunch instability may become a real concern, because the number of bunches is enormous (about 17000 per beam) and the transverse emittance is very small (1π mm-mrad, rms, normalized).

II. IMPEDANCE BUDGET

A. Impedance budget of the baseline design

Each component in the vacuum, rf, diagnostic and injection/extraction systems have been carefully analyzed. Computer models for each component have been built. Measurements for some critical components (*e.g.*, the bellows and the liner) have been carried out. Two groups of simulation codes have been put in use. One is numerical, *e.g.*, MAFIA and HFSS.[3] Another is based on a boundary perturbation method and called BPERM, which was developed at the SSC.[4] The results obtained from different codes are in agreement.

The impedance budget is listed in Table 1, where $Z_{||}/n$ is the longitudinal impedance and Z_{\perp} the transverse one. There are several remarks about this budget.

1. Every effort has been made to make the beam pipe as smooth as possible: the bellows are shielded; the valves have rf fingers; the vacuum pump ports are screened; the transitions between two pipes of different sizes are tapered; and the ceramic pipes in the kicker sections are coated with thin metallic layers.
2. Table 2 lists the impedances of two different designs for the bellows rf shield. The reduction comes from a smaller gap

and a smoother taper. The specification of the maximum lateral offset is 2.8 mm. Assuming a uniform distribution in misalignment, the resulting increase in impedance is also listed in Table 2.

3. In order to accommodate unforeseen sources, the calculated total impedance is multiplied by a factor of two, which is then used in the safety margin estimate.

B. Impedance in the presence of a liner

A perforated liner inside the beam pipe would increase the impedance in two ways:

1. The holes or slots would introduce additional impedance. Below the cutoff, small holes/slots behave like a pure inductance. For a given pumping area, short slots give less impedance than circular holes. Above the cutoff, resonant peaks in the impedance spectrum are observed when the holes or slots are periodically placed. These peaks can be greatly suppressed when the periodicity is destroyed. It is thus concluded that randomly distributed short slots would be the choice for the pattern of the perforation.
2. The installation of a liner would also reduce the inner radius (ID) of the pipe. Consequently, the transverse impedance would increase.

For an area coverage of the holes on the liner surface 4%, the impedance increase is listed in Table 3.

C. Single bunch instability threshold and safety margin

The instability threshold impedances are listed in Table 1. The ratio of the threshold to the impedance budget, called the safety margin, is listed in Table 3. Several measures could be taken to increase this margin, *e.g.*, a larger liner ID, a bigger longitudinal emittance and a higher rf voltage at injection.

III. COUPLED-BUNCH INSTABILITY

In order to suppress the coupled-bunch instability, four types of rf cavities — multiple-cell and single-cell, superconducting (sc) and normal conducting (nc) — have been compared. The rf committee has endorsed the single cell, sc cavity as the choice for the SSC.

The higher order modes (HOM) may also be generated if the beam pipes in the dipole and quadrupole sections have different cross sections, which is called the trapped mode effect. The result could be a continuous beam emittance growth. Therefore, it was decided to use a beam pipe of uniform cross section throughout the entire cold region.

IV. RESISTIVE WALL INSTABILITY

The beam tube of the Collider is made of stainless steel, which is coated on its inner surface with a thin copper layer in order

*Operated by Universities Research Association Inc. under Contract No. DE-AC02-76CHO3000 with the U.S. Department of Energy.

Table 1. Impedance Budget (per ring)

Component	Number	Impedance	
		Z_{\parallel}/n (Ω)	Z_{\perp} (M Ω /m)
RF cavity (HOM)	8×5 -cell	0.036	0.016
Transition (tapered)	4	0.004	0.003
Bellows (shielded)	6000	0.12	10
BPM (15 cm, 55°)	968	0.05	4.6
Weldment	12000	0.002	0.2
Valve (shielded)	128	1E-4	0.01
Pump port (screened)	650	0.02	2
Flange gap	12000	TBD	TBD
Resistive wall		0.02	1.7
Scrapers		1.8E-4	0.02
Collimators		2.6E-4	0.08
Injection Lambertson (laminated)		1.5E-3	1.4
Abort Lambertson (solid iron)		—	—
Injection kicker		0.06	2.0
Abort kicker		0.2	4.7
Joint to Lambertson		TBD	TBD
Conical section near IP		—	—
Total		0.51	27
Impedance budget = Total \times 2		1.0	54
Instability threshold:			
At 2 TeV		4.0	270
At 20 TeV		16	1200

Table 2. Comparison of Bellows (shielded) Impedance

Case	Z_{\parallel}/n (Ω)	Z_{\perp} (M Ω /m)
Baseline design	0.12	10
New design		
No misalignment	0.03	2.5
Max lateral offset 2.8mm	0.06	6.5

Table 3. Transverse Impedance with/without Liner

Case	$Z_{\perp}^{(liner)}$ (M Ω /m)	$Z_{\perp}^{(others)}$ (M Ω /m)	$Z_{\perp}^{(total)}$ (M Ω /m)	Safety Margin
Baseline	—	54	54	5
With liner	37	94	131	2

Table 4. Resistive Wall Impedance Budget

Component	Z_{\perp} (M Ω /m)	
	2 TeV	20 TeV
Cold beam pipe	4300	4300
Warm beam pipe (stainless steel)	1300	1300
Graphite shadows:		
Upstream to abort Lambertson	7.1	7.1
Upstream to collimator	10	323
Scrapers (copper)	1.4	46
Collimators (stainless steel)	7.7	250
Abort Lambertson (solid iron):		
Symmetric	22	22
Asymmetric	4.6	4.6
Total	5700	6300

to have low electrical resistivity. The resistive wall instability growth time can be approximately written as

$$\tau_w = \left(\frac{2\pi\gamma v_\beta b^3}{N_{\text{tot}} c r_p} \frac{\mu\omega}{2} \right) \sigma_e \Delta \quad (1)$$

where γ is the relativistic energy of the particles, v_β the beta-tron tune, b the beam tube radius, μ the vacuum permeability, ω the angular frequency, N_{tot} the total number of particles, c the velocity of light, r_p the classical radius of proton, σ_e the wall conductivity, and Δ the coating layer thickness. The specification is $\sigma_e \Delta \geq 1 \times 10^5 \Omega^{-1}$, which corresponds to a wall impedance of 4300 M Ω /m in the cold region. Table 4 is a list of the wall

impedance budget, which gives a growth time of 25 ms, or 88 turns, during the about one hour injection period.

An alternative is to use an aluminum beam tube. There are several reasons for considering this option: saving the coating cost, solving the vacuum problem without a liner, and avoiding the adhesion problem in a bi-layer tube. The quantity $\sigma_e \Delta$ remains about the same.

V. FEEDBACK SYSTEMS

The feedback systems serve four different purposes:

1. Correction of the injection errors — The feedback must have enough power to kick the beam back to the orbit before any significant decoherence occurs.
2. Damping of the resistive wall instability — Because this is a fast beam blowup, a feedback system with a large gain is needed.
3. Damping of the coupled-bunch instability — The feedback system needs a wide bandwidth.
4. Control of emittance growth — This feedback system must have very low noise level. The emittance growth rate due to the feedback noise is:

$$\frac{1}{\tau_{\text{noise}}} = 0.64 f_0 \left(\frac{x_N}{\sigma_\beta} \right)^2 \Delta v^2 \quad (2)$$

in which f_0 is the revolution frequency, x_N the noise level at the pickup, σ_β the rms beam size and Δv the total tune spread. The theoretical limit of the pickup resolution due to the thermal and electronic noises, Δx , is also calculable. In designing a feedback system, Δx must be smaller than x_N , which is determined by a specified allowable growth rate $1/\tau_{\text{noise}}$.

The specifications of the power, bandwidth, gain and noise level of the feedback systems can be found in [2].

VI. PARASITIC HEATING

The parasitic heating can be calculated by

$$P = k \frac{I_{\text{av}}^2}{M f_0} \quad (3)$$

where I_{av} is the average beam current, M the number of bunches, and k the loss factor, which is

$$k = \frac{c^2 R}{2\pi b} \int_{-\infty}^{\infty} \tilde{\lambda}^2(\omega) R_s(\omega) d\omega \quad (4)$$

in which R is the machine radius, $\tilde{\lambda}(\omega)$ the bunch spectrum. In order not to exceed the heat load budget (which is 1 kW per ring for the parasitic heating), the surface resistance must be kept below a certain level. To estimate R_s correctly, one should consider the co-existence of three extreme conditions:

- Low temperature (4 K).

The low temperature resistance is described by RRR, the residual resistance ratio. But it is meaningful only at low frequencies and low magnetic field.

- High magnetic field (6.8 T).

The magnetoresistance can be studied using a Kohler plot. At 6.8 Tesla, the RRR value is about an order of magnitude lower than that at zero field.

- High frequency (1 GHz and above).

Because of the anomalous skin effect, the surface resistance ratio $R_s(300 \text{ K})/R_s(4 \text{ K})$ at high frequencies is significantly lower than the dc value.

The measurement of R_s under these conditions was started but not completed.

VII. BEAM-BEAM EFFECTS

A. Strong beam-beam interactions

1. Inelastic scattering:

The particle loss rate is γ_{inel} , which is 10^8 s^{-1} per interaction

point (IP). The corresponding luminosity lifetime is $180/N_{\text{IP}}$ hours.

2. Elastic scattering:

This contributes to the emittance growth:

$$\frac{d\epsilon}{dt} = \frac{N_B f_0}{4\pi\epsilon} \sigma_{\text{el}} \sigma_\theta^2 \quad (5)$$

in which N_B is the number of particles per bunch, σ_{el} the elastic cross section, σ_θ the rms values of pp elastic scattering angle in the center of mass system. This gives about $4.6 \times 10^{-17} \text{ m-rad/s}$ per IP.

B. Electromagnetic beam-beam interactions

1. Incoherent effects:

- (a) Tune shift and tune spread:

The most significant beam-beam effect is the slow diffusion caused by high order betatron resonances. The budget of the total tune spread (head-on + long-range + nonlinear magnetic field) is 0.02. The calculated tune spread is well below this value.

- (b) Orbit distortion:

This is induced by long-range interactions. The calculated values are small compared with the beam size at the IP's (less than 10% σ_β).

2. Coherent effects:

The rigid dipole modes (π - and σ -mode) and high order multipole modes are studied. There are enough stability regions in the (ξ, ν_β) space.

3. Pacman effect:

There are seven injection gaps ($1.7 \mu\text{s}$ each) and one abort gap ($4.1 \mu\text{s}$) in the bunch train. Bunches near the edge of the gaps may miss collisions at some IP, thus experiencing an irregular collision sequence. This makes the orbit and tune correction difficult. But simulations show that there is enough working area in the tune space to accommodate this Pacman effect.

4. Synchro-betatron resonance due to crossing angles:

Computer simulations show that this is not a serious problem. Because the three parameters that determine the strength of the resonance are all small: (a) the beam-beam parameter $\xi = 0.0009$, (b) the synchrotron tune $\nu_s = 0.0012$, and (c) the normalized crossing angle $\alpha\sigma_s/\sigma_\beta = 0.45$.

References

- [1] "SSC Conceptual Design," SSC-SR-2020, SSC Laboratory (1986).
- [2] W. Chou, SSCL-680, SSC Laboratory (1994).
- [3] MAFIA is developed by T. Weiland and his associates, HFSS by Hewlett-Packard Company.
- [4] T. Barts and W. Chou, SSCL-MAN-0035, SSC Laboratory (1994).

COLLECTIVE EFFECTS IN THE NLC DAMPING RING DESIGNS*

T. Raubenheimer, K.L.F. Bane, J.S. Berg, J. Byrd, J. Corlett, M. Furman, S. Heifets, K. Kubo, M. Minty, B. Scott, K.A. Thompson, P.B. Wilson, F. Zimmermann
Stanford Linear Accelerator Center, Stanford University, Stanford, CA 94309 USA,
Lawrence Berkeley Laboratory, Berkeley, CA 94720 USA

I. INTRODUCTION

In this paper, we give an overview of collective effects and related issues in the damping rings for the NLC[1]. The main damping ring will have a maximum average current of 1 A in four bunch trains which are separated by 60-80 ns, allowing the fast kickers to inject and extract individual trains. Each bunch train consists of 75-90 bunches, separated by 1.4 ns, with a maximum bunch population of 1.5×10^{10} . Because of the large average current, coupled bunch instabilities are a potential problem; these can be driven by the ring impedance or by a collective beam-ion instability. In addition, because the ring has a very small momentum compaction and synchrotron tune, potential well distortion and the microwave instability could be important. Finally, because of the very small beam emittances, the intrabeam scattering is significant.

In the next sections, we will describe the present state of our calculations. We begin by describing the vacuum chamber design and RF cavities. We then discuss the longitudinal and transverse coupled bunch instabilities, the potential well distortion and the microwave instability, and finally, mode-coupling, ion effects, and intrabeam scattering.

II. VACUUM SYSTEM

The vacuum system is designed for an average operating pressure of 1 nTorr; see discussion of ion trapping. This pressure must be maintained under conditions of very intense synchrotron photon bombardment which produces a large gas load. For example, 2600L/s of pumping per bend magnet is required in the arcs to maintain the desired pressure.

The dynamic gas load and the aperture of the beam channel (25mm) are such that the required pressure can only be attained by pumping via an ante-chamber. The beam and ante-chambers are interconnected by a 5mm high slot; this height is determined from consideration of both the bunch length and the radiation spot size including allowances for mis-steering of the beam and misalignments of the vacuum chamber.

Discrete photon absorbers are located in the ante-chamber to intercept the synchrotron photons. Most of the gas load to the system is released from these absorbers. The most efficient pumping of the system is thus obtained by locating the pumps in close proximity to the absorbers. The absorbing surface will be inclined at a grazing incidence angle to the incoming photons to reduce the power density to a manageable level. A high strength copper alloy, such as Glidcop, will be required to resist thermal stresses.

Upon consideration of the pressure profile it was found desirable to evenly distribute the thermal load (and thus the gas load) between each absorber. By using an ante-chamber, the

required average operating pressure was obtained with only a small rise in pressure between pumps. The static pressure without beam was calculated to be an order of magnitude below the dynamic pressure.

To minimize the ring impedance, close attention is being given to eliminating mechanical discontinuities in the beam channel design. The ante-chamber and coupling slot are not interrupted through each of the two arcs. The magnet poles are designed to fit around the ante-chamber in a manner similar to that used in the Advanced Light Source at Berkeley. The expansion bellows between vacuum chamber modules is being modeled on those proposed for the SLAC B-factory LER [2].

III. RF CAVITIES

The narrow-band impedance of the storage ring is dominated by the radio-frequency cavities. In order to minimize this impedance, we choose to use a "monochromatic" cavity, which uses waveguides mounted on the cavity body to suppress the cavity higher order modes (HOM's). In addition, we incorporate a tapered beam pipe near the cavity, which substantially reduces the transverse impedance. The basic cavity shape is a re-entrant structure with nose cones and is based on the PEP-II cavity design. The beam pipe has a 3.1 cm radius at the cavity and is then tapered down to the main chamber radius of 1.25 cm over 15 cm length. Absorbing material will be needed to absorb the propagating HOM's.

Three waveguides are attached to the cavity body for the purpose of damping the higher order modes. These waveguides are dimensioned to have a cut-off frequency above the frequency of the accelerating mode of the cavity, but below the frequency of the lowest HOM. Thus the HOM power may couple through the apertures in the cavity wall to the waveguides, where it is absorbed in a lossy material. The location of the absorptive material is at a sufficient distance from the cavity aperture to minimize dissipation of the fundamental mode power from an evanescent waveguide mode. Experience with the PEP-II cavities shows that Q values of the HOM's can be damped to the order of a few 100's in most cases [3].

We have scaled the dimensions of the PEP-II cavities to achieve a resonant frequency of 714 MHz. The addition of the damping waveguides can be expected to reduce the fundamental shunt impedance and unloaded Q value by roughly 30%. We then calculate a shunt impedance of $R_s = 3.3 \text{ M}\Omega$, $Q_0 = 24500$, and $R/Q = 135 \Omega$ for the NLC damping ring RF cavities.

The total loss parameter for each cavity is computed to be $k_l = 1.7 \text{ V/pC}$ for a bunch length of 3.3 mm, of which the fundamental mode contributes 0.26 V/pC and modes below cut-off contribute 1.1 V/pC. The transverse kick factor is 39.4 V/pC/m. Tables 1 and 2 list the strongest monopole and dipole mode frequencies and R/Q 's.

*Work supported by the Department of Energy, contracts DE-AC03-76SF00515 (SLAC) and DE-AC03-76SF00098 (LBL)

The determination of the number of cavities required involves a compromise between their power handling capabilities and the beam impedance presented by the cavities. We expect that two cavities per ring will be sufficient to attain the required 1 MV RF voltage [1].

Table 1. Strongest monopole HOM's.

Frequency (MHz)	R/Q (Ω)
1932	7.3
2362	4.9
3150	4.8
4673	3.2

Table 2. Strongest dipole HOM's.

Frequency (MHz)	(R/Q)/(kr)**2 (Ω)
1194	17
1995	4.2
2312	0.9
2404	0.8
2509	6.7

IV. COUPLED BUNCH INSTABILITIES AND FEEDBACK

A. Longitudinal $m = 0$

In the case of longitudinal beam oscillations, the RF cavities provide the only sources of impedance strong enough to drive coupled bunch (CB) instabilities. As described above, we are using the measured parameters of the HOM's of the 476 MHz PEP-II RF cavity scaled to 714 MHz to estimate the growth rates in the NLC damping ring. For calculations of the CB growth rates, we have assumed that all HOM's have been damped to Q 's of 200.

In this case, we find that all CB growth rates fall below the radiation damping rate of 400/sec except for a few CB modes which are driven by the HOM at 3150 MHz and have growth rates of 450/sec. Because the bandwidth of the HOM's is large compared to the revolution frequency, we do not expect any change in the growth rate from frequency variations of the HOM's. All growth rates for higher mode CB ($m > 0$ modes) oscillations fall well below the radiation damping threshold.

Because the fastest growth rates are only slightly above the radiation damping threshold, we are not planning for a longitudinal CB feedback although the situation must be reevaluated once an actual RF cavity is available. Also, although most CB modes are stable, it is possible that their transient response following injection has unacceptably large amplitudes, resulting in an emittance increase or beam loss. This is especially important because of the relatively short time the beam is in the damping ring. We are currently evaluating this problem.

B. Transverse $m = 0$

In the transverse plane, the principal impedances for driving CB oscillations are the dipole HOM's of the RF cavities and the resistive wall impedance. For the expected aluminum beam pipe with a radius of 1.25 cm, the real part of the resistive wall

impedance is estimated to be $Z_{rw} = 0.47 M\Omega/m$. As for the monopole HOM's, we assume the dipole HOM's are damped to Q 's of 200.

We find the fastest growth rates of $\sim 1400/\text{sec}$ to be driven by the resistive wall impedance. This is about ten times the radiation damping rate of 216/sec in the vertical plane. The CB modes driven by cavity HOM's all have growth rates less than the radiation damping rate except for a mode at 1194 MHz which is roughly three times higher.

A transverse CB feedback system or a large transverse bunch-to-bunch tune variation is needed to stabilize the fast CB growth rates. Because the CB growth is dominated by the resistive wall impedance, it may be possible to design a lower bandwidth system (~ 50 MHz) to deal only with those CB modes rather than a broadband system (357 MHz) which would cover all possible CB modes.

C. Transverse $m = 1$

The method described in [4] and [5] was used to compute $m = 1$ (head-tail) coupled bunch growth rates. The $m = 1$ modes are especially important since they are very hard to damp with a feedback system. If the cavity Q 's are less than 300, the $m = 1$ growth rates are negligible. If instead we assume cavity Q 's of 3000, there is one cavity mode (2509 MHz) which drives an $m = 1$ mode above the radiation damping rate at a beam current of roughly 1.3 A. This is probably not a significant limitation.

V. IMPEDANCE AND MICROWAVE INSTABILITY

Usually the microwave instability is considered to be a benign instability, leading an increased bunch length and energy spread. But, there is some concern that the instability can exhibit a bursting behavior [6]. This can be a severe limitation in a damping ring since the extracted beam energy and phase fluctuates pulse-to-pulse.

To calculate the potential well distortion and the threshold for the microwave instability, we need to know the details of the vacuum chamber geometry. As was the case for the SLC damping rings, small changes in vacuum chamber cross-section can dominate in their contribution to the ring impedance over larger objects such as the rf cavities[7]. In the SLC rings, we were able to model the important elements and construct an accurate wake function; using this wake function the calculated bunch shape and basic properties of the microwave instability generally agreed well with measurements [8][9].

At this time, we are assembling detailed designs of the BPMs, bellows, masks, etc., so that we can perform a similar calculation for the NLC rings. Although this task is not yet complete, as a zeroth order approximation, we have assumed that the impedance is dominated by RF cavities. Using the wakefield of these cavities, and solving the Haissinski equation[10] we find that the potential well distortion is small, hardly perturbing the distribution from the nominal, gaussian shape. Next, using the perturbation approach of [11] to solve the linearized, time independent Vlasov equation, which includes the potential well distortion as a zeroth order effect, we find a microwave threshold at roughly 3.5 times the nominal current. While these results are

encouraging, they are obviously incomplete and we need to calculate the full wakefield to perform more realistic estimates.

VI. OTHER ISSUES

A. Mode-coupling

We use the method described in [4] and [5] to compute the single bunch mode-coupling threshold. For the transverse impedance, we use the model described in [12] which consists of the transverse HOM's, the resistive wall, and a high frequency tail due to the cavities. The effect is most severe in the vertical plane where we find a threshold at roughly 28 mA; this is about an order of magnitude above the actual single bunch current.

B. Ion Effects

Because of the high beam current and the small beam emittances, ion effects can be significant. Although the 60 ns gap separating the bunch trains clears the ions between trains and prevents 'ion trapping', ions generated within the passage of a single bunch train will affect the dynamics. There are two primary issues: tune shifts due to the focusing from the ions and a fast beam-ion collective instability that can arise in both the electron and positron rings and grows as $\exp(\sqrt{t/\tau_c})$ [13].

At a vacuum pressure of 10^{-9} Torr, the ions will produce a variation in betatron tune of $\Delta\nu_y \approx 0.002$ across the electron bunch train; although this is small, it can have an appreciable effect and may even stabilize some of the transverse coupled bunch instabilities. At this same vacuum pressure, the predicted characteristic times τ_c for the collective instability are 500 ns in the electron ring and 120 μ s in the positron ring; the characteristic times are inversely proportional to the vacuum pressure and decrease by an order of magnitude at a pressure of 10^{-8} Torr. Methods of alleviating this instability are discussed in Ref. [13].

C. Intrabeam Scattering and Touschek Lifetime

Because of the small emittances, intrabeam scattering and Touschek effects are significant. With a single bunch population of 1.54×10^{10} , intrabeam scattering increases the equilibrium horizontal emittance of the beam core by about 25% and the equilibrium vertical emittance by about 5%; the scattering has a much smaller effect on the vertical emittance, which is mainly determined by the vertical dispersion because $\langle \mathcal{H}_y \rangle / \langle \mathcal{H}_x \rangle \ll \epsilon_y / \epsilon_x$, where $\mathcal{H}_{x,y}$ is the Courant-Snyder dispersion invariant [14]. In addition, the scattering populates large amplitude tails in the particle distribution that need to be collimated before the IP [15].

Similarly, the Touschek lifetime is only 100 seconds. Although this is very short, it is long compared to the store time of 22 ms. If stored beam is desired for commissioning or diagnostic purposes, the Touschek lifetime can be lengthened by introducing vertical dispersion in the wigglers and increasing the equilibrium vertical emittance.

D. Beam-Gas Scattering

With vacuum $\leq 10^{-8}$ Torr, beam-gas scattering has no significant effect on the emittances. It only contributes to large amplitude tails in the particle distribution [16], [17]. These tails must be collimated before the IP to prevent backgrounds in the detector.

VII. SUMMARY AND FUTURE WORK

Baseline designs for the vacuum chamber and RF cavities are given for the NLC damping ring, from which instability estimates were made. We find that coupled bunch instabilities can be handled by reasonable feedback systems. Preliminary estimates indicate that the beam is below the microwave instability threshold, but more detailed calculations need to add in numerous small contributions. Simulations indicate that ion effects could put stringent requirements on the vacuum; here experimental verification is desirable.

References

- [1] T.O. Raubenheimer, et.al., "A Damping Ring Design for the SLAC Next Linear Collider", this conference.
- [2] D. Hunt, et. al., "Design of the PEP-II LER Arc Vacuum System," these proceedings.
- [3] R.A. Rimmer, , "RF Cavity Development for the PEP-II B-Factory," *Proc. Int. Workshop on B-Factories*, KEK, Tsukuba, Japan (1992).
- [4] J.S. Berg and R.D. Ruth, "Transverse instabilities for multiple nonrigid bunches in a storage ring", Submitted to *Phys. Rev. Lett.*
- [5] J.S. Berg and R.D. Ruth, "Transverse Multibunch Instabilities for Non-Rigid Bunches", this conference.
- [6] P. Krejcik, et. al., *Proc. of the 1993 IEEE Particle Acc. Conf.*, Washington, D.C. (1993) p. 3240.
- [7] K. Bane, *Proc. of the 1st European Particle Acc. Conf.*, Rome, Italy (1988) p. 637.
- [8] K. Bane and R. Ruth, *Proc. of the 1989 IEEE Particle Acc. Conf.*, Chicago, IL (1989) p. 789.
- [9] K. Bane and K. Oide, *Proc. of the 1993 IEEE Particle Acc. Conf.*, Washington, D.C. (1993) p. 3339.
- [10] J. Haissinski, *Il Nuovo Cimento* **18B**, No. 1, 72 (1973).
- [11] K. Oide and K. Yokoya, KEK-Preprint-90-10, 1990.
- [12] S. Heifets, "Study of the NLC DR impedance and collective effects", NLC-Note 8, SLAC, Dec 1994.
- [13] F. Zimmermann, et. al., "A Fast Beam-Ion Instability," these proceedings.
- [14] T.O. Raubenheimer, et. al., *Nucl. Meth. Instr.*, **A335**: 1 (1993).
- [15] T.O. Raubenheimer, *Part. Acc.*, **45**: 111 (1994).
- [16] K. Hirata, K. Yokoya, *Part. Acc.*, **39**: 147 (1992).
- [17] T.O. Raubenheimer, KEK Report 92-7 (1992).

EMITTANCE AND ENERGY CONTROL IN THE NLC MAIN LINACS*

C. Adolphsen, K.L.F. Bane, K. Kubo, T. Raubenheimer, R.D. Ruth, K.A. Thompson, F. Zimmermann,
Stanford Linear Accelerator Center, Stanford University, Stanford, CA 94309 USA

Abstract

We discuss tolerances and correction schemes needed to control single- and multi-bunch emittance in the NLC main linacs. Specifications and design of emittance diagnostic stations will be presented. Trajectory correction schemes appropriate to simultaneously controlling the emittance of a multibunch train and the emittance of individual bunches within the train will be discussed. We discuss control of bunch-to-bunch energy spread using a ramped RF pulse generated by phase-modulating the SLED-II input. Tolerances on ions, wake fields, quadrupole alignment, and accelerating structure alignment will be given.

I. INTRODUCTION

The X-band linacs in the NLC will accelerate low emittance electron and positron bunch trains from 10 GeV to 250 GeV in the initial phase of running, and from 10 GeV to 500 GeV after upgrades to the rf system. For initial (upgraded) operation, trains of 90 (75) bunches with 0.65×10^{10} (1.1×10^{10}) particles per bunch, and a 1.4 ns spacing between bunches, will be accelerated at a repetition rate of 180 (120) Hz. The X-band accelerator structures that will provide the high acceleration gradient (50 MeV/m unloaded during initial operation and 85 MeV/m after upgrades), will also heavily load the beam (25% by the last bunch) and produce strong long-range and short-range transverse wakefields when the beams are off-axis. The preservation of the emittance of the beams (nominally $\gamma\epsilon_x = 3 \times 10^{-6}$ and $\gamma\epsilon_y = 3 \times 10^{-8}$) and the energy spread ($\sim 0.1\%$) will require tight alignment and rf control tolerances. Meeting these tolerances will require that various beam-based corrections schemes be employed during operation. In the following sections, we discuss some of the tolerances and correction schemes after giving a brief description of the linac layout.

II. LINAC LAYOUT

The main linac will be basically an array of X-band accelerator structures interleaved with a FODO quadrupole lattice and interspersed with beam diagnostic devices. In order to provide maximum flexibility for using beam-based methods to control beam emittance growth, the accelerator structures and quadrupole magnets (quads) will contain beam position monitors (BPMs) and will be supported on remotely controlled mechanical movers.

The current design for the NLC main linac accelerating structure incorporates both detuning and damping, where the damping is accomplished by coupling all cells in the structure to four parallel manifolds[2][3]. The Q 's of the modes in the lowest dipole passband are lowered to about 1000, which is sufficient to control multibunch beam break-up. The manifolds will also

serve as BPMs that provide measures of the beam position relative to the structure axes. The 1.8 m long accelerator structures will be supported in pairs on a common strongback, and the strongback itself will be supported by movers that have independent horizontal and vertical positioning control at two points along the strongback. The structure movers will attach to a common girder, which itself will attach to the beam line support pedestal via manually adjustable supports. These girder supports will be used to set the initial position and orientation of the structure pairs.

At the beginning of the linacs, a quadrupole magnet will be located after each structure pair. The separation of the quads will increase in two-structure increments along the linacs, from one pair of structures to five pairs at the end of the linacs. The magnet lengths will likewise increase, from about 0.1 m to 1 m. Each quad will contain a stripline BPM in its bore, and each quad/BPM unit will be mounted on a magnet mover, which in turn will be mounted on a manually adjustable support. Together this system will have the same adjustment capability as the structures.

III. ALIGNMENT AND TRAJECTORY CORRECTION

Misalignments of the quadrupole magnet centers about the nominal linac axis will produce dispersion and hence beam emittance growth because of the non-zero energy spread. Methods that are generally used to align the quads have accuracies that depend on the distance scale of the alignment, so it is useful to characterize the alignment tolerance in terms of the wavelength of the misalignments. In computing these tolerances, we assume that the quad offsets are sinusoidal with wavelength λ , and that bunches are steered to zero in the BPMs, which themselves are centered in the quads. Figure 1 shows the tolerance on the misalignment amplitude for a 3% vertical emittance growth as a function of λ . The rapid rise in the tolerance above 160 m occurs since λ becomes larger than the longest betatron wavelength in the linac, so the dispersion averages out.

The initial placement of the quads and structures will be done with conventional surveying techniques. Most likely, triangulation and leveling methods will be used in combination with Global Positioning System (GPS) data from satellites. The long-range alignment accuracy will be within the dispersion related tolerances shown in Figure 1. However, at wavelengths less than a few hundred meters, the accuracy will level off to values that approach 100 microns on a 20 m scale. At these wavelengths, beam-based methods will be used to control the quad alignment (these methods tend to be sensitive to systematic errors at longer wavelengths and hence it is better to rely on placement accuracy to achieve these tolerances). The quad alignment corrections computed by these methods are generally highly correlated, so one does not usually refer to the absolute level of quad align-

*Work supported by the Department of Energy, contract DE-AC03-76SF00515.

ment, but instead to the residual dispersion remaining after alignment, which is a function of the BPM resolution and the alignment accuracy of the BPMs relative to the quad centers.

The quickest and simplest beam-based quad alignment algorithm is one that uses only the beam trajectory data taken with the nominal linac lattice. Having readings from N BPMs in N quads allows one to determine $N-1$ quad offsets, with the alignment end-points being the beam position in the first quad and the BPM zero of the last quad: the outgoing beam angle is unconstrained. One would align $N-1$ quads at a time, one group after the next, using the magnet movers to control the quad positions to the micron level. Values of N that would be practical range from 50 to 100, or $1/14$ to $1/7$ of the total number of quads in each linac.

Although this method would only require that the quad BPMs have resolutions of a few microns, it also requires that their mechanical plus electronic offsets relative to the quad magnetic centers be known to this same level. These offsets can be computed in a beam-based manner as well, but this requires changing the linac quad settings and would slow down the quad alignment process and disrupt colliding beam operation. To minimize the impact of such measurements, the BPM system will be designed to either insure that any drifts in the offsets after measurement will be accurately monitored, or that the changes will not be significant on at least a 24 hour time scale so that at most one measurement a day would be needed. Achieving stable BPM offsets will be especially important if the quad alignment algorithm needs to be implemented as a feedback loop in order to keep up with the effect of ground motion changes on short (hourly) time scales.

Another potentially large contributor to beam emittance growth in the NLC linacs is the transverse wakefield that is generated as the bunches travel off-axis through the structures. The wakefield degrades both the beam emittance (i.e., it generates bunch-to-bunch orbit variations) and the bunch emittances (i.e., it generates differential kicks along the longitudinal bunch profiles). Although the structure detuning and damping will significantly suppress the strength of the long-range wakefield, and BNS damping will effectively cancel the effect of the short-range wakefield on betatron motion, the alignment tolerances for the structures are still tight.

In computing these tolerances, we suppose that the quads and BPMs are perfectly aligned, and that the net wakefield kick to the beam is removed locally by steering the beam centroid to zero in the BPMs. As in the dispersion case, we consider misalignments on different length scales, although in this case we assume piecewise misalignments as opposed to sinusoidal, where the piece lengths vary from sub-structure sizes to multi-structure groups [4]. Using conventional optical alignment techniques, it would be extremely difficult to achieve the required tolerances (of order 10 microns) at scales greater than a few structure lengths. Instead, the structure mover system will be used to align the two structures as a whole relative to the beam trajectory based on the dipole mode signals from the structure damping manifolds. Signals from two modes near the ends of the structure will be selected with filters and measured so that both the position and orientation of the structure relative to the beam can be determined. The average of the measurements from the two structures will be

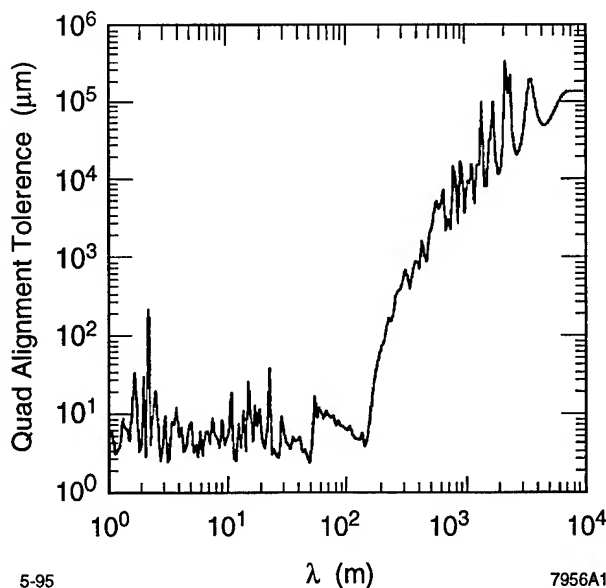


Figure 1. Misalignment tolerance for a 3% vertical emittance growth as a function of misalignment scale λ .

used to remotely adjust the mover positions at the micron level to better center the pair about the beam trajectory. This procedure will be iterated with the quad alignment algorithm if significant orbit changes occur.

The difference in the measurements from each structure pair will be used to monitor the relative structure alignment on the strongback. This alignment and the internal alignment of each of the two structures will be established prior to installation by optical means. There will be six supports on each structure that can be adjusted to meet the required tolerances; the tolerances on shorter length scales will be achieved by precision assembly of the cells prior to brazing. Adjustments to the six supports on each structure will still be possible in-situ, although not easily given the precision required.

IV. ION EFFECTS

In the NLC linacs, ions are created by collisional ionization of the residual gas. Light ions, such as hydrogen, are overfocused and lost between bunches, while, in the first part of the linac, heavier ions are trapped within a bunch train. Trapped ions affect the beam dynamics in three different ways. First, the additional focusing of the trailing bunches due to the ions will lead to an increased filamentation which is insignificant only for a vacuum pressure below 10^{-8} Torr [5]. Second, the ions cause a nonlinear octupole-like coupling of horizontal and vertical betatron motion, whose effect is greatly reduced when the horizontal and vertical phase advances are separated by about 5% [5]. Third, the coupled motion of beam and ions may result in a fast transverse multi-bunch instability of the electron bunch train in the linacs. If the pressure is 10^{-8} torr, the expected instability rise time at the start of the main linac is about 160 ns [6], assuming 90 bunches of $6.6 \cdot 10^9$ particles each and carbon monoxide ions (CO). The beam-ion instability disappears when the ions are no longer trapped within the train. The distance at which this happens depends on the beam current and on the ion mass. As an

example, for a bunch train of 90 bunches and $6.6 \cdot 10^9$ particles per bunch, CO ions are trapped up to a beam energy of about 38 GeV, which corresponds to a distance of about 800 m in the main linac. For an average CO pressure of $2 \cdot 10^{-8}$ torr and an initial bunch-to-bunch offset of $0.01\sigma_y$, the expected total dilution of the vertical emittance due to the beam-ion instability is then about 4%. At $5 \cdot 10^{-8}$ torr the dilution would exceed 100%. For higher beam intensities fewer ions are trapped over a shorter distance, and the pressure tolerance is looser.

V. MULTIBUNCH ENERGY CONTROL

The method of multibunch energy compensation is to linearly ramp the input RF pulse during one filling time just prior to injection of the beam [7]. Without such compensation, there would be a drop of energy of about 25% from the head of a train to the tail, due to beam loading of the accelerating mode. The bandwidth of the present NLC final focus design is $\pm 0.7\%$ [8]. Thus, the multibunch energy spread and the variation in the average energy of the beam must both be controlled to a few tenths of a percent. The simple linear ramp gives quite good compensation, but the RF pulse could be further corrected to improve the compensation (and maintain it via feedback as conditions vary).

Parameters used in the simulations are as follows: RF frequency, $f_{rf} = 11.424$ GHz, section length = 1.8 m, attenuation $\tau = 0.505$, fundamental mode $Q = 7107$, fundamental mode loss factor $\kappa_1 = 203.75$ V/pC, filling time, $T_f = 100$ ns, bunch spacing = $16\lambda_{rf} \approx 42$ cm, bunch charge = 1×10^{10} . We model the linac as made up of CG sections, with $2\pi/3$ phase advance per cell.

The bunches must be placed ahead of the RF crest (by about 13° for the parameters used here), to compensate the intrabunch energy spread. When the energy spread is optimized, there is a residual rms fractional energy spread (including both intrabunch and bunch-to-bunch spread) of about 0.2%.

We examined the sensitivity of the rms energy spread and the mean energy of the multibunch beam to bunch length, bunch charge variations, and ripple of the incoming RF pulse. The optimum energy compensation is not very sensitive to bunch length. A 20% change in bunch length away from the nominal value of $100 \mu\text{m}$ produces an additional rms energy spread of about 0.1%.

The compensation is quite sensitive to systematic changes in bunch charge, i.e., changes that are similar for all bunches in the train. Changing all the bunch charges by 2% from their optimum value increases the rms fractional energy spread from 0.2% to 0.3%. Changing all the bunch charges by 0.3% from their optimum value produces a shift of about 0.1% in the centroid energy of the beam.

The sensitivity to RF phase and amplitude ripple was studied as a function of time scale and amplitude of the ripple. The tightest tolerances occur for ripple that has large variations on a time scale comparable to the 100 nsec filling time, i.e. if the ripple is taken to be sinusoidal, the tightest tolerances occur for sinusoids with periods of 200 to 400 nsec. For shorter time scales, the ripple partly averages out over a filling time, loosening the tolerances. For longer time scales, the rms energy spread tolerances loosen somewhat, while the centroid energy tolerances remain about the same. The tolerances also depends on whether the ripple is similar in all accelerating sections — if it is random from

section to section, the tolerances are of course looser. The most pessimistic estimate, assuming a tolerance of 0.1% increment to the rms energy spread, is $\pm 0.5^\circ$ for the phase ripple and $\pm 0.3\%$ for the field-amplitude ripple. The most pessimistic estimate, assuming a tolerance of 0.1% energy centroid shift, is $\pm 0.3^\circ$ for the phase ripple and $\pm 0.3\%$ for the field-amplitude ripple.

References

- [1] T.Raubenheimer, et.al., "Parameters for the SLAC Next Linear Collider", this conference.
- [2] N.Kroll, et.al., "Manifold Damping of the NLC Detuned Accelerating Structure", 6th Workshop on Advanced Accelerator Concepts, Lake Geneva, WI, 12-18 June 1994; SLAC-PUB-6660.
- [3] K.Ko, et.al., "Design Parameters for the Damped Detuned Accelerating Structure", this conference.
- [4] K.Kubo, et.al., "Alignment Tolerances of Accelerating Structures and Correction Schemes for Future Linear Colliders", this conference.
- [5] T. Raubenheimer and P. Chen, "Ions in the Linacs of Future Linear Colliders", presented at LINAC 92, Ottawa, (1992); SLAC-PUB-5893.
- [6] T.Raubenheimer and F.Zimmermann, "A Fast Beam-Ion Instability", this conference.
- [7] K.A. Thompson and R.D. Ruth, Proceedings of the 1993 Particle Accelerator Conference, May 17-20, 1993, Washington, D.C.; SLAC-PUB-6154.
- [8] F.Zimmermann et.al., "A Final Focus System for the Next Linear Collider", this conference.

Digital Signal Processing for the APS Transverse and Longitudinal Damping System*

D. Barr and W. Sellyey†

Advanced Photon Source, Argonne National Laboratory
9700 South Cass Ave., Argonne, IL 60439

Abstract

The Advanced Photon Source (APS) at Argonne National Laboratory will be a 7-GeV machine. It is anticipated that for beam operations beyond the baseline design of 100 mA stored beam current, a transverse and longitudinal damping system is needed to damp instabilities. A key part of this digital damping system is digital signal processing. This digital system will be used to process samples taken from the beam and determine appropriate correction values to be applied to the beam. The processing will take the form of a transversal digital filter with adaptable filter weights. Sampling will be done at 176 MHz with a possible correction bandwidth of 88 MHz. This paper concentrates on the digital processing involved in this system, and especially on the adaptive algorithms used for determining the digital filter weights.

I. INTRODUCTION

If there are no interactions between circulating bunches of a synchrotron, the motion of each bunch can be described by three harmonic oscillators corresponding to the three tune frequencies. In real synchrotrons, coupling will be present, and proper description is in terms of the normal modes. If there are N bunches, there will be N modes and N tunes. It turns out however, that in many practical cases the tune shift from the non-coupled frequency is either nearly the same for all modes, or very small. Thus, all coupled modes can be taken as having the same frequency. All coupled bunches can thus be described, as in the uncoupled case, as three harmonic oscillators characterized by the same three tune-shifted frequencies.

This is the case in the APS storage ring [1]. In one simulation of the resistive wall instability, 54 evenly spaced bunches were assumed circulating in the ring to achieve the maximum design current of 300 mA. The fractional vertical tune, $\nu_y=0.3$, was reduced by an average of 6% for the 54 modes. The tune spread however, was only 0.7%. Under the same circumstances, a growth rate of 400/s in the longitudinal motion due to a single cavity higher-order mode (HOM) will result in a maximum of 2% tune shift in an affected coupled bunch mode. In the APS ring, HOM-induced longitudinal growth rates are expected to usually be below 200/s resulting in a maximum tune spread of 2%.

Since all bunches can be treated as having the same three tune frequencies, a bunch-by-bunch damping system can be implemented with one filter for each of the two transverse

tunes and a third for the longitudinal tune. For APS the same digital transversal filter design can be used for all three tunes. This paper deals with the design of filter coefficients.

It is natural to use a single pickup for this type of system. One stripline can readily be used to measure the two transverse displacements and longitudinal phase of each bunch on each turn. Two turns of information can be used to calculate the kick which needs to be applied to the bunch in order to cancel its transverse velocity. Let

$$y_1 = A \sin \phi \quad (1)$$

be the displacement of a bunch on one turn. On the next turn the displacement will be

$$y_2 = A \sin(2\pi\nu + \phi), \quad (2)$$

where ν is the fractional tune. The transverse velocity of this bunch at the kicker will be

$$y_3 = B \cos(2\pi\nu + \phi + \kappa), \quad (3)$$

where κ and B are determined from the betatron amplitude and phase considerations. It is straightforward to show that

$$(A/B)y_3 = a_1 y_1 + a_2 y_2, \quad (4)$$

where

$$a_1 = [\sin(2\pi\nu + \kappa) - \cot(2\pi\nu) \cos(2\pi\nu + \kappa)] \quad (5)$$

$$a_2 = \cos(2\pi\nu + \kappa) / \sin(2\pi\nu). \quad (6)$$

Thus, a two-term transversal filter is adequate for dealing with the transverse motion.

There are a number of reasons why more than two terms are desirable. One is that the detrimental effects of noise and digitizing granularity can be reduced. A second is that offset errors can be reduced. A third is that greater flexibility in the coefficient set is achieved, thus allowing a greater amount of adaptability due to the larger number of coefficients.

II. TRANSVERSAL FILTER

A. Theory

A general way to arrive at a useful set of coefficients is suggested by the following. Suppose there is a continuous signal

$$s(t) = s_0 \cos(\omega t + \phi). \quad (7)$$

At $t=0$ this will have the value

$$s(0) = s_0 \cos(\phi). \quad (8)$$

In order to phase shift the value of the signal at $t=0$ by θ , one can take a second signal

* Work Supported by the U.S. Department of Energy, Office of Basic Energy Sciences, under contract No. W-31-109-ENG-38.

† Present address: 902 Hillview Dr., Lemont, IL 60439.

$$r(t) = \frac{2}{T} \cos(\omega t + \theta), \quad (9)$$

where $\omega = 2\pi/T$ (T is the period of the cosine wave). Now compute the integral

$$I = \int_{-T}^0 s(t) r(t) dt = s_0 \cos(\phi - \theta) \quad (10)$$

and the desired phase shift is accomplished. By changing $r(t)$, the amplitude of I can also be controlled.

If the signal is sampled, one can achieve the phase shifting by a sum of products. This is accomplished by using a transversal filter. Thus, if a signal were taken for N revolutions,

$$x[n] = D \cos(2\pi n v + \phi) \quad n = -(N-1), \dots, 0 \quad (11)$$

and we use weights

$$b_j = \frac{2}{N} \cos(2\pi j v + \theta), \quad (12)$$

then

$$I = \sum_{n=-(N-1)}^0 b_n x[n] \quad (13)$$

should give us the desired phase-shifted signal. To calculate the proper kick, one simply chooses the appropriate θ and adjusts the amplitude to take the beta function into account. Thus, suppose the transverse velocity at the kicker is

$$v = v_0 \sin(2\pi n v + \phi + \kappa) = v_0 \cos\left(2\pi n v + \phi + \kappa - \frac{\pi}{2}\right). \quad (14)$$

The phase shift is

$$\theta = \frac{\pi}{2} - \kappa. \quad (15)$$

The term v_0/D is determined from the beta functions at the pickup and kicker.

B. Application of Filter Design

The main goal of the digital signal processing, or DSP, is to develop a transversal filter to process the incoming data [2]. The filter should be adaptive in order to deal with changes in the beam. Specifically, tune shifts could warrant an update to the filter. The main goal of the filter is to provide the proper phase and amplitude shift to the incoming signal that will produce the desired output for the kicker. Any DC offset must also be minimized. The input signal is of the form

$$x_i[n] = D_i \cos(2\pi n v + \phi_i) + E_i, \quad (16)$$

where i is the bunch number, n is the turn number, v is the fractional tune, ϕ is the reference phase, and D and E are constants. It is desired for the filter to produce some output $x'_i[n]$ such that

$$x'_i[n] = D_i F \sin(2\pi n v + \phi_i + \kappa). \quad (17)$$

F is known *a priori* and so is κ . The value of κ is related to the change in the betatron phase from the pickup to the kicker. It is possible to synthesize $x'_i[n]$ independently from $x_i[n]$ if ϕ_i is known accurately enough. This would allow for

perfect DC offset cancellation (E_i in Eq. (16)). The problem is that D_i in Eq. (16) is not known and must be derived from multiple measurements of $x_i[n]$. At least two measurements would be required and probably more would be used in practice. Unfortunately, it will take too long to solve for D_i and synthesize $x'_i[n]$. This leaves some sort of real-time filtration of $x_i[n]$ to produce $x'_i[n]$.

The transversal filter will take the form of

$$x'_i[n] = \sum_{j=0}^{N-1} b_j x_i[n-j], \quad (18)$$

where N is the number of filter weights. The filter operates on data from past turns as well as the present turn (assuming $N > 1$). Each bunch in the ring will have to be dealt with separately, but will use the same filter.

The goal now is to design the filter weights (the b_j 's in Eq. (18)) in order to model Eq. (17). The filter must effectively implement the gain, the phase shift (this also includes transforming the cosine to a sine), and the DC offset rejection. From the derivation in the previous section, a sine wave in the filter coefficients will be used. From Eqs. (12) and (15), take the weights to be

$$b_j = \frac{2}{N} \cos\left(2\pi j v + \frac{\pi}{2} - \kappa\right). \quad (19)$$

Using Eqs. (16) and (19), Eq. (18) becomes

$$x'_i[n] = D_i F \frac{2}{N} \sum_{j=0}^{N-1} \cos\left(-2\pi j v + \frac{\pi}{2} - \kappa\right) \left[\cos\left(2\pi(n-j)v + \phi_i\right) + E_i \right]. \quad (20)$$

If Eq. (20) is simulated using a digital computer, it is seen that the chosen filter effectively accomplishes the desired goal. Note that the sum of b_j over all j produces the attenuation factor for E_i . In other words if all the filter weights summed to 0.2, the DC offset would be reduced to 20% of its previous value.

III. SIMULATIONS AND RESULTS

Figure 1 shows the calculated and simulated data using four weights with $D_i = F = 1.0$, $\phi = 0.0$, $\kappa = 0.7$, and $v = 0.3$. The graphs show the actual calculated beam position at the kicker (calculated) versus the filtered prediction at the kicker (simulated). This result is typical in that small but significant errors result by using weights defined by Eq. (19). These errors can be eliminated by introducing an additional multiplicative constant, B , for each coefficient and requiring that the calculated and simulated results be equal. In particular, letting $n=0$, $D_i = F = 1.0$, $E_i = 0.0$, and $\phi_i = \phi$, one gets, using Eqs. (14), (17), and (20),

$$\cos\left(\phi + \kappa - \frac{\pi}{2}\right) = \frac{2}{N} \sum_{j=0}^{N-1} B_j \cos\left(-2\pi j v + \frac{\pi}{2} - \kappa\right) \cos(-2\pi j v + \phi). \quad (21)$$

Expanding this and requiring that this be true for any κ and any ϕ , one gets three equations:

$$\sum B_i \cos^2(2\pi v_i) = \frac{N}{2}, \quad (22)$$

$$\sum B_i \sin^2(2\pi v_i) = \frac{N}{2}, \quad (23)$$

$$\sum B_i \sin(4\pi v_i) = 0. \quad (24)$$

Thus for $N=2$, Eqs. (5) and (6) are used for calculating the weights. For $N=3$, Eqs. (22), (23) and (24) are used. For $N>3$, the above expressions, combined with additional conditions would be used. In particular, for $N \geq 4$ one can impose the additional condition that

$$\sum B_i \cos\left(-2\pi v_i + \frac{\pi}{2} - \kappa\right) = 0. \quad (25)$$

This assures complete DC offset cancellation. Figure 2 compares the calculated and simulated results for $N=4$ after solving for the B_i 's from Eqs. (22), (23), (24), and (25). As expected, there is complete overlap.

As discussed earlier, the largest expected tune spread will be about 2% of the fractional tune. Figure 3 was generated by using the same weights as in Figure 2 ($v=0.3$), but letting $v=0.3 \times 98\%$ for generating the measured positions of the bunch (for the simulated data). The ratio of the sum of the magnitude of the difference at each turn, over the sum of magnitudes is 6%.

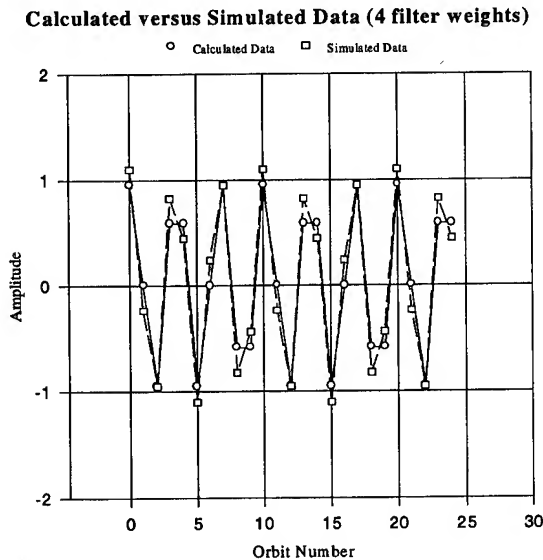


Figure 1. Calculated versus Simulated Data (4 filter weights)

IV. CONCLUSIONS

Multi-tap programmable transversal filters are useful for calculating the required kick in damping systems. The larger the number of taps (or filter weights), the greater the flexibility. In particular, four or more taps can be used to assure the elimination of the detrimental effects associated with DC offsets. Effects of noise and digitizing granularity can be reduced. Large tune shifts can be accommodated. A

single filter design can accommodate both transverse and longitudinal damping.

Calculated versus Simulated Data (4 filter weights)

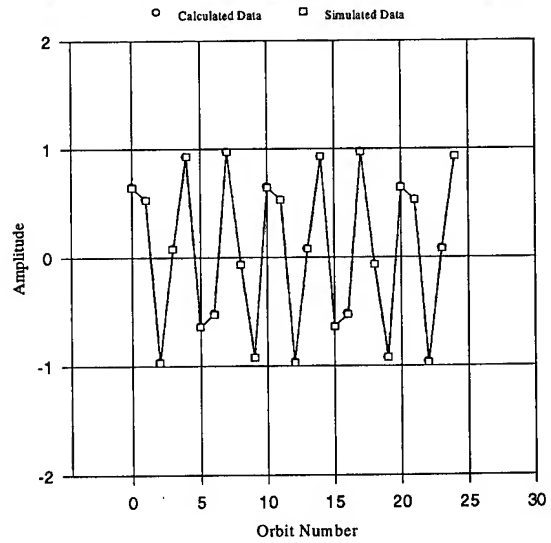


Figure 2. Corrected Calculated versus Simulated Data ($v=0.3$)

Calculated versus Simulated Data (4 filter weights)

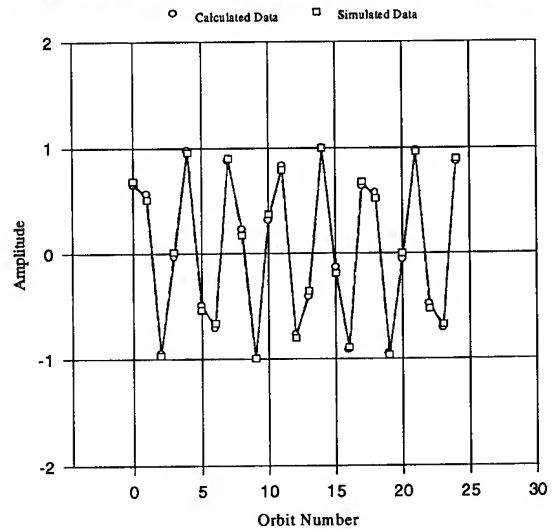


Figure 3. Corrected Calculated versus Simulated Data ($v=0.3 \times 98\%$)

V. REFERENCES

1. W. Sellyey, D. Barr, E. Kahana, and A. Votaw, "Design of the APS Transverse and Longitudinal Damping System," *Proc. of the Beam Instrumentation Workshop*, Vancouver, Canada, 1994.
2. D. Barr, *Beam Position and Angle Jitter Correction in Linear Particle Beam Accelerators*, Ph.D. Dissertation, Texas Tech University, 1992, UMI order #9226291.

LONGITUDINAL COUPLING IMPEDANCE OF A HOLE IN AN INFINITE PLANE SCREEN*

Yong-Chul Chae

Argonne National Laboratory, 9700 So. Cass Ave., Argonne, Illinois 60439, U.S.A.

Abstract

An analytical formula for the longitudinal coupling impedance of a hole is developed using a variational method. We show that the coupling impedance can be expressed as a sum of functional series, whose argument is the dimensionless quantity kd alone, where k is the free-space wave number and d is the radius of the hole. When expanded in powers of kd , we recover the long wavelength result as a limiting case. The numerical evaluation reveals that the impedance can be well modeled by an RLC-resonator circuit. We also show the qualitatively good agreement between the theory and the MAFIA-T3 simulation for the geometry of a hole in a coupled waveguide with rectangular cross section.

I. PROBLEM STATEMENT

The geometry of our problem is shown in Fig. 1 where a charge is moving in the z -direction with velocity close to the speed of light. The distance between the plane screen and the beam path is b , and the origin of the coordinate is at the center of the hole with radius d . The local cylindrical coordinate system (ρ, θ, y) is also shown. We calculate the longitudinal coupling impedance for this geometry.

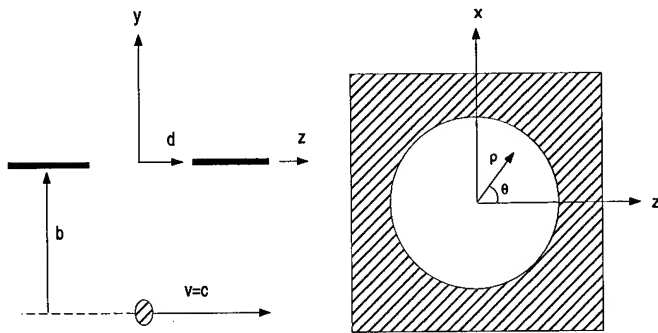


Figure 1. Infinite Flat Screen with a Hole.

II. LOW FREQUENCY SOLUTION

Denoting \mathbf{E}_1 and \mathbf{H}_1 as the fields without the hole and \mathbf{E}_2 and \mathbf{H}_2 as the fields with the hole, we can express the longitudinal coupling impedance as [1]

$$|I_0|^2 Z(k) = \int_{hole} (\mathbf{n} \times \mathbf{E}_2) \cdot \mathbf{H}_1^* dS, \quad (1)$$

where $\mathbf{n} \times \mathbf{E}_2 \equiv \mathbf{J}_m$ is the magnetic current induced in the hole, which is not known until we solve the problem.

Assuming a small hole, namely $kd = 2\pi d/\lambda \ll 1$, Bethe obtained the solution for the magnetic current in the hole as [2]

$$\mathbf{n} \times \mathbf{E} = - \underbrace{\frac{\rho}{\pi \sqrt{d^2 - \rho^2}} \mathbf{e}_\rho \times \mathbf{E}_0}_{\mathbf{J}_{m,E}} + j \underbrace{\frac{2kZ_0}{\pi} \sqrt{d^2 - \rho^2} \mathbf{H}_0}_{\mathbf{J}_{m,H}}, \quad (2)$$

where \mathbf{E}_0 and \mathbf{H}_0 are the field evaluated at the center of the hole in the absence of the hole, and $\mathbf{J}_{m,E}$ and $\mathbf{J}_{m,H}$ denote the magnetic current induced in the hole due to the incident electric and magnetic fields, respectively.

The magnetic field from the unit source current can be obtained using the image principle. In the plane of the hole, it becomes

$$H_x = -\frac{I_0}{\pi} \frac{b}{x^2 + b^2} e^{-jkz}, \quad H_z = 0, \quad (3)$$

where the coordinate system defined in Fig. 1 is used.

Assuming a small hole in which the field strength is uniform but the phase is varying, we may rewrite the source field as

$$\mathbf{H}_1 = \mathbf{H}_0 - jkz\mathbf{H}_0 + \mathcal{O}(k^2), \quad \text{where } \mathbf{H}_0 = -\frac{I_0}{\pi b} \mathbf{e}_x. \quad (4)$$

Then, the longitudinal coupling impedance becomes

$$|I_0|^2 Z_H(k) = \int_{hole} \mathbf{J}_{m,H} \cdot \mathbf{H}_1^* dS = j \frac{4Z_0 d^3 H_0^2}{3} k, \quad (5)$$

$$|I_0|^2 Z_E(k) = \int_{hole} \mathbf{J}_{m,E} \cdot \mathbf{H}_1^* dS = -j \frac{2Z_0 d^3 H_0^2}{3} k, \quad (6)$$

$$|I_0|^2 Z(k) = Z_H(k) + Z_E(k) = j \frac{2Z_0 d^3 H_0^2}{3} k, \quad (7)$$

which results in $Z(k) = (2Z_0 d^3 / 3\pi^2 b^2) k$.

If we apply the above formula to a cylindrical beam pipe of radius b with a hole of radius d , the longitudinal coupling impedance becomes, with $H_0 = \frac{I_0}{2\pi b}$ in Eq. (7),

$$Z(k) = j \frac{Z_0 d^3}{6\pi^2 b^2} k, \quad (8)$$

which is exactly the same as the well-known results [1].

III. VARIATIONAL SOLUTION

A. Variational Formalism

We begin by defining an "impedance functional" which is stationary with respect to the unknown quantity (magnetic current density in the hole).

We define the impedance functional Z as

$$Z = - \int \mathbf{J} \cdot (\mathbf{E}_2 - \mathbf{E}_1) dV. \quad (9)$$

*Work supported by U.S. Department of Energy, Office of Basic Energy Sciences under contract No. W-31-109-ENG-38.

In the above definition, as we subtracted the contribution from the source field, the entire contribution is from the scattered field which satisfies the homogeneous Maxwell's equations. We note that if the electric field is real, the longitudinal impedance is the complex conjugate of the impedance functional, $Z(k) = Z^*(k)^1$.

If the integrating surface is chosen to coincide with the plane of the screen where \mathbf{E}_1 satisfies the boundary condition $\mathbf{n} \times \mathbf{E}_1 = 0$, Z reduces to

$$Z = \int \mathbf{H}_1 \cdot (\mathbf{n} \times \mathbf{E}_2) dS. \quad (10)$$

By using Rumsey's reaction concept [3], [4], we can derive the variational expression for Z as [5]

$$Z = \frac{1}{4j\omega\epsilon} \frac{\left[\int_{S_a} \mathbf{H}^i \cdot (\mathbf{n} \times \mathbf{E}^a) dS \right]^2}{\int_{S_a} \int_{S_a} [\mathbf{n} \times \mathbf{E}^a(\mathbf{r})] \cdot \overline{\mathbf{G}}_0(\mathbf{r}|\mathbf{r}') \cdot [\mathbf{n} \times \mathbf{E}^a(\mathbf{r}')] dS dS'}, \quad (11)$$

where \mathbf{H}^i is the incident magnetic field on the screen (previously denoted as \mathbf{H}_1), \mathbf{E}^a is the assumed electric field in the hole, and $\overline{\mathbf{G}}_0(\mathbf{r}|\mathbf{r}')$ is the free-space dyadic Green's function.

The above formula is a homogeneous equation in the sense that the result does not depend on the amplitude of the assumed electric field \mathbf{E}^a . If a proper dyadic Green's function is used, this is a general expression for the impedance functional of an aperture in a conducting plane as long as the plane is the symmetry plane separating two regions, namely, an infinite plane or coupled waveguide structure. Details of the calculation depend on the shape of the aperture and the assumed tangential electric field in the aperture.

B. Results

In order to evaluate the variational expression represented by Eq. (11), we assume a trial function for \mathbf{E}^a based on the Bethe's solution in Eq. (2):

$$\mathbf{n} \times \mathbf{E}^a = \mathbf{e}_\theta \sum_{n=1}^{n=\infty} b_n \rho^n \left(1 - \frac{\rho^2}{d^2}\right)^{\frac{1}{2}-n} + \mathbf{e}_x \sum_{n=1}^{n=\infty} a_n \left(1 - \frac{\rho^2}{d^2}\right)^{n-\frac{1}{2}}. \quad (12)$$

This field satisfies Meixner's "edge-field" condition [6].

The coefficients a_n and b_n are unknown quantity and dependent on the frequency. We used the method developed by Levine and Schwinger [7] to determine these coefficients, and the detailed results can be found in [5].

Once the a_n and b_n coefficients are determined, we can use them to calculate the longitudinal coupling impedance. It turns out that the coupling impedance is numerically equal to the impedance functional. We also found that the magnetic current from the electric and magnetic field does not couple in contribution to the coupling impedance. Thus we write the impedance as

$$Z^{(N+M)} = Z_E^{(N)} + Z_H^{(M)}, \quad (13)$$

where M or N denotes the order of approximation or the number of terms used for trial fields.

It may be interesting to compare $Z_E^{(1)}(k)$ and $Z_H^{(1)}$ expanded in powers of kd . We find that

$$\begin{aligned} Z_H^{(1)} &= \frac{32Z_0 d^2 H_0^2}{27\pi} (kd)^4 \left(1 + \frac{22}{25}(kd)^2 - \dots\right) \\ &\quad + j \frac{4Z_0 d^2 H_0^2}{3} (kd) \left(1 + \frac{2}{5}(kd)^2 - \dots\right), \\ Z_E^{(1)} &= \frac{8Z_0 d^2 H_0^2}{27\pi} (kd)^4 \left(1 - \frac{19}{25}(kd)^2 + \dots\right) \\ &\quad - j \frac{2Z_0 d^2 H_0^2}{3} (kd) \left(1 - \frac{2}{5}(kd)^2 + \dots\right). \end{aligned}$$

In the low frequency range, it is found that $Z^{(2)} \simeq j(2Z_0 d^3 H_0^2/3)k$, which is the same as the low frequency result found in the previous section.

Since $H_0 \sim b^{-1}$, the above result shows that the impedance scales as $(d/b)^2$.

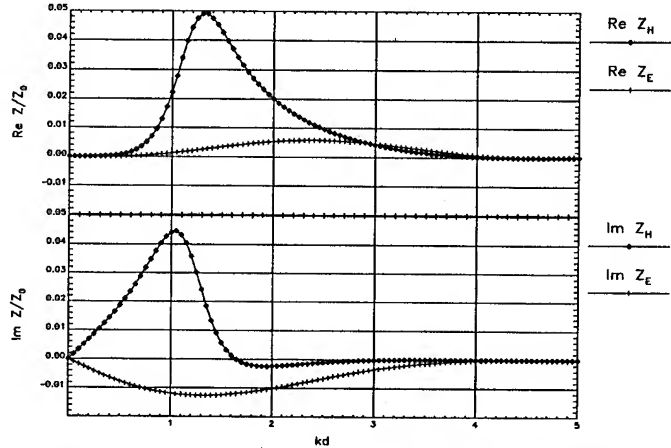


Figure 2. Comparison of Impedances due the Incident Magnetic Field, Z_H , and Electric Field, Z_E .

Numerical results of $Z_H^{(1)}$ and $Z_E^{(1)}$ are presented in Fig. 2. It shows that the impedance of magnetic type Z_H is mainly inductive ($\text{Im } Z_H > 0$), and the electric type Z_E exhibits capacitive behavior ($\text{Im } Z_E < 0$).

The results, using the three terms $Z^{(3)} = Z_E^{(1)} + Z_H^{(2)}$, are shown in Fig. 3, from which we find that the maximum value of $\text{Re } Z(k)$ is $\text{Re } Z(k)_{\max} = 0.216Z_0$. For all other d/b , it becomes $\text{Re } Z(k, d/b)_{\max} = 0.216Z_0(d/b)^2$.

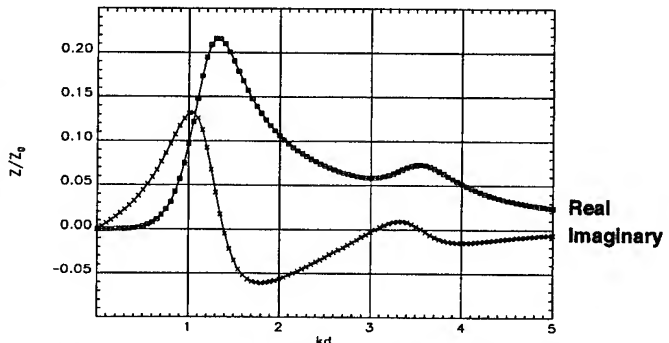


Figure 3. Variational Results Using Three-Term Electric Field. (The ratio $d/b=1.0$ is used.)

¹We found that the coupling impedance does not have the stationary property in general.

IV. BROADBAND RESONATOR MODEL

Since the impedance shown in Fig. 3 is similar to the impedance of a parallel RLC-resonator circuit, it would be useful if we described the impedance in terms of circuit parameters. The impedance of an RLC-resonator circuit is

$$Z(\omega) = \frac{R}{1 + jQ \left(\frac{\omega}{\omega_r} - \frac{\omega_r}{\omega} \right)}, \quad (14)$$

where R is the shunt impedance, Q is the quality factor, and ω_r is the resonant frequency.

The resonant frequency and the quality factor can be read from Fig. 3. For the Q value, we used the definition $Q = \omega_r / 2\Delta\omega$, where $|Z(\omega)|$ at the frequency $\omega = \omega_r + \Delta\omega$ is 0.707 of its maximum value. The shunt impedance can be determined in two ways. We can either use the impedance in the low frequency limit, $Z(k) = j(2Z_0 d^3 H_0^2 / 3)k$, or the impedance at resonance, $Z(k) = 0.216 Z_0 (d/b)^2$. Denoting these two models as BBR-1 and BBR-2, respectively, the circuit parameters are shown in Table I.

Table I
Circuit Parameter Based on BBR Model

Model	ω_r	Q	R
BBR-1	$1.35(c/d)$	1.8	$0.164 Z_0 (d/b)^2$
BBR-2	$1.35(c/d)$	1.8	$0.216 Z_0 (d/b)^2$

We compared the impedances from the two models with the variational result, which is shown in Fig. 4. Note that $(Z(k)/Z_0)/kd$ is plotted, which is the useful quantity in the instability calculation.

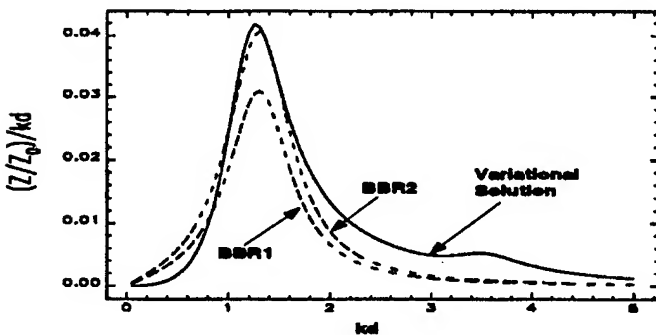


Figure 4. Comparison of Impedances from Variational Solution and Broadband Resonator Model.

V. APPLICATION TO ACCELERATOR CHAMBER

We also applied the above results to the accelerator chamber. As a model geometry we considered the rectangular waveguides coupled by the hole in the common wall. In the analysis, we used the image charges in order to remove the waveguide wall. By doing so we could investigate the contributions from the real charge and the image charges to the impedance separately. We found that the image-charge contribution is small, as long as d/b is small [5].

We compared the variational results with a MAFIA-T3 [8] simulation. The geometry used in the MAFIA-T3 simulation has a 2 cm-by-1 cm rectangular waveguide with a hole of varying radius on the 1-mm-thick common wall.

The results for the hole with a radius of 1 mm corresponding to $d/b=0.2$ are shown in Fig. 5. The agreement between the two results is qualitatively good. From the range of frequency we can conclude that the appropriate length scale is the size of the hole and not the size of the waveguide. Thus the scaling we found in the previous section also applies to the waveguide geometry.

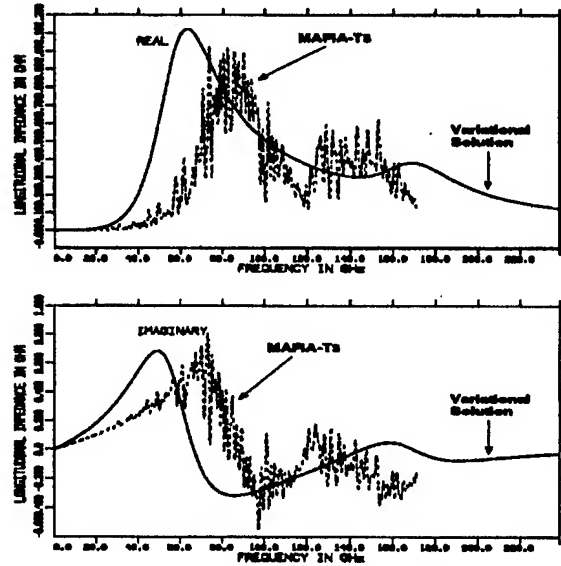


Figure 5. Coupling Impedance of the Hole with a Radius of 1 mm in the Coupled Waveguide.

References

- [1] Gluckstern, R. L., CERN SL/AP 92-05, 1992.
- [2] Bethe, H. A., *Phys. Rev.*, Vol. 66, 163, 1944.
- [3] Rumsey, V. H., *Phys. Rev.*, Vol. 94, 1483, 1954.
- [4] Harrington, R. F., *Time Harmonic Electromagnetic Fields*, McGraw-Hill Book Company, Inc., New York, 1961.
- [5] Chae, Y.-C., ANL Report LS-242, 1993.
- [6] Bouwkamp, C. J., *Reports on Progress in Physics*, Vol. XVII, 35, 1954.
- [7] Levine, H. and J. Schwinger, *Commun. Pure Appl. Math.*, Vol. 3, 355, 1950.
- [8] Klatt, R. and et al., *Proc. of the 1986 Linear Accel. Conf.*, 276, 1986.

Investigation of Resistive Wall Instability in the 7-GeV APS Storage Ring*

Yong-Chul Chae

Argonne National Laboratory, 9700 So. Cass Ave., Argonne, Illinois 60439, U.S.A.

Abstract

The Advanced Photon Source (APS) storage ring is a 7-GeV light source with 40 straight sections. Intense x-ray beams will be delivered by 34 insertion devices installed in these straight sections. The vacuum chamber for the insertion devices has an elliptical cross section with the gap equal to 8 mm. With this narrow gap, we estimate that the transverse impedance of the ring at the revolution frequency could be as high as $36 M\Omega$ from the resistive wall. By increasing the (unnormalized) chromaticity to 7, we cure the head-tail modes of order up to $m=1$ for all 60 coupled bunch mode patterns around the ring. Tracking results show that the increased sextupole strength resulting from a higher chromaticity does not significantly reduce the dynamic aperture. Since increased chromaticity alone cannot cure all the head-tail modes, the APS storage ring will have a feedback system to damp the rigid-bunch modes.

Introduction Resistive wall impedance can cause the coupled bunch instability due to the peak near the origin (long range wakefield or multi-turn effects) as well as the higher-order head-tail modes via the broad-band tail (short range wakefield or single-turn effects). Since the growth rate from the resistive wall instability is in general slow, the strategy is to damp the fastest growing mode of the coupled bunch oscillation by adjusting the chromaticity slightly above zero, causing the unstable head-tail modes to become stabilized by the radiation damping and/or Landau damping.

However, we found that this is not the case for the APS storage ring.

Resistive Wall Impedance R. Gluckstern, J. Zeitz and B. Zotter [1] have derived expressions for the longitudinal and transverse resistive wall coupling impedance for a beam pipe of arbitrary cross section in the ultra-relativistic limit. Explicit results for the transverse impedance for the beam pipe of elliptic cross section with the major axis a and the minor axis b may be written

$$\begin{aligned} Z_{x,y}(\omega) &= (1+j) \frac{Z_0 \delta L}{2\pi b^3} F_{x,y}(q) \\ &\equiv Z_{\perp, circular}(b, \omega) F_{x,y}(q), \end{aligned} \quad (1)$$

where $Z_{\perp, circular}(b, \omega)$ is the transverse impedance for the cylindrical beam pipe of radius b and $F_{x,y}(q)$ is the form factor expressed in terms of "nome" $q = (a-b)/(a+b)$. The subscripts x and y denotes the horizontal and vertical impedance, respectively. Denoting Z_y as Z_{\perp} and using the fact that the vertical form factor, $F_y(q)$ is bounded by 0.8 and 1.0 for the entire range of q , we may approximate Eq. (1) as

$$Z_{\perp}(\omega) \simeq Z_{\perp, circular}(b, \omega). \quad (2)$$

Then, Eq. (2) may be rewritten as

$$Z_{\perp}(\omega) = (\text{sign}(\omega) + j) Z_{\perp}(\omega_0) \sqrt{\frac{\omega_0}{\omega}}, \quad (3)$$

where $Z_{\perp}(\omega_0)$ is the impedance evaluated at the revolution frequency. The APS storage ring consists of 34 straight sections for insertion devices (IDs) with half gap, b , equal to 4 mm and length equal to 6.5 m per each straight section and the remaining sections with b equal to 2 cm. Then the resistive wall impedance, $Z_{\perp}(\omega_0)$, from the 34 ID vacuum chambers and the remaining sections are $34.5 M\Omega/m$ and $1 M\Omega/m$, respectively. We estimate that the total impedance for the APS storage ring due to the resistive wall is $36 M\Omega/m$. In the estimation we used the resistivity of Al at room temperature is $3 \cdot 10^{-8} \Omega m$, and the skin depth at revolution frequency of 0.2715 MHz is $168 \mu m$.

Rigid Bunch Case Consider a single rigid bunch is circulating in the ring. The "rigid" bunch means no internal motion inside the bunch, and the bunch can be approximated as a macro particle with charge Q . The equation of motion including the wakefield effects may be written as

$$\frac{d^2 y}{dt^2} + \omega_{\beta}^2 y = \frac{eQ}{\gamma m_0} \sum_{k=1}^{\infty} y(t - kT_0) \frac{W_{\perp}(kT_0)}{2\pi R}, \quad (4)$$

where ω_{β} is the free betatron oscillation frequency, T_0 is the revolution period, Q is the total charge of a bunch, and m_0 is the rest mass of a particle. The contributions from all previous turns are included as a sum in the equation.

Equation (4) may be solved by assuming that y varies harmonically as $e^{j\Omega t}$. The resulting coherent frequency shift may be written as

$$\Delta\omega_c = \Omega - \omega_{\beta} = jC_T \sum_{p=-\infty}^{+\infty} Z_{\perp}(p\omega_0 + \omega_{\beta}), \quad (5)$$

where

$$C_T = \frac{cI_0}{4\pi v_{\beta} E/e},$$

c is the velocity of light, I_0 is the average current of a single bunch, E is the total energy of a particle, and v_{β} is the vertical betatron tune.

Substituting the resistive wall impedance into Eq. (5),

$$\tau^{-1} \equiv -Im\Delta\omega_c = -C_T Z_{\perp}(\omega_0) \sqrt{\omega_0} \sum_p \frac{\text{sign}(p\omega_0 + \omega_{\beta})}{\sqrt{|p\omega_0 + \omega_{\beta}|}}. \quad (6)$$

Separating the tune into the integral and fractional parts denoted as $v_{\beta} = n_{\beta} + \Delta_{\beta}$ and absorbing the integral part into the summation indices, we find that

$$\tau^{-1} = -C_T Z_{\perp}(\omega_0) G(2\pi, \Delta_{\beta}), \quad (7)$$

*Work supported by U.S. Department of Energy, Office of Basic Energy Sciences under Contract No. W-31-109-ENG-38.

where $G(2\pi, \Delta\beta)$ is the familiar Courant-Sessler bunch function [2]. For M evenly spaced bunches, we replace I_0 by MI_0 and the mode frequency changes to $\omega_p = (Mp + n)\omega_0 + \omega_\beta$ including the coupled bunch mode number n ranging from 0 to $M - 1$. The resulting expression for the growth rate is

$$\tau^{-1} = -C_T Z_\perp(\omega_0) \sqrt{M} G(2\pi, \text{mod}(\frac{n + \nu_\beta}{M})). \quad (8)$$

The growth rate is positive when $\frac{n + \nu_\beta}{M}$ lies between an integer and next lower half-integer, and negative in the other half-interval. We can easily show that, if M is even, half the coupled bunch modes are stable and the other half are unstable.

When we applied the above formula to the APS storage ring, we assumed $I_0 = 5 \text{ mA}$, $\nu_\beta = 14.3$, and $E = 7 \text{ GeV}$ and used $Z_\perp(\omega_0) = 36 \text{ M}\Omega$. We found that

$$\tau^{-1} = -42.84 \sqrt{M} G(2\pi, \text{mod}(\frac{n + \nu_\beta}{M})).$$

Assuming sixty bunches circulating in the ring, the growth rate for the fastest growing mode of $n=45$ becomes

$$\tau^{-1} \simeq 3072 \text{ s}^{-1} > \tau_R^{-1} = 106 \text{ s}^{-1},$$

where τ_R^{-1} is the (synchrotron) radiation damping rate. Hence we conclude that some of the coupled bunch modes grow indefinitely resulting in possible beam loss. However, by assuming rigid bunch we ignored an important stabilizing mechanism due to the internal motion of particles inside the bunch. This is the subject of the next section with application to the APS storage ring.

Non-Rigid Bunch Case

The general expression for the coherent frequency shift [3] without considering mode coupling can be written as

$$\Delta\omega_{m,n} = \frac{j}{1+m} C_T M \frac{\sum Z_\perp(\omega) H_m(\omega_p - \omega_\xi)}{B \sum H_m(\omega_p - \omega_\xi)}, \quad (9)$$

where

$$\omega_p = (Mp + n)\omega_0 + \omega_\beta + m\omega_s,$$

$$n = \text{(coupled) bunch mode number,}$$

$$m = \text{head-tail mode number,}$$

$$\omega_\xi = \text{chromaticity frequency } (\xi\omega_0/\eta),$$

$$\xi = \text{chromaticity } (\Delta\nu_\beta/(\Delta p/p)),$$

$$B = \text{bunching factor (bunch length/circumference),}$$

$$H_m(\omega) = \text{self-power density } (|\lambda(\omega)|^2).$$

For a beam with Gaussian distribution, we take Hermitian line-density mode with the Fourier transforms

$$\lambda_m(\omega) = C_m j^{-m} (\omega\sigma_\tau)^m \exp(-\omega^2\sigma_\tau^2/2), \quad (10)$$

where σ_τ is the rms bunch length in time. The factor C_m may be determined such that the denominator in Eq. (9) becomes unity, i.e. $B \sum H_m(\omega_p - \omega_\xi)$. The summation was evaluated by Zotter [4] who found that

$$C_m^2 = \frac{2\pi}{r\Gamma(m + \frac{1}{2})}, \quad (11)$$

where

$$r = \frac{\tau_L}{\sigma_\tau} = \begin{cases} 4 & \text{for protons} \\ 3\sqrt{\pi/2} \approx 3.76 & \text{for electrons,} \end{cases}$$

and τ_L is the baseline bunch length. Then the normalized power spectrum has a peak at $\omega = \sqrt{m}/\sigma_\tau + \omega_\xi$ with values of 0.943, 0.694, 0.681, and 0.676 for $m = 0, 1, 2$, and 3, respectively. We note that these are equivalent to the maximum values of Sacherer's form factor [3] for the electron beam.

Denoting ω_{p0} as the lowest mode frequency and $\omega^\pm = \omega_{p0} \pm M\omega_0$, we may rewrite Eq. (9) as

$$\Delta\omega_{m,n} = \frac{j}{1+m} C_T \left(\underbrace{\frac{1}{\omega_0} \int_{-\infty}^{\omega^-} (\dots) + \frac{1}{\omega_0} \int_{\omega^+}^{+\infty} (\dots)}_{\text{"single-turn effect"}} \right. \\ \left. + \underbrace{M Z_\perp(\omega_{p0}) H_m(\omega_{p0} - \omega_\xi)}_{\text{"multi-turn effect"}} \right)$$

If the chromaticity is zero, the growth rate from the rigid bunch approximation and the growth rate from the multi-turn effect should be close to each other. It turns out $\tau^{-1} = 3072 \text{ sec}^{-1}$ and 3021 sec^{-1} , respectively, showing that the single spectrum line located nearest the origin has the dominant effect. The numerical results were obtained by using the program BBI [5].

The stabilization of the lowest mode ($m=0$) can be achieved by adjusting the chromaticity to the value greater than zero. The single-turn effect provides a large damping effect. It is shown in Fig. 1, where the chromaticity is equal to 1. The maximum growth rate is still greater than the radiation damping rate.

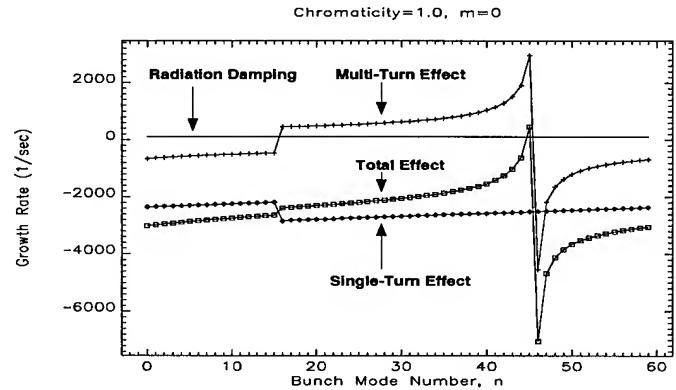


Figure 1. Single- and Multi-Turn Effects on $m = 0$ Mode at $\xi_y = 1.0$.

Thus, we further increase the chromaticity up to 7 in order to stabilize both the $m=0$ and $m=1$ head-tail modes. The results are shown in Fig. 2.

However, at chromaticity equal to 7 we found that the higher head-tail modes become unstable. Figure 3 shows the unstable modes, $m = 3$ and $m = 4$, together with the damped modes, $m = 0$ and $m = 1$.

Even though the excitation of such high head-tail modes was never observed in the electron storage ring, it is prudent to cure the instability using the feedback-damper system. The feedback system has to damp the $m = 0$ growing mode with the chromaticity adjusted at zero, where all higher modes, $m \geq 1$, are naturally damped.

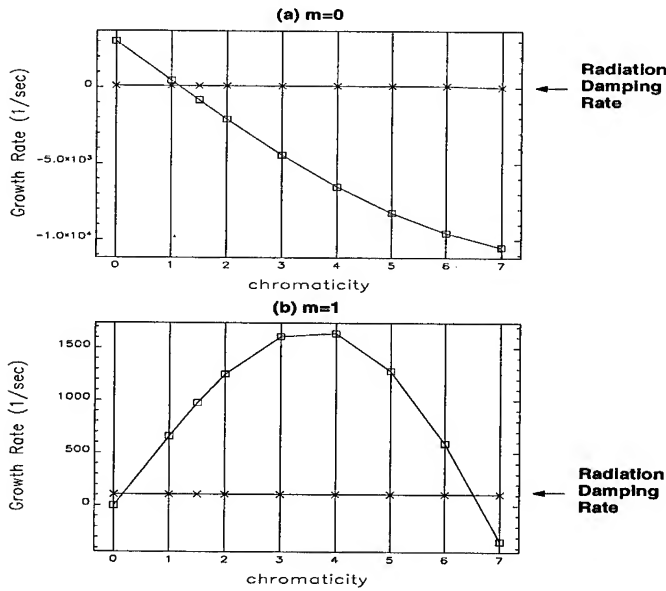


Figure 2. Growth Rate vs. Chromaticity for $m = 0$ (a) and $m = 1$ (b) Head-Tail Modes.

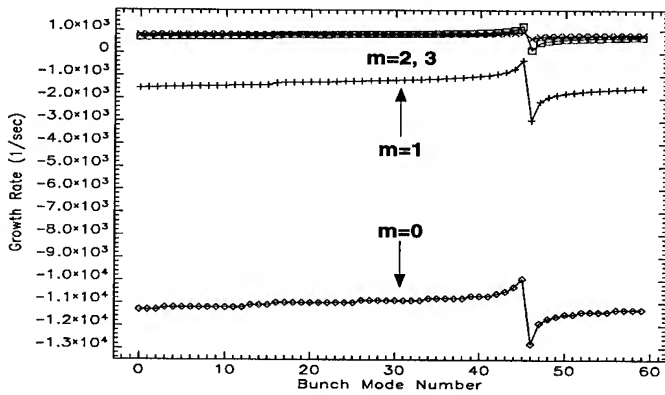


Figure 3. Growth Rate for Various Head-Tail Modes at $\xi_y = 7.0$.

During early operation of the APS storage ring when there are only 16 narrow ID chambers instead of 34, we may not need the feedback-damper system because we found that we can stabilize all head-tail modes up to a beam current of 100 mA by shifting ξ_y to ~ 0.32 .

Dynamic Aperture With the provision of operating the ring in high chromaticity, we need to make sure that the ring has large dynamic aperture. The chromaticity-correcting sextupoles in the APS storage ring can adjust the chromaticity anywhere in the triangular region bounded by the three vertices, namely $(\xi_x, \xi_y) = (0, 0)$, $(20, 0)$ and $(0, 16)$, including the diagonal line up to $\xi_x = \xi_y = 10$. The original design value of chromaticity for the APS storage ring is equal to zero. The nominal strengths of the horizontally focusing sextupole (SF) and defocusing sextupole (SD) are

$$\frac{B''l}{(B\rho)} = 4.6 \text{ m}^{-2} \text{ (SD)}, 4.2 \text{ m}^{-2} \text{ (SF)}.$$

In order to obtain a chromaticity equal to 7 in both horizontal and vertical planes, we need to increase the strengths by 14% in the SF and 10% in SD.

Dynamic aperture reduction due to increased sextupole

strengths, shown in Fig. 4, is not much even without readjusting the strength of the harmonic-correction sextupoles.

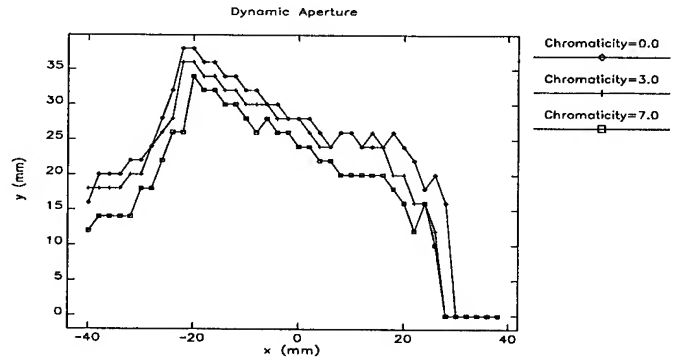


Figure 4. Dynamic Aperture at Various Chromaticities.

References

- [1] R. Gluckstern, J. Zeijts and B. Zotter, "Coupling Impedance of a Hole in an Elliptical Beam Pipe," CERN SL/AP 92-25 (1992).
- [2] E. D. Courant and A. M. Sessler, "Transverse Coherent Resistive Instabilities of Azimuthally Bunched Beams in Particle Accelerators," *Rev. of Sci. Inst.*, Vol. 37, No. 11 (1966), 1579.
- [3] F. Sacherer, "Transverse bunched-beam instability - theory," *Proc. 9th Int. Conf. on High Energy Accelerators*, Stanford (1974).
- [4] B. Zotter, CERN/ISR-TH/82-10 (1982).
- [5] B. Zotter, CERN/LEP-TH/89-74 (1989).

LONGITUDINAL INSTABILITY ANALYSIS FOR THE IPNS UPGRADE *

K. Harkay, Y. Cho, E. Lessner, Argonne National Laboratory, Argonne, IL 60439 USA

Abstract

The proposed 1-MW spallation neutron source upgrade calls for a 2-GeV rapidly-cycling synchrotron (RCS) with an intensity of 1.04×10^{14} protons per pulse [1]. Due to the high intensity, the potential exists for collective instabilities. Emphasis is placed on controlling these by (a) minimizing the machine impedance by using a contour-following rf shield and (b) maximizing the momentum spread to make use of Landau damping. The coupling impedance is estimated and is dominated by space charge effects. It is found that the longitudinal microwave stability limit can be exceeded unless the momentum spread is sufficient. A longitudinal tracking code was developed to simulate injection and acceleration, including the effects of space charge and other sources of impedance [2]. With the aid of the simulation, and under the assumptions of the instability theory, we arrive at an rf voltage profile and beam injection parameters which avoid both the instability and beam loss through the entire cycle. The limitations of the analysis are explored.

I. INTRODUCTION

Of the several known longitudinal instabilities, only the single-bunch instabilities need to be considered since the RCS operates with a harmonic number $h=1$. The microwave instability is potentially the most dangerous, and it is analyzed in detail. This instability should not occur in a machine operating below transition energy, such as the RCS, if the coupling impedance is purely capacitive (space charge). However, it could occur in the RCS when there are resistive components. The instability growth rate then depends on the momentum distribution of the beam, particularly the shape of the distribution tails. A detailed analysis of this instability requires not only knowledge of the coupling impedance seen by the beam, but also the peak current and energy spread of the beam. At this stage, this beam information was obtained through Monte Carlo simulations [2].

A conservative approach is adopted to prevent the onset of instability:

- The contributions to the coupling impedance from the various RCS components are estimated.
- The Keil-Schnell criterion, modified for bunched beams, is used to obtain the $\Delta p/p$ required to raise the threshold current, although it overestimates the severity of the instability below transition energy.
- Using the peak current and energy spread of the circulating beam obtained from the longitudinal tracking studies, a detailed analysis of the stability diagram is made.

II. COUPLING IMPEDANCE ESTIMATION

The longitudinal coupling impedance, $Z_{||}$, is estimated using the standard approximations [3-5]. The impedance for the

RCS is dominated by space charge effects. The beam position monitors (BPMs), rf cavities, and the rf shield also contribute to the impedance. The contribution of the extraction kickers is negligible. The impedance due to other components, such as vacuum ports and bellows, is expected to be negligible because these are isolated from the beam by the rf shield.

The results for the longitudinal coupling impedance are summarized in Table 1. The impedance is normalized by the mode numbers, $n = \omega/\omega_0$, where ω_0 is the revolution frequency (1.1 to 1.5 MHz). The coupling impedance of interest corresponds to the mode numbers $n \leq 500$, using the cutoff frequency $\omega_c = c/b$, where b is the rf shield radius and c is the velocity of light. The results in the table correspond to injection energy (400 MeV), unless otherwise noted. The space charge impedance is purely capacitive, while the others are inductive, and include a resistive term.

Table 1: RCS Longitudinal Impedance Estimation (at ω_c)

	$\text{Re}(Z_{ }/n)$ (Ω)	$\text{Im}(Z_{ }/n)$ (Ω)
Space charge (injection)	—	— 220
Space charge (extraction)	—	— 50
Rf shield	0.01	0.01
Rf cavities	14 **	†
BPMs ††	0.1	0.06

** decreasing to zero at $\omega \ll \omega_c$ and $\omega \gg \omega_c$

† inductive for $\omega < \omega_c$, capacitive for $\omega > \omega_c$

†† valid up to 125 MHz

The impedance due to the rf cavity higher-order modes (HOMs) was found using URMEI-T [1]. The calculations correspond to a fundamental frequency of 1.3 MHz, which is about midway through the acceleration cycle and for which the ratio R_{sh}/Q is found to be 105. The frequencies and R_{sh}/Q for the first few HOMs are listed in Table 2. The value of 14 Ω for the rf cavities listed in Table 1 is the rf-equivalent broadband impedance ($Q = 1$) and corresponds to 10 cavities.

Table 2: Ratio of Shunt Impedance and Q of First Few HOMs for an RF Cavity

$\omega_{res}/2\pi$ (MHz)	R_{sh}/Q (Ω)
5.6	5.5
10.5	0.8
14.8 ***	0.2

*** Extrapolation of ferrite properties beyond normal operating range of 0.5 to 10 MHz.

To minimize the impedance due to space charge, the vacuum chamber is constructed with a special rf shield, shown

* Work supported by U.S. Department of Energy, Office of Basic Energy Sciences under Contract No. W-31-109-ENG-38.

in Figure 1. The shield consists of Be-Cu wires which follow the beam envelope at an aperture equal to the beam-stay-clear (BSC), given by $A = \sqrt{2\beta\epsilon/\pi} + |\eta_D \Delta p/p| + \text{COD}$, where β is the lattice function, $\epsilon = 375\pi$ mm-mr is the beam emittance, η_D is the dispersion function, and COD is the closed orbit distortion (≤ 1 mm). The space charge impedance is calculated using the standard assumption of a uniform, round, unbunched beam of radius a in a vacuum chamber of radius b . The geometrical factor is given by $g_0 = 1 + 2\ln(b/a)$ [3,4]. Compared to a fixed-radius rf shield, this contour-following scheme reduces the longitudinal space charge impedance by 30% at injection and 20% at extraction.

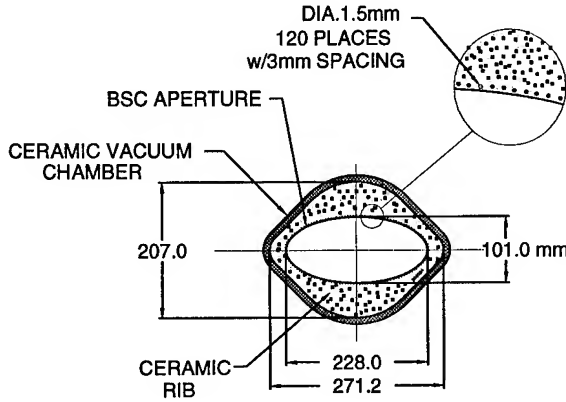


Figure 1: Ceramic vacuum chamber cross section in the focusing quadrupole magnet.

A number of corrections to the geometrical factor have been proposed to account for the wires and the more realistic elliptical beam cross-section. The electrostatic fields due to a uniform beam propagating inside a round rf-screening wire cage have been derived by T. Wang [6]. A second correction, derived by H. Okamoto, takes into account the varying elliptical shape of beam in a smooth, metallized vacuum chamber without wires and with a fixed radius [7]. These corrections result in a difference of less than 2% in the longitudinal impedance, and can be neglected [8].

III. STABILITY CRITERION

A simplified criterion for the longitudinal stability threshold, commonly referred to as the Keil-Schnell (K-S) criterion, is independent of the details of the particle phase space distribution and is given by [3,4]

$$\left| \frac{Z_{||}}{n} \right| \leq F \frac{|\eta| \beta^2 E/e}{I_{pk}} \left(\frac{\Delta p_{FWHM}}{p} \right)^2, \quad (1)$$

where local values of the current and momentum are used for bunched beams. Here $F \approx 1$ is a form factor, I_{pk} is the peak current, and η is the slip factor.

The K-S criterion imposes a lower bound on the ratio $(\Delta p)^2/I_{pk}$. For a given bunch area, increasing the momentum spread is more effective in achieving stability than is lowering

the peak current. Therefore, the stability requirement drives the peak rf voltage. The optimal injected beam parameters and rf voltage profile through the cycle are obtained through the simulation studies [2]. The injected beam is chopped, with an energy spread of ± 2.5 MeV and a length of 75% of the circumference. The time-varying peak current, obtained from the simulation, and the rf voltage are shown in Figure 2a.

The momentum spread corresponding to the threshold for the microwave instability is computed by substituting the impedance listed in Table 1 and the peak current from Figure 2a into Eq. (1). The time-variation in the threshold momentum spread is plotted in Figure 2b together with the momentum spread obtained from the simulation. The beam remains in the stable region through the cycle. The requirement that beam losses be less than 0.1% is also met.

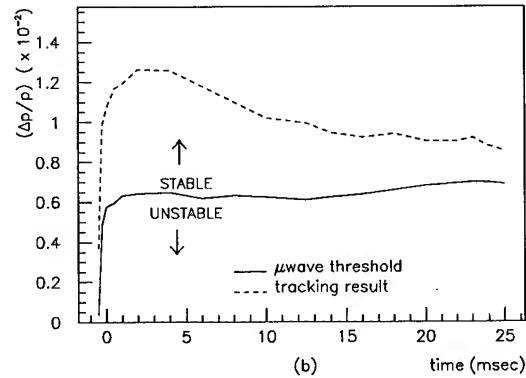
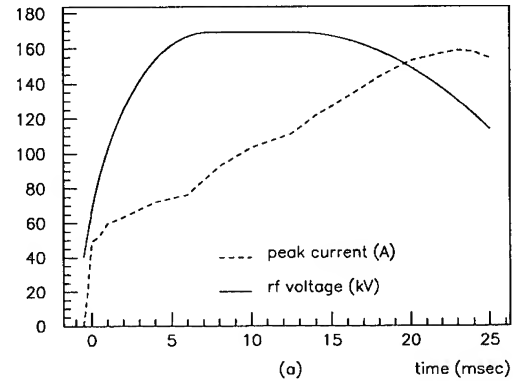


Figure 2: (a) Variation of the rf voltage and peak current and (b) threshold $\Delta p/p$ compared to that obtained from tracking. The small variations are due to the Monte Carlo statistics.

IV. STABILITY DIAGRAM

Below transition, it is possible to operate the machine outside the K-S boundary and preserve stability. The stable region is dependent on both the resistive component of the impedance and the shape of the distribution tails. The details are discussed below.

The response of a beam to a periodic perturbation, $\exp(j(\Omega t - n\phi))$, is given by the Vlasov equation, where ϕ is the azimuthal phase coordinate and Ω is the driving frequency of the perturbation. The solution to the small-amplitude Vlasov equation leads to a dispersion relation, which, for a coasting beam, is given by [9]

$$1 = -\frac{2}{\pi} \frac{I}{(E/e)\beta^2 |\eta| (\Delta p/p)^2} \frac{Z_{\parallel}}{n} I_D' \quad (2)$$

I_D' is the normalized dispersion integral, given by

$$I_D' = j \int \frac{\partial f / \partial x}{x - x_1} dx,$$

where $x = (n\omega - n\omega_0)/(nS)$, $x_1 = (\Omega - n\omega_0)/(nS)$, the full spread at half maximum of the revolution frequency distribution is given by $2S = -\eta\omega_0(\Delta p/p)$, and $f(x)$ is the normalized beam density distribution in frequency space. The imaginary part of the driving frequency leads to growth of the perturbation. A finite spread in the revolution frequency or, equivalently, in momentum, gives rise to Landau damping. The stability boundary is obtained using Eq. (2) evaluated with $\text{Im}\Omega = 0$.

The stability diagram for the RCS at 2 GeV is plotted in Figure 3a in the impedance plane for the quartic momentum spread shown in Figure 3b. Also shown in Figure 3a is the stability region which satisfies the K-S criterion. The positive vertical axis denotes capacitive impedance, and the longitudinal coupling impedance listed in Table 1 is plotted near the vertical axis as a large dot. The particle momentum distribution in Figure 3b is obtained from the simulation.

The stability boundary depends specifically on the momentum distribution and can give a higher limit than the K-S criterion. However, the upper portion of the stability boundary, which corresponds to the tails of the distribution, is highly sensitive to the beam distribution. This can be seen in Figure 4a, which shows the stability boundary using a different, smoothed distribution, shown in Figure 4b. Sections of the stability diagram are marked according to the corresponding section of the momentum distribution. Experience shows that in measured data, the tails in the line density can be rather unpredictable.

The RCS is dominated by the capacitive space charge impedance, which then determines the resistive $\text{Re}(Z_{\parallel}/n)$ limit for stability. The stable boundary satisfying the K-S criterion in Figure 3a suggests that the beam is stable at 2 GeV to a threshold $\text{Re}(Z_{\parallel}/n)$ of 70 Ω . This can readily be achieved in the RCS. A similar analysis at 400 MeV gives a resistive limit of 550 Ω . The stability criterion is most critical near extraction because the peak current increases by a factor of five, while the momentum spread decreases by 30%.

V. DISCUSSION

The microwave instability is avoided in the RCS by ensuring that the coupling impedance is within the stable region defined by the K-S criterion. This conclusion is valid within the assumptions of the theory and the impedance estimate. Rigid, longitudinal displacements of the bunch and possible emittance growth could occur in the latter part of the cycle, such as due to a fixed-frequency rf cavity HOM not analyzed by URMEL-T. The rf bucket produced by the rf voltage in Figure 2a grows significantly after the midpoint in the cycle, and would be sufficient to contain the bunch. Also,

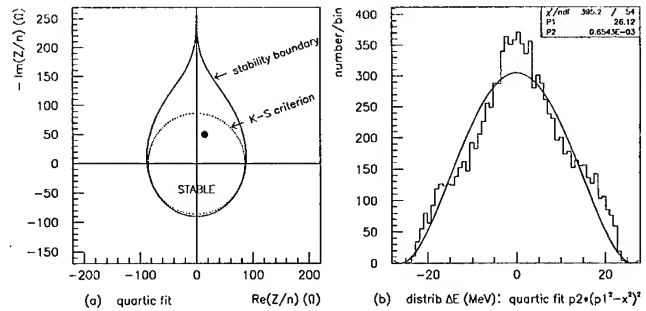


Figure 3: Longitudinal stability boundary (a) for a quartic momentum distribution (b).

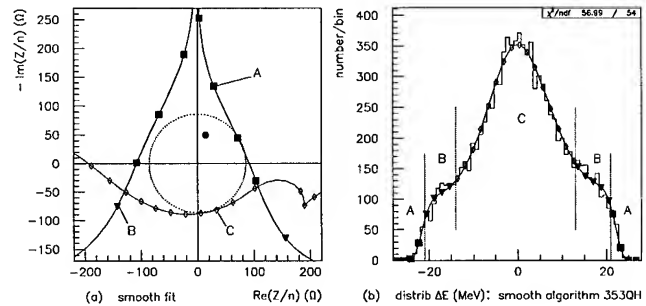


Figure 4: Dependence of the longitudinal stability boundary (a) on momentum distribution, using the distribution in (b).

active control is provided by the phase feedback system of the RCS rf system.

The authors would like to thank K. Thompson for providing Figure 1.

VI. REFERENCES

- [1] "IPNS Upgrade: A Feasibility Study," ANL-95/13, (April 1995).
- [2] Y. Cho, E. Lessner, K. Symon, "Injection and Capture Simulations for a High Intensity Proton Synchrotron," *Proc. of EPAC*, 1228, (1994).
- [3] V.K. Neil and A.M. Sessler, "Longitudinal Resistive Instabilities of Intense Coasting Beams in Particle Accelerators," *Rev. Sci. Instrum.*, **36** (4), 429, (1965).
- [4] E. Keil and W. Schnell, "Concerning Longitudinal Stability in the ISR," CERN TH-RF/69-48, (1969).
- [5] K.-Y. Ng, "Fields, Impedances, and Structures," *The Physics of Particle Accel.*, AIP Conf. Proc. 184, (1989).
- [6] T-S. F. Wang, "Electrostatic Field of a Perturbed Beam with RF-Screening Wires," CERN/PS 94-08 (DI), (1994).
- [7] "AUSTRON Accelerator Feasibility Study," AUSTRON/PS/PJB, Chapter 4, p. 145, (October 1994).
- [8] K.C. Harkay, "Study of Corrections to the Geometrical Factor in the Space Charge Impedance for the IPNS Upgrade," ANL Report NS-95-4, (March 1995).
- [9] A. Hoffman, "Single-beam collective phenomena - longitudinal," *Proc. of Theoretical Aspects of the Behavior of Beams in Accel. and Storage Rings*, CERN 77-13, (November 1976).

TRANSVERSE INSTABILITY ANALYSIS FOR THE IPNS UPGRADE *

K. Harkay and Y. Cho, Argonne National Laboratory, Argonne, IL 60439 USA

Abstract

The proposed 1-MW spallation neutron source upgrade calls for a 2-GeV rapidly-cycling synchrotron (RCS) with an intensity of 1.04×10^{14} protons per pulse [1]. The potential exists for the excitation of collective, intensity-dependent transverse instabilities. These can normally be controlled by introducing a betatron tune shift or spread, where care is exercised to avoid single-particle resonance effects. Adjusting the chromaticity using sextupoles to vary the head-to-tail phase shift is compared to introducing Landau damping by octupoles. An option for a feedback system is also examined. The momentum spread used for the transverse analysis was obtained from the requirements for longitudinal stability [2].

I. INTRODUCTION

The head-tail effect has been observed at other low energy, rapidly-cycling synchrotrons: the 500-MeV IPNS [3], KEK Booster [4], and ISIS [5]. Therefore, it is analyzed in some detail for the IPNS Upgrade. An estimation of the coupling impedance, which characterizes the interaction between the beam and its surroundings, is given first. The head-tail instability, driven by the resistive wall and kicker impedance, is discussed next using Sacherer's bunched beam formalism [6]. Further discussion of damping transverse instabilities considers the coasting beam stability criterion. The requirements for stability are dominated by the impedance due to space charge effects. It is found that passive means, which include minimizing the coupling impedance and introducing a tune shift or spread, are sufficient to ensure stability. Finally, the requirements for an active feedback kicker are given as an option.

II. COUPLING IMPEDANCE ESTIMATION

The transverse coupling impedance is estimated by using the standard approximations [7]. The impedance is dominated by space charge effects. The rf shield, extraction kickers, and the beam position monitors (BPMs) also contribute to the impedance. The kickers are traveling-wave structures with a characteristic impedance of 3.28Ω . The impedance due to other components, such as vacuum ports and bellows, is expected to be negligible because these are isolated from the beam by the rf shield. The contribution to the transverse impedance due to the rf cavity higher-order modes was found by URMEL-T calculations to be negligible. The coupling impedance of interest for instability analysis corresponds to the frequencies $\omega = (p + \nu)\omega_0$, or about 1 MHz for the RCS, where p is a negative integer near ν , the horizontal or vertical tune. The results are summarized in Table 1 and correspond to injection energy (400 MeV), unless otherwise noted. The space charge impedance is purely capacitive, while the others are inductive and include a resistive term.

Table 1: RCS Transverse Impedance Estimation (at 1 MHz)

	$\text{Re}(Z_{\perp})$ (k Ω /m)	$\text{Im}(Z_{\perp})$ (k Ω /m)
Space charge (injection)	—	—2800
Space charge (extraction)	—	—1500
Rf shield	20	20
Extraction kickers	30	50
BPMs	0.003	110

To minimize the impedance due to space charge, the vacuum chamber is constructed with a special rf shield, similar in principle to that used at ISIS [1,2]. The shield consists of a Be-Cu wire cage which follows the beam envelope. The space charge impedance is calculated using the standard assumption of a uniform, round, unbunched beam of radius a in a vacuum chamber of radius b . The geometrical factor is given by $g_{\perp} = 1/a^2 - 1/b^2$. Compared to a fixed-radius rf shield, this contour-following scheme reduces the transverse space charge impedance by 35% at injection and 10% at extraction.

A number of corrections to the geometrical factor have been proposed to account for the wires and the more realistic elliptical beam cross section. The electrostatic fields due to a uniform beam propagating inside a round rf-screening wire cage have been derived by T. Wang [8]. A second correction, derived by H. Okamoto, takes into account the varying elliptical shape of beam in a smooth, metallized vacuum chamber without wires and with a fixed radius [9]. Wang's method results in a +15% correction in the transverse impedance and Okamoto's method results in a -20% correction [10]. Until a rigorous derivation is performed for a contour-following wire rf shield, the above corrections are treated as an uncertainty.

III. HEAD-TAIL INSTABILITY

In the absence of a tune spread, the growth rate for the head-tail instability, assuming a time dependence of $\exp(j\Omega_m t)$, is given by the imaginary part of [6]

$$\Omega_m = \frac{j}{(1+m)} \frac{c I Z_{\perp}(\omega_p)}{4\pi v(E/e)} F'_m,$$

$$\text{where } F'_m = \frac{1}{B} \frac{h_m(\omega_p - \omega_{\xi})}{\sum_p h_m(\omega_p - \omega_{\xi})}$$

is a form factor and m is a mode number denoting the number of nodes along the bunch. This expression assumes that the instability is dominated by the contribution from the impedance at a single frequency, $\omega_p = (p + \nu)\omega_0$. The total growth involves a convolution of this impedance with the envelope (form factor) of the bunch spectra, h_m , which are

* Work supported by U.S. Department of Energy, Office of Basic Energy Sciences under Contract No. W-31-109-ENG-38.

shifted by the chromatic frequency, $\omega_\xi = (\xi/\eta)v\omega_0$. The chromaticity is $\xi = (\Delta v/v)/(\Delta p/p)$ and B is the ratio of bunch length to ring circumference.

For the RCS at 400 MeV, the form factor for $m = 0$ has a half-width of about 2 MHz, and the form factor for $m = 1$ peaks around 1 MHz. The chromaticity is normally corrected to zero in order to avoid a large betatron tune spread in the large-momentum particles. When the chromaticity is zero, the bunch spectra are centered at zero frequency, where the rf shield and kicker impedances are important.

In the vertical plane, the largest instability growth due to the rf shield and kicker impedances occur when $p = -6$ and -7 , respectively. Figure 1 shows the impedances and the frequency, ω_p , for the two values of p . The BPM impedance does not contribute significantly to the growth. The growth rates of the first few head-tail modes are given in Table 2 for the corrected and natural chromaticities at the end of injection. The impedance and the frequency giving the largest growth are also listed. Similar results are found for the horizontal plane.

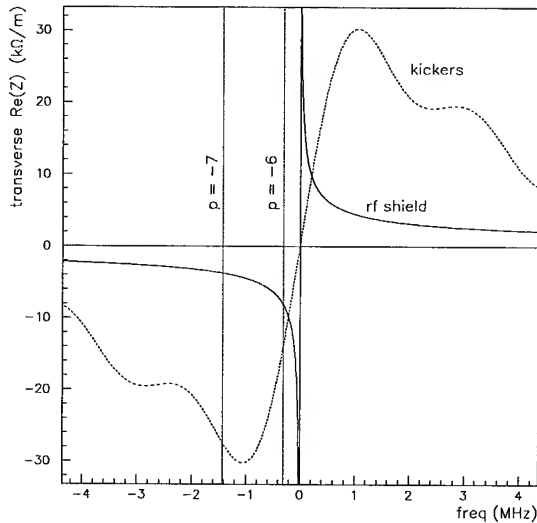


Figure 1: Real part of the transverse impedance due to the rf shield and kickers.

Table 2: Head-tail instability growth rate vs. chromaticity.

mode number, m	$\text{Re}(Z_\perp)$ (kΩ/m)	frequency (MHz)	source of impedance	growth rate (s) ⁻¹ $\xi = 0$	$\xi = -1.2$
0	8	0.3	rf shield	350	0
0	14	0.3	kickers	620	0
1	28	1.4	kickers	730	0
2	28	1.4	kickers	590	0

The lowest modes are stabilized at the natural chromaticity, $\xi = -1.2$. Using the maximum value of $\Delta p/p$ of 1.2% obtained from the longitudinal tracking [2], the corresponding betatron tune spread is 0.1. With tune values of $\nu_x = 6.821$ and $\nu_y = 5.731$ and an incoherent Laslett space charge tune shift of

about 0.15, one must consider the half-integer resonance. Therefore, the chromaticity is adjusted to be between 0 and -1.2 to shift the bunch spectrum to higher-order head-tail modes, which have lower growth rates, while at the same time ensuring that the tune spread remains inside a resonance-free working region. The stability of modes $m \leq 2$ is assured with $\xi \leq -0.35$. This gives a betatron tune spread of 0.024. The inverse growth rate of the first unstable mode, $m = 3$, is then about 14 ms. This gives less than two e-folding times during the total acceleration cycling time of 25 ms.

IV. STABILITY CRITERION

Discussed next is the transverse stabilization of the beam, achieved by using a betatron tune spread or shift. An amplitude-dependent tune spread is introduced by octupoles and second-order effects in the sextupoles, leading to Landau damping. A momentum-dependent tune shift results from a finite chromaticity, leading to stability as discussed above. The stability criterion derived for coasting beams is extended heuristically to bunched beams, and is given by

$$(\Delta v)_{\text{thresh}} = \frac{c I_{pk} |Z_\perp|}{4\pi v \omega_0 (E/e)}.$$

Since the impedance is dominated by space charge effects, this expression is equivalent to the coherent Laslett tune shift (due to image charges only.) For the RCS, the expected growth rates (Table 2) are of the order of the synchrotron frequency, ω_s ; therefore, we use the peak current, I_{pk} , to be conservative. The results for the threshold tune spread are presented in Table 3 for the vertical plane at 400 MeV and 2 GeV. The impedance is taken from Table 1.

Table 3: Threshold tune spread according to the coasting beam stability criterion

time in cycle (ms)	$\text{Im } Z_\perp$ (MΩ/m)	$(\Delta v)_{\text{thresh}}$
0	2.7	0.06
25	1.4	0.03

The threshold tune spread can be met using the chromatic contribution and/or the octupolar contribution. Our strategy requires that each term satisfy the stability criterion independently, if possible.

First, we consider a solution using the chromatic term only, where $\Delta v_\xi = [(p - v)\eta + v\xi](\Delta p/p)$. Using the condition $\Delta v_\xi \geq \Delta v_{\text{thresh}}$ and the natural chromaticity, with $p = 6$ (vertical plane), the required momentum spread becomes:

$$\frac{\Delta p}{p} \geq \begin{cases} 0.8\% & 400 \text{ MeV} \\ 0.6\% & 2 \text{ GeV} \end{cases}.$$

This is to be compared to a $\Delta p/p$ of about 1% obtained from the longitudinal tracking study. Conversely, using the $\Delta p/p$ from the tracking, the required chromaticity becomes:

$$\xi \leq \begin{cases} -0.97 & 400 \text{ MeV} \\ -0.66 & 2 \text{ GeV} \end{cases}$$

Next, we consider a solution using octupoles only with the chromaticity corrected to zero. The required octupole tune spread is $\Delta\nu_{\text{oct}} \geq \Delta\nu_{\text{thresh}}$, where $\Delta\nu_{\text{oct}} = (\beta_y a_y^2 / 32\pi) k_{\text{oct}}$, and $k_{\text{oct}} = (B'''l/B\rho)$ is the octupole strength. Using a beta-function, β_y , of 12 m and beam size, a_y , of 0.07 m at 400 MeV and 0.04 m at 2 GeV, the integrated octupole strength per super-period (= 4) required for stability is given by

$$k_{\text{oct}} \geq \begin{cases} 24 \text{ m}^{-3} & 400 \text{ MeV} \\ 44 \text{ m}^{-3} & 2 \text{ GeV} \end{cases}$$

This assumes that the octupoles are located at each defocusing quadrupole (QD). The approximate limiting value of the octupole strength at injection is shown in a plot of the dynamic aperture in Figure 2. The dynamic aperture with full-strength sextupoles and no octupoles is also shown.

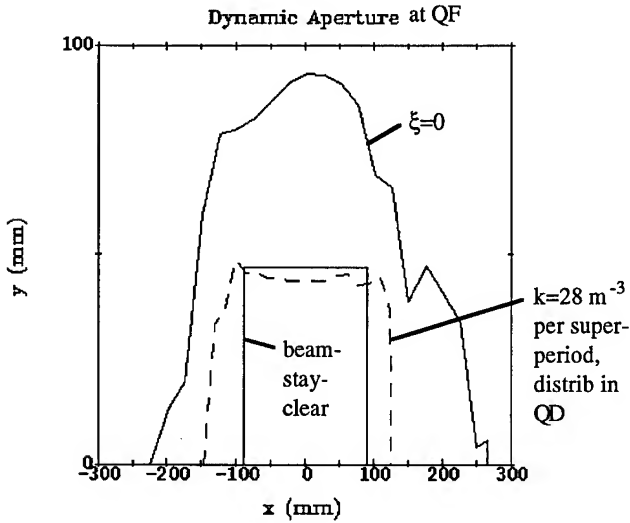


Figure 2: Dynamic aperture at a focusing quadrupole (QF).

V. BEAM FEEDBACK SYSTEM

Active beam feedback is an option to suppress or damp the head-tail instability. A typical feedback system consists of a beam position detector, processing electronics and a delay unit, a power amplifier, and a deflection kicker. Other considerations for the system include noise sensitivity and maintaining synchronicity with the rapidly-varying revolution frequency. Only the kicker strength is analyzed. The parameters of the feedback system have not been optimized, nor have space limitations been studied.

Assuming an instability rise time of 1 msec and a revolution period of 1 μ s, the instability amplitude growth is $\Delta x/x_0 = \tau_{\text{rev}}/\tau_{\text{growth}} = 10^{-3}$, where x_0 is the minimum

detected beam deviation, assumed to be 0.5 mm. The electric field, E_k , for the kicker can be written as:

$$E_k \geq 10^{-3} \frac{x_0}{\beta_x} \frac{2\beta^2(E_b/e)}{l},$$

where E_b is the beam energy and l is the length of the kicker. This gives 230 V/m for a 0.5 m kicker length at 400 MeV, and 950 V/m at 2 GeV, using the average value $\beta_x = 6$ m. It is customary in practice to allow a factor of 5 to 10 increase in the electric field.

VI. SUMMARY

An analysis of transverse instabilities in the RCS for the IPNS Upgrade is performed, including an estimation of the coupling impedance. The results show that stability is achievable through a choice of the chromaticity between the natural value and zero or through the addition of octupoles. Beam feedback is also an option. It has long been observed in other low-energy accelerators that the current required in the correction octupoles is found to be less than that predicted by the theory [4,11]. In other studies, the head-to-tail phase shift and form factors observed are not consistent with the theory [5]. Further refinement of the theory for bunched beams is required.

The authors would like to thank E. Crosbie for the dynamic aperture calculation and figure.

REFERENCES

- [1] "IPNS Upgrade: A Feasibility Study," ANL-95/13, (April 1995).
- [2] K. Harkay, Y. Cho, E. Lessner, "Longitudinal Instability Analysis for the IPNS Upgrade," these proceedings.
- [3] Y. Cho and A.V. Raichas, "Observations and Cure of the Head-Tail Effect in the Argonne Rapid Cycling Synchrotron," *IEEE Trans. Nucl. Sci.*, NS-28 (3), 2585, (1981).
- [4] Y. Kimura, et al, "Transverse Coherent Instability in the KEK Booster," *Proc. 10th Int'l Conf. High Energy Accel.*, 2, 30, (1977).
- [5] G.H. Rees, "Interpretation of the Higher-Order Mode, Head-Tail Motion Observed on ISIS," *Particle Accelerators*, 39, 159, (1992).
- [6] B. Zotter and F. Sacherer, "Transverse Instabilities of Relativistic Particle Beams in Accelerators and Storage Rings," CERN 77-13, (1977).
- [7] K.-Y. Ng, "Fields, Impedances, and Structures," *The Physics of Particle Accel.*, AIP Conf. Proc. 184, (1989).
- [8] T-S. F. Wang, "Electrostatic Field of a Perturbed Beam with RF-Screening Wires," CERN/PS 94-08 (DI), (1994).
- [9] "AUSTRON Accelerator Feasibility Study," AUSTRON/PS/PJB, Chapter 4, p. 145, (October 1994).
- [10] K.C. Harkay, "Study of Corrections to the Geometrical Factor in the Space Charge Impedance for the IPNS Upgrade," ANL Report NS-95-4, (March 1995).
- [11] D. Möhl and H. Schonauer, "Landau Damping by Non-Linear Space-Charge Forces and Octupoles," *Proc. 9th Intl. Conf. High Energy Accel.*, 380, (1974).

LONGITUDINAL EMITTANCE MEASUREMENTS IN THE FERMILAB BOOSTER

D.A. Herrup
Fermi National Accelerator Laboratory*
P.O. Box 500, Batavia, Illinois 60510

Abstract

I have installed a system to measure the longitudinal emittance over the entire acceleration cycle in the Fermilab Booster Accelerator. Measured inputs to the system are the total beam current, the RF voltage per turn seen by the beam, and a diode-detected resistive wall signal. These signals are digitized by an oscilloscope and transferred to the Fermilab control system computers. The bucket area is calculated using the measured RF voltage per turn and the design synchronous phase and ramp rate. The bunch length is taken as the ratio of the total charge to the peak-detected current and, together with the bucket area, can be used to calculate the longitudinal emittance. This system can measure the emittance or bunch length over the entire booster cycle at a 1 KHz sampling rate or over shorter periods (for example, around extraction) at up to a 10 MHz rate. We discuss operational uses of this system.

INTRODUCTION

Longitudinal beam dynamics play an important role in the Booster Synchrotron at Fermi National Accelerator Laboratory (FNAL). We desire the smallest longitudinal emittance (ϵ_l) possible. However, many processes occur naturally in the Booster acceleration cycle which can increase the ϵ_l . The 400 MeV beam injected into the Booster from the Linac is debunched and must be captured in RF buckets. The Booster is a 15 Hz. resonant accelerator, so capture occurs while the RF and magnetic fields are ramping, making adiabatic capture difficult and possibly leading to phase space dilution. Transition occurs at 5.4 GeV, in the middle of the Booster ramp, and passage through transition can excite synchrotron oscillation. Finally, at high energies and intensities longitudinal coupled bunch motion is excited. If the coupled bunch motion leads to instabilities that filament within the Booster cycle, ϵ_l will increase. Even if they do not filament and lead to a measureable emittance growth in the Booster, they can still lead to decreased efficiency in the Main Ring as the individual bunches are injected with different phase errors. In order to evaluate the effects of these processes, it is necessary to measure and understand the longitudinal emittance throughout the entire acceleration cycle.

The moving bucket area in a synchrotron is given by

$$\epsilon_l = 16 \left(\frac{R}{hc} \right) \sqrt{\frac{EV}{2\pi h\eta}} \alpha(\Gamma)$$

where R is the radius of the synchrotron, h the harmonic number, c the speed of light in vacuum, E the particle energy, V the RF voltage/turn, η the frequency slip factor, and α is the function of the synchronous phase angle Γ that relates the stationary bucket area to the moving bucket area. The bunch area (ϵ_l) is the phase space area actually occupied by the beam and can be calculated from the bucket area if the bunch length is known [1].

In the rest of this paper I will describe a system which measures the Booster longitudinal emittance over the entire cycle.

SYSTEM DESCRIPTION

The system I have designed requires knowledge of the bunch length and RF voltage throughout the cycle. The bunch length is calculated as

$$\tau = \frac{\text{total circulating charge}}{\text{peak current}},$$

so three quantities must be measured: the total circulating charge, the peak current, and the RF voltage. The peak current is derived from a diode-detected 5 GHz bandwidth resistive wall signal, the total charge from a DCCT, and the RF voltage is the phase-summed detected voltage from all gaps. These three quantities are digitized using an HP 54501A Digitizing Oscilloscope which is interfaced to the FNAL Accelerator Control System (ACNET) [2]. The system is shown in Fig. 1.

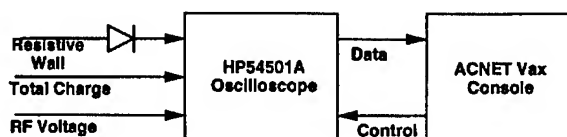


Figure 1. Schematic diagram of measurement system.

The HP 54501A scope is a 4-channel oscilloscope with 2 8-bit ADCs capable of digitizing at up to 10 MHz. On any given trigger, 2 of the inputs are digitized, and the other 2 are digitized on the next trigger. In principle it is important to measure all quantities simultaneously, but the RF voltage never changes with intensity as long as the anode voltage program is unchanged. The total charge and the peak current are measured on one cycle and the RF voltage on the next.

After digitization the data are read by an application running on an ACNET Vax where all further calculations are done. τ as calculated above is in arbitrary units, and is converted to ns. by applying a calibration factor determined once by measuring the bunch profiles directly with a 500 MHz digitizing scope and

*Operated by the Universities Research Association under contract with the U. S. Department of Energy

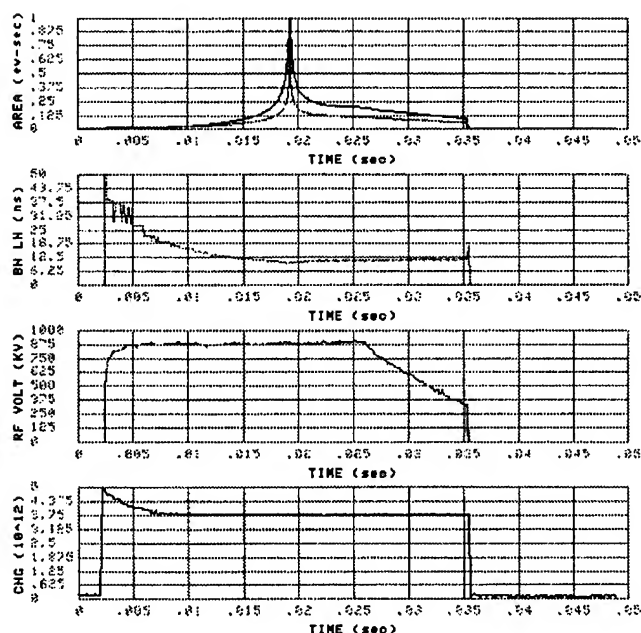


Figure 2. Data used in the ϵ_l calculation.

comparing with τ measured simultaneously. Calculation of the bucket area requires knowledge of the Booster energy gain/turn and the synchronous phase. These are determined assuming that the Booster excitation is a 15 Hz sine wave. An example of the calculation for a complete cycle is shown in Fig. 2. The plots are, from bottom up, the total charge, the RF voltage per turn, the bunch length, and the bucket and bunch areas (the bucket area is always larger). Note that the simple formula used to calculate the bucket area is singular at transition. More accurate approximations to the bucket area near transition exist [3] but have not been used in this work. The application allows zoom views and FFT calculations on any portion of the data.

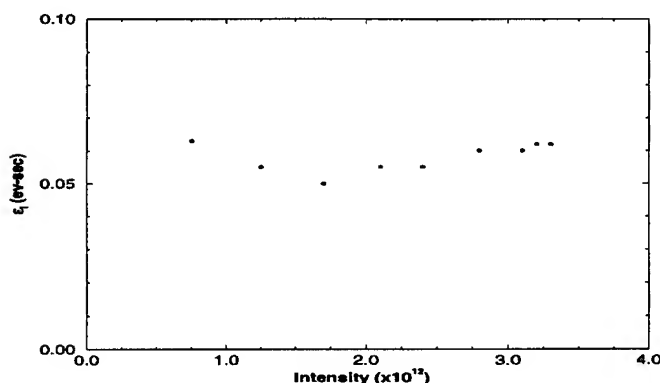


Figure 3. Intensity vs. Long. Emittance.

ϵ_l determined in this way is subject to few systematic errors. Errors due to the 8-bit resolution of the ADCs are negligible, and the RF waveform does not change from pulse to pulse with intensity. The Booster ramp is well approximated by a 15 Hz sine wave, and the only real source of error is the calibration of the diode-detected bunch length with the bunch length measured on a digitizing oscilloscope. The bunch profiles are non-gaussian,

and I have taken the bunch length to be the time during which the profile is above the baseline value. This leads to an error of about 1 ns, or 10%, in the bunch length. The function relating (bunch length/bucket length) to (bunch area/bucket area) has nearly unity slope over the region in which the Booster operates, so the 10% error in the bunch length calibration leads to a similar error in ϵ_l .

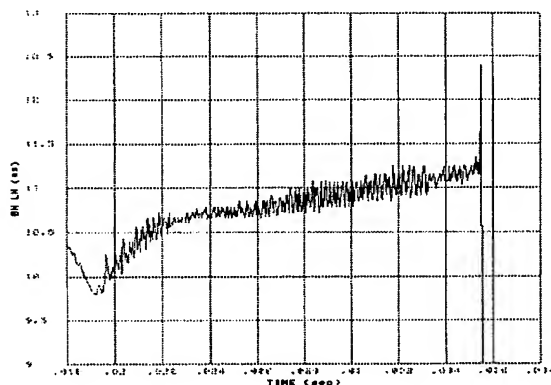


Figure 4. Bunch length oscillations at transition. Note the suppressed 0.

MEASUREMENTS

In this section I will show examples of some of the phenomena which can be studied with this system. The phenomena of interest vary with time in the cycle. In studying extracted beam one examines ϵ_l whereas oscillations at transition and the bunch rotation at the end of the cycle are best studied through the bunch length.

Extracted Emittance

Figure 3 is a plot of the longitudinal emittance at extraction as a function of the extracted intensity. There seems to be a small decrease in ϵ_l for intermediate intensities. This decrease in ϵ_l is also observed in measurements made in a dispersive section of the extraction line [4], a measurement with completely different systematic and statistical errors. It is possible that at low intensities noise in the RF feedback loops leads to emittance growth, producing the anomalously large emittances.

Prior to 1994, ϵ_l had increased rapidly with intensity, limiting the intensity to about 2.5×10^{12} . This growth was attributed to longitudinal coupled bunch instabilities which decohered during the Booster cycle. In early 1994 several narrow band dampers [5] operating on the unstable modes were installed, and the lower ϵ_l is due to their successful operation.

Oscillations at Transition

In Figure 4 I have zoomed in on the bunch length measurement from near transition to the end of the cycle. The frequency of the oscillations which appear after transition is roughly 4 KHz, or twice the synchrotron frequency of 2 KHz. Thus they are quadrupole synchrotron oscillations induced by the mismatching of the bunch and bucket before and after transition. The Booster has a γ_t -jump system which could be used to eliminate this os-

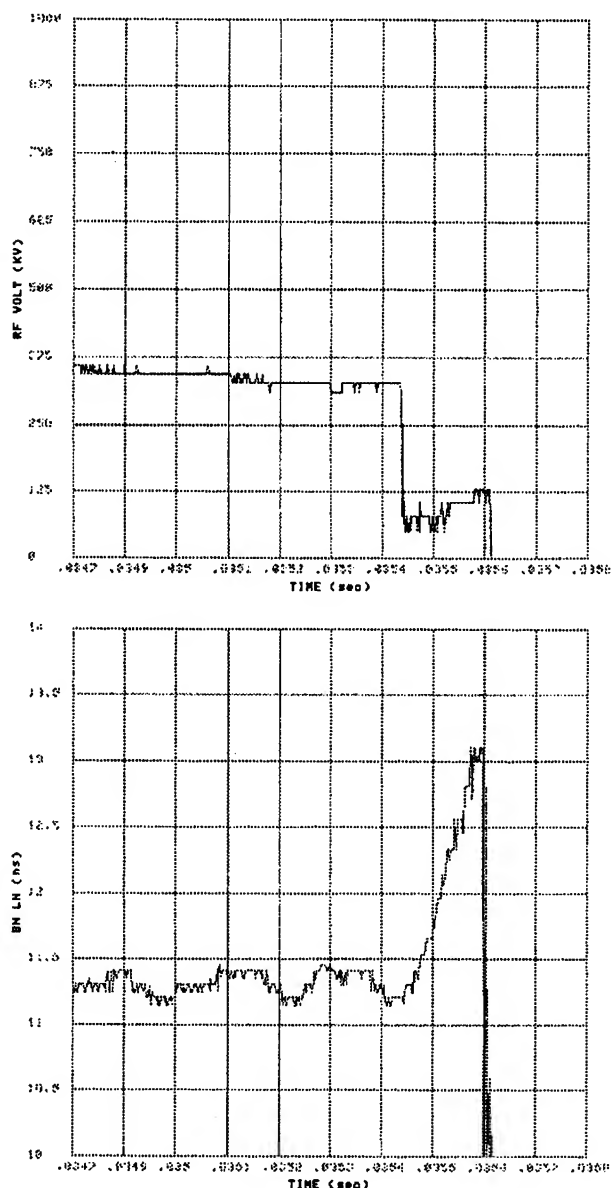


Figure 5. RF voltage (upper) and bunch length (lower) for the bunch rotation at extraction. Note the suppressed 0.

cillation, but since the oscillation does not lead to emittance growth, it is not used.

Bunch Rotation at Extraction

Extracted beam from the Booster is injected into the Main Ring. The momentum aperture of the Main Ring has long been known as a limitation, and as a result the Booster attempts to provide as low a $\Delta p/p$ as possible. $\Delta p/a$ is normally determined by the RF voltage, and throughout the last half of the Booster cycle the voltage is kept as low as possible to avoid beam loss. In addition, at the very end of the cycle a bunch rotation is performed to provide an even lower $\Delta p/p$. The rotation consists of a step drop in the RF voltage $1/4$ of a synchrotron period ($125 \mu\text{sec}$) before extraction. During this interval the bunch rotates in longitudinal phase space, exchanging energy spread ($\Delta p/p$) for time (bunch length).

This process is illustrated in Fig. 5a, the RF waveform for the bunch rotation, and Fig. 5b, the bunch length during the rotation. Immediately before the rotation one observes a bunch length of roughly 11 nsec, with a small quadrupole synchrotron oscillation. During the last $1/4$ synchrotron, while the RF voltage has been reduced, one can see the bunch "tumble", resulting in a larger bunch length and smaller $\Delta p/p$. After making this bunch rotation operational, the Main Ring intensity and pulse-to-pulse stability increased noticeably.

CONCLUSIONS

We have developed a system capable of making detailed bunch length and longitudinal emittance measurements in the Fermilab Booster. This system allows us to make detailed studies of longitudinal beam dynamics.

References

- [1] S. Ohnuma, Fermilab TM-1381.
- [2] D. Bogert, "The Fermilab Accelerator Control System", Proceedings of the Second International Workshop on Accelerator Control Systems, NIM A247 (1986), p. 133.
- [3] E.D. Courant, Fermilab FN-187.
- [4] D. McGinnis, private communication.
- [5] D.A. Herrup et. al., Analog Dampers in the Fermilab Booster, this conference.

ANALOG DAMPERS IN THE FERMILAB BOOSTER

D.A. Herrup, D. McGinnis, J. Steimel, R. Tomlin
Fermi National Accelerator Laboratory*
P.O. Box 500
Batavia, Illinois 60510

Abstract

With the increase in intensity of the Fermilab Booster accelerator to over 3×10^{12} p/s/pulse, active dampers have been required to control several transverse and longitudinal instabilities. The damper systems currently in use are: one narrow-band horizontal damper for the $(+Q_h)$ mode, a wideband horizontal damper for all modes, and four channels of narrow-band longitudinal dampers for coupled bunch modes 1, 48, 49, and 50. We discuss the observations that indicated that damper systems were necessary, the designs and operations of the systems, and their effects on beam quality in the Booster.

INTRODUCTION

The Fermilab Booster Accelerator is the lowest energy synchrotron in the Fermilab complex. The injected beam consists of (400 MeV protons provided by the Linac, and the 8 GeV extracted beam is injected into the Main Ring. The desired quality of the extracted beam is determined by the apertures of the Main Ring. In order to extract 3×10^{12} p/s/pulse from the Main Ring, the Booster transverse emittances must be less than 17π mm-mr and $\Delta p/p$ must be less than 1.5×10^{-3} .

At Booster intensities of 3×10^{12} p/s/pulse (much below the 4×10^{12} p/s/pulse needed to extract 3×10^{12} p/s/pulse from the Main Ring) we observed coherent instabilities in the Booster which severely degraded the quality of the beam injected into the Main Ring. The horizontal emittance often exceeded 35π mm-mr, and the longitudinal coupled bunch oscillations led to beam loss due to the restricted momentum aperture of the Main Ring. We undertook an effort to identify the unstable modes and provide active damping to counteract them.[1] Partly as a result of this program, the Booster has run with intensities of over 4.0×10^{12} p/s/pulse with emittances acceptable to the Main Ring.

We have installed three different types of damper systems: a narrow band horizontal damper acting upon the $(+Q_h)$ mode, a wideband horizontal damper, and longitudinal narrow band dampers acting on non specific coupled bunch modes. We will describe the measurements indicating the existence of the unstable modes and the designs of the damper systems.

UNSTABLE MODES AND DAMPERS

Horizontal Modes

The first horizontal mode identified was a mode which appeared during the last half of the Booster accelerating cycle at a frequency of approximately 180 KHz, corresponding to the lowest horizontal sideband. The horizontal tune is normally 6.7,

the revolution frequency during the second half of the cycle 626 KHz, so the unstable mode is $(7-Q_h)$. We believe that this is a resistive wall mode which is strongly driven at low frequencies. This instability is very strong and dominates the horizontal spectrum.

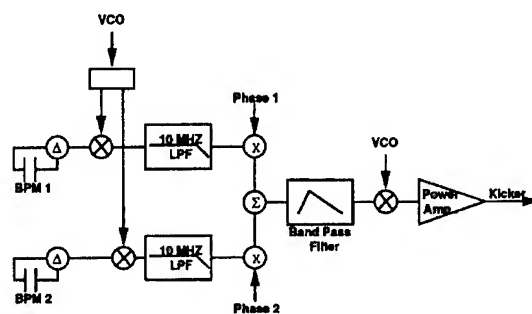


Figure 1. Schematic diagram of the horizontal narrow band damper system.

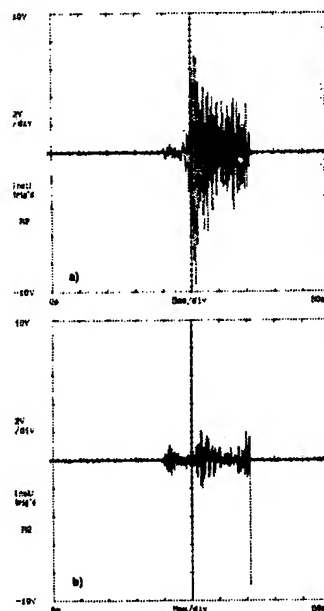


Figure 2. Signal on a horizontal BPM before (a) and after (b) installation of the horizontal narrowband amper.

Fig. 1 is a diagram of the damper system used to reduce this oscillation. The beam oscillations are detected using the difference signals on two BPMs 104° apart in betatron phase. After mixing to baseband with the Booster VCO and filtering, the proper phase is established using the two time-dependent ramps

*Operated by the Universities Research Association under contract with the U. S. Department of Energy

which multiply the processed BPM signals. The signals are then summed, put through a bandpass filter centered at 120 KHz to reject the synchrotron frequency on the low frequency side and the (Q_h-6) line at approximately 450 KHz on the high frequency side, mixed back up to 53 MHz, and then put into a power amplifier and sent to the kickers. The overall system gain is roughly 112 db.

Figs. 2a and 2b are plots of the signal on a single BPM before (a) and after (b) installation of the damper system.

Once installed, this damper eliminated any significant mode $(+Q_h)$ oscillation (Fig. 1b). However, the emittance was still larger than acceptable for the Main Ring. Examination of the frequency spectrum of a BPM showed that although the mode $(+Q_h)$ frequency was completely absent, oscillations developed at the other mode frequencies, indicating the need for a wideband damper. The system we installed (Fig. 3) uses the difference signal for a BPM. After being mixed down to baseband, filtered, and delayed, the output signal is summed with the signal from the narrow band damper and applied to the same kicker. The phase response of this damper is flat over the frequency range 0-26 MHz and the gain ranges from 20 db at low frequencies to about 7 db at 26 MHz. It has not been necessary to install equalizers. With the installation of this damper system, horizontal instabilities do not appear at intensities of 4.0×10^{12} .

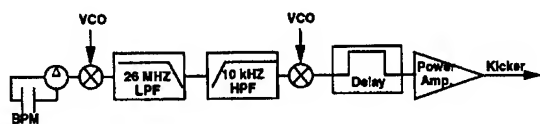


Figure 3. Schematic diagram of the horizontal wide band damper system.

Longitudinal Modes

Longitudinal coupled bunch modes have long been known to exist in the Booster. Several attempts to control them have been made, the most recent being the installation of passive dampers flaps in the RF cavities to remove the energy of the driving modes. [2] This modification eliminated instabilities up to an intensity of about 2.5×10^{12} p's/pulse, but above this intensity the coupled bunch modes 1, 48, 49, and 50 appeared. Narrowband active damper systems, each acting on a different revolution harmonic, were designed to damp these modes. Fig. 4 is a diagram of the basic damper. It is designed around a single side-band mixer whose inputs are the time derivative of the phase and a direct digital synthesizer operating at a different revolution harmonic for each damper channel. The processed signal is then input into the RF system and applied to the beam through the RF cavities. The gains of the systems vary by mode, but are at least 80 db. These systems have been effective in reducing the coupled bunch oscillations to a tolerable level. Fig. 5 is a plot of the error signal at the phase detector for the 4 systems installed with and without the damper system turned on. With these dampers operating longitudinal stability is ensured at intensities of 4×10^{12} p's/pulse the extracted $\Delta p/p$ has been as low as 0.001.

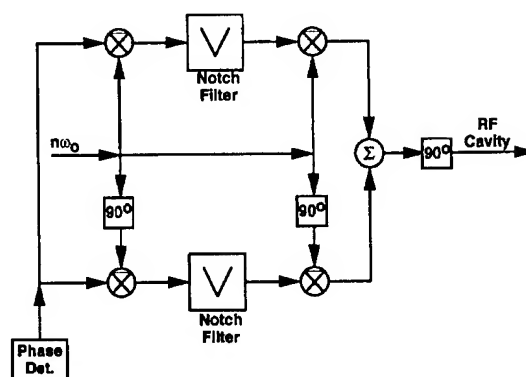


Figure 4. Schematic diagram of the longitudinal narrow band damper system.

CONCLUSIONS

Elimination of transverse and longitudinal instabilities has allowed the Booster to produce extracted intensities of 4×10^{12} p's/pulse with low emittances. We look forward to increasing the intensities and dealing with the next set of instabilities.

References

- [1] For a summary of earlier work on active dampers in the Fermilab Booster, see J. Steimel Jr. and D. McGinnis, Proceedings of the 1993 Particle Accelerator Conference, p. 2100.
- [2] K. Harkay, A Study of Longitudinal Instabilities and Emittance Growth in the Fermilab Booster Synchrotron, Ph.D Thesis, Purdue University, 1993.

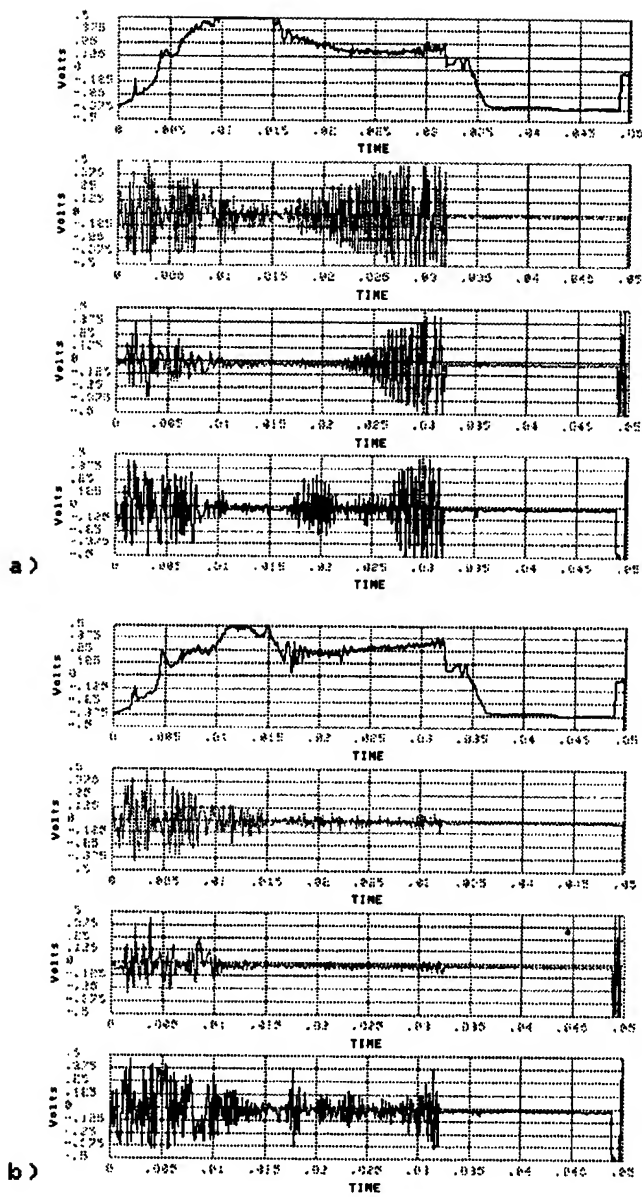


Figure 5. Error signals for the longitudinal dampers with dampers off (a) and on (b). From top to bottom, the modes are 1, 48, 49, and 50.

A STUDY OF THE LONGITUDINAL COUPLED BUNCH INSTABILITY IN THE FERMILAB MAIN RING

K. Junck, J. Marriner, D. McGinnis, Fermi National Accelerator Laboratory, Batavia, IL 60510 USA

Longitudinal synchrotron oscillations of proton bunches in the Fermilab Main Ring have been observed during various portions of the acceleration cycle. These oscillations have an effect upon the ability to coalesce 11 proton bunches into one bucket for subsequent transfer into the Tevatron. The oscillations appear to be caused by a longitudinal coupled bunch instability. We report measurements made to characterize the instability as well as design of a narrow-band feedback system.

I. INTRODUCTION

The Main Ring coalesces one high intensity bunch from 11 bunches [1]. Once the 8.9 GeV injected beam is accelerated to 150 GeV, the 53 MHz RF cavities are counterphased to a low voltage and coalescing cavities at 2.5 MHz are turned on. After bunch rotation occurs, the 53 MHz cavities are rephased to recapture the single coalesced bunch. This procedure is sensitive to the longitudinal emittance of the beam and thus maintaining a small and constant longitudinal emittance is desirable.

Uncoalesced proton beam in the Main Ring has been observed to undergo a sudden growth in bunch length during the flat-top portion of the 2B cycle (acceleration to 150 GeV for transfer to the Tevatron). The bunch size is determined by measuring the ratio of the 53 MHz (fundamental) and 159 MHz (third harmonic) components of the beam signal generated from a strip-line detector. Throughout the course of Collider Run IB, beam intensity has increased resulting in an earlier onset of this bunch length growth. The onset of bunch length growth is also dependent upon the number of bunches, with an earlier growth corresponding to a larger number of bunches.

It is thought that this phenomena is due to a coupled bunch instability. As a bunch passes through the RF cavity it sees not only the accelerating voltage applied to the cavity but fields excited by the previous bunches. A bunch is coupled to all of the previous bunches by these wakefields. Many higher order modes have been measured in the Main Ring RF cavities[2]. The 4 HOMs with the largest shunt impedance are at 67, 84, 127, and 227 MHz.

II. CHARACTERIZATION OF MODES

To characterize the oscillations of the beam, a 2 GHz Tektronix digitizer and LabView software with a Macintosh computer are used to capture and store the beam profile from a Resistive Wall Current Monitor. From this

data (Figure 1) it can be seen that individual bunches are undergoing dipole synchrotron oscillations. By following the oscillations of one particular bunch (Figure 2) a growth in the oscillation amplitude can be seen.

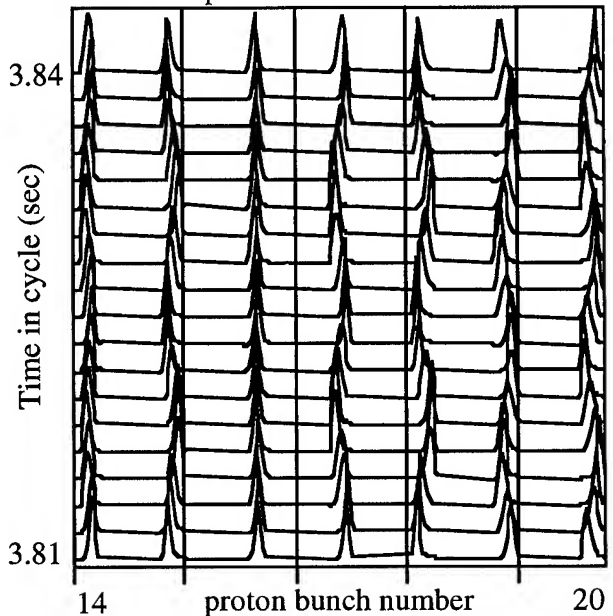


Figure 1. Mountain Range plot of proton bunches 14 through 20 showing synchrotron oscillations.

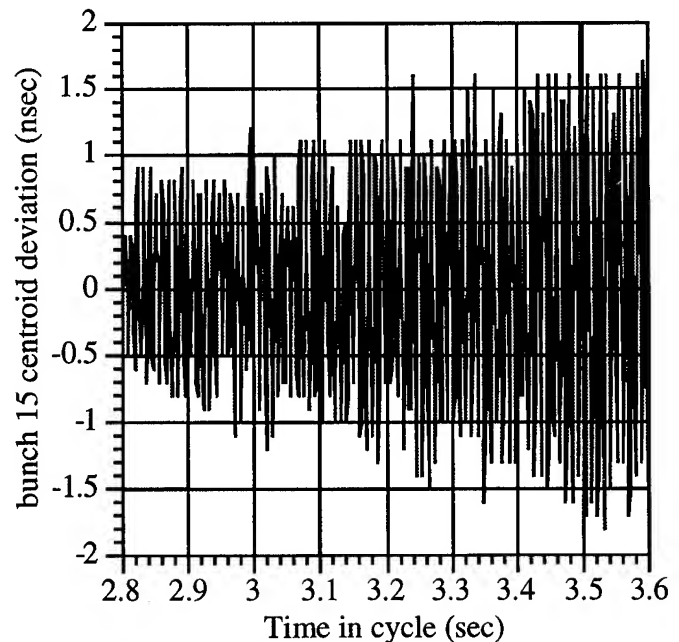


Figure 2. Growth in amplitude of synchrotron oscillation for an individual bunch. 1 nsec deviation is 19 degrees of RF phase.

At a given instant in time, the centroid of each bunch with respect to the RF bucket center will vary from bunch to bunch. Figure 3 shows data from an 84 bunch beam at a single moment. In a full ring with coupled bunch mode 1 present, this plot of deviation versus bunch number would have 1 full oscillation. A Fourier transform of this data and other snapshots in time, yields the power spectrum of the coupled bunch modes and is shown in Figure 4 [3]. The four major HOM of the RF cavities would be expected to produce modes 291, 465, 436, and 306. However Figure 4 shows that the dominant mode is 174. Although pulse to pulse variation is very common, under a wide variety of conditions (beam intensity, number of bunches, and applied RF cavity voltage) mode 174 is most prevalent. The exponential growth of this mode has been found to have a rise time on the order of 200 to 400 ms.

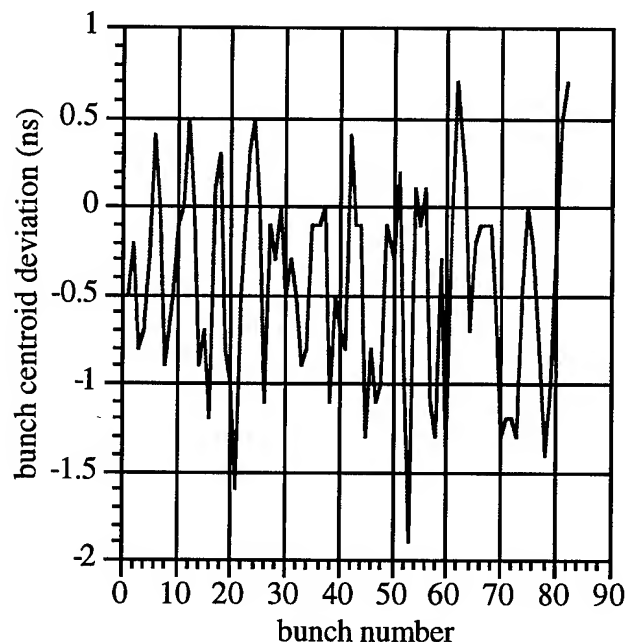


Figure 3. Bunch centroid deviation from center of RF bucket versus bunch number at a single point in time.

III. DAMPER CIRCUITRY

The signature of a coupled bunch mode N in frequency space is the presence of a sideband at the synchrotron frequency above or below the N th revolution line above or below a multiple of the rf frequency [4]. In order to detect this signal and create a narrowband damping system for these coupled bunch modes, a two-path circuit has been constructed. A schematic of this circuit is shown in Figure 5. A programmable direct digital synthesizer (DDS) provides two outputs (sine and cosine) that are used to select the mode to be damped.

After mixing the beam signal with the DDS, the output mode signal should be at the synchrotron frequency and have an amplitude proportional to the mode intensity. An example of this signal is shown in Figures 6 and 7. Figure 6 shows that the mode initially is excited at transition and Figure 7 shows further growth later in the cycle after acceleration has been completed.

IV. DAMPER SYSTEM

A first attempt to damp these oscillations considered the use of the existing power amplifiers and accelerating RF cavities to kick the beam. However the high Q of the cavities (1000-4500) and the bandwidth of the power amplifiers (50 to 90 MHz) do not provide sufficient gain for the damper system. Construction of dedicated kicker cavities will be necessary for the next phase of the project.

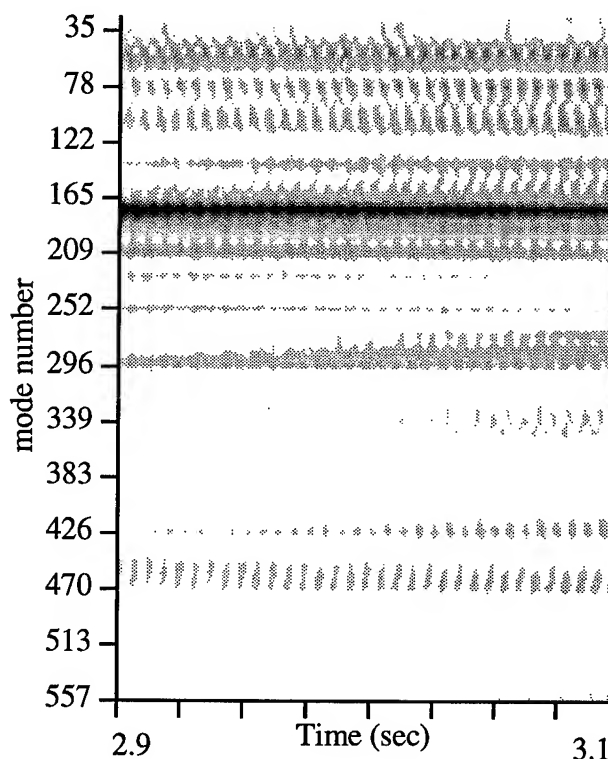


Figure 4. Power spectrum of coupled bunch modes with darkness indicating intensity.

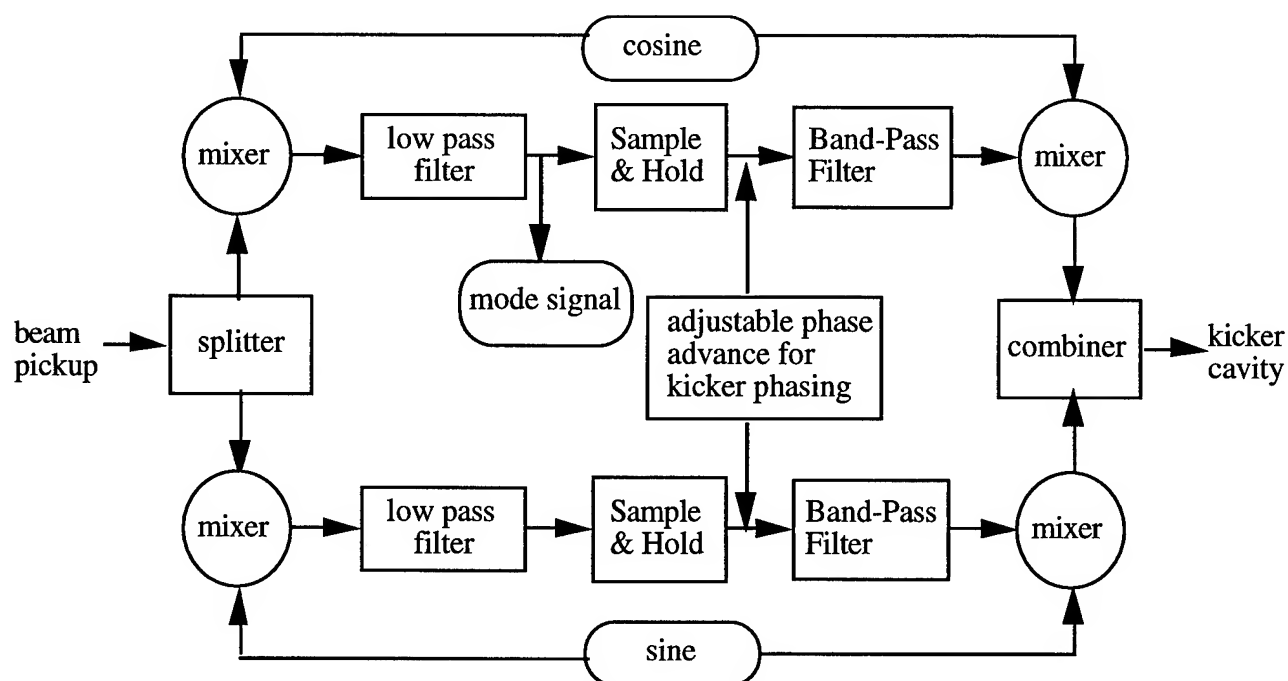


Figure 5. Schematic diagram of two-path damper circuitry.

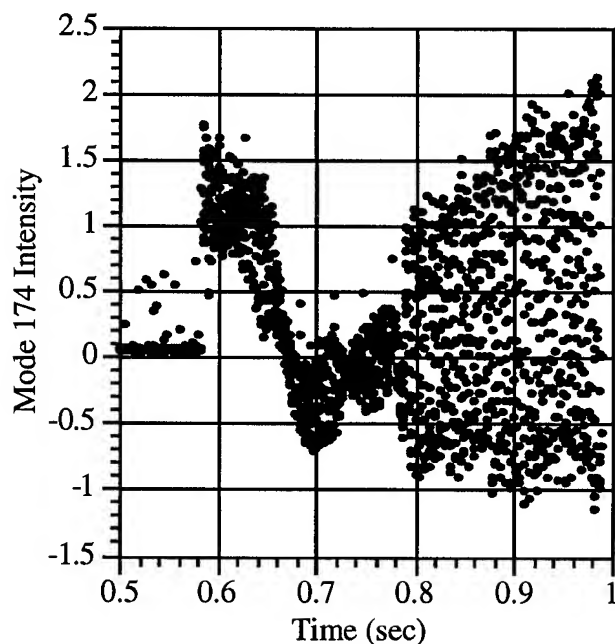


Figure 6. Intensity of Mode 174 signal during acceleration cycle. Signal increases dramatically at transition time (0.779 sec).

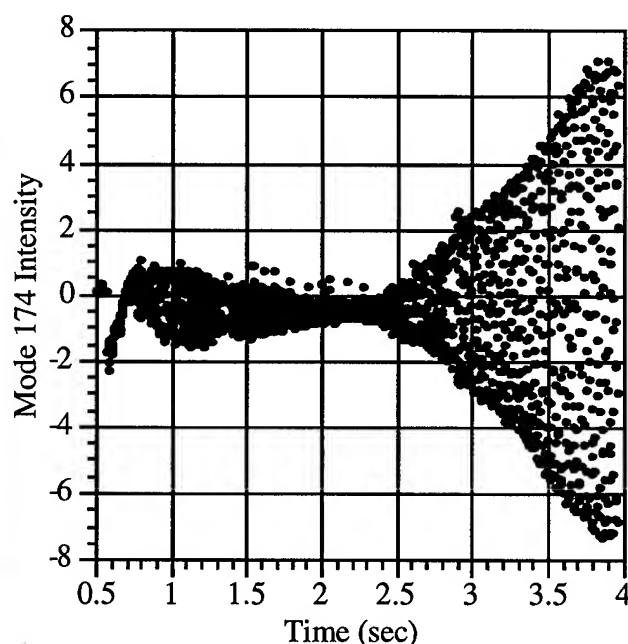


Figure 7. Growth of mode 174. Signal begins after transition and goes through exponential growth at the end of the acceleration portion of the cycle (2.4 sec).

IV. REFERENCES

- [1] I. Kourbanis, "Improvements in Bunch Coalescing in the Fermilab Main Ring", Paper RAQ13, these proceedings.
- [2] J.Dey, D. Wildman, "Higher Order Modes of the Main Ring Cavity at Fermilab", Paper WPP09 these proceedings.

- [3] D.P. McGinnis, "Coupled Bunch Mode Instabilities Measurement and Control", 1991 Accelerator Instrumentation Conference, AIP Conf. Proc. 252, W. Barry, editor, 1992, p. 65.

- [4] J.N. Galayda, "Feedback Control of Multibunch Instabilities", 1989 & 1990 USPAS, AIP Conference Proc. 249, M. Month, ed., 1992, p. 664.

INFERENCE OF WAKE FIELD STRUCTURE BY DRIVING LONGITUDINAL COUPLED BUNCH MODES IN MAIN RING*1

S. Assadi, K. Junck, P. Colestock, J. Marriner
Fermi National Accelerator Laboratory, Batavia, IL 60510, USA.

Here, we present a qualitative study of coupled bunch effects for a partially filled Main Ring. Individual bunches interact with their environment via wake fields generated by the fundamental and higher parasitic structural modes. Bunches at the front of the train influence the motion of the following bunches. We employ a two-point correlation method [1] to measure the phase oscillation between the reference bunch (bunch one) and a given bunch within the train, as a function of the bunch separations. The result of this analysis is a measure of the short range wakefield generated by the bunches.

I. ANALYSIS

Wake fields generated by a longitudinal kick to a train of proton bunches can be measured by the method of two-point correlation technique. Data are collected by observing signals from a resistive wall current monitor with a Tektronix 2 GHz digitizer. The digitizer is triggered every 32 turns to capture ~10 synchrotron periods worth of longitudinal profiles of the bunches (Fig. 1).

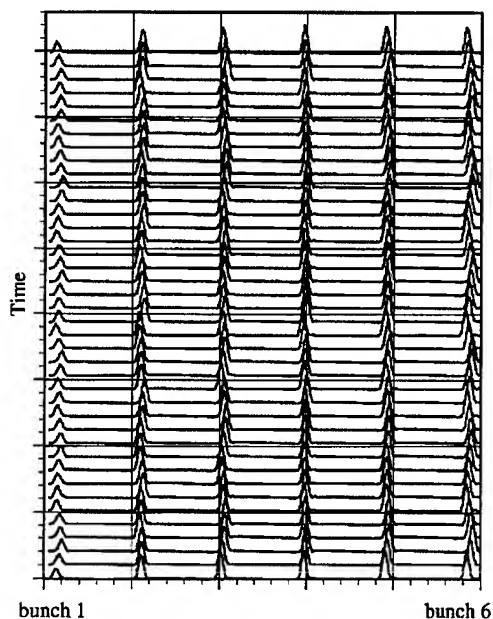


Fig. 1) Waterfall plot of the first 6 bunches.

*1 Operated by University Research Association Inc., under contract with the U.S. Department of Energy.

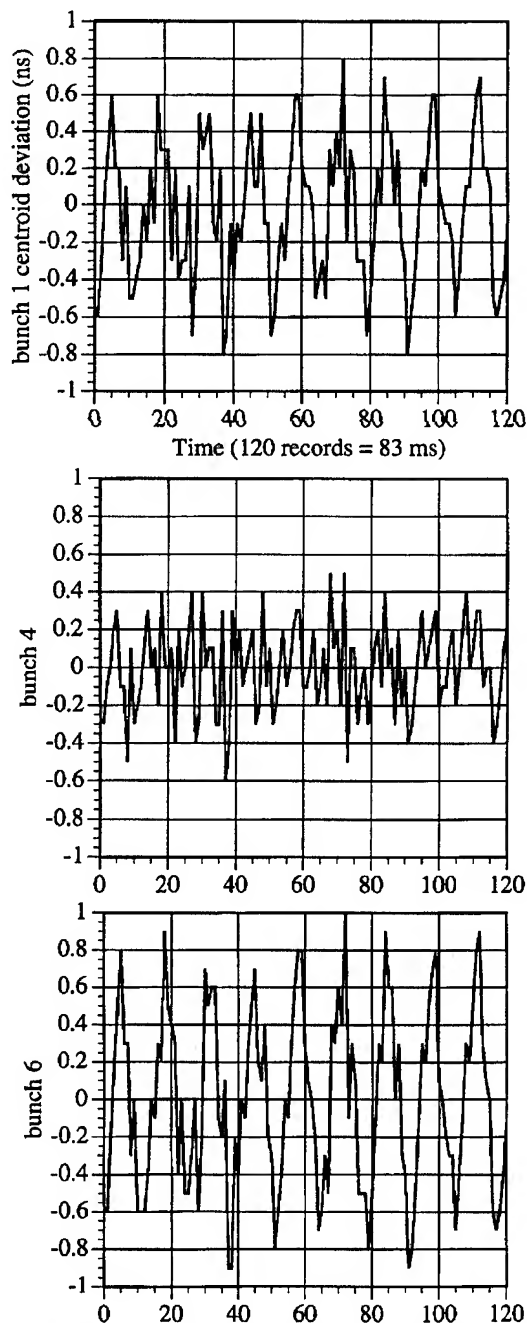


Fig. 2) The deviation of bunch centroid from bucket center for bunches 1,4,6. For the RF frequency of 53 MHz, 1 ns is equal to 19 degrees of phase.

Readout and the storage of the data is done by Macintosh computer using Labview software. The beam is given an initial kick by a programmable digital phase shifter which shifts the phase of all 18 RF cavities by 20 degrees for 200 μ sec (10 turns). The centroid position of each bunch can be found and longitudinal dipole oscillations at the synchrotron frequency are evident (Fig. 2).

The resulting time series is then broken up into 1000 realizations. Each realization contains the turn by turn data for each bunch (Fig. 3) which are then individually Fourier transformed. A cross power estimate $C_j(f)$ for each realization j is formed using the formula $C_j(f) = \phi_{j,1} \phi_{j,2}^*$ where $\phi_{j,1}$ is the Fourier transform of the signal from realization j , bunch 1 and frequency f and similarly for bunch "n" where $n > 1$. The cross power spectrum $C_j(f)$ is in general a complex quantity and can be written alternatively as $C_j(f) = |C_j(f)| \exp[\theta_j(f)]$ where $\theta_j(f)$ is known as the cross phase. An estimate of the wavenumber $k_j(f)$ is formed from each realization using $k_j(f) = \theta_j(f) / \Delta x$. Here Δx is the longitudinal separation of the bunches in centimeters. The spectral power $S(k, f)$ is then formed by summing the power $|C_j(f)|$ according to its wavenumber k and frequency f , $S(k, f) = \sum_j (\delta_{k,k_j} \delta_{f,f_j}) |C_j(f)|$ where δ_{k,k_j} is the Kronecker delta function and the sum runs over all realizations j . Normalizing $S(k, f)$ by the total power $S_{tot} = \sum_{k,f} S(k, f)$ produces the spectral density function $s(k, f) \Delta k \Delta f$ which can be thought of as the probability of finding a fluctuation in the wavenumber and frequency band $[k, k + \Delta k]$ and $[f, f + \Delta f]$. Finally, the average value of the wavenumber $k_{\theta j}$ is produced using the spectral density $s(k, f)$:

$$k_{\theta} = \sum_k k S(k)$$

where the sum runs over all wavenumbers k and

$$s(k) = \sum_f S(k, f)$$

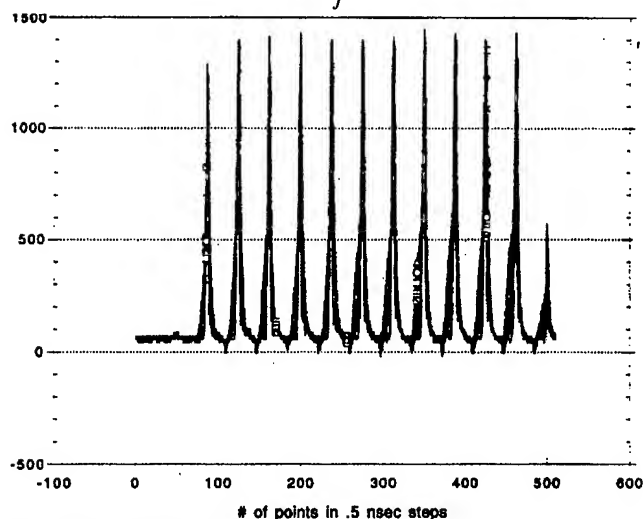


Fig. 3) A digitized batch of 12 bunches is shown.

II. RESULTS

Figure 4 shows an individual bunch oscillating within the RF bucket. The two-point correlation is done by determining the phase difference between the reference bunch (bunch one) and another bunch. For example, Figure 5 shows bunch one profile (top) and bunch 3 profile (bottom).

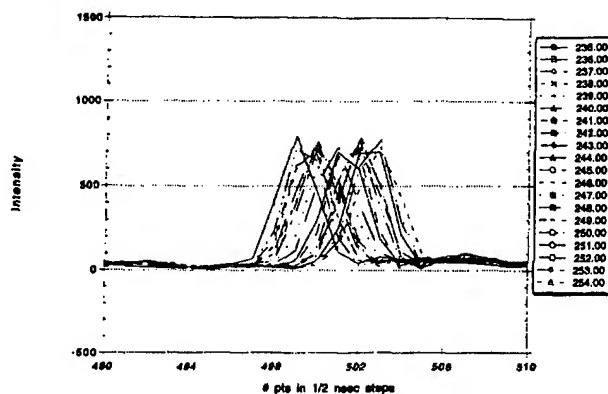


Fig. 4) Bunch oscillation within the bucket for many turns is shown.

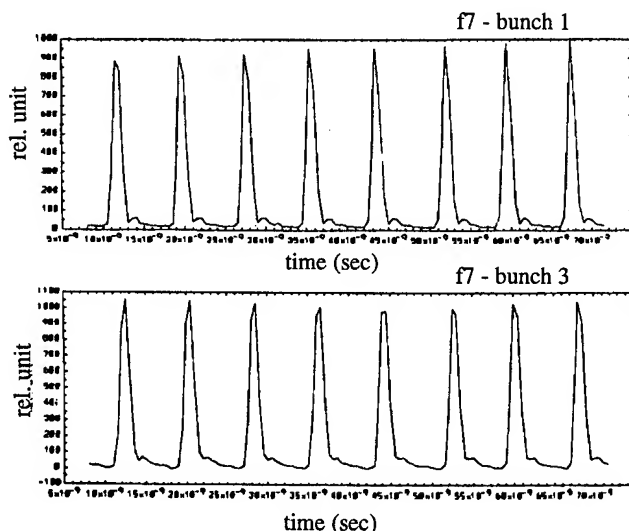


Fig. 5) Train of bunch one (top) is digitally formed from the turn by turn profiles. Same is performed for bunch three (bottom).

The wavenumber spectrum between bunch one and bunch two is shown in Figure 6. Only one peak, the dipole mode is observed. In figure 7, the wavenumber spectrum between bunch 2 and bunch 4 shows wavenumbers associated with dipole and quadrupole mode. A small peak associated with sextupole moment is also present but it is within the noise level of the measurement.

Figures 8 and 9 show the spectrum for other bunch combinations. Figure 9 shows a lack of the quadrupole mode which may have been eliminated by the superposition of the wakefields generated by the leading bunches.

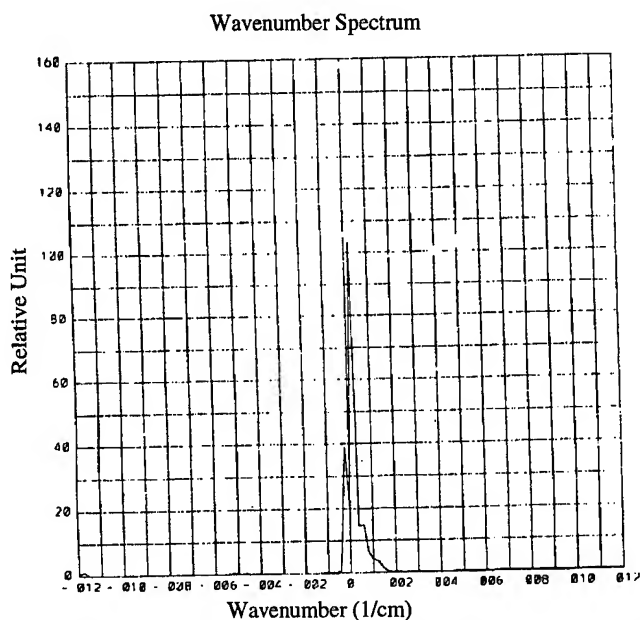


Fig.7) Shown peak associated with dipole mode is measured from the two-point correlation between the two adjacent bunch 1 and 2.

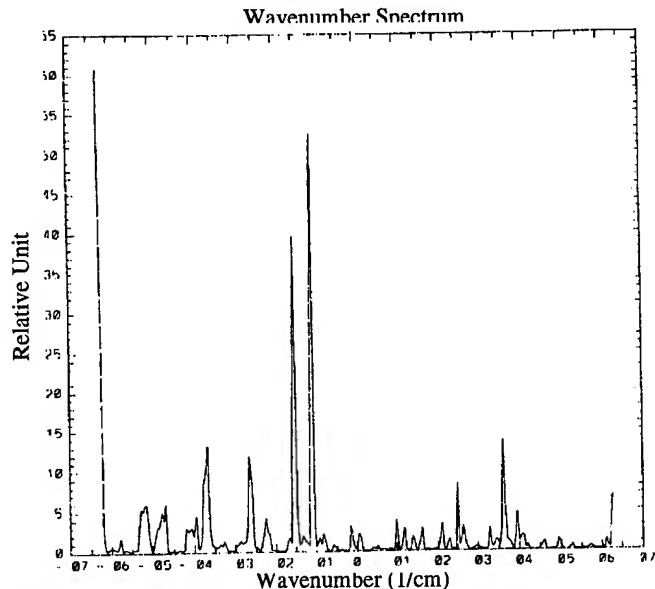


Fig.8) Measured two peaks associated with dipole and quadrupole oscillations between bunch 1 and 3 is shown.

III. CONCLUSION

From the difference in phase oscillation between bunches, the two-point correlation technique can estimate the wavenumber associated with low order short range wakefields.

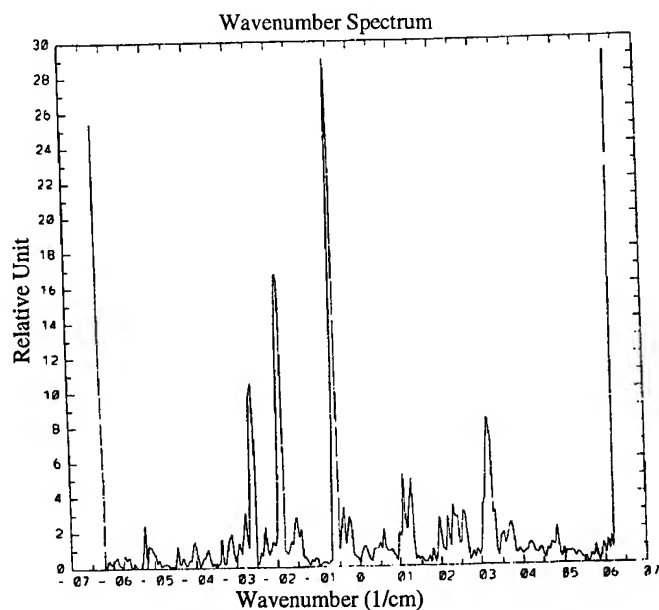


Fig.8) Three modes measured between bunch one and bunch five. $m=2$. Note, quadrupole mode is missing

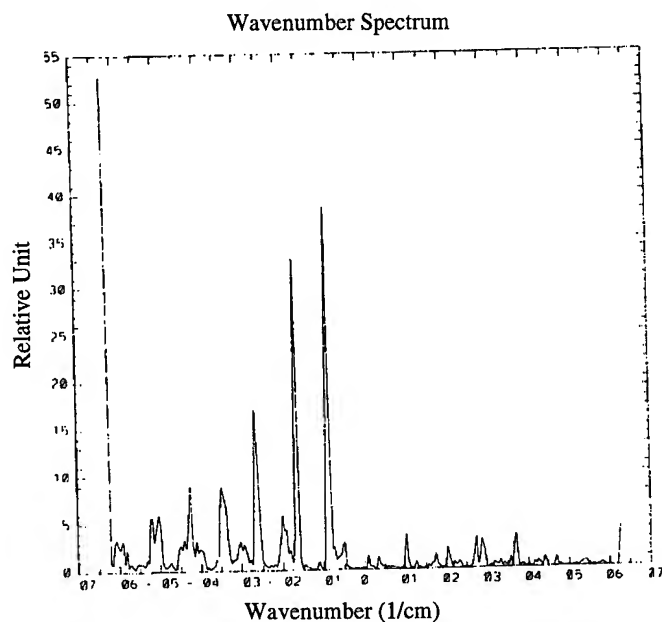


Fig.9) Three modes between bunches one and six are measured.

IV. REFERENCES

- 1) J.M. Beall, et al., Journal of Applied Physics, 53, 3933 (1982).

SIMULATION OF TRANSVERSE COUPLED BUNCH INSTABILITIES *

S. Khan, BESSY II, Rudower Chaussee 5, Geb.15.1, 12489 Berlin, Germany

Abstract

Numerical simulations of transverse coupled bunch instabilities caused by the resistive wall of the vacuum chamber are presented. These simulations confirm the results obtained analytically and extend them to cases which are not easily accessible by analytical methods.

I. INTRODUCTION

Transverse coupled bunch oscillations in a storage ring are driven by wake fields due to the interaction with cavity-like structures or with the resistive wall of the vacuum vessel. Concentrating on the latter case, the dipole wake function for a cylindrical vacuum chamber of length L , radius b and conductivity σ (in cgs units) is given by (see e.g. [1])

$$W_{\perp}(z) = -\frac{2}{\pi b^3} \sqrt{\frac{c}{\sigma}} \frac{1}{\sqrt{z}} L \quad (1)$$

where c is the velocity of light and z is the distance behind the charge causing the wake.

Due to its strong dependence on the chamber size, the resistive wall effect is in particular of interest for modern synchrotron light sources with small wiggler/undulator gaps. In this case, the radius b in equation 1 is replaced by an effective half-height of the flat vacuum chamber.

In a system of M bunches, each containing N particles, a bunch i oscillates according to the equation of motion

$$\ddot{x}_i(t) + \omega_i^2 x_i(t) = \frac{-Nr_0 c}{\gamma t_0} \sum_{j=1}^M \sum_{n=0}^{\infty} x_j(t - t_{ij} - n t_0) \cdot W_{\perp}(-c t_{ij} - n c t_0), \quad (2)$$

where r_0 is the classical electron radius, γ the Lorentz factor, t_0 the revolution time and $c t_{ij}$ the distance at which bunch j follows i . The term including the wake functions summed over all bunches and over all previous revolutions causes the oscillation to grow or decrease, depending on the phase relationship between the bunches.

In the following discussion, the BESSY II electron storage ring serves as an example. BESSY II is a 1700 MeV synchrotron light source currently under construction at Berlin [2]. The storage ring will be 240 m in circumference ($t_0 = 0.8 \mu s$) and can be filled with max. 400 bunches. In this case, the coupled bunch system has 400 oscillation modes, some of which may be excited and some damped. If the growth of any mode exceeds the rate of radiation damping or Landau damping, the beam will be unstable.

*Funded by the Bundesministerium für Bildung, Wissenschaft, Forschung und Technologie and by the Land Berlin.

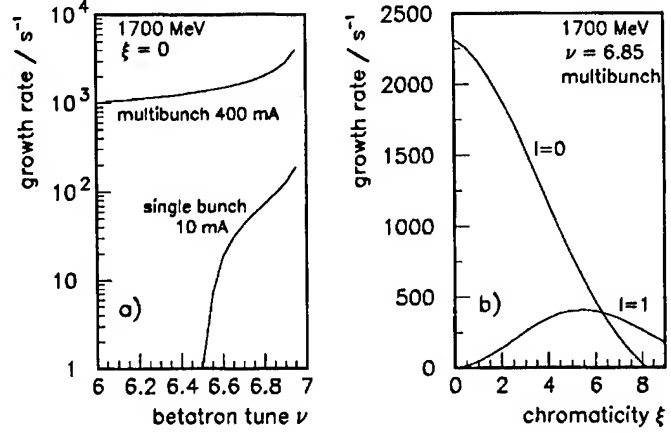


Figure 1. Growth rate of transverse coupled bunch instabilities as function of the vertical betatron tune ν (left) and of chromaticity $\xi = \Delta\nu/(\Delta p/p)$ (right).

II. ANALYTICAL EVALUATION

Fourier transformation of equation 2 into the frequency domain yields an analytical expression for the growth rate of the most unstable multibunch mode, provided the bunches are equally spaced and their motion is a harmonic oscillation (ω_i constant). Application of this well-known theory [3] leads to the following general results:

A. Single Bunch Mode

A single bunch has only one oscillation mode which is driven by its own wake from previous revolutions. This mode is damped if the fractional part of the tune δ is below 0.5; for $\delta > 0.5$ the beam is unstable.

Considering the finite size of the bunch has several consequences: As an extended object, the bunch has internal modes l . Furthermore, a finite bunch length implies a finite spectrum. Its central frequency is a function of the chromaticity ξ . A small positive chromaticity is sufficient to stabilize the $l = 0$ mode (head-tail effect), whereas the weaker $l > 0$ modes require larger values of ξ to be damped.

B. Multiple Bunches

For any tune, half of the multibunch modes are damped and half are unstable. The growth rate of the most unstable mode follows roughly $1/\sqrt{\delta}$. This is shown in the left part of figure 1 for the BESSY II storage ring, assuming an aluminium chamber in the insertion device region and a half-height of $b = 0.01$ m.

A large positive chromaticity reduces the growth rate and can even stabilize all multibunch modes for $l = 0$, while the $l = 1$ mode is still unstable, as shown in the right part of figure 1.

III. TIME DOMAIN SIMULATION (HARMONIC OSCILLATION)

A numerical simulation of the growing instability allows to study its time evolution, starting from different initial configurations and under the influence of different damping mechanisms. Furthermore, a simulation is required in cases where the growth rate cannot be determined analytically.

The simulation presented in this section maintains the assumption of a simple harmonic motion. It is meant to study the case of a fractional bunch filling and the effect of two damping mechanisms: (i) Radiation damping, where a factor $\exp(-t_0/\tau_R)$ is applied to the oscillation amplitudes after each turn, thus neglecting the stochastic nature of the radiation process. (ii) A non-linear tune shift with the amplitude $\Delta\nu \sim x^2$.

Equation 2 is iterated for all bunches in time steps of 2 ns (~ 60 steps per oscillation period). If all bunches perform a harmonic oscillation with the nearly unperturbed betatron frequency, the force experienced by a particular bunch i (given by the sum in eq. 2) just oscillates with the same frequency. In the course of the simulation, its amplitude and phase have to be recalculated from time to time, which requires little computational effort.

A. Time Evolution

Starting from a random configuration, the 400 bunches considered in figure 2 behave very differently. Some grow in amplitude, while others nearly stop oscillating. It takes about 0.2 ms for the bunches to "find" the most unstable mode μ at which they oscillate with the same exponentially growing amplitude and a fixed relative phase of $2\pi\mu/M$ between adjacent bunches. Once this state is reached, the growth rate in the simulation is consistent with the analytical result. If the bunches are initiated with the proper phase relationship, the exponential growth starts without delay.

B. Damping

The figures 2b-2d show the influence of damping on the system described above. In figure 2b, the growth of the instability is slowed down by radiation damping.

In figure 2c, a tune shift with amplitude has been introduced. All amplitudes grow up to a certain value, at which they start to diverge and their phase relationship becomes distorted. The averaged amplitude, however, remains constant.

A combination of both damping effects leads to a highly irregular motion, as shown in figure 2d.

C. Fractional Bunch Filling

If the storage ring is fractionally filled with bunches in order to leave an ion clearing gap, the coupled bunch oscillations are not easily described analytically. It has been shown that – for a given total current – the complete filling represents the worst case [4].

In a time domain simulation with 320 bunches in 400 rf buckets (figure 3), the bunches oscillate with different amplitudes and the spectrum shows a fine structure which is not present in the case of a complete filling. However, the growth rate of the instability, the phase relationship between the bunches and the gross features of the spectrum are the same for both cases.

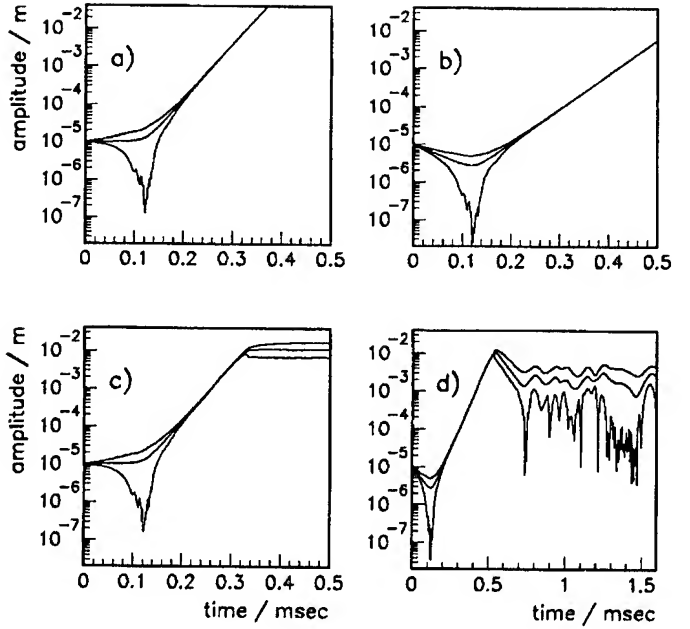


Figure 2. Smallest, largest and average amplitude in a system of 400 evenly spaced bunches with a) no damping, b) radiation damping, c) tune shift with amplitude, d) both damping effects.

IV. TIME-DOMAIN SIMULATION (BETATRON OSCILLATION)

In a realistic betatron oscillation, the frequency ω_i in equation 2 depends on the position in the lattice. Therefore, the phase relationship between bunches changes all the time, which should reduce the effective driving force.

In order to simulate this effect, all bunches are tracked through the magnetic lattice using linear transfer matrices for each time step (2 ns, corresponding to 0.6 m). To prevent the effect in question from being obscured by non-linear lattice effects, sextupole kicks were not applied. The consequences of the tune shift caused by sextupole fields were studied in [5].

With the wake function of equation 1 inserted into equation 2, the driving force for bunch i is essentially given by

$$F_i(t) \sim \sum_{j=1}^N \sum_{n=0}^{\infty} \frac{1}{\sqrt{t_{ij}/t_0 + n}} x_j(t - t_{ij} - nt_0). \quad (3)$$

Keeping track of all bunch positions over many turns and evaluating the twofold sum for all bunches at each time step would clearly require too much computer memory and time. However, a simplification can be made by expressing the transverse position of bunch j at the n^{th} previous passage as

$$x_j(t - t_{ij} - nt_0) = x_j(t - t_{ij}) \{ \cos(n\delta_j) + \alpha \sin(n\delta_j) \} + x'_j(t - t_{ij}) \beta \sin(n\delta_j), \quad (4)$$

where α and β are the Twiss parameters at the location of bunch j , and δ_j is the phase advance over one revolution backward in time. Then, equation 3 can be rewritten as

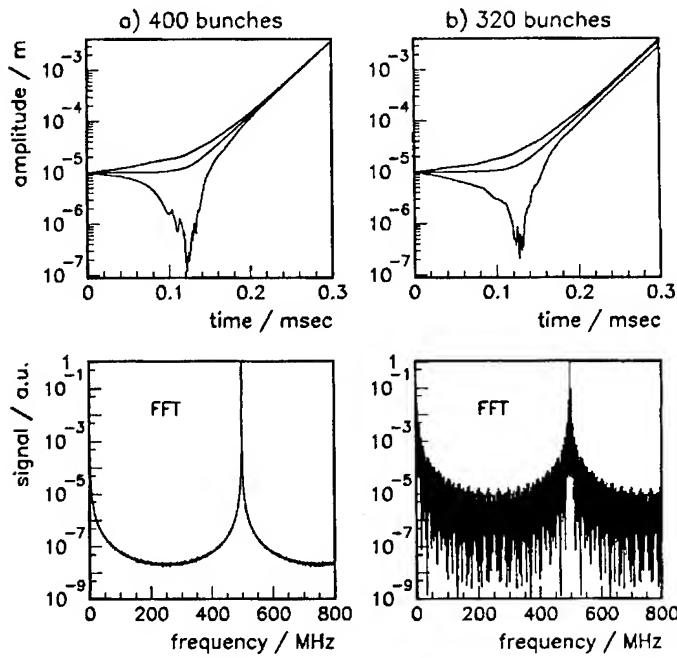


Figure 3. Amplitudes (upper part) and the Fourier transformed signal seen at a fixed location of the storage ring (lower part) for a) 400 evenly spaced bunches, and b) 320 bunches in 400 rf buckets with the same total current.

$$F_i(t) \sim \sum_{j=1}^N \left[\left\{ \sum_{n=0}^{\infty} \frac{\cos(n\delta_j)}{\sqrt{t_{ij}/t_0 + n}} \right\} \cdot x_j(t - t_{ij}) + \left\{ \sum_{n=0}^{\infty} \frac{\sin(n\delta_j)}{\sqrt{t_{ij}/t_0 + n}} \right\} \times (\alpha x_j(t - t_{ij}) + \beta x'_j(t - t_{ij})) \right]. \quad (5)$$

This allows to perform the sum over n beforehand and store the result for all required values of t_{ij} and δ_j in a look-up table. This is justified if δ_j is constant over a reasonable time scale – an assumption also made in the analytical theory.

A. First Results

In the simulation shown in figure 4, a system of 400 evenly spaced bunches was initiated with a phase relationship corresponding to the most unstable mode. The amplitudes first diverge and grow more slowly than they do in the harmonic oscillator model. The relative phases also diverge and fill a certain range (figure 4b), while the growth rate increases and settles at a value well below the theoretical rate (figure 4c).

In conclusion, an improved description of coupled bunch oscillations has been obtained and further refinements of the model are within reach, in particular the inclusion of damping mechanisms: (i) radiation damping, (ii) sextupole kicks to produce the tune shift that was included rather arbitrarily in the harmonic oscillator model, and (iii) the head-tail effect by splitting the bunches into macro-particles.

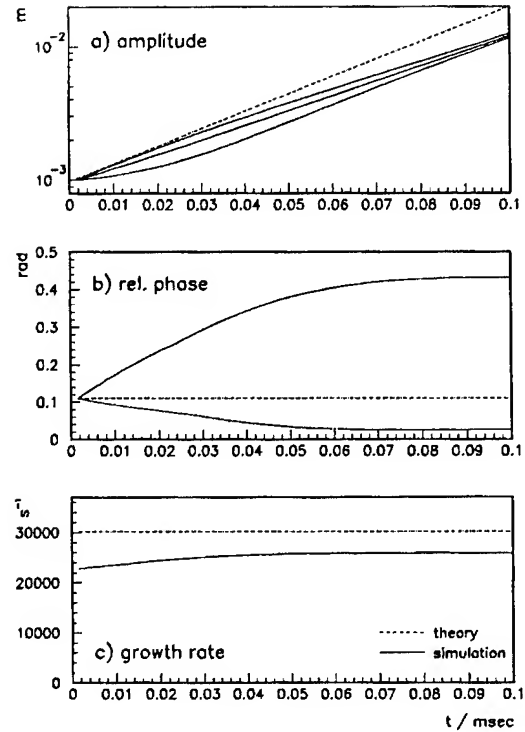


Figure 4. Transverse resistive wall instability with 400 bunches, assuming a harmonic motion (dashed lines) and a more realistic betatron oscillation (solid lines): a) smallest, largest and average amplitude, b) smallest and largest phase difference between adjacent bunches, and c) growth rate versus time.

References

- [1] Chao, A. W., *Physics of Collective Beam Instabilities in High Energy Accelerators*, New York, 1993.
- [2] E. Jaeschke, *Status of the High Brilliance Synchrotron Radiation Source BESSY II*, these proceedings.
- [3] B. Zotter and F. Sacherer, in: *Theoretical Aspects of the Behaviour of Beams in Accelerators and Storage Rings*, CERN 77-13, 1977.
- [4] R. D. Kohaupt, *On Multi-Bunch Instabilities for Fractionally Filled Rings*, DESY 85-139, 1985.
- [5] M. Meddahi and J. Bengtsson, *Studies of Transverse Coherent Bunch Instabilities for the Advanced Light Source (ALS)*, LBL-35703, 1994.

THE TRANSITION JUMP SYSTEM FOR THE AGS*

W.K. van Asselt, L.A. Ahrens, J.M. Brennan, A. Dunbar, E. Keith-Monnia, J.T. Morris,
M.J. Syphers, Brookhaven National Laboratory, Upton, NY 11973 USA

Abstract

In an attempt to generate a lossless crossing of an accelerator's transition energy, one procedure is to alter the transition energy of the accelerator quickly as the beam passes through this energy region by changing the optics of the lattice – a so-called “transition jump,” or “ γ_t -jump” scheme. Such a system was first implemented at CERN[1] and later adopted at other accelerator laboratories. A scheme for the AGS was developed in 1986. The system has become operational during the 1994 high intensity proton run. It consists of three quadrupole doublets, each magnet having an individual power supply and crowbar circuit. After a brief theoretical description of the jump system for the AGS, we describe the engineering aspects of the hardware and our experience with the system during its commissioning.

I. FIRST PRINCIPLES

Changing the transition energy in the AGS amounts to changing the average value of the dispersion function, D_x , in the bending magnets of the accelerator. The value of γ_t for a synchrotron with sector bending magnets is given by

$$\frac{1}{\gamma_t^2} \equiv \frac{\Delta C/C}{\Delta p/p} = \left\langle \frac{D_x}{\rho} \right\rangle, \quad (1)$$

where the average is taken over the circumference of the accelerator. The value of ρ is path length dependent, and has infinite value in straight sections. Hence, it is the value of the dispersion function in the bending magnets which one is after in this exercise of altering γ_t .

A. Lattice Perturbations

By introducing quadrupoles in the normal AGS lattice, one can perturb the dispersion function and hence, hopefully, alter γ_t in a constructive way. The choice of quadrupole locations for this purpose in the AGS resulted from a study in 1986[2],[3]. The AGS system alters the dispersion function as shown in Fig. 1.

By varying the strength of the six quadrupoles, one can tune the accelerator to various values of γ_t . Perturbations to the lattice functions of the AGS will have approximate values given by[4]:

$$\Delta \hat{D} \approx \frac{D_0(\beta_0 q)}{2} \sqrt{1 + \tan^2\left(\frac{\pi\mu}{2}\right)}, \quad (2)$$

$$\left| \frac{\Delta\beta}{\beta} \right|_{max} \approx \left| \frac{\beta_0 q}{2} \right| \quad (3)$$

where $q \equiv \Delta B' \ell / (B\rho)$, $\mu = \nu/3$ is the tune across one-third of the ring (the new superperiod), and D_0 and β_0 are the unperturbed lattice functions at the quadrupole locations. As an example, taking $\beta_0 q = 1$ (approximate value of the AGS γ_t quads running at 1500 A near the AGS transition energy), we get $\Delta \hat{D} \approx$

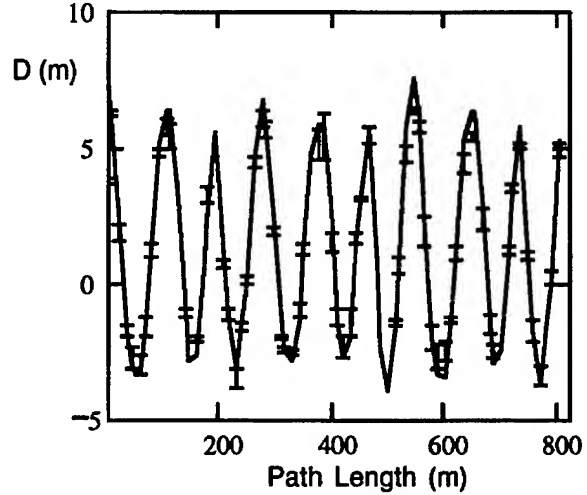


Figure. 1. Measured AGS dispersion function during the γ_t -jump. The solid curve is the dispersion function predicted using SYNCH.

7.5 m, and $\Delta\beta/\beta \approx 0.5$. Detailed calculations of the jump system using the code SYNCH[5] are in agreement with these predictions.

B. Estimation of Tune Shift

According to the well-known tune shift formula, $\Delta\nu = \beta q / 4\pi$, there should be no tune shift from six regularly spaced, alternating gradient quadrupoles in the AGS. However, the strength of these quadrupoles can be large enough that second order effects come into play, and results in

$$\Delta\nu_{x,y} \approx \frac{3 \tan \pi\mu}{8\pi} (\beta_0(x,y)q)^2. \quad (4)$$

As an example, for the AGS with a tune of 8.75, and for $q = 1/20\text{m}$, we get $\Delta\nu_x = -0.03$, and $\Delta\nu_y = -0.007$. Notice that both tune shifts are of the same sign, since they depend upon the square of the quadrupole strength.

C. Estimation of Shift in Transition Energy

To obtain an estimate of how much one can change γ_t with the AGS system, we can use Eq. 1 to see that

$$\Delta\gamma_t \approx \frac{-\gamma_{t0}^3}{2\rho} \Delta\langle D \rangle \quad (5)$$

for small variations in the lattice parameters. For the AGS system, consider the change in the dispersion function, ΔD , across one new superperiod (one third of the ring). By computing the change in the dispersion function at a “positive” quad, and propagating this change through two standard superperiods of the

*Work performed under the auspices of the U.S. Department of Energy.

AGS, summing up the changes ΔD in the bending magnets between two consecutive "positive" quads, say, and taking their average, one can employ Eq. 5 above to estimate $\Delta\gamma_t$. Doing so, we obtain:

$$\Delta\gamma_t \approx \frac{\gamma_{t0}^3 D_0}{32\rho} \left(\frac{\tan \pi\mu}{\cos^3 \frac{\pi\mu}{2}} \right) \langle A \rangle_{\text{bends}/6} (\beta_0 q)^2. \quad (6)$$

where $A_i \equiv$

$$\sqrt{\frac{\beta_i}{\beta_0}} \left[\sin(\psi_i - \frac{3\pi\mu}{2}) + \left(\cos \frac{\pi\mu}{2} - \alpha_0 \sin \frac{3\pi\mu}{2} \right) \sin \psi_i \right]. \quad (7)$$

Here, β , β_0 , α_0 , and D_0 are unperturbed values of the lattice functions (β_0 , α_0 and D_0 are at a γ_t -quad), $\Delta\psi$ is the phase advance from the nearest upstream γ_t -quad, $\mu = \nu/3$, and the average taken in the above expression is over the bending magnets in one sixth of the AGS circumference.

For the AGS, with $\nu = 8.75$,

$$\langle A \rangle_{\text{bends}/6} \approx 0.025 \quad (8)$$

and taking $\nu = 8.75$, $\gamma_{t0} = 8.5$, $\rho = 85.38$ m, and $D_0 = 2.1$ m, we get

$$\Delta\gamma_t \approx 1.7 (\beta_0 q)^2. \quad (9)$$

Quick estimates of system parameters for a nominal AGS horizontal tune of 8.75 can be made using the following summary:

$$\Delta\gamma_t = 1.7 (\beta_0 q)^2 \quad (10)$$

$$\hat{D} = \hat{D}_0 (1 + 3.2\sqrt{\Delta\gamma_t}) \quad (11)$$

$$\hat{\beta} = \hat{\beta}_0 (1 + 0.4\sqrt{\Delta\gamma_t}) \quad (12)$$

$$\Delta\nu_x = -0.02\Delta\gamma_t, \quad \Delta\nu_y = -0.005\Delta\gamma_t \quad (13)$$

II. ENGINEERING ASPECTS OF THE JUMP SYSTEM

The design of the transition jump system called for 3 quadrupole doublets, with one magnet in every other superperiod at a horizontal β_{max} location. This geometry was achieved by redesigning the tune correcting quadrupoles in a more compact way such that two quadrupole magnets could be installed in the #17 straight sections of each superperiod in the AGS. Total tune shifting quad strength has not been sacrificed by acquiring higher rated power supplies.

The power supply for each magnet is comprised of a remotely programmed charging supply connected to the magnet through a triggerable switch (see Fig. 2). The power supply is ramped to the desired current, at which time the switch is opened and the current is crowbarred through a power resistor. The time constant of this current has been a central design issue and a value of 600 μsec has been achieved.

To handle the switching requirement of 3 kA a solid state Gate Turn-off Thyristor (GTO) was selected. GTO's possess the current and voltage handling capabilities needed and can be rapidly triggered on and off. The Marconi DG758BX45 was selected for at the time of the design it had the highest on-state current of any GTO on the market. Two GTO's in parallel are used in the switch (GT01 and GT02). These GTO's were purchased in

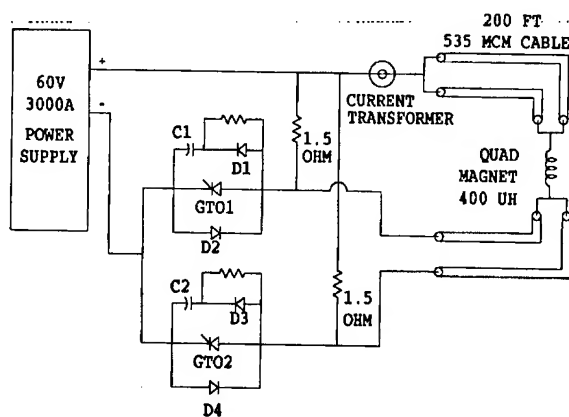


Figure. 2. Schematic diagram of the main components of the transition jump system.

matched pairs to optimize current sharing. Delay and storage times as well as on-state voltage were the matching parameters.

Integral to the switch design was the snubber design. For reliable GTO turn-off, the rate of rise of the off-state voltage ($dV/dt=500$ V/ μsec) can not be exceeded. The capacitor selected for the circuit was a Maxwell mini double ended 37600. Four of these 2 μF , 5 kV capacitors are connected in parallel using copper bus (C1,C2). Each capacitor has an inductance of less than 20 nH and a shot life of greater than 10^8 . This inductance is important because the rapidly falling GTO anode current at turn-off is transferred to the snubber circuit until the capacitor is fully charged. The overall circuit inductance dictates the magnitude of the voltage spike across the GTO at this time. This spike must be minimized to protect the GTO from excessive turn-off power dissipation. The component interconnections also contribute to the circuit inductance. Care was taken to mount all snubber components as close as possible to each other. Large buswork and component heatsinks were used as connections to eliminate wire connections. Buswork inductance is estimated to be 100 nH, well below the manufacturer's recommended value of 200 nH. Also adding to the GTO turn-off voltage spike is the forward recovery voltage of the snubber diode (D1,D3). This transient voltage is developed after forward voltage is applied to the diode and before it fully conducts. The International Rectifier R52KF45 was selected for its low forward recovery voltage of approximately 100 V. This fast recovery diode is rated for 990 A, 4500 V and has a recovery time of 5 μsec . Using this design, GTO turn-off voltage spikes of less than 300 V were obtained when switching 3 kA.

The crowbar resistor proved to be another design challenge. Two 1.5 Ω , 2 kW resistors were needed. High voltage, high energy dissipation ceramic disc resistors of 0.125 Ω each were selected. When purchased they were mounted as stacks of 12 on an insulating non-reinforced polyimide rod. During testing resistors failed due to arcing. This was caused by the fact that the torque keeping the discs in place could not be maintained due to the inherent creeping properties of the polyimide material. A brass rod was used as replacement and G-10 was used to insulate the rod from the discs. Belleville washers were used to keep

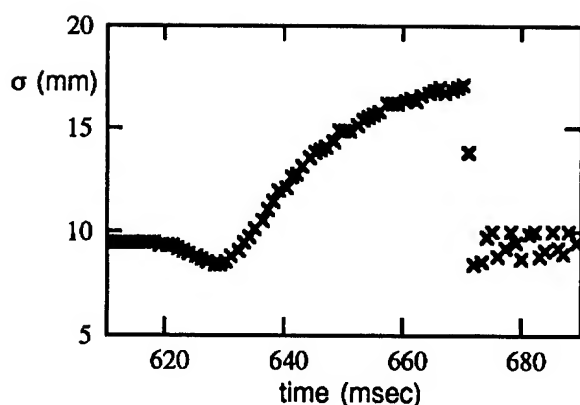


Figure. 3. The beam size measured by the IPM, during the ramp and discharge time of the transition quadrupoles.

the torque constant on the discs by compensating for any thermal cycling during operation. As an added measure, fans were installed to cool the length of the resistors.

The power supplies are located in the service buildings closest to each magnet. A quadruplex 535 MCM cable run with an average length of 200 ft connects the supplies to the magnets. The cable resistance (5 m Ω) and inductance (20 μ H) only marginally contribute to the time constant of the current decay.

III. COMMISSIONING OF THE JUMP SYSTEM

The power supplies became available in early 1994 and the commissioning of the system began in March during the startup period of the FY94 high energy physics run. After verifying polarities and timing of the individual quad systems, it was found that beam loss occurred while the entire system was pulsed at currents well below the design value. The BPM system showed orbit excursions well over 10 mm during the ramp of the quadrupoles, which were found to be caused by rather large excursions of the orbit with respect to the quadrupole magnets. To reduce this effect the AGS main dipole magnets have been realigned. To minimize this steering effect even further, the quadrupole magnets themselves have been moved to center the orbit as well as possible in the magnets.

As illustrated in Fig. 1 there are large excursions of the dispersion function during the time when the transition energy is modified. At the Ionization Profile Monitor (IPM) location, the dispersion changes from the nominal 2 m to about -5 m, when the magnets are ramped to 1500 A, corresponding to a change in the transition energy of 1.5 units. In Fig. 3 the measured beam size is plotted during the

ramping of the currents in the quadrupoles. At first the beam size decreases with the dispersion, but increases significantly later when the absolute value of the dispersion becomes larger than for the nominal machine. For a given momentum spread, this effect limits the maximum size of the transition jump, because it leads to beam scraping.

By the same token, for a given jump size the maximum acceptable momentum spread is set by the beam losses at transition. To reduce this increase, part of the longitudinal beam dilution process using the Very High Frequency (VHF) cavity, which is re-

quired for stability later in the acceleration cycle, is exercised after transition. In addition, the voltage of the main RF system is decreased during the time before the jump.

IV. STATUS AND OUTLOOK

The intensity in the AGS has reached the design goal of 6×10^{13} and the transition jump system has been one of several systems which have been essential in achieving this. Because the beam size increases with intensity the beam blowup due to the jump also increases, causing beam losses in the vicinity of transition. During the present FY95 high energy physics proton run transition losses of 2 to 3% at intensities above 5×10^{13} are typical.

Under typical operating conditions the quadrupoles are ramped to approximately 1500 A, which is far below the capacity of the jump system. The system has been used at full capacity during acceleration of gold ions when the field at which transition occurs is much higher.

Experimental studies and modeling of non-linear chromatic effects associated with the present jump system are described in a separate paper.[6]

With the outlook of even higher intensities in the future and the demand for the lowest possible beam losses, the consequences of the large excursions of the dispersion function with the present system are imminent. For that reason an investigation towards the possibility of implementing a linear jump system [7] for the AGS has started.

References

- [1] W. Hardt, "Gamma Transition-Jump Scheme of the CPS," proc. Ninth Intl. Conf. on High Energy Part. Acc., Stanford, 1974.
- [2] P. Yamin, et al., AGS Accel. Div. Tech. Note 265, Sept. 1986.
- [3] P. Yamin, et al., "A Fast Transition Jump Scheme at the Brookhaven AGS," proc. 1987 IEEE Part. Accel. Conf., 87CH2387-9, p. 134.
- [4] M. J. Syphers, et al., "The AGS γ_t -jump System," BNL report BNL-60824, September 1994.
- [5] A. A. Garren, et al., "SYNCH User's Guide - 1993," SSCL-MAN-0030 Rev, SSC Laboratory, 1993.
- [6] J. Wei, et al., these proceedings.
- [7] V. Visnjic, Phys. Rev. Lett., 73 (1994) 2860.

Measurements of Longitudinal Phase Space in the SLC Linac*

R.L. Holtzapple, F-J. Decker, R.K. Jobe, and C. Simopoulos
Stanford Linear Accelerator Center, Stanford University, Stanford, CA 94309 USA

I. Abstract

The electron and positron bunch distributions in the Stanford Linear Collider (SLC) linac have been measured using a Hamamatsu, model N3373-02, 500-femtosecond streak camera[1]. The distributions were measured at the end of the SLC linac versus the bunch compressor RF voltage. The energy spread at the end of the linac was also measured using a wire scanner. The effects of the bunch compressor on the shape of the bunch distribution are also presented.

II. Bunch Compression in the SLC Linac

In a linear collider the transverse emittance needs to be small for high luminosity. Damping rings are used to damp the emittance. The bunch extracted from the damping ring is too long for acceleration in an S-band linear accelerator. To reduce the bunch length after extraction, the bunch is compressed.

The bunch distribution in the SLC linac is determined from the distribution in the damping rings, and the bunch compressor. The bunch compression system at the SLC consists of two parts: 1) a non-isochronous transport line from the damping ring to the linac (referred to as the transport line), and 2) an S-band RF accelerating section at the beginning of the transport line (referred to as the compressor). The electron and positron damping rings have separate transport lines and compressors.

Bunch compression is determined by the relationship

$$z_f = z_i + R_{56} \frac{\Delta E}{E}$$

where R_{56} is determined by the optics in the transport line, z_i is the location of a particle in the bunch before compression, $\frac{\Delta E}{E}$ is the energy offset of a particle after the compressor, and z_f is the location of a particle in the bunch after compression.

When the bunch is extracted from the damping ring it passes through the compressor RF accelerating section where the mean of the bunch distribution is centered on the zero crossing of the compressor RF wave. The compressor voltage gives the distribution a correlated head-tail energy spread (tail of distribution is lower in energy than head). After the compressor the bunch travels through the non-isochronous transport line where the longitudinal phase space rotates. Phase space rotation occurs from the high

energy particles (head) taking a longer path than lower energy particles (tail) through the dispersive transport line. The compressor voltage amplitude can be varied so that the bunch is under-compressed, fully-compressed, or over-compressed.

III. Bunch Length Measurement

The streak camera uses synchrotron light produced in the splitter magnet at the end of the linac to determine the longitudinal bunch distribution. The projections of the longitudinal distribution are saved and analyzed off-line.

The mean and σ of the projections are estimated by fitting the entire profile to an asymmetric Gaussian function

$$I(z) = I_0 + I_1 \exp \left\{ -\frac{1}{2} \left(\frac{(z - \bar{z})}{(1 + \text{sgn}(z - \bar{z})A)\sigma} \right)^2 \right\}$$

where I_0 =pedestal, and I_1 =peak of the asymmetric Gaussian. The term $\text{sgn}(z - \bar{z})A$ is the asymmetry factor which parameterizes the shape of the asymmetric Gaussian. Since the shape deviates considerably from an asymmetric Gaussian, a better estimate of the bunch length is provided by the root mean square width

$$\sigma_z = \sqrt{\sum_i^N (z_i - \bar{z})^2 I(z_i)}$$

where N is the number of CCD pixels within $\pm 3\sigma$ of the mean \bar{z} , z_i is the location of the pixel, and $I(z_i)$ is the projection height.

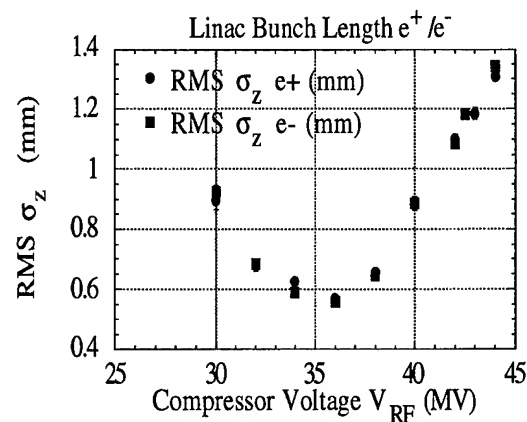


Figure 1. The bunch length as a function of the compressor voltage for the electron and positron bunch at the end of the linac.

* Work supported by Department of Energy
Contract DE-AC03-76SF00515.

The streak camera measurement consists of taking 30 longitudinal profiles at compressor voltage settings 2 MV apart. Plotted in figure 1 is the mean RMS bunch length and the root mean error for currents of $I=3.4 \times 10^{10}$ and 3.3×10^{10} particles per bunch for the electrons and positrons respectively. The accelerating RF voltage in the damping rings during this measurement was 820 and 880 kV for the electron and positron rings respectively.

A compressor voltage setting of 30 MV gives a bunch distribution that is under-compressed, 36 MV is a fully-compressed, and 42 MV gives an over-compressed distribution. The longitudinal distribution of the positrons and electrons (see figures 2 and 3) is a sum of 30 plots where the means of the distribution are shifted to a common origin.

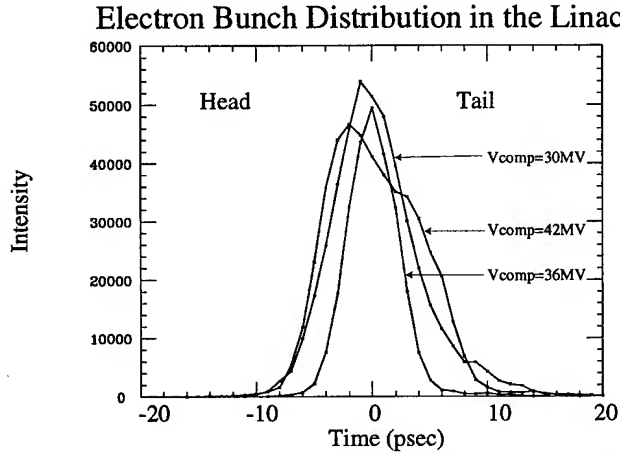


Figure 2. The electron bunch distributions at the end of the linac for compressor voltage settings of 30, 36, and 42 MV.

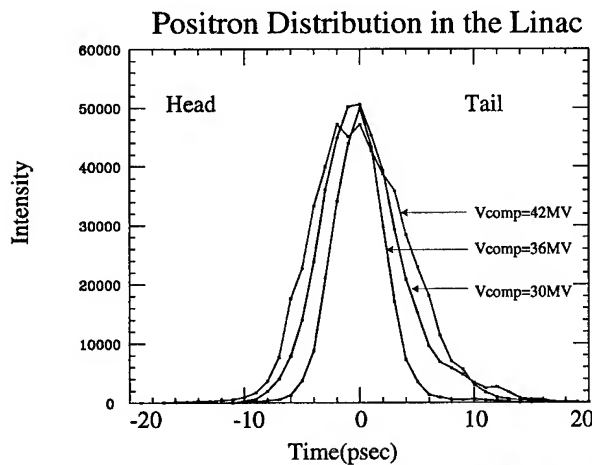


Figure 3. The positron bunch distributions at the end of the linac for compressor voltage settings of 30, 36, and 42 MV.

The systematic errors using the streak camera are discussed in reference 2. The dispersion in the glass optics limits the resolution of the streak camera as seen in figure

4. The effect of the dispersion can be minimized by using a narrow band (10nm FWHM) interference filter.

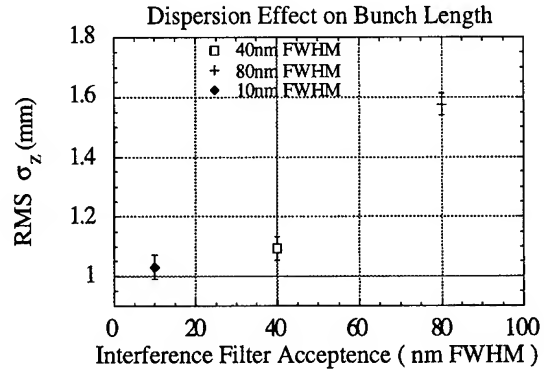


Figure 4. The electron bunch length at the end of the linac as a function of interference filter acceptance.

IV. Energy Spread

A. Ring to linac transport line

The energy spread in the transport line determines the degree of compression. It is determined by the compressor's voltage. A linearized expression for the energy spread is

$$\frac{\sigma_E}{E} = 2\pi \left(\frac{\sigma_z}{\lambda E} \right) V_{rf}$$

where σ_z is the damping ring bunch length, $\lambda = 105\text{mm}$ is the S-band wavelength, V_{rf} is the RF voltage amplitude, and E is the beam energy (1.19GeV). During the 1994 run the compressor voltage amplitude was 43 MV and the bunch length out of the linac is 7.0mm. This results in an energy spread of 1.5% in the compressor transport line. The energy aperture in the transport line at the high dispersion regions is $\pm 2.5\%$ which results in current losses for the high and low energy tails.

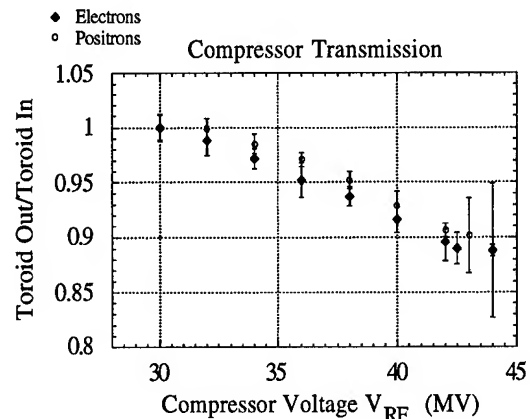


Figure 5. Electron and positron compressor transport line transmission as a function of compressor RF voltage.

Transmission through the positron and electron transport lines was measured versus compressor voltage with a toroid at the entrance and exit of the transport line. The ratio of the toroid readings (figure 5) determines the current loss. An over-compressed bunch results in a current loss of about 10% over an under-compressed bunch.

B. End of Linac

The energy spread at the end of the linac is determined from the RF amplitude in the linac, the phase of the bunch on the RF accelerating wave, and the energy loss due to longitudinal wake fields. The bunch has a longitudinal distribution in z and the energy of a particle at location z is given by[3]

$$E(z) = E_{inj}(z) + \sum_i^N E_i \cos\left(\frac{2\pi z}{\lambda} + \phi_i\right) - E_{wake}(z).$$

Where N is the number of accelerating sections, $E_{inj}(z)$ is the energy of the particle entering the linac, E_i is the maximum RF amplitude from an accelerating section, ϕ_i is the phase with respect to the crest of the RF wave, λ is the S-band wavelength, and $E_{wake}(z)$ is the energy loss or gain due to the longitudinal wake fields.

The energy spread at the end of the linac is minimized if

$$\frac{dE(z)}{dz} = 0$$

Minimizing the energy spread is done by shaping the initial distribution with the bunch compressor and by adjusting the beam phase ϕ_i . The distribution that gives the minimum energy spread can be shown to be an over-compressed distribution[4,5].

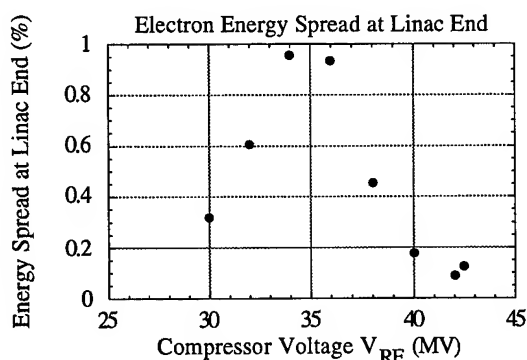


Figure 6. The minimized electron energy spread at the end of the linac as a function of compressor voltage.

The energy spread measurement at the end of the linac was made by a wire scanner at a location where the dispersion is large. The wire scanner measures the transverse bunch size, and the energy spread is determined from the Twiss parameters. At each compressor voltage

the energy spread was minimized by adjusting the phase of the bunch ϕ_i . Once the energy spread was minimized, it was measured using the wire scanner. The energy spread (see figure 6) is approximately 0.09% when minimized with an over-compressed bunch distribution (42 MV).

V. Conclusion

The measurements of the bunch distributions and the current losses in the compressor transport line for positrons and electrons are in excellent agreement with each other. The advantage of a greatly reduced energy spread from over-compression far outweighs the 10% current loss in the transport line. The reduced energy spread allows for a lower tolerance on chromatic issues in the SLC arcs as well as the interaction region. The current losses in the transport line suggest that further investigation into increasing the aperture should be done for future high current running.

VI. Acknowledgment

The authors would like to thank P. Krejcik, M. Ross, R. Siemann for valuable discussions and helpful advice, and D. Whittum for helping with the measurement of the energy spread.

VII. REFERENCES

- [1] Hamamatsu Photonic Systems Corp., 360 Foothill Rd., Bridgewater, NJ 08807-6910.
- [2] C. Simopoulos, R.L. Holtzapple, "Measurements of Longitudinal Dynamics in the SLC Damping Rings", SLAC-PUB-95-6834, 1995.
- [3] J. Seeman, "Observation of High Current Effects in High Energy Linear Accelerators", SLAC-PUB 5707, 1991.
- [4] G. Loew, J.W. Wang, "Minimizing the Energy Spread within a Single Bunch by Shaping its Charge Distribution", SLAC-PUB 3598, 1985.
- [5] F-J. Decker, et al., "Over-Compression, a Method to Shape the Longitudinal Bunch Distribution for a Reduced Energy Spread", SLAC-PUB 6604, 1994.

OBSERVATION OF INDUCED BEAM OSCILLATION FROM ACTIVELY DISPLACED RF ACCELERATING STRUCTURES

John T. Seeman, Henk Fischer, and William Roster

Stanford Linear Accelerator Center, Stanford University, Stanford, CA 94309 USA

At high beam currents the alignment of the accelerating structure in a linear collider relative to the lattice quadrupoles and position monitors dominates all other alignment issues. These structure misalignments drive wakefield emittance growth. Consequently, great efforts have been spent at SLAC to align the accelerating structure¹ of the Stanford Linear Collider (SLC). As an accelerator test, remote controlled mechanical movers have been installed on several RF structures to study wakefield effects. Experimental tests of induced beam wakefields and the resulting oscillations downstream generated by these remotely displaced structures have been performed. The observed wakefield and have been compared with a computer model. The results from displacements at the beam's betatron frequency are particularly exciting as that frequency strongly excites emittance growth. In general, a control mechanism can be made to move the structure at that spatial frequency, thus providing sine and cosine adjustments for cancellation of alignment errors in the accelerator of a future collider². A similar method to control emittance growth by changing the beam trajectory has already been tested and is in daily use³.

I. STRUCTURE DISPLACEMENTS

A displaced accelerating structure produces beam wakefields which ultimately increase the emittance of the beam and reduce the luminosity of a linear collider. A schematic of this effect is seen in Figure 1. The equation of motion for particles⁴ in the beam which are deflected by wakefields within the beam and by displaced accelerating structures is given by

$$\frac{d^2}{ds^2} x(z, s) + k^2 x(z, s) = \frac{r_e}{\gamma(z, s)} \int_z^\infty dz' \rho(z') W(z' - z) [x(z', s) + X(s)]$$

where x is the transverse displacement of the particles in the bunch, s the distance along the accelerator, z the longitudinal displacement along the bunch, k the lattice focusing, γ is the particle energy, r_e the classical radius of the electron, ρ the longitudinal particle density in the bunch, W the transverse wake potential, and X the structure displacement. If the accelerating structure also

has RF fields inside then there will be deflections due to those fields as well.⁵ In the considerations and measurements here we will keep the RF fields turned off.

The SLAC accelerating structure is made with 12 m long girders which are supported at the ends. We have placed motorized jacks in the center which are eccentric CAMs with a stroke of ± 1 mm. These are remotely controllable. The geometry of the girders is shown in Figure 2 and a close-up of the remote mover CAM is shown in Figure 3. These movers have located in a 100 m section of the linac at about 500 m from the beginning where the beam energy is about 6 GeV. Eight adjacent girders have been equipped with these movers in both the horizontal and vertical planes.

II. OBSERVATIONS

The SLC beam has been made to pass through displaced accelerator structures and the ensuing oscillations observed. The measured displacements are emphasized by subtracting a nominal trajectory from the displaced trajectory. The observed oscillations are on the order of a few hundred microns for a single offset of about 1 mm over about the center half of the girder. The resolution is about 20 microns for individual BPM readings. The SLC beam has about 3×10^{10} electrons in a single bunch with a length of about 1 mm. The energy spread is about 1.5% at this location due to the need for BNS damping. The longitudinal head of the bunch has a higher energy than the tail by about 3%.

Moving a single girder from its nominal location produces a deflection as seen in Figure 4. The effect of the displacement can be seen along the linac as oscillations persist to the end. The deflections depend on the sign of the displacement, i.e. the placement of the CAM, as seen in Figures 5 and 6. Vertical and horizontal displacements show similar results in their respective planes.

A simulation of the effect of these accelerator displacements has been made and the results of the displacement of the girder of Figure 5 are shown in Figure 7. The measured displacements agree with the simulation to about 20%. A detailed knowledge of the energy spread along the accelerator is needed to produce an exact comparison over a long distance.

If multiple movers are used to produce a deflected beam, significantly different effects can be seen. First, if two adjacent movers are displaced together the observed deflection is roughly twice as large, as expected. However, if the displacements are spread over a full betatron wave length, the beam displacements can have internal mixing

* Work supported by US Department of Energy contract DE-AC03-76SF00515.

of the transverse offsets along the bunch so that the average displacement of the entire bunch can show trajectory beats downstream as seen in Figure 8. This means that the different longitudinal slices at the end of the displaced sections of the linac are on different sides of the nominal center line of the original beam or have significantly different angular trajectories. A more detailed analysis of these multiple mover trajectories is under way.

III. CONCLUSIONS

Displacements of an electron beam have been observed from displaced accelerating structures. The deflections agree quantitatively with the predictions. Significantly more complicated trajectories can result from a coherently produced deflections using several (eight) movers spread over a betatron wavelength. Finally, the effects of RF deflections will be added in the on-going analysis as they are expected to further complicate the observed trajectories.

IV. ACKNOWLEDGMENTS

The authors wish to thank the SLC Operations Group for providing the beam and Diana Roger for her help in producing this document.

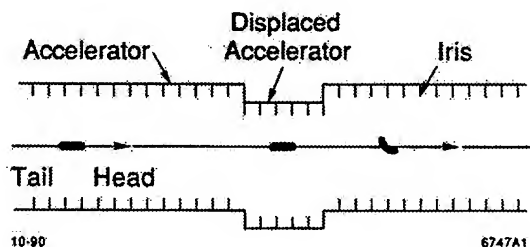


Figure 1: Schematic view of a displaced accelerating structure inducing wakefield effects in a bunch.

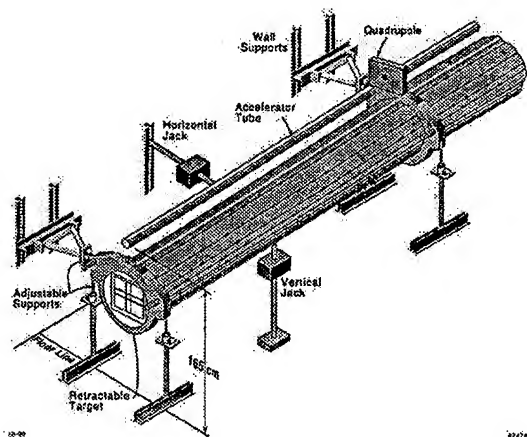


Figure 2: Schematic view of the SLAC accelerator girder with vertical and horizontal movers. The movers produce a "bow" in the girder, i.e. the ends are fixed and the center is displaced. One klystron feeds one of these girders.

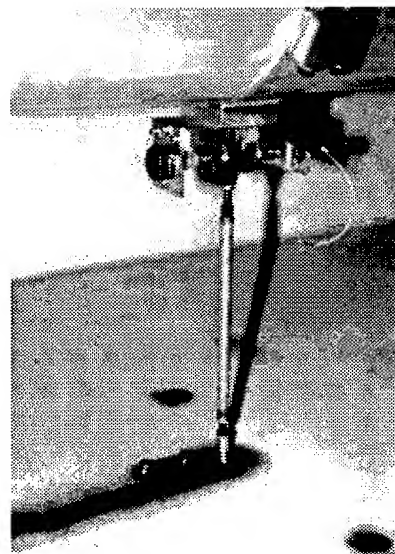


Figure 3: Close-up photograph of the remotely control motorized CAM to move the accelerating structure center by ± 1 mm. Both vertical and horizontal movers have been placed on 8 adjacent RF girders covering 100m of the SLAC linac.

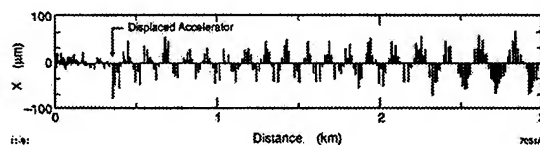


Figure 4: Measured displacement of a beam from a moved accelerator structure.

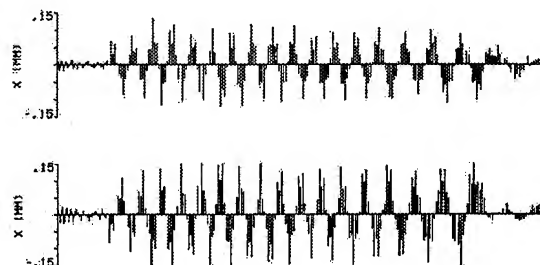


Figure 5: Examples of the beam trajectory produced by up and down single displacements of a 12 m long accelerator in Sector 5 of the SLAC linac. The upper plot results from an downward girder movement and the lower plot from an upward girder movement.

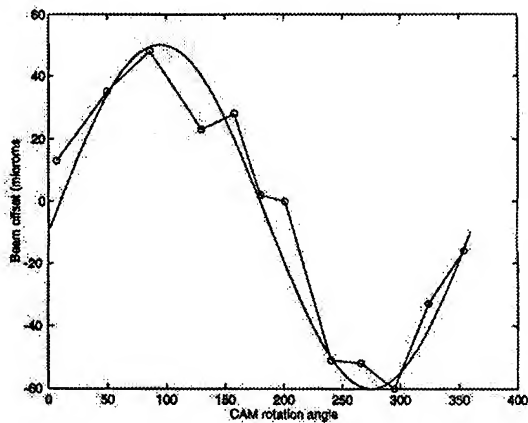


Figure 6: Displacement of an SLC bunch downstream (about 90 degrees in betatron phase) on a single position monitor from a displaced mover in Sector 5 as a function of the rotation angle of the CAM mover. The mover peak amplitude is 1 mm.

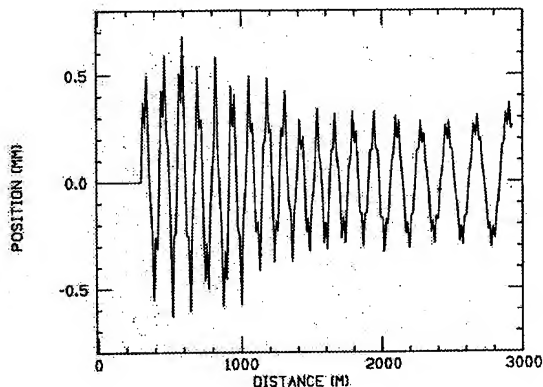


Figure 7: Simulated displacement of an SLAC beam using the accelerator displacement of Figure 3 using a 25 particle (longitudinal) model. The scales between the two plots are not the same.

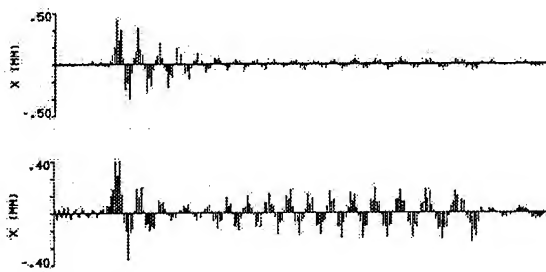


Figure 8: Examples of two trajectories produced by combined accelerator displacements. The upper plot corresponds to eight movers displaced in a sine wave pattern at the betatron frequency ($\sim 100\text{m}$). The lower plot shows an example with eight movers displaced with the first six at +1 mm and the last two at -1 mm.

V. REFERENCES

- [1] J. Seeman, et al, "Alignment Issues of the SLC Linac Accelerating Structure," 1991 IEEE USPAC, San Francisco, 91CH3038-7, p. 2949.
- [2] J. Seeman, "New Compensation of Transverse Wakefield Effects in a Linac by Displacing Accelerator Structures," 1990 Linear Accel. Conf., Albuquerque, LA-12004-C, p. 390.
- [3] J. Seeman, et al, "The Introduction of Trajectory Oscillations to Reduce Emittance Growth in the SLC Linac," XV International Conference on High Energy Accelerators, Hamburg, Germany, July 20-24, 1992, p. 879.
- [4] K. Bane, "Wakefield Effects in a Linear Collider," SLAC-PUB-4169, Dec. 1986.
- [5] J. Seeman, et al, "RF Beam Deflections Measurements and Corrections in the SLC Linac," USPAC, Vancouver, B.C., May 1985, p. 2629.

MEASUREMENT OF THE EFFECT OF COLLIMATOR GENERATED WAKEFIELDS ON THE BEAMS IN THE SLC *

K. L. F. Bane, C. Adolphsen, F.-J. Decker, P. Emma, P. Krejcik, F. Zimmermann,
Stanford Linear Accelerator Center, Stanford University, Stanford, CA 94309 USA

I. INTRODUCTION

Collimators with adjustable jaws are used in the SLC linac, arcs, and final focus to eliminate the tails of the beams that produce backgrounds in the SLD detectors. However, if the beams are not centered within the jaws of the collimators, transverse wakefields are generated which act to increase the beam emittances. The sensitivity to the beam offset is largest in the vertical collimators in the linac where the small beam sizes ($< 100 \mu\text{m}$) require that the gap between the jaws be reduced to about a millimeter for effective background reduction.

To study the wakefield effect of the collimators, measurements of the induced mean angular kick were made as function of the beam offset in one of the SLC collimators. We are interested in both the linear (dipole) behavior near the axis of the collimator and the non-linear behavior near the jaws of the collimator. In this paper we present the results together with a comparison to theoretical predictions. Besides helping us to quantify the effect of the collimators in the SLC these results are also useful in understanding their effect in future linear colliders, in which collimators will also be important components. (For a related paper, see Ref. [1].)

II. THEORY

Consider a vertical (y) collimator that has a pair of rectangular, metallic jaws separated by a distance $2a$ and that is set in a cylindrical tube of radius b , with $b \gg a$. Let the distance between the leading and trailing edges L be large compared to a , but not large compared to the local beta function β_y . Now consider an ultra-relativistic electron beam moving parallel and close to the axis of the beam tube (in the z direction) at vertical offset y_0 . Let the beam have a longitudinal charge distribution that is gaussian, and a transverse dimension that is small compared to a (for a sketch of the layout, see Fig. 1). As the beam passes the collimator it will, due to the wakefields, experience a kick in y with an amplitude that varies along the bunch (*i.e.* that depends on longitudinal position within the bunch, s), and which therefore results in a growth in projected emittance.

The wakefield of the collimator is due to the discontinuities at the leading and trailing edge of the jaws, and to the resistance of the metallic material. At present there is no good way of finding the wakefield due to both of these effects taken together. However, when the jaws are far apart the kick is due mostly to the jaw discontinuity and is approximately the same as that of a perfectly conducting collimator, and when they are close together it is due mostly to the wall resistance and can be approximated by the usual resistive wall wake. Let us call these two types of wakefields, respectively, the geometric wake and the resistive wall wake of the collimator. In the intermediate regime one might,

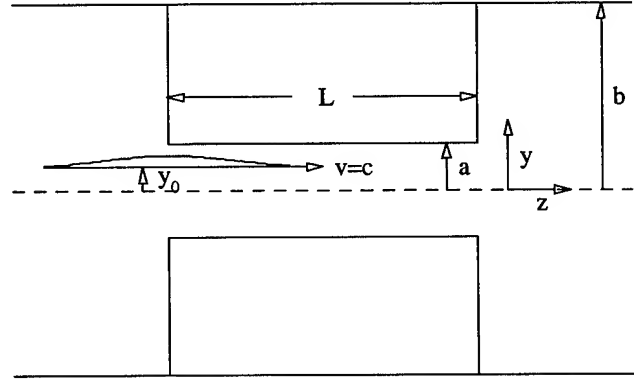


Figure 1. A sketch of the beam and collimator.

as an approximation, add the two contributions together. (Such an approach has been applied to studying the effect of the NLC collimators; see Ref. [2].)

Let us consider first the effect of the geometric wake. For a gaussian beam, with rms length $\sigma_z \text{ versusim} > a$ (which is satisfied in our experiment described below), passing near the axis of a rectangular, deep ($b \text{ versusim} > 5a$), perfectly conducting collimator the kick $\Delta y'(s)$ can be approximated by[3]

$$\Delta y'(s) \approx \left(\frac{\pi}{2}\right)^{\frac{3}{2}} \frac{r_e N}{\sigma_z \gamma} e^{-s^2/2\sigma_z^2} \left(\frac{y_0}{a}\right) \quad y_0/a \ll 1, \quad (1)$$

with r_e the electron radius ($= 2.8 \times 10^{-15} \text{ m}$), N the bunch population, and γ the beam energy parameter. In Eq. 1 we have multiplied the result for a round collimator by $\pi^2/8$. (Note that in a gently tapered collimator, such as will likely be used in future linear colliders a somewhat modified formula is appropriate.[4]) Note that the average value of the gaussian factor, when weighted by the gaussian charge distribution, is 0.71.

In the resistive wall wake regime we use the kick near the axis between two resistive plates of length L and conductivity σ (ignoring the end conditions):[5]

$$\Delta y'(s) = \frac{\pi r_e N L}{4a^2 \gamma} \left(\frac{c}{\sigma \sigma_z}\right)^{\frac{1}{2}} f(s/\sigma_z) \left(\frac{y_0}{a}\right) \quad y_0/a \ll 1 \quad (2)$$

with

$$f(x) = \frac{1}{\sqrt{2\pi}} \int_0^\infty \frac{e^{-(y-x)^2/2}}{\sqrt{y}} dy \quad (3)$$

(In a round collimator the result is $8/\pi^2$ smaller.) It is due to the extra factor of $1/a^2$ in Eq. 2 that for large a the geometric wake component dominates, while for small a the resistive

*Work supported by the Department of Energy, contract DEAC0376SF00515

wall wake component dominates. Note that the average value of $f(s/\sigma_z)$, when weighted by the gaussian charge distribution, is 0.78.

When the beam passes not near the axis of the collimator, but rather near one of its jaws, the above formulas do not hold. In the case of the geometric wakefield the general solution is not known, though simulations suggest that the kick will diverge $\sim 1/(a - y_0)$ as y_0 approaches a . [6] In the resistive wall case the solution is to replace the factor y_0/a in Eq. 2 by the factor [7]

$$\frac{1}{\pi} \left(\frac{\pi y_0/a + \sin \pi y_0/a}{1 + \cos \pi y_0/a} \right), \quad (4)$$

which diverges as $1/(a - y_0)^2$ as y_0 approaches a . The asymptotic formula is:

$$\Delta y'(s) = \frac{r_e N L}{2\pi(a - y_0)^2 \gamma} \left(\frac{c}{\sigma \sigma_z} \right)^{\frac{1}{2}} f(s/\sigma_z), \quad y_0 \rightarrow a. \quad (5)$$

We expect that, even for large a , as the beam moves close to one jaw the resistive wall wake will eventually dominate.

III. MEASUREMENTS

A collimator two-thirds of the way down the SLC linac, in Sector 18, was used for the measurements. It is a y collimator of the type indicated in Fig. 1, with length $L = 7.9$ cm, positioned in a beam tube of radius $b = 3.5$ cm. Unlike in the figure the jaw surfaces are not perfectly flat; they are rounded slightly, with a maximum excursion in the center of $40 \mu\text{m}$. The collimator body is made of titanium, and on the jaw surfaces a $25 \mu\text{m}$ layer of gold has been deposited. The collimator jaws can be moved independently in the vertical direction.

For the measurements the beam was first steered as well as possible over the first 20 sectors of the SLC linac with the collimator jaws open, using wakefield bumps to try to tune out any transverse beam tails that had been generated in earlier parts of the linac. Unfortunately, on the day of the measurement we were only partially successful in this; after tune-up tails could still be seen on downstream video screens. After tune-up the collimator jaws were set to a fixed separation and then scanned across the beam position. At each position, on each pulse, 8 upstream and 8 downstream beam position monitors (BPM's) were read, and the average wakefield kick of the collimator $\langle \Delta y' \rangle$ was obtained by fitting to a betatron oscillation. In this manner we could separate out incoming pulse-to-pulse jitter and obtain an accuracy of about $1/3 \mu\text{rad}$. At each measurement the beam intensity was measured using downstream BPM's, and any data points with more than 10% beam loss were discarded. The beam position half way between the 10% loss points was taken to be the center of the collimator, and the results were shifted to give $\langle \Delta y' \rangle = 0$ at this position.

For our measurements the bunch population is nominally $N = 3.5 \times 10^{10}$, the rms bunch length $\sigma_z = 1.3$ mm (though the bunch distribution is not gaussian; probably more like a flattened and truncated gaussian), the energy $E = 33$ GeV; the beam is roughly round, with the x and y rms bunch sizes $\sigma_x = \sigma_y = 80 \mu\text{m}$, and the rms y divergence $\sigma_{y'} = 1.35 \mu\text{r}$. The conductivity at room temperature of gold is $4.4 \times 10^{17} \text{ s}^{-1}$, that of titanium $0.21 \times 10^{17} \text{ s}^{-1}$.

IV. RESULTS

Our first measurement was to check on the linear dependence of the kick on bunch population, to see that we really have a wakefield effect. We plot in Fig. 2 the measured kick of the beam, but scaled inversely as N , as function of offset between collimator jaws, for $N = 1 \times 10^{10}$ and $N = 3.5 \times 10^{10}$. Here, $a = 1$ mm. Repeated measurements confirm the result shown here. We notice two things from Fig. 2: First, the curves are not perfectly anti-symmetric, contrary to what we expect from the symmetry of the problem. This can be due to the beam having a $y - z$ tilt or tail due to wakefields in the upstream portion of the linac and/or due to y dispersion in the linac. Or it can be due to some asymmetry in the collimator geometry. Secondly, the two curves in Fig. 2 agree quite well, confirming that we are measuring a wakefield effect. The differences that we see can be due to: (i) a lower current beam will be shorter in the damping ring and therefore of a slightly different length in the linac, and (ii) any $y - z$ tilt or tails the beam has obtained in the upstream part of the linac can be very different for beams with such different bunch populations.

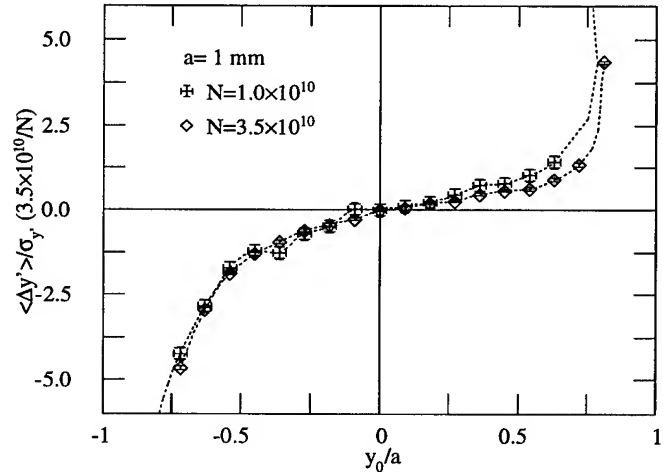


Figure 2. Kick of the beam, but scaled inversely as N , vs. y_0/a , for $N/10^{10} = 1$ and 3.5 ; $a = 1$ mm.

Next the dependence of the wakefield kick on the collimator half-aperture a was measured. In Fig. 3 we plot the kick as function of vertical offset for half apertures $a = 0.5$ mm, 1.0 mm, and 1.5 mm keeping the bunch population at $N = 3.5 \times 10^{10}$. In this data we again note the lack of symmetry mentioned above. Note that when plotting the kick as function of y_0/a if we are in the geometric wakefield regime then the curves will fall on the same straight line near the origin (see Eq. 1). And, in fact, the two curves for the larger jaw openings do roughly coalesce to one straight line over a region, though not a symmetric one, near the origin. Substituting for the parameters in Eq. 1 we find that the slope of this line should be 1.2 (the straight line in Fig. 3), which agrees fairly well with the data points.

The curve in Fig. 3 that represents the measurements using the smallest jaw opening ($a = 0.5$ mm) has a slope near the origin that is more than twice that of the other two curves. Substituting into the resistive wall wake equation, Eq. 2, taking for conductivity that of gold, we obtain, for this aperture, a contri-

bution to the slope of 0.15, which is not significant when compared to the geometric wake contribution. However, if in fact the gold layer were damaged, for example by the beam hitting it, and if the real conductivity were more like that of the underlying titanium, then the resistive wall contribution to the slope becomes 0.7, which is comparable to the geometric wakefield contribution. Although the real slope of this curve near the origin is somewhat larger than the sum of these two contributions, the results do suggest that when reaching the smallest aperture we are in a domain where the resistive wall wakefield is becoming significant, even at small offsets.

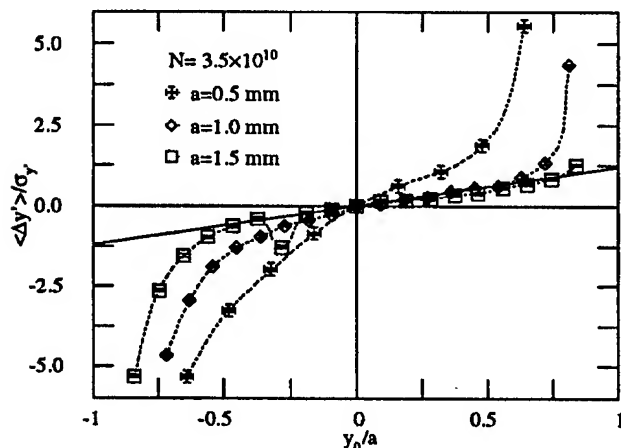


Figure 3. Kick of the beam vs. y_0/a for $a = 0.5$ mm, 1.0 mm, and 1.5 mm; $N = 3.5 \times 10^{10}$.

We plot in Fig. 4 the same data of Fig. 3, but now as a function of distance from the lower collimator jaw. Asymptotically we expect all data points to fall on the same curve, one that varies as $1/(a - y_0)^2$. We see that all data points roughly do follow this power law, the two larger aperture data sets on one curve and the smallest aperture data set roughly on a curve a factor of two less in amplitude, possibly due to a partial cancellation of the force by the other collimator jaw. On the same plot we show the resistive wall asymptotic contribution, Eq. 5, using the conductivity of titanium, 5.5 times this curve, and 11 times it. Even if we were to suppose that the geometric wake contribution (which we don't precisely know) were as large as the resistive wall wake contribution the calculated results would still be much lower in amplitude than the measured data. Due to the asymmetry of the data there seems to be less information about the asymptotic behavior near the upper jaw. The kick again seems to be consistent with a -2 power of distance, but this time with an amplitude of 3.5 times the resistive wall asymptote for titanium. We need to redo this measurement with good beam quality to resolve this.

V. CONCLUSIONS

We have performed preliminary measurements of the average wakefield kick of SLC collimators as function of beam offset within the jaws. We have demonstrated that the kick depends linearly on current, as it should for a wakefield effect. For larger jaw apertures we have demonstrated that near the center of the jaws there is a linear regime of kick dependence on offset, the

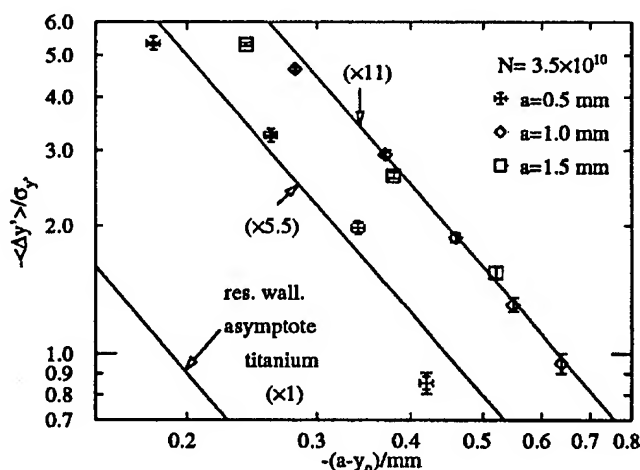


Figure 4. The same data as in Fig. 3, but plotted as distance from the lower collimator jaw. Also plotted are the resistive wall asymptotic formula for titanium, the formula times 5.5, and it times 11.

slope of which agrees with the analytical result for the geometric wakefield of collimators. For a smaller jaw aperture the slope in the linear regime is larger than can be accounted for by the geometric wakefield, which suggests that, for this case, the resistive wall wake has become important. However, this is consistent with calculations only if the $25 \mu\text{m}$ gold layer on the surface of the collimator jaws has been damaged. We also find that the kick when the beam is near the metallic surface is consistent with an inverse square dependence on distance; the amplitude, however, is much larger than we can account for with our theory. Finally, we should also point out that all our results have some unexpected asymmetry, which may be due to poor beam quality during the measurement or some asymmetry in the collimator geometry.

In the near future we will investigate the surface of the collimator, to see if it is indeed damaged. These measurements were preliminary and should be repeated.

References

- [1] A. Chao and H. Henke, WAB11, these proceedings.
- [2] J. Irwin, *et al*, 1993 Part. Accel. Conf., Washington D.C., p. 185.
- [3] K. Bane and P. Morton, 1986 Linear Accelerator Conf., SLAC, p. 490.
- [4] K. Yokoya, CERN SL/90-88, July 1990.
- [5] See, for example, A. Chao, *Physics of Collective Beam Instabilities in High Energy Accelerators*, (J. Wiley & Sons, Inc., New York, 1993), Chap. 2.
- [6] C.-K. Ng, private communication.
- [7] A. Piwinski, DESY-HERA-92-04, January 1992.

BEAM TRAJECTORY JITTER IN THE SLC LINAC*

Chris Adolphsen and Tim Slaton

Stanford Linear Accelerator Center, Stanford University, Stanford, CA 94309 USA

We present model-independent measurements of the vertical trajectory jitter of the positron beam in the Stanford Linear Collider (SLC) linac and discuss the results of studies aimed at isolating its source.

I. INTRODUCTION

In March 1993, the SLC began flat beam operation which reduced the vertical emittance at the beginning of the linac by an order of magnitude to about 3×10^{-6} m-rad. Although this improved the average luminosity, it made the luminosity more sensitive to vertical beam jitter, that is, to the variations of the vertical orbits that are faster than the few second response time of the feedback loops that are used to stabilize the orbits. The rms of the vertical jitter, which had been observed to grow in size along the linac, now became a significant fraction of the vertical beam size. In this paper, we present some of the jitter measurements and discuss the results of studies aimed at isolating its source. In particular, we examine the positron jitter since the analysis of the electron jitter is complicated by its dependence on the positron motion via long-range wakefields. However, the electron results do not differ greatly.

II. MEASUREMENTS

To characterize the jitter, we wanted an empirical method since the linac beam transport is difficult to accurately model due to uncertainties in the linac energy profile and the strong transverse wakefield effects. Our solution was to measure the beam transport properties by inducing betatron oscillations near the injection point to the linac and recording the beam trajectory changes along the linac. Using these data, we characterized trajectory changes that were measured in different regions of the linac in terms of an equivalent injection jitter, and thus mapped how the jitter varied along the linac in common units. To make the measurements more relevant to SLC operation, we normalized the results to the beam size measured at injection. However, when interpreting the results, we also had to keep in mind the non-jitter emittance growth that occurred in the linac and in the subsequent transport of the beams to the collision point.

In the study of the positron vertical jitter, betatron oscillations were measured in five regions along the linac. The regions each span about two betatron oscillation wavelengths and are separated by about four wavelengths. Each region contained a series of 24 beam position monitors (BPMs) with an average resolution of about $10 \mu\text{m}$ at the nominal beam intensity of 3.4×10^{10} positrons per bunch. Prior to the measurements, data were taken to obtain the R33 and R34 TRANSPORT matrix elements from an upstream reference point to the BPMs in each of the regions (the x-y coupling is negligible in the linac and so the other matrix elements were ignored). The reference point was chosen as the location of first beam size monitor (BSM) in the linac which is part of a set that is used to monitor beam emittance.

The R33 and R34 matrix elements for the positron beam were measured using two vertical steering dipole magnets (YCORs) in the injection line to the linac that are 90 degrees apart in betatron phase advance. The setting of each YCOR was varied in 11 steps while the linac BPMs were recorded with a five pulse average. The induced oscillations at the extreme YCOR settings were made much larger than the nominal beam jitter and BPM resolution so an accurate measurement could be made. The slopes of the BPM -vs- YCOR data were then fit for each BPM and the results used to compute the TRANSPORT elements. Because the YCORs are upstream of the BSM, this transformation can be done independently of the YCOR settings with only a knowledge of the distance of the BSM to its two neighboring BPMs. The resulting values for R33 and R34 agree well with the linac optics model near the beginning of the linac but lag in phase and increase in amplitude further along the linac.

After measuring the coefficients, several sets of jitter data were taken during 120 Hz operation in which the BPM readings in the five regions were simultaneously recorded on 200 consecutive pulses. In each region, the mean orbit was subtracted from the BPM data and results were fit using the measured R33 and R34 matrix elements to obtain the orbit parameters y and y' at the BSM. The orbit parameters were then normalized using typical values of the measured vertical beam size, $\sigma_y = 132 \mu\text{m}$, and TWISS parameters, $\beta_y = 13.5 \text{ m}$ and $\alpha_y = -5.8$, at the BSM (the TWISS parameter calculation uses beam size data from the other BSMs in the set as well). Specifically, $Y \equiv y/\sigma_y$ and $Y' \equiv (\alpha_y y + \beta_y y')/\sigma_y$ were computed for each region of the linac from the data from each pulse. For jitter with a

* Work supported by Department of Energy contract DE-AC03-76F00515.

phase space distribution equal to that of the beam, Y and Y' would each have an rms of unity and be uncorrelated.

Figure 1 shows examples of the distributions from a set of data that were taken with the linac feedback loops disabled. Here Y' -vs- Y is plotted for the first and last region of the linac, which are denoted by the linac sector at the center of the region (note that the main linac is divided into 29 sectors: LI02 to LI30). The measurement errors on the data points, which are not shown in the plots, are much smaller than the rms variation of the data. A comparison of the two plots clearly shows that only a small portion of the trajectory variation at the end of the linac can be attributed to injection jitter. The results for data taken with the linac feedback loops enabled are similar.

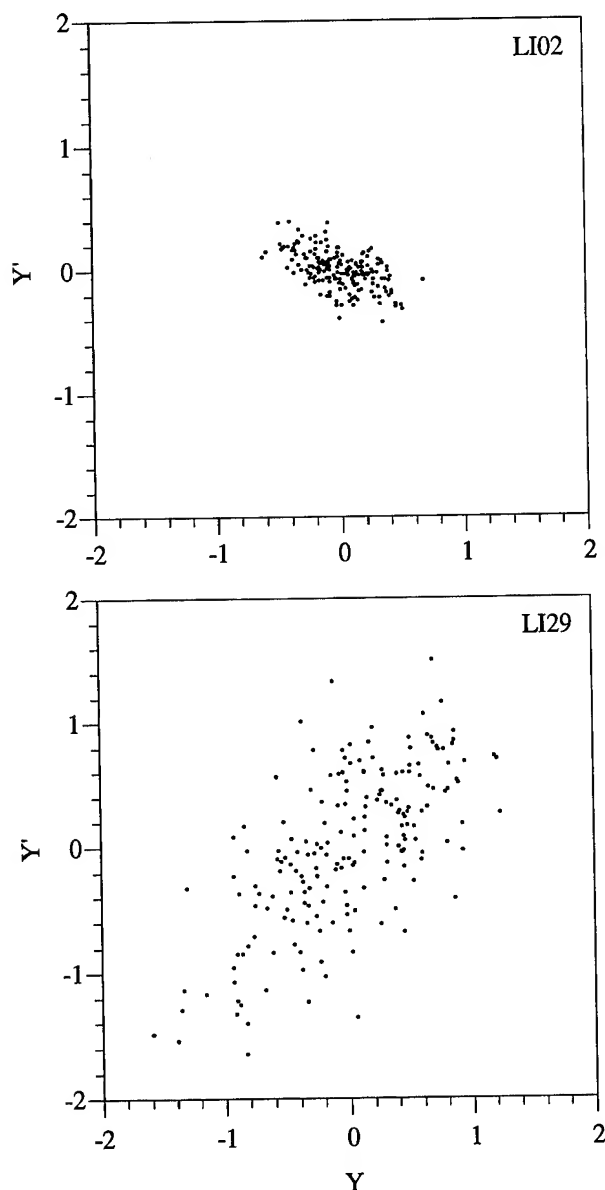


Figure 1: Phase space of vertical positron jitter measured in linac sectors LI02 and LI29.

To quantify the jitter, we computed an rms of the rms variation of Y and Y' ,

$$T_s \equiv \sqrt{\langle Y^2 \rangle + \langle Y'^2 \rangle} / \sqrt{2},$$

which is related to the time-averaged beam emittance growth in the presence of jitter, $\Delta \epsilon / \epsilon \approx T_s^2$. The values of T_s for the feedback-disabled data are plotted in Figure 2 for the five linac regions. One sees that much of the positron vertical jitter growth occurred near the end of the linac. The LI29 value of 60% would have contributed 36% to the time-averaged beam emittance in LI29 if no other emittance growth had occurred in the linac. However, the vertical emittance typically doubled in the linac, independent of the jitter, so the addition of the jitter had increased the time-averaged emittance by 18% in LI29. At the interaction point (IP), the jitter was about the same as in LI29 but the vertical emittance was typically a factor of three larger, so the jitter related emittance growth was only 6%. The size of the vertical electron IP jitter was similar to, and essentially uncorrelated with the positron jitter, so the collision luminosity was reduced by about 4% due to vertical jitter (the horizontal jitter reduced it by an additional 3% in quadrature) [1].

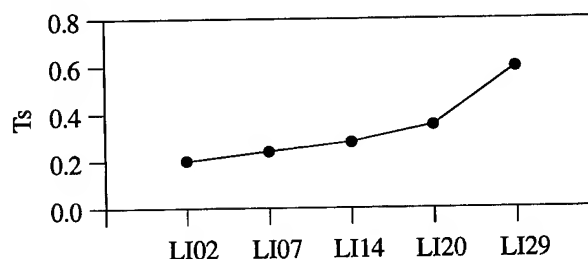


Figure 2: T_s values measured in five regions of the linac.

To study the temporal dependence of the jitter, Fourier transforms of the jitter data from the five regions were computed. The time dependence of the projections of the jitter along the major and minor axes of the phase space ellipses were analyzed in addition to Y and Y' . As an example, Figure 3 shows the power spectrum (PS) and integral of the power spectrum (IS) for the LI02 and LI29 jitter projected along the major axes of their phase space ellipses. Note that for this analysis the jitter data was normalized to have an rms of unity, so the integrated spectrum, which sums the power spectrum above the frequency plotted, is unity at 0 Hz. The relative rms jitter due the Fourier components above a given frequency is therefore the square root of the IS value at that frequency. In general, the measured spectra are essentially white noise with a few prominent frequency components in some cases. However, these components seldom contribute more than 10% to the total rms.

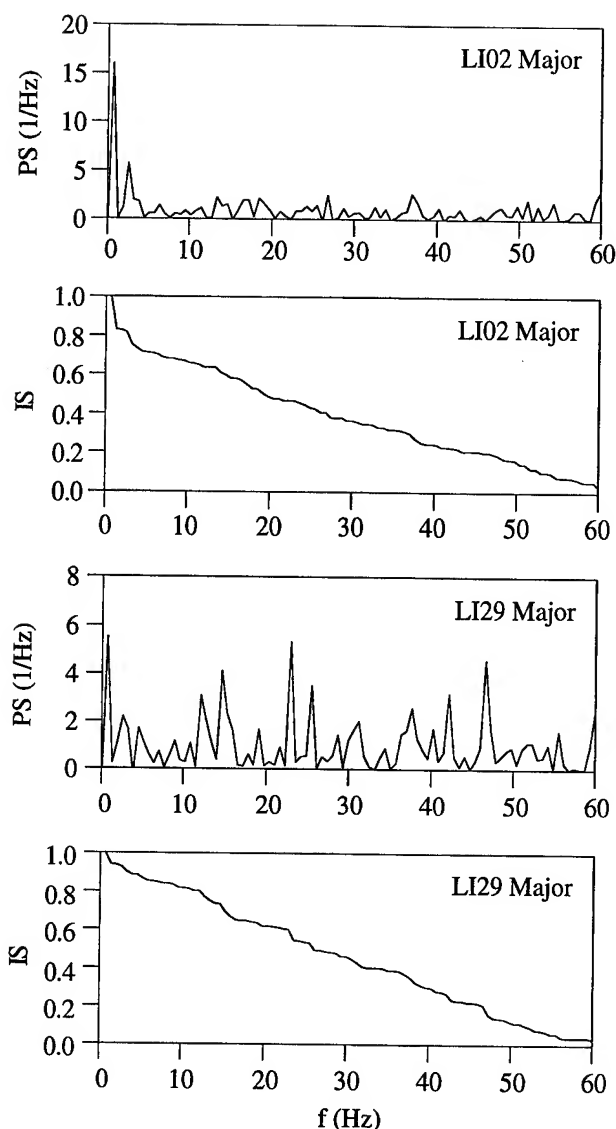


Figure 3: Normalized power spectrum (PS) and integral of the power spectrum (IS) for the LI02 and LI29 jitter projected along the major axes of their phase space ellipses.

III. DISCUSSION

Although the source of the jitter growth in the linac is not yet understood, the results from various studies have narrowed down the possibilities. For example, the size of the jitter was found to be independent of the amplitude of the orbits in the linac, so energy jitter coupled with linac dispersion is not the source, nor is fluctuations in quadrupole magnet (quad) currents. The possible contributions from quad vibrations led to measurements of the quad vertical motion [2]. Although the vibrations were found to be larger than expected, about 300 nm rms for some quads, simulations showed that even if all quads vibrated randomly by this amount, the resulting beam jitter

could only account for a small fraction of the measured growth. Also, the frequency spectrum of the quad motion is highly peaked in the 8 to 14 Hz range which would not explain the relatively flat spectra of the beam jitter.

Computing the correlations of the jitter in each region of the linac with the jitter in other regions and with the jitter of other beam properties provided further clues. No strong correlation was found between the orbit jitter and the positron intensity, energy, or bunch length jitter. The correlations measured among the orbit data suggest that the growth is incoherent along the linac. Thus, the growth is not likely to be the result of large resonant amplification of betatron motion due to transverse wakefields. In fact, measurements of this amplification for oscillations induced at various points along the linac showed that it did not differ greatly from that expected, which is a factor of 2 to 3 at most.

One possible source that has not been ruled out is the transverse rf fields in the S-band accelerator structures that result from dark currents. An rms kick of about 1 keV per structure (12 m long) is needed to explain the observed level of jitter growth in the linac. Such a kick would be 2×10^5 times smaller than the accelerating field and would likely have a white noise spectrum. Another jitter source may be damping ring instabilities that produce y-z correlations in the beam phase space that vary pulse-to-pulse. These correlations could vary in a manner that would not produce injection jitter but would nonetheless cause orbit changes in the linac due to the effect of the wakefields there. Further measurements will be made to assess the magnitude of these effects.

IV. SUMMARY

Using a model-independent method, we have measured the positron vertical trajectory jitter in the SLC linac. We observe that the jitter grows three-fold by the end of the linac, increasing the time-averaged vertical beam emittance there by about 18%. The trajectory jitter is essentially random pulse-to-pulse and is not strongly correlated with the positron intensity, energy, or bunch length jitter. Studies are continuing in an effort to determine the source of the jitter growth.

V. REFERENCES

- [1] P. Raimondi, private communication (1995).
- [2] J. Turner et. al., *Vibration Studies of the Stanford Linear Accelerator*, these proceedings (1995).

EMITTANCE GROWTH DUE TO DECOHERENCE AND WAKEFIELDS *

M.G. Minty, A.W. Chao, and W.L. Spence

Stanford Linear Accelerator Center, Stanford University, Stanford, CA 94309 USA

Abstract

Suddenly induced coherent centroid oscillations about the closed orbit will decohere due to nonlinearities in the magnetic optics—at the expense of a stored beam's emittance. Collective effects mediated by the vacuum chamber wakefield and dependent on the beam current, can however damp the coherent oscillations—ameliorating the emittance growth. Closed form expressions for both the beam centroid and the beam size are obtained in the absence of collective effects. Simultaneous turn-by-turn measurements of beam centroid and size in the SLC damping ring are presented, and the importance and intricacy of collective effects is discussed.

I. NONLINEAR DETUNING AND CHROMATICITY

In the absence of collective effects, decoherence is dominated by nonlinear detuning and chromaticity. The evolution of the beam centroid has been described in [1-4]. We here extend these results to the rms beam size. Consider a beam with a gaussian distribution in the (x, x') phase space. At turn $M = 0$, the beam is kicked by an angle $\Delta x'$. We normalize the coordinates by the unperturbed rms beam size σ_x as $\bar{x} = x/\sigma_x$ and $\bar{p} = (\alpha_x x + \beta_x x')/\sigma_x$, where β_x and α_x are the Courant-Snyder parameters. We normalize the kick by defining $Z = \frac{\beta_x}{\sigma_x} \Delta x'$. The amplitude $a = \sqrt{\bar{x}^2 + \bar{p}^2}$, and ϕ is the betatron phase. The beam distribution after the kick is

$$\rho_k(\phi, a) = \frac{a}{2\pi} e^{-(a^2 + Z^2 + 2Za \sin \phi)/2} \quad (1)$$

The nonlinearity is assumed to result from an amplitude-dependent betatron tune and a relative energy offset δ of a particle which modifies the betatron tune through the chromaticity ξ :

$$\Delta\nu = -\mu a^2 + \xi \delta \quad (2)$$

with detuning μ ; μ/σ_x^2 is determined by the lattice.

For single particle motion the amplitude a is an invariant. The time dependence of the energy offset is

$$\delta(M) = \delta_0 \cos(2\pi\nu_s M + \phi_0), \quad (3)$$

while the betatron phase advances [1] as

$$\Delta\phi = 2\pi M(\nu_0 - \mu a^2) + \frac{2\xi}{\nu_s} \delta_0 \sin(\pi\nu_s M) \cos(\pi\nu_s M + \phi_0). \quad (4)$$

The beam centroid motion after the kick is given by

$$\begin{aligned} [\langle \bar{x} \rangle + i \langle \bar{p} \rangle] &= \int_0^\infty da \int_0^{2\pi} d\phi a e^{-i\phi - i\Delta\phi(a, M)} \rho_k(\phi, a) \\ &= \frac{iZF_1}{(1-i\theta)^2} \exp\left(-i2\pi M\nu_0 + \frac{Z^2}{2} \frac{i\theta}{1-i\theta}\right), \end{aligned} \quad (5)$$

where we have defined a time variable in units set by the nonlinearity,

$$\theta = 4\pi\mu M \quad (6)$$

and a form factor differing from 1 when $\xi \neq 0$

$$F_1 = \int_0^{2\pi} d\phi_0 \int_0^\infty d\delta_0 \rho(\delta_0) e^{-i2\frac{\xi}{\nu_s} \delta_0 \sin(\pi\nu_s M) \cos(\pi\nu_s M + \phi_0)} \quad (7)$$

Assuming a gaussian distribution for δ_0 with rms σ_δ ,

$$F_1 = \exp\left[-2\left(\frac{\xi\sigma_\delta}{\nu_s}\right)^2 \sin^2(\pi\nu_s M)\right] \quad (8)$$

Equation (5) gives the decoherence behavior of the beam centroid.[1-4]

We next compute the rms beam size after the kick,

$$\begin{aligned} \begin{bmatrix} \langle \bar{x}^2 \rangle \\ \langle \bar{x}\bar{p} \rangle \\ \langle \bar{p}^2 \rangle \end{bmatrix} &= \begin{bmatrix} 1 + \frac{Z^2}{2} \\ 0 \\ 1 + \frac{Z^2}{2} \end{bmatrix} + \frac{F_2 Z^2/2}{(1+4\theta^2)^{3/2}} \exp\left(-\frac{2Z^2\theta^2}{1+4\theta^2}\right) \\ &\times \begin{bmatrix} -\cos(4\pi M\nu_0 - \frac{Z^2\theta}{1+4\theta^2} - 3\tan^{-1}(2\theta)) \\ \sin(4\pi M\nu_0 - \frac{Z^2\theta}{1+4\theta^2} - 3\tan^{-1}(2\theta)) \\ \cos(4\pi M\nu_0 - \frac{Z^2\theta}{1+4\theta^2} - 3\tan^{-1}(2\theta)) \end{bmatrix} \end{aligned} \quad (9)$$

where $F_2 = F_1^4$ for the gaussian δ_0 distribution; therefore the rms size is more strongly modulated by the chromaticity than the centroid.

The instantaneous beam size is given by $\sigma_{\bar{x}} = \sqrt{\langle \bar{x}^2 \rangle - \langle \bar{x} \rangle^2}$. This gives

$$\begin{aligned} \sigma_{\bar{x}}^2 &= 1 + \frac{Z^2}{2} \left\{ 1 - \frac{F_2}{(1+4\theta^2)^{3/2}} \exp\left(-\frac{2Z^2\theta^2}{1+4\theta^2}\right) \right. \\ &\times \cos\left[4\pi M\nu_0 - \frac{Z^2\theta}{1+4\theta^2} - 3\tan^{-1}(2\theta)\right] \\ &\quad - \frac{2F_1^2}{(1+\theta^2)^2} \exp\left(-\frac{Z^2\theta^2}{1+\theta^2}\right) \\ &\left. \times \sin^2\left[2\pi M\nu_0 - \frac{Z^2\theta}{2(1+\theta^2)} - 2\tan^{-1}\theta\right] \right\} \end{aligned} \quad (10)$$

*Work supported by the Department of Energy, contract DE-AC03-76SF00515.

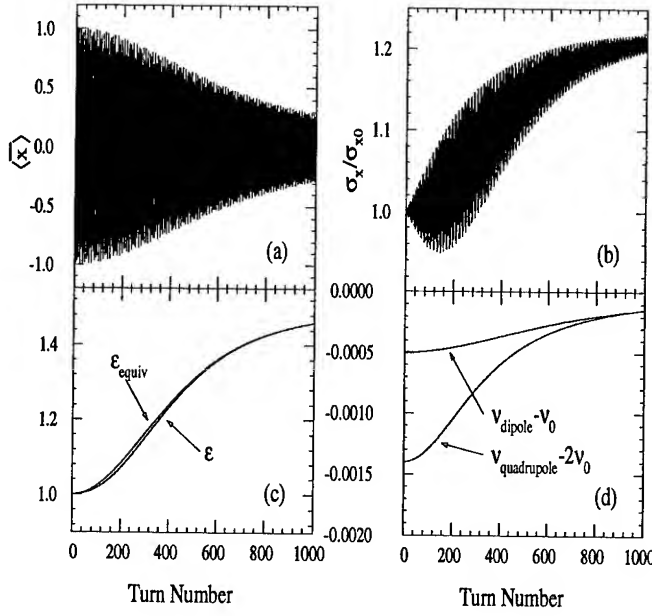


Figure 1. Beam evolution; the first 1000 turns after a kick: (a) $\langle \bar{x} \rangle$, (b) $\sigma_{\bar{x}}$, (c) ϵ_{equiv} and ϵ , (d) $\nu_{\text{dipole}} - \nu_0$ and $\nu_{\text{quadrupole}} - 2\nu_0$. Parameters used are $Z = 1$, $\xi = 0$, $\nu_s = 0.01$, $\sigma_\delta = 0.001$, $\nu_0 = 0.18$, and $\mu = 1 \times 10^{-4}$.

The amplitude of the beam centroid is, from Eq. (5),

$$A_{\bar{x}} = \sqrt{\langle \bar{x}^2 \rangle + \langle \bar{p}^2 \rangle} = \frac{ZF_1}{1 + \theta^2} \exp \left[-\frac{Z^2 \theta^2}{2(1 + \theta^2)} \right] \quad (11)$$

For small θ this amplitude decoheres approximately as a gaussian in time. For large θ , it decoheres roughly $\sim \frac{1}{\theta^2}$. When the kick is weak and the chromaticity is small, the beam filaments on a time scale of $\frac{1}{4\pi\mu}$ turns.

Note from Eq. (9) that $\langle \bar{x}^2 \rangle + \langle \bar{p}^2 \rangle = 2 + Z^2$ is an invariant after the kick. If one defines a 'matched equivalent' beam emittance [5] as $\epsilon_{\text{equiv}} = \frac{1}{2}(\sigma_{\bar{x}}^2 + \sigma_{\bar{p}}^2)$, then

$$\epsilon_{\text{equiv}}(M) = \frac{1}{2}(\langle \bar{x}^2 \rangle - \langle \bar{x} \rangle^2 + \langle \bar{p}^2 \rangle - \langle \bar{p} \rangle^2) = 1 + \frac{Z^2}{2} - \frac{A_{\bar{x}}^2}{2} \quad (12)$$

One may also define an instantaneous emittance as

$$\epsilon(M) = \sqrt{\sigma_{\bar{x}}^2 \sigma_{\bar{p}}^2 - (\langle \bar{x} \bar{p} \rangle - \langle \bar{x} \rangle \langle \bar{p} \rangle)^2} \quad (13)$$

When $M = 0$, we have $\epsilon_{\text{equiv}} = \epsilon = 1$. When $M \rightarrow \infty$, we have $\epsilon_{\text{equiv}} = \epsilon = 1 + \frac{Z^2}{2}$.

One can define an 'instantaneous' dipole tune as $\frac{1}{2\pi} \times$ (phase advance per turn of the centroid oscillation when $\xi = 0$):

$$\nu_{\text{dipole}} = \nu_0 - \frac{\mu}{1 + \theta^2} \left[4 + \left(\frac{1 - \theta^2}{1 + \theta^2} \right) Z^2 \right] \quad (14)$$

Note that if one measures the dipole tune by kicking the beam and analyzing its subsequent centroid motion, the measured dipole tune will be a function of time.

The 'instantaneous' quadrupole tune can likewise be defined as $\frac{1}{2\pi} \times$ (phase advance per turn of the beam size oscillation when $\xi = 0$),

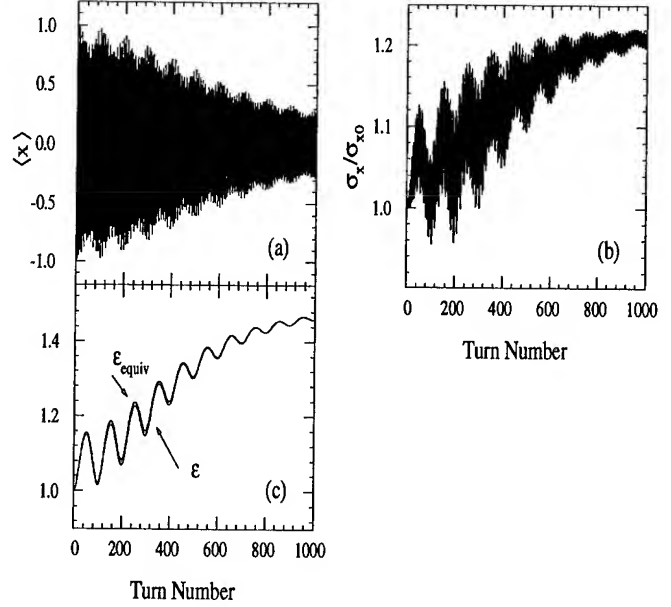


Figure 2. $\xi = 3$, otherwise as in Fig. 1.

$$\nu_{\text{quadrupole}} = 2\nu_0 - \frac{2\mu}{1 + 4\theta^2} \left[6 + \left(\frac{1 - 4\theta^2}{1 + 4\theta^2} \right) Z^2 \right] \quad (15)$$

In general, the quadrupole tune is close, but not equal, to twice the dipole tune. For $M = 0$, we have $\nu_{\text{dipole}} = \nu_0 - (4 + Z^2)\mu$ and $\nu_{\text{quadrupole}} = 2\nu_0 - 2(6 + Z^2)\mu$. When $M \rightarrow \infty$, we have $\nu_{\text{dipole}} = \nu_0$ and $\nu_{\text{quadrupole}} = 2\nu_0$.

Figures 1–2 show the time behavior of various quantities after a kick using the analytic expressions. The beam size modulation at the synchrotron frequency is a result of "recoherence" [2,3]. Despite the prominent β -beat evident in Figs. 1(b) and 2(b), the difference between the instantaneous and the matched equivalent emittances is small.

II. COLLECTIVE EFFECTS AND EXPERIMENT

Both the horizontal centroid and beam size were measured by digitizing the synchrotron light image [6] of the positron beam in the SLC damping ring. A fast-gated camera detected the radiation emitted on a single pass of the particle bunch, although each image corresponds to a different machine pulse because of the limited bandwidth of the data acquisition system. Observations were made in the neighborhood of a time in the SLC damping cycle during which the beam is accidentally kicked by spurious transients in the injection/extraction fast kicker pulses. Data for various beam currents and chromaticities are shown in Fig. 3.

The data were analyzed by the method of [5] to find ϵ_{equiv} , which is plotted in Fig. 4 in the ratio $X = (\epsilon_{\text{equiv}} - 1)/\frac{1}{2}Z^2$, which we expect to asymptote to 1 for $M \rightarrow \infty$ in the case of pure decoherence (cf. Eq. 12). But when the chromaticity is positive, as in the data, there will be collective "head-tail" damping of the centroid motion. As the coherent motion damps, rather than decoheres, there is less motion to filament and the emittance growth may be significantly inhibited, as seen decisively in the data. The extent to which $X < 1$ as $M \rightarrow \infty$ indicates that the

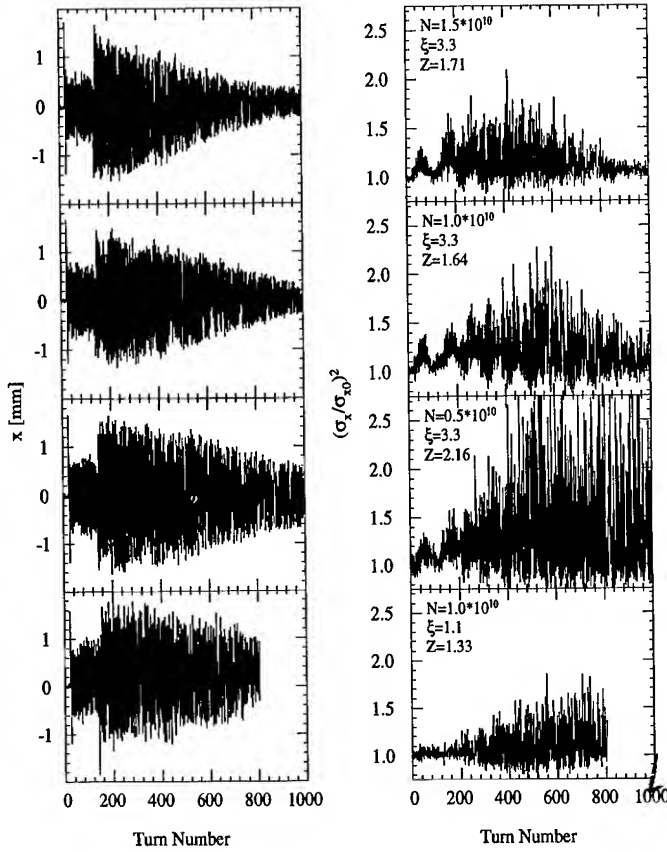


Figure 3. Measured horizontal centroid and rms size as functions of turn number in the SLC positron damping ring. The beam was kicked transversely at turns 25 and 135.

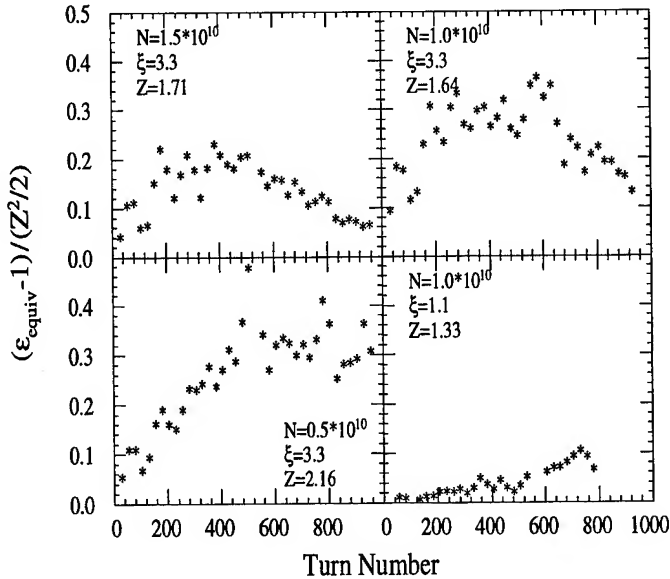


Figure 4. Matched equivalent emittance growth determined from the data in Fig. 3, relative to the maximum expected in the absence of collective damping.

time scale for collective damping is relatively 'fast' compared to that for decoherence. The decoherence in turn has a quenching influence on the collective damping in that the detuning phase competes with the accumulating head-tail phase causing the instantaneous damping rate to decrease. (For $\xi < 0$ this raises the instability threshold [7].) Thus naively we do not expect filamentation once-occurring, to be reversed; however the data in Fig. 4 appear to show an emittance drop at higher current. It may be notable that the "strong" head-tail strength $\Upsilon = \frac{Nr_0\beta_x\xi\sigma_zW_0}{4\sqrt{2}\nu_s\gamma}$ [8] takes on values of 0.27, 0.18, 0.09, and 0.18 in our four cases—below the instability threshold $\Upsilon = 2$. More work, both in theory and experiment, is needed to completely understand the collective aspects of these phenomena.

If head-tail damping dominates the centroid damping, the SLC damping ring wakefield $W_\perp(z) = W_0z$, ($z < 0$) (reasonable for short bunches) follows from the data since the damping rate [8]

$$\frac{1}{M_D} \approx \frac{4}{\pi^2} \frac{Nr_0\beta_x\xi\sigma_zW_0}{\nu_s\gamma}. \quad (16)$$

A rough fit yields $W_0 = 6 \times 10^7 \text{ m}^{-3}$, giving damping times of 670, 1000, 2000, and 3000 turns for the four cases of Fig. 3. (We use $\sigma_\delta = 0.73 \times 10^{-3}$, $\sigma_z = 6 \text{ mm}$, $\nu_s = 0.01275$, the β -function at the impedance source $\beta_x = 3 \text{ m}$, and $\gamma = 2350$.) The expected β -tron tune shift with current

$$\frac{d\nu_x}{dN} = -\frac{r_0\beta_x\sigma_zW_0}{8\sqrt{2}\pi\gamma} = -3.6 \times 10^{-14} \quad (17)$$

then is -0.0007 at $N = 2 \times 10^{10}$, e.g..

We thank Franz-Josef Decker and Marc Ross for useful discussions and support throughout the course of this work, and the Operations section of the SLAC Accelerator Department for their assistance during the data-taking.

References

- [1] R. E. Miller, A. W. Chao, J. M. Peterson, S. G. Peggs, and M. Furman, SSC-N-360 (1987).
- [2] S. Y. Lee, SSCL-N-749 (1991).
- [3] Ian C. Hsu, *Part. Accel.* **34** (1990) 43.
- [4] H. Moshhammer, *Phys. Rev. E* **48** (1993) 2140.
- [5] M. G. Minty and W. L. Spence, these proceedings.
- [6] M. G. Minty *et al.*, *AIP Conf. Proc.* **281** (1992) 158.
- [7] G. V. Stupakov and A. W. Chao, these proceedings.
- [8] A. W. Chao, *Physics of Collective Beam Instabilities in High Energy Accelerators*, Wiley, New York, 1993.

A WEAK MICROWAVE INSTABILITY WITH POTENTIAL WELL DISTORTION AND RADIAL MODE COUPLING

Alex Chao, Stanford Linear Accelerator Center, Stanford University, Stanford, CA 94309 USA
 Bo Chen, Superconducting Super Collider Laboratory, Dallas, TX 75237 USA
 Katsunobu Oide, KEK, National Laboratory for High Energy Physics, Tsukuba, Japan

I. INTRODUCTION

In attempts to minimize the impedance of an accelerator by smoothing out its vacuum chamber, improvements are typically first made by reducing the inductive part of the impedance. As the inductance is reduced, however, the impedance becomes increasingly relatively resistive, and as a consequence, the nature of potential well distortion changes qualitatively. An inductive impedance lengthens the bunch (above transition) while maintaining more or less a head-tail symmetry of the bunch longitudinal distribution. A resistive impedance does not change the bunch length as much, but tends to cause a large head-tail asymmetry.

The details of how potential well is distorted, particularly the head-tail asymmetry, affects the mechanism of the longitudinal microwave instability. Without a head-tail asymmetry, the microwave instability mechanism relies on the coupling among the "azimuthal" modes. The coupling is strong but the mode frequencies have to shift by large amounts (comparable to the synchrotron frequency ω_s) before the instability threshold is reached. With a head-tail asymmetry, the instability can be triggered by coupling of the "radial" modes. The coupling is weak, but the mode frequency shifts involved are small ($\ll \omega_s$). One then may have the following situation: as one tries to minimize the impedance, the impedance becomes resistive; the longitudinal bunch shape acquires a large head-tail asymmetry; the nature of microwave instability changes from a strong one (that involves azimuthal mode coupling) to a weak one (that involves head-tail asymmetry and radial mode coupling), but the threshold of the instability is not raised or is even lowered.[1,2] The gain of reducing the impedance is reflected only in the fact that the instability growth rate above threshold is slower.

The instability effect due to potential-well distortion and radial mode coupling has been analyzed before.[3-7] Our analysis is based on a technique[7,8] developed for the treatment of the longitudinal head-tail instability effect. To treat the coupling among radial modes, we introduce a "double water-bag" model for the simplicity of analysis.

The analysis is applied to the SLC Damping Ring. The wake function, as shown in Fig.1, is the present model used [9] taking into account the recent changes made on the vacuum chamber.[10] The calculated bunch shape distortion (particularly the head-tail asymmetry), as well as the calculated instability threshold, seem to agree with the observations.[10,11]

We explored two ways which might in principle alleviate this instability mechanism. (i) add a higher harmonic cavity: A higher harmonic rf voltage with appropriate phase and amplitude may compensate for the head-tail asymmetry and thus raise the instability threshold. (ii) operate the accelerator with a negative

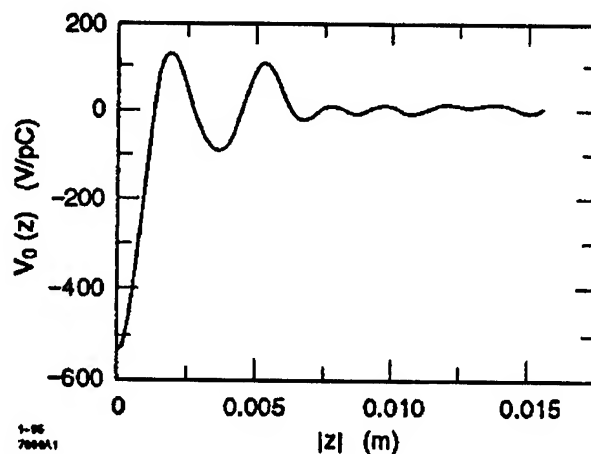


Figure 1. Wake function (in volts/pC) versus $|z|$ (in meters) used in the analysis for the SLC Damping Ring.

momentum compaction factor η : [12] With $\eta > 0$, the distorted beam distribution leans toward the head of the bunch; the bunch tail sees large wake fields. Operating with $\eta < 0$ could conceivably help because the beam distribution now leans toward the tail of the bunch. Both ways (i) and (ii) were explored in this paper. We found that a higher harmonic cavity of a modest voltage can indeed eliminate this instability, while the advantage of operating with $\eta < 0$ is less obvious.

II. SUMMARY OF ANALYSIS

Details of the analysis has been given in [2]. A brief summary is given below. We need to first compute the potential well distortion effects. Let $\psi_0(z, \delta)$ be the potential-well distorted beam distribution in the longitudinal phase space (z, δ) . The corresponding wake potential is

$$V_0(z) = e \int_{-\infty}^{\infty} dz' W'_0(z - z') \int_{-\infty}^{\infty} d\delta \psi_0(z', \delta) \quad (1)$$

We have assumed that the wake function $W'_0(z)$ is short, i.e. we consider single-bunch, single-pass instabilities. Later when we add a higher harmonic rf voltage to counteract the potential-well distortion, we will add it to V_0 . The Hamiltonian for the potential-well distorted beam is

$$H(z, \delta) = \frac{\eta}{2} \delta^2 + \frac{\omega_s^2}{2\eta c^2} z^2 - \frac{e}{T_0 E c} \int_0^z dz' V_0(z') \quad (2)$$

where ω_s is the unperturbed synchrotron frequency, T_0 is the revolution period, E is the beam energy, and c is the speed of light.

We now apply the technique developed in [7,8] and change variables from (z, δ) to (Φ, H) by a canonical transformation,

where H is given by Eq.(2), and Φ is the canonical variable conjugate to H :

$$\Phi = \frac{\partial F(\delta, H)}{\partial H} = - \int_0^\delta d\delta' \frac{\partial z(\delta', H)}{\partial H} \quad (3)$$

where $z(\delta, H)$ is obtained by inverting Eq.(2). The motion of a particle is periodic in Φ with period

$$\Phi_0(H) = \oint d\delta' \frac{\partial z(\delta', H)}{\partial H} \quad (4)$$

Note this period depends on the value of H of the particle under consideration.

In the double water bag model, ψ_0 has the form

$$\psi_0(H) = 2N[(1 - \Gamma)\Theta(\hat{H}_1 - H) + \Gamma\Theta(\hat{H}_2 - H)] \quad (5)$$

where $\Theta(x)$ is the step function, Γ is a parameter between 0 and 1 that specifies the relative amount of particles in each of the waterbags, and

$$N = \frac{N/2}{(1 - \Gamma) \int_0^{\hat{H}_1} dH \Phi_0(H) + \Gamma \int_0^{\hat{H}_2} dH \Phi_0(H)} \quad (6)$$

with N the number of particles in the beam bunch. We choose $\Gamma = 0.45$, and \hat{H}_1 and \hat{H}_2 to correspond to one- and two-sigma particles, such that the weak-beam limit of ψ_0 approximates a gaussian distribution.

Consider the ℓ -th azimuthal mode ($\ell = 1, 2, 3$ means dipole, quadrupole, sextupole modes) in the longitudinal phase space. There are two radial modes allowed in the double water bag model, one at $H = \hat{H}_1$, another at $H = \hat{H}_2$. The two radial mode frequencies are determined by the solutions of

$$\det \begin{bmatrix} \Omega^{(\ell)} - \frac{2\pi\ell c}{\Phi_0(\hat{H}_1)} + M_{11} & M_{12} \\ M_{21} & \Omega^{(\ell)} - \frac{2\pi\ell c}{\Phi_0(\hat{H}_2)} + M_{22} \end{bmatrix} = 0 \quad (7)$$

where we have defined the matrix elements

$$M_{ij} = - \frac{4r_0\eta N}{T_0\gamma\Phi_0(\hat{H}_i)} \int_0^{\frac{\Phi_0(\hat{H}_i)}{2}} d\Phi \delta(\Phi, \hat{H}_i) \sin \left[2\pi\ell \frac{\Phi}{\Phi_0(\hat{H}_i)} \right] \int_0^{\frac{\Phi_0(\hat{H}_j)}{2}} d\Phi' W'_0(z(\Phi, \hat{H}_i) - z(\Phi', \hat{H}_j)) \cos \left[2\pi\ell \frac{\Phi'}{\Phi_0(\hat{H}_j)} \right] \quad (8)$$

It can be shown that all elements M_{ij} are real. The beam is stable if both solutions for $\Omega^{(\ell)}$ are real. The instability growth rate is given by the imaginary part of $\Omega^{(\ell)}$.

In writing down Eq.(7), we have assumed that azimuthal mode coupling (coupling among different ℓ 's) can be ignored. This assumption is valid if the mode frequencies do not shift much away from the unperturbed value $\ell\omega_s$ (i.e. the mode frequency shifts $\ll \omega_s$).

The potential-well distortion can be considered to have two effects on the particle motion. First, it causes a "detuning" effect, i.e., Φ_0 now depends on H . Second, it causes a distortion of the phase space topology, i.e., the constant- H contours in phase space are no longer ellipses. It can be shown that the instability

is a result of the second effect alone. In other words, *distortion* of phase space from elliptical contours is a necessary condition for instability. This observation suggests that one way to alleviate this instability is to introduce an external higher harmonic rf to reduce the net phase space distortion.

III. APPLICATION TO SLC DAMPING RING

We have applied the analysis to the SLC Damping Rings. The following assumptions are made: (a) synchrotron radiation damping can be ignored; (b) the linearized Vlasov equation applies below the instability threshold; (c) this is a single-bunch, single-turn instability; (d) the wake field is as shown in Fig.1; (e) coupling among the azimuthal modes can be ignored; (f) we include two and only two radial modes with a double water-bag beam.

Unless specified otherwise, the parameters we used for the Damping Ring are $\eta = 0.0145$, $V_{rf} = 1.0$ MV, $\nu_s = 0.01275$, $cT_0 = 35.268$ m, $E = 1.19$ GeV. The unperturbed gaussian beam is assumed to have $\sigma_\delta = 0.73 \times 10^{-3}$. We mostly have studied the case of the quadrupole azimuthal mode with $\ell = 2$. The $\ell = 1$ case is determined by the Robinson damping mechanism and is not the subject of our study.

Figure 2 shows one set of results of our calculations. Figure 2(c) shows the complex mode frequency shifts $Y = (\frac{\Omega^{(\ell)}}{\omega_s} - \ell)$ as functions of the beam intensity N . The solid curves show the real part of Y . The two radial modes have separate frequencies for small beam intensities. At a threshold value of $N_{th} = 1.4 \times 10^{10}$, the two mode frequencies merge, and the beam becomes unstable. The instability growth rate τ^{-1}/ω_s is given by the dotted curve above threshold. The portion of the solid curve below threshold in Fig.2(b) shows the relative bunch lengthening factor σ_z/σ_{z0} versus N , where σ_{z0} is the unperturbed rms bunch length. The dotted curve above threshold is an under-estimate because the calculated σ_z took into account of potential-well distortion but ignored bunch lengthening due to microwave instability. (The solid curve above threshold will be explained later.) Figure 2(a) shows the shift of synchronous phase z_s versus N . The dotted portion of the curve gives an over-estimate of z_s .

The longitudinal radiation damping rate of the Damping Ring gives $\tau_{rad}^{-1}/\omega_s = 0.00095$. The effect of radiation damping on N_{th} is presumably small.

The instability threshold was studied as a function of the rf Voltage V_{rf} . It was found that $N_{th} = 1.7 \times 10^{10}$ when $V_{rf} = 0.8$ MV and 2.1×10^{10} when $V_{rf} = 0.6$ MV.

We have also calculated the case for the sextupole azimuthal mode $\ell = 3$ and $V_{rf} = 1.0$ MV. The instability threshold is found to be $N_{th} = 1.6 \times 10^{10}$, slightly higher than the threshold for $\ell = 2$. The beam is first unstable in its quadrupole motion, but the sextupole mode threshold is not far away. The behavior is similar when V_{rf} is lowered to 0.6 MV. At 0.6 MV, the $\ell = 3$ threshold is found to be $N_{th} = 2.6 \times 10^{10}$.

Our analysis describes the beam behavior at or below the instability threshold. By an ad hoc consideration, however, we may try to extend its application to cases *above* threshold by conjecturing that, above threshold, the bunch would lengthen just enough to stabilize the beam. The beam is therefore constantly staying at the edge of instability. The extension of the solid curve

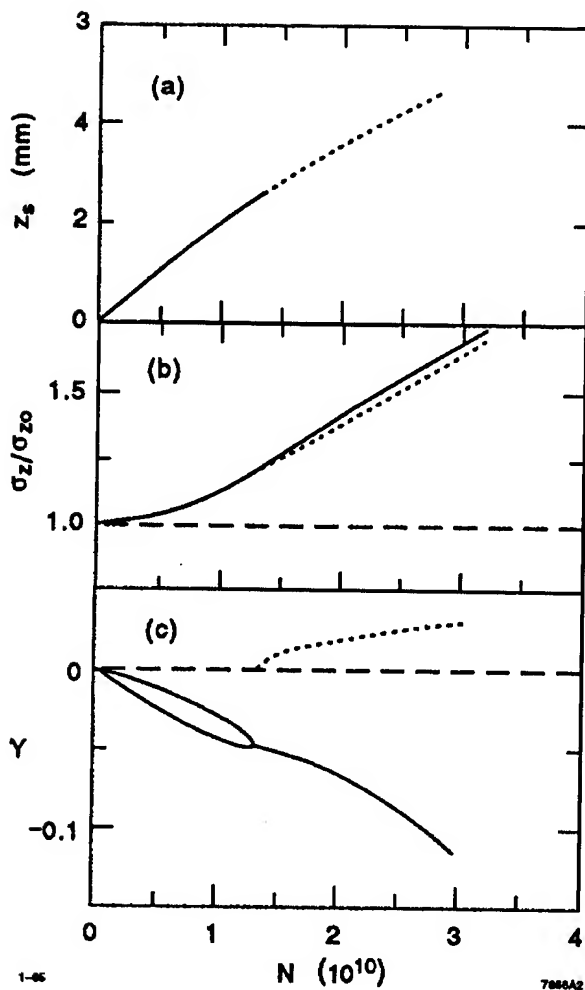


Figure 2. (a) Shift of synchronous phase z_s , in mm as a function of beam intensity N . (b) Bunch lengthening factor (due to potential-well distortion) versus N . (c) The complex mode frequency shifts versus N .

in Fig.2(b) beyond threshold represents the conjectured bunch lengthening due to microwave instability. Note that the region between the dotted and the solid curves is relatively small, indicating that this instability is weak and a small increase of the bunch length beyond the potential-well distortion stabilizes the beam. One also expects that the same small relative increase would occur in the energy spread above threshold. Furthermore, if there is a mechanism which causes the beam to execute a sawtooth oscillation, as observed in the Damping Ring,[10,11] the amplitude of the sawtooth oscillation is likely to correspond to the region between the dotted and solid curves of Fig.2(b).

To further study the instability mechanism, and to explore possible cures, we considered the following two possibilities: (i) add a high harmonic rf voltage to counteract the potential-well distortion, and (ii) operate the accelerator below transition with $\eta < 0$. [12]

We found that a higher harmonic rf is quite effective in raising the instability threshold. For example, by introducing a 12 GHz rf system (considered e.g. for the NLC at SLAC), which is phased 4 mm ahead of the main rf, a voltage of 6.5 kV pushes the threshold intensity to 3×10^{10} .

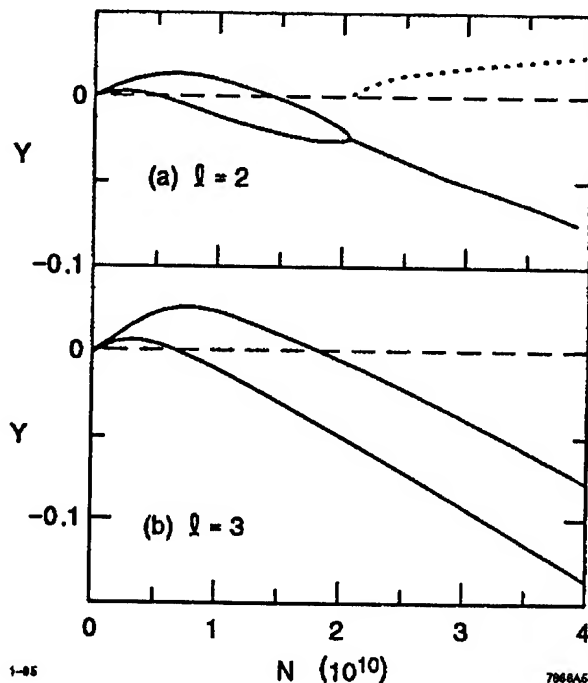


Figure 3. Mode frequencies when $\eta = -0.0145$.

Operating the accelerator with $\eta < 0$ turned out less conclusive. Figure 3(a) shows the mode frequencies with $\eta = -0.0145$. The instability threshold is raised from 1.4×10^{10} to 2.0×10^{10} . Figure 3(b) shows what happens to the $\ell = 3$ modes. Operating with $\eta < 0$ seems to improve the instability threshold somewhat in the present study. However, whether this is a general trend needs more investigation.

We thank B. Zotter, S.X. Fang, K. Bane, R. Siemann, M. Minty, W. Spence for many helpful discussions.

References

- [1] K. Oide, private communications, 1994, to be published.
- [2] A. Chao, B. Chen, and K. Oide, to appear in Proc. Workshop on Beam Instabilities in Storage Rings, NSRL, Hefei, China, 1994.
- [3] K. Oide, AIP Proc. 45, Nonlinear Dynamics and Particle Acceleration, Tsukuba, Japan, 1990, p.266.
- [4] K. Oide and K. Yokoya, KEK Preprint 90-10 (1990).
- [5] X.T. Yu and J.S. Wurtele, IEEE Part. Accel. Conf., Washington D.C., 1993, p.3327.
- [6] R. Baartman and M. D'yachkov, IEEE Part. Accel. Conf., Washington D.C., 1993, p.3330. See also these proceedings.
- [7] Bo Chen, Ph.D. thesis, Univ. of Texas at Austin, 1995.
- [8] B. Chen and A. Chao, Part. Accel. 43, 77 (1993).
- [9] K. Bane, private communications, 1994.
- [10] K. Bane et al., these proceedings.
- [11] R.L. Holtzapple, R. Siemann, C. Simopoulos, these proceedings.
- [12] S.X. Fang, private communications, 1994, to be published.

WAKE FIELD AND THE DIFFRACTION MODEL DUE TO A FLAT BEAM MOVING PAST A CONDUCTING WEDGE

A.W. Chao, Stanford Linear Accelerator Center, Stanford University, Stanford, CA 94309 USA
H. Henke, Technische Universitaet, Berlin, Germany

I. INTRODUCTION

To clean a beam of its excessive tail particles, one often uses a collimator. If the beam intensity is high enough or if the beam is brought too close to the collimator, however, the wake fields generated by the beam-collimator interaction can cause additional beam tails to grow, thus defeating, or even worsening the beam-tail cleaning process.

The wake field generated by a sheet beam moving past a conducting wedge has been obtained in closed form by Henke using the method of conformal mapping.[1] This result is applied in the present work to obtain the wake force and the transverse kick received by a test charge moving with the beam. For the beam to be approximated as sheet beams, it is assumed to be flat and the collimator is assumed to have an infinite extent in the flat dimension. We will derive an exact expression for the transverse wake force delivered to particles in the beam bunch. Implication of emittance growth as a beam passes closely by a collimator is discussed.

We consider two idealized wedge geometries. Section 2 is when the wedge has the geometry as a disrupted beam pipe. Section 3 is when it is like a semi-infinite screen. Unfortunately we have not solutions for more realistic collimator geometries such as when it is tapered to minimize the wake field effects. Our results however should still serve as pessimistic limiting cases.

An interesting opportunity is offered by our exact calculation of the wake fields: it can be used to confront the diffraction model[2,3,4] used to estimate the high frequency impedance of a cavity structure. It is shown that the field pattern, as well as the impedance, agree with those obtained by the diffraction model in appropriate limits.

We would like to thank K. Bane, R. Warnock, and P. Wilson for their help.

II. DISRUPTED PIPE

Consider a metal wedge and a rod beam as shown in Fig.1(a). Both the wedge and the beam are considered to be infinitely long in the z -direction. The beam has a line charge density λ_0 and is assumed to move with the speed of light in the x -direction. Following [1], we define

$$\lambda = \frac{\pi}{2\pi - \theta} \quad \text{and} \quad R = \left(\frac{ct - \sqrt{c^2t^2 - r^2}}{r} \right)^\lambda \quad (1)$$

The parameters have the ranges $0 < \phi < 2\pi - \theta$, $1 > R > 0$, $\pi > \theta > 0$, and $1 > \lambda > \frac{1}{2}$. We have shown the coordinates in Fig.1(a).

In the region $r < ct$ (inside the "light cylinder"), the electromagnetic field components are found by an extension of the

analysis of [1] to be

$$\begin{aligned} E_r &= -8\lambda\lambda_0 \sin \pi\lambda \sin \lambda\phi \frac{\frac{1}{R} - R}{rQ} \\ E_\phi &= 8\lambda\lambda_0 \sin \pi\lambda \frac{\frac{ct}{r}[2\cos \pi\lambda - (\frac{1}{R} + R)\cos \lambda\phi]}{Q\sqrt{c^2t^2 - r^2}} \\ B_z &= \frac{r}{ct} E_\phi, \quad E_x = -E_r \cos \phi + E_\phi \sin \phi \\ E_y &= -E_r \sin \phi - E_\phi \cos \phi \end{aligned} \quad (2)$$

where $Q = (\frac{1}{R} - R)^2 \sin^2 \pi\lambda + [(\frac{1}{R} + R)\cos \pi\lambda - 2\cos \lambda\phi]^2$. The fields are independent of the y -separation between the rod beam and the wedge.

Consider a test charge e which follows behind the rod beam at a distance D ($D > 0$) and has a vertical distance Y from the edge of the wedge ($Y > 0$), as shown in Fig.1(b). Let the test charge move with the beam at the speed of light. The Lorentz force seen by the test charge has the components

$$F_x = eE_x, \quad F_y = eE_y - eB_z, \quad \text{and} \quad F_z = 0 \quad (3)$$

We want to calculate the integrated longitudinal and transverse impulses received by the test charge as it passes by the wedge.

When $ct \rightarrow \infty$, the test charge sees $E_x \rightarrow 1/\sqrt{ct}$. It follows that the longitudinal impulse received by the test charge is infinite. This means the beam loses an infinite amount of energy to generate the wake field. The infinity does not go away with a finite wedge angle θ , or with a finite bunch length in x ; it comes from the infinite bunch width in z .

The total transverse impulse, on the other hand, converges and gives the surprisingly simple result

$$c\Delta p_y(Y, D) = \int_{(Y^2+D^2)/2D}^{\infty} F_y d(ct) = 2\pi e\lambda_0 \quad (4)$$

The transverse impulse is independent of Y or D . It is even independent of the wedge angle θ .

If the beam has a surface charge density $\Sigma(x)$, its wake effects can be obtained from the rod beam result by superposition. Consider a beam particle at location x relative to the beam center. It receives a transverse impulse from all particles in front of it. Thus

$$c\Delta p_y(x) = 2\pi e \int_x^{\infty} dx' \Sigma(x') \quad (5)$$

The previous results become simpler for the case of infinitely thin wedge when $\theta = 0$ (or $\lambda = \frac{1}{2}$):

$$B_z = -\frac{4\lambda_0 \cos \frac{\phi}{2}}{r\sqrt{2(\frac{ct}{r} - 1)(\frac{ct}{r} + \cos \phi)}}$$

$$\begin{aligned}
E_x &= -\frac{4\lambda_0 \sin \frac{\phi}{2}}{r\sqrt{2(\frac{ct}{r}-1)}}, & E_y &= \frac{4\lambda_0 \cos \frac{\phi}{2}(\frac{ct}{r}-1+\cos \phi)}{r\sqrt{2(\frac{ct}{r}-1)}(\frac{ct}{r}+\cos \phi)} \\
E_r &= \frac{ct}{r}B_z, & E_\phi &= -\frac{4\lambda_0}{r\sqrt{2(\frac{ct}{r}-1)}}\sin \frac{\phi}{2}\frac{\frac{ct}{r}-1}{\frac{ct}{r}+\cos \phi} \\
F_x &= -\frac{4e\lambda_0 \sin \frac{\phi}{2}}{r\sqrt{2(\frac{ct}{r}-1)}}, & F_y &= \frac{4e\lambda_0 \cos \frac{\phi}{2}}{r\sqrt{2(\frac{ct}{r}-1)}}
\end{aligned} \quad (6)$$

The sign of the Lorentz force is such that the test charge always sees a retarding force ($F_x < 0$). Also the transverse deflecting force deflects it toward the plate ($F_y > 0$).

III. SEMI-INFINITE SCREEN

The arrangement of the wedge and a rod beam is now shown in Fig.2. We have $\theta < \frac{\pi}{2}$ and $\frac{1}{2} \leq \lambda \leq \frac{2}{3}$. For a rod beam, inside the light cylinder, the field components are found by an extension of [1] to be

$$\begin{aligned}
E_r &= -4\lambda_0\lambda \sin \frac{\lambda\pi}{2} \frac{1}{r} [2f(\lambda\phi) \\
&\quad + f(\lambda\phi - \lambda\pi) + f(\lambda\phi + \lambda\pi)] \\
E_\phi &= -4\lambda_0\lambda \sin \frac{\lambda\pi}{2} \frac{ct}{r\sqrt{c^2t^2 - r^2}} [2g(\lambda\phi) \\
&\quad + g(\lambda\phi - \lambda\pi) + g(\lambda\phi + \lambda\pi)] \\
B_z &= \frac{r}{ct}E_\phi, & E_x &= -E_r \sin \phi - E_\phi \cos \phi \\
E_y &= E_r \cos \phi - E_\phi \sin \phi
\end{aligned} \quad (7)$$

where

$$\begin{aligned}
f(u) &= \frac{(\frac{1}{R} - R) \sin u}{(\frac{1}{R} - R)^2 \sin^2 \frac{\lambda\pi}{2} + [(\frac{1}{R} + R) \cos \frac{\lambda\pi}{2} - 2 \cos u]^2} \\
g(u) &= \frac{(\frac{1}{R} + R) \cos u - 2 \cos \frac{\lambda\pi}{2}}{(\frac{1}{R} - R)^2 \sin^2 \frac{\lambda\pi}{2} + [(\frac{1}{R} + R) \cos \frac{\lambda\pi}{2} - 2 \cos u]^2}
\end{aligned} \quad (8)$$

The transverse impulse as seen by a test charge shown in Fig.2(b) is found to be

$$c\Delta p_y(Y, D) = \int_{(Y^2+D^2)/2D}^{\infty} F_y d(ct) = \pi e\lambda_0 \quad (9)$$

Again this is independent of Y , D , and θ . Note Eq.(9) is exactly half of Eq.(4). It also follows that for a beam with surface charge density $\Sigma(x)$, a particle at position x receives a transverse kick which is half of Eq.(5).

IV. GENERAL WAKE CONSIDERATIONS

The fact that the integrated transverse wake force is independent of the transverse and the longitudinal locations of the test charge has its origin in the Maxwell equations. By our assumptions, we know that (a) the beam current density \vec{j} and the charge density ρ are related by $\vec{j} = c\rho\hat{x}$, (b) the only non-vanishing field and force components are B_z , E_x , E_y , F_x and F_y , (c) all quantities do not depend on z , and (d) the integrated field and force components $\vec{\mathcal{E}}, \vec{\mathcal{B}}, \vec{\mathcal{F}} \equiv \int (\vec{E}, \vec{B}, \vec{F}) d(ct)$ depend on x and t only

through $x - ct$. By linearly combining the Maxwell equations into equations in terms of eB_x , \mathcal{F}_x , \mathcal{F}_y , and \mathcal{F}_z , we find

$$\frac{\partial}{\partial y}\mathcal{F}_x = \frac{\partial}{\partial x}\mathcal{F}_y = \frac{\partial}{\partial y}\mathcal{F}_y = 0 \quad (10)$$

This means \mathcal{F}_y can not depend on x or y , i.e. it has to be constant. Also, \mathcal{F}_x does not depend on y , although it can depend on x . This conclusion is valid independent of the boundary conditions, as long as the boundary is independent of the z -coordinate.

It can also be shown from a general wake consideration [5] that the wake function does not depend on Y . Observing that the wake integral scales with the ratio of Y and D , it can be concluded that the wake integral must also not depend on D . The specific value of the wake integral then follows easily by setting $Y = 0$ and $\phi = \pi$.

V. THE DIFFRACTION MODEL

A diffraction model has been proposed and used to estimate the high frequency impedance of a cavity structure in the beam pipe.[2,3,4] Consider a cylindrical beam pipe of radius b and a cavity structure of total gap length g , and a beam current $\sim e^{ik(x-ct)}$. This model suggests: (a) The wake field created as the beam passes the entrance edge of the cavity populates mainly the region in the forward direction into the open cavity space. By the time the wake field reaches the exit edge of the cavity, the radial spread of the region is

$$\Delta y \sim \sqrt{g/k} \quad (11)$$

(b) The longitudinal impedance at high frequencies is given by

$$Z_0^{\parallel}(k) = \frac{Z_0}{2\pi^{3/2}b} [1 + \text{sgn}(k)i] \sqrt{\frac{g}{|k|}} \quad (12)$$

where $Z_0 = \frac{4\pi}{c} = 377 \Omega$.

Our results offer an opportunity to check the diffraction model with exact Maxwell solutions. (Our result is not a rigorous proof of the diffraction model because we do not have a cylindrical geometry.) Consider a surface charge beam with $\Sigma(x, t) = \Sigma_0 e^{ik(x-ct)}$, which moves with the speed of light c . The wake fields can be obtained from the rod-beam results by superposition. Take the disrupted beam case with $\theta = 0$ for example. We have

$$\begin{aligned}
B_z &= -\frac{4 \cos \frac{\phi}{2}}{\sqrt{2r}} \Sigma_0 e^{ik(r-ct)} \int_0^\infty du \frac{e^{iku}}{\sqrt{u(\frac{u}{r} + 1 + \cos \phi)}} \\
E_y &= \frac{4 \cos \frac{\phi}{2}}{\sqrt{2r}} \Sigma_0 e^{ik(r-ct)} \int_0^\infty du \frac{e^{iku}(\frac{u}{r} + \cos \phi)}{\sqrt{u(\frac{u}{r} + 1 + \cos \phi)}}
\end{aligned} \quad (13)$$

Significant contributions to the integrals (13) come from the region $u < \frac{1}{|k|}$. This in turn means that the components B_z and E_y are strong when ϕ is close to π with

$$|\pi - \phi| < \sqrt{\frac{2}{|k|r}} \quad (14)$$

Equation (14) in turn gives the diffraction pattern (11).

The component E_x , however, is somewhat different. It does not have the diffraction pattern (11). In fact,

$$E_x = -\frac{4 \sin \frac{\phi}{2}}{\sqrt{2r}} \Sigma_0 e^{ik(r-ct)} \int_0^\infty du \frac{e^{iku}}{\sqrt{u}} \\ = -\frac{4 \sin \frac{\phi}{2}}{\sqrt{2r}} \Sigma_0 e^{ik(r-ct)} \sqrt{\frac{\pi}{2|k|}} [1 + \text{sgn}(k)i] \quad (15)$$

The magnitude of E_x however is smaller than those of B_z and E_y by a factor of $|k|r \gg 1$.

One can estimate the high frequency impedance as follows. Consider a test charge which passes position $x = -D$ at time $t = 0$ with a vertical separation Y from the wedge. Assume the test charge move in the x -direction at the speed of light. The energy loss of the test charge as it traverses the cavity can be estimated as (assume $g \gg D, g \gg Y, |k|g \gg 1$)

$$\Delta \mathcal{E} \approx \int_0^g d(ct) e E_x \approx -4 \sqrt{\frac{\pi g}{|k|}} [1 + \text{sgn}(k)i] e \Sigma_0 e^{-ikD} \quad (16)$$

Although (16) is for a geometry with infinite z -dimension, the impedance of a cylindrical cavity can be estimated by

$$Z_0^{\parallel}(k) = \frac{\Delta \mathcal{E}/e}{2\pi b c \Sigma_0 e^{-ikD}} \quad (17)$$

which is identical to (12). One can show that (12) applies also to arbitrary θ . The diffraction model is therefore re-established. Further exploring of more details of the diffraction model should be possible using the exact solutions given in the previous sections.

VI. EMITTANCE GROWTH

We now estimate the emittance growth when a flat beam is being collimated by a metal collimator. Let the horizontal distribution of the beam be uniform with a total width L_z . We assume the vertical beam dimension is $\ll L_z$, and it is the vertical dimension which is being collimated. The vertical separation between the flat beam and the edge of the collimator is assumed to be $\ll L_z$. We ignore the resistive wall effect here.[6,7]

Consider the case of a semi-infinite screen wedge. Let the surface charge density of the beam be written as $\Sigma(x) = \frac{Ne}{L_z} \rho(x)$, where N is the total number of particles in the beam bunch, and $\int_{-\infty}^\infty dx \rho(x) = 1$. The kick angle received by a particle in the beam located at longitudinal position x is, according to Eq.(9),

$$\Delta y'(x) = \frac{\pi N r_0}{L_z \gamma} \int_x^\infty dx' \rho(x') \quad (18)$$

where r_0 is the classical radius of the particle, γ is the Lorentz energy factor.

The maximum kick is received by particles in the trailing tail $x = -\infty$. Independent of the details of the longitudinal distribution $\rho(x)$, this kick is given by

$$\Phi \equiv \Delta y'(-\infty) = \frac{\pi N r_0}{L_z \gamma} \quad (19)$$

The growth in the effective emittance of the beam is also independent of the details of $\rho(x)$:

$$\Delta \epsilon = \int_{-\infty}^\infty dx \rho(x) \beta \Delta y'^2(x) = \frac{1}{3} \beta \Phi^2 \quad (20)$$

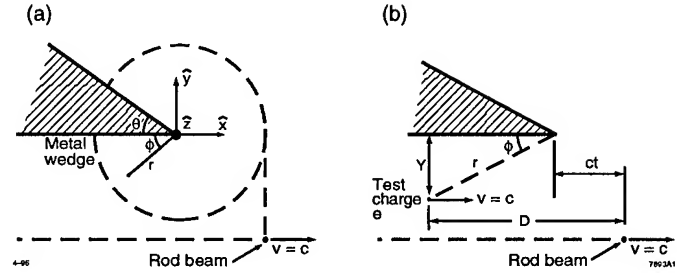


Figure 1. A rod beam passing a disrupted pipe wedge.

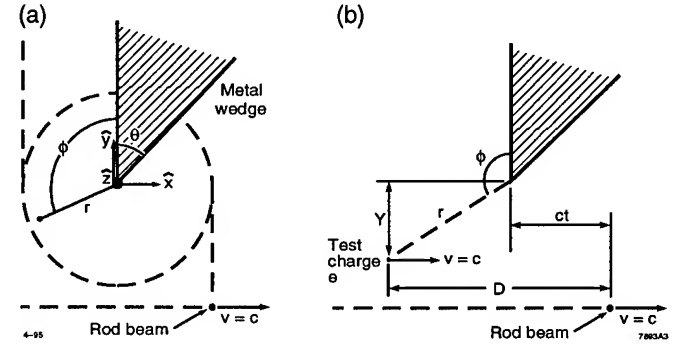


Figure 2. A rod beam passing a semi-infinite screen wedge.

where β is the β -function at the collimator.

As a numerical example, take an electron beam bunch with $N = 5 \times 10^{10}$, $L_z = 1$ mm, and $\gamma = 10^5$. We assume that the vertical beam height and the vertical distance of the beam from the collimator are $\ll 1$ mm. If we further assume the collimator has a semi-infinite screen geometry, then the wake field kick delivered to a trailing particle in the bunch is $4 \mu\text{rad}$. If $\beta = 10$ m, the effective emittance growth is found to be 0.6×10^{-10} m-rad, which corresponds to a growth of normalized emittance of 0.6×10^{-5} m-rad. As mentioned in Section 1, this can be detrimental for a high quality, low-emittance beam.

References

- [1] H. Henke, Proc. IEEE Part. Accel. Conf., San Francisco, 1991, p.380.
- [2] J.D. Lawson, Rutherford Lab. Report RHEL/M 144 (1968), and Part. Accel. 25, 107 (1990).
- [3] Karl Bane and Matthew Sands, Part. Accel. 25, 73 (1990).
- [4] A.W. Chao, "Physics of Collective Beam Instabilities in High Energy Accelerators", Wiley, New York, 1993.
- [5] S. Vaganian and H. Henke, to be published in Part. Accel., 1995.
- [6] A. Piwinski, DESY report 94-068 (1994).
- [7] K. Bane, private communications, 1995.

a result. The problem was corrected by increasing the open loop gain.

Tuner Feedback Loops

Until recently the cavity tuners were not carefully regulated. Difficulties arising from beam-related heating of the rf cavities however have necessitated careful control. The tuners, which regulate the phase between the generator and cavity voltages, are sampled and held once per cycle. Initially the tuner dead band was about 8° which was limited by the noise level in the phase measurement. To improve the signal-to-noise ratio, a filter was added after the sample and hold module which allowed the dead band to be reduced to 1° . The speed of the tuners, motor-driven tuning plungers, has also been decreased to prevent oscillations. These modifications resulted in a greater degree of stability in the loading angle. Occasional problems related to loss of regulation, however, still persist upon recovery from an extended period without beam.

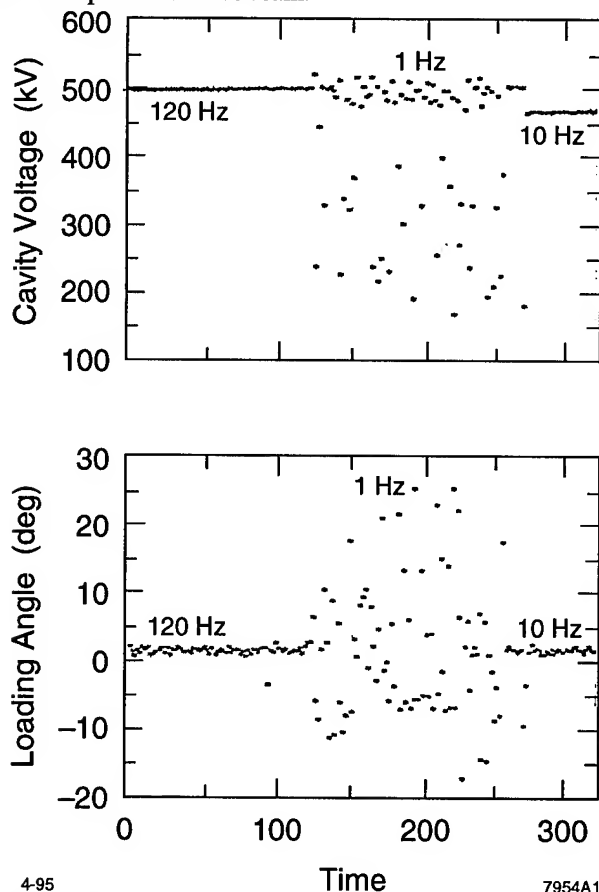


Figure 2. Measured cavity voltage and loading angle during rate limiting.

III. COMPENSATION FOR REPETITION RATE CHANGES

To avoid damage to accelerator components from beam heating, the repetition frequency is occasionally reduced

from 120 Hz to 10 Hz or 1 Hz. At low rate the slow tuner feedback loops could respond to changes in the loading angle. As shown in Fig. 2 the tuner positions and cavity voltage lost regulation under 1 Hz operation. In this example the loading angle was nominally regulated to $\phi_l = 0^\circ$ while the tuning angle, the phase between the voltage and the current, was $\phi_z = -45^\circ$. When the beam was extracted therefore, the tuners would move and the cavity would be unregulated at injection. To avoid this, a beam-presence condition was added which fixed the tuner positions in the absence of beam.

With direct rf feedback, the long absence of beam due to rate limiting also caused problems. Because the instantaneous power requirements are higher with direct rf feedback, a limiter just upstream of the klystron was added to prevent klystron saturation in the 1993 run. Initial high current experiments at the end of the 1993 run showed that simple limiting was insufficient for maintaining stability during rate-limiting at even higher beam currents. Instead, an intermediate level voltage was summed with the reference input to the amplitude feedback loop (V_{des} in Fig. 1) during rate-limiting.

IV. MINIMIZATION OF TRANSIENT LOADING EFFECTS

With the steady-state defined by operation with beam, the dominant transient loading effects are caused by injection and extraction of the beam.^{5,6} Because direct rf feedback effectively deQ's the cavity and therefore decreases the cavity fill time, this feedback proved useful in minimizing the effect of beam loading since the rf system is rapidly able to compensate for the fast changes. Without direct rf feedback and with high currents substantial beam losses resulted from the large cavity voltage oscillations induced by injection. Transients in the cavity voltage are shown in Fig. 3 with the direct rf feedback loop off ($G = 0$ dB) and on ($G = 20$ dB). Beam extraction is indicated by the initial discontinuity near $30 \mu s$. The next discontinuity $13 \mu s$ later corresponds to beam injection. Without direct rf feedback the voltage oscillated by about 400 kV peak-to-peak. With $G = 20$ dB the oscillations were reduced to 220 kV peak-to-peak. Numerical analysis results showing the effect that direct rf feedback has in reducing these transient oscillations are presented in Ref. 5.

Transient oscillations may be further reduced by ensuring that the beam is properly injected into the center of the rf bucket. The beam phase at extraction is regulated by feedback to ensure proper injection into the linear accelerator. At extraction the rf phase is reset to prepare for injection which is $13 \mu s$ later. The phase at injection is a relative phase offset between the damping ring and injection linac. Typically this phase offset (ϕ_{inj} in Fig. 1) is checked periodically and adjusted by minimizing the amplitude of the transient oscillations while viewing the rf waveform on an oscilloscope.

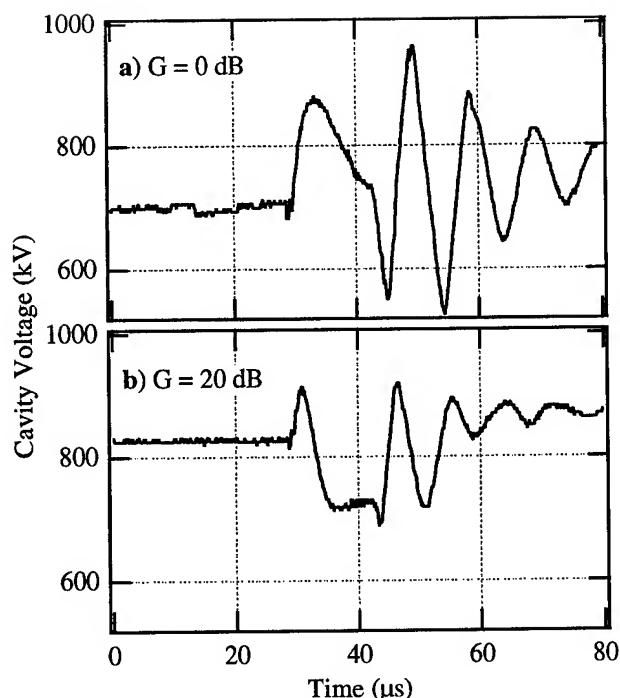


Figure 3. Cavity voltage with two different direct rf feedback gains. $\phi_l = 0^\circ$; $\phi_{inj} = 45^\circ$.

Finally, transient oscillations were minimized by intentional detuning of the loading angle. As shown in Fig. 3 a large voltage error on the accelerating cavity resulted when the direct rf feedback loop was on. By adjusting the tuner feedback loop set point to positive loading angle under nominal conditions with beam, this problem was alleviated. Transient oscillations in the cavity voltage are plotted as a function of time with direct rf feedback on at different loading angles in Fig. 4. As the loading angle increased, the amplitude of the transients decreased as expected.⁵ In the first two plots, when the beam was extracted the cavity voltage was not maintained. As a result, the voltage at injection was out of regulation. At $\phi_l = +10^\circ$ the voltage was regulated when the beam was absent. At $\phi_l = 23^\circ$ the cavity voltage was already out of regulation before the beam was extracted. At extraction the cavity voltage increased towards its regulated value.

V. SUMMARY

Modifications to the rf systems in the SLC damping rings were required to overcome instabilities related to heavy beam loading. The rf system was tuned to minimize transient beam loading effects. For future running at higher beam currents, we will try to ensure that the klystron is capable of operating at higher power levels (as in 1993). Modifications to the amplitude feedback hardware and logic are also being considered to provide better stability.

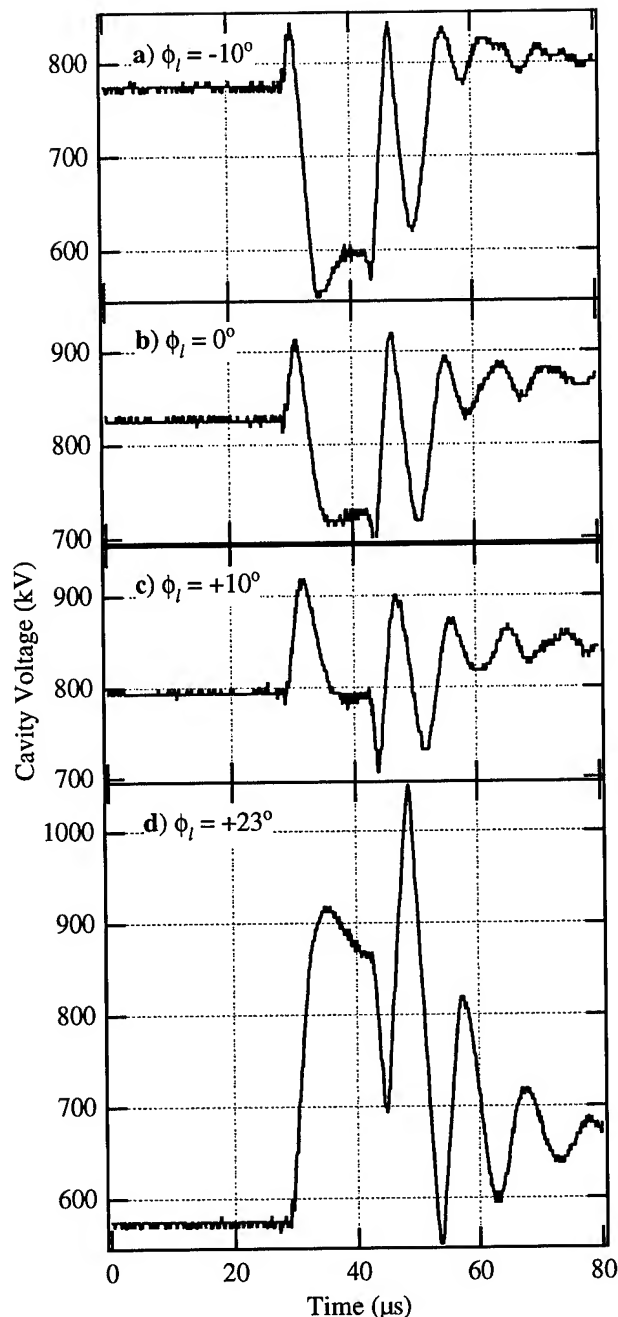


Figure 4. Cavity voltage as a function of time with $G = 20$ dB and variable loading angle ϕ_l . $\phi_{inj} = 45^\circ$.

VI. REFERENCES

1. P. Krejcik *et al*, *Proc 1993 PAC*, 3240 (1993).
2. F. Pederson, *IEEE Tran. on Nucl. Sci.*, NS-32, 2138 (1985).
3. P. Krejcik *et al*, *Proc 1993 PAC*, 2370 (1993).
4. K. Bane *et al*, *WAC17 1995 PAC*.
5. M. Minty & R.H. Siemann, *TPA09 1995 PAC*.
6. M. Minty & R.H. Siemann, *RAP10 1995 PAC*.

DEFLECTING FORCES FOR THE CASE OF MULTI MODE BEAM - RF CAVITY INTERACTION IN LINEAR ACCELERATORS

V.G.Kurakin, Lebedev Physical Institute, Leninsky Prospect 53, 117924 Moscow, Russia

Abstract

The formulae for the deflecting rf forces have been derived for the train of charged bunches, traversing a rf cavity. These forces originate from the deflection action of non symmetrical modes excited by the misaligned bunches, the infinite set of the cavity eigen modes being taken into account. Various dependencies are explored, including the effect of "mode saturation" and non linearity of rf deflecting gradient, followed by the appropriate plots.

1. INTRODUCTION

High intensity proton linacs to be used in future facilities (for example, neutron spallation sources, nuclear waste transmutation etc.) assume very low beam losses to make it possible to handle such accelerators. This in turn puts forward the problems not essential for relatively low intensity machines but of vital importance for new generation of accelerators, the formation and evolution of beam halo being among them. To this end new approaches to old problems seem to be reasonable to investigate anomalies in beam dynamics. Cumulative beam instability in rf linacs [1-4] might be one of the possible mechanism contributing to beam losses. Single mode approximation traditionally used in cumulative beam break up theories can not be justified in non resonance case, if the process takes place below the regenerative threshold. Under such conditions the choice of any particular mode responsible for beam - cavities interactions becomes completely uncertain. Many of excited deflecting modes may contribute to resulting field and deflecting gradient as well, and multi mode approach suggests itself.

The paper generalises the results had been obtained in [5]. The general expression for the deflecting gradient for any bunch from the bunch train traversing the cavity is derived. Linear approximation is not used any more, because non linear character of the beam interaction with radial modes is the principle consequence of multi mode approach, determining many features of deflecting forces. Numerical calculations are performed for cylindrical resonator, followed by various plots to illustrate quantitatively multi mode beam - cavity interaction.

2. THE EQUATIONS OF BEAM - CAVITY INTERACTION

Our aim is the derivation of the expression for deflecting electromagnetic force produced by the charged bunches train in a cavity and experienced by the particles forming this train. It is assumed in the analysis below that there is not more than one bunch in the cavity at any moment. The influence of cavity holes on field distribution is neglected. It

is assumed also that the beam is frozen in transverse direction inside cavity, so that the particle orbit is not substantially affected in its passage through the cavity. In such an approximation the electromagnetic field inside cavity acts on a particle moving with the velocity v with the average transverse force [6,7]:

$$\langle f_x \rangle = \frac{ev}{d} \int_0^d \frac{\partial A_z}{\partial x} (x, 0, z, \tau + \frac{z}{v}) dz, \quad (1)$$

where \vec{A} is vector potential and the integration is performed along the cavity of length d . (MKS units are used throughout this work.) Here, x is particle transverse displacement from cavity axis, x -axis of the basis used is assumed to coincide with it; z denotes the particle coordinate along the longitudinal axis, τ is the moment at which particle with charge e enters the cavity.

Following [8] let us represent the vector potential in (1) in the form of infinite sum of eigenvectors $\vec{A}_\lambda(\vec{r})$:

$$\vec{A}(\vec{r}, t) = \sum_\lambda q_\lambda(t) \vec{A}_\lambda(\vec{r}) \quad (2)$$

with the time dependent amplitudes $q_\lambda(t)$ satisfying the differential equation

$$\ddot{q}_\lambda + \frac{\omega_\lambda}{Q_\lambda} \dot{q}_\lambda + \omega_\lambda^2 q_\lambda = \frac{1}{\epsilon_0} \frac{\int_V \vec{j} \cdot \vec{A}_\lambda dV}{\int_V A_\lambda^2 dV} \quad (3)$$

and with \vec{A}_λ satisfying the condition $\text{div} \vec{A}_\lambda = 0$ as well as the Helmholtz equation:

$$\Delta \vec{A}_\lambda + \frac{\omega_\lambda^2}{c^2} \vec{A}_\lambda = 0. \quad (4)$$

Here, ω_λ and Q_λ are frequency and quality factor of a mode respectively, ϵ_0 is electrical permeability of free space, c is the light velocity. The solution of (3,4) for the bunch of the radius a and length l with uniform charge q distribution within it can be represented in the form:

$$q_\lambda(t) = q \text{Im} \int_{0 D(x,a)}^d \int dS A_{\lambda,z}(x, y, z) \exp \left[\frac{\omega_\lambda z}{v} \left(\frac{1}{2Q_\lambda} - i \right) \right] dz \times \\ \exp \left[\omega_\lambda (t - \tau) \left(i - \frac{1}{2Q_\lambda} \right) \right] \exp \frac{l}{v} \omega_\lambda \left(\frac{1}{2Q_\lambda} - i \right) - 1 \quad (5) \\ \frac{\pi a^2 \omega_\lambda \epsilon_0 \int_V \vec{A}_\lambda^2 dV}{\frac{l}{v} \omega_\lambda \left(\frac{1}{2Q_\lambda} - i \right)}$$

where D is the area occupied by the beam in transverse plane, and V is the cavity volume. The formula is valid for the moment when the bunch has left the cavity. After passages N bunches, following with the time interval T , the induced field acts on the particles within $N+1$ bunch (at the distance Δl from the bunch head) with the force:

$$\langle f \rangle = \frac{eqv}{d} \text{Im} \sum_{\lambda} \sum_{n=1}^N Z_{\lambda}(x_n, a) Y_{\lambda}(x_{N+1}) F_{\lambda} \times \exp \left[\omega_{\lambda} \left((N-n+1)T + \frac{\Delta l}{v} \right) \left(i - \frac{1}{2Q_{\lambda}} \right) \right], \quad (6)$$

where the following designations are used:

$$Z_{\lambda}(x, a) = \frac{\int_0^d \int_{D(x,a)} dS A_{\lambda,z}(x, y, z) \exp \left[\frac{\omega_{\lambda} z}{v} \left(\frac{1}{2Q_{\lambda}} - i \right) \right] dz}{\pi a^2 \omega_{\lambda} \epsilon_0 \int_V A_{\lambda}^2 dV}, \quad (7)$$

$$Y_{\lambda}(x) = \int_0^d \frac{\partial}{\partial x} A_{\lambda,z}(x, 0, z) \exp \left[\frac{z \omega_{\lambda}}{v} \left(i - \frac{1}{2Q_{\lambda}} \right) \right] dz, \quad (8)$$

$$F_{\lambda} = \frac{\exp \left[\frac{l}{v} \omega_{\lambda} \left(\frac{1}{2Q_{\lambda}} - i \right) \right] - 1}{\frac{l}{v} \omega_{\lambda} \left(\frac{1}{2Q_{\lambda}} - i \right)}. \quad (9)$$

For steady state case formula (6) is turned to

$$\langle f \rangle_{st} = \frac{eqv}{d} \text{Im} \sum_{\lambda} Z_{\lambda}(x, a) Y_{\lambda}(x) F_{\lambda} \times \frac{\exp \left[\omega_{\lambda} \left(T + \frac{\Delta l}{v} \right) \left(i - \frac{1}{2Q} \right) \right]}{1 - \exp \omega_{\lambda} T \left(i - \frac{1}{2Q} \right)}. \quad (10)$$

3. NUMERICAL RESULTS FOR CYLINDRICAL CAVITY

We shall use cylindrical cavity to explore quantitatively the influence of the beam and cavity parameters on rf gradient for steady case state. For such a cavity the components of eigenvectors of deflecting TM modes are:

$$\begin{aligned} A_r &= -\frac{k_z}{k_c} J'_n(r k_c) \cos n\varphi \sin k_z z, \\ A_{\varphi} &= \frac{k_z n}{k_c^2} \frac{J_n(r k_c)}{r} \sin n\varphi \sin k_z z, \\ A_z &= J_n(r k_c) \cos n\varphi \cos k_z z, \end{aligned} \quad (11)$$

and formula for rf gradient $\langle g \rangle_{rf} = \langle f \rangle / evx$ looks like

$$\langle g \rangle_{rf} = \frac{Ip}{\epsilon_0 d \Lambda c^2} G, \quad (12)$$

where I is the average beam current, $I = q / T$,

$$G = \frac{1}{\rho^4 \xi} \text{Im} \sum_{n,m,p} \frac{v_{n,m}^3 W_{n,m,p} S_{n,m} F_{n,m} \Sigma_{n,m,p} J'_n \left(v_{n,m} \frac{\xi}{\rho} \right)}{k_{n,m,p} J_{n,m,p}} \quad (13)$$

and

$$\begin{aligned} W_{n,m,p} &= \left(i \frac{k_{n,m,p}}{\beta} - \frac{k_{n,m,p}}{2\beta Q_{n,m,p}} \right)^2 \times \\ &\quad \left\{ (-1)^p \exp \left(\frac{\delta k_{n,m,p}}{2\beta Q_{n,m,p}} - i \frac{\delta k_{n,m,p}}{\beta} \right) - 1 \right\} \times \\ &\quad \left(-\frac{ip\pi}{\delta} + \frac{ik_{n,m,p}}{\beta} - \frac{k_{n,m,p}}{2\beta Q_{n,m,p}} \right)^2 \times \\ &\quad \left\{ (-1)^p \exp \left(-\frac{\delta k_{n,m,p}}{2\beta Q_{n,m,p}} + i \frac{\delta k_{n,m,p}}{\beta} \right) - 1 \right\} \times \\ &\quad \left(\frac{ip\pi}{\delta} + \frac{ik_{n,m,p}}{\beta} - \frac{k_{n,m,p}}{2\beta Q_{n,m,p}} \right)^2 \times \end{aligned}$$

$$\Sigma_{n,m,p} = \frac{\exp \left[k_{n,m,p} (1 + \theta / \beta) \left(i - 1 / 2Q_{n,m,p} \right) \right]}{1 - \exp k_{n,m,p} \left(i - 1 / 2Q_{n,m,p} \right)} \quad (14)$$

$$F_{n,m,p} = \frac{\exp \left[\frac{\eta k_{n,m,p}}{\beta} \left(\frac{1}{2Q_{n,m,p}} - i \right) \right] - 1}{\frac{\eta k_{n,m,p}}{\beta} \left(\frac{1}{2Q_{n,m,p}} - i \right)}$$

$$\begin{aligned} S_{n,m} &= \frac{2\rho^2}{v_{n,m}^2 \pi \alpha^2} \int_0^{\psi} \cos(n\varphi) d\varphi \int_r^b J_n(z) z dz, \quad \text{where} \\ b &= \frac{v_{n,m}}{\rho} \left(\xi \cos \varphi + \sqrt{\alpha^2 - \xi^2 \sin^2 \varphi} \right), \end{aligned}$$

$$\psi = \pi, \quad r = 0 \quad \text{for } \alpha \geq \xi \quad \text{while } \psi = \arcsin \frac{\alpha}{\xi}$$

$$\text{and } r = \frac{v_{n,m}}{\rho} \left(\xi \cos \varphi - \sqrt{\alpha^2 - \xi^2 \sin^2 \varphi} \right) \quad \text{for } \alpha < \xi.$$

Here, lower case Greek letters designate normalised values, $R = \rho \Lambda$, $d = \delta \Lambda$, $x = \xi \Lambda$, $l = \eta \Lambda$, $\Delta l = \theta \Lambda$, $a = \alpha \Lambda$, Λ is the wavelength of the TM_{010} mode, $\Lambda = cT$, $v_{n,m}$ is the m -th null of Bessel function of the n -th order $J_n(x)$, $\beta = v/c$, $k_z = \pi p / d$, $k_c = v_{n,m} / R$, $p = 0, 1, \dots, m$, $n = 1, 2, \dots$, and

$$J_{m,p} = \frac{\pi^3 \rho^2 p^2}{2\delta v_{n,m}^2} (A_{n,m} + B_{n,m}) + \pi \delta C_{n,m} \times \begin{cases} 1, p=0 \\ \frac{1}{2}, p \neq 0 \end{cases}$$

$$A_{n,m} = \int_0^{v_{n,m}} J_n^2(x) x dx, \quad B_{n,m} = \int_0^{v_{n,m}} \frac{J_n^2}{x} dx, \quad (15)$$

$$C_{n,m} = \int_0^{v_{n,m}} J_n^2(x) x dx, \quad k_{n,m,p} = \sqrt{\frac{v_{n,m}^2}{\rho^2} + \frac{\pi^2 p^2}{\delta^2}},$$

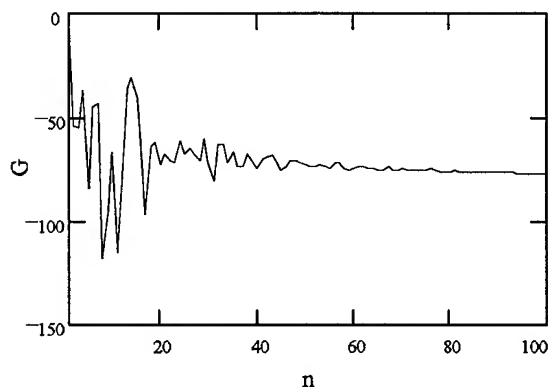


Fig. 1. Dependence of rf gradient on the number of modes. $Q=100$, $\delta=0.5$, $\rho=0.383$, $\alpha=0.002$, $\xi=0.005$, $\eta=0$, $\theta=0$.

As numerical calculations have shown, the quadruple and higher symmetry modes contribute to deflecting gradient as small perturbations to the value, determined by dipole modes. Fig. 1 represents the dependence of resulting gradient on the modes number, n being equal to maximum value of radial and longitudinal modes in the sum (13). The affect of "mode saturation" is seen from the plot. The next plot (Fig. 2) illustrates the variation of rf gradient along the bunch, calculated for saturation case. Fig. 3 demonstrates strong dependence of gradient on beam offset, originating from contribution of high orders radial modes to resulting force.

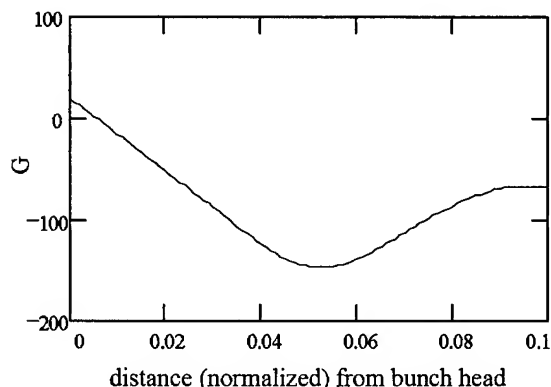


Fig. 2. Rf gradient variation along the bunch. $Q=100$, $\delta=0.5$, $\rho=0.383$, $\alpha=0.002$, $\xi=0.005$, $\eta=0.05$.

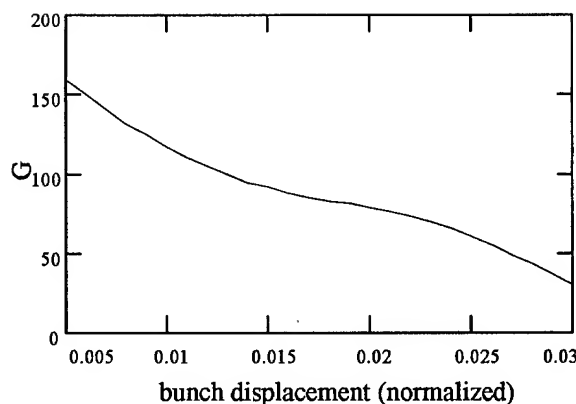


Fig. 3. Dependence of deflecting gradient on bunch displacement. $Q=500$, $\delta=0.5$, $\rho=0.383$, $\alpha=0$, $\eta=0.05$, $\theta=0$.

4. CONCLUSION

Multi mode approach has been demonstrated to result in new features of beam cavity interaction in rf accelerators. In particular, these are strong dependence of deflecting gradient on particle location within a bunch as well as non linearity of deflecting force that manifests itself as the radial dependence of rf gradient.

5. ACKNOWLEDGEMENTS

The work is supported by Russian Foundation for Fundamental Research, project No 94-02-04466.

6. REFERENCES

- [1] W.K.H.Panofsky and M.Bander, "Asymptotic Theory of Beam Break Up in Linear Accelerators", The Review of Scientific Instruments, vol. 39, pp. 206-212, February, 1968.
- [2] A.W.Chao, B.Richter and C.Y.Yao, "Beam emittance growth caused by transverse deflecting fields in a linear accelerator", Nuclear Instruments and Methods, vol. 178, pp. 1-8, 1980.
- [3] R.L.Gluckstern, R.K.Cooper and P.J.Channel, "Cumulative beam breakup in rf linacs", particle Accelerators, vol. 16, pp. 125-153, 1985.
- [4] C.L.Bohn and J.R.Delany, "Cumulative beam breakup in linear accelerators with periodic beam current", Physical Review A, vol. 45, No 8, pp. 5964-5993, April, 1992.
- [5] V.G.Kurakin, "Multi Mode Approach in Cumulative Beam Break up Theory", in Proceedings of Fourth European Particle Accelerator Conference, London, 27 June to 1 July, 1994, pp. 1123 -1125.
- [6] W.K.H.Panofsky and W.A.Wenzel, "Some Considerations Concerning the Transverse Deflection of Charged Particles in Radio-Frequency Fields", The Review of Scientific Instruments, vol. 27, No 11, p. 967, November, 1956.
- [7] M.Jean Browman, "Using the Panofsky-Wenzel Theorem in the Analysis of Radio-Frequency Deflectors", in Proceedings of 1993 Particle Accelerator Conference, Washington, May 17 - 20, 1993, pp. 800 - 802.
- [8] V.M.Lopuchin, The excitation of electromagnetic oscillations and waves by electron beams, Moscow: The publisher of technical and theoretical literature, 1953, 324 pp., in Russian.

PHOTOELECTRON TRAPPING MECHANISM FOR TRANSVERSE COUPLED BUNCH MODE GROWTH IN CESR*

J.T. Rogers

Laboratory of Nuclear Studies, Cornell University, Ithaca, NY 14853 USA

Abstract

An anomalous damping or growth of transverse coupled bunch modes has long been observed in CESR. The growth rates and tune shifts of these modes are a highly nonlinear function of current. The effect is associated with the operation of the distributed ion pumps, as it disappears when the pumps are not powered. We show that this effect can be explained by the presence of electrons trapped in the CESR chamber by the field of the dipole magnets and the electrostatic leakage field of the distributed ion pumps. Photoelectrons are introduced into the chamber by synchrotron radiation and can be ejected from the chamber by the passage of an e^+ or e^- bunch. The transverse position of the beam thus modulates the trapped photoelectron charge density, which in turn deflects the beam, creating growth or damping and a tune shift for each coupled bunch mode. Predictions of the dependence of growth rate and tune shift on bunch current, bunch pattern, and mode frequency by a numerical model of this process are in approximate agreement with observations.

I. INTRODUCTION

An anomalous horizontal coupled bunch instability [1] in CESR has growth rates and tune shifts which are nonlinear in beam current. It is strongest at the intermediate currents encountered during CESR injection, and becomes dramatically weaker at higher currents. It is present only when the distributed ion pumps are powered [2]. The absolute values of both the growth rate and tune shift are largest for the lowest frequency mode. They drop rapidly for higher frequency modes.

Here we present the hypothesis that slow electrons trapped in the CESR beam chamber are responsible. We show that photoelectrons from synchrotron radiation striking the beam chamber walls will be trapped in the combined dipole magnetic field and electrostatic leakage field from the distributed ion pumps, and calculate their interaction with the beam.

II. PHOTOELECTRON TRAPPING

Slow photoelectrons in the CESR chamber will be confined to very small orbits in the horizontal plane by the 0.2 T magnetic field of the CESR dipoles. The quadrupole component of electrostatic leakage field from the distributed ion pump slots, calculated to be 2.1×10^4 V/m² at the center of the beam chamber [3], confines the electrons vertically. Positive ions are expelled by this field. The combination of these fields acts as a Penning trap for electrons, much like the ion pump itself. Because there is a horizontal dipole component of the pump leakage field (320 V/m at the center of the beam chamber), the trapped electrons

undergo an $\mathbf{E} \times \mathbf{B}$ drift down the length of the magnet, with a velocity of the order of 1.6×10^3 m/s. Thus a trapped electron is lost from the 6.5 m long magnets in about 2 ms. We will later show that electrons are removed by interactions with the beam on a far shorter time scale, so their drift velocity may be neglected. The cyclotron frequency of the trapped electrons is 5.6 GHz, so their cyclotron motion is unimportant at the frequencies of the coupled bunch modes. The vertical motion, with frequencies of the order of 10 MHz or less, dominates the dynamics.

In addition to producing photoelectrons through synchrotron radiation, the beam has an essential role in trapping the electrons. An electron which is emitted from the chamber wall will soon collide with the chamber unless perturbed by the time-dependent force provided by the beam. Electrons which are deflected by the beam opposite to their vertical velocities are trapped on orbits of lower amplitude. Other electrons are excited to higher amplitudes and may be lost in collisions with the beam chamber.

The magnitude of the impulse from the beam depends on the position of the beam relative to the trapped electrons. Thus the oscillating beam position modulates the trapped charge density, which in turn drives the transverse oscillation of the beam. Coupled bunch modes are damped, driven unstable, or shifted in tune, depending on the phase of the trapped charge density relative to the beam motion.

III. SIMULATION

A simplified numerical model was produced to calculate the coupled bunch mode growth. In this model, we calculate the trajectories of photoelectrons moving under the influence of the electric field gradients of the distributed ion pumps, a bunched positron beam, and the other photoelectrons. Because several simplifying assumptions are used, the calculated growth rates and tune shifts should be regarded as estimates.

We divide the beam chamber into slices along the x direction from the pump slots to the center of the chamber. In each time increment δt :

1. a photoelectron macroparticle is started in each x slice at $y = y_{wall}$ with vertical velocity $v_y = 0$;
2. the electric field gradient $\partial E_y / \partial y$ is calculated for each x slice;
3. y and v_y are updated for each macroparticle using the calculated $\partial E_y / \partial y$; and
4. any macroparticle for which $y \geq y_{wall}$ is removed.

No horizontal motion of the macroparticle is allowed because of the strong vertical magnetic field. An approximate model is used for the field gradients in which $\partial E_y / \partial y$ falls off as the square of the distance from the distributed pump slots and the beam, and the effect of the photoelectron macroparticles is to screen the field due to the pump slots. The beam position x_{beam} is made to

*This work has been supported by the National Science Foundation.

oscillate sinusoidally with amplitude 4 mm. The constants used in the simulation are listed in Table 1.

Table 1: Simulation physical constants

y_{wall}	Beam chamber half-height	20 mm
x_{center}	Position of center of chamber	45.2 mm
Q_x	Horizontal tune	≈ 10.5
T_0	Revolution period	$2.56 \mu s$
β_x	Average β in dipole magnets	19 m
p	Beam momentum	5.3 GeV/c
L_{slot}	Total pump slot length	408 m
q_{slot}	Eff. slot linear charge density	4.79 nC/m
R_{pe}	Photoemission rate	$0.92 m^{-1}$

All of the physical constants used in the simulation are based on measured quantities except R_{pe} , the photoelectron charge injected per unit time, length, and beam current. No attempt was made to calculate or directly measure this quantity. It was treated as a free parameter, and was adjusted so that the maximum growth rate for the 7 bunch pattern occurred 5 mA as experimentally observed. It was then held fixed at this value for all simulations. No other free parameters were used, and no other changes of any sort were made to the original numerical model to bring it in closer agreement with experimental observations.

IV. SIMULATION RESULTS

A. Time dependence of trapped charge density

The calculated photoelectron charge density as a function of time for the 7 bunch pattern is shown in Fig. 1. The horizontal scale is in units of $\delta t = 1.4$ ns. The abrupt loss of trapped charge following each bunch passage is clearly seen, as is the slow variation due to the horizontal beam oscillation.

The reason that the instability growth rate falls off rapidly at higher beam currents is apparent from these plots. The rate at which photoelectrons are injected into the beam chamber is proportional to the synchrotron radiation flux, which is in turn proportional to the beam current. When the average photoelectron charge density is sufficient to completely screen the pump leakage field, no more electrons can be trapped. The charge density reaches an approximately constant level, extinguishing the variation needed to drive the beam.

The trapped photoelectron density depends strongly on the details of the bunch pattern. The effect of a very small gap in the bunch pattern can be seen in the sudden drop every turn (1830 increments) in Fig. 1b (the interval between bunches 7 and 1 is 378 ns as opposed to 364 ns for all other bunches). The characteristic recovery time of the photoelectron charge is of the order of 50 ns, as shown in Fig. 2, where the data of Fig. 1c are plotted on a finer time scale.

B. Current dependence of growth rate and tune shift

The growth rates α_x and tune shifts $\delta\omega_x$ for the 7 bunch pattern are shown in Figs. 3 and 4. We also simulated 9 trains of two bunches each, with a 28 ns interval between bunches. Because the recovery time of the photoelectron charge is longer than the interval between bunches, the bunches within a train act coher-

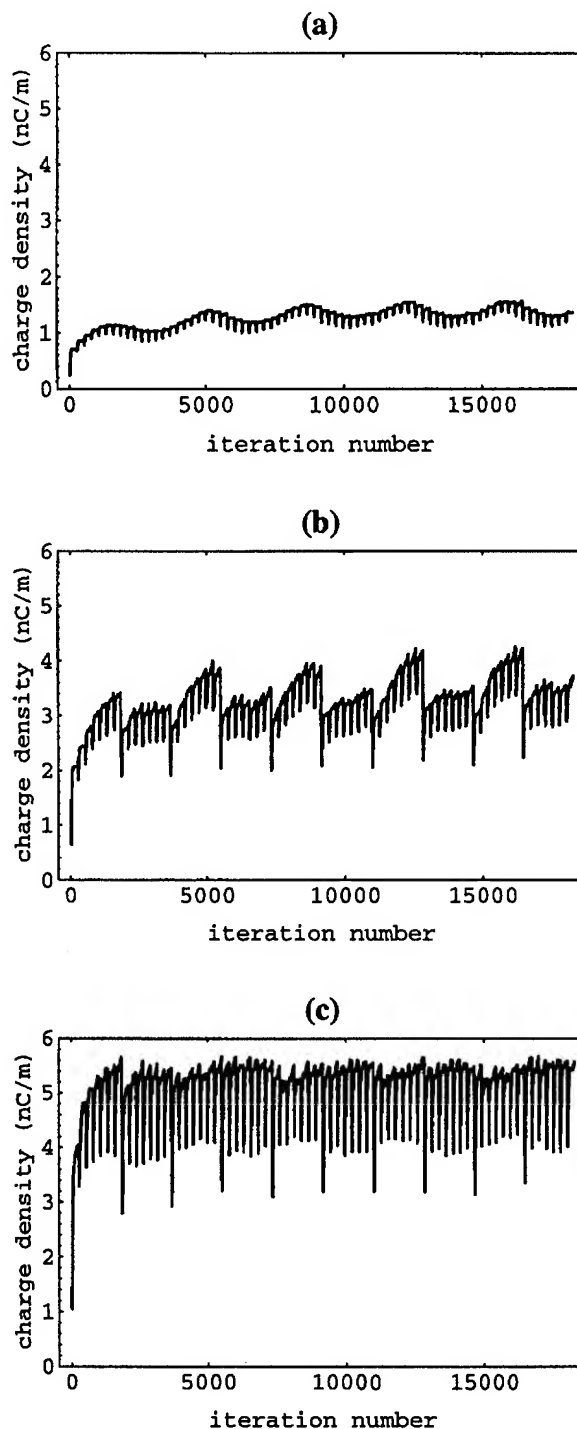


Figure 1. Photoelectron linear charge density vs. time. The horizontal scale is in units of the 1.4 ns simulation increment. The total time is 10 CESR revolutions. The beam is moving horizontally with frequency $f_0/2$. Beam currents are: (a) 3; (b) 5; and (c) 6 mA/bunch.

ently. The current at which the growth rate peaks is half that of the 7 bunch case.

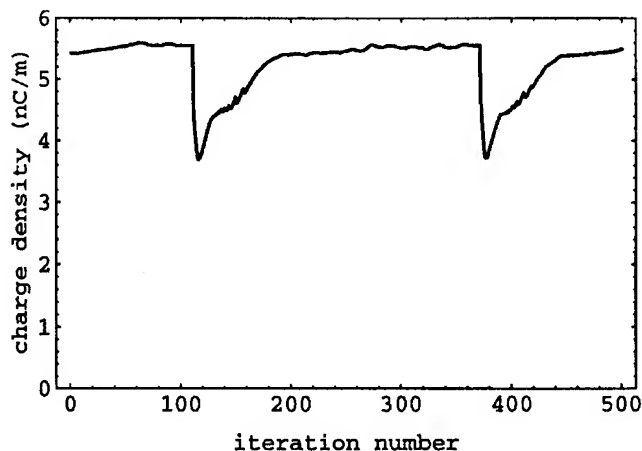


Figure 2. Photoelectron linear charge density vs. time in units of 1.4 ns (data of Fig. 1c plotted on a finer scale).

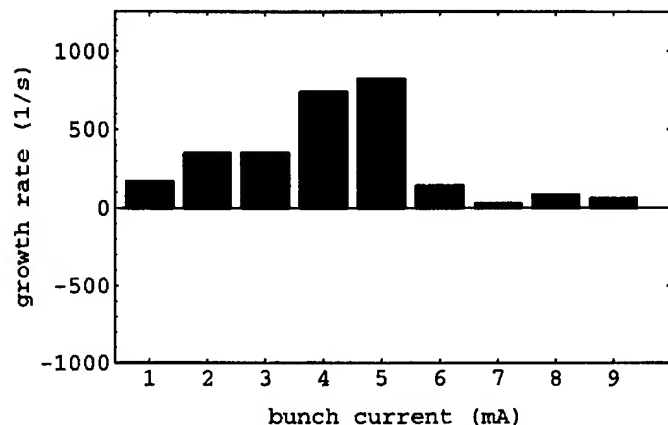


Figure 3. Growth rate vs. bunch current.

C. Frequency dependence of growth rate and tune shift

To determine the dependence of the growth rate and tune shift on the coupled-bunch frequency we followed the same procedure for coupled bunch modes with frequencies of $f_0/2$, $3f_0/2$, and $5f_0/2$, where $f_0 = 390$ kHz is the CESR revolution frequency. We used the 7 bunch pattern with 3 mA/bunch. The results are shown in Table 2. The magnitude of both the growth rate and tune shift fall off rapidly with increasing frequency, in qualitative agreement with observation.

Table 2: Frequency dependence of α_x and $\delta\omega_x$

Mode frequency	α_x (s^{-1})	$\delta\omega_x/2\pi$ (Hz)
$f_0/2$	291.1	78.2
$3f_0/2$	-37.8	0.7
$5f_0/2$	2.2	2.0

V. CONCLUSIONS

The photoelectron trapping model successfully describes the qualitative features of the observed instability. The numerical model provides estimates of growth rates which are in approximate agreement with observations in spite of a number of simplifying assumptions. For example, the calculated growth rate

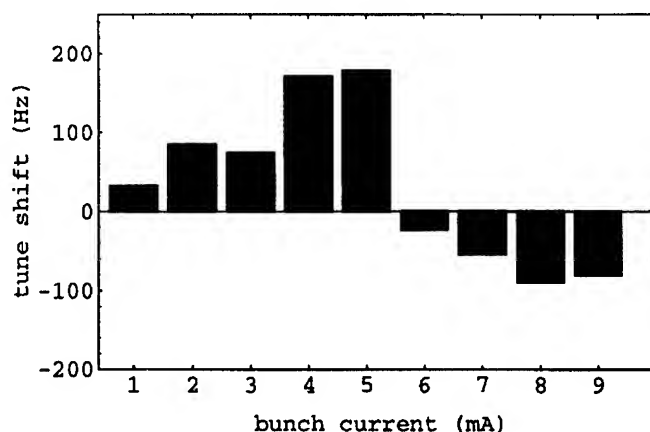


Figure 4. Tune shift vs. bunch current.

for the 7 bunch pattern at 4 mA/bunch is $740 s^{-1}$, while the observed rate is $520 s^{-1}$ [1]. The numerical model reproduces the observed behavior of the tune shift, which changes sign at the same current at which the growth rate starts to diminish, and predicts that the magnitude of the growth rate falls rapidly with frequency.

It has been observed that the $m = 1$ vertical head-tail mode is stabilized by the operation of the distributed ion pumps [2]. We note that the peak of the frequency spectrum for this mode occurs at approximately 2.4 GHz, with substantial spectral density at the 5.6 GHz cyclotron frequency of the trapped photoelectrons. The photoelectrons may be damping this mode by absorbing energy from the head-tail mode before being lost by collision with the chamber.

The author wishes to thank the many members of the CESR Operations Group, with special thanks to M. Billing, for stimulating discussions on observations and possible causes of the anomalous antidamping effect.

References

- [1] L.E. Sakazaki, R.M. Littauer, R.H. Siemann, and R.M. Talman, IEEE Trans. Nucl. Sci. **32** (1985) 2353-2355; L.E. Sakazaki, Ph.D. thesis, Cornell Univ. (1985).
- [2] R. Littauer, Cornell LNS report CLNS 88/847 (1988).
- [3] D. Sagan and J.J. Welch, Cornell LNS report CBN 92-01 (1992).

ELECTRON COOLER IMPEDANCES

A. Burov, Budker INP, 630090, Novosibirsk, Russia

Abstract

An electron beam of a cooler in an ion storage ring can be considered as a medium which responds to fields generated by an ion beam. Electron density perturbations awoken by the ion beam act back on it, which can give rise to instabilities. This reaction can be described in terms of an impedance introduced in the ring by the electron beam. Longitudinal and transverse impedances of an electron cooler are derived here, increments and thresholds of corresponding instabilities are estimated.

I. Introduction

The interaction of an ion beam with different elements of the vacuum chamber can give rise to coherent instabilities of the beam. If the beam temperature is sufficiently high, its collective modes are stabilized due to the Landau damping. Under cooling, the temperature is going down and the Landau damping is switching off; but the cooling brings about its own decrement in the collective motion of the beam. However, if the decrement of some mode is smaller than its increment caused by the interaction with the environment, the beam is either stopped at the instability threshold or lost. So, these increments determine a minimum cooling rate needed to achieve a beam temperature below the Landau damping threshold.

In a relativistic case, a significant contribution in the beam-surrounding interaction is given by a broad-band wall impedance. For a moderate relativism $\gamma - 1 \leq 1$, this impedance is shown to be exponentially damped, $\propto \exp(-4.8/(\beta\gamma))$ [3]. The influence of the wall resistivity is too small to play any role in the cooling process. Therefore, the electron cooler itself can be the main reason of instabilities; this problem was discussed in Ref. [4], [5], [6], [7].

The longitudinal and transverse impedances of the cooler are calculated here and shown to be normally orders of magnitude higher than the resistive wall ones. In the result, increment rates of the corresponding instabilities can be higher than typical cooling rates [8], [9], [10], even for rather low ion currents (e. g. \sim few μ A).

II. Main Equations

The dynamics of the magnetized electron medium of a cooler excited by fluctuations of the cooled ion beam can be described in a reference frame by the following set of equations [11]:

$$\begin{aligned} \frac{\partial \tilde{n}_e}{\partial t} + \tilde{n}_e \frac{\partial \tilde{v}_e}{\partial z} &= 0 \\ \frac{\partial \tilde{v}_e}{\partial t} - \frac{e}{m} \frac{\partial \Phi}{\partial z} &= 0 \end{aligned} \quad (1)$$

$$\frac{1}{r} \frac{\partial}{\partial r} \left(r \frac{\partial \Phi}{\partial r} \right) + \frac{\partial^2 \Phi}{\partial z^2} + \frac{1}{r^2} \frac{\partial^2 \Phi}{\partial \phi^2} = 4\pi e (\tilde{n}_e - \tilde{n}_i)$$

Here \tilde{n}_e is an electron density, \tilde{n}_e, \tilde{n}_i are electron and ion density perturbations, \tilde{v}_e is a perturbation of electron velocity, Φ is an electrostatic potential. In the impedance calculations ions are assumed to be protons, the impedances are linear response functions and do not depend on the charge of exciting particles. Unperturbed velocities of the beams are supposed to be equal, the solenoidal magnetic field assumed to be directed along the longitudinal axis z everywhere. The former assumption is justified if the velocities coincide with a sufficiently good accuracy, the criterium is discussed in the next chapter. The later assumption is only warranted for long-wave perturbations, $ka \ll 1$, where k is a longitudinal wavenumber, a is a radius of the electron beam. It is demonstrated in the following, that cooler impedances reach their maxima somewhere in the intermediate region, $ka \simeq 1$. In this wave band the results obtained from Eqs.(1) can serve only as estimations with accuracy about $\simeq 100\%$. More accurate results in the intermediate band could be found with the electron beam curvature in the ions entrance to be taken into account, this rather complicated problem is not considered here.

The solution of the problem (Eqs.1) with proper boundary conditions can be presented in the following form:

$$\begin{aligned} \Phi &= \sum_{\mu \pm} A_{l\mu \pm} J_l(\kappa_{l\mu} r/a) \cos(l\phi) \exp(iq_{l\mu \pm} z \mp i\omega_{l\mu} t) \\ \tilde{v}_e &= -\frac{e}{m} \sum_{\mu \pm} \pm \frac{A_{l\mu \pm}}{u_{l\mu}} J_l(\kappa_{l\mu} r/a) \cos(l\phi) \exp(iq_{l\mu \pm} z \mp i\omega_{l\mu} t) \\ \tilde{n}_e &= \tilde{n}_{il} \cos(l\phi) \exp(ikz) - \\ &\quad - \frac{\omega_e^2}{4\pi} \sum_{\mu \pm} \frac{A_{l\mu \pm}}{u_{l\mu}^2} J_l(\kappa_{l\mu} r/a) \cos(l\phi) \exp(iq_{l\mu \pm} z \mp i\omega_{l\mu} t) \end{aligned} \quad (2)$$

Here the subscript $\mu = 1, 2, \dots$ is a counter of radial wavenumbers, \pm corresponds to waves travelling along and against the beams, \tilde{n}_{il} is an amplitude of the ion perturbation, $\kappa_{l\mu}$ are zeroes of a Bessel function J_{l-1} , with $\kappa_{01} \approx \sqrt{2/\ln(1/(ka))}$, if an aperture radius $b \gg 1/k$. In the opposite case of adjoining aperture, $b - a \ll a$, the radial numbers $\kappa_{l\mu}$ are zeroes of J_l .

The connection between electron and ion longitudinal wavenumbers is determined by the Doppler condition, which gives:

$$q_{l\mu \pm} = k/(1 \pm \alpha_{l\mu}), \quad \alpha_{l\mu} = \omega_e a / (\kappa_{l\mu} v), \quad (3)$$

where v is the beams velocity in the laboratory frame. The eigenfrequencies are described by sound-like dispersion equations:

$$\omega_{l\mu \pm} = \pm q_{l\mu} u_{l\mu}, \quad u_{l\mu} = \alpha_{l\mu} v = \omega_e a / \kappa_{l\mu}. \quad (4)$$

It follows from a zero boundary condition on \tilde{v}_e at the ion entrance, that $A_{l\mu+} = A_{l\mu-} = A_{l\mu}$. The amplitudes $A_{l\mu}$ have to

be found from the zero boundary condition imposed on the density perturbation \tilde{n}_e .

III. Longitudinal Impedance

In this section longitudinal perturbations are considered, $l = 0$. Making use of the orthogonality properties of the Bessel functions, the amplitudes of excited modes can be found:

$$A_\mu = 2\tilde{\rho}_{i0}/(\kappa_\mu^2 F_\mu^2), \quad (5)$$

$\tilde{\rho}_{i0}$ is a linear density perturbation of the ion beam. An average of the electric field over a time τ of the flight through the cooler

$$\langle E_z \rangle = -\frac{1}{\tau} \int_0^\tau \frac{\partial \Phi}{\partial z} \Big|_{z=0} dt \quad (6)$$

gives cooler's longitudinal impedance Z^\parallel [1]:

$$\langle E_z \rangle \tau = -e\tilde{\rho}_{i0} Z^\parallel \quad (7)$$

Real parts of impedances responsible for instabilities are of the main interest:

$$\text{Re} Z^\parallel = 2 \sum_\mu \frac{(1 - \cos(\omega_{\mu+}\tau) - (1 - \cos(\omega_{\mu-}\tau))}{\kappa_\mu^2 F_\mu^2 u_\mu}. \quad (8)$$

The contributions in the real part of the impedance (8) from the positive (+) and negative (−) waves can be seen to have opposite signs: an emission of the positive wave takes away a longitudinal momentum of ions, i. e. decelerates them; on the contrary, radiation of the negative wave with a negative momentum accelerates the ion beam. The phase advances of the positive and negative waves $\omega_{\mu\pm}\tau$ normally can be rather close: $(\omega_{\mu-} - \omega_{\mu+})\tau/2 \ll 1$. In this case the (+) and (−) contributions in the impedance almost cancel each other, the series over radial modes (8) converges as $1/\mu^2$, which gives:

$$\text{Re} Z^\parallel = -4\omega\tau \frac{\sin(\omega\tau)}{\kappa^2 F^2 v} = -\frac{Z_0\omega\tau}{\pi\beta\kappa^2 F^2} \sin(\omega\tau), \quad (9)$$

where the counter $\mu = 1$ is omitted, $Z_0 = 4\pi/c = 377\Omega$, $\beta = v/c$ and $\omega = \omega_e ka/\kappa$ is the frequency of the first radial mode. The impedance (Eq.9) linearly increases with the longitudinal wave number k up to $k \simeq 1/a$.

In the short wave band ($ka > 1$), the part of the electron beam with the transverse size $\simeq 1/k$ only effectively interacts with ions. It follows, that the impedance achieves the maximum at $ka \simeq 1$, the later can be estimated from (Eq.9) with $\kappa = 2.4$, $F = 0.5$:

$$|\text{Re} Z^\parallel|_{\max} \simeq 0.1 Z_0 \frac{\omega_e \tau}{\beta}, \quad (10)$$

where $\omega\tau \gg 1$ was assumed.

Substituting, for example, $n_e = 3 \cdot 10^7 \text{ cm}^{-3}$, $g = 1\text{m}$, $\beta = v/c = 0.06$ (Li⁷⁺ in the CRYSTAL ring [13]), it gives the cooler impedance

$$\text{Re} Z^\parallel = 10\text{K}\Omega,$$

which is three orders of magnitude more than typical values of the resistive-wall impedance.

Velocities of the electron and ion beams are assumed to be zero in this calculations. It is warranted, if an additional difference between phase advances of the (+) and (−) modes introduced by a discrepancy of the velocities δv is smaller then this difference for equal velocities: $k\delta v < \alpha^2 kv$, or $\delta v/v < \alpha^2$.

The real part of the impedance is responsible for a coherent instability with an increment [12]:

$$\Lambda_k = \left| k u_i \text{Re} Z^\parallel / (2Z_{sc}) \right|, \quad Z_{sc} = iZ_0 L_i k R / \beta, \quad (11)$$

$$L_i = \ln(1/(ka_i)), \quad u_i = c\sqrt{2\tilde{\rho}_i r_0 (\gamma^{-2} - \gamma_t^{-2})},$$

where r_0 is a classical radius of the ion, R is a radius of the storage ring, a_i is a radius of the ion beam, $\tilde{\rho}_i$ is its linear density. The increment rate for the coasting Li beam with $2 \cdot 10^7$ particles, $L_i = 4$, $\text{Re} Z^\parallel = 10\text{K}\Omega$, is found to be: $\Lambda = 5\text{s}^{-1}$.

To damp the instability and to continue a cooling process, the cooling rate λ_\parallel needs to be twice more than the increment [4], [7], $\lambda_\parallel > 10\text{s}^{-1}$ in the last example.

IV. Transverse Impedance

An excitation of transverse dipole modes ($l = 1$) of the electron beam and their back action on ions can be described in terms of a transverse impedance Z^\perp [2]:

$$\langle E_x \rangle \tau = -\frac{1}{\tau} \int_0^\tau \frac{\partial \Phi}{\partial x} \Big|_{x=0} dt = i e \tilde{\rho}_i x_i Z^\perp, \quad (12)$$

where $\tilde{\rho}_i$ is a linear density of the ion beam, x_i is an amplitude of its deviation along the x -direction. The potential Φ is given by Eq.(2) with $l = 1$. The wave amplitudes A_μ are found from the zero boundary conditions on \tilde{v}_e, \tilde{n}_e at the entrance, which give: $A_\mu = -2\tilde{\rho}_i x_i / (\kappa_\mu a F_\mu^2)$ Asymptotically, at $\kappa_\mu \gg 1$, $F_\mu = (\pi\kappa_\mu/2)^{-1/2}$ and A_μ tends to be a constant: $A_\mu \simeq A = -\pi\tilde{\rho}_i x_i / a$. From here, the real part of the transverse impedance is found:

$$\text{Re} Z^\perp = -\frac{Z_0}{4\beta a} \sum_\mu \frac{\kappa_\mu v}{a} \int_0^\tau dt \{ \sin(\omega_{\mu-}t) - \sin(\omega_{\mu+}t) \}. \quad (13)$$

This series is diverging. It means a large number of the contributing modes and approves an application of the asymptotic $\mu \gg 1$.

An upper limit of the summation $\mu_{\max} = m$ is determined by an account of a finite transverse size of the ion beam a_i , it gives $m \simeq a/a_i$. If the difference of \pm phase advances at $\mu \simeq m$ is small, $(\psi_- - \psi_+)/2 = (\omega_- \tau - \omega_+ \tau)/2 < 1$, the expression (13) can be simplified:

$$\text{Re} Z^\perp = -\frac{Z_0 \omega_e \tau}{4\beta a} S, \quad S = \sum_{\mu=1}^m \begin{cases} \sin(\omega_\mu \tau) & \text{if } \omega_\mu \tau \gg 1 \\ \omega_\mu \tau / 2 & \text{if } \omega_\mu \tau \leq 1 \end{cases} \quad (14)$$

The result of the summation depends on the phase advance ψ and its difference between neighbor modes $\Delta\psi$ at the upper limit of the summation $m \simeq a/a_i$:

$$|S| \simeq \begin{cases} \sqrt{\frac{m}{2}}, & \text{if } m < m_r \\ \sqrt{\frac{m_r}{2}} + \frac{m^2}{m_r^2}, & \text{if } m_r < m < m_r^2 \\ \sqrt{\frac{m_r}{2}} + m_r^2 + \frac{m_r^2}{2} \ln\left(\frac{m}{m_r^2}\right) & \text{if } m > m_r^2 > 1 \\ \frac{m_r^2}{2} \ln m & \text{if } m_r^2 < 1 \end{cases}$$

$$m \simeq a/a_i, \quad m_r \simeq \sqrt{\omega_e \tau k a / \pi}. \quad (15)$$

Turning back to Eq.(14) and assuming, for instance, the electron density $\bar{n}_e = 3 \cdot 10^7 \text{ cm}^{-3}$, the cooler length $g = 1 \text{ m}$, the velocity $v = 2 \cdot 10^9 \text{ cm/s}$, the electron beam radius $a = 1 \text{ cm}$, taking the sum factor $S = 10$, the transverse impedance is found:

$$|\text{Re}Z^\perp| \simeq 30 \text{ M}\Omega/\text{m}. \quad (16)$$

Generally, a real part of an impedance is responsible for an instability, an increment for the coasting beam is [2]:

$$\Lambda^\perp = \frac{\bar{\rho}_i r_0 c}{\gamma Q_b} \frac{|\text{Re}Z^\perp|}{Z_0}, \quad (17)$$

where Q_b is a betatron tune, r_0 is the classical radius of an ion of the beam.

Taking as an example the mentioned Li^{+1} beam, $Q_b \simeq 2$, assuming the transverse impedance of $\text{Re}Z^\perp = 30 \text{ M}\Omega/\text{m}$, the increment is calculated: $\Lambda^\perp = 3 \text{ s}^{-1}$.

To suppress the instability at low temperatures, where the Landau damping does not exist, a transverse cooling rate of the electron cooler λ_c^\perp has to be twice higher than the increment [4]: $\lambda_c^\perp/2 > \Lambda^\perp$, for an example above $\lambda_c^\perp > 6 \text{ s}^{-1}$ has to be achieved.

V. Conclusions

Longitudinal and transverse impedances introduced in a storage ring by the electron beam of an electron cooler have been found here; both of them occurs to be orders of magnitude higher than resistive-wall ones. The corresponding values of coherent increments can be comparable with the cooling decrements even for such small ion currents, which are usually suggested for crystallization.

VI. Acknowledgments

The report has been done in the framework of the CRYSTAL project. The author is thankful to N. S. Dikansky, V. V. Parkhomchuk, L. Tecchio, G. Bisoffi, M. Grieser, G. Lamanna and S. Gustafsson for discussions and information.

References

- [1] A. Sessler and V. Vaccaro, CERN Report ISR-RF/67-2 (1967)

- [2] A. W. Chao, *Physics of Collective Beam Instabilities in High Energy Accelerators*, J. Wiley & Sons, Inc., New York, 1993.
 [3] A. V. Burov, *Wall Impedance for Low and Moderate Beam Energies*, CSR Note, Dec. 1994.
 [4] N. S. Dikansky, D. V. Pestrikov, *The Physics of Intense Beams and Storage Rings*, AIP Press, New York, 1994.
 [5] V. V. Parkhomchuk, private communication, 1992.
 [6] V. V. Parkhomchuk, D. V. Pestrikov, in *Proc. of the Workshop on Beam Cooling and Related Topics*, p. 327, Montreux, 1993.
 [7] A. V. Burov, in *Proc. of the Workshop on Beam Cooling and Related Topics*, p. 230, Montreux, 1993.
 [8] G. I. Budker et al. In *Proc. of 10 Int. Conf. on High Energy Accel.*, v. 1, p. 498, Serpukhov, 1977.
 [9] M. Grieser, private communication.
 [10] D. Reistad, private communication.
 [11] L. S. Bogdankevich, A. A. Rukhadze, *Sov. Uspekhi Phys. Nauk*, **103**, 4, p. 609 (1971).
 [12] P. L. Morton, V. K. Neil and A. M. Sessler, *J. Appl. Phys.* **37**, 3875 (1966).
 [13] L. Tecchio, G. Bisoffi et al., *CRYSTAL. A Storage Ring for Crystalline Beams. Feasibility Study*. LNL-INFN Int. Rep., 1994.

WALL IMPEDANCES FOR LOW AND MODERATE ENERGIES

A. Burov, Budker INP, 630090, Novosibirsk, Russia

Abstract

Properties of the wall impedance of a storage ring are studied for a low relativism, $\gamma - 1 \leq 1$. Both broad and narrow band impedances are shown to be damped at low energies, the damping factors are found. Coherent motion of a coasting beam is discussed; Landau decrements are calculated.

I. INTRODUCTION

The impedance of a vacuum chamber [1] depends on a beam velocity. This dependence vanishes in an ultrarelativistic limit, where all the fields excited by a point charge lag behind it, which is referred to as the causality principle for wake fields, see e. g. [2]. This causality principle does not work for low and moderate energies, where the relativistic factor $\gamma \simeq 1$: the Coulomb field is not here a δ -function of a longitudinal coordinate, but smoothly increase and decrease during the time $\tau \simeq r/\gamma v$, where r is an impact parameter. It follows that a broad band wall impedance $Z(\omega)$ is exponentially depressed at frequencies $\omega \geq \gamma v/b$, where b is an aperture radius. A pure space charge impedance is the only remaining at these frequencies, but it does not lead to instabilities of itself. A narrow band impedance is shown to be depressed to a lesser extent, then the broad band one, due to a rather sharp boundary of the eigenfield at the entrance, $\Delta z = b/2.4$.

A coherent motion of coasting beam is discussed; the Landau damping of both longitudinal and transverse oscillations is lost when a space charge of the beam separates coherent and incoherent frequencies [6], [9], [10]. Longitudinal and transverse Landau decrements are asymptotically calculated here for a thermal equilibrium.

II. IMPEDANCE DAMPING FACTORS

A. Wall Resistivity

Assuming the field dependence on the longitudinal coordinate and time as $e^{ik(z-vt)}$, Maxwell's equations reduce to the Poisson equation for a longitudinal electric field E_z excited by a charge linear density perturbation. Applying Leontovich boundary condition at the resistive wall surface, [3], $E_z(b) = \sqrt{-ikv/(4\pi\sigma)} B_\theta$, the electric field E_z in a perfectly conducting tube and its perturbation \tilde{E}_z due to a finite walls conductivity σ [4] can be found.

The fields E_z , \tilde{E}_z and the current perturbation J are connected by corresponding impedances, $E_z C = -Z^{\parallel} J$, $\tilde{E}_z C = -\tilde{Z}^{\parallel} J$, where C is the ring circumference, which gives:

$$\frac{Z^{\parallel}(kv)}{C} = \frac{2ikL}{\gamma^2 v}; \quad \frac{\tilde{Z}^{\parallel}(kv)}{C} = \frac{1 - ik/|k|}{2\pi b \delta \sigma} f(\kappa) \quad (1)$$

where $\delta = c/\sqrt{2\pi\sigma kv}$ is the skin depth, $L = \ln(r_{max}/a) + 1/2$ is the logarithmic factor with $r_{max} = \min(b, 1/k)$, a is

the beam radius. Here a high frequency damping factor $f(\kappa)$ has been introduced:

$$f(\kappa) = \kappa \frac{K_1(\kappa)I_0(\kappa) - K_0(\kappa)I_1(\kappa)}{I_0^2(\kappa)} = \begin{cases} 1, & \text{if } \kappa \ll 1 \\ \pi e^{-2\kappa}, & \text{if } \kappa \gg 1 \end{cases} \quad (2)$$

$K_m(\kappa)$, $I_m(\kappa)$ are modified Bessel functions.

The transverse resistive-wall impedance \tilde{Z}^{\perp} is found by the similar way; for any relativism $\tilde{Z}^{\perp} = 2\tilde{Z}^{\parallel}/(kb^2)$.

The real part of $\tilde{Z}^{\parallel}(\kappa)$ achieves its maximum at the dimensionless wavenumber $\kappa = 0.43$,

$$\text{Re}\tilde{Z}_{\max}^{\parallel} = 0.24Z_0(R/b)\sqrt{\gamma v/(2\pi\sigma b)},$$

$Z_0 = 4\pi/c = 377\Omega$. Assuming $\beta = 0.4$, $\sigma = 1.3 \cdot 10^{16} \text{ s}^{-1}$, $R = 10 \text{ m}$, $b = 5 \text{ cm}$, it gives $\text{Re}\tilde{Z}_{\max}^{\parallel} = 3\Omega$.

B. Broad Band Impedances

The resistive wall impedance \tilde{Z}^{\parallel} (Eq.1) can be represented in terms of its ultra relativistic value $\tilde{Z}_{ur}^{\parallel}$ and the damping factor $f(\kappa)$ (Eq.2):

$$\tilde{Z}^{\parallel}(\omega) = \tilde{Z}_{ur}^{\parallel} f(\kappa), \quad \kappa = \omega b/(\gamma v). \quad (3)$$

The factor $f(\kappa)$ reflects the strong decrease of the incident field energy flux at the distance $r = b$ as $\sim \exp(-2kb/\gamma)$. The incident field of the beam, damped near the walls as $f^{1/2} \sim \exp(-kb/\gamma)$, produces proportionally to itself a perturbation of the surface current density. The energy loss which is a product of the field \tilde{E}_z and the current induced, is damped quadratically, as $f^{1/2} \cdot f^{1/2} = f \simeq \pi \exp(-2kb/\gamma)$. The energy loss is proportional to the real part of the impedance, so the last one is damped in the same way.

Thus, Eq.(3) follows from the symple physical consideration, which is the same for all the types of the wall imperfections. The only importance is that field perturbations introduced by these imperfections are small, which practically can be applied to all broad band wall impedances.

The real part of the broad band impedance has non-zero value only above the low frequency cut-off: $\omega \geq \omega_c$. For the circular cross-section of the vacuum chamber $\omega_c = 2.4c/b$. Taking into account that $\omega = kv$, the damping factor f near the lowest possible frequency (cut-off) occurs to be:

$$f \simeq \pi \exp(-4.8/(\gamma\beta))$$

So, the broad band impedance of wall imperfections (discontinuities, shallow cavities, irises, etc.) cannot play any role for insufficiently relativistic particles. Even for $\beta = 0.4$, the damping factor $f = 2 \cdot 10^{-5}$, which makes the broad band impedance completely negligible.

For a transverse broad band impedance, \tilde{Z}^{\perp} the low energy suppression is actual even to the greater extent. The cut-off frequency for unsymmetrical modes of the vacuum pipe ω_c^{\perp} is significantly higher, than for symmetrical ones, $\omega_c^{\perp} = 3.8c/b$ for

the circular pipe, which gives the following transverse broad band damping factor:

$$\tilde{Z}^\perp(\omega) = \tilde{Z}_{ur}^\perp(\omega) f_\perp(\kappa), \quad f_\perp(\kappa) \simeq \exp(-7.6/(\gamma\beta)). \quad (4)$$

C. Narrow Band Impedances

Another possibility for energy loss and for instabilities is connected with the radiation in low frequency ($\omega < \omega_c$) modes of some elements of the vacuum chamber. At the resonance, the impedance is pure real, it achieves here its maximum, the shunt impedance $R_s(v)$. The velocity dependence of the shunt impedance is determined by a transite time factor $T(v)$ (see, e. g. [5]):

$$R_s(v) = R_s(c) \left| \frac{T(v)}{T(c)} \right|^2, \quad T(v) = \int_{-\infty}^{\infty} E(z) e^{-i\omega z/v} dz, \quad (5)$$

where $E(z)$ is an arbitrary normalized eigenfield distribution. It follows the estimation:

$$\frac{R_s(v)}{R_s(c)} = [\beta \sin(\omega g/(2v)) / \sin(\omega g/(2c))]^2 \left\{ \frac{\delta\psi}{\sinh(\delta\psi)} \right\}^2,$$

where $\psi = \omega g/v$, g is a gap length, $\delta\psi = \pi\omega\Delta z/v$, longitudinal variation of the eigenfield in the gap assumed to be $\ll \omega/v$. The $\{\dots\}$ -factor reflects an influence of a width of the field boundary $\Delta z = b/2.4$ at the entrance and exit of the narrow band element.

III. COHERENT STABILITY

A. Longitudinal Oscillations

The dispersion relation can be found from the kinetic equation, which is the Vlasov equation plus cooling-diffusion Fokker-Planck term [6]. In the reference frame:

$$\frac{\partial f}{\partial t} + w \frac{\partial f}{\partial z} + \frac{Z_i e}{M_{||}} E \frac{\partial f_0}{\partial w} = \frac{\partial}{\partial w} \left(\lambda_{||} w f + d_{||} \frac{\partial f}{\partial w} \right), \quad (6)$$

where f_0 is the beam phase density, f is its perturbation, w is a deviation of the particle velocity from the beam velocity v , $M_{||} = M_i(1/\gamma^2 - 1/\gamma_t^2)^{-1}$ is a longitudinal mass of an ion of the beam, $M_i = A_i M_p$ is its mass, A_i and Z_i are the mass and charge numbers, $\lambda_{||}$ is the cooling rate and $d_{||}$ is the diffusion coefficient. Assuming the oscillations to be mainly determined by the space charge impedance $Z^{||}$, the corrections introduced by the cooling, temperature (Landau damping) and the impedance $\tilde{Z}^{||}$ can be found as perturbations. It gives the following dispersion relation for longitudinal coherent modes in a coasting beam [7]:

$$\Omega(k) = \pm k u_{||} \left\{ 1 + \frac{\pi i}{2} \frac{k}{|k|} u_{||}^2 f_0'(\Omega/k) - i \frac{\tilde{Z}^{||}}{2|Z^{||}|} \right\} - i \frac{\lambda_{||}}{2},$$

$$u_{||} = c \sqrt{2\bar{\rho} r_0 L (\gamma^{-2} - \gamma_t^{-2})}, \quad r_0 = Z_i^2 e^2 / (M_i c^2), \quad (7)$$

where $\bar{\rho} = N/C$ is a linear density of the beam.

According to Eq.(7), instabilities caused by the real part of the impedance $\text{Re}\tilde{Z}^{||}$ can be avoided due to the Landau damping or due to cooling. In the first case longitudinal temperature of the beam must be sufficiently high. Assuming the distribution function to be Gaussian, $f_0(u) = (2\pi\Delta w^2)^{-1/2} \exp(-u^2/2\Delta w^2)$, the stability condition can be expressed as:

$$\frac{u_{||}^2}{\Delta w^2} \leq 2 \ln \left(\sqrt{\frac{\pi}{2}} \frac{u_{||}^3}{\Delta w^3} \frac{|Z^{||}|}{\text{Re}\tilde{Z}^{||}} \right) \quad (8)$$

The factor $|Z^{||}|/\text{Re}\tilde{Z}^{||}$ is usually pretty large. Therefore the stability condition (8) is almost independent on the impedance. In terms of a temperature it can be expressed as:

$$T^{||} \geq T_{th}^{||}(K) = 0.02 \frac{I(\mu A) Z_i L}{\beta(1 - \gamma^2/\gamma_t^2)} f_Z \quad (9)$$

where the factor $f_Z \approx 1$ reflects the weak logarithmic dependence on the impedance. For instance, longitudinal oscillations in a $1 \mu A$ beam of Li_7^{+1} [8] with $\beta = 0.06$, $L = 4$, will be Landau-damped if its longitudinal temperature $T^{||} \geq T_{th}^{||} = 1.6$ K. For 1 mA beam of C_{12}^{+6} at TSR with $\beta = 0.041$ the threshold temperature calculated from (9) with $L = 5$, $f_Z = 1.5$ is: $T_{th}^{||} = 2 \cdot 10^4$ K, which is rather close to the experimental value of $T^{||} = 3 \cdot 10^4$ K.

This limit can be removed if the cooling rate is high enough:

$$\lambda_{||} > 2\Lambda_k = \frac{u_{||} \beta \text{Re}\tilde{Z}_k^{||}}{L R Z_0} \quad (10)$$

If this is satisfied for all the wavenumbers $k = n/R$, the oscillations are stable even without Landau damping. For a given $\lambda_{||}$ the restriction (10) can be treated as a safe condition imposed on the impedance $\tilde{Z}^{||}$. Assuming $\lambda_{||} = 10 \text{ s}^{-1}$, for the Li_7^{+1} beam it gives: $\text{Re}\tilde{Z}^{||} < 10 \text{ K}\Omega$.

B. Transverse Oscillations

Transverse oscillations of ions of a coasting beam can be described by the following equation:

$$\ddot{x} + \omega_b^2 x - \omega_{sc}^2 (x - \bar{x}) = (\bar{\rho} r_0 c^2 / \gamma) \int W_\perp(s-s') \bar{x}(s') ds' - \lambda_\perp \dot{x}, \quad (11)$$

where x, \bar{x} are transverse coordinates of an individual ion and a center of mass of the beam, $\dot{x} = dx/dt = (-i\Omega + in\omega_0\eta w/v)x$ is a transverse velocity of the ion, $\eta = \gamma^{-2} - \gamma_t^{-2}$, w is a deviation of a longitudinal velocity from its average value v , $\omega_b = \omega_{b0} + \xi\omega_0 w/v$ is a betatron frequency with a chromaticity accounted, $\bar{\rho}$ is a linear density of the beam, ω_{sc}^2 describes a space charge defocusing, $W_\perp(s)$ is a transverse wake function, λ_\perp is a transverse cooling rate. From here, a dispersion equation follows:

$$1 = \int \frac{dI dw f_{\perp 0}(I) f_{|| 0}(w) (\omega_{sc}^2(I) + \omega_c^2)}{(\Omega - n\eta\omega_0 \frac{w}{v} + i \frac{\lambda_\perp}{2})^2 - (\omega_{b0} + \omega_0 \xi \frac{w}{v})^2 + \omega_{sc}^2(I)}, \quad (12)$$

where $\omega_c^2 = 2i\bar{p}r_0c\omega_0\gamma^{-1}(Z^\perp/Z_0)$, I is a transverse action, $f_{\perp 0}(I)$, $f_{\parallel 0}(w)$ are unperturbed distribution functions, $\int dIdwf_{\perp 0}(I)f_{\parallel 0}(w) = 1$. For small Landau damping and cooling corrections, the equation (12) can be solved:

$$\Omega = -(\omega_{b0} + \Delta\Omega_c)n/|n| - i\lambda_\perp/2 - i\delta_\perp$$

$$\Delta\Omega_c = i\frac{\bar{p}r_0c}{\gamma Q_b} \frac{Z^\perp}{Z_0}, \quad Q_b = \frac{\omega_{b0}}{\omega_0}$$

$$\delta_\perp = \pi\Delta\omega_L \int dIdwf_{\perp 0}(I)f_{\parallel 0}(w)\Delta\omega_{sc}(I) \cdot \delta(\Delta\omega_{sc}(I) + \text{Re}\Delta\Omega_c - \xi\omega_0w/v + |n|\eta\omega_0w/v). \quad (13)$$

Here $\Delta\omega_{sc}(I) = \omega_{sc}^2(I)/(2\omega_{b0})$ is an incoherent space charge betatron shift for ions with the action I , $\Delta\omega_L = \Delta Q_L\omega_0 = \Delta\omega_{sc}(0)$ is the Laslett shift.

The Landau damping term δ_\perp is seen to be lost when the incoherent and coherent frequencies are separated more than a width of the distribution. Typically, at low relativism $\Delta\omega_L \gg \Delta\Omega_c$, which follows the stability threshold for the Laslett shift [9], [10]. Actually, the situation is similar to the longitudinal case, where the space charge separates velocities of particles and waves, also causing the threshold to be almost independent on the ring impedance (Eq.9).

The Landau decrement δ_\perp can be asymptotically calculated from Eq.(13) for a thermal equilibrium, with some longitudinal and transverse temperatures $T_\parallel = M\Delta w^2$, T_\perp :

$$\delta_\perp = \pi\sqrt{\frac{2}{3}}\Delta\omega_L p^{2/3} \exp(-3p^{2/3}), \quad p = \frac{\Delta Q_L}{|-\xi + |n|\eta|} \frac{v}{\Delta w}. \quad (14)$$

From here, the stability condition for the Landau suppression of the instability can be presented as:

$$\Delta Q_L \leq \Delta Q_{th} \approx 0.2|-\xi + |n|\eta|\frac{\Delta w}{v} \ln^{3/2} \left(\frac{5\Delta\omega_L}{\Lambda_n} \right), \quad (15)$$

where $\Lambda_n = \text{Im} \Delta\Omega_c$. The limit value for the Laslett tune shift is determined by the mode with the minimum longitudinal number n , which has the increment higher than cooling decrement: $\Lambda_n > \lambda_\perp/2$. Due to a large argument of the logarithm ($\sim 10^5 \div 10^7$), the result is almost insensitive on it; the logarithmic factor itself is a large constant: $\ln^{3/2}(\dots) \approx 50 \div 60$. Assuming the cooling rate to be smaller than long wave ($n \leq |\xi|$) increments, the threshold Laslett shift is found:

$$\Delta Q_{th} \approx 10|\xi|\Delta w/v. \quad (16)$$

Taking as an example typical for TSR at the threshold $\Delta w/v = 10^{-3}$ and $|\xi| = 5$, it gives $\Delta Q_{th} = 0.05$, which is close to the observed value [11]. The restriction on the Laslett tune shift (15) is removed for sufficiently low currents, with the cooling rate higher then coherent increments: $\lambda_\perp > 2\Lambda$. For the mentioned Li beam, with $\lambda_\perp = 1s^{-1}$, it gives the restriction for the impedance: $\text{Re}Z^\perp < 15M\Omega/m$.

IV. CONCLUSIONS

The concept of the storage ring impedance, developed mainly for ultrarelativistic beams cannot be at once applied to low and moderate energy cases. The reason is that the causality principle for wake fields generally is not valid here, which cause an exponential damping of impedances above a certain threshold. The approach suggested gives the possibility to find the wall impedance for an arbitrary energy if its ultrarelativistic value is known. At low energies, $\beta \leq 0.5 \div 0.8$ the broad-band wall impedance is exponentially damped and too weak to cause instabilities of a cooled beam. A narrow-band impedance could be dangerous if its eigenfrequency ω_r is rather low: $\omega_r b/v \leq 1$.

Space charge of a beam switches-off the Landau damping, above certain thresholds, for both longitudinal and transverse oscillations. For typical cooling rates, low current (μA) beams could be cooled below the thresholds.

V. ACKNOWLEDGMENTS

The report has been done in the framework of the CRYSTAL project. The author is particularly grateful to L. Tecchio, N. S. Dikansky, A. Aleksandrov, G. Bisoffi, S. Gustafsson, G. Lamanna, A. Lombardi and A. V. Novokhatski for discussions and information.

References

- [1] A. Sessler and V. Vaccaro, CERN Report ISR-RF/67-2 (1967).
- [2] A. W. Chao *Physics of Collective Beam Instabilities in High Energy Accelerators*, Wiley, N.- Y. 1993.
- [3] J. D. Jackson, *Classical Electrodynamics*, Wiley, N.- Y. and London, 1962.
- [4] P. L. Morton, V. K. Neil, and A. M. Sessler, J. Appl. Phys. **37**, 3875 (1966).
- [5] L. Palumbo, V. Vaccaro and M. Zobov *Wake Fields and Impedance*, LNF-INFN Report 94/041, 1994
- [6] N. S. Dikansky, D. V. Pestrikov. *The Physics of Intense Beams and Storage Rings*, AIP, N.- Y. 1994.
- [7] A. Burov, in *Proc. of the Workshop on Beam Cooling and Related Topics*, p.230, 1994.
- [8] L. Tecchio et al. *CRYSTAL. A Storage Ring for Crystalline Beams*. LNL-INFN Int. Rep., 1994.
- [9] L. J. Laslett, A. M. Sessler, D. Möhl, NIM, **121**, p. 517.
- [10] B. Zotter, F. Saherer, CERN Report 77-13, p.175, 1977
- [11] M. Grieser, in *Coll. of Transp. of Disc. on Cold Stored Ion Beams*, Heidelberg, July 7-8, 1994.
- [12] A. Burov, *Electron Cooler Impedances, these Proceedings*.

IMPEDANCE ANALYSIS OF THE PEP-II VACUUM CHAMBER*

C.-K. Ng and T. Weiland†

Stanford Linear Accelerator Center, Stanford University, Stanford, CA 94309

Abstract

The PEP-II high energy ring (HER) vacuum chamber consists of a copper tube with periodically spaced pumping slots. The impedance of the vacuum chamber due to the slots is analyzed. Both narrow-band and broad-band impedances are considered as well as longitudinal and transverse components thereof. It is found that although the broad-band impedance is tolerable, the narrow-band impedance may exceed the instability limit given by the natural damping with no feedback system on. Traveling wave modes in the chamber are the major source of this high value narrow-band impedance. We also study the dependences of the impedance on the slot length and the geometrical cross section.

I. ABOUT SMALL IMPEDANCES

In order to create a "feeling" about the magnitude of *small* impedances, we shall start with a general note of caution showing that even a tiny little cavity in a beam pipe can easily create $k\Omega$ of impedance. Thus one such small cavity by itself might be capable of driving the beam unstable. Let us consider for simplicity a circular symmetric beam pipe with a small pill-box cavity in it. Such a cavity (see Fig. 1) has one trapped mode [1] for each m , where m is the azimuthal mode number. We restrict our consideration to the TM_{010} mode here for simplicity and obtain by numerical analysis with MAFIA the trapped mode as shown in Fig. 2. The trapped mode parameters are listed in Table 1. It can be seen that a tiny cavity with only 3 mm dent at the outside of the beam pipe can exceed the tolerable impedance limit in a B-factory machine without feedback by a significant factor. A deeper dent of 10 mm over the length of 20 mm is even 12 times higher and becomes relevant even if there is a powerful feedback.

*Work supported by the Department of Energy, contract DE-AC03-76SF00515.

†Permanent address: University of Technology, FB18, Schlorgortenstr.8, D64289, Darmstadt, Germany.

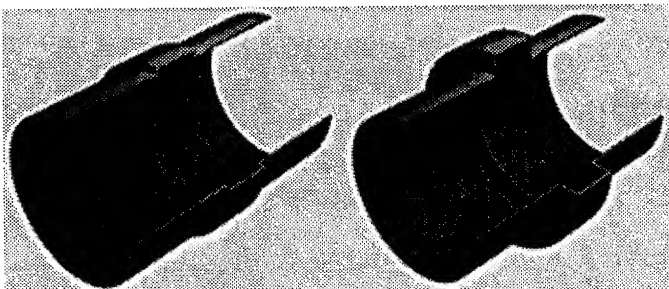


Figure 1. Three dimensional cutaway view of two very small cavities in a circular beam pipe. The cavity is 20 mm long. Their inner radius is 35 mm, and the outer radii are 38 mm and 45 mm for the two cases.

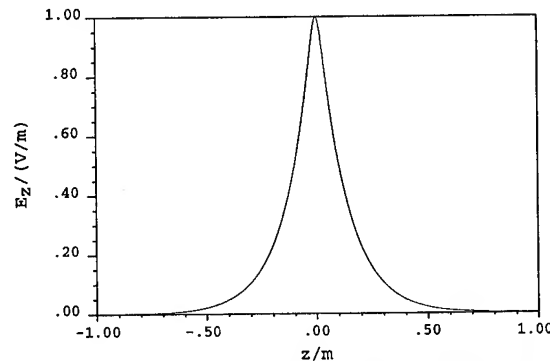


Figure 2. Longitudinal component of the electric field of the trapped mode TM_{010} in a small "cavity" ($r_{outer}=45$ mm) in a circular beam pipe. Note the exponential decay over a long distance at both sides.

Gap length (mm)	20	20
r_{inner} (mm)	35	35
r_{outer}	38	45
f_{res} (GHz)	3.258	3.062
R_s (k Ω)	7	88
Q	27000	20000
k_0 (V/pC)	0.003	0.042

Table 1: Small cavity trapped mode parameters.

II. VACUUM CHAMBER MODELS

Various models of the vacuum chamber have been analyzed for PEP-II. However, as the basic physical picture is the same for all the different models, only a generic one is considered here. Fig. 3 shows the three-dimensional view of a generic vacuum chamber with slots on one side. The dimensions have been chosen close to the PEP-II design[2], but may be considered as a generic chamber layout for electron/positron storage rings. Actually, the vacuum chamber of PEP, PETRA and HERA are almost identical in size. All results presented here are per vacuum chamber slotted section and not for the full length of the final chamber. Thus depending on the slot length one has to multiply the single section results with an appropriate factor. For PEP-II this factor is approximately $1000/L_{slot}$ (m).

III. LONGITUDINAL BROAD-BAND IMPEDANCE

The impedance in general depends on the slot length and it saturates when the length is about 1-2 times of its width [3]. The pumping requirements normally only are set by a total pumping channel cross section. Thus it is worthwhile to investigate the influence of the length of a slot in order to find an optimum slot length from the impedance point of view. The wakefield is found to be purely inductive in nature. From the low frequency

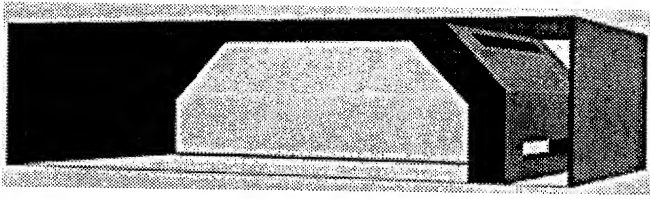


Figure 3. Three dimensional view of a generic vacuum chamber model with four pumping slots connecting the beam chamber with a side chamber. The side chamber houses vacuum pumps. For the purpose of impedance analysis the pumps are replaced by a conducting wall. The inner width is 9 cm, the inner height 5 cm, the slot width 3 mm, and the longitudinal slot spacing 1 cm. The only free parameter is the slot length L_{slot} and the number of slotted sections.

spectrum of the wakefield, the inductance is determined and its length dependence is shown in Fig. 4. The inductance converges very quickly to a saturated value of 4.0×10^{-5} nH. The loss parameter has similar variation behavior and its saturated value is 7.9×10^{-7} V/pC. This parameter is a good indication of the effective real part of the impedance weighted with the bunch spectrum. The real part of the impedance is obviously rather small compared to the imaginary part.

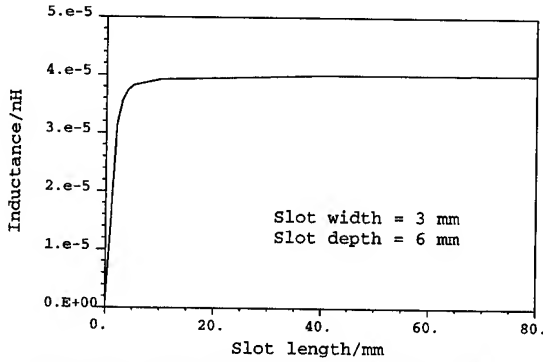


Figure 4. Inductance as a function of slot length.

IV. LONGITUDINAL NARROW-BAND IMPEDANCE

Narrow-band impedances are mostly locally confined resonant modes in cavities. A second type of resonant impedance is given by the waveguide character of a vacuum chamber. Basically being a periodic structure, it carries traveling waves with longitudinal and transverse modes just like any traveling wave accelerating structure. There are two possibilities to address this particular impedance, namely frequency and time domain approaches. Strong effects may be found by time domain simulations of a few sections, and weaker effects by modeling the chamber as a periodic structure in frequency domain.

(a) Section-to-section resonant effects

In order to identify strong section-to-section effects the wake potentials were computed for pieces consisting of 1,2,4 and 8 sections, with 4 slots per section (see Fig. 3). On the scale where the wake potential is inductive, no significant build-up of a resonant type of impedance has been observed. However, this does not mean that the resonant impedance is negligible but only that it is small compared to the inductive broad-band impedance.

Mode	$\phi / ^\circ$	f/GHz	$k/(\text{V/C})$	Q	$R_s/m\Omega$
1	163	3.27	1892	5000	1
2	143	3.63	383	35000	1
3	133	3.80	20170	15000	25
4	120	4.00	148000	27000	318
5	120	4.00	3129	8000	2
6	97	4.37	8129	10000	6
7	75	4.74	23960	37000	60

Table 2. First seven synchronous modes and the associated impedances, quality factors, loss parameters and shunt impedances.

Very narrow impedances cannot be found this way but need to be analyzed by frequency domain approaches.

(b) Traveling Wave Analysis

As a single mechanical unit, a vacuum chamber is made from 100-200 sections, and an analysis based on infinitely repeating structure is adequate. Thus we can compute traveling waves for any given phase advance per cell. Such a computation results in a Brillouin diagram as one normally finds in linear accelerator designs where similarly long structures (100-200 cavity cells) are used in one unit.

For the vacuum chamber there exist two types of modes. One group shows almost "empty waveguide" mode patterns. A second group shows fields concentrated in the slot region with almost no field in the center of the vacuum chamber. Examples of these modes for 40 mm slot length are shown in Figs. 5 and 6. In Fig. 7, we show the Brillouin diagram for the structure. The loss parameters, quality factors and shunt impedances for the first seven synchronous waves are listed in Table 2. The mode shown in Fig. 6, a TM_{11} -like mode, has a strong beam coupling. Its impedance is comparable to the acceptable value.



Figure 5. The real part of the electric field of mode 2 with $f = 3.616$ GHz and phase advance 120° per section.

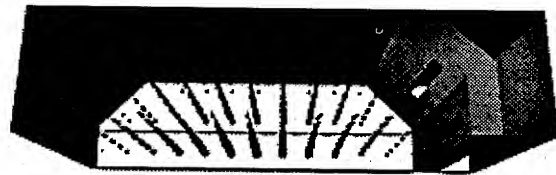


Figure 6. The real part of the electric field of mode 4 with $f = 3.996$ GHz and phase advance 120° per section.

V. TRANSVERSE BROAD-BAND IMPEDANCE

Since the vacuum chamber is symmetric with respect to the horizontal axis, the vertical forces vanish exactly when the particles pass the chamber on axis. In the horizontal plane the sit-

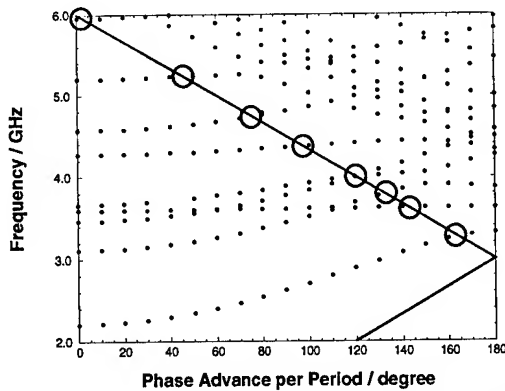


Figure 7. The Brillouin diagram for the vacuum chamber with a slot length of 40 mm and a period length of 50 mm. The line light is the solid straight curve. The synchronous modes are marked by circles.

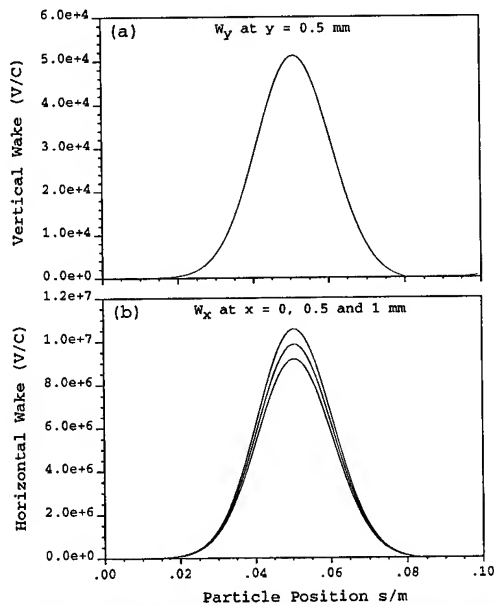


Figure 8. Transverse wake potentials as functions of s .

uation is more complex. As there is no right-left symmetry in the vacuum chamber, transverse wake forces act on the particles all the time, wherever they pass with respect to the center of the chamber. The impedance is split into a constant and x -dependent part. These portions can be obtained by computing the wake potentials at different horizontal beam positions. The difference of the wake potentials between off-axis and on-axis divided by the offset gives an impedance compatible with the standard theory for transverse impedances. The constant remaining part and the linearly rising part of the wake potentials have different effects on the beam dynamics. The vertical and horizontal components of the transverse wake potential are shown in Fig. 8.

The effects of the transverse wakes can be evaluated by the effective transverse kick parameter defined as $k_{\perp} = \int_{-\infty}^{\infty} \rho(s) w_{\perp}(s) ds / (\int_{-\infty}^{\infty} \rho(s) ds)^2$. The horizontal and transverse k_{\perp} are found to be 0.00087 and 0.00003 V/pC/m respectively. The horizontal k_{\perp} is higher because of the large non-varying part of the wake potential. For a typical single-cell 500 MHz cavity, $k_{\perp} \sim 3$ V/pC/m. Thus the transverse kicks of the vacuum chamber have very small effects on beam dynamics properties such as tune shift.

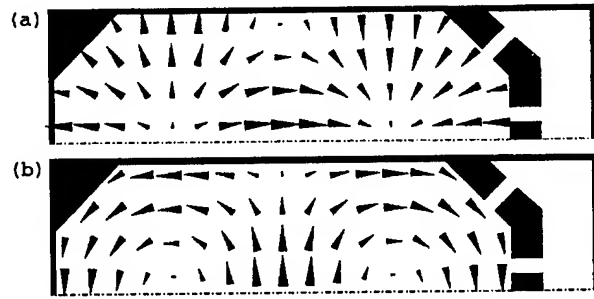


Figure 9. Real part of the (a) electric; (b) magnetic field of mode 7 ($f=4.737$ GHz) at the synchronous phase of 75° .

VI. TRANSVERSE NARROW-BAND IMPEDANCE

One of the first traveling wave modes mentioned in section IV is investigated here as an example, being likely a candidate for a strong transverse narrow-band impedance. The fields are shown in Fig. 9. The longitudinal loss parameter as a function of horizontal position is shown in Fig. 10. The transverse impedance of this mode is found to be $0.134 \text{ M}\Omega/\text{m}^2$, which should be compared with $340 \text{ M}\Omega/\text{m}^2$ of a typical single-cell 500 MHz cavity.

VII. DISCUSSIONS

The broad-band and narrow-band impedances can be further reduced by orders of magnitude by using hidden slots [4] embedded half-way in a continuous longitudinal groove. In fact, the PEP-II design has chosen this approach. Furthermore, the effects of transverse impedances on beam dynamics remain to be investigated.

Acknowledgements

We thank A. Chao, E. Daly, S. Heifets, G. Lambertson, M. Nordby and G. Stupakov for useful discussions.

References

- [1] T. Weiland, Single Mode Cavities - A Possibility for Fighting Collective Beam Instabilities, DESY Vol. 83(073), Sep 1983.
- [2] An Asymmetric B Factory, Conceptual Design Report, LBL-PUB-5379 or SLAC-418, June 1993.
- [3] K. L. F. Bane and C.-K. Ng, Impedance Calculations for the Improved SLC Damping Rings, Proc. 1993 PAC, p3432.
- [4] T. Weiland, Low Impedance Vacuum Chambers, PEP-II Technical Note No. 59, 1994.

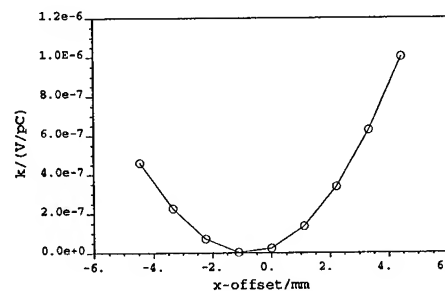


Figure 10. The longitudinal loss parameter as a function of horizontal position x . The functional dependence is nearly quadratic. Due to the mechanical asymmetry, the minimum of the wake is not at the center $x=0$, but is slightly shifted away from the slotted side of the vacuum chamber.

Microwave Instabilities in Electron Rings with Negative Momentum Compaction Factor

S. X. Fang, K. Oide, K. Yokoya, B. Chen*, J. Q. Wang
KEK, National Laboratory for High Energy Physics
Oho, Tsukuba, Ibaraki, 305 Japan

Abstract

Bunch lengthening (or shortening) caused by the potential well distortion and the microwave instability in electron rings with negative momentum compaction factor is discussed in detail based on the resonator impedance model; further, a comparison with rings of positive momentum compaction factor is given. It was found that the bunch shape is less deformed and the current threshold of the microwave instability is higher in the rings with negative momentum compaction factor over a very wide range of the impedance parameters. The results also show that even within the range where the threshold for positive momentum compaction is higher than that for negative momentum compaction, the bunch lengthening is still less serious in most cases. Finally, an example of bunch lengthening in the case that $\alpha < 0$ with a real wake field of the SLC damping ring (old vacuum chamber) is given in contrast to the case in which $\alpha > 0$.

Introduction

In most of the existing low energy electron-positron colliders, a positive momentum compaction factor ($\alpha > 0$) is usually adopted. Bunch lengthening in such machines is one of the most important factors which limit the luminosity performance and its upgrade. Using negative momentum compaction is one of the hopeful approaches[1] to shorten the bunch length.

The method and computer program developed by K. Oide and K. Yokoya[2] were used to study the longitudinal bunch behaviour. The potential well distortion (PWD) and the threshold of microwave instabilities with a resonator impedance model for both the $\alpha > 0$ and $\alpha < 0$ cases are discussed and compared in detail in the first and second sections. Finally, as an example, bunch lengthening in a ring with a real wake field of the SLC damping ring (old vacuum chamber) for $\alpha > 0$ and $\alpha < 0$ is demonstrated. Generally speaking, bunch lengthening is less serious in rings with $\alpha < 0$.

I. Potential well distortion

When the beam intensity is low enough, the bunch behaviour is determined by its own potential well field. The bunch shape is deformed and its length changed. A self-consistent solution of the bunch shape is found by applying numerical solution of the Haissinski equation[2][3]. Using the well-known dimensionless Keil-Schnell criterion parameter, $I_{k,s} = \frac{IR_s}{\eta\sigma_{E0}^2(\frac{E}{e})}$, where I is

the current intensity, R_s the shunt impedance of a broad-band resonator, and $\frac{E}{e}$ the nominal beam energy in unit of Volts, we

give the typical distribution of the particles in the bunch vs $I_{k,s}$ in the Figs. 1(a) and 1(b) for the resonator impedance model with $Q = 1$ and $K = 1$. Here Q is the quality factor, $K = \omega_r \frac{\sigma_{z0}}{c}$, ω_r is the resonator frequency, σ_{z0} is rms natural bunch length, c is the speed of light, respectively. One can see the cases $\alpha > 0$ and $\alpha < 0$ are quite different.

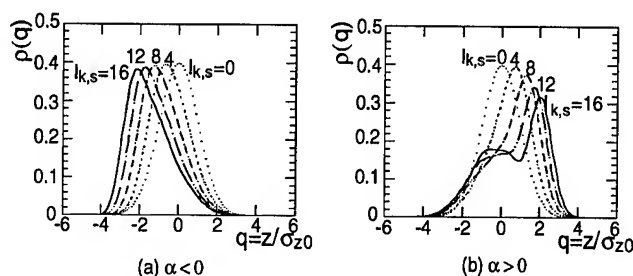


Figure 1. Bunch shape (density distribution within the bunch) for various intensities.
%vspace-2.5mm

1. As usual, the bunch leans forward to compensate for the energy loss by the RF voltage in the case $\alpha > 0$, and backward at $\alpha < 0$.
2. The bunch shape is seriously distorted for $\alpha > 0$; for high intensity, sometimes two peaks appear. However, it is less distorted for $\alpha < 0$.

The reason is obvious: in the case $\alpha > 0$, most particles move to the front part of the bunch; then, the wake field produced by them disturbs the tail part of the beam, and a large deformation occurs at the tail part at high intensity. However, in the case $\alpha < 0$, most particles move to the back of the bunch; since the wake field generated by these particles is mostly located outside of the beam, only a portion of the beam is disturbed. A calculation shows that the two peaks never appear in the $\alpha < 0$ case, and that the beam always remains in good order.

Figs. 2(a) and 2(b) give the bunch length variation vs the current. Bunch lengthening is very serious in the case that $\alpha > 0$; at high intensity¹, the lengthening factor is between 1.45 to 1.65. However, it is between 1.05 to 1.25 for $\alpha < 0$. A similar phenomenon occurs for different Q . This can be explained as follows.

For a long bunch ($K > 1$), in the case $\alpha > 0$, the spectrum of the bunch is mainly in the inductive part of the impedance, which causes the bunch to lengthen and moves the spectrum even further to the inductive part of the impedance. It is like a "positive feedback", which causes the bunch length to increase exponentially with the intensity. However, in the case $\alpha < 0$,

*Superconducting Super Collider Laboratory, Dallas.

¹For example, $I_{k,s} = 16$ corresponds to 40 mA for BEPC

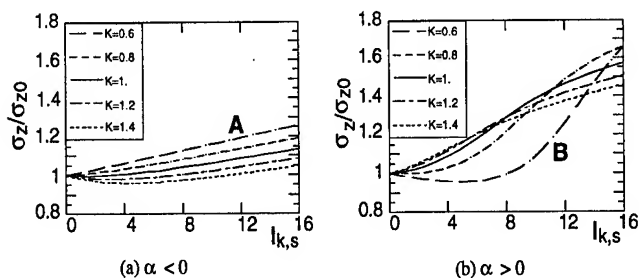


Figure 2. Bunch length vs current, $Q = 1$.

most of the spectrum of a long bunch is in the negative-inductive part of the impedance, which causes the bunch to shrink, thus forming a “negative feedback”. As a result, the bunch length increase is nearly linear and very slightly.

For a short bunch ($K < 1$), the situation is similar in the case $\alpha < 0$, in that most of the spectrum of the short bunch overlaps with the negative-capacitive part of the impedance, which causes bunch lengthening. The spectrum thus moves to the negative-inductive part of the impedance, which partly cancels the negative-capacitive part and a “negative feedback” mechanism is formed, so that the lengthening becomes weaker. This is why bunch lengthening of a short bunch is always mild, as shown in Fig. 2(a), curve “A”. However, it is quite different in the case $\alpha > 0$; it seems there should be a “positive feedback” mechanism to push the bunch length so as to become shorter. However, it is not true when the bunch is shortened to some extent; in this case the wake field generated by the head part of the bunch is so strong that it causes a serious deformation of its tail part. The bunch shortening is then stopped and lengthening starts. Once the bunch becomes lengthened, “positive feedback” plays an important role, and the bunch length increases even more significantly (curve “B” in Fig. 2(b)).

II. Microwave Instability

Above the current threshold of the microwave instability, the main results for the resonator impedance model with various parameters are described as follows:

1. In the case $\alpha < 0$, the mechanism of microwave instabilities is mainly due to radial mode coupling within a single azimuthal band; in the case $\alpha > 0$, however, besides the radial mode coupling belonging to same azimuthal band, instabilities are sometimes excited by the mixture of radial and azimuthal mode coupling. Qualitative analysis has been given in Ref. [4]. Here only the brief results are given in Figs. 3(a) and 3(b) for $Q = 1$ and $K = 1$.

One can see, the adjacent azimuthal modes remain separated until a very high current in the case $\alpha < 0$, whereas different modes merge even at a very low intensity in the case $\alpha > 0$. Usually the azimuthal mode coupling instabilities are stronger, the growth rate rapidly increases with the intensity. This is also shown in Figs. 3(a) and 3(b).

2. From a general point of view the threshold of microwave instabilities is higher over a rather wide range of K values for the case $\alpha < 0$. Even in the range where the threshold is lower than in the case $\alpha > 0$, in most cases bunch lengthening is still much

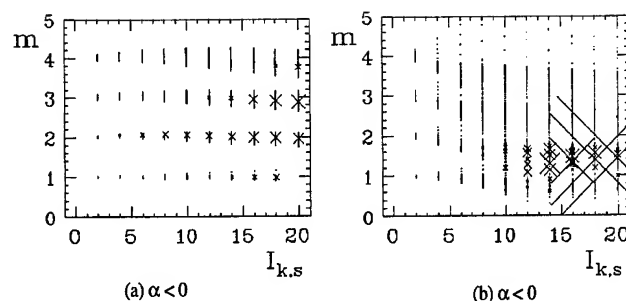


Figure 3. Adjacent azimuthal modes merge with the intensity and the magnitude of the growth rate (proportional to the size of the cross).

less serious than in the case $\alpha > 0$, if the machine is operated at the same intensity.

Comparisons of the current thresholds between both $\alpha > 0$ and $\alpha < 0$ cases are given in Fig. 4. In this comparison, the growth rate 5×10^{-3} (in units of ω_{s0}) is chosen as the threshold for all instabilities modes, and radiation damping is omitted. Similar characters have been obtained for different Q , so we take

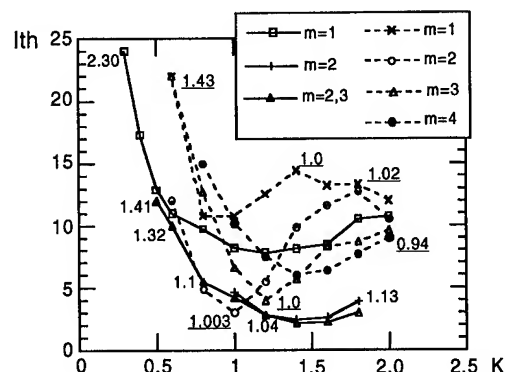


Figure 4. Current threshold vs K for different $Q = 0.6$ (Solid lines for $\alpha > 0$ and dashed lines for $\alpha < 0$).

the more typical one, $Q = 0.6$, as an example for a detailed description. From this picture, one can find three different regions: $K < 0.75$; $0.75 < K < 1.1$; $K > 1.1$.

1). $K > 1.1$. In this region the threshold of $\alpha < 0$ is higher than the threshold of $\alpha > 0$, and the system appears to be inductive (or negative inductive) for $\alpha > 0$ (or $\alpha < 0$).

In the case where $\alpha < 0$, since all of the azimuthal modes are fully separated, a total of four pure radial mode instabilities (each occurs in its own azimuthal band), appear in this region. All of these instabilities are not strong. The lowest threshold among the four instabilities is $I_{k,s} = 4$ at $K = 1.2$.

In the case where $\alpha > 0$, two pure radial mode and one azimuthal mode instabilities appear in this region. The azimuthal mode instability is the strongest; it occurs in the merging region of mode 2 and mode 3 when the intensity is high. Nevertheless, its threshold is not the lowest one. The lowest threshold which becomes the boundary in this region is determined by one of the

two pure radial modes which occur when azimuthal modes 1 and 2 are separated at low intensity. They finally both disappear at $K > 1.8$; mode 2 also disappears at $K < 1.0$. The corresponding threshold with different K is lower than that in the case $\alpha < 0$.

The bunch lengthening ($\frac{\sigma_z}{\sigma_{z0}}$) at the threshold is also shown in Fig. 4, the numbers attached to the marks with underline for $\alpha < 0$ and without that for $\alpha > 0$. Obviously, the bunch lengthening is much stronger in the case $\alpha > 0$.

2). $0.75 < K < 1.1$. The threshold of $\alpha < 0$ is lower than that of $\alpha > 0$; in this region the resistive character is dominant. In the case $\alpha < 0$, although the four pure radial mode instabilities still exist, the threshold of mode 2 decreases very rapidly with decreasing K , and arrives at its minimum at $K = 1$, giving the lowest threshold value. For $\alpha > 0$, only mode 1 still exists, and gives the boundary of the threshold.

The maximum difference in the threshold value between $\alpha < 0$ and $\alpha > 0$ is less than 50 % that at $K = 1$; the former is $I_{k,s} = 3$, and the latter is $I_{k,s} = 4.2$. If a machine with $\alpha > 0$ is operated at the same intensity as the threshold of $\alpha < 0$, i.e., $I_{k,s} = 3.0$, the bunch lengthening is 1.07, which is higher than 1.001 for $\alpha < 0$.

For increasing the threshold of $\alpha < 0$ in this region, the simplest way is to increase the energy spread of the beam; one can roughly estimate the bunch lengthening at the new higher threshold by the scaling. A calculation shows that it is effective in most cases; only about a 5~10% energy spread increment is needed. One can thus easily increase the threshold of the $\alpha < 0$ case to the same value as in the $\alpha > 0$ case. In the meantime, the bunch lengthening is still less than that in the case $\alpha > 0$.

3). $K < 0.75$. The threshold of $\alpha < 0$ is higher than that for $\alpha > 0$, and the capacitive character is dominant in this region. The lowest threshold boundary in the case that $\alpha < 0$ is determined by the pure radial mode 2 instability; in the case that $\alpha > 0$ it is determined mainly by the azimuthal mode instability, which is very strong, and the bunch shape is seriously deformed and two peaks appear.

It is surprising that the threshold is unbelievably high in this region. This may not be true for a realistic machine; first, a smaller K means a weaker wakefield, which may not be reasonable in practical cases. Second, because the real impedance cannot be correctly described sufficiently by the simple resonator impedance model, a small K means that the system appears to be more capacitive for a short natural bunch length; it may also not be true. It was pointed out in Ref. [5] that the wakefield of a realistic machine is always determined by many small discontinuities, and most of them are inductive. It is quite different from the resonator impedance. Thus, in practice, most realistic machine parameters are located at the right-hand side of the picture i.e., $K > 0.9$.

A real example is given here by using the wake field of the old vacuum chamber of the SLC damping ring[5]. Figs. 5(a) and 5(b) give the microwave thresholds for both cases; the result coincides with the analysis mentioned above.

Another very interesting phenomenon is that even above the threshold the bunch length behavior is very similar to that described by a pure potential well distortion; about half the bunch lengthening is contributed by PWD in most cases.

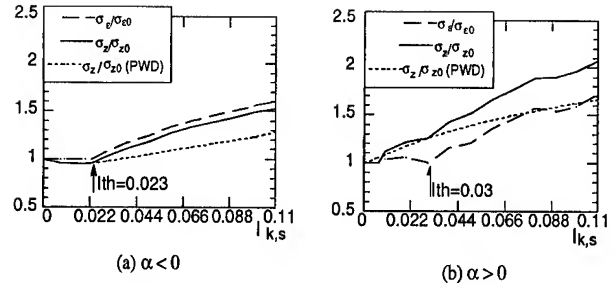


Figure 5. Threshold and bunch length behaviour for $\alpha < 0$ and $\alpha > 0$ with the wake field of the old vacuum chamber of SLC damping ring.

Conclusion

The longitudinal bunch shape is less deformed and bunch lengthening is less serious in electron rings with negative momentum compaction factor. A natural "negative feedback" mechanism can explain the above mentioned phenomenon. Even above the threshold the intrinsic shape of the potential well field plays an important role.

Acknowledgments

The author, Dr. Fang, would like to thank Dr. Alex. Chao, Dr. L. C. Teng, Dr. K. Y. Ng, Dr. T. Suzuki, Dr. Y. H. Chin, Dr. R. Baartman, Mr. M. D'yachkov for their discussions. Special thanks are given to Dr. K. L. Bane for his kindness to provide the old vacuum chamber wakefield of the SLC damping ring.

References

- [1] G. X. Li, "Design of BEPC Mini- β Schemes and Research to the Bunched Beam Longitudinal Instability with negative momentum compaction factor", Ph. D. Dissertation, IHEP, CAS, June 1993.
- [2] K. Oide and K. Yokoya, KEK-preprint 90-10 (1990); K. Oide, KEK preprint 94-138 (1994); K. Oide, in Nonlinear Dynamics and Particle Acceleration, AIP Conf. Proc. 230, P. 266 (1990).
- [3] B. Chen, "The Longitudinal Collective Instabilities of Non-linear Hamiltonian Systems in Circular Accelerators", Ph. D. Dissertation, Oct. 1994.
- [4] S.X. Fang, K. Oide, K. Yokoya et al, KEK Preprint 94-190, Feb. 1995.
- [5] K.L. Bane and K. Oide, Proceeding of the 1993 Particle Accelerator Conference, Washington D.C., 17-20 May 1993, (1993) p. 3339.

MICROWAVE STABILITY AT TRANSITION

J. A. Holt and P. L. Colestock
Fermi National Accelerator Laboratory*
P. O. Box 500, Batavia, IL 60510, USA

Abstract

The question of microwave stability at transition is revisited using a Vlasov approach retaining higher order terms in the particle dynamics near the transition energy. A dispersion relation is derived which can be solved numerically for the complex frequency in terms of the longitudinal impedance and other beam parameters. Stability near transition is examined and compared with simulation results.

I. INTRODUCTION

The question of microwave stability at transition has long been an issue for machines which must pass through transition energy. Due to the fact that the relative motion of particles at transition goes to zero, Landau damping is presumed to vanish. However, growth rates may also be sufficiently long to prevent significant mode growth. Recent theoretical studies have suggested that transition is absolutely stable against microwave modes owing to a particular cancellation of resonant contributions [1], although this analysis was based on a truncated model of the particle dynamics.

In this work we would like to reconsider microwave stability at transition including a necessarily higher-order expansion of the particle motion around the transition point. This is done in order to resolve the pole-cancellation issue referred to above. In particular, we find that while a portion of the distribution may indeed be stable near transition, those particles which exist slightly off transition in a distribution of finite momentum spread will always lead to instability. By retaining higher-order terms in the particle motion, we find an extension of the usual linear stability model for longitudinal modes which shows the appearance of a new unstable branch. The resulting dispersion relation is solved numerically for the stability boundary in the impedance plane.

As a confirmation of the analytical results, we have performed particle simulations in a coasting beam, consistent with the notion of short-wavelength modes associated with microwave instability. Using this approach, we find that regions of instability always occur above transition that can lead to longitudinal emittance blowup.

II. THEORY

The following dispersion relation can be derived from the Vlasov equation [1] which expresses the relation between the impedance and the coherent frequency of the collective mode.

$$1 = \left(\frac{e\omega_0}{2\pi}\right)^2 N Z_n \int_C d\epsilon \frac{\frac{\partial}{\partial \epsilon} \psi(\epsilon)}{i[n\omega(\epsilon) - \Omega_n]} \quad (1)$$

*Operated by the Universities Research Association, Inc., under contract with the U.S. Department of Energy

where N is the number of particles, n is the harmonic number, Z_n is the impedance associated with the n th harmonic, ψ is a normalized distribution function which is a solution to the Vlasov equation, ϵ is the energy deviation from the synchronous particle which is referred to by the subscript 0, and Ω_n is the coherent frequency. The integral contour is chosen so that Ω_n is continuous while crossing the real axis. The frequency $\omega(\epsilon)$ in terms of the dispersion coefficients is given by

$$\omega(\epsilon) = \omega_0 - \omega_0 \eta_0 \delta - \omega_0 \frac{\eta_1}{2} \delta^2 \quad (2)$$

where

$$\eta_0 = \alpha_0 - \frac{1}{\gamma_0^2}, \quad (3)$$

$$\frac{\eta_1}{2} = \alpha_0 - \alpha_1 - \eta_0 \alpha_0 \frac{3}{2} \frac{\beta_0^2}{\gamma_0^2} \quad (4)$$

and

$$\delta = \frac{\Delta p}{p} = \frac{1}{\beta^2} \frac{\epsilon}{E_0}. \quad (5)$$

The quantities α_0 and α_1 are the momentum compaction factors.

We have solved Eqn. 1 for Z_n/n assuming a Gaussian distribution

$$\psi(\epsilon) = \frac{1}{\sigma\sqrt{2\pi}} e^{-\frac{\epsilon^2}{2\sigma^2}}. \quad (6)$$

The integral can be reduced to evaluating the plasma dispersion integral which can be expressed in terms of the complex error function. The details are outlined in the appendix. The results are

$$\frac{Z_n}{n} = \left[\frac{-ie^2 \omega_0^2 N}{\sqrt{2}(2\pi)^2 \sigma^3} \frac{\beta^4 E_0^2}{\eta_1} \times \left(A \cdot Z\left(\frac{\epsilon_1}{\sqrt{2}\sigma}\right) + B \cdot Z\left(\frac{\epsilon_2}{\sqrt{2}\sigma}\right) \right) \right]^{-1} \quad (7)$$

The quantities A , B , ϵ_1 and ϵ_2 are defined in Eqns. 15-17.

III. CALCULATIONS

A. Stability Diagram

A program was written to plot the real part of Z_n/n vs. the imaginary part for Eqn. 7 for different values of the coherent frequency Ω_n and different places near transition. Figure 1 is a plot of the stability diagram below transition. The dots are for a real coherent frequency and the pluses are for a complex coherent frequency. The beam is stable.

Figure 2 is a plot of the stability diagram above transition. The dots are for a real coherent frequency and the pluses are for a complex coherent frequency. There are regions of instability.

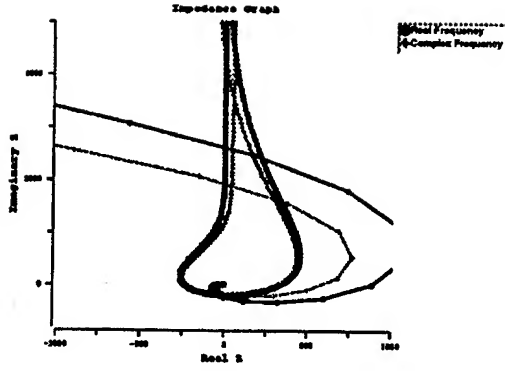


Figure 1. Stability diagram below transition. There are no regions of instability.

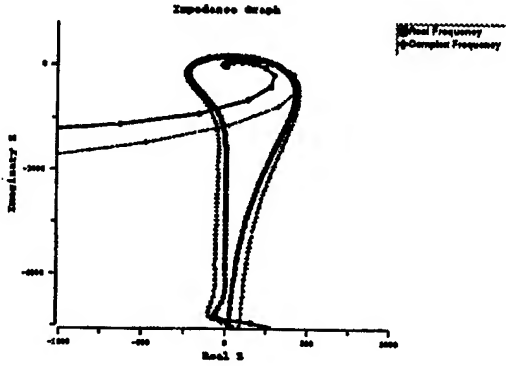


Figure 2. Stability diagram above transition.

B. Particle Simulation

Simulations of coherent phenomena in coasting beams were first reported in 1975 [2]. The essential physics is contained in the character of the incremental kicks given to the particle's position and energy per turn, relative to the central momentum particle. These may be expressed in the form

$$\delta\theta = -\eta(\epsilon)\epsilon \quad (8)$$

$$\delta\epsilon = \frac{e^2}{(2\pi)^2 E_0} \sum_n e^{in\theta} \int_{-\infty}^{\infty} Z_{||n}(\omega) e^{-i\omega t} d\omega \quad (9)$$

where $Z_{||}$ is the longitudinal impedance and is the Fourier transform of the wake function given by

$$Z_{||}(\omega) = \int_{-\infty}^{\infty} e^{\frac{is}{c}} W'_0(-s) ds \quad (10)$$

It is readily shown that Eqs. (8) and (9), in the case of small perturbations, lead to the linear dispersion relation for longitudinal modes. We note that η is a function of ϵ and may go to zero, which is the formal definition of transition. We keep both first and second-order corrections to η in our simulation to correspond to the analytical model described previously.

The time domain representation of the wake field is most convenient for computational purposes and this is given in the form [3]

$$V(\theta) = \frac{\omega_r R}{\omega_0 Q} \int_{\theta}^{2\pi+\theta} d\theta' I(\theta') e^{-\frac{\omega_r}{2Q\omega_0}\theta'} \times$$

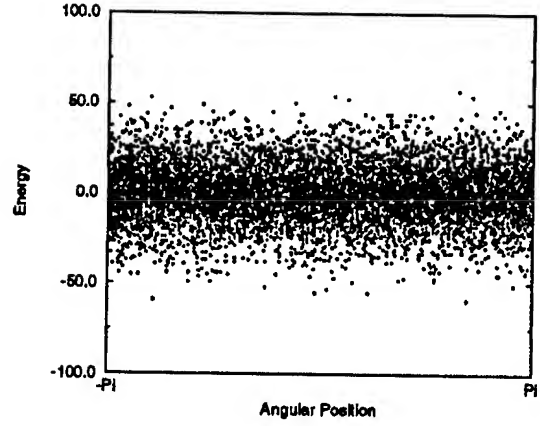


Figure 3. Particle simulation below transition. The distribution is stable.

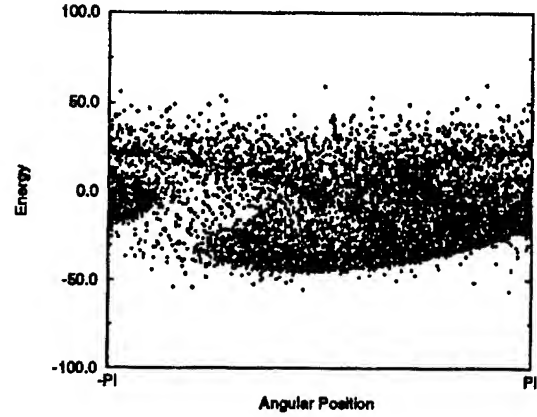


Figure 4. Particle simulation above transition. An instability has developed.

$$\left(\cos \frac{\tilde{\omega}_r}{\omega_0} \theta' - \frac{1}{2Q} \left[1 - \frac{1}{4Q^2} \right]^{-\frac{1}{2}} \sin \frac{\tilde{\omega}_r}{\omega_0} \theta' \right) \quad (11)$$

where

$$\tilde{\omega}_r = \omega_r \left(1 - \frac{1}{4Q^2} \right)^{\frac{1}{2}}, \quad (12)$$

$I(\theta)$ is the current distribution and ω_0 is the revolution frequency. The integration over angle is carried out at a fixed time each turn and may be extended into previous turns for long-range wakes (sufficiently high Q).

For the simulations in this work, we typically use $10^4 - 10^5$ particles and invoke periodic boundary conditions associated with the lowest revolution harmonic of interest. Figure 3 is a simulation of a beam before transition. The beam is stable confirming the results of Figure 1. Above transition, the simulation (Figure 4) shows that there is instability confirming the results of Figure 2.

IV. CONCLUSIONS

We have revisited the question of microwave stability at transition and have shown by including higher-order terms of the expansion of particle motion around the transition point that parti-

cles which are slightly off transition in a distribution of finite momentum spread will always lead to instability above transition.

V. Appendix

The integral in Eqn. 1 can be written with some factorization as

$$\int_C \epsilon e^{-\frac{\epsilon^2}{2\sigma^2}} d\epsilon \left[\epsilon^2 + \frac{\beta^2 E_0 \eta_0}{\eta_1} \epsilon - \frac{\beta^4 E_0}{\eta_1} \left(1 - \frac{\Omega_n}{n\omega_0} \right) \right]^{-1} \quad (13)$$

The integral can be broken up into pieces by the method of partial fractions and reduces to

$$A \cdot Z\left(\frac{\epsilon_1}{\sqrt{2}\sigma}\right) + B \cdot Z\left(\frac{\epsilon_2}{\sqrt{2}\sigma}\right) \quad (14)$$

where

$$A = \frac{\epsilon_1}{\epsilon_1 - \epsilon_2}, B = \frac{\epsilon_2}{\epsilon_1 - \epsilon_2}, \quad (15)$$

$$\epsilon_1 = -\frac{\beta^2 E_0 \eta_0}{2\eta_1} + \sqrt{\left(\frac{\beta^2 E_0 \eta_0}{2\eta_1}\right)^2 + 4\frac{\beta^4 E_0}{\eta_1} \left(1 - \frac{\Omega_n}{n\omega_0}\right)} \quad (16)$$

and

$$\epsilon_2 = -\frac{\beta^2 E_0 \eta_0}{2\eta_1} - \sqrt{\left(\frac{\beta^2 E_0 \eta_0}{2\eta_1}\right)^2 + 4\frac{\beta^4 E_0}{\eta_1} \left(1 - \frac{\Omega_n}{n\omega_0}\right)} \quad (17)$$

The function

$$Z(\xi) = \int_{-\infty}^{\infty} \frac{e^{-x^2}}{x - \xi} \quad (18)$$

is the plasma dispersion function which can be evaluated numerically in terms of the complex error function.

References

- [1] A. Bogaz, "Microwave Stability at Transition - Stability Diagram Approach", *1991 IEEE Particle Accelerator Conference*, p 1815, 1991.
- [2] E. Keil and E. Messerschmid, *Nucl. Inst. and Methods*, Vol 128, p203.
- [3] J. A. MacLachlan, FN-446, Fermilab (1987).

Experimental Observations of Nonlinear Coupling of Longitudinal Modes in Unbunched Beams

Linda Klamp Spentzouris, Patrick L. Colestock, Francois Ostiguy

*Fermi National Accelerator Laboratory, P.O. Box 500, MS 341, Batavia, IL 60510 **

Abstract

In an unbunched beam in a synchrotron, under conditions where the beam distribution is marginally stable, coherent fluctuations can cause a nonlinear coupling of longitudinal modes. Experimental observations of this parametric resonance have been reported previously.[1] Frequency domain measurements in the Fermilab Main Ring show pathological beam distributions associated with regions of marginal stability in longitudinal phase space; these are believed to be a requirement for the manifestation of the observed coupling. We have extended this investigation to the case of the beam response to an impulse excitation. The temporal development of the response indicates the formation of soliton-like structures within the beam distribution whose characteristics depend on beam conditions and the machine impedance.

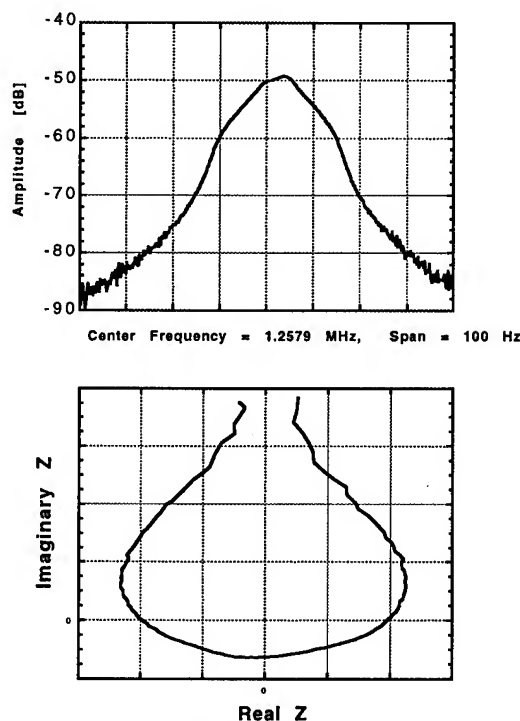
I. INTRODUCTION

A certain type of nonlinear resonance, known as a parametric resonance[2], is a process whereby energy present in oscillatory modes of a system can be transferred into another mode through frequency mixing, provided the difference frequency mode is also a normal mode of the system. In our case, these modes are the longitudinal modes of an unbunched coasting beam in a synchrotron, and the observation of this type of coupling in the Fermilab Tevatron has been documented.[1] The purpose here is to suggest conditions under which parametric coupling is likely to arise, and to present new time domain observations which provide further information concerning the phenomena. Besides clarifying the temporal sequence of energy transfer, these observations show an interesting non-linear self-bunching effect.[3] Aspects of this self-bunching are favorably compared to results from a particle tracking simulation which includes wakefields in the dynamics in order to provide a mechanism for the nonlinear resonance and self-bunching of the beam.

II. FREQUENCY DOMAIN MEASUREMENTS

Parametric coupling in the Tevatron and Main Ring was stimulated by applying an excitation to the beam at a single revolution harmonic. Once the initial oscillation was excited, it spontaneously transferred its energy into other revolution harmonics, and became damped as other modes grew. It was

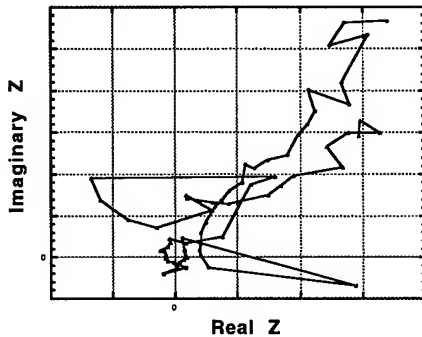
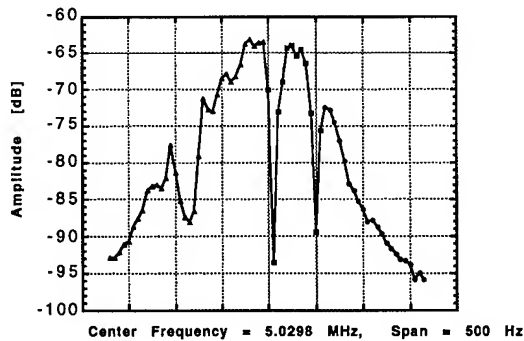
not possible to achieve parametric coupling in the Fermilab Accumulator using the same technique. The coupling coefficient for this specific kind of nonlinear coupling is dependent on the machine impedance at the frequencies of the excited modes, and is also extremely sensitive to the form of the beam distribution. Beam transfer function measurements were used to examine the beam distribution and to investigate the linear stability boundary. Results from a measurement in the Accumulator are shown in Figures 1a and 1b. These are, respectively, the magnitude response of the beam at $h=2$, and the corresponding stability boundary plotted in the complex impedance plane.



Figs. 1a and 1b Transfer function results from the Fermilab Accumulator, magnitude response and stability boundary

In contrast, the results of beam transfer function measurements in the Main Ring are shown in Figures 2a. and 2b. These are, respectively, the magnitude response of the beam at $h=106$, and an attempted construction of the linear stability boundary using the magnitude and phase information from the transfer function measurement.

* Operated by the Universities Research Association under contract with the U.S. Department of Energy.



Figs 2a and 2b Transfer function results from the Fermilab Main Ring, magnitude response and stability boundary

The magnitude response in Main Ring, unlike the Accumulator, shows deep notches in the beam distribution. These notches indicate that there are unstable regions in the phase space that would otherwise be occupied by the beam. Further investigation determined that the chromaticity and horizontal tune affected the position and depth of the notches, implying that certain momenta particles were unstable due to their mapping into tune space. The stability boundary in Figure 2b. displays large loops which correspond exactly to the notches in the beam distribution shown in Figure 2a.

III. TIME DOMAIN MEASUREMENTS

A series of measurements was performed in the Main Ring where an external voltage was applied at a single frequency for .5 ms, approximating an impulse excitation. The drive frequency was at $h=106$, since this is the center frequency of the broadband cavity ($Q \sim 42$) which was being used as the longitudinal kicker. The beam was not bunched, and the energy of the beam was constant at 8.9 GeV.

One result of these experiments was the demonstration that the parametric coupling was occurring in such a way that harmonics on the lower side of $h=106$ were excited sequentially. The initial impulse first caused the power in mode $h=106$ to grow, followed by modes $h=105$ to $h=93$ in sequential order. There was no significant excitation of harmonics at frequencies higher than $h=106$. This pattern of sequential excitation is shown in Figure 3, which is an overlay of six spectrum analyzer traces. Only the odd harmonics are shown for clarity.

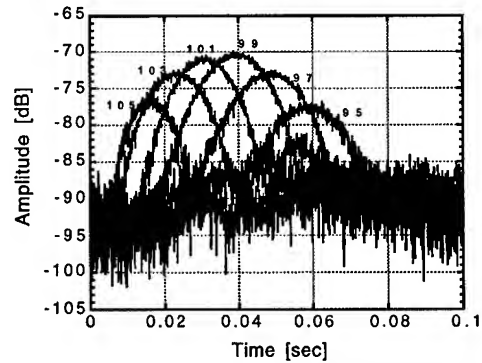


Fig 3 Power vs. Time for odd Main Ring harmonics 105-95. Growth of these harmonics occurs in sequential order.

For each trace the spectrum analyzer was set to monitor power at a particular harmonic as a function of time. This can be done by choosing the center frequency of the rotation harmonic as the center frequency of the sweep and setting the frequency span to zero. Since rotation harmonics in the Main Ring are 47 kHz apart, the resolution bandwidth was set to 30 kHz. The trigger occurred at the same time relative to the applied impulse, with the sweep time set to 100 ms. So, the relative timing shown by the overlaid traces is also the actual timing.

It is likely that the magnitude of the response at successive harmonics is in part due to the impedance of the 5 MHz cavity used to apply the initial kick. The resonant response of this cavity is shown in Figure 4. Nine harmonics away from the center frequency of the cavity the response is already 26 dB down.

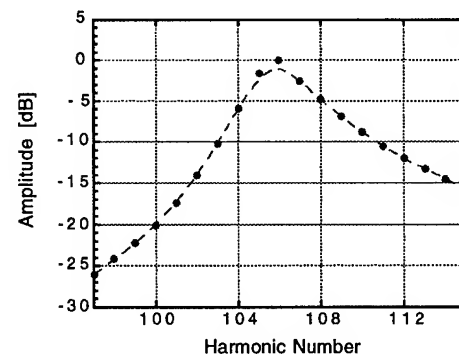


Fig. 4 Response of the Main Ring 5 MHz cavity

There are other interesting features of the beam response which are more evident upon examination of the power development at a single harmonic. The growth and decay of oscillation at $h=105$ is shown in Figure 5. The impulse excitation (at $h=106$) was applied at .0055 s with respect to the zero of the time axis, and lasted for .001 s. As energy is transferred from $h=106$, the coherent response at $h=105$ grows, but it does not continue to grow as there is a finite amount of energy available. The oscillation eventually decays due to power transfer to lower harmonics and dissipation. Note that there are several bounces in the signal level while it is losing power. This is a manifestation of a phase space rotation in which there is an exchange between the energy and phase coordinates of particles which have been bunched at $h=105$.

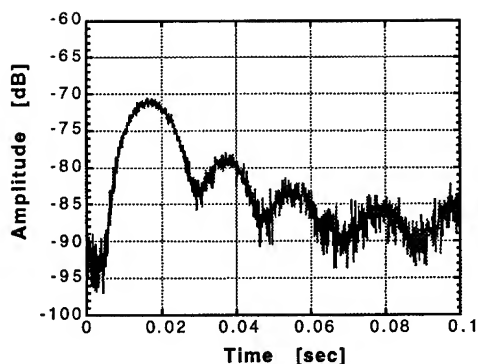


Fig. 5 Power vs. Time for mode $h=105$

The oscillation of the power level of a beam signal such as that shown in Figure 5 has been successfully reproduced with a particle tracking simulation. Besides generating output showing power level versus time for selected harmonics, the simulation also produces a phase space diagram which develops in time. An example of the phase space output is shown in Figure 6.

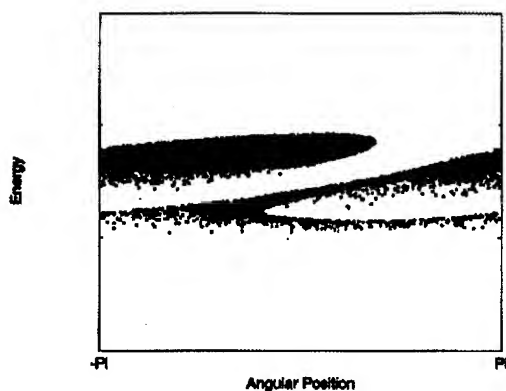


Fig. 6 Phase space output of particle tracking simulation

Inspection of Figure 6 reveals a tight clumping of particles on the higher energy side of the beam distribution. Guided by the simulation, a search for these high frequency bunchlets, and for this asymmetry in the phase space, was successfully undertaken. While much of the energy flow from the initial perturbation is governed by parametric coupling, if the initial pulse length is long enough, there is also significant higher harmonic generation. For example, with a 45 ms applied pulse, it was possible to see up to 40 higher harmonics of $h=105$; that is, $h=2 \times 105$, $h=3 \times 105$, up to $h=40 \times 105$. Examination of these higher harmonics on either side of the center frequency yielded the projected asymmetry and characteristic signature of bunch rotation. These results are shown in Figure 7.

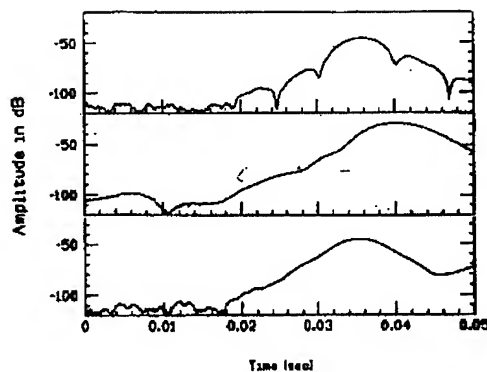


Fig. 7 From top to bottom respectively; the upper, middle, and lower portions of the frequency distribution of the beam at higher harmonic 5×105

The center trace of Figure 7 shows the time development of power at the center frequency of the 5×105 harmonic. For all three traces the spectrum analyzer had a narrow resolution bandwidth (300 Hz) for the purpose of monitoring only a fraction of the beam distribution. The upper and lower traces were taken in a manner similar to the center trace, except they were taken at the center frequency plus .5 kHz and at the center frequency minus .5 kHz, respectively. The power signal at the upper frequency has structure which indicates bunchlets of particles rotating in phase space. An exchange between energy and phase as a bunchlet rotates can cause this faster modulation of the current envelope.

IV. CONCLUSION

In machines with moderate impedances as well as regions of marginal stability in the phase space distribution of the beam, nonlinear effects may be observed. In particular, nonlinear frequency mixing otherwise known as parametric decay, higher harmonic generation, and self-bunching effects at high frequencies have been observed. Since these phenomenon are in part dependent on wakefields, perhaps these nonlinear effects may be used to quantify impedances.

V. ACKNOWLEDGEMENTS

The authors would like to thank Leo Michelotti, J. Holt, J. Beda, and A. Gerasimov for help with the simulations; and D. Wildman, G. Jackson and S. Assadi for their assistance with experimental techniques.

REFERENCES

- [1] Patrick L. Colestock and Linda Klamp, Proc. 1993 Particle Accelerator Conf., Vol. 5, p. 3384
- [2] Ron C. Davidson, "Methods in Nonlinear Plasma Theory", Academic Press, 1972
- [3] T. M. O'Neil, Phys. Fluids, 8, 12, (1965)
- [4] E. Keil and E. Messerschmid, Nucl. Inst. and Methods, Vol. 128, p. 203, (1975)

DAMPING RATE MEASUREMENTS IN THE SLC DAMPING RINGS*

C. Simopoulos, R.L. Holtzapple,
Stanford Linear Accelerator Center, Stanford University, Stanford, CA 94309 USA

Abstract

The transverse damping rates of the SLC electron and positron damping rings have been measured during the high current physics run at, $I = 3.5 \times 10^{10}$ particles per bunch. The measurements, done over a period of two months, show large fluctuations exceeding the statistical uncertainty of each measurement. The longitudinal damping rate of the positron damping was also measured.

I. DESCRIPTION OF THE OPTICS

The synchrotron light produced in a bend magnet is reflected by a water cooled molybdenum mirror which resides inside the vacuum chamber. The light exits the vacuum chamber through a synthetic fused silica window. Subsequently it is collected by an achromatic lens of focal length $f=1.33$ m which functions as the objective lens of the optical system. The objective is located 1.47 m away from the emission point. The light is transported outside the ring vault by a succession of mirrors and through an evacuated pipe which is terminated on both ends by two synthetic fused silica windows. Finally the light reaches the fast gated camera lens [1], which was used in the transverse damping times measurements, and the image of the beam is formed on the photocathode. In order to increase the field of view and prevent vignetting by the camera lens a large field lens of 1.5 m focal length and 10 cm diameter was placed 1.5 m in front of the camera lens. The total distance between the objective and field lens was 13.4 m. The camera was focused on the field lens which, within 1 m, was also the position of the image of the beam formed by the objective. In the horizontal plane, the aperture was limited by a mask, 2 cm wide, placed in front of the objective. In the vertical direction the opening angle of synchrotron radiation determines the aperture. The focal length of the camera lens in the electron damping ring was chosen to be 300 mm and the whole system provided an overall magnification of 1:2.5. The positron damping ring camera lens had a focal length of 100 mm and the system provided a magnification of 1:1. The smaller magnification of the positron damping ring system was necessitated by the bigger size of the injected positron beam.

For the longitudinal damping time measurement a streak camera was used [2]. The optics configuration for the streak camera differed because the small slit width required that the light was focused to a smaller spot. The $f=1.5$ m lens was removed and an $f=50$ cm lens was placed in front of the streak camera at a distance which provided the maximum illumination on the slit. The slit is imaged onto the photocathode of the streak camera by a pair of $f=50$ mm lenses which provide 1:1 magnification.

The resolution of the system in the horizontal plane is $13 \mu\text{m}$ determined by depth of field [3]. The depth of field depends on the beam trajectory curvature and the horizontal aperture of the optical system, which is approximately 13.7 mrad. The diffraction limited resolution, using Raleigh's criterion, is $68 \mu\text{m}$ determined by the natural opening angle of 4.0 mrad at a wavelength of 550 nm [4]. The rms contribution due to diffraction is therefore estimated to be $34 \mu\text{m}$. The critical wavelength for a 1.19 GeV beam and bending radius 2.04 m is 0.68 nm. The resolution in the vertical plane due to depth of field is determined by the length of the portion of orbit observed and the opening angle of synchrotron radiation in the vertical plane. The rms contribution is estimated to be $27 \mu\text{m}$. The resolution due to the gated camera CCD pixel size is $13 \mu\text{m}$ for the electron damping ring setup and $45 \mu\text{m}$ for the positron damping ring. Adding all these contributions in quadrature the horizontal rms resolution is $18 \mu\text{m}$ and $47 \mu\text{m}$ for the electron and positron rings respectively. The rms contribution to the width in the vertical plane is $45 \mu\text{m}$ and $64 \mu\text{m}$.

II. DATA ANALYSIS

A. Transverse

The data were acquired in a random sequence of intervals of the time elapsed between injection and the gated camera trigger. This was done so that the data would not be biased by slow variations of the transverse beam size, during the data acquisition time, which was 20 min for 300 frames. Each frame of the beam image represents a different injected bunch. The electron bunch is stored for 8 msec and the positron bunch is stored for 16 msec. The video signal of the gated camera was digitized by a transient waveform digitizer. The projections on the horizontal and vertical axes were fitted to a function of the form

$$f(x; A, B, C, \sigma, x_0) = \frac{A}{\sqrt{2\pi}\sigma} e^{-\frac{1}{2}\left(\frac{x-x_0}{\sigma}\right)^2} + B + Cx.$$

The pedestal term was not constant because of the electrically noisy environment in the building where the camera was located. A χ^2 minimization was performed for each frame with

$$\chi^2 = \sum_i^n \frac{(f(x_i; A, B, C, \sigma, x_0) - v_i)^2}{v_i}$$

Where v_i is the rescaled digitized video signal so that the χ^2 per degree of freedom distribution would peak around one. The statistical error on the measured sigma was determined from the correlation matrix derived from the minimization of the χ^2 . The square of the width was plotted against the time the bunch has spent circulating in the ring and the data was fitted to a curve of the form

$$\sigma(t)^2 = (\sigma_{inj}^2 - \sigma_{eq}^2) e^{-\frac{2t}{\tau}} + \sigma_{eq}^2$$

*Work supported by the Department of Energy, contract DE-AC03-76SF00515

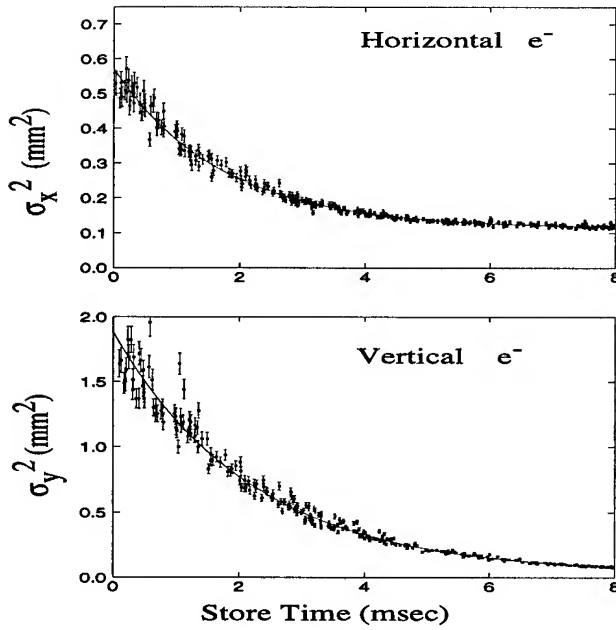


Figure 1. Sample of data for the electron damping ring. The vertical scale represents the size of the bunch image on the photocathode. The bunch itself is 2.5 times smaller

The fitted parameters are σ_{inj} the width of the injected bunch, σ_{eq} the equilibrium width of the bunch, and τ the damping time, see figures 1, 2 for a sample of data and fits.

B. Longitudinal

The analysis of the longitudinal damping time is similar. The projection of the image of the bunch on the time axis was fitted to a function of the form

$$\frac{A}{\sqrt{2\pi}\sigma} e^{-\frac{1}{2}\left(\frac{x-x_0}{\sigma(1+S)}\right)^2} + B$$

Where $S = |S| \left| \frac{x-x_0}{x-x_0} \right|$ representing the asymmetric shape of the bunch. The damping time is derived by a nonlinear exponential fit. The data consist of ten measurements of bunch length at each store time. The ten measurements at each point are averaged. The standard deviation of the ten measurements divided by $\sqrt{10}$ is used to weight the contribution of each point to the χ^2 in the exponential fit, see figure 3.

III. ERROR ANALYSIS

A. Transverse

The uncertainty in the transverse measurements has statistical as well as contributions due to systematic errors. Despite the large contribution from resolution to the width measurements the damping time determination is not affected. The resolution adds in quadrature to the width, therefore the square of the width still follows an exponential damping law. However if the resolution depends on the transverse dimensions of the beam then the above statement is no longer true. In principle there is a dependence due to the fact that the depth of field decreases as the horizontal dimension of the beam decreases but the variation is smaller

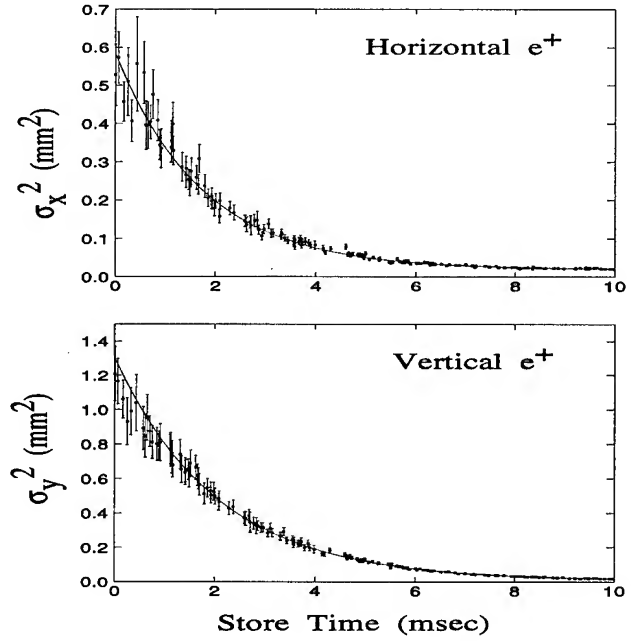


Figure 2. Sample of data for the positron damping ring. The vertical scale represents the real size of the bunch.

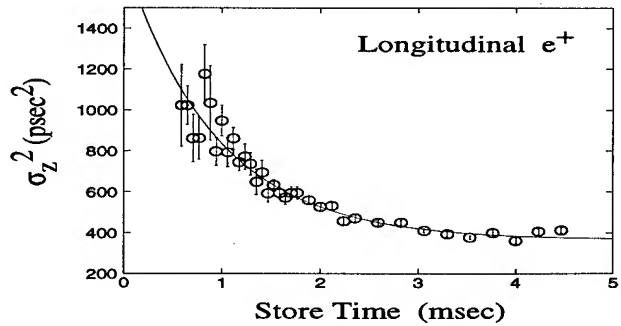


Figure 3. Longitudinal damping time data. The origin of the horizontal axis represents injection time.

than 1% due to the small angular acceptance of the optical system and the small angular spread of the synchrotron radiation in the vertical plane. Effects due to the damping of the angular divergence of the beam are also small since in the worst case of the injected positron bunch the angular divergence is 1.5 mrad, which is small compared to the light angular divergence.

The dynamic range for linear operation of the gated camera was rather limited. Even with the optimum amount of filtering, the photocathode showed signs of saturation as evidenced by the decreasing amount of light detected for increasing store time. The dependence of the width with intensity was measured and no clear plateau was found. Filtering was chosen so that the overall width variation due to this effect would stay below 10%. From simulated data, this effect tends to decrease the measured damping times by 3%.

The horizontal damping time can be influenced by the presence of dispersion which at the emission point is $\eta=5$ cm. The energy spread of the injected beam is 1×10^{-2} which rapidly

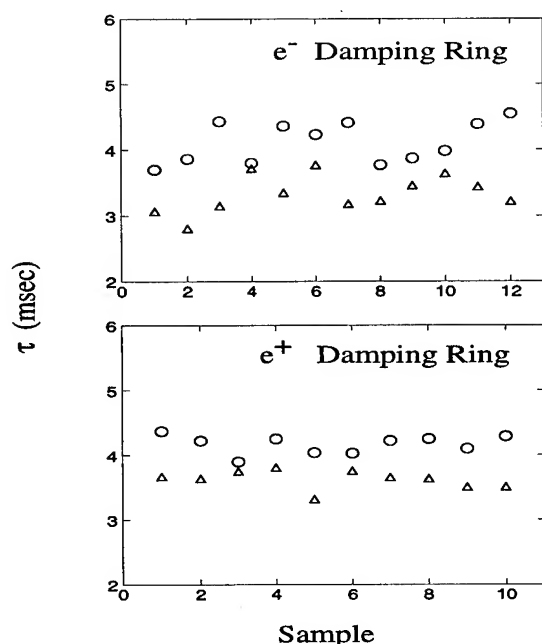


Figure 4. The horizontal damping times are represented by triangles and the vertical damping times by circles. The statistical error for each measurement is comparable to the size of the symbols

damps to the equilibrium energy spread 7×10^{-4} . In order to determine whether this effect is significant, the data were fitted to the sum of two exponentials where the damping time of one of the exponentials was fixed to be equal to 1.8 msec, the longitudinal damping time. The fits preferred a small negative weight for the second exponential. This indicates that any effect due to dispersion was masked by the nonlinear behavior of the gated camera and the low statistical weight of the points near injection.

In figure 4 the measurements are shown ordered in time. There is a large variation not explained by statistical errors indicating an additional unknown time dependent source of systematic error. Statistical errors are determined by the exponential fits, with properly weighted χ^2 , and on the average are 0.06 msec. For reasons of comparison with calculations of damping times [5] the measurements are averaged and summarized in the table above. The error quoted is the standard deviation of the corresponding set of measurements.

B. Longitudinal

Systematic errors due to photocathode saturation were eliminated by attenuating the light enough so that the camera was operated in the linear regime. The use of an interference filter centered at 500 nm and with a 40 nm bandwidth, ensured that the contribution to resolution from dispersion in the glass optics was negligible. There was only one measurement of the longitudinal damping time and the error quoted is the statistical uncertainty.

IV. CONCLUSIONS

It is impossible on the basis of these measurements alone to distinguish whether the damping time fluctuations are due to instrumental effects or to orbit changes, or beam excitation from

Damping time measurements (msec)

Ring	τ_x	τ_y	τ_z
Electron	3.32 ± 0.28	4.11 ± 0.31	-
Positron	3.60 ± 0.15	4.17 ± 0.14	1.87 ± 0.13
Calculation	3.52	3.56	1.79

the extraction kicker magnets or interaction between the two bunches in the rings.

In order to understand the origin of the large fluctuations in the damping time measurements, and the discrepancy with the calculations, the orbit, tune and pressure in the vacuum chamber dependence should be studied.

The authors would like to thank F-J Decker, K. Jobe, P. Krejčík, M. Minty, M. Ross, R. Siemann, W. Spence and J. Spencer, for useful discussions and helpful suggestions and V. Brown for technical support during the course of this work.

References

- [1] M. Minty et al., "Using a fast-gated camera for the measurements of transverse beam distributions and damping times", AIP Conference Proceedings No. 281, pp 158-167, 1993.
- [2] R.L. Holtzapple et al., "Measurements of longitudinal dynamics in the SLC damping rings", these proceedings.
- [3] A.P. Sabersky, "The geometry and optics of synchrotron radiation", Part . Acc., vol. 5, pp 199, 1973.
- [4] A. Hofmann and F. Meot, "Optical resolution of beam cross-section measurements by means of synchrotron radiation", Nucl. Instr. and Meth. vol. 203, pp 483-493, 1982.
- [5] R. Early et al, "Proposed emittance upgrade for the SLC damping rings", SLAC-PUB-6559

Transverse Multibunch Instabilities for Non-Rigid Bunches*

J. Scott Berg and Ronald D. Ruth

Stanford Linear Accelerator Center, Stanford University, Stanford, CA 94309

Abstract

In this paper, we present a method for computing growth rates and frequency shifts of a beam containing multiple non-rigid bunches. With this approach, we calculate non-rigid multibunch effects which can impact phenomena which are traditionally treated as single-bunch effects, such as the transverse mode-coupling instability. This approach is important for high current storage rings such as PEP-II at SLAC (the B-Factory) which have very strong inter-bunch forces. Typical calculations treat multibunch and single bunch effects separately, and thus eliminate important interactions between the two. To illustrate the technique, we calculate growth rates and frequency shifts using PEP-II as an example.

I. Introduction

In [1], we describe a method for computing transverse multibunch instabilities. This method allows us to include the effects of internal degrees of freedom of the bunches, including coupling between the resulting modes. Previous work by other authors has either considered coupling between internal degrees of freedom for only a single bunch, or multiple bunches where the internal degrees of freedom are not coupled (see [1] for references and more discussion).

In this paper, we briefly describe the formalism, leaving the reader to [1] for more details. We then describe in detail the effects that are seen due to transverse multibunch mode coupling. This is done by plotting the mode frequencies and growth rates versus current for previously studied cases (transverse single bunch mode coupling and transverse multibunch modes without coupling), and comparing those plots to similar plots obtained by finding the transverse multibunch modes including coupling between internal degrees of freedom.

II. The eigenvalue equation

We can write a Vlasov equation describing the time evolution of the distribution for each bunch in terms of all the bunch distributions. The bunch distribution is assumed to be a time-independent stable distribution which satisfies the Vlasov equation for zero current, plus a small time-dependent perturbation.

That Vlasov equation can then be turned into a nonlinear eigenvalue equation for the coherent mode frequencies Ω . If we assume that 1) the bunches are identical and equally spaced, 2) the non-wakefield forces are all linear and independent of position in the ring, and 3) the bunch distribution we're perturbing about is Gaussian and only depends on the non-wake Hamiltonian, then

our eigenvalue equation becomes [1]

$$\phi_m(\Omega) = \sum_{n=0}^{\infty} K_{m+n}(\Omega + p\omega_0) F_n(\Omega) \phi_n(\Omega) \quad (1)$$

$$F_n(\Omega) = \frac{1}{2^n n!} \sum_{k=0}^n \binom{n}{k} \frac{[\omega_y + (n-2k)\omega_z]^2}{\Omega^2 - [\omega_y + (n-2k)\omega_z]^2} \quad (2)$$

$$K_k(\omega) = -i \frac{r_0 c^2 \beta_y N M}{\gamma_0 L^2 \omega_y} \sum_{\alpha} \left(\frac{\sigma_l}{\beta_0 c} \right)^k (\omega + M\alpha\omega_0)^k Z_{\perp}(\omega + M\alpha\omega_0) e^{-\sigma_l^2 (\omega + M\alpha\omega_0)^2 / \beta_0^2 c^2} \quad (3)$$

where ω_0 is the angular revolution frequency of the ring, ω_y is the betatron frequency, ω_z is the synchrotron frequency, r_0 is the classical radius of the electron, c is the speed of light, β_y is the average beta-function, N is the number of particles in a bunch, M is the number of bunches, γ_0 is the nominal beam energy divided by the rest mass energy of the particle, L is the length around the ring, σ_l is the bunch length, $\beta_0 c$ is the nominal particle velocity, and Z_{\perp} is the transverse impedance. Feedback can be added by adding an additional term to K_k with $Z_{\perp}(p\omega_0 + \Omega)$ replaced by $Z_{FB}(p\omega_0 + \Omega)e^{-2\pi i p \Delta s / L}$, where Z_{FB} is the Fourier transform of the feedback response, and Δs is the distance between the pickup and kicker.

III. Illustrative Example

We will use the PEP-II B-Factory low energy ring [2] to illustrate the effects that arise from multibunch mode coupling. We have used an estimate for the broadband impedance using parameters from [3] and higher-order mode impedances for the cavities from [2], [4]. For this example, we truncate equation (1) at $m = 1$.

Fig. 1 shows mode coupling appearing when we consider only a single bunch. For small currents, the growth rates of the modes are negligible, and the mode frequencies change with increasing current. At the current where the mode frequencies coincide,

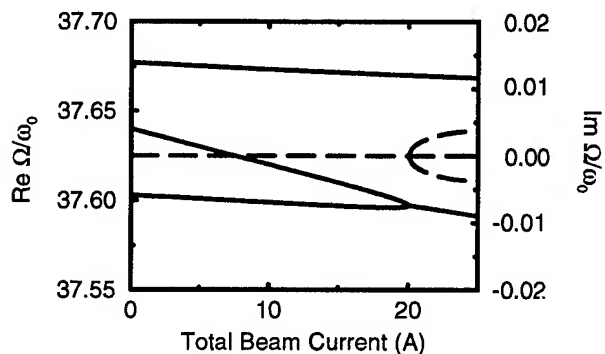


Figure 1. Single bunch mode coupling. Solid lines are real part, dashed lines are imaginary part.

*Work supported by the Department of Energy, contract DE-AC03-76SF00515.

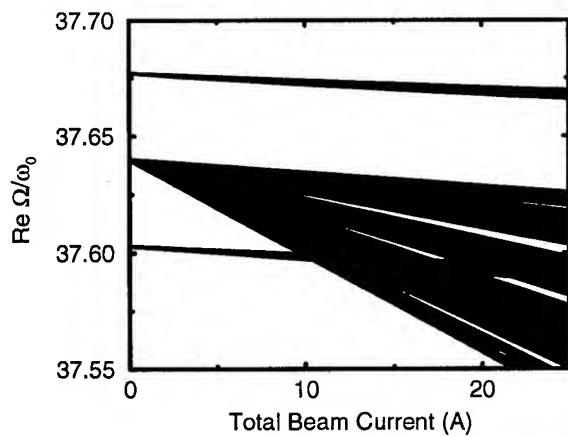


Figure 2. Multibunch mode frequencies, no coupling.

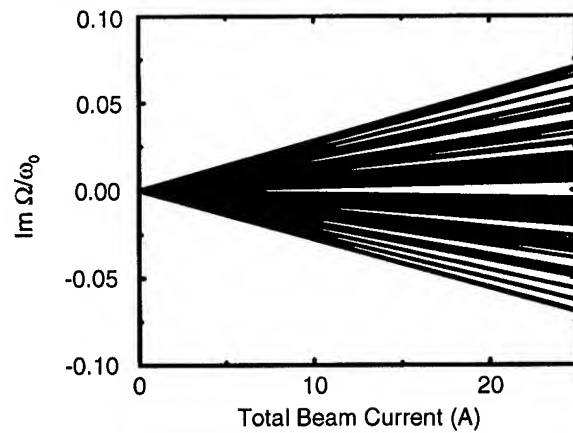


Figure 4. Multibunch $m = 0$ growth rates, no coupling.

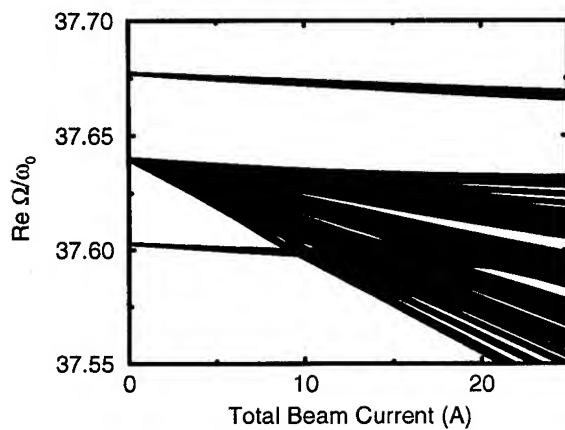


Figure 3. Multibunch mode frequencies, with coupling.

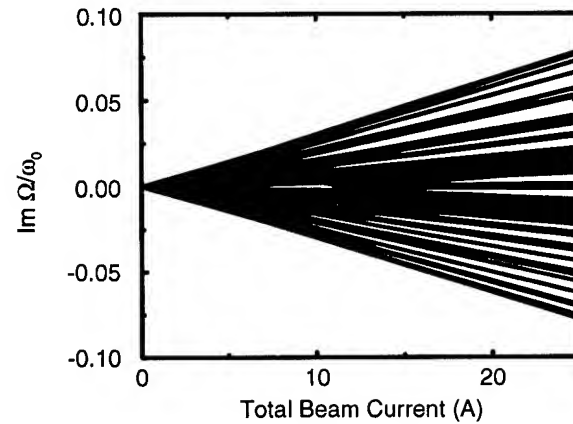


Figure 5. Multibunch $m = 0$ growth rates, with coupling.

two of the modes resonantly drive one another, and exponential growth results.

Now consider multiple bunches. In all the following diagrams, we have only shown the modes with the largest growth rates. If we ignore coupling between the $m = 0$ and $m = 1$ multibunch modes, Fig. 2 demonstrates that for many of the multibunch modes, the frequencies of the $m = 0$ and one of the $m = 1$ modes coincide at currents much lower than where the frequencies coincide in the single bunch case of Fig. 1. When we allow the multibunch modes to couple, then Fig. 3 shows the real parts having nearly identical behavior to the uncoupled case. In the uncoupled case, the frequency shifts were nearly linear with current. Once coupling occurs, the curvature of the mode frequencies with current increases, and so we notice that in Fig. 3, the current where the mode frequencies intersect is even lower than what we see in the uncoupled case. Note that this current is still well above the intended operating current of the PEP-II low energy ring [2].

Now we examine the growth rates of the multibunch modes. First we look at the $m = 0$ modes. In the uncoupled case, Fig. 4 shows the growth rates increasing nearly linearly with current.

If we allow the modes to couple, there are minimal changes to the growth rates of the $m = 0$ modes, as can be seen in Fig. 5. This is largely due to the fact that the largest growth rates are significantly larger than the growth rates due to mode coupling

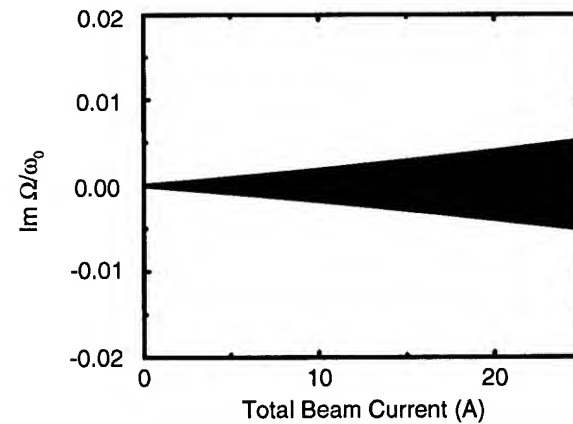


Figure 6. Multibunch $m = 1$ growth rates, no coupling.

(compare Fig. 1). In fact, if we were to look at modes with very small growth rates, we would see behavior almost identical to the single bunch case in Fig. 1.

Next, consider the $m = 1$ modes. In the uncoupled case, we see the growth rates increasing linearly with current in Fig. 6. Notice also that the growth rates are much smaller than they were in the $m = 0$ case. In fact, they are comparable to what one sees in single bunch mode coupling (Fig. 1). When we include coupling, we in fact see significant increases in the growth rate

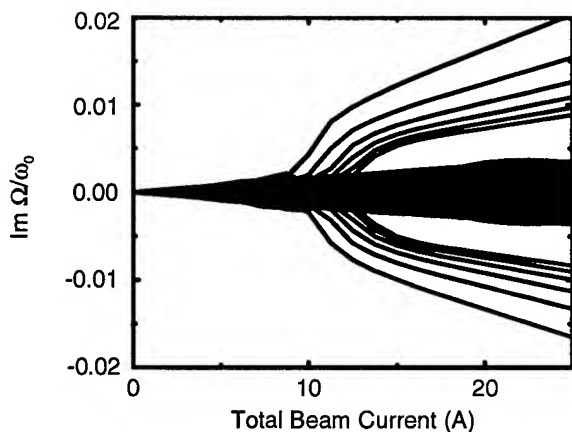


Figure 7. Multibunch $m = 1$ growth rates, with coupling.

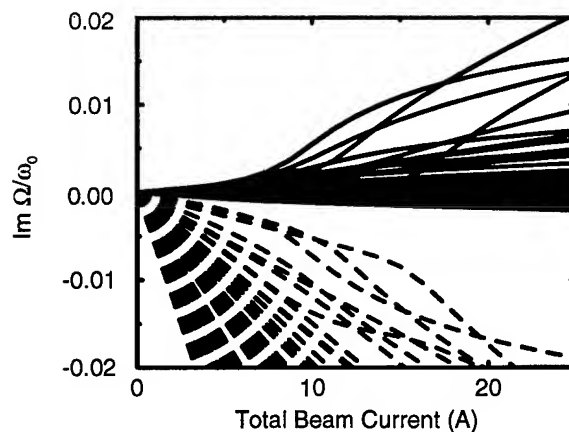


Figure 9. Multibunch growth rates, with feedback. Dashed lines are $m = 0$ modes, solid lines are $m = 1$.

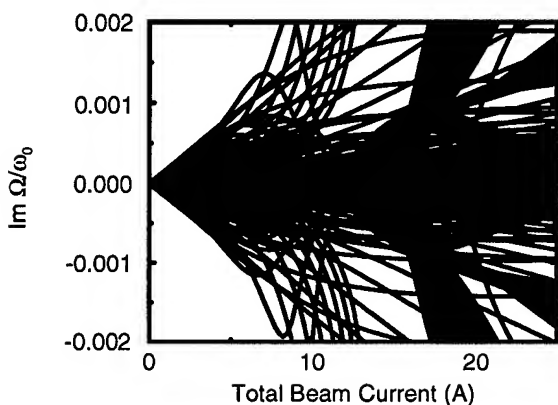


Figure 8. Multibunch $m = 1$ growth rates, with coupling. Expanded vertical scale shows curvature of mode lines with current even at low currents.

of the $m = 1$ modes, as shown in Fig. 7. Notice that the growth rates increase sharply at just the point where the real part of the mode frequencies coincide (see Fig. 3). The multibunch mode coupling also causes the mode frequencies to no longer increase linearly with current, even for currents well below the current where the real part of the frequencies coincide. This is demonstrated in Fig. 8. This can cause $m = 1$ growth rates to be significantly increased over their uncoupled values, even at very small currents.

Finally, we can consider the effects of adding a feedback system. Typically, a transverse feedback system does not operate at frequencies sufficiently high to damp $m = 1$ modes. Thus, using parameters similar to those proposed for the PEP-II B-factory, Fig. 9 shows how the $m = 0$ modes are well damped, but the $m = 1$ modes still exhibit significant growth rates due to multibunch mode coupling.

References

- [1] J. S. Berg and R. D. Ruth, "Transverse instabilities for multiple rigid bunches in a storage ring," Tech. Rep. SLAC-PUB-95-6829, SLAC, April 1995. Submitted to Phys. Rev. Lett.
- [2] "PEP-II, an asymmetric B factory," Tech. Rep. SLAC-418, SLAC, June 1993.

- [3] S. Heifets *et al.*, "Impedance study for the PEP-II B-factory," Tech. Rep. SLAC/AP-99, SLAC, March 1995.
- [4] Y. Cai. Private communication.

SIMULATIONS OF TRANSITION CROSSING IN THE MAIN INJECTOR

C.M. Bhat and J.A. MacLachlan,
Fermi National Accelerator Laboratory *
P.O. Box 500, Batavia, IL 60510

Abstract

The design goal for the Fermilab Main Injector (FMI) is to accelerate a minimum of 6×10^{10} protons per bunch through the transition. We present here the results from simulation studies of the transition crossing in the FMI using the particle tracking code ESME[1].

I. INTRODUCTION

The Fermilab Main Injector (FMI)[2] that is under construction is intended to be a high intensity 150 GeV proton injector to the Tevatron. The beam in the FMI will be accelerated from 8 GeV to 150 GeV through a transition energy of 20.48 GeV. The longitudinal emittance of the proton beam at injection is about 0.1 eVs, and the intensity will be more than 6×10^{10} protons per bunch. Maintaining the beam intensity as well as its longitudinal emittance through the acceleration cycle is very important for the FMI operation. In the past, preserving the beam emittance and the intensity through transition crossing in a proton synchrotron has been one of the major problems. A number of techniques have been suggested to cure these problems[3,4]. Two of the suggested techniques viz., a) γ_t -jump scheme[3] and b) focus free transition crossing(FFTC) [4] have been investigated in some detail for proton synchrotron along with the normal transition phase jump (NTPJ) scheme. Here, the particle tracking code ESME[1] has been used to study the longitudinal beam dynamics of the transition crossing in the FMI for these three different schemes.

The condition of non-adiabaticity[5] exists in a proton synchrotron when,

$$\left| \frac{\gamma - \gamma_t}{\gamma_t} \right| \leq \left[\frac{\gamma_t (eV_{rf} \sin \phi_s)^2}{4\pi h E_o e V_{rf} |\cos \phi_s|} \right]^{1/3} \quad (1)$$

where γ_t is the relativistic quantity γ at transition, V_{rf} is the peak rf voltage at transition, ϕ_s is the synchronous angle of the beam with the rf wave form, h is the harmonic number of the machine and E_o is the rest mass of proton. By assuming that the γ is increasing linearly near transition at a rate $\dot{\gamma}$ this expression can be converted to a non-adiabatic time period in the vicinity of the transition time,

$$T_{na} = \pm T_s \left[\frac{f_s E_o \gamma_t^4}{4\pi h \dot{\gamma} e V_{rf} |\cos \phi_s|} \right]^{1/3} \quad (2)$$

where $f_s = 1/T_s$ is the revolution frequency of the synchronous particle. Since all the particles in a bunch do not pass through

the transition at the same time, there will be a non-linear period during which some particles are above the transition energy while others are below it. The non-linear time is given by,

$$T_{nl} = \pm \gamma_t \left[\frac{\beta^2 + \alpha_1/\alpha_o + 1/2}{\dot{\gamma}} \right] \frac{\Delta p}{p} \quad (3)$$

where β is the ratio of particle velocity and the velocity of light. α_1 is the second order term in the expansion of path length in $\Delta p/p$ and $\alpha_o = \gamma_t^{-2}$. During this time the rf focusing force causes increased momentum spread and a number of different instabilities come into play. Since the non-adiabatic and non-linear time decrease with increased $\dot{\gamma}$, the simulations have been carried out for two different values of $\dot{\gamma}$ for the FMI operating scenarios.

II. ESME SIMULATIONS OF TRANSITION CROSSING

In ESME, the collective behavior of the beam particles is treated using a pair of Hamilton-like difference equations describing synchrotron oscillations in the energy-angle ($\Delta E, \phi$) phase space, (where $\Delta E = E - E_o$ and $0 \leq \phi \leq 2\pi$). The particles in a bunch are assumed to have an elliptical distribution which is a good representation of the beam bunches coming from the Fermilab Booster. For a cylindrical beam pipe of radius 'b' and a co-axial beam of radius 'a', the impedance, Z_ω seen by a single Fourier component of the beam current at a frequency $\omega/2\pi$, is,

$$\frac{Z_\omega}{n} = -j \frac{Z_o g}{2\beta \gamma^2} + \frac{Z_W}{n} + \frac{Z_{||}(\omega)}{n} \quad (4)$$

where $Z_o = 377$ Ohm (Impedance of free space), Z_W is total wall impedance of the beam pipe and the geometry factor $g = 1 + 2 \ln(b/a)$. The average values of 'a' and 'b' are listed in Table I. The $Z_{||}$ is given by,

$$Z_{||}(\omega) = \frac{R_s}{1 + jQ \left(\frac{\omega_c}{\omega} - \frac{\omega}{\omega_c} \right)} \quad (5)$$

For quality factor $Q=1$, Equation 5 represents the broad-band impedance. R_s is the strength of the effective shunt impedance. For the FMI we have taken design value $R_s = 5$ Ohm which is almost surely a considerable over estimate with enough safety margin.

The effect of transverse space charge force producing horizontal betatron tune shift is proportional to the particle density distribution in a bunch at a longitudinal position ϕ . Very close to the transition, η goes to zero. Therefore even a very small correction to γ_t becomes a sensitive parameter to determine the longitudinal beam dynamics. In the present calculations the dispersion of momentum compaction factor was taken into account by expanding,

*Operated by the Universities Research Association, under contracts with the U.S. Department of Energy

Table I

The parameters used for ESME simulations.

Parameter	Values
Mean radius of FMI	528.3019 m
γ_t (nominal)	21.838
$\dot{\gamma}$ at transition	167(Slow Ramp) sec^{-1} 300 (Fast Ramp) sec^{-1}
α_1	0.002091
Principal rf sys.	53 MHz 4 MV (max)
Init. emittance and Bunch intensity	0.1 and 0.2 eVs 6×10^{10}
Coup. imp. $Z_{ }/n$	5 Ω 2.17 GHz cutoff
Transverse Beam size(a)	0.0022 (m)
Beam pipe Radius (b)	0.03 (m)
FFTC : Shaping rf for FFTC	159 MHz 280 kV (max)
Type of Tran. Crossing	Non-symmetric
γ_t - jump : $\Delta\gamma$ Type of Tran. Crossing	1.0 Non-symmetric

$$\alpha_p \approx \alpha_o + (\alpha_o + 2\alpha_1 - \alpha_o^2) \frac{\Delta p}{p} \quad (6)$$

For the Main Injector we take α_1 to be 0.002091. This corresponds to a Johnsen parameter[3] of 0.8. Thus, each particle has its characteristic γ_t depending on the deviation of its momentum from that of the synchronous particle. Table I lists the parameters used in the present simulation studies. The results of ESME simulations have been displayed in Table II. The FFTC and γ_t -jump scheme prefer symmetric settings for beam emittance larger than 0.2 eVs. For smaller emittance beam, where the space charge forces play important role in emittance blow up, the non-symmetric transition crossing is essential. Figure 1 shows a comparison of evolution of ϵ_l for NTPJ, FFTC and γ_t -jump schemes in the Main injector for initial longitudinal emittance of 0.1 eVs. All these calculations have been performed by incorporating both space charge effects and the broad band Z/n . Since the $\Delta p/p$ increases as a bunch approaches transition energy, it is necessary to take into account the momentum acceptance of the FMI. From these simulations we find that the γ_t -jump scheme is preferable compared to FFTC. However, for emittance ≤ 0.1 eVs, and with the fast ramps the benefits are limited. With the FFTC scheme the emittance growth will be in between those for NTPJ and the γ_t -jump scheme. For emittance ≥ 0.2 eVs we find that the FFTC and γ_t -jump schemes give almost no emittance growth, while, with the NTPJ there is a max-

Table II

The results of the longitudinal beam dynamics simulations for transition crossing using ESME. The fractional growth $\Delta\epsilon/\epsilon$ for different schemes is listed.

$\dot{\gamma} _{trans.}$ (sec^{-1})	Init. Long. Emittance (eVs)	NTPJ	FFTC	γ_t -jump
167	0.1	3.0	0.6 ^a	0.15
	0.2	0.09	0.04 ^a	0.02
300	0.1	1.6	-	0.25
	0.2	0.06	-	0.02

^a In these cases the ESME simulations have been carried out for $\dot{\gamma}|_{transition} = 169/\text{sec}$.

Comparison between Gamma_t, FFTC and NTPJ Schemes
For FMI Using ESME, $\epsilon_l(\text{initial}) = 0.1\text{eV-sec}$

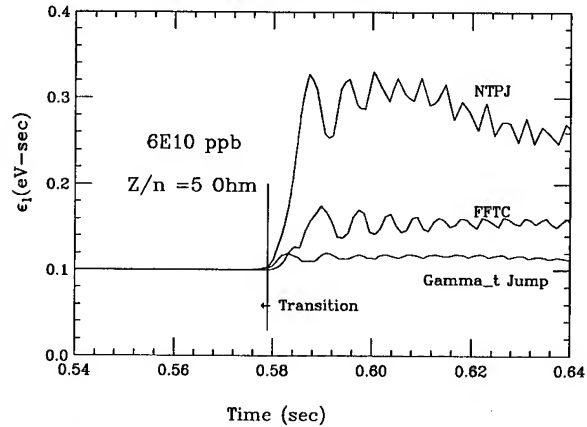


Figure 1. A comparison between γ_t -jump, FFTC and NTPJ schemes for the FMI. The initial emittance is 0.1 eVs, number of protons per bunch = 6×10^{10} . The $\dot{\gamma}|_{transition} = 167/\text{sec}$.

imum of about 10% emittance growth. Thus, with $\dot{\gamma}|_{transition} = 300/\text{sec}$ and with $\epsilon_l \geq 0.2$ eVs we may not need any of the schemes like FFTC or the γ_t -jump for transition crossing in the FMI.

In a separate set of calculations we have estimated the negative mass instability using ESME. Our results confirm the calculations of Ng[6], who employed the analysis of Hardt[7]. We find for 6×10^{10} protons/bunch a limit of $\epsilon_l \leq 0.16$ eVs for $\dot{\gamma}|_{transition} = 167/\text{sec}$ and $\epsilon_l \leq 0.12$ eVs for $\dot{\gamma}|_{transition} = 300/\text{sec}$.

III. SUMMARY AND CONCLUSIONS

We have simulated the transition crossing for the proton beam with 6×10^{10} particle/bunch. Three different schemes of transition crossing in the FMI have been investigated. We find that

for an operating scenario of $\dot{\gamma}_{transition}=300$ /sec and $\epsilon_l \geq 0.2$ eVs we do not need any special schemes like γ_t -jump or FFTC.

Authors would like to acknowledge Dr. K.Y. Ng for useful discussions, especially the treatment of negative mass instability.

References

- [1] J.A. MacLachlan, User's Guide to ESME v.8.13, Fermilab TM-1856(1994).
- [2] D. Bogert, W. Fowler, S. Holmes, P. Martin and T. Pawlak, 'The status of the Fermilab Main Injector Project' (these proceedings).
- [3] A. Sorensen, Part. Accelerators. Vol. 6 (1975) 141.
- [4] J. Griffin, Synchrotron Phase Transition Crossing Using an RF Harmonic, Fermilab TM 1734 (1991).
- [5] E.D. Courant and H.S. Snyder, Annals of Phys. 3(1958) page 1.
- [6] I. Kourbanis and K.Y.Ng, Proc. Part. Accel. Conf. (1993) 3630.
- [7] W. Hardt, Proc. 9th Int. Conf. on High Energy Accelerators, Stanford 1974.

IMPEDANCE BUDGET FOR THE KEK B-FACTORY

Y. H. Chin and K. Satoh, KEK, 1-1 Oho, Tsukuba-shi, Ibaraki-ken, 305, Japan

Abstract

In this paper, we deal with impedances of various beamline elements in the KEK B-Factory. We will also discuss the power deposition generated by a beam in the form of the higher-order-mode (HOM) losses by interacting with its surroundings.

I. INTRODUCTION

The KEK B-Factory (KEKB) is an electron-positron collider with unequal beam energies (8 and 3.5 GeV) for study of B meson physics[1]. The dominant issues in the KEKB in terms of beam instabilities and impedance are the very high beam current (2.6 A in the low energy ring (LER) and 1.1 A in the high energy ring (HER)) to achieve the high luminosity of $10^{34} \text{ cm}^{-2} \text{ s}^{-1}$, and a short bunch ($\sigma_z = 4 \text{ mm}$) to avoid a degradation of the luminosity by the hour-glass effect. Since the charges are distributed over many (5120) bunches, the bunch current is not unusually high. As a consequence, single-bunch effects are expected to be relatively moderate: their stability limits are beyond the design values with comfortable margins. The main concern, in turn, is on coupled-bunch instabilities due to high-Q resonant structures such as RF cavities and the transverse resistive-wall instability at very low frequency (lower than the revolution frequency). The short bunch can pick up the impedance at very high frequency ($f \sim 20 \text{ GHz}$) and thus may create an enormous heat deposition by the higher-order mode (HOM) losses. This heating problem requires serious efforts to reduce the impedance of various beam components or eliminate candidates for trapping modes all together.

II. IMPEDANCE OF COMPONENTS

In this section, we summarize our estimate of impedances and loss factors of various beamline components. Among impedance-generating elements of the rings, the largest contributors are RF cavities, the resistive wall, masks at arc, pumping slots and bellows (because of their large number).

A. RF cavities

Two types of RF cavities are under consideration for the KEKB. The ARES (Accelerator Resonantly coupled with Energy Storage) cavity is a normal-conductive cavity with an energy storage cavity to reduce the detuning of the accelerating frequency due to a large beam loading effect. Another candidate is a superconductive cavity with HOM absorbers made of ferrite material attached to the beam pipe. Although a final decision on which cavity will be employed in the KEKB has not yet been made, we only deal with the impedance and loss factor of the ARES cavity in this paper. The beam power of 5.2 MW will be provided by 20 and 40 cells of the ARES cavities in the LER (with wiggler) and HER, respectively. The impedance of the HOMs in the ARES have been calculated using a computer code MAFFIA. Most HOMs are significantly de-Qed, typically much less than 100, by the HOM damper consisting of a coaxial wave

guide equipped with a notch filter. Using the program ABCI[2], we have estimated that the main body of the ARES cavity produces a loss factor of 0.529 V/pC at bunch length $\sigma_z = 4 \text{ mm}$. If this cavity is connected to the beam chamber (radius=50 mm) at both ends with 100 mm long tapers, the additional loss factor will be 0.363 V/pC. In total, the loss factor of one cell of the ARES cavity is 0.892 V/pC.

B. Resistive-wall

The material of the KEKB beam chamber was chosen to be copper because of its low photon-induced gas desorption coefficient, its high thermal conductivity, and its large photon absorption coefficient. Its high electrical conductivity also helps to reduce the resistive-wall impedance. Nevertheless, this is still the dominant source of transverse impedance for the coupled-bunch instability. The total transverse resistive-wall impedance of the circular pipe with an inner radius b is given by

$$Z_{RW}(\omega) = Z_0(\text{sgn}(\omega) - i) \frac{\delta R}{b^3}, \quad (1)$$

where $Z_0 (\cong 377 \Omega)$ is the characteristic impedance of vacuum, δ is the skin depth, R is the average radius of the ring, and $\text{sgn}(\omega)$ denotes the sign of ω . For the LER vacuum chamber ($b = 50 \text{ mm}$), Eq. (1) gives the resistive-wall impedance of 0.3 M Ω /m at the revolution frequency 100 kHz, while the impedance decreases to 2 k Ω /m at the cutoff frequency 2.3 GHz of the chamber. The HER chamber of racetrack shape may be approximated by a circular one with a diameter of 25 mm.

C. Masks at arc

Each bellows has a mask (5 mm high) located in its front to be shielded from the synchrotron radiation from a nearby bending magnet. There are about 1000 bellows (one bellows on both sides of each quadrupole magnet. There will be no mask for BPMs). The cross section of the mask in the medium plane is shown in Fig. 1. For accurate calculations of wake potentials and loss factors, a 3-D program MASK30 has been developed which solves the Maxwell equations directly in time domain. Using this code, we have found that the total longitudinal impedance of 1000 masks is

$$\text{Im} \left[\frac{Z(\omega)}{n} \right] = 2.8 \times 10^{-3} \Omega, \quad (2)$$

where n expresses the frequency ω divided by the revolution frequency ω_0 , $n = \omega/\omega_0$. The total loss factor is

$$k_L = 4.6 \text{ V/pC}, \quad (3)$$

which corresponds the total HOM power of 62 kW in the LER.

D. Pumping slots

The current design of pumping slots adopts the so-called "hidden holes" structure similar to those of HERA and PEP-II. A slot

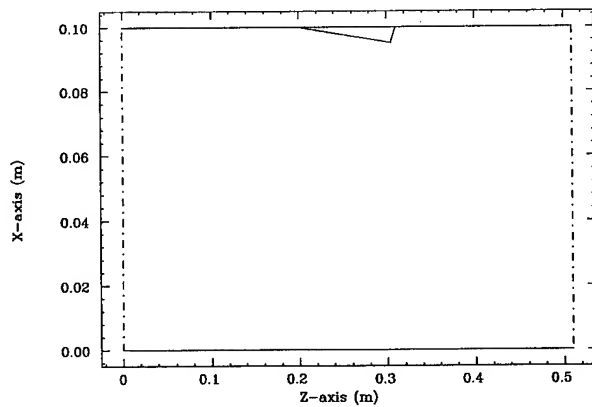


Figure 1. Mask at arc

has a rectangular shape with rounded edges, which is long in the beam-axis direction (100 mm long, 4 mm wide). The slot is patched on the pumping chamber side by a rectangular grid. They help to prevent the microwave power generated somewhere else from penetrating through the slots to the pumping chamber and then depositing the energy in the NEG pumps. There are analytic formulae for impedance and loss factor of such a narrow slot by Kurennoy[3]. We found that the total inductive impedance of the pumping slots (there are 8 slots per meter over the total length of 1800 m) with thickness correction is

$$\text{Im}\left[\frac{Z(\omega)}{n}\right] = 0.8 \times 10^{-3} \Omega. \quad (4)$$

The total loss factor was calculated to be

$$k_L = 10.6 \text{ V/pC}. \quad (5)$$

E. BPMs

The annular gap (or groove) in a BPM between the button electrode and the supporting beam chamber can be approximated by a regular octagon. The impedance of a BPM can be thus calculated from the same formula for a narrow slot considering it as a combination of eight narrow slots (two transverse, two longitudinal, and four tilted)[4]. If we neglect small contributions from the longitudinal slots, and consider four tilted slots as two transverse ones, the impedance of the BPM becomes equivalent to that of the four transverse slots. For 400 four-button BPMs (radius=6.5 mm, gap=1 mm, and thickness=1 mm), the total inductive impedance is

$$\text{Im}\left[\frac{Z(\omega)}{n}\right] = 1.3 \times 10^{-4} \Omega. \quad (6)$$

The total loss factor of BPMs is

$$k_L = 0.71 \text{ V/pC}. \quad (7)$$

F. Mask at IP

There are four masks (two large and two small) on both side of the beryllium chamber at the interaction point (IP) to shield it from the direct synchrotron radiation. Figure 2 shows their geometry. The loss factor due to these masks has been calculated using the code MASK30 and was found to be

$$k_L = 5.2 \times 10^{-2} \text{ V/pC}. \quad (8)$$

This value is about one-fourth of that obtained by ABCI using the axis-symmetrical model. The ratio of the two loss factors coincides with the ratio of the opening angle of the IP mask from the beam axis (about 90 degrees) to that of the entire circle. Based on this observation, we have learned that we can make a rough estimate of the loss factor for a 3-D structure by multiplying the opening angle ratio to a result for its axis-symmetrical model.

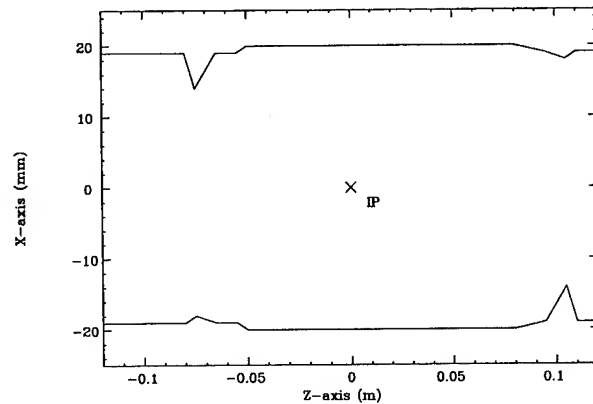


Figure 2. Mask at the IP

Not all of the power generated at the IP will be deposited there. It depends on Q-values of modes excited between the masks. The beam chamber at the IP has the cutoff frequency at 6.04 GHz, and the tips of the taller masks creates another cutoff frequency at 8.202 GHz. If the wake fields between these two frequencies are trapped, the deposited energy will be (using ABCI and the translation law)

$$k_L \approx 0.1 \times \frac{1}{4} \text{ V/pC} = 0.025 \text{ V/pC}. \quad (9)$$

The corresponding power deposition at the IP in the LER is $P=343$ W, which is 70 % more than the design tolerance of 200 W for the beryllium window. However, if one takes a close look at the impedance of these modes, all the modes except the lowest one near 6.04 GHz have Q-values much smaller than the one determined by the finite conductivity of the beryllium window. This is because the radius of the beam chamber remains the same inside and outside of the IP region separated by the masks, and thus the modes can escape to the outside region by making a bridge over the masks. The only trapped mode at 6.04 GHz has a loss factor of 0.003 V/pC and will deposit 41 W of the power at the IP. This amount of power deposition is acceptable provided that the frequency of the trapped mode is carefully detuned so that it will not resonate with the bunch frequency. The actual 3-D masks at the IP has a more open structure than the axis-symmetrical model, and thus the power deposition might be even smaller.

G. IR chamber

The experimental chamber at the IR makes two large shallow tapers. Its impedance has been calculated using ABCI and found to be mostly inductive. They are

$$\text{Im}\left[\frac{Z(\omega)}{n}\right] = 1.0 \times 10^{-3} \Omega. \quad (10)$$

The loss factor without the contribution from the IP masks is

$$k_L = 2.94 \times 10^{-1} \text{ V/pC}, \quad (11)$$

which corresponds to the HOM power loss of 3 kW. This power deposition must be taken care of by e.g., putting an absorber in the chambers.

H. Y-shaped recombination chambers

The LER and HER chambers are combined to a single chamber on both sides of the IP (about 3 m away). The impedance and loss factor of two recombination chambers were modeled as axi-symmetrical structures, and the results by ABCI then were averaged proportional to the azimuthal filling factors. That gives a large loss factor almost equivalent to that of two ARES cavities:

$$k_L = 1.6 \text{ V/pC}. \quad (12)$$

I. Bellows

As explained in the subsection for the masks at arc, there are about 1,000 shielded bellows in both rings (one bellows on both sides of every quadrupole). We have adopted so called sliding-finger structure for bellows. These bellows produce predominantly inductive impedance. Their impedance has been calculated with use of ABCI. The imaginary part of the total impedance and the total loss factor for 1,000 bellows in the LER ring are

$$\text{Im}\left[\frac{Z(\omega)}{n}\right] = 4.23 \times 10^{-3} \Omega \quad (13)$$

and

$$k_L = 2.5 \text{ V/pC}. \quad (14)$$

Additional impedance is generated by the slits between the sliding fingers of the bellows. Using the same formula for a narrow slot, we found that their contributions are negligible.

III. IMPEDANCE BUDGET

The inductive impedances and the loss factors of the individual elements in the LER are tabulated in Table I. The total longitudinal wake potential for the LER is plotted in Fig. 3. The total HOM power deposition in the LER (corresponding to the loss factor of 42.2 V/pC) is $P=570$ kW. In the HER, the total inductive impedance would be comparable to that of the LER. The total loss factor in the HER is larger than that of the LER by 18 V/pC due to additional 20 RF cavities, leading to 60 V/pC. The corresponding total HOM power deposition is 150 kW. These numbers should be used in designing RF parameters.

References

- [1] *The KEKB Design Report* in preparation.
- [2] Y. H. Chin, *Users's Guide for ABCI Version 8.8*, CERN SL/94-02(AP) and LBL-35258 (1994).
- [3] S. Kurennoy and Y. H. Chin, KEK Preprint 94-193 (1995). To be submitted to Part. Accelerators.
- [4] S. Kurennoy, Report SSCL-636, Dallas (1993).

Table I
LER inductive impedance and loss factor budgets.

Component	Inductive impedance $\text{Im}[Z/n] (\Omega)$	Loss factor (V/pC)
Cavities	—	17.84
Resistive-wall	5.2×10^{-3} at 2.3 GHz	4.0
Masks at arc	2.8×10^{-3}	4.6
Pumping slots	8.0×10^{-4}	10.6
BPMs	1.3×10^{-4}	0.71
Mask at IP	negligible	5.2×10^{-2}
IR chamber	1.0×10^{-3}	2.9×10^{-1}
Y-chambers	-8.0×10^{-4}	1.6
Bellows	4.23×10^{-3}	2.5
Total	0.014	42.2

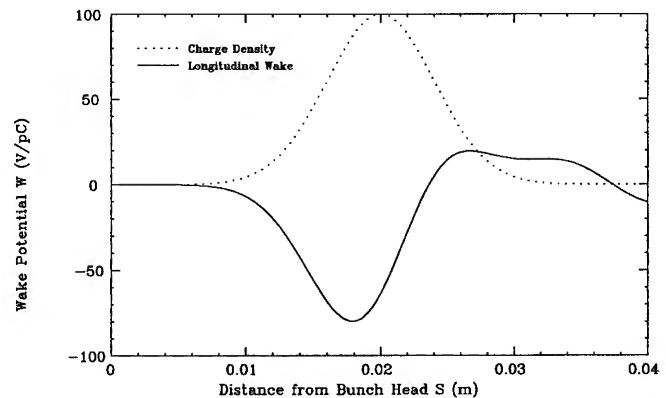


Figure 3. Total longitudinal wake potential for the KEKB LER.

SINGLE-BEAM COLLECTIVE EFFECTS IN THE KEK B-FACTORY

Y. H. Chin, K. Akai, Y. Funakoshi, K. Oide and K. Satoh
KEK, 1-1 Oho, Tsukuba-shi, Ibaraki-ken, 305, Japan

Abstract

In this paper, we deal with the issues of single-beam collective effects (the bunch lengthening and the transverse mode-coupling instability) and coupled-bunch beam instabilities due to RF cavities and the resistive-wall beam pipes in the KEK B-factory. The transit ion problem and coupled-bunch instabilities due to photo-electrons will be discussed in other publications.

I. INTRODUCTION

The KEK B-factory (KEKB) is an electron-positron collider with unequal beam energies (8 and 3.5 GeV) for study of B meson physics[1]. The dominant issues in the KEKB in terms of beam instabilities are the very high beam current (2.6 A in the low energy ring (LER) and 1.1 A in the high energy ring (HER)) to achieve the high luminosity of $10^{34} \text{cm}^{-2} \text{s}^{-1}$, and a short bunch ($\sigma_z = 4 \text{ mm}$) to avoid a degradation of the luminosity by the hour-glass effect. Since the charges are distributed over many (5120) bunches, the bunch current is not unusually high. As a consequence, single-bunch effects are expected to be relatively moderate: their stability limits are beyond the design values with comfortable margins. The main concern, in turn, is on coupled-bunch instabilities due to high-Q resonant structures such as RF cavities and the transverse resistive-wall instability at very low frequency (lower than the revolution frequency).

II. SINGLE-BUNCH COLLECTIVE EFFECTS

In this section, we review our predictions of single-bunch collective effects, namely, the bunch lengthening and the transverse mode-coupling instability. As mentioned in the introduction, these instabilities are expected to impose no fundamental limitation on the stored current, since the bunch current is relatively low compared with other large electron rings. However, the requirement of the short bunch ($\sigma_z = 4 \text{ mm}$) demands a careful attention at any possible causes for deviation from the nominal value.

A. Bunch lengthening

There are two mechanisms to alter the bunch length from the nominal value. One is the potential-well distortion of the stationary bunch distribution due to the longitudinal wake potential. The deformed bunch distribution can be calculated by solving the Haissinski equation. The bunch can be either lengthened or shortened depending on the type of the wake potential. Another mechanism is the microwave instability and has a clear threshold current for the onset of the instability.

Oide and Yokoya have developed a theory to include both the potential-well distortion effect and the microwave instability[2]. A program is now available to compute the bunch length according to their theory. Figure 1 shows the calculated bunch length in the LER as a function of the number of particles in a bunch,

N_p . As can be seen, there is a constant bunch lengthening due to the potential-well distortion and the microwave instability takes off at $N_p = 1.2 \times 10^{11}$, which is about three times larger than the proposed number of particles per bunch. At the design intensity, the bunch is lengthened only by 20%.

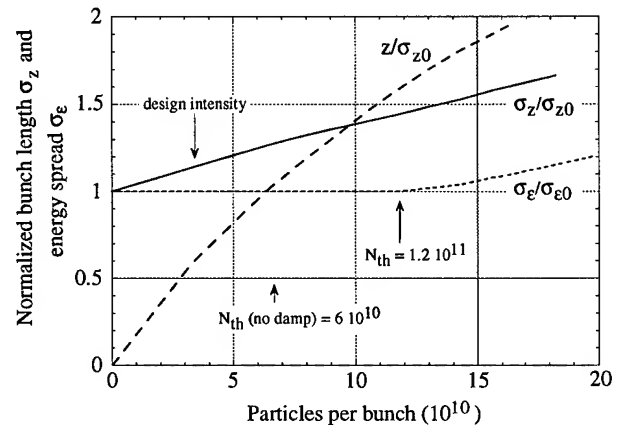


Figure 1. Bunch length and energy spread in the LER.

B. Transverse mode-coupling instability

The transverse mode-coupling instability is known to be responsible for limiting the single-bunch current in large electron rings such as PEP[3] and LEP. This instability takes place when two head-tail modes ($m=0$ and $m=-1$ modes in most cases) share the same coherent frequencies. In a short bunch regime where the KEKB will be operated, the coherent frequency of the $m=-1$ mode keeps almost constant as a function of the bunch current, while that of the $m=0$ mode keeps descending until it meets with the $m=-1$ mode. Using the estimated transverse wake potential and the averaged beta function of 10 m, we found that the coherent tune shift of the $m=0$ dipole mode is only ~ -0.0002 at the design bunch current. This value is much smaller than the design value of the synchrotron tune (~ 0.017). Thus, the transverse mode-coupling instability will not impose a serious threat on the performance of the KEKB.

III. COUPLED-BUNCH INSTABILITIES

As mentioned earlier, the coupled-bunch instabilities due to high-Q structures such as RF cavities and the resistive-wall beam pipes are the main concerns in the KEKB rings because of the unusually large beam current. We have adopted the so-called damped-cavity-structure to sufficiently lower the Q-values of higher-order parasitic modes, typically less than 100. As a result, the growth time of the fastest-growing mode in the LER (HER) becomes about 60 msec (150 msec) longitudinally and 30 msec (80 msec) transversely. They are longer than or comparable to the radiation damping time of 20 msec (longitudinally) or 40 msec

(transversely) in the two rings (with wiggler in the LER). More details on the calculation results will be available in ref. [1]. In this section, we focus on the transverse coupled-bunch instability due to the resistive-wall impedance and coupled-bunch instabilities (both transverse and longitudinal) excited by the crabbing mode of the crab cavity.

A. Transverse resistive-wall instability

The growth rate of the instability in terms of the rigid particle model is given by

$$\tau_{RW}^{-1} = -\frac{\beta_{\perp} \omega_0 I_b}{4\pi E_b/e} \sum_{p=-\infty}^{\infty} \text{Re}[Z_{RW}(\omega_{p,\mu,\nu_{\beta}})], \quad (1)$$

where

$$\omega_{p,\mu,\nu_{\beta}} = (pM + \mu + \nu_{\beta})\omega_0. \quad (2)$$

Here, β_{\perp} is the averaged beta function over the ring, ω_0 is the angular revolution frequency, $\text{Re}[Z_{RW}]$ is the real part of the resistive-wall impedance, I_b is the beam current, E_b is the beam energy, ν_{β} is the betatron tune, μ is the mode number of the coupled-bunch oscillation and M is the number of bunches in the beam. In the above formula, it is assumed that the RF buckets are uniformly filled with the equal number of particles (we ignore effects of the gap in the bunch filling which may be necessary to suppress the ion trapping).

In Figs. 2 and 3, the growth time of the most unstable mode in the LER and HER, respectively, are shown as a function of the betatron tune. In the current design of the LER (HER), the horizontal and vertical tunes are 45.52 (46.52) and 45.08 (46.08), respectively. The most unstable mode (5074 mode) in the LER has the growth time 5.9 and 8.1 msec at these tunes, respectively. On the other hand, the most unstable mode in the HER is the 5073 mode, and has the growth time of 4.0 and 5.6 msec at the horizontal and vertical tunes, respectively. Conversely, we plot the growth time as a function of the coupled-bunch mode number at the tunes 45.52 and 46.52 for the LER and the HER in Figs. 4 and 5, respectively.

One possible cure for this instability is a bunch-by-bunch feedback system. The growth rates obtained in the above are, however, close to the limit of design capability of our feedback system. Fortunately, the coherent frequencies of the unstable modes

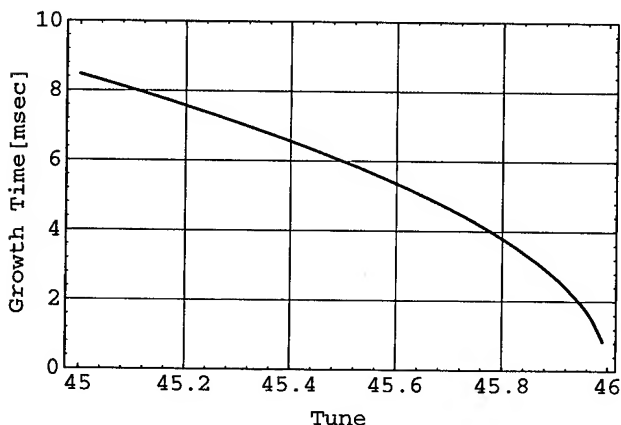


Figure 2. Growth time of the resistive-wall instability as a function of betatron tune in the LER.

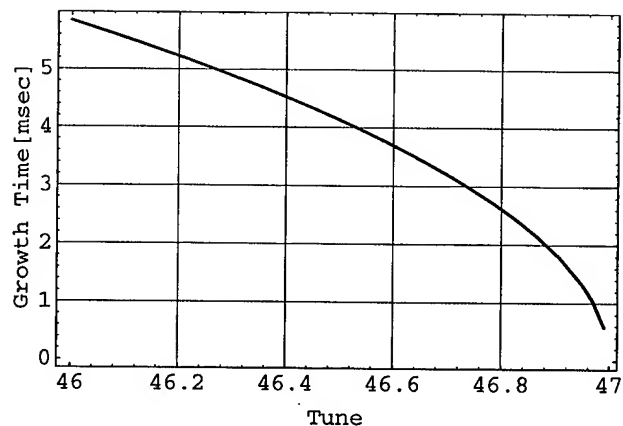


Figure 3. Growth time of the resistive-wall instability as a function of betatron tune in the HER.

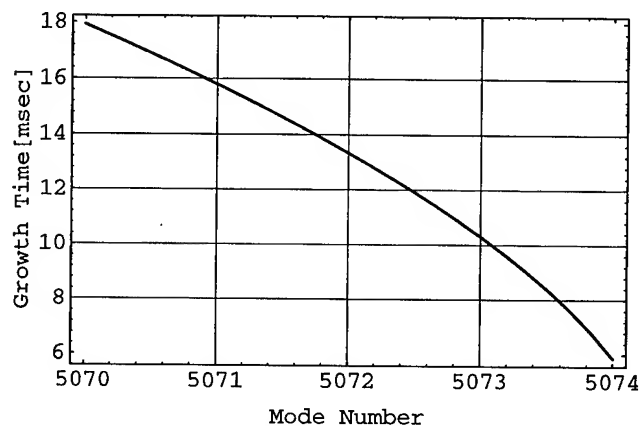


Figure 4. Growth time of the resistive-wall instability as a function of the mode number at the betatron tune of 45.52 in the LER.

stay in a narrow frequency range at low frequency, and thus these modes may be stabilized by a narrow-band mode feedback system rather than a wide-band bunch-by-bunch feedback system. If the bunch-by-bunch feedback system can perform at the damping time of 10 msec, the mode feedback system must cover only one unstable mode in the LER and three modes in the HER, as seen from Figs. 4 and 5. Then, the combination of the two feedback system is expected to provide a damping time of 1 msec for the fastest-growing modes.

B. Coupled-bunch instability by crabbing mode

In this section, we deal with only the instability due to the impedance of the crabbing mode. The instability due to the HOMs can be treated in a similar manner to those in accelerating cavities. The transverse coupling-impedance of a deflecting crabbing mode is expressed as

$$Z_{\perp}(\omega) = \frac{\omega_r}{\omega} \cdot \frac{\frac{R_{\perp}}{Q_0} Q_L}{1 + i Q_L \left(\frac{\omega}{\omega_r} - \frac{\omega_r}{\omega} \right)}, \quad (3)$$

where ω_r is the resonant frequency of the crabbing mode, R_{\perp} is the transverse shunt impedance, Q_0 is the unloaded Q-value

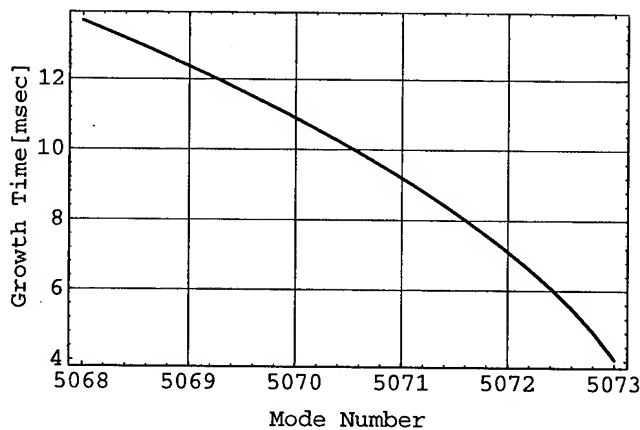


Figure 5. Growth time of the resistive-wall instability as a function of the mode number at the betatron tune of 46.52 in the HER.

and Q_L is the loaded Q-value. The most characteristic feature of the crabbing mode is that it operates at the same frequency as the accelerating mode unlike the HOMs. This feature renders this mode harmless by cancellation between the two betatron sidebands in both sides of the impedance peak, just like for the fundamental accelerating mode of a cavity. Unlike the accelerating mode which must be detuned by a large amount of frequency to compensate the heavy beam loading, we need not detune the crabbing mode. The growth rate of all coupled-bunch modes then almost vanishes as far as the resonant frequency of the crabbing mode is kept near the accelerating frequency. The main parameters of the crab cavity together with some machine parameters of LER are summarized in Table 1. The growth time of the most unstable mode (the 5074 mode for positive detuning, and the 5075 mode for negative detuning) in the LER is depicted in Fig. 6 as a function of the detuning frequency. In this figure, the radiation damping time (40 msec, with wiggler) is shown by the thick solid line. From this figure, it is clear that all modes are stable in the wide range of detuning from -6.5 kHz to 6.5 kHz. The growth time in the HER is even longer than in the LER. We can therefore conclude that the transverse coupled-bunch instability due to the crabbing mode will cause no serious problem as far as its frequency is well controlled.

Another problem may arise when the beam orbit has some offset at the cavity. In this case, longitudinal wake fields are excited which may cause a longitudinal coupled bunch instability. Even so, this type of instability can be stabilized by the fundamental mode of the accelerating cavities or by detuning the crab cavities to the lower frequency.

IV. SUMMARY

We have seen that neither bunch lengthening nor the transverse mode-coupling instability will impose a significant limitation on the stored bunch current. The luminosity performance of the KEKB is rather affected by the couple-bunch instabilities due to RF cavities (longitudinally) and the resistive-wall instability (transversely). Our carefully designed damped-cavity-structure helps to reduce the longitudinal growth to a manageable level. Even the most unstable mode has the growth time (60 msec)

Table I
Main parameters of the crab cavity in the LER.

Beam energy	3.5 GeV
Beam current	2.6 A
Horizontal beta-function at crab cavities	100 m
Horizontal betatron tune	45.52
Number of crab cavities	2
Accelerating frequency	508.88 MHz
Harmonic number	5120
R_{\perp}/Q_0	277.4 Ω/m
Q_L	1×10^6

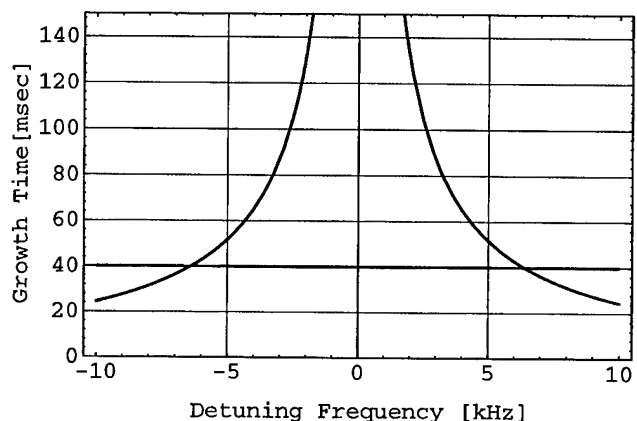


Figure 6. Growth time of the coupled bunch instability due to the crabbing mode in the LER versus the detuning frequency.

longer than the radiation damping time of 20 msec in the LER with wiggler. Transversely, however, the growth time of the resistive-wall instability (~ 5 msec) is far shorter than the radiation damping time of 40 msec. The design of the fast feedback system which can deal with the remaining growth is one of the most challenging problems for the KEKB.

References

- [1] *The KEKB Design Report* in preparation.
- [2] K. Oide and K. Yokoya, KEK Preprint 90-10 (1990).
- [3] M. S. Zisman et. al., *Study of Collective Effects for the PEP Low-Emittance Optics*, LBL-25582 and SSRL ACD Note-59 (1988).

BEAM TRANSFER FUNCTION AND TRANSVERSE IMPEDANCE MEASUREMENTS IN THE FERMILAB MAIN RING

P. J. Chou and G. Jackson

Fermi National Accelerator Laboratory*, MS 345, P.O.Box 500, Batavia, IL 60510 USA

ABSTRACT

Knowledge of the Main Ring(MR) impedance is crucial for the understanding of beam instabilities. Beam transfer function measurements provide a direct measurement of beam impedance[1, 2]. With proper calibration procedures, values for the transverse impedances can be extracted from beam transfer function measurements. The principle of measurements is reviewed and results are presented.

I. REVIEW OF MEASUREMENT PRINCIPLES

A. Beam transfer function

Beam transfer function(BTF) measurement is performed by driving the beam with an external RF excitation, then one measures the induced signal from a transverse pickup. We use the vertical feedback system of Fermilab Main Ring to drive the beam. The measurement setup is depicted in Figure 1.

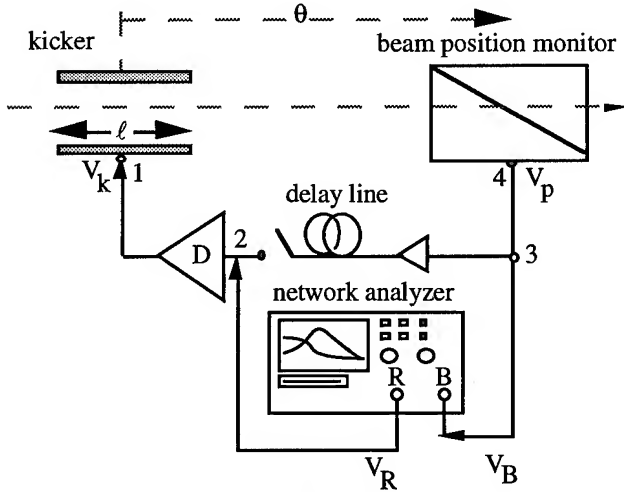


Figure 1: The setup for open-loop beam transfer function measurement. θ is the betatron phase advance from kicker to pickup.

The equation of motion for a single particle driven by external excitation at the location of kicker is given by:

$$\frac{d^2 y}{dt^2} + Q^2 \Omega^2 y = G e^{-i\omega t} + i \frac{e I_b}{\gamma m_0} \frac{Z_{\perp}(\omega)}{L} \langle y \rangle$$

where e =charge of proton, I_b =beam current, m_0 =rest mass of particle, γ =Lorentz relativistic factor, $\langle y \rangle$ =averaged beam displacement, L =accelerator circumference, Q =betatron tune of individual particle, Ω =angular revolution frequency of individual particle, ω =angular frequency of external RF

excitation and Z_{\perp} is the transverse impedance of accelerator. The beam transfer function[3] is defined as:

$$B(\omega) = -i Q_0 \Omega_0 \left\langle \frac{\tilde{y}}{G} \right\rangle$$

For zero accelerator impedance the BTF is given by[1]:

$$B_0(\omega) = \frac{(-/+)}{2} [\pi \rho(\omega) + i \cdot p v \int \frac{\rho(\omega_{\beta})}{\omega_{\beta} - \omega} d\omega_{\beta}]$$

where $\rho(\omega_{\beta})$ is the normalized betatron frequency distribution of particle beam, ω_{β} is the betatron frequency of individual particle. When ω_{β} is near the $\Omega(n+Q)$ sideband, the minus sign is used. The plus sign is used for the $\Omega(n-Q)$ sideband.

If one inverts the BTF and plots the imaginary part vs. real part, one will get the stability diagram. The equation of the stability diagram is given by:

$$\frac{1}{B(\omega)} = \frac{1}{B_0(\omega)} + \frac{e I_b(\omega)}{\gamma m_0 Q_0 \Omega} \frac{Z_{\perp}(\omega)}{L}$$

From the equation of the stability diagram one can determine the accelerator impedance simply by measuring the displacement of the contour from the origin of the complex plane.

B. Calibration

The driven beam response can be measured by the induced voltage on beam position monitor(BPM) at point 4:

$$V_p = I_b \langle y \rangle S_{\perp}$$

where S_{\perp} is the detector sensitivity[4]. The actual signal measured by the network analyzer is V_B . From the definition of the beam transfer function, the induced voltage V_p can be rewritten as:

$$V_p = \frac{I_b(\omega) S_{\perp}(\omega) B(\omega)}{-i Q_0 \Omega_0} G$$

If h denotes the cable length from port 4 of BPM to port B of the network analyzer, then the S_{21} parameter can be written as:

$$S_{21} = \frac{e I_b(\omega) S_{\perp} K_{\perp} D}{-i \gamma m_0 \ell Q_0 \Omega_0} B(\omega) e^{-i\omega h/c}$$

where ℓ is the length of kicker plate, K_{\perp} is the kicker constant[4] which characterizes the response of the kicker and D is the voltage gain factor of the amplifier.

* Operated by Universities Research Association Inc., under contract with the U.S. Department of Energy.

One can compensate the cable delay during data analysis. Since the frequency span for a BTF measurement is much smaller than the 3 dB frequency bandwidth of feedback system, S_{21} parameter and $B(\omega)$ is only different by a proportionality constant. One can just do a linear fit to determine the proportional constant, which is given by the following:

$$\frac{eI_b(\omega)S_{21}K_{\perp}D}{-i\gamma m_0\ell Q_0\Omega_0}$$

The above arguments will not hold if the frequency span of the BTF measurement is beyond the 3 dB bandwidth of feedback system. To improve the signal to noise ratio, a time domain gating technique[5] is applied to the analysis. Because we are interested in the low frequency range of the transverse impedance, a detector optimized for low frequency signals was built as depicted in Figure 2.

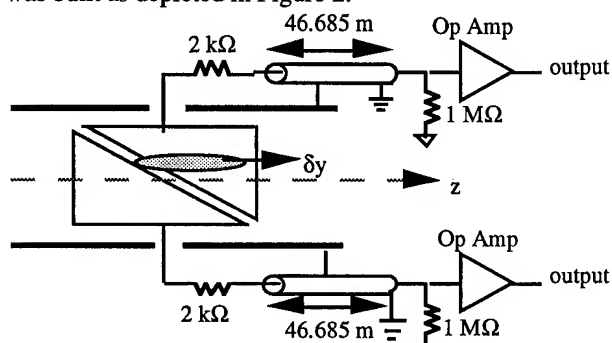


Figure 2: The configuration of beam position monitor used for BTF measurements.

II. RESULTS OF BEAM EXPERIMENTS

Vertical BTF measurements were done at the injection energy of the MR, 8 GeV, with debunched beam. Figure 4 and 5 are examples of measured raw data. Figure 6 is the stability diagram after the time domain gating technique is applied. The signal is still quite noisy. The fitting results are shown as dashed lines in Figures 6-9. Only the central portion of resonance response is used for fitting because of the noise. The fitting result for vertical impedance is shown in Figure 10.

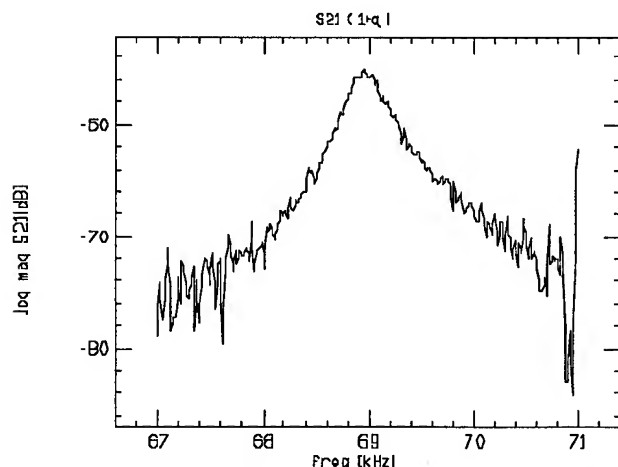


Figure 3: Amplitude of S_{21} (raw data) for the $n=1+q$ sideband.

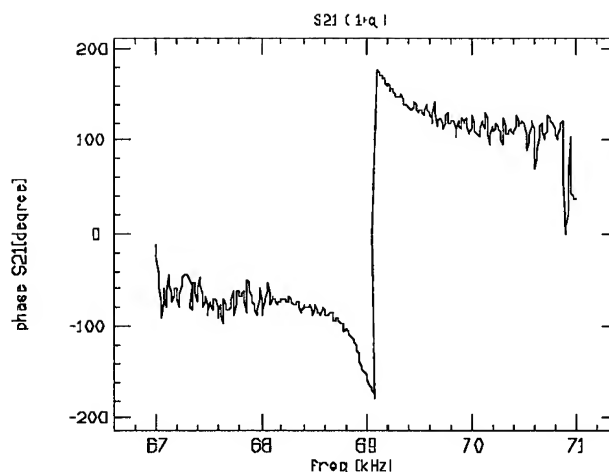


Figure 4: Phase of S_{21} (raw data) for the $n=1+q$ sideband.

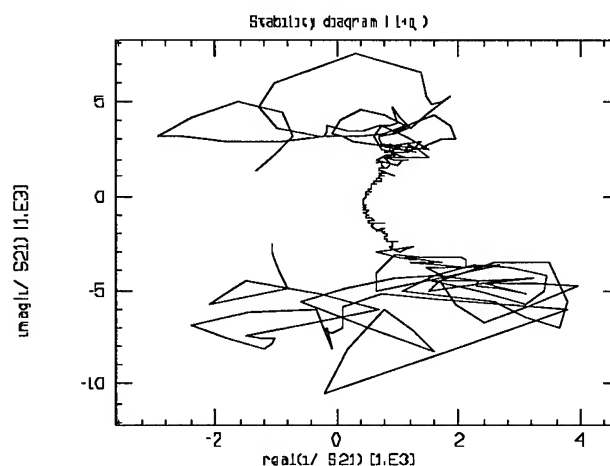


Figure 5: Stability diagram for the $n=1+q$ betatron sideband processed by applying the time domain gating technique.

The revolution frequency of Main Ring is 47.4 kHz and the fractional tune is 0.4 . The beam pipe is made of stainless steel and the thickness is 0.065". If we assume only beam pipe of circular cross section is used around the accelerator, we can calculate the vertical impedance. The result is depicted in Figure 11.

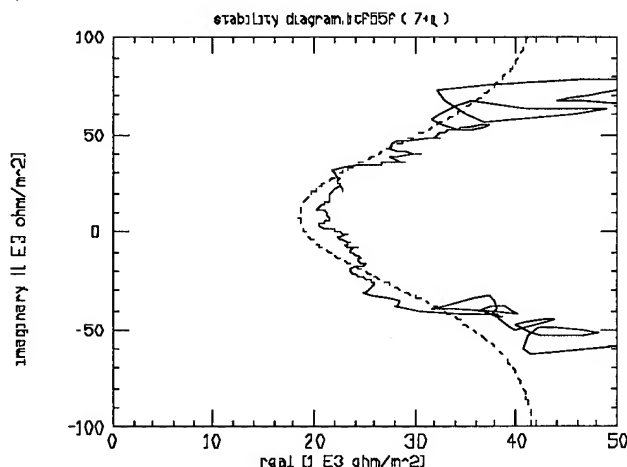


Figure 6: Stability diagram for the $n=7+q$ betatron sideband.

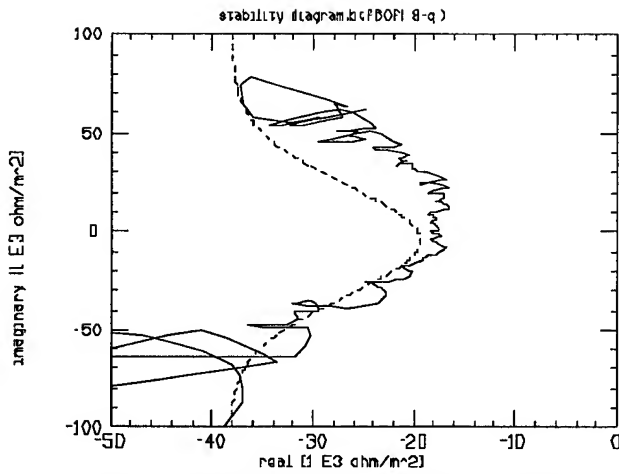


Figure 7: Stability diagram for the $n=8-q$ betatron sideband.

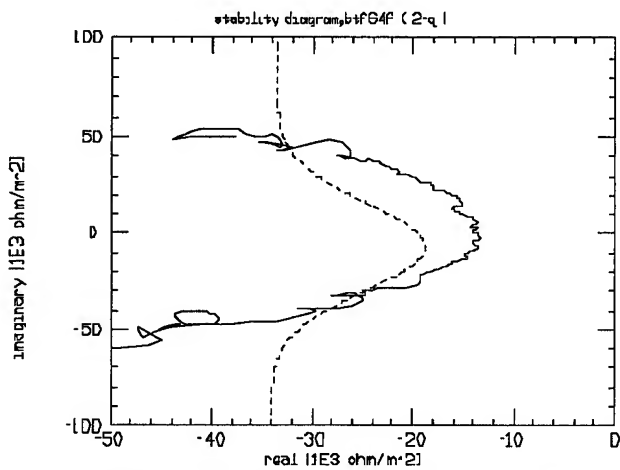


Figure 8: Stability diagram for the $n=2-q$ betatron sideband.

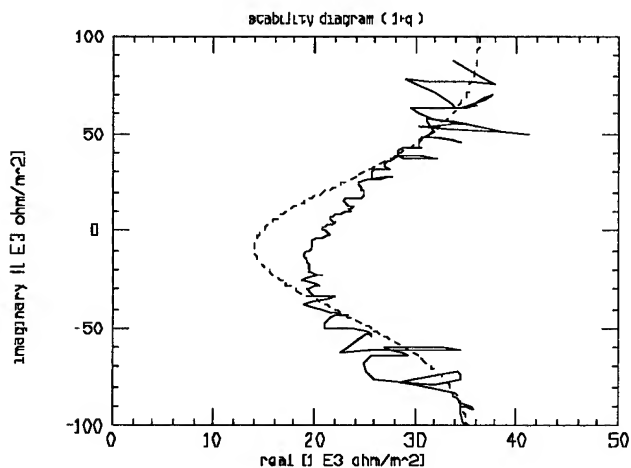


Figure 9: Stability diagram for the $n=1+q$ betatron sideband.

We are particularly interested in the vertical impedance of the first few betatron sidebands because of evidence showing the signs of collective beam instabilities due to the resistive wall impedance[6]. The results from BTF measurements do not show the characteristic $\omega^{-1/2}$ dependence of resistive wall impedance. Other sources besides wall resistance of the beam

pipe may contribute to the observed phenomena. Work is still underway to improve the accuracy of measurements.

III. ACKNOWLEDGEMENT

The authors would like to thank U. Oeftiger for many helpful discussions.

IV. REFERENCES

- [1] A. Hofmann, B. Zotter, IEEE Transactions NS-24, No.3 (1977)1487.
- [2] M. Chanel, U. Oeftiger, CERN/PS 93-44(AR).
- [3] D. Boussard, CERN SPS/86-11(ARF).
- [4] M. Month, M. Dienes(eds.), AIP Conference Proceedings, No.249, p.537, American Institute of Physics, 1992.
- [5] U. Oeftiger, F. Caspers, CERN/PS/AR/Note 92-19.
- [6] G. Jackson, IEEE Particle Accelerator Conference, vol.3, (1991)1755.

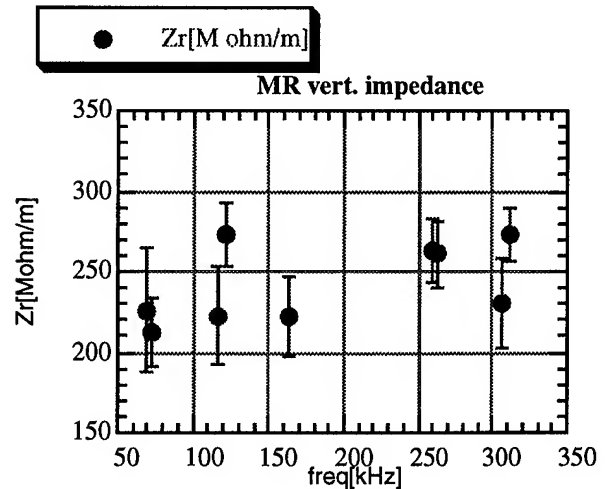


Figure 10: The vertical impedance of the Fermilab Main Ring from BTF measurements. The unit of y axis is in M Ω /m.

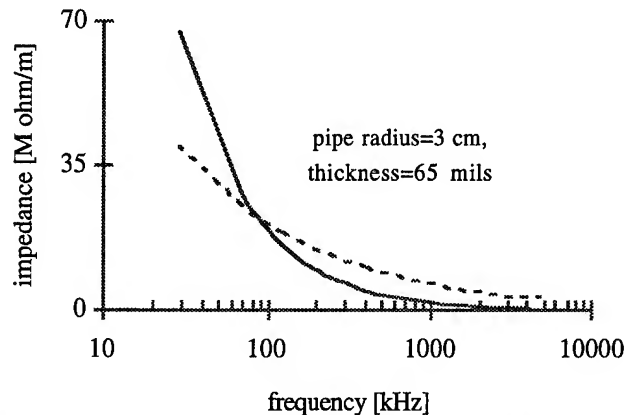


Figure 11: Theoretical calculation of vertical impedance for Main Ring. Only the real part is plotted. The dashed line is the value for thick wall model and the solid line is the thin wall model.

EXPERIMENTAL STUDIES OF TRANSVERSE BEAM INSTABILITIES AT INJECTION IN THE FERMILAB MAIN RING

P. J. Chou and G. Jackson

Fermi National Accelerator Laboratory*, MS 345, P.O.Box 500, Batavia, IL 60510 USA

ABSTRACT

Transverse beam instabilities at injection prevent the Fermilab Main Ring from storing higher intensity proton beam. It is essential to understand the nature of existing beam instabilities in order to increase the stored beam intensity. Results of experimental studies are presented and the nature of beam instabilities is depicted. Possible cures are discussed.

I. THE OBSERVED PHENOMENA

The existence of transverse collective instabilities in the Main Ring (MR) has been known for years[1, 2]. The most severe effects occur in the vertical plane because of the smaller width of beam pipe in the vertical direction. Two damper systems were built to combat the instabilities. One is slow damper which covers the frequency from DC to 1.5 MHz. The other is the super damper which is a bunch-by-bunch feedback system using digital technology. Evidence of collective beam instabilities has been shown in Ref[2].

A. Growth rate vs. beam intensity

The growth rate of the amplitude of vertical betatron oscillation clearly shows strong dependence on the total beam in the MR as depicted in Figure 1 and 2.

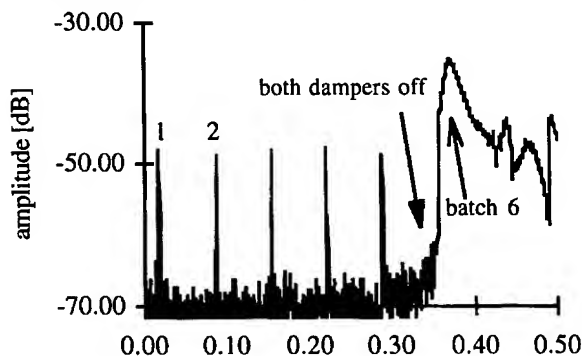


Figure 1: The amplitude of vertical betatron oscillation for $n=1-q$ sideband, batch spacing=8 RF buckets.

B. Growth rate vs. batch spacing

The separation between adjacent batch also plays an important role in the growth rate of vertical instability. The beam batches were injected in a successive order. A longer spacing between adjacent batch certainly helps to deter the onset of vertical instability. Each batch contains 84 beam bunches in the data shown in Figure 3 and 4.

C. Growth rate vs. bunch length

* Operated by Universities Research Association Inc., under contract with the U.S. Department of Energy.

The growth rate of the vertical instability also shows dependence on the bunch length. This indicates that there may be single bunch motion in the vertical plane too.

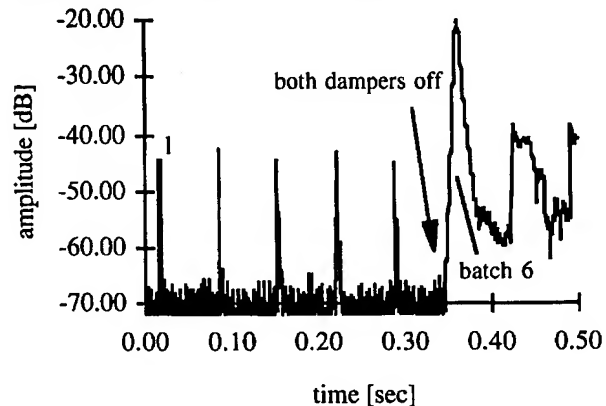


Figure 2: The amplitude of vertical betatron oscillations for the $n=1-q$ sideband. The experiment setup is the same as in Figure 1 except the beam intensity is doubled.

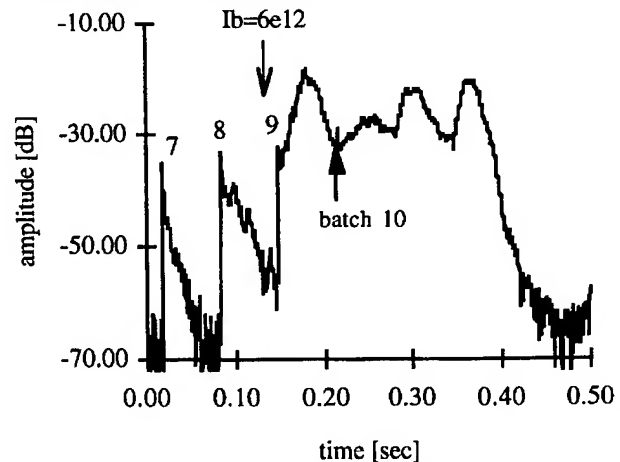


Figure 3: The amplitude of vertical betatron oscillation for the $n=1-q$ sideband. The batch spacing is 8 rf buckets. Both dampers were on during the measurement.

D. Growth rate vs. betatron tune

The growth rate as a function of the vertical tune was measured and depicted in Figure 8. The horizontal tune was 19.48 and the initial vertical tune was 19.49. There were 12 batches in the MR with a batch spacing of 8 rf buckets. Each batch was fully filled up. The chromaticity settings were -12 for the horizontal and 0 for the vertical plane.

From results shown in Figures 1 -6, we believe that both coupled bunch mode and single bunch head-tail instabilities exist in the MR.

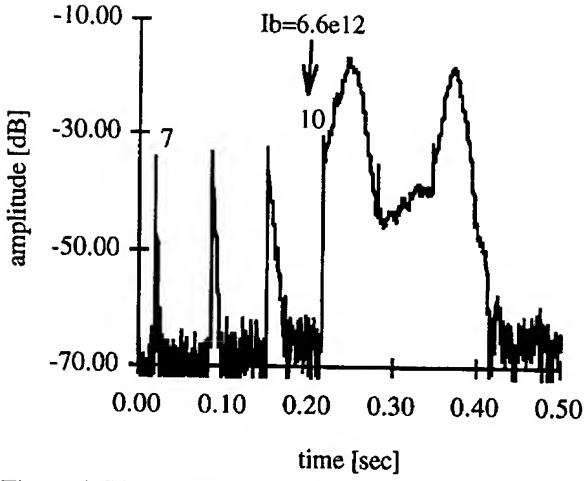


Figure 4: The amplitude of vertical betatron oscillation for the $n=1-q$ sideband. The experiment setup is the same as in Figure 3 except the batch spacing is 376 rf buckets.

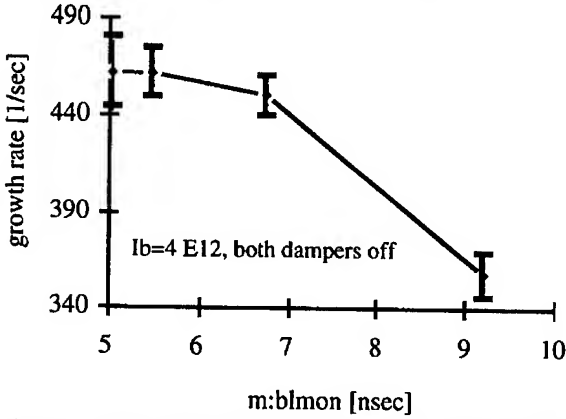


Figure 5: The measured growth rate as a function of the bunch length.

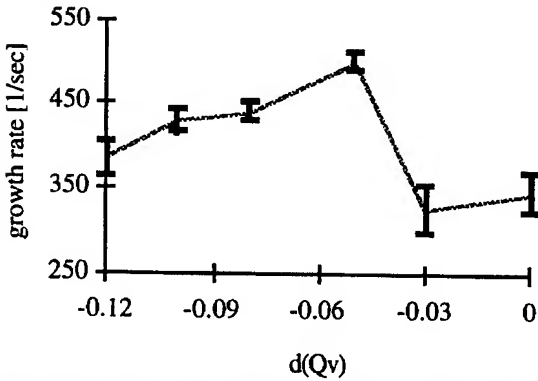


Figure 6: The growth rate vs. the changes in the vertical tune.

II. DATA ANALYSIS

A. Coupled bunch instability

A qualitative analysis was developed to help identify the unstable mode of coupled bunch instability.

Suppose there are m' batches in the accelerator, each has

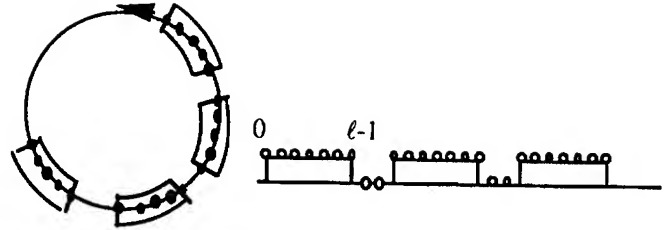


Figure 7: The bunch configuration of multibatch injection.

ℓ bunches. Each batch is separated by g rf buckets. The bunch configuration is depicted in Figure 7. The right side of Figure 7 is the cut-away view of the configuration. If we only consider the equilibrium condition, i.e. there is no damping or growth in the amplitude of betatron oscillation. We also use a macroparticle to represent a bunch. Then the transverse motion of the beam centroid for bunch p observed by a beam position monitor (BPM) at a fixed location can be expressed as:

$$d_p(t) = A_\beta Q \sum_{n=-\infty}^{\infty} e^{-i\psi(t)} \delta(t - nT - p\frac{T}{M} - \hat{\tau} \cos(\omega_s t + \phi_p))$$

$$\psi(t) = q\beta\omega_0 t + \omega_\xi \hat{\tau} \cos(\omega_s t + \psi_p)$$

where $q\beta$ is the fractional part of betatron tune, ω_0 is the angular revolution frequency, ω_ξ is the chromatic frequency, ω_s is the synchrotron frequency, ϕ_p is the initial synchrotron phase, ψ_p is the initial betatron phase, $\hat{\tau}$ and A_β is the amplitude of synchrotron oscillation and betatron oscillation respectively. Q is the total charge of a beam bunch, T is the revolution period and M is the harmonic number of accelerator. The signal observed by the beam position monitor is given by:

$$d(t) = \sum_{m=0}^{m'-1} \sum_{p=m(\ell+g)}^{m(\ell+g)+\ell-1} d_p(t)$$

For a closed-loop coupled bunch mode, we can write the coherent phase advance θ between the adjacent bunches as $2\pi\mu/M$ where μ is an integer ranging from 0 to $M-1$. Then the frequency spectrum of transverse signal for the multibatch configuration with missing bunches is given by[3]:

$$D(\omega) = \sum_{n,k=-\infty}^{\infty} A_\beta Q \omega_0 (-i)^k J_k((q\beta\omega_0 - \omega + \omega_\xi)\hat{\tau}) \cdot$$

$$F(n - \mu, \ell) B(n - \mu, \ell, g, m')$$

which is just the single bunch result multiplied by two extra factors F and B . F is the form factor for a single batch with many consecutive bunches. B is the form factor for the multibatch configuration. When there is only one batch in the accelerator, the value of B converges to one. Therefore, the frequency spectrum of transverse signal with coupled bunch coherence is just shifted by the mode factor μ . The explicit expressions for the form factors are:

$$F(n, \ell) = \left| \frac{e^{i2\pi n\ell/M} - 1}{e^{i2\pi n/M} - 1} \right|$$

$$B(n, \ell, g, m') = \frac{e^{i2\pi n(\ell+g)m'/M} - 1}{e^{i2\pi n(\ell+g)/M} - 1}$$

Figure 8 shows good agreement between the analysis and measurement data. It was found that $\mu=1$ gave the best fit. Therefore, the dominant unstable mode is the $n=1-q$ betatron sideband. Figure 9 is the time domain picture of the vertical betatron oscillation measured with a stripline BPM. The bunch oscillation was recorded up to five revolutions.

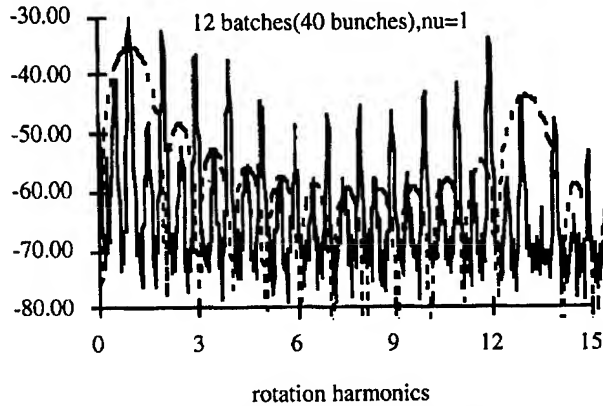


Figure 8: The frequency spectrum of vertical motion when each batch was only half filled. Both dampers were off. The dashed line is the calculated form factor with $\mu=1$.

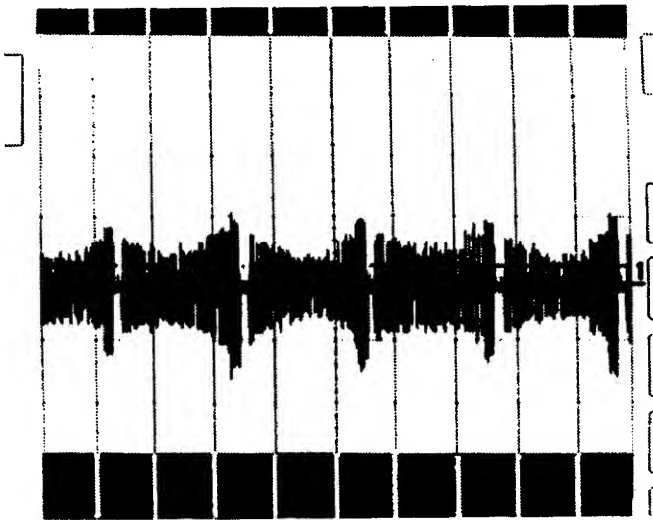


Figure 9: The vertical oscillation of 12 equally spaced batches. The horizontal scale is 10 $\mu\text{s}/\text{div}$. Signal was measured by a stripline BPM. Due to the reflected pulse from the downstream end of BPM, the period of oscillation is about 40 μs instead of 20 μs . The frequency of the $n=1-q$ betatron sideband is around 26 kHz. The revolution period of MR is 21 μs .

B. Head-tail instability

Various modes of vertical head-tail instability were also observed in the MR. Signals were measured by a quarter wavelength stripline BPM and digitized by a Tektronix digitizer RTD720 running at 2 GSample/sec. The time step used in Figures 10 and 11 is 500 ps/unit.

Figure 10 depicts the $m=0$ head-tail mode and Figure 11 is the $m=1$ mode. Both dampers were turned off during the measurements.

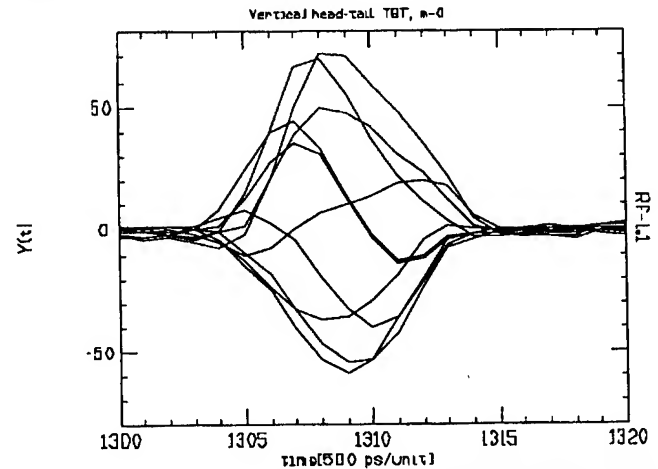


Figure 10: Vertical chromaticity=3.6, bunch length=5 nsec, beam intensity/bunch=1.07 E10 protons.

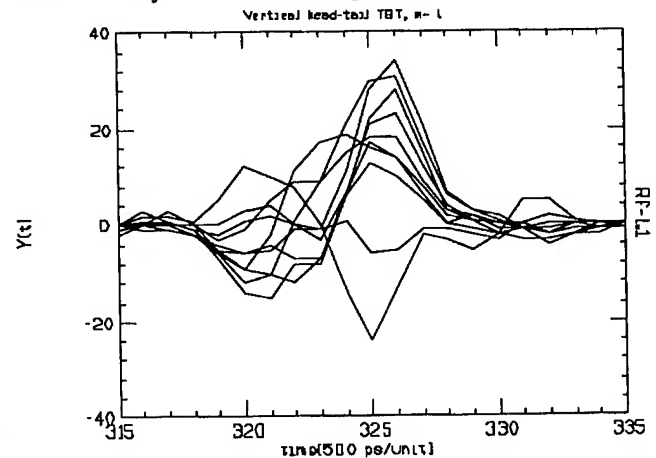


Figure 11: Vertical chromaticity=-40, bunch length=5 nsec, beam intensity/bunch=1.67 E10 protons.

C. Discussions

The measurements presented here confirm the previous suggestions that MR suffers from the vertical instabilities due to the resistive wall impedance[2]. Measurements of the accelerator impedance also show large resistive impedance in the low frequency range[4]. Design work for a new damper system is currently underway.

III. REFERENCES

- [1] R. Stiening, E. J. N. Wilson, Nucl. Instr. and Methods **121** (1974) 283-285.
- [2] G. Jackson, Proc. IEEE Part. Acc. Conf., San Francisco (1991), p.1755.
- [3] P. J. Chou, unpublished manuscript.
- [4] P. J. Chou, G. Jackson, "Beam transfer function and transverse impedance measurements in the Fermilab Main Ring", in this proceedings.

Longitudinal Multibunch Feedback Experiment with Switched Filter Bank*

A. Pei, M. Ball, M. Ellison, X. Kang, S.Y. Lee, D. Li, J. Liu, A. Riabko, L. Wang
Indiana University Cyclotron Facility, Indiana University, Bloomington, IN 47405 USA

Abstract

Fast bunch to bunch feedback is necessary to control instabilities caused by coupled bunch oscillations in high intensity machines. A time domain active feedback scheme is discussed with focus on effective error detection using simple analog filters. Fast electronic switches direct each beam bunch signal from a beam pickup to a corresponding filter. The filters are excited at steady states. The output of the filters are steady sine waves tracking the phase and amplitude variations of individual bunches, allowing easy phase comparison with a reference rf signal. Amplitude detection of the signals yields valuable information of higher order beam oscillation modes. The beam motion information is processed and multiplexed to a fast phase or amplitude modulator that drives a wideband kicker. The feedback system can also be used to correct individual bunch oscillations caused by injection errors in larger machines filled by a number of booster cycles.

I. INTRODUCTION

Classical global rf beam feedbacks are effective in damping the coherent synchrotron oscillations and are widely used in modern synchrotrons [1]. When the oscillations vary from bunch to bunch, such as in the case of coupled bunch oscillations [2], coherent feedback is no longer effective. The feedback in such a case needs to be bunch specific and can be implemented in either frequency or time domain [3].

In the frequency domain method, sidebands responsible for the oscillations of various modes are identified, processed and fed back to a wideband correction kicker. Elaborate filters, usually realized by digital signal processing technology, are used to provide the necessary transfer function of the feedback loop. The technique can possibly damp very fast instability growths relative to the synchrotron tune. No instantaneous error detectors and modulators are necessary since the feedback works entirely in the frequency domain. The signal processing filters, however, need to know accurate information about the oscillations since prescribed phase and amplitude characteristics must be realized at various sideband

frequencies.

The time domain method treats individual beam bunch as a harmonic oscillator coupled to adjacent bunches. The motion of the bunch can be described as that of an undamped simple harmonic oscillator:

$$\ddot{x} + \omega_s^2 x = f(t) \quad (1)$$

where x can be either the phase or energy variations caused by oscillations, ω_s the synchrotron oscillation frequency, and $f(t)$ the driving term. If the driving term $f(t)$ can be made to contain a term that is proportional to the first time derivative of x , damping can be achieved. In practice this is realized by detecting x and phase-shifting it by 90 degrees, resulting in a net differentiated term. The signal is then used to modulate a wideband rf cavity. In this method, exact information of oscillations is not necessary and a properly designed system can cover synchrotron tunes varying with time.

So far as damping is concerned, the two methods are equivalent and output the same correction signals to the wideband kicker [3].

II. IMPLEMENTATION OF TIME DOMAIN FEEDBACK

Our damping experiment uses the time domain method, with focus on effective error detection.

For the dipole mode oscillations, the time domain method must pick up the beam phase or energy error with respect to a reference. Energy errors can be picked up by position detectors in a region of high dispersion. The post-detection signal processing, however, has to be able to subtract the component of betatron oscillations. This adds complexity to the implementation.

The detection of phase errors is thus employed in our experiment. The hardware needs to detect the instantaneous phases of individual beam bunches and have a fast phase shifter that provides different correction phase values for each bunch.

A simple measurement of time difference between rf and a preset level of beam profile cannot produce the precise location of the centroid of the beam bunch due to the short

*Work supported in part by NSF Grant No. PHY-92-21402.

time involved and the complexity of beam profile. When a beam is tightly bunched in an rf bucket, such as in many electron rings, the precision of timing measurement can be improved by generating a train of pulses with a suitable bandpass filter (such as a Bessel constant delay type), or a microwave pulse to comb generator [4] [5]. The resulting pulse train is then compared with an rf reference by a phase detector. The timing measurement has very good accuracy due to error averaging over many cycles by phase detection.

In our experiment we pick a specified harmonic component of a beam profile (usually the fundamental revolution frequency) as a reference to the position of a relative wide beam bunch. This is often a reasonable measurement of beam bunch centroids for many types of complex beam profiles with certain symmetry.

Fig. 1 is a block diagram of our experimental scheme. The beam signal is taken from a wall gap monitor. The ring operating rf frequency is divided by the ring harmonic number. A digital counter is used to accomplish the task. The state of the digital counter is decoded to drive the switches connected to filters, so that each switch closes when a corresponding beam bunch arrives. The filter bank consists of n filters, corresponding to n bunches in the ring. Each filter only sees the beam profile of its corresponding bunch in the period of one particle revolution due to fast switching and tracks the fundamental (or other harmonic) component of a single beam bunch. The filters can either be lowpass or bandpass to obtain the desired harmonic component of the beam bunch.

Since the filters operate in the steady state instead of transient state, the parameters of the filters are quite tolerant. The filter output frequency will be locked to the revolution frequency in our setup. Properly designed filters can cover the frequency swing of machines of relativistic energies. For lower energy machines in which the velocities of particles vary a lot, the filters can be electronically tuned due to their simplicity.

The rf system frequency is divided down to the same frequency as that of filters and distributed to the phase comparators in each channel. Because the synchrotron oscillations are relatively slow, the phase errors vary slowly and can be processed by normal op-amp circuits for 90 degree phase-shifting and offset compensations.

The output of the signal processors is fed into another array of fast electronic switches operating synchronously with the demultiplexing switches. The time-multiplexed signal is then used to modulate a high speed phase modulator that drives a wideband rf kicker. The time delay between the demultiplexing switches and multiplexing switches is set as such that a beam bunch sees the correction signal generated by its error. A delay of some integer numbers of revolution

periods is allowed since the synchrotron tune is usually much smaller than unity.

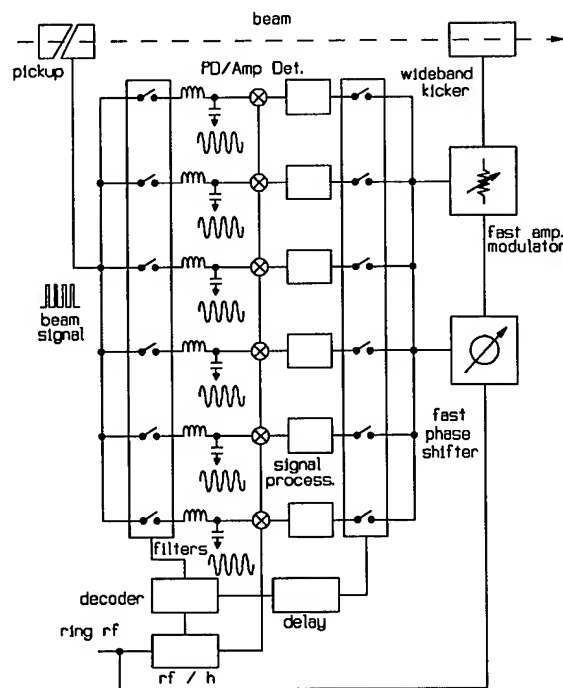


Figure 1. Block diagram of fast bunch to bunch feedback experiment.

The amplitude information of the filter output reflects higher mode bunch oscillations and is very useful, too. As shown in Fig.1, it can be amplitude detected and processed in the same fashion as the phase errors. A multiplexed fast amplitude modulator can then amplitude-modulate the wideband rf kicker to damp the oscillations.

III. HARDWARE CONSIDERATIONS

The success of the approach depends heavily on the quality of high speed electronic switches. Thanks to the state of microwave technologies, switches with excellent on/off characteristics and a couple of nanosecond switching time are readily available commercially.

Fig.2 is a scope picture of a switched beam signal. The top trace is an electron cooled 140 MeV polarized proton beam signal from the IUCF Cooler Ring. The signal is obtained from a wall gap monitor. The lower trace shows that every fourth bunch seen by the wall gap monitor is being switched to a filter. The bunches shown were in fact the same beam bunch passing through the beam monitor at the revolution frequency since the synchrotron was operating at the harmonic $h=1$. The switch was in fact being switched on every

four revolution periods. So far as switching is concerned, however, there is no difference between such a setup and true individual bunch switching.

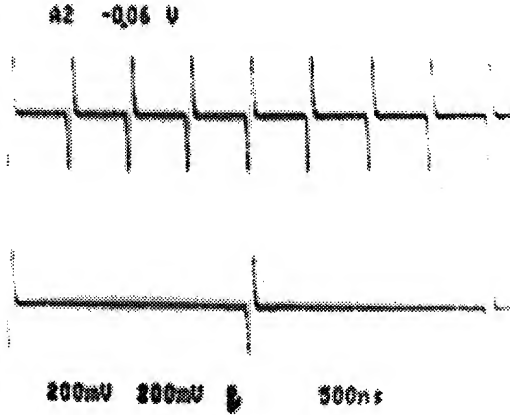


Figure 2. Every fourth bunch of beam in this scope picture is switched into a filter.

The filters are simple LC types. The phase at the output of the filters is delayed by the phase delay of the filters at the operating frequency and shows up as a DC offset at the phase detector output. The group delay of the filters delays the amplitude envelop of the filter output and is usually not a concern since the bunch oscillation periods are relatively long. If the fundamental revolution frequency is chosen from the beam profile, the filters can be lowpass types. Other harmonics usually require bandpass filters at the harmonic frequency. The Q of the bandpass filter must be such that $f/2Q > f_s$. In other words, the synchrotron sidebands must be able to pass the filter. The expression of a given harmonic of a phase modulated beam signal is:

$$x(t) = A_h \sum_{n=-\infty}^{\infty} J_n(m) \cos(\omega_h + n\omega_s) t \quad (2)$$

where J_n is the n th Bessel function of the first kind, n the n th harmonic of f_s , m the phase excursion in radian and A_h the amplitude of the h th harmonic. When the phase excursion is large, the filter bandwidth needs to cover all the higher order sidebands with significant amplitudes.

Because real beam with coupled bunch oscillations is not readily available, an electronic signal source is set up to simulate the individual bunch oscillations. Fig.3 is a block diagram of such a simulator source. Two beam bunch signals capable of independent phase modulations are simulated in this setup with a "bunch spacing" of $1/f$. An $f/2$ rf signal is split two ways. One channel is being phase modulated directly

while the other channel is delayed by $1/f$ and then phase modulated. Two one-shot pulse generators are triggered by the phase modulated signals. The output of the pulse generators are added by a combiner, forming the desired simulation signal. N bunches can be simulated in a similar fashion from an f/N rf source that is split N channels and then recombined.

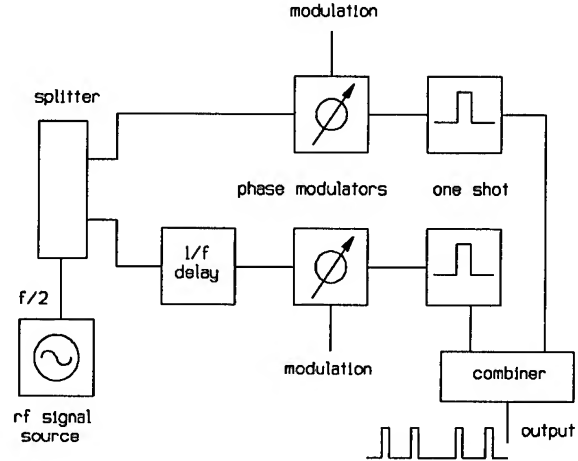


Figure 3. Block diagram of a beam signal simulation source with two independent oscillation modes.

IV. EXPERIMENTAL PLANS

We have been focusing on the error detection of coupled bunch oscillations. A wideband longitudinal kicker is needed to conduct beam experiments. A principle demonstration experiment can be conducted in the IUCF Cooler Ring attempting to damp the non-coherent bunch oscillations induced by an intentional injection phase mismatch. Further experiments can then be conducted in facilities with sufficiently high beam intensities and high impedance elements.

V. REFERENCES

- [1] D. Boussard, "Design of a Ring Rf System", CERN 91-04, Julich, 1990.
- [2] A. Hofmann, "Single-Beam Collective Phenomena -- Longitudinal", CERN 77-13, p. 165, Geneva, 1977.
- [3] J. Fox et al., "Feedback Control of Coupled-Bunch Instabilities", Proc. PAC 93, p. 2076, 1993.
- [4] H. Nuhn et al., "A Longitudinal Multibunch Feedback System for PEP", Proc. PAC 91, p. 1410, 1991.
- [5] D. Briggs et al., "Prompt Bunch by Bunch Synchrotron Oscillation Detection", Proc. PAC 91, p. 1404, 1991.

FIELD PROPAGATION EFFECTS AND RELATED MULTIBUNCH INSTABILITY IN MULTICELL CAPTURE CAVITIES

M. Ferrario[#], A. Mosnier^{*}, L. Serafini[#], F. Tazzioli[#], J.-M. Tessier^{*}

[#]Infn, Frascati and Milano -- ^{*}Cea/Dapnia/Sea, Ce-Saclay

Field propagation effects during the filling and re-filling of the cavity are not harmful for a relativistic beam accelerated in a multicell standing wave cavity. On the opposite the beam dynamics of a non relativistic beam injected into a capture cavity can be significantly affected by the interaction with other modes of the fundamental passband, under beam-loading conditions. In fact, the dominant beating provided by the passband mode nearest to the accelerating π -mode introduces fluctuations on the accelerating voltage. The phase slippage occurring in the first cells, between the non relativistic beam and the lower modes, produces an effective enhancement of the shunt impedances, which are usually negligible for a relativistic beam in a well tuned cavity. In some cases simulations show a significant oscillation of the energy spread and transverse normalized emittance along the bunch train. As an example, we have applied our computational models to the beam-loading problem in the Tesla Test Facility (TTF) superconducting capture cavity.

I. INTRODUCTION

In addition to single bunch effects, induced in particular by space charge forces, multi-bunch effects due mainly to RF field propagation inside the cavity, will affect the quality of a non relativistic beam accelerated by standing wave structures. The study of these beam loading effects, which could limit the performances of injectors involving SW cavities, led to the development of numerical codes [1]: HOMDYN, which includes space charge effects and transverse motion and MULTICELL, which involves the longitudinal motion.

After a cavity filling time, the cavity is periodically refilled by RF power during the bunch to bunch interval. Although the generator frequency is set close to the accelerating π -mode, all the modes of the TM_{010} pass-band will be excited. Recently, in the aim to study the beam loading effect in the superconducting cavity TESLA for a relativistic beam, the multi-mode problem was solved by using systems of first order differential equations [2] or Laplace transforms [3].

In this paper, we use however a different approach, by directly solving the differential equations relative to each usual mode of the pass-band, provided that an intermode coupling term is taken into account. It can be shown in fact [4] with the help of the theory of coupled resonators, that the usual modes of the pass-band, found in the steady-state regime, are coupled through the external Q of the first cell, where the coupler is located, and not through the intrinsic wall losses of the cells.

The excitations Z_m of these normal modes of index m are then found by solving the following system (1) of coupled differential equations:

$$\ddot{Z}_m + \frac{\omega_0}{Q_0} \dot{Z}_m + T_{1m} \frac{\omega_0}{Q_{ex}} \sum_k T_{1k} \dot{Z}_k + \omega_m^2 Z_m = \frac{T_{1m}}{N\epsilon} \frac{d}{dt} \int_{S'} (\vec{n} \times \vec{H}_n(\vec{r}, t)) \cdot \vec{E}_{an}(\vec{r}) dS + \frac{1}{\epsilon} \frac{d}{dt} \int_{V_{cav}} \vec{J}(\vec{r}, t) \cdot \vec{E}_a^m(\vec{r}) dV \quad (1)$$

The first driving term represents the generator current, while the second integral over the whole cavity represents the beam interaction with the mode m and will be computed during each bunch passage. The coefficient T_{nm} is the normalized excitation of mode m ($m=1, M$) at the center of cell n ($n=1, N$). The evolution of the M field amplitudes during the cavity filling and refilling driven by the generator current, together with the perturbation due to beam-loading, are found by numerical integration of system (1) coupled to the beam equations of motion. Since we are particularly interested in the evolution of amplitude and phase envelopes of the RF fields of the fundamental pass-band, which are slowly varying functions, this second order system can be easily transformed to a first order differential equations system [1].

II. RELATIVISTIC BEAM

In a well tuned cavity interacting with a relativistic beam, the average accelerating field vanishes for all modes, except of course for the π -mode. However, since the π -mode is coupled to the other excited modes through the Q_{ex} , some fluctuations remain.

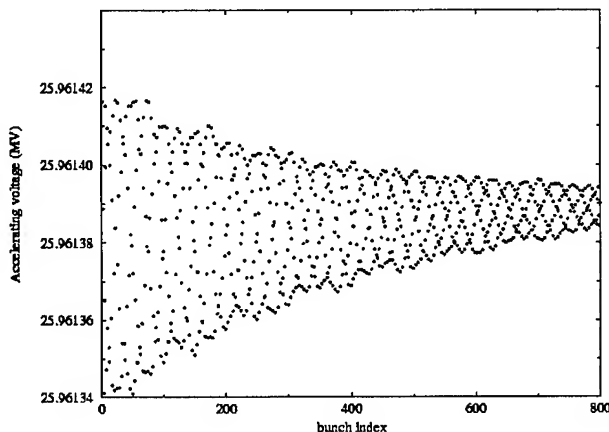


Figure 1 : Accelerating voltage evolution during 800 bunches

Figure 1 is a plot of the total accelerating voltage during the entire TESLA beam passage in a 9-cells SC cavity (bunch charge: 8 nC, bunch spacing: 1 μ s, accelerating gradient: 25 MV/m), and points out the residual oscillations, mainly caused by the mode of the pass-band nearest to the π -mode, decaying according to the mode time constants $\tau = 2Q_{ex} / \omega$. The induced bunch-to-bunch energy spread is nevertheless very small, from $3 \cdot 10^{-6}$ at the beginning to $0.5 \cdot 10^{-6}$ at the end.

III. NON-RELATIVISTIC BEAM

With a non-relativistic beam the situation changes completely: the effects of the modes lower than the π -mode do not cancel any more. The phase slippage occurring in the first cells, between the non relativistic beam and the lower pass-band modes, produces an effective enhancement of the shunt impedances, which is usually negligible for a relativistic beam in a well tuned cavity. Furthermore, since the beam phase is slipping all along the structure, the field jumps and the detuning due to the off-crest beam vary from cell to cell. Some appreciable fluctuation of the output energy during the beam pulse is then expected. This multi-bunch energy spread is here estimated for the SC capture cavity of the low charge injector I of the Tesla Test Facility [5], (bunch charge: 37 pC, bunch spacing: 4.615 ns, accelerating gradient: 10 MV/m).

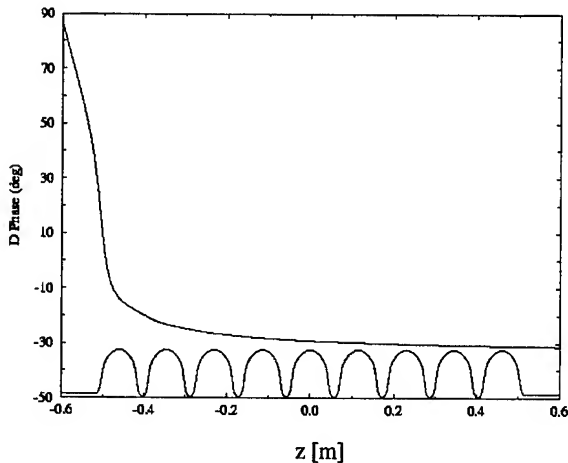


Figure 2 : Beam phase shift along the SC capture cavity (the cavity profile is also shown)

Figure 2 shows typical plots of the beam phase with respect to the RF wave for a single bunch crossing the 9-cell capture cavity. An injection energy of 240 KeV was assumed. Before reaching a stable value, the phase shift varies rapidly especially in the first cells. The total frequency detuning is about 110 Hz, i.e. almost one third of the cavity bandwidth.

Figure 3 shows the evolution of the energy gain on a short-time scale (1000 bunches), with the coupler linked to the cell n.1 or the cell n.9. The accelerating voltage exhibits fluctuations with a main beating due to the nearest $8\pi/9$ mode spaced 0.76 MHz apart from the π -mode.

The beam loading effect is different according whether the power coupler is located upstream or downstream with respect

to the beam. The shapes of the oscillations are similar and the multi-bunch energy spread amounts to $9 \cdot 10^{-4}$ in both cases.

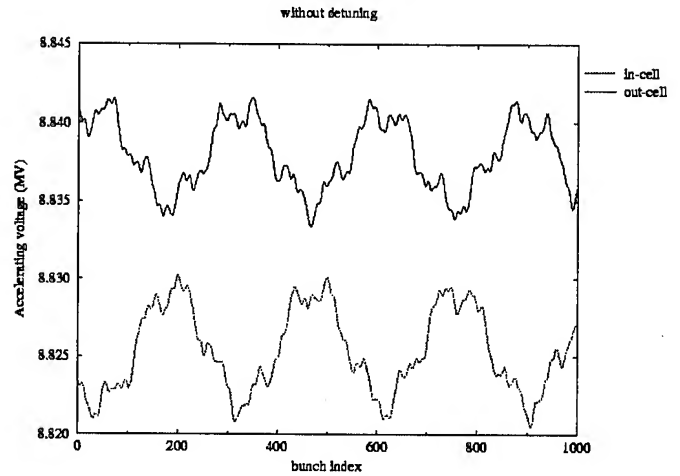


Figure 3 : Energy gain evolution during 1000 bunches

Figures 4 shows the accelerating voltage evolution on a longer time-scale, like the TTF beam pulse duration of 0.8 ms (about 173 333 bunches with injector I). The average compensation of the beam loading, by adjustment of the different parameters (generator, beam voltage or injection time), is not possible, resulting in a large slope on the cavity voltage at the beginning or at the end of the beam pulse.

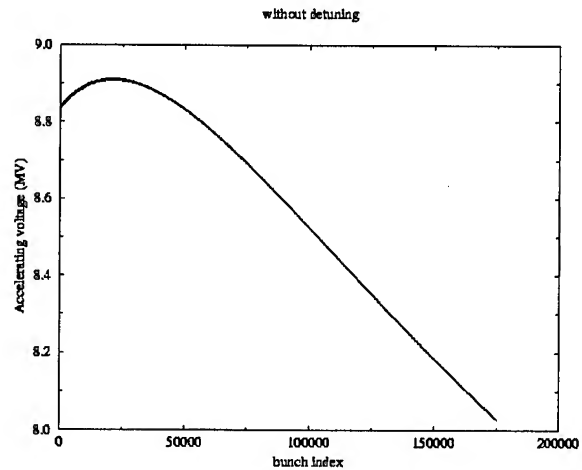


Figure 4 : Energy gain evolution on a long time-scale

IV. BEAM DETUNING COMPENSATION

When a beam is running off-crest, a cavity detuning, in addition to the critical coupling, is generally introduced [6] in order to cancel the reflected RF power and thus to minimize the RF power fed by the klystron. In the steady-state regime and for critical coupling, the tuning angle must be set to the RF phase with respect to the beam phase according to:

$$-\tau \Delta\omega_{\pi} = \tan \psi = \tan(\phi_{rf} - \phi_b)$$

The generator and the cavity voltages are then in-phase. Furthermore, it will be shown later that this beam-detuning compensation will decrease the cavity voltage fluctuations. The phasors diagrams are drawn on Figure 5, without (a) and with (b) cavity detuning.

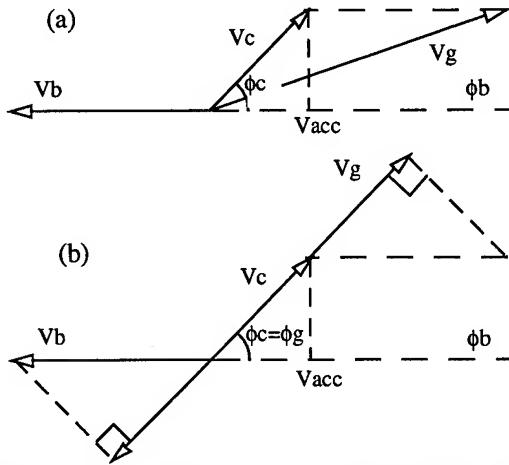


Figure 5 : Phasors diagram without (a) and with cavity detuning (b)

In order to have a constant accelerating voltage during the beam pulse, by balancing the rising generator voltage and the beam voltage, the beam should be injected after the beginning of the RF power pulse with a delay $t_0 = \tau \ln 2$ with cavity detuning or $t_0 = \tau \ln(V_g \cos \phi_g / V_b)$ without cavity detuning. Both conditions, however, neglect the other modes than the π -mode

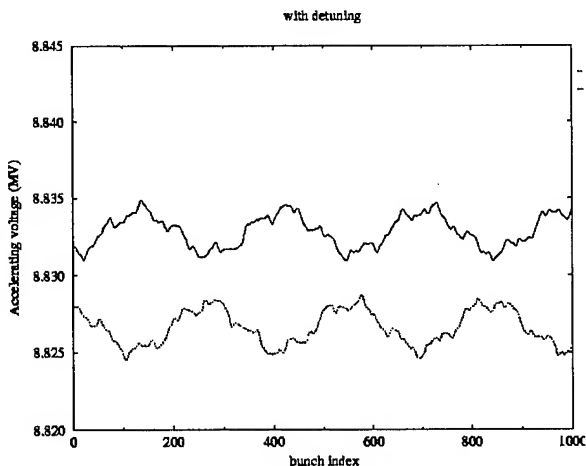


Figure 6 : Energy gain evolution with cavity detuning, solid line: out-cell, dotted line in-cell.

Figure 6 shows the energy gain with a cavity detuning of -110 Hz. The phase of the generator is assumed to track the cavity phase, at least during the field rise time. We note that the accelerating voltage fluctuations are about two times lower, giving a multi-bunch energy spread of $4 \cdot 10^{-4}$.

Figures 7 shows the accelerating voltage evolution on a longer time-scale: an average beam loading compensation can be obtained when the proper cavity detuning is introduced. We

note again that the voltage oscillations decay with the time constants of the other modes of the pass-band.

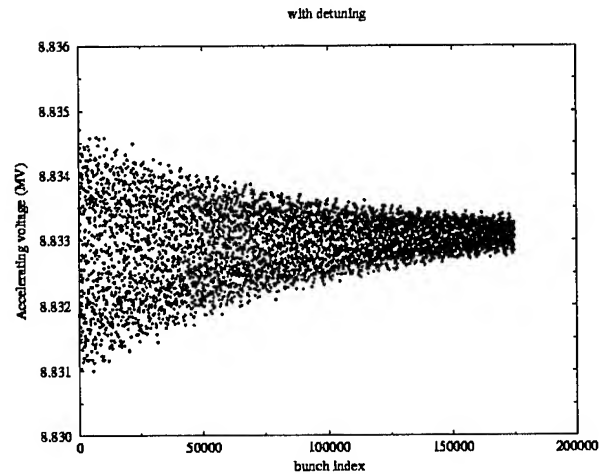


Figure 7 : Energy gain evolution on a long time-scale with cavity detuning

V.CONCLUSIONS

Although the propagation effects are not harmful for a relativistic beam accelerated in a multicell cavity, they have to be taken into account with non relativistic beams. In the latter case, the modes other than the π -mode introduce larger cavity voltage beatings. For the low charge TTF injector, the resulting bunch-to-bunch energy spread will be lower than 0.1% in any case. This value is nevertheless very small in comparison with the single-bunch energy spread of 3% , found with PARMELA simulations [5]. The impact on the transverse dynamics is also small: an rms normalized emittance fluctuation of 1% has been computed [1]. The TESLA cavity geometry is thus well suited to the capture section of the TTF injector.

With a larger number of cells or a smaller cell-to-cell coupling, stronger effects would have been obtained. On the other hand, we could imagine larger energy spreads induced by more critical beam parameters, like the bunch charge or the input energy.

VI.REFERENCES

- [1] M. Ferrario, A. Mosnier, L. Serafini, F. Tazzioli, J.-M. Tessier "Multi-bunch Energy Spread induced by Beam Loading in a Standing Wave Structure", submitted to Particle Accelerators.
- [2] H. Henke and M. Filtz, TESLA 93-26, 1993.
- [3] J. Sekutowicz, Particle Accelerators, 1994, Vol. 45.
- [4] A. Mosnier, Coupled Mode equations for RF Transients Calculations in Standing Wave Structures , CEA/DAPNIA/SEA 94-30, see also [1]
- [5] M. Bernard, B. Aune, S. Buhler et al., The TESLA Test Facility Linac Injector , Proc. of EPAC, London, 1994.
- [6] P.B. Wilson, AIP Conf. Proc. No 87 (AIP, New York, 1982), p. 474

Cure of Transverse Instabilities by Chromaticity Modulation

T. Nakamura
RIKEN-JAERI Spring-8 Project Team
Ako-gun, Hyogo JAPAN

abstract

Landau damping by betatron tune spread suppress transverse instabilities. To create this tune spread, we propose a new method; modulating chromaticity with synchrotron frequency.

I. INTRODUCTION

To introduce static tune spread inside of a bunch, we propose the modulation of the chromaticity by synchrotron frequency.

In usual cases, The energy modulation by synchrotron motion and chromaticity can modulate the betatron tune. But the phase shift of the betatron motion becomes zero after one synchrotron period. This means that this modulation of the betatron tune does not effectively suppress the coherent motion or transverse instabilities.

But introducing the chromaticity modulation by synchrotron frequency, the electrons whose synchrotron phase are different each other has different betatron tune and this tune difference is static and does not change.

The other scheme which are used in several storage rings to introduce tune spread inside of a bunch are installation of octupole magnets which cause amplitude dependent tune shift or ion trapping phenomena which introduce nonlinear field just inside and neighborhood of a bunch.

In small emittance rings, the strong octupole fields must be required for the octupole magnet scheme and it cause serious reduction of dynamic apertures. And ion-trapping sometimes causes unwanted motion of the beam.

On the other hand, this scheme, modulating chromaticity with synchrotron frequency, requires some fast sextupole magnets of moderate strength but it does not reduce dynamic apertures seriously[1].

II. CHROMATICITY MODULATION

The chromaticity ξ which is modulated by the synchrotron frequency ω_s is

$$\xi(t) = \xi_0 + \hat{\xi}_1 \cos \omega_s t. \quad (1)$$

The relative energy $(E-E_0)/E_0$ of a synchrotron oscillation of the electrons is

$$\varepsilon(t) = \hat{\varepsilon} \cos(\omega_s t + \phi). \quad (2)$$

The tune of this electron is

$$\begin{aligned} \nu(t) &= \xi(t)\varepsilon(t) \\ &= [\xi_0 + \hat{\xi}_1 \cos \omega_s t] \hat{\varepsilon} \cos(\omega_s t + \phi) \\ &= \xi_0 \hat{\varepsilon} \cos(\omega_s t + \phi) + \frac{1}{2} \hat{\xi}_1 \hat{\varepsilon} \cos \phi + \frac{1}{2} \hat{\xi}_1 \hat{\varepsilon} \cos(2\omega_s t + \phi). \end{aligned} \quad (3)$$

The second term in equation (3) shows it is the static tune spread and it depends on the phase of the synchrotron motion.

If the distribution of the electron in the phase space of the synchrotron motion is Gaussian;

$$f(\hat{\varepsilon}, \phi) d\hat{\varepsilon} d\phi = \frac{1}{2\pi\sigma_\varepsilon^2} e^{-\frac{\hat{\varepsilon}^2}{2\sigma_\varepsilon^2}} \hat{\varepsilon} d\hat{\varepsilon} d\phi, \quad (4)$$

then, the r.m.s. of this static tune spread is

$$\sigma_\nu = \sqrt{\iint \left(\frac{1}{2} \hat{\xi}_1 \hat{\varepsilon} \cos \phi \right)^2 f(\hat{\varepsilon}, \phi) d\hat{\varepsilon} d\phi} = \frac{1}{2} \hat{\xi}_1 \sigma_\varepsilon. \quad (5)$$

In the SPring-8 storage ring, σ_ε is 1×10^{-3} and revolution frequency f_0 is 208kHz. If ξ_1 is set to 1, then we get $\sigma_\nu = 0.5 \times 10^{-3}$. and the damping time τ_L by the Landau damping with this tune spread is $\tau_L \sim 1/(2\pi f_0 \sigma_\nu) = 1/(2\pi \times 208\text{kHz} \times 0.5 \times 10^{-3}) = 2\text{ms}$. This damping time is faster than the radiation damping time, 8ms. Figure 1,2,3 and 4 are the result of the tracking simulation of this damping.

Figure 5 is the result of the simulation of multi-bunch instabilities caused by cavity higher-mode transverse impedance. The preliminary study by the simulations for single-bunch instabilities also shows the effectiveness of this scheme to suppress instabilities.

III. CONCLUSION

The chromaticity modulation with synchrotron frequency is shown to be effective to create Landau damping and suppress transverse instabilities.

IV ACKNOWLEDGMENT

The author thanks to H. Tanaka and the people of the SPring-8 beam physics group for the fruitful discussion and suggestion from the point of view of the transverse single particle dynamics.

IV REFERENCES

- [1] H. Tanaka, SPring-8, Private communication

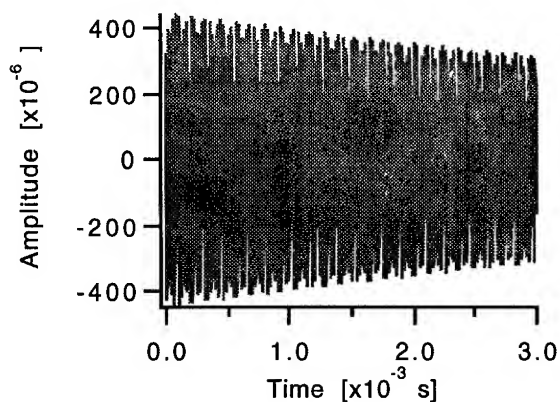


Figure 1

Betatron oscillation without chromaticity modulation.
 $\xi_0 = 0$ and $\xi_1 = 0$. The radiation damping only ($\tau \sim 8\text{ms}$).

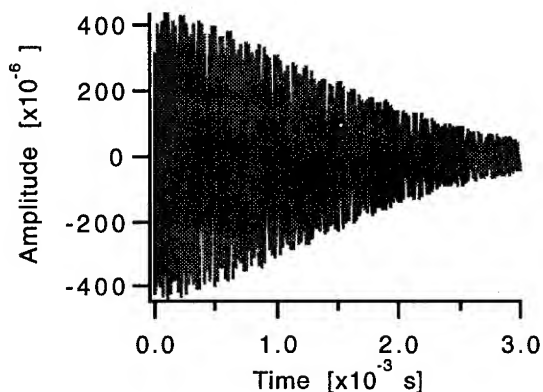


Figure 2

Betatron oscillation with chromaticity modulation.
 $\xi_0 = 0$ and $\xi_1 = 1$. The faster damping can be seen.

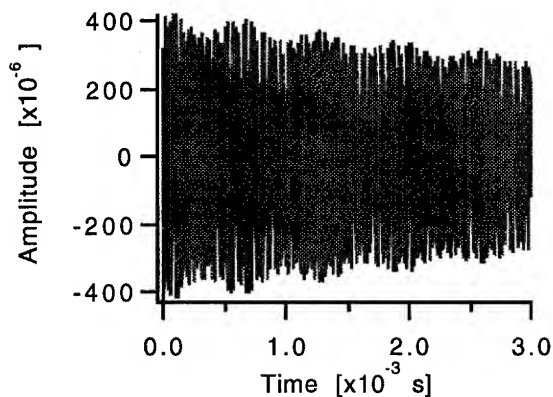


Figure 3

Betatron oscillation without chromaticity modulation.
 $\xi_0 = 2$ and $\xi_1 = 0$. The radiation damping only ($\tau \sim 8\text{ms}$).

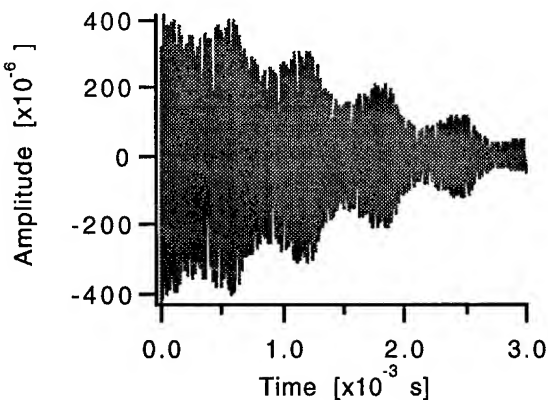


Figure 4

Betatron oscillation with chromaticity modulation.
 $\xi_0 = 2$ and $\xi_1 = 1$. The faster damping can be seen.

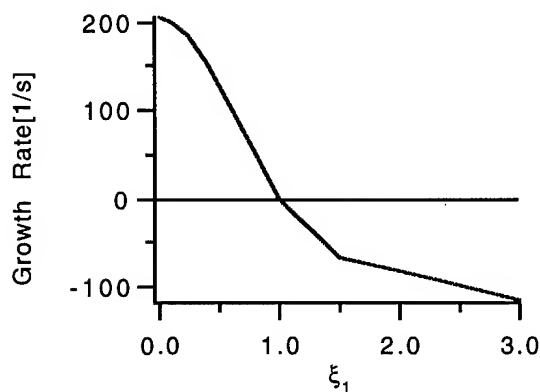


Figure 5

Transverse coupled-instabilities simulation result. This result include radiation damping($\tau \sim 8\text{ms}$). Parameters are of the SPring-8 storage ring. $\xi_0 = 2$, $E=8\text{GeV}$, $R/Q=2000$, $Q=13000$, $f=1\text{GHz}$, $\beta_{\text{cav}}=10\text{m}$, $f_{\text{rev}}=208 \times 10^3\text{Hz}$, $v_x=51.22$, $v_s=0.01$.

A FAST BEAM-ION INSTABILITY *

F. Zimmermann, T. O. Raubenheimer, and G. Stupakov,
Stanford Linear Accelerator Center, Stanford University, Stanford, CA 94309

Abstract

Mutually driven transverse oscillations of an electron beam and residual gas ions may result in a fast transverse instability. This effect arises either during a single pass of a train of electron bunches or it is caused by ionization electrons oscillating within a single positron bunch. In both cases, the beam oscillations grow exponentially with an exponent proportional to the square root of time. In this report, instability rise times are calculated analytically and compared with computer simulations. The effect considered could be a significant limitation in many future designs.

I. INTRODUCTION

The effect we describe arises during the passage of a single electron bunch train or a single positron bunch; ions (or ionized electrons) created by the head of the train (bunch), via ionization of the residual gas, perturb the tail. Under certain conditions a fast transverse beam-ion instability can develop. The instability mechanism is the same in linacs and storage rings where we assume that the ions are not trapped from turn to turn. It differs from instabilities previously studied [4], where the ions, usually treated as being in equilibrium and trapped over many turns, interact with a circulating electron or antiproton beam. By contrast, the instability discussed in this report occurs in a transport line, linac, or a storage ring with a clearing gap to prevent ion trapping. In this paper we outline the basic ideas. For more details we refer to Refs. [1] and [2].

In Section II, instability rise times are calculated analytically. Section III compares the results of computer simulations with the analytical prediction. In Section IV rise times are evaluated for several operating or proposed storage rings and linear accelerators. Section V is devoted to a brief discussion of possible remedies. A summary is given in Section VI.

II. ANALYTICAL TREATMENT

The vertical motion of the beam and the ions or electrons that are generated during the beam passage via ionization may, in linear approximation, be described by two equations of motion. The first equation reads:

$$\left(\frac{d^2}{ds^2} + \omega_\beta^2 \right) y_b(s, z) = K \Gamma(z) (y_i(s, s+z) - y_b(s, z)). \quad (1)$$

The coordinate s denotes the longitudinal position along the beam line or storage ring. Equation (1) represents the vertical motion of the beam centroid $y_b(s, z)$ at a distance z from the bunch (or bunch train) center. In our convention positive values of z refer to trailing particles. The motion is a combination of: a betatron oscillation due to external focusing, represented by a harmonic

oscillator of frequency $\omega_\beta \approx 1/\beta_y$; and a driving force that is proportional to the distance of beam and ion centroids, and also to the number of generated ions and thus to an integral over the beam density, $\Gamma(z) \equiv \int_{-\infty}^z \rho(z') dz'$, normalized such that $\Gamma(\infty) = 1$. Here, and in the following, the term "ions" is understood as "ions or electrons, respectively." Finally, the coefficient K is

$$K \equiv \frac{2\lambda_{ion}(p_{gas})r_e}{\gamma \Sigma_y(\Sigma_y + \Sigma_x)} \approx \frac{4\lambda_{ion}(p_{gas})r_e}{\gamma 3\sigma_y(\sigma_x + \sigma_y)}, \quad (2)$$

where γ denotes the relativistic factor $\gamma = E/(mc^2)$ for the beam, r_e is the classical electron radius, and $\Sigma_{x,y}^2 \approx \frac{3}{2}\sigma_{x,y}^2$ is the sum of the squares of rms ion-cloud size and beam size $\sigma_{x,y}$. Assuming a cross section for collisional ionization of about 2 Mbarns (corresponding to carbon monoxide at 50 GeV) the density λ_{ion} of ions per meter at the end of the bunch (or bunch train) is $\lambda_{ion} \approx 6Np_{gas}[\text{torr}]$, where N is the total number of particles in the beam and p_{gas} the residual gas pressure in torr. The second equation,

$$\frac{d^2 \tilde{y}_i(s, t)}{dt^2} + \omega_i^2(t-s)\tilde{y}_i(s, t) = \omega_i^2(z)y_b(s, t-s), \quad (3)$$

describes the oscillation of a transverse slice of ions inside the beam. It is here written as an equation in time t for a fixed position s . The variable $\tilde{y}_i(s, t)$ is the vertical centroid of the transverse slice of ions. For convenience, here and in the following, the time t is quoted in units of length obtained from the actual time by multiplication with the velocity of light c . At a certain time t , beam particles at a distance $z = t - s$ from the bunch center reach the location s . Their centroid position is therefore $y_b(s, t-s)$. The oscillation frequency $\omega_i(t-s) = \omega_i(z)$ is proportional to the square root of the beam density ρ . In the case of electrons oscillating inside a single positron bunch, ω_i is given by $(4N\rho(z)r_e/(3\sigma_y(\sigma_x + \sigma_y)))^{1/2}$. For ions and an electron bunch train we have $\omega_i \equiv ((4N_b r_p/(3L_{sep}\sigma_y(\sigma_x + \sigma_y)A))^{1/2}$ where A designates the atomic mass number of the ions, N_b the number of particles per bunch, L_{sep} the bunch spacing, and r_p the classical proton radius.

The solution to Eq. (3) for a slice of ions generated at time $t' = s + z'$ is denoted as $\tilde{y}_i(s, t|s+z')$. The centroid of the ions $y_i(s, t)$ (or electrons) used in Eq. (1) is obtained by averaging $\tilde{y}_i(s, s+z')$ over all possible creation times:

$$y_i(s, t) = \frac{\int_{-\infty}^z dz' \rho(z') \tilde{y}_i(s, t|s+z')}{\int_{-\infty}^z \rho(z') dz'}. \quad (4)$$

Several approximations have been made so far. For instance, the force between beam and ions is assumed to be linear. Any Landau damping caused by the lattice is ignored. It is supposed that inside a bunch train the ions are not overfocused, but that they are lost between different trains. Ions generated by synchrotron

*Work supported by Department of Energy contract DE-AC03-76SF00515.

radiation are ignored. To further simplify the calculations, we will now approximate the longitudinal bunch density $\rho(z)$ by a homogeneous rectangular distribution of length $2z_0$. The oscillation frequency ω_i is then constant inside the bunch (or along the bunch train). Equations (1), (3), and (4), can be combined into a single integral equation for the beam centroid $y_b(s, z)$ alone. The latter can be solved either as a perturbation series in K/ω_β [1] or by an averaging method [2]. The asymptotic solution for large distances s is

$$y_b(s, z) \approx \hat{y} \frac{1}{4\sqrt{\pi}} \frac{1}{\eta^{\frac{1}{4}}} e^{2\sqrt{\eta}} \sin(\omega_i z - \omega_\beta s + \theta), \quad (5)$$

where \hat{y} is the initial Fourier component at frequency ω_i in the longitudinal beam distribution, and $\eta(s, z)$ denotes the dimensionless function $\eta(s, z) \equiv (K\omega_i(z + z_0)^2/(\omega_\beta 16z_0))$. Asymptotically, the oscillation amplitude grows roughly as $\exp(\sqrt{s/\tau_{asym}})$, where τ_{asym} is the time at which the exponent $2\sqrt{\eta}$ in Eq. (5) equals one. Note that τ_{asym} is not an e-folding time because the exponent is proportional to the square root of time. In the multi-bunch case, the asymptotic rise time τ_{asym} for trailing bunches can be expressed in terms of more basic parameters as [1]

$$\tau_{asym, e-}[s] \approx \left[\frac{6p[\text{torr}] N_b^{\frac{3}{2}} n_b^2 r_e^{\frac{1}{2}} L_{sep}^{\frac{1}{2}} c}{\gamma \sigma_y^{\frac{3}{2}} (\sigma_x + \sigma_y)^{\frac{3}{2}} A^{\frac{1}{2}} \omega_\beta} \right]^{-1}, \quad (6)$$

where N_b denotes the number of particles per bunch and n_b is the number of bunches. All quantities, except for the pressure, are given in SI units. A similar expression can be found for a single positron bunch. [1] In the asymptotic limit, ion and beam motion are of similar amplitude and in phase.

III. COMPUTER SIMULATIONS

To study this instability, we have written a computer simulation. The simulation treats the beam, the ions, and the ionized electrons as collections of macroparticles whose distributions are allowed to evolve self-consistently. Each bunch in the beam is divided into slices in z . Each slice is then represented by macroparticles whose number is chosen to reflect a Gaussian distribution between $\pm 3\sigma_z$. The initial macroparticle coordinates are random with Gaussian distributions. At four locations in each FODO cell, calculations are performed using a grid in x and y centered at the bunch train centroid. As each beam slice passes, macroparticles are created at the grid points representing the ions and ionized electrons generated by collisional ionization. The beam and ion fields are mapped onto the grid and then interpolated to the macroparticle positions. Ref. [1] presents details of the simulations.

Simulations have been performed for the PEP-II HER, the SLC Positron Arc and the NLC Damping Ring, typically using about 160 000 macroparticles. The results are consistent with the analytical calculation, and confirm the expected scaling of the amplitude growth with time, pressure, ion mass, and longitudinal position z . The absolute rise times found in the simulations agree with the analytical result to within a factor 2 or 3, which is smaller than the spread of values obtained for different random seeds. The analytical solution, Eq. (5), does not include the

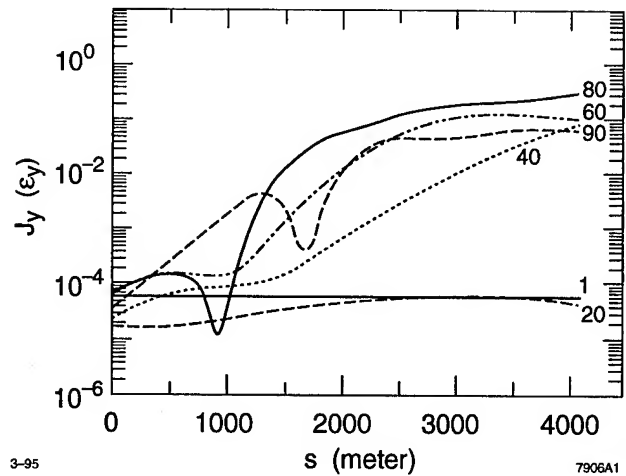


Figure 1. Action of the vertical centroid as a function of distance for every twentieth bunch of a train of 90 bunches in the NLC-DR with a pressure of 10^{-8} torr.

filamentation of ions: due, for instance, to the variation of the ion oscillation frequency with horizontal position. An approximative analytical solution which takes this ion-decoherence into account [2] predicts a rise time which is about a factor 2 or 3 larger than that of Eq. (6).

Figure 1 shows a simulation result for the NLC Damping Ring (DR). The average action $\langle J_y(s, z) \rangle$ is depicted as a function of the distance s for every twentieth bunch in the train of 90 bunches and a pressure of 10^{-8} torr. The initial amplitudes are due to the finite number of macroparticles. From this figure, the rise time for the trailing bunches is about 170 ns; within the uncertainty of the simulation this is close to the estimate of 47 ns obtained from Eq. (6). In the NLC-DR an average vacuum pressure of or below 10^{-9} torr has to be maintained, in order to sufficiently reduce the growth rate of the beam-ion instability; emittance dilutions due to other gas or ion effects do not require a pressure below 10^{-8} torr.

IV. RISE TIMES FOR SOME ACCELERATORS

Table I shows basic parameters and the asymptotic rise times for several accelerators proposed or under construction at SLAC and KEK: namely for the NLC Electron Damping Ring, the NLC main linac, the PEP-II HER, and for the ATF Damping Ring. Due to its much higher vacuum pressure, the smallest rise time is expected for the ATF Damping Ring. Values for the NLC systems vary between 40 ns and 1 μ s. If the initial perturbation is purely due to Schottky noise, it takes about 200 rise times until the bunches oscillate at an amplitude comparable to the beam size. Even with the additional factor 200, the growth times are still very short.

A similar evaluation indicates that the beam-ion instability is not expected to occur in most of the existing accelerators [1]. For instance, the estimated rise time for the SLC e+ Damping Ring, is much larger than the synchrotron period, in which case the instability cannot develop, while the predicted rise time in the HERA electron ring at DESY is about a factor 1–2 larger than the damping time of the transverse multi-bunch feedback. From all the existing machines considered, only the ALS at LBL should

show a significant fast beam-ion instability with a rise time of about 2 μ s for an average pressure of 10^{-9} torr. Experience so far is unclear. Transverse instabilities are observed, but these are not necessarily caused by ions.

accelerator	NLC e- DR	NLC ML	HER	ATF
n_b	90	90	1658	60
N_b	$1.5 \cdot 10^{10}$	$1.5 \cdot 10^{10}$	$3 \cdot 10^{10}$	10^{10}
$\beta_{x,y}$ [m]	0.5, 5	8	15	0.5, 5
σ_x [μ m]	62	35	1,060	22
σ_y [μ m]	4	3.5	169	7
z_0	19 m	19 m	1000 m	25 m
E [GeV]	2	10	9	1.54
p [torr]	10^{-9}	10^{-8}	10^{-9}	$6 \cdot 10^{-8}$
τ_{asym}	465 ns	46 ns	6 μ s	29 ns

Table I

Parameters and rise times for some future accelerators.

V. POSSIBLE CURES

If the oscillation amplitude of the trailing electron bunches, or positrons, saturates at about $1 \sigma_y$ due to the nonlinear character of the coupling force—not included in the analytical treatment—a reduction of the design vertical emittance by a factor of 2 results in about the desired projected final emittance after filamentation [8]. However, it is not yet known if the beam will continue to blow-up (though with decreasing growth rate) after partial filamentation. A second possibility is to use an optical lattice in which the product of the horizontal and vertical beta functions, and thus ω_i , vary substantially. Third, if additional gaps are introduced in the bunch train, the ions are over-focused between the shorter trains [9]. As an example, 10 additional bunch gaps in PEP-II increase the instability rise time from 5 μ s to 0.5 ms, which is inside the bandwidth of the feedback system. Finally, in linear accelerators the trailing bunches might be realigned by use of fast kickers and feed-forward.

VI. SUMMARY AND ACKNOWLEDGMENT

The interaction of an electron bunch train or a single positron bunch with ions or ionization electrons can cause a fast transverse instability, which is characterized by an exponential growth of the vertical amplitude. The exponent is proportional to the position along the bunch train (or bunch) and to the square root of time, and is inversely proportional to the 3/4th power of the beam sizes.

The expected rise time of the instability is exceedingly short. For instance, for the various NLC rings and linacs, it varies between 40 ns and 800 ns, while, for the PEP-II HER, it is estimated at 5 μ s.

The analytical model used is a linearized approximation and does not include nonlinearities of the ion-beam force or the lattice. However, these nonlinearities are included in the simulations which, for the parameter regimes compared, yield rise times that are in good agreement with the analytical model. In Ref. [2] the linear model is extended to include Landau damping due to the nonlinearity of the beam-ion force; this decreases the growth rate by a factor of two. A large number of questions remain to be answered; among them are the emittance growth due to filamentation and detuning as the oscillation saturates, the effect of

synchrotron motion on the growth rate, the rise time in the presence of different ion species, the possible damping due to the nonlinearity of the beam-beam interaction in circular colliders, and the study of coherent oscillation modes of higher order.

We thank A. Chao and S. Heifets for helpful discussions.

References

- [1] T.O. Raubenheimer and F. Zimmermann, "A Fast Beam-Ion Instability in Linear Accelerators and Storage Rings," submitted to *Phys. Rev. E*, SLAC-PUB-6740, 1995.
- [2] G. Stupakov, T.O. Raubenheimer and F. Zimmermann, "Effect of Ion Decoherence on Fast Beam-Ion Instability," submitted to *Phys. Rev. E*, SLAC-PUB-95-6805, 1995.
- [3] A. Chao, Burton Richter, Y. Yao, *Int. Conf. on High-Energy Accelerators*, CERN, July 7-11, 1980; A. Chao, *Physics of Collective Beam Instabilities in High-Energy Accelerators*, Wiley, New York, 1993.
- [4] E. Keil and B. Zotter, CERN ISR-TH 71-58 1971; G. Koshkarev and P. Zenkevich, *Part. Acc.* 3 1, 1972; L. J. Laslett et al., *NIM A* 121 517, 1974; R. Alves Pires et al., *Proc. of 1989 IEEE PAC*, Chicago, 800, 1989; E. Jones et al., *Proc. of 1985 IEEE PAC*, Vancouver, 2218, 1985; A. Poncet, *Proc. of the 1989 CERN Accelerator School*, Uppsala, Sweden, CERN 90-04, 1990; A. Poncet, in M. Dienes, M. Month, S. Turner (ed.), "Frontiers of Particle Beams," *Proc. Hilton Head Island*, South Carolina 1990; D. Sagan and A. Temnykh, *NIM A* 344, 3 459, 1994.
- [5] T. O. Raubenheimer and P. Chen, *Proc. of LINAC92*, Ottawa, vol. 2, 630, SLAC-PUB-5893 1992.
- [6] M. Bassetti, G. Erskine, CERN-ISR-TH-80-06 (1980).
- [7] P. Emma, T. Raubenheimer, F. Zimmermann, *Proc. of EPAC 94*, p. 1162, SLAC-PUB-6522, 1994.
- [8] K. Oide, private communication, 1994.
- [9] J. Seeman, private communication, 1994.

SIMULATIONS OF THE LONGITUDINAL INSTABILITY IN THE NEW SLC DAMPING RINGS*

K.L.F. Bane and K. Oide†

Stanford Linear Accelerator Center, Stanford University, Stanford, CA 94309 USA

I. INTRODUCTION

In 1992 a longitudinal, single bunch instability was observed in the SLC damping rings. [1] Beyond a threshold current of 3×10^{10} a "saw-tooth" variation in bunch length and energy spread was observed, a phenomenon that made it practically impossible to operate the SLC collider above threshold. For the 1994 run a new, low-impedance vacuum chamber was installed in both damping rings both to alleviate this problem and to shorten the bunch length. According to recent measurements the bunch length has indeed become shorter, but the "saw-tooth" instability is still seen, now beginning at currents of $1.5 - 2.0 \times 10^{10}$. [2] Fortunately, it appears to be benign and does not seem to limit SLC performance.

In an earlier paper we investigated the single bunch behavior of the SLC damping rings with the old vacuum chamber using time domain tracking and a Vlasov equation approach. [3] When compared to measurements we found: good agreement in the average values of bunch length, energy spread, and synchronous phase shift as functions of current; a 30% discrepancy in threshold current; in agreement, a mode with frequency near 2.5 times the synchrotron frequency (the so-called "sextuple" mode) as signature of the instability and the slope of the mode frequency as function of current. ¹

In the present paper we repeat the exercise of the earlier paper but with a new wakefield. The impedance which used to be inductive has become resistive, leading to different phenomena.

In a recent paper the instability in a purely resistive ring is analyzed using a Vlasov equation approach. [5] It is demonstrated that such an instability is a weak instability, with a growth rate proportional to intensity squared, and one that can be described as the coupling of two quadrupole modes with different radial mode numbers. We will compare our results with this paper. For related papers, see also Refs. [6], [7].

II. THE WAKEFIELD

In the vacuum chamber upgrade of the SLC damping rings primarily small objects that are inductive at nominal bunch lengths (~ 5 mm) were removed or modified, [2] [8] changing the character of the rings from inductive to resistive. As before, we have attempted to find an approximate Green function wakefield $W(z)$ for the new ring using the time-domain parts of the MAFIA family of computer programs, [9] taking as driving bunch a short, gaussian bunch with rms length of 1 mm. To make it causal, the part in front of bunch center ($z < 0$) was reflected and added to the back (see Fig. 1), a transformation that

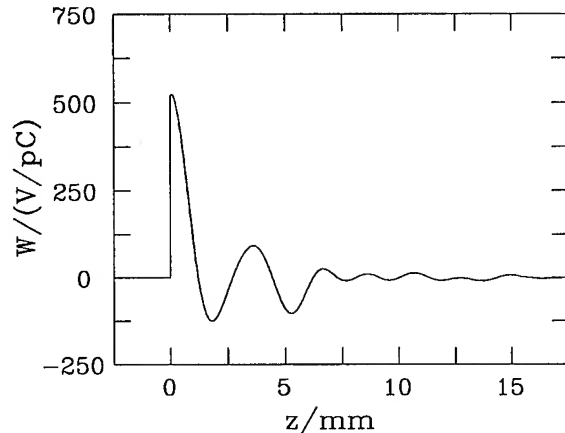


Figure 1. The wakefield used for the simulations.

preserves the real part of the impedance. We expect to be able to find beam instabilities down to wavelengths of about 1 cm.

We have had difficulty obtaining an accurate wakefield, and we are not very satisfied with what we have; it should be considered only preliminary. As we have removed the grosser, cylindrically symmetric objects (45° transitions, masks, etc.) we are left with a machine dominated by objects for which it is difficult to obtain an accurate wake function, such as, for example, the beam position monitors. Also, difficult vacuum chamber objects that could previously be ignored, such as the septum chamber, may now be important. In spite of these misgivings, and even though (as we will see) the results do not agree with the SLC measurements as well as before, we feel that this wakefield is still useful for studying the basic character of the damping ring current dependent behavior.

The induced voltage on any turn is given by

$$V_{ind}(z) = -eN \int_{-\infty}^z W(z-z') \lambda_z(z') dz', \quad (1)$$

with N the bunch population and $\lambda_z(z)$ the longitudinal charge distribution. To see that it is resistive in character at typical bunch lengths we plot in Fig. 2, λ_z and V_{ind} , for $N = 2 \times 10^{10}$ and nominal length $\sigma_{z0} = 5$ mm, the solution to the Haissinski equation. [10] We note that roughly V_{ind} can be written as $V_{ind} \approx -eN R c \lambda_z$, with R the resistance, a constant. In fact, if we take a pure resistance with $R = 880 \Omega$, and repeat the potential well calculation, we obtain almost the same bunch shape (the dashes in Fig. 2).

III. SIMULATIONS

For tracking we let the beam be represented by N_p macro-particles; each particle i has position and energy coordinates

*Work supported by Department of Energy contract DE-AC03-76SF00515.

†From KEK.

¹In Ref. [3] it was stated that the measured slope was three times smaller than the calculations. However, subsequent, more accurate measurements are in agreement with the calculations. [4]

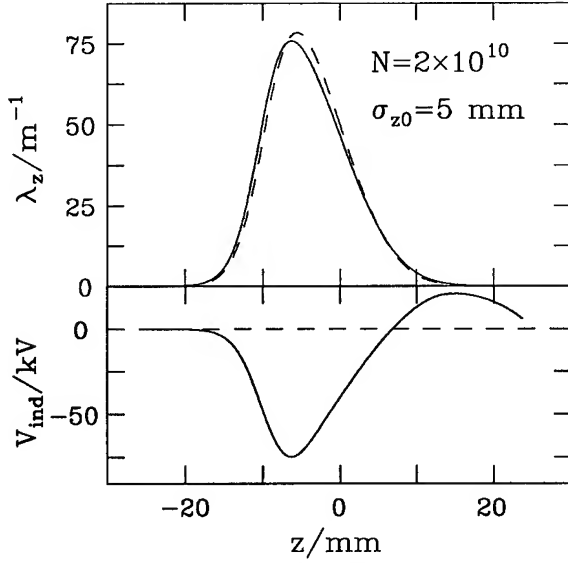


Figure 2. A potential well example.

(z_i, ϵ_i) . The properties of particle i are advanced on each turn according to the equations: [11]

$$\Delta \epsilon_i = -\frac{2T_0}{\tau_d} \epsilon_i + 2\sigma_{\epsilon 0} \sqrt{\frac{T_0}{\tau_d}} r_i + V'_{rf} z_i + V_{ind}(z_i) \quad (2)$$

$$\Delta z_i = \frac{\alpha c T_0}{E_0} (\epsilon_i + \Delta \epsilon_i) \quad , \quad (3)$$

with T_0 the revolution period, τ_d the damping time, $\sigma_{\epsilon 0}$ the nominal rms energy spread, V'_{rf} the slope of the rf voltage (a negative quantity), α the momentum compaction factor, and E_0 the machine energy; r_i is a random number from a normal set with mean 0 and rms 1. To calculate λ_z on each turn we bin the macro-particles in z .

For the simulations we take $T_0 = 118$ ns, $E_0 = 1.15$ GeV, rf frequency $\nu_{rf} = 714$ MHz, $\sigma_{\epsilon 0} = 0.07\%$, and $\tau_d = 1.7$ ms. We choose $V_{rf} = 0.8$ MV, where $\sigma_{z0} = 4.95$ mm, and the synchrotron frequency $\nu_{s0} = 99$ kHz. Therefore $\nu_{s0} T_0 = 85$ turns, $\tau_d/T_0 = 14450$ turns. We take $N_p = 30,000$, and for λ_z we use 100 bins extending over $10\sigma_z$. We let the program run for 3 damping times.

As a second method of calculation we use a computer program that solves perturbatively the time independent, linearized Vlasov equation, including the effects of potential well distortion, looking for unstable modes. [12] Beyond the threshold current we assume the average energy distribution remains gaussian, with the rms width σ_ϵ increasing to keep the beam just at the threshold condition.

IV. RESULTS

A. The Instability Threshold

For this wakefield the instability threshold is normally easy to find from the turn-by-turn tracking results. Below threshold the moments of the distributions are well behaved, above threshold they undergo macroscopic oscillations (see Fig. 3). The threshold $N_{th} \approx 1.15 \times 10^{10}$.

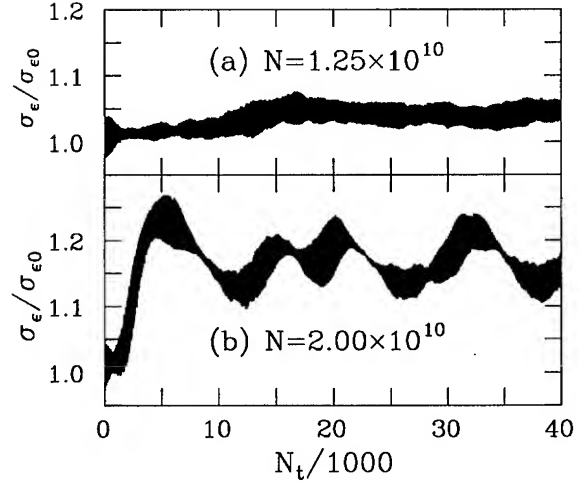


Figure 3. The turn-by-turn rms energy spread just above threshold (a) and at a higher current. (b)

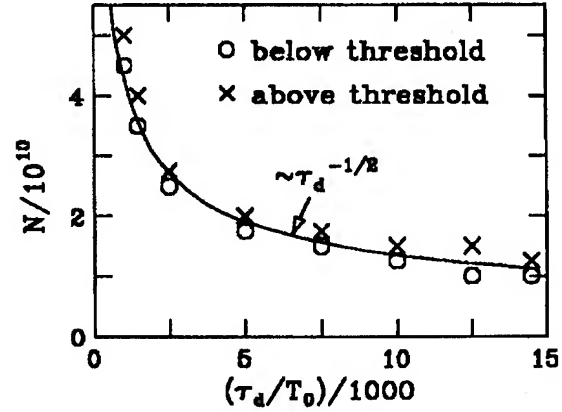


Figure 4. N_{th} vs. τ_d obtained by tracking.

When we artificially reduce the damping time in tracking we find that the threshold N_{th} increases significantly (see Fig. 4). Fitting to a power law we find that N_{th} varies approximately as $\tau_d^{-1/2}$ (the curve in Fig. 4). This agrees with the weak growth expected in a purely resistive machine, which varies as $\sim e^{aN^2t}$, with a a constant and t time. [5] Note that when we repeat the tracking procedure for the old, inductive vacuum chamber the threshold increases by only 30% as the damping time is decreased by a factor of 15. The two instabilities are quite different: the old was a strong instability and the new a weak one.

According to a formula in Ref. [5] (Eq. 27) we can raise the threshold by $\sim 1 \times 10^{10}$ if we add a pure inductance of $L = 2$ nH (by adding a term $-cL\lambda'_z$ to V_{ind}). This is roughly what we find; and at $N = 4 \times 10^{10}$ $\sigma_\epsilon/\sigma_{\epsilon 0}$ has decreased from 1.5 to 1.1. This suggests that even a small amount of tune spread can damp this instability.

B. Average Bunch Properties

Above threshold the oscillations in the moments of the distributions obtained by tracking can be large (at $N = 3.5 \times 10^{10}$ the variation in σ_z is $\pm 28\%$) and the pattern can vary greatly. It depends sensitively on, for example, N_p , which (for practical rea-

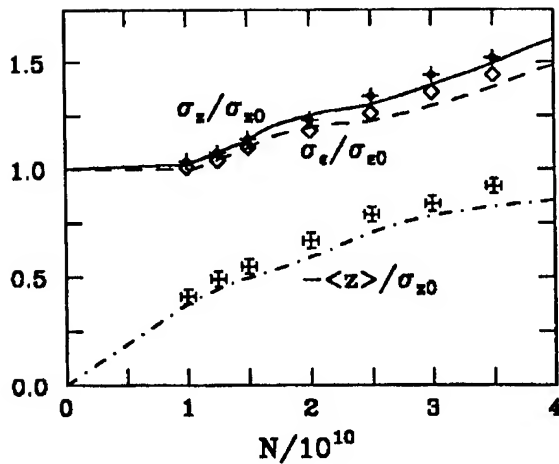


Figure 5. Average bunch properties vs N . Shown are tracking results (plotting symbols) and the Vlasov method results (curves).

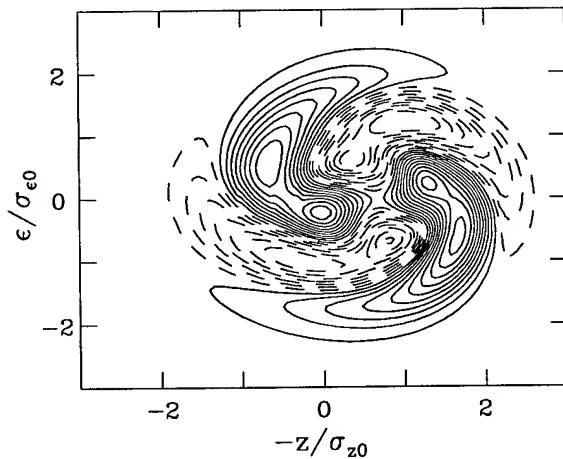


Figure 6. Mode shape at $N = 2 \times 10^{10}$.

sons) it is difficult for us to increase significantly, while keeping τ_d fixed. However, the average amplitudes appear to be rather insensitive to changes in N_p . Fig. 5 gives the average values of σ_z , σ_e , and $\langle z \rangle$ as functions of N , and also shows the Vlasov equation solution for comparison. The agreement is quite good. Note that for such a resistive impedance the potential well distortion is small; the bunch lengthening is largely due to the increase in energy spread above threshold. Thus, by adding 2 nH of pure inductance to reduce the energy spread at 4×10^{10} the 60% increase in σ_z is reduced to 30%.

Fig. 6 gives contours of phase space of the unstable mode at $N = 2 \times 10^{10}$ as calculated by the Vlasov method. Tracking gives a similar result. We see a quadrupole mode, with a slight asymmetry, that has been shifted forward.

C. The Spectrum

The mode frequencies as function of N , as obtained by the Vlasov method are shown in Fig. 7. A dot represents a stable mode, an 'X' an unstable mode, with its size proportional to the growth rate. The strongest unstable mode is a quadrupole mode beginning at $N = 1 \times 10^{10}$ with $\nu = 1.95\nu_{s0}$, and then

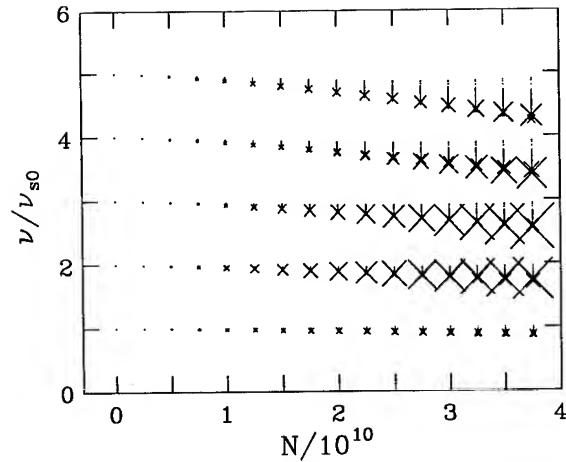


Figure 7. Modes obtained by the Vlasov method.

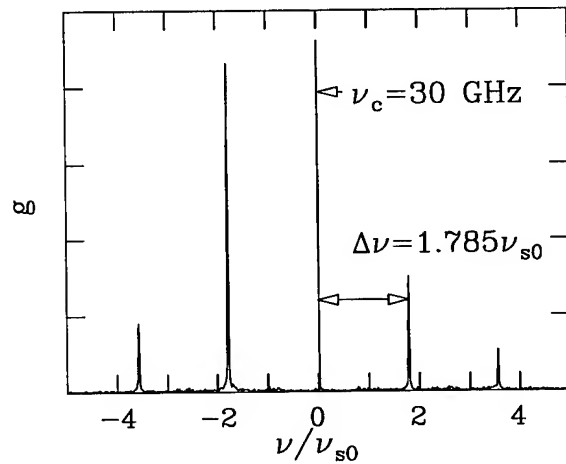


Figure 8. Spectrum for $N = 4 \times 10^{10}$, $\tau_d/T_0 = 1450$.

continuing with a slope of $-0.07\nu_{s0}/10^{10}$. As was the case for a purely resistive machine the instability can be described by coupling of two radial modes with the same azimuthal mode number.

For the tracking results, by Fourier transforming any of the turn-by-turn moments of the distribution we can obtain the spectrum. Alternatively, we can simulate what a spectrum analyzer does by calculating [13]

$$g(\omega) = \left| \sum_k e^{i\omega k T_0} \tilde{\lambda}_{zk}(\omega) \right| \quad (4)$$

with k the turn number and $\tilde{\lambda}_{zk}(\omega)$ the Fourier transform of the distribution on the k^{th} turn. We find sidebands at $1.9\nu_{s0}$, but because of numerical noise we have poor resolution. To give an example with good resolution let us set $N_p = 150,000$, artificially reduce τ_d by a factor of 10, and consider $N = 4 \times 10^{10}$. In Fig. 8 we display the result near a central frequency $\nu_c = 30$ GHz. We see sidebands of the revolution frequency separated by $1.785\nu_{s0}$. Note that the sideband amplitudes are not of equal height. In general, potential well distortion tends to result in an asymmetric mode shape; therefore, for frequencies $\nu_c \gtrsim c/2\pi\sigma_z$ we expect the sidebands to be of unequal height.

V. COMPARISON WITH MEASUREMENTS [2]

In the measurements the bunch length is smaller and the beam profile more asymmetric than before, and above threshold a frequency just below $2\nu_{s0}$ is observed, which are consistent with a resistive wakefield and our simulations. In detail, the agreement is not good unless we assume our wake is missing about 2 nH ($|Z/n| = 0.1 \Omega$) of pure inductance. The measurements give: $N_{th} = 1.5 - 2.0 \times 10^{10}$, and at $N = 4 \times 10^{10}$ $\sigma_e/\sigma_{e0} = 1.15$, and $\sigma_z/\sigma_{z0} = 1.25$; the calculations including the inductance give: $N_{th} = 2.0 \times 10^{10}$, and at $N = 4 \times 10^{10}$ $\sigma_e/\sigma_{e0} = 1.10$, and $\sigma_z/\sigma_{z0} = 1.30$. The unstable mode frequency at threshold and the slope, given by measurements (calculations, including 2 nH): $1.77 (1.87) \nu_{s0}$ and $-.06 (-.07) \nu_{s0}/10^{10}$.

Finally, how can we understand the reduction of the measured threshold when the damping ring impedance was reduced? In the old, inductive machine there was a strong instability observed at 3×10^{10} . In an inductive machine there is a large incoherent synchrotron tune spread which will Landau damp weaker instabilities which otherwise might appear at lower currents. By removing mostly inductive elements, and thereby changing the character of the ring to a resistive one, we have removed this tune spread, and presumably are now able to observe one of these weaker instabilities.

VI. ACKNOWLEDGEMENTS

The authors thank the members of the SLC Damping Ring group for helpful discussions.

References

- [1] P. Krejcik, *et al.*, Proc. of the 1993 IEEE Particle Acc. Conf., Washington D.C., 1993, p. 3240.
- [2] K. Bane, *et al.*, WAC17, this conference.
- [3] K. Bane and K. Oide, Proc. of the 1993 IEEE Particle Acc. Conf., Washington D.C., 1993, p. 3339.
- [4] M. Minty, private communication.
- [5] K. Oide, KEK-PREPRINT-94-138, Nov. 1994.
- [6] A. Chao, *et al.*, WAB10, this conference.
- [7] B. Chen, WAC31, this conference.
- [8] K. Bane and C.-K. Ng, Proc. of the 1993 IEEE Particle Acc. Conf., Washington D.C., 1993, p. 3432.
- [9] F. Ebeling, *et al.*, MAFIA Users Guide, 1992.
- [10] J. Haïssinski, *Il Nuovo Cimento*, **18B**, No. 1, 72 (1973).
- [11] See e.g. R. Siemann, *Nucl. Instr. Meth.*, **203**, 57 (1982).
- [12] K. Oide and K. Yokoya, KEK-Preprint-90-10, 1990.
- [13] A. Chao, *Physics of Collective Beam Instabilities in High Energy Accelerators*, (J. Wiley & Sons, New York, 1993).

High-Intensity Single Bunch Instability Behavior In The New SLC Damping Ring Vacuum Chamber*

K. Bane, J. Bowers, A. Chao, T. Chen, F. J. Decker, R. L. Holtzapple, P. Krejcik, T. Limberg, A. Lisin, B. McKee, M. G. Minty, C.-K. Ng, M. Pietryka, B. Podobodov, A. Rackelmann, C. Rago, T. Raubenheimer, M. C. Ross, R. H. Siemann, C. Simopoulos, W. Spence, J. Spencer, R. Stege, F. Tian, J. Turner, J. Weinberg, D. Whittum, D. Wright, F. Zimmermann
Stanford Linear Accelerator Center, Stanford University, Stanford, CA 94309 USA

New low-impedance vacuum chambers were installed in the SLC damping rings for the 1994 run after finding a single bunch instability with the old chamber. Although the threshold is lower with the new vacuum chamber, the instability is less severe, and we are now routinely operating at intensities of 4.5×10^{10} particles per bunch (ppb) compared to 3×10^{10} ppb in 1993. The vacuum chamber upgrade is described, and measurements of the bunch length, energy spread, and frequency and time domain signatures of the instability are presented.

I. VACUUM CHAMBER UPGRADE

The old vacuum chamber is described in Ref. 1. Although there are resistive elements such as the RF cavities and complex, hard to characterize elements such as septa, the calculated impedance was predominantly inductive with the contributions of different elements given in Table 1.

Table 1. Vacuum Chamber Inductance (nH)

Element	Old Chamber [†]	New Chamber*
Synch. Radiation Masks	9.5	----
Bellows	----	1.1
Quadrupole to Dipole Chamber Transitions	9.3	2.4
Ion Pump Slots	0.2	0.05
Kicker Magnet Bellows	4.1	----
Flex Joints	3.6	----
Beam Position Monitors	3.5	0.2
Other	2.4	2.4
TOTAL	33	6

[†] From ref 1. Bellows included in Table 1 of [1] were shielded in a previous upgrade. Changes to that table from recent calculations are included here.

* Many of the impedance calculations are in ref 2.

The synchrotron radiation masks and flex joints were associated with chamber flexibility. The masks protected bellows at one end of each four-foot long chamber section, and the flex joints added flexibility to the middle of each section. Flexibility was needed to compensate for limited precision in the adjustment of magnet positions and variations in chamber geometry during fabrication. Part of the upgrade was installation of new magnet and vacuum

chamber mounts capable of being surveyed and positioned to $\pm 100 \mu\text{m}$. In addition, the chambers were assembled in eight foot sections in a precision fixture that positioned parts prior to welding and provided a jig for minor adjustments after welding. By using these techniques flex joints became unnecessary and the number of bellows could be reduced by a factor of two. Synchrotron radiation masking was incorporated into the bellows RF shield, so the net change in the inductance from bellows and flex joints was from 13.1 nH to 1.1 nH.

The vacuum chamber profile must be rectangular in the dipoles for maximum damping and circular in the quadrupoles for adequate aperture. Modern materials and machining techniques allowed these transitions to be made over 5 cm versus 6 mm in the old chamber. Glidcop³ was chosen for the combination of strength and thermal conductivity needed to conduct away heat from synchrotron radiation. The transition was made smoothly by electrodischarge machining a continuous change from a circular to a rectangular profile over the length of the transition.

Other changes were the redesign of the beam position monitors and the slots between the beam and distributed ion pump chambers. The beam position monitors were made at the same radius as the beam pipe itself instead of being recessed. The pump slots were made narrower and deeper to cut-off higher frequency fields, and several slots were used instead of one to maintain the pumping speed. The pump slot impedance is strongly frequency dependent, and this change is important even though it does not appear so in Table 1. Finally, the bellows at the ends of the ceramic beam pipes for the injection and extraction kicker magnets were shielded.

All of these changes were made to fit within the mechanical constraints of existing magnets and other beam line hardware.

II. INSTABILITY PROPERTIES

A damping ring instability limited the SLC beam to 3×10^{10} ppb with the old vacuum chamber. The characteristics of that instability were: i) threshold $I \approx 3 \times 10^{10}$ ppb, ii) signals at about three times the synchrotron frequency, f_s , indicating a predominantly sextupole structure in phase space, and iii) transient behavior with the instability amplitude building up in several synchrotron periods and

* Work supported by the Department of Energy, contract DE-AC03-76SF00515.

then relaxing with roughly the radiation damping time.⁴ Based on simulations it was expected that the threshold with the new vacuum chamber would be $5 - 6 \times 10^{10}$ ppb. However, the threshold was reduced to $1.5 - 2 \times 10^{10}$ ppb, but with the redeeming feature that the consequences for the SLC were less dramatic. Towards the end of the 1994 - 1995 run we were running with bunches of up to 4.5×10^{10} ppb in the damping rings and colliding beams of up to 3.8×10^{10} ppb. The SLC intensity limit was not due to the damping ring instability, and there was at best marginal evidence of a correlation between the instability and linac performance. Details of the instability follow.

The energy spread was measured with a wire scanner in a dispersive region of the extraction line. It should be constant below the instability threshold which based on the data in Fig. 1 is between 1.5 and 2.0×10^{10} ppb for an accelerating voltage $V_{RF} = 945$ kV.

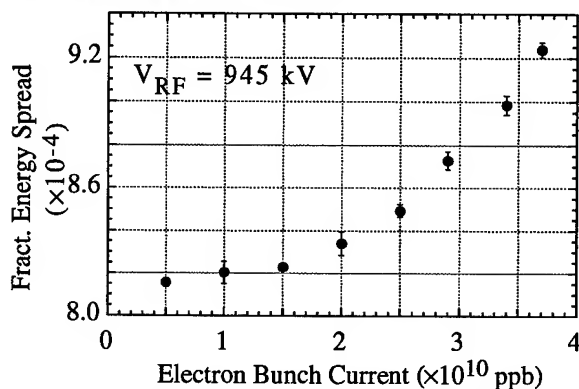


Figure 1: Energy spread as a function of current.

Bunch length was measured with a streak camera⁵ and a wire scanner in the extraction line following an accelerating section phased to produce a time-energy correlation.⁴ The distributions are not Gaussian, and the results in Fig. 2 are based on the FWHM. There is a small systematic offset between the wire scanner and streak camera data, but there is good agreement on the current dependence. Clearly there is a significant reduction in bunch lengthening with the new chamber.

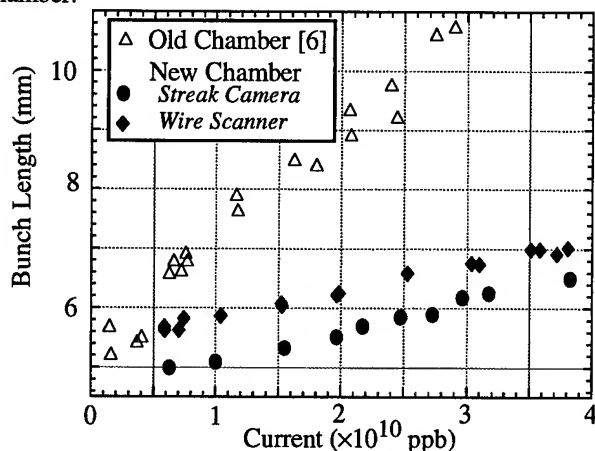


Figure 2: Bunch length dependence on current. Bunch lengths are FWHM/2.35. $V_{RF} = 800$ kV.

A study was made of the image-by-image variation of the streak camera profile. The conclusion was that the bunch length varied less than $\pm 3\%$ image-by-image. This variation and the differences in images were consistent with those expected from camera noise.

A third diagnostic was spectral analysis of a beam position monitor electrode. The spectrum analyzer was used in three different modes: i) as a swept frequency analyzer, ii) as a fixed frequency receiver, and iii) as a down converter input to a digital signal processing system.⁷ Figure 3 is a DSP output when the instability was present.

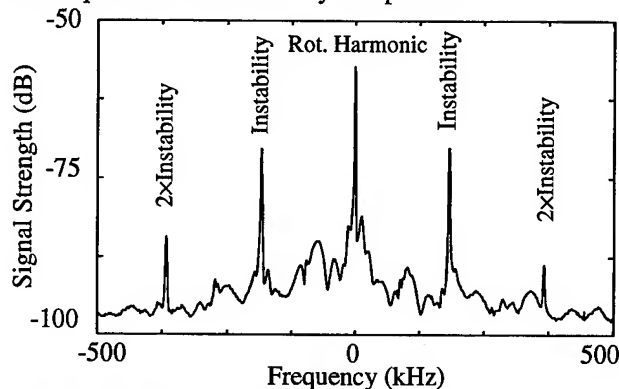


Figure 3: Spectrum centered around a rotation harmonic at 23 GHz. The current and synchrotron frequency at that time were $I = 2.9 \times 10^{10}$ ppb and $f_s = 104$ kHz.

The sidebands associated with the instability are clearly visible. They are at $f = 184$ kHz $= 1.77f_s$ from the rotation harmonic. This is the signature of a predominantly quadrupole mode in contrast to the sextupole mode with the old vacuum chamber. The frequency increases with decreasing current; the slope is $df/dI \sim -6$ kHz/ 10^{10} . This is opposite to the current dependence with the old chamber which had a slope $df/dI \sim 9$ kHz/ 10^{10} .⁴ The second harmonics in this spectrum are seen whenever the instability is strong. We have measured differences in the amplitudes of the positive and negative frequency sidebands also, and we have established that there are differences characteristic of the instability rather than being due to variation in beam position monitor sensitivity. Which sideband is stronger can depend on how far the current is above threshold.

Spectra have been taken under a number of conditions, and some conclusions can be reached from these data. First, there are no significant differences between the electron and positron damping rings. The impedances of these two rings are expected to be close, but there could be ion effects in the electron ring. We conclude that possible ion effects are not contributing to the instability.

Second, with two bunches the sidebands of adjacent rotation harmonics are roughly equal in amplitude while the rotation harmonics themselves display the alternating pattern expected with two bunches. We conclude from this that the instability is a single bunch instability.

The transient nature of the instability was studied by using the spectrum analyzer as a receiver set to a sideband

frequency. Figure 4 is one example of the output. The transient at injection/extraction time is due to the kicker noise and phase space mismatch at injection. The instability signal rises out of the noise at about 3 ms and oscillates in amplitude by about 10 dB with rise and fall times in the range of 250 to 500 μ s. This is a common pattern seen with both one and two bunches and is reminiscent of the "sawtooth" behavior we saw with the old vacuum chamber.

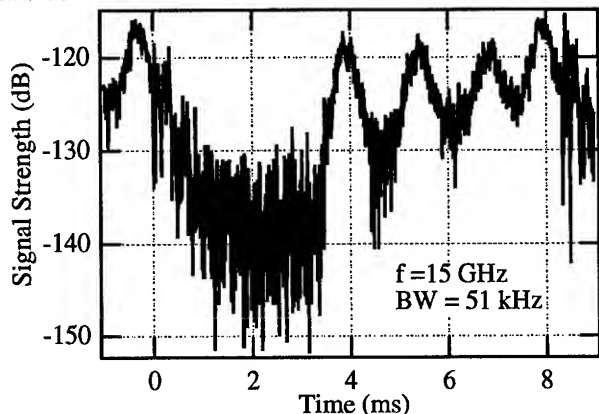


Figure 4: Video output of the spectrum analyzer tuned to a sideband frequency. The beam had two bunches, $I = 3.5 \times 10^{10}$ ppb. Injection and extraction are at 0 and 8.3 ms.

However, the sawtooth is not the only behavior that has been seen. Figure 5 shows a different set of conditions. The common feature of Figs. 4 and 5 is the appearance of the instability at roughly 3 ms into the store indicating that it takes about 2 damping times for the peak current to reach the critical value for instability.

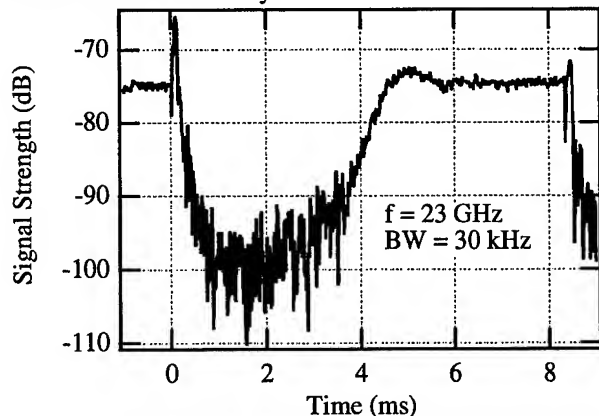


Figure 5: Video output for analyzer tuned to one of the sidebands. One bunch, $I = 3.9 \times 10^{10}$ ppb. Injection and extraction are at 0 and 8.3 ms.

We have studied the dependence of the threshold on a number of parameters, and, although our understanding is incomplete, there is clear evidence that the RF accelerating voltage is one of the key factors. Figure 6 is a graph of the signal amplitude just before extraction as a function of the accelerating voltage. There is no measurable signal below 800 kV, and the instability is present on every pulse at 865 kV ($V_{RF} = 865$ kV in Fig. 5). In between the amplitude of

the instability is not constant, and whether it is present on a given pulse depends on the phase of the transient at extraction time.

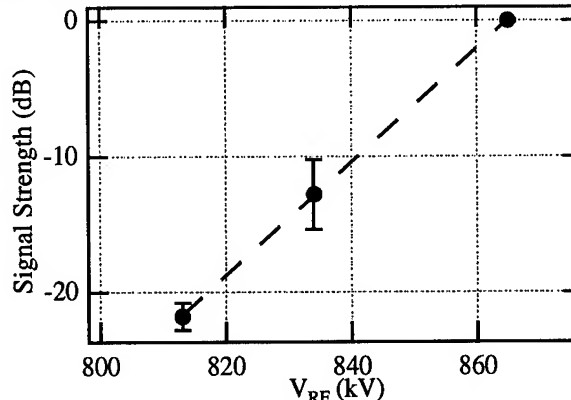


Figure 6: Instability signal amplitude 50 μ s before extraction. The beam had 1 bunch of $I = 3.9 \times 10^{10}$ ppb. Noise level ~ -25 dB. Error bars show RMS signal variation.

III. SUMMARY AND CONCLUSIONS

We have described the changes in the damping ring impedance and the observations of instability with the new vacuum chamber. Some of the results with the old chamber⁴ and some preliminary results with the new one have been or could be interpreted with the ideas in a number of theoretical and simulation papers.⁸⁻¹³ We look forward to quantitative comparisons with the data in this paper.

Finally, we are relieved that we could increase the SLC current despite this unexpected instability.

IV. ACKNOWLEDGEMENTS

The upgrade we described would not have been successful without the high quality, dedicated work of the SLAC machinists, surveyors, vacuum technicians, and mechanical technicians. They have our sincere thanks.

V. REFERENCES

1. Karl L. F. Bane, *Proc 1988 EPAC*, 637 (1988).
2. K. Bane & C. Ng, *Proc 1993 PAC*, 3432 (1993).
3. SCM Metal Products.
4. P. Krejcik *et al*, *Proc 1993 PAC*, 3240 (1993).
5. R. L. Holtzapple *et al*, WXE05, 1995 PAC.
6. L. Rivkin *et al*, *Proc 1988 EPAC*, 634 (1988).
7. R. Stege *et al*, *1992 Accel Inst Workshop*, 217 (1992).
8. X. T. Yu & J. S. Wurtele, *Proc 1993 PAC*, 3327 (1993).
9. K. Oide, KEK-preprint-94-138 (Nov, 1994).
10. R. Baartman, M. D'Yachkov, WAC20, 1995 PAC.
11. K. L. F. Bane, K. Oide, WAC16, 1995 PAC.
12. A. Chao *et al*, WAB10, 1995 PAC.
13. B. Chen, WAC31, 1995 PAC.

Alignment tolerance of accelerating structures and corrections for future linear colliders,*

K. Kubo†, C. Adolphsen, K.L.F. Bane, T.O. Raubenheimer and K.A. Thompson,
Stanford Linear Accelerator Center, Stanford University, Stanford, CA, 94309 USA

Abstract: The alignment tolerance of accelerating structures is estimated by tracking simulations. Both single-bunch and multi-bunch effects are taken into account. Correction schemes for controlling the single and multi-bunch emittance growth in the case of large misalignment are also tested by simulations.

I. ALIGNMENT TOLERANCE

Emittance growth caused by random misalignments of accelerating structures for NLC (Next Linear Collider, being designed at SLAC) main linacs are considered. Both single-bunch effects and multi-bunch effects are taken into account. The effect of other errors, for example misalignment of quadrupoles and injection jitter, are not discussed in this paper.

A. Tracking

A tracking program has been developed to simulate phase space beam dynamics in main linacs of future linear colliders[1]. Parameters for a 250 GeV NLC linac, which are used in our simulations, are listed in Table 1.

To simulate single-bunch effects, each bunch is divided into five slices and each slice has five macro particles with different initial energies. For multi-bunch simulations without single bunch effects, each bunch is treated as being rigid.

The accelerating structures are misaligned randomly and the average of the emittance growth of 100 randomly misaligned machines is used to estimate the alignment tolerance. The tolerance depends on the length of an "alignment unit" which is aligned independently. Each alignment unit is assumed to consist of either (a) M structures or (b) 1/M structure ($M=1,2,3, \dots$). Long scale misalignment is simulated in Case (a). Alignment of girders can also be simulated in the case where M structures are on a girder and each girder is aligned independently, with random errors, while the structures are perfectly aligned on each girder. Fabrication errors of each structure are simulated in Case (b). Each structure is divided into M pieces and each piece is "aligned" independently. The situation corresponds to, for example, each structure consisting of M pieces brazed together with random errors, with each piece fabricated error-free. Each slice of the beam is kicked by wakefields at the center of each structure in Case (a) and at the center of each piece of structure in Case (b).

The transverse short range wakefunction was assumed to be a linear function. Though the shape of the cells changes

along a structure, only averages over a structure were used for both longitudinal and transverse short range wakefunctions.

Frequencies, kick factors and Q 's of the modes of the first pass band of the "damped detuned structure"[2] for the NLC were used to obtain the long range transverse wakefield, which was used to calculate the inter-bunch effect. In the case of simulations for fabrication errors (a structure is divided into pieces), each mode is assumed to be localized in that piece in which the centroid of the field amplitude is located. Because fields of some modes are distributed widely, this approximation will not be appropriate for very short pieces of structures. Though we do not discuss it here, it is possible to use a more precise method to calculate a wakefield with fabrication errors[3].

The lattice is a FODO lattice with a phase advance of about 90° /cell and with a beta function that varies approximately as the square root of the beam energy.

Table 1. Parameters used for the simulation.

Accelerating frequency	11.424 GHz
Beam energy	from 10 to 250 GeV
Loaded gradient	37 MV/m
Phase advance/cell	90°
Length of a FODO cell	from 8 to 40 m
Charge per bunch	$0.7 \times 10^{10} e$
Bunch length	100 μm
Number of bunches	90
Bunch spacing	1.4 ns
Normalized emittance	3×10^{-8} m-rad
Length of acc. structure	1.8 m
Number of cell /structure	206
Structure type	Damped detuned
Average aperture radius	4.9 mm
Slope of transverse wake	8.4×10^{19} V/C/m ³

One-to-one trajectory steering is assumed to be always performed so that the beam centroid goes through the center of every focusing quadrupole magnet. Because all quadrupole magnets are assumed to be perfectly aligned, alignment tolerances obtained here should be regarded as tolerances with respect to the beam or required accuracy of beam based alignment of the accelerating structures.

Figure 1 shows the alignment tolerances for averaged emittance growth of less than 25% as function of alignment unit length. The solid line shows tolerances considering both single- and multi-bunch effects. Tolerances for the single-bunch effect alone, and multi-bunch effect alone are also shown here. Comparing the three curves, it is noticed that the single-bunch effect is dominant for longer alignment lengths

*Work supported by the Department of Energy, contract DE-AC0376SF00515

†Permanent address: KEK, 1-1, Oho, Tsukuba, Ibaraki, 305 Japan

and the multi-bunch effect is important only for pieces in each structure. The curves have a minimum at an alignment length of 16 structures or 32 m, which is about the betatron function at the end of the linac. This is expected since, when the alignment unit becomes longer than the beta function, the effects of the wakefield begin to cancel. And the end of the linac is the most sensitive region because of the weakly focusing lattice. The single-bunch curve for short alignment lengths varies according to the $-1/2$ power up to the length of about 16 structures. This is because the effect of the kick by wakefield depends only on the average offset of the beam with respect to the structure center over the length comparable to beta function. However, the multi-bunch curve drops for alignment length less than one structure. This is because, with the misalignment (fabrication error) of pieces in a structure, the designed cancellation of the 206 dipole modes of each structure is disturbed.

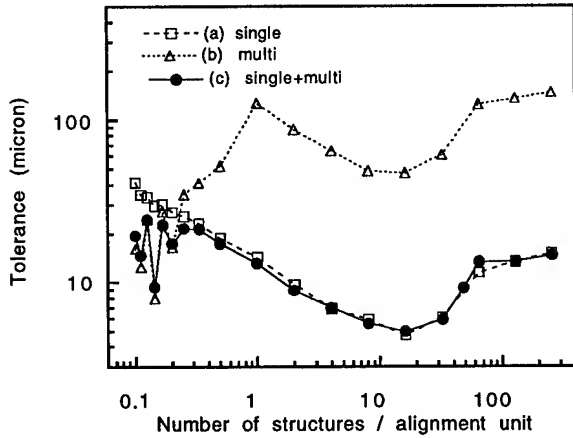


Figure 1. Tolerance of misalignment of damped-detuned structures for 25% emittance growth as function of alignment unit length, (a) considering only the single-bunch effects, (b) only the multi-bunch effects, and (c) considering both effects together. Each symbol represents the average of tracking with 100 random seeds.

The minimum alignment tolerance is $5 \mu\text{m}$ for an alignment unit length of about 32 m. The tolerance for each structure is $13 \mu\text{m}$. The minimum tolerance for short pieces (fabrication) is $9 \mu\text{m}$ in the case of 7 pieces per structure.

B. Numerical Method

In order to save calculation time, a numerical method to estimate the alignment tolerance has been developed. The essential approximation of this method is that the amplitude of betatron oscillation is negligibly small compared to the misalignment of structures. This assumption is the same as in the analytical method presented elsewhere[4].

We consider the tolerance for alignment units each of which consists of several short pieces. The expected emittance growth from kicks by wakefields due to the misalignment of accelerating structures are given as follows.

$$\langle \Delta \epsilon \rangle = e^2 \sum_i a_i^2 \sum_{\lambda \in i} \sum_{\lambda' \in i} B_{f,\lambda\lambda'} L_{\lambda} L_{\lambda'} T_{\lambda\lambda'} / E(\lambda) E(\lambda')$$

where i is index for alignment unit, λ index for short piece and a_i r.m.s. misalignment of structures.

$$B_{f,\lambda\lambda'} \equiv \frac{1 + \alpha_f^2}{2\beta_f} R_{\lambda,12} R_{\lambda',12} + \alpha_f R_{\lambda,12} R_{\lambda',22} + \frac{\beta_f}{2} R_{\lambda,22} R_{\lambda',22}$$

where α_f and β_f are twiss parameters at the end of linac and $R_{\lambda,12}$ and $R_{\lambda,22}$ are 12 and 22 elements of transfer matrix from λ to the end of linac.

$$T_{\lambda\lambda'} \equiv \sum_m q_m S_{a,m}(\lambda) S_{a,m}(\lambda') / \sum_m q_m$$

$$S_{a,m}(\lambda) \equiv S_m(\lambda) - \sum_m q_m S_m(\lambda) / \sum_m q_m$$

$$S_m(\lambda) \equiv \sum_k q_k W(\lambda, z_m - z_k)$$

where q_m is the charge of m -th slice of the beam, $W(\lambda, z)$ the transverse wake function of λ at distance z . L_{λ} the length of the piece and $E(\lambda)$ the beam energy at λ . Assuming continuous focusing and that the alignment units are short compared with beta function, we obtain an analytical expression in Ref. [4].

This method was compared with tracking for the NLC design in the cases of considering only single-bunch effects, only multi-bunch effects, and both effects together. The estimated tolerances agree well for any alignment unit length.

Fabrication errors were studied more carefully using numerical methods. Two curves in figure 2 show the tolerances as functions of alignment length for two different approximations. In both cases the wakefield of each mode is assumed to be localized in one piece, but (a) assumes that that piece is where the centroid of amplitude is, and (b) assumes that it is where the phase velocity of the mode is closest to the velocity of light[5]. The two curves are different in detail but, generally, both have similar behavior with a minimum tolerance of about $10 \mu\text{m}$.

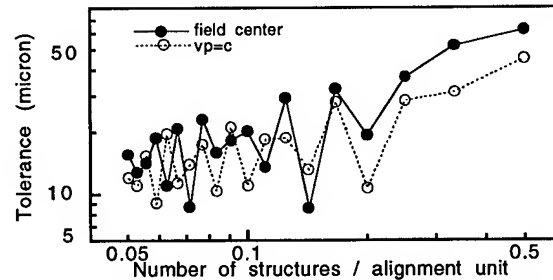


Figure 2. Tolerance of fabrication of damped-detuned structures for 25% emittance growth as function of alignment length, considering only multi-bunch effects from the numerical method, (a) assumed the field is at the center of the amplitude and (b) assumed the field is where $v_p=c$.

II. CORRECTIONS

It is expected that one can achieve the required alignment[6]. But if this is not the case, some additional correction can be done. One technique of beam based alignment has been suggested[7], in which bunch current and/or the bunch length are changed, and the trajectories are measured. However this technique may be difficult to implement. Another possible approach is a combination of : (1) for single bunch correction, trajectory bumps or moving structures, tuned by emittance measurements and (2) for multi-bunch correction, fast kickers tuned by a bunch-by-

bunch position measurement[8]. The emittance and bunch-by-bunch positions are measured at several locations in the linac. In technique (1), a beam offset with respect to structures is intentionally produced at some parts of the linac to compensate the effects of wakefield due to misalignment of other parts. In (2), the beam is kicked bunch-by-bunch so that all bunches have the same trajectory.

Tracking simulations were performed to test these techniques for the 250 GeV NLC linac. Again, note that we concentrate only on corrections for the misalignment of accelerating structures.

A. Single-bunch

In this tracking, some accelerating structures were moved instead of trajectory bumps, because of ease of simulation. Though, in reality, it may be more flexible and reliable to introduce trajectory bumps, both methods have almost the same effects.

We assumed emittance measurement at five locations, at beam energy of 30, 60, 100, 150 and 250 GeV. Two sets of accelerating structures were moved just before each location to minimize the emittance. Each set consisted of all structures between two quadrupole magnets and the two sets were separated by one FODO cell or about 90° betatron phase. The r.m.s. of misalignment of each structure was set to be 30 μm , where the expected emittance growth without corrections is 130%. The movement of each set of structures was performed in 20 μm steps and limited to $\pm 300 \mu\text{m}$.

Figure 3 shows emittance growth as a function of resolution of beam size where the resolution of emittance measurement was calculated from $\epsilon = \sigma^2 / \beta$, assuming β at focusing magnets near each station. It is shown that precise measurement of the emittance is essential for this correction.

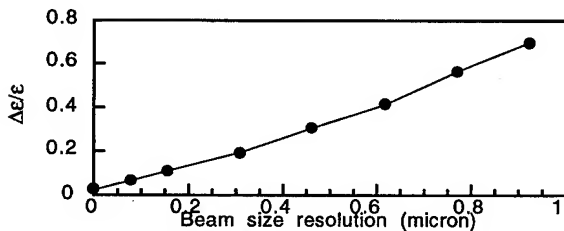


Figure 3. Emittance growth as function of resolution of beam size measurement. Each symbol represents the average of tracking with 100 random seeds.

B. Multi-bunch

Bunch-by-bunch trajectories were assumed to be measured by two fast BPMs located at consecutive focusing quadrupole magnets (90° phase difference) at each of the same five locations as the single-bunch correction. Two fast kickers were also located at consecutive focusing quadrupoles just before the BPMs and the beam was kicked bunch-by-bunch (except the first bunch) so that all bunches have the same trajectories. One-to-one trajectory correction was also performed to make the beam centroid go through the center of every focusing quadrupole magnet. Tracking was performed with 90 bunches including both single- and multi-bunch

effects. Each structure was divided into 7 pieces and the pieces were aligned independently with an r.m.s. error of 25 μm . This misalignment was chosen so that the multi-bunch effects are much stronger than single-bunch effects because we are concentrating here on multi-bunch correction. But, because it is possible that single-bunch effects become significant due to a large bunch offset caused by the multi-bunch effects, the single-bunch effects were also considered in this simulation. The expected emittance growth without corrections was estimated as $\Delta\epsilon/\epsilon = 1.33$.

Figure 4 (a) and (b) show emittance growth as function of BPM resolution and kicker speed, respectively, where the limit of kicker strength is 56 kV. A kicker speed 250 MHz and strength limit of 56 kV are our tentative design values and the bunch-by-bunch BPM resolution is expected to be better than 0.2 μm . The results show our design will be effective.

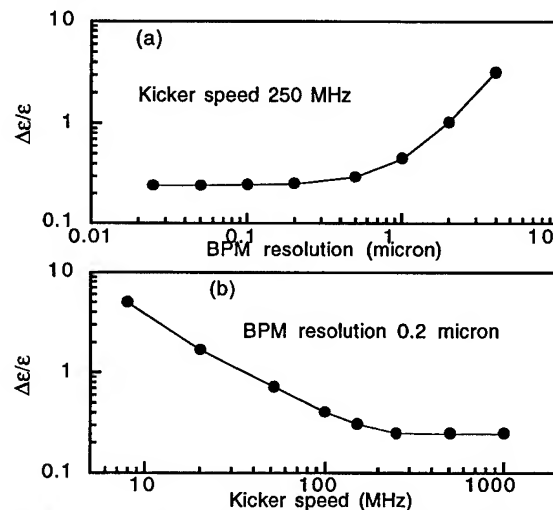


Figure 4. Emittance growth vs. (a) BPM resolution and (b) Kicker speed, with the strength limit 56 kV. Each structure was divided into 7 pieces and misalignment of pieces is 25 μm . Each symbol represents the average of tracking with 25 random seeds.

References

- [1] K. Kubo et. al., "A simulation program for Phase Space Dynamics in Future Linear Colliders," in progress.
- [2] K. Ko et. al., "Design parameters for the damped detuned accelerating structure", this conference.
- [3] K.A. Thompson, et. al., "Multibunch Beam Breakup in Detuned Structures", PAC93, SLAC-PUB-61533 (1993)
- [4] K.L.F. Bane et. al., "Issues in Multi Bunch Emittance Preservation in the NLC", EPAC94, SLAC-PUB-6581 (1994)
- [5] R. Miller private communication.
- [6] C. Adolphsen et. al., "Emittance and Energy Control in the NLC Main Linacs", this conference.
- [7] T.O. Raubenheimer and K. Kubo, "A Technique of Measuring and Correcting Emittance Dilutions due to Accelerator Structure Misalignments", SLAC-PUB-95-6523 (1994)
- [8] T.O. Raubenheimer and K. Kubo, "Proc. of 5th International Workshop on Next Generation Linear Colliders", SLAC-Report-436, p275 (1993)

REFINEMENTS TO LONGITUDINAL, SINGLE BUNCH, COHERENT INSTABILITY THEORY

S. R. Koscielniak, TRIUMF, 4004 Wesbrook Mall, Vancouver, B.C. V6T 2A3, Canada

Abstract

For the case of a bunched beam confined to a quadratic potential well, we demonstrate the necessity for considering mode-coupling to correctly obtain the threshold current for the d.c. instability. Further we find the effect upon growth rate and coherent tune shift of evaluating the impedance at a complex frequency. For the case of a bunched beam confined to a cosine potential well, we give an exact analytic expression for the dispersion integral, and calculate (with no approximations), the stability diagram for the Robinson instability taking into account Landau damping. This paper comprises extracts from a lengthy internal report[1].

I. SIMPLE HARMONIC OSCILLATOR CASE

We consider the stability of a single bunch confined in a quadratic potential well that is truncated at rf-phase $x = \pm\pi$. Let ω_s be the synchrotron frequency. We shall investigate the stability of the system through use of the linearized Vlasov equation in which products of two perturbation terms will be ignored. Let the phase-space steady-state and perturbation distribution functions be $\Psi_0(J)$ and be Ψ_1 , respectively. In action-angle coordinates (J, θ) , the Vlasov equation becomes:

$$[\partial/\partial t + (d\theta/dt)\partial/\partial\theta]\Psi_1 = (\partial\Psi_0/\partial J)(\partial H/\partial\theta). \quad (1)$$

We shall assume Ψ_1 to have time dependence e^{st} with the complex perturbation Laplace frequency $s = \sigma + i\omega$. Let $i = \sqrt{-1}$ and take $\mathcal{R}[\dots]$ to mean "form the real part".

Henceforward, we shall employ the symbols q and p as integer indices for Fourier harmonics.

Let $\xi = 2\pi I_{d.c.}/V_{rf}$.

The beam current perturbation signal is $\lambda(x, t) = \mathcal{R}[e^{st} \sum_q \lambda_q e^{iqx}]$ and leads to perturbing forces $\partial H/\partial\theta = \omega_s^2 w(x, t)$ where the wakefields are:

$$w(x, t) = \xi \mathcal{R}[e^{st} \sum_q w_q] \quad \text{with} \quad w_q = Z_q(\omega, \sigma) \lambda_q e^{iqx}. \quad (2)$$

The arguments of the complex impedance Z_q are used to indicate the modulation sideband frequency. Hence $Z_{+q}(\omega, \sigma) = Z(+q\omega_{rf} + \omega, \sigma) = Z(+q\omega_{rf} + \omega - i\sigma)$ is the complex impedance evaluated at the $\omega - i\sigma$ sideband of the q^{th} harmonic of the radio-frequency ω_{rf} .

As a trial solution of the Vlasov equation we take

$$\Psi_1 = \mathcal{R}[\psi e^{st}] \quad \text{with} \quad \psi(J, \theta) = \sum_m \psi_m(J) e^{im\theta}; \quad (3)$$

where m is the azimuthal mode index, and $m = 0$ is excluded. After separating the Vlasov equation, we find the radial functions

$$\psi_{+n}(J) = \frac{\omega_s^2 \xi n}{[s + in\omega_s]} \Psi'_0 \sum_p Z_p(\omega, \sigma) \frac{1}{p} \lambda_p J_{+n}(+p\pi k). \quad (4)$$

where $k^2 = J/J_0$ and $J_0 = \omega_s \pi^2/2$ is an action value, but the $J_n(\dots)$ with an argument are Bessel functions. The prime notation indicates a derivative with respect to action J . The Fourier harmonics are:

$$2\pi \lambda_q(n) = \int \psi_n(J) e^{-iqx} e^{in\theta} d\theta dJ, \quad (5)$$

and so the eigenvalue problem is

$$\lambda_q(n) = \frac{\omega_s \xi n}{[s + in\omega_s]} \sum_p Z_p(\omega, \sigma) \frac{1}{p} \lambda_p I_n(q, p). \quad (6)$$

Note, in the above equation the λ_p without arguments is the sum over the $\lambda_p(n)$ with arguments.

A. Single azimuthal mode and narrowband impedance

Consider the case of a solitary azimuthal $\psi(J, \theta) = \psi_m(J) e^{im\theta}$. Consider the case of a narrowband impedance such that Z_p is only significant in the vicinity of $p = q > 0$. This results in an eigenfrequency equation:

$$(s + im\omega_s) = m\omega_s I_m(q, q) \xi [Z_{+q} - Z_{-q}]/q. \quad (7)$$

$$\text{where } I_m(q, q) = \omega_s \int_0^{J_0} \Psi'_0 J_{+m}^2(q\pi k) dJ. \quad (8)$$

The combination ξZ and integral I_m are both dimensionless. If and only if both $Z_{-q} \neq 0$ and $Z_{+q} \neq 0$, then equation (7) has the property that if $m \Rightarrow -m$, then $s \Rightarrow s^*$.

Let the impedance $Z = R + iX$ be composed of a resistive part R and a reactive part X , then we find the eigenfrequency:

$$\omega/(m\omega_s) = I_m \xi [X(q\omega_{rf} + \omega) + X(q\omega_{rf} - \omega)]/q - 1 \quad (9)$$

$$\sigma/(m\omega_s) = I_m \xi [R(q\omega_{rf} + \omega) - R(q\omega_{rf} - \omega)]/q. \quad (10)$$

These equations have to be solved recursively for s . At high enough current, there is a solution with mode frequency $s = 0$, which satisfies the condition:

$$q = 2\xi X(q\omega_{rf}) I_m(q, q). \quad (11)$$

B. $\pm m$ mode-coupling and narrowband impedance

Consider the case of two azimuthal modes,

$$\psi(J, \theta) = [\psi_{+m} e^{+im\theta} + \psi_{-m} e^{-im\theta}]. \quad (12)$$

Consider the case that impedance Z_p is only significant in the vicinity of $p = q > 0$. This results in an eigenfrequency equation.

$$i \frac{(s^2 + m^2 \omega_s^2)}{(m \omega_s)^2} = 2\xi [Z(q\omega_{rf} + \omega, \sigma) - Z(-q\omega_{rf} + \omega, \sigma)] \frac{1}{q} I_m(q, q) \quad (13)$$

The equation separates into imaginary and real parts as:

$$\frac{\omega^2 - \sigma^2}{(m \omega_s)^2} = 1^2 - 2 I_m \xi [X(q\omega_{rf} + \omega) + X(q\omega_{rf} - \omega)]/q$$

$$\omega \sigma / (m \omega_s)^2 = + I_m \xi [R(q\omega_{rf} - \omega) - R(q\omega_{rf} + \omega)]/q \quad (14)$$

At high enough current, there is a solution with mode frequency $s^2 \equiv 0$.

$$q = 4 \xi X(q\omega_{rf}) I_m(q, q) \quad (15)$$

The value of the threshold differs by a factor 2 from the case of no mode coupling, expression (11).

II. IMPEDANCE AT COMPLEX FREQUENCY

If we continue Z into the complex plane, given the functional form $Z(\omega, 0)$, then the response to $\exp(\sigma + i\omega)t$ is $Z(\omega, \sigma) = Z(\omega - i\sigma)$. Actually, one does not need to know the form, but only the derivatives of resistance R and reactance X with respect to frequency ω . We denote derivatives with respect to real angular frequency ω by ∂_ω . Let $Z(\omega, \sigma) = R + iX$. We may then employ the Cauchy-Riemann conditions for analytic complex functions:

$$\partial R / \partial \sigma = -\partial X / \partial \omega \quad \text{and} \quad \partial X / \partial \sigma = +\partial R / \partial \omega,$$

to find the first order Taylor expansion

$$Z(\omega', \sigma') \approx Z(\omega', 0) + (-i\sigma') \times \partial_\omega Z \Big|_{\sigma=0} \quad (16)$$

A. Eigenvalues with narrowband impedance

Consider a narrowband impedance that is still sufficiently broad to include both the upper and lower sideband. An approximation of $[Z_{-q} - Z_{+q}]$ is

$$Z_{-q}(\omega, \sigma) - Z_{+q}(\omega, \sigma) \approx -2[iX(q\omega_{rf}) + (\omega - i\sigma)\partial_\omega R(q\omega_{rf})] \quad (17)$$

Substitution of (17) into (14) leads to the eigenvalue

$$[\omega^2 + \sigma^2] / (m \omega_s)^2 = 1^2 - 4 I_m \xi X(q\omega_{rf}) / q \quad (18)$$

$$\sigma / (m \omega_s) = -2 I_m \xi m \omega_s [\partial_\omega R(q\omega_{rf})] / q \quad (19)$$

These forms show that, to first order, and for single bunch instability, evaluation of the impedance at a complex frequency alters the coherent tune, but does not change the growth rate.

III. SIMPLE PENDULUM OSCILLATOR

Consider the stability of a single bunch confined in a sinusoidal potential well. The unperturbed Hamiltonian is:

$$H(x, y) = y^2/2 + \omega_s^2 [1 - \cos x] = y^2/2 + 2\omega_s^2 \sin^2(x/2) \quad (20)$$

We shall investigate the stability of a multi-particle system of oscillators through use of the Vlasov equation; the equation is simplified if we employ action-angle coordinates.

$$\sin(x/2) = k \operatorname{sn} \theta = \sqrt{J/J_0} \operatorname{sn} \theta \quad (21)$$

$$y = 2\omega_s k \operatorname{cn} \theta = 2\omega_s \sqrt{J/J_0} \operatorname{cn} \theta \quad (22)$$

$J_0 = 2\omega_s$ and sn , cn dn are Jacobean elliptic functions.

The time variation of θ is $\theta = \omega_s(t - t_0)$ where t_0 is a constant of integration.

The trial solution ψ must be separable after integrating θ over the interval $[-2\mathcal{K}, +2\mathcal{K}]$. Hence, we take:

$$\Psi_1 = \mathcal{R}[e^{st} \sum_{-\infty}^{+\infty} \psi_m(J) e^{im\pi\theta/2\mathcal{K}}] \quad (23)$$

After separation, we find the radial functions ψ_n :

$$\psi_n(J) = \frac{\omega_{s0}^2 \xi n}{[s + in\omega_s(J)]} \left[\frac{\pi}{2\mathcal{K}} \right] \Psi'_0 \sum_p Z_p(\omega) \frac{1}{p} \lambda_p \mathcal{J}_n(p, k) \quad (24)$$

Using the Jacobean elliptic analogue of the Hankel transform we find a particular case of Lebedev's [2] expression:

$$\lambda_q(n) = \omega_{s0}^2 \xi \sum_p Z_p(\omega) \lambda_p \left[\frac{n}{p} \right] \int_0^{J_0} \frac{\mathcal{J}_n(p, k) \Psi'_0 \mathcal{J}_n(q, k)}{s + in\omega_s(J)} dJ \quad (25)$$

If we sum this equation over mode number n , we obtain an eigenvalue problem for the harmonics λ_q . The form factors are

$$\mathcal{J}_{+n}(+q, k) \times 4\mathcal{K} = \int_{-2\mathcal{K}}^{+2\mathcal{K}} e^{-iqx} e^{+in\pi\theta/2\mathcal{K}} d\theta$$

$$= \int_{-2\mathcal{K}}^{+2\mathcal{K}} [\operatorname{dn} \theta - ik \operatorname{sn} \theta]^{+2q} e^{+in\pi\theta/2\mathcal{K}} d\theta;$$

and have the properties: $\mathcal{J}_n(q, 0) = 0$ and $\mathcal{J}_n(q, 1) = 0$.

A. Narrowband impedance at cavity radio-frequency

In general, the integrals $\mathcal{J}_n(q, k)$ are awkward to evaluate analytically. To simplify, we shall consider an impedance that is significant only at the $p = \pm 1$ harmonics of the cavity radio-frequency. For odd- n we find:

$$\mathcal{J}_n(1, k) = n \left[\frac{\pi}{\mathcal{K}} \right]^2 \frac{q^{n/2}}{1 + q^n} \quad \text{with } q = \exp \left[\frac{-\pi \mathcal{K}(k')}{\mathcal{K}(k)} \right] \quad (27)$$

Here q is the 'nome' and $(k')^2 = 1 - k^2$. Expressions for even- n are rather complicated, but

$$\mathcal{J}_2(1, k) \approx [2\pi/\mathcal{K}]^2 q / [2(1 + q)^2] \quad (28)$$

B. $\pm m$ mode coupling and narrowband impedance

Previously, we saw that a mode-coupling theory is essential when the tune shifts and growth rates are comparable with the unperturbed synchrotron frequency. Consequently, we shall not bother to consider the cases of the $-m$ and the $+m$ modes in isolation. Let the mode index m be single sided and valued and take the trial distribution function (12). For the narrowband impedance we obtain the eigenfrequency equation:

$$i = \xi[Z_{+1} - Z_{-1}]2m^2\omega_{s0}^2 \int_0^{J_0} \frac{\omega_s(J)\Psi'_0 \mathcal{J}_m^2(1, k)}{s^2 + m^2\omega_s^2(J)} dJ. \quad (29)$$

Let us search for a threshold and take $s = i\omega$ pure imaginary. Let the value of action at which the integral is singular be $\tilde{J}(\omega)$ and define $\tilde{k} = \sqrt{\tilde{J}/J_0}$. Then we have the eigenequation:

$$i = \xi[Z(-\omega_{rf} + \omega) - Z(+\omega_{rf} + \omega)] \times [f(\omega) + ig(\omega)] \quad (30)$$

where the quantities f and g are:

$$f(\omega) = 2m^2\omega_{s0}^2 \mathcal{P} \int_0^{J_0} \frac{\omega_s(J)\Psi'_0 \mathcal{J}_m^2(1, k)}{\omega^2 - m^2\omega_s^2(J)} dJ \quad (31)$$

$$g(\omega) = \omega_{s0}^2 \pi \Psi'_0(\tilde{J}) \mathcal{J}_m^2(1, \tilde{k}) / [\partial\omega_s / \partial J]_{\tilde{J}}. \quad (32)$$

Here \mathcal{P} indicates the principal value, and g is the residue.

C. Power limited instability

For the power limited instability, the eigenfrequencies are $\omega^2 = 0$. Now zero frequency is either outside the spread of incoherent frequencies, or (for a full bucket) at the very edge of the bunch where there are no particles. Consequently, this particular instability is not Landau damped. We substitute $\omega^2 = 0$ and find the Fourier components are equal $\lambda_{-1}(-m) = \lambda_{-1}(+m)$, and that the threshold current is given by

$$1 = 4\xi X(\omega_{rf}) \omega_{s0}^2 \int_0^{J_0} \Psi'_0 \frac{\mathcal{J}_m^2(1, k)}{\omega_s^2(J)} dJ. \quad (33)$$

This only differs from the linear oscillator case by virtue of the exact value of the integral.

D. Stability Diagram for $m = \pm 1$ mode coupling

We can generate constraints on the allowable impedance by considering

$$U(\omega) + iV(\omega) = \frac{i}{[f + ig]} \frac{I_{a.c.}}{I_{d.c.}} = \frac{2\pi I_{a.c.}}{V_{rf}} [Z_{-1} - Z_{+1}]. \quad (34)$$

Here V_{rf} is the cavity voltage summed about the ring, and U, V have been normalized so that the excitation current is independent of bunch length. The method is to plot contours of constant growth rate in the U, V -plane by scanning ω . The instability threshold is given by the curve of zero growth rate and is a function of \tilde{J} . If on the same plot, the curve $Z(\omega)$ lies wholly inside the threshold curve, then that mode is stable. As shown in

figures 1–4, for the case $|m| = 1$, we have evaluated the threshold diagrams for some of the binomial functions

$$\Psi_0(J) \propto (1 - J/\hat{J})^\alpha \quad \text{for } J \leq \hat{J} \quad (35)$$

The contours depict the ten cases $\hat{J}/J_0 = 0$ to 1 in steps of 0.1. The innermost and outermost contours correspond to $\hat{J} = 0$ and $\hat{J}/J_0 = 1$, respectively. For the case $\alpha < 1$ the upper intercept $\hat{V} = V(\hat{\omega})$ must be zero, while for $\alpha > 1$ intercept $\hat{V} > 0$; for $\alpha = 1$ intercept \hat{V} is undefined. For constant FW bunch length, the r.m.s. frequency spread diminishes as α increases and so the stable U, V region grows smaller; hence the plots have different scales.

References

- [1] S. Koscielniak: *Foundations of and revisions to longitudinal, single-bunch, coherent instability theory*; TRI-DN-95-13.
- [2] A.N. Lebedev: *Longitudinal instability in the presence of an r.f. field* Atomnaya Energija, Vol.25, p.100 (1968).

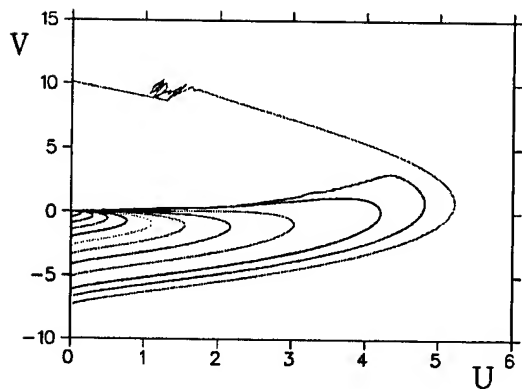


Figure 1. Stability diagram for $\alpha = 1/2$ as function of \hat{J} .

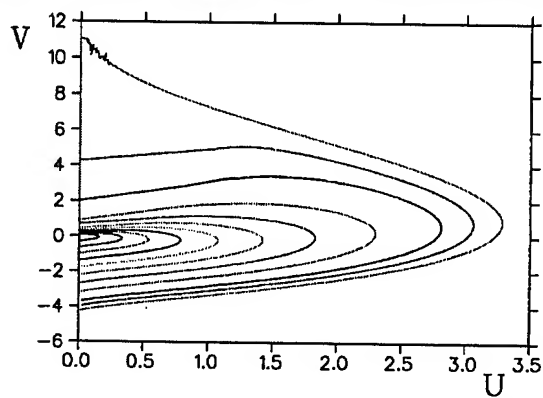


Figure 2. Stability diagram for $\alpha = 1$ as function of \hat{J} .

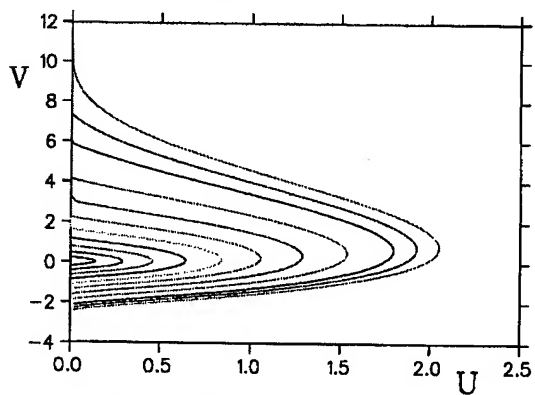


Figure 3. Stability diagram for $\alpha = 2$ as function of \hat{J} .

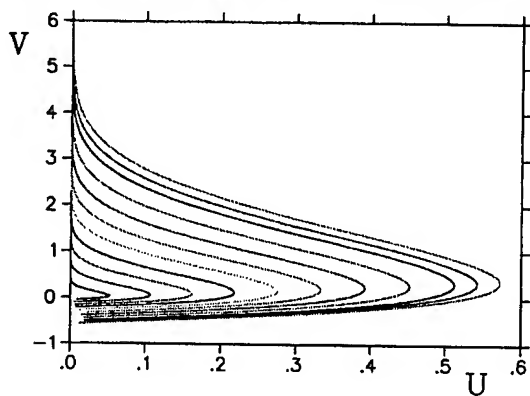


Figure 4. Stability diagram for $\alpha = 10$ as function of \hat{J} .

Simulations of Sawtooth Instability

R. BAARTMAN and M. D'YACHKOV,
TRIUMF, 4004 Wesbrook Mall, Vancouver, B.C. Canada, V6T 2A3

Abstract

The equilibrium self-consistent distribution of particles in a high intensity electron synchrotron can be found using the Haissinski equation and the wake field. At some threshold intensity the bunch becomes unstable. However, radiation damping causes the particles to be confined and the instability does not necessarily cause loss of particles.

It was observed in simulations with a very simple wake field and short bunches, that energy spread and bunch length oscillate in a sawtooth fashion. We find that this is due to the double-peaked nature of the stationary distribution. Over many synchrotron oscillations, particles diffuse from the head peak to the tail to the point where the tail peak becomes as large as the head. The two resulting sub-bunches then collapse together in less than one synchrotron oscillation, causing a net blow-up in emittance. Radiation damping reduces the emittance and diffusion begins again.

I. Introduction

A so-called 'sawtooth' instability has been observed in the SLC damping rings [1] and there is evidence that it has been observed in other electron synchrotrons as well [2]. This instability appears as a periodic fast blow-up in bunch length, followed by damping. We studied the origins of this effect using multi-particle tracking. Rather than trying to describe an actual machine, as was done by Bane and Oide [3], we simplified the model to determine which features of the wake field lead to a sawtooth behaviour.

We describe the results of the simulation and then give a qualitative discussion of the origins of the instability.

II. Numerical Simulations

A. Model

To simulate the electron's motion in a synchrotron we use a standard multi-particle tracking scheme [4]. The beam is represented by N macroparticles each with phase and energy coordinates (z_i, e_i) . These coordinates are recalculated every turn according to the following equations.

$$\Delta e_i = -\frac{2T_0}{\tau_e} e_i + 2\sigma_{e0} \sqrt{\frac{T_0}{\tau_e}} r_i + V'_{rf} z_i + V_{ind}(z_i) \quad (1)$$

$$\Delta z_i = \frac{\alpha c T_0}{E_0} (e_i + \Delta e_i) \quad (2)$$

T_0 is the revolution period, τ_e is the damping time, σ_{e0} the rms energy spread in the absence of a wake, V'_{rf} the slope of the rf voltage, α is the compaction factor, and E_0 is the mean energy; r_i is a random number with a standard normal distribution.

To calculate V_{ind} we have used the same method used by Bane [3], i.e. binning the macroparticles in z without smoothing. Then

the voltage V_{ind} induced by the beam is given by

$$V_{ind}(z) = -e \sum_i N_k W(z - z_k), \quad (3)$$

where N_k is number of particles in the k^{th} bin and $W(z)$ is the Green function wake field. Other methods of finding V_{ind} [4] give smoother results for a given number of macroparticles, but are more CPU-intensive.

For this study, we used a resonator wake field:

$$W(z) = \frac{\omega_0 R}{Q} e^{-\frac{k_0 z}{2Q}} \left[\cos(k_1 z) - \frac{\sin(k_1 z)}{\sqrt{4Q^2 - 1}} \right] \quad (4)$$

where R is shunt resistance, ω_0 the resonant frequency, $k_0 = \omega_0 \sigma_z / c$ is roughly the bunch length in units of the vacuum chamber size, and $k_1 = k_0 \sqrt{1 - 1/4Q^2}$.

In order to be able to relate the results of this paper with earlier work [6], [7], it is convenient to use as intensity the dimensionless parameter $I = eN\omega_0(R/Q)/(V'_{rf}\sigma_{z0})$.

The radiation damping usually takes tens or even hundreds of synchrotron oscillations. However, such long damping times require in general too much CPU time to simulate easily. Fortunately, the damping rate does not play a significant role in instabilities which are fast compared with synchrotron motion. This is the regime of the present study. To optimize computation time versus simulation accuracy, we used artificial radiation damping times on the order of 5 to 10 times the synchrotron oscillation period.

We found that a reasonable accuracy is achieved with as few as 5,000 macroparticles. This depends upon the wake field being fairly smooth: many times more macroparticles are required for wake fields which have many oscillations in one bunch length.[3]

For our analysis we have chosen a resonator wake field with a quality factor $Q = 1$ and bunch length parameter $k_0 = 0.5$. The radiation damping time τ_e was set to 500 turns and other parameters V'_{rf} , α , E_0 in eqn. 2 have been chosen to obtain a synchrotron period of 100 turns.

B. Results

We start with a large emittance and allow the beam to damp. At low intensities the beam relaxes to a thermodynamically stationary distribution which is well described by the Haissinski equation [5]. However when the intensity increases it takes more time for particles to reach a thermodynamical equilibrium particularly when this distribution has a two-peak line density profile. In the case $k_0 = 0.5$ the second peak in the line density appears approximately at $I = 10$. This is near the stability threshold found by solving the Vlasov equation [7]. See Fig. 5.

The region close to threshold is difficult to model because of the slow growth rate of the instability. Above approximately

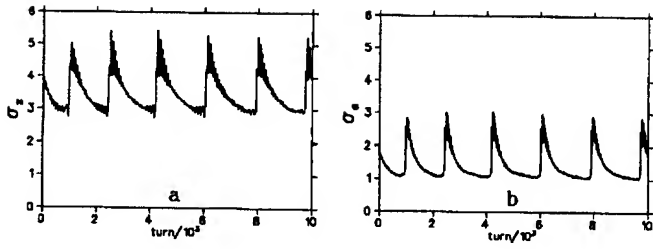


Figure 1. RMS bunch length (a) and rms energy spread (b) in case of resonator impedance ($Q = 1$, $k_0 = 0.5$) at $I = 30$. Radiation damping time is $\tau_e = 5T_s$.

$I = 20$, the sawtooth instability becomes apparent. As intensity is raised, the sawtooth periodicity also increases. A typical example showing rms bunch length and energy spread is in fig.1 for $I = 30$. At very high intensity, the behaviour becomes irregular: the case of $I = 45$ is shown in fig.2.

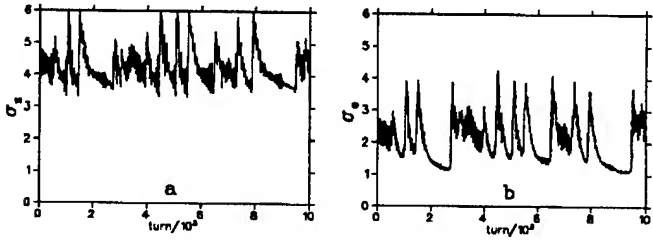


Figure 2. RMS bunch length and energy spread for the same parameters as Fig. 1, except that $I = 45$.

We found that the sawtooth repetition rate is mainly determined by the diffusion process and not by radiation damping. To illustrate this point, the case of a 10/3 times stronger radiation damping is shown on Fig.3. Comparing Fig.3 with Fig.1, one can see that the sawtooth frequency has not changed.

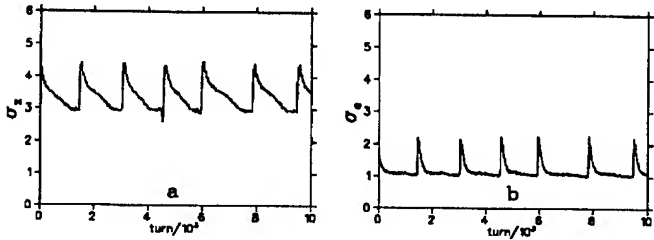


Figure 3. RMS bunch length and energy spread for an increased damping rate: $I = 30$ and $\tau_e = 1.5T_s$. Compare with Fig. 1.

A complete cycle corresponding to one 'tooth' is shown on Fig. 4:

- **a → b:** The downstream cloud damps down (about 5 synchrotron oscillations).
- **b → c:** Diffusion populates the second peak until it is approximately equal to the first (about 30 synchrotron oscillations). Note that the two peaks have started to move toward each other and a third peak is already beginning to form.

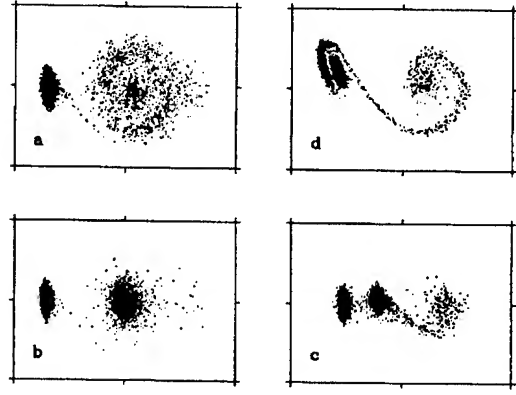


Figure 4. A complete cycle of the sawtooth instability for the case shown in Fig. 1: $I = 30$ and $\tau_e = 5T_s$. The time sequence is anticlockwise.

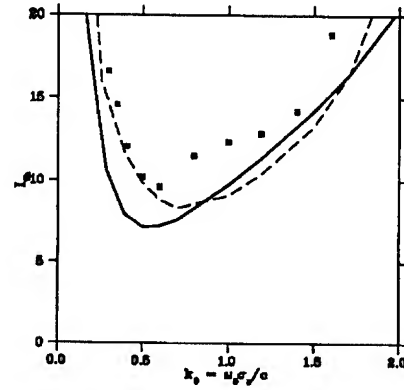


Figure 5. Threshold intensity vs. bunch length parameter k_0 in the case of a broad-band ($Q = 1$) resonator. The points and different curves are the results of different calculations. See [7]

- **c → d** In about 1/3 of a synchrotron period the two main sub-bunches collapse together.
- **d → a** The combined bunch throws out a large cloud of particles as it executes large synchrotron oscillations (less than a synchrotron period).

The sawtooth behaviour was most clearly seen in the region $0.4 < k_0 < 0.6$. For $k_0 < 0.4$, the diffusion process was too slow. For $k_0 > 0.6$, where the threshold intensity increases with bunch length (Fig. 5), sawtooth behaviour is not seen either; instead, the bunch length oscillates chaotically.

III. Analysis

Qualitatively, the instability can be understood by considering the wake of an extremely short bunch (Fig. 6, upper). In order for the energy lost by the bunch to the wake field to be compensated by the rf cavities, the rf waveform (here drawn as a straight line) must intersect the wake voltage at half the maximum. This is the location of the centre of this very short bunch, and is of course a stable fixed point. Situations for various rf voltage values can be considered by pivoting the rf waveform (line) about this point, as indicated in Fig. 6. Situations with differing beam intensities can be simulated in the same way, since amplifying the wake field

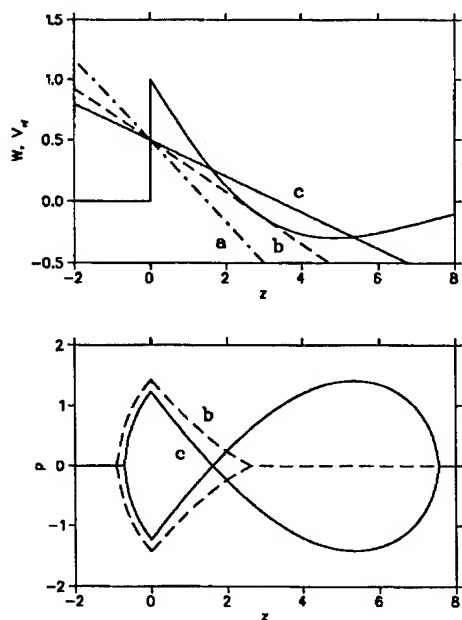


Figure 6. Green function wake field (upper window), including 3 rf waveform slopes; (a) is stable, (b) is just above threshold, and (c) is in the sawtooth regime. Looking from left to right, there is a stable fixed point if the wake field crosses the rf waveform from below, and an unstable fixed point if it crosses from above. The separatrices created by the wake fields corresponding to cases (b) and (c) have been plotted in the lower window. In case (a), there is only one stable fixed point so the wake field does not create a separatrix. Note that these curves are for a Green function wake and therefore are only suggestive. Any accumulation of a finite charge density will deform the separatrices.

has the same effect on the diagram as reducing the rf slope. At low intensity or large rf voltage, there is only the one fixed point. At high intensity or low rf voltage, the wake field intersects the rf waveform at three points; there is an unstable fixed point behind the bunch, and a stable one farther along. Separatrices created by the extra fixed points are shown in the lower window in Fig. 6.

Because of the random excitation due to emission of synchrotron radiation, particles can diffuse through the unstable fixed point and collect at the downstream stable fixed point. These particles begin to create their own wake, and will have to move forward as they lose energy to their own wake field. At the same time, the remaining particles in the head sub-bunch will move backwards as they decrease in number and no longer need as large energy gain from the rf field. At some point, the potential barrier between the two sub-bunches becomes small enough that the diffusion turns into an avalanche and the sub-bunches suddenly coalesce. The resulting bunch is over-dense and at the wrong phase with respect to the needed energy gain. It begins to execute a large synchrotron oscillation, while beginning again to lose particles to diffusion. This results in a large cloud of particles and a large rms bunch length and energy spread. The cloud condenses again at the downstream stable fixed point and diffusion continues.

IV. Conclusion

We have developed a qualitative picture of the sawtooth instability. The wake field creates its own unstable and stable fixed points, particles diffuse to the second fixed point, and then the resulting second sub-bunch collapses into the head sub-bunch. The sawtooth frequency is therefore determined not primarily by radiation damping, but by a subsequent diffusion process.

The sawtooth effect is most readily seen when the bunch length is comparable with the wake field length. Qualitatively quite different behaviours can be seen when the bunch is either short or long compared with the wake. In the former case, for example, the two sub-bunches can sometimes pass through each other instead of collapsing, thus leading to a sustained quadrupole oscillation. This may be the type of behaviour seen in LEP [8]. These regimes as well as other types of wake fields are still under investigation.

References

- [1] P. Krejcik et al., *High Intensity Bunch Length Instability in the SLC Damping Rings* Proc. PAC93 (Washington D.C.) p. 3240.
- [2] G. Rakovsky and L.R. Hughey, *SURF's up at NBS: a Progress Report* IEEE Trans Nucl. Sci. NS-26 (1979) p. 3845.
- [3] K.L.F. Bane and K. Oide, *Simulations of the Longitudinal Instability in the SLC Damping Rings*, Proc. PAC93 (Washington D.C.) p. 3339.
- [4] R. Siemann, *Computer Simulation of Bunch Lengthening in SPEAR* Nucl. Instr. Meth., **203** (1982) p. 57.
- [5] J. Haissinski, *Exact Longitudinal Equilibrium Distribution of Stored Electrons in the Presence of Self-Fields* Il Nuovo Cimento **18B** (1973) p. 72.
- [6] K. Oide and K. Yokoya, *Longitudinal Single Bunch Instability in Electron Storage Rings* KEK Preprint 90-10.
- [7] M. D'yachkov and R. Baartman, *Method for Finding Bunched Beam Instability Thresholds* Proc. EPAC94 (London) p. 1075.
- [8] D. Brandt, K. Cornelis and A. Hofmann, *Experimental Observations of Instabilities in the Frequency Domain at LEP* Proc. EPAC92 (Berlin) p. 345.

CHARACTERISATION OF A LOCALISED BROAD-BAND IMPEDANCE PHENOMENON ON THE SRS

S.F. Hill, Daresbury Laboratory, Warrington, WA4 4AD, UK

A major perturbation to the SRS vacuum envelope was required to install a second superconducting wiggler in 1992. As part of this, all of the new wiggler straight (straight 16) vacuum vessels were re-designed to give a good match to the small elliptical chamber of the wiggler, including the sector vacuum isolation valve. Because of engineering problems this valve was not fitted and a standard circular aperture valve of much larger diameter had to be installed. This caused a localised impedance, which manifested itself by gross overheating due to the energy dissipated in it from the beam. A study of the effect of this valve has been conducted and is summarised. All data from the period of installation in the ring is collated, including beam heating and instability data. On removal from the ring a bench measurement of the effective broad-band impedance has been made, using time-domain measurement techniques.

I. INTRODUCTION

The installation of a second superconducting wiggler in the SRS in 1992 [1] was the second major upgrade to the light source, the first having been a lattice upgrade to achieve higher brightness in 1986/87. The insertion of the 1 m wiggler vessel into straight 16 had a large impact on the rest of the ring, including the rearrangement of the 4 D-sextupole magnets; the design of 3 new ultra-short kickers and a new septum; as well as the relocation of components such as the dump collimator and the betatron tune driver vessel. The vacuum system of the ring is divided into 4 main sectors, isolatable by sector vacuum valves. These could not be rearranged in the ring, so a special valve was specified for the wiggler straight, with an elliptic section to match the wiggler beam tube shape. The upstream (D-Quadrupole) and downstream (F-Quadrupole) straight assemblies were already being modified with elliptic flare sections to match to the wiggler tube.

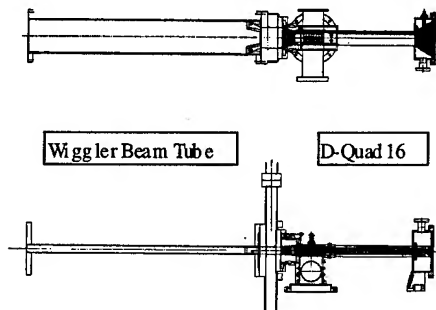


Figure 1. Upstream Straight 16 Layout

Figure 1 shows the planned layout of the chambers in the vicinity of the valve. Unfortunately this valve failed during the installation shutdown so was replaced by a standard sector valve with a circular aperture. Figure 2 illustrates the cross-section differences.

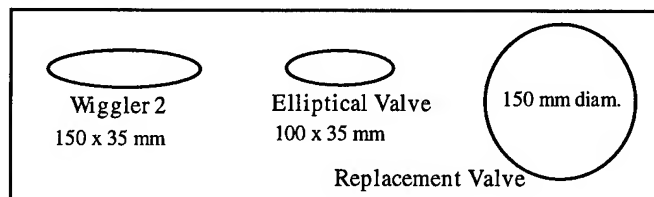


Figure 2. Cross Sections of Relevant Vessels

II. EXPERIENCE WITH BEAM

The first evidence of a large energy dissipation occurred in January 1993, some 4 months after first beam in the wiggler 2 lattice. Whilst experimenting with different fill structures (to remove a vertical beam blow-up due to ion trapping) a 300 mA beam in ~ 30 bunches (out of 160) caused a vacuum seal on the sector valve to fail due to excessive heating of the valve.

Some time was then spent on characterising this phenomenon in subsequent beam studies and operations periods [2], where valve temperatures in excess of 150 °C were seen. A measurement with a probe immediately after a beam dump indicated a localised hot spot on the upstream flange of the valve.

A temperature-time model for the effect was suggested:-

$$\frac{dT}{dt} = -a(T - T_a) + bI_b \quad (1)$$

where T = temperature at time t
 T_a = ambient temperature
 and a, b are coefficients of cooling and heating respectively.

This model gave some limited success in assessing the nature of the heating effects. Some data was taken to assess the cooling rate as a function of average temperature, yielding a value of (0.016 °C/minute) per °C above ambient temperature (estimated @ 26 °C in beam studies and slightly higher during operations time). Measurements of heating rates were made with single bunch, multibunch and partial fill beams at low and high currents at injection energy (600 MeV),

summarised in Table 1. This shows that full multi-bunch (160 bunches) gave small heating rates, essentially of small variation over a wide current range. The ~30 bunch fill gave increased heating rates and single bunch gave the greatest heating, with a strong non-linear dependence on bunch current.

Temp. (°C)	Current (mA)	Fill Structure	Rate ($\times 10^{-3}$ °C/mA/minute)
32	65	Multi-	0.6
29-34	100-300	Multi-	~1.0
44.3	283	~30 bunches	2.2
37.5	264	~30 bunches	2.5
29.3	2	Single	2.4
33.8	51.1	Single	11

Table 1. Heating Rates at 600 MeV

The ~30 bunch fill results were surprising, since its power spectrum is not very different to the full multi-bunch case. A second investigation looked at the variation with energy, at 0.6, 1.125 and 2 GeV. Despite the change in synchrotron radiation emission at these energies, the available data still suggests that a modest single bunch current gives greater heating than a higher current multi-bunch beam.

III. BENCH TEST OF VACUUM VALVE

Impedance measurements at Daresbury are performed in the time domain, using a Tektronix 7854 sampling oscilloscope fitted with a 7S12 Time Domain Reflectometry (T.D.R.) insert. This is configured with an S52 step pulse generator ($t_r \leq 25$ ps) and an S6 sampling head ($t_r \leq 30$ ps). Loss parameter measurements are made using an Impulse Forming Network (I.F.N.) which produces a near gaussian output pulse by differentiating a fast step input pulse. This allows a simulated beam measurement to be made at $\sigma \sim 20$ ps. The full system and planned upgrades is described elsewhere [3] as is the theory used to calculate the loss parameter [4], summarised below:-

The loss parameter $k(\sigma)$ is calculated from :-

$$k(\sigma) = \frac{2Z_0}{Q^2} \int_{-2\sigma}^{+2\sigma} I_0(I_0 - I_s) dt \quad (2)$$

- where I_0 = Current pulse launched through an ideal vacuum vessel (the reference vessel)
 I_s = Current pulse launched through the vessel under test
 Z_0 = Characteristic impedance of the coaxial line section (the reference vessel)

$$\text{and } Q = \int_{-2\sigma}^{+2\sigma} I_0 dt = \text{charge in the reference vessel pulse}$$

with a broad-band impedance contribution estimated using a resonator model with an appropriate Q centred at the cut-off frequency of the beam pipe under test.

The system chosen for the test and reference vessel assemblies was the upstream straight 16 assembly: the D-quadrupole and wiggler tube located either side of the vacuum valve under test. The reference system used an aluminium block with the elliptic aperture cut into it, whilst the test assembly used the circular aperture vacuum valve. Impedance matching to this system was done using thin steel cones supported within rigid copper cones which bolt to the vessel flanges. The present SRS D-Quadrupole cone was the only one available for upstream matching and a new elliptic cone to match to a the wiggler tube ellipse was constructed. The measurement system is shown in Figure 3.

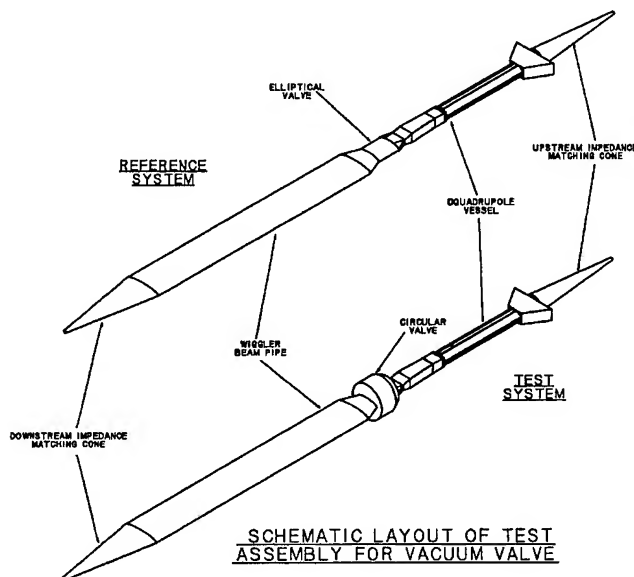


Figure 3. Measurement System Layout

The D-Quadrupole vessel was first fitted with all internal components, vacuum cleaned and tested, then impedance tested to check that no undue contribution would arise from it.

The loss parameter $k(\sigma)$ measured was within a few percent of that measured at wiggler installation time (March 1992). The vessel system was then assembled with a central conductor of 1.22 mm diameter copper wire (the 5 mm rod normally used for vessel measurements could not be easily supported in the 3 m long assembly) and T.D.R. data taken. Figure 4 shows the reference vessel assembly (elliptical valve) measured from the downstream (wiggler) end.

IV. SUMMARY AND CONCLUSIONS

The installation of a standard circular sector valve in the wiggler 2 straight in the SRS gave rise to a large energy dissipation and overheating of the vessel. Beam measurements at different energies indicates that synchrotron radiation was not the probable cause, whilst the enhanced heating rates seen with partial fills as well as single bunch cannot be explained easily with a simple broad-band impedance model. Bench measurements of the valve were carried out, which whilst showing that the vessels were not well matched to the 50 Ω measurement system, gave T.D.R. data clearly indicating the effect of the valve. Loss parameter data acquired with this system allowed an estimate of the broad-band impedance (Z/n) contribution to be made, suggesting that any change to the ring impedance to be small ($< 5\%$ of the most recent estimate [5]). Inspection of beam data leads to the suggestion that the effects were (partially) due to an interaction with a resonant structure with $Q \gg 1$ which is plausible when the valve and its connecting vessel sections are examined. Further work will involve an assessment of the resonance behaviour of the valve system.

V. ACKNOWLEDGEMENT

I would like to thank D.M. Dykes and S.L. Smith for their help and support in this work.

VI. REFERENCES

- [1] M.W. Poole et al. Commissioning a Second Superconducting Wiggler in the Daresbury SRS. Proc. IEEE Particle Accelerator Conference, Washington 1993, p1638-1640.
- [2] S.L. Smith, Investigation of Valve Flange Heating. Daresbury Internal Note SRS/APES/93/09.
- [3] S.F. Hill and M.J. Pugh, Improvements in Vessel Impedance Measurements at Daresbury. Proc. European Particle Accelerator Conference, London 1994, p1339-1341.
- [4] M. Sands and J. Rees, SLAC-Report PEP-95, August 1974.
- [5] J.A. Clarke, Bunch Lengthening Thresholds on the Daresbury SRS, these proceedings.

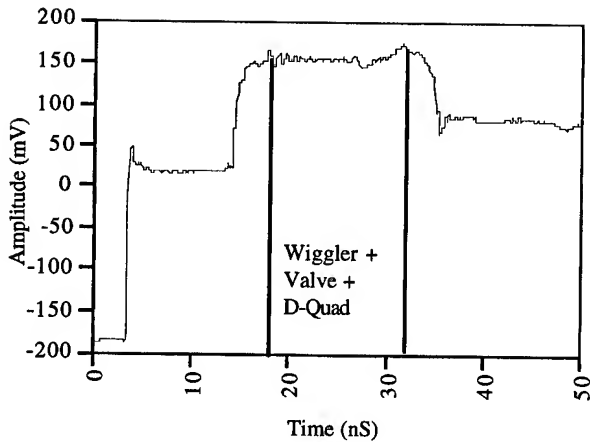


Figure 4. Full Downstream T.D.R. of Reference System

This shows that the impedance matching to the system is poor, with large reflections. However inspection of the aligned T.D.R. waveforms from the reference and test systems shows clearly the effect of the circular vacuum valve (Figure 5).

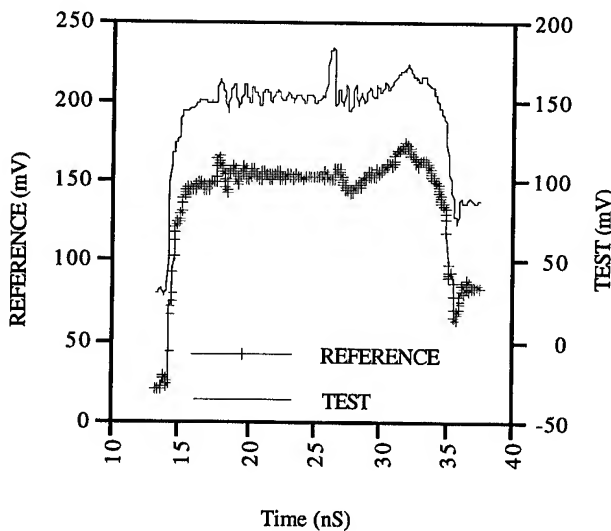


Figure 5. Comparison of Aligned T.D.R. Data

The 7854 scope T.D.R. system was then reconfigured to launch gaussian pulses through the two systems.

Applying (2) with $Z_0 = (213 \pm 11) \Omega$ (average value calculated from the T.D.R. data) gave a loss parameter result $k(\sigma) = (0.93 \pm 0.05) \text{ VpC}^{-1}$, for $\sigma = 20 \text{ ps}$. Using an assumed vessel cut-off frequency $f_c = 2 \text{ GHz}$ this gives an estimated broad-band impedance contribution of $Z/n = (0.12 \pm 0.01) \Omega$.

CAVITY-BEAM INSTABILITIES ON THE SRS AT DARESBUURY.

P A McINTOSH and D M DYKES, Daresbury Laboratory, Daresbury, Warrington WA4 4AD, UK.

Abstract

Malfunctions in the water control circuitry on the RF cavities have induced beam movements in both the horizontal and vertical planes which have been observed by users. A possible cause of such movements could be a cavity Higher Order Mode (HOM). The SRS cavity HOM spectra exhibits some Dipole modes which could produce such an effect and investigations have been performed on the SRS which have tried to identify a HOM as the cause of the beam position movement. The data presented here is the result of these investigations, whereby, cavity tuner position, cavity temperature and cavity HOM spectra have been monitored (with beam) as a function of electron beam and photon beam positions.

I. INTRODUCTION

As the temperature of the cavity 'cooling' water changes, the physical dimensions of the cavity are altered, and to keep the cavity on tune (the phase of the cavity is kept fixed w.r.t. the phase of the input waveguide) an automatic tuner loop moves a mechanical plunger. This plunger not only changes the frequency of the fundamental mode, but also the HOM's.

Beam movements in the horizontal and vertical planes have been observed and have been attributed to malfunctions in the water control circuitry on cavities 1 and 3. Undulator beam line station scientists have reported smearing of the undulator output spectrum under these conditions, similar to what has been experienced at ELETTRA[1], a possible cause of such movements could be a cavity HOM.

The effect on the electron beam position of varying the cavity tuner has been monitored using electron beam position monitors (BPM) and tungsten vane photon beam position monitors (TVM).

Preliminary investigations of the SRS cavity HOM spectra indicate that some Dipole modes exist which have comparatively large frequency shifts as a function of tuner position and which act in both planes.

II. BEAM STUDIES INVESTIGATIONS.

A. Effect of Cavity Tuner on Electron and Photon BPM's.

A one minute sawtooth was introduced onto the tuner control position of a cavity and its effect on BPMs and TVMs were recorded. Fig.1 illustrates the behaviour of cavity tuner position and its effect on TVM photon beam position. The 6 μ m oscillation observed on the TVM was more importantly, observed by station scientists on the beam line.

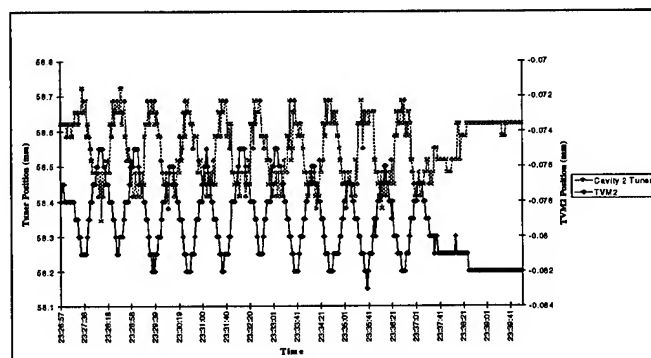


Figure 1. Cavity Tuner Position and Measured Oscillation on TVM.

Fig. 2 is a typical example of the horizontal and vertical beam movements at the BPMs recorded during this experiment.

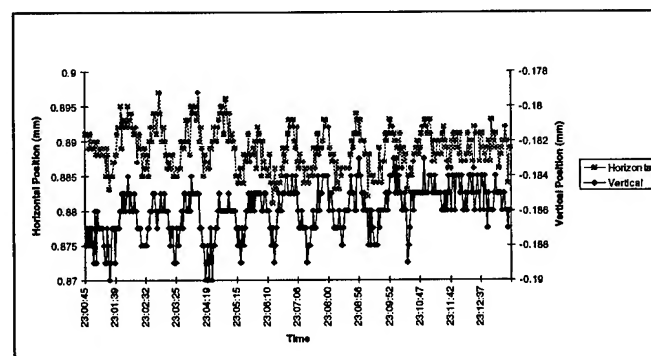


Figure 2. Corresponding Electron Beam Position Movements.

B. The Effect of Varying Cavity Temperature on Electron and Photon BPM's.

By operating a cavity at a temperature different to nominal, similar observations were made of the BPM and TVM readings. Precise measurements were made of the electron beam output spectrum so that the difference in output spectrum when the cavity was at nominal temperature and when it was at a different temperature, would indicate particular resonances that could be causing the electron beam movements.

The cavity temperature was reduced by 5°C and then brought back to nominal operating temperature in 1°C increments; at each point recording BPM, TVM and beam spectra.

Fig.3, shows TVM2 position for a 10 minute period, for each of the cavity temperature settings. The starting point offsets for each cavity temperature plot, is a function of the time needed for the cavity temperature to stabilise. It is not until the cavity temperature reaches 47°C, that oscillations are apparent in the photon beam position monitor. These oscillations are visible at most of the SRS beam lines and are typically 10-20µm p-p amplitude.

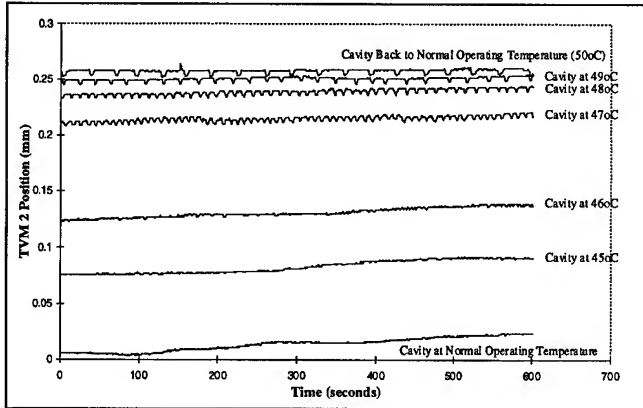


Figure 3. TVM2 Position Readings at Different Cavity Temperatures.

The beam spectra output at this new cavity temperature was compared with the spectra at normal cavity operating temperature and the differences observed in Fig's 4 and 5.

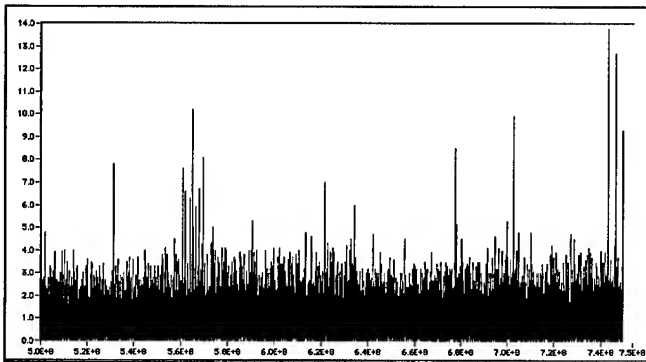


Figure 4. Difference in Beam Spectra between Cavity at Nominal Operating Temperature and 45°C.

Fig.4 shows the difference in beam spectra when the cavity temperature was moved to 45°C. The span of Fig's. 4 and 5 is 250MHz with a resolution bandwidth on the HP8568B High Frequency Spectrum Analyser of 3KHz.

The differences that appear in Fig.4 are isolated orbit harmonics about the 499.71MHz RF source signal with an amplitude <15dB. These difference peaks are very close to the noise floor in this sort of measurement and are considered to be negligible.

When one looks at the beam spectra difference when the cavity temperature is at 47°C, then large differences are

observed at 608.96MHz and orbit harmonics about this peak (see Fig.5).

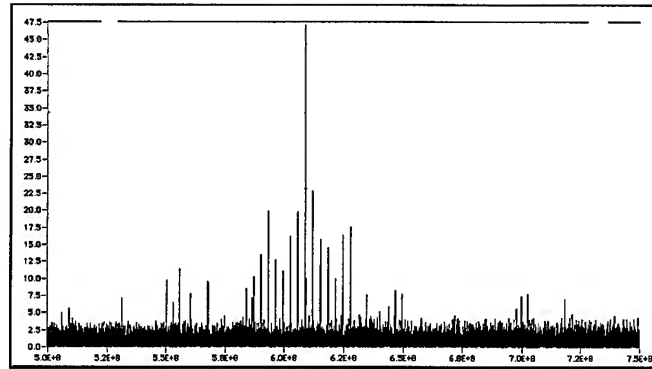


Figure 5. Difference in Beam Spectra between Cavity at Nominal Operating Temperature and 47°C.

The difference is clear and it shows that the instability observed on the photon beam appears to be as a result of this resonance. The oscillatory behaviour of the photon beam position is not yet fully understood as some oscillation is still present when the cavity temperature is brought back to its normal operating temperature, investigations are ongoing.

III. MAFIA PREDICTED CAVITY HOM's..

MAFIA simulations of the SRS cavity have been used to provide HOM information as well as predicting e-m field orientations of these HOM's which can lead to an understanding of their interaction on the electron beam, see Table 1 [2]. Relating these HOM's to the results of Fig. 5, shows that one mode in particular could be responsible for the observed instability. The 1390MHz HOM, which when wrapped around the 499.711MHz fundamental RF frequency and its harmonics, produce resonances at 1610MHz, 1110MHz, 890MHz and 610MHz.

Mode	Frequency (MHz)	R_s^1 (MΩ)
Mono	498.8	3.95
Dip (V)	791.5	6.2
Dip (H)	797.1	7.2
Mono	809.5	1.15
Dip (V)	1059.2	12.3
Dip (H)	1059.3	12.3
Dip (V)	1285.0	1.85
Dip (H)	1286.0	1.9
Mono	1333.0	0.4
Dip	1390.0	~0.9

Table 1. SRS Cavity HOM's as Predicted by MAFIA.

¹ Shunt Impedance determination assumes r.m.s. voltage

i.e. $R_s = \frac{V^2}{2P}$ where: P = Cavity Power Dissipation (W)

MAFIA has found that some dipole modes are split into two polarisations, with a null plane in the longitudinal electric field. Their action on the electron beam will be to deflect it horizontally or vertically, hence the H and V denotation.

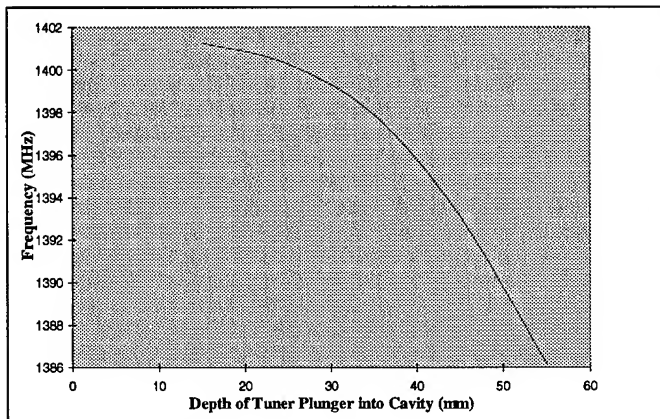


Figure 6. Frequency Variation of 1390MHz HOM as a Function of Tuner Position.

When one examines the shift in frequency of the 1390MHz mode, as a function of tuner position, the range over which the tuner operates on the actual cavity causes quite large frequency variations. Which gives this particular HOM a large operating frequency range.

The e-m field orientations of this mode are complex and its action on the electron beam is not fully understood. The mode does contain some skew dipole action and it is this property that is believed to be causing the electron beam movements.

The SRS operates with an orbit harmonic of 3.123MHz and the 286th orbit harmonic coincides with this HOM.

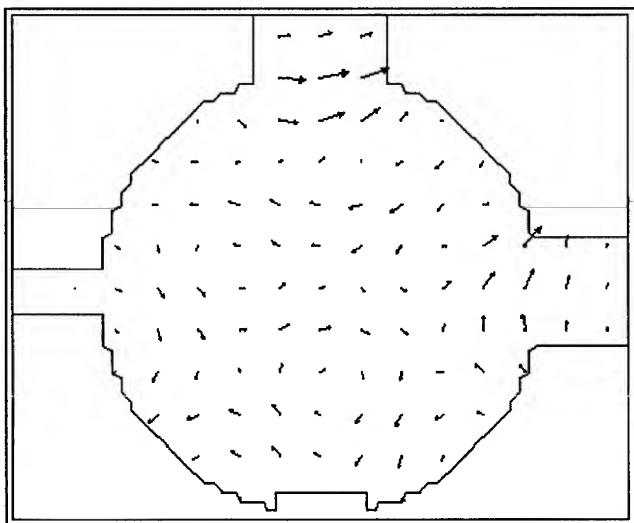


Figure 7. E field Orientation of 1390MHz HOM.

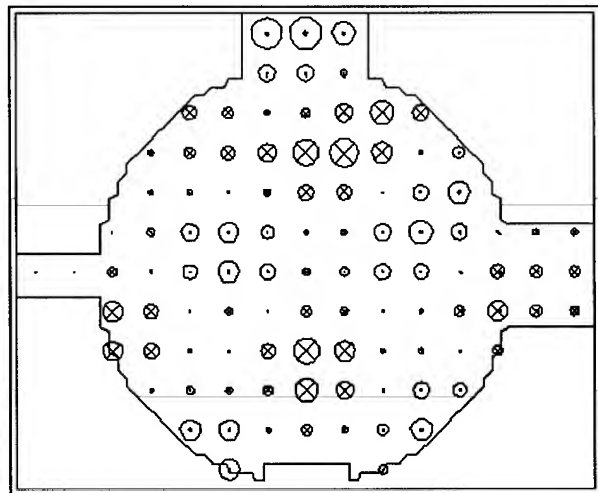


Figure 8. H field Orientation of 1390MHz HOM.

IV. CONCLUSIONS.

Under normal operating conditions, the cavity temperature is chosen such that the normal range of tuner plunger position does not enable the beam to excite any dangerous HOM's. The experiment varied the cavity temperature by $\pm 2^\circ\text{C}$ and clearly the 1390MHz mode was excited. The beam movements were observed on all TVM's and BPM's.

It is clear that a malfunction in the cavity water cooling system causing the cavity temperature to vary outside the specified limits ($\pm 0.2^\circ\text{C}$), will cause the position of the cavity tuner plunger to vary. The detailed HOM spectra is dependent on cavity tuner plunger position.

The fault was quickly rectified and since new higher precision water temperature controllers have been fitted to all cavity water cooling circuits, the temperatures are now maintained to better than $\pm 0.1^\circ\text{C}$.

V. REFERENCES

- [1] Second Annual Workshop on Synchrotron Radiation Light Sources, Grenoble 15th and 16th November 1994, by: M. Svandrik, ELETTRA.
- [2] Higher Order Modes in the SRS 500MHz Accelerating Cavities, J. N. Corlett, presented at the 1989 Particle Accelerator Conference on Accelerator Science and Technology, Chicago. DL/SCI/P627A

BUNCH LENGTHENING THRESHOLDS ON THE DARESBUURY SRS

J. A. Clarke, CCL Daresbury Laboratory, Warrington, WA4 4AD, UK.

The bunch length of the SRS has been studied over a large range of beam currents at energies between 0.6 GeV and 2.0 GeV. Longitudinal microwave instability thresholds have been observed and used to estimate the broadband impedance of the SRS. The results are compared with measurements based on other effects.

I. INTRODUCTION

The behaviour of single bunch beams in the SRS have been studied in some detail [1, 2]. This behaviour is largely dependent upon the basic impedances of the vacuum chamber experienced by the electron beam. This paper presents recent results which provide further information on these impedances and their effects. In particular, the data clearly demonstrates microwave instability thresholds and potential well distortion.

The bunch length data has been collected with a photodiode based system [3] which measures a significantly shorter value than the previously used stroboscopic image dissector [4]. Earlier data has been revised and re-evaluated in the light of these discrepancies.

II. BUNCH LENGTHENING THEORY

The length of an electron bunch in a storage ring is dependent upon the peak current of the bunch. The two effects which alter the length are potential well distortion and microwave instability. For potential well distortion the bunch length varies due to the electro-magnetic fields induced by the electrons altering the RF voltage seen by the bunch. This effect is present even at very low currents. The second effect, microwave instability, is only observed after a certain threshold current has been reached. Above this threshold the energy spread of the beam increases until the peak current of the bunch reduces to equal the threshold current again.

A. Potential Well Distortion

At very small currents the electron beam is described by the natural bunch length, σ_{l_0} :

$$\sigma_{l_0} = \frac{c\alpha}{\omega_{s_0}} \sigma_{p_0} \quad (1)$$

where c is the speed of light, α is the momentum compaction, σ_{p_0} is the natural relative energy spread of the beam and ω_{s_0} is the associated synchrotron oscillation frequency. The bunch length, σ_l , modified by the potential well distortion is given by [5]:

$$\left(\frac{\sigma_l}{\sigma_{l_0}}\right)^3 - \left(\frac{\sigma_l}{\sigma_{l_0}}\right) + I_b \frac{e\alpha \text{Im}\{[Z/n]_{\text{eff}}\}}{\sqrt{2\pi}Ev_{s_0}^2} \left(\frac{R}{\sigma_{l_0}}\right)^3 = 0 \quad (2)$$

where I_b is the average beam current, e the electron charge, R the ring average radius, E the beam energy and v_{s_0} is the synchrotron tune. The size of the effect is dependent upon the reactive part of the effective longitudinal coupling impedance $[Z/n]_{\text{eff}}$.

B. Microwave Instability

If the peak current of the beam exceeds the so-called microwave instability threshold then the energy spread of the beam, σ_p , increases thus increasing the bunch length (from Eqn (1)). The bunch length continues to grow until the peak current reduces to equal the threshold current. The threshold current, written in terms of the average beam current, is given by [6]:

$$I_b = \frac{\sqrt{2\pi}\alpha E \sigma_p^2 \sigma_l}{eR[Z/n]_{BB}} \quad (3)$$

where $[Z/n]_{BB}$ is the longitudinal broadband impedance. Combining Eqns (1) (for σ_p) and (3) leads to the dependence of the bunch length purely on the microwave instability:

$$\sigma_l^3 = \frac{ec^2\alpha R[Z/n]_{BB}}{\sqrt{2\pi}E\omega_{s_0}^2} I_b \quad (4)$$

Since the instability increases the energy spread of the beam the horizontal beam size, σ_x , is also increased. The dependence of σ_x on σ_p is given by:

$$\sigma_x^2 = \varepsilon_x \beta_x + \eta_x^2 \sigma_p^2 \quad (5)$$

where ε_x is the horizontal emittance, β_x is the horizontal betatron function and η_x is the horizontal dispersion function. Note that since in general the bunch length depends upon two effects at high current, the horizontal beam size gives a more direct observation of the broadband impedance.

C. Combination of Both Effects

Above the microwave threshold the bunch length is modified by a combination of both effects. The potential well distortion alters the synchrotron frequency and the microwave instability increases the energy spread. When both effects are present Eqn (1) can be rewritten as:

$$\sigma_l = \frac{c\alpha}{\omega_s} \sigma_p \quad (6)$$

By deriving ω_s from Eqns (1) and (2) and σ_p from Eqns (1) and (3) it is possible to show that the bunch length dependence upon the two effects is given by:

$$\sigma_l^3 = \frac{ec^2 \alpha R}{\sqrt{2\pi E \omega_{s_0}^2}} \left\{ [Z/n]_{BB} - \text{Im}[Z/n]_{eff} \right\} I_b \quad (7).$$

III. BUNCH LENGTHENING BELOW THRESHOLD

In order to determine the contribution that potential well distortion has on the bunch length of the SRS an experiment was carried out below the threshold current. The length of a single bunch beam was recorded as a function of beam current at 1.7 GeV. Throughout the experiment σ_x remained constant, confirming that the beam was indeed below the threshold of microwave instability. The variation of the bunch length with the beam current is given in figure 1. The solid line on the figure is a curve derived using Eqn (2) for $[Z/n]_{eff} = -0.7 \Omega$.

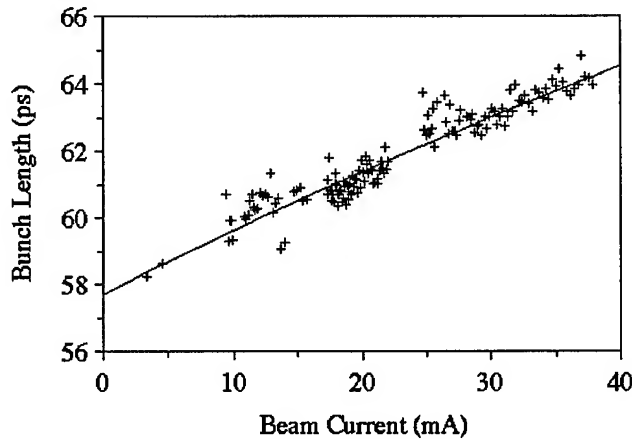


Figure 1. The bunch length as a function of beam current at 1.7 GeV.

IV. BUNCH LENGTHENING ABOVE THRESHOLD

A similar experiment to the one above was carried out at the lower energy of 0.6 GeV. The microwave threshold in this case was expected to be ≈ 1 mA so all of the measurements were taken well above this value. The bunch lengthening observed is shown in figure 2. The solid line shows the best fit to be to a power of 0.295. If the fit is forced to a one-third dependence following Eqn (7) then a combined vacuum chamber impedance of 3.1Ω is estimated. Subtracting the contribution from the effective longitudinal coupling impedance derived in section III gives a value for the longitudinal broadband impedance of 2.4Ω .

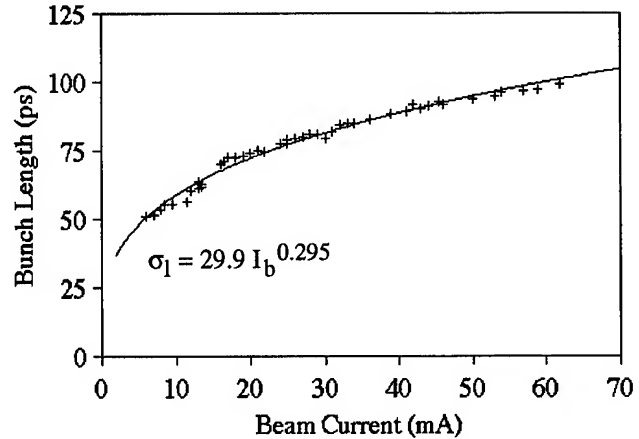


Figure 2. The bunch length as a function of beam current at 0.6 GeV.

V. OBSERVATION OF BUNCH LENGTHENING THRESHOLD

Direct observation of the onset of microwave instability in the SRS is only possible at an intermediate energy. Measurements have been carried out between 1.0 and 1.375 GeV. In these experiments all three beam dimensions were recorded. Surprisingly the threshold was clearly visible on the vertical beam size as well as the horizontal one. A subsequent experiment confirmed the presence of finite vertical dispersion in the SRS lattice [7].

The bunch length measured as a function of current at 1.125 GeV is shown in figure 3. The microwave instability threshold appears at around 19 mA. The bunch length data above threshold has been fitted to the model described by Eqn (7). This implies a combined impedance of 2.9Ω . Again subtracting 0.7Ω due to the effective longitudinal coupling impedance gives a longitudinal broadband impedance of 2.2Ω , similar to the value found earlier in section IV.

The horizontal beam size growth should be entirely due to the microwave instability (ie no potential well distortion term) so the data can be used to derive the broadband impedance directly. By substituting the value for σ_p^2 from Eqn (3) into (5) it is clear that a plot of σ_x^2 against I_b/σ_l should give a linear graph with gradient proportional to $[Z/n]_{BB}$. The horizontal beam size data is shown in this form in figure 4. The gradient implies a longitudinal broadband impedance of 1.2Ω , significantly less than the values derived above.

It is also possible to derive the value for $[Z/n]_{BB}$ from the microwave threshold current itself (see Eqn (3)). If the threshold current is taken to be 19 mA then this produces a value for the longitudinal broadband impedance of 1.5Ω .

The data taken at 1.375 GeV was not so clear as the 1.125 GeV values. The bunch length data was not recorded correctly due to a triggering failure and the horizontal beam size was unusually noisy. However, the threshold was clearly observed

in the vertical plane, due to the unexpected finite vertical dispersion in the SRS. A threshold of 28 mA is apparent in figure 5. This leads to a value for the longitudinal broadband impedance of 1.9Ω

One further set of data was recorded at 1.0 GeV. The microwave instability threshold was observed to occur at 9 mA in this instance, implying a value for the longitudinal broadband impedance of 1.8Ω .

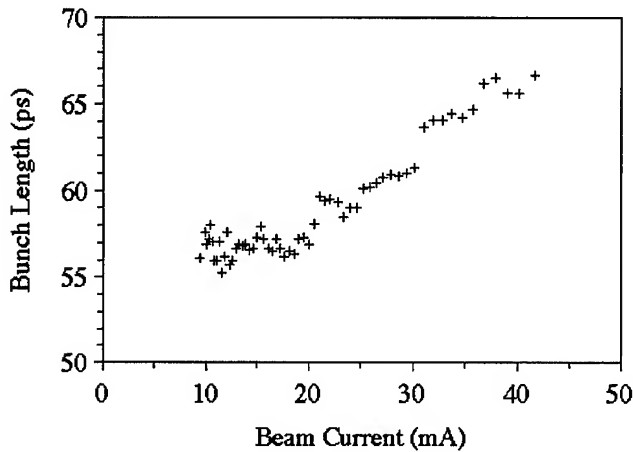


Figure 3. The bunch length as a function of beam current at 1.125 GeV.

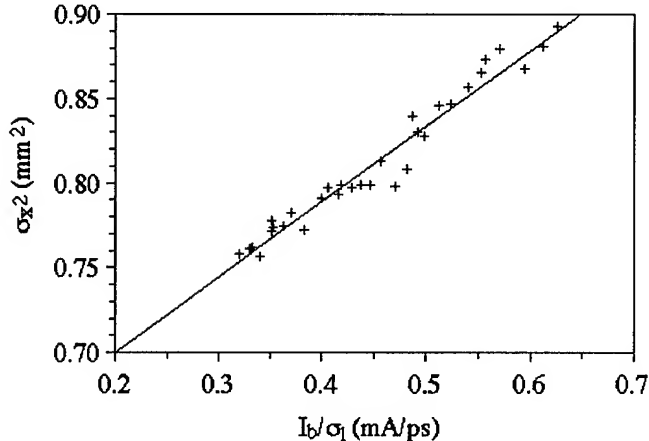


Figure 4. The horizontal beam size dependence upon the ratio of the beam current to the bunch length at 1.125 GeV.

Energy (GeV)	Technique	$[Z/n]_{BB}$ (Ω)	$[Z/n]_{BB} - \text{Im}[Z/n]_{eff}$ (Ω)
0.6	σ_l growth	2.4 ± 0.7	3.1 ± 0.5
1.0	threshold	1.8 ± 0.5	2.5 ± 0.7
1.125	σ_l growth	2.2 ± 1.1	2.9 ± 0.9
1.125	σ_h growth	1.2 ± 0.4	1.9 ± 0.6
1.125	threshold	1.5 ± 0.4	2.2 ± 0.6
1.375	threshold	1.9 ± 0.5	2.6 ± 0.7

Table 1. Summary of the impedances measured in the SRS.

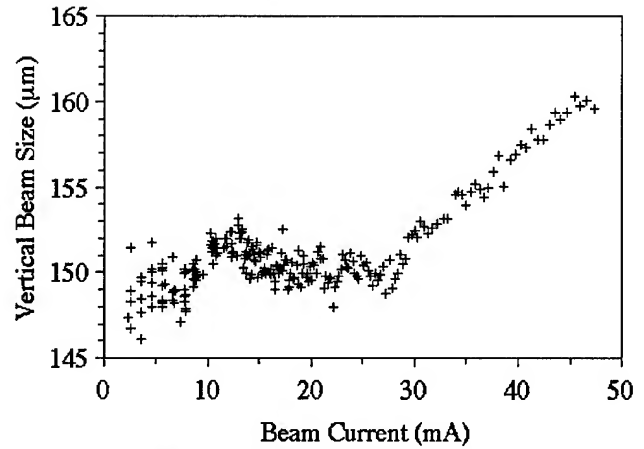


Figure 5. The vertical beam size as a function of beam current at 1.375 GeV.

VI. SUMMARY AND CONCLUSIONS

Two types of bunch lengthening have now been evaluated on the SRS in single bunch mode. Potential well distortion has been observed at high energy. The bunch lengthening measured has been used to estimate a value for the reactive part of the longitudinal coupling impedance to be $-0.7 \pm 0.2 \Omega$.

The microwave instability has been observed over a wide range of energies. Bunch lengthening and beam size growth in both planes has been noted. The increases to the beam dimensions and the threshold currents have been used to derive estimates for the longitudinal broadband impedance. The values derived are summarised in Table 1. It appears that the best estimate for the broadband impedance of the SRS is $1.8 \pm 0.6 \Omega$. This value is significantly smaller than that previously published since the earlier work was largely based upon incorrect bunch length data [3].

VII. REFERENCES

- [1] J. A. Clarke et al, "Revised SRS Impedance Estimates", in Proc Euro Part Accel Conf, London, 1994, p 1096.
- [2] L. A. Welbourne et al, "Single Bunch Effects in the Daresbury SRS", in Proc IEEE Part Accel Conf, Washington, 1993, p 3672.
- [3] J. A. Clarke, "A New Picosecond Bunch Length Monitor on the SRS", in Proc Euro Part Accel Conf, London, 1994, p 1682.
- [4] G. S. Brown et al, "Measurement of Bunch Length with an Image Dissector Tube", IEEE Trans. Nucl. Sci., NS-30, No. 4, p 2348, August 1983.
- [5] B. Zotter, "Potential-Well Bunch Lengthening", CERN SPS/81-14 (DI), 1981.
- [6] J. LeDuff et al, "Single Beam Collective Effects on DCI", Proc 11th Int Conf High Energy Accel, CERN, 1980, p 566.
- [7] J. A. Clarke, Internal Note SRS/APES/95/13, March 1995.

ESTIMATION OF COLLECTIVE INSTABILITIES IN RHIC *

W.W. MacKay, M. Blaskiewicz, D. Deng, V. Mane, S. Peggs,
A. Ratti, J. Rose, T. J. Shea, J. Wei,
Brookhaven National Laboratory, Upton NY, 11973-5000

Abstract

We have estimated the broadband impedance in RHIC to be $|Z/n| < 1.2 \Omega$ for frequencies above 100 MHz. The Z/n threshold is set for Au^{+79} ions at transition with an estimated 10% growth in emittance for $Z/n = 1.5 \Omega$. We summarize the sources of broad and narrow band impedances in RHIC and investigate the multibunch instability limits throughout the machine cycle. The largest contribution to the broadband impedance comes from the abort and injection kickers (see [1]). Since RHIC is designed to accelerate fully stripped ions from H^+ up to Au^{+79} we give results for both protons and gold ions; other ions should give results somewhere between these two extremes. All ion species are expected to be stable during storage. At lower energies damping systems and chromaticity corrections will limit any growth to acceptable levels during the short time it takes to inject and accelerate the beams.

I. INTRODUCTION

The Relativistic Heavy Ion Collider (RHIC) is designed (see [2]) to collide fully stripped ions from protons to gold, at a maximum energy of 250 GeV (protons) or 100 GeV/u (Au^{+79}). Counter-rotating beams of particles will collide head-on at up to six interaction regions. The two intersecting superconducting rings have a circumference of 3.834 km with a maximum revolution frequency, $f_{\text{rev}} = 78.2 \text{ kHz}$. The rf system consists of a set of 26.7 MHz cavities for injection and acceleration, and a set of 196 MHz cavities for storage. Some typical values of parameters including tunes, chromaticities, and emittances are given in Table I.

Table I. Typical operating parameters.

	Injection	Storage
$\gamma(\text{p})$	31.2	268.2
$\gamma(\text{Au})$	12.6	108.4
Q_x	28.18	28.18
Q_y	29.18	29.18
$f_{\text{sync}}(\text{p})$	55 Hz	333 Hz
$f_{\text{sync}}(\text{Au})$	121 Hz	388 Hz
$dQ_{x,y}/d\delta(\text{p})$	~ 2	~ 2
$dQ_{x,y}/d\delta(\text{Au})$	~ -3	~ 2
$\sigma_p/p(\text{p})$	0.0005	0.0003
$\sigma_p/p(\text{Au})$	0.0003	0.0005
$\pi\epsilon_{95\%}^N(\text{p})$	$15\pi\mu\text{m}$	$15\pi\mu\text{m}$
$\pi\epsilon_{95\%}^N(\text{Au})$	$10\pi\mu\text{m}$	$15\pi\mu\text{m}$

The machine cycle may be broken into four phases: injection, acceleration, rebucketing, and storage. Vulnerability to instabilities is greatest during injection, storage, and transition crossing.

*Work performed under the auspices of the US DoE.

Injection of 54 bunches ($\sim 10^{11}$ nucleons per bunch) into both rings is expected to take about 30 s for protons and about 120 s for other ions. Ion species other than protons will cross transition during the acceleration part of the cycle, when the Lorentz factor $\gamma = \gamma_t = 22.89$. Rebucketing occurs at top energy when beam is transferred from the 26.7 MHz rf buckets used for injection and acceleration, to the 196 MHz buckets used for storage.

II. BROADBAND IMPEDANCES

The dominant contribution to broadband impedance is expected to be from the injection kicker magnets. There are four 1.1 m long injection kickers (see [3, 4]) in each ring. Each module is constructed from alternating ferrite and ceramic C-shaped elements with an inner and outer conductor. Inside the kicker is a ceramic beam pipe with a 41.3 mm diameter aperture. With no shielding added to the ceramic pipes, $|Z/n| < 0.25 \Omega$. The five abort kickers in each ring have larger apertures and should make a smaller contribution to the overall impedance; however, for impedance estimation we have assumed that they give a contribution identical to the injection kickers. We are actively pursuing the use of image current strips on the ceramic beam pipes to reduce the impedances of these elements.

Over three quarters of the beam pipe circumference is cold, with an inner diameter of 6.9 cm. For the most part the remainder is warm with an aperture of 12.3 cm. The beampipe cutoff frequency for TM modes is 3.3 GHz. The resistive wall impedance versus frequency is estimated to be

$$Z^{\parallel}(f) = (1 - i)f^{1/2}748 \Omega[\text{GHz}]^{-1/2}.$$

The beam position monitors contribute about $-0.6i\Omega$ to Z/n at very low frequencies ($\ll 0.65 \text{ GHz}$). For high frequencies the monitors contribute as

$$|Z^{\parallel}/n| \leq 0.12f^{-1}[\Omega \text{ GHz}], \text{ for } f \gg 0.65 \text{ GHz}.$$

Since unshielded bellows would contribute $\sim 1 \Omega$ to $|Z/n|$, almost all of the bellows are to be shielded, resulting in an estimated contribution of only 0.02Ω . Vacuum ports, gate valves, and collimators will also be shielded, and most pipe transitions will be tapered with a transition length at least five times as long as the change in pipe radius.

III. RF CAVITY IMPEDANCES

The accelerating and storage rf systems (see [5]) have narrow band cavities with high shunt impedances which contribute to coupled-bunch instabilities, requiring the design of passive higher order mode dampers to detune the high Q resonances. The rf system must be capable of capturing, accelerating, and storing for 10 hours the nominal load of 54 bunches of particles with an average current of 70 mA. For each ring there are two

26.7 MHz cavities for injection and acceleration. There are also seven 196 MHz cavities per ring for storage. (Four are common to both rings.) An additional broadband system will be used to damp out injection momentum errors.

IV. FEEDBACK AND DAMPING SYSTEMS

The transverse damping system will employ strip-line kickers which produce both electric and magnetic deflection and can support a wide system bandwidth capable of damping individual bunches. The maximum expected injection errors will lead to betatron oscillations with an amplitude of 2 mm. To avoid emittance dilution of the beam, a damping time equivalent to 100 revolutions (1.3 ms) is required. Transverse head-tail modes could be damped with a minimal upgrade to the feedback circuits.

Longitudinal emittance blowup can occur during injection when a bunch injected off-center in a bucket starts a dipole oscillation. The bunches in each AGS cycle are transferred into the RHIC rings one by one. The acceptable uncorrected injection $\Delta p/p$ error is 10^{-5} for negligible longitudinal emittance blowup. However, it is quite possible that the errors will be as large as 10^{-4} which, if uncorrected, would lead to a 30% blowup for a 0.2 eVs/u gold beam (95% emittance). This higher limit sets a goal for the damping system. Simulations show that the damping time is approximately $5\tau_s = 0.05$ s at 1 kV per kick, and that the resultant emittance blowup at the end of damping is only 5%.

V. STABILITY CALCULATIONS

For purposes of stability calculations we consider protons and fully stripped gold ions. The other species are expected to lie somewhere in between these two cases.

Beam-induced fields with wavelengths short compared to the bunch length may induce microwave instabilities in a single bunch. For a specified beam intensity, this phenomenon imposes a limit on the longitudinal impedance, $|Z^{\parallel}/n|$, within the frequency range from the average bunch-spectrum frequency of 400 MHz to the beam-pipe cut-off frequency of about 3.3 GHz.

Intrabeam scattering (IBS) will cause a bunch of 10^{11} protons to grow from 0.3 to 0.7 eV-s during a 10 hour storage (see [8]). For gold ions after 10 hours, the intensity will have dropped 40% from IBS, and the longitudinal emittance will be about 1 eV-s.

The microwave threshold $|Z^{\parallel}/n| \simeq 2.1 \Omega$ is set by protons at the top end of acceleration before switching to the 196 MHz rf system. A lower limit of 1.5Ω results from limiting longitudinal emittance growth to 10% for gold ions crossing transition in the presence of a γ_t -jump. The total broadband impedance is less than $\sim 1 \Omega$ at 400 MHz and drops to 0.6Ω at 3 GHz.

Longitudinal coupled-bunch instability growth rates were calculated analytically following Baartman (see [9]) and compared with results obtained by the code ZAP[10]. Impedance limits for the 26.7 MHz accelerating cavities were set by limiting the growth rate to 2 s^{-1} , which is a factor of five below the capability of the damping system. Higher order mode dampers are being developed to satisfy this requirement. During storage, longitudinal coupled-bunch instabilities are expected to be Landau damped.

It is not as straightforward to apply transverse instability theory to RHIC as it is to apply longitudinal instability theory. Calculations are easiest in the *weak-coupling limit*, when the frequency shift of a mode is small compared to the synchrotron frequency. This is not always the case for RHIC, especially at low energies during injection. On the other hand, calculations (see [11]) which include mode coupling and which are not in the weak-coupling limit are not yet fully reliable. At low energies the space-charge tune shift (see [12]) is large compared to the synchrotron tune, further complicating mode coupling calculations.

Using the ZAP formalism in the weak-coupling limit, we obtain a maximum growth rate of 27 s^{-1} for protons at injection with zero chromaticity and no transverse damper. Halfway up the acceleration ramp the growth rate for protons drops to 5.6 s^{-1} . Gold gives slightly lower values. Increasing (decreasing) the chromaticity above (below) transition can greatly decrease the growth rates, and with a slight amount of help from the transverse dampers, growth can be virtually eliminated for both protons and gold ions.

During storage, the largest contribution to impedance is due to the transverse space-charge effect: $8 \text{ M}\Omega/\text{m}$ and $19 \text{ M}\Omega/\text{m}$ for protons and gold, respectively. Here the resulting tune shifts are small compared to the synchrotron tune, $Q_s \simeq 0.005$. Any coherent motion should be Landau damped as long as the betatron tune spread is at least twice as large as the space-charge tune shifts calculated when the tune spread is neglected (see [10]). Multiplying by a safety factor of two results in a minimum rms betatron tune spread of 0.002, which is reasonable to expect in practice.

The head-tail instability (see [13]) couples the longitudinal and transverse motion of a single bunch together. Although practically all storage rings observe this phenomenon, it is universally found to depend strongly on the horizontal and vertical chromaticities. We expect that a chromaticity of -3 units below transition and $+2$ units above transition should ensure stability. A slew rate of 5 units in 30 ms will be achievable by the RHIC sextupoles. This will allow a complete chromaticity shift at transition crossing within one synchrotron oscillation period. (The use of a transition tune jump minimizes the crossing to only 1300 turns.) In reality it would take several synchrotron oscillation periods for a head-tail instability to set in.

VI. CONCLUSIONS AND COMMENTS

The RHIC narrowband impedance spectrum is dominated by rf cavities. The resonances from the 26.7 MHz cavities used during injection and acceleration are somewhat stronger than those from the 196 MHz cavities used during storage.

The broadband impedance spectrum is dominated by the resistive wall effect at very low frequencies and by kicker magnets in the intermediate frequency range up to 3 GHz.

The threshold for longitudinal microwave instabilities is lowest for protons during rebucketing, with a $|Z^{\parallel}/n|$ broadband impedance limit of 2.1Ω in the frequency range 400 MHz to 3 GHz. If we limit the longitudinal emittance growth for gold ions at transition to about 10%, the broadband impedance limit then becomes 1.5Ω .

Longitudinal coupled-bunch growth rates are worst for protons at injection. Calculations show that the passive higher order mode dampers on the 26.7 MHz cavities will limit the worst case growth rate to 2 s^{-1} , well within the range of the active longitudinal damping system that will have a maximum damping rate of 10 s^{-1} . At storage the 196 MHz cavities will give a worst case growth rate of less than 1 s^{-1} , well within the parameters of the active damping system, if not Landau damped.

Transverse coupled-bunch growth rates are also worst for protons at injection, when the resistive wall impedance may lead to a growth rate of about 30 s^{-1} . The transverse damper system is designed to handle growth rates up to 720 s^{-1} and so will easily stabilize any emittance growth from the resistive wall instability at injection and during acceleration. At storage the beams will be Landau damped. Calculations performed in the weak coupling limit show that the stored beam is stabilized against transverse coupled-bunch instabilities by adjusting the chromaticity.

Space charge is a very significant effect, since it places a limit on the longitudinal impedance for gold ions at transition. Space charge also produces a tune spread that can be much larger than the synchrotron tune, especially at injection energies. Calculations of mode coupling instabilities in this regime are less reliable than in the traditional weak coupling regime. We continue to develop the strong coupling model and to compare our results with other machines.

All species of ion beams are expected to be stable during storage. At lower energies the damping systems and chromaticity corrections will limit any growth to acceptable levels during the short time it takes to get from injection to storage.

References

- [1] "Collective Instabilities in RHIC", Eds. S. Peggs & W. W. MacKay, RHIC/AP/36 (1994).
- [2] "RHIC Design Manual".
- [3] E. B. Forsyth, J. Tuozzolo, and W. Zhang, "The RHIC Injection Fast Kicker", these proceedings.
- [4] V. Mane et al., "Fast Kicker Impedance Reduction", these proceedings.
- [5] J. Rose et al., "RF Systems for RHIC", these proceedings.
- [6] J. Rose et al., "The Design of the 26.7 MHz RF Cavity for RHIC", these proceedings.
- [7] V. Rodel et al., "Higher-order modes and tuning of the SPS 200 MHz single-cell cavity", CERN SL/RFS/91-08, (1991).
- [8] J. Wei, "Evolution of a Hadron Beam Under IBS", p. 3651, Proc. of PAC93, Washington (1993).
- [9] R. Baartman, "Effect of the Beam on RF", US Particle Accelerator School, Florida State University, (1992).
- [10] M. Zisman et al., "ZAP User's Manual", LBL-21270 UC28, (1986).
- [11] M. Blaskiewicz and W. T. Weng, Phys. Rev. E 50, 4030 (1994).
- [12] G. F. Dell and S. Peggs, "Simulation of the Space Charge Effect in RHIC", these proceedings.
- [13] S. Peggs and V. Mane, "KRAKEN, a Numerical Model of RHIC Impedances", these proceedings.

RHIC Injection Kicker Impedance

V. Mane, S. Peggs, D. Trbojevic, W. Zhang
Brookhaven National Laboratory, *
Upton, NY 11973, USA

I. Introduction

The longitudinal impedance of the RHIC injection kicker is measured using the wire method up to a frequency of 3 GHz. The mismatch between the 50 ohm cable and the wire and pipe system is calibrated using the TRL calibration algorithm. Various methods of reducing the impedance, such as coated ceramic pipe and copper strips are investigated.

II. Kicker Parameters

The RHIC injection kicker is a pulsed transmission line kicker, consisting of 15 ferrite sections and 14 ceramic sections. The length of the kicker is 1.1 m and there are 4 such units in each ring. Figure 1 shows the kicker cross section with the outer conductor, C-shaped ferrite, inner conductor and the ceramic beam pipe [1]. The design characteristic impedance of the transmission line kicker is 25 ohm. Each kicker will be pulsed with a Blumlein pulser and terminated by a matched resistor. The ferrite material used is Ceramic Magnetics CMD5005. The initial permeability of the ferrite is 1600 at low frequencies, and the dielectric constant is 12. The ceramic is manufactured by Trans-Tech and has a high dielectric constant of 100. The wave propagation velocity in the magnet is approximately 1/15 the speed of light. The design field risetime in the magnet is 80 nsec, and the flattop is about 40 nsec. The nominal integrated magnetic field is 1900 G-m from 4 units [2].

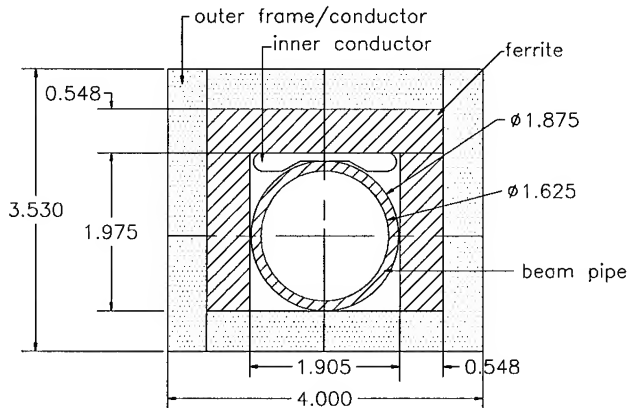


Figure 1. RHIC injection kicker cross section, Dimensions in inches

III. Test Setup

Figure 2 gives a plot of the experimental setup. The kicker is placed between two rectangular side pipes with the same dimension as the outer conductor of the kicker. The wire is placed on

the axis of the ceramic beam pipe. The characteristic impedance of the wire and rectangular pipe system is 280 ohm. The system is connected to the Network Analyzer through a 50 ohm cable. In order to calibrate the mismatch between the 50 ohm cable and the wire-pipe system, the following set of measurements are performed

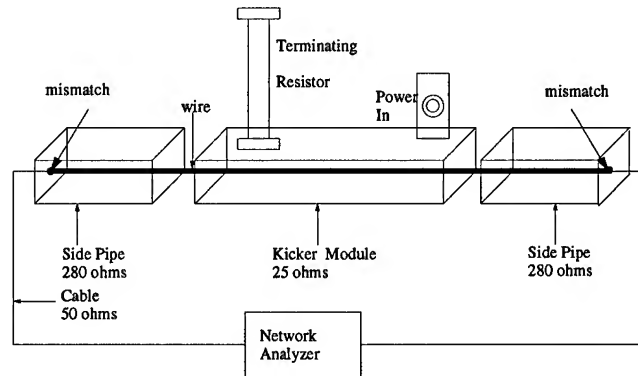


Figure 2. Bench Setup for Wire Measurement

Through Measurement: The side pipes are connected directly to each other.

Reflect Measurement: A reflective load is connected to each side pipe.

Line (Delay) Measurement: A straight pipe of arbitrary length is connected between the side pipes. Measurement is done with two pipes of different lengths.

Reference Measurement: The device is replaced by a reference pipe of the same length.

The kicker is then calibrated using the TRL calibration algorithm [3]. The impedance is obtained from the transmission coefficient S_{21} using the following relation

$$Z(\omega) = 2Z_c \frac{(S_{21}(ref) - S_{21}(DUT))}{S_{21}(DUT)} \quad (1)$$

where Z_c is the characteristic impedance of the reference pipe, $S_{21}(DUT)$ is the transmission coefficient of the Device Under Test (DUT) and $S_{21}(ref)$ is the transmission coefficient of the reference pipe.

IV. Measurement Results

The kicker impedance has to be measured carefully, as several factors contribute to the complexity of the impedance. If the

*Operated by Associated Universities Incorporated, under contract with the U.S. Department of Energy.

kicker outer conductor is isolated from the beam pipe, return currents flow outside the outer conductor, causing the beam to see the external environment. Therefore the outer conductor of the kicker is grounded to the beam pipe. To simulate this in the measurement setup, the side pipes are electrically connected to the outer conductor of the kicker. The cables from the Blumlein power supply to the kicker are 75 m long and are open when the kicker is switched off. The bench measurements are performed, with cables of length 15.5 cm. Some measurements were also done with 40.5 cm long cables and 75 m long cable. The length of the cable does not seem to have any effect on the impedance of the magnet. The measurements presented in this paper were done on a half length prototype (60 cm long).

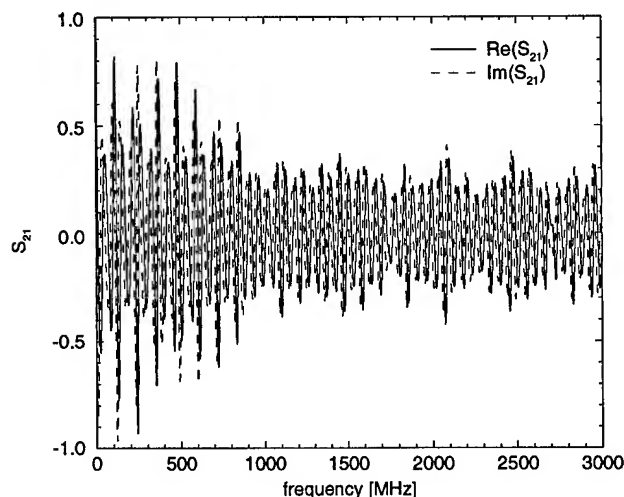


Figure 3. Uncalibrated S_{21} Parameter of the Kicker Half Module

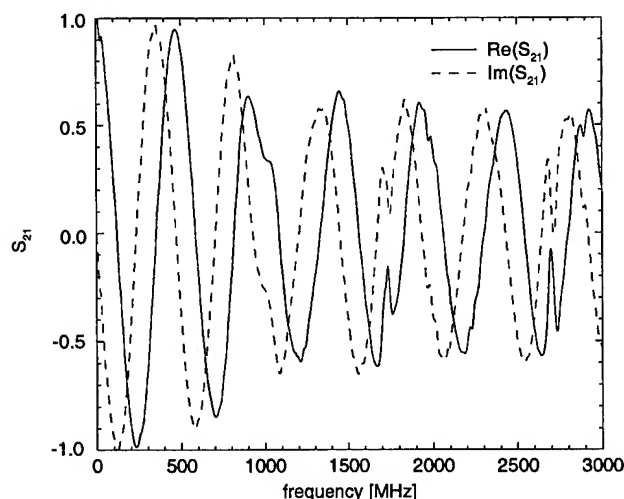


Figure 4. Calibrated S_{21} Parameter of the Kicker Half Module

The cutoff frequency of the RHIC standard beam pipe of diameter 6.91 cm is 3.3 GHz. Therefore the kicker impedance is measured up to 3 GHz. Figure 3 gives a plot of the uncalibrated transmission coefficient S_{21} of the kicker and Figure 4 gives the transmission coefficient S_{21} after TRL calibration.

Figure 5 gives a plot of the measured impedance up to a

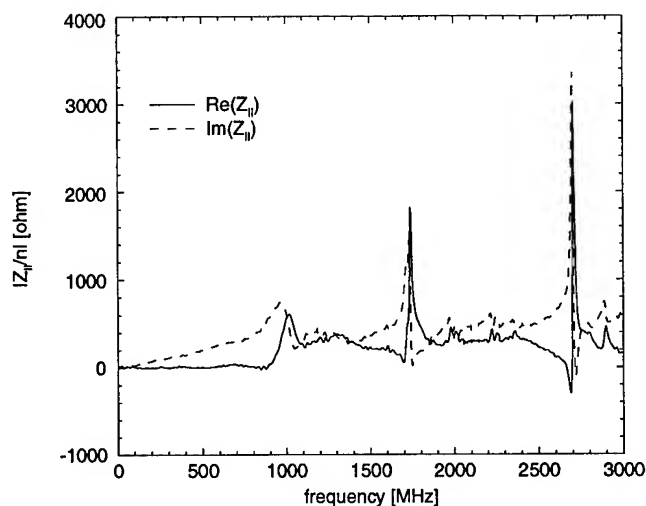


Figure 5. Injection Kicker Half Module Impedance

frequency of 3 GHz. The half length kicker has an inductive impedance with an inductance of 63 nHenry. Therefore the total contribution to the longitudinal broadband impedance $|Z_{||}/n|$ from all 4 units is .25 ohms. Note also that the impedance shows resonances at high frequencies, between 1 and 3 GHz. The frequency f , shunt impedance R_{sh} , and Q of the resonances are given in Table I. Although the ferrite is lossy at high frequencies, the resonances are not completely damped. These resonances are presumed to be higher order TM-like modes of the kicker. The frequency of the resonances is high enough and the R is low enough so as not to be fatal to the beam. In RHIC, the microwave instability sets a limit on $|Z_{||}/n|$ for gold ions at transition crossing to be 1.5 ohm. At present, the kickers make a dominant contribution to the machine broadband impedance [6].

Table I
Longitudinal Resonances of the Injection Kicker

f [MHz]	R_{sh} [Ω]	Q	R_{sh}/Q [Ω]
1000	607	9	67
1740	1816	83	22
2704	3004	208	14

V. Impedance Reduction

The following two methods for impedance reduction are being explored:

A. Conductive Coating

The inside surface of the ceramic beam tube is coated with a palladium/silver conductive paste. As described in [4] and [5], the surface resistivity of the paste is selected so that the total resistance of the coating is 20 ohm, and the measured change in kicker risetime is 5 nsec. Figure 6 gives a plot of the impedance with the coated ceramic pipe. The resonances are completely damped, and the broadband $|Z_{||}/n|$ is reduced to .012 ohm. The total broadband impedance from all 4 units is .1 ohm, reduced by a factor of 3. However, with the high conductive coating, the kicker shows a breakdown at a voltage much lower than its

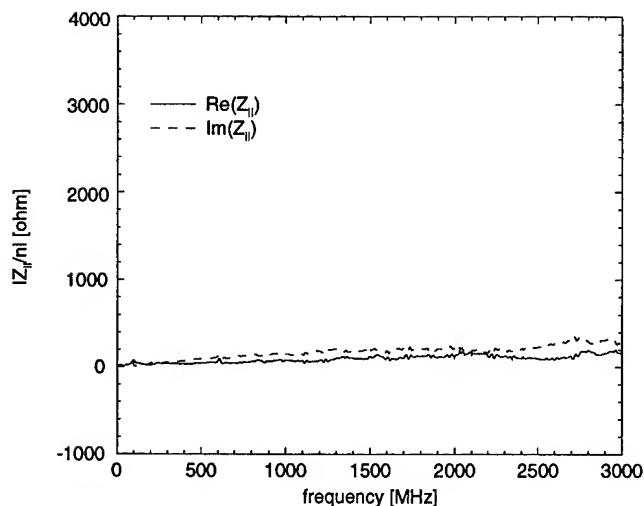


Figure 6. Kicker Impedance with Conductively Coated Ceramic Pipe

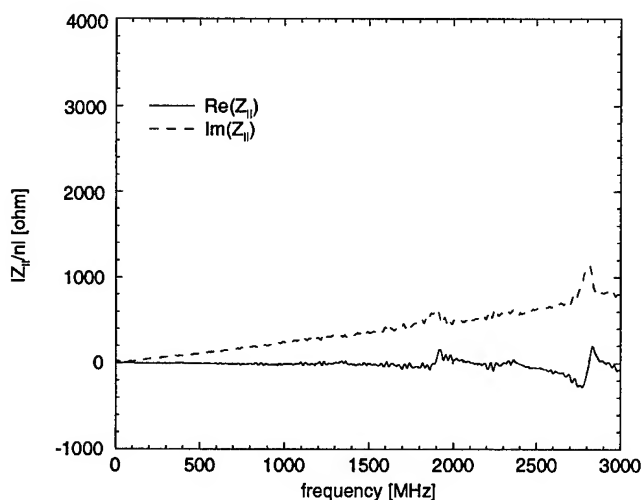


Figure 7. Kicker Impedance with Copper Strips

nominal operating voltage of 60 kV. Therefore, this solution to the impedance reduction problem is disfavored.

B. Copper Strips

Two copper strips of width .5 cm and thickness 3 mil were placed inside the ceramic pipe, at the left and the right sides (Figure 1), along the length of the kicker. Figure 7 shows a plot of the kicker impedance with the strips. The resonances have been damped substantially, and the broadband impedance $|Z_{||}/n|$ is .018 ohm. The total broadband impedance from all 4 units is .14 ohm, reduced by a factor of 1.8. The copper strips show no significant effect on the field risetimes. With the strips in place, the kicker breaks down at just below its nominal operating voltage. With some slight modifications to the kicker, the strips could be possibly used to reduce impedance.

VI. Conclusion

The kicker impedance shows resonances between 1 and 3 GHz. The frequencies of these resonances are high enough and the R

is low enough so as not to affect the beam. With a broadband impedance of .26 ohm, the injection kickers make a dominant contribution to the broadband impedance. The high conductivity coating damps the resonances completely and reduces the broadband impedance by a factor of 3, but there is breakdown at relatively low voltage. The copper strips damp the resonances, and reduce the broadband impedance by almost a factor of 2. However, these also show some breakdown behavior at high voltage. We are currently working on resolving the breakdown problem, and the strips could possibly be used as a solution to the impedance reduction problem.

VII. Status

Work is in progress with H. Hahn to understand the measured resonances better.

VIII. Acknowledgements

The authors would like to thank M. Harrison, P. Colestock and F. Caspers for helpful discussions. We would also like to thank members of the RHIC Instrumentation Group, RF Group and K. Hartmann, C. Pappas and J. Tuozzolo for their help with measurements.

References

- [1] E. B. Forsyth, "RHIC Injection Kicker", unpublished, December 1992.
- [2] "RHIC Design Manual", May 1994.
- [3] V. Mane, T. Shea, PAC, May 1993, pp. 3438-3440.
- [4] S. Kurennoy, PAC, May 1993, pp. 3420-3422.
- [5] A. Piwinski, IEEE Trans Nuclear Science, Vol.NS-24, No. 3, June 1977, pp. 1364-1366.
- [6] W. W. MacKay et al., "Estimation of Collective Instabilities In RHIC", these proceedings.

KRAKEN, a Numerical Model of RHIC Impedances

S. Peggs, V. Mane,
Brookhaven National Laboratory, *
Upton, NY 11973, USA

I. THE KRAKEN MODEL

Consider two particles, with charges q_1 and q_2 , circulating in the \hat{s} direction, horizontally and longitudinally displaced by (x_1, z_1) and (x_2, z_2) from the center of the same bunch. The equation of motion of the second particle is

$$\frac{d^2 x_2}{dt^2} + k(s) x_2 = \frac{q_1 q_2}{m\gamma} W_1(s, z_1 - z_2) x_1 \quad (1)$$

where $k(s)$ represents quadrupole focusing, m is the particle mass, γ is the Lorentz factor, and $\beta \approx 1$ is assumed. The "transverse wake field" W_1 characterises the way that the first particle interacts with the environment, to modify the transverse motion of the second particle. It is always positive for particles that are very close together, $W_1(s, +\epsilon) > 0$, defocusing a trailing particle that is in phase with the source particle. Causality demands that $W_1 = 0$ if $z_1 < z_2$, and if multi-turn wakes are neglected.

When a wake field generating device at $s = 0$ is short, it is natural to talk of its "transverse wake potential",

$$V_1(z_1 - z_2) \equiv \int_{\text{device}} W_1(s, z_1 - z_2) ds \quad (2)$$

since then the equation of motion becomes

$$x_2'' + K(s) x_2 = \frac{q_1 q_2}{mc^2\gamma} V_1(z_1 - z_2) x_1 \delta(s) \quad (3)$$

where a prime denotes differentiation with respect to s . The numerical code KRAKEN models this motion in RHIC, the Relativistic Heavy Ion Collider, by giving each of N_m macroparticles an angular kick once per turn. If there are N_b ions of atomic number Z and atomic weight A in each bunch, then the net angular kick to particle i is

$$\Delta x_i' = \frac{N_b Z^2 e^2}{Am_u c^2 \gamma} \frac{1}{N_m} \sum_{j=1}^{N_m} V_1(z_j - z_i) x_j \quad (4)$$

This numerical model is valid even if the device is long - for example, with a constant resistive wall wake field - if the synchrotron period in turns is long ($T_s \gg 1$), and the beta function at the kick point is the linearly weighted average beta over the device. To simplify the comparison of analytical and numerical results, it is assumed from here on that there are only two proton macroparticles ($N_m = 2$, $Z = A = 1$), so that

$$\Delta x_2' = \frac{N_b e^2}{2mc^2\gamma} V_1(z_1 - z_2) x_1 \quad (5)$$

II. GENERAL HEAD-TAIL RESULTS

If the chromaticity $\chi = dQ/d\delta$ is zero (where δ is the off-momentum parameter, $\Delta p/p$), the motion is stable for increasing N_b , until the *strong head-tail* threshold is passed. Unstable motion above this threshold has a rise time of $\tau \sim T_s$, the time scale on which the macroparticles exchange their "drive" and "response" roles. The strong head-tail instability, also known as the "transverse mode coupling", "transverse turbulent", or "transverse microwave" instability, has only been observed at electron storage rings.

The transverse motion of two macroparticles can be decomposed into "+" and "-" eigenmodes, in which the particles oscillate in or out of phase. When a small chromaticity χ is introduced, one eigenmode grows and the other is damped, with a slow timescale $\tau \gg T_s$. This is the *head-tail* instability.

The situation is conveniently parameterised by the dimensionless quantity

$$\Upsilon(\chi, \hat{z}) = \frac{\beta_D N_b Z^2 e^2}{4Am_u c^2 \gamma} \times \int_{t=0}^{T_s/2} V_1(z_1 - z_2) \exp \left[i (2\chi \hat{\delta} T_s) \sin \left(\frac{2\pi t}{T_s} \right) \right] dt \quad (6)$$

where β_D is the Twiss function at the device [1]. The longitudinal distance between macroparticles,

$$z_1 - z_2 = 2\hat{z} \sin \left(\frac{2\pi t}{T_s} \right) \quad (7)$$

is related to $\hat{\delta}$, the maximum off momentum parameter of a macroparticle, through the relationship

$$\beta_z \equiv \frac{\hat{z}}{\hat{\delta}} = \frac{\eta C T_s}{2\pi} \quad (8)$$

where η is the slip factor and C is the circumference of the accelerator.

Two macroparticles with longitudinal amplitude \hat{z} do not suffer from strong head-tail instability if

$$\text{Re } \Upsilon(\chi, \hat{z}) < 2 \quad (9)$$

while the head-tail eigenmode growth rates, *per turn*, are

$$\tau_{\pm}^{-1} = \mp \frac{\text{Im } \Upsilon(\chi, \hat{z})}{T_s} \quad (10)$$

These results hold for a general transverse wake field. Fortunately, τ_{-}^{-1} is overestimated, and in practice both modes are stabilised (above transition) by a slightly positive chromaticity.

*Operated by Associated Universities Incorporated, under contract with the U.S. Department of Energy.

A. STEP FUNCTION WAKE POTENTIAL

Various authors have reported analytic and simulation head-tail results for the linear (and analytically soluble) case of a step function wake potential [1], [2], [3], [4].

$$V_1(z) = V_1 \quad z > 0 \quad (11)$$

$$V_1(z) = 0 \quad z < 0 \quad (12)$$

In this case $\Upsilon(\chi)$ is independent of \hat{z} . Fig. 1 shows the horizontal “+” mode growth rate of simulated motion as a function of chromaticity, and compares it with the prediction of Eqn. 10, when $Re \Upsilon(0) = 0.03$, $\delta = 0.001$, and $T_s = 300$ turns.

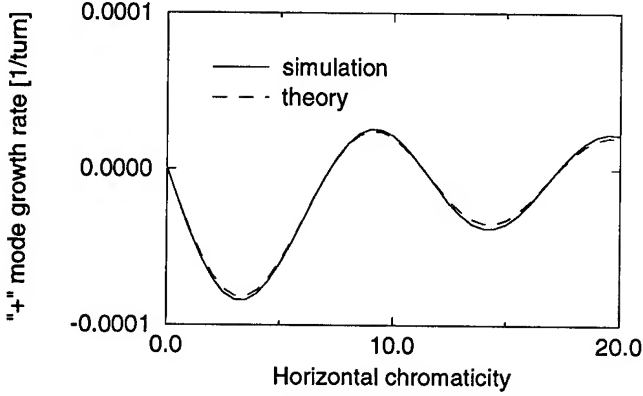


Figure 1. The head-tail growth rate τ_+^{-1} versus chromaticity χ , for a step function wake potential.

III. NEW CRITERIA WITH MOMENTUM DEPENDENT COUPLING

It is usually implicitly assumed that linear coupling is unimportant in the head-tail effect, by treating only one transverse dimension at a time. However, the Tevatron experience is that linear coupling, and its variation with momentum, are important in routine operation close to the tune diagonal [5], [6]. When coupling is important, it is reasonable to conjecture that head-tail stability is only guaranteed if the eigenchromaticities are positive for all momenta within the beam [7], [8]. A weaker conjecture is that only on-momentum particles must have positive eigenchromaticities, or that it is the average eigenchromaticity over one synchrotron period that must be positive.

The extreme values for the eigenchromaticities χ_+ and χ_- (for the worst possible combination of momentum, skew quadrupole, and normal quadrupole settings) are

$$\chi_{\pm extreme} = \frac{1}{2}(\chi_x + \chi_y) \pm \frac{1}{2}\sqrt{k^2 + (\chi_x - \chi_y)^2} \quad (13)$$

where the “skew chromaticity” vector k parameterises the variation of the closest approach of eigentunes, ΔQ_{min} , as a function of momentum. This is analogous to the way that the “normal chromaticities”, χ_x and χ_y , parameterise the tune versus momentum, far from the tune diagonal. Insisting that both of the extreme eigenchromaticities are positive leads to the **new and strong criteria** [7], [8] that

$$\chi_x + \chi_y > 0 \quad (14)$$

$$4\chi_x\chi_y > k^2 \quad (15)$$

If true, neither eigenchromaticity can ever become negative. As such, these criteria are “sufficient but often not necessary”. Both χ_x and χ_y must be positive to meet the criteria, even when $k = 0$, thereby recovering the standard uncoupled head-tail result (above transition).

KRAKEN has been used, with a step function wake potential, to test the new criteria. Fig. 2 shows what happens with equal design chromaticities $\chi_x = \chi_y \equiv \chi_0$, a skew chromaticity of $|k| = 3.8$, and other typical Tevatron parameters [6], [8]. With the same wake potential as in Fig. 1, the simulated region of stability is shifted to the right. The horizontal “+” mode growth rate goes negative at $\chi_0 \approx 2.0$, in remarkably good agreement with the predicted condition $\chi_0 > 1.9$ that comes from the new stability criteria. Clean simulation data, as shown here, are only obtained when the initial macroparticle conditions correspond to a pure local eigenmode of the coupled system.

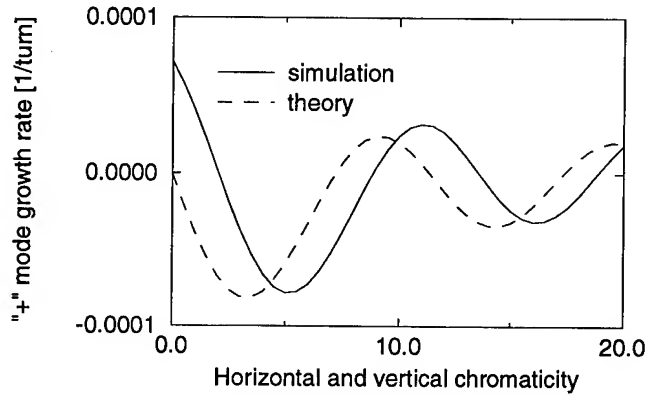


Figure 2. The head-tail growth rate τ_+^{-1} versus common chromaticity χ_0 , with momentum dependent coupling typical of Tevatron operation. The design tunes are equal.

IV. RESISTIVE WALL WAKE

The transverse resistive wall wake potential is given by

$$V_1(z) = \frac{8L}{r^4\epsilon_0(4\pi)^{3/2}} z \quad 0 < z \ll z_c \quad (16)$$

$$V_1(z) = \frac{2L}{\pi r^3} \sqrt{\frac{c}{4\pi\epsilon_0\sigma}} z^{-1/2} \quad z \gg z_c \quad (17)$$

where L , r , and σ are, respectively, the length, radius, and conductivity of the beam pipe [1]. The critical length z_c , given by

$$z_c = \left(\frac{c\epsilon_0}{\sigma}\right)^{1/3} r^{2/3} \quad (18)$$

tends to be very short. For example, $z_c = 0.12$ mm for the dominant (cold) beam pipe in RHIC, with $L = 2955$ m, $r = 0.0346$ m, and $\sigma = 2.0 \Omega^{-1}\text{m}^{-1}$.

Table I lists the nominal RHIC parameters for protons at injection, when RHIC is especially vulnerable to head-tail effects. When these values are substituted into Eqn. 6, with $\delta = \sigma_p/p$ and $\hat{z} = \sigma_z$, they lead to the variation of Υ with chromaticity recorded in Figure 3. Since the maximum value of $Re \Upsilon = 0.3$, RHIC is expected to be about an order of magnitude short of strong

Table I
RHIC parameters during proton injection.

Parameter	units	value
Bunch population, N_b		1.0×10^{11}
Lorentz factor, γ		31.17
Transition gamma, γ_T		22.89
Average device beta, β_D	m	30.0
Circumference, C	m	3833.8
Synchrotron period, T_s	turns	1414
RMS momentum error, σ_p/p		4.66×10^{-3}
RMS bunch length, σ_z	m	0.353

head-tail instability. Chromaticity values of $\chi \approx 2$ appear to be optimal. Figure 4 compares the growth rates predicted by Eqn. 10 with the rates measured by KRAKEN. The agreement is good in most cases, except that when $\chi \approx 1.5$, the anti-damping of the “+” mode is about 50% stronger than expected.

V. SUMMARY AND PLANS

The simulation code KRAKEN confirms analytical predictions of head-tail stability criteria, Eqns. 14 and 15, in the presence of momentum dependent linear coupling. It also confirms that resistive wall transverse wake fields are not a serious threat to strong head-tail stability in RHIC, at the vulnerable stage of proton injection.

Equation 10, derived from the perspective of two macroparticles, *potentially* offers a very convenient semi-numerical evaluation of the effects of arbitrary transverse wake potentials. It remains to be seen how well the two macroparticle results correlate with simulations using, say, 100 macroparticles.

KRAKEN is still under rapid development. Future plans are to include resonant wakefields, multiple bunches, space charge wakefields, betatron detuning, and a connection to the detailed RHIC impedance database.

References

- [1] A. Chao, Physics of Collective Beam Instabilities in High Energy Accelerators, New York: John Wiley and Sons, 1993.
- [2] D. Edwards and M. Syphers, An Introduction to the Physics of High Energy Accelerators, New York, John Wiley and Sons, 1993.
- [3] R. Kohaupt, DESY Report M-80/19, Hamburg, 1980.
- [4] R. Talman, CERN Report ISR-TH/81-17, Geneva, 1981; R. Talman, Nucl. Instr. Meth., **193**, 423, 1982.
- [5] S. Peggs, “Head-Tail Stability and Linear Coupling”, Fermilab AP Note 90-007, 1990.
- [6] G.P. Goderre et al, “Head-Tail Stability and Linear Coupling in the Tevatron”, IEEE Particle Accelerator Conference, San Francisco, 1991, p. 1848.

- [7] S. Peggs and G.F. Dell, “Skew Chromaticity”, Proceedings of the LHC Collective Effects Workshop, Montreux, 1994; RHIC/AP/57, 1994.
- [8] S. Peggs and G.F. Dell “Skew Chromaticity in Large Accelerators”, these proceedings.

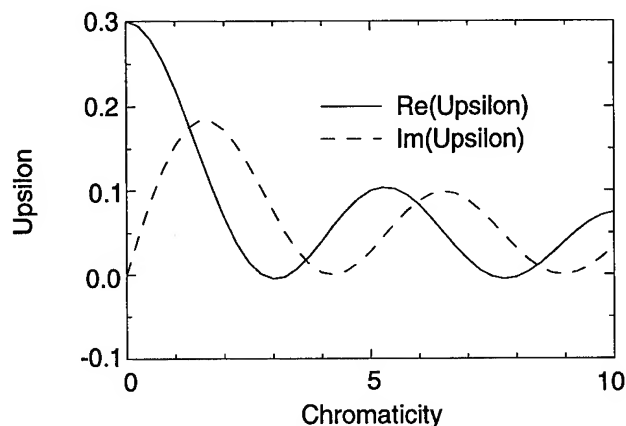


Figure 3. Υ versus chromaticity χ for protons at injection, due to the transverse resistive wall wake.

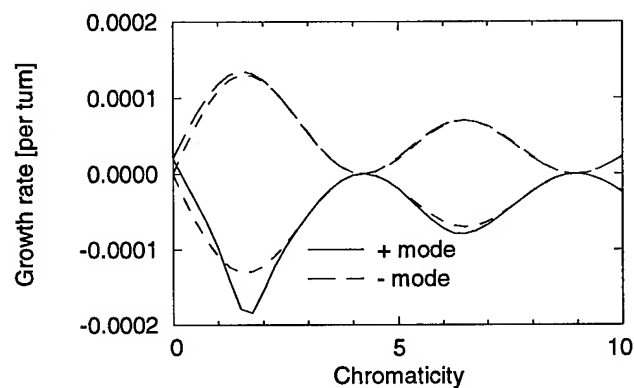


Figure 4. Two macroparticle growth rates under proton injection conditions. Simulation observations are in good agreement with theory (short dashed lines).

Lattice Design of Beijing Light Source

N. Huang, L. Jin, D. Wang, L. Wang, A. Xiao, G. Xu

Institute of High Energy Physics, Chinese Academy of Sciences
P. O. Box 918-9, Beijing 100039, China

ABSTRACT

In this paper the preliminary design of magnet lattice of Beijing Light Source(BLS) is described. Beijing Light Source is a new generation light source with the energy of 2.2GeV-2.5GeV. By choosing the FBA(five bend achromat) and TBA(triplet bend achromat) structure very low nature horizontal emittance is reached with using superconducting dipole magnets. Having made some harmonic correction the acceptable dynamic aperture is obtained though further improvement is being done to enlarge horizontal aperture.

1. DESIGN GOAL OF BLS

Since 1990 China has been planned to build a new generation light source within the medium energy range(1.5GeV-2.0GeV).[1][2] Recently the synchrotron radiation user community in China has been showing more and more interest to hard X-ray synchrotron radiation light. On the other hand it is difficult for China to afford a 6-8GeV light source which can provide 20-50KeV critical energy photons from normal dipoles and IDs. Inspired by the ideas from some Laboratories (PSI, LBL, Daresbury, etc.)[3] we adopted the design philosophy that integrate several superconducting magnets into lattice of storage ring to provide many hard X-ray beamlines for synchrotron radiation users. Meanwhile we try to keep the horizontal emittance very small to yield high brightness VUV and soft X-ray synchrotron radiation light from insertion devices(undulators and wigglers).

The overall design goal of Beijing Light Source is listed as follows:

- * Energy: 2.2GeV - 2.5 GeV
- * Nature horizontal emittance: <10nm, better less than 5nm
- * Circumference: < 250 m
- * Number of straight sections: ≥ 8
- * Length of straight sections: two long straight, ~15m >6.0m for the rest
- * Number of superconducting dipole: 4 at least
- * Beam current: ~300 mA

The figure 1 gives a comparison of the spectrum of BLS to that of two existing synchrotron light sources in China: BSRF(dedicated synchrotron radiation mode of Beijing Electron-Positron Collider, 2.2 GeV) and NSRL(0.8 GeV synchrotron light source)

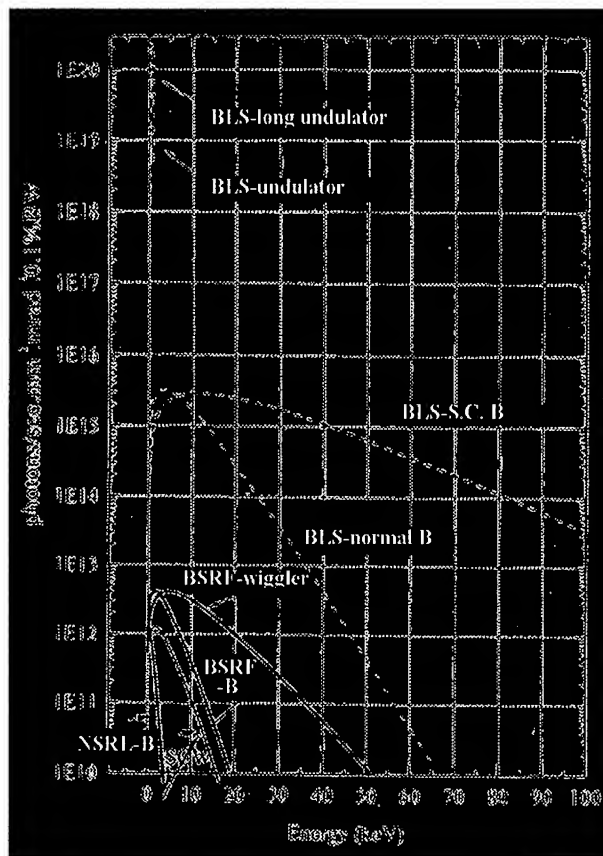


Figure 1 Comparison of the synchrotron radiation spectrum of BLS, BSRF and NSRL

2. FBA LATTICE DESCRIPTION

We have chosen the achromat structure with odd number of dipole magnets($N=3, 5$) in order to arrange a superconducting dipole by replacing the central normal dipole. FBA(Five Bend Achromat) structure can lead to a very low nature emittance even with the presence of superconducting bending magnets. Table 1 gives the main lattice parameters of BLS storage ring based on this kind of structure.

Each FBA cell consists of 5 bending magnets. The bending angle of outer dipoles for dispersion suppression and the central dipole which can be replaced by a superconducting dipole is chosen to be 8° . The bending angle of the rest 2

dipoles is 10.5° . Such a distribution of bending angle is to optimize the contribution from different dipoles to emittance. The combined function dipole is adopted to save some space therefore make it possible to arrange eight FBA cells in such a rather limited circumference. The exception is that the superconducting dipoles are flat type to avoid some technological complexities. Two extra quadrupoles for each superconducting dipole are added to provide necessary focusing.

The circumference of storage ring is fixed to 240.4m which is equal to that of Beijing Electron-Positron Collider therefore the design is also suitable for the case that a Tau-charm Factory is built at IHEP site(build BLS in BEPC tunnel).[4][5] However we found that a little bit longer circumference(250m or 260m) is more comfortable for the matching and element arrangement.

Table 1 Main lattice parameters of BLS storage ring

Nominal Beam Energy	2.2 GeV
Maximum Beam Energy	2.5 GeV
Circumference	240.4 m
Nature Horizontal Emittance	3.3 nm-rad
Number of Straight Section	8
Length of Long Straight	15.0 m
Length of short straight section	6.4 m
Number of S.C. dipole	4
Field Strength of S.C. Dipole	4.4 Tesla
Momentum Compaction	0.00834
Energy Spread	0.00105
Qx	18.38
Qy	7.15
Energy Loss per turn	441KeV
Jx/Jy/Jz	1.21/1.0/1.79
RMS Beam Size at ID	0.162/0.036mm
Chromaticities	-47.2/-19.3
Harmonic number	400
RF frequency	498.83 MHz

Table 2 The effect of s.c. dipole on nature hori. emittance

Num. of SCB	2.0 GeV	2.2 GeV	2.5 GeV
0	1.9 nm-rad	2.3 nm-rad	3.0 nm-rad
4	2.7 nm-rad	3.3 nm-rad	3.7 nm-rad
8	3.3 nm-rad	4.2 nm-rad	5.2 nm-rad

3. CHROMATICITY CORRECTION AND DYNAMIC APERTURE

The correction of chromaticity with two families of sextupoles results in a rather small dynamic aperture(~ 7 mm in horizontal direction and ~ 6 mm in vertical direction). Having applied two harmonic correction sextupole families located in the dispersion-free region the dynamic aperture is doubled in both directions. Further studies are being performed to enlarge the dynamic aperture by increasing the number of families of both chromaticity correction and harmonic correction sextupoles.

4. TBA LATTICE CONFIGURATION

As a comparison to FBA structure the TBA(Triplet Bend Achromat) configuration is done. A small nature horizontal emittance 8.5nm-rad at 2.2 GeV with 4 superconducting dipoles integrated in lattice is achieved by applying strong focusing strength. This configuration gives 4 more straight sections than FBA lattice though the adjustment of beta-functions in the straight section is not very flexible. By using 8 sextupole families a good dynamic aperture is obtained(20 mm in horizontal and 8 mm in vertical). This configuration also has two 15m long straight sections as FBA configuration.

ACKNOWLEDGMENT

The authors wish to thank the other members of accelerator physics group of IHEP for their useful discussions.

REFERENCES

- [1] L. Chen, S. Fang, D. Wang, W. Wang, Mainland-Taiwan joint workshop on synchrotron radiation, 1993
- [2] D. Ding, S. Fang, D. Xian, Internal report, 1993
- [3] A. Baldereschi et al., Conceptual Design of the Swiss Synchrotron Light Source,
- [4] S. Wang, this conference
- [5] N. Huang et al., this conference

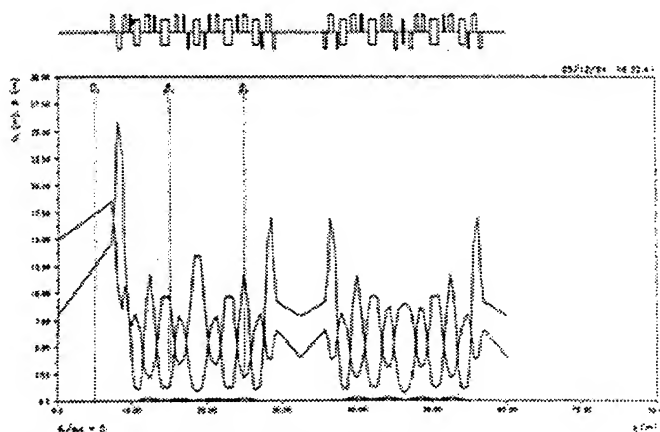


Figure 2 Lattice of 1/4 ring of BLS

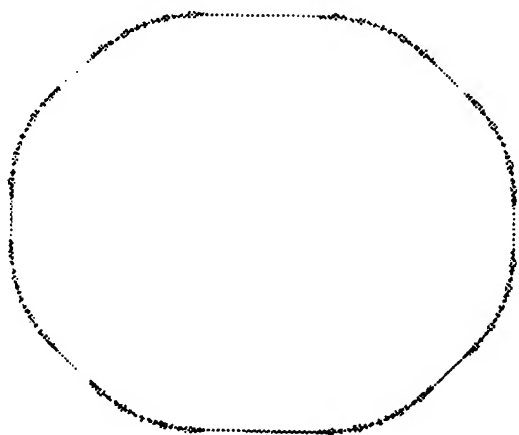


Fig. 3 Layout of the storage ring of BLS

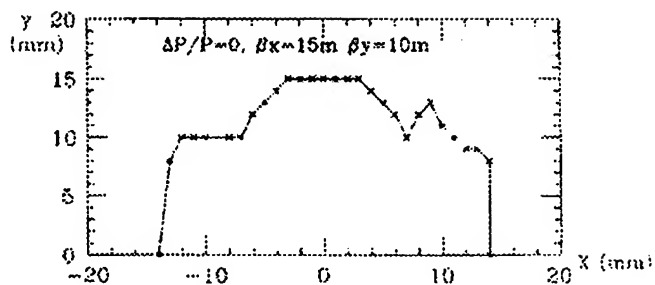


Fig. 4 Dynamic aperture of on momentum particle

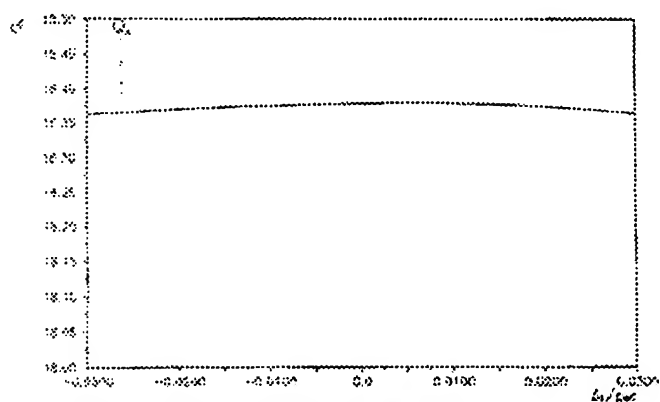


Fig. 5 Q_x vs. momentum deviation

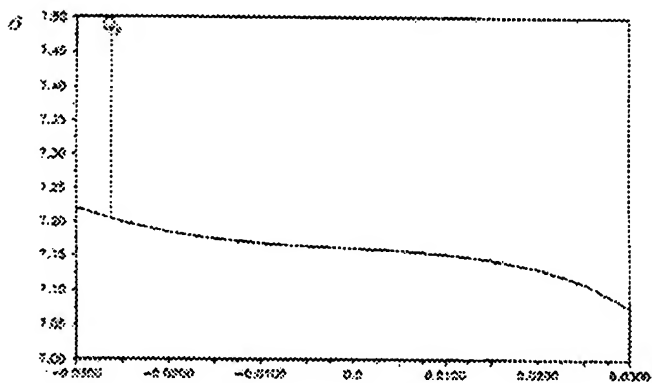


Fig. 6 Q_y vs. momentum deviation

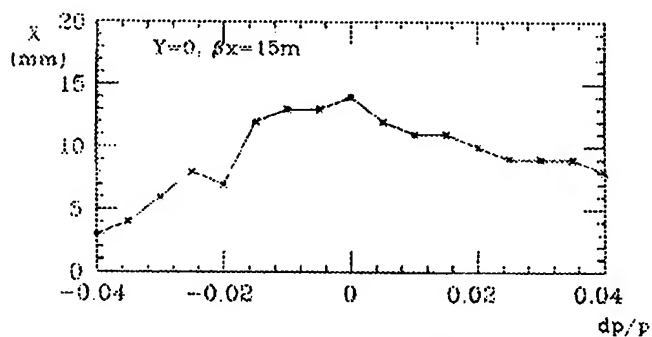


Fig. 7 Hori. dynamic aperture vs. momentum deviation

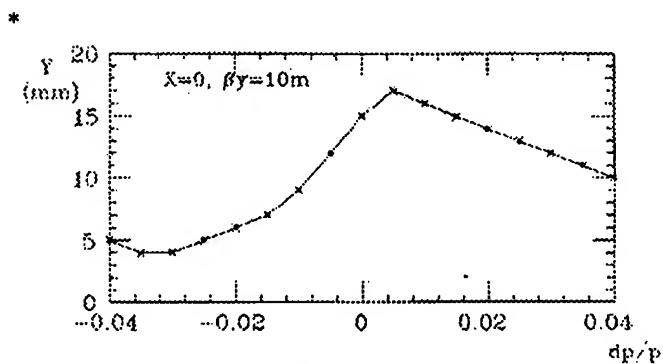


Fig. 8 Vert. dynamic aperture vs. momentum deviation

A THEORETICAL STUDY OF THE ELECTRON-PROTON INSTABILITY IN A LONG PROTON PULSE*

Tai-Sen F. Wang

AOT-1, MS H808, Los Alamos National Laboratory
Los Alamos, New Mexico 87545, USA

Abstract

The electron-proton instability of a long, intense, and partially neutralized proton bunch is studied by numerically solving the equations of motion for the line centroid of the proton beam and the line centroid of the trapped electrons. The formalism takes into account the effects of variable line densities and alternating-gradient (AG) focusing. Good qualitative agreement between the computational results and experimental observations was obtained when applying the theory to the Los Alamos Proton Storage Ring (PSR). Both the case of a clean extraction gap and the case with a few percent of protons in the extraction gap were studied. It is found that with only a few percent neutralization, the PSR beam can become unstable in both cases. The same equations and method were used to study the stability of the proton beam in the accumulator ring of the proposed LANSCE II spallation-neutron source. The results indicate that the e - p instability can also occur in the LANSCE II accumulator ring for only a few percent neutralization.

I. INTRODUCTION

Coherent transverse instability has been observed in the PSR in both bunched and unbunched beams.[1-3] Spectrum analyses of the vertical beam position monitor (BPM) signals from unstable beams indicate that the peak of the frequency distribution may vary from several ten MHz to about three hundred MHz. The fast growth of the instability and the dependence of the frequency spectrum peak on the beam conditions suggest that the instability is more likely caused by the trapped electrons in the proton bunch instead of fixed-frequency impedances. The results from a previous injection-foil biasing experiment and a beam-shaking experiment on stabilizing the marginally stable beams also suggest that the instability in the PSR could be aroused by the electrons trapped in the proton beam.

Since the e - p instability has been previously observed in the Bevatron at LBL[4,5] and at CERN[6-8] and now appears to occur in the PSR, precaution must be taken in designing the next generation spallation neutron sources such as the Los Alamos LANSCE II and the European Spallation Source (ESS) to avoid such kind of instability.

This report documents a theoretical investigation on the e - p instability in a long proton bunch like the one in the PSR or in the proposed LANSCE II. We will present the results of solving the coupled equations of motion for the centroid of the proton beam and the centroid of the trapped electrons. An example will be given for PSR.

*Work supported by Los Alamos National Laboratory Institutional Supporting Research, under the auspices of the US Department of Energy.

II. THEORETICAL MODEL

We consider a bunched proton beam of total length L with a round cross-section of radius a , propagating with a constant speed v inside a perfect conducting pipe of radius b . Protons are focused in the transverse direction by an external force that depends linearly on the radial distance. A Cartesian coordinate system is adopted such that the z -axis is in the direction of proton propagation and the y -axis is perpendicular to the ring. The origin of the coordinate system coincides with the center of the beam cross section. The proton bunch is partially neutralized by electrons possibly produced by secondary emission, gas ionization, or the charge-change injection process. We assume that in the equilibrium state, electrons are trapped in the proton beam (no electrons between beam and pipe), and both species of particles are distributed uniformly in the transverse direction. Both the population line-densities of protons and electrons, λ_p and λ_e , can be functions of z along the proton beam. We also assume that the proton beam is unstable against the perturbation in only one transverse direction, so we need to concentrate only in one direction of the transverse motion, say the y -direction. The axial motion of electrons and the synchrotron motion of protons are neglected for simplicity. The study of the e - p instability here is based on the investigation of the motion of the line centroid of the proton beam $Y_p(z, t)$ and the line centroid of the trapped electrons $Y_e(z, t)$ defined as the averaged displacements of the electrons and protons, respectively, at the location z and at the time t .

Taking the perturbation into account, we can derive the following two equations for Y_p and Y_e by averaging the equations of motion for single particles and adding the damping terms (e.g. from energy spread, tune spread, and non-linear forces):

$$\left(\frac{\partial}{\partial t} + v\frac{\partial}{\partial z}\right)^2 Y_p - C_{dp} \left(\frac{\partial Y_p}{\partial t} + v\frac{\partial Y_p}{\partial z}\right) + \omega_\beta^2 Y_p = \left(\frac{2g\lambda_p r_p \chi c^2}{a^2 \gamma}\right) Y_e, \quad (1)$$

and

$$\frac{d^2 Y_e}{dt^2} - C_{de} \frac{dY_e}{dt} + \omega_e^2 Y_e = \left(\frac{2g\lambda_p r_e c^2}{a^2}\right) Y_p, \quad (2)$$

where

$$\omega_\beta^2 = \omega_{\beta o}^2 + \frac{2\lambda_p r_p c^2}{a^2} \left[\frac{\chi}{\gamma} - \frac{1}{\gamma^3} \left(\frac{a}{b}\right)^2 \right], \quad (3)$$

C_{dp} and C_{de} are the damping constants for the proton and electron motions, respectively, $\omega_{\beta o}$ is the betatron frequency due to the external focusing force only, $\omega_e^2 = \omega_{eo}^2(1 - \chi)$, $\omega_{eo} =$

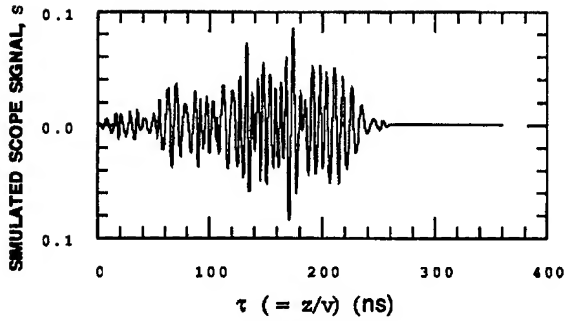


Figure 3. The simulated the scope signals corresponding to the displacement shown in Fig. 2.

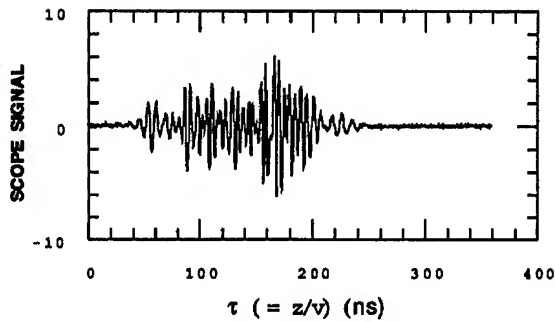


Figure 4. A BPM signal of an unstable beam in the PSR.

(ii) A gap empty of protons does not always ensure the beam stability, and the multi-turn trapping of electrons is not a necessary condition for the e - p instability to develop. If a proton beam bunch is sufficiently neutralized (a few percent in the PSR and LANSCE II cases), the e - p instability still may occur even when the gap is empty. The instability grows slightly faster and the stability threshold is slightly lower when there are a small number of protons in the gap.

(iii) The wavelength of the e - p oscillation varies with the proton line-density - short wavelength in the high density region and long wavelength in the low density region. In a proton bunch of non-uniform density, the frequency spectrum is relatively wide. This is a distinct characteristic of the oscillations that involve more than one species of particles.

(iv) The e - p instability grows both in time and space. Therefore, most of the oscillation growth occurs in the later part or in the tail of a proton bunch.

(v) We have studied the situation of non-uniform electron production around the ring. Comparing with the case of uniform electron production, we found that for the same number of electrons, the e - p oscillation is slightly more unstable when the electron production is concentrated in part of the ring.

(vi) We found that a proton bunch is more unstable and has a higher growth rate in an AG focusing system than in a continuous, uniform focusing system.

(vii) In several cases, we have included a low-level random noise at the beginning of each turn to check its effects. We observed that the noise can slightly lower the instability threshold and increase the growth rate.

IV. CONCLUSIONS

We have studied the electron-proton instability in a long proton bunch by solving the equations of motion for the centroid of the proton beam and the centroid of the trapped electrons. For PSR, we have examined both the cases of filled gap and empty gap. We found that in either case a few percent neutralization can lead to instabilities of fast growth rates. We found that the threshold is lower and the growth rate is higher when the gap is filled in. In the numerical solutions, we saw the wavelength of the e - p oscillation depends on the local proton line-density. Wavelengths are long (short) in the low (high) density region. Therefore the frequency spectrum can be wide-banded. Our numerical results seem to agree well with the experimental observations qualitatively. We have also found that both the AG focusing and random noise can lower the threshold and increase the growth rate of the e - p instability. For LANSCE II, we also found that the threshold of neutralization for the e - p instability is only a few percent.

References

- [1] T. Wang et al., Proc. of 1993 Particle Accelerator Conf., IEEE Catalog No. 93CH3279-7, Vol. 5, p. 3297.
- [2] D. Neuffer et al., Nucl. Instr. and Meth. A321, 1 (1992).
- [3] E. Colton et al., Proc. of 1991 IEEE Particle Accelerator Conf., IEEE Catalog No. 91CH3038-7, Vol. 3, p. 1896.
- [4] H. Grunder and G. Lambertson, Proc. 8th Intl. Conf. on High Energy Accelerators, CERN, 1971, p. 308.
- [5] L. J. Laslett, A. M. Sessler and D. Möhl, Nucl. Instrum. Meth., **121**, 517 (1974).
- [6] H. G. Hereward, CERN Internal Report 71-15 (1971).
- [7] E. Keil and B. Zotter, CERN Internal Note CERN-ISR-TH/71-58, December 1971.
- [8] H. Schönauer and B. Zotter, CERN Internal Note, May 1972.

RECENT PROGRESS ON BEAM STABILITY STUDY IN THE PSR*

T. Wang, P. Channell, R. Cooper, D. Fitzgerald, T. Hardek, R. Hutson
A. Jason, R. Macek, M. Plum, C. Wilkinson, and E. Colton†
Los Alamos National Laboratory, Los Alamos, New Mexico 87545

Abstract

A fast transverse instability has been observed in the Los Alamos Proton Storage Ring (PSR) when the injected beam intensity reaches more than 2×10^{13} protons per pulse. Understanding the cause and control of this instability has taken on new importance as the neutron-scattering community considers the next generation of accelerator-driven spallation-neutron sources, which call for peak proton intensities of 10^{14} per pulse or higher. Previous observations and theoretical studies indicate that the instability in the PSR is most likely driven by electrons trapped within the proton beam. Recent studies using an experimental electron-clearing system and voltage-biased pinger-electrodes for electron clearing and collection support this hypothesis. Experiments have also been performed to study the instability threshold when varying the electron production rate. Theoretical studies include a computer simulation of a simplified model for the $e-p$ instability and the investigation of possible electron confinement in the ring-element magnetic fields. This paper reports some recent results from these studies.

I. INTRODUCTION

The PSR is a fast-cycling high-current storage ring designed to accumulate beam over a macropulse of the LAMPF linac (~ 1 ms) by multi-turn injection through a stripper foil and compress that beam into a short single-turn extracted pulse ($\sim 0.25 \mu\text{s}$), which drives a neutron source. Key PSR parameters include kinetic energy of 797 MeV, circumference of 90.1 m, revolution frequency of 2.875 MHz, betatron tunes ν_x and $\nu_y \approx 3.17$ and 2.13, respectively, and present operation with $N \approx 2.35 \times 10^{13}$ stored particles. The design intensity is 100 μA on target at 12 Hz, which implies 5.2×10^{13} protons/pulse. Average and peak intensities have been somewhat less (80 μA at 20 Hz and 4×10^{13} maximum pulse size). The average current is limited by slow beam losses, and individual pulse intensities are limited by a fast instability [1-3].

The instability occurs when more than $\sim 2 \times 10^{13}$ protons are stored in bunched mode (rf on), and when more than $\sim 5 \times 10^{12}$ are stored in unbunched mode. Transverse oscillations at ~ 100 MHz are seen, and grow exponentially at time scales of 10–100 μs , causing beam losses. Searches for a possible impedance source were unsuccessful. Much evidence has been observed which supports the theory that the instability is caused by the coupled oscillation between the proton beam and trapped electrons – the “ $e-p$ ” instability that has been previously observed in some other proton facilities [4-6]. Supporting observations include the following: degrading the vacuum makes the beam

become more unstable, biasing the foil to a voltage sufficient to clear electrons in the vicinity increases the stability threshold; and moving halo scrapers into the beam pipe to produce more secondary electrons decreases the threshold. Theoretical calculations have also shown that the conditions for an $e-p$ instability may occur in the PSR. However, a dominant electron source has not yet been identified. Understanding of this instability and methods of controlling it have taken on new importance as the neutron scattering community considers the next generation of accelerator-driven spallation-neutron sources, which call for peak proton intensities of $\sim 2 \times 10^{14}$ per pulse or higher.

A theory proposed in the early nineties conjectured that a small amount of the beam in the PSR may leak into the gap to form a smooth, overall density distribution and an electric potential sufficient for electron trapping to cause instability [1,7]. A later computer simulation indicated that neither the multi-turn trapping of electrons nor the gap-filling is necessary for the $e-p$ instability to develop if there are sufficient electrons trapped in the proton bunch, but the instability threshold can be lowered by having electrons trapped for more than one turn [3,8]. Observations did show that the instability is associated with bunch leakage; with bunched beam (rf on), we observed that instability occurs when the inter-bunch gap has filled in. Measurements taken under various conditions indicate that gap filling occurs either before or simultaneously with the beginning of growing oscillations.

In the recent years, experiments were performed by using the “pinger” to sweep the leakage out of the inter-bunch gap during storage and by lowering the machine transition gamma to prevent protons to make leakage difficult [3]. In the relatively low-intensity regime, results from these experiments seem to confirm the conjecture that the gap leakage does induce the instability in the PSR. Yet at high beam intensity, neither the gap sweeping nor the low transition gamma was able to stabilize the beam. One possible explanation is that keeping the gap absolutely clean at high beam intensity is difficult. However, the results of these experiments can not exclude other mechanisms to drive the instability; whether the beam in PSR will be stable with a clean gap at the intensity of 5.2×10^{13} protons/pulse remains to be resolved, and identifying the source of electrons still needs further study.

Recently experimental studies of beam stability in the PSR were carried out by using a newly installed electron clearing system and by bumping the beam close to the wall to create electrons that may induce the instability. Our recent theoretical study covers a simple simulation of the $e-p$ instability, a study of possible electron trapping in the magnetic field of the focusing elements, and an estimation of the secondary emission of electrons from protons lost in the ring. This paper reports some of the progress made in these recent studies.

*supported by Los Alamos National Laboratory Institutional Supporting Research under the auspices of the United States Department of Energy.

†US DOE.

II. EXPERIMENTAL OBSERVATIONS

A. Electron Clearing

Since a charge-change injection method with foil stripping is used in the PSR, we believed that the injection section should have more electrons than other part of the ring. Recently an experimental clearing system, including two pairs of electrodes, two bending magnets for directing the convoy electrons from the stripping process, and an injection foil biasing capability, was implemented in this section to study the effect of electron clearing on the beam stability. The system setup and the experimental details are reported in a separate paper [9].

The results of applying this clearing system to the beam apparently depends on the machine and beam conditions. In the most effective case, we have observed a more than 20% increase of the instability threshold current of a continuous coasting beam. In this case, we only applied moderate biasing voltages on the foil and clearing electrodes. For bunched beams, we have tried higher voltages on the foil and the clearing electrodes; we found no significant effect on the instability threshold, except that the growth rate of the instability was lowered. A lack of sufficient machine development time did not allow more thorough studies on the bunched beam. Nonetheless, the results of this experiment do provide strong support to the e - p assumption.

B. Electron Collection

We performed the experiments of electron collection by using the plates of the clearing electrodes in the injection Section and the pinger in Section 3 as electron collectors. Synchronized signals from the collectors and the wall current monitor or the BPM were recorded and studied.

In the coasting-beam experiments, we observed a large current collected by the pinger electrodes during the later stage of the storage. When the stored beam went unstable, we observed that the loss of beam current was preceded by a sudden rise in the pinger current. In the bunched mode, when the stored beam was marginally stable, we found the collected currents from the pinger and from the clearing electrodes increased with the amplitude of the vertical oscillation. For unstable bunched beams, we observed that the loss of beam current is always accompanied by a fast increase in the current collected on the pinger electrodes.

C. Beam Bump Experiment

The purpose of this experiment was to prove that an excessive amount of the secondary electrons generated by the protons lost to the wall can induce the e - p instability. A similar experiment was carried out some years ago by moving a beam scraper close to the core of the beam to generate secondary electrons to induce the instability.

We created a horizontal beam bump in Section 3 of the ring where a pinger was used as an ion chamber to collect the secondary electrons. A fast instability was observed when the orbit was bumped to more than a half centimeter toward the ring center. When we bumped the orbit away from the ring center, the stored beam remained stable up to more than one centimeter of bump. The pinger collected a substantial amount of current when the beam was stable, and a large amount of current when

the beam was unstable. The stability property of the beam observed in this experiment is consistent with results of the beam scraping experiment before.

III. THEORETICAL STUDY

A. Instability Simulation

A simple computer simulation of the e - p instability in a long proton bunch has been performed by numerically solving the equations of motion for the centroid of the proton beam and the centroid of the trapped electrons. A preliminary result has been reported earlier. Recent studies include using refined line-density models, investigating the effects of the AG focusing and noise, and a study of the BPM signal. Details are documented in a separate paper [8] and in an internal report [10].

B. Electron Trapping Study [11]

The partial success in stabilizing the beam by gap sweeping with the pinger motivated the search for other mechanisms besides gap-filling, for multi-turn trapping of electrons in the PSR. A recent study investigated the possibility that electrons could be trapped in the field of lattice quadrupoles. Computer tracking of the electron motion in the combined quadrupole and beam fields indicates that a fraction of the electrons generated in the quadrupole region, including the gas ionization and secondary emission, can be trapped in the quadrupole field over several turns. The total amount of electrons trapped in all the quadrupoles can possibly reach a few percent of the amount of the protons stored, enough to trigger the e - p instability in the PSR.

C. Study on Possible Electron Source [12]

We have studied the possibility of secondary electrons generated by the protons lost to walls as an electron source in the PSR. In this estimate, we applied Sternglass' theory [13] on the yield of secondary emission. We found that the yield for the secondary emission in the PSR, due to a proton lost to the beam pipe, is about 200. Using the experimental data of beam loss in the PSR, and the theoretically estimated yield, we inferred that the electrons generated in one accumulation cycle in a typical PSR production condition is about 230 nC. The charge collected by using the pinger as an ion chamber, ranges from 90 to 550 nC. Thus, the estimated electron production is in the range of the measured data. This implies that the secondary emission due to the lost proton can be a significant electron source in the PSR.

IV. SUMMARY AND CONCLUSIONS

Our recent experiments included electron clearing in the injection section, electron collection, and beam bumping for inducing the instability. Our recent theoretical study covers instability simulation, a study of multi-turn electron trapping in the quadrupole field, and a study of secondary emission as a possible electron source. Results from our recent experimental and theoretical studies further confirm that the observed instability in the PSR is an e - p instability. Based on these observations and the results from other experiments as well as theoretical estimations, we tend to conclude that secondary emission could be one of the major electron sources in the PSR. If this is true, a hypothesis for

creating the large amount of electrons collected in the PSR can be conjectured: Initially, any small perturbation can start a relative oscillation between the injected protons and the electrons created due to injection, gas ionization, and secondary electrons produced by lost protons. This oscillation together with the increasing beam emittance due to the repetitive scattering by the injection foil cause proton loss and the production of more secondary electrons around the ring. These secondary electrons, in turn can increase the beam oscillation to cause more proton loss. Thus, the beam oscillation and the secondary emission of electrons due to the lost protons mutually enhance each other to increase the amount of electrons in the ring above the threshold of the e - p instability.

We plan to upgrade the beam injection section of the PSR to improve the quality of the injected proton beam for reducing the proton loss and machine activation. This upgrade may change the characteristics of the beam stability in the PSR and lead to a better understanding of the instability. Understanding this instability and methods of controlling it have fundamental importance in both the future operation of the PSR and the design of the next generation of accelerator-driven spallation-neutron sources. Study of the PSR instability will be continued in the future.

References

- [1] D. Neuffer, *Conf. Record of the 1991 IEEE Particle Accelerator Conf.*, Vol. 2, p. 1077, and references cited therein.
- [2] D. Neuffer et al., *Nucl. Instr. and Meth.*, **A321**, 1 (1992).
- [3] T. Wang et al., *Conf. Record of the 1993 IEEE Particle Accelerator Conf.*, Vol. 3, p. 1896.
- [4] H. Grunder and G. Lambertson, *Proc. 8th Intl. Conf. on High Energy Accelerators*, CERN, 1971, p. 308.
- [5] H. G. Hereward, CERN Internal Report 71-15 (1971).
- [6] H. Schönauer and B. Zotter, CERN Internal Note, May 1972.
- [7] D. Neuffer and C. Ohmori., *Nucl. Instr. and Meth.*, **A343**, 390 (1994).
- [8] T. Wang et al., these proceedings.
- [9] M. Plum et al., these proceedings.
- [10] T. F. Wang, Los Alamos Accelerator Theory Note, in preparation.
- [11] P. Channell and A. Jason, AOT-3 Technical Note: 93-11, AOT Division, Los Alamos National Laboratory, 1993.
- [12] M. Plum, Los Alamos PSR Technical Note, PSR-95-001, 1995.
- [13] E. J. Sternglass, *Phys. Rev.* **108**, 1 (1957).

HALOS OF INTENSE PROTON BEAMS *

Robert D. Ryne, Salman Habib and Thomas P. Wangler
Los Alamos National Laboratory
Los Alamos, NM 87545 USA

Abstract

Beam halo is an important issue for accelerator driven transmutation technologies and other applications of CW proton accelerators. These projects include, for example, the accelerator transmutation of waste, accelerator-based conversion of plutonium, accelerator production of tritium, and the development of a next-generation spallation neutron source. To keep radioactivation within acceptable limits these accelerators must operate with a very low beam loss (less than a nanoampere per meter). Beam loss is associated with the presence of a low density halo far from the beam core. Understanding the physics of halo production and determining methods to control beam halo are important to these projects. In recent years significant advances have been made, both analytically and computationally. In the following we describe recent developments in beam halo theory and simulation, including results from multi-million particle simulations.

I. THE BEAM HALO ISSUE

Beam halo is an important issue for many proposed projects including the accelerator transmutation of waste (ATW), accelerator-based conversion of plutonium (ABC), accelerator production of tritium (APT), and the development of next-generation accelerator-driven spallation neutron sources. All of these projects utilize proton linacs with currents of order 100 mA and energies of order 1 GeV. Small beam losses in the linac and in the high energy beam transport section following the linac can produce radioactivation which can degrade accelerator components and hinder or prevent hands-on maintenance. Much beam loss is due to the formation and interception of a low density beam halo at a large radial distance (4 or more times the rms beam radius) from the beam core. At 1 GeV, losses must be kept below 1 nA/m (preferably 0.1 nA/m) so that hands-on maintenance can be performed shortly after accelerator shutdown. To design accelerators in this ultra-low loss regime we must understand the causes of beam halo.

II. THE PARTICLE-CORE MODEL IN A CONSTANT FOCUSING CHANNEL

Early studies of mismatched charged particle beams showed that such beams could undergo emittance growth and develop a large halo surrounding the beam core [1][2]. Beam mismatch is now believed to be a major source of halo formation. A popular model used to study beam halo is the particle-core model of halo evolution[3]-[8]. In this model halo particles interact with a beam core that is assumed to oscillate because of an initial ra-

dial mismatch; the fields inside the core are roughly proportional to r (in the two-dimensional case), while they are inversely proportional to r outside the core. Thus, a halo particle moving in and out of the core sees a strongly time-dependent nonlinear field superposed on a linear external focusing field. As one might imagine such a system exhibits a variety of dynamical phenomena including chaos. In the particle-core model the core is assumed to have a radial density profile that does not change except in an rms sense. In other words, the beam is always a KV distribution, or always a Gaussian, etc., but the rms size of the beam is allowed to change in accord with the rms envelope equations. In addition to this approximate treatment of the core, the model is not self-consistent since the halo particles do not affect the motion of the core. However, as will be shown below results from the particle-core model are in excellent agreement with results from high resolution particle simulations. A useful way to study this model is to make a stroboscopic plot, in which test particles are plotted once each cycle of the core oscillation. (This technique was first used in halo studies by Lagniel [4][5].) As an example, consider the case of a mismatched KV beam. Figure 1 shows a stroboscopic plot of 32 test particles that were initialized with 16 on the x -axis and 16 on the p_x -axis. The main features of the plot are: (1) a central region that has an extent somewhat larger than the core radius; (2) a large amplitude region where particles exhibit betatron motion perturbed by the core space charge; (3) a period-2 resonant region associated with the fixed points to the left and right of the central region; and (4) a separatrix with an inner branch that encloses the central region and outer branches that separate the period-2 resonance from the betatron-like trajectories. The period-2 resonance is a parametric resonance corresponding to the fact that resonant particles have an oscillation frequency which is one half the envelope frequency, as has been shown analytically by Gluckstern [7]. In Figure 1 the separatrix is actually a narrow chaotic band, and the outer edge of the band has the approximate shape of a peanut. This "peanut diagram" provides a useful picture for describing halo formation: if particles in an initially well-defined core reach the separatrix (by transport mechanisms not included in the model), then they will be carried to large amplitudes along the outer branch of the separatrix. Also, since a real beam would not have an exactly uniform core, the injected beam could already have a low density tail that extends into the resonance region, and under the dynamics of the model these particles would be carried to large amplitude and form a halo.

Despite its simplicity, the particle-core model in a constant focusing channel predicts a maximum halo amplitude that is in excellent agreement with high resolution particle simulations run on the CM-5 massively parallel computer at the Los Alamos Advanced Computing Laboratory [9]. Figure 2 shows particle simulation results for a mismatched KV beam having the same

*Work supported by the U.S. Department of Energy, Office of High Energy Physics and Office of Mathematics, Information and Computer Science

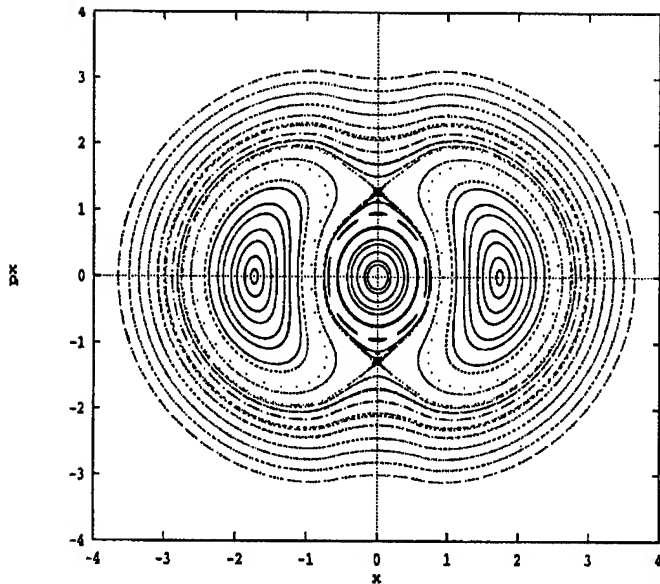


Figure 1. Stroboscopic phase space plot based on the particle-core model with a tune depression of 0.5 and an initial radius 0.62 times the matched radius. The location of 32 test particles is plotted every time the beam envelope reaches a minimum, for a total of 1000 oscillations.

parameters as Figure 1 (a tune depression of 0.5 and an initial beam size that is 0.62 times the matched value). Though the initial distribution has the property that it is uniform in (x, p_x) -space, it is unstable for the parameters chosen, and the resulting phase space of Figure 2 is highly nonuniform. (The threshold for this instability has recently been determined analytically by Gluckstern and his colleagues [10].) The first curve bounding the chaotic band in Figure 1 is also shown in Figure 2 for comparison. The CM-5 results show that for this simple configuration (an axially symmetric beam in a constant focusing channel) the maximum particle amplitudes are in excellent agreement with the amplitude of the separatrix in the particle-core model.

III. THE PARTICLE-CORE MODEL IN A QUADRUPOLE CHANNEL

The application of the particle-core model to a periodic focusing channel is much more complicated than in a constant focusing channel: In a constant focusing channel there is one frequency driving the dynamics, namely the frequency of the oscillating core; the same is true for a *matched* beam in a periodic transport system. But a mismatched beam in a periodic channel does not normally oscillate at a single frequency, and this means that stroboscopic plots, which were so useful in illuminating the underlying physics in the constant focusing case (e.g. the period-2 resonance) are not as applicable here. It should be noted, however, that if one linearizes the mismatch then it is possible to excite a single “even” or “odd” mode by a careful choice of initial conditions. This has been done by Lagniel [11].

In the case of a matched beam with little or moderate tune depression, i.e. a tune depression between 1 (no space charge) and 0.5, the envelope flutter does not appear to be a source of halo formation. Consider for example a matched KV beam in a

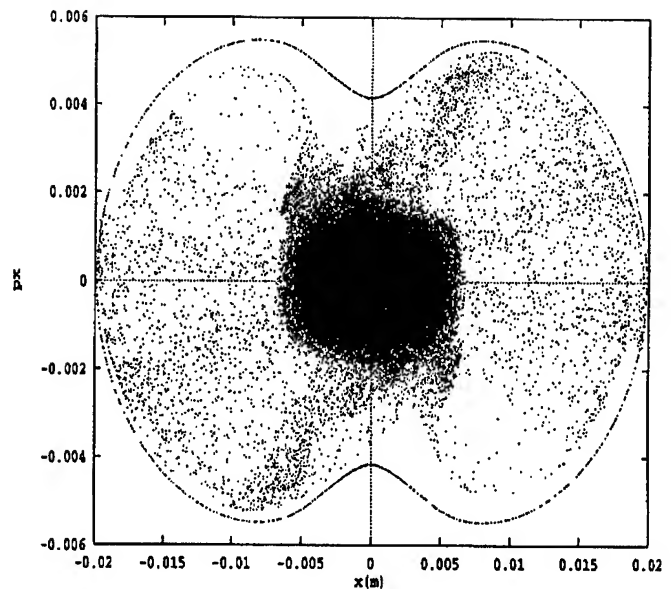


Figure 2. Beam phase space from a 2 million particle simulation on the CM-5 (65536 points are plotted). The outer peanut-shaped set of points were obtained from the particle-core model. The CM-5 results show that, for this configuration (an axially symmetric beam in a constant focusing channel), the particle-core model provides a good estimate of the maximum particle amplitudes.

FODO channel with a zero-current phase advance per focusing period of 70 degrees/cell which is depressed by space charge to 35 degrees/cell. A stroboscopic plot for a collection of test particles in such a system is shown in Figure 3; the data points are recorded at the center of each horizontally focusing quadrupole where the matched horizontal beam size is $x_{\text{edge}} = 4.6\text{mm}$ (i.e. $x_{\text{rms}} = 2.3\text{mm}$). It is clear that the period-2 resonant structure is not present in this case. Though other resonances and weak chaos are present, they do not provide a path by which particles can be transported to large amplitudes. Figure 4 shows particle simulation results for an initially rms matched Gaussian beam in this channel after 22 periods. A large amplitude halo is *not* present. In contrast, Figure 5 shows the situation when the initial beam has the horizontal and vertical rms envelopes too small by a factor of 0.6. Now a significant halo is present. It is worth noting that in the matched case the emittance growth (due to charge redistribution) is only 6%, while in the mismatched case it is approximately a factor of 2.

Since most of the projects mentioned previously will operate with somewhat modest space charge (i.e. tune depressions greater than 0.5) envelope flutter in matched beams is not expected to cause halo formation. However, it is important to note that, in the more space charge dominated regime, matched beams in FODO channels can in fact develop halos [12]. This has important ramifications for heavy ion fusion drivers.

IV. NUMERICAL MODELING OF BEAM HALO USING MASSIVELY PARALLEL PROCESSORS

For many of the projects mentioned above the fraction of particles lost in the accelerator must be kept below one part in 10^5 .

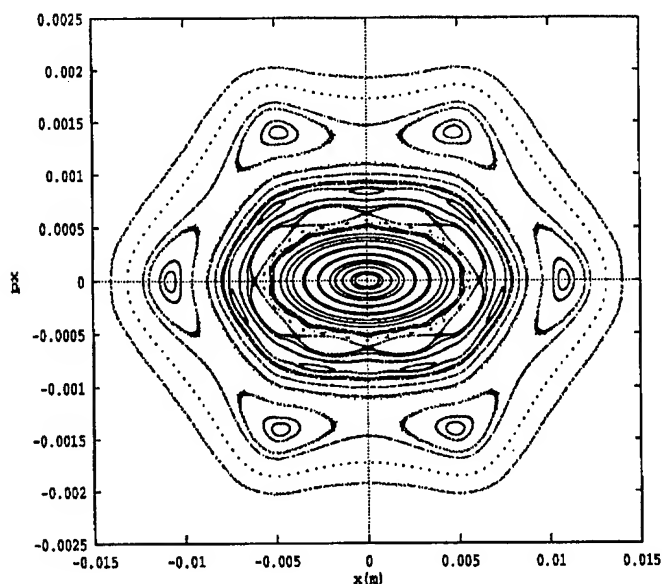


Figure 3. Stroboscopic phase space plot based on the particle-core model for a matched KV beam in a quadrupole channel. Zero-current phase shift/cell and depressed phase shift/cell are $\sigma_0 = 70$ deg, $\sigma = 35$ deg, respectively.

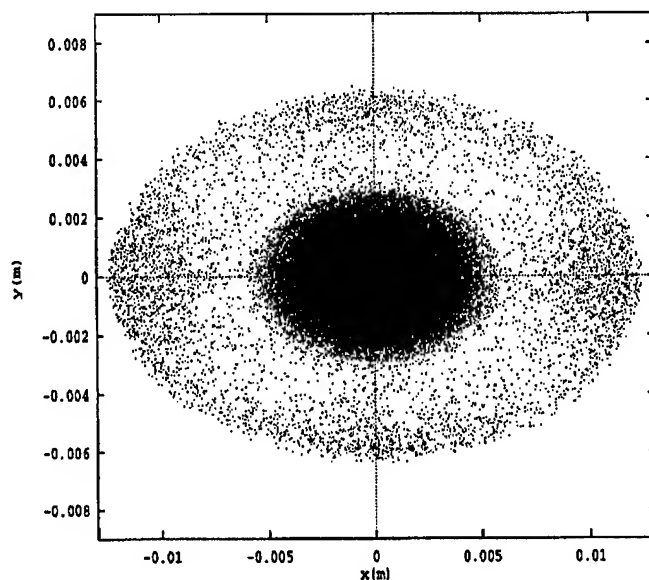


Figure 5. Simulation results showing the beam phase space after 22 focusing periods in a FODO channel. The initial distribution is an rms mismatched Gaussian beam. ($\sigma_0 = 70$ deg, $\sigma = 35$ deg)

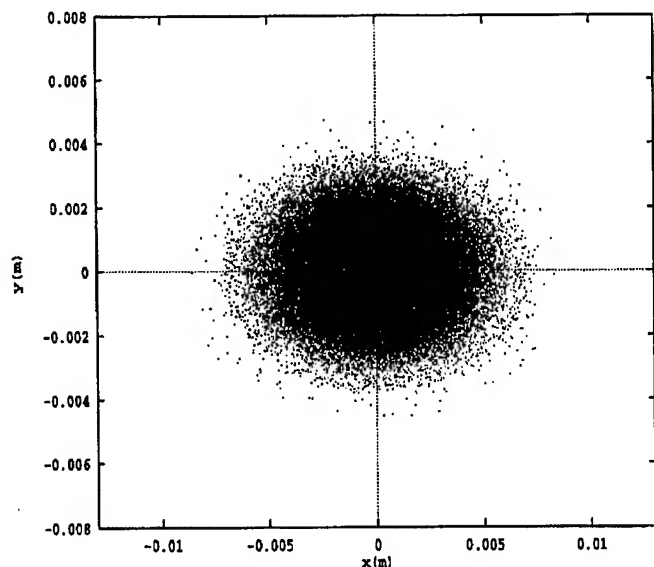


Figure 4. Simulation results showing the beam phase space after 22 focusing periods in a FODO channel. The initial distribution is an rms matched Gaussian beam. ($\sigma_0 = 70$ deg, $\sigma = 35$ deg)

This suggests that one would like to perform numerical simulations with at least 10^7 particles: If the simulation resulted in there being 100 particles in the halo (corresponding to a fractional loss of 10^{-5}), then the error associated with that number would be roughly $1/\sqrt{100} = 10\%$, which is adequate for beam halo studies. (Of course, one has to question whether or not the codes contain all the relevant physics needed to accurately predict halo formation.) Such large scale simulations are well suited to massively parallel processors. Particle simulation codes that are used to study beam halo have been developed for the CM-5 at the Los Alamos Advanced Computing Laboratory [13]. The codes perform numerical integration

of the particles' equations of motion using a second order or fourth order symplectic integration algorithm [14][15]. In a one-dimensional (radially symmetric) version of the code the space charge field is found using Gauss's law, and it involves simply using a mathematical library routine for ordering the particles in radius. In two- and three-dimensional Particle-In-Cell versions of the codes an area weighting scheme is used for the charge deposition and field interpolation; for performance reasons this is implemented using a somewhat complicated scheme that was originally developed for cosmological simulations [16].

Besides using particle simulations, it is possible to solve the Vlasov/Poisson equations directly, and this has also been implemented on the CM-5 in one and two dimensions. A Vlasov/Poisson code solves the equation

$$\frac{\partial f}{\partial t} + (\vec{p} \cdot \partial_{\vec{x}})f - (\nabla V \cdot \partial_{\vec{p}})f = 0, \quad (1)$$

where $f(\zeta, t)$ is a distribution function on phase space ($\zeta = (\vec{x}, \vec{p})$). The potential V is a sum of an externally applied potential and a space charge potential which is obtained self-consistently from Poisson's equation. To solve this equation on the CM-5, we utilize a spectral method coupled with split-operator symplectic integration algorithms [14]. For example, a second-order accurate stepping algorithm for the Vlasov/Poisson equation is given by

$$f(\zeta, t) = \mathcal{M}(t)f(\zeta, t=0). \quad (2)$$

where the mapping \mathcal{M} is given by

$$\mathcal{M}(t) = e^{-\frac{t}{2}(\vec{p} \cdot \partial_{\vec{x}})} e^{t(\nabla V \cdot \partial_{\vec{p}})} e^{-\frac{t}{2}(\vec{p} \cdot \partial_{\vec{x}})}. \quad (3)$$

In the context of symplectic integration algorithms, Yoshida showed how to take an algorithm of order $2n$ and use it to construct an algorithm of order $2n+2$ [15]. For example, the above

second-order algorithm can be used to construct a fourth order algorithm,

$$f(\zeta, t) = \mathcal{M}(z_0 t) \mathcal{M}(z_1 t) \mathcal{M}(z_0 t) f(\zeta, t=0), \quad (4)$$

where

$$z_0 = \frac{1}{2 - 2^{1/3}}, \quad (5)$$

$$z_1 = -\frac{2^{1/3}}{2 - 2^{1/3}}. \quad (6)$$

Output from a two dimensional Vlasov/Poisson code is shown in Figure 6. The initial distribution was a Gaussian in four-dimensional phase space that was mismatched into a quadrupole channel. The simulation utilized a 128^4 grid for a total of 268 million grid points.

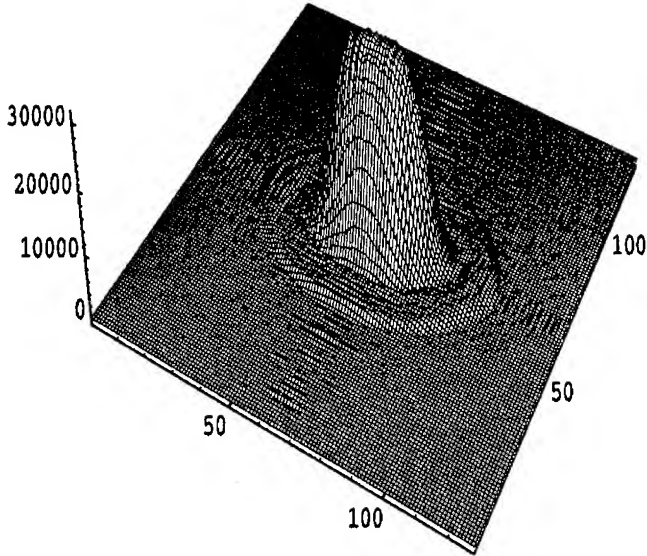


Figure 6. Output from a direct Vlasov/Poisson simulation performed on the CM-5 showing the beam density at one location in a quadrupole channel. The four-dimensional distribution function was integrated over momenta to obtain the beam density on a 128×128 grid.

Though this paper emphasizes modeling beam halo, it is worth pointing out that this approach can be applied to several other classical and quantum systems. For example, the Vlasov code can be modified to study gravitating systems. Also, to model the Schrödinger equation,

$$i\hbar \frac{\partial \psi}{\partial t} = -\frac{\hbar^2}{2m} \nabla^2 \psi + V\psi, \quad (7)$$

a second-order algorithm is given by

$$\psi(\vec{x}, t) = e^{\frac{i\hbar}{4m} \nabla^2} e^{-\frac{it}{\hbar} V(\vec{x})} e^{\frac{i\hbar}{4m} \nabla^2} \psi(\vec{x}, t=0). \quad (8)$$

In fact, this is precisely the algorithm used by Feit and Fleck to study a variety of quantum systems, including the vibrational energy levels of triatomic molecules [17]. Using Yoshida's technique, it is in principle possible to obtain high order Schrödinger codes, and a fourth order Schrödinger code has already been developed for the CM-5. Similar codes for evolving the density matrix and the Wigner distribution function, both in the absence and presence of dissipation and noise, have also been developed.

V. THREE DIMENSIONAL MODELING OF RF LINACS

Most beam halo studies have previously dealt with one- and two-dimensional systems. In the future it will be important to model beam halo in linacs in three dimensions. High resolution simulations should utilize a few times 10^7 particles and a three-dimensional grid (for space charge calculations) whose size is roughly 256^3 ; this is based on the assumption that, if the beam occupies some reasonable fraction of the grid points (e.g. one half) then there will be a few particles per grid point, as has been found to be adequate for modeling intense beams with PIC codes. (It is interesting to note, however, that for gravitational N-body codes used to model large scale structure formation in the early universe one normally requires only 1/8 particle per grid point.)

Recently there has been much progress in modeling rf linacs, including accurate treatment of the dynamics in the rf gaps [18][19][20]. Also, even when there is acceleration it is still possible to use split operator symplectic integration algorithms to evolve the particles, but it is useful to perform an additional transformation on the Hamiltonian before applying the algorithm. For example, suppose the vector potential for an rf gap is given by

$$\begin{aligned} A_x &= \frac{e'(z)}{2\omega_\alpha} x \sin(\omega_\alpha t + \theta) \\ A_y &= \frac{e'(z)}{2\omega_\alpha} y \sin(\omega_\alpha t + \theta) \\ A_z &= -\frac{1}{\omega_\alpha} \left\{ e(z) - \frac{r^2}{4} [e''(z) + \frac{\omega_\alpha^2}{c^2} e(z)] \right\} \sin(\omega_\alpha t + \theta), \end{aligned} \quad (9)$$

where $e(z)$ denotes the spatial part of the electric field at $r=0$,

$$E_z(r=0) = e(z) \cos(\omega_\alpha t + \theta), \quad (10)$$

and where a prime denotes d/dz . Then the transformed Hamiltonian for a system consisting of magnetic quadrupoles and rf gaps, paraxial in the external fields, is given by $H = H_x + H_y + H_\phi + H_{sc}$, where

$$H_x = \frac{1}{2l} \tilde{p}_x^2 + \frac{l\Omega_x}{2} \tilde{x}^2 + \frac{qlg_m}{2p_o} \tilde{x}^2, \quad (11)$$

$$H_y = \frac{1}{2l} \tilde{p}_y^2 + \frac{l\Omega_y}{2} \tilde{y}^2 - \frac{qlg_m}{2p_o} \tilde{y}^2, \quad (12)$$

$$H_\phi = \frac{\tilde{p}_\phi^2}{2l} + \frac{l\Omega_\phi}{2} \tilde{\phi}^2, \quad (13)$$

$$H_{sc} = \frac{q\Psi}{l\delta\gamma_o^2\beta_o c}. \quad (14)$$

In the above equations g_m denotes the magnetic quadrupole gradient, Ψ denotes the space charge potential, l is a scale length, and p_o is the momentum of the synchronous particle. The quantities Ω_x , Ω_y , and Ω_ϕ are given by

$$\begin{aligned} \Omega_x = \Omega_y &= \frac{(q/mc^2)(\omega_\alpha/c)}{2\beta_o^3\gamma_o^3} e \sin \phi_s \\ &+ \frac{1}{2} \left(1 + \frac{\gamma_o^2}{2}\right) \left(\frac{(q/mc^2)e \cos \phi_s}{\beta_o^2\gamma_o^2} \right)^2, \end{aligned} \quad (15)$$

$$\Omega_\phi = \frac{(\beta_o^2 + \frac{1}{2})}{\beta_o^3 \gamma_o} (q/mc^2) (\omega_\alpha/c) e \sin \phi_s \quad (16)$$

$$- \frac{3}{2} \frac{q/mc^2}{\beta_o^2 \gamma_o} e' \cos \phi_s + \frac{3}{2} \left(1 - \frac{\gamma_o^2}{2}\right) \left(\frac{(q/mc^2) e \cos \phi_s}{\beta_o^2 \gamma_o^2} \right)^2,$$

where β_o and γ_o are the relativistic factors on the synchronous trajectory, and where $\phi_s = \omega_\alpha t_o(z) + \theta$ is the phase of the synchronous particle. The above single particle Hamiltonian was used as a starting point for deriving three-dimensional envelope equations in rf linacs, and this was in turn used to develop a procedure, based on a Hamiltonian formulation of the envelope equations, to find matched beams in rf linacs [21]. The concept of an envelope Hamiltonian has also been used in analytical studies of halo formation [22],[23].

VI. SUMMARY

Much has been learned about the physics of beam halo, both from a theoretical and computational viewpoint. Most importantly, beam mismatch has been identified as a major source of beam halo. The particle-core model predicts a maximum halo extent which is in excellent agreement with multi-million particle simulations. Also, it has been found that envelope flutter associated with alternating gradient channels is not a significant source of halo formation. Previous work has emphasized one- and two-dimensional analysis and modeling of beam halo. In the future, more difficult three-dimensional issues will have to be addressed.

References

- [1] D. Kehne, M. Reiser, and H. Rudd, 1991 Particle Accelerator Conference, San Francisco, CA, p. 248 (1991).
- [2] A. Cucchetti, M. Reiser, and T. Wangler, 1991 Particle Accelerator Conference, San Francisco, CA, p. 251 (1991).
- [3] J. O'Connell *et al*, 1993 Particle Accelerator Conference, Washington, DC, p. 3657 (May 1993).
- [4] J. Lagniel, *Nucl. Inst. Meth.* A345, 46 (1994).
- [5] J. Lagniel, *Nucl. Inst. Meth.* A345, 405 (1994).
- [6] T. Wangler, Los Alamos Report LA-UR-94-1135 (1994).
- [7] R. Gluckstern, *Phys. Rev. Lett.* **73**, p. 1247 (1994).
- [8] R. Jameson, US-CERN-Japan Topical Course on Accelerator Physics and Technology (1994).
- [9] R. Ryne, T. Wangler, and S. Habib, International Conference on Accelerator Driven Transmutation Technologies and Applications, Las Vegas, NV (July 1994).
- [10] R. Gluckstern, private communication.
- [11] J. Lagniel, private communication.
- [12] Q. Qian, R. Davidson and C. Chen, *Phys. Plasma*, **2**, p.2674 (1995).
- [13] R. Ryne, and S. Habib, Energy Research Power Users Symposium, Rockville, MD (July 1994).
- [14] E. Forest and R. Ruth, *Physica D* **43**, 105 (1990).
- [15] H. Yoshida, *Phys. Lett. A* **150**, 262 (1990); E. Forest *et al*, *Phys. Lett. A* **158**, 99 (1991).
- [16] R. Ferrell and E. Bertschinger, *Intl. J. Mod. Phys. C* (1994).
- [17] M. Feit and J. Fleck, Jr., *J. Chem. Phys.* **78**, 301 (1983); M. Feit *et al*, *J. Comp. Phys.* **47**, 412 (1982); M. Hermann and J. Fleck, Jr., *Phys. Rev. A*, **38**, 38 (1988).

- [18] R. Ryne, Los Alamos Report LA-UR-95-1523, April 1995.
- [19] J. van Zeijts, these proceedings.
- [20] P. Lapostolle, E. Tanke, and S. Valero, *Particle Accelerators* **44**, p. 215 (1994).
- [21] R. Ryne, Los Alamos Report LA-UR-95-391, February 1995.
- [22] S. Lee and A. Riabko, *Phys. Rev. E* **51**, p. 1609 (1995).
- [23] A. Riabko *et al.*, *Phys. Rev. E* **51**, p. 3529 (1995).

POLARIZED PROTON BEAMS*

T. Roser, Brookhaven National Laboratory, Upton, N.Y. 11973, USA

Abstract

The acceleration of polarized proton beams in circular accelerators is complicated by the presence of numerous depolarizing spin resonances. Careful and tedious minimization of polarization loss at each of these resonances allowed acceleration of polarized proton beams up to 22 GeV. It has been the hope that Siberian Snakes, which are local spin rotators inserted into ring accelerators, would eliminate these resonances and allow acceleration of polarized beams with the same ease and efficiency that is now routine for unpolarized beams. First tests at IUCF with a full Siberian Snake showed that the spin dynamics with a Snake can be understood in detail. We now have results of the first tests of a partial Siberian Snake at the AGS, accelerating polarized protons to an energy of about 25 GeV. These successful tests of storage and acceleration of polarized proton beams open up new possibilities such as stored polarized beams for internal target experiments and high energy polarized proton colliders.

I. INTRODUCTION

The acceleration of polarized beams in circular accelerators is complicated by the presence of numerous depolarizing resonances. During acceleration, a depolarizing resonance is crossed whenever the spin precession frequency equals the frequency with which spin-perturbing magnetic fields are encountered. There are two main types of depolarizing resonances corresponding to the possible sources of such fields: imperfection resonances, which are driven by magnet errors and misalignments, and intrinsic resonances, driven by the focusing fields.

The resonance conditions are usually expressed in terms of the spin tune ν_s , which is defined as the number of spin precessions per revolution. For an ideal planar accelerator, where orbiting particles experience only the vertical guide field, the spin tune is equal to $G\gamma$ [1], where $G = 1.7928$ is the anomalous magnetic moment of the proton and γ is the relativistic Lorentz factor. The resonance condition for imperfection depolarizing resonances arise when $\nu_s = G\gamma = n$, where n is an integer. Imperfection resonances are therefore separated by only 523 MeV energy steps. The condition for intrinsic resonances is $\nu_s = G\gamma = kP \pm \nu_y$, where k is an integer, ν_y is the vertical betatron tune and P is the superperiodicity. For the AGS, $P = 12$ and $\nu_y \approx 8.8$. For most of the time during the acceleration cycle, the precession direction, or stable spin direction, coincides with the main vertical magnetic field. Close to a resonance, the stable spin direction is perturbed away from the vertical direction by the resonance driving fields. When a polarized beam is accelerated through an isolated resonance, the final polarization can be calculated analytically[2] and is given by

$$P_f/P_i = 2e^{-\frac{\pi|\epsilon|^2}{2\alpha}} - 1,$$

where P_i and P_f are the polarizations before and after the resonance crossing, respectively, ϵ is the resonance strength obtained from the spin rotation of the driving fields, and α is the change of the spin tune per radian of the orbit angle. When the beam is slowly ($\alpha \ll |\epsilon|^2$) accelerated through the resonance, the spin vector will adiabatically follow the stable spin direction resulting in spin flip. However, for a faster acceleration rate partial depolarization or partial spin flip will occur. Traditionally, the intrinsic resonances are overcome by using a betatron tune jump, which effectively makes α large, and the imperfection resonances are overcome with the harmonic corrections of the vertical orbit to reduce the resonance strength ϵ [3]. At high energy, these traditional methods become difficult and tedious.

By introducing a 'Siberian Snake' [4], which is a 180° spin rotator of the spin about a horizontal axis, the stable spin direction remains unperturbed at all times as long as the spin rotation from the Siberian Snake is much larger than the spin rotation due to the resonance driving fields. Therefore the beam polarization is preserved during acceleration. An alternative way to describe the effect of the Siberian Snake comes from the observation that the spin tune with the Snake is a half-integer and energy independent. Therefore, neither imperfection nor intrinsic resonance conditions can ever be met as long as the betatron tune is different from a half-integer.

Such a spin rotator can be constructed by using either solenoidal magnets or a sequence of interleaved horizontal and vertical dipole magnets producing only a local orbit distortion. Since the orbit distortion is inversely proportional to the momentum of the particle, such a dipole snake is particularly effective for high-energy accelerators, e.g. energies above about 30 GeV. For lower-energy synchrotrons, such as the Fermilab booster and the Brookhaven AGS with weaker depolarizing resonances, a partial snake[5], which rotates the spin by less than 180°, is sufficient to keep the stable spin direction unperturbed at the imperfection resonances.

II. IUCF SIBERIAN SNAKE TESTS

The IUCF Cooler ring operates at a kinetic proton beam energy between 40 MeV and 500 MeV, which spans two spin resonances: $G\gamma = 2$ and $G\gamma = 7 - \nu_y$. The low energy and the availability of long straight sections and also of polarized proton beam made this ring ideal for a first proof-of-principle test of Siberian Snakes. A solenoidal spin rotator was installed that was capable of rotating the spin by 180° around the beam direction and a internal target and a detector with full azimuthal coverage. Over the course of many detailed experiments it was clearly established that the spin dynamics and, in particular, the spin tune of a stored polarized beam can be manipulated using a local spin rotator. Most significantly the spin tune is indeed a half-integer with a full Siberian Snake as is shown in Fig. 1. To measure the spin tune an artificial spin resonance with adjustable driving field and frequency is used. Since the driving field for the ar-

*Work performed under the auspices of the U.S. Department of Energy

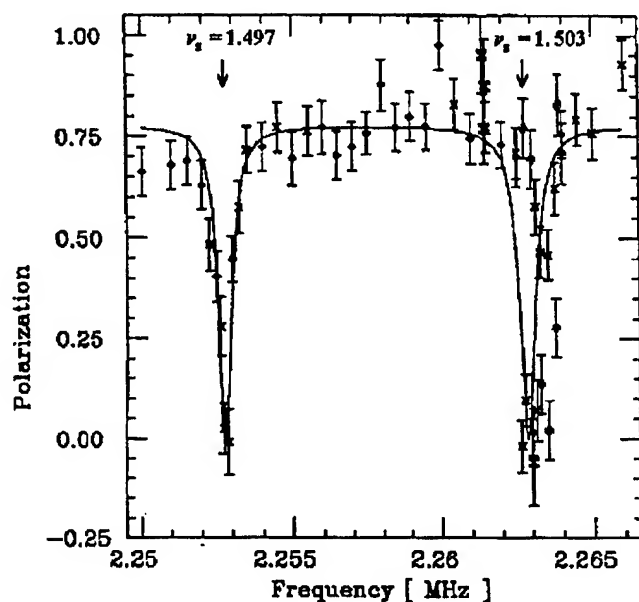


Figure 1. Measured beam polarization vs. frequency of an artificial spin resonance. The depolarizing resonance indicates the spin tune ν_s .

tificial spin resonance was in fact a oscillating horizontal field it simultaneously produced two resonances corresponding to the decomposition into two counter-rotating fields. By adjusting the current in the solenoid Snake the spin tune can easily be tuned to be exactly a half-integer. However, this adjustment is not critical as long as the betatron tune is chosen appropriately.

The ability to excite an artificial resonance is also very useful for experiments that use stored polarized proton beams with a long lifetime such as internal target experiments or colliding beam experiments. In these cases the artificial resonance can be used to reverse or flip the polarization of the stored beam periodically to minimize systematic errors of the experiments. The team at IUCF successfully used their artificial resonance driving field to demonstrate the feasibility of reversing the polarization multiple times without significant polarization loss[6]. Fig. 2 shows the result of repeated spin reversals of the stored polarized beam which was accomplished by slowly ramping the frequency of the artificial resonance through the resonance condition. In a ring with a Siberian Snake and therefore with a half-integer spin tune such a spin flipper resonance would need to be created with a true rotating field to generate only a single resonance. Designs for such devices that can be used in high energy accelerators would typically consist of orbit bumps that are excited at the spin precession frequency[7].

III. AGS PARTIAL SIBERIAN SNAKE TESTS

Two polarized beam test runs of experiment E-880 at the AGS have recently demonstrated the feasibility of polarized proton acceleration using a 5% partial Siberian Snake. During the first run[8] in April 1994 it was shown that a 5% Snake is sufficient to avoid depolarization due to the imperfection resonances without using the harmonic correction method. Fig. 4 shows the evolution of the beam polarization as the beam energy and therefore

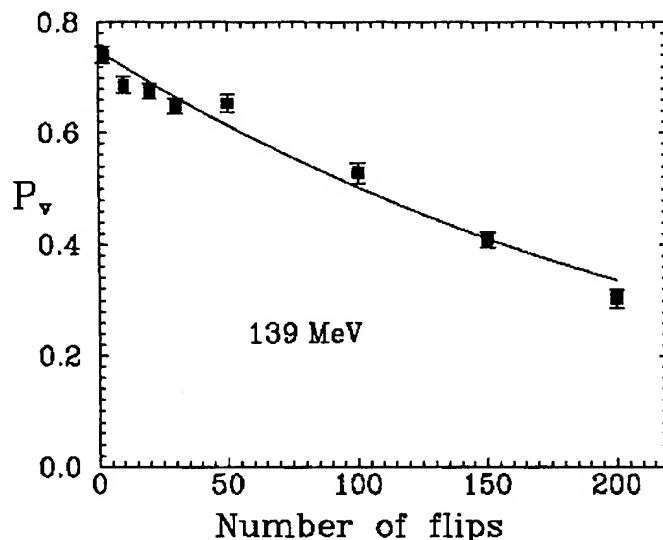


Figure 2. Final measured polarization as a function of spin flips[6].

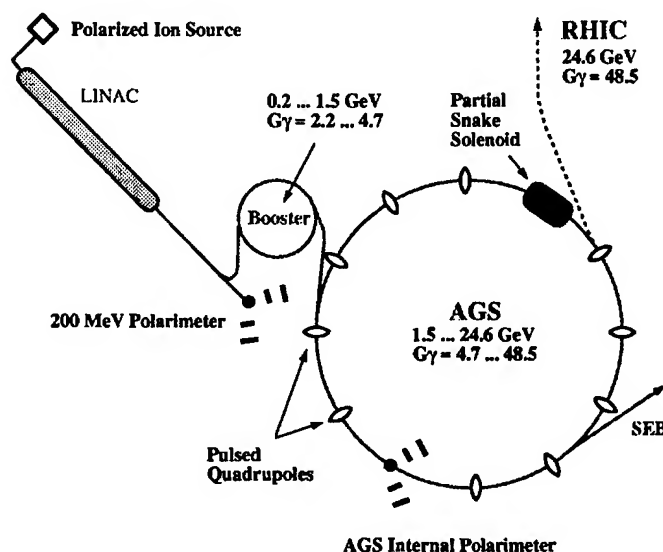


Figure 3. Layout of the AGS accelerator complex showing the location of the Partial Siberian Snake, the pulsed quadrupoles, and the AGS internal polarimeter

$G\gamma$ is increased. As predicted the polarization reverses the sign whenever $G\gamma$ is equal to an integer.

Fig. 5 shows the achieved polarization as a function of beam energy. It shows that no polarization was lost at the imperfection resonances. The only polarization loss occurred at the location of the intrinsic resonances for which the pulsed quadrupoles are required for the tune jump method. During the first run the pulsed quadrupoles were not available. During the second run in December 1994 it was shown that it is possible to use the tune jump method in the presence of the partial Snake. A new record energy for accelerated polarized beam of 25 GeV was reached with about 12% beam polarization left. Again no polarization was lost due to the imperfection resonances and depolarization

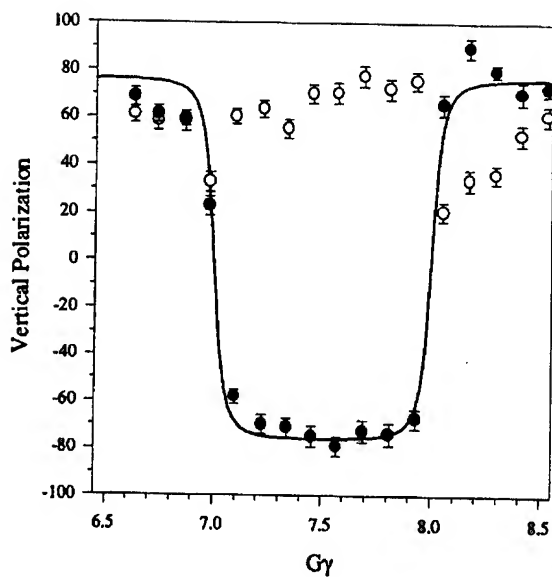


Figure 4. The measured vertical polarization as a function of the spin tune $G\gamma$ for a 10% snake is shown with and without a snake. Note here that partial depolarization at $G\gamma = 8$ is avoided by using a 10% snake. The solid line is the predicted energy dependence of the polarization.

from most intrinsic resonances was avoided with the tune jump quadrupoles. However, as can be seen from Fig. 5, significant amount of polarization was lost at $G\gamma = 0 + \nu_y$, $12 + \nu_y$ and $G\gamma = 36 + \nu_y$. The first two of these three resonances were successfully crossed previously and it will require further study to explain the unexpected polarization loss. The strength of the tune jump quadrupoles is not sufficient to jump the last resonance. We attempted to induce spin flip at this resonance but were only partially successful. During the next study run the method of inducing spin flip at intrinsic resonances will be further investigated[9].

IV. TOWARDS A POLARIZED PROTON COLLIDER

With the successful tests of Siberian Snakes the stage is set for the acceleration of polarized proton beams to much higher energies to be used in collider experiments to explore spin effects at the highest energies attainable. Two efforts are presently underway to develop Snakes designs for high energy accelerators. In the first project polarized protons from the Brookhaven AGS will be injected into the two RHIC rings to allow for up to $\sqrt{s} = 500 \text{ GeV}$ collisions with both beams polarized[10]. Fig. 6 shows the lay-out of the Brookhaven accelerator complex highlighting the components required for polarized beam acceleration.

Of particular interest is the design of the Siberian Snakes (two for each ring) and the spin rotators (four for each collider experiment) for RHIC. Proposed by V. Ptitsin and Yu. Shatunov from BINP[11], it is based on helical dipole magnet modules each having a full 360 degree helical twist. Using helical magnets minimizes orbit excursions within the extend of the Snake or spin rotator[12] which is most important at injection energy. Fig.

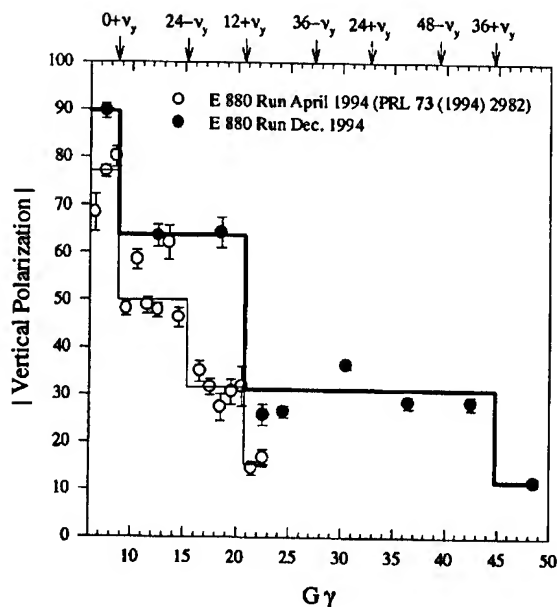


Figure 5. The measured absolute value of the vertical polarization at $G\gamma = n + \frac{1}{2}$ up to $G\gamma = 48.5$ which corresponds to an energy of 25 GeV . The partial depolarization is due to intrinsic spin resonances at $G\gamma$ values indicated at the top of the figure. The results from the Dec. 1994 run are preliminary.

7 shows the aluminum former for the prototype helical dipole magnet now under construction at Brookhaven. The construction of a large bore high field helical dipole presents a formidable challenge for present superconducting magnet technology.

The second project consists of accelerating polarized protons in the Tevatron replacing some of the Tevatron dipole magnets with higher field magnets to gain space to install the six required Siberian Snakes[13]. The project focuses on single spin collider experiments since at this time it is not feasible to polarize anti-protons, although the results discussed in the following section could open up the possibility of polarized anti-protons in the future.

With one or two Snakes all depolarizing resonances should be avoided since the spin tune is a half-integer independent of energy. However, if the spin disturbance from small horizontal fields is adding up sufficiently between the Snakes depolarization can still occur. This is most pronounced when the spin rotation from all the focusing fields add up coherently which is the case at the strongest intrinsic resonances. At RHIC two Snakes can still cope with the strongest intrinsic resonance whereas at the Tevatron six Snakes will be needed. At the energies of these strongest intrinsic resonances the betatron tune has to be adjusted very carefully to avoid the accumulation of the spin rotation of the focusing fields over more than one turn which would occur for a fractional part of the betatron tune of $\Delta\nu_y = (\frac{1}{2} \pm k)/n$, where both k and n are integers. These so called 'Snake resonances' conditions[14] are now energy independent and are the same as the location of the stop-band resonances. Therefore, with Siberian Snakes orbit and polarization stability conditions coincide.

Polarized Proton Collisions at BNL

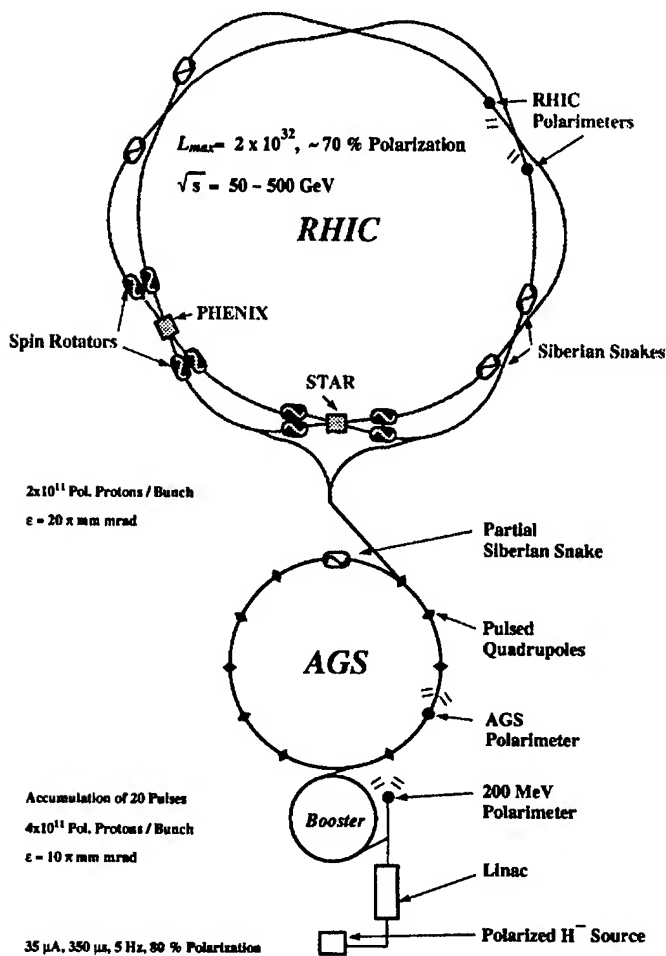


Figure 6. The Brookhaven hadron facility complex, which includes the AGS Booster, the AGS, and RHIC. The RHIC spin project will install two snakes per ring with four spin rotators per detector for achieving helicity-spin experiments.

V. POLARIZATION BUILD-UP IN STORAGE RINGS

Several people have proposed schemes to build-up the polarization of a stored beam using the fact that a small spin effect can lead to a sizable polarization if it accumulates over many million revolutions. In fact, high levels of electron polarization are being achieved routinely using the very small spin flip probability during the emission of synchrotron radiation. The motivation for such schemes is two-fold: by polarizing the beam after acceleration the depolarization from passing through the many spin resonances can be avoided and, maybe more importantly, such a scheme could also be used to produce a polarized anti-proton beam. Now, for the first time, a positive result was achieved at the Test Storage Ring in Heidelberg[15]. A polarized internal hydrogen gas target was inserted and the polarization of the circulating proton beam started to build-up reaching a maximum value of about 2% after about 90 minutes. This result is shown in Fig. 8. The beam polarization was measured before and after

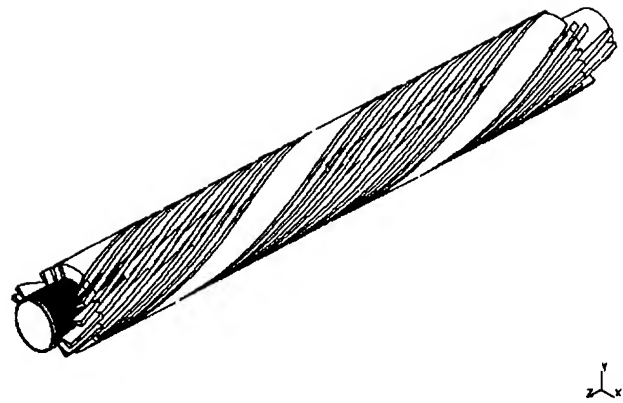


Figure 7. Aluminum former for the helical dipole magnet prototype under construction at BNL

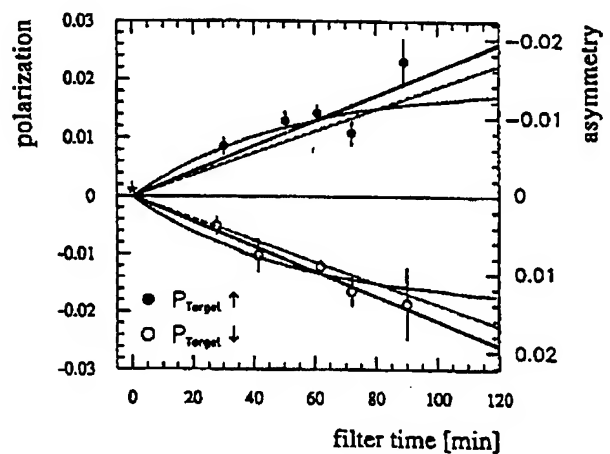


Figure 8. Polarization build-up measurements at the Heidelberg Test Storage Ring.

the build-up process using proton-alpha scattering as analyzing reaction. Three different processes contribute to the polarization build-up. The first process is spin dependent beam loss due to proton-proton scattering out of the storage ring acceptance. The remaining two effects are due to polarization transfer from either the proton or the electron to the beam proton. The polarization transfer from the electron has the opposite sign of the other two effects. The combination of all three effects is in very good agreement with the measured result.

There is no data available on the nuclear spin dependent effects between anti-proton and protons. However, the polarization transfer from polarized electrons to anti-protons can be calculated[16]. For the first time, we seem to have a realistic scheme to produce polarized anti-proton beams.

VI. CONCLUSIONS

Over the last years several new tools have become available for the acceleration and manipulation of polarized proton beams. The Siberian Snake concept has been proven to be correct and the first partial Snake has been used in a high energy accelerator. Artificial spin resonances have been used extensively as diagnostic

tools and also for spin flipping. And, in the more distant future, it might even be possible to create polarized anti-proton beams for use in high energy accelerators. With all these advances, polarized beam operation should become more of an integral part of future high energy proton accelerators.

References

- [1] L.H. Thomas, Phil. Mag. **3**, 1 (1927); V. Bargmann, L. Michel, V.L. Telegdi, Phys. Rev. Lett. **2**, 435 (1959).
- [2] M. Froissart and R. Stora, Nucl. Instr. Meth., **1**, 297 (1960).
- [3] T. Khoe et al., Part. Accel. **6**, 213 (1975); J.L. Laclare et al., J. Phys. (Paris), Colloq. **46**, C2-499 (1985); H. Sato et al., Nucl. Instr. Meth., Phys. Res. Sec **A272**, 617 (1988); F.Z. Khiari, et al., Phys. Rev. D **39**, 45 (1989).
- [4] Ya.S. Derbenev et al., Part. Accel. **8**, 115 (1978).
- [5] T. Roser, AIP Conf. Proc. No. 187, ed. K.J. Heller p.1442 (AIP, New York, 1988).
- [6] D.D. Caussyn et al., Phys. Rev. Lett. **73**, 2857 (1994)
- [7] T. Roser, Nucl. Instr. and Methods, **A 342**, 343 (1994), R.A. Phelps p.225 and T. Roser p. 73 in Proc. 3. Workshop on Siberian Snakes and Spin Rotators (A.Luccio and T.Roser Eds.) Upton, NY, Sept. 12-13, 1994, BNL-52453.
- [8] H.Huang et al., Phys. Rev. Lett. **73**, 2982 (1994)
- [9] T. Roser, in Proc. of the 10th Int. Symp. on High Energy Spin Physics, Nagoya, Japan, p. 429 (1992).
- [10] Proposal on Spin Physics Using the RHIC Polarized Collider (R5), submitted to the BNL PAC October 1992
- [11] V.I.Ptitsin and Yu.M.Shatunov, Helical Spin Rotators and Snakes, Proc. 3. Workshop on Siberian Snakes and Spin Rotators (A.Luccio and T.Roser Eds.) Upton, NY, Sept. 12-13, 1994, BNL-52453, p.15
- [12] A. Luccio and F. Pilat, 'Insertion of Helical Siberian Snakes in RHIC', this conference
- [13] 'Acceleration of Polarized Protons to 1 TeV in the Fermilab Tevatron', University of Michigan Report, August 1994.
- [14] S. Tepikian, AIP Conf. Proc. No. 187, ed. K.J. Heller p.1450 (AIP, New York, 1988).
- [15] F. Rathmann et al., Phys. Rev. Lett. **71**, 1379 (1993)
- [16] C.J. Horowitz and H.O. Meyer, Phys. Rev. Lett. **72** 3981 (1994)

BEAM DYNAMICS IN HEAVY ION FUSION

Peter Seidl, Lawrence Berkeley Laboratory, Berkeley, CA 94720 USA

Abstract

A standard design for heavy ion fusion drivers under study in the US. is an induction linac with electrostatic focusing at low energy and magnetic focusing at higher energy. The need to focus the intense beam to a few-millimeter size spot at the deuterium-tritium target establishes the emittance budget for the accelerator. Economic and technological considerations favor a larger number of beams in the low-energy, electrostatic-focusing section than in the high-energy, magnetic-focusing section. Combining four beams into a single focusing channel is a viable option, depending on the growth in emittance due to the combining process. Several significant beam dynamics issues that are, or have been, under active study are discussed: large space charge and image forces, beam wall clearances, halos, alignment, longitudinal instability, and bunch length control. .

I. HEAVY ION FUSION SYSTEM BASED ON INDUCTION LINEAR ACCELERATORS

A standard design for heavy ion fusion drivers under study in the U.S. is sketched in Fig. 1. An ion source and injector supplies 2-3 MeV beams to an electrostatically focused induction linac section (~64 beams). This is followed by a ~16 beam, magnetically focused induction linac section. The 64, later 16, beams are accelerated inside common induction cores. Finally, a compression section shortens the beams to a pulse length appropriate to the constraints of target ignition physics, and the last focusing elements bring the beams to a $r=2-3$ mm spot size.

Because the cost of the induction cores necessary for acceleration to 10 GeV is substantial, there is a premium on compact transverse packing of the parallel beams. Economic and technological considerations favor a larger number of beams in the low-energy, electrostatic-focusing section than in the high-energy, magnetic-focusing section. Combining four beams into a single focusing channel is a viable option, depending on the growth in emittance due to the combining process. (Other driver designs omit beam combining, and some of those use only electric or magnetic focusing, rather than both.)

RF based accelerator technology is the alternative principal heavy-ion driver approach. Storage rings are used

for current multiplication, and it is there that the main challenges of beam dynamics are found. It is being studied in Europe, Russia, and Japan, and is discussed in ref. [1].

II. TARGET CONSTRAINTS ON THE DRIVER BEAM

We consider here indirect-drive targets[2], which have a frozen deuterium-tritium fuel shell inside a radiation enclosure, or hohlraum. The beam energy is deposited in converter material, and secondary, soft x-radiation propagates through the hohlraum, uniformly irradiating and imploding the fuel. Direct-drive targets are heated by the driver beams. In the latter situation, the illumination uniformity on the capsule is tightly coupled to the geometry of the incoming ion beams, and is generally considered to be a less conservative target design. Target design studies show that the driver must deposit ~400 TW for ~10 ns with a ~20 ns prepulse of <100 TW in order to achieve an energy gain of 10-100, or sufficient to make the economics work out favorably for commercial energy production.

Working backwards from ballistic transport with little or no neutralization leads to ~10 GeV kinetic energy with an ion atomic mass of 200. The target constraints establish an emittance budget in the transverse and longitudinal planes, approximately 6π -mm-mrad and 1 eV-s, respectively.

Common to most variants of this 'standard' design are the assumptions of conservatively designed, conventional focusing systems throughout the driver. Another conservative assumption is ballistic transport of un-neutralized beams in the reactor chamber.

More exotic final focusing and chamber transport systems that rely on significant charge and current neutralization could make beam quality control easier. They are being investigated mainly for application near the end of the driver as a means for transporting the beams into the reactor chamber and to the target. Because these techniques are not applicable to most of the driver, much of the accelerator design would remain unchanged with a neutralized final focus at the end. However, the constraints on the number of beams, ion kinetic energy, and emittance could be relaxed. Fewer beams would simplify the interface between the driver and the reactor. The techniques, which are beyond the scope of this paper, include plasma lens focusing [3], and electron co-injection using a grid cathode [4].

* This work was supported by the Director, Office of Energy Research, Office of Fusion Energy, U.S. Dept. of Energy, under Contract No. DE-AC03-76SF00098.

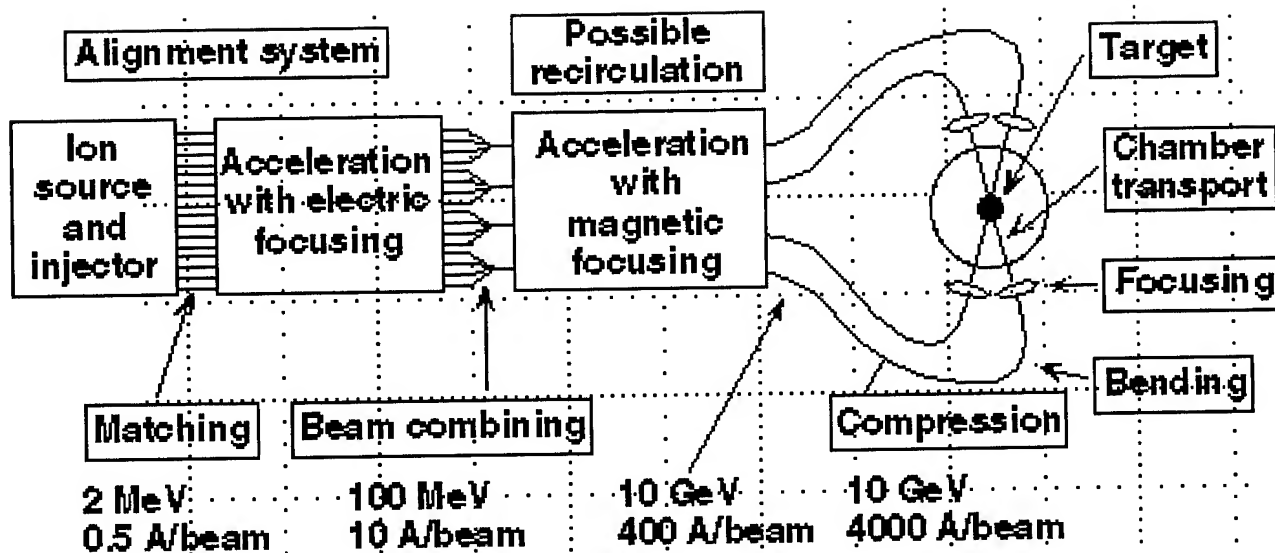


Figure 1: Block diagram of a heavy ion fusion driver. There are 64 beams in the electric focusing section, and 16 beams in the magnetic focusing section.

III. BEAM TRANSPORT

The characteristics of the beam in most of the driver are shown in table 1. The most current is transported when the space charge repulsion of the beam nearly balances the focusing force. The choice of $\sigma_0 < 90$ deg avoids well established instabilities of highly space charge depressed beams for higher tunes. The line charge density is relatively uniform for most of the pulse and quickly drops to zero near the beam ends. Longitudinal repulsion at the ends is balanced by confining voltage pulses timed to coincide with the passage of the ends through the acceleration gaps.

σ_0	70-90 deg
σ	< 20 deg.
λ_{Debye}	~ 1 mm
beam potential	$\sim 3 - 120$ keV
λ (electric section)	$0.20 - 0.30 \mu\text{C/m}$
λ (magnetic section)	$\sim 1 \mu\text{C/m}$ at start $10 \mu\text{C/m}$ near end

Table 1: Beam characteristics in a heavy-ion fusion induction linear accelerator. σ_0 is the single particle tune, or phase advance per lattice period, σ is the space-charge depressed tune, and λ is the line charge density.

The electrostatically focused induction linac section has many parallel beams transported in a common induction linac core as shown in Fig. 2. Adjacent beams share electrodes and almost purely quadrupolar fields can be made from cylindrical electrodes inside much of the physical aperture by judiciously choosing the ratio of the

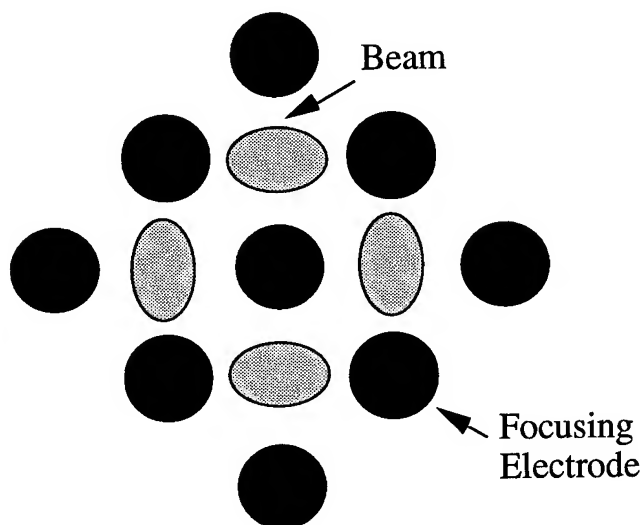


Figure 2: Schematic of part of a multiple beam electrostatic focusing array, showing the elliptical beams.

diameter of the physical aperture to that of the electrodes. The docecapole component of the electric field can be eliminated with an $7/8$ ratio. Because such electrostatic quadrupoles should be cheaper to fabricate than magnetic quadrupoles, and also because the focusing elements are closely spaced longitudinally at the low energy end of the accelerator, electric quadrupoles are favored over magnetic ones. The number of beams is determined by the high-voltage breakdown characteristics of the electric array and the need to transport a certain amount of charge in a pulse length that is initially $\sim 30 \mu\text{s}$ long. The breakdown constraint in a multi-beam array should be that between adjacent electrodes of opposite polarity. Based on

breakdown tests[5] of several electrode sizes and spacing (in the absence of beam), the estimated optimum is $R_{ap}=2.3$ cm, $R_{el}=2.6$ cm, $V_q = \pm 70$ kV. Unacceptable emittance growth from the non-linear image force occurs when the beam radius is $>80\%$ of the physical aperture. The beam-wall clearance should be increased by an additional 0.2 - 1 cm to accommodate mismatch oscillations that accumulate. They are caused by machining and alignment errors. Thus, with these clearance constraints, the maximum envelope radius in this part of the accelerator is 1.0 - 1.7 cm.

For higher velocity ions, magnetic focusing is stronger than electrostatic focusing. Since superconducting magnets would be economical, the additional space required for insulation and coils lead to an optimum with fewer beams and with larger transverse dimensions for the beams and quadrupoles. Another advantage of magnetic transport is that the maximum transportable line charge density is proportional to $B\beta a$, where B is the pole tip field, β is the relativistic factor, and a is the beam radius. Thus, for a constant beam radius, the pulse length may be reduced in proportion to increases in β , allowing the induction cores to be used more efficiently. System studies have shown that the transition from the electric section to the magnetic section with fewer beams should occur at 50-100 MeV. The electrostatically focused section is a few hundred meters long, and the magnetic section is several km long, with an average acceleration gradient of ~ 1 MV/m. The development of cost-effective beam sensing and steering systems to (infrequently) compensate for the machining and alignment imperfections would reduce the required beam clearance, lead to smaller quadrupoles, and decrease the required core material. The 16 beams in the magnetic section are consistent with the beam focusing constraints near the target and in the last focusing elements. Thus, the merging of beams into fewer transport channels is one of the main economically relevant beam manipulations in the driver, and it has critical beam dynamics issues that will be addressed below.

A slow growing longitudinal instability in induction linacs is due to longitudinal bunching of the beam. The seed for the instability may arise from an accelerating waveform imperfection. Then the perturbed distribution acts back on itself through the e.m.f. it induces in the induction cores, creating a growing wave backwards in the beam pulse rest frame. The growth rates are predicted to be greatest at frequencies below 30 MHz, but could be corrected by feed-forward control of the accelerating waveforms [6].

The beam pulse spans many lattice periods near the entrance to the electrostatically focussed accelerator (the lattice period is 0.45-0.6 m and the pulse length is ~ 25 m).

Meanwhile, the increasing lattice period allows for an increase of λ by a few percent, and a corresponding small bunch compression. This implies that the acceleration gradient should be gentle enough so that the velocity variation along the bunch length at a fixed point in the lattice should be $\delta v/v < 0.2$. A higher initial gradient would introduce intolerable transverse mismatches for parts of the beam.

The increase in λ can be controlled by setting acceleration voltage waveforms to put a smooth head to tail velocity variation, or tilt on the bunch. Compression of the bunch by a factor of ~ 4 in the magnetic focusing part of the linac can be done in the same way. The final compression to the 10 ns pulse length (30 ns including the pre-pulse) occurs in a few hundred meters and requires a larger tilt. This part of the lattice is designed so that the longitudinal compression of the beam is overcome by the space charge repulsion at the capsule. This last compression occurs while the beams are bent towards the target, and achromatic designs have been developed to maintain the focal spot requirements, in the presence of the velocity and current variations of the bunch.

A variation on the linac design is one which includes a beam-recirculating induction linac. It potentially could reduce the cost of a driver by making use of the induction cores of the ring many times for each target shot. The induction core material would be reduced, and the total accelerator length would decrease. Unresolved beam dynamics issues in the recirculator are emittance growth and beam loss at injection and extraction and in the bends. The large space charge tune shift implies the crossing of many low-order resonances, but this is mitigated by the rapid variation of the betatron wavelength due to acceleration.

IV. MERGING OF BEAMS

Beam dynamics issues that are present throughout the accelerator are also important in designing a beam combiner: Space charge, image forces and aberrations of applied fields are critical in a lattice with little beam-to-wall clearance. Beam halo should be suppressed before the beam energy makes it an activation problem. The longitudinal velocity variation required for beam compression can be handled by designing an achromatic merging lattice. Another strategy would be to remove any tilt on the beam just before the combiner, and apply a tilt appropriate for the magnetic focusing lattice downstream.

Emittance growth and beam loss are the primary issues in determining the feasibility of merging beams which bears similarity to multi-turn injection in high energy physics storage rings. However, consideration of

resonance crossing keeps the practical space charge tune shift lower in the storage ring case than in the situation described here. Experience with large contact ionization and alkali emitting alumino-silicate sources indicates that it is technically feasible to make a source and injector with a sufficiently high current density and transverse emittance limited mainly by the temperature of the emitting surface, or 0.15π mm-mrad.

The contribution to emittance growth from space charge adds in quadrature to that from the geometric configuration of the beams at the merging point [7], or

$$\Delta(\epsilon_n^2) = (\Delta\epsilon_{sc}^2 + \Delta\epsilon_{geom}^2) \quad ,$$

so the transverse phase space finally occupied by the merged beams is larger than what would be attributed to single particle dynamics filling in voids between beams ($\Delta\epsilon_{geom}$). In a driver $\Delta\epsilon_{geom} < \Delta\epsilon_{sc}$ due to the large potential energy of the four-beam configuration that is converted into transverse thermal motion.

A critical issue for minimizing the emittance growth is the allowable clearance between the beam edge and the physical aperture. A substantial halo on the beam entering the combining hardware would necessitate a greater clearance between the beam and a septum of the combiner elements, and ultimately a greater emittance dilution downstream.

Beam loss in the merging process can occur directly by beam wall interactions in the combiner hardware, or via halo formation downstream. In either case it must be compensated by accelerating more charge initially. At 50-100 MeV, activation is not a concern but halo that forms after the combiner should be scraped before the particle kinetic energy reaches the Coulomb barrier.

The lattice elements of the combiner would need at least two dipole elements; one to displace the beams from the axes of their original transport channels and the second to aim the four beams onto a trajectory parallel to their common transport channel. The design of the last one or two elements is the most difficult, due to the spatial constraints and the desire to bring the beams close together. The envelope angles are largest when the beams are round, which is undesirable for the last element. The final element should bring the beams together when they are elliptical, and have relatively small envelope angles. A combined function dipole and quadrupole element appears feasible, by approximating the desired potential distribution at the beam boundaries by a large number of discrete conductors or electrodes.

In the case of an electrostatic combined function dipole-quadrupole element, the unwanted space charge and applied fields from neighboring beam channels can be

effectively shielded by the conductors. Field and particle-in-cell simulations indicate that the beam edge to beam edge separation could be ~ 5 mm by using 1 mm diameter electrodes. On the other hand for a combiner to be used at the 50 MeV point of a driver, the difficulty presented by the high (~ 150 kV/cm) fields near the electrodes is serious.

A more tractable technical solution would be a (pulsed, warm) magnetic version of the combined function element. It would have peak fields of ~ 1.5 T, and field isolation between adjacent channels could be achieved with 1-2 mm of iron where adjacent beams are closest to one another.

A small scale beam combining experiment using entirely electrostatic focusing and dipole elements is underway at LBL [8].

V. OUTLOOK

After almost twenty years of theoretical and experimental research into heavy ion fusion with induction linacs, there are no dynamical problems that do not have a solution that fits into the driver scenario described here. Further work will help to weigh the merits among various design options. In all cases, the impact on the eventual cost of electricity will continue to be an important consideration.

At LBL, the ILSE accelerator [9] will be built to provide the beams that will enable testing many of the elements and manipulations of a fusion driver. Funding for the electric focusing section of ILSE (called Elise) has been approved, and a full engineering design will commence in 1995. The purpose of building ILSE is to explore the physics and engineering questions of the presently-conceived driver. The results will help determine and adjust the accelerator design. The ILSE beams will be equal to a driver in linear charge density, so a number of critical beam dynamics issues will be investigated at driver scale. However, to minimize cost, ILSE will have 10 MeV beams and fewer beams than a driver. It will consist of a 2 MeV, four beam injector, followed by an electrostatically focused matching section and induction linac. Each beam will initially have $\sim 0.25 \mu\text{C/m}$, and a bunch length of 1.5 μs . Except for bunch length and the number of beams, this part of ILSE is driver scale. The transition to the single-beam magnetic focusing section will occur at 5 MeV. A 4:1 beam combining experiment will be a central part of the ILSE experimental program. Drift compression, bending, and final focusing experiments will be carried out downstream of the 10 MeV point. A possible recirculation upgrade would increase the ion energy to ~ 100 MeV and address dynamics issues such as injection, extraction, and emittance growth due to bending.

VI. ACKNOWLEDGEMENTS

Discussions with Andy Faltens on various beam physics topics are gratefully acknowledged.

V. REFERENCES

- [1] G. Plass, "A Review of European Heavy Ion ICF Driver Development", these proceedings.
- [2] R. O. Bangerter, *Il Nuovo Cimento*, V106A, N. 11 (1993) 1445; J. D. Lindl, *Il Nuovo Cimento*, V106A, N. 11 (1993) 1467.
- [3] M. Stetter et al., *Il Nuovo Cimento*, V106A, N. 11, (1993) 1719.
- [4] A. Faltens and G. Krafft, "Current and Charge Neutralization of the HIF Beam after Final Focus" (1984), unpublished.
- [5] P. Seidl and A. Faltens, *Proceedings of the 1993 Particle Accelerator Conference*, V. 1, 721.
- [6] E. P. Lee, *Il Nuovo Cimento*, V106A, N. 11 (1993) 1679.
- [7] C. M. Celata et al., *Proc. of the 1987 Part. Acc. Conf.*, V. .2, 1167.
- [8] C. M. Celata et al., "Transverse Beam Combining of Four Beams in MBE-4", these proceedings.
- [9] C. M. Celata et al., *Il Nuovo Cimento*, V106A, N. 11 (1993) 1631.

CRYSTALLINE BEAMS*

John P. Schiffer

Physics Division, ANL, Argonne IL 60439 and University of Chicago

A beam of confined charged particles, that are cooled to the extreme of the space-charge dominated regime, where the relative motion of particles within the beam is small compared to their Coulomb potential energies, will crystallize in a unique form of condensed matter [1]. Such a system of particles can be simulated using the method of Molecular Dynamics, which explicitly includes the interaction between all pairs of particles and uses repeating cells to simulate the effects of a long beam. Within the molecular dynamics simulations typically a few thousand particles are followed in time, allowed to equilibrate, and then the velocities are gradually scaled down while still allowing the system to maintain equilibrium. To reach a cold equilibrium value requires 10-100 thousand iterations, corresponding to real times on the order of a few thousand betatron periods.

I. THE BASIC CRYSTALLINE STRUCTURES

The configuration of ions in such a cold beam will depend primarily on the number of particles per unit length relative to the strength of the average confining force (whose magnitude determines the betatron frequency). For few particles, the Coulomb repulsion is weak and at low (transverse as well as longitudinal) temperatures the beam particles will arrange themselves in a string on the beam axis. As the density of particles is increased, at a critical density, the repulsion between the ions will force them into a two-dimensional zig-zag pattern, and then at a yet higher density into three-dimensional arrays on the surface of a cylinder. The radius of the cylinder grows and eventually a new string forms on the axis, then gradually, more and more concentric equally-spaced cylindrical shells of particles appear. Such a system is illustrated in figure 1. The number of shells is proportional to the square root of the number of particles, each shell has the same surface density, and the particles form a triangular pattern on the mantle of the cylinder characteristic of two-dimensional Coulomb solids [2]. Thus while the system is ordered, it does not have the normal type of crystallographic order with a unit cell repeating by translation along the crystal axes. These configurations appear to be close to the classical 'ground states' of these systems; though the true quantum-mechanical ground states (having the same configurations) with no phonon excitations, are at considerably lower temperatures. This type of order was predicted to occur in all cold confined ionic systems such as in laser-cooled ion traps, where the confinement is three-dimensional [3] and where spherical or spheroidal shells of

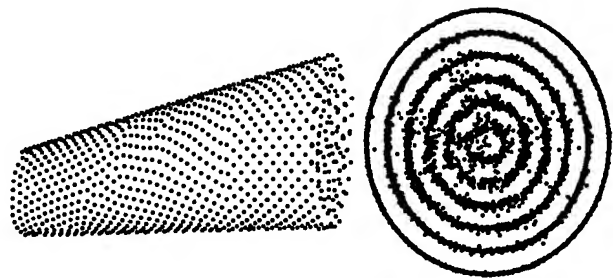


Figure 1. The result of a simulations showing a segment of beam with 5 shells. On the left is a perspective drawing of the beam with only the particles that appear on the surface shown, on the right is a projection of the beam segment onto a perpendicular plane. Typical spacings between particles and shells are on the order of tens of microns.

particles have been observed. At some point, in the interior of very large systems, the shell structure should transform into a body centered cubic lattice. Shell structure has been seen in a special "ring ion trap" [4] for stationary ions with rf quadrupole focusing which has the "beam" geometry, and the detailed patterns and the transitions between them were quantitatively confirmed.

Unequal Confining Field

In the case where the focusing forces are not equal in the two (vertical and horizontal) directions, the above shell structure is modified and the shells become elliptical in cross section instead of circular, but the pattern is otherwise very similar. As the eccentricity increases it becomes possible for the innermost structure to become planar, larger than the simple zig-zag for the cylindrically symmetric case.

II. NORMAL MODES OF THE CYLINDRICAL LATTICE

A lattice confined by a force field that is constant in time is, of course, a idealized simplification. Before considering a more realistic focusing lattice it is appropriate to discuss the simple degrees of freedom associated with a cylindrically confined beam. While many complex modes are possible, the details of these modes will depend on particular configurations. The hydrodynamic multipole modes that are characteristic of a charged fluid are more universal and of these two that are illustrated in figure 2 appear to be dominant for all but the thinnest (one- or two-dimensional) beams.

Monopole Mode

A cylindrically symmetric volume oscillation of the beam is seen at the plasma frequency (which is $\sqrt{2}$ times the betatron frequency for a single ion in the same

*This work was supported by the U.S. Department of Energy, Nuclear Physics Division, under contract W-31-109-ENG-38.

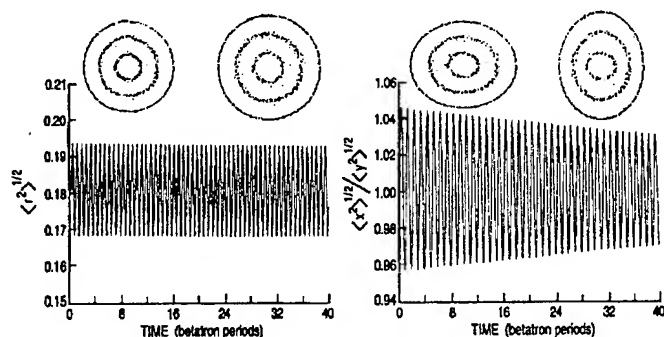


Figure 2. Simulations of the two normal modes discussed in the text followed in time; the left shows the monopole mode, the right the quadrupole.

focusing field). For a sufficiently cold beam this mode appears to be a true eigenmode — with no mixing into thermal excitation, as is illustrated in figure 2.

Quadrupole mode

The other mode that is readily excited is a volume-conserving quadrupole mode, where the beam oscillates between elliptical cross sections, elongated alternately in the horizontal and vertical directions. The frequency of this mode is equal to the betatron frequency and its damping, also shown in figure 2, is indicative of interactions with more complicated excitations.

III. MORE REALISTIC APPROXIMATIONS TO AN ACCELERATOR LATTICE

Several aspects of an accelerator need to be considered in order to approach the reality of a storage ring or similar device in which a moving cold beam may be confined. So far no effect has been found that suggests an insurmountable obstacle to achieving the condensed state of the beam discussed above.

Focusing Lattice

The fact that the accelerator lattice consists of finite focusing elements means that the confining force is not constant in time. However, the question is the time scale in which the force changes and whether the periodicity of these changes is at a harmonic of the eigenmodes of the system. While the periods within an accelerator lattice are typically shorter than the normal mode frequencies, harmonics of the lattice frequency may excite the normal modes and thus place some restrictions on particular lattices, but in general they do not significantly alter the conclusions for a static confining force mentioned above. The ordered system does undergo a slight micro-motion: oscillations with the periods imposed by the time-dependence of the focusing lattice and analogous to the "micromotion" in rf ion traps. The ordered system is a plastic one and these oscillations do not seem to couple into the random thermal degrees of peaks. The question of what constitutes a random "temperature" and what collective motion is somewhat fuzzy.

Cooling and Longitudinal-Transverse Coupling

In the Molecular Dynamics simulations cooling is a simple matter, applied uniformly to the beam under the most favorable circumstances. In a real accelerator, cooling is much less straightforward. In storage rings, where the coldest beams are obtained, unidirectional cooling is applied in a relatively short section on the beam. Simulations suggest that this may not be a serious problem — what matters is that the random kinetic energy of the beam is removed. For a hot beam the beam radius is a function of the transverse temperature, but once the temperature of the beam is low enough such that the beam radius is within an order of magnitude of the space-charge limit the coupling between the longitudinal and transverse degrees of freedom is sufficient to make the longitudinal cooling effective, as long as the number of particles is sufficient to produce multiple shells in the cold limit. When the number of particles is low (corresponding to a string when they are cold) the coupling becomes much weaker and it is perhaps problematic whether present longitudinal cooling techniques will be able to produce an ordered beam in the string-like regime.

Bending

The bending of the beam in dipole elements is an inevitable consequence of a storage ring. The co-moving coordinate frame thus becomes non-inertial and cooling the beam to a constant linear velocity causes an apparent shear, with particles on the inside of the bend moving forward and ones outside the mean ray moving backward. This shear presents a problem, and suggests that there is a limit to normal cooling techniques. Whether the condensed state of a particular beam cooled to a constant velocity can withstand the forces of bending in a particular ring depends largely on the strength of the focusing as compared to the bending shear — and is thus determined by the betatron tune ν_β for the ring. Simulations summarized in figure 3 indicate that with a small betatron tune in the vicinity of $\nu_\beta = 2-3$ only a single or two-shell beam will withstand the shearing distortion, but with larger storage rings with betatron tunes of 30 or more many shells can survive. The details of the accelerator lattice can slightly modify these conditions [5]. When the shear is overcome, and if strong longitudinal cooling is applied, the beam separates into a set of strings that slip past each other, and are ordered in a triangular pattern with respect to each other as shown in figure 4. Such ordering is characteristic of sheared colloids, but it is not clear whether the cooling in a beam could ever be sufficiently strong to produce such a system. Ideally, one would like to have a beam cooled to a constant angular velocity, where only the fluctuations in discrete bending elements would cause a much smaller problem of shear oscillations. The stability of such systems has been explored in simulations for relatively modest beams [5].

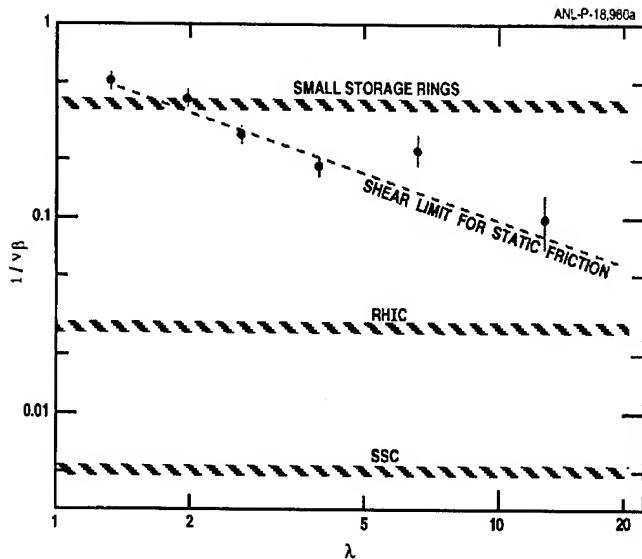


Figure 3. Limits (in $1/v\beta$) at which an ordered beam can withstand bending shear as a function of the linear particle density λ . A beam with a single shell would be in the vicinity of $\lambda = 1-2$. The points with error bars represent the results of simulation.

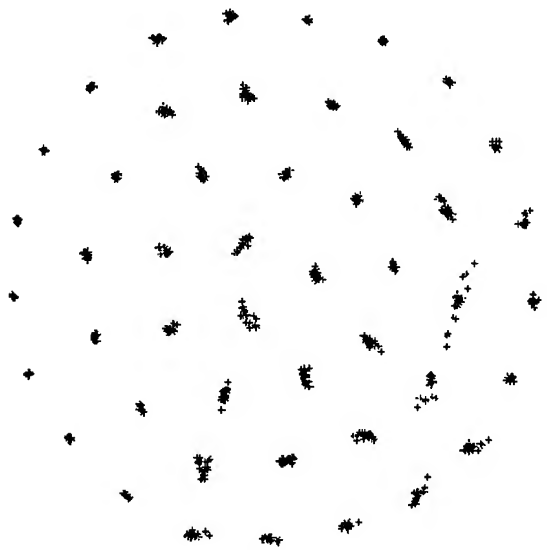


Figure 4. The projection onto a perpendicular plane of particles in a simulated beam beyond the shear limit with continuous cooling.

Ordering in Bunched Beams

In a storage ring it is also possible to cool a bunched beam. This is a case of a three-dimensional confinement similar to ion traps, but with the longitudinal confining force much less than the transverse ones. The fact that the bunching is applied in perhaps only one place in the ring matters even less than the periodicity of the transverse focusing lattice, because the relevant time scale is much longer: the period for synchrotron oscillations. A cold beam

bunch is a very elongated spheroid in the cold hydrodynamic limit. Simulations show that for discrete particles the beam will be multi-shelled in the center of a bunch, as before, gradually thinning out, and eventually ending in one-dimensional strings at the ends as shown in figure 5.

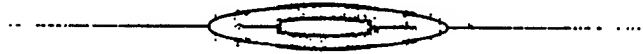


Figure 5. Simulation of a beam bunch, roughly 20 cm long and 0.2 mm in radius.

IV. EXPERIMENTAL PROGRESS AND FUTURE PROSPECTS

Considerable progress has been made in recent years in the cooling of beams in small storage rings. With laser cooling, work at the TSR in Heidelberg [6] has reached longitudinal temperatures in the fractional Kelvin regime, work at ASTRID in Aarhus in the milliKelvin regime [7] which is in the crystalline regime, however the transverse temperatures are not known. The suppression of Schottky noise has been observed for continuous beams at ASTRID [8] and the space-charge limit in the length of cooled bunched beam has also been seen [9], along with related work with electron cooling at Indiana [10]. The transverse temperature and thus the three-dimensional ordering are not firmly established, some simulations indicate that the longitudinal-transverse coupling is strong for the space-charge limited beams that have apparently been achieved, and then the transverse temperature could be similar to the longitudinal one. However better diagnostics on the transverse properties of the beam are needed and with these more quantitative measurements will become possible.

REFERENCES

- [1] A. Rahman and J.P. Schiffer, Phys. Rev. Letts. **57**, 1133 (1986); Physica Scripta **T22**, 133 (1988); J.P. Schiffer, *Proc. of Workshop on Crystalline Ion Beams*, Wertheim, FRG, Oct. 4-7, 1988, GSI-89-10 Report, April 1989, ISSN 0171-4546, p.2.
- [2] R.W. Hasse and J.P. Schiffer *Annals, of Physics* **203**, 419 (1990).
- [3] S.L. Gilbert et al., Phys. Rev. Letts. **60**, 2022 (1980).
- [4] G. Birkel, S. Kassov, and H. Walther, *Nature* **357**, 310 (1992).
- [5] J. Wei, T.P. Li, and A. Sessler, Phys. Rev. Letts. **73**, 3089 (1994).
- [6] S. Schröder et al, Phys. Rev. Letts. **64**, 2901 (1990).
- [7] J. S. Hangst et al., Phys. Rev. Letts. **67**, 1238 (1991).
- [8] J. S. Hangst et al., Phys. Rev. Letts. **74**, 86 (1995).
- [9] J. S. Hangst et al., Phys. Rev. Letts. **74**, (1995).
- [10] T.S.P. Ellison et al., Phys. Rev. Letts. **73**, 3089 (1994).

INJECTING A KAPCHINSKIY-VLADIMIRSKIY DISTRIBUTION INTO A PROTON SYNCHROTRON*

E. Crosbie and K. Symon¹

Argonne National Laboratory, 9700 South Cass Avenue, Argonne, IL 60439 USA

I. INTRODUCTION

Recently it has been suggested that the Kapchinskij-Vladimirskij (KV) distribution [1] may be of practical interest for high intensity machines in that it may provide the maximum space charge limit for such a machine. One can make a plausible argument that the maximum beam intensity is obtained for a distribution for which all particles have the same tune, at least when the resonance is approached. Therefore, the following steps should be taken: first, reduce the chromaticity of the accelerator ring as much as possible, and second, make the betatron frequencies independent of amplitude, i.e., make the focusing forces linear.

One way to make the focusing forces linear is to start with external focusing forces which are linear, and then make the space charge forces also linear by using a KV distribution [1]. Sections II and III describe two injection scenarios which produce a KV distribution (if we neglect beam-beam interactions during the injection process.) Simulations of these injection scenarios verify that the resulting distribution produces a uniform circular beam in xy-space.

A simulation code was written which also includes the space charge interactions between the 500 injected turns in the proposed scenarios; the results are given in section IV. The space charge forces have a substantial effect on the resulting distribution.

II. PAINTING SCENARIO

The KV distribution is essentially a microcanonical distribution with the beam distributed uniformly over a three-dimensional energy shell corresponding to a fixed total energy in the four-dimensional phase space of the x and y betatron oscillations. We need to construct a scenario which allows us to paint the energy shell uniformly. Let us start from the simple Hamiltonian

$$H(x, p_x, y, p_y) = \frac{p_x^2}{2} + \frac{v_x^2 x^2}{2} + \frac{p_y^2}{2} + \frac{v_y^2 y^2}{2} \quad (1)$$

Assuming that the focusing forces are linear, the space charge forces for the KV distribution will also be linear and

* Work supported by the U.S. Department of Energy, Office of Basic Energy Sciences, under Contract No. W-31-109-ENG-38.

¹permanent address: Dept. of Physics, University of Wisconsin-Madison, Madison, WI 53706 USA.

are included in the constants v_x, v_y . The independent variable is the angle $\theta = s/R$ around the ring. To simplify the algebra, v_x, v_y are assumed to be constant. (For a more complete analysis, including a derivation of the KV distribution for the alternating gradient case with an elliptical beam, see Ref. [2].)

Introduce angle-action variables:

$$\begin{aligned} x &= (2J_x / v_x)^{1/2} \sin \gamma_x, & p_x &= (2v_x J_x)^{1/2} \cos \gamma_x, \\ y &= (2J_y / v_y)^{1/2} \sin \gamma_y, & p_y &= (2v_y J_y)^{1/2} \cos \gamma_y, \end{aligned} \quad (2)$$

where the actions J_x, J_y are constants of the motion.

The necessary KV distribution can be written in the form

$$D(J_x, J_y, \gamma_x, \gamma_y) = A \delta(2J_x \cos^2 \zeta + 2J_y \sin^2 \zeta - J_0), \quad (3)$$

where J_0 is constant and ζ is an angle which may be chosen (almost) arbitrarily to change the aspect ratio of the elliptical beam boundary in xy space. If $\zeta = \pi/4$ then this is a microcanonical distribution. If the distribution in Eq. (3) is written as a function of x, y, p_x, p_y and integrated over p_x and p_y , the result is a uniform distribution over the spatial coordinates x, y within the ellipse

$$v_x x^2 \cos^2 \zeta + v_y y^2 \sin^2 \zeta = J_0. \quad (4)$$

Note that we can make the beam cross section circular by choosing

$$\tan \zeta = (v_x / v_y)^{1/2}. \quad (5)$$

If the beam is injected at a fixed point in the phase space, the betatron oscillations will spread the beam over the $\gamma_x \gamma_y$ phase plane. In order to spread it over the three-dimensional energy surface, the action variables need to vary in an appropriate way. To this end, the following variables are introduced:

$$\begin{aligned} J_0 &= 2 \cos^2 \zeta J_x + 2 \sin^2 \zeta J_y, \\ J_m &= 2 \cos^2 \zeta J_x - 2 \sin^2 \zeta J_y. \end{aligned} \quad (6)$$

The Jacobian of this transformation is constant, so if area is conserved in the $J_x J_y$ phase plane then it is also conserved in the $J_0 J_m$ phase plane.

The total action J_0 is to be held constant and J_m is to be varied slowly. If the variation of J_m is slow compared with the betatron frequencies, then near each value of J_m the betatron motion will distribute the injected beam uniformly over the $\gamma_x \gamma_y$ phase plane, provided there is no rational

relation with small denominator between γ_x and γ_y . In order to paint the J_0 shell uniformly, dJ_m/dt is required to be constant:

$$J_m = J_0 \left(1 - \frac{2t}{T} \right), \quad (7)$$

where T is the total injection time. Note that we want to paint both positive and negative values of J_m . Equation (7) is adjusted for the case in which $J_m = J_0$ initially, i.e., the x amplitude is maximum and the y amplitude is zero. The injected x, y actions are given by

$$\begin{aligned} J_x &= \frac{1}{2 \cos^2 \zeta} J_0 \left(1 - \frac{t}{T} \right), \\ J_y &= \frac{1}{2 \sin^2 \zeta} J_0 \frac{t}{T}. \end{aligned} \quad (8)$$

This scheme is easily accomplished using stripping injection into a proton accelerator. The desired distribution is achieved using a local orbit bump to control the horizontal amplitude and a steering magnet in the injection beamline to control the vertical amplitude.

A program was written to simulate this scenario as applied to the IPNS Upgrade [3]. The injection time T corresponds to 500 injected turns. The maximum injected amplitude is 50 mm. The tunes are $\nu_x=6.81$, $\nu_y=5.73$. Figure 1 shows the resulting distribution in xy space at the end of injection. Each of the small circles represents one injected turn. The spatial density is fairly uniform and has a circular cross section. Figure 2 shows the result for a scenario in which the painting is accomplished by using both horizontal and vertical orbit bumps at the stripper location. Since both orbits must move away from the stripper during injection, the resulting distribution cannot lie on the energy shell and is neither circular nor uniform.

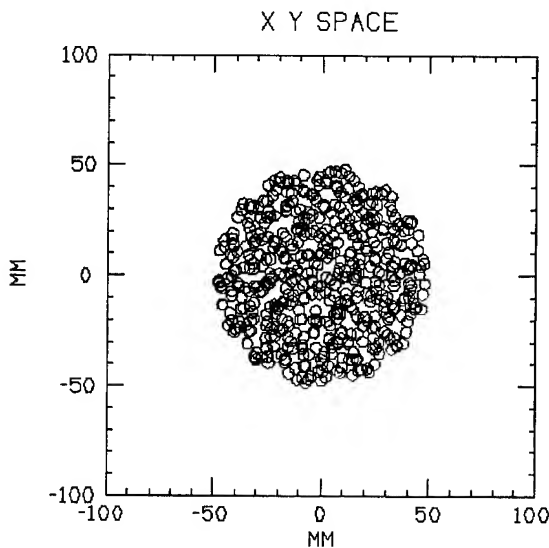


Fig. 1: Spatial distribution resulting from the painting scenario.

III. COUPLING SCENARIO

Cho [4] has suggested an elegant, practical way to produce a KV distribution. He proposes making the x and y betatron tunes equal, providing a small coupling between them, and then injecting with zero y amplitude and at a large fixed x amplitude. The coupling causes the y oscillation energy to increase at the expense of the x energy. This has two effects. First, it causes the previously injected beam to move away from the inflector and remain away for one beat period, thus permitting multi-turn injection. Second, it results in a distribution in which all particles have the same total oscillation energy.

In order to fill the entire energy shell a careful analysis is required similar to that in the previous section. A suitable scenario has been derived; the details can be found in Ref. [2]. Simulations again show that this scenario can achieve a KV distribution with a uniform spatial density within a circular beam.

IV. SIMULATIONS INCLUDING SPACE CHARGE FORCES

A simulation code which includes the effects of the forces exerted by the 500 injected turns on one another has also been written. In this simulation each injected turn is represented as a tube of charge. Each tube exerts forces on all other tubes that are present in the machine during the injection process. The forces are inversely proportional to the distances between the tubes for separations larger than the tube sizes. For separations smaller than the tube sizes, the forces vary linearly with the separation. If one first injects the beam and turns on the space charge forces after all 500 turns have been injected, the resulting distribution of tune shifts is in good agreement with the expected results and shows clearly the advantage of injecting with a uniform spatial distribution.

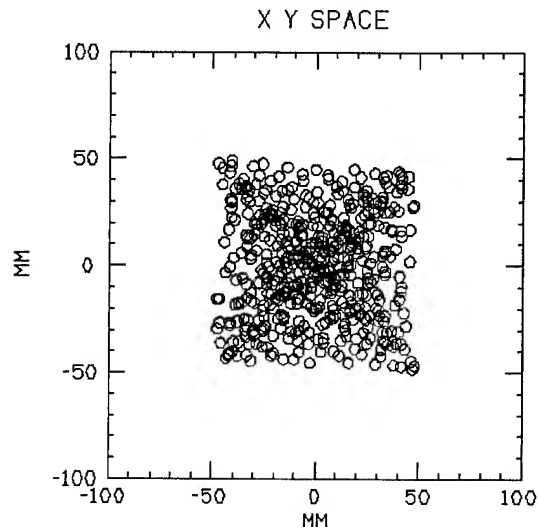


Fig. 2: Spatial distribution resulting from a non-KV injection.

If, more realistically, we include the space charge forces during the injection process, we do not reach a true KV distribution. This can be seen in Fig. 3, which shows the final distribution after injection with the painting scenario. The total injected current is about half of the calculated space charge limit for a uniform beam cross section. The space charge forces substantially affect the resulting distribution. (Compare Fig. 3 with Fig. 1.) However, the distribution is still fairly uniform over the nearly circular cross section. Figure 4 presents a similar calculation with a current two times the calculated space charge limit. The space charge forces have tuned the beam to the half-integral resonance, resulting in increased beam size and reducing the beam density enough to prevent the tunes from remaining in the stop band.

With a beam intensity exceeding the space charge limit we are able to see clearly the effect of the approach to the resonance, particularly in the tunes of the beam particles which tend to remain near the edge of the stop band. When the magnet error which drives the bump is small, and we inject a large beam, say four times the space charge limit, the resonant growth rate may not be large enough to prevent the beam from crossing the resonance. However the resulting beam cross section is not much different. If we turn off the gradient error which drives the resonance, the tunes cross the resonance and end up well below it, but the beam cross section is still not much different. We conclude that the beam-beam interactions dominate the final beam distribution.

If we inject using a non-KV scenario, the effect of the approach to resonance is to modify the distribution so as to produce a beam more uniform in spatial cross section than would otherwise result. The non-KV scenario differs in that the tune may approach resonance much sooner during the injection process, but the final result is not much different from the KV scenario. We conclude that after almost any injection scenario a beam exceeding the space charge limit will tend to adjust its distribution to produce a fairly uniform cross sectional distribution. There seems to be little advantage in using a scenario intended to produce a KV distribution.

V. REFERENCES

- [1] I. M. Kapchinskij and V. V. Vladimirskij, "Limitations of Proton Beam Current in a Strong Focusing Linear Accelerator Associated with the Beam Space Charge," *Proc. CERN Symposium on High Energy Accelerators*, 1959.
- [2] K. R. Symon, "Kapshinskij-Vladimirskij Distribution," Argonne National Laboratory Neutron Source Accelerator Note NSA-95-5 (available on request).
- [3] "IPNS Upgrade - A Feasibility Study," ANL-95/13, April 1995.
- [4] Y. Cho, private communication.

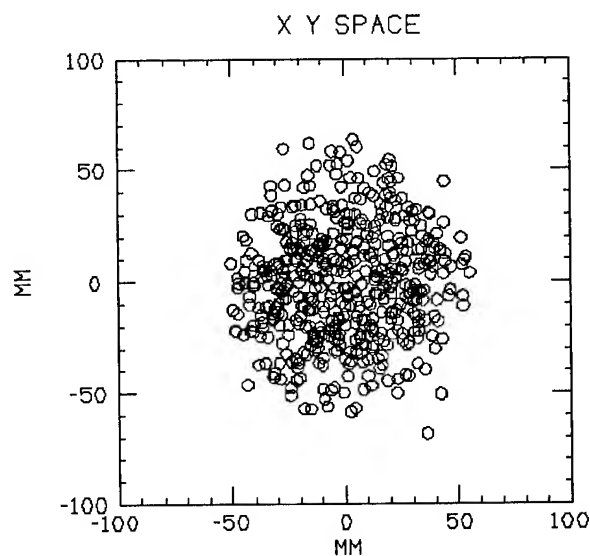


Fig. 3: Spatial distribution including the effect of space charge forces (painting scenario).

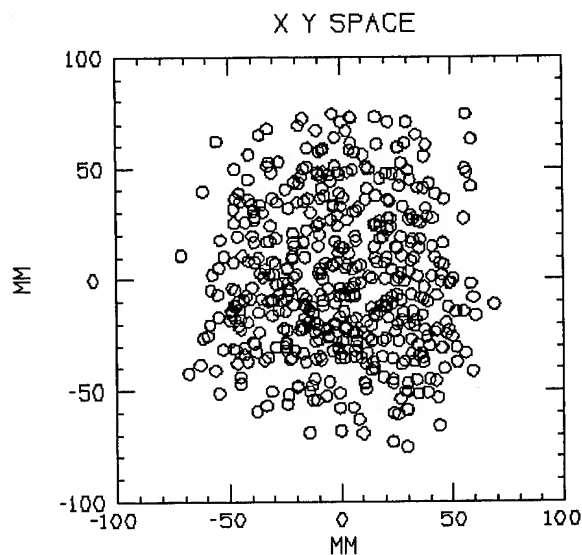


Fig. 4: Spatial distribution with space charge forces for a beam above the space charge limit.

Halo of a High-Brightness Electron Beam

G. Haouat, N. Pichoff, C. Couillaud, J.P. De Brion, J. Di Crescenzo, S. Joly, A. Loulergue, C. Ruiz, S. Seguin, and S. Striby, CEA-BIII/SPTN, BP 12, 91680 Bruyères-le-Châtel. France.

ABSTRACT

The experimental study of transverse profile of the ELSA-linac electron beam has been undertaken in order to analyze the mechanisms of halo formation and development in the generation, acceleration and transport of a high-intensity, high-brightness charged-particle beam. Measurements are reported in which the beam profile is observed over four to five decades. They were performed using an imaging technique in which light emitted from an optical transition radiation (OTR) screen placed in the beam path is transported through conventional optics to an intensified video camera. The electron-density distribution is shown to be dependent on the beam current, through space charge effects, initial conditions and transport configuration.

I. INTRODUCTION

Technology of high-intensity linear accelerators has progressed so rapidly in the past decade that they are now being considered for use in a number of applications. Possible applications are isotopic separation or plasma heating with high-power free electron lasers fed by electron linacs, or nuclear waste management, production of tritium, transmutation of defense and commercial plutonium stocks with intense spallation-neutron sources driven by large proton or light-ion linear accelerators. However, experimental observations and multiparticle simulations indicate that high-intensity beams in accelerators develop a low-density halo at the periphery of the central core of the beam. This outer part of the distribution leads to particle losses in the accelerator which, for a high-energy beam, may induce enough activity or radiation damage in the structures to complicate considerably maintenance and operation of the machine. The major challenge is to control the beam profile, which implies a better knowledge of the phenomena involved in halo formation.

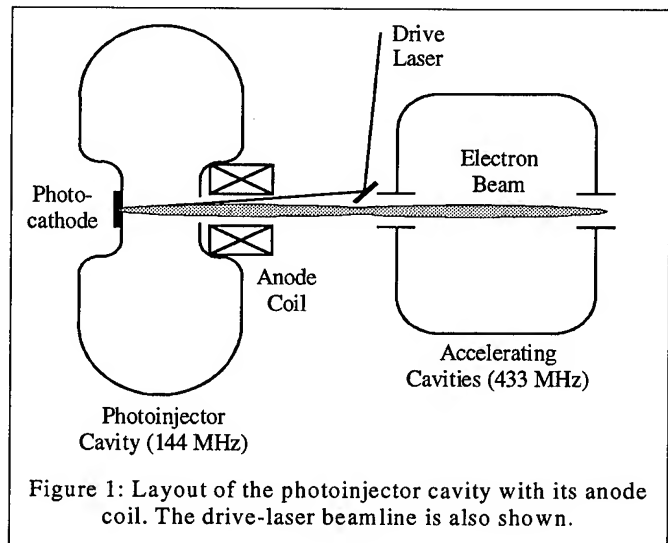
Several theoretical studies and numerical-simulation works have addressed the problem of beam halo formation and development in high-intensity linear accelerators. However, predictions of the simulations may be quantitatively incorrect since, because of computer capabilities, halo properties are described by only a few particles. Therefore, experimental study of beam halo is necessary to check theoretical predictions and complement simulations.

Few experiments, to date, have been dedicated to precise determination of the beam structure extending in the very low density regions constituting the halo. We have undertaken, at Bruyères-le-Châtel, an experimental study of the transverse

spatial distribution of the high-intensity, high-brightness electron beam delivered by the ELSA linac. The objective of this study is to analyze the beam profile over a very large dynamic range under varying conditions in the generation, acceleration and transport of the beam. An experiment is described in which the beam profile has been observed over at least four decades.

II. EXPERIMENTAL TECHNIQUE

The ELSA facility has been described previously [1]; only features peculiar to our halo experiment are given here. The accelerator, which consists in a photoinjector cavity followed by three accelerating cavities, delivers a high-brightness space-charge dominated electron beam. The 2-MeV photoinjector cavity and its anode coil are shown schematically in Figure 1. The focusing anode coil is of particular importance since it counteracts the space-charge defocusing effect on the beam, which is important at low electron energy.



The experimental apparatus designed for the halo measurements was installed at the end of the linac. It is a modified version of the devices used to diagnose transverse profile on the ELSA facility [2]. The setup, which has been described in detail in a previous paper [3], consists of an electron/photon conversion screen, a transport optics and a video camera. The converter, which is moved in the beam path by an actuator, is an optical transition radiation (OTR) screen. This type of screen is suitable for accurate halo measurements since it has an excellent linear response over a

wide dynamic range, good spatial resolution, a reasonable sensitivity, and does not suffer saturation effects or image smearing induced by thermal effects. The screen plane is oriented at 45° with respect to the beam axis so that the backward lobe of radiation is observed at 90° to the beam through a quartz window and conventional image-transport optics to a variable-gain video camera coupled to a data-acquisition system. The optical system has been designed for an observation field of 16 mm at the screen, corresponding to roughly 10 times the core diameter of a beam of 20π -mm.mrad normalized emittance transported under optimum conditions.

III. THE HOLE-BORED SCREEN METHOD

The hole-bored screen method was used for the halo measurements. The experimental procedure consists in moving an OTR screen into the beam path. The screen has the form of a stainless-steel disk, 1-mm thick and 50-mm in diameter, with a hole bored in the center. The disk is polished to optical standards. The electron-beam core is first observed with its image below saturation, by appropriate setting of the light intensifier. In this measurement, the beam is slightly off-center with respect to the hole in the disk. The beam is then steered toward the hole through which most of the core electrons pass. Then, the halo can be properly observed by increasing amplification of the light intensifier. This method yields better results than the saturated-core method, described in reference [3], since undesirable phenomena, which can spoil observation of the halo, are eliminated and background light is considerably reduced.

The measurements were performed with three OTR screens having hole diameters of 2.5, 4.0 and 6.0 mm. They were changed, during the experiment, to fit the size of the beam core to be observed. These three screens together with a light intensifier with 7-decade dynamic range permitted the observation of density profiles over five orders of magnitude. The electron beam, of 17.5 MeV energy, consisted of macropulses of 100- μ s duration, at a repetition rate of 1 Hz. The macropulse train was composed of ~ 20 -ps long bunches spaced 69.2 ns apart; the bunch temporal profile was gaussian. Bunch charges of 0.5 to 3 nC, corresponding to peak currents of 25 to 150 A, were obtained by adjusting the drive-laser beam intensity. The laser spot at the photocathode was circular with a diameter of 4 mm, and illumination was almost uniform over the spot surface.

IV. DATA ACQUISITION AND PROCESSING

For each setting of the accelerator parameters, images were taken with two to three different combinations of OTR screens and light intensifier gains in order to cover the largest electron-density range. Background images were also taken by switching off the drive-laser light. In off-line data processing the profile images were normalized one to the other, by using the precise calibration of the light intensifier,

to finally yield the electron-beam transverse distribution after background has been subtracted.

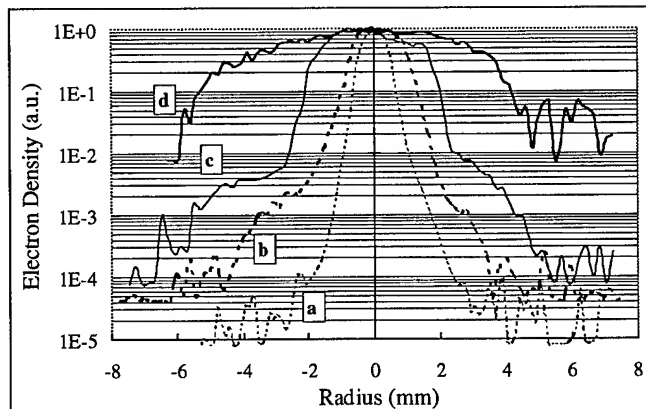


Figure 2: Density distributions for four settings of the couple of parameters Q (Bunch charge), B (Anode-coil current) which are:
a) $Q = 0.5$ nC, $B = 16.0$ A, b) $Q = 0.9$ nC, $B = 17.5$ A,
c) $Q = 1.8$ nC, $B = 19.0$ A, d) $Q = 2.8$ nC, $B = 19.7$ A.

Once the transverse profile has been reconstructed horizontal or vertical cross sections of the electron-density distribution can be deduced. Beam profiles, which were measured for different values of the two parameters, bunch charge and anode-coil current, are presented in Figure 2 and will be discussed below. This figure shows that our experimental setup is capable of measuring density distributions over 4 to 5 decades.

V. RESULTS AND INTERPRETATION

In the present work we have investigated the influence on the beam transverse profile of the electron-bunch charge and of the current in the focusing anode coil of the ELSA photoinjector.

A. Results

The transverse profile has been observed for bunch charges (Q) ranging from 0.5 to 3.0 nC and anode-coil current (B) varying between 15.0 and 19.7 A. Data were taken in four separate runs for 20 sets of Q, B values. Horizontal cross sections of the transverse density distribution have been extracted from the reconstructed profile images. Characteristic spectra are displayed in Figure 2, showing important changes in the beam density profile.

Observation of the data leads to two remarks:

- Beam size changes strongly. At low anode-coil currents (~ 15 A), there is a linear beam-spot broadening with increasing bunch charge, while, at higher anode-coil currents (> 18 A), the spot size is large and almost constant with charge. The low-coil-current behaviour has been observed before and attributed to space-charge effects [3].

- Profile shapes look quite different with the anode-coil current. i) At low currents (< 16 A), the density profile

decreases almost exponentially from the center of the beam towards outside. *ii)* At mid currents (~ 18 A), the density profile seems to be composed of two gaussian shapes, as if two beams, with different transport properties, were travelling together. The more dense beam could be called the "core", the other one, the "halo". Curves b) and c) of Figure 2 exhibit this bi-gaussian shape. *iii)* At high currents (>19.5 A), the core and the halo seem to be completely mixed.

B. Interpretation

The density profiles have been processed to yield an estimate of the fraction of the beam that extends beyond a given distance from the centroid of the beam. The resulting data have been used to deduce, for each measurement, the beam radii enclosing 90%, 99%, 99.9% and 99.99% of the particles. The 20 measurement results have then been analyzed using an interpolation-extrapolation technique to yield the radii variations in the Q,B space. Variations of the beam radius enclosing 99% of the particles are displayed in Figure 3 as a 3D contour plot; the data are labelled as "EXPERIMENT".

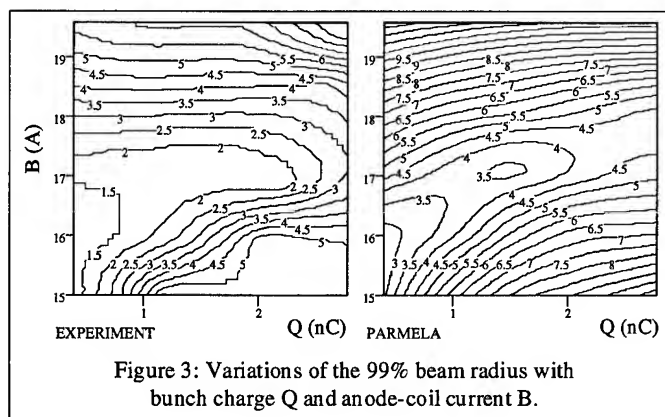


Figure 3: Variations of the 99% beam radius with bunch charge Q and anode-coil current B.

The experiment has been simulated with the code PARMELA, in order to explain our results and to try to understand the physical phenomena involved in the halo formation and development. Because of the limited numerical capabilities of the code contour plots could not be obtained for beam radii enclosing more than 99% of the particles. The data for a beam radius enclosing 99% of the particles are presented in Figure 3; they are labelled as "PARMELA". Comparison of contour plots for measured data and simulation results shows good qualitative agreement, but the simulation yields radii systematically larger than the experiment by a factor of roughly 2. This discrepancy may be explained by a crude simulation of the photoinjector or an unrealistic estimate of the transverse focusing strength of the accelerating cavities.

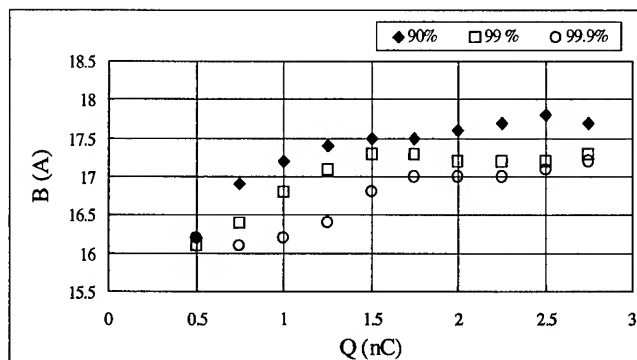


Figure 4: Experimental curves $B = f(Q)$ corresponding to minimum radii enclosing 90%, 99%, 99.9% of the particles.

Both plots exhibit a valley at the same location in the Q,B space. The bottom of this valley represents the optimum anode-coil current at a given bunch charge for transporting an electron beam of minimum size. The curves corresponding to the lowest path in the valley have been estimated for both experimental and simulation results, and they compare satisfactorily. The experimental $B = f(Q)$ curves corresponding to minimum beam-radii enclosing 90%, 99% and 99.9% of the particles are displayed in Figure 4. It indicates that the anode current should be higher if the objective is to optimize the transport of the beam core only, and relatively lower if the objective is to optimize the transport of the core+halo.

VI. CONCLUSION

The hole-bored OTR screen and the imaging technique constitute powerful tools for measuring electron-beam transverse distributions over four to five orders of magnitude and for studying the halo in the transport of a high-brightness beam. The analysis of the influence on the beam profile of the bunch charge and the focusing strength of the ELSA photoinjector yields interesting results. Further work is planned to investigate the role of other parameters controlling the beam, and to use more extensively the simulation tools in order to understand the physics of the halo.

VII. REFERENCES

- [1] R. Dei-Cas et al., "Status report on the low-frequency photo-injector and on the infrared FEL experiment ELSA", Nucl. Inst. Meth. **A296** 209 (1990).
- [2] G. Haouat, C. Couillaud, J. Di Crescenzo, J. Raimbourg and S. Seguin., Proc. First European Workshop on Beam Diag. and Inst. for Part. Acc., Montreux, Switzerland. CERN PS/93-35 (BD) - CERN SL/93-35 (BI) (1993) 180.
- [3] G. Haouat, N. Pichoff, C. Couillaud, J. Di Crescenzo, S. Joly, S. Seguin and S. Striby, "Experimental study of the ELSA electron-beam halo", BIW94, Beam Instrumentation Workshop - Vancouver, B.C., Canada, 2 - 6 Oct. 1994.

Studies on Halo Formation in a Long Magnetic Quadrupole FODO Channel First Experimental Results

P-Y Beauvais¹, D. Bogard¹, P-A Chamouard¹, R. Ferdinand¹,
G. Haouat², J-M Lagniel¹, J-L Lemaire², N. Pichoff², C. Ruiz².

1) CEN SACLAY-DSM/LNS and GECA, BP 2, 91191 Gif-sur-Yvette. France.

2) CEA-BIII/PTN, BP 12, 91680 Bruyères-le-Châtel. France.

ABSTRACT

A study is in progress to prepare an experiment on the transport of an intense proton beam, with high optical qualities, through a periodic magnetic quadrupole FODO channel (29 periods). It is intended to provide a better understanding of how halo develops and can be controlled as a crucial issue for the design of high-intensity linear accelerators. Simulations were done showing that this experiment can be performed with a high-brightness proton beam produced by a duoplasmatron source, with an energy of 500 keV and a current of tens of mA. Beam pulse length will be less than 1 ms and normalized emittance better than $1. \pi$ mm.mrad (90% of total beam). Thus, transverse tune can be sufficiently depressed in the transport channel to allow instabilities to grow and halo to develop or stay under control.

The overall experiment is divided in two phases. Phase 1, the subject of this paper, is dedicated to precise measurements on initial beam conditions, such as emittance, for the beam entering the FODO channel. Phase 2, concerning the halo formation phenomena will be carried on later, if results of phase 1 are satisfactory.

I. INTRODUCTION

For many years, experimental studies on emittance growth of beams transported under space charge conditions have been done at different laboratories [1]. The aim was, and is still, to test the calculations and the simulations made for long focusing continuous channels and alternating strong focusing quadrupole channels both for electron and heavy ion beams. Of course, the cost of such transport lines strongly limits the experiments and they have to be achieved in several steps. Previous results seem to be limited by the sensitivity of the experimental setups. Therefore, more sensitive diagnostics are needed for these tests. With the growing interest for dedicated high-intensity CW-beam linear accelerators, linacs must achieve very low beam losses to insure the maintainability of the structure. Instabilities in the beam that lead to a halo are still a real concern; so, understanding of halo formation, and controlling its development is a key issue for all designers. Recently new insights [2,3] suggested that similar experiments should be performed again with better beam instrumentation. Efforts have to be put into diagnostics better adapted to the requirements of measuring the low density part of the beam

included in the halo along with the optical qualities of the initial beam (emittance, profile, mismatching and missteering).

Because of budget constraints, a proposal was made, early in 1994, to use an existing quadrupole channel of 29 periods. This system consists of the focusing quadrupoles of the LNS 20.MeV Alvarez linac not powered with RF [3]. All the existing hardware was available and the only major modification was to update the quadrupole system. The power supplies offered all the flexibility that was necessary to cover a wide range of tuning.

II. THEORETICAL ASPECTS - BEAM SIMULATIONS

The FODO channel has a variable period because spacing of the quadrupoles increases along the structure due to the location of the drift tubes. Matching between adjacent cells has to be done to obtain the stable envelopes for different phase advances at zero beam current (σ_0) and desired transported current (σ_1). We chose $\sigma_0 = 60^\circ$ and 100° . The core envelope is optimized for a K.V distribution. Simulations are done using the particle core model (PCM) for three concentric distributions of 2000 particles each: the first distribution treats the core, the second one the border part and the third one the outer part of the beam. These test particles are uniformly distributed in the phase space and tracked along the structure. It is expected by many authors that above $\sigma_0 = 90^\circ$, instabilities develop and emittance grows. This is very well demonstrated in our simulations [3]. It is observed that phase space deteriorates and emittance grows with increasing beam current. The envelope

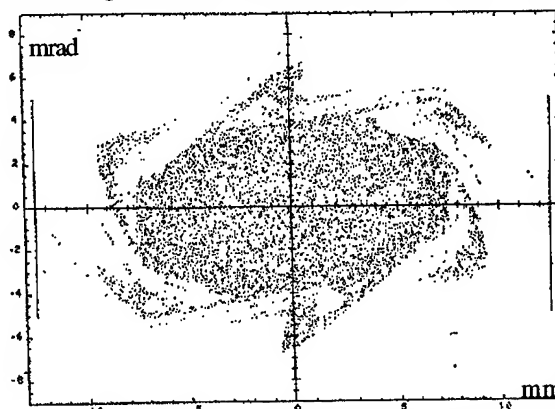


Figure 1 : Transverse phase space portrait at the end of the FODO channel. Halo which forms tails can be seen

starts to oscillate and a halo grows around the core. Studies of these phenomena are in progress but it is beyond the scope of this paper to recall all the theoretical aspects.

III. EXPERIMENTAL SET-UP

The experimental set-up corresponding to phase 1 is shown in Figure 2. It consists of a duoplasmatron source housed in a high voltage terminal **1** delivering, for the purpose of the experiment, a proton beam up to 50mA at 500 keV. The pulse duration is set to 500 μ s to allow for transient effects to die before any measurements are performed on the beam. In this respect, we can consider that we are dealing with an equivalent DC beam for both simulation and measurement. The intermediate section between the FODO channel **2** and the beam source holds all the instrumentation required for beam diagnostics during phase 1. It will become the matching section for phase 2. At present time, the only focusing element is a quadrupole triplet **3** used to form the beam image downstream. A dipole magnet **4** allows for beam analysis: its diagnostic is put in viewing box **5**. The other viewing boxes house the main beam diagnostics:

- box **6** contains a Faraday cup, collimators and a sampling hole,
- box **7** contains collimators, sampling holes, and a slit,
- box **8** contains a pepper-pot to sample the beam
- box **9** holds the instrumentation dedicated to emittance, beam profile and beam current measurements.

For phase 2 experiment, viewing box **9** will be replaced by a set of magnetic quadrupole lenses to properly match the beam to the FODO channel.

IV. EXPERIMENTAL METHODS

A. Beam Instrumentation

Usual methods are applied for beam current and beam centroid measurements; which are: Faraday cups, current transformers located at positions **6**, **8** and **9** and multi-wire profile monitors, scintillating screen located at position **9**. At places **6** and **7**, variable apertures allow for limitation of the transverse emittance. The main effort was done to achieve a maximum sensitivity on beam emittance measurements. Two methods were used for cross-checking the measurements: i) the hole-profile method (HPM) which gives good accuracy on beam brightness and on beam aberrations, ii) the pepper-pot method (PPM) where a scintillating screen gives a full video information in only one beam shot. Unfortunately, the HPM takes a long time (about 30 minutes) since a sampling hole has to be stepped across the beam. The latter method is inspired of an imaging method widely used on the ELSA linac[4] and should be capable, for phase 2, of measuring density distributions over at least 4 decades.

B. Pepper-pot Method

The 300- μ m thick graphite sampling plate with 200 μ m diameter holes spaced by 2 mm is used for the pepper-pot method. The scintillator is 64 cm behind. It is chromium doped alumina covered by a 300. \AA gold deposit to eliminate the charges. Beamlet spots are visualized with a CCD intensified camera. The measurement integrates over the beam pulse duration.

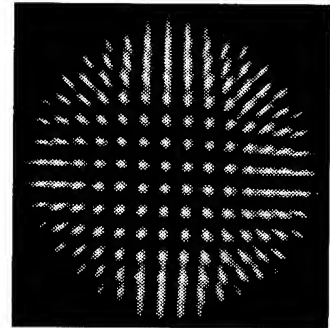


Figure 3: Pepper-pot image of beam on scintillating screen.

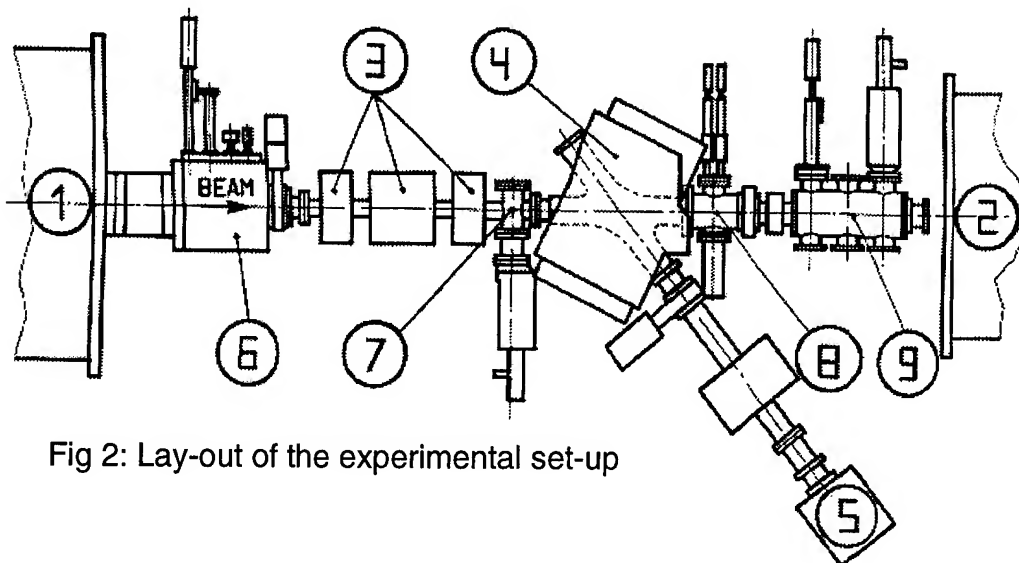


Fig 2: Lay-out of the experimental set-up

C. Profile-Hole Method

A multi wire profile monitor is placed 3m behind a 200*200 μm square sampling hole[5]. This monitor is made of 64 wires (gold covered tungsten of 30 μm diameter), spaced by 300 μm in the center and 500 μm at the edges. A 100V bias eliminates the secondary-electron emission. The sampling step size of the apparatus is .2 mm.

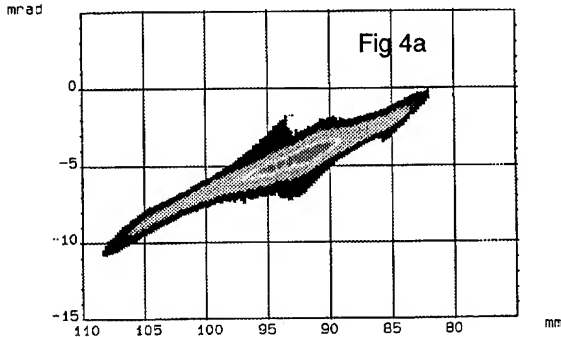


Figure 4a shows a typical emittance contour including 90% of the beam. It corresponds to a 30 mA, 500 keV beam with a normalized emittance of $\epsilon_n/p = .6 \text{ mm.mrad}$.

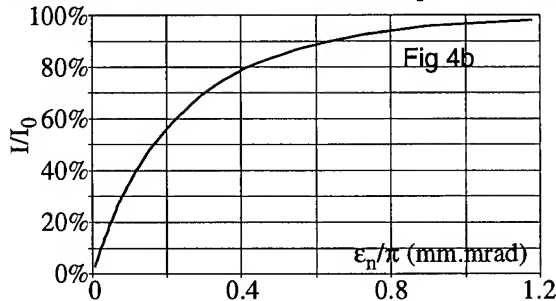


Figure 4b represents the brightness curve corresponding to the emittance shown on figure 4a. I/I_0 is the relative intensity of the beam included in this emittance contour.

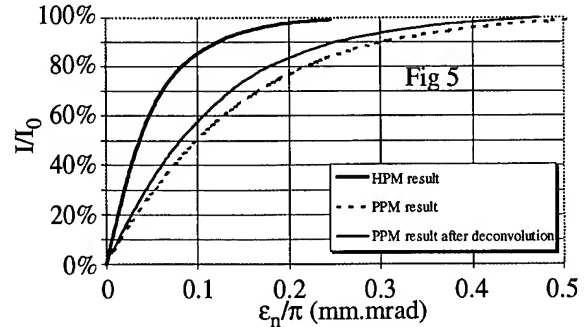
V-. EXPERIMENTAL RESULTS

We measured the relative amount of the different species produced by the ion source. It turned out that H^{2+} and H^{3+} represent respectively about 10% and 1% of the beam. The highest H^{+} percentage was reached for 50 mA total beam current. For future experiments we will have to deal with these unwanted species.

Comparison of the two emittance-measurement methods was done for a typical full beam of 20 mA. One cannot use the triplet magnet in the PPM because separation of the species produces an unacceptable background. However, without the triplet magnet, the beam was too wide on the scintillator, so it was decided to collimate the beam with a $\varnothing 4 \text{ mm}$ collimator, in order to compare the emittance measurement methods (space charge effects due to the difference between species was negligible).

Figure 5 shows the collimated-beam brightness obtained by the two methods. The PPM leads to a measured brightness 2 times greater than that measured by the HPM. After having corrected the data from diffusion effects in the scintillator, we

assume that this difference comes from the fact that the PPM data are integrated over the whole pulse duration even though the HPM samples during only 5 μs in the stable part of the pulse. Further experiments are in progress to verify this hypothesis.



VI. CONCLUSION

The present emittance results are good enough (.6 mm.mrad for 90% of the particle of a 30 mA beam) to allow experiment of phase 2 to be done with a sufficiently large excursion of the tune depression. Nevertheless some more measurements will be performed to find the best sets of source parameters which minimize the transverse emittance.

The chromium-doped alumina scintillators, which were used for the present experiment, will be replaced by faster scintillators in order to measure time-resolved profiles and emittances. These are needed to explain differences between the two experimental methods, and to allow measurements of the halo evolution during the beam pulse.

To eliminate the undesirable species in the proton beam a Wien filter has been designed. It will be installed before starting phase 2 of FODO experiment.

ACKNOWLEDGEMENTS

The authors want to express their thanks to S.Joly for encouraging and supporting the FODO experiment. It is also a pleasure to acknowledge the help of P.Hardy, S.Seguin and S.Striby

V. REFERENCES

- [1].see for example, D.Kehne, M.Reiser and H.Rudd, "Experimental studies of emittance growth due to initial mismatch of a space-charge dominated beam in a solenoidal focusing channel", PAC91 Conf.Proc; p248.
- [2] J-M Lagniel, "Chaotic behaviour induced by space charge", EPAC94, Conf.Proc, p1177
- [3] J-M Lagniel, "Etude expérimentale du halo crée par la charge d'espace, proposition", LNS-SM-94-06, int.rep.
- [4] G.Haouat and al., "Halo of a high-brightness electron beam", this conference
- [5] P-Y.Beauvais, R.Ferdinand, J-L.Lemaire, "Mesure fine de l'émittance d'un faisceau d'ions", LNS/SM 93-08, int.rep

RADIAL MODE EVOLUTION IN LONGITUDINAL BUNCHED BEAM INSTABILITY*

S. Y. Zhang and W. T. Weng,
Brookhaven National Laboratory, Upton, New York 11973 U.S.A.

I. INTRODUCTION

An indispensable aspect of the bunched beam instability mechanism is the variation of the particle distribution with respect to the beam intensity. This density variation can be shown as the evolution of radial modes. The radial modes, which are determined by the stationary particle distribution and the impedance, represent the coherence of the particle density variation governed by the Vlasov equation. Using this coherence in the beam instability analysis gives rise to not only the computational efficiency but also the physical insight into the instability mechanism. The evolution of the radial modes displays several interesting properties for the cases without and with synchrotron frequency spread. If the azimuthal mode coupling cannot be neglected, then corresponding to each coherent frequency shift there exists an extended radial mode which includes the interactions from other azimuthal modes. In this article, the radial mode evolution and the related physical implications will be discussed, which are useful for the understanding of the beam instabilities, and also useful for the beam diagnostics.

II. RADIAL MODE

If the azimuthal mode coupling is neglected, then the Sacherer integral equation can be written as an eigenvalue problem [1-4],

$$(\omega - m\omega_s)\alpha^{(m)} = M^{(m)}\alpha^{(m)} \quad (1)$$

where ω is the coherent frequency shift, m is the azimuthal mode number, ω_s is the synchrotron frequency. The system matrix $M^{(m)}$ represents a feedback determined by the particle distribution of the beam and the impedance, and it is proportional to the beam intensity. The eigenvector $\alpha^{(m)} = [\alpha_0^{(m)} \dots \alpha_{\bar{k}}^{(m)}]^T$, where \bar{k} denotes truncation and the superscript T denotes transpose, represents the radial mode defined on the basis of the normalized orthogonal polynomials $f_k^{(m)}(r)$,

$$R^{(m)}(r) = W(r) \sum_{k=0}^{\infty} \alpha_k^{(m)} f_k^{(m)}(r) \quad (2)$$

Note that the weight function is defined as $W(r) = -d\psi_0/(dr \cdot r)$, where ψ_0 is the stationary particle distribution. The radial mode together with the rotation factor $e^{jm\theta}$ determine the perturbation particle distribution in the phase space,

$$\psi_p(r, \theta) = \sum_{m'=-\infty}^{\infty} R^{(m')}(r) e^{jm'\theta} \quad (3)$$

The projection of this perturbation on the phase deviation axis is the line density, which can be observed to obtain the information of the radial mode variation.

Given stationary distribution and impedance, the radial modes represent coherent particle density evolution, governed by the Vlasov equation. This coherence implies the discreteness of the modes and the corresponding frequency shifts. The orthogonal polynomials used in [2,3], i.e. for a Gaussian distribution, the generalized Laguerre polynomials, and for a parabolic, the Jacobi, can guarantee the convergence. In Fig. 1, the weighted orthogonal polynomials for a Gaussian distribution and the Hankel spectra of these orthogonal polynomials are shown for the azimuthal mode $m=1$. We may observe that the spectra of the polynomials cover from the low frequency to the high, therefore, the larger dimension expansion of the radial modes implies to include higher frequency components. For some impedances such as the RF cavity, the convergence is very fast. Usually an expansion of a few dimension gives rise to a good approximation, and a few radial modes represent the whole system well.

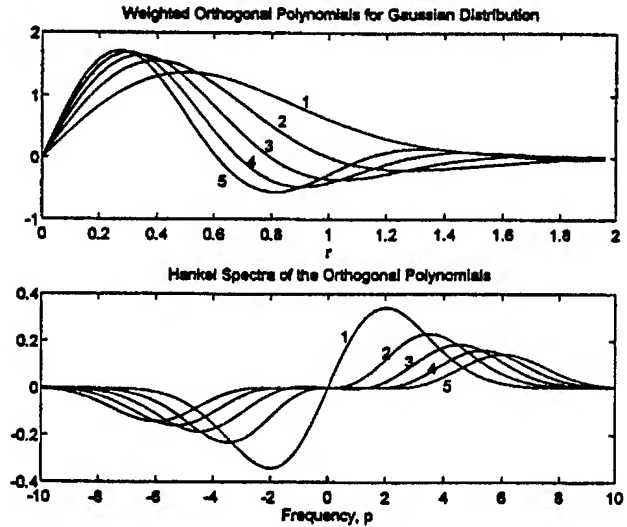


Fig. 1 Orthogonal Polynomials and Spectra

Using the coherence of the particle density evolution, solving of the eigenvalue problem in (1) is equivalent to decoupling the system into several independent subsystems, each one with its own inherent frequency and representation of its radial mode.

In general, different orthogonal basis can be chosen for the radial mode expansion, the convergence will however be affected. The problem will be discussed in Section V.

Several properties associated with the radial mode are mentioned at this point. 1) For a non-zero beam intensity, the coherent frequency shift ω is linearly proportional to

the intensity. 2) The eigenvectors and therefore the radial modes are invariant with respect to the intensity. 3) The amplitude of the radial mode is arbitrary, since the scaling of the eigenvector is arbitrary. 4) The damping or antidamping of these modes are independent for each other.

The eigenvalue problem shown in (1) is the simplest one in the perturbation problem, it also has a most popular application, especially in a regime of low intensity. It, however, cannot satisfy the situations with synchrotron frequency spread, or if the radial modes are affected by other azimuthal modes, i.e. mode coupling, or if due to high intensity the potential well is distorted. Under these conditions, equation (1) needs to be modified.

III. FREQUENCY SPREAD

For the synchrotron frequency spread due to the RF nonlinearity, the equation (1) is modified as,

$$(\omega = m\omega_{SC})\alpha^{(m)} = (mN^{(m)} + M^{(m)})\alpha^{(m)} \quad (4)$$

where $N^{(m)}$ represents the frequency dispersion, which does not depend on the beam intensity. This matrix introduces no instability mechanism, and it is dominant at low intensity. At high intensity the dominance is transferred to the matrix $M^{(m)}$, and the transition process shows the Landau damping.

We note that some properties associated with the radial modes are changed. 1) The eigenvalues are no longer linearly proportional to the beam intensity. 2) The radial modes are no longer invariant to the intensity.

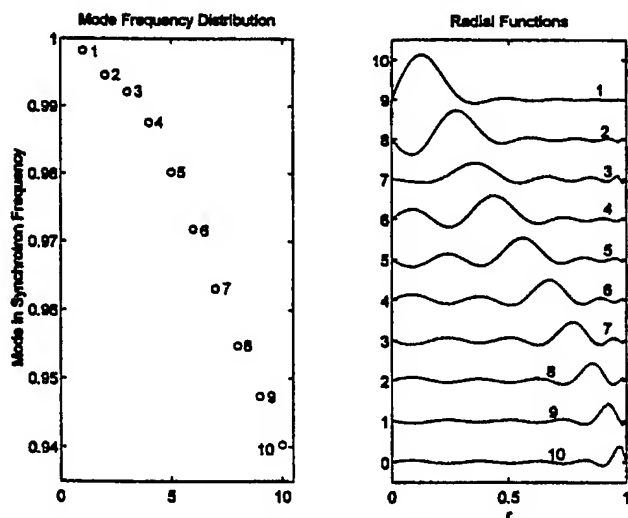


Fig. 2 Frequency Spread and Radial Modes

An example of the $m=1$ mode with RF non-linearity induced synchrotron frequency spread is shown in Fig. 2, where the coherent frequency distribution together with the corresponding radial functions at low intensity are shown. In Fig. 3 a comparison of the unnormalized perturbation line densities with and without frequency spread is shown. It can be shown that for a narrow-band impedance such as the RF cavity, an antidamping mode involves more the

particles in the bunch center, and a damping mode involves the bunch edge [5], which can be observed through the line density variation. In a case of antidamping, the radial modes responsible for the instability gradually expand from the beam center to the edge, as the beam intensity is increased, which can be used to interpret the Landau damping.

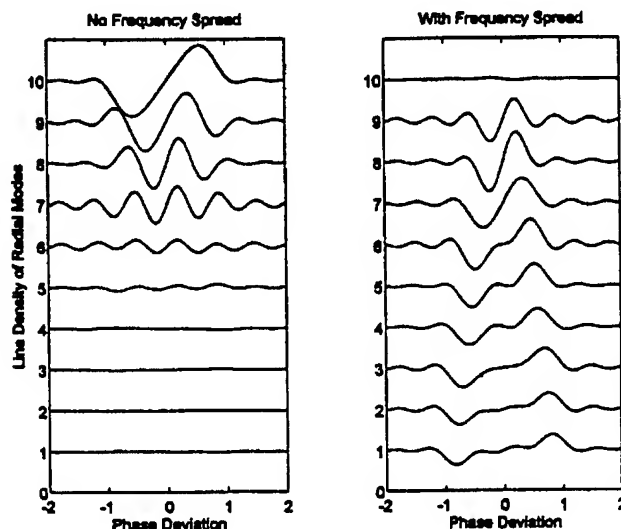


Fig. 3 Comparison of Line Densities

The effect of frequency spread itself generates no coherent distribution density evolution. As the beam intensity increases, the feedback governed by the Vlasov equation becomes effective, and coherence is taking place. The approach used in (4) is to approximate the system by a number of subsystems. This approach is convenient for the computation, and also allows physical insight into Landau damping. For most impedances, such as resonators with not too high resonances, only a small dimension of expansion is needed to get a good result [5].

IV. MODE COUPLING

When mode coupling is considered, we can write,

$$\omega \begin{bmatrix} \alpha^{(m)} \\ \alpha^{(m')} \end{bmatrix} = \begin{bmatrix} m\omega_S I & 0 \\ 0 & m'\omega_S I \end{bmatrix} \begin{bmatrix} \alpha^{(m)} \\ \alpha^{(m')} \end{bmatrix} + \begin{bmatrix} M^{(m,m)} & M^{(m,m')} \\ M^{(m',m)} & M^{(m',m')} \end{bmatrix} \begin{bmatrix} \alpha^{(m)} \\ \alpha^{(m')} \end{bmatrix} \quad (5)$$

where only the coupling between the mode m and m' is included. The equation can, however, be easily extended to multi-mode coupling and to the case with frequency spread. Comparing (5) with (4), we find some similarities, such as that both are different from (1) with an intensity independent matrix in the system matrix. There are also differences such as that the matrix M in (5) is not symmetric as is the case in (4).

In general the orthogonality of the orthogonal polynomials between different azimuthal modes is not

necessarily guaranteed. To qualify (5) as an eigenvalue problem, the rotation factors $e^{jm\theta}$ has to be included in the orthogonal basis. Therefore, the radial modes in a mode coupling situation are implicitly defined by the following distribution,

$$\psi_p^{(m)}(r, \theta) = \sum_{m'=-\infty}^{\infty} R^{(m, m')}(r) e^{jm'\theta} \quad (6)$$

We observe that the radial mode in a mode coupling lost its sole dependence on r , it, however, kept the most important characteristic, which is that the whole distribution pattern of a radial mode in the phase space bears an identical coherent frequency ω .

Consider coupling between the modes $m=1$ and $m=2$. As an example, as the intensity increases from 1 to 9, the line densities of the two responsible radial modes in the two azimuthal modes are shown in Fig. 4. The evolutions of these modes can be observed.

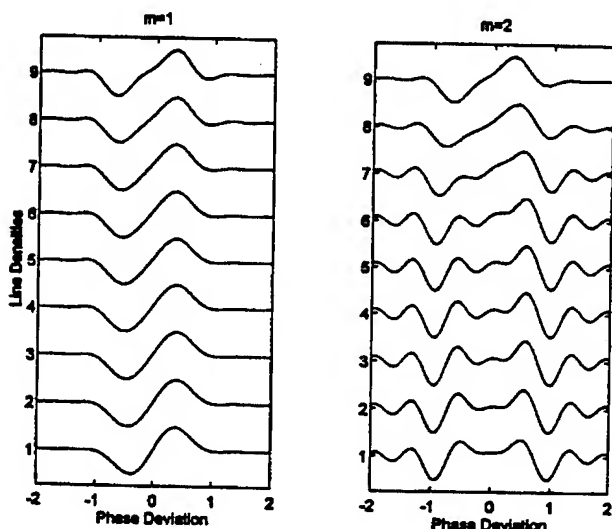


Fig. 4 Line Density Evolution for Mode Coupling

An interesting aspect of experimentally observed radial modes is reported in [6]. The observed modes are discrete, which agrees with the concept of the radial modes applied in this article. Also reported are some problems in observing these modes. We note that below the instability threshold often the radial modes responsible to the coupling are more difficult to observe, because usually before the coupling they are damped, not antidamped. Meanwhile there are other modes, which are less damped or not damped at all, therefore if the beam is excited, these modes are easily observed. They, however, have different coherent frequencies from the modes responsible for the instability thresholds. This can be shown by an example for the coupling between the $m=1$ and $m=2$ modes. The damping is especially strong for the $m=\pm 1$ coupling, which is in fact the first Robinson criterion.

V. POTENTIAL WELL DISTORTION

With potential well distortion, two things happened. First, the stationary distribution may depend on not only r but also θ . For a Gaussian distribution, this problem can be easily treated. Second, the synchrotron frequency becomes dependent on several variables, including the stationary distribution, which itself is nonlinearly dependent on the beam intensity. Considering that the stable phase shift can be corrected by the RF phase feedback, and assuming that the distortion is not so severe that the original orthogonal polynomial expansion still can be used, the problem can be formulated similarly to equation to (4) as,

$$(\omega - m\omega_{SC})\alpha^{(m)} = (mG^{(m)} + M^{(m)})\alpha^{(m)} \quad (7)$$

where $G^{(m)}$ can be calculated from the spectrum of the stationary distribution. Since the stationary distribution is distorted by the beam intensity induced feedback, this matrix is no longer constant, but non-linearly intensity dependent. It is, however, still real and symmetric. A radial mode evolution can be studied for this formulation.

In [7] a method using meshes in the radial direction as the orthogonal basis in the expansion is proposed, which has a potential to include perhaps more extended instability mechanisms. Although the general convergence is not considered as a problem if a large dimension expansion is used, the very concept of the radial modes is, however, buried in the large amount of eigenvectors, most of them represent in fact incoherent motions [8].

By using well established orthogonal polynomials for a non-distorted stationary distribution and using (7), the radial modes can be obtained and used to help the understanding of the mechanism of the instabilities. The convergence and the efficiency in using these polynomials with potential well distortion should be studied analytically and experimentally.

VI. REFERENCES

- [1] F. Sacheren, CERN/SI-BR/72-5, 1972.
- [2] G. Besnier, Nucl. Instru. Methods, Vol.164, p.235, 1979.
- [3] B. Zotter, CERN SPS/81-(18-20), 1981.
- [4] S.Y. Zhang, these proceedings.
- [5] S.Y. Zhang and W.T. Weng, Hefei Workshop, China, July, 1994, to be published.
- [6] D. Brandt, K. Cornelis, and A. Hofmann, EPAC, 1992.
- [7] K. Oide and K. Yokoya, KEK Preprint 90-10, 1990.
- [8] M. D'yachkov and R. Baartman, EPAC, 1994.

STABILITY OF A BREATHING K-V BEAM *

Robert L. Gluckstern and Wen-Hao Cheng

Physics Department, University of Maryland, College Park, MD 20742, USA

Abstract

Many explanations of halo formation in high current ion beams require the existence of particles which are outside the beams central core. We propose a mechanism which is capable of moving some particles outside the core. Specifically, we consider a 2-D KV beam which is started into a uniform density breathing oscillation by some mismatch in the transverse focusing pattern. We then consider perturbations with non-linear space charge density and find that they can be unstable against small oscillations for certain ranges of mismatch and tune depression. The stability limits in the mismatch/tune depression space have been computed for the first three azimuthally symmetric modes with non-linear charge density. It appears that even modest values of mismatch and tune depression can lead to instabilities which are capable of moving particles outside the core of the beam.

I. INTRODUCTION

Interest has arisen recently in using ion linacs in high current applications. In order to keep the beam loss to the order of 1 ppm to avoid serious linac activation, it is necessary to understand emittance growth and halo formation in great detail in order to produce an acceptable design.

Accordingly, recent attention has been focused on understanding the mechanism(s) by which halos are produced. This includes a review of observations and related simulations[1], a variety of simulations and experiments[2], [3]. Several models have been constructed to explore resonances between particle oscillation frequencies and the periodicity of the focusing system or core oscillation modes[4], [5]. Many of the simulations show the onset of chaotic motion at high space charge levels.

In a recent publication[6], we proposed a simple model in which a K-V beam, excited into a uniform density "breathing" mode by some sort of mismatch, interacts resonantly with individual oscillating ions. If the ions find themselves outside the core for part of their oscillation, the resulting non-linearity of the ion oscillations can lead to a phase lock with the breathing oscillation, producing a halo whose parameters can be predicted and whose appearance matches that in simulations performed by Wangler and by Ryne [7]. The unanswered question is: "What is the mechanism by which ions initially escape from the core in order to participate in the formation of the halo?"

Obviously, any unstable longitudinal or transverse collective modes involving the core are capable of moving particles outside the core. Studies of the transverse stability of a matched K-V beam[8], [9] have shown that instabilities exist for tune depressions (ratio of ion oscillation frequency with space charge to that without space charge) of 0.4 or less. In the present paper, we analyze the instabilities of a breathing K-V beam for various collective modes involving non-uniform charge density and find

that modes involving a significant breathing amplitude will be unstable at tune depressions as high as 0.7 or 0.8.

II. BREATHING MODE

The envelope equation of a KV beam is

$$a'' + k^2 a = \frac{I}{a} + \frac{\epsilon^2}{a^3}, \quad (1)$$

where a is the beam radius, the prime stands for d/dz , k is the tune due to the external linear restoring force, I is the perveance defined by $I = eI_0 Z_0 c / 2\pi m v_0^3$, and where $\pi\epsilon$ is the transverse emittance of the beam. Here $Z_0 = 120\pi$ ohms is the impedance of free space, I_0 is the beam current and v_0 is the particle's axial velocity. We assume that k^2 is independent of z in the present work. If we start with $a(0) = a_1$, $a'(0) = 0$, an integral of Eq. (1) gives

$$a'^2 = 2I\ell n \frac{a}{a_1} + k^2(a_1^2 - a^2) + \epsilon^2 \left(\frac{1}{a_1^2} - \frac{1}{a^2} \right), \quad (2)$$

which enables us to obtain the other value of $a(\equiv a_2)$ at which $a' = 0$, as well as the period of the breathing motion.

We now set $a^2 = \beta\epsilon$, and change the independent and dependent variables from z, x, y to $\phi = \int dz/\beta$, $u(\phi) = x(z)/\sqrt{\beta\epsilon}$, $v(\phi) = y(z)/\sqrt{\beta\epsilon}$, such that

$$\ddot{u} + u = 0, \quad \ddot{v} + v = 0, \quad (3)$$

where the dot denotes derivative with respect to ϕ . Thus the breathing mode can be described by specifying β as a function of ϕ , with period ϕ_0 . The transformation clearly depends on the size of the "mismatch", that is, on the relative amplitude of the breathing oscillation. If we scale β so that $\beta(\phi) = \sigma(\phi)/k$ and define $\alpha = I/k\epsilon$, The envelope equation can be written as

$$\frac{\ddot{\sigma}}{2\sigma} = 1 + \alpha\sigma - \sigma^2 + \frac{3}{4} \frac{\dot{\sigma}^2}{\sigma^2}. \quad (4)$$

We note that a matched beam (zero breathing amplitude) has the matched amplitude $\sigma_0 = \alpha/2 + \sqrt{1 + \alpha^2/4}$ and that the tune depression for a matched beam is given by $\eta \equiv \sqrt{k^2 - I/a_0^2}/k = 1/\sigma_0 = \sqrt{1 + \alpha^2/4} - \alpha/2$.

III. PHASE SPACE DISTRIBUTION

We now wish to consider small perturbations from a uniform charge density breathing mode in the phase space distribution. For this purpose, we use the variables $u(\phi)$, $v(\phi)$ and ϕ and write

$$f(u, v, \dot{u}, \dot{v}, \phi) = f_0(u, v, \dot{u}, \dot{v}) + f_1(u, v, \dot{u}, \dot{v}, \phi), \quad (5)$$

where the unperturbed distribution (including the breathing mode) is

$$f_0(u, v, \dot{u}, \dot{v}) = (\tau_0/\pi^2) \delta(u^2 + v^2 + \dot{u}^2 + \dot{v}^2 - 1). \quad (6)$$

*Work Supported by U.S. Department Of Energy.

Here $\tau_0 = I_0/v_0$ is the line charge density of the beam. The charge density (in the x, y space) is then

$$\rho_0 = \frac{I_0}{\pi v_0 \beta \epsilon} \begin{cases} 1 & , \quad u^2 + v^2 < 1 \\ 0 & , \quad u^2 + v^2 > 1 \end{cases} \quad (7)$$

and

$$\rho_1 = \frac{1}{\beta \epsilon} \int du \int dv f_1(u, v, \dot{u}, \dot{v}, \phi). \quad (8)$$

We assume that the electric field due to ρ_1 is derivable from a scalar potential $G(u, v, \phi)$ such that

$$\begin{aligned} \nabla \cdot \vec{E}_\perp &= \frac{1}{\sqrt{\beta \epsilon}} \left(\frac{\partial E_x}{\partial u} + \frac{\partial E_y}{\partial v} \right) = \frac{\rho_1}{\epsilon_0} \\ &= -\frac{1}{\beta \epsilon} \left(\frac{\partial^2 G}{\partial u^2} + \frac{\partial^2 G}{\partial v^2} \right) = \frac{1}{\beta \epsilon \epsilon_0} \int du \int dv f_1. \end{aligned} \quad (9)$$

The equations of motion, including the force due to the non-uniform charge distribution, are

$$\ddot{u} + u = -\frac{e}{mv_0^2} \frac{\beta}{\epsilon} \frac{\partial G}{\partial u}, \quad \ddot{v} + v = -\frac{e}{mv_0^2} \frac{\beta}{\epsilon} \frac{\partial G}{\partial v}. \quad (10)$$

If we now write

$$f_1(u, v, \dot{u}, \dot{v}, \phi) = g(u, v, \dot{u}, \dot{v}, \phi) f_0(u^2 + v^2 + \dot{u}^2 + \dot{v}^2), \quad (11)$$

keeping only terms linear in f_1 or ρ_1 (or G), the Vlasov equation becomes

$$\frac{\partial g}{\partial \phi} + \dot{u} \frac{\partial g}{\partial u} + \dot{v} \frac{\partial g}{\partial v} - u \frac{\partial g}{\partial \dot{u}} - v \frac{\partial g}{\partial \dot{v}} = R(u, v, \dot{u}, \dot{v}, \phi), \quad (12)$$

where the right hand side is

$$R(u, v, \dot{u}, \dot{v}, \phi) = \frac{2e}{mv_0^2} \frac{\beta}{\epsilon} \left[\dot{u} \frac{\partial G}{\partial u} + \dot{v} \frac{\partial G}{\partial v} \right]. \quad (13)$$

Equations (9) and (12) are coupled integro-differential equations. Since the operator on the left side of Eq. (12) corresponds to the sinusoidal orbits in Eq. (3), Eq. (12) has a formal solution which can be written as

$$g(u, v, \dot{u}, \dot{v}, \phi) = \int_{-\infty}^{\phi} d\psi R(u', v', \dot{u}', \dot{v}', \psi), \quad (14)$$

where $u' = uc - \dot{u}s$, $v' = vc - \dot{v}s$, $\dot{u}' = \dot{u}c + us$, $\dot{v}' = \dot{v}c + vs$, with $c \equiv \cos(\phi - \psi)$, $s \equiv \sin(\phi - \psi)$.

We now proceed, as in the analysis for a matched K-V beam[8], to guess at the form of the potential $G(u, v, \phi)$ and to determine the perturbed phase space distribution $g(u, v, \dot{u}, \dot{v}, \phi)$ using Eq. (14). Using Eqs. (11) and (9), we then obtain $\partial^2 G / \partial u^2 + \partial^2 G / \partial v^2$ and require that it agree with our guess for G .

Remarkably, our guess, which is almost identical to the form used for the matched K-V beam, works once again.

We now conjecture that $G(u, v, \phi)$ is

$$G(u, v, \phi) = P(\phi) F(u, v) \quad (15)$$

with

$$\begin{aligned} F(u, v) &= (u + iv)^m {}_2F_1(-j, m + j; m + 1; u^2 + v^2) \\ &= d_{jm} \sum_{\ell} \frac{(-1)^{\ell} (m + j + \ell - 1)!}{\ell! (m + \ell)! (j - \ell)!} (u + iv)^{\ell + m} (u - iv)^{\ell}, \end{aligned} \quad (16)$$

where $d_{jm} = j! m! / (m + j - 1)!$. Here $P(\phi)$ is a function periodic in ϕ (with period ϕ_0 , the same as that of the breathing oscillation) which is yet to be determined. The corresponding charge density, according to Eq. (9), is

$$\begin{aligned} \rho_1(u, v, \phi) &= \frac{4\epsilon_0}{\epsilon} \frac{P(\phi)}{\beta(\phi)} d_{jm} \sum_{\ell} \frac{(-1)^{\ell} (m + j + \ell)!}{\ell! (m + \ell)! (j - 1 - \ell)!} \times \\ &\quad (u + iv)^{\ell + m} (u - iv)^{\ell}, \end{aligned} \quad (17)$$

with m and $j - 1$ being the number of azimuthal and radial nodes in the perturbed charge density.

Requiring the self-consistency of Eqs. (9) and (14), we obtain an integral equation for $P(\phi)$

$$P(\phi) = -\alpha \int_{-\infty}^{\phi} d\psi P(\psi) \sigma(\psi) \frac{\partial Q}{\partial \psi}, \quad (18)$$

where

$$\begin{aligned} Q(\phi - \psi) &= \sum_r \frac{(-1)^{j+r} (m + j + r - 1)!}{r! (m + r)! (j - r)!} \cos^{m+2r}(\phi - \psi) \times \\ &= (-1)^j [d_{jm}]^{-1} \cos^m(\phi - \psi) \times \\ &\quad {}_2F_1(-j, m + j; m + 1; \cos^2(\phi - \psi)). \end{aligned} \quad (19)$$

To recapitulate, we have confirmed that the conjecture for the electrostatic potential in Eq. (15) leads to a perturbed phase space density in Eq. (11) which reproduces the perturbed space charge density corresponding to the potential in Eq. (15), provided $P(\phi)$ satisfies the integral equation in Eq. (18).

IV. DIFFERENTIAL EQUATION FOR $P(\phi)$

The integral equation for $P(\phi)$ in Eq. (18) can be converted to a linear differential equation with periodic coefficients. As an illustration, we consider the case $j = 2$, $m = 0$, and take successive derivatives of Eq. (18) with respect to ϕ , obtaining contributions from both the upper limit of the integral and the integrand. And then we construct a linear combination of $P(\phi)$, $\dot{P}(\phi)$ and $P^{iv}(\phi)$ in which the integrals cancel. Specifically

$$P^{iv} + (20 + 2\alpha\sigma)\ddot{P} + 4\alpha\dot{\sigma}\dot{P} + (64 - 4\alpha\sigma + 2\alpha\ddot{\sigma})P = 0. \quad (20)$$

Since $\sigma(\phi)$ in Eq. (4) is a periodic function of ϕ with period ϕ_0 , Eq. (20) is a Mathieu-like equation for $P(\phi)$. If we let V be the four-component vector $(P, \dot{P}, \ddot{P}, \ddot{\ddot{P}})$, Eq. (20) can then be written as the single 4×4 matrix equation $V = TV$ where the matrix T depends on ϕ because σ depends on ϕ .

For general j and m , by taking $2j + m$ or $2j + m + 1$ derivatives of $P(\phi)$, it is always possible to construct a linear combination which eliminates all the integrals, as we did in Eq. (20). The order of the resulting differential equation is $2j + m$ for m even or $2j + m + 1$ for m odd, as is also the dimension of the vector V and the matrix T .

V. NUMERICAL STUDIES

To determine the stability of a specific mode of density perturbation, we first need to solve the equation of the envelope oscillation shown in Eq. (4) numerically. With the solutions of $\sigma(\phi)$, we can numerically integrate the matrix form of the differential equation for $P(\phi)$. The eigenvalues of the transfer matrix \mathcal{T} for a breathing period then determines the stability of the mode denoted by j, m for the space charge α and the mismatch parameter σ_1 . Specifically, the mode will be unstable if the absolute value of any of the eigenvalues of \mathcal{T} is greater than 1.

Starting from the integral equation for $P(\phi)$ in Eq. (18), we can also make the transformation to differential equations for $(j, m) = (3, 0)$ and $(4, 0)$, and thus determine their stabilities with respect to different parameters.

As for the matched beam, i.e., $\sigma = \sigma_0 = \text{constant}$, the stability limits of the modes $(j, m) = (2, 0)$, $(3, 0)$ and $(4, 0)$, are where $\eta_{\text{limit}} = 0.2425$, 0.3859 and 0.3985 respectively. In fact, $m = 0$ is the most restrictive mode for all m , and $j = 4$ is the most serious mode that gives the the largest threshold value of η , i.e. the smallest space charge limit, for all $(j, 0)$ modes[8]. Therefore, the $(4, 0)$ mode is the least stable mode for the space charge limit of a KV beam. In Figs. 1, we show the stability diagram for these three cases in the $\mu - \eta$ space, where $\mu \equiv a_1/a_0$. The values of η_{limit} on the $\mu = 1$ axis for each case is confirmed in the figures.

The cusps appearing in these diagrams are caused by resonances of the mode frequency. In Fig. 1(a), the deep fissure down to the matched parameter $\mu = 1$ is where the phase advance of the $(2, 0)$ mode oscillation during one period of the breathing mode is π , when $\eta_{\text{limit}} = 0.5235$. Note that for this resonance the breathing frequency is twice the mode frequency. We believe that the other slits appearing in the stable domains are also due to resonance for particular parameters of tune depression and mismatch. As for the higher modes $(3, 0)$ and $(4, 0)$, the $\phi = \pi$ resonance occurs outside of their stability limits. That is why the deep fissure that meets the $\mu = 1$ axis is not seen in either the $j = 3$ or the $j = 4$ cases. One can also see that, as j increases, not only does η_{limit} moves "backward", i.e., to smaller space charge, but also the stable band width for the mismatch parameter μ becomes narrower. This implies, at least up to $j = 4$ for a KV beam, that the area of stability decreases as j increases.

We are currently using numerical orbit simulations to confirm the stability regions shown in Fig. 1.

References

- [1] R.A. Jameson, Los Alamos Report LA-UR-93-1209.
- [2] M. Reiser, Proc. of the Part. Accel. Conf., San Francisco, CA, p.2497 (1991); A. Cucchetti, M. Reiser and T. Wangler, *ibid.* p. 251; D. Kehne, M. Reiser, and H. Rudd, Proc. of the Part. Accel. Conf., Washington, DC, p. 65 (1993).
- [3] J.S. O'Connell, T.P. Wangler, R.S. Mills and K.R. Crandall, Proc. of the Part. Accel. Conf., Washington, DC, p. 3657 (1993).
- [4] C. Chen and R.C. Davidson, Phys. Rev. Letters **72**, 2195 (1994).
- [5] J.M. Lagniel, Nucl. Instrum. & Meth. **A345**, 46 (1994); **A345**, 405 (1994).
- [6] R.L. Gluckstern, Phys. Rev. Letters **73**, 1247 (1994).
- [7] Private communication.
- [8] R.L. Gluckstern, Proc. of the Linac Conf., Fermilab, 1970, p. 811.
- [9] I. Hofmann, L.J. Laslett, L. Smith and I. Haber, Particle Accelerators **13**, 145 (1983).

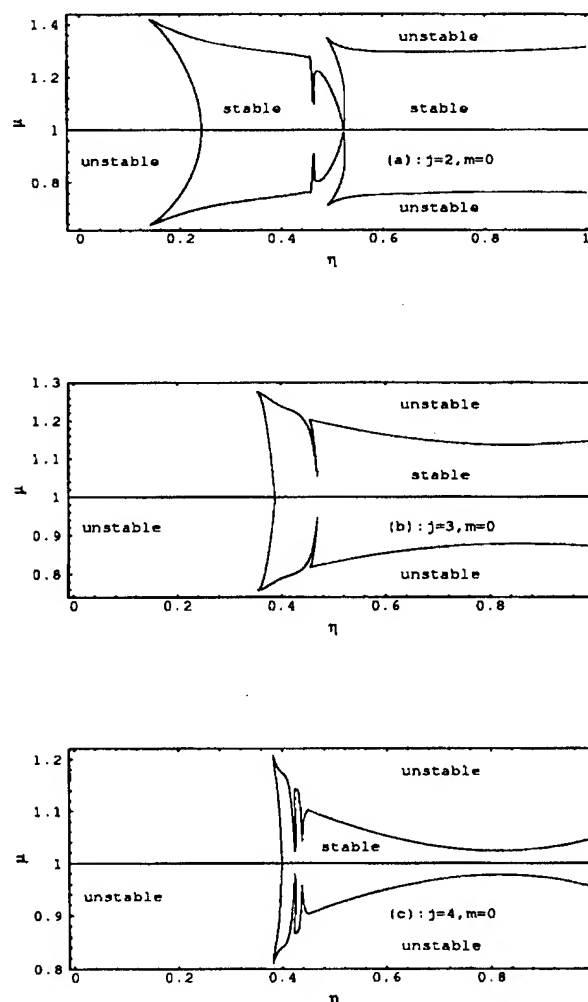


Figure 1. Stability diagram of $\mu - \eta$ space, for (a) $j = 2, m = 0$, (b) $j = 3, m = 0$, and (c) $j = 4, m = 0$.

HAMILTONIAN FORMALISM FOR SPACE CHARGE DOMINATED BEAMS IN A UNIFORM FOCUSING CHANNEL*

A.Riabko, M.Ellison, X.Kang, S.Y.Lee, J.Y.Liu, D.Li, A.Pei, L.Wang
Department of Physics, Indiana University, Bloomington, IN 47405

Abstract

Halo formation for a test particle in a mismatched KV beam is studied. Parametric resonances of the particle Hamiltonian due to envelope modulation are studied with particular emphasis on period 2 resonance which plays dominant role in Halo formation. It is shown that the onset of global chaos exhibits a sharp transition when the amplitude of modulation is larger than a critical value which is a function of a single parameter, κ , i.e., the ratio of the space charge perveance to the focusing strength.

I. INTRODUCTION

The interest in intense charged particle beams has grown in past few years due to demand in high brightness and high intensity ion sources. For beams dominated by the self-space-charge force Kapchinskij and Vladimirskij have constructed a self-consistent equilibrium distribution function which obeys the KV equation governed by the external focusing field and the self space charge force [1]. In order to understand the motion of a test particle in KV beam simultaneous numerical integration of envelope and particle equations of motion can be used. The assumption is that the envelope evolution will affect the particle dynamics, while the particle motion does not affect the envelope. The results of numerical simulations indicate that the halo formation arises mainly from resonance excitations [2-5].

This paper is organized as follows. In Sec. II, we review properties of the envelope Hamiltonian and study a motion of a weakly mismatched beam in a uniform focusing channel. In Sec. III, the particle Hamiltonian is separated into autonomous Hamiltonian and time dependent perturbation; the condition on existence of primary parametric resonances is obtained. Conditions for global chaos and estimation of halo diameter as function of modulation amplitude are considered. Conclusion is given in Sec. IV.

II. THE HAMILTONIAN FOR THE ENVELOPE PHASE SPACE

The KV envelope Hamiltonian for a uniform focusing channel is given by

$$H_e = \frac{P^2}{2} + \frac{\mu^2 R^2}{2} - K \ln(R) + \frac{\epsilon^2}{2R^2} \quad (1)$$

(where μ is the external focusing field, ϵ is the emittance of the beam and $K = \frac{2Nr_d}{\beta^2\gamma^3}$ is the space charge perveance parameter).

Using scaling transformation, we obtain the following expression for the envelope Hamiltonian

$$H_e = \frac{P^2}{2} + \frac{R^2}{2} - 2\kappa \ln(R) + \frac{1}{2R^2} \quad (2)$$

where $\kappa = \frac{K}{2\mu\epsilon}$. The matched beam radius R_o and the frequency of small amplitude envelope oscillations ν_e are given by

$$R_o = \sqrt{\sqrt{\kappa^2 + 1} + \kappa} \quad (3)$$

$$\nu_e = 2\sqrt{1 - \kappa(\sqrt{\kappa^2 + 1} - \kappa)} \quad (4)$$

Because of the nonlinear space charge force the envelope tune $Q_e(J_e)$ varies from $Q(J_e = 0) = \nu_e$ to $Q(J_e \rightarrow \infty) \rightarrow 2$. When $\kappa = 0$, the envelope dynamics is linear and $Q_e = 2$; at the infinite space charge limit $\nu_e = \sqrt{2}$.

III. THE HAMILTONIAN FOR THE PARTICLE PHASE SPACE

The Hamiltonian for a test particle is given by

$$H_p = \frac{p_r^2}{2} + \frac{L^2}{2r^2} + \frac{r^2}{2} - \frac{\kappa(r^2 - R^2)}{R^2} \Theta(R - r) - 2\kappa \ln\left(\frac{r}{R}\right) \Theta(r - R) \quad (5)$$

For a beam with mismatch parameter $M \ll 1$ envelope radius changes harmonically with time $R(t) = R_o(1 - M \cos(\nu_e t))$; the particle Hamiltonian can be separated into autonomous Hamiltonian $H_{po}(p_r, r)$ (can be rewritten in terms of canonical action-angle variables) and time-dependent perturbation $\Delta H(p_r, r, t)$.

$$H_{po}(p_r, r) = \frac{p_r^2}{2} + \frac{L^2}{2r^2} + \frac{r^2}{2} - \frac{\kappa(r^2 - R_o^2)}{R_o^2} \Theta(R_o - r) - 2\kappa \ln\left(\frac{r}{R_o}\right) \Theta(r - R_o) \quad (6)$$

$$\Delta H(p_r, r, t) = -\frac{\kappa(r^2 - R_o^2)}{R_o^2} M \cos(\nu_e t) \Theta(R_o - r) \quad (7)$$

Below we consider only $L = 0$ case (we replace coordinate r by y). For a beam with a matched envelope radius R_o particle motion inside the core ($|y| < R_o$ or equivalently $J_p < \frac{1}{2}$) is linear with

$$\nu_p = \sqrt{\kappa^2 + 1} - \kappa \quad (8)$$

*Work supported by grants from NSF PHY-9221402 and DOE DE-FG02-93ER40801.

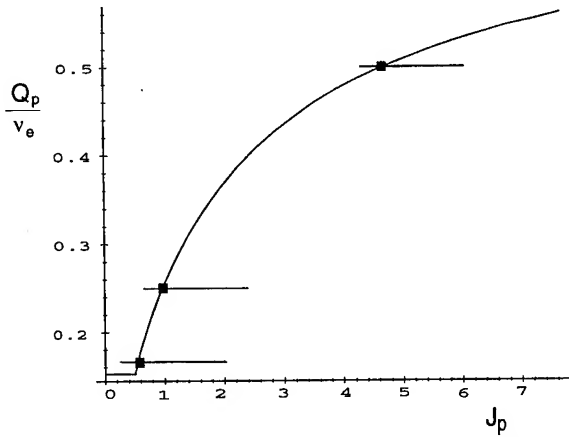


Figure 1. $\frac{Q_p}{v_e}$ vs J_p for $\kappa = 2.19$. Intersections of horizontal lines with $\frac{Q_p}{v_e}$ mark locations of parametric resonances.

On the other hand in the limit of large amplitude oscillations the space-charge force is not important; particle motion is almost harmonic with $Q_p = 1$. Thus the tune of a test particle outside the core lies within the range $[\nu_p, 1)$.

Note that functional dependence of particle tune vs. action has a cusp at $r = R_o$ (see Figure 1); this suggests that a simple power expansion may not be applicable. On the other hand the sharp rise of the particle tune outside the core will bear important implications to parametric resonances when the system is subject to harmonic perturbations (such as wake fields or envelope modulation).

In terms of action-angle variables the particle Hamiltonian becomes

$$H_p = H_{po}(J) - M\kappa \cos(\nu_e t) \sum_{n=-\infty}^{\infty} G_n(J) e^{in\psi} \quad (9)$$

where the strengths of primary resonances $G_n(J)$ are

$$G_n(J) = \frac{1}{2\pi} \int_{-\pi}^{\pi} \left(\frac{y^2}{R_o^2} - 1 \right) \Theta(R_o - y) e^{-in\psi} d\psi \quad (10)$$

Because the Hamiltonian is symmetric with respect to $y \rightarrow -y$ all odd harmonics vanish. The location of primary parametric resonances for particle motion can be found from:

$$nQ_p(J_{FP}) - \nu_e + nM\kappa G'_n(J_{FP}) = 0 \quad (11)$$

If $M\kappa G'_n(J_{FP})$ is small, the threshold of existence of n -th order primary parametric resonance is given by $\frac{\nu_p}{\nu_e} = \frac{1}{n}$. Therefore as κ increases more high order resonances appear (see Figure 2). In general n -th order primary resonance exists only if

$$\kappa > \frac{n^2 - 4}{\sqrt{8(n^2 - 2)}} \quad (12)$$

This has an important implication for Halo formation which is enhanced when many high order resonances overlap creating large chaotic area in the phase space. Also as it was found in numerical simulations the resonance strength will increase as well. Finally we see that for a beam with a very large space charge parameter many resonances appear near the core and create a large

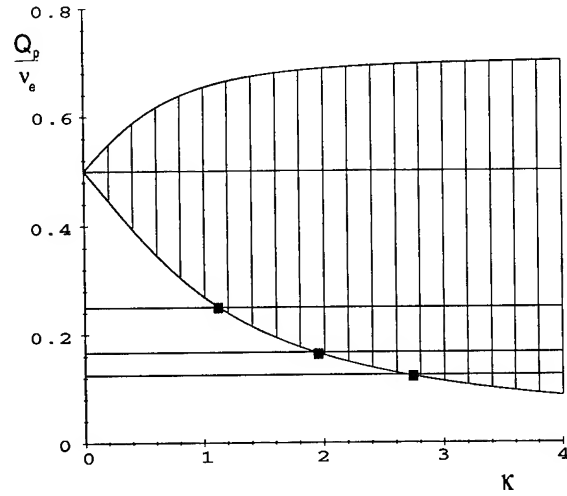


Figure 2. The range of ratios of the particle tune to the envelope tune as function of effective space charge strength κ .

region of stochasticity. Though motion inside the core is stable, the dynamics of the particle from the diffusive tail is determined by the presence of this chaotic regions.

A. Halo and global chaos

We examine particle motion in Poincaré surfaces of section at the minimum envelope radius locations; Poincaré energy for particle motion is defined as energy calculated at the minimum radius locations. The Poincaré energy of a test particle outside the core is always larger than $E_P = \frac{\nu_p}{2(1-M)^2}$ maximum energy of core particles. We now consider the motion of a particle with Poincaré energy $E = \eta E_P$. For a given mismatch parameter M and κ there is a critical number η_{cr} such that all test particles with $\eta > \eta_{cr}$ will orbit about the 2 : 1 resonance (which exists for all values of κ) and thus become halo particles. Numerical simulations indicate that η_{cr} is a smooth function of mismatch parameter M (Figure 3 a) if $\kappa < 2.2$. However for $\kappa > 2.2$, we can always observe very sharp transition when M exceeds some critical value $M_{cr}(\kappa)$ (Figure 3 b). When κ is small there are few resonances near the core. Since the width of period 2 resonance and width of stochastic layer varies smoothly with the modulation amplitude, η_{cr} will decrease smoothly as M increases. On the other hand when κ is large there are many primary and secondary resonances and local chaos is formed near the core. Once the stochastic layer layer of period 2 resonance overlaps with local chaos, global chaos occurs.

B. Period 2 resonance and Halo diameter

It is evident from numerical simulations that Halo diameter is determined mainly by period 2 resonance. Though the location of SFP of this resonance is shifted when modulation amplitude increases, this shift is linearly proportional to M (Figure 4) and is omitted for the sake of simplicity. So we can estimate the maximum transverse energy of Halo particles by $E(J_r) + \frac{\Delta E}{2}$ where $E(J_r)$ is the energy of resonance particle and ΔE is the energy width of the resonance :

$$\Delta E = Q_p(J_r) \Delta J = 4 Q_p(J_r) \sqrt{\frac{M G_2(J_r)}{Q'_p(J_r)}} \quad (13)$$

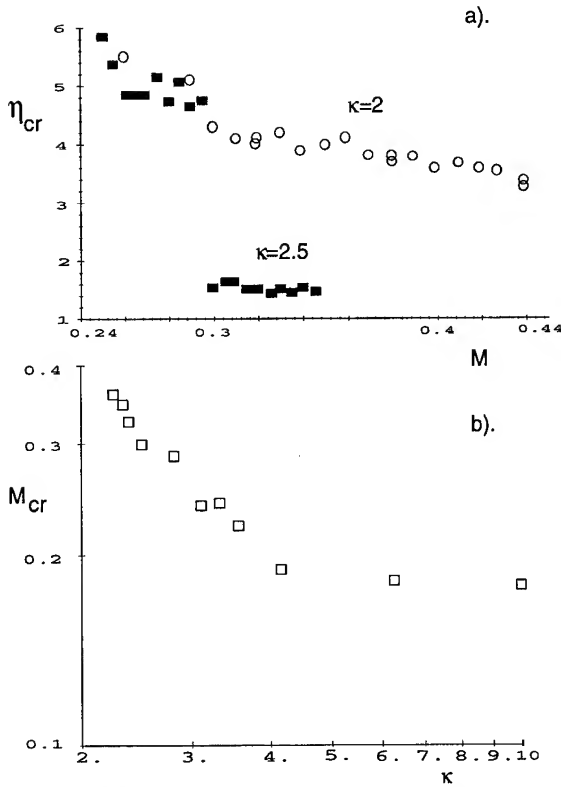


Figure 3. a). η_{cr} as function of M for $\kappa = 2$ (boxes) and 2.5 (circles). b). M_{cr} vs space charge parameter κ obtained from numerical simulations.

Taking advantage of the fact that dynamics of the system is defined by a single parameter κ we can use the following approximate formula for maximum transverse energy of Halo particles (Figure 4) :

$$E_{max} = \epsilon \mu E_r(\kappa) + \epsilon \mu \nu_e(\kappa) \sqrt{M} \beta \kappa \quad (14)$$

where $\beta \approx 2.5$ obtained from numerical simulations.

IV. CONCLUSION

In conclusion, we studied the beam transport problem solving simultaneously the dynamic equations for the KV envelope and a test particle. Parametric resonances for particle motion can be generated by a mismatched envelope oscillations. The resonance condition is found to depend only on a single effective space charge parameter κ . Due to the mismatched beam envelope oscillations, the period 2 resonance occurs at all values of space charge perveance. From our numerical simulations, it is observed that the critical Poincaré energy for the halo particle exhibits a sharp transition when plotted as a function of envelope mismatch parameter what is related to the onset of global chaos. The relation between the critical mismatch parameter M_c and the effective space charge parameter κ is obtained from numerical simulations. Halo diameter is estimated. Effects of angular momentum are considered in other publications [6].

We have studied the halo formation for a space charge dominated beams in a uniform focusing channel. This method can readily be applied to study the beam transport problems in a periodic focusing channel, where Floquet transformations is needed before analytic solution can be obtained [6].

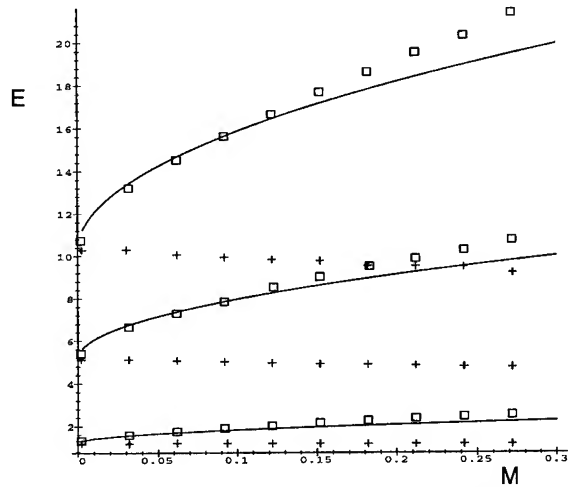


Figure 4. Maximum energy of Halo particles (boxes), equation 14(line) and location of SFP of period 2 resonance (crosses) as function of modulation amplitude M for $\kappa = 1.25, 6.25, 12.5$.

References

- [1] I.M. Kapchinskij and V.V. Vladimirkij, *Proceedings of the International Conf. on High Energy Accelerators*, p. 274 (CERN, Geneva, 1959).
- [2] R.A. Jameson, in *Proc. of the 1993 Part. Accel. Conf.* p.3926 (IEEE, Piscataway, 1993); Los Alamos Report No. LA-UR-93-1209 (1993) (unpublished).
- [3] J.S. O'Connell, T.P. Wangler, R.S. Mills and K.R. Crandall, in *Proceedings of the Particle Accelerator Conf.* edited by J. Bisognano, p.3657 (IEEE, Piscataway, NJ, 1993).
- [4] J.M. Lagniel, Nucl. Inst. and Meth. in Phys. Res. **A345**, 46 (1994), *ibid.* 405 (1994).
- [5] I. Hofmann, L.J. Laslett, L. Smith, and I. Haber, *Particle Accelerators*, **13**, 145 (1983); J. Struckmeier and M. Reiser, *Particle Accelerators*, **14**, 227 (1983).
- [6] S.Y.Lee, A.Riabko, *Phys.Rev.* **E51**, 1609 (1995); A.Riabko, *et al.*, *Phys. Rev.* **E51**, May (1995).

SIMULATION STUDIES OF THE LAMPF PROTON LINAC

R. W. Garnett, E. R. Gray, L. J. Rybarczyk, and T. P. Wangler
Accelerator Operations and Technology Division,
Los Alamos National Laboratory, Los Alamos, NM 87545 USA*

I. INTRODUCTION

The LAMPF accelerator consists of two 0.75-MeV injectors, one for H^+ and the other for H^- , a separate low-energy beam transport (LEBT) line for each beam species, a 0.75 to 100-MeV drift-tube linac (DTL) operating at 201.25 MHz, a 100-MeV transition region (TR), and a 100 to 800-MeV side-coupled linac (SCL) operating at 805 MHz. Each LEBT line consists of a series of quadrupoles to transport and transversely match the beam. Each LEBT also contains a prebuncher and an electrostatic deflector, but share a common main buncher. The deflector is used to gate beam into the linac. The DTL consists of four rf tanks (modules 1-4), each driven by a separate rf amplifier, and uses singlet FODO transverse focusing. The focusing period is doubled in the last two tanks by placing a quadrupole only in every other drift-tube. Doublet FDO transverse focusing is used in the SCL. The SCL tanks are bridge-coupled together into rf modules with a single klystron powering each module. Modules 5-12 consist of four coupled-cavity tanks bridge-coupled together with 32-36 cells/tank. Modules 13-48 consist of two bridge-coupled tanks with 49-61 cells/tank. The TR consists of separate transport lines for the H^+ and H^- beams. The path lengths for the two beams differ, by introducing bends, so the arrival of both beams is properly phased relative to the rf field. Peak H^+ beam currents typically range from 12 to 18 mA for varying duty factor, which give an average beam current of 1 mA. The number of particles per bunch is of the order 10^8 .

The work presented here is an extension of our previous work [1]. We have attempted to do a more complete simulation by including modeling of the LEBT. No measurements of the longitudinal structure of the beam, except phase-scans, are performed at LAMPF. Transverse measurements include slit and collector emittance measurements, and wire scans to determine beam size and centroids. Comparison of simulations to beam loss data suggest that the primary causes of beam spill are incomplete longitudinal capture and the lack of longitudinal matching. Measurements to support these claims are not presently made at LAMPF. However, agreement between measurement and simulation for the transverse beam properties and transmissions serve to benchmark the simulations.

*Work supported by Los Alamos National Laboratory Directed Research and Development, under the auspices of the United States Department of Energy.

II. SIMULATION TECHNIQUES

The LEBT, DTL, and TR were modeled using the PARMILA code and the operational set points obtained from the operations group. All simulations began with an initial distribution of either 10,000 or 100,000 macroparticles. The transverse beam was generated as a Gaussian distribution in 4-D transverse space and was truncated at 3σ . A uniform longitudinal distribution was generated with zero energy spread. Simulations were done separately for H^+ and H^- , and were started with a dc beam at the center of the prebuncher in each LEBT. The beam was initially propagated to the center of the endwall quadrupole of the first tank of the DTL. A comparison was then made between the simulation results and transverse emittance measurements just downstream of the prebuncher and just upstream of the first DTL tank. The prebuncher and main buncher voltages used in the simulations were estimated for the actual cavities from Q and input power measurements, and SUPERFISH calculations. The prebuncher and main buncher voltages were 2.8 kV and 8.2 kV, respectively. Because the level of space-charge neutralization in the LEBT is unknown and no measurements of longitudinal beam parameters are made, there is some uncertainty in the conditions in the LEBT. We examined the effect of space-charge in the LEBT, however, the best agreement between simulations and measurements was achieved when a fully neutralized beam was assumed. An iterative procedure to determine the initial transverse-beam Twiss parameters (α, β) at the prebuncher center gave the best agreement with measured emittances. In general, during emittance measurements, most of the beam is stopped in the deflector beam dump. We believe this results in a copious source of electrons. Therefore, it is not unreasonable to assume that the beam may be nearly fully neutralized in the region of the deflector during these measurements.

At LAMPF, the operators generally reduce the DTL tank rf amplitudes below the design values to reduce beam spill in the SCL above 100 MeV. The 1993 relative rf amplitudes, as determined from power measurements, were estimated to be 0.93, 0.94, 0.90, and 0.98 of the design amplitudes for modules 1-4, respectively. These settings were used in the simulations when comparing to measurements taken under nominal operating conditions.

The output distributions from the PARMILA DTL simulations were used as input for the coupled-cavity code, CCLDYN. The design values for rf amplitudes and quadrupole gradients were used in the SCL simulations. It

was assumed that the effects of misalignments of tanks and magnets in the SCL are small and therefore these data were not used in the simulations.

III. COMPARISON WITH MEASUREMENTS

A. H^+ Beam Simulation

Table 1 shows the results of both measurements and simulations for the H^+ beam at 100 MeV. The measured rms normalized (true rms with no factor of 4) emittance values were obtained by the slit and collector method. These measurements were made at the entrance to the DTL (0.75 MeV) and in the TR (100 MeV). Normally, emittance measurements are not recorded at 800 MeV. The simulated emittance values agree with the measurements to within 46% and 11% for ϵ_x and ϵ_y , respectively. The simulated transmission through the DTL agrees with measurements to within 3%.

Table 1 - H^+ 100 MeV Measurement and Simulation Results. The initial transverse rms normalized emittance at 0.75 MeV of 0.0063 π -cm-mrad was used in simulations.

	Measured	Simulated
$\epsilon_x(\pi - \text{cm} - \text{mrad}, \text{rms}, \text{norm})$	0.026	0.038
$\epsilon_y(\pi - \text{cm} - \text{mrad}, \text{rms}, \text{norm})$	0.020	0.018
$\epsilon_{x-out} / \epsilon_{x-in}$	4.2	9.7
$\epsilon_{y-out} / \epsilon_{y-in}$	5.3	4.7
DTL Transmission	67%	70%

B. H^- Beam Simulation

The two LEBT lines (H^+ and H^-) converge into one single line with the two beams bent by a common dipole magnet. There is an aperture restriction in the H^- beam line just before the convergence point. Downstream of the dipole magnet, there are four quadrupoles which are adjusted to match the H^+ beam into the DTL. The tuning of the H^- beam is a compromise between maximizing transmission through the aperture restriction and its match to the DTL. This is accomplished by varying the settings of quadrupoles which are upstream of the dipole magnet. Simulations suggest that some of the observed emittance growth of the H^- beam is due to the transverse mismatch at injection to the DTL. Table 2 shows the results of both measurements and simulations for the H^- beam at 100 MeV. The measured emittance growths are larger than that determined from the simulations using the nominal operating parameters. However, in the simulations, a 3% variation in the gradients of the quadrupoles just upstream of the DTL produces good agreement with the measured emittance growth. Unfortunately, this sensitivity was not seen in a later experimental test on the machine.

A few percent variation in some of the 140 quadrupole magnets of the DTL from the nominal operating gradients was required, in the simulations, to produce an output beam with Twiss parameters matching the measured beam. These variations in the quadrupole gradients are well within the known accuracy of their measured values.

Table 2 - H^- 100 MeV Measurement and Simulation Results. The initial transverse rms normalized emittance at 0.75 MeV of 0.019 π -cm-mrad was used in simulations.

	Measured	Simulated
$\epsilon_x(\pi - \text{cm} - \text{mrad}, \text{rms}, \text{norm})$	0.059	0.038
$\epsilon_y(\pi - \text{cm} - \text{mrad}, \text{rms}, \text{norm})$	0.042	0.034
$\epsilon_{x-out} / \epsilon_{x-in}$	3.2	1.8
$\epsilon_{y-out} / \epsilon_{y-in}$	2.2	1.5

C. Beam Loss at LAMPF

Simulations and operational data both show that the majority of beam loss after the DTL occurs at three locations along the linac: 1) In the transition region (TR), where the beam is transported from the DTL to the SCL at 100 MeV, 2) In module 5, at injection to the SCL at 100 MeV, and 3) near module 13 (212 MeV), where the SCL transverse focusing becomes weaker by a factor of two. The simulations give 1.2% losses in the SCL for the H^+ beam. Experimental results based on activation measurements predict 0.1% losses for H^+ . Better agreement is achieved in the simulations for the H^- beam, where the simulations predict 0.2-1.0% losses depending on the assumed initial conditions. Experimental data predict approximately 1% losses for H^- . We believe that magnetic stripping of the H^- beam can be ignored, but a contribution to beam loss from residual gas stripping cannot yet be ruled out.

Before the beam from the ion source is injected into the DTL, it must be bunched and matched transversely. The present two-buncher system in the low-energy beam transport line is not capable of 100% bunching of the beam. The fraction of the beam which lies outside of the longitudinal acceptance of the DTL will not be captured or accelerated. This has been verified in the simulations. Figure 1 shows the DTL output distributions at 100 MeV from the H^+ simulations; the longitudinal phase space plot is in the lower-right corner. It should be noted that the particles which populate the tail of the longitudinal output distribution originated from the outer edges of the longitudinal acceptance at injection. Due to the factor of four decrease in the longitudinal acceptance at injection to the SCL (transition from 201.25 MHz to 805 MHz), some of these particles will be outside of the longitudinal acceptance of the SCL and will be lost there.

Simulation studies were used to determine the effect

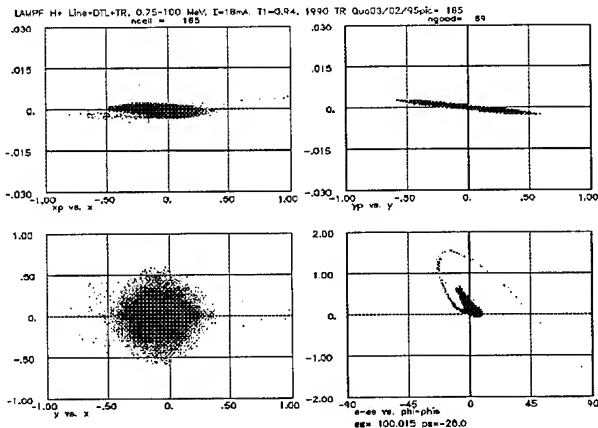


Figure 1: DTL output phase space and xy distributions at 100 MeV. The lower right plot is the longitudinal phase space. Note the long tail in the distribution.

of the DTL-module amplitudes on the DTL output longitudinal emittance at 100 MeV. It was found that there is a broad minimum in longitudinal emittance near 96% of design amplitude for module 1. This module was operated near 0.94 times the design-amplitude value during the 1993 run cycle. The result from the simulation is rather dramatic. A 6% reduction in module-1 amplitude reduces the transmission by 30% and reduces the longitudinal emittance by 60%. The transverse output emittance is not affected.

Figure 2 shows the energy spectrum of only particles lost in the SCL from H^+ simulations. It can be seen that these particles have energies of approximately 100 MeV. Figure 3 shows the energy spectrum of particles lost in both the TR and the SCL from simulations. This distribution has a low-energy tail with particle energies extending down to approximately 15 MeV. The particles in the low-energy tail are lost in the first two dipoles of the TR and therefore cause structure activation in the TR only. The particles in Fig. 3, with energies near 100 MeV, are not captured longitudinally in the SCL and are lost at the SCL entrance provided, they originated at the outer edge of the transverse distribution. Otherwise, these particles drift in the SCL until they are sufficiently deflected to the beam pipe or structure wall near module 13.

IV. A POSSIBLE UPGRADE PATH

We have done H^+ simulations where the first tank of the DTL was replaced with a 5.39-MeV RFQ and a bunch-rotator cavity was placed in the TR for longitudinal matching into the SCL. Fig 4 shows the DTL output distributions at 100 MeV from simulations with the RFQ. The longitudinal phase space plot is shown in the lower right corner and should be compared to Fig. 1. The longitudinal tail of the distribution is much reduced.

Because the beam is bunched adiabatically over many synchrotron-oscillation periods in the RFQ, the bunching process is more complete. In the simulations, the DTL

modules were at full design amplitude and the simulated DTL transmission was found to be 100%. The simulated losses in the SCL were found to be 1.4% without longitudinal matching into the SCL at 100 MeV. However, simulations including the effect of a single multi-gap bunch-rotator cavity in the TR reduced the SCL losses to 0.005%, compared to 1.2% for simulations of the existing machine. These simulations demonstrate the importance of good longitudinal capture and matching.

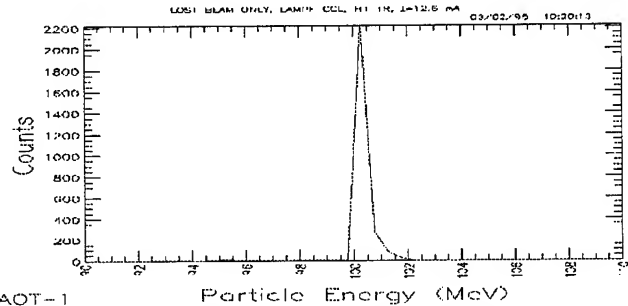


Figure 2: Energy spectrum of particles lost only in the SCL as determined from H^+ simulations.

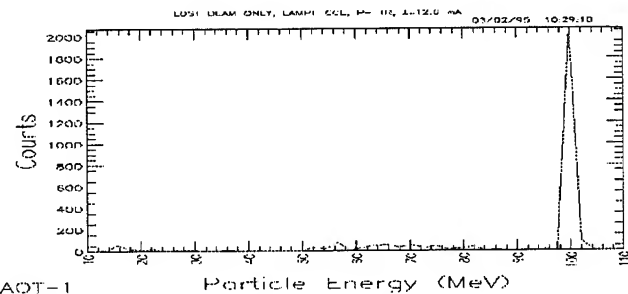


Figure 3: Energy spectrum of particles lost in the TR and the SCL as determined from H^+ simulations.

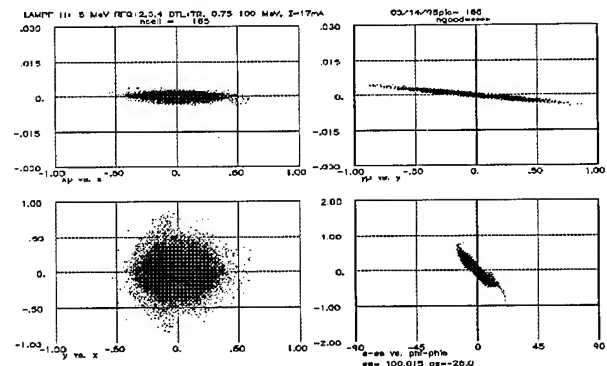


Figure 4: DTL output phase space and xy distributions at 100 MeV for the 5.39-MeV RFQ. Note the lack of a long tail in the longitudinal distribution compared to Fig. 1.

IV. REFERENCES

- [1] R. W. Garnett, R. S. Mills, and T. P. Wangler, "Beam Dynamics Simulation of the LAMPF Linear Accelerator," Proceedings of the 1990 Linac Conference, Sept. 9-14, 1990, Albuquerque, NM.

FUNCTIONAL DEPENDENCE OF WAKEFUNCTIONS FOR $v < c^*$

Zenghai Li and Joseph J. Bisognano
CEBAF, 12000 Jefferson Avenue, Newport News, VA 23606

Abstract

In evaluating the wakefield effects of medium energy particles interacting with a cavity, the integral for the wakefunction must be carried out on the pipe radius in order to avoid an infinity due to the finite space charge effect. To obtain the wakefunctions at other radial positions, a proper extrapolation algorithm is needed. This paper presents the extrapolation method for calculating wakefunctions of $v < c$. For cases with low energies, the slippage between the particle and the fields induces longitudinal smearing of the wakefunctions, and the wakefunctions inside the beam pipe are found to be weighted averages of the wakefunctions calculated on the pipe radius. The smearing effect for calculating the wakefunctions on the axis is related to $R = \frac{\sigma_z \gamma}{a}$, with the smearing effect negligible for large R . The usual ultrarelativistic assumption is found to be reasonable for $R \geq 1.5$. For cases with $R \leq 1.5$, a weighted average must be taken to calculate the wakes inside the beam pipe.

I. INTRODUCTION

When a bunch of charged particles traverses a discontinuity in an accelerator, electromagnetic fields are excited. The particles experience an energy loss and a momentum change due to these fields. The longitudinal and transverse wakefunctions describe these effects and are defined as

$$w_l(s, r) = \frac{1}{qv} \int_{-\infty}^{+\infty} dz \mathbf{v} \cdot \mathbf{E}(\mathbf{r}, z, t) |_{t=(z+s)/v} \quad (1)$$

$$w_\perp(s, r) = \frac{1}{q} \int_{-\infty}^{+\infty} dz (\mathbf{E} + \mathbf{v} \times \mathbf{B})_\perp(z, \mathbf{r}, t) |_{t=(z+s)/v} \quad (2)$$

In most cases, the wakefunctions are calculated under the assumption of $v = c$, which is a good approximation for high energy beams. However, there are cases of interest where the ultrarelativistic approximation is not reasonable although $v \approx c$. For example in some FEL scenarios [1], the energy of the electron beam in the accelerator is in the order of 10^{-10^2} MeV, and the beam bunch length is very short. In these circumstances, the effect of $v < c$ can be important.

For this medium energy range, the velocity of the particle is less than c and both the space charge and wake fields exist. The total field satisfies the inhomogeneous wave equation. The solution of the inhomogeneous equation can be separated into two parts - a special solution that satisfies the inhomogeneous equation and the general solutions that satisfy the homogeneous equation. There is a certain freedom of choosing the special solution. It is preferable, however, to choose a special solution that satisfies the \mathbf{E} boundary conditions at the beam pipe radius, and the solution for such a system can be obtained analytically [2].

*This work was supported by the U.S. Department of Energy, under contract No. DE-AC05-84ER40150.

The special solution then represents the synchronous part (or the space charge) of the field and the general solution represents the radiated (propagating) part of the field. For cases with $v < c$, integrating the fields within the beam pipe will in general be infinite since the space charge effect is finite inside the beam pipe. In order to get meaningful results, one has to separate the effects of the synchronous field and the propagating field. The effect of the propagating fields can be separated from the synchronous field by integrating the fields at the pipe radius. The contribution of the synchronous fields at the pipe radius is zero. This is numerically advantageous in using codes like TBCI [3] and ABCI [4]. In wakefunction calculations, it is essential to integrate only the z component of the \mathbf{E} field, which gives the longitudinal wakefunction. The transverse wakefunction is related to the longitudinal one through the Panofsky-Wenzel [5] theorem. Since the E_z field is nonzero only in the open gap region of the cavity, the integral at the pipe radius need only be carried out within a finite distance. The wakefunctions at other radii can be extrapolated from the one integrated at the pipe radius. The extrapolation gives the functional dependence of the wakefunction on the integral path and the smearing effects of the wakefunction due to $v < c$. (The dependence on the radial position of the source particle is explicitly calculated numerically because it is well behaved) The total effect of the fields is the summation of the extrapolated wakefunction and the space charge effect (within the length of the structure). The space charge effect can be obtained analytically, and we will not address it here. Other issues related to the numerical calculation of the wakefunction for $v < c$ include open boundary conditions at the beam pipe ends to simulate an infinitely long beam pipe and a higher-order finite-difference algorithm to reduce the frequency dependent truncation errors for short bunches. These issues are discussed in Ref. [6]. In this paper, we focus on the extrapolation of the wakefunction from the pipe radius to the inside of the beam pipe and the smearing effects due to $v < c$

II. FUNCTIONAL DEPENDENCE OF THE WAKEFUNCTION

The derivations of the functional dependence of the wakefunctions presented here assumes that the trajectories of the particles be straight lines. We study the fields that satisfy the homogeneous wave equation. For the longitudinal component of the \mathbf{E} field, the equation is [7]

$$(\nabla_\perp^2 - (\zeta_z^2 - k^2))E_z(r, \phi, z, t) = 0 \quad (3)$$

The general solution of Eq. 3 in a cylindrical coordinate system can be expressed as the follows:

$$E_z(r, \phi, z, t) = \sum_{m=-\infty}^{+\infty} \int_{-\infty}^{+\infty} d\omega d\zeta_z A(\zeta_z) G_m(k_r r) \cdot e^{-j\omega t + j\zeta_z z} e^{jm\phi} \quad (4)$$

where

$$k = \frac{\omega}{c}$$

$$k_r = \sqrt{\zeta_z^2 - k^2}$$

$$G_m(k_r r) = \begin{cases} I_m(k_r r), & \text{if } \zeta_z^2 - k^2 \geq 0 \\ J_m(k_r r), & \text{if } \zeta_z^2 - k^2 < 0 \end{cases}$$

I_m and J_m are the modified Bessel function and the Bessel function of the first kind, respectively. The longitudinal wakefunction of the m th mode at $(r, \phi, s = vt - z)$ is

$$w_{l,m}(r, \phi, s) = 2\pi \int_{-\infty}^{+\infty} d\omega A\left(\frac{\omega}{v}\right) I_m(k_r r) e^{-j\frac{\omega}{v}s} e^{jm\phi} \quad (5)$$

with

$$k_r = \sqrt{\frac{\omega^2}{v^2} - \frac{\omega^2}{c^2}} = \frac{\omega}{\gamma\beta c} \quad (6)$$

At the pipe radius $r = a$

$$w_{l,m}(a, \phi, s) = 2\pi \int_{-\infty}^{+\infty} d\omega A\left(\frac{\omega}{v}\right) I_m(k_r a) e^{-j\frac{\omega}{v}s} e^{jm\phi} \quad (7)$$

Fourier transforming Eq. (7), we have

$$A\left(\frac{\omega}{v}\right) = \frac{e^{jm\phi}}{(2\pi)^2 v I_m(k_r a)} \int_{-\infty}^{+\infty} w_{l,m}(a, \phi, s') e^{j\frac{\omega}{v}s'} ds' \quad (8)$$

By substituting Eq. (8) into Eq. (5) we have the wakefunction at radius r

$$w_{l,m}(r, \phi, s) = \int_{-\infty}^{+\infty} ds' w_{l,m}(a, \phi, s') W_{l,m}(\gamma, a, r, s - s') \quad (9)$$

where

$$W_{l,m}(\gamma, a, r, s - s') = \frac{\gamma}{2\pi a} \int_{-\infty}^{+\infty} \frac{I_m(q \frac{r}{a})}{I_m(q)} e^{-jq \frac{(s-s')}{a/\gamma}} dq \quad (10)$$

From Panofsky-Wenzel [5] theorem, the transverse wakefunction is related to the longitudinal one as

$$w_{\perp}(r, \phi, s) = - \int_{-\infty}^s \nabla_{\perp} w_l(r, \phi, z') dz' \quad (11)$$

We have

$$w_{r,m}(r, \phi, s) = -\frac{m}{a} \int_{-\infty}^s dz' \int_{-\infty}^{+\infty} ds' w_{l,m}(a, \phi, s') \cdot W_{2,m}(\gamma, a, r, s - s') \quad (12)$$

$$w_{\phi,m}(r, \phi, s) = -j \frac{m}{r} \int_{-\infty}^s dz' \int_{-\infty}^{+\infty} ds' w_{l,m}(a, \phi, s') \cdot W_{1,m}(\gamma, a, r, s - s') \quad (13)$$

with

$$W_{2,m}(\gamma, a, r, s - s') = \frac{\gamma}{2\pi a} \int_{-\infty}^{+\infty} dq \left(\frac{a}{r} \frac{I_m(q \frac{r}{a})}{I_m(q)} + \frac{q}{m} \frac{I_{m+1}(q \frac{r}{a})}{I_m(q)} \right) e^{-jq \frac{(s-s')}{a/\gamma}} \quad (14)$$

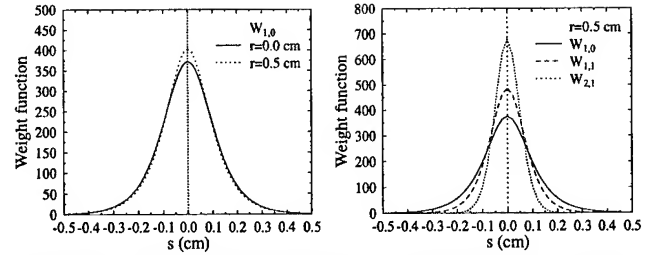


Figure 1. Weight functions for $\beta = 0.9948$, $a = 1.74$ cm.

It is clear now that the wakefunction at radius r is a weighted average of the wakefunction on the pipe radius. The weight function has finite width, which means that there is smearing effect along the s direction due to $v < c$. The profile of the weighting function is independent of the bunch length and is a function of r/a and a/γ only. The weight functions for mode $m = 0, 1$ for $\beta = 0.9948$, $a = 1.74$ cm are shown in Fig. 1. The halfwidth of the weight function for a given r/a is linear on a/γ .

At ultrarelativistic limit, the Bessel functions in the weight functions reduce to

$$\frac{I_m(q \frac{r}{a})}{I_m(q \frac{a}{\gamma})} = \left(\frac{r}{a} \right)^m \quad (15)$$

The longitudinal wakefunction is independent of r for $m = 0$ and scales as r^m for other modes whereas the transverse wakefunctions scale as r^{m-1} . There is no smearing effect along the s direction.

III. THE SMEARING EFFECTS FOR $v < c$

Since the width of the short range wakefunction is roughly proportional to the bunch length, while the width of the weight function depends only on the energy and the cavity structure, the smearing effect is bunch length dependent. If the width of the weight function is much smaller than the bunch length, the smearing effect will be small, but if the width of the weight function is larger than the bunch length, the smearing effect is strong. Fig. 2 shows the wakefunctions of a 3 mm (rms) bunch with $\beta = 0.9948$ in the CEBAF 5-cell cavity at radii $r = 1.74$ cm and $r = 0$ cm. The halfwidth of the weight function for this case is 1.2 mm, which is smaller than the rms bunch length, and the smearing effect is negligible in this case. Fig. 3 shows the radial dependence of the wakefunctions of a pillbox cavity for a short bunch with bunch length of 0.5 mm (rms) and $\beta = 0.9948$ at radii $r = 1$ and $r = 0$ cm. The halfwidth of the weight function for this case is 0.66 mm, which is larger than the rms bunch length. The smearing effect is significant. The peak of the wakefunction becomes wider and lower at $r = 0$. The wakefunctions also show the slippage effects between the charge and the fields, which results in none zero wakefields ahead of the bunch.

The smearing effect of the short range wakefunction for a given energy depends not only on the energy (γ) of the beam, but also on the bunch length. The ratio

$$R = \frac{\sigma_z \gamma}{a} \quad (16)$$

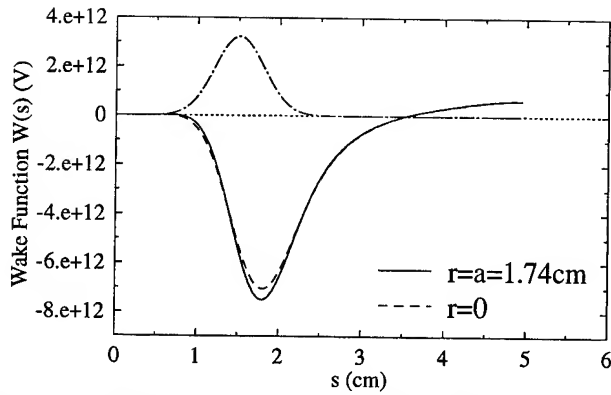


Figure 2. Wakefunctions for $\beta = 0.9948$ (5 MeV), $\sigma_z = 3$ mm. CEBAF 5-cell cavity.

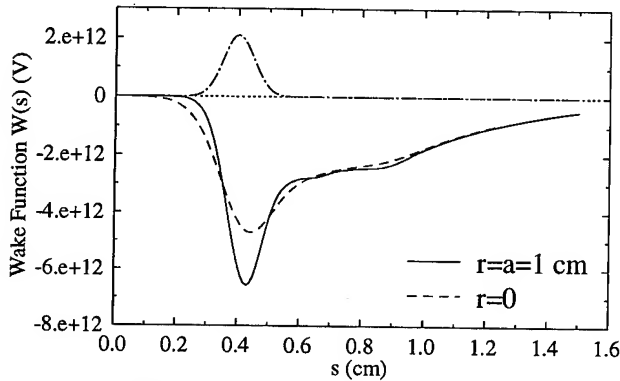


Figure 3. Wakefunctions for $\beta = 0.9948$. $\sigma_z = 0.5$ mm. Pillbox cavity.

provides a measure of the smearing effect. Large R implies weak smearing. The relative difference of the peaks of the short range wakefunctions calculated at the pipe radius and on the axis of a pillbox cavity as a function of R is shown in Fig. 4. For $R = 1.5$, the relative difference is less than 10%.

The R value of Eq.(16) can be used to determine whether the beam can be treated as ultrarelativistic in the wakefield calculation. The relative difference of the wakefunctions as a function of R may be slightly different from the one shown in Fig. 4 for different structures and bunch length. It is found from the numerical simulations that a difference of the peak of less than 10% can in general be obtained for $R > 1.5$, and the beam can be assumed ultrarelativistic. For $R < 1.5$, the smearing effect is not negligible, and wakefunctions at $r < a$ should be calculated by use of the weighted average. For example, consider the CEBAF cavity with a beam pipe of $a = 1.74$ cm. For $\sigma_z = 3$ mm, the beam can be treated as being ultrarelativistic for $\gamma > 8.7$ or $E > 4.5$ MeV. For $\sigma_z = 0.5$ mm, however, the beam can be treated as being ultrarelativistic only for $\gamma > 52$ or $E > 26.5$ MeV.

IV. CONCLUSION

The effects of slippage between the beam and the fields are important in the cases of low energies and short bunches. The R value defined in Eq. (16) provides a measure of the smearing effect on the wakefields for a non-relativistic beam. The particle

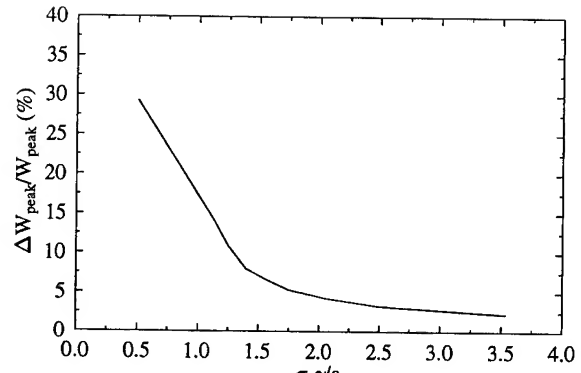


Figure 4. Relative difference $\frac{\sigma_z \gamma / a}{W_{pipe}} \frac{W_{pipe} - W_{axis}}{W_{pipe}}|_{peak}$ vs. $R = \frac{\sigma_z \gamma}{a}$. (calculated from the wakefunctions of a pillbox cavity; $(r=3 \text{ cm}) \times (L=4 \text{ cm})$, pipe radius = 1 cm).

can only be assumed ultrarelativistic for cases with large R .

References

- [1] Proposal, "High-power UV and IR Free Electron Lasers Using the CEBAF Superconducting Accelerator," Vol. 1, May 1992.
- [2] J. A. Stratton, Electromagnetic Theory, McGraw-Hill, New York, (1941).
- [3] T. Weiland, "Comment on Wake Field Computation in Time Domain," Nucl. Inst. and Meth. 216, p31-34, 1983.
- [4] Y. H. Chin, User's Guide for ABCI, LBL-35258.
- [5] W. K. H. Panofsky and W. A. Wenzel, "Some Considerations Concerning the Transverse Deflection of Charged Particle Radio-Frequency Fields," Rev. Sci. Instr. 27, 967 (1956).
- [6] Z. Li, Beam Dynamics in the CEBAF Superconducting Cavities, Ph.D. thesis, The College of William and Mary, 1995.
- [7] J. D. Jackson, Classical Electrodynamics, John Wiley, New York, (1962).

Betatron Transients Caused by Rapid Changes in the Closed Orbit

James J. Welch, *Cornell University, Ithaca NY 14853 **

Introduction

During a normal cycle of operation of CESR there are three occasions when the closed orbit is deliberately changed: Electrostatic separators create the appropriate pretzel for injection, pre-collision and luminosity conditions. At the same time the separator voltages are varied corrector magnets create orbit distortions that help reduce radiation sources. In addition to the deliberate changes there are occasional undesired closed orbit alterations due to separator high voltage sparking or magnet power supply anomalies. The analysis in this paper shows that a rapid change of the closed orbit, whether intentional or not, generates betatron motion. The amplitude of the betatron motion is such that at least twice the aperture is required to make a rapid change than a slow one.

Analysis

For clarity, in this analysis I describe the motion of interest as horizontal, but it could equally well have been vertical. Imagine an instantaneous change in the closed orbit caused by suddenly turning on and leaving on a angle kick $\Delta\theta$ at a location where the betatron phase is $\phi = \phi(s) = \phi_i$ and the beta function is $\beta = \beta(s) = \beta_i$. The new closed orbit measured with respect to the old closed orbit is constructed by finding a betatron trajectory which has $x(\phi_i + 2\pi\nu) = x(\phi_i)$ and $x'(\phi_i + 2\pi\nu) = x'(\phi_i) - \Delta\theta$. The well known result is:

$$x_c(\phi - \phi_i) = \Delta\theta\sqrt{\beta\beta_i} \frac{\cos(\phi - \phi_i - \pi\nu)}{2\sin\pi\nu} \quad (1)$$

where $\phi - \phi_i$ is evaluated *modulo* $2\pi\nu$, and ν is the phase advance per turn. The closed orbit is then periodic in ϕ with period $2\pi\nu$. It has a 'kink' in it at $\phi = \phi_i + 2\pi\nu N$, ($N = 1, 2, \dots$) where the kick is applied but otherwise is a smooth free betatron orbit. After several damping times a particle which had no betatron amplitude before the kick was turned on closely follows the new closed orbit given by equation 1. However, immediately following the turn on, the particle is not on the new closed orbit and instantaneously gets a betatron amplitude about the new closed orbit.

When the angle kick is first turned on and the particle has passed the kick point only once, the motion may be well described as a free betatron oscillation about the original closed orbit. In this case the net about the original closed orbit for the first turn only is,

$$x = \Delta\theta\sqrt{\beta\beta_i} \sin(\phi - \phi_i) \quad (2)$$

Work Supported by the National Science Foundation

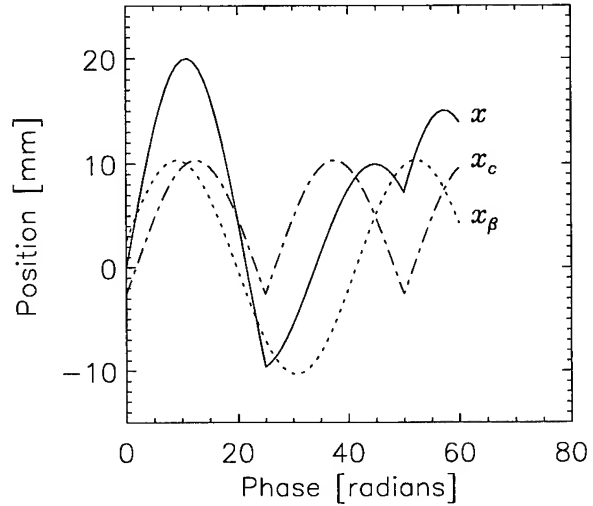


Figure 1: The closed orbit, betatron motion and the total transient motion are plotted as a function of $\phi - \phi_i$ with constant $\beta = 20m$ assumed. A kink occurs in x and x_c once each turn. Note that the peak excursion of x is about twice the peak closed orbit excursion. The fractional part of the tune is .58, the kick angle is 0.001 radians, and the initial position is $x(\phi_i) = 0$.

assuming there was no betatron motion present before the kick was turned on. Since $x = x_\beta + x_c$, for $0 \leq (\phi - \phi_i) \leq 2\pi\nu$ the particle motion about the new closed orbit is,

$$x_\beta = \Delta\theta\sqrt{\beta\beta_i} \sin(\phi - \phi_i) - \Delta\theta\sqrt{\beta\beta_i} \frac{\cos(\phi - \phi_i - \pi\nu)}{2\sin\pi\nu} \quad (3)$$

Here I have dropped the *modulo* operation implicit in equation 1. Nevertheless equation 3 is valid for all $\phi > \phi_i$. This expression for x_β has been constructed to give the correct initial value and slope at the kick point. It clearly solves the betatron equations of motion for all $\phi - \phi_i > 0$ as it is made of two pieces each of which is a valid betatron trajectory. So equation 3 must be valid for all $\phi - \phi_i > 0$, not just the first turn.

Now we can easily compute the net position of the particle for all $\phi - \phi_i > 0$ using equations 1 and 3 and $x = x_\beta + x_c$, but we must keep in mind that equation 1 is evaluated with $\phi - \phi_i$ *modulo* $2\pi\nu$. A simple example of these motions assuming constant β is shown in figure 1.

Amplitude of Transient Motion

To calculate the effects of the transients it is useful to know the size of its invariant betatron amplitude. Once that is known the maximum excursion at any point in the ring can be calculated quite easily.

In a constant guide field and with no radiation, particles follow trajectories about a closed orbit of the form

$$x_\beta = a\sqrt{\beta} \cos(\phi - \phi_0) \quad (4)$$

where a and ϕ_0 determine the particular trajectory and a is the invariant betatron amplitude. Under these conditions at any point in the ring the peak value of x_β will eventually be reached when the argument of the cosine happens to be near 0. The peak amplitude is then simply $a\sqrt{\beta}$.

I will directly calculate the invariant amplitude about the new closed orbit just after the kick is applied. As before, I assume that before the kick is turned on the particle is on the design orbit with no betatron motion. Just after the kick, we have at $\phi = \phi_i$ using equation 1

$$\begin{aligned} x(\phi_i) &= 0, & x'(\phi_i) &= \Delta\theta \\ x_c(\phi_i) &= \Delta\theta \frac{\beta_i}{2} \cot \pi\nu \\ x_\beta(\phi_i) &= x(\phi_i) - x_c(\phi_i) \\ &= -\Delta\theta \frac{\beta_i}{2} \cot \pi\nu \end{aligned} \quad (5)$$

An expression for $x'_\beta(\phi_i)$ may be derived by differentiating $x_\beta = x - x_c$. The algebra is somewhat tedious but the result is

$$x'_\beta(\phi_i) = \frac{\Delta\theta}{2} \left(1 - \frac{\beta'_i}{2} \cot \pi\nu\right) \quad (6)$$

Another handy formula, borrowed from Sands but simple to derive is

$$a^2 = \frac{x_\beta^2}{\beta} + \beta \left(x'_\beta - \frac{\beta'}{2\beta} x_\beta\right)^2 \quad (7)$$

Plugging 5 and 6 into 7 yields:

$$|a| = \left| \frac{\Delta\theta}{2} \sqrt{\beta_i} \csc \pi\nu \right| \quad (8)$$

This result can also be obtained with less algebra if one imagines turning on the kick just after the passage of the particle. Then for the rest of the turn $x = 0$ so $x_\beta = -x_c$. This leads to $|a| = |a_c|$ where a_c is the invariant betatron amplitude of the closed orbit trajectory equation 1.

Equation 8 gives the invariant betatron amplitude about the new closed orbit after the closed orbit has been suddenly changed by a single kick of $\Delta\theta$ and before damping or feedback have had any effects. Note I have also assumed that there was no betatron motion before the closed orbit was changed. If there were no further changes to the closed orbit after the kick was applied, at each point in the ring the particle position would 'oscillate' about the new closed orbit eventually approaching peak values of

$$\hat{x}_\beta(s) = \left| \frac{\Delta\theta}{2} \sqrt{\beta_i \beta(s)} \csc \pi\nu \right| \quad (9)$$

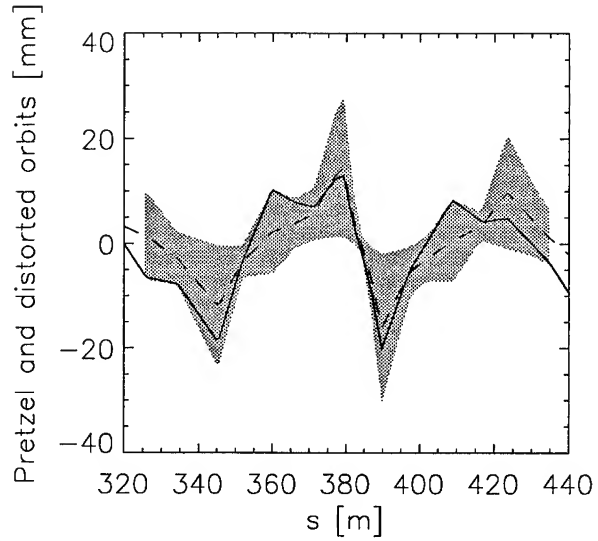


Figure 2: The original pre-spark pretzel (solid line) and the distorted post-spark pretzel (dashed line) are plotted with the resulting betatron motion represented by shading. Here the separator at 45W was assumed to spark during e^- injection.

Using equations 1 and 9 we have the ratio of peak betatron motion to the closed orbit at every point in the ring:

$$\frac{\hat{x}_\beta(s)}{|x_c|} = \left| \frac{1}{\cos \phi - \phi_i - \pi\nu} \right| \geq 1 \quad (10)$$

So $\hat{x} \geq 2x_c$ in general, where \hat{x} is the maximum value that x can reach at each point in the ring. Near a closed orbit maximum, the ratio is close to 2.

After a few turns, the number depending on the choice of tune, the phase of the betatron motion and that of the closed orbit distortion combine to give a maximum orbit excursion which is at least twice the peak closed orbit change. This means that a rapid change in the closed orbit at requires twice the aperture of a slow change.

Examples

When a separator sparks in CESR the voltage goes very rapidly to zero, recovering a few tens of milliseconds later. The size of the transient generated depends on which separator sparks. To calculate the transient we first calculate the change to the closed orbit by setting one separator at zero voltage, then add the betatron transient motion from equation 9, (see figure 2). Note that in this case the transient amplitude is not greater than or equal to the original pretzel because only one of four separators sparked. Nevertheless the transient still brings the beam center out well beyond the original pretzel maximum to over 30 mm in the region of the north interaction point ($s = 384$ m). The vacuum chamber wall is at 45 mm.

A table of maximum amplitudes for various configurations of CESR undergoing sparking any of four separators is shown in table 1. Electron injection conditions are the most dangerous for the beam. A spark at 8E would swing the beam center within 7

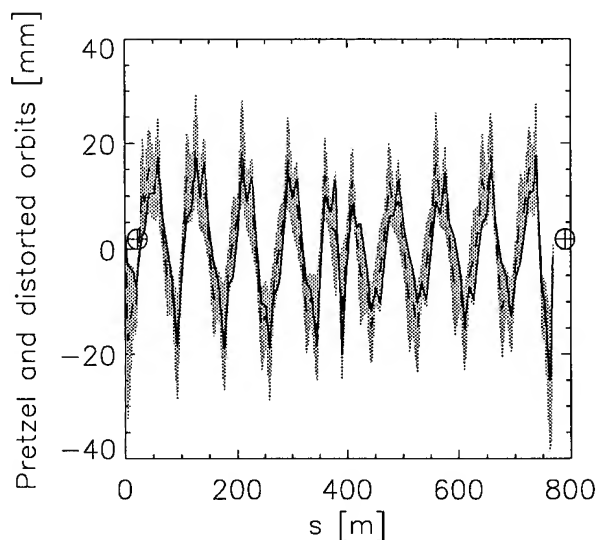


Figure 3: A spark in the separator at 8E would cause this distortion of the pretzel (dashed line) and transient betatron motion about the distorted pretzel (shaded region). The pre-spark pretzel is shown in solid line. The interaction point is marked with a \oplus .

Condition	Location of spark			
	8E	45E	45W	8W
e^- injection	38.6	25.5	29.9	22.6
pre-collision	33.3	22.6	26.0	27.8
collision	18.3	20.2	18.8	25.3

Table 1: The maximum excursion in millimeters of the beam center including the transient from a separator spark at various locations. Note that magnetic bumps were not taken into account and could further increase the maximum excursion. The vacuum chamber wall is at 45 millimeters.

mm of the vacuum chamber wall near the east IR. This is shown in figure 3.

Beam loss is also likely during pre-collision if the 8E separator sparks. The excursions are calculated for the positron beam.

An even more dangerous situation occurs if the separator voltages rise too fast. Then the amplitude of the transient is indeed more than twice the amplitude of the full pretzel and the peak excursion will be at least 32 millimeters. However the high voltage power supplies are not capable of raising the voltage arbitrarily fast and some damping reduces the maximum excursion the beam reaches.

Acknowledgements

I wish to thank David Sagan for his thoughtful review of this paper and suggestions for simplifications of the analysis.

PHENOMENOLOGY OF CRYSTALLINE BEAMS IN SMOOTH ACCELERATORS *

A.F. Haffmans, D. Maletić, A.G. Ruggiero,
Brookhaven National Laboratory, Upton, NY 11973 USA

Abstract

We present a phenomenology of crystalline beams in storage rings. We use the smooth approximation to solve the equations of a test particle moving in the focussing potential of the storage ring, and in that of the other ions. We find simple confinement, and stability conditions.

I. GENERAL OVERVIEW

When ions in a storage ring are cooled sufficiently, they undergo a phase transition to a crystalline ion beam. These crystalline beams have already been observed in Molecular Dynamics simulations and ion trap experiments [1], [2], [3]. Among other things, crystalline beams provide a new way to obtain intense ion beams. We present an analytical study of ground state crystalline beams. We examine the stability of the motion of a test particle in the crystalline beam in a storage ring consisting of linear elements. We find the beam's confinement and stability conditions. Using simple arguments from classical dynamics, we obtain a succession of beam structures, as the ion density is increased.

We start with a collection of ions with mass number A , and atomic number Q already near zero-temperature equilibrium position. The crystalline beam consists of a bundle of substrings, with ions placed a distance λ apart in the longitudinal direction. The space-charge force on a test particle in the beam is included as a perturbation in the familiar single particle equations of motion [4]. We perform a "Gedanken Experiment" in which we systematically increase the number of ions in the crystalline beam, and hence decrease λ . At each step we determine the stability of the equilibrium of the test particle. At a critical value λ , the focussing forces no longer balance the space charge and the orbits along which the substrings lie, undergo a *pitchfork bifurcation* [5]. Two new stable orbits with the same period originate out of the unstable orbit, according to the Poincaré-Bendixson theorem [6]. As the number of ions is increased further, the process repeats itself: each stable orbit will become unstable, and undergo a pitchfork bifurcation, doubling the number of substrings.

Therefore, the specifics of the ground state of the crystalline beam is a function of the ion density, and focussing properties of the storage ring. Each crystalline beam is characterized by a range of values of the inter-ion spacing λ . The upper limit is the ion spacing when the structure is formed, and the lower limit is the ion spacing when the structure becomes unstable, and undergoes a bifurcation. In this bifurcation picture, the lower limit of a structure corresponds roughly to the upper limit of the next structure.

*Work performed under the auspices of the U.S. D.O.E.

II. EQUATIONS OF MOTION

We use a curvilinear orthogonal coordinate system [7],[4], where x and y denote the horizontal and vertical direction, respectively, σ the path length difference and δ , the momentum error. The equations of motion of the test particle are derived from the quadratic Hamiltonian discussed in [7], viz.:

$$y'' + K_v(s)y + \frac{Qr_0}{eA\beta^2\gamma^3} \frac{\partial \Phi_{sc}}{\partial y} = 0; \quad (1)$$

$$x'' + K_h(s)x + \frac{Qr_0}{eA\beta^2\gamma^3} \frac{\partial \Phi_{sc}}{\partial x} = h(s)\delta; \quad (2)$$

$$\sigma' = \frac{\delta}{\gamma^2} + h x; \quad (3)$$

$$\delta' = \frac{Qr_0}{eA\beta^2\gamma^3} \frac{\partial \Phi_{sc}}{\partial \sigma}. \quad (4)$$

The derivatives are with respect to the curvilinear longitudinal coordinate s ; β and γ are the usual relativistic factors, $h(s)$ is the curvature, and $K_{v,h}(s)$ the focussing functions which describe the storage ring. Φ_{sc} is the space-charge potential, and r_0 is the classical proton radius.

We expand the space charge potential Φ_{sc} to second order in small deviations around the (conjectured) equilibrium position of the test particle. After putting these expansions in the equations of motion, we obtain two sets of equations: The *envelope equations* determining the equilibrium position of the test particle in the storage ring, and those for the motion around this equilibrium.

For storage rings with smooth lattice functions and smooth bending we may use the *smooth approximation*. That is, we replace the local focussing forces $K_{h,v}(s)$ with their averages around the ring. The average value of the amplitude function is $\nu_{h,v}/R$. In addition, we replace the local curvature $h(s)$ by $1/R$, i.e. its average around the ring. We will use this below to obtain estimates of the tune shift.

III. CONFINEMENT

Confinement in the transverse direction is provided by the focusing of the storage ring. The crystalline beam has to be closed, and have the same periodicity as the storage ring. We can use this closure, or *isochronism* condition $-\sigma' = 0$ – to approximately integrate Eq. (3). We find, that the momentum error δ_l of the test particle varies linearly with its horizontal displacement from the (dilute beam) reference trajectory x_l . This approximation is appropriate only for a sufficiently smooth lattice [7]. Substituting our approximate expression for δ_l in Eq. (2) gives the envelope equations:

$$x_l'' + [K_h(s) - \frac{\gamma^2}{R^2} - \frac{4\lambda_c^3}{g_0 R^2 \lambda^3} \mathcal{F}_h] x_l = 0, \quad (5)$$

$$y_l'' + [K_v(s) - \frac{4\lambda_c^3}{g_0 R^2 \lambda^3} \mathcal{F}_v] y_l = 0. \quad (6)$$

The kinematic term proportional to γ^2 is entirely due to the *isochronism* condition across one super-period. λ_c is the characteristic length of the crystalline beam:

$$\lambda_c = \left(\frac{Q^2 r_0 g_0 R^2}{A \beta^2 \gamma^5} \right)^{\frac{1}{3}}, \quad (7)$$

R is the radius of the storage ring, and g_0 is a numerical factor, approximately equal to 1.2. \mathcal{F}_h and \mathcal{F}_v are proportional to the first order derivative of the space charge potential around the equilibrium. These equations are identical to those of a test particle perturbed by a space charge force. Because the period of the crystalline beam has to be the same as that of the storage ring, the tune shift induced by the space charge should be large enough to reach the integral stopband [7], [4]. Using the smooth approximation, together with the familiar incoherent tune shift estimate to impose this condition, we obtain the *horizontal and vertical confinement conditions*:

$$\frac{\lambda^3}{F_{h,v}} = (\lambda_c \overline{c_{h,v}})^3, \quad (8)$$

with:

$$\overline{c_{h,v}} = (\nu_{h,v} \overline{\delta_{h,v}})^{-\frac{1}{3}}, \quad (9)$$

$$\overline{\delta \nu_h} = \frac{1}{2} (\nu_h - m N_p) - \frac{\gamma^2}{2 \nu_h} \quad (10)$$

$$\delta \nu_v = \frac{1}{2} (\nu_v - m N_p), \quad (11)$$

N_p is the super-period of the storage ring, and m an integer. $\nu_{h,v}$ are the dilute beam tunes, and correspond to the working point of the storage ring. The term in γ^2 is subtracted from the actual distance of the horizontal working tune to the nearest stopband. Therefore, for the appearance of a horizontally extended "Crystalline Beam", the following condition needs to be satisfied:

$$\gamma < \sqrt{2 \nu_h \delta \nu_h} \quad (12)$$

This generalizes the condition obtained by Wei, Li and Sessler [3], and in particular implies that the storage ring has to be operated below the transition energy.

λ is the same for all substrings, and we can combine the horizontal and vertical confinement condition into the envelope function W :

$$W = \frac{\mathcal{F}_h}{\mathcal{F}_v} = \frac{\overline{c_v^3}}{\overline{c_h^3}} = 1 - \Delta \propto \frac{K_h}{K_v}, \quad (13)$$

where Δ is the defocussing. Furthermore, this implies that the solutions of the envelope equations are invariant under reflections, and rotations.

The confinement in the longitudinal direction is provided by the repulsion between the ions in the "Crystalline Beam". In the absence of curvature, there is no net longitudinal force when the ions are in their equilibrium position. The longitudinal force between the different strings in the crystalline beam is zero, when the longitudinal shift between them is either 0 or $\lambda/2$. Right after a bifurcation, some of the substrings have a relative shift of $\lambda/4$, or $3\lambda/4$. However, we find, that as these substrings move away from each other, their final shifts will be 0, or $\lambda/2$.

IV. Stability

A. The Stability Equations

The motion of the test particle around the equilibrium is described by the equations:

$$y'' + [K_v(s) - \frac{4\lambda_c^3}{g_0 R^2 \lambda^3} \eta_v] y = 0, \quad (14)$$

$$x'' + [K_h(s) - \frac{4\lambda_c^3}{g_0 R^2 \lambda^3} \eta_h] x = h \delta, \quad (15)$$

$$\sigma' = h x - \frac{\delta}{\gamma^2}, \quad (16)$$

$$\delta' = 2\gamma^2 \frac{4\lambda_c^3}{g_0 R^2 \lambda^3} \eta_e \sigma. \quad (17)$$

$\eta_{h,v,e}$ are proportional to the second order expansion of Φ_{sc} around the equilibrium of the test particle. The space charge force of the crystalline beam perturbs the free-oscillation motion of the test particle. Again, we can use the smooth approximation to find out when the tune crosses the stopband. Only an integral stopband, corresponds to a pitchfork bifurcation. A half integral stopband corresponds to a period doubling, and this violates the confinement conditions, since crystalline beams need to have the same periodicity as the storage ring. The lower limit λ_l of the ion spacing in the crystalline beam is given by:

$$\lambda_l = \eta_{h,v}^{\frac{1}{3}} \lambda_c c_{h,v}. \quad (18)$$

V. Results and Discussion

We investigated a succession of crystalline beams for weak ($\Delta = 0.001$), and moderate ($\Delta = 0.25$) defocussing. To obtain the envelope we solved Eqs. (8) and (13). The stability followed from Eq. (18). Our results are shown in Figs. 1, and 2. We consider gold ions ($Q = 57$, $A = 157$) in a storage ring with a magnetic rigidity of 1.2 Tm, a radius of 6.46 m, a superperiod of 16, and tune $\nu_h = 4.8$. $\nu_v = 4.8$, for $\Delta = 0.001$, and 5.54, for $\Delta = 0.25$; $\lambda_c = 47 \mu\text{m}$. $\frac{\gamma^2}{R^2}$ is small, so we have ignored it.

In our analysis, we start with the string. There is no upper limit to λ ; the string is formed even by very dilute ion clouds. In the smooth approximation, the lower limit is determined by the horizontal, and vertical stopband of the storage ring. Using transfer matrices, we determined however, that for most realistic storage rings, the coupling resonance between the longitudinal, and transverse motion in the horizontal plane is quite important.

The focussing in the vertical direction is the largest, and the next structure is a horizontal zigzag. Using transfer matrices we determined that only extremely smooth storage rings can support horizontal zigzags. Therefore, for storage rings that support higher order crystalline beams, the smooth approximation must be accurate.

At the point of bifurcation, we find that the ion spacing of the zigzag is roughly twice that of the string from which it originates. In addition, to balance the longitudinal forces, the two substrings are shifted by half an ion spacing. This is all in agreement with the bifurcation picture. For large defocussing ($\Delta > 0.5$), the zigzag bifurcates in the plane. For $\Delta < 0.5$, the zigzag bifurcates in the vertical direction, and goes over into a helix. Again, the ion spacing roughly doubles at bifurcation.

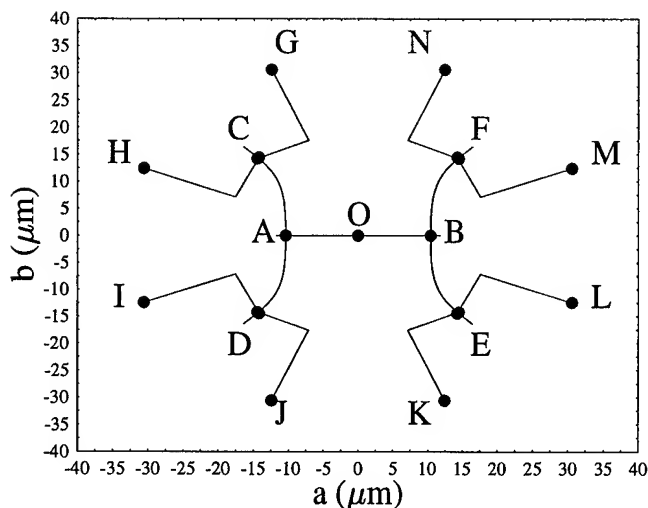


Figure 1. The transition from string (0), to horizontal zigzag (AB), to helix (CDEF), and to shell(16) (GHIKL ...) using the smooth approximation, for $\Delta = 0.001$.

To balance the longitudinal forces, the four substrings shift a little bit longitudinally as they move away from each other. This transition region is very small.

Eventually, the helix will become unstable, and its four substrings will each split in two, to form a shell consisting of eight substrings. We call this structure shell(8), to distinguish it from other shells. The ion spacing doubles again, and the substrings shift longitudinally as they move away from each other, in order to maintain longitudinal equilibrium.

The next shell structure, shell(16), is formed when the eight substrings of the shell(8) split. It is unstable right from the start. Therefore, a shell with eight substrings is the largest hollow crystalline beam we obtained.

Putting a string in the middle of the shell(16), along the reference orbit, stabilizes it. This is in agreement with the MD simulations of Wei et al. [3].

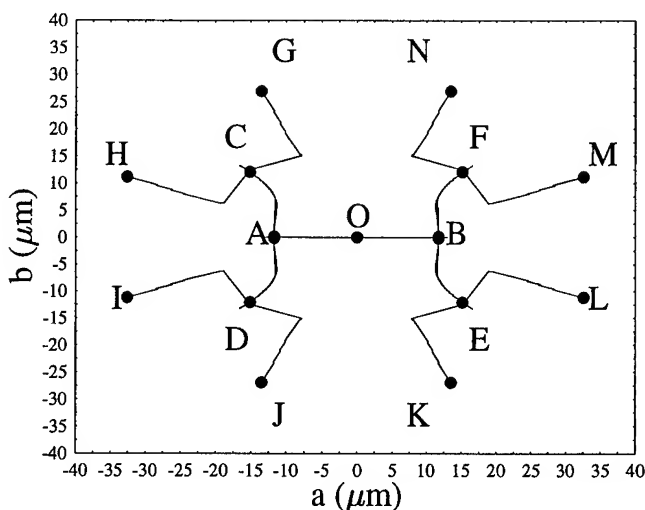


Figure 2. The transition from string (0), to horizontal zigzag (AB), to helix (CDEF), and to shell(16) (GHIKL ...) using the smooth approximation, for $\Delta = 0.25$

References

- [1] J.P. Schiffer and A. Rahman, Feasibility of a Crystalline Condensed State in Cooled Ion Beams of a Storage Ring. PHY-5121-ME-88, Feb. 1988, Argonne National Laboratory. R.W. Hasse and J.P. Schiffer, Ann. of Phys. **203**, 419 (1990).
- [2] H. Walther, Phase Transitions of Laser-Cooled Ions, in Advances in At. Mol. and Opt. Physics, **31**, p.137, (1993), and, Atoms in Cavities and Traps, in Advances in At. Mol. and Opt. Physics, **32**, p. 379, (1994).
- [3] J.Wei, X.P.Li, A.M.Sessler, Crystalline Beam Ground State, BNL-52381, June 1993.
- [4] E.D. Courant and H.S. Snyder, Ann. of Phys. **3**, 1 (1958).
- [5] John Guckenheimer and Philip Holmes, Nonlinear Oscillations, Dynamical Systems, and Bifurcations of Vector Fields, Springer-Verlag, New York, 1983.
- [6] J.A.G. Roberts and G.R.W. Quispel, Phys. Rep. **216**, 63 (1992).
- [7] A.F. Haffmans, D. Maletić, and A.G. Ruggiero, Informal Report, BNL-60436, April 1994, Informal Report, BNL-60619, April 1994, Informal report, BNL-60743, May 1994, Informal report, BNL-60876, May 1994; Confinement and Stability of Crystalline Beams in Storage Rings, To appear in the "Proceedings of the 6th Workshop on Advanced Accelerator Concepts", June 12-18, 1994, BNL-60878, September 1994.

BEAM DYNAMICS IN THE 1.3 GeV HIGH INTENSITY ESS COUPLED CAVITY LINAC

M. Pabst and K. Bongardt, Forschungszentrum Jülich GmbH, 52425 Jülich, Germany

The 700 MHz coupled cavity linac (CCL) of the European Spallation source (ESS) accelerates H^- ions up to 1.334 GeV. The bunch current is 214 mA and the average current 3.84 mA. Four tanks are fed by one 4 MW klystron. The phase slip of 4° at injection is not critical. After every second tank a doublet is installed for transverse focusing providing a 'round' beam. The other intertank sections are used for beam diagnostic elements and steering. To find the smallest injection energy rms and total emittances are studied by multiparticle calculations and by varying the injection energy between 70 and 150 MeV. In addition the influence of field and phase errors is considered. For the low loss injection into the following compressor rings the problem of partly filled bunches is examined.

LAYOUT OF ESS AND LINAC

The need for a future pulsed neutron source in Europe has led users and machine designers to propose the following parameters for the ESS[1,2]:

- An average beam power of 5.1 MW
- A beam pulse at the target less than 3 μ sec long
- A repetition rate of 50 Hz
- Two target stations, one operating at 50 MHz, 5.1 MW and a second one at 10 Hz, 1 MW

These parameters will be achieved by a combination of a linear accelerator and two storage rings. The linear accelerator accelerates H^- ions in pulses of 1.2 msec length up to 1.334 GeV. With a 50 Hz repetition rate the beam is injected into two accumulator rings [3].

The layout of the linac is shown in Fig. 1. To achieve 107 mA peak current and at the same time small emittances, funneling is proposed with two front end legs. Each leg will deliver 54 mA.

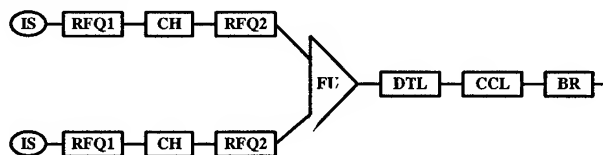


Fig. 1 ESS linac layout: IS: ion source, CH: chopper, FU: funneling, BR: bunch rotator

CCL PARAMETER AND DESIGN

Basis of the 700 MHz CCL design are the 805 MHz side coupled linacs operating successful and reliable at Los Alamos and Fermilab. Table 1 lists the main parameters of the CCL.

TABLE 1
CCL parameter

Input energy	70 MeV
Output energy	1334 MeV
Frequency	700 MHz
Repetition rate	50 Hz
duty cycle	6.0 %
Bunch current	214 mA
Effective pulse current	64 mA
Average current	3.84 mA
Acc. grad. E_0T	2.8 MV/m
Synchronous phase	-25°
Shunt impedance	29...41 $M\Omega/m$
Transit time factor	0.83
Peak power beam	81 MW
Peak power structure	113 MW
Average CCL power	12 MW
Eff. peak power per klystron	3 MW
Number of klystrons	66
Number of tanks	264
Tank length	1.3...2 m
Cell number per tank	16...10
Focusing	doublets
Quadrupole gradient	25...15 T/m
CCL length	≤ 663 m
Bore hole diameter	4.4 cm

The design of the CCL is ruled mainly by the minimization of costs and losses. Costs are minimized by choosing an accelerating gradient $E_0T = 2.8$ MV/m. These costs include structure, rf, ten years of operation and buildings without extensive shielding [4]. Concerning losses one has to be aware of 'matching' losses in the transverse and longitudinal direction resulting from the change of the transverse focusing period and the accelerating gradient between the 350 MHz DTL and the 700 MHz CCL. The matching losses occur mainly after injection. Therefore the input energy of the CCL has to be low as possible, here 70 MeV, to be far below the neutron production threshold of about 120 MeV.

As power sources 4 MW multiple beam klystrons can be chosen [6]. 3 MW are for beam and structure and 1 MW will be foreseen as control power for stabilizing the transient behaviour. The tank length is determined by a required peak power of 0.75 MW for the chopped pulse mode. One klystron feeds four tanks coupled by three bridge couplers. The tank length varies between 1.27 m and 1.95 m and has cells of constant length. The shunt impedance values have been calculated with SUPERFISH [5]. The maximum phase slip is 4° in the first tank. Another possibility is to use conventional 2 MW klystrons feeding two tanks only.

Transverse focusing is provided by doublets located after every second tank in $5\beta\lambda/2$ long intertank sections. Doublets are

favoured over singlets giving a more round beam with smaller average diameter and beam envelope oscillations. Diagnostic equipment and steering elements are placed in short intertank sections. The length of those is $3\beta\lambda/2$. The klystron power will be coupled into bridge couplers at long intertank sections. The increase of the intertank sections with β allows to install scrapers at the high β end and the use of less compact doublets which can be supplied by stable dc power supplies. For this layout the total length of the CCL is 663 m.

Shortening the linac is possible for choosing a less flexible layout. By skipping the short diagnostic intertank sections the tank length will be doubled. To get reasonable phase slip the length of cells has to be changed within the first tanks. Diagnostic and steering has to be placed in the focusing sections. This reduces the CCL length by about 60 m.

BEAM DYNAMICS IN THE CCL LINAC

Due to the frequency of 700 MHz which is twice the frequency of the DTL a bunch current of 214 mA has to be accelerated by the CCL. At input the normalized transverse rms emittance is 0.6π mm mrad and the longitudinal rms emittance is 1.2π ° MeV. Following the line of minimizing losses the tunes have to be set in a way avoiding beam resonances and other sources of emittance growth.

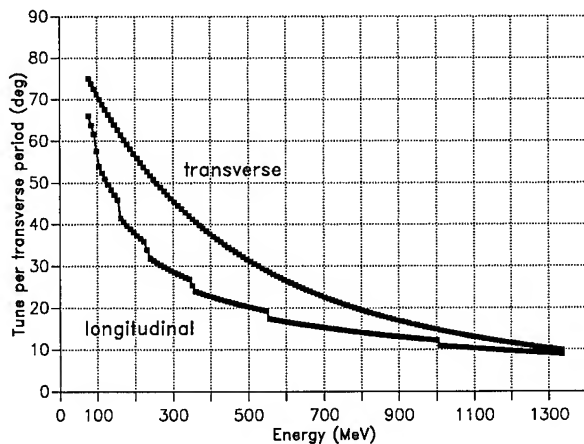


Fig. 2 Transverse and longitudinal tune as a function of energy

Several designs with varying injection energies between 70 and 150 MeV have been set up and tested by multiparticle calculation. For setting up the design we had to handle several problems. First, a constant transverse tune is not possible along the CCL. Due to a decreasing beam radius in case of a constant tune space charge increases at higher energies and the beam becomes unstable longitudinally. We solve the problem by decreasing the transverse tune σ_t with β according to $\sigma_t = \sigma_{t0}(\gamma_0/\gamma)^{-2.5}$. γ is the relativistic factor and γ_0, σ_{t0} are the values at input energy. Second, to avoid energy exchange between transverse and longitudinal direction the beam has to be equipartitioned at injection. With the given emittances the transverse tune σ_{t0} at input has to be large but less than 90° per

transverse focusing period. The large tune has a useful side effect of a fast betatron oscillation which favors a loss of halo particles as soon as possible after injection.

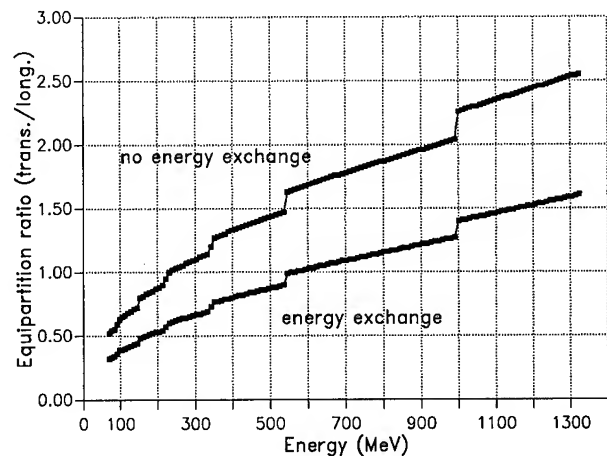


Fig. 3 Ratio of transverse to longitudinal energy (equipartition ratio)

In all cases the growth of normalized rms emittances is less than 10 % transversely and longitudinally. We finally have chosen 70 MeV as an appropriate input energy of the CCL. The transverse tune at injection was set to 75° . The energy dependence of the tunes is shown in Fig. 2. The tune depressions are moderate and stay between 0.7 and 0.8 along the CCL for the transverse and longitudinal direction. The ratio of transverse to longitudinal energy (equipartition ratio) $E_t\sigma_t/E_l\sigma_l$ is shown in Fig. 3. We recognized that for having no energy exchange the ratio has to be larger than 0.5 at injection. No exchange of rms emittances is seen at higher energies even if the ratio increases up to 2.5 corresponding to a nonequipartitioned beam. As a counterexample we present a beam with a ratio of 0.3 at injection, shown in Fig. 3. An energy exchange is seen from the oscillations of the rms emittances plotted in Fig. 4.

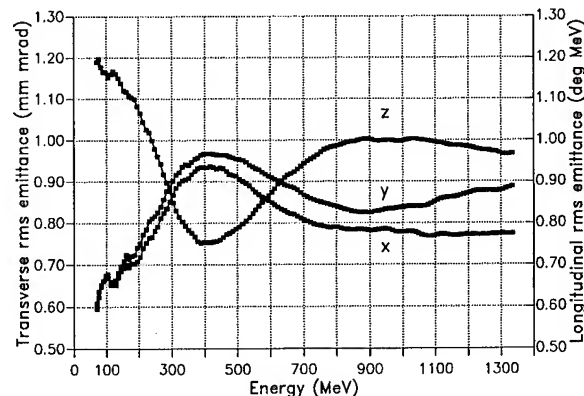


Fig. 4 Normalized transverse (x and y) and longitudinal (z) rms emittances for a nonequipartitioned beam at injection

For the total emittance the input distribution of the multiparticle calculation is important. We have chosen a 4-d waterbag

transversely and a 2-d waterbag longitudinally. As a result for the equipartitioned case the total emittance increases by a factor 2.5 in all three planes. In the nonequipartitioned case we have a larger growth factor of about 3.

Concerning transverse and longitudinal acceptance for the full current we have the following data. The average beam radius is 3 mm while the bore hole radius is 22 mm. This gives a factor 7 between rms radius and aperture and a factor 50 between rms emittance and acceptance. Longitudinally the situation is somewhat different. Due to phase damping the rms phase width decreases from 6° down to 2° and the rms energy spread increases from 0.2 MeV up to 0.6 MeV. The phase acceptance is about $\pm 25^\circ$ and constant along the CCL. The energy acceptance increases from about 0.5 MeV up to 6 MeV. The resulting acceptance increases from $12.5 \pi^\circ \text{ MeV}$ to $160 \pi^\circ \text{ MeV}$ giving a factor 10 between the longitudinal rms emittance and the acceptance at injection and a factor 130 at the linac end.

ERRORS AND PARTLY FILLED BUNCHES

We also studied field and phase errors. For each tank a field error $\leq 1\%$ and a phase error $\leq 1^\circ$ is assumed. The errors are distributed randomly within the limits. This type of errors will effect mainly the motion of the bunch center longitudinally. Fig. 5 shows the oscillation of the bunch center around the synchronous energy. At the end of the CCL the amplitude has grown up to 0.6 MeV which is of same order as the rms energy spread. If no errors are present the amplitude is by a factor 10 smaller. As the rms energy spread is reduced by a factor 3 in the transfer line after the CCL, errors of 1% for field and 1° for phase are the upper limit. Rms values of emittances, radii, phase width and energy spread do not differ much if errors are present or not. An effect can be seen for the total emittances. Here the growth factor is 3.5, larger as if no errors are present.

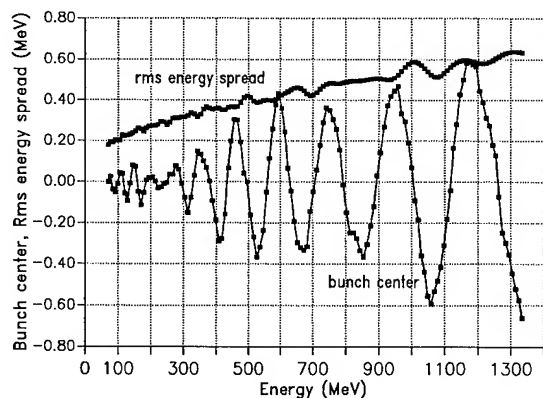


Fig. 5 Energy of the bunch center in the longitudinal phase space and rms energy spread

For the injection into the compressor rings the beam pulse has to be chopped at around 2 MeV. During switching the chopper can create bunches carrying less current than the design value. Those partly filled bunches cause problems in the transfer line between the CCL and the compressor rings [7].

If a bunch carries not the full current the bunch is mismatched mainly in transverse direction. However, because the current is less the average beam radius is somewhat reduced. We simulated two cases, one with half the design current and another one with 1% of the design current. As a result we see larger oscillations of the rms radii but the maxima of the rms radii decreases with the current. Also, we see no effect at the emittances. Unfortunately the partly filled bunches pass the CCL and cause problems in the following transfer line. Therefore, the low energy chopping system has to avoid partly filled bunches.

SUMMARY

We studied the beam dynamics of the 700 MHz, 214 mA bunch current, 1.334 GeV coupled cavity linac of the European Spallation Source. The major goal is the minimization of losses. We approach this goal by avoiding all known sources of emittance growth. For the CCL mainly two conditions have to fulfilled:

- The beam has to be equipartitioned at injection to avoid exchange of energy
- The transverse tune has to be decreased with increasing energy to avoid longitudinal instability

As a consequence of those conditions the increase of the rms emittance is less than 10%. Total emittances grow by a factor 2.5. Field and phase errors cause mainly an oscillation of the longitudinal bunch center. The errors should not be larger than 1% for the accelerating field and 1° in phase. The low energy chopping system has to avoid partly filled bunches, because those bunches pass the CCL and cause problems in the transfer line to the compressor rings.

REFERENCES

- [1] H. Lengeler, "Proposals for Spallation Sources in Europe", Fourth European Particle Accelerator Conference, London, 1994, World Scientific, p.249-253
- [2] H. Klein, "Spallation Neutron Sources", Proceedings of the 1994 International Linac Conference, Tsukuba, 1994, p. 322-327
- [3] G. Rees, "Important Design Issues of High Output Current Proton Rings", see Ref. 1, p. 241-245
- [4] K. Bongardt and M. Pabst, "Design Criteria for High Intensity H^- - Injector Linacs", this conference
- [5] R. de Leeuw and J. Botman, "Cavity Modelling for the Side Coupled Cavity Linac of the ESS", TU Eindhoven internal report, VDF/NK 95.06
- [6] G. Clerc et al., "Considerations Regarding the Efficiency of High Power RF Sources for Particle Accelerators", Proceedings of the Particle Accelerator Conference, Washington D.C., 1993, p. 1184
- [7] K. Bongardt and M. Pabst, "Final Bunch Rotation and Momentum Spread Limitation in the ESS High β Transfer Line", this conference

FINAL BUNCH ROTATION AND MOMENTUM SPREAD LIMITATION FOR THE ESS FACILITY

K. Bongardt and M. Pabst, Forschungszentrum Jülich GmbH, 52425 Jülich, Germany

The key issue of the accelerator part of the European Spallation Source (ESS) is the loss free ring injection. In the transfer line between linac and compressor rings two rf cavities, phased independently, are installed followed by an achromatic collimator. This two-stage system allows an optimum energy spread limitation under varying beam current and energy ramping conditions. The system aims to have less than 10^{-4} particles outside an energy spread of ± 2 MeV at ring injection. Longitudinal space charge forces are still present and cause an increase of the energy spread and the longitudinal emittance. Multiparticle calculations with varying beam currents are presented for the 130 m long straight transfer line after the linac end.

INTRODUCTION

The most critical part of the accelerator of the European Spallation Source [1] is the loss free injection into the compressor rings. Due to the 5.1 MW average beam power at 1.334 GeV, particle loss above $10^{-7}/\text{m}$ forbids unconstrained hands on maintenance of accelerator components. At the injection of the 1.2 msec long linac pulse into the two compressor rings the loss must be here at the 10^{-5} level. For achieving this with a 1000 turn H^- - injection scheme the linac beam has to be truncated in both transverse planes. The mean kinetic energy has to be varied by 4 MeV during injection, corresponding to 2×10^{-3} $\Delta p/p$ ramping. Less than 10^{-4} particles above an energy spread of ± 2 MeV should be accepted by the stripping foil. The linac pulse has to be chopped at the 1.67 MHz revolution frequency with 60 % chopping efficiency [2].

The longitudinal halo collimation puts stringent conditions on the design of the high energy transfer line between linac end and compressor rings. The layout of this line consists of three parts:

- a straight transfer line of 75 m from the linac end up to a 700 MHz bunch rotation cavity
- a 42.5π m circumference, 180 deg achromatic collimation system
- a 75 m final matching section up to the H^- - stripping foils

At the stripping foils the two 0.6 msec long linac pulses are separated vertically, with a final vertical separation of 1.5 m for the two accumulator rings. Longitudinal halo scraping is obtained by a two stage collimation system. First are two independently phased energy ramping and bunch rotating cavities which reduce considerably the particle number outside the wanted ± 2 MeV value. The remaining particles are stripped and collected in an achromatic collimation system.

FINAL BUNCH ROTATION

The beam motion was studied for a 130 m straight transfer line including a bunching cavity. The rms values of the energy

spread and the longitudinal emittance are shown in Fig. 1 and 2 for the ESS linac design parameters: 214 mA bunch current at 700 MHz and 1.334 GeV [3]. For the multiparticle calculation the linac output phase space distribution is used as the input distribution for the transfer line simulation [4]. The same focusing was adopted as at the coupled cavity linac end: a quadrupole doublet every 5.4 m resulting in an initial average transverse radius of 3.5 mm.

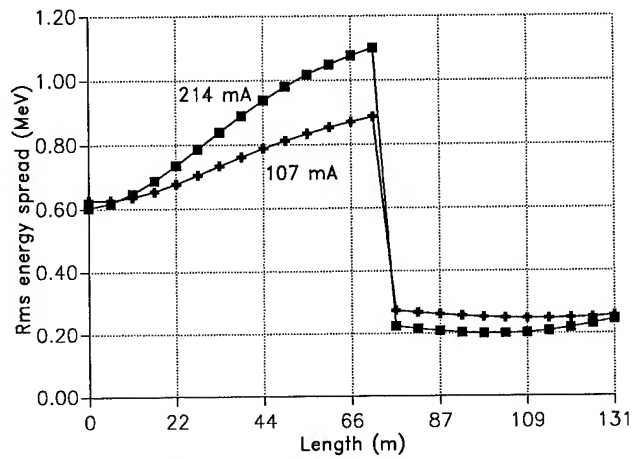


Fig. 1 Rms energy spread for full bunch current (214 mA) and half bunch current (107 mA) in the transfer line

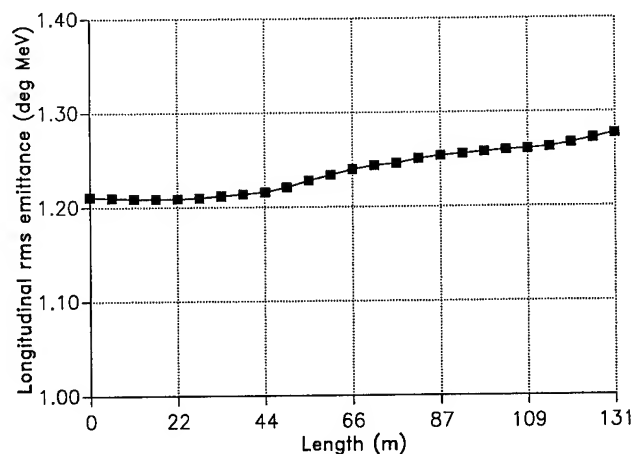


Fig. 2 Rms emittance for 214 mA in the transfer line

The rms energy spread and the longitudinal rms emittance are not constant along the transfer line as expected in a simple drift space. Due to small, but still not negligible, space charge forces the particles are not 'drifting' longitudinally but moving instead in a 'plasma channel' with decreasing strength. The envelope equation for the dense beam core with its mainly linear space charge forces is space charge dominated and not

emittance dominated in spite of the high kinetic energy. The rms phase changes from 2° to 6° (10° without bunching cavities), see Fig. 3. For constants quadrupole gradients, there is a reduction of the transverse beam size. The shielding of the conducting boundary is neglected, as the initial value of 0.5 cm for the bunch length is shorter than the pipe radius.

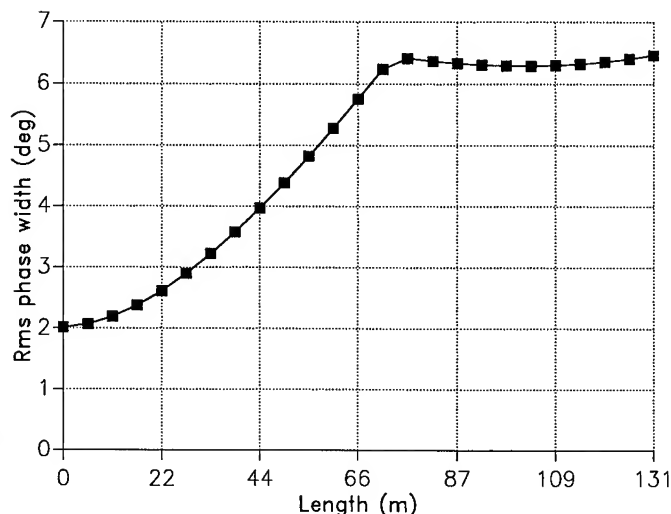


Fig. 3 Rms phase width for 214 mA in the transfer line

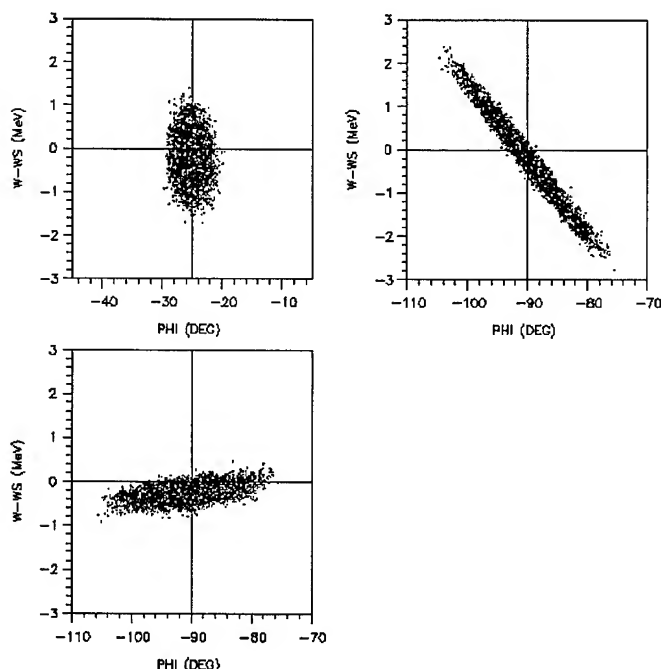


Fig. 4 Longitudinal rms emittances at end of CCL, before and after the buncher (upper left, upper right, lower left)

Along the 130 m long transfer line, the longitudinal rms emittance increases by the same amount as along the whole coupled cavity linac [4]. This increase is caused by the longitudinal mismatch along the line. The unexpected situation cannot be avoided easily as the rms energy spread of 0.6 MeV at the linac exit is too large for loss free ring injection. With a

bunch rotation cavity, placed after 75 m at 6° rms phase width, see Fig. 1, the rms energy spread is reduced to 0.2 MeV. About 11 MV rotation voltage is applied to a 4 m long 700 MHz coupled cavity. After the bunch rotation cavity the rms energy spread is not constant for a 50 m long transfer line. In Fig. 4 the longitudinal phase space is plotted at the linac end, before and after the bunch rotation cavity.

LONGITUDINAL HALO COLLIMATION BY ENERGY RAMPING AND BUNCH ROTATION

As pointed out before the main task of the bunch rotation cavity is not to reduce the rms energy spread to its smallest allowed value, but to limit the total energy spread to ± 2 MeV at the H^- - stripping foils. In addition the mean energy has to be ramped by 4 MeV during the pulse. The energy spread limitation must be fulfilled under varying beam current and ramping conditions.

In Fig. 1 the bunch rotation is shown also for a 'partly' filled bunch having 50% of its design current. Those bunches can be created by a chopping system at low energies [5].

As there is only a 20 % tune depression at full current for all three planes along the CCL, the output parameters for the 50 % current value will not differ very much to those for full current. However, due to less space charge, the phase width and energy spread, see Fig. 1, are increasing much slower. By keeping the rotation voltage unchanged this bunch cannot be rotated properly.

The required 4 MeV energy ramping can, in principle, be done with bunch rotation cavity by changing the synchronous phase by 21° . But as the 95 % phase width is around $\pm 13^\circ$ at the cavity position, see Fig. 4, this would result in a deformed phase space boundary which could lead to more particles outside the ± 2 MeV limit at the stripping foil for the ramped beam.

For a beam at the design intensity and emittance, with no ramping and field errors in the accelerating structures, only particles with emittances above 100 times the rms emittance are outside the ± 2 MeV limit directly after the rotation cavity, see Fig. 4. However, 5% of the particles are outside the collimation limit before the bunch rotation cavity. For the partly filled bunch, see Fig. 1, the safety margin is 64 only. If random amplitude errors of 1% and phase errors of 1° are present in the CCL, the mean energy of the bunch center could be shifted by 0.6 MeV at the linac end [4]. This would drastically reduce the safety margin by 50%. As the phase width of the outermost particles is smaller than 60° , 10 times the rms value, the cavity can operate with a sinusoidal field. Placing the cavity at larger phase values will increase the safety margin only, if higher harmonic field components are superimposed.

In order to keep this large safety margin also for half the beam current and for a energy ramped beam, a second independently phased 700 MHz cavity will be placed after the CCL. E.g., this allows to bring the 107 mA beam to the same orientation in phase space after the bunch rotation cavity as the 214 mA beam. At the new 100 MeV transfer

line at Fermilab two bunching cavities are synchronized for routine operation. By varying amplitude and phase of both cavities, there are four independent knobs for achieving the longitudinal halo collimation under varying beam current and ramping conditions, including the influence of field errors and mismatch effects. As the design goal is the particle limitation outside the ± 2 MeV limit and not the smallest possible rms energy spread, it could well be that the bunch has to be under- or overrotated. For allowing this operational flexibility the large safety margin (100 for a matched beam at full intensity) is of great importance.

ACHROMATIC COLLIMATION SYSTEM

After the bunch rotation cavity, the 75 m long line for vertical beam separation could, in principle, follow. Due to the enlarged rms phase width of about 6° the value for the bunch-length is increased to 1.5 cm, comparable to the pipe radius. Then, the space charge forces can neither be approximated by the short bunch limit for direct forces nor by the long bunch limit for image forces. In this transition region, the linear part of the forces is smaller than predicted by the direct Coulomb force assumption. However, the nonlinear part is larger than the Coulomb part [6]. The effect on the rms energy spread when using the short bunch approach is shown in Fig. 1. Here the rms energy spread is increased by 25%. The long bunch approach is calculated in [7]. Both calculations agree, that after the rotation cavity longitudinal forces are present. Therefore the large quoted safety margin at the position of the rotation cavity cannot be easily transformed to the H^- – stripping foils position, 75 m downstream.

To overcome this serious difficulty an achromatic collimation system has been designed [8], where the longitudinal halo limitation is made by stripping away the unwanted particles at a position of large normalized dispersion. This two stage longitudinal beam collimation is quite superior to all other discussed possibilities. With the ramping and rotation cavity the number of particles outside ± 2 MeV is reduced considerably. The remaining particles are stripped and collected afterwards. For 5.1 MW average beam power scraping away 10^{-4} of the

current results in 500 W average power, to be collected at a small spotsize. Even more important is the flexibility of the two stage system. Here it seems to be possible to find optimal solutions under various beam current and ramping conditions.

The transverse beam parameters have to be matched carefully to the achromatic conditions. The change from a doublet focusing system with small β -values to a triplet with large β -values has to be made in the transfer line between linac end and rotation cavity. A current dependent matching is mandatory. As the transverse particle distributions are not changing significantly along the transfer line, horizontal beam scraping is foreseen before the rotation cavity, vertical scraping is applied after the achromatic collimation section. Long low field gradient bending magnets are used in order to avoid unwanted Lorentz dissociation of the H^- – particles.

REFERENCES

- [1] H. Lengeler, "Proposals for Spallation Sources in Europe", Fourth European Particle Accelerator Conference, London, 1994, World Scientific, p.249–253
- [2] G. Rees, "Important Design Issues of High Output Current Proton Rings", see Ref. 1, p. 241–245
- [3] H. Klein, "Spallation Neutron Sources", Proceedings of the 1994 International Linac Conference, Tsukuba, 1994, p. 322–327
- [4] M. Pabst and K. Bongardt, "Beam Dynamics in the 1.3 GeV High Intensity ESS Coupled Cavity Linac", this conference
- [5] M. Pabst and K. Bongardt, "Design Criteria for High Intensity H^- – Injector Linacs", this conference
- [6] A. W. Chao, "Physics of Collective Beam Instabilities in High Energy Accelerators", Wiley, New York; M. Reiser, "Theory and Design of Charged Particle Beams", Wiley, New York
- [7] G. Rees, J. V. Trotman, "Longitudinal Envelope Equation", ESS-95–25–R report, February 1995
- [8] V. Lebedev, G. Rees, "Transfer Line from Linac to Accumulator", ESS-95–18 R report, February 1995

DESIGN CRITERIA FOR HIGH INTENSITY H^- - INJECTOR LINACS

K. Bongardt and M. Pabst, Forschungszentrum Jülich GmbH, 52425 Jülich, Germany

All proposed pulsed spallation source projects include a high power H^- - linac followed by one or more compressor rings [1] or a rapid cycling cyclotron [2]. A key issue for the whole accelerator facility is the loss free ring injection which can be achieved by $H^- - H^+$ charge exchange. The design of an H^- - injector differs remarkably from the layout of an high intensity H^+ - linac [3]. At the low energy end a fast chopper operating at the ring revolution frequency has to be installed. No partly filled bunches are allowed. Funneling of two beams is preferred as it relaxes the conditions for the chopping system. The linac itself has to be designed for no emittance growth and small halo production. In order to ensure a loss free injection into the rings, the linac pulse has to be limited in energy and truncated transversely. The energy spread reduction is made by a bunch rotator after the linac. A cost saving option is to use pulsed superconducting cavities for the high β linac [4].

INTRODUCTION

All proposed pulsed spallation source projects consists of a high power H^- - linac, followed by one (or more) compressor rings or rapid cycling synchrotrons. In Fig. 1, as a typical example the layout of the ESS linac is shown [5]. The low energy part consists of two H^- - ion sources with 70 mA peak current each, a 2 MeV bunched beam transfer line between two RFQs for installing a fast chopping device and a 5 MeV funneling line afterwards. The drift tube linac (DTL) operates at 350 MHz, the coupled cavity linac (CCL) at 700 MHz. The transition energy is 70 MeV. In the 1.334 GeV high energy transfer line, a 4 m long 700 MHz cavity is positioned after 75 m, acting as a bunch rotator. The linac operates at 50 Hz with 6% duty cycle. All the mentioned parameters are more or less typical for high intensity H^- - injector linacs.

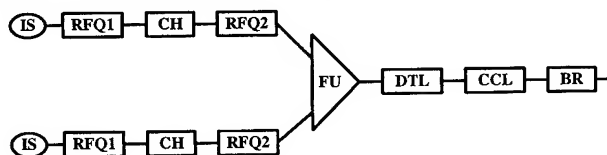


Fig. 1 ESS linac layout: IS: ion source, CH: chopper, FU: funneling, BR: bunch rotator

Different from high intensity proton linacs is the injector part; two H^- - sources and the two bunched beam transfer lines and the bunch rotation cavity at the linac end. For achieving loss free ring injection, the linac pulse has to be chopped at the ring revolution frequency and the energy spread has to be limited [6]. Energy ramping of the injected pulse is also foreseen for most scenarios.

FRONT END OF THE H^- - INJECTOR LINAC

For any loss free ring injection scheme at about 1.3 GeV, the number of injected turns is limited to about 1000. As

in addition the linac pulse has to be chopped with about 60% chopping efficiency, the required peak current from the H^- - source has to be about 100 mA. Even at 50 mA peak current a cesiated source is not available at this moment [7].

Due to the strict loss limitation in the following rings, a 'clean' pulse has to be provided, including sharp voids created by the chopping system. After each void the beam current is built up in about 50 μ sec depending somewhat on the source parameters. The leading edge particles can be seen at ring injection, even with an RFQ as the first accelerator. This is absolutely unwanted for a typical tolerable loss rate of 10^{-4} at ring injection. Switching on the RFQ sometimes later, may not remove this 'leading' edge problem completely due to the RFQ filling time. A similar argument holds for chopping the ion source. For a clean chopped beam, the rise and fall time must be shorter than the RFQ bunching time, typically about 5 nsec. Large distortions of the beam emittance, due to chopping in space charge neutralized transport system, have been observed [8]. Increasing the extraction voltage might overcome some of the problems, but it is not in favour of the required energy spread limitation at the linac end, as it increases the longitudinal emittance drastically.

An achievable solution for getting a beam with no 'leading' edge particles, sharp edges created by the chopper and a small longitudinal emittance is the design of a bunched beam transfer line. The fast chopping element [9] and the mandatory collector afterwards are located in drift spaces, obtained by a triple waist design in all 3 directions [10]. Prechopping of the ion source reduces the heat load at the collector. The beam is kept bunched in order to maintain the small output RFQ-emittance. The correct phasing of independent bunching cavities is routine at the Fermilab 400 MeV linac upgrade [11] and was also demonstrated successfully with beam at the 5 MeV Los Alamos single leg funnel experiment [12].

The use of a funneling scheme implies a second bunched beam transfer line, but relaxes the constraints of the chopping line considerably. The peak current is halved and the first RFQ operates at a lower frequency. Both bunched beam lines are emittance dominated and not space charge dominated. Therefore, the energy spread is almost constant between two bunching cavities. The phase width must be limited to 40° in order to avoid filamentation in the longitudinal phase space. This limits the free drift space to the value of the longitudinal beta-function at the buncher position, proportional to the bunching wavelength. Low frequencies and high energies, obtainable by using segmented RFQs [13], are preferred for both lines. Due to the pulsed operation, the thermal layout of the rf-deflector cavity and a two gap, two hole bunching cavity is quite relaxed compared to cw operation [14].

As both bunched beam lines are emittance dominated, they are very insensitive against operation at reduced current lev-

els during a start-up period [10,15]. Variable electromagnetic quads allow current depending matching.

NORMALCONDUCTING HIGH β LINAC

The most cost expensive and on the other hand most sensitive part of any injector linac is the high β one. A frequency jump and operating at higher gradient is preferred in order to reduce the capital and operating costs. But this can cause longitudinal halo production due to mismatch, absolutely unwanted for the required energy spread limitation afterwards. Both conflicting requirements can be overcome by an almost optimized layout, emphasizing the high quality design [16].

A new developed cost effective, reduced in size, high efficient modulator system can be used for the pulsed operation [17]. This modulator has delivered 10 MW peak power for 2 msec with 85% efficiency. Together with a cathode modulated klystron, this results in a high overall rf-efficiency even for pulse length up to 2 msec. Based on this assumption, in Fig. 2 the investment and operating costs for the normal conducting ESS high β linac are plotted as a function of the accelerating gradient. For 50.000 h or 10 years operating time, about the lifetime of a pulsed klystron, the cost optimum is shifted considerably towards a lower gradient.

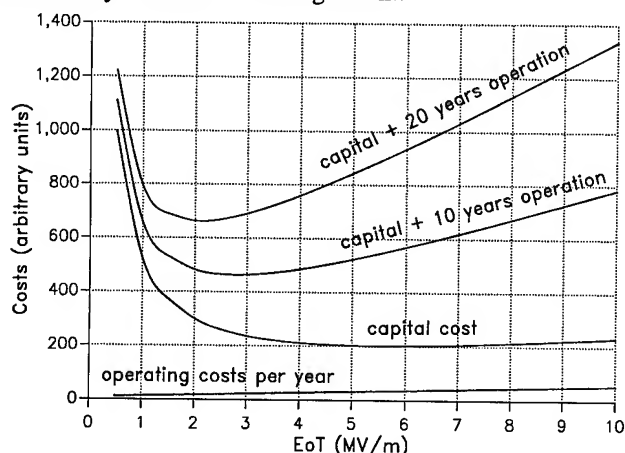


Fig. 2 Costs for the ESS 700 MHz normalconducting coupled cavity linac. Capital costs include structures, rf and buildings without extensive shielding

The rf-control system has to be designed for beamloading parameters up to 3 and an abrupt change of beam current due to chopping. About 30% additional power of the generator power, applied for reducing the cavity filling time, seems to be adequate to control 1% amplitude and 1° phase stability [18]. These are the upper limits for keeping the fluctuation of the mean beam energy below the rms energy spread [16].

Operating the high β linac at higher frequencies is not in favour from the beam dynamics point of view. It increases the bunch current without substantial gain in rf-efficiency, as the shunt impedance is almost constant for constant aperture radius. The effective longitudinal emittance is increased too, absolutely unwanted for the energy spread limitation in the high energy transfer line.

BEAM COLLIMATION IN THE HIGH ENERGY TRANSFER LINE

In order to ensure a loss free injection scheme, the outgoing linac pulse has to be limited in energy spread and truncated in both transversal planes. Energy ramping during the injection time is also foreseen for most scenarios.

The energy spread reduction can be done by placing a dephasing section, consisting of a coupled cavity after the linac. Due to, still present, longitudinal space charge forces the energy spread is not constant. We have a space charge dominated motion instead of a emittance dominated one in this high energy transfer line [19].

Most of the spallation source facilities require a curved transfer line from the linac to the rings. The dipoles should be placed only after the bunch rotation cavity, where the energy spread is changing slowly. The dipole field has to be limited in order to avoid Lorentz dissociation of the H^- particles. Due to the increased bunch length, image forces are more dominant than the direct Coulomb forces. They can lead to an increased number of particles outside the energy limit at the stripping foil. To overcome this difficulty, a two stage collimation system is proposed for the ESS facility. At the first stage, the combination of energy ramping and bunch rotation cavity, as many particles as possible are brought within the ± 2 MeV collimation limit at the stripping foil. The few ones, still remaining outside the limit, are scraped away by a stripping foil at a position of large normalized dispersion in an achromatic collimation section [20].

SUPERCONDUCTING HIGH β LINAC

Especially for accelerator layouts with a long linac and compressor ring, superconducting cells are a very interesting option for the high part. In the normal conducting ESS high β linac the total rf power is 2.4 times the beam power cw. Superconducting cavities are now being routinely used in many accelerators. Experience gained during the building of these machines strongly suggests that rf superconductivity is approaching already mature technology, even if it is still from its limit.

For accelerating a high intensity pulsed H^- beam from 100 MeV to about 1.3 GeV various technical and physical difficulties have to overcome which aren't existing in the acceleration of low intensity, cw, relativistic electron beams.

Superconducting iris loaded cavities can operate at the low DTL frequency of about 350 MHz with aperture openings of 5 cm radius [21]. This is certainly an advantage for reduced activation by particle losses. The accelerating gradient can be substantially higher than in a normalconducting cell, but the available space is used less effectively. A bunched beam transfer line between the DTL and the SC linac is required, as the transverse and longitudinal focusing parameters differ substantially in both sections.

Due to pulsed operation, the rf pulse length has to be increased by the filling time. If the rf input coupler is matched to have no power reflections during acceleration, then the filling time is proportional to the accelerating gradient/bunch current.

A higher gradient means a shorter linac, less investment costs, but increased operating costs. For a constant average current, the increase in rf pulse length is independent of the bunch current. During the start-up period with reduced current, and therefore reduced power, the filling time for half the current is 30% larger than the filling time at full current. For an optional ESS 350 MHz superconducting high β linac the rf-pulse length is increased by 50% for full intensity.

Due to the high effective pulse current of up to 65 mA, the input coupler requires special attention. Peak power levels can be greater than 400 kW, exceeding the present performance data obtained so far with beam [22]. The multipactor threshold is proportional to the 4th power in frequency [23]. As the filling time is not negligible compared to the pulse length, the behaviour of the high power input coupler under various load conditions must be studied, including the start-up period with 50% current only.

The arrangement of cells and rf units must be solved for cell length varying with β . For a constant number of cells/input coupler and a constant number of input couplers/klystron, the accelerating gradient must be ramped down with β . This increases the linac length substantially. By operating at higher frequencies, solutions can be found with increasing gradient, but decreasing number of cells/input coupler [24]. This is more favourable, as it keeps the peak surface field below its critical value all along the linac.

Most attention has to be given to the dynamic behaviour of the radiation pressure or Lorentz force detuning. With a time constant of 1 msec, measured at the MASCE accelerator at Saclay, the caused phase deviation is not constant during the beam pulse [25]. Even for stiffened cavities, where the static detuning is well inside the loaded cavity bandwidth, the dynamic effect must be examined in great detail. For a spallation source linac with energy spread limitation requirements, the accelerating phase has to be stabilized within 1° over the beam pulse. If more than one cryomodule are connected to a klystron, microphonic noise must be considered too.

A 8 mA, pulsed, 500 MeV electron linac with 1.3 GHz superconducting cells, the TESLA test facility, is under construction at DESY [26]. The first beam is expected at end of 95. 16 power couplers are connected to one klystron. At the design gradient of 25 MW/m, the peak power per input coupler is 200 kW. As a SASE FEL is foreseen afterwards, controlling the dynamic Lorentz force detuning and microphonic noise is of great importance.

ACKNOWLEDGEMENT

We would like to thank our colleagues from the ESS linac and ring group for many stimulating, fruitful and critical discussions. Many thanks are given to H. Lengeler for his advice in understanding pulsed superconductivity and to H. Klein for discussions about the layout of the ESS linac. Special thanks are given to G. Rees for clarifying the longitudinal halo collimation system.

REFERENCES

- [1] A. Jason, "Linac Driven Spallation Sources", these proceedings
- [2] P. J. Bryant, "Synchrotron-Driven Spallation Sources", these proceedings
- [3] G. Lawrence, "Transmutation and Energy Production with High Power Accelerators", these proceedings
- [4] H. Lengeler, EPAC 1994, London, p. 249-253
- [5] H. Klein, Linac 94, Tsukuba, p. 322-327
- [6] G. Rees, EPAC 1994, London, p. 241-245
- [7] L. Schroeder, K. H. Leung, J. Alonso, Proc. Workshop on Ion Source Issues Relevant to a Pulsed Neutron Source, Berkeley, 1994, LBL-36347 conf. rep.
- [8] J. M. Brennan et al., EPAC 1988, Rome, p. 1003
- [9] S. Nath, T. P. Wangler, R. R. Stevens, "Conceptual Design of Beam Choppers for RFQ Linacs", these proceedings
- [10] K. Bongardt, Proc. ICANS XII, 1993, RAL rep. 94-025, p. A-115,
- [11] M. P. Popovic, L. Allen, C. Schmidt, "Fermilab Linac Injector, Revisited", these proceedings
- [12] K. F. Johnson et al., Part. Acc., 37-38, 1992, p. 261
- [13] L. M. Young, Linac 94, Tsukuba, p. 178
- [14] F. L. Krawczyk, Los Alamos internal note, AOT-1:94-171, September '94
- [15] R. W. Garnett, P. Smith, Linac 94, Tsukuba, p. 107
- [16] M. Pabst, K. Bongardt, "Beam Dynamics in the 1.3 GeV High Intensity ESS Coupled Cavity Linac", these proceedings
- [17] H. Pfeffer et al., "A long Pulse Modulator for Reduced Size and Cost", Proc. 21th Int. Power Modulator Symposium, June 94, Costa Mesa
- [18] Y. N. Senichev, Contribution to the 3rd General ESS Meeting, Baden, March '95
- [19] K. Bongardt, M. Pabst, "Final Bunch Rotation and Momentum Spread Limitation for the ESS Facility", these proceedings
- [20] V. Lebedev, G. Rees, ESS-95-18-R report, February '95
- [21] H. Heinrichs et al., VI th Workshop on RF Superconductivity, CEBAF 93
- [22] J. Kirchgessener, "Review of the Development of RF Cavities of High Current", these proceedings
- [23] E. Somersalo, P. Yla-Oijala, D. Proch, TESLA rep. 94-14, July 94
- [24] G. Swain, see ref. 21
- [25] A. Mosnier, J. M. Tessier, EPAC 1994, London
- [26] TESLA test facility linac design report, ed. D. A. Edwards, TESLA rep. 95-01, March 95
- H. Weise, "The TESLA Test Facility Linac", these proceedings

Measurements of Vacuum Chamber Impedance Effects on the Stored Beam at CESR*

M. Billing, Z. Greenwald, W. Hartung, W. R. Lou, M. Pisharody, J. Rogers, D. Sagan, J. Sikora
Laboratory of Nuclear Studies, Cornell University, Ithaca, NY 14853 USA

Within the last year CESR (Cornell Electron Storage Ring) has changed its mode of operation from 7 nearly equally spaced bunches in the two counter-rotating beams to 9 trains of 2 bunches in each of the beams as the next step in the upgrade of the facility toward higher beam currents and increased luminosity. The upgrade program has included work to understand and document the transverse stability of a single beam composed of trains of bunches. Initial results from this work will be reported here.

EIGEN MODES OF OSCILLATION FOR TRAINS OF BUNCHES

One of the most common methods for studying single beam collective effects consists of observing the change of the tune and of the damping rate for each of the eigen modes of oscillation of the beam as a function of the beam current. To make these measurements the eigen modes for trains of bunches and the eigen mode frequencies must be known. Although for brevity the following arguments will treat transverse dipole modes of oscillation, these arguments can be trivially generalized to higher transverse head-tail modes as well as to longitudinal modes of oscillation.

Following the formulation by Siemann[1], we may describe the betatron motion of a single bunch of particles driven by a sinusoidal excitation from a kicker as observed at a single beam position monitor (BPM) in the ring. On time scales much longer than the bunch length, the position signal from the BPM, $d(t)$, can be represented as a complex phasor proportional to a sequence of delta-functions spaced at the revolution period T and modulated by the average position of the bunch times its current,

$$d(t) = x_0 Q_b e^{j\omega_b t} \sum_{n=-\infty}^{\infty} \delta(t + nT)$$

where x_0 is the betatron oscillation amplitude at the angular frequency ω_b and Q_b is the charge in the bunch. The frequency spectrum of this dipole moment $d(\omega)$ is calculated by Fourier transformation to be

$$d(\omega) = x_0 Q_b \sum_{n=-\infty}^{\infty} e^{jnT(\omega_b - \omega)} = x_0 Q_b \omega_r \sum_{n=-\infty}^{\infty} \delta(\omega - \{\omega_b + n\omega_r\})$$

where $\omega_r = 2\pi / T$. This is a line spectrum with the lines occurring at the upper betatron sidebands of the rotation harmonics. When this signal is connected to a spectrum analyzer, negative frequencies are not observed directly but are reflected about zero into the positive frequency domain causing the negative frequency part of the spectrum to occur at the lower betatron sidebands of the rotation harmonics.

For the case of N_t trains of N_b bunches having a uniform spacing in time of T/N_t between the lead bunches of subsequent trains and a spacing of T_{bb} between the bunches

within each train, the time domain signal will be the sum of dipole moments for each of the bunches giving us N_t times N_b sets of these delta-function sequences. The eigen modes of the betatron oscillations for this ensemble of bunches (charge Q_b per bunch) will be occur as stationary temporal patterns of displacements having the same maximum for each bunch in the beam. A stationary pattern of displacements means that each eigen mode must excite the bunches in an oscillation pattern that, if on one given turn the kicker's excitation was in phase with one of the bunches in the ensemble, a change of this excitation to be in phase with some other bunch would simply translate the pattern; this implies the displacements must satisfy periodic boundary conditions. The lowest eigen frequency of each eigen mode must then have a constant phase advance between lead bunches in adjacent trains of $2\pi (L/N_t)$ where $L = 0, 1, \dots, N_t - 1$ and a constant phase advance between bunches within the train of $2\pi (K/N_b)$ where $K = 0, 1, \dots, N_b - 1$. Thus the dipole moment of the ensemble of bunches, $d_{N_t, N_b}(L, K, t)$, driven at the lowest eigen frequency specified by mode parameters (L, K) is

$$d_{N_t, N_b}(L, K, t) = x_0 Q_b \sum_{l_t=0}^{N_t-1} \sum_{k_b=0}^{N_b-1} \delta\left(t + \frac{l_t}{N_t} T + k_b T_{bb}\right) * \exp\left[j\omega_b \left(\frac{l_t}{N_t} T + k_b T_{bb}\right) + 2\pi j \frac{l_t L}{N_t} + 2\pi j \frac{k_b K}{N_b}\right]$$

where the last two terms in the exponential arise from the phase advances from train to train and from bunch to bunch within each train. The Fourier transform of $d_{N_t, N_b}(L, K, t)$ is

$$d_{N_t, N_b}(L, K, \omega) = S(\omega_b, L) I(\omega, K)$$

In this form $S(\omega_b, L)$ selects the spectral lines which are associated with the mode parameter L and these identify what we will call "train modes" of oscillation since there is a phase advance of $2\pi (L/N_t)$ from train to train. In this equation $I(\omega, K)$ is the envelope function for the "bunch modes" of oscillation which have phase advances of $2\pi (K/N_b)$ from bunch to bunch within each train. $S(\omega_b, L)$ and $I(\omega, K)$ are

$$S(\omega_b, L) = x_0 Q_b \omega_r N_t \sum_{n=-\infty}^{\infty} \delta(\omega - \omega_b - \{nN_t + L\} \omega_r)$$

$$I(\omega, k) = \frac{\sin \frac{1}{2} [(\omega - \omega_b) N_b T_{bb} - 2\pi K]}{\sin \frac{1}{2} \left\{ (\omega - \omega_b) T_{bb} - 2\pi \frac{K}{N_b} \right\}}$$

$$* \exp \left\{ -\frac{j}{2} \left[(\omega - \omega_b) (N_b - 1) T_{bb} - 2\pi \frac{K(N_b - 1)}{N_b} \right] \right\}$$

* Work Supported by the National Science Foundation.

Notice for a given mode L that $S(\omega_b, L)$ selects every N_L -th spectral line to associate with this mode while the $N_L - 1$ intervening lines correspond to the other train modes. The form of $I(\omega, K)$ gives an interference pattern, whose first global maximum occurs at $\omega = 2\pi K / (N_b T_{bb})$ with a periodicity of $\Delta\omega = 4\pi / (N_b T_{bb})$ in the frequency spectrum, and is analogous to the well known spatial interference pattern of light passing through an array of multiple slits. This interference envelope function also has the property for mode K that betatron sidebands in the neighborhood of each global maximum will have zero or nearly zero amplitudes for all other $N_b - 1$ modes. Therefore to find a spectral line for mode (L, K) , which has minimum coupling to other modes, select one of the betatron sidebands that satisfies

$$\omega_{L,K} = (nN_L + L)\omega_r + \omega_b$$

where n is an integer and which is the nearest one to the interference function's global maxima, ω_r , where

$$\omega_r = \frac{(2\pi K + i N_b)}{N_b T_{bb}}$$

where i is an integer. So it is possible to find a single betatron sideband for each eigen mode which will best represent the dynamics of that eigen mode.

MEASUREMENT TECHNIQUES

Observations of dipole coupled bunch-train modes of oscillation were made using spectrum analyzers connected to horizontal and vertical processed BPM signals that were sufficiently broadband to be able to detect bunches with a 14 nsec spacing. The tracking generator output of the spectrum analyzers were connected to modulators, which can gate the generator signal on continuously or on for a pulse of duration one to a few milliseconds. The modulated signals are then fed to broadband drivers (either shaker magnets or stripline kickers.) To observe the tune shift as a function of beam current the analyzers were set to scan across the betatron sidebands corresponding to each bunch-train mode using a continuous excitation for the drivers. The frequency corresponding to either the spectral peak or, if different, the intensity weighted centroid of the spectrum were recorded. The damping rate measurements were made using the spectrum analyzers set up as narrowband receivers tuned to the same betatron sideband with the drivers modulated on to excite the beam for a few milliseconds and then turned off to measure decay time of the amplitude of each mode. If there were no coupling to other bunch-train modes, we would expect this decay to be exponential over a few orders of magnitude. With the spectrum analyzer set up as a tuned receiver, the swept trace displayed the amplitude as a function of time and by recording two amplitude readings and their time difference, the damping rate could be calculated.

OBSERVATIONS

A large number of measurements of the tune shift and damping rate vs. positron current have been performed at CESR. The accelerator conditions corresponded to routine High Energy Physics operating parameters, i.e. beam energy of 5.3 GeV, horizontal tune of 10.541, vertical tune of 9.592, bunch length of 18 mm and a spacing of 28 nsec between

bunches within a train. During these sets of measurements the bunches which were populated ranged from a single bunch (1t1b, i.e. 1 train 1 bunch) to 1t2b, 1t3b, 3t2b, 9t1b and 9t2b. The spacing between the first bunches in each of the trains were equal for 3 trains and had an extra 42 nsec between the last and first trains for 9 trains of bunches.

The betatron mode spectrum for trains of bunches has been observed for these cases and is in agreement with the predictions above. Figure 1 presents the example of 1 train of 2 bunches where one of the betatron spectral lines was excited and the resulting beam spectrum was observed for each of the bunch modes. The nodes of the frequency spectra are visible at 18 MHz for the $K=0$ mode and at 0 and 36 MHz for the $K=1$ mode as expected for a 28 nsec spacing between 2 bunches. The roll off of the amplitude at higher frequencies is due to the finite width of the BPM signal as processed for the spectrum analyzer.

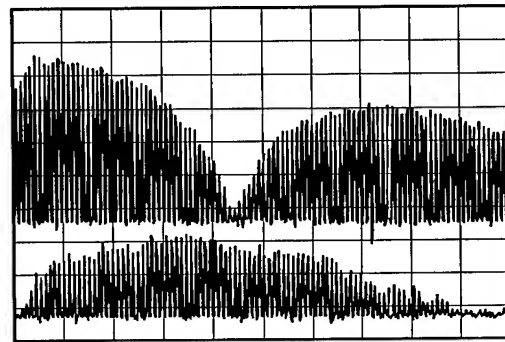
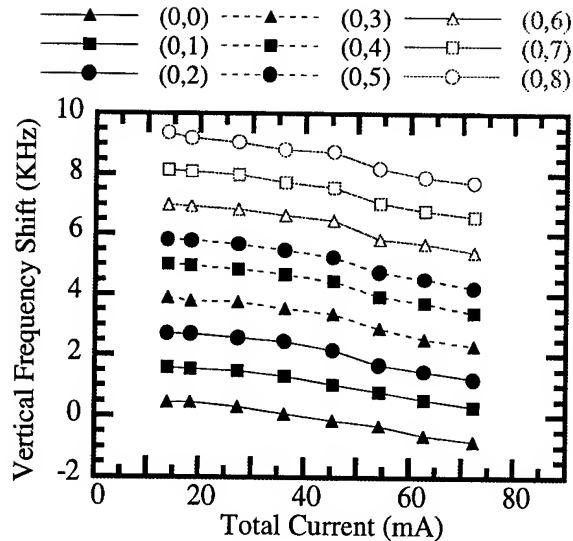


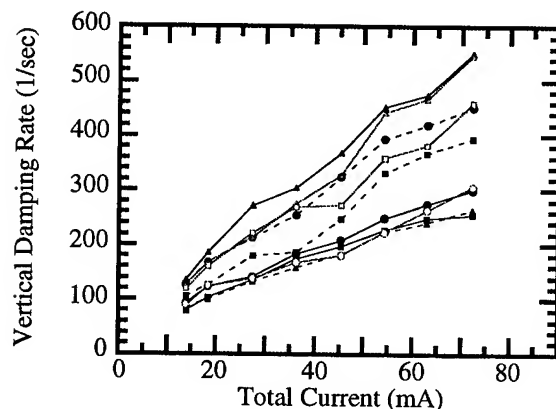
Figure 1: Betatron frequency spectra for the $K=0$ eigen mode (upper trace) and $K=1$ eigen mode (lower trace) for 1 train of 2 bunches with a 28 nsec spacing. Horizontal scale: 0 to 40 MHz. Vertical scale: 5 dB/division.

Typical results for the measurements of tune shift and damping rate vs. total beam current are presented in Figure 2A and 2B for the vertical eigen modes for the case of 9 trains of one bunch. The vertical tune shift data in figure 2A is plotted with an arbitrary offset for each of the eigen modes in order to separate them on the graph. Notice that all the eigen modes have essentially the same slope vs. current, a result which is typical of the horizontal and vertical tune shifts for all the cases studied. The vertical damping rates, α_v , in figure 2B have not been corrected for the small head-tail damping from chromaticity; the slopes of these damping rates do show a significant variation over the set of modes. Both of these sets of data were taken with the distributed ion pumps OFF to eliminate the predominantly horizontal effect known as Anomalous Antidamping (AA) [2]. Measured with the beam stabilization feedback system ON, figure 2C gives the difference in horizontal damping rates α_h for pumps ON minus OFF for all eigen modes again for 9t1b. Total beam currents in the range of 40-50 mA show the most extreme difference in α_h from mode to mode and in this range the instability is strongest becoming weaker at higher currents.

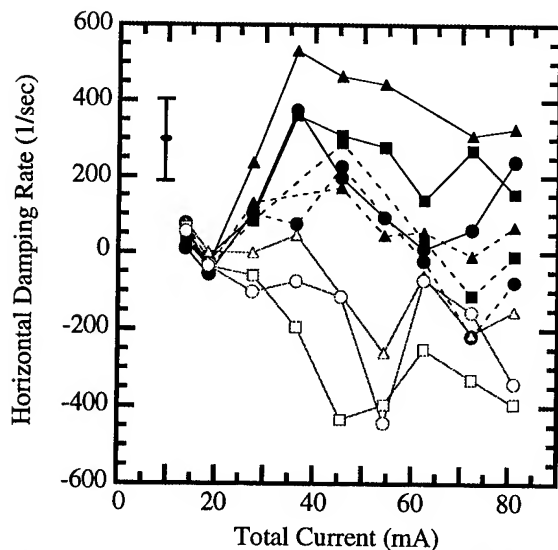
Measurements for 2 bunches per train found some added features. The spectrum of each eigen frequency is split into two separate peaks, one for the lead and one for the trailing bunch; this was easily observed in the vertical spectrum as these peaks are sufficiently narrow that the splitting can be a few times the width of the peaks. In the damping rate



2A



2B



2C

Figure 2: Vertical tune shift vs. total current (2A), vertical damping rate vs. total current (2B), and horizontal damping rate vs. total current (2C) shown for each of the 9 coupled train modes of oscillation (L,0) for 9 trains of a single bunch. Distributed ion pumps are OFF for figures 2A and 2B while figure 2C is the difference of pumps ON minus OFF.

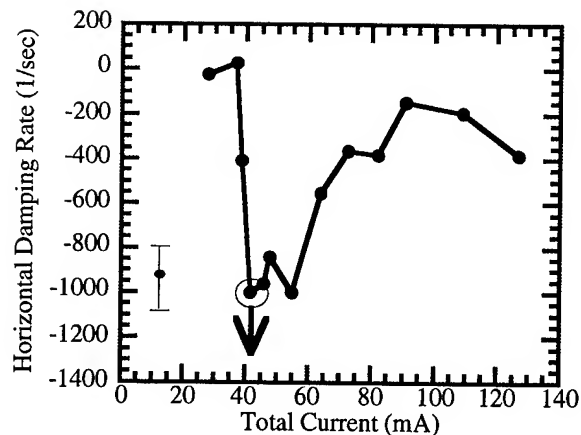


Figure 3: Horizontal damping rate difference for distributed pumps ON minus OFF vs. total beam current for the most unstable eigen mode in the case of 9 trains of 2 bunches. The circled point designates an upper limit for α_h at 42 mA.

measurements one observes an interference beat pattern in time at the difference frequency between the two spectral peaks which modulates the expected exponential decay. In the horizontal case this decay rate can be comparable to the decoherence time from the beating of the two betatron frequencies making damping rate measurements difficult and subject to larger systematic errors. Figure 3 shows α_h vs. current for 9t2b for the (L,K)=(8,0) eigen mode. Notice that the peak of the instability occurs at the same total beam current as the case of 9t1b; this implies that AA is affected by the total current per train or in other words the initial decay of the wakefield for AA is longer than 28 nsec.

All the measurements thus far have shown that AA will be the dominant mechanism for single beam instabilities for trains of single or multiple bunches. Since the present feedback system is able to stabilize the beam during filling as the current passes through the region of maximum instability, we can expect that this feedback system will be suitable for at least 5 bunches in 9 trains.

ACKNOWLEDGMENTS

The authors wish to thank P. Prymmer and Z. Hubert for their help with the data collection and analysis.

REFERENCES

- [1] R. H. Siemann, "Bunched Beam Diagnostics," *AIP Conference Proceedings* 184, pp. 430-471.
- [2] M. Billing, et al, "Interaction of the CESR Vacuum Chamber with Stored Beam, *Proceedings of the 1989 PAC*, pp. 1163-5.

THE STUDY OF NONLINEAR EFFECTS INFLUENCED BY SPACE CHARGE IN HIGH INTENSITY LINAC

A. A. Kolomiets, S. G. Yaramishev, P. R. Zenkevich, A. P. Korolev
Institute for Theoretical and Experimental Physics, Moscow, Russia

INTRODUCTION

Beam halo formation in high intensity linacs is now extensively studied due to the problem of particle losses is a critical condition for design of high current cw linacs for nuclear waste transmutation and power production facilities. The beam losses less than 1 nA/m for high energy part of linac are considered now as acceptable level. It is clear that requirement of such low level losses leads either to beam current limitation or such set of linac parameters, which can considerably decrease its efficiency.

As it follows from the previous and recently carried out investigations the main reasons of the beam halo formation are nonlinear effects. The latest review of these works is given in [1]. These effects have their origin in influence of the space charge forces, mismatched initial distribution, nonlinear external focusing, etc. In many cases as this takes place Hamiltonian becomes time dependent:

$$H = H_0(I) + \varepsilon V(I, \theta, t) \quad (1)$$

where H_0 - Hamiltonian of nonperturbed system, ε - perturbation parameter, $V(I, \theta, t)$ - time periodic function, I, θ - action - angle variables, t - time.

This leads to appearance of nonlinear resonances which makes beam dynamics much more complicated. The simulations show that for rather big perturbation parameter (high beam current for example) this is reflected in the fact that beam emittance grows. Nevertheless there is certain range of perturbation for which simulations do not show any emittance growth but appearance of the beam halo is experimentally observed.

It is known [2] that even for very small perturbation parameter there exist stochastic trajectories which correspond to the destroyed tori whose measure, however, is exponentially small. To clear up the low particle losses problem it is necessary to investigate the beam dynamics at rather small perturbation. In present paper the using of the correlation function for analysis of beam dynamics simulation results is discussed.

SPECTRAL PROPERTIES OF DYNAMICAL SYSTEMS

The consideration of some specific spectral properties of dynamical systems in the transition region from order to chaos is given in [3]. In this work the simplest map that arises in the nonlinear oscillation theory has been studied:

$$\begin{aligned} I_{n+1} &= I_n + K \sin \vartheta_n, \\ \vartheta_{n+1} &= \vartheta_n + I_{n+1} \mod 2\pi, \end{aligned} \quad (2)$$

where K is parameter of the problem and n is discrete time.

For some sequence $x_k = f(I_k, \vartheta_k)$ the spectral density of the correlation function is determined by the expression

$$\begin{aligned} R_N(\omega_m) &= \frac{1}{N} \sum_{-\frac{1}{2}N \leq k \leq \frac{1}{2}N} R_N(k) e^{-ik\omega_m} \\ R_N(k) &= \frac{1}{N} \sum_{-\frac{1}{2}N \leq j \leq \frac{1}{2}N} x_j x_{j+k}, \quad \omega_m = 2\pi \frac{m}{N} \end{aligned} \quad (3)$$

In this expression N determines the maximum of map steps.

It follows from given in [3] qualitative analysis of spectrum of correlation function that it is determined by structure of the phase space. Inside it one can see the stability islands which correspond to the resonances of different orders. They point out in spectrum for $K \ll 1$ the local maxima with corresponding resonant frequencies. As K increases the spectrum becomes wider and nearly uniform.

There is one more universal spectral property of mapping (2). Well marked peak appears for zero frequency when $K \approx 1$ (so called „central peak“). It is due to some trajectories pass the vicinity of hyperbolic point of the separatrix for a very long time. This peak is a good indicator of stochastic motion region appearance.

ANALYSIS OF THE BEAM DYNAMICS SIMULATION RESULTS

Let us consider now spectral properties of particle trajectories in periodic focusing channels. It is well known that trajectory is defined by expression

$$\begin{aligned} x &= \sqrt{\frac{2I_x L}{\varepsilon_x}} |\varphi_x| \cos(\mu\tau + \theta_x) \\ I_x &= \frac{2\varepsilon_x |\tilde{c}_x|^2}{L}; \quad \theta_x = \arg \tilde{c}_x, \end{aligned} \quad (4)$$

where \tilde{c}_x - complex amplitude of oscillation, L - length of focusing period, φ_x - Flouquet function, which depends on Coulomb parameter h and on type of initial particle distribution in phase space, μ - phase advance of Flouquet function on the focusing period, ε_x - emittance in corresponding plane and τ - dimensionless time.

Coulomb parameter depends on phase density of beam current and on focusing channel parameters [4]:

$$h = \frac{\lambda k}{\mu_0 \beta \gamma^2 J_0} \frac{J}{\varepsilon_{x,y}}. \quad (5)$$

here λ - wave length of accelerating field, $k = \frac{L}{\beta \lambda}$, J - beam current, β, γ - relativistic parameters, μ_0 - phase advance for

$J=0$, J_0 - characteristic current.

It is shown in [1] that dependence of phase advance μ on Coulomb parameter is expressed by

$$\mu = \mu_0 \left(\sqrt{1+h^2} - h \right) \quad (6)$$

In [5] the influence of structural resonances in periodic focusing structures on beam dynamics are considered. In this work the analytical study has been carried out for smooth approximation and for uniform distribution of particles in phase space. Following [5] the Hamiltonian in the vicinity of resonance with number k can be determined by expression

$$H = \frac{2\pi I_{max}}{L} \left[\sum_{n=1} \frac{v_n}{n} \tilde{I}^n + \frac{g_k}{k} \tilde{I}^k \cos[2k(2\pi\delta\tau + \theta_x)] \right] \quad (7)$$

where $\delta = \frac{\mu}{2\pi} - \frac{1}{2k}$, $\tilde{I} = \frac{I_x}{I_{max}}$, g_k - depended on h width of the k -th resonance, v_1 - linear shift of the transverse oscillation frequency, $v_{n>1}$ - nonlinear frequency shift for particles with maximum amplitude influenced by $2n$ -th nonlinearity of potential $V(I, \vartheta, t)$.

Following the procedure given in [2] one can write the mapping for (7):

$$\begin{aligned} \vartheta_{n+1} &= \vartheta_n + 2\pi(v_1 + v_2 \tilde{I}_n) + g_k 2\pi \tilde{I}_n^k \cos[2k(2\pi n\delta - \theta_n)] \\ \tilde{I}_{n+1} &= \tilde{I}_n + g_k 4\pi \cdot \tilde{I}_n^k \sin[2k(2\pi n\delta) - \vartheta_n] \end{aligned} \quad (8)$$

The described above correlation function can be applied for analysis of the results of computer simulations in different accelerating and focusing structures. Simulations give usually particles trajectories as some discrete sequence of coordinates of particles in phase space $x_n = f(I_n, \vartheta_n, \tau)$. In this case x_n can represent any coordinate of phase space. It is the most convenient to choose as step of sequence integer number of focusing periods of structure ($\tau_{n+1} = \tau_n + n$). It corresponds to averaged over focusing period trajectories of particles. If initial conditions corresponds to the case $I_{n+1} = I_n$ and $\vartheta_{n+1} = \vartheta_n$ (zero current matched beam) the expression (4) becomes a sinusoid with constant amplitude and initial phase shift ϑ_0 . The appearance of space charge forces leads to determined by (8) amplitude and frequency modulation of trajectories. Modulation rate is determined by mapping (8).

The spectra of correlation function of particle trajectories are shown in fig. 1. The trajectories are the result of simulations of the beam dynamics in the test focusing channel. This test channel corresponds to the intermediate part of the linac for nuclear waste transmutation proposed in [6]. The parameters of the channel and beam are the following:

Type of focusing structure	FODO
Frequency of the accelerating field	300 MHz
Relative velocity of the particles	0.4282
Normalized input emittance	2 mm mrad
Phase advance	0.9866

The represented in fig.1 results have been obtained by simulations with constant longitudinal particle velocities (no

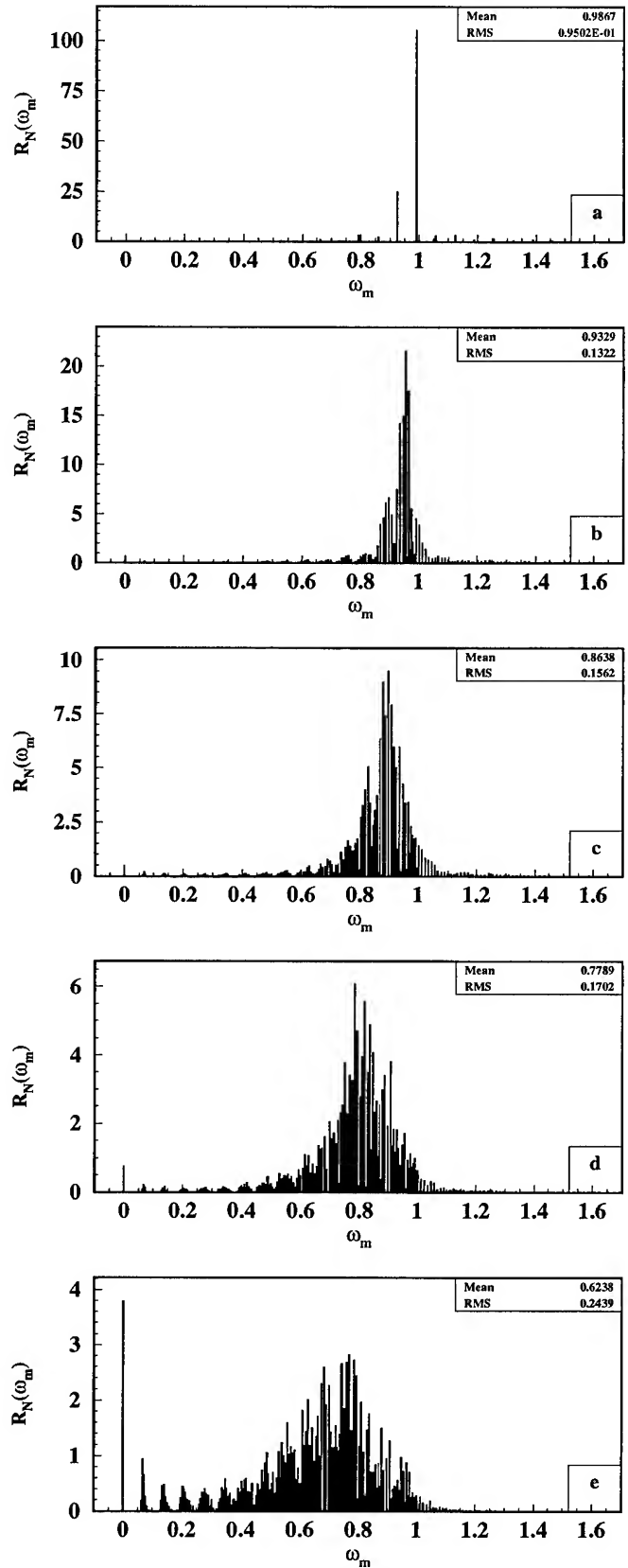


Figure 1. Spectra of correlation function $R_N(\omega_m)$ calculated for particle trajectories from test channel simulations at $h=0$ (a), $h=0.05$ (b), $h=0.124$ (c), $h=0.248$ (d), $h=0.496$ (e)

acceleration) and for space charge forces calculated only for transverse planes. The simulations were carried out by means written in ITEP code „PROTON“ [7]. Test channel consists of 100 focusing periods and only 300 particles were used. The spectral densities of the correlation function in fig.1 have been calculated for the Coulomb parameter $h=0, 0.05, 0.124, 0.248, 0.496$. The frequencies of the correlation function ω_m coincide in our case with phase advances at focusing period.

Fig.1 shows that mean value of phase advance decreases due to linear shift and spectra width increases due to phase advance modulation with increasing of parameter h . The most noticeable feature of the spectra is the appearance of the central peak even for very small value of Coulomb parameter. This effect testifies that even for low Coulomb parameter there is the noticeable region in phase space where the behavior of the trajectories becomes chaotic.

The linear shift of phase advance depending on h obtained from spectra is in a good accordance with analytical formula (6) as it is shown in fig.2.

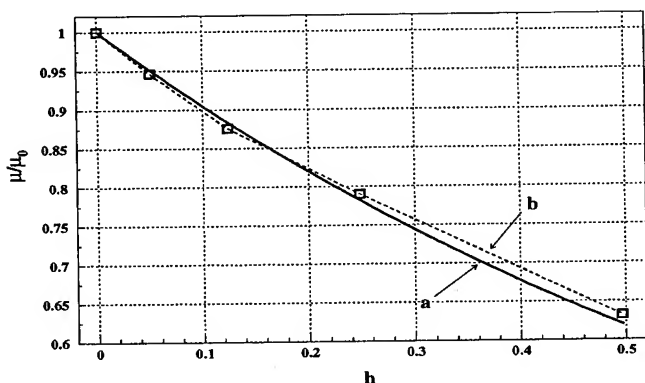


Figure 2. The phase advance dependence on h . a - calculated by formula (6), b - mean values of the spectra of correlation function $R_N(\omega_m)$.

The analysis of the results shows that there is considerable range of the parameter h where simulations did not show any emittance growth. Nevertheless the relative power of the central peak significantly increases with h . This value allows to evaluate a relative size of regions of phase space with stochastic movement of particles. By assuming that this regions are responsible for beam halo appearance, the relative central peak power can be considered as a useful tool for comparison of different accelerating and focusing structures in terms of low level particle losses.

The dependence of central peak relative power and emittance growth in the test channel on h is shown in fig.3. It can be seen that there is no threshold for appearance of the central peak whereas the emittance growth begins at $h>0.24$. When comparing the emittance growth curve with spectra, one can notice that at h corresponding to the beginning of the rapid emittance growth, the low frequency border of the spectrum approaches to zero.

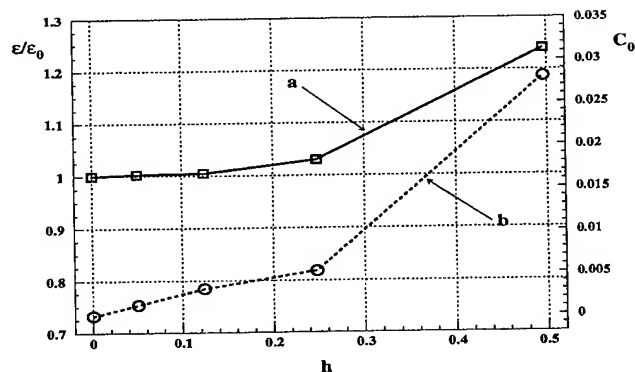


Figure 3. The dependence of the emittance growth (a) and the central peak relative power (b) on h .

CONCLUSION

The use of the correlation function is relatively simple procedure for analysis of spectral properties of particle trajectories calculated by simulations of beam dynamics in linacs. It does not need a big number of particles and can be used for the relatively short structures. This procedure allows to evaluate the influence of different nonlinear effects on beam dynamics. The relative measure of phase space regions where dynamics becomes stochastic can be estimated. It can be useful for the analysis of low level particle losses in different types of accelerating and focusing structures.

REFERENCES

- [1] R. A. Jameson, „Self-Consistent Beam Halo Studies & Halo Diagnostic Development in a Continuous Linear Focusing Channel“, Los-Alamos Report LA-UR-94-3753.
- [2] G. M. Zaslavskii, R. Z. Sagdeev, „Introduction to Nonlinear Physics“, „Nauka“, Moscow, 1988.
- [3] V. V. Beloshapkin, G. M. Zaslavskii, „On The Spectral Properties of Dynamical Systems in The Transition Region from Order to Chaos“, Physics Letters, v.97a, N°4, 1983.
- [4] I. M. Kapchinskiy, „Theory of Linear Resonant Accelerators“, Moscow, „Energoizdat“, 1982.
- [5] P. R. Zenkevich, A. P. Korolev, „Coulomb Structural Resonances in High Current Channels“, Preprint ITEP N°10, Moscow, 1988.
- [6] I. M. Kapchinskiy et al., „Linear Accelerator for Transmutation of Nuclear Power Production Wastes“, Preprint ITEP 100-92, Moscow, 1992.
- [7] Vorobjev et al., Beam Dynamics Simulations in ITEP RFQ“, Preprint ITEP-52, Moscow, 1986.

Beam Size Versus Intensity for Resonant Extracted Beam At the Brookhaven AGS*

K.A. Brown and R. Thern, Brookhaven National Laboratory
H. Huang, Indiana University

I. Abstract

Transverse beam sizes were measured in the AGS prior to the initiation of the third order resonance ($\nu_H = 8 \frac{2}{3}$; driven by sextupoles) used for the slow extraction and again in the external beam lines. The measurements were made using the AGS Ionization Profile Monitor (IPM) and an External Profile Monitor (EPM). Both of these monitors use the ionized residual gas to image the beam on arrays of wires that are aligned parallel to the direction of the beam. The effects of space charge on the IPM are significant at the intensities measured, but the EPM measurements are not affected by space charge. Two measurements are reported. First is the intensity dependence of the resonant beam size, and secondly, an indirect measure of the space charge effect on the IPM. A differential comparison of the two monitors in the vertical plane allows unfolding the effect of the space charge on the measurements. These measurements were made over an intensity range between 15×10^{12} and 36×10^{12} protons per AGS pulse.

II. Data Collection

The AGS IPM is located in the AGS ring and measures beam profiles of the circulating beam.^[1] The EPM is located in the transport channel after beam is extracted from the AGS. Both instruments work on the same principle. Residual gas ions are collected on wires which are aligned parallel to the direction of the beam, as the beam passes between two planes of wires at some potential difference. The major difference between the two instruments is that one measures the high current circulating beams while the other measures the low current extracted beam.

The AGS IPM has a dedicated application which interfaces with the AGS controls system to control the device parameters and to collect data. The EPM is only available as an analog signal which can be displayed on an oscilloscope. Using a Lecroy 9404 digital oscilloscope and capturing the data via GPIB into a National Instruments® LabVIEW® virtual instrument running on a Sun SPARC station IPX, we were able to put together a simple but powerful system which allowed analysis similar

*Work performed under the auspices of the U.S. Department of Energy.

to that which is done in the IPM application software. Since we were only interested in getting accurate width and integrated areas of the EPM, we only built the LabVIEW application to do simple least squares analysis of a gaussian distribution on the profiles captured from the Lecroy 9404. We then captured profiles from the EPM at the same time that we took IPM scans for a series of different intensities.

The beam before it is debunched for extraction has peak currents of as high as 30 A while after beam is extracted the currents are only a few microampere. The high current bunched beams cause significant space charge effects in the IPM measurement,^[2] while the low currents after extraction cause no space charge effects in the EPM measurements.^[3]

III. Results

Figure 1 shows the emittance growth in the vertical plane on the EPM versus intensity. Values shown are of ϵ (E.G.; area = 0.15π) and are un-normalized. To get normalized emittance multiply by $\beta\gamma = 25.7$.

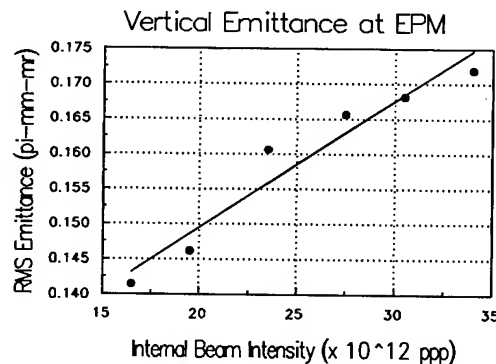


Figure 1: Vertical Emittance vs Intensity

This shows the emittance increasing linearly at a rate of $1.71 \times 10^{-3} \pi$ mm-mr/TP (RMS), or a 20 % increase over a factor of two in intensity.

Figure 2 shows the emittance growth in the horizontal plane at the EPM.

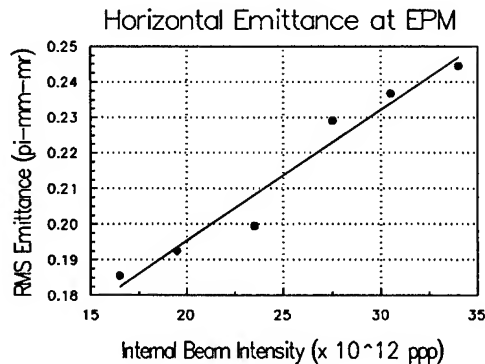


Figure 2: Horizontal Emittance vs Intensity

This shows the emittance increasing linearly at a rate of $3.33 \times 10^{-3} \pi$ mm-mr/TP (RMS), or a 26 % increase over a factor of two in intensity. This measurement represents the growth of the horizontal emittance observed after the extraction process. This growth is roughly twice that seen in the vertical plane, although the percentage increase is about the same.

The uncertainty in the above emittances from the EPM is approximately ± 30 %. This uncertainty is primarily due to the uncertainty in β at the EPM. What is of interest, though, is the relative variations with intensity, which can be measured very well, as seen by the scatter of the points around the straight line in figures 1 and 2.

The IPM shows the vertical beam size changing in the process of debunching the beam for extraction. The IPM measurement suffers substantial distortion from the space charge forces of the beam at these high intensities and small beam sizes. It is believed that the actual vertical size does not change during the debunching process, and thus the size difference is a manifestation of the change in space charge distortion in changing from a bunched beam which is small horizontally to an unbunched beam which is large horizontally (due to the large dp/p attained during the debunching).

Figure 3 shows the inferred beam size, where the correction has been made by a Monte-Carlo simulation of the ion collection process in the IPM. At this small beam size and high intensity, the simulation is only feasible for the unbunched beam. For a bunched beams this narrow and intense, the distortion is very sensitive to several parameters that are insufficiently well known to allow a meaningful unfolding of the effect.

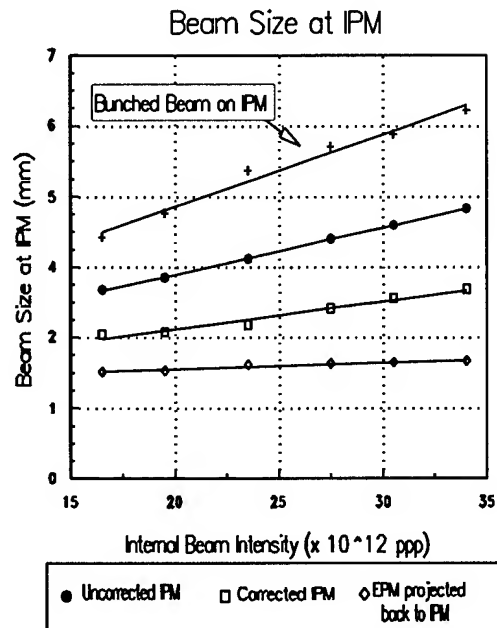


Figure 3: Vertical Beam Size for Debunched Beam versus Intensity.

IV. Conclusions

The growth in the emittance observed after resonant extraction is approximately 20 to 30 % over a range of intensities of 15 to 35×10^{12} protons/AGS repetition period, both vertically and horizontally. The AGS IPM also shows a modest growth, but unfolding the actual beam sizes is extremely difficult. In general, though, and given the uncertainties in both instruments, the agreement is very good.

V. References

- [1] H. Weisberg, E. Gill, P. Ingrassia, and E. Rodger, IEEE Trans. Nucl. Sci., NS-30 (1983) 2179.
- [2] R.E. Thern, 1987 Particle Accelerator Conf., Wash., D.C., p. 646.
- [3] I.H.Chiang, Private Communication

REVIEW OF LONGITUDINAL PERTURBATION FORMALISM*

S. Y. Zhang, Brookhaven National Laboratory, Upton, New York 11973 U.S.A.

I. INTRODUCTION

The foundation of the beam perturbation formalism was established on the Sacherer integral equation [1]. The original solution was obtained by using simplified radial functions, and the results can be used to explain several important beam instability problems. To solve the instabilities caused by high beam intensities calls for more complete solution and the extension to the formalism as well. For the non-coupled perturbation problem without frequency spread, two different eigenvalue type solutions were proposed. The formalism is also modified to solve the azimuthal mode coupling instability and the beam instability with synchrotron frequency spread, where both dispersion type and eigenvalue type solutions were proposed. In this article, a brief review of longitudinal perturbation formalism based on Sacherer integral equation is given. Some perspectives will also be discussed.

II. SACHERER INTEGRAL EQUATION

At the low intensity regime, the azimuthal mode coupling can be neglected, and the Sacherer integral equation is written as [2-4],

$$(\omega - m\omega_s) R^{(m)}(r) = jm\omega_s \xi W(r) \times \sum_{p=-\infty}^{\infty} \frac{Z(p)}{p} J_m(pr) \Lambda^{(m)}(p) \quad (1)$$

where ω is the coherent frequency shift, m is the azimuthal mode number, ω_s is the synchrotron frequency, and $R^{(m)}(r)$ is the radial function defined on the amplitude of oscillation, r . The scaling factor ξ is defined as $\xi = 2\pi I_0 / (V \cos \phi_s)$, where I_0 is the average beam current, ϕ_s is the synchronous phase and V is the total RF voltage. The weight function is defined as $W(r) = -d\psi_0 / (dr)$, where ψ_0 is the stationary particle distribution. $Z(p)$ in (1) is the impedance with p representing the frequency samplings. The Hankel spectrum $\Lambda^{(m)}(p)$ is related to the radial function by,

$$\Lambda^{(m)}(p) = \int_0^\infty R^{(m)}(r) J_m(pr) r dr \quad (2)$$

where $J_m(pr)$ is the m th order Bessel function.

2.1 Sacherer's Solution

The equation (1) is an eigenvalue problem, which has two unknown variables ω and $R^{(m)}(r)$, and therefore, cannot be

solved straightforwardly. To get approximate solutions, Sacherer assumed simplified modes, for example sinusoidal line densities, and solved the equation [1]. The result is very useful in many applications. For high intensity applications, more exact solution is needed, which appears to be in two different forms of eigenvalue problems.

2.2 Solution Using Orthogonal Polynomials

Using orthogonal polynomial expansion of radial modes is a conventional approach in treating an integral equation such as the Sacherer's. For the weight function $W(r)$, a set of normalized orthogonal polynomials $f_k^{(m)}(r)$ can always be found. The radial function can be expanded on these polynomials as,

$$R^{(m)}(r) = W(r) \sum_{k'=0}^{\infty} \alpha_{k'}^{(m)} f_{k'}^{(m)}(r) \quad (3)$$

and the Bessel function $J_m(pr)$ can be written as,

$$J_m(pr) = \sum_{k'=0}^{\infty} \Lambda_{k'}^{(m)}(p) f_{k'}^{(m)}(r) \quad (4)$$

where the Hankel spectrum of the orthogonal polynomial is,

$$\Lambda_k^{(m)}(p) = \int_0^\infty W(r) f_k^{(m)}(r) J_m(pr) r dr \quad (5)$$

After some manipulations, the equation (1) can be written as an eigenvalue problem [4],

$$(\omega - m\omega_s) \alpha^{(m)} = M^{(m)} \alpha^{(m)} \quad (6)$$

with the eigenvector $\alpha^{(m)} = [\alpha_0^{(m)} \dots \alpha_{\bar{k}}^{(m)}]^T$ where \bar{k} denotes truncation and the superscript T denotes transpose. The k th element of the system matrix $M^{(m)}$ is,

$$M_k^{(m)} = jm\omega_s \xi \sum_{p=-\infty}^{\infty} \frac{Z(p)}{p} \Lambda_k^{(m)}(p) \Lambda_l^{(m)}(p) \quad (7)$$

In solving $|(\omega - m\omega_s) I - M^{(m)}| = 0$, the eigenvalues can be found. A similarity transformation can be applied to the matrix $M^{(m)}$, which yields both the eigenvalues and eigenvectors simultaneously. If we take only the first orthogonal polynomial, then (6) becomes a scalar equation. The solution obtained under the conditions such as a long bunch and narrow-band impedances is comparable to Sacherer's solution using the simplified model, with only small differences.

2.3 Solution Using Handel Samplings

Another eigenvalue type of formalism in solving (1) is as follows [5],

$$(\omega - m\omega_s) \Lambda_p^{(m)} = K^{(m)} \Lambda_p^{(m)} \quad (8)$$

* Work performed under the auspices of the U.S. Dept. of Energy.

where $\Lambda_p^{(m)} = [\Lambda^{(m)}(-\bar{p}) \dots \Lambda^{(m)}(\bar{p})]^T$ represents Hankel harmonic samplings, and the p,qth element of the system matrix $K^{(m)}$ is,

$$K_{p,q}^{(m)} = jm\omega_s \xi \frac{Z(p)}{p} \int_0^\infty W(r) J_m(pr) J_m(qr) r dr \quad (9)$$

To find the relation between the two approaches, we write the impedance matrix as,

$$Z = \text{diag} \left\{ \frac{Z(-\bar{p})}{-\bar{p}} \frac{Z(-\bar{p}+1)}{-\bar{p}+1} \dots \frac{Z(\bar{p})}{\bar{p}} \right\} \quad (10)$$

and the Hankel spectrum matrix,

$$\Lambda^{(m)} = \begin{bmatrix} \Lambda_0^{(m)}(-\bar{p}) & \Lambda_0^{(m)}(-\bar{p}+1) & \dots & \Lambda_0^{(m)}(\bar{p}) \\ \vdots & \vdots & \ddots & \vdots \\ \Lambda_k^{(m)}(-\bar{p}) & \Lambda_k^{(m)}(-\bar{p}+1) & \dots & \Lambda_k^{(m)}(\bar{p}) \end{bmatrix} \quad (11)$$

then we get,

$$M^{(m)} = jm\omega_s \xi \Lambda^{(m)} Z \Lambda^{(m)T} \quad (12)$$

$$K^{(m)} = jm\omega_s \xi \Lambda^{(m)T} \Lambda^{(m)} Z \quad (13)$$

Note that we have $\Lambda_p^{(m)} = \Lambda^{(m)T} \alpha^{(m)}$. By left multiplying $\Lambda^{(m)T}$ to (6), we have,

$$(\omega - m\omega_s) \Lambda_p^{(m)} = \Lambda^{(m)T} M^{(m)} \alpha^{(m)} = K^{(m)} \Lambda_p^{(m)} \quad (14)$$

which is the same as (8).

To compare the two different eigenvalue problems, we note that the dimension of $M^{(m)}$ is determined by the number of orthogonal polynomials, and the dimension of $K^{(m)}$ is determined by the frequency harmonic number. In general, the dimension of the latter is larger than the former, but the computational load is about the same. The calculation of $K_{p,q}^{(m)}$ of (9) does not require the truncation in k , and therefore it can be more accurate. On the other hand, sometimes $M_{k,l}^{(m)}$ can be directly calculated on the line densities, avoiding the truncation on p [4].

III. MODE COUPLING

When the beam intensity increases, the coupling between the azimuthal modes can no longer be neglected. The equation (1) becomes,

$$(\omega - m\omega_s) R^{(m)}(r) = j^{m+1} m \omega_s \xi W(r) \times \sum_{p=-\infty}^{\infty} \frac{Z(p)}{p} J_m(pr) \sum_{m'=-\infty}^{\infty} j^{-m'} \Lambda^{(m')}(p) \quad (15)$$

This equation can be solved as either an eigenvalue problem [6] or a dispersion relation problem [3].

3.1 Eigenvalue Type Solution

To be not overwhelmed by large dimensions, we only consider the coupling between m and m' , which can be easily extended to include any and all necessary modes. Using orthogonal polynomial expansion, the following equation is obtained.

$$\begin{bmatrix} (\omega - m\omega_s)I & 0 \\ 0 & (\omega - m'\omega_s)I \end{bmatrix} \begin{bmatrix} \alpha^{(m)} \\ \alpha^{(m')} \end{bmatrix} = \begin{bmatrix} M^{(m,m)} & M^{(m,m')} \\ M^{(m',m)} & M^{(m',m')} \end{bmatrix} \begin{bmatrix} \alpha^{(m)} \\ \alpha^{(m')} \end{bmatrix} \quad (16)$$

where the k,l th element in $M^{(m,m')}$ is,

$$M_{k,l}^{(m,m')} = j^{m+1-m'} m \omega_s \xi \times \sum_{p=-\infty}^{\infty} \frac{Z(p)}{p} \Lambda_k^{(m)}(p) \Lambda_l^{(m')}(p) \quad (17)$$

The equation (16) is formally an eigenvalue problem. It is noted that in general the orthogonality between the polynomials of the different azimuthal modes is not guaranteed. Since the polynomials of the azimuthal mode m is further modulated by the rotation factor $e^{jm\theta}$, which itself is orthogonal for m , the orthogonality between the polynomials in different azimuthal modes is implicitly implied, and therefore (16) can be treated as an eigenvalue problem.

The coupling between the modes $m = \pm 1$ in fact is the same problem the conventional Robinson approach handled, which leads to the well known second Robinson criterion. The following is a brief comparison between the two approaches. In the Robinson approach, only the fundamental modes are concerned, the impedances are considered in a form of second order transfer function, and the particle distribution is only reflected in the ratio of the beam DC current and the fundamental current. In the mode coupling approach, more than fundamental modes are included, the impedances are considered with the real and imaginary parts, and the particle distribution is used in the calculation. Examples can be found to show that the mode coupling is a more reliable treatment of the problem.

3.2 Dispersion relation Type Solution

The following equation is derived from (15), similarly to (8),

$$(\omega - m\omega_s) j^{-m} \Lambda_p^{(m)} = K^m \sum_{m'=-\infty}^{\infty} j^{-m'} \Lambda_p^{(m')} \quad (18)$$

Dividing (18) by $\omega - m\omega_s$ and summing over m , we get an equation for the azimuthal mode coupling,

$$\sum_{m=-\infty}^{\infty} j^{-m} \Lambda_p^{(m)} = \sum_{m=-\infty}^{\infty} K^{(m)} / (\omega - m\omega_s) \sum_{m'=-\infty}^{\infty} j^{-m'} \Lambda_p^{(m')} \quad (19)$$

Because of the denominator on the right side of the equation, it is clear that (19) is a dispersion relation type equation. To find the relation between the dispersion equation (19) and the eigenvalue problem (16), we move the factor $(\omega - m\omega_s)$ in the equation (16) to the right side, then multiply from the left by $[j^{-m}\mathbf{A}^{(m)T} j^{-m'}\mathbf{A}^{(m')T}]$.

IV. FREQUENCY SPREAD EFFECT

Taking the synchrotron frequency spread into consideration, we write $\omega_s(r) = \omega_{sc} + D(r)$, where ω_{sc} is the synchrotron frequency at the beam center, and the frequency dispersion function $D(r)$ represents the dependence of the synchrotron frequency on the amplitude of oscillation.

4.1 Eigenvalue Type Solution

Substituting $\omega_s(r)$ into (1), moving $D(r)R^{(m)}(r)$ to the right side, and using orthogonal polynomial expansion, we get [2,7],

$$(\omega - m\omega_{sc})\alpha^{(m)} = (mN^{(m)} + M^{(m)})\alpha^{(m)} \quad (20)$$

where $N^{(m)}$ is called the frequency dispersion matrix, whose elements are,

$$N_{kl}^{(m)} = \int_0^\infty D(r)W(r)f_k^{(m)}(r)f_l^{(m)}(r)rdr \quad (21)$$

Note that $M^{(m)}$ is proportional to the beam intensity, therefore, at very low intensity, the system is dominated solely by $N^{(m)}$. This matrix is real and symmetric, which decomposes the original system into several lossless resonators with slightly difference inherent oscillation frequencies, and introduces no instability mechanism. When the beam intensity increases, the matrix $M^{(m)}$ becomes dominant, and the system shows the stability or instability. The transition of the two different status shows the property of Landau damping. The equation (20) can be used for study of Landau damping in the process of antidamping, damping, and the combined situation, with a reasonable computational load [7]. To include mode coupling, $\omega_s(r)$ is substituted into the equation (15). The result is shown to be the same as (16), except the following matrix is used as the system matrix,

$$\begin{bmatrix} mN^{(m)} & 0 \\ 0 & m'N^{(m')} \end{bmatrix} + \begin{bmatrix} M^{(m,m)} & M^{(m',m)} \\ M^{(m,m')} & M^{(m',m')} \end{bmatrix} \quad (22)$$

4.2 Dispersion Relation Type Solution

The equation (20) can also be solved by the dispersion relation [8]. Substituting $\omega_s(r)$ into (1) and moving $\omega - m\omega_s(r)$ to the right side, we get,

$$\alpha^{(m)} = A^{(m)}M^{(m)}\alpha^{(m)} \quad (23)$$

where the elements of the matrix $A^{(m)}$ are,

$$A_{kl}^{(m)} = \int_0^\infty \frac{W(r)f_k^{(m)}(r)f_l^{(m)}(r)rdr}{\omega - m\omega_s(r)} \quad (24)$$

This matrix shows the dispersion relation. By carefully handling the singularity problem, the solution for any mode of each azimuthal mode can be obtained. To reach a comprehensive solution including all necessary modes seems to be difficult.

V. DISCUSSION

For all previously treated problems, eigenvalue type solutions exist, which provides convenience in the calculation, and also physical insight into the problem. The synchrotron frequency spread alone doesn't generate coherent motion, when the beam intensity increases, however, the feedback force becomes effective and an eigenvalue equation can be used to approximate the system by several subsystems. The convergence is guaranteed, and for most impedances the required expansion dimension is not large.

If the effect of the stationary beam distribution cannot be neglected, the formalism has to be revised. One approach [9] is to use the meshes in the r direction, which itself is an orthogonal basis. This method is straightforward but the computational load is drastically increased. It is of interest to search for more efficient methods.

Various formalisms and the related solutions of the perturbation have been briefly reviewed. All formalisms have applications under certain conditions, and also all are subjected to limitations. These conditions and limitations need to be clearly specified.

VI. REFERENCES

- [1] F. Sacherer, CERN/SI-BR/72-5, 1972
- [2] G. Besnier, Nucl. Instr. Methods, Vol.164, p. 235, 1979.
- [3] B. Zotter, CERN SPS/81-(18-20), 1981.
- [4] S.Y. Zhang and W.T. Weng, BNL Informal Report, No. 60557, July 1994.
- [5] J.L. Laclare, CERN 87-03, p. 264, 1987.
- [6] T. Suzuki, Y. Chin and K. Satoh, Particle Accelerators, Vol. 13, p. 179, 1983.
- [7] S.Y. Zhang and W.T. Weng, Hefei Workshop, July 1994, to be published.
- [8] Y. Chin, K. Satoh, and K. Yokoya, Particle Accelerators, Vol. 13, p. 45, 1983.
- [9] K. Oide and K. Yokoya, KEK Preprint 90-10, 1990.

KLYSTRON POWER SPECIFICATIONS BASED ON TRANSIENT BEAM LOADING ANALYSIS IN DAMPING RINGS*

M.G. Minty, R.H. Siemann

Stanford Linear Accelerator Center, Stanford University, Stanford, CA 94309 USA

Abstract

A useful diagram is presented and used to study rf cavity voltage regulation in a damping ring or other circular accelerator where large beam currents are injected and extracted rapidly. With conventional feedback systems and high particle beam currents, the maximum beam current can be limited by the ability of the klystron to maintain constant gap voltage at high currents, low currents, or in the absence of beam. Techniques for storing high current beams are suggested when the maximum klystron output power is predetermined. Alternately, these techniques may be applied and used to specify the performance requirements of the klystron if the desired particle beam current and nominal rf cavity voltage are known.

I. INTRODUCTION

Experience^{1,2} with high current beams and transient beam loading in the Stanford Linear Collider (SLC) damping rings has motivated studies of the rf system and beam stability with a nonlinear power source². As beam currents in fast cycling accelerators are increased, the absence of beam is the dominant perturbation to the rf system, where slow tuner feedback loops around each cavity have insufficient bandwidth to track the changes. The beam may be absent due to machine repetition rate changes, due to time required between fills, or due to gaps between bunch trains. With standard feedback and direct rf feedback³ for regulation of the cavity voltage, the klystron output power can increase substantially when the beam is absent. While the behavior without beam is of little concern, missing pulses can leave the rf system out of regulation when the next pulse arrives. The beam can then become unstable with both the bunch length and the beam phase at extraction varying with time.

The phasor diagram corresponding to the generic circuit model of the beam cavity interaction is shown in Fig. 1. The current used in the equivalent circuit^{3,4} \vec{I}_b is 180° out of phase with the actual beam current. The generator current \vec{I}_g is summed with \vec{I}_b to give the total cavity current \vec{I}_c . The beam current, or magnitude of \vec{I}_b , is twice the dc beam current: $I_b = 2I_{dc}$. The phase of the beam ϕ_b is measured with respect to the crest of the rf. The equilibrium value of ϕ_b is the synchronous phase ϕ_s . The projection of \vec{I}_c onto the cavity voltage is the shunt resistor current, $I_0 = \frac{V_c}{R}$. The tuning angle is the angle between \vec{I}_c and the cavity voltage \vec{V}_c :

$$\phi_z = \tan^{-1} \left[2Q \frac{(\omega_0 - \omega_{rf})}{\omega_0} \right], \quad (1)$$

in which Q and ω_0 are the quality factor and resonance frequency of the cavity, respectively, while ω_{rf} is the accelerating

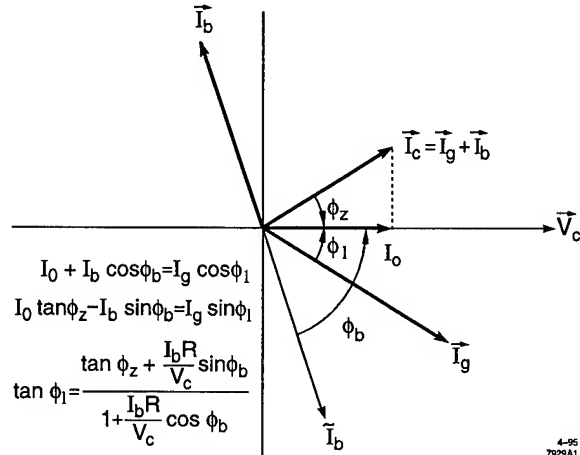


Figure. 1. Phasor diagram for a capacitive cavity and a beam above transition.

frequency. The angle between \vec{I}_g and \vec{V}_c is the loading angle, ϕ_1 .

II. PARAMETER SPACE FOR VOLTAGE REGULATION

A relationship between the beam current \vec{I}_b , generator power P_g , and cavity voltage \vec{V}_c can be derived using the equations developed in reference 5. The result is

$$I_b = \frac{V_c}{R \cos \phi_z} \left[-\cos(\phi_z - \phi_b) \pm \sqrt{\cos^2(\phi_z - \phi_b) + \left(\frac{8R\beta_c P_g}{V_c^2(1 + \beta_c)} \right) \cos^2 \phi_z - 1} \right], \quad (2)$$

in which β_c is the cavity coupling coefficient. This expression remains valid in the presence of feedback loops. The parameter space for voltage regulation in the steady state is shown in Fig. 2 for the SLC damping rings. The solid curve bounding regions 1, 2, and 3 shows Eq. (2) for a 60 kW klystron output power. In order to operate outside this region, either the klystron power would have to be increased or the gap voltage lowered. The curve with circles is a simulation^{2,4} result which takes into account the dynamics of the beam-cavity interaction in the presence of multiple feedback loops and a nonlinear power source. Region 3, which is bounded from above by Eq. (2) and below by the simulation results, is unstable against perturbations to the system.

The vertical line separating regions 1 and 2 represents a practical limit associated with missing pulses. Consider an rf current of magnitude $I_b = I_m$ or $I_b = I_n$. When this pulse is extracted, the loading angle becomes large and negative as the slow tuner feedback loops have insufficient bandwidth to track the change;

*Work supported by Department of Energy contract DE-AC03-76SF00515.

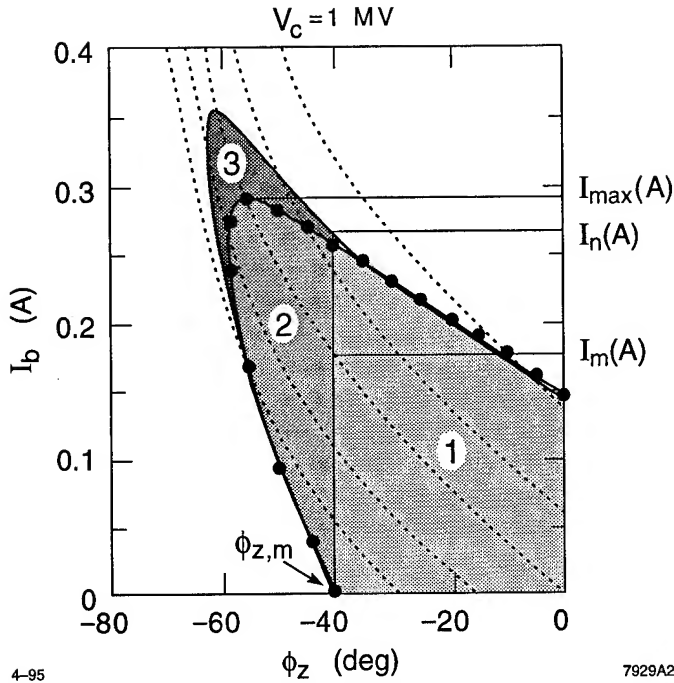


Figure 2. Parameter space for voltage regulation subdivided into three characteristic regions. The dotted lines indicate contours of constant loading angle ϕ_l . From left to right these are $\phi_l = -30^\circ$, -15° , 0° , $+15^\circ$, and $+30^\circ$.

the operating point moves downward (towards $I_b = 0$) on this vertical line. A voltage error related to the change in the beam-induced voltage is detected by the feedback loops that regulate the cavity voltage. If direct rf feedback is used or if the cavity and amplitude loop bandwidth are fast relative to the time during which the beam is absent, then the klystron is driven to larger output power in an attempt to compensate for this error. Because the gain of the amplitude feedback loops depends on the local slope of the klystron saturation curve, as the feedback drives the klystron harder, the gain of the loop is simultaneously decreasing. In particular, if the klystron is improperly limited, then a missing pulse or current jitter can lead to a situation of positive feedback.

III. KLYSTRON POWER REQUIREMENTS

Analysis of the available operating space for voltage regulation may be used to make an estimate of the required output power from a klystron. At high beam current and high cavity voltage, however, the estimate may be unrealistic. Methods of optimizing the stability of the rf system at high currents, while minimize the power requirements of the klystron will now be considered.

A. Power Requirements with $\phi_l = 0$

A conservative estimate for the required klystron power may be determined from the missing pulse limit; for a properly matched cavity ($\phi_l = 0$) and known operating voltage, the klystron should deliver as much power as required such that the beam current is less than I_m . Rewriting Eq. (2),

$$P_g = \frac{V_c^2(1 + \beta_c)}{8R\beta_c \cos^2 \phi_z} \left[\left(\frac{I_b R}{V_c} \right)^2 \cos^2 \phi_z \right]$$

$$+ \frac{2I_b R}{V_c} \cos \phi_z \cos(\phi_z - \phi_b) + 1], \quad (3)$$

which gives the required generator power in terms of the rf current I_b , the cavity voltage V_c , and the cavity tuning angle ϕ_z . The tuning angle at $\phi_l = 0$ and $I_b = I_m$ is

$$\phi_{z,m} = -\tan^{-1} \left(\frac{I_m R}{V_c} \sin \phi_b \right). \quad (4)$$

Substituting $\phi_{z,m}$ into (3) and putting $I_b = 0$ gives the klystron power required to be stable against missing pulses when the nominal rf current is I_m :

$$P_m = \frac{V_c^2(1 + \beta_c)}{8R\beta_c} \left[1 + \left(\frac{I_m}{I_0} \right)^2 \sin^2 \phi_b \right], \text{ with } \phi_l = 0. \quad (5)$$

With beam, the klystron output power in the steady state is Eq. (3) evaluated at I_m , which is less than P_m .

B. Power Requirements with Cavity Detuning ($\phi_l \neq 0$)

By detuning the cavity to $\phi_l > 0$, more beam current can be stored stably for the same maximum klystron power while maintaining stability against missing pulses. At I_b just less than I_n , the klystron power with and without beam is approximately the same, however much of the output power however is reflected back into the isolator. From Eq. (2) the maximum current I_c operable while maintaining stability against missing pulses results when the two terms in the square brackets are equal. Then

$$I_n = -\frac{2V_c}{R \cos \phi_z} \cos(\phi_z - \phi_b). \quad (6)$$

The klystron power required is Eq. (3) evaluated at $I_b = I_c$.

C. Optimal Use of Klystron Power by RF Conditioning with $\phi_l = 0$

To achieve higher beam currents for the same maximum klystron output power, the klystron must be made to operate more efficiently. For operation in region 2 of Fig. 2, the hard limit due to missing pulses or absence of beam must be overcome. This may be accomplished by lowering the reference to the direct rf feedback loop in the case of a missing pulse. Highlighted in Fig. 3 are the voltage error ΔV and the phase error $\Delta \phi$ that result from an absent beam. Ideally, one might raise \vec{V}_g when the beam is absent to equal the steady state cavity voltage with beam \vec{V}_c . If the klystron is power limited, however, this is impossible. Alternatively, the output of the amplitude loop can be lowered by changing the reference input during the time $I_b = 0$. The output of the amplitude feedback loop is the reference for the direct rf feedback loop. Along $\phi_l = 0$ the change in the cavity voltage setpoint required for correction is

$$\Delta V = V_c + V_b \frac{\sin(\phi_b - \phi_z)}{\sin \phi_z}. \quad (7)$$

The change in the phase reference setpoint required for correction is $\Delta \phi = \phi_z - \phi_l$. The corrections should be disabled at injection of the next pulse. More generally, transients arising from beam intensity fluctuations could be minimized by applying voltage and phase corrections which depend on the input current. In

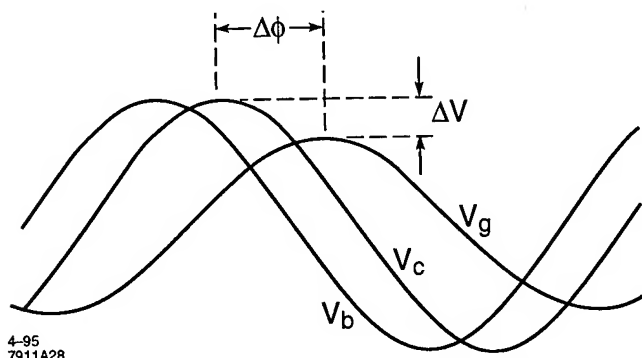


Figure 3. Cavity voltages highlighting errors in the voltage ΔV and phase $\Delta\phi$ resulting from beam extraction.

practice the amount by which to lower the voltage setpoint would be to that value for which the control voltage from the amplitude feedback loop is unchanged by the change in beam current at injection. The amount by which to change the phase setpoint would be to minimize the change in the cavity voltage phase angle.

Simulation results using rf conditioning are shown in Fig. 4 for the case of a missing pulse. Without rf conditioning, the klystron operates well beyond the knee of the saturation curve during the time $I_b = 0$. When the beam is injected, the gain of the amplitude and direct rf feedback loops are zero and the cavity voltage does not regulate. Poor regulation is also evidenced in the amplitude feedback loop control voltage which exhibits runaway during the time the beam is missing. With conditioning of the rf voltage, the voltage reference is reduced when the missing pulse is detected. The next pulse is anticipated and the reference is raised. During the time in which the beam was absent the klystron is brought out of saturation. The cavity voltage is then well regulated when the beam is injected.

IV. RF PARAMETER OPTIMIZATION

As beam currents in damping rings are increased, specifications for the klystron power and feedback loop parameters should involve analysis of the effects of transient loading on the rf system. Using the plot of the parameter space, effects arising from the largest possible transient, that of pulse extraction, may be analyzed. Equation 2 shows that the available operating area changes as a function of cavity voltage, cavity impedance, cavity coupling, klystron power, and synchronous phase. Tradeoffs between klystron output power and these other parameters can be considered in the design of the rf system.

References

- [1] M.G. Minty et al., WAB12 1995 PAC.
- [2] M. Minty and R.H. Siemann, RAP10 1995 PAC.
- [3] F. Pederson, *IEEE Tran. on Nucl. Sci.*, NS-32, No. 3 (1985) 2138.
- [4] M.G. Minty, R.H. Siemann, "Heavy Beam Loading in Storage Ring RF Systems," to be submitted to *Nucl. Instr. and Methods*.

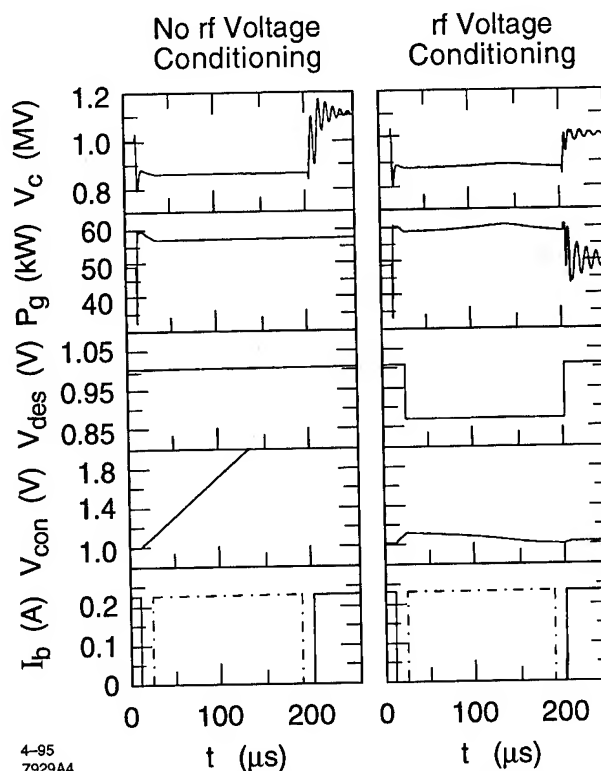


Figure 4. Cavity regulation and voltage transient reduction in the SLC with and without rf conditioning in the event of a missing pulse. Plotted as a function of time are the cavity voltage V_c , the klystron output power P_g , the reference input to the amplitude feedback loop V_{des} , the amplitude feedback control voltage V_{con} , and the rf current I_b . The dot-dashed curve in I_b indicates the missing pulse.

- [5] P. Wilson, "High Energy Electron Linacs; Application to Storage Ring RF Systems and Linear Colliders," in *Phys. of High-Energy Part. Acc.*, AIP Conf. Proc. No. 87 (AIP, NY 1982), pp.450-563. SLAC-PUB-2884 (1982).

TRANSVERSE COMBINING OF FOUR BEAMS IN MBE-4*

C.M. Celata, W. Chupp, A. Faltens, W.M. Fawley, W. Ghiorso, K.D. Hahn, E. Henestroza, C. Peters, and P. Seidl, Lawrence Berkeley Laboratory, University of California, Berkeley, CA 94720

ABSTRACT

Transverse beam combining is a cost-saving option employed in many designs for induction linac heavy ion fusion drivers. But resultant transverse emittance increase, due predominantly to anharmonic space charge forces, must be kept minimal so as not to sacrifice focusability at the target. A prototype combining experiment has been built, using the MBE-4 experiment. Four sources produce four 4 mA Cs^+ beams at 200 keV. The ion sources are angled toward each other, so that the beams converge. Focusing upstream of the merge consists of 4 quadrupoles and a final combined-function element (quadrupole & dipole). All lattice elements are electrostatic. Due to the small distance between beams at the last element (~ 2 mm), the electrodes here are a cage of small wires, each at different voltage. The beams emerge into the 30 period transport lattice of MBE-4 where emittance growth due to merging, as well as the subsequent evolution of the distribution function, can be diagnosed. The combiner design, simulation predictions, and preliminary results from the experiment are presented.*

MOTIVATION

Transverse beam combining is an important cost-saving feature of standard driver designs for heavy ion fusion. At the low-energy end of a driver, electrostatic quadrupoles are used to focus each beam of the multiple-beam array. Voltage breakdown and economics considerations dictate a small aperture for these quadrupoles, and thus a large number of beams. At higher energies it is more economical to accelerate fewer fatter beams through large-aperture magnetic quadrupoles. Thus at some energy ~ 100 MeV, transverse beam combining occurs.

Since space charge dominates beam dynamics for these intense beams, the interactions between particles during merging serve as a source of emittance growth, along with the usual "phase space filling" seen, for instance, in beam stacking in storage rings. As shown in previous work, transverse emittance growth is minimized by packing the beams as tightly as possible. Near the merge point the small space between beams makes it difficult to insert focusing structures with good field quality. The experimental challenge is to position the beams to sufficient accuracy to allow tight packing, and to keep them focused as their centroids converge.

DESCRIPTION OF THE EXPERIMENT

At Lawrence Berkeley Laboratory an experiment to demonstrate 4-to-1 transverse beam combining is being

installed on the old MBE-4 accelerator. A "combiner", consisting of a Cs^+ source, 200 keV diode, and focusing transport channel for each of the four 4 mA beams, replaces the old MBE-4 diode and matching system. The beamlines converge with angle of 6° relative to the combiner centerline. A diagram of one of the beamlines is shown in Fig. 1. Four electrostatic quadrupoles, followed by an electrostatic combined-function quadrupole + dipole, are used to focus each beam and straighten its trajectory so that the beams emerge from the combiner almost parallel to the centerline. The design configuration for the beam cross sections as they emerge from the combiner is shown in Fig. 2. As can be seen, the cross section is x-y asymmetric to allow for good packing of the elliptical beams. After the combiner the merged beam is transported (without acceleration) and diagnosed in one transport channel of the remaining 30 lattice periods of MBE-4.

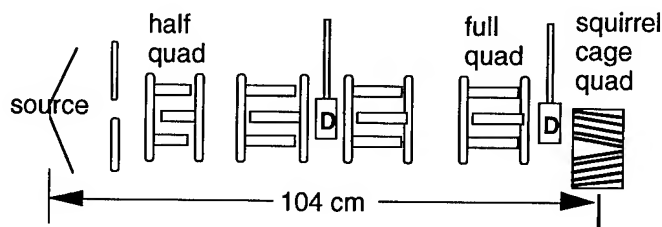


Figure 1. One combiner beamline. Diagnostics are on paddles marked "D".

Due to length restrictions, matching is done in the combiner, rather than in a separate matching system. For the same reason, the need for an initial dipole for each beam has been removed by aiming the sources toward a common point of convergence.

As the separation between beams decreases with distance down the combiner, the design of the lattice elements must change. The first three combiner quadrupoles are of standard design, and consist of circular electrodes, with the ratio of electrode radius to aperture set to minimize the lowest order 2D nonlinear field component-- the dodecapole. The first quadrupole is half the length of succeeding quads to facilitate matching. At the fourth quadrupole, the space between beams is too small for standard electrodes, so that small-aperture hyperbolic electrodes have been designed which both shield the beams from each other and produce minimal nonlinearity. Taking advantage of the elliptical shape of the beam, the electrodes in the focusing plane have also been moved closer to the beam to allow space for adjacent quadrupoles, thus making an asymmetric aperture. Voltages on the first four quadrupoles are all less than 5 kV.

* This work was supported by the Director, Office of Energy Research, Office of Fusion Energy, U.S. Dept. of Energy, under Contract No. DE-AC03-76SF00098.

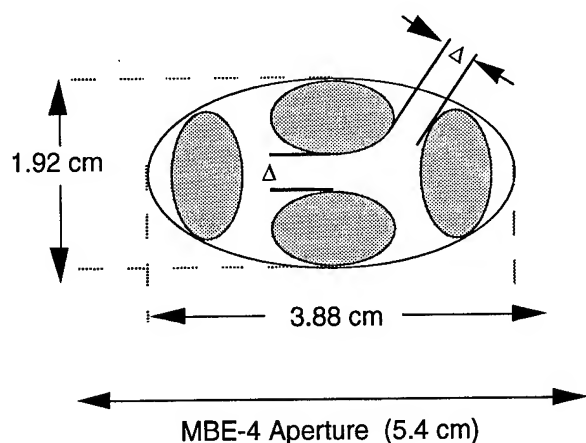


Figure 2. Design configuration of four beams as they emerge from combiner. Beam radii are 6.5 and 3.7 mm. $\Delta=4$ mm.

The small spacing between the beams at the downstream end of the fifth lattice element does not allow adequate space for solid electrodes. Quadrupole and dipole fields are instead produced by surrounding the beams with an elliptical "squirrel cage" of 1 mm diameter wires, at a spacing of approximately 1 mm, approximately parallel to the beam path. The voltage on each wire is set so that the wires approximately produce the correct Dirichlet boundary condition for the electric field, and therefore the correct field. Voltage differences of up to 1.5 kV from wire to wire are needed. Figure 3 shows a transverse view of the squirrel cage element. Note that the cross section shrinks in a self-similar fashion as the beam centroids converge.

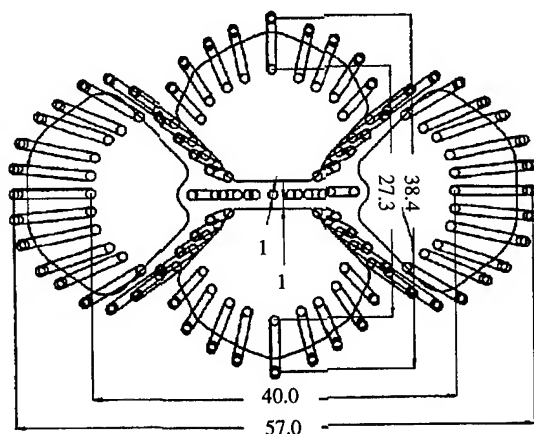


Figure 3. Transverse view of squirrel cage, showing wires converging as z increases. Dimensions are in millimeters.

Alignment is accomplished with sources mounted on gimbals which allow them to rotate about their centers, followed by articulation in x and y of the second quadrupole. Both operations can be done in vacuum. Since the beams emerge from the combiner separated by about 4 mm, their clearance from the wires within the squirrel cage is only about a millimeter near the exit of the cage. Thus alignment must be correct to the sub-millimeter level.

FIELDS OF THE SQUIRREL CAGE

The 3D field of the squirrel cage has been calculated in order to evaluate the effects of fringe and anharmonic interior fields on the beams. In this initial calculation the wire leads were neglected, but no extension of the technique is needed to include them at a later time. Fields were calculated using the capacitive matrix technique. This is equivalent to modeling the wires (at constant voltage) as lines of charges. The charges were spaced at intervals, Δz , of 1.25 mm along the 7 cm length of the cage. Elements of the capacitive matrix can be expressed as:

$$C_{ij} = \frac{1}{\text{Max} \left[|r_i - r_j|, r_o \right]}, \quad (1)$$

where r_i and r_j are the positions of two of the charges, and $r_o = \Delta z / (4 \log 2)$. The effective size of the charge, r_o , is chosen to produce as little variation in voltage along the wire as possible. Once the capacitive matrix is inverted, the charges can be determined, since $V(r_i) = \sum C_{ij}^{-1} Q_j$. The field is then determined using Coulomb's law.

Figure 4 shows the results of a multipole decomposition of the field about a parabolic approximation to the beam centroid orbit. The decomposition was done using the method of Hahn. The dominant nonlinear component through most of the cage is a sextupole. Near the ends of the cages the pseudo-octupole caused by the second derivative of the quadrupole moment becomes significant.

In order to obtain a measure of the emittance growth expected from the anharmonic fields, these fields were integrated along the approximate orbit of the beam centroid. When appropriately scaled, the gradient of this integrated value gives the net impulse in both x and y velocities as a function of location with respect to the beam centroid. The results show that over most of the aperture the calculated impulse in dx/dz and dy/dz is small when compared to the dipole deflection angle and comparable to the thermal angles of the incoming beam particles. Particles that come within ~ 1.5 mm of the wires can receive larger impulses, but our calculations are less trustworthy in that regime due to the 1.25 mm spacing adopted for the charges used to simulate the charged wires. The changes in angle noted here are about an order of magnitude less than those expected during merging, indicating that the anharmonic squirrel cage fields are well within acceptable tolerance levels.

SIMULATION RESULTS

Transport through the entire combiner, and subsequent merging and transport of the merged beam have been simulated using the 2D particle-in-cell code HIBEAM. Four 4 mA beams of Cs^+ with initial normalized emittance of 2×10^{-8} m-rad, and energy of 200 keV are assumed. A semi-gaussian initial distribution function is used for each beam--i.e., uniform spatial density and Maxwellian velocity distribution. One beam is followed where the beams are well separated (up to 8 cm before the squirrel cage), neglecting effects of other beams and quadrupoles. Image effects of the

focusing structures included are calculated using the capacitive matrix technique. At the fourth quadrupole the surfaces of the electrodes are modeled as hyperbolic, as in the experiment, and the fields and image fields of adjacent quadrupoles are included, due to their proximity. Because of the 2D nature of the simulation, wires in the squirrel cage are modeled by dividing their length into 16 equal segments parallel to the centerline of the combiner, but with aperture equal to that of the real combiner wires at the center of the interval.

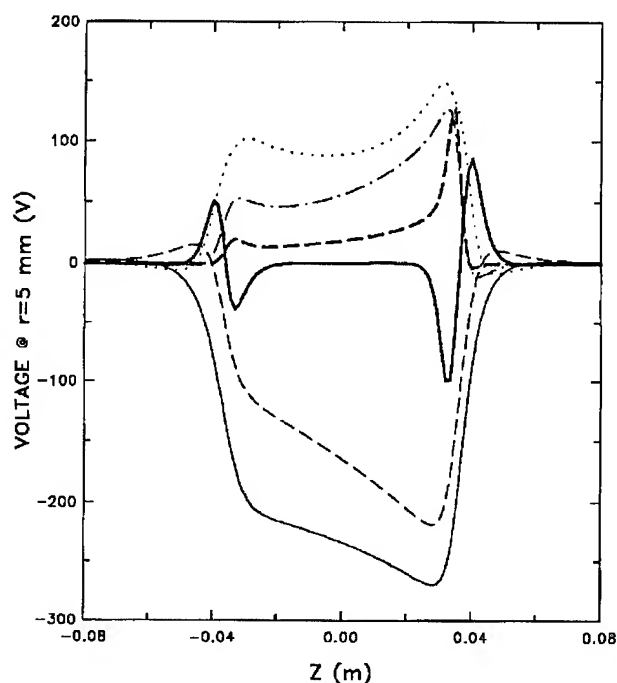


Figure 4. Squirrel cage multipole moments as a function of z . At $z=0$, in order of decreasing ordinate position, those shown are: 10 x sextupole, 10 x octupole, 10 x pseudooctupole, 10 x dodecapole, quadrupole, 0.1 x dipole.

The resulting normalized emittance as a function of z is shown in Fig. 5. Image effects of the electrodes of the first three quadrupoles cause emittance growth of about 2×10^{-9} m-rad, while the field aberrations in the squirrel cage increase the emittance to approximately 3.5×10^{-8} m-rad. Asymmetry due to adjacent quadrupole electrodes at the fourth quadrupole results in negligible displacement of the centroid. During the merging process the emittance grows, to finally attain a value of 2.4×10^{-7} m-rad. Beam loss is negligible ($<0.02\%$). Without space charge, the expected final emittance would be approximately 1.1×10^{-7} m-rad, which demonstrates that this experiment is, like the driver, in the regime where both space charge and phase-space filling contribute to the final emittance growth. It should be noted that because of the relatively large spaces between the small beams in this experiment, emittance growth is proportionately bigger than it would be in a driver, where the much larger beams are expected to have approximately the same separation. Simulations have been done which show adequately low emittance growth for the case of the driver.

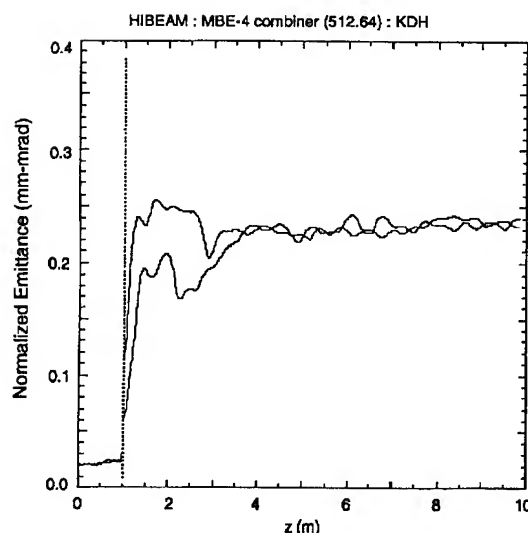


Figure 5. Normalized emittance as a function of z . Vertical line shows the end of the combiner.

STATUS OF THE EXPERIMENT

At present all components of the combiner have been fabricated and aligned with respect to the combiner center line, except the squirrel cage. The design is complete for this element as well. One of the sources, which are porous tungsten emitting surfaces saturated with an aqueous solution of CsCO_3 , has been installed in MBE-4. The effects of heat from the 1000°C emitting surface on alignment and on the source alignment adjustment motor have been found to be acceptable, but water cooling will be added to the driver motor support plates to improve the tolerance margin for the motors. A beam current of 6.7 mA at 198 keV was measured 9.4 cm downstream of the source, in agreement with E-GUN calculations. This current will be adjusted using aperture plates just downstream of the diode during the actual experiment.

As time and resources allow, the diodes and first four quadrupoles for each beam will be installed in MBE-4, and experiments will be performed to measure the distribution function of the beams at the entrance to the squirrel cage. The squirrel cage will then be added, and the effect of the combiner on one beam measured, followed by full merging experiments.

REFERENCES

- [1] C.M. Celata A. Faltens, D.L. Judd, L. Smith, and M.G. Tiefenback, Proc. of 1987 Part. Acc. Conf., Washington, D.C., 2 (1987), 1167
- [2] Thomas J. Fessenden, Denis Keefe, Charles Kim, Hermann Meuth, and Anthony Warwick, Proc. of 1987 Part. Acc. Conf., Wahington, D.C., 2 (1987), 898.
- [3] K. Hahn, Nucl. Instrum Meth. 338 (1994), 161.

ION CORE PARAMETERS IN THE BENDING MAGNETS OF ELECTRON STORAGE RINGS

E. Bulyak, National Science Centre "Kharkov Institute of Physics and Technology", Kharkov, Ukraine

Abstract

Effective methods of decreasing the density of ions neutralizing the space charge of electron beams in storage rings are improving the vacuum conditions and application of the clearing electrodes. There are presented the results of both theoretical and numerical studies of the relation of ion density with the density and composition of the residual gas in the vacuum chamber. Steady state of the ion core was investigated for the case of the dipole magnetic field and electrostatic clearing electrodes. Analytical expressions describing the longitudinal, the vertical and the horizontal shapes of the core density are presented. It is shown that the core density and ionizing rates of ions is determined by the gas-to-beam density ratio. Transverse density of ions is much sharper than the beam density, and the ion induced force is sufficiently nonlinear.

1. INTRODUCTION

Positive ions captured by electron beams cause limitations in performance of the storage rings. The most effective method of extracting ions from the beam is insertion of the clearing electrostatic electrodes into the vacuum chamber of a storage ring. This clearing is effective if there exists the longitudinal (along the beam orbit) stream of ions, because the clearing plates cover a small part of the ring circumference. In this paper we present results from both theoretical estimations and digital calculations of the ion core parameters in dipole magnet of the electron storage ring provided with clearing electrodes. Mainly we deal with the number of ions in the beam and its transverse density shape.

2. MODEL

Let us assume the electron beam to be round in the cross section of radius a and have homogeneous density $n_b(x, y, z) = n_b = \text{const}$, $x^2 + z^2 < a^2$. The frequency of bunches passing is much greater than the frequency of ion oscillations, so the beam is coasting for the ions. Thus, n_b denotes the average beam density.

This beam passes through a dipole magnet with a field strength of $B_z = B = \text{const}$, and the orbit length in the magnet is Y . At the magnet ends there are installed the electrostatic clearing electrodes. The vacuum chamber of the storage ring contains neutral gas with a density of n_0 , consisting of molecules of mass M and the ionization cross section σ_0 . The positive ions produced in collision of circulating electrons with the residual gas molecules are trapped by the electric field of the beam. These ions oscillate vertically (along the magnetic field lines) and circulate around ellipses

in the xy plane. The ellipses move along the beam axis (so-called drift in the crossed fields) and finally reach the clearing electrodes. The outer ellipses ($x_c > 0$) drift downstream the electron beam, the inner ellipses ($x_c < 0$) -- upstream. During this drift the ions impart additional focusing to the beam particles.

We limit our consideration to the case of low neutralization when the density of the ion core is negligibly lower than that of the beam, e.g. we consider the case of effective clearing.

Considering the ellipses as new objects we find the density of ellipse centers (EC) n_c at the distance y downstream the clearing station [1], which reads as:

$$n_c = \frac{cn_0\sigma_0 B(1+D)}{\pi e} y, \quad (1)$$

$$D \equiv n_b \frac{2\pi M c^2}{B^2}.$$

Integrating (1) over the beam cross section we obtain the total number of ions per unit orbit length:

$$N_{ion} = \frac{n_0\sigma_0 Y B a(1+D)}{\pi e} \left\{ \log \left[\frac{1 + \sqrt{1 - \chi^2}}{\chi} \right] - \sqrt{1 - \chi^2} \right\} \quad (2)$$

$$\chi \equiv \frac{x_m}{a} (1+D)$$

Here x_m is the minimal distance of the EC from the beam axis when the ion is considered to be drifting, i.e., reaching the clearing station.

The key point in our analysis is the determination of x_m value because the ion density in the beam is fully relevant on that parameter. The basic hypothesis of this paper consists in considering the ion core separated into 3 parts: the central rest part $-x_m < x < x_m$ and two streams mentioned above. The density of the central part is supposed equal to the average beam density (full neutralization of the beam charge). The density of both streams is matched to the central part at $x = \pm x_m$.

3. FINITE TEMPERATURE

It is essential to take into account the initial ion temperature T to eliminate divergence in the vertical density shape of the core. This temperature does not eliminate divergence in the radial shape but decreases the core density at $x_m < x < a$.

Finite-temperature taking into account does not change the distribution of EC (1). The transverse core density related to the EC distribution (1) is:

$$n_i(x,z) \sim F_x(x) \cdot F_z(x,z), \quad (3)$$

$$F_x(x) = \frac{1}{2} \int_{x_m/t_x}^{a/(1+D)t_x} \frac{B_i(y) dy}{\left(x - \left(x^2 - (1-D^2)\sqrt{1+y^2} \right) \right) \sqrt{x^2 - (1-D^2)(1+y^2)}}$$

$$F_z(x,z) = \frac{t_z}{a} \int_{-z^2/t_z}^{(a^2-z^2)/t_z^2} \frac{B_i(y) dy}{\sqrt{y + z^2/a^2}}$$

$$B_i(y) = \frac{4}{\sqrt{\pi}} \exp(y) \int_{\sqrt{\max(y,0)}}^{\infty} (u^2 - y) \exp(-u^2) du$$

$$t_x = \frac{1}{eB} \sqrt{\frac{2kTmc^2}{3(1+D)}} \quad t_z = \sqrt{\frac{kT}{3\pi e^2 n_b}}$$

The function B_i defined here describes the 'track' of the thermalised ion assemble produced at the point u with a 'zero temperature' amplitude α and the center of oscillation u_0

$$y = \frac{\alpha^2 - (u - u_0)^2}{t^2}$$

Examples of vertical and horizontal shapes are depicted in Fig.1.

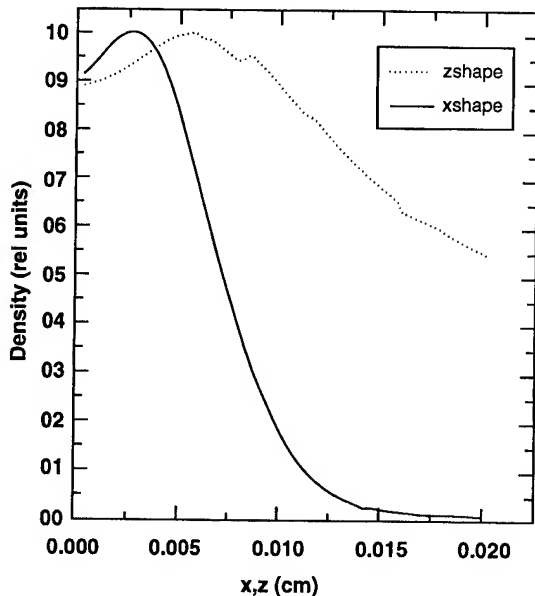


Fig.1. Transverse ion core shapes for the case: beam current $I = 50$ mA, radius $a = 0.05$ mm, field strength $B = 1$ Tesla.

4. SURVEY OF THE RESULTS

Based on the approach proposed and expressions (1) and (2), the computer code has been developed which computes the longitudinal density (the neutralization factor η) and the transverse density shape of the ion core confined by the electron beam in the dipole magnet of the storage ring with the clearing electrodes.

The results of computing are as follows:

(i) For the typical beam parameters in the synchrotron storage ring ($a=0.05$ cm, $Y=1$ meter, $B=1$ Tesla, residual gas pressure 1 nTorr of Nitrogen) ion clearing keeps the neutralization factor below the 5% limit (Fig.2). Therefore our assumption of low neutralization of the beam space charge is proved valid.

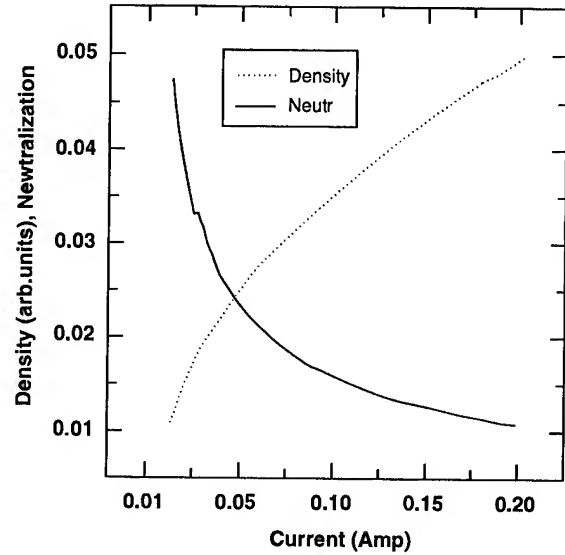


Fig.2. Neutralization factor η and density of ions n_i (in arbitrary units) versus beam current I (in Amperes), $a = 0.05$ mm, $B = 1$ Tesla, $Y = 1$ m.

(ii) The transverse core density is essentially nonlinear because the main part of ions is confined in the near-to-axis region (Fig.3);

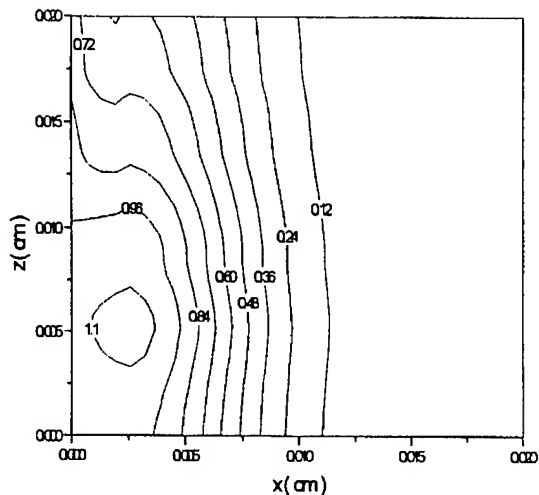


Fig. 3. Relative ion core density in the beam central quarter. $I = 50$ mA, $a = 0.05$ mm, $B = 1$ Tesla, Nitrogen molecules.

(iii) The density of ions increases very little when the beam current is increased up. So, the neutralization factor decreases as it is depicted in Fig.2;

(iv) Response of the ion density to increase in the residual gas pressure (as well as the distance between the clearing stations Y) is less than proportional, see Fig. 4.

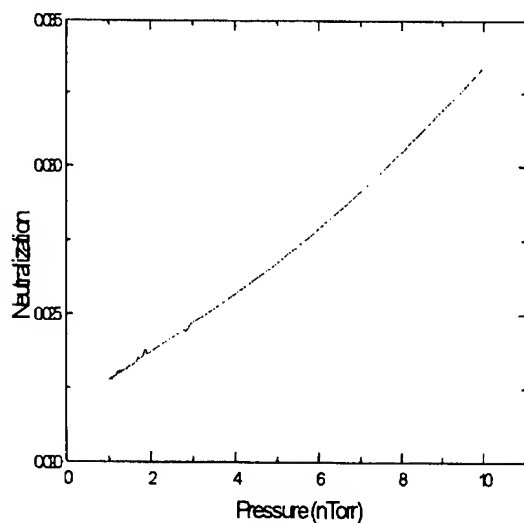


Fig. 4. Neutralization factor versus residual gas pressure (Nitrogen). $I = 50$ mA, $a = 0.05$ mm, $B = 1$ Tesla, $Y = 1$ m.

(v) The core density decreases when the magnetic field strength is increased, Fig. 5.

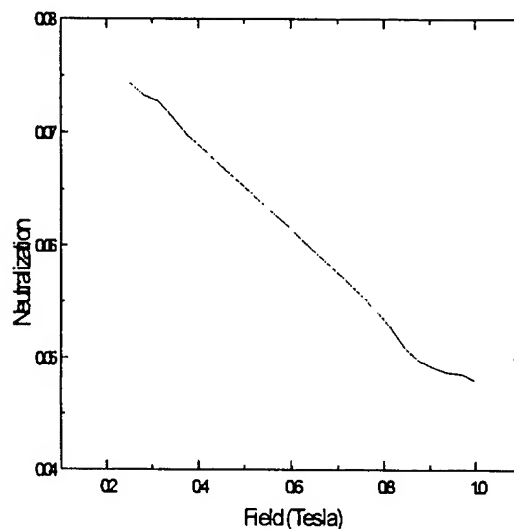


Fig.5. Neutralization factor versus magnetic field strength. $I = 100$ mA, $a = 0.05$ mm, $P = 2$ nTorr, $Y = 1$ m.

Thus, considering production of ions and their drift in the dipole magnets of the electron storage rings and supposing full neutralization of the beam charge without clearing we come to the conclusion that the clearing electrodes can de a help in keeping the ion density in the beam within the required limits of a few percents of the average beam density. Residual ions are located in the near-to-orbit region adding sufficiently nonlinear focusing forces to the beam particles [2]. Process of neutralization in the near-to-axis region of the beam needs thorough studying both analytically and experimentally.

REFERENCES

- [1] Bulyak E. *The ion core density in electron storage rings with clearing electrodes* Proc. of PAC93 (Washington DC, May 1993)
- [2] Bulyak E. *Ion driven effects in the intence electron beam circulating in storage rings* Proc. of PAC95 (Dallas TX, May 1995)

ION DRIVEN EFFECTS IN THE INTENCE ELECTRON BEAM CIRCULATING IN STORAGE RINGS

E. Bulyak, Kharkov Institute of Physics and Technology, Kharkov, Ukraine

1. INTRODUCTION.

Ion-driven effects in electron beams impose severe limitations on performance of storage rings [1]. These effects are much similar to the well-studied effects of the beam space charge. Most effects caused by the entire charge of the beam can be calculated by commonly used codes, e.g., BeamParam and ZAP [2]. We make an attempt to survey briefly in this report the scaling coefficients of the ion-driven effects related to those of the beam charge. The ion core confined by the electron beam is described by the neutralization factor η equal to the relative ion core charge:

$$\eta = \frac{\sum_{q=1}^Z q N_q}{N_b}$$

Here N_q is the number of ions within the beam per its unit length; N_b is the number of electrons per beam's unit length ($N_b = j/ce$, j is the beam current); Z is the charge of the ion nucleus.

Besides we use the relative density of the ion core ζ :

$$\zeta = \frac{\sum_{q=1}^Z N_q}{N_b}$$

We suppose that the transverse density distributions in both the beam and the core are the same and the ion core is coasting (the core density is homogeneously distributed along the beam orbit). The electron beam is considered consisting of bunches that occupy $1/B$ part of the orbit length (B is the bunching factor). So, the main ion-driven effects with their scaling to similar effects of the beam are discussed below.

2. TUNE SHIFTS

2.1. Incoherent betatron tune shifts

The incoherent shift of the betatron tune Q_u caused by the core is positive:

$$(Q_u - Q_{u0})_{ion} = -(Q_u - Q_{u0})_{beam} \eta \gamma^2/B, \quad (1)$$

where $u=(x,z)$.

While the tune shift induced by the beam space charge is negligible, the shift caused by ions is significant ($\eta \gamma^2/B \gg 1$). It is worthy of note that this shift is essentially nonlinear. For the elliptical beam cross section with the normal density distribution the shift is:

$$Q_u = Q_{u0} + \frac{N_i r_0 R^2}{Q_{u0} \gamma^2} \int_0^\infty \frac{\exp\left(-\frac{J_x}{Q_{x0}(2\sigma_x^2+t)} - \frac{J_z}{Q_{z0}(2\sigma_z^2+t)}\right)}{\sqrt{(2\sigma_x^2+t)(2\sigma_z^2+t)(2\sigma_u^2+t)}} dt$$

Thus for the round gaussian beam it is:

$$Q_u = Q_{u0} + \frac{N_i r_0 R^2}{Q_{u0} \gamma} \frac{1 - \exp\left[-\frac{1}{2\sigma^2} \left(\frac{J_x}{Q_{x0}} + \frac{J_z}{Q_{z0}}\right)\right]}{(J_x/Q_{x0}) + (J_z/Q_{z0})} \quad (2)$$

Here J_u is the square of the betatron amplitude.

Betatron amplitude vs. its tune is plotted in Fig. 1.

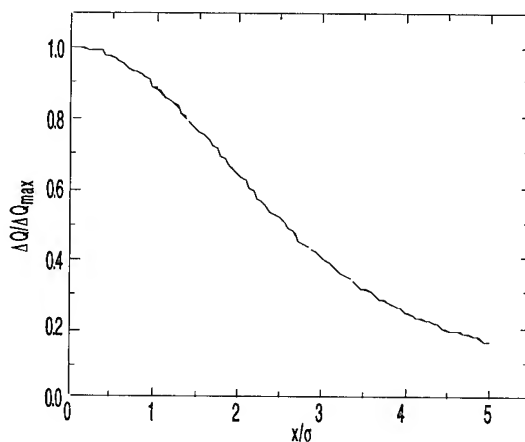


Fig. 1. Q shift vs. amplitude (square root of J over σ).

As it can be seen from Fig.1, the ion tune shift is sufficiently nonlinear at large amplitudes of oscillations. Therefore the peripheral beam particles will experience nonlinear oscillations. The maximum in the tune shift at the beam axis ($J=0$ in (2)) is equal to the maximum value of the tune spread. Major part of the tune spread in electron beams causing the Landau damping is due to trapped ions.

2.2. Tune shifts due to the beam environment

These shifts are much smaller than the beam's and negligibly smaller than those described in 2.1. So, the incoherent tune shift due to reflection in the conducting vacuum chamber walls is smaller than that due to the beam charge by a factor of $-\eta/B$. Reflection of the ion current in ferromagnetics does not take place because of a zero average longitudinal velocity of ions.

2.3. Coherent tune shifts

The ion core is at rest when the beam experiences small coherent betatron oscillations. Hence the coherent betatron shifts are equal to the incoherent ones (2) and are dominant.

3. INCREASE IN BEAM LOSSES AND EMITTANCE

Trapped ions contribute the additional density to the residual gas. The results in the increase of gas pressure in the beam. The influence of the ions is proportional to their density n_i .

$$n_i(\varepsilon_x, \varepsilon_z) = \zeta n_b = \frac{4j\zeta}{\pi Rce} \left(\frac{Q_x Q_z}{\varepsilon_x \varepsilon_z} \right)^{1/2} \quad (3)$$

where ε_u is the beam emittance.

The transverse emittances can be derived from the set of algebraic equations:

$$\begin{cases} \varepsilon_x = \varepsilon_{rad} + V(n_0 + n_i) / Q_x \\ \varepsilon_z = V(n_0 + n_i) / Q_z + \kappa \varepsilon_x \end{cases} \quad (4)$$

$$V = \frac{12\pi^3 r_0 R^2 Z^2 \ln(181.5 \cdot Z^{-1/3})}{\gamma^5 I_2} \quad (4a)$$

$$\varepsilon_{rad} = \frac{55}{32\sqrt{3}} \frac{\hbar}{m_e c} \gamma^2 \frac{I_5}{I_2(1 - I_4/I_2)} \quad (4b)$$

where κ is the coupling factor; I_p are the radiation integrals of the ring.

As it can be seen from (4a)-(4b) the radiation part of the horizontal emittance increases with energy as γ^2 while the 'gas' part decreases as γ^{-5} . Therefore, at high energies the beam emittance is not increased by the ions and the residual gas as well. The trapped ions cause increase in the gas density (3) and the ensuing losses of the beam particles.

4. ION-DRIVEN TRANSVERSE RESONANCES

The forces due to the space charge of the ion core can not only shift the working point (Q_x, Q_z) of the ring towards resonant stop-bands but also drive the specific resonances. These resonances are similar to the crossing beam resonances being studied intensively. The resonances due to the ion core forces are not so complicated for investigation because of the coasting nature of the core. As it has been shown in [3], the ion core drives the nonlinear difference resonances

$$2|mQ_x - nQ_z| < 1, \quad (5)$$

These resonances capture the peripheral beam particles. The 'transverse energy' of these particles is the constant of motion:

$$E_{\perp} = J_x Q_x^2 + J_z Q_z^2 = \text{const} \quad (6)$$

It leads to the occurrence of halo around the beam and can cause the 'resonant' increase in the beam losses when the halo tails reach the aperture of the ring. These resonances may be harmful for the machine with the low-energy multiple injection, where the injected beam with a large amplitude experiences the nonlinear forces due to the ions confined by the circulating beam. Especially it concerns the rings with $Q_z < Q_x$. Increase in a value of the relation

$$\frac{\sigma_x}{\sigma_z} \cdot \frac{Q_x}{Q_z}$$

will lead to enlarging of halo. A sketch of the beam cross section experiencing the difference resonance is presented in Fig. 2.

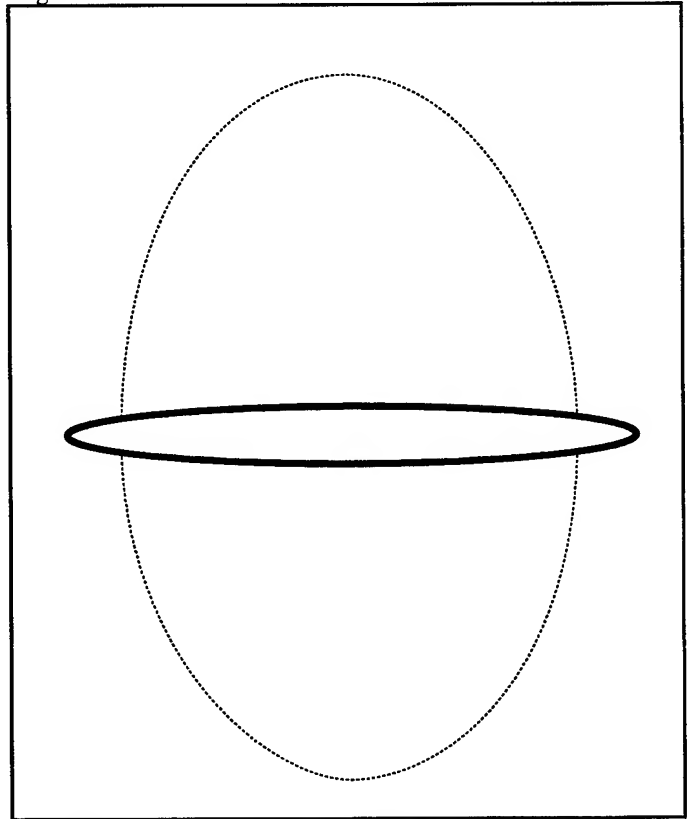


Fig. 2. Solid line represents the beam envelope, dotted line -- the halo envelope.

6. ELECTRON-ION INSTABILITY

This instability of the relative oscillations of the beam and the core is similar to the proton-electron or the antiproton-ion ones. The main difference between them consists in the bunching of the electron beams. This instability is the only

known ion driven effect dependent upon the longitudinal bunch shape. The instability of the space modes has the lowest threshold [4]. The hydrodynamic theory for the round homogeneous bunch shows that the threshold is determined by the maximum in the bunch density:

$$\max(n_{bunch}) = \frac{\gamma(p^2 - Q^2)}{4\pi r_0 R^2} \quad (7)$$

$$p=1,2,\dots; \quad p>Q$$

The increment has its largest value in the vicinity of the threshold and is proportional to the square root of the ion density:

$$\delta = \frac{\gamma(p^2 - Q^2)}{R^2 r_0 n'_{bunch}} \left(\frac{r_p n_i}{4\pi A} \right)^{1/2} \quad (8)$$

Here $n'_{bunch} \equiv dn_{bunch}/d\vartheta$, r_p is the classical proton radius; A is the ion mass number.

This phenomenon is poorly known. Experimental observations show pulsation in the beam dimensions and none additional beam losses [4].

5. CONCLUSION

The most harmful ion-driven effects among listed above are the nonlinear tune shifts and resonances especially for the rings with the multiple low energy injection. The tune spread caused by ions increases the Landau damping which stabilizes the coherent transverse instabilities. It is essential to choose properly the working point and strength of the multipole lenses such as the octupoles. Some ion-driven effects need to be studied more extensively.

REFERENCES

- [1] Baconnier Y., Poncet A., and Tavares P.F. *Neutralization of Accelerator Beams by Ionization of the Residual Gas* Proc. of CAS 1992 / CERN 94-01 (1994) vol 2, p 525
- [2] Gyggi-Hanney P. M., Jovett J. M. and Keil E. 'BeamParam' A program for computing beam dynamics CERN/LEP-TH/88-2, (1987)
- [3] Bulyak E. V., Gonchar V. Yu., Kurilko V. I. *Response of the emittance on the beam current in electron storage rings* Proc. of 13 ICHEA (Novosibirsk, 1987) vol 2, p 174 (in Russian)
- [4] Bulyak E. V. *Theory of the transverse electron-ion instability in the bunch circulating in an electron storage ring* Ukrainian Journ of Physics, (1984) vol, N 5, p 657 (in Russian)
- [5] Bulyak E. V. and Kurilko V. I. *Low-frequency transverse charge oscillations in an electron storage ring* Pis'ma Zh. Eksp. Teor. Fiz (1981) **34**, No.9, p.493

DISK-LOADED WAVEGUIDES FOR ACCELERATION HIGH INTENSITY SHORT PULSE ELECTRON BEAMS

N.I.Aizatsky, National Science Centre, Kharkov Institute of Physics & Technology (KFTI),
310108, Kharkov, Ukraine.

One of the beam loading effects in linacs is limitation on the amount of number of particles that can be accelerated in very short beam pulses. The maximum number of particles is determined the correlation between the external accelerating field amplitude and the retarding field amplitude which particles radiate passing the waveguide. For increasing this value we suggested to use disk-loaded waveguides with period D that satisfies the condition: $\lambda/2 < D < \lambda$, where λ is the wavelength of accelerating wave. Three accelerating sections of this type have been manufactured in KFTI and installed at different linacs.

INTRODUCTION

A most widely used technique for energy loss reduction is enlargement of the structure geometric sizes with an ensuing decrease of the accelerator operating frequency. For similar geometry structures the accelerating field amplitude in a certain cross-section at a fixed total rf-flow value depends in direct proportion on the operating frequency $E_a \propto f_0$, while radiation fields for similar geometry bunches vary according to the law $E_r \propto f_0^2$. After decreasing the operating frequency by the factor of n the ratio of the energy loss to the energy gain decreases by this value. Note that this inference is valid only for similar geometry bunches.

In a number of cases the radiation loss reduction by the way of operating frequency decrease is undesirable, because it entails making larger accelerating structure sizes, decreases the breakdown limit, etc. It is of considerable interest to seek out other ways of diminishing the slow-wave structure electrodynamic inhomogeneity for particle acceleration. We

suggested that energy losses to radiation of charge particles at constant operating frequency be decreased by the making smaller the number of inhomogeneities per unit length of a slow-wave guide [1, 2]. For a disk-loaded waveguide it was shown that in case of acceleration of short-pulsed beams containing several bunches ($N > 10$), when energy losses are determined by excitation of the fundamental mode, the increasing of inter-disk spacing causes the radiated wave to decrease amplitude faster than the acceleration gradient decreases. Concurrently, beginning from a certain inter-disk value one of the wave spatial harmonics becomes the accelerating one, i.e. particle-synchronous. This conformity to natural laws opens up a possibility to increase the number of accelerating particles at a constant external source power. Besides, such structures have several other advantages, namely, a better Q and presence of rf-focusing [3, 4].

However, during single-bunch acceleration, when the excited wave spectrum considerably broadens, the possibility of loss decrease owing to a sparser inhomogeneity position becomes obscure. Really, in case of single bunch acceleration of considerable importance are both excited wave amplitudes and their frequency spectrum "density". In this connection, we carried out calculations of radiation characteristics of point charged particles in disk-loaded waveguides with different inter-disk spacing.

BASIC EQUATIONS

As a main parameter chosen to be constant for the structures under consideration was considered the group velocity V_g . At constant V_g , section lengths L and external source power P one and the same value of rf-energy W

($W = P \tau_f$, $\tau_f = L / V_g$) is needed to file them. The accelerating wave amplitude in a fixed cross-section of the homogeneous slow-wave structure is known to be determined by the expression

$$E_a = \sqrt{R_s P(z)} \quad (1)$$

where $P(z)$ is the electromagnetic wave power in the given cross-section, $R_s = E_s^2(z)/P(z)$ is the consecutive impedance of the accelerating wave synchronous spatial harmonic. The longitudinal radiation field component in the wake of axis-propagating particle without consideration of the oscillation terms is equal to the sum of all exited waveguide eigen-waves [5]

$$E_r = -q c \sum_{n=0}^{\infty} R_n \frac{|\beta_{g,n}|}{|1 - \beta_{g,n}|} \cos(\omega_n(t - \frac{z}{V_0}) - \omega_n t_0) \quad (2)$$

here $\beta_{g,n} = V_{g,n} / c$, $V_{g,n}$ is the group velocity of n -th eigen wave, particle-synchronous, t_0 is the particle flight time over the cross-section considered as a start-off count marker for the longitudinal coordinate, q is the particle charge. For a value characterizing the relationship of radiation fields vs. accelerating field is taken the dimensionless value which is equal to the relationship of the radiation field in the frequency range $\omega_n < \omega$ ($0 \leq n \leq N$) in the immediate vicinity of point particle ($t - z/V_0 \approx t_0$) with the charge $q_* = 1$ nC vs. the accelerating wave amplitude that has in the cross-section under consideration the total power flow $P_* = 1$ MW:

$$F(\omega) = \frac{q_* c \sum_{n=0}^N R_n |\beta_{g,n}| / |1 - \beta_{g,n}|}{\sqrt{R_s P_*}} \quad (4)$$

Since the eigen-waves form a discrete frequency spectrum, then the function $F(\omega)$ is treated as a step-by-step one.

RESEARCH RESULTS

The calculations of eigen-wave characteristics for disk-loaded waveguide were performed according to a program

developed by the authors of this technique [6,7] in consideration of 20 eigen-oscillations in the inter-disk spacing and 101 spatial field harmonics over the flight region. Results of $F(\omega)$ -function calculations for various slow-wave structure geometries are shown in Fig.1.

As indicated above, the value of accelerating wave group velocity at the operating frequency ($f_0 = 2797,2$ MHz) is chosen to be constant

$\beta_{g,s} \approx 0,01$. Geometrical dimensions of the waveguides under consideration are given in Table 1 (a is the radius

Table 1

Type	a (mm)	t (mm)	D (mm)
B ₁	11,8	6	35,73
B ₂	11,8	6	71,45
B ₃	50	50	71,45

of the aperture in the disk, D is the structure period, t is the disk thickness).

The first-type accelerating structure ($R_s = 2245 \Omega/\text{cm}^2$, $\alpha = 0,002$ 1/cm, $\beta_{g,s} = 0,0101$, $\theta = 2\pi/3$, $n_s = 0$) resembles in its average waveguide characteristics that a constant gradient section at SLAC [8]. The second-type accelerating structure ($R_s = 878 \Omega/\text{cm}^2$, $\alpha = 0,0015$ 1/cm, $\beta_{g,s} = 0,0096$, $\theta = -2\pi/3$, $n_s = 1$) is analogous to the structure used in a high-current section of the linear accelerator LUE-300 at KFTI [1]. To date two accelerating sections of this type have been manufactured with the length $L \approx 160$ cm and group velocity $\beta_g = 0,036$ installed with the fieldback loop. Electron acceleration in this waveguide is performed by the first spatial harmonic of the counter-propagating wave. Slow-wave structures of this type were designated STRAM which stands for STRucture Accelerating Modified. The third-type structure ($R_s = 552 \Omega/\text{cm}^2$, $\alpha = 0,0024$ 1/cm, $\beta_{g,s} = 0,0099$, $\theta = -2\pi/3$, $n_s = 1$), which has non-standard parameters, has been developed, and on its base an accelerating section has been manufactured for LIC-accelerator, which stands for Laser Injector Complex designed to accelerate intense electron bunches [9].

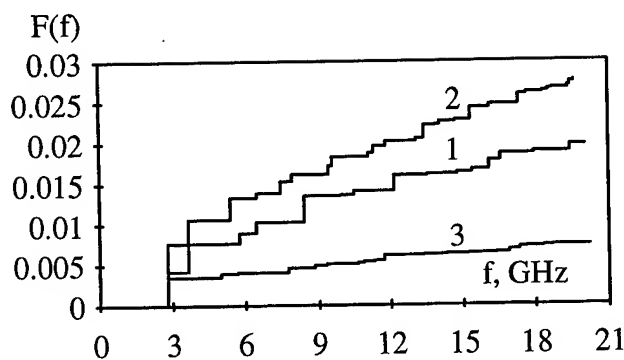


Fig.1

As follows from Table 1, disks in the waveguide B_2 are spaced twice as rare as in the waveguide B_1 . Comparison of the $F(\omega)$ -function relationships for these two structures indicates that the radiation field value in the fundamental pass band decreases faster upon increasing the inter-disk spacing than the accelerating field amplitude [1,2]. Yet, upon frequency increasing the $F(\omega)$ -function for the waveguide B_2 rises faster than for the waveguide B_1 . This is accounted for by the fact that owing to increasing of the cavity longitudinal dimension, as formed by two adjacent disks, the frequency spacing between excited eigen-waves decreases. As a result, structures of this type are no better for acceleration of single bunches than standard disk-loaded waveguides.

The third-type structure, designed and manufactured at KFTI, is much alike in its operation to the waveguide B_2 . Particle acceleration in it is also done by the first spatial harmonic of the counter-propagating wave. However, as can be seen from Fig.1, it has considerably lower losses to radiation across the entire frequency spectrum. This is achieved due to three reasons. Firstly, owing to the increased structure period the number of electrodynamic inhomogeneities overflowed by particle per unit length is decreased by a factor of two. Secondly, resulting from an increase disk thickness the cavity dimensions remained practically the same as in the structure B_1 , leaving the "spectrum density" of eigen-waves unchanged. Thirdly, removal of inhomogeneities off from the axis (increasing the

radius of the flight-through aperture) led to an additional decrease of the amplitudes of particle-excited waves. Thus, the above results of studies on charge particle radiation field relationships in periodic waveguides show that without changing the operating frequency one can decrease the losses to radiation by way of increasing the inter-spacing between electrodynamic inhomogeneities both in the fundamental band pass and in the wide frequency spectrum.

REFERENCES

1. N.I.Aizatsky, E.Z.Biller, E.V.Bulyak et al. Voprosy atomnoi Nauki i Tekniki. VANT: series, Nuclear Physics Research (Theory and Experiment), 1991, No.3(21), p.16-18.
2. N.I.Aizatsky, V.V.Volobuyev. Voprosy atomnoi Nauki i Tekniki. VANT: series, Nuclear Physics Research (Theory and Experiment), 1991, No.3(21), p.43-44.
3. L.A.Makhnenko, V.I.Pakhomov, K.N.Stepanov. ZhTF, 1965, Vol.35, No.4, p.618-622.
4. N.I.Aizatsky, E.V.Bulyak, V.I.Kurilko. Proc. 12th All-Union Seminars on Charged Particle Accelerators, Dubna, 1992, Vol.1, p.412-415.
5. E.P.Burstein, E.V.Voskresensky. Intense Beam Electron Linacs, Moscow, Atomizdat, 1970.
6. V.I.Naidenko, E.V.Guseva. Radiotekhnika i Elektronika, 1987, Vol.32, No.8, p.1735-1757.
7. V.I.Naidenko. Doklady AN Ukr.SSR, Ser.A, Phys.-Math. and Technical Science, 1990, No.9, p.58-61.
8. Loew G.A., Neal R.V. Accelerating structures.// "Linear accelerator" edited by P.M.Lapostolle, 1970, p.39-113.
9. N.I.Aizatsky, E.Z.Biller, V.N.Boriskin et al. 13th All-Union Seminars on Charged Particle Accelerators, Dubna, 1992, p.154.

THE DESCRIPTION OF HIGH CURRENT BEAM DYNAMICS USING LIE ALGEBRAIC METHODS

A.I.Borodich, A.A.Khrutchinsky, V.I.Stolyarsky
Institute of Nuclear Problems, Belorussian State University
220050, Minsk, Belarus

Abstract

A scheme to describe a nonlaminar beam dynamics in the electromagnetic field is suggested. It is based on the Lie algebraic methods and uses the quasi-equilibrium plasma model. Numerical results are represented.

I. INTRODUCTION

Using of the paraxial approximation for the description of high current beam dynamics leads to applying the Lie algebraic methods to calculate transfer map, that relates initial and final coordinates and momenta of an arbitrary particle in the sixdimensional phase space [1], [2]. The main difficulty, when dealing with a bright beam, is to take into account the influence of space charge on variation of beam characteristics. For laminar beams it was done in [3], [4] in terms of charged particle optics. In this paper the powerful methods, mentioned above, are used to describe high current (nonlaminar) beam dynamics, when space charge is altering. A beam is considered as a statistical system of charged particles. The results of numerical simulations for a beam being focused by longitudinal magnetic field are given as a simple example and compared with known facts from plasma physics.

II. BACKGROUND MATERIAL: COMPUTATION OF TRANSFER MAP

The location of any particle of a beam in six-dimensional phase-space is characterized by the vector $\xi(X, Y, T, P_X, P_Y, P_T)$. An independent variable z is the coordinate along the reference trajectory. Variables X and Y denote transverse displacement of an arbitrary particle from the reference one, T fixes the difference of their time coordinates. And the least three variables are correspondingly the canonical conjugate momenta. Using of the reference trajectory means the description of a beam dynamics in paraxial approximation.

According to the definition, transfer map M relates initial and final generalized coordinates and momenta of an arbitrary particle,

$$\xi(z) = M\xi^{in}(z).$$

The action of this operator can be considered as a canonical transformation. Taking into account the canonical transformations generate a symplectic group, we can factorize M , i.e. write it as an infinite product of Lie transformations of Lie operators associated with some homogeneous polynomials f_m [1], [2]. Since, for the first, the fundamental Poisson bracket defining Lie operators is invariant in canonical transformations, for the second, ten symplectic group generators realize the presentation of Lie algebra, it is possible to express f_m over polynomials H_m , obtained as one-particle Hamiltonian decomposition.

Particle's Hamiltonian is:

$$H(X, Y, T, P_X, P_Y, P_T; z) = -\frac{1}{c} \{ (P_T + p_t^0 + q\phi)^2 - (P_X - qA_X)^2 c^2 - (P_Y - qA_Y)^2 c^2 - m^2 c^4 \}^{\frac{1}{2}} - qA_z - \frac{P_T + p_t^0}{v^0}, \quad (1)$$

(m and q are the particle rest mass and charge, c — speed of light; reference trajectory parameters are marked by subscript 0).

Scalar and vector potentials of the electromagnetic field ϕ and A consist of two parts, that describe the influence of the external field and space charge upon a particle:

$$\begin{aligned} \phi(X, Y; z) &= \phi^{field}(X, Y; z) + \phi^{beam}(X, Y; z), \\ A(X, Y; z) &= A^{field}(X, Y; z) + A^{beam}(X, Y; z). \end{aligned} \quad (2)$$

It is assumed ϕ^{field} and A^{field} are known. Their structure is determined by given focusing systems that are used to form or to transport a beam. If the form of ϕ^{beam} and A^{beam} is also known and the decomposition on the polynomials have been done for them, we can apply the Dragt method [1], [2] to express polynomials f_m over H_m and write down transfer map M in obvious form. To find out M , for example, through the fourth order, the system of three matrix differential equations must be derived (their structure is added in [1], [2]).

III. SPACE CHARGE CALCULATION

Inasmuch mapping has been done for any particle of a beam as we will use one-particle distribution function $g(\xi, z)$ to calculate the potentials ϕ^{beam} and A^{beam} .

The Coulomb interaction dominates in comparison with mutual collisions between the particles in high current beam [5] and we can be satisfied by zero approximation for gas parameter η (ratio of average potential energy to the mean kinetic) to calculate an alteration of $g(\xi, z)$ according to the Liouville theorem:

$$\frac{d}{dz} g(\xi, z) = 0. \quad (3)$$

Now, instead of solving the Landau-Vlasov equation and the system of the Maxwell equations jointly, we choose another way. Space charge structure proves to be invariable along z within some length l , that is greater than the Debye radius, but don't exceed the range of a particle without collisions. Therefore, on every elementary length l of the interaction channel time-independent space charge acts to any particle of a beam. Moreover, the distribution function satisfies the Liouville theorem (3). Hence, moving high current beam as a statistical system passes through the consequence of equilibrium states only.

It is obviously, the volume occupied by the particles is slowly varying parameter for given adiabatic process. Thus, $g(\xi, z)$ of the quasi-equilibrium system under review assumes to obey the Boltzmann–Maxwell statistics along the whole interaction channel. Only the shape of the distribution function is altering on every length l .

To calculate A^{beam} on given elementary length the quasi-stationary approximation [6] can be used:

$$\begin{aligned} A_X^{beam}(X, Y) &= 0, A_Y^{beam}(X, Y) = 0, \\ A_z^{beam}(X, Y) &= \frac{v_0}{c^2} \phi^{beam}(X, Y). \end{aligned} \quad (4)$$

The electric part of space charge assumes to be only transverse in respect to the reference trajectory, $E^{beam} = -grad(\phi^{beam})$; the magnetic one $B^{beam} = rot(A^{beam})$ – azimuthal.

If particles are distributed according to the Boltzmann–Maxwell statistics and the decomposition of ϕ^{beam} is limited by the polynomials of the second degree, charge density of a beam $\rho(X, Y)$ has the Gaussian shape on every elementary length l . It's known that particles of a beam aren't in equilibrium, but using of the Gaussian distribution is often suitable for its description [5]. And, as it will be shown below, such simple "step by step" scheme to calculate space charge gives positive results.

The magnitude of ϕ^{beam} on given elementary length at some point (x_0, y_0) of the beam cross-section is calculated with the help of the Green function as a solution of the two-dimensional Dirichlet problem for the Poisson equation:

$$\begin{aligned} \phi^{beam}(x_0, y_0) &= \iint dx dy \frac{\rho(x, y)}{\epsilon_0} \\ &\times \frac{1}{2\pi} \ln \frac{1}{\sqrt{(x - x_0)^2 + (y - y_0)^2}}, \end{aligned} \quad (5)$$

where, ϵ_0 is a dielectric permittivity of free space.

IV. ALGORITHM TO DESCRIBE A BRIGHT BEAM DYNAMICS

So, the general scheme to describe a bright beam dynamics in external field is the following. The initial cross-section of a beam is being represented as a set of the test point particles. Their transverse coordinates and momenta satisfy the Boltzmann–Maxwell distribution. Time coordinates are the same for all test particles and for the reference one. The energy of an arbitrary test particle differ from the reference particle energy on the quantity

$$\begin{aligned} -P_T^i &= c\sqrt{(p_z^0)^2 + (P_X^i)^2 + (P_Y^i)^2 + m^2 c^2} \\ &- c\sqrt{(p_z^0)^2 + m^2 c^2}. \end{aligned}$$

According to (5) we find numerically values of ϕ^{beam} at the knots of a spatial net, that cover the cross-section of a beam, computing the two-dimensional integral by the Gauss method. Then we approximate $\phi^{beam}(X, Y)$ and $A^{beam}(X, Y)$ from (4) by the homogeneous polynomials of the fourth degree, substitute them into the Hamiltonian (1) and receive expressions for H_m . Solving numerically the system of three matrix differential equations by the Runge-Kutta-Merson method, we determine transfer

map M in obvious form for every test particle. These operators are used, we find coordinates and momenta of the test particles at the end of the first elementary length. Computing the mean values and dispersions of the transverse coordinates and momenta, energy spectrum, we obtain the initial data to execute test particles on the next elementary length of the interaction channel. Repeating the procedure for calculating space charge potentials and transfer maps we carry out computations on the following steps.

The scheme described above is an algorithm for computer code TRLIE. This code calculates a bright beam characteristics when it is passing through a set of magnetic focusing elements. Verification of this code was carried out by comparison with the results of the tests having executed by codes TRANSPORT (without space charge effects) and CHARLIE4F (with space charge effects) [4].

V. EXAMPLE: HIGH CURRENT BEAM IN MAGNETIC FIELD

Let's consider as a simple example the results given by TRLIE code, when the beam is placed at the homogeneous longitudinal magnetic field. They were obtained for the beam with current 1 kA, initial radius 2,5 cm, initial divergence of the transverse momenta of 1 % from the reference particle momentum at the magnetic field induction magnitude 100 Gs for the different kinetic energy values of the beam.

On fig.1 the beam radius evolution is shown. Obtained oscillations of a beam boundary can be identify with the surface waves in plasma with the parameter of inhomogeneity r_0 , that is restrained by the external longitudinal magnetic field. The dispersion equation for axial symmetrical modes [7] gives the following expression for spectrum of this long-wave oscillations (frequency ω is not exceed plasma frequency ω_L):

$$\omega^2 = k^2 \frac{\omega_L^2 r_0^2}{2} \ln \frac{1}{kr_0} \quad (6)$$

In the table 1 magnitudes of the wave number k and the frequency ω of the surface wave obtained by the code and the frequency ω calculated according to (6) are represented. It is obviously, the results of simulations are in good agreement with known facts from plasma physics.

VI. CONCLUSION

The description of a bright beam dynamics, accomplished above, can be applied for any flows. There is no restriction of an energy or current density of a beam. The validity of suggested method is limited by the paraxial approximation in sense of the accuracy to decompose one-particle Hamiltonian on the polynomials close to the reference trajectory.

References

- [1] A.J. Dragt, J.M. Finn, "Lie Series And Invariant Functions For Analitic Symplectic Maps," *J. Math. Phys.*, vol. 17, pp. 2215-2227, 1976.
- [2] A.J. Dragt, E. Forest, "Computation of Nonlinear Behavior of Hamiltonian System Using Lie Algebraic Methods," *J. Math. Phys.*, vol. 24, pp. 2734-2744, 1983.

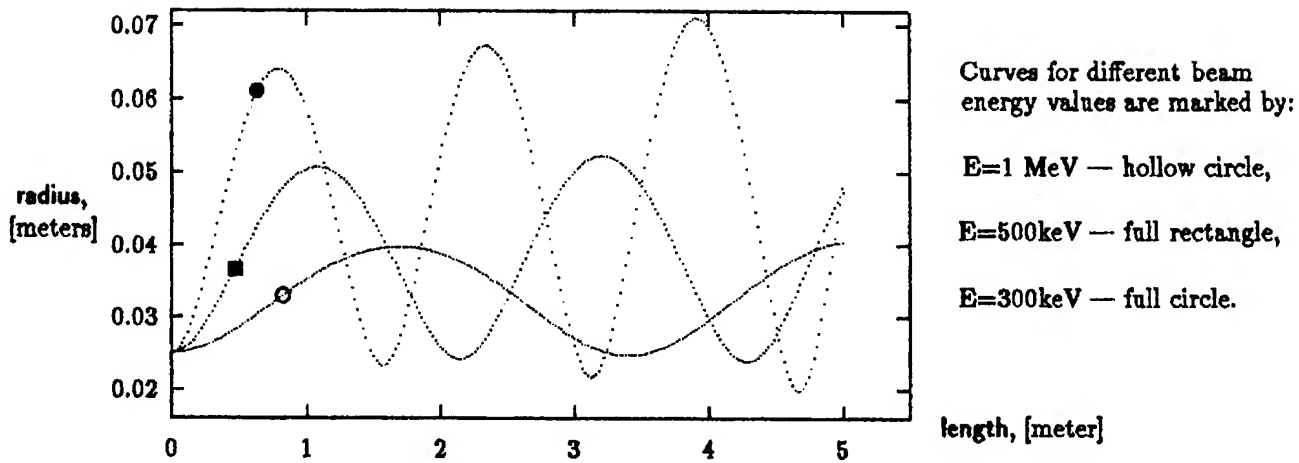


Figure. 1. Beam radius evaluation.

E , keV	k , m^{-1}	ω , sec^{-1}	w , sec^{-1}
300	3.98	1.01×10^9	0.94×10^9
500	2.86	0.81×10^9	0.76×10^9
1000	1.84	0.57×10^9	0.53×10^9

Table I

Characteristics of the surface waves in a beam and plasma.

- [3] R.D. Ryne, A.J. Dragt, *Proceedings of the 1987 IEEE Particle Accelerator Conference*, vol. 2, pp. 1063-1065, 1987.
- [4] R.D. Ryne, *AIP Conference Proceeding*, vol. 177, pp. 265-274, 1988.
- [5] J.D. Lawson, *The Physics of Charged-Particle Beams*, Clarendon Press, Oxford, 1977.
- [6] I.M. Kapchinsky, *Theory of Linear Resonant Accelerators*, Atomizdat, Moscow, 1988.
- [7] A.F. Alexandrov, L.S. Bogdankevich, A.A. Rukhadze, *Fundamentals of Plasma Electrodynamics*, Nauka, Moscow, 1988.

Chaos, a source of Charge Redistribution and Halo Formation in Space-Charge Dominated Beams

Jean-Michel LAGNIEL and David LIBAULT

Commissariat à l'Energie Atomique, Direction des Sciences de la Matière, GECA
CEN Saclay - LNS, 91191 Gif-sur-Yvette Cedex, FRANCE

Abstract

A significant breakthrough in the understanding of the space-charge dominated beam dynamics has been achieved with the introduction of the Particle-Core Model at the previous PAC (O'Connell, Wangler, Mills & Crandall, May 1993). Using this model, we have shown the chaotic behaviour of the particles for mismatched beams in continuous focusing channels (August 1993 & August 1994) and for matched beams in FODO channels (December 1993 & June 1994). In these studies, it has been settled that the recent theories developed for the analysis of nonlinear dynamic systems ("chaotic dynamics") are very useful to understand charge redistribution and halo formation phenomena. They are now used to describe the behaviour of mismatched beams in FODO channels. It is shown that a mismatch adds perturbing forces which can deeply modify the dynamics. The particle diffusion far from the beam core is studied.

1. INTRODUCTION

In numerous nonlinear dynamical systems studied in various disciplines (fluid dynamics, celestial mechanics, chemistry, biology, economy, ecology...), chaotic (stochastic) motions are generated by the dynamics itself whereas no random force is present. The chaotic behaviour of the particle trajectories (already studied in the accelerator field to understand the beam-beam effect) has been observed from numerical experiments on space-charge dominated beams [1 - 4]. This significant breakthrough in the understanding of the mechanisms leading to charge redistribution and halo formation in the new generations of high-power linacs has been achieved thanks to the Particle-Core Model (PCM) [5].

The PCM is obviously not a self consistent model but, as it is usually done to study *complex systems*, it is a simplified model which keeps the dominant properties of the real physical system and which allows an analysis of the basic phenomena. For the PCM :

- the influence of the halo on the beam core is neglected because halo particles are supposed to be a very low fraction of the total beam,
- the "breathing" mode which is the main oscillation mode excited by the quadrupoles in a real accelerator is the sole mode taken into account. All the other modes are neglected.

The first numerical experiments completed using the PCM [5, 1, 6, 2] dealt with the evolution of beams in a continuous focusing channel. As pointed out in ref.[1,2], when the envelope of a mismatched beam oscillates, space charge can be assimilated to a *nonlinear periodic perturbing force* which excites resonances. The *resonance overlap mechanism* [7] can then lead to the formation of a

halo area where the particle trajectories are stochastic. This chaotic behaviour has been clearly observed using the Poincaré surface of section technique. Sensitive dependence on initial conditions and intermitencies which characterize chaotic systems have been also shown.

In ref.[3,4], the PCM is used to analyse the behaviour of a matched beam evolving in a FODO channel. Again, the test particles trajectories are studied using the Poincaré section technique to display the chaotic areas prominently. Here, the beam envelope oscillations are naturally "excited" by the quadrupoles then, as for a mismatched beam in a continuous focusing channel, several resonances can overlap and form a halo. Therefore, it seems important to emphasize that halos can be generated even if the beam is perfectly matched, not only via non-ideal conditions as found stated in some recent papers.

In a FODO channel, both order and number of the resonances which are present around the beam core are determined by the choice of the phase advances with (σ_t) and without (σ_{0t}) space charge. Actually, the tune of the test particles which travel near the core is close to $\nu = \sigma_t/2\pi$ and it tends towards $\nu = \sigma_{0t}/2\pi$ when the transverse energy is increased because the effect of space charge becomes more and more negligible. For K-V or monotonically-decreasing distribution functions for which σ_t is the phase advance near the axis, the parametric resonances which can be excited are then in the range :

$$\sigma_t/2\pi \leq \nu < \sigma_{0t}/2\pi$$

The size of the stochastic areas, consequently the particle diffusion, is limited when the strong resonances $\nu = 1/4$ and $\nu = 1/5$ are avoided ($\sigma_{0t} < 72^\circ$) [3]. This can be done using modified octupoles to reduce the tune spread in the beam core vicinity [4] or, simply choosing $\sigma_{0t} \sim 61.9^\circ$ and $\sigma_t \sim 19.9^\circ$ for example. The resonances which surround the K-V beam core are then in the range $1/18 \leq \nu \leq 1/6$ with the $\nu = 1/18$ resonance ($\sigma = 20^\circ$) very close to the core and the $\nu = 1/6$ resonance ($\sigma = 60^\circ$) far from it. Figure 1 gives a Poincaré section for uncoupled ($x, x', y=y'=0$) test particles showing the $\nu = 1/6, 1/7$ and $1/8$ resonances. A thin stochastic layer appears around each resonance (weak chaos) but they do not overlap, they stay isolated by KAM surfaces. The perturbation is too weak to form a large stochastic sea which could lie down up to the $\nu = 1/6$ resonance area.

In Ref.[3], it has been shown that to couple the RF defocusing effect to the radial motion leads to the formation of large stochastic seas. Therefore, the dynamics is deeply modified when "coupled oscillators" are added to the system. In the following sections, the effects of an additional source of perturbation : a beam core mismatch, will be studied.

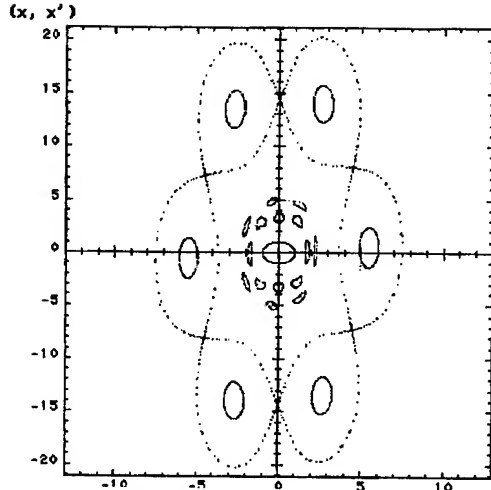


Fig. 1: Poincaré section for a matched beam.
(uncoupled particles with $\sigma_{0r} \sim 61.9^\circ$ and $\sigma_t \sim 19.9^\circ$)

2. MISMATCHED ENVELOPES

For weak mismatches, the envelope equations in smooth approximation can be linearized. When $a_0 = b_0$ are the matched beam mean radii, the envelopes in the two transverse planes can be noted $a = a_0 + \delta a$ and $b = b_0 + \delta b$. The two mismatch terms ($\delta a \ll a_0$ and $\delta b \ll b_0$) are then determined by two coupled linear differential equations :

$$\delta a'' + \sigma_a^2 \delta a + \sigma_{ab}^2 \delta b = 0 \quad \text{and} \quad \delta b'' + \sigma_b^2 \delta b + \sigma_{ab}^2 \delta a = 0$$

with $\sigma_{ab}^2 = 2K / (a_0 + b_0)^2$
and $\sigma_a^2 = \sigma_b^2 = \sigma_{0r}^2 + (3\varepsilon^2/a_0^4) + \sigma_{ab}^2$

where K is the generalized perveance and $\varepsilon = \varepsilon_x = \varepsilon_y$ is the beam emittance. Following I. Hofmann [8], the two eigen modes can be called even and odd, they are given by :

$$\sigma_e^2 = \sigma_a^2 + \sigma_{ab}^2 = 2(\sigma_t^2 + \sigma_{0r}^2) \quad \text{and} \quad \sigma_o^2 = \sigma_a^2 - \sigma_{ab}^2 = 3\sigma_t^2 + \sigma_{0r}^2$$

The K-V envelope equations have been numerically integrated (without smooth approximation) for a weak initial mismatch $\delta a = 0.1a_0$, $\delta b = \delta a' = \delta b' = 0$ and a FODO channel with $\sigma_{0r} \sim 62^\circ$ and $\sigma_t \sim 20^\circ$. The Fourier spectrum of the envelopes (fig.2) shows that, even for this weak mismatch, the amplitudes of the odd and even modes are already large compared to the one of the main mode ($f=1$). The eigen frequencies are close to those calculated using the theoretical formulas but, for larger mismatches, the envelope oscillations become rapidly chaotic leading to a more complicated frequency spectrum.

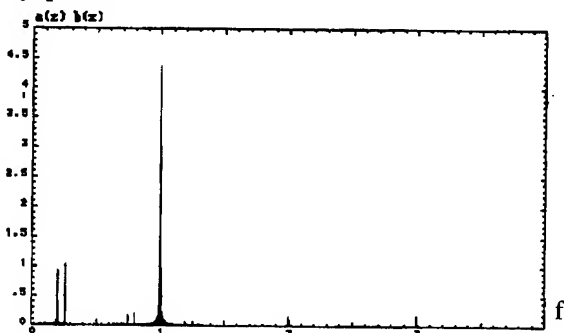


Fig. 2 : Fourier spectrum of a mismatched beam envelope.

3. RESONANCES EXCITED BY A MISMATCH

Above the resonances excited by the natural beam modulation due to the quadrupolar focusing system ($\sigma_t/2\pi \leq \nu < \sigma_{0r}/2\pi$), new resonances are excited by the two eigen frequencies of the envelope oscillations when the beam is mismatched. These additional resonances are in the range $\sigma_t/\sigma_{e,o} \leq \nu_{e,o} < \sigma_{0r}/\sigma_{e,o}$ then, with $\eta = \sigma_t/\sigma_{0r}$:

$$\eta/\sqrt{2(\eta^2+1)} \leq \nu_e < 1/\sqrt{2(\eta^2+1)} \quad \text{for the even mode}$$

$$\text{and} \quad \eta/\sqrt{3\eta^2+1} \leq \nu_o < 1/\sqrt{3\eta^2+1} \quad \text{for the odd mode.}$$

Figure 3 shows the range of resonances which can be excited by the two modes as a function of the tune spread η . As in the case of a continuous focusing channel [2], the strong $\nu_{e,o} = 1/2$ resonance is definitively always present.

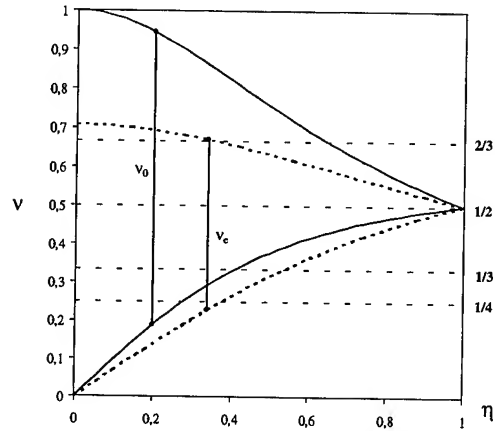


Fig. 3 : Range of excited resonances versus η .

4. CHAOS INDUCED BY A MISMATCH

The simplest way to analyse the test particle chaotic motions is to use the Poincaré section technique. For a mismatched beam in a FODO channel, it is therefore necessary to choose an initial mismatch such as only one mode (even or odd) is excited, and also to choose the channel parameters such as the beam core oscillation is periodic. An optimization code has been written to find these conditions, the case $\sigma_{0r} = 61.87659^\circ$ and $\sigma_t = 19.92206^\circ$ has been chosen for the numerical experiments. Using these parameters :

- the main resonances which are present around the K-V beam core are $1/18 \leq \nu \leq 1/6$ (see section 1 and figure 1),
- the beam core oscillation is exactly five FODO periods for an initial mismatch $\delta a = .1a_0$, $\delta b = -.1a_0$, $\delta a' = \delta b' = 0$.
- $\eta = 0.322$ and the main resonances excited by the odd mode are $\nu_o = 2/3, 1/2$ and $1/3$ (see figure 3).

Using these parameters, a Fourier analysis of the envelopes shows that the amplitude of the odd mode is about half of those of the fundamental mode. In a Poincaré section (fig.4) a large stochastic area which is created by the overlapping of resonances appears around the beam core. The $\nu_o = 1/2$ (easily recognizable in figure 4) and the $\nu_o = 1/3$ resonances overlap with the low order resonances excited by the fundamental mode. For uncoupled particles, this chaotic sea stays isolated from the $\nu = 1/6$ resonance by KAM curves which are not destroyed by the weak mismatch.

6. CONCLUSION

For the new generation of high-power accelerators, the most important aim is to limit the beam losses to an extremely low fraction of the total beam, the basic phenomena leading to emittance growth and halo formation must then be understood. In this paper as well as in ref. [1-4], we have tried to show that chaos induced by resonance overlap and Arnol'd diffusion can drive particles far from the beam core. Even if the studies are far from being exhaustive, they have shown that these phenomena become more and more significant when perturbations such as beam core modulations due to the quadrupolar focusing, synchrotron coupling or mismatches are taken into account. Nevertheless, the random character of the particle motions will not facilitate the studies. As far as we know, analytic calculation of the diffusion rates will be practically impossible and several questions can be asked on the numerical experiments :

- What is the number of test particles requested to obtain a true evaluation of the diffusion rates? Can a judicious choice of the initial conditions reduce this number?
- Can the diffusion rates for some focusing periods be deduced from a tracking over a large number of periods?
- Do the round off errors allow an accurate evaluation of the diffusion rates?

It will be also very important to take into account the (nonlinear) longitudinal motions because Arnol'd diffusion can drive particles out of the separatrix, then leads to unbounded motions. This study is in progress.

Acknowledgement.

D. Libault, student of the ESPCI, would like to thank the support provided by the CEA-DSM-GECA.

7. REFERENCES

- [1] J-M. Lagniel, "On halo formation from space-charge dominated beams", LNS/SM/93-35, August 1993 and NIM-A Vol.345 No.1, 1994, p.46.
- [2] J-M. Lagniel and A-C. Piquemal, "On the dynamics of space-charge dominated beams", LINAC94 conf. proc., August 1994.
- [3] J-M. Lagniel, "Chaotic behaviour and halo formation from 2D space-charge dominated beams", LNS/SM/93-42, December 1993 and NIM-A Vol.345 No.3, 1994, p.405.
- [4] J-M. Lagniel, "Chaotic behaviour induced by space charge", EPAC94 proc., June 1994, p.1177.
- [5] J.S. O'Connell, T.P. Wangler, R.S. Mills and K.R. Krall, "Beam halo formation from space-charge dominated beams in uniform focusing channels", PAC93 proc., May 1993, p.365.
- [6] T.P. Wangler, "Dynamics of beam halo in mismatched high-current charged-particle beams", LA-UR-94-1135, March 1994.
- [7] B.V. Chirikov, "A universal instability of many-dimensional oscillator systems", Physics reports Vol.52 No.5, May 1979.
- [8] I. Hofmann, "Transport and focusing of high-intensity unneutralized beams", in Applied charged particle optics (C), A. Septier, Academic press, 1983.

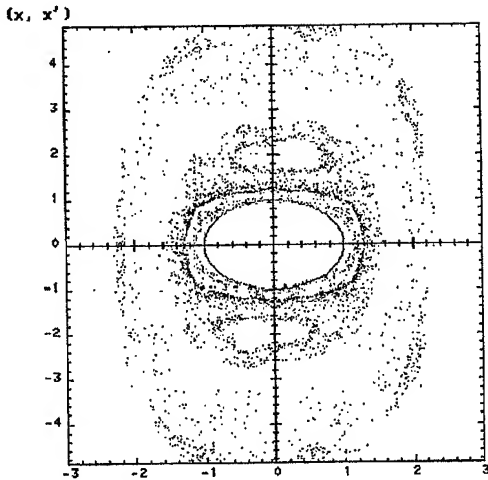


Fig. 4 : Poincaré section for a mismatched beam.
(uncoupled particle, $\sigma_{0x} = 61.87659^\circ$ and $\sigma_{0x'} = 19.92206^\circ$)

5. SEARCH FOR ARNOLD'S DIFFUSION AT LARGE AMPLITUDES

When there is more than two degrees of freedom, the KAM surfaces no longer isolate the stochastic areas which form a dense "Arnol'd web" [7, 4]. Diffusion of particles toward large amplitudes is then possible along this web with diffusion rates which increase when the size of the chaotic areas increases (due to a mismatch for example). This "Arnol'd diffusion" is a phenomenon which has been studied for numerous systems (see Ref[4] for a matched beam in a FODO channel), but the random behaviour of the particle motions along the web highly complicates the calculation of low diffusion rates.

Regarding the preliminary study presented here, the beam core and FODO channel parameters are those of the previous section. To analyse the particle diffusion, 2500 test particles have been followed over 200 FODO periods in order to analyse the maximum radius (R_{max}) reached with a given initial radius (R_0). Figure 5 gives the values of $(R_{max}-R_0)/R_0$ for initial conditions (normalized with respect to the core envelope) in the range $0 < x \text{ or } y < 6$ and $x' = y' = 0$. The large stochastic area located near the beam core and the $\nu = 1/6$ resonance area can be clearly localized. But any diffusion from one area to the other can be observed. For the chosen parameters (weak mismatch), the diffusion rate seems therefore low and very difficult to estimate.

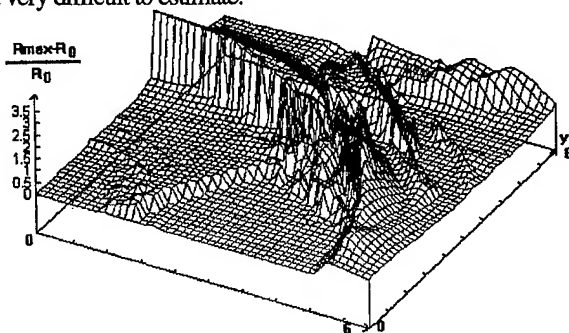


Fig. 5 : Maximum amplitudes reached by the test particles versus their initial positions ($x, y, x' = y' = 0$).

TRANSPORT OF A PARTIALLY-NEUTRALIZED ION BEAM IN A HEAVY-ION FUSION REACTOR CHAMBER*

Debra A. Callahan and A. Bruce Langdon
Lawrence Livermore National Laboratory, Livermore, CA 94550 USA

Abstract

In a heavy-ion driven, inertial confinement fusion power plant, a space-charge dominated beam of heavy ions must be transported through a reactor chamber and focused on a 2-3 mm spot at the target. The spot size at the target is determined by the beam emittance and space charge, plus chromatic aberrations in the focusing lens system and errors in aiming the beam. The gain of the ICF capsule depends on the focal spot size. We are investigating low density, nearly-ballistic transport using an electromagnetic, $r-z$ particle-in-cell code. Even at low density ($n \approx 5 \times 10^{13} \text{ cm}^{-3}$), beam stripping may be important. To offset the effects of stripping and reduce the space charge, the beam is partially charge neutralized via a pre-formed plasma near the chamber entrance. Additional electrons for charge neutralization come from ionization of the background gas by the beam. Simulations have shown that stripping can greatly increase the spot size; however, partial neutralization can offset most of this increase.

I. INTRODUCTION

In a heavy ion fusion (HIF) reactor, a space-charge dominated beams of heavy ions must be focused and transported through the reactor chamber and hit a 2-3 mm spot on the inertial confinement fusion (ICF) target. The gain of the target is a function of the spot size that can be achieved with the beams and ultimately sets the requirements on allowable beam quality in the accelerator.

The beam spot size at the target is influenced by four factors. The beam's transverse emittance and space charge, chromatic aberrations in the final focusing magnet system, and errors in aiming the beam at the target. Generally, the spot size at the target should be approximately,

$$(r_{\text{target}})^2 \approx (r_{\text{space charge + emittance}})^2 + (r_{\text{chromatic aberrations}})^2 + (r_{\text{aiming}})^2 \quad (1)$$

where r_{target} is the final spot size at the target and r_x is the spot size from effect x . We strive to achieve $r_{\text{target}} = 2-3$ mm. The target is injected into the chamber by an air gun and estimates of the aiming error give $r_{\text{aiming}} = .4$ mm[1]. A final design for the final focus system is still needed. We assume $r_{\text{chromatic aberrations}} \approx 1-1.5$ mm. For a 3 mm spot, $r_{\text{space charge + emittance}} \leq 2.8$ mm.

Our studies have revolved around low chamber density, nearly-ballistic transport. We feel that this is a more conservative option than pinched or channel transport schemes. Pinched

and channel transport schemes could drastically reduce the requirements on beam quality and the cost of electricity. The physics of these schemes is not well understood, however. An understanding of the simpler, nearly-ballistic transport will give the HIF program at least one credible scheme for chamber transport.

II. THE BICrz PARTICLE-IN-CELL CODE

The BICrz (Beam In Chamber) code was written to study HIF chamber transport. BICrz is an axisymmetric, electromagnetic particle-in-cell code. Beam ions and energetic electrons are modeled as particles to preserve kinetic effects. The code includes a model for stripping of the beam ions by the background gas and collisional ionization of the background gas molecules by the beam ions.

BICrz uses a nearly orthogonal grid which converges with the beam. In a typical chamber design, the beam radius decreases from 5 cm to 3 mm over a distance of 3 meters. The converging grid concentrates resolution near the target where it is needed.

III. HYLIFE-II REACTOR DESIGN

Our simulations are based on the HYLIFE-II reactor design[2]. In HYLIFE-II, the 4 MJ of energy in the main pulse is supplied by 10 beam of mass 200 amu, charge state +1 ions. Each beam carries 4 kA current and has a 10 nsec pulse duration. Two additional beams are used to generate the prepulse ("foot") required by the target. The chamber first wall is located 3 meters from the target. Each beam has a 1° convergence angle.

The chamber wall is protected by a liquid salt, $(\text{BeF}_2)(\text{LiF})_2$, "Flibe." Moir's studies[3] show that .5 m of liquid Flibe (density 2 g/cc) will protect the structural material from neutron damage for the full 30 year lifetime of a power plant. In addition, a thickness of .8 m of liquid Flibe will allow for shallow burial of 304 stainless steel upon decommissioning of the plant.

The chamber gas will be composed of BeF_2 and LiF molecules. At the temperatures of interest for the HYLIFE-II reactor (600 - 700° C), the gas will be rich in BeF_2 by about a factor of 10 over LiF . For 650°, the density of the chamber gas will be about $5 \times 10^{13} \text{ cm}^{-3}$.

Our simulations use a 10 GeV, mass 210, charge state +1 beam of heavy ions. The beam has a parabolic current profile with a maximum current of 4.688 kA and duration of 8 nsec. This beam is shorter than that used in the reactor (10 nsec) for computational convenience. The shorter beam requires fewer particles which makes the calculation faster. With these beam parameters, vacuum transport will produce a reasonable spot size at the target. We hope to extend the nearly-ballistic transport mode to the density of the HYLIFE-II chamber.

*Work performed under the auspices of the U.S. DoE by LLNL under contract W-7405-ENG-48.

IV. VACUUM TRANSPORT

Simulations of beam transport in vacuum can be compared with the beam envelope equation to verify the code. Figure (1) shows the beam as the head reaches 1, 2, and 3 meters along with the envelope solution. Ballistically transporting the particles forward, we find the distance at which the root-mean-square radius is the smallest. For the particles shown in figure (1), the best focus occurs at 2.82 m with 95% of the particles falling inside a 2.6 mm radius. The envelope solution agrees well with the simulation and predicts the best focus at 2.83 meters with a spot size of 2.7 mm.

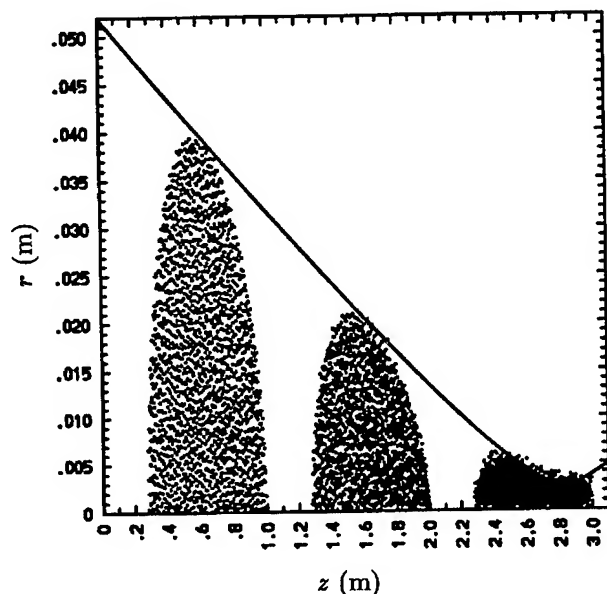


Figure 1. Beam at 3 times and envelope solution for vacuum transport

These simulations used a normalized emittance of 10.4π mm-mrad. In a 3 meter chamber, this results in a spot size of 2 mm from emittance alone. This value of the emittance was chosen for computational convenience because it prevents the beam, and hence the cell size, from becoming too small. To achieve the small spots needed in a reactor, an emittance of about half this value is necessary.

V. BEAM STRIPPING AND GAS IONIZATION

Even at the low densities of the HYLIFE-II chamber, it appears that beam stripping will be important. Cross sections for 10 GeV, Pb^{+1} ions and BeF_2 gas have been difficult to obtain. Estimates of the cross section range from $1.2-4 \times 10^{-16} \text{ cm}^2$ [4], [5], [6] and leads to a range of mean-free-paths (MFPs) of 0.5 - 1.6 m at 650° C . These MFPs are smaller than the chamber radius (3 meters) so stripping will play a role in understanding beam propagation.

While beam stripping makes chamber propagation more difficult, ionization of the background gas by the beam can partially neutralize the beam and aid transport. Cross sections for collisional ionization of BeF_2 by the beam have a larger uncertainty than stripping cross sections because calculating molecular cross sections is more difficult than calculating atomic cross

sections. Estimates of the MFP for ionizing the background gas range from 0.7 m to 25 m[4], [8], [7].

Knowing the ratio of these cross sections would be helpful because there is some flexibility in the chamber density. Reducing the temperature from 650° to 600° C reduces the density by a factor of 4.

A. Beam Stripping and Gas Ionization Sensitivity Study

Because there is uncertainty in the cross sections, we did a series of simulations to understand how these processes effect the beam spot size at the target.

Currently, BICrz does not contain an actual target. Instead, we run the simulation until the beam head reaches the distance of best focus. The particles are then ballistically transported to this same distance and the radius which contains 95% of the charge is found. This radius is then the spot size.

We found a stripping MFP of 1.2 meters increased the spot size from 2.6 mm (vacuum transport) to 8 mm. Using the same stripping MFP, but adding a background gas ionization MFP of 3.0 m reduced the spot size from 8 mm to 5.4 mm. A gas ionization MFP of .4 m (which is outside the range of MFPs discussed in the previous section) reduces the spot size from 8 mm to 3.7 mm.

We found that adding electrons to the system causes the radial electric field to become nonlinear. Figures (1) and (2) show the radial velocity deflection of particles near the beam center as a function of radius for an initially cold beam. In figure (2), there are no electrons present and the field is linear with radius. Figure (3) includes electrons from both beam stripping and collisional ionization and the field is clearly not linear. In our focusing system, we can compensate for a linear electric field by increasing the focusing angle, but we cannot compensate for the nonlinear fields in this same way. In addition, the ions have a velocity spread because they are stripped at different times. Once the ion strips, it responds more strongly to the electric fields.

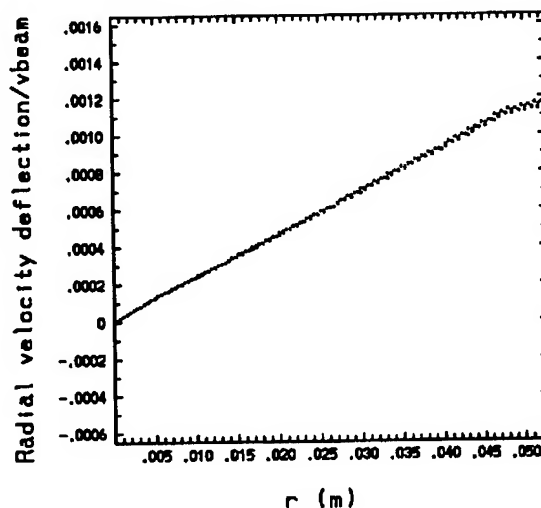


Figure 2. In vacuum transport, the radial electric field is linear. We overfocus the beam to compensate for these linear fields.

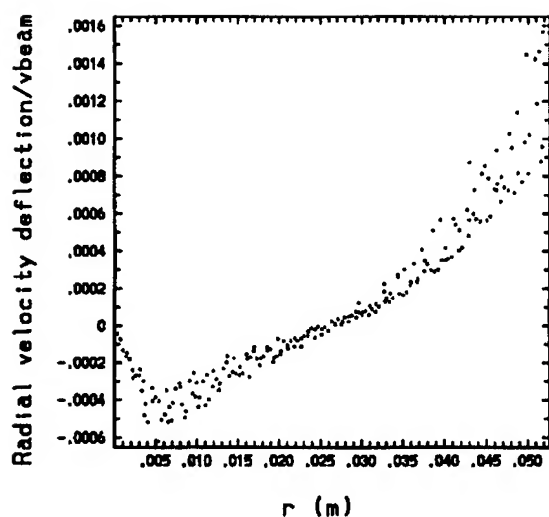


Figure 3. When electrons are added (from beam stripping and gas ionization in this case), the radial field becomes nonlinear. We cannot compensate for the nonlinear field by simply overfocusing the beam.

VI. NEUTRALIZATION VIA A PREFORMED PLASMA ANNULUS

Neutralizing an ion beam is more difficult than neutralizing an electron beam. If an electron beam passes through a plasma, the plasma electrons are moved out of the beam path by the beam's self field and leave the immobile plasma ions behind to neutralize the beam. In the case of an ion beam, electrons must be pulled in from outside the beam path in order to neutralize.

An electron produced by ionizing the background gas only reduces the net charge after the beam has left the gas ion behind. As a result, gas ionization neutralizes the beam very slowly and radial velocities develop before neutralization takes place. These radial velocities result in an increase in spot size at the target.

To neutralize the beam quickly, we added a preformed plasma annulus near the chamber entrance. As the beam enters the chamber, it pulls in electrons from the annulus and leaves a positively charged plasma behind. We found that this was quite effective at neutralizing the beam initially. However, the entrained electrons are hot ($v_{th} \approx .3c$) and do not compress as readily as the beam ions. Hence, neutralization is not as good near the target.

Our simulations used an annulus that was .3 meters long placed 5 cm inside the chamber entrance. The annulus was designed to fit between the beams in HYLIFE-II and had total electron charge of 4 times the beam charge. Adding the annulus to a simulation with a stripping MFP of 1.2 m decreased the spot size from 8 mm to 3.5 mm. Adding gas ionization should improve the spot size because the electrons produced by gas ionization are not as hot as the electrons from the plasma annulus and will aid neutralization near the target. Simulations confirm this prediction and the spot size with the plasma annulus plus a gas ionization MFP of 3 meters results in a spot size of 3.0 mm.

VII. CONCLUSIONS

Although some uncertainty remains in the cross section, beam stripping seems important at the gas density of the HYLIFE-II chamber. Simulations have shown that stripping can increase the spot size considerably. Stripping causes the beam ions to respond more strongly to any electric fields present. In addition, electrons in the chamber cause nonlinear electric fields which cannot be compensated for by the final focusing system.

Charge neutralization of the beam by both background gas ionization and a preformed plasma annulus have been studied. Neutralization via gas ionization happens slowly since the beam must ionize the gas molecule, then leave the resulting ion behind before the net charge is reduced. The spot size is reduced with gas ionization, but radial velocities develop before neutralization can occur.

A preformed plasma annulus placed near the chamber entrance is quite effective at neutralizing the beam early on. The beam pulls in electrons from the annulus quickly, before radial velocities develop. However, these electrons are hot, and become less effective at neutralizing as the beam compresses near the target. The best spot size was found with a combination of gas ionization and a preformed plasma annulus.

Future studies will include ionizing a larger volume of the background gas surrounding the entire beam path. We hope that this will result in better charge neutralization which may allow the use of higher current beams. Higher current beams, in the form of either multiply charged ions or lower energy, lighter ions (Cs for example), should reduce the cost of a heavy ion driver considerably; however, high current beams must be partially charge neutralized in the chamber even in vacuum.

References

- [1] R. W. Petzold, PhD Thesis, U.C. Davis, 1995.
- [2] R. W. Moir, et al., *Fusion Technology*, **25**, 5 (1994).
- [3] R. W. Moir, *Nuclear Engineering and Design*, **29**, 34 (1995).
- [4] N. Barboza, U.C. Berkeley, Private Comm. (1994).
- [5] W. R. Meier, et al., "Osiris and Sombrero Inertial Confinement Fusion Power Plant Designs," WJSA-92-01, DOE/ER/54100-1 (1992).
- [6] B. Badger, et al., "HIBALL-2, An Improved Conceptual Heavy Ion Beam Driven Fusion Reactor Study," UWFD-625, U. of Wisconsin (1984).
- [7] R. W. Moir, LLNL, Private Comm. (1994).
- [8] W. Ping, U. of Wisconsin, Private Comm. (1994).

EMITTANCE GROWTH FROM ROTATED QUADRUPOLES IN HEAVY ION ACCELERATORS *

John J. Barnard

Lawrence Livermore National Laboratory, L-440, Livermore, CA 94550

Abstract

We derive a set of moment equations which incorporates linear quadrupolar focusing and space-charge defocusing, in the presence of rotational misalignments of the quadrupoles about the direction of beam propagation. Although the usual beam emittance measured relative to fixed transverse x and y coordinate axes is not constant, a conserved emittance-like quantity has been found. Implications for alignment tolerances in accelerators for heavy-ion inertial fusion are discussed.

I. INTRODUCTION

One class of misalignments of interest to accelerator designers is that class characterized by a rotation of the beam optical elements about the axis of propagation. Rotated dipoles, for example, are known to cause the centroid of a particle beam to wander off axis, (since the rotations will result in momentum impulses in the positive and negative y [vertical] direction.) However rotated quadrupoles will not cause an initially aligned beam centroid to become misaligned. Quadrupole rotations do however, create a linear coupling between the two transverse directions, x (horizontal) and y , in the equations of motion. Since this coupling enters linearly in the equations of motion, individual particle oscillation frequencies can be shifted, and this has implications for resonance avoidance in synchrotrons, (see ref. [1] and references therein). In this paper, we are interested in the effects on the emittance of beams with non-negligible space charge, such as those proposed for heavy ion inertial fusion.

We derive a set of moment equations which incorporates this coupling, and which serves as a generalization to the conventional envelope equations. We show that even when the equations of motion are linear in x and y , the beam emittance measured relative to fixed x and y coordinate axes is not constant, although a conserved emittance-like quantity can be defined. If not corrected, a beam will acquire a finite angular momentum and rotation angle, before passing through a final focusing lens, thereby limiting the achievable final spot size. The results presented here will be of use in determining alignment tolerances in heavy ion accelerators.

II. EQUATIONS OF MOTION

To obtain an estimate, we assume that the force on an ion comes from two sources only: The external focusing from a purely quadrupolar field, and the space charge of the beam (image forces have been neglected). For the purposes of this calculation we assume that the space charge is distributed in a uniform

density ellipse, but we allow the semi-axes and the rotation angle of the ellipse to evolve as a function of the axial coordinate z . We assume that a quadrupole is rotated by an angle θ from the x -axis, and that the beam is rotated by an angle α from the x -axis. The relation between the coordinates in the quadrupole frame (indicated by subscript 0) and the lab frame (no subscript) are given by:

$$x = x_0 \cos \theta - y_0 \sin \theta; \quad y = y_0 \cos \theta + x_0 \sin \theta \quad (1)$$

Similarly, the relation between the coordinates in the rotated beam frame (in which the beam semi-axes are parallel to the coordinate axes and are indicated by subscript b) and the lab frame are given by:

$$x - \langle x \rangle = x_b \cos \alpha - y_b \sin \alpha; \quad y - \langle y \rangle = y_b \cos \alpha + x_b \sin \alpha \quad (2)$$

Here $\langle \rangle$ indicates a statistical average over the distribution function. For a non-relativistic beam moving at constant velocity βc along the z axis, the paraxial equations of motion can then be written as:

$$x'' = K_{qxx}x + K_{qxy}y + K_{sxx}(x - \langle x \rangle) + K_{sxy}(y - \langle y \rangle) \quad (3)$$

$$y'' = K_{qyy}y + K_{qyx}x + K_{syx}(y - \langle y \rangle) + K_{syx}(x - \langle x \rangle) \quad (4)$$

Here primes ($'$) indicate derivatives with respect to z and

$$\begin{aligned} K_{qxx} &\equiv K_{qx0} \cos^2 \theta + K_{qy0} \sin^2 \theta = K_{qx0} \cos 2\theta \\ K_{qxy} &\equiv (K_{qx0} - K_{qy0})(\sin \theta \cos \theta) = K_{qx0} \sin 2\theta \\ K_{qyx} &\equiv (K_{qy0} - K_{qx0})(\sin \theta \cos \theta) = -K_{qxy} \\ K_{qyy} &\equiv K_{qy0} \cos^2 \theta + K_{qx0} \sin^2 \theta = -K_{qx0} \cos 2\theta \\ K_{sxx} &\equiv K_{sxb} \cos^2 \alpha + K_{syb} \sin^2 \alpha \\ K_{sxy} &\equiv (K_{sxb} - K_{syb})(\sin \alpha \cos \alpha) \\ K_{syx} &\equiv (K_{sxb} - K_{syb})(\sin \alpha \cos \alpha) = K_{sxy} \\ K_{syy} &\equiv K_{syb} \cos^2 \alpha + K_{sxb} \sin^2 \alpha \end{aligned}$$

and where

$$K_{qx0} \equiv \pm \frac{B'}{[B\rho]} \quad \text{or} \quad \frac{E'}{\beta c [B\rho]}; \quad K_{qy0} \equiv -K_{qx0} \quad (5)$$

$$\begin{aligned} K_{sxb} &\equiv K/[2(\Delta x_b^2 + (\Delta x_b^2 \Delta y_b^2)^{1/2})]; \\ K_{syb} &\equiv K/[2(\Delta y_b^2 + (\Delta x_b^2 \Delta y_b^2)^{1/2})] \end{aligned} \quad (6)$$

and Δx_b^2 and Δy_b^2 are the moments in the rotated beam frame:

$$\Delta x_b^2 = \Delta x^2 \cos^2 \alpha + \Delta y^2 \sin^2 \alpha + 2\Delta xy \cos \alpha \sin \alpha \quad (7)$$

$$\Delta y_b^2 = \Delta y^2 \cos^2 \alpha + \Delta x^2 \sin^2 \alpha - 2\Delta xy \cos \alpha \sin \alpha \quad (8)$$

*Work performed under the auspices of the U.S. D.O.E. by LLNL under contract W-7405-ENG-48

Here, $K \equiv 2qI/(\beta^3 AI_0)$ is the perveance, q is the charge state of the ions, A is the atomic mass of the ions, β is the velocity of the ions in units of c , $I_0 \equiv 4\pi\epsilon_0 m_p c^3/e$ is the proton characteristic current (≈ 31 MA), I is the ion beam current, B' and E' are quadrupole magnetic or electric field gradients respectively, $[B\rho] \equiv Am_p\beta c/qe$ is the ion rigidity, m_p is the proton mass, e is the proton charge, ϵ_0 is the free space permittivity and the operator Δ is defined (as in ref. [2]) by $\Delta ab = \langle ab \rangle - \langle a \rangle \langle b \rangle$ (e.g. $\Delta x^2 \equiv \langle x^2 \rangle - \langle x \rangle^2$), where $\langle \rangle$ indicates average over particles.

Note that the space-charge force, is just the force obtained from the potential of a uniform density ellipse (ref. [3]), but where the semi-axes a and b have been replaced by $2(\Delta x_b^2)^{1/2}$ and $2(\Delta y_b^2)^{1/2}$, respectively, and where the location of the centroid determines the zero point of the space-charge force.

The beam rotation angle α may be expressed in terms of second order moments. From eq. (2), $\Delta x^2 - \Delta y^2 = (\Delta x_b^2 - \Delta y_b^2) \cos 2\alpha$ and $\Delta xy = (1/2)(\Delta x_b^2 - \Delta y_b^2) \sin 2\alpha$, so that

$$\tan 2\alpha = \frac{2\Delta xy}{\Delta x^2 - \Delta y^2} \quad (9)$$

In deriving eq. 9 we have used the fact that $\Delta xy_b = 0$.

III. MOMENT EQUATIONS

Let the distribution function f , be the number of particles dN per unit transverse phase space volume,

$$f(x, x', y, y', z) = \frac{dN}{dx dx' dy dy'}$$

The evolution of f is described by the Vlasov/Collisionless Boltzmann Equation:

$$\frac{\partial f}{\partial z} + x' \frac{\partial f}{\partial x} + x'' \frac{\partial f}{\partial x'} + y' \frac{\partial f}{\partial y} + y'' \frac{\partial f}{\partial y'} = 0, \quad (10)$$

where x'' and y'' are determined by the equations of motion (eqs. [3] and [4]).

The average of a variable ξ over the continuous distribution is given by:

$$\langle \xi \rangle(z) \equiv \frac{1}{N} \int \int \int \int \xi f(x, x', y, y', z) dx dx' dy dy'.$$

Using integration by parts, it is straightforward to calculate the evolution of the following second order moments:

$$\begin{aligned} \frac{d\Delta x^2}{dz} &= 2\Delta x x' \\ \frac{d\Delta x x'}{dz} &= \Delta x'^2 + K_{xx}\Delta x^2 + K_{xy}\Delta xy \\ \frac{d\Delta x'^2}{dz} &= 2K_{xx}\Delta x x' + 2K_{xy}\Delta x' y' \\ \frac{d\Delta y^2}{dz} &= 2\Delta y y' \\ \frac{d\Delta y y'}{dz} &= \Delta y'^2 + K_{yy}\Delta y^2 + K_{yx}\Delta xy \\ \frac{d\Delta y'^2}{dz} &= 2K_{yy}\Delta y y' + 2K_{yx}\Delta x y' \\ \frac{d\Delta xy}{dz} &= \Delta x' y' + \Delta x y' \\ \frac{d\Delta x' y'}{dz} &= \Delta x' y' + K_{xx}\Delta xy + K_{xy}\Delta y^2 \\ \frac{d\Delta x y'}{dz} &= \Delta x' y' + K_{yy}\Delta xy + K_{yx}\Delta x^2 \\ \frac{d\Delta x' y'}{dz} &= K_{xx}\Delta x y' + K_{xy}\Delta y y' + \end{aligned}$$

$$K_{yy}\Delta x' y' + K_{yx}\Delta x x' \quad (11)$$

Similarly the evolution of the first-order moments is given by:

$$\begin{aligned} \frac{d\langle x \rangle}{dz} &= \langle x' \rangle \\ \frac{d\langle y \rangle}{dz} &= \langle y' \rangle \\ \frac{d\langle x' \rangle}{dz} &= K_{qxx}\langle x \rangle + K_{qxy}\langle y \rangle \\ \frac{d\langle y' \rangle}{dz} &= K_{qyy}\langle y \rangle + K_{qyx}\langle x \rangle \end{aligned} \quad (12)$$

In eq. 11,

$$\begin{aligned} K_{xx} &\equiv K_{qxx} + K_{sxx} \\ K_{yy} &\equiv K_{qyy} + K_{syy} \\ K_{xy} &\equiv K_{qxy} + K_{sxy} \\ K_{yx} &\equiv K_{qyx} + K_{syx} = K_{xy}. \end{aligned}$$

Note that the four equations for the first order moments depend only on first order moments, and the ten equations for the second order moments depend only on second order moments, so that each set of equations forms a closed set. The centroid motion is thus decoupled from the envelope motion calculated with respect to the centroid.

The rms emittances defined along the x and y lab frame axes are defined by:

$$\begin{aligned} \epsilon_x &\equiv 4(\Delta x^2 \Delta x'^2 - (\Delta x x')^2)^{1/2} \\ \epsilon_y &\equiv 4(\Delta y^2 \Delta y'^2 - (\Delta y y')^2)^{1/2} \end{aligned}$$

Using eqs. (11) we can calculate the derivatives of ϵ_x^2 and ϵ_y^2 (again assuming constant β):

$$\begin{aligned} \frac{d\epsilon_x^2}{dz} &= 32K_{xy}(\Delta x^2 \Delta x' y' - \Delta x y \Delta x x') \\ \frac{d\epsilon_y^2}{dz} &= 32K_{yx}(\Delta y^2 \Delta x y' - \Delta x y \Delta y y') \end{aligned} \quad (13)$$

Since the rotated quadrupoles induce finite correlations between x and y the rms emittances are not conserved.

We may also define a quantity $l \equiv \Delta x y' - \Delta x' y$, which is proportional to the z component of the angular momentum. Again using eqs. (11) and some manipulations involving the definitions, and eqs. (4), (5) and (9), we find,

$$\frac{dl}{dz} = (K_{qyy} - K_{qxx})\Delta xy + K_{qxy}(\Delta x^2 - \Delta y^2) \quad (14)$$

As can be seen from eq. 14, the angular momentum is not necessarily conserved when the quadrupoles are rotated. Physically, after a beam has passed through a quadrupole the beam will in general be elliptical. On passing through a quadrupole rotated relative to the first, the principal axis of the elliptical beam will not align with the quadrupole axes and a torque will be applied to the beam, causing a rotation of the beam. (Note also that eq. 14, does not depend on the self space-charge forces of the beam, as expected).

Because the focusing strength is a function of z , the effective external potential well within which the beam travels is z dependent, and so the transverse beam energy H is also not a constant in z . However, in the hard-edge model, within each quadrupole and drift section the focusing strength is assumed constant, and therefore the transverse energy is constant. We may use the result of ref. [2], adding the kinetic and potential energy terms to

obtain a total transverse energy. To obtain the potential energy of the beam in the external quadrupole field, we transform Δx_0^2 and Δy_0^2 to the lab frame. The result is

$$2H = \Delta x'^2 + \Delta y'^2 - K_{qxo} ((\Delta x^2 - \Delta y^2) \cos 2\theta + 2\Delta xy \sin 2\theta) - K \ln ((\Delta x_b^2)^{1/2} + (\Delta y_b^2)^{1/2}) \quad (15)$$

Here Δx_b^2 and Δy_b^2 may be expressed in laboratory quantities using eqs. (7) and (8).

IV. "EMITTANCE-LIKE" CONSTANT OF THE MOTION

Although the emittance is not a constant with respect to z , a quantity which is related to the emittance is conserved. We define a generalized emittance ϵ_g by:

$$\epsilon_g^2 \equiv \frac{1}{2}\epsilon_x^2 + \frac{1}{2}\epsilon_y^2 + 16(\Delta xy \Delta x' y' - \Delta x y' \Delta x' y) \quad (16)$$

It is readily shown using eqs. 11 and 13 that $\frac{d\epsilon_g^2}{dz} = 0$.

V. EXAMPLES OF RESULTS

A code was written to integrate eqs. (11). The results for ϵ_x and ϵ_g are plotted in figure 1 for a singly charged potassium beam ($A = 39$) with a current of 2 mA, an energy of 80 kV, initial emittances $\epsilon_x = \epsilon_y = 2.5 \times 10^{-5}$ m rad, $K_{qxo} = 30.9 \text{ m}^{-2}$, and with $\langle \theta \rangle = 0.0234$ and $\Delta \theta^2 = 0.0156$. The occupancy of the quadrupoles was 0.33 and the half-lattice period was 0.36 m. The integration length was 40 half-lattice periods.

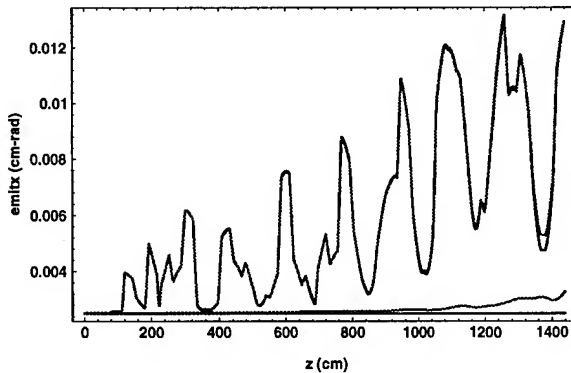


Figure 1. ϵ_x (oscillating) and ϵ_g (nearly constant) vs z for both integration of eq. 11, and particle-in-cell results.

Also shown in Figure 1 is a 2D particle-in-cell (PIC) simulation with the same parameters, for an initial distribution that is KV (ref.[3]), propagating through a pipe with circular cross section and 6 cm radius. The near identical overlap of the curves suggests that if the initial distribution is KV the assumption that the space charge field remains linear is at least a good approximation and possibly an exact result. The small increase in ϵ_g for large z is probably due to the non-linear image forces arising because of the finite pipe radius in the PIC simulations.

When these results are applied to the small recirculator of ref. [4], we find that with 2 mrad rms errors, there occurs only a 2%

increase in emittance for a beam which drifts (rather than accelerates) the nominal 15 laps. When the rotation errors are random over all 15 laps the emittance increases by about 50%. An accelerated beam will presumably show behavior somewhere in-between. A generalization of the theory presented here to include acceleration is in progress.

VI. DISCUSSION AND CONCLUSION

In inertial fusion applications, the ultimate goal is to focus the beam onto a small, 2-3 mm spot at the target. The final emittance is one of the important parameters needed to calculate the achievable final spot size (see e.g. ref.[5]). When quadrupole rotation errors are present, the beam will in general have a finite rotation angle and rotation rate, and will focus down to a more elliptical shape than in the absence of errors, reducing the power level that falls within a given spot radius. Analogous to the case of centroid displacements, it is conceivable that a system of intentionally rotated quadrupoles could compensate for the accumulated errors if the ten moments in eq. 11 are known.

In summary, we have used a formulation, in which the major assumption is that the space charge force can be calculated by assuming that the beam remains a uniform density ellipse with a shape that evolves in z . Under this assumption we have derived a set of moment equations which generalizes the conventional envelope equations. We have found the misalignments cause the beam to acquire an overall angular momentum, and an increase in emittance measured relative to fixed laboratory axes. A generalized emittance has been constructed which is a conserved quantity (when the forces remain linear). Particle-in-cell results have shown agreement with the moment equations, and have suggested that the formulation may be exact if the initial distribution is KV. We have applied this method to estimate rotation alignment tolerances in the small recirculator of ref [4], and have suggested that this formulation will be useful when setting alignment tolerances and/or correction methods in an inertial fusion driver.

VII. ACKNOWLEDGEMENTS

I wish to thank S. M. Lund for useful discussions and suggestions and for critically reading a draft version of this paper, and A. Friedman and W. M. Sharp for other useful comments.

VIII. REFERENCES

- [1]. Edwards, D.A., and Syphers, M.J., "An Introduction to the Physics of High Energy Accelerators," [John Wiley and Sons, Inc., New York], Chapter 5, (1993).
- [2]. J.J. Barnard, H.D. Shay, S.S. Yu, A. Friedman, and D.P. Grote, "Emittance Growth in Heavy Ion Recirculators," Proceedings of the 1992 Linear Accelerator Conference, 1992 August 24-28, Ottawa, Ontario, Canada, C.R. Hoffman, ed., AECL 10728 (AECL Research, Chalk River, Canada) p. 229.
- [3]. I.M. Kapchinsky and V.V. Vladimirkij, "Limitations of proton beam current in a strong focusing linear accelerator with the beam space charge," Proceedings of the International Conference on High Energy Accelerators, (CERN, Geneva, 1959), p. 274.

[4]. A. Friedman, J.J. Barnard, M. Cable, D.A. Callahan, F. Deadrick, D.P. Grote, H. Kirbie, D. Longinotti, S.M. Lund, L. Natrass, M. Nelson, M. Newton, C. Sangster, W.M. Sharp, D. Judd, S.S. Yu, "Progress Toward a Prototype Recirculating Induction Accelerator for Heavy-Ion Fusion," these proceedings.

[5].E.P. Lee, "Accelerator and Final Focus Model for an Induction Linac Based HIF System Study," in Heavy Ion Inertial Fusion, AIP Conference Proceedings 152, M. Reiser, T. Godlove, and R. Bangerter, Eds. (AIP, NY,1986), p. 461.

WAKEFIELD EFFECTS ON THE BEAM ACCELERATED IN A PHOTOINJECTOR: PERTURBATION DUE TO THE EXIT APERTURE

J.-M. Dolique* and W. Salah, Université Joseph Fourier-Grenoble I

*and CEA-Bruyères-le-Châtel. France

The influence of the photoinjector exit aperture on the wakefield generated by the strongly accelerated electron beam, has been theoretically studied in a companion paper [1]. In this communication we study the effects of such a wakefield on the beam, in that propagation stage where the beam approaches the hole and enters it, i.e. the propagation stage where the influence of the photoinjector exit hole must be taken into account. First, the perturbed wakefield map $(E, B)(x, t)$ is shown for various instants, and for photoinjector and beam parameters corresponding to typical values on ELSA [2], the CEA-Bruyères-le Châtel high-current, high-brilliance electron beam facility. Then, the effects on the beam quality are studied in terms of emittances, when the beam approaches the hole. These effects are compared to the corresponding ones, previously obtained for a wakefield map where the exit hole perturbation had been neglected [3].

I. INTRODUCTION

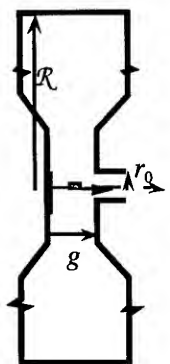


Fig. 1. Schematic of an RF photoinjector cavity

In a companion paper [1], we have analytically calculated the wakefield map $(E, B)(x, t)$ generated by the accelerated electron beam in a photoinjector, when the effects due to the exit aperture (of radius r_0 ; Fig. 1) are taken into account. Let us recall that the term wakefield has been used with a rather different meaning than it has in the most usually considered case of ultrarelativistic coasting beams. The wakefield has been defined as the total electromagnetic field undergone by a beam electron, whether this field is generated by the conducting walls under the beam influence, or by the other beam electrons (the space charge field is not negligible).

More precisely, in [1] analytical expressions of the wakefield scalar and vector potentials are given, which depend on the propagation phase considered. In the first: $t < g/c$, (where $t=0$ corresponds to the photoemission beginning), the beam-generated electromagnetic field has not yet reached the exit wall (anode). In the second: $g/c < t < t_g$, the beam-generated electromagnetic field has reached the exit wall, but the beam head is still above the exit aperture. In the third: $t_g < t < t_{gg}$ the beam penetrates the exit hole. For $E_0=30$ MV/m, $\tau=30$ ps, $g=6$ cm (typical values for the ELSA photoinjector [2]), these three phases correspond to: $t < 200$ ps, $200 < t < 250$ ps, and $250 < t < 280$ ps respectively. The corresponding expressions of

E_z, E_r and B_θ as a function of r, z, t , result from these potentials. Their numerical calculation for a given set of photoinjector and beam parameters has turned out to be a particularly difficult venture due to the very slow convergence of the various implied series or improper integrals. It is the reason why the results presented here are limited to phases 1 and 2. Calculations concerning phase 3 are still in progress.

It is also a reason to welcome possible checks of validity. Fortunately there are two of these, both very simple.

II. TWO CHECKS

There are two cases where the field maps obtained by the method described in [1] must be identical with those previously obtained [3] for a closed cavity: a) in the above "first phase", b) when the aperture radius r_0 vanishes. These two tests have been successfully carried out, as is shown in Fig. 2 and 3 given as examples (but the excellent agreement has been verified in many other cases).

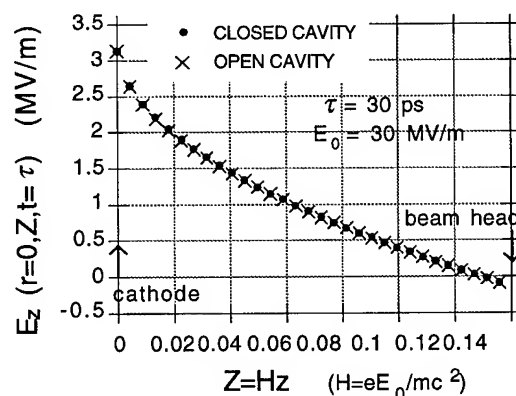


Fig. 2. $E_z(z)$ on the beam axis, as given by the closed- or open cavity modelling respectively, for $t=\tau$ (first phase)

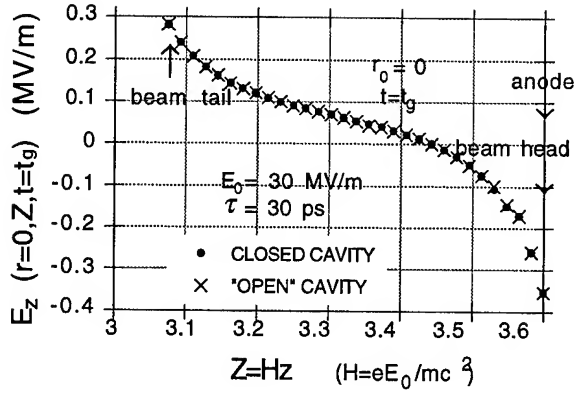


Fig. 3. $E_z(z)$ on the beam axis, as given by the closed- or open cavity modelling respectively, for $t=t_g$ (second phase) and $r_0=0$

III. SOME SAMPLE FIELD MAPS

These correspond to the following beam parameters: $I=100$ A, $\pi a^2=1$ cm², $E_0=30$ MV/m, $\tau=30$ ps, $r_0=2$ cm, and to a beam reaching the photoinjector exit aperture ($t=t_g$)

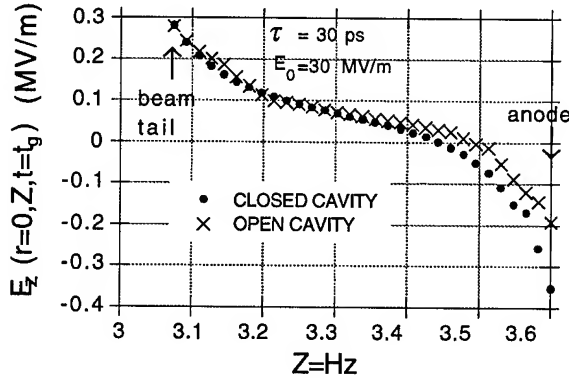


Fig. 4. $E_z(z)$ on the beam axis, as given by the closed- or open cavity modelling respectively, for $t=t_g$ (second phase)

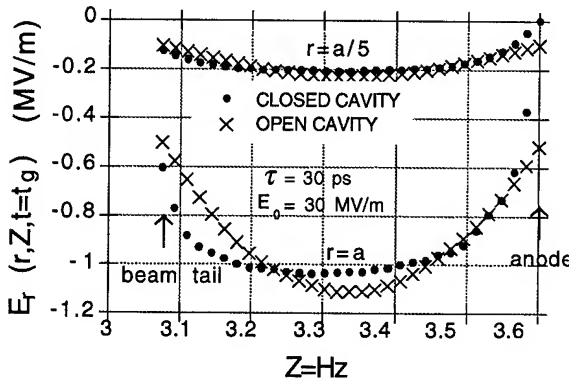


Fig. 5. $E_r(r,z)$ for $r=a$ and $r=a/5$, as given by the closed- or open cavity modelling respectively, for $t=t_g$ (second phase)

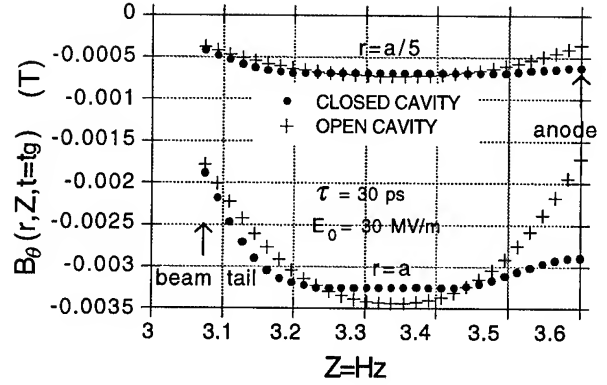


Fig. 6. $B_\theta(r,z)$ for $r=a$ and $r=a/5$, as given by the closed- or open cavity modelling respectively, for $t=t_g$ (second phase)

IV. CONSEQUENCES OF THESE APERTURE EFFECTS ON BEAM QUALITY (PHASE 2: THE BEAM PULSE APPROACHES THE EXIT APERTURE)

A. Used emittances

Beam quality will be defined by normalized whole-beam rms emittances:

$$\varepsilon_r = 2 \left[\langle r^2 \rangle \langle \left(\frac{p_r}{mc} \right)^2 \rangle - \left\langle r \frac{p_r}{mc} \right\rangle^2 \right]^{1/2}$$

$$\varepsilon_z = 4 \left[\langle \Delta z^2 \rangle \langle \left(\frac{\Delta p_z}{mc} \right)^2 \rangle - \left\langle \Delta z \frac{\Delta p_z}{mc} \right\rangle^2 \right]^{1/2},$$

where $\langle \rangle$ means an average taken over the whole beam:

$$\langle G \rangle = \int G(\mathbf{x}, \mathbf{p}|t) f(\mathbf{x}, \mathbf{p}|t) d^3x d^3p.$$

\mathbf{x} is the position, \mathbf{p} the momentum. The distribution function f is normalized to 1. $\Delta \mathbf{x} = \mathbf{x} - \langle \mathbf{x} \rangle$, $\Delta \mathbf{p} = \mathbf{p} - \langle \mathbf{p} \rangle$, where $\langle \mathbf{x} \rangle$ and $\langle \mathbf{p} \rangle$ are the beam-center position and momentum respectively.

B. Calculation of the radial and longitudinal emittances, as a function of time, with the ATRAP-LIVIE code

To study the effects on beam quality of the previously calculated wakefield, the ATRAP-LIVIE code has been used.

Taking as a starting point theoretical calculations of space-charge effects in strongly accelerated beams, based on the Liénard-Wiechert formulæ (J.-M. DOLIQUE [5]), this code has been developed by J.-L. COACOLO [6]. The use of the Liénard-Wiechert formulæ to describe the electromagnetic interaction between beam electrons provides a rigorous description of beams where (as in photoinjector beams) momenta are very spread, with important relativistic retardation- and radiation field effects.

The ATRAP-LIVIE code gives, at each time t , the positions and momenta of beam electrons, which evolve under the influence of the space-charge field, of the cathode electromagnetic reaction, and possibly of other external fields such as a magnetic focusing field.

If axisymmetry is postulated, the beam is allowed to start from the cathode with arbitrary radial and axial profiles.

In order to isolate the wakefield effects of the anode (with aperture or without) by comparison with the previously obtained analytical field map, we have imposed the approximations of the analytical model in question, i.e. a purely longitudinal motion with a uniform radial profile, on ATRAP-LIVIE. The subroutine computing the space-charge and cathode-image fields is disconnected, and the wakefield map deduced from the previous analytical model introduced as an external field.

To emphasize the specific effect of the exit aperture, wakefield maps for closed or open cavity have been successively introduced.

A. Whole-beam radial emittance

This is shown in Fig.7 as a function of time ($t=0$ corresponds to the beginning of photoemission), between $t=g/c$ and $t=t_g$.

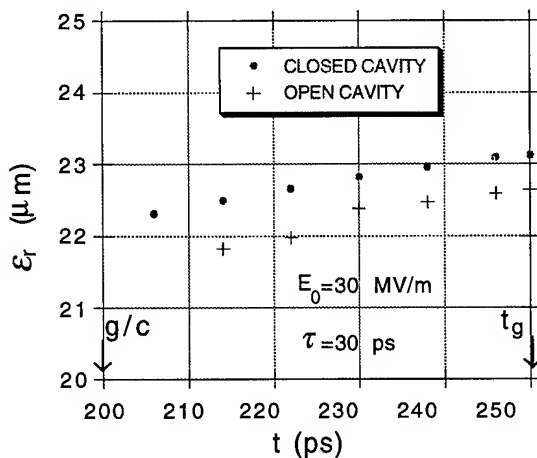


Fig. 7. Whole-beam radial emittance as a function of time. $t=0$ corresponds to the beginning of photoemission, $t=t_g$ to the time when the beam head reaches the exit aperture.

Taking the aperture into account leads to a small radial emittance decrease, of about 3% at maximum.

B Whole-beam axial emittance

This is shown in Fig. 8 as a function of time.

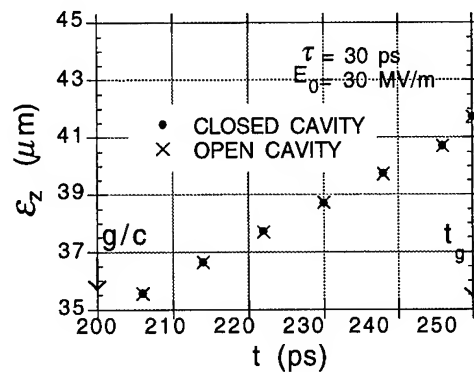


Fig. 8. Whole-beam axial emittance as a function of time.

It appears that for the parameters chosen, the influence of the exit aperture, in terms of beam quality, is slight concerning the transverse emittance: $(\Delta\epsilon_{\perp}/\epsilon_{\perp})(z) \sim 3\%$ at maximum, and negligible concerning the axial emittance.

To complete this paper, we recall the results previously obtained concerning the wakefield of a closed cavity for a beam approaching the anode [3]. They had quantitatively specified the expected deep dissymmetry between the conducting walls regarding their contribution to the total wakefield, besides the space-charge contribution. (Given that the radial walls have no time to contribute, these conducting walls are the cathode and the anode).

Thus, concerning the effects on whole-beam emittances, the correction $(\Delta\epsilon_{\perp}/\epsilon_{\perp})(z)$ entailed by taking the anode contribution into account had been found to be less than 5% at maximum (a maximum reached for $t=t_g$, and for $E_0=10$ MV/m; for $E_0=30$ MV/m, the maximum was of the order of 1 %).

The field map perturbation due to the aperture in the anode has an effect of the same order of magnitude, i.e. small, on the transverse emittance of a beam reaching this exit aperture.

As shown in Fig. 7, this correction is of the order of 3% for $E_0=30$ MV/m. It could be of the order of 10% for $E_0=10$ MV/m.

Of course, one can expect a stronger effect when the beam enters the drift tube: $t > t_g$. Calculations on this point are in progress with the theoretical model [1].

REFERENCES

- [1] J.-M. Dolique, this conference TPR05
- [2] E.g.: S. Joly, J.P. de Brion *et al.*, N.I.M. **A340**, 214 (1994)
- [3] J.-M. Dolique, EPAC 94, London, UK (1994)
- [5] J.-M. Dolique, LPPG Rept 90. 09 (1990). Also: Proceed. of the PAC 91 Conference, San Francisco, p. 233 (1991)
- [6] J.L. Coacolo, Doctorate dissertation, Université Joseph Fourier-Grenoble I (1993)

INFLUENCE OF THE PHOTOINJECTOR EXIT APERTURE ON THE WAKEFIELD DRIVEN BY AN INTENSE ELECTRON BEAM PULSE: A THEORETICAL APPROACH

J.-M. DOLIQUE, Université Joseph Fourier-Grenoble I, and CEA-Bruyères-le-Châtel. France

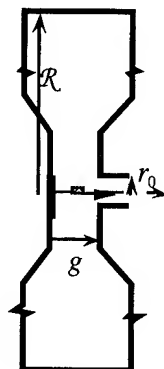
The wakefield generated in the cylindrical cavity of an RF photoinjector, by the strongly accelerated electron beam, has been analytically calculated [1] under the assumption that the perturbation of the field map by the exit hole is negligible as long as the ratio: exit hole radius/cavity radius is lower than approximately 1/3. Shown experimentally in the different context of a long accelerating structure formed by a sequence of bored pill-box cavities [2], this often quoted result must be checked for the wakefield map excited in a photoinjector cavity. Further, in the latter case, the empirical rule in question can be broken more easily because, due to the causality, the cavity radius to be considered is not the physical radius but that of the part of the anode wall around the exit hole reached by the beam electromagnetic influence. We present an analytical treatment of the wakefield driven in a photoinjector by the accelerated electron beam which takes this hole effect into account, whatever the hole radius may be.

I. INTRODUCTION

Wakefields are usually considered for ultrarelativistic coasting beams. The electromagnetic response of a discontinuous conducting wall to an exciting charged particle is only experienced by the particles located downstream, in the wake. Furthermore, the self-field, or space charge field, is negligible so that the only forces acting on a beam particle are the wakefield and a possible focusing force. At the end, the beam is assumed to be coming from $-\infty$ and going to $+\infty$.

For a photoinjector beam, the situation is very different. It is strongly accelerated from thermal to transrelativistic velocity. If intense, its self-field must be taken into account. In addition, beam electrons appear at the cathode surface at $t=0$, the time when laser illumination begins, so that causality governs both synchronous and radiation fields. If it is agreed to call wakefield once again that field experienced by a beam electron which is generated by other beam electrons in the presence of the conducting walls, this wakefield includes both the wall response and the space charge field.

Thus defined wakefield has been analytically calculated for a pill box photoinjector model [1]. Radially, this modelling is relevant because the only parts of the photoinjector RF-cavity walls that the beam field has time to reach, during beam acceleration, are located not far from the axis on both cathode and anode. On the anode however, the question arises of the exit hole influence. The latter has been neglected in [1] by putting forward an empirical rule [2] according to which hole influence is negligible as long as $r_0/\mathcal{R} < 1/3$, where r_0 and \mathcal{R} are the hole and cavity radii respectively. Though often quoted, this rule is based on a single experimental study worked out



on an ultrarelativistic coasting beam crossing a set of bored cavities. Its validity for the low- to transrelativistic- energy beam accelerated in a photoinjector is questionable.

The aim of the present work is to investigate theoretically the aperture effects on the above defined wakefield.

Fig. 1. Schematic of an RF- photoinjector cavity

II. EXPANSION OF THE ZONE OF BEAM ELECTROMAGNETIC INFLUENCE: THE THREE PHASES

Before trying to calculate the map $(\mathbf{E}, \mathbf{B})(\mathbf{x}, t)$ of the beam-generated, time-dependent electromagnetic field, in the presence of the cavity conducting walls, one has to know what parts of these cavity walls are able to play a role in the field map building. Owing to causality, three phases have to be distinguished. In the first: $t < g/c$ (where $t=0$ corresponds to the beginning of photoemission) the beam-generated electromagnetic field has not yet reached the exit wall (anode). In the second: $g/c < t < t_g$, the beam-generated electromagnetic field has reached the exit wall, but the beam head is still above the exit aperture. In the third: $t_g < t < t_{qg}$ the beam penetrates the exit hole. For $E_0=30$ MV/m, $\tau=30$ ps, $g=6$ cm, these three phases correspond to: $t < 200$ ps, $200 < t < 250$ ps, and $250 < t < 280$ ps respectively.

III. FIRST PHASE

The situation is schematized in Fig. 2. The $(\mathbf{E}, \mathbf{B})(\mathbf{x}, t)$ field map is that already calculated in this phase for the closed cavity [1].

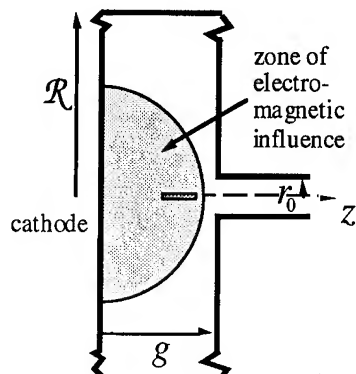


Fig.2. First phase: $t < g/c$, where $t=0$ corresponds to the beginning of photoemission ($t < 200$ ps for the above parameters)

IV. SECOND PHASE

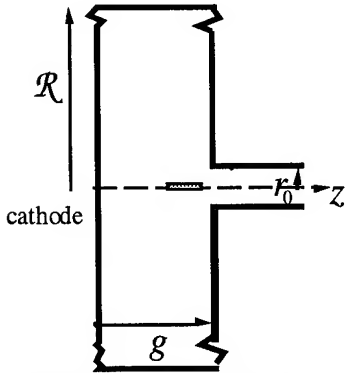


Fig. 3. Second phase: $g/c < t < t_{gg}$

The question is of solving Maxwell's equations in the unbounded domain of Fig. 3.

There is no rigorous analytical solution which would take into account the boundary conditions of the first step, as well as:

$$\Phi(r_0 \leq r \leq R, z = g, t) = 0,$$

$$\text{and: } \frac{\partial A_z}{\partial z}(r_0 \leq r \leq R, z = g, t) = 0.$$

But a good approximation is obtained by assigning these conditions to the general solution in the domain of Fig. 4.

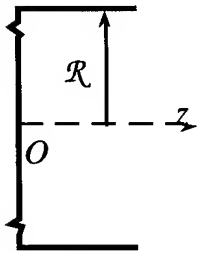


Fig. 4.

This general solution is the sum of a synchronous field and of a radiation field.

A. Synchronous field

This is the particular solution of Maxwell's equations which corresponds to the beam right-hand sides $\rho(\mathbf{x}, t)$ and $\mathbf{j}(\mathbf{x}, t)$ (charge and current densities), i.e. in terms of the scalar- and vector-potentials Φ and \mathbf{A} , and in Lorentz gauge:

$$\square \Phi = \rho/\epsilon_0, \quad \square \mathbf{A} = \mu_0 \mathbf{j}.$$

For an axisymmetric radially uniform beam, transformation and Green's function techniques lead to:

$$\begin{aligned} \Phi_{syn}(r, z, t) &= \frac{4I}{\pi^2 \epsilon_0 a R} \sum_{n=1}^{\infty} \frac{J_0(j_n \frac{r}{R}) J_1(j_n \frac{a}{R})}{j_n J_1^2(j_n)} \int_0^{\infty} \frac{\sin(hz)}{h^2 + (\frac{j_n}{R})^2} \\ &\times \int_0^t \left[1 - \cos\left[c\sqrt{h^2 + (\frac{j_n}{R})^2} (t - t_0)\right] \right] \left\{ \sin[h(\sqrt{c^2 t_0^2 + \Lambda^2} - \Lambda)] \right. \\ &\quad \left. - \sin[h(\sqrt{c^2 (t_0 - \tau)^2 + \Lambda^2} - \Lambda)] \right\} dt_0 dh, \\ A_{zsyn}(r, z, t) &= \frac{4\mu_0 I c}{\pi^2 a R} \sum_{n=1}^{\infty} \frac{J_0(j_n \frac{r}{R}) J_1(j_n \frac{a}{R})}{j_n J_1^2(j_n)} \int_0^{\infty} \frac{\cos(hz)}{h\sqrt{h^2 + (\frac{j_n}{R})^2}} \\ &\times \int_0^t \sin\left[c\sqrt{h^2 + (\frac{j_n}{R})^2} (t - t_0)\right] \left\{ \sin[h(\sqrt{c^2 t_0^2 + \Lambda^2} - \Lambda)] \right. \\ &\quad \left. - \sin[h(\sqrt{c^2 (t_0 - \tau)^2 + \Lambda^2} - \Lambda)] \right\} dt_0 dh, \end{aligned}$$

where a is the beam radius, I the current, $\Lambda = mc^2/eE_0$, and E_0 the accelerating RF field ($E_z = -E_0$), supposed to be constant during the beam photoemission $0 \leq t \leq \tau$, as it is in the 144 MHz cavity of the ELSA photoinjector [3].

B. Radiation field

This is a general solution of homogeneous Maxwell's equations. Taking the boundary conditions into account, this general solution can be written under the form:

$$\begin{aligned} \Phi_{rad}(r, z, t) &\propto \sum_{n=1}^{\infty} J_0(j_n \frac{r}{R}) \int_0^{\infty} \sin(hz) \\ &\times \left\{ A_{\Phi n}(h) \cos\left(\sqrt{h^2 + \frac{j_n^2}{R^2}} ct\right) + B_{\Phi n}(h) \sin\left(\sqrt{h^2 + \frac{j_n^2}{R^2}} ct\right) \right\} dh, \end{aligned}$$

with a similar expression for A_{zrad} , $\sin(hz)$ being replaced by $\cos(hz)$, $A_{\Phi n}(h)$ and $B_{\Phi n}(h)$ by $A_{An}(h)$ and $B_{An}(h)$. These 4 latter functions of h are, for the time being, arbitrary dimensionless integrable functions, only related by the Lorentz gauge condition which gives:

$$A_{An} = (1/hR) B_{\Phi n}, \quad B_{An} = -(1/hR) A_{\Phi n}.$$

C. Calculation of $A_{\Phi n}(h)$ and $B_{\Phi n}(h)$

At first, these integrable functions ($\int |A_{\Phi n}(h)| dh < \infty$) are expanded in Laurent series, taking into account their odd parity ($A_{\Phi n}(h)$ and $B_{\Phi n}(h)$ are sin-Fourier coefficients):

$$A_{\Phi n}(h) = (1/hR) \sum_{m=0}^{\infty} A_{\Phi nm} (hR)^{-2m}.$$

To calculate $A_{\Phi nm}$ and $B_{\Phi nm}$, the above boundary condition $\Phi(r_0 \leq r \leq R, z=g, t)$ is written for $\Phi_{tot} = \Phi_{syn} + \Phi_{rad}$, and integrated on r in its validity domain: $r_0 \leq r \leq R$. One is led to an infinite system of linear algebraic equations:

$$\sum_{n=1}^{\infty} \sum_{m=0}^{\infty} \{ \alpha_{nm}(t) A_{\Phi nm} + \beta_{nm}(t) B_{\Phi nm} \} = \zeta(t),$$

where $\zeta, \alpha_{nm}, \beta_{nm}$ are known functions of t , $A_{\Phi nm}, B_{\Phi nm}$ are the sought after unknowns. A good approximate solution is found by truncating the system to a finite size: $n \leq N, m \leq M$, with $N \sim 100$ and $M \leq 10$. The $2N(M+1)$ unknowns are then calculated by numerically solving the system of $2N(M+1)$ equations:

$$\sum_{n=1}^N \sum_{m=0}^M \alpha_{nm}(t_i) A_{\Phi nm} + \beta_{nm}(t_i) B_{\Phi nm} = \zeta(t_i), \quad i \in [1, 2N(M+1)],$$

$$t_i \in [g/c, t_g].$$

$A_{\Phi nm}$ and $B_{\Phi nm}$ being calculated, $\Phi(r, z, t)$ and $A_z(r, z, t)$ are

deduced, from which the fields result.

V. THIRD PHASE

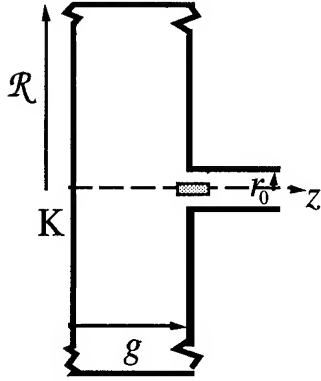


Fig. 5. Third phase: $t_g < t < t_{qg}$

The beam now penetrates the exit hole. The electromagnetic field is obtained by adding, in the cavity and in the drift tube respectively, the synchronous field and a radiation field with undetermined coefficients.

These coefficients are determined, according to the above method, by writing the boundary conditions: a) on the photoinjector anode ($z = g, r_0 \leq r \leq R$) for the

coefficients relative to the field inside the photoinjector, b) on the aperture ($z = g, 0 \leq r \leq r_0$) for the radiation field coefficients inside the drift tube.

A. Wakefield inside the cavity

a) Synchronous field

The techniques used are the same as in phase 2. Again, in Lorentz gauge, one finds for the scalar potential:

$$\Phi_{3, photoinj, syn}(r, z, t) = \frac{4cI}{\pi^2 \epsilon_0 a R} \sum_{n=1}^{\infty} \frac{J_0(j_n \frac{r}{R}) J_1(j_n \frac{a}{R})}{j_n J_1^2(j_n)} \times \int_0^{\infty} \frac{\sin(hz)}{\sqrt{h^2 + (\frac{j_n}{R})^2}} \times \int_t^{t_g + \tau} \sin[c\sqrt{h^2 + (\frac{j_n}{R})^2} (t \ominus t)] \times \int_{t \ominus \tau}^{t_g} \sin[h(\sqrt{c^2 t'^2 + \Lambda^2} - \Lambda)] dt' dt \ominus dh,$$

and for the vector potential:

$$A_{z, photoinj, syn}(r, z, t) = \frac{4\mu_0 c I}{\pi^2 a R} \sum_{n=1}^{\infty} \frac{J_0(j_n \frac{r}{R}) J_1(j_n \frac{a}{R})}{j_n J_1^2(j_n)} \times \int_0^{\infty} \frac{\cos(hz)}{\sqrt{h^2 + (\frac{j_n}{R})^2}} \times \int_t^{t_g + \tau} \sin[c\sqrt{h^2 + (\frac{j_n}{R})^2} (t \ominus t)] \times \left\{ \sin(hg) - \sin[h(\sqrt{c^2 (t \ominus \tau)^2 + \Lambda^2} - \Lambda)] \right\} dt \ominus dh.$$

b) Radiation field

This has the same form as in phase 1.

B. Wakefield inside the drift tube

a) Synchronous field

For the scalar potential, the following is found:

$$\Phi_{3, tube, syn}(r, z, t) = \frac{I r_0}{\pi \epsilon_0 c a \beta} \sum_{n=1}^{\infty} \frac{J_0(j_n \frac{r}{r_0}) J_1(j_n \frac{a}{r_0})}{j_n^3 J_1^2(j_n)} \times \left\{ 2 - \exp[-\frac{j_n}{r_0} (z - g)] - \exp[-\frac{j_n}{r_0} |z - g - \beta c(t - t_g)|] \right\},$$

and a similar expression is found for A_z

b) Radiation field

The boundary conditions to be satisfied are now:

- $\Phi=0, A_z=0$ on the tube wall
- a radiation condition for $z \rightarrow +\infty$.

This leads to adopting for the scalar potential:

$$\Phi_{3, photoinj, rad}(r, z, t) \propto \sum_{n=1}^{\infty} J_0(j_n \frac{r}{r_0}) \times \int_0^{\infty} D_{n\phi}(\omega) \exp[i(\omega t - \sqrt{\frac{\omega^2}{c^2} - \frac{j_n^2}{r_0^2}} z)] d\omega,$$

with $\omega > 0$ (wave propagating in the positive z direction).

The unknown functions $D_{n\phi}(\omega)$, expanded in Laurent series, are calculated by writing the field continuity on the aperture: ($z = g, 0 \leq r \leq r_0$). After integration on r , in the interval $0 \leq r \leq r_0$, one is led to an infinite system of linear algebraic equations:

$$\sum_{n=1, m=1}^{\infty} K_{n,m}(t) D_{n,m} = L(t)$$

Here again, a good convergence is reached by truncating at $n_{max} = N$ and $m_{max} = M$, with $N \sim 100$ and $M \leq 10$.

Sample field maps are given in a companion paper [4], in which wakefield effects on beam quality are studied.

REFERENCES

- [1] J.-M. Dolique, EPAC 94, London, UK (1994)
- [2] H. Figuera *et al.*, Phys. Rev. Lett. **60**, 2144 (1988)
- [3] E.g.: S. Joly, J.P. de Brion *et al.*, N.I.M. **A340**, 214 (1994)
- [4] J.-M. Dolique and W. Salah, this conference TPR04

INVARIABILITY OF INTENSE BEAM EMITTANCE IN NONLINEAR FOCUSING CHANNEL

Y.K.Batygin, The Institute of Physical and Chemical Research (RIKEN), Saitama 351-01, Japan

Abstract

New approach to keep emittance of a high current beam in a uniform focusing channel is presented. The matching conditions for a beam with arbitrary distribution function in a nonlinear focusing channel are examined. To obtain proper matching, it is necessary to accept that the potential of the external focusing field contains higher order terms than quadratic. The solution for external potential is obtained from the stationary Vlasov's equation for beam distribution function and Poisson's equation for electrostatic beam potential. An analytical approach is illustrated by results of a particle-in-cell simulation.

I. INTRODUCTION

The nonlinear space charge field of a beam is a serious concern for beam emittance growth in the low energy part of an accelerating facility. This effect is most pronounced in the injection region where particles are slow and space charge forces are significant. The problem of beam emittance growth due to nonstationary beam profile in a focusing channel with a linear focusing field was treated in many papers (see ref. [1-9] and cited references there). The general property of space charge dominated beam behavior is that a beam with an initial nonlinear profile tends to be more uniform and this process is associated with strong emittance growth and the appearance of beam halo.

The beam emittance is conserved if the beam is matched with the channel. The problem of matching of the nonlinear density profiled beam with linear uniform focusing channel was studied in detail in ref. [9-12]. The analytical approach is based on the fact that the Hamiltonian of the matched beam is a constant of motion, and therefore the unknown distribution function can be expressed as a function of the Hamiltonian. A general property of the solution to problem is that with increasing beam current, the profile of the matched beam has to be more and more flat while the phase space projection (beam emittance) has to be more and more close to a rectangle.

Laboratory beams are usually far from the above solution and suffer serious emittance growth. The purpose of this paper is to check whether it is possible to match the beam with a given distribution function with the uniform focusing channel. As is shown below, it is possible if we assume that the focusing field includes higher order terms than quadratic [13].

II. MATCHED CONDITIONS FOR THE BEAM WITH GIVEN DISTRIBUTION FUNCTION

The procedure to find the matching conditions for a beam with an arbitrary distribution function was discussed in ref. [13]. Let us assume that the beam is matched with the channel.

Hence, the Hamiltonian is a constant of motion but no assumptions about linearity of focusing forces are adopted:

$$H = \frac{p_x^2 + p_y^2}{2m} + q U(x, y = \text{const}) \quad (1)$$

The total potential of the structure is a combination of the external focusing potential, U_{ext} , and the space charge potential U_b of the beam, $U = U_{\text{ext}} + U_b$. The time-independent distribution function of a matched beam obeys Vlasov's equation:

$$\frac{df}{dt} = \frac{\partial f}{\partial x} v_x + \frac{\partial f}{\partial y} v_y - q \left(\frac{\partial f}{\partial p_x} \frac{\partial U}{\partial x} + \frac{\partial f}{\partial p_y} \frac{\partial U}{\partial y} \right) = 0 \quad (2)$$

where the partial derivative of the distribution function over time is omitted due to initial matched conditions. The distribution function of the beam is supposed to be given from the source of particles of the beam. Therefore, the self potential of the beam U_b is also a known function derived from Poisson's equation:

$$\frac{1}{r} \frac{\partial}{\partial r} \left(r \frac{\partial U_b}{\partial r} \right) = - \frac{\rho(r)}{\epsilon_0} \quad (3)$$

where $\rho(r)$ is the space charge density of the beam. Combining solutions of Vlasov's equation for total potential of the structure, U , and space charge potential of the beam, U_b , obtained from Poisson's equation, the external potential of the focusing structure can be found:

$$U_{\text{ext}} = U - U_b. \quad (4)$$

The solution of this problem is unique for every specific particle distribution.

III. EXAMPLE OF THE MATCHED BEAM WITH NONLINEAR SPACE CHARGE FORCES

Let us consider a z-uniform beam with a "parabolic" distribution function in four-dimensional phase space:

$$f = f_0 \left(1 - \frac{x^2 + y^2}{2 R^2} - \frac{p_x^2 + p_y^2}{2 p^2} \right) \quad (5)$$

This distribution makes an elliptical phase space projection at every phase plane and produces a decrease function of space charge density from axis which is close to experimentally

observed beam. The normalized root-mean-square (RMS) beam emittance is:

$$\epsilon = \frac{4}{mc} \sqrt{\langle x^2 \rangle \langle p_x^2 \rangle - \langle x p_x \rangle^2} = \frac{R p}{m c} \quad (6)$$

Substituting the distribution function (5) into Vlasov's equation yields an expression for the total unknown potential of the structure:

$$\frac{mc^2}{q} (x p_x + y p_y) = \frac{R^4}{\epsilon^2} \left[p_x \frac{\partial U}{\partial x} + p_y \frac{\partial U}{\partial y} \right] \quad (7)$$

Vlasov's equation can be separated into two independent parts for x- and y- coordinates respectively:

$$\frac{\partial U}{\partial x} = \frac{mc^2 \epsilon^2}{q R^4} x; \quad \frac{\partial U}{\partial y} = \frac{mc^2 \epsilon^2}{q R^4} y \quad (8)$$

Combining solutions of eq. (8), the total potential of the structure is a quadratic function of coordinates which creates linear focusing:

$$U(x,y) = \frac{mc^2 \epsilon^2}{q R^4} \left(\frac{x^2 + y^2}{2} \right) \quad (9)$$

The appearance of quadratic terms in the total potential of the structure is quite clear because phase space projections of the beam have elliptical shape and an ellipse is conserved in a linear field. The space charge field of the beam E_b is calculated from Poisson's equation using a known space charge density function of the beam ρ_b :

$$\rho_b = \frac{3 I}{2 \pi c \beta R^2} \left(1 - \frac{r^2}{2 R^2} \right)^2 \quad (10)$$

$$E_b = \frac{3 I r}{4 \pi \epsilon_0 \beta c R^2} \left[1 - \left(\frac{r}{\sqrt{2} R} \right)^2 + \frac{1}{3} \left(\frac{r}{\sqrt{2} R} \right)^4 \right] \quad (11)$$

where I is the beam current and β is the longitudinal velocity of particles. Subtraction of the space charge field from the total field of the structure gives the expression for the external focusing field of the structure which is required for conservation of beam emittance:

$$E_{ext} = -\frac{mc^2 r}{q R^2} \left[\frac{\epsilon^2}{R^2} + \frac{3 I}{I_c \beta} \left(1 - \frac{r^2}{2 R^2} + \frac{r^4}{12 R^4} \right) \right] \quad (12)$$

where $I_c = 4 \pi \epsilon_0 m c^3 / q = A / Z \cdot 3.13 \cdot 10^7$ amp is a characteristic value of the beam current. The relevant potential of the focusing field is given by the expression:

$$U_{ext} = \frac{m c^2}{q} \left[\frac{r^2}{2 R^2} \left(\frac{\epsilon^2}{R^2} + \frac{3 I}{I_c \beta} \right) + \frac{3 I}{8 I_c \beta} \left(-\frac{r^4}{R^4} + \frac{r^6}{9 R^6} \right) \right] \quad (13)$$

Let us note that the external potential of the structure consists of two parts: quadratic (which produces linear focusing) and higher order terms which describe nonlinear focusing. The

linear part depends on the values of beam emittance and beam current while the nonlinear part depends on beam current only. This means that the external field has to compensate the nonlinearity of self-field of the beam and produce required linear focusing of the beam to keep the elliptical beam phase space distribution. Fig. 1 illustrates the relationships between space charge field of the beam, total field, and focusing field of the structure. The external focusing field obtained from the above consideration is a complicated function of radius which is linear near the axis and becomes nonlinear far from the axis. One of the ideal ways to create the required focusing potential is to introduce inside the transport channel an opposite charged cloud of heavy particles with the space charge density:

$$\rho_{ext} = \frac{I_c}{2 \pi c R^2} \left[\frac{\epsilon^2}{R^2} + \frac{3 I}{\beta I_c} \left(1 - \frac{r^2}{2 R^2} \right)^2 \right] \quad (14)$$

In fig. 2 the charged particle density of the transport beam and the external focusing beam are presented.

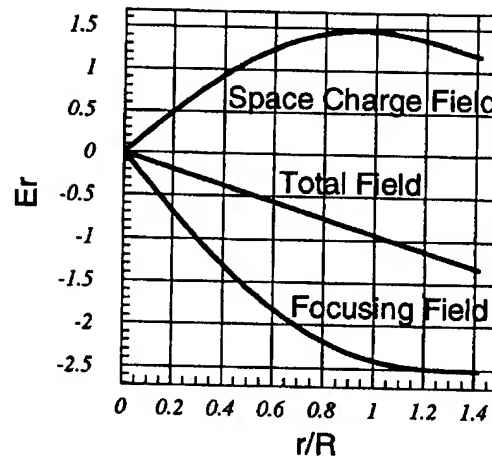


Fig. 1. Space charge field of the beam, external focusing field, and total field of the structure.

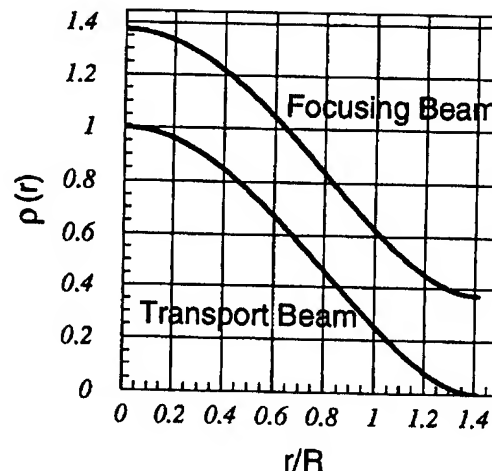


Fig. 2. Charged particle density of the transport beam and the external focusing beam.

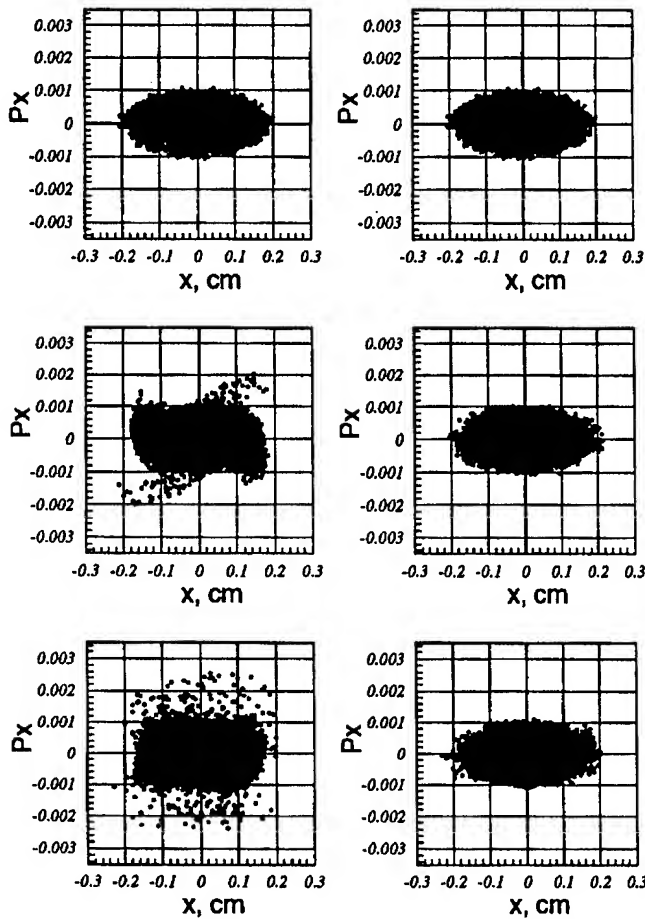


Fig. 3. Halo formation of the beam in focusing channel with linear focusing forces (left column) and perfect matching of the same beam with nonlinear focusing channel(right column).

At fig. 3 the results of particle-in-cell simulation of the beam in linear and nonlinear focusing channel using code BEAMPATH [14] are presented. A beam of particles was represented as a collection of 10000 trajectories. Space charge field of the beam was calculated from Poisson's equation on the uniform rectangular meshes of dimension $N_X \times N_Y = 256 \times 256$. The external focusing potential for the linear focusing channel was chosen as

$$U_{\text{ext}}(r) = \frac{m c^2}{q} \left(\frac{\epsilon^2}{2 R^4} + \frac{1}{I_c \beta R^2} \right) r^2 \quad (15)$$

which corresponds to the matched conditions for an equivalent KV beam with the same RMS beam emittance, ϵ , and RMS beam size, R . In the case of nonlinear focusing, the external potential is represented by eq. (13). Let us note that quadratic terms in potentials (13) and (15) are different.

From results of simulations, it is seen that in both cases the sizes of the beam in real space (beam envelopes) are close to constant which is typical for matching of the beam, taking into account RMS beam sizes. But in the case of linear focusing, the beam is mismatched in the phase plane which results in 25% emittance growth accompanied by halo formation. At the same time, the beam is completely matched with the nonlinear focusing channel, and this results in

conservation of all beam characteristics and does not suffer any serious emittance growth.

IV. CONCLUSIONS

Conservation of beam emittance was treated as a problem of proper matching of the beam with a uniform focusing channel. Matched conditions for the beam with elliptical phase space projections but nonlinear space charge forces in a uniform focusing channel require the focusing field to include nonlinear terms of higher order than quadratic. The solution for the external potential is attained from the stationary Vlasov's equation for beam distribution function and Poisson's equation for electrostatic beam potential. The focusing field produces linear focusing near the axis of the structure but has to change non-linearly away from the axis. Example of the beam with "parabolic" distributions in 4D phase space was considered. Results of a particle-in-cell simulation confirms the conservation of beam emittance in a nonlinear external field.

V. REFERENCES

- [1]. P.M.Lapostolle, IEEE Trans. Nucl. Sci. NS-18, 1101 (1971).
- [2]. J.Struckmeier, J.Klabunde, and M.Reiser, Part. Accel. 15, 47 (1984).
- [3]. T.P.Wangler, K.R.Crandall, R.S.Mills, and M.Reiser, IEEE Trans. Nucl. Sci. NS-32, 2196 (1985).
- [4]. R.A.Jameson, Proceedings of the PAC93, Washington D.C., 3926 (1993).
- [5]. J.S.O'Connell, T.P.Wangler, R.S.Mills and K.R.Crandall, Proceedings of the PAC93, Washington D.C., 3657 (1993).
- [6]. R.D.Ryne, Proceedings of the PAC93, Washington D.C., 3229 (1993).
- [7]. J.M.Lagniel, Nucl. Instr. and Meth. A 345, 46 (1994); Nucl. Instr. and Meth. A 345, 405 (1994).
- [8]. R.L.Gluckstern, Proceedings of the 1994 International Linac Conference, Vol. 1, 333, Tsukuba, Japan (1994).
- [9]. M.Reiser, Theory and Design of Charged Particle Beams, Wiley, New York, 1994.
- [10]. I.M.Kapchinsky, Theory of Resonance Linear Accelerators, Moscow, Atomizdat, 1966, Harwood, 1985.
- [11]. P.Lapostolle, VII Int. Conference on High Energy Accelerators, Yerevan, 205 (1969).
- [12]. J.Struckmeier and I.Hofmann, Part. Accel., 39, 219 (1992).
- [13]. Y.Batygin, Proceedings of the 1994 International Linac Conference, Vol. 1, 487, Tsukuba, Japan (1994).
- [14]. Y.Batygin, Proceedings of the EPAC92, Berlin, 822 (1992).

Beam Transport for Uniform Irradiation: Nonlinear Space Charge and the Effect of Boundary Conditions

D. Bruhwiler, Northrop Grumman Advanced Technology & Development Center, 4 Independence Way, Princeton NJ 08540[†]
Yuri K. Batygin, Moscow Engineering Physics Institute, 31 Kashirskoe shosse, 115409 Moscow, RUSSIA*

Proposed high-intensity ion accelerators required for Accelerator Driven Transmutation Technologies (ADTT) and the International Fusion Materials Irradiation Facility (IFMIF) demand careful control of beam shape and distribution on target; for example, uniform irradiation of a rectangular area. Nonlinear magnetic elements can yield the desired beam on target; however, nonlinear space charge forces also play a significant role. We consider the importance of boundary conditions used when modeling space charge effects in such a transport line. Simple analytical criteria are derived for determining when nonlinear space charge forces will be significant and for when proper treatment of boundary conditions is required. Two computer codes employing different boundary conditions for their respective space charge models, the PIC code BEAMPATH [1] and the high-order optics code TOPKARK [2], are used to simulate an example transport line in order to demonstrate our results.

I. BEAM INTENSITY REDISTRIBUTION

We consider a cylindrically-symmetric, unbunched beam of particles with charge q , mass m and current I , which propagates along the z -axis with velocity $v=\beta c$ and relativistic factor $\gamma=(1-\beta^2)^{-1/2}$. We assume the beam is space charge dominated, so that finite-emittance effects can be neglected.

In general, the space charge forces are nonlinear, so the density profile of the beam is changed nonlinearly along the z -axis. However, there is a distance where the different layers of the beam do not cross each other: the radial motion of the particles is nonlinear, but the beam flow is still laminar. Space charge forces distort the x - p_x phase space of a zero-emittance beam into an S-shape. The assumption of laminar flow holds as long as $p_x(x)$ remains a single-valued function.

For laminar flow, the number of particles contained in an arbitrary cylinder with initial radius r_0 remains constant. Use of Gauss' theorem yields the result:

$$r E_r(r) = \frac{1}{\epsilon_0} \int_0^{r_0} r' \rho(r') dr' = \text{const.} \quad (1)$$

Here, r is the radius of our hypothetical cylinder, which expands as the beam drifts; thus, $r=r(z)$ and $r(z=0)=r_0$.

We suppose the initial beam distribution to be Gaussian and define $R_0=2x_{\text{rms}}=2\langle x^2 \rangle^{1/2}$:

$$\rho(r_0) = \frac{2I}{\pi R_0^2 \beta c} \exp\left(-2 \frac{r_0^2}{R_0^2}\right). \quad (2)$$

Use of Eq.'s (1) and (2) yields the radial space charge force at any location in z :

$$E_r(r) = \frac{I}{2\pi\epsilon_0\beta c} \frac{f(r_0)}{r}; \quad f(r_0) \equiv 1 - \exp\left(-2 \frac{r_0^2}{R_0^2}\right). \quad (3)$$

We note that for a uniform distribution, one would obtain $f(r_0) = (r_0/R_0)^2$, and R_0 would be the initial beam radius.

The equation of motion for a single particle in a drift region under the influence of space charge forces has the form:

$$\frac{d^2 r}{dz^2} = \frac{2I}{I_0 \beta^3 \gamma^3} \frac{f(r_0)}{r}, \quad (4)$$

where $I_0=4\pi\epsilon_0 mc^3/q$ is the characteristic current. Eq. (4) is the well-known envelope equation for a zero-emittance beam spreading in a drift region due to space charge [3], but here we apply it to the motion of a single particle within the beam.

If we define the following dimensionless variables

$$\bar{R} = \frac{r}{r_0}; \quad Z = \frac{z}{r_0} \sqrt{\frac{4If(r_0)}{I_0 \beta^3 \gamma^3}}, \quad (5)$$

then we can write the first integral of Eq. (4) in the form

$$\left(\frac{d\bar{R}}{dZ}\right)^2 - \left(\frac{d\bar{R}}{dZ}\right)_{\text{init}}^2 = \ln(\bar{R}). \quad (6)$$

Assuming the Z derivative of \bar{R} vanishes initially, and for $1 \leq \bar{R} \leq 3$ ($0 \leq Z \leq 3.2$), Eq. (6) has the approximate solution [4]

$$\bar{R}(Z) \approx 1 + 0.25 Z^2 - 0.017 Z^3. \quad (7)$$

This result is valid for a single particle, and it also describes how the radius of our hypothetical cylinder evolves with z .

The number of particles dN inside a thin ring ($r, r+dr$) is constant during the drift of the beam; hence, the particle density $\rho(r) = dN / (2\pi r dr)$ at any z is connected with the initial density $\rho(r_0)$ by the following equation [5]:

$$\rho(r) = \rho(r_0) \frac{r_0}{r} \frac{dr_0}{dr} = \rho(r_0) \frac{d(r_0^2)}{d(r^2)}. \quad (8)$$

Using Eq.'s (2), (7) and (8), we can write the beam distribution at any z location in the form

$$\rho(r) = \frac{(2I/\pi R_0^2 \beta c) \exp(-2\xi_0^2)}{a_0 + a_1 F + a_2 F^2 + a_3 F^3 + a_4 F^4 + a_5 F^5 + a_6 F^6}, \quad (9)$$

where the following notation has been used:

$$\xi_0 = \frac{r_0}{R_0}; \quad F(\xi_0) = \sqrt{[1 - \exp(-2\xi_0^2)] / \xi_0^2}; \quad (10a)$$

$$\eta = \frac{4I}{I_0 \beta^3 \gamma^3} \frac{z^2}{R_0^2} = \frac{Z^2}{f(r_0)}; \quad a_0 = 1 + \eta \exp(-2\xi_0^2); \quad (10b)$$

$$a_1 = -0.102 \eta^{3/2} \exp(-2\xi_0^2); \quad a_2 = \frac{1}{4} \eta^2 \exp(-2\xi_0^2); \quad (10c)$$

$$a_3 = 0.017 \eta^{3/2} - 0.0425 \eta^{5/2} \exp(-2\xi_0^2); \quad (10d)$$

$$a_4 = 1.734 \times 10^{-3} \eta^3 \exp(-2\xi_0^2) - \frac{1}{16} \eta^2; \quad (10e)$$

$$a_5 = 0.01275 \eta^{5/2}; \quad a_6 = -5.78 \times 10^{-4} \eta^3. \quad (10f)$$

The distribution is most uniform for $\eta \approx 4$. For larger values of η , the distribution becomes progressively more hollow.

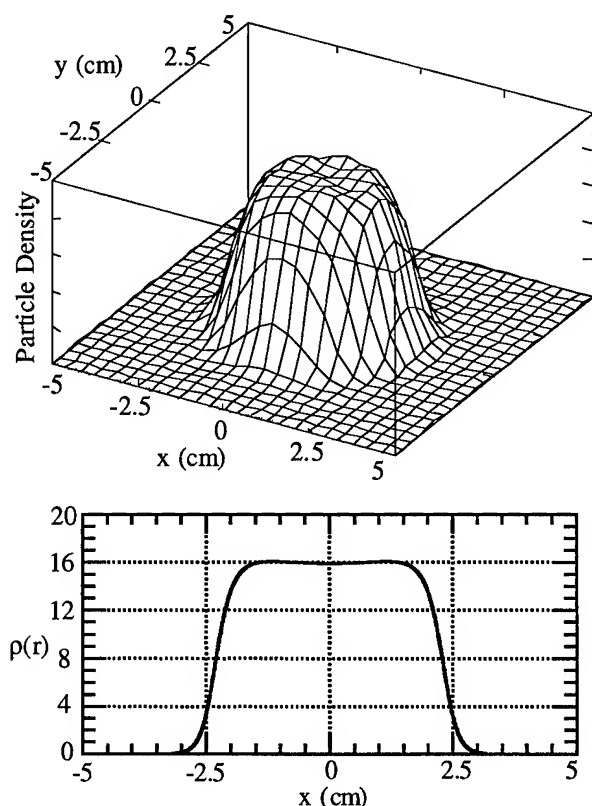


Figure 1: Initially Gaussian 2-D beam that has drifted under the influence of nonlinear space charge forces, with $\eta=3.8$; computer simulation above and analytical result below.

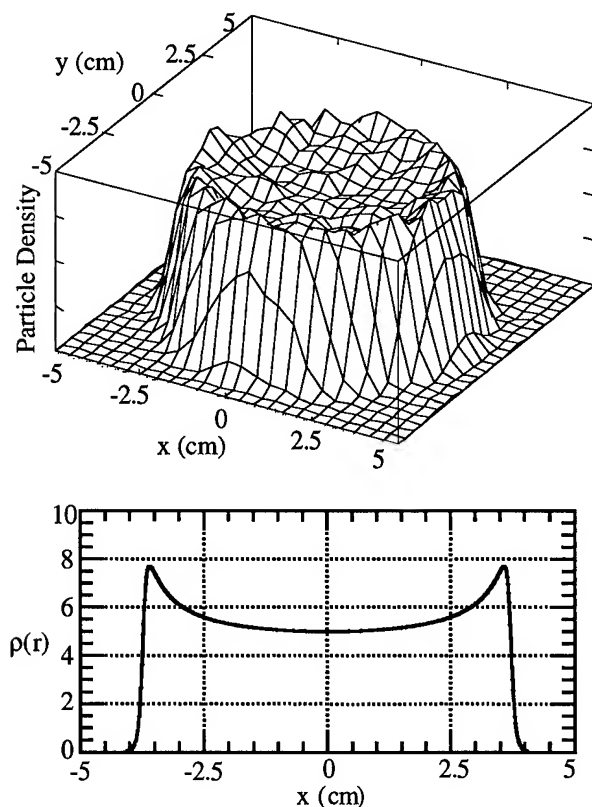


Figure 2: Same as Fig. 1, but for $\eta=10$; hollowing of the beam due to nonlinear space charge forces is shown.

Figures 1 and 2 show good comparison between theory and numerics for 35 MeV D^+ with $I=4.7$ A, $R_0=1.3$ cm and two values of η . BEAMPATH was used for the simulation, with 10^4 particles on a grid 256×256 . Treatment of bunched beams requires the use of an equivalent peak beam current: $I = I_{\text{bunch}} * 2\pi / \Delta\phi$, where $\Delta\phi$ is the phase length of the bunch.

II. GENERAL FEATURES OF THE CODES

BEAMPATH [1] is a PIC code advancing macroparticles on a 3-D rectangular grid of fixed dimensions with area-weighted charge distribution, using a combination of leap-frog and 2nd-order implicit methods. Space charge forces are found by solving Poisson's equation with FFT, imposing Dirichlet conditions at the transverse boundaries and longitudinal periodicity. For the simulation below, BEAMPATH used 10^4 particles and an $x/2, y, z$ spatial grid of $128 \times 256 \times 128$.

TOPKARK [2] is a ray-tracing code using a 4th-order Runge-Kutta integrator to advance an ensemble of particles. The Garnett and Wangler [6] ellipsoidal, Fourier-expansion space charge model is used to solve Poisson's equation with free-space boundary conditions. For the simulation below, TOPKARK used 10^4 particles and kept 10 Fourier modes.

III. LATTICE USED FOR CODE COMPARISON

The lattice considered here is one which bounces the beam first in y , and then in x . Octupole and duodecapole fields are applied at these waists in order to appropriately introduce nonlinearities into the two transverse phase planes with a minimum of x - y coupling. These nonlinearities result in a folding of the transverse phase plane distributions such that the final beam distribution $f(x,y)$ on target is approximately constant with sharp boundaries. See Table I for details.

Table I. Nonlinear lattice for code benchmarking

ELEMENT	LENGTH	SETTING	
quadrupole	0.2 m	-10.16958	T/m
drift	0.4 m		
multipole	0.2 m	11.65657	T/m
octupole		-150.0	T/m^3
duodecapole		35000.0	T/m^5
drift	0.4 m		
quadrupole	0.1 m	0.91613	T/m
drift	0.4 m		
multipole	0.2 m	-11.90051	T/m
octupole		-80.0	T/m^3
duodecapole		0.0	T/m^5
drift	0.4 m		
quadrupole	0.2 m	10.78634	T/m
drift	17.5 m		

The design of such beamlines has been previously studied in some detail [5], [7]. Our primary objectives here are to 1) consider the effects of nonlinear space charge forces on beam transport through lattices of this type and 2) benchmark two codes with very different approaches to the problem of modeling space charge and with different boundary conditions. The distribution of the initial bunch was chosen to be Gaussian,

truncated at 5 RMS. The FWHM and maximum excursion beam envelopes are shown in Fig. 3.

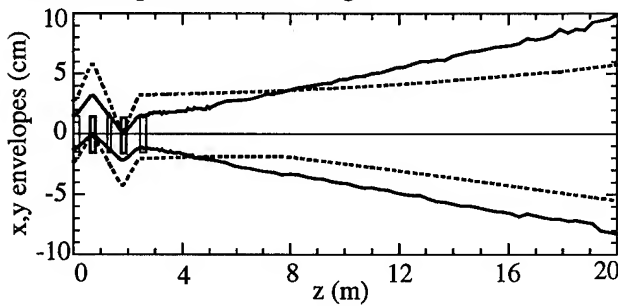


Figure 3: The FWHM (solid line) and maximum (dashed) x/y envelopes plotted above/below the axis.

IV. BOUNDARY CONDITIONS AND RESULTS

Consider a particle bunch in the beam frame with length z_b and radius r_b inside a perfectly conducting pipe of radius r_p . The impact of BC's on the space charge fields can be parameterized in terms of the geometry factor g [8]. Table I of Ref. [8] shows that for short bunches ($z_b \leq r_b$) g in the presence of a perfectly conducting pipe differs significantly from the freespace g -factor g_0 only when r_b is comparable to r_p . However, for long bunches ($z_b \gg r_b$) g can differ significantly from g_0 even when $r_p \gg r_b$.

In the region containing magnetic lenses, the grid used in BEAMPATH is 10 cm in x and y ($r_p \sim 5$ cm) and 8 cm in z . In this region, the transverse bunch width is typically 4 cm or less ($r_b \sim 2$ cm), and the bunch length is short ($z_b \sim 1$ cm). The resulting difference in the g -factors for the two codes should thus be at most a few percent. However, the maximum beam excursion does reach ~ 5 cm in x during the first multipole magnet and in y during the second multipole, so significant BC effects could arise in these two locations. In the long drift, the BEAMPATH grid is 20 cm in x and y ($r_p \sim 10$ cm) and 32 cm in z . The bunch radius grows to $r_b \sim 5$ cm and the bunch length to $z_b \sim 10$ cm, so the maximum difference in the two g -factors should be $\sim 20\%$. Differences resulting from the two types of longitudinal BC's have not yet been assessed.

In fact, the agreement between these two codes is remarkably close for this long, high-order, space-charge-dominated beamline. The beam phase space and space charge fields have been compared in detail at several critical points, showing only minor differences. We only have space to show the final x - y distribution in Fig. 4. TOPKARK was used to design the beamline and shows a very uniform beam. BEAMPATH shows a slightly hollow beam, which indicates slightly more nonlinear space charge fields due to differing BC's.

We chose a long lattice with high current to provide a rigorous comparison of the two codes, and applying the above analysis at the end of the last quadrupole yields $\eta \gtrsim 20 \gg 4$. This beam is initially diverging and has finite emittance, so the assumptions of Section I do not hold; nevertheless, one would expect the final distribution to be hollow. TOPKARK simulations with no octupoles or duodecapoles do in fact yield a hollow beam. For this beamline, the nonlinear elements are required to partially counteract the space charge nonlinearities in order to obtain a uniform distribution on target.

VI. REFERENCES

- † DLB acknowledges many useful discussions with M. F. Reusch, and the support of Northrop Grumman Corp.
- * Present address: Inst. of Physical and Chemical Research (RIKEN), Hirosawa 2-1, Saitama 351-01, JAPAN
- [1] Y. Batygin, "BEAMPATH: A program library for beam dynamics simulation in linear accelerators", Proc. of the 3rd European Part. Accel. Conf. (Berlin, 1992), p. 822.
- [2] D. Bruhwiler and M. F. Reusch, "High-order optics with space charge: the TOPKARK code", AIP Conf. Proc. 297, R. Ryne ed. (AIP, New York, 1993), p. 524.
- [3] J. R. Pierce, in *Theory and Design of Electron Beams*, ed. by D. Van Nostrand (New York, 1954).
- [4] S. I. Molokovskii and A. D. Sushkov, *Intense Electron and Ion Beams*, (Leningrad, Energia, 1972), in Russian.
- [5] Y. K. Batygin, "Beam intensity redistribution in a non-linear optics channel", Nucl. Instr. and Meth. B, 79 (1993), pp. 770-772.
- [6] R. Garnett and T. Wangler, "Space-charge calculation for bunched beams with 3-D ellipsoidal symmetry", Part. Accel. Conf. Proc., (IEEE, New York, 1991), p. 330.
- [7] B. Blind, "Production of uniform and well-confined beams by nonlinear optics", Nucl. Instr. and Meth. B, 57 (1991), pp. 1099-1102.
- [8] C. Allen, N. Brown and M. Reiser, "Image effects for bunched beams in axisymmetric systems," Part. Accel. 45 (1994), pp. 149-165.

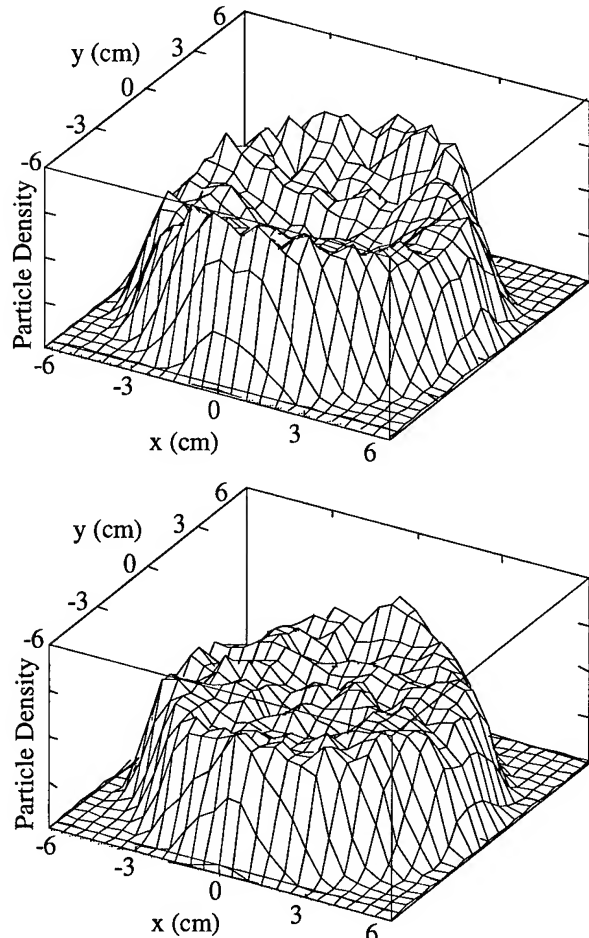


Figure 4. Final beam: BEAMPATH (above) and TOPKARK.

Transport of Bunched Beams with Space Charge through a Periodic Lattice

M.F.Reusch and D.L.Bruhweiler, Northrop Grumman Advanced Technology and Development Center, 4 Independence Way, Princeton, NJ 08540 USA

We present a numerical study of beam transport through a FODO HEBT typical of proposed large current ion linear accelerator systems. Previous studies of this problem have usually assumed uniform and linear focusing forces. In contrast, our study includes non uniform focusing as well as nonlinearities associated with space charge forces, fringe fields and RF gaps. We examine current limits, beam mismatch and emittance growth. These simulations are conducted with the high order Northrop Grumman Topkark code, which implements the Garnett and Wangler 3-D space charge model. We compare our results to the analytic studies of Hofmann[3], Reiser[4] and others.

I. INTRODUCTION

We have used the Northrop Grumman Topkark code [1] in a preliminary study of the transport of high current intensity beams through a periodic high-energy beam transport (HEBT) lattice. Such beam transport lattices, as opposed to accelerating Linacs, form part of proposed (AXY) systems for the study of fusion materials, the accelerator production of Tritium (APT) and the accelerator transmutation of radioactive waste (ATW). Some previous studies of this problem have assumed uniform and/or linear focusing forces. In contrast, our simulation includes non uniform focusing as well as nonlinearities associated with space charge forces, fringe fields and RF gaps. Our principle aims are to benchmark the Topkark code in these well studied circumstances and to examine the effect that non uniform, non linear, fully 3D focusing and 3D, bunched-beam space charge effects have on high energy beam transport.

II. TOPKARK

The Topkark code used in this study is a general optics and particle tracking version implementing essentially exact dynamical applied field models along with restricted models of space charge effects. The Garnett and Wangler[2] (G&W) space charge model used, implements a general distribution of ellipsoidal symmetry based on particle positions. Conducting wall boundary conditions are not presently implemented. The code contains combined function, i.e., including quadrupole, sextapole, octupole, etc. field moments, dipole bend and straight magnetic elements, hard and soft edge fringe field models and general misalignments[6]. The code uses both Symplectic[7] and Runge-Kutta type integrators. Topkark has been previously compared with Trace 3D in the linear limit and with Parmila, obtaining reasonable agreement. Most recently, in a paper by D. Bruhwiler and Y. Batygin at this conference, Topkark is compared to a PIC code.

III. LATTICE

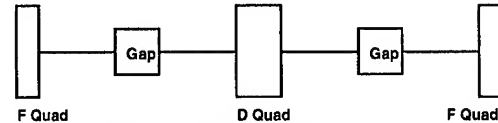


Fig. 1 - Simple FODO Lattice

For this study, we concocted a simple ~ one meter cell, 10 MeV, proton FODO lattice in which the drift spaces between the 10 cm focus and defocus quadrupoles are of equal length, the focus and defocus quadrupoles are of equal strength and an RF cavity is inserted between every quadrupole pair. This lattice treats the X and Y planes on an identical footing. The zero current transverse phase advance is normally arranged to be 72 degrees. The phase advances versus matched beam current with a linear space charge model are given in Fig. 2.

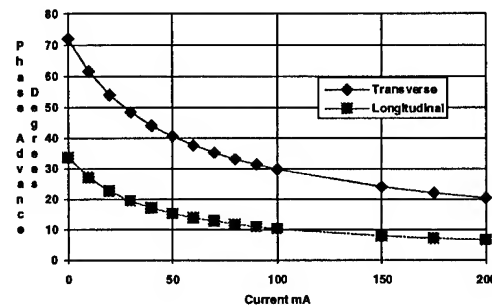


Fig. 2 - Phase advance vs current for a linear space charge model.

We confirm a number of expected phenomena in a FODO lattice with the code. The linear space charge model shows close agreement with Trace3D and exhibits very little emittance growth. With non linear space charge models, mismatched beams grow rapidly in emittance, as do unstable beams in a lattice whose zero current phase advance exceeds 90 degrees.

No precise upper limit for current is found in quiescent transport. Instead, a practical limit is provided by aperture as the matched beam size, for fixed transverse focusing strength, grows with current.

Figures 5 through 8, show the rms local transverse emittances when a matched, 100 mA beam with 2000 particles is propagated through 100 periods of this lattice. This is enough current that the transverse phase advance is depressed by a factor of one half and the longitudinal by a

factor of one third. We compare simulations with a thin, quasi-linear RF gap, Figs. 5 and 7, and a more realistic thick, single mode RF cavity, Figs. 6 and 8.

The simulation includes the non linear effects of space charge, quadrupole fringe fields and RF cavity focusing. Importantly, the emittance growth of Figs. 6 and 8 is almost entirely due to the thick RF cavity and, in magnitude, is in rough agreement with an analytical estimate [8].

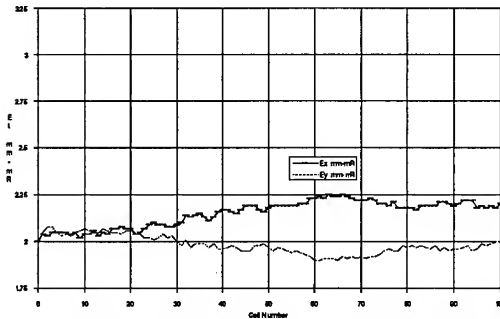


Fig. 5 Transverse Emittance vs Cell No, FODO with thin RF gap.

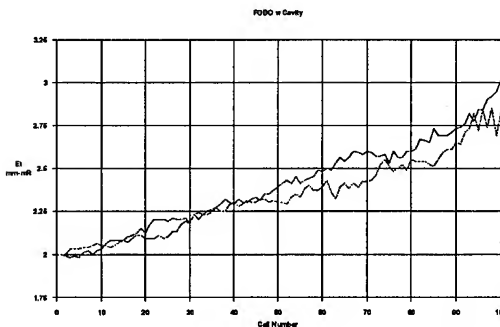


Fig. 6 - Transverse Emittance vs Cell No, FODO with thick RF cavity.

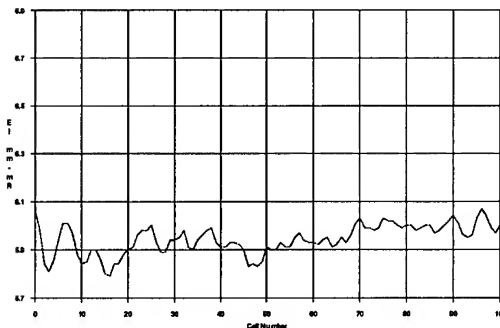


Fig. 7 - Longitudinal Emittance vs Cell No. FODO with thin RF gap.

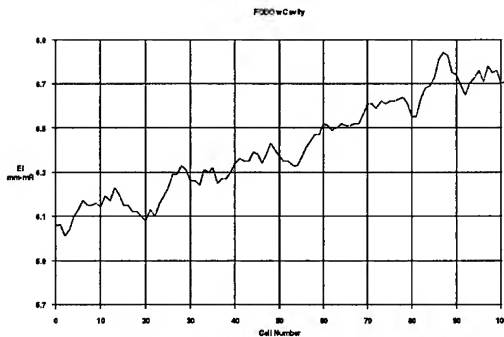


Fig. 8 - Longitudinal Emittance vs Cell No. FODO with thick RF cavity.

Multipole components in the fringe fields of the quadrupoles make very little contribution to the emittance growth suggesting that geometrical aberrations may not be significant in such HEBTs. However as more current is transported the matched beam size grows causing these non linearities to become more important.

Interestingly, in the thin gap model (Fig. 6) the transverse emittances, after tracking each other for a while, become slightly different. The reason for this transverse emittance asymmetry is not yet understood. It occurs in either plane depending on initial statistics and is not affected much by fringe fields or octupole strength in combined function magnets.

IV. BEAM MATCHING

Ordinarily an initial upward transient of as much as 100% occurs in the emittance as a linearly matched beam is introduced into a non linear lattice. This initial transient may be regarded as spurious or not according to supposed initial conditions. However, this transient, if allowed, obscures sensitive dependencies.

The lack of initial emittance growth in the above figures has been arranged by performing a heuristic rematching procedure. In its simplest form, the beam is propagated repeatedly through a lattice period. The emerging beam is phase-space culled of particles beyond 4 sigma. New particles are randomly introduced. The phase space is multiplicatively adjusted to preserve emittance. This preparatory "non linear matching" minimizes initial emittance growth. It allows the beam to adjust to a more or less self-consistent state.

With the G&W model, this matching method yields beams with spatial distributions that are neither Gaussian nor uniform, but something in between, as shown in Fig. 9. As the current is doubled from 100 mA to 200 mA, for constant emittance, there is little change in the beam distribution.

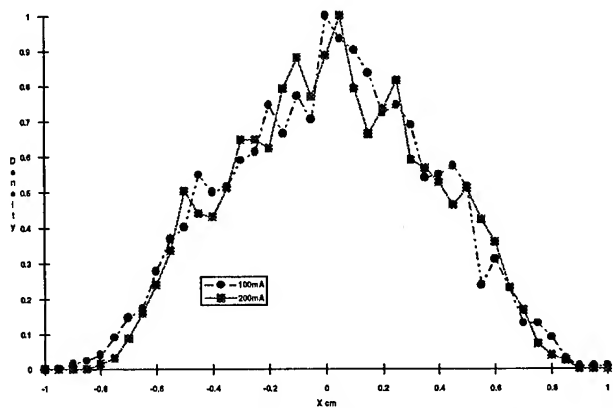


Fig. 9 - Transverse beam distributions at 100 and 200 mA.

Figure 10 gives the "tune shift" with amplitude for an 100 mA beam using the G&W model. The tunes have been deduced from an approximate transport map that has been obtained through the judicious placement of test particles and a finite difference procedure. The highly non linear G&W space charge model emphasizes repulsive space charge forces near the bunch center over the equivalent linear model. In consequence, particles near the bunch center may see an unstable lattice.

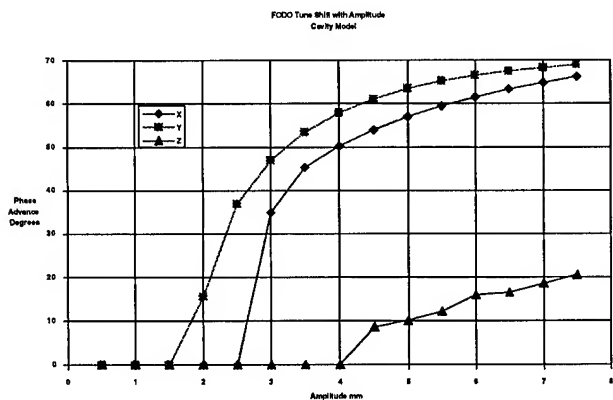


Fig. 10 - Tune shift with amplitude, G&W space charge model at 100 mA.

V. CONCLUSIONS

A preliminary study of HEBT transport and emittance growth has been carried out with the tracking version of the Northrop Grumman Topkark code. Results tend to agree with previous work encouraging the belief that Topkark will prove useful in future studies of transport lines. A non linear, emittance preserving, matching method was discussed that eliminates initial transients in bulk beam properties. With the G&W model, this matching method yields beams with spatial distributions that are neither Gaussian nor uniform, but something in between,

VI. REFERENCES

- [1] D. L. Bruhwiler and M. F. Reusch, AIP Conf. Proc. 297, R. Ryne Editor, (AIP, New York, 1993), pp. 524-531.
- [2] R. Garnett and T. Wangler, IEEE Particle Accelerator Conf. Proc., (IEEE, New York, 1991), p. 330.
- [3] I. Hofmann, in Applied Charged Particle Optics, Part C: Very High-Density Beams, A. Septier ed. (Academic Press, 1983).
- [4] M. Reiser, Theory and Design of Charged Particle Beams (John Wiley and Sons, 1994)
- [5] R. A. Jameson, Beam Intensity Limitations in Linear Accelerators, IEEE Trans. Nuclear Science, Vol. NS-28, No. 3, June 1981, pp.2408-2412.
- [6] E. Forest, M. Reusch, D. Bruhwiler and A. Amiry, Particle Accelerators, 1994, Vol. 45, pp.65-94
- [7] E. Forest, J. Bengtsson, M. Reusch, Physics Letters A, 158 (1991) 99-101.
- [8] M. Weiss, CERN/MPS/LI Report 73-2 Geneva (1978).

MODELING SPACE CHARGE IN BEAMS FOR HEAVY-ION FUSION*

W. M. Sharp

Lawrence Livermore National Laboratory L-440, Livermore, CA 94550, USA

Abstract

A new analytic model is presented which accurately estimates the radially averaged axial component of the space-charge field of an axisymmetric heavy-ion beam in a cylindrical beam pipe. The model recovers details of the field near the beam ends that are overlooked by simpler models, and the results compare well to exact solutions of Poisson's equation. Field values are shown for several simple beam profiles and are compared with values obtained from simpler models.

I. INTRODUCTION

Longitudinal confinement of space-charge-dominated beams in induction accelerators requires detailed knowledge of the beam space-charge field. Unlike radio-frequency accelerators, the accelerating fields of induction accelerators provide no longitudinal focusing, so time-varying electric fields must be added to the acceleration field in at least some induction modules to balance the space-charge force. For the ion beams considered for heavy-ion fusion (HIF), which are typically meters long and only a few centimeters in radius, these longitudinal-control fields, referred to here as "ears," are highly non-linear and must be calculated from the measured beam quantities like current and radius.

In HIF experiments [1] and some analytic work [2], the beam space-charge field has been calculated from a simple one-dimensional model. By assuming axisymmetry and a uniform charge density ρ , it can be shown that neglecting the axial derivative in Poisson's equation leads to the simple result, in SI units, that

$$\langle E_z(z) \rangle \approx -\frac{1}{4\pi\epsilon_0} \left[\ln \left(\frac{R^2}{a^2} \right) \right] \frac{\partial \lambda}{\partial z}. \quad (1)$$

Here, $\lambda = \pi\rho a^2$ is the beam line-charge density, z is axial distance in the beam frame, and the angle brackets denote averaging over the beam cross section. The logarithmic factor in Eq. (1) is called the "geometry factor" or "g-factor," and a and R in the term denote the radii of the beam and the beam pipe respectively. A slightly more sophisticated treatment, including the possible axial variation in a gives

$$\langle E_z(z) \rangle \approx -\frac{1}{4\pi\epsilon_0} \left\{ \left[\frac{1}{2} + \ln \left(\frac{R^2}{a^2} \right) \right] \frac{\partial \lambda}{\partial z} - \frac{\lambda}{a} \frac{\partial a}{\partial z} \right\}. \quad (2)$$

These simple expressions are not expected to be valid at the beam ends because neglecting the axial derivative in Poisson's equation is clearly invalid there. The failure of qs. (1) and (2)

is evident, for example, for a beam with a uniform charge density. For this case, a vanishes at the beam ends, and both $\langle E_z \rangle$ expressions unphysically become singular there.

In this paper, a Green's function is used to derive a more general expression for the radially averaged axial space-charge field $\langle E_z \rangle$ of a nonrelativistic ion beam centered in a perfectly conducting cylindrical pipe. The expression is specialized to beams, like those in induction accelerators, that are much longer than their radius, and a closed-form approximation to $\langle E_z \rangle$ is obtained for the class of beams with $a/R \gtrsim 0.05$ at all points. This calculation is done in the beam frame, but since HIF beams are nonrelativistic, $\langle E_z \rangle$ is effectively the same in the laboratory frame. The importance of beam-radius variation is illustrated by plotting the space-charge field for several beam profiles, and results of the new model are compared with predictions of the simpler g-factor models.

II. DERIVATION

A general expression for $\langle E_z \rangle$ is derived from a Green's function equivalent to that in Ref. [3]. The Green's function G for the potential of a ring of charge with unit magnitude centered in a perfectly conducting pipe of radius R is obtained from Poisson's equation, given in SI units for this case by

$$\nabla^2 G(r, z; r', z') = \frac{1}{\epsilon_0 r} \delta(r - r') \delta(z - z'), \quad (3)$$

where the primed coordinates denote the source location, and unprimed coordinates are field points. A straightforward solution gives

$$G(r, z; r', z') = \frac{1}{\epsilon_0 R} \sum_{n=1}^{\infty} \frac{J_0\left(\frac{\alpha_n}{R} r\right) J_1\left(\frac{\alpha_n}{R} r'\right)}{\alpha_n J_1^2(\alpha_n)} \exp\left(-\frac{\alpha_n}{R} |z - z'|\right), \quad (4)$$

where J_0 and J_1 are Bessel functions of the first kind, and α_n denotes the n th zero of J_0 . The potential ϕ for any axisymmetric charge distribution with density $\rho(r, z)$ is then found by integrating G over all r' and z' , and the corresponding axial space-charge field is given by $E_z(r, z) = -\partial\phi(r, z)/\partial z$. When ρ is assumed to be independent of r within some radius $a(z)$, then the E_z expression is trivially averaged over r , giving

$$\langle E_z(z) \rangle = \frac{1}{\pi\epsilon_0 R} \sum_{n=1}^{\infty} \frac{\left(\frac{2}{A_n a}\right) J_1(A_n a)}{\alpha_n J_1^2(\alpha_n)} \cdot \left[\int_{-L_b/2}^{L_b/2} dz' \operatorname{sgn}(z - z') \frac{\lambda'}{a'} J_1(A_n a') \exp(-A_n |z - z'|) \right]. \quad (5)$$

Here, the notation $A_n \equiv \alpha_n/R$ has been introduced, and z has been assumed to be zero at the beam midpoint, so that the ends of a beam of length L_b are at $\pm L_b/2$.

*The research was performed under the auspices of the U. S. Department of Energy by Lawrence Livermore National Laboratory under Contract No. W-7405-ENG-48.

The integral in Eq. (5) cannot in general be evaluated in closed form. However, for typical beams from induction accelerators, the axial scale lengths of a and λ are much longer than the exponential scale length A_n^{-1} for all n . This short exponential scale length allows us to expand the integrand linearly about the z' value where the integrand magnitude is maximum. Equating the derivative of the integrand with respect to z' to zero gives a transcendental equation for this integrand extremum. Rather than solve this equation numerically, we simplify the equation by assuming that the Bessel-function arguments are small, as is appropriate when $A_n a' \lesssim 1$. The resulting equation for the location of the integrand peak is

$$1 - \text{sgn}(z - z') A_n \zeta' \approx 0, \quad (6)$$

where $\zeta(z) = (L_b/2) - |z|$ is the axial distance from the nearest beam end. Examination of Eq. (7) shows that the integrand peak is

$$\zeta' \approx \max(\zeta, A_n^{-1}) \equiv \zeta_n. \quad (7)$$

The significance of Eq. (7) is that the integrand is expanded about the exponential maximum except very near the ends. The approximation leading to Eq. (7) proves to be excellent in cases where $a(\pm L_b/2) \ll R$, and it still is usable for larger beam-end radii because a varies slowly near the beam ends, so errors in ζ_n have little consequence.

After linear expansion of the integrand about ζ_n , the integral in Eq. (5) is evaluated in a straightforward manner and, after some algebra, gives the following Bessel-series expression for $\langle E_z \rangle$:

$$\begin{aligned} \langle E_z(z) \rangle = & \frac{1}{\pi \epsilon_0} \sum_{n=1}^{\infty} \frac{\left(\frac{2}{A_n a}\right) J_1(A_n a)}{\alpha_n^2 J_1^2(\alpha_n)} \\ & \cdot \left\{ \text{sgn}(z) \frac{\lambda_n}{a_n} J_1(A_n a_n) \exp(-A_n \zeta) \right. \\ & \left. - 2 \left[\frac{1}{A_n a} \frac{\partial \lambda}{\partial z} J_1(A_n a) - \frac{\lambda}{a} \frac{\partial a}{\partial z} J_2(A_n a) \right] \zeta_n f_n(z) \right\}, \quad (8) \end{aligned}$$

where a_n and λ_n are values at ζ_n , and

$$f_n(z) \equiv 1 - \frac{1}{2} [1 + \max(1, A_n \zeta)] \exp(-A_n \zeta). \quad (9)$$

Here, the fact that $A_n L_b \gg 1$ has been used to discard exponentially small contributions from the farther of the two beam ends. This expression is found to be in excellent agreement with the exact expression Eq. (5) for every case examined.

Eq. (9) is an important result of this paper, but the summation in general requires laborious numerical evaluation. In the following section, however, it is shown that the expression may be approximately evaluated for beams with sufficiently large radii at the beam ends.

III. SPECIAL CASES

A. Beam Profiles

The radius a of the axisymmetric beam and the line-charge density λ in Eq. (9) are in general independent quantities related by the beam transverse emittance and the accelerator lattice. In this work, λ is taken to be any non-negative function

that vanishes smoothly at the beam ends. For the equilibrium axisymmetric beams considered here, a , λ , and the normalized edge emittance ϵ_N are related approximately by the steady-state envelope equation

$$-\frac{\sigma_0^2}{4L^2} a + \frac{\kappa}{a} + \frac{\beta^2 \epsilon_N^2}{a^3} \approx 0. \quad (10)$$

Here, σ_0 is the phase advance per lattice period $2L$ in the absence of space-charge effects, and

$$\kappa = \frac{1}{4\pi\epsilon_0} \frac{2e\lambda}{\beta^2 M c^2} \equiv K \frac{\lambda}{\beta^2} \quad (11)$$

is the beam perveance, with β being the beam axial velocity scaled by c . Four cases are studied here:

(1) Uniform radius. Here, ϵ_N is obtained directly from Eq. (10) and increases toward the beam ends to balance the decreasing transverse space-charge force.

(2) Uniform normalized emittance. For this case, Eq. (10) is solved trivially for a^2 , giving

$$a^2 \approx \frac{2L^2}{\sigma_0^2} \left[K \frac{\lambda}{\beta^2} + \left(K^2 \frac{\lambda^2}{\beta^4} + \frac{\beta^2 \epsilon_0^2 \sigma_0^2}{L^2} \right)^{1/2} \right]. \quad (12)$$

(3) Uniform "transverse temperature". Even though the envelope equation Eq. (10) is derived under the assumption that the beam is cold in the transverse plane, the transverse temperature of a beam is in general proportional to $T \equiv \epsilon_N^2/a^2$. If this temperature-like quantity is treated as uniform along a beam, Eq. (10) gives

$$a^2 \approx \frac{4L^2}{\sigma_0^2} \left(K \frac{\lambda}{\beta^2} + T \right). \quad (13)$$

(4) Uniform charge density. If the charge density ρ is assumed uniform along the beam, then

$$a^2 = \frac{\lambda}{\pi \rho}, \quad (14)$$

and the normalized emittance ϵ_N from Eq. (10) vanishes at the beam ends along with λ and a .

Although these simple profiles are unlikely to match that in an experimental beam, they illustrate the sensitivity of the space-charge field to the beam radial variation. Fig. 1 shows field values calculated for beams with identical parameters and line-charge profiles, but differing radial profiles. The parameters are those of a small recirculating induction accelerator being built at the Lawrence Livermore National Laboratory [4], except that the midsection of the beam has been shortened to highlight field changes near the ends. As expected, one finds that the peak space-charge field increases for profiles that have smaller end radii. It is also evident that $\langle E_z \rangle$ for the uniform-density is qualitatively different from the others. For the cases with a finite beam-end radius, the field magnitude is seen to drop significantly in a narrow region at the beam end. In this region, which has a characteristic length of R/α_1 , the absence of charge outside the beam reduces the axial field, and at the endpoints, the field is reduced by approximately half. In contrast, $\langle E_z \rangle$

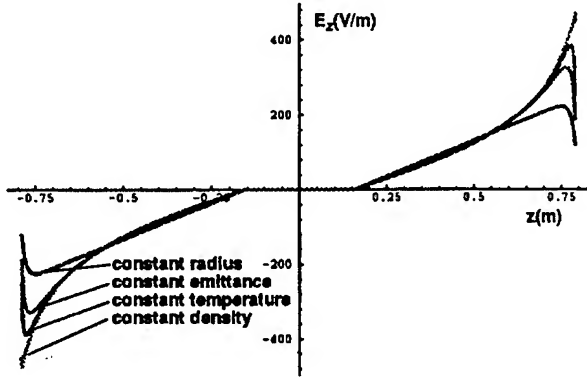


Figure 1. Radially averaged space-charge field for beams with various radial profiles but the same line-charge density.

for the uniform-density case varies monotonically near the end due to the rapidly decreasing radius. Another distinction of the uniform-density case is that about 250 terms are required for convergence of the Bessel series in Eq. (8), whereas the other cases require between 20 and 40 terms. This difference arises because the beam radial profile is poorly fit by a Bessel series when a/R is small, and many terms are needed for an adequate representation.

B. Analytic Approximations

Since the series Eq. (8) converges rapidly when $a/R \gtrsim 0.05$ for all z , it is sensible to approximate the $\langle E_z \rangle$ expression by setting $n = 1$ in f_n and in the exponential factor. Also, since a varies only slightly between the ends and ζ_1 for such beams, leading Bessel factor and the derivatives of a and λ can all be evaluated at ζ_1 with negligible error. These approximations leave two Bessel series that, remarkably, can be exactly summed. Expressed generally, these Bessel sums have been verified numerically over the range $1 \geq x > 0$:

$$4 \sum_{n=1}^{\infty} \frac{\left(\frac{2}{\alpha_n x}\right)^2 J_1^2(\alpha_n x)}{\alpha_n^2 J_1^2(\alpha_n)} = \frac{1}{2} + \ln\left(\frac{1}{x^2}\right) \quad (15a)$$

$$8 \sum_{n=1}^{\infty} \frac{\left(\frac{2}{\alpha_n x}\right) J_1(\alpha_n x) J_2(\alpha_n x)}{\alpha_n^2 J_1^2(\alpha_n)} = 1. \quad (15b)$$

Outside the specified range, these sums either fail to converge or give other values. Substituting Eq. (15) into the approximate form of Eq. (8) leads to the expression

$$\langle E_z(z) \rangle = -\frac{1}{4\pi\epsilon_0} \left\{ \left[\frac{1}{2} + \ln\left(\frac{r^2}{a_1^2}\right) \right] \left[f_1(z) \frac{\partial \lambda}{\partial z} \right]_{\zeta_1} - \text{sgn}(z) \frac{A_1 \lambda_1}{2} \exp(-A_n \zeta) \right] - f_1(z) \left[\frac{\lambda}{a} \frac{\partial a}{\partial z} \right]_{\zeta_1} \right\}. \quad (16)$$

This expression is a numerically tractable generalization of Eq. (2) and is a very good approximation to the Bessel-series expression Eq. (8) for most experimental beams. As expected, it gives an inaccurate but non-singular result for uniform-density beams.

Sufficiently far from the beam ends, the exponentials in Eq. (8) vanish, and $\zeta_n = \zeta$. In this case, the Bessel sums in

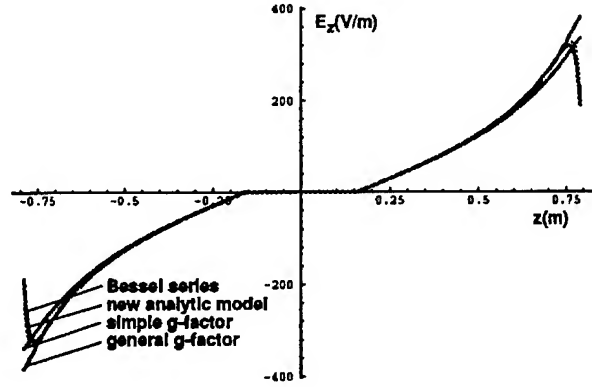


Figure 2. Radially averaged space-charge field for a constant emittance beam calculated using various approximations

Eq. (15) can be used to evaluate Eq. (8) without further approximation, and the result exactly recovers the general g-factor expression Eq. (2). It follows that Eq. (2) gives $\langle E_z \rangle$ accurately in the interior of any beam in which λ and a vary on length scales that are long compared with R/α_1 . The expression only fails within a region a few times R/α_1 in length at each end.

The various approximate expressions for $\langle E_z \rangle$ are compared in Fig. 2 for a beam with a uniform normalized emittance and the same lattice and beam parameters as the beams shown in Fig. 1. The Bessel-series approximation has been compared with the exact integral expression Eq. (5) at selected points along the beam and is found to agree within 1% everywhere. The new analytic expression Eq. (16) deviates from the Bessel-series result by a few percent near the peak magnitude of $\langle E_z \rangle$, but it nonetheless reproduces the main features of the more exact expression. Both curves overlay the general g-factor model away from the ends, as expected. The curve generated from the simple g-factor expression Eq. (1) deviates from the other approximations in the beam interior, underlining the fact that variation of the beam radius cannot in general be ignored.

References

- [1] T. J. Fessenden, D. L. Judd, D. Keefe, C. Kim, L. J. Laslett, L. Smith, and A. I. Warwick, *AIP Conference Proceedings* 152 from the 1985 Heavy-Ion Fusion Symposium, Washington, D. C., p. 145.
- [2] E. P. Lee, *Proceedings of the 1981 Linear Accelerator Conference*, Los Alamos Report LA-9234-C, p. 263.
- [3] C. K. Allen, N. Brown, and M. Reiser, *Part. Accel.* **45**, 149 (1994).
- [4] A. Friedman, J. J. Barnard, M. D. Cable, D. A. Callahan, F. J. Deadrick, S. Elon, T. J. Fessenden, D. P. Grote, D. L. Judd, H. C. Kirbie, D. B. Longinotti, S. M. Lund, L. A. Natrass, M. B. Nelson, M. A. Newton, T. C. Sangster, W. M. Sharp, and S. S. Yu, "Progress Toward a Prototype Recirculating Induction Accelerator for Heavy-Ion Fusion," in these proceedings.

IMPEDANCE OF PERIODIC IRISES IN A BEAM PIPE *

Shicheng Jiang and Robert L. Gluckstern

Physics Department, University of Maryland, College Park, MD 20742, USA

Hiromi Okamoto

Institute for Chemical Research, Kyoto University, Kyoto 611, Japan

Abstract

In a recent paper[1], we constructed a variational form to calculate both the longitudinal and transverse impedance of a thick iris in a beam pipe. Implementation of this calculation led to rapidly converging and accurate values for these impedances for a circular beam pipe and iris. We have now constructed an analogous variational form for the longitudinal and transverse impedance of periodic irises in a beam pipe, with similar convergence and accuracy properties. In this case the numerically calculated impedance is imaginary, except for isolated narrow resonances corresponding to modes propagating with the velocity of light. The real part of impedance is obtained by using causality. Analysis and numerical results are discussed and presented.

I. Introduction

In a previous publication[1], we calculated both the longitudinal and transverse coupling impedance of an iris in a beam pipe. In particular we constructed a variational formulation for the impedance, where the trial function was the transverse electric fields at the two junctions of the beam pipe and the iris. The numerical implementation of this formulation proved to be extremely well convergent for a circular beam pipe and iris, requiring only a few terms in the expansion of the trial functions in terms of TM and TE transverse modes in the iris region.

In this work, we construct a corresponding variational formulation for the longitudinal and transverse impedance of a beam pipe loaded with periodic irises. The numerical implementation for a circular beam pipe with periodic circular irises is again well convergent. The numerically calculated impedance in this case is imaginary, except for isolated narrow resonances corresponding to modes propagating with the velocity of light. However, the real part of the impedance is retrieved from the information the imaginary part carries, in the form of a sum of delta functions.

II. Analysis

We will consider a beam pipe of arbitrary cross section loaded with periodic irises of arbitrary cross section, both homogeneous in the axial direction. The planes involving the iris side walls are perpendicular to the beam pipe axis. We denote the period of irises as L , and the width of irises as g . We consider the m th iris and its following pipe cavity as the m th cell of length L . We set the coordinate origin at the center of the *zeroth* iris and the axis of the pipe as the z axis. The cross sectional area of the iris hole is denoted by S_1 while S_2 represents the side walls of the iris.

Both in the iris hole and in the pipe cavity, the electromagnetic fields are superpositions of source fields and pipe fields which can be expanded as sums over the normal modes in relevant regions. We use Latin letters as the subscripts of the quantities defined in the pipe cavity, and Greek letters for those defined in the iris hole. The time dependent factor $\exp(j\omega t)$ attached to all fields is omitted for simplicity.

In the pipe cavity region, the source fields are generated by the ultrarelativistic charged particle beam moving near or along the axis of a smooth pipe. Specifically, in the frequency domain we have:

$$\mathbf{E}_0 = Z_0 \mathbf{H}_0 \times \hat{\mathbf{z}} = A_0 e^{-jkz} \nabla_{\perp} \chi, \quad (1)$$

where Z_0 is the free-space impedance, A_0 is a constant, and $\hat{\mathbf{z}}$ is unit vector in positive z direction. ∇_{\perp} is defined as $\nabla_{\perp} = \hat{\mathbf{x}} \frac{\partial}{\partial x} + \hat{\mathbf{y}} \frac{\partial}{\partial y}$. The source field potential χ is a function of transverse coordinates which satisfies the boundary conditions on the pipe surface.

The pipe fields contain both left and right traveling waves with wave number β_n . Floquet's theorem says that in a periodic structure the electromagnetic fields in the m th cell must be identical to those in the $(m+1)$ th cell except for a constant phase factor. We then write:

$$\frac{\mathbf{E}_{\perp}}{A_0} = e^{-jkz} \nabla_{\perp} \chi + \sum_n \epsilon_n e^{-jkmL} [A_n e^{-j\beta_n(z-mL)} + B_n e^{j\beta_n(z-mL)}], \quad (2)$$

$$\frac{Z_0 \mathbf{H}_{\perp} \times \hat{\mathbf{z}}}{A_0} = e^{-jkz} \nabla_{\perp} \chi + \sum_n \epsilon_n \lambda_n e^{-jkmL} [A_n e^{-j\beta_n(z-mL)} - B_n e^{j\beta_n(z-mL)}]. \quad (3)$$

Here, ϵ_n are the transverse electric normal modes defined on the cross section of the pipe region (Its area is $S_1 + S_2$), that means $\int_{S_1+S_2} \epsilon_n \cdot \epsilon_{n'} dS = \delta_{nn'}$, A_n and B_n are expansion coefficients, and λ_n is k/β_n for TM modes, β_n/k for TE modes.

In the iris hole, the source field potential is replaced by σ which satisfies the boundary conditions on the hole surface, and we write:

$$\frac{\mathbf{E}_{\perp}}{A_0} = e^{-jkz} \nabla_{\perp} \sigma + \sum_{\mu} \epsilon_{\mu} e^{-jkmL} [C_{\mu} e^{-j\beta_{\mu}(z-mL)} + D_{\mu} e^{j\beta_{\mu}(z-mL)}], \quad (4)$$

$$\frac{Z_0 \mathbf{H}_{\perp} \times \hat{\mathbf{z}}}{A_0} = e^{-jkz} \nabla_{\perp} \sigma + \sum_{\mu} \epsilon_{\mu} \lambda_{\mu} e^{-jkmL} [C_{\mu} e^{-j\beta_{\mu}(z-mL)} - D_{\mu} e^{j\beta_{\mu}(z-mL)}]. \quad (5)$$

*Work supported by the U.S. Department of Energy

Here, e_μ are the transverse electric normal modes defined on the cross section of the iris hole (Its area is S_1), that means $\int_{S_1} e_\mu \cdot e_{\mu'} dS = \delta_{\mu\mu'}$, C_μ and D_μ are expansion coefficients, β_μ is the wave number in the iris hole, and λ_μ is k/β_μ for TM modes, β_μ/k for TE modes.

By introducing two unknown fields U and V defined as the transverse electric fields on S_1 , which can be expanded in terms of e_μ , and matching electromagnetic fields at the junctions of irises and pipe, we eventually get two integral equations:

$$\int_{S_1} \vec{K}_{11} \cdot U dS + \int_{S_1} \vec{K}_{12} \cdot V dS = G_U, \quad (6)$$

$$\int_{S_1} \vec{K}_{12} \cdot U dS + \int_{S_1} \vec{K}_{22} \cdot V dS = G_V. \quad (7)$$

Here, \vec{K}_{11} , \vec{K}_{12} and \vec{K}_{22} are tensor integral kernels:

$$\begin{aligned} \vec{K}_{11} = & \sum_n e_n e'_n \frac{2\lambda_n}{j \sin \beta_n (L-g)} [\cos k(L-g) - \cos \beta_n (L-g)] \\ & + \sum_\mu e_\mu e'_\mu \frac{2\lambda_\mu}{j \sin \beta_\mu g} [\cos kg - \cos \beta_\mu g], \end{aligned} \quad (8)$$

$$\vec{K}_{12} = \sum_n e_n e'_n \frac{2\lambda_n \sin k(L-g)}{\sin \beta_n (L-g)} + \sum_\mu e_\mu e'_\mu \frac{2\lambda_\mu \sin kg}{\sin \beta_\mu g}, \quad (9)$$

$$\begin{aligned} \vec{K}_{22} = & \sum_n e_n e'_n \frac{2\lambda_n}{j \sin \beta_n (L-g)} [\cos k(L-g) + \cos \beta_n (L-g)] \\ & + \sum_\mu e_\mu e'_\mu \frac{2\lambda_\mu}{j \sin \beta_\mu g} [\cos kg + \cos \beta_\mu g]. \end{aligned} \quad (10)$$

And G_U and G_V are respectively:

$$G_U = \sum_n e_n \frac{2\lambda_n (\rho_n + \chi_n)}{j \sin \beta_n (L-g)} [\cos k(L-g) - \cos \beta_n (L-g)], \quad (11)$$

$$G_V = \sum_n e_n \frac{2\lambda_n (\rho_n + \chi_n) \sin k(L-g)}{\sin \beta_n (L-g)} - 2 \nabla_\perp \rho, \quad (12)$$

where $\chi_n = \int_{S_2} \nabla_\perp \chi \cdot e_n dS$, $\rho_n = \int_{S_1} \nabla_\perp \rho \cdot e_n dS$, and ρ is defined as $\rho = \chi - \sigma$.

Finally, the impedance of one cell of this periodic structure can be expressed as

$$Z(k) = G_0(k) + Z_{var}(k), \quad (13)$$

where the explicit term $G_0(k)$ is a sum over the indices of the normal modes in the pipe region, and $Z_{var}(k)$ has been put into the variational form:

$$Z_{var}(k) = \frac{[\int_{S_1} G_U \cdot U dS + \int_{S_1} G_V \cdot V dS]^2}{M}, \quad (14)$$

where M is

$$\begin{aligned} M = & \int_{S_1} dS \int_{S_1} dS' U \cdot \vec{K}_{11} \cdot U + 2 \int_{S_1} dS \int_{S_1} dS' U \cdot \vec{K}_{12} \cdot V \\ & + \int_{S_1} dS \int_{S_1} dS' V \cdot \vec{K}_{22} \cdot V. \end{aligned} \quad (15)$$

III. Numerical Results

As an example, we use the formula to calculate the longitudinal and transverse impedance of a circular pipe loaded with circular irises. We obtain results for a wide range of structure parameters. We find that our computer code is well convergent over a large range of frequency for those structures. The calculated impedance is imaginary, except for isolated narrow resonances. The positions of the resonances are the intersections of dispersion curves with the light line. These are the resonant modes propagating with the velocity of light in the periodic structure. Fig. 1 presents the longitudinal impedance for a sample structure (The radius of beam pipe is a , the radius of iris hole is b . In our example, the ratios of $b/a = 0.45$, $L/a = 1.1$, and $g/a = 0.35$). The resonant modes and loss factors obtained from our calculation agree well with those from the well known computer codes KN7C and TRANSVRS [2].

IV. Discussion

The missing real part of the impedance can be retrieved from the imaginary part by using causality. Taking the longitudinal case as an example (Note: $Z = R + jX$),

$$\frac{X_{||}(k)}{Z_0} = \sum_n \frac{a_n k}{k_n^2 - k^2}, \quad (16)$$

where all a_n 's are greater than zero to satisfy Foster's Reactance Theorem[3]. If we now move the poles to a position slightly above the real axis, we can write the impedance for very small ϵ . We use the relation $Z_{||}(-k) = Z_{||}^*(k)$ and write the imaginary part in the form:

$$\frac{Z_{||}(k)}{Z_0} = \sum_n \frac{j a_n k}{k_n^2 - k^2 + j\epsilon}. \quad (17)$$

By using $\lim_{\epsilon \rightarrow 0} [\epsilon/(\epsilon^2 + x^2)] = \pi \delta(x)$, we get

$$\begin{aligned} \frac{R_{||}(k)}{Z_0} &= \lim_{\epsilon \rightarrow 0} \sum_n \frac{a_n k \epsilon}{(k_n^2 - k^2)^2 + \epsilon^2} \\ &= \pi \sum_n a_n k_n \delta(k^2 - k_n^2). \end{aligned} \quad (18)$$

We can therefore use the computed behavior of $X_{||}(k)$ near each resonance at $k = k_n$ to determine a_n by fitting $Z_0/X_{||}(k)$ as a linear function of $k - k_n$ near $k = k_n$, and from these a_n 's to obtain the real part of the impedance as a sum of delta functions with specified coefficient. Clearly these delta functions will be broadened if the wall conductivity is finite. Fig. 2 presents the delta functions of real part longitudinal impedance[4]. The first 10 resonances out of the 60 shown in Figs. 1 and 2 are identified in Table 1.

It appears that the resonances at $k = k_n$ correspond to the frequencies at which propagation of azimuthally symmetric modes through the structure produces a phase advance of kL per period of length L , in order to be in synchronism with the particle moving with velocity c . This is confirmed from the dispersion curves calculated with our geometry, using the program KN7C.

The total longitudinal impedance is therefore

$$\frac{Z_{||}(k)}{Z_0} = \pi \sum_n a_n k_n \delta(k^2 - k_n^2) + jk \sum_n \frac{a_n}{k_n^2 - k^2}, \quad (19)$$

where the sum is over all values of n corresponding to positive k_n . Clearly $Z_{\parallel}(-k) = Z_{\parallel}^*(k)$, as required.

A similar situation exists for the transverse impedance, where we find,

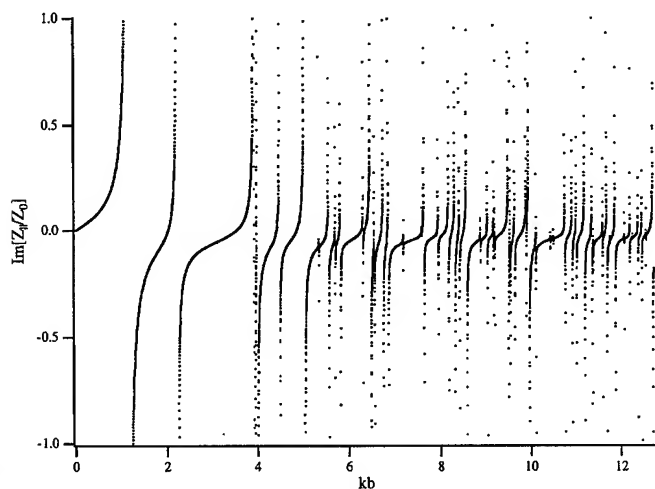


Figure. 1. The imaginary part of longitudinal impedance for $b/a = 0.45$, $L/a = 1.1$, $g/a = 0.35$.

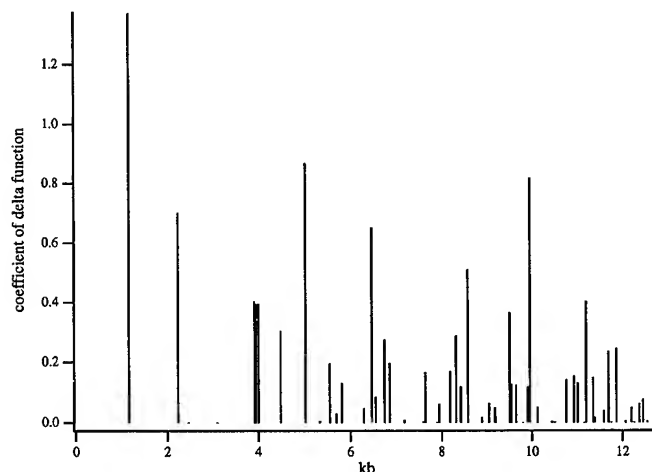


Figure. 2. The real part of longitudinal impedance for $b/a = 0.45$, $L/a = 1.1$, $g/a = 0.35$.

$$\frac{Z_{\perp}(k)}{Z_0} = \pi k \sum_n b_n \delta(k^2 - k_n^2) + j \sum_n \frac{b_n k_n}{k_n^2 - k^2}, \quad (20)$$

This time we satisfy $Z_{\perp}(-k) = -Z_{\perp}^*(k)$, and the resonances correspond to the propagation of modes proportional to $\cos \theta$, $\sin \theta$, with a phase advance of kL per period. We present the first 10 resonances of the transverse impedance in Table 2.

Acknowledgment

We are grateful to Dr. Karl L. Bane for providing the output of KN7C and TRANSVRS for our structure.

References

- [1] H. Okamoto, S. Jiang, R. L. Gluckstern, *Phys. Rev.*, **E50**, 1501(1994).
- [2] K. Bane, B. Zotter, in *Proceedings of the 11th International Conference on High Energy Accelerators*, CERN (Burhäuser Verlag, Basel, 1980), p581.
- [3] E. A. Guillemin, *Communication Networks*, John Wiley & Sons, Inc., New York, 1931.
- [4] The vertical axis is the coefficient of the delta function in Eq. 18.

	kb	$a_n(Z_0)$
1	1.16131	3.75845E-1
2	2.23213	9.99812E-2
3	2.47150	1.21422E-6
4	3.10663	4.22596E-6
5	3.91728	3.27981E-2
6	3.94055	3.18982E-2
7	3.99824	3.14555E-2
8	4.48055	2.16335E-2
9	5.02304	5.50932E-2
10	5.33543	2.46804E-4

Table. 1. The first 10 resonances of longitudinal impedance for $b/a = 0.45$, $L/a = 1.1$, $g/a = 0.35$.

	kb	$b_n(Z_0)$
1	1.57045	7.10124E-1
2	1.75736	3.14108E-2
3	2.31282	1.23584E-1
4	2.79476	2.20642E-2
5	2.98274	1.13804E-2
6	3.24850	6.87317E-3
7	3.66906	4.27322E-2
8	3.91339	3.63055E-3
9	4.08240	9.94933E-3
10	4.21653	8.24202E-3

Table. 2. The first 10 resonances of transverse impedance for $b/a = 0.45$, $L/a = 1.1$, $g/a = 0.35$.

FREQUENCY DEPENDENCE OF THE POLARIZABILITY AND SUSCEPTIBILITY OF A CIRCULAR HOLE IN A THICK CONDUCTING WALL*

Wen-Hao Cheng, Alexei V. Fedotov and Robert L. Gluckstern
Physics Department, University of Maryland, College Park, MD 20742, USA

Abstract

We calculate a generalized polarizability and susceptibility of a circular hole in a thick metallic plate as a function of hole dimensions and wavelength. In particular, we construct a variational form which allows us to obtain accurate numerical results with a minimum of computational effort. Numerical results are obtained for a variety of hole dimensions relative to the wavelength. In addition, analytic results are obtained and shown to be accurate to second order in the ratio of the hole dimension to the wavelength for a vanishingly thin wall.

I. INTRODUCTION

The penetration of electric and magnetic fields through a hole in a metallic wall plays an important role in many devices. In an accelerator, such holes in the beam pipe serve to allow access for pumping, devices for beam current and beam position measurement, coupling between cavities, etc. In much of the early work the hole dimensions were considered to be very small compared to the wavelength. The purpose of this paper is to extend the calculation to include the effects of finite wavelength, although we still confine our attention to wavelengths no smaller than the hole dimensions.

We redefine the conventional static treatment of polarizability and susceptibility in terms of the cavity detuning, defining a new generalized polarizability and susceptibility. In this way, we include the frequency dependence of the polarizability and susceptibility as well as the contributions of higher multipole moments of the hole. But these generalized polarizability and susceptibilities should only be seen as intermediate vehicles to relate the coupling integrals of interest to the detuning of the cavity by the hole. We will obtain an expression for the detuning of the modes of the symmetric cavity structure due to the presence of the hole. The symmetric cavity structure consists of two identical cavities, each of the length L and radius b . Clearly the modes will be either symmetric or antisymmetric in the axial coordinate. Our analysis will be limited to the modes near the $TM_{0N\ell}$, $TM_{1N\ell}$ and $TE_{1N\ell}$ modes of the unperturbed pillbox.

II. GENERAL ANALYSIS

Our analysis can be generalized to include cavity regions and iris regions of arbitrary cross section. Taking $z_1 = 0$ to be the left end of the left cavity, we can write the transverse electric field as

$$E_{\perp}^{(C)}(\mathbf{r}, z_1) = \sum_n a_n e_n(\mathbf{r}) \frac{\sin \beta_n z_1}{\sin \beta_n L}, \quad (1)$$

where \mathbf{r} stands for the transverse coordinates x and y , and where the modes e_n may be either TM or TE. Here $\beta_n^2 = k^2 - \gamma_n^2$, where γ_n^2 are the eigenvalues of the two dimensional scalar Helmholtz equation in the cavity region with the appropriate boundary conditions. We use Latin subscripts (n, m, N, \dots) for the cavity region, and $kc/2\pi$ is the frequency.

The transverse electric field in the iris region can similarly be written as

$$E_{\perp}^{(I)}(\mathbf{r}, z_2) = \sum_{\nu} b_{\nu} e_{\nu}(\mathbf{r}) \frac{\cos \beta_{\nu} z_2}{\cos \beta_{\nu} g/2}, \quad (2)$$

where $z_2 = 0$ is now the center of the iris region, and where we use Greek subscripts (ν, μ, σ, \dots) for the iris region. Equation (2) is appropriate for the modes in our symmetric structure for which $E_{\perp}^{(I)}$ is even in z_2 . For those modes where $E_{\perp}^{(I)}$ is odd in z_2 we need to replace the cosines by sines in Eq. (2). We express the coefficients a_n and b_{ν} in terms of $E_{\perp}(\mathbf{r}) \equiv \mathbf{u}(\mathbf{r})$ at the interface between the cavity and the iris ($z_1 = L, z_2 = -g/2$). We then write the transverse magnetic field in each region. Equating the transverse magnetic field at $z_1 = L, z_2 = -g/2$ in the region S_1 leads to the integral equation for the unknown function $\mathbf{u}(\mathbf{r})$

$$\int_{S_1} dS' \mathbf{u}(\mathbf{r}') \cdot \overleftrightarrow{K}(\mathbf{r}, \mathbf{r}') = 0, \quad (3)$$

where

$$\begin{aligned} \overleftrightarrow{K}(\mathbf{r}, \mathbf{r}') &= \sum_n \lambda_n e_n(\mathbf{r}) e_n(\mathbf{r}') \cot \beta_n L \\ &- \sum_{\nu} \lambda_{\nu} e_{\nu}(\mathbf{r}) e_{\nu}(\mathbf{r}') \tan \beta_{\nu} g/2, \end{aligned} \quad (4)$$

and

$$\begin{aligned} \lambda_n &= \frac{Z_0}{Z_n} = \begin{cases} k/\beta_n, & TM \\ \beta_n/k, & TE \end{cases}, \\ \lambda_{\nu} &= \frac{Z_0}{Z_{\nu}} = \begin{cases} k/\beta_{\nu}, & TM \\ \beta_{\nu}/k, & TE \end{cases}, \end{aligned} \quad (5)$$

with $Z_0 = \sqrt{\mu_0/\epsilon_0}$ being the impedance of free space, Z_n being the impedance of the "cavity" wave guide and Z_{ν} is the impedance of the "iris" waveguide.

By separating out the dominant term N in the sum over n , one can cast Eq. (3) into a variational form for the frequency, with the trial function being $\mathbf{u}(\mathbf{r})$. The result is the implicit equation for the frequency

$$\frac{\tan \beta_N L}{\lambda_N} = \sum_{\nu} \sum_{\mu} K_{N\nu} (M^{-1})_{\nu\mu} K_{N\mu}. \quad (6)$$

*Work supported by the U.S. Department of Energy

Here $M_{\nu\mu}$ is a symmetric matrix defined by

$$M_{\nu\mu} = - \sum_{n \neq N}' \lambda_n \cot \beta_n L K_{n\mu} K_{n\nu} + \sum_{\sigma} \lambda_{\sigma} \tan \beta_{\sigma} g/2 K_{\sigma F\mu} K_{\sigma\nu} \quad (7)$$

and

$$K_{n\nu} \equiv \int_{S_1} dS \mathbf{e}_n \cdot \mathbf{f}_{\nu}, \quad K_{\sigma\nu} \equiv \int dS \mathbf{e}_{\sigma} \cdot \mathbf{f}_{\nu}. \quad (8)$$

Note that we are looking at modes close to the cavity modes corresponding to $\beta_N L = \ell\pi$ or $k_{N\ell}^2 = \ell^2 \pi^2 / L^2 + \gamma_N^2$. Since the frequency k is also contained in $M_{\nu\mu}$, Eq. (6) must be solved by iteration.

We obtain the expression for the frequency change in the cavity and therefore generalize the concept of the static polarizability to a generalized polarizability by considering a mode which has a normal electric field, but no tangential magnetic field at the center of the hole (for example the $TM_{0N\ell}$ mode) and write

$$\chi \equiv \frac{k^2 - k_M^2}{k_M^2 E_M^2(0)}. \quad (9)$$

Similarly we obtain the generalization of the susceptibility for a circular hole (for example the $TM_{1N\ell}$ or $TE_{1N\ell}$ mode)

$$\psi \equiv \frac{k_M^2 - k^2}{k^2 H_M^2(0)}. \quad (10)$$

We obtain k from Eq. (6) and χ or ψ , for that frequency, from Eq. (9) or (10). Clearly the mode identification M stands for $0N\ell$ or $1N\ell$ as appropriate.

III. POLARIZABILITY FOR A CIRCULAR IRIS HOLE

We now specialize to TM_{0n} waveguide modes in a circular geometry in order to obtain the polarizability[1]. The cavity radius is b and the iris radius is a and we use the complete set

$$\mathbf{f}_{\nu}(r) = \mathbf{e}_{\nu}(r) = -\nabla \phi_{\nu}(r), \quad (11)$$

with

$$\phi_n(r) = \frac{J_0(s_n r/b)}{\sqrt{\pi s_n J_1(s_n)}}, \quad \phi_{\nu}(r) = \frac{J_0(s_{\nu} r/a)}{\sqrt{\pi s_{\nu} J_1(s_{\nu})}}. \quad (12)$$

Here $s_{n,\nu}$ are the roots of the equation $J_0(s_{n,\nu}) = 0$. Evaluating the kernels and matrices in Eq. (8) and Eq. (7), the frequency can now be calculated using Eq. (6) and the symmetric polarizability using Eq. (9). Similarly we can obtain the asymmetric polarizability.

The polarizabilities obtained in this way will be functions of the geometrical parameters $a/b, g/a, a/L$, and ℓ, N of the $TM_{0N\ell}$ cavity mode. In order to tie the polarizabilities to the geometry of the hole alone, it is necessary to take the limit for large b and L , but with finite frequency. This can be accomplished by letting $b, L \rightarrow \infty$, but keeping $s \equiv s_N a/b \equiv \ell\pi a/L$ finite by also allowing $N, \ell \rightarrow \infty$.

IV. SUSCEPTIBILITY FOR A CIRCULAR HOLE

We now must use the waveguide modes TM_{1n} and TE_{1n} for our complete set in the pipe region. Specifically we have

$$\mathbf{e}_n = -\nabla \phi_n,$$

$$\phi_n = \sqrt{\frac{2}{\pi}} \frac{J_1(p_n r/b) \cos \theta}{p_n J_0(p_n)} \text{ for } TM_{1n} \text{ modes}, \quad (13)$$

$$\mathbf{e}_n = \hat{\mathbf{z}} \times \nabla \psi_n,$$

$$\psi_n = \sqrt{\frac{2}{\pi}} \frac{J_1(q_n r/b) \sin \theta}{\sqrt{q_n^2 - 1} J_1(q_n)} \text{ for } TE_{1n} \text{ modes}, \quad (14)$$

where $p_{n,\nu}$ are the roots of $J_1(p_{n,\nu}) = 0$. In the iris region

$$\mathbf{e}_{\nu} = -\nabla \phi_{\nu},$$

$$\phi_{\nu} = \sqrt{\frac{2}{\pi}} \frac{J_1(p_{\nu} r/a) \cos \theta}{p_{\nu} J_0(p_{\nu})} \text{ for } TM_{1\nu} \text{ modes}, \quad (15)$$

$$\mathbf{e}_{\nu} = \hat{\mathbf{z}} \times \nabla \psi_{\nu},$$

$$\psi_{\nu} = \sqrt{\frac{2}{\pi}} \frac{J_1(q_{\nu} r/a) \sin \theta}{\sqrt{q_{\nu}^2 - 1} J_1(q_{\nu})} \text{ for } TE_{1\nu} \text{ modes}, \quad (16)$$

where $q_{n,\nu}$ are the roots of $J_1'(q_{n,\nu}) = 0$. Once again, the kernels and matrix elements can be calculated, but now n and ν can be either TM or TE in $K_{n\nu}^{\psi}$, where the superscript ψ denotes susceptibility. The frequency is again obtained from Eq. (6), but the susceptibility requires using Eq. (10).

V. DISCUSSION OF THE ANALYTIC RESULTS

The variational formulation also allows us to obtain analytically the first order correction in $k^2 a^2$ for a hole in a plate of zero thickness from the knowledge of the correct field solutions for $ka = 0$. In the case of polarizability we obtain the following approximate analytic form

$$\chi_{N\ell} \cong \frac{4a^3}{3} \left(1 - \frac{k^2 a^2}{5} - \frac{s^2}{5} + \frac{4j}{9\pi} k^3 a^3 \right). \quad (17)$$

In the case of susceptibility we obtain

$$\begin{aligned} \psi_{N\ell}^{TM} &\cong \frac{8a^3}{3} \left[1 + k^2 a^2 \left(\frac{8}{15} - \frac{p^2}{3k^2 a^2} - \frac{p^4}{15k^4 a^4} \right) \right. \\ &\quad \left. - \frac{8j}{9\pi} k^3 a^3 \right], \end{aligned} \quad (18)$$

$$\psi_{N\ell}^{TE} \cong \frac{8a^3}{3} \left[1 + k^2 a^2 \left(\frac{8}{15} - \frac{q^2}{5k^2 a^2} \right) - \frac{8j}{9\pi} k^3 a^3 \right], \quad (19)$$

where $p \equiv p_N a/b$, $q \equiv q_N a/b$. It appears that the approximate forms for polarizability and susceptibility give reasonably accurate results even for values of ka as large as 1.

The coefficients of the leading terms in Eqs. (17)-(19) for $g = 0$ and small ka appear to be well confirmed. Moreover, the coefficients of the terms in first order in $k^2 a^2$ and the coefficients of the leading imaginary terms are the same as those obtained by Eggimann[2].

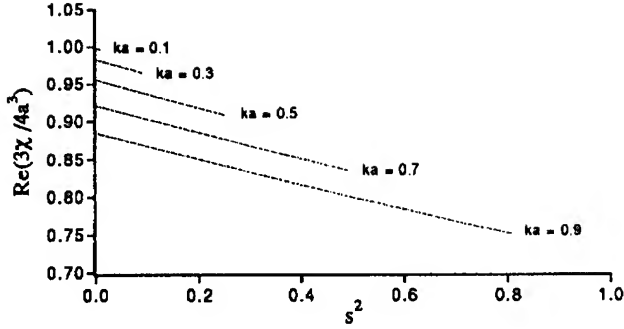


Figure 1. Real part of scaled polarizability $\tilde{\chi}$ vs. s^2 for various ka , with $g/a = 0$.

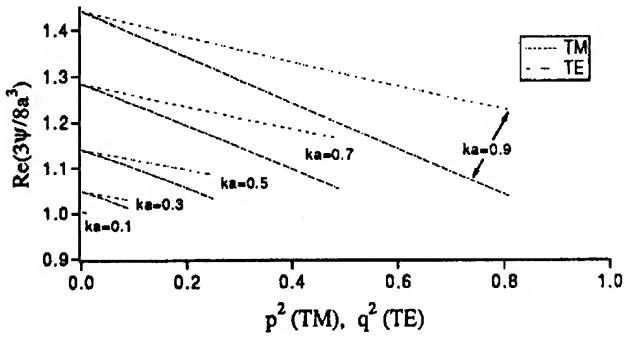


Figure 2. Real part of scaled susceptibility $\tilde{\psi}$ vs. p^2 (for TM mode) or q^2 (for TE mode) for various ka , with $g/a = 0$.

VI. NUMERICAL RESULTS FOR A HOLE IN A PLATE

We present the results in a form suggested by the predictions for $g = 0$ (zero wall thickness) and small ka , s in Eq. (17). Specifically, we define $\tilde{\chi}(ka, s) \equiv \chi/(4a^3/3)$ and plot the real part of $\tilde{\chi}$ vs. s^2 for various values of ka in Fig. 1. A similar presentation is provided for the real part of the susceptibilities. We define $\tilde{\psi} \equiv \psi/(8a^3/3)$ and plot $\tilde{\psi}$ vs. p^2 (TM) or q^2 (TE) for various values of ka in Fig. 2.

For the wall with finite thickness, the polarizability and susceptibility seen within the cavity are given by [1] $\chi_{in} = \chi_s + \chi_a$, $\psi_{in} = \psi_s + \psi_a$, while the polarizability and susceptibility seen outside the cavity are given by $\chi_{out} = \chi_s - \chi_a$, $\psi_{out} = \psi_s - \psi_a$. Here the subscripts s and a denote the solutions of the symmetric and antisymmetric potential problems [1]. In Figs. 3 and 4, we show $\tilde{\chi}_{in}$ and $\tilde{\psi}_{in}$ as functions of g/a for various ka .

The logarithmic plots of $\tilde{\chi}_{out}$ and $\tilde{\psi}_{out}$ become linear with slopes $-s_1 = -2.405$ and $-q_1 = -1.841$, respectively, as expected.

VII. SUMMARY

We have defined a generalized polarizability and susceptibility of a hole for finite wave length in terms of the frequency shift of the associated cavities due to the hole. In addition we have constructed a variational form for these frequency shifts, assuring

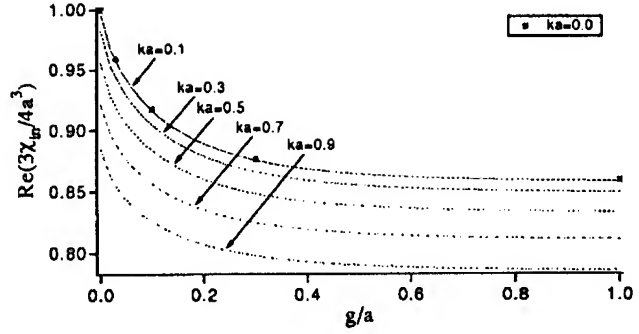


Figure 3. Real part of scaled polarizability $\tilde{\chi}_{in}$ vs. g/a for various ka , with $s = 0$.

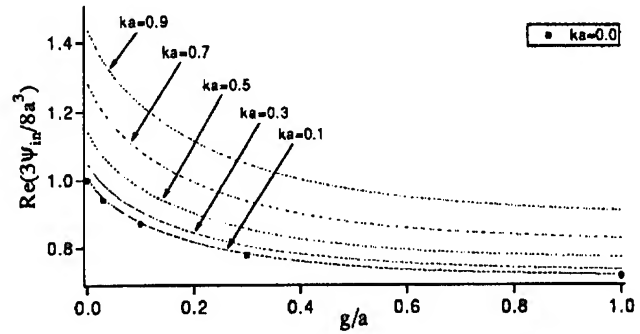


Figure 4. Real part of scaled susceptibility $\tilde{\psi}_{in}$ vs. g/a for various ka , with $p = 0$ (for TM mode) or $q = 0$ (for TE mode), where the curves are the same for both TM and TE modes.

ing good convergence for our numerical calculations. We then allow the cavity dimensions to be infinitely large, enabling us to obtain accurate numerical values of the polarizability and susceptibilities of a circular hole in an infinite plate of finite thickness. Then we obtain numerical results for various values of ka , g/a . The approximate analytic forms are given by Eq. (17) for the polarizability and by Eqs. (18), (19) for the susceptibility.

References

- [1] The analysis for a circular hole in a thick wall follows that for $k = 0$ in R.L. Gluckstern and J.A. Diamond, IEEE Transactions in Microwave Theory and Techniques, Vo. 39, No. 2, February 1991, p. 274, which contains references to earlier work.
- [2] W.H. Eggimann, Higher Order Evaluation of Electromagnetic Diffraction by Circular Disks, IRE Transactions of Microwave Theory and Techniques, vol. MMT-9, pp. 408-418, September 1961.

SPATIAL-TEMPORAL HYSTERESIS EFFECTS IN AN INTENSE ELECTRON BEAM

A. V. Agafonov, A. N. Lebedev, V. S. Voronin

P. N. Lebedev Physical Institute, Leninsky Prosp. 53, Moscow 117924, Russia

ABSTRACT

An electron gun with large compression of a thin annular beam for generation of high-power microwaves and IR radiation has been designed. Computer simulations of beam formation in the gun show some hysteresis effects: a beam with different current can exist in the same external conditions. At the upper (metastable) part of a hysteresis curve the beam current exceeds Child-Langmuir current. Experimental observation of these metastable states is possible if one has the possibility for fast control of emitted current, which is the case for photoemission cathode. The results of computer simulation are presented and physics reasons of such behaviour are discussed.

I. INTRODUCTION

In sources of electron beams of high brightness, applicable and developed for FELs and linear colliders, there have begun to be used in recent times photocathodes that permit forming "cold" beams initially. One of the important problems in these investigations concerns the magnitude of current taken from the photocathode. In a number of works — theoretical as well as experimental — there is discussed the possibility of obtaining currents exceeding the Child-Langmuir limit and is indicated that such an increase is possible only for the generation of short bunches, the length of which are less or of the order of the gap length.

Naturally, the classical CL-law is applicable only for a stationary regime with current limited by space charge for the following conditions: 1) voltage constant, 2) transverse dimensions of the emitting surface significantly exceeding (geometry close to unidimensional) the characteristic longitudinal dimensions of the accelerating region and 3) emissive power of the cathode unlimited.

Let us consider two first of the limitations. The first corresponds to constancy of current and implicitly implies that the variable quantity can be only voltage, while the value of current is determined by this voltage. It should be noted that with the appearance of efficient photoemitters and lasers, it became possible to independently vary emission current, in addition to the possibility of varying voltage. The possibility of controlling beam current in photoemission sources at fixed voltage leads to a qualitatively different situation. To a certain extent it is suggestive of the process of beam injection (although at very low initial energy) in an accelerating region rather than drawing the beam from an emitting surface.

The second limitation reduced the problem to unidimensional and, evidently, is violated under real conditions. Although the influence of the end effects is recognized, its contribution is considered to be small. At the same time, in a plane diode, when the transverse dimensions of the emitter are approximately equal to the length of the gap, the influence of fringe effects becomes determining. They are no longer simply fringe effects, they are

main effects.

In view of the non-stationary nature and multi-dimensionality of the problem, the results given below were obtained by computer simulation with electromagnetic code KARAT [1].

II. DRIFT REGION. FRINGER OR MAIN?

For a purely stationary flow that is unidimensional and unlimited in the transverse direction, the dependence of the passing current I_{out} on injection current I_{inj} is represented by the so-called "lambda-curve" (Fig. 1) [2].

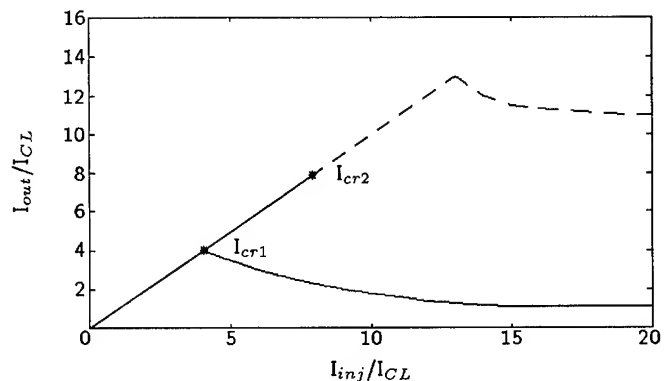


Figure 1. "Lambda" curve

Three solutions are possible for the region from I_{cr1} to I_{cr2} in such a flow. One of these is with a virtual cathode and partial passage of the beam (lower part of solid curve) and the other two (merging into one) are without a virtual cathode and with complete passage of the beam. It is considered that the last two states are unstable and when I_{cr1} is exceeded the beam always goes to the lower part of the curve with formation of a virtual cathode. For unlimited increase of injected current the virtual cathode asymptotically approaches the plane of injection and through the region there passes only current equivalent to the CL-current for a plane diode of the same dimensions, with voltage corresponding to the energy of injected electrons. For non-relativistic energy of particles, $I_{cr1} = 4I_{CL}$, $I_{cr2} = 2I_{cr1}$.

In [3], it was analytically shown that when the flow completely fills the chamber cross-section (the case of a semi-infinite plane slit with end plane was considered), the current passed can increase without limit ($I_{out} \propto \sqrt{I_{inj}}$) due to "exudation" of particles close to the chamber wall in a thin layer. The thickness of this layer decreases inversely proportionally to $\sqrt{I_{inj}}$. Close to the end plane, the central part of the beam is blocked by the space-charge field and the virtual cathode acquires the form of such a coaxial slit with rounded edges.

Let us consider the case when two-dimensional effects appear most effective. The drift region is chosen in the form of a cylindrical resonator having the diameter ($D = 5$ cm) much larger than the longitudinal dimension ($d = 1$ cm), the diameter of injected beam ($2r_e = 1$ cm) equals to the length of the resonator. We

present the results for a beam having non-relativistic energy $W = 20$ keV. In Fig. 1, the value of current is presented in units corresponding to CL-current ($I_{CL} = \pi r_e^2 j_{CL}$, $j_{CL} d^2 = 6.6$ A for 20 kV on the diode). The solid line shows the analytical dependence for unidimensional stationary flow and the dotted lines the calculated dependence for established regime when injecting beams of various currents with a 4-ns linear front. The established beam configuration for 200-A injected current is shown in Fig. 2 and is very

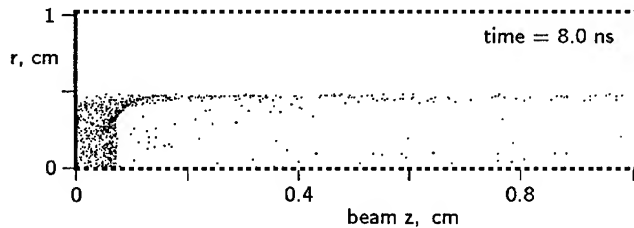


Figure 2. Beam with "whiskers"

similar to that considered in [3]. The difference is that the beam passes far from the side walls and the passed current does not increase with the injected, but remains approximately at one level. It should be noted that the main part of the current is concentrated in "whiskers", the thickness of which decreases with increasing injected current.

The time dependence of current passing through the resonator shown in Fig. 3. The interruption of current is due to the formation of a virtual cathode arising near the center of the resonator and is rapidly displaced toward the injection plane when reflected electrons appear.

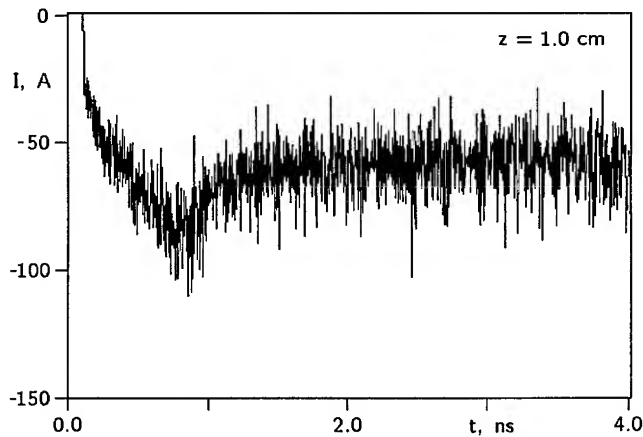


Figure 3. Transient regime in the drift region

With increasing transverse dimensions the influence of "whiskers" on the inner part of the beam is weakened due to preventing of field by electrodes and electrons with density of current close to the Child-Langmuir begin take "emitted" from the virtual-cathode region. Since the total CL-current will increase proportionally to r^2 and the current in the "whiskers" not more than r , the contribution of the "whiskers" becomes small relative to current from a larger area, but lower current density. This corresponds to unidimensional flow unlimited in the transverse direction.

III. FRINGE EFFECTS IN SIMPLE ACCELERATING REGION

The detailed exposition of the effects occurring in a drift region had as its main purpose to show that qualitative concepts about the formation of beam structure in the drift region can be transferred to the accelerating region. In any case, this is so when it is possible to rapidly control emission current, i.e., for the case of photocathodes.

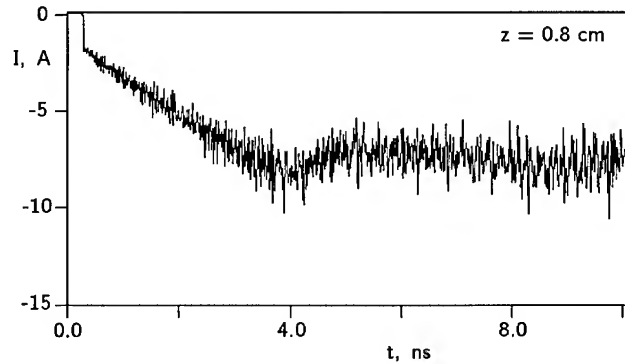


Figure 4. Transient regime in plane diode

The formation of "whiskers" in a drift region occurs particularly effectively when close to the cathode boundary there is a conducting wall and particles simply drift along it with an energy close to the energy of injection. In the case of an accelerating region, the energy of emitted electrons is low and the formation of fringe "whiskers" is made difficult because of the low energy of "injection" and strong influence of the proper field. The proximity of the electrode, at cathode potential, directly to the boundary of the emitting surface leads to screening of the proper as well as extracting field. Thus, it is necessary that the distance of side walls from emitter edges be such as to allow, on the one hand, considerable screening the influence of own space charge and, on the other, penetration of a sufficiently large external field.

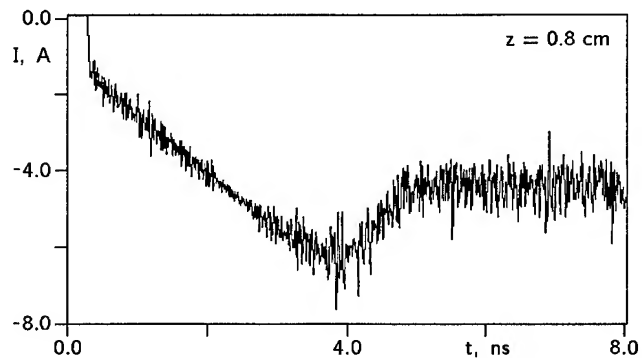


Figure 5. Transient regime in conical diode

As an example that supports such an approach, we present in Fig. 4 and Fig. 5 time dependence of beam current in a plane diode and in a diode with emitting surface in a recess. The voltage on the diode is constant and equal to 20 kV, emitter diameter is 1 cm, emission current increases linearly to 8 A in 4 ns and is then held constant. In the first case, hysteresis is practically imperceptible, but in the second it is quite pronounced.

IV. HYSTERESIS EFFECTS IN A HIGH-VOLTAGE ELECTRON GUN

Spatial-temporal hysteresis effects to a significant extent appeared in the process of developing an electron gun with large compression of a tubular beam (Fig. 6) intended for generation of powerful microwave and IR radiation [4].

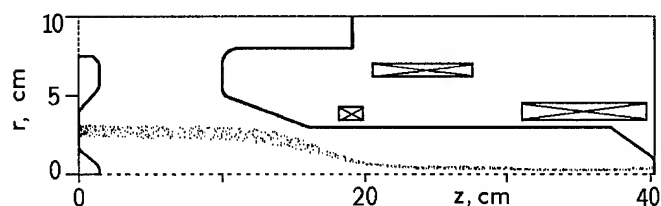


Figure 6. Schematic diagram of the gun

Electromagnetic code KARAT was used to calculate beam dynamics and the results were tested by means of stationary code SAM [5]. Simulation of emission of particles in the KARAT code could be realized by two methods: giving constant (or variable) emission current exceeding the space-charge limited current and increasing the voltage on the gun to a certain given value (thermionic cathode); giving constant voltage on the gun and increasing emission current from the cathode in time in accordance with a desired law (photocathode).

Fig. 7 shows averaged (high-frequency components filtered off) behavior of beam current at the gun output for various modelling conditions. Dependencies 1–3 correspond to conditions of photocathode operation and dependence 4 to conditions of thermionic cathode operation. Dependencies 1–3 were obtained for constant rate of emission current increase (about 28 A/ns) on the linear front, the duration of which was 7 ns (195 A), 7.5 ns (210 A) and 11 ns (310 A) for dependencies 1–3, respectively, and constant current for greater time. Current discrimination is clearly seen at 195 A, with subsequent drop to values that approximately correspond to the value of beam current in the stationary state obtained with stationary code SAM. The fourth dependence is plotted for the case when emission current is held constant at 400 A and the voltage on the diode increases from 160 kV to 400 kV in 8 ns.

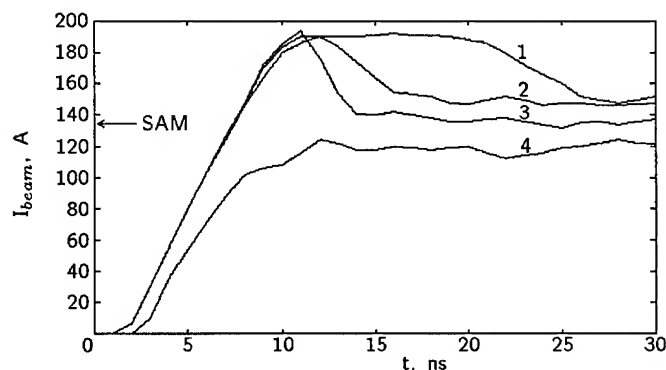


Figure 7. Hysteresis effects in high-voltage gun

course to a decrease in diode perveance, is accompanied by a sharper change in the ratio of peak to stationary value of current.

REFERENCES

- [1] P. V. Kotetashwily, P. V. Rybak, V. P. Tarakanov, "KARAT — a Means for a Computer Experiment in Electrodynamics", Institute of General Physics, Moscow, Russia, Preprint no. 44, 1991.
- [2] H. F. Ivey. *Adv. Electronic and Electron Physics*, v.6 (1954) 137–256.
- [3] V. S. Voronin, A. N. Lebedev, Y. T. Zozula. "Selfconsistent states of relativistic electron flow in a drift region", *Sov. JTP*, v.42 (1972) 546–551.
- [4] A. V. Agafonov, E. G. Krastelev, A. N. Lebedev, V. S. Voronin, A. M. Bishaev, V. A. Krasnopol'sky, P. J. M. van der Slot. "An electron gun with large compression of a thin annular beam". - *Proc. 10th Intern. Conf. on High Power Particle Beams*. June 20–24, 1994, San Diego, USA. Vol. 2, p. 522–525.
- [5] M. A. Tiunov, B. M. Fomel, V. P. Yakovlev, "SAM — an Interactive Program for the Design of Electron Guns on a Mini-computers", Institute of Nuclear Physics, Novosibirsk, Russia, Preprint no. 87–35, 1987.

It should be noted that a little screening of the cathode (for example, placing it in a 5-mm deep circular slot), leading of

GENERAL WAVE EQUATION IN THE ELECTROSTATIC APPROXIMATION

A. V. Agafonov

P. N. Lebedev Physical Institute, Leninsky Prosp. 53, Moscow 117924, Russia

ABSTRACT

Equilibria of high-current electron beams in an axial magnetic field are considered at the base of the approach [1] for the two cases of shielded and immersed cathodes. A general wave equation in the electrostatic approximation, which is valid in any selfconsistent equilibrium, was derived under the only assumption of constancy of full particle energy. This equation supplements general steady state equation [1] and allows to consider different equilibria and their wave properties in closed manner.

I. INTRODUCTION

For proper investigation of wave processes in REB it is necessary to use models of beam equilibria that could be solved analytically and would be consistent with an experimental condition. Often, the analytical solvability of a model is beyond its conformity to the real conditions. A general wave equation for selfconsistent equilibria is also important as it permits to compare the influence of different cross terms that can be omitted because of approximate solution of the steady state problem. In view of space limitations only these two problems are discussed.

II. LAMINAR FLOWS EQUILIBRIA

In cylindrical coordinates r, θ, z , under the conditions $\partial/\partial t = \partial/\partial z = \partial/\partial \theta = 0$, steady state equilibria of a beam in the longitudinal magnetic field B_{z0} are described by the following equations

$$\frac{\gamma v_\theta^2}{r} + E_r + v_\theta B_z - v_z B_\theta = 0;$$

$$\frac{dB_z}{dr} = -4\pi\rho v_\theta; \quad \frac{1}{r} \frac{d}{dr} r B_\theta = 4\pi\rho v_z; \quad \frac{1}{r} \frac{d}{dr} r E_r = 4\pi\rho,$$

where $v_\theta = \omega_0 r$, v_z are equilibrium velocities, $\omega_0 \geq 0$ is the angular velocity of the beam rotation as a whole, ρ the charge density, $B_z \leq 0$ the full longitudinal magnetic field, E_r, B_θ are self fields of the beam, $\gamma = 1/\sqrt{1 - v_\theta^2 - v_z^2}$.

The general macroscopic fluid equations describing the equilibrium of a cylindrical beam allow many solutions. Any two functions can be chosen arbitrarily or two additional relations are necessary to close this selfconsistent set of equations that permit to simulate the experimental circumstances. Here we shall follow the approach [1]. It combines a macroscopic cold fluid description and conservation laws which are in use

for a microscopic description based on the Vlasov-equation. We assume that full energy of particles conserved

$$H = \gamma + \phi = \text{const}, \quad (1)$$

(this means the emission of particles from an equipotential cathode) and that the conservation law for the canonical angular momentum is valid

$$P_\theta = r(p_\theta + A_\theta) = \text{const}, \quad (2)$$

(this means the conservation of axial symmetry), where $A_\theta = A_\theta(r)$ at the source.

Three cases, namely, 1) $P_\theta = 0$, 2) $P_\theta = \text{const}$, and 3) $P_\theta = B_0 r^2/2$ allow to simulate three cases of emission, namely, 1) magnetically shielded source, 2) hollow beam formation launched from a cathode surface coinciding with a magnetic flux surface, and 3) immersed source with a cathode immersed in the longitudinal magnetic field. These two physical relations allow to derive the next general set of equations [1]

$$(r\gamma^2 v_z')' + \gamma \left(\frac{v_\theta P_\theta'}{v_z} \right)' = 0, \quad (3)$$

$$(r\gamma^2 v_\theta')' - \frac{\gamma^2 v_\theta}{r} - r\gamma \left(\frac{P_\theta'}{r} \right)' = 0,$$

where the prime denotes d/dr . For the first two cases we get

$$r\gamma^2 v_z' = \text{const}. \quad (4)$$

The constant equals zero (i.e., $v_z = \text{const}$) in the first case, which corresponds to the model of a solid beam emitted from a shielded source and in the second case, which corresponds to a foilless magnetic-insulation diode under the conditions of no central conductor and no axial current inside the drift region. General analytical solutions in these two cases were found in [2] and later in [1]. We do not reproduce them here. Note that in the second case the general solution was represented by Jakoby-functions. Simplified solution in a case of practical interest, namely, thin-walled annular beam, can be represented by simple functions [3], which is useful for investigating wave processes.

For an immersed source P_θ depends on the radius, as A_θ varies across the emitting surface. Unfortunately, it is impossible to consider the transient region between the cathode and the drift region in the case. We can assume that there is no crossing of trajectories and that radius r_c from which an electron is launched at the cathode and radius r of this electron inside the drift region satisfy the simple relation $r = \alpha r_c$, where α is constant.

It can be shown that for this case equilibria with $v_z = \text{const}$ or $\omega_0 = \text{const}$ are impossible. Moreover, the approximate solution shows that due to beating no homogeneity along z stationary

states exists if the beam is launched in a drift region with smaller magnetic field than in the cathode region. The nature of these beats is the interaction of the beam with the B_r - component of the field. Fast cyclotron rotation of an electron around a force line of the magnetic field is affected by the rotation of the electron under the action of the B_r - component, which is paramagnetic in a decreasing field and diamagnetic in an increasing field. Inside a drift region the beam as a whole always rotates diamagnetically and the rotation induced in a decreasing field produces mismatching effects, which are seen as free oscillations of the beam envelope.

Thus, the general approach allows to simulate conditions of beam generation in high-current accelerators and provide the basis for analytical investigation of wave processes in the frame of stringent selfconsistent equilibria at least in two cases: a solid beam ($P_\theta = 0$) and a hollow beam ($P_\theta = \text{const}$). It is rather difficult to use the model of an immersed beam, which is of practical interest due to the absence an analytical solution. It is shown below that an ordinary simplification that could allow to find an analytical solution leads to the loss of necessary information about the equilibrium state and the same result in this approximation can describe initially different equilibria.

Moreover, we do not consider here a transition region that can have fantastic geometry. The comparison of analytical and numerical results with the results of computer simulation for real geometry shows that to form a beam with parameters close to those for given model, the form of the magnetic field in the transition region must be rather complicated and precise.

III. GENERAL WAVE EQUATION IN ELECTROSTATIC APPROXIMATION

The electrostatic approximation is used rather often to investigate electrostatic instabilities and slow waves. It is assumed that $\vec{B} = \nabla \times \vec{E} \approx 0$ and $\vec{E} = -\nabla\phi = \{-\partial\phi/\partial r, im\phi/r, ikz\}$ (all small perturbation is considered as $\propto \exp(i\omega t - ikz - im\theta)$ where ω is the frequency, k the longitudinal wave number and m the number of azimuthal variations).

Here, the general wave equation in the electrostatic approximation is presented and completes the general steady state equations [1]. Let us suppose that the conservation law (1) is valid and no additional assumption is used, i.e., we consider a rather wide class of equilibrium states of monoenergetic beams.

Performing routine procedures to linearize the complete set of equations, the wave equations in our case may be written in the form

$$\begin{aligned} & \frac{1}{r} \frac{\partial}{\partial r} r L^2 \left(1 + \frac{\omega_p^2 \gamma_0}{F_5 - \gamma_0^2 L^2} \right) \frac{\partial \Phi}{\partial r} - \\ & \Phi \left\{ \left(\frac{m^2}{r^2} + k^2 \right) \left(L^2 - \frac{\omega_p^2}{\gamma_0} \right) + \frac{\omega_p^2}{\gamma_0} \left(\frac{m}{r} v_\theta + k v_z \right)^2 + \right. \\ & \left. \frac{\omega_p^2}{\gamma_0} \frac{(\frac{m}{r} F_1 + k F_2)^2}{F_5 - \gamma_0^2 L^2} - \frac{L}{r} \frac{\partial}{\partial r} r \frac{\partial L}{\partial r} + \right. \\ & \left. \frac{1}{r} \frac{\partial}{\partial r} r \frac{\omega_p^2 L (\frac{m}{r} F_1 + k F_2)}{F_5 - \gamma_0^2 L^2} \right\} = 0, \quad (5) \end{aligned}$$

where $\Phi = \phi/L$, $L = \omega - k v_z - m v_\theta / r$. Functions F_i describe an equilibrium state and take the forms

$$\begin{aligned} F_1 &= B_{z0} + (v_\theta \gamma_0)' + v_\theta \gamma_0 / r = P_\theta' / r; \\ F_2 &= (v_z \gamma_0)' - B_{\theta 0} = -(P_\theta' / r) v_\theta / v_z; \\ F_3 &= F_1 - \gamma_0 (v_\theta' - v_\theta / r); \\ F_4 &= F_2 - v_z' \gamma_0; \\ F_5 &= F_1 F_3 + F_2 F_4, \end{aligned} \quad (6)$$

and $v_\theta F_1 + v_z F_2 \equiv 0$. Eqn. (5) is of general form for the given class of equilibrium states and is valid for solid as well as for hollow beams [4].

Taking into account the second conservation law (2), which was used in the first part, one can redefine functions F_i by means of P_θ . These expressions are in the right-hand member of equations (6).

Equation (5) has its simplest form under the assumption that $P_\theta = \text{const}$, which corresponds to the $v_z = \text{constant}$ class (solid beam launched from shielded source and hollow beam launched from foilless magnetic insulation diode). In the case

$$F_1 \equiv F_2 \equiv F_4 \equiv F_5 \equiv 0; \quad F_3 = -\gamma_0 (v_\theta' - \frac{v_\theta}{r})$$

and equation (5) has the form

$$\begin{aligned} & \frac{1}{r} \frac{\partial}{\partial r} r \left(L^2 - \frac{\omega_p^2}{\gamma_0} \right) \frac{\partial \Phi}{\partial r} - \Phi \left\{ \left(\frac{m^2}{r^2} + k^2 \right) \left(L^2 - \frac{\omega_p^2}{\gamma_0} \right) + \right. \\ & \left. \frac{\omega_p^2}{\gamma_0} \left(\frac{m}{r} v_\theta + k v_z \right)^2 - \frac{L}{r} \frac{\partial}{\partial r} r \frac{\partial L}{\partial r} \right\} = 0. \quad (7) \end{aligned}$$

It is an obvious nonessential simplification due to transition to the $v_z = 0$ system.

When the beam is launched from an immersed source in magnetic field B_0 we get

$$F_1 = B_0; \quad F_2 = -B_0 \frac{v_\theta}{v_z}; \quad (8)$$

$$F_5 = B_0 [B_0 (1 + \frac{v_\theta^2}{v_z^2}) - \gamma_0 \frac{v_z}{r} (\frac{r v_\theta}{v_z})'].$$

In this case the analytical solution can be found only under special approximations, for example, small currents limit and large external magnetic field. Numerical solutions of steady state equations show that under conditions $B_{ze} r_e \geq 1$ and $I \leq 0.1$ transverse distributions of the main interesting parameters (ω_p^2 , v_z , B_z , ω_0 , L , γ) are close to uniform except $v_\theta \propto r$. Note that B_0 at the cathode differs from B_z in the drift region. Using this approximate solution, one can write functions F_i as

$$\begin{aligned} F_1 &\approx \omega_v; \quad F_2 \approx -(\omega_0 B_0 / v_{zi}); \\ F_3 &\approx F_1; \quad F_4 \approx 0; \quad F_5 \approx \omega_v^2, \end{aligned} \quad (9)$$

where $\omega_v = B_{zi} + 2\omega_0 \gamma_i$, $\omega_0 = -(B_{zi} - B_0) / 2\gamma_i$. Index 'i' signifies axis value. Wave equation (5) can be written as follows

$$\begin{aligned} & \frac{1}{r} \frac{\partial}{\partial r} r \frac{\partial \phi}{\partial r} - \phi \left\{ \frac{m^2}{r^2} + \right. \\ & \left. \frac{\omega_v^2 - \gamma^2 L^2}{\omega_v^2 - \gamma^2 L^2 + \omega_p^2 \gamma} \left(k^2 \left(1 - \frac{\omega_p^2}{\gamma L^2} \right) + \right. \right. \\ & \left. \left. \frac{\omega_p^2}{\gamma L^2} (m \omega_0 + k v_z)^2 \right) \right\} = 0. \quad (10) \end{aligned}$$

Note that this equation where an approximate steady state solution of 1-st order was used, is valid at least for two other equilibria, namely 1) monoenergetic beam with $\rho = \text{const}$, 2) rigid rotor equilibrium with $v_z = \text{const}$. That is, for such a 'universal' approximation all information about special characteristics of the equilibrium was lost. It would be not surprising that in the wave 'language' all these equilibria are the same.

For this simplification, the wave equation for a beam launched from a shielded cathode will be similar to (10) if $\omega_v \equiv 0$ and differs qualitatively.

IY. ELECTROMAGNETIC WAVE EQUATION FOR A HOLLOW THIN-WALLED BEAM

It is difficult to find the electromagnetic wave equation in general form due to the cumbersome expressions. But, it is possible to find rather simple equations for a solid beam with $P_\theta = 0$, at least in the small current limit (of little practical interest) and for a high-current hollow ($P_\theta = \text{const}$), thin-walled beam, which might be useful because of practical interest.

For a thin-walled hollow beam but with large (relativistic) variation of v_θ in cross section under assumptions $d/dr \gg 1/R$, where R is the average radius of the beam, $m/R \approx \text{const}$, and $\omega_p^2/\gamma_0 \approx \text{const}$, though ω_p^2 and γ_0 do strongly vary in cross section [3]. In the $v_z = 0$ system, the result may be written in the form (here $\gamma_0 = \gamma_\perp$)

$$\begin{aligned} W''_{\theta z} + \chi^2 W_{\theta z} &= 0; \\ \left(\left(L^2 \gamma_0^2 - \frac{\omega_p^2}{\gamma_0} \right) W'_\theta \right)' + \\ \left(L^2 \gamma_0^2 - \frac{\omega_p^2}{\gamma_0} \right) \left(\chi^2 + \frac{\omega_p^2}{\gamma_0} \right) W_\theta &= 0; \end{aligned} \quad (11)$$

where $\chi^2 = \omega^2 - k^2 - m^2/R^2 - \omega_p^2/\gamma_0 \approx \text{const}$, $L = L(v_\theta)$, and

$$\begin{aligned} W_{\theta z} &= (\chi^2 + k^2) E_z + k \left(\frac{m}{r} - \frac{\omega_p^2 v_\theta}{\gamma_0 L} \right) E_\theta; \\ W_\theta &= \frac{E_\theta}{(\chi^2 + k^2) \gamma_0 L}. \end{aligned}$$

CONCLUSION

A general wave equation in the electrostatic approximation, which is valid in any selfconsistent equilibrium, was derived under the only assumption of constancy of full particle energy. This equation supplements general steady state equation and allows to consider different equilibria and their wave properties in closed manner. Equations (5) and (11) allow to investigate and compare properties of electrostatic and electromagnetic waves and instabilities in REB for different equilibrium states corresponding to experimental condition of beam generation in high-current accelerators. These equations permit to compare the influence

of different cross terms that can be omitted because of approximate solution of the steady state problem especially for resonant cases.

REFERENCES

- [1] M. Raiser, "Laminar-flow equilibria and limiting currents in magnetically focused relativistic beams", *Phys. Fluids* 20 (1977) 477.
- [2] A. V. Agafonov, V. S. Voronin, A. N. Lebedev, K. N. Pazin, "High-current electron beam transport by means of magnetic field", *Sov. JTP* 44 (1974) 1909.
- [3] A. V. Agafonov, A. N. Lebedev, "Stability of an electron beam with $v/\gamma > 1$ in a magnetic field", *Sov. JTP* 47 (1977) 1729.
- [4] A. V. Agafonov, "Equilibria and waves in high-current electron beams emitted from shielded and immersed cathodes". - *Proc. 10th International Conference on High Power Particle Beams*. June 20-24, 1994, San Diego, USA. Vol. 2, p. 511.

SPACE CHARGE EFFECTS IN THE KEK-BOOSTER SYNCHROTRON

Chihiro Ohmori

Institute for Nuclear Study, University of Tokyo, Tokyo, Japan

Toshikazu Adachi, Tadamichi Kawakubo, Motohiro Kihara and Isao Yamane

National Laboratory for High Energy Physics (KEK), Ibaraki, Japan

Space charge effects have been observed in the KEK-PS Booster synchrotron. Beam-profile measurements by the BEAMSCOPE method show that a beam blow-up in the vertical plane occurred during the RF capture process. The intensity dependence of beam blow-up and deformation of beam profile were observed.

I. INTRODUCTION

The KEK-PS Booster is a 40- to 500-MeV proton synchrotron, which is the injector of the KEK 12 GeV Proton synchrotron, and also delivers a beam to the Booster Synchrotron Utilization Facility (BSF). It is a compact alternating-gradient synchrotron operated at fixed tunes. The repetition rate is 20Hz and the synchrotron magnets are excited by a resonance circuit. The linac beam is injected by charge exchange injection and is adiabatically captured in an RF bucket. A bunch is formed in 600 μ s and the bunching factor becomes ~ 0.3 . A transverse beam blow-up at the early stage of acceleration has been observed [1]. Since the Booster synchrotron was designed for H^+ multi-turn injection, it has apertures of 272π mm mrad and 49π mm mrad in the horizontal and vertical planes, respectively [2]. This vertical emittance growth becomes crucial as the beam intensity increases. Since the acceleration period is rather short, we chose the BEAMSCOPE method [3], which can measure a beam profile in 100 μ s. It is difficult to use a wire scanner and other methods for a quick measurement. In order to measure the beam profile exactly, a precise calibration was performed [1].

II. MEASUREMENT

The beam-profile measurement system comprises a beam scraper and two pulsed bump magnets which kick the beam in the vertical direction. Figure 1 shows a plan view of the Booster synchrotron. Vertical bump magnets are installed in straight sections S2 and S4. Since the phase advance between the magnets is π radians and the beta functions at both magnets are same, a bump orbit is formed from S2 to S4 in the vertical plane. The magnets are connected in series and excited by a pulsed current having the same polarity. The pulse shape is a half-sine and

the pulse width is 200 μ s. M1-M8 are alternating-gradient magnets and have a focusing order of FDDF. The beam scraper is located in straight section S3, where the bump orbit has its extremum.

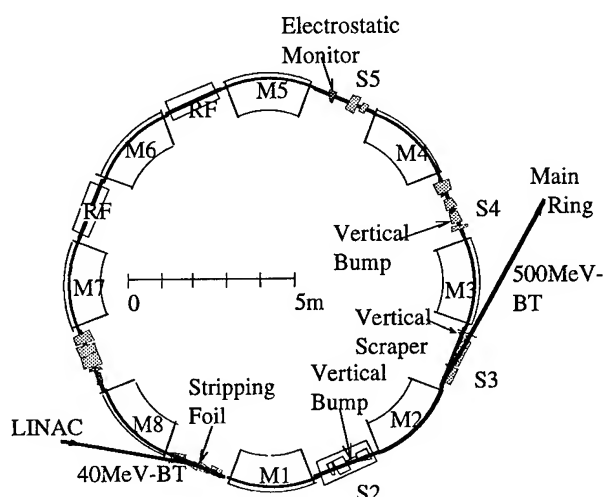


Fig. 1. Plan of the Booster synchrotron.

The ratio of the current of the bump magnets and the height of bump orbit at the scraper was precisely calibrated by means of a pencil beam, which was much smaller than the ring acceptance. In order to measure the beam profile exactly, it is essential to calibrate the bump current to the beam displacement with good accuracy. The ratio is reproducible and independent of the beam parameters, except for the energy. The beam scraper was movable and located at the optimum position where the aperture was minimum in the ring, but did not disturb the circulating beam. The current of the bump magnets was optimized to be able to scrape the whole beam as slowly as possible. Figure 2 shows a schematic view of the beam-profile measurement system. The current of the bump magnets and the beam-bunch signal were recorded simultaneously using a digital sampling oscilloscope, which records the all data during 200 μ s with a sampling rate of 200MHz. The current of the bump magnets and bunch signal were measured by a current transformer and a fast electrostatic monitor (ESM), respectively.

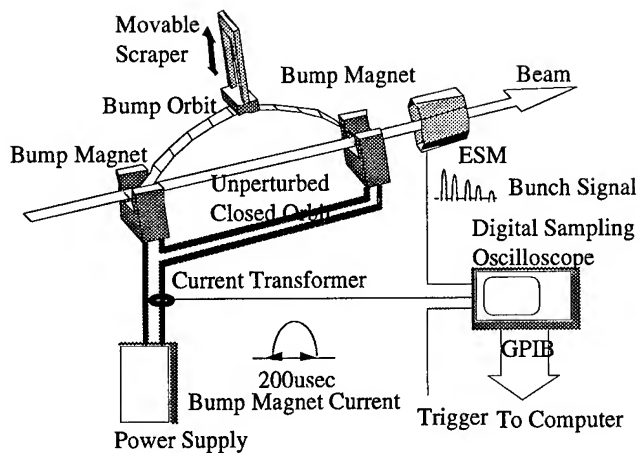


Fig. 2. Schematic of the profile measuring system.

We measured the intensity dependence of the beam profiles in the vertical plane for intensities from 1.8×10^{11} to 2.2×10^{12} particle per bunch (ppb). Since we wanted to use the same initial beam distributions for the different beam intensities, a beam slit of mesh shape was installed at the entrance of the 40-MeV Linac. Figures 3 and 4 show the normalized emittance containing 90% of the beam and normalized $1-\sigma$ emittance, respectively, against a delay time of up to 5 ms from injection for various intensities. In these figures, the emittance at injection, i.e. Delay Time = 0 ms, was obtained from the beam profile taken by moving the beam scraper without exciting the bump magnets, since the ESM cannot be available during injection where a bunch structure has not been sufficiently formed. The initial beam emittances are constant for different intensities for both 90% and $1-\sigma$ emittance (Figs. 3 and 4). The initial distribution was independent of the beam intensity. Figures 3 and 4 also show the emittance growth which occurred before ~ 1 ms.

The emittance growth is clearly observed at intensities larger than 1.66×10^{12} ppb in Fig. 3. The emittance growth between intensities of 1.4×10^{12} ppb and 1.66×10^{12} ppb is much larger than that between intensities of 1.66×10^{12} ppb and 2.2×10^{12} ppb. However, we should note that there might be a small amount of beam loss for 2.2×10^{12} ppb. The emittance growth is observed at intensities larger than 1×10^{12} ppb. The normalized $1-\sigma$ emittance becomes larger according to the increment of the beam intensity. The threshold intensity for $1-\sigma$ emittance is about 40% less than that for 90% emittance. Figure 5 shows the FWHM and the width which contains 90% of the beam against the beam intensities. It clearly shows that the intensities which cause the emittance growths are different for the beam core and edge. The difference of the threshold intensities for

emittance growths suggests that it is caused by space charge effects.

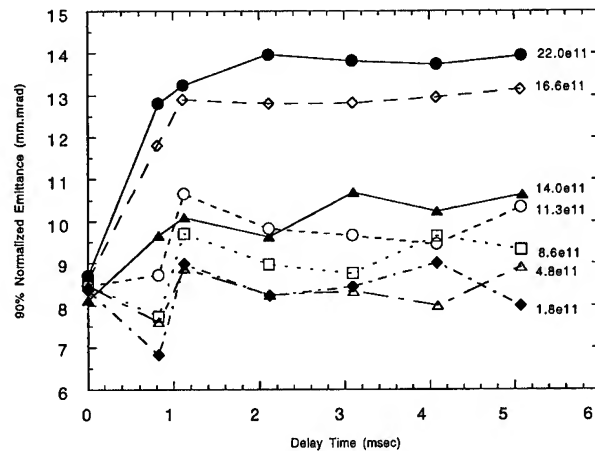


Fig. 3. Intensity dependence of the normalized emittance which contains 90% of the beam.

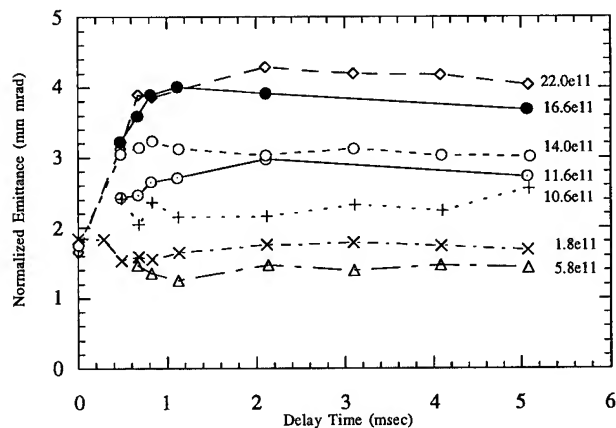


Fig. 4. Intensity dependence of the normalized $1-\sigma$ emittance.

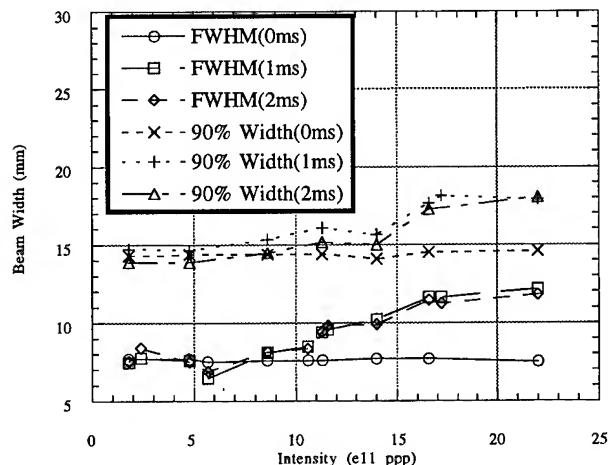


Fig. 5. Intensity dependence of the beam widths.

III. SPACE CHARGE TUNE SHIFT

The Booster tune space is shown in Fig. 6. In order to estimate the space charge detuning in the smooth approximation for $\Delta p/p=0$, we use the expression [4] $\Delta Q_{H,V} = N r_p G [\pi B \beta^2 \gamma^3 (\epsilon_{H,V} + (\epsilon_H \epsilon_V Q_{H,V} / Q_{V,H})^{1/2})]^{-1}$, where N =number of protons, $r_p = 1.535 \cdot 10^{-18}$ m, and G is a form factor which depends on the transverse intensity distribution. For $1.0 \cdot 10^{12}$ ppp at the end of injection, where $\beta^2 \gamma^3 = 0.09$ and the bunching factor is ~ 1 , the 90% beam width was 14mm. Using $G=1.56$ for the Gaussian distribution, we obtain $\Delta Q_{ySC} = -0.10$ and $\Delta Q_{xSC} = -0.05$, as shown in Fig. 6(a), bounded by the bold line. At 1 ms after injection, where emittance growth has occurred for the beam core but not for the beam tail, the beam is captured in the RF bucket and the bunching factor becomes 0.3. Then, $\Delta Q_{ySC} = -0.34$ and $\Delta Q_{xSC} = -0.17$ are obtained for the same beam widths. This is the lowest point of the region in Fig. 6(a) bounded by the solid line, and touches both $Q_x=2$ and $Q_y=2$. For $1.66 \cdot 10^{12}$ ppp at the end of injection, we obtain $\Delta Q_{ySC} = -0.17$ and $\Delta Q_{xSC} = -0.08$, as shown in Fig. 6(b), bounded by the bold line. For bunched beam showing emittance growth for both the beam core and edge, the 90% beam width became 18mm 1 ms after injection. We obtain $\Delta Q_{ySC} = -0.40$ and $\Delta Q_{xSC} = -0.26$ which cross both $Q_x=2$ and $Q_y=2$ resonances largely, as shown in Fig. 6(b).

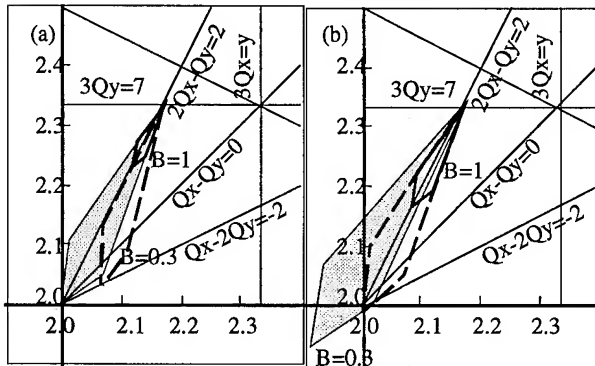


Fig. 6 KEK-PS Booster Tune Spaces at $1.0 \cdot 10^{12}$ ppp (a) and $1.66 \cdot 10^{12}$ ppp (b).

However, the real beam is not smooth and $\Delta p/p \neq 0$. For a more accurate estimation we used the computer code space SPACEX [5], which can solve envelope equations including the space charge force. The results are also shown in Fig. 6. We assume that the momentum spread was 0.30% and that the real beam was larger in the horizontal plane due to it. Using $G=1.56$ and $B=0.3$, we obtain $\Delta Q_{ySC} = -0.30$ and $\Delta Q_{xSC} = -0.11$ for $1 \cdot 10^{12}$ ppp. It is shown in Fig. 6(a), bounded by the dashed line. We also

obtained $\Delta Q_{ySC} = -0.34$ and $\Delta Q_{xSC} = -0.17$ for $1.66 \cdot 10^{12}$ ppp. This is shown in Fig. 6(b), bounded by the dashed line. Since the momentum spread was taken into account, the tune spreads obtained by SPACEX are smaller than those by Laslett formula. Since the 90% beam width during the emittance growth was smaller than 18 mm, the tune spread should have been much larger than the region in Fig. 6(b) bounded by the dashed line. It is reasonable that the large tune spread which crosses the integer and other resonances causes emittance growth, which stops when the tune spread becomes smaller.

IV. DISCUSSIONS

The emittance growth in the vertical plane can be explained based on the space charge effects. Operation at higher tunes and resonance correction techniques are used to avoid and overcome the effects. However, the Booster synchrotron is a small accelerator and has limited space. It is difficult to install the necessary instruments to change the tunes and for corrections. Reduction of the peak intensity by the second-harmonic buncher is another way, and might be possible if the instrument is designed to be compact.

V. REFERENCES

- [1] T. Adachi et al., "Beam Profile Measurement in the KEK-PS Booster Using Pulsed Bump Magnets and Movable Scraper", Proceedings of the 4th European Particle Accelerator Conference (EPAC94), London, U.K., July 1994.
- [2] T. Suzuki, "ORBIT ANALYSIS OF THE KEK SYNCHROTRON", KEK-74-4.
- [3] H. Shonauer, "Experience with the BEAMSCOPE Emittance Measurement System at the CERN-PS Booster", Proceedings of the Workshop on Advanced Beam Instrumentation, KEK, Tsukuba, Japan, April 1991, pp. 453-466.
- [4] L. J. Laslett, BNL Summer Study, BNL 7534, pp. 324-67(1963).
- [5] G. Rees, private communications.

ON THE RELAXATION OF SEMI-GAUSSIAN AND K-V BEAMS TO THERMAL EQUILIBRIUM *

S.M. Lund, J.J. Barnard, and J.M. Miller

Lawrence Livermore National Laboratory, University of California, Livermore, CA 94550, USA

Abstract

A beam propagating in a continuous, linear focusing channel tends to relax to a thermal equilibrium state. We employ nonlinear conservation constraints to theoretically analyze changes in quantities that characterize both an initial semi-Gaussian beam with a matched rms beam envelope and a K-V beam under a relaxation to thermal equilibrium. Results from particle-in-cell simulations are compared to the theoretical predictions.

I. INTRODUCTION

Semi-Gaussian (SG) beams are characterized by a thermal-like Gaussian distribution of particle momentum and uniformly distributed space-charge. In so-called K-V beams first described by Kapchinskij and Vladimirkij, all particles have the same transverse energy and the space-charge is also uniformly distributed.^{1,2} Both SG and K-V beams are widely used in the theory and simulation of charged particle beams, and a fundamental question is how these beams change on relaxation to thermal equilibrium (TE). Here we employ conservation constraints of a simple theoretical model to derive equations that connect initial SG and K-V beams to their final TE state. These equations are solved numerically to obtain universal curves describing changes in beam emittance, radius, and peak density on relaxation to TE. These curves demonstrate contexts in which these distributions may be regarded as approximations to TE. This study does not address the dynamical evolution of the beam as it relaxes to TE.

II. THEORETICAL MODEL, MOMENTS, AND CONSERVATION CONSTRAINTS

We employ an (r, θ, z) cylindrical polar coordinate system to analyze an infinitely long, unbunched ($\partial/\partial z = 0$) beam composed of a single species of particles of mass m and charge q . All particles propagate with constant axial velocity $v_b e_z$, and continuous radial focusing is provided by an external electric field that is proportional to the radial coordinate r , i.e., $\mathbf{E}_{\text{ext}} = -(mv_b^2 k_\beta^2 / q) r e_r$, where $k_\beta = \text{const}$ is the betatron wavenumber. This field can be thought of as arising from a uniform background of charges or as representing the average focusing strength of an alternating gradient lattice of electric or magnetic quadrupoles.^{1,2} For simplicity, we neglect self-magnetic fields and employ a nonrelativistic and electrostatic model where initial ($s = 0$) and final ($s \rightarrow \infty$) states of the beam can be described for a long axial propagation distance s ($s = v_b t$, where

t is the time) in terms of a single-particle distribution function f that can generally be a function of the transverse position and momentum \mathbf{x} and \mathbf{p} of a single particle and the axial coordinate s , i.e., $f = f(\mathbf{x}, \mathbf{p}, s)$. Neglecting particle correlation effects, the evolution of f is described by the Vlasov equation,¹

$$\left\{ \frac{\partial}{\partial s} + \frac{\partial H}{\partial \mathbf{p}} \cdot \frac{\partial}{\partial \mathbf{x}} - \frac{\partial H}{\partial \mathbf{x}} \cdot \frac{\partial}{\partial \mathbf{p}} \right\} f(\mathbf{x}, \mathbf{p}, s) = 0, \quad (1)$$

where

$$H(\mathbf{x}, \mathbf{p}) = \frac{\mathbf{p}^2}{2mv_b} + mv_b \frac{k_\beta^2}{2} \mathbf{x}^2 + \frac{q}{v_b} \phi \quad (2)$$

is the Hamiltonian and the self-field potential ϕ satisfies the Poisson equation

$$\left[\frac{1}{r} \frac{\partial}{\partial r} \left(r \frac{\partial}{\partial r} \right) + \frac{1}{r^2} \frac{\partial^2}{\partial \theta^2} \right] \phi(\mathbf{x}, s) = -4\pi q \int d^2 p f. \quad (3)$$

Beam Vlasov equilibria are stationary ($\partial/\partial s = 0$) solutions to the Vlasov-Poisson system (1)-(3). It follows that any distribution function f formed from the single-particle constants of the motion in the full equilibrium field configuration is a Vlasov equilibrium. Therefore, for azimuthally symmetric ($\partial/\partial \theta = 0$) beams, $f = F(H)$ is an equilibrium distribution for arbitrary functions $F(H)$. It can be shown that the equilibrium $f = F(H)$ is stable to perturbations of arbitrary amplitude if $dF(H)/dH \leq 0$.¹ Moreover, the density inversion theorem¹ shows that any beam equilibrium with a radial density profile $n(r) = \int d^2 p f$ satisfying $dn/dr \leq 0$ corresponds to a stable distribution $f = F(H)$ with $dF(H)/dH \leq 0$.

Moment descriptions of the beam can provide a simplified understanding of beam transport. Transverse statistical averages of a quantity ξ are expressed in terms of this Vlasov formulation as $\langle \xi \rangle \equiv (1/N) \int d^2 x \int d^2 p \xi f$, where $N \equiv \int d^2 x \int d^2 p f$ is the number of particles per unit axial length. A commonly employed measure of the envelope radius of beam particles is the rms radius $R \equiv \sqrt{2\langle r^2 \rangle}$. Note that R is identically equal to the edge radius of a beam with uniformly distributed space-charge. Second order moments of the Vlasov equation (1) can be employed to derive the so-called "rms envelope equation" for the evolution of R .^{1,2} For azimuthally symmetric beams (i.e., $\partial/\partial \theta = 0$), one obtains

$$\frac{d^2 R}{ds^2} + k_\beta^2 R - \frac{K}{R} - \frac{\epsilon_x^2}{R^3} = 0, \quad (4)$$

where $K = -2q\langle r\partial\phi/\partial r \rangle / mv_b^2$ is the self-field perveance [Eq. (3) can be integrated to obtain $\langle r\partial\phi/\partial r \rangle = -qN$, and thereby show that $K = 2q^2 N / mv_b^2 = \text{const}$] and

$$\epsilon_x^2 = 16[\langle x^2 \rangle \langle (dx/ds)^2 \rangle - \langle x(dx/ds) \rangle^2] \quad (5)$$

is the square of the rms x -emittance ϵ_x . For a K-V equilibrium distribution, $\pi\epsilon_x$ is constant and corresponds to the phase-space

*This research was performed under the auspices of the US D.O.E. by LLNL under contract W-7405-ENG-48. S.M. Lund was supported in part by the U.S. D.O.E. Postdoctoral Research Program administered by the Oak Ridge Institute for Science and Education.

area (in $x, dx/ds$ phase-space) of the beam. For general distributions, ϵ_x is not constant and is employed as a statistical measure of the quality of the beam.²

It is convenient to express the envelope equation (4) as $d^2R/ds^2 + \sigma^2 R - \epsilon_x^2/R^3 = 0$, where $\sigma \equiv (k_\beta^2 - K/2\langle r^2 \rangle)^{1/2}$ is the phase-advance per unit axial length of the transverse oscillations of a single particle moving in the applied and self-fields of an "equivalent" K-V beam.² For radial confinement of the beam ($n = \int d^2p f = 0$ in the limit $r \rightarrow \infty$), $\sigma^2 \geq 0$, with the limit $\sigma = 0$ corresponding to a cold-beam equilibrium with $dR/ds = 0 = d^2R/ds^2$ and $\epsilon_x^2 = 0$. In the tenuous, kinetic-dominated limit $k_\beta^2 \gg K/2\langle r^2 \rangle$, space-charge effects are negligible, and $\sigma \simeq \sigma_0$, where $\sigma_0 = |k_\beta|$ is the "undepressed" phase advance. The phase advance σ in the presence of space-charge is "depressed" from σ_0 (i.e., $\sigma^2 = \sigma_0^2 - K/2\langle r^2 \rangle$), and the phase advance ratio

$$\sigma/\sigma_0 = (1 - K/2k_\beta^2\langle r^2 \rangle)^{1/2} \quad (6)$$

provides a convenient normalized measure of space-charge effects ($0 \leq \sigma/\sigma_0 \leq 1$), with the limits $\sigma/\sigma_0 \rightarrow 0$ and $\sigma/\sigma_0 \rightarrow 1$ corresponding to a cold, space-charge dominated beam and a warm, kinetic dominated beam, respectively.

The nonlinear Vlasov-Poisson system (1)-(3) possesses the conservation constraints

$$N = \int d^2x \int d^2p f = \text{const}, \quad (7)$$

$$\mathcal{E} = \int d^2x \int d^2p \frac{p^2}{2m} f + N m v_b^2 \frac{k_\beta^2}{2} \langle r^2 \rangle + W = \text{const},$$

where $W \equiv \int d^2x |\partial\phi/\partial\mathbf{x}|^2/8\pi$ is the self-field energy. It can be verified that $dN/ds = 0 = d\mathcal{E}/ds$ follow directly from Eqs. (1)-(3). These constraints correspond to the conservation per unit axial length of particle number and system energy (particle and field) and provide powerful constraints on the nonlinear evolution of the system. Similar constraints remain valid in systems where particle correlation effects are not negligible. Note that the two-dimensional self-field energy W is logarithmically divergent since $\partial\phi/\partial\mathbf{x} \sim -(2qN/r)\mathbf{e}_r$ for $r \gg R$. For practical applications, this divergence must be removed (regularized) in an s -invariant manner. For azimuthally symmetric ($\partial/\partial\theta = 0$) beams, the divergence can be isolated by examining the work required to assemble the beam from a large radius.³ Subtracting this divergence from W , we obtain the regularized self-field energy

$$W_r = -8\pi^2 q^2 \int_0^\infty dr r \ln\left(\frac{r}{r_s}\right) n(r) \int_0^r d\bar{r} \bar{r} n(\bar{r}), \quad (8)$$

where $r_s = \text{const}$ is a scale radius and $n(r) = \int d^2p f$ is the radial density. Making the replacement $W \rightarrow W_r$ in the constraint $\mathcal{E} = \text{const}$ obtains the needed regularized energy constraint. Insofar as the same scale radius $r_s = \text{const}$ is applied, this regularized conservation constraint can be applied to connect two azimuthally symmetric states, even if the intervening states are not azimuthally symmetric.

III. BEAM THERMAL EQUILIBRIA

A beam thermal equilibrium (TE) is characterized by a radial density profile that becomes uniform in the limit of low temperature and Gaussian-like for high temperature. The single-particle distribution function describing a TE beam is^{1,2}

$$f = \frac{n_0}{2\pi m T} \exp\left\{-\frac{v_b H}{T}\right\}. \quad (9)$$

Here, $n_0 = \text{const}$ is a characteristic density and $T = \text{const}$ is the thermodynamic temperature (energy units). Specification of the charge and energy of the beam macrostate fix the constants n_0 and T . The TE distribution is a special class of stable Vlasov equilibrium.¹ Within the weak coupling approximation ($q^2/n_0^{-1/3} \ll T$) any initial distribution function $f(\mathbf{x}, \mathbf{p}, s = 0)$, however complex, relaxes to the TE form of Eq. (9). This is true regardless of the details of the intervening evolution due to both collective and collisional processes. Even stable Vlasov equilibria must ultimately relax to TE form due to effects outside the Vlasov model. In this regard, TE can be regarded as the preferred equilibrium state of the system.

Employing the TE distribution (9), one obtains

$$\epsilon_x^2 = \frac{8T}{m v_b^2} \langle r^2 \rangle, \mathcal{E}_r = NT + m v_b^2 \frac{k_\beta^2}{2} \langle r^2 \rangle + W_r, \quad (10)$$

where \mathcal{E}_r denotes the regularized system energy. The envelope equation (4) with $d^2R/ds^2 = 0$ and ϵ_x^2 calculated above then shows that

$$\langle r^2 \rangle = \frac{2T + q^2 N}{m v_b^2 k_\beta^2}. \quad (11)$$

The TE density $n(r) = \int d^2p f$ needed to explicitly calculate $N = 2\pi \int_0^\infty dr r n(r)$ and W_r is nonlinear, and must, in general, be calculated numerically. For this purpose it is convenient to express the density as $n(r) = n_0 \exp(-\psi)$, where $\psi \equiv (1/T)[m v_b^2 k_\beta^2 r^2/2 + q\phi]$ satisfies the transformed Poisson equation

$$\frac{1}{\rho} \frac{d}{d\rho} \left(\rho \frac{d\psi}{d\rho} \right) = 1 + \Delta - \exp(-\psi),$$

subject to $\psi(0) = 0$. Here, $\rho \equiv r/\lambda$ is a radial coordinate scaled to the thermal Debye length $\lambda \equiv (T/4\pi q^2 n_0)^{1/2}$ formed from the on-axis beam density n_0 , and $1 + \Delta \equiv 2v_b^2 k_\beta^2/\omega_{p0}^2$ (where $\omega_{p0}^2 \equiv 4\pi q^2 n_0/m$ is the on-axis plasma frequency-squared), is a positive, dimensionless parameter qualitatively representing the ratio of applied to space-charge defocusing forces.

IV. SEMI-GAUSSIAN AND K-V BEAMS

Semi-Gaussian (SG) and K-V beams are described by the single-particle distribution functions¹⁻³

$$f = \begin{cases} (n_b/2\pi m T_b) \Theta(r_b - r) \exp(-p^2/2m T_b), & \text{SG} \\ (n_b/2\pi m v_b) \delta(H - 2T_b/v_b), & \text{K-V} \end{cases} \quad (12)$$

Here, $\Theta(x)$ and $\delta(x)$ are theta- and Dirac delta-functions, $T_b = \text{const}$ is the beam kinetic temperature [i.e., $NT_b =$

$\int d^2x \int d^2p (p^2/2m)f]$ for both distributions, and both density profiles $n = \int d^2p f$ have a constant value n_b within the beam radius $r_b = \text{const}$ [i.e., $n = n_b$ for $0 \leq r < r_b$] and are zero outside the beam radius [i.e., $n = 0$ for $r > r_b$]. K-V distributions are exact Vlasov equilibria with $\partial/\partial s = 0$, whereas SG distributions are not and will evolve within the Vlasov model. The SG distribution must be regarded as an initial state, and the conditions $dR/ds = 0 = d^2R/ds^2$ are applied to this state for a “matched” beam envelope. Then for both the SG and K-V distributions, the envelope equation (4) becomes an initial state constraint $2T_b = mv_b^2 k_\beta^2 r_b^2/2 - q^2 \pi r_b^2 n_b/2$ [equivalent to Eq. (11) and defining r_b for K-V beams], and expressions identical in form are obtained to the TE quantities calculated in Eq. (10) with the kinetic temperature T_b replacing the thermodynamic temperature T . Additionally, for these rectangular density profile beams, one may analytically calculate $N = \pi r_b^2 n_b$, $\langle r^2 \rangle = r_b^2/2$, and $W_r = (q^2 N^2/4)[1 - 4 \ln(r_b/r_s)]$.

V. BEAM CHANGES ON RELAXATION TO THERMAL EQUILIBRIUM

The conservation constraints $N = \text{const}$ and $\mathcal{E}_r = \text{const}$ uniquely connect an initial SG beam with a matched envelope or an initial K-V beam to its final TE state. These constraints can be used with Eqs. (10) and (11) expressed in scaled form for both initial and final states to calculate ratios of final to initial state emittance-squared ϵ_x^2 , mean-square radius $\langle r^2 \rangle$, and on-axis density $n(r=0)$ in terms of the single dimensionless parameter Δ associated with the final TE. Likewise, the phase advance ratio σ/σ_0 of the initial beam can also be calculated in terms of Δ . Details of this procedure are presented elsewhere,³ and the resulting ratios are plotted versus σ/σ_0 in the figure. These curves are universal in the sense that all beam parameters fall onto a single curve and the curves apply both to an initial (matched) SG or a K-V beam. Particle-in-cell simulations of an initial SG beam are presented in the figure. These simulations provide insight on the axial propagation distance necessary for relaxation to TE and agree well with the theory for σ/σ_0 small.^{3,4} Spreads about the simulation points indicate rms fluctuations that become large as $\sigma/\sigma_0 \rightarrow 1$ due to the lack of space charge forces to induce relaxation to TE. Indeed, it has been shown that the simulations are consistent with relaxation to a virtual, phase-mixed equilibrium as $\sigma/\sigma_0 \rightarrow 1$.

The figure shows that the rms emittance and radius undergo small, space-charge dependent decreases on relaxation to TE, while the peak (on-axis) beam density can undergo a significant, space-charge dependent increase. All the ratios plotted approach unity in the space-charge dominated limit $\sigma/\sigma_0 \rightarrow 0$ because all three distributions become identical with uniform densities and zero temperatures in this limit. In the kinetic dominated limit $\sigma/\sigma_0 \rightarrow 1$, the ratios of rms emittance and mean-square radius approach unity, whereas the ratio of peak densities approaches 2. These limits are consistent with analytic calculations with the self-field potential ϕ neglected. With ϕ neglected, all second-order moments of the system are constants of the motion (the rms radius and temperature are then constants) and the final TE density profile is Gaussian with $n(r) = n_0 \exp(-2r^2/r_b^2)$, thereby showing that the ratio of final to initial peak density is 2 using

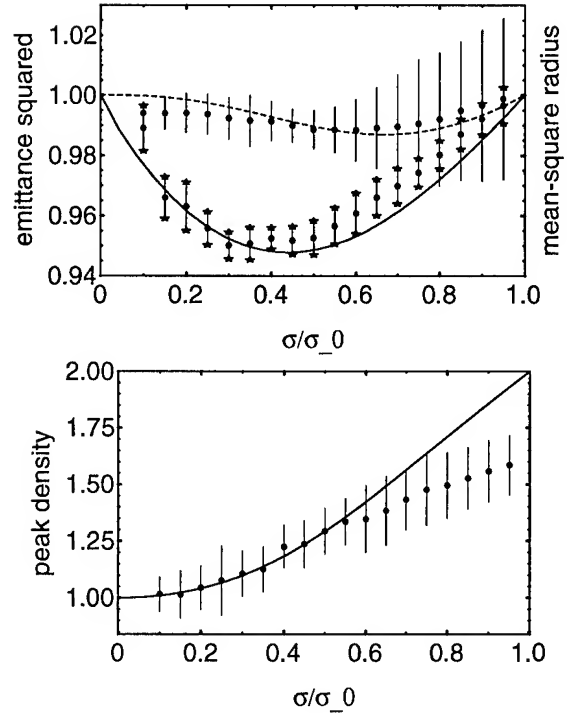


Figure 1. Ratios of final to initial state emittance squared (ϵ_x^2 , upper plot, solid curve), mean-square radius ($\langle r^2 \rangle$, upper plot, dashed curve), and peak (on-axis) density [$n(r=0)$, lower plot] versus σ/σ_0 .

$N = \pi r_b^2 n_b = \int d^2x n(r)$. For the general case of finite space-charge effects with $0 < \sigma/\sigma_0 < 1$, the figure demonstrates that on relaxation to TE, the rms radius of the beam decreases slightly, while the peak (on-axis) beam density significantly increases. Evidently, the initially uniform density beam relaxes to a diffuse radial density profile such that the characteristic thermal tail and increased core density weight to maintain nearly constant rms radius.

VI. CONCLUSIONS

An initial semi-Gaussian or K-V beam within a continuous focusing channel must ultimately relax to thermal equilibrium. We employed conservation constraints of a simple theoretical model to analyze changes in quantities characterizing the beam under this relaxation. Universal curves were calculated giving the ratio of various final to initial state quantities in terms of the ratio of depressed to undepressed phase advance of the initial beam, which provides a convenient normalized measure of space-charge effects. These curves demonstrate that the rms emittance and radius of the beam undergo a small, space-charge dependent decrease on relaxation to TE. The smallness of these decreases for σ/σ_0 small indicate that with respect to the transport of second-order moments of the system, which are of primary importance in beam physics, the SG and K-V distributions are a good approximation to the true TE distribution that can be transported without change. On the other hand, particularly for larger σ/σ_0 , it was demonstrated that higher order moments or nonmoment quantities (e.g., peak beam density) could un-

dergo significant space-charge dependent changes on relaxation to TE, thereby indicating both contexts for caution and possible measures to ascertain whether the beam has relaxed. More detailed analyses including beam rotation and magnetic focusing along with relativistic, self-magnetic, and longitudinal effects have been carried out, and the essential conclusions of this simple analysis remain unaltered.³

References

- [1] R.C. Davidson, *Physics of Nonneutral Plasmas* (Addison-Wesley, Reading, MA, 1990), and references therein.
- [2] M. Reiser, *Theory and Design of Charged Particle Beams* (John Wiley & Sons, Inc., New York, 1994), and references therein.
- [3] S.M. Lund, J.J. Barnard, and J.M. Miller, manuscript in preparation.
- [4] T.P. Wangler, K.R. Crandall, R.S. Mills, and M. Reiser, IEEE Trans. Nucl. Sci., **32**, 2196 (1985).

TRANSVERSE-LONGITUDINAL ENERGY EQUILIBRATION IN A LONG UNIFORM BEAM*

I. Haber, Naval Research Laboratory, Washington, DC 20375 USA

D. A. Callahan, A. Friedman, D. P. Grote, A. B. Langdon
Lawrence Livermore National Laboratory, Livermore, CA 94550 USA

Abstract

Evidence is presented to show the transfer, via a collective electrostatic instability, of transverse energy to the longitudinal direction if the axial temperature of a beam is sufficiently low. Two-dimensional r,z electrostatic PIC simulations of a long coasting space-charge-dominated beam propagating in a uniform focused channel are presented to illustrate, for typical parameters, the development of a coherent mode structure with an axial wavelength comparable to the beam diameter, and growth times comparable to the betatron period.

I. INTRODUCTION

In many accelerator systems it is important to carefully control the phase space volume occupied by the beam. For example, in a heavy ion accelerator which is to be used for the ignition of a thermonuclear pellet, both the transverse beam emittance and the spread in longitudinal velocities are constrained by the requirement for focusing sufficient power density onto the target. While the constraints on the transverse and longitudinal phase space are generally related in a complex way by the details of the accelerator design, it is important to limit the growth of both.

If it is noted that the addition of equal energy to each beam particle during acceleration results in a decrease in the longitudinal velocity spread in the beam frame, while the same reduction does not occur in the transverse direction, it is easy to envision the development of a substantial anisotropy in the beam temperature. While the very low beam collision frequency precludes any thermodynamic equipartitioning of the temperature anisotropy on a time scale comparable to the beam lifetime, a collective mechanism that can transfer energy from the transverse to longitudinal directions is described here.

Previous examination [1,2] of the behavior of beam bunches, where the length of the bunch is comparable to its radius, has identified possible collective mechanisms which can transfer energy between the transverse and longitudinal direction so as to reduce a temperature anisotropy. More recently, three-dimensional simulation studies [3,4] of space-charge-dominated beam dynamics have also shown evidence of a collective mechanism for energy transfer, even when the bunch length is much longer than the beam diameter. These simulations suggest that the collective mechanism does not depend on the bunch length being comparable to beam

diameter. The work discussed here attempts to clarify the nature of that mechanism by examining a space-charge-dominated beam with a transverse temperature greater than the longitudinal temperature, but in the simpler case of axisymmetric geometry and a uniform focusing channel.

As will be discussed below, the simulations show that an instability develops which transfers energy from the transverse to the longitudinal direction. The unstable mode in the example shown appears to behave like a localized envelope oscillation, with a length comparable to the beam diameter, that is driven unstable by the transverse energy. This mode appears to be only one of the potentially unstable, and possibly coupled, modes of the anisotropic beam system.

II. AXISYMMETRIC SIMULATIONS

For simplicity, the investigation described here is restricted to an axisymmetric space-charge-dominated beam in a focusing system which is linear and uniform in the longitudinal direction. The beam self-fields are assumed to be electrostatic. For further simplification, a relatively small, in the examples here 0.32 m, section of the beam is examined using periodic boundary conditions. Figure 1 is a plot of the z (longitudinal) rms. velocity of the beam particles as a function of the distance propagated by the beam as it is transported.

The beam shown in Fig. 1 is a 4.8 A beam consisting of singly charged ions with mass of 12 AMU and energy of 10 MeV. A linear inward focusing force, independent of longitudinal position, is employed, corresponding to a 7.2 m low-current betatron wavelength, which maintains a matched beam radius of 0.023 m, in the 0.05 m radius conducting pipe. The beam particles have been given an initially semi-Gaussian (uniform in space Gaussian in velocity) distribution with a transverse emittance of 2.2×10^{-4} m-rad. The initial conditions represent sufficient space charge to depress the transverse phase advance by a factor of 2.35 were the beam initially a K-V distribution with the same rms. quantities. The initial thermal velocity in the longitudinal direction is 10^3 m/sec.

The numerical simulations were performed using the electrostatic r,z WARP [5] particle-in-cell simulation code. The particular simulation shown in Fig. 1 employed 224K macroparticles. The grid consisted of 32 radial and 512 axial zones, with Gaussian smoothing employed in the axial direction to suppress the longitudinal grid instability

* Work performed under the auspices of the United States Department of Energy by NRL and LLNL under contracts DE-AI02-93ER40799, DE-AI02-94ER54232, and W-7405-ENG-48.

sometimes observed in the simulation of longitudinally cold beams.

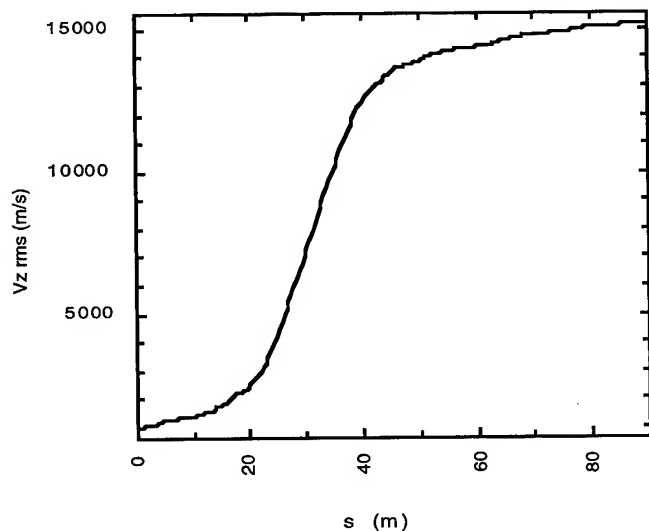


Fig 1. Longitudinal rms. velocity plotted against the distance propagated by the beam. Energy from the initially semi-Gaussian transverse distribution is transferred to the longitudinal direction.

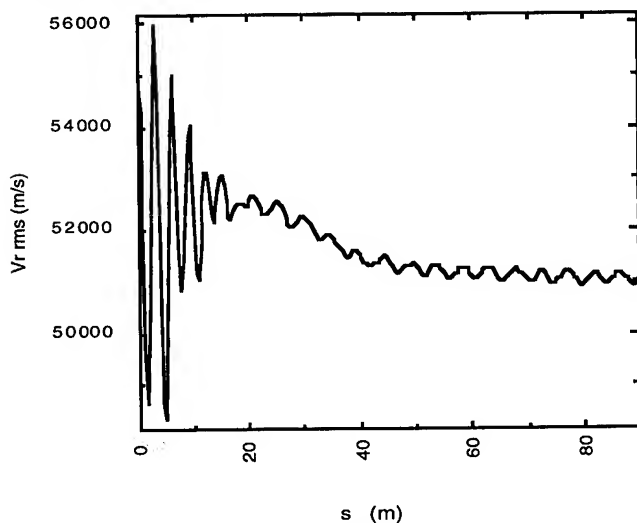


Fig. 2. Evolution of the transverse rms. velocity, showing the initial fluctuations that result from a lack of detailed force balance when the beam is prepared with an initially semi-Gaussian distribution.

The growth in longitudinal thermal energy shown in Fig. 1 can be separated into three phases, consisting of an initial short period of slow growth followed by a period of somewhat more rapid growth, and finally a slowing of this rapid growth. Because it is conjectured that the mechanism for transfer of energy is a result of a collective instability, the initial growth phase is problematic, since an instability which is not explicitly seeded will tend to grow from some small initial perturbation which is due to a nonuniformity in the initial distribution. A possible explanation for this initial behavior can be found from the examination of the transverse dynamics, as is illustrated by the plot in Fig. 2 of the

transverse rms. velocity as the beam propagates down the transport line.

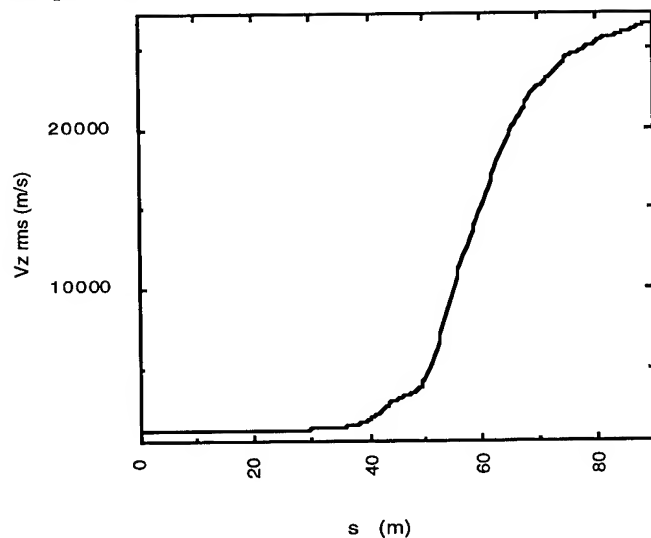


Fig 3. Longitudinal rms. velocity plotted against the distance propagated, when the beam is given an initially K-V distribution. Note the delayed onset of growth in the longitudinal thermal energy.

While a beam with an initially semi-Gaussian transverse distribution can be close to a steady state distribution, especially in the limit of small emittance, this distribution is not in local force balance with the external focusing force. An initial transient therefore will occur until the beam relaxes to an equilibrium. Since the beam in the simulation is represented by a number of particles which is far less than the number in an actual beam, the resulting granularity in the distribution causes numerical collisions which can couple momentum from the internal dynamics of the transverse beam redistribution to the longitudinal direction and therefore heat the beam longitudinally. A numerical cause for the initial growth in longitudinal energy is supported by the fact that the growth rate does decrease with an increase in the number of simulation particles used to represent the beam.

In order to remove the complications associated with any initial redistribution of a beam not in equilibrium, simulations were performed employing an initially K-V distribution, for which the beam is in local force balance with the focusing forces. Figure 3 is a plot of the evolution of the rms. z velocity for an initially K-V beam with the same rms. parameters as in the previous case shown in Figs. 1 and 2. Absent the redistribution to equilibrium present in the initially semi-Gaussian beam, the longitudinal velocity shows the quiescent period and exponentiation which is characteristic of an unstable mode growing from the small initial fluctuations in the initial distribution function. The smoother initial behavior can also be noted by examining the rms. radial velocity component shown in Fig. 4. The large initial fluctuations are now absent and the transverse cooling, as the energy is transferred to the longitudinal direction, is now evident.

A further interesting facet of the instability mechanism is the creation of large fluctuations in the beam current, as shown in Fig. 5, which is a plot of the current after the beam has propagated 60 meters, or 8.3 betatron periods. Note that the characteristic scale of these fluctuations is on the same order as the beam radius.

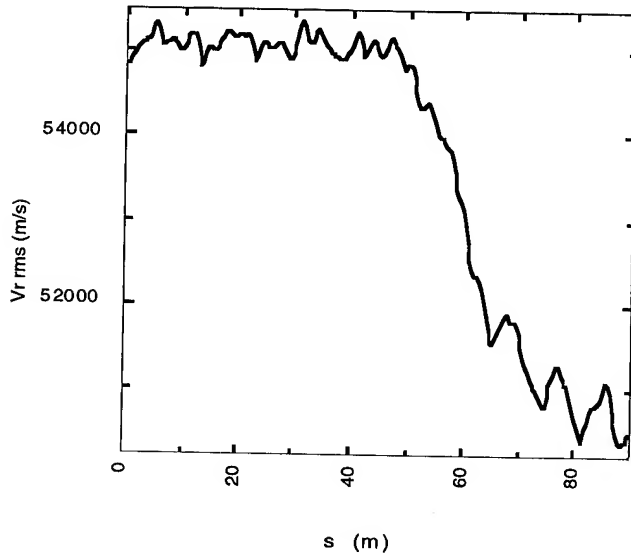


Fig. 4. Evolution of the transverse rms. velocity for the beam with an initially K-V distribution, showing the smooth transfer of energy from the transverse to the longitudinal direction.

III. DISCUSSION OF SIMULATIONS

The two simulations discussed above are representative of several that have been conducted to examine details of an instability which is responsible for the transfer of energy from the transverse to longitudinal dimensions when there is a substantial anisotropy in beam temperature. Limited space however, restricts the discussion here to describing some of the more important features which were observed.

One significant feature seen in the linear phase of the instability is that the transverse dependence of the self-electric fields within the beam strongly resemble the $J_1(kr)$ and $J_0(kr)$ Bessel functions for E_r and E_z respectively. For the parameter regime shown here, the value of k for the unstable mode is such that the longitudinal electric field, but not the transverse, reverses direction within the beam. Self-electric fields with this transverse dependence are associated with the solutions of Poisson's equation that have a real (decaying or growing) exponential dependence on z rather than being propagating modes. The local nature of the growing modes that this implies was verified by seeding the instability by a local perturbation in the beam radius. Preliminary analysis of the characteristic frequencies of such an envelope perturbation, which is localized in the axial direction, show that oscillation frequencies are consistent with what is required for the fields to resonate with the particle betatron oscillations, including the space charge depression. The beam dynamics appear to be complicated, however, by a coupling to the longitudinal space

charge waves that will propagate the energy in the growing modes. Though the mechanism appears to be similar to the Harris instability[6], with the betatron oscillations replacing the cyclotron motion in that case, the finite transverse geometry in the present case appears to substantially modify the dynamics.

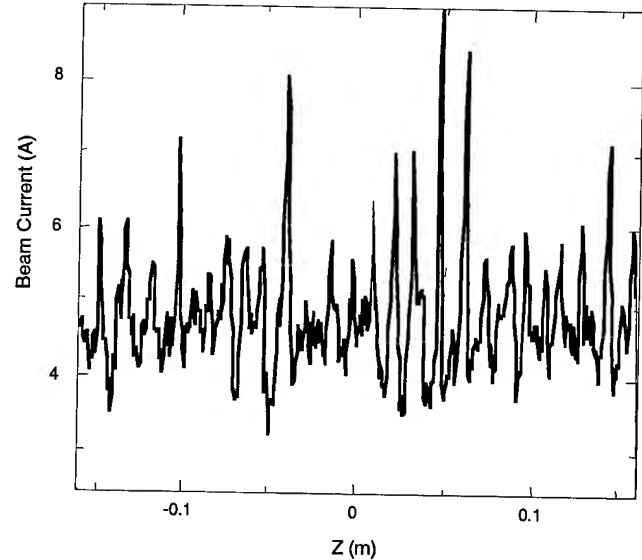


Fig. 5. Beam current plotted against axial position within the beam, after the beam has propagated 60 m.

IV. REFERENCES

- [1] I. Hofmann, "Emittance Growth of Beams Close to the Space Charge Limit," *IEEE Tran. Nucl. Sci.* **NS-28**, 2399 (1981).
- [2] R. A. Jameson, "Beam Intensity Limitations in Linear Accelerators," *op. cit.* 2408.
- [3] Alex Friedman, David P. Grote, and Irving Haber, "Three-Dimensional Particle Simulation of Heavy-Ion Fusion Beams," *Phys. Fluids B* **4**, 2203 (July, 1992).
- [4] A. Friedman, D. A. Callahan, D. P. Grote, A. B. Langdon, and I. Haber, "Studies of Equilibration Processes in Heavy Ion Beams," *Bull. Am. Phys. Soc.*, **35**, 9, 2121 (Oct. 1990).
- [5] Debra A. Callahan, A. Bruce Langdon, Alex Friedman, and Irving Haber, "Longitudinal Beam Dynamics for Heavy Ion Fusion," *Proc. 1993 Particle Accel. Conf.*, 730 (IEEE, 1993).
- [6] E. G. Harris, "Unstable Plasma Oscillations in a Magnetic Field," *Phys. Rev. Letters*, **2**, 34 (1959).

VARIANTS OF OPTICS SCHEMES AND ACCELERATOR CONFIGURATIONS FOR THE ATHENS MICROTRON: PRELIMINARY CONSIDERATIONS.

A.V. Tiunov, V.I. Shvedunov, I.V. Surma, Moscow State University, Russia
K.Hizanidis, C.Kalfas, C.Trikalinos, J.Tigelis, Institute of Accelerating Systems and Applications, Athens -- Greece (IASA)

I. INTRODUCTION.

The IASA Continuous Wave Race Track Microtron will be built from the components of 185 MeV/550 μ A NIST/LANL research RTM project. The original NIST CW RTM was designed as 15 linac passages accelerator with increase in orbit circumference per turn $\nu = 2$, 12 MeV synchronous energy gain per turn and quadrupole doublets on each return path. Being outstanding in a number of projected parameters this well-developed design differs by complexity of accelerator tuning connected with chose injection scheme and beam optics. Nuclear physics experiments planned for IASA RTM requires an increase of output beam energy to about 250 MeV, which cannot be achieved with the original design. By this report, we present the results of comparative study of the original design with other possible variants that can be realized with NIST RTM equipment and which differ in accelerator configuration and beam optics. We compared different variants from the point of view of longitudinal and transverse acceptances' values, sensitivity to misalignments, output energy attainable, RF power consumption. From different variants considered we present here original scheme (Variant 1); scheme with $\nu = 1$ and high injection energy (Variant 2); and cascade scheme (Variant 3) in which available second end magnets pair can be used. Schematic views of these variants are shown in figure 1, and their parameters are given in Table I.

Table I. RTM parameters for different configurations.

RTM variants	1	2	3 - I	3 - II
Injection energy (MeV)	5	17	5	42.5
Energy gain per turn (MeV)	12	6	1.6	8
Incremental number, ν	2	1	1	1
Number of linac passages	15	28	25	25
Output energy (MeV)	185	185	42.5	245
Maxim current (μ A)	550	100	100	100
End magnets field (Tesla)	1	1	0.266	1.33
Linac length (m)	8	4	1.6	8
Linacs RF losses (kW)	305	305	24	106
A_r (π mmx mrad)	36	105	30	90
A_{ion} (π MeVx deg)	0.6	3.6	1	10

II. RTMS VARIANTS

A. NIST RTM (variant 1).

The original goal of the NIST RTM project (figure 1a) was to investigate the feasibility of building a 1-2 GeV high current CW accelerator using beam recirculation with normal conducting accelerating cavities [1]. Tightly interconnected choice of $\nu = 2$, high energy gain per turn and focusing elements on the return paths determine the features of longitudinal and transverse beam dynamics for NIST RTM. For $\nu = 2$ region of longitudinal phase stability is about two times smaller than for $\nu = 1$; and quadrupole doublets on the return paths produce unavoidable longitudinal and horizontal motion coupling. To decrease this coupling period of betatron oscillations in the original design is chosen to be close to 8, and longitudinal - 4. First orbit problem is solved by complicated "hairpin" injection scheme - after first linac passage beam is reflected by the end magnet fringe field and accelerated in opposite direction, thus increasing effective injection energy to 21 MeV.

We have calculated RTM beam dynamics with RTMTRACE code [2] to estimate longitudinal (A_{lon}) and normalized transverse (A_r) acceptances and sensitivity of longitudinal motion to elements misalignments and errors in fields settings. We present in the Table I values of the acceptances and in Table II sensitivity factors, which are values of change in distance between end magnets Δd , change of accelerating field phase with respect to injected beam $\Delta\phi$, relative change in accelerating field amplitude $\Delta E/E$, and relative change in end magnets field $\Delta B/B$ which lead to amplitude of synchronous particle longitudinal oscillations $\sim 2^\circ$

Table II. Sensitivity factors.

Variant	Δd (mm)	$\Delta\phi$ (degr.)	$\Delta E/E$ (%)	$\Delta B/B$ (%)
1	0.15	0.9	0.1	0.06%
2	0.37	2.4	0.5	0.14
3	0.41	2.2	0.65	0.14

B. Reconfigured NIST RTM (variant 2).

Figure 1b shows RTM schemes that can be realized with minimal rework using NIST RTM equipment. In this variant one from two linacs sections is transferred from the

RTM axis to injector. Increasing the injection energy to 17 MeV with the magnetic mirror installed at the injector output and having 6 MeV synchronous energy gain per turn we get injected beam orbit diameter 7.4 cm - too small to bypass linac. The problem of linac bypass can be solved with the injection scheme originally used at MAMI RTM I [3] and schematically shown at fig. 1a. Thus, $\nu = 1, 28$ orbit RTM can be realized with the beam focusing by quadrupole doublets installed at both linacs sides on the common axis. This simple optics similar to that used in MAMI RTMs [3] posses enough strength to ensure stable transverse oscillations for our choice of injection to output energies ratio 17: 185 despite to the quadratic focusing strength decrease with the energy growth.

Our computer simulation showed that due to $\nu = 1$, high injection energy and short distance between end magnets this variant has ~ 3 times larger longitudinal acceptance, than variant 1, ~ 6 times larger normalized transverse acceptance, and is about 2 -3 times less sensitive to elements misalignments and fields errors

RTM tuning and operation is significantly simplified in considered scheme, but part of the problems connected with accelerator tuning and operation is transferred from the RTM to injector. On the other hand, high current, small longitudinal and transverse emittances beam with energy varying between 6 and 17 MeV can be obtained at the injector output in relatively short time and used in applied researches. Magnetic mirror can be realized according to one of the known schemes - it can be isochronous achromatic four magnets system, similar to that of ref. 4, or has more simple construction being one dipole magnet with special field configuration as described in [5]. To output beam from the injector three magnet chicane must be installed between the existing 5 MeV line and added accelerator section. New line to transport and inject beam to RTM must be designed and manufactured.

Linacs RF power losses in variant 2 is nearly the same as in the original scheme so output energy cannot be essentially increased

C. Cascade scheme (Variant 3).

Cascade scheme was originally suggested in [3] and successfully realized in three steps MAMI accelerator with 850 MeV output energy [6]. Accelerator tuning and operation is greatly simplified in this case as compared with the original NIST/LANL design. RF power consumption is essentially decreased thus giving possibility to increase output energy. Two pairs of end magnets available at IASA make this solution quite realistic.

View of the cascade scheme is given in figure 1c. Both RTMs are $\nu = 1, 25$ orbit machines. Original linac with it's 8 m length is installed in RTM II, operating at low energy gradient ~ 1 MeV/m, thus consuming only ~ 106 kW RF power without beam load. RTM I 1.6 m linac with the same energy gradient consumes ~ 24 kW RF power, and

matching section placed between two steps has much less power consumption.

Choice of the RTM I output energy for a given end magnet dimensions is dictated by the necessity of linac bypass for injection energy 5 MeV. In this case simplest injection scheme shown in figure 1c can be used for both RTMs.

Similar to variant 2, simple optics with beam focusing by quadrupole doublets installed at the both linacs sides on the common axis for RTM II and singlets for RTM I are used, having higher strength, than in variant 2 as the ratios of input to output energies are smaller for both cascades.

Calculated values of the longitudinal and normalized transverse acceptances and sensitivity factors are given in Tables I and II, respectively. RTM II acceptances are rather large being close to that of variant 2. For RTM I owing to large phase slip on the few first orbits and low injection energy acceptances are more close to the original design. Sensitivity factors for both steps are close to variant 2, thus cascade scheme is less sensitive to elements misalignments and field errors, than the original design.

The crucial point of cascade scheme for the present 245 MeV design is possibility to achieve high field uniformity at the field level $\sim 1.3 - 1.4$ T with the available end magnets, which were designed for 0.8 -1.2 T gap field. We have made POISSON [7] calculations which showed, that to get field homogeneity $2 \cdot 10^{-4}$ at the gap field level 1.33 T it is necessary slightly increase shim thickness as compared with the original design. For higher field levels owing to steel saturation field inhomogeneity become too high to be compensated by shim thickness. Method of current shims used for MAMI RTMs [6] can be used in this case

Comparing with previous variants cascade scheme requires much more labor for its realization. New linacs must be designed and manufactured for RTM I and matching system, though this problem can be solved by one of two 4 m main linac sections reassembling [8]. In this case ~ 6 m linac will be used for RTM II and two ~ 1 m linacs for RTM I and matching system. With the decreasing linacs length RF power consumption will proportionally grow, being within available 500 kW klystron capabilities.

III. CONCLUSION.

Possibility to get 245 MeV output energy, RTM I beam with the energy $\sim 40 - 45$ MeV, which can be used in applied researches, inherent simplicity in tuning and operation make the cascade scheme to be favorable choice. Additional calculations to get matching conditions for different variants and more extensive misalignment effects estimations will be made. The final choice of IASA RTM scheme depends both on the relative technical merits and amount of labor needed to build and operate accelerator.

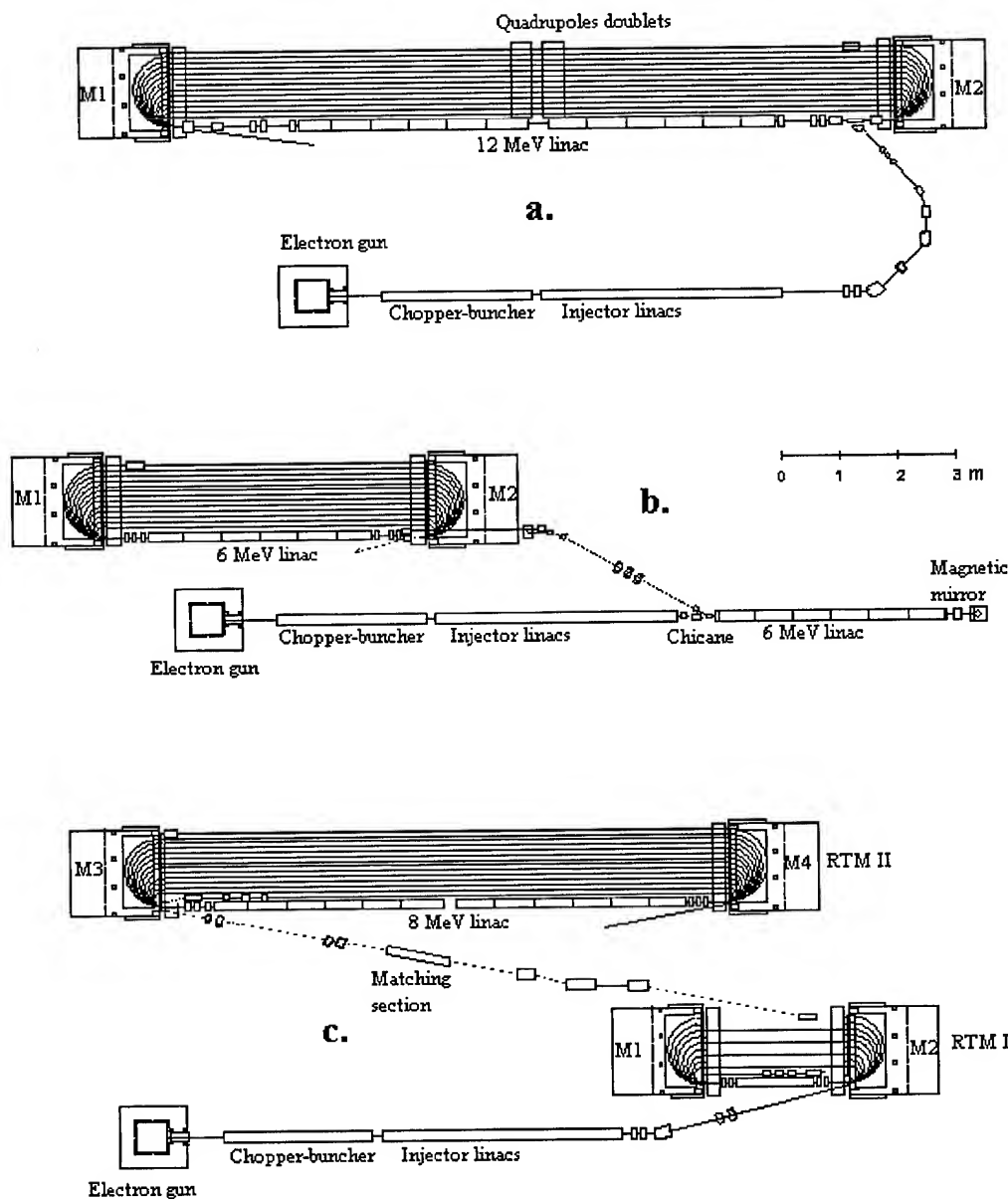


Figure 1. Variants for IASA CW RTM.

IV. REFERENCES

- [1].S. Penner et al. IEEE Trans. on Nucl. Sci., Vol.NS-32,(1985)2669-2671.
- [2].V.G. Gevorkyan et al. VINITI N 183-B89, Moscow 1989.(in Russian)
- [3].H.Herminghaus et al. Nucl. Instr. Meth., v.138,(1976)1
- [4].S.O. Schriber and E.A. Highway. IEEE Trans. NS-22, No.3(1975)1060
- [5].B.S. Ishkhanov et al Preprint INP MSU 94-37/359, Moscow, 1994, 40 p.(in Russian)
- [6]. H.Herminghaus 1988 Linear Acc. Conf. Proc., CEBAF Report-89-001, p. 247
- [7].User's Guide for the POISSON/SUPERFISH Group of Codes., LA-UR-87-115, Los Alamos, 1987.
- [8].L.S. Cardman, private communication

STUDY OF BEAM DECOHERENCE IN THE PRESENCE OF HEAD-TAIL INSTABILITY USING A TWO-PARTICLE MODEL*

G.V. Stupakov and A.W. Chao

Stanford Linear Accelerator Center, Stanford University, Stanford, CA 94309 USA

Abstract

The decoherence behavior of a beam centroid motion after a kick is studied using a two-particle model. A simple theory based on averaging of the governing equation is developed. The effects of a finite chromaticity and synchrotron motion are taken into account. Increasing the tune spread in the beam, a transition from a head-tail instability to a stable decay of an initial kick is explicitly demonstrated.

I. INTRODUCTION

When a bunched beam is kicked in a storage ring, it executes a betatron oscillation. If there is a spread in the betatron frequencies of the beam particles, it is well-known [1-4] that the centroid motion of the beam will decay in time as a result of decoherence among the oscillations of different particles. The rate of decoherence depends on the spread of the betatron frequencies.

In addition to this decoherence effect, the beam centroid motion after the kick is also affected by the collective effects if the beam is sufficiently intense [4-6]. The interplay between the decoherence and the collective effects was analyzed in Ref. 5, except that it neglected the effect of the head-tail instability by assuming a zero chromaticity. For a coasting beam, a similar problem has been treated in Ref. 6. In this note, we offer a bunched-beam analysis that includes the effect of a finite chromaticity using a simplified two-particle model of the beam. We obtain the time behavior of the beam centroid after the kick as a function of the frequency spread, the wake field strength, and the chromaticity. The results reduce to those of Ref. 5 when the chromaticity is set to zero. It is shown that by an appropriate transformation, the formalism of Ref. 5 for the case with zero chromaticity applies also to the case with finite chromaticity.

Our result demonstrates the transition from Landau-damped oscillations to instability. In particular, it gives explicitly the condition for the collective instability to be Landau damped.

II. GENERAL ANALYSIS

To study the interplay between the decoherence and the collective head-tail effects, we consider a simplified two-particle model in which the beam is modeled as two macroparticles interacting with each other through a wake field according to

$$y''_{1,2} + \frac{\omega_{1,2}^2}{c^2} y_{1,2} = \varepsilon h_{1,2} \bar{y}_{2,1}, \quad (1)$$

where y_1 and y_2 are the transverse offsets for the first and the second macroparticles respectively, and the prime designates the differentiation with respect to the longitudinal coordinate s . The

betatron frequencies ω_1 and ω_2 in Eq. (1) for each particle are modulated due to the synchrotron motion,

$$\omega_{1,2} = \omega (1 \mp \xi \delta \cos(\omega_s s/c)), \quad (2)$$

where ω is the unperturbed betatron frequency and $\delta = \hat{z}\omega_s/c\eta$ with ξ designating the chromaticity parameter, ω_s the synchrotron frequency, η the momentum compaction factor and \hat{z} the amplitude of synchrotron oscillations. We assume the two macroparticles execute their synchrotron oscillations according to $z_1 = -z_2 = \hat{z} \sin(\omega_s s/c)$. On the right hand side of Eq. (1) we have $\varepsilon = Nr_0 W_0 / 2\gamma C$, where N is the number of particles in the bunch (each macroparticle contains $N/2$ particles); r_0 is the classical radius of the particle; W_0 is the wake function at $z = 0$ (in case when $W(z = 0) = 0$, W_0 is some characteristic value of W); γ is the relativistic factor; and C is the accelerator circumference. The function $h_1(s)$ accounts for the time variation of macroparticle positions: it is equal to $W(2\hat{z}|\sin(\omega_s s/c)|)/W_0$ for $z_1 < z_2$, and $h_1(s) = 0$ for $z_1 > z_2$. The function $h_2(s)$ differs from $h_1(s)$ in that z_1 is interchanged with z_2 . Note that $h_1(s)$ ($h_2(s)$) is nonvanishing only when the first (second) macroparticle trails the other macroparticle.

We assume a frequency spread within each macroparticle which has a distribution $\rho(\omega)$ normalized so that $\int \rho(\omega) d\omega = 1$. The function $\rho(\omega)$ has a maximum at $\omega = \omega_0$ with a characteristic width $\Delta\omega_0 \ll \omega_0$. The functions $y_1 = y_1(s|\omega)$ and $y_2 = y_2(s|\omega)$ in Eq. (1) are, as a matter of fact, functions of two variables, s and ω , and the bar designates averaging over frequency,

$$\bar{y}_{1,2}(s) = \int y_{1,2}(s|\omega) \rho(\omega) d\omega. \quad (3)$$

We will be looking for solution of Eq. (1) in the following form [7]

$$y_{1,2}(s|\omega) = \bar{y}_{1,2}(s|\omega) \exp(-i\omega_0 s/c \pm i\chi \sin(\omega_s s/c)), \quad (4)$$

where $\chi = \xi \delta \omega_0 / \omega_s$ is the head-tail phase, and $\bar{y}_{1,2}(s|\omega)$ is a slowly varying amplitude. Substituting Eq. (4) into Eq. (1) and neglecting small terms we have

$$-2i \frac{\omega_0}{c} \bar{y}'_{1,2} + \frac{\omega^2 - \omega_0^2}{c^2} \bar{y}_{1,2} = \varepsilon h_{1,2} \bar{y}_{2,1} e^{(\mp 2i\chi \sin(\frac{\omega_s s}{c}))}, \quad (5)$$

where

$$\hat{y}_{1,2}(s) = \int \bar{y}_{1,2}(s|\omega) \rho(\omega) d\omega. \quad (6)$$

Assuming $\chi \ll 1$ we can expand the right hand side of Eq. (5) and average it over s . Also, because the frequency spread is assumed to be small, we have $\omega^2 - \omega_0^2 \approx 2\omega_0 \Delta\omega$, where $\Delta\omega = \omega - \omega_0$. We then have

$$\bar{y}'_{1,2} + i \frac{\Delta\omega}{c} \bar{y}_{1,2} = \frac{ic}{2\omega_0} \varepsilon (\alpha_1 + 2i\alpha_2 \chi) \hat{y}_{2,1}, \quad (7)$$

*Work supported by the Department of Energy contract DE-AC03-76SF00515

where

$$\alpha_1 = \frac{\omega_s}{2\pi W_0 c} \int_0^{c\pi/\omega_s} W \left(2\hat{z} \sin \left(\frac{\omega_s s}{c} \right) \right) ds, \quad (8)$$

$$\alpha_2 = \frac{\omega_s}{2\pi W_0 c} \int_0^{c\pi/\omega_s} W \left(2\hat{z} \sin \left(\frac{\omega_s s}{c} \right) \right) \sin \left(\frac{\omega_s s}{c} \right) ds. \quad (9)$$

For a constant wake, $W(z) \equiv W_0$, we have $\alpha_1 = 1/2$, $\alpha_2 = 1/\pi$.

It is convenient to define the center of mass Y and the relative displacement D of the macroparticles so that

$$Y = \frac{1}{2} (\tilde{y}_1 + \tilde{y}_2), \quad D = \tilde{y}_1 - \tilde{y}_2. \quad (10)$$

This reduces Eq. (7) to a pair of decoupled equations,

$$Y' + i \frac{\Delta\omega}{c} Y = r \hat{Y}, \quad D' + i \frac{\Delta\omega}{c} D = -r \hat{D}, \quad (11)$$

where

$$\begin{Bmatrix} \hat{Y}(s) \\ \hat{D}(s) \end{Bmatrix} = \int \begin{Bmatrix} Y(s|\Delta\omega) \\ D(s|\Delta\omega) \end{Bmatrix} \rho(\Delta\omega) d\Delta\omega, \quad (12)$$

and $r = i c \epsilon (\alpha_1 + 2i\alpha_2 \chi) / 2\omega_0$.

At this point, we note that averaging Eq. (5) actually assumes that the functions $\hat{y}_{1,2}$ vary on the time scale that is larger than the synchrotron period. From Eq. (11) we find that, due to the wake field, Y and D will be modulated with the frequency equal to $c \text{Im} r$. Hence, we have to require $c^2 \epsilon \alpha_1 / 2\omega_0 \ll \omega_s$, as an applicability condition of our approach. It is worth noting that the ratio $\pi c^2 \epsilon \alpha_1 / 2\omega_0 \omega_s$ is equal to the parameter Υ defined in [7], p. 180 (for a constant wake), that governs the strong head-tail instability. The above condition therefore implies that we are well below the threshold of the strong head-tail instability.

We will first focus on the behavior of the centroid of the bunch and consider the first of Eq. (11). The analysis follows closely that of Ref. 5. Integrating the equation for Y we find,

$$Y = Y_0 e^{-i\Delta\omega s/c} + r \int_0^s \hat{Y}(s') e^{-i\Delta\omega(s-s')/c} ds', \quad (13)$$

where Y_0 is a constant equal to the initial value of Y at $s = 0$. Averaging Eq. (13) according to Eq. (12) yields

$$\hat{Y} = Y_0 K(s) + r \int_0^s \hat{Y}(s') K(s-s') ds', \quad (14)$$

where $K(s)$ is the *decoherence function*

$$K(s) = \int e^{-i\Delta\omega s/c} \rho(\Delta\omega) d\Delta\omega. \quad (15)$$

Eq. (14) can now be solved by means of a Laplace transform. Defining

$$u(p) = \int_0^\infty \hat{Y}(s) e^{-ps} ds, \quad \kappa(p) = \int_0^\infty K(s) e^{-ps} ds, \quad (16)$$

the Laplace transform of Eq. (14) is

$$u(p) = Y_0 \kappa(p) + r \kappa(p) u(p), \quad (17)$$

from which we find $u(p)$, and making inverse Laplace transform yields

$$\hat{Y}(s) = \frac{1}{2\pi i} Y_0 \int_{\sigma-i\infty}^{\sigma+i\infty} \frac{\kappa(p)}{1 - r\kappa(p)} e^{ps} dp. \quad (18)$$

Since Eq. (11) for D differs only by the sign of r , all our results for Y are also applicable to D upon the substitution $r \rightarrow -r$.

III. DISTRIBUTION FUNCTIONS AND INSTABILITY

We have thus solved formally the motion of the beam centroid after a kick. The amplitude of the beam centroid motion is described by $\hat{Y}(s)$ of Eq. (18) where Y_0 is the initial kick amplitude. The parameter r contains the wake field and the chromaticity information. The function $\kappa(p)$, given by Eqs. (15) and (16), contains the information of the betatron frequency spectrum of the beam. To proceed, we assume a Gaussian distribution function,

$$\rho(\omega) = \frac{1}{\sqrt{2\pi} \Delta\omega_0} \exp \left(-\frac{\Delta\omega^2}{2\Delta\omega_0^2} \right), \quad (19)$$

where $\Delta\omega_0$ is the rms width of the spectrum. Then

$$K(s) = \exp \left(-\Delta\omega_0^2 s^2 / 2c^2 \right), \quad (20)$$

and

$$\kappa(p) = \frac{c\sqrt{\pi}}{\sqrt{2}\Delta\omega_0} \exp \left(\frac{p^2 c^2}{2\Delta\omega_0^2} \right) \left[1 - \text{erf} \left(\frac{pc}{\sqrt{2}\Delta\omega_0} \right) \right], \quad (21)$$

where $\text{erf}(x)$ is the error function. Defining the variable $\zeta = ipc/\Delta\omega_0$ and the function $w(\zeta) = -i \exp(-\zeta^2/2) [1 - \text{erf}(-i\zeta/\sqrt{2})]$, we can rewrite Eq. (18) in the following form

$$\hat{Y}(s) = \frac{\Delta\omega_0}{2\pi r c} Y_0 \int_C \frac{w(\zeta) \exp(-i\Delta\omega_0 \zeta s/c) d\zeta}{w(\zeta) + i\sqrt{2}\Delta\omega_0 / r c \sqrt{\pi}}, \quad (22)$$

where the integration goes along a straight horizontal line in the upper half plane of the complex variable ζ , above the singularities of the integrand. The function $w(\zeta)$ is an analytic function in the upper half plane of the complex variable ζ . To perform the integration we can shift the integration path down to the real axis of ζ . However, if the denominator in Eq. (22) has a root in the upper half plane, $\zeta = \zeta_0$, the integration path will have to encircle the corresponding pole, and the residue from the pole will give a contribution to $\hat{Y}(s)$ with the time dependence $\propto \exp(-i\Delta\omega_0 \zeta_0 s/c)$. This implies an instability with the growth rate equal to $\Delta\omega_0 \text{Im} \zeta_0$.

We can easily find the root of the denominator in Eq. (22) and obtain the condition for the stability assuming $|\Delta\omega_0/r| \ll 1$. In this limit, a solution to the equation $w(\zeta) = -i\sqrt{2}\Delta\omega_0 / r c \sqrt{\pi}$ is [5]

$$\zeta = -\frac{\epsilon \alpha_1 c^2}{2\omega_0 \Delta\omega_0} - \frac{i\epsilon \chi \alpha_2 c^2}{\omega_0 \Delta\omega_0} - \frac{i\sqrt{\pi} \epsilon^2 \alpha_1^2 c^4}{\sqrt{2}\omega_0^2 \Delta\omega_0^2} \exp \left(-\frac{\epsilon^2 \alpha_1^2 c^4}{2\omega_0^2 \Delta\omega_0^2} \right). \quad (23)$$

For small $\Delta\omega_0$, the last term is exponentially small, and we can neglect it. The result will be a head-tail instability in the system of two macroparticles for $\chi < 0$ with the growth rate $\gamma_{inst} = \varepsilon\alpha_2 c^2 |\chi|/\omega_0$. The last term in Eq. (23) accounts for the Landau damping effect. It overcomes the second term and suppresses the instability if

$$|\chi| \alpha_2 < \frac{\sqrt{\pi} \varepsilon \alpha_1^2 c^2}{\sqrt{2} \omega_0 \Delta\omega_0} \exp\left(-\frac{\varepsilon^2 \alpha_1^2 c^4}{2 \omega_0^2 \Delta\omega_0^2}\right). \quad (24)$$

Eq. (22) has been integrated numerically in Ref. [5] for both stable and unstable regimes. The relevant plots can be found in that paper.

We will also consider the case when the tune spread is associated with the lattice nonlinearity so that the tune is $\nu = \nu_0 - \mu a^2$, where a is the ratio of the amplitude of the betatron oscillations to the rms width of the beam, and μ is a nonlinearity parameter. In this case, for a small amplitude oscillations of the centroid, the decoherence function has a form [1]:

$$K(s) = \frac{1}{(1 - is\Delta\omega_0/c)^2}, \quad (25)$$

where $\Delta\omega_0 = 2\mu\omega_{rev}$, and ω_{rev} is the revolution frequency. The Laplace transform of Eq. (25) yields

$$\kappa(p) = \frac{ic}{\Delta\omega_0} \exp\left(\frac{ipc}{\Delta\omega_0}\right) E_2\left(\frac{ipc}{\Delta\omega_0}\right), \quad (26)$$

where $E_2(x)$ is the exponential integral function [8]. Using the variable ζ we can rewrite Eq. (18) in the following form

$$\hat{Y}(s) = \frac{\Delta\omega_0}{2\pi rc} \int_C d\zeta \frac{\exp(\zeta - i\Delta\omega_0 s \zeta/c) E_2(\zeta)}{i\Delta\omega_0/rc - \exp(\zeta) E_2(\zeta)}. \quad (27)$$

This equation is similar to Eq. (22) in that it exhibits stabilization effect for sufficiently large $\Delta\omega_0$ due to Landau damping. We will demonstrate this in the next section for a particular example considered in Ref.4.

IV. DECOHERENCE EFFECTS

As an example, we assume one set of parameters considered in Ref. 4: $N = 3 \times 10^{10}$, $\sigma_z = 6$ mm, $\nu_\beta = 8.18$, $\beta_x = 3$ m, $\gamma = 2350$, and a linear wake function, $W(z) = W_0 z$, with $W_0 = 2 \times 10^7$ m⁻³. The amplitude of the synchrotron oscillation \hat{z} is assumed to be $\hat{z} = \sqrt{2}\sigma_z$, and the betatron frequency $\omega_\beta = c/\beta_x$. This gives for the factor r , $r = 3.0 \times 10^{-5}(0.64i + 0.08\xi)$. The parameter $\Delta\omega_0$ can be expressed in terms of μ , $\Delta\omega_0/c = 8.14 \times 10^{-2} \mu$ m⁻¹.

The amplitude $|\hat{Y}(s)|$ of the beam calculated with the use of Eq. (27) is plotted in Fig. 1 for various values of μ for the unstable case $\xi = -1$. The critical value for μ that stabilizes the head-tail instability is 2.2×10^{-4} .

Figure 1 shows also a stable case, $\xi = 1$. In this case, increasing μ causes a faster decay of the initial kick.

As mentioned in Sec. II, the time behavior of $\hat{D}(s)$ is governed by the same equations as $\hat{Y}(s)$ with r substituted by $-r$. That means that $\xi = -1$ corresponds to stable oscillations of $\hat{D}(s)$, and $\xi = 1$ leads to the head-tail instability in the absence of the tune spread. Calculations show that for the parameters listed above, Landau damping stabilizes the instability of $\hat{D}(s)$ when $\mu > 6 \times 10^{-5}$.

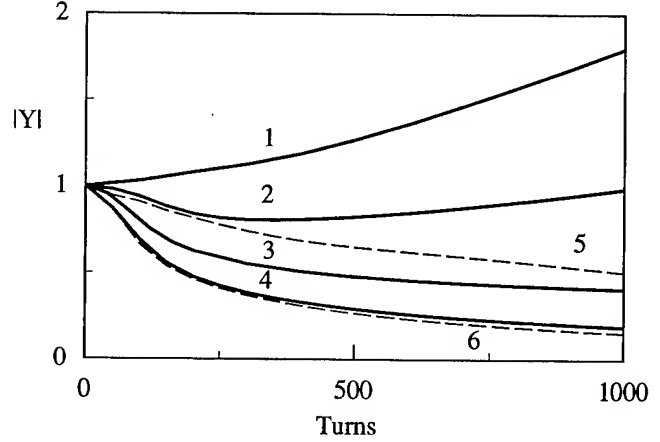


Figure 1. Plot of $|\hat{Y}(s)|$ for $\xi = -1$ (solid curves 1-4) and for $\xi = 1$ (dashed curves 5 and 6). The values of the μ are: 1 and 5 - $\mu = 5.3 \times 10^{-5}$, 2 - $\mu = 1.6 \times 10^{-4}$, 3 and 6 - $\mu = 2.7 \times 10^{-4}$, 4 - $\mu = 3.7 \times 10^{-4}$.

References

- [1] R.E. Meller, A.W. Chao, J.M. Peterson, S.G. Peggs, and M. Furman. Decoherence of kicked beams. SSC-N-360 (1987).
- [2] S.Y. Lee. Decoherence of Kicked Beams II. SSCL-N-749 (1991).
- [3] Ian C. Hsu. *Part. Acc.*, v. 34, p. 43 (1990).
- [4] M. Minty, W. Spence, and A. Chao, these proceedings.
- [5] G.V. Stupakov and A.W. Chao. SSCL Report SSCL-621, (1993).
- [6] M. Blaskiewicz. *Proceedings of the 1993 Particle Accelerator Conference* v. 5, p. 3321 (1993).
- [7] See, for example, Alexander W. Chao. *Physics of Collective Beam Instabilities in High Energy Accelerators* (Wiley, New York, 1993).
- [8] M. Abramovitz and I.A. Stegun, *Handbook of Mathematical functions*, (Dover, New York, 1968).

Beam Distribution Function after Filamentation*

T. O. Raubenheimer, F.-J. Decker, J. T. Seeman

Stanford Linear Accelerator Center, Stanford University, Stanford, CA, 94309

Abstract

In this paper, we calculate the beam distribution function after filamentation (phase-mixing) of a focusing mismatch. This distribution is relevant when interpreting beam measurements and sources of emittance dilution in linear colliders. It is also important when considering methods of diluting the phase space density, which may be required for the machine protection system in future linear colliders, and it is important when studying effects of trapped ions which filament in the electron beam potential. Finally, the resulting distribution is compared with measured beam distributions from the SLAC linac.

I. INTRODUCTION

In a conservative system, which a linear accelerator or storage ring without synchrotron radiation closely approximate, the six-dimensional phase space density is conserved. Similarly, if the three degrees of freedom are uncoupled, all two-dimensional projections of the six-dimensional phase space are also conserved. A conservative emittance dilution arises when the transverse or longitudinal degrees of freedom become coupled. In this case, the 6-D emittance is preserved, but the projected emittances are increased. It can easily be shown that coupling of two planes always increases the smaller of the two projected emittances.

Because the emittance dilutions are conservative, they can be corrected, *i.e.* the emittance can be uncoupled, provided that the dilution has not filamented (phase mixed). Filamentation arises because the beam has a spread in oscillation frequencies due to the energy spread in the beam, nonlinear fields, space charge forces, *etc.* The effect of the filamentation is to cause a phase mixing which makes it difficult to correct dilutions of the projected emittance. Once a dilution filaments, it is, for practical purposes, unrecoverable (synchrotron oscillations in a storage ring provide one obvious exception to this statement).

In this paper, we will discuss the beam distribution function arising after filamentation of a focusing mismatch. When a beam is injected into a storage ring or linac, it should be matched to the periodic or natural lattice functions. A mismatched beam will filament, with corresponding emittance growth, until it is matched to the lattice. In a storage ring, the beta function is chosen to be periodic but in a linac there is room for ambiguity since one needs to define initial values or boundary conditions. Actually, most long linacs are constructed from adiabatically varying periodic focusing cells. The natural lattice functions are simply those defined by the periodic cells.

Understanding the beam distribution function after filamentation is relevant when interpreting beam emittance measurements and locating the sources of emittance dilution. It is also important when considering methods of increasing the phase space density by deliberately mismatching the beam. Finally, it is important when studying trapped ions in an electron beam. In

the next section, we will derive the distribution function for the beam action J and the projection into the x plane. Then we will present some measurements from the Stanford Linear Collider (SLC) linac, and finally, we will discuss the applications.

II. THEORY

In a periodic linear focusing channel, a particle will perform betatron oscillations and its position and angle ($dx/ds = x'$) can be expressed in a form analogous to that of a harmonic oscillator [1]:

$$x = \sqrt{2J\beta(s)} \cos(\psi(s) + \phi) \quad (1)$$

$$x' = \sqrt{\frac{2J}{\beta(s)}} (\sin(\psi(s) + \phi) + \alpha(s) \cos(\psi(s) + \phi)) \quad (2)$$

Here, J and ϕ are the particle 'action' and 'angle' coordinates and are constants of the motion. In addition, the focusing lattice is described by the periodic lattice functions $\alpha(s)$ and $\beta(s)$ and the phase advance $\psi(s)$, where α and ψ are given by

$$\alpha \equiv -\frac{1}{2} \frac{d\beta}{ds} \quad \psi(s) \equiv \int_0^s \frac{ds'}{\beta(s')} \quad (3)$$

Finally, these equations can be inverted to solve for the action in terms of the particle coordinates

$$J = \frac{1}{2} \left(\frac{1 + \alpha^2}{\beta} x^2 + 2\alpha x x' + \beta x'^2 \right) \quad (4)$$

Next, consider a particle beam that occupies some area in x - x' phase space and has a distribution function $g(x, x')$. The rms emittance of the beam is equal to

$$\epsilon \equiv \sqrt{\langle x^2 \rangle \langle x'^2 \rangle - \langle x x' \rangle^2} \quad (5)$$

and the beam can be described with an ellipse whose orientation is specified by the second moments: $\langle x^2 \rangle$, $\langle x x' \rangle$, and $\langle x'^2 \rangle$, and whose area is given by $\pi \epsilon$. With complete generality, the second moments can be written in terms of the beam emittance and two parameters α^* and β^* which we will refer to as beam parameters:

$$\langle x^2 \rangle = \beta^* \epsilon \quad \langle x'^2 \rangle = \frac{1 + \alpha^{*2}}{\beta^*} \epsilon \quad \langle x x' \rangle = -\alpha^* \epsilon \quad (6)$$

These beam parameters α^* and β^* describe the orientation of the beam ellipse in the (x, x') phase space and are not necessarily related to the lattice functions α and β .

The beam distribution function can be expressed in terms of the action-angle coordinates, but, in general it will depend upon both J and ϕ . Instead, we can write the position and angle of particles in terms of the beam parameters α^* and β^* and an amplitude and phase, J^* and ϕ^* :

$$x = \sqrt{2J^*\beta^*} \cos \phi^* \quad (7)$$

$$x' = \sqrt{2J^*/\beta^*} (\sin \phi^* - \alpha^* \cos \phi^*) \quad (8)$$

*Work supported by the Department of Energy, contract DE-AC03-76SF00515

Now, assume that the beam distribution is rotationally symmetric in the normalized phase space x and $\alpha^*x + \beta^*x'$; this is true of bi-gaussian beams and most other distributions of interest. In this case, the distribution function will be independent of the phase ϕ^* and is just a function of J^* . Furthermore, the rms beam emittance ϵ is simply equal to the expectation of the amplitude $\langle J^* \rangle$.

The action-angle coordinates can be related to the amplitude and phase as:

$$J = J^* \left[\left(\frac{\beta^*}{\beta} + \left(\alpha \sqrt{\frac{\beta^*}{\beta}} - \alpha^* \sqrt{\frac{\beta}{\beta^*}} \right)^2 \right) \cos^2 \phi^* + 2 \left(\alpha - \alpha^* \frac{\beta}{\beta^*} \right) \cos \phi^* \sin \phi^* + \frac{\beta}{\beta^*} \sin^2 \phi^* \right] \quad (9)$$

and

$$\tan \phi = \frac{\beta}{\beta^*} \tan \phi^* + \left(\alpha - \alpha^* \frac{\beta}{\beta^*} \right). \quad (10)$$

If the beam parameters are equal to the lattice functions, then the beam is 'matched' to the lattice. In this case, the action J is equal to the amplitude J^* and the angle ϕ is equal to ϕ^* . In addition, the beam distribution function, written in action-angle coordinates, will be independent of the angle coordinate and the rms beam emittance is equal to the expectation of the particle actions $\langle J \rangle$. If the beam filaments as it is transported through the lattice, effectively randomizing the angle coordinate ϕ , the beam emittance and distribution remain unchanged.

In contrast, if the beam is mismatched to the lattice and the beam filaments, the beam distribution function will change and the filamented rms emittance ϵ_f will increase. The emittance increase is trivially calculated from Eq. (9) and can be expressed in terms of the B_{mag} parameter [2][3]:

$$\epsilon_f = B_{\text{mag}} \epsilon, \quad (11)$$

where

$$B_{\text{mag}} \equiv \frac{1}{2} \left[\frac{\beta^*}{\beta} + \frac{\beta}{\beta^*} + \left(\alpha \sqrt{\frac{\beta^*}{\beta}} - \alpha^* \sqrt{\frac{\beta}{\beta^*}} \right)^2 \right]. \quad (12)$$

The calculation of the beam distribution function after filamentation is a little more complicated. Assuming that the angle coordinate is independent of the action after the filamentation, we can express the distribution as

$$g(J)dJ = \int_0^{2\pi} \frac{d\phi^*}{2\pi} g^*(J^*) dJ^*, \quad (13)$$

where $J^* = J/X(\phi^*)$ and

$$X(\phi^*) = a \sin^2 \phi^* + 2b \sin \phi^* \cos \phi^* + c \cos^2 \phi^*, \quad (14)$$

with

$$a = \frac{\beta}{\beta^*} \quad b = \alpha - \alpha^* \frac{\beta}{\beta^*} \quad (15)$$

$$c = \frac{\beta^*}{\beta} + \left(\alpha \sqrt{\frac{\beta^*}{\beta}} - \alpha^* \sqrt{\frac{\beta}{\beta^*}} \right)^2. \quad (16)$$

If the initial beam has a bi-gaussian distribution in x and x' , then the distribution $g^*(J^*)$ is an exponential distribution:

$$g^*(J^*) = \frac{e^{-J^*/\epsilon}}{\epsilon}, \quad (17)$$

and Eq. (13) is straight forward to evaluate. In the trivial case, where $b = 0$ and $\beta^* \gg \beta$ or $\beta \gg \beta^*$, the distribution for J is just a χ -squared distribution with one degree of freedom. In the general case, we can evaluate the integral by first performing a rotation to eliminate the cross term in $X(\phi^*)$. In this case,

$$X(\phi^*) = \lambda_1 \cos^2(\phi^* - \theta) + \lambda_2 \sin^2(\phi^* - \theta), \quad (18)$$

where

$$\lambda_{1,2} = \frac{a+c}{2} \pm \frac{1}{2} \sqrt{(a-c)^2 + 4b^2} \quad (19)$$

$$\theta = \tan^{-1} \left(\frac{c-a}{2b} - \frac{1}{2b} \sqrt{(c-a)^2 + 4b^2} \right). \quad (20)$$

By changing the variable of integration from ϕ^* to $1/c^2 - 1/X$, the integral can be expressed in the form of a tabulated integral [4] and the result can be expressed in terms of the B_{mag} parameter:

$$g(J) = \frac{e^{-JB_{\text{mag}}/\epsilon}}{\epsilon} I_0 \left(\frac{J}{\epsilon} \sqrt{B_{\text{mag}}^2 - 1} \right), \quad (21)$$

where I_0 is the modified Bessel function, B_{mag} is defined in Eq. (12), and ϵ is the injected beam emittance before filamentation. As expected, when $B_{\text{mag}} = 1$, the distribution is an exponential and when $B_{\text{mag}} \rightarrow \infty$, the distribution becomes a χ -squared with one degree of freedom.

Finally, we can calculate the projection into the x plane which is the beam distribution that would be measured. The projection is

$$f(x) = \int_{-\infty}^{\infty} dx' \frac{g(J(x, x'))}{2\pi}, \quad (22)$$

where $J(x, x')$ is given in Eq. (4). In the general case, the distribution function can be expressed in terms of a degenerate hypergeometric series of two variables. Unfortunately, such an expression is not any easier to evaluate than the integral Eq. (22). In the limit where $B_{\text{mag}} \rightarrow \infty$, the projection simplifies to

$$f(x) = \frac{e^{-x^2/8\beta\epsilon_f}}{\sqrt{4\pi^3} \sqrt{\beta\epsilon_f}} K_0 \left(\frac{x^2}{8\beta\epsilon_f} \right), \quad (23)$$

where K_0 is the modified Bessel function and $\epsilon_f = B_{\text{mag}}\epsilon$. The infinite value at $x = 0$ arises because we have essentially assumed a one-dimensional injected beam. A similar expression was derived in Ref. [5] where the author was considering the distribution function for trapped ions in an electron beam.

The distribution $f(x)$ is plotted versus the rms beam size $\sqrt{\beta B_{\text{mag}}\epsilon}$ for different values of B_{mag} in Fig. 1. Notice that as the mismatch becomes larger, the relative amplitude of the central core of the beam increases while long tails contribute to the rms emittance. In the limit of large B_{mag} , the density of the core can be written:

$$\lim_{B_{\text{mag}} \rightarrow \infty} f(0) = \frac{1}{\pi^{3/2} \sqrt{B_{\text{mag}}\beta\epsilon}} \ln(\sqrt{128} B_{\text{mag}}). \quad (24)$$

The core density decreases as $\ln(B_{\text{mag}})/\sigma_x$ rather than $1/\sigma_x$ as it would if the distribution did not change as the emittance increased.

III. MEASUREMENTS

Figure 2 shows the measured profile of a filamented beam in the SLC with large non-gaussian tails. The beam was created

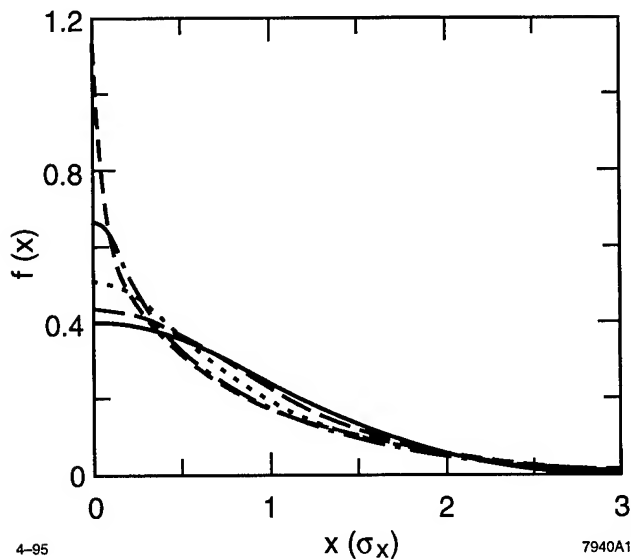


Figure 1. $f(x)$ versus the rms beam size for $B_{\text{mag}} = 1.0$ (solid), $B_{\text{mag}} = 1.25$ (dashes), $B_{\text{mag}} = 2.0$ (dots), $B_{\text{mag}} = 5.0$ (dash-dot), and $B_{\text{mag}} = 50.0$ (dashes).

by an error in a solenoid at the low energy end of the SLAC accelerator. The beam distribution was measured after the beam had filamented; this can be determined by comparing the beam profiles measured at different betatron phases. In Fig. 2, the resulting mismatch had a $B_{\text{mag}} \approx 5$. The data was fit with a phenomenological 'super-gaussian' function [6] which shows reasonable agreement. The small asymmetry that is visible in the data is likely due to transverse wakefields.

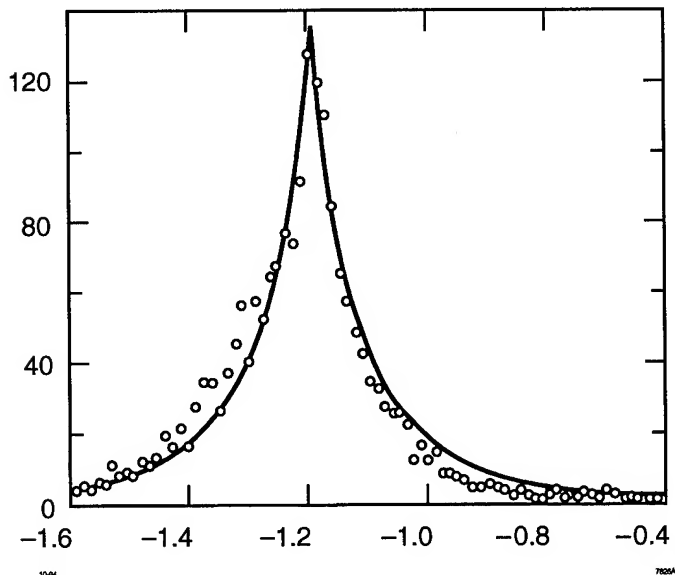


Figure 2. Strong non-gaussian tails form a 'Christmas tree' like distribution which indicates that there is a large mismatch of the beam.

IV. DISCUSSION

In this paper, we have described the beam distribution function arising from a filamented focusing mismatch. Understand-

ing the beam distribution can aid interpreting emittance measurements in a linear collider as well as assist in the diagnosis of the problem.

Another situation where this distribution is relevant occurs when considering machine protection schemes for future linear colliders. If mis-steered, the very small beams in future linear colliders could puncture the vacuum chamber in a single pulse. This is not a desirable feature when commissioning components. One possible method of protecting the collider is to generate a large mismatch $B_{\text{mag}} \sim 1000$ which would then filament and decrease the beam density. This approach has the advantage of not perturbing the beam centroid so that wakefield effects, steering, etc., are not changed. Understanding the evolution of the core density is important in evaluating this technique.

Finally, the filamented distribution also describes the distribution of ions generated by collisional ionization and trapped in a long train of bunches [5][7]. In this case, the ions are created with a transverse density profile equal to the transverse beam profile but the ion thermal energy is typically small compared to the potential energy in beam field. Thus, the ions are mismatched relative to the focusing field of the beam. As ions continue to accumulate, the density evolves into the filamented distribution with $B_{\text{mag}} = E_{\text{pot}}/E_{\text{th}} \gg 1$ and $\beta\epsilon_f = \sigma^2/2$, where σ is the rms electron beam size.

References

- [1] E. D. Courant and H. S. Snyder, "Theory of the Alternating-Gradient Synchrotron," *Annals of Phys.*, **3**, 1 (1958).
- [2] F.-J. Decker, et. al., "Dispersion and Betatron Matching into the Linac," *Proc. of 1991 IEEE Part. Acc. Conf.*, San Francisco, CA, p. 905 (1991).
- [3] M. Syphers, T. Sen, D. Edwards, "Amplitude Function Mismatch," *Proc. of 1993 IEEE Part. Acc. Conf.*, Washington, D.C., p. 134 (1993).
- [4] I. S. Gradshteyn and I. M. Ryzhik, *Tables of Integrals, Series, and Products*, Academic Press, Orlando FL (1980), integral 3.383.2 (1980).
- [5] P. F. Tavares, "Ion Trapping in Electron Storage Rings," Ph.D. Thesis, University of Campinas (1993).
- [6] F.-J. Decker, "Beam Distributions Beyond RMS," *Proc. of 6th Beam Instrumentation Workshop*, Vancouver, B.C., (1994).
- [7] T. O. Raubenheimer and Pisin Chen, "Ions in the Linacs of Future Linear Colliders," *Proc. of the 1992 Linac Conf.*, Ottawa, Canada, p. 630 (1992).

MEASUREMENT OF THE INTERACTION BETWEEN A BEAM AND A BEAM LINE HIGHER-ORDER MODE ABSORBER IN A STORAGE RING*

W. Hartung, P. Barnes, S. Belomestnykh, M. Billing, R. Chiang, E. Chojnacki, J. Kirchgessner, D. Moffat, H. Padamsee, M. Pisharody, D. Rubin, & M. Tigner
Laboratory of Nuclear Studies, Cornell University, Ithaca, New York 14853

"Underneath this chilly gray October sky,
We can make believe the SSC is still alive;
We've shootin' for the Higgs,
An' smilin' Hazel's drivin' by." [1]

I. INTRODUCTION

A phased luminosity upgrade of the CESR e^+e^- storage ring has been initiated [2]. The upgrade program calls for the eventual installation of superconducting cavities with strongly damped higher-order modes (HOMs). The cavity is designed to allow all HOMs to propagate into the beam pipe, so that they may be damped by a layer of microwave-absorbing ferrite. RF measurements with a full-size copper cavity and loads made of TT2-111R ferrite¹ indicate that the design gives adequate HOM damping [3]. The coupling impedance of the ferrite loads and the consequences for beam stability in a high-current ring have been predicted [7]. Prototypes for the cavity, cryostat, and HOM loads were subjected to a beam test in CESR [4], [5], [6]. To further test our understanding of the beam-ferrite interaction, beam measurements were done in CESR in December 1994 on a ferrite load of magnified coupling impedance. This test is described herein.

II. LOAD FABRICATION

We designed a test structure with a beam tube diameter 2.5 times smaller and a ferrite-bearing length 6 times larger than an actual "porcupine" HOM load [6]. The predicted coupling impedance of this test structure is ~ 2 times the predicted monopole impedance and ~ 10 times the predicted dipole impedance of the 8 porcupine loads to be installed in CESR. The structure was split into three units, with sections of straight beam tube (with pumping ports) between them. Each unit consisted of a copper tube with 40 TT2-111R ferrite tiles soldered to the inside and water cooling on the outside (Fig. 1), incorporating features from both the original full-size HOM load [8] and the redesigned porcupine HOM load [6]. A total of four ion pumps, each rated at 140 L/s, were adjacent to the ferrite sections during the vacuum bake and the beam test.

A prototype unit with only 10 tiles was made first for evaluation in a high power density RF test with a 500 MHz klystron. For this test, the ferrite-lined tube became the outer conductor of a coaxial line, with a short placed to produce relatively uniform dissipation in the ferrite. An average surface power density of 15 W/cm² was reached without visible damage to any of the tiles. The maximum (measured) tile surface temperature was 96°C.

*Work supported by the National Science Foundation, with supplementary support from U. S.-Japan collaboration.

¹A product of Trans-Tech, Inc.

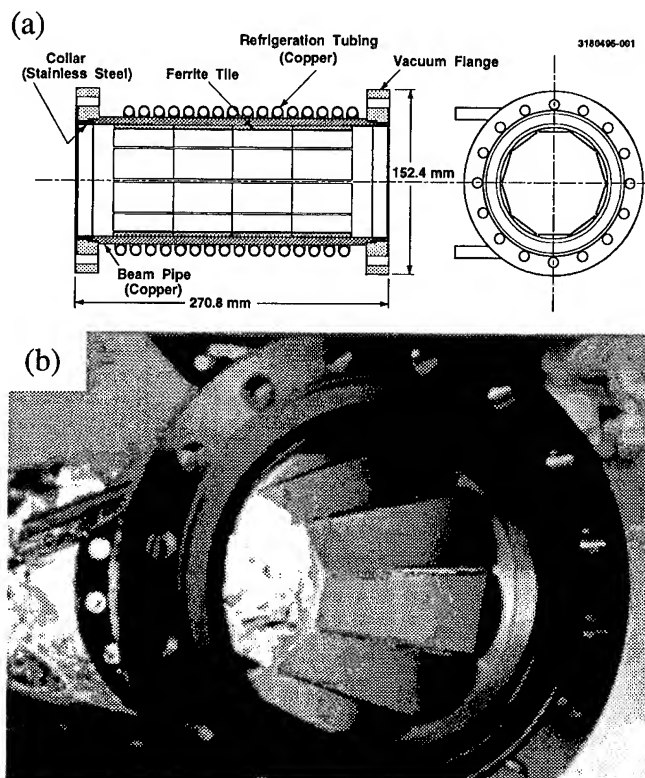


Figure 1. (a) Drawing and (b) photograph of one unit of the ferrite structure. The ID of the Cu tube is 92.1 mm; the ferrite tiles are $50.8 \times 25.4 \times 3.175$ mm³ before radiusing.

III. BEAM TEST RESULTS

The beam measurements on the ferrite section were done over several days, interleaved with machine start-up activities following a down period. Some measurements were done with 9 bunches, in addition to the 1- and 2-bunch measurements discussed herein. Positrons were used almost exclusively, because we did not have complete masking for direct synchrotron radiation from the electron beam. The predictions mentioned in this section are based on the same type of coupling impedance calculations as was done for the HOM loads, *i.e.* using the AMOS program [9] and an analytic approximation [7]. In the calculations, we assumed an axisymmetric geometry with a 3.175 mm layer of ferrite, and did not split the ferrite into three sections.

A. Calorimetric Measurements

The power dissipation in each unit was obtained calorimetrically via the flow rate, inlet temperature, and outlet temperature of the cooling water (the volume flow rate of water was ~ 50 mL/s per unit for most of the test). The monopole loss factor k_0^{\parallel}

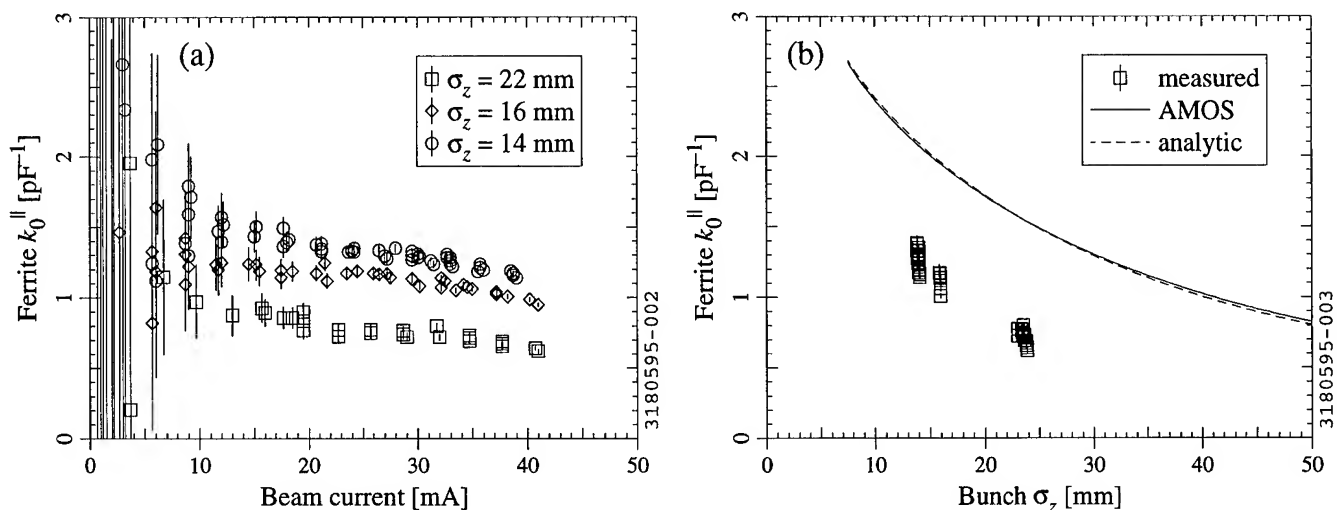


Figure 2. Calorimetrically measured single-bunch loss factor (summed over all 3 units) of the ferrite section as a function of (a) beam current, and (b) bunch length (with predictions). The RF voltage was adjusted to vary the bunch length. Noisy low-current points ($I < 20$ mA) are omitted in (b).

of the ferrite units can be obtained directly from the total power dissipation P_d and total beam current I . The measured k_0^{\parallel} as a function of I is shown in Fig. 2a for a single bunch. The noise in the data at low I is due to the poor resolution of the small ΔT values. At higher I , a slight decrease in the measured k_0^{\parallel} as function of I is visible. Possible explanations for this effect include (i) systematic error in the calorimetry, (ii) non-linearity in the ferrite response to the RF field, or (iii) the ferrite properties' temperature dependence.

Fig. 2b shows the single-bunch data plotted as a function of the longitudinal bunch size σ_z , calculated from the measured synchrotron frequency f_s (we did not have any means to measure the bunch length directly), along with the predicted k_0^{\parallel} . It can be seen that, inasmuch as f_s is a reliable indicator of the bunch length, the decrease in k_0^{\parallel} with I cannot be explained as being due to changes in σ_z as a function of I . The measured k_0^{\parallel} is smaller than predicted by about a factor of 2, perhaps because of the afore-mentioned idealisations in the model.

We used the Temnykh method [10] to sample the wake field: with two bunches of equal charge (I_b = current per bunch = 20 mA for each), we measured the power dissipation in the ferrite as a function of the spacing Δz between the bunches. In terms of a power loss factor

$$P_0^{\parallel} \equiv \frac{P_d f_0}{N_b I_b^2},$$

where N_b = number of bunches and f_0 = revolution frequency, we should have² $P_0^{\parallel} = k_0^{\parallel}$ if the wake fields have vanished by the time the second bunch arrives and $P_0^{\parallel} \rightarrow 2k_0^{\parallel}$ as $\Delta z \rightarrow 0$. The results are shown in Fig. 3, along with a prediction obtained by integrating the calculated coupling impedance with the appropriate form factor. The measurement suggests that the ferrite section's wake fields endure longer than predicted; for $\Delta z > 1$ RF bucket, however, the measurements and predictions seem to agree that the wake field has decayed to zero.

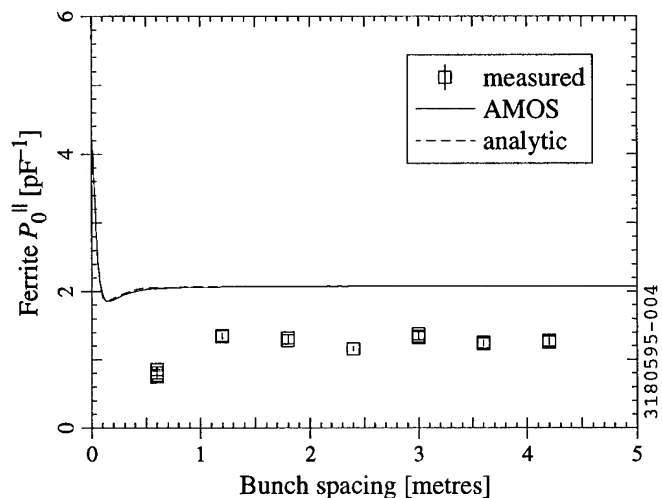


Figure 3. Calorimetrically measured and predicted 2-bunch power loss factor of the ferrite as a function of spacing, with $\sigma_z = 14$ mm (from f_s). Because the RF frequency is 500 MHz, the smallest measurable Δz is 0.6 m.

We used magnetic and electrostatic elements to produce a transverse displacement of the beam in the ferrite chamber and its vicinity. The measured calorimetric single-bunch loss factor as a function of displacement is shown in Fig. 4, along with a prediction based on the calculated monopole and dipole loss factors. Though the measurement suggests that there is some dependence on displacement, the signal-to-noise ratio is not very favourable.

B. RF Power Measurements

It is possible to infer the total loss factor of a storage ring by applying the appropriate book-keeping methods to the cavity RF power and synchrotron radiation power [11]. We applied this technique with and without the ferrite in order to get an independent measure of the power loss due to the ferrite. The results are compared in Fig. 5. The predicted k_0^{\parallel} of CESR shown in Fig. 5 was obtained from scaling laws for various machine elements

²we are (justifiably, we think) treating the single-bunch k_0^{\parallel} and the single-pass k_0^{\parallel} as synonymous.

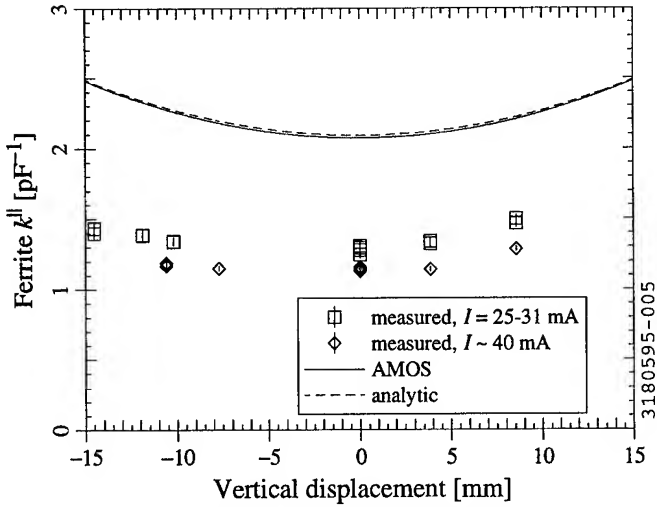


Figure 4. Calorimetrically measured and predicted loss factor of the ferrite section as a function of the vertical displacement of the beam, with $\sigma_z = 14$ mm (from f_s).

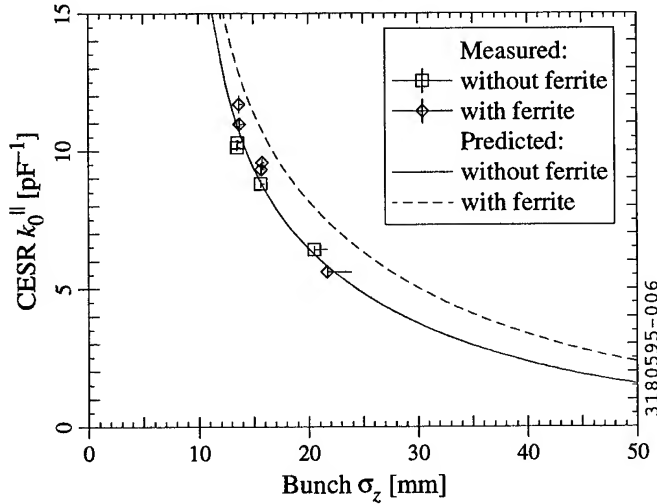


Figure 5. Measured and predicted single-bunch loss factor of CESR, with and without ferrite present.

[12] (updated to account for recent modifications). The total k_0^{\parallel} measurement gave less accuracy than the calorimetric measurement, but the results do not overtly contradict each other.

C. Tune Shift And Damping Rate Measurements

According to theory, the total ring impedance should produce shifts in the frequencies and damping rates of coupled-bunch modes. In the "effective impedance" approximation, the shift in the frequency f and damping rate α should be proportional to I . We used established techniques [13] to measure the lowest-order single-bunch transverse mode frequencies (i.e. the horizontal and vertical betatron frequencies) and corresponding α 's as a function of I , with and without ferrite. We did the measurements with the CESR distributed ion pumps turned off, in order to eliminate anomalous growth effects [13]. We believe that measured differences in slope ($\Delta f' = 0$ to 13 kHz/A and $\Delta \alpha' = -4$ to -6 ms $^{-1}$ A $^{-1}$) are below the reproducibility threshold of the measurement.

IV. LOAD PERFORMANCE

The maximum (total) power dissipation in the ferrite was 5.8 kW according to calorimetry (average power density = 3.8 W/cm 2); this was obtained with $I = 142$ mA in 9 bunches. At this current, the pressure gauges read ≤ 30 pbar, although pressures as high as 50 pbar were recorded (at lower I) during an earlier "beam processing" shift. Several vacuum "spikes" occurred in the course of the test, with the pressure rising to 100–200 pbar or higher. Prior to installation, the pressure in the ferrite assembly reached 1 pbar at 17°C after a vacuum bake-out to 150°C.

A brief inspection of the ferrite chamber after removal from CESR revealed that one corner of one tile had broken off; it was found lying on the bottom of one of the ferrite sections. The piece appeared to have been unsoldered except along one edge. The remaining tiles have not yet been closely inspected for cracks.

V. CONCLUSION

CESR beam measurements with a ferrite-lined section of magnified impedance indicate that the loss factor is a factor of ~ 2 smaller than predicted; the measured wake field endures longer than predicted, but is not visible for $\Delta z \geq 4.2$ m, which is planned for CESR. The signal-to-background ratio made it difficult to pick out effects from the ferrite via measurements on the beam only. We are working on predictions which model the actual load geometry more closely.

We wish to thank all of the Laboratory staff who helped to make this beam test possible.

References

- [1] C. Blonde, "Tomorrow, Wendy (remix)," in *Songs of the DOE: A Benefit Compilation*, Polymer Records, New York, 1995.
- [2] D. Rubin, these proceedings.
- [3] V. Veshcherevich *et al.*, *Proceedings of B Factories: The State of the Art in Accelerators, Detectors, and Physics*, SLAC-400/CONF-9204126, p. 177.
- [4] H. Padamsee, *et al.*, these proceedings.
- [5] S. Belomestnykh, *et al.*, "Wakefields and HOMs Studies...", these proceedings.
- [6] S. Belomestnykh, *et al.*, "Comparison of the Predicted and Measured Loss Factor...", these proceedings.
- [7] W. Hartung *et al.*, *Proceedings of the 1993 Particle Accelerator Conference*, p. 3450.
- [8] D. Moffat *et al.*, *ibid.*, p. 977.
- [9] J. DeFord *et al.*, *Proceedings of the 1989 IEEE Particle Accelerator Conference*, p. 1181.
- [10] A. Temnykh, Cornell LNS Report CON95-06 (1995).
- [11] D. Rice, *et al.*, *IEEE Trans. NS-28*, p. 2446 (1981).
- [12] M. Billing, Cornell LNS Report CBN84-15 (1984).
- [13] M. Billing, *et al.*, these proceedings.

A NEW ANALYTICAL MODEL FOR AXI-SYMMETRIC CAVITIES

D.Burrini, C.Pagani, L.Serafini, INFN-Milan
Via Celoria 16, 20133 Milano, Italy

In this paper we derive a general off-axis expansion valid for axi-symmetrical em. fields. With the application of general arguments a new method to determine analytically off-axis field components is presented, starting with the knowledge of the on-axis distribution of the longitudinal field component. Analytical and numerical em. fields off-axis are compared, in the case of RF monopole modes in a cavity, showing very good agreement up to a radial off-axis position which is comparable to the wavelength. The relevance of the method on applications in analytical study of particles dynamics is discussed and a calculation of the transverse momentum imparted by the field to a relativistic particle is reported: this is of interest for dark current, beam halo and RF injector analysis. Another kind of application in cavity design is mentioned.

I. GENERAL EXPANSION

In deriving a general off-axis expansion for axi-symmetrical em. field, we consider both TE-like and TM-like waves. The cylindrical symmetry of the field allows us to write:

$$\begin{aligned} \begin{pmatrix} E_z^{TM}(r, z, t) \\ H_z^{TE}(r, z, t) \end{pmatrix} &= A_0(z, t) + A_2(z, t)r^2 + \dots + A_{2N}(z, t)r^{2N} \\ \begin{pmatrix} E_r^{TM}(r, z, t) \\ H_r^{TE}(r, z, t) \end{pmatrix} &= B_1(z, t)r + B_3(z, t)r^3 + \dots + B_{2N+1}(z, t)r^{2N+1} \\ \begin{pmatrix} E_\phi^{TE}(r, z, t) \\ H_\phi^{TM}(r, z, t) \end{pmatrix} &= C_1(z, t)r + C_3(z, t)r^3 + \dots + C_{2N+1}(z, t)r^{2N+1} \end{aligned} \quad (1)$$

where $A_0(z, t) = \begin{pmatrix} E_z(r=0, z, t) - TM \\ H_z(r=0, z, t) - TE \end{pmatrix}$ is the field on-axis.

We want to obtain a formula which allows to write the field off-axis, by the knowledge of the field on-axis shown above.

To do this, the simplest way is to consider the following Maxwell equations in empty space ($\rho=0$, $J=0$, $\epsilon_r = \mu_r = 1$);

$$\begin{aligned} \nabla \cdot \mathbf{E} &= 0 \quad ; \quad \nabla^2 \mathbf{E} - \frac{1}{c^2} \frac{\partial^2}{\partial t^2} \mathbf{E} = 0 \\ \left\{ \nabla \times \begin{pmatrix} \mathbf{E}^{TE} \\ \mathbf{H}^{TM} \end{pmatrix} \right\}_z &= \begin{pmatrix} -\mu_0 \\ \epsilon_0 \end{pmatrix} \frac{\partial}{\partial t} \begin{pmatrix} H_z^{TE} \\ E_z^{TM} \end{pmatrix}(r, z, t) \end{aligned} \quad (2)$$

Assuming an harmonic time dependence as $e^{i\omega t}$ we project in cylindrical co-ordinates and replace the expressions of the fields in eq.1, obtaining the following recurrence relations:

$$\begin{aligned} 4N^2 A_{2N}(z, t) &= - \left\{ \frac{\partial^2}{\partial z^2} A_{2(N-1)}(z, t) + k^2 A_{2(N-1)}(z, t) \right\} \\ 2(N+1) B_{2N+1}(z, t) + \frac{\partial}{\partial z} A_{2N}(z, t) &= 0 \\ 2(N+1) C_{2N+1}(z, t) &= ik \begin{pmatrix} Z_0^{-1} \\ -Z_0 \end{pmatrix} A_{2N}(z, t) \end{aligned} \quad (3)$$

where $Z_0 = \sqrt{\mu_0/\epsilon_0}$ is the vacuum impedance and $k = \omega/c$. The following treatment holds for resonant modes and/or for single Fourier components (angular frequency ω) of a cylindrical wave: the time dependence left in the field coefficients A_i, B_i, C_i is meant to represent a slowly varying envelope behaviour, under the hypothesis $\partial A_i / \partial t \ll \omega A_i$.

Defining the unidimensional Helmholtz operator like $\Phi(A_0(z, t)) = \frac{\partial^2}{\partial z^2} A_0(z, t) + k^2 A_0(z, t)$ we can write the coefficients $A_{2N}(z, t)$ in a compact form as functions of the on-axis distribution field $A_0(z, t)$. This is written as

$A_{2N}(z, t) = \frac{(-1)^N}{2^{2N} N!^2} \Phi^N(A_0(z, t))$ where for $N=0$ we have $\Phi^0(A_0(z, t)) = A_0(z, t)$. Now with the recurrence relation obtained previously and the form of the em. field due to the symmetry, we finally have:

$$\begin{aligned} \begin{pmatrix} E_z^{TM} \\ H_z^{TE} \end{pmatrix} &= \text{Re} \left[\sum_{N=0}^{\infty} \frac{(-1)^N}{N!^2} \Phi^N(A_0(z, t)) \left(\frac{r}{2} \right)^{2N} \right] \\ \begin{pmatrix} E_r^{TM} \\ H_r^{TE} \end{pmatrix} &= \text{Re} \left[\sum_{N=0}^{\infty} \frac{(-1)^{N+1}}{N!^2 (N+1)} \Phi^N \left(\frac{\partial}{\partial z} A_0(z, t) \right) \left(\frac{r}{2} \right)^{2N+1} \right] \\ \begin{pmatrix} H_\phi^{TM} \\ E_\phi^{TE} \end{pmatrix} &= \text{Re} \left[ik \begin{pmatrix} Z_0^{-1} \\ -Z_0 \end{pmatrix} \sum_{N=0}^{\infty} \frac{(-1)^N}{N!^2 (N+1)} \Phi^N(A_0(z, t)) \left(\frac{r}{2} \right)^{2N+1} \right] \end{aligned} \quad (4)$$

These are the most general expressions for off-axis expansion of any axis-symmetrical wave. Taking $k=0$ in the previous expressions, the Helmholtz operator becomes

$\Phi(A_0(z)) = \frac{d^2}{dz^2} A_0(z) = A_0''(z)$ and we get the case of electrostatic field for TM modes, and the magnetostatic field for TE modes:

$$\begin{aligned} \begin{pmatrix} E_z^{STA} \\ H_z^{STA} \end{pmatrix} &= A_0 - A_0'' \left(\frac{r}{2} \right)^2 + \frac{1}{4} A_0'''' \left(\frac{r}{2} \right)^4 - \frac{1}{36} A_0'''''' \left(\frac{r}{2} \right)^6 + \dots \\ \begin{pmatrix} E_r^{STA} \\ H_r^{STA} \end{pmatrix} &= \frac{-r}{2} A_0' + \frac{1}{2} A_0''' \left(\frac{r}{2} \right)^3 - \frac{1}{12} A_0'''' \left(\frac{r}{2} \right)^5 + \frac{1}{128} A_0'''''' \left(\frac{r}{2} \right)^7 + \dots \end{aligned}$$

The above expressions are written for a few terms of expansion and are in agreement with ref.[1]: they can be used to obtain off-axis fields in magnetostatic and/or electrostatic lenses.

II. SPATIAL HARMONICS EXPANSION AND TM₀₁₀- π MODE

In a multi-cell accelerating structure, we know that under certain conditions the field on-axis can be expressed in Floquet form, see [2], so $A_0 = \text{Re} \left[\sum_{n=-\infty}^{\infty} b_n \exp i(\omega t - k_n z) \right]$, with

$k_n = \left(\frac{\psi + 2\pi n}{d} \right)$ while ψ is the phase shift per cavity cell.

Applying the Helmholtz operator to the Floquet form we obtain:

$$\Phi^N(A_0(z, t)) = k^{2N} \text{Re} \left[\sum_{n=-\infty}^{+\infty} b_n (1 - \kappa_n^2)^N \exp i(\omega t - k_n z) \right]$$

where $\kappa_n = k_n/k$. Substituting in the expressions of the general expansion (eqs.4), we have:

$$\begin{pmatrix} E_z^{TM} \\ H_z^{TE} \end{pmatrix}(r, z, t) = \text{Re} \left[\sum_{n=-\infty}^{+\infty} b_n e^{i(\omega t - k_n z)} \sum_{N=0}^{\infty} \frac{(\kappa_n^2 - 1)^N}{N!^2} \left(\frac{kr}{2} \right)^{2N} \right]$$

$$\begin{pmatrix} E_r^{TM} \\ H_r^{TE} \end{pmatrix}(r, z, t) = \text{Re} \left[-i \sum_{n=-\infty}^{+\infty} \kappa_n b_n e^{i(\omega t - k_n z)} \sum_{N=0}^{\infty} \frac{(\kappa_n^2 - 1)^N}{N!^2 (N+1)} \left(\frac{kr}{2} \right)^{2N+1} \right]$$

$$\begin{pmatrix} H_\phi^{TM} \\ E_\phi^{TE} \end{pmatrix}(r, z, t) = \text{Re} \left[i \begin{pmatrix} Z_0^{-1} \\ -Z_0 \end{pmatrix} \sum_{n=-\infty}^{+\infty} b_n e^{i(\omega t - k_n z)} \sum_{N=0}^{\infty} \frac{(\kappa_n^2 - 1)^N}{N!^2 (N+1)} \left(\frac{kr}{2} \right)^{2N+1} \right]$$

This is the spatial harmonics expansion for a general axisymmetric em. field, which is described by the spatial harmonics coefficients b_n . Setting $b_{-(n+1)} = b_n^*$ and $\psi = \pi$, we obtain the well-known TM₀₁₀- π standing mode used in many accelerating structures.

The accelerating field on-axis, $A_0(z, t)$, in this particular case

$$\text{becomes } A_0(z, t) = \text{Re} \left[\left(\sum_{n=\text{odd}} a_n \exp \left(\frac{i\pi n}{d} z \right) \right) \exp i(\omega t + \phi_0) \right],$$

where ϕ_0 is the initial phase of the wave and a_n are the harmonics satisfying the relation above. Since the Helmholtz operator doesn't act on the time variables, we may omit the exponential factor for simplicity. Defining $k' = \pi/d$ we apply it on this expression obtaining:

$$\begin{aligned} E_z^\pi(z, r) &= \text{Re} \left[\sum_n a_n e^{ik'nz} \sum_{N=0}^{\infty} \frac{(n^2 k'^2 - k^2)^N}{N!^2} \left(\frac{r}{2} \right)^{2N} \right] \\ E_r^\pi(z, r) &= \text{Re} \left[-i \sum_n n a_n e^{ik'nz} \sum_{N=0}^{\infty} \frac{k'(n^2 k'^2 - k^2)^N}{N!^2 (N+1)} \left(\frac{r}{2} \right)^{2N+1} \right] \\ H_\phi^\pi(z, r) &= \text{Re} \left[\frac{1}{Z_0} \sum_n a_n e^{ik'nz} \sum_{N=0}^{\infty} \frac{k(n^2 k'^2 - k^2)^N}{N!^2 (N+1)} \left(\frac{r}{2} \right)^{2N+1} \right] \end{aligned} \quad 5)$$

In multi-cell structures for relativistic particles we have $d = \lambda/2$ so $k = k'$, and the above expressions become simpler as follows:

$$\begin{aligned} E_z^\pi(z, r) &= \begin{cases} \sum_n a_n \cos(nkz) & ; r=0 \\ \sum_n a_n \cos(nkz) \sum_{N=0}^{\infty} \frac{(n^2 - 1)^N}{N!^2} \left(\frac{kr}{2} \right)^{2N} & ; r \neq 0 \end{cases} \\ E_r^\pi(z, r) &= \sum_n n a_n \sin(nkz) \sum_{N=0}^{\infty} \frac{(n^2 - 1)^N}{N!^2 (N+1)} \left(\frac{kr}{2} \right)^{2N+1} \\ H_\phi^\pi(z, r) &= \frac{1}{Z_0} \sum_n a_n \cos(nkz) \sum_{N=0}^{\infty} \frac{(n^2 - 1)^N}{N!^2 (N+1)} \left(\frac{kr}{2} \right)^{2N+1} \end{aligned} \quad 6)$$

For $n=1$ and $N=0$ these expressions give the linear field expansion used in several beam dynamics studies, see [2]. If $v \rightarrow \infty$, the series in eqs.5 converge to modified Bessel functions of first kind, setting $\kappa = k'/k$ we have:

$$\begin{aligned} E_z^\pi(r, z) &= \sum_n a_n \cos(nk'z) I_0 \left(kr \sqrt{(n\kappa)^2 - 1} \right) \\ E_r^\pi(r, z) &= \sum_n n a_n \sin(nk'z) \frac{\kappa I_1 \left(kr \sqrt{(n\kappa)^2 - 1} \right)}{\sqrt{(n\kappa)^2 - 1}} \\ H_\phi^\pi(r, z) &= \frac{1}{Z_0} \sum_n a_n \cos(nk'z) \frac{\kappa I_1 \left(kr \sqrt{(n\kappa)^2 - 1} \right)}{\sqrt{(n\kappa)^2 - 1}} \end{aligned}$$

where the first harmonic term is obtained as limit for $n \rightarrow 1$; if $\kappa=1$ we obtain expressions in agreement with previous studies [2]. We compared the analytic field expression $r \cdot H_\phi^\pi(r, z)$ (eqs.6) with the corresponding numerical values generated by SUPERFISH in the case of a typical superconducting multicell cavity whose boundary is shown in fig.2 (solid line). The range of application of the method is $kr/2 < 1$, the maximum order of expansion is about $v \equiv n$ for a chosen set of harmonics. The result of the comparison is shown in fig.1, for a set of nine harmonics and seventh-order expansion.

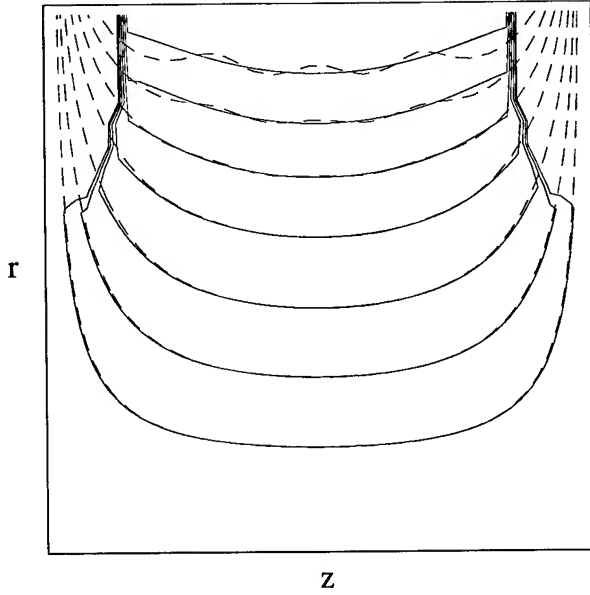


Figure 1: Comparison of the analytical expanded field (dashed line) with SUPERFISH predicted field (solid line) at a maximum radius 0.24λ , maximum error is 6.7%.

III. AN APPLICATION TO BEAM DYNAMICS IN RF GUNS

The field expansion off-axis derived in eq.6 may be used to obtain higher order components in the transverse momentum p_r imparted by the RF field to a photo-electron accelerated in a RF gun cavity. Assuming that the particle of charge q and rest mass m travels at $v = c$ on a trajectory parallel to the z -axis, the transverse momentum p_r at the cavity exit ($z = z_f$), can be easily computed via the Panofsky-Wentzel theorem [3]:

$$p_r = \frac{q}{mc} \left\{ \left[A_r(z = z_i) - A_r(z = z_f) \right] + \int_{z_i}^{z_f} \nabla_{\perp} A_z dz \right\} \quad (7)$$

Where the RF gun cavity starts with the metallic cathode wall at $z = z_i$, where the particles are generated. Since $A_r(z = z_i) = 0$, and $A_r(z = z_f) = -E_r/\omega$, p_r comes out to be not vanishing as in a standard multi-cell structure with open ends. Using the off-axis expansion of TM_{010} - π mode for the case $k = k'$ of eq.6, we obtain:

$$p_r = \alpha \sin \phi \left\{ a_1 k r + \sum_{n \geq 3} a_n \sum_{N=1}^{\infty} \frac{(n^2 - 1)^{N-1}}{4^N N!^2 (N+1)} \left[(n^2 - 1)(kr)^{2N+1} + 4N(N+1)(kr)^{2N-1} \right] \right\} \quad (8)$$

It is interesting to note that the first and third order components in eq.8, obtained setting $n = 3$ and $N = 1$, have been already evaluated in ref.[4],[5]

The interest of considering higher order terms in p_r is relevant for all beam dynamics studies involving trajectories

close to the cavity irises as in dark currents, beam halos, RF guns studies.

IV. DESIGN OF THE CAVITY

Writing the family of the lines perpendicular to the equipotential lines of the field in the cavity, and setting initial conditions by specifying the iris aperture and radius of cavity equator, we obtain a system of parametric differential equation in $\zeta = \zeta(s) = kz$ and $\rho = \rho(s) = kr$ variables, written as follows:

$$\begin{cases} \frac{d\rho(s)}{dt} = \frac{\rho(s)}{Z_0} \sum_n a_n \cos(n\zeta(s)) \sum_{N=0}^{\infty} \frac{(n^2 - 1)^N}{N!^2} \left(\frac{\rho(s)}{2} \right)^{2N} \\ \frac{d\zeta(s)}{dt} = -\frac{\rho^2(s)}{2Z_0} \sum_n n a_n \sin(n\zeta(s)) \sum_{N=0}^{\infty} \frac{(n^2 - 1)^N}{N!^2 (N+1)} \left(\frac{\rho(s)}{2} \right)^{2N} \end{cases}$$

Whose solution gives the analytical approximation for the iris shown in fig.2, see [6]:

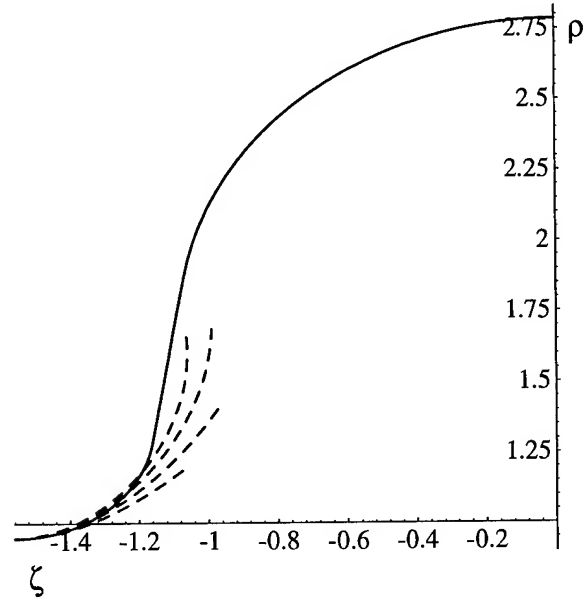


Figure 2: Comparison between actual cavity boundary (solid line) and analytical predictions (dashed lines) for different order of expansion ($N=0,1,2,3$).

VI. REFERENCES

- [1] S.Humphries "Principles of charged particle acceleration", John Wiley & sons- New York, 1985
- [2] P.M.Lapostolle, A.L.Septier "Linear accelerators", North-Holland Publishing company - Amsterdam, July 1969 and S.C.Hartman, J.B.Rosenzweig, Phys.Rev.E-47 (1993) 2031
- [3] W.K.H.Panofsky, W.A.Wenzel, Rev.Sci.Instr.-27(1956)967
- [4] L.Serafini, NIM A304(1991) 353-356, and ref. therein
- [5] J.Gao, NIM A304(1991) 348-352
- [6] D.Burrini, Grad. Thesis, University of Milan, Feb.1995

IMPURITY GROWTH IN SINGLE BUNCH OPERATION OF PF

M. Tobiyama, A. Higuchi, T. Mitsuhashi, T. Kasuga and S. Sakanaka
National Laboratory for High Energy Physics, 1-1 Oho, Tsukuba 305, Japan

Abstract

Growth of the single bunch impurity was observed in the Photon Factory storage ring. The phenomenon caused by recapture of electrons that are thrown out of the main bucket by Touschek effect was analyzed theoretically. Agreement of the observed rate of the impurity growth and the theoretical estimation was fairly well. In order to cure the effect, the RF knockout method was employed. The betatron tune of a bunch depends on the number of electrons in it. If the knockout frequency is adjusted to that corresponds to weak bunches to remove them, the betatron motion of the main bunch is scarcely affected. This method is routinely used in the single bunch operation of Photon Factory.

I. INTRODUCTION

In the single-bunch-mode operation of a synchrotron light source, it is highly necessary to establish a 'pure' single bunch because undesirable bunches cause unwanted reactions in the time resolved experiments such as photoluminescence or light absorption. The single-bunch impurity, which is defined as the ratio of the number of electrons (positrons) in undesirable bunches to that in the main bunch, is the order of 10^{-4} and the increase of the ratio is much smaller. Then the measuring system with very wide dynamic range is essential. We have constructed a single photon counting system in the beamline 21 in the KEK-PF. An excellent dynamic range is obtained when enough events are collected and high time resolution is achieved because of the fast photomultiplier with microchannel plate.

The increase in a single-bunch impurity with the lapse of time after injection was previously studied in the UVSOR storage ring at Institute for Molecular Science and was explained as the recapture of electrons that are thrown out the main bucket by Touschek effect^{[1],[2]}. The effect was estimated to be small enough for high energy storage ring such as PF ring because the Touschek effect decreases rapidly with the energy increase. However when we have measured the change in the impurity, unexpected growth was observed clearly in the PF ring. We show the theoretical treatment which takes into account of the relativistic effect on electron-electron scattering and the local machine parameters at the position where the scattering occurs. The agreement between our calculation and the observed growth rate of the impurity was fairly good^[3].

In order to cure the effect, we have employed the RF knockout method. The large difference of bunch current between the main bunch and the unwanted bunches enables us to kick only unwanted bunches because the betatron tune of a bunch depends on the bunch current. This system is used not only the time just after an injection but also during the users' time routinely without affecting the beam quality. Related parameters of the KEK-PF storage ring is listed in Table. I.

Table I
Main Parameters of KEK-PF ring

Energy [GeV]	E	2.5
Circumference [m]	C	187
RF frequency [MHz]	f_{RF}	500.1
Harmonic number	h	312
Revolution period [ns]	T	624
Synchrotron tune	ν_s	0.0227
Betatron tune	ν_x/ν_y	8.45/3.30
Momentum compaction	α	0.0157
Peak RF voltage [MV]	\hat{V}_{RF}	1.7
Synchrotron radiation loss [kV]	U_0	399
Radiation damping time [ms]	τ_x	7.79
	τ_y	7.82
	τ_e	3.92

II. PHOTON COUNTING SYSTEM AND INCREASE IN IMPURITY

The photon counting system installed in the beamline 21 in KEK-PF and the increase in impurity measured with the system have already been described in ref.[3] in detail, therefore only a brief outline is explained here. The system is shown schematically in Fig. 1.

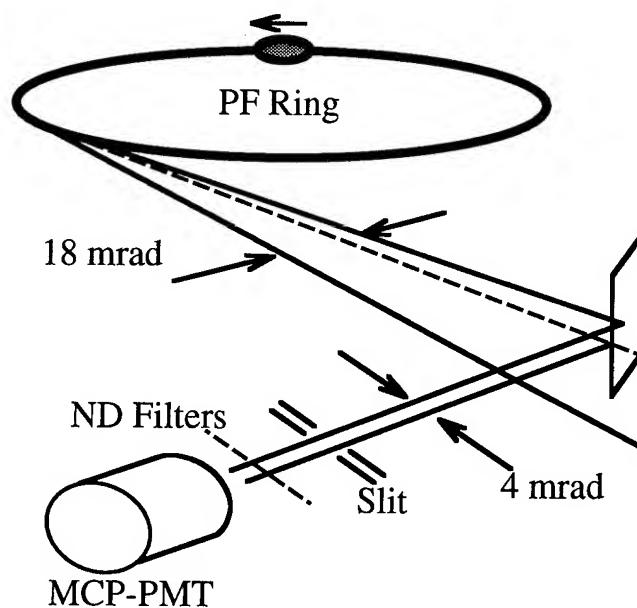


Figure 1. The photon counting system

The SR from a bending section is led to the beamline, and the visible part is reflected by a mirror made of SiC. Photons reach a microchannel-plate type photomultiplier (MCP-PMT, Hamamatsu R2809U-06) through an ICF-70 view port. The intensity

of the photons is reduced to the level of one photon detection per about a hundred revolutions of a bunch.

Pulses from a PMT are amplified by a two-stage wide-band amplifiers with a total gain of 49dB, then shaped by a constant fraction discriminator (CFD) which detects the peak of the pulse. The time interval between the output of the CFD and the timing signal synchronized to the revolution of a bunch is converted to the pulse height by a time-to-amplitude converter and analyzed with a multichannel analyzer. An example of the measured longitudinal bunch structure is shown in Fig. 2.

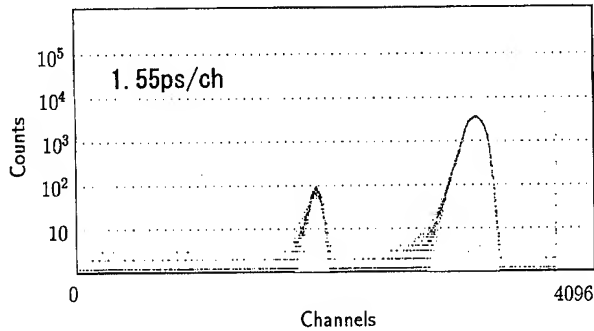


Figure 2. Longitudinal bunch structure measured by the photon counting system.

Figure 3 shows the measured increase in impurity at the bunch

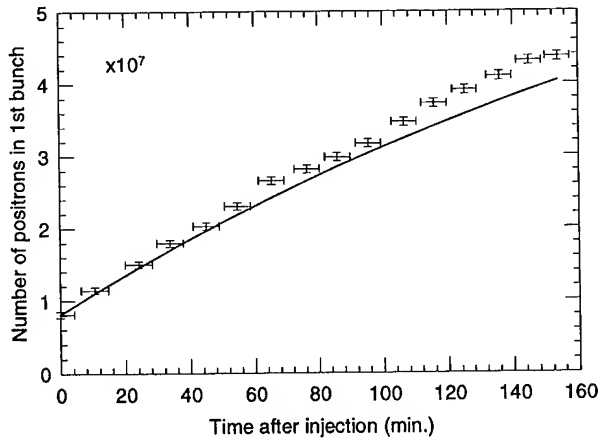


Figure 3. Increase in the population in the first bunch. The horizontal bars represent the time interval during each measurement.

The increase in impurity is not negligible small for users' experiments.

The mechanism of increase in impurity is the followings. The synchrotron motion of an electron with a momentum of $p_0 + p$, where p_0 is the design momentum, in longitudinal phase space is described as

$$\frac{d\epsilon}{dt} = \frac{1}{TE} e\hat{V}_{RF} \sin(\phi_0 - \phi) - \frac{1}{TE} U_0 - \frac{2}{\tau_e} \epsilon \quad (1)$$

$$\frac{d\phi}{dt} = -h\omega_0 \alpha \epsilon \quad (2)$$

where $\epsilon = p/p_0$, ϕ_0 and ϕ are the synchrotron phase and the phase of the RF, respectively. Owing to the radiation damping term in eq. (1), the separatrices have an opening shown in Fig. 4.

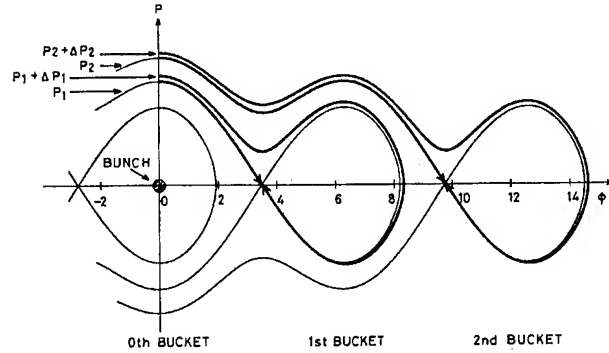


Figure 4. Trajectory of an electron thrown out from the main bunch in longitudinal phase space

If there are electrons which thrown out of the main bunch with momenta corresponding to the aperture, they are recaptured. Only the Touschek scattering mechanism can produce such electrons with significant probability.

Since it is not applicable for non-relativistic approximation for the PF ring, we used the Völkel's formula^[5] with the approximation of small RF bucket height and rectangular momentum distribution. Because the result depends linearly to the bunch volume, we included the local beam size for horizontal and vertical, and the bunch lengthening effect also measured by the photon counting system simultaneously. Additionally, the effect of intrabeam scattering was also included. The growth rate $\Delta N_i / \Delta t$ of the single-bunch impurity for i -th bucket is then

$$\frac{\Delta N_i}{\Delta t} = \frac{N_0}{2} \left(\frac{1}{\tau_T(p_i)} - \frac{1}{\tau_T(p_i + \Delta p_i)} \right) \quad (3)$$

where $\tau_T(p)$ is the Touschek lifetime for bucket height p and N_0 is number of electrons in the main bunch. Note we need the coefficient $1/2$ because one of two electrons that take part in the collision loses momentum and is never captured by the backward buckets. The solid line in Fig. 3 shows the calculated result.

III. CURE THE SINGLE-BUNCH IMPURITY

The typical single-bunch impurity just after the injection is about a few per cent and of course is not acceptable for users. To cure the impurity in the ring, we applied the RF knockout method. Under the single-bunch mode, huge bunch current deviates the betatron tune from the zero-current tune. The measured vertical betatron tune shift with the current is shown by the solid line in Fig. 5, it was about $-3 \times 10^{-4}/\text{mA}$.

As the bunch current of neighboring bunches is a few percent of the main bunch current, we are able to only excite a betatron oscillation of the unwanted bunches sweeping the knockout frequency without disturbing the main one.

In the 'purification' process, we measure the vertical betatron tune just after the injection and determine the frequency range of the knockout, that the frequency slightly higher than that of vertical betatron frequency of the main bunch to 490 kHz. The

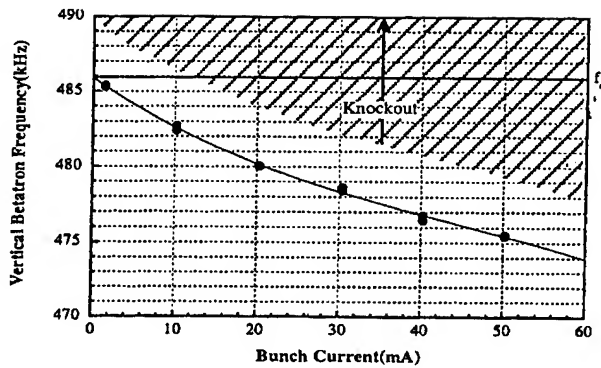


Figure 5. Measured vertical betatron tune in single-bunch mode with bunch current (solid line) and the RF knockout frequency range (shaded area).

frequency range is shown by the shaded area in Fig. 5. We sweep the frequency using the computer-control system shown in Fig. 6. The knockout frequency range is automatically controlled with the beam current from a DCCT.

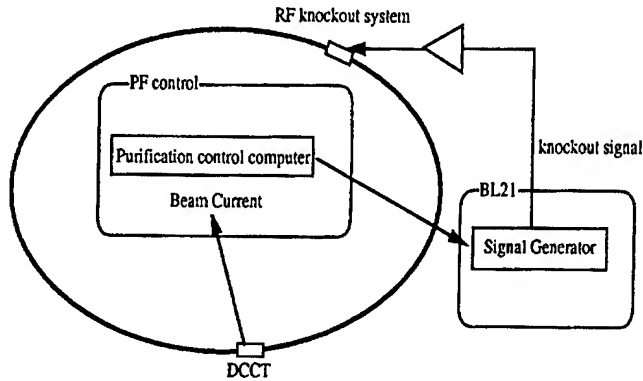


Figure 6. Automatic RF knockout system to keep the single bunch purity.

In the users' time for the single bunch operation, we enlarge the x-y coupling by exciting skew quadrupole magnets to make the Touschek lifetime long. Nevertheless, there remains unacceptable increase in impurity. Though we use the RF knockout system continuously during the users' time, the betatron amplitude growth with the system is acceptably small. Figure 7 shows an example of the change in impurity measured during a users' time using a photon counting system.

We used the avalanche photo diode in the X-ray region as the detector to improve the signal-to-noise ratio^[6]. The impurity is kept small enough compared with the requirements from users.

IV. SUMMARY

We have measured the increase in single-bunch impurity in the Photon Factory positron storage ring with the photon counting system installed in the beamline 21. The electrons thrown out of the main bunch by the Touschek effect were recaptured by the following bunches by the radiation damping effect. With employing the relativistic formula for the Touschek effect and evaluating the beam size properly, we have reconstructed the measured growth in good agreement.

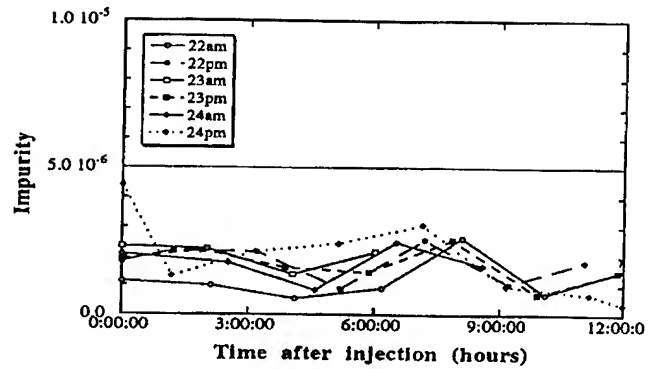


Figure 7. Increase in impurity during the users' time. The measured impurity has been kept less than 5×10^{-6} .

To cure the impurity, we have constructed computer-control RF knockout system. Using the betatron tune shift with the bunch current, the unwanted bunches are swept out clearly. This system is routinely used during the users' time without bothering the beam quality.

The authors wish to thank Dr. S. Kishimoto for his work on the photon counting system using avalanche photo diode.

References

- [1] T. Kasuga, H. Yonehara, M. Hasumoto and T. Kinoshita, Jpn. J. Appl. Phys. **28** (1989) 541
- [2] T. Kasuga, M. Tobiyama and H. Yonehara, in proceedings of the 7th Accel. Sci. Tech. Osaka, Japan pp 273
- [3] T. Obina, T. Kasuga, M. Tobiyama, T. Katsura and K. Tamura, Nucl. Instrum. Meth. **A354** (1995) 204-214
- [4] R. P. Walker, IEEE Trans. Nuc. Sci. **NS-35** (1988) 491
- [5] U. Völkel, DESY 67/5 (1967)
- [6] S. Kishimoto, Nucl. Instrum. Meth. **A351** (1994) 554-558

COUPLING IMPEDANCE OF A PERIODIC ARRAY OF DIAPHRAGMS

G. V. Stupakov, Stanford Linear Accelerator Center, Stanford University, Stanford, CA 94309 USA

Abstract

A method is presented for calculating the high-frequency longitudinal and transverse coupling impedances in a periodic array of diaphragms in a circular perfectly conducting pipe. The method is based on Weinstein's theory of diffraction of a plane electromagnetic wave on a stack of halfplanes. Using Weinstein's solution, it is shown that the problem of finding the beam field in the pipe reduces to an effective boundary condition at the radius of the diaphragms which couples the longitudinal electric field with the azimuthal magnetic one. Solving Maxwell's equations with this boundary condition leads to simple formulae for Z_{long} and Z_{tr} . A good agreement with a numerical solution of the problem found by other authors is demonstrated.

I. INTRODUCTION

Studies of the impedance at the frequencies much higher than the cutoff frequency have a long history with many theoretical and numerical results obtained for different types of accelerator structures (see e.g. a special issue of Particle Accelerators journal devoted exclusively to this subject [1]). One of the major problems addressed by several authors is the high-frequency impedance of multiple cavities or a periodic system of diaphragms [2-5]. There is a general consensus that, for large ω , the longitudinal impedance in this system scales asymptotically as $\omega^{-3/2}$. Specifically, for a periodic array of thin diaphragms, in the limit $\omega \rightarrow \infty$, the real part of Z_{long} per one cell can be approximated by the following function:

$$\text{Re} Z_{long}(\omega)/Z_0 \approx f (g/a)^3 (kg)^{-3/2}, \quad (1)$$

where $k = \omega/c$, $Z_0 = 4\pi/c = 377\Omega$, g is the distance between the diaphragm openings, a is the radius of the diaphragms, and f is a numerical factor. However, various authors find different values for f which deviate almost by the order of magnitude: $f = \pi^{-1/2}$ in Ref. [3], $f = 8\pi^{-1/2}$ in Ref. [4], and according to the Sessler - Weinstein model [2], $f = 0.67\pi^{-1/2}$.

Apart from differing numerical values for f , Eq. (1) itself gives a rather poor approximation in the region $10 < kg < 20$ typical for practical applications in accelerator physics. The reason for Eq. (1) to be relatively inaccurate is that the actual parameter in asymptotic expansion (1) is $(kg)^{1/2}$ (or even $(kg/\pi)^{1/2}$) rather than kg . This makes it necessary to seek better asymptotes than the leading term represented by Eq. (1). Refs. [2-3] indeed provide a more accurate expressions that reduce to Eq. (1) in the limit $(kg)^{1/2} \gg 1$.

In this paper an attempt is made to revise the approach to the calculation of the impedance of the periodic system of diaphragms using a more adequate physical description of the beam interaction with the diaphragms. On a qualitative level, the physics involved has been outlined in Ref. [6]. Its two basic elements are: a small angle diffraction of the beam field at the edges of the diaphragms, and depletion of the amplitude of the

field in the region close to the edges due to repeated trapping of the field energy into the space between the diaphragms. We will show that this qualitative argument can be cast into a quantitative consideration using a rigorous solution to the diffraction of a plane electromagnetic wave on an infinite stack of conducting halfplanes.

II. BASIC ASSUMPTIONS

Consider a relativistic beam with a factor of γ much larger than unity, $\gamma \gg 1$, propagating along the axis of a circular pipe with infinitely thin periodic diaphragms. The azimuthal magnetic field of such a beam is almost equal to its radial electric field, and both propagate with the speed $\approx c$. In that respect, excluding the vicinity of the axis of the pipe occupied by the beam, the electromagnetic field can be considered as a free electromagnetic wave propagating in the pipe. Accepting this point of view, we intend to apply to the beam field the results derived from the diffraction of the wave on the edges of the diaphragms.

The analysis of the diffraction is greatly simplified by the fact that we are only interested in the high frequency band. From Fresnel theory of diffraction, it is known that the area involved in the diffraction extends from the edges by distance $\sim \sqrt{g/k}$, and occupies an annulus from $r \approx a - d\sqrt{g/k}$ to $r \approx a + d\sqrt{g/k}$, where d has a value of the order of unity. As soon as $\sqrt{g/k}$ is much smaller than the radius a , we can neglect the cylindrical geometry of the problem and consider the diffraction in plane geometry. We will also assume that $\sqrt{g/k} \ll b - a$, where b is the pipe radius; in this case the pipe wall does not interfere with the diffraction process, and we can further simplify the problem eliminating the pipe walls and allowing the field to freely propagate in the radial direction to infinity [5].

As a result of these approximations we essentially reduce the problem to the diffraction of a plane electromagnetic wave on an infinite periodic array of halfplanes the solution for which can be found in Ref. [7].

III. WEINSTEIN'S THEORY

This section briefly summarizes Weinstein's results for the diffraction of a plane wave for an arbitrary incidence angle φ_0 , (φ_0 is measured from the vertical axis y so that the grazing incidence corresponds to $\varphi_0 = \pi/2$). In our case, the beam field propagates horizontally which corresponds to the limit $\cos \varphi_0 \rightarrow 0$ in the diffraction solution.

Let the position of m th halfplane be given by $z = mg$, $y \leq 0$. Consider a plane wave propagating in the halfspace $y > 0$ at an angle φ_0 with the vertical axis ($0 \leq \varphi_0 \leq \pi/2$) and polarized so that the only component of the magnetic field is directed along the x -axis,

$$H_x = A \exp [ik(z \sin \varphi_0 - y \cos \varphi_0)]. \quad (2)$$

Here and below we assume the time dependence $\propto \exp(-i\omega t)$.

The solution to the diffraction problem for the incident wave (2) [7, Chapter 7] represents the field at $y < 0$ as a sum of eigenmodes propagating between the plates:

$$H_x = A \left(T_0 e^{-iky} + \sum_{n=1}^{\infty} T_n \cos \frac{\pi n z}{g} e^{-i\kappa_n y} \right), \quad (3)$$

where $\kappa_n = \sqrt{k^2 - (\pi n/g)^2}$, $\text{Im}\kappa_n \geq 0$. Eq. (3) is valid for $0 < z < g$; the field between m th and $(m+1)$ th plates has an additional factor $\exp(ikmg \sin \varphi_0)$ on the right hand side. Complex values of κ_n imply that the corresponding eigenmode is an evanescent one; it exponentially decays when $y \rightarrow -\infty$.

The field in the upper halfspace, $y > 0$, is given by

$$H_x = A e^{ik(z \sin \varphi_0 - y \cos \varphi_0)} + A \sum_{n=-\infty}^{\infty} R_n e^{ik(z \sin \varphi_n + y \cos \varphi_n)}, \quad (4)$$

where $\cos \varphi_n = [1 - (n + q \sin \varphi_0)^2 / q^2]^{1/2}$, $q = kg/2\pi$; it is assumed that $\text{Im}(\cos \varphi_n) \geq 0$. The first term on the right side of Eq. (4) is the incident wave, and the sum represents the diffracted waves generated by the periodic structure. One of these waves having $n = 0$ is a mirror reflected image of the incident field; it has the amplitude AR_0 .

The expressions for T_n and R_n can be found in Ref. [7]. For our purposes, we will only need R_0 as a function of q and φ_0 ,

$$R_0(q, \cos \varphi_0) = -\frac{1 - \cos \varphi_0}{1 + \cos \varphi_0} e^{4iq \cos(\varphi_0) \ln 2} \times \prod_{n=1}^{\infty} \frac{1 + \frac{\cos \varphi_0}{\cos \varphi_n} \frac{1 + \frac{\cos \varphi_0}{\cos \varphi_{-n}}}{1 - \frac{\cos \varphi_0}{\cos \varphi_n} \frac{1 + \frac{\cos \varphi_0}{\cos \varphi_{-n}}}{1 - \frac{\cos \varphi_0}{\cos \varphi_{-n}}}}{1 + \frac{2\pi q \cos \varphi_0}{\kappa_n g} \frac{1 - \frac{2\pi q \cos \varphi_0}{\kappa_n g}}{1 + \frac{2\pi q \cos \varphi_0}{\kappa_n g}}}. \quad (5)$$

IV. BOUNDARY CONDITION

To consider the case of horizontal propagation of the wave we need, first, to find the limit $\cos \varphi_0 \rightarrow 0$ in Eq. (5). Using analysis of Ref. [7], after straightforward though cumbersome algebra, one can show that in this limit, for $kg \gg 1$,

$$R_0 = -1 + 2S(kg) \cos \varphi_0, \quad (6)$$

where the complex function $S(q)$ is given by

$$S(x) = \frac{1}{2} \left[1 + \frac{(1-i)}{\pi} \sqrt{\frac{x}{2}} \left((\sqrt{2}-1) F(2x) + \alpha \right) \right], \quad (7)$$

where

$$F(x) = \int_{-\infty}^{\infty} dt \left(\exp \left(\frac{t^2}{2} - ix \right) - 1 \right)^{-1}, \quad (8)$$

and

$$\alpha = -2 \int_{-\infty}^{\infty} \frac{1 - e^{t^2/2} + t^2/2}{t^2 (e^{t^2/2} - 1)} dt = 3.658. \quad (9)$$

The function $F(x)$ is a periodic function of its argument with the period equal to 2π . It has singularities $\propto |x - 2m\pi|^{-1/2}$ at the points $x = 2m\pi$, where m is an integer.

Turning now to the physical interpretation of the solution, note that in the limit $\cos \varphi_0 \rightarrow 0$, both the incident wave given by Eq. (2) and the mirror reflected wave $AR_0 \exp(ik(z \sin \varphi_0 + y \cos \varphi_0))$ in Eq. (4) propagate parallel to the horizontal axis. This observation prompts us to believe that their sum has to be identified with the electromagnetic field of the beam at the edge of the diaphragms. Using Eq. (6) we find for the magnetic component of this field:

$$H_x = A e^{ikz \sin \varphi_0} (e^{-iky \cos \varphi_0} + R_0 e^{iky \cos \varphi_0}) \approx A e^{ikz} (-2i \sin(ky \cos \varphi_0) + 2S(kg) \cos \varphi_0 e^{iky \cos \varphi_0}) \approx 2A \cos \varphi_0 e^{ikz} (S(kg) - iky). \quad (10)$$

In order to obtain a nonzero result when $\cos \varphi_0 \rightarrow 0$, we have to assume that A goes to infinity so that $2A \cos \varphi_0 \rightarrow E$ and

$$H_x = E e^{ikz} (S(kg) - iky), \quad (11)$$

where E is a constant. We see that our solution *requires* the magnetic field to be a linear function of y ; in other words, for $\varphi_0 = \pi/2$ the diffraction process imposes a certain constraint on the behavior of the electromagnetic field near the edges of the diaphragms. This constraint can be expressed as a boundary condition at $y = 0$ if one notes that Maxwell's equation $\partial H_x / \partial y = ik E_z$ combined with Eq. (11) allows to one express E in terms of the electric field: $E_z = -E \exp(ikz)$. Substituting this relation in Eq. (11) yields

$$E_z = -\frac{1}{S(kg)} H_x|_{y=0}. \quad (12)$$

Eq. (12) represents our main result. It relates the longitudinal component of the electric field to the transverse component of the magnetic field at the diaphragms.

Note a close resemblance of Eq. (12) to the boundary condition at a conducting wall in the case of high conductivity σ , $E_z = (i-1) \sqrt{\omega/8\pi\sigma} H_x|_{y=0}$, [8]. This allows us to assign the diaphragms an effective (complex) conductivity σ_{eff} , such that

$$\sqrt{\frac{2\pi\sigma_{\text{eff}}}{\omega}} = \frac{(i-1)}{2} S(kg). \quad (13)$$

Using Eq. (13), for a given solution of an electromagnetic problem in a smooth pipe with finite conductivity $\sigma(\omega)$, one can find the solution of the corresponding problem in the pipe with periodic diaphragms by substitution $\sigma \rightarrow \sigma_{\text{eff}}$.

V. IMPEDANCE

Having found the boundary condition (12) we can now return to the cylindrical geometry of the pipe with the beam and solve for the beam field in the region $0 < r < a$. In polar coordinate system, the x -component of the magnetic field H_x should be identified with the azimuthal component H_ϕ , so that Eq. (12) takes the form,

$$E_z = -\frac{1}{S(kg)} H_\phi|_{r=a} \quad (14)$$

With this boundary condition, a standard derivation (see, e.g., [9]) of the longitudinal and transverse impedances, Z_{long} and Z_{tr} ,

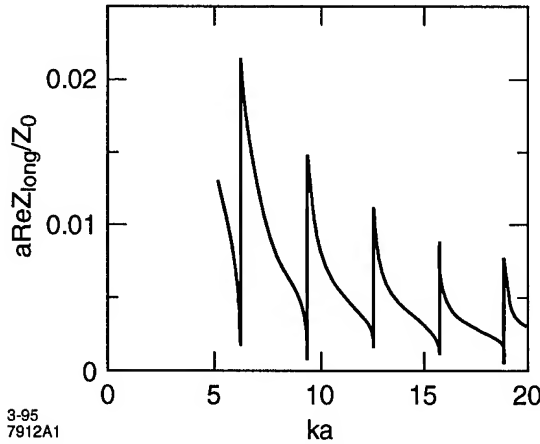


Figure 1. Real part of the longitudinal impedance.

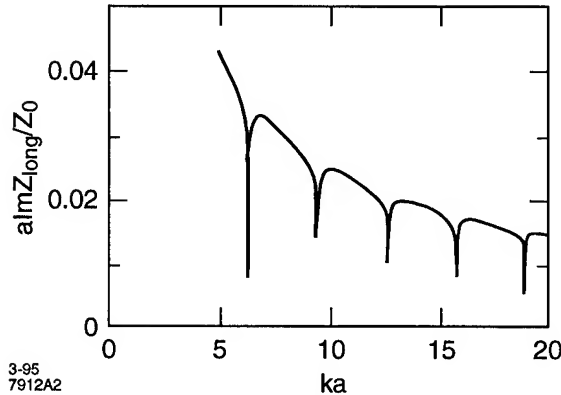


Figure 2. Imaginary part of the longitudinal impedance.

yields :

$$Z_{long} = \frac{Z_0}{2\pi a} \frac{1}{S(kg) - ika/2}, \quad (15)$$

$$Z_{tr} = \frac{Z_0}{\pi ka^3} \frac{1}{S(kg) - \frac{1}{2}ika + i(ka)^{-1}}. \quad (16)$$

Figures 1 and 2 show the real and imaginary parts of Z_{long} for the case when $a = g$. In addition to general fall off of Z_{long} with the frequency, it demonstrates peaks and jumps at $ka = m\pi$, where m is an integer. This behavior can be explained as due to a strong coupling, through diffraction, of the beam field with the modes between the diaphragms having a small radial wavenumber. These modes have the frequency close to $\pi m/a$; they represent standing waves between two adjacent diaphragms.

In the limit of very high frequency, $\omega \rightarrow \infty$, the asymptotic dependence of $Z_{long}(\omega)$ is given by

$$\text{Re}Z_{long} \approx \frac{2Z_0}{\pi k^2 a^3} \text{Re}S(kg), \quad \text{Im}Z_{long} \approx \frac{Z_0}{\pi ka^2}. \quad (17)$$

Note that on the average $\text{Re}Z_{long}$ scales asymptotically as $\omega^{-3/2}$ in agreement with Eq. (1).

Similar to longitudinal impedance, Z_{tr} has sharp peaks at $ka = m\pi$, however, it decays more rapidly than $Z_{long}(\omega)$. Asymptotically, for $\omega \rightarrow \infty$,

$$\text{Re}Z_{tr} \approx \frac{4Z_0}{\pi k^3 a^5} \text{Re}S(kg), \quad \text{Im}Z_{tr} \approx \frac{2Z_0}{\pi k^2 a^4}. \quad (18)$$

VI. DISCUSSION

We compared our result with a numerical solution of a similar problem in Ref. [5], where a repeated structure of thin irises has been studied. A close inspection of the plot of $\text{Re}Z_{long}$ in this reference shows a very good agreement with our Fig. 1, including the positions and the heights of each peak even for ka as small as 5. This agreement indicates that using a plane geometry for solution of the diffraction problem turns out to be a very accurate approximation even for relatively small values of ka .

In the limit of very large frequencies, our result agrees with Eq. (1) with $f = 0.26$ which is below both Gluckstern's result ($f = 0.56$) and Sessler-Weinstein model ($f = 0.37$).

VII. ACKNOWLEDGMENT

I thank Karl Bane, who initiated this work, for many useful discussions, and G. Dome for useful comments.

References

- [1] Part. Accel., 25, (1990)
- [2] E. Keil. Nucl. Instr. and Meth., 100, p. 419 (1972).
- [3] R.K. Gluckstern. Phys. Rev. D, 39, p. 2780 (1989).
- [4] S. A. Heifets and S. A. Kheifets. Rev. Mod. Phys., 63, p. 631-674 (1991).
- [5] G. Dome, L. Palumbo, V.G. Vaccaro and L. Verolino. Proceedings of the European Particle Accelerator Conference, Berlin 1992, 2, p. 925 (1992).
- [6] R.B. Palmer. Part. Accel., 25, p. 97, (1990).
- [7] L.A. Weinstein. The Theory of Diffraction and the Factorization Method (The Golden Press, Boulder, Colorado, 1069)
- [8] L.D. Landau and E. M. Lifshits. Electrodynamics of Continuous Media (Pergamon Press, Oxford, 1960).
- [9] A. Chao. Physics of Collective Beam Instabilities in High Energy Accelerators (Wiley, New York, 1993).

COUPLING IMPEDANCE OF A LONG SLOT AND AN ARRAY OF SLOTS IN A CIRCULAR VACUUM CHAMBER*

G. V. Stupakov, Stanford Linear Accelerator Center, Stanford University, Stanford, CA 94309 USA

Abstract

We find the real part of the longitudinal impedance for both a small hole and a long slot in a beam vacuum chamber with a circular cross section. The length of the slot can be arbitrarily large, the only requirement on the dimensions of the slots is that its width be much smaller than c/ω . Regular array of N slots periodically distributed along the pipe is also considered.

I. INTRODUCTION

Existing theory for the impedance produced by small holes in the wall of a vacuum chamber of the accelerator has been developed in papers by Kurennoy [1] and Gluckstern [2]. They applied Bethe's approach developed for study of diffraction of an electromagnetic wave on a perfectly conducting plane screen with a small hole [3] to the problem of radiation of the beam propagating in a circular pipe having a hole in its wall. The method is based on utilization of small parameters α_{el}/b^3 and α_{mg}/b^3 , where α_{el} is the electric and α_{mg} is the magnetic polarizabilities of the hole, and b is the beam pipe radius. For circular holes, $\alpha_{mg} \sim |\alpha_{el}| \sim w^3$, where w is the radius of the hole, and these ratios are of the order of $(w/b)^3$. This theory also assumes that the wavelength of the electromagnetic waves radiated by the hole is much larger than the dimensions of the hole. In the first approximation of the perturbation theory, the impedance is expressed in terms of polarizabilities α_{el} and α_{mg} and turns out to be purely imaginary¹

$$Z = -\frac{Z_0 i \omega}{2\pi c b^2} (\alpha_{el} + \alpha_{mg}). \quad (1)$$

In many cases it is necessary to know the real part of the impedance. In this paper we find $\text{Re} Z$ for small holes and slots of arbitrary length l , assuming only that the width of the slot w is much smaller than b and c/ω . We also find the impedance of a regular array of N slots. A more detailed study of relevant issues including the effect of randomization of the slot positions in the array, can be found in Ref. [4].

II. REAL PART OF THE IMPEDANCE FOR A HOLE

To calculate the longitudinal impedance of a circular beam pipe with a hole, it is convenient to consider an oscillating current traveling with the velocity of light along the axis of the pipe,

$$I(z, t) = I_0 \exp(-i\omega t + i\kappa z), \quad (2)$$

*Work supported by the Department of Energy contract DE-AC03-76SF00515

¹Our definitions of α_{el} and α_{mg} agree with the Bethe's paper [3]. They are two times larger than those used by Kurennoy [1].

where $\kappa = \omega/c$. The pipe is assumed to have a small hole located at $z = 0$ with characteristic dimensions much less than pipe radius b . Perturbation of the electromagnetic field caused by the hole can be represented as a superposition of the waveguide modes propagating away from the hole.

We choose normalization of the eigenmodes in a circular pipe such that for E modes

$$E_z^{(n,m)} = \frac{\mu_{n,m}^2}{b^2} J_n \left(\mu_{n,m} \frac{r}{b} \right) \cos(n\theta) \exp(\sigma i \kappa_{n,m} z), \quad (3)$$

and for H modes

$$H_z^{(n,m)} = \frac{\mu_{n,m}^2}{b^2} J_n \left(\mu_{n,m} \frac{r}{b} \right) \cos(n\theta) \exp(\sigma i \kappa_{n,m}' z), \quad (4)$$

where J_n is the Bessel functions of the n th order, $\mu_{n,m}$ is the m th root of J_n , $\mu_{n,m}'$ is the m th root of the derivative J_n' , $\kappa_{n,m} = \sqrt{\omega^2 - \omega_{n,m}^2}/c$, $\kappa_{n,m}' = \sqrt{\omega^2 - \omega_{n,m}'^2}/c$, $\omega_{n,m} = c\mu_{n,m}/b$, $\omega_{n,m}' = c\mu_{n,m}'/b$, and b is the radius of the waveguide. The variable σ denotes the direction of the propagation of the wave; $\sigma = +1$ corresponds to the waves propagating in the positive direction along the z -axis, and $\sigma = -1$ marks the waves traveling in the opposite direction.

In the first order of the perturbation theory, the electromagnetic field scattered by the hole into the waveguide is characterized by the amplitudes $a_{n,m}(\sigma)$ such that

$$F = h(z) \sum_{E, H} \sum_{n, m} a_{n,m}(\sigma = 1) F^{(n,m)}(r, z, \sigma = 1) + h(-z) \sum_{E, H} \sum_{n, m} a_{n,m}(\sigma = -1) F^{(n,m)}(r, z, \sigma = -1), \quad (5)$$

where $h(z)$ is the step function and F denotes any of the components E_z , E_r , or H_θ . The factors $a_{n,m}$ can be expressed in terms of the electric α_{el} and magnetic α_{mg} polarizabilities of the hole [1]

$$a_{n,m}^{(E)} = \frac{4I_0 (\kappa \alpha_{mg} + \sigma \kappa_{n,m} \alpha_{el})}{c b^2 \kappa_{n,m} \mu_{n,m} J_n'(\mu_{n,m}) (1 + \delta_{n,0})}, \quad (6)$$

for an E mode, and

$$a_{n,m}^{(H)} = -\frac{4n I_0 (\sigma \kappa_{n,m}' \alpha_{mg} + \kappa \alpha_{el})}{c b^2 \kappa_{n,m}' (\mu_{n,m}'^2 - n^2) J_n(\mu_{n,m}')}, \quad (7)$$

for an H mode. Calculating Z using Eqs. (5) – (7) with the help of the following relation,

$$Z = -\frac{1}{I_0} \int_{-\infty}^{\infty} dz E_z(z, r=0) \exp(-i\omega z/c), \quad (8)$$

gives Eq. (1).

The real part of the impedance of a hole arises in the second order of the perturbation theory based on the smallness of the parameters α_{mg}/b^3 and α_{el}/b^3 . It turns out, however, that we can find the real part of the impedance without going to higher orders if use is made of the following relation between the $\text{Re}Z$ and the energy P radiated per unit time by the hole :

$$P = \frac{1}{2} I_0^2 \text{Re}Z(\omega) . \quad (9)$$

The energy flux P in Eq. (9) should include all the waves radiated by the hole, both inside and outside of the waveguide. The outside radiation will depend on the geometry and location of the conducting surfaces in that region and cannot be computed without knowing particular details of the specific design. Here we neglect its contribution, assuming that the thickness of the pipe wall is large enough so that the electromagnetic field does not penetrate through the hole.

Inside the waveguide, we have to take into account the radiation going into all E and H modes. The energy flow in the mode of unit amplitude is equal to

$$P_{n,m}^{(E)} = \frac{1 + \delta_{0,n}}{16} \omega \kappa_{n,m} \mu_{n,m}^2 J_n^2(\mu_{n,m}) , \quad (10)$$

and

$$P_{n,m}^{(H)} = \frac{1 + \delta_{n,0}}{16} \omega \kappa'_{n,m} (\mu_{n,m}^2 - n^2) J_n^2(\mu'_{n,m}) , \quad (11)$$

respectively. The energy flux in each mode radiated by the hole is given by $|a_{n,m}(\sigma = 1)|^2 P_{n,m}$ and $|a_{n,m}(\sigma = -1)|^2 P_{n,m}$ in the forward and backward directions, respectively. It is evident that this radiation occurs only if the frequency ω is larger than the cutoff frequency $\omega_{n,m}$ (or $\omega'_{n,m}$).

The total energy flux P is

$$P = \sum_{E,H} \sum_{n,m} \sum_{\sigma=\pm 1} P_{n,m} |a_{n,m}|^2 , \quad (12)$$

where the summation is carried out over both directions of propagation, $\sigma = \pm 1$, all possible values of n and m , and also over E and H modes. Combining Eqs. (9)–(12) yields the following equation for the contribution of E and H modes into the real part of the impedance:

$$\text{Re}Z^{(E)} = \frac{Z_0}{\pi} \frac{\omega^2}{c^2 b^4} \sum_{n,m} \frac{1}{(1 + \delta_{n,0})} F^{(E)}\left(\frac{\omega}{\omega_{n,m}}\right) , \quad (13)$$

where

$$F^{(E)}(x) = \frac{\alpha_{mg}^2 x^2 + \alpha_{el}^2 (x^2 - 1)}{x \sqrt{x^2 - 1}} \quad (14)$$

for $x > 1$, and $F^{(E)}(x) = 0$ for $x < 1$. For the H modes

$$\text{Re}Z^{(H)} = \frac{Z_0}{\pi} \frac{\omega^2}{c^2 b^4} \sum_{n,m} \frac{n^2}{\mu_{n,m}^2 - n^2} F^{(H)}\left(\frac{\omega}{\omega'_{n,m}}\right) , \quad (15)$$

where

$$F^{(H)}(x) = \frac{\alpha_{el}^2 x^2 + \alpha_{mg}^2 (x^2 - 1)}{x \sqrt{x^2 - 1}} \quad (16)$$

for $x > 1$, and $F^{(H)}(x) = 0$ for $x < 1$.

Eqs. (13) and (15) apply also for short slots such that $l \ll b$ and $l\kappa \ll 1$. For a large aspect ratio, $l \gg w$, we have $\alpha_{mg} \approx -\alpha_{el}$, and $F^{(E)}(x) = F^{(H)}(x)$. In this case, the plot of the $\text{Re}(Z^{(E)} + Z^{(H)})$ measured in units $\alpha_{mg}^2 Z_0 / \pi b^6$ as a function of $\omega b / c$ is shown in Fig. 1.

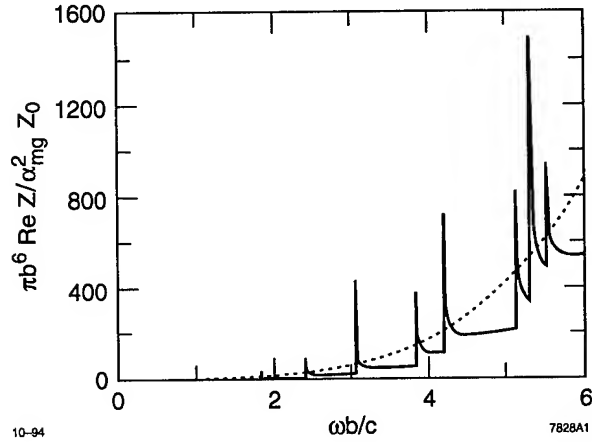


Figure. 1. Real part of the impedance of a short large-aspect-ratio slot as a function of the frequency (solid curve), and a high-frequency approximation given by Eq. (17) (dotted curve).

Because the functions $F^{(E)}(x)$ and $F^{(H)}(x)$ go to infinity when $x \rightarrow 1$, $\text{Re}Z$ has singularities at the cutoff frequencies $\omega_{n,m}$ and $\omega'_{n,m}$. Formally, this happens because the amplitude of the radiated waves given by Eqs. (6) and (7) scales as $\kappa_{n,m}^{-1}$ when ω approaches a cutoff frequency. The actual height of the cutoff peaks will be determined by higher order corrections of the theory and finite conductivity of the walls.

In the limit $\omega \gg c/b$, a large number of harmonics is involved in the sums (13) and (15). By considering them to be continuous variables, it is possible to integrate over n and m instead of summing. This integration yields

$$\text{Re}Z = \frac{2}{3\pi} Z_0 \frac{\omega^4 \alpha_{mg}^2}{c^4 b^2} . \quad (17)$$

This function is also plotted in Fig. 1; it gives a good approximation of the averaged dependence of the $\text{Re}Z$, even for small frequencies.

III. REAL PART OF THE IMPEDANCE FOR A LONG SLOT

To find the real part of the impedance of a long slot for which l is comparable or larger than b and/or κ^{-1} , we consider the long slot as a distributed system of magnetic and electric dipoles. The field radiated by the slot consists of the waves coming from different elements of the slots with a relative phase advance between them. For two infinitesimal elements located at distance z , the phase advance is composed of two parts. The first part is due to the change of phase of the driving field of the beam, and is equal to κz . The second part is caused by the relative phase shift of the two radiated waves, and is equal to $-\sigma \kappa_{n,m} z$, where $\sigma = \pm 1$ for the forward and backward propagating waves. The total

phase exponent, $\exp(i\kappa z - i\sigma\kappa_{n,m}z)$ should be integrated over the length of the slot, yielding the factor

$$f_{n,m}(\sigma) = \frac{1}{l} \int_0^l \exp(i(\kappa - \sigma\kappa_{n,m})z) dz = \frac{1}{il(\kappa - \sigma\kappa_{n,m})} [\exp(i(\kappa - \sigma\kappa_{n,m})l) - 1] \quad (18)$$

for the E modes and a similar factor $f'_{n,m}(\sigma)$, for which $\kappa_{n,m} \rightarrow \kappa'_{n,m}$ in Eq. (18), for the H modes. These factors multiply the amplitudes $a_{n,m}^{(E)}$ and $a_{n,m}^{(H)}$ in Eqs. (6) and (7). Combining all these changes, and taking into account that for a long slot, $\alpha_{el} = -\alpha_{mg}$, results in the following modifications of the functions $F^{(E)}$ and $F^{(H)}$ in Eqs. (13) and (15):

$$F^{(E)}(x) = \frac{2b^2}{\mu_{n,m}^2} \left(\frac{\alpha_{mg}}{l}\right)^2 \frac{1}{x\sqrt{x^2-1}} \left\{ \sin^2 \left[\frac{l\mu_{n,m}}{2b} \right] \times (x - \sqrt{x^2-1}) + \sin^2 \left[\frac{l\mu_{n,m}}{2b} (x + \sqrt{x^2-1}) \right] \right\}, \quad (19)$$

and $F^{(H)}$ given by the same expression with $\mu_{n,m}$ substituted by $\mu'_{n,m}$. In the limit $l \gg |\kappa - \sigma\kappa_{n,m}|^{-1}$, the effective length of the slot that contributes to the real part of the impedance turns out to be equal to $|\kappa - \sigma\kappa_{n,m}|^{-1}$, which means that $\text{Re}Z(\omega)$ does not depend on l in the limit $l \gg \kappa^{-1}$ (but $\kappa^{-1} \gg w$).

IV. REGULAR ARRAY OF SLOTS

Consider an array of N identical slots distributed along the beam pipe such that the distance between the slots is equal to d_1 . The system has a period $d = l + d_1$. The electromagnetic field scattered by the array is the sum of the fields of individual slots. In the first approximation of the perturbation theory, the impedance is equal to NZ , where Z is given by Eq. (1). However, since the energy radiated by the array of slots is a quadratic function of the amplitude of the waves, it will be shown below that, at resonant frequencies, there is a strong amplification in $\text{Re}Z$ which scales as N^2 .

To find the radiation from N slots, it is necessary to sum their fields, taking into account the relative phase advance between the fields of deferent slots. As shown in the previous section, the phase advance between two adjacent slots is equal to $\exp(i\kappa d - i\sigma\kappa_{n,m}d)$. For N slots, the amplitude of (n, m) E mode should be multiplied by the following factor:

$$g_{n,m}(\sigma) = \sum_{j=0}^{N-1} \exp[idj(\kappa - \sigma\kappa_{n,m})] = \frac{1 - \exp[idN(\kappa - \sigma\kappa_{n,m})]}{1 - \exp[id(\kappa - \sigma\kappa_{n,m})]}. \quad (20)$$

The square of the absolute value of $g_{n,m}(\sigma)$, multiplies each sine term in Eq. (19) modifying the function $F^{(E)}$ into the following expression:

$$F^{(E)}(x) = \frac{2b^2}{\mu_{n,m}^2} \left(\frac{\alpha_{mg}}{l}\right)^2 \frac{1}{x\sqrt{x^2-1}} \left\{ \sin^2 \left[\frac{l\mu_{n,m}}{2b} \right] \times (x - \sqrt{x^2-1}) + \sin^2 \left[\frac{l\mu_{n,m}}{2b} (x + \sqrt{x^2-1}) \right] \right\}.$$

$$\times (x - \sqrt{x^2-1}) \left\{ \frac{\sin^2 \left[\frac{dN\mu_{n,m}}{2b} (x - \sqrt{x^2-1}) \right]}{\sin^2 \left[\frac{d\mu_{n,m}}{2b} (x - \sqrt{x^2-1}) \right]} + \frac{\sin^2 \left[\frac{l\mu_{n,m}}{2b} (x + \sqrt{x^2-1}) \right] \sin^2 \left[\frac{dN\mu_{n,m}}{2b} (x + \sqrt{x^2-1}) \right]}{\sin^2 \left[\frac{d\mu_{n,m}}{2b} (x + \sqrt{x^2-1}) \right]} \right\}.$$

For the H modes, the function $F^{(H)}(x)$ contains $\mu'_{n,m}$ instead of $\mu_{n,m}$.

The maximum value of $|g_{n,m}|^2$ in Eq. (20) is equal to N^2 and is attained when the following condition holds

$$d(\kappa - \sigma\kappa_{n,m}) = 2q\pi, \quad (21)$$

where q is an integer. For large N , Eq. (20) represents narrow peaks with a width at half height $\Delta\omega/\omega \approx 1/(2qN)$ at the resonant frequencies. This implies that the Q factor for these resonances can be estimated as $Q \approx qN$.

If $d/b = 2\pi q/\mu_{n,m}$ (or $d/b = 2\pi q/\mu'_{n,m}$), Eq. (21) is satisfied by the cutoff frequency $\omega_{n,m}$ (or $\omega'_{n,m}$). In this case, the height of the resonant peaks will be strongly amplified because of the superposition of the cutoff singularity for a single peak with a maximum of the $|g_{n,m}|^2$ function.

In the limit of very large N , $N \rightarrow \infty$, the width of the resonances becomes so narrow that it will actually be determined by the finite conductivity of the walls σ . The transition to this regime occurs when Q becomes comparable to b/δ , where δ is the skin depth at the resonant frequency. Previously, this regime has been studied in detail for an infinitely long periodic bellow in Ref. [5], where the resonance conditions (21) have also been found.

V. Acknowledgments

I thank A. Chao, R. Gluckstern, S. Heifets, S. Kurennoy and T. Weiland for useful discussions related to this work.

References

- [1] S. S. Kurennoy, *Part. Accel.*, **39**, 1 (1992).
- [2] R. L. Gluckstern, *Phys. Rev.*, **A46**, 1106 (1992).
- [3] H. A. Bethe, *Phys. Rev.* **66**, 163 (1944).
- [4] G. V. Stupakov, Preprint SLAC-6698, Stanford (1994).
- [5] P. K. Cooper, S. Krinsky, and P. L. Morton, *Part. Accel.*, **12**, 1 (1982).

DARK CURRENTS FOR CEBAF LINACS*

Byung C. Yunn

Continuous Electron Beam Accelerator Facility
12000 Jefferson Avenue, Newport News, VA 23606, USA

Abstract

Continuing on our numerical study[1] of field emitted electrons from a superconducting CEBAF cavity we have identified all possible emission sites, magnitudes, and the energy profile of dark currents expected at CEBAF under nominal operating conditions. We find that most electrons do not survive beyond a single cryomodule which includes eight 5-cell superconducting cavities. However, some electrons can be accelerated through many cryomodules, ending up with an energy close to 100 MeV. However, no field emitted electrons can be recirculated along with an electron beam generated at the gun, due to the limited energy acceptance of CEBAF recirculation arcs.

I. INTRODUCTION

In our previous study[1], we found that most field emitted electrons from a CEBAF superconducting cavity were likely to stay in the cavity where they originated. However, some field emitted electrons could be accelerated to adjacent cavities when emitted from a few selected locations at a proper phase. Furthermore, we have identified all such emission sites in the CEBAF cavity which could become a potential source of dark currents. Our study, however, was not complete in that the tracking of electrons was not possible beyond a single cavity at the time. Dark current was estimated by calculating characteristics of a field emitted electron bunch leaving the cavity through open beam pipe. The arrival times of such a bunch at neighboring cavities determine whether the bunch can keep pace with the nominal electron beam. Even though we expect that forward moving field emitted currents from the linacs under the most favorable phase relationship with subsequent cavities in downstream cryomodules will be intercepted at the spreaders (and backward currents at the recombiners, respectively) due to low energy acceptance of less than one percent level of such beam transport modules, it is important to find out what actually happens to all dark current candidates when more than a single cavity is involved. In this paper we report on our study of following electrons throughout CEBAF linacs assuming the beam injection at 45 MeV. There is a chicane at the entrance to the linac which prevents dark currents originated at the injector reaching the linac.

II. A CEBAF CRYOMODULE

Cavities in a CEBAF cryomodule are arranged in a particular way in order to minimize emittance degradation due to rf coupler kicks. It is helpful to differentiate CEBAF cavities into 4 different groups for the purpose of describing such an arrangement, even though a CEBAF cavity has only a single configuration with no

variation in its assembly with FP and HOM couplers. A sketch of a 5-cell cavity which belongs to a group of type I cavities is shown in the following Fig. 1. A type II (III and IV respectively)

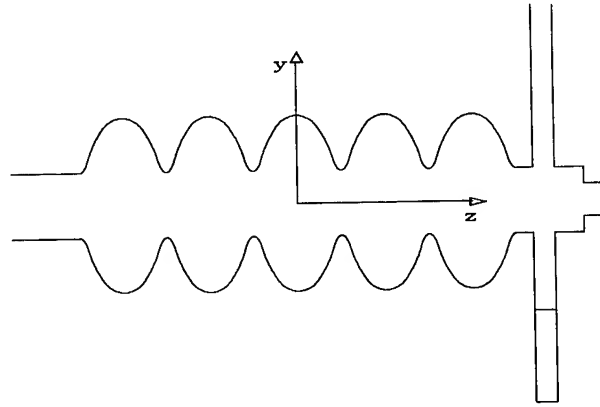


Figure 1. Type I cavity: positive x-axis is into the paper.

cavity is defined as a type 1 cavity rotated by 180° about the +y axis (+z and +x axis respectively). In a cryomodule, we have 8 cavities in the following order:

$$\text{I - II - III - IV - III - IV - I - II} \quad (\text{A})$$

Our trajectory program(FEET) requires electromagnetic fields in whole CEBAF linacs as an input. This problem is manageable because cavities are all independently powered and cross talks between cavities[2] are negligible at the operating 1497 MHz mode. First, we calculate fields for a type I cavity numerically with the computer codes URMEL and MAFIA[3]. (For a practical reason, we had to divide the cavity into two regions: one with an axial symmetry and the other with no such symmetry.) Second, fields for other types of cavities are obtained from fields for the type I cavity by the symmetry consideration. Type II:

$$\begin{aligned} E_x^{II}(x, y, z) &= -E_x^I(-x, y, -z) \\ E_y^{II}(x, y, z) &= E_y^I(-x, y, -z) \\ E_z^{II}(x, y, z) &= -E_z^I(-x, y, -z) \end{aligned} \quad (1)$$

Type III:

$$\begin{aligned} E_x^{III}(x, y, z) &= -E_x^I(-x, -y, z) \\ E_y^{III}(x, y, z) &= -E_y^I(-x, -y, z) \\ E_z^{III}(x, y, z) &= E_z^I(-x, -y, z) \end{aligned} \quad (2)$$

Type IV:

$$\begin{aligned} E_x^{IV}(x, y, z) &= E_x^I(x, -y, -z) \\ E_y^{IV}(x, y, z) &= -E_y^I(x, -y, -z) \\ E_z^{IV}(x, y, z) &= -E_z^I(x, -y, -z) \end{aligned} \quad (3)$$

*This work was supported by the U.S. Department of Energy, under contract No. DE-AC05-84ER40150.

and similar transformations for magnetic fields.

III. TRACKING THROUGH LINACS

How the program FEET handles a field emitted electron in a CEBAF cavity can be found in ref. [1]. When an electron enters a neighboring cavity through the beam pipe, forces acting on the particle are calculated from the electromagnetic fields in the cavity performing field transformations described in Eqs. (1) to (3) depending on the type of the cavity. In addition rf phase must be also adjusted. Assuming that all cavities in the linacs are set up for a maximal energy gain of 2.5 MeV per cavity, absolute phases (in units of degrees at 1497 MHz) of 8 cavities in a cryomodule at time equal to zero are 0, -90, 165.936, 75.936, -28.127, -118.127, 137.809, and 47.809, respectively, in the order noted in the layout (A) of those 8 cavities in section II. The leftmost cavity of (A), which is of the type I, is chosen as the reference here. Also, there is an rf phase shift of 76.708 degree between the last cavity in a cryomodule and the first cavity in the next cryomodule. Furthermore, in the warm region between two cryomodules there is a quadrupole for focusing the electron beam, which was turned on in the simulation. The linac lattice is a FODO type with 120 degree phase advance per cell for the 1st pass beam. Focussing effects of a quadrupole are easily simulated with the 1st order transfer matrix. We also mention aperture limits in linacs which are 3.0 inches in cavities and 1.5 inches in beam pipes, loosely stated. (The program FEET treats this in complete detail.)

IV. RESULTS

For the present study, we scan the surface of the first two cavities (They are of the type I and II, respectively. For convenience of notation, we will simply refer to them as cavity I and cavity II) of the first cryomodule in the North linac for field emission at an accelerating gradient of 5 MV/m only. It is expected that dark currents containing the highest energy electron bunches have most likely originated from these two cavities because they have the largest number of downstream cavities available. 5 MV/m is the design value for the CEBAF cavity gradient. In order to obtain a detectable field emitted electron current at this field intensity we assume cavities with field enhancement factor $\beta=300$. According to Fowler-Nordheim[4] theory, the current density J in A/m² is given by

$$J = \frac{1.54 \times 10^6 (\beta E_{\text{surf}})^2}{\phi} \exp\left(-\frac{6.83 \times 10^3 \phi^{1.5}}{\beta E_{\text{surf}}}\right) \quad (4)$$

where E_{surf} is the surface electric field in MV/m and ϕ is the work function of the metal surface in eV. For niobium we take $\phi = 4$ eV. As in our previous study, the emission from a given site is normalized to a total dissipated power of 1 Watt. In other words, $A_E \int J(\theta) E_{\text{kin}}(\theta) d\theta = 2\pi$ W, where $J(\theta)$ is the current density determined with the instantaneous field at rf phase θ , $E_{\text{kin}}(\theta)$ is the impacting energy of the electron emitted at that phase, and the integration runs from 0 to π or π to 2π depending on the location of the site in the cavity. Average impact energy is determined by $\int J(\theta) E_{\text{kin}}(\theta) d\theta / \int J(\theta) d\theta$.

We can see a typical example of generation of dark current from Fig. 2. Trajectories of electrons emitted from a site in cavity I (see the site c in Fig. 3) at all phases are shown. Most electrons

with wrong phases fan out ending at nearby cells, while a small batch of electrons emitted at right phases escape to the downstream cavity II and beyond. We should mention that a piece of beam pipe about a half meter long, which is not pictured here, connects the top and the bottom portions of Fig. 2 to complete the cryomodule. The electron bunch essentially goes through the center of the beam pipe segment in cavities downstream of it. Dark current in the particular case shown in Fig. 2 terminates at the 19th cavity with an energy gain of about 36 MeV.

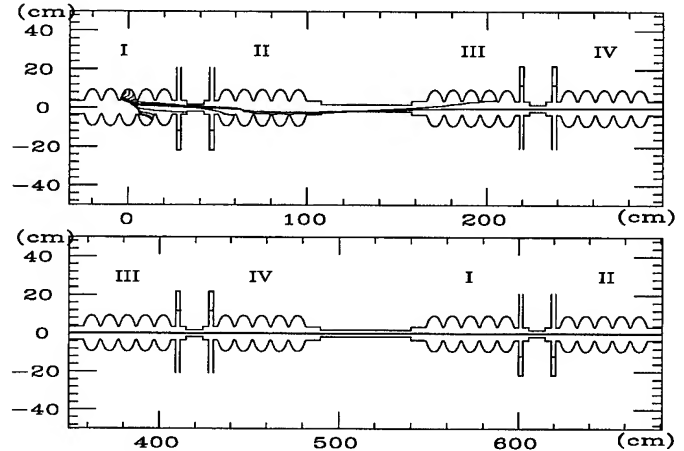


Figure 2. An example of dark current generation in a CEBAF cryomodule at 5 MV/m gradient. Roman letters on top of cavities specify the types of the cavities as explained in section II.

We have identified all emission sites on the surface of cavity I and II which could serve as a source of dark current. In this paper we report only on those sites which produce field emitted electrons traveling downstream toward the end of the linacs. A complete list of all such sites with a brief note on some characteristics of electron bunches which form dark currents can be found in the following two subsections. In Figs. 3 and 4 we also present pictorially locations of the emission sites in the cavity I and II, respectively. An emission site is really a cylindrically symmetric thin strip of the cavity surface typically about a few mm wide. A vertical line in the figures specifies the center position of such a strip. In the following each emission site is represented by a letter (from a to m) assigned next to a vertical line.

A. Emission Sites at Cavity I

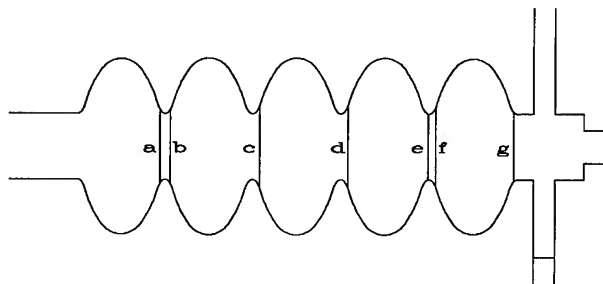


Figure 3. Dark current emission sites located in the cavity I. Vertical lines represent thin strip regions as explained in the text.

Site a: We find two distinct phase windows, one about 0.5 deg wide delivering $I_{avg} = 30$ nA and power of 10 mW, and another 1.0 deg wide with $I_{avg} = 160$ nA and power of 40 mW. Most electrons terminate at the cavity II.

Site b: The region consists of two narrow strips about 2 mm apart. In the left strip we find two phase regions, one about 0.75 deg wide with $I_{avg} = 0.5$ nA and power of 0.2 mW (all power to the cavity II), and another about 0.5 deg wide with $I_{avg} = 0.3$ nA and power of 0.2 mW. In the latter case electrons travel up to the 7th cavity but attain maximum energy of only 2.6 MeV. In the right strip, a phase window of 15 deg produces $I_{avg} = 0.3$ nA and power of 0.12 mW with all electrons ending up on the cavity II.

Site c: We find two distinct phase regions, one about 2.5 deg wide with $I_{avg} = 16$ nA and power of 6 mW, and another 18.0 deg wide with $I_{avg} = 5$ nA and power of 3 mW. Electrons mostly terminate either at the 2nd or at the 3rd cavity except a small fraction of them (about 10 pA) reaching to the 19th cavity with a peak energy of 36 MeV.

Site d: There exist three distinct phase regions, one about 7.5 deg wide with $I_{avg} = 9$ pA and power of 0.02 mW, and another about 4.0 deg wide with $I_{avg} = 0.4$ nA and power of 1 mW with electrons reaching up to the 3rd cavity. The last one is about 2.5 deg wide with $I_{avg} = 36$ pA with a negligible power of 0.01 mW even though electrons travel to the 7th cavity.

Site e: We find a phase region of about 1 deg wide with $I_{avg} = 19$ nA and power of 12 mW. About 1 nA of electrons traverse a whole cryomodule only to be lost in the warm section while most electrons do not survive beyond the 3rd cavity. Peak energy achieved is 15 MeV.

Site f: A phase window of about 5 deg wide generates $I_{avg} = 72$ nA and power of 62 mW. About 2 nA of electrons travel to the 2nd cryomodule attaining a peak energy of 32 MeV.

Site g: The region consists of two strips 2 mm apart. In the left strip we find two 3 deg wide phase regions, one with $I_{avg} = 0.5$ μ A and power of 36 mW, another with $I_{avg} = 2$ μ A and power of 380 mW. Dark current terminates at the 3rd cavity. In the right strip, we also have two windows, one about 10 deg wide with $I_{avg} = 8$ μ A and power of 615 mW delivered to nearby two cavities, another about only 0.1 deg wide with $I_{avg} = 72$ nA and power of 1.5 W with current extending to the 21st cavity.

B. Emission Sites at Cavity II

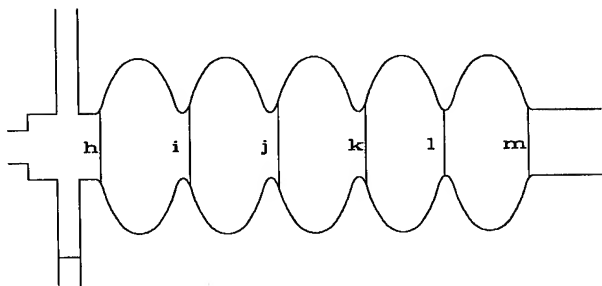


Figure 4. Dark current emission sites at the cavity II.

Site h: There exists a phase window of about 0.1 deg width. Most electrons do not survive beyond the 3rd cavity, but a few of them reach to the 28th cavity attaining energy of 48 MeV. However, the current is extremely small and the power is negligible.

Site i: We find two phase regions, one about 20 deg wide with only $I_{avg} = 0.1$ pA (most power to the 3rd cavity), another about 5 deg wide with a negligible power of 10 nW despite some electrons traversing a whole cryomodule and attaining a peak energy of 13 MeV.

Site j: A phase window about 0.5 deg wide exists. Electrons are accelerated to the 34th cavity attaining a peak energy of 75 MeV. However, power is only about 7 nW.

Site k: We find two phase regions, one about 10 deg wide with $I_{avg} = 0.3$ nA and power of 0.5 mW (about 0.5 pA of electrons reach the 4th cryomodule gaining a peak energy of 30 MeV), and another about 0.1 deg wide with electrons accelerated to the 23rd cavity. 45 MeV energy gain is achieved, but power is negligible.

Site l: $I_{avg} = 16$ nA and power of 2.5 mW is produced from a phase window about 1 deg wide. Almost all electrons are lost in the 3rd cavity.

Site m: There exist two distinct phase windows only about 0.1 deg wide, one with $I_{avg} = 80$ nA and power of 50 mW, another with $I_{avg} = 50$ nA and 30 mW. Most power is delivered to cavities in the latter part of the first cryomodule.

V. CONCLUSION

From the result presented here, we can safely assert that none of field emitted electrons can be recirculated along with an electron beam generated at the gun, due to the limited energy acceptance of CEBAF recirculation arcs.

References

- [1] B. C. Yunn and R. M. Sundelin, *Proc. 1993 Particle Accelerator Conf.*, 1092 (1993).
- [2] B. C. Yunn, "A Cross Coupling between Cavities," CEBAF TN-80 (1988).
- [3] R. Klatt *et al.*, *Proc. 1986 Linear Accelerator Conf.*, 276 (1986).
- [4] R. H. Fowler and L. Nordheim, *Proc. R. Soc. London A* **119**, 173 (1928).

IMPROVEMENTS IN BUNCH COALESCING IN THE FERMILAB MAIN RING

J. Dey, I. Kourbanis, D. Wildman, Fermi National Accelerator Laboratory*, P.O Box 500, Batavia, IL. 60510, USA

Abstract

In Fermilab's Main Ring bunch coalescing is used to produce intense proton and antiproton bunches for the Tevatron. For the bunch coalescing, 11 proton or antiproton bunches are rotated first in the fundamental rf harmonic of 53 MHz to reduce the momentum spread, then are rotated for a quarter of a period in a lower harmonic ($h=53$ or 2.5 MHz) and recaptured in a single 53 MHz bucket[1]. The 2.5 voltage available for coalescing is 22 KV. Recently 3 new 2.5 MHz coalescing cavities were installed[2] and the available 2.5 voltage was tripled. The coalescing improvements from this upgrade will be described.

I. INTRODUCTION

Recent injector improvements and upgrades helped increased the Main Ring intensity by 50% since the last collider run. The higher proton intensities resulted in higher longitudinal emittances before coalescing. Typical long. emittances of the highest intensity proton bunches are 0.30-0.32 eV-sec.

Also higher antiproton stacking efficiencies resulted in higher antiproton stacks and larger antiproton bucket sizes, for more antiprotons extracted. The 11 antiproton bunches have a parabolic distribution in emittances and intensities, the middle bunches having the greater intensities and emittances. The pbar emittances typically vary between 0.14 eV-sec for the end bunches to 0.30 eV-sec for the bunches in the middle.

With the larger proton and antiproton long. emittances, even with the introduction of a second harmonic cavity, the coalescing efficiency was in the 70-80% range resulting in satellites and DC beam. In Fig. 1 an ESME[3] simulation is shown of 11 (typical long. emittance) antiproton bunches at the moment of recapture in an 800 KV 53 MHz bucket. In Fig. 1 the distribution at recapture is wider than the standard 53 MHz bucket (18.9 nsec). Some of the particles spill into the two neighboring buckets resulting in satellites, and some are not captured and lost as DC beam.

In Fig.2 the same 11 antiproton bunches are shown at recapture rotated this time with 60 KV of 2.5 MHz. The width of the distribution is now narrow enough to fit in the single 53 MHz bucket and there are almost no satellites.

*Operated by Universities Research Association, Inc. under contract with the U.S. Department of Energy.

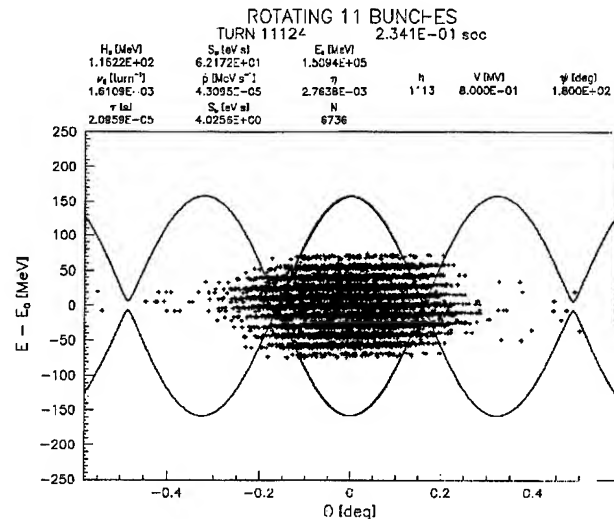


Figure 1: 11 pbar bunches rotated with 21 KV of 2.5 MHz and 4 KV of 5 MHz at the moment of recapture.

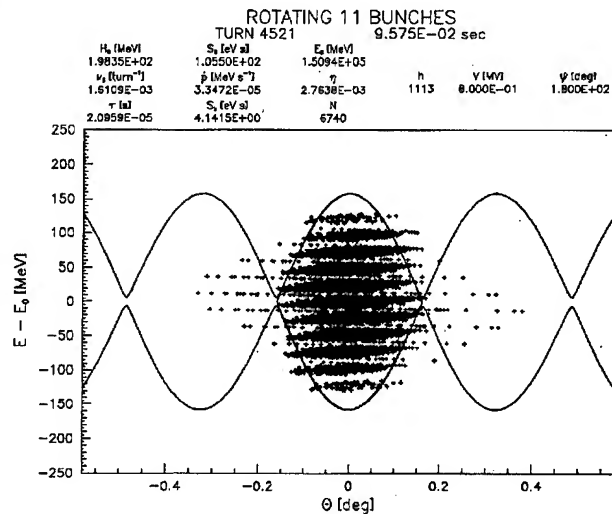


Figure 2: 11 typical pbar bunches rotated with 60 KV of 2.5 MHz and 11 KV of 5.0 MHz at the moment of recapture.

Recently a decision was made to upgrade our coalescing system by making new 2.5 MHz cavities capable of producing a total of 60 KV, three times the voltage available today. The new higher voltage would

help us reduce the width of the recaptured distribution by a factor of $\sqrt{3}$, increase the coalescing efficiency and eliminate the satellites.

III. EXPERIMENTAL RESULTS

To test if the results with the higher 2.5 MHz voltage agree with the simulations, 5 proton bunches (to eliminate the effect of the 5.0 MHz voltage) each of 0.3 eV-sec were coalesced first with the old coalescing cavities (a total of 21 KV of 2.5 MHz) and then with the old and the new cavities together (a total of 60 KV of 2.5 MHz). The digitized beam profiles at the moment of recapture for both cases are shown in Fig. 3. The rms. spread with the 60 KV is about $\sqrt{3}$ times smaller than the rms. spread of the distribution rotated with 21 KV, as in the simulations. Also the total spread of the distribution rotated with 60 KV is 17.5 nsec and fits in the recapture 53 MHz bucket (18.9 nsec wide).

The effect of the higher 2.5 MHz voltage on the pbar coalescing efficiency is shown in Fig. 4. The predicted coalescing efficiencies are from ESME simulations for 11 pbars bunches with typical emittances rotated with 21 KV of 2.5 MHz and 4 KV of 5.0 MHz (before the upgrade) and 60 KV of 2.5 MHz (after the upgrade). The results agree with the predictions, and show a 14% improvement in pbar coalescing efficiency.

The proton coalescing efficiency also increased by about 10% after the upgrade with proton bunches as large as $3.2E11$ being observed. The typical satellite bunches after the upgrade have intensities less than 2% of the main bunch intensity, compared with 8-12% before.

The proton bunch coalescing efficiency is expected to be further improved with the installation of the new 5 MHz cavity that is going to be installed in the summer of '95 along with the rest of the new 2.5 MHz cavities.

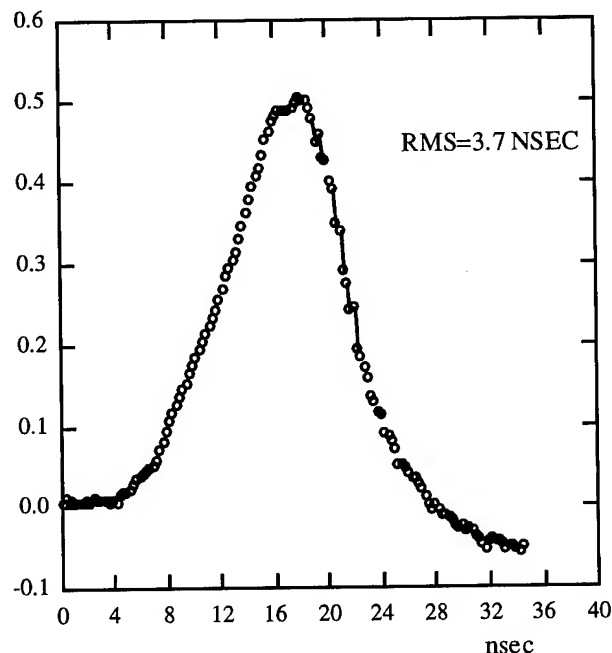
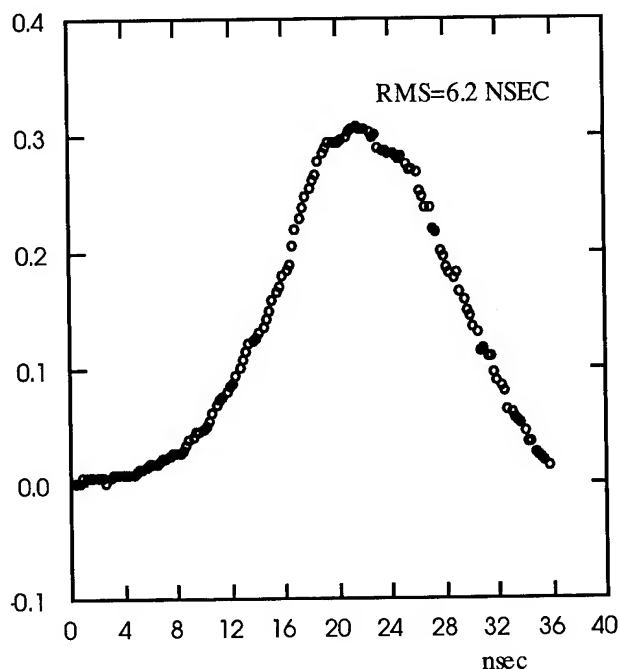


Figure 3: Profiles of the coalesced distribution of 5 proton bunches at the moment of recapture. Top: Bunches rotated with 21 KV of 2.5 MHz. Bottom: Bunches rotated with 60 KV of 2.5 MHz.

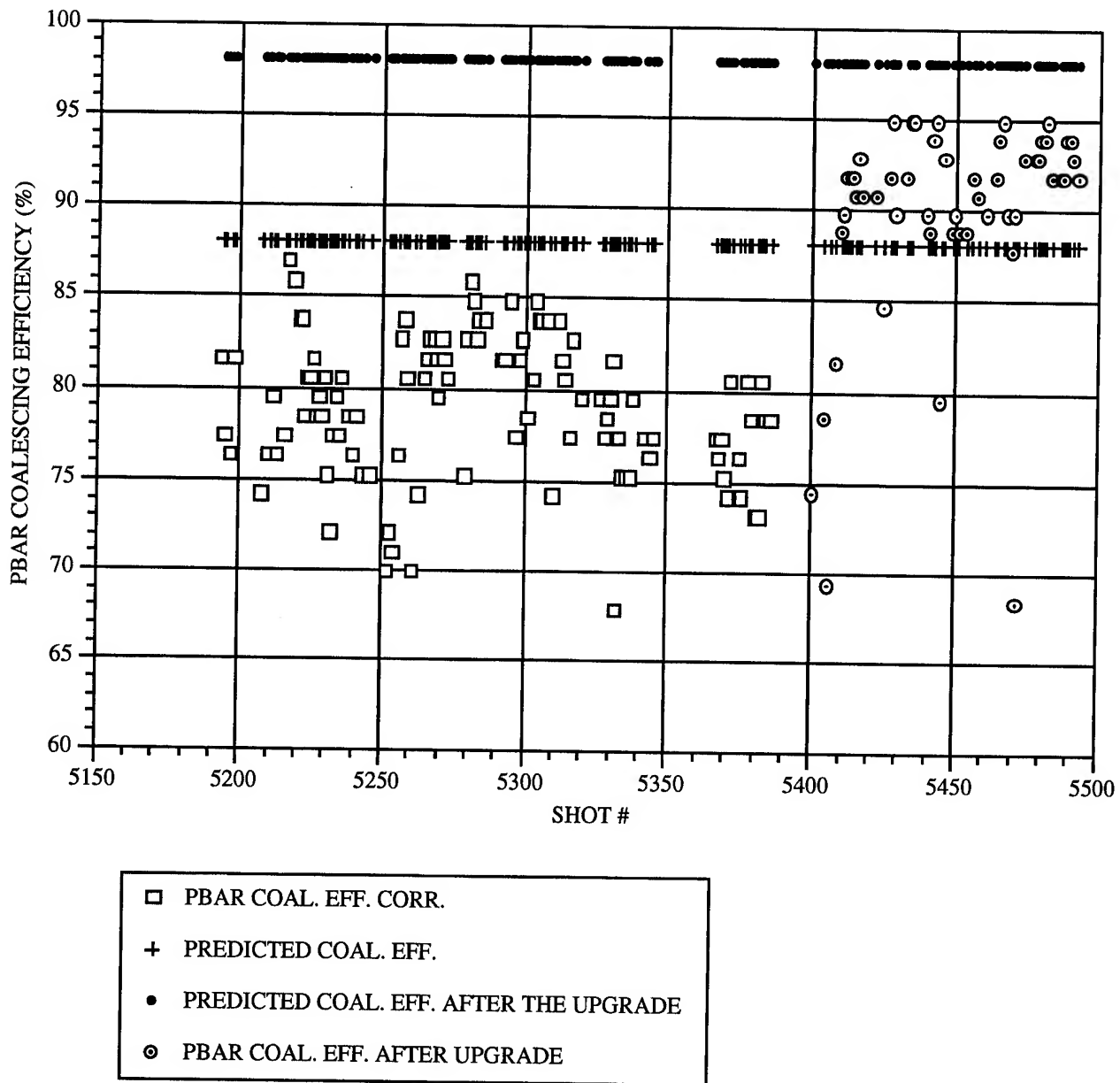


Figure 4: Pbar coalescing efficiency versus shot number before and after the coalescing upgrade.

IV. CONCLUSION

The 3 new 2.5 MHz cavities installed in Main Ring tripled the existing 2.5 MHz voltage and helped us increase the pbar coalescing efficiency by 14%, the proton coalescing efficiency by 10% and eliminate the satellite bunches.

VI. REFERENCES

- [1] "Performance and Comparison of Different Coalescing Schemes Used in the Fermilab Main Ring", I. Kourbanis, G.P. Jackson, and X. Lu. Proc. of the 1993 Particle Accelerator Conf. 3799 (1993).
- [2] "A New RF System for Bunch Coalescing in the Fermilab Main Ring" J. Dey, I. Kourbanis, and D. Wildman. These proceedings.
- [3] "Users Guide to ESME v. 7.1", S. Stahl and J. MacLachlan, Fermilab internal note TM-1650 (2/90).

SLOW EXTRACTION OF PARTICLES USING A THIN TARGET FOR DRIVING FOR RESONANCE

Yu. Severgin, W. Belov, A. Makarov, M. Tarovik

The D.V. Efremov Scientific Research Institute of Electrophysical Apparatus 189631, St.-Petersburg, Russia

Abstract

The slow extraction of particles from the accelerator using parametric resonance of betatron oscillations is investigated. A special feature of the parametric resonance is the absence of separatrix on a phase plane. Therefore frequencies of betatron oscillations of the particles to be extracted at each revolution are to change abruptly. A value of this jump is need to be sufficient to transfer the frequencies of betatron oscillations of these particles inside the band of parametric resonance from the region outside and to ensure the increase of the oscillation amplitude in two revolutions, which is required to throw the particles in a gap of the extraction septum-magnet. It can be achieved through the energy losses of the particles, as ones passes through the thin target, and the use of sextupole lenses. Suggested techniques of the slow extraction can be applied for resonance of the higher order as well.

I.

The resonance slow extraction is based on existence of both stability region for oscillations with small amplitudes and resonance growth of amplitudes on asymptotes of separatrix outside the region. For linear parametrical resonance such region is not available. Close to a band of parametrical resonance the oscillation amplitude has beats, with swing growing as the boundary of the band is approached. The amplitude grows linearly at the boundary and exponentially within the band. Therefore the slow driving for resonance involves an increase of oscillation amplitude of particles not only in the beam part being extracted but in the whole beam as well. It is necessary to have a mechanism allowing the betatron oscillation frequency for a some share of particles to be moved abruptly in the resonance band from the region outside the band, in which the beats swing is reasonably small, and to act only on this share by resonance. It is necessary also, that this mechanism acts at all times for long. The mechanism is available: the use of both thin target for a part of the beam and sextupole lenses. The target releases a jet of particles with a pulse different from that of the main beam and imparts coherent betatron oscillations to the jet. Sextupoles under certain conditions excite the parametrical resonance only for this jet. The slow extraction is performed as follows. At the close of acceleration, using bump-magnets, the beam displaces inward (or outward) of the synchrotron ring so that its edge passes through a thin wire target. The target is positioned in that part of the ring, where dispersion ψ function is distinct from zero. The thickness of target is selected so that the change in pulse $|\delta p/p|$, in its only passage through the target, to be several times greater than pulse dispersion $|\Delta p/p|$ in beam. For this share of particles the equilibrium orbit displaces inward ($\psi \gg 0$) the ring by magnitude

$$X = -\psi \left| \frac{\delta p}{p} \right|$$

and the coherent betatron oscillations about the orbit are excited with initial amplitude

$$X_0 = \sqrt{(x_0 - \psi_t \left| \frac{\delta p}{p} \right|)^2 + (x'_0 - \psi'_t \left| \frac{\delta p}{p} \right|)^2 R_0^2}$$

and angle

$$X'_0 = x'_0 - \psi'_t \left| \frac{\delta p}{p} \right|,$$

where $x'_0 = \psi'_t \Delta p/p + \alpha_t \sqrt{\epsilon/\beta_t}$, $x_0 = \sqrt{\epsilon\beta_t} + \psi_t \Delta p/p$, ϵ —emittance of the beam at the close of acceleration, $\alpha_t, \beta_t, \psi_t, \psi'_t$ —characteristic function of synchrotron in the site of target. Sextupole lenses should be installed, where the ψ function is maximum ($\psi_s \gg \psi_t$) and

$$\psi_s \left| \frac{\delta p}{p} \right| > X_s$$

$X_s = X_0 \sqrt{\beta_s/\beta_t} (\cos(\mu_s - \mu_t) + \alpha_t \sin(\mu_s - \mu_t)) + X'_0 \sqrt{\beta_s/\beta_t} \sin(\mu_s - \mu_t)$ —amplitude of coherent betatron oscillation of particles, passed through the target, on azimuth of sextupole. Then in the sextupole they move about the orbit, shifted from the axis of chamber by value $\delta X_s = -\psi_s |\delta p/p|$ and sextupole lens field can be presented as

$$H_s = \frac{1}{2} \frac{\partial^2 H_z}{\partial x^2} \left(\left(\psi_s \frac{\delta p}{p} \right)^2 - 2\psi_s \left| \frac{\delta p}{p} \right| x + x^2 \right).$$

Quadrupole component of the field H_s causes displacement of the betatron oscillation frequency for these particles by value

$$\Delta Q_x = \frac{1}{2\pi R_0} \int_0^{2\pi R_0} \frac{1}{H R} \frac{\partial^2 H_z}{\partial x^2} \psi \beta_x ds \left| \frac{\delta p}{p} \right|$$

and excitation of parametrical resonance $2Q_x = k - \delta$ with half-width $|P_k|$

$$P_k = -\frac{1}{2\pi R_0} \int_0^{2\pi R_0} \frac{1}{H R} \frac{\partial^2 H_z}{\partial x^2} \psi \beta_x \exp(-2i\chi - \frac{iks}{R_0}) ds \left| \frac{\delta p}{p} \right|$$

(ΔQ_x and $|P_k|$ for particles of main part of the beam, that has not passed through the target is several times less, on the strength of condition $|\delta p/p| \gg |\Delta p/p|$). Gradients of sextupole lenses should be chosen so that

$$\Delta Q_x = \delta - \kappa_x \frac{\delta p}{p}, \quad (1)$$

where δ —detuning from resonance, and κ_x —self-chromaticity of synchrotron (without sextupole lenses). Then the exponential growth of amplitude of coherent betatron oscillations takes place only for the share of particles, that passed through the targets, with maximum increment $|P_k|$:

$$X = X_0 \exp(|P_k|s)$$

on azimuth of synchrotron, where the phase shift of betatron oscillations from the sextupole makes $\pi/2$. In this case the oscillation amplitude of particles, which have not passed through the target, essentially does not increase if $|\Delta p/P| \ll |\delta p/p|$. When slowly driving the beam on the target, it is possible to expand the extraction greatly. The risk of the repeat passing through the target is run. At half-integer frequency of betatron oscillations this can be obviated by setting several sextupole lenses with the gradients and shifts of phases between them, so that the condition (1) would be met and increment $|P_k|$ would be sufficient to get around the target at the second revolution. Driving of the beam on target during the extraction results in change of amplitude of coherent betatron oscillations, so to keep the same throw throughout the whole time of extraction is necessary to change $|P_k|$ at constant value of ΔQ_x . Emittance of extracted beam is defined by the radial width of the target s , angular divergence of the beam, hitting in the target $(2/\beta_t)\sqrt{(2\sqrt{\epsilon\beta_t} - s)s}$, root-mean square angle of divergence on passing through the target $\langle\theta^2\rangle^{1/2}$ and can be made small

$$\epsilon_{extr} = \frac{\pi s}{2} \left(\frac{\sqrt{(2\sqrt{\epsilon\beta_t} - s)s}}{\beta_t} + \frac{1}{2}\langle\theta^2\rangle^{1/2} \right).$$

It is advisable to position the target in the interval, where $\alpha_t = 0$.

II.

Let us use the synchrotron K4, [1], to illustrate the method of slow extraction. It produces electronic cooling of the beam on accumulation, and final $\Delta p/p = \pm 10^{-4}$. Magnetic structure includes intervals with large 7.3 m and small ~ 0 m values of ψ function. The working point $Q_x = 2.4$. The self-chromaticity $\kappa_x = -2.13$. The perimeter $P = 82.97$ m, magnetic rigidity $HR = 4$ T·m. Frequency Q_x is shifted to the working magnitude $Q_x = 2.48$ by using structural quadrupole lenses, $\delta = 0.04$, and $Q_z = 2.64$. The target is installed within small straight at values of $\beta_x = 2.5$ m, $\psi = 1.0$ m. Its thickness is selected so that $\delta p/p = -2 \cdot 10^{-3}$. At energy of protons $W = 585$ MeV the thickness of carbon target makes $s = 4.4$ mm, $\Delta p/p = 10^{-4}$, $\langle\theta^2\rangle^{1/2} = 2.4 \cdot 10^{-3}$, [2]. A single sextupole lens of length $l = 0.25$ m is used. It is installed within a long straight at values of $\psi_s = 6.91$ m, $\beta_s = 12.2$ m. From the condition (1) it is found $\partial^2 H_z / \partial x^2 = 26.8$ T/m². Increment $|P_k| = 3.4 \cdot 10^{-3} \text{ m}^{-1}$. The initial amplitude of coherent betatron oscillations $X_0 = 1.0$ cm, $X_0 = 0.6$ cm when positioning the target outside and inside the closed orbit, accordingly. The value $|P_k|$ is enough to get around the target at the second revolution (amplitude increase $\sim 32\%$). At the local displacement of

orbit to the septum-magnet for a distance 1.5 cm, knife thickness of 0.2 cm and target positioned outside, extraction begins at 4-th revolution. Emittance of extracted beam $\epsilon = 1.4\pi$ mm-mrad.

The most complicated problem is an investigation of interaction of particles and a target when slow (several microns per revolution) driving the latter on a beam. The numerical simulation [2] has shown, that the incomplete passing of particles through a target causes the repassing with the greater amplitude of a throw and increase of effective emittance of extracted beam. The efficiency of slow extraction is basically determined by losses on a target resulted from the nuclear reactions (makes $\sim 3\%$, [2]). Due to resonance nature of a swing amplitude of betatron oscillations the efficiency of extraction is higher, than that in the Piccioni method [3,4]. In the work [2] the extension of the Piccioni method is proposed for the case of strongly focusing accelerators, where is the large difference of values of ψ function. That is not required for the method put forward here, that can be, in principle, used for accelerators with the weak focusing. This method is applicable providing the decrease of pulse dispersion for the beam at the close of acceleration is realizable through the performance of high-frequency stations. We have considered the slow extraction at parametrical resonance for reasons of its features noted above. However, the mechanism of extraction being suggested can be applied for resonances of higher orders as well.

III. ACKNOWLEDGEMENTS

We are grateful to I.Shukeilo for discussion.

References

- [1] The storage complex for heavy ions K4-K10. Technical proposal. Report of group K4-K10, edited by G.M.Ter-Akopian. R9-92-15. JINR, Dubna, 1992.
- [2] N.D.Malitsky, Yu.P.Severgin, I.A.Shukeilo. The beam slow extraction from a magnetic ring, based on particle-target interaction. EPAC-88, v.1, p.565, Rome 1988.
- [3] B.T.Wright. Rev.Sci.Instr.,25, p.429, (1954)
- [4] W.A.Wenzel.Proc.of the Inter.Conf.on High Energy Acceler.p.698, Dubna, (1963)

PROPERTIES OF A TRANSVERSE DAMPING SYSTEM, CALCULATED BY A SIMPLE MATRIX FORMALISM

S. Koscielniak and H.J. Tran*

TRIUMF, 4004 Wesbrook Mall, Vancouver, B.C., V6T 2A3 Canada

Abstract

In a synchrotron, proton beams with injection steering errors perform coherent betatron oscillations, possibly of large amplitude. The oscillations may be damped by using a system of a beam position monitor and a variable, fast kicker combined in a feedback loop to form a 'transverse damper'. The system of ring, beam and damper can be modeled by iteration of a matrix mapping once per turn. This paper reports the calculation of damping rates, and coherent tune shifts by analytic solution of the recursions. Two cases are treated: (i) kick proportional to beam displacement; and (ii) 'bang-bang' damping in which, above a certain threshold, the kick depends only on the sign (+/-) of the displacement. We demonstrate (under certain conditions) that the 'bang-bang' scheme provides a linear damping of the amplitude and no tune shift, and (for the same peak power) is faster than the conventional proportional damper which produces an exponential damping with time.

I. INTRODUCTION

The aim of a damping system is to reduce the betatron oscillation of a beam as fast as possible. The damper may be designed to reduce injection errors, or to combat coherent instability; often the damper services both aims and its performance is a compromise: the effect of the kick is small compared with the displacement and it takes many repeated kicks to bring the beam on axis. If the oscillation amplitude is not reduced in a short period of time, then nonlinear effects which tend to accumulate with time, can dilute the emittance and reduce the beam quality. In fact, if filamentation is great enough the coherent motion 'washes out', the dipole signal vanishes and damping stops. A further concern, is that growth rate of a coherent instability is proportional to displacement; and if the condition for instability occurs during injection, the initial errors can be large. For these reasons it is important to provide fast damping. Further, if a damper intended to combat instability (later in acceleration) is used to reduce injection errors, its response will saturate for large amplitudes; and we should still like to find the damping rate.

A. System model

We shall use the single particle model of coherent beam motion and linear optics to illustrate the working of the system and derive its properties. Figure 1 shows the essential components of a damping system. Assume, as is inevitable in practise, that a beam has been injected into the synchrotron with some error; and that it oscillates about the closed orbit. The oscillation can be damped by reducing the net divergence with a fast kicker. For simplicity, the kicker is taken as a thin element that changes only

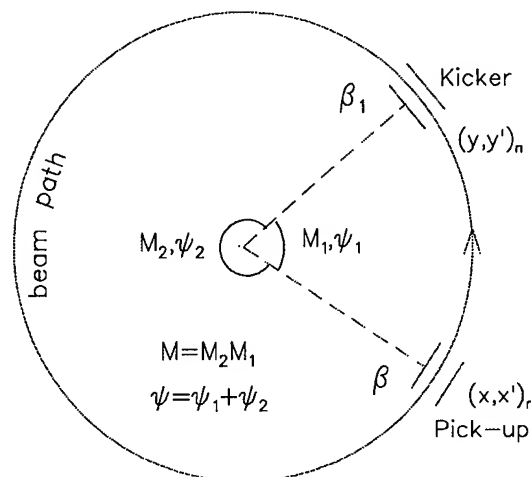


Figure 1. Schematic of a damping system.

the divergence but not the displacement at its location. Due to power limitation of the kicker, the divergence is reduced a small amount each revolution, and many kicks are required. Because the direction of the divergence can be different each time, the kick direction has to be adjusted accordingly. A beam position pick up (P.U.) at ψ_1 betatron phase advance up stream is used to provide this feedback information.

B. Kick schemes

We shall consider only two possible kick schemes: (i) the kick is proportional to upstream displacement, and (ii) the kick magnitude is constant but the sign comes from the sign of the beam displacement. The second scheme is simple to arrange: the kicker is powered by a constant supply whose output polarity is adjusted each time to damp the oscillation. This is known as 'bang-bang' damping. For the proportional kick, the P.U.-signal is used to drive a linear amplifier that powers the kicker. This eliminates the possibility of 'over kicking' the particle, as is unavoidable with a constant magnitude kick. In reality a linear amplifier will saturate at some peak power, and so above a certain threshold displacement, the magnitude of the kick becomes constant. Consequently, with this arrangement, the time sequence of kicks is a combination of proportional or constant. However, for simplicity, we only derive the damping characteristics of either purely proportional or purely constant-magnitude kicks.

*Graduate student at the University of British Columbia.

II. PROPORTIONAL KICK

Consider first the case of a proportional kick, which leads to exponential damping of the betatron oscillation. We will outline the derivation of the coherent tune shift and the dependence of the damping coefficient on the beta function and phase advance. We adopt a vector notation in which the first component is the displacement and the second the divergence.

In Figure 1, \mathbf{x}_n denotes the coordinates of the particle at the pick-up after n revolutions and likewise \mathbf{y}_n at the kicker. The magnitude of the kick is

$$\Delta y'_n = -k x_n, \quad (1)$$

where k is the kick strength proportionality constant. The displacement is assumed to be unchanged. The coordinates of the particle on the next turn become

$$\mathbf{x}_{n+1} = \mathbf{M}' \mathbf{x}_n = \{\mathbf{M}_2(\mathbf{M}_1 + \mathbf{K})\} \mathbf{x}_n, \quad (2)$$

where \mathbf{M}_1 is the linear transfer matrix from the P.U. to the kicker, \mathbf{M}_2 is that from the kicker (around the far side of the ring) back to the P.U., and \mathbf{K} is the kick matrix. The modified one-turn map, \mathbf{M}' , is linear; so applying the map n times to the initial coordinates \mathbf{x}_0 , we have

$$\mathbf{x}_n = (\mathbf{M}')^n \mathbf{x}_0. \quad (3)$$

Equation 3 is a system of 2 linear homogenous equations with constant, real coefficients and has solutions of the form

$$\mathbf{x}_n = \lambda^n \mathbf{e}, \quad (4)$$

where λ and \mathbf{e} are corresponding eigenvalue and eigenvector of \mathbf{M}' . Because \mathbf{M}' is 2×2 and real, the two eigenvalues and eigenvectors come in complex conjugate pairs. Let us write $\lambda = \exp(\alpha + i\mu)$ and $\mathbf{e} = \mathbf{u} + i\mathbf{v}$ with α , μ and \mathbf{u}, \mathbf{v} real. The complete solution can be written as

$$\mathbf{x}_n = e^{n\alpha} \{c_1 (\mathbf{u} \cos n\mu - \mathbf{v} \sin n\mu) + c_2 (\mathbf{u} \sin n\mu + \mathbf{v} \cos n\mu)\}, \quad (5)$$

where c_1 and c_2 are real constants. The oscillation is exponentially damped and has a modified one-turn phase advance μ . The damping coefficient α is given by

$$e^{2\alpha} = 1 - k(\beta\beta_1)^{1/2} \sin \psi_1, \quad (6)$$

where β and β_1 are the beta function at the pick-up and at the kicker respectively, and ψ_1 the relative phase advance between them. μ is given by

$$\cos \mu = \frac{2 \cos \psi - k(\beta\beta_1)^{1/2} \sin \psi_2}{2[1 - k(\beta\beta_1)^{1/2} \sin \psi_1]^{1/2}}, \quad (7)$$

where ψ_2 is the phase advance from the kicker, around the far side of the ring, to the P.U. and ψ is the unperturbed one-turn phase advance without damping.

III. CONSTANT MAGNITUDE KICK

When the magnitude of the kick is the same each time, \mathbf{x}_n is given by a nonlinear recursion. The mapping contains the summation over all previous revolutions of the function $\text{sgn}(x_k)$, and

does not admit an exact solution in closed form. However, we will show that to first order and under a certain phase advance, the damping of the amplitude is linear with turn number and there is no coherent tune shift.

We start with the one-turn map modified by the constant magnitude kick:

$$\mathbf{x}_{n+1} = \mathbf{M}(\mathbf{x}_n + \text{sgn}(x_n)\Delta), \quad (8)$$

where Δ is the equivalent of the kick transformed upstream to the pick-up and \mathbf{M} is the unperturbed one-turn map of the ring. The map of \mathbf{x}_n after n revolutions is thus

$$\mathbf{x}_n = \mathbf{M}^n \mathbf{x}_0 + \sum_{k=0}^{n-1} \text{sgn}(x_k) \mathbf{M}^{n-k} \Delta. \quad (9)$$

The solution \mathbf{x}_n can be written in terms of the eigenvalues and eigenvectors of \mathbf{M} . After some algebra, the complete solution of the displacement can be written

$$\begin{aligned} x_n = & C \cos(n\psi + \phi) \\ & + D \cos(n\psi + \phi) \sum_{m=0}^{n-1} \text{sgn}(x_m) \cos(m\psi + \Delta\phi) \\ & + D \sin(n\psi + \phi) \sum_{m=0}^{n-1} \text{sgn}(x_m) \sin(m\psi + \Delta\phi), \end{aligned} \quad (10)$$

where C , ϕ , are determined by the initial conditions and D , $\Delta\phi$ are determined by the kick strength and ψ_1 .

When the kick is independent of amplitude, one can profitably think of the damping as occurring not by changing the divergence, but by changing the closed orbit (C.O.) each turn to bring it closer to the displaced beam. Given that it is only the C.O. which changes we should expect no tune shift. Hence to first order, we can substitute the unperturbed oscillation $x_m = C \cos(m\psi + \phi)$ in $\text{sgn}(x_m)$ on the right hand side of equation (10). In order to evaluate the sum, we approximate $\text{sgn}[x_m]$ by $\cos(m\psi + \phi)$. After summation, collecting like terms gives four sinusoidal terms of equal phase advance per turn. Hence, to first order there is no coherent tune shift of the damped oscillation and so the trial solution is self-consistent. Neglecting the two sinusoidal terms whose amplitudes are constant and small compared to the initial beam amplitude, the damped oscillation decreases linearly as n . For the special case in which ψ_1 is an odd multiple of $\pi/2$ and the derivative of the beta function at the P.U. is zero, the damped oscillation can be written as

$$x_n \approx (A - n\Delta) \cos(n\psi + \phi), \quad (11)$$

where A is the modified initial amplitude and the linear damping rate

$$\Delta = \sqrt{\beta\beta_1} |\Delta y'|. \quad (12)$$

depends on the constant magnitude kick.

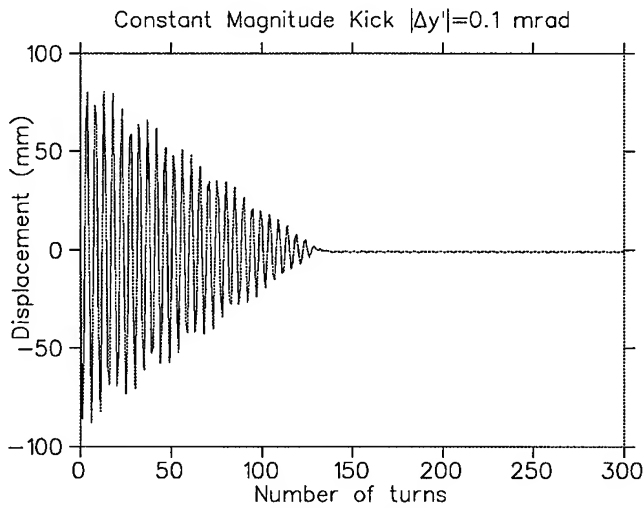


Figure 2. Linear damping by constant magnitude kick.

IV. SIMULATION OF DAMPING

We have computer simulated a damping system with constant magnitude kick to compare the results with the linear damping rate given in equation (12), and also to confirm that there is no coherent tune shift for any phase advance between P.U. and kicker. A damper subroutine was written and incorporated into the multiparticle-tracking injection-simulation code ACCSIM. The optics assumed was that of the KAON Factory Accumulator ring. As a check, the code was used to simulate the case of a proportional kick, where the damping coefficient and tune shift can be compared with exact expressions (6 and 7); and the accuracy was found to be satisfactory.

Figure 2 shows the displacement of the particle as registered by the pick-up as the oscillation is being damped with a constant magnitude kick of $|\Delta y'| = 0.1$ mrad. The large initial displacement was chosen to highlight the linear decay of the amplitude. However, to allow Fourier analysis and extraction of the tune, we have chosen $|\Delta y'| = 0.005$ mrad which damps an amplitude of about 100 mm in a few thousand turns. The results tabulated below are for five different phase advances ψ_1 between the pick-up and the kicker, including the special case of $\pi/2$. All five cases exhibit linear damping and, in all cases, the tune shift is less than 5×10^{-5} , which is the resolution limit of the FFT. This confirms that there is no tune shift.

Table I : Simulations for constant magnitude kick.

$\frac{\psi_1}{2\pi}$	β_1 (m)	$2\pi\Delta\nu$ $\times 10^{-6}$	Damping rate (10^{-3} mm/rev)
0.2347	5.262	-10.0 ± 0.1	-21.93 ± 0.05
0.2500	6.033	0.0 ± 0.10	-23.63 ± 0.05
0.3141	15.891	40.0 ± 0.1	-35.34 ± 0.05
0.4508	9.303	50.0 ± 0.1	-8.81 ± 0.05

For the special case $\psi_1 = \pi/2$, we can compare the actual damping rate to that given by the approximate formula (11). The formula gives a linear decay rate of 37.14×10^{-3} mm/rev and the actual rate (from simulation) is $(23.63 \pm 0.04) \times 10^{-3}$ mm/rev. The discrepancy is large, and is due to the approximation of $\text{sgn}(x_m)$ by $\cos(m\psi + \phi)$ in the derivation. Given that $|\text{sgn}(x_m)| \geq |\cos(m\psi + \phi)|$ and kicks in the simulation are larger than in the approximate summation, it may surprise that

the simulated damping rate is smaller. However, with a constant kick, there will be times when the kick is too large which results in temporary antidamping. However, if the kick is scaled as $\cos(n\psi + \phi)$ the resulting damping is more effective, because there is less over kicking. Hence the formula (12) slightly over estimates the damping rate, but can estimate the kick requirement $\Delta y'$ if used with care.

V. PERFORMANCE CONSIDERATIONS

According to the expression (6) for the exponential damping coefficient, the pick-up and the kicker should be placed as close as possible to where the beta function has its maximum values and the relative phase advance should be ideally an odd multiple of $\pi/2$. This arrangement produces the fastest damping because the displacement of the particle is greatest at the P.U. and this, in turn, leads to large proportional kicks. The same arrangement also works well for the case of damping with constant magnitude kick; because the given kick makes the largest possible change to the closed orbit.

If the amplifier has infinite power resources, then obviously exponential damping is faster than linear damping. In reality, the amplifier will saturate and so for the same peak power linear damping is often faster. For an oscillation amplitude at the peak power limit, and proportional kicking, the number of revolutions n_p required to damp the amplitude to $1/e$ is:

$$n_p = 2/[k\sqrt{\beta\beta_1}]. \quad (13)$$

For the same amplitude and peak power, and constant magnitude kicking,

$$n_c = 1/[k e \sqrt{\beta\beta_1}]. \quad (14)$$

Accordingly, linear damping is $\simeq 2e$ faster than exponential damping for the same peak power. A drawback of linear damping is that it does not damp the amplitude down to zero. To achieve this, some final stage exponential damping is necessary.

VI. CONCLUSION

We have derived the characteristics of damping systems with purely proportional kick and purely constant magnitude kick under certain conditions. We have found that proportional kick produces exponential damping and induces a coherent betatron tune shift; whereas the constant magnitude kick produces linear damping and no coherent tune shift. We have also considered the damping performance of these two types of kick with practical power supply constraints and found that linear damping is faster.

A. Acknowledgment

We thank Fred Jones for promptly writing and installing the damper subroutine in his ACCSIM code and we greatly appreciate his enthusiasm for this work.

A CONCEPT FOR EMITTANCE REDUCTION OF DC RADIOACTIVE HEAVY-ION BEAMS

J. A. Nolen and J. C. Dooling*, Physics Division, Argonne National Laboratory, Argonne, IL 60439

Numerical simulations indicate that it should be possible to use an electron beam to strip 1+ DC radioactive ion beams to 2+ or higher charge states with on the order of 40-80% efficiency. The device, which we call an Electron-Beam Charge-State Amplifier, is similar to an Electron Beam Ion Source, except that it is not pulsed, the beams are continuous. The 2+ beams are obtained in a single pass through a magnetic solenoid while higher charge states may be reached via multiple passes. An unexpected result of the ion optics simulations is that the normalized transverse emittance of the ion beam is reduced in proportion to the charge-state gain. Ion beams with realistic emittances and zero angular momentum relative to the optic axis before entering the solenoid will travel through the solenoid on helical orbits which intercept the axis once per cycle. With an ion beam about 2 mm in diameter and an electron beam about 0.2 mm in diameter, the ion stripping only occurs very near the optic axis, resulting in the emittance reduction.

I. INTRODUCTION

A. Motivation

The creation of accelerated beams of radioactive nuclides far from stability is an area of significant interest in nuclear physics [1,2]. Several laboratories around the world are currently developing methods for the production of high quality radioactive beams based on the extensive experience accumulated in recent years at Isotope Separator On-Line (ISOL) facilities such as ISOLDE [3]. Isotopes of many elements are available with high efficiencies and excellent emittances and energy spreads in 1+ charge states [4,5]. However, the acceleration of radioactive nuclides in the mass 120-240 range with high duty factor and good beam quality from 1+ charge states requires some development, especially at the front end of the post accelerator [6,7,8]. An ionizer capable of efficiently increasing the charge states of very low velocity heavy ions, even if only to 2+, 3+, or 4+, would be of great value in simplifying this process.

B. Background

It has been shown that a 1+ ion beam can be injected into an Electron Beam Ion Source (EBIS), "cooked" to higher charge states, and then extracted [9,10]. This is a batch transfer process with an inherently low duty factor, which is well matched to those nuclides which can be stored in certain ISOL-type ion sources, such as surface ionization sources. Recently, it has been proposed to extend this concept further to increase its efficiency by adding a Penning

trap in which to accumulate, store, and cool radionuclides from an ISOL-source before batch transfer to the EBIS charge-state breeder [11]. This concept has the potential for high efficiency and excellent beam quality, but estimates of the number of ions which can be stored in the Penning trap indicate that it may be limited to low average currents [11].

We have developed a concept for a device called an Electron-Beam Charge-State Amplifier (EBQA), an extension of the EBIS-type charge-state breeder, which has the potential for overall efficiencies of 40-80% and operates in a DC mode [12]. In the present paper we describe the EBQA qualitatively and present some of the results of computer simulations with emphasis on the fact that the EBQA reduces the normalized transverse emittance of the ion beam in proportion to the amount of charge state enhancement.

II. THE ELECTRON BEAM CHARGE-STATE AMPLIFIER CONCEPT

A. Qualitative Description

The concept is to pass a DC beam of low energy heavy ions, ^{132}Sn in the numerical examples below, through a strong magnetic solenoid and to use an EBIS-type electron beam to increase the charge state in a single pass. In the single-pass mode, indicated schematically in Fig. 1, the goal is to increase the charge state from 1+ to 2+. It is also possible to use a multipass mode by recirculating the stripped ions back through the solenoid for further charge-state enhancement. With two recirculating beamlines, for example, charge state increase to 4+ would be possible.

Ions extracted from an ion source at 60-100 keV in 1+ charge state are decelerated to 1 keV for injection into the superconducting solenoid located on a high voltage platform. As shown below the ion beam diameter in the solenoid is about 2 mm. An electron beam of about 5 keV energy and about 0.2 mm in diameter is used to strip a fraction of the ion beam to higher charge states. Using reasonable estimates for the initial ion beam emittance and cross sections for electron stripping it is shown below that as much as 40% of the 1+ beam could be stripped to 2+ in a single pass and over 80% could be stripped to 2+ or higher charge states for recirculation.

For the single-pass mode, as indicated in Fig. 1, the 2+ beam is accelerated from the platform to approximately twice the energy of the original beam. As discussed below, the normalized transverse emittance is reduced by a factor of two, so the overall ion beam brightness is increased by a factor of three (assuming 40% efficiency).

*Present affiliation: Department of Energy, Chicago Operations Office, 9800 S. Cass Ave., Argonne, IL 60439

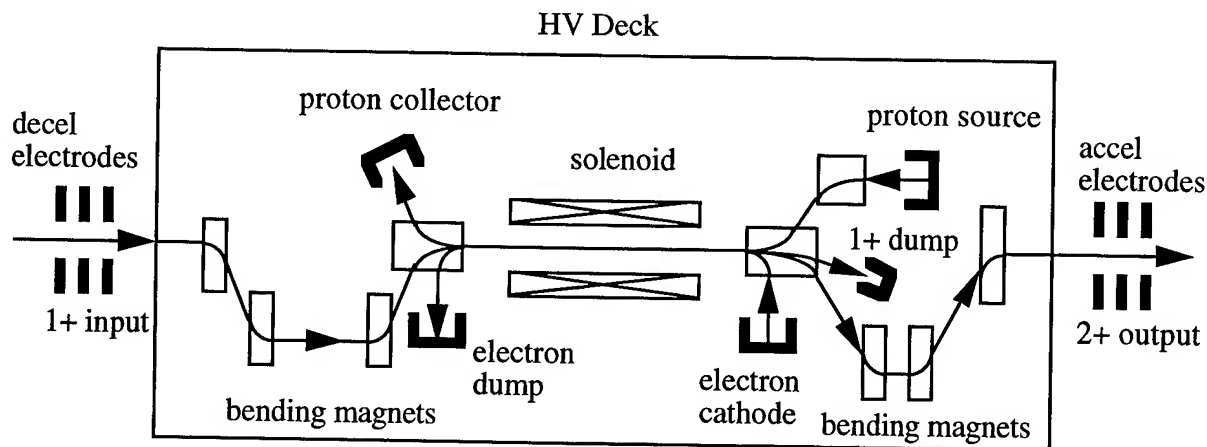


Figure 1: Electron Beam Charge State Amplifier (EBQA) single-pass configuration

The space-charge potential of the small diameter electron beam can be quite high, on the order of 1 kV, so it must be neutralized. It may be possible to use residual gas or a copropagating low energy proton beam for neutralization. The layout in Fig. 1 indicates the possible configuration of a proton beam used for this purpose.

B. Ion Orbit Dynamics

The efficiency of the EBQA for charge stripping depends critically on properly matching the ion beam into the solenoid. A simple derivation, confirmed by the simulations shown below, gives a relationship for the properly matched ion beam radius (r_0) in the solenoid in terms of the ion charge (qe), mass (m_0), ion source normalized emittance (ϵ_n), and solenoid strength (B):

$$r_0 = \left[\frac{2\epsilon_n m_0 c}{B qe} \right]^{1/2},$$

where c is the speed of light.

Several types of ISOL 1+ ion sources have emittances (unnormalized) in the 2-10 π mm-mr range at 30 keV beam energy [5]. In the numerical simulations below we have used 5 π mm-mr at 60 keV for the Sn beam from the ion source. From the equation above, the ion beam orbit in the solenoid scales as the square root of the ion source emittance.

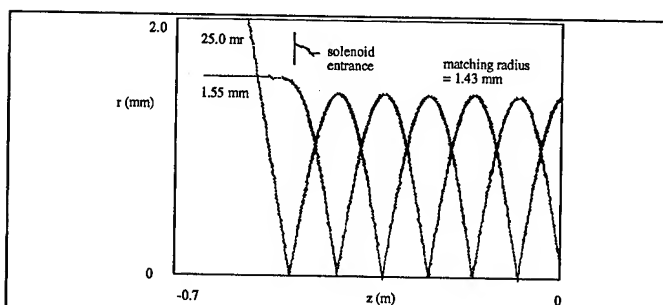


Figure 2. The orbits of ions with maximum x displacement and maximum x' divergence matched into a 2 T solenoid for a $^{132}\text{Sn}^{1+}$ beam with 38.7 π mm-mr emittance at 1 keV.

Based on conservation of generalized angular momentum, any ion which has zero angular momentum relative to the beam axis before entering the solenoid will spiral through the magnetic field on helical orbits which pass through the solenoid axis once per cycle. Numerical (ray tracing) simulations show that it is possible to match the emittance ellipse of the ion beam into the solenoid so that all ions at the perimeter of the ellipse have the same diameter helices while in the magnet, and the radius of the resulting envelope of the ion beam is given by the equation above. Results of these simulations for the ions with maximum x-value and maximum x'-value at injection are shown in Fig. 2.

C. Emittance Reduction

Figure 3 shows a calculation for the same beam as Fig. 2, but with twice the charge and half the emittance. Note that the vertical scale in Fig. 3 is one half that of Fig. 2, i.e. the projected orbit diameters are a factor of two smaller due to the higher charge state. If the charge of an ion from Fig. 2 is changed due to stripping by an electron near the solenoid axis, then its orbit changes discontinuously to one with half the projected radius, as in Fig. 3. Ions which enter the solenoid with emittance and orbits as in Fig. 2 will leave with the emittance as shown in Fig. 3, as long as the stripping occurs at radii small compared to the overall ion beam radius.

Figure 4 is an end view of the ion and electron orbits in the solenoid. The projected orbits of $q=1$ ions are circles

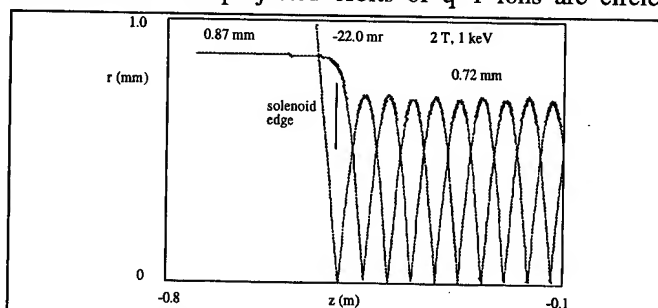


Figure 3. The orbits of ions with maximum x displacement and maximum x' divergence matched into a 2 T solenoid for a $^{132}\text{Sn}^{2+}$ beam with 19.1 π mm-mr emittance at 1 keV.

with diameters determined by the normalized emittance of the initial ion beam (the largest circle in this diagram). All orbits pass through the axis of the solenoid due to the conservation of angular momentum. The electron beam is contained within the smallest circle in this diagram. Charge state changing occurs within the small circle. Hence, ion orbit diameters decrease in proportion to the charge state increase, and orbits continue to pass through the axis of the solenoid in the approximation that the electron beam is contained within a circle which is small relative to the ion helical orbits. It is the selective stripping of ions only very near the axis which leads to the emittance reduction effect.

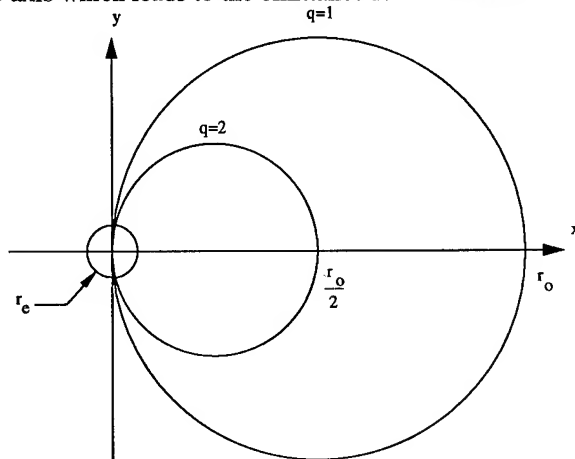


Figure 4. End view of ion and electron orbits in the solenoid.

D. Stripping Probabilities

The EBQA is potentially useful only if a significant fraction of the 1+ ions are stripped at least once in a single pass through the solenoid. With parameters given above the ions spend on the order of 30 μ sec in the solenoid, so with the relative orbit diameters also given above, cross sections estimated from the Lotz formulation [13], an 8 T, 1 meter long solenoid, and an assumed 1 ampere electron beam the calculated stripping of the 1+ beam is over 50% in a single pass. For single-pass operation the peak in the 2+ yield is predicted to be about 40% as the distribution evolves from 1+ to 2+ and then to 3+ and above. For multiple-pass operation the theoretical yield into the 4+ charge state is as high as 80%.

III. SUMMARY AND DISCUSSION

The EBQA concept is potentially very useful for an advanced, high intensity accelerated radioactive beam facility such as the one under study at Argonne [14]. It would reduce the electric fields required at the front end of the post accelerator by a factor of 2-4 for single-pass or multiple-pass configurations, respectively. It also relaxes the design specifications of this section of the post accelerator due to the increased beam brightness (reduced transverse emittance) and the higher ion velocity at the accelerator entrance.

Further simulations of the intense electron beam required for the EBQA must be carried out to determine its ultimate limitations. Trade-offs between solenoid strength and length and electron beam energy and intensity will have to be studied. The stripping cross sections are higher for low energy electron beams, but injection dynamics issues are more difficult at these low energies. Since conventional EBIS devices are dedicated to the achievement of very high, nearly fully stripped ions, most experience has been accumulated for the higher energy beams required by such applications.

Detailed neutralization of the intense electron beam is required especially to avoid energy spread in the stripped ion beam due to variation in the potential across a partially neutralized e-beam.

Informative discussions with Dr. P. van Duppen on the recent developments related to EBIS charge-state breeders are gratefully acknowledged.

This work is supported by the U.S. Department of Energy Nuclear Physics Division.

IV. REFERENCES

- [1] The IsoSpin Laboratory, Research Opportunities with Radioactive Beams, LALP report 91-51 and references therein.
- [2] European Radioactive Beam Facilities Report of NuPECC Study Group 1993.
- [3] H. L. Ravn and B. W. Allardyce, in *Treatise on Heavy Ion Science*, ed. by D. A. Bromley, Plenum, New York, 1989, Vol. 8, p 363 and H. L. Ravn, paper MPE2 at this conference.
- [4] H. L. Ravn et al., *Nucl. Instr. and Meth.* **B88**, 441 (1994).
- [5] R. Kirchner "Ion Sources for Radioactive Beams" *Proceedings of the Workshop on Post-Accelerator Issues at the IsoSpin Laboratory, Berkeley, CA, LBL-35533* (1994).
- [6] S. Arai, et al., paper RPG13 at this conference.
- [7] P.G. Bricault, et al., RPR2 at this conference.
- [8] K.W. Shepard and J.-W. Kim, paper RPR5 at this conference.
- [9] J. Faure, B. Feinberg, A. Courtois, and R. Gobin, *Nucl. Instr. Meth.*, 219, 449 (1984).
- [10] E. Beebe et al., *Nucl. Instr. and Meth.* **B93**, 378 (1994).
- [11] The REX-ISOLDE Proposal, CERN/ISC94-24 (1994).
- [12] J.A. Nolen and J.C. Dooling, to be published.
- [13] W. Lotz, *Z. Phys.*, 216, 341(1968), and *Z. Phys.*, 220, 466(1969).
- [14] J.A. Nolen, paper RPG14 at this conference.

MEASUREMENTS OF THE OCTUPOLE-INDUCED AMPLITUDE-DEPENDENT FREQUENCY SHIFT IN SPEAR*

P. Tran, C. Pellegrini, Department of Physics, UCLA, Los Angeles, CA 90024, USA
J. Yang, M. Cornacchia, and J. Corbett, SLAC, Stanford University, Stanford, CA 94309, USA

Abstract

Four octupoles are used in SPEAR to provide the frequency spread for Landau damping of coupled-bunch motions at high current. With the planned implementation of a new low-emittance lattice, the effectiveness of the octupoles needs to be quantified. The recent development of a multi-dimensional turn-by-turn phase-space monitor and the availability of an accurate frequency analysis technique have made measurement of the octupole-induced amplitude-dependent frequency shift in the new SPEAR lattice possible. This paper presents the data collection and analysis procedures, and compares experimental results to model-based simulations.

I. INTRODUCTION

The SPEAR Synchrotron Light Source has four octupoles which were designed and used for the high-energy physics collider configuration. These magnets have been reactivated recently to provide an amplitude-dependent frequency shift for the Landau damping of coupled-bunch motion in SPEAR. The result has been a dramatic improvement in transverse beam stability at high current, and raises the possibility of a 20-percent increase in useful delivered current.

The success of the octupoles in stabilizing coupled-bunch motions has prompted interest in determining their effectiveness in a new NOQ3 lattice [1] that is planned for future operations. The NOQ3 lattice has the defocusing quadrupole family removed from the insertion doublet, reducing that region from a D/2-O-F-O-D-O structure to D/2-O-F-O. Although the optical functions in the arcs stay fixed, the tunes and the IR optics will differ significantly. We wish to measure the octupole-induced amplitude-dependent frequency shift of this new lattice.

Using a synchro-betatron phase-space monitor [2], the transverse dynamics of an excited electron bunch was tracked turn-by-turn. The data were stored and post-processed using a technique called numerical analysis of fundamental frequency (NAFF) [3] to extract characteristic oscillation frequencies. Relating these frequencies to the average oscillation amplitudes and octupole strength gave a representation of the amplitude-dependent frequency shift in the NOQ3 lattice. The analysis of these measurements and model-based simulations are presented herein.

II. MEASUREMENT HARDWARE

The 6-D phase-space monitor in SPEAR is capable of recording turn-by-turn amplitude of the synchrotron and betatron oscillations of an excited electron bunch for up to 15000 turns. At present, only the transverse unit of the monitor is used.

Four 8-bit, 2-channel LeCroy 6840 waveform digitizers acquire the data. Each channel has a bandwidth of 100 MHz, a maximum sample clock rate of 40 Megasamples/second, a memory of 128 Kilosamples, and an effective resolution of ± 0.125 mm. The layout allows the digitizers to be triggered serially by a VAX software command. In turn, one of the digitizers signals to gate through one pulse of the 1.28-MHz SPEAR revolution clock to trigger a horizontal kicker. The kicker has a pulse width of approximately 2 μ s FWHM, and will excite a single-bunch twice on consecutive turns.

The transverse BPM signals at two different locations are stretched by passive filters, and processed by RF hybrid junctions to produce two sets of signals: The horizontal difference (Δx), the vertical difference (Δy), the SUM (proportional to the stored beam current), and the TRIGGER. The latter is used to clock the LeCroy 6840 waveform digitizers which sample the other three. For each of the two BPMs, the ratios (Δx /SUM) and (Δy /SUM) give the single-turn, current-independent horizontal and vertical displacements. Figure 1 shows a typical transverse tracking result for a single-bunch at one BPM.

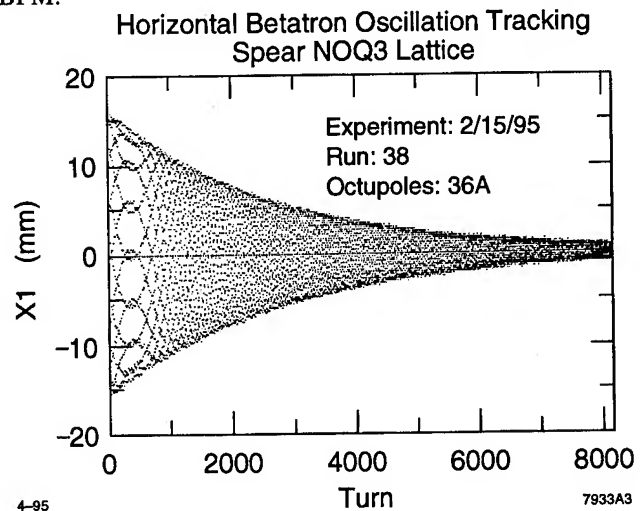


FIGURE 1. Turn-by-turn tracking of an excited single-bunch beam.

*work supported in part by US DOE grant DE-FG03-92ER40493 and contract DE-AC03-76SF00515.

III. ANALYSIS

Given a set of tracking data as shown in Fig. 1, one may perform an FFT to determine the oscillating frequency of the bunch centroid. This method of frequency analysis has an accuracy of $2\pi/n$ where n is the number of data points used in the procedure. To resolve frequencies to an accuracy of 1×10^{-3} , which is marginal for analysis of the amplitude-dependent frequency shift in SPEAR, requires more than 6200 turns. However, the typical bunch-centroid damping time in SPEAR is relatively short, approximately 2500 turns for the data set shown in Fig. 1. In this case, the FFT method of frequency analysis is not adequate. We therefore employ the more accurate NAFF technique for the purpose of frequency extraction (see section IIIB below).

A. Data Preparation

The action-angle variables (J, Φ) were used as the basis for data analysis. We first transformed the horizontal beam position data from a pair of BPMs into the Courant-Snyder normalized coordinates (x, p_x) . From there, a second coordinate transformation takes the data into the $J-\Phi$ space. These transformations are relatively straight forward. Given the horizontal displacements x_1 and x_2 at BPM_1 and BPM_2 and assuming that there are only dipoles and quadrupoles between the BPMs, x_1 and x_2 are related by [4]

$$x_2 = \sqrt{\frac{\beta_{x2}}{\beta_{x1}}} (\cos \mu_{12} + \alpha_{x1} \sin \mu_{12}) x_1 + \sqrt{\beta_{x1} \beta_{x2}} (\sin \mu_{12}) x'_1 \quad (1)$$

where x'_1 is the angle the beam made with respect to the design orbit at BPM_1 , β_{xi} is the value of the horizontal betatron amplitude function at the i^{th} BPM, $\alpha_{x1} = -\beta'_{x1}/2$, and μ_{12} is the betatron phase-advance. Equation (1) can be solved for x'_1 ,

$$x'_1 = \left(\frac{1}{\beta_{x1}} \right) \left[\left(\frac{\sqrt{\beta_{x1} / \beta_{x2}}}{\sin \mu_{12}} \right) x_2 - (\cot \mu_{12} + \alpha_{x1}) x_1 \right]. \quad (2)$$

The normalized momentum p_x is defined as: $p_x \equiv \alpha_x x + \beta_x x'$. Substituting Eq. (2) for x'_1 , we find

$$p_{x1} = \left(\frac{\sqrt{\beta_{x1} / \beta_{x2}}}{\sin \mu_{12}} \right) x_2 - (\cot \mu_{12}) x_1. \quad (3)$$

Figure 2 displays the result of transforming the data from Fig. 1 and a companion set measured simultaneously at a second BPM into the normalized phase-space coordinates (x, p_x) . The values for β_{xi} , α_{x1} , and μ_{12} were taken from a model-based simulation. Notice a gradual reversal of the spiraling direction, which is a manifestation of the amplitude-dependent frequency shift.

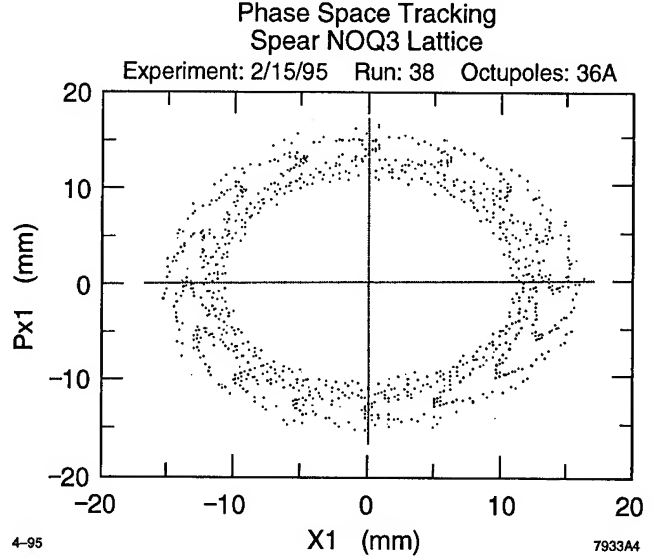


FIGURE 2. Phase-space tracking of a single electron bunch in SPEAR.

The coordinate transformation to (J, Φ) follows from the Courant-Snyder invariant,

$$J = \frac{1}{2} \left(\frac{(\alpha_x + 1)}{\beta_x} x^2 + 2\alpha_x x x' + \beta_x x'^2 \right), \quad (4)$$

which reduces to

$$J = \frac{1}{2\beta_x} (x^2 + p_x^2). \quad (5)$$

The corresponding angle Φ is

$$\Phi = \tan^{-1} \left(\frac{p_x}{x} \right). \quad (6)$$

B. NAFF Method

The Fourier series expansion of a function $f(t)$ that is piecewise regular over an interval of $[-T, T]$ is

$$\tilde{f} = \sum_{n=-\infty}^{\infty} c_n e^{in\left(\frac{\pi}{T}\right)t}, \quad n \in \{\dots, -1, 0, 1, \dots\} \quad (7)$$

where

$$c_n = \frac{1}{2T} \int_{-T}^T f(t) e^{-in\left(\frac{\pi}{T}\right)t} dt. \quad (8)$$

This expansion projects $f(t)$ onto the orthogonal basis-vectors $\{\exp(in\pi t / T)\}$. If the function $f(t)$ is periodic, say

$$f(t) = a e^{i\nu t} \quad (9)$$

where a is a complex amplitude, the projection gives

$$c_n = a \frac{\sin[(v - n\pi/T)T]}{(v - n\pi/T)T}. \quad (10)$$

We approximate the fundamental frequency of $f(t)$ by an $n\pi/T$ that corresponds to the maximum value of c_n . If v is not an integer multiple of π/T , this approximation is only accurate to π/T .

We can find v much more precisely by solving for an ω that maximizes the projection integral

$$I = \frac{1}{2} \int_{-T}^T f(t) e^{-i\omega t} dt. \quad (11)$$

For the above example, this integral is simply

$$I = a \frac{\sin[(v - \omega)T]}{(v - \omega)T}, \quad (12)$$

which has a maximum value at $\omega = v$. For cases where $f(t)$ may have more than one frequency component, the projection method still works; however, the precision depends on the separation of the frequency components since the continuum of vectors $\{\exp(i\omega t/T), \omega \in \mathbb{R}\}$ is not an orthogonal set and leakage may occur between the frequency components. As long as the separation between any two frequency components of $f(t)$ is larger than a few π/T , the distortion between the frequencies will be minimal and the NAFF method is more accurate than an FFT.

Usually the function $f(t)$ is not known a priori; only its sampled values over the interval $[-T, T]$ are available. In this case, assuming that there is no aliasing and the sampling time is small so that one can compute integrals involving $f(t)$ from the data, the projection integral in Eq. (11) can be evaluated numerically using for example an elementary algorithm of n th stage, extended trapezoidal rule.

C. Analysis of Amplitude-Dependent Frequency Shift

For this experiment, SPEAR was operated at 2.3 GeV in the NOQ3 configuration. A single-bunch 3.44-mA beam was excited by a kicker powered to 4.0 KV. The octupole currents were 36 Amps during the measurement designated as RUN 59, and 33 Amps during the measurement designated as RUN 60. The data were transformed into $x-p_x$ and then $J-\Phi$ before being subdivided into bins of 512 consecutive points for frequency analysis. We analyzed each bin using the NAFF algorithm and correlated the resulting frequencies to the average amplitude.

Figure 3 summarizes the results of the NAFF analysis. Model simulations using TRACY [5] are shown as solid lines. The top curve corresponds to a simulated octupole current of 70.4 Amps, and the bottom, 58.5 Amps.

Assuming discrepancies come entirely from horizontal beta-beating in SPEAR, the analysis suggests an average beating of 36-percent at the octupole sites.

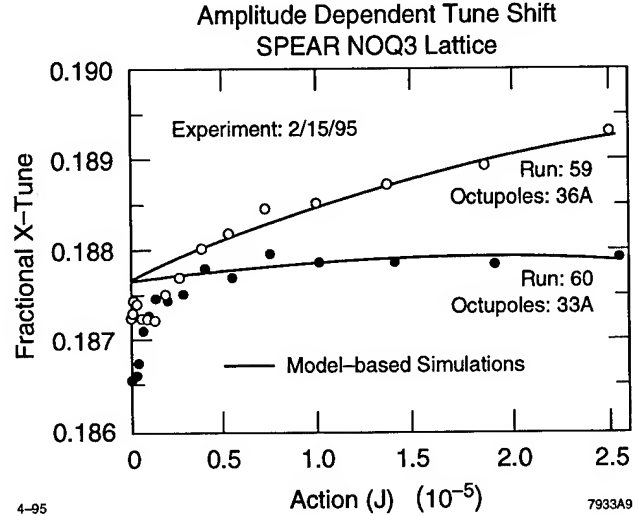


FIGURE 3. A comparison of the measured and simulated octupole-induced amplitude-dependent frequency shift in the SPEAR NOQ3 lattice.

IV. CONCLUSION

The recent development of a turn-by-turn phase-space monitor in SPEAR and implementation of the NAFF algorithm has made measurement of the octupole-induced amplitude-dependent frequency shift in the new SPEAR NOQ3 lattice possible. Discrepancies between the measured and simulated results show a possible beta beating of as much as 36 percent.

V. ACKNOWLEDGMENTS

The authors acknowledge Martin Lee for his support and valuable inputs. We would like to thank the SPEAR operators for their technical assistance in carrying out this experiment.

VI. REFERENCES

- [1] H.-D. Nuhn, "An Optimized Low Emittance Lattice for SPEAR," SLAC-PUB-6457, June, 1994.
- [2] P. Tran, C. Pellegrini, M. Cornacchia, M.J. Lee, and W.J. Corbett, "Nonlinear Beam Dynamics Experimental Program at SPEAR," SLAC-PUB-95-6720, Feb., 1995.
- [3] J. Laskar, et. al., Physica D **56**, 253 (1993).
- [4] E.D. Courant and H.S., Snyder, Ann. Phys. **3**, 1 (1958).
- [5] TRACY lattice codes written by J. Bengtsson, E. Forest, and H. Nishimura, LBL.

RADIATION DAMPING IN FOCUSING-DOMINATED SYSTEMS *

Zhirong Huang, Pisin Chen and Ronald D. Ruth

Stanford Linear Accelerator Center, Stanford University, Stanford, CA 94309 USA

Abstract

A quasi-classical method is developed to calculate the radiation damping of a relativistic particle in a straight, continuous focusing system. In one limiting case where the pitch angle of the particle θ_p is much larger than the radiation opening angle $1/\gamma$, the radiation power spectrum is similar to synchrotron radiation and the relative damping rate of the transverse action is proportional to the relative energy loss rate. In the other limiting case where $\theta_p \ll 1/\gamma$, the radiation is dipole in nature and the relative damping rate of the transverse action is energy-independent and is much faster than the relative energy rate. Quantum excitation to the transverse action is absent in this focusing channel. These results can be extended to bent systems provided that the focusing field dominates over the bending field.

I. INTRODUCTION

Radiation reaction including damping and quantum excitation has been studied extensively in synchrotrons and storage rings [1]. Recently, we demonstrated [2] that in a straight, continuous focusing channel, the radiation reaction is essentially different from that in a bending magnet. A fully quantum mechanical approach was used to investigate in detail the radiation reaction in the case $\gamma\theta_p \ll 1$ where the radiation is formed over many oscillation wavelengths. We have shown that the transverse action damps exponentially with an energy-independent damping rate, and that no quantum excitation is induced. As $\gamma\theta_p$ becomes much larger than one, the radiation is formed in a small portion of one wavelength, which can be nearly replaced by a segment of a circle. Therefore, both the radiation spectrum and the radiation damping will be similar to that from a sequence of bending magnets. In this paper, to illustrate the smooth transition between these two limiting cases, we develop a quasi-classical method to evaluate the radiation damping rate for any $\gamma\theta_p$ and obtain the expected results in both small and large $\gamma\theta_p$ limits. Then we extend these findings to focusing-dominated bent systems and consider the possibility of beam cooling based on the damping effect.

II. RADIATION

Let us consider a planar focusing system that provides a continuous parabolic potential $Kx^2/2$, where K is the focusing strength. A charged particle with energy $E = \gamma mc^2$ ($\gamma \gg 1$) oscillates in the transverse x direction while moving freely in the longitudinal z direction with a constant longitudinal momentum p_z in the absence of radiation. Define the pitch angle of the particle $\theta_p = p_{x,max}/p_z$ ($p_{x,max}$ being the maximum transverse momentum) and assume that θ_p is always much less than one. The motion of the particle can be decomposed into two

parts: a free longitudinal motion and a transverse harmonic oscillation; i.e., we have $E \simeq E_z + E_x$ with $E_z = \sqrt{m^2c^4 + p_z^2c^2}$ and $E_x = p_x^2c^2/2E_z + Kx^2/2$.

A quantum mechanical theory of radiation and radiation reaction for such a system was given in Ref. [2]. We only need to know that $E_x = (n + 1/2)\hbar\omega_z$, where $n = 0, 1, 2, \dots$ is the transverse quantum number and $\omega_z = \sqrt{Kc^2/E_z}$ is the transverse oscillation frequency. For sufficiently large quantum number n , the transverse motion is classical and the radiation can be described by classical electrodynamics provided that the typical photon energy emitted is much smaller than the energy of the particle. Thus the energy radiated per unit solid angle per unit frequency is given by [3]

$$\frac{d^2E}{d\Omega d\omega} = \frac{e^2\omega^2}{4\pi^2c} \left| \int_{-\infty}^{\infty} \vec{n} \times (\vec{n} \times \vec{\beta}) e^{i\omega(t' - \vec{n} \cdot \vec{r}/c)} dt' \right|^2, \quad (1)$$

where \vec{n} is the unit vector from the source to the observation point, $\vec{\beta}c$ and \vec{r} are the velocity and position of the particle at the retarded time t' .

We can express Eq. (1) in the form of a double integral with respect to t_1 and t_2 :

$$\frac{d^2E}{d\Omega d\omega} = \frac{e^2\omega^2}{4\pi^2c} \int_{-\infty}^{\infty} dt_1 \int_{-\infty}^{\infty} dt_2 (\vec{\beta}_1 \cdot \vec{\beta}_2 - 1) e^{i(\Phi_1 - \Phi_2)}, \quad (2)$$

where we have introduced the notation $\vec{\beta}_{1,2} = \vec{\beta}(t_{1,2})$, $\vec{r}_{1,2} = \vec{r}(t_{1,2})$ and $\Phi_{1,2} = \omega(t_{1,2} - \vec{n} \cdot \vec{r}_{1,2}/c)$. Going over to the new variables of integration t and τ via the transformation $t_1 = t - \tau/\omega_z$ and $t_2 = t + \tau/\omega_z$, and treating the integrand in the integral with respect to t as the angular spectral distribution of the radiated power at time t , we have

$$\frac{d^3E}{dt d\Omega d\omega} = \frac{e^2\omega^2}{2\omega_z\pi^2c} \int_{-\infty}^{\infty} d\tau (\vec{\beta}_1 \cdot \vec{\beta}_2 - 1) e^{i(\Phi_1 - \Phi_2)}. \quad (3)$$

The averaged radiated power is obtained by integrating over $d\Omega d\omega$ and then averaging over one oscillation period (indicated by $\langle \rangle$). In the system we consider here, it can be shown that [4]

$$\left\langle \frac{dE}{dt} \right\rangle = \frac{2ie^2}{\pi c} \omega_z^2 \gamma^2 \int_0^\infty \xi d\xi \int_{-\infty}^{\infty} \frac{d\tau}{\tau} g(\tau, \xi) e^{-if(\tau, \xi)}, \quad (4)$$

$$f(\tau, \xi) = 2\xi\tau[1 + \gamma^2\theta_p^2(1 - \sin^2\tau/\tau^2)/2],$$

$$g(\tau, \xi) = J_0(u) + \gamma^2\theta_p^2 \sin^2\tau [J_0(u) - iJ_1(u)],$$

$$u = \gamma^2\theta_p^2\xi(\sin^2\tau/\tau - \sin 2\tau/2), \quad \xi = \omega/2\gamma^2\omega_z,$$

and $J_\nu(u)$ is the Bessel function of order ν ($\nu = 0, 1, 2, \dots$).

Equation (4) is completely general for any $\gamma\theta_p$. The contour of integration with respect to τ must be displaced below the real axis around $\tau = 0$ to guarantee the vanishing radiation when the field is switched off [4]. The range of τ that gives a significant contribution to the integral can be defined as the

*Work supported by Department of Energy DE-AC03-76SF00515

ratio of the radiation formation length l_r to the oscillation wavelength $\lambda_z = 2\pi\sqrt{E_z/K} = 2\pi c/\omega_z$ [5]. Since l_r is of the order $\langle\rho\rangle/\gamma$ [1], where $\langle\rho\rangle$ is the averaged radius of curvature and can be approximated as $\langle\rho\rangle \sim E/(KA) \sim \lambda_z^2/A \sim \lambda_z/\theta_p$, the ratio l_r/λ_z is inversely proportional to $\gamma\theta_p$. We consider two opposite limits $\gamma\theta_p \gg 1$ and $\gamma\theta_p \ll 1$ where Eq. (4) can be greatly simplified.

In the case $\gamma\theta_p \gg 1$ or $l_r \ll \lambda_z$, using the integral representations of the Bessel functions and the method of stationary phase around $\tau = 0$, we obtain the asymptotic expression of Eq. (4) [5]

$$\left\langle \frac{dE}{dt} \right\rangle = \frac{4e^2\gamma^2\omega_z^2}{\sqrt{3}\pi c} \int_{-\pi}^{\pi} \frac{d\psi}{2\pi} \int_0^{\infty} \xi d\xi \int_{\chi}^{\infty} K_{5/3}(y) dy, \quad (5)$$

where $\chi = 4\sqrt{2}\xi/[3\gamma\theta_p(1 - \sin\psi)^{1/2}]$ and $K_{5/3}(y)$ is the modified Bessel function of order 5/3. This expression is very similar to the frequency spectrum of synchrotron radiation [3], with χ here playing the role of ω/ω_c . Thus the equivalent critical frequency is $\omega_c \sim \gamma^3\theta_p\omega_z$, or the equivalent rotational frequency is $\omega_0 \sim c/\langle\rho\rangle \sim \theta_p\omega_z$.

In the case $\gamma\theta_p \ll 1$ or $l_r \gg \lambda_z$, expanding the integrand in Eq. (4) to leading order in $\gamma\theta_p$ and applying contour integration in the complex τ plane, we get [5]

$$\left\langle \frac{dE}{dt} \right\rangle = \frac{e^2\gamma^4\theta_p^2\omega_z^2}{c} \int_0^{\infty} d\xi \xi [1 + 2\xi(\xi - 1)]\Theta(1 - \xi), \quad (6)$$

where $\Theta(1 - \xi)$ is the Heaviside step function. Since $\xi = \omega/2\gamma^2\omega_z$, we conclude that the radiation frequency distribution has a sharp cutoff at $\omega_d = 2\gamma^2\omega_z$, which is the characteristic of dipole radiation.

In both cases, we can carry out the integrals in Eq. (5) and (6) and find the averaged radiation power $\langle dE/dt \rangle = e^2\gamma^4\theta_p^2\omega_z^2/3c$. By using relations $\theta_p^2 \simeq 2E_x/E \simeq 2n\hbar\omega_z/E$ and $\omega_z^2 \simeq Kc^2/E$, we see that the rate of energy loss agrees with that in Ref. [2].

III. RADIATION DAMPING

The differential radiation power spectrum (i.e., Eq. (3)) can be used to define the differential number rate of photon emissions as follows: Let $R(\omega, \Omega)$ be the number of photons emitted per unit time with energies between $\hbar\omega$ and $\hbar(\omega + d\omega)$ in the directions between Ω and $\Omega + d\Omega$, i.e.,

$$R(\omega, \Omega) = \frac{1}{\hbar\omega} \frac{d^3E}{dt d\Omega d\omega}, \quad (7)$$

then the average rate of change of any physical quantity, say F , is given by

$$\left\langle \frac{dF}{dt} \right\rangle = \int_0^{2\pi/\omega_z} \frac{\omega_z dt}{2\pi} \int d\Omega |\Delta F(\omega, \Omega)| R(\omega, \Omega), \quad (8)$$

where $\Delta F(\omega, \Omega)$ is the change of F after a photon with energy $\hbar\omega$ is emitted in the direction Ω . For example, the rate of energy loss $\langle dE/dt \rangle$ is obtained by replacing ΔF with $\Delta E = \hbar\omega$ and is given in the previous section.

The transverse action J_x is defined through the relation $J_x = E_x/\omega_z = (n + 1/2)\hbar \simeq n\hbar$. For small change of J_x after a photon emission, we have $\Delta J_x \simeq \Delta E_x/\omega_z - \Delta\omega_z E_x/\omega_z^2$.

The energy and the longitudinal momentum conservation require $\Delta E_x \simeq \hbar\omega(1 - \beta \cos\theta)[2]$, where θ is the angle between the photon direction and the longitudinal direction. Writing $\Delta\omega_z \simeq -\hbar\omega\omega_z/2E \simeq -\hbar\omega\omega_z\theta_p^2/4E_x$, we get

$$\Delta J_x \simeq \hbar\omega(1 - \beta \cos\theta + \theta_p^2/4)/\omega_z, \quad (9)$$

which is always positive definite. Thus the transverse action always decreases after a photon emission process and the quantum excitation is absent in such a system. This result was obtained for the transverse quantum number n based on the same kinematic argument in Ref. [2].

The damping rate of transverse action $\langle dJ_x/dt \rangle$ is obtainable by replacing ΔF in Eq. (8) with ΔJ_x in Eq. (9). With the expansion $1 - \beta \cos\theta = 1/(2\gamma^2) + \theta^2/2$, $\langle dJ_x/dt \rangle$ can be written as $\langle dJ_{x1}/dt \rangle + \langle dJ_{x2}/dt \rangle$, where

$$\begin{aligned} \left\langle \frac{dJ_{x1}}{dt} \right\rangle &= \frac{1}{\omega_z} \left(\frac{1}{2\gamma^2} + \frac{\theta_p^2}{4} \right) \left\langle \frac{dE}{dt} \right\rangle, \\ \left\langle \frac{dJ_{x2}}{dt} \right\rangle &= \int_0^{2\pi/\omega_z} \frac{\omega_z dt}{2\pi} \int d\Omega \frac{1}{\omega_z} \frac{\theta^2}{2} \frac{d^3E}{dt d\Omega d\omega}. \end{aligned} \quad (10)$$

The first of the above equations is simply proportional to the rate of energy loss found in the previous section. The second one involves a more complicated angular integral. Together they account for the radiation damping for any $\gamma\theta_p$.

In the case $\gamma\theta_p \gg 1$, Eq. (10) can be simplified as [5]

$$\begin{aligned} \left\langle \frac{dJ_{x1}}{dt} \right\rangle &= \frac{1}{\omega_z} \frac{\theta_p^2}{4} \left\langle \frac{dE}{dt} \right\rangle, \\ \left\langle \frac{dJ_{x2}}{dt} \right\rangle &= \frac{ie^2}{2\pi c} \omega_z \gamma^2 \theta_p^2 \int_0^{\infty} \xi d\xi \int_{-\infty}^{\infty} \frac{d\tau}{\tau} h(\tau, \xi) e^{-if(\tau, \xi)}; \\ h(\tau, \xi) &= J_0(u) + iJ_1(u) + \gamma^2 \theta_p^2 \sin^2\tau \left[\frac{J_0(u)}{2} + \frac{J_2(u)}{2} \right]. \end{aligned} \quad (11)$$

All quantities used above are defined in Eq. (4). Similar to the calculation of the averaged radiation power, we can show [5] $\langle dJ_{x1}/dt \rangle = 2\langle dJ_{x2}/dt \rangle = e^2\gamma^4\theta_p^4\omega_z/12c$. By using the relation $J_x/E \simeq \theta_p^2/(2\omega_z)$, it is straightforward to obtain

$$\frac{1}{J_x} \left\langle \frac{dJ_x}{dt} \right\rangle = \frac{3}{4} \frac{1}{E} \left\langle \frac{dE}{dt} \right\rangle. \quad (12)$$

Thus, the relative damping rate of the transverse action is proportional to the relative energy loss rate, which depends on both energy and the transverse action. This result resembles the radiation damping in a bending magnet [1], with the numerical difference due to the chromatic effect and the sinusoidal variation of the focusing field [5].

In the case $\gamma\theta_p \ll 1$, Eq. (10) becomes [5]

$$\begin{aligned} \left\langle \frac{dJ_{x1}}{dt} \right\rangle &= \frac{1}{\omega_z} \frac{1}{2\gamma^2} \left\langle \frac{dE}{dt} \right\rangle, \\ \left\langle \frac{dJ_{x2}}{dt} \right\rangle &= \frac{e^2\omega_z}{\pi c} \int_0^{\infty} d\xi \int_{-\infty}^{\infty} \frac{d\tau}{\tau^2} g(\tau, \xi) e^{-if(\tau, \xi)}. \end{aligned} \quad (13)$$

Applying contour integration again, we can show [5] $\langle dJ_{x1}/dt \rangle = \langle dJ_{x2}/dt \rangle = e^2\gamma^2\theta_p^2\omega_z/6c$. Therefore,

$$\left\langle \frac{dJ_x}{dt} \right\rangle = \frac{1}{3} \frac{e^2\gamma^2\theta_p^2\omega_z}{c} = \frac{2}{3} \frac{r_e K}{mc} J_x, \quad (14)$$

where $r_e = e^2/mc^2$ is the classical electron radius. We see that the transverse action damps exponentially with an energy-independent damping constant $\Gamma_c = 2r_e K/3mc$. An identical result for the transverse quantum number n was obtained in Ref. [2] for the "undulator regime" where $\gamma\theta_p \ll 1$. We also notice that the relative damping rate of the transverse action is much faster than the relative energy loss rate in this regime since

$$\Gamma_c = \frac{1}{J_x} \left\langle \frac{dJ_x}{dt} \right\rangle \gg \frac{1}{E} \left\langle \frac{dE}{dt} \right\rangle = \frac{\Gamma_c}{2} \gamma^2 \theta_p^2. \quad (15)$$

We have shown that the radiation damping in a straight, continuous focusing channel is fundamentally different from that in a bending magnet. In the longitudinal direction the particle recoils against the emitted photon to conserve the longitudinal momentum between the two particles. However, in the transverse direction, the existence of the focusing force destroys the momentum balance and suppresses the direct recoil effect. As a result, the radiation reaction is not opposite to the photon emission direction, but always has a component pointing towards the focusing axis.

IV. FOCUSING-DOMINATED SYSTEMS

So far we have assumed that the focusing system is straight. In fact, the above discussion can be extended to bent systems under certain conditions. Consider a bent system with a constant radius ρ . A highly relativistic particle of energy E being bent by a uniform magnetic field, $B = E/ec\rho$, radiates at the rate $\langle dE/dt \rangle = 2r_e c E^4 / (3m^3 c^6 \rho^2)$. Thus the characteristic damping (or anti-damping) rate in all three degrees of freedom due to the bending is $\Gamma_b \sim \langle dE/dt \rangle / E = 2r_e c \gamma^3 / (3\rho^2)$.

In addition, the particle radiates while executing rapid betatron oscillations around the circular bent trajectory due to the focusing field. If the bending is adiabatic and the particle's pitch angle relative to the ideal orbit is small compared with $1/\gamma$, the transverse damping rate due to betatron oscillations can then be approximated by $\Gamma_c = 2r_e K/3mc$, as discussed in the previous section. Taking the ratio of these two rates, we obtain:

$$\frac{\Gamma_b}{\Gamma_c} = \frac{\lambda_\beta^2}{(\rho/\gamma)^2}, \quad (16)$$

where $\lambda_\beta = \lambda_\beta/2\pi = \sqrt{E/K} = c/\omega_s$ is the reduced betatron wavelength. Equation (16) shows that if $\rho/\gamma \gg \lambda_\beta$, the transverse damping due to local oscillations is much stronger than that from the global bending of the trajectory. Since $\rho/\gamma = E/\gamma ecB = mc/eB$, we conclude that in a system that satisfies $mc/eB \gg \sqrt{E/K}$ or $K \gg \gamma e^2 B^2/m$, the radiation damping is dominated by the focusing field.

To illustrate the choice of parameters for such a system, we consider a numerical example: a focusing-dominated low energy electron ring. Let us assume that the radius of the ring is $\rho = 33\text{m}$ and that $E = 0.1\text{GeV}$ electrons circulate around the ring. A rather weak magnetic field $B = 0.01\text{T}$ is required to confine the particles on the ideal circular trajectory. Suppose along the ideal trajectory, the electrons are continuously focused with the focusing strength $K = 30\text{GeV/m}^2$, so the reduced betatron wavelength λ_β is about 5.8cm and ρ/γ is about 17cm . From Eq. (16), we see that the transverse damping rate due to

the focusing field is about nine times as fast as the characteristic damping (or anti-damping) rate from the bending field.

In a straight system, quantum excitation is absent because the transverse action must decrease after every photon emission to satisfy the kinematic constraints. In a bent system, the dispersion effect may introduce a random fluctuation of the transverse action. Nevertheless, because of the discreteness of the transverse action, there seems to exist a set of consistent conditions under which quantum excitation is prohibited even in a dispersive system [2].

V. CONCLUSION

The basic results obtained here apply to straight or bent, focusing-dominated systems. The excitation-free, asymmetric radiation damping in such systems is the direct consequence of the kinematic requirements and does not depend on the various approximations used above. There may be interesting applications of this phenomenon in beam cooling. For example, in a sufficiently low-energy, focusing-dominated electron ring, this damping effect could perhaps be utilized to obtain ultra-cool beams in transverse phase space without much energy loss. Since the system is free of radiation excitation, the actual equilibrium beam emittance will depend upon the details of the application considered.

References

- [1] M. Sands, "The Physics of Electron Storage Rings," SLAC Report-121, 1970; A. A. Sokolov and I. M. Ternov, *Radiation from Relativistic Electrons*, AIP Translation Series, (AIP, New York, 1986).
- [2] Z. Huang, P. Chen and R. D. Ruth, *Phys. Rev. Lett.* **74** (1995) 1759; Z. Huang, P. Chen and R. D. Ruth, to appear in the *Proc. of the 6th Int. Workshop on Advanced Accelerator Concepts*, ed. A. M. Sessler (1994).
- [3] J. D. Jackson, *Classical Electrodynamics*, 2nd Edition, (John Wiley & Sons, Inc., 1975)
- [4] V. N. Baier, V. M. Katkov, and V. M. Strakhovenko, *Soviet Physics JETP* **53** (1981) 688.
- [5] Z. Huang, P. Chen and R. D. Ruth, in preparation.

Colliding Crystalline Beams

A. F. Haffmans, D. Maletic, and A. G. Ruggiero
Brookhaven National Laboratory, Upton, NY 11973, USA

Crystalline Beams* are an ordered state of an ensemble of ions, circulating in a storage ring, with very small velocity fluctuations [1,2]. They can be obtained from ordinary warm ion beams with the application of powerful cooling techniques (stochastic, electron, laser, ...). Depending on the focussing properties and dimensions of the storage ring, and on the ion beam density, several ground states are possible [3-4]. All of them can be visualized as a bundle of n_s symmetrically distributed, parallel *strings* [5]. The longitudinal ion separation λ is the same for all *strings*. The minimum temperature that can be achieved depends on the background noise of the cooling technique used. It is required for stability that the vibration amplitude of the ions is only a fraction of the separation λ .

I. COLLIDING CRYSTALLINE BEAMS

There are several advantages in using colliding Crystalline Beams. First, it is possible to obtain more-compact beams. Second, most importantly, the particles in each beam occupy well-defined and rigid positions. The uncertainty on the transverse location of each *string* is considerably smaller than the longitudinal spacing λ . By carefully aligning the two beams to pair countermoving *strings* in the collision, it is possible to increase the luminosity by a considerable factor. Indeed the luminosity in this case is proportional to the number of *strings* in each beam

$$L = n_s L_s \quad (1)$$

where

$$L_s = N_s^2 f_{enc} / 4\pi \sigma_{eff}^2 \quad (2)$$

is the contribution to the luminosity from each pair of countermoving *strings*; f_{enc} is the frequency of encounter, σ_{eff} is an effective cross section which is the common transverse dimension of the two *strings* during collision, and N_s is the number of circulating ions per *string* engaged in the collision at one time, assuming that the two countermoving beams are identical.

II. COLLISION BETWEEN STRINGS

The easiest example to investigate is the case of two identical Crystalline Beams sharing the same storage ring. The two beams are moving in the opposite direction along the common closed orbit. We require that the ions in the two beams have the same magnetic rigidity, mass number A , and charge state Q . But they must have opposite sign of the electric charge, if the

bending along the closed orbit is due to a common axial magnetic field. Thus, one beam is made of partially-stripped, positively-charged ions, and the other beam is made of the same ions with an excess of electrons (negative ions). We shall not debate here how this can be realized in practice, but only assume that it is possible.

It is also sufficient to investigate the case of collision between paired *strings* and neglect the presence of the others in the background which are taken to be at a sufficiently large distance. We shall assume that the two countermoving *strings* are initially separated vertically by some distance $2b$, and want to investigate the behavior and the stability of the motion of the ions when the separation distance b is reduced and the *strings* are brought closer for collision.

III. EQUATIONS OF MOTION

If the two *strings* were moving in the same direction, the configuration expected is that of a *vertical zigzag* [4] of which the properties are known. In the present case, the two strings move parallel to each other, but in opposite direction, each with velocity βc . As the ions of one *string* pass along the reference ion in the other *string*, the motion of this is modulated periodically in all directions. We shall assume that the modulation has an amplitude small compared to the separation λ , and linearize the equations of motion which apply, for symmetry, to all particles. They are [5]:

$$b'' + K_v(s) b + K_{sc} f_3(\alpha, \tau) b / g_0 = 0 \quad (3)$$

$$a'' + K_h(s) a = h(s) \delta \quad (4)$$

$$\sigma' = h(s) a - \delta / \gamma^2 \quad (5)$$

$$\delta' = -(\gamma^2 \lambda K_{sc} / 2 g_0) [df_1(\alpha, \tau) / d\tau] \quad (6)$$

The force acting on the test particle is the one generated by all the ions of the countermoving *string*. Those ions on the same *string* do not contribute to the total force. In Eq.s (3-6) the independent variable is the path length s along the common closed orbit. A prime denotes differentiation with respect to s . b is the vertical displacement from the median plane of symmetry, a is the radial displacement, σ the path length difference, and δ the momentum deviation from the reference closed orbit conditions. $K_{v,h}$ are the focussing functions which we approximate with constants $(v_{v,h} / R)^2$, where $v_{v,h}$ are the betatron tune numbers and R is the average closed orbit radius. $h(s)$ is the curvature function, which we also approximate with $1/R$. β and γ are respectively the velocity and energy relativistic factors. $g_0 = 1.3$ is a constant. The space-charge constant [5]

* Work performed under the auspices of the US DOE

$$K_{sc} = (2/R^2) (\lambda_c/\lambda)^3 \quad (7)$$

where the critical spacing [5]

$$\lambda_c = (g_0 Q^2 r_0 R^2 / A \beta^2 \gamma^5)^{1/3} \quad (8)$$

and $r_0 = 1.535 \times 10^{-18}$ m is the proton classical radius. Finally, the form factors

$$f_n(\alpha, \tau) = \Sigma_i [\alpha^2 + (i - \tau)^2]^{-n/2} \quad (9)$$

where the aspect ratios $\alpha = 2b/\lambda\gamma$ and $\tau = 2s/\lambda$. The form factors are periodic with respect to τ with a periodicity of one.

IV. CASE OF LARGE SEPARATION

In the limit of large separation among the two *strings*, that is $\alpha > 1$, f_3 is about constant, whereas $df_1/d\tau$ oscillates around zero. In the smooth and linear approximation, ignoring the curvature of the storage ring, we can decouple the vertical motion from the longitudinal one. Because the two beams have opposite charge sign and $f_3 > 0$ for all values of α and τ , it is seen that the third term at the l.h. side of Eq. (3) adds to the focusing of the storage ring. We can estimate the betatron tune-shift as

$$\delta v_v = K_{sc} \langle f_3 \rangle R^2 / 2 v_0 g_0 \quad (10)$$

where $\langle f_3 \rangle \sim 2/\alpha^2$. If the tune-shift does not exceed half of the distance Δv_v to the nearest half-integral stopband the motion is stable [5].

At the same time, particles oscillate longitudinally (σ) around their stationary position with an amplitude

$$\sigma_0/\lambda = \lambda^2 K_{sc} \Delta / 8 g_0 \quad (11)$$

where $\Delta < 0.01$ for $\alpha > 1$ and is a slow function of α . Thus, for large separation between the countermoving *strings*, the motion is stable, and the configuration of each *string* is not disrupted.

V. CASE OF CLOSE COLLISION

As the two *strings* are brought together in collision, we reach a range of aspect ratios $\alpha \ll 1$. In this range, the form factor f_3 essentially vanishes over the full period of τ , except that periodically, at $\tau = \text{integer}$, it transforms to a kick. In the smooth approximation, we can spread the kick evenly over one period. Solving Eq. (3) in the same approximation again leads to the tune-shift (10). Since $\langle f_3 \rangle \sim 2/\alpha^2$, Eq. (10) sets a limit to the aspect ratio α below which the relation cannot be satisfied. At the limit of stability of individual *strings*, $\lambda \sim \lambda_c$, there is a threshold value of the aspect ratio

$$\alpha^2 > 1/v_v \Delta v_v = \alpha_{trans}^2 \quad (12)$$

below which the configuration of the two *strings* is destroyed. As a consequence, a large betatron tune v_v and a large periodicity of the storage ring is desired (so that $\Delta v_v \sim v_v/2$) to allow the lowest possible threshold value α_{trans} .

As the separation $2b$ between the two *strings* reduces, the longitudinal force acting on the test particle has still an oscillatory behavior around zero, but with a waveform grossly distorted from a pure sine-wave. The amplitude of the oscillation increases as $\Delta \sim 1/2 \alpha^2$ for $\alpha \ll 1$. Inserting this at the r.h. side of Eq. (11) gives the amplitude of the longitudinal oscillations. To avoid disruption of both *strings*, we require $\sigma_0 < \lambda/2$. That is, at the limit of individual *string* stability, when $\lambda \sim \lambda_c$, the aspect ratio cannot be reduced below the threshold value

$$\alpha^2 > (\lambda/R)^2 / 4 g_0 = \alpha_{long}^2 \quad (13)$$

VI. CONCLUSIONS

In conclusion, two *strings*, moving in the opposite direction in the same storage ring, separated vertically by the aspect ratio α , have a stable configuration with the ions performing small-amplitude oscillations around their otherwise stationary position, provided that the vertical separation is sufficiently large. Two criteria are to be satisfied, namely Eqs (12 and 13). In a typical storage ring, it is found that the limitation is caused mainly by the transverse forces, and that the smallest separation that can be achieved between the two *strings* is set by the betatron tune

$$\alpha = 2b/\lambda\gamma \sim 1/v_v \quad (14)$$

We have seen that according to Eq. (2) the luminosity depends on the effective cross section σ_{eff} of the two *strings* colliding with each other, given by the background noise of the cooling method used. For the effective collision of the two *strings*, it is also required that the separation b , set by Eqs (12 or 13), is sufficiently smaller than σ_{eff} .

VII. REFERENCES

- [1] A. Rahman and J. P. Schiffer, Phys. Rev. Lett., **57**, (1986), 1133.
- [2] R. W. Hasse and J. P. Schiffer, Ann. of Phys., **203**, (1990), 419.
- [3] J. Wei, X. P. Li and A. M. Sessler, Phys. Rev. Lett., **73**, (1994), 3089.
- [4] A. F. Haffmans, D. Maletic, and A. G. Ruggiero, "Crystal-line Beams ...", Internal Reports BNL-60436/60619/60743/60876 (1994).
- [5] A. G. Ruggiero, "Crystalline Beams: Theory, Experiments, and Proposals", Internal Report BNL-61007 (1994)

Helical spin rotators and snakes for RHIC

V.I.Ptitsin and Yu.M.Shatunov

Budker Institute of Nuclear Physics, Novosibirsk, 630090, Russia

S.Peggs

Brookhaven National Laboratory, Upton, NY 11973, USA

Abstract

Various possible spin rotator and siberian snake schemes are considered for use at the RHIC collider, based on sequences of four helical dipole magnet modules.

I. Introduction

The RHIC collider, now under construction at BNL, will have the possibility of polarized proton-proton collisions up to a beam energy of 250 GeV. Polarized proton beams of such high energy can be only obtained with the use of siberian snakes, a special kind of spin rotator that rotates the particle spin by 180° around an axis lying in the horizontal plane [1]. Siberian snakes help to preserve the beam polarization while numerous spin depolarizing resonances are crossed, during acceleration. In order to collide longitudinally polarized beams, it is also planned to install spin rotators around two interaction regions.

Schemes based on a sequence of vertical and horizontal bending magnets have been proposed, for use as spin rotators and snakes [2,3]. The main disadvantage of such schemes is a large orbit excursion, especially at the injection energy (about 26 GeV for RHIC). From this point of view a rotator based on helical dipole magnets is more efficient [4]. Several schemes that use multipole helical magnets have been suggested in the last few years [5,6].

This paper discusses snake and spin rotator designs based on sequences of four helical magnets. The schemes that were chosen to be applied at RHIC are presented.

II. Orbital and spin motion in helical magnet

In a helical dipole magnet with a period λ and a field amplitude h , the on-axis field can be written as:

$$H_x = -h \sin kz, \quad H_y = h \cos kz, \quad H_z = 0 \quad (1)$$

where $|k| = 2\pi/\lambda$, z is the coordinate along helical magnet axis, and subscripts x and y refer to horizontal and vertical components, respectively. A helical magnet is also characterised by its helicity, $S = k/|k|$.

As a measure of the magnetic field amplitude, it is more convenient to define the field parameter

$$p = \frac{q_0 h}{c|k|} \quad (2)$$

where $q_0 = e/mc$.

Solving the equations of orbital and spin motion, one obtains the transformation for the proton orbital coordinates and the proton spin after one helical period [7]. For a particle entering the

magnet along its axis, the orbit is simply shifted by $\lambda p/\gamma$ after one period, in a direction determined by the direction of the magnetic field at the helical magnet entrance and the helicity: $y = y_0 - S \lambda p/\gamma$. The spin transformation is described by the spin rotation axis:

$$n = -\frac{1}{\sqrt{1 + p^2 A^2}} (A p e_y + S e_z) \quad (3)$$

where $A = (1 + 1/\nu_0) \cdot a$ with $a = (g - 2)/2$, and by the spin rotation angle $2\pi\nu$ around this n axis, where ν is:

$$\nu = \sqrt{1 + A^2 p^2} \quad (4)$$

These expressions for the one-period transformation of orbit and spin are the basis from which to construct spin rotators that consist of several magnets with integer numbers of periods, but with different helicities and field amplitudes. Note that when one changes the sign of the magnetic field and the helicity, the one period orbit shift does not change while the spin rotation is reversed. This gives additional flexibility during the construction of spin rotators.

III. Siberian snake

The nominal RHIC design includes 2 siberian snakes in each ring. It is assumed that one pair of snakes will be sufficient to overcome the spin depolarizing resonances during beam acceleration. In order to have the spin tune equal to $1/2$, the angle between the spin rotation axes of two snakes must be 90° .

On the basis of four helical dipoles, one can construct the analog of a "continuous axis" snake [2,3]. The internal symmetry of such a snake automatically restores the particle orbit at the snake exit, and provides a snake axis in the horizontal plane. The appropriate symmetry conditions, obtained from an analysis of the spin transformation matrix, are:

1. $S_1 = S_4, \quad S_2 = S_3$
2. $p_1 = -p_4, \quad p_2 = -p_3$
3. $N_1 = N_4, \quad N_2 = N_3$, where N_i is the number of periods of the i th magnet
4. The magnetic field at each magnet entrance is vertical

The RHIC lattice imposes additional requirements on the parameters of a siberian snake: the snake must be less than 12 meters long, and the maximum magnetic field must be less than 4 Tesla.

An analysis of all possible snake schemes shows that the best variant, from the point of view of RHIC demands, has the same helicity in all helical magnets, each with one period. Figure 1 shows the relationship between p_1 and p_2 , and shows the dependence of longitudinal snake axis projection on p_1 , for this variant.

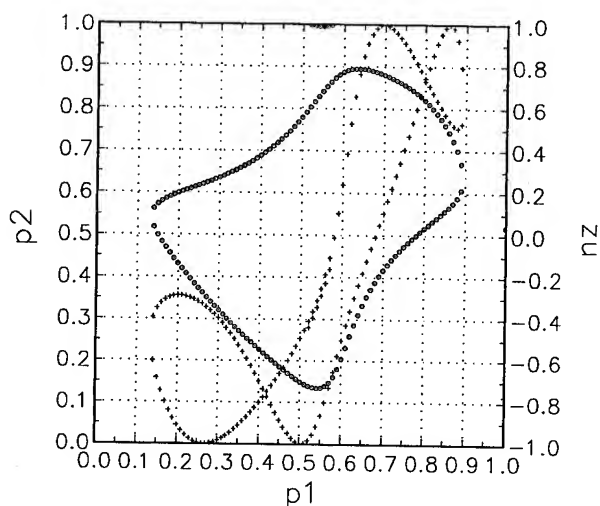


Figure 1. The dependence of p_2 (circles) and the longitudinal snake axis projection n_z (crosses) on p_1 .

Two snakes with 45° and -45° axes have been chosen for RHIC. As Fig. 1 shows, a snake with a 45° axis ($|n_z| = 0.707$) can be obtained in several ways. From the point of view of minimum orbit excursion, the best choice is $p_1 = 0.154$ and $p_2 = -0.493$. Taking the magnets to have a helical period of 2.4 m, $B_1 = 1.26\text{T}$ and $B_2 = 4.04\text{T}$, producing a 3.02 cm orbit excursion inside the snake at the RHIC injection energy. More exact values for the magnetic field and the orbit excursion have been calculated by the direct integration of particle and spin motion in a realistic helical field [8].

IV. Spin rotator

Four pairs of spin rotators are planned at RHIC, in order to have the possibility of longitudinally polarised beam collisions at two collision points.

Due to the presence of dipole magnets inserted between the rotator and the interaction point, where longitudinal beam polarization is desired, the spin orientation angle required in the horizontal plane after the rotator depends on the energy. If the spin angle from the longitudinal axis at the rotator exit is ϕ , then $\phi = 10.2^\circ$ at the lowest RHIC energy ($\gamma = 27$), and $\phi = 101.2^\circ$ at the highest energy ($\gamma = 268$). Thus the rotator must provide a spin orientation angle in the horizontal plane at its exit in the range $10.2^\circ < \phi < 101.2^\circ$.

As described in the previous section on Siberian snakes, all rotator designs discussed for use in RHIC included four helical dipole magnets, with an internal symmetry that provides the automatic restoration of the particle orbit at the spin rotator exit.

Consider a spin rotator which consists of four helical magnets, each with just one period. If the direction of the magnetic field at the entrance to each module is characterized by an angle α from the vertical, then automatic restoration of the particle orbit after the rotator implies:

$$\sum_{i=1}^4 \sin \alpha_i \cdot p_i \cdot S_i = 0$$

γ	ϕ	B_1 (T)	B_2 (T)	max.orbit (cm)
27	10.19	2.13	2.77	2.31
50	18.88	2.38	2.65	1.39
100	37.75	2.87	2.47	0.84
150	56.63	3.22	2.51	0.63
200	75.50	3.41	2.78	0.50
250	94.38	3.50	3.11	0.41

Table I
Required magnetic fields, and maximum orbit excursions, for various RHIC energies.

$$\sum_{i=1}^4 \cos \alpha_i \cdot p_i \cdot S_i = 0 \quad (5)$$

It follows from these expressions that one way to introduce symmetry into the scheme is to combine the helical magnets in two pairs, and to require that the orbit shift caused by the first pair is compensated by the second. Asserting that magnets of each pair have the same field direction angle α , it follows from Eqn. 5 that these helical dipoles must have the same field and opposite helicities, or the same helicity and opposite fields. Combining the rotator magnets in pairs does not necessarily mean that two consecutive magnets are connected to each other. For example, one can also relate the first helical module with the third, and the second module with the fourth.

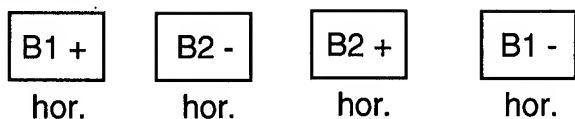
After introducing the symmetry conditions, a rotator scheme depends on two magnetic field values, which must be chosen to satisfy the spin conditions. Specifically, the particle spin after the rotator must be in the horizontal plane, with a particular spin orientation angle. Because the spin transformation matrix for helical dipoles depends on the magnetic fields in a quite complex and nonlinear way, its analysis is performed with the use of a specially written code.

Analysis shows that three variants are the best, from the point of view of minimum orbit excursion and minimum magnetic field. These schemes are shown in Figure 2.

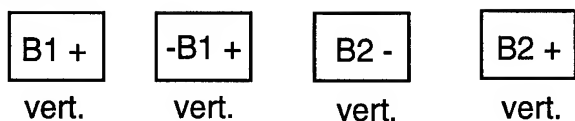
Figure 3 shows how the maximum orbit deviation depends on the final spin angle for all 3 design variants, at a fixed energy of $\gamma = 100$. Since the orbit excursion changes with particle energy as $1/\gamma$, one can obtain the maximum orbit deviation at another energy by appropriately scaling the vertical axis in Figure 3. From these graphs one can see that variant 1 provides least orbit deviation when the spin is close to the longitudinal direction, while variant 3 is best when the spin is close to transverse, and variant 2 is preferable for an intermediate range of spin angles.

Variant 1 has been chosen as the nominal spin rotator design, because it provides the smallest maximum orbit deviation at the RHIC injection energy. The magnetic field values needed to obtain the proper spin direction at the rotator exit can be extracted from diagrams that show how the final spin angle ϕ , and the second field parameter p_2 , depend on p_1 , the field of the first helical magnet. Such diagrams for the nominal spin rotator design are presented in Figures 4 and 5. Table 1 lists the magnetic field values and the maximum orbit deviation at some RHIC energies (for $\lambda = 2.4\text{m}$).

Variant 1:



Variant 2:



Variant 3:

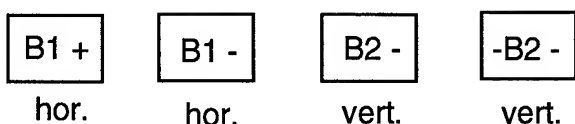


Figure 2. Three possible symmetric rotator variants. The signs (+, -) denote the magnet helicities, while "vert." and "hor." denote the field direction at the magnet entrance.

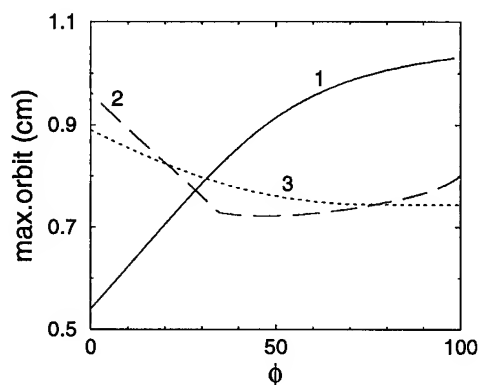


Figure 3. Maximum orbit deviation versus spin direction angle after each rotator variant, at fixed energy ($\gamma = 100$).

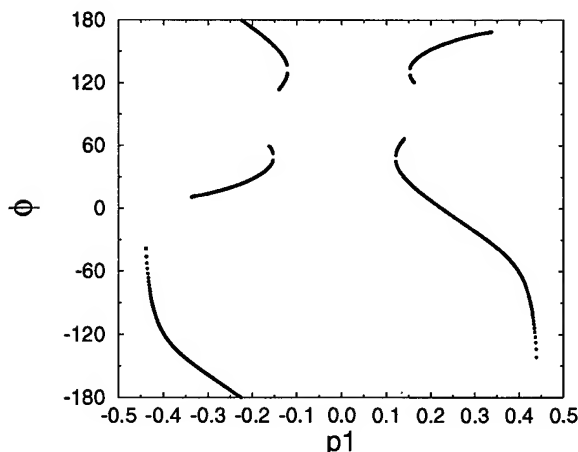


Figure 4. The relationship between the spin direction angle after the rotator, and the field p_1 of the first magnet.

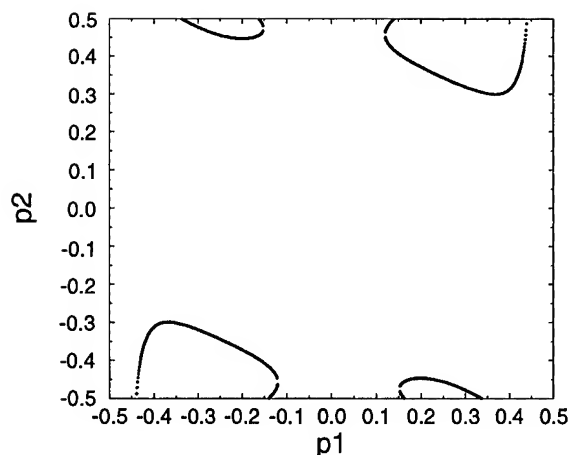


Figure 5. The relationship between p_1 and p_2 , the fields in the first and second magnets.

V. Conclusion

Spin rotator and siberian snake schemes based on helical dipole magnet modules have been adopted at RHIC. The main advantage of these schemes is that the orbit deviation is less than in bending magnet schemes.

References

- [1] Ya. S. Derbenev and A. M. Kondratenko, Part. Accel., **8**, 115 (1978).
- [2] K. Steffen, DESY Report, DESY 83-124 (1983).
- [3] S. Y. Lee, Nucl. Instr. and Meth., **A306** (1991).
- [4] Ya. S. Derbenev and A. M. Kondratenko, Proc. High Energy Physics with Polarized Beams and Targets, Argonne 1978, AIP Conf. Proc. **51**, 292.
- [5] E. D. Courant, Proc. of 8th International Symposium on High-Energy Spin Physics, Minneapolis 1988, AIP Conf. Proc. **187**, vol.2, 1085.
- [6] T. Toyama, Proc. of 10th International Symposium on High-Energy Spin Physics, Nagoya 1992, 433.
- [7] V. I. Ptitsin and Yu. M. Shatunov Proc. of 3rd Workshop on Siberian Snake and Spin Rotators, BNL 1994, 15
- [8] A. Luccio Proc. of 3rd Workshop on Siberian Snake and Spin Rotators, BNL 1994, 193

EFFECTS OF ENHANCED CHROMATIC NONLINEARITY DURING THE AGS γ_t -JUMP*

J. Wei, J.M. Brennan, L.A. Ahrens, M.M. Blaskiewicz, D-P. Deng, W.W. MacKay, S. Peggs,
T. Satogata, D. Trbojevic, A. Warner, W.K. van Asselt
Brookhaven National Laboratory, Upton, New York 11973, USA

Abstract

The γ_t -jump designed to reduce the bunch self-field mismatch and intensity loss during the AGS transition crossing can cause significant orbit and lattice distortions and dramatically enhance chromatic nonlinear effects. Employing a low-intensity, small emittance proton bunch crossing transition with the γ_t -jump quadrupoles excited, we found that the nonlinear momentum-compaction factor α_1 increases from 2.2 to about 90 in the presence of the γ_t -jump. On the other hand, this enhancement can be effectively suppressed by properly exciting the chromaticity sextupoles, reducing α_1 from 90 to 16. The experimental measurement agrees well with computer simulations using MAD and TIBETAN.

I. INTRODUCTION

During recent years, the γ_t -jump method¹ has been extensively used in hadron accelerators to improve crossing efficiency at transition energy. In the Brookhaven National Laboratory AGS, a γ_t -jump has been successfully commissioned and routinely used since 1994 in both² proton and heavy ion operations. With the γ_t -jump, bunch-shape mismatch caused by beam self fields is significantly reduced. Acceleration of high intensity protons (up to 6×10^{13} per pulse)³ can be achieved with relatively small beam loss.

During operation, it has been observed that the second-order γ_t -jump scheme² currently used in the AGS causes significant distortion in the machine lattice. The measured maximum dispersion increases from about 2.2 to 8.6 meters, and momentum aperture is significantly reduced. Even with low-intensity beam, quadrupole-mode bunch oscillations (Fig. 1) and occasional beam loss occur near transition energy when γ_t -jump is employed.

Under the hypothesis that bunch oscillations and beam loss of low-intensity beams are caused by chromatic effects,⁴ which are enhanced by the lattice distortion during the γ_t -jump, we proposed an experiment to first measure the increase in the nonlinear momentum-compaction factor α_1 in the presence of the jump, and then to demonstrate the possibility of reducing α_1 by exciting the sextupole families. Section II of this paper summarizes the experimental method used to measure the α_1 factor and the momentum aperture during the jump. The results are compared with computer simulations in Section III using the programs MAD and TIBETAN. The conclusion is given in Section IV.

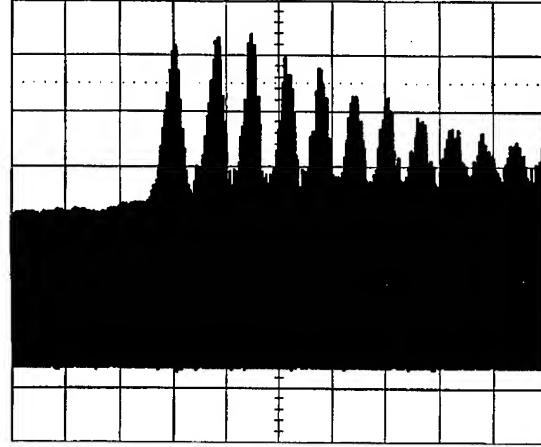


Figure 1. The envelope of the longitudinal pick-up signal during transition showing more than 100% amplitude modulation. The abscissa is time (5 ms per division).

II. EXPERIMENTAL ANALYSIS

In the low-intensity limit when multiparticle effects are negligible, the longitudinal motion of the particle can be described in terms of its rf phase ϕ and energy deviation $W \equiv \Delta E / h\omega_s$ by^{5,6} the equations

$$\begin{cases} W_{n+1} = W_n + \frac{qeV}{h\omega_s} (\sin \phi_n - \sin \phi_{s,n}) \\ \phi_{n+1} = \phi_n + \frac{2\pi h^2 \omega_s \eta (W_{n+1})}{E_s \beta_s} W_{n+1} + \phi_{s,n+1} - \phi_{s,n} \end{cases} \quad (1)$$

where ϕ_s , ω_s , $\beta_s c$, E_s are the synchronous phase, revolution frequency, velocity, and energy, respectively, and h and V are the rf harmonic and voltage. The slip factor

$$\eta(\delta) \approx \alpha_0 - \frac{1}{\gamma_s^2} + \alpha_0 \left(\alpha_1 + \frac{3}{2} \beta_s^2 \right) \delta + \left[\alpha_0 \alpha_2 + \frac{(1 - 5\beta_s^2) \beta_s^2}{2\gamma_s^2} \right] \delta^2 \quad (2)$$

includes the nonlinear dependence in momentum δ ($\equiv \Delta p / p = h\omega_s W / E \beta_s^2$) for both the machine lattice and the particle motion. Here, α_0 ($\equiv 1/\gamma_{t0}^2$), α_1 , and α_2 are the zeroth, first, and second order momentum-compaction factors.⁵

A. Measurement of the α_1 factor

The factor α_1 has been evaluated by measuring at various radial orbits (momenta) the change in time Δt when transition energy is crossed, i.e., when the minimum beam loss is measured as we vary the time to switch over the synchronous phase, as shown in Fig. 2. For small δ , we can neglect higher order nonlinear terms,

*Work performed under the auspice of the U.S. Department of Energy.

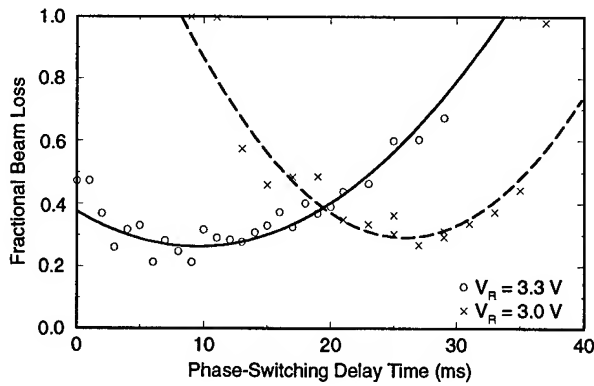


Figure 2. Beam loss versus the phase-switch delay time at radial positions $V_R = 3.3$ V (left) and 3.0 V (right), respectively, at $\dot{B} = 2.2$ T/s with γ_t -jump quadrupoles at $I_Q = 1.7$ kA. The solid and dashed lines are the fitted data.

$$\beta_s^2 \dot{B} \Delta t = - \left(\alpha_1 + \frac{1}{2} \beta_s^2 \right) B \delta. \quad (3)$$

The magnetic field B and the ramping rate \dot{B} were measured with the Gauss clock. The momentum δ was calibrated against the radial-loop voltage setting V_R by measuring the average orbit position using the beam position monitors.

As a reference, we first measure the change in γ_t without exciting the γ_t -jump quadrupoles and chromaticity sextupoles, as shown by the squares in Fig. 3. γ_{t0} is equal to 8.45, and α_1

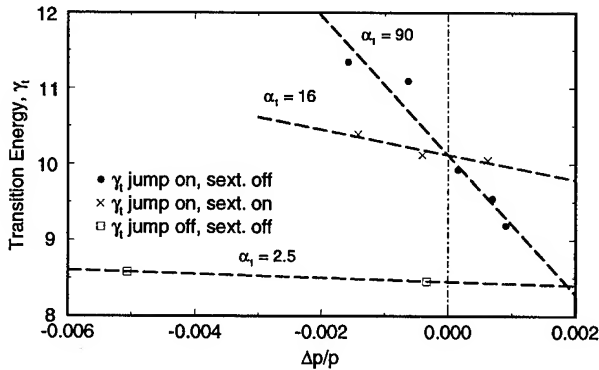


Figure 3. Measured transition energy as a function of the momentum deviation.

obtained from Eq. 3 is equal to 2.5. This result is consistent with the previous findings.⁶

To study the enhancement of α_1 during the γ_t -jump, we excited the γ_t -jump quadrupoles with a peak current of $I_Q = 1.7$ kA for about 60 ms. As shown by the solid lines in Fig. 4, the beam is made to cross transition during this period when γ_{t0} is at the maximum value of about 10.1. The measurement is performed at five different radial orbits, as shown by the dots in Fig. 3. The nonlinearity is greatly enhanced by the γ_t -jump, and α_1 is equal to 90.

The sextupoles in the machine can change the chromatic properties of the lattice and thus the α_1 factor. To study their effects, during the transition period we excited the horizontal chromatic sextupole families with a current of $I_S = 100$ A, in addition to

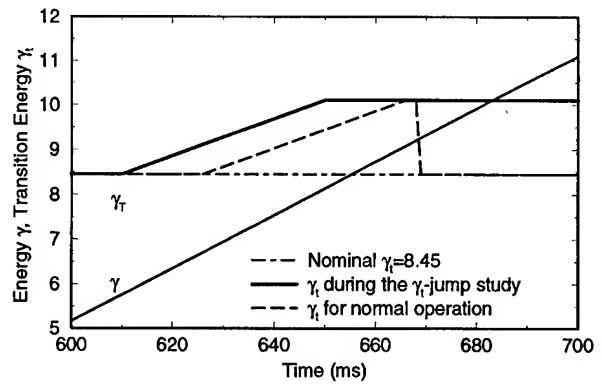


Figure 4. The excited transition energy γ_t (solid line) during the study, compared with the nominal (dot-dashed line) and the one for normal γ_t -jump operation (dashed line).

exciting the γ_t -jump quadrupoles. As shown by the crosses in Fig. 3, the nonlinearity is significantly reduced, and α_1 is equal to 16.

B. Measurement of the momentum aperture

The momentum aperture of the machine under various γ_t -jump quadrupole and chromaticity sextupole settings was explored by displacing the beam at various radial orbits while measuring the beam survival. Since the momentum spread of the beam becomes very large at transition, especially in the absence of the proper γ_t -jump (dashed line in Fig. 4), the study was performed by measuring the beam loss at transition. Taking into account the beam size of about $\Delta p/p = \pm 2.8 \times 10^{-3}$ at transition (bunch area 0.3 eV·s), the measured results are summarized in Table I. Obviously, the

Table I
Measured AGS γ_t , α_1 , and momentum aperture at various γ_t -jump quadrupole (I_Q) and sextupole (I_S) settings.

(I_Q, I_S) (A)	(0, 0)	(1700, 0)	(1700, 100)
γ_{t0}	8.45	10.12	10.12
α_1	2.5	90	16
$\Delta p/p _{ap} (\times 10^{-3})$	± 7.9	± 4.7	± 4.3

γ_t -jump significantly reduces the momentum aperture $\Delta p/p|_{ap}$. The further reduction caused by the excitation of the sextupoles is secondary.

C. Discussion

During normal high-intensity proton operation, the beam is made to occupy the entire momentum aperture to minimize the beam self fields.³ Near transition, when the γ_t -jump is excited, particles of different momenta experience dramatically different slip factors η in longitudinal motion. Consequently, emittance growth and beam loss occur in the longitudinal dimension, along with the beam loss caused by the momentum aperture reduction in the transverse dimension. With the proper excitation of the sextupole families, the nonlinearity in the longitudinal dimension can be greatly reduced. However, the limitation in the transverse dimension can only be removed by improving the γ_t -jump scheme.

III. COMPARISON WITH SIMULATIONS

A. Comparison with MAD

We have compared the measurement results (Fig. 3) with computer simulation using MAD^{7,8} (Fig. 5). Considering the simple

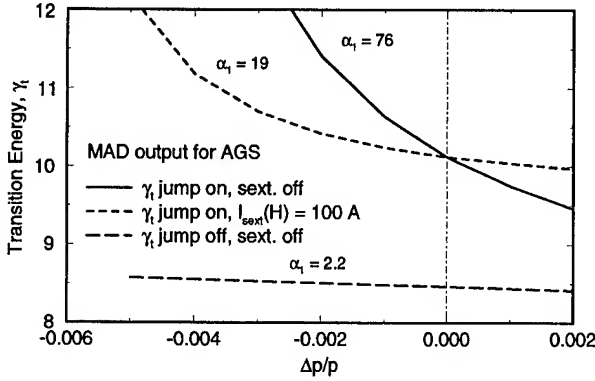


Figure 5. Transition energy as a function of the momentum deviation evaluated from the program MAD.

modeling of the AGS lattice, the agreement on the first-order nonlinear factor α_1 is excellent. On the other hand, MAD calculation also indicates significant amount of second-order nonlinearity (α_2 in Eq. 2) when γ_t -jump is used. Therefore, we extract both α_1 and α_2 from Fig. 5 using the relations

Table II

MAD calculation of AGS γ_{t0} , α_1 , α_2 and maximum dispersion $\eta_{x|max}$ at the γ_t -jump quadrupole and sextupole settings corresponding to Table 1.

(I_Q, I_S) (A)	(0, 0)	(1700, 0)	(1700, 100)
γ_{t0}	8.45	10.12	10.12
α_1	2.2	76	19
α_2	8.9	-2.7×10^3	-1.6×10^3
$\eta_{x max}$ (m)	2.2	8.6	8.6

$$\alpha_1 \approx -\gamma'_t \sqrt{\alpha_0} - \frac{1}{2}, \quad \alpha_2 \approx -\frac{2}{3} \gamma''_t \sqrt{\alpha_0} + \gamma'^2_t \alpha_0 - \frac{2}{3} \alpha_1, \quad (4)$$

where γ'_t and γ''_t are the first and second derivatives with respect to δ . Table II summarizes α_0 , α_1 , α_2 , and the maximum dispersion $\eta_{x|max}$ for the on-momentum particle. Due to the γ_t -jump, $\eta_{x|max}$ increases from 2.2 to 8.6 m, significantly reducing the momentum aperture.

B. Comparison with TIBETAN

We have performed computer simulations of the longitudinal motion using TIBETAN.⁵ In the absence of the γ_t -jump, quantitative agreement has previously been achieved⁶ on the beam loss at transition caused by chromatic nonlinearity as functions of rf voltage, ramp rate, and synchronous-phase switch-over time. With the γ_t -jump and the enhanced α_1 , the simulation shows that emittance growth and beam loss may occur. On the other hand, the reduction in nonlinearity given by the proper excitation of the sextupoles is adequate to eliminate beam loss in the longitudinal

dimension. The contribution from the second-order α_2 , however, is not significant within the currently available momentum aperture.

IV. CONCLUSION

The γ_t -jump intended to reduce the bunch mismatch and intensity loss during the AGS transition causes significant lattice distortions. Consequently, the α_1 factor is significantly increased, enhancing the chromatic nonlinear effects. Employing a low-intensity, small emittance proton bunch, crossing transition with the γ_t -jump quadrupoles excited, we measured the transition energies at different radial orbits and found that α_1 increases from 2.2 to about 90 in the presence of the γ_t -jump. The excitation of the chromaticity sextupoles significantly changes the chromatic properties of the lattice and, if performed properly, minimizes the nonlinearity. The experimental measurement of the α_1 factor agrees well with computer simulations using MAD under various circumstances.

Acknowledgment We thank C. Gardner, E. Gill, M. Harrison, T. Hayes, K. Reece, T. Roser, C. Saltmarsh, M. Syphers, S. Tepikian for many useful discussions and assistance, and the AGS operation crew for their generous support.

V. REFERENCES

- W. Hardt, et al., Proc. 7th Int. Conf. on High-Energy Accel., Yereran, 329 (1969); L.C. Teng, FN-207/400 (FNAL, Batavia, 1970); L. Thorndahl, ISR-300/LI/69-38 (CERN, Geneva, 1969); A. Sørensen, Part. Accel. 6, 141 (1975); L. Ahrens, et al., AD/No.265 (BNL, 1986); S.Y. Lee and K.Y. Ng, Proc. Fermilab III Instab. Workshop, 170 (1990).
- P. Yamin, et al., AGS Note 265 (1986); Proc. 1987 IEEE Part. Accel. Conf., 87CH2387-9, p.194; W.K. van Asselt, these proceedings.
- M. Brennan; M. Blaskiewicz, et al., these proceedings.
- K. Jøhnsen, Proc. CERN Symp. High-Energy Accel. and Pion Physics (Geneva, 1956), Vol.1, p.106; K. Takayama, Part. Accel. 14, 201 (1984); E. Ciapala, et al., IEEE Trans. Nucl. Sci. NS-26, 3571 (1979); P. Faugeras, et al., IEEE Trans. Nucl. Sci. NS-26, 3577 (1979); S.Y. Lee and J. Wei, EPAC Proc. (Rome, 1988), p.764.
- J. Wei, Ph.D thesis (1990), revised Nov. 1994; J. Wei, Proc. 3rd EPAC, Berlin, 643 (1992).
- J. Wei, et al., EPAC 1994, London, p.976 (1994); J. Wei, et al., EPAC 1994, London, p.973 (1994).
- H. Grote et al., MAD 8.13, CERN/SL/90-13 (1990).
- J.P. Shan, et al., Particle Accelerators 45 1 (1994).

EFFECT OF PARAMETRIC RESONANCES ON THE BUNCHED BEAM DILUTION MECHANISM*

L. Wang¹, M. Ball¹, B. Brabson¹, J. Budnick¹, D.D. Caussyn², G. East¹, M. Ellison¹, X. Kang¹, S.Y. Lee¹,
D. Li¹, J.Y. Liu¹, K.Y. Ng³, A. Pei¹, A. Riabko¹, D. Rich¹, T. Sloan¹, M. Syphers³

¹ IUCF, Indiana University, Bloomington, IN 47405

² Department of physics, University of Michigan, Ann Arbor, MI

³ Fermilab, Box 500, Batavia, IL 60510

Abstract

Experimental measurements of bunch dilution resulting from a modulating secondary rf cavity will be discussed. We found that parametric resonances played indeed an important role in the bunch dilution mechanism. The rms bunch length vs time did not satisfy the Einstein relation. Thus the bunch dilution may not be explained by a simple diffusion mechanism.

I. INTRODUCTION

The double rf system has been used to alleviate the space charge effect by reducing the peak current [1], [2]. It has also been used to overcome multibunch instabilities by modifying the time structure of the bunch, which changes the effective impedance experienced by the beam, and more importantly to increase the synchrotron tune spread of the beam for achieving an enhanced Landau damping [3], [4]. In past few years, there have been some theoretical studies on the double rf system for small amplitude synchrotron oscillations [6], which are valid only for synchrotron phase amplitude $\hat{\phi} \leq 50^\circ$. More recently, a method has been advanced to solve the double rf system, without small amplitude approximations, in the presence of external coherent harmonic modulations [7]. In particular, an analytic solution has been obtained for the case where the harmonic ratio is two [8]. Furthermore, a secondary high frequency rf system has also been used for controlled longitudinal beam emittance dilution [5].

Longitudinal phase space dilution is important in the operation of many synchrotrons. In particular, the longitudinal phase space dilution can minimize the negative mass instability across the transition energy. A common procedure is to modulate a secondary high frequency rf system. The phase modulation with a proper modulation frequency leads to a controlled phase space blowup before the transition energy crossing. This paper discusses experimental measurements of the evolution of bunch profile while a modulating secondary rf system is acting on the beam.

II. EXPERIMENTAL TECHNIQUE AND CALIBRATION

The experimental procedure started with 90 MeV H_2^+ strip-injected into the Indiana University Cyclotron Facility (IUCF) Cooler Ring, resulting in a proton kinetic energy of 45 MeV.

The revolution frequency for the synchronous particle, f_0 , was 1.03168 MHz. The frequency of the primary rf cavity was 1.03168 MHz with $h_1 = 1$, and the harmonic number of the secondary rf cavity was $h = 9$. The ratio of the harmonic numbers was chosen to be equal to 9 so that the secondary rf cavity would work as a perturbation to the primary rf cavity. The primary rf voltage was set at about 300 V, which resulted in a synchrotron frequency of about 705 Hz while operating with the primary rf cavity alone. The total beam current was about 100 μ A, or equivalently 6×10^8 protons per bunch. The accelerator was operated with a cycle time of 10 s. The injected beam was electron-cooled for about 3 seconds. The cooling rate has been previously measured to be about $3 \pm 1 \text{ s}^{-1}$ [9], [10], which is equivalent to a cooling time of about 300 ms.

The Hamiltonian for the double rf system is given by

$$H_0 = \frac{1}{2} \nu_s \delta^2 + \nu_s \left[(1 - \cos \phi) - \frac{r}{h} (1 - \cos[h\phi + \Delta\phi(t)]) \right], \quad (1)$$

where $\nu_s = \left(\frac{h_1 e V_1 |\eta|}{2\pi \beta^2 E} \right)^{1/2}$ is the small amplitude synchrotron tune of the primary rf system alone, $r = \frac{V_2}{V_1}$ is the ratio of the rf voltages, and $h = \frac{h_2}{h_1}$ is the ratio of the harmonic numbers. The synchrotron tune is the number of synchrotron oscillations per revolution. The conjugate phase space coordinates (ϕ, δ) are respectively the phase of the particle relative to that of the synchronous particle and the normalized off-momentum variable $\delta = -\frac{h|\eta|}{\nu_s} \frac{\Delta p}{p_0}$, where $\eta = -0.86$ is the phase slip factor. The phase of the secondary rf cavity is modulated by $\Delta\phi = A \sin \nu_m \theta + \Delta\phi_0$, where A is the modulation amplitude and $\Delta\phi_0$ is a constant.

The rf voltages of the two cavities were calibrated individually by measuring their synchrotron frequencies, when each cavity was operated alone. Since there is a lower limit of higher harmonic cavity, we choose $V_1 = 300 \text{ V}$, which gives $\nu_s = 705 \text{ Hz}$ for the primary rf system. At this rf voltage, the rms bunch length is about 20 ns at a beam current of about 100 μ A.

To measure the evolution of the bunch distribution function, we use a BPM sum signal passing through a low loss cable, called *elephant trunk*. The elephant trunk cable is a 7/8" heliax high bandwidth, low attenuation cable, made by Andrews Corp. The amp is a Burr-Brown 3553 FET buffer amp. We use a 1 Mohm resistor to ground on the front end of the circuit. Taking into account the capacitance of the pickup, it gives us a 1 kHz high pass filter. Setting the acceptance of the amp close to dc can effectively eliminate the overshoot that is commonly seen on 50 ohm amps. The amp has a bandwidth of 150 MHz.

*Work supported in part by grants from the NSF PHY-9221402 and the DOE DE-FG02-93ER40801.

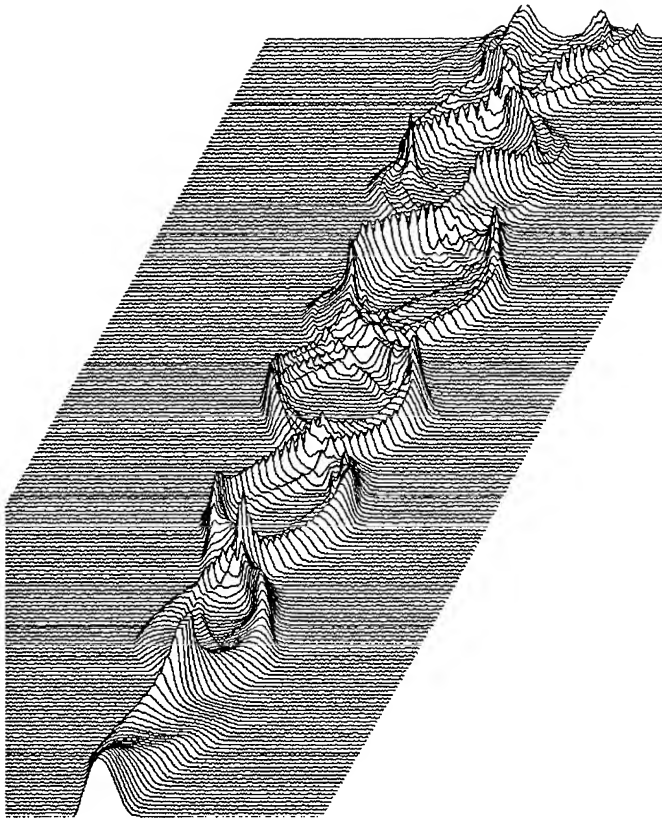


Figure 1. The bunch evolution profile as a function of time obtained from fast digital oscilloscope. The time resolution is 1 ns and the interval between each bunch profile is about 25 μ s. The modulating frequency is 1.3 kHz. We note that the effect of parametric resonances is evident from the bunch profile splitting.

The signal is digitized by a fast sampling scope at a time step of 1 ns with adjustable interval of revolution periods. We have written a program in the PC to control the data taking and data transfer from the scope to PC via GPIB control card. A data processing and replay system has been developed in the X Window environment to benefit from its portability. The digitized data can be replayed in a movie real-time style or projected in 3-D. Furthermore, the digitized data can be integrated to estimate beam loss in each run. The rms beam size can also be calculated by using the relation,

$$\sigma_t^2(t) = \oint \rho(t')(t - t_0)^2 dt. \quad (2)$$

Figure 1 shows an example of the evolution of bunch profile as a function of time when the secondary rf cavity is modulated at a frequency of 1.3 kHz. We note in particular that the bunch profile was observed to split into many beamlets which rotated about the center of the synchrotron phase space. Depending on the modulating frequency, the characteristics of bunch evolution would vary. In order to analyze these data systematically, we calculate the rms beam size of the beam.

Bunch Length vs Time

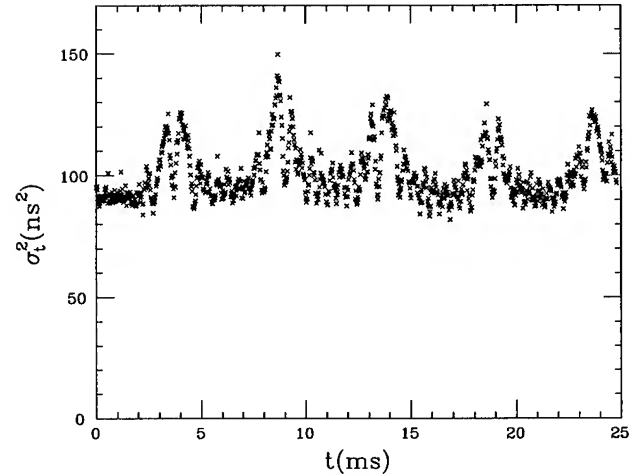


Figure 2. The rms bunch length as a function of time when the modulation frequency is 200 Hz. Note that the bunch length shows a characteristic 200 Hz modulatory peaks. The bunch shape is distorted without dilution. Since the modulation frequency is far from parametric resonances, the beam response is small.

A. Background subtraction and the evolution of the rms distribution

The initial rms bunch length is about 20 ns while the final rms bunch length can be as large as 80 ns. The digitized trace of each bunch profile is 512 ns. Thus any noise in the digitized signal will greatly distort the evolution of rms value. Thus a reliable background subtraction is necessary. This is ensured by the 512 ns sampling time of each bunch profile which is long enough to guarantee at least 100 ns pretrigger of pure background whose level is then easily estimated and subtracted for each profile. Also, a computational method is used to cut the background noise preceding and trailing the beam profile signal in order to eliminate the error introduced by these random noise in evaluation of the rms value; the error is observed to be overwhelmingly large and buries the true rms value of the beam bunch due to the quadratical contribution of these noise that spread widely towards the two ends of the sampling window.

Figure 2 shows an example of the evolution of the $\sigma_t(t)^2$ vs time t . Note that the rms size of the bunch remains constant, while the modulation frequency of 200 Hz is visible in the bunch evolution spectrum. On the other hand, when the modulation frequency was near harmonics of synchrotron frequencies, we observed a sizable emittance blowup shown in Fig. 3. Note in particular that the evolution of the bunch rms size shows two characteristic slopes. From the bunch profile evolution shown in Fig. 1, it seemed that some major parametric resonances played key roles in transporting particles into traps of small islands created by the modulating secondary rf system.

The particle transporting mechanism depends sensitively on the modulation frequency. Figure 4 shows the slope of the initial growth as a function of the modulation frequency.

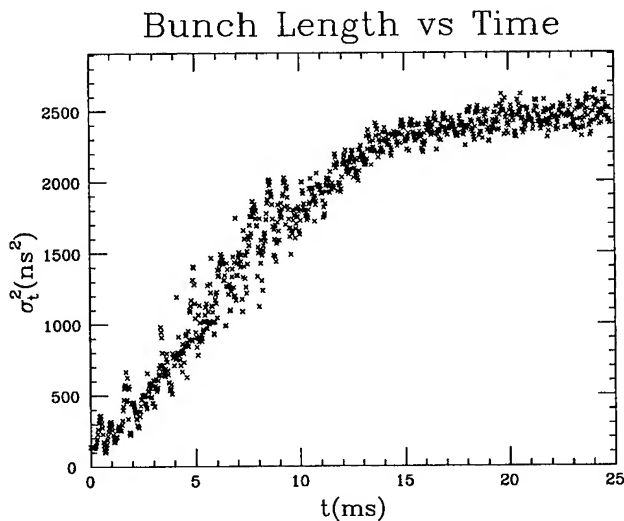


Figure 3. The rms bunch length shown as a function of time when the modulation frequency is 2.5 kHz, where the 4th order parametric resonances are important. Note in particular that there growth rate of the rms bunch length shows two distinct diffusion like behavior. The fast growth region corresponds to the parametric resonance dominant regime and the slow growth region resembles the statistically randomized motion.

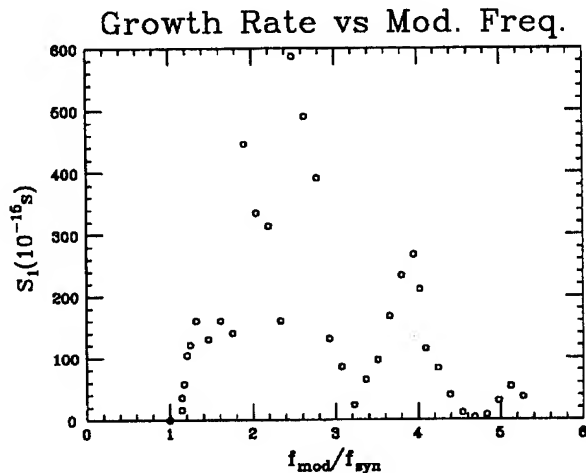


Figure 4. The measured initial growth rate plotted as a function of the modulation frequency. Note the sensitivity of the modulation frequency.

III. CONCLUSION

We have made systematic experimental observation of the bunch profile evolution when a secondary rf field is modulated. The measured bunch profile shows characteristics of dominant parametric resonances playing the role of particle transporting mechanism. Once the bunch is distributed uniformly, the beam bunch distribution function becomes less sensitive to these strong dominant resonances. We also found that the initial diffusion rate depended sensitively on the modulation frequency. In many cases, the bunch beam dilution mechanism does not exhibit the characteristics of diffusion. The abnormal diffusion played an important role in the bunch beam dilution mechanism.

References

- [1] G. Gelato, L. Magnani, N. Rasmussen, K. Schindl and H. Schönauer, Proc. IEEE Part. Acc. Conf. p.1298, March 16-19, Washington (IEEE, New York, 1987); J.M. Baillod, et al., IEEE Trans. Nucl. Sci. NS-30, 3499 (1983).
- [2] In one of our beam dynamics experiment at the IUCF Cooler Ring, we have observed a four-fold increase in beam intensity when the double rf system is used in conjunction with optimized electron cooling.
- [3] R. Averill *et al.*, Proc. of the 8th Conf. on High Energy Accelerators, edited by M.H. Blewett (CERN, Geneva, 1971) p.301.
- [4] P. Bramham *et al.*, IEEE Trans. Nucl. Sci. NS-24, 1490 (1977).
- [5] V.V. Balandin, M.D. Dyachkov, and E.N. Shaposhnikova, Particle Accelerators **35**, 1 (1991); R. Capii, R. Garoby, and E.N. Shaposhnikova, CERN/PS 92-40 (RF) (1992).
- [6] A. Hofmann, S. Myers, Proc. 11th Int. Conf. on High Energy Accelerators, CERN p.610 (1980); S. Krinsky and J.M. Wang, Particle Accelerators **17**, 109 (1984); J. Wei, Proc. of the third European Part. Accel. Conf. p.833, March 24-28 (Editions Frontières, France, 1992); A. Pauluhn, DESY report HERA 93-02 (Deutsches Electron Synchrotron, 1993), unpublished.
- [7] S.Y. Lee *et al.*, Phys. Rev. E **49**, 5717 (1994).
- [8] J.Y. Liu *et al.*, to be published (1994).
- [9] M. Ellison *et al.*, Phys. Rev. Lett. **70**, 591 (1993); H. Huang *et al.*, Phys. Rev. E **48** 4678 (1993).
- [10] Y. Wang *et al.*, Phys. Rev. E **49**, 1610 (1994); M. Syphers *et al.*, Phys. Rev. Lett. **71**, 591 (1993); D. Li *et al.*, Phys. Rev. E **48**, R1638 (1993).

PARAMETRIC RESONANCES AND STOCHASTIC LAYER INDUCED BY A PHASE MODULATION*

J.Y. Liu, M. Ball, B. Brabson, J. Budnick, D.D. Caussyn¹, P. Colestock², V. Derenchuk
G. East, M. Ellison, D. Friesel, B. Hamilton, W.P. Jones, X. Kang, S.Y. Lee, D. Li

K.Y. Ng², A. Pei, A. Riabko, T. Sloan, M. Syphers³, L. Wang

Indiana University Cyclotron Facility, Bloomington, IN 47408

¹Physics Department, University of Michigan, Ann Arbor, MI 48109

²Fermilab, Box 500, Batavia, IL 60510

³Brookhaven National Laboratory, Upton, NY 11973

Abstract

The Hamiltonian system with phase modulation in a higher harmonic rf cavity is experimentally studied on the IUCF cooler ring. The Poincaré maps in the resonant rotating frame are obtained from experimental data and compared with numerical tracking. The formation of the stochastic layer due to the overlap of parametric resonances is discussed. The dependence of the stochastic layer on the voltage of the higher harmonic rf cavity, amplitude and frequency of the phase modulation is studied.

I. INTRODUCTION

The double rf system, *i.e.* a primary rf system plus a secondary rf system working at a higher harmonic, can be used to overcome the space charge effect in low and median energy proton accelerators by reducing the peak current, and provide strong Landau damping against instabilities in high energy accelerators. It has been widely used to enhance the beam intensity in synchrotrons [1].

For particles in a double rf system, the synchrotron equations of motion with respect to the orbiting angle θ are generally given by

$$\begin{aligned}\dot{\phi} &= \nu_s \delta, \\ \dot{\delta} &= -\nu_s (\sin \phi + \epsilon \sin h\phi),\end{aligned}\quad (1)$$

where ϕ is the phase coordinate relative to the primary rf cavity, $\delta = -\frac{h_1 |\eta|}{\nu_s} \frac{\Delta p}{p}$ is the normalized momentum coordinate, and $\frac{\Delta p}{p}$ is the fractional momentum deviation from the synchronous particle, η is the phase slip factor, $\nu_s = \sqrt{\frac{h_1 e V_1 |\eta|}{2\pi \beta^2 E_0}}$ is the synchrotron tune determined by the primary rf system, $h = \frac{h_2}{h_1}$ and $\epsilon = \frac{V_2}{V_1}$ are harmonic and voltage ratios of the primary and the secondary rf cavities.

In previous reports, we have systematically studied the double rf system with $h = 2$ and discussed the stability of particle motion under the influence of parametric resonances by applying external phase and voltage modulations to both rf cavities [2]. We recently studied the controlled beam emittance dilution using the double rf system with higher harmonic ratio by modulating either the primary rf cavity or the secondary one [3]. The controlled beam blow-up is necessary in a high intensity accelerator with a small longitudinal emittance to avoid synchrotron

instabilities and reduce the beam loss during the transition crossing. In this report, we present the study of using the secondary rf cavity with a phase modulation as a perturbation to the primary rf cavity. We analysed parametric resonances and stochastic motions, based on experiment data from the beam experiment CE37F at IUCF. The controlled beam evolution will be discussed in another paper [4].

II. HAMILTONIAN ANALYSIS

With a sinusoidal phase modulation to the secondary rf system, the Hamiltonian can be written as

$$H = \frac{\nu_s}{2} \delta^2 + \nu_s (1 - \cos \phi) + \frac{\nu_s \epsilon}{h} [1 - \cos(h\phi + \phi_m(\theta))], \quad (2)$$

where $\phi_m(\theta) = a_m \sin \nu_m \theta$, a_m and ν_m are amplitude and tune (frequency) of the phase modulation respectively. For a small ϵ/h , we treat the secondary rf system as a perturbation to the primary rf cavity, and therefore we are able to expand the time dependent Hamiltonian in action-angle variables $\{J, \psi\}$ of the unperturbed Hamiltonian [5]. Rewriting the term $\cos(h\phi + \phi_m) = \cos h\phi \cos \phi_m - \sin h\phi \sin \phi_m$, we can expand $\sin h\phi$ and $\cos h\phi$ in the Fourier series,

$$\sin h\phi = \sum_n S_n(J) e^{in\psi}, \quad \cos h\phi = \sum_n C_n(J) e^{in\psi}, \quad (3)$$

where $S_n(J)$ and $C_n(J)$ are *strength functions*, given by the inverse Fourier transform,

$$\begin{aligned}S_n(J) &= \frac{1}{2\pi} \oint \sin[2h \tan^{-1}(\tan \frac{\phi_0}{2} \text{cn}\psi)] e^{-in\psi} d\psi, \\ C_n(J) &= \frac{1}{2\pi} \oint \cos[2h \tan^{-1}(\tan \frac{\phi_0}{2} \text{cn}\psi)] e^{-in\psi} d\psi,\end{aligned}\quad (4)$$

and $\text{cn}\psi$ is the elliptical function. Hence, the term $\cos h\phi$ gives rise only to even harmonics and $\sin h\phi$ to odd harmonics in the first order perturbation. Figure 1 shows the resonance strengths S_1 and C_2 which drive the lowest harmonics of parametric resonances. The small amplitude approximations are compared and found to be good for a range $\phi < 50^\circ$.

In terms of action-angle variables $\{J, \psi\}$, the Hamiltonian of Eq. (2) becomes

$$\mathcal{H} = E(J) + \frac{\nu_s \epsilon}{h} \left[\sum_n \sum_{k=0} S_n(J) J_{2k+1}(a_m) \right]$$

*Work supported in part from NSF Grant, No. PHY-9221402

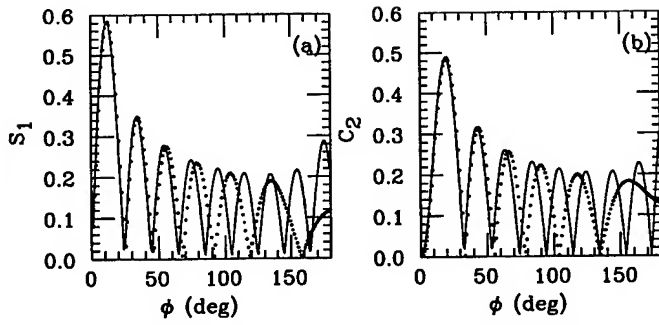


Figure 1. Resonance strengths S_1 and C_2 (solid lines) for strongest parametric resonances, compared with the small amplitude approximations (dotted lines).

$$\times \cos(n\psi - (2k+1)\nu_m\theta + \chi_n) - \sum_n \sum_{k=1} C_n(J) \times J_{2k}(a_m) \cos(n\psi - 2k\nu_m\theta + \chi_n) \quad (5)$$

where $E(J)$ is the energy of the unperturbed Hamiltonian, and $J_k(a_m)$ is the Bessel function. In Eq. (5), only terms which contribute to parametric resonances are kept. The further analysis of an isolated parametric resonance can be easily accomplished by a canonical transformation. When the modulation tune is near one of the parametric resonances, i.e. $k\nu_m \approx n\nu_s$, the perturbation coherently acts on the particle motion.

The parametric resonances are numerically studied in a basis of turn by turn tracking. Figure 2 shows parametric resonances at $\nu_m = 0.6\nu_s$ and $\nu_m = \nu_s$. The overlap of higher harmonic resonances is responsible to the stochasticity near the boundary of the bucket. However, in a dissipative dynamical system such as the IUCF cooler ring, the stochastic motion of particles will not lead a significant beam loss. Instead, particles are damped into the central region of the potential well and form a beam profile with waves on the top. In such a way, the beam emittance is blow-up, depending on the modulation amplitude and frequency. Figure 3 shows the tracking results at $\nu_m/\nu_s = 1$ with a phase damping. The damping rate $\alpha = 15 \text{ s}^{-1}$ is used. The fixed points of resonance islands become attractors as observed in previous experiments [2].

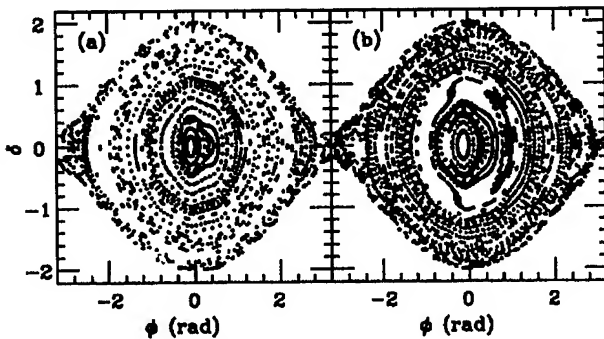


Figure 2. Parametric resonances with $\nu_s = 6.3 \times 10^{-4}$, $\epsilon = 0.2$, $h = 9$ and $a_m = 71^\circ$. In (a), $\nu_m/\nu_s = 0.6$, and in (b), $\nu_m/\nu_s = 1$.

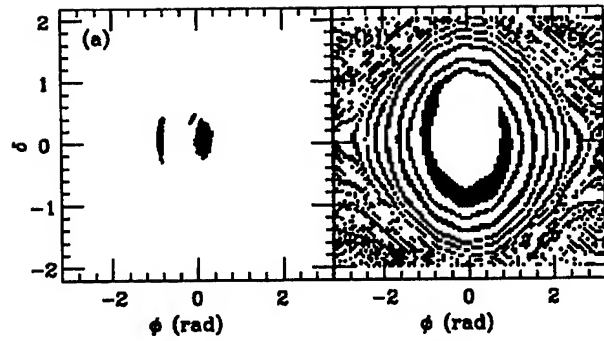


Figure 3. Attractors obtained from tracking 100×100 particles with $\alpha = 15 \text{ s}^{-1}$, $\nu_s = 6.3 \times 10^{-4}$, $\epsilon = 0.2$, $h = 9$, $\nu_m/\nu_s = 1$ and $a_m = 71^\circ$. (a) The final distribution and (b) the initial distribution showing basins of attractors.

III. EXPERIMENTAL MEASUREMENT

The IUCF cooler ring was operated with a single proton beam bunch at the energy of 45 MeV and the intensity about $100 \mu\text{A}$. The cycling time of the proton beam is about 10 seconds with injection and electron cooling being accomplished in about 5 seconds. The electron cooling time is about 300 ms. The beam emittance of the proton beam is electron-cooled to less than $0.3 \pi \text{ mm-mrad}$ in about 3 seconds. The momentum spread $\Delta p/p$ is of order 10^{-4} and the typical bunch length is about $\sigma_l = 10 \text{ ns}$. The revolution frequency is $f_0 = 1.03168 \text{ MHz}$. The primary rf cavity and the secondary rf cavity were operated at harmonics $h_1 = 1$ and $h_2 = 9$ respectively. The voltage of the primary rf cavity was set at $V_1 = 285 \text{ v}$ to achieve the synchrotron frequency of $f_s = 650 \text{ Hz}$ (or $\nu_s = 6.3 \times 10^{-4}$), and the secondary rf cavity was varied to obtain a proper voltage ratio to the primary rf cavity.

When the experiment was started, the beam bunch was longitudinally kicked to drive the synchrotron oscillation by phase shifting the control signals for both rf cavities. The phase modulation with controllable amplitude and frequency was added onto the phase shift to the secondary rf cavity. Once the beam is phase kicked, the beam closed orbit x_c was measured from the ratio of the difference (Δ) and sum (Σ) signals of a BPM at a high dispersion location with an accuracy of 0.1 mm . Then the off-momentum variable was calculated from $\Delta p/p = x_c/D_x$, where $D_x \approx 3.9 \text{ m}$. The Σ signal from this BPM was lead to a phase detector with a range of 720° which generated the phase coordinate by comparing the signal from a pickup loop in the primary rf cavity with a resolution of 0.2° . A Poincaré map then can be constructed from the digitized $\Delta p/p$ and ϕ data.

Figure 4 shows a set of a typical measured data with $\epsilon = 0.2$, $h = 9$, $a_m = 71^\circ$ and $f_m = 650 \text{ Hz}$ which gave $\nu_m/\nu_s = 1$. In Fig. 4(a) the phase space is plotted each 10 turns for 50000 turns, and in Fig. 4(b) the Poincaré phase map shows a resonance island after data being transformed to the resonance rotating frame. Because of the weak dissipative damping force of the electron cooling, the motion of the beam centroid is damped into the outer attractor as predicted in Fig. 3. The wiggling of the damping path is due to the time dependent effect. Figure 5 displays the beam profiles reconstructed from a fast sampling oscilloscope with $\epsilon = 0.2$, $h = 9$, $a_m = 125^\circ$ and $f_m = 600 \text{ Hz}$, which

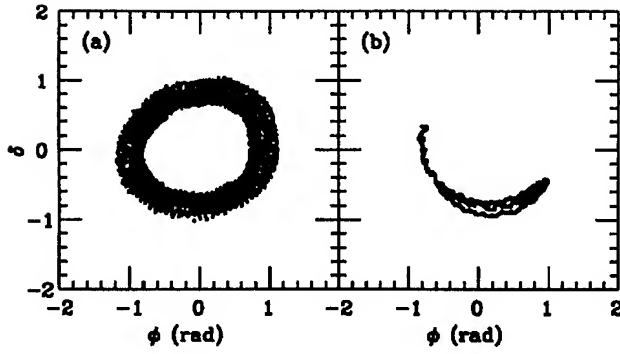


Figure 4. Measured phase space with $\epsilon = 0.2$, $h = 9$, $a_m = 71^\circ$ and $f_m = 650$ Hz ($\nu_m/\nu_s = 1$), (a) original data, and (b) Poincaré phase map after transformation.

shows the evidence of the parametric resonances. Figure 5(a) shows two beamlets obtained about 15 ms after the phase modulation was turned on, and Fig 5(b) shows the final beam profile captured after 25 ms, showing a wave structure resulted from the phase modulation. The beam profiles were extended from a half length of about 10 ns to 50 ns without beam loss.

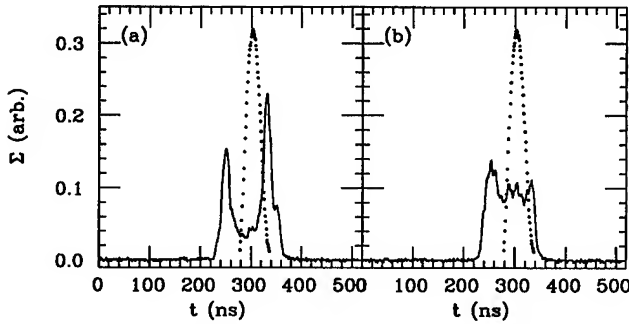


Figure 5. Beam profiles. In (a), two beamlets were due to the first harmonic resonance, and in (b), the beam profile with a wave structure was resulted from the phase modulation. The initial beam profile is plotted as dotted line.

For a given modulation frequency, the stochastic layer exists near the separatrix. As the amplitude of the phase modulation is increased, the stochastic layer increases as well. Numerical simulations indicate that when the beam is kicked inside the stochastic boundary, particle motions in the bunch decohere more rapidly. The change of the damping rates was experimentally observed to depend on the phase modulation. The measurements were done by fixing the phase kicks at $\phi = 60^\circ$, 100° , 120° and 140° and varying the modulation amplitude in a step $\Delta a_m = 18^\circ$ for given modulation frequencies $f_m = 600$ Hz, 900 Hz and 1200 Hz. Because the experiment was time-consuming, very coarse steps of the phase kick and the phase modulation were used. Figure 6 shows the measured results of the stochastic boundary versus the modulation amplitude, compared with numerical simulations.

IV. CONCLUSION

In summary, we have studied the parametric resonances due to a phase modulation in the secondary rf cavity. The resonance island was experimentally obtained, which agrees with the theoretical analysis. The beam profiles were evidently related to

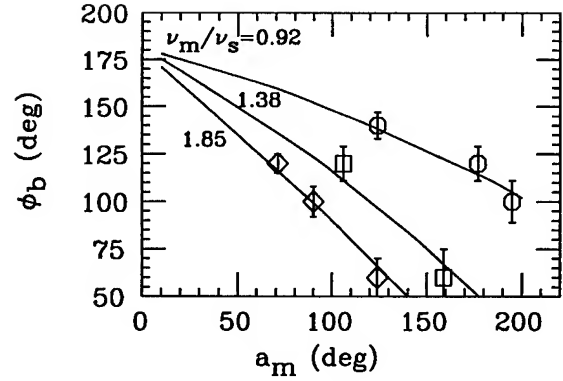


Figure 6. Stochastic boundary as a function of the modulation amplitude for given frequencies (symbols), compared with numerical simulations (solid lines).

the parametric resonances in the beam evolution process. In the measurement of the stochastic layer, we found that this dynamical system was complicated to detect. The diagnostic method of the stochastic layer is expected to work better in a simple system such as the double rf system reported in reference [2].

References

- [1] R. Averill *et al.*, Proc. 8th Int. Conf. on High Energy Accelerators, CERN (1971) p.301; P. Bramham *et al.*, IEEE Trans. Nucl. Sci. NS-24, 1490 (1977); J.M. Bailod *et al.*, IEEE Trans. Nucl. Sci. NS-30, 3499 (1983); G. Gelato *et al.*, Proc. IEEE Part. Acc. Conf., Washington (1987), p.1298.
- [2] J.Y. Liu, *et al.*, published on *Particle Accelerators*; J.Y. Liu, *et al.*, Phys. Rev. E50, R3349, (1994)
- [3] R. Cappi, R. Garoby and E.N. Shaposhnikova, CERN/PS 92-40 (RF)
- [4] L. Wang *et al.*, this proceedings.
- [5] H. Huang *et al.*, Phys. Rev. E 48, 4678 (1994); V.V. Balandin, M.B.Dyachkov and E.N. Shaposhnikova, *Particle Accelerators*, 35 1 (1991).

NONLINEAR SPACE CHARGE EFFECT OF GAUSSIAN TYPE BUNCHED BEAM IN LINAC *

Yinbao Chen, Shinian Fu, Zhibin Huang
(China Institute of Atomic Energy, P.O.Box 275(17) Beijing, China)
Zhenhai Zhang
(Tsinghua University, Beijing , China)

The nonlinear space charge effect of bunched beam with Gaussian type longitudinal distribution is discussed in this paper. Some useful formulae are derived for calculating the potential induced by a cylinder model of space charge in the waveguide of a linac with longitudinal density distribution of Gaussian type combining with transverse density distributions of Kapchinskij-Vladimirskij, waterbag, parabolic and Gaussian types, respectively.

I. INTRODUCTION

Theoretical and experimental studies on the intense beam have already found that the bunched beams always show some distributions [1]. Therefore, the nonlinear space charge effect due to the different distributions of the bunched beam is a very important subject in the intense beam research.

In Ref.[2], the general calculation formulae for the nonuniform density space charge effect in the waveguide of electron linac have been given. And in Ref.[3], we discussed the space charge effect of the disk model and the cylinder model with different transverse distributions: Kapchinskij-Vladimirskij (K-V), waterbag (WB), parabolic (PA), and Gaussian (GA), but uniform distribution in longitudinal direction. Furthermore, in Ref.[4] we developed the space charge effect of the two models with longitudinal distributions of waterbag or parabolic types combining with the above four different transverse distributions. It should be pointed out that the Gaussian distribution is of much more general importance, since, according to the central limit theorem of statistical mechanics, any processes of a random, statistically independent nature acting on a particles' positions that obey a Gaussian distribution [5]. Therefore, in this paper, the nonlinear space charge effect of longitudinal Gaussian type bunched beam combining with the above four different transverse distributions has been discussed according to the general formulae derived in the Ref.[4].

II. SPACE CHARGE EFFECT OF BUNCHED BEAM WITH LONGITUDINAL GAUSSIAN DISTRIBUTION

We use the cylinder model of space charge with b and $\pm L/2$ as its boundaries in r and z axes, respectively, in the waveguide of a linac.

The function for longitudinal Gaussian distribution can be described as follows:

$$\rho(z) = e^{-z^2/\beta^2}, \quad (1)$$

where β is the truncated distance of the longitudinal distribution.

A. Transverse uniform (K-V) distribution

The volume charge density distribution function of the space charge bunch is

$$\rho(r,z) = \rho_{kv,ga} e^{-z^2/\beta^2}, \quad (2)$$

with $\rho_{kv,ga} = q/\sqrt{2}\pi^{3/2}b^2\beta$ and the total charge q .

Now expanding the eq.(1):

$$e^{-z^2/\beta^2} = 1 + \sum_{n=1}^{\infty} \frac{(-1)^n z^{2n}}{2^n n! \beta^{2n}} \quad (3)$$

and substituting eq.(2) into the general formulae derived in Ref.[4], one can get the potentials:

$$\Phi_{1,2} = \frac{2ab\rho_{kv,ga}}{e_0} \sum_{l=1}^{\infty} \frac{J_1(k_l b) J_0(k_l r)}{(k_l \rho)^3 J_1^2(k_l \rho)} P_{2l} e^{-k_l |z|}, \quad (4)$$

* The project is supported by National Natural Science Foundation of China (NSFC) and China Science Foundation of Nuclear Industry.

$$\varphi_3 = \frac{2ab\rho_{kb,ga}}{\epsilon_0} \sum_{l=1}^{\infty} \frac{J_1(k_l b)J_0(k_l r)}{(k_l a)^3 J_1^2(k_l a)} Q_{ga}, \quad (5)$$

where

$$P_{ga} = sh \frac{k_l L}{2} + \sum_{n=1}^{\infty} A(n) \left[\sum_{k=1}^n B(k) sh \frac{k_l L}{2} - \sum_{k=1}^n C(k) ch \frac{k_l L}{2} \right], \quad (6)$$

$$Q_{ga} = (1 - e^{-k_l L/2} ch k_l z) + \sum_{n=1}^{\infty} A(n) \left\{ (e^{-k_l |z|} - e^{-k_l L/2}) ch k_l z + \sum_{k=1}^n [D(k) - B(k) e^{-k_l L/2} ch k_l z] - \sum_{k=1}^n C(k) e^{-k_l L/2} ch k_l z \right\}, \quad (7)$$

and, the subscript "1,2" stands for the potentials in the region of ($|z| > L/2$), "3" stands for the potential in the region of ($|z| < L/2$), and with

$$A(n) = \frac{(-1)^n (2n)!}{n! (2\beta^2 k_l^2)^n} \quad (8)$$

$$B(k) = \frac{(k_l L/2)^{2k}}{(2k)!} \quad (9)$$

$$C(k) = \frac{(k_l L/2)^{2k-1}}{(2k-1)!} \quad (10)$$

$$D(k) = \frac{(k_l |z|)^{2k}}{(2k)!} \quad (11)$$

It should be pointed out that the potentials are derived as usual in the frame of reference moving with the space charge bunch with the same velocity. As for the relativistic space charge effect, the formulae should be transformed into the relativistic case according to Ref.[6].

B. Transverse WB distribution

The volume charge density distribution function of the space charge bunch is

$$\rho(r, z) = \rho_{wb,ga} \left(1 - \frac{r^2}{b^2} \right) e^{-z^2/2\beta^2}, \quad (12)$$

with $\rho_{wb,ga} = 2q / \sqrt{2\pi} \beta^2 b^2 \beta$.

The potential formulae for the space charge bunch

with waterbag distribution in both longitudinal and transverse directions can be derived as follows:

$$\varphi_{1,2} = \frac{4a^2 \rho_{wb,ga}}{\epsilon_0} \sum_{l=1}^{\infty} \frac{J_2(k_l b)J_0(k_l r)}{(k_l a)^4 J_1^2(k_l a)} P_{ga} e^{-k_l |z|}, \quad (13)$$

$$\varphi_3 = \frac{4a^2 \rho_{wb,ga}}{\epsilon_0} \sum_{l=1}^{\infty} \frac{J_2(k_l b)J_0(k_l r)}{(k_l a)^4 J_1^2(k_l a)} Q_{ga}. \quad (14)$$

C. Transverse PA distribution

The volume charge density distribution function of the space charge bunch is

$$\rho(r, z) = \rho_{pa,ga} \left(1 - \frac{r^2}{b^2} \right)^2 e^{-z^2/2\beta^2}, \quad (15)$$

with $\rho_{pa,ga} = 3q / \sqrt{2\pi} \beta^2 b^2 \beta$.

The potentials can be obtained as follows:

$$\varphi_{1,2} = \frac{16a^3 \rho_{pa,ga}}{\epsilon_0 b} \sum_{l=1}^{\infty} \frac{J_3(k_l b)J_0(k_l r)}{(k_l a)^5 J_1^2(k_l a)} P_{ga} e^{-k_l |z|}, \quad (16)$$

$$\varphi_3 = \frac{16a^3 \rho_{pa,ga}}{\epsilon_0 b} \sum_{l=1}^{\infty} \frac{J_3(k_l b)J_0(k_l r)}{(k_l a)^5 J_1^2(k_l a)} Q_{ga}, \quad (17)$$

D. Transverse GA distribution

The volume charge density distribution function of the space charge bunch is

$$\rho(r, z) = \rho_{ga,ga} e^{-r^2/2\alpha^2} e^{-z^2/2\beta^2}, \quad (18)$$

with $\rho_{ga,ga} = q / (2\pi) \alpha^2 \beta^2$, $\alpha^2 = \langle x^2 \rangle$.

The potentials can be derived as follows:

$$\varphi_{1,2} = \frac{2\rho_{ga,ga} \alpha^2}{\epsilon_0} \sum_{l=1}^{\infty} \frac{J_0(k_l r) e^{-k_l^2 \alpha^2/2}}{(k_l a)^2 J_1^2(k_l a)} P_{ga} e^{-k_l |z|}, \quad (19)$$

$$\varphi_3 = \frac{2\rho_{gsa}\alpha^2}{\epsilon_0} \sum_{l=1}^{\infty} \frac{J_0(k_l r)}{(k_l \rho)^2 J_1^2(k_l \rho)} e^{-k_l^2 \alpha^2 l^2} Q_{gs}, \quad (20)$$

It is obviously that when $L/2$ approaches to infinity, we have: $P_{gs} = sh \frac{k_l L}{2}$, $Q_{gs} = (1 - e^{-k_l^2 \alpha^2 l^2}) / (k_l \rho)$. Therefore, the above potential formulae eqs.(4), (5), (13), (14), (16), (17), (19), and eq.(20) degenerated into the potentials induced by the cylindrical space charge with longitudinal uniform distribution while uniform(K-V), waterbag, parabolic and Gaussian distributions in transverse direction, respectively, in Ref.[3]. Furthermore, as $L/2$ approaches to zero, the above equations agree to the potential of a point charge in Ref.[7].

III. REFERENCES

- [1] J. D. Lawson, The Physics of Charged -Particle Beams, Second Edition, Clarendon Press, Oxford:1988.
- [2] Chen Yinbao, Xie Xi, " Space charge effect of nonuniform density distribution in waveguide" , Chinese Journal of Nuclear Physics, 1979, 1:107-128.
- [3] Chen Yinbao, " Nonlinear space charge effect of bunched beam in linac ", Chinese Journal of Nuclear Physics, 1991, 13(4):351-362.
- [4] Chen Yinbao, Fu Shinian, Huang Zhibin, et al., Space charge effect of bunched beam with nonuniform distributions in both longitudinal and transverse directions, Atomic Energy Science and Technology, 1994, 28(6):481-487.
- [5] Martin Reiser, Theory and Design of Charged Particle Beams, John Wiley & Sons, Inc., New York, 1994, p.372.
- [6] Xie Xi, Chen Yinbao and Shong Zhongheng, " Space charge effect in electron linear accelerator", Atom. Ener. Sci. and Tech., 1978, 2:127-132.
- [7] Hechtel J. " The effect of potential beam energy on the performance of linear beam devices", IEEE Trans. on electron devices, 1970, 15:999-1009.

EMITTANCE GROWTH CAUSED BY BUNCHED BEAM WITH NONUNIFORM DISTRIBUTIONS IN BOTH LONGITUDINAL AND TRANSVERSE DIRECTIONS IN LINAC*

Zhibin Huang, Yinbao Chen, Shinian Fu
(China Institute of Atomic Energy, P. O. Box 275-17, Beijing 102413, China)

The nonlinear space charge effect of bunched beam in linac is one of the important factors that induces the emittance growth due to the conversion of the field energy to kinetic energy. In this paper, using a cylinder model of space charge in linac, we derived the internal energy for a bunched beam with some nonuniform space charge distributions, such as Gaussian, waterbag and parabolic distributions in both longitudinal and transverse directions. And the emittance growth caused by these nonuniformities is worked out.

I. INTRODUCTION

The nonlinear space charge effect in a charged beam is one of the basic factors determining the beam dynamics in many intense beam facilities, such as Free Electron Laser (FEL), Inertial Confined Fusion (ICF), Heavy Ion Fusion (HIF) and some microwave devices. Theoretical and experimental studies on the intense beam have already regarded nonuniform charge distribution as a major cause of emittance growth, a nonuniform beam have higher field energy than the equivalent beam, and the particle distribution will become uniform. The difference in potential energy is converted to kinetic energy as the distribution tends to more homogeneity. A general relationship between the possible emittance growth and excess energy is given in Ref.[1]. Formulae for calculating the nonlinear self-field energy of a space charge bunched beam with nonuniform distribution in transverse direction in linac are given in Ref.[2], and hence emittance growth caused by nonuniformities is discussed, but in the above discussion uniform distribution in longitudinal direction is assumed. Therefore, it is necessary to derive formulae for calculating the nonlinear field energy of a space charge bunched beam with the nonuniform distributions in both longitudinal and transverse directions and to calculate the possible emittance growth caused by the nonuniformities. Using a cylinder model of space charge in linac, we derived formulae for calculating the self-field energy of a space

charge bunched beam with each of different longitudinal distributions such as waterbag and parabolic distributions combining with each of different transverse distributions such as Kapchinskij-Vladimirskij (K-V), waterbag (WB), parabolic (PA) and Gaussian (GA) distributions, and gave curves of the corresponding emittance growth.

II. SELF-FIELD ENERGY FOR BUNCHED BEAM WITH LONGITUDINAL NONUNIFORM DISTRIBUTION

A cylinder model of space charge is used here to present a space charge in linac. In the waveguide of a linac, assume the cylinder model to be symmetry and let the cylindrical space charge q be set in the central position, b and $\pm L/2$ are boundaries of the bunch in r and z axes respectively.

According to the cylindrical density distribution and the potential induced by some nonuniform distributions in Ref.[3], using the formula for calculating total stationary field energy in linear medium as

$$W = \frac{1}{2} \int \rho \phi d\tau, \quad (1)$$

where ρ stands for the charge density, ϕ , the potential and $d\tau = r dr d\theta dz$. we can get the self-field energy corresponding to each of different longitudinal distributions combining with each of different transverse distributions.

A. Longitudinal Waterbag Distribution

For transverse K-V distribution we obtain the self-field energy as below:

$$W_{kv,wb} = \frac{18q^2 a^2}{\pi \epsilon_0 L b^2} \sum_{l=1}^{\infty} \frac{J_1^2(k_l b)}{(k_l \rho)^4 J_1^2(k_l \rho)} A_{wb}, \quad (2)$$

where the subscript in which before the comma presents transverse distribution and after the comma longitudinal

* The project is supported by National Natural Science Foundation of China (NSFC) and China Science Foundation of Nuclear Industry.

distribution, a is the radius of the waveguide, b and L are the radius and length of the cylinder, respectively. $J_i(k, x)$ is the Bessel function and k_i satisfies the equation: $J_0(k_i a) = 0$. Let $C = k_i L/2$, A_{wb} stands for

$$A_{wb} = \frac{2}{15} - \frac{1}{3C^2} + \frac{1}{C^3} \left[1 + \frac{1}{C} - \left(1 + \frac{1}{C} \right)^2 e^{-C} \operatorname{sh} C \right], \quad (3)$$

For transverse WB distribution we get the corresponding self-field energy as below:

$$W_{wb,wb} = \frac{288q^2 a^2}{\pi \epsilon_0 L b^4} \sum_{l=1}^{\infty} \frac{J_2^2(k_l b)}{(k_l \rho)^6 J_1^2(k_l \rho)} A_{wb}. \quad (4)$$

For transverse PA distribution we have the corresponding self-field energy as below:

$$W_{pa,wb} = \frac{10368q^2 a^2}{\pi \epsilon_0 L b^6} \sum_{l=1}^{\infty} \frac{J_3^2(k_l b)}{(k_l \rho)^8 J_1^2(k_l \rho)} A_{wb}. \quad (5)$$

For transverse GA distribution we obtain the corresponding self-field energy as below:

$$W_{ga,wb} = \frac{9q^2}{2\pi \epsilon_0 L} \sum_{l=1}^{\infty} \frac{e^{-k_l^2 a^2}}{(k_l \rho)^2 J_1^2(k_l \rho)} A_{wb}. \quad (6)$$

B. Longitudinal Parabolic Distribution

For transverse K-V distribution we get the corresponding self-field energy as below:

$$W_{kv,pa} = \frac{20q^2 a^2}{7\pi \epsilon_0 L b^2} \sum_{l=1}^{\infty} \frac{J_1^2(k_l b)}{(k_l \rho)^4 J_1^2(k_l \rho)} A_{pa}. \quad (7)$$

where A_{pa} stands for

$$A_{pa} = 1 - \frac{3}{C^2} + \frac{63}{2C^4} + \frac{954}{2C^6} + \frac{2835}{2C^7} + \frac{2835}{2C^8} - \frac{315}{2C^5} \left(1 + \frac{3}{C} + \frac{3}{C^2} \right)^2 e^{-C} \operatorname{sh} C. \quad (8)$$

For transverse WB distribution we have the corresponding self-field energy as below:

$$W_{wb,pa} = \frac{320q^2 a^4}{7\pi \epsilon_0 L b^4} \sum_{l=1}^{\infty} \frac{J_2^2(k_l b)}{(k_l \rho)^6 J_1^2(k_l \rho)} A_{pa}. \quad (9)$$

For transverse PA distribution we obtain the corresponding self-field energy as below:

$$W_{pa,pa} = \frac{11520q^2 a^6}{7\pi \epsilon_0 L b^6} \sum_{l=1}^{\infty} \frac{J_3^2(k_l b)}{(k_l \rho)^8 J_1^2(k_l \rho)} A_{pa}. \quad (10)$$

For transverse GA distribution we get the

corresponding self-field energy as below:

$$W_{ga,pa} = \frac{5q^2}{7\pi \epsilon_0 L} \sum_{l=1}^{\infty} \frac{e^{-k_l^2 a^2}}{(k_l \rho)^2 J_1^2(k_l \rho)} A_{pa}. \quad (11)$$

As $L/2$ tends to infinity, above formulae for calculating the self-field energy retrograde into those formulae^[2] with correspondence to each of above referred distributions combining with longitudinal uniform distribution.

III. EMITTANCE GROWTH

In uniform beam the cylindrical space charge holds the self-field energy as below^[2]:

$$W_{kv,kv} = \frac{2q^2 a^2}{\pi \epsilon_0 L b^2} \sum_{l=1}^{\infty} \frac{J_1^2(k_l b)}{(k_l \rho)^4 J_1^2(k_l \rho)} A_{kv}, \quad (12)$$

where A_{kv} stands for^[2]

$$A_{kv} = 1 - \frac{1}{C} e^{-C} \operatorname{sh} C. \quad (13)$$

Now let W_0 be equal to $W_{kv,kv}$, then an equation can be described as below:

$$U_n = W_n - W_0, \quad (14)$$

where the subscript n may be (kv,wb), (wb,wb), (pa,wb), (ga,wb), (kv,pa), (wb,pa), (pa,ap), or (ga,pa), respectively. U_n is the difference between the nonuniform distribution and the equivalent k-v distribution in the self-field energy. The excess field energy is transformed into particle transverse kinetic energy as the distribution inclines to become more homogeneous, causing emittance growth. Provided that U_n/W_0 would be expressed as the relative measurement of the excess field energy in nonuniform density distribution of a space charge bunched beam, using the formulae of the self-field energy, for some different distributions we can get U_n/W_0 .

The general formula for calculating the possible emittance growth caused by a space charge with nonuniform density distribution is given in Ref.[1]. The relationship between the possible emittance growth and U_n/W_0 is described as below^[1]

$$\frac{\epsilon_f}{\epsilon_i} = \left[1 + \frac{U_n}{2W_0} \left(\frac{k_0^2}{k_i^2} - 1 \right) \right]^{\frac{1}{2}}, \quad (15)$$

where ϵ_i and ϵ_f are respectively assumed to be initial and final value of emittance, k_0 represents the external focusing constant and k_i the initial focusing constant. Substituting U_n/W_0 into eq.(15) and assuming α/b to be 0.3 in Gaussian

distribution, we can obtain curves of the corresponding emittance growth ϵ_f/ϵ_i versus the ratio b/a . As k_f/k_0 equals 0.3, figure 1 shows the possible emittance growth ϵ_f/ϵ_i versus b/a for either waterbag or parabolic longitudinal distribution combining with each of different transverse distributions such as waterbag, parabolic and Gaussian distributions, figure 2 shows the possible emittance growth ϵ_f/ϵ_i versus L/a for K-V transverse distribution combining with each of different longitudinal distributions such as waterbag and parabolic distributions. In addition, from eq.(15) we find that the possible emittance growth also varies with the ratio k_f/k_0 . As an example, figure 3 shows the possible emittance growth ϵ_f/ϵ_i versus b/a for Gaussian transverse distribution combining with either waterbag or parabolic longitudinal distribution when k_f/k_0 is equal to 0.1, 0.2 or 0.3, respectively.

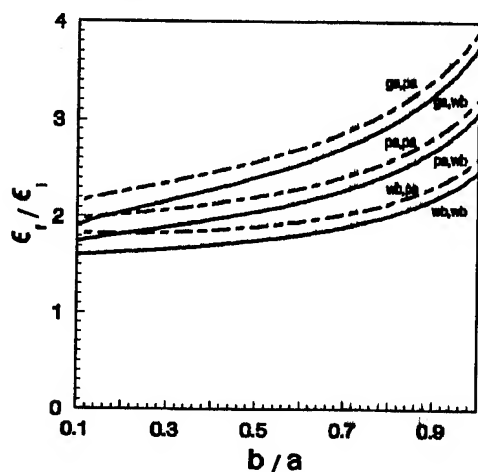


Figure 1: Emittance growth ϵ_f/ϵ_i vs b/a for different longitudinal distributions combining with different transverse distributions.

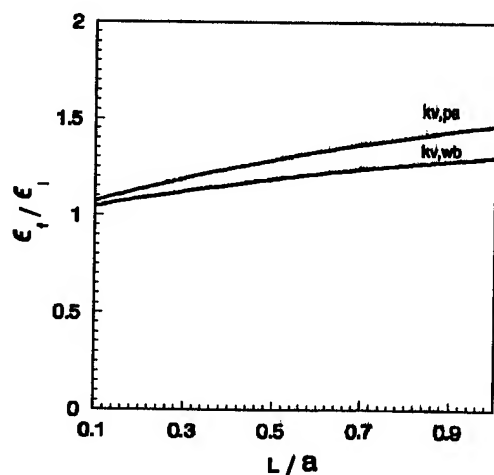


Figure 2: Emittance growth ϵ_f/ϵ_i vs L/a for transverse K-V distribution combining with different longitudinal distributions.

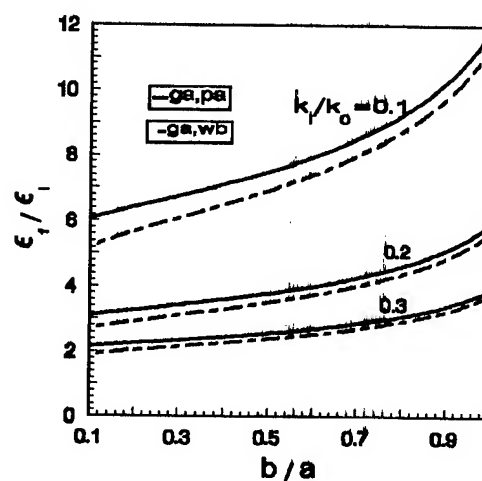


Figure 3: Emittance growth ϵ_f/ϵ_i vs b/a for transverse GA distribution combining with either WB or PA longitudinal distribution.

IV. REFERENCES

- [1] Reiser M., Free energy and emittance growth in nonstationary charged particle beams, J. Appl. Phys., 1991, 70(4):1919-1923
- [2] Chen Yinbao and Zhang Zhenhai, Emittance growth caused by the transverse nonuniform space charge distributions of bunched beam in linac, Chinese Journal of Nuclear Physics, 1994, 16(1):71-76
- [3] Chen Yinbao, Fu Shinian, Huang Zhibin, et al., Space charge effect of bunched beam with nonuniform distributions in both longitudinal and transverse directions, Atomic Energy Science and Technology, 1994, 28(6):481-487.

The ENVELOPES of BEAM MOTION in the CHARGED PARTICLE CYCLIC ACCELERATOR

Virchenko Yu.P.

Single Crystal Institute, UA-310001, Kharkov, Ukraine

Grigor'ev Yu.N.

Kharkov Institute of Physics & Technology, National Science Center,
UA-310108, Kharkov, Ukraine

Abstract.

The method for calculation of the beam motion envelopes in the six-dimensional phase space of charged particle moving in a cyclic accelerator is proposed. It is based on the invariance of the special quadratic form depending on the dynamic variables relatively to the shift along the particle trajectory. The envelopes are expressed as the explicit functions of the form coefficients.

1. Introduction

The classical problem for development of cyclic accelerator of charged particles is the calculation of the envelopes of the particle beam with respect to different dynamic variables $u_l(\theta)$, $l = 1, \dots, 6$, which are the components of the state vector $u(\theta)$ of a charged particle in the point with fixed accelerator azimuth θ . This problem is actual as before (see, for example [1-3]). The envelopes determine the maximum possible values of the respective dynamic variables in any point θ of the accelerator ring and therefore they determine various important physical characteristics of the beam: transverse sizes, divergence and energy spread [4,5]. In the present communication we propose the method for calculation of the envelopes in terms of the evolution matrix elements.

2. Evolution matrix

In general case the components of the state vector may be expressed by the set of the following values $(x, \dot{x}, \delta, \eta, z, \dot{z})$ [4], i.e. $u_1(\theta) = x(\theta)$, $u_2(\theta) = \dot{x}$, and so on. Here x, z are the particle deviations along the normal and the binormal to the closed orbit respectively; $\delta = (E - E_s)/E_s$, E is particle energy, E_s is the energy equilibrium value, $\eta = (\varphi - \varphi_s)$ is phase deviation from the equilibrium value; \dot{x}, \dot{z} are the rates connected with the coordinates x, z respectively. The charged particle dynamics in the cyclic accelerator in the one-particle approximation with negligibly small random perturbations is described by the set of linearized equations [4,5]

$$\dot{u}(\theta) = A(\theta)u(\theta), \quad (1)$$

where the 6×6 -matrix $A(\theta) = (A_{lm}(\theta))$, $l, m = 1, \dots, 6$ is the periodic function with respect to θ and it has a definite structure with the dependence on θ defined by the given accelerator design. However, the concrete form of matrix $A(\theta)$ has no importance for the below proposed method.

Determine the evolution matrix $M(\theta)$ for the above linear system by the relationship $M(\theta)u(0) = u(\theta)$. This matrix is the

unique solution of the equation

$$\dot{M}(\theta) = A(\theta)M(\theta) \quad (2)$$

with initial condition $M(0) = 1$. Since the dependence $A(\theta)$ is piecewise constant and it is periodic respective to θ [4,5], then the matrix $M(\theta)$ can be always determined explicitly on the basis of quite tedious calculations for the specified accelerator design. Further, the matrix $M(\theta)$ will be assumed known. To determine the motion envelope with respect to the u_l -phase coordinate it is necessary to calculate $\max[M_{lk}(\theta)u_k(0)]$ where the maximum is determined by the exhaustion of all possible initial data $u_k(0)$, $k = 1, \dots, 6$, which the beam particles possess at certain fixed initial moment. This calculation procedure is very inconvenient and, therefore, it is preferable to obtain the formulae for envelopes directly in terms of matrix $M(\theta)$. Such formulae are known for the case of the independent x -oscillations provided that the energy homogeneity takes place [6].

3. Invariant quadratic form

Introduce the matrix $G(\theta) = M(\theta)M(\theta)^+$ (+ denotes the matrix transposition), which according to Eq.(2) satisfies to the equation

$$\dot{G}(\theta) = A(\theta)G(\theta) + G(\theta)A(\theta)^+ \quad (3)$$

and to $G(0) = 1$. The matrix $M(\theta)$ is reversible because $d(\ln \det M(\theta))/d\theta = \text{Sp} d(\ln M(\theta))/d\theta = \text{Sp} M^{-1}(\theta)\dot{M}(\theta) = \text{Sp} A(\theta)$ and hence

$$\det M(\theta) = \exp \left\{ \int_0^\theta \text{Sp} A(\tau) d\tau \right\} \neq 0$$

Then the matrix $G(\theta)$ is reversible and it may be possible to introduce the quadratic form $I(\theta)$ depending on the state vector $u(\theta)$

$$I(\theta) = (u(\theta), G^{-1}(\theta)u(\theta)). \quad (4)$$

Using the differentiation formula $dG^{-1}(\theta)/d\theta = -G^{-1}(\theta)\dot{G}(\theta)G^{-1}(\theta)$ and Eqs.(1),(3), we find that value $I(\theta) = I_0$ is a formal invariant relative to shift along the trajectory. So, the particle moves on the six-dimensional surface the shape and the location of which in the six-dimensional phase space are regulated by matrix $G^{-1}(\theta)$ and therefore it is changed with θ . The surface is formed by the trajectories with the initial vectors $u(0)$ which give the same value of the invariant, $I_0 = (u(0), u(0))$. Since the surface under consideration is the sphere at time $\theta = 0$, then it is closed and simply connected at any time moment.

Moreover, since the surface with lesser value of the invariant I_0 at time $\theta = 0$ is putted into the surface with greater value, then this relation between these surfaces is conserved during the motion. Due to this we may set up a problem of the trajectory envelopes corresponding to the initial data u_0 which are inside the fixed six-dimensional sphere $(u(0), u(0)) = I_0$. At a fixed moment θ all these trajectories are contained inside the sphere in the u_0 -space which is formally described by the equation

$$(u(\theta, u_0), G^{-1}(\theta)u(\theta, u_0)) = I_0$$

with the vector u_0 as the surface parameter. Passing on the parametric description on the base of vector $u = u(\theta, u_0)$ we find that this surface is the face of the six-dimensional ellipsoid

$$(u, G^{-1}(\theta)u) = I_0 \quad (5)$$

at each moment θ . It is true because the above coordinate transformation is affine due to the linearity of the Eq.(2). Thus, the desired envelopes are formed by means of the motion of the surface (5).

Notice, that for the system with one degree of freedom which describes the x -oscillations one would show that $G_{22}(\theta) = \beta(\theta)$, $G_{12}(\theta) = -\dot{\beta}(\theta)/2$, $G_{11}(\theta) = \gamma(\theta)$ where γ is determined from the condition $\det G(\theta) = 1$. In this case the using of Eq.(4) gives the expression

$$I = \gamma \dot{x}^2 - \dot{\beta} x \dot{x} + \beta \dot{x}^2$$

coinciding with Courant-Snyder invariant [6]. Consequently, the surface in this case is the ordinary ellipse.

4. Envelopes of beam motion

We consider now the particle motion neglecting the friction connected with the particle radiation. Then Eq.(2) represents the canonical Hamiltonian system for which $\text{Sp}A(\theta) = 0$, i.e. $\det M(\theta) = 1$ [7], and the phase volume containing inside the surface (5) is constant due to Liouville's theorem. We assume further that system (2) is stable, i.e. the case when eigenvalues of the monodromy matrix $M(T)$ (T is the period $A(\theta + T) = A(\theta)$) have unit modulus and the set of theirs is divided on mutually conjugate pairs. The typical trajectory of the particle motion is almost periodic in general case, i.e. the eigenvalues are incommensurable. However each trajectory moves on accompanying ellipsoid (5). In turn the matrix $G(\theta)$ is not periodic also in general case, $G(T) \neq G(0) = 1$, i.e. the ellipsoid (5) does not coincide with itself after a lapse of the period. It is connected with that the monodromy matrix is not unitary in general case due to its eigenvectors are not mutually orthogonal. Then the desired envelopes are the envelopes of all possible shifts $\theta \rightarrow \theta + nT$, $n = 1, 2, 3, \dots$ of the surface (5). Since we want to determine separately the envelope relative to each dynamic variable u_l , then it is suitable to divide the solution of this problem on two stages. On first stage we determine the maximum value $\bar{u}_l(\theta) = \max[u_l(\theta)]$ of the variable $u_l(\theta)$ for all trajectories with the initial values u_0 inside the sphere (5) at $\theta = 0$. On second stage we must calculate the maximum value \bar{u}_l of the function $\bar{u}_l(\theta)$ on all possible shifts of the θ ,

$$\bar{u}_l = \sup\{\bar{u}_l(\theta + nT), n = 0, 1, 2, 3, \dots\} \quad (6)$$

This value is the desired envelope for the dynamic variable $u_l(\theta)$.

First stage of the above described procedure is reduced to the simple geometrical problem connected with the ellipsoid. We give it solution below. Under above considerations to calculate the values $\bar{u}_l(\theta)$ it is sufficient to find the value $\bar{u}_l = \max[u_l]$ where the maximum is computed for all points of the enveloping ellipsoid (5). Calculate, for example, the value \bar{u}_1 , determining the maximum of u_1 by varying u_2, \dots, u_6 over the ellipsoid surface. In this case we may consider u_1 to be the implicit function of u_2, \dots, u_6 parameters. Since in Eq.(5) the θ is fixed and, hence, we do not specify below the dependence on θ . Denote $P \equiv G^{-1}(\theta)$ and by symbol P' the truncated 5×5 - matrix which is obtained from P by crossing out the first line and the first column. Denote also $Q \equiv (P')^{-1}$. In all below formulae the summation respective to repeating indexes is performed from 2 to 5. By differentiating Eq.(5) on u_s , $s = 2, \dots, 5$ respectively and requiring the maximality of u_1 , i.e. $u_1 \rightarrow \bar{u}_1$, $\partial u_1 / \partial u_s = 0$, $s = 2, \dots, 5$, we obtain $u_l = Q_{ls} P_{s1} \bar{u}_1$, $l = 2, \dots, 5$. The substitution of these u_l - values in (5) gives the equation for the \bar{u}_1 - calculation

$$I_0 = \bar{u}_1^2 [P_{11} - r], \quad r = P_{1k} Q_{km} P_{m1}, \quad (7)$$

where we applied the identity

$$P_{lm} Q_{mk} = P'_{lm} Q_{mk} = \delta_{lk}; \quad l, k = 2, \dots, 5.$$

Now we transform the expression in square brackets. It follows from the definition of the P - matrix that

$$G_{1k} P_{1m} + G_{kl} P_{lm} = \delta_{km}, \quad G_{11} P_{11} + G_{1k} P_{1k} = 1,$$

$$G_{1k} P_{11} + G_{kl} P_{11} = 0, \quad k, m = 2, \dots, 5.$$

The first equation shows that $r = P_{1m} Q_{mk} P_{k1} + G_{1k} P_{1k} r$. Using second and third equations we obtain

$$r G_{11} P_{11} = P_{1k} G_{km} P_{m1} = -P_{1k} G_{1k} P_{11} = (1 - P_{11} G_{11}) P_{11}.$$

Substituting the expression $r = 1/G_{11} - P_{11}$ in Eq.(7) and recovering the dependence on θ , we derive the final formula

$$\bar{u}_1(\theta) = \pm(I_0 G_{11}(\theta))^{1/2}.$$

The calculations performed are related literally for every dynamic variable u_l and therefore the general formula is valid

$$\bar{u}_l(\theta) = \pm(I_0 G_{ll}(\theta))^{1/2} \quad (8)$$

Eq.(8) gives the general expression for $\bar{u}_l(\theta)$ obtaining on first stage of the above described calculation procedure. Three almost periodic functions $G_{ll}(\theta)$, $l = 1, 2, 3$ can be called the generalized magneto-optic functions of the accelerator structure.

Pass on the second stage of the envelope computation. If the monodromy matrix is unitary, then $\bar{u}_l(\theta) = \bar{u}_l(\theta)$, i.e. the envelope form is determined by the Eq.(8). But the opposite case with the nonunitary monodromy matrix takes place as a rule. And we must use Eq.(6) in order to find the envelopes. Due to the almost periodicity of the matrix $G(\theta)$, the ellipsoids (5) obtained by the consequent shifts $\theta \rightarrow \theta + nT$ do not coincide with each

other. Therefore the problem arises to find the envelope of all possible shifts mentioned for each value $\tilde{u}_l(\theta)$, $l = 1, \dots, 6$. To do this it may set up the following problem. Is there an ellipsoid (5) which coincides with itself after the shift $\theta \rightarrow \theta + T$, i.e. is there an initial matrix G_0 such that the matrix $G(\theta)$, $G(0) = G_0$ which satisfies to Eq.(3) and to $G(\theta + T) = G(\theta)$? If there are the ellipsoids with described property then we may put the initial unit sphere $(u_0, u_0) = 1$ into one of them and the next question arises. Would one to elect the matrix G_0 by an optimal way when the envelope (6) generated by the motion with initial data u_0 on the sphere will coincide with the optimal ellipsoid? Answers on these questions contain the following assertions.

Theorem 1. If the system (1) is stable, then there is always the ellipsoid (5) which is invariant relative to the transformation $\theta \rightarrow \theta + T$, along the trajectories of the motion. It is determined by the matrix $G_0^{-1}(G_0^+ = G_0, \det G_0 = 1)$ of the quadratic form coefficients. If the spectrum of the matrix $M(T)$ is not degenerate, then this ellipsoid is unique to within the isotropic dilatation.

Theorem 2. If the spectrum of the matrix $M(T)$ of the stable system is not degenerate and has not some pairs of the commensurable Floquet exponents, then there is the unique ellipsoid enveloping all trajectories with initial data u_0 lying on the sphere $(u_0, u_0) = I_0$. This ellipsoid coincides with the invariant ellipsoid mentioned in Theorem 1. and it is circumscribed round the sphere determined by the value I_0 , i.e. it is minimal among invariant ellipsoids containing the sphere.

The properties expressed by these theorems one would consider as the generalization for the linear uniform systems with periodic dependence in time of the corresponding properties of the linear autonomous Hamiltonian systems. If the oscillations of charged particle for all degrees of freedom are connected and have the incommensurable frequencies when the system parameters are in general position, then the theorem conditions take place and we may use their assertions for the finding of the motion envelopes. In particular, on the base of Theorem 2 we may consider that the union of all ellipsoids obtained by the consequent shifts on the period T from the initial sphere coincides with the circumscribed invariant ellipsoid. Therefore to find the value $\tilde{u}_l(\theta)$ it is sufficient to build the circumscribed invariant ellipsoid and after that to calculate the value $\tilde{u}_l(\theta)$ for this ellipsoid on the base of Eq.(8).

Here we'll not give the complete proofs of the theorems formulated. It will be done in other publication. We'll point out only that these proofs are based on the transformation possibility of the monodromy matrix $M(T)$ to the unitary one by means of a reversible matrix S , which does not depend on θ . This idea we illustrate below on the simple example.

Example. Consider the particular case of the linear stable Hamiltonian system for which the matrix A is constant. Then $M(\theta) = \exp(A\theta)$ and the monodromy matrix $M(T) = \exp(AT)$ is not unitary in general case, i.e. the condition $M(T)M^+(T) = 1$ does not necessarily take place, since $A \neq -A^+$ and moreover the matrices A, A^+ may be noncommuting. But there is the matrix G_0 such that $G_0^+ = G_0$ and

$$G_0^{-1}AG_0 = -A^+.$$

It permits to build the matrix $G = M(\theta)G_0M^+(\theta)$, which does not depend on θ , i.e. it coincides with the G_0 and, in particular, it is invariant relative to shift on the period. The proof of the existence of the matrix G_0 is based on the following argument. From one hand the system (1) is stable and therefore the eigenvalues of the A are imaginary and in addition they form the mutually conjugate pairs. From other hand the sets of eigenvalues of the matrices A, A^+ coincide with each other. Then for each A -eigenvalue α there is the A^+ -eigenvalue α^* such that $\alpha + \alpha^* = 0$. It is sufficient for the existence of the nontrivial solution of the matrix Lyapunov equation $AG_0 + G_0A^+ = 0$. If the spectrum of the A is not degenerate, then the eigenvalue α^* is unique for each α . and therefore the matrix G_0 is also unique due to the condition $\det G_0 = 1$. Notice that one would always represent the matrix G_0 in the form $G_0 = SS^+$ where the matrix S realizes the transformation the matrix $M(T)$ to the unitary one.

References

1. D.A.Edwards, L.C.Teng, IEEE Trans. Nucl. Sci., vol.119-20, No.3, p.885 (1973).
2. K.L.Brown, R.V.Servrancki, Particle Accelerators, 1991, vol.36, pp. 121-139.
3. F.Willeke, G.Ripken, Methods of Beam Optics, DESY 88-114 August 1988.
4. A.A.Kolomenskij, A.N.Lebedev "A Theory of Cyclic Accelerators", Gosizdat FML, Moscow, 1962.
5. Henri Bruck, Accelérateurs circulaires de particules, Presses Universitaires de France 1966.
6. B.Courant, H.Snyder. Theory of the Alternating- Gradient Synchrotron. Ann.of Phys. 3, 1-48 (1958).
7. V.A.Jakubovich, V.N.Starzhinskij, Linear Differential Equations with Periodic Coefficients and their applications, Nauka, Moscow, 1972.

A Semi-analytical Approach to the Design of Low Energy Cylindrically Symmetric Transport Lines

Pedro F. Tavares, Laboratório Nacional de Luz Síncrotron, LNLS, Campinas, Brazil

Abstract

An optimization procedure that determines the best values (i.e., those that minimize beam radius) for the focal distances of solenoidal magnetic lenses in a low-energy cylindrically symmetric transport line is presented. The procedure is based on an analysis of the RMS beam envelope equation, which accounts for space charge as well as emittance effects. Universal beam-spreading curves including emittance effects (a generalization to the well-known space-charge spreading curves) are presented in a form convenient for general use. The results are applied to the design of the gun-to-linac transport channel of the LNLS injector.

I. Introduction

LNLS is building a 1.15 GeV electron storage ring to be commissioned in early 1996 as a synchrotron light source. Injection into the storage ring takes place from a 100 MeV LINAC. The 80 keV 100 ns electron beam pulses are produced in a conventional gridded electrostatic gun and then transported to the accelerating structures by means of three iron-core solenoidal magnetic lenses.

The dynamics of the low-energy cylindrically symmetric electron beam under the action of space-charge and focussing forces along the gun-to-linac transport line can be described by the RMS envelope equation derived by Lee and Cooper[1], which also includes finite emittance effects. Although numerical solutions to this equation can be easily obtained in order to validate a given lay-out (position and excitation of lenses) of the transport line, the question remains as to whether the best possible setting of the lenses (in the sense of providing the minimum beam radius all along the line) has been chosen.

In this paper, I present a simple, semi-analytical approach to find the best possible settings for a series of (thin) magnetic lenses once the transport-line lay-out is chosen. In section (II), the RMS envelope equation is briefly reviewed and solutions are presented for field-free regions in the form of normalised beam spreading curves similar to the well know space-charge beam spread curves. The focussing action of the magnetic lenses is calculated in section (III) in the thin lens approximation and piecewise numerical minimisation of the beam radius is performed between lenses, using the lens focal length as the variable parameter. Finally, in section (IV) the particular case of the LNLS preinjector is presented and the results of a detailed (thick lens) numerical solution are compared with the thin lens approximation.

II. The envelope equation

The RMS radius of a cylindrically symmetric electron beam propagating in a *field-free* region obeys the envelope equation

$$R''(z) = \frac{K}{R(z)} + \frac{\varepsilon_0^2}{R^3(z)}, \quad (1)$$

where ε_0 is the RMS radial emittance (a constant of the motion)

$$\varepsilon_0^2 = \langle r^2 \rangle \langle r'^2 \rangle - (\langle rr' \rangle)^2, \quad (2)$$

where the angle brackets denote an average over the electron phase space distribution, and

$$K = \frac{e_0 I_0}{4\pi \epsilon_0 m_0 (\gamma \beta c)^3}, \quad (3)$$

where e_0 is the elementary charge, I_0 is the beam current, m_0 is the electron mass, and γ , β are respectively the electron energy in units of the electron rest mass and the electron velocity in units of the velocity of light.

Clearly, the solutions to Eq.(1) may present two kinds of behaviour: an initially diverging beam ($R'_0 > 0$) continues to diverge with ever increasing slope, whereas an initially converging beam reaches a waist at a certain point and diverges thereafter. In any case, a waist may be defined with respect to which the solution is symmetric.

Multiplying both terms of Eq.(1) by $2R'(z)$ and integrating from a waist at $z = 0$ (where $R'(z) = 0$, $R = R_0$), I obtain

$$R'^2(z) = 2K \int_{R_0}^R \frac{dR^*}{R^*} + 2\varepsilon_0^2 \int_{R_0}^R \frac{dR^*}{R^{*3}} \quad (4)$$

and yet another integration yields an implicit solution for $R(z)$:

$$z(R) = \int_{R_0}^R \frac{dR^*}{\sqrt{2K \ln\left(\frac{R^*}{R_0}\right) + \frac{\varepsilon_0^2}{R_0^2} \left[1 - \left(\frac{R_0}{R^*}\right)^2\right]}}. \quad (5)$$

It is convenient to introduce the dimensionless variables

$$\rho = \frac{R}{R_0}, \quad (6)$$

$$\nu = \frac{\varepsilon_0^2}{2K R_0^2}, \quad (7)$$

$$\xi = \sqrt{2K} \frac{z}{R_0}, \quad (8)$$

so that Eq.(5) becomes

$$\xi(\rho) = \int_1^\rho \frac{d\rho^*}{\sqrt{\ln \rho^* + \nu \left[1 - \left(\frac{1}{\rho^*}\right)^2\right]}}. \quad (9)$$

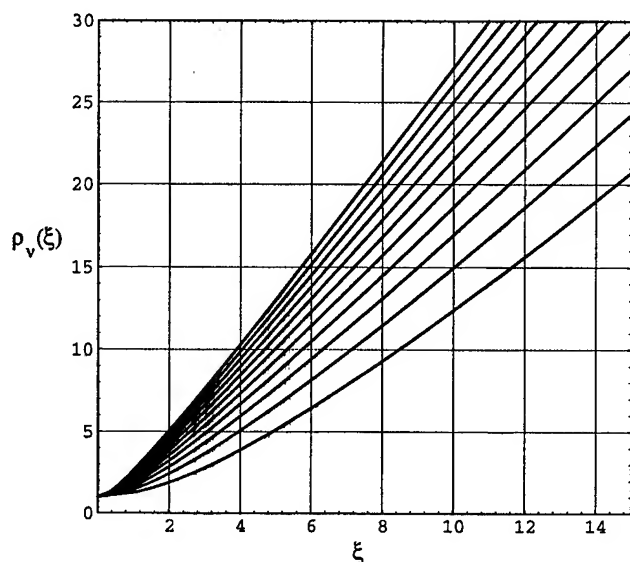


Figure 1. Normalised spreading curves for a beam under the action of space-charge and emittance. The curves correspond to (from bottom to top) $\nu = 0, 0.5, 1.0, 1.5, 2.0, 2.5, 3.0, 3.5, 4.0, 4.5, 5.0$.

Finally, it is convenient to change the integration variable to w defined by

$$w^2 = \ln \rho^*, \quad (10)$$

so that

$$\xi_v(\rho) = \int_0^{\sqrt{\ln \rho}} \frac{2e^{w^2} w dw}{\sqrt{w^2 + \nu(1 - e^{-2w^2})}}. \quad (11)$$

Fig.(1) shows beam spread curves calculated from the equation above for various values of ν . These curves reduce to those plotted by Hutter[2] in the limit of a laminar beam ($\nu = 0$). Once these curves are calculated numerically at a sequence of points, a spline interpolation provides a convenient and fast way of calculating the inverse function $\rho_v(\xi)$.

III. Optimisation of lens settings

The generalisation of Eq.(1) to include static axial magnetic fields reads

$$R''(z) = \frac{K}{R} + \frac{\varepsilon_0^2}{R^3} - \Omega^2(z)R, \quad (12)$$

where

$$\Omega(z) = \frac{e_0 B(z)}{2m_0 c \gamma \beta} \quad (13)$$

and $B(z)$ is the longitudinal magnetic field. If the magnetic field is confined to a small region around $z = z_i$, its effect may be approximated by a thin lens of focal distance

$$\frac{1}{f} = \int \Omega^2(z) dz \quad (14)$$

so that, on crossing the lens, the slope R' changes by $\Delta R' = -R/f$, whereas, in between two lenses, the functions $\xi_v(\rho)$ and $\rho_v(\xi)$ defined above describe the evolution of the envelope. Fig.(2) shows the qualitative evolution of the envelope along a

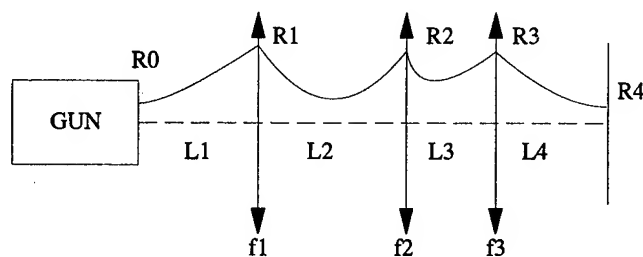


Figure 2. The beam envelope along a transport line with three thin magnetic lenses.

transport line containing three thin magnetic lenses. For simplicity, I assume that both the starting point $z = 0$ (at the output of the gun) and the end of the line are waists ($R' = 0$).

The beam radius at the first lens is

$$R_1 = R_0 \rho_v \left(\sqrt{2K} L_1 / R_0 \right). \quad (15)$$

I now consider the problem of minimising the beam radius at the second lens (R_2) by adjusting the focal length f_1 , or equivalently, by adjusting the position ($z_{wa} = L_1 + z_{ma}$) and radius R_{wa} of a beam waist to be formed after lens 1. The boundary conditions at $z = L_1$ and $z = L_1 + L_2$ are

$$\sqrt{2K} \frac{z_{ma}}{R_{wa}} = \xi_v \left(\frac{R_1}{R_{wa}} \right), \quad (16)$$

$$\sqrt{2K} \frac{|L_2 - z_{ma}|}{R_{wa}} = \xi_v \left(\frac{R_2}{R_{wa}} \right), \quad (17)$$

where the absolute value is introduced to deal with the possibility of the waist being after lens 2. The equations above can be combined to yield

$$R_2(R_{wa}) = R_{wa} \rho_v \left(\left| \frac{L_2 \sqrt{2K}}{R_{wa}} - \xi_v \left(\frac{R_1}{R_{wa}} \right) \right| \right). \quad (18)$$

Once R_{wa} , z_{ma} , and R_2 are determined by numerical minimisation of the expression above¹, the same reasoning may be applied to the region between the second and third lenses so as to determine the value of f_2 that minimises R_3 given by the equation

$$R_3(R_{wb}) = R_{wb} \rho_v \left(\left| \frac{L_2 \sqrt{2K}}{R_{wb}} - \xi_v \left(\frac{R_1}{R_{wb}} \right) \right| \right). \quad (19)$$

where now the radius at the waist is R_{wb} . A similar reasoning may be used to determine the focal length f_3 that is compatible with the assumption $R'_4 = 0$ and that yields the minimum possible R_3 , by minimising the expression

$$R_3^b(R_4) = R_4 \rho_v \left(\frac{\sqrt{2K} L_4}{R_4} \right), \quad (20)$$

¹ Clearly, since ν is actually a function of R_{wa} , a proper treatment would require that the functions $\rho_v(\xi)$ and $\xi_v(\rho)$ be interpolated as functions of two variables rather than just the 1-dim curves given above. If the emittance effect is a small correction to the space-charge effect, however, one may safely take $\nu = \text{constant}$.

where now the waist position is fixed (at L_4) and the radius at the waist is R_4 . The larger of the two values (R_3^α and R_3^β) obtained for the beam radius at the third lens (as determined by independent conditions) must be taken as the design value, since otherwise the two requirements are incompatible and cannot be satisfied simultaneously, so that

$$R_3 = \max(R_3^\alpha, R_3^\beta). \quad (21)$$

If $R_3 = R_3^\alpha$, then R_4 is obtained by solving the equation

$$R_4 \rho_v \left(\frac{\sqrt{2K} L_4}{R_4} \right) = R_3, \quad (22)$$

whereas if $R_3 = R_3^\beta$ is larger, then R_4 is just the value obtained from the minimisation in Eq.(20). Similarly, if $R_3 = R_3^\beta$, R_{wb} is obtained from the equation²

$$\frac{\sqrt{2K} L_3}{R_{wb}} = \xi_v \left(\frac{R_2}{R_{wb}} \right) + \xi_v \left(\frac{R_3}{R_{wb}} \right), \quad (23)$$

whereas if $R_3 = R_3^\alpha$, R_{wb} is simply the value obtained in the minimisation of Eq.(19). The positions of the waists are given by

$$z_{wa} = L_1 + \frac{R_{wa}}{\sqrt{2K}} \xi_v \left(\frac{R_1}{R_{wa}} \right) \quad (24)$$

$$z_{wb} = L_1 + L_2 + \frac{R_{wb}}{\sqrt{2K}} \xi_v \left(\frac{R_1}{R_{wb}} \right). \quad (25)$$

Finally, the slopes just before and after the various lenses are

$$R'_{1-} = \sqrt{2K} \sqrt{\ln R_1/R_0 + v \left(1 - \left(\frac{R_1}{R_0} \right)^2 \right)},$$

$$R'_{1+} = -\sqrt{2K} \sqrt{\ln R_1/R_{wa} + v \left(1 - \left(\frac{R_{wa}}{R_1} \right)^2 \right)},$$

$$R'_{2-} = \sqrt{2K} \sqrt{\ln R_2/R_{wa} + v \left(1 - \left(\frac{R_{wa}}{R_2} \right)^2 \right)},$$

$$R'_{2+} = -\sqrt{2K} \sqrt{\ln R_1/R_{wa} + v \left(1 - \left(\frac{R_{wa}}{R_2} \right)^2 \right)},$$

$$R'_{3-} = \sqrt{2K} \sqrt{\ln R_3/R_{wb} + v \left(1 - \left(\frac{R_{wb}}{R_3} \right)^2 \right)},$$

$$R'_{3+} = -\sqrt{2K} \sqrt{\ln R_3/R_{wb} + v \left(1 - \left(\frac{R_{wb}}{R_3} \right)^2 \right)},$$

and the focal distances are

$$f_i = \frac{R_i}{R'_{i+} - R'_{i-}}, \quad (26)$$

with $i = 1, 2, 3$.

²Here I assume $z_{mb} = z_{wb} - (L_1 + L_2) < L_3$.

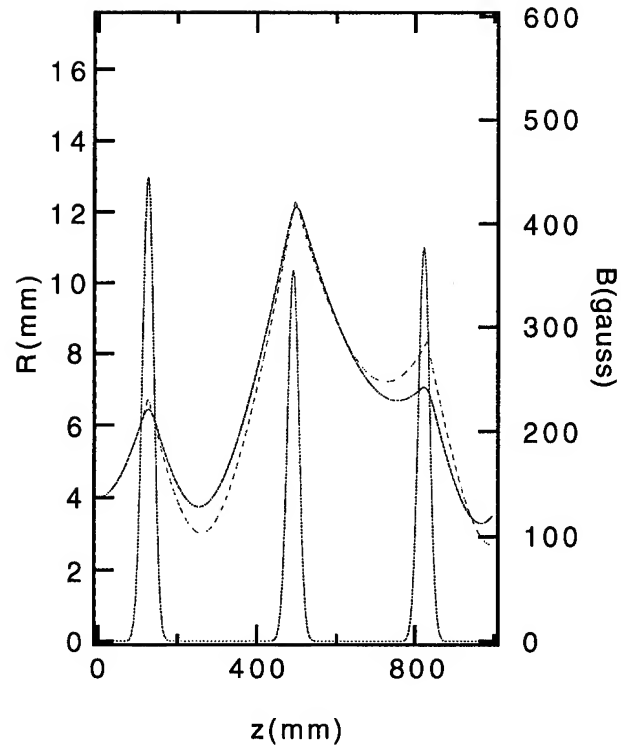


Figure 3. Beam envelope along the gun-to-LINAC transport line. The dashed line is the result of the thin lens approximation and the solid line was obtained from a full numerical solution of the envelope differential equation with a gaussian model for the longitudinal magnetic field. Also shown is the axial magnetic field.

IV. Results

Fig.(3) shows the results obtained with the method outlined above for an 80 keV 2 Amp beam, with $\epsilon_0 = 40$ mm mrad. The distances are $L_1 = 12.7$ cm, $L_2 = 33.2$ cm, $L_3 = 32.4$ cm, and $L_4 = 14.21$ cm. The optimised focal distances are $f_1 = 8.5$ cm, $f_2 = 10.5$ cm, and $f_3 = 8.4$ cm.

References

- [1] E.P.Lee and R.K.Cooper, *General Envelope Equation for Cylindrically Symmetric Charged-Particle Beams*, Part. Acc., Vol 27 pp. 83 (1976)
- [2] R. Hutter, *Beams with Space-charge*, in *Focusing of Charged Particles*, Vol II ed by A. Septier, Academic Press, New York (1967).

Stability of Trapped Ions in Electron Storage Rings in View of Parametric Resonance

Y. Miyahara, SPring-8, Kamigori, Ako-gun, Hyogo 678-12, Japan

Abstract

Stability of the trapped ions in electron storage ring was studied with a Hamiltonian formalism derived from the Mathieu equation, in which the nonlinear field of the electron beam and the Fourier component of the beam current were taken into account.

I. Introduction

Stability of positive ions trapped ion electron beam in electron storage rings can be distinguished by the matrix method. This derives the critical mass of the trapped ions, above which the ions are stable or the ions are trapped in the electron beam. It has been observed that the trapped ions can be eliminated by the partial fill mode operation, in which some RF buckets are not filled with electron beam bunches [1,2,3]. The stability of the ions in this mode can also be distinguished by the matrix method. But this method is only applicable in case of linear field. The electric field produced by the electron beam is highly nonlinear because of the Gaussian distribution of the electron beam.

Meanwhile, the stability was studied analytically on a special partial fill mode, in which the electron beam was distributed sinusoidally along the circumference of the ring [2]. In this mode, the equation of motion of the ions can be expressed with the Mathieu equation, so that the stability or instability of the ion can be derived straightforwardly. But this method was also discussed assuming linear field.

The electric field is linear only in the region $z \leq \sigma_z/2$ ($z=x$ or y), so that the ions might be still trapped in or near the electron beam even if the unstable condition is satisfied in the linear field region. In the present paper we have studied the effects of the nonlinear field with a Hamiltonian formalism derived from the Mathieu equation. In addition, the beam current was expanded in a Fourier series, so that any pattern of the beam bunch distribution can be included in the present analysis. Special attention is paid to the 1/3 fill mode being made in ESRF, which will be probably applied to SPring-8.

II. Stability Analysis of Trapped Ions

A. Hamiltonian Formalism

The electron beam current can be expanded in the Fourier series. The coefficients ϵ_m 's of the Fourier component for the 1/3 fill mode are given by $\epsilon_m = (6/m\pi)\sin(2m\pi/3)$, where m denotes the m -th component of the revolution frequency of the electron beam. The equation of motion of the trapped ion for one Fourier component can be written as

$$\frac{d^2 u}{dt^2} + \omega_0^2 [1 + \epsilon_m \cos(m\omega_0 t + \theta_m)] f(u) = 0 \quad (1)$$

where $u=x/\sigma_x$ or y/σ_y , ω_0 is the oscillation frequency of the ion in the linear field, ω_0 is the revolution frequency of the electron beam, θ_m is the initial phase and $f(u)$ is the position dependence of the electric field. Introducing the following definitions

$$\omega_m = m\omega_0/2, \quad \omega_{i0} = \omega_m + \Delta\omega \quad \text{and} \quad \theta = \omega_m t, \quad (2)$$

and taking up to the third power of the nonlinear field, at first, we can write Eq.(1) as follows,

$$\begin{aligned} \frac{d^2 u}{d\theta^2} + u + [\delta + \epsilon_m(1+\delta) \cos(2\theta + \theta_m)] u \\ - k_3(1+\delta)[1 + \epsilon_m \cos(2\theta + \theta_m)] u^3 = 0, \quad (3) \\ (\delta = 2\Delta\omega/\omega_m, \quad \epsilon_m = \Delta\omega/\omega_m) \end{aligned}$$

Equation (1) is obtained from the following Hamiltonian,

$$\begin{aligned} H = \frac{1}{2} (p_u^2 + u^2) + \frac{1}{2} [\delta + \epsilon_m(1+\delta) \cos(2\theta + \theta_m)] u^2 \\ - \frac{1}{4} k_3 (1+\delta) [1 + \epsilon_m \cos(2\theta + \theta_m)] u^4, \quad (4) \\ (p_u = \partial u / \partial \theta) \end{aligned}$$

Introducing the following canonical transformation

$$u = \sqrt{2J} \cos(\theta + \Phi) \quad \text{and} \quad p_u = -\sqrt{2J} \sin(\theta + \Phi), \quad (5)$$

and taking the average of the Hamiltonian over $\theta=0 \sim 2\pi$, we find

$$\begin{aligned} \bar{H}_1 = \frac{1}{2} J \delta + \frac{1}{4} J \epsilon_m (1+\delta) \cos(\theta_m - 2\Phi) \\ - \frac{3}{8} J^2 k_3 (1+\delta) - \frac{1}{4} J^2 k_3 (1+\delta) \epsilon_m \cos(\theta_m - 2\Phi), \quad (6) \end{aligned}$$

where we have assumed J is constant over the above period. Because of no dependence on θ , \bar{H}_1 is a constant of motion. Introducing again the following canonical transformation,

$$Z = \sqrt{2J} \cos(\Phi + \Phi_0) \quad \text{and} \quad P = -\sqrt{2J} \sin(\Phi + \Phi_0), \quad (7)$$

we obtain

$$\bar{H}_2 = A(Z^2 + P^2) + B(Z^2 - P^2) - C(Z^2 + P^2)^2 - D(Z^4 - P^4), \quad (8)$$

with $A = \delta/4$, $B = \epsilon_m(1+\delta)/8$

$$C = 3k_3(1+\delta)/32, \quad D = k_3\epsilon_m(1+\delta)/16$$

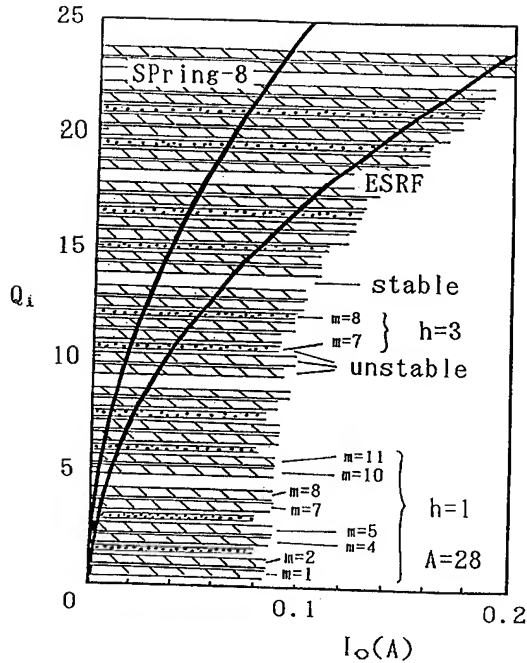


Figure 1. Stability diagram of CO^+ ion in the 1/3 fill mode in ESRF and SPring-8. The ion is unstable in the shaded and dotted regions.

B. Trajectory in the phase space and stability diagram

In case of the linear field ($k_3=0$), we have $C=D=0$, so that the trajectory in the phase space (Z, P) is ellipse (stable or trapped) or hyperbola (unstable), which is determined by the relation of A and B . The boundary of the stable and unstable regions is separated by the following function

$$g(\chi) = \frac{2\chi(2+\chi)}{(1+\chi)^2} = 4\chi - 6\chi^2 + 8\chi^3 \dots \quad (9)$$

with $\chi = \delta_m$. In case of the 1/3 fill mode the bandwidth of the unstable region can be written as

$$\delta Q_i \approx \epsilon_m m h / 4 = (3h/2\pi) |\sin(2\pi m/3)|, \quad (10)$$

where h is the resonant mode number of the Mathieu equation, and Q_i is defined as

$$Q_i = \frac{\omega_0}{\omega_b} = \left[\sqrt{2\pi} \frac{r_p}{ec} \frac{I_0}{A} \frac{R^2}{\sigma_x \sigma_y} \right]^{1/2}, \quad (11)$$

with r_p ; the classical proton radius, e ; the charge of the electron, c ; the velocity of the light, I_0 ; the average beam current, A ; the mass number of the trapped ion, and R ; the average radius of the storage ring. Figure 1 represents the stability diagram of CO^+ ions in the 1/3 fill mode of ESRF and SPring-8 determined by the linear field approximation. In the figure the ordinate is Q_i and the absciss is the average beam

current. The solid curves in the figure represent the current dependence of Q_i , and the ion is unstable in the shaded and dotted regions. In this approximation the ion is unstable at any beam current.

In case of nonlinear field with $k_3 \neq 0$, the ion is always bounded. Examples of the trajectory in the phase space (Z, P) are shown in Fig.2 for different value of δ_m 's at $\epsilon_m=0.1$. Even at $\epsilon_m=1$, the trajectory is also bounded within a few σ_z . The results are not much different even if we add the fifth power term of the nonlinear field as shown in Fig.3. The Hamiltonian becomes very complicated if we introduce higher power terms further.

Now we consider again the stability of the trapped ion in the linear field in case of an equidistant several bunch mode operation. In case of 21 bunch mode operation in SPring-8, for instance, we have $\epsilon_m \approx 1$ for $m=21, 42, 63 \dots$. Taking into account the width of the unstable region at $\epsilon_m=1$, we obtain the stability diagram shown in Fig.4. As shown with a solid circle in the figure, there are critical value Q_{ic} and I_{0c} , below which the ions are stable. From the analysis of the unstable region determined by the function $g(\chi)$, we obtain $Q_{ic} = m^*/\sqrt{6}$, where m^* is the minimum m , which is 21 in the present case. Meanwhile, we have from the above definition of Q_i

$$Q_{ic} = \alpha \sqrt{I_{0c}/A_c} = \alpha \sqrt{I_0/A_c}, \quad (12)$$

Consequently, we find the following critical mass,

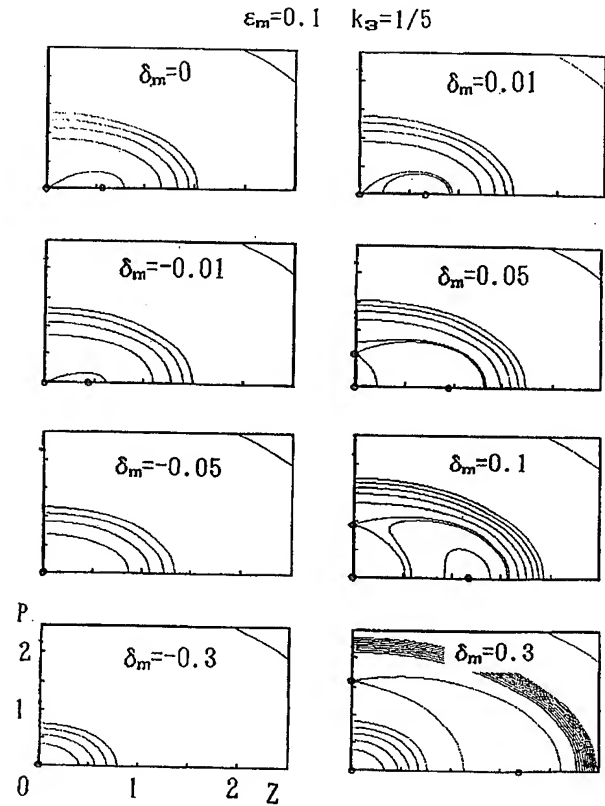


Figure 2. Ion trajectory in the phase space (Z, P). The nonlinear field was taken into account up to the third power of the field expansion.

$$A_c \approx \frac{r_p}{\sqrt{2\pi}} \frac{N_e}{N_B} \frac{2\pi R}{N_B} \frac{1}{\sigma_x \sigma_y}, \quad (13)$$

This is very close to the critical mass derived by the matrix method.

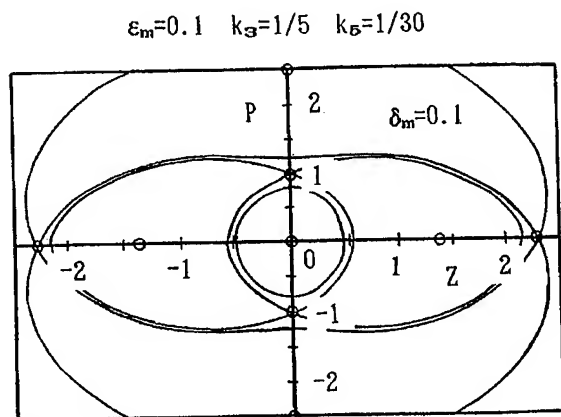


Figure 3. Ion trajectory in the phase space. The nonlinear field was taken into account up to the fifth power.

III. Conclusion

We have discussed the stability of the trapped ions in the electron beam with the Hamiltonian formalism by taking into account the nonlinear field produced by the electron beam and the Fourier component of the beam current. It was found that the ions are bounded within a few σ 's of the electron beam size so long as the nonlinear field is considered up to the fifth power of the field expansion. It is required to investigate the stability by including higher power terms further. Meanwhile, in the linear field approximation, we have derived the critical mass from the present formalism, which is close to the mass derived from the matrix method. Therefore, the present formalism is more general than the matrix method, and will be useful to make a further investigation on the ion trapping.

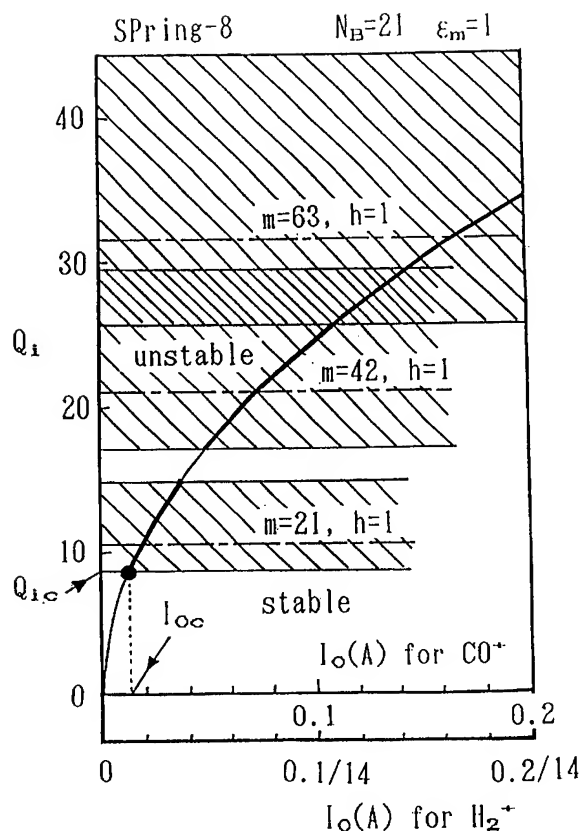


Figure 4. Stability diagram of CO^+ and H_2^+ ions in the equidistant 21 bunch mode of SPring-8.

References

- [1] M. Barton, Nucl. Instr. and Methods, A243 (1986) 278.
- [2] S.Sakanaka, KEK Preprint, 86-17, June, 1986.
- [3] J.L.Laclare, Proc. of Particle Accel. Conf. 1993, Vol 2, 1427.

ENTROPY AND EMITTANCE OF PARTICLE AND PHOTON BEAMS*

K.-J. Kim and R.G. Littlejohn, Lawrence Berkeley Laboratory, Berkeley, CA 94720 USA

Abstract

The emittance as the available phase space area is defined as the product of the elementary cell area $\delta\Omega$ and $\exp(S)$, where S is the normalized entropy of a particle beam. The definition is based on the fact that the factor $\exp(S)$ can be interpreted as the number of the occupied cells. For particle beams, a closed expression for the emittance in terms of the phase space distribution function is obtained which is independent of $\delta\Omega$. To compute the emittance of the radiation beam, it is necessary to find the eigenvalues of the correlation operator. An explicit solution is found for the case of a partially coherent radiation beam which is a stochastic superposition of coherent Gaussian beams with a Gaussian probability distribution. Such a beam is a reasonable model for undulator radiation by beam of electrons. From the requirement that the radiation emittance reproduces the particle beam emittance in the incoherent limit, the elementary cell area $\delta\Omega$ is determined unambiguously to be λ , the radiation wavelength. The emittance in the coherent limit then becomes λ .

I. INTRODUCTION

The macroscopic state of a particle beam is specified by the distribution function in phase space. However, it is often useful to have a global characterization of the beam quality by means of a few numbers. The area of phase space occupied by the beam, called the emittance, is a good representation of the beam quality as it gives a measure of the uncertainty in the state of a particle beam. It is furthermore invariant under linear beam transport transformation. On the other hand, definition of emittance has been rather arbitrary.

Let us first recall several definitions of emittance. Throughout this paper, we will, for simplicity limit our discussion to the phase space distribution in one transverse direction. Let the probability distribution function in phase space be $f(x, \phi)$, with the normalization $\int f(x, \phi) dx d\phi = 1$. Examples of the possible emittance definitions are:

1. The geometric emittance, ϵ_F defined to be the area of the phase space region containing a fraction F of the total particles.
2. The peak emittance, defined as $\epsilon_0 = 1/f(0, 0)$
3. The rms emittance

$$\epsilon_{rms} = \sqrt{\langle x^2 \rangle \langle \phi^2 \rangle - \langle x\phi \rangle^2},$$

where quantities within the angular brackets are the average values.

Each of the above definitions is suitable for certain phase space distributions, but not for others; ϵ_F could depend sensitively on the chosen value of the fraction F and could also be ambiguous for a complicated distribution, ϵ_0 is suitable only for a distribution with a well defined peak at the origin and no other

places, and ϵ_{rms} is not suitable in for general non-Gaussian distributions. Also ϵ_F and ϵ_0 cannot be generalized to radiation beams. Although ϵ_{rms} can be generalized to radiation beam, it gives an infinity for the case of a coherent beam after an aperture.

This paper is an attempt to put the emittance concept on a firmer theoretical basis by relating it to the entropy in statistical mechanics. We define emittance as the product of the elementary cell area $\delta\Omega$ and $\exp(S)$, where S is the normalized entropy of a particle beam. The definition is reasonable because the factor $\exp(S)$ can be interpreted as the number of the occupied cells. The approach provides a well defined, unified description of the beam qualities for particle and radiation beams. Such a unified understanding will be useful in describing the partially coherent beams from electron beams travelling through undulators in modern synchrotron radiation facilities.

Entropy as a measure of the quality of particle beam has been suggested before[1]. Here we provide a quantitative connection of the entropy to emittance for particle as well as radiation beam.

II. ENTROPY AND EMITTANCE

To compute the entropy of a particle beam, we divide the phase space area occupied by the beam into a large number M of elementary cells of an area $\delta\Omega$. Let N be the total number of particles in the beam, n_k is the number of the particles in the k th cell, and $p_k = n_k/N$ be the probability that a particle occupy the k th cell. The number of ways in which the particles can be partitioned into different cells to produce a given phase space distribution is

$$P = \frac{N!}{n_1! n_2! \dots n_M!}. \quad (1)$$

The entropy of the beam is given by $\ln P$. The normalized entropy, S , is obtained by dividing the entropy by N :

$$S \equiv \frac{1}{N} \ln P = - \sum_{k=1}^M p_k \ln p_k. \quad (2)$$

In the above we are assuming that N and n_k are large so that Stirling's formula is applicable.

The entropy has a well known meaning as a measure of the disorder in statistical mechanics, or as the information capacity in information theory. We will relate the entropy to emittance by noting that the quantity $\exp S$ can be interpreted as the number of the occupied cells. To see this, we construct a uniform phase space distribution associated with the original distribution such that the entropies of the two distributions are the same. The number of elementary cells in the associated distribution, denoted by \bar{M} , will be the number of the occupied cells in the original distribution. The normalized entropy for the associated distribution is $\ln \bar{M}$ which by construction is equal to S . Thus we see, indeed, that $\exp S$ is the number of the occupied cells.

Based on these considerations, we write the emittance as follows:

$$\epsilon = \delta\Omega \exp S. \quad (3)$$

*This work was supported by the Director, Office of Energy Research, Office of Basic Energy Sciences, of the U.S. Department of Energy under Contract No. DE-AC03-76SF00098.

Equation(3) is the emittance definition based on statistical mechanics adopted in this paper. In the following sections, the emittance of particle and radiation beams are computed based on this formula.

III. PARTICLE BEAMS

For a beam of non-interacting particles, the phase space distribution function $f(x_e, \phi_e)$ is a non-negative, physically measurable quantity. Here, and in the rest of the paper, the subscript e is used to distinguish the particle (electron) variables from those of radiation. We consider first the case where the distribution is a smooth function so that for a sufficiently small value of $\delta\Omega$, Eq.(2) can be replaced by the following integral [1]:

$$S = - \int dx_e d\phi_e f(x_e, \phi_e) \ln (f(x_e, \phi_e) \delta\Omega). \quad (4)$$

The emittance from Eq.(3) becomes

$$\epsilon = \exp \left[- \int dx_e d\phi_e f(x_e, \phi_e) \ln f(x_e, \phi_e) \right] \quad (5)$$

Note that the emittance in this continuous limit is independent of $\delta\Omega$, as it should be. It is also important to observe that the emittance defined by Eq.(5) is conserved for any Hamiltonian beam transport system due to Liouville's theorem.

For a uniform distribution occupying a phase space area Ω , Eq.(5) gives $\epsilon = \Omega$, as expected.

Consider a Gaussian distribution

$$f(x_e, \phi_e) = \frac{1}{2\pi\sigma_{x_e}\sigma_{\phi_e}} \exp\left(-\frac{x_e^2}{2\sigma_{x_e}^2} - \frac{\phi_e^2}{2\sigma_{\phi_e}^2}\right), \quad (6)$$

where σ_{x_e} and σ_{ϕ_e} are respectively the rms widths of the particle distribution in x_e and ϕ_e . Equation(5) becomes in this case

$$\epsilon = e 2\pi\sigma_{x_e}\sigma_{\phi_e}. \quad (7)$$

The result is a factor $e \simeq 2.72$ larger than the peak emittance $1/f(0,0)$.

In many practically important cases, the distribution could have rapid variations within experimentally realizable phase space resolution $\delta\Omega$. The emittance in those cases should then be defined as

$$\epsilon = \exp \left[- \sum_k \delta\Omega \bar{f}_k \ln \bar{f}_k \right], \quad (8)$$

where \bar{f}_k is the average of the distribution in the k th cell element of area $\delta\Omega$. The emittance defined by this equation will in general not be conserved even for a Hamiltonian system. For example, a smooth distribution at the beginning of a beam transport system can evolve into a highly filamented distribution due to non-linear transport elements. The emittance as defined by Eq.(8) will increase in such a case.

IV. RADIATION BEAM

For radiation beam, the phase space area and cells are abstract quantities[2],[3]. In this case, we proceed by noting that the

probabilities p_k are the eigenvalues of the normalized version $\hat{\Gamma}_N$ of the correlation operator $\hat{\Gamma}$. This is similar to the case of quantum statistical mechanics where the density operator plays the role of the correlation operator. Equation(2) becomes, therefore

$$S = -Tr(\hat{\Gamma}_N \ln \hat{\Gamma}_N), \quad (9)$$

To relate the quantities appearing in the above to the field quantities, consider the frequency component $E(x)$ at a given frequency of the radiation field at a fixed longitudinal position along the optical axis. Throughout this paper, we ignore polarization and treat the field as a scalar. In general the field will be a stochastic variable. The correlation function of the radiation field is given by

$$\Gamma(x, x') = \langle E(x)E(x')^* \rangle. \quad (10)$$

The angular brackets in the above imply taking the statistical average. In terms of Dirac bra-ket notation, the correlation operator and the correlation function are related by

$$\Gamma(x, x') = \langle x | \hat{\Gamma} | x' \rangle. \quad (11)$$

The normalized correlation matrix is given by

$$\Gamma_N(x, x') = \frac{\Gamma(x, x')}{\int dx \Gamma(x, x)}. \quad (12)$$

V. PARTIALLY COHERENT UNDULATOR RADIATION

A. Model for Undulator Radiation

We now apply the above formalism to radiation generated by a beam of electrons from an undulator. To permit analytical calculation, the expression for the radiation field is simplified as follows[4]: The fundamental frequency component at $\omega = \omega_1$ from a single electron with a transverse coordinate x_e from the center of the undulator gap and with an angle ϕ_e with respect to the undulator axis entering the undulator at time t_e can be approximately represented as follows [4]:

$$E(x; x_e, \phi_e) = \left(\frac{I_0}{\sigma_{x_r} \sqrt{2\pi}} \right)^{1/2} \exp \left[-\frac{(x - x_e)^2}{4\sigma_{x_r}^2} + i k_1 \phi_e (x - x_e) - i \omega_1 t_e \right], \quad (13)$$

where $k_1 = \omega_1/c$ is the reference wave number, and where σ_{x_r} is a measure of the spread in the x -direction of the radiation produced by the single electron. The quantity I_0 is a normalization constant, defined by $\int |E(x)|^2 dx = I_0$. Note that the field $E(x; x_e, \phi_e)$ is related to $E(x; 0, 0)$ by translation of the phase space coordinates. We define the Fourier transform of the radiation field by

$$\tilde{E}(\phi; x_e, \phi_e) = \int \frac{dx}{\sqrt{2\pi}} E(x; x_e, \phi_e) \exp(-i\phi k_1 x), \quad (14)$$

so that

$$\tilde{E}(\phi; x_e, \phi_e) = \left(\frac{I_0}{k_1 \sigma_{\phi_r} \sqrt{2\pi}} \right)^{1/2} \exp \left[-\frac{(\phi - \phi_e)^2}{4\sigma_{\phi_r}^2} - i k_1 x_e (\phi - \phi_e) - i \omega_1 t_e \right], \quad (15)$$

where $\sigma_{\phi r}$ is the width of the radiation field in the variable ϕ .

The radiation widths σ_{xr} and $\sigma_{\phi r}$ satisfy

$$\sigma_{xr}\sigma_{\phi r} = \frac{1}{2k_1}, \quad (16)$$

so that the Gaussian beam of Eq.(13) is a minimum uncertainty wave packet. For an undulator of length L , we have $\sigma_{xr} = \sqrt{2\lambda_1 L}/4\pi$ and $\sigma_{\phi r} = \sqrt{\lambda_1/2L}$, where $\lambda_1 = 2\pi/k_1$, the wavelength corresponding to k_1 .

The total electric field $E(x)$ is obtained by summing over contributions from different electrons $E(x; x_e, \phi_e)$.

B. Correlation and Entropy

In calculating the average in Eq.(10), terms involving product of electric fields from different electrons vanish due to random phase factors. The contributions from the same electron is averaged with the electron probability distribution $f(x_e, \phi_e)$. Thus,

$$\Gamma(x, x') = N_e \int dx_e d\phi_e f(x_e, \phi_e) E(x; x_e, \phi_e) E(x'; x_e, \phi_e)^* \quad (17)$$

where N_e is the total number of electrons. Assuming that the electron distribution is Gaussian as given by Eq.(6), the integrals can be performed, and we obtain

$$\Gamma_N(x, x') = \frac{1}{\Delta_x \sqrt{2\pi}} \exp \left[-\frac{1}{2\Delta_x^2} \left(\frac{x+x'}{2} \right)^2 - \frac{k_0^2 \Delta_\phi^2 (x-x')^2}{2} \right], \quad (18)$$

where

$$\Delta_x^2 = \sigma_{x_e}^2 + \sigma_{x_r}^2, \quad (19)$$

$$\Delta_\phi^2 = \sigma_{\phi_e}^2 + \sigma_{\phi_r}^2. \quad (20)$$

To compute the entropy we must carry out the trace in Eq.(9). For this purpose it is convenient to have the eigenvalues p_k of the operator $\hat{\Gamma}_N$, i.e., the eigenvalues which appear in the equation

$$\int dx' \Gamma_N(x, x') \phi_k(x') = p_k \phi_k(x), \quad (21)$$

where $\phi_k(x)$ are the eigenfunctions. The eigenvalues p_k are necessarily non-negative, since $\hat{\Gamma}$ is a non-negative definite operator. In fact, p_k can be identified as the probability to occupy the k th cell introduced in Section II.

It turns out that the integral eigenvalue equation, Eq.(21), can be solved by noting the similarity of the present problem with the quantum statistical mechanics of harmonic oscillators[5]. Without going into the derivation [6], we give the result for the normalized entropy for the partially coherent radiation beam as follows:

$$S = \frac{1}{2} \left[(\eta + 1) \ln \frac{\eta + 1}{2} - (\eta - 1) \ln \frac{\eta - 1}{2} \right], \quad (22)$$

where

$$\eta = 2k_1 \Delta_x \Delta_\phi \geq 1. \quad (23)$$

C. Emittance of Partially Coherent Radiation Beam

The emittance is given by Eq.(3) with S determined from Eq.(22). In contrast to the particle beam case, however, we need to specify the value of the elementary cell area $\delta\Omega$. We will prove below the very reasonable result that $\delta\Omega = \lambda_1$, the wavelength of the radiation. Indeed, we note that the radiation emittance should approach the electron beam emittance when $\eta \gg 1$. In this incoherent limit, Eq.(23) becomes

$$S = \ln \eta + 1 + O(1/\eta^2). \quad (24)$$

Therefore the emittance in the incoherent limit becomes

$$\epsilon = \delta\Omega (e\eta/2 + O(1/\eta)) \simeq \delta\Omega e k_1 \sigma_{x_e} \sigma_{\phi_e}. \quad (25)$$

This becomes identical to Eq.(7) if, and only if, $\delta\Omega = \lambda_1$, as was asserted.

In the limit of vanishing electron beam emittance, the radiation emittance becomes λ_1 , the elemental phase space area; The radiation is completely coherent.

A measure of coherence of a partially coherent beam is the coherent fraction F_{coh} , defined as the ratio of the coherent emittance to the full emittance. We obtain $F_{coh} = \exp(-S)$, with S given by Eq.(22). In the past, the rms definition of emittance was often used, in which case $F_{coh}^{rms} = 1/\eta$. We have compared F_{coh} and F_{coh}^{rms} as a function of $\xi = \sigma_{x_e}/\sigma_{x_r} = \sigma_{\phi_e}/\sigma_{\phi_r}$, and find that they do not differ much from each other.

References

- [1] J.D. Lawson, P.M. Lapostolle, and R.L. Gluckstern, *Particle Acc.*, Vol 5,61(1973).
- [2] K.-J. Kim, *Nucl. Instr. Meth.*, A 246, 71(1986).
- [3] R. G. Littlejohn, *Phys. Rep.* 138, 193(1986).
- [4] K.-J. Kim, *SPIE Proceedings*, vol. 582,2 (1986); For a review, see K.-J. Kim, "Characteristics of Synchrotron Radiation," *Physics of Particle accelerators*, Vol 184, AIP Conference Proceedings, p565(1989)
- [5] L. S. Schulman, *Techniques and Applications of Path Integration* (Wiley, New York, 1981).
- [6] K.-J. Kim and R.G. Littlejohn, to be published.

EFFECT OF THE COUPLING SLOTS ON BEAM DYNAMICS IN ACCELERATOR STRUCTURE OF MOSCOW CW RTM

V.I. Shvedunov, A.S. Alimov, A.S. Chepurnov, O.V. Chubarov, D.I. Ermakov, A.V. Tiunov, P.L. Tkachev, Institute of Nuclear Physics, Moscow State University, 119899, Moscow, Russia

We detected strong coupling slots effect on the transverse beam dynamics for on-axis coupled accelerator structure. This effect is explained by the transverse magnetic field exited on the axis of coupling cells and providing intercell coupling. We suggested method to compensate coupling slots effect with the external magnetic field. Transition radiation was used to get beam size and position in the course of experiments presented below.

I. INTRODUCTION

Effect of coupling slots on the transverse beam dynamics for on-axis coupled accelerator structure was first detected in [1] and investigated in details in [2-4]. The main manifestation of this effect is quadrupole beam focusing in one plane and defocusing in the other, which was explained by quadrupole field asymmetry in accelerating cells introduced by coupling slots. To compensate this effect coupling slots in accelerating cells should be aligned with the pair of slots at one accelerating cell web exactly against the pair at the other web.

One of the Moscow CW RTM accelerator structure peculiarity is that only one coupling slot is placed at each cells web [5]. So instead of quadrupole effect one should wait phase dependent dipole effect leading to the beam position shift during its acceleration.

II. EXPERIMENTAL SET-UP

Experiments were conducted with the accelerator sections of Moscow CW RTM injector described elsewhere [6]. Injector consists of the graded- β capture section and five $\beta = 1$ sections, each powered by its own klystron exited by the reference signal. Every section provides about 1.1-1.2 MeV maximum energy gain, so 6.7 MeV beam can be obtained at the injector output with the bunch phase length about 5°, energy spread 0.3% and normalised transverse emittance 5mmxmrads. Intercells coupling slots were positioned in vertical plane, in the lower web part at accelerating cell entrance and upper at exit.

To investigate coupling slots effect we measured dependence of the beam size and position on the last accelerator section phase at the 1 m distance from the injector output. Experimental set-up is shown in Fig. 1.

Accelerating field phase with respect to the reference signal were changed by phaseshifter Φ and measured by phasemeter ΦM . Beam energy can be measured with the analysing magnet M.

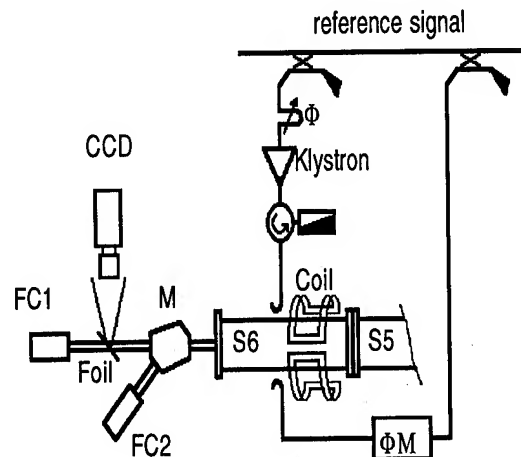


Figure 1. Schematic view (from the top) of the experimental set-up. Shown are: accelerator sections S5, S6, analysing magnet M, phaseshifter Φ , phasemeter ΦM , Faraday's caps, FC1, FC2, CCD TV camera, reference signal line, klystron, correcting coils.

For exact measurements of the beam centre gravity position and current distribution we used transition radiation [7-8] from 9 mkm Al foil placed at 45° to the beam axis. Signal from CCD camera with magnification 14:1 at 51cm TV screen was analysed with digital TV system and stored in computer memory. An example of beam current distribution obtained by this method for 6.7 MeV, 40 mA beam is shown in Fig. 2.

To compensate slots effect correcting coils shown in Fig. 1 with the effective length about 0.35m were placed at external part of section. Coils produced magnetic field on section axis in horizontal plane with the induction about 3 Gauss per 1 A of current.

III. RESULTS AND INTERPRETATION.

We have measured dependence on the accelerator section phase of (a) beam energy, (b) beam centre gravity position, and (c) value of correcting coils current returning beam to the reference position which is the beam position with the last section field switched off (beam energy 5.5 MeV). Results of this measurements are shown in Fig. 3. Accelerating field phase was arbitrary taken to be zero at maximum acceleration.

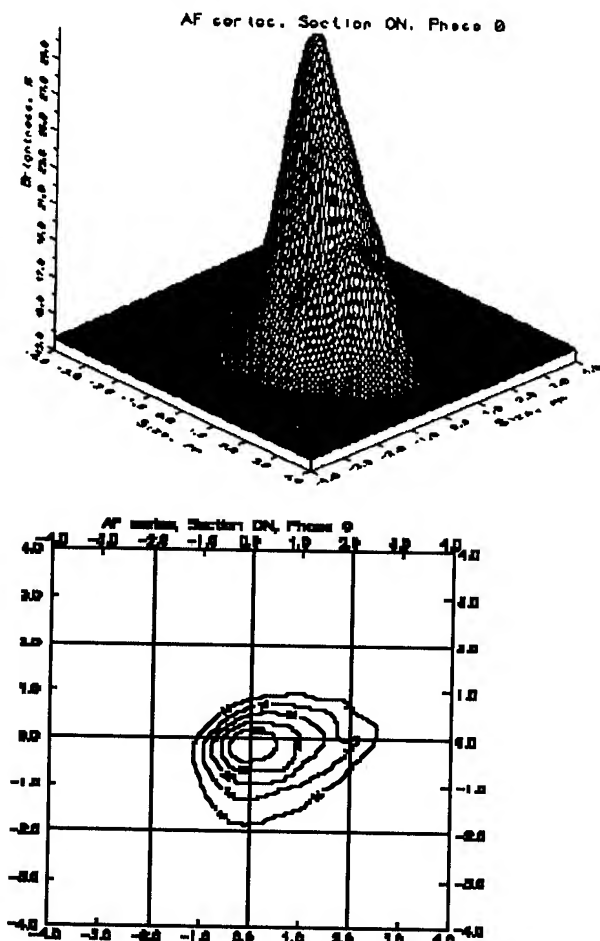


Figure 2. Current distribution in the beam (3D view and contours plot) measured by means of transition radiation.

One can see that in the accelerating phase (6.7 MeV energy) beam is shifted for about 4.5mm upwards with respect to the reference position, and in the decelerating phase (4.3 MeV energy) downward for about 7.2mm. In horizontal plane beam position was practically unchanged. Beam form changed slightly, reflecting mainly dependence of section focusing properties and beam energy on the phase. By applying current +0.8 A and -0.9 A to the correcting coils, respectively for accelerating and decelerating phases, beam can be shifted to the reference position.

To explain obtained results different possible reasons of the beam shift were considered and first of all accelerating cells field asymmetry due to the coupling slots. Electromagnetic field distribution inside the accelerating cell was calculated with the MAFIA code [9]. Calculations were made with one full accelerating cell and two coupling half cells at the ends with magnetic walls boundary conditions. In this case we neglect possible influence of the coupling cells magnetic field on beam dynamics. Radial electric and azimuthal magnetic field asymmetry of the order of 10^{-3} were investigated, and beam dynamics with RTMTRACE code [10] were calculated. Calculations showed depending on phase beam shift but with opposite sign as compared with experimental one, and about 5 times less in magnitude.

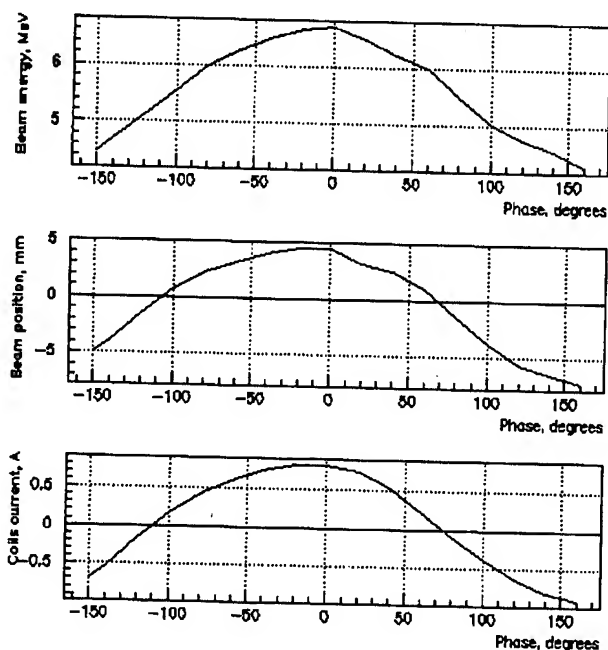


Figure 3. Dependence on the section 6 phase of beam energy (upper), beam position (middle), and correcting coils current (lower).

Influence of external parasitic magnetic fields and accelerator section misalignments on the transverse beam dynamics were analysed - this influence was found to be order of magnitude less than investigated effect.

After that we made new set of MAFIA calculations, but with one full coupling cell and two accelerating half cells at the ends with electric type boundary conditions. Results of this calculations appeared to be extremely interesting. Though in simplified models of biperiodic standing wave accelerator structure, such as lumped circuit model, coupling cells stay unexcited for $\pi/2$ mode in tuned structure (neglecting the power flow owing to finite quality factor), MAFIA calculations showed strong transverse magnetic field on the axis of coupling cells. Magnetic field distribution in the central plane of coupling cell is shown in Fig. 4.

Magnetic flux is propagating from one accelerating cell to the other through coupling slots creating near the coupling cells axis field pattern resembling TM₁₁ mode field distribution. Electric field components, both longitudinal and transverse are close to zero near the axis. Presence of the strong field in the coupling cells correlating in spatial distribution with position of coupling slots was investigated in [3].

Calculated by MAFIA code integrals show that vertical transverse momentum obtained by the relativistic particle in coupling cell is about 6×10^{-3} of the longitudinal momentum obtained in the accelerating cell - value corresponding to experimental one. Taking into account, that magnetic field reaches its maximum when particle in accelerating phase passes the centre of coupling cell and that the sign of transverse momentum obtained by the electrons corresponds to that obtained in experiment we can conclude that investigated beam shift is practically totally explained by influence of this field.

VI. CONCLUSION.

We investigated strong phase dependent beam shift for on-axis coupled accelerator structure with one coupling slot per web which can not be explained by the accelerating cells field asymmetry nor for the value of beam shift not for its sign. Calculations made with MAFIA code showed existence of the strong field in the coupling cells providing intercell coupling with transverse component of the magnetic field on the cells axis. Taking into account this field we explained our experimental data. For the accelerator structure with two coupling slots per web additional effect of coupling cells field also should be taken into account.

We would like to express our appreciation to Dr. H. Euteneuer for helpful discussions and valuable information he presented us.

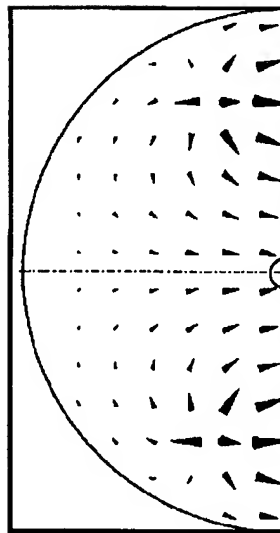


Figure 4. Magnetic field distribution in the centre of coupling cell for biperiodic on-axis coupled accelerator structure with one coupling slot per web.

V. REFERENCES.

- [1].M.M. Karliner, O.A. Nezhevenko, G.N. Ostreyko, B.M. Fomel, V.P. Yakovlev, G.I. Yasnov *Voprosi Atomnoi Nauki i Tekhniki*, 1/18/, 30(1984) (in Russian)
- [2].H. Euteneuer, private communication, and *Interne Notiz MAMI 1/89*, Institute für Kernphysik, Universität Mainz, 13p.(1989)
- [3].F.P. Adams, R.J. Burton and J. Ungrin, *Conf.Rec. of the 1991 Particle Accelerator Conference*, San Francisco, California, May 6-9, (5), 3011(1991)
- [4].R.L. Sheffield, M.J. Browman, B.E. Carlsten and L.M. Young, *Nucl. Instr. and Meth.*, **A318**, 282(1992)
- [5].A.S. Alimov, B.S. Ishkhanov, I.M. Piskarev, V.I. Shvedunov and A.V. Tiunov, *Nucl. Instr. and Meth.*, **A328**, (385)1993
- [6].A.S. Alimov, A.S. Chepurnov, O.V. Chubarov, I.V. Gribov, M.A. Sotnikov, I.V. Surma, A.V. Shumakov, V.I. Shvedunov, A.V. Tiunov and V.A. Ushkanov, *Nucl. Instr. and Meth.*, **A326**, 391(1993)
- [7].I. Frank and V. Ginzburg, *J.Phys. USSR* **9**, 353(1945)
- [8].L. Wartski, S. Roland, J. Lassale, M. Bolore, and G. Filippi, *J. of Appl. Phys*, vol.46, No.8, 3644(1975)
- [9].R.Klatt, F.Krawczyk, W.R.Novender, C.Palm, T.Weiland, B.Steffen, T.Barts, M.J.Browman, R.Cooper, C.T.Mottershead, G.Rodenz, S.G.Wipf, *Proceedings of the 1986 Linear Accelerator Conference*, SLAC-303, 276 (1986)
- [10].V.G. Gevorkyan, A.B. Savitsky, M.A. Sotnikov and V.I. Shvedunov, *VINITI*, No. 183-B89,54p (1989) (in Russian)

The Electron Beam Orbit Sensitivity of the Photon Flux of the Photon Beam Line

Ian Hsu, G.H. Luo, K.L. Tsang, C.C. Chu, C.I. Yu, W.T. Weng, and S.C. Chung

Institute of Nuclear Science, Nation Tsing-Hua University

and

Synchrotron Radiation Research Center

Hsinchu, Taiwan 30043, R.O.C.

Abstract

The effects of the electron beam position as well as the electron beam orbit slop at the source point on the photon flux of the photon beam lines were studied both by the ray tracing simulation and by the experiments. The experimental result shown that 10 μm beam position change will cause more than 1% of the photon flux change which agreed with the simulation results. However, for some distorted orbit slop (0.2 mrad), 10 μm beam position change can cause 8% of the photon flux change.

I. INTRODUCTION

The very high resolution photon beam line is one of the characteristics of a third generation light source. Due to the very high resolution requirement, the optical system of the photon beam line become very sensitive to its photon source position and slop, i.e. the electron beam orbit. Taiwan Light Source(TLS) of Synchrotron Radiation Research Center(SRRC), is one of the several third generation light sources in operation now. The photon flux fluctuation due to the instabilities of the electron beam position and slop is an essential issue of all of these light sources. In this paper, we presented the studies of the sensitivity of the photon flux due to electron beam position change as well as beam angular change (the orbit slop) at the source point of the photon beam line. Because the sensitivity of the vertical beam displacement is much higher than that of the horizontal beam displacement, the studies presented here are all in vertical dimension. The studies include the ray tracing simulations and experiments. The experiments were done by changing the size of the orbit local position bumps as well as local angular bumps and measuring the change of the photon flux of the photon beam line. This study is essential because it will provide the conversion fact of the instabilities between the machine people and the users e.g., photon beam line people. It will also provide information for decoupling the instability sources from machine and those from the photon beam line itself. By the end of the this year, we should reduce the electron beam instabilities such that the photon flux fluctuation is less than 0.5%. The final target of that value should be 0.1%.

II. THE EXPERIMENTS

The experiments were done by changing the size of the orbit local position bumps as well as local angular bumps and measuring the change of the photon flux of the photon beam line. The photon flux was measured by a photon electric detector which was located after the entrance slit. The sensitivity will certainly dependent upon the size of the entrance slit. In all the experiments presented here and in the simulation the slit size was set at 50 μm . The orbit bumps were created by using four correct magnets. Therefore, we can independently control the electron beam position and slop at the source point of the photon beam line. Figure 1 shows two of the typical orbit bumps in our experiments.

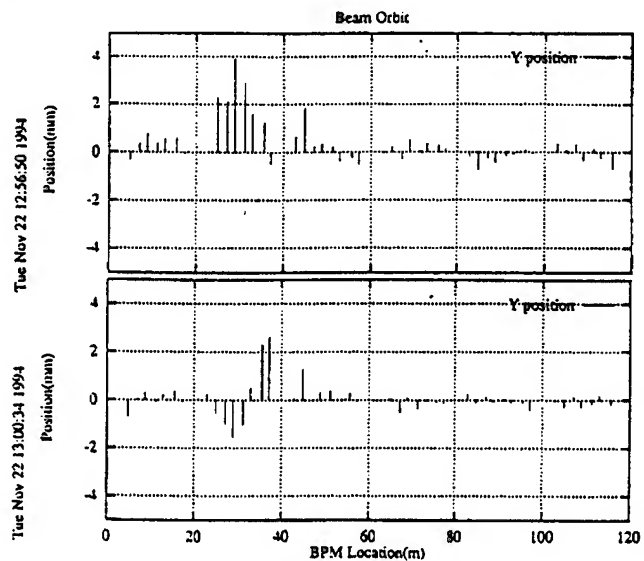


Fig. 1 The position bump and angular bump.

The electron beam position and slop at the source point of the photon beam line were calculated by read two BPMs, one up stream and one down stream of the source point. The resolution of our BPM at the time of doing the experiments was about 50 μm as shown in figure 2. For the case of position bump we moved about 50 to 100 μm in each step and for the case of the angular bump we move about 50 - 100 μrad in each step. We started with a reasonable good orbit e.g., rms. less than 300 μm . We then adjusted the vertical

focusing mirror (VFM) until we got the maximum photon flux. After each step of either the position bump change or the angular bump change, we record the photon flux change. We then adjusted the VFM until we got the maximum photon flux. Then the next step of change was proceed. To gain the maximum photon flux by adjusting the VFM is a routine fine tune done by the photon beam line people.

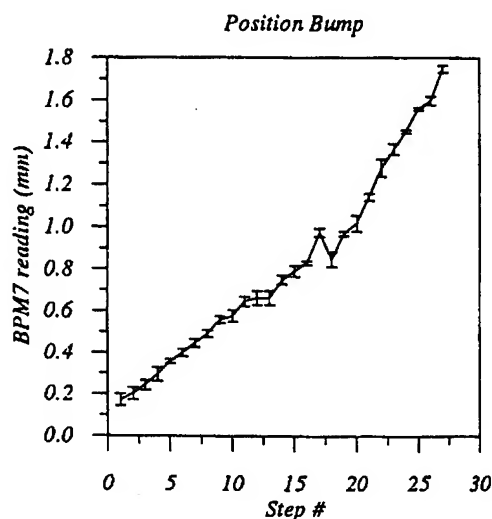


Fig. 2 The raw data of one of the BPM reading. The error bar was the standard deviation of ten measurements

In figure 3, we shown the results when only the position bump was changed. For these changes, the slop should be kept unchanged. Due to the imperfection of the bump, the slop of the beam at the source point does have some change. In the figure we also plot the slop value for each step. From the results we got, we were assured that those small change is ignoble. Therefore, from figure 3 we could conclude that 10 μm vertical beam position displacement will cause 1 to 2 % photon flux change.

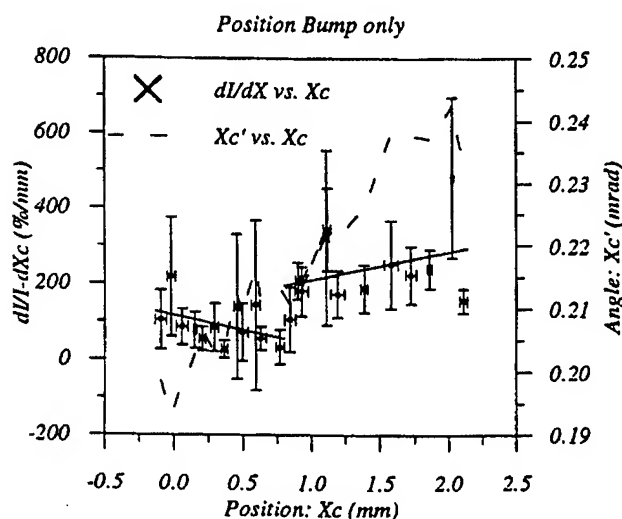


Fig. 3 The results of position bump change

In figure 4, we shown the results when only the angular bump was changed. For these changes, the position should be kept unchanged. Due to the imperfection of the bump, the position of the beam at the source point does have some change. In the figure we also plot the position value for each step. From the results we got, we were assured that those small change is ignoble, too. Therefore, from figure 4 we could conclude that 10 μrad vertical beam slop change will cause 1 to 2 % photon flux change.

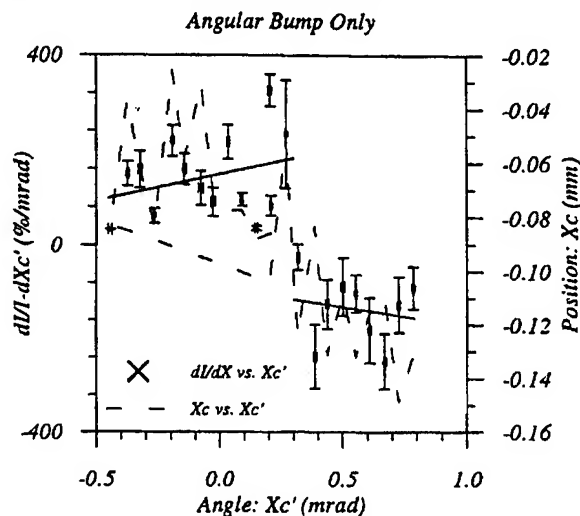


Fig. 4 The results of angular bump change

In figure 5, we shown the results when only the position bump was changed. However, in this case there was a 200 μrad angular bump on top of the position bump. Again, in the figure we also plot the slop value for each step. From figure 5 we could conclude that 10 μm vertical beam position displacement will cause 7 to 8 % photon flux change. This value is much larger than that of the figure 3. There was no extra angular bump in the latter case.

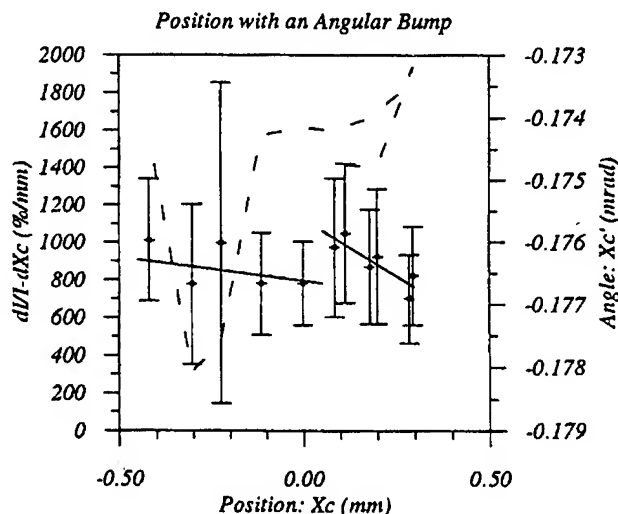


Fig. 5 The results of position bump change with an 200 mrad angular bump.

III. THE SIMULATIONS

Figure 6 is the layout of the 6m-HSGM beam line which is the photon beam line we perform the experiments. According to the optics system of this beam line, we did a ray tracing study for the case of position bump change without angular bump. The results was shown in figure 7. We had shown the results for two different electron beam size, 2σ equals to $100\text{ }\mu\text{m}$ and $50\text{ }\mu\text{m}$. For the latter case, we got that $10\text{ }\mu\text{m}$ vertical beam position displacement will cause 1.4 % photon flux loss. That agreed with the experiment results.

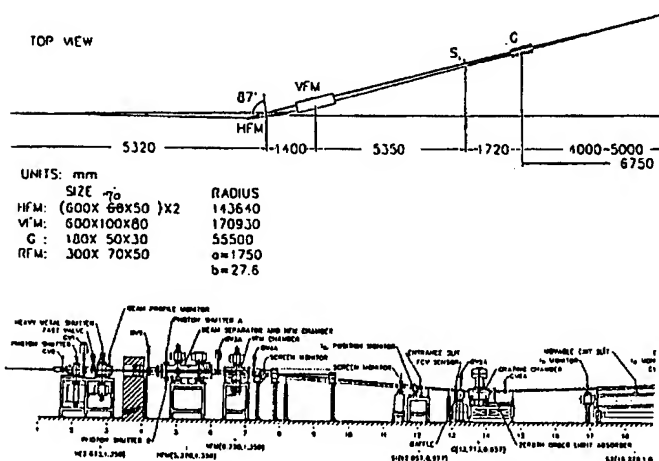


Fig. 6 The 6m-HSGM beam line layout(not complete)

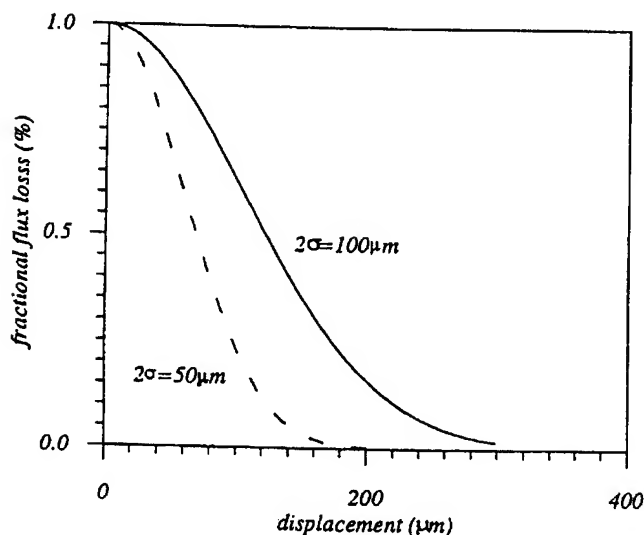


Fig. 7 The photon beam line ray tracing results

IV. RESULTS AND DISCUSSIONS

From the experiment studies and the simulation results, we learned that, for a flat electron beam orbit, $10\text{ }\mu\text{m}$ vertical beam position displacement will cause 1 to 2 % photon flux change. However, if the orbit is not flat the sensitivity could be enhanced by a fact of 10. This fact will strongly dependent on the photon beam line optics.

During the experiments, we also found that when doing the position bump change, in a large range of displacement, the photon flux could be brought back to the original value, e.g., the value before the orbit was changed, by adjusting the VFM. However, when doing the angular bump change, in most of the case, we could not get back the previous maximum value by adjusting the VFM. This was understood by that when the source slop was changed by introducing the angular bump, part of the photon beam was fall outside the VFM, therefore there is no way to bring the photon flux back to previous value by adjusting the VFM. However, for the case of changing source position by introducing the position bump, the photon flux was reduced due to that part of the focused photon beam was fall out side the entrance slit, therefore we could bring the photon flux back to previous value by adjusting the VFM. The origin of this difference is because that the photon beam are incident into the VFM with a very small grazing angle and the distance between the source point and the mirror is large. The above understanding was conformed by the ray tracing studies.

V. ACKNOWLEDGMENT

We would like to thank Ms. Jenny Chen of SRRC for the help of the BPM data acquisition program.

GROUND MOTION IN LEP AND LHC

L. Vos, CERN, Geneva, Switzerland.

I. INTRODUCTION

It is well known that large colliders, linear or circular, with small beam sizes are prone to ground motion effects. The effect of seismic perturbations on machine performance has been the subject of several studies[1,2,3,4].

The object of this paper is to report on the results obtained with a dedicated beam position monitor, concerning ground motion effects on the LEP beams. Since the ultimate objective of this study is the LHC it is appropriate to say that LEP is used as a test bench for LHC. The organisation of the report is as follows. It starts with some properties of ground vibrations which are relevant to the observation of the phenomenon in LEP. Then the transformation of ground motion power into beam motion power is calculated. Based on the properties of the transverse monitor the magnitude of the phenomenon can be measured with sufficient precision. The results of the observations will be presented both at the betatron frequencies and at very low frequencies centred around the common mode. They are compared with published data on direct ground motion to check the plausibility of the hypothesis that ground motion is indeed the primary cause of the observed signals. Finally a discussion on the influence of the effect on the LHC beams is presented.

II. GROUND MOTION

From correlation measurements between two probes for varying distances as a function of frequency it is possible to derive the velocity of the ground waves. Indeed, the correlation between two probes at distance l drops to zero for a frequency such that this distance is a quarter wavelength:

$$l = \frac{\lambda}{4} = \frac{v}{4f}.$$

It is interesting to note that in the TT2A tunnel an average speed of 1500 m/s is found [6], while in two points in the LEP tunnel this speed has increased to 4000 m/s [7]. This is due to a different quality of rock in which the tunnels have been excavated.

The effect of ground motion in a large accelerator is vehicled by the uncorrelated motion of quadrupoles of a focusing family F or D. It follows that the effect will decrease quickly for frequencies below the coherence limit:

$$f_m = \frac{v}{4l},$$

where l is the cell length. For LEP $l=79$ m so that the lower limit of the coherence is reached for a frequency of 12.6 Hz (upper limit) or 4.7 Hz (lower limit). In LHC $l=90$ m and the coherent limits are 11Hz and 4 Hz. The absolute cut-off frequency is reached when the whole machine fits within a quarter wave length, that is for $l=\text{machine diameter}$. This limit for LEP/LHC is 1/8 Hz. The famous '7 s hum' will be next to invisible.

The spectral power density S_{gm} has been measured at many places. A common characteristic is the fact that it falls off by about three orders of magnitude per decade[5,6,7,8]. The dispersion in the results spans over several decades.

Assuming a logarithmic frequency slope of -2.5, the expected power at 2 kHz (close to betatron frequency in LEP) is $S_{gm} = 110^{-14} \mu^2/\text{Hz}$ and at 100Hz $S_{gm} = 110^{-11} \mu^2/\text{Hz}$.

III. FROM GROUND TO BEAM MOTION

Ground vibrations at frequencies higher than 12.6 Hz will cause uncorrelated motions of the quadrupoles in LEP. A quadrupole displacement provokes a displacement of the beam. If the frequency of the vibration lies in the betatron frequency band of the beam, then the beam will oscillate with an amplitude depending on the power of the exciter(ground motion) and on the frequency spread in the beam.

A quadrupole that is displaced by an amount ϵ will cause a beam displacement with amplitude x :

$$x = \sqrt{\beta_o \beta_Q} K \ell \epsilon,$$

where $K \ell$ is the integrated normalised quadrupole strength, β_Q and β_o respectively are the β function at the quadrupole and at the observation point. The contributions of many quadrupoles add quadratically:

$$x^2 = \beta_o \sum \beta_Q (K \ell)^2 \epsilon^2.$$

Response at β frequencies for beam with tune spread can be computed as follows. Consider a beam with tune spread δQ . The frequency of the external excitation x lies in the frequency band of the β oscillation of the beam. From the study of the transverse stability diagram and for a reasonable distribution function, following expression holds for the oscillation amplitude of the ensemble:

$$\bar{x} = \frac{x}{2\delta Q}.$$

This can be applied to the previous result to give:

$$\bar{x}^2 = \frac{\beta_o \sum \beta_Q (K \ell)^2}{4\delta Q^2} \epsilon^2.$$

To compute the effect on the closed orbit it is sufficient to replace the optic amplification factor $1/\delta Q$ by the optic orbit amplification factor $1/|\sin(\pi q)|$, yielding:

$$x_{co}^2 = \frac{\beta_o \sum \beta_Q (K \ell)^2}{4\sin^2(\pi q)} \epsilon^2.$$

The data on ground motion are given in the form of spectral densities. Previous formulae can be rewritten taking this aspect into account. Indeed,

$$S_{gm}(f) = \frac{\epsilon^2}{df}$$

$$\text{and } \frac{\bar{x}^2}{df} = \frac{\beta_o \sum \beta_Q (K \ell)^2}{4\delta Q^2} S_{gm}(f). \quad (1)$$

$$\frac{x_{co}^2}{df} = \frac{\beta_o \sum \beta_Q (K \ell)^2}{4\sin^2(\pi q)} S_{gm}(f) \quad (2)$$

It is worth pointing out that \bar{x} and x_{co} are quantities that are measurable by a beam position monitor. The next step is to estimate the various constants in the expressions.

The parameter $\beta_o \sum \beta_q (K\ell)^2$ depends on the machine optics. It has been computed for the 1993 Pretzl optics used in LEP during physics runs. The result for the vertical plane is 18700 and for the horizontal one 16600.

As far as the tune spread δQ is concerned a pragmatic attitude is adopted in the sense that it is taken to be 0.015 which is some average value based on the actual observations. It is realised that this is in contradiction with the expectations for beams influenced by a beam-beam tune spread generated by four interaction points.

The fractional tune q in LEP varies between 0.1 and 0.3. Hence the orbit amplification factor $\sin(\pi q)$ varies between 0.3 and 0.8, say an average of 0.5.

This then leads finally to a value for the expected spectral density of the beam motion at the betatron frequencies of:

$$\frac{\bar{x}}{\sqrt{df}} = 0.43 \text{ nm}/\sqrt{\text{Hz}}$$

while the orbit motion around 100 Hz will have a spectral density of:

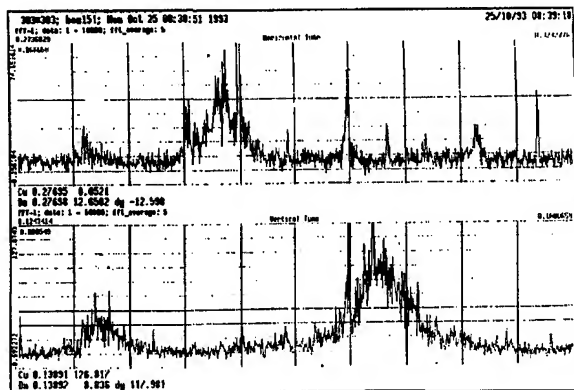
$$\frac{x_{co}}{\sqrt{df}} = 0.55 \text{ nm}/\sqrt{\text{Hz}}.$$

IV. PROPERTIES OF THE BEAM POSITION MONITOR SYSTEM

A beam position monitor of the directional coupler type had been installed in LEP for general purpose use. The properties of this monitor and its associated acquisition system can be analysed in great detail for a single lepton bunch coasting in LEP. Special care has been taken to maximise the sensitivity. A resolution of $0.16 \text{ nm}/\sqrt{\text{Hz}}$ is obtained for a bunch intensity of 300 μA , sufficient to observe the expected excitation by ground motion.

V. OBSERVATIONS

A typical FFT plot of the β oscillations is shown in Figure 1



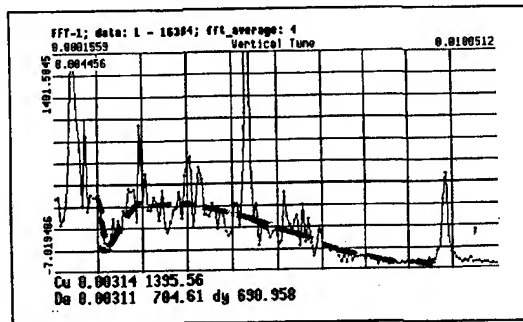
Typical FFT plot of beam signals excited by ground motion
Figure 1

This and similar plots can be analysed using previous expressions to yield a value of S_{gm} . The results are presented in next table.

i_b	frequency	δQ	peak signal	S_{gm}
μA	Hz		bit	$10^{-14} \mu^2/\text{Hz}$
260	1720	0.016	540	550
240	1760	0.012	84	8.8
300	1800	0.014	80	7
117	1870	0.006	40	2.1
289	1900	0.014	67	5.3
300	1940	0.02	45	4.5
230	1940	0.015	93	18.4
324	2210	0.018	65	6.5
190	1090	0.004	400	400
240	3150	0.006	44	6.8
260	3160	0.015	140	370
300	3200	0.008	43	7.4
340	3300	0.01	32	5
300	3300	0.008	30	3.6

Table 1: Results at β oscillation frequencies

A typical FFT plot of the closed orbit spectrum is shown in Figure 2.



Vertical spectrum at low frequencies(0 to 112 Hz)
Figure 2

A clear valley at $q=0.001$, or $f=11.2$ Hz can be seen. It is very likely that this corresponds with the coherence limit that was calculated before and found to be at 12.6 Hz. In table 4 measurements at frequencies 45 and 90 Hz are shown.

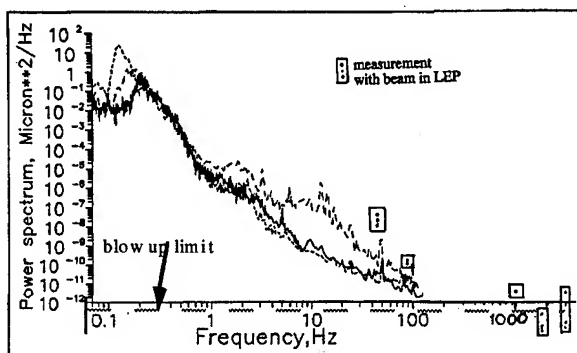
i_b	$f=90$ Hz		$f=45$ Hz	
	peak sig.	S_{gm}	peak sig.	S_{gm}
μA	bit	$10^{-10} \mu^2/\text{Hz}$	bit	$10^{-10} \mu^2/\text{Hz}$
340	170	3.1	1400	210
200	86	2.3	970	290
300	120	2.0	1280	230
80	40	3.1	370	260
135	70	3.4	450	140

Table 2: Results from low frequency measurement of ground motion effect

This is the moment to make a small digression. It can be shown that Schottky noise is 20 to 30 dB below the noise level of the observation system. Hence, it cannot be at the

origin of the observed signals. A second contender can now be ruled out for the excitation of the beam at a few kHz. That one is power supply noise. Power supplies in LEP are essentially low frequency devices with a bandwidth of a few Hz only. While it is not unreasonable that their effect may be visible at these low frequencies it is to be expected that their strength decreases at a rate of at least two orders of magnitude per decade. At 2kHz the skin effect of the Al chamber will cause a further attenuation in the order of a factor of 10. All this adds up to a signal density which is a lot smaller than the resolution of the system.

In Figure 3 the measurement results with beam are assembled in a comparison plot with direct seismic measurements[7].



Comparison plot between seismic measurements in LEP and beam motion measurements
Figure 3

The correspondence between the direct seismic measurement results and the beam measurements is astonishing. Even the logarithmic slope of 2.5 shows up clearly in the beam measurements. Of course, the vertical scale is very compressed. It is not even sure that the scatter of the results is due to the measurement. Indeed, there is no good reason why the spectral density of the seismic activity should be constant in time. On several occasions, highlighted in Table 2 and 3, a much higher activity was noted.

VI. CONSEQUENCES FOR THE LHC

The transverse excitation source for LEP and LHC is obviously the same S_{gm} . The effect of uncorrected ground motion in the LHC is beam blow up since damping is very small. The blow up can be computed with following formula :

$$\tau^{-1} = \sum \beta_Q (K\ell)^2 \left(\frac{f_{rev}}{2} \right)^2 \frac{\gamma}{\epsilon} S_{gm}(f),$$

where ϵ is the normal beam emittance and γ mass to rest mass ratio.

Assuming that the growth rate should not be less than 40 hours, allowing for a damping time of around 25 hours and an emittance of $3.75 \mu\text{radm}$ and $\gamma=8000$ we find an upper limit for S_{gm} :

$$S_{gm} \leq 70 \cdot 10^{-14} \mu^2 / \text{Hz}.$$

In Figure 3 this level is designated by the label 'blow up limit'.

This result shows that most of the time at fractional tunes of 0.15 and above this condition is met. However, seismic activity is not constant and cases were observed where the limit has been exceeded considerably over many hours. The impressive scatter of the results shown in Figure 1 is maybe partially due to power variations of seismic vibrations. Moreover, even if the source of the effect is the same in LEP and LHC it is not sure that the motion of the quadrupoles is identical. It is well known that the magnet supports can enhance the motion considerably [1,2]. Therefore, it may be wise to consider a narrow band low power and low noise transverse feedback system that will keep the persistent oscillation amplitude \bar{x} below a level that corresponds to an acceptable growth rate. The feasibility study of such a system goes beyond the scope of this report.

VII. CONCLUSIONS

The excitation of the beam in LEP by seismic vibrations has been measured rather accurately. Its effect on the blow up of the LHC coasting beams has been estimated. In view of large temporal variations of the power of seismic vibrations it is suggested that a special feedback is envisaged to keep the effect within acceptable bounds at all times.

VIII. ACKNOWLEDGEMENTS

I thank the following persons for their interest, encouragement and assistance: C. Boccard, T. Bogey, C. Bovet, W. Fischer, B. Halvarsson, H. Jakob, I. Milstead, J-P. Papis and F. Schmidt.

IX. REFERENCES

- [1] Ground Motion and Its Effect in Accelerator Design, G.E. Fischer, AIP Conference Proceedings 153, Fermilab Summer School, 1984.
- [2] Ground Motion Tolerances for the SSC, G.E. Fischer and P. Morton, SLAC-PUB-3870, January 1986.
- [3] Suppression of emittance growth caused by mechanical vibrations of magnetic elements in presence of beam-beam effects in the SSC, V.A. Lebedev, V.V. Parchomchuk, V.D. Shiltsev, A.N. Skrinsky, Pre-print 91-120, Budker Institute of Nuclear Physics, 1991.
- [4] Emittance Growth Issues, K-Y Ng, FERMILAB-FN-588, April 1992.
- [5] Fast Ground Motion at HERA, J. Rossbach, DESY 89-023, February 1989.
- [6] Measurements of seismic vibrations in the CERN TT2A tunnel for linear collider studies, Balakin V.E., et al, Branch of Institute of Nuclear Physics, Protvino, Russia, W. Coosemans, et al, CERN, CLIC Note 191, June 1993.
- [7] Investigations of power and spatial correlation characteristics of seismic vibrations in the CERN LEP tunnel for linear collider studies, Juravlev V.M., et al, Branch of Institute of Nuclear Physics, Protvino, Russia, W. Coosemans, et al, CERN, CLIC Note 217, December 1993.
- [8] Seismic Vibration Studies for Future Linear Colliders, Juravlev V.M., et al, CLIC Note 234, July 1994.

Cosmic Particle Acceleration at Very High Energies*

K.O. Thielheim
 Institut für Reine und Angewandte Kernphysik
 Abteilung Mathematische Physik
 University of Kiel
 Otto-Hahn-Platz 3
 24118 Kiel
 Germany

I. High Energy Cosmic Particles and Fields

In very strong electromagnetic fields, near to the magnetic poles of a neutron star, for example, where the magnetic field strength may well exceed 10^{12} G, and thus the corresponding mass equivalent of field energy be higher than 200 g cm^{-3} , mechanisms can evolve, that are interesting for a number of reasons:

Something may be learnt about electromagnetism at extremely high energy densities,

Astrophysicists want to understand the structure and dynamics of pulsar magnetospheres in terms of underlying physics,

Rotating cosmic magnets, rotation-powered radio pulsars, for example, are possible candidates for high energy cosmic particle accelerators [1],

The physics at work may be helpful for the designing of new types of man-made accelerators.

The present paper is directed to a better understanding of the classical equation of motion for particles in very strong electromagnetic fields at its possible rôle in the generation of gamma ray bursts and in the formation of plasma jets.

II. Self-Consistent Electrodynamics

According to the conventional interpretation of Maxwell theory, electromagnetic radiation is 'generated' through shear acceleration of an electromagnetically interacting particle, irrespective of the nature of accelerating forces.

Consequently, Larmor's radiation formula

$$P^{RAD} = m\tau_0(d\mathbf{v}_{MRS}/dt)^2 = m\tau_0\|d\mathbf{u}/d\tau\|^2 \quad (1)$$

then contains the (four-) vector of 'kinematical' acceleration, $d\mathbf{u}/d\tau$. $d\mathbf{v}_{MRS}/dt$ is the corresponding (three-) vector in the momentary rest frame, MRS, of that particle. m is its mass and $\tau_0 = 2e^2/3mc^3$ is the radiation constant.

Also in agreement with this interpretation, the equation of motion

$$du_j/d\tau = \eta_0 F_{jk}^{EXT} u^k + \tau_0 G_{jk} u^k, \quad (2)$$

contains a radiation force tensor

$$G_{jk} = G_{jk}^{L-D} := ([d^2 u_j/d\tau^2] u_k - u_j [d^2 u_k/d\tau^2])/c^2 \quad (3)$$

*Paper delivered to the Particle Accelerator Conference, May, 1-5, 1995, Dallas, Texas. Due to the shortage of space, numerical and graphical results shown at the conference will be reproduced elsewhere.

which is governed by (this time the second) kinematical acceleration¹. F_{jk}^{EXT} is the tensor of the external field² in an arbitrary inertial frame of reference (IS) and $\eta_0 = e/mc$. If acceleration is due to external *electromagnetic* fields, Larmor's radiation formula (1) specializes to

$$P^{RAD} = m\tau_0(c\eta_0 \mathbf{E}_{MRS}^{EXT})^2 = m\tau_0\|\underline{u}^L\|^2, \quad (4)$$

where $\underline{u}^L := \eta_0 F_{jk}^{EXT} u^k$ is used as an abbreviation for the 'Lorentz acceleration'. \mathbf{E}_{MRS}^{EXT} is the electric field vector of the external field, in the MRS.

Accordingly, the radiation force tensor (3) specializes to

$$G_{jk} = G_{jk}^{EXT} := \eta_0 u^l \partial_l F_{jk}^{EXT} + G_{jk}^T, \quad (5)$$

with

$$G_{jk}^T := (u_j^{LL} u_k - u_j u_k^{LL})/c^2 \quad (6)$$

and $u_j^{LL} := \eta_0^2 F_{jk}^{EXT} F^{EXTkl} u_l$ as an abbreviation for the 'second Lorentz acceleration'.

In what follows I shall, tentatively, suggest that (I) *radiation is generated and radiation reaction may be felt only if and insofar as acceleration is due to external electromagnetic fields* [2], [5], [6].

As a consequence of this suggestion, (4) is expected to be the correct form of Larmor's radiation formula, (at least in the lowest order of the interaction constant) and (5) is expected to be the correct form of the radiation force tensor.

When the external field is a *wave* field, radiation from a charged particle is often looked upon as the *scattered* wave field ('synchro-Compton radiation') and the fourth-order component of radiation reaction force in this special case is seen as the *knock-on* force due to many-photon Thomson- (or Compton-) scattering³,

$$\mathbf{K}_{MRS}^T = (\sigma^T/c) \mathbf{S}_{MRS}^{EXT}, \quad (7)$$

where $\sigma^T = 8\pi e^4/3m^2 c^4$ is the Thomson cross-section and \mathbf{S} is the Poynting vector.

Here it will be shown how this interpretation can be extended also to electromagnetic fields of *arbitrary* shape, namely that (II)

¹Equation (2) with (3) sometimes is called Lorentz-Dirac equation (L-D equation) or Abraham-Lorentz equation. Equation (2) with (5) sometimes is referred to as Lorentz-Dirac-Landau equation (L-D-L equation). A review is given in: [3].

²The external field is understood as the field due to all other electromagnetically interacting particles around.

³As one might expect, (6) can be deduced from (7) by Lorentz transformation [4].

radiation emitted from an electromagnetically interacting particle in general can be understood as the result of the scattering of an external electromagnetic field.

Suggestions (I) and (II) will be integrated in a Schrödinger picture of the photon and referred to as *self-consistent electrodynamics*.

III. Wave Mechanics of the Photon

In Maxwell's equations

$$\begin{aligned} [\nabla, \mathbf{E}] &= -(1/c)\partial_t \mathbf{H} - (4\pi/c)\mathbf{j}^{(m)}, \\ [\nabla, \mathbf{H}] &= (1/c)\partial_t \mathbf{E} + (4\pi/c)\mathbf{j}^{(e)}, \\ (\nabla, \mathbf{E}) &= 4\pi\rho^{(e)}, \\ (\nabla, \mathbf{H}) &= 4\pi\rho^{(m)}, \end{aligned}$$

the electromagnetic field is represented by the electric and magnetic vectors \mathbf{E} and \mathbf{H} , respectively. $\mathbf{j}^{(e)}$ and $\mathbf{j}^{(m)}$ are the electric and magnetic current vectors, and $\rho^{(e)}$ and $\rho^{(m)}$ are the electric and magnetic charge densities, respectively.

As is well known, these classical field equations may be written⁴

$$i\hbar\partial_t\psi = \mathcal{H}^+\psi - 4\pi i\hbar\zeta, \quad (8)$$

where $(\nabla, \psi) = 4\pi\eta$. $\psi := C(\mathbf{E} + i\mathbf{H})$ is the wave function of the photon and $\psi^\dagger = C^*(\mathbf{E}^T - i\mathbf{H}^T)$ is its adjoint. Correspondingly, the source terms⁵ are defined through the electric and magnetic charges $\eta = C\{\rho^{(e)} + i\rho^{(m)}\}$ and the respective currents $\zeta = C\{\mathbf{j}^{(e)} + i\mathbf{j}^{(m)}\}$, respectively⁶. $s := ((s_\lambda)_{\mu\nu}) := -i\hbar(\epsilon_{\lambda\mu\nu})$ is the spin and $\mathbf{p} := ((p_\lambda)_{\mu\nu}) := -i\hbar((\partial_\lambda)\delta_{\mu\nu})$ is the momentum of the photon. $\mathcal{H}^+ := (c/\hbar)(s, \mathbf{p})$.

In a source-free region, Schrödinger's equations is

$$i\hbar\partial_t\psi = \mathcal{H}^+\psi. \quad (9)$$

Alternatively, one might have written

$$i\hbar\partial_t\tilde{\psi} = \mathcal{H}^-\tilde{\psi} \quad (10)$$

with the wave function $\tilde{\psi} := C^*(\mathbf{E} - i\mathbf{H})$ and its adjoint $\tilde{\psi}^\dagger := C(\mathbf{E}^T + i\mathbf{H}^T)$. Then, $\mathcal{H}^- := -(c/\hbar)(s, \mathbf{p})$.

Only waves corresponding to positive energy \mathcal{E} of the photon have a physical counterpart in classical electromagnetic fields⁷

⁴For example, in: A. Messiah, Quantum Mechanics, Vol. I & II, North Hollandish Publ. Comp. (1970).

⁵Magnetic charges and currents are admitted for reasons of symmetry, but their appearance is not essential in the following argumentations. Brackets [.] are for the vector product, (.) for the scalar product. In what follows, Latin indices are running from 0 through 3, Greek indices are running from 1 through 3. T stands for transposition and $*$ for complex conjugate. \mathcal{H} will be used for the Hamiltonian to distinguish it from the magnetic vector \mathbf{H} . Also, \mathcal{E} will be used for the energy of a photon to distinguish it from the energy density of the electromagnetic field ϵ . $\epsilon_{\lambda\mu\nu}$ are the Levi-Civita symbols.

⁶With this definition of ψ through \mathbf{E} and \mathbf{H} we have not given privilege to any of these two field vectors \mathbf{E} or \mathbf{H} since the norm of the wave function, as well as expectation values are numerically invariant, and the field equations are form-invariant under the transformation $\psi \rightarrow \psi' = e^{i\alpha}\psi$, so that $\mathbf{E} \rightarrow \mathbf{E}' = \mathbf{E} \cos \alpha - \mathbf{H} \sin \alpha$, and $\mathbf{H} \rightarrow \mathbf{H}' = \mathbf{E} \sin \alpha + \mathbf{H} \cos \alpha$, (with corresponding transformation rules for the source terms). Moreover, these invariances also exist under unitary transformations, $\psi \rightarrow \psi' = \mathcal{A}\psi$, with $\mathcal{A} \in U(3)$, from where it looks 'natural' that the corresponding irreducible representations 'appear' as 'elementary entities' which take part in electromagnetic interaction.

⁷In addition, one has to consider wave functions which are independent from the coordinates in space and time, in the normalization volume. They correspond to the limit of vanishing photon energy, $\mathcal{E} \rightarrow 0$.

and thus need to be selected from the solutions of (9) and (10). Among these, the ones with positive sense of rotation of the electric vector with respect to the direction of propagation (i.e. left-circularly polarized waves in the usual notation, corresponding to positive helicity of the photon) are delivered by (9), while those with negative sense of rotation (i.e. right-circularly polarized waves, corresponding to negative helicity) are described by (10).

Here, it will be more comfortable, to make use of a one-to-one correspondence of solutions from (9) and (10), restricting to solutions of (9)

$$i\hbar\partial_t\psi = \mathcal{H}\psi, \quad (11)$$

where $\mathcal{H} := (c/\hbar)\chi(s, \mathbf{p})$, and χ distinguishes between states of positive and negative helicity.

IV. Normalization and Statistical Interpretation

The quantum Schrödinger picture can be related to the classical Maxwell picture through a statistical interpretation. Multiplication of the Schrödinger equation (9) with ψ^\dagger and of the adjoint equation with ψ after subtraction delivers,

$$\partial_\mu w_\mu + \partial_t w = q, \quad (12)$$

where $w(\mathbf{x}, t) := \psi^\dagger\psi = (\psi^*, \psi)$, and $\mathbf{w}(\mathbf{x}, t) = (w_\mu) := -ic[\psi^*, \psi]$, and $q := -8\pi\text{Re}(\psi^*, \zeta)$, where $\text{Re}()$ stands for the real part.

If the wave packet of the particle constituting the electric charge does not grow too fast within time intervals considered, w is *quasi-source free*. In that case, normalization

$$\int_V \psi^\dagger\psi d^3\mathbf{x} = 1 \quad (13)$$

is possible with the help of

$$|C|^2 = 1/\int_V \{\mathbf{E}^2 + \mathbf{H}^2\} d^3\mathbf{x}, \quad (14)$$

where $V \subseteq \mathbf{R}_3(\mathbf{x})$ is an appropriately chosen normalization volume in 3-dimensional coordinate space⁹. Then, w is interpretable as the *position probability density* of the photon and w_μ as the corresponding *position probability current* and the expectation value for energy, e.g., is

$$\langle \mathcal{H} \rangle = \int_V \psi^\dagger \mathcal{H} \psi d^3\mathbf{x}. \quad (15)$$

Multiplying (9) with $\psi_\mu^* \epsilon_{\kappa\eta\mu}$ and subtraction of the complex conjugate delivers

$$\partial_\nu w_{\mu\nu} + \partial_t w_\mu = q_\mu, \quad (16)$$

where $w_{\mu\nu} := (\psi^*, \psi)\delta_{\mu\nu} - (\psi_\mu^* \psi_\nu + \psi_\nu^* \psi_\mu)$ and¹⁰ $q_\mu := C\{\psi_\mu^* (\nabla, \psi) + \psi_\mu (\nabla, \psi^*)\}$.

⁸Corresponding to $q = -8\pi|C|^2\{(\mathbf{E}, \mathbf{j}^{(e)}) + (\mathbf{H}, \mathbf{j}^{(m)})\}$.

⁹Singularities from point-like sources can be avoided by taking into account the finite extension of the wave packet of the corresponding physical particle.

¹⁰Corresponding to $q_\mu = 8\pi c|C|^2\{E_\mu \rho^{(e)} + H_\mu \rho^{(m)}\}$

Since, in a source-free region, each component of $\mathbf{w} = (c/\hbar)\psi^\dagger \mathbf{s} \psi$ obeys the continuity equation (16), \mathbf{w} may also be interpreted as a density, in this case, of $c := (c/\hbar)\mathbf{s}$.

For an interpretation of the conserved quantity c , we note that with (11) the only possible eigenvalue of $c = (c/\hbar)\mathbf{s}$ is $+c$. Thus, c_μ may be understood as the velocity operator of the photon with $c_\mu c_\mu = c^2$. \mathbf{w} can be seen as the velocity density and $w_{\mu\nu}$ as the corresponding velocity current.

We thus arrive at the classical continuity equation $\partial_\mu S_\mu^\# + \partial_t \varepsilon^\# = 0$ for the density $\varepsilon^\# := N < \mathcal{H} > w$, and the current $S_\mu^\# := N < \mathcal{H} > w_\mu$, of *expected* energy, and at the classical continuity equation $\partial_\nu \sigma_{\mu\nu}^\# + \partial_t P_\mu^\# = 0$, for the density $P_\mu^\# := N < \mathcal{H} > w_\mu/c$, and the current $\sigma_{\mu\nu}^\# := N < \mathcal{H} > w_{\mu\nu}/c$, of *expected* momentum, where N is the ratio of classical field energy in the normalization volume to the expectation value of photon energy.

V. Reproduction of the Equation of Motion

We now have the means to reinterpret radiation generation and radiation reaction within a field of arbitrary shape in terms of *many photon Thomson scattering*.

If, in the MRS, $O(V')$ is the surface separating a (sufficiently small spherical) scattering volume $V' \subset V$ from $V \setminus V'$, then the rate of *expected* momentum transfer onto the charged particle is

$$K_{MRS\mu} = - \oint_{O(V')} \sigma_{\mu\nu}^\# d^2 o_\nu. \quad (17)$$

Through arguments analogous to those applied earlier [2], [5], [6], contributions from the external field and from the Coulomb field deliver the Lorentz (Coulomb) force

$$\mathbf{K}_{MRS}^{LOR} = e \mathbf{E}_{MRS}^{EXT}, \quad (18)$$

and transformation of (18) from the MRS to an arbitrary IS leads to the covariant form of the Lorentz force

$$K_j^{LOR} = m \eta_0 F_{jk}^{EXT} u^k, \quad (19)$$

while contributions from the radiation field and from the Coulomb field reproduce the radiation reaction force

$$\mathbf{K}_{MRS}^{RAD}(t) = \tau_0 d\mathbf{K}_{MRS}^{LOR}(t)/dt. \quad (20)$$

Transformation of (20) analogously leads to

$$K_j^{RAD} = m \tau_0 G_{jk}^{EXT} u^k, \quad (21)$$

and thereby back to the classical equation of motion (2) with (5).

VI. A Possible Mechanism for the Formation of Jets and the Generation of Gamma Ray Bursts by Rotating, Magnetized Neutron Stars

Near the surface of a rotating, magnetized neutron star, the magnetic field may be extremely strong [7], typically of the order of $10^{12}G$, and also the electric field may be very strong, though considerably less, typically of the order of $10^{10}G$. Under such conditions particles tend to follow magnetic field lines and, as I

have suggested earlier [6], [5], an upper limit of particle energy is created *locally* by radiation reaction.

In the polar region, $\theta = 0$, of an *orthogonal rotator*, this limit is $\max(\gamma^{\text{ortho}}) \cong 2.4 \cdot 10^3$ for the electron, and $\max(\gamma^{\text{ortho}}) \cong 3.6 \cdot 10^5$ for the proton¹¹.

For a *parallel rotator*,

$$\max(\gamma^{\text{para}}) \cong 2\sqrt{r_L/c\tau_0} \cdot \left(\frac{r_N}{r_T}\right) \text{ctg} \theta_0 \frac{\sqrt{\cos^2 \theta_0 (3\cos^2 \theta_0 + 1)}}{(1 + \cos^2 \theta_0)}. \quad (22)$$

In the polar region, $\theta = 0$, of a parallel rotator, the upper limit of the Lorentz factor is $\max(\gamma^{\text{para}}) \cong 2.9 \cdot 10^3 \text{ctg} \theta_0$ for the electron, and $\max(\gamma^{\text{para}}) \cong 4.4 \cdot 10^5 \text{ctg} \theta_0$ for the proton.

Unlike the orthogonal rotator, the parallel rotator develops a very narrow *nozzle* around the axis, $\theta = 0$, through which very energetic particles can be ejected from the surface. This mechanism may play a rôle in both, the generation of gamma ray bursts¹² as well as the formation of jets.

References

- [1] K.O. Thielheim, *Fundamentals of Cosmic Physics*, **13**, 357 (1989).
- [2] K.O. Thielheim, *Il Nuovo Cimento*, **109 B**, N. 1. 103 (1994).
- [3] A.D. Yaghjian, *Relativistic Dynamics of a Charged Sphere*, Springer Verlag, Berlin, Heidelberg, New York (1992).
- [4] K.O. Thielheim, *Int. Journ. of Modern Physics D* **3.1**, 289 (1993).
- [5] K.O. Thielheim, *Physica Scripta* **T52**, 123 (1994).
- [6] K.O. Thielheim, *Proc. EPAC*, London, **1**, 808 (1994).
- [7] A.J. Deutsch, *Ann. d'Astrophys.* **18**, 1 (1955).
- [8] K.O. Thielheim, *Nucl. Phys. (Proc. Suppl.)*, **22B**, 60 (1991).

¹¹ As in [8], numerical values given here are for the 'standard set of parameters', e.g., for the radius of the neutron star: $r_N = 10^6 \text{cm}$, for the light radius: $r_L = 4.8 \cdot 10^8 \text{cm}$, and for the 'typical radius': $r_T = 2.4 \cdot 10^{13} \text{cm}$ (electrons) and $r_T = 5.6 \cdot 10^{11} \text{cm}$ (protons), corresponding to $\nu = 10 \text{sec}^{-1}$ and $\mu = 10^{30} G \text{cm}^3$.

¹² One may think of thin beams of very energetic particles from spinning neutron stars distributed in the volume of the galactic halo, which randomly hit the location of the observer. But, of course, one has to keep in mind that this suggestion is based on results from particle dynamics in vacuum fields ('stage one'). As mentioned before, modifications of the fields are expected through plasma effects.

TRAPPED MODES IN THE VACUUM CHAMBER OF AN ARBITRARY CROSS SECTION

Sergey S. Kurennoy

Physics Department, University of Maryland, College Park, MD 20742, USA

and Gennady V. Stupakov

SLAC, Stanford, CA 94309, USA

Abstract

A recent study [1] has shown that a small discontinuity such as an enlargement or a hole on circular waveguides can produce trapped electromagnetic modes with frequencies slightly below the waveguide cutoff. The trapped modes due to multiple discontinuities can lead to high narrow-band contributions to the beam-chamber coupling impedance, especially when the wall conductivity is high enough. To make more reliable estimates of these contributions for real machines, an analytical theory of the trapped modes is developed in this paper for a general case of the vacuum chamber with an arbitrary single-connected cross section. The resonant frequencies and coupling impedances due to trapped modes are calculated, and simple explicit expressions are given for circular and rectangular cross sections. The estimates for the LHC are presented.

I. Introduction

Previous computer studies of cavities coupled to a beam pipe indicated that the impedance of small chamber enlargements exhibits sharp narrow peaks at frequencies close to the cutoff frequencies of the waveguide, see references in [1]. For a single small discontinuity, such as an enlargement or a hole, on a smooth circular waveguide, an analytical theory has been developed [1], which shows that these peaks can be attributed to trapped modes localized near the discontinuity. A trapped mode is an eigenmode of the waveguide with a discontinuity, with the eigenfrequency slightly below the waveguide cutoff, which can exist in addition to the continuous spectrum of the smooth waveguide. The existence of trapped modes depends on a relation between the conductivity of the chamber walls and a typical size of the discontinuity, and in the limit of perfectly conducting walls the trapped modes exist even for very small perturbations.

The trapped modes in a circular waveguide with many discontinuities have also been studied [2], and it was demonstrated that the resonance impedance due to N close discontinuities in the extreme case can be as large as N^3 times that for a single discontinuity. This phenomenon is dangerous for the beam stability in large superconducting proton colliders like the LHC, where the design anticipates a thermal screen (liner) with many small pumping holes inside the beam pipe. In such structures with many small discontinuities and a high wall conductivity, the trapped modes can exist and contribute significantly to the beam-chamber coupling impedances.

In the present paper we develop an analytical description of the trapped modes for a waveguide with an arbitrary single-connected cross section. We also derive particular results for cir-

cular and rectangular waveguides from our general formulas.

II. General Analysis

Let us consider a cylindrical waveguide with a transverse cross section S , having a small hole in its perfectly conducting walls. We assume that the z axis is directed along the waveguide axis, the hole is located at the point $(\vec{b}, z = 0)$, and its typical size h satisfies $h \ll b$. The fields of a source with time dependence $\exp(-i\omega t)$ in the waveguide without hole can be expressed as a series in TM- and TE-modes. The fields of the TM_{nm} mode are [3]

$$\begin{aligned} E_z^\mp &= k_{nm}^2 e_{nm} \exp(\pm \Gamma_{nm} z); & H_z^\mp &= 0; \\ \vec{E}_t^\mp &= \pm \Gamma_{nm} \vec{\nabla} e_{nm} \exp(\pm \Gamma_{nm} z); \\ Z_0 \vec{H}_t^\mp &= ik\hat{z} \times \vec{\nabla} e_{nm} \exp(\pm \Gamma_{nm} z), \end{aligned} \quad (1)$$

where \pm indicates the direction of the mode propagation, k_{nm}^2 , $e_{nm}(\vec{r})$ are eigenvalues and orthonormalized eigenfunctions (EFs) of the 2D boundary problem in S :

$$(\nabla^2 + k_{nm}^2) e_{nm} = 0; \quad e_{nm}|_{\partial S} = 0, \quad (2)$$

and propagation factors $\Gamma_{nm} = (k_{nm}^2 - k^2)^{1/2}$ are to be replaced by $-i\beta_{nm}$ with $\beta_{nm} = (k^2 - k_{nm}^2)^{1/2}$ for $k > k_{nm}$. Here $\vec{\nabla}$ is the 2D gradient in plane S ; $k = \omega/c$; $\hat{\nu}$ means an outward normal unit vector, $\hat{\tau}$ is a unit vector tangent to the boundary ∂S of the chamber cross section S , and $\{\hat{\nu}, \hat{\tau}, \hat{z}\}$ form a RHS basis. Similarly, TE_{nm} fields are expressed in terms of EFs h_{nm} satisfying the boundary problem (2) with the Neumann boundary condition $\nabla_\nu h_{nm}|_{\partial S} = 0$, and corresponding eigenvalues $k_{nm}^{\prime 2}$ [3].

A. Frequency Shifts

In the presence of the hole, there is a solution of the homogeneous, i.e., without external currents, Maxwell equations for this structure with the frequency Ω_s ($s \equiv \{nm\}$) slightly below the corresponding cutoff frequency $\omega_s = k_s c$, so that $\Delta\omega_s \equiv \omega_s - \Omega_s \ll \omega_s$ — the s th trapped TM-mode. At distances $|z| > b$ from the discontinuity the fields of the trapped mode have the form

$$\begin{aligned} \mathcal{E}_z &= k_s^2 e_s \exp(-\Gamma_s |z|); & \mathcal{H}_z &= 0; \\ \vec{\mathcal{E}}_t &= \text{sgn}(z) \Gamma_s \vec{\nabla} e_s \exp(-\Gamma_s |z|); \\ Z_0 \vec{\mathcal{H}}_t &= ik\hat{z} \times \vec{\nabla} e_s \exp(-\Gamma_s |z|), \end{aligned} \quad (3)$$

where $k = \Omega_s/c$, and the propagation constant Γ_s satisfies the equation

$$\Gamma_s \simeq \frac{1}{4} \psi_\tau (\nabla_\nu e_s^h)^2. \quad (4)$$

Here ψ_τ is the transverse magnetic susceptibility of the hole, cf. [4], and superscript 'h' indicates that the field is taken at the hole. Typically, $\psi_\tau = O(h^3)$, while $\nabla_\nu e_s^h = O(1/b)$, and as a result, $\Gamma_s b \ll 1$. This means that the field of the trapped mode extends in the waveguide over the distance $1/\Gamma_s$ large compared to the waveguide transverse dimension. Conditions like Eq. (4) were obtained in [1], [2] for a circular waveguide using the Lorentz reciprocity theorem, but there are other ways to derive them. For example, they follow in a natural way from a general theory for the impedances of small discontinuities [4]. In such a derivation, the physical mechanism of this phenomenon becomes clear: a tangential magnetic field induces a magnetic moment on the hole, and the induced magnetic moment support this field if the resonance condition (4) is satisfied. Thus, the mode can exist even without an external source, see in [4]. Note that the induced electric moment P_ν is negligible for the TM-mode, since $P_\nu = O(\Gamma_s)M_\tau$, as follows from Eq. (3).

The equation (4) gives the frequency shift $\Delta\omega_s$ of the trapped s th TM-mode down from its cutoff ω_s ,

$$\frac{\Delta\omega_s}{\omega_s} \simeq \frac{1}{32k_s^2} \psi_\tau^2 (\nabla_\nu e_s^h)^4. \quad (5)$$

In the case of a small hole this frequency shift is very small, and for the trapped mode (3) to exist, the width of the resonance should be smaller than $\Delta\omega_s$. Contributions to the width come from energy dissipation in the waveguide wall due to its finite conductivity, and from energy radiation inside the waveguide and outside, through the hole. Radiation escaping through the hole is easy to estimate [1], and for a thick wall it is exponentially small, e.g., [5]. The damping rate due to a finite conductivity is $\gamma = P/(2W)$, where P is the time-averaged power dissipation and W is the total field energy in the trapped mode, which yields

$$\frac{\gamma_s}{\omega_s} = \frac{\delta}{4k_s^2} \oint dl (\nabla_\nu e_s)^2, \quad (6)$$

where δ is the skin-depth at frequency Ω_s , and the integration is along the boundary ∂S . The evaluation of the radiation into the lower waveguide modes propagating in the chamber at given frequency Ω_s is also straightforward [6], if one makes use of the coefficients of mode excitation by effective dipoles on the hole, e.g., Eqs. (6)-(9) in Ref. [4]. It shows that corresponding damping rate $\gamma_R = O(\psi_\tau^3)$ is small compared to $\Delta\omega_s$. For instance, if there is only one TE_p-mode with the frequency below that for the lowest TM_s-mode, like in a circular waveguide (H_{11} has a lower cutoff than E_{01}),

$$\frac{\gamma_R}{\Delta\omega_s} = \frac{\psi_\tau \beta'_p}{k_p'^2} (\nabla_\nu h_s^h)^2, \quad (7)$$

where $\beta'_p \simeq (k_s^2 - k_p'^2)^{1/2}$ because $k \simeq k_s$.

The frequency of the trapped TE_p-mode is given by the condition [4]

$$\Gamma'_p \simeq \frac{1}{4} \left[\psi_z k_p'^2 (h_p^h)^2 - \chi (\nabla_\tau h_p^h)^2 \right], \quad (8)$$

provided the RHS of Eq. (8) is positive. Here ψ_z and χ are the longitudinal magnetic susceptibility and the electric polarizability of the hole.

B. Impedance

The trapped mode (3) gives a resonance contribution to the longitudinal coupling impedance at $\omega \approx \Omega_s$,

$$Z_s(\omega) = \frac{2i\Omega_s \gamma_s R_s}{\omega^2 - (\Omega_s - i\gamma_s)^2}, \quad (9)$$

where the shunt impedance R_s can be calculated as

$$R_s = \frac{\sigma \delta \left| \int dz \exp(-i\Omega_s z/c) \mathcal{E}_z(z) \right|^2}{\int_{S_w} ds |\mathcal{H}_\tau|^2}. \quad (10)$$

The integral in the denominator is taken over the inner wall surface, and we assume here that the power losses due to its finite conductivity dominate. Integrating in the numerator one should include all TM-modes generated by the effective magnetic moment on the hole using Eqs. (6)-(9) from [4], in spite of a large amplitude of only the trapped TM_s mode. While all other amplitudes are suppressed by factor $\Gamma_s b \ll 1$, their contributions are comparable to that from TM_s, because this integration produces the factor $\Gamma_q b$ for any TM_q mode. The integral in the denominator is dominated by TM_s. Performing calculations yields

$$R_s = \frac{Z_0 \tilde{e}_\nu^2 \psi_\tau^3 k_s (\nabla_\nu e_s^h)^4}{8\delta \oint dl (\nabla_\nu e_s)^2}, \quad (11)$$

where $\tilde{e}_\nu \equiv -\sum_s e_s(0) \nabla_\nu e_s(\vec{b})/k_s^2$ is the normalized electric field produced at the hole location by a filament charge on the chamber axis, see [7] and [4].

Results for a particular shape of the chamber cross section are obtained from the equations above by substituting the corresponding eigenfunctions.

III. Circular Chamber

For a circular cross section of radius b the eigenvalues $k_{nm} = \mu_{nm}/b$, where μ_{nm} is m th root of the Bessel function $J_n(x)$, and the normalized EFs are

$$e_{nm}(r, \varphi) = \frac{J_n(k_{nm}r)}{\sqrt{N_{nm}^E}} \begin{Bmatrix} \cos n\varphi \\ \sin n\varphi \end{Bmatrix}, \quad (12)$$

with $N_{nm}^E = \pi b^2 \epsilon_n J_{n+1}^2(\mu_{nm})/2$, where $\epsilon_0 = 2$ and $\epsilon_n = 1$ for $n \neq 0$. For TE-modes, $k'_{nm} = \mu'_{nm}/b$ with $J'_n(\mu_{nm}) = 0$, and

$$h_{nm}(r, \varphi) = \frac{J_n(k'_{nm}r)}{\sqrt{N_{nm}^H}} \begin{Bmatrix} \cos n\varphi \\ \sin n\varphi \end{Bmatrix}, \quad (13)$$

where $N_{nm}^H = \pi b^2 \epsilon_n (1 - n^2/\mu_{nm}^2) J_n^2(\mu'_{nm})/2$. In this case $\tilde{e}_\nu = 1/(2\pi b)$, which follows from the Gauss law. Assuming the hole located at $\varphi = 0$, we get from Eq. (4)

$$\Gamma_{nm} = \frac{\psi_\tau \mu_{nm}^2}{2\pi \epsilon_n b^4}, \quad (14)$$

and from Eq. (11)

$$R_{nm} = \frac{Z_0 \psi_\tau^3 \mu_{nm}^3}{32\pi^4 \epsilon_n \delta b^8}. \quad (15)$$

For TE-modes from Eq. (8)

$$\Gamma'_{nm} = \frac{\psi_z \mu_{nm}^{1/4}}{2\pi \epsilon_n b^4 (\mu_{nm}^{1/2} - n^2)} \quad (16)$$

Note that only the modes with $\cos n\varphi$ can be trapped, while sin-modes just do not "see" the hole.

The results of this section coincide with those of [1], [2], except R_s in [1], where the contribution of only the trapped mode to Eq. (10) was taken into account. Formulas for an axisymmetric enlargement with area A of the longitudinal cross section are easily obtained from Eqs. (14)-(15) with $n = 0$ by substitution $\psi_\tau \rightarrow 4\pi b A$.

IV. Rectangular Chamber

For a rectangular chamber of width a and height b the eigenvalues $k_{nm} = \pi\sqrt{n^2/a^2 + m^2/b^2}$ for $n, m = 1, 2, \dots$, and the normalized EFs are

$$e_{nm}(x, y) = \frac{2}{\sqrt{ab}} \sin \frac{\pi nx}{a} \sin \frac{\pi my}{b}, \quad (17)$$

with $0 \leq x \leq a$ and $0 \leq y \leq b$. Let a hole be located in the side wall at $x = a$, $y = y_h$. Then Eq. (4) gives

$$\Gamma_{nm} = \frac{\psi_\tau \pi^2 n^2}{a^3 b} \sin^2 \left(\frac{\pi m y_h}{b} \right), \quad (18)$$

and from Eq. (11) the impedance is

$$R_{nm} = \frac{Z_0 \psi_\tau^3 \pi^3 n^2 \sqrt{n^2 b^2 + m^2 a^2}}{2 \delta a^4 b^2 (n^2 b^3 + m^2 a^3)} \Sigma^2 \left(\frac{a}{b}, \frac{y_h}{b} \right) \sin^4 \left(\frac{\pi m y_h}{b} \right) \quad (19)$$

where

$$\Sigma(u, v) = \sum_{l=0}^{\infty} \frac{(-1)^l \sin[\pi(2l+1)v]}{\cosh[\pi(2l+1)u/2]} \quad (20)$$

is a fast converging series; see pictures in [7]. Both the frequency shift and especially the impedance decrease very fast if the hole is displaced closer to the corners of the chamber, i.e. when $y_h \rightarrow b$ or $y_h \rightarrow 0$.

V. Estimates

In a vacuum chamber with many discontinuities their mutual interaction is very important. For trapped modes in a circular pipe this interaction was studied in [2], but the results are applicable for any cross section of the chamber. A few holes in one cross section work as a single combined discontinuity. If the average distance g between adjacent cross sections with holes is shorter than $1/\Gamma_s$, the number of the cross sections with holes which work as an effective combined discontinuity is $N_{eff} = \sqrt{2/(\Gamma_s g)}$. Referring to [2] for more detail, in this case we use the following estimate for the reduced impedance of a cyclic accelerator due to the trapped modes

$$Re \frac{Z}{n} = \frac{4\pi}{\Gamma_s k_s g^2} R_s, \quad (21)$$

where Γ_s , k_s , and R_s are given by the formulas above.

For the LHC liner we consider a model having a square cross section with side $a = 36$ mm. The liner wall has thickness

$t = 1$ mm and the inner copper coating. There are 666 narrow longitudinal slots with width $s = 1.5$ mm and length $s = 6$ mm per meter of the liner, with $M = 8$ slots in one cross section, which makes spacing $g = 12$ mm. The slots are located at distance $a/4$ from corners. Using $\psi_\tau = w^2 s / \pi$ for a long slot in the thick wall [8], we get for the lowest E-mode (TM₁₁) near 5.9 GHz

$$Re \frac{Z}{n} = 9.2 \sqrt{RRR} \text{ Ohms}, \quad (22)$$

where $RRR = 30 - 100$ for copper. The estimate for the model with the circular cross section of radius $b = 18$ mm was $16.5 \sqrt{RRR}$ Ohms [2]. These estimates presume identical slots. A distribution of slot areas/lengths reduces $Re Z/n$ significantly: e.g., for the Gaussian distribution with RMS $\sigma_A/A_{ave} = 0.1$, the above result $16.5 \sqrt{RRR}$ Ohms turns into 7 Ohms, independent of RRR , see [2].

VI. Conclusions

The trapped modes in waveguides with an arbitrary single-connected cross section are considered. The formulas for the frequency shift and the resonance impedance are derived in a general case, and the results for circular and rectangular chambers are given.

The transverse coupling impedance due to trapped modes is calculated in a similar way, see formulas for the case of a circular chamber in [2].

References

- [1] G.V. Stupakov and S.S. Kurennoy, *Phys. Rev. E* **49** (1994) 794.
- [2] S.S. Kurennoy, *Phys. Rev. E* **51** (1995) 2498.
- [3] R.E. Collin, *Field Theory of Guided Waves* (IEEE, NY, 1991).
- [4] S.S. Kurennoy, R.L. Gluckstern, and G.V. Stupakov, *These Proceedings*.
- [5] R.L. Gluckstern, *Phys. Rev. A* **46** (1992) 1106, 1110.
- [6] G.V. Stupakov, Preprint SLAC-6698, Stanford (1994); *Phys. Rev. E*, to be published.
- [7] S.S. Kurennoy, *Proceed. of EPAC* (Berlin, 1992) 871; more details in IHEP 92-84, Protvino (1992).
- [8] S.S. Kurennoy and G.V. Stupakov, *Part. Acc.* **45** (1994) 95.

A GENERAL APPROACH FOR CALCULATING COUPLING IMPEDANCES OF SMALL DISCONTINUITIES

Sergey S. Kurennoy and Robert L. Gluckstern

Physics Department, University of Maryland, College Park, MD 20742, USA

and Gennady V. Stupakov

SLAC, Stanford, CA 94309, USA

Abstract

A general theory of the beam interaction with small discontinuities of the vacuum chamber is developed taking into account the reaction of radiated waves back on the discontinuity. The reactive impedance calculated earlier is reproduced as the first order, and the resistive one as the second order of a perturbation theory based on this general approach. The theory also gives, in a very natural way, the results for the trapped modes due to small discontinuities obtained earlier by a different method.

I. Introduction

A common tendency in design of modern accelerators is to minimize beam-chamber coupling impedances to avoid beam instabilities and reduce heating. Even contributions from tiny discontinuities like pumping holes have to be accounted for, due to their large number, which makes analytical methods for calculating the impedances of small discontinuities very important. According to the Bethe theory of diffraction by small holes [1], the fields diffracted by a hole can be found as those radiated by effective electric and magnetic dipoles. The coupling impedance of pumping holes in the vacuum chamber walls has been calculated earlier [2], [3], [4] using this idea. The imaginary part of the impedance is proportional to the difference of hole polarizabilities $(\psi - \chi)$, where the magnetic susceptibility ψ and the electric polarizability χ are small compared to the cubed typical dimension b^3 of the chamber cross section. From considerations of the energy radiated into the chamber and through the hole, the real part of the hole impedance comes out to be proportional to $(\psi^2 + \chi^2)$, being usually much smaller than the reactance.

In the present paper we further develop this analytical approach by taking into account the reaction of radiated waves back on the discontinuity. It leads to a more general theory, and allows us to reproduce easily all previous results, including those about trapped modes due to small discontinuities [5]. While our consideration here is restricted to small holes, it can be readily applied to other small discontinuities like enlargements or irises because the idea of effective polarizabilities works equally well in these cases also [6].

II. General Analysis

Let us consider an infinite cylindrical pipe with an arbitrary cross section S and perfectly conducting walls. The z axis is directed along the pipe axis, a hole is located at the point $(\vec{b}, z = 0)$, and a typical hole size h satisfies $h \ll b$. To evaluate the coupling impedance one has to calculate the fields induced in the chamber by a given current. If an ultrarelativistic point charge

q moves along the chamber axis, the fields harmonics \vec{E}^b, \vec{H}^b produced by this charge on the chamber wall without hole would be

$$E_v^b(z; \omega) = Z_0 H_\tau^b = -Z_0 q e^{ikz} \sum_{n,m} \frac{e_{nm}(0) \nabla_v e_{nm}(\vec{b})}{k_{nm}^2}, \quad (1)$$

where $k_{nm}^2, e_{nm}(\vec{r})$ are eigenvalues and orthonormalized eigenfunctions (EFs) of the 2D boundary problem in S :

$$(\nabla^2 + k_{nm}^2) e_{nm} = 0; \quad e_{nm}|_{\partial S} = 0. \quad (2)$$

Here $\vec{\nabla}$ is the 2D gradient in plane S ; $k = \omega/c$; \hat{v} means an outward normal unit vector, $\hat{\tau}$ is a unit vector tangent to the boundary ∂S of the chamber cross section S , and $\{\hat{v}, \hat{\tau}, \hat{z}\}$ form a RHS basis.

A. Fields

At distances l such that $h \ll l \ll b$, the fields radiated by the hole into the pipe are equal to those produced by effective dipoles [1], [7]¹

$$\begin{aligned} P_v &= -\chi \varepsilon_0 E_v^h/2; & M_\tau &= (\psi_{\tau\tau} H_\tau^h + \psi_{\tau z} H_z^h)/2; \\ M_z &= (\psi_{z\tau} H_\tau^h + \psi_{zz} H_z^h)/2, \end{aligned} \quad (3)$$

where superscript 'h' means that the fields are taken at the hole. In general, ψ is a symmetric 2D-tensor. If the hole is symmetric, and its symmetry axis is parallel to \hat{z} , the skew terms vanish, i.e. $\psi_{\tau z} = \psi_{z\tau} = 0$.

When the effective dipoles are obtained, e.g., by substituting beam fields (1) into Eqs. (3), one can calculate the fields in the chamber as a sum of waveguide eigenmodes excited in the chamber by the dipoles, and find the impedance. This approach has been carried out in [2], and for an arbitrary chamber in [8]. However, a more refined theory should take into account the reaction of radiated waves back on the hole. The TM-eigenmodes contribution to the radiated fields is a series

$$\vec{F} = \sum_{nm} \left[A_{nm}^+ \vec{F}_{nm}^+ \theta(z) + A_{nm}^- \vec{F}_{nm}^- \theta(-z) \right], \quad (4)$$

where \vec{F} means either \vec{E} or \vec{H} and superscripts ' \pm ' denote waves radiated respectively in the positive (+, $z > 0$) or negative (−, $z < 0$) direction. The fields of $\{n, m\}$ th TM-eigenmode in Eq. (4)

¹Polarizabilities ψ, χ are related to the effective ones α_e, α_m used in [7], [2] as $\alpha_e = -\chi/2$ and $\alpha_m = \psi/2$, so that for a circular hole of radius a in a thin wall $\psi = 8a^3/3$ and $\chi = 4a^3/3$.

are expressed [7] in terms of EFs (2)

$$\begin{aligned} E_z^\mp &= k_{nm}^2 e_{nm} \exp(\pm \Gamma_{nm} z); & H_z^\mp &= 0; \\ \vec{E}_t^\mp &= \pm \Gamma_{nm} \vec{\nabla} e_{nm} \exp(\pm \Gamma_{nm} z); \\ \vec{H}_t^\mp &= \frac{ik}{Z_0} \hat{z} \times \vec{\nabla} e_{nm} \exp(\pm \Gamma_{nm} z), \end{aligned} \quad (5)$$

where propagation factors $\Gamma_{nm} = (k_{nm}^2 - k^2)^{1/2}$ should be replaced by $-i\beta_{nm}$ with $\beta_{nm} = (k^2 - k_{nm}^2)^{1/2}$ for $k > k_{nm}$. For given values of dipoles (3) the unknown coefficients A_{nm}^\pm can be found [8] using the Lorentz reciprocity theorem

$$A_{nm}^\pm = a_{nm} M_\tau \pm b_{nm} P_v, \quad (6)$$

$$a_{nm} = -\frac{ikZ_0}{2\Gamma_{nm}k_{nm}^2} \nabla_v e_{nm}^h; \quad b_{nm} = \frac{1}{2\varepsilon_0 k_{nm}^2} \nabla_v e_{nm}^h. \quad (7)$$

In a similar way, the contribution of TE-eigenmodes to the radiated fields is given by an analogue of Eq. (4) with the excitation coefficients

$$B_{nm}^\pm = \pm c_{nm} M_\tau + d_{nm} P_v + q_{nm} M_z, \quad (8)$$

$$\begin{aligned} c_{nm} &= \frac{1}{2k_{nm}^2} \nabla_\tau h_{nm}^h; & q_{nm} &= \frac{1}{2\Gamma_{nm}'} h_{nm}^h; \\ d_{nm} &= -\frac{ik}{2Z_0 \varepsilon_0 \Gamma_{nm}' k_{nm}^2} \nabla_\tau h_{nm}^h, \end{aligned} \quad (9)$$

where EFs h_{nm} satisfy the boundary problem (2) with the Neumann boundary condition $\nabla_v h_{nm}|_{\partial S} = 0$, and k_{nm}^2 are corresponding eigenvalues.

Now we can add corrections to the beam fields (1) due to the radiated waves in the vicinity of the hole. It gives

$$E_v = \frac{E_v^b + \psi_{\tau\tau} \Sigma'_x Z_0 H_\tau + \psi_{zz} \Sigma'_x Z_0 H_z}{1 - \chi(\Sigma_1 - \Sigma'_1)}, \quad (10)$$

$$H_\tau = \frac{H_\tau^b + \psi_{\tau z}(\Sigma_2 - \Sigma'_2) H_z}{1 - \psi_{\tau\tau}(\Sigma_2 - \Sigma'_2)}, \quad (11)$$

$$H_z = \frac{\chi \Sigma'_x E_v / Z_0 + \psi_{\tau\tau} \Sigma'_3 H_\tau}{1 - \psi_{zz} \Sigma'_3}, \quad (12)$$

where $(s = \{n, m\})$ is a generalized index

$$\begin{aligned} \Sigma_1 &= \frac{1}{4} \sum_s \frac{\Gamma_s (\nabla_v e_s^h)^2}{k_s^2}; & \Sigma_2 &= \frac{k^2}{4} \sum_s \frac{(\nabla_v e_s^h)^2}{\Gamma_s k_s^2}; \\ \Sigma'_1 &= \frac{k^2}{4} \sum_s \frac{(\nabla_\tau h_s^h)^2}{\Gamma_s' k_s^2}; & \Sigma'_2 &= \frac{1}{4} \sum_s \frac{\Gamma_s' (\nabla_\tau h_s^h)^2}{k_s^2}; \\ \Sigma'_x &= i \frac{k}{4} \sum_s \frac{h_s^h \nabla_\tau h_s^h}{\Gamma_s'}; & \Sigma'_3 &= \frac{1}{4} \sum_s \frac{k_s^2 (h_s^h)^2}{\Gamma_s'}. \end{aligned} \quad (13)$$

Since this consideration works at distances not shorter than l , and $l > h$, the summation in Eq. (13) should be restricted to values of $s = \{n, m\}$ such that $k_s h \leq 1$ and $k'_s h \leq 1$.

B. Impedance

The longitudinal impedance of the hole is defined as

$$Z(k) = -\frac{1}{q} \int_{-\infty}^{\infty} dz e^{-ikz} E_z(0, z; \omega), \quad (14)$$

where the field at the axis is given by Eq. (4) with coefficients (6) and (8) in which the corrected near-hole fields (10)-(12) are substituted. It yields

$$\begin{aligned} Z(k) &= -\frac{ikZ_0 \tilde{e}_v^2}{2} \left[\frac{\psi_{\tau\tau}}{1 - \psi_{\tau\tau}(\Sigma_2 - \Sigma'_2)} \right. \\ &\quad \left. + \psi_{\tau z}^2 \Sigma'_3 - \frac{\chi}{1 - \chi(\Sigma_1 - \Sigma'_1)} \right], \end{aligned} \quad (15)$$

where $\tilde{e}_v \equiv E_v^b / (Z_0 q) = -\sum_s e_s(0) \nabla_v e_s(\vec{b}) / k_s^2$ is merely the normalized electric field produced at the hole location by the beam moving along the chamber axis, cf. Eq. (1). In deriving this result we have neglected the coupling terms between E_v , H_τ and H_z , cf. Eqs. (10)-(12), which contribute to the third order of an expansion discussed below, and also have taken into account that $\psi_{\tau z} = \psi_{z\tau}$.

For a small discontinuity, polarizabilities ψ , $\chi = O(h^3)$, and they are small compared to b^3 . If we expand the impedance in a perturbation series in polarizabilities, the first order gives

$$Z_1(k) = -\frac{ikZ_0 \tilde{e}_v^2}{2} (\psi_{\tau\tau} - \chi), \quad (16)$$

that is exactly the inductive impedance obtained in [8] for an arbitrary cross section of the chamber. For a particular case of a circular pipe, from either direct summation in (1) or applying the Gauss law, we get $\tilde{e}_v = 1/(2\pi b)$, substitution of which into Eq. (16) leads to a well-known result [2], [3]. From a physical point of view, keeping only the first order term (16) corresponds to dropping out all radiation corrections in Eqs. (10)-(12).

These corrections first reveal themselves in the second order term

$$\begin{aligned} Z_2(k) &= -\frac{ikZ_0 \tilde{e}_v^2}{2} \left[\psi_{\tau\tau}^2 (\Sigma_2 - \Sigma'_2) + \psi_{\tau z}^2 \Sigma'_3 \right. \\ &\quad \left. + \chi^2 (\Sigma'_1 - \Sigma_1) \right], \end{aligned} \quad (17)$$

which at frequencies above the chamber cutoff has both a real and imaginary part. The real part of the impedance is

$$\begin{aligned} \text{Re } Z_2(k) &= \frac{k^3 Z_0 \tilde{e}_v^2}{8} \left\{ \psi_{\tau z}^2 \sum_s \frac{k_s^2 (h_s^h)^2}{k^2 \beta_s'} \right. \\ &\quad + \psi_{\tau\tau}^2 \left[\sum_s \frac{(\nabla_v e_s^h)^2}{\beta_s k_s^2} + \sum_s \frac{\beta_s' (\nabla_\tau h_s^h)^2}{k^2 k_s^2} \right] \\ &\quad \left. + \chi^2 \left[\sum_s \frac{\beta_s (\nabla_v e_s^h)^2}{k^2 k_s^2} + \sum_s \frac{(\nabla_\tau h_s^h)^2}{\beta_s' k_s^2} \right] \right\}, \end{aligned} \quad (18)$$

where the sums include only a finite number of the eigenmodes propagating in the chamber at a given frequency, i.e. those with $k_s < k$ or $k'_s < k$.

The real part of the impedance is related to the power P scattered by the hole into the beam pipe, $\text{Re } Z = 2P/q^2$, and can

be calculated in an alternative way from energy considerations: $P = \sum_s (A_s^2 P_s^{(E)} + B_s^2 P_s^{(H)})$, where we sum over all propagating modes in both directions, and P_s means the time-averaged power radiated in s th eigenmode: $P_s^{(E)} = k\beta_s k_s^2 / (2Z_0)$ and $P_s^{(H)} = Z_0 k\beta_s k_s^2 / 2$. Substituting beam fields (1) into Eqs. (6)-(9) for the coefficients A_s and B_s and performing calculations gives the result (18). Such an alternative derivation of the real part has been first carried out in Ref. [4] for a circular pipe with a symmetric untilted hole ($\psi_{\tau z} = 0$). The result (18) for this particular case coincides with that of [4]. Moreover, in this case at high frequencies the series can be summed approximately [4] to give $Re Z = Z_0 k^4 \tilde{e}_v^2 (\psi_{\tau\tau}^2 + \chi^2) / (12\pi)$, which can also be obtained by calculating the energy radiated by the dipoles in a half-space [8]. Note that the additional $\psi_{\tau z}^2$ -term in Eq. (18) could give a leading contribution to $Re Z$, e.g., for a long and slightly tilted slot.

C. Trapped Modes

So far we considered the perturbation expansion of Eq. (15) implicitly assuming that correction terms $O(\psi)$ and $O(\chi)$ in the denominators of its RHS are small compared to 1. Under certain conditions this assumption is incorrect, and it leads to some non-perturbative results. Indeed, at frequencies slightly below the chamber cut-offs, $0 < k_s - k \ll k_s$, — or the same with replacement $k_s \rightarrow k'_s$, — a single term in sums Σ'_1 , Σ_2 , or Σ'_3 becomes very large, due to very small $\Gamma_s = (k_s^2 - k^2)^{1/2}$ (or Γ'_s) in its denominator, and then the “corrections” $\psi \Sigma$ or $\chi \Sigma$ can be of the order of 1. As a result, one of the denominators of the RHS of Eqs. (15) can vanish, which corresponds to a resonance of the coupling impedance. On the other hand, vanishing denominators in Eqs. (10)-(12) mean the existence of non-perturbative eigenmodes of the chamber with a hole, since non-trivial solutions $E, H \neq 0$ exist even for vanishing external (beam) fields $E^b, H^b = 0$. These eigenmodes are nothing but the trapped modes studied in [5] for a circular waveguide with a small discontinuity (see [9] for waveguides with an arbitrary cross section).

Let us for brevity restrict ourselves to the case $\psi_{\tau z} = 0$ and consider Eq. (11) in more detail. For $H^b = 0$ we have

$$H_\tau \left[1 - \psi_{\tau\tau} \frac{k^2 (\nabla_v e_{nm}^h)^2}{4\Gamma_{nm} k_{nm}^2} + \dots \right] = 0, \quad (19)$$

where \dots means all other terms of the series Σ_2, Σ'_2 . At frequency $k \simeq k_{nm}$ slightly below the cutoff k_{nm} of the TM_{nm} -mode, the fraction in Eq. (19) is large due to small Γ_{nm} in its denominator, and one can neglect the other terms. Then the condition for a non-trivial solution $H_\tau \neq 0$ to exist is

$$\Gamma_{nm} \simeq \frac{1}{4} \psi_{\tau\tau} (\nabla_v e_{nm}^h)^2. \quad (20)$$

This equation gives us the frequency shift Δf of the trapped TM-mode down from the cutoff $f_{nm}^{(E)}$

$$\frac{\Delta f}{f_{nm}^{(E)}} \simeq \frac{1}{32k_{nm}^2} \psi_{\tau\tau}^2 (\nabla_v e_{nm}^h)^4. \quad (21)$$

One can easily see that denominator $[1 - \chi(\Sigma_1 - \Sigma'_1)]$ in Eq. (10) does not vanish because singular terms in Σ'_1 have a

“wrong” sign. However, due to the coupling between E_v and H_z , a non-trivial solution $E_v, H_z \neq 0$ of simultaneous equations (10) and (12) can exist, even when $E^b = 0$. The corresponding condition has the form

$$\Gamma'_{nm} \simeq \frac{1}{4} \left[\psi_{zz} k_{nm}^2 (h_{nm}^h)^2 - \chi (\nabla_\tau h_{nm}^h)^2 \right], \quad (22)$$

which gives the frequency of the trapped TE_{nm} -mode.

One can easily show that for the particular case of a circular pipe the results (20)-(22) coincide with those obtained by a different method in Ref. [5]. For more detail, a physical picture of, and resonance impedances due to trapped modes, see [5] and [9].

III. Conclusions

The analytical approach discussed above provides a general picture for the coupling impedance of a small discontinuity of the vacuum chamber. It gives the real and imaginary part of the impedance, as well as trapped modes. Results for typical shapes of the chamber cross section (circular or rectangular) are easily obtained from the expressions above using specific EFs, see, e.g., in [7] or [9]. The transverse impedance can be derived in a similar way [8].

We have not considered explicitly effects of the wall thickness, assuming that the hole polarizabilities are the inside ones [3], and they include these effects. We also neglected the radiation escaping through the hole, contributions of which to the real part of the impedance are estimated [2], [3], [5], and usually are small.

At high frequencies (near or above the chamber cutoff) the mutual interaction of many holes is important and can cause resonances if the hole pattern is periodic, e.g. [10], [4]. A more complete theory should take this interaction into account.

References

- [1] H.A. Bethe, *Phys. Rev.* **66** (1944) 163.
- [2] S.S. Kurennoy, *Part. Acc.* **39** (1992) 1.
- [3] R.L. Gluckstern, *Phys. Rev. A* **46** (1992) 1106, 1110.
- [4] G.V. Stupakov, Preprint SLAC-6698, Stanford (1994); *Phys. Rev. E*, to be published.
- [5] G.V. Stupakov and S.S. Kurennoy, *Phys. Rev. E* **49** (1994) 794.
- [6] S.S. Kurennoy and G.V. Stupakov, *Part. Acc.* **45** (1994) 95.
- [7] R.E. Collin, *Field Theory of Guided Waves* (IEEE, NY, 1991).
- [8] S.S. Kurennoy, *Proceed. of EPAC* (Berlin, 1992) 871; more details in IHEP 92-84, Protvino (1992).
- [9] S.S. Kurennoy and G.V. Stupakov, *These Proceedings*.
- [10] S.S. Kurennoy, *Proceed. of PAC* (Washington, DC, 1993) 3417.

POLARIZABILITIES OF AN ANNULAR CUT AND COUPLING IMPEDANCES OF BUTTON-TYPE BEAM POSITION MONITORS

Sergey S. Kurennoy

Physics Department, University of Maryland, College Park, MD 20742, USA

Abstract

The longitudinal and transverse coupling impedances of a small discontinuity on the accelerator chamber wall can be expressed in terms of the electric and magnetic polarizabilities of the discontinuity. The polarizabilities are geometrical factors and can be found by solving a static (electric or magnetic) problem. However, they are known in the explicit analytical form only for a few simple-shaped discontinuities, for example, for an elliptic hole in a thin wall. In the present paper the polarizabilities of a ring-shaped cut in the wall are obtained. The results are applied to calculate the coupling impedances of button-type beam position monitors.

I. Introduction

The coupling impedances of a small discontinuity on the wall of the vacuum chamber of an accelerator have been calculated in terms of the polarizabilities of the discontinuity [1], [2], [3]. The basic idea of the approach used is related with the Bethe theory of diffraction by small holes [4], which shows that fields produced by a hole can be approximated by those due to effective dipoles induced on the hole by an incident (beam) field. The magnitudes of the effective electric P and magnetic M dipoles are expressed through the incident fields E_v^h , H_t^h at the hole location without hole [4], [5]

$$P_v = -\chi \varepsilon_0 E_v^h / 2; \quad M_t = \psi H_t^h / 2, \quad (1)$$

where χ is the electric polarizability and ψ is the magnetic susceptibility of the hole, \hat{v} is the normal vector to the hole plane, and \hat{t} is the tangential one. In general, ψ is a symmetric 2D-tensor, but we will consider here only axisymmetric holes.

The hole polarizabilities are known in an analytical form only for a few simple cases. For a circular hole of radius b in a thin wall $\psi = 8b^3/3$ and $\chi = 4b^3/3$ [4]. There are also analytical results for elliptic holes in a thin wall [5]. The polarizabilities for the case of a thick wall have been studied using a variational technique in [6] for circular holes, and in [7] for elliptic holes. There are also some approximate formulae for slots [8].

In the present paper, the polarizabilities of an annular cut in a thin wall are obtained and used to estimate the beam coupling impedances of the button-type beam position monitors (BPMs).

II. General Analysis

When the wavelength is large compared to the hole size, the polarizabilities can be obtained from the electro- or magnetostatic problem: find the fields due to an aperture (hole) in a metal plane when it is illuminated from one side by a homogeneous static (normal electric or tangential magnetic) field.

A. Integral Equations

Let a hole in the plane $z = 0$ be illuminated by a far magnetic field H_0 from $z > 0$ side. We assume that the hole center coincides with the origin of the plane coordinates (u, v) , and the field is directed along \hat{u} . One can decompose this far field as $H_0/2 + H_0/2 = H_0$ for $z > 0$, and as $H_0/2 - H_0/2 = 0$ for $z < 0$, and consider two separate problems — the symmetric and the antisymmetric one [6], [9]. For a zero thickness plane, the symmetric magnetic problem is trivial (the field is $H_0/2$ everywhere). The antisymmetric problem can be reduced to the integral equation [9] for the function $G(\vec{r}) = 2H_z(\vec{r}, 0)/H_0$

$$\int_h d\vec{r}' G(\vec{r}') K(\vec{r}, \vec{r}') = u, \quad (2)$$

where $\vec{r} = (u, v)$, the integration runs over the aperture, and the kernel is symmetric

$$K(\vec{r}, \vec{r}') = \frac{1}{4\pi^2} \int \frac{d\vec{\sigma}}{\sigma} e^{i\vec{\sigma}(\vec{r}-\vec{r}')} = \frac{1}{2\pi|\vec{r}-\vec{r}'|}. \quad (3)$$

If Eq. (2) is solved, the magnetic susceptibility is [9]

$$\psi_u = \int_h d\vec{r}' u G(\vec{r}'). \quad (4)$$

For an axisymmetric aperture, one can simplify Eq. (2) using $u = r \cos \varphi$, substituting $G(\vec{r}) = g(r) \cos \varphi$, and integrating over the polar angle φ . It yields

$$\int_{[h]} dr' r' g(r') K_m(r, r') = r, \quad (5)$$

with the following kernel

$$\begin{aligned} K_m(x, y) &= \int_0^\infty d\sigma J_1(\sigma x) J_1(\sigma y) \\ &= \theta(y-x) \frac{x}{2y^2} {}_2F_1\left(\frac{3}{2}, \frac{1}{2}; 2; \frac{x^2}{y^2}\right) + \{x \leftrightarrow y\} \\ &= \frac{xy}{2(x+y)^3} {}_2F_1\left(\frac{3}{2}, \frac{3}{2}; 3; \frac{4xy}{(x+y)^2}\right), \end{aligned} \quad (6)$$

where $J_n(x)$ is the n -th order Bessel function of the first kind, and ${}_2F_1$ is the Gauss hypergeometric function. This kernel has a ln-singularity at $x = y$

$$\begin{aligned} K_m(x, y) &\simeq \frac{8xy}{\pi(x+y)^3} \left(\ln \frac{x+y}{|x-y|} + 2 \ln 2 - 2 \right) \\ &+ O(|x-y| \ln |x-y|). \end{aligned} \quad (7)$$

The magnetic susceptibility in this case is

$$\psi = \pi \int_{[h]} dr r^2 g(r). \quad (8)$$

In Eqs. (5) and (8) symbol $[h]$ denotes the interval of the radius-vector variation: $[h] = [0, b]$ for a circular hole of radius b , and $[h] = [a, b]$ for an annular cut with inner radius a and outer radius b .

In a similar way, a solution $f(r)$ of the electrostatic problem satisfies the integral equation

$$\int_{[h]} dr' r' f(r') K_e(r, r') = 1, \quad (9)$$

with a more singular $[O((x-y)^{-2})]$ kernel

$$K_e(x, y) = \int_0^\infty d\sigma \sigma^2 J_0(\sigma x) J_0(\sigma y). \quad (10)$$

The electric polarizability of the axisymmetric hole is

$$\chi = 2\pi \int_{[h]} dr r f(r). \quad (11)$$

A solution $g(r)$ of the integral equation (5) must have the correct singular behavior near the thin metal edge: $g(r) \propto \Delta^{-1/2}$ when $\Delta = b - r \rightarrow 0$ or $\Delta = r - a \rightarrow 0$. For the problem (9), the function $f(r)$, which is proportional to the electric potential, must behave as $\sqrt{\Delta}$ near the edge to provide for the correct singularity $\Delta^{-1/2}$ of the electric field. In the case of a circular hole of radius b the exact solutions of Eqs. (5) and (9) are known [4]. They are $g(r) = 4r/(\pi\sqrt{b^2 - r^2})$ and $f(r) = 2\sqrt{b^2 - r^2}/\pi$, substituting of which in (8) and (11) gives the polarizabilities of a circular hole cited in Introduction.

B. Narrow Cut: Analytical Solution

Suppose the width $w = b - a$ of the gap is small, $w \ll b$. For a narrow annular cut, the electric polarizability can be approximated by that of a narrow (yet bented) slot of width w and length $2\pi b \gg w$ as $\chi \simeq \pi^2 w^2 b/4$, see [8]. It is obvious that χ is small compared to ψ , since the normal electric field does not penetrate far through the narrow gap, unlike the tangential magnetic field on the parts of the annular cut which are parallel to its direction.

Introducing dimensionless variables $x = r'/b$ and $y = r/b$, we are looking for a solution of Eq. (5) in the form $g(x) = C(x)/\sqrt{(1-x)(x-\rho)}$, where $\rho = a/b$, and $C(x)$ is a regular function in the interval $[\rho, 1]$. For a narrow gap $\delta \equiv 1 - \rho \ll 1$, and one can expand $C(x)$ as $C(x) = C + O(\delta)$. Substituting this into Eq. (5) and keeping only the singular part (7) of the kernel (the rest would give corrections $O(\delta)$ to the RHS) leads to the equation

$$1 = \frac{C}{\pi} \int_\rho^1 \frac{dx [\ln(8/|x-y|) - 2]}{\sqrt{(1-x)(x-\rho)}}, \quad (12)$$

where we neglected terms $O(\delta \ln \delta)$ in the RHS. Replacing variables $x = 1 - u\delta$, $y = 1 - v\delta$, and using the identity

$$\int_0^1 \frac{du \ln|u-v|}{\sqrt{u(1-u)}} = -2\pi \ln 2,$$

we get from (12)

$$C = [\ln(32/\delta) - 2]^{-1}. \quad (13)$$

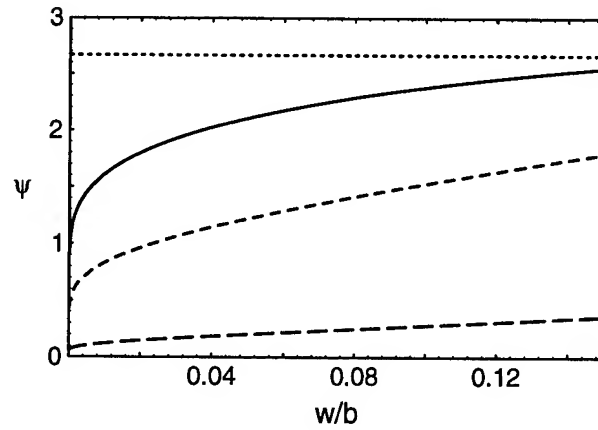


Figure 1. Magnetic susceptibility (in units of b^3) of a narrow annular cut versus its relative width w/b : solid line for (14), long-dashed line for octagon model (15), and short-dashed line for slot model (16). The dotted line shows the susceptibility of the circular hole $\psi/b^3 = 8/3$.

Then from Eq. (8) the magnetic susceptibility of a narrow ($w = b - a \ll b$) annular cut in a thin plate is

$$\psi = \frac{\pi^2 b^2 a}{\ln(32b/w) - 2}. \quad (14)$$

It is interesting to compare Eq. (14) with the estimate [8] obtained by approximating the annular cut with an octagon and using the magnetic susceptibilities for narrow slots:

$$\psi_o = \frac{4}{3} \left(\frac{\pi}{4}\right)^4 \frac{b^3}{\ln(2\pi b/w) - 7/3}. \quad (15)$$

While the behavior is similar, this estimate is a few times smaller than (14), see Fig. 1. Moreover, even a more extreme model — two long slots of length $2b$ and width w oriented parallel to the magnetic field — give the susceptibility

$$\psi_m = \frac{4}{3} \frac{\pi b^3}{\ln(16b/w) - 7/3}, \quad (16)$$

which is still smaller than Eq. (14), see Fig. 1.

As seen from Fig. 1, the susceptibility (14) becomes close to that of a circular hole for relatively narrow gaps, $w/b \geq 0.1$. To check this surprising result, and to find the applicability range for Eq. (14), we proceed below with a variational study of Eq. (5).

C. Wide Cut: Variational Approach

An elegant variational technique for polarizabilities has been developed in [6]. Multiplying Eq. (5) by $rg(r)$ and integrating over r , we convert it to the following variational form for the magnetic susceptibility ψ

$$\frac{\pi b^3}{\psi} = \frac{\int_\rho^1 x dx \int_\rho^1 y dy g(x) K_m(x, y) g(y)}{\left[\int_\rho^1 x^2 dx g(x) \right]^2}. \quad (17)$$

A solution $g(x)$ of Eq. (5) minimizes the RHS of Eq. (17). We are looking for it in the form of a series

$$g(x) = \sum_{n=0}^{\infty} c_n g_n(x) \quad \text{with} \quad (18)$$

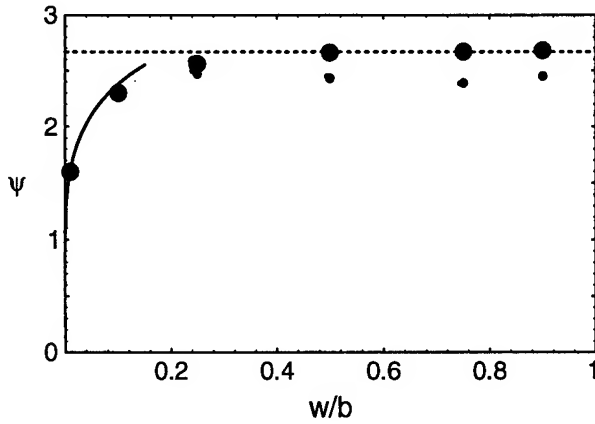


Figure 2. Magnetic susceptibility (in units of b^3) of an annular cut versus its relative width w/b . Thin points show the zeroth iteration, and thick points are for the second one. The solid line corresponds to Eq. (14) for narrow gaps, and the dotted line is the limit of a circular hole, $w = b$.

$$g_0(x) = \frac{1}{\sqrt{(1-x)(x-\rho)}}, \quad g_k(x) = T_{k-1}\left(\frac{2x-\rho-1}{1-\rho}\right),$$

where c_n are unknown coefficients, and $T_n(x)$ are Chebyshev's polynomials of the first kind. Denoting $d_n = \int_{\rho}^1 dx x^2 g_n(x)$ and $a_n = c_n d_n$, we define the matrix

$$K_{kn} = \int_{\rho}^1 x dx \int_{\rho}^1 y dy g_k(x) K_m(x, y) g_n(y) / (d_k d_n), \quad (19)$$

and convert Eq. (17) into the following form

$$\frac{\pi b^3}{\psi} = \frac{\sum_{k,n} a_k K_{kn} a_n}{(\sum_n a_n)^2}. \quad (20)$$

Following [6], one can prove that minimizing the RHS of Eq. (20) yields

$$\psi = \pi b^3 \sum_{k,n} (K^{-1})_{kn}, \quad (21)$$

where matrix K^{-1} is the inverse of the matrix K , Eq. (19). The further procedure is straightforward: n th iteration ($n = 0, 1, 2, \dots$) corresponds to the matrix (19) truncated to the size $(n+1) \times (n+1)$. In the zeroth iteration the truncated matrix is merely a number, K_{00} ; it corresponds to the analytical study of Sect. II.B. All integrations and matrix inversions have been carried out using *Mathematica*. Calculations show that only even terms of the series (18) contribute, i.e. $c_1 = c_3 = \dots = 0$, and, effectively, one can use $g = g_0 + c_2 T_1 + c_4 T_3 + \dots$, and squeeze matrix K removing odd lines and rows. The results for ψ versus the cut width are shown in Fig. 2. As one can see, the zeroth iteration, as well as the analytical solution (14), is good for narrow gaps, $w/b \leq 0.15$, but it is also not bad for wide ones. The process practically converges in three iterations (effective 0,1,2) for the whole range of the cut width $0 \leq w/b \leq 1$.

III. Impedances

The beam-chamber coupling impedances can be obtained using formulas from [1], [2], [3] and polarizabilities found in

Sect. II. For example, a narrow annular cut of radius b and width $w \ll b$ on the thin wall of a circular pipe of radius $r \gg b$ produces the longitudinal impedance

$$Z(\omega) = -\frac{i Z_0 \omega (\psi - \chi)}{8\pi^2 c r^2} \simeq -\frac{i Z_0 \omega b^3}{8c r^2 [\ln(32b/w) - 2]}. \quad (22)$$

This result can be used to estimate the impedance of a button-type BPM. Taking into account the wall thickness reduces the estimate, cf. [6], [8]. For other cross sections of the chamber, $Re Z$, and the transverse impedance, see [3] and references therein. Note that the impedance (22) of a narrow cut with $w/b > 0.05$ is larger than (but less than twice) that of a circular hole with radius b , and tends to the last one when $w \rightarrow b$.

IV. Conclusions

The magnetic susceptibility of an annular cut in a thin wall is calculated using the analytical and variational methods. The estimate for the coupling impedance of a button-type BPM is obtained.

The electro- and magnetostatic problems considered above can also be solved numerically. With boundary conditions which ensure a given homogeneous field far from the aperture plane, a static electric or magnetic potential can be computed using standard codes. We have done this for the electric polarizability of an axisymmetric aperture, in which case the problem is effectively a 2-D one, using the *POISSON* code. Results for a narrow gap and a hole coincide with the expected ones. The case of a thick wall can be also studied in this way. Unfortunately, for the magnetic problem, as well as for an arbitrary aperture, this approach requires 3-D codes and cumbersome computations.

We plan a further study using different methods to take into account the effects due to the wall thickness.

The author would like to thank Dr. R.L. Gluckstern and Dr. R.K. Cooper for useful discussions.

References

- [1] S.S. Kurennoy, *Part. Acc.* **39** (1992) 1.
- [2] R.L. Gluckstern, *Phys. Rev. A* **46** (1992) 1106, 1110.
- [3] S.S. Kurennoy, R.L. Gluckstern, and G.V. Stupakov, *These Proceedings*.
- [4] H.A. Bethe, *Phys. Rev.* **66** (1944) 163.
- [5] R.E. Collin, *Field Theory of Guided Waves* (IEEE, NY, 1991).
- [6] R.L. Gluckstern and J.A. Diamond, *IEEE Trans. MTT* **39** (1991) 274.
- [7] B. Radak and R.L. Gluckstern, *IEEE Trans. MTT* **43** (1995) 194.
- [8] S.S. Kurennoy, Report SSCL-636, Dallas (1993).
- [9] R.L. Gluckstern, R.Li and R.K. Cooper, *IEEE Trans. MTT* **38** (1990) 186.

The Effect of Coupling on Luminosity*

David Sagan

Laboratory of Nuclear Studies, Cornell University, Ithaca, NY 14853

Abstract

In a storage ring the existence of skew quadrupoles, solenoids, and other coupling elements breaks the independence of the horizontal and vertical motions. With the flat beams used in electron/positron colliding beam storage rings this coupling results in an increase in the vertical beam size with an attendant loss in luminosity. By defining a 'badness' parameter B_c the luminosity loss can be directly related to measurements of the coupling.

Introduction

The coupling of horizontal and vertical motions in colliding beam storage rings results in an unwanted increase in vertical beam size and hence in a loss of luminosity. It is useful in dealing with coupling to be able to relate how severe the luminosity degradation is for a given amount of coupling. To this end it is useful to define a 'badness' parameter B_c :

$$B_c \equiv \frac{\mathcal{L}(\text{BBI}) - \mathcal{L}(\text{BBI}+\text{Coupl})}{\mathcal{L}(\text{BBI})}, \quad (1)$$

where $\mathcal{L}(\text{BBI}+\text{Coupl})$ is the luminosity obtained with coupling present, and $\mathcal{L}(\text{BBI})$ is the luminosity without coupling and only the beam-beam interaction to determine the beam size (and hence the luminosity). With this definition for B_c the condition needed so that the coupling is negligible is simply

$$B_c \ll 1. \quad (2)$$

The usefulness of B_c comes when we can relate it directly to the coupling. This is the problem to be addressed in the rest of the paper.

Assuming equal beam sizes with $\sigma_Y \gg \sigma_X$ one finds[1]

$$\mathcal{L} = \frac{f N^2}{4\pi\sigma_X\sigma_Y} \left(1 + \left(\frac{\sigma_X \cdot \delta\theta}{\sigma_Y} \right)^2 \right)^{-1/2}, \quad (3)$$

where N is the number of particles in each beam, σ_X and σ_Y are the beam sigmas along the principal axes, and $2\delta\theta \equiv (\theta_+ - \theta_-)$ is the angle between the beams due to the coupling. This differential rotation is not present if the opposing beams follow the same trajectory since, in this case, there is time reversal symmetry. However, with a pretzeled orbit, or with a two ring machine, the coupling each beam sees is different and the symmetry is lost. Using Eq. (3) in Eq. (1) and using the fact that, for weak coupling, σ_X is independent of the coupling gives

$$B_c \approx \frac{\sigma_Y^*(\text{BBI}+\text{Coupl}) - \sigma_Y^*(\text{BBI})}{\sigma_Y^*(\text{BBI}+\text{Coupl})} + \quad (4)$$

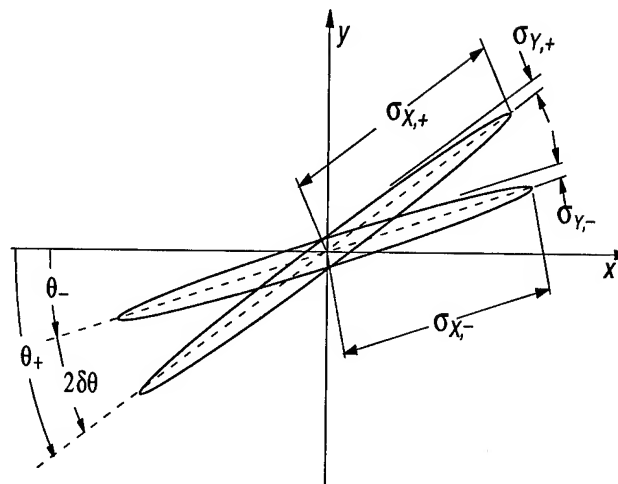


Figure 1: 1σ beam envelopes

$$\frac{1}{2} \left(\frac{\sigma_X^* \cdot \delta\theta^*}{\sigma_Y^*(\text{BBI}+\text{Coupl})} \right)^2,$$

where '*' indicates the quantity must be evaluated at the IP. There are two components to B_c : The first term on the RHS of Eq. (4) is due to the vertical blow-up of the beams and the second term is due to the decrease in overlap when the beams are rotated with respect to one another.

Vertical Beam Blowup

Consider first the vertical blow-up term in Eq. (4). The problem with this term is that it is not an easy matter to compute $\sigma_Y(\text{BBI}+\text{Coupl}) - \sigma_Y(\text{BBI})$. The reason for this is that the beam blowup due to coupling is essentially a linear phenomena while the beam-beam induced blowup is highly nonlinear in nature. It is a nontrivial matter to determine how the beam-beam interaction couples with the coupling to affect the beam height. One option is to simply assume that the beam-beam interaction and the coupling can be taken as independent processes so that the the beam height scales in quadrature:

$$\sigma_Y^2(\text{BBI}+\text{Coupl}) = \sigma_Y^2(\text{BBI}) + \sigma_Y^2(\text{Coupl}), \quad (5)$$

where $\sigma_Y(\text{Coupl})$ is the vertical beam height with coupling but without the beam-beam interaction. The problem is now simpler since $\sigma_Y(\text{BBI}+\text{Coupl})$ can be approximated using the design or observed beam-beam tune shift parameter and $\sigma_Y(\text{Coupl})$ can be obtained from coupling data. In order to test

*Work supported by the National Science Foundation

Eq. (5) computer simulations were performed using the weak-strong model developed by Krishnagopal and Siemann[2] modified to include coupling. The results of the simulations show more of a linear rather than a quadratic dependence. This is reasonable since the coupling changes the strength of some of the resonances driven by the beam-beam interaction. A more conservative formula would then be to take

$$\sigma_Y(\text{BBI}+\text{Coup}) = \sigma_Y(\text{BBI}) + \sigma_Y(\text{Coup}). \quad (6)$$

In the spirit that B_c is to be used as a first check on whether the coupling is significantly degrading the luminosity, Eq. (6) will be used. Putting Eq. (6) in Eq. (4) gives

$$B_c \approx \frac{\sigma_Y^*(\text{Coup})}{\sigma_Y^*(\text{BBI}+\text{Coup})} + \frac{1}{2} \left(\frac{\sigma_X^* \cdot \delta\theta^*}{\sigma_Y^*(\text{BBI}+\text{Coup})} \right)^2. \quad (7)$$

The computation of $\sigma_Y(\text{Coup})$ is relatively straightforward. The normal mode coordinate transformation for the 4x4 coupled one-turn transfer matrix \mathbf{T} is written as[3, 5]

$$\begin{aligned} \mathbf{T} &= \mathbf{V} \cdot \mathbf{U} \cdot \mathbf{V}^{-1} \\ &= \begin{pmatrix} \mathbf{I}_\gamma & \mathbf{C} \\ -\mathbf{C}^\dagger & \mathbf{I}_\gamma \end{pmatrix} \begin{pmatrix} \mathbf{A} & \mathbf{0} \\ \mathbf{0} & \mathbf{B} \end{pmatrix} \begin{pmatrix} \mathbf{I}_\gamma & -\mathbf{C} \\ \mathbf{C}^\dagger & \mathbf{I}_\gamma \end{pmatrix}, \end{aligned} \quad (8)$$

where \mathbf{I} is the identity matrix, '†' denotes the symplectic conjugate, and γ is given by $\gamma^2 + \|\mathbf{C}\|^2 = 1$. Eigenmode a is the nearly horizontal mode and b is the nearly vertical mode. To remove the beta dependence \mathbf{a} can be transformed to $\bar{\mathbf{a}}$ via

$$\bar{\mathbf{a}} = \mathbf{G} \mathbf{a}, \quad (9)$$

where

$$\mathbf{G} = \begin{pmatrix} \mathbf{G}_a & \mathbf{0} \\ \mathbf{0} & \mathbf{G}_b \end{pmatrix}, \quad \mathbf{G}_a \equiv \begin{pmatrix} \frac{1}{\sqrt{\beta_a}} & 0 \\ \frac{\alpha_a}{\sqrt{\beta_a}} & \sqrt{\beta_a} \end{pmatrix}, \quad (10)$$

and similarly for \mathbf{G}_b where β_a is the beta for eigenmode a . \mathbf{T} is now written in terms of the normalized normal modes as

$$\mathbf{T} = \mathbf{G}^{-1} \bar{\mathbf{V}} \bar{\mathbf{U}} \bar{\mathbf{V}}^{-1} \mathbf{G}, \quad (11)$$

where

$$\begin{aligned} \bar{\mathbf{V}} &= \mathbf{G} \mathbf{V} \mathbf{G}^{-1} \\ &= \begin{pmatrix} \mathbf{I}_\gamma & \mathbf{G}_a \mathbf{C} \mathbf{G}_b^{-1} \\ -\mathbf{G}_b \mathbf{C}^\dagger \mathbf{G}_a^{-1} & \mathbf{I}_\gamma \end{pmatrix} \\ &\equiv \begin{pmatrix} \mathbf{I}_\gamma & \bar{\mathbf{C}} \\ -\bar{\mathbf{C}}^\dagger & \mathbf{I}_\gamma \end{pmatrix}. \end{aligned} \quad (12)$$

Since the coupling is weak the following approximations can be made:

$$\beta_a = \beta_{X,a} = \beta_x, \quad \beta_b = \beta_{Y,b} = \beta_y, \quad \epsilon_a = \epsilon_x, \quad (13)$$

where β_x and β_y are the horizontal and vertical betas without coupling, and $\beta_{X,a}$ and $\beta_{Y,b}$ are the betas for the a and b modes projected onto the X and Y axes respectively with X and Y lying along the principal axes of a beam (cf. figure 2).

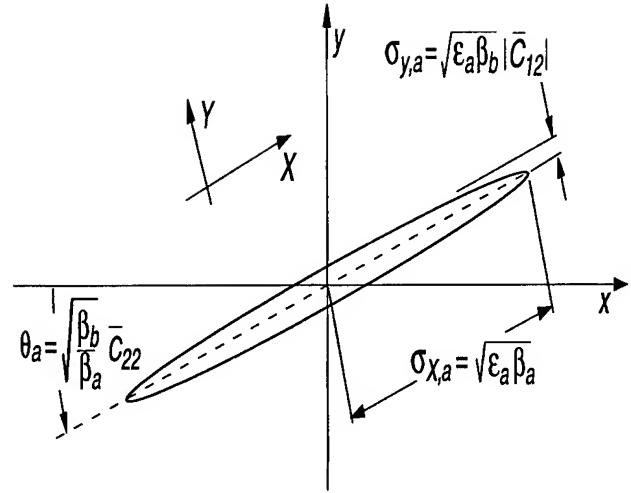


Figure 2: 1σ envelope for eigenmode a . Adapted from Bagley and Rubin figure 1.

Without the beam-beam interaction the normal mode motions are independent so the total sigma is the quadrature sum of the mode sigmas:

$$\begin{aligned} \sigma_Y^2(\text{Coup}) &= \epsilon_a \beta_{Y,a} + \epsilon_b \beta_{Y,b} \\ &\equiv \sigma_{Y,a}^2 + \sigma_{Y,b}^2, \end{aligned} \quad (14)$$

where ϵ_a and ϵ_b are the emittances for the normal modes

Consider first the a eigenmode. Since $\epsilon_a \gg \epsilon_b$ the motion due to the a mode dominates so, to a good approximation, $\sigma_x = \sigma_{X,a}$ and the Y -axis coincides with the minor axis of the a mode. From figure 2, which is adapted from Bagley and Rubin[3] figure 1, we have

$$\sigma_{Y,a} = \sqrt{\epsilon_a \beta_b} |\bar{C}_{12}|, \quad (15)$$

For the b motion $\sigma_{Y,b}$ is calculated from Eq. (14):

$$\sigma_{Y,b} = \sqrt{\epsilon_b \beta_b}. \quad (16)$$

Combining Eqs. (14), (15), and (16), and using Eq. (13) gives at the IP

$$\sigma_Y^*(\text{Coup}) = \sqrt{\epsilon_a \beta_y^*} \left(\bar{C}_{12}^{*2} + \frac{\epsilon_b}{\epsilon_a} \right)^{1/2}. \quad (17)$$

With knowledge of the $\bar{\mathbf{C}}$ matrix around the ring one can calculate ϵ_a/ϵ_b [4, 6] and hence $\sigma_Y^*(\text{Coup})$.

How does the contribution to σ_Y^* from $\sigma_{Y,a}^*$ and $\sigma_{Y,b}^*$ compare? Both $\sigma_{Y,a}$ and $\sigma_{Y,b}$ scale linearly with $\bar{\mathbf{C}}$ in the sense that if $\bar{\mathbf{C}}$ around the ring is scaled by some factor then both $\sigma_{Y,a}$ and $\sigma_{Y,b}$ will be scaled by the that factor[1]. However, it is important to note that $\sigma_{Y,b}^*$ is dependent upon the coupling matrix around the ring as opposed to $\sigma_{Y,a}^*$ which is determined solely by the coupling matrix at the IP. Thus, it is always possible to make the a mode contribution to σ_Y^* equal to zero by using a single skew quad but the b mode contribution will always be present unless the ring is totally ('locally') decoupled.

Ignoring the tilt term for the moment, the calculation of B_c from Eqs. (7) and (17) and from knowledge of the coupling is

straight forward if somewhat cumbersome. If one only wants a rough number, one can first assume that the $\sigma_{Y,a}$ contribution has been zeroed out using a skew quad. It can be shown that[1]

$$\frac{\epsilon_b}{\epsilon_a} \approx 2 \left\langle \overline{C}_{12}^2 \right\rangle_s, \quad (18)$$

where $\langle \dots \rangle_s$ is an average over the ring. Using this in Eqs. (7) and (17) then gives for the vertical blowup term

$$B_c \approx \sqrt{\frac{2\epsilon_x}{\epsilon_y(BBI+Couple)}} \left\langle \overline{C}_{12}^2 \right\rangle_s^{1/2}. \quad (19)$$

Using Eq. (19) along with data on \overline{C}_{12} [3, 7] for the Cornell Electron/positron Storage Ring CESR shows that with a modest amount of global coupling B_c can be as high as 0.3 and with local decoupling can be decreased to as low as 0.07[1]. This is in line with the qualitative observation that local decoupling is necessary to obtain the highest luminosity[7].

$\delta\theta$ Calculation

For a given beam since $\epsilon_a \gg \epsilon_b$ the a eigenmotion dominates. Therefore, with negligible error we can take the angle of a beam, θ to correspond to θ_a — the angle for the a mode ellipse. θ_a is related to \overline{C}_{22} as shown in figure 2. Using this gives

$$\delta\theta^* \equiv \frac{1}{2}(\theta_+^* - \theta_-^*) = \sqrt{\frac{\beta_y^*}{\beta_x^*}} \delta\overline{C}_{22}^*, \quad (20)$$

where

$$\delta\overline{C}_{22} \equiv \frac{1}{2}(\overline{C}_{22,+} - \overline{C}_{22,-}). \quad (21)$$

Since $\delta\theta^*$ depends upon the difference in the \overline{C}_{22}^* , with pretzeled orbits $\delta\theta^*$ may be zeroed using a single skew sextupole.

The critical $\delta\theta^*$ is defined as the angle needed to give a badness of 0.1. From Eq. (7) this is found to be

$$\delta\theta_{crit}^* = 0.46 \frac{\sigma_Y^*(BBI+Couple)}{\sigma_X^*}. \quad (22)$$

Combining Eq. (22) with Eq. (20) gives

$$\begin{aligned} \delta\overline{C}_{22,crit}^* &= 0.46 \sqrt{\frac{\beta_x^*}{\beta_y^*}} \frac{\sigma_Y^*(BBI+Couple)}{\sigma_X^*} \\ &= 0.46 \sqrt{\frac{\epsilon_y(BBI+Couple)}{\epsilon_x}}. \end{aligned} \quad (23)$$

Eq. (23) shows that $\delta\overline{C}_{22,crit}^*$ is independent of β_x^* or β_y^* . This is just a reflection of the fact that the \overline{C} 's are properly normalized. This is an important point: From measurement of the $\delta\overline{C}_{22}$ 'wave' outside of the IP one can get a sense of whether $\delta\overline{C}_{22}$ is too large. Unfortunately, \overline{C}_{22} is hard to measure accurately[3]. However, \overline{C}_{12} is relatively easy to measure and since the \overline{C} matrix can be represented as the superposition of two rotating phasors[5] the magnitude of the $\delta\overline{C}_{12}$ wave should be very close

to the magnitude of the $\delta\overline{C}_{22}$ wave. Furthermore, for a given $\delta\overline{C}_{22}$ at any point in the ring, it is easily shown that the percentage change in the overlap integral due to a finite $\delta\theta$ is independent of the local β_x and β_y . The conclusion is that a quick visual inspection of synchrotron light signals from the bends in the arcs will give an indication of how the beams are overlapping at the IP. One must always remember, however, that it is possible for the phases to be such that there is no tilt at one point in the arcs but unacceptable tilt at the IP (or vice versa).

Acknowledgements

My thanks to Dave Rubin and Alexander Temnykh for some very helpful discussions. My thanks to Flora Sagan for editorial assistance.

References

- [1] D. Sagan, "The Effect of Coupling on Luminosity," Cornell LNS report CBN 95-01 (1995).
- [2] S. Krishnagopal and R. Siemann, "Bunch-length effects in the beam-beam interaction," Phys. Rev. D, **41**, 2312 (1990).
- [3] P. Bagley and D. Rubin, "Correction of Transverse Coupling in a Storage Ring," Proc. 1989 Part. Acc. Conf. (San Francisco) p. 874, (1989).
- [4] Y. Orlov and D. Sagan, "Calculation of the Crab Rotation Angle from the One Turn Transport Matrix," Cornell CBN 91-04, (1991).
- [5] M. Billing, "The Theory of Weakly, Coupled Transverse Motion in Storage Rings," Cornell CBN 85-2, (1985).
- [6] M. Billing, " 'Vertical' Emittance due to Linear Lattice Coupling," Cornell CON 86-6, (1985).
- [7] D. Rubin, private communication.

RFQ-DTL MATCHING SOLUTIONS FOR DIFFERENT REQUIREMENTS *

D. Raparia, Brookhaven National Laboratory, Upton, NY 11973, USA

Abstract

The Radio-Frequency Quadrupole (RFQ) has a FODO lattice and Drift-Tube-Linacs (DTL) in general also have FODO lattices. Therefore the natural solution for the matching between these is a FODO lattice. For matching in all three planes one then needs sixteen degrees of freedom. However, different requirements, depending on the applications, may change this solution. For example, in the production environment (like medical and industrial applications), one needs fixed current and fixed beam quality. On the other hand, in the research environment one not only needs all degrees of freedom, but may also want to chop of beam pulse. This paper discusses matching solutions for these different requirements.

I. INTRODUCTION

To provide successful beam delivery from one device to another, one generally needs a beam-line matching section connecting these two devices. The main functions of matching section (MS) are (1) to match the beam into the following device in all phase space, and (2) to provide space for useful (necessary) diagnostics. A good MS should have these functions decoupled. The MS should provide sixteen degree of freedom: ten are machine parameters, namely $\alpha_x, \beta_x, \alpha_y, \beta_y, \alpha_z, \beta_z$ (amplitude function) and D_x, D'_x, D_y, D'_y (dispersion function) and six trajectory matching parameters $\Delta x, \Delta x', \Delta y, \Delta y', \Delta z, \Delta z'$. If the RFQ and DTL are in a straight line (no horizontal or vertical bend), then one only has ten constraints, namely six amplitude functions and four trajectory matching parameters. If the number of variables (*knobs*) is equal to number of constraints, we will call this solution an optimum solution (OS), and if the number of variables is less than the number of constraints, the solution is called over constrained (OCS). Finally if the number of the variables is more than the constraints, the solution will be an under constrained solution (UCS). These solutions may have different lattices, such as FODO [1], [2], [5], [6], [7], [11], FOFODOD [10] or triplet [9].

The choice of solution will depend upon requirements and limitations such as space, emittance growth, funding, etc. The important ingredients which go into the choice of the solution to minimize the emittance growth and particle loss are: (1) Physical beam size; there should not be a sudden change in beam size. In other words, the zero current phase advance per unit length (σ/L) should have no discontinuity. (2) Space charge forces; the tune depression ($\frac{\sigma}{\sigma_0}$) should not be too low, (3) Neutralization; in the case of H^- , neutralization should be avoided, particularly when the beam energy is low, (4) Diagnostics; there should be enough space left for necessary diagnostics.

The most sensitive errors are the trajectory position matching errors. Emittance growth and particle losses are relatively less

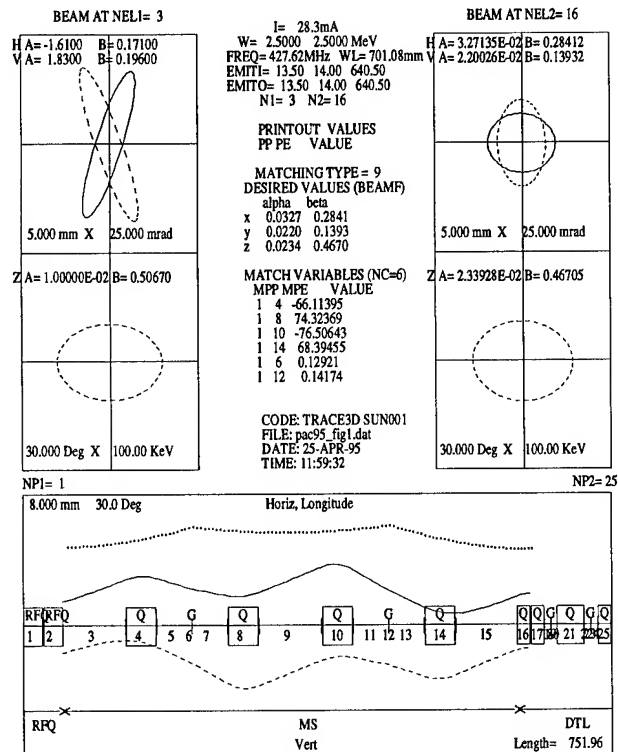


Figure 1. TRACE3D Beam profiles for OS (SSC MS)

sensitive to the amplitude function matching errors. One can estimate the effect of these errors as follows: Position mismatch, $\frac{\sigma_x^2}{\sigma_0^2} = 1 + \frac{1}{2} \left(\frac{\Delta X_{eq}}{\sigma_0} \right)^2$, and amplitude function mismatch, $\frac{\sigma_x^2}{\sigma_0^2} = 1 + \frac{1}{2} \left(\frac{\left(\frac{\Delta \beta}{\beta} \right)}{\sqrt{1 + \left(\frac{\Delta \beta}{\beta} \right)^2}} \right)^2$. Where $\Delta X_{eq}^2 = \Delta x^2 + (\alpha \Delta x + \beta \Delta x')^2$, and σ and σ_0 are the rms beam sizes for unmatched and matched beam respectively.

II. MATCHING SOLUTIONS

RFQs have FODO lattices and, generally, DTLs also have FODO lattices. Therefore, the natural choice lattice for MS is FODO. To provide matching in all phase spaces, one needs two FODO cells, two bunchers between quadrupoles, and four steerers [1] (OS). The number of FODO cells may be less than two, depending upon the requirements and limitations (OCS) [8] [6]. The number of cells may also be more than two [2], in order to provide extra constraints such as space for chopper, bending magnet [5], etc (UCS).

In this section we will consider solutions of each type. We will use the SSC RFQ [4] and SSC DTL Tank1 [3]. The output energies of the RFQ and Tank1 are 2.5 MeV and 13.4 MeV, respectively and the nominal current is 25 mA.

*work performed under the auspices of the U. S. Dept. of Energy.

Quadrupole No.	5 cm	7 cm	9 cm
Q1 (T/m)	-125.01	-126.47	-126.80
Q2 (T/m)	149.63	155.41	141.82
Q3 (T/m)	-125.82	-108.06	-38.22
Q4 (T/m)	140.29	112.07	7.581

Table I
DTL First Four Quad. Grad. for 5, 7, 9 cm, MS(OCS)

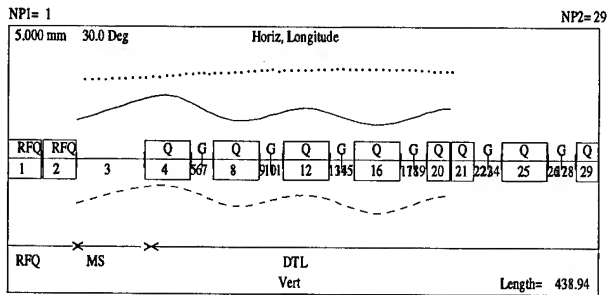


Figure 2. TRACE3D Beam profiles for 5 cm MS(OCS)

A. Optimum Solution (OS)

Figure 1 shows the TRACE3D beam profiles for the SSC MS. This MS has four variable PMQs and two bunchers, to provide six variables for amplitude function. The variable PMQs were also movable transversely to provide four steering variables to match trajectory. It had enough space to provide diagnostics. The phase advance per $\beta\lambda$ at the end of RFQ is 22.40 deg, and at the beginning of DTL was 20.85 deg. The tune depression in this section is 0.92.

B. Over Constrained Solution (OCS)

In the production environment, one needs reliability rather than flexibility. The fewer the variables, the better the reliability. Partial or full matching may be accomplished by altering a few end cells of the RFQ and the first few cells of the DTL.

In the following examples we have only drift lengths of 5, 7, and 9 cm between the RFQ and the DTL and have used the first four quadrupoles in the DTL for the matching in the following cells. The first four quadrupole gradients for these cases are given in Table I. TRACE3D profiles for case of 5 cm MS(OCS) are shown in Figure 2.

C. Under Constrained Solution (UCS)

In this situation, one might have to accommodate other constraints. For example, one might have to chop the beam pulse length [9], or the DTL lattice is not FODO [10], or σ_0/L is quite different in the RFQ and DTL [7].

We consider an RF chopper to chop the beam. We have tried two solutions namely, (1) FODO lattice where choppers are placed between quadrupoles and, (2) triplets to provide long drift space for one chopper. In the first case, a systematic search was made for minimum number of choppers which could kick the beam centroid at least 0.8 cm (beam pipe radius). The TRACE3D beam profiles are shown in Figure 3 for the FODO solution which was optimized for the minimum emittance growth. In this case we have four choppers, having plates which are 6 cm

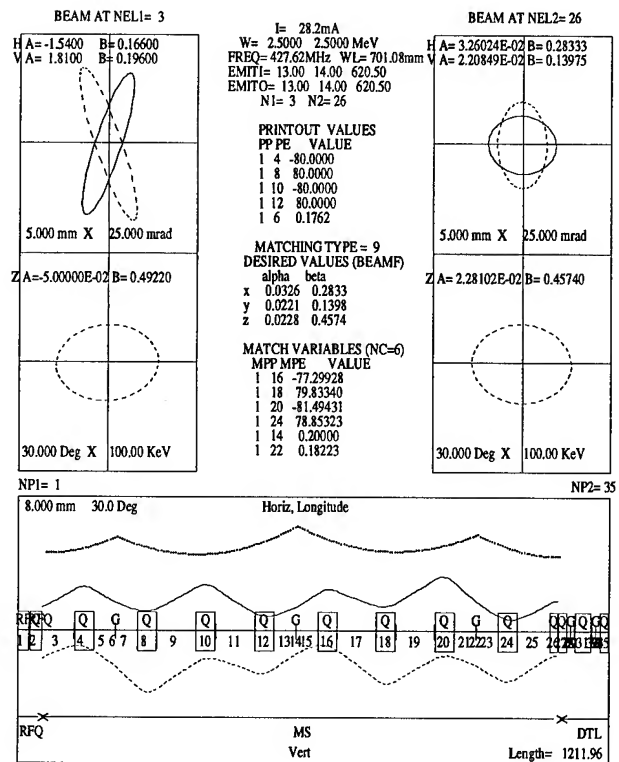


Figure 3. TRACE3D Beam Profiles for UCS (FODO).

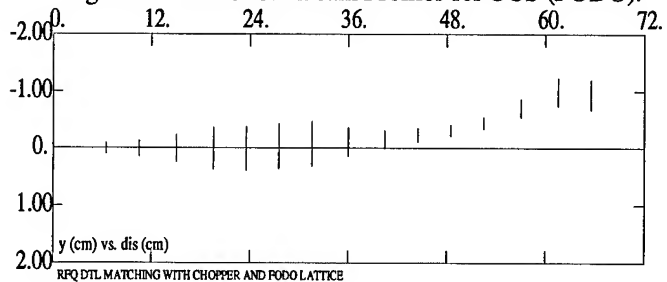


Figure 4. PARTRACE Beam profile for UCS (FODO) with chopper.

long and 2.54 cm apart. The chopper pulse is about 5kV at few MHz. These choppers are located at element numbers 9, 11, 17 and 19 in Figure 3. This arrangement could kick the beam centroid 1 cm off axis as shown in Figure 4.

For the second solution, to provide 30 cm long drift space with beam size less than 0.8 cm, we have used two triplets, and four quadrupoles to bring the beam size slowly to match to the DTL. Again this solution is also optimized for the minimum emittance growth. Figure 5 shows the TRACE3D profiles for the triplet lattice. Again, the chopper operating parameters are same as above, but, instead four 6 cm long plates, it uses one 30 cm long plate, corresponding to element number 9 in Figure 5. Figure 6 shows the beam profiles through this section. In this case also the beam centroid is kicked 1 cm off axis.

III. CONCLUSIONS

We have also done PARMTEQ and PARMILA calculations for these cases. 1000 macro-particles were used to form a matched beam into the RFQ. The same particles were followed in the MS and DTL. Table II shows the output emittances at the

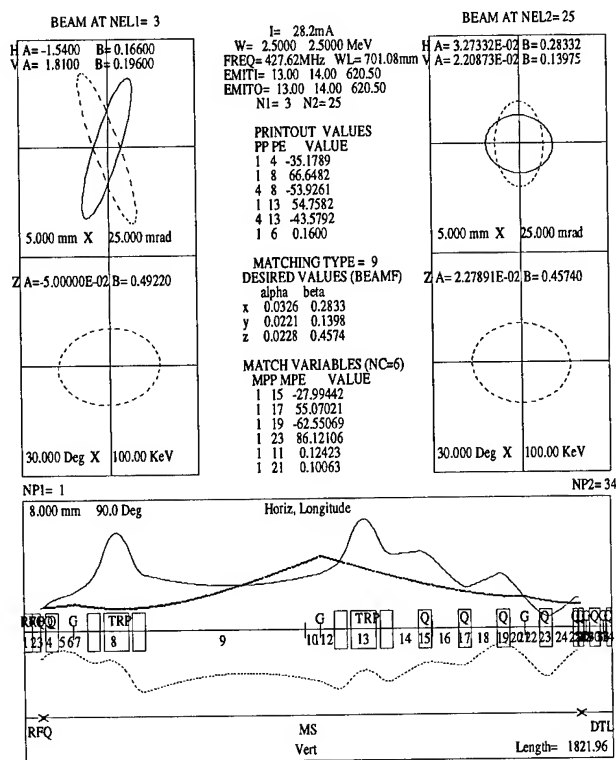


Figure 5. TRACE3D Beam Profiles for UCS (Triplet).

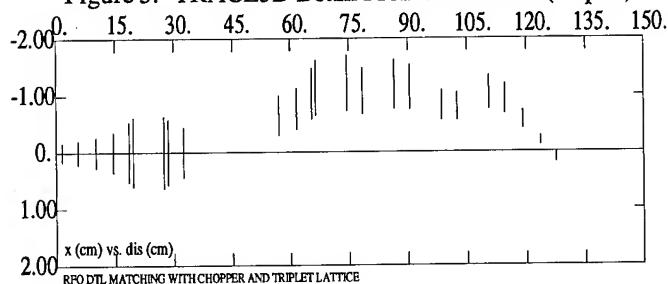


Figure 6. PARTRACE Beam Profiles for UCS (Triplet) with chopper.

end of TANK 1. In MS and DTL no particle loss occurred except in the case of UCS triplet where particle loss is about 0.5%. The emittance growth in cases of OS, OCS (5 cm) and UCS (FODO) are reasonable.

IV. ACKNOWLEDGEMENTS

We would like to thank J. Alessi and A. Kponou for their valuable suggestions and discussions.

References

- [1] R. C. Sethi, *et al*, "Design of the RFQ-DTL Matching Section for the SSCL Linac", p 482, Proceeding of the 1992 Linear Accelerator Conference, AECL-10728, August 1992, Ottawa, Ontario, Canada.
- [2] O. R. Sander, *et al*, "Commissioning the GTA Accelerator", p 535, *ibid*.
- [3] D. Raparia, *et al*, "SSC Drift-Tube Linac Design", p 199, *ibid*.

Solutions	ϵ_x	ϵ_y	ϵ_z	$\Delta\epsilon_t$	$\Delta\epsilon_z$
RFQ	0.189	0.208	0.124	-	-
OS	0.202	0.219	0.124	5.0%	0.0%
OCS (5 cm)	0.194	0.214	0.149	4.0%	20.0%
OCS (7 cm)	0.213	0.215	0.161	10.0%	30.0%
OCS (9 cm)	0.347	0.215	0.188	44.0%	52.0%
UCS (FODO)	0.208	0.217	0.139	6.0%	12.0%
UCS (Triplet)	0.193	0.243	0.150	12.0%	21.0%

Table II

DTL Tank 1 output normalized rms emittances. ϵ_x, ϵ_y are in units of π mm-mrad, ϵ_z is in units of π MeV deg. $\Delta\epsilon_t$ is the average emittance growth in x and y plane with respect to the RFQ output.

- [4] T. S. Bhatia, *et al*, "Beam Dynamics Design of an RFQ for the SSCL", p 1884, Proceeding of the IEEE Particle Accelerator Conference, May 1991, San Francisco, CA.
- [5] D. Raparia, "RFQ-DTL Matching Section", Preliminary Design Review for SSC Linac, January 29, 1991.
- [6] E. Boltezar, *et al*, "Experimental RFQ As Injector To The CERN Linac 1", p 302, Proceeding of the 1981 Linear Accelerator Conference, AECL-10728, October 1981, Santa Fe, New Mexico, USA.
- [7] M. Weiss, "The RFQ2 Complex: the Future Injector to CERN Linac2", p 539, Proceeding of the 3rd European Particle Accelerator Conference, March 1992, Berlin.
- [8] R. Hamm, Private Communication.
- [9] J. Alessi, *et al*, "The AGS H⁻ RFQ Preinjector", p 196, Proceeding of the 1988 Linear Accelerator Conference, CEBAF-Report-89-001, October 1988, Newport News, Virginia.
- [10] R. W. Garnett and P. Smith, "Design of a Current-Independent Matching Section for APDF", p 107, Proceeding of the 1994 Linear Accelerator Conference, August 1994, Tsukuba, Japan.
- [11] Takao Kato, "Design of Beam-Transport Line Between the RFQ and the DTL for the PHP 1-GeV Proton Linac", p 59, *ibid*.

Low-Dispersion γ_t Jump for the Main Injector

K.Y. Ng and A. Bogacz

Fermi National Accelerator Laboratory,* P.O. Box 500, Batavia, IL 60510

Abstract

A bipolar γ_t -jump design is reported for the Fermilab Main Injector (Lattice MI-17). The total amount of jump is 1.3 units. Both the betatron and dispersion waves are confined, while the betatron tunes remain nearly unchanged.

I. Introduction

The Fermilab Main Injector has been designed to overcome some of the unfavorable effects on the particle motion around transition energy. Unlike the Main Ring, the Main Injector has a very large aperture, so that beam loss due to scraping can be avoided. The bunch area at transition will be less than 0.1 eV-sec, so that the nonlinear Johnson effect [1] can be avoided. Also rapid ramping across transition is possible, so that the nonadiabatic time can be reduced. Nevertheless, negative-mass instability will develop when the bunch intensity is high enough. The only way to avoid this instability is to incorporate a γ_t jump.

During a γ_t jump, it is difficult to confine the betatron waves and dispersion wave, and at the same time preserve the betatron tunes. The existing γ_t jumps at the CERN PS and the Fermilab Booster have been performed at the expense of creating unfavorable increases in dispersions. In the scheme to be presented below, such unpleasant dispersion increase has been avoided by utilizing the dispersion-free regions in the Main Injector. Similar scheme had been considered by Bogacz et al and Peggs et al. [2],[3]

II. Review of Theory

An off-momentum particle will pass through the special quads for γ_t jump off-centered and acquire a kick, thus changing its path length around the ring. The change in γ_t has been given by Risselada: [4]

$$C_0 \Delta(\gamma_t^{-2}) = - \sum_{i=1}^N K_i (1 + M + M^2 + \dots) D_i^2, \quad (1)$$

with the matrix M defined as

$$M_{ij} = - \frac{K_i \sqrt{\beta_{xi} \beta_{xj}}}{2 \sin \pi \nu_x} \cos(\pi \nu_x - |\phi_i - \phi_j|_x). \quad (2)$$

In the above, C_0 is the circumferential length of the ring, K_i is the strength of the special quad at location s_i , while β_{xi} , ϕ_{xi} , and D_i are the horizontal beta function, phase advance, and dispersion at s_i , and ν_x the horizontal betatron tune, all before the pulsing

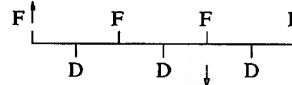
of the special quads. Thus, Eq. (1) is an expansion in terms of $O(K\beta)$.

During the jump, naturally we would like little or no change in the betatron tunes ν_x and ν_y , while keeping the dispersion and the horizontal and vertical beta functions below reasonable values.

For small quad strength K_i 's, the changes in tunes are

$$\Delta \nu_{x,y} = \pm \frac{1}{4\pi} \sum_{i=1}^N K_i (\beta_i)_{x,y}. \quad (3)$$

To keep $\Delta \nu_x = 0$ and $\Delta \nu_y = 0$, we can go with doublets, each having $\beta_1 K_1 + \beta_2 K_2 = 0$. The Main Injector has 90° cells. So we can put one special quad of strength K at the F quad of one cell and another of strength $-K$ at the F quad of some later identical cell as follows:



F quads are used because β_x and D are usually at a maximum there; so $\Delta \gamma_t$ will be maximized.

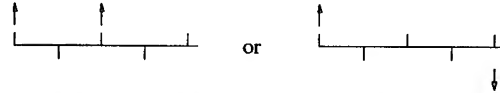
For a special quad of strength K_i , the betatron waves downstream are

$$\Delta \beta_{x,y}(s) = \mp (\beta(s) \beta_i)_{x,y} K_i \sin[2(\phi(s) - \phi_i)_{x,y}], \quad (4)$$

whereas the dispersion wave downstream is

$$\Delta D(s) = -\sqrt{\beta_x(s) \beta_{xi}} D_i K_i \sin[\phi(s) - \phi_i]_x. \quad (5)$$

To confine betatron waves in 90° cells, we can place a doublet of special quads of the *same* sign at successive identical cells, or place one at F of one cell and the other of *opposite* sign at F of the 3rd cell that is 180° downstream:

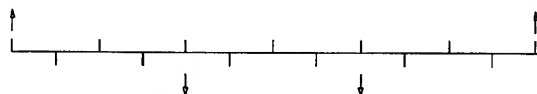


The latter is preferred since ν_x and ν_y are preserved.

On the other hand, dispersion wave can only be confined between two special quads of the *same* sign placed at 90° cells 180° apart, or of *opposite* sign placed 360° apart:



One possible way to accommodate all these restrictions is



But, unfortunately, these 4 quads give $\Delta \gamma_t = 0$. Thus, it appears that there is no way to satisfy all the restrictions.

*Operated by the Universities Research Association under contracts with the U.S. Department of Energy.

For the γ_t jumps in the CERN PS and the Fermilab Booster, doublets of special quads are used to null the tune changes and confine betatron wave but *not* the dispersion wave. This scheme gives $M^2 = 0$ and simplifies Eq. (1):

$$\Delta\gamma_t^{-2} = \frac{1}{2C_0 \sin \pi \nu_x} \sum_{i=1}^N D_i^2 \beta_{xj} K_i K_j \cos(\pi \nu_x - |\phi_i - \phi_j|_x),$$

so that the change in γ_t is second order in M or $(K\beta)^2$. In order to have a bipolar jump, two families of doublets must be needed. This scheme had also been considered by Holmes for the Main Injector. [5]

For machines with dispersion-free regions, there is another scheme. [2] Here, groups of 4 quads are used to confine both the betatron and dispersion waves, but changes in betatron tunes are ignored for the time being:



Next, we place in dispersion-free regions another family of special quad doublets at F 's 90° apart. Here, betatron waves are again confined. But no dispersion wave will be created and $\Delta\gamma_t$ will be unaffected. The strength of this second family is adjusted to null out $\Delta\nu_x$ and $\Delta\nu_y$. In this scheme, all orders of M or $K\beta$ contribute. But the first order usually dominates. This scheme is termed *matched* by Bogacz et al, and the first one *unmatched*. [2]

III. Application to Main Injector

The Main Injector will be ramped at $\dot{\gamma} = 163 \text{ s}^{-1}$ when crossing transition. The nonadiabatic time is $t_c = 1.96 \text{ ms}$. For a bunch of emittance $0.1 \text{ eV}\cdot\text{sec}$, the nonlinear time is $t_n = 1.06 \text{ ms}$, assuming that the nonlinear momentum compaction $\alpha_1 = \frac{1}{2}$. Thus, we need a γ_t jump of at least $\Delta\gamma_t \approx 2\dot{\gamma}_t(t_c + t_n) = 1.0$. Numerical simulations show that a much cleaner crossing will result if the jump is ~ 1.3 . In this bipolar application, our aim is therefore $\Delta\gamma_t \approx \pm 0.65$.

The Main Injector lattice MI-17 is two-fold symmetric, so we need only to study one half. We start at location MI52. There are 19 90° cells in a row in the arc; we put in 20 special quads (5 sets of 4's). After a dispersion-free neutrino-extraction region at MI40, there are 6 90° cells in a row; we put in 4 special quads (1 set of 4's). The second family of doublets is placed in the dispersion-free regions: 2 quads at MI40 (ν extraction), 2 quads at MI32 (opposite to kicker), 4 quads at MI30 (rf region), and 2 quads at MI22 (opposite to kicker). The results are listed in Table 1. The lattice functions $\beta_x^{1/2}$ and D before the jump, at jump-up, and jump-down are plotted in Fig. 1(a), (b), and (c), respectively. We see that a γ_t jump of $+0.683$ and -0.625 has been achieved with dispersion well-confined within 2.2 m and β_x within 78 m . Both betatron tunes are matched up to < 0.002 . In fact, the MI-17 lattice is not well-matched; the dispersion-free regions are not exactly at $D = 0$, and the betatron functions do not repeat themselves exactly for every FODO cell. In addition, the cells are not exactly 90° . If these were corrected, the confinements of the betatron and dispersion waves could have been very much improved. Nevertheless, these results are much

Table 1: A bipolar γ_t jump scheme for MI-17

	MI-17	up	down
ν_x	26.40748	26.40606	26.40940
ν_y	25.40998	25.40836	24.41182
$\beta_x \text{ Max (m)}$	59.86643	78.04456	68.88534
$\beta_y \text{ Max (m)}$	63.17612	64.12093	65.25474
$D \text{ Max (m)}$	1.97820	2.04025	2.20696
γ_t	21.58789	+0.6826	-0.6254
$\int B'd\ell (1)$		+0.1822 T	-0.1586 T
$\int B'd\ell (2)$		-0.4305 T	+0.3724 T

better than those obtained in Ref. 2 for the MI-15 lattice. There, the dispersion reaches a maximum of 2.64 m and the β_x reaches 97.5 m .

IV. Jump Rate

During the process of the γ_t jump, the special quads are first pulsed at the roughly the machine ramping rate so that γ_t is raised slowly by 0.68 unit. Near the transition energy, the current in the special quads are reversed suddenly, so that γ_t drops to a value which is 0.63 unit below. After that, the pulse current is slowly reduced to zero. The rate of jump is limited only by the allowable flux change in the laminations of the quads, which is roughly 1.5 T at 100 Hz , or $\dot{B} \approx 942 \text{ T/s}$, provided that good silicon steel is used. From Table 1, we see that the largest integrated change in flux gradient is 0.803 T in the second family. If we assume the quads are of length 1 m and the distance to pole tips is 2 in , the change in flux at pole tips is $\Delta B = 0.041 \text{ T}$. Therefore, the fastest jump or reversal of current can be made in $43 \mu\text{s}$ or about 4 turns.

For the design of Holmes [5], the dispersion increases by 4.8 m per unit $\Delta\gamma_t$. In order that the horizontal emittance does not increase appreciably, one needs to limit the rate of jump. However, since the change in dispersion is so small in the present design, this restriction no longer applies.

References

- [1] K. Johnsen, Symposium on High Energy Accel., CERN, 1956, Vol. 1, p.106
- [2] A. Bogacz, F. Harfoush, and S. Peggs, Proc. Fermilab III Instabilities Workshop, 1990, p.177.
- [3] S. Peggs, S. Tipikian, and D. Trbojevic, Proc. PAC 93, Washington, 1993, p.168
- [4] T. Risselada, CERN 4th General Accel. School, Jülich, Germany, 1990, p.161.
- [5] S. Holmes, Fermilab Internal Report MI-0008, 1989.

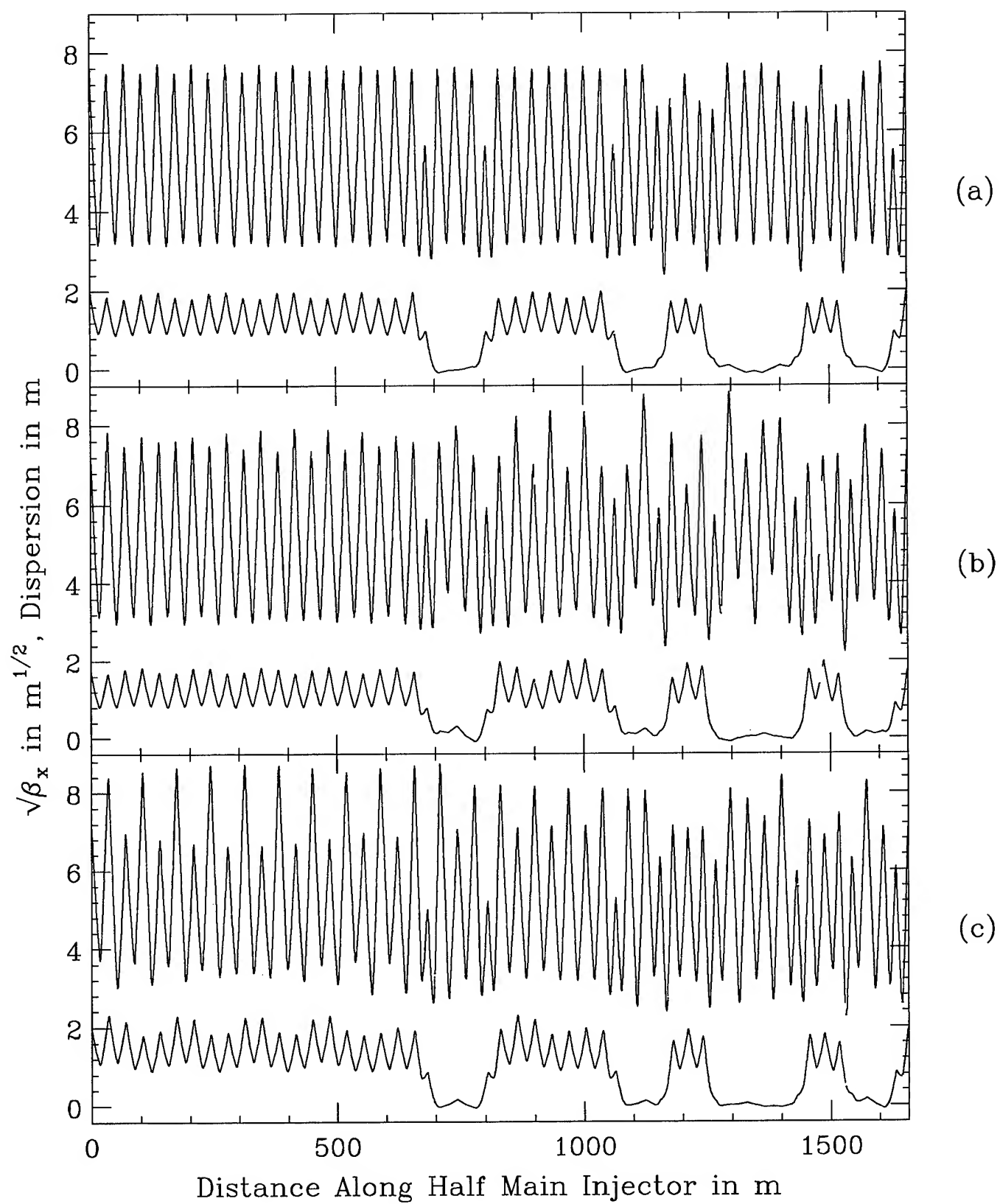


Fig. 1. $\sqrt{\beta_x}$ and D of the Main injector M-17 (a) before transition jump, (b) at jump-up, and (c) at jump-down.

Wakefields and HOMs Studies of a Superconducting Cavity Module with the CESR Beam*

S. Belomestnykh[†], W. Hartung, G. Flynn[‡], J. Kirchgessner, H. Padamsee, and M. Pisharody
Laboratory of Nuclear Studies, Cornell University, Ithaca, NY 14853 USA

Abstract

Several aspects of the beam-cavity interaction were investigated in a beam test of the superconducting accelerating cavity module for the CESR upgrade: the time structure of the cavity wake potential, sampled with two bunches, the effect of the module on the total machine loss factor, and the influence of the cavity tuner position on the frequencies and damping times of coupled bunch modes. The spectra of some of higher-order modes excited by the beam were also recorded. The results are discussed.

I. INTRODUCTION

The CESR luminosity upgrade plan calls for increasing the average current to 500 mA per beam and shortening the bunch length to 1 cm [1], in comparison with the present operating conditions of approximately 150 mA per beam and 1.8 cm bunch length. At the higher current, the parasitic interaction of the bunched beams with the surrounding structure will be much stronger. We therefore pay special attention to the design and testing of new components for operation at higher current. Four cells of superconducting (SC) cavities with specially designed higher-order mode (HOM) dampers [2-4] will be installed in the CESR to replace the existing 20 cells of copper cavities. This reduce the parasitic impedance of the RF system and its parasitic interaction with the beam. Calculations [5] and measurements of the copper model of the cavity [6] indicate that the design is adequate to the requirements of a high current storage ring.

The beam test of the superconducting cavity took place recently at the CESR storage ring [7, 8]. Experiments were undertaken in an effort to understand the time structure of the cavity's wake potential and to observe the interaction of the beam with the cavity HOMs. Beam stability studies were done for different bunch patterns. No instabilities due to the SRF cavity were encountered. The spectra of some HOMs were recorded and no resonant excitation of those modes was found.

II. TOTAL CESR LOSS FACTOR

Studies of the higher mode losses for CESR have been done by M. Billing [9]. Scaling laws for the loss factor of different components in the vacuum chamber are in good agreement with experimental data; we used them to predict the total loss factor of the machine under the conditions of our test. Both the predictions and the separate calorimetric mea-

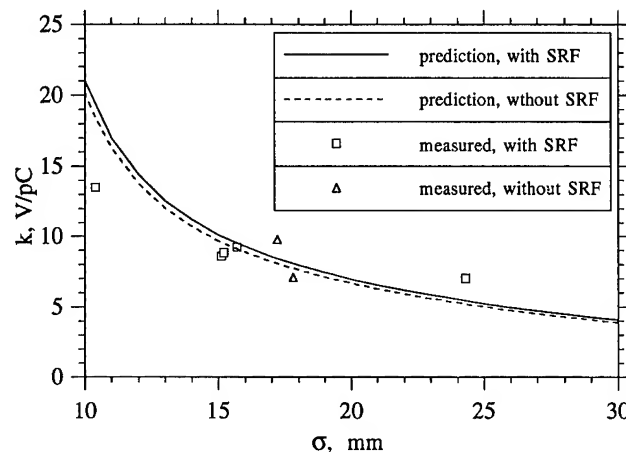


Figure 1. The total CESR loss factor (experimental data and prediction).

surements of the loss factor of the superconducting cavity module [8] show that the loss factor of the SC cavity is much less than the total CESR loss factor. Nevertheless we measured the total loss factor of the machine before and after installation of the SC cavity, to make sure that there were no gross errors in the calorimetric measurements. The predicted and measured total CESR loss factors are shown in the Fig. 1.

III. TIME STRUCTURE OF THE WAKE POTENTIAL

An elegant method of wake potential sampling, proposed by A. Temnykh [10], was used in the beam test: with two bunches of equal current, placed close to each other, one can measure the power loss due to the HOMs of some discontinuity of vacuum chamber. By using different bunch spacings we can obtain information about the time structure of the wake potential. Also, we can calculate the loss factor and wake potentials for the two-bunch case using computer codes like ABCI [11] and AMOS [12] and compare these calculations with the measured values. Let us define the loss factor for this case as

$$k = \frac{N P f_{rev}}{I_o^2},$$

where I_o is the average beam current; f_{rev} is the revolution frequency; N is the number of bunches, and P is the HOM power.

The loss factor will be equal to the loss factor of a single bunch if the wake potential decays completely before the arrival of the second bunch, or if the HOMs with high R/Q s are all detuned far enough from harmonics of one half the RF frequency (so that the wake fields are not close to being completely in phase or completely out of phase).

* Work supported by the National Science Foundation, with supplementary support from the US-Japan Collaboration

[†] On leave from Budker Institute of Nuclear Physics, 630090 Novosibirsk, Russia

[‡] Present address: LURE, 91405 Orsay, France

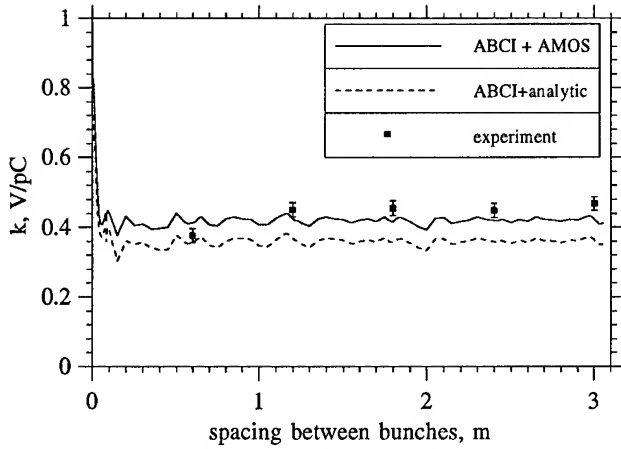


Figure 2. The loss factor of the SRF cavity assembly sampled by two bunches (experimental data and prediction).

The minimum spacing between two bunches is equal to the wavelength of the RF system, i.e. 60 cm for CESR. We measured the power dissipation in the HOM loads of the cavity module calorimetrically [8] and varied the bunch spacing from 1 to 5 buckets. The measurements were done for a beam energy of 5.3 GeV and for three different total beam currents: 10, 20, and 30 mA. Figure 2 shows the measured loss factor in comparison ABCI and AMOS calculations. The agreement is very good.

IV. OTHER TESTS

A. Influence of the Cavity Tuner Position on the Beam Dynamics

Using the cavity's fundamental mode frequency tuner, we changed the HOM frequencies to investigate the influence of the HOMs on the beam dynamics and to look for any unexpectedly dangerous (high $R/Q \cdot Q$) HOMs. In these tests, the RF power for the SC cavity was switched off and the fundamental mode frequency remained detuned. While scanning the tuner position, we were able to maintain a 100 mA beam, and there were no beam instabilities. We continuously monitored the HOM power deposited by the beam. The loss factor was calculated from the temperature of the HOM load. The dependence of the loss factor on tuner position is shown in Figure 3. The small variation of the loss factor shows that there was no resonant excitation of HOMs as their frequencies changed. In addition, we measured the tunes and damping times of coupled bunch modes with a nine bunch beam, using a spectrum analyzer, for two positions of the tuner. The technique of these measurements is the same as described in [13]. No significant changes in damping times or tunes were observed between the two tuner positions: all changes were within the repeatability of the measurements.

B. Dipole loss factor

We tried to investigate the dipole component of the cavity loss factor by displacing a 120 mA (in 9 bunches) beam (with a bunch length of about 15 mm) horizontally and vertically by ± 10 mm in the SC cavity. According to calculations, the monopole component of the loss factor is 0.43 V/pC, and the dipole component is 0.006 V/pC for a 10

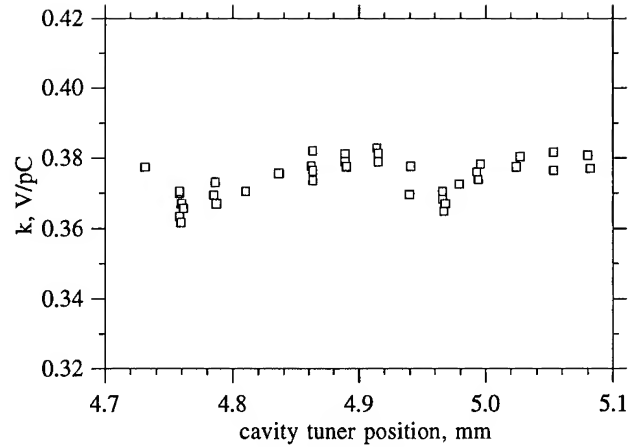


Figure 3. Dependence of the cavity loss factor on the cavity tuner position.

mm beam displacement. The cooling water ΔT was about 3.5°C for each HOM load. That means that the contribution from the dipole component should be of order of 0.05°C , according to the prediction. The resolution of our calorimetry is 0.03°C , and the noise level is of the same order. No changes in the cooling water ΔT were seen in excess of the resolution and noise level of the measurement.

C. Spectra of HOMs

Experiments were done to search for dangerous HOMs by exciting the cavity via a single-bunch beam of 30 mA, with a varying transverse displacement of the beam. The HOM spectra were observed and recorded using a spectrum analyzer.

We used results of URMEL [14] and CLANS (for monopole HOMs) [15] calculations and measurements of the copper cavity model [6] to compare with the beam test measurements. Unfortunately we did not succeed very much in exact identifying of the HOMs though we can say that for monopole HOMs Q -factors are of order of one hundred, and for dipole and quadrupole HOMs Q -factors are typically less than one thousand. That is consistent with previous measurements. No resonant excitation of HOMs or beam instabilities were observed.

V. CONCLUSIONS

Several aspects of the beam-cavity interaction were investigated in the beam test of the superconducting accelerating cavity module for the CESR upgrade, in an attempt to find dangerous HOMs, to understand the time structure of the cavity wake potential, and to check the effect of the module on the total machine loss factor. The loss factor results are in a good agreement with the predictions. The results of wake potential sampling indicate that the wake fields of the SRF cavity will not limit the CESR performance in bunch train operation[1]. No beam instabilities or dangerous HOMs were encountered while sweeping the HOM frequencies using the cavity tuner or exciting multipole HOMs by displacing the beam off axis horizontally and vertically.

VI. REFERENCES

- [1] D. Rubin, "CESR Status and Plans", *these proceedings*
- [2] H. Padamsee, et al., "Accelerating Cavity Development for the Cornell B-Factor, CESR-B", *Conference Record of the 1991 Particle Accelerator Conference*, Vol. 2, pp. 786-788, San Francisco, CA, May 1991
- [3] H. Padamsee, et al., "Design Challenges for High Current Storage Rings", *Particle Accelerators*, 1992, Vol. 40, pp. 17-41
- [4] H. Padamsee, et al., "Development and Test of a Superconducting Cavity for High Current Electron Storage Rings", *Proceedings of the Fourth European Particle Accelerator Conference*, Vol.3, pp. 2048-2050, London, Great Britain, June 1994
- [5] V. Veshcherevich, et al., "Higher Order Modes Damping in CESR B Cavity", *Proceedings of B Factories: The State of the Art in Accelerators, Detectors and Physics*, SLAC-400/CONF-9204126, pp. 177-180, Stanford, CA, April 1992
- [6] W. Hartung, et al., "The Interaction of a Beam with a Beam Line High-Order Mode Absorber", *Proceedings of the 1993 Particle Accelerator Conference*, Vol. 2, pp. 3450-3452, Washington, D.C., May 1993
- [7] H. Padamsee, et al., "Beam Test of a Superconducting Cavity for the CESR Luminosity Upgrade", *these proceedings*
- [8] S. Belomestnykh, et al., "Comparison of the Predicted and Measured Loss Factor of the Superconducting Cavity Assembly for the CESR Upgrade", *these proceedings*
- [9] M. Billing, "Higher Mode Power Loss Limitations for Beam Currents in CESR", *CBN 84-15* (1984)
- [10] A. Temnykh, "Wake function study using two spaced bunches", *CON 95-06* (1995)
- [11] Y. H. Chin, "Advances and Applications of ABCI", *Proceedings of the 1993 Particle Accelerator Conference*, Vol. 2, pp. 3414-3416, Washington, D.C., May 1993
- [12] J. DeFord, et al., "The AMOS (Azimuthal Mode Simulator) Code", *Proceedings of the 1989 IEEE Particle Accelerator Conference*, Vol. 2, pp. 1181-1183, Chicago, IL, March 1989
- [13] M. Billing, et al., "Measurements of Vacuum Chamber Impedance Effects on the Stored Beam at CESR", *these proceedings*
- [14] U. Laustroer, et al., "URMEL and URMEL-T User Guide (Modal Analysis of Cylindrically Symmetric Cavities; Evaluation of RF-Fields in Waveguides)", *DESY M-87-03* (1987)
- [15] D. G. Myakishev, V. P. Yakovlev, "The New Possibilities of SuperLANS Code for Evaluation of Axisymmetric Cavities", *these proceedings*

Comparison of the Predicted and Measured Loss Factor of the Superconducting Cavity Assembly for the CESR Upgrade*

S. Belomestnykh[†], W. Hartung, J. Kirchgessner, D. Moffat, H. Muller, H. Padamsee, and V. Veshcherevich[†]

Laboratory of Nuclear Studies, Cornell University, Ithaca, NY 14853 USA

I. INTRODUCTION

Superconducting cavities have been chosen to replace the existing copper cavities for the future upgrade of CESR. The use of superconducting cavity modules, specially designed for a high current collider, allows us to lower the cavity impedance and the loss factor of the accelerating system and thereby increase the threshold for multi- and single-bunch instabilities [1, 2]. The prototype superconducting cavity assembly was developed at the Laboratory of Nuclear Studies, Cornell University [3, 4] and successfully tested recently in a beam test in the CESR storage ring [5].

Figure 1 shows a schematic of the entire module which includes the cavity, the 24 cm round beam pipe, the fluted beam pipe, the ferrite HOM loads, sliding joints, gate valves and tapers to the CESR beam pipe.

The beam tubes were designed so that all of the higher order modes (HOMs) propagate out of the cavity and are damped by ferrite HOM loads which are located outside the cryostat and which are an integral part of the beam tube.

Systematic studies were done to estimate the interaction of a bunched beam with the cavity module including the HOM load [6, 7]. ABCI, TBCI and AMOS were used for calculating the loss factor as a function of the bunch length. Also, an analytical approach was developed to estimate the coupling impedance and loss factor of the HOM loads.

The loss factor has been measured in a beam test using calorimetric method; we measure the water temperature rise and the flow rate of the cooling water to the HOM load. To measure the loss factor vs. bunch length (10 to 25 mm), we used two different sets of CESR optics and different RF voltages. The experimental data points are in a good agreement with predicted values.

II. HOM LOADS

In the high power RF test of the first HOM load prototype [8], several ferrite tiles cracked. Subsequent examination revealed that the solder bond between the ferrite and the tin-plated stainless steel shell was poor. The HOM load was therefore redesigned. A new, so-called "porcupine" load was developed (see Figures 2). It consists of a stainless steel shell with 18 copper plates bolted along the inside. Each copper plate carries two 2" long or four 1" long soldered TT-111R ferrite tiles¹. The width of the tiles is 1.5" and the thickness is 0.125". Copper tubing is brazed to each plate for water cooling. This modular design is more tolerant of soldering

* Work supported by National Science Foundation, with supplementary support from the US-Japan Collaboration.

[†] Visitor from Budker Institute of Nuclear Physics, 630090 Novosibirsk, Russia

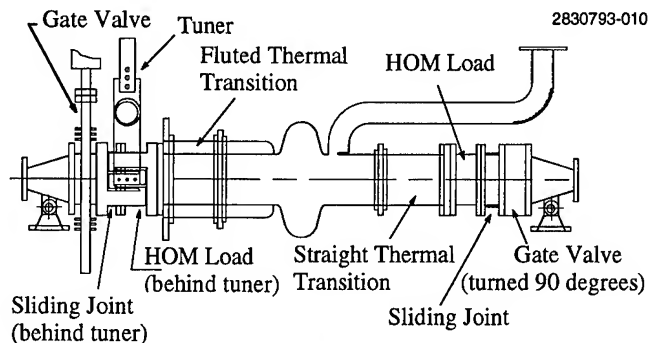


Figure 1. Schematic of the SRF cavity module.

problems than its predecessor.

Three loads have been fabricated. We used two of them in the beam test. The third was subjected to a separate high power test. An inner conductor was placed concentric to the HOM load and the assembly was connected to 50 Ohm coaxial line terminated by 30 kW water load (see Figure 3). We used a 500 MHz klystron as a source of RF power. The dissipated power was measured via RF (directional couplers) and calorimetry (temperature rise and flow rate of the cooling water). Tile surface temperature measurements were done with "button" type temperature-indicating labels. The test load reached an average power density of 20 W/cm² and measured surface temperatures were excess of 150°C, at which point the water ΔT was 55°C. The water flow rate was equal to 0.9 gpm during this test. The test was done in air, not in vacuum. The agreement between the RF and calorimetric measurements of the dissipated power was quite good.

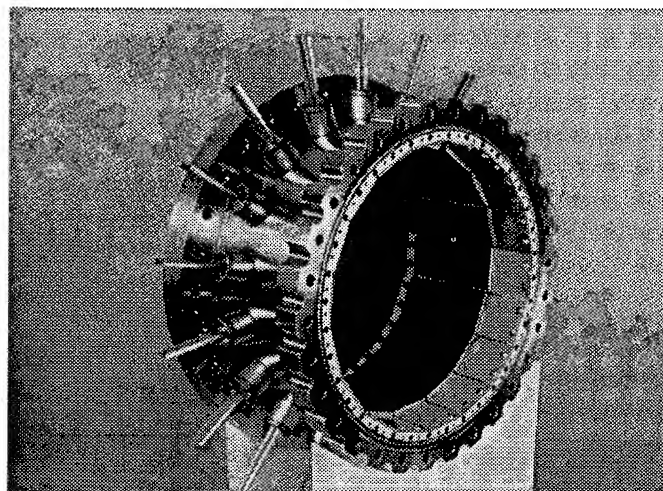


Figure 2. Higher order mode load.

¹Product of Trans-Tech Inc., Adamstown, MD 301-695-9400

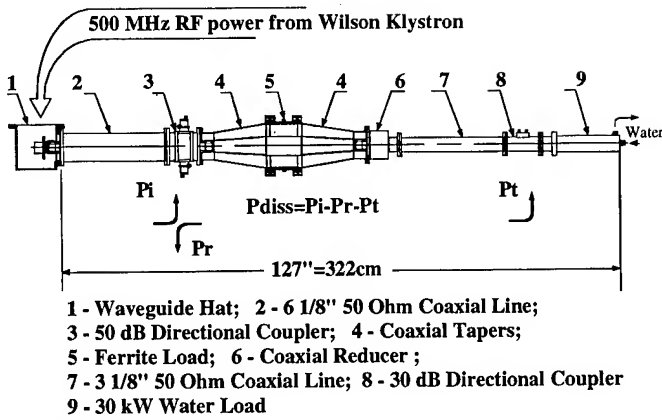


Figure 3. Layout of the HOM load high power test.

III. CALCULATIONS OF THE LOSS FACTOR

One can calculate the loss factor of an axially symmetric accelerating structure using TBCI [9] or ABCI [10, 11]. Unfortunately, these programs do not allow us to calculate wake fields in the presence of absorbing materials such as ferrite. On the other hand, AMOS [12] can handle such materials but we have not yet successfully applied it to complex geometries. In the mean time we are using a palliative measure: we calculate the loss factor of the simplified geometry (we did not take into account the RF coupler and flutes) of the cavity module without ferrite and of the ferrite load alone adding results to get the total loss factor of the assembly. As an alternative to AMOS, we also used an analytical approach [7].

A. The Loss Factor of the Cavity Module

Initial calculations of the loss factor for the cavity module were done using TBCI [6]. The RF coupler, the flutes on one of the beam tubes, and ferrite were not taken into account. Moreover, the cavity module had to taper to two different beam pipe cross-sections, because of variation in the CESR vacuum chamber dimensions. We averaged TBCI results for bunches travelling in each direction to obtain the "irreversible" contribution. We found that the cavity's loss factor is larger than that of the tapers for long bunches ($\sigma_f > 1.4$ cm), but smaller for short bunches.

We did further calculations with ABCI, the latest version of which has such advantages as a moving mesh, an improved method for calculating the wake potentials, and variable radial mesh size. ABCI results for the geometry used in [6] are consistent with the TBCI results.

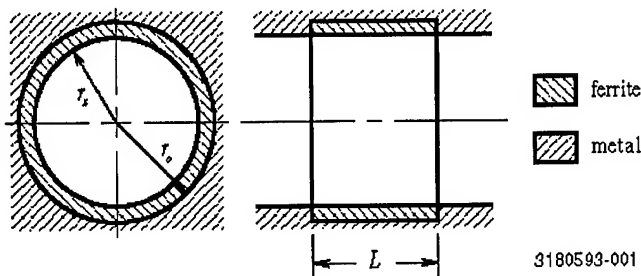


Figure 4. Simplified geometry of the HOM load for AMOS: $L = 101.6$ mm, $r_x = 114.0968$ mm, and $r_o = 117.2718$ mm.

B. The Loss Factor of the HOM Load

As mentioned above, the new HOM loads have ferrite tiles attached to copper plates which are placed at a slightly smaller radius than that of the beam tube. At present AMOS deals only with the axisymmetric case when a lossy material fills an outward protrusion in the beam pipe. Therefore we used the modified geometry shown in Figure 4 for the calculation.

The predicted loss factors for the cavity module (ABCI) and the HOM load (AMOS and analytical) are shown in Figure 5.

IV. LOSS FACTOR MEASUREMENTS IN A BEAM TEST

We measured the temperature of the input and output cooling water for each HOM load, along with the water flow rate. The values yield the power transferred to the water from the ferrite:

$$P = \sum_{i=1}^2 \dot{V}_f^i C \rho (T_{out}^i - T_{in}^i),$$

where P is the power transferred to the cooling water from the ferrite of two HOM loads; \dot{V}_f is the water flow rate; C is the specific heat capacity of the water; ρ is the water density; T_{out} and T_{in} are the output and input temperatures of the cooling water.

This power should be approximately equal to the power lost by the beam due to its interaction with the cavity structure below the cutoff frequencies of the beam pipes because (i) in our HOM load design (Figure 2) other heat transfer mechanisms (conduction through the copper plate to the stainless steel shell, and heat radiation) should not give a significant contribution in comparison with water cooling, and (ii) the HOMs with resonance frequencies below cutoff frequencies of the nearby beam pipes (2.2 GHz and 3.4 GHz) are trapped inside the accelerating structure, so all their energy should be dissipated in the lossy material of the HOM loads.

We used two different sets of CESR optics to obtain bunch lengths between 10 and 25 mm. Some machine parameters for these optics are given in Table 1. Uniformly-filled bunches were used. Most measurements were done with one bunch or 9 bunches. For uniformly-filled bunches, the loss factor is given by

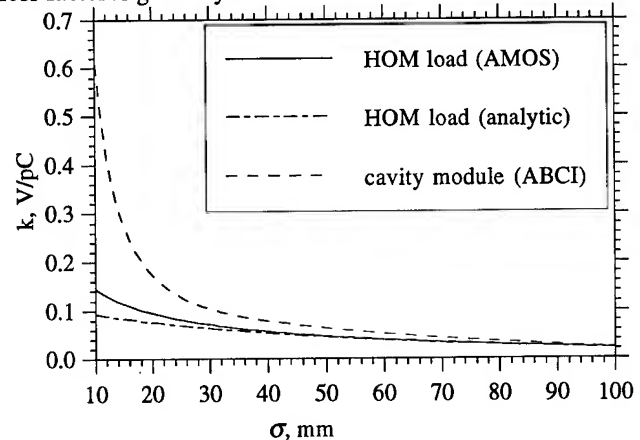


Figure 5. The calculated loss factor of the cavity module (ABCI), and HOM load (AMOS and analytical) as a function of bunch length.

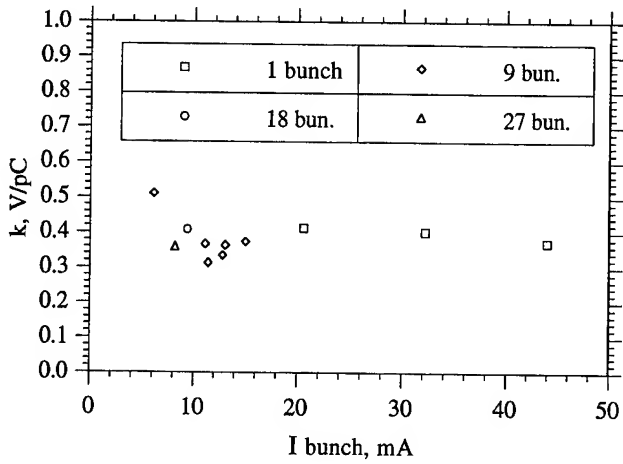


Figure 6. The loss factor of the SRF cavity vs. current per bunch.

$$k = \frac{N P f_{rev}}{I_o^2},$$

where I_o is the average beam current; f_{rev} is the revolution frequency; N is the number of bunches.

We do not have a bunch length monitor for CESR, but previous measurements [13, 14] indicate that there is no bunch lengthening in the storage ring; so we can calculate bunch length via

$$\sigma_l = \frac{\alpha c}{\Omega_s} \cdot \frac{\sigma_E}{E_o},$$

$$\Omega_s^2 = \omega_{rev}^2 \cdot \frac{\alpha h e \sqrt{V_{RF}^2 \cdot (U_o/e + U_{coh}/e)^2}}{2\pi E_o},$$

where α is the momentum compaction factor; c is the speed of light; Ω_s is the synchrotron frequency; σ_E/E_o is the relative energy spread; h is the RF harmonic number, E_o is the beam energy; V_{RF} is the RF voltage; U_o is the energy loss per turn due to synchrotron radiation; and U_{coh} is the coherent energy loss per turn due to the total loss factor of the ring.

To verify that we do not have bunch lengthening, the loss factor was plotted as function of bunch current for the same machine optics (high energy lattice) and RF voltage (Fig. 6). The theoretical bunch length σ_l is equal to 15.3 mm for this case. One can see that the loss factor does not depend on current, i.e. there is no evidence of the bunch lengthening.

The experimental results for the loss factor versus bunch length are compared with the predictions in Figure 7. One can see that there is some disagreement for the shortest bunch length. That disagreement may be due to propagation of some portion of the HOM power into the beam pipes for frequencies

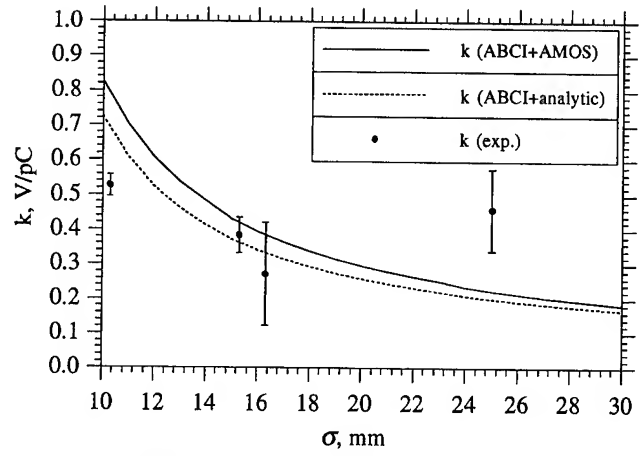


Figure 7. The loss factor of the SRF cavity assembly (experimental data and prediction).

above cutoff. Also, there is a big disagreement for the 25 mm bunch length. That data point was obtained with the low-energy CESR lattice, using only the SRF voltage (the CESR NRF system was switched off and the NRF cavities were detuned). Unfortunately, the accelerating voltage was not high enough to allow us make measurements with high beam current: the total current was limited to 29 mA in 9 bunches due to poor life time. Therefore the signal was small and this data point may have a big systematic error.

V. CONCLUSIONS

The calorimetric method was successfully applied to measure the loss factor of the superconducting cavity assembly in the CESR beam test. The results are consistent with predicted values.

VI. REFERENCES

- [1] H. Padamsee, et al., *Conf. Record of the 1991 Part. Accel. Conf.*, Vol. 2, p. 786 (1991)
- [2] H. Padamsee, et al., *Particle Accelerators*, Vol. 40, p. 17 (1992)
- [3] D. Moffat, et al., *Proc. of the 1993 Part. Accel. Conf.*, Vol. 2, p. 763, (1993)
- [4] H. Padamsee, et al., *Proc. 4th Europ. Part. Accel. Conf.*, Vol. 3, p. 2048 (1994)
- [5] H. Padamsee, et al., *these proceedings*
- [6] V. Veshcherevich, et al., *SRF-931013/11* (1993)
- [7] W. Hartung, et al., *Proc. of the 1993 Part. Accel. Conf.*, Vol. 2, p. 3450 (1993)
- [8] D. Moffat, et al., *Proc. of the 1993 Part. Accel. Conf.*, Vol. 2, p. 977 (1993)
- [9] T. Weiland, *DESY 82-015* (1982)
- [10] Y. H. Chin, *Proc. of the 1993 Part. Accel. Conf.*, Vol. 2, p. 3414 (1993)
- [11] Y. H. Chin, *LBL-35258, CBP Note-069, CERN SL/94-02 (AP)*
- [12] J. DeFord, et al., *Proc. of the 1989 IEEE Part. Accel. Conf.*, Vol. 2, p. 1181 (1989)
- [13] E. B. Blum, et al., *Nucl. Instr. and Meth.*, Vol. 207, p. 321 (1983)
- [14] Z. Greenwald, et al., *Conf. Record of the 1991 Part. Accel. Conf.*, Vol. 2, p. 1246 (1991)

Table 1. Selected Parameters of the CESR Storage Ring

Parameter	High Energy Lattice	Low Energy Lattice
Revolution frequency	390.14788 kHz	
Beam energy	5.265 GeV	4.400 GeV
SR energy loss per turn	1.0105 MeV	0.4928 MeV
Momentum compaction	0.01142	0.00926
Energy spread	$6.122 \cdot 10^{-4}$	$5.116 \cdot 10^{-4}$

CONTROL OF TRAPPED ION INSTABILITIES IN THE FERMILAB ANTIPROTON ACCUMULATOR

Steven J. Werkema, Fermi National Accelerator Laboratory[†], Batavia, IL 60510 USA

Significant progress has been made in the control and understanding of trapped ion induced instability in the Fermilab Antiproton Accumulator. In addition to a clearing electrode system, a novel method of clearing Hydrogen ions by lightly bunching the beam with RF has been developed. These ion clearing techniques have eliminated trapped ion induced instability as a limiting factor in antiproton source performance. A brief description of these techniques and why they work is presented in this paper.

I. INTRODUCTION

The residual gas in the Fermilab Antiproton Accumulator is ionized by coulomb interactions with the antiprotons in the beam at a rate of one unit of charge per antiproton every 2 to 5 seconds. The production process imparts substantially less than thermal transverse energy to the resultant ions [1]. The ions, therefore, will have a Maxwellian velocity distribution at the temperature of the vacuum chamber. Virtually all the ions produced in this manner are trapped in the space charge potential well of the antiproton beam where they will oscillate at a frequency which, among other things, depends on the mass and charge of the ion (see Equation 3).

Approximately half of the ions produced are hydrogen. The mass and charge of hydrogen ions (H_2^+ and H^+) is such that, over a large range of beam sizes and intensities, the frequency of ion oscillations about the center of the beam will coincide with the low order betatron resonance frequencies of the beam. The motion of hydrogen ions will therefore drive coherent oscillation of the beam [2].

II. MEASUREMENT OF TRAPPED ION EFFECTS

It is difficult to directly observe any parameter of the ion motion in the beam. What is usually observed are beam phenomena caused by ion motion. The impact of trapped ion motion on global accumulator beam parameters such as transverse emittance and betatron tune, have been described elsewhere [3],[4]. More directly connected to the ion motion is the beam coherent oscillation spectrum induced by the motion of ions in the beam. A determination has been made of which beam oscillation modes the trapped ions couple to. Measurements of the transverse beam transfer function have also been made at the beam dipole betatron resonance frequencies both in the presence of trapped ions and without trapped ions.

[†] Operated by the Universities Research Association, Inc under contract with the U.S. Department of Energy.

A. Beam Coherent Oscillation Spectrum

The transverse coherent oscillation spectrum of the antiproton beam induced by the motion of trapped ions is shown in Figure 1.

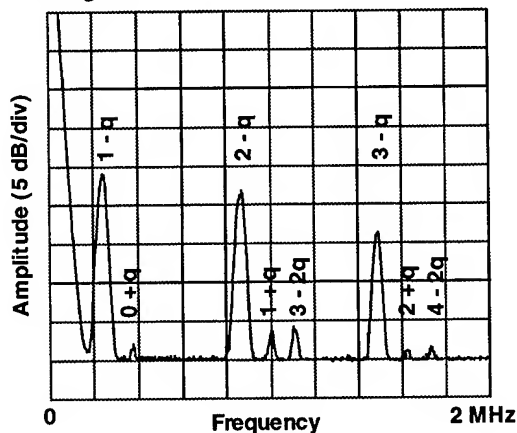


Figure 1: Ion driven horizontal coherent oscillation spectrum. q is the fractional part of the betatron tune.

The spectrum includes both slow and fast wave dipole oscillation. There is also an indication of quadrupole motion (i.e. the $3-2q$ and $4-2q$ lines). This spectrum was measured using transverse dipole pickups and differentially driven electronics which attenuate common mode signals, such as quadrupole oscillation, by at least 27 dB. Therefore, it can be concluded that the amplitude of the quadrupole motion is very large. Transverse beam quadrupole oscillation is in fact an expected and serious consequence of the presence of trapped ions [5].

B. Beam Transfer Function Measurements

The motion of ions in the beam and the coupling of the ions to the dynamics of the beam is non-linear [2]. The non-linearity is manifest in the transverse beam transfer function. Figure 2 shows the transverse response of 52 mA of protons circulating in the antiproton accumulator. Due to the positive charge of the beam, no trapped ion effects are expected.

By contrast, Figure 3 shows the transverse response for 68 mA of antiprotons. The double peaked characteristic is believed to be due to the influence of trapped ions on the response of the beam to a transverse stimulus. This effect is enhanced if any of the various ion clearing mechanisms are made less effective or turned off (see Figure 4). This characteristic is observed up to very high frequencies (up to ~100 MHz).

A self consistent theory which explains the details of the ion modified beam transfer function is still under development [6]. The double peaked feature may be qualita-

tively understood by considering the non-linearity of the ion motion in the beam.

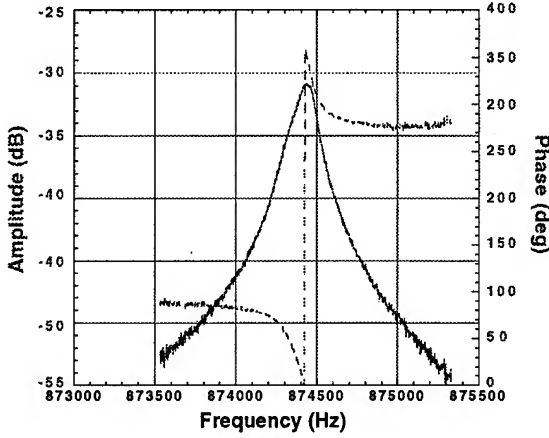


Figure 2: Beam transfer function at the $(2-q)f_{rev}$ resonance with 52 mA of protons in the accumulator.

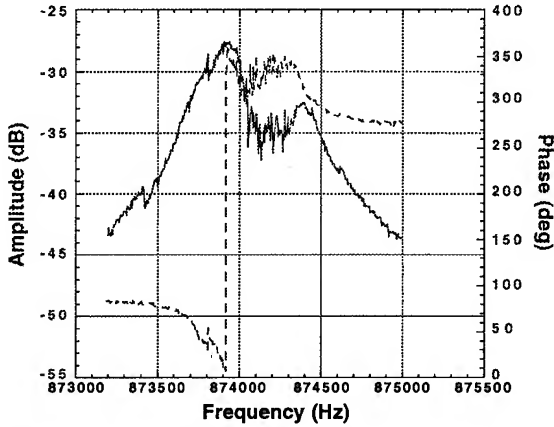


Figure 3: Beam transfer function at the $(2-q)f_{rev}$ resonance with 68 mA of antiprotons in the accumulator.

For a transversely cylindrical Gaussian beam of width σ in a vacuum chamber of infinite radius, the radial electric field due to the beam line charge density λ is given by:

$$E(r) = \frac{\lambda}{2\pi\epsilon_0} \frac{1 - e^{-r^2/2\sigma^2}}{r} \quad (1)$$

The equation of motion, to second order in r/σ , for an ion of charge to mass ratio Z/A in the presence of this field is:

$$Am_p \ddot{r} = ZeE(r) \quad (2)$$

$$\ddot{r} + \left[\omega_b^2 - \frac{1}{4} \left(\frac{r}{\sigma} \right)^2 + \dots \right] r = 0$$

m_p is the proton mass. ω_b is the ion linear bounce frequency, and is given by:

$$\omega_b = \sqrt{\frac{Z}{A} \cdot \frac{e|\lambda|}{4\pi\epsilon_0 m_p \sigma^2}} \quad (3)$$

All higher order terms in Equation (2) are even powers of r/σ . Thus, large amplitude motion occurs with a smaller oscillation frequency than the zero amplitude motion.

During a beam transfer function measurement the beam is driven near its resonant frequency by a network

analyzer. The ensuing transverse oscillation of the beam drives the ion motion at that frequency to larger amplitudes [7] causing a downward shift in the ion oscillation frequency. This depletes the ion population oscillating near the beam resonance. The effect of the network analyzer drive is to temporarily increase the transverse stability of the beam by depopulating the ion distribution near the beam resonance.

III. CLEARING TRAPPED IONS BY RF MODULATION OF BEAM

To date, the most successful strategy for dealing with trapped ion instabilities in the Fermilab Antiproton Accumulator has been to eliminate the ions from the beam. There are two primary techniques in routine use which accomplish this. The first technique is the use of clearing electrodes placed at most of the longitudinal minima in the beam space charge potential [4]. The clearing electrodes allow operation of the Antiproton Accumulator up to antiproton intensities of approximately 130 mA.

The second ion clearing technique is to destabilize the ion motion by modulating the line charge density of the beam by the application of a small amount of RF voltage. Ion clearing with RF has permitted stable operation the Accumulator with antiproton intensities as high as 220 mA (the intensity limit has not yet been reached).

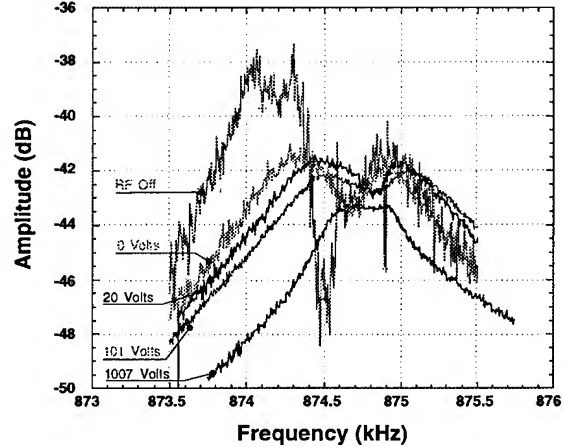


Figure 4: Beam transfer function at the $(2-q)f_{rev}$ resonance with 132 mA of antiprotons in the accumulator. The voltage of the ion clearing RF system is varied from OFF to 1007 V.

The impact of RF ion clearing on the transverse stability of the beam is illustrated in Figure 4. As the RF voltage is increased the magnitude of the beam response is reduced and the beam response approaches the linear/ion-free response shown in Figure 2. The removal of ions from the beam also gives rise to a defocusing tune shift which is evident from the increase in the frequency of the maximum response as the RF voltage is raised.

An important property of RF ion clearing is that most of the stabilizing benefit is realized just by turning the RF

system on[†]. Relatively little stability is gained by further turning up the RF voltage. This feature of RF ion clearing is not quantitatively understood.

A. Stability of Small Amplitude Ion Motion

In order to understand the effect of a small RF modulation of the beam on the ion motion it is instructive to begin with small amplitude motion such that the non-linear terms in Equation (2) are negligible. To account for the bunching of the beam, λ in Equations (1) and (3) is replaced with $\lambda = \lambda_0(1 - \delta \cos \omega_{RF} t)$, where δ is the fraction of the beam in the RF bucket, and $\omega_{RF} = 2\pi h f_{rev}$. The RF harmonic, h , is 2 for the results presented in this paper. With this modification Equation (2) becomes:

$$\ddot{r} + \omega_b^2(1 - \delta \cos \omega_{RF} t)r = 0 \quad (4)$$

Making the change of variable $x = \omega_{RF} t / 2$, the linearized equation of motion becomes:

$$\frac{d^2 r}{dx^2} + (a - 2q \cos 2x)r = 0 \quad (5)$$

where

$$a = 4 \left(\frac{\omega_b}{\omega_{RF}} \right)^2 \quad \text{and} \quad q = \frac{a\delta}{2} \quad (6)$$

Equation (5) is the Mathieu equation. A pertinent property of the Mathieu equation is that the motion is unbounded for certain regions in (a, q) parameter space. The condition that ion motion is unstable at the $(n - q)f_{rev}$ resonance of the beam for all values of the bunching parameter δ is given by:

$$a = 4 \left(\frac{n - q}{h} \right)^2 = 1, 4, 9, \dots \quad (7)$$

This condition is not met at the three modes most relevant to ion induced instability (see Figure 1). Accordingly, small amplitude ion motion is stable.

B. Monte Carlo Analysis of Trapped Ion Motion

In order to investigate the nature of relatively large amplitude ion motion a Monte Carlo simulation of the ion motion was written which numerically solves the non-linear equations of motion in a vacuum chamber of finite radius. The simulation generates the initial ion positions according to a Gaussian distribution with the same σ as the beam. The beam σ is chosen to give a linear ion bounce frequency equal to the frequency of a beam resonance. The initial ion velocities are generated according to a 300°K Maxwellian distribution. A simulated ion is tracked until it has either undergone many thousands of oscillations or is lost to the vacuum chamber wall.

The results of the Monte Carlo suggest that RF modulation of the beam has the effect of shrinking the amplitude range for stable ion motion. Deeper RF modulation results

in a smaller stable phase space area for ion motion (see Figure 5).

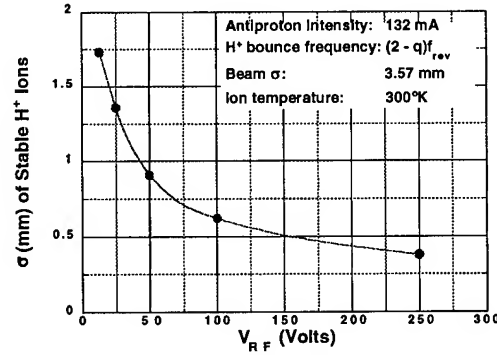


Figure 5: Width of the ion initial amplitude distribution for stable simulated ion motion as a function of applied RF voltage. At 250 Volts, approximately 92% of the beam is bunched.

The Monte Carlo also shows that RF clearing is ineffective for clearing heavy ions ($\frac{Z}{A} < \frac{1}{2}$). Cleared hydrogen ions will therefore be replaced by heavier, less harmful, ion species. Any pockets of ions which are not cleared by the clearing electrode system will be partially neutralized by ions which do not adversely impact beam stability.

IV. REFERENCES

- [1] P. Zhou, A Study of Ion Trapping and Instability in the Fermilab Antiproton Accumulator, Ph.D. Thesis, p8-11, December (1993).
- [2] P. Zhou, P. Colestock, and S. Werkema, Trapped Ions and Beam Coherent Instability, Proceedings of the 1993 Particle Accelerator Conference, p3303, May (1993).
- [3] S. Werkema, D. Peterson, and P. Zhou, Transverse Emittance Growth in the Fermilab Antiproton Accumulator with High-Current Antiproton Stacks, Proceedings of the 1993 Particle Accelerator Conference, p3573, May (1993).
- [4] S. Werkema, K. Fullett, and P. Zhou, Measurement of Trapped Ion Pockets and Control of Ion Instabilities in the Fermilab Antiproton Accumulator, Proceedings of the 1993 Particle Accelerator Conference, p3309, May (1993).
- [5] R. Alves-Pires, et. al., On the Theory of Coherent Instabilities due to Coupling between a Dense Cooled Beam and Charged Particles from the Residual Gas, Proceedings of the 1989 IEEE Particle Accelerator Conference, p800, March (1989).
- [6] J. Myra, et. al., Quasilinear Theory of Trapped Ions, Beam Emittance Growth and Trapped Ion Removal in Antiproton Storage Rings, Paper in preparation (1995).
- [7] R. Alves-Pires and R. Dilão, Elimination of Transverse Beam Instabilities in Accumulation Rings by Application of an External Periodic Force, Phys. Rev. A45, p2567, February (1992).

[†] When the RF cavity is off it is also shorted. When the cavity is turned on the beam will see some small voltage due to excitation of the cavity by the beam.

LONGITUDINAL EMITTANCE OSCILLATION IN A SUPERCONDUCTING DRIFT TUBE LINAC

J.W. Kim and K.W. Shepard, Argonne National Laboratory, Argonne, IL 60439 USA

In drift tube linacs a beam energy spread results from the finite beam size. Radial variation of the axial accelerating field induces a beam energy spread, which, in general, will accumulate as the beam passes through successive drift tubes. This paper shows that under some conditions of periodic transverse focusing and longitudinal phase focusing, the correlation between the longitudinal and transverse motion can be used to correct the energy spread. The process of achieving such a correction is first described in a simplified situation, and then demonstrated for a particular tuning using a ray-tracing program which models a low velocity and low charge state linac designed for radioactive ion beams.

I. INTRODUCTION

The design of an ISOL-type radioactive beam facility utilizing the present ATLAS accelerator as a secondary beam accelerator is described in several papers at this conference [1] [2]. One requirement for such a project is a low charge state injector linac for the ATLAS superconducting linac. A key issue with such an injector linac is to maintain small longitudinal emittance while maximizing transverse acceptance. These two requirements tend to conflict since acceleration of a finite size beam through a drift tube linac increases the beam energy spread because of radial variation of the accelerating field. The variation is quadratic in the lowest order, causing longitudinal beam quality to deteriorate rapidly with increasing beam radius. The beam energy spread is inversely proportional to the wavelength of the slow wave in the drift tube structure, thus becoming worst at low particle velocities.

The longitudinal emittance increase could in principle accumulate throughout the acceleration process. However, by proper matching of longitudinal phase focusing to the periodic transverse focusing structure, emittance growth can be limited by using the correlation between longitudinal and transverse phase spaces. This process is clearly manifested in numerical ray-tracing studies performed in the design of the low charge state ($q/A \geq 1/66$), low velocity ($\beta \geq 0.004$) injector linac described in reference [2]. In what follows, first a simplified version of the correction mechanism is described, and then numerical ray-tracing results are presented.

II. A MECHANISM OF LONGITUDINAL EMITTANCE CORRECTION

Figure 1 shows schematically a linac in which transverse focusing elements alternate with short drift tube accelerating structures, resonant cavities, which are operated in a phase focusing mode. The cell length is $l_{cell} (=l_{res} + l_{drift})$, and the stability

condition of transverse motion in such a structure is that $f/l_{cell} \geq 1/4$, where f is the focal length [3].

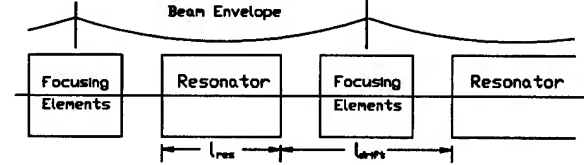


Figure 1: A periodic focusing structure in a drift tube linac along with a matched beam envelope.

In considering the behavior of a beam through the structure, we make several simplifying assumptions. First, the transverse focal length is a half of the cell length so that the phase advance of the transverse motion is 90° , which implies that all particles have the same radial displacements every other cell. Second, we consider only the energy spread induced by the first and third resonators (i.e. assume the second resonator has no radial variation in accelerating field).

A correction mechanism is depicted in Figure 2 for a three cell structure. The upper graphs show the longitudinal phase space, and the lower graphs display the correlation, showing energy spread versus radial displacement. Figure 2 (a) shows a beam energy spread induced at the first resonator. The longitudinal emittance increase is indicated by shading. On going through the second resonator, shown in Figure 2 (b), the matched phase focusing action of the resonator effectively inverts the energy spread. On arrival at the third resonator, the particles have advanced 180° in transverse motion so that the particles repeat the displacement they had in the first resonator, but the energy spread is inverted. The beam bunch is thus effectively 'pre-compensated' for the radial variation in energy gain about to be experienced in traversing the third resonator. The beam energy spread is then perfectly corrected at the third resonator as shown in Figure 2 (c).

We can examine the action of the second resonator more quantitatively as follows. We define $U(\phi_{op})$ to be a slope of the energy gain versus operating phase angle at ϕ_{op} . An approximate condition for matched phase focusing for ions of velocity β is then

$$U(\phi_{op}) \simeq \frac{A m c^3 \beta^3}{q \omega l_{cell}}, \quad (1)$$

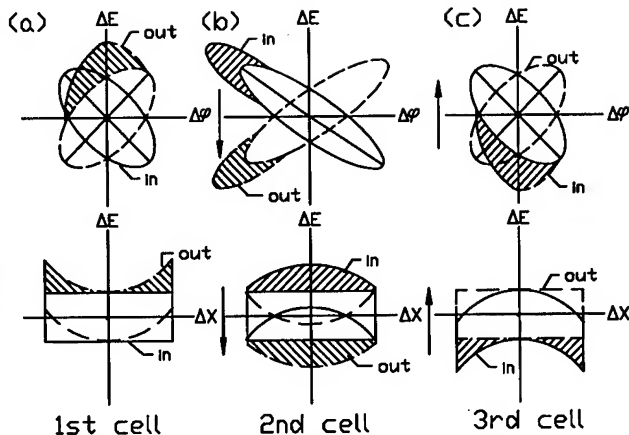


Figure 2: A simplified model for demonstrating the mechanism for correcting the energy spread resulting from radial variation of the accelerating field. The solid line indicates the phase space at the entrance of the resonator, and the dashed line at the exit. See the text for details.

where ω is the angular radio frequency. This condition can be satisfied by adjusting the operating phase angle ϕ_{op} . The above relation has two implications of interest:

1) in going to low particle velocities, we must reduce the drift length, or $U(\phi_{op})$ by shifting the operating phase angle closer to the maximum energy gain phase (e.g. see Figure 3 in the next section),

2) in going to smaller q/A , however, we require stronger phase focusing for matching, which requires increasing the operating phase angle,

In the present application, 2) above is beneficial in allowing the operating phase angle to be sufficiently large to provide good linearity in the phase focusing. These effects have been observed with the ray-tracing calculations in a low charge state linac described in the next section.

When the phase focusing is not well matched to the linac structure, emittance correction is weaker, and correction period spreads out over more cells.

III. NUMERICAL SIMULATIONS

The above corrective process clearly appears in numerical simulations of a proposed low energy injector linac for ATLAS [2]. Phase space motion in such a linac was calculated using a ray-tracing program developed at ATLAS. The design particle is $^{132}\text{Sn}^{2+}$, and the initial velocity (β) is 0.008. The focusing element is a quadrupole triplet, perfect quadrupole fields with hard edges being assumed in the program. A realistic quadrupole design [4] can give a phase advance of 60° with $f = l_{cell}$. The drift tube structures modeled in the program are the quarter wave superconducting resonators used at the low energy end of PII linac at ATLAS [5]. The linac parameters which are input to the pro-

Table 1: Input parameters for the ray-tracing program

Resonator	48.5 MHz, 4 gap
β_{in}, ϕ_0	0.008, -20°
Quadrupole strength	350 T/m
Triplet length (cm)	(Q1,Q2,Q3)=(4,7,4)
l_{res}, l_{drift}	14 cm, 29 cm
β_{out} , after 7 resonators	0.013

gram are listed in Table.1. The operating phase and energy gain relationship of the I1-type resonator is shown in Figure 3 for $^{132}\text{Sn}^{2+}$ at a mean energy gain of 4.5 MeV/m. The slope $U(\phi_{op})$ is roughly 0.2 MeV/rad/q at an operating phase of -20° , which satisfies the condition (1) for β near 0.009.

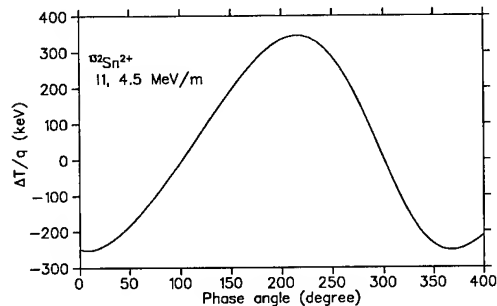


Figure 3: The operating phase angle-energy gain curve of I1 resonator for $^{132}\text{Sn}^{2+}$ at an average energy gain of 4.5 MeV/m

Figure 4 shows the longitudinal phase space and Figure 5 the coupled phase space at the entrance and exit of the first, second, and fifth resonators. The normalized transverse emittance is $0.6 \pi \text{ mm} \cdot \text{mrad}$, and the longitudinal emittance is $5\pi \text{ keV} \cdot \text{nsec}$. In (a) of Figure 4 and 5 the beam energy spread at the exit of the first resonator is clearly shown. In (b) of Figure 4 and 5 the process of inversion of the energy spread through phase focusing is manifested. In (c) of Figure 4 and 5 we clearly see that the energy spread is cancelled by the effect of the radial variation in energy gain through the fifth resonator.

The longitudinal emittance on the first seven resonators of the injector linac is displayed in Figure 6. The emittance increase and correction extends over the first five resonators. In fact the emittance correction process continues throughout the linac ($0.008 \geq \beta \geq 0.03$), and longitudinal emittance appears to be oscillatory [2]. The oscillation amplitude becomes larger for a beam having larger transverse emittance.

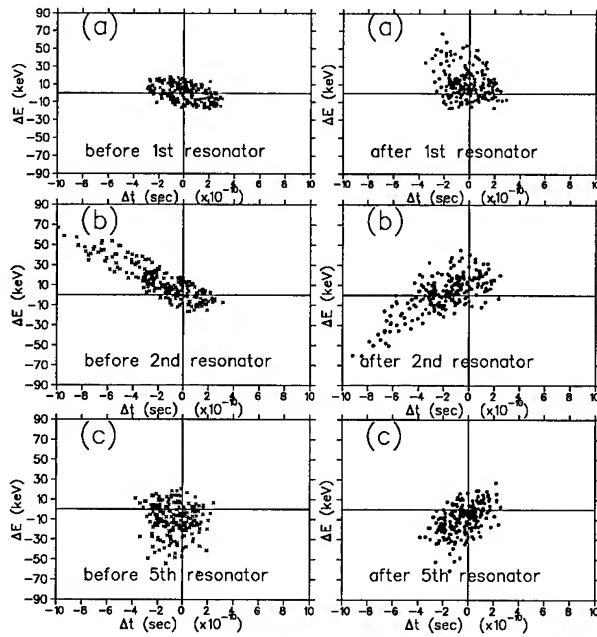


Figure 4: Longitudinal phase spaces at the entrance and the exit of the first, second and fifth resonators shown in the left and right graphs, respectively.

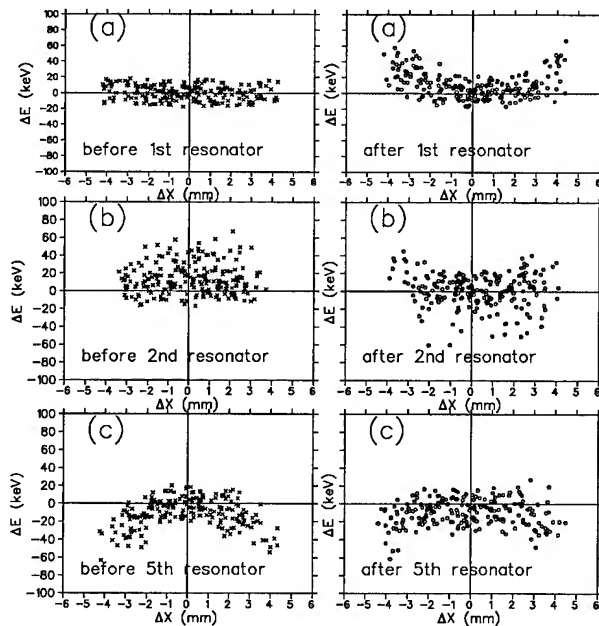


Figure 5: Coupled phase spaces displayed for the corresponding resonators of Figure 4

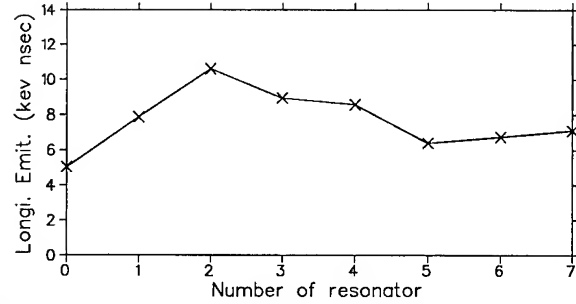


Figure 6: Longitudinal emittance in the first seven resonators of the injector linac.

IV. CONCLUSION

If the beam size is sufficiently smaller than the wavelength of the slow wave, a beam energy spread due to non-linear radial variation of energy gain in a drift tube linac can be negligible. However, for low q/A ions at low energies it can be difficult to obtain transverse focusing to insure an adequately small beam. The resulting emittance growth can be corrected using the correlation between transverse and longitudinal phase spaces that we have discussed. This correlation is beneficial for the design of a low energy injector for a radioactive beam facility proposed at ANL, in which high beam quality and large transverse acceptance are essential.

References

- [1] J. Nolen, Accelerator Complex for a Radioactive Ion Beam Facility at ATLAS, in these proceedings.
- [2] K. Shepard and J. Kim, A low-charge-state injector linac for ATLAS, in these proceedings.
- [3] M. Reiser, *Theory and Design of Charged Particle Beams*, p142, John Wiley & Sons, Inc. (1994)
- [4] J.W.Kim and K.W.Shepard, High Field Superconducting Quadrupole for a Low Charge State Linac, in these proceedings.
- [5] L.M. Bollinger, et.al., Nucl. Instr. and Meth., **A328**, 221 (1993)

ELECTRIC FIELDS, ELECTRON PRODUCTION, AND ELECTRON MOTION AT THE STRIPPER FOIL IN THE LOS ALAMOS PROTON STORAGE RING

M. PLUM

Accelerator Operations and Technology Division
Los Alamos National Laboratory, Los Alamos, NM 87545

The beam instability at the Los Alamos Proton Storage Ring (PSR) most likely involves coupled oscillations between electrons and protons. For this instability to occur, we must have a strong source of electrons, and so we have begun to investigate the various sources of electrons in the PSR. We expect copious electron production in the injection section because this section contains the stripper foil. This foil is mounted near the center of the beam pipe, and both circulating and injected protons pass through it, thus allowing ample opportunity for electron production. In this paper we will discuss various mechanisms for electron production, beam-induced electric fields, and electron motion in the vicinity of the foil.

I. INTRODUCTION

In the PSR, the stripper foil is a 200 $\mu\text{g}/\text{cm}^2$ carbon foil suspended near the center of the beam pipe by a web of carbon fibers. Many electrons are created when both the circulating and injected protons pass through this foil, as shown in Table 1. We have identified four sources: "convoy" electrons stripped from the injected H^0 beam, secondary-emission (SEM) electrons due to the injected and circulating particles passing through the foil, thermionic electrons due to foil heating, and delta-ray (knock-on) electrons due to the injected and circulating protons passing through the foil. We also expect SEM from any beam-pipe surfaces the beam may interact with, and electron-ion pairs from residual-gas ionization.

II. ELECTRON PRODUCTION

The convoy electron-production rate is the same as the incoming H^0 particle rate, minus the 7% to 10% stripping inefficiency. During normal production conditions, the peak

H^0 current is about 10 mA over the 250-ns chopping period, or about 7 mA averaged over the entire macropulse. In contrast to the other electron-production processes, there is no net charge deposited on the foil due to convoy-electron production. The kinetic energy of the convoy electrons is 430 keV.

The SEM coefficient for 800-MeV protons incident on carbon is about 0.006. Our foil has two surfaces, so we expect to see about 0.012 electrons leaving the surfaces of the foil for each proton that passes through the foil. During production conditions [1], the peak rate of SEM emission is about 0.12 A, and the average rate (over a one second interval) is about 270 μA . The SEM electrons have kinetic energies up to about 20 eV.

To get the knock-on-electron production rate, we apply the equations of F. Sauli [2]: the number of electrons created with energy greater than E_0 , in carbon of thickness $\rho t = 200 \mu\text{g}/\text{cm}^2$, from a proton of velocity βc , is

$$N = (0.154 \text{ MeV cm}^2 / \text{g}) \cdot \frac{\rho t}{\beta^2} \cdot \left(\frac{1}{E_0} - \frac{1}{(2.45 \text{ MeV})} \right)$$

We are interested in knock-on electrons with kinetic energies large enough to escape from the foil. If we take the case of a knock-on electron created near the center of the foil, E_0 must be slightly greater than 5 keV for the electron to escape. Using this value for E_0 , $N = 0.004$. The rate of knock-on electron emission from the foil is therefore about one third of the SEM emission rate. The knock-on electrons have kinetic energies up to about 2.4 MeV. The probability of the electron having kinetic energy E is approximately proportional to $1/E^2$, so most of the electrons are concentrated at low kinetic energies.

To calculate the rate of electron emission due to thermionic emission, we note that the peak foil temperature is about 1900 $^\circ\text{K}$ during production conditions. At this temperature the thermionic electron current density is 8.4 $\mu\text{A}/\text{cm}^2$, and even if we assume the entire 16 mm x 16 mm foil is heated this gives us peak current of just 22 μA , about four orders of magnitude less than the peak SEM current. The foil temperature does not change much over the 360-ns period of the PSR. The thermionic current is highly sensitive to the foil temperature – for a foil temperature just 100 $^\circ\text{K}$ higher, the current density will be 45 $\mu\text{A}/\text{cm}^2$. The kinetic energies of these electrons is about 0.24 eV.

Table 1. Electron production per injected H^0 particle.

Electron source	no. per injected H^0	Kinetic Energy.	Average Current
Convoy electrons	1.0	430 keV	75 μA
Secondary electrons	3.6	up to ~20 eV	270 μA
Knock-on electrons from the foil	1.2	up to 2.4 MeV	90 μA
Thermionic electrons	<0.002	~0.24 eV	<0.12 μA
Res. gas electron-ion pairs	0.0037	up to 2.4 MeV	0.28 μA

To calculate the current we expect from residual-gas ionization, we use the simple formula [3] $I_{ION} = n \sigma d I_{BEAM}$. In our case, for production conditions, the gas density $n = 9.7 \times 10^{15} / \text{m}^3$, the ionization cross section $\sigma = 94 \times 10^{-24} \text{m}^2$, the length of the ionization volume $d = 4.5 \text{m}$, and the average current $I_{BEAM} = 5.2 \text{A}$. Using these parameters, the average ionization current $I_{ION} = 21 \mu\text{A}$. The various electron production rates can also be expressed in terms relative to the number of injected H^0 particles, as shown in Table 1. The distribution of kinetic energies for these electrons is similar to the knock-on electrons - up to 2.4 MeV.

III. E-FIELD AT THE FOIL SURFACE

To find out what happens to electrons emitted from the foil, we need to calculate the E-fields. We start by simplifying the problem by assuming that the foil completely covers the beam-pipe aperture, that it is perfectly conducting, and that it is at zero potential. We also assume an electrostatic case, since the beam intensity does not vary much over the distance of several beam-pipe diameters, and since the magnetic field due to the beam is weak (for a 43 A beam passing through a circle of radius 0.5 cm, the B-field at 0.5 cm is only $1.7 \times 10^{-3} \text{Tesla}$). These assumptions simplify the problem enough to allow us to easily calculate the perpendicular component of the electric field at the surface of such a foil. The parallel component of the E-field is of course zero, since we are assuming the foil is perfectly conducting.

To calculate the E-field at the surface of the foil, we assume a uniform, centered distribution of charge of radius b , in a perfectly conducting beam pipe of radius a , that extends in the z direction. The charge density ρ is a function of r and z only. Due to the lack of space, we cannot go into more detail (see ref. 4 for more details), but we have solved [5] Poisson's equation to get the electric potential:

$$\phi_{beam}(r, z, d) = - \sum_{n=1}^{\infty} \frac{2\rho ab J_1(j_{0n} a/b) J_0(j_{0n} r/b)}{\epsilon_0 j_{0n}^3 J_1(j_{0n})^2 \sinh(j_{0n} d/b)} \times$$

$$(\sinh(j_{0n} z/a) - \sinh(j_{0n} (z-d)/a) - \sinh(j_{0n} d/a))$$

where ϵ_0 is the permittivity constant, J_0 and J_1 are Bessel functions, and j_{0n} is the n^{th} zero of J_0 . Figure 1 shows a plot of $\phi_{beam}(0, z, d)$, using realistic parameters from the PSR ($\rho = 2.2 \times 10^{-9} \text{coul/cm}^3$, $a = 7.5 \text{cm}$, $b = 0.5 \text{cm}$, $r = 0$, $z = 0$, $d = 50 \text{cm}$ [larger values of d will not change the result]). We see that once we get about 25 cm away from the foil our potential has reached a maximum of 9800 V, and that the potential climbs very steeply during the first couple of centimeters.

To get the E-field, we differentiate ϕ_{beam} to get

$$E_z(r, z) = - \sum_{n=1}^{\infty} \frac{2b\rho J_0(j_{0n} r/a) J_1(j_{0n} b/a) \sinh(j_{0n} (z-d/2)/a)}{\epsilon_0 j_{0n}^2 J_1^2(j_{0n}) \cosh(j_{0n} d/2a)}$$

Evaluating this expression using the same realistic parameters above, we get $1.2 \times 10^6 \text{V/m}$ for the E-field at the surface of the foil at the center of the beam.

IV. BIASING THE STRIPPER FOIL

Because of the suspected e-p instability, we would like to either prevent electrons from leaving the foil, or efficiently collect them. In most situations the preferred method would be to use clearing electrodes or clearing rings, but with the foil located in the middle of a metal frame, the electric field lines emanating from any clearing electrodes or rings would mostly terminate on the frame, and not on the surface of the foil where we need them. So the solution we adopted was to bias the foil.

However, with an E-field of about 10^6V/m at the surface of the foil, it is very difficult to bias it enough to prevent the SEM and thermionic electrons from boiling off. To calculate the effect of a biased foil, we assume a perfectly conducting "soup can" with one lid biased to a potential V_0 , and solve Laplace's equation. There is no beam present in this calculation. The end result is

$$\phi_{foil}(r, z) = \sum_{n=1}^{\infty} \frac{2V_0}{j_{0n} J_1(j_{0n})} J_0(j_{0n} r/a) \frac{\sinh(j_{0n} z/a)}{\sinh(j_{0n} d/2a)}$$

Figure 1 shows $\phi_{foil}(0, z)$ using our now familiar parameters from the PSR. Differentiating to get the E-field in the z direction,

$$E_z(r, z) = \sum_{n=1}^{\infty} \frac{2V_0}{a J_1(j_{0n})} J_0(j_{0n} r/a) \frac{\cosh(j_{0n} (d/2 - z)/a)}{\sinh(j_{0n} d/2a)}$$

This calculation shows that if we put a 10,000 V bias on the foil, the E-field at the center of the surface of the foil will be about 170,000 V/m. This is not nearly high enough to prevent electrons from leaving the foil, since the field due to the beam is over 10^6V/m . To overcome the field due to the beam, we would need a bias voltage of at least 57 kV! So the best we can do with our present foil ladder is to create a potential well near the surface of the foil, by biasing the foil below the depth of the beam's potential well, which, we see from Fig. 1, is about 10 kV.

From Fig. 1 we see that if the foil is biased with no beam present, low-energy electrons leaving the foil are pushed back onto the foil due to the triangle-shaped potential well. If the beam is present and the foil is grounded, low-energy electrons will be pulled off the foil due to the sharp drop in the potential well caused by the beam. If the beam is present and the foil is biased below the depth of the beam's potential, then we create a potential well a couple of centimeters from the surface of the foil. Low-energy electrons pulled off the foil will be trapped in this well until the proton bunch has gone by, and the electrons will then be pushed back onto the foil to be reabsorbed.

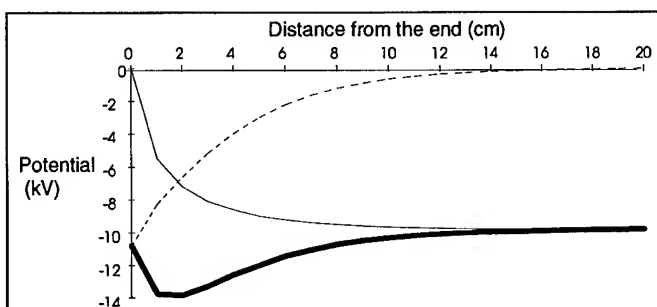


Fig. 1. A plot of the potential due to the beam (solid line), the biased foil (dashed line) and the sum (bold). We assume a 7.5-cm-radius beam pipe with a full-aperture, perfectly conducting foil at one end, a foil bias of 10,000 V, and a beam radius of 0.5 cm with a charge density of $2.2 \times 10^{-9} \text{ C/cm}^3$ (43 A). The dashed line does not contact the y axis at -10,000 because of convergence problems at $z=0$. The polarities of all the potentials have been reversed to make the concept clearer.

V. A RESISTIVE FOIL

Of course the PSR stripper foil is not perfectly conducting. The 16-mm x 16-mm x 200 $\mu\text{g/cm}^2$ carbon postage-stamp foil presently in use at the PSR is supported by about 115 ea. 5-micron-diameter carbon fibers, spaced at 2-mm intervals, and stretched across a rectangular metal frame with inside dimensions of 15.4 cm x 17.0 cm. The fibers form two planes of webbing that support the foil, and the average fiber length between the foil and the frame is about 7.5 cm. We have measured the bulk resistivity of the fibers to be 1.2 m Ω -cm, or 6 k Ω /cm. If we assume the fibers make good electrical contact with the frame and the foil, the total resistance is about 200 Ω . The carbon foil starts out as amorphous carbon with a very high bulk resistivity of about 4 or 5 Ω -cm. It may anneal after spending some time in the beam, and therefore reduce the bulk resistivity, but this effect has not been studied. From all of this we see that the minimum resistance between the foil and the frame is about 200 Ω , and that it could be a lot higher due to marginal electrical contact between the foil and the fibers and between the fibers and the frame. To help minimize the resistance, in 1993 we started using conductive epoxy to fasten the fibers to the frame.

Because of the resistance between the foil and the frame, the potential of the foil will jump around as electrons are emitted from it. If the potential jumps are large enough, they can affect the electrons emitted from the foil. To estimate the magnitude of the jumps, we consider the case of a grounded foil frame, with no cable leading to any test equipment, with a perfectly-conducting foil sitting at the end of a 200 Ω resistor. For a peak SEM and knock-on current of 0.16 A, the potential of the foil should jump up by just 32 V. This is not enough of a change in potential to significantly alter the electron trajectories. The time constant is less than 1 ns, so the time structure of the potential fluctuations match the time structure of the beam.

VI. SUMMARY

We have identified five different sources of electrons in the injection section of the PSR: convoy electrons, SEM electrons, knock-on electrons, thermionic electrons, and electrons from residual-gas ionization. We have characterized these sources with simple calculations of their energies and production rates. The three most prolific sources are the SEM, the knock-on, and the convoy electrons. We have also made some simple calculations of the potential and electric fields in the vicinity of a perfectly conducting, full-aperture, biased stripper foil with a beam passing through it. We found that by biasing the foil, we can create a potential well that will trap low-energy electrons emitted from the foil. This technique has been successfully applied [6] to control the electrons created in the injection section of the PSR.

This paper is just a beginning. More work is needed on modeling the E-field and potential distributions for a resistive foil, modeling the fields for an asymmetric gaussian beam distribution (as opposed to the uniform cylindrical distributions assumed in this note), and modeling the effect of a foil that covers only a fraction of the full aperture. More work is also needed to investigate sources of electrons other than those due to interactions of the beam with the stripper foil.

VII. ACKNOWLEDGMENTS

I would like to acknowledge the help of R. Cooper with solving Laplace's and Poisson's equations.

- [1] Production conditions are characterized by an accumulation time of about 650 μs , a storage time of 10 μs , a rep rate of 20 Hz, and an average current of about 75 μA of 800-MeV protons delivered to the spallation target.
- [2] F. Sauli, "Principles of Operation of Multiwire Proportional and Drift Chambers," CERN 77-09, May 3, 1977.
- [3] G Guinard, "Selection of Formulae Concerning Proton Storage Rings", CERN 77-10, June 6, 1977.
- [4] M. Plum, "Electric Fields, Electron Production, and Electron Motion at the PSR Stripper Foil", PSR Tech Note PSR-94-001, March 10, 1994.
- [5] R. Cooper, private communication.
- [6] M. Plum et. al., "Electron Clearing in the Los Alamos Proton Storage Ring", 1995 IEEE Particle Accelerator Conference, these proceedings.

ELECTRON CLEARING IN THE LOS ALAMOS PROTON STORAGE RING

M. PLUM, J. ALLEN, M. BORDEN, D. FITZGERALD, R. MACEK, T.S. WANG

Accelerator Operations and Technology Division
Los Alamos National Laboratory, Los Alamos, NM 87545

The instability observed in the Los Alamos Proton Storage Ring (PSR) has been tentatively identified as an electron-proton instability. A source of electrons must exist for this instability to occur. The PSR injection section contains the stripper foil, and therefore provides several strong sources of electrons. We have installed an electron clearing system in the injection section to clear out these electrons. The system comprises: 1) a foil biasing system to clear the SEM and thermionic electrons, 2) a pair of low-field bending magnets with a Faraday cup to clear the convoy electrons, and 3) two pairs of clearing electrodes, one upstream and one downstream of the stripper foil, to clear the remaining electrons. In this paper we will discuss the design and performance of the Electron Clearing System, and its effect on the instability. We will also present some results from other charge-collection experiments that suggest there is also substantial electron production in parts of the ring other than the injection section.

I. INTRODUCTION

Electrons are an important issue for the PSR because we suspect our instability is an e-p instability. In this instability, background low-energy electrons are trapped in the space-charge potential of the proton beam. Above a certain threshold, the electrons and protons develop coupled oscillations that grow in time, eventually leading to beam loss. The biggest sources of electrons are probably in the injection section, which contains the 16-mm x 16-mm x 200 $\mu\text{g}/\text{cm}^2$ carbon stripper foil. Because of this foil, we have [1] electrons due to secondary emission (SEM) from the stripper foil, "convoy" electrons stripped from the incoming H^+ beam, thermionic electrons from energy deposition in the stripper foil, and knock-on electrons from interactions of the circulating and injected protons with the stripper foil. We also have residual-gas ionization and SEM from any beam-pipe surfaces the proton beam may interact with. The SEM and thermionic electrons have low energies (a few eV), the convoy electrons have kinetic energies of 430-keV, and the knock-on electrons have kinetic energies that range from a few eV to 2.4 MeV. For each H^0 particle injected into the ring, we expect from the foil 1.0 convoy electrons, 3.6 SEM electrons, 1.2 knock-on electrons, and less than 0.002 thermionic electrons. We also expect about 0.0074 electron-ion pairs created over the length of the section from residual-gas ionization.

II. ELECTRON CLEARING SYSTEM

To control these electrons we built three subsystems, illustrated in Fig. 1: 1) clearing electrodes (two pair) for the ions and electrons from residual gas ionization, and the electrons from SEM off the beam-pipe walls caused by beam halo scraping; 2) a stripper-foil-biasing system to control the thermionic and SEM electrons from leaving the foil; and 3) a bending magnet and Faraday cup for the 430-keV convoy electrons. We will now briefly discuss each of these three subsystems.

III. CLEARING ELECTRODES

The purpose of the clearing electrodes is to clear the charged particles caused by residual-gas ionization and the SEM electrons caused by the beam halo scraping on the beam-pipe walls. These electrodes must create an electric field (E-field) strong enough to overcome the E-field due to the space charge of the beam. In high-intensity machines, these space-charge fields can be considerable. For the PSR the maximum space-charge electric field is about 250,000 V/m. We installed two pair of clearing electrodes, one upstream and one downstream of the stripper foil. Our aluminum electrodes are curved to match the cross section of the beam pipe, and each one covers 90 degrees of the circumference. Each electrode can be biased up to 30 kV. The electrodes upstream of the stripper foil are separated by 10 cm, and the electrodes downstream of the stripper foil are separated by 14 cm. These separations correspond to maximum E-fields of 600,000 V/m and 430,000 V/m, respectively.

IV. STRIPPER-FOIL BIASING

The purpose of the stripper-foil biasing subsystem is to control the SEM, thermionic, and low-energy knock-on electrons emitted from the foil. We cannot simply use clearing electrodes or clearing rings for this purpose, since the foil is suspended in the center of a metal frame, and the E-field created by the electrodes would be strong between the foil frame and the electrodes but weak at the center of the foil, where we need it the most. So we chose instead to bias the stripper foil. With our high beam intensities, the electric field at the center of the surface of the foil is about 1 MV/m [1], assuming a perfectly-conducting, full-aperture foil. We cannot bias it enough to prevent electrons from being pulled off the foil, but if we bias it below the depth of the beam's potential well (≈ 10 kV), we can create a potential well 1 to 2 cm away

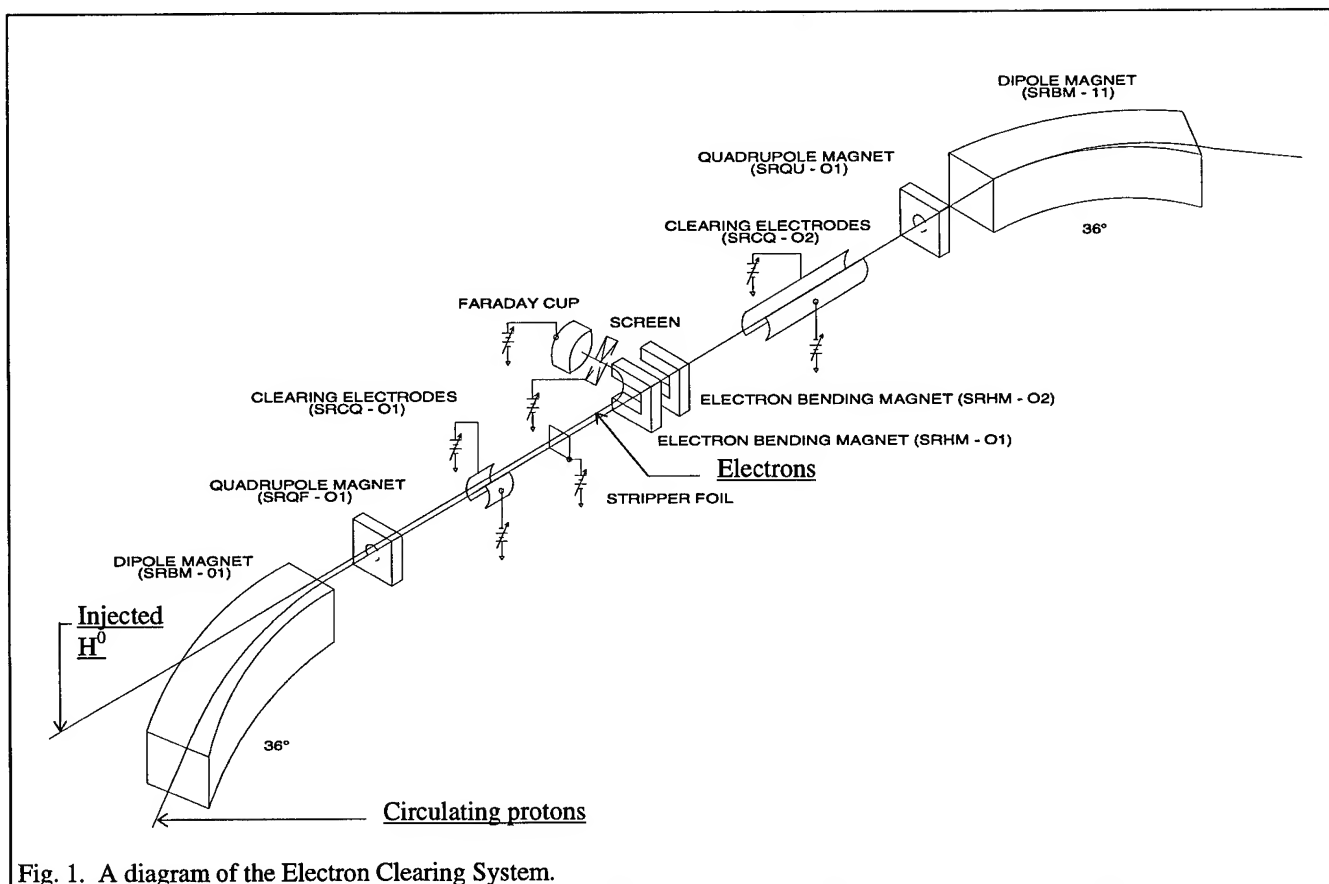


Fig. 1. A diagram of the Electron Clearing System.

from the foil to trap the electrons. Then, when the beam intensity drops at the end of the beam bunch the bias E-field will be strong enough to attract the electrons and reabsorb them. The electrons are therefore cleared after each revolution of the beam around the ring, or about every 360 ns. We can bias the foil up to about 11 kV, limited by the insulating properties of the foil-mounting system.

V. FARADAY CUP

The purpose of the faraday-cup subsystem is to collect the 430-keV convoy electrons. The energy of these electrons is too high to clear with electrodes, so we bend them 90° with a low-field bending magnet into a Faraday Cup. A second magnet identical to the first, but opposite in polarity, and located just downstream of the first, cancels the closed-orbit distortion and the effects of the non-linear magnetic fields. We also installed a screen at the entrance to the Faraday cup, flush with the inside of the beam pipe, to avoid any wake-field effects. We can bias this screen to reduce the SEM effects when the convoy electrons hit the Faraday cup, and also to attract any low-energy electrons and negative ions from within the beam pipe. We found that a Faraday cup bias of +200 V, a screen bias of -100 V, and a magnetic field of 420 Gauss, is sufficient to clear the convoy electrons.

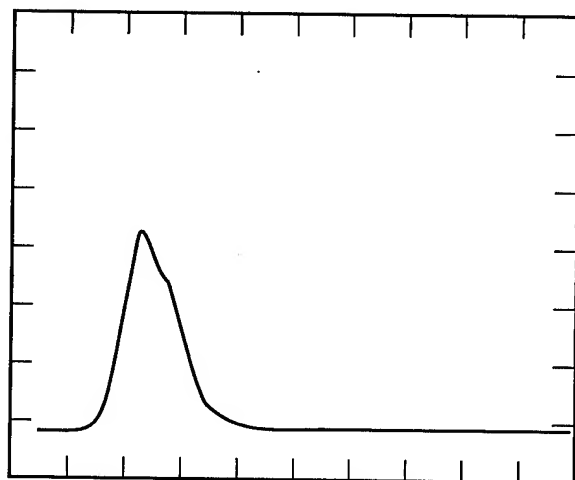
VI. WHAT ABOUT THE DELTA RAYS?

The three subsystems discussed above deal effectively with all the electron sources but one — the delta-ray (or high-energy knock-on) electrons. These electron energies span the range from a few eV to 2.4 MeV. Most of the delta rays from the foil have low kinetic energy, and they will be trapped between the foil and the Faraday-cup magnets, and should eventually be cleared by the biased foil. The medium-energy delta rays will be deflected into the Faraday cup, and the few (about 3×10^{-5} per proton) high-energy delta rays that pass through the Faraday-cup magnets will be lost on the beam-pipe walls. After commissioning the electron-clearing system in 1993, we believe we can collect almost all the electrons created in the PSR injection section (Section 0).

VII. THE RESULTS

During machine development tests in 1993, we performed experiments with both bunched and coasting (dc) beams. Some examples of signals from the stripper foil are shown in Fig. 2. We found that the Electron Clearing System does a good job at effectively clearing the electrons. We found that we can raise the threshold of the coasting-beam instability by about 20%, and increase the growth time of the bunched-beam instability by almost an order of magnitude (but not alter its threshold). The instability was *not* cured. We suspect that

50 mV / div

500 μ s / div

50 mV / div

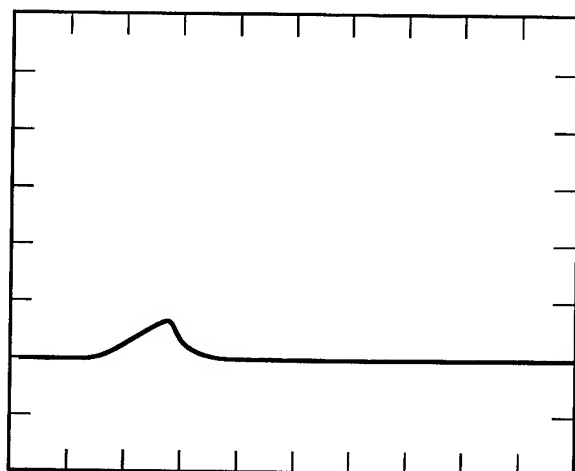
500 μ s / div

Fig. 2. Signals from the stripper foil, using capacitive coupling to the HV cable. The top signal is for 0 V bias, and the bottom signal is for 3 kV bias. Note that biasing the foil reduces the signal caused by electron emission from the foil. Beam parameters: Injection time = 500 μ s, storage time = 300 μ s.

although we were able to clear the electrons from Section 0, there are probably other strong sources of electrons in one or more other sections. To search for other sources, we have initiated a new set of experiments of identify and characterize them.

VIII. OTHER SOURCES OF ELECTRONS

In another section of the ring (Section 3) we have a pinger [2] with two 4-m long electrodes. By biasing the electrodes we can use the pinger as an ion chamber to collect charge from

Charge collected (nC)

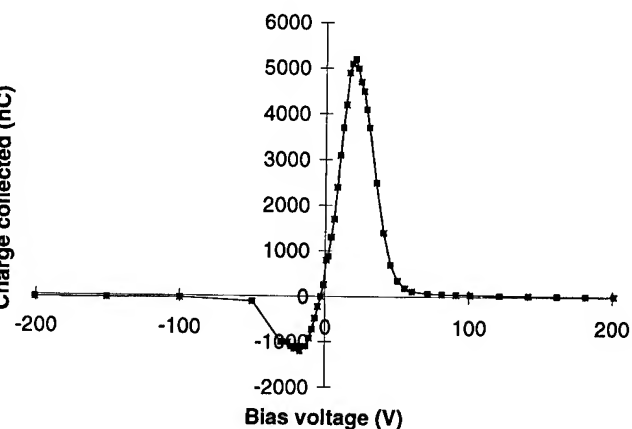


Fig. 3. An example of the charge collected from Section 3 of the PSR. This data was taken during production conditions, with a maximum charge of about 3.75 μ C in the ring. The data remain flat above 200 V and below -200 V.

within the beam pipe. Poisoning the vacuum at low beam intensities gives the result expected for residual gas ionization, but at higher beam intensities we have observed unusual and unexplained results for bunched beams. An example [3] is shown in Fig. 3, where a small change in the electrode biasing makes a big change in the amount of charge collected. In another case, with the same setup, we collected charge equivalent to 25% of the total beam charge in the ring!

IX. SUMMARY

The Los Alamos Proton Storage Ring has an instability at high beam intensities that we have tentatively identified as an e-p instability. We built an Electron Clearing System to attempt to cure the instability. We found that although we effectively cleared the electrons from the most prolific section of the ring, we made only small improvements in the instability threshold. We have identified other, surprisingly strong, sources of electrons, and we are working to understand them.

- [1] M. Plum, "Electric Fields, Electron Production, and Electron Motion at the Stripper Foil in the Los Alamos Proton Storage Ring", 1995 IEEE Particle Accelerator Conference, these proceedings.
- [2] T.W. Hardek and H.A. Thiessen, "A Pinger System for the Los Alamos Proton Storage Ring", 1991 IEEE Particle Accelerator Conference, IEEE Conference Record 91CH3038-7, p. 866.
- [3] M. Plum et. al., "Pinger Ion Chamber Development", PSR Tech Note PSR-94-03, Los Alamos National Laboratory, June 22, 1994.

Advanced Photon Source Insertion Device Field Quality and Multipole Error Specification*

Yong-Chul Chae and Glenn Decker

Argonne National Laboratory, 9700 So. Cass Ave., Argonne, Illinois 60439, U.S.A.

Abstract

The Advanced Photon Source (APS) storage ring is a 7-GeV light source with forty straight sections. Intense x-ray beams will be delivered by insertion devices installed in these straight sections. Installation of insertion devices in the APS storage ring produces several effects which can degrade overall performance. Rigid ring performance requirements exist which can be used to set limits on insertion device field quality, i.e. the first- and second-field integrals of the transverse magnetic field. Individual multipole error specifications can be determined by considering the lifetime of the beam. For nominal operation of the APS storage ring, the vertical aperture corresponding to a 10-hour lifetime is approximately 3.35 mm, which limits the level of multipole error. We find that the skew-octupole error has the most significant effect on the reduction of the aperture; the reasons are discussed in this paper.

I. Introduction

Installation of insertion devices (IDs) into the APS storage ring produces several effects which can degrade overall performance. Rigid ring performance requirements already exist which can be used to set limits on insertion device field quality. Shown in Table 1 is a list of insertion device properties and the storage ring parameters affected.

Table 1
Ring Performance Parameters Affected by Insertion Device Field Quality.

Insertion Device Property	Ring Parameter Affected
Field Integral, $I_{1,y,x} = \int B_{y,x} dl$	Horizontal/Vertical Beam Position Stability
Second Field Integral, $I_{2,y,x} = \int \int B_{y,x} dl dl'$	Horizontal/Vertical Beam Position Stability
Quadrupole Integral, $\int dB_y/dx dl$	Tune, Beam Size
Skew Quadrupole Integral, $\int dB_x/dx dl$	Coupling, Beam Size
Sextupole Integral, $\int d^2 B/dx^2 dl$	Dynamic Aperture, Lifetime
Octupole Integral, $\int d^3 B/dx^3$	Dynamic Aperture, Lifetime

It is important to take into account the anticipated manner of

Work supported by U.S. Department of Energy, Office of Basic Energy Sciences under Contract No. W-31-109-ENG-38.

operation of the insertion devices once they are installed in the ring, specifically the expectation that gaps will be scanned during operation. This places significantly tighter constraints on field quality than for the fixed gap operation, and dictates to a certain extent how the field quality specification should be written. The requirement that the interaction between a given insertion device and other beamlines be consistent with beam stability criterion limits the allowable field errors in that device. The maximum allowable changes in beam properties caused by insertion device operation place the strictest requirements on field quality.

II. Effects of an Ideal Insertion Device

Since in an ideal insertion device (ID) the first- and second-field integrals vanish, the device does not distort the equilibrium orbit. However it is well known that IDs have a vertical focusing effect on the beam. This can be illustrated by writing the Hamiltonian with respect to the oscillating equilibrium orbit suggested by L. Smith [1] as

$$H = \frac{1}{2}(p_x^2 + p_y^2) + \frac{1}{2} \left(\frac{1}{2\rho^2} - \frac{p_x k}{\rho} \sin ks \right) y^2 \quad (1)$$

$$+ \frac{k^2}{12\rho^2} y^4 + \frac{k^4}{90\rho^2} y^6 + \dots,$$

where $k = 2\pi/\lambda_w$, λ_w is the period length, and ρ is the radius of curvature in the ID peak field. If we neglect the fast oscillating (compared to betatron oscillation) term contained in $\sin ks$, we may treat the ID as a long quadrupole with all nonlinear elements lumped at the center. The tracking studies [2] based on this model showed identical results from the full-blown numerical integration through the ID field. The same study also showed that the ultimate dynamic aperture is limited by the nonlinear effects of the ID.

For the Type-A undulator which is one of the major IDs installed in APS storage ring, the effective integrated focusing strength is equal to 242 Gauss, which is two orders of magnitude smaller than the typical quadrupole strength in the ring. Thus, the perturbation of linear lattice functions due to the ID is negligible. However, the effective integrated octupole strength is equal to 600 Gauss/cm², which has a serious effects on the dynamic aperture. In the specification of multipole tolerances of ID, the allowable multipole components will be compared with these values.

III. Field Integral Specifications

A. Beam Position Stability

The fundamental beam performance requirement from which ID field quality specifications can be inferred is beam position stability. This has been stated for the APS storage ring as shown in Table 2.

Table 2
APS Storage Ring Beam Stability Requirements

Δx	$\Delta x'$	Δy	$\Delta y'$
$16 \mu m$	$1.2 \mu rad$	$4.4 \mu m$	$0.45 \mu rad$

These requirements are derived from the need for the beam to be stable to within 10% of its emittance, which translates to 5% of its rms size. Table 2 assumes $\beta_x = 14 m$ and $\beta_y = 10 m$, which are the values at the IDs.

It is important that these stability specifications be interpreted as the maximum amount that the beam position can change with time. For example, it is acceptable to install a device which has a relatively large field integral, provided it does not change with time. If it does change appreciably with time, for example when scanning the gap, several things can still be done to stabilize the beam. First, because the amount of field integral change with gap is approximately known, one can introduce local steering compensation which tracks with gap, producing a net field integral which is independent of gap to the first order. This type of stabilization might be called "open loop" compensation.

It would be imprudent to assume that the open loop compensation of ID steering can be done significantly better than a factor of ten. Therefore, to generate an ID field integral specification guaranteed to meet beam stability requirements without being overly restrictive, the following procedure is proposed. First, compute the amount of field integral for one insertion device which will move the beam around the ring at most by the amounts in Table 2. If we allow the uncompensated field integral to be ten times this amount, stability requirements can be met since it is safe to place a requirement of a factor of ten reduction from open loop compensation.

In fact, the APS storage ring will not have one ID, but rather thirty-four IDs. Because the contributions of these devices to the overall orbit motion is quasi-random, one would expect the net orbit motion to be on the order of $\sqrt{34}$ multiplied by the effect of a single ID. To compensate for this, we will rely on the real-time closed orbit feedback system using the photon beam position monitors. Since $\sqrt{34}$ is less than ten and we can assume that the feedback system will reduce the orbit distortion by a factor of ten, the requirement still can be met. Also, it is unlikely that all 34 beamlines will scan their gaps simultaneously, improving the situation further.

Of all the quantities in Table 2, the restriction on vertical beam motion forms the tightest constraint. Specifically, a change in insertion device field integral, gap open vs. gap closed, of 11.2 Gauss-cm (I_{1x}) will produce $4.4 \mu m$ of vertical beam motion somewhere around the ring. Horizontally, one arrives at 26.5 Gauss-cm of I_{1y} to produce $16 \mu m$ of motion. A conservative specification for the uncompensated field integral, as described above, is therefore 100 Gauss-cm.

Similar arguments for the second field integral indicate that 11,200 Gauss-cm² of I_{2x} will produce $4.4 \mu m$ of vertical beam motion. Also, 37,400 Gauss-cm² of I_{2y} produces $16 \mu m$ of horizontal beam motion. A reasonable requirement for the uncompensated second field integral is therefore 100,000 Gauss-cm²,

or 0.001 Tesla-m².

The results of this section are summarized in Table 3. Specifications both before and after open-loop compensation are stated. Clearly, it is desirable to have insertion devices whose first- and second-field integrals do not require compensation. This may not be realistic, because it is extremely difficult to measure the integrals of B_x in the presence of large B_y .

Table 3
First- and Second-Field Integral Specification.

Quantity	Before Compensation	After Compensation
$I_{1x,y}$	100 Gauss-cm	10 Gauss-cm
$I_{2x,y}$	100,000 Gauss-cm ²	10,000 Gauss-cm ²

B. Good Field Region

The values in Table 3 give the allowable amount of variation with gap of field integrals for particles moving along the geometric axis of the device. An equally important concept is the allowable variation in field integral over a "good field region" at fixed gap. A reasonable "good field region" is $\pm 5 mm$ horizontally, and $\pm 2 mm$ vertically. Considering that the horizontal and vertical beam sizes are $\sigma_x = 330 \mu m$ and $\sigma_y = 89 \mu m$, respectively, this allows for 10 $\sigma_{x,y}$ plus a missteering allowance of 2 mm horizontally and 1.1 mm vertically.

If one could specify that the first field integral not change by more than 10 Gauss-cm over this region, and that the second field integral not change by more than 10,000 Gauss-cm², it would be insured that the compensation would not have to be modified when orbit changes are made. This represents the ideal situation, because it is extremely difficult to construct such a device, or even to confidently measure it without using beam.

Since insertion device photons will be accurately aligned relative to beamline x-ray beam position monitors and held fixed with a high degree of reproducibility from fill to fill, one can specify a more relaxed tolerance, and perform careful first- and second-field integral compensation vs. gap for a signal trajectory through the device. For the APS, the tolerances will be fixed at 100 Gauss-cm and 100,000 Gauss-cm² across $\pm 5 mm$ horizontally and $\pm 2 mm$ vertically, including variation with gap. In terms of the normal (b_n) and skew (a_n) multipole coefficients defined at APS:

$$\int (B_y + i B_x) dl = B_0 L \sum_{n=0}^{\infty} (b_n + i a_n) (x + i y)^n. \quad (2)$$

These requirements translate to $B_0 L b_n = 100$ Gauss-cm, 200 Gauss, 400 Gauss/cm, and 800 Gauss/cm² for $n=0, 1, 2, 3$, respectively. These tolerances should be compared with the lattice magnet tolerances and the effective strength of the ID itself. For example, the tolerances on the quadrupole magnets at APS are $B_0 L b_n = 58$ Gauss, 12 Gauss/cm, and 6 Gauss/cm² for $n=1, 2, 3$, respectively. Recalling the effective strength of the ID is $B_0 L b_1 = 242$ Gauss and $B_0 L b_3 = 600$ Gauss/cm², we can set reasonable tolerances as $B_0 L b_n = 100$ Gauss-cm, 50 Gauss, 200 Gauss/cm, and 600 Gauss/cm². At this stage, the tolerances on skew components can be the same.

This requirement places bounds on allowable multipole components which are necessary, but not sufficient.

IV. Multipole Tolerances

In the previous section we considered the constraints on the field quality based on beam position stability. The other requirements listed in Table 1 will also limit the multipole tolerances. These tolerances should be compared with the allowable multipole components specified in the previous section.

Since the lattice perturbation from the effective quadrupole strength of the ID is negligible, $B_0Lb_1 = 50$ Gauss is acceptable.

The requirement on the vertical beam size is that the change of beam size should be less than 5% of the natural beam size, assuming 10% emittance coupling from the lattice magnets. The corresponding skew quadrupole strength is $B_0La_1 = 157$ Gauss. Thus $B_0La_1 = 50$ Gauss specified in the previous section also satisfies this requirement.

The design beam lifetime at the APS is 10 hours. The study [3] showed that the required vertical aperture is 3.3 mm during nominal operation. Even though the vertical vacuum chamber size (half gap of the ID chamber) is 4 mm, a particle with horizontal oscillation amplitude of 5 mm should be stable within the required vertical aperture of 3.3 mm.

In order to determine the physical aperture including the integrated multipole components in the ID, a tracking study was done. We first studied the effects on the physical aperture due to the individual multipole components, whose strengths are specified in the previous section. The result obtained by using the program RACETRACK [4] is shown in Fig. 1. In the tracking studies, we assume 34 IDs installed in the ring and consider the particle lost if its amplitude is larger than 4 mm at the ID section. From the figure we find that we need to tighten the skew multipole tolerances. The skew multipoles have more effects on reducing the physical aperture because the lattice tunes are close to the sum- and/or difference-resonance line caused by the skew multipoles. After a few iterations we found that the aperture requirement can be met at $B_0Lb_2 = 200$ Gauss/cm, $B_0La_2 = 100$ Gauss/cm, $B_0Lb_3 = 300$ Gauss/cm², and $B_0La_3 = 50$ Gauss/cm². Taking into account all effects, i.e. tune shift, beam size change, dynamic aperture, and beam position stability, we arrive at the reasonably consistent set of multipole tolerances shown in Table 4.

Table 4
ID Integrated Multipole Tolerance Specifications.

n	Normal Component B_0Lb_n	Skew Component B_0La_n
0	100 Gauss-cm	100 Gauss-cm
1	50 Gauss	50 Gauss
2	200 Gauss/cm	100 Gauss/cm
3	300 Gauss/cm ²	50 Gauss/cm ²

A conclusion is that, if the requirements on the first- and second-field integrals are satisfied, the requirement on the mul-

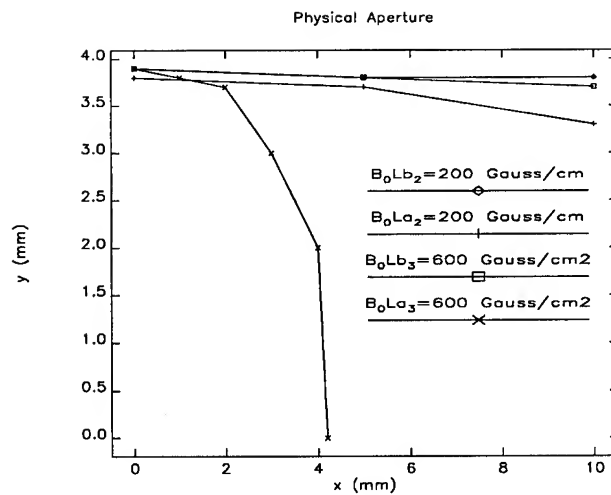


Figure 1
Physical Aperture with Multipole Component.

tipole tolerance is also satisfied.

V. References

- [1] L. Smith, "Effects of Wigglers and Undulators on Beam Dynamics," LBL ESG TECH Note-24 (1986).
- [2] Y.-C. Chae and E. A. Crosbie, "Tracking Studies of Insertion Device Effects on Dynamic Aperture in the APS Storage Ring," *Proc. of the 1993 Part. Accel. Conf.*, Washington, D. C. (1993), also in ANL Report LS-196 (1992).
- [3] H. M. Bizek, *private communication*, (1994).
- [4] F. Iazzourene, et al., "RACETRACK User's Guide, Version 4," Sincrotrone Trieste ST/M-92/7 (1992).

Study of Field Ionization in the Charge Exchange Injection for the IPNS Upgrade*

Yong-Chul Chae and Yanglai Cho

Argonne National Laboratory, 9700 So. Cass Ave., Argonne, Illinois 60439, U.S.A.

Abstract

The proposed 1-MW neutron spallation source is a rapid-cycling synchrotron (RCS) with a design intensity of 1.04×10^{14} protons. A H^- beam from the linac is injected into the synchrotron via the charge exchange process. Due to the high intensity of the beam, the minimization of beam loss is one of the primary concerns. In this paper, we study a possible beam loss associated with field ionization, which includes estimates of the charge fraction and level distribution of the excited hydrogen atoms after stripping, and an estimate of lifetime of the excited hydrogen atoms in the transverse magnetic field.

I. INTRODUCTION

Minimization of beam losses is one of the major goals at the proposed neutral spallation source at Argonne. Among the various injection-loss mechanisms, the beam loss due to field ionization has recently received a great deal of attention after Hutson and Macek at Los Alamos reported that the measured 0.2-0.3% of beam loss at the Proton Storage Ring (PSR) [1] was attributed to field ionization of the $n \geq 3$ excited hydrogen atoms in the 1.2-Tesla bending magnet located downstream of the stripping foil.

If the foil strips the electrons of injected H^- ions completely, we will not have the field-ionization loss. However, for a given foil thickness, the stripping efficiency is less than 100% resulting in the fraction of neutral hydrogen in the various excited states. It is these hydrogen atoms that will be ionized in the magnetic field and, following a wrong orbit, eventually lost.

II. FIELD IONIZATION

Let's consider an energetic hydrogen atom moving through the uniform magnetic field B whose direction is normal to the velocity v . Magnetic field in the lab frame is transformed to mostly electric field in the rest frame according to:

$$F(V/m) = \gamma\beta cB(T), \quad (1)$$

where γ and β are the usual relativistic quantities, c is the speed of light, B is the magnetic field in the lab frame, and F is the electric field in the rest frame. This external electric field puts the hydrogen atom in Stark states.

The Hamiltonian for the hydrogen atom in a Stark state may be written as

$$\begin{aligned} H &= H_0 + H' \\ H_0 &= \frac{p^2}{2m} - \frac{e^2}{r} \\ H' &= -eFz = -eFr \cos \theta, \end{aligned} \quad (2)$$

Work supported by U.S. Department of Energy, Office of Basic Energy Sciences under Contract No. W-31-109-ENG-38.

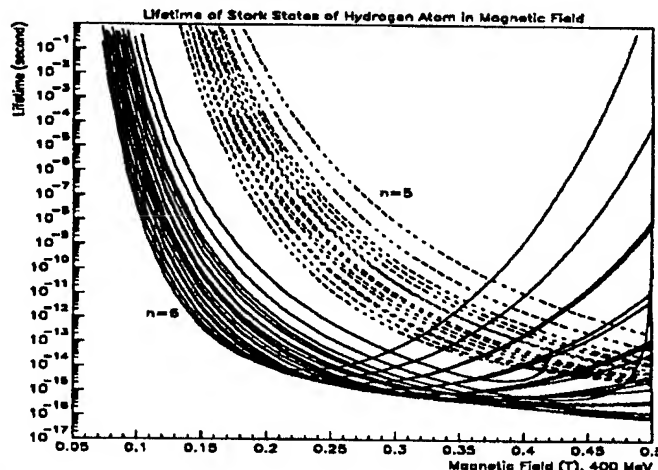


Figure 1
Lifetime of Stark States ($n=5, 6$) of Hydrogen Atom in the Magnetic Field at 400 MeV. (The group of lines represents $n(n+1)/2$ energy states for a given n .)

where we assume the external field is in the z -direction. Due to the external field, the potential well of unperturbed hydrogen atoms is distorted in such a way that the width of the barrier becomes finite, which in turn allows the possibility of ionization via tunneling.

In order to include the effect of ionization in the solution of the Schrödinger equation, Landau [2] introduced the complex energy values defined as

$$E = E_0 - \frac{1}{2}i\Gamma, \quad (3)$$

where E_0 and Γ are two constants, which are positive. The physical significance of the complex energy can be seen by writing the time factor in the wave function of the form

$$e^{-(i/\hbar)Et} = e^{-(i/\hbar)E_0t} e^{-(\Gamma/\hbar)t/2}. \quad (4)$$

It can be seen that the probability of finding the electron inside the barrier decreases with time as $e^{-(\Gamma/\hbar)t}$. Thus Γ determines the lifetime of the state defined by $\tau = \hbar/\Gamma$, whose relation satisfies Heisenberg's uncertainty relation. If we measure the energy state, the spectrum will be centered at E_0 with width Γ . In the literature E_0 is commonly called Stark energy and Γ is linewidth (of the spectrum).

Damburg and Kolosov [3] solved Schrödinger equation in the parabolic coordinate system¹ for E_0 and Γ using the perturbation method. They obtained the series in F for the Stark energy and derived a semiempirical formula for Γ .

Damburg and Kolosov's formula was used to calculate the Stark energy and the lifetime of hydrogen atoms in excited states

¹The choice of parabolic coordinates for the Stark-effect problem is not incidental. For a clear exposition of choosing a proper coordinate system, see p. 1676 in Ref. [4]

[5]. The results for n , the principal quantum number, equal to 5 and 6 are shown in Fig. 1, where the lifetimes of $n(n+1)/2$ energy states for a given n are plotted as a function of magnetic field.

In the calculation, we assumed the injection energy of 400 MeV and considered the magnetic field strength up to 0.5 T. However, the ionization lifetime greater than 10^{-8} sec should be interpreted carefully, for the average radiation transition lifetime of a hydrogen atom is of the order of 10^{-8} sec or greater for $n \geq 3$ [6]

III. CHARGE FRACTION OF H^- IONS

When H^- ions traverse a carbon foil, charge exchange processes occur. Assuming that the electron capturing process, governed by the E^{-3} law, is negligible, there are three important electron loss processes:

- (i) $H^- \rightarrow H^0$, with cross section σ_{-10} ,
- (ii) $H^- \rightarrow H^+$, with cross section σ_{-11} ,
- (iii) $H^0 \rightarrow H^+$, with cross section σ_{01} .

In terms of these cross sections, the charge fractions can be written as

$$\begin{aligned} N_{H^-} &= e^{-(\sigma_{-10} + \sigma_{-11})x}, \\ N_{H^0} &= \frac{\sigma_{-10}}{(\sigma_{-10} + \sigma_{-11}) - \sigma_{01}} \left[e^{-\sigma_{01}x} - e^{-(\sigma_{01} + \sigma_{-11})x} \right], \\ N_{H^+} &= 1 - N_{H^-} - N_{H^0}, \end{aligned} \quad (5)$$

where x is the foil thickness (the number of target atoms/cm²), and N_{H^-} , N_{H^0} and N_{H^+} are the three charge fractions in the beam.

Theoretical calculations for electron loss cross section have been worked out by several authors. One of these theories is due to Gillespie [7]. His results agreed well with the measurements in the wide range of energy including the measurements done at Fermilab with 200-MeV beam and the one at Los Alamos with 800-MeV beam. These measured cross sections are presented in Table 1, which indicates that cross section varies as β^{-2} . Gillespie's theory also shows such a scaling law².

Table 1
Electron Loss Cross Sections.

Kinetic Energy (MeV)	$\sigma_{-10} + \sigma_{-11}$ ($\times 10^{-18}$ cm ²)	σ_{01} ($\times 10^{-18}$ cm ²)
200 (Measured, [8])	1.56 ± 0.14	0.60 ± 0.10
400 (Fitted)	0.98	0.38
800 (Measured, [9])	0.67	0.33

But both sets of data with beam at 200 MeV and 800 MeV show slightly smaller values than the theory [8]. In order to estimate the cross section for 400-MeV beam, instead of using the theoretical result directly (which may be all right), we fit two measurement data with the β^{-2} scaling law. The result obtained

² Stopping power of the foil is also governed by the same scaling law, which indicates that the two processes are similar. In fact, both processes are dominated by electron-electron elastic scattering.

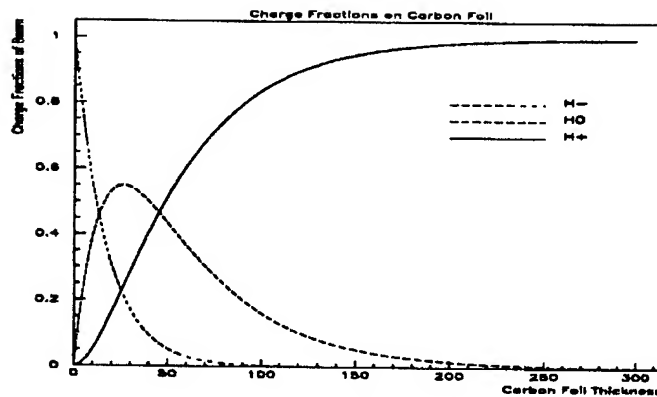


Figure 2
Charge Fractions vs. Foil Thickness at 400 MeV.

is also included in Table 1. The accuracy of this fit is within one standard deviation of measurement.

Substituting the estimated cross section into Eq. (5), we obtain the charge fractions as functions of foil thickness. These results are shown in Fig. 2. Numerical values for the interesting range of foil thicknesses are also summarized in Table 2.

Table 2
Charge Fraction after Carbon Foil of Various Thicknesses.

Foil Thickness ($\mu\text{g}/\text{cm}^2$)	N_{H^-} (%)	N_{H^0} (%)	N_{H^+} (%)
200	0.0007	1.7	98.3
210	0.0004	1.3	98.7
220	0.0002	1.1	98.9
230	0.0001	0.85	99.15
240	0.00007	0.67	99.33
250	0.00004	0.54	99.46

IV. n -DISTRIBUTION

After the foil, the neutral hydrogen atoms are distributed (or populated) in different states. At present no theory exists for excited-state production using the beam-foil method. However, we may mention the atomic-collision theory for radiative capture of free electrons by bare nuclei in the high velocity limit, which shows n^{-3} dependence on the principal quantum number of the capture cross section [6]. Even if it is not clear whether we can apply this approach to beam-foil interaction, the early measurement results at low energy (less than 1 MeV/au) showed such a dependence on principal quantum number³. An interesting theoretical analysis [11] of post-foil measurement of electromagnetic radiation and ion charge also suggests that the level populations decrease as n^{-3} and depend universally on the kinetic energy of the incoming beam. From these early studies we learn [11]:

•dependence of the level population on principal quantum number according to n^{-3} is observed frequently but not exclu-

³ June Davidson [10] used neutral helium at 0.275 MeV in order to measure the absolute population in $3 \leq n \leq 6$ after $6 \mu\text{g}/\text{cm}^2$ carbon foil.

sively,

- dependence of the level population on foil thickness is unknown,
- dependence of the level population on kinetic energy of the incident beam was not observed.

Since the above studies are not conclusive enough to apply the findings to 400 MeV H^- ions passing the carbon foil as proposed for the neutral spallation source at Argonne, we pay attention to the recent experimental study on beam-foil interaction [12]. Assuming that the n distribution is governed by a power law n^{-p} , the exponent of the power law p is measured for a given foil at 800 MeV. The results are found to be:

for a given $25.0 \mu\text{g}/\text{cm}^2$ carbon foil

$$\begin{cases} p = 3.41 & \text{for } n=2,\dots,5 \\ p = 8.0 & \text{for } n=10,\dots,14 \end{cases}$$

for a given $198.0 \mu\text{g}/\text{cm}^2$ carbon foil

$$\begin{cases} p = 1.29 & \text{for } n=2,\dots,5 \\ p = 8.0 & \text{for } n=10,\dots,14. \end{cases}$$

It is interesting to note that a single power law is unable to characterize the n distribution of excited states over a wide range of n and the low-lying states become more evenly populated for the thicker foils.

V. APPLICATION

The injection orbit in the IPNS-Upgrade RCS [13] is shown in Fig. 3. With a $250\text{-}\mu\text{g}/\text{cm}^2$ stripper foil, about 0.54% of the H^- beam emerges from the foil as partially stripped neutral hydrogen atoms, some of which are in the ground state and some of which are in excited states. If these particles are allowed to enter a normal bending magnet field, they will become stripped and either hit the vacuum chamber wall or, if not lost, form a halo of large betatron oscillation around the normal proton beam.

Figure 3 shows that the neutrals pass through the center of one quadrupole (QD) and enter the next quadrupole (QF) at -11 cm, where the field is 0.3 T, unless the H^0 -catcher is installed. This field over a length of 0.5 m is enough to strip all electrons with $n \geq 5$, or about 20% of the H^0 beam. In this estimation, we assumed that n -distribution follows n^{-p} dependence, and, since the foil thickness is $250 \mu\text{g}/\text{cm}^2$, we used $p = 1.29$ for the conservative estimate. The catcher, therefore, is placed upstream of this quadrupole (QF) as shown in Fig. 3.

The relatively short bumper magnets, B3 and B4 shown in Fig. 3, can also ionize the H^0 beam. However, the beam loss due to the field ionization in these bumper magnets is negligible.

VI. CONCLUSION

In order to minimize the beam loss in the proposed IPNS-Upgrade RCS due to field ionization, we propose to use the relatively thick stripper foil with thickness of $250 \mu\text{g}/\text{cm}^2$ and to install a H^0 -catcher in the ring together with the careful trajectory control of the neutral hydrogen atoms.

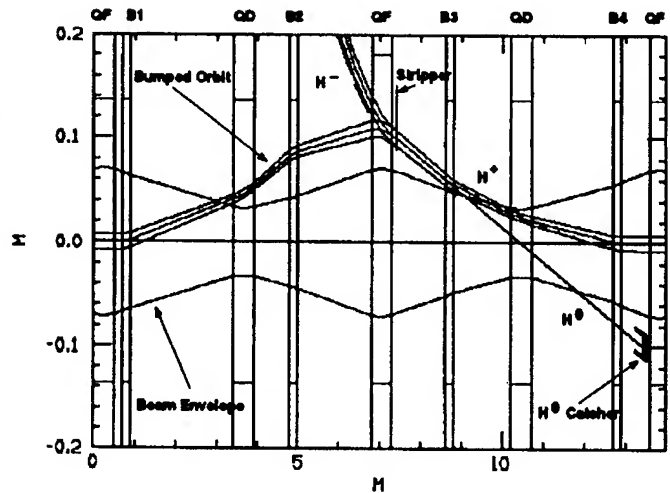


Figure 3
Injection Orbit in the IPNS-Upgrade RCS.

VII. REFERENCES

- [1] R. Hutson and R. Macek, *Proc. 1993 Part. Accel. Conf.*, 363, 1993.
- [2] L. D. Landau and E. M. Lifshitz, *Quantum Mechanics* 3rd Ed., Pergamon Press, 1977.
- [3] R. J. Damburg and V. V. Kolosov, in *Rydberg States of Atoms and Molecules*, edited by R. F. Stebbings, Cambridge University Press, 1983.
- [4] P. M. Morse and H. Feshbach, *Methods of Theoretical Physics*, McGraw-Hill Book Company, 1953.
- [5] Y.-C. Chae, ANL Report NSA-94-2, 1994.
- [6] H. A. Bethe and E. E. Salpeter, *Quantum Mechanics of One- and Two-Electron Atoms*, Plenum Pub. Corp., 1977.
- [7] G. H. Gillespie, *Phys. Rev.*, **A 16**, 943, 1977.
- [8] R. C. Webber and C. Hojvat, *IEEE Trans. Nucl. Sci.*, **NS-26**, No. 3, 4012, 1979.
- [9] O. B. van Dick *et al.*, AIP Conf. Proc. No. 69, 985, 1980.
- [10] June Davidson, *Phys. Rev.*, **A 12**, 1350, 1975.
- [11] T. Aberg and O. Goscinski, *Phys. Rev.*, **A 24**, 801, 1982, and references therein.
- [12] A. H. Mohagheghi *et al.*, *Phys. Rev.*, **A 43**, 1345, 1991.
- [13] IPNS Upgrade-A Feasibility Study, ANL-95/13 (Draft), April 1995.

Lattice Considerations for a Tau-Charm Factory*

L. C. Teng and E. A. Crosbie

Advanced Photon Source, Argonne National Laboratory
9700 South Cass Avenue, Argonne, Illinois 60439 USA

Abstract

The magnet lattice appropriate for a tau-charm factory had been studied extensively [1]. Here we discuss two possible simplifying features which make the design, construction, and operation of the machine simpler without sacrificing performance. These two features may be characterized and identified as a) luminosity optimization in the "monochromatic" mode, and b) chromaticity correction with sextupoles only in the arcs.

I. INTRODUCTION

A tau-charm factory is a high luminosity ($L \geq 10^{33} \text{ cm}^{-2} \text{ s}^{-1}$) e^+e^- collider with a center-of-mass energy, $2E$ (E = beam energy), adjustable from 3 to 6 GeV. The lower limit is set by the charmonium, J/ψ , production threshold of 3.1 GeV and the upper limit is set by the production threshold for pairs of charmed baryons, e.g. at 2×2.74 GeV for $(\bar{\Omega}_c^-, \Omega_c^-)$. The high luminosity requires that the two beams be stored in separate rings, here assumed to be located one directly above the other. Because of the extremely narrow width of J/ψ ($\Gamma = 0.086$ MeV), it has been proposed [1] that for J/ψ production the lattices of the two rings be tuned to have large equal and opposite vertical dispersion functions, $\pm D_y$, for the two beams at the collision point. The collision energy spread would then arise only from the vertical betatron width $\sigma_{y\beta}$ of the beams. To keep the energy spread within the J/ψ width, we must have

$$\sigma_{y\beta} \leq \left(\frac{\Gamma}{2E} \right) D_y. \quad (1)$$

This so-called "monochromatic" tuning was considered necessary for J/ψ production even at a sacrifice of luminosity. We will show that, properly optimized, the achievable luminosity is actually higher for the "monochromatic" tune.

II. OPTIMIZATION OF LUMINOSITY

For the head-on collision of two identical beam bunches containing N particles each, the beam-beam tune shifts are

$$\begin{cases} \xi_x = NK \frac{\beta_x}{\sigma_x(\sigma_x + \sigma_y)}, \\ \xi_y = NK \frac{\beta_y}{\sigma_y(\sigma_x + \sigma_y)}, \end{cases} \quad (2)$$

where $K \equiv r_0/2\pi\gamma = 1.48 \times 10^{-19} \text{ m}$ at the beam energy of $E = 1.55$ GeV for J/ψ production. In these equations and throughout this paper all symbols have their conventional meanings and all quantities are evaluated at the collision point. The luminosity is

$$L = \frac{f}{4\pi} \frac{N^2}{\sigma_x \sigma_y}, \quad (3)$$

where f is the bunch collision frequency. The luminosity is clearly largest when $\xi_x = \xi_y \equiv \xi$ = empirical maximum attainable value $\equiv 0.04$. This condition gives

$$\frac{\beta_y}{\sigma_y} = \frac{\beta_x}{\sigma_x}. \quad (4)$$

When this condition is satisfied, we have

$$N = \frac{\xi}{K} \frac{\sigma_x^2}{\beta_x} \left(1 + \frac{\beta_y}{\beta_x} \right) \quad (5)$$

and

$$L = \frac{f}{4\pi} \frac{N^2}{\beta_y} \frac{\beta_x}{\sigma_x^2}. \quad (6)$$

For the standard tuning $D_x = D_y = 0$ and Eq. (4) gives $\beta_y/\beta_x = \epsilon_y/\epsilon_x$ = a value generally much less than unity. In this case, we should take $\beta_y = 0.01 \text{ m}$ = the smallest practicable value in one of the two dimensions. Taking further, $f = 30 \text{ MHz}$ (10-m bunch spacing) and $\epsilon_x = 250 \times 10^{-9} \text{ m-rad}$ we obtain

$\beta_x(\text{m})$	β_y/β_x	N	$L (\text{cm}^{-2}\text{s}^{-1})$
0.02	0.5	1.02×10^{11}	0.98×10^{33}
0.05	0.2	0.81×10^{11}	0.63×10^{33}

This shows that with these parameters one can barely reach the desired luminosity of $10^{33} \text{ cm}^{-2} \text{ s}^{-1}$.

For the "monochromatic" tuning, the example lattice we studied gives $D_y = 0.4 \text{ m}$ and $\sigma_E \equiv 0.6 \text{ MeV}$ at the beam energy $E = 1.55 \text{ GeV}$ for J/ψ . Equations (1) and (4) then give

$$\sqrt{\beta_y \epsilon_y} = \frac{\Gamma}{2E} D_y \equiv 11 \mu\text{m} \quad (7)$$

* Work supported by the U.S. Department of Energy, Office of Basic and Energy Sciences, under Contract No. W-31-109-ENG-38.

$$\frac{\beta_y}{\epsilon_y} = \left[1 + \left(\frac{2\sigma_E}{\Gamma} \right)^2 \right] \frac{\beta_x}{\epsilon_x} \cong 190 \frac{\beta_x}{\epsilon_x}. \quad (8)$$

It is unlikely that ϵ_y can be made smaller than $\epsilon_x/190$. Equation (8) then says that β_x must be smaller than β_y . We therefore set β_x equal to the minimum practical value of 0.01 m. Equations (7) and (8) then give

$$\beta_y \cong 0.03 \text{ m} \quad \text{and} \quad \epsilon_y \cong 4 \times 10^{-9} \text{ m}, \quad (9)$$

and Eqs. (5) and (6) give

$$N \cong 2.7 \times 10^{11} \quad \text{and} \quad L \cong 2.3 \times 10^{33} \text{ cm}^{-2} \text{ s}^{-1}. \quad (10)$$

The higher luminosity is derived, of course, from the higher beam intensity which is, however, allowed by the beam-beam effect for this design.

The very small collision energy spread is desirable at all energies and for all experiments. There is no need ever for the zero-dispersion design.

III. ARC LATTICE

The linear lattice is conventional and consists of two 180° arc sections joined by two 118.4-m-long straight sections: one for injection and rf, the other for beam collision and the detector assembly. The arc sections are composed of ten 60° 7.4-m FODO cells each (including the horizontal dispersion suppressor cells) with parameters adjusted to give a natural horizontal emittance of $\sim 250 \times 10^{-9}$ m.

IV. COLLIDING STRAIGHT LATTICE

The injection straight lattice is conventional and straightforward and will, therefore, not be discussed. The collision or interaction straight lattice is developed along the following guiding features:

1. The collision is head-on. The strong low- β quadrupole doublets next to the collision point are superconducting, and are common to and have identical focal actions on both beams. The lattice is, thus, symmetric. Outboard of the common quadrupole doublets, the beams are separated vertically, first by electrostatic separators followed by septum dipoles. The linear orbit functions are adjusted to $D_x = 0$, $D_y = \pm 0.4$ m, $\beta_x = 0.01$ m, $\beta_y = 0.03$ m, $\epsilon_y \leq 4 \times 10^{-9}$ m and, since the lattice is symmetric, $D'_x = D'_y = \alpha_x = \alpha_y = 0$. (Here, as before, all values given are those at the collision point.)
2. We choose not to cross the beams so that a) the central collision energy can be fine-adjusted (up to $\sim 2\sigma_E \cong 1.2$ MeV) by vertically parallel-displacing one beam against the other, and that b) the no crossing geometry in the injection straight is more convenient for injection and for accommodating rf cavities. The design of the matched linear lat-

tice offers essentially no special difficulties and is shown in Fig. 1. However, some special attention is required for chromaticity correction and dynamic aperture problems.

V. CHROMATICITY CORRECTION AND DYNAMIC APERTURES

Without correction the natural chromaticities of the linear lattice are approximately -27 (horizontal) and -39 (vertical). The major contribution comes from the very strong superconducting low- β quadrupoles. The traditional wisdom is to correct the chromaticity "at the source." To do this, many additional complicated and difficult matching conditions must be met in the linear straight lattice

For this tau-charm factory we tried to avoid this complication by locating the sextupoles in the arcs only. Since the arcs consist of 60° FODO cells, we can place two pairs of sextupoles in each arc such that the two members in each pair are identical in strength, located at identical β values, and separated by π phase-advance. In this way, the chromaticity correcting effects of the two members add, but their resonance driving effects cancel. With one pair placed at high β_x and the other at high β_y , we can adjust the strengths of the two pairs to correct the x- and y-chromaticities simultaneously. We found, indeed, that after correcting the chromaticities to zero, the dynamic apertures are $> 80\sigma$ ($\sigma =$ larger of σ_x and σ_y) at the central energy and $> 25\sigma$ at $\pm 10\sigma_E$ from the central energy.

Actually, with the rather large vertical dispersions at the superconducting low- β quadrupoles, one can provide chromaticity corrections "at the source" by inserting superconducting skew-sextupole coils in these low- β quadrupoles, except it is now impossible to cancel their resonance-driving harmonics by other skew-sextupoles located π -phase advance away.

VI. REFERENCE

- [1] J. M. Jowett, Frontiers of Particle Beams: Factories with e+e- Rings, edited by M. Dienes, M. Month, B. Strasser, S. Turner (Springer Verlag, 1994); and the many references given in this paper.

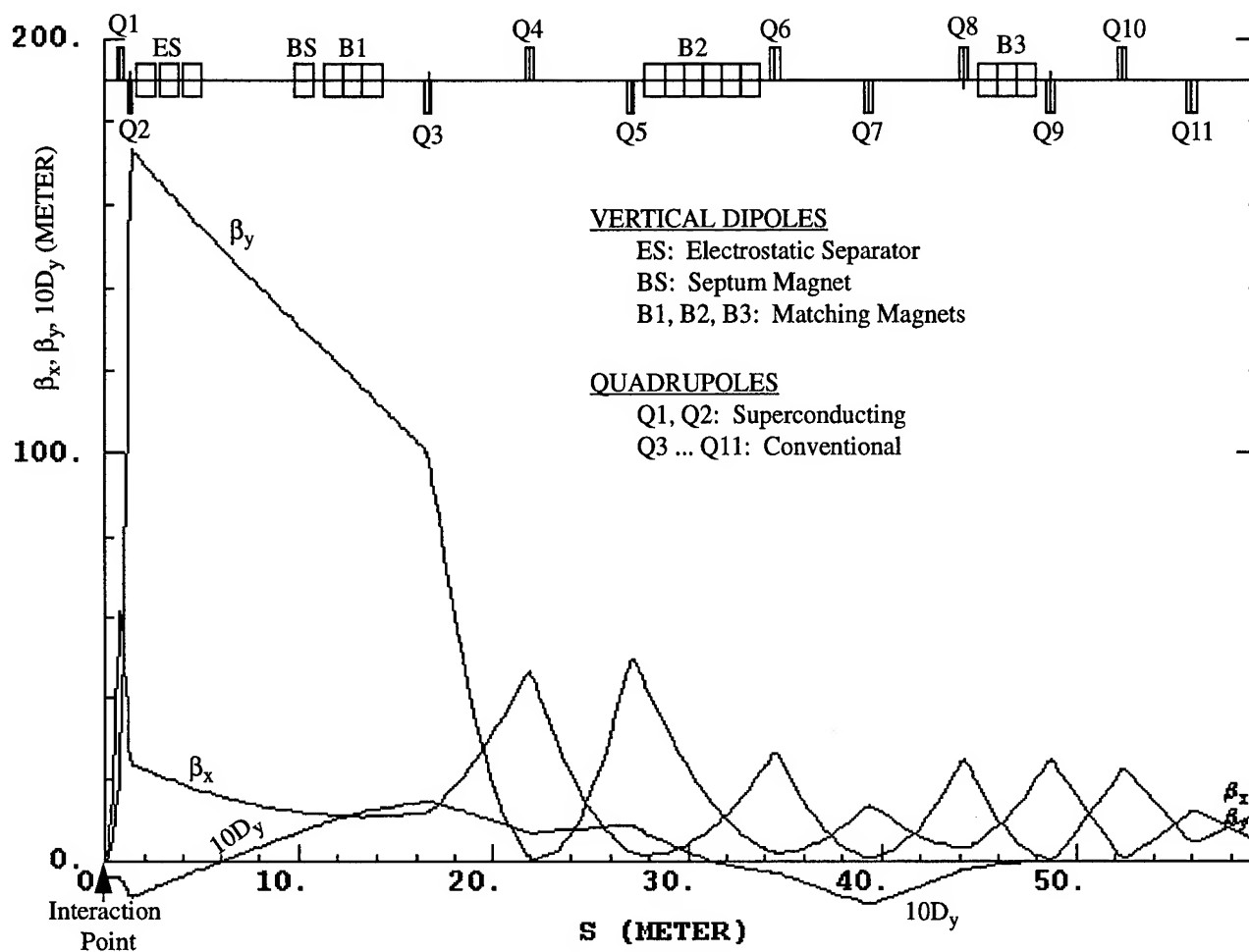


Figure 1: Linear orbit functions across one-half of the interaction straight section.

At the collision point $\beta_x = 1$ cm, $\beta_y = 3$ cm, $D_x = 0$, $D_y = 0.4$ m.

For the complete ring, $\epsilon_x = 252$ nm, $\epsilon_y = 3.8$ nm, and $\sigma_E/E = 0.38 \times 10^{-3}$.

The vertical separation of the rings is ~ 1.23 m.

Effects of Vertical Aperture on Beam Lifetime at the Advanced Photon Source (APS) Storage Ring*

Hana M. Bizek

Advanced Photon Source, Argonne National Laboratory
9700 South Cass Avenue, Argonne, Illinois 60439 USA

Abstract

When a positron's energy deviation $\delta E/E$ exceeds the rf acceptance, or when it receives an angular kick for the betatron motion that exceeds some limiting admittance, the positron will be lost. The main contributions to the total beam lifetime come from single Coulomb and Touschek scattering. In this report we investigate the dependence of the residual gas pressure and the vertical aperture of the Advanced Photon Source storage ring on the total beam lifetime. We present results of calculating the total beam lifetime as a function of vertical aperture for varying average ring pressure, beam current, and coupling coefficient.

I. INTRODUCTION

The vertical aperture and pressure enter the lifetime calculation through the single Coulomb scattering. In particular, the variation in vertical aperture is due to elastic scattering on nuclei. The Touschek lifetime numbers do not vary with vertical aperture and are read from the table in Ref. [1]. The total beam lifetime is calculated and plotted as a function of the vertical aperture.

The so-called SPEAR scaling calculation is also included. Experimental observations [2] at the SPEAR storage ring seem to suggest that, for short bunches with rms bunch length σ_l smaller than the beam pipe radius b , the effective longitudinal broadband impedance seen by the beam at frequencies beyond $\omega_c = c/b$ (c being the speed of light) is scaled down by a factor of $(\sigma_l/b)^{1.68}$. This phenomenological power law is referred to as the "SPEAR scaling law."

II. METHOD OF CALCULATION

The single Coulomb scattering lifetime for a pressure of 1 nTorr, T , is calculated for a range of vertical apertures. Included are elastic and inelastic scattering on nuclei and electrons. The vertical aperture is taken from 1 mm to 20 mm, in 1-mm increments. The highest value of the vertical aperture corresponds to the aperture in the insertion straight sections. The vertical aperture values and the corresponding single-Coulomb scattering lifetime values are used to obtain the single-Coulomb scattering lifetime as a function of the assumed pressure from the formula

$$\tau_{\text{gas}} = \frac{T}{P} \quad (1)$$

where P is the assumed pressure in nTorr. The single-Coulomb scattering lifetime and Touschek lifetime are inserted into the following equation

$$\frac{1}{\tau_{\text{total}}} = \frac{1}{\tau_{\text{gas}}} + \frac{1}{\tau_{\text{Touschek}}} \quad (2)$$

in order to obtain the total beam lifetime.

The Touschek lifetime is calculated for the APS storage ring, by use of the code ZAP [3]. For the SPEAR scaling calculations, one needs to find the rms value of the lengthened bunch, σ_l , and its corresponding rms momentum spread, σ_p . Once these numbers are obtained from Option 2 of the ZAP code, they are input into the Touschek scattering routine of ZAP. The results are used in the present work.

In each case, the calculated rms minimum bunch length σ_l is 0.58 cm and the corresponding rms momentum spread σ_p is 0.96×10^{-3} . In the case of SPEAR scaling, σ_l and σ_p increase, respectively, to 0.89 cm and 1.48×10^{-3} for 5.22 mA current, and, respectively, to 1.51 cm and 2.50×10^{-3} for 10.44 mA current.

III. ANALYSIS OF RESULTS

Each plot shows the total beam lifetime, as a function of vertical aperture, for pressures of 1 nTorr, 2 nTorr, 3 nTorr, and 4 nTorr; for currents of 1 mA, 5.22 mA, and 10.44 mA; and for 10% and 1% coupling. The total beam lifetime for 10.44-mA current and 1% coupling is not shown. In this case, the current is too high and the coupling too low to obtain interesting results. The bucket height is assumed to be $\pm 2\%$. As may be seen in Figs. 1 through 5, the beam lifetime decreases with increasing current and decreasing coupling. In the case of SPEAR scaling, holding the coupling fixed and increasing the current will not appreciably change the lifetime. This may be seen by comparing Fig. 6 with Fig. 8 and Fig. 7 with Fig. 9.

Each of these graphs also shows a vertical bar, at the total beam lifetime of 10 hours. This is the minimum allowed lifetime for optimum APS storage-ring operation. Clearly, lifetimes below 10 hours for given vertical apertures are too low. Such vertical apertures are to be avoided. Therefore, this method may predict what kinds of bunches may be sustained at what apertures by estimating the aperture for which a given bunch will operate at exactly 10 hours. For the APS storage ring we consider three phases [4]: the commissioning phase, for which the vertical aperture is 40.7 mm, Phase I, for which the vertical aperture is 12 mm, and Phase II, for which the vertical aperture is 8 mm. According to the APS list of param-

* Work supported by the U.S. Department of Energy, Office of Basic Energy Sciences, under Contract No. W-31-109-ENG-38.

ters [5], the maximum circulating current for a single bunch is 5 mA.

From Figs. 1-9 it is immediately seen that a 0.58-cm bunch will not be sustained under 4-nTorr pressure at all, and a 0.58-cm, 5-mA bunch cannot be sustained under a pressure of 3 nTorr either (Figs. 3 and 4). For SPEAR scaling, both 0.89-cm and 1.51-cm bunches having 10% coupling can be sustained under 3-nTorr pressure in the insertion straight sections (Figs. 6 and 8), while the 0.89-cm bunch with 10% coupling can also be sustained under this pressure in Phase I (Fig. 6).

For the pressures of 1 nTorr and 2 nTorr and 10% coupling, the 0.58-cm bunches, as well as the SPEAR-scaled 0.89-cm and 1.51-cm bunches, are sustained for vertical apertures of all three phases. Moreover, for the lowest pressure (1 nTorr), only the 0.58-cm bunches with 5-mA current and 1% coupling are not sustained (Fig. 4).

As can be expected, the 0.58-cm bunches with the best lifetimes are those with 1-mA current and 10% coupling. As Fig. 1 shows, they can be sustained in the ring environment of 1-, 2- and 3-nTorr pressure for all three phases. Figure 2 shows that the 1-mA current bunches with 1% coupling also do well; however, at 3 nTorr they cannot be sustained in Phase II. On the other hand, the 0.58-cm, 10-mA bunches do rather poorly. From Fig. 5 it is seen that only bunches having 10% coupling are sustained at 1-nTorr pressure. Longer bunches stand a better chance under these conditions.

IV. ACKNOWLEDGEMENT

We would like to acknowledge Drs. Edwin A. Crosbie and Glenn Decker for continued assistance in this work. Drs. Michael Borland and Louis Emery provided assistance with ZAP.

V. REFERENCES

- [1] Bizek, Hana M., private communication.
- [2] Chao, A. W., "Coherent Instabilities of a Relativistic Bunched Beam," *Physics of High Energy Particle Accelerators*, SLAC Summer School 1982, AIP Conf. Proc. No. 105, 1983, p. 353.
- [3] Zisman, M. S., Chattopadhyaya, S., Bisognano, J. J., "ZAP User's Manual," LBL-21270, December 1986.
- [4] "7-GeV Advanced Photon Source Conceptual Design Report," ANL-87-15, April 1987.
- [5] *Ibid*, Appendix A.

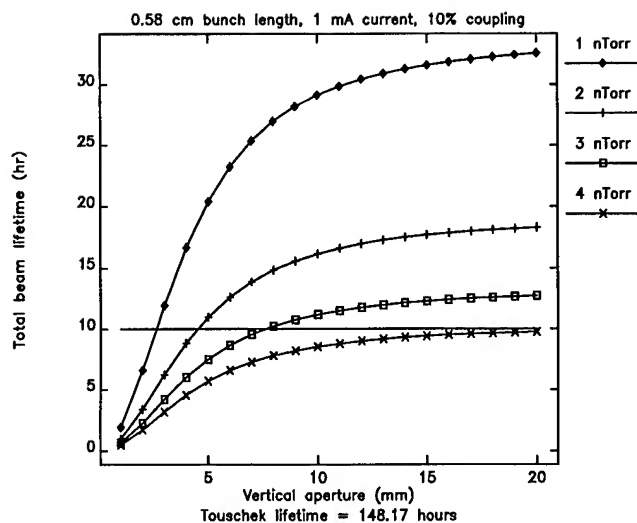


Figure 1

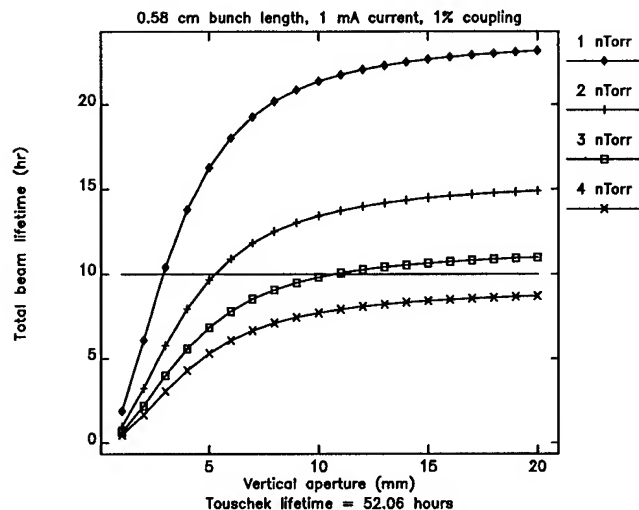


Figure 2

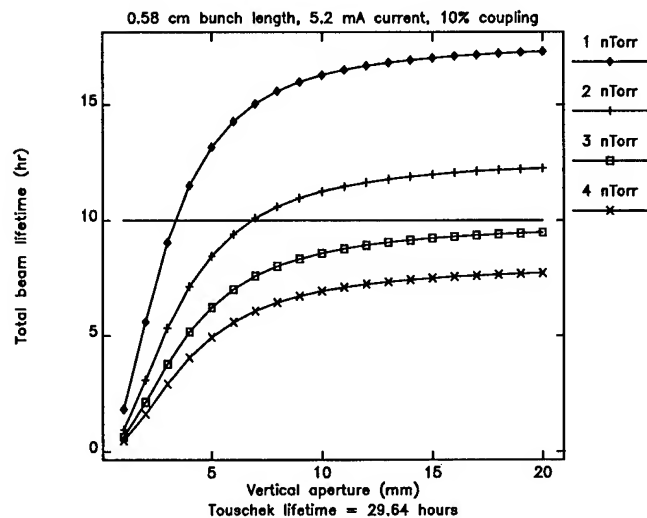


Figure 3

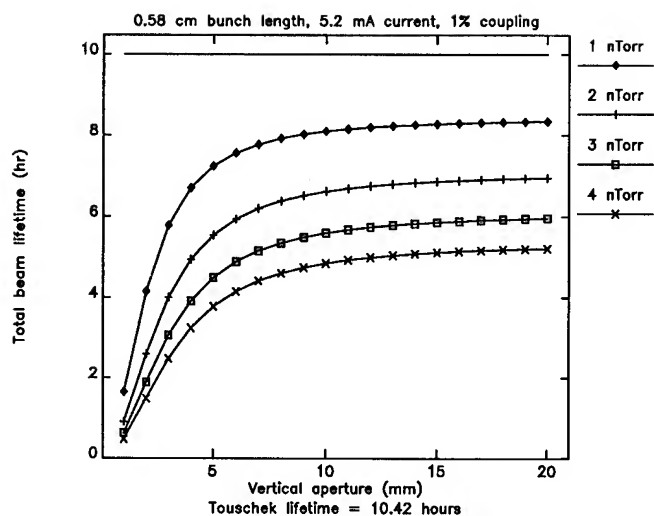


Figure 4

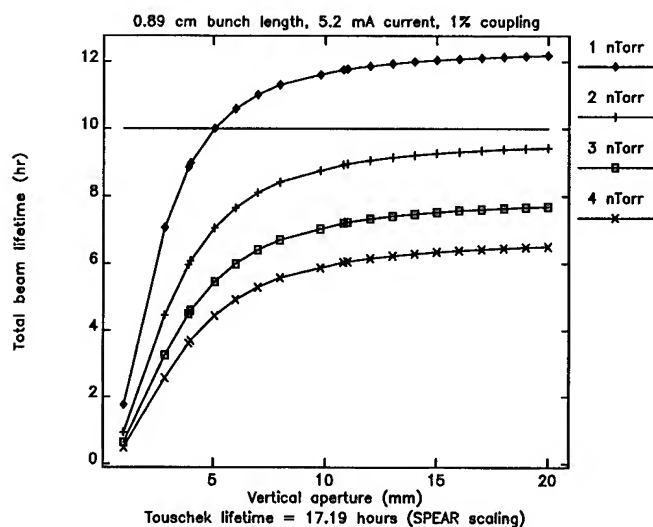


Figure 7

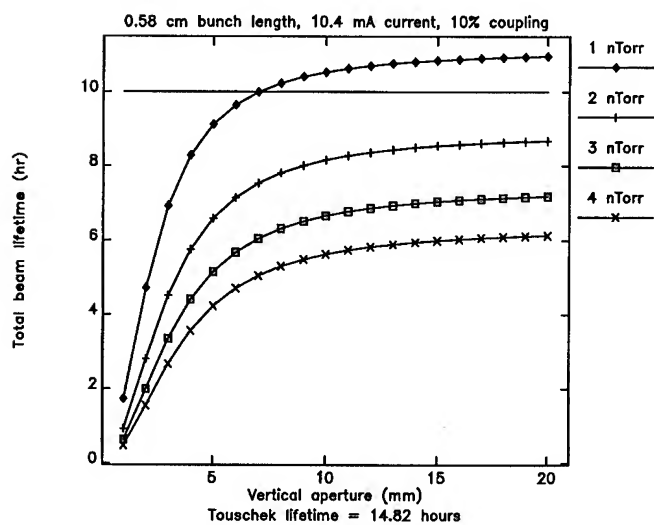


Figure 5

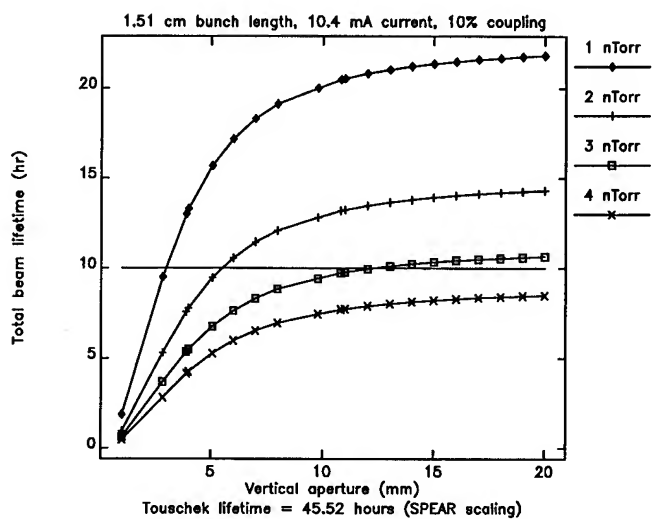


Figure 8

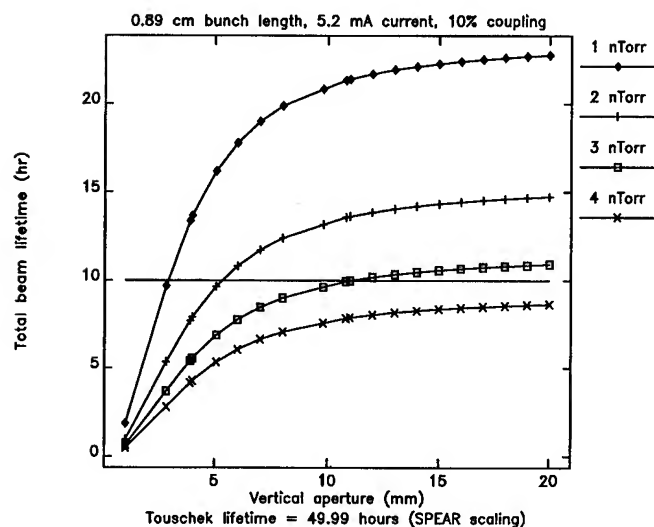


Figure 6

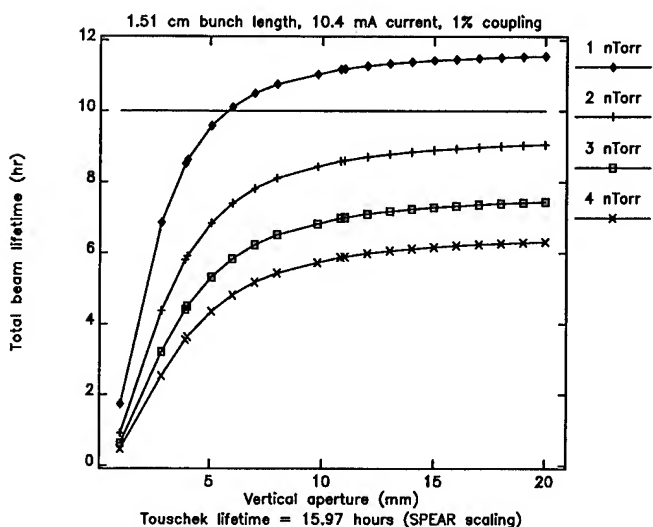


Figure 9

Rebucketing after transition in RHIC*

D.-P. Deng and S. Peggs
Relativistic Heavy Ion Collider
Brookhaven National Laboratory
Upton, NY 11973-5000

Abstract

Rebucketing in the Relativistic Heavy Ion Collider, *RHIC*, describes the process of moving the beam from the 26MHz accelerating system to the 196MHz storage system with as little beam loss as possible. This puts a stringent requirement on the beam longitudinal area done at top energy. The ample bucket space after, but not too close to, transition is explored by computer simulation to relax such stringent conditions.

I. Introduction

The ultimate task of the *RHIC* RF systems, which has one set of accelerating cavities and a set of storage cavities [1], is to put the bunches in storage cavities, with as little beam loss as possible, for physics experiments. The longitudinal emittance determines how difficult it is to make such a "handoff" between accelerating cavities and storage cavities [2].

The storage system buckets are approximately 5 ns long. Therefore, given a margin of 80% for safety, the bunches have to be made no greater than 4 ns long in order for the storage system to rebucket them. The bunch length is defined as containing 95% of the particles in a bunch. The nominal bunch length for gold beam at top energy is greater than 5 ns. Means have to be sought to make shorter bunches. Away from the immediate transition region in which the bunch is naturally short, the bunch length can be shortened (or lengthened) by manipulating the bucket height or the bucket phase relative to the bunch center.

Since the bunch length is inversely proportional to $V^{\frac{1}{4}}$, the adiabatic compression of bunch length has a quartic power law for the voltage required. For instance, a bunch is 6ns long, which is typical for gold at top energy, at voltage of 300kV. To compress it down to 4ns, the voltage has to increase to $300 * (\frac{6}{4})^4 = 1.5MV$, which is excessive in comparison with the maximum available voltage from the accelerating cavities.

The bunch rotation technique is a non-adiabatic way to shorten the bunches. Its main advantages are speed, and lower requirements on the available voltage from the cavities. Its limitation is that it develops long tails if the bunch area is too large. In this note, we explore by means of computer simulation the region after transition where ample bucket area is available to suppress the long tails, and thus eliminate large beam losses.

II. Beam dynamics after transition

The longitudinal particle dynamics are governed by the single particle Hamiltonian

$$H = \frac{1}{2E_0} \left(\frac{hc}{R_0} \right)^2 \frac{\eta}{\gamma} W^2 + \frac{eV_{rf}}{2\pi h} [\cos \phi - \cos \phi_s + (\phi - \phi_s) \sin \phi_s] + O(W^3) \quad (1)$$

where γ is the Lorenz factor of the beam, E_0 is the particle rest energy, h is the rf harmonic number, R_0 is the average radius of the ring, $W = \frac{E-E_s}{\omega_{rf}}$, E_s is the synchronous energy, ω_{rf} is the angular rf frequency, $\eta = \frac{1}{\gamma_{tr}^2} - \frac{1}{\gamma^2}$ is the phase slip factor, and ϕ_s is the synchronous phase. In the case of a constant speed magnet ramp (\dot{B}) and constant rf gap voltage (V_{rf}), the behavior of a particle is complete determined by the ratio of $\frac{\eta}{\gamma}$. Solving the equation with respect to the top energy ($\gamma = 108$, $\gamma_{tr} = 22.8$)

$$\frac{\eta}{\gamma} = \left(\frac{\eta}{\gamma} \right)_{top} \quad (2)$$

we find that equivalent point $\gamma \approx 26$, where the particle dynamics behave exactly the same as at top energy.

The bucket size scales inversely proportional to the square root of how close it is to transition, i.e. $A_{bkt} \propto \frac{1}{\sqrt{\gamma - \gamma_{tr}}}$. It's clear that if we move from the equivalent point down close to transition, the bucket size increases dramatically comparing with that of around top energy where the bucket size hardly changes.

III. Simulation Results

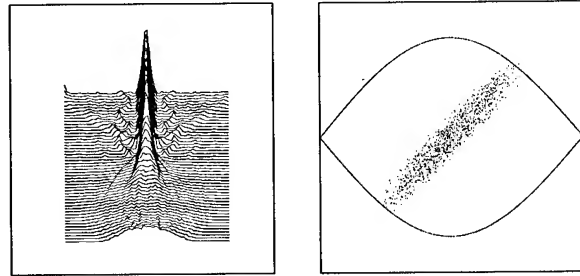


Figure 1. On the left: mountain range plot of the bunch shape in a rebucketing process from simulation. On the right: phase space plot when the bunch is mismatched after shifting the stable fixed point back to the center of the bunch

The basic idea of bunch rotation is to first lengthen the bunch and then make it mismatched to the bucket. In *RHIC* rebucketing, the procedure goes as follows. First we lengthen the bunch by shifting the unstable fixed point of the bucket to the bunch center. After a fraction of a synchrotron period the bunch has elongated along the separatrix of the bucket. The stable fixed point is then shifted back to the bunch center again. The bunch,

*Work performed under the auspices of the US Department of Energy.

being mismatched, starts to rotate in the phase space. After the bunch rotates $3/8$ of a synchrotron period to reach its minimum bunch length position, the storage cavities are turned on and the accelerating cavities are turned off. Figures 1 and 2 illustrate the rebucketing process, for a particularly large bunch area, to illustrate the beam loss situation.

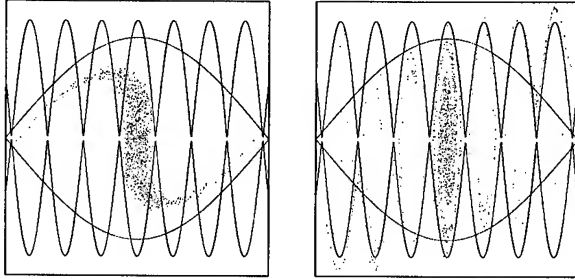


Figure 2. On the left: phase space plot when the bunch is at its narrowest. On the right: phase space plot several synchrotron periods later after rebucketing.

We simulate the rebucketing process for gold beam in three cases: stationary bucket, stationary bucket with the nonlinear $\alpha_1 = -0.6$ [3] and moving bucket. In each case, we scan for bunch areas of 0.6, 0.7, 0.8 and 1.0 eVs/u , and for each bunch area we scan at 6 different points away from transition range from $\Delta\gamma = \gamma - \gamma_{tr} = 0.7$ to $\Delta\gamma = 3.2$. In all cases the rf voltage is 600kV, and $\dot{B} = 0.05T/s$ for the moving bucket, the nominal ramp rate for RHIC.

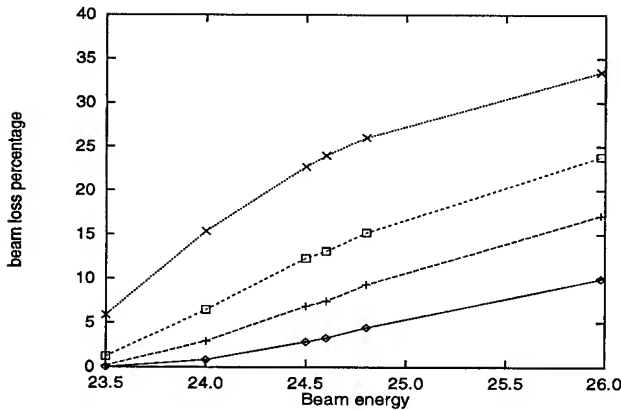


Figure 3. In a stationary bucket. Percentage of beam loss vs. γ . The curves from top to bottom correspond to bunch area of 1.0, 0.8, 0.7, 0.6 eVs/u .

For case 1, in Figure 3, we plot the beam loss as a function of how far away from transition for various bunch areas. Upon close examination, these curves are united through a reduced variable $\epsilon^x \Delta\gamma^{1-x}$, where ϵ is the bunch area and $x = 0.71$ from data fitting. In Figure 4, we plot the beam loss with respect to the reduced variable. Figures 5 and 6 are for the cases 2 and 3 respectively. As expected, when the non-linear factor is considered, the beam in the phase space distorted more, and thus the beam loss becomes worse. If we use a moving bucket to accomplish the rebucketing, the bucket size is reduced, and the beam loss increases.

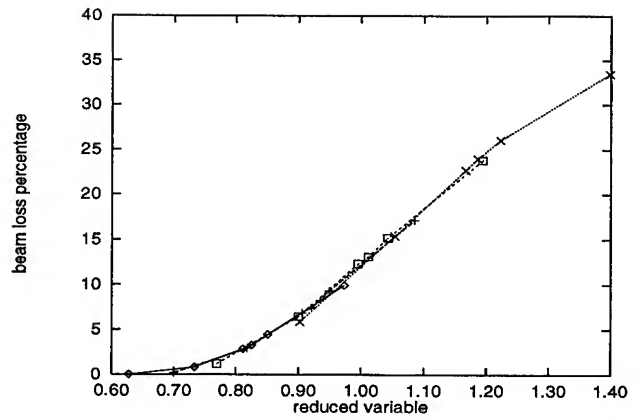


Figure 4. In a stationary bucket. Percentage of beam loss vs. reduced parameter $\epsilon^x \Delta\gamma^{1-x}$.

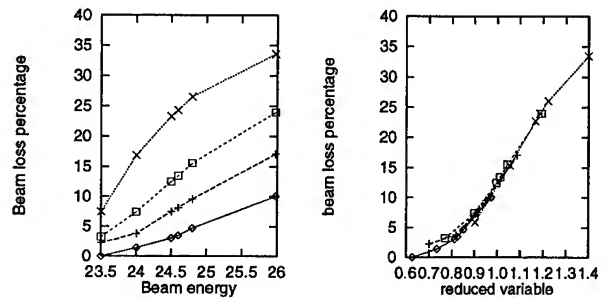


Figure 5. In a stationary bucket with $\alpha_1 = -0.6$. Left figure: Percentage of beam loss vs. γ . The curves from top to bottom correspond to bunch area of 1.0, 0.8, 0.7, 0.6 eVs/u . Right figure: Percentage of beam loss vs. reduced parameter $\epsilon^x \Delta\gamma^{1-x}$.

From these beam loss curves and the reduced variable, we can plot curves for constant beam loss in the space of bunch area and $\Delta\gamma$. Such a plot allows us to choose where rebucketing should take place. Each point on a curve represents at what energy the rebucketing takes place and the maximum bunch area that will give rise of the amount of beam loss. For example, if we choose to tolerate 5% beam loss while rebucketing at energy $\gamma = 25.5$, following on the 5% curve, the maximum bunch area will then be 0.55 eVs/u . That is, any bunch area greater than 0.55 eVs/u will result more than 5% beam loss. It's clear from Figure 7 that the closer toward transition ($\gamma_{tr} = 22.8$) the less beam loss will occur, and the larger bunch area that it can tolerate. Of course, we can't arbitrarily get too close to transition, because of other complications associated with transition itself.

IV. Conclusion

Comparing with rebucketing at top energy, rebucketing after transition has some good features. First, it does not require any new hardware investment, it is just a matter performing the same task at a lower energy. Second, since it is performed at low energy, any beam loss has less impact on the performance of the superconducting magnets. Third, it opens up the emittance bottleneck. Depending on what bunch area will result from transition, we can choose many different points to rebucket the beam.

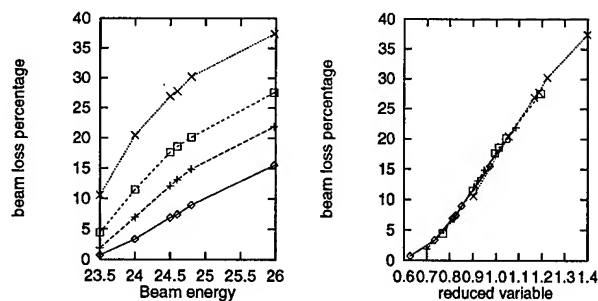


Figure. 6. In a moving bucket. Left figure: Percentage of beam loss vs. γ . The curves from top to bottom correspond to bunch area of 1.0, 0.8, 0.7, 0.6 eVs/u. Right figure: Percentage of beam loss vs. reduced parameter $\epsilon^x \Delta \gamma^{1-x}$.

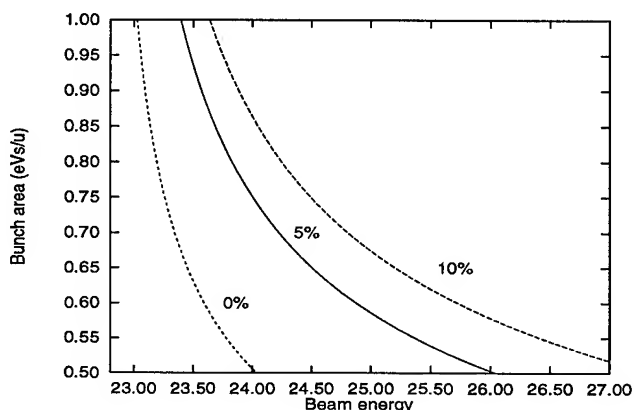


Figure. 7. Constant beam loss curves for rebucketing in a stationary bucket.

Fourth, it can be conducted both with stationary buckets (zero magnet ramp) and moving bucket (nonzero magnet ramp). The subsequent acceleration is done by the storage system.

V. Acknowledgment

The authors would like to thank fruitful discussions with M. Brennan.

References

- [1] The Conceptual RHIC RF design. Tech Note, RHIC/RF-22, 1994.
- [2] D. P. Deng Gold Beam Longitudinal Emittance Limit at Rebucketing. Tech Note RHIC/RF-18, 1994
- [3] J. Wei *et. al.* in these proceedings for its effects.

CLOSED-ORBIT DRIFTS IN HERA IN CORRELATION WITH GROUND MOTION

V. Shiltsev, B. Baklakov, P. Lebedev, Budker INP, 630090, Novosibirsk, RUSSIA
and C. Montag, J. Rossbach, DESY, 22603 Hamburg, GERMANY

Abstract

This article describes the results of orbit motion measurements in HERA e - p collider. Power spectral density of vertical drifts of HERA proton beam orbit was obtained in a frequency range from $6 \cdot 10^{-5}$ Hz up to 250 Hz. The slow closed-orbit drifts were found to have diffusive character and to grow as the square root of time interval. Simultaneous measurement of ground vibrations at HERA tunnel has shown significant correlation of the orbit drifts with the ground motion. It was observed that the orbit motion substantially affects the proton loss rate.

I. INTRODUCTION

Quadrupole vibrations due to ground motion cause distortion of beam orbits in HERA and beam-beam separation at the interaction point. The goal of these measurements was to reveal directly the correlation between the HERA tunnel vibrations and the closed orbit distortions (COD). To do this, the signals of beam position monitors (BPM) and seismometers were recorded with high precision. The search was performed in a very broad frequency band of almost 7 decades from $6 \cdot 10^{-5}$ Hz to 250 Hz. At the same time, the dependence of the particle loss rate in the ring on the orbit motion is a point of keen interest, therefore, we recorded and took in processing the signal from a proton loss monitor. During the measurements, most of the data on beams were obtained under luminosity run conditions of HERA with the typical parameters: proton current of 30-45 mA at 820 GeV, electron (positron) current of 10-25 mA at 28 GeV. The measurements are described in detail in [1].

II. INSTRUMENTS AND METHODS

Sensors for the ground motion were four SM-3KV type velocity meters (a pair of vertical and a pair of horizontal) which allow us to obtain data in 0.1 – 140 Hz frequency band with a sensitivity of about 80 mV/(μ m/s); and a pair of three component CMG-3T geophones made by Guralp Systems Co. with a flat velocity response of 0.75 mV/(μ m/s) in the band 0.003 Hz – 50 Hz. The noises of the probes were found to be much less than the ground motion signals in the corresponding frequency ranges [1]. The vibration detectors were set in the HERA Hall North (H1 detector area) and in the HERA Hall West at the depth of about 25 m.

The transverse proton beam closed orbit was detected by a pick-up BPM at WR35 sector of HERA ($\beta_h = 227$ m, $\beta_v = 25$ m). The BPM sensitivity was 1.5 mV/ μ m in respect to $\beta = 1$ m. (Further, the orbit motion will be normalized to the point of a lattice with $\beta = 1$ m. It is about the HERA interaction point values of $\beta_v^* = 0.7$ m and $\beta_h^* = 1.4$ m). The rms BPM noises are

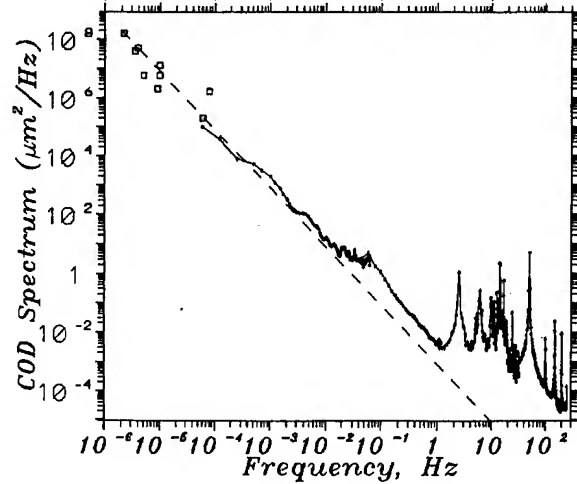


Figure 1. Spectrum of vertical COD of proton beam (normalized to $\beta=1$ m). Squares are for the data from Ref. [3].

about 0.1 μ m in a frequency band of 0.5 Hz and about 0.5 μ m for a 100 Hz band.

The HERA proton loss monitor detects the beam halo particles scattered in the material of a collimator. Note, that the loss rate variation depends on beam shaking as well as on the beam shape (cross section) deformations because the collimator "jaw" was from the only side of the beam. The monitor is described in detail in [2].

The signals from all the monitors were digitized simultaneously by ADCs with variable sampling frequency (from 0.1 Hz to 1 kHz) and then were sent to the memory for storage. To get information in different frequency ranges, the low-pass filters at 200 Hz, 20 Hz, 2 Hz, and 0.5 Hz were applied.

The properties of noises can be described by the power spectral density (PSD) $S(f)$. Its dimension is power in a unit frequency band, for example, m^2/Hz for the PSD of displacement. The value of $S(f)$ relates to the rms value of the signal $X_{rms}(f_1, f_2)$ in frequency band from f_1 to f_2 as $X_{rms}(f_1, f_2) = \sqrt{\int_{f_1}^{f_2} S(f) df}$. The normalized spectrum of the correlation $K(f)$ of two signals $x(t)$ and $y(t)$ is defined as

$$K(f) = \frac{\langle X(f)Y^*(f) \rangle}{\sqrt{\langle X(f)X^*(f) \rangle \langle Y(f)Y^*(f) \rangle}}, \quad (1)$$

where the brackets $\langle \dots \rangle$ mean the time averaging over the different measurement data, and $X(f)$ and $Y(f)$ are the Fourier transformations of $x(t)$ and $y(t)$. Note, that correlation is a complex function $K(f) = Co(f) \exp(-i\Delta\phi(f))$. The coherence $Co(f)$ of the two signals is equal to the modulus of $K(f)$. By the definition, the value of the coherence does not exceed 1.0.

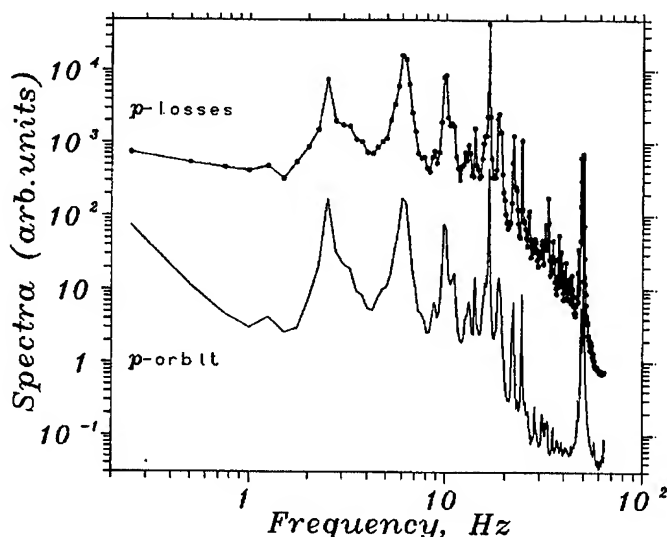


Figure 2. Spectra of proton loss rate and p -BPM signals.

The value of $\Delta\phi(f)$ reflects phase advance between the corresponding Fourier harmonics of the two signals.

III. RESULTS

The power spectral density of the vertical motion of the HERA proton beam closed orbit (scaled for $\beta = 1$ m) from $6 \cdot 10^{-5}$ Hz up to 250 Hz (almost 7 decades in frequency) is shown in Fig.1. In order to get better estimation of the PSD at the lowest frequency three-day data record (29.09 – 01.10.1994) were processed. It is interesting to note that the measured PSD is well consistent with the analysis of weekly orbit drifts all over the HERA- p ring [3], those data are marked by squares in Fig.1. The spectrum can be divided in two parts: continuum below 1 Hz and a series of peaks at frequencies above 1 Hz. The continuous part can be approximated by the formula (see dashed line in Fig.1)

$$S_{COD}(f) = \frac{1.2 \cdot 10^{-3}}{f^2} \quad [\mu\text{m}^2/\text{Hz}], \quad (2)$$

This part of spectra describes the slow drift of the HERA proton orbit that looks like a “random walk” process, and its PSD corresponds to the rms orbit displacement proportional to the square root of the time interval of observation \sqrt{T} .

The Fourier processing of the proton loss signal (see Fig.2) shows that at frequencies above 1 Hz the spectrum of proton orbit vibrations (solid line in Fig.2) and the spectrum of proton losses variations (solid line marked by points) follow each other. For example, the spectral lines at 2.5 Hz, 6.25 Hz, 9.8 Hz, 12 Hz, 16 Hz, 18 Hz, 19 Hz, 22 Hz, 24.4 Hz, 48.8 Hz, 50 Hz, etc, are clearly seen in both PSDs. This coincidence points to certain connection (correlation) of the particle losses and orbit motion. Results of direct correlation measurements allow us to conclude that below 50 Hz the most of these peaks are caused by mechanical vibrations (for, example, 24.4 Hz and 48.8 Hz harmonics are due to mechanical pumps in HERA), and above 50 Hz they are due to the multiples of 50 Hz in magnet power supplies.

The spectrum of the coherence between the vertical ground motion (detected by CMG-3T and SM3-KV probes at the tun-

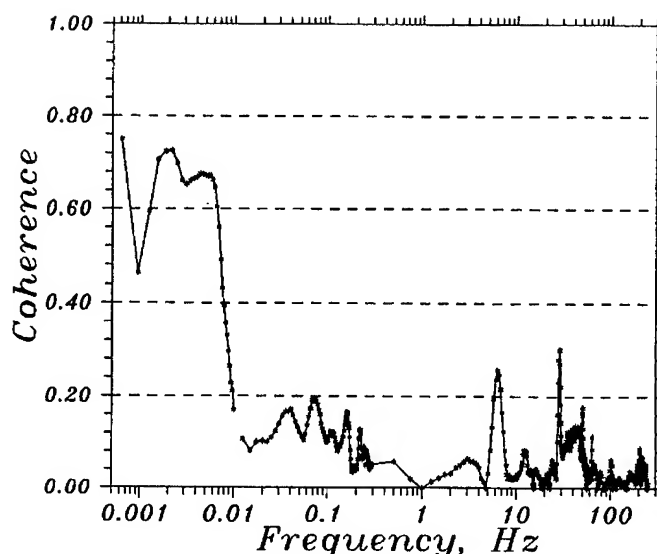


Figure 3. Spectrum of the coherence between vertical ground motion and vertical closed-orbit drifts of p -beam.

nel depth in the Hall West pit) and proton closed orbit vibrations measured by the BPM is shown in Fig.3. The measurements were performed during 5 days (September 16 – 21, 1994), and the spectrum covers a frequency band of 0.001 Hz – 200 Hz. A number of FFTs of the data records was about 60 – 90, and it allowed us to reduce the statistical error of the coherence measurement down to $\sigma \approx 0.1$. As it is seen in Fig.3, the significant coherence (above 2σ) was detected at frequencies 24.4 Hz and 6.25 Hz. There is no valuable correlation at frequencies of the *microseismic ground waves* which occupy a band of 0.1–0.3 Hz in the PSD of the HERA tunnel motion, and their amplitudes are about $2 \mu\text{m}$ [1]. The reason is that their wavelength of 20–30 km is much longer than the betatron wavelength in HERA (about 200 m). In spite of the PSD of the tunnel vibrations, there is no peak due to these waves in the COD PSD which is shown in Fig.1.

It is hard to conclude definitely on the COD–ground correlation at frequencies of 0.02 – 0.3 Hz, where the value of $Co(f)$ is about $1-2 \sigma$. The remarkable phenomena in this frequency region are the waves from the remote earthquakes that happened some dozen times during the period of the experiments. In spite of their large amplitude (up to $400 \mu\text{m}$) these seldom events produced no effect on HERA beams because their wavelength is above hundreds of km.

Below a frequency of 0.01 Hz, the coherence is as big as 0.6 – 0.7, what is above 3σ limit. This allows us to consider the slow tunnel motion to be a governing source of the closed orbit drifts in HERA.

Fig.4 demonstrates that the proton losses are due to the orbit motion at the frequencies of 0.01 – 0.3 Hz and 1–30 Hz. The harmonics observed in the PSD of the proton losses (Fig.2) are clearly seen in the coherence spectrum. Nevertheless, this connection is not still fully understood. For example, there is no a reasonable model to describe fast changes of the phase shift $\Delta\phi(f)$ between the BPM and the p -loss monitor signals over a frequency range of 0.01–30 Hz – see Fig.5.

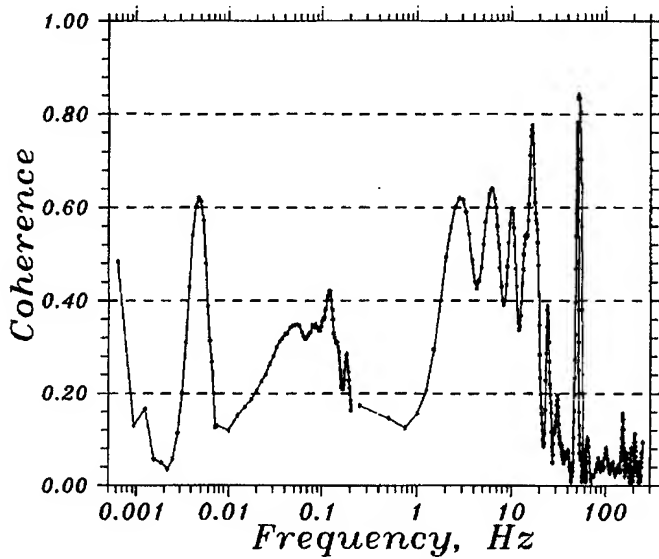


Figure 4. Spectrum of coherence between proton orbit motion and proton loss rate.

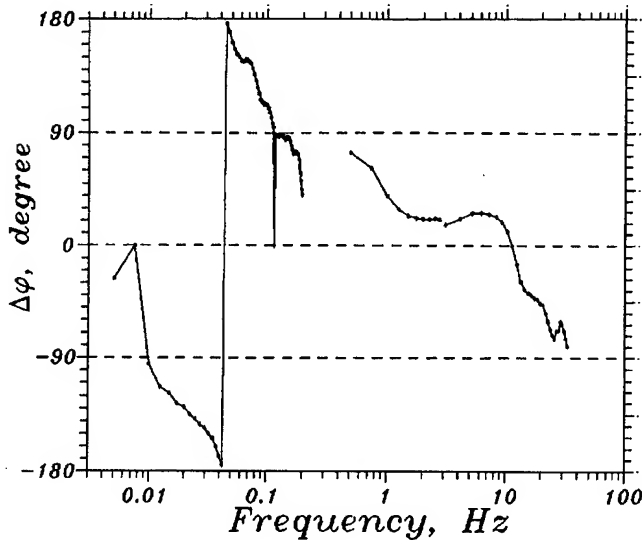


Figure 5. Phase advance between p -orbit motion and proton loss rate signals vs. frequency.

IV. DISCUSSION

The observed orbit drifts in HERA and the conclusion on their ground motion origin are in agreement with predictions of the *ATL law* [4]. This empirical rule states that besides the regular correlated ground motion there is a diffusion of *relative* positions of two points of the ground. The rms value of the displacement dX depends on the distance between the points L and the observation time interval T as $dX^2 = A \cdot T \cdot L$, where the constant somewhat depends on the site and typically $A \approx 10^{-5} \div 10^{-4} \mu m^2 / (s \cdot m)$. Due to a small value of the coefficient A , this diffusion usually takes place as a background for the large regular processes; however, it was properly measured in long-term observations in geophysics laboratories and in accelerator tunnels [4]. At present time, the interval of distances $L=7 - 2000$ m and the corresponding time interval from

some hours to 17 years are considered to be within the limits of validity of the law.

The ground diffusion leads to the closed orbit distortion $X_{COD} \propto \sqrt{ATC}$, where C is the accelerator circumference (6.3 km for HERA). Thus, the PSD of the COD is inversely proportional to the squared frequency $S_{COD} = A \cdot P / f^2$. The factor P contains machine lattice parameters and is derived analytically in [4]. For the HERA proton ring with vertical tune $\nu_y=33.298$, this parameter is about $P \approx 60$. Finally, from the approximation (2) of measured HERA proton COD spectrum $S_{COD}(f) = 1.2 \cdot 10^{-3} / f^2 [\mu m^2 / Hz]$, one can get the value of the ground diffusion constant $A = 1.2 \cdot 10^{-3} / P \approx 0.2 \cdot 10^{-4} \mu m^2 / (s \cdot m)$. It is within the range of previous results on the *ATL* diffusion and close to the HERA- e data [3].

V. ACKNOWLEDGEMENTS

We express our acknowledgement to Y. Soloviev, I. Shevyakov, S. Herb, M. Seidel, W. Radloff, M. Lomperski, S. Kazaryan (DESY), N. Dikansky, V. Parkhomchuk, S.igmatuulin, A. Chupira (INP) for their assistance in preparing the measurements in DESY. We would like to thank G.-A.Voss, F.Willeke (DESY) and A.Skrinsky (INP) for useful discussions.

References

- [1] V. Shiltsev *et. al.*, to appear as DESY HERA Report, 1995; see also this conference.
- [2] K.-H. Mess, M. Seidel, *Nucl. Instr. Meth.*, A310 (1994), p.279.
- [3] R. Brinkmann, J. Rossbach, *Nucl. Instr. Meth.*, A350 (1994), No. 1-2, p.8.
- [4] V. Parkhomchuk, V. Shiltsev, G. Stupakov, *Part. Accel.*, vol. 46 (1994), No.4, pp.241.

Simulation of the Acceleration of Polarized Protons In Circular Accelerators

Yu. Shatunov, V. Yakimenko,

Budker Institute of Nuclear Physics, Novosibirsk, 630090, Russia

Abstract

An acceleration of high energy polarized protons is a long term issue of spin physics. The application of Lie algebra method for the calculation of the strength spin resonances (both intrinsic and imperfection) in the high energy proton ring is discussed. The simulation results of the polarized proton acceleration in RHIC with two Siberian snakes are presented.

I. Introduction

Beam polarization can be lost during acceleration, when the particles pass the spin resonance. These resonances appear in the case, where the spin precession number $G\gamma$ ($G = 1.793$ is the anomalous magnetic moment for protons) is the integer or is equal to $kP \pm Q_y$. Here P is the number of superperiods, Q_y is the vertical betatron frequency, and k is the integer. Depolarization (in the case of the vertically polarized beam) is caused by horizontal magnetic fields being always present in the rings. Under resonance conditions, the action of these fields is coherent, and they force the spin to deviate from the stable vertical direction. The spin-betatron resonances are due to the horizontal fields generated by the vertical betatron motion.

During proton acceleration at RHIC[5] from a 20 GeV injection energy to a 250 GeV experimental energy, the beam passes several thousand spin resonances. The most important intrinsic resonances are approximately within $G\gamma = kP \pm Q_y \approx mPM \pm Q_b$, where k and m are the integers, P is the superperiodicity, M is the number of the FODO cells in the superperiod, and $2\pi Q_b = (2\pi Q_y - 6)$ is the phase advance in all the FODO cells containing the bending magnets. Position of the three most powerful resonances is the following:

$G\gamma$	E [GeV]
$3 \times 81 + (Q_y - 6)$	139
$5 \times 81 - (Q_y - 6)$	200
$5 \times 81 + (Q_y - 6)$	224

where 81 is the product of the superperiodicity (3) and the effective number of the FODO cells in the superperiod (27), which comprise insertions for dispersion suppression. The simulation results are given for $E = 224$ GeV. The most important imperfection resonances are near the powerful intrinsic ones. Therefore, the analysis of the region $E = 224 \pm 2$ GeV considers all the important aspects.

There are a lot of studies devoted to description of depolarization due to the isolated spin resonance crossing [1]. However, with a sufficiently large force the resonances become overlapping, so the analytical results do not work. There is a possibility of suppressing these resonances using the Siberian snakes [2]. However, the predicted so called "snake's resonances" [3], [4] expected at sufficiently powerful ordinary spin resonances require the special examination. The contradictory data obtained by a model tracking [3] impelled us to use the code SpinLie [6] to

simulate the conservation of polarization during the proton beam acceleration at RHIC with the Siberian snakes.

II. Simulation Model

The simulation was linear in order to save the computer time. The betatron frequencies were $Q_x = 28.19$ and $Q_y = 29.18$, respectively. For resonance strength estimation we introduced next machine imperfections: quads rotation angles relative to the longitudinal axis and quads vertical displacement have Gaussian distributions (truncated at two standard deviations) and with the amplitudes of 0.3 mrad and 0.25 mm, respectively. These imperfections cause the RMS orbit disturbance of about a 8 mm. The residual after correction RMS orbit deviation was approximately a 0.3 mm. The normalized emittance (according to [5]) was assumed to be equal to $\epsilon_{nx} = \epsilon_{ny} \equiv 6\pi\beta\sigma_{x,y}/\beta_{x,y} = 20\pi$ mm mrad.

III. Simulation Results

The spin resonance force [1] can be characterized by the dependence of the root-mean-square spin spread $\Delta\vec{n}_{rms} \equiv \langle (\vec{n}(\theta, \vec{z}) - \vec{n}_0(\theta))^2 \rangle^{1/2}$, where $\vec{n}_0(\theta)$ is the periodic spin solution for a synchronous particle on an ideal orbit and $\vec{n}(\theta, \vec{z})$ is the periodic spin solution for a off-axis particle, $\langle \rangle$ denote the averaging over the beam distribution. In this notations a resonance strength is the half-width of the dependence $\Delta\vec{n}_{rms}$ on the level $\Delta\vec{n}_{rms} \approx 0.6$, which corresponds to the angle between the vectors \vec{n} and \vec{n}_0 of the order $\pi/4$. Figure 1 illustrates the simulation of the imperfection resonances (for $\epsilon_{nx} = \epsilon_{ny} = 0$). The dashed curve in this figure shows complete suppression of these resonances by two Siberian snakes, which are placed diametrically opposite in the collider magnet system and rotate the spin by π relative to the longitudinal and horizontal axes, respectively.

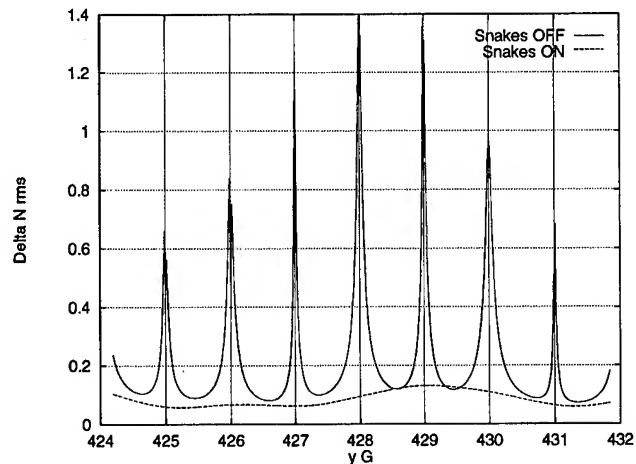


Figure 1. Imperfection resonances and their suppression by two Siberian snakes.

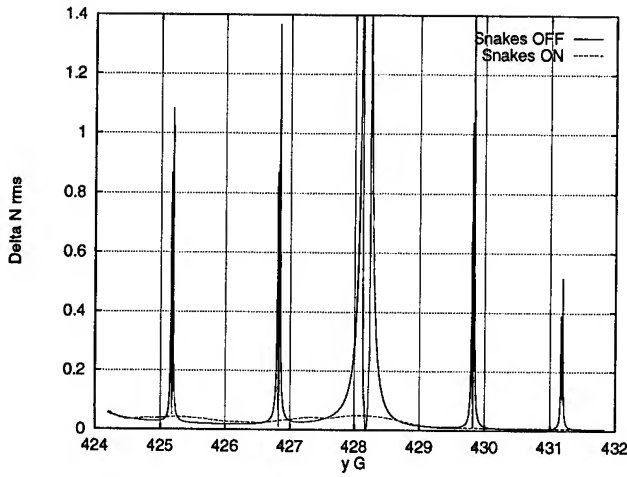


Figure 2. Intrinsic resonances without orbit disturbances and their suppression by two Siberian snakes

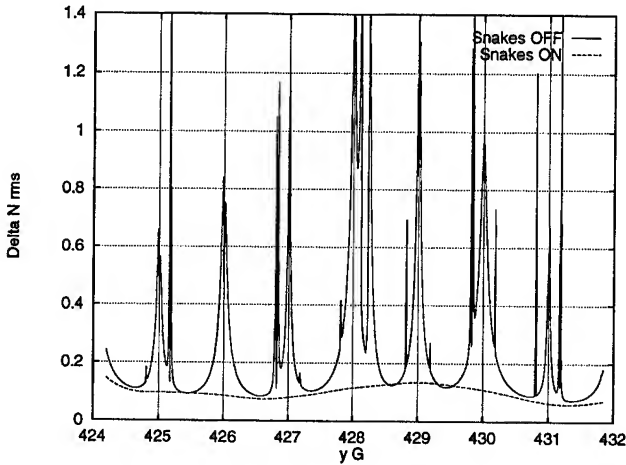


Figure 3. Intrinsic and imperfection resonances, and their suppression by two Siberian snakes

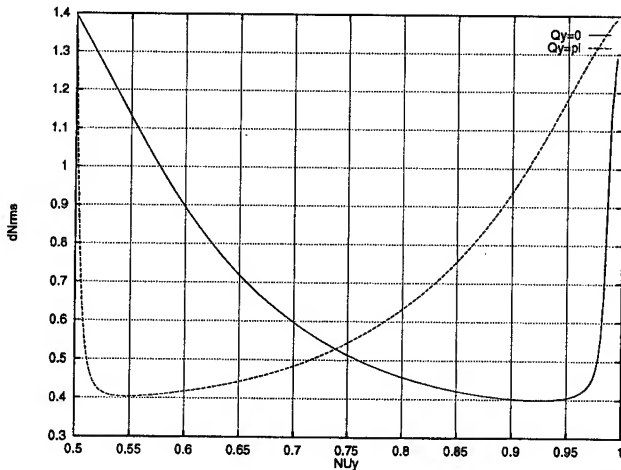


Figure 4. The root-mean-square spin spread versus vertical betatron frequency under the resonance condition $Q_{spin} = 399 + Q_y$. Snakes ON. Two cases are presented: the vertical phase advantage on snakes are 0 and π correspondently.

Figure 2 shows the simulation of the intrinsic resonances without C.O. disturbances with two Siberian snakes on and off (for $\epsilon_{nx} = \epsilon_{ny} = 20\pi$). The joint of the intrinsic and imperfection resonances with two Siberian snakes on and off is presented in Fig. 3.

In calculations, the snake is assumed to be ideal, i.e., it is a thin snake with a zero betatron phase advance ($\Delta Q_x = 0$ and $\Delta Q_y = 0$). The length and phase advance on the snake should be specially studied. As Fig. 4 shows, the different phase advance is favorable for different values of the full betatron frequency. This figure presents the root-mean-square spin spread versus the vertical betatron frequency under the resonance condition $Q_{spin} = 399 + Q_y$ (expected spin resonance point). Two curves correspond to two values of the vertical betatron phase advance on the snake $\Delta Q_y = 0$ and $\Delta Q_y = 1/2$.

IV. Spin Tracking

Additionally to estimation of the resonance strength Lie algebra techniques was applied for spin tracking while particle accelerating. The below results are obtained in the assumption that the beam consists of 50 particles with the Gaussian distribution in the phase space. The particle coordinates are prescribed relative to a zero (ideal) orbit.

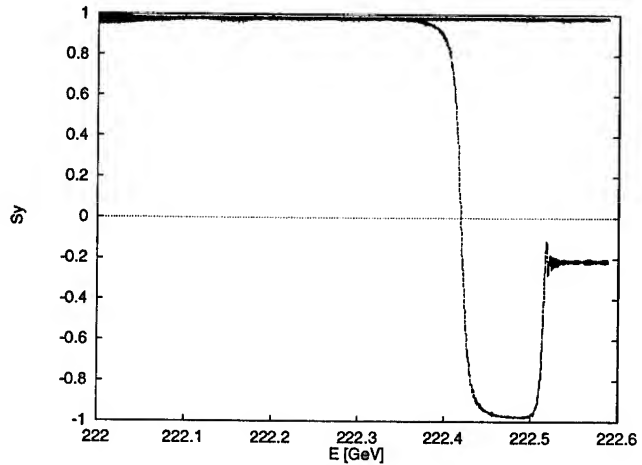


Figure 5. Spin-flip due to crossing imperfection resonance ($\gamma G = 425$) and its canceling by two snakes

The acceleration rate of about 120 keV/turn is close to a lower boundary of the designed rate. The alignment errors and the orbit compensation are taken into account. Figure 5 shows a spin-flip due to the adiabatical imperfection resonance crossing and then strong depolarization from nearest intrinsic resonance. When Siberian snakes are on we did not see spin-flip and depolarization (upper curve). Corresponding beam spin spread is presented on Figure 6.

V. Conclusion

The obtained results show that the Lie algebra method is applicable to calculating the dynamics of a spin motion. Moreover, they confirm the ability of the Siberian snakes concept and the possibility of a polarized proton beam acceleration at RHIC up

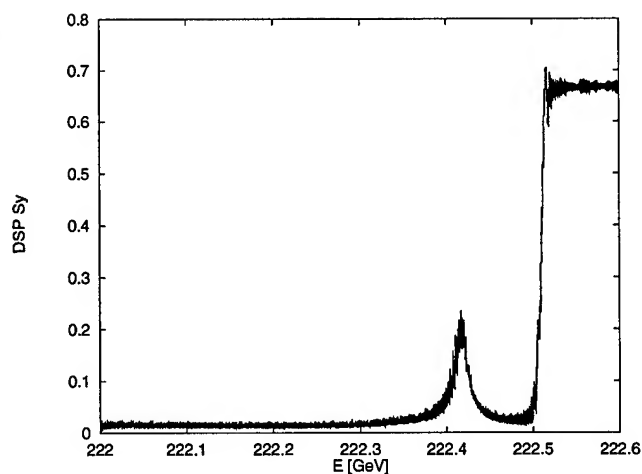


Figure. 6. Spin dispersion in the beam crossing imperfection resonance ($\gamma G = 425$)

to top energy. However, the validity of the simulation depends on whether the conditions correspond to the real ones.

References

- [1] E.D.Courant, R.D.Ruth *Acceleration of Polarized Protons In Circular Accelerators*, BNL Report 51270, UC-28 (1980).
- [2] Ya.S.Derbenev and A.M.Kondratenko, *JETP* **35**, 230 (1970).
- [3] S.Y.Lee, S.Tepikian, *Phys.Rev.Lett.*, **56**, 1635, (1986).
- [4] S.Y.Lee, *High Energy Spin Physics*, AIP Conf Proc., No.187, p.1105, (1988).
- [5] *RHIC Design Manual*, Brookhaven National Laboratory, Upton, (1994).
- [6] Yu.Eidelman, V.Yakimenko, *SPINLIE - New Code for Polarization Calculation*, PAC93, Washington, 1994, pp.430-433.

Abe, H. FAP13, 1358
Abe, S. TAQ35, 1608
Abraham, W. WPA01, 902
Abramenko, N. RPR10, RPR15, 1143, 1155
Abramsky, P. WPP11, 1681
Adachi, Toshikazu TPR16, 3275
Adamski, J. FAA27, 248
Adamski, J.L. FAA28, 251
Adolphsen, C. WAG11, RPB03, RPB04, RPC01, RAE03, TPQ17, WAB07, WAC18, 646, 662, 665, 698, 2389, 2989, 3031, 3112
Adolphsen, Chris WAB08, 3034
Afanasiev, O. FAQ06, 1399
Agafonov, A.V. TPR13, TPR14, 3269, 3272
Ahrens, L.A. TAP11, TAP12, TAP13, WAB04, RAQ22, 378, 381, 383, 3022, 3334
Aizatsky, N.I. WPQ22, TPA14, 1773, 3229
Akai, K. FAE09, WPQ08, WPQ09, WPQ17, WPR05, WPR09, RPQ06, WAC08, 1503, 1735, 1738, 1759, 1797, 1806, 2675, 3085
Akasaka, N. RPA20, FAE09, WPQ09, WPQ17, WPR05, WPR09, TPC08, TPC29, TAG01, 1099, 1503, 1738, 1759, 1797, 1806, 2613, 2655, 2742
Akemoto, M. WPR02, WPR03, 1788, 1791
Akimov, V. WAA17, 1263
Akre, J. FAQ24, FAQ25, 1444, 1447
Akre, R. WPR15, WAB12, 1821, 3046
Alessi, J. WPC09, 1013
Alexahin, Y. RAA17, 560
Alexandrof, V.A. TAG01, 2742
Alimov, A. RPA19, 1096
Alimov, A.S. RAR04, 3361
Alinovsky, N.I. TAC06, 143
Allen, C.W. RPA24, 1111
Allen, Christopher K. MPC04, 2324
Allen, J. RAR23, 3406
Allen, L. WPA06, 917
Allen, M.A. WPQ06, 1729
Allen, Ray TPP13, 1645
Alley, R. MPE10, 887
Allison, Paul W. TAE08, 1207
Allison, S. RAE03, 2389
Alonso, Jose R. WPE01, 58
Alton, G.D. MPE05, WPC12, WAQ26, 871, 1022, 1897
Altuna, X. WAP12, WAP13, 464, 467
Amankath, H. RPA26, 1116
Amiranoff, F. WAG07, 634
Anderson, David E. TAE07, 1204
Anderson, K. WAQ22, WAR17, 1888, 1939
Ando, A. RPQ15, 2699
Andreev, V.G. WPP19, 1702
Andreev, V.V. FAC09, 2856
Andriishchin, A. FAQ06, 1399
Anerella, M. TPE04, FAQ04, 1293, 1396
Angerth, B. RPE02, 1999
Ankenbrandt, C. FAG06, 86
Anthouard, Ph. TAE09, 1210
Antonsen, T.M. WAG04, 621
Aoki, T. FAP13, 1358
Arai, S. RPG13, 351
Arbuzov, V. WPP11, 1681
Ardonceanu, J. WAG07, 634
Argyakis, J. FAP03, 1328
Arinaga, M. RAB13, 779
Arnold, N. RPA11, RPA14, MPQ08, 1073, 1082, 2467
Asano, K. TPP03, TPP16, 1620, 1652
Ashton, J.R. RPB05, 668
Assadi, S. TAG10, RAP03, WAB01, 2777, 2886, 3016
Asseev, A.A. WAR23, 1955
Assmann, R. RAA19, WAG11, RPB02, 567, 646, 659
Astapov, A.A. RPE13, 2029
Auble, R.L. WAQ26, 1897
Auch, S. RPR06, 1131
Aune, B. WPB22, 998
Ausset, P. WPQ26, 1781
Austin, R.H. FAA19, FAA31, 234, 260
Autin, B. RPC11, WAE09, 722, 2178
Averill, R. RPG05, RAA31, 327, 600
Azorsky, N.I. TAQ34, 1605
Baartman, R. RPG12, WAQ07, WAC20, 348, 1858, 3119
Baba, T. WAQ06, 1855
Babzien, M. MPE11, 890
Backmor, Rudolf TAQ13, 1550
Bailey, J.D. TAP07, TAP08, TAP09, 366, 369, 372
Bailey, R. WAP12, WAP13, RAA11, 464, 467, 548
Bainan, Ding FAA26, 246
Baiod, R. FAP04, FAP06, FAP07, FAP09, MPB06, 1331, 1337, 1340, 1346, 2285
Bak, J.S. RPA06, 1061
Baker, S. WAR19, 1945
Bakker, R. RPG06, 330
Baklakov, B. TAA01, RAR30, 2078, 3424
Balakin, V. TAG01, 2742
Balewski, K. FAR07, 275
Balhan, B. RAA15, 557
Ball, M. TPB24, RAP21, RAP22, WAC12, RAQ23, RAQ24, 2583, 2934, 2937, 3094, 3337, 3340
Ballauff, M. FAR06, 272
Bamblevski, V.P. RPE13, 2029
Bane, K. RPA04, WAC17, 1058, 3109
Bane, K.L.F. RPA20, TPQ16, TPQ17, WAB07, WAC16, WAC18, 1099, 2986, 2989, 3031, 3105, 3112
Bangerter, R.O. WAQ04, 1852
Baptiste, K. TAR03, 801
Baranov, V.I. MPG10, WAR21, 426, 1949
Baranova, L.A. TAP16, 389
Barber, D.P. WPG08, 511
Bardy, J. TAE09, 1210
Barker, D. MPR13, 2265
Barklow, T. RPB01, 656
Barletta, W. TAA28, 2135
Barlow, T.A. TPC13, 2628
Barnard, J. TAR17, 837
Barnard, J.J. TAR14, TPB14, TPR18, 828, 2557, 3278
Barnard, John J. TPR02, 3241
Barnes, P. FAE13, WPQ02, RAQ04, 1515, 1720, 3294
Barov, N. WAG06, WPB11, 631, 976
Barr, D. MPQ03, RPQ16, TPQ19, 2452, 2702, 2992
Barry, W. RAE13, RPQ08, 2423, 2681
Barts, T. MPB10, 2294
Batchelor, K. MPE11, WPB13, RAE09, WXE03, TPB01, 890, 982, 2411, 2432, 2530
Batskikh, G. FAP24, 1387

Batskikh, G.I. RPR07, 1134
 Batygin, Y. WPC01, 1001
 Batygin, Y.K. TPR06, 3251
 Batygin, Yuri K. TPR07, 3254
 Beadle, Edward R. TPB08, TPB09, 2545, 2548
 Beauvais, P.-Y. RAG07, 3173
 Becher, D. MPE05, 871
 Bechstedt, U. TPB20, 2574
 Bechtold, V. FAR06, 272
 Becker, T. FAP02, 1325
 Becker, U. TAQ06, WAE13, 1533, 2190
 Beebe, E. WPC09, 1013
 Behne, D. MPP12, MPP20, 2064, 2075
 Beisel, U. WPA04, 911
 Bekefi, G. TPG14, RPC15, 192, 734
 Belkovets, V. TAC16, 152
 Beloglazov, V.I. TAE14, 1225
 Belomestnykh, S. FAE13, WPP11, RAQ04, RAR18, RAR19, 1515, 1681, 3294, 3391, 3394
 Belov, W. RAQ14, 3315
 Belova, Nadya G. WAA01, 1227
 Belser, C. RAA04, 530
 Belser, F.C. WPQ06, TAA22, 1729, 2129
 Belugin, V.M. RPR07, 1134
 Ben-Zvi, I. MPE11, WPB13, RAE09, WXE03, TPB01, 890, 982, 2411, 2432, 2530
 Benesch, J. FAE12, 1512
 Benjamin, J. TAP11, 378
 Benjegerdes, R. WPA01, FAP17, 902, 1369
 Bennett, L. TAE06, 1201
 Bennett, Lawrence F. TAE07, 1204
 Benson, S. FAG11, FAA25, WPA17, WPC24, 102, 243, 942, 1052
 Benvenuti, C. FAE11, TPP12, 1509, 1642
 Bercher, M. WAG07, 634
 Berenc, T. WPB06, 961
 Berezin, A.K. RAB15, 782
 Berg, J. TAA22, 2129
 Berg, J.S. FAB06, TPQ16, 2804, 2986
 Berg, J. Scott TPQ07, WAC05, 2962, 3076
 Berg, W. RPA11, MPQ10, 1073, 2473
 Berger, D.D. WPQ06, 1729
 Bergher, M. RAP19, 2928
 Berkelman, K. FAE13, 1515
 Bernal, Santiago TAA17, 2117
 Bernard, D. WAG07, 634
 Bernard, M. WPB01, WPB22, 945, 998
 Berridge, S. TAA28, 2135
 Bertagnolli, H. FAR06, 272
 Bertinelli, F. RPE02, 1999
 Bertolini, L. RAA03, 527
 Bertsche, K. TPE05, FAP21, WAQ09, MPQ21, TPB19, 1298, 1381, 1864, 2503, 2572
 Bertuzzi, J.-P. MPP15, 2069
 Berwald, D. RPR20, 1164
 Berz, Martin MPC09, 2336
 Bessonov, E.G. RAP06, 2895
 Beveridge, J.L. RPG12, 348
 Beyer, K.A. TPC13, 2628
 Bharadwaj, V. MPG02, WAP04, RPC20, RPC21, WPB08, TAG01, 396, 443, 749, 752, 967, 2742
 Bhat, C.M. FAP05, WAR02, TAA12, WAC06, 1334, 1903, 2105, 3079
 Bialowons, W. RPE08, 2017
 Bialy, J. FAR06, 272
 Bickley, M. MPA12, MPR19, 2220, 2276
 Bieniosek, F.M. WAR17, WAR18, 1939, 1942
 Biggs, J. FAP03, 1328
 Billen, J.H. RPR08, RPR09, 1137, 1140
 Billen, James H. MPB16, 2306
 Billing, M. FAE13, FAB12, TPA04, RAQ04, 1515, 2820, 3206, 3294
 Billing, M.G. RAE14, 2426
 Binns, B. WAA16, TPB04, 1260, 2536
 Birukov, I.N. RPR01, 1119
 Biryukov, V.M. MPG10, WAR20, WAR21, 426, 1948, 1949
 Biryukov, Valery WAR24, 1958
 Biscardi, R. TPP06, WPP03, 1626, 1660
 Bisognano, J. FAG11, FAA25, WPA17, 102, 243, 942
 Bisognano, J.J. RPQ11, 2690
 Bisognano, Joseph J. MPC25, RAG12, 2370, 3188
 Bizek, Hana M. RAR27, 3418
 Bjerklie, S. FAG06, 86
 Black, E. FAP03, 1328
 Black, W.M. TAE10, 1213
 Blanchard, R. WAP12, WAP13, 464, 467
 Blas, F. MPG09, 423
 Blaskiewicz, M. TAP11, TAP12, TAP13, WAC24, 378, 381, 383, 3131
 Blaskiewicz, M.M. RAQ22, 3334
 Blastos, J. TPG14, 192
 Blazhevich, S.V. FAG12, 105
 Bleser, E.J. TAP13, WAR13, 383, 1930
 Bloess, D. TPP12, 1642
 Blondel, A. RAA19, 567
 Bloom, E. WAQ15, 1876
 Blosser, H. RPG11, 345
 Bluem, H.P. TAA32, 2141
 Blum, E. FAR10, 284
 Blum, E.B. FAR01, MPQ01, 263, 2450
 Bocchetta, C. FAR06, 272
 Bocchetta, C.J. FAA13, FAR21, TAG05, 222, 309, 2762
 Boehnlein, D. FAG06, 86
 Boer-Rookhuizen, H. MPQ17, 2491
 Boers, Jack E. MPB18, 2312
 Bogacz, A. FAP05, WAR19, RAR17, 1334, 1945, 3388
 Bogacz, S.A. RAB20, TAR20, 790, 843
 Bogard, D. RAG07, 3173
 Bogaty, J.M. TPC12, 2625
 Bogdanovich, B. RPR10, RPR15, TAQ24, 1143, 1155, 1575
 Bogdanovich, B.Yu. TAB13, TAQ23, 125, 1572
 Böge, M. RAP08, 2901
 Bogert, D. MPG01, 391
 Bohl, T. WAP12, WAP13, RAA11, FAE10, 464, 467, 548, 1506
 Bohlen, H. FAE07, 1497
 Bohn, C.L. FAG11, 102
 Bojon, J.-P. RPE06, 2014
 Bolme, G.O. WPA08, RPR19, 923, 1161
 Bolotin, I. WPR19, 1833
 Bolser, C. MPC01, 2317
 Bonati, R. WAR11, 1924
 Bondarev, B.I. RPR07, 1134
 Bongardt, K. TPA01, TPA02,

TPA03, 3197, 3200, 3203
Boni, R. RPA26, 1116
Bonifacio, R. FAA12, 219
Bonin, B. TPP09, 1632
Bonnafond, C. TAE09, 1210
Bonnafond, Ch. TPC17, 2640
Bookwalter, V. MPR13, 2265
Borden, M. RAR23, 3406
Borland, M. FAR11, WAE11,
 MPQ10, 287, 2184, 2473
Borodich, A.I. TPA15, 3232
Bortnyansky, A. TAA18,
 2120
Bosch, R.A. FAR20, 306
Bosotti, A. TAA07, 2093
Bossard, P. MPG09, 423
Bossart, R. RPC10, 719
Bosser, J. RAP23, RAP24,
 2940, 2943
Bostic, D. MPP10, 2057
Bothe, W. FAR06, 272
Botman, J.I.M. WAQ19,
 WAQ20, RPP04, RPQ31, 1882,
 1885, 1970, 2738
Bourdon, J.C. WPB22, 998
Boussard, D. FAE10, TPP12,
 1506, 1642
Bowden, G.B. RPB04, RPA23,
 665, 1108
Bowers, J. WAC17, 3109
Bowling, B. MPR13, 2265
Bowling, B.A. WAE10, 2181
Bowling, S. RPR19, 1161
Boyd, John K. MPC13, 2339
Boyes, John D. TAE07, 1204
Bozoki, Eva RPQ14, 2696
Brabson, B. RAP21, RAQ23,
 RAQ24, 2934, 3337, 3340
Bracco, R. FAQ19, 1432
Bradley, S. RPG05, 327
Brandt, D. RAA17, RAA20,
 FAC03, 560, 570, 2841
Brauer, S.O. RPE09, 2020
Braun, A. RPC21, 752
Braun, H. RPC09, RPC10, 716,
 719
Brefeld, W. FAA02, FAR07,
 195, 275
Brennan, J.M. TAP11, TAP13,
 FAE05, MPQ30, RPQ17, RPQ25,
 WAB04, RAQ22, 378, 383,
 1489, 2518, 2705, 2723,
 3022, 3334
Bricault, P.G. RPG12, RPR02,
 RPR03, 348, 1122, 1125
Bridges, J.F. WPP16, 1693
Brillson, L.J. FAG11, 102
Brinker, F. FAA02, 195
Brinkmann, R. MPG04, RPB07,
 RPE08, 406, 674, 2017
Brodowski, J. WPP07, WPQ19,
 RPQ17, 1669, 1765, 2705
Brogle, R. WAG09, WPC20,
 640, 1039
Broome, W. TPP06, 1626
Brouet, M. MPP15, 2069
Brouzet, E. WAP13, 467
Browman, A. TAR12, TPB13,
 822, 2554
Brown, B. TPE05, 1298
Brown, B.C. FAP05, FAP06,
 FAP07, MPB05, MPB06, 1334,
 1337, 1340, 2282, 2285
Brown, D. TPB13, 2554
Brown, K. RPC06, MPR13,
 707, 2265
Brown, K.A. TPA06, 3212
Brown, Nathan RPR23, 1170
Brown, R. WPC08, 1010
Brown, V.W. WPA08, 923
Bruhwieler, D. RPR20, TPR07,
 1164, 3254
Bruhwieler, D.L. TPR08, 3257
Brunelle, P. FAR14, 293
Brunet, J.-C. RPE02, 1999
Brüning, O. TAG09, 2774
Brüning, O.S. MPG07, 420
Brunner, O. WPG09, 514
Bruns, Warner RPA15,
 RPA16, 1085, 1088
Bryant, P.J. RPG03, 322
Budilin, V. WPR19, 1833
Budnick, J. RAP21, RAQ23,
 RAQ24, 2934, 3337, 3340
Bugg, W. TAA28, 2135
Bugorsky, A.P. MPG10, 426
Buhler, S. WPB22, 998
Bula, C. TAA28, 2135
Bulfone, D. TPG11, FAR21,
 186, 309
Bulos, F. WAQ15, TAG01,
 1876, 2742
Bulyak, E. FAR17, TPA12,
 TPA13, 299, 3223, 3226
Buon, J. RPC20, TAG01, 749,
 2742
Burke, D. RPC01, RPC20,
 TAA08, WXE07, TAG01, 698,
 749, 2096, 2444, 2742
Burkhardt, H. WAP12, WAP13,
 RAA11, 464, 467, 548
Burlet, A. MPP15, 2069
Burnham, B. FAA08, RAA01,
 RAB22, MPA10, MPA11,
 MPQ06, FAC20, 213, 524, 796,
 2214, 2217, 2461, 2877
Burnside, C. MPP15, 2069
Burov, A. WAB16, WAB17,
 3055, 3058
Burrini, D. RAQ05, 3297
Burton, A. RAA15, 557
Bushuyev, A. WPP11, 1681
Bussa, M.P. WAP14, 470
Butteris, J. FAQ32, 1465
Buxton, W.E. MPA19, 2235
Byrd, J. RPC02, MPC01,
 RAE12, RAE13, RPQ08, TPQ16,
 701, 2317, 2420, 2423, 2681,
 2986
Byrd, J.M. WXE06, RPQ09,
 2441, 2684
Byrne, M. WPR15, 1821
Cable, M.D. TAR14, 828
Cai, Y. RAA22, RAA25, RAA26,
 RAA27, 576, 585, 588, 591
Cain, T.D. FAG05, 83
Calabrese, R. RAE05, 2399
Calame, J. TAQ17, 1561
Calame, J.P. TAQ18, TAQ19,
 1563, 1566
Calder, R. RPE02, 1999
Calish, S. TAR18, 840
Callahan, D.A. TAR14, TPR19,
 828, 3282
Callahan, Debra A. TPR01,
 3238
Callin, R.S. TAQ28, 1587
Camas, J. TPC21, 2649
Cameron, P. TAA09, 2099
Cameron, P.R. MPQ05, 2458
Campbell, R. WAA16, 1260
Capone, D. FAQ14, 1417
Caporaso, G. RPC16, MPE14,
 WPC16, WAA19, TAA20, 737,
 899, 1027, 1269, 2123
Cappi, R. TAP14, MPG09, 386,
 423
Carboni, G. WAP14, 470
Carder, B. WAA19, TAA20,
 1269, 2123
Cardman, L. FAG11, WPA17,
 102, 942
Cardman, L.S. WPC17, 1030
Cargnello, F. TPG11, 186
Carlier, E. RAA15, 557
Carlsten, Bruce E. WPB15,
 FAE06, 985, 1494
Carnegie, D.W. TPE08, 1310
Carrigan, D. WAR19, 1945
Carroll, Frank E. FAG04, 80
Carson, J.A. FAP06, FAP07,

1337, 1340
Carter, A. RPG05, 327
Carter, F. FAA08, RPA17, MPA11, 213, 1090, 2217
Caruette, A. TPP11, TPP14, 1639, 1648
Carwardine, J.A. WAA08, RPP03, RPQ18, 1242, 1967, 2708
Caryotakis, G. FAE07, 1497
Casella, R. RPP02, 1964
Caspers, F. RPE02, RAP24, 1999, 2943
Caspi, S. FAQ23, 1441
Cassel, R.L. WAR06, 1915
Castellano, M. TPG11, 186
Castillo, V. RPQ07, 2678
Castle, M. TAQ18, TAQ19, 1563, 1566
Castro, P. RAA20, FAC03, 570, 2841
Catravas, P. TPG14, 192
Caussyn, D.D. RAP21, RAQ23, RAQ24, 2934, 3337, 3340
Cayla, J.N. WPB01, 945
Celata, C.M. TPA10, 3220
Cevenini, F. TPG11, 186
Chae, Y.-C. TAP05, FAB09, 363, 2811
Chae, Yong-Chul TPQ20, TPQ21, RAR24, RAR25, 2995, 2998, 3409, 3412
Chamouard, P.-A. RAG07, 3173
Chan, A. TAR18, 840
Chan, K.C.D. FAA16, TAR12, 228, 822
Chanel, M. RAP24, 2943
Chang, C.H. FAQ26, 1450
Chang, H.P. FAA07, RAA24, TPQ10, 210, 582, 2971
Chang, L.H. FAA04, RAA24, FAQ26, TPQ08, 201, 582, 1450, 2965
Chang, Peace TAR04, 804
Chang, Y.M. MPQ32, 2524
Channell, P. WAC29, 3146
Chao, A. MPC01, WAC17, 2317, 3109
Chao, A.W. WAB09, WAB11, RAQ02, 3037, 3043, 3288
Chao, Alex FAC02, WAB10, 2838, 3040
Charruau, G. WPQ26, 1781
Chattopadhyay, S. TPG07, RPC16, TAA28, 174, 737, 2135
Chautard, F. RPC10, 719
Chavanne, J. TPE10, 1319
Chehab, R. WPB22, 998
Chen, B. WAB20, 3064
Chen, Bo WAB10, 3040
Chen, C.-I. TPC15, 2634
Chen, D. WAR19, 1945
Chen, J.R. FAA07, 210
Chen, J.S. MPR10, TPB29, 2256, 2592
Chen, Jenny MPR10, MPQ16, TPB29, 2256, 2488, 2592
Chen, P. RPC01, TAA28, RAP15, 698, 2135, 2919
Chen, Pisin RAQ18, 3326
Chen, R.-C. TPC15, 2634
Chen, S.C. MPE12, WPB03, WPB04, 893, 951, 954
Chen, T. RAA26, TAG06, RAP09, RAP11, RAP12, WAC17, 588, 2765, 2904, 2910, 2913, 3109
Chen, Y. RPC16, WPC16, WAA19, 737, 1027, 1269
Chen, Yinbao FAA21, RAQ25, RAQ26, 237, 3343, 3346
Cheng, J. TAQ18, TAQ19, 1563, 1566
Cheng, Wen-Hao RAG09, TPR12, 3179, 3266
Cheng, Y. FAA04, FAA07, 201, 210
Chepurnov, A. RPA19, 1096
Chepurnov, A.S. FAG12, RAR04, 105, 3361
Cherenshchikov, S.A. WPA15, WPA16, 938, 939
Chernikov, V.I. WAR09, 1918
Chernogubovsky, M.A. WPP04, 1663
Chertok, I. TPE09, 1316
Chertok, I.L. TAC06, 143
Chesnokov, Yu.A. MPG10, WAR20, WAR21, 426, 1948, 1949
Chester, N.S. FAP06, FAP07, 1337, 1340
Chiang, R. RAQ04, 3294
Chiaveri, E. FAE11, 1509
Chin, A. TPG07, 174
Chin, Y.H. TPC08, WAC07, WAC08, 2613, 3082, 3085
Chiou, T.C. RAB02, RAB08, 761, 773
Chirkov, P.N. FAB02, 2792
Cho, M.H. TAR07, RPA06, TAQ15, 813, 1061, 1556
Cho, Y. TAP05, TPQ22, TPQ23, 363, 3001, 3004
Cho, Y.S. FAA10, 216
Cho, Yanglai RAR25, 3412
Choi, J. TAR07, RPA06, 813, 1061
Choi, Sewan RPP11, 1985
Chojnacki, E. WPB11, WPB12, WPQ02, RAQ04, 976, 979, 1720, 3294
Chou, P.J. MPQ13, WAC09, WAC10, 2479, 3088, 3091
Chou, W. WAP02, WAP03, MPB10, TPQ15, 437, 440, 2294, 2983
Chowdhary, M. MPR14, RAE11, 2268, 2417
Chu, C.C. MPQ26, RAR05, 2515, 3364
Chu, C.-C. TPC15, 2634
Chu, W.T. RAE04, 2394
Chubar, O.V. RAE06, WXE08, 2402, 2447
Chubarov, O. RPA19, 1096
Chubarov, O.V. RAR04, 3361
Chumakov, S.N. TAC06, RPP08, 143, 1979
Chung, K.H. FAA10, 216
Chung, S.C. RAR05, 3364
Chung, Y. MPQ03, MPQ08, TPC03, RPQ15, RPQ16, 2452, 2467, 2598, 2699, 2702
Chupp, W. TPA10, 3220
Church, M. TAR16, 834
Church, Mike RPG07, 333
Ciardullo, D.J. MPQ30, 2518
Cieslik, W. MPQ11, 2476
Ciocci, F. TPG11, 186
Clark, D.C. WPA08, 923
Clark, G.S. RPG12, 348
Clarke, J.A. TPG09, WAC23, 180, 3128
Claus, J. FAP11, 1352
Claus, R. RAE12, RPQ01, RPQ05, 2420, 2660, 2672
Clayton, C. TPB18, 2569
Clayton, C.E. WAG08, RAB01, RAB02, RAB04, RAB05, 637, 758, 761, 767, 770
Clendenin, J. MPE10, WPC21, 887, 1043
Clendenin, J.E. MPE08, WPC18, 877, 1033
Cleveland, E.K. FAG05, 83
Cliff, B.E. TPC12, 2625
Cline, D. TAA28, 2135
Cline, D.B. TAB06, WPG11, RAB20, TAR21, 119, 520, 790,

- Codutti, A.** FAQ19, 1432
Colby, E. WPB05, WPB08, 957, 967
Colestock, P. WPP01, RAP21, WAB01, RAQ24, 1655, 2934, 3016, 3340
Colestock, P.L. TAG04, WAC01, 2757, 3067
Colestock, Patrick L. WAC02, 3070
Collier, P. WAP12, WAP13, RAA10, RAA11, RAA12, RAA13, 464, 467, 545, 548, 551, 554
Collins, J. TPB24, 2583
Colton, E. WAC29, 3146
Coluzza, C. FAR06, 272
Comunian, M. RPC10, 719
Conde, M. WAG06, WPB08, WPB11, 631, 967, 976
Conkling, C.R. MPA16, 2226
Connolly, R. RPR19, WPP07, 1161, 1669
Connolly, R.C. RPR22, TPC06, 1167, 2607
Cooper, R. WAC29, 3146
Cooper, Ronald WPB15, 985
Corbett, J. RPQ21, RPQ22, RAQ17, 2714, 2717, 3323
Corcoran, P. TAE06, 1201
Corlett, J. RPC02, WPR14, MPC01, RAE12, RAE13, RPQ08, TPQ16, 701, 1818, 2317, 2420, 2423, 2681, 2986
Corlett, J.N. WXE06, 2441
Corley, J.P. TAE06, 1201
Cornacchia, M. FAA25, RAA18, RAQ17, 243, 564, 3323
Cornelis, K. WAP12, WAP13, RAA11, RAA17, RAA20, FAC03, 464, 467, 548, 560, 570, 2841
Corredoura, P. RPQ02, RPQ03, RPQ05, 2663, 2666, 2672
Corsini, R. RPC09, RPC11, 716, 722
Corvin, C. TAA16, 2114
Cosso, R. FAE11, 1509
Couillaud, C. RAG06, 3170
Cours, A. RPA11, 1073
Cours, Alexander TAQ16, 1559
Coverdale, C.A. RAB01, 758
Cox, G. WAG06, WPB11, 631, 976
Craddock, M.K. FAB14, 2823
Craddock, W. TAA28, 2135
Crandall, K.R. RPG10, 342
Crane, G. TAR18, 840
Crawford, J. WAP04, 443
Crawford, K. RPQ29, 2732
Cremer, T. FAP20, 1378
Crofford, M. WXE01, 2429
Cromer, K.D. RAP01, 2880
Cros, B. WAG07, 634
Crosbie, E. TAP05, RAA29, RAG05, 363, 597, 3167
Crosbie, E.A. RAR26, 3415
Crowe, T. TPC04, 2601
Cruikshank, P. RPE02, 1999
Cutolo, A. TPG11, 186
Cyvot, G. MPG09, 423
d'Amico, E.T. RPC12, 725
D'Auria, G. TPG11, FAA13, FAR21, 186, 222, 309
D'Ottavio, T. MPR20, 2279
D'Yachkov, M. WAC20, 3119
Daclon, F. TPG11, FAR21, 186, 309
Dalin, J.-M. RPE02, 1999
Daly, E. TAA22, MPC01, 2129, 2317
Daly, E.F. MPP08, MPP10, MPP12, MPP20, 2051, 2057, 2064, 2075
Dangor, A.E. WAG08, 637
Danilewsky, A.N. FAR06, 272
Danilov, O. TAQ21, 1569
Danly, B.G. MPE12, 893
Darrow, C.B. WAG08, RAB01, 637, 758
Datskov, V.I. MPP01, 2034
Dattoli, G. TPG11, TPC03, 186, 2598
Davies-White, W. RAA04, 530
Davis, P. WPC20, RPA21, RPA22, 1039, 1102, 1105
Dawson, J. WAG09, TPC16, 640, 2637
De Angelis, A. TPG11, 186
De Brion, J.P. RAG06, 3170
de Groen, P. TAQ12, 1547
de Jager, C. RPG06, 330
de Leeuw, R.W. WAQ19, WAQ20, RPP04, RPQ31, 1882, 1885, 1970, 2738
De Martinis, C. TPC10, 2619
De Mascureau, J. TAE09, 1210
De Rijk, G. RAA11, 548
de Rijk, G. WAP12, WAP13, 464, 467
de Wijs, M.C.J. WAQ19, 1882
Deadrick, F. RPC18, TAR17, WPA02, TAE01, 743, 837, 905, 1178
Deadrick, F.J. TAR14, TPB14, 828, 2557
DeBarger, S. FAP16, 1366
Debraine, A. WAG07, 634
Decker, C.D. RAB01, RAB02, 758, 761
Decker, F.J. WAG11, RPB04, WAC17, 646, 665, 3109
Decker, F.-J. RPB02, WPR15, TPC20, RAP15, RAP16, RAP17, WAB05, WAB07, RAQ03, 659, 1821, 2646, 2919, 2922, 2925, 3025, 3031, 3291
Decker, G. FAR13, FAR19, MPQ03, MPQ08, MPQ10, RPQ16, 290, 303, 2452, 2467, 2473, 2702
Decker, Glenn RAR24, 3409
Decking, W. FAA02, FAB01, FAC19, 195, 2789, 2874
DeCobert, J. WAA16, 1260
Degen, C.M. TPB12, 2551
Dehnel, M. WAQ07, 1858
Dehning, B. WAP14, RAA19, 470, 567
Deitinghoff, H. WPA04, RPR06, RPR18, 911, 1131, 1158
Dejus, R. TPC03, 2598
Delahaye, J.P. RPC10, 719
Delahaye, J.-P. RPC09, 716
delaRama, F. TAE01, 1178
Dell, G.F. MPC05, FAB20, 2327, 2829
Dellwo, J. MPE05, WPC12, 871, 1022
Delsart, Ph. TAE09, 1210
Deluen, J.-P. RAA15, 557
Demko, J.A. MPP01, 2034
Den Hartog, P. MPP16, 2072
Deng, D. WAC24, 3131
Deng, D.P. WPP07, WPQ19, 1669, 1765
Deng, D.-P. MPB08, RAQ22, RAR29, 2288, 3334, 3421
Deppe, G. TPP11, 1639
Derenchuk, V. WPC08, RAP22, RAQ24, 1010, 2937, 3340
Desavouret, E. FAP06, FAP07, MPB06, 1337, 1340, 2285
Desmons, M. WPB22, 998
Despe, O. FAQ18, 1429
Deviatilov, V. WAA18, 1266
Devin, A. TAE09, TPC17,

1210, 2640
Dewa, H. FAR08, RPA13, WAQ01, 278, 1079, 1843
Dey, J. WPP08, WPP09, WPP23, RAQ13, 1672, 1675, 1714, 3312
Di Bona, A. WPC23, 1049
Di Crescenzo, J. RAG06, 3170
Dickey, C. FAA08, RPA17, WAA10, MPA11, 213, 1090, 1248, 2217
Dieperink, J. RAA15, 557
Dieulot, J.M. WAG07, 634
Dikansky, N. WPG06, TAR11, 500, 819
Dikansky, N.S. TAC06, WAA17, 143, 1263
DiMarco, J. FAP06, FAP07, 1337, 1340
Dinehart, M.R. WAQ26, 1897
Dinkel, J. WAA05, WAR01, 1236, 1900
Dinkel, J.A. WAA07, 1239
Dipace, A. TPG11, 186
Diviacco, B. FAQ19, 1432
Dobbe, N. MPQ17, 2491
Dobbins, J.A. RAE14, 2426
Dobeck, N. RPP06, 1973
Dobrovodsky, J. TAA18, 2120
Dodson, G. RPG05, 327
Dohlus, M. RPB15, RPB16, TAQ06, WPP05, WAE13, MPC16, 692, 695, 1533, 1666, 2190, 2345
Doinikov, N. MPC21, 2359
Dolbilov, G.V. WAA20, TAQ34, 1272, 1605
Dolique, J.-M. TPR04, TPR05, 3245, 3248
Donald, M. RAA22, 576
Donald, M.H.R. RAA27, 591
Donaldson, A.R. RPB05, WAA11, WAR06, RPP07, 668, 1251, 1915, 1976
Donaldson, T. WAQ15, 1876
Dooling, J.C. RAQ16, 3320
Doolittle, L. MPR13, MPR14, 2265, 2268
Doornbos, J. RPG12, 348
Doose, C. TPE08, 1310
Doria, A. TPG11, 186
Douglas, D. FAA25, WAQ14, 243, 1873
Douglas, D.R. WXE01, 2429
Dovbnaya, A.N. WPA15, WPA16, WPB16, 938, 939, 988
Dow, K. RPG05, 327
Dowell, D.H. FAA27, FAA28, WPB20, 248, 251, 992
Dowling, D.T. TAP07, WAQ26, 366, 1897
Doyle, E. FAE07, 1497
Drago, A. RAE12, RPQ01, 2420, 2660
Drees, A. RAA19, 567
Dressler, J. RAA03, 527
Drevlak, M. RPB14, 689
Drury, M. FAE12, 1512
Du, W. FAP01, 1322
Dugardin, F. TAB04, 116
Dunbar, A. WAB04, 3022
Dunham, B. MPR15, TPC07, 2271, 2610
Dunham, B.M. WPC17, 1030
Dunnam, C.R. RAE14, 2426
Dunning, F.B. WPC21, 1043
Durand, R. TPP04, WPQ02, 1623, 1720
Durfee III, C.G. WAG04, 621
Durieau, L. TAP14, 386
Durkin, A.P. RPR07, 1134
Dutto, G. RPG12, MPE03, WAQ07, 348, 864, 1858
Dykes, D.M. WPQ18, WAC22, 1762, 3125
Dylla, F. WPA17, 942
Dylla, H.F. FAG11, FAA25, 102, 243
Early, R. RPC02, 701
East, G. RAP21, RAP22, RAQ23, RAQ24, 2934, 2937, 3337, 3340
Ecklund, S. RPB01, RPC01, 656, 698
Ecklund, S.D. WPC18, 1033
Edighoffer, J. RPA26, 1116
Efimov, S. FAR17, RAA08, 299, 542
Egawa, K. RAA33, 603
Ehrlich, R. FAE13, 1515
Ehrlichmann, H. RPE08, 2017
Eichenberger, C. WAA19, 1269
Eichhorn, K.D. FAR06, 272
Eigenmann, B. FAR06, 272
Einfeld, D. TPG08, FAR06, WPQ24, 177, 272, 1776
Ekelöf, Tord TPC11, 2622
Elias, L.R. FAA29, 254
Elizondo, J. WAA19, TAA20, 1269, 2123
Elleauume, P. TPE10, 1319
Ellison, M. WPP20, WPP21, RAP21, RAP22, WAC12, RAG10, RAQ23, RAQ24, 1705, 1708, 2934, 2937, 3094, 3182, 3337, 3340
Ellison, T. TPB24, RAP22, 2583, 2937
Elsener, K. WAP14, 470
Emamian, M. FAA08, TAA02, 213, 2081
Emery, L. MPR01, MPB17, MPQ10, 2238, 2309, 2473
Emma, P. WAG11, RPB01, RPC03, RPC06, WAB07, 646, 656, 704, 707, 3031
Emma, Paul WAG01, 606
Emoto, T. TAQ08, 1539
Enchevich, I.B. WPP18, 1699
Engels, O. WPA04, WPA05, 911, 914
Engwall, D. FAG11, WPA17, 102, 942
Enjeti, Prasad N. RPP11, 1985
Enomoto, A. TAQ08, TAQ25, TAA04, 1539, 1578, 2087
Erdman, K. WAQ07, 1858
Eremeev, I.P. FAG10, TAC11, 98, 146
Erg, G.I. FAQ17, 1426
Erickson, R. RPA24, FAP16, 1111, 1366
Ermakov, D. RPA19, 1096
Ermakov, D.I. RAR04, 3361
Erochin, A. FAQ06, 1399
Escallier, J. FAQ03, 1393
Esin, S.K. RPR24, RPR25, RAE08, 1173, 1175, 2408
Estrin, B. WAA17, 1263
Etz Korn, F.J. WPQ26, 1781
Evans Jr., K. MPQ03, 2452
Evans, L.R. FPD04, 40
Everett, M. RAB05, 770
Everett, M.J. RAB04, 767
Evtushenko, Yu.A. FAQ17, 1426
Eyharts, Ph. TAE09, 1210
Eyl, P. TAE09, 1210
Eylon, S. TAR14, WPA02, WPA09, TAE01, TAE11, WAQ04, 828, 905, 926, 1178, 1216, 1852
Ezura, E. FAE09, TPP16, WPQ08, WPQ17, WPR05, WPR09, RPQ06, 1503, 1652, 1735, 1759, 1797, 1806, 2675
Fabris, A. FAR21, WPQ04,

TAG05, 309, 1723, 2762
Fabris, R. FAR21, 309
Fackler, O. RAA03, 527
Fahmie, M. RPQ08, 2681
Fainberg, Ya.B. RAB15, WAA02, WAA03, 782, 1230, 1233
Fallis, M.C. WPR20, 1835
Faltens, A. FAP17, FAP18, TPA10, 1369, 1372, 3220
Fan, T.C. FAQ26, 1450
Fang, C.S. MPQ32, 2524
Fang, S. MPR16, 2273
Fang, S.X. WAB20, 3064
Fang, Si J. FAP05, 1334
Fang, Ye TAR22, 850
Fant, K. WPR08, 1803
Farias, R.H.A. FAP14, 1361
Farkas, Z.D. WPR15, 1821
Farkhondeh, M. RPG05, 327
Farvacque, L. TPG05, 167
Farvid, A. MPP09, 2054
Fateev, A.A. WAA20, TAQ34, 1272, 1605
Fathizadeh, M. TAP05, 363
Faugeras, P. TPE03, 1288
Faugier, A. WAP12, WAP13, RAA11, 464, 467, 548
Faure, J. FAR14, 293
Fawley, W. FAP17, 1369
Fawley, W.M. FAA12, RAB03, FAP18, TPA10, 219, 764, 1372, 3220
Fazio, Michael V. FAE06, 1494
Fedin, O.L. MPG10, 426
Fedotov, A.P. RPR07, 1134
Fedotov, Alexei V. TPR12, 3266
Fedotov, Yu. MPR11, 2259
Feerick, B. WAQ15, 1876
Feldl, E. TPC04, 2601
Feldman, Donald W. WPB15, 985
Fellenz, B. MPQ13, 2479
Feng, W. WAR12, 1927
Feng, W.Q. WAA15, 1257
Ferdinand, R. RPR11, RAG07, 1146, 3173
Ferguson, M. RPP12, 1988
Ferianis, M. TPG11, FAR21, 186, 309
Feroli, F. WAP13, 467
Fernow, Richard MXG03, 53
Ferrario, M. WAC13, 3097
Feschenko, A.V. RAE08, 2408
Fessenden, R.W. TAB17, 131
Fessenden, T. TAR17, 837
Fessenden, T.J. TAR13, TAR14, TPB14, 825, 828, 2557
Fidecaro, G. WAP14, 470
Fieguth, T. WAQ15, 1876
Field, R. TAG01, 2742
Field, R.C. WXE07, 2444
Fietier, N. FAG09, 95
Filatov, B.A. WAA21, 1274
Filtz, M. MPC28, 2373
Fink, C.L. FAG14, 110
Fiorentini, G. WPB10, 973
Firjahn-Andersch, A. WPA03, 908
Fischer, C. RPC14, TPC21, 731, 2649
Fischer, Henk WAB06, 3028
Fischer, W. TAG07, 2768
Fisher, A. TPG14, RAA04, 192, 530
Fitzgerald, D. WPC10, WAC29, RAR23, 1016, 3146, 3406
Fitzgerald, J.B. TPG09, RAE10, 180, 2414
Flanz, J.B. RPE03, 2004
Flechtner, D. WPC19, 1036
Fleckner, K. RPA26, 1116
Filiflet, A.W. TAQ37, 1611
Flood, R. RPP13, 1991
Flora, R. WAE07, 2172
Flöttmann, K. TAA08, TAG01, 2096, 2742
Flynn, G. FAE13, RAR18, 1515, 3391
Fockler, J. WAA19, 1269
Foelsche, H. FAQ15, 1420
Foelsche, H.W. FAP11, 1352
Foley, M. FAG06, WPP01, 86, 1655
Fomin, M. WPP11, 1681
Fong, K. MPR16, 2273
Forest, E. RAA22, RAA25, FAB06, 576, 585, 2804
Forsyth, E.B. WAA15, WAR10, WAR12, 1257, 1921, 1927
Foster, G.W. MPG11, WAP16, TPE05, 428, 473, 1298
Foster, J. WPB06, 961
Foster, W.B. FAP21, 1381
Fouaidy, M. TPP09, TPP11, TPP14, 1632, 1639, 1648
Fougeron, C. WPQ26, 1781
Fowkes, W.R. FAE07, TAQ28, 1497, 1587
Fowler, W. MPG01, 391
Fox, J. RAA04, RAE12, RAE13, RPQ01, RPQ08, 530, 2420, 2423, 2660, 2681
Fox, T. MPR13, 2265
Frachon, D. FAQ17, FAQ18, 1426, 1429
Franks, R.M. WPQ06, 1729
Franzke, B. MPC15, 2342
Freund, A. WAP14, 470
Fricks, R. MPA11, 2217
Friedman, A. TAR14, TAR15, TAR17, FAQ17, TPR19, 828, 831, 837, 1426, 3282
Friedman, Aharon RPQ14, 2696
Friedrich, L. FAR06, 272
Friedsam, H. TAP05, TAA03, 363, 2084
Friesel, D. WPP20, WPP21, RAQ24, 1705, 1708, 3340
Friesel, D.L. RPG08, TAP03, WAQ08, 336, 357, 1861
Frisch, J. WAG11, MPE10, 646, 887
Fu, Shinian FAA21, RAQ25, RAQ26, 237, 3343, 3346
Fugitt, J. FAG11, FAA25, WPA17, RPQ30, 102, 243, 942, 2735
Fuja, R. RPA10, RPA11, MPQ08, MPQ10, 1070, 1073, 2467, 2473
Fuja, R.E. TPC01, 2595
Fujino, T. TPP07, 1629
Fujita, H. FAR08, RPA13, WAQ01, 278, 1079, 1843
Fukuma, H. RAA33, 603
Fukutomi, M. TPP16, 1652
Fullett, K. WAR17, WAR18, 1939, 1942
Funahashi, Y. TPP07, 1629
Funakoshi, Y. MPQ31, WAC08, 2521, 3085
Furman, M. RPC02, TPQ16, 701, 2986
Furman, Miguel A. RAP14, 2916
Furuya, T. TPP03, 1620
Fusellier, J. WAG07, WPB22, 634, 998
Gai, W. WAG06, WPB11, MPQ11, 631, 976, 2476
Galayda, J. RPQ16, 2702
Galayda, John N. MAD02, 4
Gallardo, Juan C. MXG03, WPB21, 53, 995
Gallerano, G.P. TPG11, 186
Gamo, N. TPP03, 1620
Ganetis, G. TPE04, FAQ02,

FAQ03, FAQ04, FAQ15, 1293, 1390, 1393, 1396, 1420
Ganetis, G.L. TAA09, 2099
Gangeluk, M. WPR13, 1815
Gao, J. RPA03, 1055
Gao, Jie WPQ01, 1717
Garcia, R.C. TPC06, 2607
Gardner, C.J. TAP11, TAP13, 378, 383
Garnett, R.W. RAG11, 3185
Garoby, R. MPG09, 423
Garosi, F. TPG11, 186
Garrel, N. WAP12, RAA15, 464, 557
Garren, A. WPG11, 520
Garren, A.A. TAB06, 119
Garvey, J.D. FAP06, FAP07, 1337, 1340
Garvey, T. WPA14, WPB22, 935, 998
Gavaggio, R. MPP15, 2069
Gavrilov, N.G. FAQ17, 1426
Gay, T. WPC21, 1043
Gayet, Ph. MPP02, 2037
Geisik, C. WPC10, 1016
Gelato, G. MPG09, 423
Gelfand, N.M. RAB19, 787
Gelfand, Norman M. WAP07, 452
Geller, J. WAR11, RPP02, 1924, 1964
Geng, X. MPA01, 2193
Genova, L. RAA04, 530
Georges, J.P. TAB04, 116
Georges, P. WPB01, 945
Geschonke, G. TPP12, 1642
Gevchuk, A. FAR17, 299
Ghiorso, W. TPA10, 3220
Ghosh, A. TPE04, FAQ03, FAQ04, 1293, 1393, 1396
Giacuzzo, F. MPP04, 2042
Giannessi, L. TPG11, 186
Giannini, M. TPG11, FAR21, 186, 309
Gilgenbach, R.M. TAQ32, 1599
Gillespie, G.H. RPR20, 1164
Gillespie, George H. FAG13, MPB14, 107, 2300
Gilpatrick, J.D. RPR19, RPR22, TPB16, TPB22, 1161, 1167, 2563, 2580
Giordano, G. RPC17, 740
Giovannozzi, M. FAC06, 2847
Giove, D. TAA07, TPC10, 2093, 2619
Giovenale, E. TPG11, 186
Gladkikh, P. FAR17, 299
Glass, H. TPE05, 1298
Glass, H.D. FAP05, FAP06, FAP07, MPB05, MPB06, 1334, 1337, 1340, 2282, 2285
Glazov, A. WPC13, WPR19, 1025, 1833
Glenn, J.W. TAP13, WAR13, 383, 1930
Glock, H.-W. RPB15, RPB16, 692, 695
Glover, E. TPG07, 174
Gluckstern, R. RPA04, 1058
Gluckstern, R.L. TPQ14, 2980
Gluckstern, Robert L. RAG09, TPR11, TPR12, RAR12, 3179, 3263, 3266, 3376
Gluskin, E. TPE06, FAQ17, MPP16, 1301, 1426, 2072
Goddard, B. RAA15, 557
Goderre, G. WAP08, 455
Goderre, G.P. WAP05, 446
Godfrey, G. WAQ15, 1876
Godlove, T.F. TAE10, 1213
Godlove, Terry F. TAA17, 2117
Godot, J.C. RPC10, 719
Goffeney, N. RPC17, 740
Gold, C. RPA10, 1070
Gold, S.H. TAQ37, 1611
Goldberg, D.A. WPQ13, 1747
Goldman, M.A. TAA09, 2099
Goldstein, J.C. FAA16, 228
Golkowski, Cz. TAQ01, 1518
Golubev, I.I. WAA20, 1272
Golubev, V. WPC03, 1004
Goncharov, A.D. TAC06, RPP08, 143, 1979
Gonichon, J. MPE12, 893
Gonin, I.V. RPR01, 1119
Goral, J. RPA11, 1073
Gordeeva, M.A. MPG10, 426
Gordon, D. RAB04, RAB05, 767, 770
Gorelov, D.V. RPR01, 1119
Gorev, V.V. MPE06, 874
Gorin, M.Yu. WAR23, 1955
Gorniker, E. WPP11, 1681
Gorski, A. FAP03, 1328
Goto, A. WPC01, 1001
Gougnaud, F. WPB22, 998
Gournay, J.F. WPB22, 998
Govil, R. TPG07, RAB10, 174, 776
Gower, E. RPA26, 1116
Graber, J. FAE03, 1478
Gracia, J. RAA04, 530
Granatstein, V.L. TAQ17, TAQ18, TAQ19, 1561, 1563, 1566
Gras, J.J. TPC21, 2649
Grassi, R. FAC06, 2847
Grau, M.C. MPQ05, 2458
Graves, W.S. FAQ13, 1414
Gray, E.R. RAG11, 3185
Green, M. WPG11, 520
Green, M.A. TAB06, 119
Greene, A. TPE04, FAQ03, FAQ04, FAQ15, 1293, 1393, 1396, 1420
Greenly, John B. TAE07, 1204
Greenwald, Z. FAE13, TPA04, 1515, 3206
Grelick, A. RPA11, 1073
Grelick, A.E. RPA10, RPA14, RPE09, 1070, 1082, 2020
Greth, V.N. WAR20, 1948
Gridasov, V. FAQ06, 1399
Grieser, M. RPR06, 1131
Grigor'ev, Yu.N. RAA07, RAQ28, 539, 3349
Grimm, T. RPG11, 345
Grimmer, J. RPE09, 2020
Grishin, V.K. FAG12, FAA14, 105, 225
Gröbner, O. RPE02, 1999
Gromme, T. RAE03, 2389
Gross, G. WAR06, 1915
Grossberg, P. RAE03, 2389
Grosse-Wiesmann, P. RAA19, 567
Grote, D. TAR17, TAE01, 837, 1178
Grote, D.P. TAR13, TAR14, TAR15, WPA09, TPR19, 825, 828, 831, 926, 3282
Grote, H. RAA19, 567
Grudiev, A. MPB09, 2291
Grunder, Hermann A. MAD01, 1
Gubin, K. WAA17, 1263
Guckel, H. WPE02, 63
Gudkov, K. RPA19, 1096
Gudkov, K.A. FAG12, 105
Guharay, Samar K. MPC04, 2324
Guidi, V. RAE05, 2399
Guignard, G. RPC09, RPC12, RPC13, 716, 725, 728
Guinand, R. RAA15, 557
Guo, H. TAQ17, 1561
Guo, Z. TPQ03, 2955
Gupta, R. TPE04, FAQ04,

FAQ16, TAA09, 1293, 1396,
 1423, 2099
Gupta, R.C. WAP10, 461
Gur'yev, M.P. MPG10, 426
Gurov, G. MPG06, 416
Güsewell, D. MPP02, 2037
Gusinskli, G.M. TAP16, 389
Gustafson, Dick TPE05, 1298
Gustavsson, J. FAA08, 213
Guy, F.W. RPG10, 342
Gyr, M. WAP14, WAQ24, 470,
 1891
Haber, I. TAR15, TPR19, 831,
 3282
Haberichter, W. TPC16, 2637
Habib, Salman RAG01, 3149
Habs, D. RPR06, 1131
Haddock, C. FAQ14, 1417
Haebel, E. TPP12, 1642
Haffmans, A.F. RAG14,
 RAQ20, 3194, 3329
Hafizi, B. TAQ37, 1611
Haga, K. RPQ23, 2720
Hagedoorn, H.L. WAQ19,
 WAQ20, RPP04, RPQ31, 1882,
 1885, 1970, 2738
Hahn, H. TPQ02, 2952
Hahn, K.D. TPA10, 3220
Hahn, U. FAR07, 275
Halmson, J. RPC22, TAQ03,
 755, 1524
Hairapetian, G. WPC20,
 RPA21, RPA22, 1039, 1102,
 1105
Hakota, M. TAQ35, 1608
Hall, P.J. FAP06, FAP07,
 MPB06, 1337, 1340, 2285
Haller, M. FAR06, 272
Halling, M. RPC20, RPC21,
 TAG01, 749, 752, 2742
Hamilton, B. TPB24, RAP21,
 RAP22, RAQ24, 2583, 2934,
 2937, 3340
Hammel, E. TPB07, 2542
Han, Bumsoo TAB09, FAR03,
 122, 269
Han, D.H. WPR11, 1812
Hanna, B. WAR01, 1900
Hanna, S.M. RPA23, 1108
Hanne, G.F. WPC21, 1043
Haouat, G. RAG06, RAG07,
 3170, 3173
Hardek, T. WAC29, 3146
Hardek, T.W. TAQ31, 1596
Harding, D.J. FAP04, FAP05,
 FAP06, FAP07, FAP09, MPB05,
 MPB06, 1331, 1334, 1337,
 1340, 1346, 2282, 2285
Harkay, K. TAP05, TPQ22,
 TPQ23, 363, 3001, 3004
Harrison, M. MPG03, TAA09,
 401, 2099
Harrison, M.A. MPG12, 431
Hartill, D.L. RAE14, 2426
Hartley, R. FAA19, 234
Hartley, R.A. FAA31, 260
Hartman, S. RPB02, RPC20,
 WXE07, TAG01, 659, 749,
 2444, 2742
Hartman, S.C. RPB04, TPC29,
 665, 2655
Hartnagel, H.L. MPC15, 2342
Hartung, W. FAE13, TPA04,
 RAQ04, RAR18, RAR19, 1515,
 3206, 3294, 3391, 3394
Harwood, S.L. WXE01, 2429
Hasegawa, K. RPG09, 339
Haseroth, H. MPG09, 423
Haseroth, H.D. MPG05, 411
Hashimoto, S. FAQ21, 1438
Hathaway, D. MPP12, MPP20,
 2064, 2075
Hawkins, A. WAA16, 1260
Hayakawa, A. WXE07, 2444
Hayano, H. RPA20, WPR03,
 TPC05, TAG01, 1099, 1791,
 2604, 2742
Hayashi, E.K.C.S. MPQ33,
 2527
Hayashi, S. FAP13, 1358
Haynes, D.L. WAQ26, TPC18,
 1897, 2643
Haynes, W. Brian FAE06,
 1494
Hays, S. WAE07, 2172
Hays, T. FAE13, TPP02,
 WPQ02, 1515, 1617, 1720
Hayward, T.D. FAA27, FAA28,
 WPB20, 248, 251, 992
Hedblom, K. WPP20, WPP21,
 WAQ08, RAP21, 1705, 1708,
 1861, 2934
Heese, R. FAR10, 284
Heifets, S. MPC01, MPC08,
 TPQ16, 2317, 2333, 2986
Heifets, S.A. TAA22, MPC02,
 MPC03, MPC18, 2129, 2319,
 2321, 2351
Heim, J. RAA03, 527
Heimlinger, G. TAG01, 2742
Heine, E. TAQ12, MPQ17,
 1547, 2491
Heinrichs, G. TPB20, 2574
Helm, R. RAA22, RPC06,
 RPC07, RPC20, TAA08, TAG01,
 576, 707, 710, 749, 2096,
 2742
Helvajian, H. FAG11, 102
Hemelseoet, G.H. WAE09, 2178
Hémery, J.-Y. TAP14, 386
Hemmer, M.F. TAA09, 2099
Henderson, S. FAE13, 1515
Henderson, T. FAP01, 1322
Hendrickson, L. RAE03, 2389
Hendrickson, L.J. WAG11,
 RPB03, 646, 662
Henestroza, E. RPC16, RPC17,
 RPC19, WPA02, WPA09, TAE01,
 TAE11, MPC01, MPC08, TPA10,
 737, 740, 746, 905, 926,
 1178, 1216, 2317, 2333, 3220
Henke, H. TAQ30, WPQ14,
 WAB11, 1593, 1750, 3043
Henkel, D.P. FAG11, 102
Hentges, M. MPP01, 2034
Herold, W. WPA12, 929
Herr, W. WAP14, WPG09, 470,
 514
Herrup, D.A. TPQ25, TPQ26,
 3007, 3010
Hershcovitch, A. WPC09,
 1013
Herz, P. TPB07, 2542
Hettel, R. MPQ22, RPQ21,
 RPQ22, 2506, 2714, 2717
Heutenik, B. TAQ12, 1547
Heydari, Huschang WAP09,
 458
Higashi, Y. WPQ15, 1753
Higgins, D.S.G. WPQ18, 1762
Higgins, S. MPR13, 2265
Higo, T. FAQ08, WPQ15,
 WPR02, WPR03, 1405, 1753,
 1788, 1791
Higo, Toshiyasu FAE02, 1474
Higuchi, A. RAQ06, 3300
Higuchi, T. TPP07, 1629
Hilaire, A. WAP12, WAP13,
 464, 467
Hill, B.W. RPR20, 1164
Hill, Barrey W. MPB14, 2300
Hill, S.F. WAC21, 3122
Hilleret, N. TPP12, 1642
Himel, T. RAE03, 2389
Hindi, H. RAE12, 2420
Hinode, F. WPQ16, WPR02,
 WPR03, TPC05, 1756, 1788,
 1791, 2604
Hipple, R. WPA01, TAE01,
 902, 1178
Hiramoto, K. TAB03, WPQ21,

113, 1770
Hirano, K. TAQ08, 1539
Hirata, K. RAP02, 2883
Hirata, Y. WPR02, 1788
Hirota, J.I. TAB03, WPQ21, 113, 1770
Hizanidis, K. RAQ01, 3285
Ho, C. WPB11, 976
Ho, C.H. WPB07, 964
Hoag, H. RPA04, WPQ05, 1058, 1726
Hoag, H.A. RPA23, 1108
Hobson, B. RAA03, 527
Hodges, T. RPG12, 348
Hodgkins, D. MPE04, WPA08, 867, 923
Hodgson, J. WPR08, 1803
Hoeflich, J. RAE12, 2420
Hoffstätter, G.H. FAB07, 2807
Hofler, A. MPR13, 2265
Hofmann, A. RAA17, RAA18, RAA20, FAC03, 560, 564, 570, 2841
Hogan, B. TAQ18, TAQ19, 1563, 1566
Hogan, M. FAA23, RPA21, RPA22, 240, 1102, 1105
Hogrefe, R. TPE08, 1310
Hohbach, R. TAQ33, 1602
Holdener, F.R. MPP12, MPP20, TAA22, 2064, 2075, 2129
Holmes, C. WAA19, 1269
Holmes, S. MPG01, 391
Holmes, S.D. WAP01, 434
Holmquist, T. RAE14, 2426
Holsinger, R.F. TPE07, 1305
Holt, J. RPC20, 749
Holt, J.A. WAP01, WAP08, RPC21, TAG01, WAC01, 434, 455, 752, 2742, 3067
Holtkamp, N. FAR06, RPB12, RPB13, RPB15, RPB16, WPA12, WPP05, MPC16, 272, 683, 686, 692, 695, 929, 1666, 2345
Holtzapple, R.L. WXE05, WAB05, WAC04, WAC17, 2438, 3025, 3073, 3109
Honda, T. RPQ23, 2720
Honecker, V. FAR06, 272
Hopster, H. WPC21, 1043
Horan, D. TAP05, RPP12, 363, 1988
Hori, T. WPC22, MPA07, 1046, 2208
Houck, T. RPC16, RPC17, WPC16, 737, 740, 1027
Houck, T.L. TAQ03, 1524
Hovater, C. FAE12, TPC26, RPQ29, 1512, 2652, 2732
Howell, J. TAR08, 816
Hower, N. FAA08, RPA17, TAA02, MPQ06, 213, 1090, 2081, 2461
Hower, Nelson WPA13, 932
Hoyer, E. FAQ24, FAQ25, 1444, 1447
Hoyt, E. MPP09, MPP12, MPP20, 2054, 2064, 2075
Hoyt, M. MPP09, MPP12, MPP20, 2054, 2064, 2075
Hseuh, H.C. TAP11, TAP12, MPP11, 378, 381, 2060
Hsieh, H. RAA05, RPA26, 533, 1116
Hsiung, G.-Y. TPC15, 2634
Hsu, I. TAA28, 2135
Hsu, Ian MPQ26, TPC15, RAR05, 2515, 2634, 3364
Hsu, K.T. FAA04, FAA07, RAA23, RAA24, MPR10, MPQ16, MPQ19, MPQ32, TPB29, TPQ08, TPQ09, TPQ10, 201, 210, 579, 582, 2256, 2488, 2497, 2524, 2592, 2965, 2968, 2971
Hsu, R.-C. TPC15, 2634
Hsu, S.Y. WPB07, 964
Hsue, C.S. RAA24, TAR04, TPQ09, TPQ10, 582, 804, 2968, 2971
Huang, Gloria MPR10, 2256
Huang, H. TPA06, 3212
Huang, J.Y. TPG06, 171
Huang, N. RAA21, WAC27, 573, 3140
Huang, Zhibin FAA21, RAQ25, RAQ26, 237, 3343, 3346
Huang, Zhirong RAQ18, 3326
Huffman, G. FAE07, 1497
Hughes, Thomas P. TAE08, 1207
Hülsmann, P. RPB15, RPB16, 692, 695
Humbert, J. FAP03, 1328
Hümmer, K. FAR06, 272
Humphries, D. FAQ24, FAQ25, 1444, 1447
Hunt, D. MPP13, 2067
Hustache, R. WAP14, 470
Hutson, R. WAC29, 3146
Hutson, R.L. TAR12, 822
Huttel, E. FAR06, 272
Hutton, A. TPC26, 2652
Hwang, J.I. WPB07, 964
Hwang, O.H. TAQ14, 1553
Hwu, K.H. MPQ19, 2497
Iazzourene, F. FAR21, TAG05, 309, 2762
Ieiri, Takao TPB17, 2566
Igarashi, Y. TAQ25, 1578
Igarashi, Z. WPC07, 1007
Ignatyev, A. TAB13, TAQ23, TAQ24, 125, 1572, 1575
Ihloff, E. RPG05, 327
Iida, S. TPP03, 1620
Ikegami, K. WPC07, 1007
Ikegami, M. FAR08, RPA13, WAQ01, 278, 1079, 1843
Ilijinov, A.N. RPR01, 1119
Imai, Y. FAQ08, 1405
Imanishi, A. RPG13, 351
Imel, G.R. TAC12, 149
Inagaki, S. TPP16, 1652
Inaguchi, T. FAQ08, 1405
Ingalls, W. WPC10, 1016
Ingwersen, Pete TAE07, 1204
Inman, T.K. RPA24, 1111
Ino, H. RPG09, 339
Inoue, H. TPP07, 1629
Inoue, M. FAR08, RPA13, RPA18, WPQ21, WAQ01, 278, 1079, 1093, 1770, 1843
Irwin, J. RAA22, RAA25, RAA26, RAA27, RPC01, RPC06, RPC07, RPC08, RPC20, TAA08, TAG01, TAG06, FAC18, RAP09, RAP11, RAP12, 576, 585, 588, 591, 698, 707, 710, 713, 749, 2096, 2742, 2765, 2871, 2904, 2910, 2913
Irwin, John MPC31, 2376
Irwin, M. WPQ13, 1747
Isagawa, S. TPP16, 1652
Ishi, Y. TAP04, TPP03, 360, 1620
Ishida, T. MPQ18, 2494
Ishihara, N. TAG01, 2742
Ishii, H. MPQ31, 2521
Ishkhanov, B. RPA19, 1096
Ishkhanov, B.S. FAG12, FAA14, 105, 225
Issinsky, I.B. WAR09, FAC12, 1918, 2863
Ito, I. TAQ35, 1608
Ito, N. RPG09, 339
Itoh, Y. MPA07, 2208
Ivanov, A. TAC16, 152
Ivanov, A.A. WAR20, 1948
Ivanov, A.S. TAE13, 1222

Ivanov, I.N. WAA20, 1272
Ivanov, P. RAA31, 600
Ivanov, P.M. FAQ17, FAQ18, 1426, 1429
Ivanov, S. WPP05, MPC16, TPQ01, TPQ04, 1666, 2345, 2949, 2958
Ivanov, Yu.D. RPR07, 1134
Ivers, J.D. WPC19, TAE12, 1036, 1219
Iverson, R. RPC20, TAA28, WXE07, TAG01, 749, 2135, 2444, 2742
Iwashita, Y. FAR08, RPA13, RPA18, WPQ21, WAQ01, 278, 1079, 1093, 1770, 1843
Izawa, M. TPP03, WPQ07, WPR04, 1620, 1732, 1794
Jablonka, M. WPA14, WPB22, 935, 998
Jackson, A. FAA03, FAA05, RPC02, 198, 204, 701
Jackson, G. MPG11, WAP16, TPE05, WAR19, MPQ13, RAP20, WAC09, WAC10, 428, 473, 1298, 1945, 2479, 2931, 3088, 3091
Jackson, L.T. RPP01, RPP07, 1961, 1976
Jackson, T. RAA04, FAQ24, 530, 1444
Jacob, J. TPG05, FAR06, 167, 272
Jacobs, K. RPG05, RAA31, 327, 600
Jacquemard, B. WPB22, 998
Jacquet, F. WAG07, 634
Jaeschke, E. RPR06, FAQ12, 1131, 1411
Jaffery, T.S. FAQ32, 1465
Jagger, J. FAP03, 1328
Jain, A. WAP10, TPE04, FAQ03, FAQ04, FAQ16, TAA09, 461, 1293, 1393, 1396, 1423, 2099
Jamison, R.A. RPR20, 1164
Jan, G.J. MPR10, MPQ16, TPB29, 2256, 2488, 2592
Jang, J.S. TPG06, 171
Jarvis, H. WPR15, 1821
Jason, A. WAC29, 3146
Jason, Andrew J. TAE02, 1183
Jayamanna, K. MPE03, WAQ07, 864, 1858
Jean, Benedikt FAG03, 75
Jeanjean, J. RPC20, TAG01, 749, 2742
Jeanneret, B. FAC04, 2844
Jenner, D. WPP20, WPP21, 1705, 1708
Jensen, C. WAR01, 1900
Jensen, C.C. WAA07, 1239
Jensen, D. FAQ08, 1405
Jensen, E. MPG09, 423
Jiang, D.M. RPE10, 2023
Jiang, Shicheng TPR11, 3263
Jiang, W.S. MPP11, 2060
Jiang, Y. FAP01, 1322
Jianjun, Deng FAA26, 246
Jin, K. WPP05, 1666
Jin, L. RAA21, WAC27, 573, 3140
Jinsui, Shi FAA26, 246
Jobe, K. WPR15, 1821
Jobe, R.K. WAB05, 3025
Joffe, D. RPR02, 1122
Joh, Kihun TAB09, FAR03, 122, 269
Johnson, B. WPC21, 1043
Johnson, C. RPC09, 716
Johnson, D. RPG11, 345
Johnson, D.E. TAB06, FAP04, FAP09, FAP10, 119, 1331, 1346, 1349
Johnson, J. WPR14, RAE13, RPQ08, 1818, 2423, 2681
Johnson, J.W. WAQ26, 1897
Johnson, K.F. RPR19, RPR22, TPC06, 1161, 1167, 2607
Johnston, M. WPC21, 1043
Johnstone, C. FAG06, 86
Johnstone, J. WAP01, 434
Joho, W. FAB14, 2823
Joly, J.M. WAG07, WPA14, WPB22, 634, 935, 998
Joly, S. RAG06, 3170
Jones, C.M. TPC18, 2643
Jones, G.S. RPP06, 1973
Jones, R.M. TAA33, MPC03, 2144, 2321
Jones, W.P. TPB24, RAQ24, 2583, 3340
Jongewaard, E. FAE07, 1497
Jonker, M. WAP12, WAP13, RAA11, 464, 467, 548
Jordan, K. FAG11, FAA25, WPA17, 102, 243, 942
Joshi, C. WAG08, WAG09, RAB01, RAB02, RAB03, RAB04, RAB05, WPC20, RPA21, RPA22, TPB18, 637, 640, 758, 761, 764, 767, 770, 1039, 1102, 1105, 2569
Judd, D.L. TAR14, 828
Judkins, J. WPQ10, WPR08, 1741, 1803
Juillard, M. WAG07, WPB22, 634, 998
Junck, K. TPQ28, WAB01, 3013, 3016
Jung, R. TPC21, 2649
Junquera, T. WPB22, TPP09, TPP11, TPP14, 998, 1632, 1639, 1648
Juras, R.C. WAQ26, MPA05, 1897, 2202
Juras, S. TPP12, 1642
Jurgens, T.G. MPB15, 2303
Kachtanov, E. FAQ06, 1399
Kadnikov, A. WAA18, WPR13, MPA04, 1266, 1815, 2199
Kadokura, E. MPQ18, 2494
Kageyama, T. FAE09, WPQ09, WPQ17, WPR05, WPR09, 1503, 1738, 1759, 1797, 1806
Kahana, E. MPQ03, MPQ10, RPQ15, 2452, 2473, 2699
Kahn, S. TPE04, FAQ16, 1293, 1423
Kakigi, S. FAR08, RPA13, WAQ01, 278, 1079, 1843
Kako, E. TPP07, 1629
Kalashnikov, V.V. TPB25, 2586
Kalbreier, W. RAA15, 557
Kalfas, C. RAQ01, 3285
Kaltchev, D. FAB14, 2823
Kamber, I. RPC10, 719
Kaminsky, A. TAC16, 152
Kamiya, Y. FAR09, FAP22, WPQ07, WPR04, 281, 1384, 1732, 1794
Kando, M. FAR08, RPA13, WAQ01, 278, 1079, 1843
Kandrunin, V.N. WPR17, 1827
Kaneda, T. FAP13, 1358
Kang, Kyungwoo TAB09, FAR03, 122, 269
Kang, Woung TAB09, FAR03, 122, 269
Kang, X. TAP03, WPP20, WPP21, RAP21, WAC12, RAG10, RAQ23, RAQ24, 357, 1705, 1708, 2934, 3094, 3182, 3337, 3340
Kang, Y.G. FAR19, FAQ18, 303, 1429
Kang, Y.W. WAG10, WPP16, RPE09, 643, 1693, 2020
Kang, Yoon WPP12, 1684

Kaplan, R. FAE13, WPQ02, 1515, 1720
 Karantzoulis, E. FAR21, TAG05, 309, 2762
 Karantzoulis, Emanuel MPR12, 2262
 Karas', V.I. WAA02, WAA03, 1230, 1233
 Karas', Vyacheslav I. WAA01, 1227
 Karetnikov, M. RPR10, RPR15, 1143, 1155
 Karev, A.I. TAR05, FAP19, WPR17, 807, 1375, 1827
 Karl, F.X. TAA09, 2099
 Karn, J. MPR15, 2271
 Karnaukhov, I. FAR16, FAR17, RAA08, 296, 299, 542
 Karpenko, V. TAR17, 837
 Karshev, Yu. MPR11, 2259
 Kashikin, V. FAR06, 272
 Kasuga, T. RPQ23, RPQ26, RAQ06, 2720, 2726, 3300
 Katoh, M. RPQ23, 2720
 Katoh, T. MPA06, 2205
 Katsouleas, T. WAG09, RAB02, RAB08, TAA28, TPB18, 640, 761, 773, 2135, 2569
 Kaul, O. FAA02, FAC19, 195, 2874
 Kawai, M. RPG09, 339
 Kawakubo, T. RAB13, WAR04, MPQ18, 779, 1909, 2494
 Kawakubo, Tadamichi TPR16, 3275
 Kazarezov, I. WAA17, 1263
 Kazimi, R. WXE01, TPC07, 2429, 2610
 Keane, J. FAR10, TPP06, 284, 1626
 Keeley, D. RPQ21, RPQ22, 2714, 2717
 Keffeler, D. TAQ02, 1521
 Keffeler, D.R. WPA08, 923
 Kehne, D. FAG11, FAA25, WPA17, 102, 243, 942
 Keil, E. WPG09, 514
 Keith-Monnica, E. WAB04, 3022
 Keizer, R. WAP12, 464
 Kelley, M.J. FAG11, 102
 Kelly, D.R.C. RPE08, 2017
 Kelly, E. TPE04, FAQ03, FAQ04, FAQ15, 1293, 1393, 1396, 1420
 Kelly, K.W. TAA32, 2141
 Kemper, A.H. RPP04, 1970
 Kendall, M. RAA03, 527
 Kennedy, K. MPP13, 2067
 Kerner, T.M. MPA18, 2232
 Kerns, C. WPR21, 1838
 Kerns, J.A. TAA22, 2129
 Kerns, Q. WPR21, 1838
 Kerslick, G.S. WPC19, TAE12, TAQ01, 1036, 1219, 1518
 Kewisch, J. MPR20, 2279
 Khabiboulline, T. WPP05, 1666
 Khan, S. FAQ12, WAQ17, WAB03, 1411, 1879, 3019
 Kheifets, S.A. MPC18, 2351
 Khomyakov, E.A. TAE14, 1225
 Khrutchinsky, A.A. TPA15, 3232
 Kihara, Motohiro TPR16, 3275
 Kijima, Y. TPP03, 1620
 Kikuchi, M. RAA33, 603
 Kikutani, E. RPQ26, 2726
 Kikuzawa, N. TPG02, 159
 Kim, Byungmun TAB09, FAR03, 122, 269
 Kim, C. FAA03, FAA06, 198, 207
 Kim, C.H. FAA05, 204
 Kim, G.N. TAR07, 813
 Kim, J. TAA11, 2102
 Kim, J.W. RPR05, FAQ09, RAR21, 1128, 1408, 3400
 Kim, Jinsoo TAB09, FAR03, 122, 269
 Kim, K. TPE08, 1310
 Kim, K.-J. TPG07, TAG13, RAR02, 174, 2786, 3358
 Kim, Keeman TAB09, FAR03, 122, 269
 Kim, Kwang-Je RAP06, 2895
 Kim, S. FAR19, TAP05, FAB09, 303, 363, 2811
 Kim, S.H. FAA10, TPE08, 216, 1310
 Kim, Sungmyun TAB09, FAR03, 122, 269
 Kim, T.H. FAQ08, 1405
 Kim, T.Y. FAA10, 216
 Kim, Y.S. WPR11, 1812
 Kim, Younghee TAB09, FAR03, 122, 269
 Kim, Yuri TAB09, FAR03, 122, 269
 Kimura, W.D. WAG05, 626
 Kindermann, H.P. TPP12, 1642
 Kinkead, A.K. TAQ37, 1611
 Kinross-Wright, John M. WPB15, 985
 Kinsho, M. WPC07, WAQ06, 1007, 1855
 Kinter, R. RAB02, 761
 Kirbie, H.C. TAR14, 828
 Kirby, R. MPE10, MPP09, 887, 2054
 Kircher, J. FAR06, 272
 Kirchgessner, J. FAE01, FAE13, WPQ02, RAQ04, RAR18, RAR19, 1469, 1515, 1720, 3294, 3391, 3394
 Kirchman, J. RPQ15, RPQ16, 2699, 2702
 Kirk, Harold G. WPB21, 995
 Kiseljov, V.A. RAB15, 782
 Kishkek, R. TAQ32, 1599
 Kishiyama, K. MPP12, MPP20, 2064, 2075
 Kiver, A. MPP03, 2040
 Kleffner, C.-M. RPR06, 1131
 Klein, H. RPB15, RPB16, 692, 695
 Klein, W.B. WAE08, 2175
 Klem, J. WAP14, 470
 Kleman, K.J. WPR01, 1785
 Klewe-Nebenius, H. FAR06, 272
 Klippert, T. MPP16, 2072
 Klopenkov, M. TAA18, 2120
 Kneisel, Peter TPP13, 1645
 Knobloch, J. FAE13, TPP04, 1515, 1623
 Knöchel, A. FAR06, 272
 Knuth, T. TPE09, 1316
 Ko, I.S. TAR07, RPA06, MPA02, 813, 1061, 2196
 Ko, K. RPA04, RPA11, RPA14, TAQ06, WPQ05, WPQ12, WPR07, MPC01, 1058, 1073, 1082, 1533, 1726, 1744, 1800, 2317
 Kobayashi, A. FAA30, 257
 Kobayashi, T. RAB13, WPQ17, 779, 1759
 Kobayashi, Y. FAR09, RPQ23, 281, 2720
 Kodaira, M. FAP13, 1358
 Koga, A. FAA30, 257
 Kogan, M. TPB04, 2536
 Kohaupt, Rolf-Dieter RPQ32, 2741
 Koike, S. WPQ15, 1753
 Koiso, H. TAG11, 2780
 Kokoulin, V. WAA17, 1263

Kokura, S. TPP03, 1620
Kolomiets, A.A. TPA05, 3209
Kolonko, J. WPG11, 520
Kolonko, J.J. TAB06, 119
Komarov, V. MPP03, MPR11, 2040, 2259
Komori, K. TPP16, 1652
Konecny, R. WAG06, WPB11, WPB12, 631, 976, 979
Kononenko, S. FAR16, FAR17, RAA08, 296, 299, 542
Konovalov, V.A. RPR07, 1134
Koontz, R. WPR15, 1821
Koopman, J. TPC21, 2649
Korchuganov, V. WAA18, FAP02, 1266, 1325
Korepanov, V.M. WAA21, 1274
Korolev, A.P. TPA05, 3209
Kos, N. RPE02, 1999
Koscielniak, S. RPG12, RAQ15, 348, 3317
Koscielniak, S.R. WAC19, 3115
Koseki, T. FAP22, WPQ07, WPR04, 1384, 1732, 1794
Köbler, V. RPR06, 1131
Kosterin, S.A. FAG12, 105
Kostin, D.V. WPR18, 1830
Kosukhin, V.V. WAA20, 1272
Kot, N. WAA17, 1263
Kotaki, H. WPC22, 1046
Kotov, V.I. MPG10, WAR20, WAR21, 426, 1948, 1949
Kouptsidis, J. RPE08, 2017
Kourbanis, I. WPP08, WPP23, RAQ13, 1672, 1714, 3312
Koutchouk, J.P. RAA17, 560
Koutchouk, J.-P. FAC04, 2844
Kovach, P. TAA18, 2120
Kovachev, V. FAQ14, 1417
Kovalev, V.P. WAA21, 1274
Kowalski, S. RPG05, RAA31, 327, 600
Kozawa, T. RAB13, 779
Kozin, V. FAR17, 299
Kozlov, O.S. WAR09, 1918
Kponou, A. WPC09, 1013
Krafft, G.A. WAQ14, RAE11, WXE01, TPC04, TPC07, 1873, 2417, 2429, 2601, 2610
Krämer, D. TPE09, FAP02, FAQ12, WAQ17, 1316, 1325, 1411, 1879
Kramer, S.L. MPQ23, 2509
Krasnopolsky, V. WPC13, WPR19, 1025, 1833
Krasnykh, A. TAC01, TAC16, 134, 152
Krauter, K. RAE03, 2389
Kravchuk, L.V. RPR24, RPR25, 1173, 1175
Krawczyk, Frank L. MPB16, MPC22, 2306, 2361
Krebs, G. FAB01, 2789
Krejcik, P. WAG11, RPB02, RPC02, WAB07, WAB12, WAC17, 646, 659, 701, 3031, 3046, 3109
Kreps, G. WPP05, 1666
Kriens, W. WPA12, 929
Krienstein, B. RPB16, TAQ06, 695, 1533
Krinsky, S. FAR10, FAQ17, WXE04, TPQ14, 284, 1426, 2435, 2980
Krishnaswamy, J. FAA19, FAA31, 234, 260
Krivchikov, V.P. TAE14, 1225
Kroc, T. FAG06, 86
Kroes, F. RPG06, TAQ12, MPQ17, 330, 1547, 2491
Krogh, M. WAA19, 1269
Kroll, N. RPA04, 1058
Kroll, N.M. WPQ10, TAA33, 1741, 2144
Kroll, Norman M. WPR10, 1809
Kruijjer, A. TAQ12, 1547
Krüssel, A. FAR06, 272
Krutikhin, S. WPP10, 1678
Krycuk, A. RPQ29, 2732
Krylov, Y. MPA04, 2199
Krylov, Yu. WPR13, 1815
Kuba, A. MPA07, 2208
Kubo, K. WAG12, RPC02, RPA20, WPR03, TPQ16, TPQ17, WAC18, 649, 701, 1099, 1791, 2986, 2989, 3112
Kubo, T. MPQ18, 2494
Kuchar, J. TAP08, 369
Küchler, S. FAP02, 1325
Kudo, M. TPP03, 1620
Kuijt, J. MPQ17, 2491
Kukhtin, V. MPC21, 2359
Kulevoy, T. TAC05, 140
Kulikov, A. RPE14, TAA22, 2032, 2129
Kulikov, A.V. WPC18, 1033
Kulipanov, G.N. FAQ17, 1426
Kumada, M. RPP09, 1982
Kumagai, S. TPP16, 1652
Kumpe, G. FAR06, 272
Kunkel, W.B. TPB07, 2542
Kuo, C. RAA24, 582
Kuo, C.C. FAA04, FAA07, RAA23, TPQ08, TPQ10, 201, 210, 579, 2965, 2971
Kuo, C.H. MPR10, MPQ16, TPB29, 2256, 2488, 2592
Kuo, T. WAQ07, 1858
Kuptsov, I. WPP10, WPP11, 1678, 1681
Kurakin, V.G. WAB14, 3049
Kurennoy, Sergey S. RAR11, RAR12, RAR13, 3373, 3376, 3379
Kurita, N. MPP07, MPP08, TAA22, MPC01, MPQ15, MPQ25, 2048, 2051, 2129, 2317, 2485, 2512
Kurkin, G. WPP11, 1681
Kurkin, Grigori WPR22, 1841
Kurokawa, S.-I. MPA06, 2205
Kurokawa, Shin-ichi WPG04, 491
Kurz, M. RPB15, RPB16, 692, 695
Kusano, J. RPG09, 339
Kushin, V. TAC05, 140
Kushnir, V.A. WPB16, 988
Kustom, R. TAP05, WPP13, WPP14, RPP12, 363, 1687, 1690, 1988
Kustom, R.L. WAG10, 643
Kustom, Robert WPP12, 1684
Kuznetsov, M.I. WPP18, 1699
Kuznetsov, N. FAP02, 1325
Kuznetsov, S. WPR13, MPA04, 1815, 2199
Kuznetsov, V.S. TAE13, 1222
Kvasha, A.I. RPR24, RPR25, 1173, 1175
Kwiatkowski, S. WPP07, WPQ19, 1669, 1765
Kwok, P. TAA28, 2135
Kwon, M. TPG06, WPR11, 171, 1812
Kwon, Y.S. WAQ26, 1897
Labrousche, J. TAE09, 1210
Lacarrere, D. FAE11, 1509
Lackey, J. FAG06, 86
Laclare, J.L. TPG05, 167
Laffin, M. RAA15, 557
Lagniel, J.-M. RPR11, RAG07, 1146, 3173
Lagniel, Jean-Michel TPA17, 3235
Lahti, G. MPR13, MPR14, 2265, 2268

Lai, A.-T. TPC15, 2634
Lai, C.H. WAG09, 640
Lai, P. RAB02, TAA28, 761, 2135
Lal, A. RAB04, RAB05, 767, 770
Lam, R. TPC16, 2637
Lambertson, G. MPC01, RAE13, RPQ08, 2317, 2423, 2681
Lamont, M. WAP12, WAP13, WPG09, RAA11, RAA15, 464, 467, 514, 548, 557
Lampel, M. RAB03, RPA21, RPA22, 764, 1102, 1105
Lamzin, E. MPC21, 2359
Lancaster, C. FAA27, 248
Lane, S.N. TAP07, 366
Langdon, A.B. TPR19, 3282
Langdon, A. Bruce TPR01, 3238
Langton, J. MPP08, 2051
Lara, P. MPE04, 867
Lara, P.D. WPA08, 923
Larbalestier, D.C. TPE01, 1276
Lasutin, E.V. FAG12, 105
Latypov, T. FAP24, 1387
Lau, W.C. FAA04, 201
Lau, W.K. RAA23, RAA24, WPB07, TPQ08, TPQ10, 579, 582, 964, 2965, 2971
Lau, Y.Y. TAQ32, 1599
Lauer, E. WAA19, 1269
Launspach, J. TAE09, 1210
Lauritzen, T. RPE12, 2026
Laverty, M. MPR16, 2273
Lavrent'ev, B.M. WAA21, 1274
Lawrence, G.P. FPD03, 35
Lawson, W. TAQ17, TAQ18, TAQ19, 1561, 1563, 1566
Lawton, D. RPG11, 345
Laxadal, R. WAQ07, 1858
Laxdal, R.E. WAR15, 1936
Le Diberder, F. RPC20, 749
Le Goff, A. TPP09, 1632
Le Taillandier, P. TAE09, 1210
Lebedev, A.N. TPR13, 3269
Lebedev, N.I. WAA20, TAQ34, 1272, 1605
Lebedev, O.P. WPP02, 1658
Lebedev, P. TAA01, RAR30, 2078, 3424
Leblond, B. WPB01, 945
LeCroy, C.T. TPC18, 2643
LeDiberder, F. TAG01, 2742
Lee, Edward P. FAC01, 2835
Lee, H.S. RPA06, TAQ14, 1061, 1553
Lee, J.C. FAA07, RAA24, TAR04, TAR06, TPQ09, TPQ10, 210, 582, 804, 810, 2968, 2971
Lee, P.J. TPE01, 1276
Lee, S.Y. RPG08, TAP03, WPP20, WPP21, RAP21, WAC12, RAG10, RAQ23, RAQ24, 336, 357, 1705, 1708, 2934, 3094, 3182, 3337, 3340
Lee, Sangil TAB09, FAR03, 122, 269
Lee, T. TPG06, TAQ06, WPQ05, 171, 1533, 1726
Lee, Terry G. TAQ27, 1584
Lee, Y. TPB07, 2542
Lee, Y.Y. MXG03, TAP11, WAR13, 53, 378, 1930
Leemans, W. TPG07, RAB10, WAQ04, TAA28, 174, 776, 1852, 2135
Legg, R. WAQ14, WXE01, TPC07, 1873, 2429, 2610
Lehrman, I.S. FAA19, FAA31, 234, 260
Lemaire, J.-L. RAG07, 3173
Len, L.K. TAE10, 1213
Lenci, S. FAE07, 1497
Lenisa, P. RAE05, 2399
Lenkszus, F. MPQ07, RPQ16, 2464, 2702
Lennox, A. FAG06, 86
Lenz, J.W. RPG10, 342
Lepeltier, V. RPC20, TAG01, 749, 2742
Lessner, E. TAP05, FAB09, TPQ22, 363, 2811, 3001
Letoumellin, R. TAB04, 116
Letta, P. MPR13, 2265
Leung, E.M. TAB06, 119
Leung, K.N. TPB07, 2542
Levashov, Y. TAA02, 2081
Levchenko, V.D. WAA02, WAA03, 1230, 1233
Level, M.-P. FAR14, 293
Leveling, A. FAG06, 86
Levichev, E. FAP02, 1325
Levy, C.D.P. MPE03, 864
Ley, R. RAP24, 2943
Leyh, G. WAQ15, 1876
Leyh, G.E. RPP07, 1976
Li, D. TAP03, WPA04, WPP20, WPP21, RAP21, WAC12, RAG10, RAQ23, RAQ24, 357, 911, 1705, 1708, 2934, 3094, 3182, 3337, 3340
Li, H. RPC16, RPC17, RPC19, 737, 740, 746
Li, N. FAP01, 1322
Li, Rui WAQ12, MPB11, 1870, 2297
Li, W.M. RPE10, 2023
Li, Xiao-Ping RAP25, 2946
Li, Z. FAG11, FAA25, 102, 243
Li, Zenghai MPC25, RAG12, 2370, 3188
Liang, C. TPC07, 2610
Libault, David TPA17, 3235
Lien, E. FAE07, 1497
Limberg, T. RAP08, WAC17, 2901, 3109
Lin, C.L. MPE12, 893
Lin, G. TPQ09, 2968
Lin, Glory MPQ16, 2488
Lin, K.K. FAA07, MPQ19, MPQ32, 210, 2497, 2524
Lin, Leon C.-L. WPB03, WPB04, 951, 954
Lin, Liu FAP14, 1361
Lin, T.F. TAA14, MPQ16, 2108, 2488
Lin, X. MPC01, 2317
Lin, X.E. WPQ12, 1744
Lin, X.T. RPA04, 1058
Lin, Xintian E. WPR10, 1809
Lindner, M. FAQ04, 1396
Linebarger, W. RPA24, 1111
Linnecar, T. WAP12, WAP13, FAE10, 464, 467, 1506
Linnik, A.F. RAB15, 782
Linscott, I. RAE12, RPQ01, RPQ22, 2420, 2660, 2717
Liou, R. WAG09, TAA28, 640, 2135
Lisin, A. MPP10, WAC17, 2057, 3109
Littlejohn, R.G. RAR02, 3358
Littmann, B. TAQ30, 1593
Littmann, Bengt WPP22, 1711
Litvinenko, V. MPA11, 2217
Litvinenko, V.N. FAA08, RAA01, RAB22, RPA17, MPA10, MPQ06, FAC20, 213, 524, 796, 1090, 2214, 2461, 2877
Liu, H. FAG11, WPA17, WAQ11, 102, 942, 1867
Liu, H.-X. FAA25, 243
Liu, J. TPP16, WPP20, WPP21, WAC12, 1652, 1705, 1708,

3094
Liu, J.Y. TAP03, RAP21, RAG10, RAQ23, RAQ24, 357, 2934, 3182, 3337, 3340
Liu, W. MPA01, 2193
Liu, Y.C. FAA04, FAA07, RAA24, WPB07, 201, 210, 582, 964
Liu, Y.-C. TPC15, 2634
Liu, Zuping FAQ29, FAQ30, 1456, 1459
Lo, C.C. TAR03, 801
Lobov, I. MPR11, 2259
Loew, G. RPC01, 698
Loew, G.A. WAG13, 653
Loewen, R. RPA23, 1108
Loewen, R.J. WAG13, 653
Lofnes, T. TPC31, 2658
Long, H. WPA14, 935
Longinotti, D. TAR17, 837
Longinotti, D.B. TAR14, 828
Lopez, F. FAP12, 1355
Lorenz, R. TPC14, 2631
Lou, W. FAB12, 2820
Lou, W.R. TPA04, 3206
Lou, Weiran TAA29, 2138
Louie, W. TAA09, 2099
Loulergue, A. RAG06, 3170
Lovato, Richard WPB15, 985
Lu, J.J. TAQ33, 1602
Lucas, Peter W. WAP06, 449
Luccio, A. FAQ28, 1453
Ludmirsky, E. RAB21, 793
Luger, G. WAE08, 2175
Luijckx, G. RPG06, 330
Lumpkin, A. MPQ08, MPQ09, MPQ10, MPQ11, TPC03, RPQ15, RPQ16, 2467, 2470, 2473, 2476, 2598, 2699, 2702
Lund, S. TAR17, 837
Lund, S.M. TAR14, TPR18, 828, 3278
Luo, G.H. FAA07, RAA24, RAR05, 210, 582, 3364
Luo, Gwo-Huei FAA04, 201
Luo, H. MPA01, 2193
Luo, X. FAC04, 2844
Luong, M. TPP09, 1632
Lussignol, Y. WPB22, 998
Lütgert, S. WAE13, 2190
Lykke, Keith R. WPC11, 1019
Lyons, S. TAB17, RPA26, 131, 1116
Lysenko, W.P. RPR19, RPR22, 1161, 1167
Maas, R. RPG06, TPB03, 330, 2533
Maccaferri, R. RAP24, 2943
Macek, R. TPB13, WAC29, RAR23, 2554, 3146, 3406
Macek, R.J. TAR12, 822
MacGregor, I. TAR18, 840
Machida, S. TAP04, WPC07, WAR05, 360, 1007, 1912
MacKay, W.W. WAC24, RAQ22, 3131, 3334
MacKenzie, R. RAE03, 2389
MacLachlan, J.A. WAC06, 3079
Madert, M. RPR06, 1131
Madey, J.M.J. FAA08, RAB22, RPA17, FAC20, 213, 796, 1090, 2877
Madlung, J. WPA03, 908
Madsen, J. RPC09, 716
Madsen, J.H.B. RPC10, 719
Madura, D. WPG11, 520
Madura, D.D. TAB06, 119
Magugumela, M. WPC21, 1043
Mahoney, K. TPC26, 2652
Maier, R. TPB20, 2574
Maines, J. FAQ17, 1426
Mair, R. MPE10, 887
Maïssa, S. TPP09, 1632
Maj, J. WPP13, 1687
Makarov, A. RAQ14, 3315
Mako, F.M. TAE10, 1213
Malakhov, N. TAC16, 152
Maletic, D. RAG14, RAQ20, 3194, 3329
Malka, V. WAG08, 637
Malone, R. MPE11, 890
Malygin, A.N. RPP08, 1979
Mamaev, G. FAP24, 1387
Mammosser, J. FAE12, TPC07, 1512, 2610
Manca, J.J. WPR20, 1835
Manca, J.P.J. WPR20, 1835
Mandrillon, P. FAG09, 95
Mane, V. WAC24, WAC25, WAC26, 3131, 3134, 3137
Mangili, P. TPC10, 2619
Manglunki, D. MPG09, 423
Mangra, D. FAR19, 303
Mao, N. WAQ09, 1864
Mapes, M. MPP11, 2060
Margaritondo, G. TPG11, 186
Marhauser, F. WPA05, 914
Mariotti, E. RAE05, 2399
Markiewicz, T. RPC01, 698
Markov, V. FAR17, 299
Marks, S. FAQ24, FAQ25, 1444, 1447
Marneris, I. WAR11, RPP02, 1924, 1964
Marone, A. FAQ03, 1393
Marriner, J. WAP01, TPQ28, WAB01, 434, 3013, 3016
Marsh, K.A. WAG08, RAB01, 637, 758
Martens, M. WAP01, 434
Martens, M.A. WAP05, WAP08, 446, 455
Marti, F. RPG11, TAP08, TAP10, 345, 369, 375
Martin, D. MPQ15, MPQ25, 2485, 2512
Martin, E.J. RPP06, RPP13, 1973, 1991
Martin, K. WAE07, 2172
Martin, P. MPG01, 391
Martin, P.S. FAP04, FAP05, FAP06, FAP07, FAP09, WAR02, TAA12, 1331, 1334, 1337, 1340, 1346, 1903, 2105
Martini, M. TAP14, WAE09, 386, 2178
Martlew, B.G. RAE10, 2414
Maruyama, T. MPE10, 887
Marx, M. RPB15, 692
Masalov, V. WPC13, 1025
Mashiko, K. FAR08, RPA13, 278, 1079
Massarotti, A. TPG11, FAR21, WPQ04, 186, 309, 1723
Massoletti, D. FAA05, 204
Mastovsky, I. TPG14, RPC15, 192, 734
Masunov, E.S. RPR12, 1149
Matheson, R. MPQ22, 2506
Mathewson, A. RPE02, 1999
Matricon, P. WAG07, 634
Matsuda, K. FAR09, 281
Matsumoto, H. WAG12, RPA20, WPR03, 649, 1099, 1791
Matsumoto, S. RPB04, RPA20, 665, 1099
Matsuoka, M. TPP07, 1629
Mattei, P. RPR11, 1146
Matthews, P.J. WAG10, 643
Matthews, Paul WPP12, 1684
Matthieussent, G. WAG07, 634
Mattison, T. RPC02, 701
Mattison, T.S. WAR06, 1915
Matveev, Yu. WAA18, 1266
Matyukov, A.V. TAP16, 389
Mau, R. WAP04, 443
Maury, S. RAP23, RAP24, 2940, 2943

Maury, Stephan RPG07, 333
 May, Lisa M. FAE06, 1494
 May, M. TPE05, FAP09, 1298, 1346
 Mazaheri, G. RPB04, 665
 Mazarakis, M.G. TAE06, 1201
 Mazur, P.O. FAP06, FAP07, 1337, 1340
 McAllister, B. RPG05, 327
 McCormick, D. RPB01, RPB04, 656, 665
 McCrory, E. FAG06, 86
 McCrory, Elliot S. WAP06, 449
 McCune, E. FAE07, 1497
 McDaniel, B.D. RAE14, 2426
 McDaniel, M.R. TAA22, 2129
 McDonald, K.T. TAA28, 2135
 McDonald, M. MPE03, 864
 McDowell, W. TAP05, 363
 McGhee, D. FAR19, TAP05, 303, 363
 McGhee, D.G. RPP03, 1967
 McGinnis, D. WAP01, TPQ26, TPQ28, 434, 3010, 3013
 McIntosh, P.A. MPC19, WAC22, 2353, 3125
 McInturff, A.D. FAQ07, 1402
 McIntyre, Peter M. FAQ31, 1462
 McKee, B. WAC17, 3109
 McManus, A. WAR19, 1945
 McMichael, G.E. TAC12, 149
 McMichael, Gerald E. FAG13, 107
 Mead, J. TPB12, 2551
 Mecklenburg, B. RPC22, TAQ03, 755, 1524
 Meddahi, M. WPG09, RAA17, 514, 560
 Medvedko, A.S. FAQ17, 1426
 Medvedko, E.A. FAQ17, FAQ18, 1426, 1429
 Meigs, M.J. WAQ26, MPA05, TPC18, 1897, 2202, 2643
 Melekhin, V.N. TAR05, FAP19, WPR17, 807, 1375, 1827
 Mencick, M. WPB22, 998
 Mendelsohn, S.L. RPR20, 1164
 Menshikov, L. TAC16, 152
 Méot, F. FAC04, 2844
 Meredith, J. TAR17, 837
 Meredith, J.W. TPB14, 2557
 Merl, R. FAR19, TPE08, 303, 1310
 Merle, E. TAE09, TPC17, 1210, 2640
 Merminga, L. FAG11, FAA25, RPQ11, RPQ30, 102, 243, 2690, 2735
 Mertens, V. RAA15, 557
 Merz, W. RPP13, 1991
 Meshcherov, R. WPC13, 1025
 Meshkov, I. RAP23, RAP24, 2940, 2943
 Metz, H. TAQ19, 1566
 Metzmacher, K. MPG09, 423
 Meuth, H. WPQ26, 1781
 Meyer, J. RPQ15, 2699
 Meyer, S. TAR18, 840
 Meyerer, Thomas WPB21, 995
 Meyerhofer, D.D. TAA28, 2135
 Meyers, T. RPR20, 1164
 Mezi, L. TPG11, 186
 Michailov, S. TPE09, 1316
 Michelato, P. WPC23, 1049
 Michelotti, L. WAP08, 455
 Michelotti, Leo FAB15, 2826
 Michine, A.V. TAB15, 128
 Michnoff, R. MPA17, 2229
 Micklich, B.J. FAG14, 110
 Miertusova, J. MPP04, MPP05, 2042, 2045
 Mikhailichenko, A. TAG01, 2742
 Mikhailichenko, A.A. RAB18, 784
 Mikhailov, V.A. WAR09, FAC12, 1918, 2863
 Milchberg, H.M. WAG04, 621
 Milder, M.L. WPA08, 923
 Milder, Martin L. WPB15, 985
 Miller, H. TAQ11, 1544
 Miller, J.M. TPR18, 3278
 Miller, R. TAB17, RPB02, RPC01, MPE10, RPA04, RPA26, 131, 659, 698, 887, 1058, 1116
 Miller, R.A. WPC18, 1033
 Miller, R.H. WPB13, WXE03, 982, 2432
 Millich, A. WPQ25, 1779
 Milliman, L. FAA27, 248
 Millo, D. FAQ19, 1432
 Mills, F. TAP05, 363
 Mills, G.D. MPE05, WAQ26, 871, 1897
 Milton, B. WAQ07, 1858
 Milton, B.F. FAG07, 89
 Milton, S. MPQ10, 2473
 Milton, S.V. RAA28, FAP12, RPP03, RPQ18, 594, 1355, 1967, 2708
 Mimashi, T. MPA06, 2205
 Minagawa, Y. RPQ26, 2726
 Minamihara, Y. FAQ24, FAQ25, 1444, 1447
 Minato, T. FAQ08, 1405
 Miné, Ph. WAG07, 634
 Minehara, E.J. TPG02, 159
 Mingalev, B. MPC21, 2359
 Minty, M. WAG11, RPC02, RAE03, TPQ16, 646, 701, 2389, 2986
 Minty, M.G. RAA06, RPB03, RAP10, WAB09, WAB12, WAC17, TPA09, 536, 662, 2907, 3037, 3046, 3109, 3217
 Miram, G. FAE07, 1497
 Mirzoev, K. MPP03, 2040
 Mishin, A.V. RPA25, 1114
 Mishra, C.S. FAP06, MPB05, MPB06, TAG10, RAP03, 1337, 2282, 2285, 2777, 2886
 Mishra, S. FAP04, FAP07, 1331, 1340
 Mitchell, M. WPR15, 1821
 Mitra, A.K. TAQ33, 1602
 Mitrochenko, V.V. WPB16, 988
 Mitsuhashi, T. RAQ06, 3300
 Mitsunobu, S. TPP03, 1620
 Miura, T. WPR02, 1788
 Miya, K. RAB13, 779
 Miyahara, Y. FAQ20, FAQ21, RAQ30, 1435, 1438, 3355
 Miyai, Y. TAQ35, 1608
 Miyauchi, Y. FAA30, 257
 Mizumoto, M. RPG09, 339
 Mizuno, A. WPC22, MPA07, 1046, 2208
 Mizuno, H. FAQ08, TAQ29, 1405, 1590
 Mocheshnikov, N. FAR17, 299
 Modena, A. WAG08, 637
 Moe, H. TAP05, 363
 Moe, H.J. RPA07, 1064
 Moffat, D. FAE13, RAQ04, RAR19, 1515, 3294, 3394
 Möhl, D. RAP23, 2940
 Mohr, J. FAR06, 272
 Moi, L. RAE05, 2399
 Moibenko, A. WAE07, 2172
 Moir, David C. TAE08, 1207
 Moiseev, V.A. RPR01, 1119
 Moisseev, V. WPR13, 1815
 Moisseev, V.I. TPB25, 2586
 Mokhov, N.V. RAB19, 787

Mokhtarani, A. FAP06, FAP07, 1337, 1340
Molinari, G. RAP24, 2943
Möller, K.D. FAR06, 272
Møller, S.P. WAP14, 470
Möller, W-D. TPP11, 1639
Molodkin, V. FAR16, FAR17, 296, 299
Montag, C. TAA01, TAA06, RAR30, 2078, 2090, 3424
Montès, B. WAG07, 634
Montjar, B. MPR13, 2265
Moog, E.R. TPE06, 1301
Mora, P. WAG04, WAG07, 621, 634
Morano, R. WAG07, 634
Morcombe, P. FAA08, WAA10, MPA11, MPQ06, 213, 1248, 2217, 2461
Morcombe, Peter WPR22, 1841
Moretti, A. WPA07, 920
Morgan, G. TPE04, FAQ03, FAQ04, FAQ16, 1293, 1393, 1396, 1423
Morgan, J. TAR16, 834
Morgillo, A. FAQ03, 1393
Mori, W.B. WAG09, RAB01, RAB02, RAB08, TPB18, 640, 758, 761, 773, 2569
Mori, Y. TAP04, MPE03, WPC07, WAQ06, WAR05, 360, 864, 1007, 1855, 1912
Morii, Y. TAQ35, 1608
Morillo, J. WAG07, 634
Morpurgo, G. RAA20, FAC03, 570, 2841
Morris, J.T. WAB04, 3022
Mortazavi, P. TPP06, WPQ20, 1626, 1768
Morvillo, M. MPQ05, 2458
Moser, H.O. FAR06, 272
Moshammer, W. RPC02, 701
Mosko, S.W. TAP07, WAQ26, 366, 1897
Mosnier, A. WPB22, WAC13, 998, 3097
Mostowfi, D. RPQ21, RPQ22, 2714, 2717
Moulin, F. WAG07, 634
Mouton, B. WPB22, 998
Mufel, V.B. TAE14, 1225
Mugge, M. MPP12, MPP20, 2064, 2075
Muggli, P. WAG09, WPC20, 640, 1039
Mulhall, S. FAQ15, TAA09, 1420, 2099
Mulhollan, G. MPE10, WPC21, 887, 1043
Muller, H. FAE13, TPP04, RAR19, 1515, 1623, 3394
Müller, W.F.O. RPB15, 692
Munasypov, R.N. WAA21, 1274
Munneke, B. TAQ12, 1547
Murata, H. RPG09, 339
Muratore, J. TPE04, FAQ02, FAQ03, FAQ04, 1293, 1390, 1393, 1396
Murin, B.P. RPR07, 1134
Murphy, C.T. WAR19, 1945
Murphy, J.B. FAR10, TPQ14, 284, 2980
Murray, S.N. MPE05, 871
Mustafin, E. RAP23, 2940
Myakishev, D. RPA12, 1076
Myakishev, D.G. MPC17, 2348
Myers, S. WPG01, 476
Mytsykov, A. FAR17, 299
Myznikov, K. FAQ06, 1399
Nadji, A. FAR14, 293
Nagaenko, M. FAR06, 272
Nagafuchi, T. FAP13, 1358
Nagai, A. FAA30, 257
Nagai, R. TPG02, 159
Nagaitsev, S. RAP22, 2937
Nagaoka, R. FAR21, TAG05, 309, 2762
Nagatsuka, T. FAP22, WPQ07, 1384, 1732
Nagchaudhuri, A. MPA11, 2217
Naidenov, V.O. TAP16, 389
Naito, F. FAE09, WPQ17, WPR05, WPR09, 1503, 1759, 1797, 1806
Najmudin, Z. WAG08, 637
Nakajima, K. RAB13, TAA28, 779, 2135
Nakamura, N. RPQ23, 2720
Nakamura, T. WAC14, 3100
Nakamura, T.T. MPA06, 2205
Nakanishi, H. RAB13, TPP16, TAA28, 779, 1652, 2135
Nakata, K. TAQ35, 1608
Nakayama, H. WAR03, TAG01, 1906, 2742
Nam, S.H. TPG06, 171
Namkung, W. TAR07, RPA06, TAQ14, TAQ15, MPA02, 813, 1061, 1553, 1556, 2196
Naqvi, S. TAQ01, 1518
Nasonov, N.N. FAG12, 105
Nassiri, A. WPB06, RPA10, WPP16, 961, 1070, 1693
Nath, S. RPR08, RPR09, 1137, 1140
Nath, Subrata WAQ02, 1846
Nation, J.A. WPC19, TAE12, TAQ01, 1036, 1219, 1518
Nattrass, L. TAR17, 837
Nattrass, L.A. TAR14, 828
Nawrocki, G. MPQ08, 2467
Nawrocky, R.J. MPQ23, 2509
Neau, Eugene L. TAE03, 1188
Neil, G. FAA25, WPA17, RPQ30, 243, 942, 2735
Neil, G.R. FAG11, 102
Neil, George R. TAC03, 137
Nelson, D. WAQ15, 1876
Nelson, M. TAR17, 837
Nelson, M.B. TAR14, 828
Nemoshkalenko, V. FAR16, FAR17, 296, 299
Nesemann, H. FAA02, FAC19, 195, 2874
Nesterov, N. TAC05, 140
Nesterov, V.V. WAA11, 1251
Nesterovich, A. RPR10, RPR15, 1143, 1155
Nett, D. TAB17, RPA26, 131, 1116
Neubauer, M. WPQ10, WPR07, WPR08, 1741, 1800, 1803
Neuffer, D. FAG11, WPA17, WAQ11, 102, 942, 1867
Neuffer, D.V. FAA25, 243
Neuffer, David MXG03, 53
Newton, M.A. TAR14, 828
Nezhevenko, O. RPA12, TAQ21, 1076, 1569
Ng, C. WPR07, MPC01, MPQ25, 1800, 2317, 2512
Ng, C.K. TAA28, 2135
Ng, C.-K. WPQ10, WPQ12, MPP07, MPQ15, WAB18, WAC17, 1741, 1744, 2048, 2485, 3061, 3109
Ng, K.Y. RAP21, TPQ12, RAQ23, RAQ24, RAR17, 2934, 2977, 3337, 3340, 3388
Ng, K.-Y. TAR20, 843
Nghiem, P. FAR14, 293
Nguyen, D.C. FAA16, 228
Nicol, T. WPB08, 967
Nielsen, R. TAP05, 363
Nieuwenkamp, H. MPQ17, 2491
Niki, K. RPG13, 351
Nikiforov, S. WPC03, 1004

Niquille, C. WAP13, 467
 Nishi, M. TAB03, WPQ21, 113, 1770
 Nishida, Y. RAB13, TAA28, 779, 2135
 Nishihara, S. FAA30, 257
 Nishimura, H. MPR03, MPR04, 2244, 2247
 Nishimura, Hiroshi WAE04, 2162
 Nobel, R.J. WPA07, 920
 Noda, A. FAR08, RPA13, RPA18, WPQ21, WAQ01, 278, 1079, 1093, 1770, 1843
 Noda, K. TAB03, 113
 Nogiec, J.M. FAP06, FAP07, MPB06, 1337, 1340, 2285
 Noguchi, S. TPP07, 1629
 Nolen, J.A. RPG14, FAQ09, TPC13, RAQ16, 354, 1408, 2628, 3320
 Noomen, J. RPG06, 330
 Noomen, J.G. MPQ17, 2491
 Noonan, J. RPE09, 2020
 Nordberg, E. FAE13, 1515
 Nordby, M. MPP08, MPP12, MPP20, TAA22, MPC01, MPQ25, 2051, 2064, 2075, 2129, 2317, 2512
 Nordby, M.E. MPP07, 2048
 Norek, G. TAP05, 363
 Norem, J. RAA29, TAA28, TPC16, 597, 2135, 2637
 Norris, B.L. WAE02, 2152
 Norton, M. TAA20, 2123
 Norum, B.E. RAP01, 2880
 Norum, Blaine E. RAE07, 2405
 Nosochkov, Y. RAA22, RAA25, RAA27, 576, 585, 591
 Nosyrev, S. WPP10, WPP11, 1678, 1681
 Novikov, A. WPP10, 1678
 Novikov, S.A. WAR09, 1918
 Novikova, T.A. FAA14, 225
 Novokhatsky, A. WAA17, 1263
 Nuhn, H.-D. FAA12, FAA17, 219, 231
 Nusinovich, G.S. TAQ17, 1561
 Nyman, M. RPQ08, 2681
 O'Connor, T. RAA03, 527
 O'Day, S. WAQ22, 1888
 O'Shea, P. FAA08, MPA11, 213, 2217
 O'Shea, P.G. RPA17, TAQ07, 1090, 1536
 O'Shea, Patrick G. WPA13, WPB09, TAG12, 932, 970, 2783
 O'Sullivan, M. RPP13, 1991
 O'Sullivan, M.K. RPP06, 1973
 Obina, T. TPC08, RPQ26, 2613, 2726
 Oerter, B. MPA16, 2226
 Ogata, A. RAB13, TAA28, 779, 2135
 Ogawa, Y. TAA04, 2087
 Ogitsu, T. FAQ02, FAQ08, 1390, 1405
 Oguri, H. RPG09, 339
 Oh, J.S. TAQ15, 1556
 Ohgaki, H. MPR04, 2247
 Ohmi, K. RAP02, 2883
 Ohmori, Chihiro TPR16, 3275
 Ohshita, E. TAQ35, 1608
 Oide, K. RPC20, RPA20, TAA08, WXE07, TAG01, TAG11, WAB20, WAC08, WAC16, 749, 1099, 2096, 2444, 2742, 2780, 3064, 3085, 3105
 Oide, Katsunobu WAB10, 3040
 Okada, M. RPG13, 351
 Okamoto, H. FAR08, RPA13, RPA18, WAQ01, 278, 1079, 1093, 1843
 Okamoto, Hiromi TPR11, 3263
 Okuma, S. FAA30, TAQ35, 257, 1608
 Okumura, Y. RPG09, 339
 Okun, L. FPD05, 45
 Olivieri, D.N. TAR16, 834
 Olsen, D.K. RPG01, TAP07, WAQ26, 312, 366, 1897
 Olsen, J. RAE12, 2420
 Omeich, M. WPA14, WPB22, 935, 998
 Onillon, E. RPQ17, RPQ25, 2705, 2723
 Onishchenko, I.N. RAB15, 782
 Onken, R. WPQ24, 1776
 Ono, M. TPP07, 1629
 Opanasenko, A.N. WPA15, WPA16, 938, 939
 Oren, W. WXE01, 2429
 Oreshnikov, A. TAC05, 140
 Orris, D. TPE05, 1298
 Orris, D.F. FAP06, FAP07, 1337, 1340
 Ortiz, R. MPQ22, 2506
 Osborn, J. FAP01, 1322
 Oshita, E. FAA30, 257
 Ostanin, V.P. RPP08, 1979
 Ostiguy, F. TAG04, 2757
 Ostiguy, Francois WAC02, 3070
 Ostiguy, J.F. WPB08, 967
 Ostiguy, J.-F. TAR20, TPE05, FAP10, FAP21, MPC07, 843, 1298, 1349, 1381, 2330
 Ostojic, R. FAC04, 2844
 Ostroumov, P.N. RPR01, RPR24, RAE08, 1119, 1173, 2408
 Otake, Y. TAQ29, 1590
 Otock, R. TAA11, 2102
 Otock, R.D. RPE09, 2020
 Ottarson, J. TAP08, 369
 Ottaviani, P.L. TPG11, 186
 Oude Velthuis, R.G.J. RPP04, 1970
 Ovchinnikov, V.P. TAE13, 1222
 Owen, H.L. TPG09, 180
 Oxoby, G. RAE12, RPQ01, 2420, 2660
 Ozaki, Y. WXE07, 2444
 Pabst, M. TPA01, TPA02, TPA03, 3197, 3200, 3203
 Pachnik, J.E. FAP06, FAP07, MPB06, 1337, 1340, 2285
 Padamsee, H. FAE13, TPP02, TPP04, WPQ02, RAQ04, RAR18, RAR19, 1515, 1617, 1623, 1720, 3294, 3391, 3394
 Pagani, C. WPB10, WPC23, TAA07, RAQ05, 973, 1049, 2093, 3297
 Pai, C. MPP11, 2060
 Palkovic, J. TPB19, 2572
 Palmer, D. RPA26, 1116
 Palmer, D.T. WPB13, WXE03, 982, 2432
 Palmer, Robert B. MXG03, 53
 Palrang, M. MPP10, 2057
 Pan, K.T. MPQ16, 2488
 Pang, A.W. WPC21, 1043
 Pangos, N. FAR21, MPP05, 309, 2045
 Pankuch, P. TAE06, 1201
 Pantazis, R. MPA11, 2217
 Pantenburg, F.J. FAR06, 272
 Pappas, G.C. WAR10, WAR12, 1921, 1927
 Papureanu, S. RPR06, WPQ26, TPB20, 1131, 1781, 2574
 Paramonov, V.V. WPP17, WPP18, WPP19, 1696, 1699, 1702
 Parazzoli, C. FAA27, 248
 Parazzoli, C.G. FAA28, 251
 Pardo, R.C. WAQ03, 1849
 Park, H.J. WPR11, 1812

Park, Heunggyu TAB09, FAR03, 122, 269
Park, Jongpil TAB09, FAR03, 122, 269
Park, S. RPA21, RPA22, 1102, 1105
Park, S.H. FAA08, RAB22, TAQ14, 213, 796, 1553
Park, S.S. TAQ15, 1556
Park, Sanghyun WPB02, 948
Parkhomchuk, V. TAR11, 819
Parzen, G. FAB03, FAB04, FAB05, 2795, 2798, 2801
Pasotti, C. WPQ04, TAG05, 1723, 2762
Pasquinelli, Ralph J. RAE01, 2379
Patavalis, N. MPR13, 2265
Paterson, E. RPC01, 698
Patteri, P. TPG11, 186
Patterson, D. MPQ10, 2473
Paulson, C.C. RPR20, 1164
Pavlovets, M. TAA18, 2120
Pawlak, T. MPG01, 391
Payet, J. FAR14, 293
Peacock, M.A. RPR20, 1164
Pearson, C. FAE07, 1497
Pearson, Pauline MPR07, 2250
Peck, S. FAE13, 1515
Pedersen, F. MPG09, 423
Peggs, S. MPG12, TAA09, MPC05, FAB20, FAB22, WAC24, WAC25, WAC26, RAQ21, RAQ22, RAR29, 431, 2099, 2327, 2829, 2832, 3131, 3134, 3137, 3331, 3334, 3421
Peggs, S.G. WAP10, 461
Pei, A. TAP03, WPP20, WPP21, RAP21, WAC12, RAG10, RAQ23, RAQ24, 357, 1705, 1708, 2934, 3094, 3182, 3337, 3340
Pei, Yuan Ji RPE10, 2023
Pekeler, M. TPP11, 1639
Pelaia, T.A. RAE14, 2426
Pellegrini, C. FAA23, RAB03, RPA21, RPA22, RAQ17, 240, 764, 1102, 1105, 3323
Pendleton, R. WPR07, WPR16, 1800, 1824
Penicka, M. TAA03, 2084
Pennacchi, R. WPR15, 1821
Perin, R. TPE02, 1282
Perkins, C. RAA04, MPP09, MPP10, MPP12, MPP20, TAA22, MPC01, MPQ25, 530, 2054, 2057, 2064, 2075, 2129, 2317, 2512
Perkins, L. TPB07, 2542
Peschke, C. RPB16, 695
Peters, C. RPC16, RPC18, WPA01, TAE01, FAP17, FAP18, TPA10, 737, 743, 902, 1178, 1369, 1372, 3220
Peters, F. TAG01, 2742
Peterson, K.J. TAP05, 363
Petracca, S. WAE12, 2187
Petrenko, I.I. FAB02, 2792
Petrenko, V. WPR13, 1815
Petrenko, V.V. TPB25, 2586
Petri, H. WPC08, 1010
Petrov, S.P. FAQ17, 1426
Petrov, V. WPP11, 1681
Petrov, V.A. WAA20, TAQ34, 1272, 1605
Petty, L. MPP15, 2069
Pfeffer, H. WAE07, 2172
Pflüger, J. FAR07, 275
Phillips, R. FAE07, 1497
Phinney, N. WAG11, RPB01, RPC01, 646, 656, 698
Phung, B. WPB22, 998
Piaszczyk, C. RPR20, 1164
Piataev, V. TAC16, 152
Pichoff, N. RAG06, RAG07, 3170, 3173
Pickard, D. TPB07, 2542
Pietryka, M. RAA04, WAC17, 530, 3109
Pilat, F. FAQ28, FAB22, 1453, 2832
Pilyar, N. TAC16, 152
Pinto, I.M. WAE12, 2187
Pipersky, P. FAQ24, FAQ25, 1444, 1447
Pirkil, W. WPP07, WPQ19, 1669, 1765
Pirovano, R. TAQ12, 1547
Pisharody, M. FAE13, WPQ02, RAE14, TPA04, RAQ04, RAR18, 1515, 1720, 2426, 3206, 3294, 3391
Piskarev, I. RPA19, 1096
Pitel, Ira J. RPP11, 1985
Placidi, M. RAA19, RPB01, 567, 656
Plass, G. FAG08, 92
Plate, D. FAQ24, FAQ25, 1444, 1447
Plate, S. FAQ15, 1420
Plato, John G. WPB15, 985
Platonov, Yu.P. MPG10, 426
Plesko, M. TPG08, FAA13, FAR06, 177, 222, 272
Plesko, Mark MPR12, 2262
Plotnikov, S. TAC05, 140
Plouviez, E. TPG05, RPQ15, 167, 2699
Plum, M. TPB13, WAC29, RAR22, RAR23, 2554, 3146, 3403, 3406
Podebrad, O. RPB16, 695
Podobedov, B. WAC17, 3109
Poelman, A. MPQ17, 2491
Pogorelsky, I. MPE11, 890
Poilleux, P. WAG07, 634
Poirier, R.L. TAQ33, WPP18, 1602, 1699
Polyakov, V. RAP24, 2943
Poncet, A. RPE02, MPP15, 1999, 2069
Ponds, M. TAQ07, 1536
Poole, J. WPG09, RAA15, WAE03, 514, 557, 2157
Poole, M.W. TPG09, 180
Popik, V.M. FAQ17, 1426
Popov, Yu. TAC16, 152
Popovic, M. FAG06, WPA06, WPA07, WPR21, 86, 917, 920, 1838
Porterfield, D. TPC04, 2601
Portmann, G. FAQ24, RPQ13, FAB01, 1444, 2693, 2789
Potter, James M. FAE06, 1494
Poukey, J.W. TAE06, 1201
Pourre, J.L. TAB04, 116
Power, J. WAG06, WPB11, WPB12, RPR19, 631, 976, 979, 1161
Power, J.F. TPB22, 2580
Powers, T. FAE12, 1512
Powers, Tom TPP13, 1645
Pozdeev, M. TPQ04, 2958
Prabhakar, S. RAE12, 2420
Preble, J. FAE12, 1512
Prelec, K. WPC09, 1013
Prescott, C. MPE10, 887
Price, E. TPC04, 2601
Prieto, P. WAE07, 2172
Primdahl, K. WPP13, WPP14, 1687, 1690
Proch, D. FAE08, TPP11, WPQ24, 1500, 1639, 1776
Prodell, A. TPE04, 1293
Pruyn, J. WPA01, 902
Ptitsin, V.I. RAQ21, 3331
Puchkov, A. RPR10, 1143
Pullia, M. TPC10, 2619
Puntus, V. WPP05, 1666
Puzo, P. RPC20, TAG01, 749,

2742
Qian, Y.L. RPA08, RPA11, 1067, 1073
Qian, Zubao TPP01, 1614
Qin, Q. TPQ03, 2955
Qing, Li FAA26, 246
Qiu, X. MPE11, 890
Qiu, X.Z. RAE09, TPB01, 2411, 2530
Queralt, X. TPG09, 180
Quinn, P.D. RAE10, 2414
Qunell, D. WAR01, 1900
Rackelmann, A. WAC17, 3109
Radloff, W. TPC09, 2616
Radusewicz, P. FAQ08, 1405
Rafael, F.S. MPQ33, 2527
Rago, C. WAC17, 3109
Raimondi, P. WAG11, RPB01, RPC20, TAA08, TAG01, RAP15, RAP16, 646, 656, 749, 2096, 2742, 2919, 2922
Rakowsky, G. FAQ17, WXE04, 1426, 2435
Ramachandran, S. WAR19, 1945
Ramamoorthy, S. MPA15, 2223
Ramamoorthy, Susila MPR07, RPQ14, 2250, 2696
Ramirez, G. WPP03, 1660
Ramirez, J.J. TAE05, TAE06, 1198, 1201
Raparia, D. RAR16, 3385
Rasmussen, J.O. WAQ04, 1852
Rasmussen, N. MPG09, 423
Ratti, A. WPP07, WPQ19, RPQ17, WAC24, 1669, 1765, 2705, 3131
Raubenheimer, T. RPB02, RPC01, RPC03, TPQ16, TPQ17, WAC17, 659, 698, 704, 2986, 2989, 3109
Raubenheimer, T.O. RPC02, TAG03, WAC15, WAC18, RAQ03, 701, 2752, 3102, 3112, 3291
Rauchas, A. TAP05, 363
Ravn, Helge L. MPE02, 858
Razuvakin, V.N. WAA20, 1272
Reece, C. FAE12, 1512
Reece, R.K. TAP11, TAP13, 378, 383
Reed, L. TPC16, 2637
Rees, D. WPA08, TAQ02, TAQ31, 923, 1521, 1596
Reginato, L. RPC16, RPC18, WPA01, TAE01, FAP17, WAQ04, 737, 743, 902, 1178, 1369, 1852
Rehak, M. TPE04, 1293
Reid, J. TAQ11, 1544
Reilly, J. FAE13, WPQ02, 1515, 1720
Reilly, R. WAA05, WAR01, 1236, 1900
Reiser, M. TAE04, TAQ17, TAQ18, TAQ19, TPQ11, 1193, 1561, 1563, 1566, 2974
Reiser, Martin RPR23, TAA17, MPC04, 1170, 2117, 2324
Renieri, A. TPG11, 186
Renken, D. TPP11, 1639
Renner, T. WXE06, 2441
Repnaw, R. RPR06, 1131
Repond, J. RAA29, 597
Repose, G. TAR17, 837
Reusch, M.F. RPR20, TPR08, 1164, 3257
Reuter, E. RAA04, TAA22, 530, 2129
Revol, J.L. TPG05, 167
Reyermier, C. RPE02, 1999
Rhoades, J. WAR19, 1945
Riabko, A. TAP03, WPP20, WPP21, RAP21, WAC12, RAG10, RAQ23, RAQ24, 357, 1705, 1708, 2934, 3094, 3182, 3337, 3340
Rice, D. FAE13, FAB12, 1515, 2820
Rich, D. RAQ23, 3337
Richard, Frank FAC07, 2850
Riche, A.J. MPC24, 2367
Richter, R. FAR21, 309
Rimmer, R. WPR07, WPR14, 1800, 1818
Rimmer, R.A. WPQ06, WPQ13, WPR08, 1729, 1747, 1803
Rindi, A. TPG11, 186
Ringwall, A.D. RPG10, 342
Rinolfi, L. RPC10, 719
Rintamaki, J. TPB14, 2557
Risselada, T. FAC04, 2844
Ritson, D. RAA26, 588
Ritson, D.M. RAA22, RAA27, 576, 591
Riunaud, J.-P. TAP14, 386
Rizawa, T. WPR16, 1824
Robin, D. FAA06, RPC02, RPQ13, FAB01, 207, 701, 2693, 2789
Rode, Claus H. RPE01, 1994
Rodger, E. FAP11, 1352
Rodier, J. WPB22, 998
Rogers, J. FAE13, TPA04, 1515, 3206
Rogers, J.T. RAE14, WAB15, 2426, 3052
Rojak, M. MPB09, 2291
Rokni, S. TAG01, 2742
Romanov, G. MPC16, 2345
Romasko, V.P. WPA15, 938
Rookhuizen, H. Boer RPG06, 330
Root, L. RPG12, WAQ07, 348, 1858
Ropert, A. TPG05, 167
Roques, A. TAE09, 1210
Rose, J. WPP07, WPQ19, RPQ17, WAC24, 1669, 1765, 2705, 3131
Rosei, R. TPG11, 186
Rosenblum, B. WAA19, 1269
Rosenzweig, J. FAA23, WPB05, WPB08, RPA21, RPA22, TAA28, 240, 957, 967, 1102, 1105, 2135
Rosenzweig, J.B. WAG06, MPE13, 631, 896
Roser, T. TAP11, TAP12, TAP13, RPQ07, RAG02, 378, 381, 383, 2678, 3154
Rosing, M. WPB11, 976
Ross, M. RPB01, RPB04, RPC01, WPR15, WAQ15, TAA28, 656, 665, 698, 1821, 1876, 2135
Ross, M.C. WAG11, WAC17, 646, 3109
Ross, W. RAE12, RPQ01, 2420, 2660
Roßbach, J. FAC19, 2874
Roszbach, J. TPG12, WAG02, TAA01, TAA06, RAR30, 189, 611, 2078, 2090, 3424
Rossi, C. FAA13, FAR21, 222, 309
Rossmannith, R. FAR07, 275
Rossmannith, Robert RAE07, 2405
Roster, William WAB06, 3028
Rotela, E. MPQ07, 2464
Rotela, R. TAR08, 816
Rothman, J.L. MPQ01, 2450
Roudier, P. WPB22, 998
Roy, G. WAP12, WAP13, RAA11, RAA17, TAG01, 464, 467, 548, 560, 2742
Roybal, W. TAQ02, 1521

Rubbia, C. FAG09, TPG11, 95, 186
Rubin, D. FAE13, RAQ04, 1515, 3294
Rubin, David L. WPG02, 481
Rudenko, V. TAC16, 152
Ruemmler, J. WAR14, 1933
Rufer, C. FAC04, 2844
Ruggiero, A.G. RAG14, RAQ20, 3194, 3329
Ruggiero, F. RPE02, WAE12, 1999, 2187
Rulz, C. RAG06, RAG07, 3170, 3173
Ruland, Robert E. RPE04, 2009
Rusnak, Brian TPP10, 1636
Russell, A. MPB06, 2285
Russell, A.D. FAP06, FAP07, WAR02, MPB05, 1337, 1340, 1903, 2282
Russell, S.J. TPB22, 2580
Russell, Steven WPB15, 985
Russell, T. RPA11, RPE09, 1073, 2020
Russell, Thomas J. TAQ16, 1559
Rusthoi, D.P. RPR22, TPC06, 1167, 2607
Ruth, R. RPC01, RPA04, 698, 1058
Ruth, R.D. WAG13, TPQ17, 653, 2989
Ruth, Ronald D. WAG03, TAQ26, TAQ27, WAC05, RAQ18, 616, 1581, 1584, 3076, 3326
Ruth, Thomas J. WPE03, 67
Ryan, W.A. MPQ04, 2455
Rybarcyk, L.J. RAG11, 3185
Ryne, Robert D. MPB16, RAG01, 2306, 3149
Ryu, C.M. TAQ14, 1553
Saab, A.H. RPP01, 1961
Saadatmand, K. FAG05, 83
Saba, J. WPQ06, 1729
Saban, R. WAE01, 2147
Sabbi, G.L. RAA20, FAC03, 570, 2841
Sabia, E. TPG11, 186
Sachtschale, R. RPA17, TAQ07, MPA11, 1090, 1536, 2217
Sachtschale, R.J. WAA10, 1248
Sachtshale, R. FAA08, 213
Sackett, J. FAE07, 1497
Saeki, K. FAA30, 257
Saewert, G.W. MPB15, 2303
Sáez, P. MPE10, WPC21, 887, 1043
Safa, H. TPP09, 1632
Safranek, J. FAR02, RPQ19, FAB11, 266, 2711, 2817
Sagan, D. FAE13, TPA04, RAR15, 1515, 3206, 3382
Sagan, David RAP04, 2889
Sah, R. FAG05, 83
Saile, V. TAA32, 2141
Saito, K. TPP07, 1629
Sakae, T. MPE03, 864
Sakai, H. WPQ15, 1753
Sakai, I. WAR05, 1912
Sakaki, H. WPC22, MPA07, 1046, 2208
Sakanaka, S. WPQ16, WPR02, WPR03, RAQ06, 1756, 1788, 1791, 3300
Salah, W. TPR04, 3245
Saltmarsh, C. MPR20, 2279
Sampayan, S. MPE14, WPC16, WAA19, TAA20, 899, 1027, 1269, 2123
Sampson, W. TPE04, FAQ03, FAQ04, 1293, 1393, 1396
Sandberg, J.N. WAR11, RPP02, 1924, 1964
Sander, O.R. RPR19, RPR22, TPC06, 1161, 1167, 2607
Sanders, D.A. RAB20, 790
Sandler, P.H. RAB20, 790
Sandoval, D.P. TPC06, 2607
Sangster, C. TAR17, 837
Sangster, T.C. TAR14, 828
Sannibale, F. RPA26, 1116
Sapozhnikov, L. RAE12, RPQ01, RPQ05, 2420, 2660, 2672
Sapp, W. RPG05, 327
Sarantsev, V.P. TAQ34, 1605
Saraph, G. TAQ19, 1566
Sarau, B. FAA02, 195
Sarstedt, M. TPB07, 2542
Sasaki, S. FAQ21, RPQ15, 1438, 2699
Sasaki, Y. FAP13, 1358
Sass, R. RPB03, RAE03, 662, 2389
Sathe, S. MPR20, 2279
Sato, H. WAR04, WAR05, 1909, 1912
Sato, I. TAQ08, TAQ25, TAA04, 1539, 1578, 2087
Satogata, T. MPR20, TPB21, RAQ22, 2279, 2577, 3334
Satoh, K. WPR02, WAC07, WAC08, 1788, 3082, 3085
Satoh, Kotaro MPQ14, 2482
Satti, J.A. FAP08, 1343
Saulter, Q. WAQ14, 1873
Saury, J.L. WPB22, 998
Sawamura, M. TPG02, 159
Scandale, W. WAP14, FAC04, FAC06, 470, 2844, 2847
Scanlan, R.M. FAQ07, 1402
Schachinger, L. MPR04, RPQ13, 2247, 2693
Schachinger, L.C. TAB06, 119
Schächter, L. WPC19, TAE12, TAQ01, 1036, 1219, 1518
Schaffner, S. MPR13, 2265
Schafstall, P.J. WPA08, 923
Schank, C.V. TPG07, 174
Schaper, J. TPG08, FAR06, 177, 272
Scharlemann, E.T. FAA12, FAA17, 219, 231
Scheidt, K. TPG05, RPQ15, 167, 2699
Schempp, A. WPA03, WPA04, WPA05, RPR06, 908, 911, 914, 1131
Schiffer, John P. RAG04, 3164
Schindl, K. MPG09, 423
Schirm, K.M. FAE11, 1509
Schirmer, D. FAQ12, WAQ17, 1411, 1879
Schlösser, K. FAR06, 272
Schlueter, R. FAQ23, FAQ24, FAQ25, 1441, 1444, 1447
Schlüter, R. FAA17, 231
Schmenk, E.G. TAA32, 2141
Schmickler, H. WAP12, WAP13, RAA10, RAA11, RAA13, 464, 467, 545, 548, 554
Schmidt, C. FAG06, 86
Schmidt, C.W. WPA06, 917
Schmidt, F. TAG07, 2768
Schmidt, R. WPG09, RAA19, 514, 567
Schmieder, R. WPC09, 1013
Schmitz, M. WPA12, 929
Schmor, P. WAQ07, 1858
Schmor, P.W. RPG12, MPE01, MPE03, 348, 853, 864
Schnase, A. WPQ26, TPB20, 1781, 2574
Schneider, G.C. MPG09, 423
Schneider, H.R. RPG12, RPR02, RPR03, 348, 1122,

1125
Schneider, J.D. MPE04,
WPA08, 867, 923
Schnell, W. RPC09, 716
Schoenlein, R. TPG07, 174
Schoessow, P. WAG06,
WPB11, 631, 976
Scholl, E.H. TPB21, 2577
Scholz, T. RPE02, 1999
Schönauer, H. MPG09, WAQ25,
423, 1894
Schönfeld, Frank WPP22,
1711
Schreiber, S. RPC10, 719
Schreuder, H.W. RPG02, 317
Schulte, Elmar TPC11, 2622
Schultheis, R. MPC15, 2342
Schultz, D. WPC21, WAQ15,
1043, 1876
Schulz, G. FAR06, 272
Schulze, M.E. FAG05, 83
Schumburg, N. RPP02, 1964
Schuppler, S. FAR06, 272
Schwalm, D. RPR06, 1131
Schwandt, P. RAP22, 2937
Schwarz, H. RAA04, WPQ06,
WPR07, WPR08, RPQ05, 530,
1729, 1800, 1803, 2672
Schweickert, H. FAR06, 272
Scott, B. RPC02, TPQ16, 701,
2986
Sears, J. FAE13, WPQ02,
1515, 1720
Sebek, J. MPQ22, RPQ22,
2506, 2717
Sedlyarov, I. WPP10, WPP11,
1678, 1681
Seeman, J. RAA27, RPE14,
MPP12, MPP20, MPC01,
MPC02, 591, 2032, 2064,
2075, 2317, 2319
Seeman, J.T. WPG10, RAA04,
TAA22, RAQ03, 517, 530,
2129, 3291
Seeman, John T. WPG03,
WAB06, 486, 3028
Segreto, A. TPG11, 186
Seguin, S. RAG06, 3170
Seidel, I. FAR06, 272
Seidl, P. TPA10, 3220
Seidl, Peter RAG03, 3159
Selesnev, V.S. WAR20, 1948
Seleznev, D. TAC05, 140
Sellyey, W. MPQ10, TPQ19,
2473, 2992
Sen, T. TAG09, 2774
Senichev, Yu.V. WPP18, 1699

Sennyu, K. TPP03, 1620
Senyukov, V. TAB13, TAQ23,
TAQ24, 125, 1572, 1575
Serafini, L. MPE13, WPB10,
WAC13, RAQ05, 896, 973,
3097, 3297
Sereno, N. RPA14, 1082
Sereno, N.S. RPA10, RPA11,
1070, 1073
Serio, M. RAE12, RPQ01,
2420, 2660
Sermes, L. MPG09, 423
Serov, V.L. RPR24, RPR25,
1173, 1175
Sertore, D. WPC23, 1049
Servranckx, R.V. FAB14,
2823
Sessler, A. FAA06, RPC16,
RPC17, TAA28, 207, 737, 740,
2135
Sessler, Andrew RAP25,
2946
Sessler, Andrew M. FPD02,
30
Settles, R. TAG01, 2742
Severgin, Y. FAR06, 272
Severgin, Yu. MPC21, RAQ14,
2359, 3315
Sgobba, S. RPE02, 1999
Shalnov, A. TAB13, RPR10,
RPR15, TAQ23, TAQ24, 125,
1143, 1155, 1572, 1575
Shapiro, Alan WPB15, TPP10,
985, 1636
Sharma, S. FAR19, TAR08,
303, 816
Sharonov, S.A. FAP06,
FAP07, 1337, 1340
Sharp, W. TAR17, 837
Sharp, W.M. TAR13, TAR14,
TPR09, 825, 828, 3260
Shatilov, D.N. RAP05, 2892
Shatunov, Yu. RAA31, RAR31,
600, 3427
Shatunov, Yu.M. RAQ21, 3331
Shchedrin, I.S. RPA25, 1114
Shchepunov, V.A. FAC12,
2863
Shcherbakov, A. FAR16,
FAR17, RAA08, 296, 299, 542
Shea, D. MPR20, 2279
Shea, T.J. MPQ04, MPQ05,
TPB12, WAC24, 2455, 2458,
2551, 3131
Sheehan, J. MPE11, MPA15,
890, 2223
Sheffield, Richard L. MPE09,

882
Shen, Weijun FAQ31, 1462
Sheng, I.C. TAR08, 816
Shenzong, Hu FAA26, 246
Shepard, K.W. RPR05, FAQ09,
RAR21, 1128, 1408, 3400
Sheppard, J. RPC01, WAQ15,
698, 1876
Sheppard, R. RPA26, 1116
Sherman, J. MPE04, 867
Sherman, J.D. WPA08, 923
Sherwood, Boyd WPB15, 985
Sheu, R.J. TPQ09, 2968
Sheynin, S. FAP12, 1355
Shibata, H. RAB13, 779
Shiltsev, V. TAA01, TAA21,
RAR30, 2078, 2126, 3424
Shimer, D. RAA04, 530
Shimer, D.W. RPP01, 1961
Shinas, M.A. TPC06, 2607
Shinn, M. FAG11, FAA25,
WPC24, 102, 243, 1052
Shintake, T. WAG12, RPC20,
RPA20, FAE09, WPQ09, WPQ17,
WPR05, WPR09, TAA28,
WXE07, TPC08, TPC29, RPQ04,
TAG01, 649, 749, 1099, 1503,
1738, 1759, 1797, 1806,
2135, 2444, 2613, 2655,
2669, 2742
Shinto, K. WPC07, WAQ06,
1007, 1855
Shirai, T. FAR08, RPA13,
RPA18, WAQ01, 278, 1079,
1093, 1843
Shirakata, M. WAR05, 1912
Shishido, T. TPP07, 1629
Shoae, H. WAE10, RAE03,
RAE11, 2181, 2389, 2417
Shoji, Y. TAP12, WAR04,
WAR05, 381, 1909, 1912
Shpak, A. FAR16, FAR17, 296,
299
Shu, D. MPQ08, 2467
Shu, Q.S. TPP11, TPP14,
1639, 1648
Shukeilo, I. FAR06, 272
Shumakov, A. RPA19, 1096
Shumakov, I.V. RPR07, 1134
Shurina, E. MPB09, 2291
Shurter, R.B. TPB22, 2580
Shvedov, D. WAA18, 1266
Shvedunov, V. RPA19, 1096
Shvedunov, V.I. FAA14,
TAR05, FAP19, WPR17, RAQ01,
RAR04, 225, 807, 1375, 1827,
3285, 3361

Shvets, G. RAB08, 773
 Shvetsov, V.S. WAA20, TAQ34, 1272, 1605
 Sibley, C. RPG05, 327
 Siemann, R.H. WXE05, RAP10, RAP11, RAP12, WAB12, WAC17, TPA09, 2438, 2907, 2910, 2913, 3046, 3109, 3217
 Sigov, Yu.S. WAA02, WAA03, 1230, 1233
 Sikora, J. TPA04, 3206
 Sikora, J.P. RAE14, 2426
 Sikora, R.E. MPQ05, 2458
 Sim, J. FAP05, 1334
 Sim, J.W. FAP06, FAP07, MPB05, MPB06, 1337, 1340, 2282, 2285
 Simopoulos, C. WXE05, WAB05, WAC04, WAC17, 2438, 3025, 3073, 3109
 Simpson, J. WAG06, WPB11, WPB12, 631, 976, 979
 Simrock, S. RPQ29, RPQ30, 2732, 2735
 Simrock, S.N. MPR14, RAE11, 2268, 2417
 Simrock, Stefan MPB11, 2297
 Sinclair, C. FAG11, FAA25, WPA17, TPC07, TPC26, 102, 243, 942, 2610, 2652
 Sinclair, C.K. WPC17, 1030
 Singh, A. TAQ17, 1561
 Singh, O. FAQ17, MPA15, RPQ19, 1426, 2223, 2711
 Singh, Om V. RPQ27, 2729
 Singleterry Jr., R.C. TAC12, 149
 Sisson, D. TPG14, 192
 Skaritka, J. MPE11, 890
 Skarpaas, K. MPP10, 2057
 Skrinsky, A. MAD04, TAR11, 14, 819
 Skuratov, V. WPR19, 1833
 Slaton, T. WAG11, RPB01, RPB03, 646, 656, 662
 Slaton, Tim WAB08, 3034
 Sloan, T. RAQ23, RAQ24, 3337, 3340
 Sloth, K. TAE10, 1213
 Sluijk, T. TAQ12, MPQ17, 1547, 2491
 Smirnov, A. RAP24, 2943
 Smirnov, A.I. MPG10, 426
 Smirnov, A.V. RPR13, 1152
 Smith, D. FAA27, 248
 Smith, D.L. TAE06, 1201
 Smith, David L. TAE07, 1204
 Smith, G.A. RPQ07, 2678
 Smith, H. WPR15, TPC20, 1821, 2646
 Smith, I. TAE06, 1201
 Smith, J. MPA15, 2223
 Smith, J.D. MPR08, 2253
 Smith, John MPR07, 2250
 Smith, M. RPR22, TPC06, 1167, 2607
 Smith, P. WAQ15, 1876
 Smith, R. WAQ03, 1849
 Smith, S. MPQ15, MPQ25, 2485, 2512
 Smith, S.L. TPG09, RAE10, 180, 2414
 Smith, T.L. WPP16, 1693
 Smithe, D.N. WPC12, 1022
 Snyder, S.L. TAP10, 375
 Snyderstrup, L. MPP11, 2060
 Sobczynski, S. RPG05, 327
 Sobenin, N.P. TAR05, FAP19, WPR17, WPR18, 807, 1375, 1827, 1830
 Solnyshkov, D. WPC03, 1004
 Solomon, L. FAQ13, WXE04, RPQ19, 1414, 2435, 2711
 Soloveichik, Yu. MPB09, 2291
 Somersalo, E. FAE08, 1500
 Sommer, M. FAR14, 293
 Somov, L. TAC16, 152
 Song, J.J. RPA10, WPP16, TAA11, 1070, 1693, 2102
 Sotnikov, G.V. RAB15, 782
 Soukas, A. TAP11, WAR11, WAR13, RPP02, 378, 1924, 1930, 1964
 Specka, A. WAG07, 634
 Spence, David WPC11, 1019
 Spence, P. TAE06, 1201
 Spence, W. WAG11, RPC20, TAG01, WAC17, 646, 749, 2742, 3109
 Spence, W.L. RAA06, WAB09, 536, 3037
 Spencer, C. WAQ15, 1876
 Spencer, C.M. FAP16, 1366
 Spencer, J. RPC02, RPC08, TAA28, TPC16, WAC17, 701, 713, 2135, 2637, 3109
 Spencer, J.E. RPB06, 671
 Spentzouris, L.K. TAG04, 2757
 Spentzouris, Linda Klamp WAC02, 3070
 Sprehn, D. WAE13, 2190
 Spyropoulos, B. TAA15, 2111
 Srinivasan-Rao, T. MPE11, 890
 Stanek, M. RPA24, TPC20, 1111, 2646
 Stefan, P.M. WXE04, 2435
 Stege, R. WAG11, RPB04, WAC17, 646, 665, 3109
 Steimel, J. TPQ26, 3010
 Steimel Jr., James M. RAE02, 2384
 Stein, P. TPP11, 1639
 Steinbach, Ch. TAP14, 386
 Steinbock, L. FAR06, 272
 Steinhäuser, N. WPQ24, 1776
 Steininger, R. FAR06, 272
 Stelzer, J.E. WPC10, 1016
 Stenz, C. WAG07, 634
 Stepashkin, O. RAP24, 2943
 Stephenson, E. WPC08, 1010
 Stepin, D.L. WPB16, 988
 Stepp, J. MPQ08, 2467
 Stevens Jr., R. MPE04, 867
 Stevens Jr., R.R. WPC10, 1016
 Stevens Jr, Ralph R. WAQ02, 1846
 Stevens, R.R. WPA08, 923
 Stevens, T. MPP13, 2067
 Stevenson, G.R. WAQ24, 1891
 Stevenson, N.R. FAG07, 89
 Stierlin, U. TAG01, 2742
 Still, D. RPC21, 752
 Stillman, A. TPB15, 2560
 Stillman, Arnold MPA09, 2211
 Stirbet, M. TPP12, 1642
 Stockhorst, H. TPB20, 2574
 Stoeffl, W. WPG10, RAA03, MPP12, MPP20, TAA22, MPC01, MPC02, 517, 527, 2064, 2075, 2129, 2317, 2319
 Stoker, J. WPA01, 902
 Stoker, J.D. TAE01, 1178
 Stolyarsky, V.I. TPA15, 3232
 Stolzenburg, C. TPP11, 1639
 Stoner, R. TPG14, 192
 Stovall, J.E. RPR08, RPR09, MPC23, 1137, 1140, 2364
 Stover, G. RAE12, 2420
 Stover, G.D. WAA14, 1254
 Straub, D. FAA08, 213
 Striby, S. RAG06, 3170
 Strohman, C.R. RAE14, 2426
 Strönisch, U. FAP02, 1325
 Strubin, P.M. RPE06, 2014
 Struckmeier, Jürgen FAC10, 2860
 Stuart, M. FAP17, FAP18,

1369, 1372
Studebaker, Jan WPB15, 985
Stupakov, G. MPC01, WAC15, 2317, 3102
Stupakov, G.V. RAQ02, RAQ09, RAQ10, 3288, 3303, 3306
Stupakov, Gennady V. RAR11, RAR12, 3373, 3376
Sturges, Ronald WPB15, 985
Su, J.J. TAA28, 2135
Suberlucq, G. RPC10, 719
Sudan, Ravi N. TAE07, 1204
Sugimoto, M. TPG02, 159
Suk, H. TPQ11, 2974
Sukhina, B. TPE09, 1316
Sukhina, B.N. TAC06, RPP08, 143, 1979
Suller, V.P. TPG09, 180
Sullivan, M. RAA25, 585
Sumbaev, A. TAC16, 152
Sun, D. WPP01, 1655
Sun, Y. FAP01, 1322
Surma, I.V. RAQ01, 3285
Sutter, S. RPA26, 1116
Suzuki, H. FAP13, 1358
Suzuki, S. WPC22, 1046
Suzuki, T. FAA30, TPP07, 257, 1629
Svandriik, M. FAR06, FAR21, WPQ04, TAG05, 272, 309, 1723, 2762
Svinin, M. WPC03, TAA18, 1004, 2120
Svinjin, M.P. TAE13, 1222
Swan, T. RAA03, 527
Swenson, D.A. RPG10, 342
Swenson, D.R. WPC10, 1016
Swift, G. FAA08, RPA17, TAQ07, 213, 1090, 1536
Symon, K. TAP05, RAG05, 363, 3167
Syphers, M. RAP21, RAQ23, RAQ24, 2934, 3337, 3340
Syphers, M.J. TAP13, MPG12, WAB04, 383, 431, 3022
Syresin, E. RAP23, RAP24, 2940, 2943
Sytchev, V. FAQ06, 1399
Sytchevsky, S. MPC21, 2359
Tachibana, S. TPP03, 1620
Tadano, M. RPQ23, 2720
Tadokoro, M. TAB03, 113
Tajima, T. TPP03, 1620
Takagi, A. WPC07, WAQ06, WAR05, 1007, 1855, 1912
Takahashi, T. TPP03, 1620
Takaki, H. FAR09, 281
Takao, M. FAQ20, FAQ21, 1435, 1438
Takashima, T. RPQ06, 2675
Takashina, H. TPP03, 1620
Takatomi, T. WPQ15, 1753
Takeda, H. FAA16, RPR08, RPR09, MPC23, 228, 1137, 1140, 2364
Takeda, Harunori MPB16, 2306
Takeda, O. WAG12, 649
Takeda, Y. RPG13, 351
Taketani, A. RPQ15, 2699
Takeuchi, Y. FAE09, WPQ17, WPR05, WPR09, TAG01, 1503, 1759, 1797, 1806, 2742
Tallerico, P.J. TAR12, TAQ02, 822, 1521
Talman, R. RAP03, 2886
Tambini, U. RAE05, 2399
Tan, J. TPP09, 1632
Tanabe, J. FAP01, 1322
Tanaka, M. WAR13, 1930
Tang, Cha-Mei WPE05, 70
Tang, H. WAG11, RPC01, MPE10, WPC18, WPC21, 646, 698, 887, 1033, 1043
Tang, J. MPR13, 2265
Tang, Y.N. MPR08, 2253
Tani, N. FAP13, 1358
Taniuchi, T. WPC22, 1046
Taniyama, N. TPP03, 1620
Tantawi, S. WPQ05, 1726
Tantawi, S.G. TAQ28, 1587
Tantawi, Sami G. TAQ26, TAQ27, TAA27, 1581, 1584, 2132
Tarabrin, V. TAC16, 152
Tarakanov, M.V. MPG10, WAR20, WAR21, 426, 1948, 1949
Tarasenko, A. RAA08, 542
Tarnetsky, V. RPA12, TAQ21, 1076, 1569
Tarovik, M. RAQ14, 3315
Tatchyn, R. FAP20, FAQ23, 1378, 1441
Tatum, B.A. TAP07, WAQ26, MPA05, 366, 1897, 2202
Taufer, M. FAE11, 1509
Taurel, E. RPQ15, 2699
Taurigna-Quere, M. WPB22, 998
Tauschwitz, A. WAQ04, 1852
Tavares, Pedro F. RAQ29, 3352
Taylor, B. TAR03, 801
Taylor, T. RAA04, FAC04, 530, 2844
Tazzari, S. TPG11, 186
Tazzioli, F. TPG11, WAC13, 186, 3097
Tecimer, M. FAA29, 254
Tecker, F. RAA19, 567
Tejima, M. RAA33, MPQ31, TPC05, 603, 2521, 2604
Tejima, Masaki MPQ14, 2482
Telegin, Yu. FAR17, 299
Temkin, R.J. MPE12, 893
Temnykh, Alexander B. TAG08, 2771
Tenenbaum, P. RPC06, RPC20, TAA08, WXE07, TAG01, 707, 749, 2096, 2444, 2742
Teng, L. RAA29, 597
Teng, L.C. RAR26, 3415
Teng, Lee C. FAB10, 2814
Tenyakov, I. FAP24, 1387
Tepikian, S. TAA09, MPR20, FAB22, 2099, 2279, 2832
Terada, Y. FAP22, WPQ07, 1384, 1732
Terashima, A. FAQ02, 1390
Terekhov, V. MPP03, 2040
Terekhov, V.I. MPG10, WAR20, 426, 1948
Tereshkin, Y. FAP24, 1387
Terrell, R. MPR14, 2268
Terunuma, N. WAR03, TPC05, 1906, 2604
Tessier, J.-M. WAC13, 3097
Teytelman, D. RAE12, RPQ01, RPQ08, 2420, 2660, 2681
Thern, R. TPA06, 3212
Theuws, W. RPQ31, 2738
Theuws, W.H.C. WAQ19, RPP04, 1882, 1970
Thevenot, M. TAE09, 1210
Thieberger, P. TAP11, 378
Thielheim, K.O. RAR09, 3370
Thiery, Y. WPB22, 998
Thivent, M. MPG09, 423
Thomas, M. TPP06, WPQ20, 1626, 1768
Thomas, M.D. TAB17, 131
Thomas, P. WPB01, 945
Thomas, R. TPE04, TAA09, 1293, 2099
Thompson, K. TAP05, RPC01, RPC02, RPA04, FAP03, 363, 698, 701, 1058, 1328
Thompson, K.A. TPQ16, TPQ17, WAC18, 2986, 2989,

3112
Thompson, P. TPE04, FAQ03, FAQ04, FAQ16, 1293, 1393, 1396, 1423
Thorndahl, L. RPC09, 716
Thur, W. RPE12, 2026
Tian, F. WAG11, RPB01, TPC20, WAC17, 646, 656, 2646, 3109
Tiefenback, M. MPR15, 2271
Tiefenback, M.G. WAQ12, 1870
Tieger, D. RPG05, 327
Tigelis, J. RAQ01, 3285
Tighe, R. RPQ03, RPQ05, 2666, 2672
Tigner, M. FAE13, RAQ04, 1515, 3294
Timmer, Carl WPB15, 985
Timmermans, C.J. WAQ19, WAQ20, RPP04, RPQ31, 1882, 1885, 1970, 2738
Timossi, C. MPR03, 2244
Tinsley, D. WAR01, 1900
Titcomb, Ch. MPP02, 2037
Tiunov, A.V. RPR01, RAQ01, RAR04, 1119, 3285, 3361
Tiunov, M. MPB09, 2291
Tkachev, P.L. RAR04, 3361
Tkatchenko, A. FAR14, 293
Tobiyama, M. RPQ26, RAQ06, 2726, 3300
Todd, A.M.M. RPR20, 1164
Todesco, E. FAC06, 2847
Toge, N. RPB01, RAP02, 656, 2883
Tojyo, E. RPG13, 351
Tokarev, Yu. WAA17, 1263
Tokuda, N. RPG13, TAP04, 351, 360
Tokumoto, S. TAQ29, WPR02, WPR03, 1590, 1788, 1791
Tölle, R. TPB20, 2574
Tolstun, N.G. TAE13, 1222
Tomimasu, T. FAA30, TAQ35, 257, 1608
Tomlin, R. TPQ26, 3010
Tompkins, J.C. FAP06, FAP07, 1337, 1340
Tongu, E. FAA30, 257
Torre, A. TPG11, 186
Torun, Yagmur MXG03, 53
Tosa, M. TPP16, 1652
Tosello, F. WAP14, 470
Tosi, L. FAA13, FAR21, TAG05, 222, 309, 2762
Tosin, G. FAP14, FAP15, 1361, 1364
Touchi, Y. RPG09, 339
Toyama, T. WAR05, 1912
Trahern, C.G. WAP10, MPR20, 461, 2279
Trakhtenberg, E. FAQ17, MPP16, 1426, 2072
Tran, H.J. RAQ15, 3317
Tran, P. RAQ17, 3323
Tranquille, G. RAP24, 2943
Trantham, K. WPC21, 1043
Travier, C. WPB01, 945
Travish, G. FAA23, RPA21, RPA22, 240, 1102, 1105
Trbojevic, D. WAP10, TAA09, FAB22, WAC25, RAQ22, 461, 2099, 2832, 3134, 3334
Treas, P. TAB17, RPA26, 131, 1116
Tremblay, K. WXE01, 2429
Trenkler, T. FAC04, 2844
Trikalinos, C. RAQ01, 3285
Trimble, D. MPE14, WAA19, TAA20, 899, 1269, 2123
Trombly-Freytag, K. FAP06, FAP07, MPB05, MPB06, 1337, 1340, 2282, 2285
Tronc, D. TAB04, 116
Trotz, S.R. MPE12, 893
Trower, W.P. TAR05, FAP19, WPR17, 807, 1375, 1827
Trzeciak, W.S. FAR20, 306
Tsai, H.J. TPQ10, 2971
Tsang, K.L. FAA07, RAR05, 210, 3364
Tsarik, S.V. MPG10, WAR20, WAR21, 426, 1948, 1949
Tschalaer, C. RPG05, 327
Tseng, P.K. FAA04, 201
Tseng, P.-K. TPC15, 2634
Tsentlovich, E. RPG05, 327
Tsoupas, N. FAP11, 1352
Tsuchiya, K. FAQ02, 1390
Tubaev, M. RPR15, 1155
Tückmantel, J. TPP12, 1642
Tuozzolo, J.E. WAR10, 1921
Tupikov, V.S. RPP08, 1979
Tur, Yu. WPB17, 990
Tur, Yu.D. WPB16, TAE14, 988, 1225
Turchinets, W. RPG05, RAA31, 327, 600
Turner, J. WAG11, RPB01, WAC17, 646, 656, 3109
Turner, J.L. RPB04, 665
Turner, L.R. FAQ17, 1426
Tzeng, K.-C. RAB01, RAB02, 758, 761
Ueda, T. RAB13, 779
Uemura, T. FAQ08, 1405
Ueng, T.S. MPQ19, MPQ32, 2497, 2524
Uesaka, M. RAB13, 779
Ueyama, Y. FAP13, 1358
Uggerhoj, E. WAP14, 470
Uhm, Han S. TAQ04, TAQ05, 1527, 1530
Umezawa, H. TPP07, 1629
Urakawa, J. WPR02, WPR03, WAR03, TPC05, 1788, 1791, 1906, 2604
Ursic, R. TPC26, 2652
Ushkov, V. WPR13, 1815
Uskov, V.V. RAB15, 782
Uythoven, J. TPP12, 1642
v. Blanckenhagen, P. FAR06, 272
v. Es, J. MPQ17, 2491
v. Hartrott, M. WAQ17, 1879
v. Rienen, U. RPB16, 695
Vacca, J.H. RPA07, 1064
Valdez, M. MPR03, 2244
Valentinov, A. MPA04, 2199
Valeri, S. WPC23, 1049
Van Asselt, W. RPQ07, 2678
van Asselt, W.K. WAB04, RAQ22, 3022, 3334
van Bibber, K. MPP12, MPP20, 2064, 2075
v.d. Laan, J. MPQ17, 2491
van der Laan, J. RPG06, 330
van Greevenbroek, H.R.M. WAQ20, 1885
van Oers, W.T.H. MPE03, 864
van Oort, J.M. FAQ07, 1402
van Rooij, M. MPG09, MPP15, 423, 2069
Van Vaerenbergh, P. TPE10, 1319
van Zeijts, J. WAE10, 2181
van Zeijts, Johannes MPR02, MPC20, 2241, 2356
VanAsselt, W. TAP13, 383
Vanecek, D. RPC18, WPA01, TAE01, 743, 902, 1178
Varenne, F. RAP23, RAP24, 2940, 2943
Varfolomeev, A. FAA23, 240
Varisco, G. TAA07, 2093
Vasilevsky, A. MPP03, 2040
Vasiljev, A.A. RPR07, 1134
Vasserman, I. FAQ17, FAQ18, 1426, 1429
Vasserman, S. WAA17, 1263

Vassiliev, L. FAQ06, 1399
Vaziri, K. FAG06, 86
Vella, M.C. FAP18, 1372
Veluri, V.R. RPA07, 1064
Verdier, A. WPG09, RAA17, FAC03, 514, 560, 2841
Verdier, André FAC07, FAC08, 2850, 2853
Verhagen, H. RAA15, 557
Verkooyen, J. TAQ12, 1547
Vescovi, M. RPA26, 1116
Veselov, O. FAQ06, 1399
Veshcherevich, V. WPP10, WPP11, RAR19, 1678, 1681, 3394
Vetter, A.M. FAA27, FAA28, WPB20, 248, 251, 992
Vignola, G. WPG05, RPA26, 495, 1116
Villate, D. TAE09, TPC17, 1210, 2640
Vincent, J. RPG11, 345
Vinokurov, N.A. FAQ17, 1426
Virchenko, Yu.P. RAQ28, 3349
Virostek, S. RPB04, 665
Visintini, R. TPG11, FAR21, 186, 309
Vlieks, A.E. WAG13, RPA23, TAQ26, TAQ27, TAA27, 653, 1108, 1581, 1584, 2132
Vobly, P. MPB09, 2291
Vodopianov, F.A. TAR02, TAQ10, 799, 1542
Voisin, L. TAE09, 1210
Volfbeyn, P. TPG07, RPC15, RAB10, 174, 734, 776
Völker, F. MPG09, 423
von Hahn, R. RPR06, 1131
von Holtey, G. WPG09, 514
Vormann, H. WPA04, 911
Vorogushin, M.F. WPP04, 1663
Voronin, G. WPC03, 1004
Voronin, V.S. TPR13, 3269
Vos, L. RAR07, 3367
Voss, G.-A. TAG01, 2742
Voss, Gustav-Adolf FPD01, 27
Votaw, A. MPQ08, MPQ10, 2467, 2473
Votaw, A.J. RPQ16, 2702
Voykov, G. TPC03, 2598
Vuagnin, G. WAP14, 470
Wachter, J. MPQ22, 2506
Wadlinger, E.A. RPR19, 1161
Wagner, S.R. TAG01, 2742
Wake, M. FAQ32, TPP07, 1465, 1629
Wakisaka, K. FAA30, 257
Wakita, K. FAA30, TAQ35, 257, 1608
Walbridge, D.G.C. FAP06, FAP07, MPB05, MPB06, 1337, 1340, 2282, 2285
Waldschmidt, G. WPB06, 961
Walker, N. RPB01, 656
Walker, R.P. TPG11, FAA13, FAR21, FAQ19, TAG05, 186, 222, 309, 1432, 2762
Wallén, E. RPE02, 1999
Walling, L.S. RPG10, 342
Walters, G.K. WPC21, 1043
Walther, R. WPA12, 929
Walton, J. WAR01, 1900
Walz, D. RPC08, WXE07, TAG01, 713, 2444, 2742
Wan, Weishi MPC09, 2336
Wanderer, P. WAP10, TPE04, FAP11, FAQ02, FAQ04, FAQ16, TAA09, 461, 1293, 1352, 1390, 1396, 1423, 2099
Wanderer, P.J. FAQ03, 1393
Wang, B. MPA01, 2193
Wang, C. MPA01, 2193
Wang, C.J. MPR10, TPB29, 2256, 2592
Wang, C.-P. TPC15, 2634
Wang, Ch. FAA04, RAA24, FAQ26, TPQ08, 201, 582, 1450, 2965
Wang, Chun-xi MPC31, 2376
Wang, Chunxi FAC02, 2838
Wang, D. WAA16, WXE01, TPB04, TPC04, WAC27, 1260, 2429, 2536, 2601, 3140
Wang, D.X. MXG02, 48
Wang, J. RPA04, WAA08, WAA09, 1058, 1242, 1245
Wang, J.G. TAE04, TPQ11, 1193, 2974
Wang, J.M. TPP06, 1626
Wang, J.P. TAA14, 2108
Wang, J.Q. WAB20, 3064
Wang, J.W. WAG13, RPA23, 653, 1108
Wang, L. TAP03, WPP20, WPP21, RAP21, WAC12, WAC27, RAG10, RAQ23, RAQ24, 357, 1705, 1708, 2934, 3094, 3140, 3182, 3337, 3340
Wang, M.H. RAA24, TAR06, TPQ08, TPQ09, TPQ10, 582, 810, 2965, 2968, 2971
Wang, P. FAA08, RPA17, 213, 1090
Wang, Ping WPA13, WPR22, 932, 1841
Wang, Shu-Hong WPG07, 506
Wang, T. WAC29, 3146
Wang, T.S. RAR23, 3406
Wang, Tai-Sen F. WAC28, 3143
Wang, X. MPQ07, MPQ08, MPQ10, 2464, 2467, 2473
Wang, X.J. MPE11, WPB13, RAE09, WXE03, TPB01, 890, 982, 2411, 2432, 2530
Wang, X.-J. TPG14, 192
Wang, X.Q. RPE10, 2023
Wang, Y. TAB17, MPA01, RAP21, 131, 2193, 2934
Wang, Y.L. TAQ08, 1539
Wangler, T.P. RAG11, 3185
Wangler, Thomas P. WAQ02, RAG01, 1846, 3149
Wanzenberg, R. RPB14, 689
Ward, C. TAR17, 837
Warkentien, R. MPA18, 2232
Warner, A. RAQ22, 3334
Warner, D. TAP05, 363
Warnock, R.L. FAB06, 2804
Warnock, Robert L. TPQ07, 2962
Warren, David WPB15, 985
Warwick, A. FAA03, 198
Watson III, William A. WAE05, 2167
Watson, W. WAE10, MPR13, MPR19, 2181, 2265, 2276
Watson, W.A. RAE11, 2417
Webber, Robert C. RPQ10, 2687
Weber, M. TPB07, 2542
Webers, G.A. WAQ19, WAQ20, RPQ31, 1882, 1885, 2738
Wedekind, M. WPC08, 1010
Wehrle, U. FAE10, 1506
Wei, F. FAR21, 309
Wei, J. WAP10, FAB22, WAC24, RAQ22, 461, 2832, 3131, 3334
Wei, Jie RAP25, 2946
Weidemann, A.W. TAA28, 2135
Weihreter, E. TPE09, WAQ17, 1316, 1879
Weiland, T. RPB16, TAQ06, WAE13, MPC01, MPQ15, WAB18, 695, 1533, 2190, 2317, 2485, 3061

Weinberg, J. WAQ15, WAC17, 1876, 3109
Weingarten, W. FAE11, 1509
Weinstein, A. TAR18, 840
Weise, H. RPB08, 677
Weisend, J.G. MPP01, 2034
Weiss, R. RPR22, 1167
Weisse, E. WAP14, WAQ24, 470, 1891
Weisz, S. WAP14, FAC04, 470, 2844
Welch, J. FAE13, 1515
Welch, James J. TAA29, TAG08, FAC14, RAG13, 2138, 2771, 2866, 3191
Welton, R.F. MPE05, WPC12, 871, 1022
Welz, J. MPE03, 864
Wendt, M. TPC09, 2616
Weng, W.T. FAA07, RAA23, RAA24, RAG08, RAR05, 210, 579, 582, 3176, 3364
Wenjun, Zhu FAA26, 246
Wenninger, J. WAP12, RAA11, RAA19, RAA20, 464, 548, 567, 570
Werkema, Steven J. RAR20, 3397
Wermelskirchen, C. RPQ22, 2717
Wesolowski, W. RPA11, 1073
West, C. MPR13, 2265
Westenskow, G. RPC16, RPC17, MPE14, WPC16, TAA28, 737, 740, 899, 1027, 2135
Westenskow, G.A. TAQ03, 1524
Westervelt, R.T. WAE08, 2175
Wetherholt, D. MPR13, 2265
Wharton, K. RAB04, 767
White, K. MPA12, MPR13, 2220, 2265
White, M. TAP05, RPA07, RPA08, RPA10, RPA11, RPA14, TPC01, 363, 1064, 1067, 1070, 1073, 1082, 2595
Whitham, K. TAB17, RPA26, 131, 1116
Whittum, D. RAB13, TAA28, WAC17, 779, 2135, 3109
Widgren, J. FAA08, 213
Wiemerslage, G. MPP16, 2072
Wienands, H.-U. RAA27, 591
Wienands, U. RAA04, TAA22, MPC01, 530, 2129, 2317
Wight, G.W. MPE03, 864
Wildman, D. WPP08, WPP09, WPP23, RAQ13, 1672, 1675, 1714, 3312
Wildner, E. MPG09, WAE09, 423, 2178
Wilkinson, C. WAC29, 3146
Wilkinson, C.A. TAR12, 822
Willeke, F. MPG07, TAG02, TAG09, 420, 2747, 2774
Willen, E. TPE04, FAQ03, FAQ04, FAQ15, FAQ16, 1293, 1393, 1396, 1420, 1423
Williams, C.E. WAQ26, 1897
Williams, G. FAR06, 272
Williams, M.D. TPB07, 2542
Williams, Mel WPB15, 985
Williams, R. TAA28, 2135
Williams, S. TAG01, 2742
Wilson, I. WAG13, RPC09, RPC10, RPC15, 653, 716, 719, 734
Wilson, K. FAR06, 272
Wilson, P. RPC01, RPC02, RPC06, 698, 701, 707
Wilson, P.B. FAE04, TAA33, TPQ16, 1483, 2144, 2986
Winick, H. WPB13, WXE03, 982, 2432
Winje, R.A. FAG05, 83
Winkler, G. MPP02, 2037
Winn, David MXG03, 53
Wise, M. MPR13, 2265
Wiseman, M. FAG11, FAA25, WPA17, 102, 243, 942
Witherspoon, S. WAE10, MPR13, 2181, 2265
Witkover, R. RPQ07, 2678
Witkover, R.L. TPB26, 2589
Witte, K. MPE10, 887
Wolf, Z. FAP16, FAQ08, 1366, 1405
Wolff, D. WAE07, 2172
Wolff, S. RPB09, 680
Wollnik, H. WAQ26, 1897
Wong, J. TAR18, 840
Wong, V. RPQ07, 2678
Woo, B. MPC18, 2351
Wood, P. TPC04, 2601
Wood, R.L. RPR08, RPR09, 1137, 1140
Woodle, M. WPB13, WXE03, 982, 2432
Woodley, M. WAG11, RPB01, RPB03, RPB04, RAE03, 646, 656, 662, 665, 2389
Woods, M. RPC08, 713
Woody, K.A. TPC13, 2628
Wright, D. MPP09, MPP12, MPP20, MPC01, WAC17, 2054, 2064, 2075, 2317, 3109
Wright, E. FAE07, 1497
Wright, E.L. TAQ28, 1587
Wrulich, A. TPG11, FAA13, FAR21, TAG05, 186, 222, 309, 2762
Wu, X. RPG11, 345
Wu, Y. FAA08, RPG06, RAA01, RAA21, RAB22, RPA17, MPA10, MPA11, MPQ06, FAC20, 213, 330, 524, 573, 796, 1090, 2214, 2217, 2461, 2877
Wu, Y.Y. TPB03, 2533
Wu, Ying WPR22, 1841
Wuensch, W. WAG13, RPC09, RPC10, RPC15, 653, 716, 719, 734
Wurtele, J. TAA28, 2135
Wurtele, J.S. RAB08, MPE12, WPB03, WPB04, 773, 893, 951, 954
Wüstefeld, Godehard FAC16, 2868
Wyss, C. TPP12, 1642
Xi, Boling RPP04, 1970
Xiao, A. WAC27, 3140
Xie, Jialin TPG04, 162
Xie, Ming TPG10, 183
Xu, G. RAA21, TPQ03, WAC27, 573, 2955, 3140
Xu, J. MPA01, 2193
Xu, S. MPP16, 2072
Yakimenko, V. TAR11, RAR31, 819, 3427
Yakovlev, V. RPA12, TAQ21, 1076, 1569
Yakovlev, V.P. MPC17, 2348
Yamada, R. MPC07, 2330
Yamada, S. MAD03, 9
Yamaguchi, H. MPQ18, 2494
Yamaguchi, S. TAQ25, 1578
Yamamoto, N. RPC20, MPA06, WXE07, TAG01, 749, 2205, 2444, 2742
Yamane, Isao TPR16, 3275
Yamazaki, Y. FAE09, WPQ08, WPQ09, WPQ17, WPR05, WPR09, 1503, 1735, 1738, 1759, 1797, 1806
Yan, Y. RAA22, 576
Yan, Y.T. RAA26, RAA27, TAG06, 588, 591, 2765
Yanagida, K. WPC22, 1046
Yang, B. MPQ09, MPQ10,

MPQ11, TPC03, 2470, 2473,
 2476, 2598
 Yang, J. RAQ17, 3323
 Yang, Ming-Jen MPQ20, 2500
 Yang, X.-F. TPC16, 2637
 Yano, Y. WPC01, 1001
 Yaramishev, S.G. TPA05,
 3209
 Yarba, V.A. FAP06, FAP07,
 1337, 1340
 Yarygin, N. FAQ06, 1399
 Yarygin, S.N. WPR18, 1830
 Yasumoto, M. FAA30, 257
 Yavor, S.Ya. TAP16, 389
 Yazynin, I. WAR22, 1952
 Yee, D. FAP01, 1322
 Yeremian, A.D. WPC18, 1033
 Yi, He FAA26, 246
 Yifang, Wang TAR22, 850
 Yin, Yan TPC11, 2622
 Ylä-Oijala, P. FAE08, 1500
 Yokomizo, H. WPC22, FAP13,
 MPA07, 1046, 1358, 2208
 Yokoya, K. RPA20, WAB20,
 1099, 3064
 Yokoyama, M. RPQ23, 2720
 Yokoyama, S. FAQ08, 1405
 Yonehara, H. FAP13, 1358
 Yoon, M. TPG06, WPR11, 171,
 1812
 York, R.C. RPG11, 345
 York, R.L. WPC10, 1016
 Yoshida, Y. RAB13, 779
 Yoshihara, K. TPP16, 1652
 Yoshii, J. TPB18, 2569
 Yoshii, M. TAP04, WPC07,
 WAR05, 360, 1007, 1912
 Yoshikawa, H. WPC22,
 MPA07, 1046, 2208
 Yoshimoto, S. RPQ06, 2675
 Young, E. RAP07, 2898
 Young, L.M. RPR08, RPR09,
 1137, 1140
 Young, Lloyd M. MPB16, 2306
 Yourd, R. FAP01, 1322
 Yourd, R.B. RAA05, 533
 Yu, C.I. MPQ26, RAR05, 2515,
 3364
 Yu, C.-I. TPC15, 2634
 Yu, I.H. WPR11, 1812
 Yu, S. RPC16, RPC17, RPC18,
 WPA01, TAE01, 737, 740, 743,
 902, 1178
 Yu, S.S. RPC19, TAR14,
 WPA09, WAQ04, 746, 828,
 926, 1852
 Yu, Y. MPA01, 2193
 Yuan, D. WAQ07, 1858
 Yuan, V. RPR19, 1161
 Yuan, V.W. RPR22, TPC06,
 1167, 2607
 Yudin, I.P. MPB19, FAC09,
 2314, 2856
 Yugami, N. RAB13, 779
 Yuldashev, O.I. MPB19, 2314
 Yuldasheva, M.B. MPB19,
 2314
 Yule, T.J. FAG14, 110
 Yunn, B. WPA17, 942
 Yunn, Byung C. MPB11,
 RAQ11, 2297, 3309
 Yupinov, Y. MPA04, 2199
 Yupinov, Yu. WPR13, 1815
 Yurkov, M.V. WAA20, TAQ34,
 1272, 1605
 Zako, A. FAA30, 257
 Zakutin, V.V. WPA15, TAE14,
 938, 1225
 Zangrando, D. TPG11, FAQ19,
 186, 1432
 Zante, A. TAB17, RPA26, 131,
 1116
 Zaugg, T. WPA08, 923
 Zavadtsev, A.A. WPR18, 1830
 Zazula, J.M. WAQ24, 1891
 Zegenhagen, J. FAR06, 272
 Zelenski, A.N. MPE03, 864
 Zelinsky, A. FAR17, RAA08,
 299, 542
 Zelinsky, A.Yu. RAA07, 539
 Zeller, A.F. RPG11, 345
 Zenkevich, P. RAP23, 2940
 Zenkevich, P.R. TPA05, 3209
 Zeno, K. TAP12, 381
 Zhan, M. MPA01, 2193
 Zhang, C. WPG09, TPQ03, 514,
 2955
 Zhang, R. RAB03, RPA21,
 RPA22, 764, 1102, 1105
 Zhang, S.Y. TAP13, RAG08,
 TPA08, 383, 3176, 3214
 Zhang, W. WAR10, WAC25,
 1921, 3134
 Zhang, Zhenhai RAQ25, 3343
 Zhao, Aihua FAQ29, FAQ30,
 1456, 1459
 Zhao, J. MPA01, 2193
 Zhao, S. TAA03, 2084
 Zhidkov, E.P. MPB19, 2314
 Zhiglo, V.F. WPA15, 938
 Zholents, A. RAA03, RAA22,
 FAB01, 527, 576, 2789
 Zholents, A.A. RAP05, 2892
 Zhou, J. WPB06, TAA11, 961,
 2102
 Zhou, Ping TPB05, 2539
 Zimmermann, F. WPG10,
 WAG11, RPB01, RPC03, RPC06,
 RPC07, TPQ16, TPQ17, WAB07,
 WAC15, WAC17, 517, 646,
 656, 704, 707, 710, 2986,
 2989, 3031, 3102, 3109
 Ziomek, C. TAQ31, RPQ02,
 RPQ05, 1596, 2663, 2672
 Zisman, M. MPC01, 2317
 Zisman, M.S. RAA03, RAA05,
 527, 533
 Zolfaghari, A. RPG05, WAA16,
 TPB04, 327, 1260, 2536
 Zolotorev, M. WPG10, RPE14,
 MPC01, MPC08, 517, 2032,
 2317, 2333
 Zolotorev, Max TAQ27, 1584
 Zotter, B. RAA20, RPC09,
 570, 716
 Zubovskiy, V. TAC05, 140
 Zwart, T. RPG05, RAA31, 327,
 600
 Zyngier, H. TPG01, FAR14,
 155, 293



